INTEGRATIVE PHARMACOLOGY-BASED RESEARCH ON TRADITIONAL MEDICINE: METHODOLOGIES, MEDICAL AND PHARMACOLOGICAL APPLICATIONS, 2nd Edition

EDITED BY: Hai Yu Xu, Chang-xiao Liu, Yanqiong Zhang, Yan Xu and Takashi Sato

PUBLISHED IN: Frontiers in Pharmacology

frontiers Research Topics

frontiers

Frontiers eBook Copyright Statement

The copyright in the text of individual articles in this eBook is the property of their respective authors or their respective institutions or funders. The copyright in graphics and images within each article may be subject to copyright of other parties. In both cases this is subject to a license granted to Frontiers.

The compilation of articles constituting this eBook is the property of Frontiers.

Each article within this eBook, and the eBook itself, are published under the most recent version of the Creative Commons CC-BY licence. The version current at the date of publication of this eBook is CC-BY 4.0. If the CC-BY licence is updated, the licence granted by Frontiers is automatically updated to the new version.

When exercising any right under the CC-BY licence, Frontiers must be attributed as the original publisher of the article or eBook, as applicable.

Authors have the responsibility of ensuring that any graphics or other materials which are the property of others may be included in the CC-BY licence, but this should be checked before relying on the CC-BY licence to reproduce those materials. Any copyright notices relating to those materials must be complied with.

Copyright and source acknowledgement notices may not be removed and must be displayed in any copy, derivative work or partial copy which includes the elements in question.

All copyright, and all rights therein, are protected by national and international copyright laws. The above represents a summary only. For further information please read Frontiers' Conditions for Website Use and Copyright Statement, and the applicable CC-BY licence.

ISSN 1664-8714
ISBN 978-2-8325-3551-6
DOI 10.3389/978-2-8325-3551-6

About Frontiers

Frontiers is more than just an open-access publisher of scholarly articles: it is a pioneering approach to the world of academia, radically improving the way scholarly research is managed. The grand vision of Frontiers is a world where all people have an equal opportunity to seek, share and generate knowledge. Frontiers provides immediate and permanent online open access to all its publications, but this alone is not enough to realize our grand goals.

Frontiers Journal Series

The Frontiers Journal Series is a multi-tier and interdisciplinary set of open-access, online journals, promising a paradigm shift from the current review, selection and dissemination processes in academic publishing. All Frontiers journals are driven by researchers for researchers; therefore, they constitute a service to the scholarly community. At the same time, the Frontiers Journal Series operates on a revolutionary invention, the tiered publishing system, initially addressing specific communities of scholars, and gradually climbing up to broader public understanding, thus serving the interests of the lay society, too.

Dedication to Quality

Each Frontiers article is a landmark of the highest quality, thanks to genuinely collaborative interactions between authors and review editors, who include some of the world's best academicians. Research must be certified by peers before entering a stream of knowledge that may eventually reach the public - and shape society; therefore, Frontiers only applies the most rigorous and unbiased reviews.
Frontiers revolutionizes research publishing by freely delivering the most outstanding research, evaluated with no bias from both the academic and social point of view. By applying the most advanced information technologies, Frontiers is catapulting scholarly publishing into a new generation.

What are Frontiers Research Topics?

Frontiers Research Topics are very popular trademarks of the Frontiers Journals Series: they are collections of at least ten articles, all centered on a particular subject. With their unique mix of varied contributions from Original Research to Review Articles, Frontiers Research Topics unify the most influential researchers, the latest key findings and historical advances in a hot research area! Find out more on how to host your own Frontiers Research Topic or contribute to one as an author by contacting the Frontiers Editorial Office: frontiersin.org/about/contact

INTEGRATIVE PHARMACOLOGY-BASED RESEARCH ON TRADITIONAL MEDICINE: METHODOLOGIES, MEDICAL AND PHARMACOLOGICAL APPLICATIONS, 2nd Edition

Topic Editors:
Hai Yu Xu, Institute of Chinese Materia Medica, China Academy of Chinese Medical Sciences, China
Chang-xiao Liu, Tianjin Institute of Pharmaceutical Research, China
Yanqiong Zhang, Institute of Chinese Materia Medica, China Academy of Chinese Medical Sciences, China
Yan Xu, Cleveland State University, United States
Takashi Sato, Tokyo University of Pharmacy and Life Sciences, Japan

Publisher's note: This is a 2nd edition due to an article retraction.

Citation: Xu, H. Y., Liu, C.-x., Zhang, Y., Xu, Y., Sato, T., eds. (2023). Integrative Pharmacology-Based Research on Traditional Medicine: Methodologies, Medical and Pharmacological Applications, 2nd Edition. Lausanne: Frontiers Media SA. doi: 10.3389/978-2-8325-3551-6

Table of Contents

10 ***An Integrative Pharmacology-Based Analysis of Refined Qingkailing Injection Against Cerebral Ischemic Stroke: A Novel Combination of Baicalin, Geniposide, Cholic Acid, and Hyodeoxycholic Acid***
Chongyang Ma, Xueqian Wang, Tian Xu, Shuang Zhang, Shuling Liu, Changming Zhai, Zisong Wang, Jie Mu, Changxiang Li, Fafeng Cheng and Qingguo Wang

24 ***Screening for Susceptibility-Related Factors and Biomarkers of Xianling Gubao Capsule-Induced Liver Injury***
Chun-yu Li, Ming Niu, Ya-lei Liu, Jin-fa Tang, Wei Chen, Geng Qian, Ming-yu Zhang, Ya-fei Shi, Jun-zhi Lin, Xing-jie Li, Rui-sheng Li, Xiao-he Xiao, Guo-hui Li and Jia-bo Wang

37 ***Pharmacological Activity, Pharmacokinetics, and Toxicity of Timosaponin AIII, a Natural Product Isolated From* Anemarrhena asphodeloides *Bunge: A Review***
Yan Lin, Wai-Rong Zhao, Wen-Ting Shi, Jing Zhang, Kai-Yu Zhang, Qian Ding, Xin-Lin Chen, Jing-Yi Tang and Zhong-Yan Zhou

53 ***Treating Different Diseases With the Same Method—A Traditional Chinese Medicine Concept Analyzed for Its Biological Basis***
Xing Zhai, Xi Wang, Li Wang, Linlin Xiu, Weilu Wang and Xiaohan Pang

69 ***Traditional Asian Herbs in Skin Whitening: The Current Development and Limitations***
Yibo Hu, Hongliang Zeng, Jinhua Huang, Ling Jiang, Jing Chen and Qinghai Zeng

79 ***Inhibitory Effect of Cudratrixanthone U on RANKL-Induced Osteoclast Differentiation and Function in Macrophages and BMM Cells***
Eun-Nam Kim, Jaeyoung Kwon, Hyun-Su Lee, Sooyeun Lee, Dongho Lee and Gil-Saeng Jeong

93 ***Antioxidant Phytoconstituents From* Onosma bracteata *Wall. (Boraginaceae) Ameliorate the CCl_4 Induced Hepatic Damage:* In Vivo *Study in Male Wistar Rats***
Ajay Kumar, Varinder Kaur, Kritika Pandit, Hardeep Singh Tuli, Katrin Sak, Subheet Kumar Jain and Satwinderjeet Kaur

111 ***Unsupervised Learning and Multipartite Network Models: A Promising Approach for Understanding Traditional Medicine***
Mohieddin Jafari, Yinyin Wang, Ali Amiryousefi and Jing Tang

121 ***Jian-Pi-Bu-Xue-Formula Alleviates Cyclophosphamide-Induced Myelosuppression* via *Up-Regulating NRF2/HO1/NQO1 Signaling***
Qiuju Huang, Lizhi Feng, Hang Li, Liang Zheng, Xiaoxiao Qi, Ying Wang, Qian Feng, Zhongqiu Liu, Xiaohong Liu and Linlin Lu

136 ***Huoxue Huatan Decoction Ameliorates Myocardial Ischemia/Reperfusion Injury in Hyperlipidemic Rats* via *PGC-1α–PPARα and PGC-1α–NRF1–mtTFA Pathways***
Fei Lin, Yu-Qing Tan, Xuan-Hui He, Li-Li Guo, Ben-Jun Wei, Jun-Ping Li, Zhong Chen, Heng-Wen Chen and Jie Wang

153 ***Traditional Chinese Medicine in Treating Influenza: From Basic Science to Clinical Applications***
Yibai Xiong, Na Xiao Li, Naifang Duan, Bin Liu, Hui Zhu, Chi Zhang, Li Li, Cheng Lu and Luqi Huang

162 **Veratrilla baillonii** ***Franch Could Alleviate Lipid Accumulation in LO2 Cells by Regulating Oxidative, Inflammatory, and Lipid Metabolic Signaling Pathways***
Xian-ju Huang, Cai-jing He, Shuai Liang, Jing Wang, Jun Li, Guang-zhong Yang and Zhang Zhao

176 ***Gastrointestinal Motility, Muscle Relaxation, Antipyretic and Acute Toxicity Screening of Amyrin Type Triterpenoid (Daturaolone) Isolated From*** **Datura metel** ***Linnaeus (Angel's Trumpet) Fruits***
Saud Bawazeer, Abdur Rauf and Sami Bawazeer

184 ***Tripterygium Ingredients for Pathogenicity Cells in Rheumatoid Arthritis***
Yujun Tang, Qiuping Liu, Yuxiang Feng, Yi Zhang, Zhenghao Xu, Chengping Wen and Yun Zhang

200 ***Onion Bulb Extract Downregulates EGFR/ERK1/2/AKT Signaling Pathway and Synergizes With Steroids to Inhibit Allergic Inflammation***
Ahmed Z. El-Hashim, Maitham A. Khajah, Khaled Y. Orabi, Sowmya Balakrishnan, Hanan G. Sary and Ala A. Abdelali

218 ***An Integrative Serum Pharmacology-Based Approach to Study the Anti-Tumor Activity of*** **B. paniculatum** ***Aqueous Bulb Extract on the Human Hepatocellular Carcinoma Cell Line BEL-7404***
Xuesong Feng, Guangyuan Ma, Hailong Shi, Yuewen Wang and Xu Chao

230 ***The Interventional Effects of Tubson-2 Decoction on Ovariectomized Rats as Determined by a Combination of Network Pharmacology and Metabolomics***
Fan Yang, Xin Dong, Feixiang Ma, Feng Xu, Jie Liu, Jingkun Lu, Chunyan Li, Ren Bu and Peifeng Xue

243 ***Regulation of $GABA_A$ and 5-HT Receptors Involved in Anxiolytic Mechanisms of Jujube Seed: A System Biology Study Assisted by UPLC-Q-TOF/MS and RT-qPCR Method***
Liang Chen, Xue Zhang, Chun Hu, Yi Zhang, Lu Zhang, Juntao Kan, Bo Li and Jun Du

259 ***Integrating Pharmacology and Gut Microbiota Analysis to Explore the Mechanism of Citri Reticulatae Pericarpium Against Reserpine-Induced Spleen Deficiency in Rats***
Yuying Zheng, Xuan Zeng, Pan Chen, Tingting Chen, Wei Peng and Weiwei Su

277 ***A Novel Strategy for Decoding and Validating the Combination Principles of Huanglian Jiedu Decoction From Multi-Scale Perspective***
Ke-Xin Wang, Yao Gao, Wen-Xia Gong, Xiao-Feng Ye, Liu-Yi Fan, Chun Wang, Xue-Fei Gao, Li Gao, Guan-Hua Du, Xue-Mei Qin, Ai-Ping Lu and Dao-Gang Guan

295 ***Hydroxysafflor Yellow A: A Systematical Review on Botanical Resources, Physicochemical Properties, Drug Delivery System, Pharmacokinetics, and Pharmacological Effects***
Feng Zhao, Ping Wang, Yuanyuan Jiao, Xiaoxiao Zhang, Daquan Chen and Haiyu Xu

316 ***Bufei Jianpi Formula Improves Mitochondrial Function and Suppresses Mitophagy in Skeletal Muscle via the Adenosine Monophosphate-Activated Protein Kinase Pathway in Chronic Obstructive Pulmonary Disease***
Jing Mao, Ya Li, Suxiang Feng, Xuefang Liu, Yange Tian, Qingqing Bian, Junzi Li, Yuanyuan Hu, Lanxi Zhang, Huige Ji and Suyun Li

333 ***Quality Markers for Astragali Radix and Its Products Based on Process Analysis***
Yuntao Dai, Dongbo Wang, Manjia Zhao, Lihua Yan, Chao Zhu, Pengyue Li, Xuemei Qin, Rob Verpoorte and Shilin Chen

343 ***Network Pharmacology Reveals the Mechanism of Activity of Tongqiao Huoxue Decoction Extract Against Middle Cerebral Artery Occlusion-Induced Cerebral Ischemia-Reperfusion Injury***
Si-peng Wu, Ning Wang and Li Zhao

356 ***An Integrated Strategy for Effective-Component Discovery of Astragali Radix in the Treatment of Lung Cancer***
Bing Yang, Nan Yang, Yaping Chen, Maomao Zhu, Yuanpei Lian, Zhiwei Xiong, Bei Wang, Liang Feng and Xiaobin Jia

375 ***Clinical Practice Guideline for* Tripterygium *Glycosides/*Tripterygium wilfordii *Tablets in the Treatment of Rheumatoid Arthritis***
Na Lin, Yan-Qiong Zhang, Quan Jiang, Wei Liu, Jian Liu, Qing-Chun Huang, Kuan-Yu Wu, Sheng-Hao Tu, Zu-Shan Zhou, Wei-Heng Chen, Xiao-Xia Li, Ying Ding, Yong-Fei Fang, Jian-Ping Liu, Zhen-Bin Li, Dong-Yi He, Yao-Long Chen, Yu-Qian Lou, Qing-Wen Tao, Qing-Wen Wang, Ying-Hui Jin, Xing Liao, Tai-Xian Li and Xiao-Yue Wang

382 ***Effects of* Guanxinshutong *Capsules as Complementary Treatment in Patients With Chronic Heart Failure: Study Protocol for a Randomized Controlled Trial***
Yu Wang, Jiaping Xu, Jiehong Yang, Ling Zhang, Yuanjiang Pan, Liping Dou, Peng Zhou, Yizhou Xu, Chang Li, Yu He, Huifen Zhou, Li Yu, Jingwen Chen, Shuwei Huang, Wei Fu and Haitong Wan

392 ***Network Patterns of Herbal Combinations in Traditional Chinese Clinical Prescriptions***
Ning Wang, Ninglin Du, Yonghong Peng, Kuo Yang, Zixin Shu, Kai Chang, Di Wu, Jian Yu, Caiyan Jia, Yana Zhou, Xiaodong Li, Baoyan Liu, Zhuye Gao, Runshun Zhang and Xuezhong Zhou

404 ***The Traditional Chinese Medicine Fuyou Formula Alleviates Precocious Puberty by Inhibiting GPR54/GnRH in the Hypothalamus***
Guo-liang Bai, Kai-li Hu, Yi Huan, Xing Wang, Lei Lei, Meng Zhang, Chun-yan Guo, Hong-sheng Chang, Li-bo Zhao, Jing Liu, Zhu-fang Shen, Xiao-ling Wang and Xin Ni

416 ***Paeonol Protects Against Myocardial Ischemia/Reperfusion-Induced Injury by Mediating Apoptosis and Autophagy Crosstalk***
Chin-Feng Tsai, Hsing-Hui Su, Ke-Min Chen, Jiuan-Miaw Liao, Yi-Ting Yao, Yi-Hung Chen, Meilin Wang, Ya-Chun Chu, Yi-Hsin Wang and Shiang-Suo Huang

427 ***Integrating Network Pharmacology and Experimental Validation to Investigate the Effects and Mechanism of* Astragalus *Flavonoids Against Hepatic Fibrosis***
Lin An, Yuefang Lin, Leyan Li, Muyan Kong, Yanmei Lou, Jinjun Wu and Zhongqiu Liu

444 ***The Efficacy and Mechanism of Chinese Herbal Medicines in Lowering Serum Uric Acid Levels: A Systematic Review***
Liqian Chen, Zhengmao Luo, Ming Wang, Jingru Cheng, Fei Li, Hanqi Lu, Qiuxing He, Yanting You, Xinghong Zhou, Hiu Yee Kwan, Xiaoshan Zhao and Lin Zhou

468 ***Epigallocatechin Gallate During Dietary Restriction — Potential Mechanisms of Enhanced Liver Injury***
Zhuo Shi, Jing-xiao Zhu, Yu-ming Guo, Ming Niu, Le Zhang, Can Tu, Ying Huang, Peng-yan Li, Xu Zhao, Zi-teng Zhang, Zhao-fang Bai, Guang-qin Zhang, Yang Lu, Xiao-he Xiao and Jia-bo Wang

481 ***An Integrative Pharmacology-Based Approach for Evaluating the Potential Effects of Purslane Seed in Diabetes Mellitus Treatment Using UHPLC-LTQ-Orbitrap and TCMIP V2.0***
Jinli Hou, Xiang Zhou, Ping Wang, Chunhui Zhao, Yuewen Qin, Feng Liu, Liping Yu and Haiyu Xu

499 ***Chemical Characteristics of* Platycodon grandiflorum *and its Mechanism in Lung Cancer Treatment***
Yaling Deng, Xianwen Ye, Yufan Chen, Hongmin Ren, Lanting Xia, Ying Liu, Minmin Liu, Haiping Liu, Huangang Zhang, Kairui Wang, Jinlian Zhang and Zhongwei Zhang

515 ***Review of the Efficacy and Mechanisms of Traditional Chinese Medicines as a Therapeutic Option for Ionizing Radiation Induced Damage***
Xiaomeng Zhang, Xiaoying Chen, Lei Wang, Changhao He, Zhongyu Shi, Qian Fu, Wenhui Xu, Shujing Zhang and Sumin Hu

533 ***An Integrative Pharmacology-Based Pattern to Uncover the Pharmacological Mechanism of Ginsenoside H Dripping Pills in the Treatment of Depression***
Libin Zhao, Rui Guo, Ningning Cao, Yingxian Lin, Wenjing Yang, Shuai Pei, Xiaowei Ma, Yu Zhang, Yingpeng Li, Zhaohui Song, Wuxun Du, Xuefeng Xiao and Changxiao Liu

551 ***Deciphering the Pharmacological Mechanisms of Guizhi-Fuling Capsule on Primary Dysmenorrhea Through Network Pharmacology***
Siqin Zhang, Xinxing Lai, Xin Wang, Gang Liu, Zhenzhong Wang, Liang Cao, Xinzhuang Zhang, Wei Xiao and Shao Li

565 ***The Protective Effects of Shengmai Formula Against Myocardial Injury Induced by Ultrafine Particulate Matter Exposure and Myocardial Ischemia are Mediated by the PI3K/AKT/p38 MAPK/Nrf2 Pathway***
Lina Chen, Yuan Guo, Shuiqing Qu, Kai Li, Ting Yang, Yuanmin Yang, Zhongyuan Zheng, Hui Liu, Xi Wang, Shuoqiu Deng, Yu Zhang, Xiaoxin Zhu and Yujie Li

582 ***Inhibition of TLR4/MAPKs Pathway Contributes to the Protection of Salvianolic Acid A Against Lipotoxicity-Induced Myocardial Damage in Cardiomyocytes and Obese Mice***
Zhen Yang, Yanli Chen, Zhaoyuan Yan, Tian Tian Xu, Xiangyao Wu, Aiwen Pi, Qingsheng Liu, Hui Chai, Songtao Li and Xiaobing Dou

592 **Palmul-*Tang, a Korean Medicine, Promotes Bone Formation via BMP-2 Pathway in Osteoporosis***
La Yoon Choi, Mi Hye Kim, Yeon Kyung Nam, Ju Hee Kim, Hea-Young Cho and Woong Mo Yang

601 ***An Integrative Pharmacology-Based Strategy to Uncover the Mechanism of Xiong-Pi-Fang in Treating Coronary Heart Disease With Depression***
Lihong Zhang, Yu Zhang, Mingdan Zhu, Limin Pei, Fangjun Deng, JinHong Chen, Shaoqiang Zhang, Zidong Cong, Wuxun Du and Xuefeng Xiao

618 ***The Treatment of Rhodiola Mimics Exercise to Resist High-Fat Diet-Induced Muscle Dysfunction via Sirtuin1-Dependent Mechanisms***
Baiyang You, Yaoshan Dun, Siqian Fu, Dake Qi, Wenliang Zhang, Yuan Liu, Ling Qiu, Murong Xie and Suixin Liu

629 ***Galectin-3 Mediated Inflammatory Response Contributes to Neurological Recovery by QiShenYiQi in Subacute Stroke Model***
Yule Wang, Shuang He, Xinyan Liu, Zhixiong Li, Lin Zhu, Guangxu Xiao, Xiaoli Du, Hongxia Du, Wen Zhang, Yiqian Zhang, John Orgah, Yuxin Feng, Boli Zhang and Yan Zhu

645 ***An Effective Workflow for Differentiating the Same Genus Herbs of Chrysanthemum morifolium Flower and Chrysanthemum Indicum Flower***
Jiao He, Qian Zhang, Cuiying Ma, Gabriel I. Giancaspro, Kaishun Bi and Qing Li

656 ***Yi-Qi-Jian-Pi Formula Suppresses RIPK1/RIPK3-Complex-Dependent Necroptosis of Hepatocytes Through ROS Signaling and Attenuates Liver Injury* in Vivo *and* in Vitro**
Feixia Wang, Li Tang, Baoyu Liang, Chun Jin, Liyuan Gao, Yujia Li, Zhanghao Li, Jiangjuan Shao, Zili Zhang, Shanzhong Tan, Feng Zhang and Shizhong Zheng

672 ***Network Pharmacology-Based Strategy for Elucidating the Molecular Basis Forthe Pharmacologic Effects of Licorice (*Glycyrrhiza *spp.)***
Jia Chen, Lin-Fu Li, Xiao-Ru Hu, Feng Wei and Shuangcheng Ma

687 ***Qing-Yi Decoction in the Treatment of Acute Pancreatitis: An Integrated Approach Based on Chemical Profile, Network Pharmacology, Molecular Docking and Experimental Evaluation***
Tian-Fu Wei, Liang Zhao, Peng Huang, Feng-Lin Hu, Ju-Ying Jiao, Kai-Lai Xiang, Zhi-Zhou Wang, Jia-Lin Qu and Dong Shang

700 ***Evaluation of the Efficacy and Safety of Chinese Herbal Injection Combined With Trimetazidine for Viral Myocarditis: A Network Meta-Analysis***
Kerui Wu, Dingwei Deng, Binghui Yu, Ziyun Han, Lanlin Huang, Yaxing He, Xia Yan and Dawei Wang

713 ***Gegen Qinlian Decoction Ameliorates Hyperuricemia-Induced Renal Tubular Injury via Blocking the Inflammatory Signaling Pathway***
Xiao-Jun Wang, Yi-Ding Qi, Hao-Chen Guan, Hua-Gang Lin, Pei-Qing He, Kang-Wei Guan, Lei Fu, Mao-Qing Ye, Jing Xiao and Tao Wu

727 ***Integrated Pharmacological Analysis on the Mechanism of Fuyou Formula in Treating Precocious Puberty***
Chunyan Guo, Ning Sun, Kaili Hu, Guoliang Bai, Meng Zhang, Qian Wang, Qian Ding, Jing Liu, Xiaoling Wang and Libo Zhao

738 ***Clinical Efficacy of* Cortex Daphnes *(*Zushima*) Patch in Patients With Symptomatic Knee Osteoarthritis: A Multicenter Non-Inferiority Randomized Controlled Clinical Trial***
Yan-Ting Li, Juan Jiao, Yi Zhang, Ci-Bo Huang, Hai-Dong Wang, Bei Wang, Xiao Su, Hui Song, Mian-Song Zhao, De-Xun Jiang, Jia-Qiang Wang and Quan Jiang

749 ***Comparative Efficacy of Oral Chinese Patent Medicine for Chronic Prostatitis/Chronic Pelvic Pain Syndrome With Sexual Dysfunction: A Bayesian Network Meta-Analysis of Randomized Controlled Trials***
Yang Zhang, Hongzhao Ma, Tao Nan, Yongqiang Li, Wei Zheng, Zhihui Zhou and Xiaoyong Gong

764 ***Exploring the Mechanism of Zhibai Dihuang Decoction in the Treatment of Ureaplasma Urealyticum-Induced Orchitis Based on Integrated Pharmacology***
Dong-hua Bin, Shi-ying Zhang, Min Zhan, Ling Li, Ying-qiu Li, Xing Zhou, Fang-guo Lu, Qing Zhou and Qing-hu He

781 ***Efficacy of Chinese Herbal Injections for Elderly Patients With pneumonia—A Bayesian Network Meta-analysis of Randomized Control Trials***
Yang Yuan, Quan Zheng, Zhilin Si, Juhua Liu, Zhi Li, Lian Xiong, Pan Liu, Xu Li, Chengshi He and Jinghong Liang

790 ***Traditional Chinese Medicine Qingre Huoxue Treatment vs. the Combination of Methotrexate and Hydroxychloroquine for Active Rheumatoid Arthritis: A Multicenter, Double-Blind, Randomized Controlled Trial***
Xun Gong, Wei-Xiang Liu, Xiao-Po Tang, Jian Wang, Jian Liu, Qing-Chun Huang, Wei Liu, Yong-Fei Fang, Dong-Yi He, Ying Liu, Ming-Li Gao, Qing-Jun Wu, Shi Chen, Zhen-Bin Li, Yue Wang, Yan-Ming Xie, Jun-Li Zhang, Cai-Yun Zhou, Li Ma, Xin-Chang Wang, Chi Zhang and Quan Jiang

802 ***Identification of the Main Active Components and Mechanism of Wang Bi Tablet in Treating Rheumatoid Arthritis Based on Integrative Pharmacology***
Yuanyuan Jiao, Jia Xu, Hong Chen, Qiuyan Guo, Xiaofang Deng, Tong Zhang, Jingbo Zhang, Chenjing Shi and Ping Wang

815 ***Qian Yang Yu Yin Granule Improves Renal Injury of Hypertension by Regulating Metabolic Reprogramming Mediated by HIF-1α/PKM2 Positive Feedback Loop***
Lichao Qian, Shuai Ren, Zhongchi Xu, Yawei Zheng, Lihua Wu, Ying Yang, Yixuan Wang, Jie Li, Shihai Yan and Zhuyuan Fang

832 ***Synthesis of Icariin-Zinc and its Protective Effect on Exercise Fatigue and Reproductive System Related Glands in Male Rats***
Juntao Zhang, Chao Zhang, Aifeng Liu, Qiang Ji, Lixia Ren, Chuanrui Ma, Hengyu Zhang, Chaochao Wu, Donglin Zhang, Man Shang and Feng He

842 ***Developing Placebos for Clinical Research in Traditional Chinese Medicine: Assessing Organoleptic Properties of Three Dosage Forms (Oral Liquid, Capsule and Granule)***
Mengli Xiao, Jiake Ying, Yang Zhao, Qingna Li, Yingpan Zhao, Rui Gao and Fang Lu

850 ***Metabolic and Network Pharmacological Analyses of the Therapeutic Effect of* Grona styracifolia *on Calcium Oxalate-Induced Renal Injury***
Wei Chen, Yachen Si, Jin Cheng, Jiarong Ding, Hongxia Zhao, Wenrui Liu, Qishan Lin, Jiebin Hou and Zhiyong Guo

863 ***Exploring the Regulatory Mechanism of* Hedysarum Multijugum Maxim.-Chuanxiong Rhizoma *Compound on HIF-VEGF Pathway and Cerebral Ischemia-Reperfusion Injury's Biological Network Based on Systematic Pharmacology***
Kailin Yang, Liuting Zeng, Anqi Ge, Yi Chen, Shanshan Wang, Xiaofei Zhu and Jinwen Ge

882 ***Components and Pharmacodynamical Mechanism of Yinfupian Based on Liquid Chromatography-Mass Spectrometry and Proteomics Analyses***
Heng-li Tong, Hao Chen, Fei-peng Gong, Ling-yun Zhong, Jing Zhu and Song-hong Yang

900 ***TCMIP v2.0 Powers the Identification of Chemical Constituents Available in Xinglou Chengqi Decoction and the Exploration of Pharmacological Mechanisms Acting on Stroke Complicated With Tanre Fushi Syndrome***
Ping Wang, Shuang Wang, Hong Chen, Xiaofang Deng, Luoqi Zhang, Haiyu Xu and Hongjun Yang

916 ***Feasibility and Mechanism Analysis of Shenfu Injection in the Treatment of Idiopathic Pulmonary Fibrosis***
Peipei Liu, Shengnan Yang, Zai Wang, Huaping Dai and Chen Wang

931 **Poria cum Radix Pini *Rescues Barium Chloride-Induced Arrhythmia by Regulating the cGMP-PKG Signalling Pathway Involving ADORA1 in Zebrafish***
Ning-Juan Yang, Yan-Ru Liu, Zhi-Shu Tang, Jin-Ao Duan, Ya-Feng Yan, Zhong-Xing Song, Ming-Geng Wang, Yu-Ru Zhang, Bai-Jin Chang, Meng-Li Zhao and Yan-Ting Zhao

944 ***Efficacy and Safety of Chinese Patent Medicine Combined With Oseltamivir in Treatment of Children With Influenza: A meta-Analysis***
Nai-fan Duan, Bin Liu, Xiao-na Li, Yi-bai Xiong, Yan Zhang, Chi Zhang, Li Ll, Cheng Lu and Jueni Lyu

962 ***A Systematic Study of the Mechanism of Acacetin Against Sepsis Based on Network Pharmacology and Experimental Validation***
Yuanshuo Ouyang, Yi Rong, Yanming Wang, Yanli Guo, Liya Shan, Xiushi Yu, Li Li, Junqiang Si, Xinzhi Li and Ketao Ma

973 ***Study on the Effect of Macrophages on Vascular Endothelium in Mice With Different TCM Syndromes of Dyslipidemia and its Biological Basis Based on RNA-Seq Technology***
Jing Chen, Chao Ye, Zheng Yang, Tieshan Wang, Bing Xu, Pengyang Li, Shan Zhang and Xiaolin Xue

987 **Kaempferia galanga *L.: Progresses in Phytochemistry, Pharmacology, Toxicology and Ethnomedicinal Uses***
Si-Yu Wang, Hui Zhao, Hong-Tao Xu, Xiao-Dong Han, Yun-Shan Wu, Fang-Fang Xu, Xiao-Bo Yang, Ulf Göransson and Bo Liu

1004 ***Circadian Pharmacological Effects of Paeoniflorin on Mice With Urticaria-like Lesions Circadian Pharmacological Effects of Paeoniflorin***
Li Peng, Lijuan Wen, Jie Zhang, Xiaotong Zhang, Qin Wei, Jing Guo and Jinhao Zeng

frontiers in Pharmacology

ORIGINAL RESEARCH
published: 08 May 2020
doi: 10.3389/fphar.2020.00519

An Integrative Pharmacology-Based Analysis of Refined Qingkailing Injection Against Cerebral Ischemic Stroke: A Novel Combination of Baicalin, Geniposide, Cholic Acid, and Hyodeoxycholic Acid

Chongyang Ma[1†], Xueqian Wang[2†], Tian Xu[2†], Shuang Zhang[2], Shuling Liu[2], Changming Zhai[3], Zisong Wang[4], Jie Mu[2], Changxiang Li[2], Fafeng Cheng[2] and Qingguo Wang[2*]*

[1] School of Traditional Chinese Medicine, Capital Medical University, Beijing, China, [2] School of Traditional Chinese Medicine Department, Beijing University of Chinese Medicine, Beijing, China, [3] Department of Liver Disease, Guangdong Province Hospital of Traditional Chinese Medicine Zhuhai Branch, Zhuhai, China, [4] Department of Traditional Chinese Medicine, Beijing Chaoyang Hospital, Capital Medical University, Beijing, China

OPEN ACCESS

Edited by:
Hai Yu Xu,
China Academy of Chinese Medical Sciences, China

Reviewed by:
Liang Feng,
China Pharmaceutical University, China
Ming Niu,
302 Military Hospital, China

***Correspondence:**
Fafeng Cheng
fafengcheng@gmail.com
Qingguo Wang
wangqg8558@163.com

†These authors have contributed equally to this work

Specialty section:
This article was submitted to Ethnopharmacology, a section of the journal Frontiers in Pharmacology

Received: *07 February 2020*
Accepted: *02 April 2020*
Published: *08 May 2020*

Citation:
Ma C, Wang X, Xu T, Zhang S, Liu S, Zhai C, Wang Z, Mu J, Li C, Cheng F and Wang Q (2020) An Integrative Pharmacology-Based Analysis of Refined Qingkailing Injection Against Cerebral Ischemic Stroke: A Novel Combination of Baicalin, Geniposide, Cholic Acid, and Hyodeoxycholic Acid. Front. Pharmacol. 11:519. doi: 10.3389/fphar.2020.00519

Stroke is the second leading cause of death after heart disease globally and cerebral ischemic stroke accounts for approximately 70% of all incident stroke cases. We selected four main compounds from a patent Chinese medicine, Qingkailing (QKL) injection, including baicalin from *Scutellaria baicalensis* Georgi (Huang Qin), geniposide from *Gardenia jasminoides* J. Ellis (Zhizi), and cholic acid and hyodeoxycholic acid from *Bovis Calculus* (Niuhuang) with a ratio of 4.4:0.4:3:2.6 m/m, to develop a more efficacious and safer modern Chinese medicine injection against ischemic stroke, refined QKL (RQKL). In this study, we investigated multiple targets, levels, and pathways of RQKL by using an integrative pharm\acology combining experimental validation approach. In silica study showed that RQKL may regulate PI3K-Akt, estrogen, neurotrophin, HIF-1, MAPK, Hippo, FoxO, TGF-beta, NOD-like receptor, apoptosis, NF-kappa B, Wnt, chemokine, TNF, Toll-like receptor signaling pathways against ischemic stroke. The experimental results showed that RQKL improved neurological function and prevented infract volume and blood-brain-barrier damage. RQKL inhibited microgliosis and astrogliosis, and protected neurons from ischemic/reperfusion injury. RQKL also inhibited cell apoptosis and affecting the ratio of the anti-apoptosis protein B-cell lymphoma-2 (Bcl2) and pro-apoptosis protein Bcl2-associated X protein (Bax). Western blot analysis showed that RQKL activated AKT/PI3K signaling pathway and antibody array showed RQKL inhibited inflammatory response and decreased proinflammatory factor Tnf, Il6, and Il1b, and chemokines Ccl2, Cxcl2, and Cxcl3, and increased anti-inflammatory cytokine Il10. In conclusion, RQKL protected tissue against ischemic stroke through multiple-target, multiple signals, and modulating

multiple cell-types in brain. This study not only promoted our understanding of the role of RQKL against ischemic stroke, but also provided a pattern for the study of Chinese medicine combining pharmaceutical Informatics and system biology methods.

Keywords: network pharmacology, ischemic stroke, combination of drug, Chinese medicine, protein protein-interaction (PPI) network, topological analysis, Qingkailing, modern Chinese medicine

INTRODUCTION

Stroke is the second leading cause of death after heart disease globally and is associated with the highest disability-adjusted life-years lost of any disease in China (Wu et al., 2019). Approximately 795,000 new stroke cases are reported in the US yearly and 4.3 times this number was recently surveyed by the nationwide community-based study, NESS-China (Wang W. et al., 2017). Cerebral ischemic stroke accounts for approximately 70% of all incident stroke cases. Since the 1990s, intravenous alteplase has been considered the only evidence-based therapeutic agent for improving the prognosis of patients with cerebral ischemic stroke and accepted as standard of care all around the world (Powers et al., 2019). However, its short therapeutic window and high risk of hemorrhagic complications have hampered its widespread adoption in China. Therefore, exploring novel therapeutic strategies to treat ischemic stroke is an urgent need.

Qingkailing (QKL) injection, is a patent traditional Chinese medicine formulation approved by the China Food and Drug Administration to treat ischemic stroke for over 30 years. We previously study screened a novel modern drug combination (refined Qingkailing, RQKL) consisting of four compounds, baicalin (CAS number 21967-41-9) from *Scutellaria baicalensis* Georgi (Huang Qin), geniposide (CAS number 24512-63-8) from *Gardenia jasminoides* J. Ellis (Zhizi), and cholic acid (CAS number 81-25-4) and hyodeoxycholic acid (CAS number 83-49-8) from *Bovis Calculus* (Niuhuang) with a ratio of 4.4:0.4:3:2.6 m/m. Our previous study showed that RQKL protected the brain against ischemia-reperfusion (I/R) injury *in vivo* and *in vitro* (Cheng et al., 2012; Cheng et al., 2018). However, the underlying mechanisms and core signaling pathways mediating the multi-linked and multi-targeted effects of RQKL against ischemic stroke are still unknown.

Generally, natural bioactive compounds exert therapeutic effects through multiple targets and pathways that cannot be accurately detected solely using conventional pharmacological approaches.

Integrative pharmacology could enhance the comprehension and facilitate the prediction of potential targets, pathways, and consequences, which might provide clues for designing subsequent research studies. In this work, we used an integrative pharmacology approach with the goal of understanding the systemic, organ-related, and molecular effects of RQKL. This approach combined the prediction of multiple drug targets, visualization of compound-target network and target-cell-type network, topological analysis of protein-protein interaction (PPI) networks and gene ontology (GO), and KEGG pathway analysis of core targets. Importantly, our experimental results largely validated the mechanism of action of RQKL, as predicted by the integrative pharmacology analysis (**Figure 1**).

MATERIALS AND METHODS

Materials and Reagents

The RQKL used in this study was a mixture of baicalin, geniposide, cholic acid, and hyodeoxycholic acid (4.4:0.4:3:2.6). Baicalin (CAS number 21967-41-9), geniposide (CAS number 24512-63-8), and cholic acid (CAS number 81-25-4), and hyodeoxycholic acid (CAS number 83-49-8) were purchased from Shanghai Aladdin Biochemical Technology Co., Ltd. (Shanghai China). Protease inhibitor, radioimmunoprecipitation assay (RIPA) lysis buffer, and enhanced chemiluminescence (ECL) reagent were obtained from Applygen Technologies Inc. (Beijing China). The antibodies against B-cell lymphoma-2 (Bcl2, 12789-1-AP) and glyceraldehyde-3-phosphate dehydrogenase (GAPDH, 10494-1-AP) were obtained from Proteintech Group, Inc (Rosemont, USA). The antibodies against BCL2-associated X protein (BAX, #2772), serine-threonine protein kinase (AKT, #9272), phosphorylated-AKT (pAKT, #9271), phosphatidylinositol-4,5-Bisphosphate 3-kinase (PI3K, #4249), and phosphorylated-PI3K (pPI3K, #4228) were obtained from Cell Signaling Technology (Boston, USA). The antibodies against glial fibrillary acidic protein (GFAP, ab7260) was obtained from Abcam (Cambridge, USA). The antibodies against GFAP labeled Alexa Fluor 488 (MAB3402X) and neuronal nuclei antigen (NEUN, MAB37) were purchased form Millipore (Darmstadt, Germany) and the antibody against ionized calcium binding adaptor molecule-1 (IBA1, 019-19741) was purchased from WAKO CHEMICAL, CO., LTD. (Japan). Terminal deoxynucleotidyl transferase (TdT)-mediated deoxyuridine triphosphate (dUTP) nick-end labeling (TUNEL) apoptosis detection kit was purchased from Roche Applied Science (Mannheim, Germany). Rat cytokine array antibody arrays (GSR-CAA-67) were purchased from RayBiotech Life (California, USA).

Construction of the Compound-Target and Disease-Target Databases

To identify the corresponding targets of the four active ingredients of RQKL, several approaches combined with a chemometric method, information integration, and data-mining were implemented. First, the biological targets of the active ingredients were obtained from SEA (http://sea.bkslab.org/) (Keiser et al., 2007), STITCH (http://stitch.embl.de/) (Szklarczyk et al., 2016), DrugE-Rank (http://datamining-iip.

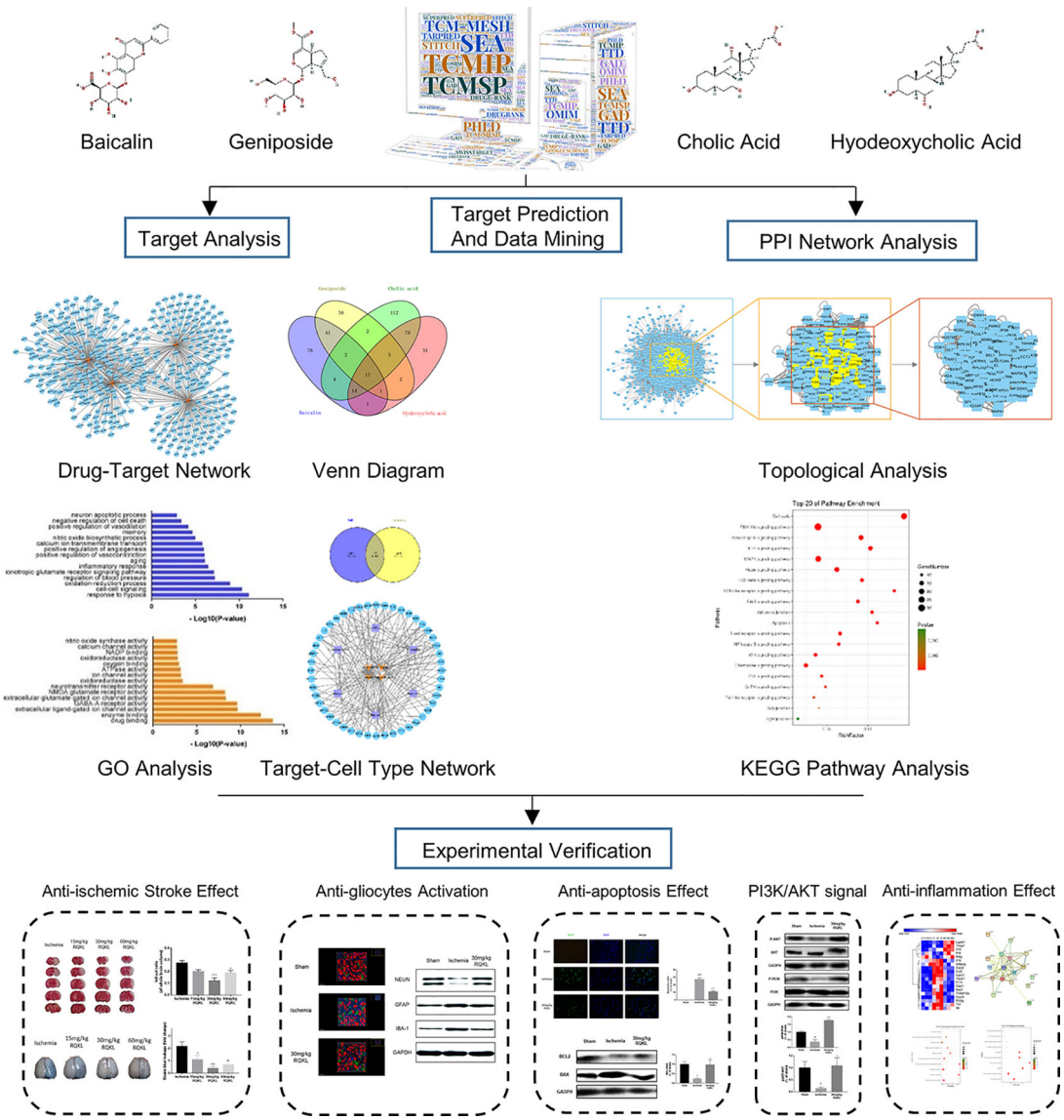

FIGURE 1 | Schematic diagram of combining integrative pharmacology and experimental approach used in this work.

fudan.edu.cn/service/DrugE-Rank) (Yuan et al., 2016), PhlD (http://phid.ditad.org/) (Hu et al., 2014), SuperPred (http://prediction.charite.de/index.php?site=home) (Nickel et al., 2014), SwissTarget (http://www.swisstargetprediction.ch/) (Gfeller et al., 2014), and TarPred (http://www.dddc.ac.cn/tarpred) (Liu et al., 2015). All active compounds were also sent to TCMIP (http://www.tcmip.cn/TCMIP/index.php/Home/Index/index.html) (Xu et al., 2019) TCM-Mesh (http://mesh.tcm.microbioinformatics.org/) (Zhang et al., 2017), TCMSP (http://tcmspw.com/tcmsp.php) (Ru et al., 2014), and Google Scholar to mine compound-target interactions. Please see detailed information in **Supplementary Table S1**.

Known therapeutic targets for ischemic stroke were collected from the DrugBank (http://www.drugbank.ca/) (Wishart et al., 2018), Online Mendelian Inheritance in Man (OMIM) (http://www.omim.org) (Hamosh et al., 2005), Genetic Association (GAD, http://geneticassociationdb.nih.gov/) (Becker et al., 2004), and Therapeutic Target Database (TTD, https://db.idrblab.org/ttd/) (Yang et al., 2016) databases. After deleting the redundant information, 321 known therapeutic targets for the treatment of ischemic stroke were included in this study. Please see detailed information in **Supplementary Table S2**.

Screening of Target Related Cell-Type

AlzData (http://www.alzdata.org/) database contains gene expression data of different cell-types from human brain single cell RNA-seq (GSE67835) and was used to recognize target related cell-type in the present study (Xu et al., 2018). In

briefly, after overlapping compound-target and disease-target databases, we input the obtained targets into AlzData database to investigate each target related cell-types.

Network Construction

Two kinds of networks in this study were established using Cytoscape (version 3.2.1) software (Shannon et al., 2003): compound-target network and target-cell-type network. Compound-target network was composed of compounds and their potential targets, which was built to reveal the compound-target interactions. Target-cell-type network was built based on the potential targets and their related cell-types.

Protein-Protein Interaction Network Construction

PPI data were imported from six currently available PPI databases, including the Biological General Repository for Interaction Datasets (BioGRID), Biomolecular Interaction Network Database (BIND), Molecular INTeraction Database (MINT), Human Protein Reference Database (HPRD), and Database of Interacting Proteins (DIP), which were searched using BisoGenet, a Cytoscape plugin (Martin et al., 2010). An interactive network for the candidate drug targets and known ischemic stroke-related targets of RQKL was constructed based on their interaction data and was visualized using the Cytoscape software.

Definition of Topological Feature Set for the Network

As previously mentioned the topological properties of every node in the interaction network were analyzed by calculating six measures: "betweenness centrality (BC)," "degree centrality (DC)," "eigenvector centrality (EC)," "closeness centrality (CC)," "network centrality (NC)," and "local average connectivity (LAC)" using CytoNCA (Wang X. et al., 2017). The definitions and computation equations of these six parameters represent the topological importance of a node in the network. More important nodes receive higher quantitative values within the network than less important nodes did (Tang et al., 2015).

Gene Oncology Enrichment and Pathway Analysis

Further, we performed GO analysis of the 438 non-repetitive putative targets of RQKL using the Database for Annotation, Visualization, and Integrated Discovery (DAVID) to gain insights into their involvement in two different categories namely, biological processes (BP) and molecular function (MF) (Sherman and Lempicki, 2009). Tissue enrichment analysis was performed using FunRich software (http://www.funrich.org) (Pathan et al., 2015). Then, we performed Kyoto Encyclopedia of Genes and Genomes (KEGG) signaling pathway enrichment analysis of the 189 candidate targets of RQKL after the topological analysis. A $P < 0.05$ was considered significant, and the enriched GO terms were identified using the hypergeometric test. A Bubble Chart was plotted using the OmicShare tools, a free online platform for data analysis (www.omicshare.com/tools).

Animals

Adult male Sprague-Dawley rats (220–230 g), provided by Vital River Laboratory Animal Technology (number SCXK 2016-0006, Beijing, China), were housed in the laboratory animal room and maintained at 25 ± 1°C with 65 ± 5% humidity on a 12-h light/dark cycle (lights on from 07:30 to 19:30) for at least 1 week before the experiments. Animals were provided food and water *ad libitum*. The animal experimental design and protocols used in this study were approved by the Ethics Review Committee for Animal Experimentation of Beijing University of Chinese Medicine (BUCM-4-2017090116-3016).

Transient Middle Cerebral Artery Occlusion

All animals were fasted overnight but allowed free access to water and were then randomly assigned to five groups: low-, medium-, and high-dose RQKL treatment; ischemic, and control groups. The transient middle cerebral artery (tMCA) occlusion (tMCAO) model was established as described previously to induce focal cerebral I/R injury (Zheng et al., 2014). The right MCA was occluded using a poly-L-lysine-coated nylon suture, which was inserted from the external carotid artery into the common carotid artery, and after a 90-min occlusion, the MCA-suture was carefully removed for reperfusion. The body temperature of the rats was maintained at 37°C. The sham group was subjected to the same procedure except for the nylon thread insertion. Rats in the low-, medium, and high-dose RQKL groups were administered intraperitoneal injections of RQKL dissolved in saline water at doses of 15, 30, and 60 mg/kg, respectively, and those in the ischemic group were administered physiological saline at the same volume. The first injection was performed immediately after model establishment, followed by administration after 4 h, and once every 12 h after that. At 24 h after reperfusion, 10 rats in each group were euthanized, and the brains were rapidly excised for histomorphological assay or protein detection.

Neurological Assessment

The neurological deficit score of each rat was measured 24 h after tMCAO induction in a blinded fashion according to a well-established five-point neurological scale (Longa et al., 1989): 0 = no apparent deficits, 1 = failure to fully extend the right forepaw, 2 = circling to the right, 3 = falling or leaning over to the right, 4 = no spontaneous walking and a depressed level of consciousness, and 5 = death.

Infarct Volume Assessment

Following neurological function evaluation, the rats were euthanized, and the brains were harvested for triphenyltetrazolium chloride (TTC) staining. The percentage infarct volume relative to the entire brain represented the degree of cerebral infarction. Serial coronal sections (2 mm thick) were prepared and soaked in 2% TTC phosphate buffer at 37°C for 10 min in the dark. Normal brain tissues were stained red while infarct tissues were not stained (white). The sections were soaked in 4%

paraformaldehyde (PFA) phosphate buffer for 30 min, arranged in order and scanned (Tsinghua Unisplendour A688, Xi'an, China). Areas of red and white staining were measured using a computer color multimedia image analysis system (Image-Pro Plus 6.0, Media Cybernetics, WY, USA). The percentage of the infarction was calculated using the following equation: infarct volume (%) = infarct volume/total volume of slice × 100.

Blood-Brain-Barrier Permeability

The blood-brain barrier (BBB) permeability was determined using Evans blue (EB) extravasation 24 h after tMCAO. In brief, EB dye (2%, 4 ml/kg) was injected over a 2-min period into the left femoral vein at a dose of 2 ml/kg and allowed to circulate for 1 h. Rats were anesthetized and perfused transcardially using saline to remove the intravascular EB dye. After decapitated, the entire brain of each animal was removed, homogenized in physiological phosphate-buffered saline (PBS), trichloroacetic acid was added to precipitate the protein, and then the tissue homogenates were cooled and centrifuged. The EB absorbance of the resulting supernatant was measured at 620 nm using a spectrophotometer.

Nissl Staining

Coronal brain sections from four equidistant brain levels, 1 mm apart, were stained with cresyl violet according to a standard protocol. For Nissl staining, air-dried sections were fixed in 4% PFA solution for 15 min; immersed in 100, 95, 85, and 70% ethanol, followed by double distilled water for 3 min each; stained for 15 min with filtered cresyl violet solution [Sigma, 0.2% (w/v)]); and then briefly rinsed in double distilled water. Finally, the sections were dehydrated again in 70, 95, and 100% ethanol for 1 min each; placed in xylene for another 10 min; and then coverslipped. Nissl staining was performed to examine the neuronal injury, and necrotic neurons (red triangles) showed the absence of Nissl's bodies in the cytoplasm, a shrunken intercellular space, and deep staining. The following four scores were used to evaluate necrotic neurons in the infarct area: 0, normal; 1, damaged neurons were < 25%; 2, damaged neurons were 25–50%; 3, damaged neurons were 50–75%; and 4, damaged neurons were > 75%(Sun et al., 2009).

Terminal Deoxynucleotidyl Transferase-Mediated Deoxyuridine Triphosphate Nick-End Labeling Staining

Ischemic stroke-induced DNA fragmentation was quantified in frozen sections using the TdT-mediated dUTP nick-end labeling (TUNEL) assay according to the manufacturer's instructions. Briefly, air-dried sections were fixed with methanol-free 4% PFA at room temperature for 15 min and washed twice with PBS. The sections were immersed in equilibration buffer for 10 min, which was then replaced by a mixture of 1 μl TdT enzyme, 5 μl nucleotide mix, and 45 μl equilibration buffer. The sections were then kept at 37°C for 90 min, and then SSC (2×) was added for 15 min at room temperature to terminate the TdT enzyme reaction.

Confocal Microscopy and Morphology Analysis

Brains were cut into coronal sections (40 μm) on a cryostat, placed in 1 ml of anti-freeze solution (40% PBS, 30% ethylene-glycol, 30%, glycerol, v/v) and stored at −20°C until immunohistochemistry. Triple immunostaining was performed on coronal slices with the free-floating method as previously described (Lana et al., 2014). The following primary antibodies were used a mouse monoclonal anti-neuronal nuclei (NeuN, 1:200; Millipore, Billerica, MA) for neurons; a rabbit polyclonal anti-glial fibrillary acidic protein (GFAP, 1:1,000; DakoCytomation, Glostrup, Denmark) for astrocytes; a rabbit polyclonal anti-IBA1 (1:300, WAKO Pure Chem. Ind., Osaka, Japan) for microglia. Slices were observed under a ZEISS LSM 5 confocal laser scanning microscope. Confocal scans were taken at 0.5 μm z-steps keeping pinhole, contrast, and brightness constant. Semi-automated image analysis was performed using Bitplane IMARIS 7.4 3D image analysis software (Oxford Instruments, Concord, MA) and the 3-D reconstructed images of microglia and astrocyte were using surface function based on previously described (Radford et al., 2015).

Western Blotting

The cortical tissue in the penumbra was collected for western blot analysis. The protein was extracted using RIPA lysis buffer containing protease inhibitor, and the concentration was measured using a bicinchoninic acid (BCA) protein assay kit (#CW0014, CWBio, China). Protein samples (50 μg) were separated on sodium dodecyl sulfate (SDS)-polyacrylamide gels and transferred onto a polyvinylidene fluoride membrane (Millipore Corporation, Billerica, MA, USA). The membrane was blocked with 5% nonfat dry milk in Tris-buffered saline containing 0.05% Tween-20 (TBST) buffer and then incubated with primary antibodies against BCL2, BAX, pAKT, AKT, pPI3K, PI3K, NEUN, GFAP, IBA-1, and GAPDH overnight at 4°C. Subsequently, the membranes were incubated for 1 h at room temperature with secondary antibodies coupled to horseradish peroxidase (1: 10,000). The antigen-antibody complexes were then exposed to the ECL reagent and visualized using a c600 western blot imaging system (Azure Biosystems, Dublin, CA, USA). The protein levels of pro-inflammatory mediators were expressed as relative integrated intensity and were normalized to that of GAPDH.

Cytokine Antibody Microarray

Rat cytokine array antibody arrays were used to analyze cytokine expression profiles in brain samples according to the manufacturer's instructions. A digital imaging system (InnoScan 300 Microarray Scanner, Innopsys) was used to detect chemiluminescent signals which were analyzed using ImageJ software (NIH). Measured cytokines included the following: ADIPOQ, AGER, CCL11, CCL2, CCL27, CCL3, CCL5, CD48, CD80, CD86| CDH3, CNTF, CSF2, CX3CL1, CXCL1, CXCL2, CXCL3, CXCL5, DCN, EPHA5, EPO, F11R, FGFBP1, FLT3LG, GAS1, GFRA1, HAVCR1, HGF, ICAM1,

IFNG, IGDCC4, IL10, IL13, IL17F, IL1A, IL1B, IL1RL2, IL1RN, IL2, IL22, IL2RA, IL3, IL4, IL6, IL6ST, IL7, INHBA, KITLG, LGALS1, LGALS3, NGF, NOTCH1, NOTCH2, NRP1, NRP2, PDGFA, PPBP, PRL, PRLR, SELL, TIMP1, TIMP2, TNF, TNFRSF9, TNFSF12, TNFSF9, TREM1, VEGFA.

Statistical Analysis

Statistical analysis was performed using the GraphPad Prism 5 software. Normally distributed data and homogeneous variances were expressed as means ± standard error of the mean (SEM). These data were analyzed by one-way analysis of variance (ANOVA) followed by a *post hoc* Bonferroni multiple comparison test or Dunnett's test. Nonnormally distributed data were expressed as the median. Kruskal–Wallis test was used for the within-group differences comparation, and the Wilcoxon rank test was used to compare two groups. A $P < 0.05$ was considered significant.

RESULTS

Network Pharmacological Analysis of Refined Qingkailing

Construction and Analysis of Compound-Target Network of Refined Qingkailing

RQKL is composed of baicalin, geniposide, cholic acid, and hyodeoxycholic acid, which have all been identified to be crucial bioactive natural compounds of a famous patent Chinese medicine, QKL injection. In this work, we explored the therapeutic targets of RQKL predicted using multiple online databases as previously described. Then, a network of potential targets of the compounds in RQKL was constructed using Cytoscape software as shown in **Figure 2A**, and 652 compound-target interactions were generated between the four compounds and 438 non-repetitive targets: 156, 129, 226, and 141 for baicalin, geniposide, cholic acid, and hyodeoxycholic acid, respectively. As shown in **Figure 2B**,

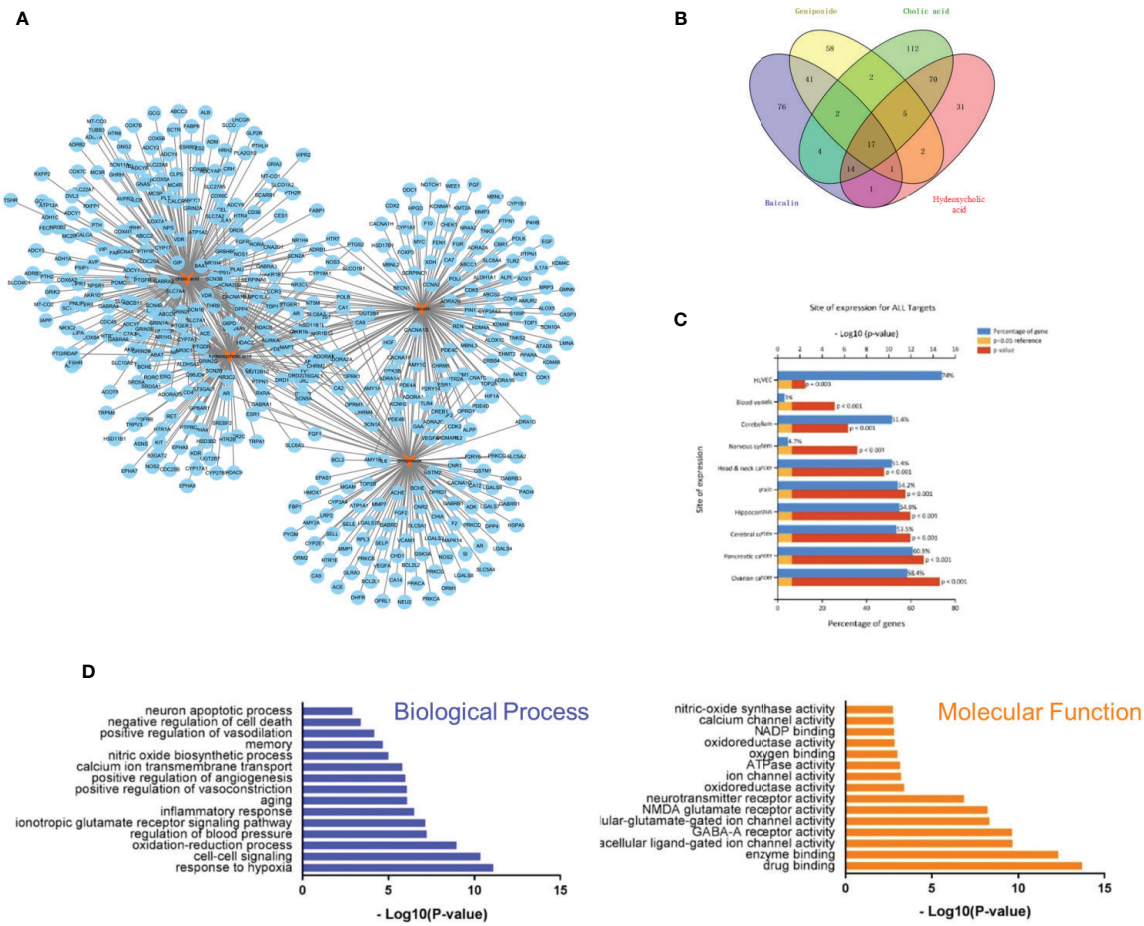

FIGURE 2 | Compound-target interaction network and preliminary gene ontology (GO) analysis of drug targets. **(A)** Compound-target network of refined Qingkailing (RQKL). **(B)** Preliminarily screening targets of four compounds in RQKL. **(C)** Tissue enrichment analysis of drug target **(D)** GO analysis of drug targets classified into two categories, biological process (BP), and molecular function (MF).

we found that 16 differential genes were overlapping among all the targets of each compound, indicating a synergistic effect of RQKL compounds on these targets, such as the dopamine receptor D2 (DRD2) and estrogen receptor 1 (ESR1), adenosine A1 receptor (ADORA1), and retinoid X receptor alpha (RXRA).

Tissue and Gene Ontology Enrichment of Refined Qingkailing Targets

Tissue enrichment using the FunRich software (http://www.funrich.org) showed in **Figure 2C**, indicated that all targets of the four compounds were located in the cerebral cortex, hippocampus, and blood vessels, especially human umbilical vein endothelial cells (HUVEC), indicating a therapeutic effect on brain disease. GO analysis of the putative RQKL targets described based on BP and MF terms were constructed using the DAVID database. In total, 597 BPs and 183 MFs that were enriched for this dataset were identified, which consisted of 449 BPs and 145 MFs with P <0.05. **Figure 2D** illustrates an overview of the GO analysis with 15 remarkably enriched terms in the BP and MF categories. We noticed that some BPs and MFs might be associated with the pathogenesis of ischemic stroke such as response to hypoxia, inflammatory response, negative regulation of cell death, and calcium channel activity, indicating the potential mechanisms of action of RQKL in ischemic stroke.

Construction and Analysis of Compound-Target-Cell Type Network of Refined Qingkailing Against Ischemic Stroke

To evaluate targets of RQKL against ischemic stroke, we collected 321 ischemic stroke-related targets from four existing databases, namely the DrugBank, Online Mendelian Inheritance in Man, Genetic Association, and Therapeutic Target database. A Venn diagram was shown in **Figure 3A** and 47 targets were found overlapped between compound

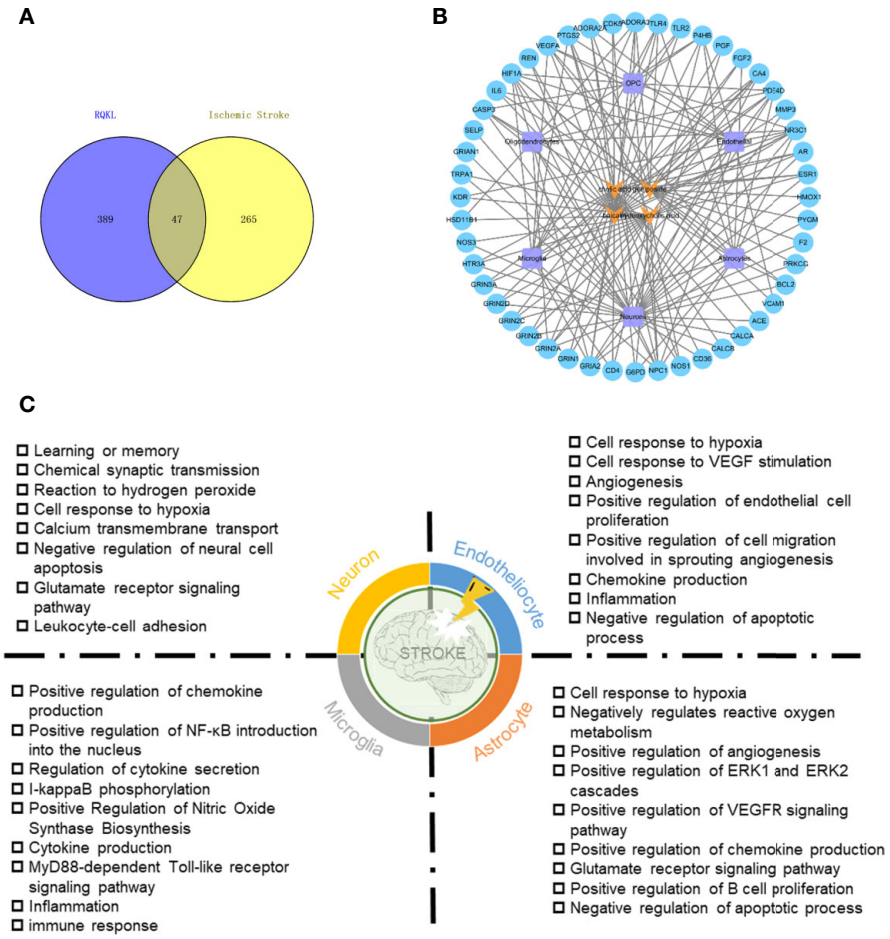

FIGURE 3 | Ischemic stroke-related targets of refined Qingkailing (RQKL) regulated multiple cell type *via* multiple biological processes. **(A)** Veen diagram of compound targets of RQKL and ischemic stroke-related targets. **(B)** The compound-target-cell-type network of RQKL anti-ischemic stroke effect. The yellow refers to the compounds of RQKL. The purple represents six cell-types in brain and the blue represents intersectant targets of RQKL and ischemic stroke. **(C)** Biological process enrichment analysis of targets related to different cell-types in brain.

targets and ischemic stroke targets. AlzData online database was used to understand the relationship between these 47 targets and cell types in brain. A compound-target-cell type network was constructed in **Figure 3B**, and we found 31 targets were related to neurons, 14 targets were related to astrocytes, 13 targets were related to endothelial cells, and 11 targets were related to microglia, indicating an effect of RQKL on these cells. BP enrichment showed in **Figure 3C** indicated different effects of RQKL on different cell type. In neuron, RQKL may involve in learning or memory, chemical synaptic transmission, response to hydrogen peroxide, cellular response to hypoxia, calcium transmembrane transport, negative regulation of neural cell apoptosis, and glutamate receptor signaling pathway. In astrocyte, cell response to hypoxia, negatively regulates reactive oxygen metabolism, positive regulation of angiogenesis, positive regulation of ERK1 and ERK2 cascades, positive regulation of VEGFR signaling pathway, positive regulation of chemokine production, glutamate receptor signaling pathway, positive regulation of B cell proliferation, and negative regulation of apoptotic process. In endotheliocyte, cell response to hypoxia, cell response to VEGF stimulation, angiogenesis, positive regulation of endothelial cell proliferation, positive regulation of cell migration involved in sprouting angiogenesis, chemokine production, inflammation, and negative regulation of apoptotic process. In microglia, RQKL may involve in some inflammation process, including positive regulation of chemokine production, positive regulation of NF-κB introduction into the nucleus, regulation of cytokine secretion, I-kappaB phosphorylation, positive regulation of nitric oxide synthase biosynthesis, cytokine production, MyD88-dependent Toll-like receptor signaling pathway, inflammation, and immune response.

Identification of Core Anti-Ischemic Stroke Targets *via* Protein-Protein Interaction Network

Ischemic stroke-related targets are interconnected, and the PPI network has been shown to organize all protein-coding genes into a large network, which provides a better understanding of the role of various proteins in complex diseases such as ischemic stroke [29, 30]. Therefore, a compound-related target network (6,605 nodes and 158,668 edges) and a known ischemic stroke-related target network (2,861 nodes and 57,981 edges) were constructed using the PPI data. Further, we intersected both networks, consisting of 2,260 nodes and 51,966 edges. We identified nodes with degrees that were more than twice the median degree (58) of all nodes as significant targets as previously described. Thus, we constructed a network of significant targets for RQKL against ischemic stroke that had 564 nodes and 21,028 edges. Further, we calculated the topological features of each hub namely, "degree centrality (DC)," "betweenness centrality (BC)," "closeness centrality

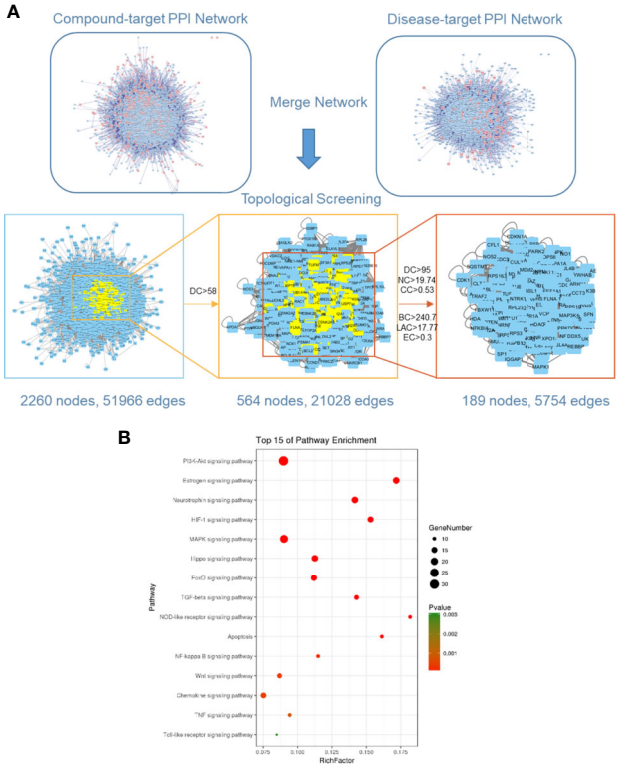

FIGURE 4 | Core target identification *via* protein-protein network and Kyoto Encyclopedia of Genes and Genomes (KEGG) pathway analysis. **(A)** Topological screening of protein-protein interaction (PPI) network. **(B)** KEGG pathway analysis of core targets for RQKL in treating ischemic stroke.

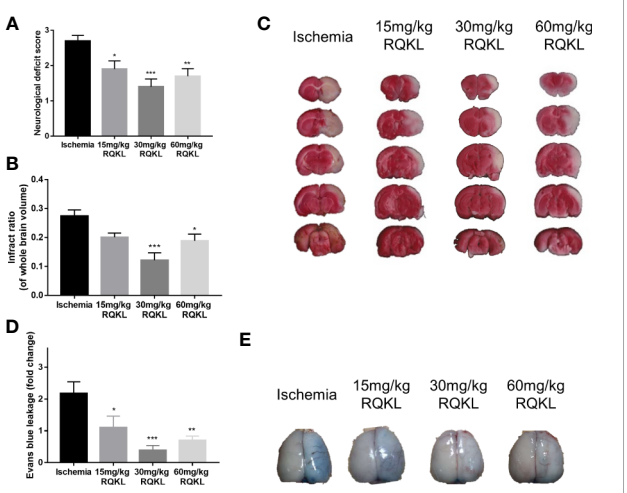

FIGURE 5 | Effects of different doses of refined Qingkailing (RQKL) on ischemia/reperfusion injury. **(A)** Effects RQKL on neurological deficits score **(B)** Quantitative analysis of cerebral infarct areas. **(C)** Representative pictures of brain sections stained with 2% TTC. **(D)** Evans blue (EB) leakage analysis to evaluate prevention of blood-brain barrier (BBB) damage by RQKL. **(E)** Representative pictures of EB leakage. Data points indicate means±SEM. *Vs.* ischemia group: *p<0.05, **p<0.01, ***p<0.001. At least three independent experiments were performed for each group.

(CC)," "eigenvector centrality (EC)," "network centrality (NC)," and "local average connectivity (LAC)." The median values of "DC," "BC," "CC," "EC," "NC," and "LAC" were 95, 240.7, 0.53, 0.3, 19.74, and 17.77, respectively. A flowchart of the core target screening is presented in **Figure 4A**. Detailed topological features of the core PPI and 189 core targets are shown in **Supplementary Table S3**.

Kyoto Encyclopedia of Genes and Genomes Enrichment Analysis of Core Targets for Refined Qingkailing Against Ischemic Stroke

To further clarify the possible roles of the 189 core targets, we performed an enrichment analysis of their KEGG pathways. Specifically, we obtained signaling pathways related to PI3K-Akt, estrogen, neurotrophin, HIF-1, MAPK, Hippo, FoxO, TGF-beta, NOD-like receptor, apoptosis, NF-kappa B, Wnt, chemokine, TNF, Toll-like receptor, shown in **Figure 4B**. Based on the p-values, the PI3K-Akt signaling pathway was the most probable candidate for RQKL function targeting ischemic stroke.

Experimental Validation

Refined Qingkailing Treatment Attenuated Ischemia-Reperfusion Injury

To determine whether RQKL treatment improved neurological function after ischemic stroke, neurological deficit scoring was carried out. As shown in **Figure 5A**, obvious neurological deficits were observed in the ischemic group. Furthermore, while 15 mg/kg RQKL reduced the neurological deficits without a significant difference, treatment with 30 and 60 mg/kg remarkably decreased the neurological deficit score.

The infarct volume rate was assessed using TTC staining, and normal tissues were stained red, whereas the infarction area was unstained (white, **Figure 5C**). As shown in **Figure 5B**, after the 24 h tMCAO, the infarct ratio of the 30 and the 60 mg/kg groups declined obviously compared with that of the ischemic group. No significant neuroprotective effect was observed at the lowest dose.

After determining that RQKL inhibits cell death after I/R, we further investigated whether it affects the BBB integrity. In **Figures 5D, E**, the quantitative data showed that RQKL significantly decreased Evans blue extravasation leakage in the ipsilateral cortex, indicating that RQKL reduced the BBB permeability

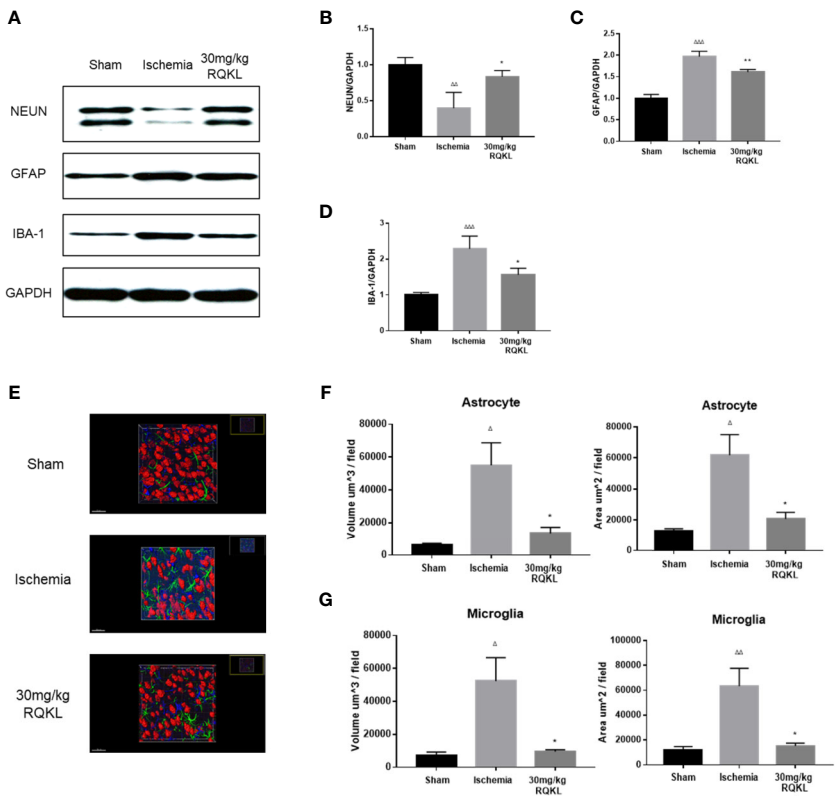

FIGURE 6 | Anti-gliacyte response effect of refined Qingkailing (RQKL) on ischemia/reperfusion injury. **(A)** Representative pictures of expression of NUEN, GFAP, and IBA-1. **(B)** Quantitative analysis of NEUN expression. **(C)** Quantitative analysis of GFAP expression. **(D)** Quantitative analysis of IBA-1 expression. **(E)** Representative pictures of 3D reconstruction of astrocytes, microglia and neuron nuclei. Green represented astrocytes labeled by GFAP. Blue represented microglia labeled by INA-1. Red represented neuron nuclei labeled by NEUN. **(F)** Volume and surface area of astrocytes. **(G)** Volume and surface area of microglia. Data points indicate means±SEM. *Vs*. Sham group: $^{\triangle}p < 0.05$, $^{\triangle\triangle}p < 0.01$, $^{\triangle\triangle\triangle}p < 0.001$, *vs*. ischemia group: $^{*}p < 0.05$, $^{**}p < 0.01$. At least three independent experiments were performed for each group.

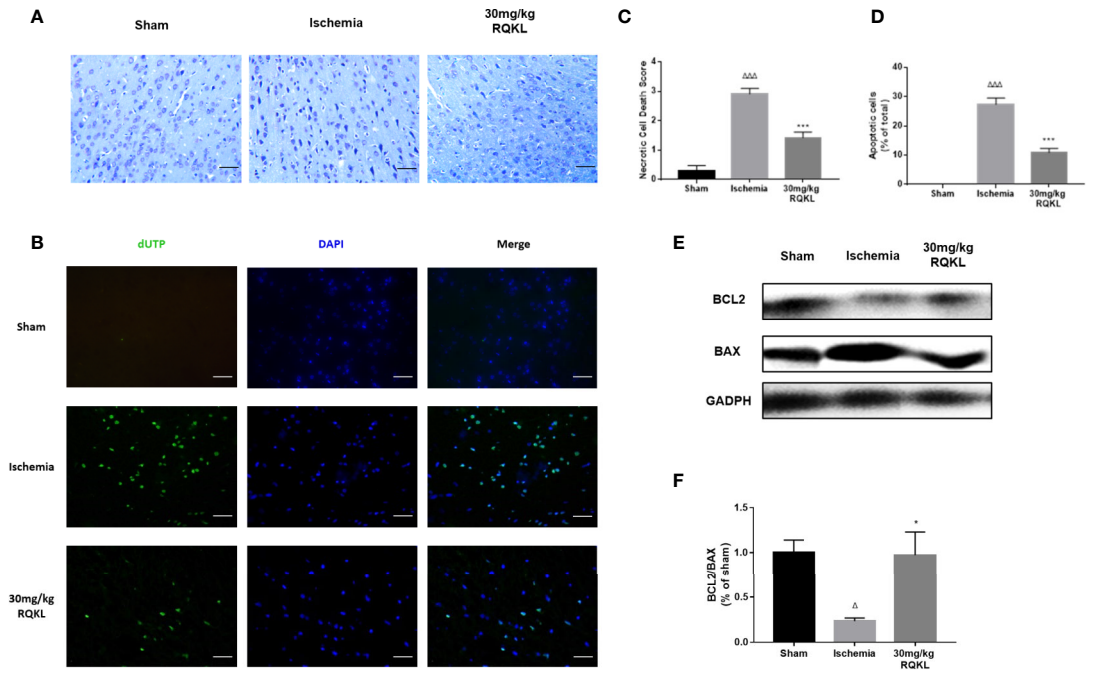

FIGURE 7 | Anti-apoptosis effect of refined Qingkailing (RQKL) on ischemia/reperfusion injury. **(A)** Representative pictures of Nissl staining and **(B)** representative images of cell apoptosis stained by terminal deoxynucleotidyl transferase-mediated deoxyuridine triphosphate nick-end labeling TUNEL method. **(C)** Relevant quantitative analysis based on pathological four-score scale and **(D)** rate of apoptotic cells in each group. **(E)** Western blot analysis of B-cell lymphoma 2 (BCL2) and BCL2-associated X protein (BAX). **(F)** Quantitative analysis of BCL2: BAX expression ratio. Data points indicate means±SEM. *Vs*. Sham group: $^{\triangle}p < 0.05$, $^{\triangle\triangle\triangle}p < 0.001$, *vs*. ischemia group: *p <0.05, ***p < 0.001. At least three independent experiments were performed for each group.

after ischemic stroke. Dose of 30 mg/kg RQKL was choose for further biological experiment because of its optimal effect.

Refined Qingkailing Treatment Decreased Glia Activation After Ischemic Stroke

To evaluate RQKL on neuron, astrocyte, and microglia, we evaluated expression level of protein marker of neuron, astrocyte, and microglia *via* western blot. As shown in **Figures 6A–D**, RQKL increased the expression level of NEUN compared to ischemia group, indicating a neuroprotective effect of QKL against ischemic stroke. And RQKL decreased expression level of GFAP and IBA-1 compared to ischemia group, indicating RQKL inhibited activation of astrocyte and microglia. Next we discussed RQKL on morphology of astrocyte and microglia. After 3D reconstructing astrocyte and microglia *via* software, the volume and surface area were calculated automatically. As shown in **Figures 6E–G**, ischemic stroke significantly increased the volume and surface area of astrocyte and microglia, and RQKL significantly decreased above index compared to ischemia group. These data suggested RQKL decreased glia activation after ischemic stroke.

Refined Qingkailing Treatment Inhibited Cell Apoptosis Induced by Ischemic Stroke

Integrative pharmacology showed RQKL neuroprotective effect involved in cell apoptosis signal. In the present work, Nissl staining of the cerebral cortex (**Figures 7A, C**) was used to assess the cellular protective effect of treatment with the medium-dose RQKL (30 mg/kg). The results showed that RQKL significantly decreased the necrotic cell death score based on a published four-point scale evaluating necrotic neurons in the infarct area. The TUNEL staining (**Figures 7B, D**) showed no apparent positively stained cells in the cerebral cortices of the sham group, whereas numerous apoptotic cells with positively stained nuclei were observed in the ischemic group, which also showed shrinkage of the nuclei or chromatin margination. RQKL treatment induced the percentage of apoptotic cells compared to ischemia group.

Moreover, the analysis of alterations in apoptosis-related proteins showed that RQKL dramatically increased the Bcl-2/Bax ratio in ischemic animals (**Figures 7E, F**). Thus, the overall effect of RQKL in ischemic stroke was likely mediated by both the elevation of anti-apoptotic signaling and suppression of cellular death progress.

Refined Qingkailing Treatment Activated PI3K/AKT Signaling Pathways

Previous integrative pharmacology analysis showed that the PI3K/Akt signaling pathway is the main signaling pathway mediating the biological effects of RQKL on ischemic stroke. Therefore, we designed a western blot experiment to detect the activation of this signaling pathway. As shown in **Figures 8A–C**, the results of the western blotting showed that the expression

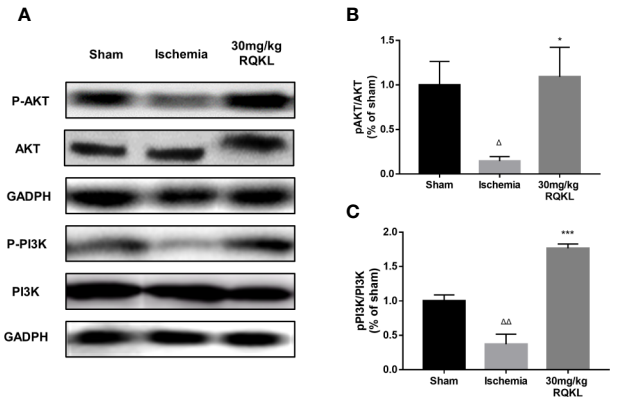

FIGURE 8 | Refined Qingkailing (RQKL) activated phosphoinositide 3-kinase (PI3K)/AKT signal pathway. **(A–C)** Western blot and quantitative analysis of phosphorylated AKT (p-AKT) and p-PI3K by normalization to AKT and PI3K levels, respectively. Data points indicate means±SEM. *Vs.* Sham group: $^{\triangle}p < 0.05$, $^{\triangle\triangle}p < 0.01$, *vs.* ischemia group: $^{*}p < 0.05$, $^{***}p < 0.001$. At least three independent experiments were performed for each group.

levels of p-AKT/AKT ratio and p-PI3K/ PI3K ratio in the ischemic group were significantly decreased 24 h after ischemic stroke. Moreover, RQKL significantly increased the level of the two, indicating RQKL activated PI3k/Akt signaling suppressed by ischemic stroke.

Refined Qingkailing Treatment Reduced Inflammatory Response

To evaluate RQKL on inflammatory response, an antibody microarray containing 67 cytokines and chemokines was used. As shown in **Figures 9A–D**, 19 proteins were identified as different expression proteins of RQKL treatment compared to ischemia group. A PPI network was constructed, and BP and KEGG enrichment analysis was illustrated in bubble plots. Some BP and KEGG signals mentioned in integrative pharmacology part were obtained, including inflammatory response, response to hypoxia, TNF signaling pathway, NOD-like receptor signaling pathway, NF-kappa B signaling pathway, Toll-like receptor signaling pathway.

DISCUSSION

QKL injection is a famous traditional Chinese medicine formulation that has been widely used in China for more than 30 years. However, some adverse drug reactions and events have been reported, which has limited the clinical use of QKL injection since 2001 (Hao et al., 2010). Therefore, the development of a considerably safer and more efficacious QKL injection is urgently required. Therefore, we refined QKL into a novel medicine, RQKL, also targeted at treating acute ischemic stroke, one of the indications of QKL. RQKL is composed of only four main components of QKL and has the advantage of quality stabilization and clinical safety. In

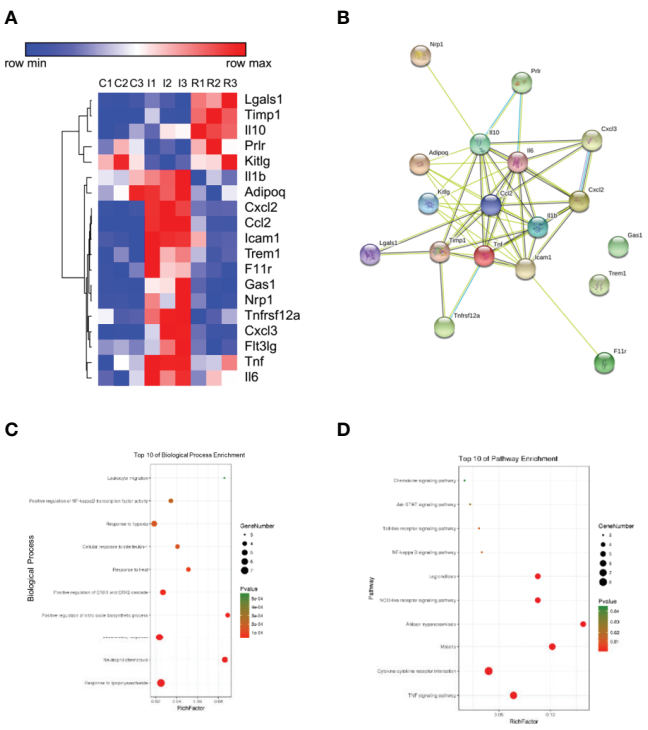

FIGURE 9 | Anti-inflammation effect of refined Qingkailing (RQKL) on ischemia/reperfusion injury. **(A)** Different expression genes (DEGs) based on antibody array. **(B)** protein-protein interaction network of DEGs. **(C)** biological process enrichment of DEGs. **(D)** Kyoto Encyclopedia of Genes and Genomes (KEGG) pathway enrichment of DEGs.

this study, we evaluated the neuroprotective effect of RQKL in a tMCAO rat model. We observed not only the effect of RQKL in improving neurological deficits and decreasing infract ratio but also on the BBB permeability following BBB injury in a dose-independent manner. And our unpublished *in vitro* data showed that RQKL protected neurons from ischemia/reperfusion injury with a dosage-independent manner, which was consistent with this study. And we also tested the efficacy of ingredients in RQKL against ischemia/reperfusion injury, only geniposide was found to have dose-dependent manner.

Most natural compounds are known to affect more than one gene or protein and have the potential to potently affect the entire biological process without severe side effects or excessive inhibition of certain single signaling pathway. Unfortunately, traditional methods have failed to reveal the obscure mechanisms of multi-target medicines in the systemic analysis. Recently, integrative pharmacology has provided an efficient approach for determining the underlying molecular mechanisms of multi-target medicine. We applied a integrative pharmacology approach that included target prediction, PPI analysis, GO enrichment analysis, network analysis, and experimental verification to decipher the mechanisms of the combination of four bioactive components derived from QKL injection (RQKL) for the therapy of ischemic stroke.

In this work, we built a network of 652 compound-target interactions generated between the four compounds and 438 non-repetitive targets, and numerous targets located in the cerebral cortex, hippocampus, and blood vessels, indicating a pharmacological efficacy of RQKL in treating cerebral vascular disease. GO analysis showed the multi-effects of RQKL including response to hypoxia, as well as negative regulation of cell death and inflammatory responses. Based on single cell RNA-seq data, we found RQKL could influence different cell-type, including neuron, astrocyte and microglia. Experimental data suggested an increased level of NEUN in penumbra of cortex, indicating a neuroprotective effect of RQKL treatment. According to previous studies, after ischemic stroke, astrocytes was activated into hypertrophic morphology with extended processes and swollen cell bodies and microglia was activated into hypertrophic morphology with thickened and retracted processes (Tian et al., 2019; Zhang et al., 2019). In the present study, we used 3D reconstruction software to reveal the morphology of astrocyte and microglia. We found RQKL treatment altered hypertrophic morphology of astrocyte and microglia in ischemic stroke model, indicating RQKL inhibited glia cells activation. Crucially, it is not clear whether the structural alteration of glia cells, is the cause or the consequence of protection of neurons in ischemic stroke. Further studies should focus on potential molecular mechanisms on modulating microgliosis and astrogliosis of RQKL.

After merging the PPI network of ischemic stroke- and RQKL-related targets, 189 candidate targets of RQKL treatment were characterized based on topological features. Enrichment analysis of their KEGG pathways highlighted the PI3K/Akt signaling pathway as the most probable candidate mediating the effects of RQKL on ischemic stroke. According to previous studies, suppression of PI3k/Akt signaling has been associated with the neuronal death induced by cerebral I/R. Therefore, enhanced Akt activity contributes to the anti-apoptotic and neuroprotective effects on the ischemic brain (Sun et al., 2018). Experiments showed that RQKL treatment activated PI3K/Akt signaling pathway and inhibited apoptosis progress. There are number literature reports of the cellular protective effect of compounds in RQKL *via* PI3K/Akt signal. Baicalin was reported to alleviate the neuronal apoptosis induced by ketamine toxicity (Zuo et al., 2016) and protect neonatal brains against hypoxic-ischemic injury *via* activation of PI3K/Akt signaling pathway (Zhou et al., 2017). A recent study showed that baicalin might directly bind to the pleckstrin homology domain of AKT and activate the phosphorylation of AKT on Ser473 site (Yang et al., 2019). Geniposide was reported to protect against hypoxic-ischemia-induced brain injury through the activation of PI3K/Akt signaling pathway (Liu et al., 2019). And the anti-apoptotic effects of geniposide mediated *via* the PI3K/AKT signaling pathway were also reported in H9c2 cells in response to the H/R injury (Jiang et al., 2016; Huang et al., 2017). Furthermore, numerous kinds of bile acids have been reported to activate the PI3k/Akt signaling pathway and attenuate certain kinds of brain injury (Hanafi et al., 2016; Sun et al., 2017). Activation of TGR5, a receptor of cholic acid and hyodeoxycholic acid, phosphorylate AKT at Ser473 and activate PI3K/Akt signal (Li et al., 2020). Consistent with the observation of these studies, our data showed that RQKL promoted the phosphorylation of PI3K/AKT and upregulated the ratio of the anti-apoptotic protein Bcl2 and pro-apoptotic protein Bax, which was confirmed by the downstream phosphorylation of Akt (Huang et al., 2015; Chen et al., 2017).

Our data confirmed some inflammation related signal was regulated by RQKL treatment, including TNF signaling pathway, NOD-like receptor signaling pathway, NF-kappa B signaling pathway, and Toll-like receptor signaling pathway. Ischemic stroke leads to the release of danger-associated molecular patterns (DAMPs) from dying neurons and other damaged cells. These molecules trigger the activation of resident microglia and astrocytes and leads to secretion of chemokines and cytokines, formation of an inflammatory environment, and damage amplification (Xiong et al., 2019). Modulating these inflammatory signals is a promising area of therapeutics research against ischemic stroke.

CONCLUSION

In conclusion, in this study, we combined a method of Big data discovery with biological validation to study the mechanism of the actions of RQKL against ischemic stroke at the systemic level. We confirmed the neuroprotective effect of RQKL against cerebral I/R injury, which was associated with its attenuation of brain damage, cell apoptosis and activation of glia cells, modulation of the PI3K/Akt pathway, TNF signaling pathway, NOD-like receptor signaling pathway, NF-kappa B signaling pathway, and Toll-like receptor signaling pathway. Whether other pathways or mechanisms predicted in this network pharmacological approach participate in the beneficial effects of RQKL needs to be further investigated.

However, this study has some limitations that are worth mentioning. First, the reliability of the drug- and disease-related targets and protein-protein interaction database was of great importance in analyzing the underlying mechanisms of the effects of RQKL against ischemic stroke. The accuracy of GO and pathway analyses depends on *a priori* biological knowledge. Secondly, different data mining machines lead to different results. Therefore, biological verification is necessary to evaluate the reliability of bioinformatic analysis *in silico*. Lastly, more specific evidence should be considered in determining the exact effect of these drugs on this signaling pathway. Furthermore, quantitative analysis of the synergistic effect of the four compounds should be investigated in the future.

DATA AVAILABILITY STATEMENT

All datasets generated for this study are included in the article/ **Supplementary Material**.

ETHICS STATEMENT

The animal study was reviewed and approved. The animal experimental design and protocols used in this study were approved by the Ethics Review Committee for Animal Experimentation of Beijing University of Chinese Medicine (BUCM-4-2017090116-3016).

AUTHOR CONTRIBUTIONS

CM, XW, and TX wrote and modified the manuscript. FC and QW designed the experiment and provided fund support. CM, TX, SZ, and CZ helped to complete the animal experiment. SL carried out the western blot analysis. ZW, JM, and CL helped to construct the illustration and revised the manuscript.

FUNDING

The present study was supported by grants from the National Natural Science Foundation of China (81973789, 81430102, 81774122, 81774030, 81373886, and 81303260).

ACKNOWLEDGMENTS

The authors thank Elsevier Language Services for providing language assistance and for proofreading the manuscript.

SUPPLEMENTARY MATERIAL

The Supplementary Material for this article can be found online at: https://www.frontiersin.org/articles/10.3389/fphar.2020.00519/full#supplementary-material

REFERENCES

Becker, K. G., Barnes, K. C., Bright, T. J., and Wang, S. A. (2004). The genetic association database. *Nat. Genet.* 36 (5), 431–432. doi: 10.1038/ng0504-431

Chen, L., Cheng, L., Wei, X., Yuan, Z., Wu, Y., Wang, S., et al. (2017). Tetramethylpyrazine analogue CXC195 protects against dopaminergic neuronal apoptosis via activation of PI3K/Akt/GSK3β signaling pathway in 6-OHDA-induced Parkinson's disease mice. *Neurochem. Res.* 42 (4), 1141–1150. doi: 10.1007/s11064-016-2148-x

Cheng, F., Zhong, X., Lu, Y., Wang, X., Song, W., Guo, S., et al. (2012). Refined Qingkailing protects MCAO mice from endoplasmic reticulum stress-induced apoptosis with a broad time window. *Evidence-Based Complement. Altern. Med.* 2012, 567872. doi: 10.1155/2012/567872

Cheng, F., Ma, C., Sun, L., Zhang, X., Zhai, C., Li, C., et al. (2018). Synergistic neuroprotective effects of Geniposide and ursodeoxycholic acid in hypoxia −reoxygenation injury in SH−SY5Y cells. *Exp. Ther. Med.* 15 (1), 320–326. doi: 10.3892/etm.2017.5395

Gfeller, D., Grosdidier, A., Wirth, M., Daina, A., Michielin, O., and Zoete, V. (2014). SwissTargetPrediction: a web server for target prediction of bioactive small molecules. *Nucleic Acids Res.* 42 (W1), W32–W38. doi: 10.1093/nar/gku293

Hamosh, A., Scott, A. F., Amberger, J. S., Bocchini, C. A., and McKusick, V. A. (2005). Online Mendelian Inheritance in Man (OMIM), a knowledgebase of human genes and genetic disorders. *Nucleic Acids Res.* 33 (suppl_1), D514–D517. doi: 10.1093/nar/gki033

Hanafi, N., Mohamed, A., Noor, J. M., Hasani, N. A. H., Siran, R., Osman, N., et al. (2016). Ursodeoxycholic acid upregulates ERK and Akt in the protection of cardiomyocytes against CoCl2. *Genet. Mol. Res.* 15 (2), gmr.15028150. doi: 10.4238/gmr.15028150

Hao, Y., Kong, X., and Wu, T. (2010). Assessment of the safety of Qin Kai Ling injection: a systematic review. *J. Evidence-Based Med.* 3 (2), 105–116. doi: 10.1111/j.1756-5391.2010.01074.x

Hu, Q. N., Deng, Z., Tu, W., Yang, X., Meng, Z. B., Deng, Z. X., et al. (2014). VNP: interactive visual network pharmacology of diseases, targets, and drugs. *CPT: Pharmacometrics Syst. Pharmacol.* 3 (3), 1–8. doi: 10.1038/psp.2014.1

Huang, J., Kodithuwakku, N. D., He, W., Zhou, Y., Fan, W., Fang, W., et al. (2015). The neuroprotective effect of a novel agent N2 on rat cerebral ischemia associated with the activation of PI3K/Akt signaling pathway. *Neuropharmacology* 95, 12–21. doi: 10.1016/j.neuropharm.2015.02.022

Huang, B., Chen, P., Huang, L., Li, S., Zhu, R., Sheng, T., et al. (2017). Geniposide attenuates post-ischaemic neurovascular damage via GluN2A/AKT/ERK-dependent mechanism. *Cell. Physiol. Biochem.* 43 (2), 705–716. doi: 10.1159/000480657

Jiang, Y.-Q., Chang, G.-l., Wang, Y., Zhang, D.-Y., Cao, L., and Liu, J. (2016). Geniposide prevents hypoxia/reoxygenation-induced apoptosis in H9c2 cells: improvement of mitochondrial dysfunction and activation of GLP-1R and the PI3K/AKT signaling pathway. *Cell. Physiol. Biochem.* 39 (1), 407–421. doi: 10.1159/000445634

Keiser, M. J., Roth, B. L., Armbruster, B. N., Ernsberger, P., Irwin, J. J., and Shoichet, B. K. (2007). Relating protein pharmacology by ligand chemistry. *Nat. Biotechnol.* 25 (2), 197–206. doi: 10.1038/nbt1284

Lana, D., Melani, A., Pugliese, A. M., Cipriani, S., Nosi, D., Pedata, F., et al. (2014). The neuron-astrocyte-microglia triad in a rat model of chronic cerebral hypoperfusion: protective effect of dipyridamole. *Front. Aging Neurosci.* 6, 322. doi: 10.3389/fnagi.2014.00322

Li, J., Cheng, R., and Wan, H. (2020). Overexpression of TGR5 alleviates myocardial ischemia/reperfusion injury via AKT/GSK-3β mediated inflammation and mitochondrial pathway. *Biosci. Rep.* 40 (1), BSR20193482. doi: 10.1042/BSR20193482

Liu, X., Gao, Y., Peng, J., Xu, Y., Wang, Y., Zhou, N., et al. (2015). TarPred: a web application for predicting therapeutic and side effect targets of chemical compounds. *Bioinformatics* 31 (12), 2049–2051. doi: 10.1093/bioinformatics/btv099

Liu, F., Wang, Y., Yao, W., Xue, Y., Zhou, J., and Liu, Z. (2019). Geniposide attenuates neonatal mouse brain injury after hypoxic-ischemia involving the

activation of PI3K/Akt signaling pathway. *J. Chem. Neuroanat.* 102, 101687. doi: 10.1016/j.jchemneu.2019.101687

Longa, E. Z., Weinstein, P. R., Carlson, S., and Cummins, R. (1989). Reversible middle cerebral artery occlusion without craniectomy in rats. *stroke* 20 (1), 84–91. doi: 10.1161/01.STR.20.1.84

Martin, A., Ochagavia, M. E., Rabasa, L. C., Miranda, J., Fernandez-de-Cossio, J., and Bringas, R. (2010). BisoGenet: a new tool for gene network building, visualization and analysis. *BMC Bioinf.* 11 (1), 91. doi: 10.1186/1471-2105-11-91

Nickel, J., Gohlke, B.-O., Erehman, J., Banerjee, P., Rong, W. W., Goede, A., et al. (2014). SuperPred: update on drug classification and target prediction. *Nucleic Acids Res.* 42 (W1), W26–W31. doi: 10.1093/nar/gku477

Pathan, M., Keerthikumar, S., Ang, C. S., Gangoda, L., Quek, C. Y., Williamson, N. A., et al. (2015). FunRich: An open access standalone functional enrichment and interaction network analysis tool. *Proteomics* 15 (15), 2597–2601. doi: 10.1002/pmic.201400515

Powers, W. J., Rabinstein, A. A., Ackerson, T., Adeoye, O. M., Bambakidis, N. C., Becker, K., et al. (2019). Guidelines for the early management of patients with acute ischemic stroke: 2019 update to the 2018 guidelines for the early management of acute ischemic stroke: a guideline for healthcare professionals from the American Heart Association/American Stroke Association. *Stroke* 50 (12), e344–e418. doi: 10.1161/STR.0000000000000211

Radford, R., Rcom-H'cheo-Gauthier, A., Wong, M. B., Eaton, E. D., Quilty, M., Blizzard, C., et al. (2015). The degree of astrocyte activation in multiple system atrophy is inversely proportional to the distance to α-synuclein inclusions. *Mol. Cell. Neurosci.* 65, 68–81. doi: 10.1016/j.mcn.2015.02.015

Ru, J., Li, P., Wang, J., Zhou, W., Li, B., Huang, C., et al. (2014). TCMSP: a database of systems pharmacology for drug discovery from herbal medicines. *J. Cheminf.* 6 (1), 13. doi: 10.1186/1758-2946-6-13

Shannon, P., Markiel, A., Ozier, O., Baliga, N. S., Wang, J. T., Ramage, D., et al. (2003). Cytoscape: a software environment for integrated models of biomolecular interaction networks. *Genome Res.* 13 (11), 2498–2504. doi: 10.1101/gr.1239303

Sherman, B. T., and Lempicki, R. A. (2009). Systematic and integrative analysis of large gene lists using DAVID bioinformatics resources. *Nat. Protoc.* 4 (1), 44. doi: 10.1038/nprot.2008.211

Sun, M., Zhao, Y., Gu, Y., and Xu, C. (2009). Inhibition of nNOS reduces ischemic cell death through down-regulating calpain and caspase-3 after experimental stroke. *Neurochem.y Int.* 54 (5-6), 339–346. doi: 10.1016/j.neuint.2008.12.017

Sun, D., Gu, G., Wang, J., Chai, Y., Fan, Y., Yang, M., et al. (2017). Administration of tauroursodeoxycholic acid attenuates early brain injury via Akt pathway activation. *Front. Cell. Neurosci.* 11, 193. doi: 10.3389/fncel.2017.00193

Sun, M., Izumi, H., Shinoda, Y., and Fukunaga, K. (2018). Neuroprotective effects of protein tyrosine phosphatase 1B inhibitor on cerebral ischemia/reperfusion in mice. *Brain Res.* 1694, 1–12. doi: 10.1016/j.brainres.2018.04.029

Szklarczyk, D., Santos, A., von Mering, C., Jensen, L. J., Bork, P., and Kuhn, M. (2016). STITCH 5: augmenting protein–chemical interaction networks with tissue and affinity data. *Nucleic Acids Res.* 44 (D1), D380–D384. doi: 10.1093/nar/gkv1277

Tang, Y., Li, M., Wang, J., Pan, Y., and Wu, F.-X. (2015). CytoNCA: a cytoscape plugin for centrality analysis and evaluation of protein interaction networks. *Biosystems* 127, 67–72. doi: 10.1016/j.biosystems.2014.11.005

Tian, X., Liu, H., Xiang, F., Xu, L., and Dong, Z. (2019). β-Caryophyllene protects against ischemic stroke by promoting polarization of microglia toward M2 phenotype via the TLR4 pathway. *Life Sci.* 237, 116915. doi: 10.1016/j.lfs.2019.116915

Wang, W., Jiang, B., Sun, H., Ru, X., Sun, D., Wang, L., et al. (2017). Prevalence, incidence, and mortality of stroke in china clinical perspective. *Circulation* 135 (8), 759–771. doi: 10.1161/CIRCULATIONAHA.116.025250

Wang, X., Yu, S., Jia, Q., Chen, L., Zhong, J., Pan, Y., et al. (2017). NiaoDuQing granules relieve chronic kidney disease symptoms by decreasing renal fibrosis and anemia. *Oncotarget* 8 (34), 55920. doi: 10.18632/oncotarget.18473

Wishart, D. S., Feunang, Y. D., Guo, A. C., Lo, E. J., Marcu, A., Grant, J. R., et al. (2018). DrugBank 5.0: a major update to the DrugBank database for 2018. *Nucleic Acids Res.* 46 (D1), D1074–D1082. doi: 10.1093/nar/gkx1037

Wu, S., Wu, B., Liu, M., Chen, Z., Wang, W., Anderson, C. S., et al. (2019). Stroke in China: advances and challenges in epidemiology, prevention, and management. *Lancet Neurol.* 18 (4), 394–405. doi: 10.1016/S1474-4422(18)30500-3

Xiong, X., Fang, W., Zhu, X., Liu, R., Jian, Z., Semerin, D., et al. (2019). The Involvement and Therapy Target of Immune Cells After Ischemic Stroke. *Front. Immunol.* 10, 2167. doi: 10.3389/fimmu.2019.02167

Xu, M., Zhang, D.-F., Luo, R., Wu, Y., Zhou, H., Kong, L.-L., et al. (2018). A systematic integrated analysis of brain expression profiles reveals YAP1 and other prioritized hub genes as important upstream regulators in Alzheimer's disease. *Alzheimer's Dementia* 14 (2), 215–229. doi: 10.1016/j.jalz.2017.08.012

Xu, H.-Y., Zhang, Y.-Q., Liu, Z.-M., Chen, T., Lv, C.-Y., Tang, S.-H., et al. (2019). ETCM: an encyclopaedia of traditional Chinese medicine. *Nucleic Acids Res.* 47 (D1), D976–D982. doi: 10.1093/nar/gky987

Yang, H., Qin, C., Li, Y. H., Tao, L., Zhou, J., Yu, C. Y., et al. (2016). Therapeutic target database update 2016: enriched resource for bench to clinical drug target and targeted pathway information. *Nucleic Acids Res.* 44 (D1), D1069–D1074. doi: 10.1093/nar/gkv1230

Yang, S., Zhang, Y., Shen, F., Ma, X., Zhang, M., Hou, Y., et al. (2019). The flavonoid baicalin improves glucose metabolism by targeting the PH domain of AKT and activating AKT/GSK 3β phosphorylation. *FEBS Lett.* 593 (2), 175–186. doi: 10.1002/1873-3468.13305

Yuan, Q., Gao, J., Wu, D., Zhang, S., Mamitsuka, H., and Zhu, S. (2016). DrugE-Rank: improving drug–target interaction prediction of new candidate drugs or targets by ensemble learning to rank. *Bioinformatics* 32 (12), i18–i27. doi: 10.1093/bioinformatics/btw244

Zhang, R.-z., Yu, S.-J., Bai, H., and Ning, K. (2017). TCM-Mesh: the database and analytical system for network pharmacology analysis for TCM preparations. *Sci. Rep.* 7 (1), 1–14. doi: 10.1038/s41598-017-03039-7

Zhang, Y., Liu, J., Yao, M., Song, W., Zheng, Y., Xu, L., et al. (2019). Sailuotong Capsule Prevents the Cerebral Ischaemia-Induced Neuroinflammation and Impairment of Recognition Memory through Inhibition of LCN2 Expression. *Oxid. Med. Cell. Longevity* 2019, 8416105. doi: 10.1155/2019/8416105

Zheng, Y., Hou, J., Liu, J., Yao, M., Li, L., Zhang, B., et al. (2014). Inhibition of autophagy contributes to melatonin-mediated neuroprotection against transient focal cerebral ischemia in rats. *J. Pharmacol. Sci.* 124 (3), 354–364. doi: 10.1254/jphs.13220FP

Zhou, Z.-q., Li, Y.-L., Ao, Z.-B., Wen, Z.-L., Chen, Q.-W., Huang, Z.-G., et al. (2017). Baicalin protects neonatal rat brains against hypoxic-ischemic injury by upregulating glutamate transporter 1 via the phosphoinositide 3-kinase/protein kinase B signaling pathway. *Neural Regenerat. Res.* 12 (10), 1625. doi: 10.4103/1673-5374.217335

Zuo, D., Lin, L., Liu, Y., Wang, C., Xu, J., Sun, F., et al. (2016). Baicalin attenuates ketamine-induced neurotoxicity in the developing rats: Involvement of PI3K/Akt and CREB/BDNF/Bcl-2 pathways. *Neurotoxic. Res.* 30 (2), 159–172. doi: 10.1007/s12640-016-9611-y

Conflict of Interest: The authors declare that the research was conducted in the absence of any commercial or financial relationships that could be construed as a potential conflict of interest.

Copyright © 2020 Ma, Wang, Xu, Zhang, Liu, Zhai, Wang, Mu, Li, Cheng and Wang. This is an open-access article distributed under the terms of the Creative Commons Attribution License (CC BY). The use, distribution or reproduction in other forums is permitted, provided the original author(s) and the copyright owner(s) are credited and that the original publication in this journal is cited, in accordance with accepted academic practice. No use, distribution or reproduction is permitted which does not comply with these terms.

frontiers in Pharmacology

ORIGINAL RESEARCH
published: 29 May 2020
doi: 10.3389/fphar.2020.00810

Screening for Susceptibility-Related Factors and Biomarkers of Xianling Gubao Capsule-Induced Liver Injury

Chun-yu Li[1†], Ming Niu[2†], Ya-lei Liu[2], Jin-fa Tang[3], Wei Chen[1], Geng Qian[1], Ming-yu Zhang[1], Ya-fei Shi[1], Jun-zhi Lin[4], Xing-jie Li[5], Rui-sheng Li[5], Xiao-he Xiao[2], Guo-hui Li[1] and Jia-bo Wang[2*]*

[1] National Cancer Center, National Clinical Research Center for Cancer, Cancer Hospital, Chinese Academy of Medical Sciences and Peking Union Medical College, Beijing, China, [2] China Military Institute of Chinese Medicine, Fifth Medical Center of Chinese PLA General Hospital, Beijing, China, [3] The First Affiliated Hospital of Henan University of Chinese Medicine, Zhengzhou, China, [4] Central Laboratory, Hospital of Chengdu University of Traditional Chinese Medicine, Chengdu, China, [5] Research Center for Clinical and Translational Medicine, Fifth Medical Center of Chinese PLA General Hospital, Beijing, China

OPEN ACCESS

Edited by:
Rong-Rong He,
Jinan University, China

Reviewed by:
Luyong Zhang,
China Pharmaceutical University, China
Jianbo Wan,
University of Macau, China

***Correspondence:**
Guo-hui Li
tcm_sci@126.com
Jia-bo Wang
pharm_sci@126.com

[†]These authors have contributed equally to this work

Specialty section:
This article was submitted to Ethnopharmacology, a section of the journal Frontiers in Pharmacology

Received: 04 February 2020
Accepted: 18 May 2020
Published: 29 May 2020

Citation:
Li C-y, Niu M, Liu Y-l, Tang J-f, Chen W, Qian G, Zhang M-y, Shi Y-f, Lin J-z, Li X-j, Li R-s, Xiao X-h, Li G-h and Wang J-b (2020) Screening for Susceptibility-Related Factors and Biomarkers of Xianling Gubao Capsule-Induced Liver Injury. Front. Pharmacol. 11:810. doi: 10.3389/fphar.2020.00810

Although increasing reports from the literature on herbal-related hepatotoxicity, the identification of susceptibility-related factors and biomarkers remains challenging due to idiosyncratic drug-induced liver injury (IDILI). As a well-known Chinese medicine prescription, Xianling Gubao Capsule (XLGB) has attracted great attention due to reports of potential liver toxicity. But the mechanism behind it is difficult to determine. In this paper, we found that XLGB-induced liver injury belongs to IDILI through the analysis of clinical liver injury cases. In toxicological experiment assessment, co-exposure to XLGB and non-toxic dose of lipopolysaccharide (LPS) could cause evident liver injury as manifested by significantly increased plasma alanine aminotransferase activity and obvious liver histological damage. However, it failed to induce observable liver injury in normal rats, suggesting that mild immune stress may be a susceptibility factor for XLGB-induced idiosyncratic liver injury. Furthermore, plasma cytokines were determined and 15 cytokines (such as IL-1β, IFN-γ, and MIP-2α etc) were acquired by receiver operating characteristic (ROC) curves analysis. The expression of these 15 cytokines in LPS group was significantly up-regulated in contrast to the normal group. Meanwhile, the metabolomics profile showed that mild immune stress caused metabolic reprogramming, including sphingolipid metabolism, phenylalanine metabolism, and glycerophospholipid metabolism. 8 potential biomarkers (such as sphinganine, glycerophosphoethanolamine, and phenylalanine etc.) were identified by correlation analysis. Therefore, these results suggested that intracellular metabolism and immune changes induced by mild immune stress may be important susceptibility mechanisms for XLGB IDILI.

Keywords: Xianling Gubao capsule, idiosyncratic drug-induced liver injury, susceptibility-related factors, metabolomics, biomarkers

INTRODUCTION

Recently, with a deep belief that traditional Chinese medicines (TCM) are safe because they are "natural," TCM and related products are applied more and more widely in the world, especially in the fields of tonics, health products, and food (Luo et al., 2019). However, TCM-related hepatotoxicity issues have also become increasingly prominent, causing widespread concern among researchers and drug regulatory authorities. Xianling Gubao (XLGB) is extensively applied to treat osteoporosis, osteoarthritis, menopausal syndrome, aseptic bone necrosis and bone fracture for about 20 years, and has definite therapeutic effect (Cheng et al., 2013). However, many cases of liver injury associated with XLGB have emerged in recent years. The China Food and Drug Administration (CFDA) has also warned of the risk of liver damage from XLGB in 2016.

The formulation of XLGB consists of six herbs: Epimedii folium (*Epimedium brevicornu* Maxim., *Epimedium koreanum* Nakai, *Epimedium pubescens* Maxim., *Epimedium sagittatum* (Siebold & Zucc.) Maxim., or *Epimedium wushanense* T.S.Ying), Psoraleae fructus (*Cullen corylifolium* (L.) Medik.), Dipsaci radix (*Dipsacus asperoides* C.Y.Cheng & T.M.Ai or *Dipsacus inermis* Wall.), Salvia miltiorrhiza radix et rhizoma (*Salvia miltiorrhiza* Bunge), Anemarrhenae rhizoma (*Anemarrhena asphodeloides* Bunge), and Rehmanniae radix preprarata (*Rehmannia glutinosa* (Gaertn.) DC.) (Guan et al., 2011). No toxic herbs were found in the routine recipe. Moreover, no obvious adverse effects or toxicity developed in ovariectomized rats administrated XLGB at dosages 1000 mg/kg for 26 weeks (Cheng et al., 2013) or 1200 mg/kg/day for 12 months and up to 1800 mg/kg/day for 26 weeks (equivalent to six times the daily-recommended dose) (Wu et al., 2017). The safety and effectiveness of XLGB in treating osteoporosis has been proven in a randomized, multicenter, double-blind, placebo-controlled clinical trial (Li et al., 2018). Currently, in spite of predictable liver toxicity is often found in preclinical and clinical testing for drugs, it is extremely difficult to recognize or assess Chinese herbs-related to hepatotoxicity, especially idiosyncratic liver injury. Therefore, the underlying mechanisms of XLGB-induced liver injury remain unknown. Our previous research has indicated that mild inflammation might be one of the factors related to susceptibility of Chinese herbs (He shou wu in Chinese)-induced liver injury (Li et al., 2016; Li et al., 2017). Simultaneous exposure to small doses of LPS can serve on a susceptibility-related determinant of many chemicals to intoxication, such as trovafloxacin and monocrotaline (Yee et al., 2003; Poulsen et al., 2014). A critical need exists to predict IDILI of Chinese herbs and understand the mechanisms behind it. Here, we investigated the objectivity of XLGB-induced liver injury by analyzing clinical liver injury cases and simultaneously evaluated XLGB susceptibility on previously established animal models of mild immune stress. As a follow-up, we employed a metabolomics strategy in order to explore the susceptibility related biomarkers of XLGB-induced liver toxicity from the perspective of metabolic reprogramming. The immune cytokines and differentially expressed biomarkers associated with the susceptibility factors of XLGB-induced liver injury were identified.

MATERIALS AND METHODS

Chemicals and Reagents

Xianling Gubao Capsule (batch number 1601046) was produced by Guizhou Tongjitang Pharmaceutical Co., Ltd (Guizhou, China). Epimedin A, Epimedin B; Epimedin C, icariin, psoralen, angelicin, icarisid II and anhydroicaritin were from Chengdu Pufei De Biotechnology Co., Ltd. (Chengdu, China). Sodium pentobarbital (cat 57-33-0) and LPS [derived from Escherichia coli, 055:B5 (lot 086M4159V)] were supplied by Sigma Chemical Company. Methanol and formic acid are both HPLC grade, purchased from Fisher Chemicals (Pittsburg, PA, USA); Acetonitrile is also HPLC grade, obtained from Merck (Darmstadt, Germany); Water was purified by a Millipore's ultrapure water system (Millipore, Bedford, MA, USA). Luminex multiplex cytokine analysis kits was from R&D Systems (MN, United States). Alanine aminotransferase (ALT) and aspartate aminotransferase (AST) detection kits were acquired from Jiancheng Biological Technology, Co., Ltd (Nanjing, China).

Data Sources of Adverse Drug Reactions Cases

A total of 55,388 cases of drug-induced liver injury were collected from the National Adverse Drug Reaction (ADR) Monitoring Database (2012–2016), of which 63 cases of XLGB-related liver injury were found and included in the study. All cases were evaluated and included using the integrated evidence chain-based identification of traditional Chinese medicine in the "Guideline for diagnosis and treatment of herb-induced liver injury" issued by the China Association of Chinese Medicine and "Technical guidelines for clinical evaluation of liver injury induced by traditional Chinese medicine" issued by National Medical Products Administration (Wang et al., 2014; Wang et al., 2016; Zhu et al., 2016b). Retrospective analysis was performed for statistical analysis in this study.

Animals and Treatment Protocol

Male, Sprague-Dawley Rats weighing 180 to 250 g (Laboratory Animal Center of the Academy of Military Medical Sciences, License No. SYXK 2007- 004, Beijing, China) were used for this research. Rats were given continual access to water and food *ad libitum*. Animals were maintained in a 12 h light/dark cycle for one week of acclimatization. They received humane care according to the Guiding Principles for the Care and Use of Laboratory Animals of China and Institutional Animal Care, and procedures were approved by the Use Committee of 302 hospital of PLA. The powder of Xianling Gubao Capsule was suspended in 0.5% sodium carboxymethyl cellulose solution.

Evaluation of idiosyncratic liver injury was according to literature and our previously reported rat model and adjusted appropriately (Luyendyk et al., 2006; Li et al., 2015). Doses of LPS

and XLGB were selected from our preliminary range-finding studies. Briefly, the animals were given normal saline or 2.8 mg/kg LPS by tail vein injection. Two hours later, 1.62 g/kg Xianling Gubao Capsule or an equivalent volume of normal saline was administered intragastrically. Rats were anesthetized (sodium pentobarbital, 50 mg/kg, ip) after six hours later. Blood was gathered from the inferior vena cava using a syringe filled with 0.38% sodium citrate. Plasma was collected after centrifugation (3,000 rpm, 10 min) and stored at 20°C until use. The left lateral liver lobe (3–4 mm) were removed and performed histopathological examination after fixing in 10% neutral buffered formalin for at least 72 h (He et al., 2018).

Assessment of Hepatic Injury and Analysis of Cytokines in Plasma

Hepatic parenchymal cell damage is assessed by an increase in ALT and AST activity in plasma, which is determined in accordance with the procedures of the microplate assay kit. Formalin-fixed liver lobes were embedded in paraffin, cut at a 4 μm, and stained with hematoxylin and eosin. Resulting slides were coded, and evaluated by light microscopy. Plasma cytokine/chemokine profiles, including IL-18A, MIP-2, MIP-2α, Rantes, MCP-3, MCP-1, IP-10, IL-6, VEGF-α, GRO-α, IL-4, IFN-γ, IL-2, IL-13, TNF-α, IL-1β, GM-CSF, IL-5, IL-11, IL-12p70, and Eotaxin were deterimined according to the manufacturer's instructions of the Cytokine array of Luminex Assays Kit.

Sample Handling of Metabolomics Study

The plasma samples were thawed at room temperature, and 600 μl of methanol was added to the 200 μl sample for extraction. The mixture were vortexed for 1 min and centrifuged (10,000 rpm,10 min) at 4°C. Then, the supernatants were collected and filtered through a 0.22-μm syringe filter.

Chromatography and Mass Spectrometry Conditions

The metabolic profiling analysis was performed on a Waters I-Class UPLC system (Waters Corporation, Milford, USA). The sample sequence is random, and all samples were separated on a reverse phase HSS T3 C18 column (100 mm × 2.1 mm, 1.8 μm particle size). The column temperature was maintained at 40 °C. To ensure the stability and repeatability of the system, 10 μl of each sample was combined for quality control (QC), which was inserted and analyzed in every 10 samples. The mobile phase used 0.1% formic acid in water as solvent A and 0.1% formic acid in acetonitrile as solvent B. The flow rate was 0.3 mL/min. The gradient program was as follows: 0 to 1 min, 5 to 5% B, 1 to 9 min, 5 to 40% B, 9 to 19 min, 40 to 90% B, 19 to 21 min, 90 to 100% B, 21 to 25 min, 100 to 100% B. The sample inject volume was 4 μl. During the whole experiment, all the samples were held at 4°C.

For mass spectrometry analysis, Waters Xevo G2-XS QTOF/MS with positive and negative electrospray ionization sources (ESI) was used (Waters Corporation, Manchester, UK). The data collection was controlled by the UNIFI informatics platform (Waters Corporation, Manchester, UK), and the data range was 50-1200 Da. Capillary voltages were at 2.5 and 2.2 kV in positive and negative modes, respectively. For positive mode and negative mode, the cone voltage was 40 V. The applied source temperature was 130°C. The desolvation gas flow was set to 800 L/h, and the desolvation temperature was 350°C. The high collision energy scan was set at a ramp energy scan from 10 to 55 eV, and the low collision energy scan was set at 4 eV. The scan time for each function was 0.20 s. Leucine enkephalin (100 pg/μl) was applied as the lock mass, generating reference ions in negative mode of 554.2610 and positive mode of m/z 556.2771, and introducing reference ions at 10 μl/min at by a lockspray for accurate mass acquisition.

Multivariate Pattern Recognition Analysis and Identification of Biomarkers

UNIFI informatics platform was used to pre-process all data. Normalize the intensity of each ion in relation to the total number of ions to generate a data matrix consisting of normalized peak area, m/z value, and retention time (Wang et al., 2012). Then the data was introduced into (Umetrics, Umea, Sweden) software for principal component analysis (PCA) and orthogonal partial least squares-discriminant analysis (OPLS-DA) (Zhang et al., 2016; Huang et al., 2018). To screen variables that have a significant contribution to distinguishing potential biomarkers between the two groups (LPS vs Normal group or XLGB vs Normal group), only variables with $|p(corr)| \geq 0.5$ and VIP values > 1 were chose and applied for further data analysis in the OPLS-DA model. Meanwhile, significant variables with p values <0.05 and folder changes> 2 or <0.5 were considered potential biomarkers. Biochemical databases, HMDB (http://www.hmdb.ca/) and METLIN (http://metlin.scripps.edu/) were used to identify potential biomarkers. Metabolic pathway analysis was performed by the KEGG (www.genome.jp/kegg/) pathway database, which was carried out using MetaboAnalyst 3.0 (http://www.metaboanalyst.ca/) in line with the pathway library of Rattus norvegicus (rat) (Wang et al., 2012).

Correlation Analysis

Pearson's correlation coefficient is a statistical measure of the strength of the linear relationship between paired data (Han et al., 2018; Li et al., 2019). To quantify the association between two consecutive variables, correlation analysis, a common statistical method, was applied to analyze the relevance between concentrations of cytokines and the peak area values from the UPLC-Q-TOF/MS in this study. Then, Pearson's correlation coefficient was obtained and further used to explore important related metabolites.

Statistical Analysis

One-way analysis of variance (ANOVA, Student's t-test) was used to assess the significant difference of potential biomarkers between groups (SPSS version 15.0; IBM: Chicago, IL, USA, 2006). $P < 0.05$ was considered statistically significant, and $P < 0.01$ was considered highly significant.

RESULTS

Chemical Compositions Determination of XLGB

The chemical compositions of XLGB were determined by HPLC method. The representative HPLC chromatograms of mixed standards and XLGB were shown in **Supplementary Figures 1A, B**. The results showed that there was a roughly separation within different chromatographic peaks of XLGB. Eight major components in XLGB including Epimedin A, Epimedin B, Epimedin C, icariin, psoralen, angelicin, icarisid II and anhydroicaritin were ditermined and quantified, and the relative proportion of these compounds in the preparation is 0.058%, 0.015%, 0.012%, 0.373%, 0.155%, 0.056%, 0.058% and 4.937%, respectively.

Clinical Features of XLGB-Induced Liver Injury

As shown in **Figure 1A**, of the 63 cases of XLGB-induced liver injury, 36 cases were treated with XLGB alone, and 27 cases were used in combination with diclofenac sodium, omeprazole, and cisapride. Since diclofenac sodium itself is prone to liver damage, in order to reveal the objective authenticity of XLGB-induced liver injury, it is necessary to rule out the effects of other combination drugs, and only 36 cases of XLGB alone are included in the next study. Serious adverse reactions occurred

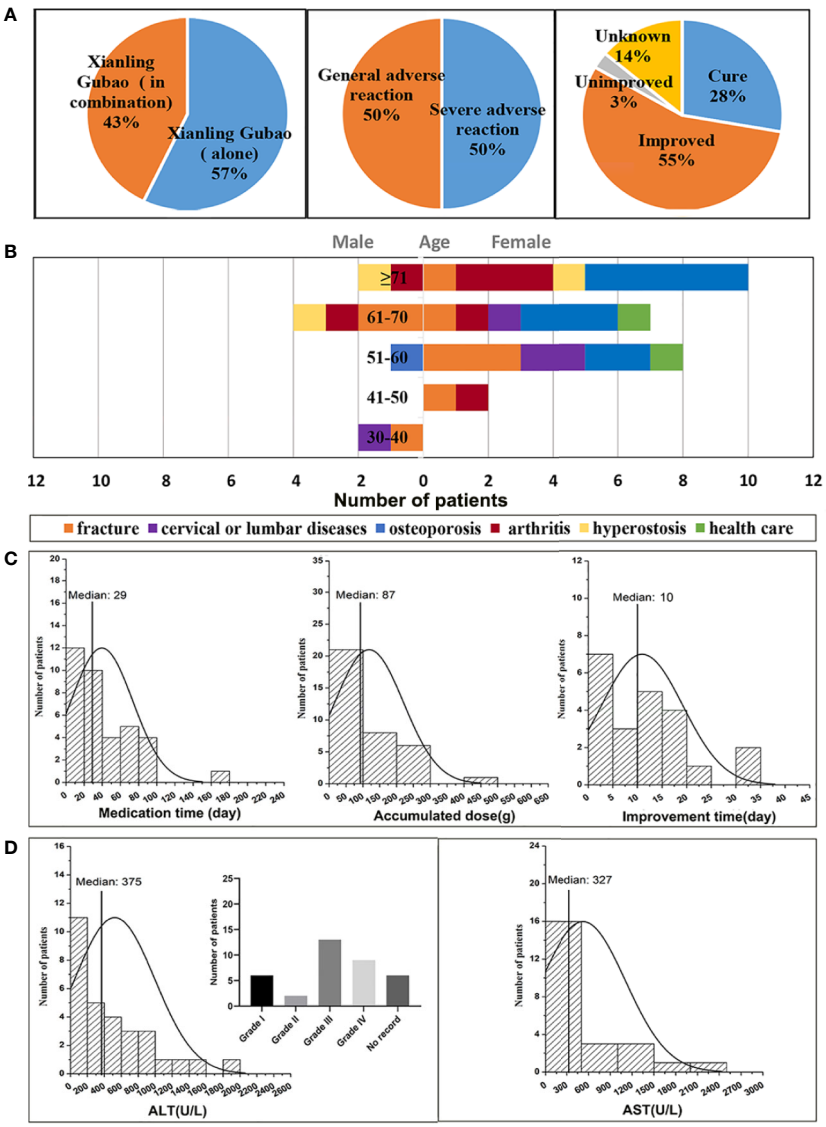

FIGURE 1 | Analysis of clinical features of XLGB-induced liver injury **(A)** the incidence of XLGB-induced liver injury, drug compatibility, degree of adverse drug reaction, prognosis; **(B)** gender, age, and the purpose of medications; **(C)** Medication time, accumulated dose and improvement time; **(D)** biochemical indicators (ALT and AST).

in 50% of cases, and the general adverse reactions were the same. After treatment, most patients had a good prognosis, 55% of cases improved, 3% did not improve, the cure rate was 28%, and 14% of cases were unknown (**Figure 1A**).

The age distribution characteristics of liver injury cases indicated that the median age of onset was 64 years (range, 20-91 years), the ratio of males to females was 1:3.5, and the percentage is 6% in the 30-40 year-olds, 6% in the 41-50 year-olds, 25% in the 51-60 year-olds, 30% in the 5-60 year-olds, 33% in the more than 71 years old. Thus, the XLGB-induced liver injury was more common in women, and the peak age of which occurred at more than 71 years of age (**Figure 1B**). The purpose of XLGB medication included osteoporosis (30.6%), fracture (25%), arthritis (19.4%), cervical lumbar spondylosis (11.1%), hyperostosis (8.3%), and health care (5.6%), which were all in the scope of the instructions except health care (**Figure 1B**). As depicted in **Figure 1C**, the median duration of administration was 29 days. Obvious dose-to-toxic relationship was not observed between the duration of administration and the cumulative dosage. The median time of improvement after treatment drug or discontinuation was 10 days. Clinical biochemical indicators can be found in **Figure 1D**, the median of the ALT and AST levels were 10 and 9 times greater than the upper limit of the normal range (**Figure 1D**). Moreover, the higher ratio of grade 3/4 liver enzyme elevation were observed in 22/36(ALT) of patients in accordance with National Cancer Institute Common Terminology Criteria for Adverse Events (CTCAE) (Ahn et al., 2017).

Liver Functional and Histologic Changes of XLGB

As shown in **Figures 2A, B**, compared with normal group, plasma ALT, and AST activities were not increased significantly by XLGB treatment alone ($P > 0.05$). Likewise, LPS administration did not cause increase in ALT and AST activities ($P > 0.05$). However, as marked by increased ALT and AST activities in plasma, liver injury from XLGB and LPS coexposure occurred in contrast with LPS group.

The results of histopathology displayed that no significant lesions were observed in the saline (control) and XLGB treatment groups. LPS-treated group showed evidence of mild leukocyte infiltration in portal area but no evident hepatocytes

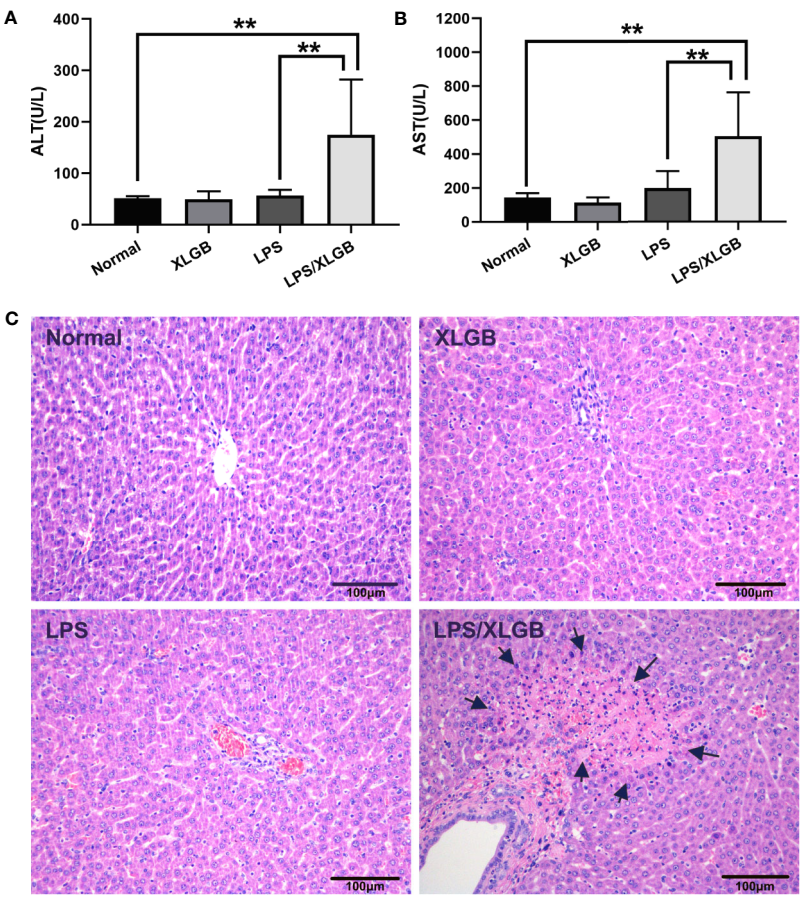

FIGURE 2 | (A, B) Influence of co-treatment with LPS (2.8 mg/kg, i.v.) and XLGB (1.62 g/kg, i.g.) on plasma ALT and AST activities. **(C)** Representative microphotographs of liver sections isolated from rats. The arrows indicate multifocal midzonal necrosis of hepatocytes caused by co-treatment XLGB (1.62 g/kg, i.g.) and LPS (2.8 mg/kg, i.v.). HE staining (×200). n = 10, x ± s. $^{**}P < 0.01$ vs normal group or vs LPS group.

injury. However, When combined with LPS and XLGB, the severity of histologic changes was pronounced, such as multifocal midzonal necrosis of hepatocytes andmany inflammatory cell infiltration (**Figure 2C**). These data suggested that the LPS-induced inflammation activation presumably plays a crucial part in the pathogenesis of XLGB IDILI.

Screening for Susceptibility-Related Cytokines of XLGB-Induced Liver Injury

To observe possible cytokine/chemokine profiles in the normal, LPS, XLGB, and LPS/XLGB groups, the PCA analysis was performed to visualize cytokines/chemokines differences between the above four groups (**Figure 3A**). The results indicated that the LPS group and LPS/XLGB group were able to significiantly distinguished from the normal group and XLGB group. The susceptibility of XLGB-induced liver injury was therefore evident from the cytokine expression profiles. Next, The susceptibility-related cytokines of XLGB-induced liver injury were screened by a Receiver Operating Characteristic (ROC) Curve analysis (**Figure 3B**). Finally, MCP-1, IL-11, Rantes, IL-1β, IFN-γ, GRO-α, MIP-2α, IP-10, MCP-3, IL-4, MIP-2,GM-CSF, IL-18A, VEGF-α, and TNF-α were seen as potential factors (AUC > 0.9) (**Figure 3C**). Meanwhile, we performed cluster analysis of plasma-derived samples and cytokines and represented the result as a heat map. The resluts showed that there was a clear separation between the above two groups in line with cytokine expression profiles. The sample tree was divided into two clusters: cluster1: the normal group with relatively low (cold spots) cytokine expression; cluster 2: the LPS group with relatively high (hot spots) cytokine expression (**Figure 3C**).

Metabolomic Analysis of Plasma

The unsupervised PCA and supervised method OPLS-DA were performed in positive and negative ion modes. **Figure 4A** showed the score plots of PCA analysis in ESI+ mode. QC samples were chosen to assess the stability and accuracy of metabolomics methods because they contain a wide range of m/z values and chemical polarities. The RSD % results showed that the within-run precision, between-run precision and stability of m/z values, retention times, and peak areas were within the error range, respectively, which verified the feasibility of the method. In addition, QC samples clustered closely in PCA score plots indicating that the LC/MS system was stable throughout the experiment. Plasma samples from normal, LPS, XLGB, and XLGB/LPS groups could be divided into different blocks by PCA, which indicated that metabolic profiles vary greatly between the four groups. In addition, there was a clear separation between the normal group and the LPS group from PCA1, indicating that the metabolic environment was significantly affected by different physiological states. Similar results in ESI- were displayed in **Supplementary Figure 2A**. Moreover, as shown in **Figure 4B** and **Supplementary Figure 2D**, the four groups (normal, LPS, XLGB, and LPS/XLGB groups) in both ESI+ and ESI-modes could also be obviously distinguished by the clustering heatmaps based on these metabolites.

To further investigate the potential metabolites of the susceptibility-related XLGB-induced liver injury, OPLS-DA was applied to classifiy or discriminate analysis. As displayed in **Figure 5A**, and XLGB and normal groups can be clearly separated (in ESI+mode) and showed a good predictive ability with a R2Y (cum) of 0.981, R2X (cum) of 0.764, and Q2 (cum) of 0.523. Meanwhile, the LPS group could also be obviously

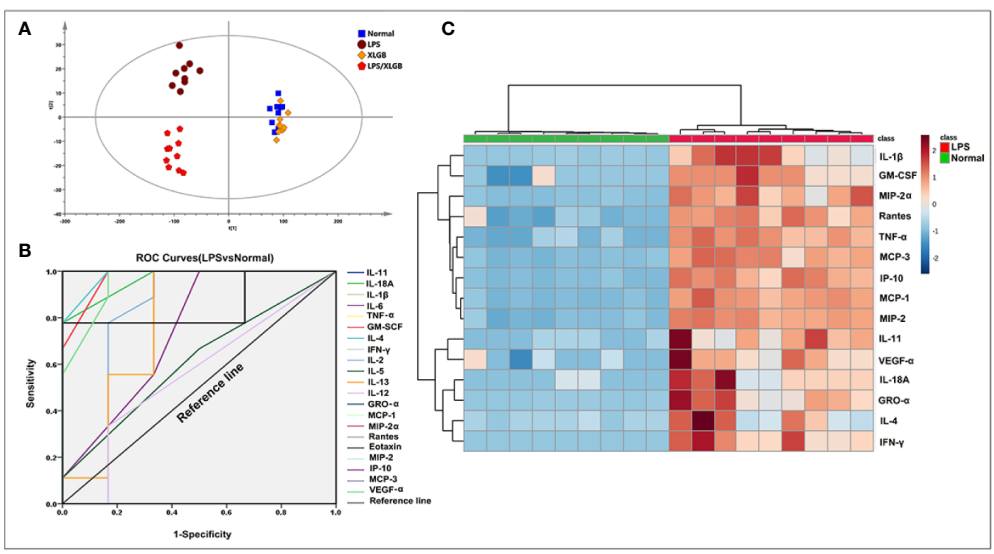

FIGURE 3 | Screening for susceptibility-related cytokines of XLGB-Induced liver injury. **(A)** principal component analysis (PCA) of plasma cytokines; **(B)** receiver operating characteristic (ROC) curves of susceptibility-related to cytokines (LPS group vs normal group); **(C)** cluster analysis of susceptibility-related to cytokines (ROC > 9); the heat map colours represent concentration of cytokines relative to the minimum and maximum of all values in this analysis.

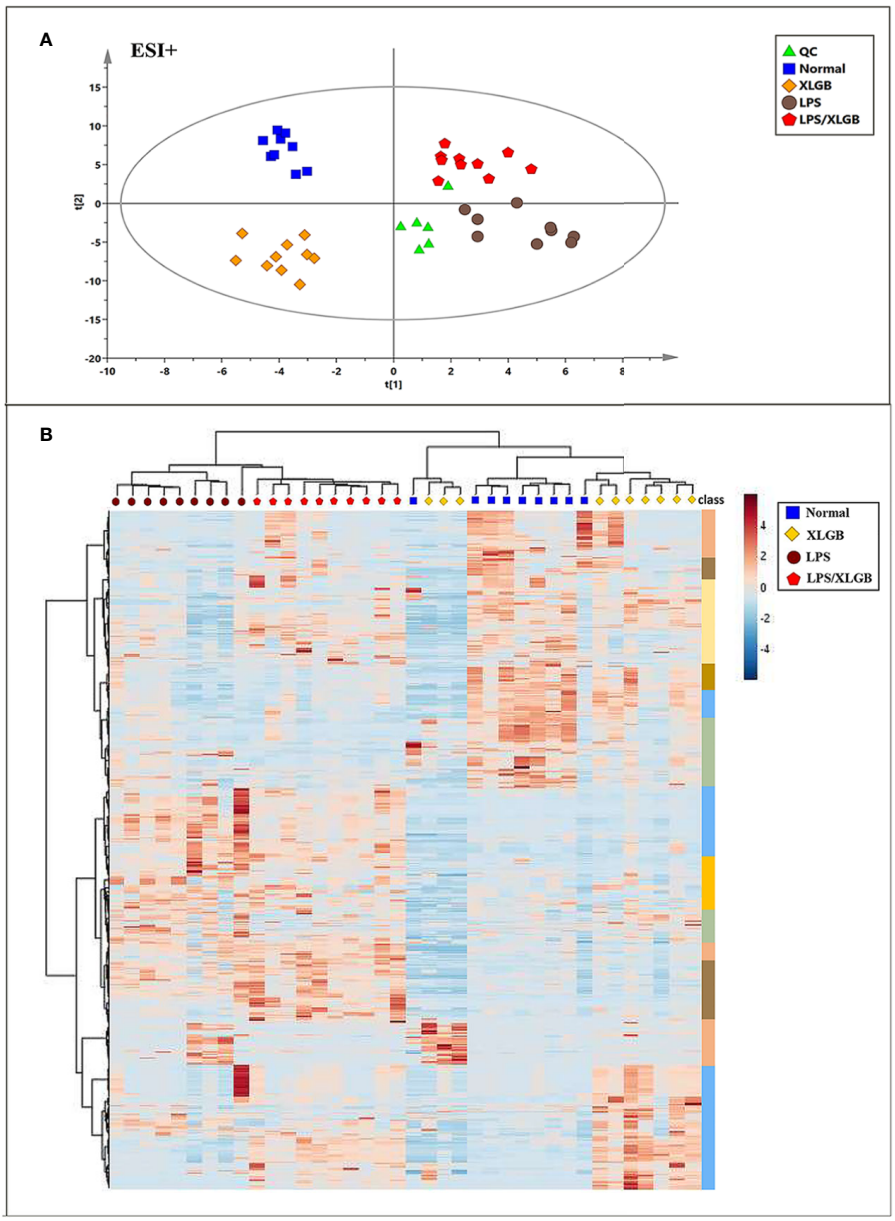

FIGURE 4 | Metabolomic Profile Analysis of XLGB-induced liver injury. **(A)** PCA score plots ofof different groups in positive ESI mode; **(B)** cluster analysis of the 654 significantly changed ions among the normal, LPS, XLGB, and LPS/XLGB groups. The colors from blue to red indicate the relative contents of metabolites.

detached from normal group. The R2Y (cum), R2X (cum), and Q2 (cum) were 0.969, 0.73, and 0.576, respectively, indicating that the OPLS-DA model was reliable. The S-plots for LPS vs normal and XLGB vs normal are shown in **Figures 5A, B**. Data analysis of ESI- mode was also performed and described in **Supplementary Figures 3A, B**. Then, the variables with a |p (corr)|≥0.5,VIP value > 1, $P < 0.05$ and fold change (FC) > 2 or <0.5 were selceted as the potential biomarkers for further analysis. Next, area-proportional 3-Venn diagrams have been used to analyze differences and similarities between differential metabolites in two different groups. The results depicted that there were 424 (LPS *vs* normal) and 231 (XLGB *vs* normal) differential ions in two independent comparisons of the ESI+ mode (**Figure 5C**), while the above comparisons were 403 and 188 in the ESI-mode, respectively (**Supplementary Figure 3C**). Therefore, the results showed that 126 differential variables were affected by the synergistic effect of LPS and XLGB, not just the individual effects of XLGB or LPS, so they could be used as potential biomarkers related to susceptibility to XLGB IDILI.

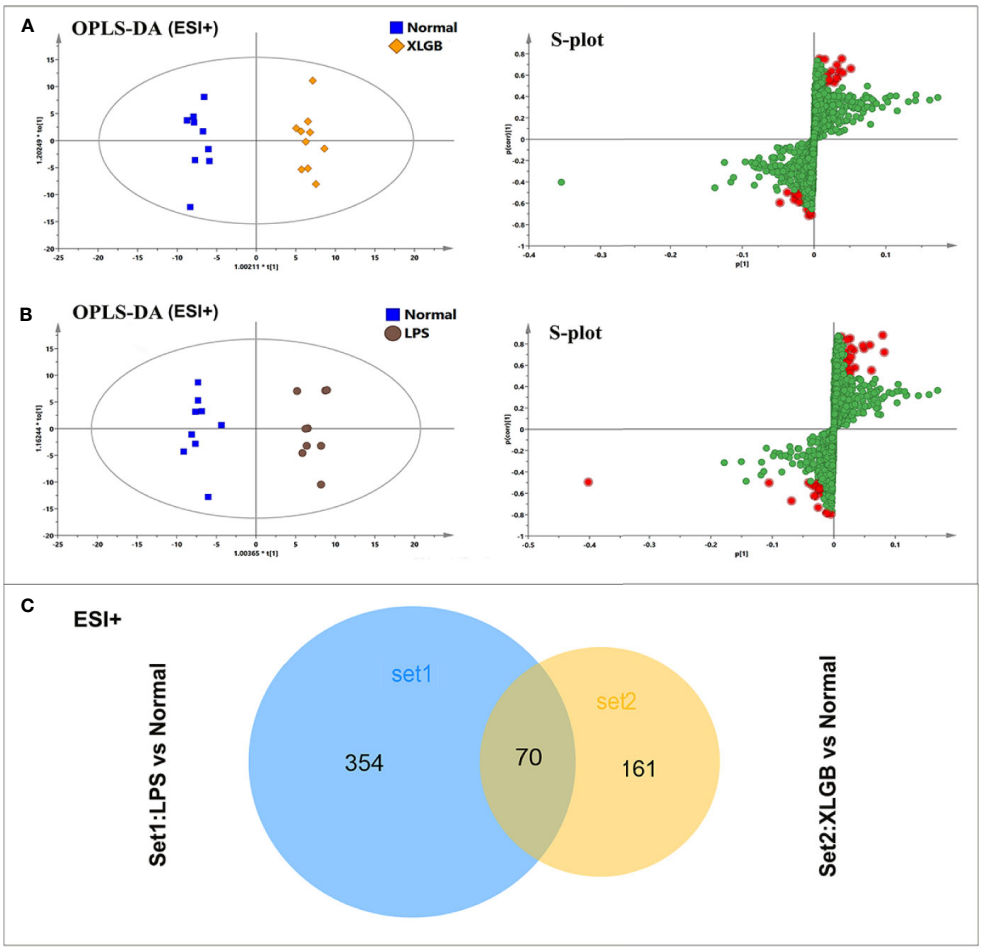

FIGURE 5 | Analysis of potential biomarkers associated with susceptibility to XLGB-induced liver injury. OPLS-DA analysis of the data generated from the XLGB vs normal **(A)**, LPS vs normal **(B)** in the ESI+ mode. S-score plots constructed from the supervised OPLS analysis, the axes that are plotted in the S-plot from the predictive component are p1 vs p (corr)1, representing the magnitude and reliability respectively. Metabolite ions with VIP value >1 were marked with a red square. **(C)** The shared and unique numbers of metabolites were also visualized in Venn diagram from LPS vs normal and XLGB vs normal.

Identification Potential Biomarkers and Enrichment Pathway

The acquired metabolites were combined and tentatively identified with the accurate mass charge ratio. Finally, 77 variables were considered candidates for potential biomarkers and then imported into MetaboAnalyst 3.0 and enriched in the KEGG pathway to further explore the metabolic pathways. Of these, 12 significant metabolites were obtained, including calcitriol, pregnenolone, spermidine, ceramide, sphinganine, glycerophosphoethanolamine, phenylalanine, phosphatidylethanolamine, stearidonic acid, γ-linolenic acid,glycocholic acid,5'-methylthioadenosine (**Supplementary Table 1**). In order to more intuitively compare the metabolite differences between the LPS group and the normal group, a spider diagram of the differential metabolites was constructed based on their relative abundance (**Figure 6A**). The results showed that except for pregnenolone, spermidine, ceramide, and glycocholic acid, the expression of differential metabolites in the LPS group was notably higher than that in the normal group. A schematic diagram of disturbed metabolic pathways was displayed in **Figure 4B**. Meanwhile, a complex network was constructed based on enriched metabolic pathways and the identifed differential metabolites, which contributed to contrast the differences between the LPS group and the normal group in metabolic profles (**Figure 6C**).

Correlation Analysis of Susceptibility-Related Cytokines and Biomarkers

To further screen for susceptibility-related metabolites of XLGB-Induced liver Injury, correlation analysis was used to evaluate metabolite-cytokine relationships between area values of 12 metabolites and concentrations of 15 cytokines. From the results depicted in **Figure 7**, the correlation coefficients demonstrated that five metabolites, sphinganine, 5'-methylthioadenosine, calcitriol, phenylalanine, and glycerophosphoethanolamine were significantly positively correlated, while pregnenolone, spermidine, ceramide, and glycocholic acid were negatively correlated. Besides, there was no

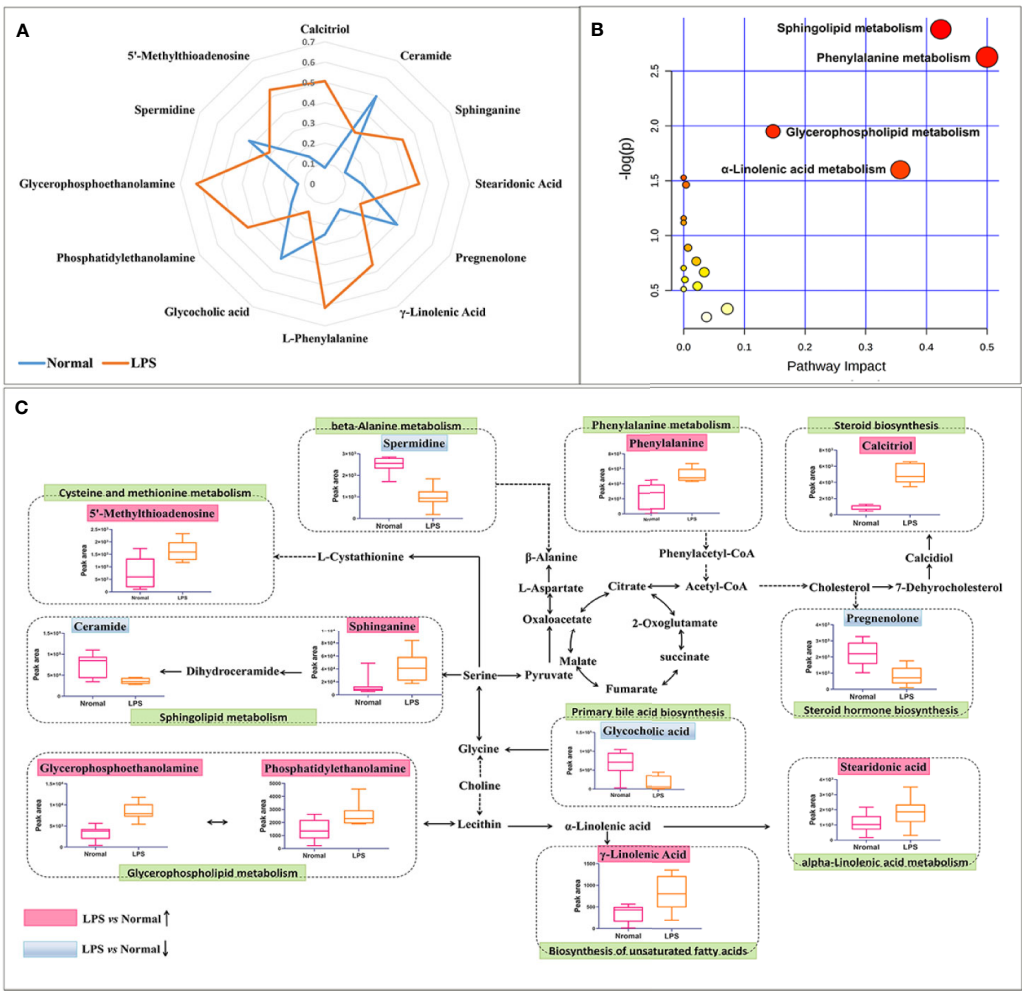

FIGURE 6 | Overall metabolic profle. **(A)** spider plot of 12 metabolites of which the change in relative abundance best diferentiated between the LPS group and normal group. Blue line represents normal group, orange line represents LPS group. **(B)** Schematic diagram of the disturbed metabolic pathways. **(C)** Network map of metabolic pathways and metabolites. The notations are as follows: (↑) in red, metabolite higher in the LPS-treated group than in the normal group; (↓) in, metabolite lower in the LPS-treated group than in the normal group. The related metabolic pathways are cycled in a green box.

correlation between γ-linolenic acid and 15 cytokines ($P > 0.05$). Compared with the normal group, the content of the five positively related metabolites increased significantly, while the content of the other four negatively related metabolites decreased. These data suggest that the change trend of the content is consistent with the positive and negative correlation of cytokines. In addition, sphinganine and 5′-methylthioadenosine were significantly correlated with 15 cytokines. Stearidonic acid and calcitriol were not correlated with 15 cytokines except for TNF-α. Specially, TNF-α was related to 9 metabolites except for phosphatidylethanolamine and γ-linolenic acid.

DISCUSSION

IDILI is one type of drug-related adverse reaction, which is relatively rare but may be severe or even fatal in some cases (Andrade et al., 2019). IDILI is determined by the interaction of environmental and host factors with the drug. As the significant individual differences and susceptibility of the liver to adverse drug reactions, it is still a formidable challenge to predict IDILI (Uetrecht, 2019). Despite many cases of TCM-induced hepatotoxicity have been reported, preclinical studies have not revealed and predicted their hepatotoxicity in normal experimental animals. Therefore, it is speculated that the hepatotoxicity of TCM may belong to IDILI. Our study demonstrated that the ratio of XLGB-induced liver injury in all DILI cases was very low, only 0.06% (36 in 55388), and not dose- or time-dependent by virtue of the retrospective statistics of DILI cases in the National Adverse Drug Reaction (ADR) Monitoring Database (2012-2016). Moreover, all patients took the drugs according to the instructions, and there was no overdose. Thus, XLGB-induced liver injury might be IDILI.

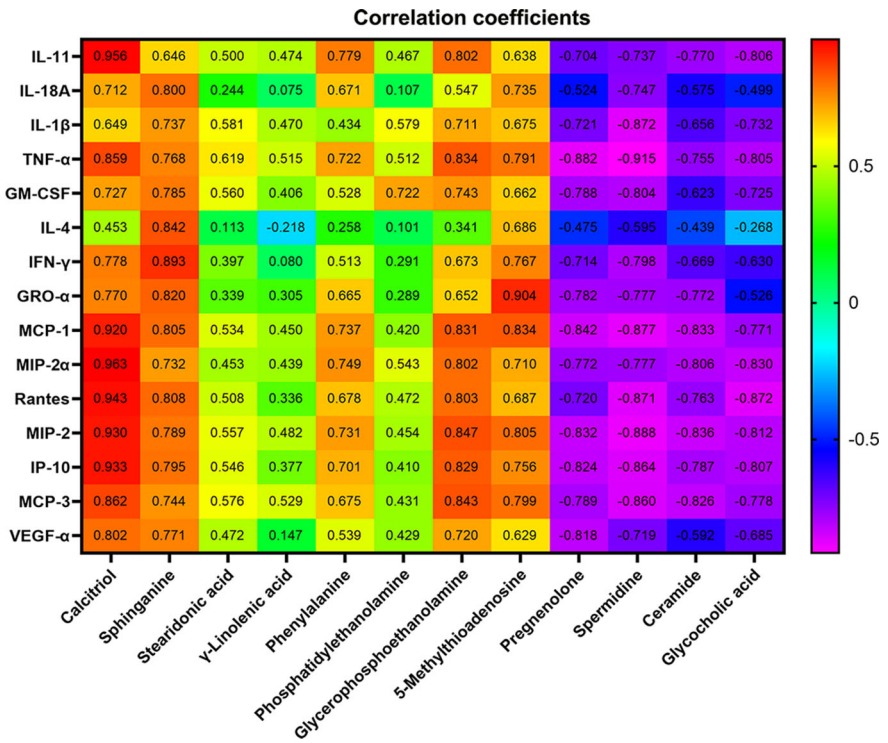

FIGURE 7 | Pearson correlation coefficient of 12 metabolites and concentrations of 15 cytokines. $P > 0.05$ or $P > 0.01$(the correlation coefficient > 0.6).

Currently, combined treatment of rats with endotoxin (LPS) and a model drug related to drug idiosyncrasy inpatients, led to severe hepatotoxicity in toxicological experiment assessment (Ramm et al., 2015). This model has been applied to assess IDILI of some drugs, including trovafloxacin, pyrrolizidine alkaloids, ranitidine, nefazodone, nimesulide, clarithromycin, and telithromycin successfully (Tukov et al., 2007; Guo et al., 2013; Hammad et al., 2013). In our previous work, Polygoni multiflora radix (*Reynoutria multiflora* (Thunb.) Moldenke), Epimedii folium (*Epimedium brevicornu* Maxim.), and Psoraleae fructus (*Cullen corylifolium* (L.) Medik.) could induce acute liver injury in the LPS rats, suggesting that this model could evaluate the susceptibility of the liver to hepatotoxic chemicals from TCM (Li et al., 2015). In this study, we found that a single administration of XLGB or LPS did not develop a significant liver injury phenotype, but co-administration of XLGB with LPS to rats resulted in an increase in the plasma ALT and AST levels and the severity of histologic changes. Additionally, LPS led to a slight infiltration of inflammatory cells in portal area and upregulation of cytokines such as IL-11, GRO-α, IL-1β, MCP-3, IFN-γ, MCP-1, Rantes, MIP-2, IL-4, GM-CSF, IP-10, MIP-2α, IL-18A, VEGF-α, and TNF-α. Given the effect of cytokines in regulating inflammatory responses, changes in cytokine expression modes may be as potential biomarkers for DILI (Laverty et al., 2010). During the exploration of the LPS/Trovafloxacin model, neutrophil recruitment and activation, and increased cytokines such as IL-18, IFN-γ, and PAI-1 played an important role in the pathogenesis of liver damage (Shaw et al., 2009). LPS alone led to an obvious increase in the levels of IL-1, IL-6, TNF-α, CINC-1, which were remarkably amplified by co-administration with diclofenac and closely related to the observed liver injury (Ramm et al., 2015). Inflammatory stress has the potential to interact with co-exposure drug treatment and might be a susceptibility factor participated in the mechanism of IDILI (Shaw et al., 2010). As far as XLGB is concerned, a lot of patients have inflammatory-related diseases, including osteoarthritis and rheumatoid arthritis. This result is consistent with diclofenac, which is well known to induce IDILI (Kishida et al., 2012). In addition, our previous epidemiological investigations have shown that many patients with immune or inflammation-related diseases such as osteoarthritis, psoriasis, and systemic lupus are prone to cause liver injury after taking Polygoni multiflora radix (*Reynoutria multiflora* (Thunb.) Moldenke) (Zhu et al., 2016a). Accordingly, inflammatory mediators evoked by concurrent LPS exposure should alter liver homeostasis to provide the cells more susceptible to toxic chemicals in XLGB.

Inflammation is not only a physiological response to harmful stimuli but also an important factor to the pathogenesis of various metabolic disorders (Kim et al., 2017). As shown in **Figure 6B**, 12 significant metabolites accountable for class discrimination were enriched into 10 metabolic pathways. Sphingolipid metabolism, phenylalanine metabolism, and glycerophospholipid metabolism are the top 3 important pathway. Emerging experimental evidence suggests that sphingolipids can be intimately involved in

inflammation (Sakamoto et al., 2019). It has been reported that LPS can increase the levels of sphinganine in serum, indicating that LPS induces the release of TNF-α and IL-1β, thereby activating a variable sphingosine kinase (Jang et al., 2007). As a second messenger molecule of sphingolipids, ceramide also acts as a systemic mediator of inflammation (Lightle et al., 2003). The production of ceramide in the liver increased the secretion of cytokines such as IL-6, TNF-α, and IL-1β, which should contribute to enhancing inflammatory responses in metabolic diseases (Schilling et al., 2013). Ceramide synthase catalyzes the N-transacylation of sphinganine to form dihydroceramides and then to ceramide in the *de novo* sphingolipid biosynthesis pathway (Tolleson et al., 1999). In the present study, the results demonstrated that sphinganine levels increased and ceramide decreased after LPS-treatment. Therefore, the concentration of sphinganine decreased in LPS group may be relevant to sphingosine accumulation. Glycerophospholipids and sphingolipids are structural units of biological membranes and act as bioactive mediators and signaling molecules in inflammation process (Dang et al., 2016). Glycerophosphoethanolamine (PE) is an important lipid marker of inflammation in glycerophospholipid metabolism. Increased concentrations of PE was detected in systemic circulation of Nonalcoholic steatohepatitis patients (Anjani et al., 2015). Inflammation is characterized by elevated plasma levels of PE and elevated proinflammatory cytokines IL-6, MCP-1, IL-8, and TNF-α (Ruiz et al., 2015). The results revealed that LPS dramatically altered numerous metabolic pathways that were associated with inflammatory response, immune modulation, and nutrient metabolism, which all may play a crucial part in the susceptibility of XLGB-induced liver injury.

At present, the hepatotoxic chemicals attributed to XLGB-induced liver injury are not still clarified. Epimedii folium (*Epimedium brevicornu* Maxim.) and Psoraleae fructus (*Cullen corylifolium* (L.) Medik.) could amplify inflammation cytokines such as TNF-α, IL-6, and IL-1β individually or in combination, resulting in liver injury in the LPS rat model (Gao et al., 2020). These two herbs are also contained in XLGB. Whether they are the main hepatotoxic drugs for XLGB-induced liver damage needs further study.

However, there are some limitations in this experiment. Although factors and biomarkers related to XLGB susceptibility have been explored, they still need to be validated and systematically clarified in the clinic. Additionally, the importance of mild immune stress should be validated through immunodeficiency animal models. The material basis of XLGB IDILI and its related biological mechanisms are also required for further illumination.

DATA AVAILABILITY STATEMENT

All datasets generated for this study are included in the article/ **Supplementary Material**.

ETHICS STATEMENT

The animal study was reviewed and approved by: All procedures on animals and their care complied with the Guiding Principles for the Care and Use of Laboratory Animals of China and Institutional Animal Care and Use Committee of 302 hospital of PLA. Fifth Medical Center of Chinese PLA General Hospital (formerly named as 302 hospital of PLA).

AUTHOR CONTRIBUTIONS

C-yL and MN performed the experiments, analyzed the data and wrote the manuscript. Y-lL, J-fT, and WC, and collected and prepared samples. GQ, M-yZ, and Y-fS performed the analyses. J-zL, X-jL, and R-sL amended the paper. X-hX, G-hL, and J-bW designed the study and amended the paper.

FUNDING

This research is supported by the National Key R&D Program of China (No. 2018YFC1707000), the National Natural Science Foundation of China (Nos. 81630100, 81721002, and 81503350), CAMS Innovation Fund for Medical Sciences (CIFMS) (Grant no. 2016-I2M-1-001) and Beijing Nova Program (No. Z171100001117114).

SUPPLEMENTARY MATERIAL

The Supplementary Material for this article can be found online at: https://www.frontiersin.org/articles/10.3389/fphar.2020.00810/full#supplementary-material

REFERENCES

Ahn, M. J., Sun, J. M., Lee, S. H., Ahn, J. S., and Park, K. (2017). EGFR TKI combination with immunotherapy in non-small cell lung cancer. *Expert Opin. Drug Saf.* 16 (4), 465–469. doi: 10.1080/14740338.2017.1300656

Andrade, R. J., Chalasani, N., Bjornsson, E. S., Suzuki, A., Kullak-Ublick, G. A., Watkins, P. B., et al. (2019). Drug-induced liver injury. *Nat. Rev. Dis. Primers* 5 (1), 58. doi: 10.1038/s41572-019-0105-0

Anjani, K., Lhomme, M., Sokolovska, N., Poitou, C., Aron-Wisnewsky, J., Bouillot, J. L., et al. (2015). Circulating phospholipid profiling identifies portal contribution to NASH signature in obesity. *J. Hepatol.* 62 (4), 905–912. doi: 10.1016/j.jhep.2014.11.002

Cheng, Y., Liu, Y., Wang, H., Li, J., Ren, J., Zhu, L., et al. (2013). A 26-week repeated dose toxicity study of Xian-ling-gu-bao in Sprague-Dawley rats. *J. Ethnopharmacol.* 145 (1), 85–93. doi: 10.1016/j.jep.2012.09.055

Dang, V. T., Huang, A., Zhong, L. H., Shi, Y., and Werstuck, G. H. (2016). Comprehensive Plasma Metabolomic Analyses of Atherosclerotic Progression Reveal Alterations in Glycerophospholipid and Sphingolipid Metabolism in Apolipoprotein E-deficient Mice. *Sci. Rep.* 6, 35037. doi: 10.1038/srep35037

Gao, Y., Wang, Z., Tang, J., Liu, X., Shi, W., Qin, N., et al. (2020). New incompatible pair of TCM: Epimedii Folium combined with Psoraleae Fructus induces idiosyncratic hepatotoxicity under immunological stress conditions. *Front. Med.* 14 (1), 68–80. doi: 10.1007/s11684-019-0690-z

Guan, X. Y., Li, H. F., Yang, W. Z., Lin, C. H., Sun, C., Wang, B. R., et al. (2011). HPLC-DAD-MS(n) analysis and HPLC quantitation of chemical constituents in Xian-ling-gu-bao capsules. *J. Pharm. BioMed. Anal.* 55 (5), 923–933. doi: 10.1016/j.jpba.2011.03.021

Guo, Y., Ma, Z., Kou, H., Sun, R., Yang, H., Smith, C. V., et al. (2013). Synergistic effects of pyrrolizidine alkaloids and lipopolysaccharide on preterm delivery and intrauterine fetal death in mice. *Toxicol. Lett.* 221 (3), 212–218. doi: 10.1016/j.toxlet.2013.06.238

Hammad, M. A., Abdel-Bakky, M. S., Walker, L. A., and Ashfaq, M. K. (2013). Tissue factor antisense deoxyoligonucleotide prevents monocrotaline/LPS hepatotoxicity in mice. *J. Appl. Toxicol.* 33 (8), 774–783. doi: 10.1002/jat.2728

Han, X., Jiang, H., Han, L., Xiong, X., He, Y., Fu, C., et al. (2018). A novel quantified bitterness evaluation model for traditional Chinese herbs based on an animal ethology principle. *Acta Pharm. Sin. B.* 8 (2), 209–217. doi: 10.1016/j.apsb.2017.08.001

He, Y. N., Zhang, D. K., Lin, J. Z., Han, X., Zhang, Y. M., Zhang, H. Z., et al. (2018). Cardiac function evaluation for a novel one-step detoxification product of Aconiti Lateralis Radix Praeparata. *Chin. Med.* 13, 62. doi: 10.1186/s13020-018-0219-4

Huang, H. Z., Zhao, S. Y., Ke, X. M., Lin, J. Z., Huang, S. S., Xu, R. C., et al. (2018). Study on the stability control strategy of Triphala solution based on the balance of physical stability and chemical stabilities. *J. Pharm. BioMed. Anal.* 158, 247–256. doi: 10.1016/j.jpba.2018.06.008

Jang, S., Lee, J. H., Choi, K. R., Kim, D., Yoo, H. S., and Oh, S. (2007). Cytochemical alterations in the rat retina by LPS administration. *Neurochem. Res.* 32 (1), 1–10. doi: 10.1007/s11064-006-9215-7

Kim, M. H., Ahn, H. K., Lee, E. J., Kim, S. J., Kim, Y. R., Park, J. W., et al. (2017). Hepatic inflammatory cytokine production can be regulated by modulating sphingomyelinase and ceramide synthase 6. *Int. J. Mol. Med.* 39 (2), 453–462. doi: 10.3892/ijmm.2016.2835

Kishida, T., Onozato, T., Kanazawa, T., Tanaka, S., and Kuroda, J. (2012). Increase in covalent binding of 5-hydroxydiclofenac to hepatic tissues in rats co-treated with lipopolysaccharide and diclofenac: involvement in the onset of diclofenac-induced idiosyncratic hepatotoxicity. *J. Toxicol. Sci.* 37 (6), 1143–1156. doi: 10.2131/jts.37.1143

Laverty, H. G., Antoine, D. J., Benson, C., Chaponda, M., Williams, D., and Kevin Park, B. (2010). The potential of cytokines as safety biomarkers for drug-induced liver injury. *Eur. J. Clin. Pharmacol.* 66 (10), 961–976. doi: 10.1007/s00228-010-0862-x

Li, C. Y., Li, X. F., Tu, C., Li, N., Ma, Z. J., Pang, J. Y., et al. (2015). The idiosyncratic hepatotoxicity of Polygonum multiflorum based on endotoxin model. *Yao Xue Xue Bao* 50 (1), 28–33. doi: 10.16438/j.0513-4870.2015.01.006

Li, C., Tu, C., Gao, D., Wang, R., Zhang, H., Niu, M., et al. (2016). Metabolomic Study on Idiosyncratic Liver Injury Induced by Different Extracts of in Rats Integrated with Pattern Recognition and Enriched Pathways Analysis. *Front. Pharmacol.* 7, 483. doi: 10.3389/fphar.2016.00483

Li, C., Niu, M., Bai, Z., Zhang, C., Zhao, Y., Li, R., et al. (2017). Screening for main components associated with the idiosyncratic hepatotoxicity of a tonic herb, Polygonum multiflorum. *Front. Med.* 11 (2), 253–265. doi: 10.1007/s11684-017-0508-9

Li, Z. R., Cheng, L. M., Wang, K. Z., Yang, N. P., Yang, S. H., He, W., et al. (2018). Herbal Fufang Xian Ling Gu Bao prevents corticosteroid-induced osteonecrosis of the femoral head-A first multicentre, randomised, double-blind, placebo-controlled clinical trial. *J. Orthop. Translat.* 12, 36–44. doi: 10.1016/j.jot.2017.11.001

Li, C., Tu, C., Che, Y., Zhang, M., Dong, B., Zhou, X., et al. (2019). Bioassay based screening for the antiplatelet aggregation quality markers of Polygonum multiflorum with UPLC and chemometrics. *J. Pharm. BioMed. Anal.* 166, 264–272. doi: 10.1016/j.jpba.2019.01.005

Lightle, S., Tosheva, R., Lee, A., Queen-Baker, J., Boyanovsky, B., Shedlofsky, S., et al. (2003). Elevation of ceramide in serum lipoproteins during acute phase response in humans and mice: role of serine-palmitoyl transferase. *Arch. Biochem. Biophys.* 419 (2), 120–128. doi: 10.1016/j.abb.2003.08.031

Luo, C., Xu, X., Wei, X., Feng, W., Huang, H., Liu, H., et al. (2019). Natural medicines for the treatment of fatigue: Bioactive components, pharmacology, and mechanisms. *Pharmacol. Res.* 148, 104409. doi: 10.1016/j.phrs.2019.104409

Luyendyk, J. P., Lehman-McKeeman, L. D., Nelson, D. M., Bhaskaran, V. M., Reilly, T. P., Car, B. D., et al. (2006). Coagulation-dependent gene expression and liver injury in rats given lipopolysaccharide with ranitidine but not with famotidine. *J. Pharmacol. Exp. Ther.* 317 (2), 635–643. doi: 10.1124/jpet.105.096305

Poulsen, K. L., Olivero-Verbel, J., Beggs, K. M., Ganey, P. E., and Roth, R. A. (2014). Trovafloxacin enhances lipopolysaccharide-stimulated production of tumor necrosis factor-alpha by macrophages: role of the DNA damage response. *J. Pharmacol. Exp. Ther.* 350 (1), 164–170. doi: 10.1124/jpet.114.214189

Ramm, S., Morissey, B., Hernandez, B., Rooney, C., Pennington, S. R., and Mally, A. (2015). Application of a discovery to targeted LC-MS proteomics approach to identify deregulated proteins associated with idiosyncratic liver toxicity in a rat model of LPS/diclofenac co-administration. *Toxicology* 331, 100–111. doi: 10.1016/j.tox.2015.03.004

Ruiz, M., Jove, M., Schluter, A., Casasnovas, C., Villarroya, F., Guilera, C., et al. (2015). Altered glycolipid and glycerophospholipid signaling drive inflammatory cascades in adrenomyeloneuropathy. *Hum. Mol. Genet.* 24 (24), 6861–6876. doi: 10.1093/hmg/ddv375

Sakamoto, W., Canals, D., Salamone, S., Allopenna, J., Clarke, C. J., Snider, J., et al. (2019). Probing compartment-specific sphingolipids with targeted bacterial sphingomyelinases and ceramidases. *J. Lipid Res.* 60 (11), 1841–1850. doi: 10.1194/jlr.M094722

Schilling, J. D., Machkovech, H. M., He, L., Sidhu, R., Fujiwara, H., Weber, K., et al. (2013). Palmitate and lipopolysaccharide trigger synergistic ceramide production in primary macrophages. *J. Biol. Chem.* 288 (5), 2923–2932. doi: 10.1074/jbc.M112.419978

Shaw, P. J., Ganey, P. E., and Roth, R. A. (2009). Tumor necrosis factor alpha is a proximal mediator of synergistic hepatotoxicity from trovafloxacin/lipopolysaccharide coexposure. *J. Pharmacol. Exp. Ther.* 328 (1), 62–68. doi: 10.1124/jpet.108.143792

Shaw, P. J., Ganey, P. E., and Roth, R. A. (2010). Idiosyncratic drug-induced liver injury and the role of inflammatory stress with an emphasis on an animal model of trovafloxacin hepatotoxicity. *Toxicol. Sci.* 118 (1), 7–18. doi: 10.1093/toxsci/kfq168

Tolleson, W. H., Couch, L. H., Melchior, W. B.Jr., Jenkins, G. R., Muskhelishvili, M., Muskhelishvili, L., et al. (1999). Fumonisin B1 induces apoptosis in cultured human keratinocytes through sphinganine accumulation and ceramide depletion. *Int. J. Oncol.* 14 (5), 833–843. doi: 10.3892/ijo.14.5.833

Tukov, F. F., Luyendyk, J. P., Ganey, P. E., and Roth, R. A. (2007). The role of tumor necrosis factor alpha in lipopolysaccharide/ranitidine-induced inflammatory liver injury. *Toxicol. Sci.* 100 (1), 267–280. doi: 10.1093/toxsci/kfm209

Uetrecht, J. (2019). Mechanistic Studies of Idiosyncratic DILI: Clinical Implications. *Front. Pharmacol.* 10, 837. doi: 10.3389/fphar.2019.00837

Wang, X., Zhang, A., Han, Y., Wang, P., Sun, H., Song, G., et al. (2012). Urine metabolomics analysis for biomarker discovery and detection of jaundice syndrome in patients with liver disease. *Mol. Cell Proteomics* 11 (8), 370–380. doi: 10.1074/mcp.M111.016006

Wang, J. B., Xiao, X. H., Du, X. X., Zou, Z. S., Song, H. B., and Guo, X. X. (2014). Identification and early diagnosis for traditional Chinese medicine-induced liver injury based on translational toxicology. *Zhongguo Zhong Yao Za Zhi* 39 (1), 5–9. doi: 10.4268 /cjcmm20140102

Wang, J. Bo, LI, C., Zhu, Y., Song, H. Bo, Bai, Z., and He, X. X. (2016). Integrated evidence chain-based identification of Chinese herbal medicine-induced hepatotoxicity and rational usage: Exemplification by Polygonum Multiflorum(He shou wu). *Chin. Sci. Bull.* 61 (9), 971. doi: 10.1360/N972015-01289

Wu, H., Zhong, Q., Wang, J., Wang, M., Fang, F., Xia, Z., et al. (2017). Beneficial Effects and Toxicity Studies of Xian-ling-gu-bao on Bone Metabolism in Ovariectomized Rats. *Front. Pharmacol.* 8, 273. doi: 10.3389/fphar.2017.00273

Yee, S. B., Harkema, J. R., Ganey, P. E., and Roth, R. A. (2003). The coagulation system contributes to synergistic liver injury from exposure to monocrotaline and bacterial lipopolysaccharide. *Toxicol. Sci.* 74 (2), 457–469. doi: 10.1093/toxsci/kfg129

Zhang, C. E., Niu, M., Li, R. Y., Feng, W. W., Ma, X., Dong, Q., et al. (2016). Untargeted Metabolomics Reveals Dose-Response Characteristics for Effect of Rhubarb in a Rat Model of Cholestasis. *Front. Pharmacol.* 7, 85. doi: 10.3389/fphar.2016.00085

Zhu, Y., Li, Y. G., Wang, Y., Wang, L. P., Wang, J. B., Wang, R. L., et al. (2016a). Analysis of Clinical Characteristics in 595 Patients with Herb-induced Liver Injury. *Zhongguo Zhong Xi Yi Jie He Za Zhi* 36 (1), 44–48. doi: 10.7661/CJIM.2016.01.0044

Zhu, Y., Niu, M., Chen, J., Zou, Z. S., Ma, Z. J., Liu, S. H., et al. (2016b). Hepatobiliary and pancreatic: Comparison between Chinese herbal medicine and Western medicine-induced liver injury of 1985 patients. *J. Gastroenterol. Hepatol.* 31 (8), 1476–1482. doi: 10.1111/jgh.13323

Conflict of Interest: The authors declare that the research was conducted in the absence of any commercial or financial relationships that could be construed as a potential conflict of interest.

Copyright © 2020 Li, Niu, Liu, Tang, Chen, Qian, Zhang, Shi, Lin, Li, Li, Xiao, Li and Wang. This is an open-access article distributed under the terms of the Creative Commons Attribution License (CC BY). The use, distribution or reproduction in other forums is permitted, provided the original author(s) and the copyright owner(s) are credited and that the original publication in this journal is cited, in accordance with accepted academic practice. No use, distribution or reproduction is permitted which does not comply with these terms.

frontiers in Pharmacology

REVIEW
published: 03 June 2020
doi: 10.3389/fphar.2020.00764

Pharmacological Activity, Pharmacokinetics, and Toxicity of Timosaponin AIII, a Natural Product Isolated From *Anemarrhena asphodeloides* Bunge: A Review

Yan Lin[1,2†], *Wai-Rong Zhao*[1†], *Wen-Ting Shi*[1†], *Jing Zhang*[1], *Kai-Yu Zhang*[1], *Qian Ding*[3], *Xin-Lin Chen*[1], *Jing-Yi Tang*[1*] *and Zhong-Yan Zhou*[1,4*]

[1] Department of Cardiovascular Research Laboratory, Longhua Hospital, Shanghai University of Traditional Chinese Medicine, Shanghai, China, [2] Department of Oncology, The Fourth Affiliated Hospital of Xinjiang Medical University, Urumqi, China, [3] College of Basic Medicine, Guizhou University of Traditional Chinese Medicine, Guiyang, China, [4] State Key Laboratory of Quality Research in Chinese Medicine and Institute of Chinese Medical Sciences, University of Macau, Macao, Macau

Anemarrhena asphodeloides Bunge is a famous Chinese Materia Medica and has been used in traditional Chinese medicine for more than two thousand years. Steroidal saponins are important active components isolated from *A. asphodeloides* Bunge. Among which, the accumulation of numerous experimental studies involved in Timosaponin AIII (Timo AIII) draws our attention in the recent decades. In this review, we searched all the scientific literatures using the key word "timosaponin AIII" in the PubMed database update to March 2020. We comprehensively summarized the pharmacological activity, pharmacokinetics, and toxicity of Timo AIII. We found that Timo AIII presents multiple-pharmacological activities, such as anti-cancer, anti-neuronal disorders, anti-inflammation, anti-coagulant, and so on. And the anti-cancer effect of Timo AIII in various cancers, especially hepatocellular cancer and breast cancer, is supposed as its most potential activity. The anti-inflammatory activity of Timo AIII is also beneficial to many diseases. Moreover, VEGFR, X-linked inhibitor of apoptosis protein (XIAP), B-cell-specific Moloney murine leukemia virus integration site 1 (BMI1), thromboxane (Tx) A2 receptor, mTOR, NF-κB, COX-2, MMPs, acetylcholinesterase (AChE), and so on are identified as the crucial pharmacological targets of Timo AIII. Furthermore, the hepatotoxicity of Timo AIII was most concerned, and the pharmacokinetics and toxicity of Timo AIII need further studies in diverse animal models. In conclusion, Timo AIII is potent as a compound or leading compound for further drug development while still needs in-depth studies.

Keywords: Timosaponin AIII, autophagy, apoptosis, angiogenesis, inflammation

OPEN ACCESS

Edited by:
Yan Xu,
Cleveland State University,
United States

Reviewed by:
Baiping Ma,
Academy of Military Medical Sciences, China
Shao-Jiang Song,
Shenyang Pharmaceutical University, China
Mamdouh Moawad Ali,
National Research Centre, Egypt

***Correspondence:**
Jing-Yi Tang
dr_tang@163.com
Zhong-Yan Zhou
biozzy@126.com

†*These authors have contributed equally to this work*

Specialty section:
This article was submitted to Ethnopharmacology, a section of the journal Frontiers in Pharmacology

Received: *21 February 2020*
Accepted: *07 May 2020*
Published: *03 June 2020*

Citation:
Lin Y, Zhao W-R, Shi W-T, Zhang J, Zhang K-Y, Ding Q, Chen X-L, Tang J-Y and Zhou Z-Y (2020) Pharmacological Activity, Pharmacokinetics, and Toxicity of Timosaponin AIII, a Natural Product Isolated From Anemarrhena asphodeloides Bunge: A Review. Front. Pharmacol. 11:764. doi: 10.3389/fphar.2020.00764

INTRODUCTION

Timosaponin AIII (Timo AIII, IUPAC name: (2*S*,3*R*,4*S*,5*S*,6*R*)-2-[(2*R*,3*R*,4*S*,5*R*,6*R*)-4,5-dihydroxy-6-(hydroxymethyl)-2-[(1*R*,2*S*,4*S*,5'*S*,6*R*,7*S*,8*R*,9*S*,12*S*,13*S*,16*S*,18*R*)-5',7,9,13-tetramethylspiro[5-oxapentacyclo[10.8.0.0^{2,9}.0^{4,8}.0^{13,18}]icosane-6,2'-oxane]-16-yl]oxyoxan-3-yl]oxy-6-(hydroxymethyl)oxane-3,4,5-triol, CAS no: 41059-79-4) is a natural steroidal saponin with multiple-pharmacological activities, and it is primary isolated from Chinese Materia Medica *Anemarrhena asphodeloides* Bunge (well-known as Zhimu in Chinese) (**Figure 1**) which has been used for treatment various diseases including arthralgia, hematochezia, cough, hemoptysis, and so on, in traditional Chinese medicine (Wang et al., 2014). Phytochemistry studies have identified more than 100 compounds from *A. asphodeloides* Bunge, and the main constitutes are steroidal saponins, flavonoids, phenylpropanoids, alkaloids, steroids, organic acids, anthraquinones, and so on (Wang et al., 2014). The total saponins, which are rich in rhizome, could be extracted by hot water under reflux and purified by EtOAc, n-BuOH, and H_2O, and the content of saponins is more than 6% (Wang et al., 2014; Yang et al., 2016; Nian et al., 2017). Timo AIII, Timosaponin BII (Timo BII) and sarsasapogenin are three main active saponins isolated from *A. asphodeloides* Bunge (**Figure 1**), and they have been identified as quality control and pharmacokinetic markers of diverse *A. asphodeloides* Bunge-contained Chinese herb formulas, such as TongGuanWan, Rhizoma Anemarrhenae-Phellodendron herb pair, guizhi-shaoyao-zhimu herb pair, zhimu-baihe herb pair, and so on (Tang et al., 2012; Wang et al., 2014; Tang et al., 2015; Yang et al., 2018). The biotransformation of Timo AIII from Timo BII could been mediated by β-D-glycosidase (Lu et al., 2016). Lu et al. also developed an enzyme associated five-step preparation method to produce high yield and purity Timo AIII from *A. asphodeloides* Bunge, which allowed us obtain efficient amount of Timo AIII for further study and product development (Lu et al., 2016). Although Timo AIII and Timo BII are mainly metabolized to sarsasapogenin *in vivo*, the sugar chain plays important roles in their pharmacological activities (Sy et al., 2008; Lee et al., 2010; Wang et al., 2010). The sugar chain in Timo AIII is indispensable to its pharmacological activities, and conversion of Timo BII to Timo AIII enhanced its cytotoxicity (King et al., 2009). So, Timo AIII presented most potential anti-cancer activity due to its specific sugar chain binding site. However, the hydrophobicity and low bioavailability of Timo AIII limited its efficacy *in vivo*, and many studies also focused on derivatization or drug delivery system design based on Timo AIII (Wang et al., 2010; Hu et al., 2011; Kim et al., 2014; Lu et al., 2018).

Timo AIII affected different numerous cellular signaling pathways and presented efficacy in different cell types and various disease models both *in vitro* and *in vivo*, such as cancer, Alzheimer's disease, depression, diabetic mellitus, colitis, and so on. Timo AIII dramatically inhibited the cancer cell growth at micromole level of concentration and selectively reduced the cancer cell viability but not normal cell (King et al., 2009). Thus, Timo AIII was proposed as a potent anti-cancer agent, and its anti-cancer activity and underlying mechanisms were most investigated in the previous studies (Han et al., 2018). In this review, we comprehensively summarized the pharmacological activity, pharmacokinetics, and toxicity of Timo AIII according to the literatures in the recent decades. And this review provides an overview of the previous research related to Timo AIII, which is benefit for its further study and drug development.

PHARMACOLOGICAL ACTIVITIES OF TIMO AIII

Cancer

Cytotoxicity

Timo AIII and Timo BII are two well-known steroidal saponins in *Anemarrhena asphodeloides* Bunge while Timo BII presented less cytotoxic effect than Timo AIII in cancer cells (King et al., 2009). Induction of tumor cell death by cytotoxicity agent is the important mechanism of current cancer chemotherapy (Wang et al., 2013). Selectively kill cancer cell, regardless of normal cell, is the basic principle in cytotoxic anti-cancer drug development. Timo AIII could cause cell death in cancer cell but not in normal cell in the certain concentration (King et al., 2009; Wang et al., 2013; Zhou et al., 2020). In addition, previous studies indicated that Timo AIII presented cytotoxicity effects in various kinds of cancer cells including breast cancer, hepatocellular cancer, cervical cancer, colon cancer, nasopharyngeal cancer, pancreatic cancer, lung cancer, renal cancer, chronic myelogenous leukemia, ovarian carcinoma, osteosarcoma, leukemia, melanoma, and so on. The detection methods and corresponding concentrations which presented cytotoxicity effect and/or IC50 in cancer and normal cell lines were summarized in **Tables 1** and **2**. And the anti-cancer effects and underlying mechanisms of Timo AIII were most studied in breast cancer and hepatocellular cancer. However, only a small part of studies employed a positive control when evaluating the cytotoxicity of Timo AIII in their studies (**Tables 1** and **2**). These results also indicated that the cytotoxic effect of Timo AIII to both cancer and normal cells were not all the same in the different contexts. In addition, the dosage of Timo AIII examined in animal models including mice, rat, and zebrafish were listed in **Table 3**.

Abbreviations: AChE, acetylcholinesterase; AMPK, 5' AMP-activated protein kinase; BCRP, breast cancer resistance protein; BMI1, B-cell-specific Moloney murine leukemia virus integration site; CDK, cyclin-dependent kinase; COX-2, Cyclooxygenase-2; IAP, inhibitor of apoptosis protein; ISVs, intersegmental vessels; MDR1, multi-drug resistance protein 1; MMP, matrix metalloproteinase; MRP1, MDR-associated protein 1; PARP, poly-(ADP ribose) polymerase; PCA, passive cutaneous anaphylaxis; PCNA, proliferating cell nuclear antigen; PRC1, polycomb repressive complex 1; SIVs, subintestinal vessels SIVs; SMC1, structural maintenance of chromosomes protein 1; TORC1 target of rapamycin complex 1; VEGFR, vascular endothelial growth factor receptor; XIAP, X-linked inhibitor of apoptosis protein.

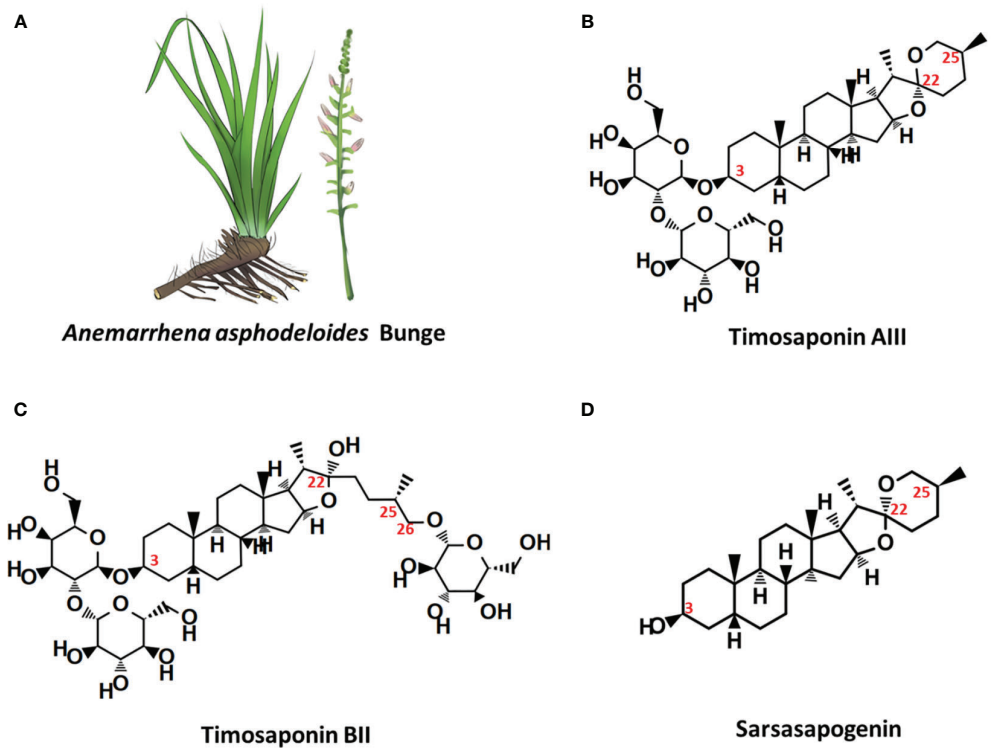

FIGURE 1 | *Anemarrhena asphodeloides* Bunge and the chemical structures of its main steroidal saponin ingredients. **(A)** *A. asphodeloides* Bunge. **(B)** Timosaponin AIII, Pubchem CID: 71306914, MF: $C_{39}H_{64}O_{13}$. **(C)** Timosaponin BII, Pubchem CID: 44575945, MF: $C_{45}H_{76}O_{19}$. **(D)** Sarsasapogenin, Pubchem CID: 92095, MF: $C_{27}H_{44}O_3$.

Promotion of Cell Apoptosis and Cell Cycle Arrest

Induction of cell apoptosis and cell cycle arrest, which stops cancer cell proliferation and causes cell death, is the current main strategy in cancer treatment. The anti-cancer effect of Timo AIII was firstly reported ten years ago in 2008 by Sy et al. They identified that prolong treatment Timo AIII increased cytochrome c release and caspase activation in HeLa cells, and this pro-apoptosis effect of Timo AIII was mediated by over production of ROS and mitochondrial dysfunction (Sy et al., 2008). However, the anti-cancer effects of Timo AIII were most studied in breast cancer and hepatocellular cancer in the past decades. King et al. found that Timo AIII promoted breast cancer cell BT474, MDAMB231 and MCF10A apoptosis in a concentration-dependent manner, and the underlying mechanisms was co-related with target of rapamycin complex 1 (TORC1) inhibition and endoplasmic reticulum (ER) stress stimulated-apoptosis as well as the inhibition of major cell proliferation signaling transduction pathways (King et al., 2009). In the research field of hepatocellular cancer, Wang et al. found that Timo AIII enhanced the apoptosis cell population by activation of poly-ADP ribose polymerase (PARP) and caspase 3, and Z-VAD-FMK which is a cellular apoptosis inhibitor suppressed Timo AIII-induced cytotoxicity in human hepatocellular cancer cell lines including HepG2, MHCC97L, PLC/PRF/5 and Hep3B (Wang et al., 2013). And Timo AIII induced tumor cell apoptosis and increased cleavage PARP and caspase 3 expression in xenografted tumor mice model (Wang et al., 2013). In addition, Wang et al. proved that Timo AIIII reduced the expression of X-linked inhibitor of apoptosis protein (XIAP), which is one of the inhibitor of apoptosis proteins (IAP), in both hepatocellular cancer cells *in vitro* and *in vivo*, and suppression of XIAP by siRNA reduced the toxic sensitivity of Timo AIII in hepatocellular cancer cells (Wang et al., 2013). These results indicated that Timo AIII reduced the tumor growth by modulation of XIAP-mediated cellular caspase active apoptosis in hepatocellular cancer. Moreover, Kyoung et al. found that the anti-cancer effect of Timo AIII was most effective in HepG 2 liver cancer cell among MDA-MB-231 breast cancer cell, A549 no-small-cell lung cancer cell and Hep3B liver cancer cell (Nho et al., 2016). Timo AIII induced more than 90% cell apoptosis on the concentration of 15 μM, and the IC 50 (24h) was 15.41 μM in HepG2 cell. And Timo AIII-promoted cell apoptosis was associated with the decreased expression of Bcl-2, Mcl-1 and IAP family, and the increased release of cytochrome c and activities of caspase family including caspase 3, 7, 8, and 9 (Nho et al., 2016).

In addition, Timo AIII also presented efficacy in colon cancer, pancreatic cancer, lung cancer, osteosarcoma, melanoma, and leukemia. In colon cancer, human colon cancer HCT-15 cells treated various concentrations of Timo AIII for 12 or 24 h appeared different degree of G_0/G_1 and G_2/M phase cell cycle arrest, and the cell cycle regulation effect of

TABLE 1 | The cytotoxicity effects of Timo AIII in different cancer cell lines.

Cell line	Species	Category	Detection method	Tested concentration or IC50	Positive control	Reference
BT474	Human	Breast cancer	Annexin-PI staining	1~10 μM (24 h) and IC50 < 2.5μM(24 h)	None	(Kang et al., 2011)
MDA-MB-231	Human	Breast cancer	Annexin-PI staining	1~10 μM (24 h)	None	(Kang et al., 2011)
			CCK-8 assay	6–20 μM (24 h)	None	(Nho et al., 2016)
			MTT assay	0.001–1 μM (48 h)	None	(Tsai et al., 2013)
			MTT assay	2–4 μM and IC50, 2 μM (48 h)	None	(Gergely et al., 2018)
MCF10A	Human	Breast cancer	Annexin-PI staining	1–10 μM (24 h)	None	(King et al., 2009)
MCF-7	Human	Breast cancer	MTT assay	1–100 μM and IC50=~ 10 μM (48 h)	None	(Sy et al., 2008)
			MTT assay	2–4 μM and IC50 = 2 μM (48 h)	None	(Gergely et al., 2018)
HepG2	Human	Hepatocellular cancer	MTT assay	1–100 μM and IC50=~ 10 μM (48 h)	None	(Sy et al., 2008)
			MTT assay	3.125–50 μM (24 and 48 h)	None	(Wang et al., 2013)
			CCK-8 assay	6–20 μM (6, 24, and 48 h) and IC50 = 15.41 μM (24 h)	None	(Nho et al., 2016)
Hep3B	Human	Hepatocellular cancer	MTT assay	3.125~50 μM (24 and 48 h)	None	(Wang et al., 2013)
PLC/PRF/5	Human	Hepatocellular cancer	MTT assay	3.125~50 μM (24 and 48 h)	None	(Wang et al., 2013)
MHCC97L	Human	Hepatocellular cancer	MTT assay	3.125~50 μM (24 and 48 h)	None	(Wang et al., 2013)
HeLa	Human	Cervical cancer	MTT assay	1–100 μM and IC50=~ 10 μM (48 h)	Sarsasapogenin (50 μM)	(Sy et al., 2008)
SUNE-1	Human	Nasopharyngeal cancer	MTT assay	1–100 μM and IC50=~ 10 μM (48 h)	None	(Sy et al., 2008)
HCT-15	Human	Colon cancer	SRB protein staining	2.5–20 μM and IC50 = 6.1 μM (3 days)	None	(Kang et al., 2011)
HCT-116	Human	Colon cancer	SRB protein staining	IC50 = 5.5 μM (3 days)	None	(Kang et al., 2011)
HT-29	Human	Colon cancer	SRB protein staining	IC50 = 10.1 μM (3 days)	None	(Kang et al., 2011)
SW-480	Human	Colon cancer	SRB protein staining	IC50 = 13.1 μM (3 days)	None	(Kang et al., 2011)
SW-620	Human	Colon cancer	SRB protein staining	IC50 = 11.1 μM (3 days)	None	(Kang et al., 2011)
A549	Human	Lung cancer	CCK-8 assay	3–30 μM (24 h) and IC50 = ~10 μM	None	(Jung et al., 2016)
			CCK-8 assay	6–20 μM (24 h)	None	(Nho et al., 2016)
A549/T	Human	Lung cancer	MTT assay	1.56–100 μM and IC50 = 5.12 μM (24 h)	None	(Song et al., 2019)
A375-S2	Human	Melanoma	MTT assay	1–8 μM (24 h)	None	(Wang et al., 2017)
B16-F10	Murine	Melanoma	MTS assay	10–100 nM (24 h)	None	(Kim et al., 2016)
WM-115	Human	Melanoma	MTS assay	10–100 nM (24 h)	None	(Kim et al., 2016)
PANC-1	Human	Pancreatic cancer	Modified MTT assay*	5–20 μM (24 and 48 h)	Gemcitabine (1 mM)	(MarElia et al., 2018)
BxPC-3	Human	Pancreatic cancer	Modified MTT assay*	5–20 μM (24 and 48 h)	Gemcitabine (1 mM)	(MarElia et al., 2018)
AsPC-1	Human	Pancreatic cancer	MTT assay	0–100 μM and IC50 = 22.1 μM (24 h)	Gemcitabine (5 μM)	(Kim et al., 2019b)
786-O	Human	Renal cancer	MTT assay	2–8 μM (24 h)	None	(Chiang et al., 2019)
A-498	Human	Renal cancer	MTT assay	2–8 μM (24 h)	None	(Chiang et al., 2019)
ACHN	Human	Renal cancer	MTT assay	2–8 μM (24 h)	None	(Chiang et al., 2019)
K562	Human	Chronic myelogenous leukemia	CCK-8 assay	0.2–1.6 mg/L and IC50 = 1.01 mg/L (24h)	Adriamycin (4-32μg/m)	(Chen et al., 2016)
K562/ADM	Human	Chronic myelogenous leukemia	CCK-8 assay	16–128 mg/L and IC50 = 32.18 mg/L (24h)	Adriamycin (4-32μg/m)	(Chen et al., 2016)
A2780/T	Human	Ovarian carcinoma	MTT assay	1.56–100 μM and IC50 = 4.64 μM (24 h)	None	(Song et al., 2019)
MG63	Human	Osteosarcoma	CCK-8 assay	3–15 μM (24 h) and IC50 = 12 μM	None	(Jung and Lee, 2019)
U2OS	Human	Osteosarcoma	CCK-8 assay	3–15 μM (24 h)	None	(Jung and Lee, 2019)
Jurkat cell	Human	T–cell acute lymphoblastic leukemia	CCK-8 assay	2–32 μM (24, 48, and 72 h)	None	(Wang et al., 2019)

*SRB, sulforhodamine-B; *CellTiter 96 non-radioactive cell proliferation assay (MTT, Promega).*

Timo AIII was associated with the down-regulation of cyclin A, cyclin B1, CDK2, CDK4, pRb, proliferating cell nuclear antigen (PCNA) and c-Myc (Kang et al., 2011). Moreover, Timo AIII promoted cell apoptosis by induction of DNA fragmentation, activation of caspases, induction of cleaved-PARP and reduction of Bcl-xL and Bcl-2 expression in HCT-15 cells *in vitro*. In line with this results, Timo AIII significantly decreased the tumor volume in HCT-15 cell-bearing athymic nude mice *in vivo* (Kang et al., 2011). In melanoma, Timo AIII arrested the cell cycle at G_0/G_1 phase and enhanced the cell apoptosis by up-regulation of cleavage-caspase 3 expression in human melanoma A375-S2 cells (Wang et al., 2017). And Timo AIII enhanced the expression of iNOS which resulted in the elevated release of NO, and Timo AIII-induced cleavage of caspase 3 was attenuated by iNOS inhibitors DTT and 1400W in A375-S2 cells. Timo AIII increased the expression of JNK and ERK, and their inhibitors enhanced Timo AIII-induced cell death but decreased cleavage-caspase 3 expression in A375-S2 cells (Wang et al., 2017). Thus, JNK and ERK seem play protective roles in the Timo AIII-induced cell death. In

TABLE 2 | The cytotoxicity effects of Timo AIII in various normal cells.

Cell line	Species	Category	Detection method	Tested concentration or IC50	Positive control	Reference
MRS-5	Human	Normal lung epithelial	SRB protein staining	IC50 > 50 μM (3 days)	None	(Kang et al., 2011)
Hs68	Human	Normal lung fibroblast	SRB protein staining	IC50 > 50 μM (3 days)	None	(Kang et al., 2011)
L-02	Human	Normal hepatocyte	MTT assay	8–512 μM and IC50 > 128 μM (24 h)	None	(Wang et al., 2013)
Chang	Human	Normal hepatocyte	CCK-8 assay	6–20 μM (24 h)	None	(Nho et al., 2016)
hPBMC	Human	Peripheral blood mononuclear cells	MTT assay	2.5–40 μM (24 h)	5-FU and paclitaxel (2.5–40 μM)	(Wang et al., 2017)
HUVEC	Human	Umbilical vein endothelial cell	MTT assay	0.5–8 μM (24 h)	None	(Zhou et al., 2020)
SK-N-SH	Human	Neuroblastoma	Western blot assay	2.5–10 μM (1 h)	Tacrine (5 μM)	(Lee et al., 2009)
HEK	Human	Epidermal keratinocyte	MTT assay	1–200 nM (24 h)	None	(Kim et al., 2019a)
HDF	Human	Dermal fibroblast	Cell migration assay	5–20 nM (12 h)	None	(Kim et al., 2019a)
Primary macrophage	Mice	Peritoneal macrophage	Trypan blue method	2–5 μM (20 h)	None	(Lim et al., 2015)
BV-2	Mice	Neuronal microglia	Western blot assay	2.5–10 μM (1 h)	Tacrine (5 μM)	(Lee et al., 2009)
RBL-2H3	Rat	Cancerous basophil cells	ELISA assay	20 and 50 μM (4 h)	Dexamethasone (10 μM)	(Lee et al., 2010)

SRB, sulforhodamine-B.

TABLE 3 | The dose range of Timo AIII examined in animal models.

Animal	Species	Administration approach	Experimental duration	Tested dosage	Reference
Tübingen (TU) (1 dpf)	Zebrafish	Immersed in drug-contained culture medium	24 h	0.5, 1, and 2 μM	(Zhou et al., 2020)
Tg(Fli-1: EGFP)y1 (1 dpf)	Zebrafish	Immersed in drug-contained culture medium	12 h	0.5, 1, 2, and 3 μM	(Zhou et al., 2020)
Nude mice (female)	Mice	Intraperitoneal injection (3 times per week)	3 weeks	7.5 mg/kg	(Wang et al., 2013)
BALB/c nude mice (male, 5 weeks old)	Mice	Intraperitoneal injection (3 times per week)	30 days	2 and 5 mg/kg	(Kang et al., 2011)
C57BL / 6	Mice	Intraperitoneal injection	14 days	12.5 and 25 mg/kg	(Kim et al., 2016)
BALB/c nude mice (male)	Mice	Intraperitoneal injection (every two days)	10 days	2.5 and 5 mg/kg	(Song et al., 2019)
ICR (male)	Mice	Oral administration or intraperitoneal injection	1 h	5, 20, and 50 mg/kg	(Lee et al., 2010)
BALB/c nude mice (male, 7 weeks old)	Mice	Oral administration (twice daily)	5 days	10, 20, and 40 mg/kg	(Cong et al., 2016)
Wistar (male, 8 weeks old)	Rat	Oral administration (twice daily)	5 days	10, 20, and 40 mg/kg	(Cong et al., 2016)
BALB/c nude mice (5–6 weeks old)	Mice	Intraperitoneal injected (3 times per week)	30 days	7.5 mg/kg	(Lu et al., 2018)
ICR (6-8 weeks old)	Mice	Oral administration (once daily)	7 days	30, 90, and 270 mg/kg	(Han et al., 2015)
KK-Ay	Mice	Oral administration (once daily)	8 weeks	30, 90, and 270 mg/kg	(Han et al., 2015)
SD (male)	Rat	Oral administration	14 days	100 mg/kg	(Wu et al., 2014)
BALB/c nude mice (male)	Mice	Intraperitoneally injected (every two days)	10 days	2.5 and 5 mg/kg	(Song et al., 2019)
ICR (male)	Mice	Oral administration	1 and 5 h	10, 20, or 40 mg/kg	(Lee et al., 2009)
SD (6 weeks old)	Rat	Oral administration (once a day)	7 days	50–200 μg/kg	(Shin et al., 2008)
ddY (male,4 weeks old)	Mice	Intravenously Injected	4-5 weeks	10 mg/kg	(Kimura et al., 1996)

dpf, day post fertilization; ICR, Institute of Cancer Research.

pancreatic cancer, Kim et al. demonstrated that Timo AIII increased the number of apoptotic cells which accompanied with the reduction of mRNA expression of anti-apoptosis proteins survivin, Bcl-2 and Bcl-xl, and Timo AIII elevated cell cycle distribution at sub-G1 phase which might result from the down-regulation of cell cycle regulators cyclin-D and upregulation of cyclin-dependent inhibitor p21 in human pancreatic cancer cell AsPC-1 (Kim et al., 2019b). And combination commercial available anti-cancer drug dasatinib, which is a Src inhibitor, with Timo AIII enhanced the pro-apoptosis effect by regulation of PARP and caspase 3 expressions in AsPC-1 cells (Kim et al., 2019b). Interestingly, Timo AIII enhanced the ERK/Src phosphorylation at low concentration while decreased both the amount of phosphorylated and total protein at high concentration (Kim et al., 2019b), which revealed that high concentration of Timo AIII mainly resulted in cell death. Timo AIII also inhibited the tumor growth by activation of caspase-3 which stimulated cellular apoptosis on pancreatic cancer PANC-1 cell-xenograft nude mice model (Pan et al., 2013). In osteosarcoma and lung cancer, Timo AIII significantly induced cell apoptosis by regulation of caspase 3, caspase 7 and PARP expressions in MG63 human osteosarcoma cells (Jung and Lee, 2019), and induced cell apoptosis and cell cycle arrest at G_0/G_1 phase in human no-small-cell lung cancer cell A549 (Jung et al., 2016). Timo AIII also concentration-dependently induced cell apoptosis by upregulation of Bax and down regulation of Bcl-2 in T−cell acute lymphoblastic leukemia Jurkat cells (Wang et al., 2019).

Thus, we could conclude that the anti-cancer efficacy of Timo AIII was well studied, especially hepatocellular cancer and breast cancer, and the mainly underlying mechanism was induction of cell apoptosis (**Figure 2**) and cell cycle arrest (**Figure 3**). In addition, the XIAP might be potential pharmacological target of Timo AIII.

Induction of ER Stress, ROS Generation, and Mitochondrial Dysfunction

Normal endoplasmic reticulum (ER) function is essential for maintaining the cellular homeostasis, and ER stress presents in cancer cells due to its nutrient limitative and hypoxic tumor micro-environment (Cubillos-Ruiz et al., 2017). However, chronic ER stress stimulated activation of cellular apoptosis pathways which could result in cancer cell death, and the anti-cancer effects of various natural products were resulted from the induction of intracellular ER stress (Kim and Kim, 2018). King et al. found that Timo AIII time-dependently enhanced the ER stress by up-regulating the protein levels of PDI, calreticulin, GRP78, ATF4, and TRIB3 and the phosphorylation levels of eIF2α and PERK, which are ER stress markers (King et al., 2009). And Timo AIII also enhanced the genes expression in cholesterol biosynthesis pathways in breast cancer cell BT474, MDAMB231 and MCF10A. However, the total cholesterol levels were not changed and the cholesterol biosynthesis regulator SREBP-2 was significantly activated in Timo AIII treated cell (King et al.,

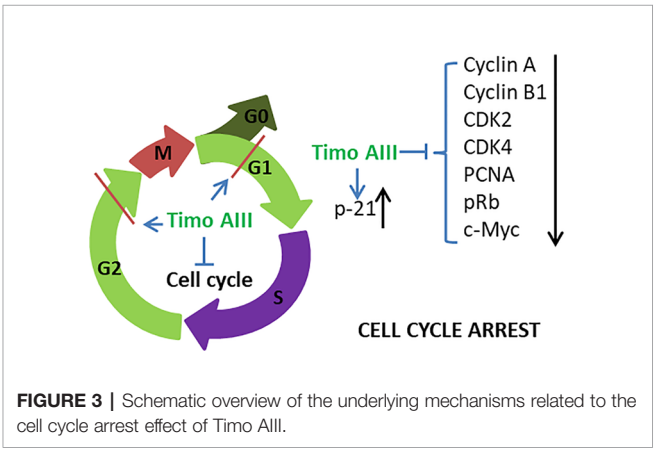

FIGURE 3 | Schematic overview of the underlying mechanisms related to the cell cycle arrest effect of Timo AIII.

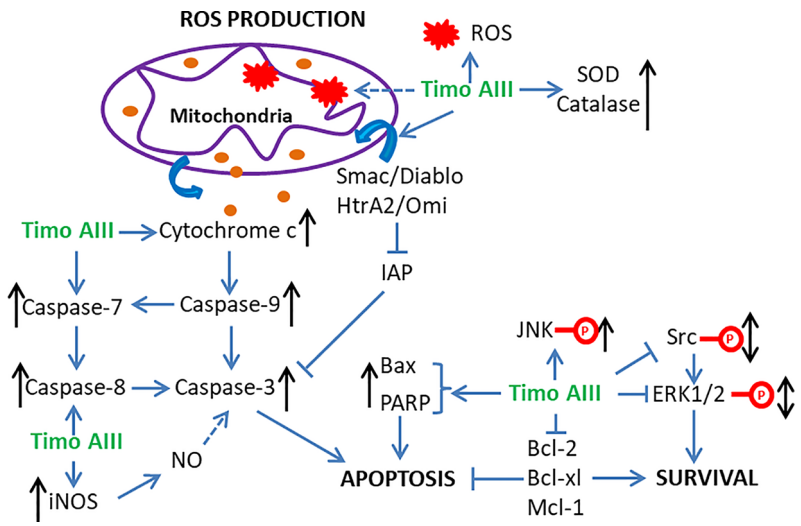

FIGURE 2 | Schematic overview of the underlying mechanisms related to the induction of apoptosis, ROS production, and mitochondrial dysfunction by Timo AIII.

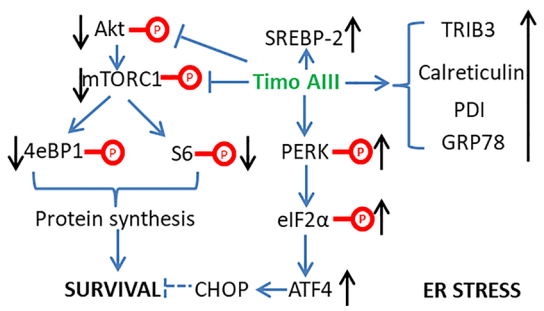

FIGURE 4 | Schematic overview of the underlying mechanisms related to the induction of ER stress by Timo AIII.

2009). Thus, the cell death induced by Timo AIII was not due to the biosynthesis of cholesterol, and the regulation of cholesterol biosynthesis by Timo AIII supported its ER stress induction activity (**Figure 4**).

Mitochondria regulates many cellular physical functions including energy metabolism, reactive oxidant species (ROS) generation and apoptosis, and Chiu et al. claimed that mitochondria played a central role in cancer development and suggested that mitochondria-targeted therapeutic approach was valuable in cancer (Chiu et al., 2020). Kyoung et al. found that Timo AIII dramatically induced apoptosis in HepG2 cells, which might be co-related to the translocation of Smac/Diablo and HtrA2/Omi from cytosol to mitochondria consequently triggered cell apoptosis (Nho et al., 2016). ROS could be either cause or result of mitochondria dysfunction which promotes disruption of intracellular homeostasis and cancer cell death (Kudryavtseva et al., 2016; Park et al., 2019; Zhou J. et al., 2019). Timo AIII induced intracellular ROS accumulation which could be cleared by anti-oxidant NAC and might be an important cause of cell death in triple negative breast cancer cell MDA-MB-231 (Tsai et al., 2013). Consistently, Timo AIII concentration-dependently increased the intracellular ROS and anti-oxidant enzymes including SOD and catalase in HeLa cells, which indicated that Timo AIII impaired intracellular redox homeostasis (Sy et al., 2008). In addition, Timo AIII destroyed mitochondrial membrane potential, mitochondrial permeability transition, and release of cytochrome c, and the mitochondria was the main sources of ROS-induced by Timo AIII in HeLa cells (Sy et al., 2008). So, targeting ROS production and mitochondria dysfunction might be essential mechanisms for Timo AIII-caused cancer cell death (**Figure 2**).

Anti-Angiogenesis

Tumor angiogenesis, which is triggered by tumor-secreted angiogenic factors, transports nutrient to tumor and promotes tumor growth and metastasis. Targeting tumor angiogenesis and vascular normalization have been a promising anti-cancer drug development strategy, and several agents have been developed (Viallard and Larrivee, 2017; Jaszai and Schmidt, 2019). The anti-tumor effect of Timo AIII on pancreatic cancer cell PANC-1 bearing nude mice model was co-related to the down-regulation of mRNA and protein levels of the angiogenic factor VEGF (Pan et al., 2013). Timo AIII inhibited the mRNA expression of VEGF-1, and suppressed the EGF-triggered Src/STAT3/ERK signaling pathway activation in a concentration-dependent manner in pancreatic cancer cell AsPC-1 (Kim et al., 2019b). Zebrafish and vascular endothelial cell have been considered as the well-known *in vivo* and *in vitro* models for anti-angiogenesis activity evaluation with the advantages of low cost, time saving, and easy observation (Norrby, 2006; Delvecchio et al., 2011). Zhou et al. found that Timo AIII presented anti-angiogenesis effect in zebrafish *in vivo* and human umbilical vein endothelial cells (HUVECs) *in vitro* (Zhou et al., 2020). Timo AIII inhibited the intersegmental vessels (ISVs) and sub-intestinal vessels (SIVs) growth in transgenic zebrafish line Tg(Fli-1: EGFP)^{y1} which expressed enhanced green fluorescence protein (EGFP) in vascular endothelial cells. Timo AIII also inhibited the endothelial cell proliferation, migration, invasion, and tube formation in HUVECs. And the underlying mechanism might be closely related to the down-regulation of VEGFRs and suppression of VEGF/PI3K/Akt/MAPK signaling pathway. So, the anti-tumor angiogenesis effect of Timo AIII also contributes to its anti-cancer capability, and VEGFR might be potential pharmacological target of Timo AIII (**Figure 5**).

Anti-Metastasis

Most of the cancer patients die from cancer metastasis which consists of multiple physical processes and have long been associated with cancer cell migration and invasion (Guan, 2015). Matrix metalloproteinase (MMP) is the vital pharmacological target in cancer progression, which degrades extracellular matrix, affects the cancer microenvironment, and initiates cancer metastasis (Shay et al., 2015; Lyu et al., 2019). Various signaling pathways, including MAPKs, src/FAK, beta-catenin, NF-κB, STAT3, and so on are involved in the regulation of MMPs expressions (Pan et al., 2011; Merchant et al., 2017). Timo AIII significantly inhibited the proteolytic activity and mRNA expression of MMP-2/9 which are key regulators in cell migration and invasion in human no-small-cell lung cancer cells A549 and H1299, and the underlying mechanisms might be related to the suppression of ERK1/2, Src/FAK, and beta-catenin signaling pathways (Jung et al., 2016). Consistently, Timo AIII significantly decreased MMP-2/9 expression, and inhibited cell migration and invasion in human osteosarcoma cells MG63 and U2OS. The underlying mechanism was involved in suppression of Src/FAK/MAPKs signaling pathway and down-regulation of transcription factors CREB and b-catenin (Jung and Lee, 2019). In addition, Timo AIII decreased mRNA expression of MMP-9 in human pancreatic cancer cell AsPC-1 (Kim et al., 2019b) and suppressed HGF-induced MMP-9 expression in triple negative breast cancer cell MDA-MB-231 (Tsai et al., 2013).

MicroRNAs (miRNAs), which are small-noncoding RNA molecules and regulate the target genes expression, are classified as oncomiRs (tumor inducers) and tumor suppressor miRNA. And miRNA were well recognized for cancer treatment and diagnose in recent decades (Katz et al., 2015; Qadir and Faheem, 2017; Daoud et al., 2019). The expression level of cancer stem cell phenotype regulator B-cell-specific Moloney murine

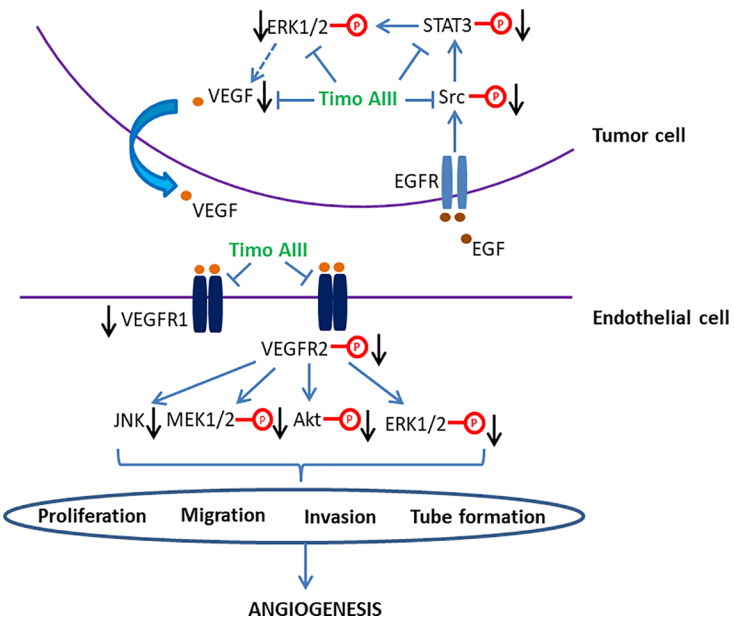

FIGURE 5 | Schematic overview of the signaling pathways related to the anti-angiogenesis activity of Timo AIII.

leukemia virus integration site 1 (BMI1), which is also a component of the polycomb repressive complex 1 (PRC1) and its transcription is dramatically regulated by Myc, is up-regulated in various cancers especially breast cancers (Dimri et al., 2015; Hiraki et al., 2017). Dimiri et al. suggested that the oncogenic activity of BMI1 was also mediated by miR-200c/141 cluster-BMI1 auto-regulatory loop in cancer cells (Dimri et al., 2016). Timo AIII concentration-dependently induced tumor cell senescence and inhibited cell oncogenic phenotypes, including migration, invasion, and colonies formation in soft-agar in both triple negative cancer cell MDA-MB-231 and non-triple negative cancer cell MCF-7 (Gergely et al., 2018). Gergely et al. proved that the inhibitory effect of Timo AIII on cell oncogenic phenotype was mediated by the up-regulation of miR-200c/141 cluster and down-regulation of BMI1, mono-ubiquitination of histone H2A at lysine 119 (H2AUb) and Myc in both MDA-MB-231 and MCF-7 cells (Gergely et al., 2018). There are also accumulated evidences which revealed the tumor suppressive role of miR-129-5p in various cancers (Liu et al., 2019; Qiu et al., 2019; Shi et al., 2019). Timo AIII inhibited cell migration and invasion among the concentration range of 2 to 6 μM in which Timo AIII not affected the cell viability and cell cycle distribution in human renal cancer cells 786-O and A-498 (Chiang et al., 2019). And this non-toxic inhibitory effect of Timo AIII on cell migration and invasion was co-related with the down-regulation of cysteine protease cathepsin c expression, which was regulated by PI3K/Akt/miR-129-5p signaling axis (Chiang et al., 2019).

The inflammatory infiltration state of cancer microenvironment plays crucial role in cancer growth, metastasis, and resistance, which is mainly regulated by COX2/PGE2/EP and NF-κB signaling cascades (Hsu et al., 2017; Tong et al., 2018). The inhibition of these processes presented potential therapeutic effect in various cancers (Yun et al., 2016; Liu et al., 2018). Timo AIII suppressed the migration capability of murine melanoma cell B16-F10 and human melanoma cell WM-115, which were induced or not induced by COX-2 stimulator 12-O-tetradecanoylphorbal-13-acetate (TPA), and it was closely associated with its concentration-dependent inhibitory effect on endogenous COX-2 expression and PGE2 production (Kim et al., 2016). Timo AIII also reduced protein levels of NF-κB, IKKα, IκBα, and PGE2 receptors including EP2 and EP4 in B16-F10 cells (Kim et al., 2016). In line with these *in vitro* experiment results, Timo AIII significantly inhibited the metastasis of B16-F10 cells to lung with reduction of COX2 and NF-κB expression in mice *in vivo* (Kim et al., 2016). Many growth factors induce cancer cell proliferation, migration, and invasion, which contribute to cancer cell motility and intravasation (Guan, 2015). Hepatocyte growth factor (HGF), which promotes various cancer cell metastasis, triggered cancer cell migration and invasion *via* cMet-ERK-COX2 and MAPK signaling pathways (Siegfried et al., 2007; Kuang et al., 2017). Timo AIII concentration-dependently inhibited HGF-induced cell migration and invasion which were blocked by COX2 inhibitor NS398 and ERK inhibitor PD98059 in triple negative breast cancer cell MDA-MB-231 (Tsai et al., 2013). Timo AIII also significantly attenuated HGF-induced intracellular p-cMet and COX2 expressions as well as nuclear ERK phosphorylation and ATF2 expression in MDA-MBA-231 cells (Tsai et al., 2013).

Thus, Timo AIII inhibited cancer stem cell phenotype, including cell migration and invasion, and subsequently suppressed cancer metastasis by targeting MMPs, BMI1, and cancer inflammatory infiltration (**Figure 6**).

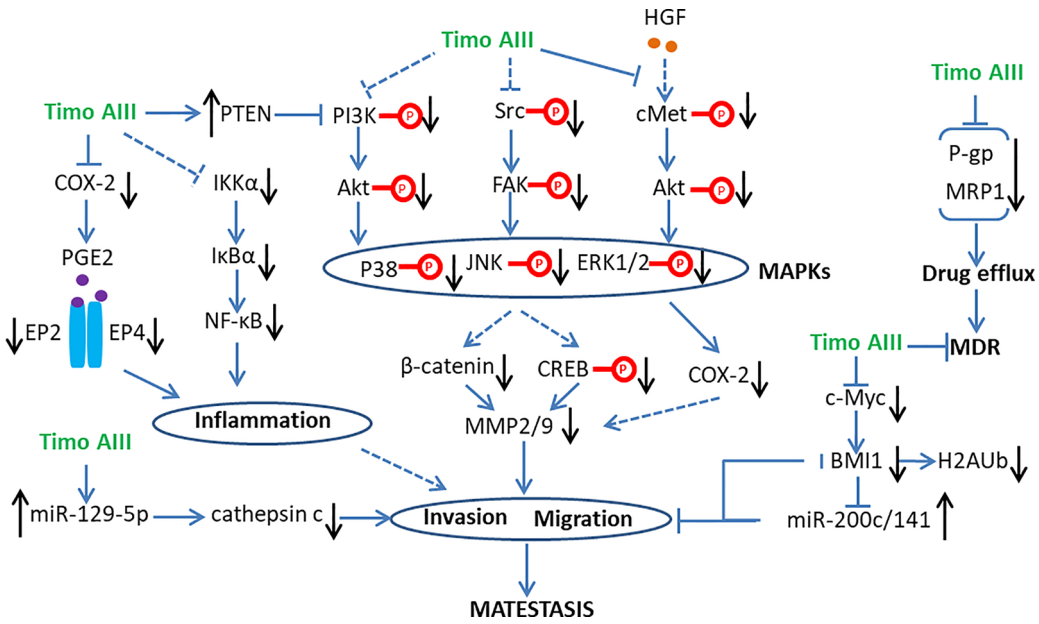

FIGURE 6 | Schematic overview of the signaling pathways related to the anti-metastasis and anti-multi drug resistance (MDR) activity of Timo AIII.

Anti-Resistance and Synergistic Anti-Cancer Effect

Multiple drug resistance (MDR) is a severe problem in current cancer therapy (Gottesman, 2002; Vasan et al., 2019). Elevating the sensitivity of therapeutic drug to resistant-cancer cell by combination with other agents might be a promising therapeutic strategy. Timo AIII concentration-dependently caused cytotoxicity, cell cycle arrest, and caspase-dependent apoptosis in PANC-1 and BxPC-3 cells, which were resistance to gemcitabine in different degree, and enhanced the sensitivity to gemcitabine in these pancreatic cancer cells (MarElia et al., 2018). The underlying mechanism of Timo AIII enhanced the sensitivity of gemcitabine on cell cycle dysfunction, and apoptosis was involved in activation of pro-apoptotic proteins in PI3K/Akt signaling cascade (MarElia et al., 2018). Timo AIII also inhibited PI3K/Akt signaling pathway on adriamycin (ADM)-resistant human chronic myelogenous leukemia cell K562 (Chen et al., 2016). And the anti-tumor effects of Timo AIII on taxol-resistance lung and ovarian cancers were co-related to the suppression of PI3K/AKT/mTOR and Ras/Raf/MEK/ERK signaling pathways (Song et al., 2019). In addition, Ginsenosides including compound K, Rb1, and Rc enhanced the cytotoxicity of Timo AIII in MG63 human osteosarcoma cells, in which Rb1 and Rc increased the population of apoptosis cell caused by Timo AIII (Jung and Lee, 2019). Thesis results indicate that Timo AIII could enhance the cancer cell apoptosis and suppressed the cell survival signaling, and ginsenoside might present synergistic effect on Timo AIII-induced cancer cell death and metastasis.

The metabolism and transport of intracellular drug to extra cell contributes to MDR, which is also called drug efflux. The ATP-binding cassette (ABC) transporter family including multi-drug resistance protein 1 (MDR1; also known as P-glycoprotein and ABCB1), MDR-associated protein 1 (MRP1; also known as ABCC1) and breast cancer resistance protein (BCRP; also known as ABCG2) regulates the process of drug efflux, which also overexpresses in many drug-resistant cancer cells (Holohan et al., 2013). Timo AIII increased intracellular adriamycin (ADM) concentration and presented reversal effect on ADM-resistant human chronic myelogenous leukemia cell K562 in a concentration-dependent manner, and the underlying mechanisms were related to the down-regulation of P-glycoprotein (P-gp) and MRP1 (Chen et al., 2016). Moreover, Timo AIII attenuated the expression of P-gp and enhanced cell apoptosis in taxol-resistance human lung cancer cell A549/T and human ovarian cancer A2780/T *in vitro* and A549/T cell injected nude mice *in vivo* (Song et al., 2019). Thus, the inhibition of drug efflux by down-regulation of drug transporters expression was a key mechanism account for the anti-resistant capability of Timo AIII in cancer cells (**Figure 6**).

Negative Regulated Cell Death by Autophagy

Autophagy characterized by the formulation of autophagic vacuoles which degrade and recycle the dysfunctional proteins and damaged organelles subsequently maintains the intracellular homeostasis (Antunes et al., 2018). Autophagy is a double-edged sword in cancer development, progression, and treatment, which could be tumor-suppressive, tumor-promoting, or neutral under different conditions (Amaravadi et al., 2016). PI3K/Akt/mTOR signaling pathway plays a key role in regulation of autophagy (Colhado Rodrigues et al.,

2019). Timo AIII notably induced cellular autophagic morphology *via* inhibition of PI3K/Akt/mTOR signaling pathway in Jurkat cells (Wang et al., 2019). Lok et al. found that Timo AIII suppressed the mTOR signaling and trigged autophagy while this process was not all the same with rapamycin-induced autophagy in HeLa cells (Lok et al., 2011). Timo AIII modulated specific transcriptional mechanisms and caused the up-regulation of cholesterol biosynthesis pathways for supporting the formation of autophagic vacuoles which capture ubiquitin proteins (Lok et al., 2011). Timo AIII-induced autophagy was co-related with elevated intracellular calcium concentration and accelerated the clearance of ubiquitin protein aggregation which induced by proteinase inhibitor MG132 (Lok et al., 2011). In addition, Timo AIII inhibited the mTORC1 and promoted selective protective autophagy in breast cancer cells (King et al., 2009). The inhibition of autophagy by chloroquine enhanced the cytotoxicity of Timo AIII in MDA-MB-231 and MCF 10A cells regardless of BT474 cell (King et al., 2009). In line with this result, Timo AIII increased the accumulation and conversion of cytosol LC3 I to autophagosome membrane located LC3 II, which revealed the autophagy induction effect in HeLa cells (Lok et al., 2011), and Timo AIII-induced apoptosis was potentiated in the presence of autophagy inhibitor 3-methyladenine (3-MA) or silenced beclin-1 gene which is a key regulator of autophagy (King et al., 2009). Moreover, Timo AIII induced autophagy in hepatocellular cancer cells both *in vitro* and *in vivo*, which mediated by AMPKα activation and mTOR inhibition (Wang et al., 2013). The inhibition of autophagy by Atg5 silence increased the cytotoxicity of Timo AIII in hepatocellular cancer cells, which revealed the cyto-protective role of autophagy in Timo AIII-induced hepatocellular cancer cell death (Wang et al., 2013). Timo AIII increased autophagy vacuoles, Beclin-1 and LC3 levels in human melanoma A375-S2 cells, and Timo AIII-induced apoptosis was accelerated by the autophagy inhibitor 3-MA (Wang et al., 2017). These results indicated that Timo AIII-induced autophagy might act as the role to promote tumor cell survival *in vitro*, and mTORC1 might be the potential target of Timo AIII (**Figure 7**).

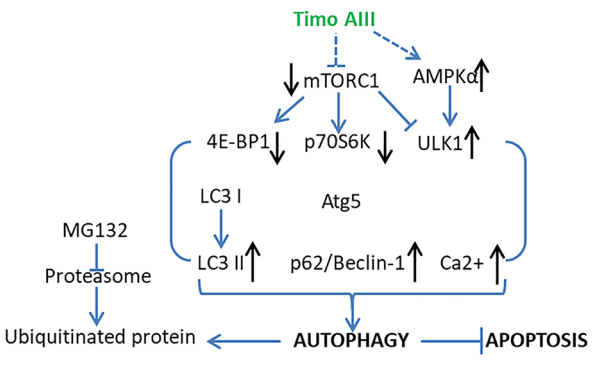

FIGURE 7 | Schematic overview of the underlying mechanisms and signaling pathways related to the cellular protective autophagy activity of Timo AIII.

Neuronal Disorders

Alzheimer's Disease

Alzheimer's disease (AD), which is a progressive neurodegeneration disease and characterized by disorder of memory and cognitive functions, is the most common type of dementia with poor therapeutic efficacy until now (Oboudiyat et al., 2013). Several pathology features, including neuro-inflammation, accumulation of β-amyloid plaques and tau protein, and deficient cholinergic transmission were found in the brain of AD patients (Tundis et al., 2016). Acetylcholinesterase (AChE) degrades acetylcholine and lowers cholinergic activity and its selective inhibitor donepezil has been used for AD treatment in clinics (Arvanitakis et al., 2019). Lee et al. found that orally administration of Timo AIII (10, 20 and 40 mg/kg) significantly ameliorated the scopolamine-caused mice memory impairment in both passive avoidance test and Morris water maze test, and tacrine (10 mg/kg)-treated mice served as the positive control (Lee et al., 2009). Timo AIII elevated the acetylcholine level in scopolamine-treated mice brain which was correlated to its concentration dependently inhibition of the AChE activity (IC 50 = 35.4 μM). In addition, the elevation levels of pro-inflammatory cytokines including TNF-α, IL-6 and IL-1β have been found in the AD brain, and microglia triggered neuro-inflammation has been considered contribution to AD progression (Webers et al., 2019). Timo AIII decreased the expression of pro-inflammatory cytokines TNF-α and IL-1β in the brain of scopolamine-treated mice, and the underlying mechanism was associated with the suppression of NF-κB signaling pathway activation in both microglia and neuron (Lee et al., 2009). Though the anti-AD activity of Timo AIII was demonstrated *in vivo*, whether Timo AIII could cross blood-brain barrier need to be further studied. Thus, we could conclude that Timo AIII was potentially for AD therapy due to its inhibition on AChE activity and NF-κB-mediated neuro-inflammation (**Figure 8**).

Depression

Depression is a serious psychiatric disease and dramatically disrupted the quality of life (Smith, 2014). Although these are multiple pharmacological and physical strategies for depression treatment in clinic, various side effects accompany with the positive outcomes (Tomlinson et al., 2019). Timosaponin B-III (Timo B-III) which is also one of the main natural steroidal saponins in *A. asphodeloides* Bunge prevented from depression in a mouse postpartum depression model (Zhang et al., 2017). Timo AIII (30 mg/kg) also presented anti-depression activity according to the experiment results from open field test, tail suspension test and forced swimming test in mice, and fluoxetine-treated mice served as the positive control. However, the anti-depression effect of Timo B-III was more effective than Timo AIII (Jiang et al., 2014). Thus, further studies about the anti-depression effect of Timo B-III are more valuable than Timo AIII.

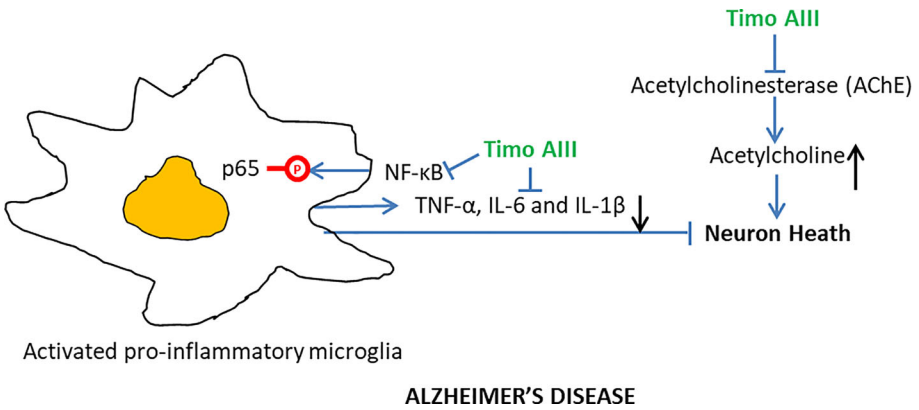

FIGURE 8 | Overview of the underlying mechanisms of the Alzheimer's disease protective effect of Timo AIII.

Diabetic Mellitus

Anemarrhena asphodeloides Bunge is an important constitute of herb medicine formulas, like TongGuanWan, Bai-Hu-Jia-Rensheng-Tang, Rhizoma Anemarrhenae-Phellodendron herb pair and guizhi-shaoyao–*A. asphodeloides* herb pair, which have been applied for treatment of diabetic mellitus for thousands of years in China (Kimura et al., 1996; Shin et al., 2008; Tang et al., 2012; Han et al., 2015; Zhao et al., 2015). But the active constitutes of *A. asphodeloides* Bunge for diabetic mellitus treatment was not fully elucidated. The diabetic mellitus protective effect of Timo AIII was firstly investigated on streptozocin (STZ)-induced diabetic and normal mice in 1996 (Kimura et al., 1996). In diabetic mice model, Timo AIII (1 and 10 mg/kg) significantly promoted the salivary flow. And combination of $CaCl_2$ (2 and 4 mg/kg) with Timo AIII (0.1 mg/kg) enhanced the pilocarpine-induced saliva secretion when compared with Timo AIII alone (Kimura et al., 1996). However, Nian et al. found that the glucosidase inhibitory effect of flavones, including mangiferin and isomangiferin, were more effective than steroidal saponins including Timo AIII and Timo BII, which revealed the more potent anti-diabetic mellitus effects of flavones than saponins isolated from *A. asphodeloides* Bunge (Nian et al., 2017). And Yuan et al. found Timo BII prevent from diabetic nephropathy by suppression the inflammation in alloxan-induced mice (Yuan et al., 2015). These results revealed that the anti-diabetic mechanisms were different between steroidal saponins and flavones ingredients of *A. asphodeloides* Bunge and the anti-diabetic mellitus activity of Timo AIII might be due to its anti-inflammatory property.

Others

Anti-Platelet and Anti-Thrombotic Activity

Platelet activation and aggregation have been considered as the main pathology of many cardiovascular diseases, such as coronary heart disease, atherosclerosis, and strokes (Yeung et al., 2018). The inhibition of thromboxane prostaglandin (TP) receptor which blocked thromboxane (Tx) A2 pathway has been suggested as the efficient drug target for inhibition of platelet activation and aggregation (Fu et al., 2017; Kashiwagi et al., 2019). Timo AIII inhibited U46619-induced platelet aggregation by reduction of ADP secretion *in vitro* and prevented thrombus formation in mice *in vivo* (Cong et al., 2016). The thromboxane (Tx) A2 receptor activity and Gq signaling pathway were suppressed by Timo AIII, and the anti-platelet aggregation activity was enhanced by combination Timo AIII with current known antiplatelet agents including PGE1 and SQ29548. So, Timo AIII might be potential for development of cardiovascular drugs for its anti-platelet and anti-thrombotic activity targeting thromboxane (Tx) A2 receptor.

Anti-UVB Radiation

UVB radiation was harmful to skins which resulted in cellular damage, mutation, inflammation, photoaging, and consequently, photocarcinogenesis progression (Lan, 2019). Natural herbs were precious library for discovery of UV protective agents (Li et al., 2019; Mohan and Gupta, 2019). Kim et al. found that Timo AIII, which isolated from Chinese herb *A. asphodeloides* Bunge, protected against UVB-induced cell migration and invasion in both human epidermal keratinocytes (HEKs) and dermal fibroblasts (HDF), and the underlying mechanism were involved in the inhibition of Akt/MAPK signaling pathway and down-regulation of MMP9 (Kim et al., 2019a). Timo AIII reduced UVB-induced up-regulation of COX2 and inflammatory cytokines including TNF-α and IL-6 expressions, which was associated with the down-regulation of pro-inflammatory factor NF-κB. In addition, Timo AIII reduced UVB-induced DNA damage and deposition of 8-oxo-7, 8-dihydro-2'-deoxyguanosine (8-oxo-dG), which were mediated by down regulation of cell cycle arrest–related genes PCNA and SMC1. Thus, the UBV-radiation protective effect of Timo AIII might be mainly due to its anti-inflammatory, anti-cell migration, and anti-cell invasion capabilities.

Anti-Colitis

Timo AIII concentration-dependently inhibited in LPS- or peptidoglycan-stimulated upregulation of COX2, iNOS, and pro-inflammatory cytokines TNF-α and IL-6 expressions in mice peritoneal macrophages, which accompanied with suppression of MAPKs and NF-κB signaling pathways activation (Lim et al., 2015). Moreover, Lim et al. found that Timo AIII reduced the amount of LPS binding to TLR and restored the balance of Th17/Treg cells in mice peritoneal macrophages, and these *in vitro* experiment results were in line with the anti-inflammatory effects of Timo AIII on 2,4,6-trinitrobenzene sulfonic acid (TNBS)-induced colitis in mice *in vivo* (**Figure 9**).

Anti-Allergy

Timo AIII inhibited the passive cutaneous anaphylaxis (PCA) reaction and scratching behaviors in mice while further studies revealed that sarsasapogenin, one of the metabolites of Timo AIII, was the active metabolic compound in Timo AIII-induced anti-allergy (Lee et al., 2010). Lim et al. also found that Timo AIII inhibited the differentiation of T cell to Treg cell *in vitro* (Lim et al., 2015). Thus, Timo AIII might also be able to regulate the immune system (**Figure 9**).

Anti-Virus

Respiratory syncytial virus (RSV) has been identified as the most important cause of lower respiratory tract infections and results in some mortality in young children and elderly (Jorquera et al., 2016; Broor et al., 2018). Although several inhibitors targeting RSV has been found over decades, there is still no antiviral drugs or vaccines approved for the prevention or treatment of RSV infections (Heylen et al., 2017). Joung et al. isolated the Timo AIII from the BuOH fraction of *A. asphodeloides* Bunge and found that Timo AIII significantly inhibited the propagation of RSV in HEp-2 cells (IC50 = 1.0 μM) (Joung et al., 2011). Furthermore, ribavirin–treated group served as the positive control with the IC50 value of 1.15 μM, which was higher than Timo AIII. Thus, we could conclude that Timo AIII presented potential anti-virus activity while its action mechanisms still needs further studies.

PHARMACOKINETICS AND TOXICITY

Pharmacokinetics and toxicity studies play vital roles in the process of drug development. Several analytical methods were developed for detection of the saponins including Timo AIII and Timo BII in animal blood plasma after administration of single compound or herb formulas (Liu Y. et al., 2013; Sun et al., 2013; Feng et al., 2014). Timo AIII is one of the important active ingredients of Baihe Zhimu decoction which was used for depression treatment in traditional Chinese medicine for a long history in China (Yang et al., 2018). Yang et al. found that Timo AIII presented in the blood after oral administration of Baihe Zhimu decoction by an AB Sciex QTRAP ((R)) 5500 mass spectrometer in both normal and depression rats (Yang et al., 2018). Lee et al. detected the blood concentration of Timo AIII using LC-MS in mice, and they found that its maximum blood concentration was 104.7 ± 20.7 ng/μL after oral administration of Timo AIII (50 mg/kg) for 4 to 6 h (Lee et al., 2009). And this result was consistent with efficacy results that the memory-enhancing effect of Timo AIII after orally administration for 5 h was more effective than 1 h. However, Liu et al. found that the Cmax, Tmax, t1/2, and MRT (mean residence time) of Timo AIII were 18.2 ± 3.1 ng/mL, 2.3 ± 0.57 h, 4.9 ± 2.0 h, and 7.1 ± 1.4 h respectively after oral administration of Timo AIII (6.8 mg/kg) in health male SD rat (Liu Z. et al., 2013). Moreover, Timo AIII presented slow eliminated rate in the liver and caused hepatotoxicity which might result from its induction of intracellular ROS and down-regulation of bile acid transporters capabilities (Wu et al., 2014; Xie et al., 2018). And mangiferin, which is an active component in *A. asphodeloides* Bunge and presented anti-oxidant ability, attenuated Timo AIII-induced hepatotoxicity. The absorption, distribution, metabolism, and elimination (ADME) processes and toxicity of

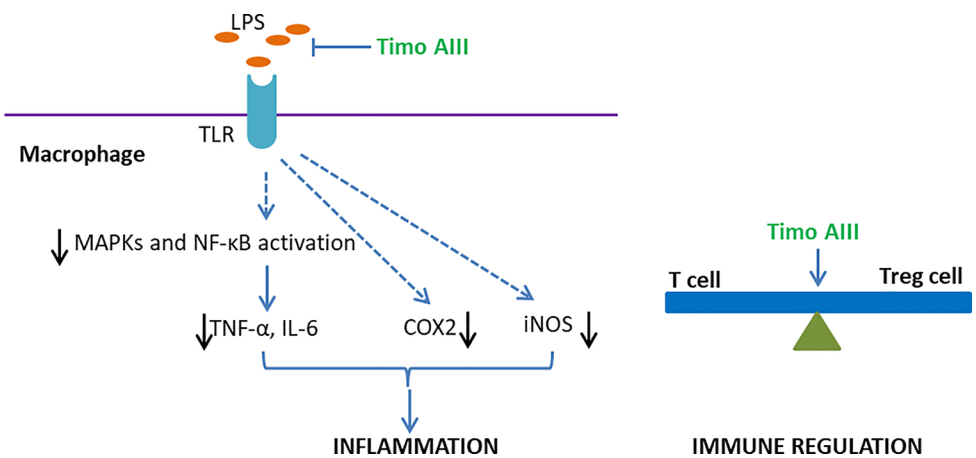

FIGURE 9 | Overview of the underlying mechanisms of the anti-inflammation and immune regulation effects of Timo AIII.

Timo AIII still need further study in both health and disease models including mice, rat, and human.

DISCUSSION

Timo AIII presented various pharmacological activities including anti-cancer, anti-AD, anti- diabetic mellitus, anti-colitis, anti-coagulant, and so on, while these researches were mainly conducted *in vitro*. The most effective activity of Timo AIII is anti-cancer, especially breast cancer and hepatocellular cancer, and the underlying mechanism are co-related with its anti-metastasis, anti-resistance, cytotoxicity, pro-apoptosis, and induction of cell cycle arrest, ROS, ER stress, and mitochondria dysfunction. Previous studies revealed that Timo AIII-induced autophagy might act as the role to promote tumor cell survival *in vitro*. These lack the *in vivo* evidence that explore whether inhibition of autophagy could elevate the anti-cancer effect of Timo AIII. And the autophagy induction effect of Timo AIII might contribute to other diseases, like AD and PD, in which activation of autophagy accelerates clearance of misfolding proteins. We also identified VEGFR, XIAP, BMI1, thromboxane (Tx) A2 receptor, mTOR, NF-κB, COX-2, MMPs, AChE, and so on are as the vital pharmacological targets of Timo AIII. Moreover, the anti-inflammatory effect of Timo AIII is also wealth for further studies, which accounts for its anti-AD, anti-metastasis, ant-metastasis, anti-UVB radiation, and anti-colitis activities. The toxicity, especially hepatotoxicity, and pharmacokinetics including ADME of Timo AIII are worth to investigate in diverse animal models. In conclusion, Timo AIII is potent as a compound or leading compound for further drug development while still needs in-depth studies.

DATA AVAILABILITY STATEMENT

The raw data supporting the conclusions of this article will be made available by the authors, without undue reservation, to any qualified researcher.

AUTHOR CONTRIBUTIONS

YL and W-RZ wrote the manuscript. W-TS, JZ, K-YZ, and QD collected the related articles and summarized the figures and tables. W-TS, X-LC, J-YT, and Z-YZ designed the study and revised the manuscript.

FUNDING

This study was supported by the National Health Commission of Shanghai (GWIV-28, ZY-(2018-2020)-FWTX-8001, XHLHGG201803) and Shanghai University of Traditional Chinese Medicine (A1-N19205010302). The authors thank Mr. Hua Chaofeng from School of Management, Jiangxi Agricultural University for drawing the features of *Anemarrhena asphodeloides* Bunge according to Compendium of Materia Medica.

REFERENCES

Amaravadi, R., Kimmelman, A. C., and White, E. (2016). Recent insights into the function of autophagy in cancer. *Genes Dev.* 30 (17), 1913–1930. doi: 10.1101/gad.287524.116

Antunes, F., Erustes, A. G., Costa, A. J., Nascimento, A. C., Bincoletto, C., Ureshino, R. P., et al. (2018). Autophagy and intermittent fasting: the connection for cancer therapy? *Clinics* 73 (suppl 1), e814s. doi: 10.6061/clinics/2018/e814s

Arvanitakis, Z., Shah, R. C., and Bennett, D. A. (2019). Diagnosis and Management of Dementia: Review. *Jama* 322 (16), 1589–1599. doi: 10.1001/jama.2019.4782

Broor, S., Parveen, S., and Maheshwari, M. (2018). Respiratory syncytial virus infections in India: Epidemiology and need for vaccine. *Indian J. Med. Microbiol.* 36 (4), 458–464. doi: 10.4103/ijmm.IJMM_19_5

Chen, J. R., Jia, X. H., Wang, H., Yi, Y. J., Wang, J. Y., and Li, Y. J. (2016). Timosaponin A-III reverses multi-drug resistance in human chronic myelogenous leukemia K562/ADM cells *via* downregulation of MDR1 and MRP1 expression by inhibiting PI3K/Akt signaling pathway. *Int. J. Oncol.* 48 (5), 2063–2070. doi: 10.3892/ijo.2016.3423

Chiang, K. C., Lai, C. Y., Chiou, H. L., Lin, C. L., Chen, Y. S., Kao, S. H., et al. (2019). Timosaponin AIII inhibits metastasis of renal carcinoma cells through suppressing cathepsin C expression by AKT/miR-129-5p axis. *J. Cell Physiol.* 234 (8), 13332–13341. doi: 10.1002/jcp.28010

Chiu, H. Y., Tay, E. X. Y., Ong, D. S. T., and Taneja, R. (2020). Mitochondrial Dysfunction at the Center of Cancer Therapy. *Antioxid. Redox Signal* 32(5), 309–330. doi: 10.1089/ars.2019.7898

Colhado Rodrigues, B. L., Lallo, M. A., and Perez, E. C. (2019). The Controversial Role of Autophagy in Tumor Development: A Systematic Review. *Immunol. Invest.* 14, 1–11. doi: 10.1080/08820139.2019.1691222

Cong, Y., Wang, L., Peng, R., Zhao, Y., Bai, F., Yang, C., et al. (2016). Timosaponin AIII induces antiplatelet and antithrombotic activity *via* Gq-mediated signaling by the thromboxane A2 receptor. *Sci. Rep.* 6, 38757. doi: 10.1038/srep38757

Cubillos-Ruiz, J. R., Bettigole, S. E., and Glimcher, L. H. (2017). Tumorigenic and Immunosuppressive Effects of Endoplasmic Reticulum Stress in Cancer. *Cell* 168 (4), 692–706. doi: 10.1016/j.cell.2016.12.004

Daoud, A. Z., Mulholland, E. J., Cole, G., and McCarthy, H. O. (2019). MicroRNAs in Pancreatic Cancer: biomarkers, prognostic, and therapeutic modulators. *BMC Cancer* 19 (1), 019–6284. doi: 10.1186/s12885-019-6284-y

Delvecchio, C., Tiefenbach, J., and Krause, H. M. (2011). The zebrafish: a powerful platform for *in vivo*, HTS drug discovery. *Assay Drug Dev. Technol.* 9 (4), 354–361. doi: 10.1089/adt.2010.0346

Dimri, M., Cho, J. H., Kang, M., and Dimri, G. P. (2015). PLK1 inhibition down-regulates polycomb group protein BMI1 *via* modulation of the miR-200c/141 cluster. *J. Biol. Chem.* 290 (5), 3033–3044. doi: 10.1074/jbc.M114.615179

Dimri, M., Kang, M., and Dimri, G. P. (2016). A miR-200c/141-BMI1 autoregulatory loop regulates oncogenic activity of BMI1 in cancer cells. *Oncotarget* 7 (24), 36220–36234. doi: 10.18632/oncotarget.8811

Feng, Y., Chen, B., Lin, A., and Liu, Y. (2014). Simultaneous determination of timosaponin B-II and A-III in rat plasma by LC-MS/MS and its application to pharmacokinetic study. *J. Chromatogr. B. Analyt. Technol. BioMed. Life Sci.* 965, 119–126. doi: 10.1016/j.jchromb.2014.06.017

Fu, J., Zhu, X., Wang, W., Lu, H., Zhang, Z., Liu, T., et al. (2017). 1, 6-di-O-caffeoyl-beta-D-glucopyranoside, a natural compound from Callicarpa

nudiflora Hook impairs P2Y12 and thromboxane A2 receptor-mediated amplification of platelet activation and aggregation. *Phytomedicine* 36, 273–282. doi: 10.1016/j.phymed.2017.10.012

Gergely, J. E., Dorsey, A. E., Dimri, G. P., and Dimri, M. (2018). Timosaponin A-III inhibits oncogenic phenotype *via* regulation of PcG protein BMI1 in breast cancer cells. *Mol. Carcinog.* 57 (7), 831–841. doi: 10.1002/mc.22804

Gottesman, M. M. (2002). Mechanisms of cancer drug resistance. *Annu. Rev. Med.* 53, 615–627. doi: 10.1146/annurev.med.53.082901.103929

Guan, X. (2015). Cancer metastases: challenges and opportunities. *Acta Pharm. Sin. B.* 5 (5), 402–418. doi: 10.1016/j.apsb.2015.07.005

Han, J., Yang, N., Zhang, F., Zhang, C., Liang, F., Xie, W., et al. (2015). Rhizoma Anemarrhenae extract ameliorates hyperglycemia and insulin resistance *via* activation of AMP-activated protein kinase in diabetic rodents. *J. Ethnopharmacol.* 172, 368–376. doi: 10.1016/j.jep.2015.05.016

Han, F. Y., Song, X. Y., Chen, J. J., Yao, G. D., and Song, S. J. (2018). Timosaponin AIII: A novel potential anti-tumor compound from Anemarrhena asphodeloides. *Steroids* 140, 125–130. doi: 10.1016/j.steroids.2018.09.014

Heylen, E., Neyts, J., and Jochmans, D. (2017). Drug candidates and model systems in respiratory syncytial virus antiviral drug discovery. *Biochem. Pharmacol.* 127, 1–12. doi: 10.1016/j.bcp.2016.09.014

Hiraki, M., Maeda, T., Bouillez, A., Alam, M., Tagde, A., Hinohara, K., et al. (2017). MUC1-C activates BMI1 in human cancer cells. *Oncogene* 36 (20), 2791–2801. doi: 10.1038/onc.2016.439

Holohan, C., Van Schaeybroeck, S., Longley, D. B., and Johnston, P. G. (2013). Cancer drug resistance: an evolving paradigm. *Nat. Rev. Cancer* 13 (10), 714–726. doi: 10.1038/nrc3599

Hsu, H. H., Lin, Y. M., Shen, C. Y., Shibu, M. A., Li, S. Y., Chang, S. H., et al. (2017). Prostaglandin E2-Induced COX-2 Expressions *via* EP2 and EP4 Signaling Pathways in Human LoVo Colon Cancer Cells. *Int. J. Mol. Sci.* 18 (6), 1132. doi: 10.3390/ijms18061132

Hu, Y. M., Yu, Z. L., and Fong, W. F. (2011). Stereoselective biotransformation of timosaponin A-III by Saccharomyces cerevisiae. *J. Microbiol. Biotechnol.* 21 (6), 582–589. doi: 10.4014/jmb.1101.12041

Jaszai, J., and Schmidt, M. H. H. (2019). Trends and Challenges in Tumor Anti-Angiogenic Therapies. *Cells* 8 (9), 1102. doi: 10.3390/cells8091102

Jiang, W., Guo, J., Xue, R., Zhu, K., Li, Z., Chen, M., et al. (2014). Anti-depressive activities and biotransformation of timosaponin B-III and its derivatives. *Nat. Prod. Res.* 28 (18), 1446–1453. doi: 10.1080/14786419.2014.910663

Jorquera, P. A., Anderson, L., and Tripp, R. A. (2016). Understanding respiratory syncytial virus (RSV) vaccine development and aspects of disease pathogenesis. *Expert Rev. Vaccines* 15 (2), 173–187. doi: 10.1586/14760584.2016.1115353

Joung, U., Jang, J.-E., Nam, J.-W., Yoo, J., Young, M., Son, H., et al. (2011). Anti-respiratory syncytial virus (RSV) activity of timosaponin A-III from the rhizomes of Anemarrhena asphodeloides. *J. Med. Plant Res.* 5, 1062–1065. doi: 10.1002/cmdc.201000444

Jung, O., and Lee, S. Y. (2019). Synergistic anticancer effects of timosaponin AIII and ginsenosides in MG63 human osteosarcoma cells. *J. Ginseng Res.* 43 (3), 488–495. doi: 10.1016/j.jgr.2018.11.002

Jung, O., Lee, J., Lee, Y. J., Yun, J. M., Son, Y. J., Cho, J. Y., et al. (2016). Timosaponin AIII inhibits migration and invasion of A549 human non-small-cell lung cancer cells *via* attenuations of MMP-2 and MMP-9 by inhibitions of ERK1/2, Src/FAK and beta-catenin signaling pathways. *Bioorg. Med. Chem. Lett.* 26 (16), 3963–3967. doi: 10.1016/j.bmcl.2016.07.004

Kang, Y. J., Chung, H. J., Nam, J. W., Park, H. J., Seo, E. K., Kim, Y. S., et al. (2011). Cytotoxic and antineoplastic activity of timosaponin A-III for human colon cancer cells. *J. Nat. Prod.* 74 (4), 701–706. doi: 10.1021/np1007735

Kashiwagi, H., Yuhki, K. I., Imamichi, Y., Kojima, F., Kumei, S., Tasaki, Y., et al. (2019). Prostaglandin F2alpha Facilitates Platelet Activation by Acting on Prostaglandin E2 Receptor Subtype EP3 and Thromboxane A2 Receptor TP in Mice. *Thromb. Haemost.* 119 (8), 1311–1320. doi: 10.1055/s-0039-1688906

Katz, B., Trope, C. G., Reich, R., and Davidson, B. (2015). MicroRNAs in Ovarian Cancer. *Hum. Pathol.* 46 (9), 1245–1256. doi: 10.1016/j.humpath.2015.06.013

Kim, C., and Kim, B. (2018). Anti-Cancer Natural Products and Their Bioactive Compounds Inducing ER Stress-Mediated Apoptosis: A Review. *Nutrients* 10 (8), 1021. doi: 10.3390/nu10081021

Kim, H. J., Park, S. R., and Jang, Y. P. (2014). Extraction-free *in situ* derivatisation of timosaponin AIII using direct analysis in real time TOF/MS. *Phytochem. Anal.* 25 (4), 373–377. doi: 10.1002/pca.2488

Kim, K. M., Im, A. R., Kim, S. H., Hyun, J. W., and Chae, S. (2016). Timosaponin AIII inhibits melanoma cell migration by suppressing COX-2 and *in vivo* tumor metastasis. *Cancer Sci.* 107 (2), 181–188. doi: 10.1111/cas.12852

Kim, K. M., Im, A. R., Park, S. K., Shin, H. S., and Chae, S. W. (2019a). Protective Effects of Timosaponin AIII against UVB-Radiation Induced Inflammation and DNA Injury in Human Epidermal Keratinocytes. *Biol. Pharm. Bull.* 42 (9), 1524–1531. doi: 10.1248/bpb.b19-00222

Kim, Y., Kim, K. H., Lee, I. S., Park, J. Y., Na, Y. C., Chung, W. S., et al. (2019b). Apoptosis and G2/M cell cycle arrest induced by a timosaponin A3 from Anemarrhena asphodeloides Bunge on AsPC-1 pancreatic cancer cells. *Phytomedicine* 56, 48–56. doi: 10.1016/j.phymed.2018.08.006

Kimura, M., Kimura, I., and Chem, F. J. (1996). Combined potentiating effect of byakko-ka-ninjin-to, its constituents, rhizomes of Anemarrhena asphodeloides, tomosaponin A-III, and calcium on pilocarpine-induced saliva secretion in streptozocin-diabetic mice. *Biol. Pharm. Bull.* 19 (7), 926–931. doi: 10.1248/bpb.19.926

King, F. W., Fong, S., Griffin, C., Shoemaker, M., Staub, R., Zhang, Y. L., et al. (2009). Timosaponin AIII is preferentially cytotoxic to tumor cells through inhibition of mTOR and induction of ER stress. *PloS One* 4 (9), 0007283. doi: 10.1371/journal.pone.0007283

Kuang, W., Deng, Q., Deng, C., Li, W., Shu, S., and Zhou, M. (2017). Hepatocyte growth factor induces breast cancer cell invasion *via the* PI3K/Akt and p38 MAPK signaling pathways to up-regulate the expression of COX2. *Am. J. Transl. Res.* 9 (8), 3816–3826.

Kudryavtseva, A. V., Krasnov, G. S., Dmitriev, A. A., Alekseev, B. Y., Kardymon, O. L., Sadritdinova, A. F., et al. (2016). Mitochondrial dysfunction and oxidative stress in aging and cancer. *Oncotarget* 7 (29), 44879–44905. doi: 10.18632/oncotarget.9821

Lan, C. E. (2019). Effects and interactions of increased environmental temperature and UV radiation on photoageing and photocarcinogenesis of the skin. *Exp. Dermatol.* 1, 23–27. doi: 10.1111/exd.13818

Lee, B., Jung, K., and Kim, D. H. (2009). Timosaponin AIII, a saponin isolated from Anemarrhena asphodeloides, ameliorates learning and memory deficits in mice. *Pharmacol. Biochem. Behav.* 93 (2), 121–127. doi: 10.1016/j.pbb.2009.04.021

Lee, B., Trinh, H. T., Jung, K., Han, S. J., and Kim, D. H. (2010). Inhibitory effects of steroidal timosaponins isolated from the rhizomes of Anemarrhena asphodeloides against passive cutaneous anaphylaxis reaction and pruritus. *Immunopharmacol. Immunotoxicol.* 32 (3), 357–363. doi: 10.3109/08923970903383889

Li, L., Huang, T., Lan, C., Ding, H., Yan, C., and Dou, Y. (2019). Protective effect of polysaccharide from Sophora japonica L. flower buds against UVB radiation in a human keratinocyte cell line (HaCaT cells). *J. Photochem. Photobiol. B.* 191, 135–142. doi: 10.1016/j.jphotobiol.2018.12.001

Lim, S. M., Jeong, J. J., Kang, G. D., Kim, K. A., Choi, H. S., and Kim, D. H. (2015). Timosaponin AIII and its metabolite sarsasapogenin ameliorate colitis in mice by inhibiting NF-kappaB and MAPK activation and restoring Th17/Treg cell balance. *Int. Immunopharmacol.* 25 (2), 493–503. doi: 10.1016/j.intimp.2015.02.016

Liu, Y., Pu, Y., Zhang, T., Ding, Y., Wang, B., and Cai, Z. (2013). Rapid and Sensitive Determination of Timosaponin AIII in Rat Plasma by LC-MS/MS and Its Pharmacokinetic Application. *Int. J. Mol. Sci.* 14 (2), 3656–3670. doi: 10.3390/ijms14023656

Liu, Z., Dong, X., Ding, X., Chen, X., Lv, L., Li, Y., et al. (2013). Comparative pharmacokinetics of timosaponin B-II and timosaponin A-III after oral administration of Zhimu-Baihe herb-pair, Zhimu extract, free timosaponin B-II and free timosaponin A-III to rats. *J. Chromatogr. B. Analyt. Technol. BioMed. Life Sci.* 926, 28–35. doi: 10.1016/j.jchromb.2013.03.003

Liu, Q., Tong, D., Liu, G., Gao, J., Wang, L. A., Xu, J., et al. (2018). Metformin Inhibits Prostate Cancer Progression by Targeting Tumor-Associated Inflammatory Infiltration. *Clin. Cancer Res.* 24 (22), 5622–5634. doi: 10.1158/1078-0432.CCR-18-0420

Liu, Y., Liang, G., Wang, H., and Liu, Z. (2019). MicroRNA-129-5p suppresses proliferation, migration and invasion of retinoblastoma cells through PI3K/AKT signaling pathway by targeting PAX6. *Pathol. Res. Pract.* 215 (12), 4. doi: 10.1016/j.prp.2019.152641

Lok, C. N., Sy, L. K., Liu, F., and Che, C. M. (2011). Activation of autophagy of aggregation-prone ubiquitinated proteins by timosaponin A-III. *J. Biol. Chem.* 286 (36), 31684–31696. doi: 10.1074/jbc.M110.202531

Lu, L., Liu, Y., Ding, Y., Hou, J., Zhang, Y., Xue, H., et al. (2016). Preparation of highly purified timosaponin AIII from rhizoma anemarrhenae through an enzymatic method combined with preparative liquid chromatography. *Nat. Prod. Res.* 30 (20), 2364–2367. doi: 10.1080/14786419.2016.1169416

Lu, L., Ding, Y., Zhang, Y., Ho, R. J., Zhao, Y., Zhang, T., et al. (2018). Antibody-modified liposomes for tumor-targeting delivery of timosaponin AIII. *Int. J. Nanomed.* 13, 1927–1944. doi: 10.2147/IJN.S153107

Lyu, Y., Xiao, Q., Yin, L., Yang, L., and He, W. (2019). Potent delivery of an MMP inhibitor to the tumor microenvironment with thermosensitive liposomes for the suppression of metastasis and angiogenesis. *Signal Transduct Target Ther.* 4 (26), 019–0054. doi: 10.1038/s41392-019-0054-9

MarElia, C. B., Sharp, A. E., Shemwell, T. A., Clare Zhang, Y., and Burkhardt, B. R. (2018). Anemarrhena asphodeloides Bunge and its constituent timosaponin-AIII induce cell cycle arrest and apoptosis in pancreatic cancer cells. *FEBS Open Bio* 8 (7), 1155–1166. doi: 10.1002/2211-5463.12457

Merchant, N., Nagaraju, G. P., Rajitha, B., Lammata, S., Jella, K. K., Buchwald, Z. S., et al. (2017). Matrix metalloproteinases: their functional role in lung cancer. *Carcinogenesis* 38 (8), 766–780. doi: 10.1093/carcin/bgx063

Mohan, S., and Gupta, D. (2019). Role of Nrf2-antioxidant in radioprotection by root extract of Inula racemosa. *Int. J. Radiat. Biol.* 95 (8), 1122–1134. doi: 10.1080/09553002.2019.1607607

Nho, K. J., Chun, J. M., and Kim, H. K. (2016). Induction of mitochondria-dependent apoptosis in HepG2 human hepatocellular carcinoma cells by timosaponin A-III. *Environ. Toxicol. Pharmacol.* 45, 295–301. doi: 10.1016/j.etap.2016.06.012

Nian, S. H., Li, H. J., Liu, E. H., and Li, P. (2017). Comparison of alpha-glucosidase inhibitory effect and bioactive constituents of Anemarrhenae Rhizoma and Fibrous Roots. *J. Pharm. BioMed. Anal.* 145, 195–202. doi: 10.1016/j.jpba.2017.06.039

Norrby, K. (2006). In vivo models of angiogenesis. *J. Cell Mol. Med.* 10 (3), 588–612. doi: 10.1111/j.1582-4934.2006.tb00423.x

Oboudiyat, C., Glazer, H., Seifan, A., Greer, C., and Isaacson, R. S. (2013). Alzheimer's disease. *Semin. Neurol.* 33 (4), 313–329. doi: 10.1055/s-0033-1359319

Pan, X., Han, H., Wang, L., Yang, L., Li, R., Li, Z., et al. (2011). Nitidine Chloride inhibits breast cancer cells migration and invasion by suppressing c-Src/FAK associated signaling pathway. *Cancer Lett.* 313 (2), 181–191. doi: 10.1016/j.canlet.2011.09.001

Pan, H. J., Nie, X. Q., Liu, D., and Bian, K. (2013). [Effects of four kinds of Chinese medicine monomer on growth of PANC-1 xenograft tumor and studying of molecular mechanism]. *Zhongguo Zhong Yao Za Zhi* 38 (2), 245–248. doi: 10.4268/cjcmm20130220

Park, W., Park, S., Song, G., and Lim, W. (2019). Inhibitory Effects of Osthole on Human Breast Cancer Cell Progression *via* Induction of Cell Cycle Arrest, Mitochondrial Dysfunction, and ER Stress. *Nutrients* 11 (11), 2777. doi: 10.3390/nu11112777

Qadir, M. I., and Faheem, A. (2017). miRNA: A Diagnostic and Therapeutic Tool for Pancreatic Cancer. *Crit. Rev. Eukaryot. Gene Expr.* 27 (3), 197–204. doi: 10.1615/CritRevEukaryotGeneExpr.2017019494

Qiu, Z., Wang, X., Shi, Y., and Da, M. (2019). miR-129-5p suppresses proliferation, migration, and induces apoptosis in pancreatic cancer cells by targeting PBX3. *Acta Biochim. Biophys. Sin.* 51 (10), 997–1007. doi: 10.1093/abbs/gmz096

Shay, G., Lynch, C. C., and Fingleton, B. (2015). Moving targets: Emerging roles for MMPs in cancer progression and metastasis. *Matrix Biol.* 46, 200–206. doi: 10.1016/j.matbio.2015.01.019

Shi, Y., Gong, W., Lu, L., Wang, Y., and Ren, J. (2019). Upregulation of miR-129-5p increases the sensitivity to Taxol through inhibiting HMGB1-mediated cell autophagy in breast cancer MCF-7 cells. *Braz. J. Med. Biol. Res.* 52 (11), e8657. doi: 10.1590/1414-431x20198657

Shin, M. S., Kim, S. K., Kim, Y. S., Kim, S. E., Ko, I. G., Kim, C. J., et al. (2008). Aqueous extract of Anemarrhena rhizome increases cell proliferation and neuropeptide Y expression in the hippocampal dentate gyrus on streptozotocin-induced diabetic rats. *Fitoterapia* 79 (5), 323–327. doi: 10.1016/j.fitote.2008.02.014

Siegfried, J. M., Gubish, C. T., Rothstein, M. E., Queiroz de Oliveira, P. E., and Stabile, L. P. (2007). Signaling pathways involved in cyclooxygenase-2 induction by hepatocyte growth factor in non small-cell lung cancer. *Mol. Pharmacol.* 72 (3), 769–779. doi: 10.1124/mol.107.034215

Smith, K. (2014). Mental health: a world of depression. *Nature* 515 (7526), 181. doi: 10.1038/515180a

Song, X. Y., Han, F. Y., Chen, J. J., Wang, W., Zhang, Y., Yao, G. D., et al. (2019). Timosaponin AIII, a steroidal saponin, exhibits anti-tumor effect on taxol-resistant cells *in vitro* and *in vivo*. *Steroids* 146, 57–64. doi: 10.1016/j.steroids.2019.03.009

Sun, Y. G., Du, Y. F., Yang, K., Chang, L., Cao, L., Ren, Y. P., et al. (2013). A comparative study on the pharmacokinetics of a traditional Chinese herbal preparation with the single herb extracts in rats by LC-MS/MS method. *J. Pharm. BioMed. Anal.* 82, 34–43. doi: 10.1016/j.jpba.2013.03.022

Sy, L. K., Yan, S. C., Lok, C. N., Man, R. Y., and Che, C. M. (2008). Timosaponin A-III induces autophagy preceding mitochondria-mediated apoptosis in HeLa cancer cells. *Cancer Res.* 68 (24), 10229–10237. doi: 10.1158/0008-5472.CAN-08-1983

Tang, Y. H., Sun, Z. L., Fan, M. S., Li, Z. X., and Huang, C. G. (2012). Anti-diabetic effects of TongGuanWan, a Chinese traditional herbal formula, in C57BL/KsJ-db/db mice. *Planta Med.* 78 (1), 18–23. doi: 10.1055/s-0031-1280268

Tang, Z., Li, G., Yang, J., Duan, J., Qian, D., Guo, J., et al. (2015). Anemarrhena asphodeloides Non-Steroidal Saponin Components Alter the Pharmacokinetic Profile of Its Steroidal Saponins in Rat. *Molecules* 20 (7), 11777–11792. doi: 10.3390/molecules200711777

Tomlinson, A., Efthimiou, O., Boaden, K., New, E., Mather, S., Salanti, G., et al. (2019). Side effect profile and comparative tolerability of 21 antidepressants in the acute treatment of major depression in adults: protocol for a network meta-analysis. *Evid. Based Ment. Health* 22 (2), 61–66. doi: 10.1136/ebmental-2019-300087

Tong, D., Liu, Q., Wang, L. A., Xie, Q., Pang, J., Huang, Y., et al. (2018). The roles of the COX2/PGE2/EP axis in therapeutic resistance. *Cancer Metastasis Rev.* 37 (2-3), 355–368. doi: 10.1007/s10555-018-9752-y

Tsai, C. H., Yang, C. W., Wang, J. Y., Tsai, Y. F., Tseng, L. M., King, K. L., et al. (2013). Timosaponin AIII Suppresses Hepatocyte Growth Factor-Induced Invasive Activity through Sustained ERK Activation in Breast Cancer MDA-MB-231 Cells. *Evid. Based Complement Alternat. Med.* 421051 (10), 25. doi: 10.1155/2013/421051

Tundis, R., Bonesi, M., Menichini, F., and Loizzo, M. R. (2016). Recent Knowledge on Medicinal Plants as Source of Cholinesterase Inhibitors for the Treatment of Dementia. *Mini Rev. Med. Chem.* 16 (8), 605–618. doi: 10.2174/1389557515666150709104731

Vasan, N., Baselga, J., and Hyman, D. M. (2019). A view on drug resistance in cancer. *Nature* 575 (7782), 299–309. doi: 10.1038/s41586-019-1730-1

Viallard, C., and Larrivee, B. (2017). Tumor angiogenesis and vascular normalization: alternative therapeutic targets. *Angiogenesis* 20 (4), 409–426. doi: 10.1007/s10456-017-9562-9

Wang, Y. Z., Feng, B., Huang, H. Z., Kang, L. P., Cong, Y., Zhou, W. B., et al. (2010). Glucosylation of steroidal saponins by cyclodextrin glucanotransferase. *Planta Med.* 76 (15), 1724–1731. doi: 10.1055/s-0030-1249938

Wang, N., Feng, Y., Zhu, M., Siu, F. M., Ng, K. M., and Che, C. M. (2013). A novel mechanism of XIAP degradation induced by timosaponin AIII in hepatocellular carcinoma. *Biochim. Biophys. Acta* 12 (10), 29. doi: 10.1016/j.bbamcr.2013.07.018

Wang, Y., Dan, Y., Yang, D., Hu, Y., Zhang, L., Zhang, C., et al. (2014). The genus Anemarrhena Bunge: A review on ethnopharmacology, phytochemistry and pharmacology. *J. Ethnopharmacol.* 153 (1), 42–60. doi: 10.1016/j.jep.2014.02.013

Wang, Y., Xu, L., Lou, L. L., Song, S. J., Yao, G. D., Ge, M. Y., et al. (2017). Timosaponin AIII induces apoptosis and autophagy in human melanoma A375-S2 cells. *Arch. Pharm. Res.* 40 (1), 69–78. doi: 10.1007/s12272-016-0763-3

Wang, H., Dong, R., Fan, W. W., Zheng, X. C., Li, A. M., and Wang, W. D. (2019). Timosaponin AIII induces autophagy of Tcell acute lymphoblastic leukemia Jurkat cells *via* inhibition of the PI3K/Akt/mTOR pathway. *Oncol. Rep.* 41 (5), 2937–2944. doi: 10.3892/or.2019.7072

Webers, A., Heneka, M. T., and Gleeson, P. A. (2019). The role of innate immune responses and neuroinflammation in amyloid accumulation and progression of Alzheimer's disease. *Immunol. Cell Biol.* 26 (10), 12301. doi: 10.1111/imcb.12301

Wu, Z. T., Qi, X. M., Sheng, J. J., Ma, L. L., Ni, X., Ren, J., et al. (2014). Timosaponin A3 induces hepatotoxicity in rats through inducing oxidative stress and down-regulating bile acid transporters. *Acta Pharmacol. Sin.* 35 (9), 1188–1198. doi: 10.1038/aps.2014.65

Xie, Y., Zhou, X., Pei, H., Chen, M. C., Sun, Z. L., Xue, Y. R., et al. (2018). Metabolism, pharmacokinetics, and hepatic disposition of xanthones and saponins on Zhimu treatments for exploratively interpreting the discrepancy between the herbal safety and timosaponin A3-induced hepatotoxicity. *Acta Pharmacol. Sin.* 39 (12), 1923–1934. doi: 10.1038/s41401-018-0012-z

Yang, B. Y., Zhang, J., Liu, Y., and Kuang, H. X. (2016). Steroidal Saponins from the Rhizomes of Anemarrhena asphodeloides. *Molecules* 21 (8), 1075. doi: 10.3390/molecules21081075

Yang, B., Liu, Z., Wang, Q., Chai, Y., and Xia, P. (2018). Pharmacokinetic comparison of seven major bioactive components in normal and depression model rats after oral administration of Baihe Zhimu decoction by liquid chromatography-tandem mass spectrometry. *J. Pharm. BioMed. Anal.* 148, 119–127. doi: 10.1016/j.jpba.2017.09.031

Yeung, J., Li, W., and Holinstat, M. (2018). Platelet Signaling and Disease: Targeted Therapy for Thrombosis and Other Related Diseases. *Pharmacol. Rev.* 70 (3), 526–548. doi: 10.1124/pr.117.014530

Yuan, Y. L., Guo, C. R., Cui, L. L., Ruan, S. X., Zhang, C. F., Ji, D., et al. (2015). Timosaponin B-II ameliorates diabetic nephropathy *via* TXNIP, mTOR, and NF-kappaB signaling pathways in alloxan-induced mice. *Drug Des. Devel. Ther.* 9, 6247–6258. doi: 10.2147/DDDT.S96435

Yun, E. J., Song, K. S., Shin, S., Kim, S., Heo, J. Y., Kweon, G. R., et al. (2016). Docosahexaenoic acid suppresses breast cancer cell metastasis by targeting matrix-metalloproteinases. *Oncotarget* 7 (31), 49961–49971. doi: 10.18632/oncotarget.10266

Zhang, X. L., Wang, L., Xiong, L., Huang, F. H., and Xue, H. (2017). Timosaponin B-III exhibits antidepressive activity in a mouse model of postpartum depression by the regulation of inflammatory cytokines, BNDF signaling and synaptic plasticity. *Exp. Ther. Med.* 14 (4), 3856–3861. doi: 10.3892/etm.2017.4930

Zhao, N., Li, J., Li, L., Niu, X. Y., Jiang, M., He, X. J., et al. (2015). Molecular network-based analysis of guizhi-shaoyao-zhimu decoction, a TCM herbal formula, for treatment of diabetic peripheral neuropathy. *Acta Pharmacol. Sin.* 36 (6), 716–723. doi: 10.1038/aps.2015.15

Zhou, J., Zhang, L., Wang, M., Zhou, L., Feng, X., Yu, L., et al. (2019). CPX Targeting DJ-1 Triggers ROS-induced Cell Death and Protective Autophagy in Colorectal Cancer. *Theranostics* 9 (19), 5577–5594. doi: 10.7150/thno.34663

Zhou, Z. Y., Zhao, W. R., Xiao, Y., Zhou, X. M., Huang, C., Shi, W. T., et al. (2020). Antiangiogenesis effect of timosaponin AIII on HUVECs *in vitro* and zebrafish embryos *in vivo*. *Acta Pharmacol. Sin.* 41 (2), 260–269. doi: 10.1038/s41401-019-0291-z

Conflict of Interest: The authors declare that the research was conducted in the absence of any commercial or financial relationships that could be construed as a potential conflict of interest.

Copyright © 2020 Lin, Zhao, Shi, Zhang, Zhang, Ding, Chen, Tang and Zhou. This is an open-access article distributed under the terms of the Creative Commons Attribution License (CC BY). The use, distribution or reproduction in other forums is permitted, provided the original author(s) and the copyright owner(s) are credited and that the original publication in this journal is cited, in accordance with accepted academic practice. No use, distribution or reproduction is permitted which does not comply with these terms.

frontiers in Pharmacology

ORIGINAL RESEARCH
published: 26 June 2020
doi: 10.3389/fphar.2020.00946

Treating Different Diseases With the Same Method—A Traditional Chinese Medicine Concept Analyzed for Its Biological Basis

Xing Zhai[1], *Xi Wang*[2], *Li Wang*[1], *Linlin Xiu*[3]*, *Weilu Wang*[3] *and Xiaohan Pang*[3]

[1] School of Management, Beijing University of Chinese Medicine, Beijing, China, [2] College of Humanities, Beijing University of Chinese Medicine, Beijing, China, [3] College of Traditional Chinese Medicine, Beijing University of Chinese Medicine, Beijing, China

OPEN ACCESS

Edited by:
Hai Yu Xu,
China Academy of Chinese Medical Sciences, China

Reviewed by:
Yulong Xu,
Henan University of Traditional Chinese Medicine, China
Yong Wang,
Beijing University of Chinese Medicine, China

***Correspondence:**
Linlin Xiu
xiulinlin1231@126.com

Specialty section:
This article was submitted to Ethnopharmacology, a section of the journal Frontiers in Pharmacology

Received: 31 March 2020
Accepted: 10 June 2020
Published: 26 June 2020

Citation:
Zhai X, Wang X, Wang L, Xiu L, Wang W and Pang X (2020) Treating Different Diseases With the Same Method—A Traditional Chinese Medicine Concept Analyzed for Its Biological Basis. Front. Pharmacol. 11:946. doi: 10.3389/fphar.2020.00946

Introduction: The fundamental theory of traditional Chinese medicine (TCM) implies that when different diseases have the same pathogen, the syndromes of these individual diseases will be the same. "Treating different diseases with the same method" is a TCM principle suggesting that when different diseases have similar pathological changes during different stages of their development, the same method of treatment can be applied. Our study aims to analyze the concept "treating different diseases with the same method" from a molecular perspective, in order to clarify its biological basis and to objectively standardize future TCM syndrome research.

Objective: The TCM syndromes Qi deficiency and blood stasis have similar pathogenesis in relation to coronary heart disease (CHD) and stroke. We aim to use big data technology and complex network theory to mine the genes specifically relevant to these TCM syndromes. This study aims to explore the correlation between the biological indicators of CHD and stroke from a scientific perspective.

Methods: Mining the relevant neuroendocrine-immune (NEI) genes by means of gene entity recognition, complex network construction, network integration, and decomposition to categorize relevant syndrome terms and establish a digital dictionary of gene specifically related to individual diseases. We analyzed the biological basis of "treating different diseases with the same method" from a molecular level using the TCMIP v2.0 platform in order to categorize the TCM syndromes most relevant to CHD and stroke.

Results: We found 46 genes were involved in the TCM syndromes of Qi deficiency and blood stasis of CHD and stroke. The same genes and their molecular mechanism also appeared to be in close relation to inflammatory response, apoptosis, and proliferation.

Conclusion: By using information extraction and complex network technology, we discovered the biological indicators of the TCM syndromes Qi deficiency and blood stasis of CHD and stroke. In the era of big data, our results can provide a new method for the researchers of TCM syndrome differentiation, as well as an effective and specific methodology for standardization of TCM.

Keywords: treating different diseases with the same method, traditional Chinese medicine, information extraction, complex network, TCMIP v2.0

PREFACE

"Treating different diseases with the same treatment" is an important part of the fundamental theory of TCM, embodying the spirit of "treatment by syndrome differentiation". A similar point of view can be seen in modern medicine where it is academically accepted that certain disease mechanisms lead to various diseases. For example, insulin resistance exists in obesity, diabetes, dyslipidemia, and other metabolic diseases. Another example is that the inflammatory response mechanism can be found in infections, atherosclerosis, glomerulosclerosis, hypertension, and ischemia-reperfusion of heart and brain. The knowledge that certain diseases have shared pathological mechanisms has a significant impact on the study of pathology both in modern medicine and TCM. From their respective perspectives both TCM and modern medicine acknowledge the importance of shared pathological mechanism of diseases. Therefore, the concept of "treating different diseases with the same method" can be seen as a focal point of the integration and unification of TCM and modern medicine (Xuezhong et al., 2004).

In the era of big data, the acknowledgment of TCM theory is closely related to informatics. The standardization and digitalization of TCM diagnosis need information and big data to improve the research. Information technology is needed to make a breakthrough in the fundamental research of TCM syndrome differentiation and biology. Getting research results published is common procedure for any scholar to have their research known and acknowledged, TCM is no exception. To this day, a large number of research documents related to TCM are stored in WOS, PubMed, and other international medicine databases. However, only a small amount of these papers and their knowledge can be found by the means of Artificial Intelligence (AI) and algorithms and has to be individually searched and found by humans. It will be of great significance for the medical society to discover the relationship between TCM syndrome differentiation and modern molecular biology. We aim to discover and compare a vast number of medical journals and texts to explore "treating different diseases with the same method" from the perspective of microbiology by using information technology (including machine learning, text mining, complex network, etc.)

To begin our research of "treating different diseases with the same method", we chose diseases and syndromes with a high incidence rate, complex treatment and which have a major impact on the health of the general population. With the rapid development of the Chinese national economy peoples living conditions and lifestyles have changed dramatically, ultimately resulting in a shift of the most common diseases. The incidence rate of coronary heart disease (CHD) and stroke is increasing. According to the China Health and Family Planning Statistical Yearbook, released by the national health and family planning commission, stroke and CHD have become the leading cause of death among Chinese citizens. Additionally, a WHO survey points out that the incidence rate of stroke is ranked first among diseases in China and is now trending toward younger parts of the population. How to effectively prevent and treat these two diseases has become a key point in the medical field.

Qi deficiency and blood stasis are important syndromes in the diagnosis and treatment of TCM. These two TCM syndromes are common in CHD, stroke, tumor, hypertension, cerebral infarction, and other multi-system diseases. To treat the above diseases, TCM doctors use prescriptions to invigorate Qi and activate blood. For example, *Buyang Huanwu Decoction* is a commonly used formula for the treatment of the syndromes of Qi deficiency and blood stasis, which in turn has a good effect on CHD and stroke. This principle of treating different diseases in their respective stage of development with the same method principle is the essence of "treating different diseases with the same method". In this paper, we chose the common mechanism of CHD and stroke as our focal point to discover the biological basis of "treating different diseases with the same method". This paper is divided into four chapters. Chapter 1, Introduction of research in China and abroad. Chapter 2, Introduction of data and methods used in this study. Chapter 3, Study results. Chapter 4, Summarization of research and suggestions for future research.

LITERATURE REVIEW

Information Extraction (IE) and Its Applications in the Biomedical Field

IE refers to the process of extracting, integrating and processing relevant information from existing data in order to store the specific information in a new data structure for future use and consultation (Bin, 2002). In IE, the uttermost important is to discover and extract the relationship between various entries. At present, relationship extraction generally applies to relationship extraction in dictionaries, as part of pattern matching and by means of machine learning. The dictionary based approach matches the words in the corpus with those in the professional dictionary in order to identify the words

and/or their relationships. By matching the relevant literature and gene dictionaries related to Qi deficiency and blood stasis syndromes of CHD, Zhao (Xing et al., 2015) identified the genes most relevant to these syndromes. Using relationship extractions based on dictionaries is simple and fast, but in the era of big data, the speed that information updated is even faster leading to dictionaries lacking behind the current information. Thus it can be understood that this method is not suitable for scenarios where the data of dictionaries is updated on a regular basis.

Relation extraction of pattern matching is based on the observation and analysis of entries by linguistic experts to define the specific rules and extract the correlation of biomedical entries. For example, in 2001, Ono et al. (2001) created an extraction model base on relations between protein-protein interaction (PPI) relationships by observing regular expressions, shallow syntactic patterns, and pattern matching method. Although methods based on pattern matching can extract the relationship between biomedical entities more accurately, it is difficult to identify the relationships outside of the defined set of rules. Therefore, the accuracy is often high but at the same time the recall rate is low.

Based on machine learning, the relevant features and parameters are calculated from the sample data and following used to identify and establish the new model. Machine learning can be further divided into eigenvector based methods and kernel based methods. Feature vector based method, which belongs to supervised machine learning and eigenvector based method, is a commonly used machine learning method applied in biomedical entity relationship extraction. Feature vector based method is used to change the relation of linguistic information into plane features, and following to create a high-dimensional map in vector space. This is done in order to translate information of the natural language into recognizable vector classifiers. For example, using support vector machine (SVM) models Xiao et al. (2005) extracted PPI relationship by applying a combination of lexical, syntactic, and semantic features in combination with maximum entropy classifiers. Although feature vector based relation extraction method is flexible and has good performance, the spectrum of feature selection often directly determines the extent of relation extraction. At the same time, the quantity and quality of labeled corpus usually determines the performance of extraction. The core function is used to calculate the similarity of two candidate relationship instances in potential vector space. For example, Bunescu and Mooney (2005a) proposed the idea of applying kernel function method to extract protein relations. Based on kernel function they managed to isolate PPI relationships by extracting the dependency pathways between specific proteins. The kernel based method has better performance because it has more flexibility to extract correlating information between entities. However, per definition kernel function has a direct impact on the result of relation extraction. It can be seen that there is a common problem in relation extraction methods based on machine learning. It gives rise to similar issues, whether using eigenvector or kernel function for relation extraction. Due to the need of large quantity of labeled corpora the quality of these functions will deteriorate along with the quality of the labels.

Use of Complex Network in Biomedical Research

The complex network theory is a method based on graph theory and complex system theory. Large-scale nodes, complex network structures, and dynamic spatiotemporal evolution of networks are the main characteristics of complex network. They coincide with the characteristics of data complexity, diversity, and the dynamic changes of informatics. Applying the theory and method of complex network to data analysis helps analysts to pinpoint what exact problems should be researched, and as a whole to improve the efficiency of their analytic tasks.

Complex network theory is not only applied to climate, politics, economy, society, military, and management, but also widely used in biomedical research. At present, the research of complex network in the biomedical field mainly focuses on the location of disease gene, disease-related sub-network recognition, network-based disease control research and drug target predictions. For example, Lim et al. (2006) used pathway information to discover pathogenic proteins. Deng et al. (2004) predicted a drug target method based on network topology. Artzy-Randrup et al. (2004) constructed the pin sub-network of Huntington's disease (HTT) and by these means discovered a new HTT pathogenic gene

Regarding TCM research, Li (Li et al., 2007) applied the information technology of text mining to prove that "disease" and "syndrome" have the possibility of a "disease syndrome combination" at the level of biological networks. Zhou et al. (Xuezhong et al., 2004) processed and integrated the database of TCM literature to find the gene related to kidney Yang deficiency and thereby provided an effective way to understand the function of this specific gene and its significance regarding the TCM syndrome. From the perspective of "interaction network function", Li (Shao, 2007) explored and established the relevant method to apply computational system biology on TCM. He discovered through the excavation and research of the TCM syndromes of "cold and heat", diseases, and prescriptions that the biological network of somatic angiogenesis is closely related to the TCM concept of" collateral disease". Ding et al. (Fan et al., 2014) used network analysis method to study *Buyang Huanwu Decoction* from three aspects: chemical composition, target tissue, and related diseases to discover its potential in cancer treatment.

Since the 1970s, modern medicine has recognized the concept and interconnection of the neuro-endocrine-immune (NEI) systems. In 1973, Isaković and Janković (1973) firstly proposed the relationship between these three systems by injuring different parts off rat brains with bilateral symmetrical electrolysis and following observing their effects on lymphoid organs. The discovery and acknowledgment of NIE coincide with the overall concept advocated by TCM for thousands of years, and to a certain extent, it validates the theory of TCM, that has been developed through millennial of clinical practice. In 1990, Wang (Lan and Yusheng, 1990) firstly drew parallels between NEI network and

TCM theory. Afterward, more scholars have researched the connection between TCM theory and NEI network, such as the study of "cold and heat" syndromes (Ma et al., 2010) and the study of therapeutic mechanism of acupuncture (Ding et al., 2013). The key of "treating different diseases with the same method" is that although diseases are different, the syndromes can be the same. By using NEI network to explore the correlation between biological indicators of different diseases, we got a deeper understanding of TCM which assists to its modernization and internationalization.

Through the use of information technology in biomedical science, this TCM research has achieved good results. We still see the need for improvements. The main problems are as follows: 1) although there are many experiments of TCM using information technology, modern medicine and molecular biology most of them lack the effective combination of the mathematical modeling of precise result mining. This in turn leads to the biological significance of TCM syndromes and diseases being undiscovered. In other words, there are no clear indicators of the correlation between the perspectives of macro biology and microbiology in the research. 2) In the current research on biological networks the constructed networks are large and complex in scale. Due to the complexity of the network indicators, the results are difficult to analyze. There is no known method to compress networks and define the similarity between nodes ones the networks are compressed. We proposed to apply machine learning, information extraction and complex network technology to construct gene networks based on TCM syndromes, as well as use data mining by combining decomposition and combination throughout these networks. Our hypothesis is that by using these technologies to discover common genetic nodes through calculations, analysis and mining it will be possible to discover the genes specifically related to the syndromes of Qi deficiency and blood stasis of CHD and stroke.

Mesh (Medical Subject Headings) technology was used to mine the specific genes of NEI throughout PubMed database to construct the biological network. We also explored the mechanism of the concept "treating different diseases with the same method" from the perspective of microbiology. This has deepened the understanding of the theoretical system of TCM syndrome differentiation, and promoted the studies of TCM syndromes.

MATERIALS AND METHODS

This article was based on biomedical literature downloaded from http://www.ncbi.nlm.nih.gov/entrez/query.fcgi, including the two target syndromes. This was chosen due to vast PubMed database managed by the United States National Library of Medicine and the National Institutes of Health, providing free catalogs of biomedical papers worldwide. With the increasing internationalization of TCM research, the biomedical literature in PubMed contains a large number of articles related to Traditional Chinese medicine (A total of 148,000 articles related to Traditional Chinese medicine dated from 2010 to 2020 found by searching the keywords "*Traditional Chinese medicine*", "*herbal medicine*", "*aspiration*" and "*prescriptions*"). These articles are valuable to TCM scientific research and innovation, TCM technological innovation and the understanding of the current situation of TCM clinical practice in and outside of China. The free and easy access to vast biomedical literature related to TCM and modern medicine is why we chose PubMed as our data source. In order to precisely mine the genetic data of the two target syndromes, and to improve the accuracy of the data mining, the author proposed a data mining model based on the combination of "network decomposition" and "symptom combination" to mine the NEI genetic data in PubMed database (Xing et al., 2015; Liu et al., 2019). Then, the author combined the results of the two methods to draw a final conclusion. The methods of mining are described below.

Network Decomposition

In order to reduce the complexity of network analysis, the network was divided into sub networks according to the network categories and the specific genes and their functions. Each sub network was individually analyzed and the results of each sub network were combined to find the genes related to the target syndromes. See **Figure 1**.

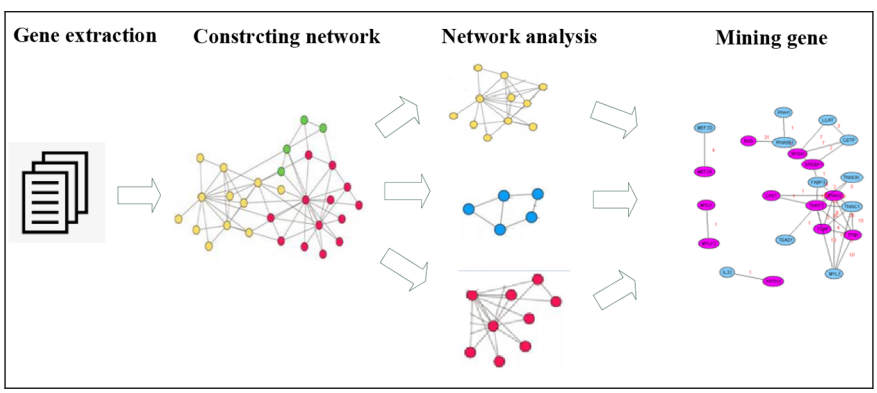

FIGURE 1 | Flow chart of network decomposition method.

Data Collection

According to the *Guidance Principle of Clinical Studies of New Drug of Traditional Chinese Medicine* (Xiao-yu, 2002), the terms of the target syndromes were selected. Then, two TCM experts weighted the rationality of these terms according to their personal clinical experiences to decisively determine the terms to be used in this paper. As the TCM terms chosen were all in Chinese and PubMed database in English, it was necessary to translate them into English. However, due to the specificity of TCM terminology many translated terms could not be searched in PubMed. Therefore, it was necessary to convert these TCM terms into corresponding modern medicine terminology. In this paper, Symmap database was used to finalize the translation of TCM terms into modern medicine terms. Symmap database (Wu et al., 2018) was developed by Chen Jian-xin, Professor of Beijing University of Chinese Medicine. Through Symmap and its classifications of internal molecular mechanism and external symptom, the database charted 1,717 TCM symptoms and allocated them to 961 modern medicine symptoms. For example, "red tongue" of TCM diagnosis is translated through Symmap database into "Glossitis" of western medicine (**Figure 2**).

The key terms were loaded into PubMed database according to the search format. We searched the Mesh subject terms and downloaded the literature summary. Following we downloaded the documents and converted them into a unified formation order to generate the corpus intended for mining.

Gene Information Extraction

According to the basis of this paper, the entity of NEI genes that needed extraction from the literature was relatively defined and had little change. For improvements of efficiency and accuracy of entity extraction we used a dictionary matching method. The downloaded documents were pre-processed, and following divided into independent sentences that were further segmented by using the *Jieba* word, a python segmentation package. After this process the separated words were matched with the key words of the NEI gene Dictionary. The NEI gene dictionary was downloaded from dbNEI (http://bioinfo.au.tsinghua.edu.cn/dbNEIweb/) A total of 1,435 NEI genes were downloaded and used for comparison (**Figure 3**).

Gene relationship extraction is used to identify the possible gene relationships in literature abstracts (In this paper it mainly refers to the gene relationships recognized in the abstracts). We found the relationships between genes and understood their potential usage through analysis and identification of the specific genes and their interrelations. We used sparse multi-instance learning algorithm (SMIL) (Wu et al., 2018) to extract gene relationships based on the summaries of previous relationship extraction algorithms. This approach can be applied to relationship extraction. By assessing whether or not a specific group of genes have interactions, and whether or not these interactions are of identical genes.

In this study, each grouping contained multiple relationships. If the relationship between two or more genes were observed, then the group was labeled positive. If no relationships between genes were observed, the package was labeled negative. E.g. A study has two genes that may be mentioned several times throughout the abstract, but generally speaking a specific relationship will only be mentioned once. Therefore, the information regarding these two specific genes will be relative sparse. We decided to use SMIL to extract the genetic relationship and avoid overlooking important information in the literature abstracts acquired from PubMed.

In addition to the data packages, "knowledge base" and "file data" are needed to extract relationships using SMIL algorithm. "File data" is a data source that contains data relations. "Knowledge

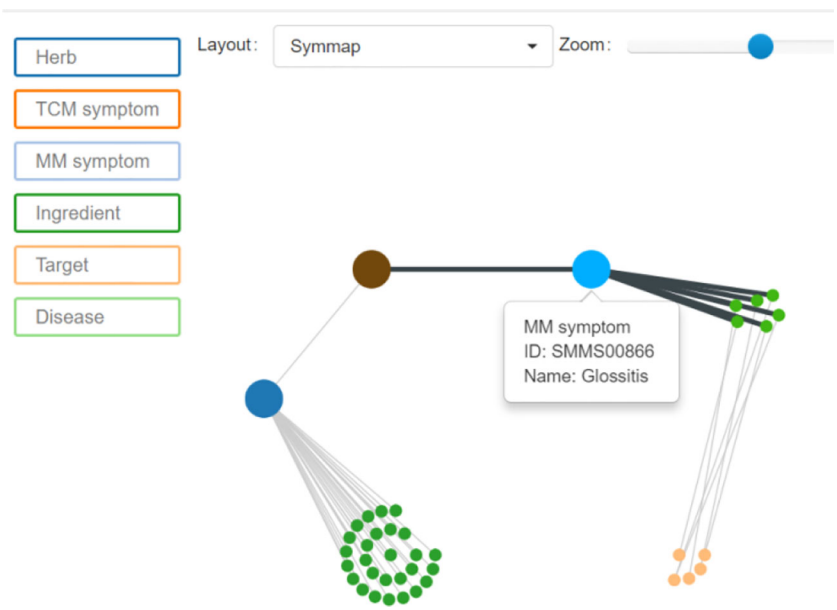

FIGURE 2 | Symmap query interface.

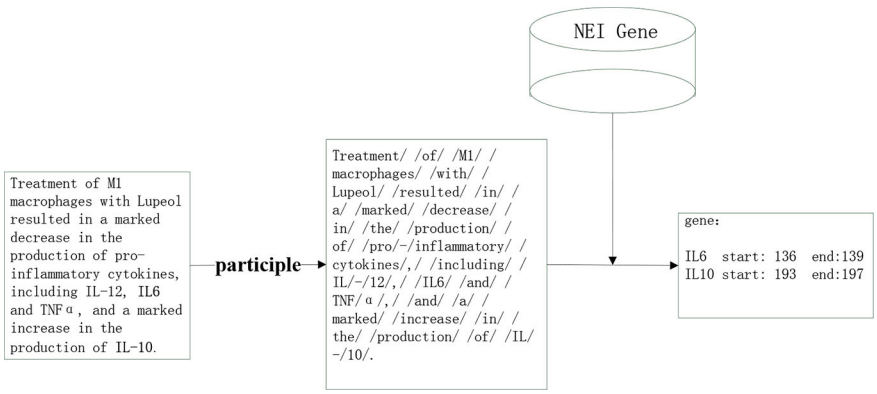

FIGURE 3 | Gene entity recognition.

base" has the ability to replace manual labeling of existing relationships. Therefore, the "knowledge base" must contain the exact same relationships as the relationships examined for extraction.

There are many industry databases about the relationship between genes in the field of bioinformatics. Therefore, to obtain the industry knowledge base was easy. After the comparative analysis of these specific gene databases, we finally decided to build a knowledge base from the string database. String database (http://string-db.org/) can analyze protein-protein interaction and includes 5,090 organisms. It not only contains the protein-protein interaction data known through validated experiments, but the database also includes predictions of unknown protein-protein interaction. We copied and pasted all NEI genes into the string database through the "multiple proteins by names/identifiers" option, selected the set species as Homosapiens before beginning the search. The outcome of the protein relationship search was 823 nodes, 7,616 edges and the relationship values of each paired protein. We then downloaded the protein relationship data and used it to construct the knowledge base which contains the relationship between all NEI genes. The method of constructing the instance package is shown in algorithm 1. When two genes appear in the same paper abstract the whole text is traversed through the algorithm and the two genes added to a specific bag. If the specific gene relationship in bag exists in STRING knowledge base, the bag is flag as 1, otherwise as 0. We carried out this task until all the gene relationships in the knowledge base were mapped.

The algorithm used for word bag model generation is as follows (Lamurias et al., 2017):

```
function generate_bag (corpus,string)
begin
    bags=[]
    for abstract in corpus do
    begin
     for gene in abstract do
    begin
        bag= (gene_i,gene_j)
        if bag not in bags then
        begin
            if bag in string then
                bag.flag=1
            else
                bag.flag=0
           end
            bags.add(bag)
           end
    end
    retrun bags
end
```

Network Analysis

The adjacency matrix was constructed based on the gene relationship mined by SMIL method and following converted into Pajek recognized.net file. The file was imported into Pajek software to generate a visualized gene network map. We applied the method of "decomposition integration" because the complexity of the genetic network. This method was used to divide the genetic network into sub networks (community nodes), that in turn were separately analyzed. Finally, the results of each sub network were recombined to analyze the results of the whole network. Referring to the results of Yi's research (YIDH, 2017), we calculated the community node centrality index, subnet weight index, standardized weight, and node genetic weight index. This was done according to the following formulas:

$$CMI = CD*CB*(1/CC) + CE \quad \text{(formula 1)}$$

$$SW = N + ZJW \quad \text{(formula 2)}$$

$$ZSW = (SW - MIN)/(MAX - MIN) \quad \text{(formula 3)}$$

$$GW = CMI + ZSW \quad \text{(formula 4)}$$

(CMI) comprehensive measurement indicator; (CD)centrality degree; (CB) betweenness centrality; (CC) closeness centrality; (CE) centrality eigenvector; (SW) subnet weight; (ZSW) standardized weight of SW; (N) number of nodes in subnet; (ZJW) The correlation between subnet function and the problem to be studied problem, which is scored by experts; (GW) gene weight.

Combination Method

Combination method is an analytic method used to combine equations and set aside variables to discover a unified value. We assumed that multiple genes would correspond to each individual symptom (key), and that multiple symptoms would in turn correspond to one TCM syndrome. We investigated the most relevant genes (**Figure 4**) through the research concept of "gene symptom syndrome". The key words of target syndromes in modern medicine were regarded independently. Firstly, we discovered the genes related to the modern medicine syndrome, and following referred the data to the standard of TCM diagnosis for re-matching. As a final step we uncovered the specific gene which existed in each combination. This specific gene is the key gene and the result of these mentioned methods.

Search for Symptom Specific Gene

The search for symptom specific gene was done by the use of GenCliP software. GenCliP is a literature mining tool that can be used to form a list of genes with the use of keywords. These lists were then extracted by the software from their related literature and then manually verified. GenCliP displays specified genes and keywords mentioned in literature for manual association verification (Huang et al., 2008). We used the software to input all NEI genes in the "Upload Gene List", and input each target syndrome and their symptom into the search box "Word Related Gene Search". This was done to explore the NEI gene related to each specific symptom, and to define the symptom and the accompanying gene as "Abstract". The results of these searches included two parts: "Gene" and "Hit". "Gene" refers to the name of the searched gene, "Hit" refers to the number of documents in which the gene and the correlated searched symptom have appeared simultaneous. This concept can also be understood as the "weight of the gene".

Symptomatic Combination

In TCM each disease and syndrome are composed of many symptoms, and these symptoms can be further divided into primary and secondary symptoms. Under the guidance of TCM experts, we combined the individual symptoms according to the TCM diagnostic standards to better reflect the essential characteristics of the disease related to this study. The TCM experts divided the target syndromes into three parts: main syndrome, Qi deficiency syndrome and blood stasis syndrome. According to the TCM diagnosis standard, experts combined the symptoms of these three sections in different models to extract the gene information of each individual combination. We used this information to plot the intersection of the symptom combinations, and to screen out the genes existing in each combination. Finally, combining the method of Li (Li et al., 2007) and the experience of TCM experts, we discovered the core genes of each individual target syndrome. We following compared the genes of two respective target syndromes by "combination" and "decomposition" methods to extract the relevant genes.

TABLE 1 | Key words of Qi deficiency and blood stasis syndrome of coronary heart disease.

TCM symptoms	胸痛, 胸闷, 气短,心悸, 乏力, 畏寒/肢冷, 自汗, 不寐, 舌淡紫, 偏瘫, 瘀斑, 头晕目眩
Symptoms of modern medicine	Chest pain, chest heaviness, respiratory abnormality, palpitation, lassitude, typhoid fever/monoparesis/chills, sweating, insomnia, tongue disorder, hemiplegia, ecchymoses, dizziness

TABLE 2 | Key words of Qi deficiency and blood stasis syndrome of stroke.

TCM symptoms	头晕目眩, 头痛, 易怒, 肢体麻木, 痰多, 气短, 乏力, 自汗, 便秘, 口干口渴, 舌质红, 舌质暗, 半身不遂, 口舌歪斜, 面色淡白, 瘀斑
Symptoms of modern medicine	Dizziness, headache, irritability, numbness of extremity, sputum, respiratory abnormality, lassitude, perspiration, constipation, xerostomia, glossitis, tongue disorder, hemiplegia, stroke, ecchymoses

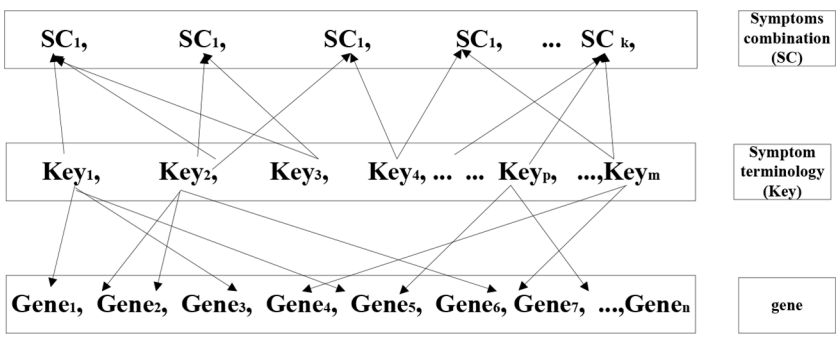

FIGURE 4 | Schematic diagram of combination method.

RESEARCH RESULTS

Results of "Decomposition Method"

We retrieved the relationships between TCM symptoms and modern medicine symptoms based on the SymMap database. **Tables 1** and **2** show translation from Chinese of symptom keywords in English based on TCM terminology. These keywords were used for literature search in PubMed.

We used these keywords for Mesh retrieval in PubMed database. A total of 85,733 documents related to syndromes of Qi deficiency and blood stasis of CHD and 96,038 documents related to Qi deficiency and blood stasis syndromes of stroke were retrieved. We downloaded the documents (including author, title, key words, abstract, and so forth) and used them to generate the document library in XML format. A total of 84 NEI genes relevant to Qi deficiency and blood stasis syndrome of CHD and 199 NEI genes relevant to Qi deficiency and blood stasis syndrome of stroke were extracted by the mining method shown in *Gene Information Extraction*. Through the relationship recognition method shown in *Gene Information Extraction*, 109 gene pairs relevant to Qi deficiency and blood stasis syndrome of CHD and 313 gene pairs relevant to Qi deficiency and blood stasis syndrome of stroke were identified. The adjacency matrix of gene relationship was constructed and converted into a.net file recognized by Pajek software to generate a visualized gene network diagram (**Figure 5**).

Calculations of four centrality indexes per network were made from the gene nodes, and then, according to Formula 1 the comprehensive measurement value of the centrality index was calculated. As a final step each of the two networks were individually divided into sub networks according to the community division algorithm of complex network. The results showed that the genetic network of Qi deficiency and blood stasis syndromes of CHD was divided into 14 sub networks (left of **Figure 6**). Among them, there were three large communities with more than 10 nodes, four with 5–10 nodes, and seven small communities with less than 5 nodes. A total of 21 sub networks (right of **Figure 6**) were discovered from the gene division of Qi deficiency and blood stasis syndromes of stroke. Among them, there were nine large communities with more than 10 nodes, three with 5–10 nodes, and nine small communities with less than 5 nodes. We then calculated the GW values of the target syndromes (**Tables 3** and **4**) according to formula 4.

Results of "Combination Method"

Since TCM diseases and syndromes are composed of a variety of symptoms, and these can be divided into primary and secondary symptoms. Under the guidance of TCM experts|, we clarified what symptoms are allocated to our two target syndromes, according to the criteria of TCM diagnostic, and following combined all target

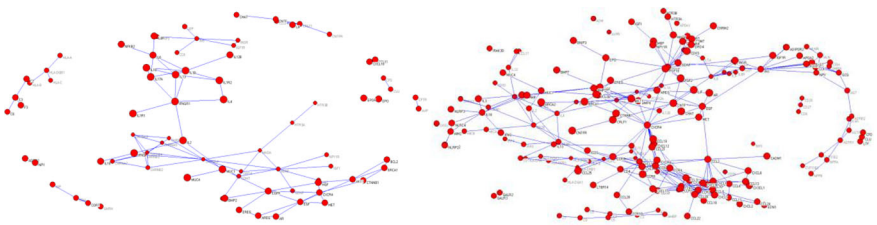

FIGURE 5 | Gene network of (left) Qi deficiency and blood stasis in coronary heart disease and (right) Qi deficiency and blood stasis in stroke.

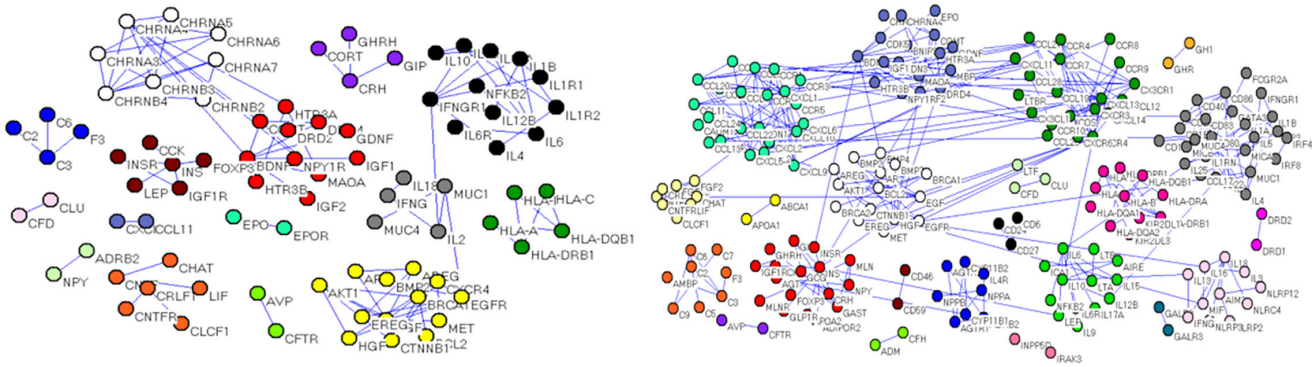

FIGURE 6 | Gene sub network divisions, (left) Qi deficiency and blood stasis in CHD and (right) Qi deficiency and blood stasis in stroke.

TABLE 3 | Top rated genes GW values in Qi deficiency and blood stasis of coronary heart disease.

Id	Gene	Degree	Closeness	Betweeness	Hub	CMI	ZSW	GW
1	CHRNA4	1	1	0.29	1	1.29	1	2.29
2	BDNF	0.8	0.92	0.29	0.5	0.752174	1	1.75
3	CHRNB4	0.6	0.69	0	0.7	0.7	1	1.70
4	CHRNA5	0.5	0.62	0	0.64	0.64	1	1.64
5	CHRNB3	0.5	0.62	0	0.62	0.62	1	1.62
6	CHRNA6	0.4	0.62	0	0.54	0.54	1	1.54
7	COMT	0.5	0.77	0.14	0.44	0.530909	1	1.53
8	CHRNA3	0.5	0.62	0	0.52	0.52	1	1.52
9	CHRNB2	0.4	0.62	0	0.5	0.5	1	1.5
10	MAOA	0.4	0.77	0.14	0.38	0.452727	1	1.45

TABLE 4 | Top rated genes GW values in Qi deficiency and blood stasis of stroke.

Id	Gene	Degree	Closeness	Betweeness	Hub	CMI	ZSW	GW
1	CXCR4	1	0.99	0.91	0.78	1.70	0.88	2.58
2	CXCL13	0.92	0.94	0.65	0.88	1.52	0.88	2.40
3	CCR7	0.85	0.88	0.27	1	1.06	0.88	1.94
4	CCL2	0.69	0.87	0.4	0.83	1.26	0.63	1.89
5	CXCL1	0.77	0.75	0.05	1.01	0.91	0.88	1.79
6	CCR4	0.62	0.87	0.16	0.93	0.85	0.88	1.73
7	CXCL9	0.62	0.75	0.04	0.88	0.85	0.88	1.73
8	CCL5	0.69	0.72	0.08	0.83	1.04	0.63	1.67
9	CCR2	0.54	0.72	0.02	0.87	0.75	0.88	1.63
10	CCR1	0.54	0.72	0.01	0.86	0.55	1	1.55

symptoms. By combining these main symptoms, the results can better reflect the essential characteristics of the target diseases.

1. Results of symptoms classification of Qi deficiency and blood stasis syndromes in CHD.
a. Main symptoms: chest pain, chest tightness.
b. Symptoms of Qi deficiency: shortness of breath, fatigue, perspiration, dizziness, cold limbs, insomnia, palpitation.
c. Blood stasis: light purple tongue body, hemiplegia, ecchymosis.

2. Results of symptoms classification of Qi deficiency and blood stasis syndrome in stroke; stroke
a. Main symptoms: hemiplegia, deviated mouth and/or tongue.
b. Qi deficiency: shortness of breath, fatigue, perspiration, pale complexion, dizziness, thirst, phlegm, white and greasy tongue coating.
c. Blood stasis: ecchymosis, red tongue body, numbness, irritability, constipation.

We firstly used Genclip software to obtain the genes corresponding to each symptom and their respective keywords. This was done according to the method in *Combination Method* (see **Table 5**). Unfortunately, no genes were related to "tongue disorder", "insomnia" and "chest heaviness" by using Genclip. These three symptoms were found in Genclip, but since our aim was to analyze the combination, rather than individual symptoms removing these three aforesaid symptoms from the symptom combination would not impact our subsequent research.

TABLE 5 | Number of genes discovered by keyword.

Id	Symptoms	Count
1	Dizziness	166
2	Constipation	210
3	Headache	338
4	Xerostomia	87
5	Irritability	122
6	Glossitis	19
7	Extremity Numbness	4
8	Hemiplegia	65
9	Sputums	4
10	Stroke	699
11	Respiratory Abnormality	76
12	Anemic	169
13	Lassitude	31
14	Ecchymoses	24
15	Sweating	129
16	Hemiplegia	65
17	Chest pain	225
18	Palpitation	49
19	Typhoid Fever	82
20	Chest Symptom Heaviness	0
21	Tongue Disorder	0
22	Insomnia	0

3. Symptom Combination Results of Qi Deficiency and Blood Stasis Syndromes in CHD

Using the formula combination of "main symptoms" + "Qi Deficiency" + "blood stasis" in Qi deficiency and blood stasis of CHD, 10 individual symptom combinations were obtained after

deleting the keywords "Chest heaviness, insomnia and tongue disorder".

Combination 1:
Chest pain + Respiratory abnormality + Palpitation + Hemiplegia
Combination 2:
Chest pain + Respiratory abnormality + Palpitation + Ecchymoses
Combination 3:
Chest pain + Lassitude + Palpitation + Hemiplegia
Combination 4:
Chest pain + Lassitude + Palpitation + Ecchymoses
Combination 5:
Chest pain + Sweating + Palpitation + Hemiplegia
Combination 6:
Chest pain + Sweating + Palpitation + Ecchymoses
Combination 7:
Chest pain + Dizziness + Palpitation + Hemiplegia
Combination 8:
Chest pain + Dizziness + Palpitation + Ecchymoses
Combination 9:
Chest pain + Typhoid fever + Palpitation + Hemiplegia
Combination 10:
Chest pain + Typhoid fever + Palpitation + Ecchymoses

4. Symptom Combination Results of Qi Deficiency and Blood Stasis Syndrome in Stroke

Using the formula combination of "main symptoms" + "Qi deficiency" + "blood stasis" in Qi deficiency and blood stasis in stroke, six different combinations of symptoms were obtained after deleting the keywords "Chest heaviness, insomnia and tongue disorder".

Combination 1:
Hemiplegia + Stroke + Respiratory abnormality + Lassitude + Constipation + Xerostomia + Headache + Sputum + Ecchymoses + Extremity Numbness
Combination 2:
Hemiplegia + Stroke + Respiratory abnormality
+ Lassitude + Constipation + Xerostomia + Headache + Sputum + Glossitis + Irritability
Combination 3:
Hemiplegia + Stroke + Sweating + Constipation + Xerostomia + Headache + Sputum + Ecchymoses + Numb extremities
Combination 4:
Hemiplegia + Stroke + Sweating + Constipation + Xerostomia + Headache + Sputums + Glossitis + irritability
Combination 5:
Hemiplegia + Stroke + Anemic + Constipation + Xerostomia + Headache + Sputum + Ecchymoses + Numb extremities
Combination 6:
Hemiplegia + Stroke + Anemic + Constipation + Xerostomia + Headache + Sputum + Glossitis + Irritability

Comparing these combinations and removing any data repeated between them a total of 373 genes related to the syndrome of Qi deficiency and blood stasis of CHD and 804 genes relevant to the syndrome of Qi deficiency and blood stasis of stroke were obtained.

Results Combination of "Decomposition" and "Combination"

According to the results of "decomposition method" and "combination method", "decomposition method" had 84 genes related to the syndrome of Qi deficiency and blood stasis of CHD and 199 genes related to the syndrome of Qi deficiency and blood stasis of stroke, "combination method" had 373 genes related to the syndrome of Qi deficiency and blood stasis of CHD and 804 genes related to the syndrome of Qi deficiency and blood stasis of stroke. By matching the results of "decomposition method" and "combination method" a total of 84 genes related to Qi deficiency and blood stasis syndrome of CDH and 161 genes related to Qi deficiency and blood stasis syndrome of stroke were found.

Even though Qi deficiency and blood stasis syndrome of CHD is different from that of stroke, the same treatment can be used according to TCM. Since different diseases can have the same treatment there evidently should be similar pathological changes and pathogenic mechanisms between these diseases. Therefore, we decided to investigate the common genes of these two target syndromes (see **Figure 7**) for specific similarities. After comparison, 46 genes in both diseases were identified: CXCR4, HGF, EGF, BDNF, IL10, INS, IL12B, IL13, IGF2, IGF1R, CTNNB1, IFNG, HTR3A, EGFR, HLA-B, HLA-DQB1, HLA-DRB1, IFNGR1, IGF1, CRLF1, GDNF, FOXP3, AKT1, F3, BMP2, AR, CNTF, BCL2, IL6, COMT, CHRNA4, CLCF1, CNTFR, MET, MUC1, MAOA, LEP, CCK, IL4, BRCA1, C3, IL18, IL2, IL1B, INSR, IL17A.

We further analyzed the functions and biological pathways affected by the above 46 genes. An online software (https://www.kegg.jp/) was used to analysis the pathways of related genes (see **Table 6**).

It can be seen from the above table that genes related to different diseases share certain common pathways. Nine shared signaling pathways (including AMPK, FoxO, ErbB, HIF-1, Jak-STAT, PI3K-Akt, Rap1, Ras, T cell receptor), 30 shared disease pathways (7 tumor related pathways, 13 infectious disease related pathways, 6 immune system disease related pathways, 4 endocrine disease pathways).

Genes Related to Traditional Chinese Materia Medica

We searched the "TCM target database" of TCMIP v2.0 in order to further study the relevance of traditional Chinese materia medica to the target syndromes. Using the reverse search function of TCMIP v2.0 led us to the discovery of

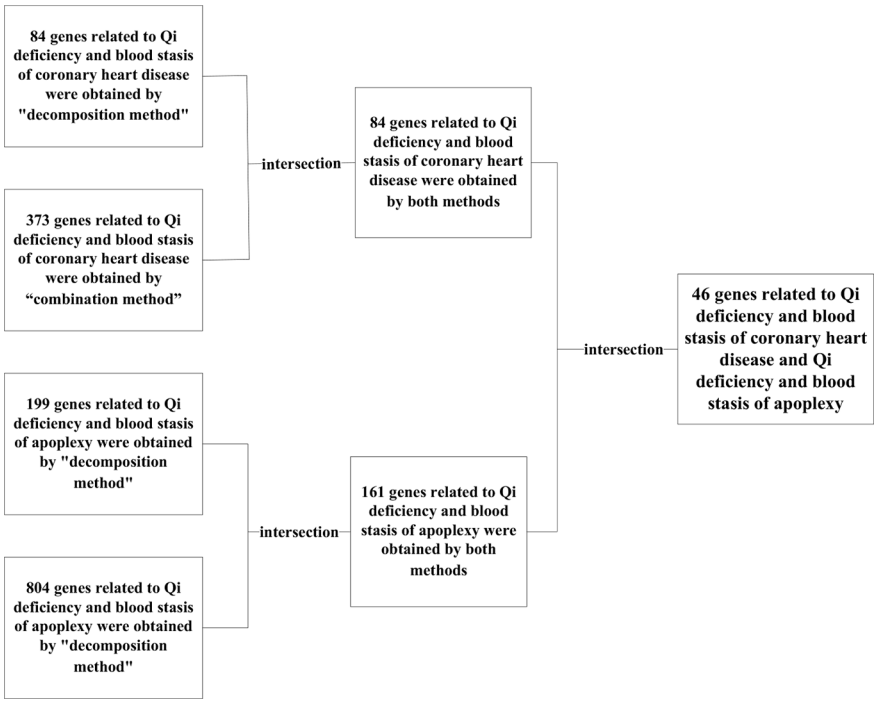

FIGURE 7 | Gene integration steps.

the medical components related to the 46 genes involved in our target syndromes.

TCMIP v2.0 (Xu et al., 2019) is an intelligent data platform, which is embedded with a broad spectrum of authoritative algorithms including drugs physical and chemical properties, evaluation of drug composition, and prediction of drug targets. In addition, the system is also able to analyze functions and pathways related to drug targets and disease targets. This function allows for cross retrieval from traditional Chinese materia medica → formula → ingredients → target gene → function/pathway → disease. This cross search function can uncover the relevance of syndromes and drugs related to specific diseases, as well as rate the medicines' compatibility with target molecular groups. As shown in the **Figure 8**, a target gene was inserted into TCMIP v2.0 "TCM target database". For example, insert "AR", now the database will show the results of gene name, the specific genes corresponding to Chinese materia medica compounds and its corresponding prescription. With this search we found a total of 25 types of traditional Chinese materia medica related to the target syndromes;

Arestemona root, pinellia tuber, danshen root, common rush, adhesive rehmannia root, garden burnet root, barbary wolfberry fruit, seaweed extract, puncturevine caltrop fruit, Indian Quassiawood twing and leaf, lotus seed, pyrola herb, European verbena herb, dwarf lilyturf tuber, hogfennel root, ginseng, mulberry twig, common yam rhizome, inula root, longstamen onion bulb, inula flower, yanhusuo, Yào Wáng; Chá, poppy shell, and milkwort root.

DISCUSSIONS

According to TCM CHD belongs to the category of chest arthralgia, palpitation, and subjective fatigue, it is located in the heart and blood vessels and mostly caused by the invasion of external evils, internal injury of emotions, improper diet, stress, and deficiency of viscera. In the development of CHD, Qi deficiency is the main factor, with inseparable bonds to phlegm and blood stasis (Houde, 2017).*Yilin Gaicuo* said "deficiency of vital energy(Qi) will lead to Qi not reaching the blood vessels, blood vessels without Qi will accumulate and form blood stasis", the etiology and pathogenesis of cardiovascular disease are mostly related to Qi deficiency and blood stasis (Jianqi and Yu, 2016), a vast amount of TCM literature point out that, according to TCM Qi deficiency and blood stasis are the two main pathological changes causing CHD. Stroke is located in the brain, and is according to TCM closely related to the heart, liver, spleen and kidney. Wind, fire, phlegm, blood stasis, deficiency and toxin are the main pathogenic factors of stroke (Zhe, 2010). Wang Qingren believed that the root of hemiplegia induced by stroke could be found in the deficiency of vital energy (Qi), based on this theory, he composed the *Buyang Huanwu Decoction* for the treatment of Qi deficiency and blood stasis syndromes of stroke (Zhengtai et al., 2017).

Our study shows that Qi deficiency and blood stasis of CHD and stroke includes some inflammatory factors: IL-10, FOXP3, cell apoptosis, differentiation, and proliferation. Cell apoptosis, differentiation, and proliferation: BCL-2, AKT1, CLCF1, HGF,

TABLE 6 | Recurring genes and pathways of target syndromes.

Channel Name	Genes	P Value
Inflammatory bowel disease (IBD)	IL4, IL17A, IL6, IL18, IFNG, IL13, IL12B, FOXP3, IFNGR1, IL10, IL2	2.49E-13
Cytokine-cytokine receptor interaction	LEP, IL4, IL17A, IL6, CNTF, CLCF1, CXCR4, IL18, IFNG, IL13, CNTFR, IL12B, IL10, IFNGR1, IL2	3.59E-13
HIF-1 signaling pathway	AKT1, EGFR, IGF1R, IL6, INS, BCL2, IFNG, IGF1, EGF, INSR, IFNGR1	3.07E-11
Jak-STAT signaling pathway	AKT1, IL4, LEP, IL6, CNTF, IFNG, IL13, CNTFR, IL12B, IFNGR1, IL10, IL2	5.4E-11
PI3K-Akt signaling pathway	AKT1, IL4, EGFR, IGF1R, IL6, INS, BCL2, MET, IGF1, HGF, EGF, INSR, BRCA1, IL2	3.34E-09
Prostate cancer	AKT1, EGFR, IGF1R, AR, INS, BCL2, IGF1, EGF, CTNNB1	7.76E-09
Pathways in cancer	AKT1, EGFR, IGF1R, AR, IL6, BMP2, CXCR4, BCL2, MET, IGF1, HGF, EGF, CTNNB1	2.36E-07
FoxO signaling pathway	AKT1, EGFR, IGF1R, IL6, INS, IGF1, EGF, INSR, IL10	2.66E-07
Rap1 signaling pathway	AKT1, EGFR, IGF1R, INS, MET, IGF1, HGF, EGF, INSR, CTNNB1	6.56E-07
Chagas disease (American trypanosomiasis)	AKT1, IL6, C3, IFNG, IL12B, IFNGR1, IL10, IL2	9.27E-07
Melanoma	AKT1, EGFR, IGF1R, MET, IGF1, HGF, EGF	1.04E-06
Tuberculosis	AKT1, IL6, C3, BCL2, IL18, IFNG, IL12B, IFNGR1, IL10	2.07E-06
Measles	AKT1, IL4, IL6, IFNG, IL13, IL12B, IFNGR1, IL2	3.82E-06
Proteoglycans in cancer	AKT1, EGFR, IGF1R, MET, IGF1, IGF2, IL12B, HGF, CTNNB1	4E-06
Focal adhesion	AKT1, EGFR, IGF1R, BCL2, MET, IGF1, HGF, EGF, CTNNB1	4.5E-06
Malaria	IL6, IL18, IFNG, MET, HGF, IL10	5.88E-06
Ras signaling pathway	AKT1, EGFR, IGF1R, INS, MET, IGF1, HGF, EGF, INSR	1.18E-05
Leishmaniasis	IL4, C3, IFNG, IL12B, IFNGR1, IL10	1.41E-05
African trypanosomiasis	IL6, IL18, IFNG, IL12B, IL10	2.45E-05
Allograft rejection	IL4, IFNG, IL12B, IL10, IL2	3.45E-05
Intestinal immune network for IgA production	IL4, IL6, CXCR4, IL10, IL2	6.3E-05
Toxoplasmosis	AKT1, BCL2, IFNG, IL12B, IFNGR1, IL10	0.00018
Glioma	AKT1, EGFR, IGF1R, IGF1, EGF	0.000249
AMPK signaling pathway	AKT1, LEP, IGF1R, INS, IGF1, INSR	0.000298
Adherens junction	EGFR, IGF1R, MET, INSR, CTNNB1	0.000448
Type I diabetes mellitus	INS, IFNG, IL12B, IL2	0.001164
Influenza A	AKT1, IL6, IL18, IFNG, IL12B, IFNGR1	0.001507
T cell receptor signaling pathway	AKT1, IL4, IFNG, IL10, IL2	0.001813
Endometrial cancer	AKT1, EGFR, EGF, CTNNB1	0.001956
Ovarian steroidogenesis	IGF1R, INS, IGF1, INSR	0.002195
Legionellosis	IL6, C3, IL18, IL12B	0.003836
Signaling pathways regulating pluripotency of stem cells	AKT1, IGF1R, BMP2, IGF1, CTNNB1	0.004221
Pertussis	IL6, C3, IL12B, IL10	0.006069
Asthma	IL4, IL13, IL10	0.006078
Salmonella infection	IL6, IL18, IFNG, IFNGR1	0.008094
Non-alcoholic fatty liver disease (NAFLD)	AKT1, LEP, IL6, INS, INSR	0.008759
Rheumatoid arthritis	IL17A, IL6, IL18, IFNG	0.009541
Progesterone-mediated oocyte maturation	AKT1, IGF1R, INS, IGF1	0.009847
Graft-versus-host disease	IL6, IFNG, IL2	0.013008
Herpes simplex infection	IL6, C3, IFNG, IL12B, IFNGR1	0.0136
Amoebiasis	IL6, IFNG, IL12B, IL10	0.01594
Oocyte meiosis	IGF1R, AR, INS, IGF1	0.018058
Aldosterone-regulated sodium reabsorption	INS, IGF1, INSR	0.018591
Insulin resistance	AKT1, IL6, INS, INSR	0.019401
Autoimmune thyroid disease	IL4, IL10, IL2	0.026985
Non-small cell lung cancer	AKT1, EGFR, EGF	0.027996
Regulation of lipolysis in adipocytes	AKT1, INS, INSR	0.03438
mTOR signaling pathway	AKT1, INS, IGF1	0.035495
Central carbon metabolism in cancer	AKT1, EGFR, MET	0.040091
Pancreatic cancer	AKT1, EGFR, EGF	0.041274
Fc epsilon RI signaling pathway	AKT1, IL4, IL13	0.041274
Renal cell carcinoma	AKT1, MET, HGF	0.04247
Transcriptional misregulation in cancer	IGF1R, IL6, MET, IGF1	0.042499
Colorectal cancer	AKT1, BCL2, CTNNB1	0.047383
ErbB signaling pathway	AKT1, EGFR, EGF	0.070363
Choline metabolism in cancer	AKT1, EGFR, EGF	0.088362
Systemic lupus erythematosus	C3, IFNG, IL10	0.088362
Toll-like receptor signaling pathway	AKT1, IL6, IL12B	0.094642

EGF, IGF1, CXCR4, and CTNNB1. Neurotrophic factors includes; CNTF, BDNF, and GDNF. Our results verify that the inflammatory responses, apoptosis, proliferation, and other mechanisms are shared by the two target syndromes.

Interleukin is involved in regulating the activation, proliferation, inflammatory response, and differentiation of immune cells. Interleukin-10 (IL-10) plays an important role in the pathogenesis of CHD, acute cerebral infarction, and other

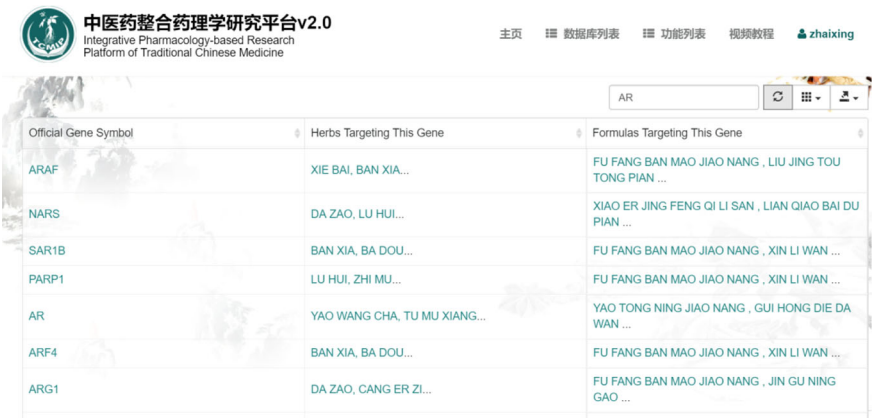

FIGURE 8 | TCMIP v2.0 Query interface.

diseases (Chao et al., 2013; Dong et al., 2015). FoxP3 regulates T-cell specific transcription factor that can secrete IL-10 as well as regulate immune functions and cause immune tolerance (Huehn et al., 2009). Other research has found that for coronary artery disease patients with low IL-10/TNF-α ratio has low left ventricular ejection fraction, with high incidence of cardiac related diseases within 10 years. It is therefore speculated that the imbalance of IL-10 and TNF α may be relevant to the pathological development of atherosclerosis and heart failure (Dopheide et al., 2015).

The Bcl-2 gene is involved in apoptosis. Some scholars (Zhongfu et al., 2001) believe that oxygen free radicals and calcium excess can induce apoptosis during myocardial ischemia-reperfusion. Bcl-2 can inhibit apoptosis by interaction with antioxidants, inhibiting the production of oxygen free radicals, changing the cell outflow of $Ca2^{+,}$ and by regulating cGMP. Hepatocyte growth factor (HGF), insulin-like growth factor (IGF), epidermal growth factor (EGF), and other cytokines can activate PI3-Akt, Jak-STAT, and other signal pathways that are active in the facilitation of cell differentiation, angiogenesis, and apoptosis inhibition (Hosui et al., 2006). Cardiac nutrition literacy cytokine (CLCF1) is mainly involved in the Jak-STAT signaling pathway, cytokine, and chemokine mediated signaling pathway and negative regulation of apoptosis (Elsaeidi et al., 2014). Chemokine receptor (CXCR4) promotes cell proliferation. It has been suggested that up regulation of CXCR4 signaling pathway may be an important mechanism in the treatment of CHD (Hristov et al., 2007). CTNNB1 is a β-catenin. The stable expression of β-catenin in cells can up-regulate the survival rate of regulatory T cells, induce the apoptosis of non-conditional T cells, accelerate cell cycles and promote cell proliferation (Ding et al., 2008).

Neurotrophic factors can induce, regulate and control the survival, growth, and migration of neurons as well as establish functional connections with other cells by regenerating axons as part of nerve regeneration (Lichtman, 1987). As an important neurotrophic factor, glial cell-derived neurotrophic factor (GDNF) can reduce the area of infarction during the acute stage of stroke (Gunther et al., 2005). The increased expression of brain-derived neurotrophic factor (BDNF) may be relevant to the recovery of neural function and plasticity after cerebral ischemia (Ergul et al., 2012).

By searching the KEGG database, we further confirmed the interrelations of the above mentioned genes and their pathways. PI3K-Akt signal path (**Figure 9**) involves FoxO, ErbB, Ras, and other sub modules, while FoxO, ErbB, HIF-1, and Jak-STAT also contain signals of the sub module PI3K-Akt. It is known that PI3K-Akt signaling pathway can promote endothelial regeneration, vasodilation, and platelet adhesion in cardiomyocyte, hence improve their survival rate and functionality (PAN et al., 2017). In addition, PI3K-Akt signaling pathway is also involved in cerebral infarction and other diseases (Zhang Hong and Junjian, 2011).

We found, through our analysis that the traditional Chinese herbs related to the 46 specific genes includes; Qi replenishing herbs *ginseng* and *yam*; blood activating herb *danshen* root; resuscitation herb *milkwort* root; phlegm dissolving herbs *pinellia* tuber, *hogfennel* root, and inula flower. This indicated that Qi replenishing, blood activating, resuscitation, and phlegm dissolving herbs have close connection to Qi deficiency and blood stasis syndrome. This discovery is consistent with TCM theory and clinical practice. Some scholars (Mengna et al., 2017) think that CHD is caused by Qi deficiency, Yang deficiency, blood deficiency, and Yin deficiency with Qi deficiency as the common denominator. Qi is the driving force of blood circulation. When Qi flows, blood flows. Weak Qi leads to blood not flowing smoothly that in turn leads to stagnation and pain. Qi deficiency, phlegm coagulation and blood stasis constitute the key pathogenesis of CHD and stroke. In the treatment of these diseases, emphasis should be given on Qi and blood circulation in order to tonify the body and resolve blood stasis. Modern pharmacological research validates that ginseng contains *ginsenoside*, ginseng polysaccharide, volatile oil, and other components. These chemicals can regulate the heart function, blood vessels, blood pressure, and central nervous

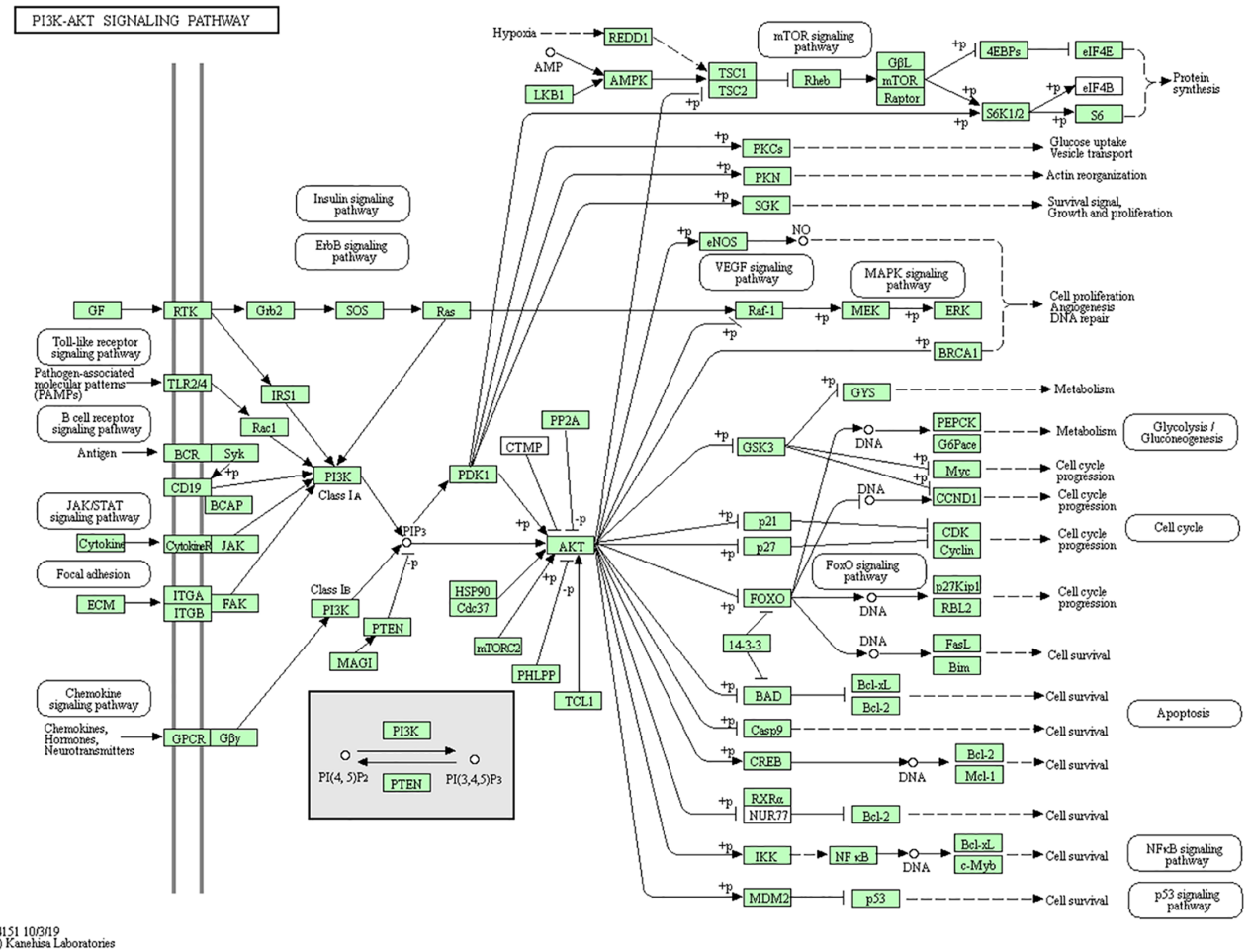

FIGURE 9 | PI3K-Akt signal pathways.

system. *Ginsenoside* as the main component of ginseng has proven *in vivo* to protect cardiomyocytes, improve myocardial metabolism, and to increase stroke volume (Wang et al., 2015). *Ginsenoside* Rb1 prevents lipopolysaccharide induced cardiomyocyte inflammation by inhibiting the PI3K/Akt signaling pathway (Zhiyang et al., 2018). Tanshinone, *Danshensu* and other water-soluble components in *danshen* root can improve myocardial metabolism, increase coronary blood flow, and reduce the incidence of myocardial ischemia and myocardial infarction. *Jiawei Danshen Yin* (ruoxia et al., 2020) can activate the PI3K/Akt signaling pathway through negative regulation of PTEN that in turn inhibit apoptosis of myocardial cells during ischemia-reperfusion and improve the survival rate of myocardial cells during ischemia and hypoxia. This leads to improvements of the heart and reduces the injury of cardiovascular disease to the heart. Pinellia tuber can regulate blood lipid metabolism leading to improved hemodynamics, reduce blood viscosity, and inhibition of RBC aggregation (Wenyue et al., 2002).

This study preliminarily clarified that the pathological mechanism of Qi deficiency and blood stasis is involved in cell necrosis, apoptosis and inflammatory responses. As well as involving FoxO, ErbB, HIF-1, Jak-STAT, PI3K-Akt signal pathways. We aim to reveal the molecular mechanism based on biological research to provide a scientific basis for the TCM theory of "treating different diseases with the same method".

SUMMARY AND PROSPECT

Using Qi deficiency and blood stasis as our fundamental concepts to analyze the extensive online literature and big data with "decomposition" model, "combination" model, "information extraction," and "complex network". Ultimately, leading to discussions on the biological basis of the TCM theory "treating different diseases with the same method". This study provides a bridge between TCM and modern medicine, and also

demonstrates the use of information technology to study the TCM term "syndrome".

It is a new approach to use big data and complex network as a method to analysis the biological basis of the TCM concept "treating different diseases with the same method". Follow up research will be needed to verify and validate the genes related to the two target syndromes as well as the practicality of our method. We plan to conduct more in-depth researches on the relationship between traditional Chinese materia medica—genes–syndromes–diseases by exploring their common molecular mechanism. Then, we will get a deeper biological understanding of the TCM concept "treating different diseases with the same method".

DATA AVAILABILITY STATEMENT

The datasets presented in this study can be found in online repositories. The names of the repository/repositories and accession number(s) can be found in the article/ **Supplementary Material**.

AUTHOR CONTRIBUTIONS

XZ: Put forward research ideas and write papers. XW: Paper revision. LW: thesis writing. WW: Thesis writing. XP: Thesis writing. LX: Put forward research ideas and write papers.

FUNDING

This work was supported by the Fundamental Research Funds for the Central Universities (2020-JYB-ZDGG-070, 2019-JYB-JS-031) and the National Natural Science Foundation of China (No. 81603499).

SUPPLEMENTARY MATERIAL

The Supplementary Material for this article can be found online at: https://www.frontiersin.org/articles/10.3389/fphar.2020.00946/full#supplementary-material

REFERENCES

Artzy-Randrup, Y., Fleishman, S. J., Ben-Tal, N., and Stone, L. (2004). Comment on "Network motifs: simple building blocks of complex networks" and "Super families of evolved and designed networks". *Science* 305 (5687), 1107. doi: 10.1126/science.1099334

Bin, S. (2002). Overview of information extraction technology. *Terminology Standardization Inf. Technol.* 3 (1), 28–32.

Bunescu, R., and Mooney, R. (2005a). "Subsequence kernels for relation extraction A," in *In Proceedings of NIPS C]*, vol. 2005. (Vancouver Canada: MIT Press), 171–178.

Chao, Y, Tong, C., and Kexia, Z. (2013). Correlation between serum IL-6 and carotid atherosclerosis in patients with acute cerebral infarction. *J. Modern Lab. Med.* 28 (2), 152–153,156. doi: 10.3969/j.issn.1671-7414.2013.02.049

Deng, M., Tu, Z., Sun, F., and Chen, T. (2004). Mapping Gene Ontology to proteins based on protein-protein interaction data. *Bioinformatics.* 20 (6), 895–902. doi: 10.1093/bioinformatics/btg500

Ding, S. S. , Hong, S. H., Wang, C., Guo, Y., Wang, Z. K., and Xu, Y. (2013). Acupuncture modulates the Neuro-Endocrine-Immune network. *QJM* 107 (5), 341–345. doi: 10.1093/qjmed/hct196

Ding, Y., Shen, S., and Lino, A. C. (2008). Stable expression of β-catenin promotes regulatory T cell survival and induces non conditional T cell apoptosis. *Chin. J. Tumor Biother.* (02), 168.

Dong, G., Xiaodong, W., Guangyi, J., and Wenqi, J. (2015). Research progress in the structure of Toll like receptor ligand complex. *J. Cell Mol. Immunol.* 31 (4), 553–556.

Dopheide, J. F., Knopf, P., Zeller, G. C., Vosseler, M., Abegunewardene, N., Münzel, T., et al. (2015). Low IL-10/TNF-α Ratio in Patients with Coronary Artery Disease and Reduced Left Ventricular Ejection Fraction with a Poor Prognosis After 10 Years. *Inflammation* 38 (2), 911–922. doi: 10.1007/s10753-014-0053-5

Elsaeidi, F., Bemben, M. A., Zhao, X. F., and Goldman, D. (2014). Jak/Stat signaling stimulates zebrafish optic nerve regeneration and overcomes the inhibitory actions of Socs3 and Sfpq. *Neurosci* 34 (7), 2632–2644. doi: 10.1523/JNEUROSCI.3898-13.2014

Ergul, A., Alhusban, A., and Fagan, S. C. (2012). Angiogenesis: a harmonized target for recovery after stroke. *Stroke* 43 (8), 2270–2274. doi: 10.1161/STROKEAHA.111.642710

Fan, D., Qianru, Z., Yuanjia, H, and Yitao, W. (2014). Study on the mechanism of Buyang Huanwu Decoction in the prevention and treatment of Qi deficiency and blood stasis based on network analysis. *Chin. J. Traditional Chin. Med.* 39 (22), 4418–4425. doi: 10.4268/cjcmm20142227

Gunther, A., Kuppers-Tiedt, L., Schneider, P. M., et al. (2005). Reduced infarct volume and differential effects on glial cell activation after hyperbaric oxygen treatment in rat permanent focal cerebral ischaemia. *Eur. J. Neurosci.* 21 (11), 3189–3194. doi: 10.1111/j.1460-9568.2005.04151.x

Hosui, A., Takehara, T., Ohkawa, K., Kanazawa, Y., Tatsumi, T., and Yamaguchi, S. (2006). Suppressive effect on hepatocyte differentiation of hepatitis C virus core protein. *Biochem. Biophys. Res. Commun.* 346 (4), 1125–1130. doi: 10.1016/j.bbrc.2006.05.114

Houde, R. (2017). Treatment of cardiovascular diseases from the perspective of integration of Chinese and Western Medicine. *Clin. Res. Traditional Chin. Med.* 9 (10), 145–146. doi: 10.3969/j.issn.1674-7860.2017.10.070

Hristov, M., Zernecke, A., Bidzhekov, H., Liehn, E. A., Shagdarsuren, E., Ludwig, A., et al. (2007). Importance of CXC chemokine receptor 2 in the homing of human peripheral blood endothelial progenitor cells to sites of arterial injury. *Circ. Res.* 100 (4), 590–597. doi: 10.1161/01.RES.0000259043.42571.68

Huang, Z. X., Tian, H. Y., Hu, Z. F., Zhou, Y. B., Zhao, J., and Yao, K. T. (2008). GenCLiP: a software program for clustering gene lists by literature profiling and constructing gen eco-occurrence networks related to custom keywords. *BMC Bioinf.* 13 (9), 308. doi: 10.1186/1471-2105-9-308

Huehn, J., Polansky, J. K., and Hamann, A. (2009). Epigenetic control of FOXP3 expression: the key to a stable regulatory T-cell lineage? *Nat. Rev. Immunol.* 9 (2), 83–89. doi: 10.1038/nri2474

Isaković, K., and Janković, B. D. (1973). Neuro-Endocrine Correlates of Immune Response. *Int. Arch. Allergy Immunol.* 45 (3), 373–384. doi: 10.1159/000231055

Jianqi, L, and Yu, S. (2016). Research progress on the prevention and treatment of cardiovascular diseases by the method of Supplementing Qi and activating blood circulation. *J. Guangxi Univ. Traditional Chin. Med.* 19 (01), 78–80. doi: 10.7501/j.issn.0253-2670.2015.10.027

Lamurias, A., Clarke, L. A., and Couto, F. M. (2017). Extracting microRNA-gene relations from biomedical literature using distant supervision. *PloS One* 12 (3), e0171929. doi: 10.1371/journal.pone.0171929

Lan, W., and Yusheng, Z. (1990). The role of doubtful nucleus in the regulation of cellular immunity by acupuncture at Zusanli. *J. OVeterinary Univ.* 10 (2), 146–148.

Li, S., Zhang, Z. Q., Wu, L. J., Zhang, X. G., Li, Y. D., and Wang, Y. Y. (2007). Understanding ZHENG in traditional Chinese medicine in the context of neuro-endocrine -immune network. *Syst. Biology IET* 1 (1), 51–60. doi: 10.1049/iet-syb:20060032

Lichtman, J. W., and Taghert, P. H. (1987). Developmental neurobiology.Trophic factor theory matures. *Nature* 326 (6111), 336. doi: 10.1038/326336a0

Lim, J., Hao, T., Shaw, C., Patel, A. J., Szabó, G., Rual, J.-F., et al. (2006). A protein-protein interaction network for human inherited ataxias and disorders of Purkinje cell degeneration. *Cell* 125 (4), 801–814. doi: 10.1016/j.cell.2006.03.032

Liu, J., Zhai, X., and Liao, X. (2019). Bibliometric analysis on cardiovascular disease treated by traditional Chinese medicines based on big data. *Int. J. Parallel Emergent Distributed Syst*. 1, 1–17 doi: 10.1080/17445760.2019.1606912

Ma, T., Tan, C., Zhang, H., Wang, M. Q., Ding, W. J., and Li, S. (2010). Bridging the gap between traditional Chinese medicine and systems biology: the connection of Cold Syndrome and NEI network. *Mol. Biosyst.* 6 (4), 613–619. doi: 10.1039/b914024g

Mengna, J., Li, Y., and Zetao, C. (2017). Professor Shao nianfang's experience in the treatment of coronary heart disease with the method of Invigorating Qi and promoting blood circulation. *J. Guangxi Univ. Traditional Chin. Med.* (3), 020(003), 5–6. doi: 10.3969/j.issn.2095-4441.2017.03.003

Ono, T., Hishigaki, H., Tanigami, A., and Takagi, T. (2001). Automated extraction of information on protein-protein interactions from the biological literature. *Bioinformatics* 17 (2), 155–161. doi: 10.1093/bioinformatics/17.2.155

Pan, Y., Yin, J., Cai, X. M., Li, L., Xu, Y., and Yu, C. (2017). Research progress on interven-tion of traditional hinese medicine on coronary heart diseasethrough PI3K / Akt signaling pathway. *China Tradit Herb Drugs* 48 (19), 4100–4104. doi: 10.7501/j.issn.0253-2670.2017.19.030s

Ruoxia, W., Zhengyang, L., Weisi, B., Wenyao, Z., Jing, L., Xiang, W., et al. (2020). Study on the inhibitory effect of Jiawei Danshen drink on IRI through PTEN / PI3K / Akt signal pathway. *Hunan J. Traditional Chin. Med.* 36 (03), 137–140. doi: 10.16808/j.cnki.issn1003-7705.2020.03.058

Shao, L. (2007). Computational system biology of traditional Chinese medicine and cold heat syndrome. *World Sci. Technol. - Modernization Traditional Chin. Med.* 9 (1), 105–111. doi: 10.11842/wst.2007.1

Wang, R. X., He, R. L., Jiao, H. X., Dai, M., Mu, Y.-P., Hu, Y., et al. (2015). Ginsenoside Rb1 attenuates agonist-induced contractile response via inhibition of store-operated calcium entry in pulmonary arteries of normal and pulmonary hypertensive rats. *Cell Physiol. Biochem.* 35 (4), 1467–1481. doi: 10.1159/000373966

Wenyue, J., Yu, Y., and Yanyan, L. (2002). Effects of pinellia, Guawei, Fritillaria thunbergii and Acorus tatarinowii on Hemorheology in rats. *J. Traditional Chin. Med.* 43 (3), 215–225.

Wu, Y., Zhang, F., Yang, K., Fang, S., Bu, D., Li, H., et al. (2018). SymMap: an integrative database of traditional Chinese medicine enhanced by symptom mapping. *Nucleic Acids Res.* 47, D1110–D1117. doi: 10.1093/nar/gky1021

Xiao, J., Su, J., Zhou, G. D., and Tan, C. L. (2005). "Protein-protein interaction extraction: a supervised learning approach A," in *Proceedings of the First International Symposium on Semantic Mining in Biomedical C* (Turku, Finland: SMBM), 51–59.

Xiao-yu, ZHENG (2002). *Guidance Principle of Clinical Study on NewDrug of Traditional Chinese Medicine* (Beijing: Chinese Medical and Pharmaceutical Science Press).

Xing, Z., Xuanchao, F., Jingwei, L., Gao, K., Jia, Z., Zhao, H., et al. (2015). Neuro-Endocrine-Immune Biological Network Construction Of Qi Deficiency Pattern And Qi Stagnation Pattern In Traditional Chinese Medicine. *J. Biol. Syst.* 23 (2), 305–321. doi: 10.1142/S0218339015500163

Xu, H. Y., Zhang, Y. Q., Liu, Z. M., Chen, T., Lv, C. Y., Tang, S. H., et al. (2019). ETCM: An encyclopaedia of traditional Chinese medicine. *Nucleic Acids Res.* 47 (D1), D976–D982. doi: 10.1093/nar/gky987

Xuezhong, Z., Zhaohui, W, and Baoyan, L. (2004). Knowledge Diseovery in Biomedieal Literature:Survey and ProsPeet. *Complex Syst. ComPlexity Seienee* 1, 3, 1–3.

YIDH, CHENGH (2017). A Research on Comprehensive Measurement Of Complex Network Structure Relationship Based on Social Network Analysis. *Stat. Decision* (7), 14–17. doi: 10.13546/j.cnki.tjyjc.2017.07.003

Zhang Hong, S., and Junjian, Z. (2011). Research progress of PI3K / Akt signaling pathway in nervous system diseases. *Med. Rev.* 17 (18), 2732–2735.

Zhe, Z. (2010). Preliminary discussion on the evolution of stroke pathogenesis. *World Traditional Chin. Med*. 5 (1), 3–4. doi: 10.3969/j.issn.1673-7202.2010.01.002

Zhengtai, Z., Shihuan, T., and Yuexiang, M. (2017). Research progress of Buyang Huanwu Decoction in treating stroke of Qi deficiency and blood stasis type. *Shandong J. Traditional Chin. Med.* 36 (1), 71–73. doi: 10.16295/j.cnki.0257-358x.2017.01.024

Zhiyang, Z., ran, G, and lulu, Y. (2018). Ginsenoside Rb1 protects lipopolysaccharide induced myocardial inflammatory response by inhibiting PI3K / Akt signaling pathway. *Chin. J. Evidence Based Cardiovasc. Med.* 10 (07), 823–826. doi: 10.3969/j.issn.1674-4055.2018.07.13

Zhongfu, M, Hong, M., Rengao, Y., Bin, L., Quansheng, Z., and Jinlang, W. (2001). Study on apoptosis of myocardial cells in elderly patients with acute myocardial infarction. *Chin. J. Gerontol.* (01), 6–9. doi: 10.3969/j.issn.1005-9202.2001.01.003

Conflict of Interest: The authors declare that the research was conducted in the absence of any commercial or financial relationships that could be construed as a potential conflict of interest.

The reviewer YW declared a shared affiliation, with no collaboration, with the authors to the handling editor at the time of the review.

Copyright © 2020 Zhai, Wang, Wang, Xiu, Wang and Pang. This is an open-access article distributed under the terms of the Creative Commons Attribution License (CC BY). The use, distribution or reproduction in other forums is permitted, provided the original author(s) and the copyright owner(s) are credited and that the original publication in this journal is cited, in accordance with accepted academic practice. No use, distribution or reproduction is permitted which does not comply with these terms.

frontiers in Pharmacology

REVIEW
published: 07 July 2020
doi: 10.3389/fphar.2020.00982

Traditional Asian Herbs in Skin Whitening: The Current Development and Limitations

Yibo Hu[1], *Hongliang Zeng*[2], *Jinhua Huang*[1], *Ling Jiang*[1], *Jing Chen*[1]* and *Qinghai Zeng*[1]*

[1] Department of Dermatology, Third Xiangya Hospital, Central South University, Changsha, China, [2] Institute of Chinese Materia Medica, Hunan Academy of Chinese Medicine, Changsha, China

In Asia, the market for whitening cosmetics is expanding rapidly, more and more people prefer to use natural products. Driven by natural product demand and technical advances, herbal research is also developing fast. Lots of studies reported that Asian herbal reagents can reduce melanogenesis, these findings provide evidence for the whitening application of Asian herbs. However, the current development status and challenges of herbal research need attention too. By reviewing these studies, different problems in studying herbal formulas, extracts, and active ingredients were presented. One of the most influential troubles is that the components of herbs are too complex to obtain reliable results. Thus, an understanding of the overall quality of herbal research is necessary. Further, 90 most cited Asian herbal studies on whitening were collected, which were conducted between 2017 and 2020, then statistical analysis was carried out. This work provided a comprehensive understanding of Asian herbal research in skin whitening, including the overall status and quality, as well as the focuses and limitations of these studies. By proactively confronting and analyzing these issues, it is suggested that the focus of herbal medicine research needs to shift from quantity to quality, and the new stage of development should emphasize transformation from research findings to whitening products.

Keywords: skin whitening, Asian herbs, traditional herbs, pigmentation, melanogenesis

OPEN ACCESS

Edited by:
Hai Yu Xu,
China Academy of Chinese Medical Sciences, China

Reviewed by:
Yujie Li,
China Academy of Chinese Medical Sciences, China
Sayeed Ahmad,
Jamia Hamdard University, India

***Correspondence:**
Jing Chen
43700351@qq.com
Qinghai Zeng
zengqinghai@csu.edu.cn

Specialty section:
This article was submitted to Ethnopharmacology, a section of the journal Frontiers in Pharmacology

Received: *13 February 2020*
Accepted: *17 June 2020*
Published: *07 July 2020*

Citation:
Hu Y, Zeng H, Huang J, Jiang L, Chen J and Zeng Q (2020) Traditional Asian Herbs in Skin Whitening: The Current Development and Limitations. Front. Pharmacol. 11:982. doi: 10.3389/fphar.2020.00982

INTRODUCTION

Due to economic development and aesthetic needs, the global cosmetics market is unprecedentedly prosperous at present; likewise, the variety of cosmetics has also increased (Lee et al., 2016; Peltzer et al., 2016). Traditional herb-based natural products are putting into practical use as a new type of cosmetics, especially in skin whitening (Kanlayavattanakul and Lourith, 2018). Meanwhile, studies have screened abundant components from traditional herbs, most of them show favorable effects on pigmentation reduction. These findings have developed several hot products, such as arbutin and kojic acid (Leyden et al., 2011). In Asia, the application of traditional herbs in skin whitening has gotten more attention, two outstanding factors may contribute to this situation. One of them is local culture and aesthetic manner, generally, most Asians prefer white skin; the other factor is that Asia has a long history of using herbal medicine (Scarpa and Guerci, 1987; Gao et al., 2018).

Driven by the booming whitening market in Asia, many studies focus on the effects of traditional herbs; meanwhile, Asian consumers show strong need and trust for herbal reagents (Kanlayavattanakul and Lourith, 2018).

However, reliable herbal reagents are still in short supply. Though studies provide a basic guarantee for whitening effects and safety of many Asian herbs, there are still a lot of issues to be addressed before they transformed into products. The problems come from several aspects, for example, many natural ingredients are unstable and only show mild effects, the limitations of research methods are also a tough issue (Bent and Ko, 2004; Efferth, 2017; Espinosa-Leal and Garcia-Lara, 2019). It's not just that, we need to know the potential obstacles to the application of Asian herbs in skin whitening. Thus, this review provided a comprehensive understanding of the development status and problems of herbal research. In addition to summarizing the current findings, this work mainly focused on finding problems, which might help promote the application of traditional Asian herbs.

THE INCREASE OF ASIAN COSMETICS MARKETS AND SKIN WHITENING DEMAND

The Asian cosmetics market is growing rapidly. Immediately behind Europe and the United States, China, Japan, India, and Korea are major consumers of cosmetics. In China, the total retail sales of cosmetics exceeded 40 billion dollars over the past three years and still maintained a high growth rate according to the National Bureau of Statistics (NBS) (China, 2018). These statistics are impressive enough, it suggests that the Asian cosmetics market is unprecedentedly prosperous. In Asia, the whitening product is an important part of cosmetics, besides, natural products have great potential in the whitening market. From the perspective of consumers, natural products are more skin-friendly, so herbal reagents are readily accepted (Kanlayavattanakul and Lourith, 2018). Meanwhile, increased skin whitening demand leads to the explosion of herbal research.

REGULATION OF MELANOGENESIS

Skin whitening is affected by many factors, but the whitening effect of most herbs depends on regulating melanin synthesis. As an important pigment, melanin is widely distributed in mucosa, retina, and ovary (Slominski et al., 2004), but it mainly deposits in the skin and plays a role in resisting ultraviolet radiation (UVR) (Pinkert and Zeuss, 2018). Melanin is a kind of indole derivative of 3,4 di-hydroxy-phenylalanine (DOPA) produced by melanocytes. It derives from tyrosine through a series of oxidative reactions in melanosomes (Sealy et al., 1982). The first step is known as the Raper-Mason pathway, which depends on tyrosinase (TYR) (Miranda et al., 1988), the key rate-limiting enzyme. Besides, several proteins are involved in the maturation of melanosomes, such as tyrosinase-related protein 1 (TYRP1) and dopachrome tautomerase (DCT or TYRP2) (Bertolotto et al., 1998). After that, melanosomes will be transported to nearby keratinocytes and deposit around the nucleus, where they work and eventually degrade. Proteins involved in this step are Ras-Related Protein Rab-27A (RAB27A), Myosin VA (MYO5A), Fascin Actin-Bundling Protein 1 (FSCN1) (Slominski et al., 2004), and so on. The complete process is called melanogenesis.

The regulation of melanogenesis is complex and can be divided into three aspects: melanin synthesis, transport, and degradation. Melanin synthesis is the most studied area, while transport and degradation are not well understood. First of all, the expression and activation of TYR have the most immediate impact on melanin synthesis and determines the color of human skin (Pavan and Sturm, 2019); second, oxidative stress is another vital factor in promoting melanin synthesis, though it also causes cell damage (Schalka, 2017). Moreover, Microphthalmia-associated transcription factor (MITF) is an important transcription factor that can upregulate the expression of TYR, TYRP1, and TYRP2. It's known that several signaling pathways can regulate MITF, such as the MAPKs (ERK, JNK, and p38) signaling pathway (Kim et al., 2017; Xu et al., 2018); the canonical Wnt signaling pathway, and the cAMP/PKA/CREB signaling pathway (Wang et al., 2017b; Yun et al., 2018). Besides, neighboring keratinocytes and fibroblasts have great impacts (Joly-Tonetti et al., 2018; Koike et al., 2018). It is partly due to the effects of endocrine and paracrine cytokines secreted by keratinocytes and fibroblasts, such as alpha-melanocyte-stimulating hormone (α-MSH), stem cell factor (SCF) and endothelin1 (ET1) (Pei et al., 2018; Yuan and Jin, 2018). The regulating system also plays a role in hyperpigmentation diseases, such as freckles, chloasma, and sunburn (Slominski et al., 2004; Sulem et al., 2007). Most whitening cosmetics work *via* part of the regulating system. For example, ascorbic acid (AA) is a famous antioxidant, arbutin and kojic acid can inhibit tyrosinase activity (Seo et al., 2012; Qu et al., 2018). As reported, the mechanisms of other natural reagents are similar to these cosmetics, the details will be shown later.

THE EFFECTS AND PROBLEMS OF TRADITIONAL ASIAN HERBS IN SKIN WHITENING

The application of herbs in skin whitening starts quite early in Asia. The book *Shen Nong's Herbal Classic* written in more than 2,000 years suggested that semen platycladi, the seed kernel of *Platycladus orientalis (L.) Franco*, can improve people's complexion and appearance. The book *Theory of Medicine Nature* recorded that the rhizome of *Atractylodes macrocephala Koidz.* can ameliorate dark skin (Zhen, 2006). After thousands of years' attempts in developing whitening reagents, lots of useful Asian traditional herbs have been recorded, and some of them have been studied in recent years (Xie and Yu, 1996). Generally, how traditional herbs are used can be divided into three types: formula (consisted of several herbs); extract (a mixture of several components, or a class of compounds, from the same herb), and active ingredient (a purified compound that has a definite molecular structure).

Herbal Formulas

Herbal formulas work *via* the synergy of all components, each herb is necessary, the composition of formulas will follow a particular principle to increase efficacy and reduce side effects (Zhang, 1994). Herbal formulas account for a large proportion of herb use, but the formula-based study in whitening is rare. In Ye's study, researchers screened 50 herbal reagents (32 herbs and 18 herbal formulas) and successfully identified three useful tyrosinase inhibitors: Qian-wang-hong-bai-san, Qiong-yu-gao, and San-bai-tang (Ye et al., 2010a). The authors further revealed that Qian-wang-hong-bai-san could inhibit the p38 MAPK and PKA signaling pathway, and San-bai-tang could inhibit the p38 MAPK signaling pathway (Ye et al., 2010b; Tsang et al., 2012). This formula exists for a long time, but it is the first time to reveal the mechanisms. In addition, a Thai herbal formula AVS073 was reported to affect melanogenesis *via* suppressing the activity of tyrosinase, as well as neutralize ROS *via* increasing glutathione (GSH) biosynthesis and glutathione S-transferase (GST) activity (Panich et al., 2013). A Korean formula LASAP-C exhibited anti-melanogenic efficacy *via* inhibiting melanogenic proteins (TYR, TYRP1, and TYRP2) both in cells and zebrafish (Kim et al., 2016). Moreover, India also has a long history of using herbal formulas and an ancient medical systems: Ayurveda. Therefore, many Indian formulas have been studied in recent years. Ubtan, a traditional formula, was reported to have anti-tyrosinase and antioxidant effects (Biswas et al., 2016). (The composition of formulas showed in **Table 1**.)

These studies provide evidence for further research. However, some problems should be noted. First, the formulas processing, such as water decocting, is mainly based on ancient records or personal experience, but not a uniform standard. Apparently, differences in processing will affect the final composition (Bent and Ko, 2004). Moreover, the composition of formulas is incredibly complex (Yu et al., 2019), it brings uncontrollable interference to research. The inadequate knowledge of herbal formulas is a thorny issue for scientists under current conditions (Dai et al., 2019).

Herbal Extracts

Due to the development of extraction techniques such as High Performance Liquid Chromatography (HPLC) and Ultra Performance Liquid Chromatography (UPLC), the components of herbal extracts can be identified now (Wang et al., 2017a). These techniques help separate crude herbal extracts into several classes: saccharides, glycosides, phenylpropanoids, quinones, flavonoids, terpenes, triterpenes, steroids, and alkaloids (Li et al., 2019). No doubt it is conducive to further research. Different from formulas, there are a lot of research reports on herbal extracts. For example, ginseng (*Panax ginseng* C.A.Mey.) leaves extract is found to be effective in moisturizing, anti-aging, freckle-removing, and skin whitening (Jimenez-Perez et al., 2018). Ganoderma lucidum polysaccharides can reduce melanogenesis by inhibiting cAMP/PKA and ROS/MAPK signaling pathways, as well as inhibiting paracrine effects

TABLE 1 | The information of Asian herbal formulas.

Study	Formula	Species, concentration	Mechanisms	Models
Ye et al. (2010a); Tsang et al. (2012)	Qian-wang-hong-bai-san	tubers of *Bletilla striata* (Thunb.) Reichb. f., tubers of ***Sauromatum giganteum*** **(Engl.) Cusimano & Hett. (syn**. *Typhonium giganteum* Engl.**)**, pericarps of *Punica granatum* L., fruits of *Benincasa hispida* (Thunb.) Cogn., With the ratio of 1:1:1:1.	suppressing tyrosinase activity and expression; inhibiting p38 MAPK signaling pathway; inhibiting PKA/CREB signaling pathway	mushroom tyrosinase; B16 cells
Ye et al. (2010a)	Qiong-yu-gao	roots and rhizomes of *Panax ginseng* C. A. Mey., roots of *Rehmannia glutinosa* Libosch., rhizomes of *Smilax glabra* Roxb. With the ratio of 1:1:1.	suppressing tyrosinase activity	mushroom tyrosinase; B16 cells
Ye et al. (2010a); Ye et al. (2010b)	San-bai-tang	rhizomes of *Atractylodes macrocephala* Koidz., rhizomes of *Smilax glabra* Roxb., roots of *Paeonia lactiflora* Pall., With the ratio of 1:1:1.	suppressing tyrosinase activity and expression; inhibiting p38 MAPK signaling pathway and MITF expression	mushroom tyrosinase; B16 cells
Panich et al. (2013)	Ayurved Siriraj Brand Wattana formula (AVS073)	*Piper nigrum* (L.), *Boesenbergia rotunda* (L.) Manf., *Cyperus rotundus* (L.), *Tinospora crispa* **(L.) Hook.f. & Thomson**, *Terminalia chebula* Retz., *Cladogynos orientalis* **Zipp. ex Span.**, *Derris scandens* (Roxb.) Benth., *Anamirta cocculus* (L.) **Wight & Arn.**, ***Putranjiva roxburghii*** **Wall. (syn.** *Drypetes roxburghii* (Wall.)**)**, *Cinnamomum siamense* Craib., ***Ferulaa*** *assa-foetida* L., *Aegle marmelos* (L.) **Corrêa**, ***Conioselinum vaginatum*** **(Spreng.) Thell. (syn.** *Conioselinum univittatum* Turcz. **ex Kar. & Kir.)**, ***Aucklandia costus*** **Falc. (syn.** *Saussurea lappa* **(Decne.) Sch.Bip.)**, ***Cryptolepis dubia*** **(Burm.f.) M.R.Almeida (syn.** *Cryptolepis buchananii* Roem. & Schult.). Concentration not provided.	suppressing tyrosinase activity and mRNA; inhibiting ROS formation	G361 cells
Kim et al. (2016)	LASAP-C	root of *Rehmannia glutinosa* Libosch. var. purpurea Makino, 100g fruit of *Lycium chinense* Mill., 50 g root of *Scutellaria baicalensis* Georgi, 50 g root of *Angelica dahurica* (Hoffm.) Benth. & Hook.f. **ex Franch. & Sav.** 35 g	suppressing tyrosinase activity and expression	B16F10 cells zebrafish
Biswas et al. (2016)	Ubtan (UF-1 to UF-4)	rhizome of *Curcuma longa* L. seeds of *Cicer arietinum* L. heartwood of *Santalum album* L. With the ratio of 2:2:2 (UF-1), 1:2:2 (UF-2), 2:1:2 (UF-3) and 2:2:1 (UF-4)	antioxidant; sun protection; suppressing tyrosinase activity	*in vitro*: mushroom tyrosinase

(Hu et al., 2019; Jiang et al., 2019). Goji berry (*Lycium chinense* Mill.) root extract can result in depigmentation *via* suppressing oxidation, MAPK and PKA signaling pathways (Huang et al., 2014). *Gastrodia elata* Blume and *Foeniculum vulgare* **Mill**. fruits extracts can resist α-MSH or UV-induced melanogenesis (Nam and Lee, 2016; Shim et al., 2017). Essential oils from the leaves of *Pogostemon plectrantoides* Desf. were tyrosinase inhibitors (Suganya et al., 2015). What is more, a clinical study reported that polypodium leucotomos extract treatment is safe and effective for melasma patients (Goh et al., 2018).

As we all know, growing conditions (soil, water, climate), growth time, and harvest time have great impacts on herbs in cultivation (Yuan et al., 2016; Olennikov et al., 2017; Zhang et al., 2017). These factors will subsequently influence the components of herbal extracts, so do their effects (Bent and Ko, 2004). Furthermore, different extraction methods yield different ingredients (Lin et al., 2019). For instance, Wang et al. compared the effects of water and ethanol extracts of *Cuscuta chinensis* **Lam.** seeds in B16F10 cells and zebrafish; it is impressive that water extract inhibited tyrosinase activity, but ethanol extract worked oppositely (Wang et al., 2014). What is more, many ingredients widely exist in herbs, thus different herbal extracts may have similar components (Yuan et al., 2012; Wu et al., 2018), while the content of special ingredients tends to be lower (Ho et al., 2013; Tian et al., 2019). For these reasons, it is hard to guarantee the reliability of experimental results.

Active Ingredients

With the renovation of extraction techniques, such as Enzyme-Assisted Extraction (EAE), Supercritical-Fluid Extraction (SFE), and Microwave-Assisted Extraction (MAE) (Bilal and Iqbal, 2020), a large number of active ingredients have been purified and identified, some of them show good performance in anti-tumor, anti-inflammatory, antioxidation, and skin whitening (Gao et al., 2019; Zeng et al., 2019b). Many famous herbs have been well studied, such as licorice (*Glycyrrhiza* uralensis **Fisch. ex DC.**), ginseng, and aloe (*Aloe vera* (L.) Burm.f.). Chen et al. confirmed that glabridin (extracted from licorice) reversibly inhibits tyrosinase in a non-competitive manner (Chen et al., 2016). Besides, floralginsenoside A (extracted from ginseng) showed anti-melanogenesis effects in cells and zebrafish *via* regulating MITF expression and ERK activation (Lee et al., 2017). Moreover, aloin (extracted from aloe) led to skin lightening *via* alpha-adrenergic receptor stimulation (Ali et al., 2012). Betulinic acid (extracted from *Dillenia indica* L.) exhibited non-competitive mode of tyrosinase inhibition (Biswas et al., 2017). Bixin and norbixin (from *Bixa orellana* L.) inhibited both melanin synthesis and tyrosinase activity (Anantharaman et al., 2016). 2-hydroxy-4-mehoxybenzaldehyde (MBALD) and its crude extract (extracted from *Hemidesmus indicus* [L.] R. Br. ex Schult.) could inhibit monophenolase activity (Kundu and Mitra, 2014). As the research object is more clear, these findings are more convincing to support the whitening effect of herbs.

Screening active ingredients is an important part of the herbal study, and it has great application prospects. But unlike the success in research, there are still many problems with herbal ingredients before they can be used. First, most natural ingredients are difficult to extract and purify on a large scale (Bai et al., 2014), and extraction costs are a key factor limiting the conversion of ingredients into products. Second, many herbal ingredients only show moderate effects and are unstable under normal conditions, their performance depends on the structure and properties (Manda et al., 2014; Ho et al., 2016; Lyles et al., 2017). Thus, the molecular structure of some ingredients will be further improved before use, research in this area is under development.

THE STATUS OF ASIAN HERBAL RESEARCH IN SKIN WHITENING

In addition to finding problems by reviewing previous studies, it is also important to have a comprehensive understanding by statistics. Thus, we collected Asian herbal studies published between January 2017 and May 2020 and conducted a multifaceted analysis, aiming to understand the research status of Asian herbs in skin whitening, as well as to assess the overall quality and value of these studies. We used "skin whitening" and/or "Asian herb" as keywords to retrieve articles by Web of Science, the selected databases were Web of Science Core Collection, BIOSIS Citation Index, and MEDLINE®, the time frame was from January 2017 to May 2020. After that, we sorted the lists by academic citations and reviewed the 300 most cited articles in detail, then removed studies that were not associated with Asian herbs. Finally, we collected 90 studies for subsequent analysis. (The information of studies we collected were provided in *Supplementary Materials*.)

Overview of Asian Herbal Research

Similar to the size of cosmetics markets, 72 studies were conducted in South Korea (42 studies, 46.7%), China (19 studies, 21.1%), Thailand (6 studies, 6.7%), and Japan (5 studies, 5.6%); 9 studies were conducted in Turkey, Pakistan, Iran, India, and Kuwait; the other 9 studies were cooperative projects between several Asian countries (**Figure 1A**). The geographical distribution of studies is related to the scientific research level, to some extent, it also can reflect the cosmetic market size and whitening demand. In another perspective, though only a few studies were conducted in countries other than Korea, China, Thailand, and Japan, the optimistic explanation is that the whitening markets in these countries have potential, and their herbal research are developing. It is known that India also has a lot of studies focused on herbs and depigmentation (Mukherjee et al., 2018). Further, we grouped studies based on reagent types. Unsurprisingly, studies mainly focused on herbal extracts (38 studies, 42.2%) and active ingredients (38 studies, 42.2%), and they share the same proportion. Besides, there are 13 studies reported both extracts and active ingredients (14.4%, labeled "Combined"), but only 1

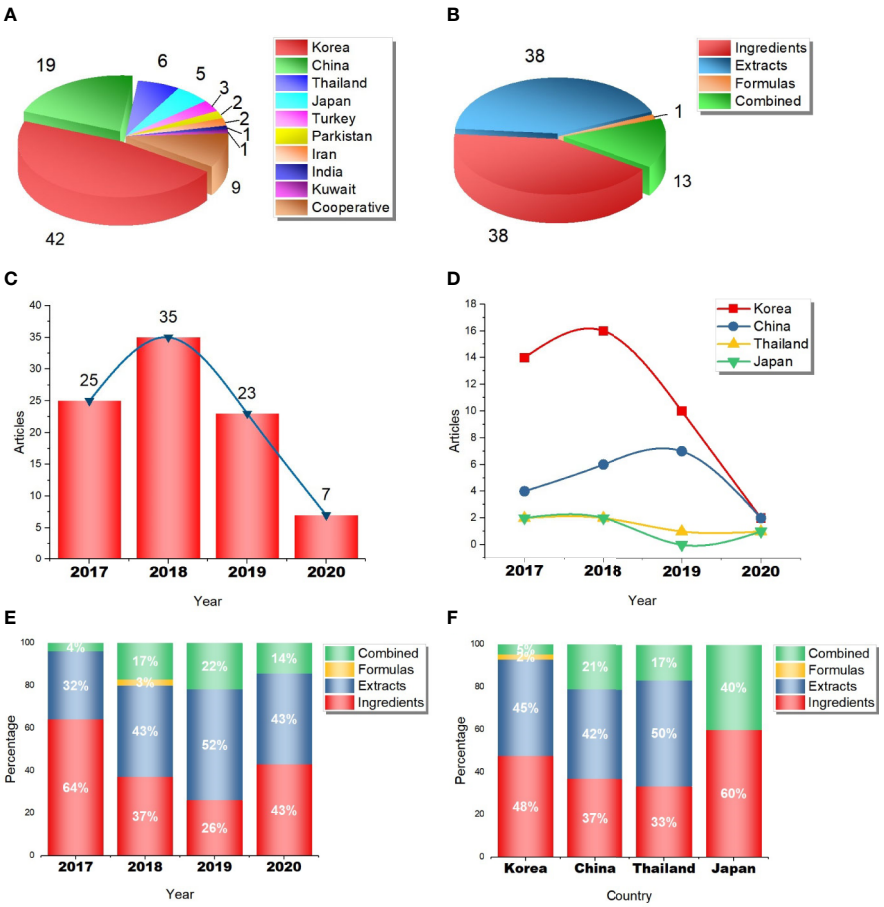

FIGURE 1 | Overview of 90 Asian herbal studies in skin whitening. **(A)** The number of studies in different countries; **(B)** the number of studies on different reagent types; **(C)** the number of studies from 2017 to 2019; **(D)** the studies in four countries from 2017 to 2019; **(E)** the percentage of different reagent types from 2017 to 2019; **(F)** the percentage of different reagent types in four countries.

study involved herbal formulas (**Figure 1B**). The result may have something to do with the difficulties in studying three types of herbal reagents. As mentioned above, there are too many distractions in studying formulas.

The whitening market is still growing in Asia, research advances and market trends complement each other. According to our data, from 2017 to 2018, the number of studies increased from 25 to 35; but curiously, the number fell to 23 in 2019 and was not getting better in the first half of 2020 (**Figure 1C**). However, on the one hand, this could be a mistake caused by article collection, because we only reviewed the 300 most cited articles; on the other hand, we can't rule out the impacts of delay in database updating of Web of Science. Likewise, studies in Korea was increased in 2018 and decreased in 2019, but China was still on the rise (**Figure 1D**). Partly because China's scientific research, as a rising star, is developing fast. Though herbal research has not met a bottleneck, we should be aware that we already face some challenges. With the explosion of studies in skin whitening, the requirements are getting higher now.

Then, we further subdivided the studies by three reagent types and analyzed the differences between years and countries. Though the overall attention paid to herbal extracts and active ingredients is almost the same (**Figure 1B**), it seems like the proportion of extract-related studies was increasing from 2017 to 2019, so did that of combined studies (reported both extracts and active ingredients). In contrast, the proportion of ingredient-related studies had a clear decline (**Figure 1E**). We don't yet know what this change means but have speculation. As new techniques and research facilities become more readily available, researchers may prefer to screen raw herbal materials rather than purchase purified ingredients, this helps to discover new reagents. Moreover, the attention paid to herbal extracts and active ingredients is slightly different between Korea and China, while Thailand and Japan have too few studies to be representative (**Figure 1F**).

Quality and Value of Asian Herbal Studies

There is no doubt that Asian herbal research is developing well in skin whitening, and plenty of effective reagents have been found. But sadly, scattered studies are easy to ignore, their findings may also have limitations. Thus, to learn more about the overall quality of Asian herbal studies, we moved on and evaluated the scientificity and academic value of 90 collected studies.

First, we divided studies into two groups: active ingredients and mixtures (including herbal extracts, formula, and combined studies). The evaluation criteria include information about (1) the source of herbal materials and ingredients (Source), (2) the processing method of raw materials (Processing), (3) the composition determination method of herbal extracts and ingredients, such as HPLC and UPLC (Quality control). For purchased herbal reagents, we assumed they met three criteria if detailed merchant information was provided. In this way, about 80% of the studies stated the sources and processing methods of herbal materials (**Figures 2A, B**). But only 65% of mixture-related studies provided quality control information (**Figure 2B**), which means that nearly 1/3 of the studies can not guarantee the quality of herbal extracts. Moreover, 82% of ingredient-related studies performed quality control (**Figure 2A**), but that does not mean they are scientific enough, because few of them stated the purity of the compounds. Therefore, we should be cautious about the credibility of these studies.

To assess the academic value, we also calculated the research models in 90 studies. It is surprised to find that only 10 (11.1%) of them carried out *in vivo* experiments (**Figure 2C**), the models include volunteers, zebrafish, mice, and guinea pigs (**Figure 2D**). The other 80 studies conducted *in vitro* experiments (**Figure 2E**), 57 (71.3%) of them used only mushroom tyrosinase, 13 (16.3%) of them used only mice cell lines (mostly B16 cells) and human melanoma cell lines, with or without mushroom tyrosinase; only 9 studies used human epidermal melanocytes (HEMs) and 3-dimensional human skin equivalents (3D skin). That is to say, only 1/10 of the studies showed the *in vivo* effects of herbs, and another 1/10 showed whitening evidence in human melanocytes. Although this is an acceptable proportion, there is room for further improvement.

In the 90 studies we collected, most herbal reagents regulate melanogenesis *via* part of the mechanisms previously mentioned. About 81% of the studies reported a decrease in tyrosinase activity, 40% reported antioxidant effect, and 49% observed downregulation of MITF expression. Otherwise, about 2% of the studies explored the sunscreen effect. When it comes to further mechanisms, only 20% of the studies reported a change in MAPK signaling pathway (mostly ERK and p38), and 13% involved CREB/AKT signaling pathway, etc. (**Figure 2F**). The main mechanisms of these herbal reagents are showed in **Figure 3**. Besides, the data show that studies are mainly focused on the ani-tyrosinase and antioxidant effects of herbal reagents, which are common characteristics of most herbs, thus their biological effects have not been thoroughly explored.

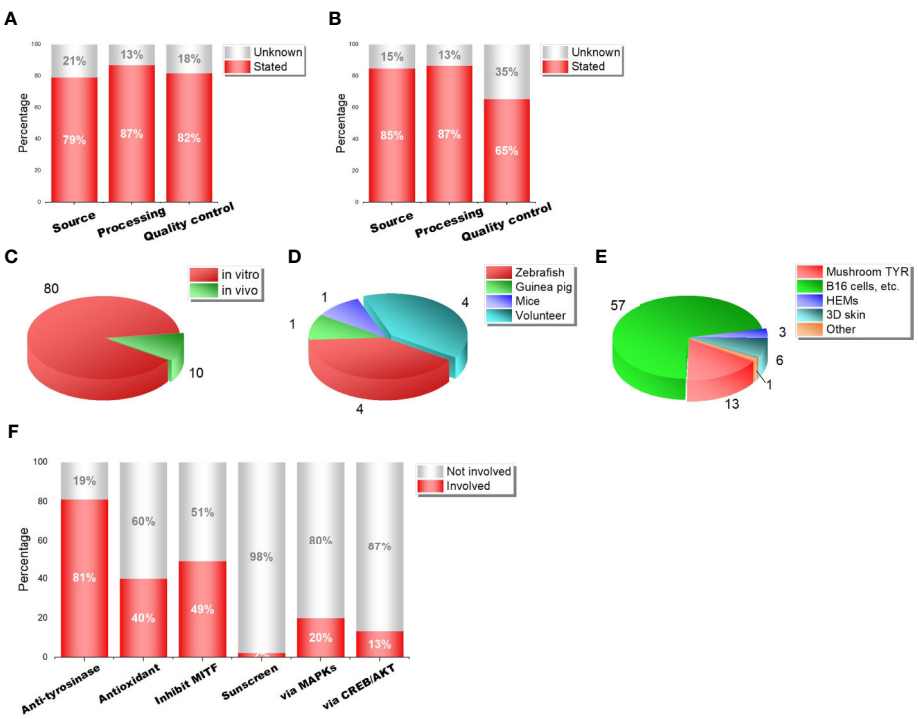

FIGURE 2 | Scientificity and academic value of 90 Asian herbal studies. **(A)** the quality control of ingredient-related studies; **(B)** the quality control of mixture-related studies (herbal formula, extracts, and combined studies); **(C)** the number of *in vitro* and *in vivo* studies; **(D)** the models of *in vivo* studies; **(E)** the models of *in vitro* studies; **(F)** the percentage of different mechanisms involved in studies.

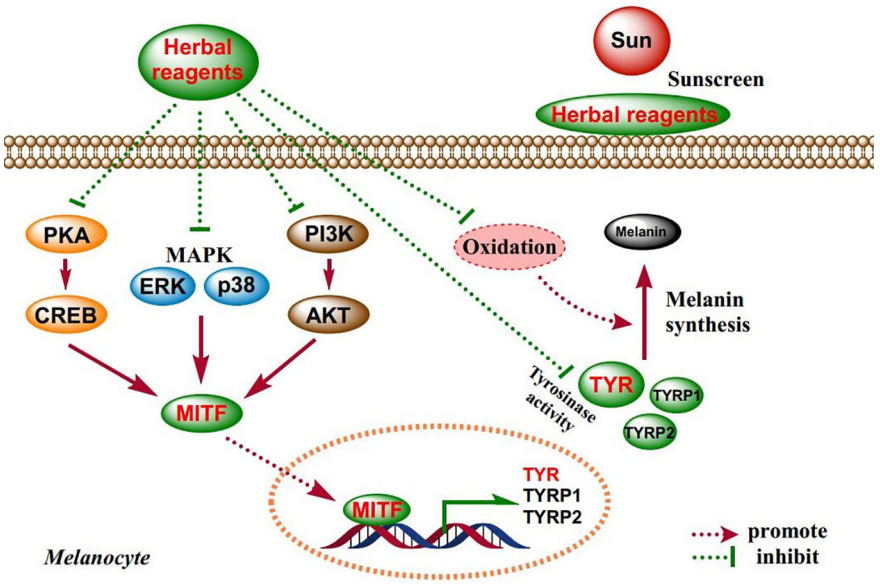

FIGURE 3 | Schematic diagram of the mechanisms of herbal reagents in 90 studies.

CHALLENGES AND PROSPECTS

In Asia, whitening cosmetics are in high demand, and leading to great progress in herbal research. However, the downside also deserves attention. In this work, we reviewed whitening-related studies from a comprehensive view and found some problems. One of them is that herbal components are complex and easily affected by multiple factors, which brings problems to studying herbal formula and extract, and also affects the reliability of the results. In contrast, active ingredients are the focus of research. The quality of most studies is reliable, but ingredient purification is a tough job. In a big way, Asian herbal research is not deep and systematic enough, because studies still focus on the discovery of new ingredients, rather than mechanism exploration and application. Also, there are few clinical studies on whitening. At present, the market for natural whitening cosmetics is a mess. On the one hand, research findings rarely translate into products; on the other hand, substandard products emerge one after another due to supervision loopholes (Desmedt et al., 2016). Many herbal reagents exhibit pharmacological properties (Zeng et al., 2019a) and can affect the structure and function of cells and organs, including the skin (Imokawa, 2008). Although herbal reagents are moderate, their side effects should be taken seriously, which have been ignored in the past.

In order to promote the application and development of traditional Asian herbs in whitening, all issues should be addressed carefully. Such as, the focus of herbal research should shift from quantity to quality and promote achievements transformation. At present, researchers are trying to synthesize herbal ingredients and derivatives, aiming to enhance their advantages and improve defects (Gonzalez-Sabin et al., 2011). From another point of view, synthetic and semi-synthetic natural ingredients may become a new hotspot in the future (Lee et al., 2016; Pillaiyar et al., 2017). In Asia, traditional herbs have been used over thousands of years, but have been ignored in the past century. In skin whitening, the discovery of natural ingredients such as arbutin was a surprise (Akiu et al., 1991; Chakraborty et al., 1998). In China alone, more than 10,000 herbs have been recorded (Xie and Yu, 1996), compared with this huge "herbal ingredient pool," the findings so far have only scratched the surface (Zhao et al., 2020). Given the advances of techniques and the explosion of research, traditional Asian herbs need a new stage towards application.

SEARCH STRATEGIES

Most materials in this review were obtained from Web of Science and PubMed; only documents covered by Science Citation Index (SCI) were selected. A few materials were obtained from ancient medical books, which were collected in the library of Central South University. Some keywords used in retrieving are provided below: Asian herbs, traditional herbs, melanogenesis, skin whitening. The 90 studies collected for statistical purposes were not directly cited in the paper, and their information were provided in the **Supplementary Materials**.

AUTHOR CONTRIBUTIONS

YH: collected the materials and drafted the manuscript. HZ: participated in the collection and screening of studies and provided analytical methods. JH: guided the analysis and

arrangement of literature. LJ: recorded information and made tables. QZ and JC: put forward ideas, provided a framework for writing, checked and corrected writing problems. All authors contributed to the article and approved the submitted version.

FUNDING

The authors thank the financial support from the National Natural Science Foundation of China (No. 81703101), the New Xiangya Talent Projects of the Third Xiangya Hospital of Central South University (No. JY201623 and No. 20170301), the Natural Science Foundation of Hunan Province (No. 2018JJ3788 and No. 2018JJ3793), the Project of Health and Family Planning Commission of Hunan Province (No. C2019173), and the Fundamental Research Funds for the Central Universities of Central South University (No. 2020zzts199).

SUPPLEMENTARY MATERIAL

The Supplementary Material for this article can be found online at: https://www.frontiersin.org/articles/10.3389/fphar.2020.00982/full#supplementary-material

REFERENCES

Akiu, S., Suzuki, Y., Asahara, T., Fujinuma, Y., and Fukuda, M. (1991). Inhibitory effect of arbutin on melanogenesis–biochemical study using cultured B16 melanoma cells. *Nihon Hifuka Gakkai Zasshi* 101, 609–613.

Ali, S. A., Galgut, J. M., and Choudhary, R. K. (2012). On the novel action of melanolysis by a leaf extract of Aloe vera and its active ingredient aloin, potent skin depigmenting agents. *Planta Med.* 78, 767–771. doi: 10.1055/s-0031-1298406

Anantharaman, A., Hemachandran, H., Priya, R. R., Sankari, M., Gopalakrishnan, M., Palanisami, N., et al. (2016). Inhibitory effect of apocarotenoids on the activity of tyrosinase: Multi-spectroscopic and docking studies. *J. Biosci. Bioeng.* 121, 13–20. doi: 10.1016/j.jbiosc.2015.05.007

Bai, Y., Bi, H., Zhuang, Y., Liu, C., Cai, T., Liu, X., et al. (2014). Production of salidroside in metabolically engineered Escherichia coli. *Sci. Rep.* 4, 6640. doi: 10.1038/srep06640

Bent, S., and Ko, R. (2004). Commonly used herbal medicines in the United States: a review. *Am. J. Med.* 116, 478–485. doi: 10.1016/j.amjmed.2003.10.036

Bertolotto, C., Abbe, P., Hemesath, T. J., Bille, K., Fisher, D. E., Ortonne, J. P., et al. (1998). Microphthalmia gene product as a signal transducer in cAMP-induced differentiation of melanocytes. *J. Cell Biol.* 142, 827–835. doi: 10.1083/jcb.142.3.827

Bilal, M., and Iqbal, H. M. N. (2020). Biologically active macromolecules: Extraction strategies, therapeutic potential and biomedical perspective. *Int. J. Biol. Macromol.* 151, 1–18. doi: 10.1016/j.ijbiomac.2020.02.037

Biswas, R., Mukherjee, P. K., Kar, A., Bahadur, S., Harwansh, R. K., Biswas, S., et al. (2016). Evaluation of Ubtan - A traditional indian skin care formulation. *J. Ethnopharmacol.* 192, 283–291. doi: 10.1016/j.jep.2016.07.034

Biswas, R., Chanda, J., Kar, A., and Mukherjee, P. K. (2017). Tyrosinase inhibitory mechanism of betulinic acid from Dillenia indica. *Food Chem.* 232, 689–696. doi: 10.1016/j.foodchem.2017.04.008

Chakraborty, A. K., Funasaka, Y., Komoto, M., and Ichihashi, M. (1998). Effect of arbutin on melanogenic proteins in human melanocytes. *Pigment. Cell Res.* 11, 206–212. doi: 10.1111/j.1600-0749.1998.tb00731.x

Chen, J., Yu, X., and Huang, Y. (2016). Inhibitory mechanisms of glabridin on tyrosinase. *Spectrochim. Acta A Mol. Biomol. Spectrosc.* 168, 111–117. doi: 10.1016/j.saa.2016.06.008

China, N.B.O.S.O. (2018). *Total Retail Sales of Consumer Goods*, [Online]. http://www.stats.gov.cn/english/. [Accessed].

Dai, Y., Li, Q., Tong, J., Verpoorte, R., Zhao, S. J., Qin, X. M., et al. (2019). Quality marker identification based on standard decoction of differently processed materials of Ephedrae Herba. *J. Ethnopharmacol.* 237, 47–54. doi: 10.1016/j.jep.2019.03.025

Desmedt, B., Courselle, P., De Beer, J. O., Rogiers, V., Grosber, M., Deconinck, E., et al. (2016). Overview of skin whitening agents with an insight into the illegal cosmetic market in Europe. *J. Eur. Acad. Dermatol. Venereol.* 30, 943–950. doi: 10.1111/jdv.13595

Efferth, T. (2017). From ancient herb to modern drug: Artemisia annua and artemisinin for cancer therapy. *Semin. Cancer Biol.* 46, 65–83. doi: 10.1016/j.semcancer.2017.02.009

Espinosa-Leal, C. A., and Garcia-Lara, S. (2019). Current Methods for the Discovery of New Active Ingredients from Natural Products for Cosmeceutical Applications. *Planta Med.* 85, 535–551. doi: 10.1055/a-0857-6633

Gao, S. M., Liu, J. S., Wang, M., Cao, T. T., Qi, Y. D., Zhang, B. G., et al. (2018). Traditional uses, phytochemistry, pharmacology and toxicology of Codonopsis: A review. *J. Ethnopharmacol.* 219, 50–70. doi: 10.1016/j.jep.2018.02.039

Gao, T., Zhao, P., Yu, X., Cao, S., Zhang, B., and Dai, M. (2019). Use of Saikosaponin D and JNK inhibitor SP600125, alone or in combination, inhibits malignant properties of human osteosarcoma U2 cells. *Am. J. Transl. Res.* 11, 2070–2080.

Goh, C. L., Chuah, S. Y., Tien, S., Thng, G., Vitale, M. A., and Delgado-Rubin, A. (2018). Double-blind, Placebo-controlled Trial to Evaluate the Effectiveness of Polypodium Leucotomos Extract in the Treatment of Melasma in Asian Skin: A Pilot Study. *J. Clin. Aesthet. Dermatol.* 11, 14–19.

Gonzalez-Sabin, J., Moran-Ramallal, R., and Rebolledo, F. (2011). Regioselective enzymatic acylation of complex natural products: expanding molecular diversity. *Chem. Soc. Rev.* 40, 5321–5335. doi: 10.1039/c1cs15081b

Ho, L. J., Chang, W. L., Chen, A., Chao, P., and Lai, J. H. (2013). Differential immunomodulatory effects by Tripterygium wilfordii Hook f-derived refined extract PG27 and its purified component PG490 (triptolide) in human peripheral blood T cells: potential therapeutics for arthritis and possible mechanisms explaining in part Chinese herbal theory "Junn-Chenn-Zuou-SS". *J. Transl. Med.* 11, 294. doi: 10.1186/1479-5876-11-294

Ho, N. H., Inbaraj, B. S., and Chen, B. H. (2016). Utilization of Microemulsions from Rhinacanthus nasutus (L.) Kurz to Improve Carotenoid Bioavailability. *Sci. Rep.* 6, 25426. doi: 10.1038/srep25426

Hu, S., Huang, J., Pei, S., Ouyang, Y., Ding, Y., Jiang, L., et al. (2019). Ganoderma lucidum polysaccharide inhibits UVB-induced melanogenesis by antagonizing cAMP/PKA and ROS/MAPK signaling pathways. *J. Cell Physiol.* 234, 7330–7340. doi: 10.1002/jcp.27492

Huang, H. C., Huang, W. Y., Tsai, T. C., Hsieh, W. Y., Ko, W. P., Chang, K. J., et al. (2014). Supercritical fluid extract of Lycium chinense Miller root inhibition of melanin production and its potential mechanisms of action. *BMC Complement. Altern. Med.* 14, 208. doi: 10.1186/1472-6882-14-208

Imokawa, G. (2008). Recent advances in characterizing biological mechanisms underlying UV-induced wrinkles: a pivotal role of fibrobrast-derived elastase. *Arch. Dermatol. Res.* 300 (Suppl 1), S7–20. doi: 10.1007/s00403-007-0798-x

Jiang, L., Huang, J., Lu, J., Hu, S., Pei, S., Ouyang, Y., et al. (2019). Ganoderma lucidum polysaccharide reduces melanogenesis by inhibiting the paracrine effects of keratinocytes and fibroblasts via IL-6/STAT3/FGF2 pathway. *J. Cell Physiol.* 234 (12), 22799–22808. doi: 10.1002/jcp.28844

Jimenez-Perez, Z. E., Singh, P., Kim, Y. J., Mathiyalagan, R., Kim, D. H., Lee, M. H., et al. (2018). Applications of Panax ginseng leaves-mediated gold nanoparticles in cosmetics relation to antioxidant, moisture retention, and whitening effect on B16BL6 cells. *J. Ginseng Res.* 42, 327–333. doi: 10.1016/j.jgr.2017.04.003

Joly-Tonetti, N., Wibawa, J. I. D., Bell, M., and Tobin, D. J. (2018). An explanation for the mysterious distribution of melanin in human skin: a rare example of asymmetric (melanin) organelle distribution during mitosis of basal layer progenitor keratinocytes. *Br. J. Dermatol.* 179, 1115–1126. doi: 10.1111/bjd.16926

Kanlayavattanakul, M., and Lourith, N. (2018). Plants and Natural Products for the Treatment of Skin Hyperpigmentation - A Review. *Planta Med.* 84, 988–1006. doi: 10.1055/a-0583-0410

Kim, M. K., Bang, C. Y., Kim, M. Y., Lee, J. H., Ro, H., Choi, M. S., et al. (2016). Traditional herbal prescription LASAP-C inhibits melanin synthesis in B16F10 melanoma cells and zebrafish. *BMC Complement. Altern. Med.* 16, 223. doi: 10.1186/s12906-016-1209-7

Kim, Y. M., Cho, S. E., Kim, S. C., Jang, H. J., and Seo, Y. K. (2017). Effects of Extremely Low Frequency Electromagnetic Fields on Melanogenesis through p-ERK and p-SAPK/JNK Pathways in Human Melanocytes. *Int. J. Mol. Sci.* 18. doi: 10.3390/ijms18102120

Koike, S., Yamasaki, K., Yamauchi, T., Inoue, M., Shimada-Ohmori, R., Tsuchiyama, K., et al. (2018). Toll-like receptors 2 and 3 enhance melanogenesis and melanosome transport in human melanocytes. *Pigment. Cell Melanoma Res.* 31, 570–584. doi: 10.1111/pcmr.12703

Kundu, A., and Mitra, A. (2014). Evaluating tyrosinase (monophenolase) inhibitory activity from fragrant roots of Hemidesmus indicus for potent use in herbal products. *Ind. Crops Prod.* 52, 394–399. doi: 10.1016/j.indcrop.2013.10.053

Lee, S. Y., Baek, N., and Nam, T.-G. (2016). Natural, semisynthetic and synthetic tyrosinase inhibitors. *J. Enzyme Inhib. Med. Chem.* 31, 1–13. doi: 10.3109/14756366.2015.1004058

Lee, D. Y., Lee, J., Jeong, Y. T., Byun, G. H., and Kim, J. H. (2017). Melanogenesis inhibition activity of floralginsenoside A from Panax ginseng berry. *J. Ginseng Res.* 41, 602–607. doi: 10.1016/j.jgr.2017.03.005

Leyden, J. J., Shergill, B., Micali, G., Downie, J., and Wallo, W. (2011). Natural options for the management of hyperpigmentation. *J. Eur. Acad. Dermatol. Venereol.* 25, 1140–1145. doi: 10.1111/j.1468-3083.2011.04130.x

Li, Y., Huang, J., Lu, J., Ding, Y., Jiang, L., Hu, S., et al. (2019). The role and mechanism of Asian medicinal plants in treating skin pigmentary disorders. *J. Ethnopharmacol.* 245, 112173. doi: 10.1016/j.jep.2019.112173

Lin, D., Wang, S. H., Song, T. Y., Hsieh, C. W., and Tsai, M. S. (2019). Safety and efficacy of tyrosinase inhibition of Paeonia suffruticosa Andrews extracts on human melanoma cells. *J. Cosmet. Dermatol*. doi: 10.1111/jocd.12902

Lyles, J. T., Kim, A., Nelson, K., Bullard-Roberts, A. L., Hajdari, A., Mustafa, B., et al. (2017). The Chemical and Antibacterial Evaluation of St. John's Wort Oil Macerates Used in Kosovar Traditional Medicine. *Front. Microbiol.* 8, 1639. doi: 10.3389/fmicb.2017.01639

Manda, V. K., Avula, B., Ali, Z., Khan, I. A., Walker, L. A., and Khan, S. I. (2014). Evaluation of in vitro absorption, distribution, metabolism, and excretion (ADME) properties of mitragynine, 7-hydroxymitragynine, and mitraphylline. *Planta Med.* 80, 568–576. doi: 10.1055/s-0034-1382760

Miranda, M., Amicarelli, F., Poma, A., Ragnelli, A. M., and Arcadi, A. (1988). Liposome-entrapped tyrosinase: a tool to investigate the regulation of the Raper-Mason pathway. *Biochim. Biophys. Acta* 966, 276–286. doi: 10.1016/0304-4165(88)90077-3

Mukherjee, P. K., Biswas, R., Sharma, A., Banerjee, S., Biswas, S., and Katiyar, C. K. (2018). Validation of medicinal herbs for anti-tyrosinase potential. *J. Herb. Med.* 14, 1–16. doi: 10.1016/j.hermed.2018.09.002

Nam, J. H., and Lee, D. U. (2016). Foeniculum vulgare extract and its constituent, trans-anethole, inhibit UV-induced melanogenesis via ORAI1 channel inhibition. *J. Dermatol. Sci.* 84, 305–313. doi: 10.1016/j.jdermsci.2016.09.017

Olennikov, D. N., Chirikova, N. K., Kashchenko, N. I., Gornostai, T. G., Selyutina, I. Y., and Zilfikarov, I. N. (2017). Effect of Low Temperature Cultivation on the Phytochemical Profile and Bioactivity of Arctic Plants: A Case of Dracocephalum palmatum. *Int. J. Mol. Sci.* 18. doi: 10.3390/ijms18122579

Panich, U., Pluemsamran, T., Tangsupa-a-Nan, V., Wattanarangsan, J., Phadungrakwittaya, R., Akarasereenont, P., et al. (2013). Protective effect of AVS073, a polyherbal formula, against UVA-induced melanogenesis through a redox mechanism involving glutathione-related antioxidant defense. *BMC Complement. Altern. Med.* 13, 159. doi: 10.1186/1472-6882-13-159

Pavan, W. J., and Sturm, R. A. (2019). The Genetics of Human Skin and Hair Pigmentation. *Annu. Rev. Genomics Hum. Genet.* 20, 41–72. doi: 10.1146/annurev-genom-083118-015230

Pei, S., Huang, J., Chen, J., Hu, S., Lei, L., Fu, C., et al. (2018). UVB-inhibited H19 activates melanogenesis by paracrine effects. *Exp. Dermatol.* 27, 1120–1125. doi: 10.1111/exd.13749

Peltzer, K., Pengpid, S., and James, C. (2016). The globalization of whitening: prevalence of skin lighteners (or bleachers) use and its social correlates among university students in 26 countries. *Int. J. Dermatol.* 55, 165–172. doi: 10.1111/ijd.12860

Pillaiyar, T., Manickam, M., and Namasivayam, V. (2017). Skin whitening agents: medicinal chemistry perspective of tyrosinase inhibitors. *J. Enzyme Inhib. Med. Chem.* 32, 403–425. doi: 10.1080/14756366.2016.1256882

Pinkert, S., and Zeuss, D. (2018). Thermal Biology: Melanin-Based Energy Harvesting across the Tree of Life. *Curr. Biol.* 28, R887–R889. doi: 10.1016/j.cub.2018.07.026

Qu, Z., Na, W., Liu, X., Liu, H., and Su, X. (2018). A novel fluorescence biosensor for sensitivity detection of tyrosinase and acid phosphatase based on nitrogen-doped graphene quantum dots. *Anal. Chim. Acta* 997, 52–59. doi: 10.1016/j.aca.2017.10.010

Scarpa, A., and Guerci, A. (1987). Depigmenting procedures and drugs employed by melanoderm populations. *J. Ethnopharmacol.* 19, 17–66. doi: 10.1016/0378-8741(87)90136-X

Schalka, S. (2017). New data on hyperpigmentation disorders. *J. Eur. Acad. Dermatol. Venereol.* 31 (Suppl 5), 18–21. doi: 10.1111/jdv.14411

Sealy, R. C., Hyde, J. S., Felix, C. C., Menon, I. A., Prota, G., Swartz, H. M., et al. (1982). Novel free radicals in synthetic and natural pheomelanins: distinction between dopa melanins and cysteinyldopa melanins by ESR spectroscopy. *Proc. Natl. Acad. Sci. U.S.A.* 79, 2885–2889. doi: 10.1073/pnas.79.9.2885

Seo, D. H., Jung, J. H., Lee, J. E., Jeon, E. J., Kim, W., and Park, C. S. (2012). Biotechnological production of arbutins (alpha- and beta-arbutins), skin-lightening agents, and their derivatives. *Appl. Microbiol. Biotechnol.* 95, 1417–1425. doi: 10.1007/s00253-012-4297-4

Shim, E., Song, E., Choi, K. S., Choi, H. J., and Hwang, J. (2017). Inhibitory effect of Gastrodia elata Blume extract on alpha-melanocyte stimulating hormone-induced melanogenesis in murine B16F10 melanoma. *Nutr. Res. Pract.* 11, 173–179. doi: 10.4162/nrp.2017.11.3.173

Slominski, A., Tobin, D. J., Shibahara, S., and Wortsman, J. (2004). Melanin pigmentation in mammalian skin and its hormonal regulation. *Physiol. Rev.* 84, 1155–1228. doi: 10.1152/physrev.00044.2003

Suganya, P., Jeyaprakash, K., Mallavarapu, G. R., and Murugan, R. (2015). Comparison of the chemical composition, tyrosinase inhibitory and anti-inflammatory activities of the essential oils of Pogostemon plectranthoides from India. *Ind. Crops Prod.* 69, 300–307. doi: 10.1016/j.indcrop.2015.02.045

Sulem, P., Gudbjartsson, D. F., Stacey, S. N., Helgason, A., Rafnar, T., Magnusson, K. P., et al. (2007). Genetic determinants of hair, eye and skin pigmentation in Europeans. *Nat. Genet.* 39, 1443–1452. doi: 10.1038/ng.2007.13

Tian, X., Liu, H., Qiao, S., Yin, H., Chen, M., Hu, P., et al. (2019). Exploration of the hepatoprotective chemical base of an orally administered herbal formulation (YCHT) in normal and CCl4-intoxicated liver injury rats. Part 2: Hepatic disposition in vivo and hepatoprotective activity in vitro. *J. Ethnopharmacol.* 236, 161–172. doi: 10.1016/j.jep.2019.02.022

Tsang, T. F., Ye, Y., Tai, W. C., Chou, G. X., Leung, A. K., Yu, Z. L., et al. (2012). Inhibition of the p38 and PKA signaling pathways is associated with the anti-melanogenic activity of Qian-wang-hong-bai-san, a Chinese herbal formula, in B16 cells. *J. Ethnopharmacol.* 141, 622–628. doi: 10.1016/j.jep.2011.08.043

Wang, T. J., An, J., Chen, X. H., Deng, Q. D., and Yang, L. (2014). Assessment of Cuscuta chinensis seeds effect on melanogenesis: comparison of water and ethanol fractions in vitro and in vivo. *J. Ethnopharmacol.* 154, 240–248. doi: 10.1016/j.jep.2014.04.016

Wang, L., Liu, L. F., Wang, J. Y., Shi, Z. Q., Chang, W. Q., Chen, M. L., et al. (2017a). A strategy to identify and quantify closely related adulterant herbal materials by mass spectrometry-based partial least squares regression. *Anal. Chim. Acta* 977, 28–35. doi: 10.1016/j.aca.2017.04.023

Wang, Y., Viennet, C., Robin, S., Berthon, J. Y., He, L., and Humbert, P. (2017b). Precise role of dermal fibroblasts on melanocyte pigmentation. *J. Dermatol. Sci.* 88, 159–166. doi: 10.1016/j.jdermsci.2017.06.018

Wu, X., Chan, S. W., Ma, J., Li, P., Shaw, P. C., and Lin, G. (2018). Investigation of association of chemical profiles with the tracheobronchial relaxant activity of Chinese medicinal herb Beimu derived from various Fritillaria species. *J. Ethnopharmacol.* 210, 39–46. doi: 10.1016/j.jep.2017.08.027

Xie, Z. W., and Yu, Y. C. (1996). *National herbal medicine name* (Beijing, China: People's Medical Publishing House).

Xu, Z., Chen, L., Jiang, M., Wang, Q., Zhang, C., and Xiang, L. F. (2018). CCN1/Cyr61 Stimulates Melanogenesis through Integrin alpha6beta1, p38 MAPK, and ERK1/2 Signaling Pathways in Human Epidermal Melanocytes. *J. Invest. Dermatol.* 138, 1825–1833. doi: 10.1016/j.jid.2018.02.029

Ye, Y., Chou, G. X., Mu, D. D., Wang, H., Chu, J. H., Leung, A. K., et al. (2010a). Screening of Chinese herbal medicines for antityrosinase activity in a cell free system and B16 cells. *J. Ethnopharmacol.* 129, 387–390. doi: 10.1016/j.jep.2010.04.009

Ye, Y., Chu, J. H., Wang, H., Xu, H., Chou, G. X., Leung, A. K., et al. (2010b). Involvement of p38 MAPK signaling pathway in the anti-melanogenic effect of San-bai-tang, a Chinese herbal formula, in B16 cells. *J. Ethnopharmacol.* 132, 533–535. doi: 10.1016/j.jep.2010.09.007

Yu, C., Xu, Y., Wang, M., Xie, Z., and Gao, X. (2019). Application of characteristic fragment filtering with ultra high performance liquid chromatography coupled with high-resolution mass spectrometry for comprehensive identification of components in Schisandrae chinensis Fructus. *J. Sep. Sci.* 42, 1323–1331. doi: 10.1002/jssc.201801203

Yuan, X. H., and Jin, Z. H. (2018). Paracrine regulation of melanogenesis. *Br. J. Dermatol.* 178, 632–639. doi: 10.1111/bjd.15651

Yuan, Y., Song, L., Li, M., Liu, G., Chu, Y., Ma, L., et al. (2012). Genetic variation and metabolic pathway intricacy govern the active compound content and quality of the Chinese medicinal plant Lonicera japonica thunb. *BMC Genomics* 13, 195. doi: 10.1186/1471-2164-13-195

Yuan, Y., Huang, M., Pang, Y. X., Yu, F. L., Chen, C., Liu, L. W., et al. (2016). Variations in Essential Oil Yield, Composition, and Antioxidant Activity of Different Plant Organs from Blumea balsamifera (L.) DC. at Different Growth Times. *Molecules* 21. doi: 10.3390/molecules21081024

Yun, C. Y., Mi Ko, S., Pyo Choi, Y., Kim, B. J., Lee, J., Mun Kim, J., et al. (2018). alpha-Viniferin Improves Facial Hyperpigmentation via Accelerating Feedback Termination of cAMP/PKA-Signaled Phosphorylation Circuit in Facultative Melanogenesis. *Theranostics* 8, 2031–2043. doi: 10.7150/thno.24385

Zeng, P., Chen, Y., Zhang, L., and Xing, M. (2019a). Ganoderma lucidum polysaccharide used for treating physical frailty in China. *Prog. Mol. Biol. Transl. Sci.* 163, 179–219. doi: 10.1016/bs.pmbts.2019.02.009

Zeng, P., Li, J., Chen, Y., and Zhang, L. (2019b). The structures and biological functions of polysaccharides from traditional Chinese herbs. *Prog. Mol. Biol. Transl. Sci.* 163, 423–444. doi: 10.1016/bs.pmbts.2019.03.003

Zhang, X., Zhao, Y., Guo, L., Qiu, Z., Huang, L., and Qu, X. (2017). Differences in chemical constituents of Artemisia annua L from different geographical regions in China. *PloS One* 12, e0183047. doi: 10.1371/journal.pone.0183047

Zhang, Z. J. (1994). *Treatise on Febrile and Miscellaneous Diseases* (Shijiazhuang, China: Hebei science and technology press).

Zhao, N., Su, X., Wang, Y., Chen, J., and Zhuang, W. (2020). Traditional Chinese Herbal Medicine for Whitening. *Natural Prod. Commun.* 15. doi: 10.1177/1934578X20905148

Zhen, Q. (2006). *The Theory of Medicine Nature* (Hefei, China: Anhui science & technology press).

Conflict of Interest: The authors declare that the research was conducted in the absence of any commercial or financial relationships that could be construed as a potential conflict of interest.

Copyright © 2020 Hu, Zeng, Huang, Jiang, Chen and Zeng. This is an open-access article distributed under the terms of the Creative Commons Attribution License (CC BY). The use, distribution or reproduction in other forums is permitted, provided the original author(s) and the copyright owner(s) are credited and that the original publication in this journal is cited, in accordance with accepted academic practice. No use, distribution or reproduction is permitted which does not comply with these terms.

frontiers in Pharmacology

ORIGINAL RESEARCH
published: 05 August 2020
doi: 10.3389/fphar.2020.01048

Inhibitory Effect of Cudratrixanthone U on RANKL-Induced Osteoclast Differentiation and Function in Macrophages and BMM Cells

Eun-Nam Kim[1], *Jaeyoung Kwon*[2], *Hyun-Su Lee*[1], *Sooyeun Lee*[1], *Dongho Lee*[3] *and Gil-Saeng Jeong*[1]*

[1] College of Pharmacy, Keimyung University, Daegu, South Korea, [2] Natural Constituents Research Center, Korea Institute of Science and Technology (KIST), Gangneung, South Korea, [3] Department of Biosystems and Biotechnology, College of Life Sciences and Biotechnology, Korea University, Seoul, South Korea

OPEN ACCESS

Edited by:
Hai Yu Xu,
China Academy of Chinese Medical Sciences, China

Reviewed by:
An Qin,
Shanghai Ninth People's Hospital, China
Sang-Hyun Kim,
Kyungpook National University, South Korea

***Correspondence:**
Gil-Saeng Jeong
gsjeong@kmu.ac.kr

Specialty section:
This article was submitted to Ethnopharmacology, a section of the journal Frontiers in Pharmacology

Received: *22 April 2020*
Accepted: *26 June 2020*
Published: *05 August 2020*

Citation:
Kim E-N, Kwon J, Lee H-S, Lee S, Lee D and Jeong G-S (2020) Inhibitory Effect of Cudratrixanthone U on RANKL-Induced Osteoclast Differentiation and Function in Macrophages and BMM Cells. Front. Pharmacol. 11:1048. doi: 10.3389/fphar.2020.01048

Cudratrixanthone U (CTU) is a prenylated xanthone compound isolated from *Maclura tricuspidata* Bureau (Moraceae). Prenylated xanthones have been reported to exhibit a variety of biological activities. However, the effects of prenylated xanthone on osteoclast differentiation and function are still unclear. Excessive bone resorption by osteoclasts is considered a major cause of diseases such as osteoporosis. Accordingly, suppression of excessive osteoclast formation and function is one of strategies for treating osteoclast related bone diseases. In this study, CTU inhibited osteoclast differentiation and function in RAW264.7 macrophages and BMM cells induced by receptor activator of nuclear factor-κB ligand (RANKL). CTU regulated the formation of TRAF6-TAK1 complex in RANKL-induced RAW264.7 macrophages and BMM cells. Osteoclast-specific genes including those encoding matrix metallopeptidase 9 (MMP-9), dendritic cell-specific transmembrane proteins (DC-STAMP), cathepsin K (CTSK) and chemokine CC motif ligand 4 (CCL4) play an important role in bone resorption and migration, and were effectively regulated by CTU. These results suggest that CTU is a potential therapeutic agent in osteoporosis.

Keywords: Cudratrixanthone U, TRAF6, TAK-1, RANKL, CCL4, osteoclast

INTRODUCTION

Bone homeostasis is associated with a balance between bone resorption by osteoclasts and bone formation by osteoblasts. Bone resorption by excessive osteoclast differentiation can lead to disorders such as osteoporosis and rheumatoid arthritis (Boyce et al., 2005; Warren et al., 2015). Therefore, inhibition of bone resorption by excessive osteoclast differentiation plays a key role in the treatment of osteoporosis. Osteoclasts are giant multinucleated cells derived from the mononuclear macrophage family *via* continual proliferation, differentiation and fusion of hematopoietic stem cells. They are involved in bone resorption, and play an essential role in bone formation and control of bone density (Novack and Teitelbaum, 2008; Geng et al., 2017).

Osteoclast formation requires specific activation of the RANKL/RANK (receptor activator of NF-κB ligand and its receptor) system of macrophage or monocyte lineage. These osteoclasts play an essential role in various diseases (Teitelbaum, 2000). Among the TNF receptor-related factors (TRAF) molecules, TRAF6 is an important component of the RANK signaling pathway. When RANKL binds to RANK in preosteoclasts, TRAFs 2, 3, 5, and 6 are recruited, which induces mitogen-activated protein kinase (MAPK) and nuclear factor kappa-light-chain-enhancer of activated B cells (NF-κB) pathways (Kim et al., 1999), and the activation of various signaling pathways. In addition, RANKL stimulation not only activates transforming growth factor beta-activated kinase 1 (TAK1), which is a member of the mitogen-activated protein kinase (MAPK) family, but also activates the TRAF6-TAK1 complex associated with RANK to induce both c-Jun N-terminal kinase (JNK) and NF-kB activation and downstream signaling pathway activator protein 1 (AP-1), and c-Fos/c-Jun dimer induces the expression of primary osteoclast regulatory nuclear factor of activated T cells c1 (NFATc1) (Takayanagi et al., 2002; Kanzaki et al., 2017). Thus, inhibition of these signaling pathways prevents pathological bone loss induced by excessive osteoclast formation. Activated NFATc1 regulates a variety of genes, such as tartrate-resistant acid phosphatase (TRAP), cathepsin K (CTSK), and dendritic cell-specific transmembrane proteins (DC-STAMP), which are essential for osteoclast differentiation and function (Li et al., 2006). Also, the matrix metalloproteinase (MMP)-9 and integrin β3 secreted by osteoclasts are known to promote osteoclast migration and mediate osteoclast bone resorption (Ishibashi et al., 2006). Previous studies have suggested that the inhibition of osteoclast migration is a potential therapeutic target in bone disease, including osteoporosis, and the chemokine CC motif ligand 4 (CCL4) is known to promote the migration and viability of pre-osteoclast cells (Lee et al., 2018). Therefore, inhibition of these genes may play an important therapeutic role in osteoporosis in order to disrupt the differentiation and function of activated osteoclasts.

Maclura tricuspidata Bureau (Moraceae) is a traditional medicinal plant native to Northeast Asia that has long been used for lumbago, hemoptysis, and hematemesis (Jung and Shin, 1990; Chang et al., 2008). In particular, *M. tricuspidata* root is known as "Chuan-po-shi" in traditional Chinese medicine and has been used to treat rheumatism and lumbago, and is one of the most common traditional remedies for cancer in Korea (Kim et al., 2009; Xin et al., 2017). Previous studies have reported that the roots and fruits of *M. tricuspidata* showed various pharmacological activities, such as anti-inflammatory effects (Jeong et al., 2010), cytotoxicity inhibition (Lee et al., 2005), and hepatoprotection (Tian et al., 2005). The major constituents of *M. tricuspidata* include prenylated xanthones and flavonoids, alkaloids, and organic acids (Xin et al., 2017; Li et al., 2018). Prenylated xanthones isolated from *M. tricuspidata* have been reported to inhibit neurotoxicity (Jeong et al., 2008), and exhibit neuroprotective (Kwon et al., 2014), and anti-cancer effects (Seo et al., 2001). Despite these pharmacological activities, studies on bone diseases are still incomplete. Therefore, this study investigated the effect of cudratrixanthone U isolated from *M. tricuspidata* on osteoclast differentiation, migration and bone resorption in RANKL-stimulated RAW264.7 and bone marrow-derived macrophages (BMM) cells.

MATERIALS AND METHODS

Chemicals and Reagents

Minimum Essential Medium Eagle—Alpha Modification (Alpha MEM), fetal bovine serum (FBS), penicillin, and streptomycin were purchased from Welgene Inc. (Korea). Mouse RANKL was purchased from PeproTech (Rocky Hill, NJ, USA). 3-(4,5-Dimethylthiazol-2-yl)-2,5-diphenyltetrazoliumbromide (MTT) was obtained from Amresco Inc. (Solon, OH, USA). Fast Red-violet LB salt, naphthol AS-MX phosphate 4-6-diamidino-2-phenylindole (DAPI) and ρ-nitro-phenylphosphate were obtained from Sigma-Aldrich Fine Chemicals (St. Louis, MO, USA). Antibodies against p-ERK, ERK, p-p38, p38, p-JNK, JNK, NFATc1, c-Fos, integrin β3, MMP-9, CTSK and β-actin were purchased from Cell Signaling Technology (Danvers, MA, USA). Anti-TRAF6, anti-TAK1, IκB-α, p-IκB-α, and NF-κB p65 were obtained from Santa Cruz Biotechnology (Santa Cruz, CA, USA). Also, Antibodies of DC-STAMP and CTSK were obtained Abcam (Cambridge, UK). Secondary antibodies were purchased from Santa Cruz and Cell Signaling Technology. Nuclear and cytoplasmic extraction reagent kit and enhanced chemilu-minescence kit were provided by Pierce Biotechnology (Rockford, IL, USA). Protease inhibitors were purchased from Roche (Hoffmann, NC, USA). Alexa fluor-488 palloidin was acquired from Invitrogen (Waltham, MA, USA). Osteo assay surface multiwell plates were obtained from Corning Inc. (NY, USA). Radioimmunoprecipitation (RIPA) assay buffer and protease and phosphatase inhibitor cocktail were purchased from Fisher Scientific Inc. (Waltham, MA, USA).

Plant Materials and Isolation of Compounds

A voucher specimen (accession number KH1-4-090814) was deposited at the Department of Biosystems and Biotechnology, Korea University, Seoul, Korea. We isolated cudratrixanthone U (CTU) from the bark of *M. tricuspidata*. CTU was extracted as reported previously and structurally identified using nuclear magnetic resonance (NMR) and high-resolution electrospray ionization mass spectrometry (HRESIMS) (Kwon et al., 2016).

Cell Culture and Viability Assays

RAW 264.7 and BMM cells (ATCC, Manassas, VA, USA) were cultured in alpha-MEM supplemented with 10% heat-inactivated FBS, 2 mM L-glutamine, and 100 U/ml penicillin/streptomycin. Incubations were carried out at 37°C in 5% CO_2. We performed an MTT assay following the manufacturer's instructions to detect CTU cytotoxicity. RAW264.7 and BMM cells were seeded on a 96-well plate at a concentration of 5×10^3 cells/ml, followed by treatment with different concentrations and

incubation for 120 h. The concentration of MTT solution was 50 mg/ml, and the absorbance at 490 nm was measured by an ELISA plate reader (Männedorf, Swiss).

Osteoclast Differentiation

RAW 264.7 and BMM cells were seeded on 24-well plates (5×10^3 cells/well) with complete alpha-MEM containing RANKL (50 ng/ml) in the presence of CTU for 5 days at 37°C and 5% CO_2.

Tartrate-Resistant Acid Phosphatase (TRAP) Staining and Activity

After differentiation and osteoclast formation as described above, cells were washed and fixed with 4% paraformaldehyde for 10 min, permeabilized with 0.1% Triton X-100, and finally stained for TRAP with the Leukocyte Acid Phosphatase Kit (Sigma, Cat. No. 387A-1KT). Fixed cells were assayed for tartrate-resistant acid phosphatase (TRAP) activity, according to the manufacturer's instructions (Saint Louis, MO, USA).

Actin Ring and DAPI Staining

RAW264.7 and BMM cells were cultured in alpha-MEM, with or without CTU for 5 days. The cells were washed three times with phosphate-buffered saline (PBS) and fixed in 4% formalin for 15 min. The cells were then stained with fluorescein isothiocyanate (FITC)-phalloidin solution for 1 h, and the nuclei were sequentially stained with 2.5 μg/ml 4′,6-diamidino-2-phenylindole (DAPI) solution for 10 min. The images were captured using a fluorescence Olympus IX microscope 71-F3 2PH (Tokyo, Japan).

Bone Resorption Assay

RAW264.7 and BMM cells were seeded with alpha-MEM containing RANKL (50 ng/ml) in the presence of CTU (0.5, 1, 2, 5 μm) into the wells of an osteo assay surface well for 12 days at 37°C and 5% CO_2. After 10 days, RAW 264.7 cells were removed by 5% sodium hypochlorite (Saint Louis, MO, USA) treatment and resorption pits were visualized under a light Olympus IX microscope 71-F3 2PH. The resorption area was calculated and analyzed using Image-J software Version 1.52i (USA).

Cell Migration Assay

RAW264.7 and BMM cells (1.5×10^4 cells/well) were incubated in a 24-well plate for 24 h, followed by constant scratching. Next, cells were treated with α-MEM and 10% FBS with or without RANKL (50 ng/ml) and CTU, and the cells migrating for 5 days were counted with Incucyte® Live-Cell analysis systems (Göttingen, Germany).

Quantitative Real-Time Polymerase Chain Reaction (qRT-PCR)

Total RNA was extracted from the cells using TRIzol reagent (Bioneer, Korea) according to the manufacturer's instructions. PCR reaction conditions included 1 μl primer, 11 μl nuclease-free ultrapure water, 4 μl 5× reaction buffer, 1 μl RiboLock RNA enzyme inhibitor (20 U/μl), 2 μl 10mM dNTP mix, and 1 μl RevertAid M-MuLV reverse transcriptase (200 U/μl) (Thermo Fisher Scientific, USA). The cycling conditions were 40 cycles at 50°C for 2 min, 95°C initial denaturation for 10 min, 95°C denaturation for 15 s, and 60°C annealing for 30 s. The primer sequences used are listed in **Table 1**.

Cytosolic and Nuclear Protein Extraction

RAW 264.7 and BMM cells were seeded on culture dishes at a density of 2.5×10^5 cells/dish and treated with indicated concentrations of CTU (0.5, 1, 2, and 5 μM), stimulated with RANKL (50 ng/ml), incubated at 37°C with 5% CO_2, and then lysed using the RIPA buffer. We prepared the cytosolic and nuclear extracts using an NE-PER nuclear and cytoplasmic extraction reagents kit, according to the manufacturer's instructions.

Co-Immunoprecipitation (Co-IP)

RAW264.7 and BMM cells treated with or without RANKL in the presence or absence of CTU (2, 5 μM) was digested using RIPA buffer and centrifuged for 30 min. First, the antibody for the targets TRAF6 and TRAF6-specific IgG was incubated with the Thermo dynabead protein G kit in a tube for 10 min, and the antibody was washed away by placing the tube in a Dynamagnet and removing the supernatant. For immunoprecipitation, cell lysates extracted were incubated with anti-TRAF6 or anti-TAK1 antibody for 1 h at 4°C, followed by 1 h incubation at 4°C with the Thermo Fisher Scientific (Waltham, MA, USA) dynabeads protein G kit, following the manufacturer's instructions.

Western Blot Analysis

RAW 264.7 and BMM cells were lysed in RIPA buffer containing protease inhibitors and centrifuged at 14,000 rpm for 30 min. Protein concentration was measured by Bradford assay using a Bio-Rad Bradford assay reagent (Hercules, CA, USA). Amounts of each lysate were separated by sodium dodecyl sulfate polyacrylamide gel electrophoresis (SDS-PAGE). After electrophoresis, proteins were transferred using polyvinylidene difluoride (PVDF) membranes (Hercules, CA, USA). After blocking with TBS-T buffer containing skim milk (5%), we incubated with the primary antibody overnight at 4°C. It was

TABLE 1 | Primer sequences.

Target gene		Sequence
DC-STAMP	Forward (5'-3')	GCTGTATCGGCTCATCTCCT
	Reverse (3'-5')	AAGGCAGAATCATGGACGAC
ATP6v0d2	Forward (5'-3')	AAGCCTTTGTTTGACGCTGT
	Reverse (3'-5')	TTCGATGCCTCTGTGAGATG
Acp5	Forward (5'-3')	CACTCCCACCCTGAGATTTGT
	Reverse (3'-5')	AAGTAGTGCAGCCCGGAGTA
CTSK	Forward (5'-3')	TCCGCAATCCTTACCGAATA
	Reverse (3'-5')	AACTTGAACACCCACATCCTG
MMP-9	Forward (5'-3')	GATGCGTGGAGAGTCGAAAT
	Reverse (3'-5')	CACCAAACTGGATGACGATG
CCL4	Forward (5'-3')	CTTCTGCGATTCAGTGCTGTCA
	Reverse (3'-5')	GCAAAGGCTGCTGGTCTCATAGTAA
GAPDH	Forward (5'-3')	ACCCAGAAGACTGTGGATGG
	Reverse (3'-5')	CACATTGGGGGTAGGAACAC

washed, incubated with a secondary antibody (horseradish peroxidase-conjugated anti-rabbit IgG and anti-mouse IgG), and detected with Healthcare Life Science ECL-plus (Tokyo, Japan). Immunoreactive bands were analyzed by LAS 4000 (GE Healthcare Life Science, Tokyo, Japan).

Statistical Analysis

Each experiment was performed in triplicate and expressed as mean value and standard deviation. Statistical analysis was conducted using SPSS Statistics 19.0 software, and correlations were considered significant at $p < 0.05$.

RESULTS

Inhibitory Effect of CTU on RANKL-Induced Osteoclast Formation

To measure CTU (**Figure 1A**) cell viability, we treated RAW264.7 and BMM cells with various concentrations of CTU (0.5, 1, 2, and 5 μM) for 5 days. As shown in **Figure 1B**, there was no significant cytotoxicity due to CTU, also it was confirmed that the morphology of osteoclasts differentiated by RANKL was also inhibited by CTU (**Figure 1C**). Therefore, to verify the effect of CTU on osteoclast formation at the indicated concentrations, we treated CTU with RANKL at different concentrations in RAW264.7 and BMM cells.

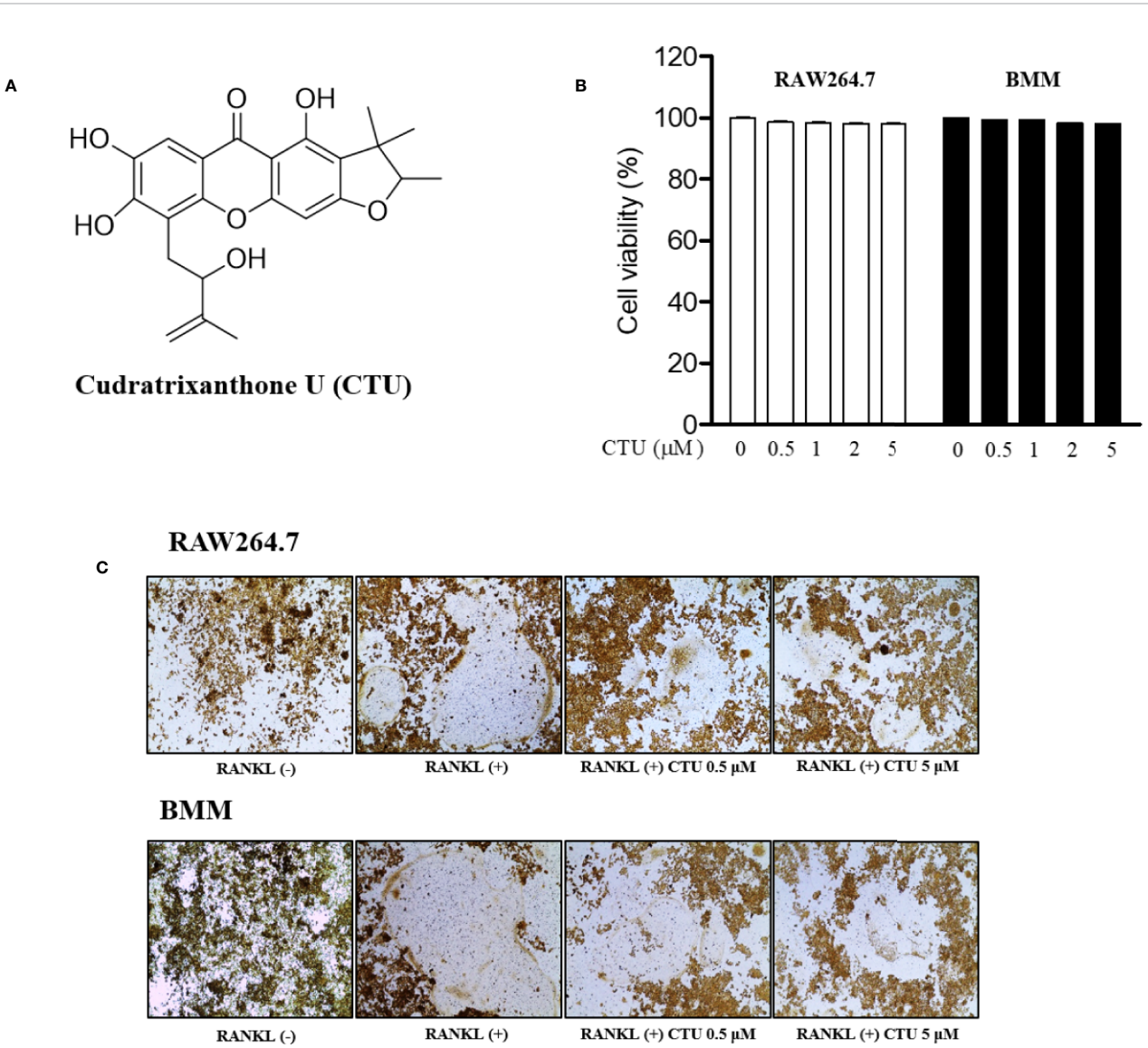

FIGURE 1 | The viability of CTU in RAW264.7 and BMM cells. The chemical structure of cudratrixanthone U (CTU) **(A)**. Effect of CTU on cell viability measured by MTT assay. RAW 264.7 and BMM cells were incubated with various concentrations of CTU for 5 days **(B)**. The effect of CTU in differentiated osteoclasts on morphology **(C)**.

After 5 days of culture, we measured TRAP staining and activity of mature osteoclasts. Osteoclast differentiation and activity were significantly inhibited by CTU treatment in a dose-dependent manner (**Figures 2A, B**).

CTU Suppresses Formation of RANKL-Stimulated Osteoclastic F-actin Rings

The F-actin ring is a characteristic structure of mature osteoclasts, and therefore we measured the area *via* fluorescence staining of mature osteoclasts to investigate the effect of CTU on RANKL-induced osteoclasts. We found that the formation of the F-actin ring and the pit area were significantly inhibited by CTU in a dose-dependent manner (**Figures 3A, B**). Increased F-actin ring formation by RANKL treatment was concentration-dependently reduced by CTU in RAW264.7 cells and In BMM cells, CTU 0.5 μM and 1 μM treatment group showed similar level of inhibition, and 5 μM treatment group significantly reduced the pit area.

CTU Inhibited Osteoclast Differentiation and Function

Because CTU inhibited the formation of osteoclasts and F-actin rings, we measured pit formation by inducing osteoclasts on a bone-biomimetic synthetic surface to investigate their effects on bone resorption. We found that CTU significantly inhibited the pit area in a concentration-dependent manner, and there was almost no pit area at the highest concentration (**Figures 4A, B**). Therefore, CTU inhibited osteoclast differentiation and function in bone resorption in RAW264.7 and BMM cells induced by RANKL.

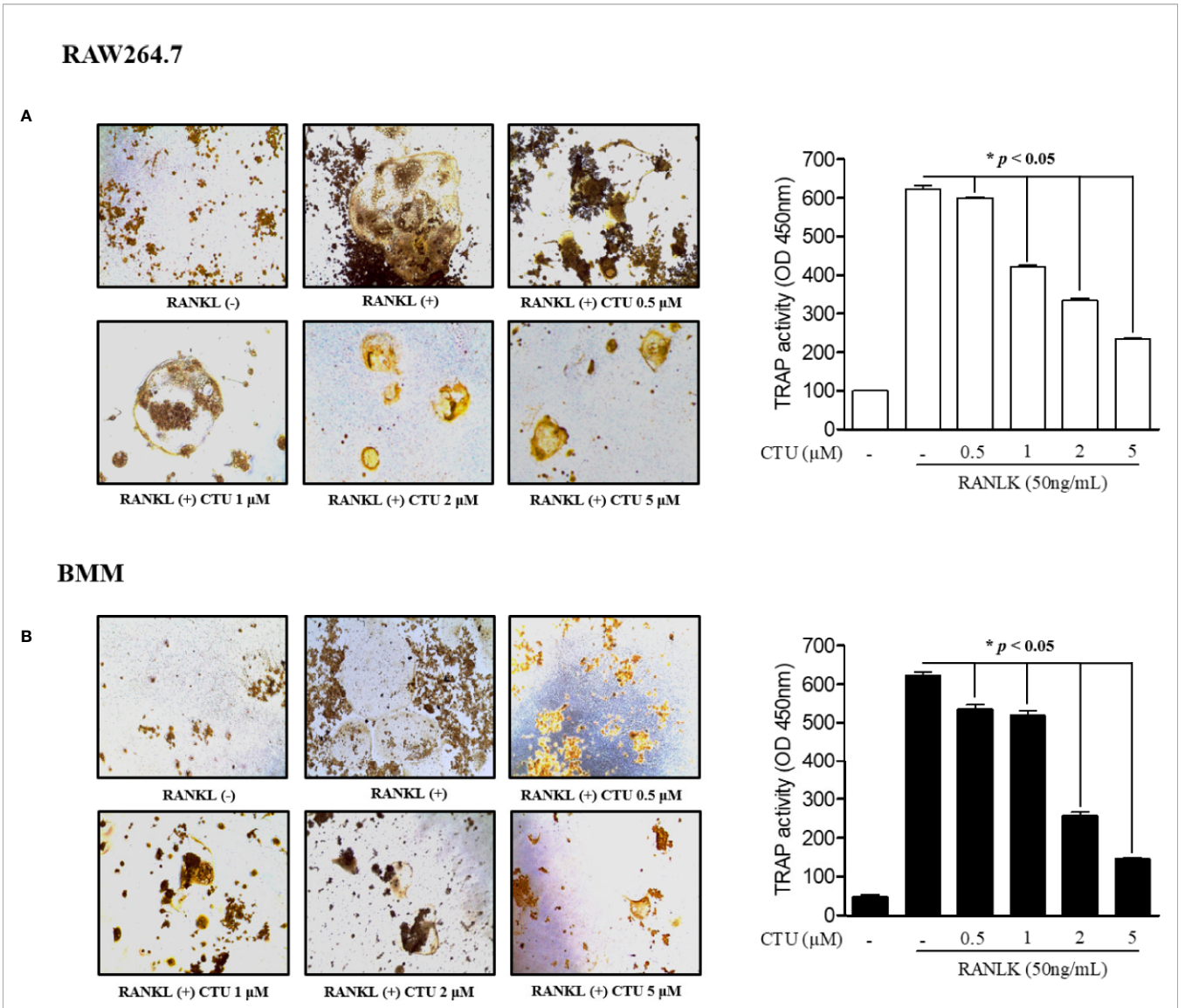

FIGURE 2 | The effect of CTU on osteoclast differentiation in RANKL-induced RAW 264.7 **(A)** and BMM **(B)** cells. The cells were incubated with 50 ng/ml RANKL or both RANKL and various concentrations of CTU for 5 days and then stained for TRAP. TRAP activity was measured using an ELISA reader (optical density, 405 nm). *$p < 0.05$ compared with the only RANKL-treated group.

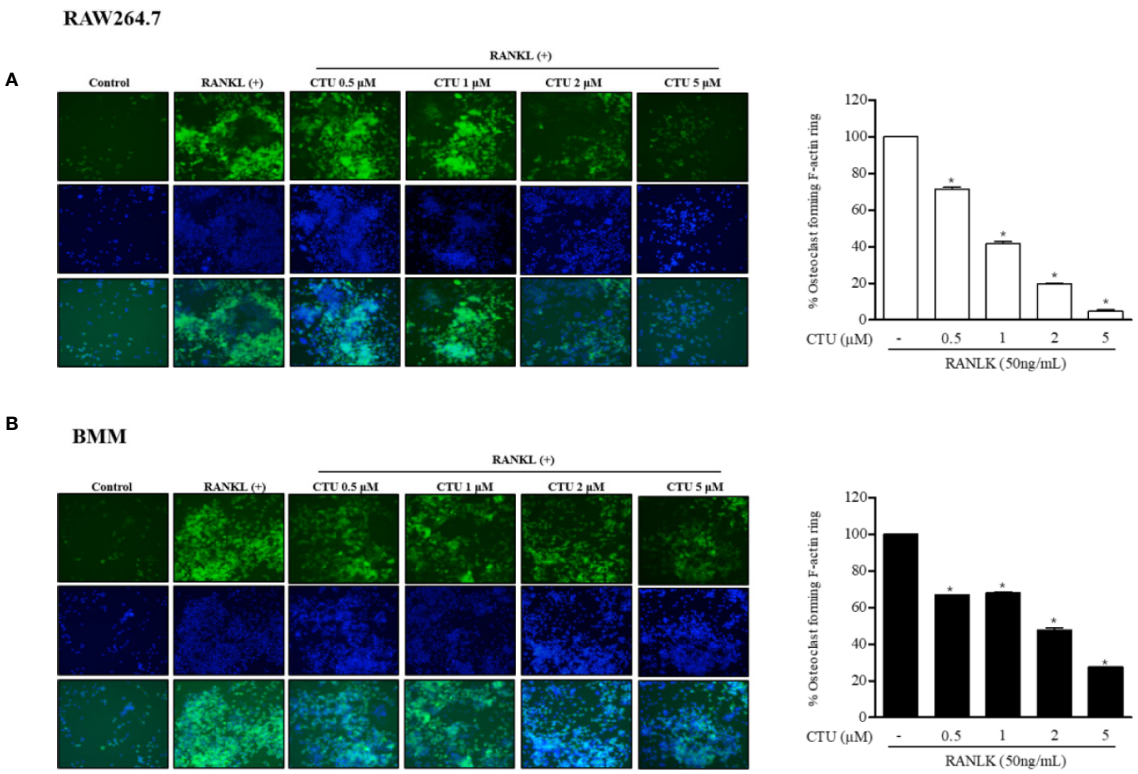

FIGURE 3 | The effect of CTU on osteoclast-actin ring structures in RANKL-induced RAW 264.7 **(A)** and BMM **(B)** cells. RAW 264.7 cells were treated with different concentrations of CTU in the presence of RANKL. After fixation and incubation with Alexa Fluor 488-conjugated phalloidin stained with DAPI, cells were visualized under a fluorescence microscope. Quantitative analysis shows percentage of osteoclasts forming F-actin rings. *$p < 0.05$ compared with the only RANKL-treated group.

CTU Inhibits Osteoclast Migration by Regulating CCL4

Chemokine CCL4 has been suggested to play an important role in osteoclast migration. Therefore, we measured the RNA expression of CCL4 in RANKL-treated RAW264.7 and BMM cells. As a result, the expression of CCL4 increased the most after 5 days of RANKL treatment. On day 5 of RANKL treatment, CTU inhibited CCL4 in a concentration-dependent manner (**Figures 5C, D**). CTU effectively inhibited the expression of integrin β3 in RANKL-treated RAW264.7 and BMM cells (**Figures 5A, B**). In addition, to measure the inhibitory effect of osteoclast migration on CTU, the coefficient of migrated cells was measured, as a result, the increased migration coefficient by RANKL on day 5 in RAW264.7 and BMM cells was reduced by concentration-dependent treatment of CTU (**Figures 5E, F**).

CTU Inhibits the Expression of RANKL-Induced Osteoclast-Specific Genes

The maturation of osteoclasts is accompanied by the expression of specific genes and protein, ATP6VOD2 and ACP5, DC-STAMP, CTSK and MMP-9, which are essential for osteoclast formation and function. Therefore, we investigated the role of specific genes and protein in osteoclast formation and function under the inhibitory effect of CTU on osteoclast differentiation and bone resorption. Treatment with CTU significantly down-regulated the expression of ATP6VOD2 and ACP5, DC-STAMP, CTSK, and MMP-9 more than in RANKL-treated group (**Figures 6A, B**). As a result, CTU suppressed differentiation and function by down-regulating the expression of osteoclast specific genes and proteins.

CTU Suppress RANKL-Induced TRAF6-TAK1 Complex Formation

TRAF6/TAK1 complex formation is an important step prior to RANKL-mediated MAPK and NF-κB activation. Therefore, we used co-precipitation to investigate the effects of CTU on the formation of RANKL-induced TRAF6/TAK1 complex. In pull-down assays, co-immunoprecipitation of TAK1 with anti-TRAF6 antibody (and of TRAF6 with anti-TAK1) was increased in the presence of RANKL. However, CTU inhibited co-precipitation of RANKL-induced TRAF6/TAK1 complexes in a concentration-dependent manner (**Figures 7A, B**).

CTU Suppresses RANKL-Induced Activation of NF-κB and MAPKs

Downstream of TRAF6 signaling complexes, the activation of MAPK (ERK, JNK and p38 MAPK) and NF-κB plays an important role in osteoclast differentiation. Therefore, we used

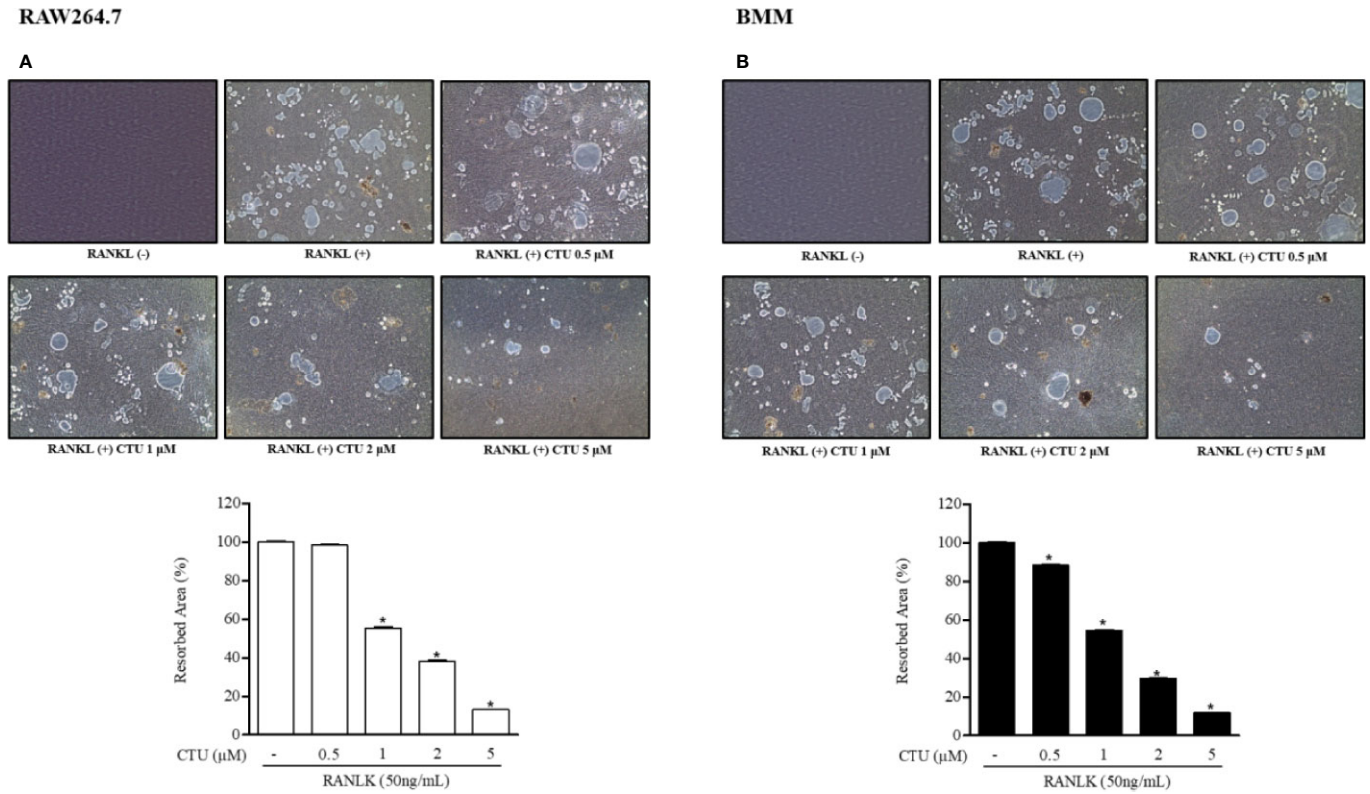

FIGURE 4 | The effect of CTU on osteoclast bone resorption in RANKL-induced RAW 264.7 **(A)** and BMM **(B)** cells. The cells were treated with different concentrations of CTU in the presence of RANKL. Total resorption pit area was measured and the results are shown as % of RANKL treatment. Pit formation assay of osteoclasts and quantification of pit area. *$p < 0.05$ compared with the only RANKL-treated group.

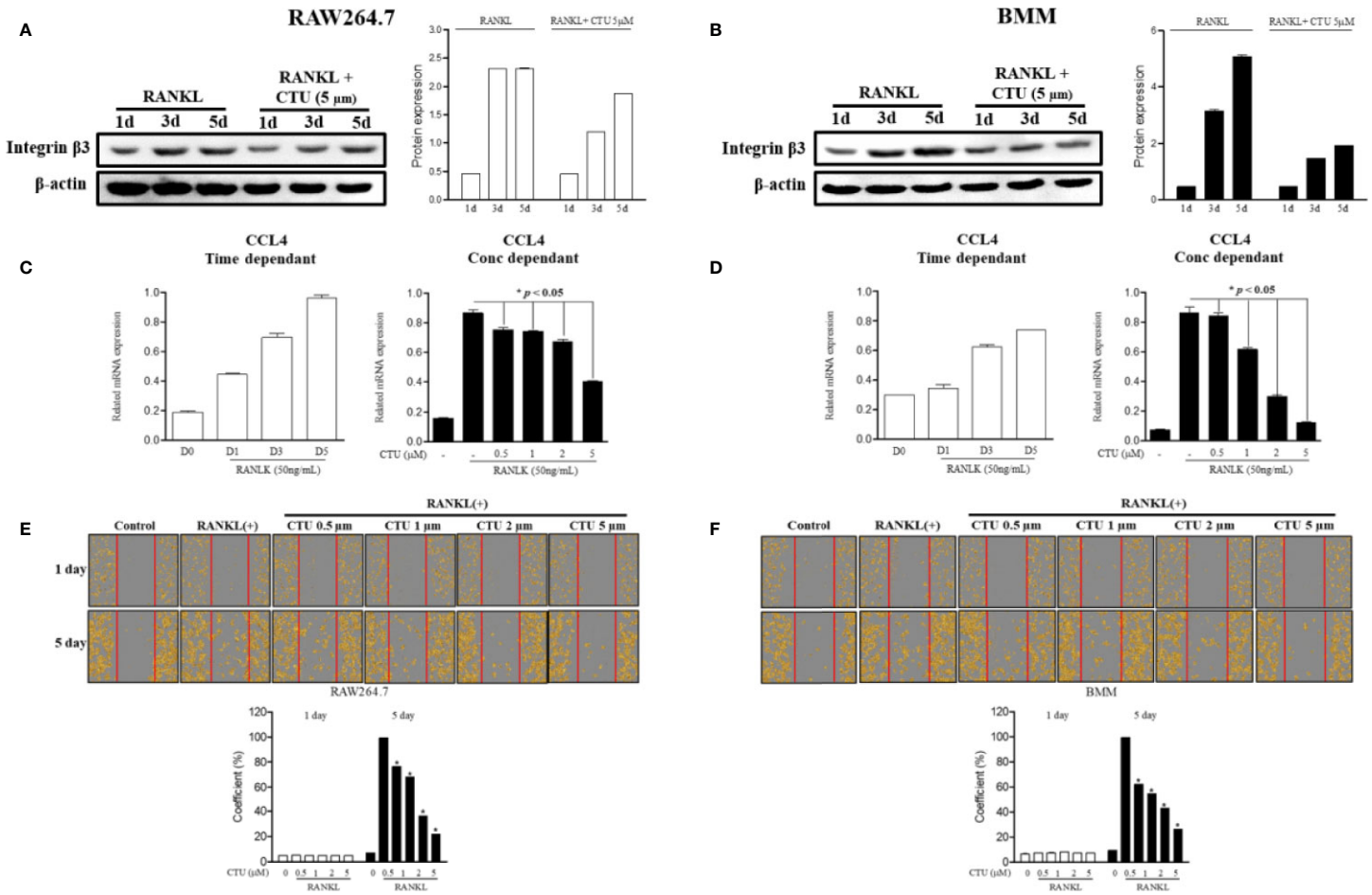

FIGURE 5 | The effect of CTU on RANKL-induced osteoclast migration. RAW 264.7 and BMM cells were cultured in the presence of CTU and RANKL for 1–5 days to induce osteoclast differentiation, and the protein expression of integrin β3 was measured by Western blot **(A, B)**, and the levels of CCL4 mRNA were measured by real-time PCR **(C, D)**. RAW264.7 and BMM cells were cultured without or with RANKL for 3 d, and further incubated for 24 h in the presence of CTU (0.5, 1, 2, and 5 μM) after gentle scratching **(E, F)**. The number of migrated cells was averaged using IncuCyte-image marking software. *p < 0.05 compared with the only RANKL-treated group.

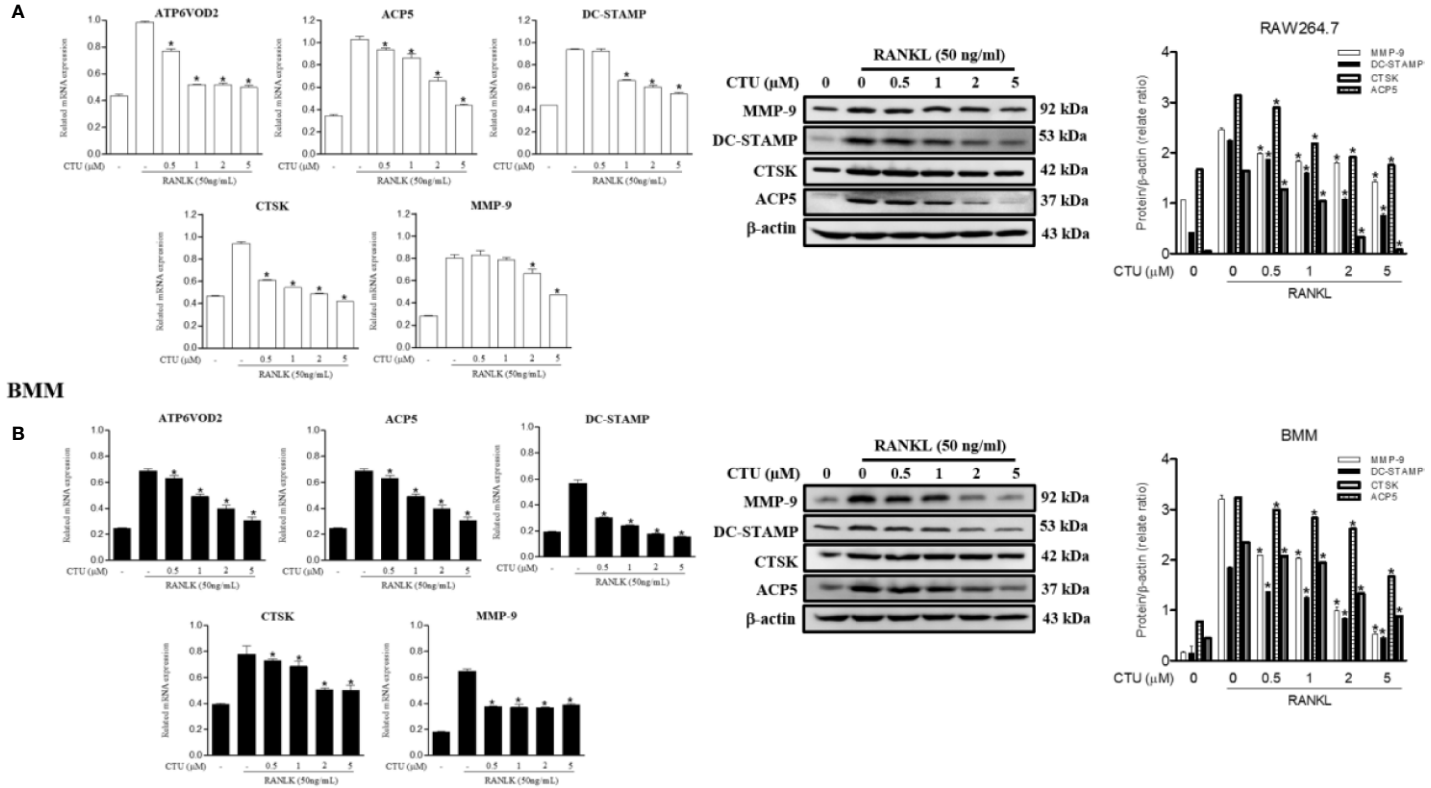

FIGURE 6 | The effect of CTU on osteoclast-specific gene and protein expression in RANKL-induced RAW 264.7 **(A)** and BMM **(B)** cells. The cells were treated with different concentrations of CTU in the presence of RANKL, and osteoclast-specific gene expression was measured by real-time PCR. The results were normalized to GAPDH expression. *$p < 0.05$ compared with only RANKL-treated group.

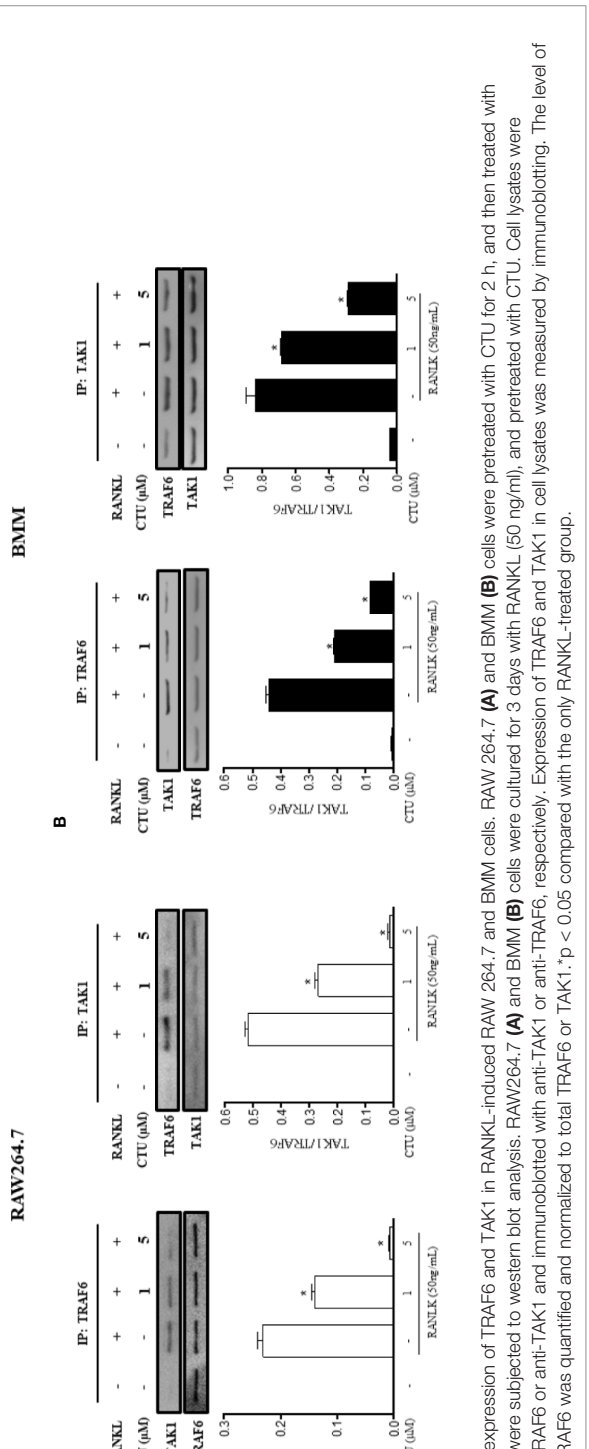

FIGURE 7 | The effect of CTU on expression of TRAF6 and TAK1 in RANKL-induced RAW 264.7 and BMM cells. RAW 264.7 **(A)** and BMM **(B)** cells were pretreated with CTU for 2 h, and then treated with RANKL for 24 h. The cell extracts were subjected to western blot analysis. RAW264.7 **(A)** and BMM **(B)** cells were cultured for 3 days with RANKL (50 ng/ml), and pretreated with CTU. Cell lysates were immunoprecipitated (IP) with anti-TRAF6 or anti-TAK1 and immunoblotted with anti-TAK1 or anti-TRAF6, respectively. Expression of TRAF6 and TAK1 in cell lysates was measured by immunoblotting. The level of co-immunoprecipitated TAK1 or TRAF6 was quantified and normalized to total TRAF6 or TAK1.*$p < 0.05$ compared with the only RANKL-treated group.

western blots to further explore the activation of the MAPKs and NF-κB pathways by which CTU regulates osteoclast differentiation and function. Phosphorylation of MAPKs and NF-κB p65 activity were induced in RANKL-stimulated RAW264.7 and BMM cells, and the expression of p-ERK, p-JNK, and p-p38 was inhibited by CTU (**Figures 8A, B**). CTU also inhibited the activity of p65 and the phosphorylation of IκB-α (**Figures 8C, D**). Thus, the osteoclast-differentiation and bone-resorption functions of CTU were related to MAPKs and NF-κB activity.

CTU Downregulates RANKL-Induced Expression of NFATc1 and c-Fos

NFATc1 and c-Fos are the most important osteoclast-specific transcription factors following RANKL binding to RANK. Therefore, we used the western blot to evaluate the effects of CTU on the two transcription factors. RAW 264.7 and BMM cells induced by RANKL for 24 h significantly increased the expression of c-Fos and NFATc1, whereas in the group treated with CTU 0.5 and 1 μM in RAW264.7 and BMM cells, similar levels of NFATc1 and c-Fos expression were suppressed, and 2 and 5 μM treatment group showed a marked inhibitory effect (**Figures 9A, B**).

DISCUSSION

Disruption of bone homeostasis is caused by increased bone resorption by osteoclasts rather than new bone formation by osteoblasts, and RANKL is a major pro-osteoclastogenic cytokine that mediates osteoclast differentiation (Park et al., 2017; Ono and Nakashima, 2018). Thus, the inhibition of osteoclast formation, bone resorption and migration by inhibiting RANKL signaling and downstream pathways is an important target in the treatment of osteoporosis (Zou et al., 2001; Xuan et al., 2017). In the present study, we evaluated the mechanism of CTU inhibition of osteoclast differentiation and migration in a RANKL-induced RAW 264.7 and BMM cell line. Osteoclast differentiation by RANKL activates TRAP, a representative osteoclast marker involved in bone resorption, forms and maintains actin ring formation on the bone surface, and promotes bone resorption (Hayman, 2008). In our study, CTU attenuated osteoclast differentiation and function by inhibiting TRAP activity, F-actin formation, and bone resorption. Also, proteolytic enzymes, such as cathepsin K and MMP-9, and osteoclastogenesis-related markers, such as ACP5, DC-STAMP, and ATP6V0d2 play an important role in bone resorption and osteoclast differentiation. CTU inhibited these osteoclast gene markers in a concentration dependent manner.

In osteoclast signaling by RANKL, the cytoplasmic domain of RANK recruits TRAF6 to initiate complex formation with TAK1, activates NF-κB and MAPK, and plays a critical signaling role in osteoclast maturation (Mizukami et al., 2002; Nakashima et al., 2012). The TRAF family consists of six proteins each. TRAF6 is a unique member of the RING domain ubiquitin ligase family, which catalyzes the poly-ubiquitin chain linked *via* ubiquitin Lys-63 (Arch et al., 1998; Lamothe et al., 2007; Landstrom, 2010). In addition, the TRAF6 pathway induces phosphorylation of

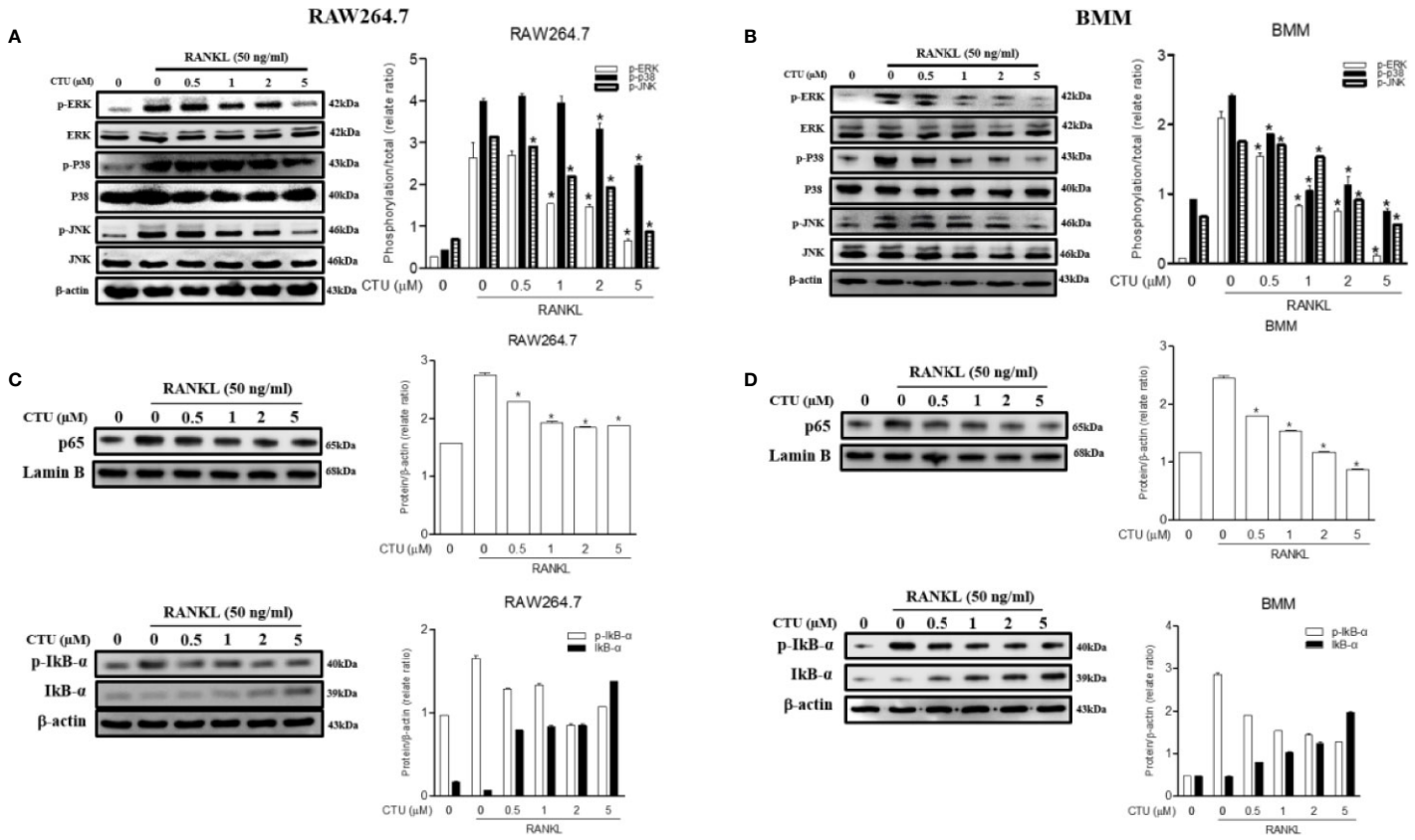

FIGURE 8 | Effect of CTU on MAPKs **(A, B)** and NF-kB **(C, D)** activation in RANKL-induced RAW 264.7 and BMM cells. The cells were pre-incubated with or without CTU for 2 h, followed by treatment with 50 ng/ml RANKL for 30 min. The protein expression of cytosolic and nuclear p65, IκB¥á, and p-IκB¥á was compared with that of controls subjected to western blot analysis. *p < 0.05 compared with the only RANKL-treated group.

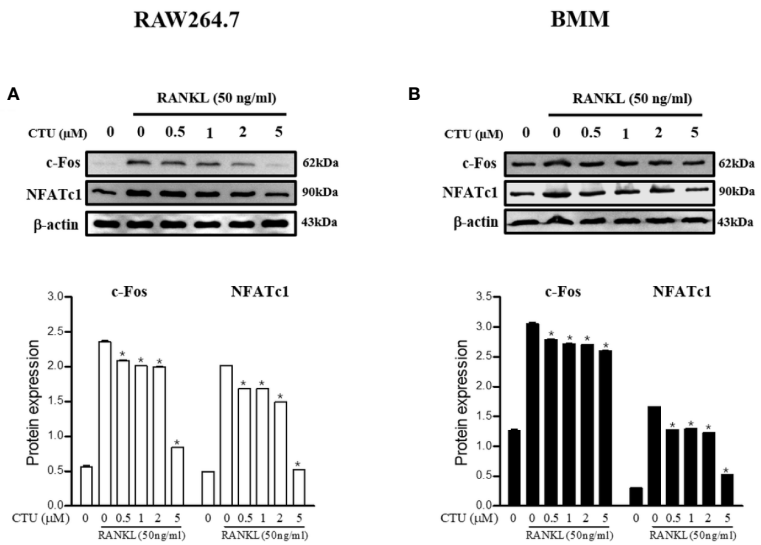

FIGURE 9 | The effects of CTU on NFATc1 and c-Fos protein expression in RANKL-induced RAW 264.7 **(A)** and BMM **(B)** cells. The cells were cultured in the presence of RANKL with the CTU. After 24 h, the total protein was isolated and the protein expression levels were evaluated by western blots.*$p < 0.05$ compared with the only RANKL-treated group.

MAPKs, such as ERK, p38, and JNK, and regulates the expression of transcription factors such as NF-κB upon binding of RANKL and RANK in osteoclast precursor cells (Kobayashi et al., 2001). During RANKL signaling, MAPK is an important target for osteoclast differentiation as a major regulator of various cellular responses, including cell proliferation, apoptosis, and differentiation (Sui et al., 2014; Thummuri et al., 2015).We found that CTU inhibited the formation of TRAF6-TAK1 complex by RANKL stimulation in RAW264.7 and BMM cells and inhibited phosphorylation and transcription of NF-κB and phosphorylation of MAPK (JNK, ERK, p38) in a concentration-dependent manner. In addition, NFATc1 inhibition by CTU may be caused by down-regulation of c-Fos. Therefore, inhibition of the TRAF6-TAK1 complex formation plays an important role in osteoclast differentiation. In our immunoprecipitation assay, RANKL increased TRAF6 and TAK1 association, which was inhibited by CTU. These results suggest that CTU targets TRAF6-TAK1 complex formation to inhibit osteoclast differentiation.

RANKL regulates a variety of transcription factors, such as NF-κB, c-Fos, and NFATc1, and induces NFATc1 early to form mature and active osteoclasts (Teitelbaum and Ross, 2003). NFATc1 has been reported to regulate genes, such as TRAP, cathepsin K, and integrin β3 involved in osteoclast differentiation and function (Kim et al., 2014). In addition, osteoclast migration plays an important role in diseases associated with abnormal bone resorption such as rheumatoid arthritis and osteoporosis. In recent studies, chemokine CCL4 has been shown to mediate cell migration and bone invasion in RANKL-induced bone resorption (Xuan et al., 2017). In this study, CTU downregulated the expression of transcription factors and genes involved in RANKL-induced osteoclast differentiation and migration.

Recent studies investigating the osteoclast-differentiation inhibitory effects of natural compounds, such as flavonoids or polyphenols, have been actively conducted (Kim et al., 2018). However, prenylated xanthones have yet to be investigated for their role in inhibition of bone disease or osteoclast differentiation, despite their various antioxidant, anti-atherosclerotic, anti-inflammatory, and hepatoprotective activities (Lee et al., 2009; Jeong et al., 2010; Kim et al., 2019). Therefore, in this study, CTU isolated from *M. tricuspidata* suggests a potential therapeutic agent for osteoporosis by inhibiting proteins and specific genes that play an important role in the regulation of osteoclast differentiation and bone resorption and migration.

DATA AVAILABILITY STATEMENT

The original contributions presented in the study are included in the article/supplementary material; further inquiries can be directed to the corresponding author.

AUTHOR CONTRIBUTIONS

E-NK performed the experiments and wrote the manuscript. H-SL and JK performed the statistical analysis. G-SJ, DL, and SL participated in study design and coordination as well as drafting the manuscript. All authors contributed to the article and approved the submitted version.

FUNDING

This research was supported by Basic Science Research Program through the National Research Foundation of Korea (NRF) funded by the Ministry of Education (NRF-2016R1A6A1A03011325).

REFERENCES

Arch, R. H., Gedrich, R. W., and Thompson, C. B. (1998). Tumor necrosis factor receptor-associated factors (TRAFs); a family of adapter proteins that regulates life and death. *Genes Dev.* 12, 2821–2830. doi: 10.1101/gad.12.18.2821

Boyce, B. F., Yamashita, T., Yao, Z., Zhang, Q., and Li, F. (2005). Roles for NFkappaB and c-Fos in osteoclasts. *J. Bone Miner. Metab.* 23, 11–15. doi: 10.1016/j.canrad.2016.07.082

Chang, S. H., Jung, E. J., and Lim, D. G. (2008). Anti-inflammatoryaction of *Cudraniatricuspidata* on spleen cell and T lymphocyteproliferation. *J. Pharm. Pharmacol.* 60, 1221–1226. doi: 10.1211/jpp.60.9.0015

Geng, H., Chang, Y. N., and Bai, X. (2017). Fullerenol nano particle ssuppress RANKL-induced osteoclastogenesis by inhibiting differentiation and maturation. *Nanoscale* 9, 12516–12523. doi: 10.1039/c7nr04365a

Hayman, A. R. (2008). Tartrate-resistant acid phosphatase (TRAP) and the osteoclast/immune cell dichotomy. *Autoimmunity* 41, 218–223. doi: 10.1080/08916930701694667

Ishibashi, O., Niwa, S., Kadoyama, K., and Inui, T. (2006). MMP-9 antisense oligodeoxynucleotideexerts an inhibitory effect on osteoclastic bone resorption by suppressing cell migration. *Life Sci.* 79, 1657–1660. doi: 10.1016/j.lfs.2006.05.024

Jeong, G. S., An, R. B., Pae, H. O., Chung, H. T., Yoon, K. H., Kang, D. G., et al. (2008). Cudratricusxanthone A protects mouse hippocampal cells against glutamate-induced neurotoxicity via the induction of heme oxygenase-1. *Planta Med.* 74, 1368–1373. doi: 10.1055/s-2008-1081315

Jeong, C. H., Choi, G. N., Kim, J. H., Kwak, J. H., Jeong, H. R., Kim, D. O., et al. (2010). Protective effects of aqueous extract from *Cudrania tricuspidata* on oxidative stress-induced neurotoxicity. *Food Sci. Biotechnol.* 19, 1113–1117. doi: 10.1007/s10068-010-0158-z

Jung, B. S., and Shin, M. K. (1990). *Encyclopedia of illustrated korean naturaldrugs* (Seoul: Young Lim Sa), 544–545.

Kanzaki, H., Shinohara, F., Itohiya, K., Yamaguchi, Y., Katsumata, Y., Matsuzawa, M., et al. (2017). RANKL induces Bach1 nuclear importand attenuates Nrf2-mediated antioxidant enzymes, thereby augmenting intracellular reactive oxygen species signaling and osteoclastogenesis in mice. *FASEB J.* 31, 781–792. doi: 10.1096/fj.201600826r

Kim, H. H., Lee, D. E., Shin, J. N., Lee, Y. S., Jeon, Y. M., Chung, C. H., et al. (1999). Receptor activator of NF-kB recruits multiple TRAF family adaptors and activates c-Jun N-terminal kinase. *FEBS Lett.* 443, 297–302. doi: 10.1016/s0014-5793(98)01731-1

Kim, T. J., Han, H. J., Lim, Y., Song, M. C., Kim, J., Hong, J. T., et al (2009). Antiproliferative action of cudraflavone B, isolated from *Cudrania tricuspidata*, through the downregulation of pRb phosphorylation in aortic smooth muscle cell proliferation signaling. *J. Cardiovasc. Pharmacol.* 53, 341–348. doi: 10.1097/FJC.0b013e31819fd4cb.

Kim, J. Y., Cheon, Y. H., Yoon, K. H., Lee, M. S., and Oh, J. (2014). Parthenolide inhibits osteoclast differentiation and bone resorbing activity by down-regulation of NFATc1 induction and c-Fos stability, during RANKL-mediated osteoclastogenesis. *BMB Rep.* 47, 451–456. doi: 10.5483/bmbrep.2014.47.8.206

Kim, H. R., Kim, B. M., Won, J. Y., Lee, K. A., Ko, H. M., Kang, Y. S., et al. (2018). Quercetin, a plant polyphenol, has potential for the prevention of bone destruction in rheumatoid arthritis. *J. Med. Food* 22, 1–10. doi: 10.1089/jmf.2018.4259

Kim, P. S., Nam, Y. J., Kim, W. J., Kim, J. K., Lee, G. B., Song, M. J., et al. (2019). Edgeworthiapapyrifera regulates osteoblast and osteoclast differentiation in vitro and exhibits anti-osteoporosis activity in animal models of osteoporosis. *Planta Med.* 85, 766–773. doi: 10.1055/a-0942-1960

Kobayashi, N., Kadono, Y., Naito, A., Matsumoto, K., Yamamoto, T., Tanaka, S., et al. (2001). Segregation of TRAF6-mediated signaling pathways clarifies its role in osteoclastogenesis. *EMBO J.* 20, 1271–1280. doi: 10.1093/emboj/20.6.1271

Kwon, J. Y., Hiep, N. T., Kim, D. W., Hwang, B. Y., Lee, H. J., Mar, W. C., et al. (2014). Neuroprotective xanthones from the root bark of *Cudrania tricuspidata*. *J. Nat. Prod.* 77, 1893–1901. doi: 10.1021/np500364x.

Kwon, J. Y., Hiep, N. T., Kim, D. W., Hong, S. G., Guo, Y. Q., Hwang, B. Y., et al. (2016). Chemical constituents isolated from the root bark of *Cudrania tricuspidata* and their potential neuroprotective effects. *J. Nat. Prod.* 79, 1938–1951. doi: 10.1021/acs.jnatprod.6b00204

Lamothe, B., Webster, W. K., Gopinathan, A., Besse, A., and Campos, A. D. (2007). TRAF6 ubiquitin ligase is essential for RANKL signaling and osteoclast differentiation. *Biochem. Biophys. Res. Commun.* 359 (4), 1044–1049. doi: 10.1016/j.bbrc.2007.06.017

Landstrom, M. (2010). The TAK1-TRAF6 signalling pathway. *Int. J. Biochem. Cell Biol.* 42, 585–589. doi: 10.1016/j.biocel.2009.

Lee, B. W., Lee, J. H., and Lee, S. T. (2005). Antioxidant and cytotoxic activities of xanthones from *Cudrania tricuspidata*. *Bioorg. Med. Chem. Lett.* 15, 5548–5552. doi: 10.1016/j.bmcl.2005.08.099

Lee, Y. J., Kim, S., Lee, S. J., Ham, I., and Whang, W. K. (2009). Antioxidant activities of new flavonoids from *Cudrania tricuspidata* root bark. *Arch. Pharmacal. Res.* 32, 195–200. doi: 10.1007/s12272-009-1135-z

Lee, D. B., Shin, K. J., Kim, D. W., Yoon, K. A., Choi, Y. J., Lee, B. N. R., et al. (2018). CCL4 enhances preosteoclast migration and its receptor CCR5 downregulation by RANKL promotes osteoclastogenesis. *Cell Death Differ.* 2018, 495. doi: 10.1038/s41419-018-0562-5

Li, C. Y., Jepsen, K. J., Majeska, R. J., Zhang, J., Ni, R., Gelb, B. D., et al. (2006). Mice lacking cathepsin K maintain bone remodeling but develop bone fragility despitehigh bone mass. *Offic. J. Am. Soc Bone Miner. Res.* 21, 865–875. doi: 10.1359/jbmr.060313

Li, X., Yao, Z., Jiang, X., Sun, J., Ran, G., Yang, X., et al. (2018). Bioactive compounds from *Cudrania tricuspidata*: A natural anticancer source. *Crit. Rev. Food Sci. Nutr.* 22, 1–21. doi: 10.1080/10408398

Mizukami, J., Takaesu, G., Akatsuka, H., Sakurai, H., Ninomiya-Tsuji, J., Matsumoto, K., et al. (2002). Receptor activator of NF-kappaB ligand (RANKL) activates TAK1 mitogen-activated protein kinase kinase kinase through a signaling complex containing RANK, TAB2, and TRAF6. *Mol. Cell Biol.* 22, 992–1000. doi: 10.1128/mcb.22.4.992-1000.

Nakashima, T., Hayashi, M., and Takayanagi, H. (2012). New insights into osteoclastogenic signaling mechanisms. *Trends Endocrinol. Metab.* 23, 582–590. doi: 10.1016/j.tem.2012.05.005.

Novack, D. V., and Teitelbaum, S. L. (2008). The osteoclast: friend or foe. *Annu. Rev. Pathol.* 3, 457–484. doi: 10.1146/annurev.pathmechdis.3.121806.151431

Ono, T., and Nakashima, T. (2018). Recent advances in osteoclast biology. *Histochem. Cell Biol.* 149, 325–341. doi: 10.1007/s00418-018-1636-2

Park, J. H., Lee, N. K., and Lee, S. Y. (2017). Current understanding of RANK signaling in osteoclast differentiation and maturation. *Mol. Cells* 40, 706–713. doi: 10.14348/molcells.2017.0225

Seo, W. G., Pae, H. O., Oh, G. S., Chai, K. Y., Yu, Y. G., Chung, H. T., et al. (2001). Ethyl acetate extract of the stem bark of *Cudrania tricuspidata* induces apoptosis in human leukemia HL-60 cells. *Am. J. Chin. Med.* 29, 313–320. doi: 10.1142/S0192415X01000332

Sui, X., Kong, N., Ye, L., Han, W., Zhou, J., Zhang, Q., et al. (2014). p38 and JNK MAPK pathways control the balance of apoptosis and autophagy in response to chemotherapeutic agents. *Cancer Lett.* 344, 174–179. doi: 10.1016/j.canlet.2013.11.019

Takayanagi, H., Kim, S., Koga, T., Nishina, H., Isshiki, M., Yoshida, H., et al. (2002). Induction and activation of the transcription factor NFATc1 (NFAT2) integrate RANKL signaling in terminal differentiation of osteoclasts. *Dev. Cell* 3, 889–901. doi: 10.1016/s1534-5807(02)00369-6

Teitelbaum, S. L. (2000). Bone resorption by osteoclasts. *Science* 289, 1504–1508. doi: 10.1126/science.289.5484.1504

Teitelbaum, S. L., and Ross, F. P. (2003). Genetic regulation of osteoclast development and function. *Nat. Rev. Genet.* 4, 638–649. doi: 10.1038/nrg1122

Thummuri, D., Jeengar, M. K., Shrivastava, S., Nemani, H., Ramavat, R. N., Chaudhari, P., et al. (2015). Thymoquinone prevents RANKL-induced osteoclastogenesis activation and osteolysis in an in vivo model of inflammation by suppressing NF-κB and MAPK signalling. *Pharmacol. Res.* 99, 63–73. doi: 10.1016/j.phrs.2015.05.006

Tian, Y. H., Kim, H. C., Cui, J. M., and Kim, Y. C. (2005). Hepatoprotective constituents of *Cudrania tricuspidata*. *Arch. Pharmacal. Res.* 28, 44–48. doi: 10.1007/bf02975134

Warren, J. T., Zou, W., Decker, C. E., Rohatgi, N., Nelson, C. A., Fremont, D. H., et al. (2015). Correlating RANK ligand/RANK binding kinetics with osteoclast formation and function. *J. Cell. Biochem.* 116, 2476–2483. doi: 10.1002/jcb.25191

Xin, L. T., Yue, S. J., Fan, Y. C., Wu, J. S., Yan, D., Guan, H. S., et al. (2017). *Cudrania tricuspidata*: An updated review on ethnomedicine, phytochemistry and pharmacology. *RSC Adv.* 7, 31807–31832. doi: 10.1039/C7RA04322H

Xuan, W. H., Feng, X., Qian, C., Peng, L. Y., Shi, Y., Xu, L. X., et al. (2017). Osteoclast differentiation gene expression profiling reveals chemokine CCL4 mediates RANKL-induced osteoclast migration and invasion via PI3K pathway. *Cell Biochem. Funct.* 35, 171–177. doi: 10.1002/cbf.3260

Zou, W., Hakim, I., Tschoep, K., Endres, S., and Bar-Shavit, Z. (2001). Tumor necrosis factor-αmediates RANK ligand stimulation of osteoclast differentiation by an autocrine mechanism. *J. Cell. Biochem.* 83, 70–83. doi: 10.1002/jcb.1202

Conflict of Interest: The authors declare that the research was conducted in the absence of any commercial or financial relationships that could be construed as a potential conflict of interest.

Copyright © 2020 Kim, Kwon, Lee, Lee, Lee and Jeong. This is an open-access article distributed under the terms of the Creative Commons Attribution License (CC BY). The use, distribution or reproduction in other forums is permitted, provided the original author(s) and the copyright owner(s) are credited and that the original publication in this journal is cited, in accordance with accepted academic practice. No use, distribution or reproduction is permitted which does not comply with these terms.

frontiers in Pharmacology

ORIGINAL RESEARCH
published: 21 August 2020
doi: 10.3389/fphar.2020.01301

Antioxidant Phytoconstituents From *Onosma bracteata* Wall. (Boraginaceae) Ameliorate the CCl_4 Induced Hepatic Damage: *In Vivo* Study in Male Wistar Rats

Ajay Kumar[1], *Varinder Kaur*[2], *Kritika Pandit*[1], *Hardeep Singh Tuli*[3], *Katrin Sak*[4], *Subheet Kumar Jain*[5] *and Satwinderjeet Kaur*[1]*

[1] Department of Botanical & Environmental Sciences, Guru Nanak Dev University, Amritsar, India, [2] Indigenous Education and Research Centre, James Cook University, Townsville, QLD, Australia, [3] Department of Biotechnology, Maharishi Markandeshwar (Deemed to be University), Ambala, India, [4] NGO, Praeventio, Tartu, Estonia, [5] Department of Pharmaceutical Sciences, Guru Nanak Dev University, Amritsar, India

OPEN ACCESS

Edited by:
Yan Xu,
Cleveland State University,
United States

Reviewed by:
Wentzel Christoffel Gelderblom,
Cape Peninsula University of Technology, South Africa
Chan-Min Liu,
Jiangsu Normal University, China

***Correspondence:**
Satwinderjeet Kaur
satwinderjeet.botenv@gndu.ac.in;
sjkaur2011@gmail.com

Specialty section:
This article was submitted to Ethnopharmacology, a section of the journal Frontiers in Pharmacology

Received: 02 June 2020
Accepted: 05 August 2020
Published: 21 August 2020

Citation:
Kumar A, Kaur V, Pandit K, Tuli HS, Sak K, Jain SK and Kaur S (2020) Antioxidant Phytoconstituents From Onosma bracteata Wall. (Boraginaceae) Ameliorate the CCl_4 Induced Hepatic Damage: In Vivo Study in Male Wistar Rats. Front. Pharmacol. 11:1301. doi: 10.3389/fphar.2020.01301

Onosma bracteata Wall. (Boraginaceae) is a highly valuable medicinal herb that is used for the treatment of fever, bronchitis, asthma, rheumatism, stomach irritation, and other inflammatory disorders. The present study aims to explore the hepatoprotective potential of ethanolic extract (*Obeth*) from *O. bracteata* aerial parts against carbon tetrachloride (CCl_4) which causes hepatic damage in the male Wistar rats. *Obeth* showed effective radical quenching activity with an EC_{50} of 115.14 and 199.33 µg/mL in superoxide radical scavenging and lipid peroxidation analyses respectively along with plasmid DNA protective potential in plasmid nicking assay. The *Obeth* modulated mutagenicity of 2 Aminofluorine (2AF) in the pre-incubation mode of investigation (EC_{50} 10.48 µg/0.1 mL/plate) in TA100 strain of *Salmonella typhimurium*. In *in vivo* studies, pretreatment of *Obeth* (50, 100, and 200 mg/kg) had the potential to normalize the biochemical markers aggravated by CCl_4 (1mL/kg b.wt.) including liver antioxidative enzymes. Histopathological analysis also revealed the restoration of CCl_4-induced liver histopathological alterations. Immunohistochemical studies showed that the treatment of *Obeth* downregulated the expression levels of p53 and cyclin D in hepatocytes. and downregulation in the Western blotting analysis revealed the downregulation of p-NF-kB, COX-2, and p53. HPLC data analysis showed the supremacy of major compounds namely, catechin, kaempferol, epicatechin, and Onosmin A in *Obeth*. The present investigation establishes the hepatoprotective and chemopreventive potential of *O. bracteata* against CCl_4-induced hepatotoxicity *via* antioxidant defense system and modulation of the expression of proteins associated with the process of carcinogenesis in hepatic cells.

Keywords: antimutagenicity, apoptosis, carcinogenesis, hepatoprotective effect, *Onosma bracteata*, phytoconstituents

INTRODUCTION

Global increase in the demand of industrial solvents in pharmaceuticals, paint and coating industry can raise the global solvent market to an estimated USD 12.31 billion by year 2026 as per Global Market Outlook report (2018). Recently, the use of industrial solvents has brought higher risks to both humans and animals. Industrial solvents cause environmental pollution and their acute and chronic exposure can cause cellular injuries and progressive genetic alterations (mutations) *via* activation of reactive oxygen species (ROS) with significant changes that may transform healthy cells to cancerous cells (Pizzino et al., 2017). The mutations caused alter the DNA which along with oxidative stress triggers destruction of tumor-suppressor genes and/or the stimulation of proto-oncogenes which contribute to the initiation of liver, breast, colon and prostate cancer (Maron and Ames, 1983; Canli et al., 2017).

The liver is the main organ essential for survival, which plays a crucial function in the body's metabolism and detoxification process. The liver is a primary site in the body that is mostly involved in modulation and biotransformation of xenobiotic compounds mediated by cytochrome P_{450} (CYP) family of enzymes (Gu and Manautou, 2012). The chemicals like carbon tetrachloride (CCl_4), acetylaminofluorene, thioacetamide, and polycyclic aromatic hydrocarbons are biotransformed into the transitional molecules and generate reactive oxygen species (ROS), including oxygen free radicals that induce hepatic damage (Karakus et al., 2011; Kaur et al., 2017; Kaur S. et al., 2019). Various hepatotoxic compounds and transitional radicals of oxidative reactions affect many proteins and encourage negative effects *via* oxidative stress (OS) or DNA damage (Rahal et al., 2014). The homeostatic balance of cellular redox is the main feature for combating the lethal insults of ROS, which are internally maintained by antioxidative defense systems. Any aberrant functioning to curb stress can lead to malfuctioning like cancer (Snezhkina et al., 2019). Carbon tetrachloride (CCl_4) is a typical solvent which is used in the research for hepatic ailments. Firstly, liver can metabolize CCl_4 by cytochrome P_{450} enzyme complex to produce toxic metabolites such as trichloromethyl free radicals ($CCl_3^{\bullet}$) and trichloromethyl peroxyl radicals ($CCl_3OO^{\bullet}$). These free radicals have capacity of eliminating hydrogen ions from fatty acids to induce lipid peroxidation. Hence, mutually $CCl_3^{\bullet}$ and $CCl_3OO^{\bullet}$ cause injury in the cell membrane, alteration in enzyme action and lastly cause hepatic damage or necrosis (Chao et al., 2019). The treatment of hepatic cancer still is one of the important tasks despite the newest developments in recognizing its biological basis. The deregulation of p53, COX-2, and NF-κB signaling is one of the central factors for the beginning of hepatic cancer (Alqahtani et al., 2019). p53 (a tumor suppressor gene) associated mutations are found in most of the hepatocellular carcinoma (HCC) (Aravalli et al., 2008). From the past few decades, the natural phytoconstituents from plants are recognized for restoring the health of humans (Che and Zhang, 2019). So, the diet rich in natural compounds has been shown to exert various healing effects *via* activating redox-signaling, phase-II detoxification enzymes, antioxidants, anti-inflammatory, and anti-carcinogenic properties (Wu et al., 2017).

Onosma bracteata Wall. family Boraginaceae widely knowns as 'gaozaban' is mainly distributed in India and Nepal in high altitude regions, spread in Jammu & Kashmir, Himachal Pradesh and Uttar Pradesh in north-western Himalayas (Ved et al., 2016). It is used as the main component for the preparation of drug in Unani and Ayurvedic medicinal system. It is usually used in Indian traditional medication due to its medicinal benefits *viz*. demulcent, diuretic, anti-aging, antioxidant, antibacterial, wound healing, antileprotic, spasmolytic, and tonic nature (Fareed et al., 2012). The entire parts of *O. bracteata* have pharmacological properties like anthelmintic, anti-inflammatory, antimicrobial, antiperoxidative, and radical scavenging (Albaqami et al., 2018; Imran et al., 2018; Farooq et al., 2019). It is reported that *Onosma* genus is a rich source of flavonoids, benzoquinones, naphthoquinones, shikonins, and onosmins (Kumar et al., 2013). However, to date, there are no records about its hepatoprotective activity.

Thus, we planned to explore the protective effects of *Obeth* from *O. bracteata* by using *in vitro* assays *viz*. antioxidant, antimutagenic and DNA protective potential. Further, *in vivo* studies were carried out to explore the hepatoprotective effects of *Obeth via* evaluation of serum marker enzymes, antioxidative enzymes and histopathological parameters. Modulatory effects on the expression level of p53, COX-2, NF-κB, and Cyclin D were studied using immunohistochemical (IHC) and Western blotting.

MATERIALS AND METHODS

Chemical and Reagents

1-chloro-2, 4- dinitrobenzene (CDNB), 2- thiobarbituric acid (TBA), 5, 5-dithiobisnitrobenzoic acid (DTNB), Bovine Serum Albumin (BSA), Hydrogen peroxide (H_2O_2), malondialdehyde, nitro blue tetrazolium (NBT), and Silymarin were procured from Sigma (St. Louis, MO, USA). Carbon tetrachloride (CCl_4), ethidium bromide (EtBr), low melting point agarose (LMPA), malondialdehyde (MDA), nicotinamide adenine dinucleotide (NADH), normal melting point agarose (NMPA), hydroxylamine hydrochloride, oxidized glutathione (GSSG), phenazine methosulfate (PMS), reduced glutathione (GSH), sodium pyruvate, and xylenol orange were obtained from HiMedia Pvt. Ltd., (Mumbai, India). The pBR322

Abbreviations: 2AA, 2-aminoanthracene; 2-AF, 2-aminofluorene; AA, Ascorbic acid; BC, bacterial culture; b.wt., body weight; CCl_4, carbon tetrachloride; COX-2, cyclooxygenase-2; CPCSEA, committee for the Purpose of Control and Supervision of Experiments on Animals; ANOVA, analysis of variance. CYP, cytochrome P_{450}; df, Degree of freedom; EDTA, ethylenediamine tetraacetic acid; ECL, Enhanced chemiluminescence; $FeCl_3$, Ferric chloride; GSH, reduced glutathione; GSSG, oxidized glutathione; HPLC, high-performance liquid chromatography; i.p, intraperitoneal; MDA, malondialdehyde; NBT, nitro blue tetrazolium; NF-κB, nuclear factor-kappaB; NPD, 4- Nitro-o-phenylenediamine; PAGE, polyacrylamide gel electrophoresis; PBS, phosphate buffer saline; PMS, Phenazine methosulfate; PVDF, polyvinylidene fluoride; ROS, reactive oxygen species; rpm, revolutions per minute; SA, sodium azide; SDS, sodium dodecyl sulphate; TA, top agar; TCA, trichloroacetic acid; WB, western blotting.

(plasmid) DNA was purchased from Genei Pvt. Ltd. Bangalore, India. Cyclin-D (cyclin-dependent), p53 (tumor suppressor p53), COX-2, and Nf-κB antibodies were purchased from Cell signaling technology (Danvers, MA, USA). (PVDF) membrane (MDI, Ambala), ECL kit was procured from (Biorad, USA). Kits for analysis of serum parameters were purchased from Erba Mannheim (London, UK). The other chemicals used in the experiments were of Analytical grade.

Collection, Identification, and Authentication of Plant Material

The aerial parts including stems and leaves of *Onosma bracteata* Wall. were collected from Herbal Health Research Consortium (HHRC) Pvt. Ltd. Amritsar, Punjab (India), a Government of India approved Drug analysis laboratory. Mr. Viney (Research Officer), at the HHRC Pvt, Ltd. identified and authenticated the plant material by analyzing organoleptic, microscopic and pharmacognostic characteristics. The specimen with accession no: GAZ-03 was submitted in the herbarium of HHRC Pvt. Ltd. Amritsar, Punjab (India).

Extraction Procedure

The plant material was washed with running tap water and dried at 40°C. The material was crushed to powder form (2 Kg) and soaked with 80% ethanol by using the maceration method. The filtered material was evaporated using Rotavapor (Buchi Rotavapor R-210, Switzerland) and was dried to yield 120 g (6%) of the ethanolic extract (*Obeth*).

Antioxidant Assays

Superoxide Radical Anion Scavenging Assay

The radical scavenging activity of *Obeth* was conducted according to the method suggested by Nishikimi et al. (1972), with little modifications. Initially, 0.06 M NBT and 0.156 M NADH were mixed to the different *Obeth* concentrations (25–400 μg/mL), along with the addition of 0.468 M PMS. In the control samples, *Obeth* was substituted by methanol in all of the above solutions. The mixtures were kept at room temperature for 20 min. In the incubation phase, the yellow-colored NBT was reduced to blue colour and the absorbance was recorded at 560 nm.

The percentage decrease of NBT was represented as:

$$\text{Percent change} = ((OD_C - OD_S)/OD_C) \times 100$$

where OD_C = Absorbance of control solution.
OD_S = Absorbance of the sample solution.

Lipid Peroxidation (TBARS) Assay

For this experiment, the procedure was adopted as proposed by Halliwell and Gutteridge (1989), with a little amendment. The lipid origin (10% homogenous egg), 150 mM KCl, and *Obeth* (25–400 mg/mL) were combined in this assay. In place of *Obeth*, methanol was used as a control. To continue lipo-oxidation to the above reaction mixture, 10 mM $FeCl_3$ was added followed by incubation at 37°C for 30 min. Subsequently, HCl solution (comprising TCA, TBA and BHT) was added to the mixture and the resultant mixture was heat treated for 1 h at 90°C accompanied by cooling and centrifugation at 2,500 rpm for 15 min. Lastly, the absorbance of pink coloured supernatant formed was recorded at 532 nm.

The estimation of the percent inhibition (anti-lipoperoxidation activity) was based on the formula below:

$$\text{Percent change} = ((OD_C\text{-}OD_S)/OD_C) \times 100$$

where OD_C = Absorbance of control solution.
OD_S = Absorbance of the sample solution.

Plasmid Nicking Assay

To determine the DNA protective ability of *Obeth* or capacity to scavenge the hydroxyl radical (•OH), the plasmid nicking assay was conducted as per the procedure given by Lee et al. (2002) with few amendments recommended by Robin et al. (2015). Different concentrations (25–100 μg/mL) of *Obeth* from *O. bracteata* were mixed with freshly prepared Fenton's reagent (30 mM H_2O_2, 50 mM Ascorbic acid, and 80 mM $FeCl_3$) and pBR322 plasmid DNA, followed by incubation for 30 min at 37 °C. The samples were resolved onto 1% (w/v) agarose gel using electrophoresis unit at 60 V for 1 h. For this assay, rutin (100 μg/mL) was used as a standard. Immediately, DNA bands were viewed with Gel Doc XR (Bio-Rad, USA), and the band density was determined by using LabImage Bioimaging Platform (Version: 4.1.1) software.

Antimutagenic Activity

The antimutagenic potential of *Obeth* from *O. bracteata* was studied using Ames test, with two *Salmonella typhimurium* strains as per the method given by Maron and Ames (1983) with few amendments recommended by Kaur et al. (2000). The strains of *S. typhimurium* were procured from Microbial Type Culture Collection (MTCC), Chandigarh. Under sterile conditions, direct-acting mutagens, i.e., 4- Nitro-o-phenylenediamine and sodium azide were used for TA98 and TA100, respectively. The antimutagenic activity of *Obeth*, at different concentration levels (25–250 μg/0.1 mL/plate), was studied using two experimental approaches *viz*. co-incubation and pre-incubation modes to distinguish between the bio-antimutagenicity and desmutagenicity, respectively. Negative control contains only bacterial culture, *Obeth* and top agar which showed that *Obeth* did not exhibit mutagenic characteristics. In co-incubation mode, mutagen with *Obeth* was blended into 2mL of top agar containing bacterial culture whereas, in pre-incubation, the mixture of *Obeth* and mutagen was incubated at 37 °C for 30 min before adding to the top agar with bacterial culture. The positive control contains bacterial culture and mutagens which help to assess the dosage rate of toxicity/mutagenicity. *Obeth* antimutagenicity was also tested using S9-mix in the top agar as per the procedure suggested by Garner et al. (1972). The protocol includes a similar method as previously mentioned, except with the inclusion of S9-mix among other components of top agar for the activation of indirect acting mutagens. The reverting colonies were counted using a colony counter.

Antimutagenic Effect

Antimutagenic activity is defined by the percentage decrease in the number of colonies as shown below:

Percentage of Antimutagenic activity of *Obeth*

$$= (a\text{-}b)/(a\text{-}c) \times 100$$

where,

a= number of mutagenic-induced colonies (positive control)

b= number of colonies induced with mutagen and different concentration of *Obeth*

c= number of colonies in (negative control).

Hepatoprotective Activity

Animal Ethics Statement

This experiment was performed in compliance with the guideline of the Committee for the Purpose of Control and Supervision of Experiments on Animals (CPCSE), Ministry of Environment and Forestry, Government of India, and authorized by Institutional Animal Ethics Committee (IAEC), GNDU (approval number 226/CPCSEA/2014/06). As indicated by the IAEC, all rats were entitled to humane care.

Procurement and Care of Experimental Animals

Male Wistar rats, weighing between 150–240 g were purchased from the National Institute of Pharmaceutical Education and Research (NIPER), S.A.S. Nagar, Mohali, Punjab (India). The acclimatization of rats was conducted for one week in polypropylene cages containing husk in the aerated Central Animal House of Guru Nanak Dev University, Amritsar. Commercial rodent feed was provided for the rats, and water was given *ad libitum* with an environmentally regulated condition (55 ± 5 percent humidity, 23 ± 2° C) with a 12 h light/dark cycle photoperiod.

Experimental Design

After acclimatization, rats were divided into 7 groups (n=6). Group, I served as control; Group II intoxicated with 1 mL kg^{-1} CCl_4 (mixed in same volume of olive oil *via* intraperitoneal (i.p.) doses, 3 days in a week) which induced liver mutilation and is mostly used for analyzing the hepatoprotective potential of various drugs (Ritesh et al., 2015; Zamzami et al., 2019); Group III was provided pretreatment of 50 mg kg^{-1} body weight (b.wt.) of silymarin (natural chemopreventive compound) for 21 days *via* oral route accompanied by CCl_4 (i.p.) doses, 3 days in week without fasting of rats; Group IV was administered with an oral dose of only *Obeth* (100 mg kg^{-1} b.wt.) of *O. bracteata* as negative control; Group V was provided with the *Obeth* (50 mg kg^{-1} b.wt.) accompanied by CCl_4 (i.p.) doses; Group VI was provided *Obeth* (100 mg kg^{-1} b.wt.) intoxicated with CCl_4; Group VII was given *Obeth* (200 mg kg^{-1} b.wt.) accompanied with CCl_4 (i.p) treatment. The experimental concentrations of *Obeth* have been decided based on the literature report on *O. bracteata* in *in vivo* studies (Asif et al., 2019).

Blood Extraction and Serum Marker Enzyme Analysis

The rats were kept on fasting overnight before termination of experiment, the blood was extracted from retro-orbital venous puncture into heparinized tubes under moderate diethyl-ether anesthesia. The blood samples were centrifuged at 3,000 rpm for 20 min for the separation of serum. The extracted serum was used for examining the different hepatic markers enzymes (Serum Glutamic Pyruvic Transaminase (SGPT), Serum Glutamic-Oxaloacetic Transaminase (SGOT), Alkaline Phosphatase (ALP), total bilirubin, total protein, Albumin, urea, creatinine, and cholesterol) using Erba diagnostics kits with Bene Sphera autoanalyzer.

Animal Sacrifice and Preparation of Liver Homogenate

The liver was dissected after euthanizing by cervical dislocation. The collected liver was washed with ice-cold saline solution. After this, the liver was rinsed with the mixture of (150 mM KCl + 10 mM Tris-HCl) buffer. Finally, 10 percent (w/v) of dried liver homogenate was mixed with chilled Tris-KCl buffer and centrifugation at 2,500 rpm for 10 min. Supernatant was separated and used for further analysis.

Biochemical Analysis of Liver Functions

Protein Quantification

The standard protocol given by Bradford, 1976 was used for the quantification of protein concentration in the liver. In this experiment, 900 µL of Bradford reagent was mixed with 100 µL of homogenate. The reaction solution was then kept for 30 min at room temperature and the absorbance was calculated on ELISA plate reader at 595/450 nm.

Estimation of Lipid Peroxidation

To check lipid peroxidation in liver homogenate, TBARS (thiobarbituric reactive species) procedure recommended by Devasagayam et al. (1983) was used. 2 mL of TBA solution was mixed to 500 µL of the sample. The mixture was fully stirred and incubated for 30 min at 80°C followed by centrifugation for 15 min at 2,000 rpm. Lastly, supernatant reading was taken at 532 nm and 600 nm. MDA was used as a standard for measuring the amount of TBARS represented as MDA value (MDA equal µmol/g of tissue).

Estimation of Lipid Hydroperoxides

Lipid hydroperoxide generation in liver homogenate was assessed as a method proposed by Jiang et al. (1992). 900 µL of Fox reagent (0.1 M Xylenol orange, 0.025M of H_2SO_4, 0.25 M of $(NH_4)_2$ $Fe(SO_4)_2.6H_2O$, and 0.004 M of $C_{15}H_{24}O$) was mixed to 100 µL of liver homogenate. This reaction mix was kept for 40 min at 37°C and final reading was measured at 560 nm. The lipid hydroperoxide generation is shown as nM H_2O_2 equivalent/g of tissue.

Estimation of Reduced Glutathione Content (EC1.6.4.2)

The reduced glutathione content in liver homogenate was detected as per the protocol given by Anderson (1985) with little changes. Potassium phosphate buffer (200 µM, pH 8) and DTNB solution (600 µM) were mixed to 100 µL homogenate, preceded by incubation for 10 min and the absorbance was recorded at 412 nm. Glutathione was used as a reference for making a standard curve and total GSH content was expressed as µmol of GSH content/g of tissue.

Phase I Enzymes

Evaluation of Cytochrome P_{450} and P_{420} Content

Phase I enzymes were determined as per the method performed by Choi et al. (2003). In this protocol, the liver homogenate was added into two 96-well plates. In one plate 15 µL of sodium hydrosulphite (500 mM) was added in each well preceded with 30–35 bubbles of carbon monoxide. Another plate was saturated with only 30–35 bubbles of carbon monoxide without adding sodium hydrosulphite. The absorbance was observed at 420 nm, 450 nm, and 490 nm.

Cytochrome b5 Analysis

The cytochrome b5 (Cyt b5) quantities were analyzed as the method suggested by Omura and Sato (1964). In this experiment, 500 µL of liver homogenate was added to 4.3 mL of Tris-HCl buffer. After that, 50 µL of this mixture was poured onto two separate 96-well plates. Now, 50 µL of NADPH (500 mM) was added in each well of one plate and 50 µL of Tris-HCl in each well in the other plate followed by incubation for 20 min. The absorbance was measured at 409 nm and 424 nm. The enzyme activity was determined by using the extinction coefficient (6.22 mM^1 cm^1).

NADPH Cytochrome b5 Reductase

The NADPH Cyt b5 was determined using procedure recommended by Mihara and Sato (1972) with little modification. For this, 200 µL of NADPH (100 µM) and 200 µL of Potassium ferricyanide (200 µM) were mixed with 500 µL of potassium phosphate buffer (300 mM). The process was initiated with the addition of 100 µL of homogenate. The NADPH Phase II Enzymes

Glutathione-S-Transferase (EC 2.5.1.18)

Phase II metabolic isozyme glutathione-S-transferase (GST) was quantified as per the method suggested by Habig et al. (1974). In this experiment, 2.7 mL of sodium phosphate buffer (100 mM) was mixed with 100 µL each of 1-Chloro-2,4-dinitrobenzene (CDNB) (0.03 M) and 100 µL reduced glutathione (0.03 M) followed by incubation at 37°C for 5 min. After incubation, 100 µL of homogenate was added to initiate the reaction and enzyme activity was recorded at 340 nm at 30 s interval for 3 min.

Antioxidative Enzymes

Catalase (CAT) (EC 1.11.1.6)

Catalase was analyzed in the liver homogenate as the method described by Aebi (1984) with little modifications. 300 µL of H_2O_2 (150 mM) and 2.6 mL of 50 mM potassium phosphate buffer (50 mM) were mixed thoroughly. After this, homogenate was added to initiate the reaction. Eventually, the absorbance was recorded for the catalase activity at an interval of 15 s, for 2 min at 240 nm.

Glutathione Reductase (GR) (EC 1.6.4.2)

A slight modification was done to assess the GR level in the samples using the protocol given by Carlberg and Mannervik (1975). In this assay, the reaction mixture was prepared by adding 1.2 mL of sodium phosphate buffer (200 mM), 200 µL oxidized glutathione (10 mM), 200 µL EDTA (20 mM), and 200 µL of homogenate. Finally, 200 µL NADPH (1000 µM) was mixed in a reaction solution and at an interval of 15 s, absorbance was measured at 340 nm for 3 min.

Lactate Dehydrogenase (EC 1.1.1.27)

To determine the lactate dehydrogenase (LDH) activity in liver homogenate, the protocol recommended by Kaur S. et al. (2019) with slight modifications was adopted. In this experiment, reaction mixture comprising of 2.3 mL of Tris HCl buffer (100 mM, pH 7.1), 300 µL of sodium pyruvate (100 mM), 100 µL Triton X (7.5%), and 300 µL of NADH (3 mM) was incubated at 30°C for 15 min. In this reaction mixer, 100 µL of homogenate was added and absorbance was measured at an interval of 10 s at 340 nm for 1 min.

Guaiacol Peroxidase (EC 1.11.1.7)

Guaiacol peroxidase activity in liver homogenate was determined as per the method suggested by Gee et al. (1970) with slight modifications. The reaction mixture was prepared by adding 75 µL (20 mM) of guaiacol solution to 25 µL 100 mM phosphate buffer with 100 µL of liver homogenate and then 25 µL of H_2O_2 was added. The absorbance was taken at 436 nm.

Histopathological Assessment

To check the hepatocytes' structural integrity, the isolated livers from the respective groups were fixed in a 10% buffered formalin solution, dipped in ethanol for dehydration and implanted in paraffin wax. The microtome was used to make sections of the livers (0.4 mm thick) using paraffin blocks and stained with H&E (hematoxylin and eosin) by the standard procedure. The slides were observed with a Nikon Eclipse E200 Compound microscope.

Immunohistochemical (IHC) Examination

To evaluate the pattern of expression of p53 and cyclin D proteins (after treatment with CCl_4 and *Obeth*) in hepatocytes, IHC analysis was performed. In this method, the liver sections (3-6 µm) were deparaffinized on glass slides. The sections were kept for 30 min in H_2O_2 (0.3% of methanol). The section slides were blocked with 5% skimmed milk for 30 min. Finally, slides were incubated overnight with anti-p53 and anti-cyclin D antibodies at 4°C. Slides were then washed twice with 1 x PBS followed by the addition of anti-rabbit IgG HRP- conjugated secondary antibody and incubated for 30 min and washed thrice with 1x PBS. The expression of proteins was developed by using 3-diaminobenzidine (DAB) for 2–3 min and washed with 1 x PBS. The slides were observed under a Nikon Eclipse E200, Japan microscope.

Single-Cell Gel Electrophoresis (Comet Assay)

The comet assay (single-cell gel electrophoresis) was performed according to the protocol given by Collins and Dušinská (2002) with slight modifications. In this assay, 500 mg of rat liver was minced in trypsin solution and kept for 15–20 min at room temperature. The homogenate was passed through a muslin cloth to remove tissue debris followed by centrifugation at 2,500 rpm for 10 min to obtain a cell pellet. After that, 50 µL of cell suspension was added to a low melting point agar (LMPA) solution and transferred to normal melting point agar (NMPA) coated glass slides. The slides were kept in the fridge for 10–15

min. The slides were immersed in lysine buffer (100 mM EDTA, 10 mM Tris-HCl, 1% Triton X-100, 250 mM NaCl, 10 percent DMSO; pH 10) at 4°C for 3- 4 hr. Now slides were dipped in electrophoresis buffer for 10-15 min before starting electrophoresis (voltage = 25 V, current = 300 mA, time = 20 min). After electrophoresis, the slides were dried and kept in neutralization buffer for 15 min (thrice). After 24 h slides were stained with 100 µL (20 µg/mL) ethidium bromide and observed in the fluorescent microscope (Nikon, Tokyo, Japan). Per slide thirty cells were selected randomly to assess DNA impairment, tail length, tail DNA (%) and tail moment using Comet Assay Software Project (CASP) Lab version CASP1.2.3 beta 1.

Western Blot Analysis

The liver was dissected and rapidly stored according to respective groups at -80°C. The samples were homogenized in RIPA lysis buffer followed by centrifugation at 12,000 rpm for 20 min and the upper transparent solution was then poured into new tubes. The quantity of proteins was analyzed using Bradford method. Equal concentration of protein (40 µg) was resolved by SDS-PAGE and transferred to PVDF membrane through western bloting. After that, the membrane was blocked using BSA (5% in TBST, 0.1% Tween-20) for 2 h at 25°C and kept overnight with antibodies against p53 (1:1,000), NFκB (1:2,000) and COX-2 (1:500). After that, the membrane was washed thrice with TBST and HRP-conjugated secondary antibody (1:1,500) was added followed by incubation for 2 hr at room temperature. ECL reagent was used to develop blots and imaging was done using Image-Quant LAS 4000, GE Healthcare. Band densities were quantified with Alphaease FC Software (version 4.0). β-actin (1:500) as endogenous control was used for normalizing the expression of the protein of interest.

Phytochemical Analysis

HPLC Analysis

The filtered *Obeth* was analyzed for the presence of polyphenols using UHPLC Nexera system (Shimadzu, MA, USA), column (C18). The solvent used in mobile phase consisted of solvent A (0.2% acetic acid) and solvent B (methanol). The flow rate of 1.0 mL/min was sustained for 21 min of running time. The gradient flow used was: 20% B (0–10 min), 55% B (10–12 min), 70% B (12–14 min), 50% B (14–15 min), 40% B (15–17 min), and 30% B (17 –21 min). For testing, the injection volume of the sample was 10 µL with column temperature maintained at 25°C. The spectra were observed at 280 nm with a photodiode array (PDA) analyzer. The peaks of the compound were identified by comparing retention time and distribution of UV-VIS spectra of samples with those of standard compounds.

Statistical Analysis

All results are represented as Mean ± SE of minimum three independent replicates. To compare difference among the means, one-way and two-way analysis of variance (ANOVA) with Tukey's test was used at 5% confidence level (p-value ≤ 0.05).

RESULTS

Antioxidant Potential of *Obeth*

Superoxide radical scavenging and lipid peroxidation activity of *Obeth* is shown in **Figure 1**, **Table S1**. SRS assay there is dose-dependent increase in free radical scavenging activity *via* NBT inhibition with EC_{50} (115.14 µg/mL) whereas EC_{50} of Rutin was observed to be 46.18 µg/mL. The lipid peroxidation activity of Rutin and *Obeth* was EC_{50} (115.68 µg/mL) and EC_{50} (199.33 µg/mL) respectively (**Table S2**) exhibiting *Obeth* with better antioxidant activity as compared to standard rutin.

Plasmid Nicking Assay

DNA protective effect of *Obeth* at various concentrations *viz*. 25, 50, 100 µg/mL was demonstrated in **Figure 2**. It was observed that the *Obeth* exhibits quite strong radical scavenging properties with the highest tested concentration (100 µg/mL) on pBR322 plasmid DNA. The experiment exhibited the formation of nicked DNA because of hydroxyl (•OH) radicals produced by Fenton's

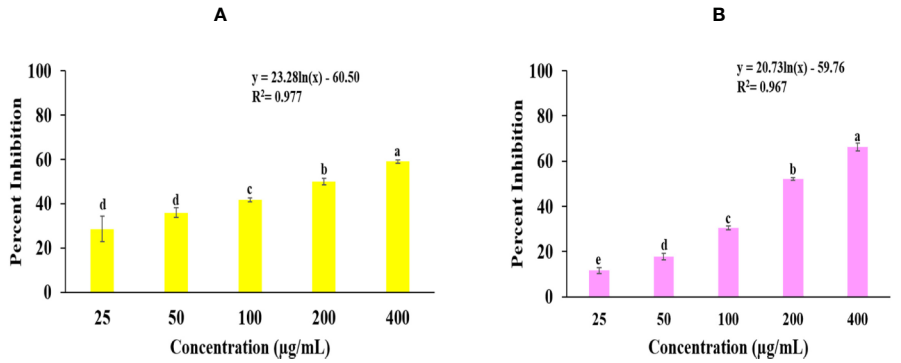

FIGURE 1 | Graphs shows the *in vitro* antioxidant potential of *Obeth* from *O. bracteata*. **(A)** Superoxide radical scavenging assay. EC_{50} = 115.14 µg/mL; F-ratio = 187.19; HSD = 8.77. **(B)** Lipid peroxidation inhibition assay. EC_{50} = 199.33 µg/mL; F-ratio = 331.68; HSD = 5.89. Values are expressed as Mean ± SE at level of significance p ≤ 0.05. Data labels with different letters represent significant difference among them.

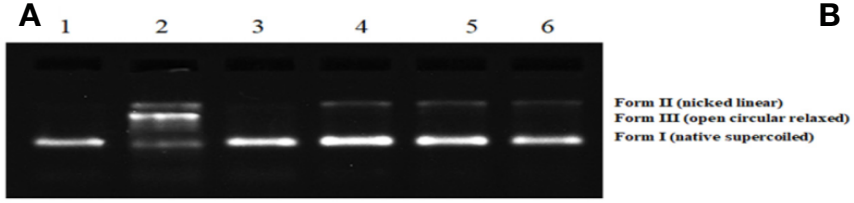

B

Lane No	Treatment	Native Supercoiled	Nicked Linear	Open Circular Relaxed
1	DNA	100	-	-
2	Rutin+DNA+FR	33.33	21.74	44.92
3	FR+DNA	100	-	
4	DNA+FR+ (*Obeth*) 25 µg/mL	82.21	17.78	-
5	DNA+FR+ (*Obeth*) 50 µg/mL	81.53	18.46	-
6	DNA+FR+ (*Obeth*) 100 µg/mL	81.76	18.23	-

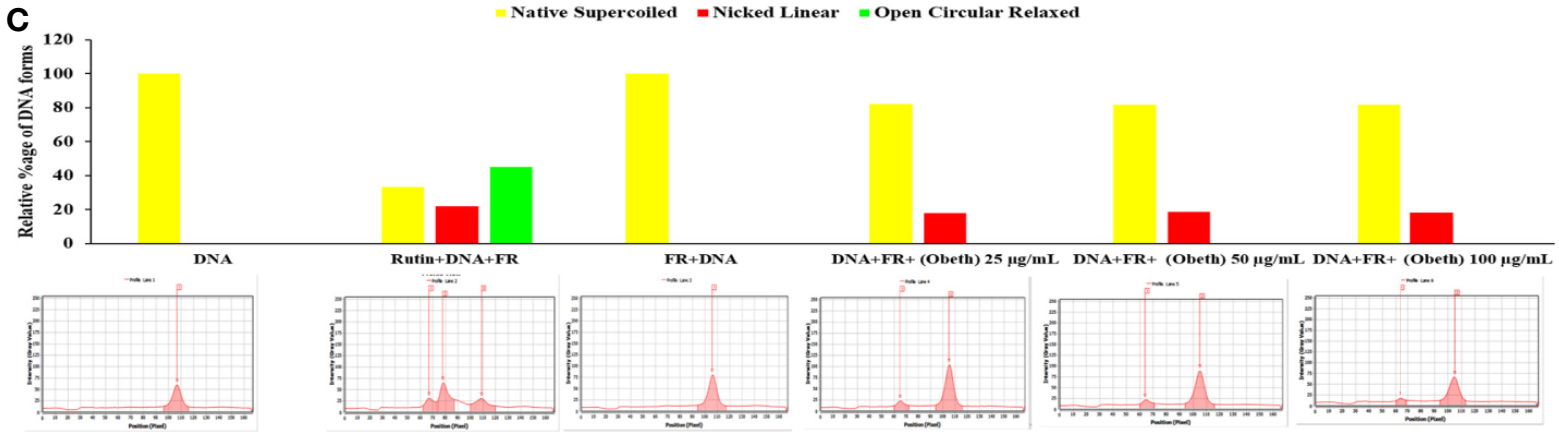

FIGURE 2 | Effect of *Obeth* from *O. bracteata* on DNA protection against oxidative damage caused by Fenton's reagent (FR) in DNA nicking assay. **(A)** Relative mobility of different forms of plasmid DNA exposed to *Obeth* extract in electrophoresis. Lane 1: Negative control (pBR322 DNA + distilled water); Lane 2: Positive control (pBR322 DNA + FR); Lane 3: pBR322 DNA + FR + 100 µg/mL rutin; Lanes 4, 5, 6: pBR322 DNA + FR + 25, 50, 100 µg/mL *Obeth* fraction respectively. **(B)** Densitometric analysis showing relative percentage of different DNA forms in plasmid after treatment with various concentrations of *Obeth* fraction in the form of table and **(C)** graph respectively (software used = Lab Image). CN = Control, FR=Fenton reagent.

reagent. The various concentrations of *Obeth* showed a dose-dependent minimization of supercoiled DNA to open circular.

Ames Assay

The antimutagenic potential of *Obeth* was tested against sodium azide and 2-aminofluorene mutagenicity in *S. typhimurium* strains as shown in **Table S3**. The *Obeth* in TA100 strain (-S9 mix) displayed a high inhibition rate (82.30% at 250 µg/0.1 mL/plate) showing strong modulation of genotoxicity of base-pair substitution mutagen sodium azide as compared to NPD (frame-shift mutagen) in TA98 tester strain **Table 1**. The *Obeth* exhibited high antimutagenicity potential for preincubation mode than in co-incubation approach without -S9 in both TA100 and TA98 as shown in **Figure 3A** and with +S9 mix in **Figure 3B**. Minimum EC_{50} values were depicted by the extract against 2AF mutagenicity in pre-incubation mode in TA100 strain as shown in **Table S3**. In case of TA98 strain also, *Obeth* showed good antimutagenic potential in pre-incubation experiments as compared to co-incubation approach (**Figure 3**, **Table 1**). The calculated EC_{50} value showed the high suppression of mutagenicity with a minimum EC_{50} value (29.51 µg/0.1 mL/plate) with TA98 (+S9) in the pre-incubation approach of treatment as shown in **Table S3**. The evaluation between all treatments, with and without S9, is shown in **Figure 3**, **Table S3** respectively. The assessment permits noticeable potential of *Obeth* +S9, even at minimum concentrations, as compared to -S9 treatments. Therefore, the complete investigation showed the conspicuous activity of *Obeth*, with S9 mix in pre-incubation approach. The findings were statistically evaluated by two-way ANOVA for statistical difference and the interactions as seen in **Table 1**, **S3**. The study revealed a statistically significant difference between co-incubation and pre-incubation methods of investigation, in addition to among different treatments used. So, the *Obeth* of *O. bracteata* exhibited marked antimutagenicity potential.

Variations in Body Weight (b.wt.) of Animals

In the present study CCl_4 treated group, the percentage fold decrease in b. wt. of rats was recorded after 3 weeks, and a statistically significant difference was observed in the b.wt. of CCl_4 rats treated group (0.88-fold) relative to control group I (one-fold). Additionally, dose-dependent variability in the b.wt.

TABLE 1 | Percentage inhibition of mutagenicity by *Obeth* extract of *O. bracteata* in TA98 and TA100 tester strains of *Salmonella typhimurium* with and without S9.

Treatment	Dose/0.1 mL/plate	TA 100 (without S9) % Inhibition	TA 98 (without S9) % Inhibition	TA 100 (with S9) % Inhibition	TA 98 (with S9) % Inhibition
Co-incubation	25 µg	42.01 ± 4.25^{b}	23.07 ± 3.42^{c}	53.02 ± 5.71^{c}	40.40 ± 3.42^{c}
	50 µg	50.69 ± 4.24^{b}	39.92 ± 3.76^{b}	66.85 ± 1.66^{b}	50.35 ± 2.05^{b}
	100 µg	65.71 ± 2.48^{a}	50.98 ± 1.65^{ab}	74.48 ± 2.59^{ab}	60.37 ± 1.40^{a}
	250 µg	74.47 ± 2.51^{a}	58.97 ± 1.81^{a}	83.37 ± 1.21^{a}	61.51 ± 2.08^{a}
Pre-incubation	25 µg	49.77 ± 2.88^{c}	35.53 ± 2.79^{c}	60.91 ± 2.01^{c}	46.39 ± 2.45^{c}
	50 µg	60.51 ± 2.06^{b}	47.60 ± 2.76^{b}	70.66 ± 3.44^{b}	57.74 ± 1.79^{b}
	100 µg	75.28 ± 2.91^{a}	58.79 ± 1.74^{a}	85.01 ± 1.11^{a}	73.43 ± 3.45^{a}
	250 µg	82.30 ± 1.63^{a}	62.85 ± 3.33^{a}	91.41 ± 1.26^{a}	82.56 ± 2.24^{a}

Values are represented as Mean ± SE, level of significance $p \leq 0.05$. Means with different superscripts represent significant difference among them in all groups.

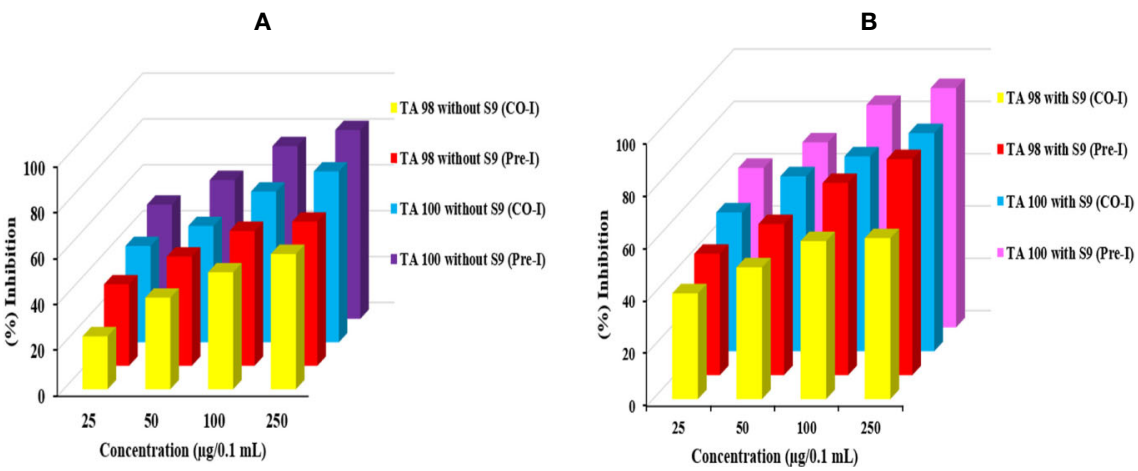

FIGURE 3 | Graph represents the antimutagenic potential of *Obeth* using *S. typhimurium* in Ames assay. **(A)** Represents the TA100 and TA98 without S9 (Pre and Co-incubation). **(B)** Represents TA100 and TA98 with S9 (Pre and Co-incubation). **(A)** Represent the percent inhibition between co- and pre-incubation in TA98 and TA100 strain without S9. **(B)** Represent the percent inhibition between co- and pre-incubation in TA98 and TA100 strain with S9.

of *Obeth* + CCl_4 intoxicated groups was maintained b.wt. as the control group (**Table S4**).

Serum Marker Enzymes

Effect of *Obeth* and CCl_4 on SGOT, SGPT, and ALP Levels

Group II (CCl_4) significantly increased the amount of SGOT, SGPT, and ALP to 351.45 ± 21.01, 133.86 ± 29.88, and 529.16 ± 56.74 IU/L respectively in comparison with Group I (control) at 5% level of significance ($p \leq 0.05$) (**Table S5**). Increased concentration of these enzymes in serum, highlighted the poor functioning of the liver and liver injury because of their seepage into the blood. However, the results showed that the treatment of *Obeth* minimized the amount of these enzymes relative to the CCl_4 Group II. III and IV exhibited the amounts of SGOT, SGPT, and ALP in serum in the acceptable limits, signifying reduction in liver injury (**Figure 4A**).

Direct Bilirubin and Total Bilirubin Enzymes in *Obeth* and CCl_4 Treated Rats

Obeth pretreatment followed by CCl_4 doses in Groups V, VI, and VII was effective in maintaining natural level of direct bilirubin and total bilirubin disturbed in Group II (**Figure 4B**). In Group III and *Obeth* treated Group VII indicated an optimum capacity for regeneration by stopping a rise in these enzymes (**Table S6**).

Total Protein and Albumin Level in Serum

CCl_4 stimulated changes in the hepatic enzymes resulting in decreased albumin (2.15 ± 0.3 g/dL) and protein (5.93 ± 0.34 g/dL) content that lead to hepatic injury (**Table S7**). Pretreatment of *Obeth* followed by CCl_4 intoxication exhibited substantial protective capacity retaining the normal levels of these enzymes as identified in Groups V, VI, and VII (**Figure 4C**).

Effect of *Obeth* and CCl_4 on Serum Proteins, Urea, Creatinine, and Cholesterol

The levels of urea, creatinine and cholesterol in the serum of various groups is given in **Table S8**. There was a significant increase in the level of urea, creatinine and cholesterol in CCl_4 treated Group II. As depicted from the results of Group IV pretreated with *Obeth* followed by CCl_4 showed a restored level of urea, creatinine and cholesterol, hence showing the recovered hepatic damage in a dose-dependent manner (**Figure 4D**).

Biochemical Parameters

Estimation of Protein Content in Liver Homogenate

The protein content in the CCl_4-treated group (24.89 ± 4.16 mg/g tissue) was observed to decrease significantly as compared to the control group (52.74 ± 11.37 mg/g tissue) **Table S9**. Group IV, however, showed a high protein content of 53.38 ± 4.21 mg/g. On the other side, pretreated groups (V, VI, and VII) were shown to greatly recover the normal protein amount as seen in **Figure 5A**.

Estimation of Lipid Peroxidation in Liver Homogenate

The level of MDA content exhibited the level of lipid peroxidation. Group II revealed a significant increase ($p \leq 0.05$) in the MDA content relative to the Group I. Group IV *Obeth* treated exhibited less concentration of MDA content (0.67 ± 0.33 nM MDA equivalent/g of tissue). However, pretreatment of *Obeth* followed by CCl_4 resulted in a dose-dependent decrease in raised MDA content as seen in **Figure 5B** and **Table S9**.

Estimation of Lipid Hydroperoxide in Liver Homogenate

It was observed that the group treated with CCl_4 displayed a substantial increase in the lipid hydroperoxide content (23.24 ± 2.54 nM equivalent H_2O_2/g of tissue) relative to the control

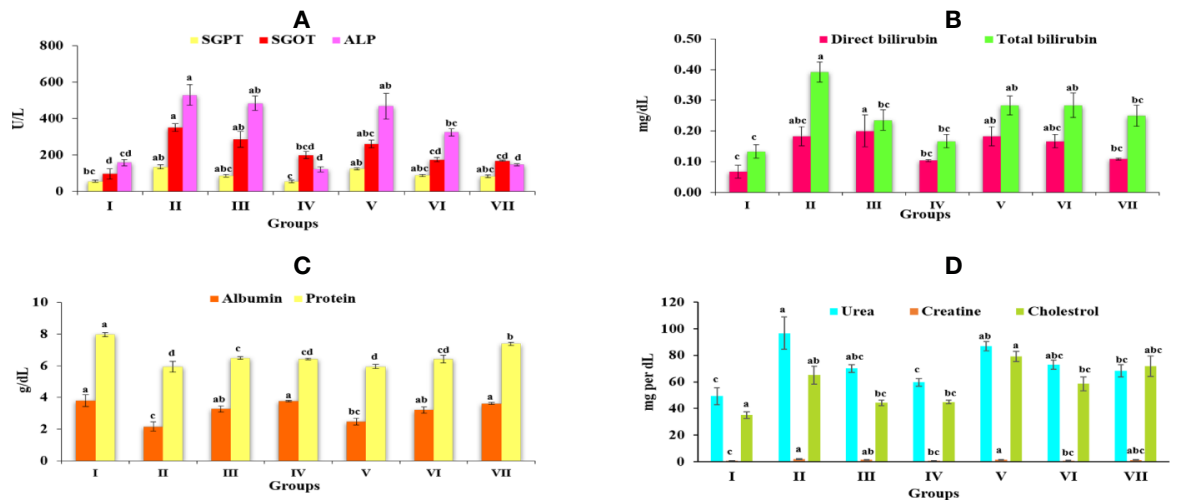

FIGURE 4 | Graph represents the effect of *Obeth* of *O. bracteata* on level of serum enzymes level in CCl_4-treated male Wistar rats. **(A)** Represent the levels of SGOT, SGPT, and ALP. **(B)** Represent the levels of direct bilirubin and total bilirubin. **(C)** Represent the levels of albumin and total protein. **(D)** Represent the levels of urea, creatine and cholesterol. Values are expressed as Mean ± SE at level of significance $p \leq 0.05$. Data labels with different letters represent significant difference among them.

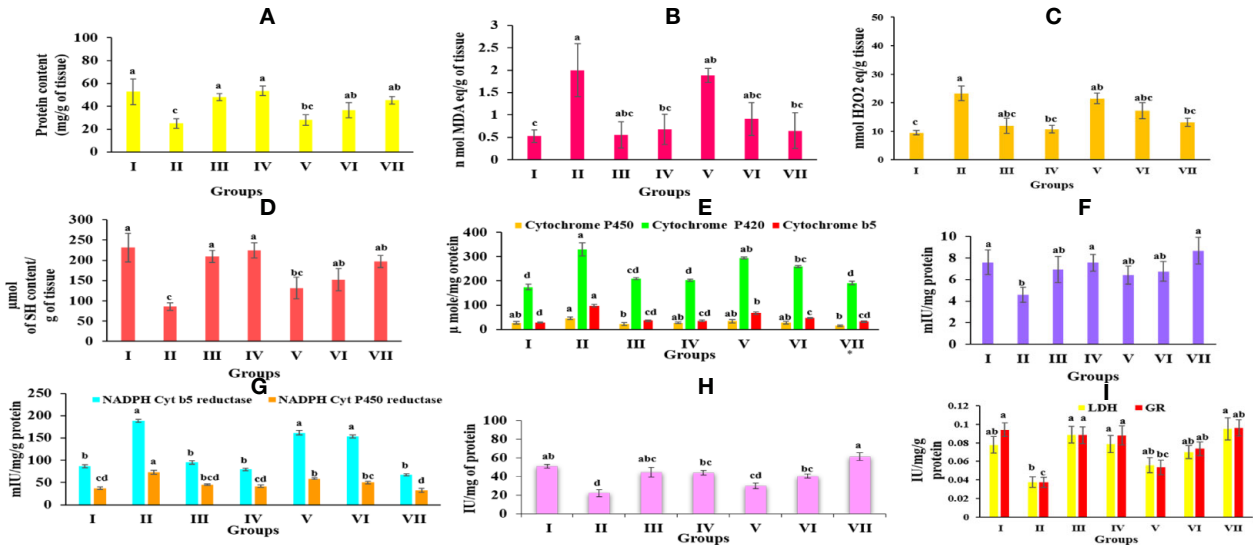

FIGURE 5 | Graph represents the effect of *Obeth* of *O. bracteata* on level of enzymes in CCl_4-treated male Wistar rats. **(A)** Represent the levels of protein in liver homogenates. **(B)** Represent the levels of malondialdehyde (MDA) content in liver homogenate. **(C)** Represent the levels of lipid hyperoxide in liver homogenates. **(D)** Represent the levels of reduced glutathione (GSH) in liver homogenate. **(E)** Represent the levels of NADH Cyt b5 and NADH Cyt P_{450} in liver homogenate of Wistar rats. **(F)** Represent the levels of GST in liver homogenate of Wistar rats. **(G)** Represent the levels of NADH Cyt b5 and NADH Cyt P_{450} in liver homogenate of Wistar rats. **(H)** Represent the levels of Catalase in liver homogenate. **(I)** Represent the levels of lactate dehydrogenase and glutathione reductase in liver homogenate. Values are expressed as Mean ± SE at level of significance $p \leq 0.05$. Data labels with different letters represent significant difference among them.

group (9.43 ± 0.79 nM equivalent H_2O_2/g of tissue). Pretreatment by *Obeth* maximum dose showed to decrease CCl_4 toxic impact by exhibiting a maximal decrease in lipid peroxide content (**Figure 5C** and **Table S9**).

Reduced Glutathione (GSH) Content

The group administered with silymarin displayed substantial improvement in GSH content (209.75 ± 14.71 µmol of SH content/g of tissue) compared with CCl_4-treated group with GSH content of 85.99 ± 9.57 µmol of SH content/g of tissue (**Table S9**). *Obeth* recovered the reduced amount of GSH effectively as close to that of the control group (**Figure 5D**).

Phase I Enzymes

As shown in **Table S10**, *Obeth* exhibited a dose-dependent effect on cytochrome P_{450}, b5 and P_{420} levels in the liver homogenate. CCl_4-treated group exhibited reduction in the level of cytochrome P_{450} (45.90 ± 5.07 µmol) and P_{420} (329.18 ± 26.63 µmol) as compared to the control group. Pre-treatment of *Obeth* followed by CCl_4, showed increasing cytochrome levels P_{450} and P_{420} showing an important defensive effect against hepatic toxicity (**Figure 5E**). A rise in the production of cytochrome b5 (98.32 ± 5.74 µmol) in CCl_4 treated group compared to the control group (29.34 ± 2.27 µmol) was observed. NADH cytochrome P_{450} reductase activity showed an increase in the CCl_4-intoxicated group relative to the control group. Silymarin (45.27 ± 1.91 mIU) and *Obeth* Group IV (41.82 ± 3.23 mIU) showed same activity as compared to the control group of rats (37.23 ± 2.96 mIU) whereas group VII showed decrease in level of enzyme (32.47 ± 4.99 mIU) as shown in **Table S11**. Moreover, the CCl_4-treated group exhibited an increase in the specific action of NADH cytochrome b5 reductase to 188.43 ± 3.86 mIU in comparison to the control group (86.40 ± 3.17 mIU) whereas group VII exhibited minimization in level of enzyme (67.20 ± 2.36 mIU) as shown in (**Figure 5G**, **Table S11**).

Phase II Enzymes

Glutathione S-Transferase (GST)

CCl_4 treated group showed decreased GST behavior (4.59 ± 0.684 mIU/mg protein) compared to the control group (7.6 ± 1.14 mIU) (**Table S12**) (**Figure 5F**). However, it was observed that there was a significant increase in GST activity in group III, IV, and VII which showed enhancement of hepatic antioxidant enzymes to combat the increased level of reactive oxygen species.

Antioxidative Enzymes

Catalase

As shown in **Table S13**, the catalase activity decreased in the CCl_4-intoxicated group (21.92 ± 3.76 IU/mg protein) as compared to control group (50.76 ± 1.95 IU/mg protein). The higher pretreated dose of *Obeth* (200 mg/kg b.wt.) followed by CCl_4 showed an increase in catalase function over the untreated group, thereby offering protective activity against CCl_4 intoxication (**Figure 5H**).

Glutathione Reductase (GR)

The enzymatic expression of GR in the CCl_4-administered group showed 0.03 IU of GR level as compared to control group (0.09 IU). The increased GR specific activity was detected in groups VI and VII which suggested *Obeth* has a protective role against hepatic damage done by CCl_4 (**Table S13**, **Figure 5I**).

Lactate Dehydrogenase (LDH)

The level of lactate dehydrogenase is correlated with the integrity of the cell membrane. The increased LDH level in the CCl_4-intoxicated group (0.03 IU) mediated cell injury occurred due to the lethal metabolites created by Phase I and II enzyme stimulation. Pre-treated groups with different doses of *Obeth* were shown to significantly reduce the level of LDH equivalent to the control group (**Table S13**) and (**Figure 5I**).

Histopathological Studies

The histopathological analysis showed supportive results for the biochemical and serum enzyme markers. The liver of the CCl_4-treated group showed necrosis, inflammation and loss of hepatocytes with vacuolization when observed between central vein and portal traid area with hematoxylin and eosin staining (**Figure 6B**). In **Figure 6**, compared to other groups, CCl_4-intoxicated group showed a maximum region of fibrotic markers and collagen localization. *Obeth* and Silymarin treated groups maintained normal liver hepatocyte architecture relative to control group around the central vein area (**Figures 6C–G**).

Immunohistochemical (IHC) Analysis

Within hepatocytes, over-expression of p53 protein and cyclin-D contribute to hepatocellular carcinoma development. In this experiment, CCl_4-treated group exhibited an upregulated expression level of cyclin D (**Figure 7A**) and p53 markers (**Figure 7B**) which finally show fibrosis and lobular inflammation whereas, treatment of *Obeth* decreased the CCl_4 induced p53 and cyclin D protein expression dose-dependently in liver hepatocytes as compared to the toxic group (**Figures 7A**, **c–g** and **7B**, **c–g**).

Comet Assay

As shown in **Figure 8**, larger Comet tail length in CCl_4 treated groups indicated the higher necrosis, apoptosis and DNA fragmentation in hepatocytes. Whereas, reduced Comet tail length in *Obeth* + CCl_4 treated groups (100 mg/kg b.wt. and 200 mg/kg b.wt.) showed inhibition of necrosis, apoptosis and DNA fragmentation.

Western Blotting

Protein Expression of p-53, Cox-2, and NfκB

To explore the relationship between p53, COX-2, and NfκB and the hepatoprotective effects of *Obeth* on toxicity induced by CCl_4, we studied protein expression using western blotting. As shown in **Figure 9**. there was a significant increased ($p < 0.05$) in p53, Cox-2, and NfκB protein expression in CCl_4 treated group as compared to the untreated control group. However, there was a dose-dependent decrease in the expression of proteins on administration of *Obeth* with CCl_4 treated groups as compared to only CCl_4 intoxicated group.

Phytochemical Analysis by HPLC Analysis

The phytochemical analysis by HPLC exhibited the occurrence of catechin, epicatechin, Onosmin A, rutin and kaempferol as major phytoconstituents in *Obeth* (**Figure 10**, **Table 2**).

DISCUSSION

The active polyphenols present in the plants act as scavengers of ROS, DNA protective agents and help to maintain the expression of genes/proteins that break down toxins and keep cellular redox homeostasis (Liu et al., 2018). These polyphenols have the antioxidant, antimutagenic and chemopreventive properties that might help to protect and conserve the constancy of genome (Mehta et al., 2010; Rodríguez-García et al., 2019). Previous studies have reported the potential of *Onosma* genus as antioxidant compounds and their use in averting numerous pharmacological situations (Naz et al., 2006; Ebrahimzadeh et al., 2010; Ahmad et al., 2013; Imran et al., 2018; Farooq et al., 2019).

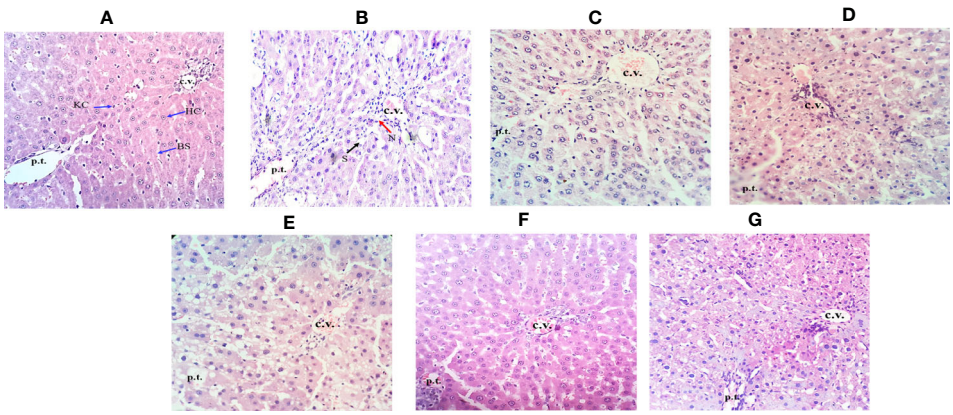

FIGURE 6 | Effect of *Obeth* from *O. bracteata* on histology of liver tissues as assessed by H & E staining. **(A)** Control group (tap water ad libitum) (GI) showing normal lobular architecture with clear portal triad. **(B)** CCl_4: Olive oil (1:1; 1mL kg^{-1}b.wt.) induced necro-inflammatory activity in GII was noted. Treatment of *Obeth* extract was associated with diminution of portal hypertension with increasing dose. **(C)** Silymarin (100 mg kg^{-1}b.wt.) + CCl_4, **(D)** low dose (50 mg kg^{-1}b.wt.) + CCl_4, **(E)** medium dose (100 mg kg^{-1}b.wt.) + CCl_4, **(F)** High dose (200 mg kg^{-1}b.wt.) + CCl_4, **(G)** Negative (only extract 100 mg kg^{-1}b.wt. Arrows indicate Kupffer cell (KC), central vein (CV), hepatic cells (HC), blood sinusoids (BS), steatosis (S) (black arrow), and necrosis (N) (red arrow).

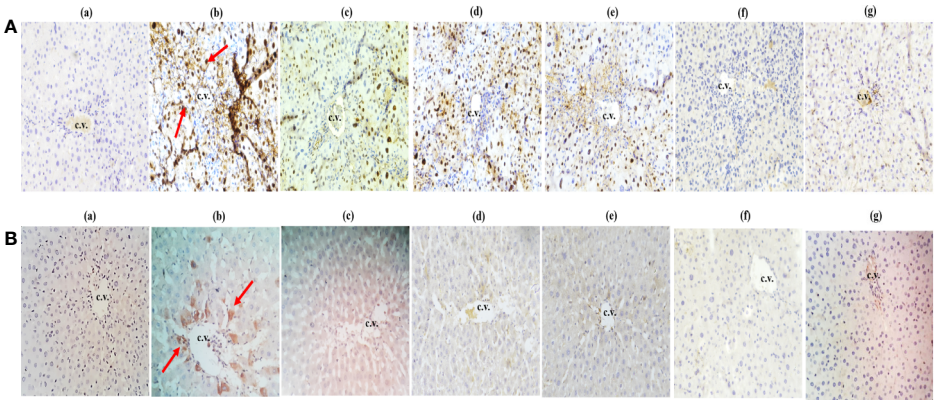

FIGURE 7 | Effect of *Obeth* from *O. bracteata* on expression levels of proteins using immunohistochemical analysis of liver tissues. **(A)** shows cyclin (d) and **(B)** shows p53 antibodies. Arrows showed the increase in expression of cyclin D and p53 proteins in CCl_4 treated liver samples (Original magnification = 40 x). Expression of these proteins was downregulated when observed in liver samples co-treated with CCl_4 and *Obeth* (200 mg/kg b.wt.). Red arrow indicates the increase in the expression of protein in the CCl_4 treated group. (b) Control group (tap water ad libitum) (GI) showing normal lobular architecture with clear portal triad. (b) CCl_4: Olive oil (1:1; 1mL kg^{-1} b.wt.) induced elevation in the expression level of cyclin D was noted. Treatment of *Obeth* extract was associated with diminution of portal hypertension with increasing dose. (c) Silymarin (100 mg kg^{-1}b.wt.) + CCl_4, (d) low dose (50 mg kg^{-1}b.wt.) + CCl_4, (e) medium dose (100 mg kg^{-1}b.wt.) + CCl_4, (f) High dose (200 mg kg^{-1}b.wt.) + CCl_4, (g) Negative (only extract 100 mg kg^{-1} b.wt.).

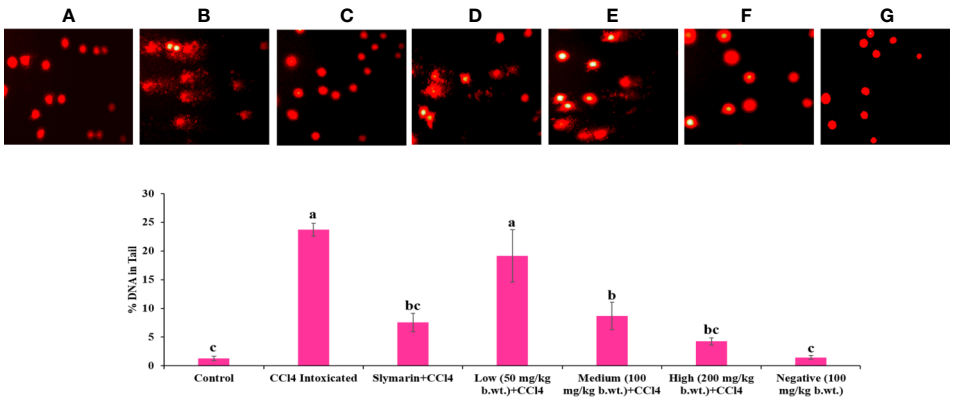

FIGURE 8 | Single cell gel electrophoresis assay was used for determined DNA damage/protect in liver of rats. Results of the comet assay confirm that pretreatment with *Obeth* decreases CCl_4-induced hepatotoxicity in rats. **(A)** Control group (tap water ad libitum) (GI), **(B)** CCl_4: Olive oil (1:1; 1mL kg^{-1}b.wt.) in GII, **(C)** Silymarin (100 mg kg^{-1}b.wt.) + CCl_4, **(D)** low dose (50 mg kg^{-1}b.wt.) + CCl_4, **(E)** medium dose (100 mg kg^{-1}b.wt.) + CCl_4, **(F)** High dose (200 mg kg^{-1}b.wt.) + CCl_4, **(G)** Negative (only extract 100 mg kg^{-1}b.wt.). Histograms showing densitometric analysis of % of DNA in tail in comet assay. Values are expressed as Mean ± SE at level of significance $p \leq 0.05$. Data labels with different letters represent significant difference among them.

In the current study, we investigated the antioxidant, antimutagenic, genoprotective, and hepatoprotective properties of *Obeth* from *Onosma bracteata* along with evaluation of the expression of proteins involved in the inflammation and apoptotic induction in *in vivo* studies using male Wistar rats. In antioxidant assays, *Obeth* had shown potential to scavenge free radicals, namely in SRS and LPO assays. *Obeth* showed strong radical scavenging activity with EC_{50} (115.14 µg/mL) whereas LPO inhibition activity with EC_{50} (199.33 µg/mL) (**Tables S1** and **S2**). Radical scavenging potential of *Obeth* might be correlated to the nature of phenolics, contributing to their electron transfer/hydrogen donating ability.

Plants contain natural antioxidants, primarily flavonoids, which are being explored to inhibit various diseases *viz.* chronic inflammation and cancer (Surh, 2003). *Onosma* genus plants are enriched with bioactive components *viz.* flavonoids, alkannin, and shikonin responsible for wound healing, analgesic and its antibacterial actions (Kumar et al., 2013). The HPLC analysis of *Obeth* revealed the existence of different phytoconstituents *viz.*, kaempferol, Onosmin A, catechin and epicatechin. Numerous reports have shown that *Onosma* genus and its isolated compounds are responsible for excellent antioxidant activities (Riedl et al., 2004; Kandemir and Türkmen, 2008; Menghani et al., 2011). The ethyl acetate, methanol and water extracts from *Onosma heterophylla*

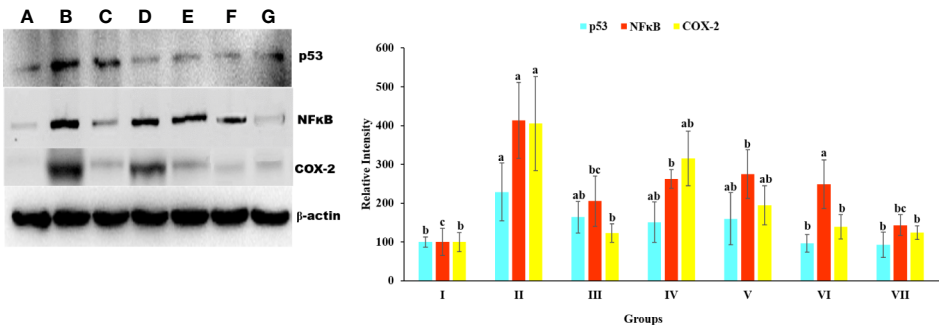

FIGURE 9 | Expression level p53, NFκB, and COX-2 protein in liver homogenate of Wistar rats detected using Western blotting. **(A)** Control group (tap water ad libitum) (GI), **(B)** CCl_4: Olive oil (1:1; 1mL kg^{-1}b.wt.) induced elevation in the expression level of p53 was noted. **(C)** Silymarin (100 mg kg^{-1}b.wt.) + CCl_4, **(D)** low dose (50 mg kg^{-1}b.wt.) + CCl_4, **(E)** medium dose (100 mg kg^{-1}b.wt.) + CCl_4, **(F)** High dose (200 mg kg^{-1}b.wt.) + CCl_4, **(G)** Negative (only extract 100 mg kg^{-1} b/wt.). Histograms showing densitometric analysis of p53, NFκB, and COX-2 protein bands using western blotting. Band density was measured and normalized to that of β-actin. Values are expressed as mean ± SE at level of significance $p \leq 0.05$. Data labels with different letters represent significant difference among them.

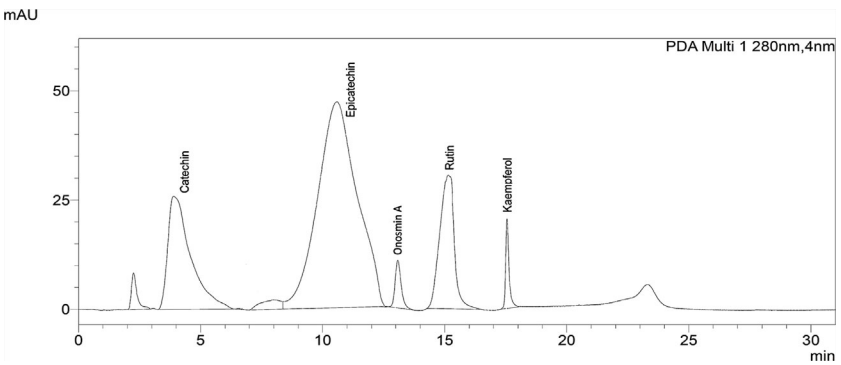

FIGURE 10 | Chromatogram of *Obeth* of *O. bracteata* showing presence of polyphenols as identified using HPLC analysis by reference compound.

TABLE 2 | Amount (mg/L) of different phytochemical quantified by HPLC in different *Obeth* of *O. bracteata*.

Compounds (*Obeth*)	Concentration (mg/L)
Gallic acid	–
Catechin	203.29
Chlorogenic acid	–
Epicatechin	844.04
Caffeic acid	–
Umbelliferone	–
Rutin	49.84
Ellagic acid	–
Quercetin	–
Onosmin A	21.82
Kaempferol	34.82
Coumaric acid	–

Griseb. have an appreciable amount of kaempferol, caffeic acid, o-Coumaric acid, rutin and rosmarinic acid which are responsible for antioxidant activity (Ozer et al., 2018). Saravanakumar et al., 2019 also reported that the methanol extract of *Onosma isaurica* Boiss. & Heldr. and *Onosma bracteosa* Hausskn. & Bornm. showed effective free radical scavenging ability due to the presence of the phytoconstituents. This plant has been widely used because of its medicinal properties.

In Ames assay, the antimutagenic potential of *Obeth* against sodium azide, 4-nitro-o-phenylenediamine and 2- aminofluorene mutagens was evaluated against two *Salmonella typhimurium* strains, i.e., TA100 and TA98. The study showed that *Obeth* effectively modulated the mutagenicity of direct-acting base-pair mutagen, sodium azide with 82.30% inhibition at 250 µg/0.1 mL/plate (**Table S3**) in TA 100 while it showed moderate antimutagenic effect against 4NPD with 62.85% inhibition at the same concentration in TA98 tester strain. *Obeth* exhibited antimutagenicity against 2AF (S9 dependent) in both the tester strains. Kaur et al., 2001 reported that phenolic fractions isolated from *Terminalia arjuna* showed mutagen specificity *via* decreasing the frameshift mutagen NPD whereas it failed in the prevention of sodium azide (base pair substitution)-induced his^+ revertants. Kaur et al., 2016 described that ethyl acetate fraction of *Cassia fistula* (CaFE) showed strong antimutagenic and antioxidant properties due to the presence of polyphenolic compounds

(umbelliferone, catechin and epicatechin). *Obeth* also demonstrated the potential to protect plasmid DNA against free radicals of Fenton's reagent in plasmid DNA nicking assay. *Obeth* at 100 μg/mL concentration efficiently retained DNA's supercoiled form.

In *in vivo* studies, serum analysis showed that the oxidative stress serum markers (SGOT, SGPT, ALP, creatinine and direct bilirubin) were significantly increased, following the dosage of CCl_4 to rats (Group II) (**Tables S5**, **S6**, and **S8**). The potential to produce albumin proteins (which function as transport molecules) vanished in damaged hepatocytes, and the capacity to make inflammatory proteins increased. CCl_4 generated free radicals (trichloromethyl and peroxytrichloromethyl) that induced damage in hepatocytes resulting in leakage of cytoplasmic SGPT and SGOT into the bloodstream (Shah et al., 2015). *Obeth* ameliorated the toxic effects of CCl_4 by enhancing the activity of antioxidant molecules in the liver. *Obeth* significantly decreased the damage caused by CCl_4 (Group II) in cellular TBARS. A decrease in GSH enzymes and protein levels was observed in the CCl_4 treated group (Group II), while an increase in these markers was observed following *Obeth* treatment (**Table S9**). Sabir et al. (2017) reported in their study that aqueous extracts of *Zanthoxylum armatum* DC. (syn. *Zanthoxylum alatum* Roxb.) restored the level of glutathione and showed hepatoprotective property against paracetamol-induced hepatic damage in albino mice which decreased the hepatic glutathione level. The activation of lipid hydroperoxides, Cytochrome P_{450}, P_{420}, and b5 were observed in CCl_4 treated group whereas *Obeth* treatment declined the level of these markers (**Table S10**). The values of the above parameters in the *Obeth*-treated group were the same as of the control (GroupI) which reflects a high safety potential of *Obeth*. CCl_4 treated group showed decline GST levels as compared to control but in a dose-dependent manner whereas *Obeth* treated groups exhibited restored level of GST. Allocati et al., 2018 reported that GSTs can protect DNA against oxidative stress and eliminate toxic molecules that can led to mutations or carcinogenesis. Laouar et al., 2017 reported that treatment of CCl_4 lead to significantly reduced levels of hepatic GSH, GPx, and GST activities than control group in Wistar rats, whereas aqueous extract of *Juniperus phoenicea* L. berries treatment significantly restored the levels of these enzymes. The Group II showed a significant increase in the amount of NADPH cytochrome b5 and NADH cytochrome 450, whereas, *Obeth* treated groups exhibited a dose-dependent decline in the level of these enzymes (**Table S11**). The CCl_4 treatment generates $CCl_3^{\bullet}$ radicals which not only damaged DNA but also caused necrosis and apoptosis as evidenced from increase in Comet tail length in CCl_4 treated group whereas in case of *Obeth* -treated groups, the reduced Comet tail length showed the DNA protective activity of *Obeth* in a dose-dependent manner (**Figure 8**). Damage of cells by $CCl_3^{\bullet}$ free radical (toxic) formed by the reduction of CCl_4, in hepatocytes has also been reported Brai et al. (2014) and Josan et al. (2015). The previous report from Younis et al., 2018 showed that CCl_4 treated rats showed a high degree of DNA damage and remarkable changes in (comet, head, tail) length and %DNA in the tail, while methanolic extract of *Fraxinus xanthoxyloides* (G.Don) Wall. ex A.DC. ameliorates the effect of CCl_4 similar to that of control group.

Histopathological studies showed that *Obeth* was itself non-toxic and showed close histological similarity to the control group and displayed the same histological arrangement with no sign of inflammation (**Figure 6G**). In contrast, CCl_4 treated group displayed steatosis, necrosis, inflammation in blood sinusoids and vacuolization (**Figure 6B**). However, pretreatment of *Obeth* followed by CCl_4 treatment effectively restored the regular hepatocytes' architecture and also reduces the vacuoles formation between the central vein and portal triad indicating hepatoprotective potential of *Obeth*, as shown in **Figures 6D–F**. Earlier, Josan et al. (2015) reported that CCl_4 treated Sprague Dawley rats showed necrosis of hepatocytes nearby central vein and increased the level of alanine transaminase (ALT) whereas control group showed normal architecture of hepatocytes. Ganaie et al., 2015 also reported that dose-dependent treatment of ethanolic extract of *Rumex vesicarius* L. showed a restored pattern of histological architecture, while silymarin treatment followed by CCl_4-intoxication in Wistar rats showed less disarrangement of hepatocytes. The results of the Immunohistochemistry (IHC) studies showed that p53 protein and Cyclin D expressions in the liver tissues were maximum in the CCl_4 intoxicated group. Upregulated expression of pro-apoptotic p53 in CCl_4 treated group might be formed in response to hepatocyte inflammation and the induction of necrosis in liver cells (**Figures 7A, B**). Similar results were observed in western blotting studies showing p53 upregulation in the CCl_4 group as compared with the control group. The tumor suppressor gene p53 is upregulated in response to DNA damage, and its upregulated expression is only found in cells that show mutant forms (Aly et al., 2019). The upregulated expression of Cyclin D protein in the CCl_4 intoxicated group also highlighted the mutation in hepatocytes while *Obeth* treatment showed the downregulation of Cyclin D exhibiting its protective effects against CCl_4 intoxication. Cyclin D has been described to have the main role in cell progression through the G1/S phase of the cell cycle, and its deregulation can lead to tumorigenesis (Ying et al., 2008; Chibazakura et al., 2011; Gao et al., 2016).

The expression of p53, COX-2, and NF-κB was upregulated due to cellular stress, inflammation and mutation in cellular DNA (Banerjee et al., 2002; Cha and DeMatteo, 2005). Hepatic cancer can be controlled by the suppression of COX-2, NF-κB and p53 which might offer an effective control approach. The investigation of the effects of *Obeth* towards stimulated forms of p53, cyclin-D, COX-2 and NF- κB proteins was performed. The expression levels of COX-2 and NF-κB proteins were upregulated after CCl_4 administration (**Figure 9**) highlighting the production of mediator cytokines which facilitate tumor growth *via* inhibiting apoptosis and promoting cell proliferation (Brücher et al., 2019; Lerdwanangkun et al., 2019). Eltahir et al. (2020) reported that CCl_4 treated Wistar rats showed significantly high expression levels of NF- κB and COX-2 while *Boswellia serrata* Roxb. (BS) gum resin treatment followed by CCl_4 significantly restored the level of NF- κB and

COX-2 expression due to the presences of a natural compound that exhibited anti-inflammatory effects by targeting multiple pathways. The stressed cells promoted the overactivation of signaling proteins or inflammatory cytokines including, IL-6, TNFα, and IL-1β that stimulate the overproduction of IL-6 in Kupffer cells leading to the enhanced proliferation of hepatocytes, some of which harbor oncogenic mutations (Sun and Karin, 2008). *Obeth* has efficient antioxidant properties that protect the hepatocytes against any damage by inducing antioxidative mechanisms. Previous reports have proved the connotation among natural compounds isolated from plants and cancer inhibition *via* antioxidant properties (Seufi et al., 2009). In the present study, it was found that the *Obeth* contains catechin, epicatechin, rutin, kaempferol, and Onosmin A (**Figure 10**, **Table 2**). All these compounds have antioxidant potential are known to ascertain their remedial effects by scavenging the free radical species due to the presence of H donating hydroxyl groups on the different polyphenolic rings of these molecules stabilize the negative charge on the different reactive species and hence, nullify their damaging consequences (Kaur P. et al., 2019). One such study showed catechin to regulate the expression of NF-κB and Cox-2 by scavenging the ROS and hence delivering the anti-inflammatory and antioxidant effects (Chu et al., 2017). Similarly, rutin has also proven as an effective hepatoprotective agent against CCl_4 induced Wistar rat liver damage by altering the expression of IL-6/STAT3 pathway genes expression due to its antioxidative, anti-inflammatory and anti-apoptotic properties (Hafez et al., 2015). On the other hand, epicatechin has the potential to inhibit Sprague-Dawley rat liver inflammation *via* NFκB signaling pathway initiated by HSP60 (Huang et al., 2019). Zang et al., 2018 reported that soybean leaves and its isolated compound kaempferol galactoside and kaempferol have the ability to reduce serum parameters (serum aspartate aminotransferase and serum alanine aminotransferase) increased by CCl_4 intoxication. In addition to this, all these compounds were also found to ameliorate the lipid peroxidation and regulate the levels of different liver enzymes (Sinha et al., 2012; Khan et al., 2012; Liu et al., 2015; Wang et al., 2015). The polyphenolics such as catechin, caffeine, epicatechin (EC), epigallocatechin gallate (EGCG), and epicatechin gallate (ECG) showed preventive effects of Liubao Tea against CCl_4 -induced liver injury in Kunming mice, comparable to silymarin (Pan et al., 2018). Ahmad et al., 2005, reported that Onosmin A isolated from *Onosma hispida* Wall. ex G.Don has potential to inhibit lipogenase enzyme in a concentration-dependent manner. It can be stated that the chemical association of phytochemicals, presumable flavonoids in *Obeth* from *O. bracteata* have protective effects on liver damage *via* suppression of CCl_4-induced oxidative stress (**Figure 11**). This study reported that antioxidant, antimutagenic, DNA protective, and anti-inflammatory properties of *Obeth* are correlated with the phytoconstituents present in and have also been shown to have modulatory impact on pro-carcinogenic proteins p53, NF-κB, and COX-2 for the first time.

CONCLUSIONS

In the current study, *Obeth* of *O. bracteata* has shown significant antioxidant, genoprotective, antimutagenic and hepatoprotective properties. As revealed by HPLC investigations, *Obeth* harbors catechin, epicatechin, rutin, Onosmin A and kaempferol as major phytoconstituents. *Obeth* exerted its protective potential *via* its radical scavenging and DNA protective abilities, minimizing oxidative stress through induction of antioxidative enzymes and ameliorating the hepatic changes triggered by CCl_4. The modulation of crucial proteins such as p53, cyclin D, Cox-2, and NF-κB demonstrated potential of *Obeth* as an effective chemotherapeutic agent against hepatic cancer.

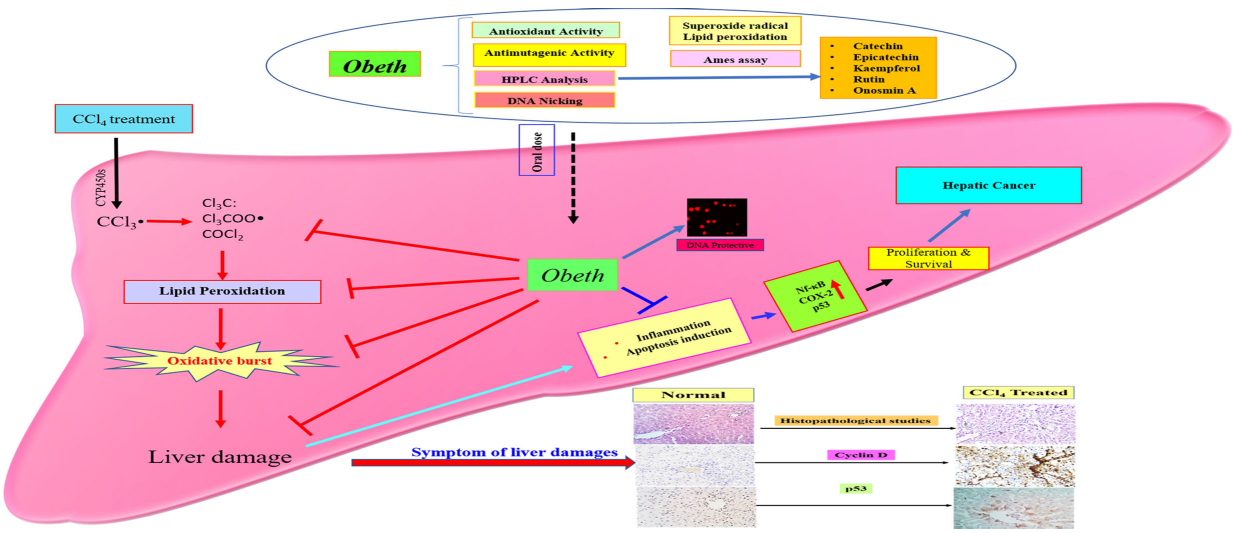

FIGURE 11 | Schematic proposed mechanisms for hepatoprotective property of *Obeth* from *O. bracteata*. *Obeth* phytoconstituents ameliorated hepatic oxidative stress and suppressed inflammation, apoptosis, and DNA damage in CCl_4-injured hepatocytes.

DATA AVAILABILITY STATEMENT

The raw data supporting the conclusions of this article will be made available by the authors, without undue reservation, to any qualified researcher.

ETHICS STATEMENT

The animal study was reviewed and approved by Committee for the Purpose of Control and Supervision of Experiments on Animals (CPCSE), Ministry of Environment and Forestry, Government of India, and authorized by Institutional Animal Ethical Committee (IAEC), Guru Nanak Dev University, Amritsar, India (approval number 226/CPCSEA/2014/06).

AUTHOR CONTRIBUTIONS

AK: formal analysis, investigation, methodology, data curation, and writing—original draft. HT and KS: helped to revise the manuscript, reviewing, and editing. VK: intellectual contribution and reviewing manuscript. KP: formal analysis. SJ: conceptualization and project administration. SK: conceptualization, supervision, project administration, reviewing, editing, and resources. All authors contributed to the article and approved the submitted version.

ACKNOWLEDGMENTS

The authors are thankful to the University Grants Commission (UGC)- Basic Scientific Research (BSR), DST-PURSE, and DST-FIST (Grant No. SR/FST/LSI-691/2016(C) programme for providing financial assistance. We also like to acknowledge UGC, New Delhi for the instrumentation facility provided under UGC-DRS V (Grant No. F4-13/2015/DRS-II (SAP-II), CPEPA, RUSA 2.0 scheme, UPE program, and Centre of Emerging Life Sciences, Guru Nanak Dev University, Amritsar (India) for providing the required support and facilities.

SUPPLEMENTARY MATERIAL

The Supplementary Material for this article can be found online at: https://www.frontiersin.org/articles/10.3389/fphar.2020.01301/full#supplementary-material

REFERENCES

Aebi, H. (1984). Catalase in vitro. *In Methods Enzymology*. (USA: Academic Press), 105, 121–126. doi: 10.1016/S0076-6879(84)05016-3

Ahmad, I., Nawaz, S. A., Afza, N., Malik, A., Fatima, I., Khan, S. B., et al. (2005). Isolation of onosmins A and B, lipoxygenase inhibitors from *Onosma hispida*. *Chem. Pharm. Bull.* 53 (8), 907–910. doi: 10.1248/cpb.53.907

Ahmad, S., Khan, M. A., Ayaz, S., and Ahamd, I. (2013). Antibacterial and antifungal studies of the crude extract and solvent fractions of *Onosma khyberianum*. *Pharmacologica* 4 (9), 525–528. doi: 10.5567/pharmacologia.2013.525.528

Albaqami, J., Myles, L. E., and Tiriveedhi, V. (2018). The Effect of *Onosma bracteatum* in cancer cells. *MOJ Bioequiv. Availab.* 5 (6), 321–325. doi: 10.15406/mojbb.2018.05.00122

Allocati, N., Masulli, M., Di Ilio, C., and Federici, L. (2018). Glutathione transferases: substrates, inihibitors and pro-drugs in cancer and neurodegenerative diseases. *Oncogenesis* 7 (1), 1–15. doi: 10.1038/s41389-017-0025-3

Alqahtani, A., Khan, Z., Alloghbi, A., S Said Ahmed, T., Ashraf, M., and Hammouda, M. (2019). Hepatocellular carcinoma: Molecular mechanisms and targeted therapies. *Medicina* 55 (9):526. doi: 10.3390/medicina55090526

Aly, S. M., Fetaih, H. A., Hassanin, A. A., Abomughaid, M. M., and Ismail, A. A. (2019). Protective Effects of Garlic and Cinnamon Oils on Hepatocellular Carcinoma in Albino Rats. *Anal. Cell. Pathol.* 2019, 1–15. doi: 10.1155/2019/9895485

Anderson, M. E. (1985). Determination of glutathione and glutathione disulfide in biological samples. *Methods Enzymology* 113, 548–555. doi: 10.1016/S0076-6879(85)13073-9.

Aravalli, R. N., Steer, C. J., and Cressman, E. N. (2008). Molecular mechanisms of hepatocellular carcinoma. *Hepatology* 48 (6), 2047–2063. doi: 10.1002/hep.22580

Asif, H. M., Hayee, A., Aslam, M. R., Ahmad, K., and Hashmi, A. S. (2019). Dose-dependent, antidepressant, and anxiolytic effects of a traditional medicinal plant for the management of behavioral dysfunctions in animal models. *Dose-Response* 17 (4), 1–6. doi: 10.1177/1559325819891262

Banerjee, T., Valacchi, G., Ziboh, V. A., and Van Der Vliet, A. (2002). Inhibition of TNFα-induced cyclooxygenase-2 expression by amentoflavone through suppression of NF-κB activation in A549 cells. *Mol. Cell. Biochem.* 238 (1–2), 105–110. doi: 10.1023/a:1019963222510

Bradford, M. M. (1976). A rapid and sensitive method for the quantitation of microgram quantities of protein utilizing the principle of protein-dye binding. *Anal. Biochem.* 72 (1–2), 248–254. doi: 10.1016/0003-2697(76)90527-3

Brai, B.II, Adisa, R. A., and Odetola, A. A. (2014). Hepatoprotective properties of aqueous leaf extract of Persea americana, mill (lauraceae)'avocado'against CCl 4-induced damage in rats. *Afr. J. Tradit. Complement. Altern. Med.* 11 (2), 237–244. doi: 10.4314/ajtcam.v11i2.2

Brücher, B. L., Lang, F., and Jamall, I. S. (2019). NF-κB signaling and crosstalk during *carcinogenesis*. *4open* 2, 13. doi: 10.1051/fopen/2019010

Canli, Ö., Nicolas, A. M., Gupta, J., Finkelmeier, F., Goncharova, O., Pesic, M., et al. (2017). Myeloid cell-derived reactive oxygen species induce epithelial mutagenesis. *Cancer Cell* 32 (6), 869–883. doi: 10.1016/j.ccell.2017.11.004

Carlberg, I. N. C. E. R., and Mannervik, B. E. N. G. T. (1975). Purification and characterization of the flavoenzyme glutathione reductase from rat liver. *J. Biol. Chem.* 250 (14), 5475–5480.

Cha, C., and DeMatteo, R. P. (2005). Molecular mechanisms in hepatocellular carcinoma development. *Best Pract. Res. Clin. Gastroenterol.* 19 (1), 25–37. doi: 10.1016/j.bpg.2004.11.005

Chao, W. W., Chen, S. J., Peng, H. C., Liao, J. W., and Chou, S. T. (2019). Antioxidant Activity of *Graptopetalum paraguayense* E. Walther Leaf Extract Counteracts Oxidative Stress Induced by Ethanol and Carbon Tetrachloride Co-Induced Hepatotoxicity in Rats. *Antioxidants* 8 (8), 251. doi: 10.3390/antiox8080251

Che, C. T., and Zhang, H. (2019). Plant natural products for human health. *Int. J. Mol. Sci.* 20, 1–4. doi: 10.3390/ijms20040830

Chibazakura, T., Kamachi, K., Ohara, M., Tane, S., Yoshikawa, H., and Roberts, J. M. (2011). Cyclin A promotes S-phase entry via interaction with the replication licensing factor Mcm7. *Mol. Cell. Biol.* 31 (2), 248–255. doi: 10.1128/MCB.00630-10

Choi, S. J., Kim, M. R., Kim, S.II, and Jeon, J. K. (2003). Microplate assay measurement of cytochrome P450-carbon monoxide complexes. *BMB Rep.* 36 (3), 332–335. doi: 10.5483/BMBRep.2003.36.3.332

Chu, C., Deng, J., Man, Y., and Qu, Y. (2017). Green tea extracts epigallocatechin-3-gallate for different treatments. *BioMed Res. Int.* 2017, 1–9. doi: 10.1155/2017/5615647

Collins, A. R., and Dušinská, M. (2002). "Oxidation of cellular DNA measured with the comet assay", In: *Oxidative stress biomarkers and antioxidant protocols*. 186, 147–159. doi: 10.1385/1-59259-173-6:147

Devasagayam, T. P., Pushpendran, C. K., and Eapen, J. (1983). Differences in lipid peroxidation of rat liver rough and smooth microsomes. *Biochim. Biophys. Acta (BBA)-Lipids Lipid Metab.* 750 (1), 91–97. doi: 10.1016/0005-2760(83)90207-2

Ebrahimzadeh, M. A., Nabavi, S. F., Nabavi, S. M., Eslami, B., and Asgarirad, H. (2010). In vitro antioxidant and free radical scavenging activity of Leonurus

cardiaca subsp. *Persicus, Grammosciadium platycarpum* and *Onosma demawendicum*. *Afr. J. Biotechnol.* 9 (51), 8865–8871. doi: 10.5897/AJB10.782

Eltahir, H. M., Fawzy, M. A., Mohamed, E. M., Alrehany, M. A., Shehata, A. M., and Abouzied, M. M. (2020). Antioxidant, anti-inflammatory and anti-fibrotic effects of Boswellia serrate gum resin in CCl_4-induced hepatotoxicity. *Exp. Ther. Med.* 19 (2), 1313–1321. doi: 10.3892/etm.2019.8353

Fareed, S., Siddiqui, H. H., Haque, S. E., Khalid, M., and Akhtar, J. (2012). Psychoimmunomodulatory Effects of *Onosma bracteatum* Wall. (Gaozaban) on Stress Model in Sprague Dawley Rats. *J. Clin. Diagn. Res.* 6 (7), 1356–1360.

Farooq, U., Pan, Y., Disasa, D., and Qi, J. (2019). Novel Anti-Aging Benzoquinone Derivatives from *Onosma bracteatum* Wall. *Molecules* 24 (7), 1428. doi: 10.3390/molecules24071428

Ganaie, M. A., Khan, T. H., Siddiqui, N. A., and Ansari, M. N. (2015). Ameliorative effect of methanol extract of Rumex vesicarius on CCl4-induced liver damage in Wistar albino rats. *Pharm. Biol.* 53 (8), 1163–1167. doi: 10.3109/13880209.2014.967782

Gao, X., Fan, L., Li, H., Li, J., Liu, X., Sun, R., et al. (2016). Hepatic injury is associated with cell cycle arrest and apoptosis with alteration of cyclin A and D1 in ammonium chloride-induced hyperammonemic rats. *Exp. Ther. Med.* 11 (2), 427–434. doi: 10.3892/etm.2015.2931

Garner, R. C., Miller, E. C., and Miller, J. A. (1972). Liver microsomal metabolism of aflatoxin B1 to a reactive derivative toxic to Salmonella typhimurium TA 1530. *Cancer Res.* 32 (10), 2058–2066.

Gee, J. B. L., Vassallo, C. L., Bell, P., Kaskin, J., Basford, R. E., and Field, J. B. (1970). Catalase-dependent peroxidative metabolism in the alveolar macrophage during phagocytosis. *J. Clin. Invest.* 49 (6), 1280–1287. doi: 10.1172/JCI106340

Green Solvents & Bio Solvents - Global Market Outlook (2017-2026) (2018). Available at: https://www.researchandmarkets.com/reports/4655796/green-solvents-and-biosolvents-global-market (Accessed May 05,2020).

Gu, X., and Manautou, J. E. (2012). Molecular mechanisms underlying chemical liver injury. *Expert Rev. Mol. Med.* 14, 1–21. doi: 10.1017/S1462399411002110

Habig, W. H., Pabst, M. J., and Jakoby, W. B. (1974). Glutathione S-transferase—the first enzymatic step in mercapturic acid formation. *J. Biol. Chem.* 249 (22), 7130–7139.

Hafez, M. M., Al-Harbi, N. O., Al-Hoshani, A. R., Al-Hosaini, K. A., Al Shrari, S. D., Al Rejaie, S. S., et al. (2015). Hepato-protective effect of rutin via IL-6/STAT3 pathway in CCl4-induced hepatotoxicity in rats. *Biol. Res.* 48 (1), 1–10. doi: 10.1186/s40659-015-0022-y

Halliwell, B., and Gutteridge, J. M. C. (1989). *Free radicals in biology and medicine. 2nd edn* (Oxford, United Kingdom: Clarendon Press).

Huang, Z., Jing, X., Sheng, Y., Zhang, J., Hao, Z., Wang, Z., et al. (2019). (-)-Epicatechin attenuates hepatic sinusoidal obstruction syndrome by inhibiting liver oxidative and inflammatory injury. *Redox Biol.* 22, 101117. doi: 10.1016/j.redox.2019.101117

Imran, H., ur Rahman, A., Sohail, T., Taqvi, S.II, and Yaqeen, Z. (2018). Onosma bracteatum wall: A Potent analgesic agent. *Bangladesh J. Med. Sci.* 17 (1), 36–41. doi: 10.3329/bjms.v17i1.35276

Jiang, Z. Y., Hunt, J. V., and Wolff, S. P. (1992). Ferrous ion oxidation in the presence of xylenol orange for detection of lipid hydroperoxide in low density lipoprotein. *Anal. Biochem.* 202 (2), 384–389. doi: 10.1016/0003-2697(92)90122-N

Josan, S., Billingsley, K., Orduna, J., Park, J. M., Luong, R., Yu, L., et al. (2015). Assessing inflammatory liver injury in an acute CCl4 model using dynamic 3D metabolic imaging of hyperpolarized [1-13C] pyruvate. *NMR Biomed.* 28 (12), 1671–1677. doi: 10.1002/nbm.3431

Kandemir, A., and Türkmen, Z. (2008). The Flora of Üzümlü-Sakaltutan (Erzincan-Gümüşhane). *Turkish J. Bot.* 32 (4), 265–304.

Karakus, E., Karadeniz, A., Simsek, N., Can, I., Kara, A., Yildirim, S., et al. (2011). Protective effect of Panax ginseng against serum biochemical changes and apoptosis in liver of rats treated with carbon tetrachloride (CCl4). *J. Hazard. Mater.* 195, 208–213. doi: 10.1016/j.jhazmat.2011.08.027

Kaur, S. J., Grover, I. S., and Kumar, S. (2000). Modulatory effects of a tannin fraction isolated from Terminalia arjuna on the genotoxicity of mutagens in Salmonella typhimurium. *Food Chem. Toxicol.* 38 (12), 1113–1119. doi: 10.1016/s0278-6915(00)00104-6

Kaur, S., Grover, I. S., and Kumar, S. (2001). Antimutagenic potential of extracts isolated from Terminalia arjuna. *J. Environ. Pathol. Toxicol. Oncol.* 20 (1), 1–6. doi: 10.1615/JEnvironPatholToxicolOncol.v20.i1.20

Kaur, S., Kumar, M., Kaur, P., Kaur, V., and Kaur, S. (2016). Modulatory effects of Cassia fistula fruits against free radicals and genotoxicity of mutagens. *Food Chem. Toxicol.* 98, 220–231. doi: 10.1016/j.fct.2016.10.027

Kaur, V., Kumar, M., Kaur, P., Kaur, S., Singh, A. P., and Kaur, S. (2017). Hepatoprotective activity of Butea monosperma bark against thioacetamide-induced liver injury in rats. *Biomed. Pharmacother.* 89, 332–341. doi: 10.1016/j.biopha.2017.01.165

Kaur, S., Sharma, D., Singh, A. P., and Kaur, S. (2019). Amelioration of hepatic function, oxidative stress, and histopathologic damages by Cassia fistula L. fraction in thioacetamide-induced liver toxicity. *Environ. Sci. Pollut. Res.* 26 (29), 29930–29945. doi: 10.1007/s11356-019-06158-y

Kaur, P., Mehta, R. G., Singh, B., and Arora, S. (2019). Development of aqueous-based multi-herbal combination using principal component analysis and its functional significance in HepG2 cells. *BMC Complement. Altern. Med.* 19 (1), 18. doi: 10.1186/s12906-019-2432-9

Khan, R. A., Khan, M. R., and Sahreen, S. (2012). CCl 4-induced hepatotoxicity: protective effect of rutin on p53, CYP2E1 and the antioxidative status in rat. *BMC Complement. Altern. Med.* 12 (1), 178. doi: 10.1186/1472-6882-12-178

Kumar, N., Kumar, R., and Kishore, K. (2013). Onosma L.: A review of phytochemistry and ethnopharmacology. *Pharmacognosy Rev.* 7 (14), 140. doi: 10.4103/0973-7847.120513

Laouar, A., Klibet, F., Bourogaa, E., Benamara, A., Boumendjel, A., Chefrour, A., et al. (2017). Potential antioxidant properties and hepatoprotective effects of Juniperus phoenicea berries against CCl_4 induced hepatic damage in rats. *Asian Pac. J. Trop. Med.* 10 (3), 263–269. doi: 10.1016/j.apjtm.2017.03.005

Lee, J. C., Kim, H. R., Kim, J., and Jang, Y. S. (2002). Antioxidant property of an ethanol extract of the stem of Opuntia ficus-indica var. saboten. *J. Agric. Food Chem.* 50 (22), 6490–6496. doi: 10.1021/jf020388c

Lerdwanangkun, P., Wonganan, P., Storer, R. J., and Limpanasithikul, W. (2019). Combined effects of celecoxib and cepharanthine on human colorectal cancer cells in vitro. *J. Appl. Pharm. Sci.* 9 (04), 117–125. doi: 10.7324/JAPS.2019.90415

Liu, J., Lu, J. F., Wen, X. Y., Kan, J., and Jin, C. H. (2015). Antioxidant and protective effect of inulin and catechin grafted inulin against CCl4-induced liver injury. *Int. J. Biol. Macromol.* 72, 1479–1484. doi: 10.1016/j.ijbiomac.2014.09.066

Liu, Z., Ren, Z., Zhang, J., Chuang, C. C., Kandaswamy, E., Zhou, T., et al. (2018). Role of ROS and nutritional antioxidants in human diseases. *Front. Physiol.* 9, 477. doi: 10.3389/fphys.2018.00477

Maron, D. M., and Ames, B. N. (1983). Revised methods for the Salmonella mutagenicity test. *Mutat. Research/Environmental Mutagenesis Relat. Subj.* 113 (3-4), 173–215. doi: 10.1016/0165-1161(83)90010-9

Mehta, R. G., Murillo, G., Naithani, R., and Peng, X. (2010). Cancer chemoprevention by natural products: how far have we come? *Pharm. Res.* 27 (6), 950–961. doi: 10.1007/s11095-010-0085-y

Menghani, E., Sudhanshu, R. N., and Mittal, S. (2011). Free radical scavenging capacity and antioxidant activity of *Onosma bracteatum*. *Int. J. Pharm. Res. Dev.* 4, 16–20.

Mihara, K., and Sato, R. (1972). Partial purification of NADH-cytochrome b5 reductase from rabbit liver microsomes with detergents and its properties. *J. Biochem.* 71 (4), 725–735. doi: 10.1093/oxfordjournals.jbchem.a129819

Misra, H. P., and Fridovich, I. (1972). The role of superoxide anion in the autoxidation of epinephrine and a simple assay for superoxide dismutase. *J. Biol. Chem.* 247 (10), 3170–3175.

Naz, S., Ahmad, S., Rasool, S. A., Sayeed, S. A., and Siddiqi, R. (2006). Antibacterial activity directed isolation of compounds from *Onosma hispidum*. *Microbiol. Res.* 161 (1), 43–48. doi: 10.1016/j.micres.2005.05.001

Nishikimi, M., Rao, N. A., and Yagi, K. (1972). The occurrence of superoxide anion in the reaction of reduced phenazine methosulfate and molecular oxygen. *Biochem. Biophys. Res. Commun.* 46 (2), 849–854. doi: 10.1016/S0006-291X(72)80218-3

Omura, T., and Sato, R. (1964). The carbon monoxide-binding pigment of liver microsomes I. Evidence for its hemoprotein nature. *J. Biol. Chem.* 239 (7), 2370–2378.

Ozer, M. S., Kirkan, B., Sarikurkcu, C., Cengiz, M., Ceylan, O., Atılgan, N., et al. (2018). Onosma heterophyllum: Phenolic composition, enzyme inhibitory and antioxidant activities. *Ind. Crops Prod.* 111, 179–184. doi: 10.1016/j.indcrop.2017.10.026

Pan, Y., Long, X., Yi, R., and Zhao, X. (2018). Polyphenols in Liubao tea can prevent CCl4-induced hepatic damage in mice through its antioxidant capacities. *Nutrients* 10 (9), 1280. doi: 10.3390/nu10091280

Pizzino, G., Irrera, N., Cucinotta, M., Pallio, G., Mannino, F., Arcoraci, V., et al. (2017). Oxidative stress: harms and benefits for human health. *Oxid. Med. Cell. Longevity* 2017, 1–13. doi: 10.1155/2017/8416763

Rahal, A., Kumar, A., Singh, V., Yadav, B., Tiwari, R., Chakraborty, S., et al. (2014). Oxidative stress, prooxidants, and antioxidants: the interplay. *BioMed. Res. Int.* 1–19. doi: 10.1155/2014/761264

Riedl, H., Binzet, R., and Orcan, N. (2004). A new species of Onosma (Boraginaceae–Lithospermeae) from southern Turkey. *Edinburgh J. Bot.* 61 (2-3), 127–130. doi: 10.1017/S0960428605000211

Ritesh, K. R., Suganya, A., Dileepkumar, H. V., Rajashekar, Y., and Shivanandappa, T. (2015). A single acute hepatotoxic dose of CCl4 causes oxidative stress in the rat brain. *Toxicol. Rep.* 2, 891–895. doi: 10.1016/j.toxrep.2015.05.012

Robin,, Arora, S., and Vig, A. P. (2015). Inhibition of DNA oxidative damage and antimutagenic activity by dichloromethane extract of Brassica rapa var. rapa L. seeds. *Ind. Crops Prod.* 74, 585–591. doi: 10.1016/j.indcrop.2015.05.038

Rodríguez-García, C., Sánchez-Quesada, C., and Gaforio, J. J. (2019). Dietary flavonoids as cancer chemopreventive agents: an updated review of human studies. *Antioxidants* 8 (5), 137. doi: 10.3390/antiox8050137

Sabir, S. M., Rocha, J. B. T., Boligon, A. A., and Athayde, M. L. (2017). Hepatoprotective activity and phenolic profile of Zanthoxylum alatum Roxb. fruit extract. *Pakistan J. Pharm. Sci.* 30 (5), 1551–1556.

Saravanakumar, K., Sarikurkcu, C., Sarikurkcu, R. T., and Wang, M. H. (2019). A comparative study on the phenolic composition, antioxidant and enzyme inhibition activities of two endemic Onosma species. *Ind. Crops Prod.* 142, 111878. doi: 10.1016/j.indcrop.2019.111878

Seufi, A. M., Ibrahim, S. S., Elmaghraby, T. K., and Hafez, E. E. (2009). Preventive effect of the flavonoid, quercetin, on hepatic cancer in rats via oxidant/antioxidant activity: molecular and histological evidences. *J. Exp. Clin. Cancer Res.* 28 (1), 80. doi: 10.1186/1756-9966-28-80

Shah, M. D., Gnanaraj, C., Haque, A. E., and Iqbal, M. (2015). Antioxidative and chemopreventive effects of Nephrolepis biserrata against carbon tetrachloride (CCl4)-induced oxidative stress and hepatic dysfunction in rats. *Pharm. Biol.* 53 (1), 31–39. doi: 10.3109/13880209.2014.909502

Sinha, M., Das, D. K., Manna, K., Datta, S., Ray, T., Sil, A. K., et al. (2012). Epicatechin ameliorates ionising radiation-induced oxidative stress in mouse liver. *Free Radical Res.* 46 (7), 842–849. doi: 10.3109/10715762.2012.684245

Snezhkina, A. V., Kudryavtseva, A. V., Kardymon, O. L., Savvateeva, M. V., Melnikova, N. V., Krasnov, G. S., et al. (2019). ROS Generation and antioxidant defense systems in normal and malignant cells. *Oxid. Med. Cell. Longev.* 2019, 1–17. doi: 10.1155/2019/6175804

Sun, B., and Karin, M. (2008). NF-κB signaling, liver disease and hepatoprotective agents. *Oncogene* 27 (48), 6228–6244. doi: 10.1038/onc.2008.300

Surh, Y. J. (2003). Cancer chemoprevention with dietary phytochemicals. *Nat. Rev. Cancer* 3 (10), 768–780. doi: 10.1038/nrc1189

Ved, D. K., Sureshchandra, S. T., Barve, V., Srinivas, V., Sangeetha, S., Ravikumar, K., et al. (2016). (envis. frlht. org/frlhtenvis. nic. in). (Bengaluru: FRLHT's ENVIS Centre on Medicinal Plants), 1475–1484.

Wang, Y., Tang, C., and Zhang, H. (2015). Hepatoprotective effects of kaempferol 3-O-rutinoside and kaempferol 3-O-glucoside from Carthamus tinctorius L. @ on CCl4-induced oxidative liver injury in mice. *J. Food Drug Anal.* 23 (2), 310–317. doi: 10.1016/j.jfda.2014.10.002

Wu, J. C., Lai, C. S., Tsai, M. L., Ho, C. T., Wang, Y. J., and Pan, M. H. (2017). Chemopreventive effect of natural dietary compounds on xenobiotic-induced toxicity. *J. Food Drug Anal.* 25 (1), 176–186. doi: 10.1016/j.jfda.2016.10.019

Ying, J., Li, H., Yu, J., Ng, K. M., Poon, F. F., Wong, S. C. C., et al. (2008). WNT5A exhibits tumor-suppressive activity through antagonizing the Wnt/β-catenin signaling, and is frequently methylated in colorectal cancer. *Clin. Cancer Res.* 14 (1), 55–61. doi: 10.1158/1078-0432.CCR-07-1644

Younis, T., Rasul, A., Jabeen, F., Hussain, G., Altaf, J., Jafri, L., et al. (2018). Ameliorating role of methanolic leaves extract of Fraxinus xanthoxyloides against CCl_4-challanged nephrotoxicity in rats. *Pakistan J. Pharm. Sci.* 31, 1475–1484.

Zamzami, M. A., Baothman, O. A., Samy, F., and Abo-Golayel, M. K. (2019). Amelioration of CCl4-Induced Hepatotoxicity in Rabbits by Lepidium sativum Seeds. *Evidence-Based Complement. Altern. Med.* 2019, 1–17. doi: 10.1155/2019/5947234

Zang, Y., Hashimoto, S., Yu, C., and Igarashi, K. (2018). Protective effects of dietary kaempferol glycoside components from unripe soybean (Edamame, Glycine max L. Merrill.'Jindai') leaves and their serous metabolite on carbon tetrachloride-induced liver injury mice. *J. Food Sci. Technol.* 55 (11), 4515–4521. doi: 10.1007/s13197-018-3385-6

Conflict of Interest: The authors declare that the research was conducted in the absence of any commercial or financial relationships that could be construed as a potential conflict of interest.

Copyright © 2020 Kumar, Kaur, Pandit, Tuli, Sak, Jain and Kaur. This is an open-access article distributed under the terms of the Creative Commons Attribution License (CC BY). The use, distribution or reproduction in other forums is permitted, provided the original author(s) and the copyright owner(s) are credited and that the original publication in this journal is cited, in accordance with accepted academic practice. No use, distribution or reproduction is permitted which does not comply with these terms.

frontiers in Pharmacology

REVIEW
published: 26 August 2020
doi: 10.3389/fphar.2020.01319

Unsupervised Learning and Multipartite Network Models: A Promising Approach for Understanding Traditional Medicine

*Mohieddin Jafari, Yinyin Wang, Ali Amiryousefi and Jing Tang**

Research Program in Systems Oncology, Faculty of Medicine, University of Helsinki, Helsinki, Finland

The ultimate goal of precision medicine is to determine right treatment for right patients based on precise diagnosis. To achieve this goal, correct stratification of patients using molecular features and clinical phenotypes is crucial. During the long history of medical science, our understanding on disease classification has been improved greatly by chemistry and molecular biology. Nowadays, we gain access to large scale patient-derived data by high-throughput technologies, generating a greater need for data science including unsupervised learning and network modeling. Unsupervised learning methods such as clustering could be a better solution to stratify patients when there is a lack of predefined classifiers. In network modularity analysis, clustering methods can be also applied to elucidate the complex structure of biological and disease networks at the systems level. In this review, we went over the main points of clustering analysis and network modeling, particularly in the context of Traditional Chinese medicine (TCM). We showed that this approach can provide novel insights on the rationale of classification for TCM herbs. In a case study, using a modularity analysis of multipartite networks, we illustrated that the TCM classifications are associated with the chemical properties of the herb ingredients. We concluded that multipartite network modeling may become a suitable data integration tool for understanding the mechanisms of actions of traditional medicine.

Keywords: unsupervided learning, network modelling, precision medicine, traditional medicine, systems medicine

OPEN ACCESS

Edited by:
Hai Yu Xu,
China Academy of Chinese Medical Sciences, China

Reviewed by:
Xuezhou Zhou,
Beijing Jiaotong University, China
Xing Zhai,
Beijing University of Chinese Medicine, China

***Correspondence:**
Jing Tang
Jing.tang@helsinki.fi

Specialty section:
This article was submitted to Ethnopharmacology, a section of the journal Frontiers in Pharmacology

Received: *19 May 2020*
Accepted: *07 August 2020*
Published: *26 August 2020*

Citation:
Jafari M, Wang Y, Amiryousefi A and Tang J (2020) Unsupervised Learning and Multipartite Network Models: A Promising Approach for Understanding Traditional Medicine. Front. Pharmacol. 11:1319. doi: 10.3389/fphar.2020.01319

INTRODUCTION

Classification and clustering are our fundamental learning process to understand human biology and diseases. To achieve the ultimate goal of precision medicine, i.e., the right intervention for a patient at the right time (Stefano and Kream, 2015), there has been a long history of symptom-based diagnosis that utilizes available information to classify patients, diseases, and drugs (**Figure 1**). In the early days of traditional medicine, physicians tried to characterize diseases using empirical terms, such as temperament and meridian (Rezadoost et al., 2016; Arji et al., 2019; Wang Y. et al., 2019), based on which they prescribed corresponding herbs that are known to target them (Xu, 2011; Li and

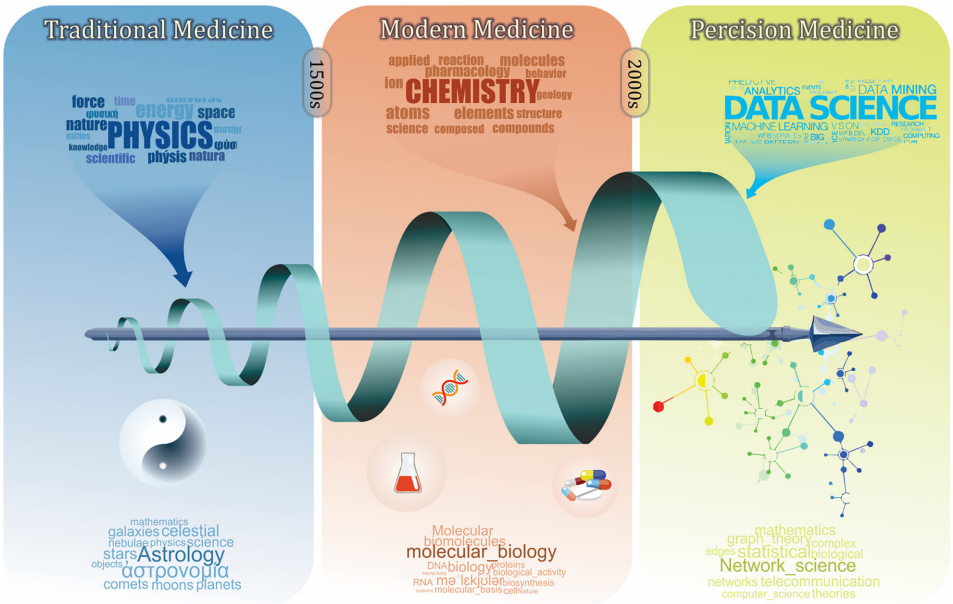

FIGURE 1 | A brief history of medicine and its relation with other branches of science. Traditional medicine as the first era of medicine was mainly built on the physical characterization of diseases and patient biographical data. The modern medicine was established by including more chemical and physical characterizations. Defining biomolecule using biochemistry and molecular biology revealed more details of diseases and pathological processes. This eventually led to the development of diagnosis codes and the pharmaceutical industry. Recently, precision medicine has emerged with the advances of data science, which involves more holistic analyses in order to understand human medicine at the systems level.

Weng, 2017). With increasing knowledge on biochemistry, the era of modern medicine has started, further advancing our understanding of human diseases to the molecular level. Molecular profiles, along with clinical phenotypes, are leveraged to formally characterize diseases, disorders, and symptoms (Steindel, 2010).

One of the greatest challenges in precision medicine is to integrate all available patient-derived data for accurate diagnosis and treatment, which would require novel data-driven approaches rather than more conventional hypothesis-driven approaches (Rouillard et al., 2015). Genomic information for patients, albeit fundamental and often necessary, may not be sufficient due to the fact that the human genome is dynamically adjusting its functions by epigenetic regulations (Jafari et al., 2017; Nussinov et al., 2019). Therefore, interactions among other molecular features including transcriptome, proteome, and metabolome should also be considered to obtain a more systematic characterization of the diseases (Eric, 2014). On the other hand, phenotypic data including cell and tissue images have been utilized for illustrating the impact of molecular alternations in human diseases (Langlois et al., 2011; De Fauw et al., 2018). Likewise, to improve our understanding on human diseases, we may also investigate sources of clinical, phenotypic, and pharmacological data that are derived from traditional medicine (Ma et al., 2010; Zhao et al., 2014). A systematic integration of all of these available information may provide a promising approach to turn precision medicine into a reality ultimately.

Here, we started by reviewing the application of clustering analysis in high-throughput biological studies in modern and traditional medicine. Next, we described the application of clustering in network modeling for the stratification of drugs or patients. We focused on the advantages and promises of a particular network modelling approach called multipartite networks which can inherently integrate heterogeneous data types at multiple levels. In a case study, a multipartite network was developed to model traditional medicine herbs. We showed that this modeling approach provides novel insights on the rationale of herb classifications, which may facilitate the drug discovery in TCM, such as discovering herb combinations or prioritization of active ingredients.

USING CLUSTERING TO IMPROVE PATIENT STRATIFICATIONS

Thanks to advanced experimental and computational technologies, we are able to collect, standardize, and integrate a variety of cell-based patient-derived datasets. For example, the LINCS program (Keenan et al., 2018) is one of the recent multi-center studies to facilitate the understanding of cancer biology by providing transcriptional and morphological changes of multiple cancer cell lines in responding to a variety of pharmaceutical agents. Moreover, there are national and international efforts to sequence patients' genomic features. For example, UK Biobank and FinnGen focused on the contributions of genetic predisposition and environmental exposure to the occurrence of common diseases for over half a

million subjects (The Finngen Research Project Takes Finns to a Discovery Trip to Genome Data; Manolio, 2018). On the other hand, with the development of computational methods such as text mining technologies, researchers are able to standardize data resources in traditional medicine, making them easily accessible and reusable (Zhou et al., 2005; Mirzaeian et al., 2019). For example, the SymMap database was constructed to provide a mapping relationship between 499 natural products, 19,595 ingredients, 1,717 clinical symptoms, and 5,235 diseases (Wu et al., 2019). This work showed the potential to integrate traditional and modern medicine at both phenotypic and molecular levels toward phenotype-based drug discovery. Another example was the UNaProd database which contains information concerning 3,411 natural products used in Iranian traditional medicine (ITM) (Naghizadeh et al., 2020).

Clustering has been commonly used to identify subpopulations of patients with distinctive genetic variants or gene expression profiles. For example, Naval et al. showed how clustering analysis helped identifying single nucleotide polymorphisms (SNPs) associated with skin properties (Naval et al., 2014). Combining transcriptomic data with images, Voineagu et al. showed how the clustering methods characterize distinct complex disease subtypes in autism spectrum disorder (Voineagu et al., 2011). Additionally, in clinical proteomics, clustering analysis also identifies a group of proteins as functional modules in pathogenesis. For example, Baldelli et al. clustered non-small cell lung cancer tumors according to the expression, activation, and phosphorylation levels of 26 signaling proteins (Baldelli et al., 2015). Implementing clustering methods in the context of precision medicine is not only applicable to omics data, but also to physiological data. For example, Xu et al. developed human stress management using clustering of physiological signals during series of task-rest cycles (Xu et al., 2015). On the other hand, image data as a major part of health records of individuals is commonly utilized (Hsu et al., 2013). For example, Enguehard et al. presented a strategy of integrating neural network and clustering analysis for automatic magnetic resonance imaging data analysis (Enguehard et al., 2019). Furthermore, it has been shown that utilizing biomedical annotations can potentially improve clustering analysis to obtain more biologically relevant disease categories (Futschik and Carlisle, 2005; Bandyopadhyay et al., 2007; Lee, 2011). Therefore, the integration of existing biomedical annotations, such as gene ontology or pathway enrichment, is also expected to improve patient disease clustering with refined distance functions (Handl et al., 2005).

As abovementioned, exploring subclasses of diseases and drugs is a prevalent task in precision medicine, and traditional medicine is no exception. For example, Liu et al. studied the gene expression signature of breast cancer cell lines for an herbal formula Si-Wu-Tang (SWT). This analysis showed that the effect of SWT is comparable to β-estradiol treatment on estrogen-responsive genes (Liu et al., 2013). Ruan et al. proposed a clustering algorithm called THCluster that can effectively discover meaningful categorization of herbs and their potential clinical indications (Ruan et al., 2017). Zhang et al. validated TCM syndrome types using a clustering method based on latent tree models, based on which they proposed a standard for syndrome differentiation in TCM which was then validated successfully in a study of kidney deficiency (Zhang et al., 2008). Likewise, Zhao et al. proposed a top-down subspace clustering for improving the precision of syndrome differentiation. Considering 5,600 symptoms and 150 syndrome elements of AIDS (acquired immune deficiency syndrome) patients, they showed that their method identified clusters of patients more precisely, compared to conventional clustering algorithms such as k-means (Zhao et al., 2014).

While identifying the heterogeneity of patients is critical, understanding the driving molecular mechanisms of such heterogeneity shall provide more rational on the design of precision medicine. To understand the underlying factors that are shared by patients with similar diseases, more information about the interaction of biological entities including genes, proteins, and drugs is required. By introducing network models, such a complex layer of information can be systematically evaluated, for which clustering analysis may further help infer the distinctive disease patterns. In the following we focused on the combination of network modeling and clustering analysis and showed that how they may contribute to the understanding for precision medicine.

EXPLORING NETWORK MODULES AS A BASIS FOR CLASSIFICATION

A simple network consists of a set of elements called nodes or vertices which are connected by a set of links or edges (Jafari et al., 2013). Depending on the definition of node and edge sets, numerous types of biological networks can be constructed and used for further analysis. For example, the degree of a node, which is defined as the number of links attached to the node, suggests the importance of node and helps detect global and provincial hubs within the network. The heterogeneity of a network which is defined as the root of the variance of degrees divided by their mean, also explains the overall topology of the network and organization of relationships among the nodes (Dong and Horvath, 2007).

One of the major network modeling approaches is the modularity analysis or community detection which is the intersection of clustering analysis and network science (Fortunato, 2010; Fortunato and Hric, 2016). In this analysis, exploring the local densely connected nodes, i.e., networks community structure is the main aim. In other words, a community within a given network includes nodes with high intra-relationship and low inter-relationship with the other nodes outside the community (Girvan and Newman, 2002). Therefore, finding network modules is important to elucidate and understand the complex topology of networks by discriminating dense and sparse local structures. The network topology determines the adjacency matrix, which can be utilized for clustering analysis alone or in combination with the similarity matrix derived from the node properties (Von Luxburg, 2006; Fortunato, 2010). Since in real biological and disease networks, there are multifunctional nodes belonging to more than one group, soft clustering is also recommended (Yang and Leskovec,

2015). In the soft clustering, overlapping communities, also called covers, are detectable because the multiple memberships for a node are allowed. There are other methods including dynamical clustering (Jeub et al., 2015). For example, the Markov Clustering algorithm (MCL) is one of the commonly used dynamic clustering algorithms based on biological annotations (Jafari et al., 2015). After exploring the modules of a given network, it is common to convert the network into its reduced version, where a node of the reduced network corresponds to a module of the original network, and an edge is inferred from the number of interactions between the modules (**Figure 2**).

Utilizing molecular information in conjunction with the module detection to predict biological functions is a common task (Vespignani, 2003; Jafari et al., 2015). The main assumption is that members of the same cluster tend to be involved in the same biological process which is known as guilt-by-association. For example, in protein-protein interaction networks, clique-based clustering was used to detect protein complexes (Altaf-Ul-Amin et al., 2006; Phan and Sternberg, 2012; Jafari et al., 2013). Hierarchical clustering was utilized to identify signaling cascades or metabolic pathways (Guimera and Amaral, 2005; Koch and Ackermann, 2013; Azimzadeh Jamalkandi et al., 2016). Also, according to the local topological features of biological networks, clustering methods are commonly used to predict cellular co-localization and co-expressed gene regulatory mechanisms (Dittrich et al., 2008; Amiri et al., 2013; Mitra et al., 2013). At the phenotypic level, network modeling linking phenotypes to molecular components of a biological system, e.g., disease-causing genetic variations is also one of the exciting research areas (Goh et al., 2007; Loscalzo and Barabasi, 2011; Goh and Choi, 2012; Emmert-Streib et al., 2013). In the context of traditional medicine, Huang et al. highlighted how network pharmacology modeling allows us to integrate concurrent and traditional knowledge of herbal medicines for the development of new drugs for complex human diseases (Huang et al., 2013). Using a network-based integration of chemical structure and omics data, they inferred novel drug-disease interactions *via* molecular targets and pathways. Similarly, Li et al. introduced a distance-based mutual information model to score herb interactions based on their frequencies and distances, and thus identify the rationale of herb combinations (Li et al., 2010).

Network biology approaches have also shown potential for exploring disease subcategories and patient subclasses in TCM. For instance, Zhou et al. constructed a clinical phenotype network to investigate the underlying mechanisms of TCM diagnosis and treatment (Zhou et al., 2014). Wang et al. proposed a co-occurrence network approach to identify the TCM symptoms as biomarkers for the fatty liver disease (Wang W. et al., 2019). Interestingly, Jiang et al. also demonstrated the association between the TCM symptoms and tongue-coating microbiome using co-occurrence networks (Jiang et al., 2012). Network modeling of cold and hot syndromes of traditional medicine has also been developed. For example, Ma et al. provided a gene expression signature of the cold syndrome in TCM associated with the neuroendocrine-immune system. By analyzing the protein interaction networks, they showed that the genes related to the cold syndrome are involved in pathways of energy metabolism, neurotransmitters, hormones, and cytokines (Ma et al., 2010). Likewise, Lu et al. provided distinctive molecular signatures in CD4-positive T cells of Rheumatoid Arthritis patients associated with the cold and heat patterns in TCM respectively (Lu et al., 2012a; Lu et al., 2012b).

MULTIPARTITE NETWORK MODELS FOR INTEGRATING HETEROGENEOUS DATA

With the development of high-throughput technologies, precision medicine has been made more plausible with increasingly diversified data sets. These data sets range from gene expression profiles to medical images, where the scales, characteristics, and formats are different since they are gathered at the different levels of biological systems (Lee, 2011). The integration of information from these heterogeneous biological and clinical data sets need to be applied in order to discover new mechanistic insights of systems medicine. For example, to predict more effective disease

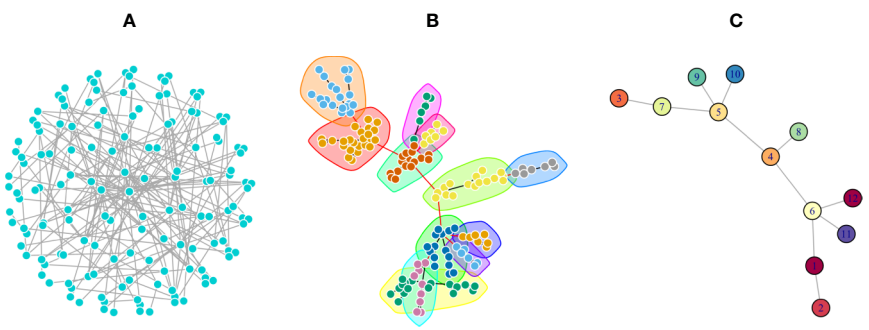

FIGURE 2 | A Poisson-distributed random network is represented in three formats. **(A)** A complex view of the network by placing nodes on a sphere layout that obscure the complexity of the network topology. **(B)** The same network using the force-directed layout algorithm in which communities were identified *via* a greedy optimization of modularity score. This representation is usually used to show the modular structure of the network. **(C)** The simplified network in which each node represents a community in the original network, and each edge denotes the interaction of communities.

treatment options using multi-targeted drug combinations (Tang and Aittokallio, 2014), we need to gather multiple data types such as *in vitro* drug response of cancer cells and *in vivo* response of patients including symptoms and molecular profiles. To predict the effectiveness of drug combinations, understanding about the signaling pathways and drug target interactions along with the pathophysiological states is essential. There is a major type of network models called multipartite networks which are commonly used in systems medicine (Junker and Schreiber, 2008). This kind of network modeling is crucial due to its flexibility to integrate mixed datasets and discover complex hidden relationships which are required for understanding precision medicine. Unlike ordinary uni-partite networks which contain single sets of nodes and edges represented by an adjacency matrix, a multipartite network constitutes of multiple sets of nodes and edges which are exemplified by incidence matrix (Agnarsson and Greenlaw, 2007). Depending on the data types, the network can represent gene-disease (Bauer-Mehren et al., 2011; Barneh et al., 2016; Chen et al., 2018), drug-target (Barneh et al., 2016), protein-cell localization (Mirzaei Mehrabad et al., 2018), drug-disease (Lamb, 2007) and drug-side effect associations (Luo et al., 2014), as well as associations at the patient level including patient-drug interactions and patient-symptom interactions (Bhavnani et al., 2010).

Based on the constructed multipartite networks, different kinds of clustering algorithms can be applied to identify the hidden subnetwork structures for each node set. For instance, Long et al. proposed a clustering method by a combination of co-clustering and probabilistic hidden Markov models (Long et al., 2007). Also, Hartsperger et al. developed a fuzzy multipartite clustering to decompose the nodes of multiple types in tripartite networks (Hartsperger et al., 2010). They showed that the fuzzy clustering algorithm was able to identify functionally correlated modules of a tripartite gene-disease-protein complex network for the identification of biologically meaningful clusters. Duan et al. identified two major subtypes of breast cancer by reconstructing a tripartite graph of drug-cell line-patient tumors. They showed how drug response data helped discover dysregulated pathways for breast cancer (Duan et al., 2013). A multipartite network can be also utilized as a visualization tool, with which one can navigate efficiently the high-throughput drug response data from public databases including Cancer Cell Line Encyclopedia (CCLE) and Genomics of Drug Sensitivity in Cancer (GDSC) (Duan et al., 2014).

Typical multipartite network analyses involve network projection, which aims for simplifying the network topology from the viewpoint of each node set separately. In **Figure 3**, the projection of a schematic bipartite network and module detection analysis is briefly presented. Constructing the projected networks facilitates the exploration of hidden relationships among each set of nodes in a multipartite network. For example, Barneh et al. constructed a drug-target network and further developed its projected version called Drug Similarity Network (DSN) and Target Similarity Network (TSN), which can be used for drug-target prediction (Barneh et al., 2016). Recently, they have applied the method to predict drug combinations, and confirmed them experimentally (Barneh et al., 2018; Barneh et al., 2019). To facilitate drug repositioning, network topological similarity-based inference (NTSIM) and its classification-equipped version, i.e., NTSIM-C methods were also proposed to unveil novel drug-disease associations (Zhang et al., 2018).

NETWORK ANALYSIS RATIONALIZES TCM CLASSIFICATIONS: A CASE STUDY

The idea of utilizing multipartite networks in traditional medicine is potentially feasible, as the data standardization and annotation has been increasingly pursued. However, to the best of our knowledge, the models are not yet utilized to provide more profound insights on traditional medicine, although some tools such as SymMap (Wu et al., 2019) may provide an appropriate dataset to build such multipartite networks. In the following, we conducted a case study to reconstruct a bipartite network of natural products and ingredients of TCM to show the potential

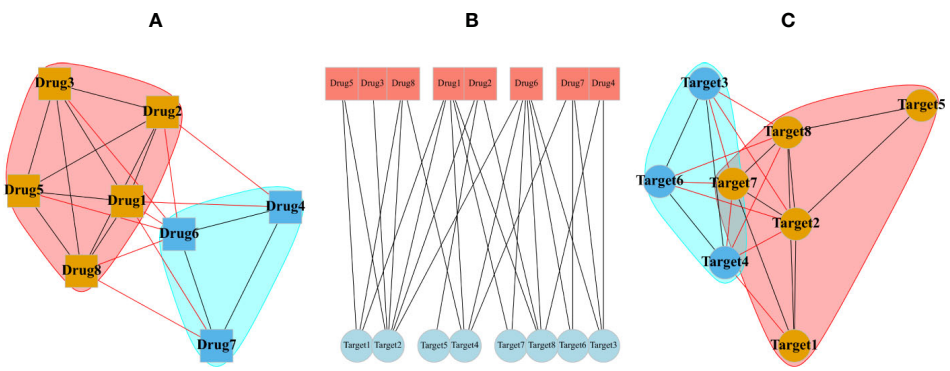

FIGURE 3 | A random bipartite graph or bigraph of drugs (square nodes) and targets (circular nodes) is represented along with two possible projections of it. The center graph **(B)** is a main bipartite graph by placing nodes in two different sets. The projection of drugs **(A)** and the projection of targets **(C)** are shown in which communities were identified *via* greedy optimization of modularity score.

of this modeling for understanding TCM rationale for disease treatment and drug discovery.

TCM-related databases provide a large set of information about the TCM herbs including their classifications and disease indications, as well as molecular characterization, such as ingredient profiles and molecular targets. Recently, this information has been successfully applied for developing computational models to understand the TCM classifications (Wang Y. et al., 2019). As a case study to show the potential of multipartite networks in the integration of heterogonous data, we obtained a list of 4,485 natural products consisting of 2,857 chemical ingredients from the TCMID database (Huang et al., 2018). We used the second version of the TCMID database, as the largest dataset in this field, which contains richer experimental data originating from ingredient-specific and herbal mass spectrometry spectra. The natural products and ingredients are considered to be the two parts of a bipartite network. After removal of disconnected nodes, we extracted a giant component of the graph consisting of 7,004 nodes and 17,555 edges. Following the projection of this bigraph as outlined in **Figure 3**, two projected graphs called the natural product similarity network (NSN) and ingredient similarity network (ISN) were reconstructed, such that each edge indicates at least one common ingredient or natural product in NSN and ISN, respectively. The NSN contains 4,308 natural products and 204,807 edges, while the ISN consists of 2,696 nodes and 78,228 edges. The community detection was subsequently done for both similarity networks *via* optimizing a modularity score (Clauset et al., 2004), resulting in 42 and 24 communities for NSN and ISN, separately. The fast greedy algorithm outperformed compared to the other high-performance algorithms, i.e., infomap and walktrap (Labatut and Balasque, 2013; Wagenseller et al., 2018) according to the highest average of modularity index in the NSN and ISN (**Supplementary file 2**). These communities reflect the internal similarity of herbs and ingredients which could be investigated further. For example, a community of NSN indicates a set of natural products with similar profiles of ingredients. Therefore, the members of the same natural product cluster can be used for therapeutic interchanging due to the similarity of ingredient profiles in the cluster. Also, members of different clusters can be candidates for new drug combinations as they are expected to affect distinctive biological pathways. Similarly, the cluster of active ingredients in ISN can be used to predict the mechanism of action of newly discovered or synthesized compounds based on TCM classifications. In other words, a functionally-unknown molecule with high structural similarity to any of active ingredient clusters indicate the analogous TCM properties and implications. Therefore, any follow-up experimental analysis can be prioritized to disclose therapeutic hits of the new molecules based on known properties and implications of the corresponding cluster. Also, the priority of active ingredients for treatment can be redefined in each cluster independently using availability, and the relevant protein targets characterizations (code and data set for this case study can be found in **Supplementary File 1**).

We sought to validate our prediction about the herb and ingredient communities, i.e., whether the herbs or active ingredients that are clustered in the same community tend to share similar features. Four types of features for the natural products and their ingredients including meridians and properties were extracted from TCMID. Furthermore, the SMILE strings of these ingredients along with the identified or predicted protein targets of them were extracted using PubChem (Kim et al., 2018) and STITCH databases (Szklarczyk et al., 2016). Then, the average of pairwise intersection of meridian and property profiles was computed separately for each cluster in NSN. Likewise, the average similarity of SMILE string using the Dice index and the pairwise intersection of their protein targets in each cluster of ISN were also calculated. We showed in **Figure 4** the average similarity of all the 42 and 24 communities in NSN (**Figures 4A, B**) and ISN (**Figures 4C, D**), as compared to that of random clustering from 100 simulations. We found that the similarity of natural products or active ingredients within a cluster is significantly higher than that for the random clustering. For example, the median of meridian-based similarity of random grouping is 0.56, while the median similarity of the 42 clusters found in NSN is 0.96 (p-value = 1.99e-05, Wilcoxon test). Similarly, in ISN, the median of the Dice similarity of SMILE strings in random groups is 0.22, while the median of the 24 clusters in ISN is 0.36 (p-value = 5.84e-05, Wilcoxon test). Our findings suggested that the clusters of ISN and NSN consist of similar ingredients or natural products, and thus validating the feasibility of bipartite modeling in analyzing TCM data.

Interestingly, these network analyses also suggested a molecular basis of TCM classifications, which originated from the physical features of natural products or empirical knowledge about the disease indications. Although the chemical and molecular characteristics of the natural products, i.e., chemical structures and protein targets have only been available recently, the TCM classification according to meridians were indeed associated with them. The same observation was found for the property classification in TCM in our findings, as the natural products in a given cluster based on ingredient profiles are associated with their property profiles. On the other hand, our approach promises to bridge a gap between pharmaceutical chemistry and traditional pharmacology in TCM. For example, we can use attributes of active ingredient profile of natural products as a rich training set, and newly discovered, or synthesized molecules can be characterized accordingly as a test set. To summarize, this bipartite network analysis provides novel insights for the understanding of molecular evidence of traditional classification in TCM. Using the bipartite network modeling, we may integrate phenotypes of different types, i.e., signs and symptoms, with the chemical knowledge of drug molecules in order to provide a formal framework for phenotype-based drug discovery in TCM.

SUMMARY AND OUTLOOK

Nowadays, TCM, along with the other traditional medical schools, was modernized and expanded by the molecular shreds of evidence provided by experimental biology (Xue et al., 2013). These

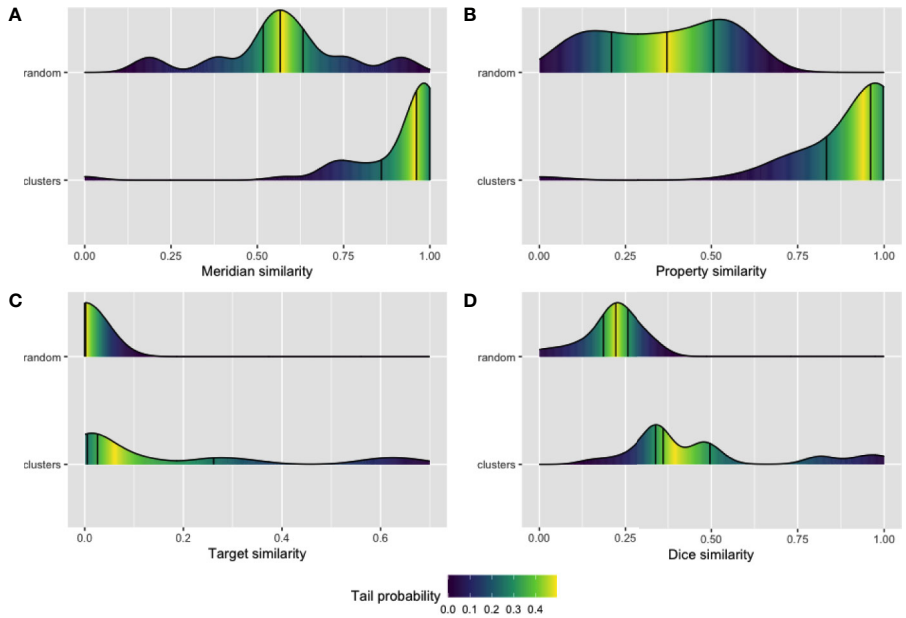

FIGURE 4 | Validation of the network communities in TCM herbs. The distribution of Meridian similarity **(A)** and Property similarity **(B)** within the communities of NSN (natural product similarity network) compared to random groups; The distribution of drug target similarity **(C**, **D)** the Dice index similarity within the communities of ISN (ingredient similarity network) compared to random groups. Lines indicate the quartiles values and gradient color represent the probability of values within the empirical cumulative density function for the distributions.

experiments usually are started by extraction and fractionation techniques such as chromatography, and followed by identification methods such as mass spectrometry to determine a comprehensive profile of ingredients within the natural products (Jafari et al., 2016; Kabiri et al., 2017). The challenging part of this experimental design is identifying the ingredients responsible for the bioactivities of natural products. To further explore the drug-target interactions of these ingredients, high-throughput omics is now a preferable approach to study the effects on gene expression and protein activity. Through these experimental techniques, large volumes of molecular features related to disease indications can be disclosed, including antimicrobial, antiviral, antioxidant, anti-inflammatory, and neurological activities (Neghabi-Hajiagha et al., 2016; Pourramezan et al., 2018). In the next step, we always face the challenge of applying appropriate data integration methods to associate these molecular features with the phytochemical and pharmacological properties of the TCM ingredients.

A remarkable portion of biological studies deal with generating, organizing, and retrieving patient data, which is usually large scale and noisy. Data mining algorithms such as clustering and classification are being applied. Furthermore, the integration of heterogeneous biological data is imperative. Rigorous and efficient analysis tools are required for the integration of different data characteristics and formats as standard statistical inference techniques may be limited (Lee, 2011; Eric, 2014). Harnessing the network modeling in computational biology becomes a feasible strategy for data integration to navigate the complex space of biological systems (Barabási et al., 2011). Here, we highlighted the application of the multipartite network reconstruction for data integration in biomedical researches, particularly in traditional medicine. More specifically, we demonstrated how we can combine current chemical knowledge of ingredients and TCM classifications of natural products to bridge the gap between traditional and modern medicine. We provided a case study to show its potentials for uncovering TCM concepts and discovering potential treatments.

Although network science, and more precisely, network medicine is on its developing stage, using multipartite network modeling may provide more rational on the therapies in traditional medicine. Generally in traditional medicine, much efforts are spent on collecting the symptoms of patients, while in modern medicine, biochemical profiles and image data are more relied on. Providing a framework for integrating all these data using multipartite network model shall facilitate the interchange of knowledge from traditional and modern medicine. Reconstructing multipartite networks is a convenient way to characterize patient similarity, which serves the basis for further explorations on their diseases mechanisms (Pai and Bader, 2018). Depending on the nature of the node sets, a multipartite network can be utilized to investigate complex interactions, that might be critical for understanding diseases with high-level patient heterogeneity such as cancer (Yaffe, 2019). Considering all available data from cellular behaviors to patient responses using multipartite network modeling can play a significant role

in the integration of these heterogeneous datasets, a successful application of which may make precision medicine a reality ultimately.

AUTHOR CONTRIBUTIONS

Study design: MJ, YW, JT. Data analysis: YW, MJ. Writing: MJ, YW, AA, JT.

FUNDING

The work has been supported by the China Scholarship Council (No. 201706740080) and the Finland EDUFI Fellowship (No. TM-18-10928).

ACKNOWLEDGMENTS

The authors would like to express their gratitude to Dr. Mehrdad Karimi for his helpful comments, and Ehsan Zanganeh and Minoo Ashtiani for graphical designing of **Figure 1**.

SUPPLEMENTARY MATERIAL

The Supplementary Material for this article can be found online at: https://www.frontiersin.org/articles/10.3389/fphar.2020.01319/full#supplementary-material

SUPPLEMENTARY FILE 1 | R code and dataset for section "Network analysis rationalizes TCM classifications: a case study".

SUPPLEMENTARY FILE 2 | Modularity index of the clustering algorithms used for the present case study.

REFERENCES

Agnarsson, G., and Greenlaw, R. (2007). *Graph theory: Modeling, applications, and algorithms* (Upper Saddle River, New Jersey: Pearson/Prentice Hall).

Altaf-Ul-Amin, M., Shinbo, Y., Mihara, K., Kurokawa, K., and Kanaya, S. (2006). Development and implementation of an algorithm for detection of protein complexes in large interaction networks. *BMC Bioinf.* 7, 207. doi: 10.1186/1471-2105-7-207

Amiri, M., Jafari, M., Azimzadeh Jamalkandi, S., and Davoodi, S. M. (2013). Atopic dermatitis-associated protein interaction network lead to new insights in chronic sulfur mustard skin lesion mechanisms. *Expert Rev. Proteomics* 10, 449–460. doi: 10.1586/14789450.2013.841548

Arji, G., Safdari, R., Rezaeizadeh, H., Abbassian, A., Mokhtaran, M., and Hossein Ayati, M. (2019). A systematic literature review and classification of knowledge discovery in traditional medicine. *Comput. Methods Prog. Biomed.* 168, 39–57. doi: 10.1016/j.cmpb.2018.10.017

Azimzadeh Jamalkandi, S., Mozhgani, S. H., Gholami Pourbadie, H., Mirzaie, M., Noorbakhsh, F., Vaziri, B., et al. (2016). Systems biomedicine of rabies delineates the affected signaling pathways. *Front. Microbiol.* 7, 1688. doi: 10.1101/068817

Baldelli, E., Haura, E. B., Crino, L., Cress, D. W., Ludovini, V., Schabath, M. B., et al. (2015). Impact of upfront cellular enrichment by laser capture microdissection on protein and phosphoprotein drug target signaling activation measurements in human lung cancer: Implications for personalized medicine. *Proteomics Clin. Appl.* 9, 928–937. doi: 10.1002/prca.201400056

Bandyopadhyay, S., Mukhopadhyay, A., and Maulik, U. (2007). An improved algorithm for clustering gene expression data. *Bioinformatics* 23, 2859–2865. doi: 10.1093/bioinformatics/btm418

Barabási, A. L., Gulbahce, N., and Loscalzo, J. (2011). Network medicine: a network-based approach to human disease. *Nat. Rev. Genet.* 12, 56–68. doi: 10.1038/nrg2918

Barneh, F., Jafari, M., and Mirzaie, M. (2016). Updates on drug-target network; facilitating polypharmacology and data integration by growth of DrugBank database. *Briefings Bioinf.* 17, 1070–1080. doi: 10.1093/bib/bbv094

Barneh, F., Salimi, M., Goshadrou, F., Ashtiani, M., Mirzaie, M., Zali, H., et al. (2018). Valproic acid inhibits the protective effects of stromal cells against chemotherapy in breast cancer: Insights from proteomics and systems biology. *J. Cell. Biochem.* 119, 9270–9283. doi: 10.1002/jcb.27196

Barneh, F., Mirzaie, M., Nickchi, P., Tan, T. Z., Thiery, J. P., Piran, M., et al. (2019). Integrated use of bioinformatic resources reveals that co-targeting of histone deacetylases, IKBK and SRC inhibits epithelial-mesenchymal transition in cancer. *Briefings Bioinf.* 20, 717–731. doi: 10.1093/bib/bby030

Bauer-Mehren, A., Bundschus, M., Rautschka, M., Mayer, M. A., Sanz, F., and Furlong, L. I. (2011). Gene-disease network analysis reveals functional modules in mendelian, complex and environmental diseases. *PloS One* 6, e20284–e20284. doi: 10.1371/journal.pone.0020284

Bhavnani, S. K., Bellala, G., Ganesan, A., Krishna, R., Saxman, P., Scott, C., et al. (2010). The nested structure of cancer symptoms. *Methods Inf. Med.* 49, 581–591. doi: 10.3414/ME09-01-0083

Chen, X., Xie, D., Wang, L., Zhao, Q., You, Z. H., and Liu, H. (2018). BNPMDA: bipartite network projection for MiRNA–disease association prediction. *Bioinformatics* 34, 3178–3186. doi: 10.1093/bioinformatics/bty333

Clauset, A., Newman, M. E., and Moore, C. (2004). Finding community structure in very large networks. *Phys. Rev. E.* 70, 066111. doi: 10.1103/PhysRevE.70.066111

De Fauw, J., Ledsam, J. R., Romera-Paredes, B., Nikolov, S., Tomasev, N., Blackwell, S., et al. (2018). Clinically applicable deep learning for diagnosis and referral in retinal disease. *Nat. Med.* 24, 1342. doi: 10.1038/s41591-018-0107-6

Dittrich, M. T., Klau, G. W., Rosenwald, A., Dandekar, T., and Müller, T. (2008). Identifying functional modules in protein–protein interaction networks: an integrated exact approach. *Bioinformatics* 24, i223–i231. doi: 10.1093/bioinformatics/btn161

Dong, J., and Horvath, S. (2007). Understanding network concepts in modules. *BMC Syst. Biol.* 1, 24. doi: 10.1186/1752-0509-1-24

Duan, Q., Kou, Y., Clark, N., Gordonov, S., and Ma'ayan, A. (2013). Metasignatures identify two major subtypes of breast cancer. *CPT: Pharmacometr. Syst. Pharmacol.* 2, 1–10. doi: 10.1038/psp.2013.11

Duan, Q., Wang, Z., Fernandez, N. F., Rouillard, A. D., Tan, C. M., Benes, C. H., et al. (2014). Drug/Cell-line Browser: interactive canvas visualization of cancer drug/cell-line viability assay datasets. *Bioinformatics* 30, 3289–3290. doi: 10.1093/bioinformatics/btu526

Emmert-Streib, F., Tripathi, S., R.d.M. Simoes, A. F., and Dehmer, M. (2013). The human disease network: Opportunities for classification, diagnosis, and prediction of disorders and disease genes. *Syst. Biomed.* 1, 20–28. doi: 10.4161/sysb.22816

Enguehard, J., O'Halloran, P., and Gholipour, A. (2019). Semi-Supervised Learning With Deep Embedded Clustering for Image Classification and Segmentation. *IEEE Access* 7, 11093–11104. doi: 10.1109/ACCESS.2019.2891970

Eric, J. (2014). Topol, Individualized Medicine from Prewomb to Tomb. *Cell* 157, 241–253. doi: 10.1016/j.cell.2014.02.012

Fortunato, S., and Hric, D. (2016). Community detection in networks: A user guide. *Phys. Rep.* 659, 1–44. doi: 10.1016/j.physrep.2016.09.002

Fortunato, S. (2010). Community detection in graphs. *Phys. Rep.* 486, 75–174. doi: 10.1016/j.physrep.2009.11.002

Futschik, M. E., and Carlisle, B. (2005). Noise-robust soft clustering of gene expression time-course data. *J. Bioinf. Comput. Biol.* 3, 965–988. doi: 10.1142/S0219720005001375

Girvan, M., and Newman, M. E. (2002). Community structure in social and biological networks. *Proc. Natl. Acad. Sci.* 99, 7821–7826. doi: 10.1073/pnas.122653799

Goh, K. I., and Choi, I. G. (2012). Exploring the human diseasome: the human disease network. *Briefings Funct. Genomics* 11, 533–542. doi: 10.1093/bfgp/els032

Goh, K. I., Cusick, M. E., Valle, D., Childs, B., Vidal, M., and Barabási, A.-L. (2007). The human disease network. *Proc. Natl. Acad. Sci.* 104, 8685–8690. doi: 10.1073/pnas.0701361104

Guimera, R., and Amaral, L. A. N. (2005). Functional cartography of complex metabolic networks. *nature* 433, 895. doi: 10.1038/nature03288

Handl, J., Knowles, J., and Kell, D. B. (2005). Computational cluster validation in post-genomic data analysis. *Bioinformatics* 21, 3201–3212. doi: 10.1093/bioinformatics/bti517

Hartsperger, M. L., Blöchl, F., Stümpflen, V., and Theis, F. J. (2010). Structuring heterogeneous biological information using fuzzy clustering of k-partite graphs. *BMC Bioinf.* 11, 522. doi: 10.1186/1471-2105-11-522

Hsu, W., Markey, M. K., and Wang, M. D. (2013). Biomedical imaging informatics in the era of precision medicine: progress, challenges, and opportunities. *J. Am. Med. Inf. Assoc.* 20, 1010–1013. doi: 10.1136/amiajnl-2013-002315

Huang, C., Zheng, C., Li, Y., Wang, Y., Lu, A., and Yang, L. (2013). Systems pharmacology in drug discovery and therapeutic insight for herbal medicines. *Briefings Bioinf.* 15, 710–733. doi: 10.1093/bib/bbt035

Huang, L., Xie, D., Yu, Y., Liu, H., Shi, Y., Shi, T., et al. (2018). TCMID 2.0: A comprehensive resource for TCM. *Nucleic Acids Res.* 46, D1117–D1120. doi: 10.1093/nar/gkx1028

Jafari, M., Sadeghi, M., Mirzaie, M., Marashi, S. A., and Rezaei-Tavirani, M. (2013). Evolutionarily conserved motifs and modules in mitochondrial protein-protein interaction networks. *Mitochondrion* 13, 668–675. doi: 10.1016/j.mito.2013.09.006

Jafari, M., Mirzaie, M., and Sadeghi, M. (2015). Interlog protein network: an evolutionary benchmark of protein interaction networks for the evaluation of clustering algorithms. *BMC Bioinf.* 16, 319–319. doi: 10.1186/s12859-015-0755-1

Jafari, M., Mirzaie, M., Khodabandeh, M., Rezadoost, H., Ghassempour, A., and Aboul-Enein, H. Y. (2016). Polarity-based fractionation in proteomics: hydrophilic interaction vs reversed-phase liquid chromatography. *Biomed. Chromatogr.* 30, 1036–1041. doi: 10.1002/bmc.3647

Jafari, M., Ansari-Pour, N., Azimzadeh, S., and Mirzaie, M. (2017). A logic-based dynamic modeling approach to explicate the evolution of the central dogma of molecular biology. *PloS One* 12, e0189922–e0189922. doi: 10.1371/journal.pone.0189922

Jeub, L. G., Balachandran, P., Porter, M. A., Mucha, P. J., Mahoney, M. W., and locally, T. (2015). act locally: Detection of small, medium-sized, and large communities in large networks. *Phys. Rev. E.* 91, 012821. doi: 10.1103/PhysRevE.91.012821

Jiang, B., Liang, X., Chen, Y., Ma, T., Liu, L., Li, J., et al. (2012). Integrating next-generation sequencing and traditional tongue diagnosis to determine tongue coating microbiome. *Sci. Rep.* 2, 936. doi: 10.1038/srep00936

Junker, B. H., and Schreiber, F. (2008). *Analysis of biological networks, Wiley Online Library*. (John Wiley & Sons, Inc.). doi: 10.1002/9780470253489

Kabiri, M., Rezadoost, H., and Ghassempour, A. (2017). A comparative quality study of saffron constituents through HPLC and HPTLC methods followed by isolation of crocins and picrocrocin. *LWT* 84, 1–9. doi: 10.1016/j.lwt.2017.05.033

Keenan, A. B., Jenkins, S. L., Jagodnik, K. M., Koplev, S., He, E., Torre, D., et al. (2018). The library of integrated network-based cellular signatures NIH program: system-level cataloging of human cells response to perturbations. *Cell Syst.* 6, 13–24. doi: 10.1016/j.cels.2017.11.001

Kim, S., Chen, J., Cheng, T., Gindulyte, A., He, J., He, S., et al. (2018). PubChem 2019 update: improved access to chemical data. *Nucleic Acids Res.* 47, D1102–D1109. doi: 10.1093/nar/gky1033

Koch, I., and Ackermann, J. (2013). On functional module detection in metabolic networks. *Metabolites* 3, 673–700. doi: 10.3390/metabo3030673

Labatut, V., and Balasque, J. M. (2012). Detection and Interpretation of Communities in Complex Networks: Methods and Practical Application. *Computational Social Networks: Tools, Perspectives and Applications*. (Springer), 81–113. doi: 10.1007/978-1-4471-4048-1_4

Lamb, J. (2007). The Connectivity Map: a new tool for biomedical research. *Nat. Rev. Cancer* 7, 54–60. doi: 10.1038/nrc2044

Langlois, R., Pallesen, J., and Frank, J. (2011). Reference-free particle selection enhanced with semi-supervised machine learning for cryo-electron microscopy. *J. Struct. Biol.* 175, 353–361. doi: 10.1016/j.jsb.2011.06.004

Lee, J. K. (2011). *Statistical bioinformatics: for biomedical and life science researchers* (John Wiley & Sons).

Li, F. S., and Weng, J. K. (2017). Demystifying traditional herbal medicine with modern approach. *Nat. Plants* 3, 1–7. doi: 10.1038/nplants.2017.109

Li, S., Zhang, B., Jiang, D., Wei, Y., and Zhang, N. (2010). Herb network construction and co-module analysis for uncovering the combination rule of traditional Chinese herbal formulae. *BMC Bioinf.* 11, S6. doi: 10.1186/1471-2105-11-S11-S6

Liu, M., Fan, J., Wang, S., Wang, Z., Wang, C., Zuo, Z., et al. (2013). Transcriptional profiling of Chinese medicinal formula Si-Wu-Tang on breast cancer cells reveals phytoestrogenic activity. *BMC Complement. Altern. Med.* 13, 11. doi: 10.1186/1472-6882-13-11

Long, B., Zhang, Z. M., and Yu, P. S. (2007). *A probabilistic framework for relational clustering, Proceedings of the 13th ACM SIGKDD international conference on Knowledge discovery and data mining* (California, USA: ACM, San Jose), 470–479.

Loscalzo, J., and Barabasi, A. L. (2011). Systems biology and the future of medicine. *Wiley Interdiscip. Rev.: Syst. Biol. Med.* 3, 619–627. doi: 10.1002/wsbm.144

Lu, C., Niu, X., Xiao, C., Chen, G., Zha, Q., Guo, H., et al. (2012a). Network-based gene expression biomarkers for cold and heat patterns of rheumatoid arthritis in traditional chinese medicine. *Evidence-Based Complement. Altern. Med.* 2012, 203043. doi: 10.1155/2012/203043

Lu, C., Xiao, C., Chen, G., Jiang, M., Zha, Q., Yan, X., et al. (2012b). Cold and heat pattern of rheumatoid arthritis in traditional Chinese medicine: distinct molecular signatures indentified by microarray expression profiles in CD4-positive T cell. *Rheumatol. Int.* 32, 61–68. doi: 10.1007/s00296-010-1546-7

Luo, Y., Liu, Q., Wu, W., Li, F., and Bo, X. (2014). "Predicting drug side effects based on link prediction in bipartite network," in *2014 7th International Conference on Biomedical Engineering and Informatics*. (IEEE), 729–733.

Ma, T., Tan, C., Zhang, H., Wang, M., Ding, W., and Li, S. (2010). Bridging the gap between traditional Chinese medicine and systems biology: the connection of Cold Syndrome and NEI network. *Mol. Biosyst.* 6, 613–619. doi: 10.1039/b914024g

Manolio, T. A. (2018). UK Biobank debuts as a powerful resource for genomic research. (Nature Publishing Group). *Nature Med.* 24 (12), 1792–1794.

Mirzaei Mehrabad, E., Hassanzadeh, R., and Eslahchi, C. (2018). PMLPR: A novel method for predicting subcellular localization based on recommender systems. *Sci. Rep.* 8, 12006. doi: 10.1038/s41598-018-30394-w

Mirzaeian, R., Sadoughi, F., Tahmasebian, S., and Mojahedi, M. (2019). Progresses and challenges in the traditional medicine information system: A systematic review. *J. Pharm. Pharmacogn. Res.* 7, 246–259.

Mitra, K., Carvunis, A. R., Ramesh, S. K., and Ideker, T. (2013). Integrative approaches for finding modular structure in biological networks. *Nat. Rev. Genet.* 14, 719. doi: 10.1038/nrg3552

Naghizadeh, A., Hamzeheian, D., Akbari, S., Mohammadi, F., Otoufat, T., Asgari, S., et al. (2020). UNaProd: A Universal Natural Product Database for Materia Medica of Iranian Traditional Medicine. *Evid. Based. Complement. Alternat. Med. Accepted*. 2020. doi: 10.1155/2020/3690781

Naval, J., Alonso, V., and Herranz, M. A. (2014). Genetic polymorphisms and skin aging: The identification of population genotypic groups holds potential for personalized treatments. *Clin. Cosmetic Investigational Dermatol.* 7, 207–214. doi: 10.2147/CCID.S55669

Neghabi-Hajiagha, M., Aliahmadi, A., Taheri, M. R., Ghassempour, A., Irajian, G., Rezadoost, H., et al. (2016). A bioassay-guided fractionation scheme for characterization of new antibacterial compounds from Prosopis cineraria aerial parts. *Iranian J. Microbiol.* 8, 1.

Nussinov, R., Jang, H., Tsai, C. J., and Cheng, F. (2019). Review: Precision medicine and driver mutations: Computational methods, functional assays and conformational principles for interpreting cancer drivers. *PloS Comput. Biol.* 15, 1–54. doi: 10.1371/journal.pcbi.1006658

Pai, S., and Bader, G. D. (2018). Patient Similarity Networks for Precision Medicine. *J. Mol. Biol.* 430, 2924–2938. doi: 10.1016/j.jmb.2018.05.037

Phan, H. T., and Sternberg, M. J. (2012). PINALOG: a novel approach to align protein interaction networks—implications for complex detection and

function prediction. *Bioinformatics* 28, 1239–1245. doi: 10.1093/bioinformatics/bts119

Pourramezan, Z., Kermanshahi, R. K., Oloomi, M., Aliahmadi, A., and Rezadoost, H. (2018). In vitro study of antioxidant and antibacterial activities of Lactobacillus probiotic spp. *Folia Microbiol.* 63, 31–42. doi: 10.1007/s12223-017-0531-x

Rezadoost, H., Karimi, M., and Jafari, M. (2016). Proteomics of hot-wet and cold-dry temperaments proposed in Iranian traditional medicine: a Network-based Study. *Sci. Rep.* 6, 30133–30133. doi: 10.1038/srep30133

Rouillard, A. D., Wang, Z., and Ma'ayan, A. (2015). Abstraction for data integration: Fusing mammalian molecular, cellular and phenotype big datasets for better knowledge extraction. *Comput. Biol. Chem.* 58, 104. doi: 10.1016/j.compbiolchem.2015.06.003

Ruan, C., Wang, Y., Zhang, Y., Ma, J., Chen, H., Aickelin, U., et al. (2017). "THCluster: Herb supplements categorization for precision traditional Chinese medicine," in *2017 IEEE International Conference on Bioinformatics and Biomedicine (BIBM)*. (Kansas City, MO, USA), 417–424.

Stefano, G. B., and Kream, R. M. (2015). Personalized- and one- medicine: bioinformatics foundation in health and its economic feasibility. *Med. Sci. Monit.* 21, 201–204. doi: 10.12659/MSM.893207

Steindel, S. J. (2010). International classification of diseases, 10th edition, clinical modification and procedure coding system: descriptive overview of the next generation HIPAA code sets. *J. Am. Med. Inf. Assoc.* 17, 274–282. doi: 10.1136/jamia.2009.001230

Szklarczyk, D., Santos, A., von Mering, C., Jensen, L. J., Bork, P., and Kuhn, M. (2016). STITCH 5: augmenting protein-chemical interaction networks with tissue and affinity data. *Nucleic Acids Res.* 44, D380–D384. doi: 10.1093/nar/gkv1277

Tang, J., and Aittokallio, T. (2014). Network Pharmacology Strategies Toward Multi-Target Anticancer Therapies: From Computational Models to Experimental Design Principles. *Curr. Pharm. Design* 20, 23–36. doi: 10.2174/13816128113199990470

The Finngen Research Project Takes Finns to a Discovery Trip to Genome Data. (Nature Publisher Group). *Nature Med.* 24 (12), 1792–1794.

Vespignani, A. (2003). Evolution thinks modular. *Nat. Genet.* 35, 118–119. doi: 10.1038/ng1003-118

Voineagu, I., Wang, X., Johnston, P., Lowe, J. K., Tian, Y., Horvath, S., et al. (2011). Transcriptomic analysis of autistic brain reveals convergent molecular pathology. *Nature* 474, 380–384. doi: 10.1038/nature10110

Von Luxburg, U. (2006). A tutorial on spectral clustering. *Max Planck Institute Biol. Cybernet. Tech. Rep.*

Wagenseller, P., Wang, F., and Wu, W. (2018). Size Matters: A Comparative Analysis of Community Detection Algorithms. *IEEE Trans. Comput. Soc. Syst.* 5, 951–960. doi: 10.1109/TCSS.2018.2875626

Wang, Y., Jafari, M., Tang, Y., and Tang, J. (2019). Predicting Meridian in Chinese traditional medicine using machine learning approaches. *PloS Comput. Biol.* 15, e1007249–e1007249. doi: 10.1371/journal.pcbi.1007249

Wang, W., Li, C., Xu, J., and Li, X. (2019). "Bridging Fatty Liver Disease and Traditional Chinese Medicine: A Complex Network Approach," in *2019 IEEE International Symposium on Circuits and Systems (ISCAS)*. (IEEE), 1–5.

Wu, Y., Zhang, F., Yang, K., Fang, S., Bu, D., Li, H., et al. (2019). SymMap: an integrative database of traditional Chinese medicine enhanced by symptom mapping. *Nucleic Acids Res.* 47, D1110–D1117. doi: 10.1093/nar/gky1021

Xu, Q., Nwe, T. L., and Guan, C. (2015). Cluster-based analysis for personalized stress evaluation using physiological signals. *IEEE J. BioMed. Health Inform* 19, 275–281. doi: 10.1109/JBHI.2014.2311044

Xu, Z. (2011). Modernization: one step at a time. *Nature* 480, S90–S92. doi: 10.1038/480S90a

Xue, R., Fang, Z., Zhang, M., Yi, Z., Wen, C., and Shi, T. (2013). TCMID: Traditional Chinese Medicine integrative database for herb molecular mechanism analysis. *Nucleic Acids Res.* 41, D1089–D1095. doi: 10.1093/nar/gks1100

Yaffe, M. B. (2019). Why geneticists stole cancer research even though cancer is primarily a signaling disease. *Sci. Signaling* 12, eaaw3483. doi: 10.1126/scisignal.aaw3483

Yang, J., and Leskovec, J. (2015). Defining and evaluating network communities based on ground-truth. *Knowledge Inf. Syst.* 42, 181–213. doi: 10.1007/s10115-013-0693-z

Zhang, N. L., Yuan, S., Chen, T., and Wang, Y. (2008). Latent tree models and diagnosis in traditional Chinese medicine. *Artif. Intell. Med.* 42, 229–245. doi: 10.1016/j.artmed.2007.10.004

Zhang, W., Yue, X., Huang, F., Liu, R., Chen, Y., and Ruan, C. (2018). Predicting drug-disease associations and their therapeutic function based on the drug-disease association bipartite network. *Methods* 145, 51–59. doi: 10.1016/j.ymeth.2018.06.001

Zhao, Y., Zhang, X., Luo, L., He, L., Zhao, Y., Liu, B., et al. (2014). "'TCM syndrome differentiation of AIDS using subspace clustering algorithm," in *2014 IEEE International Conference on Bioinformatics and Biomedicine (BIBM)*. (IEEE), 219–224.

Zhou, X., Liu, B., and Wu, Z. (2005). "Text mining for clinical Chinese herbal medical knowledge discovery," in *International Conference on Discovery Science*. (Berlin, Heidelberg: Springer), 396–398.

Zhou, X., Li, Y., Peng, Y., Hu, J., Zhang, R., He, L., et al. (2014). Clinical phenotype network: the underlying mechanism for personalized diagnosis and treatment of traditional Chinese medicine. *Front. Med. China* 8, 337–346. doi: 10.1007/s11684-014-0349-8

Conflict of Interest: The authors declare that the research was conducted in the absence of any commercial or financial relationships that could be construed as a potential conflict of interest.

Copyright © 2020 Jafari, Wang, Amiryousefi and Tang. This is an open-access article distributed under the terms of the Creative Commons Attribution License (CC BY). The use, distribution or reproduction in other forums is permitted, provided the original author(s) and the copyright owner(s) are credited and that the original publication in this journal is cited, in accordance with accepted academic practice. No use, distribution or reproduction is permitted which does not comply with these terms.

frontiers in Pharmacology

ORIGINAL RESEARCH
published: 26 August 2020
doi: 10.3389/fphar.2020.01302

Jian-Pi-Bu-Xue-Formula Alleviates Cyclophosphamide-Induced Myelosuppression *via* Up-Regulating NRF2/HO1/NQO1 Signaling

Qiuju Huang[1,2†], Lizhi Feng[1,3†], Hang Li[1,3], Liang Zheng[1], Xiaoxiao Qi[1], Ying Wang[1], Qian Feng[1], Zhongqiu Liu[1], Xiaohong Liu[1,3] and Linlin Lu[1*]*

[1] Joint Laboratory for Translational Cancer Research of Chinese Medicine of the Ministry of Education of the People's Republic of China, International Institute for Translational Chinese Medicine, Guangzhou University of Chinese Medicine, Guangzhou, China, [2] School of Basic Medical Sciences, Guangzhou University of Chinese Medicine, Guangzhou, China, [3] Department of Respiratory Medicine, The First Affiliated Hospital of Guangzhou University of Chinese Medicine, Guangzhou, China

OPEN ACCESS

Edited by:
Yanqiong Zhang,
China Academy of Chinese Medical Sciences, China

Reviewed by:
Gangjun Du,
Henan University, China
Yanfang Zheng,
Fujian University of Traditional Chinese Medicine, China

***Correspondence:**
Xiaohong Liu
rsclxh@gzucm.edu.cn
Linlin Lu
lllu@gzucm.edu.cn

[†]These authors have contributed equally to this work

Specialty section:
This article was submitted to Ethnopharmacology, a section of the journal Frontiers in Pharmacology

Received: 16 June 2020
Accepted: 05 August 2020
Published: 26 August 2020

Citation:
Huang Q, Feng L, Li H, Zheng L, Qi X, Wang Y, Feng Q, Liu Z, Liu X and Lu L (2020) Jian-Pi-Bu-Xue-Formula Alleviates Cyclophosphamide-Induced Myelosuppression via Up-Regulating NRF2/HO1/NQO1 Signaling. Front. Pharmacol. 11:1302. doi: 10.3389/fphar.2020.01302

Jian-pi-bu-xue-formula (JPBXF), a TCM formula composed of twelve Chinese medicinal herbs, has been used in clinic to ease patients' state of weakness and fatigue especially after receiving anti-tumor chemotherapy in China. The lack of the phytochemical characterization, detail therapeutic evaluation and mechanism of JPBXF remains the main limitation for its spreading. In this study, we systematically evaluated the effectiveness and underline mechanism of JPBXF on cyclophosphamide (CTX)-induced myelosuppression and identified the main constituents of JPBXF aqueous extract. JPBXF treatments reversed CTX-induced myelosuppression through increasing the number of haematopoietic stem cells (HSCs) and expression of C-kit in bone marrow cells. Simultaneously, JPBXF treatments alleviated CTX-induced blood cells reduction by increasing numbers of RBCs and WBCs and levels of GM-CSF, TPO and EPO in plasma. JPBXF treatments reduced CTX-induced immunosuppression by increasing expressions of CD3, CD4, and CD8a in PBMCs, and recovering structure damages of thymus and spleen. Moreover, JPBXF notably increased the expression of NRF2 compared with CTX group, and subsequently up-regulated HO1 and NQO1 both in mRNA and protein levels. In addition, eighteen compounds were recognized from JPBXF aqueous extract and the potential targets of the identified compounds were predicted. Overall, JPBXF can greatly reverse CTX-induced myelosuppression in C57BL/6 mice, especially in improving the blood and immune function through activating NRF2/HO1/NQO1 signaling pathway, which provides a reliable reference for JPBXF application in clinical. By recognizing eighteen compounds in JPBXF aqueous extract and predicting the underline mechanisms of the identified compounds, our study would provide theoretical guidance for further research of JPBXF.

Keywords: Jian-pi-bu-xue-formula, cyclophosphamide, complementary therapy, myelosuppression, NRF2

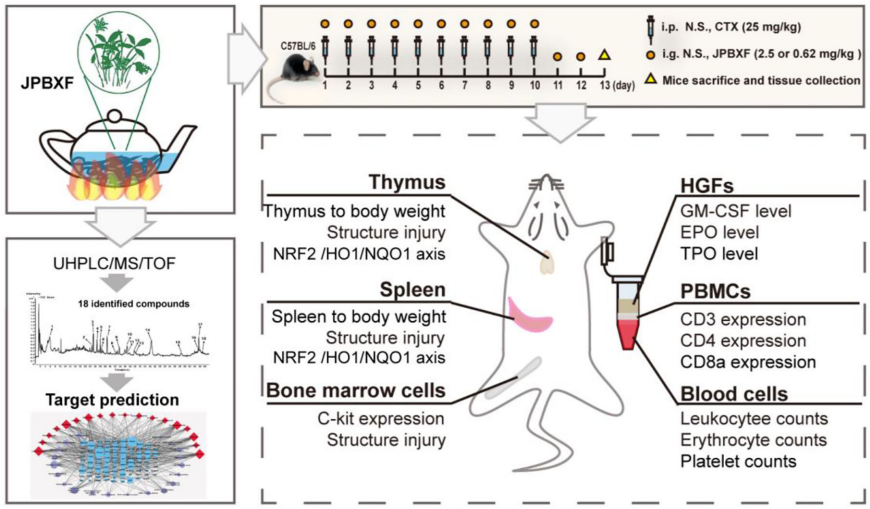

GRAPHICAL ABSTRACT |

INTRODUCTION

Cancer, an aggressive malignancy, approximately causes 4,285,033 new cases and 2,865,147 cancer-related deaths annually in China (Bray et al., 2018). The conventional therapies for cancer treatment include chemotherapy, radiotherapy and surgery. Among these treatments, chemotherapy acts as a practical method and was widely used to kill cancer cells by impeding their growth and reproduction (Potti et al., 2011). However, most of chemotherapeutic agents pose many side effects including myelosuppression, immunosuppression, gastrointestinal reaction and hepatic or renal toxicity, that greatly threaten patients' quality of life, reduce treatments' efficiency, and furthermore lead to termination of ongoing useful therapy (Tachi et al., 2015). For instance, cyclophosphamide (CTX), a common anti-cancer chemotherapeutic agent, is often used alone or in combination with platinum and paclitaxel as standard first-line therapy (Handolias et al., 2016). Myelosuppression, the most common side effect of CTX characterized by decrease of stem and progenitor cells in bone marrow, often arises complications such as neutropenia, anemia and thrombocytopenia (Carey, 2003; Neboh and Ufelle, 2015). It has proof that NRF2 deficiency deteriorated CTX-induced myelosuppression, while activation of NRF2 mitigates ionizing CTX -induced myelosuppression (Que et al., 2016). The up-regulation of HO1 and NQO1 could resist to CTX-induced bone marrow suppression, oxidative stress, inflammation and apoptosis (Chen et al., 2014; HAS et al., 2019). Therefore, methods, which could prevent or eliminate chemotherapy-induced side effects through regulating NRF2 pathway, have great significance for patients struggling against cancer.

Complementary medicine, forms of treatment that used along with standard medical treatments, is common among cancer patients to help lessen some side effects of cancer treatment (Hubner et al., 2015). In clinical, hematopoietic growth factors (HGFs) including granulocyte colony-stimulating factor (G-CSF) and granulocyte macrophage colony-stimulating factor (GM-CSF), are effective complementary medicines for therapy to alleviate chemotherapy-induced myelosuppression (Miller and Steinbach, 2014). Unfortunately, G-CSF and GM-CSF can also accelerate growth of cancer cells (Gutschalk et al., 2006). Therefore, new approaches on finding more effective and safe drugs for preventing and treating chemotherapy-induced myelosuppression are necessary. Traditional Chinese medicine (TCM) complementary treatment has been reported to alleviate chemotherapy induced side effects and improve quality of life (Zhang et al., 2007; Konkimalla and Efferth, 2008). For instance, *Ipomoea obscura* (L.) Ker Gawl. extract could reduce CTX-induced myelosuppression, improve white blood cell counts and recover bone marrow cellularity (Hamsa and Kuttan, 2010). Sip-jeon-dea-bo-tang, a traditional herbal medicine, has been reported to prevent the cisplatin-induced reduction of food intake and weight loss (Woo et al., 2016). Considering the limitations of hematopoietic growth factors, finding effective TCMs on alleviating chemotherapy-induced myelosuppression is helpful and meaningful.

Jian-pi-bu-xue-formula (JPBXF), a TCM consisted of twelve Chinese medicinal herbs, is consumed in clinical for strengthening spleen and fortifying the blood in China for decades. According to basic theories of Chinese medicine,

Abbreviations: BATMAN-TCM, Bioinformatics Analysis Tool for Molecular mechANism of Traditional Chinese Medicine; CTX, cyclophosphamide; DAVID, Database for Annotation, Visualization and Integrated Discovery; ELISA, enzyme-linked immunosorbent assay; EPO, erythropoietin; G-CSF, granulocyte colony-stimulating factor; GM-CSF, granulocyte macrophage colony-stimulating factor; JPBXF, Jian-pi-bu-xue-formula; PBMC, peripheral blood mononuclear cell; PPI, protein-protein interaction; TCM, traditional Chinese medicine; TPO, thrombopoietin.

JPBXF is a combined formula based on Si-Jun-Zi-Tang, Si-Wu-Tang and Dang-Gui-Bu-Xue-Tang without unnecessary drugs, aiming to improve the hematopoiesis effects and make it gently to patients with chemotherapy. JPBXF is composed of monarch drugs *Hedysarum multijugum Maxim* (Huang-Qi) and *Codonopsis pilosulae* (Franch.) Nannf. (*Codonopsis pilosulae* Radix, Dang-Shen), minister drugs including *Ficus simplicissima* Lour. syn. Ficus hirta Vahl (Wu-zhi-mao-tao), *Atractylodes macrocephala Koidz.* (Bai-Zhu), *Angelica sinensis (Oliv.) Diels* (Dang-Gui), and *Rehmannia glutinosa* (Gaertn.) DC. (Shu-Di-Huang), assistant drugs including *Pinellia ternata* (Thunb.) Makino syn. *Arum ternatum* Thunb. (Ban-Xia), *Citrus* × *aurantium L.* syn. *Citrus reticulata* Blanco (Chen-Pi), *Pogostemon cablin (Blanco) Benth.* (Huo-Xiang) and *Zingiber officinale Roscoe* (Sheng-Jiang), and guide drugs *Ziziphus jujuba Mill* (Da-Zao) and *Glycyrrhiza uralensis Fisch* (Gan-Cao). In JPBXF, *H. multijugum, C. pilosula* and *R. glutinosa* had been reported to enhance immunity *in vivo* after CTX t*reatment* (Cohen et al., 2002; Wang et al., 2012). *A. sinensis* has great impacts on promoting hematopoiesis (Gong et al., 2016). *Z. jujuba, Z. officinale, A. ternatum, P. cablin, C. aurantium, A. macrocephala* and *G. uralensis* are often used in formulas for antiemetic during chemotherapy (Cohen et al., 2002). Our previous study also showed that JPBXF could improve hematopoiesis of chemotherapy mice by affecting the expression levels of GM-CSF, TPO, and EPO (Feng and Liu, 2015). Although JPBXF has been used as a formula in clinical for decades, the lack of detail therapeutic evaluation and underline mechanism of JPBXF remains the main limitation for its spreading. Furthermore, the phytochemical characterization of JPBXF is still unclear.

In our study, a CTX-induced myelosuppression animal model was established to assess the effectiveness and safety of JPBXF in alleviating chemotherapy-induced myelosuppression. Changes in thymus, spleen, bone marrow, blood cell counts, expressions of T-cell surface markers such as CD3, CD4, and CD8a in peripheral blood mononuclear cells (PBMCs), expression of C-kit in bone marrow cells, as well as levels of GM-CSF, TPO, and EPO in plasma in the mice were systematically evaluated. Meanwhile, effects of JPBXF on NRF2, HO1, and NQO1 expressions in thymus and spleen were also detected. Furthermore, main chemical constituents of JPBXF aqueous extract were identified using UHPLC/MS/TOF and the underline mechanisms of the identified compounds were predicted using bioinformatics analysis.

MATERIAL AND METHODS

Reagents

Cyclophosphamide (Pude Pharmaceutical Co., Datong, Shanxi, China) was purchased from the First Affiliated Hospital of Guangzhou University of Chinese Medicine. The anti-CD3 and anti-CD4 antibodies, goat anti-rabbit and anti-mouse secondary antibody horseradish peroxidase conjugate (IgG antibodies) were purchased from Abcam (Cambridge, Massachusett, UK). The anti-CD8a antibody and anti-C-kit receptor antibody were purchased from Santa Cruz Biotechnology (Santa Cruz, California, USA). GM-CSF, TPO, and EPO Elisa kits were purchased from R&D Systems (Minneapolis, MN., USA). All other reagents were from a standard source and were analytical pure grade.

Plant Materials and JPBXF Preparation

F. simplicissima (30 g), *H. multijugum* (30 g), *C. pilosula* (20 g), *A. macrocephala* (15 g), *A. sinensis* (6 g), *R. glutinosa* (10 g), *A. ternatum* (10 g), *C. aurantium* (10 g), *P. cablin* (10 g), *Z. officinale* (6 g), *Z. jujuba* (10 g) and *G. uralensis* (10 g) were all purchased from the First Affiliated Hospital of Guangzhou University of Traditional Chinese Medicine (Guangdong, China) and identified by Institute of Chinese Materia Medica, China Academy of Chinese Medical Sciences (Beijing, China). A voucher specimen was deposited at the Laboratory of International Institute for Translational Chinese Medicine, Guangzhou University of Chinese Medicine (Guangzhou, China). The Chinese herbal mixture was immersed in a 8-fold amount of distilled water for 30 min and gently boiled for 30 min. The extract was collected. The herb residues were boiled again with a 6-fold amount of distilled water for 1 h, and the extract was collected again. Following, the collection extract were combined, filtered with three layers of gauze, and evaporated in 60 °C. After cooling at room temperature, liquid was spared and stored at 4 °C.

JPBXF Chemical Components Analysis

Characterization of main chemical components in JPBXF was detected by UHPLC/MS/TOF (Agilent Technologies 6540). Chromatographic separation was achieved on a Zorbax C18 column (100 × 3.0 mm^2, 1.8 μm) (Agilent Technologies), with column temperature maintained at 25°C. The mobile phases consisted of water (A) and acetonitrile (B) using a gradient elution. The flow rate was 0.3 ml/min. The mass spectrometer was operated in negative ion mode. The full scan setting parameters are as follows: capillary voltage, 2.5 kV; nozzle voltage, 1,000 V; gas temperature, 290°C; sheath temperature, 340°C; sheath gas flow, 11 L/min; and gas flow, 10 L/min; fragmentation voltage: 135 V. Self-building database containing mass spectrometry information of reported compounds from each herb was used for compounds matching.

Animals

Male C57BL/6 mice (4–6 weeks, 18–22 g) were purchased from the Laboratory Animal Center of Guangzhou University of Chinese Medicine (Guangzhou, China; License: SCXK, Guangdong, 2018-0034). The mice were kept in the animal facility in the SPF animal laboratory (License number: SYXK (GZ) 2019-0144) at International Institute for Translational Chinese Medicine, Guangzhou University of Chinese Medicine (Guangzhou, China). The animal experiments were approved by the International Institute for Translational Chinese Medicine Animal Care and Use Committee, Guangzhou University of Chinese Medicine (Guangzhou, China). The mice randomly

divided into five groups: control, CTX, GM-CSF, high- and low-dose JPBXF. Control group (n = 6) received treatments with 0.9% physiologic saline (i.p.) once a day for 10 days and intragastric administrations with 0.9% physiologic saline once a day for 12 days. CTX, GM-CSF, JPBXF groups (each with n = 6) received administrations with CTX (25 mg/kg, i.p.) once a day for 10 days and intragastric administrations with 0.9% physiologic saline, GM-CSF (5 μg/kg), high- and low-dose of JPBXF (2.5 g/mL and 0.62 g/mL) once a day for 12 days, respectively. The body weights of the mice were recorded every other day. Finally, the mice were sacrificed and the organs (including spleen and thymus) of each mouse were isolated and weighed.

Peripheral Blood Cell Count

Before the mice were sacrificed, the blood samples (200 μL of each mouse) were collected in heparin-treated tubes by and then stored at 4°C. After all samples collection, the numbers of leukocyte, platelet, and erythrocyte were counted using SYSMEX XT-1800I (Kobe, Japan).

Isolation of Plasma and PBMCs

After the mice were sacrificed, the whole blood of each mouse was collected in heparin-treated tubes and then centrifuged at 3,000 rpm for 10 min. The plasma samples were harvested, and stored at -80 °C. The remaining precipitation was resuspended in PBS (v/v, 1:1), and loaded into the tubes filled with Ficoll (GE Healthcare, Chicago, USA). After centrifuged at 400 g for 30 min, PBMCs were isolated, and rinsed twice with PBS.

ELISA Assay

Levels of GM-CSF, TPO, and EPO in plasma were measured by enzyme-linked immunosorbent assay (ELISA), using Quantikine ELISA kits (R&D Systems, Minneapolis, MN, USA), according to the manufacturer's instructions. Results were expressed as ng/L of plasma.

Flow Cytometry

After isolated, PBMCs were treated according our previous study (Feng et al., 2016). After incubated with anti-CD3 antibody (1:200), anti-CD4 antibody (1:200), anti-CD8a antibody (1:50), and secondary antibodies (1:200), the PBMCs samples were detected using Flow cytometry (BD Biosciences, San Diego, CA, USA).

H&E Staining

Tissues such as thymus, spleens, and femurs were treated and observed according our previous study (Feng et al., 2016). Briefly, after fixed, embedded, and sliced, sections (4 μm) of thymus, spleens, and femurs were deparaffinized and rehydrated. Following, hematoxylin and eosin staining were performed. The slices were then observed under a light microscope (Leica DM750, Wetzlar, GER).

Western Blot

Total proteins of thymus or spleens were extracted using RIPA lysis buffer and phenylmethanesulfonyl fluoride (PMSF), and quantified using Coomassie Brilliant Blue Kit (Bio-Rad, Hercules, CA, USA). Protein samples of each tissue were separated by 10% SDS-PAGE, transferred onto PVDF membranes, and blocked with 5% BSA for 1 h. The membranes were incubated with the primary antibody of NRF2 (1:1,000) at 4 °C overnight, subsequently, with the corresponding secondary antibodies (1:5,000) at room temperature for 1 h. β-actin acted as a loading control. ECL chemiluminescence reagent was applied to detect for fluorescent signals using FluorChem E (Santa Clara, CA, USA). Protein bands were quantified using Quantity One software (Bio-Rad, Hercules, CA, USA).

Real-Time PCR Analysis

Total RNA of thymus or spleens was isolated through the TRIzol extraction method. Then, RNA reverse transcribed into cDNA according to a reverse transcription kit (TaKaRa, Shiga, Japan). SYBR Green real-time PCR amplification and detection were then performed with an ABI 7500 system (Applied Biosystems, Foster City, USA). β-actin was regarded as house-keeping gene. Primers are as follows. HO1: 5'-TGATGGCTTCCTTGTA CCATATC-3' and 3'-AGCTCCTCAGGGAAGTAGAG- 5'; NQO1: 5'-GAGAAGAGCCCTGATTGTACTG-3' and 3'-ACC TCCCATCCTCT CTTCTT-5'; β-actin: 5'-CTGTCCCTGTAT GCCTCTG-3' and 5'-ATGTCACGCAC GATTTCC-3'.

Immunohistochemistry (IHC)

Thymus and spleens tissues were fixed in 4% paraformaldehyde, embedded in paraffin. After sliced up, the slices (4 μm) were dewaxed, hydrated, and then incubated with natrium citric (0.01 M) for antigen retrieval. Following, the slices were rinsed with PBS, and incubated with anti-HO1 and anti-NQO1 overnight at 4 °C. Following steps were performed using the immunostaining kit (BOSTER Biological Technology) based on the manufacturer's instructions.

Target Prediction by Network Pharmacology

The myelosuppression-related genes were obtained from the GeneCards database (https://www.genecards.org/), and the potential target genes of compounds were predicted using a Bioinformatics Analysis Tool for Molecular mechANism of Traditional Chinese Medicine (BATMAN-TCM) (http://bionet.ncpsb.org/batman-tcm/) and Swiss Target Prediction database (http://www.swisstargetprediction.ch/). Genes obtained from these three databases were analyzed using Venny 2.1 (https://bioinfogp.cnb.csic.es/tools/venny/index.html). The gene ontology (GO) and Genomes (KEGG) enrichment analyses were performed for the potential targets using the Database for Annotation, Visualization and Integrated Discovery (DAVID) (https://david.ncifcrf.gov/) and the online software Omicshare. The protein-protein interaction (PPI) among these potential targets was constructed using the STRING database (https://string-db.org/) (Du et al., 2019). The compound-target-pathway network was constructed using Cytoscape 3.7.2 (Zhang et al., 2019).

Data Analysis

All data were expressed as mean ± standard deviation (SD). Significant differences were analyzed by one-way ANOVA followed by LSD test (for more than two groups) by SPSS. Statistical difference was considered significant at $P < 0.05$.

RESULTS

Phytochemical Characterization of JPBXF

To identify the main constituents of JPBXF aqueous extract, we analyzed the JPBXF aqueous extract using UHPLC/MS/TOF. Eighteen compounds were recognized from JPBXF aqueous extract as shown in **Table 1**. The typical scaffold backbones for the eighteen compounds are flavonoids, saponins and polyphenols. Among the eighteen compounds, there are thirteen flavonoids, including liquiritin apioside, liquiritin, acteoside, naringin, isoacteoside, hesperidin, isoliquiritin apioside, isoliquiritin, liquiritigenin, calycosin, formononetin, glycycoumarin, and licoisoflavone B. Meanwhile, licoricesaponine A3, licoricesaponine G2 and glycyrrhizic acid are three saponins. Paeonol and 4-gingerol are two polyphenols. According to UHPLC/MS/TOF, liquiritin, acteoside, naringin, hesperidin, glycyrrhizic acid and 4-gingerol were identified with high contents (**Figure 1**). Three pairs of flavonoid isomers need further identification.

Effects of JPBXF on CTX-Induced Myelosuppression

To assess the effects of JPBXF on chemotherapy-induced myelosuppression in mice, body weight change and H&E staining of femurs were performed. Although there was no significant change in body weight among each group, CTX treatment induced a slight decrease in body-weight of mice compared with the control group (**Figure 2A**). However, after treated with JPBXF, the body-weight loss of mice induced by CTX was decreased slightly (**Figure 2A**). H&E staining results shown that CTX treatment significantly reduced the number of haematopoietic stem cells (HSCs) in femurs compared with control group. To the contrary, JPBXF treatments increased the number of HSCs compared with that of CTX treatment alone (**Figure 2B**). To further confirm whether JPBXF treatments could influence the number of HSCs, the expression of C-kit, a marker of HSCs, was detected in bone marrow cells. The results shown that compared with control, the expression of C-kit was markedly decreased by 57.02 ± 6.16% in CTX treated bone marrow cells ($P < 0.01$, **Figure 2C**). Meanwhile, 5 μg/kg of GM-CSF and 2.5 g/mL of JPBXF treatments increased the expression of C-kit by 35.68 ± 7.82% and 42.44 ± 8.71% respectively compared with that of CTX alone ($P < 0.05$, **Figure 2C**).

JPBXF Alleviated CTX-Induced Blood Cells Reduction

Along with myelosuppression, CTX treatments often induce blood cells reduction (Hill et al., 2011). To investigate the effects of JPBXF on blood cells, we detected the numbers of WBCs, RBCs, and PLTs and analyzed the secretion levels of hematopoietic growth factors including GM-CSF, EPO, and TPO. The whole blood analysis revealed that compared with control group, the numbers of WBCs and RBCs were significantly decreased after CTX treatments. However, 5 μg/kg of GM-CSF and 2.5 g/mL of JPBXF treatments increased the numbers of WBCs and RBCs at different degrees. Nevertheless, the number of PLTs showed a slight increase in GM-CSF group, but had few changes in CTX and JPBXF groups (**Figure 3A**). Meanwhile, ELISA assays showed that the secretion levels of GM-CSF, EPO, and TPO were significantly reduced by 35.05 ± 7.99%, 89.84 ± 2.48%, and 49.48 ± 4.79% respectively in CTX group compared with the control group. However, JPBXF treatments abrogated the suppression effect of CTX and markedly increased the secretion levels of GM-CSF, EPO, and TPO at different degrees in plasma. Compared with CTX group,

TABLE 1 | Compounds of aqueous extract from Jian-pi-bu-xue-formula (JPBXF) were identified.

No.	T_R (min)	m/z	Formula	Identification	Therotical m/z	Error (ppm)
1	5.81	165.0545	$C_9H_{10}O_3$	paeonol	165.0557	7.3
2	23.21	549.1582	$C_{26}H_{30}O_{13}$[a]	liquiritin apioside	549.1614	5.8
3	23.34	417.1170	$C_{21}H_{22}O_9$[b]	liquiritin	417.1191	5.0
4	24.74	623.1952	$C_{29}H_{36}O_{15}$[c]	acteoside	623.1981	4.6
5	26.07	579.1672	$C_{27}H_{32}O_{14}$	naringin	579.1719	8.1
6	26.64	623.1963	$C_{29}H_{36}O_{15}$[c]	isoacteoside	623.1980	2.7
7	28.74	609.1791	$C_{28}H_{34}O_{15}$	hesperidin	609.1825	5.6
8	32.37	549.1589	$C_{26}H_{30}O_{13}$[a]	isoliquiritin apioside	549.1614	4.5
9	33.67	417.1176	$C_{21}H_{22}O_9$[b]	isoliquiritin	417.1191	3.6
10	36.61	983.4429	$C_{48}H_{72}O_{21}$	licoricesaponine A3	983.4493	6.5
11	36.76	255.0659	$C_{15}H_{12}O_4$	liquiritigenin	255.0663	1.6
12	39.38	283.0604	$C_{16}H_{12}O_5$	calycosin	283.0612	2.8
13	39.91	837.3864	$C_{42}H_{62}O_{17}$	licoricesaponine G2	837.3914	6.0
14	46.48	821.3915	$C_{42}H_{62}O_{16}$	glycyrrhizic acid	821.3965	6.1
15	58.61	267.0655	$C_{16}H_{12}O_4$	formononetin	267.0663	3.0
16	65.18	367.1188	$C_{21}H_{20}O_6$	glycycoumarin	367.1187	0.3
17	65.26	265.1476	$C_{15}H_{22}O_4$	4-gingerol	265.1445	7.9
18	67.02	351.0878	$C_{20}H_{16}O_6$	licoisoflavone B	351.0874	1.1

[a,b,c]*Three pairs of flavonoids isomers.*

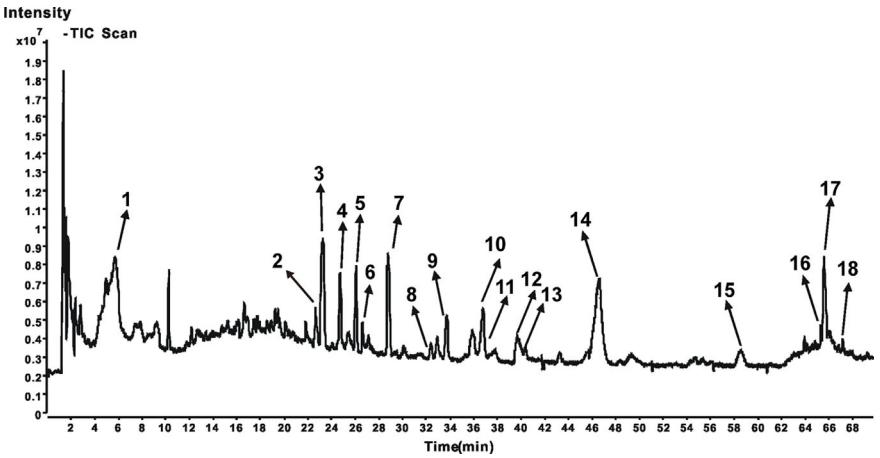

FIGURE 1 | Chromatograms of UHPLC/MS/TOF of JPBXF extract.

2.5 g/mL of JPBXF treatments increased the levels of GM-CSF, EPO and TPO by 2.94-, 69.84-, and 4.21-fold in plasma (**Figure 3B**).

JPBXF Reduced CTX-Induced Immunosuppression

According to the white blood cell analysis results, we found that JPBXF treatments might raise the immunity of mice suppressed by CTX. Among these white blood cells, T cell play important role in immunity. To further confirm the effect of JPBXF on T cells, we detected the expressions of T-cell surface markers, such as CD3, CD4, and CD8α in PBMCs. The results demonstrated that compared with control group, CTX treatment significantly decreased the expressions of CD3, CD4, and CD8α by 44.03 ± 2.96%, 14.63 ± 4.14%, and 46.70 ± 3.10%, respectively. However, CTX-induced expression decrease of CD3, CD4 and CD8α were recovered by JPBXF treatments (**Figure 4**). In detail, 2.5 g/mL of JPBXF treatments increased CD3, CD4, and CD8a expression levels by 31.33 ± 5.59%, 28.62 ± 3.44%, and 18.13 ± 2.24%, respectively. Meanwhile, 0.62 g/mL of JPBXF treatments increased the expressions of CD3, CD4, and CD8a by 37.99 ± 5.07%, 34.06 ± 3.09%, and 45.16 ± 3.29%, respectively.

Thymus and spleen are two main immune organs that play important roles in cellular and humoral immunity. To assess the effects of JPBXF on cellular and humoral immunity in mice, size comparison and H&E staining of thymus and spleen were further conducted. The pictures of thymus directly showed that CTX treatment induced a size reduce of thymus compared with that of control, however, JPBXF treatments increased the size of thymus. Compared with the control group, thymus index (ratios of thymus to body-weight) in CTX group decreased markedly. Meanwhile, thymus index in GM-CSF group and high-dose JPBXF group were significantly increased compared with CTX group; however, thymus index in the low-dose JPBXF group had no significant change (**Figure 5A**). H&E staining results showed that the tissue structures of thymus, including cortex, medulla, and thymic corpuscle, were clear observed in control group, and destroyed in CTX group. However, the structure damages of thymus by CTX were significantly recovered by JPBXF treatments (**Figure 5B**). The same as thymus, the size of spleen was reduced by CTX and increased by JPBXF. Spleen index (ratios of spleen to body-weight) in CTX group was decreased markedly compared with that of control group, meanwhile, increased in GM-CSF and JPBXF groups compared with CTX group (**Figure 6A**). In addition, white pulp atrophy, hemorrhage and necrosis were observed in spleen after CTX treatment. However, these damages were reduced in GM-CSF and JPBXF groups, especially in 2.5 g/mL JPBXF group (**Figure 6**).

JPBXF Alleviated CTX-Induced Myelosuppression Through Activating NRF2/HO1/NQO1 Signaling Pathway

NRF2, a pivotal transcription factor, is involved in regulating redox homeostasis, drug metabolism, responses to oxidative and electrophilic stress and so on (Hayes and Dinkova-Kostova, 2014). NRF2 deficiency deteriorated CTX-induced myelosuppression, while activation of NRF2 mitigated CTX-induced myelosuppression (Que et al., 2016). Herein, to further determine the underlying mechanism of JPBXF in alleviating CTX-induced myelosuppression, NRF2 expressions in thymus or spleen were evaluated. Our results showed that the expressions of NRF2 were significantly decreased by CTX both in thymus and spleen compared with control group, meanwhile, notably increased by GM-CSF and JPBXF treatments compared with CTX group, suggesting that JPBXF could mitigate CTX-induced myelosuppression through activating of NRF2 (**Figure 7A**). The up-regulation of HO1 and NQO1 could resist to CTX-induced bone marrow suppression, oxidative stress, inflammation and apoptosis (Chen et al., 2014; HAS et al., 2019), and we found that JPBXF reversed CTX-induced HO1 and NQO1 suppressions both in mRNA and protein levels (**Figures 7B–D**), indicating that JPBXF alleviated CTX-induced myelosuppression through activating NRF2/HO1/NQO1 signaling pathway.

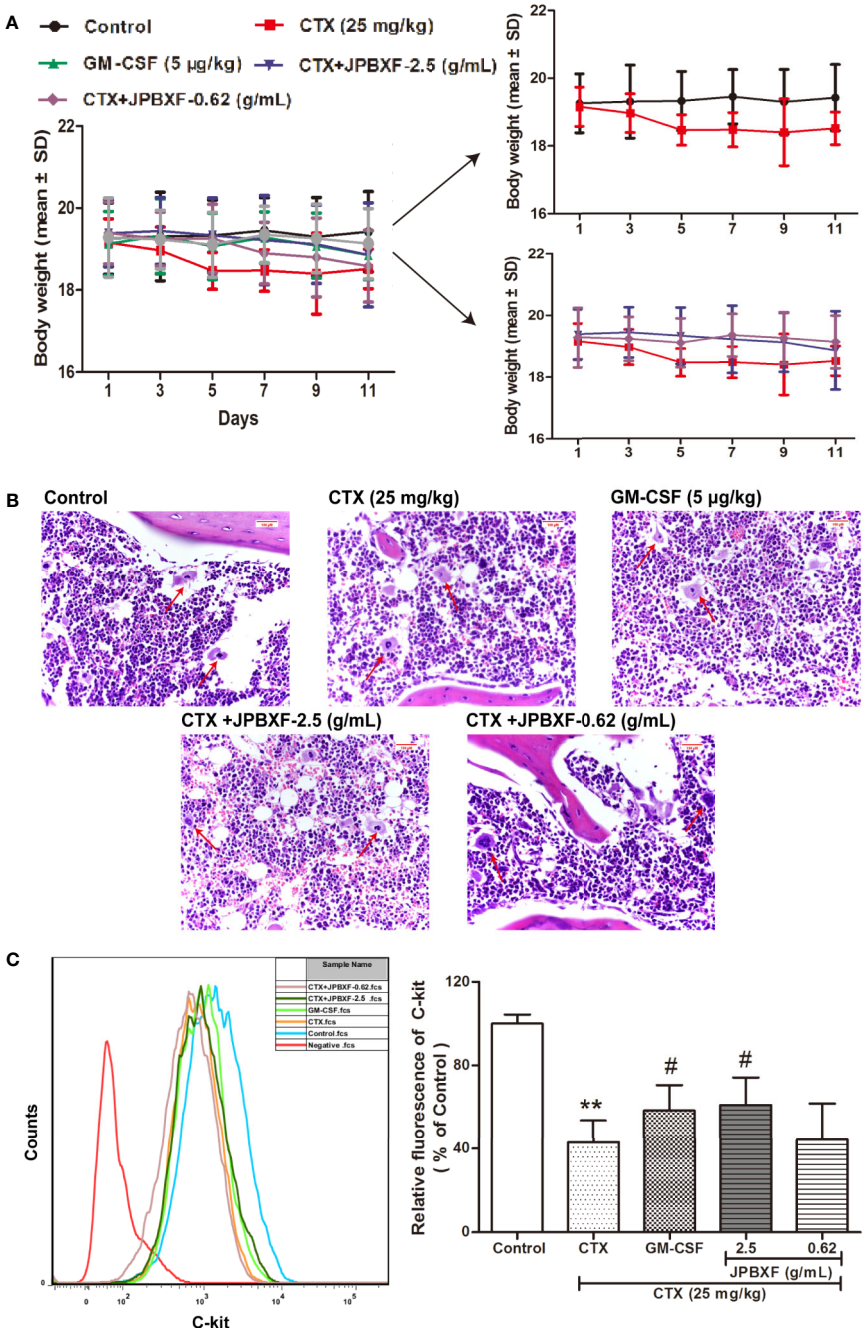

FIGURE 2 | Effects of JPBXF on myelosuppression in CTX-treated mice. **(A)** The body weight curves of CTX-treated mice after JPBXF treatments. **(B)** Histopathological changes in bone marrow tissues (stained by H&E, ×400). **(C)** Expression of C-kit in bone marrow cells. Data shown are means ± SD from day 13. $^{**}P < 0.01$ *vs.* Control, $^{\#}P < 0.05$ *vs.* CTX.

Target Prediction of Eighteen Compounds on Alleviating Myelosuppression by Network Pharmacology

We queried 3,519 genes related to myelosuppression using GeneCards database, 482 predicted target genes of compounds using BATMAN-TCM database and 582 predicted target genes of compounds using Swiss Target Prediction database. 87 of the potential targets yielded from these three database were selected for GO and KEGG analyses (**Figure 8A**). $P < 0.05$ was set as threshold criteria to identify the functional gene ontology and pathway, and Top 20 ontology and pathway were showed in **Figures 8B, C**. GO enrichment analysis indicated that the 87

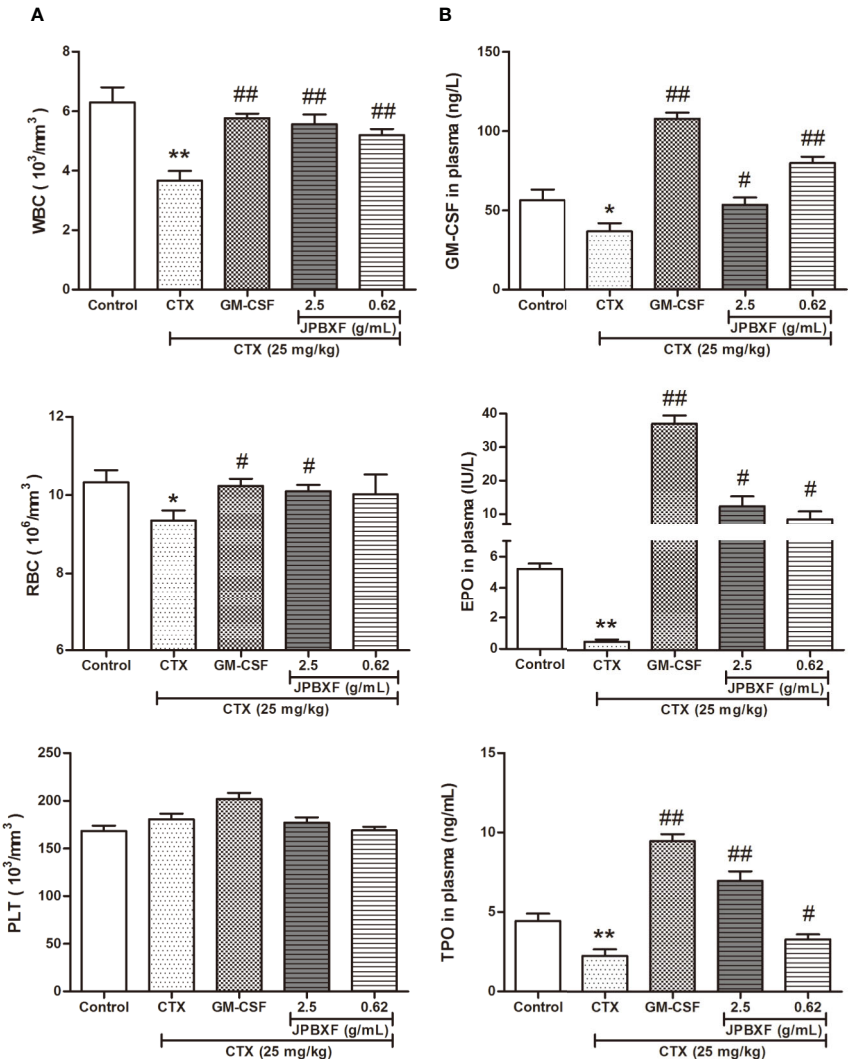

FIGURE 3 | Effects of JPBXF on blood system in CTX-treated mice. **(A)** The numbers of white blood cells, red blood cells and platelets in CTX-treated mice after JPBXF treatments. **(B)** The secretion levels of GM-CSF, EPO, and TPO in plasma in CTX-treated mice after JPBXF treatments. Data shown are means ± SD from day 13. $^{*}P < 0.05$, $^{**}P < 0.01$ *vs.* Control, $^{\#}P < 0.05$, $^{\#\#}P < 0.01$ *vs.* CTX.

potential targets were primarily associated with the "response to organic substance," "response to chemical," "multicellular organismal process," "regulation of multicellular organismal process," and "regulation of biological quality" terms. KEGG enrichment analysis revealed that the 87 potential targets were significantly enriched in the "Neuroactive ligand-receptor interaction," "Pathways in cancer," "Calcium signaling pathway" "cAMP signaling pathway" and "Vascular smooth muscle contraction" terms. The PPI network identified 14 key genes for the compounds, including AGTR2, PTGS2, MTOR, DRD2, EP300, OPRM1, AGTR1, DRD3, OPRD1, OPRK1, PPARG, PTGER3, RXRA, and TNF (**Figure 8D**). The three-level network consisted of 125 nodes (18 compounds, 87 genes and 20 pathways) and 552 edges. Among the 18 compounds, naringin showed the broadest effect on the target genes (38 genes). Liquiritin apioside, liquiritigenin, licoricesaponine G2, and isoliquiritin also affected 36, 35, 33, and 33 genes, respectively. Among the 87 genes, PRKCA, PRKCB and IMPDH1 were influenced by 16, 13, and 12 compounds, respectively. OPRD1, PPP2CA, ESR1, OPRM1, OPRK1, and ALOX5 were affected by 11 compounds. CNR2 was affected by 10 compounds. IMPDH2 was influenced by 9 compounds. DRD2, NR3C1 and TOP2A were affected by 8 compounds. While three targets were influenced by 7 compounds, one target was influenced by 6 compounds, ten targets were affected by 5 compounds, nine targets were affected by 4 compounds, twenty three targets were affected by 3 compounds, and the rest twenty seven were affected by only one compound.

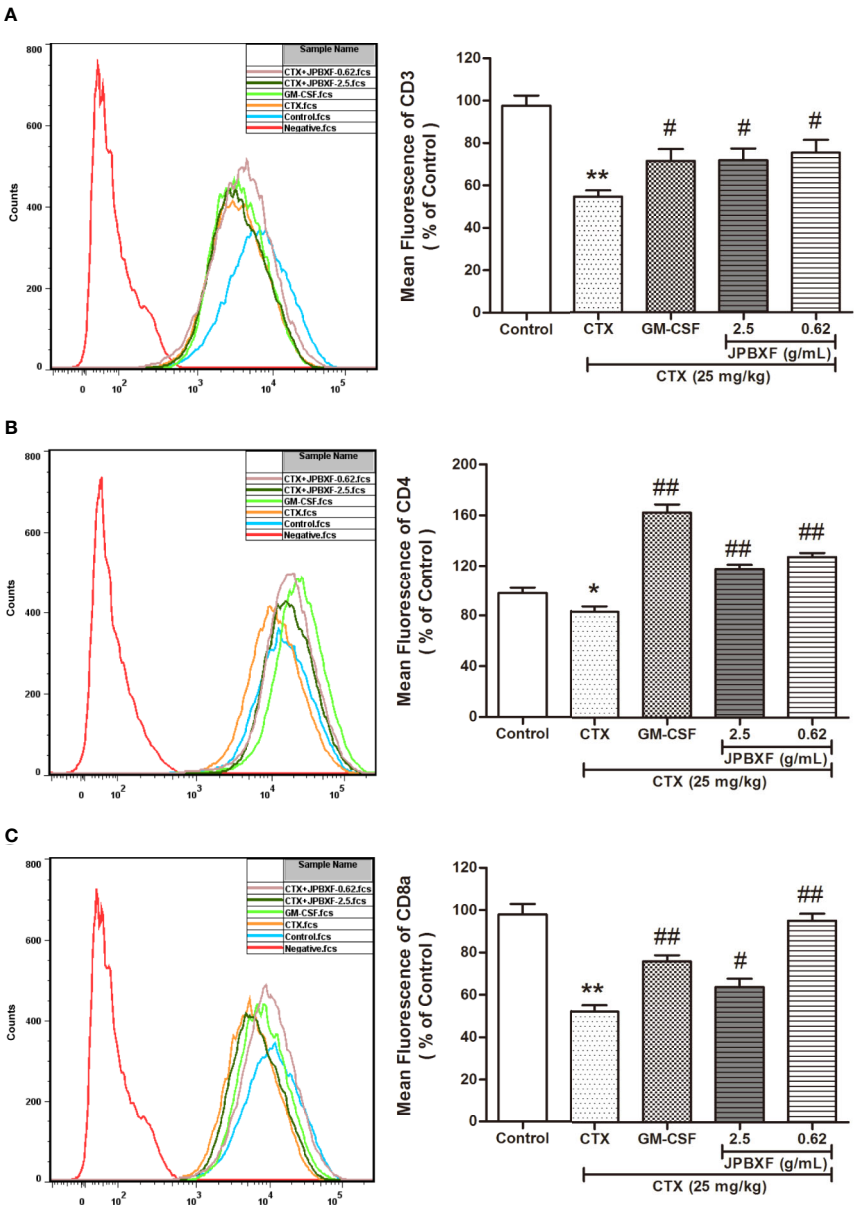

FIGURE 4 | Effects of JPBXF on the PBMCs in CTX-treated mice. The expression levels of CD3 **(A)**, CD4 **(B)**, and CD8α **(C)** in peripheral blood mononuclear cells (PBMCs) of CTX-treated mice after JPBXF treatments. Data shown are means ± SD from day 13. $^{*}P < 0.05$, $^{**}P < 0.01$ *vs.* Control, $^{\#}P < 0.05$, $^{\#\#}P < 0.01$ *vs.* CTX.

DISCUSSION

TCMs are widely used in Asian countries, especially China, Japan and Korea. With the development of medicine, Chinese medicine is gradually accepted by western countries (Dobos and Tao, 2011). Given the ability of alleviating chemotherapy-induced side effects, TCMs complementary treatment is widely adopted for patients suffering from cancers (Woo et al., 2016). To be an empirical TCM formula, JPBXF has been used to ease chemotherapy-induced weakness and fatigue for cancer patients in clinic in China for decades. However, the phytochemical characterization, detail therapeutic evaluation and underline mechanism of JPBXF remain unclear.

Our study directly provides evidence that JPBXF treatments could alleviate CTX-induced myelosuppression in C57BL/6 mice as following aspects: **(i)** JPBXF treatments increased the number of HSCs; **(ii)** JPBXF treatments recovered CTX-induced blood cells reduction; **(iii)** JPBXF treatments reduced CTX-induced immunosuppression. Cancer patients who receive CTX-chemotherapy, often suffered side effects including myelosuppression, weight loss, asthenia, and so on (Strati et al., 2013; Que et al., 2016). In our study, JPBXF treatments

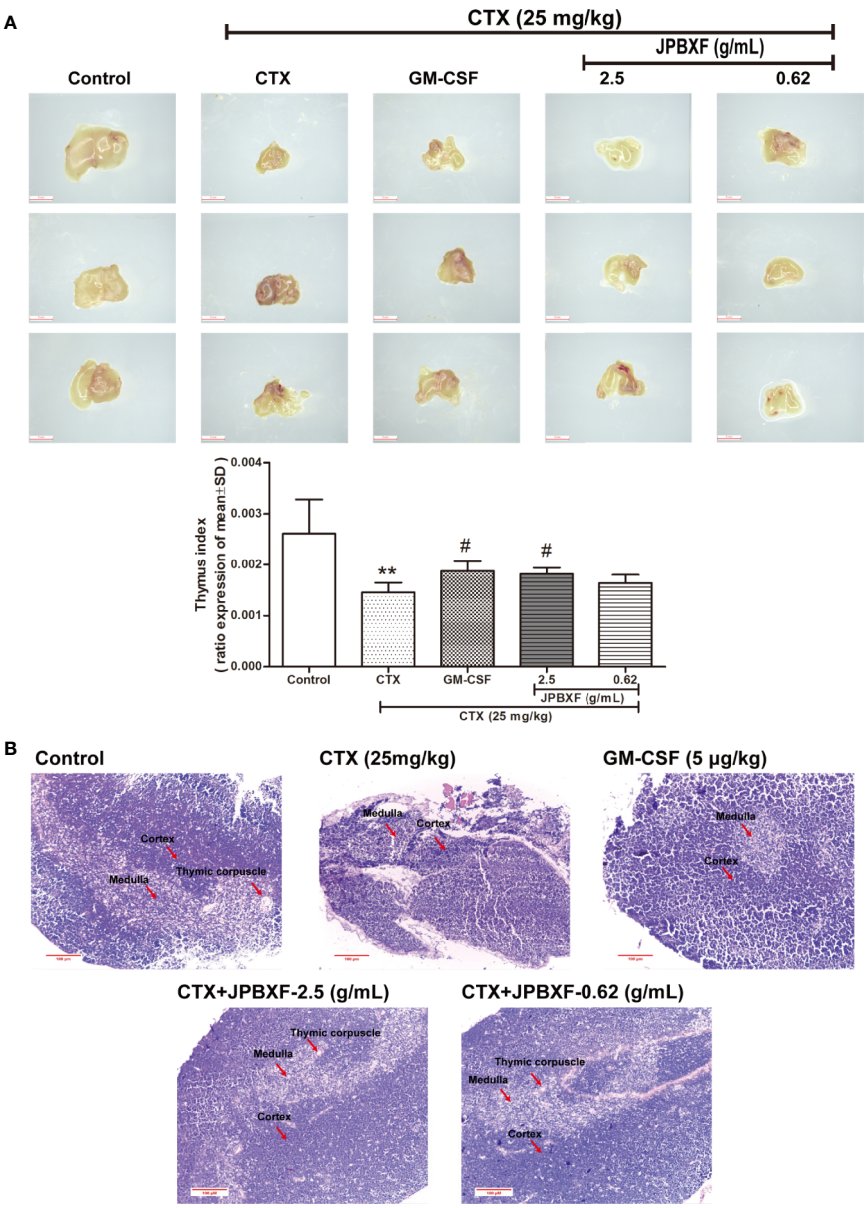

FIGURE 5 | Effects of JPBXF on the thymus in CTX-treated mice. **(A)** Sizes and index of thymus in mice (scale = 3 mm). **(B)** Histopathological changes in thymus tissues (stained by H&E, ×200). Data shown are means ± SD from day 13. $^{**}P < 0.01$ *vs.* Control, $^{\#}P < 0.05$ *vs.* CTX.

could increase the number of HSCs and the expression of HSC marker C-kit (**Figure 2**), illustrating that JPBXF could abrogate the myelosuppression induced by CTX. On the other hand, CTX treatment could significantly reduce the number of WBCs and RBCs and the secretion levels of GM-CSF, EPO and TPO in mice, which consistent with the previous reports (Botnick et al., 1981; Jantunen et al., 2003). Expectedly, JPBXF treatments increased the number of RBCs and WBCs, and the secretion levels of EPO and GM-CSF at different degrees (**Figure 3**). Except for increasing blood function, JPBXF also showed great ability on reducing CTX-induced immunosuppression in C57BL/6 mice. It is reported that CTX treatment could induce immunosuppression and inhibit the generation and function of T cells (Traverso et al., 2012; Salva et al., 2014). CD3, CD4, and CD8a are the most abundant immunity T cell in the PBMCs (Sedgmen et al., 2013). We found that the expressions of CD3, CD4, and CD8a in PBMCs were decreased by CTX, while JPBXF abrogated the decrease expressions of CD3, CD4 and CD8a (**Figure 4**). Furthermore, thymus and spleen are two main immune organs that play important roles in cellular and humoral immunity. Thymus and spleen functions can be inhibited by CTX treatment (Zhao et al., 2009). In the present study, we found that thymic atrophy and splenatrophy were obvious after CTX treatment. To the contrary, thymus and

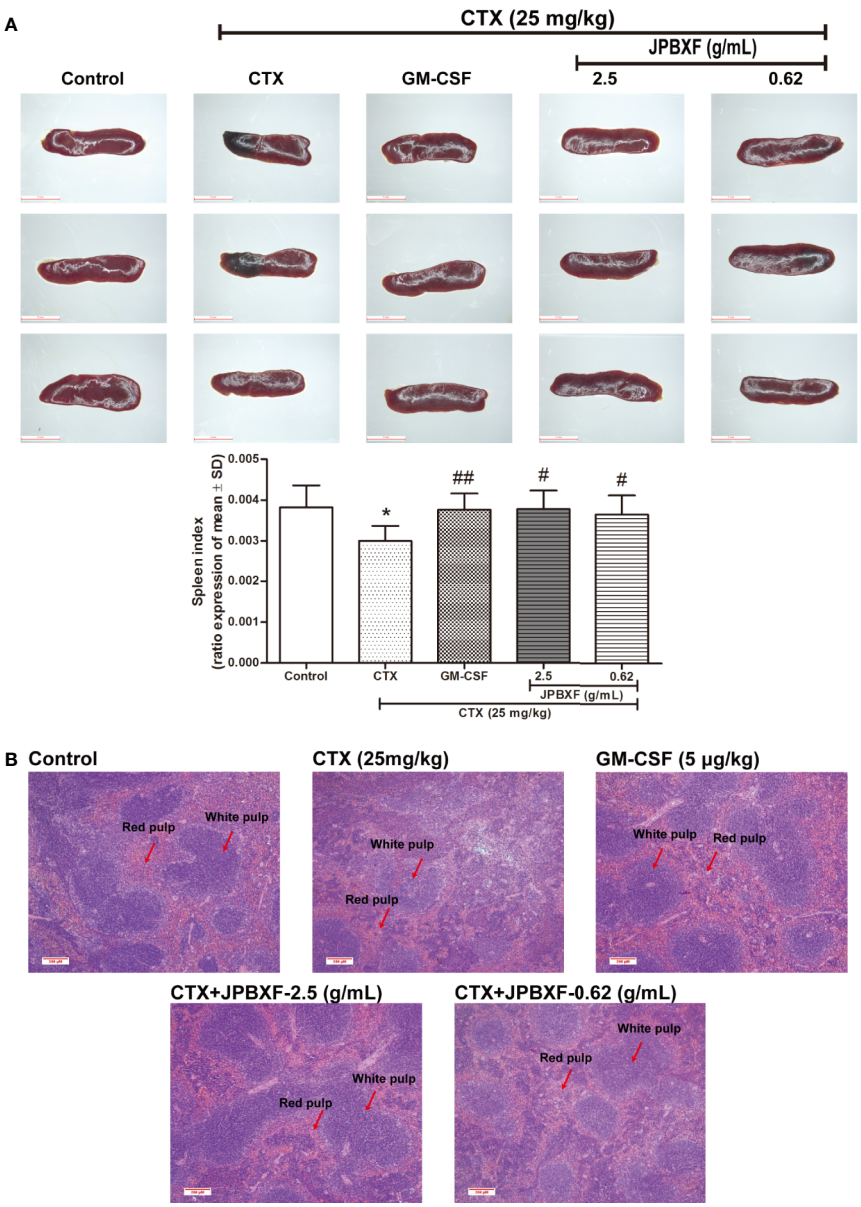

FIGURE 6 | Effects of JPBXF on the spleen in CTX-treated mice. **(A)** Sizes and index of spleens in mice (scale=5 mm). **(B)** Histopathological changes in spleens tissues (stained by H&E, ×100). Data shown are means ± SD from day 13. $^{*}P < 0.05$ *vs.* Control, $^{\#}P < 0.05$, $^{\#\#}P < 0.01$ *vs.* CTX.

spleen index increased after JPBXF treatments (**Figures 5A** and **6A**). In addition, CTX-induced structure damages, including cortex, medulla and thymic corpuscle in thymus and white pulp atrophy, hemorrhage and necrosis in spleen, were recovered by JPBXF treatments (**Figures 5B** and **6B**).

Our data also revealed that JPBXF alleviated CTX-induced myelosuppression through activating NRF2/HO1/NQO1 signaling pathway. It is reported that NRF2 deficiency deteriorated CTX-induced myelosuppression, while activation of NRF2 mitigates CTX -induced myelosuppression (Que et al., 2016). The up-regulation of HO1 or NQO1 could resist to CTX-induced bone marrow suppression, oxidative stress, inflammation and apoptosis (Chen et al., 2014; HAS et al., 2019). We observed that JPBXF treatment notably reversed CTX-induced NRF2 suppressions both in thymus and spleen, subsequently, recovered the expression of HO1 and NQO1 both in mRNA and protein levels (**Figure 7**), indicating that JPBXF alleviated CTX-induced myelosuppression through activating NRF2/HO1/NQO1 signaling pathway.

In our study, JPBXF aqueous extract showed great ability in alleviating CTX-induced myelosuppression in C57BL/6 mice.

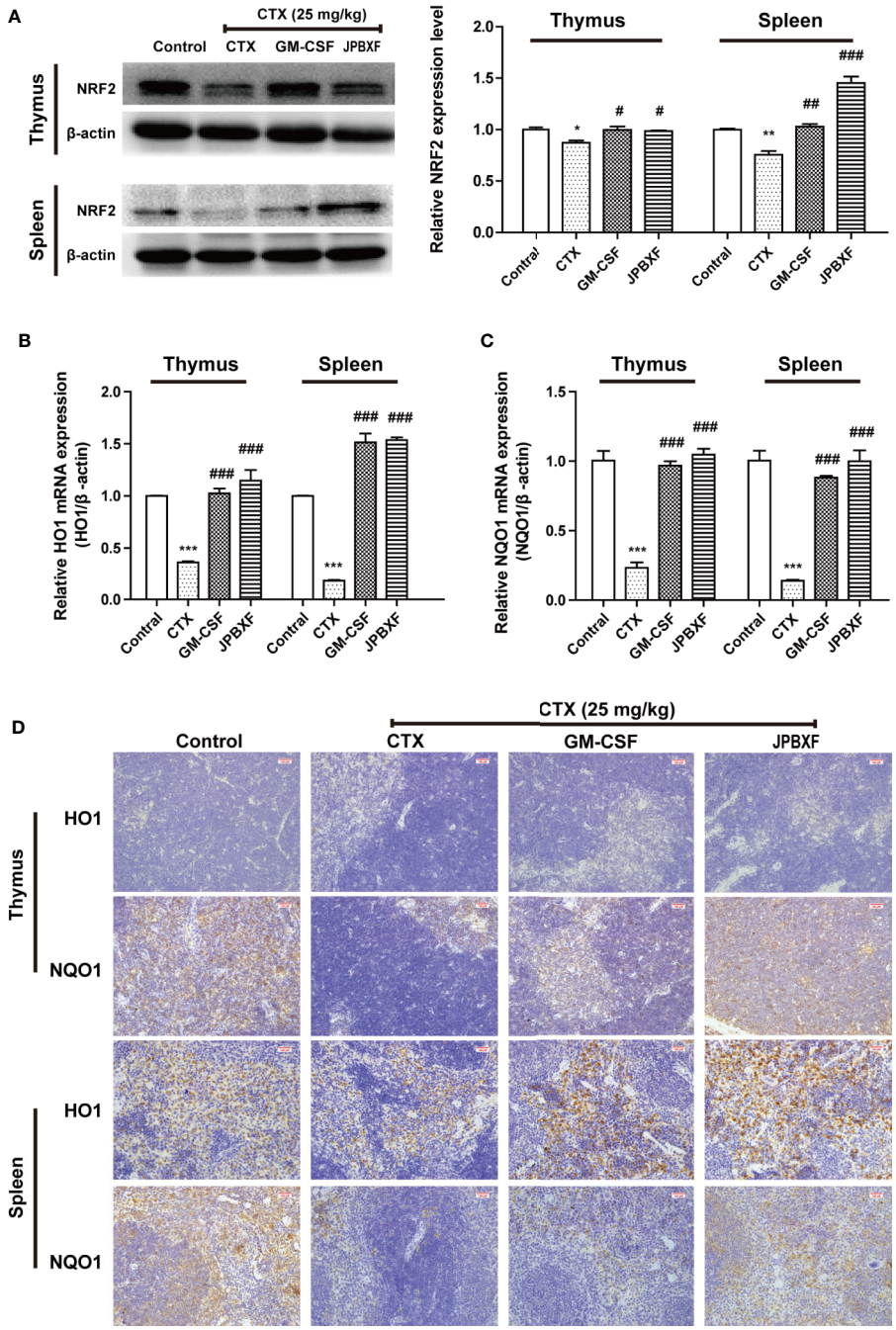

FIGURE 7 | JPBXF activated NRF2/HO1/NQO1 pathway. **(A)** Protein expressions of NRF2 in thymus or spleen tissues after treatments as design. mRNA expression levels of HO1**(B)** and NQO1 **(C)** were detected using real-time PCR analysis. **(D)** Images of HO1 and NQO1 protein expressions in thymus or spleen tissues were presented by immunohistochemistry. Data shown are means ± SD from day 13. $^{*}P < 0.05$, $^{**}P < 0.01$, $^{***}P < 0.001$ *vs.* Control, $^{\#}P < 0.05$, $^{\#\#}P < 0.01$, $^{\#\#\#}P < 0.001$ *vs.* CTX.

However, the main chemical constituents in JPBXF aqueous extract and the underline mechanisms of the main compounds on alleviating CTX-induced myelosuppression are still unclear. Herein, we identified main chemical constituents of JPBXF aqueous extract using UHPLC/MS/TOF and confirmed that the main constituents in JPBXF extracts are paeonol, liquiritin apioside, liquiritin, acteoside, naringin, isoacteoside, hesperidin, isoliquiritin apioside, isoliquiritin, licoricesaponine A3, liquiritigenin, calycosin, licoricesaponine G2, glycyrrhizic acid, formononetin, glycycoumarin,

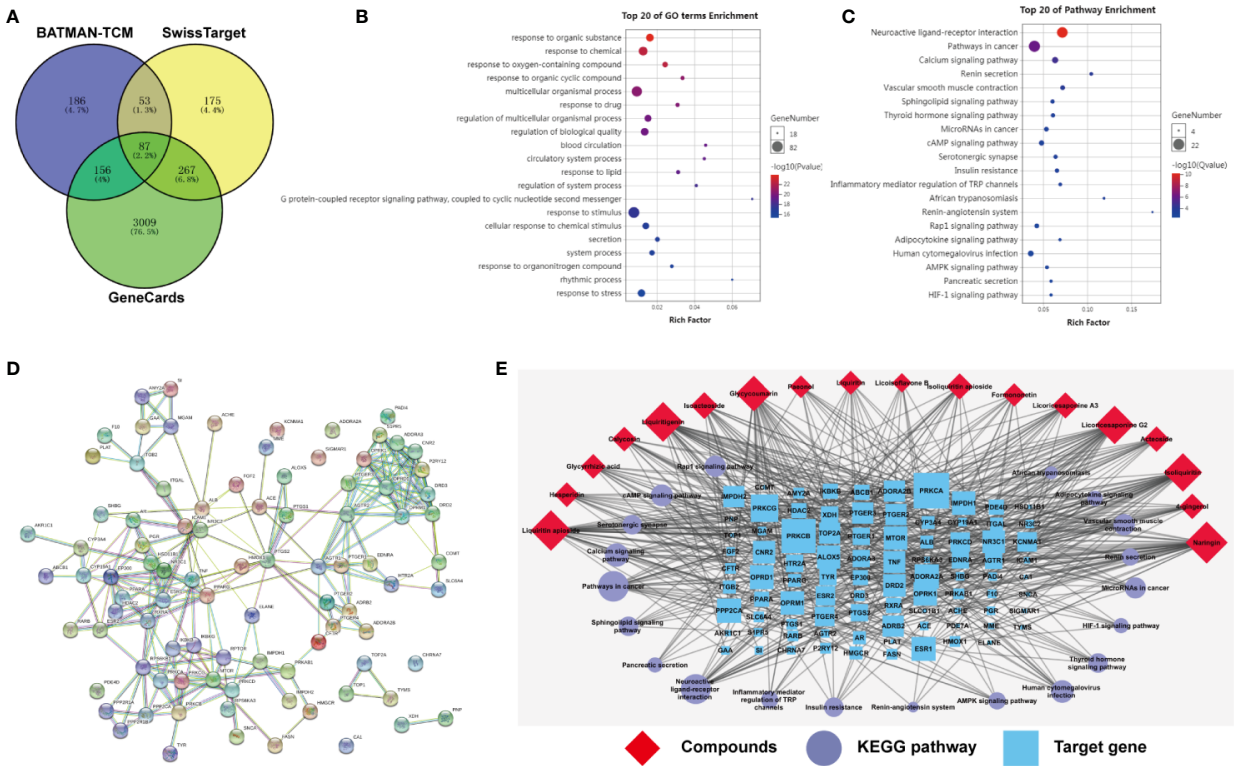

FIGURE 8 | Target prediction of eighteen compounds on alleviating myelosuppression. **(A)** The 87 potential target genes of eighteen compounds on myelosuppression were selected using Venny. **(B)** Gene ontology (GO) enrichment analysis of 87 selected genes performed by Database for Annotation, Visualization and Integrated Discovery (DAVID) and visualized by Omicshare. **(C)** KEGG enrichment analysis of 87 selected genes performed by DAVID and visualized by Omicshare. **(D)** The protein-protein interaction (PPI) network of 87 selected genes constructed by the STRING database. **(E)** The compound-target-pathway network was constructed and visualized by Cytoscape.

4-gingerol, and licoisoflavone B (**Figure 1** and **Table 1**). We also try to explain the underline mechanism by which 18 compounds on alleviating CTX-induced myelosuppression using bioinformatics analysis and found that 87 potential targets were primarily associated with the "response to organic substance," "response to chemical," "multicellular organismal process," "regulation of multicellular organismal process," and "regulation of biological quality" terms by targeting multi-protein network, such as "Neuroactive ligand-receptor interaction," "Pathways in cancer," "Calcium signaling pathway" "cAMP signaling pathway," and "Vascular smooth muscle contraction". Combining with the PPI network and the three-level network results, 24 identified genes, including AGTR2, PTGS2, MTOR, DRD2, EP300, OPRM1, AGTR1, DRD3, OPRD1, OPRK1, PPARG, PTGER3, RXRA, TNF, PRKCA, PRKCB, IMPDH1, PPP2CA, ESR1, ALOX5, CNR2, IMPDH2, NR3C1, and TOP2A (**Figure 8**), might be the key targets of 18 compounds in alleviating CTX-induced myelosuppression. To confirm these prediction results, more researches will be conducted in the future.

In conclusion, JPBXF can greatly reverse CTX-induced myelosuppression in C57BL/6 mice, especially in improving the blood and immune function through activating NRF2/HO1/NQO1 signaling pathway, which provides a reliable reference for JPBXF application in clinical. By recognizing 18 compounds in JPBXF aqueous extract and predicting the underline mechanism, our study would provide theoretical guidance for further research of JPBXF.

DATA AVAILABILITY STATEMENT

The raw data supporting the conclusions of this article will be made available by the authors, without undue reservation, to any qualified researcher.

ETHICS STATEMENT

The animal study was reviewed and approved by International Institute for Translational Chinese Medicine Animal Care and Use Committee, Guangzhou University of Chinese Medicine.

AUTHOR CONTRIBUTIONS

LL and XL designed the research. QH, LF, HL, and LZ performed the study. QH and LF analyzed the data and wrote the manuscript. ZL and QF revised the manuscript. XQ and YW provided technical support. All authors contributed to the article and approved the submitted version.

FUNDING

This work was supported by the projects of the National Natural Science Foundation of China [81720108033, 81930114, and 81874367], the Natural Science Foundation of Guangdong Province [2018B030322011], and the Natural Science Funds for Distinguished Young Scholar of Guangdong Province [2017A030306033].

REFERENCES

Botnick, L. E., Hannon, E. C., Vigneulle, R., and Hellman, S. (1981). Differential effects of cytotoxic agents on hematopoietic progenitors. *Cancer Res.* 41 (6), 2338–2342.

Bray, F., Ferlay, J., Soerjomataram, I., Siegel, R. L., Torre, L. A., and Jemal, A. (2018). Global cancer statistics 2018: GLOBOCAN estimates of incidence and mortality worldwide for 36 cancers in 185 countries. *CA Cancer J. Clin.* 68 (6), 394–424. doi: 10.3322/caac.21492

Carey, P. J. (2003). Drug-induced myelosuppression : diagnosis and management. *Drug Saf. Int. J. Med. Toxicol. Drug Exp.* 26 (26), 691–706. doi: 10.2165/00002018-200326100-00003

Chen, S., Wang, J., Fang, Q., Gao, R., Shi, Q., Zhang, H., et al. (2014). Upregulated heme oxygenase-1 expression of mouse mesenchymal stem cells resists to chemotherapy-induced bone marrow suppression. *Chin. Med. J. (Engl)* 127 (7), 1310–1316. doi: 10.3760/cma.j.issn.0366-6999.20133214

Cohen, I., Tagliaferri, M., and Tripathy, D. (2002). Traditional Chinese medicine in the treatment of breast cancer. *Semin. Oncol.* 29 (6), 563–574. doi: 10.1053/sonc.2002.50005

Dobos, G., and Tao, I. (2011). The model of Western integrative medicine: the role of Chinese medicine. *Chin. J. Integr. Med.* 17 (1), 11–20. doi: 10.1007/s11655-011-0601-x

Du, Z., Zhang, S., Lin, Y., Zhou, L., Wang, Y., Yan, G., et al. (2019). Momordicoside G Regulates Macrophage Phenotypes to Stimulate Efficient Repair of Lung Injury and Prevent Urethane-Induced Lung Carcinoma Lesions. *Front. Pharmacol.* 10, 321 doi: 10.3389/fphar.2019.00321

Feng, L., and Liu, X. (2015). Effects of Jianpi Buxue Decoction on EPO, TPO, and GM-CSF in Lewis Lung Cancer Mice Treated with Chemotherapy. *Trad. Chin. Drug Res. Clin. Pharmacol.* 26, 431–434. doi: 10.3969/j.issn.1003-9783.2015.04.002

Feng, L., Huang, Q., Huang, Z., Li, H., Qi, X., Wang, Y., et al. (2016). Optimized Animal Model of Cyclophosphamide-induced Bone Marrow Suppression. *Basic Clin. Pharmacol. Toxicol.* 119 (5), 428–435. doi: 10.1111/bcpt.12600

Gong, A. G., Lau, K. M., Zhang, L. M., Lin, H. Q., Dong, T. T., and Tsim, K. W. (2016). Danggui Buxue Tang, Chinese Herbal Decoction Containing Astragali Radix and Angelicae Sinensis Radix, Induces Production of Nitric Oxide in Endothelial Cells: Signaling Mediated by Phosphorylation of Endothelial Nitric Oxide Synthase. *Planta Med.* 82 (5), 418–423. doi: 10.1055/s-0035-1558332

Gutschalk, C. M., Heroldmende, C. C., Fusenig, N. E., and Mueller, M. M. (2006). Granulocyte Colony-Stimulating Factor and Granulocyte-Macrophage Colony-Stimulating Factor Promote Malignant Growth of Cells from Head and Neck Squamous Cell Carcinomas In vivo. *Cancer Res.* 66 (16), 8026–8036. doi: 10.1158/0008-5472.CAN-06-0158

Hamsa, T. P., and Kuttan, G. (2010). Ipomoea obscura ameliorates cyclophosphamide-induced toxicity by modulating the immune system and levels of proinflammatory cytokine and GSH. *Can. J. Physiol. Pharmacol.* 88 (11), 1042–1053. doi: 10.1139/Y10-086

Handolias, D., Quinn, M., Foo, S., Mileshkin, L., Grant, P., Dutu, G., et al. (2016). Oral cyclophosphamide in recurrent ovarian cancer. *Asia Pac. J. Clin. Oncol.* 12 (1), e154–e160. doi: 10.1111/ajco.12074

HAS, A. L., Alotaibi, M. F., Bin-Jumah, M., Elgebaly, H., and Mahmoud, A. M. (2019). Olea europaea leaf extract up-regulates Nrf2/ARE/HO-1 signaling and attenuates cyclophosphamide-induced oxidative stress, inflammation and apoptosis in rat kidney. *BioMed. Pharmacother.* 111, 676–685. doi: 10.1016/j.biopha.2018.12.112

Hayes, J. D., and Dinkova-Kostova, A. T. (2014). The Nrf2 regulatory network provides an interface between redox and intermediary metabolism. *Trends Biochem. Sci.* 39 (4), 199–218. doi: 10.1016/j.tibs.2014.02.002

Hill, B. T., Rybicki, L., Smith, S., Dean, R., Kalaycio, M., Pohlman, B., et al. (2011). Treatment with hyperfractionated cyclophosphamide, vincristine, doxorubicin, and dexamethasone combined with cytarabine and methotrexate results in poor mobilization of peripheral blood stem cells in patients with mantle cell lymphoma. *Leuk. Lymphoma* 52 (6), 986–993. doi: 10.3109/10428194.2010.551154

Hubner, J., Prott, F. J., Micke, O., and Munstedt, K. (2015). [Complementary medicine and cancer]. *Dtsch Med. Wochenschr* 140 (10), 768–769. doi: 10.1055/s-0041-102202

Jantunen, E., Putkonen, M., Nousiainen, T., Pelliniemi, T. T., Mahlamaki, E., and Remes, K. (2003). Low-dose or intermediate-dose cyclophosphamide plus granulocyte colony-stimulating factor for progenitor cell mobilisation in patients with multiple myeloma. *Bone Marrow Transplant.* 31 (5), 347–351. doi: 10.1038/sj.bmt.1703840

Konkimalla, V. B., and Efferth, T. (2008). Evidence-based Chinese medicine for cancer therapy. *J. Ethnopharmacol.* 116 (2), 207–210. doi: 10.1016/j.jep.2007.12.009

Miller, R. C., and Steinbach, A. (2014). Growth factor use in medication-induced hematologic toxicity. *J. Pharm. Pract.* 27 (5), 453–460. doi: 10.1177/0897190014546113

Neboh, E. E., and Ufelle, S. A. (2015). Myeloprotective activity of crude methanolic leaf extract of Cassia occidentalis in cyclophosphamide-induced bone marrow suppression in Wistar rats. *Adv. Biomed. Res.* 4 (5), 5–5. doi: 10.4103/2277-9175.148285

Potti, A., Dressman, H. K., Bild, A., Riedel, R. F., Chan, G., Sayer, R., et al. (2011). Retraction: Genomic signatures to guide the use of chemotherapeutics. *Nat. Med.* 17 (1), 135. doi: 10.1038/nm0111-135

Que, L., He, L., Yu, C., Yin, W., Ma, L., Cao, B., et al. (2016). Activation of Nrf2-ARE signaling mitigates cyclophosphamide-induced myelosuppression. *Toxicol. Lett.* 262, 17–26. doi: 10.1016/j.toxlet.2016.09.003

Salva, S., Marranzino, G., Villena, J., Aguero, G., and Alvarez, S. (2014). Probiotic Lactobacillus strains protect against myelosuppression and immunosuppression in cyclophosphamide-treated mice. *Int. Immunopharmacol.* 22 (1), 209–221. doi: 10.1016/j.intimp.2014.06.017

Sedgmen, B. J., Papalia, L., Wang, L., Dyson, A. R., McCallum, H. A., Simson, C. M., et al. (2013). Ex vivo restimulation of human PBMC expands a CD3 +CD4-CD8- gammadelta+ T cell population that can confound the evaluation of CD4 and CD8 T cell responses to vaccination. *Clin. Dev. Immunol.* 2013, 186420. doi: 10.1155/2013/186420 2013.

Strati, P., Wierda, W., Burger, J., Ferrajoli, A., Tam, C., Lerner, S., et al. (2013). Myelosuppression after frontline fludarabine, cyclophosphamide, and rituximab in patients with chronic lymphocytic leukemia: analysis of persistent and new-onset cytopenia. *Cancer* 119 (21), 3805–3811. doi: 10.1002/cncr.28318

Tachi, T., Teramachi, H., Tanaka, K., Asano, S., Osawa, T., Kawashima, A., et al. (2015). The Impact of Outpatient Chemotherapy-Related Adverse Events on the Quality of Life of Breast Cancer Patients. *PloS One* 10 (4), e0124169. doi: 10.1371/journal.pone.0124169

Traverso, I., Fenoglio, D., Negrini, S., Parodi, A., Battaglia, F., Kalli, F., et al. (2012). Cyclophosphamide inhibits the generation and function of CD8(+) regulatory T cells. *Hum. Immunol.* 73 (3), 207–213. doi: 10.1016/j.humimm.2011.12.020

Wang, J., Tong, X., Li, P., Cao, H., and Su, W. (2012). Immuno-enhancement effects of Shenqi Fuzheng Injection on cyclophosphamide-induced

immunosuppression in Balb/c mice. *J. Ethnopharmacol.* 139 (3), 788–795. doi: 10.1016/j.jep.2011.12.019

Woo, S. M., Choi, Y. K., Kim, A. J., Yun, Y. J., Shin, Y. C., Cho, S. G., et al. (2016). Sip-jeon-dea-bo-tang, a traditional herbal medicine, ameliorates cisplatin-induced anorexia via the activation of JAK1/STAT3-mediated leptin and IL-6 production in the fat tissue of mice. *Mol. Med. Rep.* 13 (4), 2967–2972. doi: 10.3892/mmr.2016.4889

Zhang, M., Liu, X., Li, J., He, L., Qiu, M., and Tripathy, D. (2007). Chinese medicinal herbs to treat the side-effects of chemotherapy in breast cancer patients. *Cochrane Database Syst. Rev.* 18 (2), CD004921. doi: 10.1002/14651858.CD004921.pub2

Zhang, S., Zhou, L., Zhang, M., Wang, Y., Wang, M., Du, J., et al. (2019). Berberine Maintains the Neutrophil N1 Phenotype to Reverse Cancer Cell Resistance to Doxorubicin. *Front. Pharmacol.* 10, 1658. doi: 10.3389/fphar.2019.01658

Zhao, N., Wang, L., Mou, H. Y., Liang, M., and Yue, W. (2009). [Synergism and attenuation effects of taurine on cyclophosphamide]. *Ai Zheng* 28 (3), 244–248. doi: 10.3321/j.issn:1000-467X.2009.03.004

Conflict of Interest: The authors declare that the research was conducted in the absence of any commercial or financial relationships that could be construed as a potential conflict of interest.

Copyright © 2020 Huang, Feng, Li, Zheng, Qi, Wang, Feng, Liu, Liu and Lu. This is an open-access article distributed under the terms of the Creative Commons Attribution License (CC BY). The use, distribution or reproduction in other forums is permitted, provided the original author(s) and the copyright owner(s) are credited and that the original publication in this journal is cited, in accordance with accepted academic practice. No use, distribution or reproduction is permitted which does not comply with these terms.

frontiers in Pharmacology

ORIGINAL RESEARCH
published: 15 September 2020
doi: 10.3389/fphar.2020.546825

Huoxue Huatan Decoction Ameliorates Myocardial Ischemia/Reperfusion Injury in Hyperlipidemic Rats *via* PGC-1α–PPARα and PGC-1α–NRF1–mtTFA Pathways

Fei Lin[1†], Yu-Qing Tan[2,3†], Xuan-Hui He[2], Li-Li Guo[2], Ben-Jun Wei[4], Jun-Ping Li[2], Zhong Chen[2], Heng-Wen Chen[2] and Jie Wang[2*]*

[1] Heart Center of Xinxiang Medical University, The First Affiliated Hospital of Xinxiang Medical University, Xinxiang, China, [2] Department of Cardiology, Guang'anmen Hospital, China Academy of Chinese Medical Sciences, Beijing, China, [3] Graduate School, Beijing University of Chinese Medicine, Beijing, China, [4] Key Laboratory of Ministry of Education Department of Lanzhou Province and Dunhuang Medical Transformation, Gansu University of Chinese Medicine, Lanzhou, China

OPEN ACCESS

Edited by:
Hai Yu Xu,
China Academy of Chinese Medical Sciences, China

Reviewed by:
Giuseppe Antonio Malfa,
University of Catania, Italy
Yong Wang,
Beijing University of Chinese Medicine, China

***Correspondence:**
Heng-Wen Chen
chenhengwen@163.com
Jie Wang
jiewang1001@126.com

[†]These authors have contributed equally to this work

Specialty section:
This article was submitted to Ethnopharmacology, a section of the journal Frontiers in Pharmacology

Received: 30 March 2020
Accepted: 28 August 2020
Published: 15 September 2020

Citation:
Lin F, Tan Y-Q, He X-H, Guo L-L, Wei B-J, Li J-P, Chen Z, Chen H-W and Wang J (2020) Huoxue Huatan Decoction Ameliorates Myocardial Ischemia/Reperfusion Injury in Hyperlipidemic Rats via PGC-1α–PPARα and PGC-1α–NRF1–mtTFA Pathways. Front. Pharmacol. 11:546825. doi: 10.3389/fphar.2020.546825

Objective: The aim of this study was to eluc\idate the preventive and therapeutic effects and the underlying mechanisms of Huoxue Huatan Decoction (HXHT) on myocardial ischemia/reperfusion (I/R) injury in hyperlipidemic rats.

Methods: An I/R model was established in hyperlipidemic Wistar rats. After 4–8 weeks of HXHT treatment, the physical signs of rats were observed. Lipid metabolism, myocardial enzyme spectrum, cardiac function, myocardial histomorphology, and mitochondrial biosynthesis were investigated by a biochemical method, ultrasonography, electron microscopy, pathological examination, real-time PCR, and Western blot.

Results: HXHT can affect lipid metabolism at different time points and significantly reduce the levels of cholesterol (CHO), triglyceride (TG), high-density lipid-cholesterol (HDL-C), and low-density lipid-cholesterol (LDL-C) in hyperlipidemic rats ($P < 0.05$ or $P < 0.01$); it can significantly reduce the levels of creatine kinase-MB (CK-MB) and lactate dehydrogenase (LDH), reduce the myocardial infarct size and myocardial ischemic area, and improve cardiac function. The results of myocardial histomorphology showed that HXHT could protect myocardial cells, relieve swelling, reduce the number of cardiac lipid droplets, and improve myocardial mitochondrial function. HXHT could significantly increase the levels of total superoxide dismutase (T-SOD) and succinate dehydrogenase (SDH) ($P < 0.05$ or $P < 0.01$), increase CuZn-superoxide dismutase (CuZn-SOD) and glutathione-peroxidase (GSH-Px) levels, and decrease the levels of malondialdehyde (MDA) ($P < 0.05$); it could increase the mRNA and protein expression levels of peroxisome proliferator-activated receptor-gamma coactivator 1 alpha (PGC-1α), peroxisome proliferator-activated receptor alpha (PPARα), nuclear respiratory factor 1 (NRF1), and mitochondrial transcription factor A (mtTFA) ($P < 0.05$ or $P < 0.01$), and increase the synthesis of mitochondrial DNA (mtDNA) ($P < 0.01$).

Conclusion: HXHT can reduce myocardial I/R injury in hyperlipidemic rats. The protective mechanisms may involve a reduction in blood lipids, enhancement of PGC-1α–PPARα pathway activity, and, subsequently, an increase in fatty acid β-oxidation, which may provide the required input for mitochondrial energy metabolism. HXHT can additionally enhance PGC-1α–NRF1–mtTFA pathway activity and, subsequently, increase the antioxidant capacity, promote mtDNA synthesis, and reduce mitochondrial damage. The two pathways use PGC-1α as the intersection point to protect mitochondrial structure and function, reduce I/R-induced injury, and improve cardiac function.

Keywords: Huoxue Huatan Decoction, hyperlipidemia, ischemia/reperfusion (I/R), mitochondria, PGC-1α

Coronary heart disease refers to heart disease caused by hypoxia and ischemia of the myocardium due to arterial obstruction or stenosis, which is a common type of disease caused by coronary atherosclerosis (Benjamin et al., 2018). Hyperlipidemia is closely related to the risk of coronary heart disease. At present, 50.0% of patients in China have hypertension, of whom 37.5% have coronary heart disease and more than 30.0% have peripheral arterial disease (Chen et al., 2014). The risk factors of cardiovascular disease can be broadly divided into two categories, i.e., intervenable and non-intervenable. Intervenable factors include lifestyle (smoking, blood pressure, blood sugar, and cholesterol) and medication, non-intervenable factors include age, gender, race, and family history (Derosa et al., 2020).

A high-fat diet, as a common intervenable factor, can lead to lipid accumulation, induce the inflammatory response, promote atherosclerosis, and accelerate the development of cardiovascular diseases (Cao et al., 2018). Specifically, a high-fat diet can increase plasma low-density lipoprotein (LDL) levels. LDL is oxidized and modified into oxidized LDL (Ox-LDL). Monocytes take up Ox-LDL, and the expression of adhesion molecules increases. A high-fat diet promotes the conversion of monocytes into foam cells, which is a key step in the development of atherosclerosis (Henning et al., 2018). Chronic arterial inflammation plays an important role in the pathogenesis of atherosclerosis. The secretion of atherogenic cytokines induces the expression of endothelial adhesion molecules, which mediate the attachment of monocytes and lymphocytes (Ham et al., 2019). Atherosclerosis results in thickening of the vessel wall and a reduction of lumen diameter and blood flow. The current guidelines mainly focus on the treatment of hyperlipidemia, with LDL and cholesterol levels as the main indicators (Okopień et al., 2016), and the ultimate goal is to reduce the risk of atherosclerotic cardiovascular disease. The main ways of lowering lipids are lifestyle regulation and pharmacological lipid-lowering. Studies have shown that reducing LDL-cholesterol (LDL-C) and triglyceride (TG) levels, reducing the intake of saturated fatty acids and refined carbohydrates, and increasing the intake of fruits, vegetables, cereals, and low-fat dairy products can reduce the risk of cardiovascular events and prevent coronary plaque progression. It is important to focus on whole foods and eating habits to successfully reduce the risk of cardiovascular disease (Alissa and Ferns, 2017; Welty, 2020). Pharmacological treatment is still mainly based on statins and targeted at LDL-C (Han et al., 2019).

Traditional Chinese medicine has a rich clinical history of coronary heart disease and dyslipidemia treatment. Coronary heart disease accompanied by elevated blood lipids or obesity is classified as coronary heart disease with phlegm–blood stasis syndrome, and both TG and LDL-C levels are significantly increased in patients with coronary heart disease with phlegm–blood stasis syndrome (Wang et al., 2008). The only patented medicines for the treatment of coronary heart disease with phlegm–blood stasis syndrome in China are Danlou tablets (The cardiovascular disease branch of China Association of Chinese Medicine, 2019). Mitochondria, as semi-autonomous organelles, are known as "enzyme bags" and "power plants." They are the main sites for the biological oxidation of sugars, proteins, and fats. Myocardial cells have a high demand for energy, and mitochondria account for approximately 40% (m/m) of cardiomyocytes. Abnormal structure and function of mitochondria directly affect myocardial energy metabolism, oxidative stress, ion uptake and release, and apoptosis (Goldenthal, 2016).

Huoxue Huatan Decoction (HXHT) is a commonly prescribed medicine for the treatment of coronary heart disease with phlegm–blood stasis syndrome, and has been used clinically for more than 20 years. It is composed of *Salvia miltiorrhiza* Bunge, *Astragalus mongholicus* Bunge, *Panax notoginseng* (Burkill) F.H. Chen, *Ginkgo biloba* L., *Trichosanthes kirilowii* Maxim., *Allium macrostemon* Bunge, and *Ziziphus jujuba* Mill. HXHT has the effects of invigorating qi and activating blood, resolving phlegm, and removing blood stasis.

The main components of *S. miltiorrhiza* Bunge are tanshinone IIA and *S.* miltiorrhiza polyphenols, which have antioxidant, anti-inflammatory, anticoagulant, anti-atherosclerosis, and vasodilator effects. They can also protect the myocardium and vascular endothelium, reduce adipogenesis, and reduce the proliferation and migration of vascular smooth muscle cells (Ren et al., 2019; Yuan et al., 2020). Astragaloside IV is the main active ingredient of *A. mongholicus* Bunge. It has protective effects on ischemic injury and cardiovascular disease. It has anti-inflammatory, immunomodulatory, and antioxidant effects, and exerts cardioprotective effects through multiple signaling pathways (Li et al., 2017). The main active ingredient of *P. notoginseng* (Burkill) F.H. Chen is *P. notoginseng* saponins, and its pharmaceutical preparations, such as Xueshuantong, Xuesaitong, and Naodesheng, are widely used and have cardiovascular protective effects. *P. notoginseng* saponins can reduce the formation of

atherosclerotic lesions (Liu et al., 2019; Liu et al., 2020). *G. biloba* L. can effectively improve metabolic syndrome, diabetes, hypertension, and dyslipidemia, reduce the risk of cardiovascular disease (Eisvand et al., 2020), and alleviate vascular aging-related dysfunction (Li et al., 2020). *T. kirilowii* Maxim. and *A. macrostemon* Bunge often appear as a pair in commonly used drugs, which are essential for the treatment of angina pectoris, heart failure, and myocardial infarction. *T. kirilowii* Maxim. can protect the myocardium and endothelial cells, eliminates phlegm, and has anti-oxidation, anticoagulation, and anti-inflammatory effects (Yu et al., 2018). *A. macrostemon* Bunge is a potential drug to treat hyperglycemia, hyperlipidemia, and visceral obesity (Xie et al., 2008), and can also reduce myocardial ischemic injury by regulating abnormal energy metabolism (Li et al., 2014). *Z. jujuba* Mill. has sedative and hypnotic effects, and it is clinically used to treat insomnia, forgetfulness, and dizziness. In addition, it also has anti-inflammatory, anti-oxidation, blood pressure-lowering, and blood lipid-lowering effects (He et al., 2020), and it can protect myocardial cells from acute cardiac ischemia/reperfusion (I/R) injury (Gu et al., 2019). The compatibility of the whole prescription is reasonable, it has immune regulatory effects, and it can protect myocardial cells from ischemia and hypoxia. Previous clinical and experimental studies have shown that this prescription can significantly improve the clinical symptoms of patients with coronary heart disease with phlegm–blood stasis syndrome, with good safety (Li, 2016; Zhang et al., 2016).

Therefore, in this study, we analyze the effects of HXHT on myocardial I/R injury in hyperlipidemic rats from the perspectives of lipid metabolism, the myocardial enzyme spectrum, myocardial histomorphology, and myocardial infarct size. In addition, the underlying mechanisms of HXHT in preventing and treating myocardial I/R in hyperlipidemic rats are studied from the perspectives of myocardial mitochondrial function and the expression of genes related to mitochondrial biogenesis.

MATERIALS AND METHODS

Preparation of Experimental Drugs

HXHT was provided by the Pharmacology Laboratory of Traditional Chinese Medicine, Guang'anmen Hospital, China Academy of Chinese Medical Science. It is composed of *S. miltiorrhiza* Bunge (17.4%, Specimen ID 33873, product batch number 140381391), *A. mongholicus* Bunge (7.0%, Specimen ID 106823, product batch number 140581231), *P. notoginseng* (Burkill) F.H. Chen (17.4%, Specimen ID 69689, product batch number 140581091), *G. biloba* L. (11.6%, Specimen ID 4988, product batch number 140581421), *T. kirilowii* Maxim. (17.4%, Specimen ID 15439, product batch number 140281611), *A. macrostemon* Bunge (17.4%, Specimen ID 50154, product batch number 140580301), and *Z. jujuba* Mill. (11.6%, Specimen ID 27570, product batch number 140581941) (**Table 1**). All of the medicinal names have been unified using the Kew Medicinal Plant Names Service. All of the specimens have been deposited in the Chinese National Herbarium, Institute of Botany, Chinese Academy of Sciences (20 Nanxincun, Xiangshan, Beijing 100093, China). All of the medicinal materials were provided by Beijing Kangmei Pharmaceutical Co., Ltd. (Beijing, China).

S. miltiorrhiza Bunge was extracted 10 times with 60% ethanol through heating reflux twice, each time for 1.5 h. The ethanol was recovered from the extract and concentrated to thick paste (50°C, density 1.20 g/cm^3) under reduced pressure, and the concentrated solution was separated twice using an AB-8 macroporous adsorption resin column (Tianjin NANDA Resin Technology Co., Ltd.), where 50% ethanol of the same volume as the column bed was used for elution. The eluate was concentrated into a thick paste (50°C, density 1.20 g/cm^3), and dried in vacuum at 60°C to obtain the *S. miltiorrhiza* Bunge extract. The leaves of *Ginkgo biloba* L. were extracted 8 times with 60% ethanol through heating reflux twice, each time for 2 h. After vacuum concentration, the concentrated solution was separated three times using an AB-8 macroporous adsorption resin column, where 70% ethanol of the same volume as the column bed was used for elution. The eluate was concentrated into a thick paste (50°C, density 1.20 g/cm^3), and dried in vacuum at 60°C to obtain the *Ginkgo biloba* L. extract. Then 10 volumes of water were added to the remaining material, and the medicine was extracted twice, concentrated (50°C, density 1.20 g/cm^3), and dried in vacuum at 60°C. Finally, all the extracts were crushed and mixed to obtain the HXHT extract.

The contents of active ingredients were 12.66% for tanshinone IIA, 9.25% for cryptotanshinone, 34.51% for salvianolic acid B, 5.30% for salvianolic acid A sodium, 1.64% for rosmarinic acid, 0.66% for protocatechuic aldehyde, 1.02% for ginsenoside Rg1, 0.90% for ginsenoside Rb1, 0.20% for

TABLE 1 | The composition of traditional Chinese medicine in Huoxue Huatan Decoction (HXHT).

Component	Component (Chinese)	Medicinal parts	Percentage (%)	Active ingredient content (%)
Salvia miltiorrhiza Bunge	Danshen	Dry roots and rhizomes	17.4	tanshinone IIA 0.31%, cryptotanshinone 0.25%, salvianolic acid B 3.44%
Astragalus mongholicus Bunge	Huangqi	Dry roots	7.0	astragaloside IV 0.06%, calycosin glucoside 0.04%
Panax notoginseng (Burkill) F.H. Chen	Sanqi	Dry roots and rhizomes	17.4	ginsenoside Rg1 5.26%, ginsenoside Rb1 4.00%, notoginsenoside R1 1.09%
Ginkgo biloba L.	Yinxingye	Dry leaves	11.6	total flavonols 0.41%, total lactones 0.27%
Trichosanthes kirilowii Maxim.	Gualou	Dry ripe fruit	17.4	–
Allium macrostemon Bunge	Xiebai	Dry bulb	17.4	–
Ziziphus jujuba Mill.	Suanzaoren	Dry mature seeds	11.6	jujuboside A 0.08% spinosin 0.13%

notoginsenoside R1, 0.12% for ginsenoside Re, 25.81% for *G. biloba* total flavonols, 7.01% for *G. biloba* total lactones, 0.29% for the total saponins of *Z. jujuba* Mill., 0.10% for calycosin glucoside, and 0.10% for astragaloside IV (Lin, 2015). All of the components were tested by HPLC (Agilent 1100, Agilent Technologies, Inc., CA, USA). The conditions for the measurement of all of the components and HPLC spectra are shown in **Figures 1–23** in Part 1 of the **Supplementary Materials**. As positive controls, we used a traditional Chinese medicine (Danlou tablets, 0.3 g/tablet, product batch number: 20140605, Jilin Cornell Pharmaceutical Co., Ltd.) and a Western medicine (Atorvastatin calcium tablets, 20 mg/tablet, product batch number: J28283, sub-packaging batch number: J70319, Pfizer Pharmaceuticals LLC, Pfizer Pharmaceutical Co., Ltd., imported sub-packages).

Wistar Rats

Male SPF Wistar rats ($N = 168$, weight 140 ± 10 g) were provided by Beijing Vital River Laboratory Animal Technology Co., Ltd., production license No. SCXK (Beijing) 2012-0001. The research protocol was approved by the Animal Ethics Committee of Guang'anmen Hospital of China Academy of Chinese Medicine (No. 2015EC035-02). In accordance with the Guide for the Care and Use of Laboratory Animals of the National Institutes of Health (Bethesda, MD, USA), they were raised indoors by the Animal Feeding Center of Guang'anmen Hospital, China Academy of Chinese Medical Sciences, at a constant temperature and with good ventilation, and they were fed with standard feed, with free access to food and water.

Preparation of High-Fat Feed

The high-fat feed contained 78.8% of ordinary feed, 1% of cholesterol, 10% of yolk powder, 10% of lard, and 0.2% of bile salt (People's Republic of China Ministry of Health, 2003). The nutritional composition of high-fat feed, provided by Beijing Huafukang Biotechnology Co., Ltd., is shown in **Table 2**.

Establishment of the I/R Injury Model in Hyperlipidemic Animals

After 3 days of quarantine, Wistar rats were randomly divided into the following seven groups ($n = 24$ rats per group): (i) healthy control group (Normal), (ii) hyperlipidemia model group (Model), (iii) Western medicine (Atorvastatin calcium tablets, 3.33 mg/kg) positive control group (Control A), (iv) traditional Chinese medicine (Danlou tablets, 0.75 g/kg) positive control group (Control B), (v) high-dose HXHT (3.6 g/kg, equivalent to 20.06 g/kg of the original medicinal material) group (HXHT-H), (vi) medium-dose HXHT (1.8 g/kg, equivalent to 10.03 g/kg of the original medicinal material) group (HXHT-M), and (vii) low-dose HXHT (0.9 g/kg, equivalent to 5.02 g/kg of the original medicinal material) group (HXHT-L). The calculation was based on the body surface area of humans and rats. HXHT was suspended in a 0.5% sodium carboxymethylcellulose aqueous solution (carboxymethyl cellulose nanoparticles, size 300–800 mpa·s, batch number: 20081023, manufacturer Sinopharm Chemical Reagent Co., Ltd.).

TABLE 2 | Nutrient composition of high-fat feed.

Nutrient composition	Ordinary feed (%)	High-fat feed (%)
Crude protein	20.16	18.89
Crude fat	4.24	19.34
Crude fiber	4.48	3.53
Coarse ash	6.04	4.76
Moisture	10	8.39
Calcium	1.29	1.02
Phosphorus	0.83	0.65

The Normal group was fed with ordinary feed, and the other groups were fed with high-fat feed. The rats were kept indoors with four animals per cage, at a constant temperature and under good ventilation, and they were fed with standard feed, with free access to food and water. After 4 weeks of feeding, the serum TG and LDL levels in all six high-fat groups were significantly increased compared with the Normal group. The Model group and the five treatment groups were appropriately adjusted according to the statistical results of cholesterol (CHO) and LDL levels, so that the mean values were as similar as possible. After these initial 4 weeks ($t = 0$), rats from the treatment groups were administered once a day a volume of 10 ml/kg for 4 or 8 weeks. The Normal and Model groups were simultaneously treated with an equal amount of 0.5% sodium carboxymethyl cellulose aqueous solution (10 ml/kg). Blood samples were collected from the eyeballs at the 4th, 6th, and 8th weeks to analyze biochemical indicators of blood lipids.

To establish the I/R model, the left anterior descending coronary artery of rats was ligated for 40 min (Liu et al., 2011; Du et al., 2014) and the blood flow was restored for 2 h, at the 4th and 8th weeks. The specific method was as follows.

① After weighing the rats, they were anesthetized with 10% chloral hydrate (330 mg/kg) (product batch number: 20130201, Sinopharm Chemical Reagent Co., Ltd.) by intraperitoneal injection. The rats were fixed on the operating table, the skin was prepared for disinfection, the tracheal tube was inserted, and the physiological signal acquisition system was connected.

② After tracheal intubation, the small animal ventilator was connected with a ventilator frequency of 70 breaths/min, a tidal volume of 8 ml, and a respiratory ratio of 1:3 for assisted respiration.

③ The third rib was cut at 0.5 cm from the left sternal border, the musculature was dissected, the thorax was opened with an eyelid opener to expose the heart, the needle was inserted 2–3 mm from the lower edge of the left atrial appendage with a 3/8 round needle pierced with a 4-0 suture and hooked around the main trunk of the left anterior descending coronary artery, and the needle was withdrawn from the pulmonary conus. A polyethylene tube was cut and placed between the two sutures, the sutures were tightened to form a closed loop, and reperfusion occurred by cutting the sutures 40 min later.

④ Successful criteria of model establishment were the following: the ST segment arch was elevated after ligation; the color of the ligation site was grayish or cyanotic; the ST segment regressed or was elevated after reperfusion; or the color of the ligation site changed from grayish to normal bright red.

⑤ During the whole process of myocardial I/R, a PowerLab physiological signal acquisition system was used to monitor electrocardiograms (ECGs) intermittently, and ECGs were continuously recorded before and after coronary artery ligation and after reperfusion. ST elevation was closely observed and recorded at the same time.

Detection of Biochemical Indicators of Blood Lipids in Rats

Blood samples were collected from the retro-orbital venous plexus of the rats before treatment (at $t = 0$) and after 4, 6, and 8 weeks. Blood samples were stored at room temperature for 30 min and centrifuged at 3,000 rpm for 15 min to obtain serum. Four biochemical indicators of blood lipids were measured. The detection of CHO was performed using an enzymatic method (batch number: AUZ1433); the GPO-POD method was used for detection of TG (batch number: OSR61118E); high-density lipoprotein-cholesterol (HDL-C) levels were measured by an enzymatic method (batch number: OSR6287); and LDL-C levels were measured using an LDL-C enzymatic colorimetric assay kit (batch number: OSR6283), These kits were provided by Beckman Coulter Laboratories (Suzhou) Co., Ltd.

Detection of CK-MB and LDH

Hyperlipidemic rats were anesthetized with 10% chloral hydrate (280 mg/kg) after 4 and 8 weeks, the skin was prepared, the trachea was intubated and connected to a ventilator, the chest was opened, the left coronary artery was ligated with a 4-0 sterile suture for 40 min, and perfusion was restored, while performing ECG monitoring. After 2 h of reperfusion, blood was collected from the intraocular canthus, stored for 30 min at room temperature, and centrifuged at 3,000 rpm for 15 min to obtain serum. The serum was diluted 20 times with purified water, and the creatine kinase-MB (CK-MB) and lactate dehydrogenase (LDH) levels were measured with an AU640 automatic biochemical analyzer. LDH was detected with an LDH lactate substrate assay kit (batch number: AUZ1443, Beckman Coulter Laboratories (Suzhou) Co., Ltd.); CK-MB was detected with a CK-MB enzymatic immunosuppression test kit (batch number: OSR61155, Beckman Coulter Laboratories (Suzhou) Co., Ltd.).

Cardiac Function

After 4 or 8 weeks, the left coronary artery was ligated for 40 min, and reperfusion was allowed for 2 h. The rats were anesthetized with 10% chloral hydrate (280 mg/kg), prepared for skin disinfection, and fixed on the back. The left ventricular ejection fraction (LVEF), left ventricular end-diastolic inner diameter (LVIDd), left ventricular end-systolic inner diameter (LVIDs), and other cardiac function parameters were measured by DW-350 B-mode echocardiography (Dawei Electronic Equipment Co. Ltd., Xuzhou, JS, CHN).

Calculation of Infarct Area and Ischemic Area

After 4 or 8 weeks, hyperlipidemic rats were anesthetized with 10% chloral hydrate (280 mg/kg), the left coronary artery was ligated for 40 min, and reperfusion was allowed for 2 h. The thoracic cavity was opened, the heart was exposed, the left anterior branch of the coronary artery was re-ligated along the suture, and 0.5% Evans blue (Yang et al., 2009) was intravenously injected in the left lung. The heart was stained blue about 2 min later. The heart was removed, rinsed with normal saline, frozen at −20°C, stained, and photographed using TTC. For statistical analysis, the Evans blue-stained blue area was considered as the normal area, the TTC-stained red area as the ischemic area, and the grayish white area as the infarct area. Photographs were taken with Canon PowerShot A2600 (after 4 weeks) and L2035AW Pioneer (after 8 weeks) cameras, and the myocardial ischemic, infarct, and global areas were analyzed with Image-Pro Plus 6.0 software. The ratio of the ischemic area to the global area and the ratio of the infarct area to the global area were calculated.

Standard Operating Procedures for Pathological Staining

After 8 weeks, rats in the Normal, Model, Control A, and HXHT-M groups with better pharmacodynamic results were selected for histomorphological and molecular biological mechanism studies based on the previous experimental results. Rats in each group were subjected to myocardial ischemia for 40 min. After 2 h of reperfusion, they were anesthetized with 10% chloral hydrate mixture (280 mg/kg) and thoracotomy was performed. The hearts of the rats were removed and placed on ice, and 3 × 3 mm sized samples from the apical site were rapidly taken and fixed with 3% glutaraldehyde for sectioning. The mitochondrial ultramicrostructure in the infarct tissue was observed by transmission electron microscopy, with the assistance of the Peking University School. The 0.3 cm of myocardium below the ligature was fixed with 4% paraformaldehyde for He staining (Chen et al., 2018), another ~0.3 cm of myocardium was rapidly frozen for Oil Red O staining (Wen et al., 2019), and the rest was stored in a −80°C freezer.

Detection of Oxidative Stress Indicators

After 8 weeks, after myocardial ischemia for 40 min and reperfusion for 2 h, and after anesthesia with 10% chloral hydrate (280 mg/kg), about 5 ml of blood was collected from the abdominal aorta. The artery was immediately clamped with the hemostatic forceps. The blood was allowed to stand for 40 min and centrifuged at 3,500 rpm for 10 min, and the serum was separated and stored in a −80°C freezer until analysis. The myocardial tissue samples were collected as described in the part of Standard Operating Procedures for Pathological Staining. The contents of malondialdehyde (MDA), total superoxide dismutase (T-SOD), CuZn-superoxide dismutase (CuZn-SOD), and glutathione peroxidase (GSH-Px) in rat serum and reactive oxygen species (ROS), succinate dehydrogenase (SDH), and cytochrome c oxidase (COX) in myocardial tissue were measured following the manufacturers' instructions of the respective kits (MDA kit, batch number: 20150118, T-SOD kit, batch number: 20150312, Nanjing Jiancheng Biotechnology Co., Ltd.; CuZn-SOD kit, batch number: 20150204, Shanghai Youniko Co., Ltd.; GSH-Px kit, batch number: 20150206,

Shanghai Youniko Co., Ltd.; ROS kit, batch number: GMS10096.2, Shanghai Jiemei Biological Gene Pharmaceutical Technology Co., Ltd.; SDH kit, batch number: 20150116, Nanjing Jiancheng Biotechnology Co., Ltd.; and COX kit, batch number: GMS10014.3.2, Shanghai Jiemei Biological Gene Pharmaceutical Technology Co., Ltd.).

Detection of Protein, mRNA, and mtDNA

The protein expression levels of peroxisome proliferator-activated receptor-gamma coactivator 1 alpha (PGC-1α), peroxisome proliferator-activated receptor alpha (PPARα), nuclear respiratory factor 1 (NRF1), and mitochondrial transcription factor A (mtTFA) were measured by Western blot (Chen et al., 2018). The specific methods and steps are shown in Part 2 of the Supplementary Materials. The following antibodies were used: anti-PGC-1α (batch number: ab54481), anti-PPARα (batch number: ab8934), anti-NRF1 (batch number: ab175932), and anti-mtTFA (mitochondrial marker, batch number: ab131607) were provided by Abcam (Cambridge, UK); anti-β-actin (batch number: TA-09) was supplied by Beijing Zhongshan Jinqiao Biotechnology Co., Ltd. (Beijing, China). The mRNA expression levels of PGC-1α, PPARα, NRF1, and mtTFA were measured by real-time PCR (RT-PCR) (Mocker et al., 2019). The specific methods and steps are shown in Part 3 of the Supplementary Materials. Mitochondrial DNA (mtDNA) was detected using the PCR-fluorescent probe method (Liu et al., 2016). The specific methods and steps are shown in Part 4 of the **Supplementary Materials**.

Statistical Analysis

SPSS 17.0 software was used for statistical analysis. The data are expressed as mean ± standard deviation ($\bar{x} \pm s$). One-way analysis of variance (ANOVA) or the Student's *t*-test was used for comparison between groups. Statistical results were considered to be statistically significant at $P < 0.05$. The area of myocardial infarction was analyzed with Image-Pro Plus 6.0 software, and the results were statistically analyzed with SPSS 17.0 software.

RESULTS

Observation of Physical Signs

The body weight of rats in the Model group and the treatment groups was higher than that of rats in the Normal group, but this difference was not statistically significant. No abnormalities were found in mental status, physical activity, respiration, coat color, facial features, genitalia, food intake, urine, and feces.

CHO Analysis

After 4 weeks of feeding with the high-fat diet (at $t = 0$), CHO levels were significantly higher in the Model group and the treatment groups than in the Normal group ($P < 0.01$), confirming the hyperlipidemic rat model was established successfully. The CHO serum levels were not significantly reduced in the Control A and B groups compared with the Model group during treatment ($P > 0.05$), although a decreasing trend was observed. HXHT-H could reduce CHO serum levels to different extents after 4, 6, and 8 weeks; after 6 and 8 weeks, the difference between the HXHT-H group and the Model group was statistically significant ($P < 0.05$ or $P < 0.01$). After 8 weeks, the HXHT-H, HXHT-M, and HXHT-L groups showed reductions in CHO levels of 30%, 21%, and 16%, respectively (**Figure 1**). In conclusion, HXHT significantly reduced CHO levels compared with Controls A and B.

TG Analysis

After 4 weeks of high-fat feed (at $t = 0$), the TG serum levels were significantly higher in the Model group than in the Normal group ($P < 0.01$). The TG levels in the treatment groups were lower than in the Model group, but this difference was not statistically significant ($P > 0.05$). After 6 weeks of treatment, TG levels in the treatment groups were significantly lower. TG levels in the Control A and B groups had decreased by 21% and 18%, respectively ($P < 0.01$). TG levels in the HXHT-H, HXHT-M, and HXHT-L groups had decreased by 28% ($P < 0.01$), 20% ($P < 0.01$), and 10% ($P < 0.05$), respectively. In all of the treatment groups except for HXHT-H group, TG levels were lower after 8 weeks than after 6 weeks ($P < 0.01$; **Figure 2**). HXHT significantly reduced TG levels compared with Controls A and B, and there was no significant difference among the three HXHT groups.

HDL-C Analysis

After 4, 6, and 8 weeks, HDL-C levels were significantly higher in the Model group than in the Normal group ($P < 0.01$). In all three HXHT groups, after 8 weeks, HDL-C levels were significantly lower than in the Model group ($P < 0.05$), and no significant changes were observed among the other groups (**Figure 3**). The

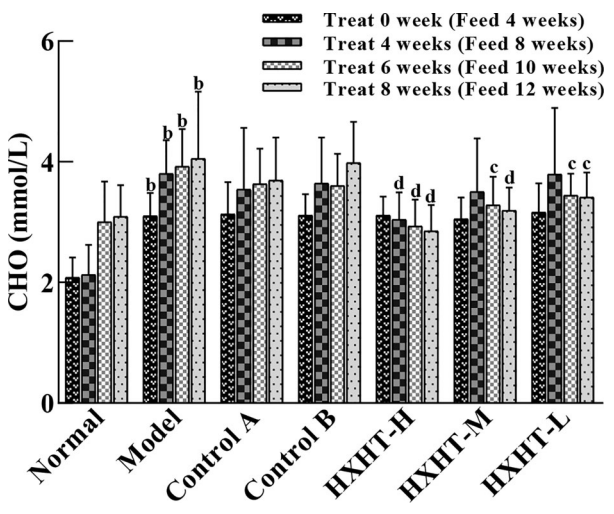

FIGURE 1 | Effects of Huoxue Huatan Decoction (HXHT) on cholesterol (CHO) serum levels in hyperlipidemic rats ($\bar{x} \pm s$). The num ber of animals per group at 4 weeks is $n = 24$; the number of animals per group at 8 weeks is $n = 16$. $^{b}P < 0.01$ compared with the Normal group; $^{c}P < 0.05$, $^{d}P < 0.01$ compared with the Model group. HXHT, Huoxue Huatan Decoction; CHO, cholesterol.

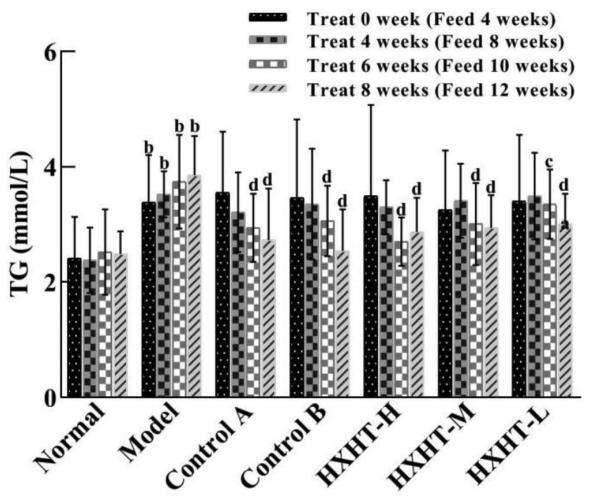

FIGURE 2 | Effects of Huoxue Huatan Decoction (HXHT) on triglyceride (TG) serum levels in hyperlipidemic rats ($\bar{x} \pm s$). The number of animals per group at 4 weeks is $n = 24$; the number of animals per group at 8 weeks is $n = 16$. $^{b}P < 0.01$ compared with the Normal group; $^{c}P < 0.05$, $^{d}P < 0.01$ compared with the Model group. HXHT, Huoxue Huatan Decoction; TG, triglyceride.

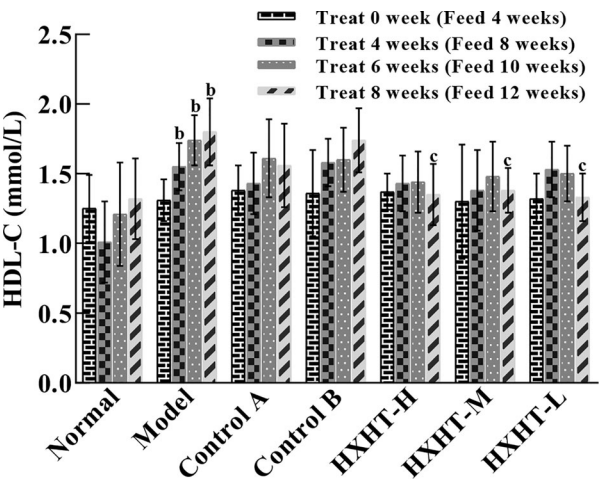

FIGURE 3 | Effects of Huoxue Huatan Decoction (HXHT) on high-density lipid-cholesterol (HDL-C) serum levels in hyperlipidemic rats ($\bar{x} \pm s$). The number of animals per group at 4 weeks is $n = 24$; the number of animals per group at 8 weeks is $n = 16$. $^{b}P < 0.01$ compared with the Normal group; $^{c}P < 0.05$ compared with the Model group. HXHT, Huoxue Huatan Decoction; HDL-C, high-density lipid-cholesterol.

reduction of HDL-C levels after 8 weeks of HXHT administration was significantly stronger than that in the Control A and Control B groups.

LDL-C Analysis

Before treatment (at $t = 0$) and after 4, 6, and 8 weeks, LDL-C levels were increased to different extents in the Model group and the treatment groups compared with the Normal group ($P < 0.05$ or $P < 0.01$), confirming the hyperlipidemic rat model was established successfully.

LDL-C levels in all of the treatment groups began to decrease after 4 weeks compared with the Model group. After 8 weeks, LDL-C levels were significantly decreased in the Control A group ($P < 0.05$), while LDL-C levels in the Control B group exhibited no significant change ($P > 0.05$). LDL-C levels in the HXHT-H, HXHT-M, and HXHT-L groups had decreased by 47% ($P < 0.01$), 30% ($P < 0.01$), and 16% ($P < 0.05$), respectively. HXHT and Control A significantly reduced LDL-C levels compared with Control B after 8 weeks of administration (**Figure 4**).

CK-MB and LDH Analysis

After 4 and 8 weeks, CK-MB levels after I/R injury were significantly higher in the Model group than in the Normal group ($P < 0.05$ or $P < 0.01$). CK-MB levels were significantly lower in the Control A, HXHT-H, and HXHT-M groups than in the Model group ($P < 0.05$ or $P < 0.01$). No significant differences were observed for other groups ($P > 0.05$; **Figure 5**). After 4 and 8 weeks, LDH serum levels after I/R injury were significantly higher in the Model group than in the Normal group ($P < 0.01$). LDH levels were significantly lower in the Control A, HXHT-H, and HXHT-M groups than in the Model group ($P < 0.05$ or $P < 0.01$). No significant changes were observed for the remaining groups ($P > 0.05$; **Figure 6**). HXHT and Control A controlled CK-MB and LDH levels significantly better than Control B after 4 and 8 weeks of administration.

Analysis of Cardiac Function

After 4 weeks and I/R, no significant changes in LVEF, LVIDd, and LVIDs were observed in any group (**Figures 7–10**). After 8

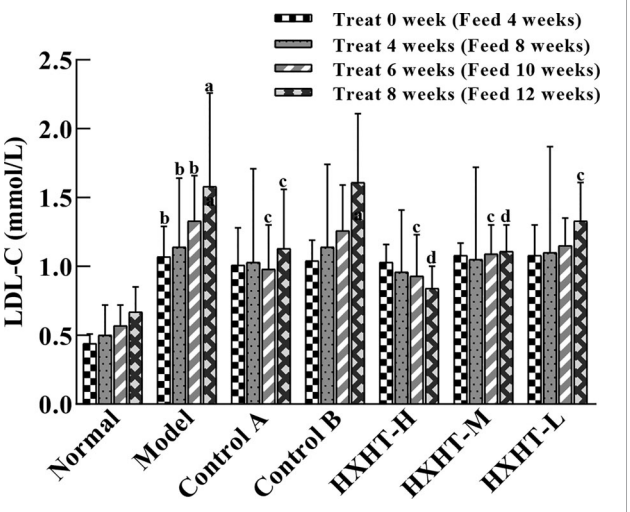

FIGURE 4 | Effects of Huoxue Huatan Decoction (HXHT) on low-density lipid-cholesterol (LDL-C) serum levels in hyperlipidemic rats ($\bar{x} \pm s$). The number of animals per group at 4 weeks is $n = 24$; the number of animals per group at 8 weeks is $n = 16$. $^{a}P < 0.05$, $^{b}P < 0.01$ compared with the Normal group; $^{c}P < 0.05$, $^{d}P < 0.01$ compared with the Model group. HXHT, Huoxue Huatan Decoction; LDL-C, low-density lipid-cholesterol.

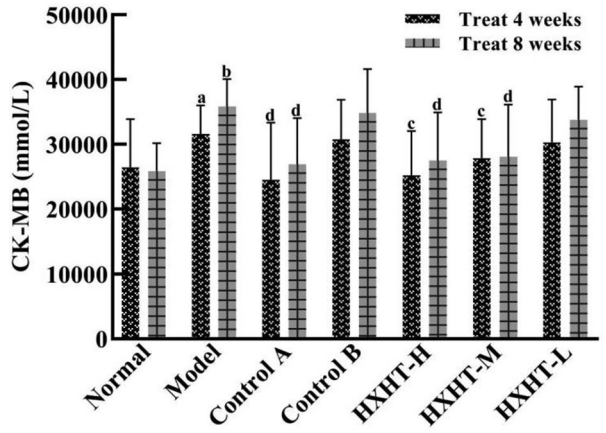

FIGURE 5 | Effects of Huoxue Huatan Decoction (HXHT) on creatine kinase-MB (CK-MB) serum levels in hyperlipidemic ischemia/reperfusion (I/R) rats ($\bar{x} \pm s$) The number of animals per group at 4 weeks is $n = 24$; the number of animals per group at 8 weeks is $n = 16$. $^{a}P < 0.05$, $^{b}P < 0.01$ compared with the Normal group; $^{c}P < 0.05$, $^{d}P < 0.01$ compared with the Model group.

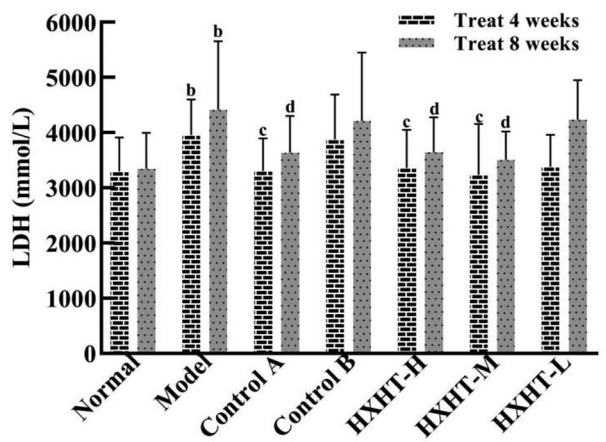

FIGURE 6 | Effects of Huoxue Huatan Decoction (HXHT) on lactate dehydrogenase (LDH) serum levels in hyperlipidemic ischemia/reperfusion (I/R) rats ($\bar{x} \pm s$). The number of animals at 4 weeks is $n_{Normal} = 8$; $n_{Model} = 7$; $n_{Control\ A} = 7$; $n_{Control\ B} = 8$; $n_{HXHT\text{-}H} = 7$; $n_{HXHT\text{-}M} = 8$; $n_{HXHT\text{-}L} = 8$. The number of animals at 8 weeks is $n_{Normal} = 16$; $n_{Model} = 15$; $n_{Control\ A} = 16$; $n_{Control\ B} = 15$; $n_{HXHT\text{-}H} = 16$; $n_{HXHT\text{-}M} = 16$; $n_{HXHT\text{-}L} = 15$. $^{b}P < 0.01$ compared with the Normal group; $^{c}P < 0.05$, $^{d}P < 0.01$ compared with the Model group. HXHT, Huoxue Huatan Decoction; CK-MB, creatine kinase-MB; LDH, lactate dehydrogenase; I/R, ischemia/reperfusion.

weeks and 2 h of I/R, the LVEF, LVIDd, and LVIDs of rats in the Model group were significantly lower than in the Normal group ($P < 0.05$); the cardiac function of rats in all of the treatment groups was significantly better than in the Model group ($P < 0.05$ or $P < 0.01$). HXHT, Control A, and Control B significantly improved cardiac function, especially HXHT-M.

Infarct Size and Ischemic Area Analysis

After 4 weeks, the area of myocardial infarction was larger in the Model group than in the Normal group, and the myocardial infarct size was reduced to different extents in the treatment groups compared with the Model group. The reduction in the area of myocardial infarction was more significantly reduced in the HXHT-M group ($P = 0.057$) than in the Control A and Control B groups. After 8 weeks, the area of myocardial infarction was significantly larger in the Model group than in the Normal group ($P < 0.05$). The area of myocardial infarction was significantly smaller in the treatment groups than in the Model group ($P < 0.05$ or $P < 0.01$; **Figure 11**).

After 4 weeks, the ischemic area of the Model group was slightly increased compared with the Normal group, but this difference was not statistically significant. The ischemic area in the Control A and HXHT-H groups was significantly smaller than in the Model group ($P < 0.05$), and was larger than that in the Control B group. After 8 weeks, no significant difference was observed between any groups. The results of our analysis of infarct size and ischemic area are presented in **Figure 11**.

HE Staining Analysis

After 8 weeks and I/R injury, HE staining of myocardial tissue revealed the following.

Normal group: Local myocardial cells had small focal necrosis, the arrangement of local myocardial fibers was disordered, wavy, or broken, and granular degeneration and vacuole degeneration could be observed locally. Myocardial capillaries were dilated and hyperemia was observed; inflammatory cell infiltration was observed under the epicardium.

Model group: Local myocardial cells had small focal necrosis, and the arrangement of local myocardial fibers was disordered, wavy, or broken, with varying degrees of granular degeneration and vacuolar degeneration. The myocardial interstitium was visibly widened, the myocardial capillaries were dilated, and congestion was obvious. Inflammatory cell infiltration was observed in myocardial interstitium, perivasculature, and epicardium, which was more pronounced than in the Normal group.

Control A group: Local myocardial cells had small focal necrosis, and the arrangement of local myocardial fibers was disordered, wavy, or broken, with a low degree of cell degeneration and varying degrees of granular degeneration and vacuolar degeneration. Capillary congestion, myocardial interstitial widening, and inflammatory cell infiltration were also observed, but these were milder than in the Model group.

HXHT-M group: Mild loose edema of myocardial cells was observed, with local small focal necrosis, occasional wavy myocardial fibers, slight granular degeneration and vacuolar degeneration, and inflammatory cell infiltration, which were milder than in the Model group (**Figure 12**).

Oil Red O Staining Analysis

After 8 weeks and I/R, the results of Oil Red O staining of myocardial tissue revealed the following:

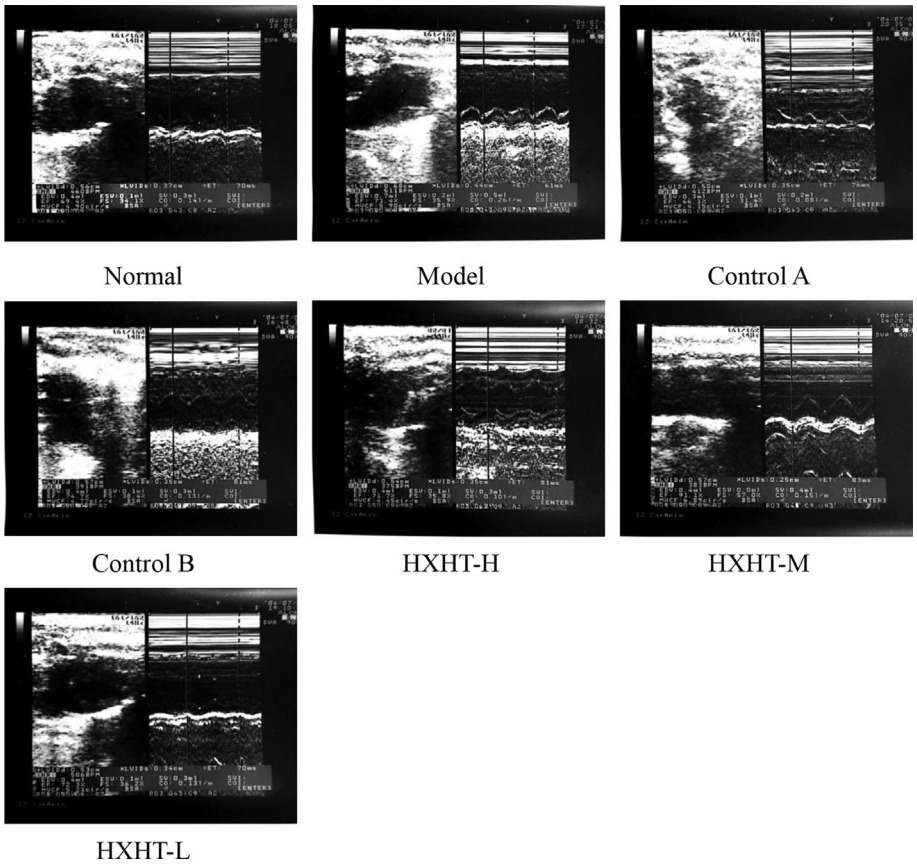

FIGURE 7 | B-ultrasound of hyperlipidemic ischemia/reperfusion (I/R) rats.

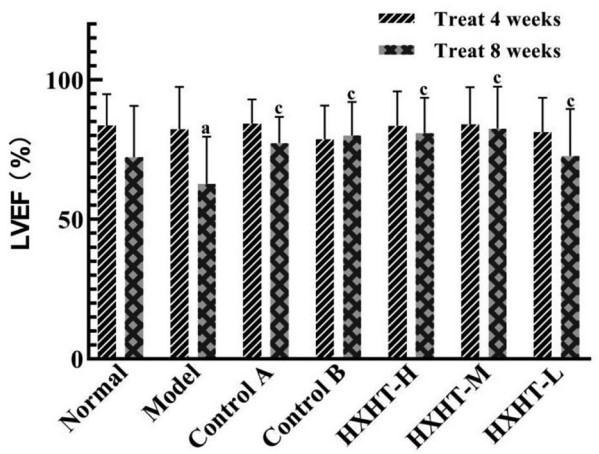

FIGURE 8 | Effects of Huoxue Huatan Decoction (HXHT) on left ventricular ejection fraction (LVEF) in hyperlipidemic ischemia/reperfusion (I/R) rats ($\bar{x} \pm s$). TThe number of animals at 4 weeks is $n_{Normal} = 8$; $n_{Model} = 7$; $n_{Control}$ A = 7; $N_{Control}$ B = 8; $n_{HXHT\text{-}H} = 7$; $n_{HXHT\text{-}M} = 8$; $n_{HXHT\text{-}L} = 8$. The number of animals at 8 weeks is $n_{Normal} = 16$; $n_{Model} = 15$; $n_{Control}$ A = 16; $n_{Control}$ B = 15; $n_{HXHT\text{-}H} = 16$; $n_{HXHT\text{-}M} = 16$; $n_{HXHT\text{-}L} = 15$. $^{a}P < 0.05$ compared with the Normal group; $^{c}P < 0.05$ compared with the Model group.

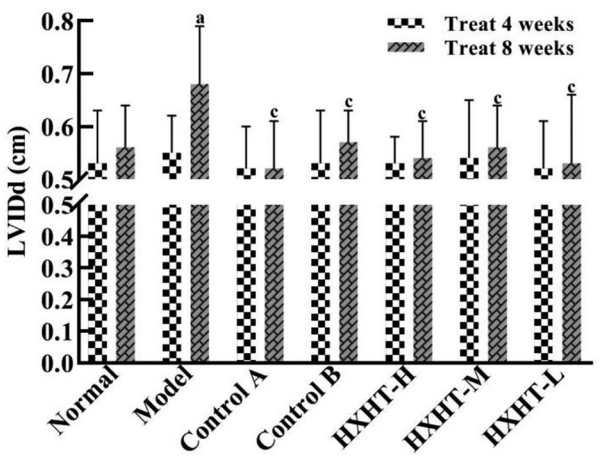

FIGURE 9 | Effects of Huoxue Huatan Decoction (HXHT) on left ventricular end-diastolic inner diameter (LVIDd) in hyperlipidemic ischemia/reperfusion (I/R) rats ($\bar{x} \pm s$). The number of animals at 4 weeks is $n_{Normal} = 8$; $n_{Model} = 7$; $n_{Control}$ A = 7; $N_{Control}$ B = 8; $n_{HXHT\text{-}H} = 7$; $n_{HXHT\text{-}M} = 8$; $n_{HXHT\text{-}L} = 8$. The number of animals at 8 weeks is $n_{Normal} = 16$; $n_{Model} = 15$; $n_{Control}$ A = 16; $n_{Control}$ B = 15; $n_{HXHT\text{-}H} = 16$; $n_{HXHT\text{-}M} = 16$; $n_{HXHT\text{-}L} = 15$. $^{a}P < 0.05$ compared with the Normal group; $^{c}P < 0.05$ compared with the Model group.

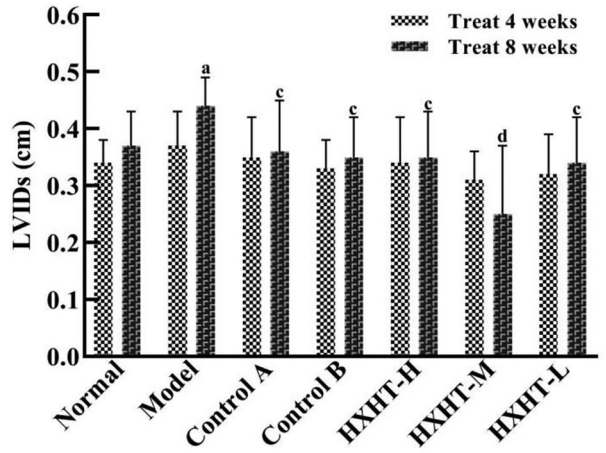

FIGURE 10 | Effects of Huoxue Huatan Decoction (HXHT) on left ventricular end-systolic inner diameters (LVIDs) in hyperlipidemic ischemia/reperfusion (I/R) rats ($\bar{x} \pm s$). The number of animals at 4 weeks is $n_{Normal} = 8$; $n_{Model} = 7$; $n_{Control\ A} = 7$; $n_{Control\ B} = 8$; $n_{HXHT\text{-}H} = 7$; $n_{HXHT\text{-}M} = 8$; $n_{HXHT\text{-}L} = 8$. The number of animals at 8 weeks is $n_{Normal} = 16$; $n_{Model} = 15$; $n_{Control\ A} = 16$; $n_{Control\ B} = 15$; $n_{HXHT\text{-}H} = 16$; $n_{HXHT\text{-}M} = 16$; $n_{HXHT\text{-}L} = 15$. $^{a}P < 0.05$ compared with the Normal group; $^{c}P < 0.05$, $^{d}P < 0.01$ compared with the Model group.

Normal group: Dark red lipid droplets were occasionally observed locally and scattered in cardiomyocytes. Occasionally, the light brown lipid droplets were connected into sheets, and light brown or tan miscellaneous droplets were observed overall.

Model group: Dark red lipid droplets were often observed scattered in cardiomyocytes, which also contained larger lipid droplets. Light reddish brown lipid droplets at the epicardium were connected into sheets, and brownish red or tan miscellaneous granules were observed overall.

Control A group: Dark red lipid droplets were occasionally scattered in cardiomyocytes, with fewer lipid droplets. The whole body was light brown, but occasionally brown red was found in the folds.

HXHT-M group: Dark red lipid droplets were occasionally scattered in cardiomyocytes, with fewer lipid droplets, and the whole body was light brown. The epicardium was reddish brown, and occasionally brown red was found in the folds.

Oil Red O staining showed that there were more lipid droplets in the Model group, while there were fewer lipid droplets in the Control A and HXHT-M groups (**Figure 13**).

Analysis of Mitochondrial Ultrastructure

After 8 weeks and I/R injury, the mitochondrial ultrastructure analysis revealed the following.

Normal group: The mitochondrial ultrastructure was relatively clear and the membrane was relatively intact, but the mitochondrial cristae were vague and disordered, fused, and damaged. Some mitochondrial cristae disappeared or vacuolized, and the ruptured membranes rarely formed vesicles or vacuoles. Occasionally, disordered intercalated discs and poor continuity were observed.

Model group: Mitochondria were significantly swollen, the inner and outer membranes were obviously damaged, or even broken and dissolved, and the contents spilled. Mitochondrial cristae were vague and disordered, and some mitochondrial cristae disappeared or vacuolized. The mitochondrial matrix was blurred, and fragmented mitochondria were observed. Myofibrils were uneven in thickness, the sarcomere structure was unclear, and some myofilaments were damaged and dissolved. Some disordered intercalated discs and

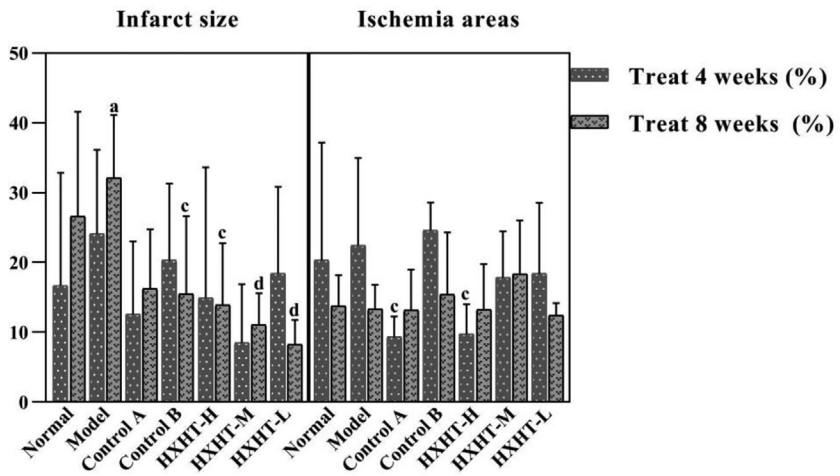

FIGURE 11 | Effects of Huoxue Huatan Decoction (HXHT) on myocardial infarct size and ischemic area in hyperlipidemic ischemia/reperfusion (I/R) rats ($\bar{x} \pm s$). The number of animals at 4 weeks is $n_{Normal} = 8$; $n_{Model} = 7$; $n_{Control\ A} = 7$; $n_{Control\ B} = 8$; $n_{HXHT\text{-}H} = 7$; $n_{HXHT\text{-}M} = 8$; $n_{HXHT\text{-}L} = 8$. The number of animals at 8 weeks is $n_{Normal} = 8$; $n_{Model} = 8$; $n_{Control\ A} = 8$; $n_{Control\ B} = 7$; $n_{HXHT\text{-}H} = 8$; $n_{HXHT\text{-}M} = 8$; $n_{HXHT\text{-}L} = 7$. $^{a}P < 0.05$ compared with the Normal group; $^{c}P < 0.05$, $^{d}P < 0.01$ compared with the Model group. HXHT, Huoxue Huatan Decoction; I/R, ischemia/reperfusion.

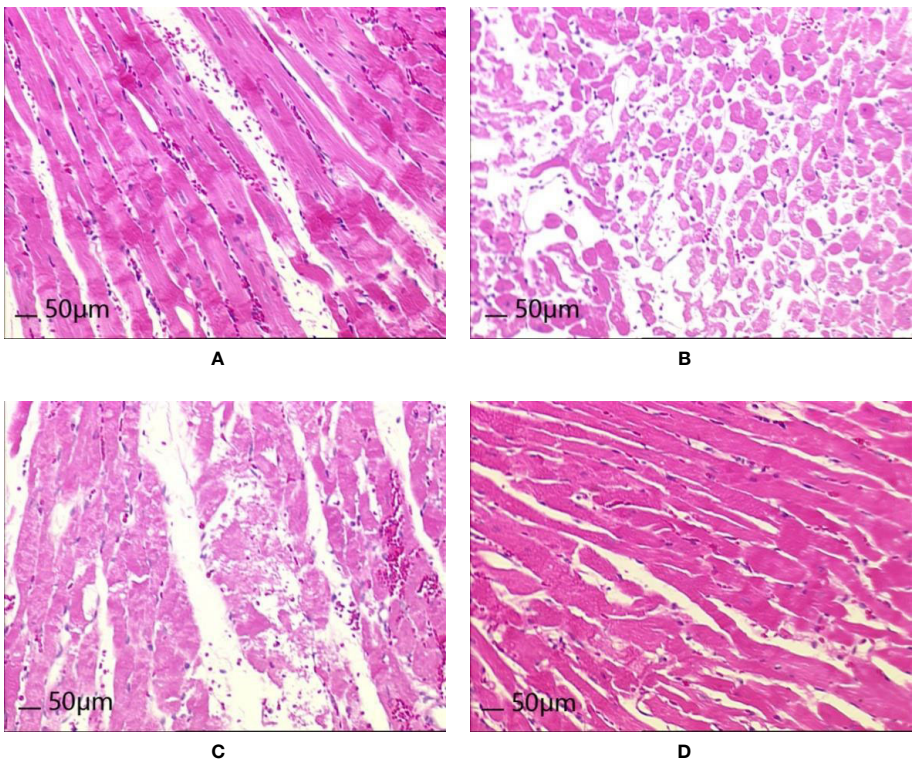

FIGURE 12 | Effects of Huoxue Huatan Decoction (HXHT) on heart histopathology after myocardial ischemia/reperfusion (I/R) injury in hyperlipidemic rats (HE staining, 200×). **(A)** Normal control; **(B)** Model control; **(C)** Control A; **(D)** HXHT-M. The number of animals at 8 weeks is $n_{Normal} = 8$; $n_{Model} = 7$; $n_{Control\ A} = 8$; $n_{HXHT\text{-}M} = 8$. HXHT, Huoxue Huatan Decoction; I/R, ischemia/reperfusion.

poor continuity were observed. Most of the myofilaments were dissolved, and the Z-line was significantly thickened extending toward the I-band.

Control A group: The mitochondrial membrane was thinned or even ruptured. The mitochondrial ridges were reduced and the ridges were blurred. Some mitochondrial cristae disappeared or vacuolized. Mitochondria were swollen, partial rhomboid cristae and longitudinal cristae were observed, and giant myocardial mitochondria, vesicles, or vacuoles formed from ruptured membranes. The intercalated discs were neat and continuous.

HXHT-M group: The ultrastructure of rat myocardial mitochondria was clear, the membrane was intact, the mitochondrial cristae were dense, the mitochondrial matrix was clear, and occasional mitochondrial cristae were blurred. The intercalated discs were neat and continuous. Mitochondria were distributed in bands and arranged neatly. The sarcomeres were well arranged.

In the Model group, mitochondria were swollen. The mitochondrial membrane was ruptured. Mitochondrial cristae fused, disappeared, or broke. These phenomena were more serious than in other groups (**Figure 14**).

Analysis of Oxidative Stress

After 8 weeks and I/R injury, MDA serum levels were significantly higher in the Model group than in the Normal group ($P < 0.01$). MDA serum levels were lower in the Control A and HXHT-M groups than in the Model group; for the HXHT-M group, this difference was statistically significant ($P < 0.05$).

T-SOD, CuZn-SOD, and GSH-Px levels were significantly lower in the Model group than in the Normal group ($P < 0.05$ or $P < 0.01$). T-SOD, CuZn-SOD, and GSH-Px levels were higher in the Control A and HXHT-M groups than in the Model group; for T-SOD in the HXHT-M group, this difference was statistically significant ($P < 0.01$).

The SDH levels in myocardial tissue after myocardial I/R were significantly lower in the Model group than in the Normal group ($P < 0.05$), and the SDH levels in the HXHT-M group were significantly higher than in the Model groups ($P < 0.05$). No significant differences in ROS and COX levels were observed between the groups (**Figure 15**).

mRNA and Protein Expression Levels of PGC-1α, PPARα, NRF1, and mtTFA

After 8 weeks and I/R injury, the mRNA and protein expression levels of PGC-1α, PPARα, NRF1, and mtTFA were significantly lower in the Model group than in the Normal group ($P < 0.01$). The mRNA expression levels of PGC-1α, PPARα, NRF1, and mtTFA were significantly increased in the Control A and HXHT-M groups compared with the Model group ($P < 0.05$;

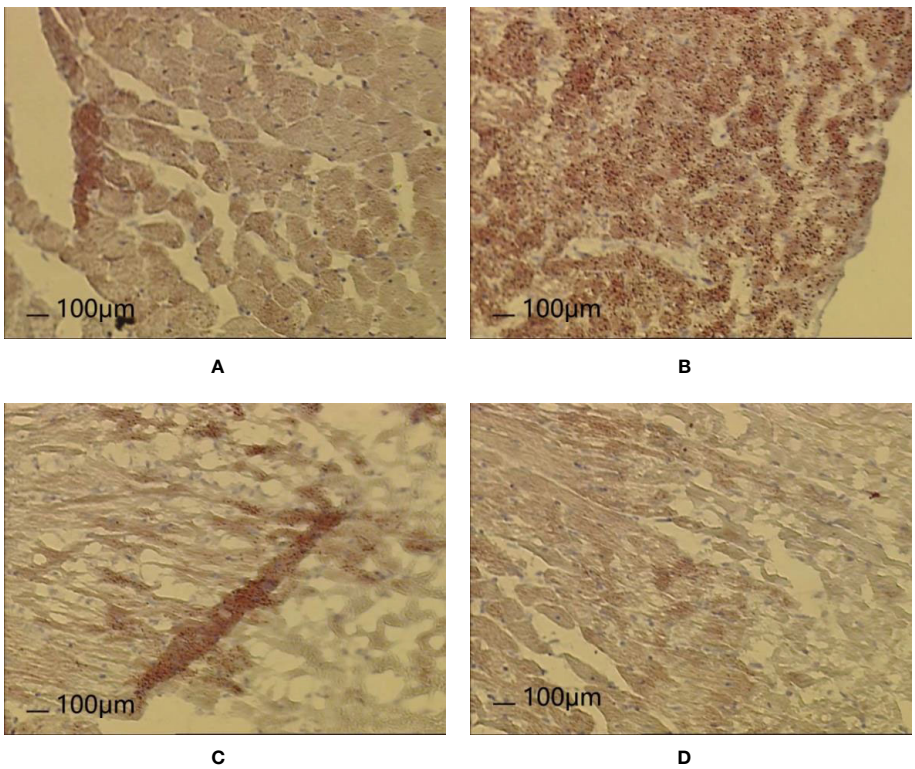

FIGURE 13 | Effects of Huoxue Huatan Decoction (HXHT) on heart histopathology after myocardial ischemia/reperfusion (I/R) injury in hyperlipidemic rats (Oil Red O staining, 100×). **(A)** Normal control; **(B)** Model control; **(C)** Control A; **(D)** HXHT-M. The number of animals at 8 weeks is $n_{Normal} = 8$; $n_{Model} = 7$; $n_{Control\ A} = 8$; $n_{HXHT\text{-}M} = 8$. HXHT, Huoxue Huatan Decoction; I/R, ischemia/reperfusion.

Figure 16). The protein expression levels of PGC-1α, NRF1, and mtTFA were significantly increased in the Control A and HXHT-M groups compared with the Model group ($P < 0.05$ or $P < 0.01$; **Figure 17**). The protein expression levels of PPARα were significantly increased in the HXHT-M group compared with the Model group ($P < 0.05$; **Figure 17**), but the increase was not significant in the Control A group.

Analysis of mtDNA Copy Number

After 8 weeks and I/R injury, the mtDNA copy number was significantly lower in the Model group than in the Normal group ($P < 0.01$), and it was significantly increased in the HXHT-M group compared with the Model group, while it was further decreased in the Control A group ($P < 0.01$; **Figure 18**).

DISCUSSION

Elevated blood lipids are one of the main pathogenic factors of atherosclerosis (Song, 2003). LDL-C has a direct relationship with atherosclerotic cardiovascular disease and is positively correlated with the incidence of the disease. The main goal of preventing and treating atherosclerotic cardiovascular disease is to reduce abnormal blood lipids, especially LDL-C. Therefore, here we conducted an in-depth study of the dynamic continuous and dose-effect relation of the effects of HXHT on lipid metabolism in hyperlipidemic rats. Our results showed that a high-fat diet could significantly increase the levels of CHO, TG, HDL-C, and LDL-C in Wistar rats. HXHT could significantly reduce blood lipids to different extents after 4, 6, and 8 weeks of administration, and the effects of high-dose HXHT were the most significant. HXHT can significantly reduce CHO, TG, LDL-C, and HDL-C after 4, 6, and 8 weeks of administration. HXHT was superior to the positive control drugs, and it had no significant effect on body weight. *S. miltiorrhiza* Bunge, *P. notoginseng* (Burkill) F.H. Chen, *T. kirilowii* Maxim., and *A. macrostemon* Bunge, which are ingredients of HXHT, have previously been reported to have hypolipidemic effects. For example, salvianolic acid B could reduce blood glucose, increase insulin resistance, reduce CHO, LDL-C, free fatty acid, liver glycogen, and muscle glycogen, and increase HDL-C in diabetic model rats (Huang et al., 2015). *P. notoginseng* (Burkill) F.H. Chen could significantly reduce CHO, TG, and LDL-C and increase HDL-C in the treatment of patients with hyperlipidemia (Si, 2015). *T. kirilowii* Maxim. and *A. macrostemon* Bunge could significantly reduce TC, TG, LDL, and arteriosclerosis index ($P < 0.01$). The combination of the two had a synergistic effect and a better lipid-lowering effect (He, 2002).

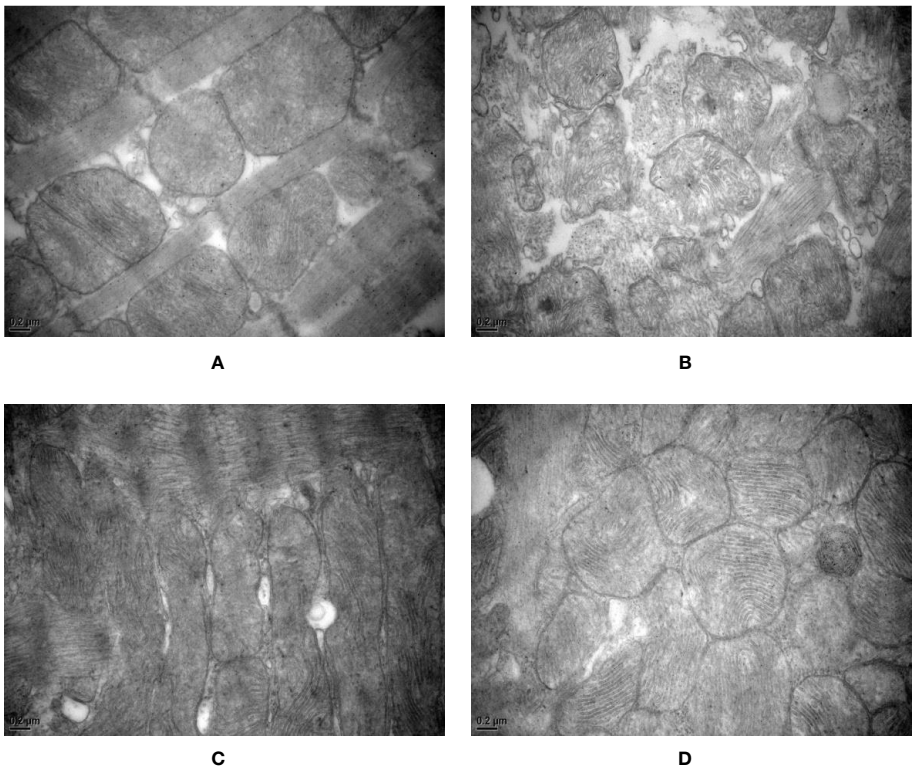

FIGURE 14 | Effects of Huoxue Huatan Decoction (HXHT) on myocardial mitochondria after myocardial ischemia/reperfusion (I/R) injury in hyperlipidemic rats (transmission electron microscopy, 40,000×). **(A)** Normal control; **(B)** Model control; **(C)** Control A; **(D)** HXHT-M. The number of animals at 8 weeks is $n_{Normal} = 8$; $n_{Model} = 7$; $n_{Control\ A} = 8$; $n_{HXHT\text{-}M} = 8$. HXHT, Huoxue Huatan Decoction; I/R, ischemia/reperfusion.

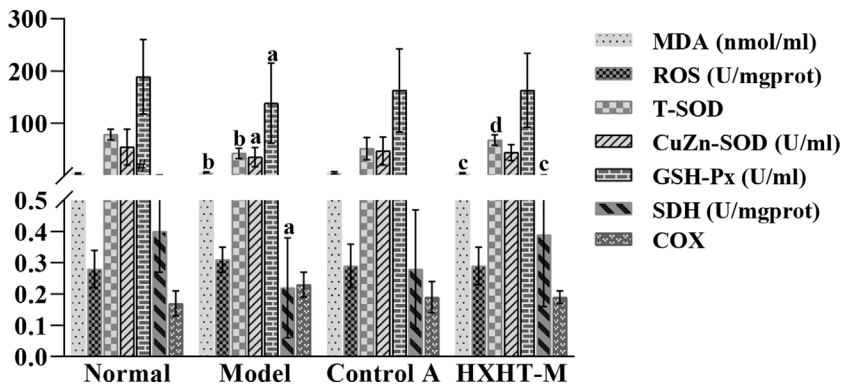

FIGURE 15 | Effects of Huoxue Huatan Decoction (HXHT) on oxidative stress indicators in hyperlipidemic ischemia/reperfusion (I/R) rats. $^{a}P < 0.05$, $^{b}P < 0.01$ compared with the Normal group; $^{c}P < 0.05$, $^{d}P < 0.01$ compared with the Model group. The number of animals at 8 weeks is $n_{Normal} = 8$; $n_{Model} = 7$; $n_{Control\ A} = 8$; $n_{HXHT\text{-}M} = 8$. HXHT, Huoxue Huatan Decoction; I/R, ischemia/reperfusion.

A high-fat and low-sugar diet did not affect non-ischemic left ventricular function, but it could aggravate myocardial injury and enhance the mortality caused by pump failure and ventricular arrhythmia during myocardial I/R in rats, which might be closely related to myocardial mitochondrial fission and fusion, calcium channel, and myocardial capacity metabolism (Liu and Lloyd, 2013; Liu et al., 2014). The effect of HXHT on myocardial I/R injury in hyperlipidemic rats was studied. The results showed that after 8 weeks and 12 weeks of feeding, the myocardial enzyme levels, cardiac function, and the

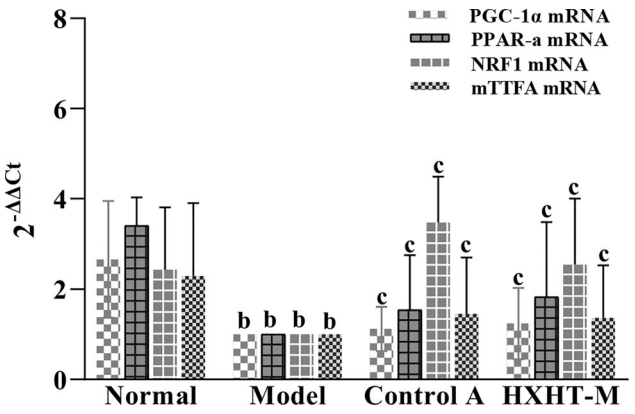

FIGURE 16 | Effects of Huoxue Huatan Decoction (HXHT) on mRNA levels in hyperlipidemic ischemia/reperfusion (I/R) rats ($\bar{x} \pm s$). The results were calculated using the $2^{-\Delta\Delta Ct}$ method, where $2^{-\Delta\Delta Ct} = (Ct_{target\ gene} - Ct_{housekeeper\ gene})$ experimental group – $(Ct_{target\ gene} - Ct_{housekeeper\ gene})$ control group. The amplification factors are presented for comparison reasons. $^{b}P < 0.01$ compared with the Normal group; $^{c}P < 0.05$ compared with the Model group. The number of animals at 8 weeks is $n_{Normal} = 8$; $n_{Model} = 7$; $n_{Control\ A} = 8$; $n_{HXHT\text{-}M} = 8$. HXHT, Huoxue Huatan Decoction; I/R, ischemia/reperfusion.

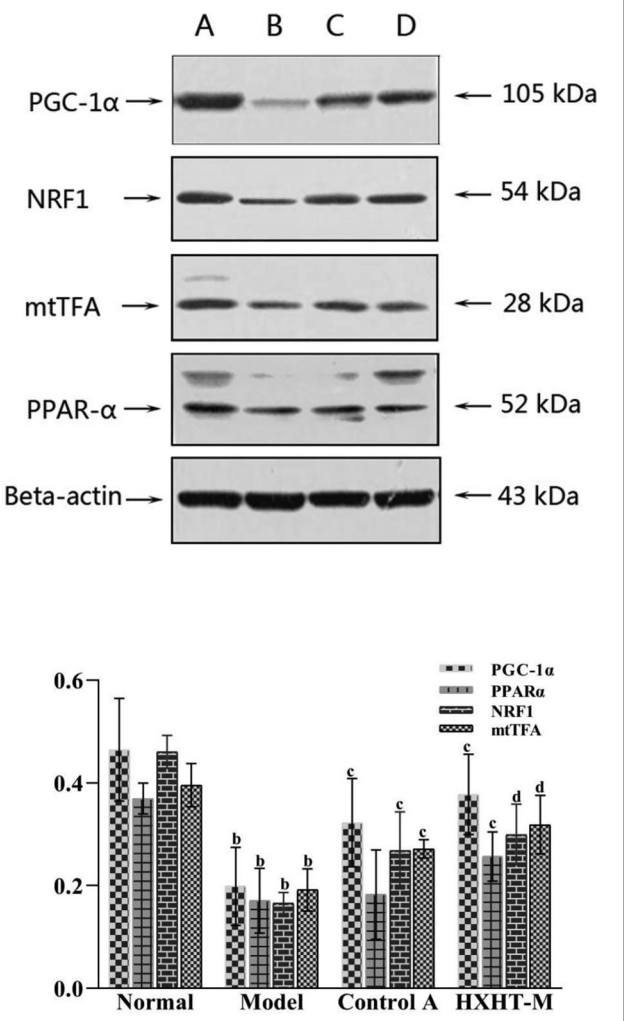

FIGURE 17 | Effects of Huoxue Huatan Decoction (HXHT) on proteins in hyperlipidemic ischemia/reperfusion (I/R) rats ($\bar{x} \pm s$). The images were scanned and analyzed with ImageJ software. The gray-scale value was calculated for each band. The relative content of each target protein was calculated by dividing the gray-scale value of the target protein by the gray-scale value of β-actin. $^{b}P < 0.01$ compared with the Normal group; $^{c}P < 0.05$, $^{d}P < 0.01$ compared with the Model group. The number of animals at 8 weeks is $n_{Normal} = 8$; $n_{Model} = 7$; $n_{Control\ A} = 8$; $n_{HXHT\text{-}M} = 8$. HXHT. **(A)** Normal control; **(B)** Model control; **(C)** Control A; **(D)** HXHT-M. HXHT, Huoxue Huatan Decoction; I/R, ischemia/reperfusion.

myocardial infarction area of the hyperlipidemia model group were significantly higher, worse, and larger than those of the Normal control group, respectively. A high-fat diet could aggravate myocardial I/R injury in rats. HXHT could prevent myocardial I/R injury in hyperlipidemic rats after 4 weeks of administration, and significantly reduce myocardial enzyme levels. After 8 weeks of administration, HXHT could significantly reduce the myocardial infarction area and improve cardiac function.

The histomorphological study showed that myocardial cell focal necrosis, myocardial vascular congestion, inflammatory cell infiltration, and lipid droplet accumulation were more serious in the hyperlipidemia model than in the other groups, while in the HXHT groups and the Control A group, these were lighter than in the hyperlipidemia model group. On the one hand, HXHT might reduce the infiltration of inflammatory cells due to its lipid-lowering effects; on the other hand, the components of HXHT may have anti-inflammatory effects. Tanshinone and salvianolic acid could promote blood circulation, dilate blood vessels, scavenge free radicals, and protect mitochondria, and they have anticoagulation and anti-inflammatory effects (Adams et al., 2006). Cryptotanshinone, which is also present in HXHT, could downregulate the expression of pro-inflammatory cytokines; cryptotanshinone and 15,16-dihydrotanshinone could inhibit the activities of nuclear transcription factor-κB and activator protein (Jeon et al., 2008). There are many ways to inhibit atherosclerosis. Salvianolic acid B and ginkgolide mainly act on inflammatory cytokines, *P. notoginseng* glycosides act on adhesion factors, and tanshinone acts on growth factors (Li et al., 2007).

Oxygen free radicals, calcium overload, and the inflammatory response are directly or indirectly related to mitochondria, which function as intracellular effectors and are protected by ischemic preconditioning. Mitochondria, as an important organelle in the regulation of energy metabolism in cells, participate in myocardial I/R injury through various pathways. The results of the present study showed that the mitochondria in the hyperlipidemia model group were swollen and the mitochondrial membrane was ruptured. HXHT could protect the morphology of mitochondria upon I/R. Excessive fat intake increases oxygen free radical levels. Free radicals cause lipid peroxidation of cell membranes, causing mitochondrial dysfunction, which in turn affects the tricarboxylic acid cycle and results in dysfunction of the myocardium. The results of this study showed that the activities of MDA, T-SOD, CuZn-SOD, and GSH-

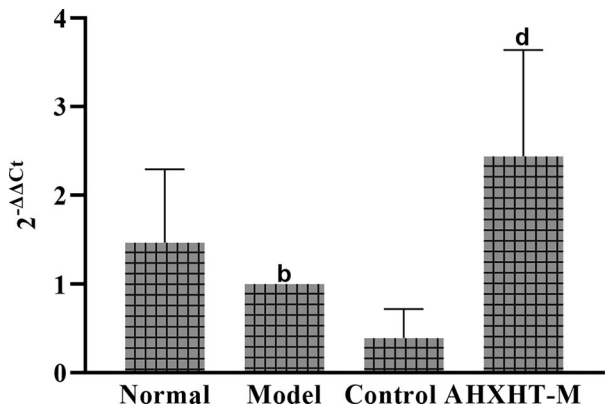

FIGURE 18 | Effects of Huoxue Huatan Decoction (HXHT) on mitochondrial DNA (mtDNA) copy number in hyperlipidemic ischemia/reperfusion (I/R) rats ($\bar{x} \pm s$). $^{b}P < 0.01$ compared with the Normal group; $^{d}P < 0.01$ compared with the Model group. The number of animals at 8 weeks is $n_{Normal} = 8$; $n_{Model} = 7$; $n_{Control\ A} = 8$; $n_{HXHT\text{-}M} = 8$. HXHT, Huoxue Huatan Decoction; I/R, ischemia/reperfusion; mtDNA, mitochondrial DNA.

PX in serum were significantly changed after myocardial I/R in the hyperlipidemia model group, and SDH levels in myocardial tissue were significantly decreased. HXHT could reduce the activity of MDA in serum, increase the activity of T-SOD, and increase the activity of SDH in myocardial tissue. It was speculated that HXHT might: (i) enhance the ability of rats to resist oxygen free radicals, (ii) prevent oxygen free radicals from invading mitochondrial membranes, and (iii) protect mitochondrial membranes, thereby protecting the function of mitochondria (Liu et al., 2014).

The results of this experimental study showed that HXHT may protect the myocardium through the PGC-1α–PPAR pathway and regulate mitochondrial biosynthesis through the PGC-1α–NRF1–mtTFA pathway. The two pathways coordinate to protect myocardial mitochondria during myocardial I/R. In the PGC-1α–PPARα pathway, PPARα could regulate myocardial energy and fat metabolism, participate in every step of myocardial utilization of fatty acids, and play a decisive role in myocardial energy generation (Barroso et al., 2013).

HXHT could increase the gene and protein expression levels of PGC-1α and downstream PPARα; these results were consistent with the lipid-lowering effects of HXHT. PPARα is mainly expressed in the liver and participates in lipid regulation, adipogenesis, and blood glucose control. PPARα affects lipid metabolism by regulating fatty acid oxidation. In addition, PPARα is expressed in various cells constituting the blood vessel wall, such as monocyte-macrophages, smooth muscle cells, and vascular endothelial cells. HXHT could promote the expression of PPARα. PPARα directly acts on the inner wall of the blood vessel, increases the antioxidant effect of the vascular wall, and plays a role in the protection of blood vessels. HXHT might regulate fatty acid β-oxidation to ensure energy supply after I/R and rapidly restore the myocardium. Previous studies on the PGC-1α–NRF1–mtTFA pathway have shown that high fat intake could reduce the mRNA and protein levels of the mitochondrial biogenesis-related genes PGC-1α, NRF1, and mtTFA (Keaney et al., 2003; Liu et al., 2014). HXHT could promote the mRNA and protein expression levels of PGC-1α, NRF1, and mtTFA in the myocardium of hyperlipidemic rats in preliminary experiments, and alleviate myocardial I/R injury. On the one hand, HXHT lowered blood lipids and reduced the damage of CHO and LDL-C to the vascular endothelium; on the other hand, it reduced oxygen free radical levels in mitochondria, and acted on other pathways through its effects on NRF1 and mtTFA. HXHT might increase the expression of mtDNA and promote mitochondrial biosynthesis by promoting the mRNA and protein expression of PGC-1α, NRF1, and mtTFA and increasing PGC-1α–PPARα pathway activity.

CONCLUSIONS

The results of this study demonstrate that a high-fat diet affects myocardial mitochondria through two pathways: PGC-1α–PPARα and PGC-1α–NRF1–mtTFA. Myocardial fatty acid biosynthesis and oxidation affect mitochondrial function and aggravate I/R injury, as revealed by a comprehensive study of lipid metabolism, the myocardial enzyme spectrum, myocardial histomorphology, and mitochondrial biogenesis. HXHT could affect lipid metabolism and reduce the levels of CHO, TG, HDL-C, and LDL-C in hyperlipidemic rats in a dose-dependent manner, affect fatty acid β-oxidation through the PGC-1α–PPARα pathway, and protect against disturbances of mitochondrial energy metabolism. At the same time, HXHT could promote the mRNA expression and protein transcription of the mitochondrial biosynthesis-related genes of PGC-1α–NRF1–mtTFA, promote mtDNA synthesis, increase T-SOD levels, protect the structure and function of mitochondria, and defend against myocardial I/R injury in hyperlipidemic rats.

DATA AVAILABILITY STATEMENT

The raw data supporting the conclusions of this article will be made available by the authors, without undue reservation, to any qualified researcher.

ETHICS STATEMENT

The animal study was reviewed and approved by Animal Ethics Committee of Guang'anmen Hospital of China Academy of Chinese Medicine.

AUTHOR CONTRIBUTIONS

All of the authors took part in the experiments. FL and Y-QT wrote the first draft of the manuscript. X-HH, L-LG, and B-JW revised the manuscript. H-WC, J-PL, and ZC revised sections of the manuscript. H-WC and JW drew article figures and tables. All authors contributed to the article and approved the submitted version.

FUNDING

This study was supported by the National Major Scientific and Technological Special Project for "Significant New Drugs Development" (No. 2012ZX09102201), the National Natural Science Foundation of China (No. 81973836), the China Association for Science and Technology Youth Talent Project (No. 2017QNRC001), and the China Academy of Chinese Medical Sciences—Traditional Chinese Medicine Science and Technology Achievement Leading Project (No. ZZ13-ZD-04).

ACKNOWLEDGMENTS

We thank LetPub (www.letpub.com) for its linguistic assistance during the preparation of this manuscript.

SUPPLEMENTARY MATERIAL

The Supplementary Material for this article can be found online at: https://www.frontiersin.org/articles/10.3389/fphar.2020.546825/full#supplementary-material

REFERENCES

Adams, J. D., Wang, R., Yang, J., and Lien, E. J. (2006). Preclinical and clinical examinations of Salvia miltiorrhiza and its tanshinones in ischemic conditions. *Chin. Med.* 1:3. doi: 10.1186/1749-8546-1-3

Alissa, E. M., and Ferns, G. A. (2017). Dietary fruits and vegetables and cardiovascular diseases risk. *Crit. Rev. Food Sci. Nutr.* 57 (9), 1950–1962. doi: 10.1080/10408398.2015.1040487

Barroso, E., Astudillo, A. M., Balsinde, J., and Vázquez-Carrera, M. (2013). PPARβ/δ Activation prevents hypertriglyceridemia caused by a high fat diet. Involvement of AMPK and PGC-1α-Lipin1-PPARα pathway. *Clin. Investig. Arterioscler.* 25 (2), 63–73. doi: 10.1016/j.arteri.2013.01.001

Benjamin, E. J., Virani, S. S., Callaway, C. W., Chamberlain, A. M., Chang, A. R., Cheng, S., et al. (2018). Heart disease and stroke statistics-2018 update: A report from the american heart association. *Circulation* 137, e67–e492. doi: 10.1161/CIR.0000000000000558

Cao, X. J., Zhang, M. J., Zhang, L. L., Yu, K., Xiang, Y., Ding, X., et al. (2018). TLR4 mediates high-fat diet induced physiological changes in mice via attenuating PPARγ/ABCG1 signaling pathway. *Biochem. Biophys. Res. Commun.* 503 (3), 1356–1363. doi: 10.1016/j.bbrc.2018.07.048

Chen, W. W., Gao, R. L., Liu, L. S., Zhu, M. L., Wang, W., Wang, Y. J., et al. (2014). Summary of cardiovascular disease report in China in 2013. *Chin. Circ. J.* 29 (07), 487–491. doi: 10.3969/j.issn.1000-3614.2014.07.003

Chen, H., Dong, Y., He, X., Li, J., and Wang, J. (2018). Paeoniflorin improves cardiac function and decreases adverse postinfarction left ventricular remodeling in a rat model of acute myocardial infarction. *Drug Des. Dev. Ther.* 12, 823–836. doi: 10.2147/DDDT.S163405

Derosa, G., Colletti, A., Maffioli, P., D'Angelo, A., Lupi, A., Zito, G. B., et al. (2020). Lipid-lowering nutraceuticals update on scientific evidence. *J. Cardiovasc. Med. (Hagerstown)* 2020. doi: 10.2459/JCM.0000000000000970

Du, P., Chang, D., and Chen, C. (2014). Protective effects of atorvastation on myocardium ischemia reperfusion injury in rats. *J. Chin. Med. Univ.* 43 (5), 407–410. doi: 10.3969/j.issn.0258-4646.2014.05.006

Eisvand, F., Razavi, B. M., and Hosseinzadeh, H. (2020). The effects of Ginkgo biloba on metabolic syndrome: A review. *Phytother. Res.* 34 (8), 1798–1811. doi: 10.1002/ptr.6646

Goldenthal, M. J. (2016). Mitochondrial involvement in myocyte death and heart failure. *Heart Fail. Rev.* 21, 137–155. doi: 10.1007/s10741-016-9531-1

Gu, M., He, P., Lyu, C., Liu, X., Xu, Y., Cheng, S., et al. (2019). Spinosin and 6'''-Feruloylspinosin protect the heart against acute myocardial ischemia and reperfusion in rats. *Mol. Med. Rep.* 20 (5), 4253–4261. doi: 10.3892/mmr.2019.10686

Ham, Y. M., Song, H. S., Kwon, J. E., Jeon, H., Baek, H. J., Kim, C. W., et al. (2019). Effects of fermented Sorghum bicolor L. Moench extract on inflammation and thickness in a vascular cell and atherosclerotic mice model. *J. Nat. Med.* 73 (1), 34–46. doi: 10.1007/s11418-018-1231-9

Han, S. N., Yang, W. H., Yin, J. J., Tao, H. L., and Zhang, L. R. (2019). Drug treatment of hyperlipidemia in chinese patients: focus on the use of simvastatin and ezetimibe alone and in combination. *Am. J. Cardiovasc. Drugs* 19 (3), 237–247. doi: 10.1007/s40256-018-00317-1

He, S. R., Zhao, C. B., Zhang, J. X., Wang, J., Wu, B., and Wu, C. J. (2020). Botanical and traditional uses and phytochemical, pharmacological, pharmacokinetic, and toxicological characteristics of ziziphi spinosae semen: A Review. *Evid. Based Complement. Alternat. Med.* 2020, 5861821. doi: 10.1155/2020/5861821

He, L. (2002). Applying factorial design to research on the lipid-reducing efficacy of snakegourd and allium macrostemon. *Hunan. Guid. J. TCMP* 8 (4), 205, 207. doi: 10.13862/j.cnki.cn43-1446/r.2002.04.040

Henning, A. L., Venable, A. S., Vingren, J. L., Hill, D. W., and McFarlin, B. K. (2018). Consumption of a high-fat meal was associated with an increase in monocyte adhesion molecules, scavenger receptors, and propensity to form foam cells. *Cytom. B. Clin. Cytom.* 94 (4), 606–612. doi: 10.1002/cyto.b.21478

Huang, M., Wang, P., Xu, S., Xu, W., Xu, W., Chu, K., et al. (2015). Biological activities of salvianolic acid B from Salvia miltiorrhiza on type 2 diabetes induced by high-fat diet and streptozotocin. *Pharm. Biol.* 53 (7), 1058–1065. doi: 10.3109/13880209.2014.959611

Jeon, S. J., Son, K. H., Kim, Y. S., Choi, Y. H., and Kim, H. P. (2008). Inhibition of prostaglandin and nitric oxide production in lipopolysaccharide-treated RAW 264.7 cells by tanshinones from the roots of Salvia miltiorrhiza bunge. *Arch. Pharm. Res.* 31 (6), 758–763. doi: 10.1007/s12272-001-1223-4

Keaney, J. F., Larson, M. G., Vasan, R. S., Wilson, P. W. F., Lipinska, I., Corey, D., et al. (2003). Obesity and systemic oxidative stress clinical correlates of oxidative stress in the framingham study. *Arterioscler. Thromb. Vasc. Biol.* 23 (3), 434–439. doi: 10.1161/01.ATV.0000058402.34138.11

Li, Y., Yang, Q., and Zhu, X. (2007). TCM anti inflammation: an effective approach for treating atherosclerosis. *World Sci. Technol./Mod. Tradit. Chin. Med. Mater. Med.* 9 (2), 22–28.

Li, F., Xu, Q., Zheng, T., Huang, F., and Han, L. (2014). Metabonomic analysis of allium macrostemon bunge as a treatment for acute myocardial ischemia in rats. *J. Pharm. Biomed. Anal.* 88, 225–234. doi: 10.1016/j.jpba.2013.09.002

Li, L., Hou, X., Xu, R., Liu, C., and Tu, M. (2017). Research review on the pharmacological effects of astragaloside IV. *Fundam. Clin. Pharmacol.* 31 (1), 17–36. doi: 10.1111/fcp.12232

Li, X., Lu, L., Chen, J., Zhang, C., Chen, H., and Huang, H. (2020). New insight into the mechanisms of Ginkgo Biloba extract in vascular aging prevention. *Curr. Vasc. Pharmacol.* 18 (4), 334–345. doi: 10.2174/1570161117666190621150725

Li, M. (2016). The clinical research and microRNA study of Huoxuehuatan'anshen prescription intervene patients with coronary heart disease (CHD) angina pectoris and phlegm and blood stasis syndrome. *Beijing Univ. Chin. Med.*, 1–80.

Lin, F. (2015). Based on the methods of harmonizing qi and blood of treatise on cold-induced diseases to study on protective effects and mechanisms of Huoxue Huatan Fang on myocardial ischemia/reperfusion injury in hyperlipidemia rats. *Hubei Univ. Tradit. Chin. Med.*, 1–165.

Liu, J., and Lloyd, S. G. (2013). High-fat, low-carbohydrate diet alters myocardial oxidative stress and impairs recovery of cardiac function after ischemia and reperfusion in obese rats. *Nutr. Res.* 33 (4), 311–321. doi: 10.1016/j.nutres.2013.02.005

Liu, J. G., Zhang, D. W., Li, J., Feng, J. T., Yang, X. P., Shi, D. Z., et al. (2011). Effects of salvia militiorrhiza and carthamus tinctorius aqueous extracts and compatibility on rat myocardial ischemic reperfusion injury. *Chin. J. Chin. Mat. Med.* 36 (2), 189–194. doi: 10.4268/cjcmm20110222

Liu, J., Wang, P., Zou, L., Qu, J., Litovsky, S., Umeda, P., et al. (2014). High-fat, low-carbohydrate diet promotes arrhythmic death and increases myocardial ischemia-reperfusion injury in rats. *Am. J. Physiol. Heart Circ. Physiol.* 307 (4), H598–H608. doi: 10.1152/ajpheart.00058.2014

Liu, J., Zou, Y., Tang, Y., Xi, M., Xie, L., Zhang, Q., et al. (2016). Circulating cell-free mitochondrial deoxyribonucleic acid is increased in coronary heart disease patients with diabetes mellitus. *J. Diabetes Invest.* 7 (1), 109–114. doi: 10.1111/jdi.12366

Liu, C., Feng, R., Zou, J., Xia, F., and Wan, J. B. (2019). 20(S)-Protopanaxadiol Saponins Mainly Contribute to the Anti-Atherogenic Effects of Panax notoginseng in apoE deficient mice. *MoleculesApplying factorial design to research on the lipid-reducing efficacy of snakegourd and allium macrostemon* 24 (20):3723. doi: 10.3390/molecules24203723

Liu, H., Yang, J., Yang, W., Hu, S., Wu, Y., Zhao, B., et al. (2020). Focus on notoginsenoside R1 in metabolism and prevention against human diseases. *Drug Des. Devel. Ther.* 14, 551–565. doi: 10.2147/DDDT.S240511

Mocker, A., Hilgers, K. F., Cordasic, N., Wachtveitl, R., Menendez-Castro, C., Woelfle, J., et al. (2019). Renal chemerin expression is induced in models of hypertensive nephropathy and glomerulonephritis and correlates with markers of inflammation and fibrosis. *Int. J. Mol. Sci.* 20, 6240. doi: 10.3390/ijms20246240

Okopień, B., Bułdak, Ł., and Bołdys, A. (2016). Current and future trends in the lipid lowering therapy. *Pharmacol. Rep.* 68 (4), 737–747. doi: 10.1016/j.pharep.2016.03.016

People's Republic of China Ministry of Health (2003). *Technical standards for testing & assessment of health food* (Beijing: People's Republic of China Ministry of Health).

Ren, J., Fu, L., Nile, S. H., Zhang, J., and Kai, G. (2019). *Salvia miltiorrhiza* in treating cardiovascular diseases: a review on its pharmacological and clinical applications. *Front. Pharmacol.* 10, 753. doi: 10.3389/fphar.2019.00753

Si, R. (2015). Effects observation of sanqi powder on hyperlipidemia. *Clin. J. Chin. Med.* 7 (3), 57–58. doi: 10.3969/j.issn.1674-7860.2015.03.027

Song, J. (2003). Research progress in prevention and treatment of atherosclerosis with traditional Chinese medicine. *Chin. J. Bas. Med. Tradit. Chin. Med.* 9 (11), 71–74.

The cardiovascular disease branch of China Association of Chinese Medicine (2019). Guideline for diagnosis and treatment of chinese medicine in stable angina coronary artery disease. *J. Tradit. Chin. Med.* 60 (21), 1880–1890. doi: 10.13288/j.11-2166/r.2019.21.015

Wang, J., He, Q. Y., Shi, Z., Xing, Y. W., Li, J., Fang, Y. T., et al. (2008). Correlation between syndrome factor combination and cardiac function as well as blood-lipid in coronary heart disease. *J. Chin. Integr. Med.* 6 (9), 897–901. doi: 10.3736/jcim20080904

Welty, F. K. (2020). Dietary treatment to lower cholesterol and triglyceride and reduce cardiovascular risk. *Curr. Opin. Lipidol.* 31 (4), 206–231. doi: 10.1097/MOL.0000000000000689

Wen, J., Lin, T., Wu, W., Yang, Y., Luo, C., Zhou, C., et al. (2019). Tiaopi huxin recipe improved endothelial dysfunction and attenuated atherosclerosis by decreasing the expression of caveolin-1 in ApoE^{-} deficient mice. *J. Cell Physiol.* 234, 15369–15379. doi: 10.1002/jcp.28184

Xie, W., Zhang, Y., Wang, N., Zhou, H., Du, L., Ma, X., et al. (2008). Novel effects of macrostemonoside A, a compound from allium macrostemon bung, on hyperglycemia, hyperlipidemia, and visceral obesity in high-fat diet-fed C57BL/6 mice. *Eur. J. Pharmacol.* 599 (1-3), 159–165. doi: 10.1016/j.ejphar.2008.09.042

Yang, F., Zhao, W. L., Mi, Q. Y., Xie, L. P., Liu, Z., Zhang, W., et al. (2009). Assessment of myocardial ischemia-reperfusion injury with two different staining methods. *Acta Univ. Med. Nanjing* 29 (8), 1055–1058. doi: CNKI:SUN:NJYK.0.2009-08-003

Yu, X., Tang, L., Wu, H., Zhang, X., Luo, H., Guo, R., et al. (2018). Trichosanthis Fructus: botany, traditional uses, phytochemistry and pharmacology. *J. Ethnopharmacol.* 224, 177–194. doi: 10.1016/j.jep.2018.05.034

Yuan, L., Li, Q., Zhang, Z., Liu, Q., Wang, X., and Fan, L. (2020). Tanshinone IIA inhibits the adipogenesis and inflammatory response in ox-LDL-challenged human monocyte-derived macrophages via regulating miR-130b/WNT5A. *J. Cell. Biochem.* 121 (2), 1400–1408. doi: 10.1002/jcb.29375

Zhang, Y. Y., Guo, H., Wang, J., Gao, J. L., and Sun, J. N. (2016). Protective effect of shenlou shuangxin pills on myocardial ischemia reperfusion injury in rats. *Chin. J. Exp. Tradit. Med. Form.* 22 (06), 94–98. doi: 10.13422/j.cnki.syfjx.2016060094

Conflict of Interest: The authors declare that the research was conducted in the absence of any commercial or financial relationships that could be construed as a potential conflict of interest.

Copyright © 2020 Lin, Tan, He, Guo, Wei, Li, Chen, Chen and Wang. This is an open-access article distributed under the terms of the Creative Commons Attribution License (CC BY). The use, distribution or reproduction in other forums is permitted, provided the original author(s) and the copyright owner(s) are credited and that the original publication in this journal is cited, in accordance with accepted academic practice. No use, distribution or reproduction is permitted which does not comply with these terms.

frontiers in Pharmacology

MINI REVIEW
published: 15 September 2020
doi: 10.3389/fphar.2020.575803

Traditional Chinese Medicine in Treating Influenza: From Basic Science to Clinical Applications

Yibai Xiong[1], Na Xiao Li[1], Naifang Duan[1], Bin Liu[1], Hui Zhu[2], Chi Zhang[3], Li Li[1], Cheng Lu[1] and Luqi Huang[2]**

[1] Institute of Basic Research in Clinical Medicine, China Academy of Chinese Medical Sciences, Beijing, China, [2] China Academy of Chinese Medical Sciences, Beijing, China, [3] Dongzhimen Hospital, Beijing University of Chinese Medicine, Beijing, China

Influenza infection is a highly contagious, acute febrile respiratory disease caused by the influenza virus. Traditional Chinese Medicine (TCM) has dominated plenty of theoretical and practical approaches in the treatment of influenza. It is, therefore, important to highlight the effects of TCM in the clinical treatment of influenza and their impact on inhibiting the growth of this virus in laboratory experiments. We scrutinized existing evidence on whether TCM is effective in clinical applications. Moreover, we described the potential mechanisms of TCM against the influenza virus. Our findings provide analytical evidence that supports the effectiveness of TCM in treating influenza infections as well as their mechanisms against this virus.

Keywords: influenza, Traditional Chinese Medicine, herbal medicine, influenza symptoms, anti-influenza virus, review

OPEN ACCESS

Edited by:
Hai Yu Xu,
China Academy of Chinese Medical Sciences, China

Reviewed by:
Xiaojun Wu,
Shanghai University of Traditional Chinese Medicine, China
Zhe-Sheng Chen,
St. John's University, United States

****Correspondence:***
Cheng Lu
cheng@163.com
Luqi Huang
hlq910@126.com

Specialty section:
This article was submitted to Ethnopharmacology, a section of the journal Frontiers in Pharmacology

Received: *24 June 2020*
Accepted: *14 August 2020*
Published: *15 September 2020*

Citation:
Xiong Y, Li NX, Duan N, Liu B, Zhu H, Zhang C, Li L, Lu C and Huang L (2020) Traditional Chinese Medicine in Treating Influenza: From Basic Science to Clinical Applications. Front. Pharmacol. 11:575803. doi: 10.3389/fphar.2020.575803

INTRODUCTION

Influenza is an acute viral respiratory infection that was first described in the 4th century BC. At the time, it was estimated to have caused nearly 60,000 mortalities in Venice, Italy. Due to the impact of this disease in Venice, it was understood by folklore to be a punishment from God and was therefore named "Influenza (Devil)" (JJ, 2010). The influenza virus belongs to the Orthomyxoviridae family. It is a single-stranded negative-sense RNA virus exhibiting an eight-segmented genetic material (Brody, 2019). Its genetic material is made up of Polymerase Basic Protein 1 (PB1), Polymerase Basic Protein 2 (PB2), Polymerase Acidic (PA), Hemagglutinin (HA), Nucleoprotein (NP), Neuraminidase (NA), Matrix Protein (M), and Nonstructural Protein (NS) (Lu, 2008). Depending on the composition of its NP and M, this virus is grouped into three types (A, B, and C). Its subtypes are determined by the antigenicity of two surface glycoproteins, the 18 HA and 11 NA (Webster et al., 1992; Kawaoka, 2006; Huang et al., 2008). It is extremely susceptible to mutations because its RNA genome lacks proof-reading ability during replication as is the case with DNA genomes. Moreover, the mutations are also attributed to antigenic drifts. These mutating types propagate this virus, leading to epidemics in certain seasons (Cox

Abbreviations: TCM, Traditional Chinese Medicine; PB1, Polymerase Basic Protein 1; PB2, Polymerase Basic Protein 2; PA, Polymerase Acidic; HA, Hemagglutinin; NP, Nucleoprotein; M, Matrix Protein; NS, Nonstructural Protein; NA, Neuraminidase; NAIs, Neuraminidase Inhibitors; WHAFS, Wind-heat affecting Fei syndrome; RCT, Randomized Controlled Trial; HCP, Houttuynia cordata polysaccharide.

and Subbarao, 2000; He et al., 2011; Kamali and Holodniy, 2013) and, notably, they hinder the development of new antiviral drugs. First-line antiviral drugs in the treatment of influenza rely on blocking the action of NP (Gaitonde et al., 2019). However, the side-effects of anti-NA drugs render many patients unavailable to treatment. In China, the broadly prescribed anti-influenza drugs include oseltamivir, zanamivir, and peramivir (Lee et al., 2017). Notably, Oseltamivir has been associated with resistance (Govorkova et al., 2001; Kiso et al., 2004; Moscona, 2004) and leads to immunocompromised conditions (Govorkova et al., 2001; Moscona, 2009; Panning, 2013). Zanamivir is administered through inhalation, and challenges over its use have been described (Shetty and Peek, 2012). Due to its limited bioavailability, peramivir can only be administered intravenously (Birnkrant and Cox, 2009). Therefore, these challenges call for more effort and attention toward developing fresh strategies to combat influenza. Previously, TCM demonstrated a positive anti-viral effect on influenza virus and alleviated the symptoms among patients (He et al., 2019; Nagai et al., 2019). In TCM theory, influenza disease was classified as "YI Disease" and was first reported in Huang Di Nei Jing. During the Han Dynasty, a theory of Shang Han (Treatise of Exogenous Febrile Diseases or Discourse on Cold-Damage Disorders) was written by Zhang Zhongjing to treat influenza. Later, during the Ming and Qing Dynasties, the emergence of "Wen Yi Lun (Analysis of Epidemic Warm Diseases)" revealed that TCM had contributed enormously to the prevention and treatment of influenza for thousands of years. Despite studies showing that TCMs are effective against influenza (Moscona, 2004; Tian et al., 2011), further studies on the development of novel anti-influenza agents are essential (Rajasekaran et al., 2013; Chang et al., 2014; Ding et al., 2014; Li C. et al., 2015). Herein, we summarize the impacts of TCM in treating influenza from basic experiments to clinical applications.

CONFIRMED IN CLINICAL APPLICATION

In Asia and some countries in Europe, TCM has been proven to be effective and secure for treating influenza (Moscona, 2004). Traditional Chinese Medicine (TCM) subdivides influenza into cold syndrome and heat syndrome. The major symptoms of wind-cold type include severe cold, light heat, lack of sweating, headache, sore limbs, and stuffy nose. On the other hand, high fever, a mild cold, headache, sore throat, cough are the primary symptoms of wind-heat type. By relying on the concept of evidence-based medicine, several clinical trials have been conducted to verify the efficacy and safety of TCM.

Meta-Analysis

A meta-analysis enrolled 30 studies consisting of 3,444 cases in all to investigate efficacy and safety of TCM in the treatment of influenza infection. Our findings indicated that the mean time fever resolution of the TCM treatment group was statistically significant compared to the control group. Additionally, the synergistic effects of TCM and conventional medicines on viral infections were better compared to the control group (Li J. H. et al., 2016). Further, a different TCM prescription from Shang Han Lun, ma-huang-tang(5 g of *ephedra equisetina bunge*, 5 g of *prunus armeniaca L.*, 4 g of *cinnamomum verum J.Presl*, and 1.5 g of *glycyrrhiza uralensis fisch. ex DC.*) was confirmed that it alleviated fever when singly administered or in combination with neuraminidase inhibitors (NAIs) and might be a well-tolerated treatment as reported by a systematic review and meta-analysis conducted by Japanese scientists (Yoshino et al., 2019). Andrographis paniculata was indicated to be beneficial and safe for relieving influenza symptoms and shortening time to symptom resolution (Hu et al., 2017).Conclusively, TCM are validated in lessening influenza symptoms, such as duration for defervescence and cough.

Randomized Clinical Trial (RCT)

Researchers conducted a randomized trial for comparing the efficacy and safety of oseltamivir and maxingshigan-yinqiaosan [6 g of *honey-fried ephedra equisetina bunge*; 10 g of *anemarrhena asphodeloides bunge*; 15 g of *artemisia annua L.*; 30 g of *gypsum fibrosum*; 15 g of *lonicera japonica thunb.*; 15 g of *scutellaria baicalensis georgi*; 15 g of *stir-baked prunus armeniaca L.*; 15 g of *forsythia suspensa (thunb.) vahl*; 6 g of *mentha canadensis L.*; 15 g of *fritillaria thunbergii miq.*; 15 g of *arctium lappa L.*; and 10 g of *glycyrrhiza uralensis fisch. ex DC.*] originating from Shang Han Lun and Wen Bing Tiao Bian, in treating uncomplicated influenza. Results have shown that singular use or combinations of oseltamivir and maxingshigan-yinqiaosan minimized defervescence time in patients diagnosed with influenza viral infections (Wang et al., 2011). It was, therefore, proposed that maxingshigan-yinqiaosan in combination with oseltamivir be utilized as an alternative medication in the treatment of influenza viral infections. In a multi-centric, randomized, double-blind, and placebo-controlled trial, a total of 480 adults with influenza symptoms were recruited. It was observed that TCM increased recovery by 17% ($p < 0.001$) and lowered disease severity (evaluated through the median symptom score) by 50% ($p < 0.001$) (Wang et al., 2010). Moreover, 136 influenza patients with wind-heat affecting Fei syndrome (WHAFS) were prescribed with Jinhua Qinggan Granules (JHG) that have been developed by experts in recent years. This preparation has been based on findings in a double-blind randomized control trial. In this trial, the duration of defervescence, the defervescence rate, the efficacy of TCM, the alleviation rate of primary symptoms and physical signs of influenza, the absence of viral nucleic acid in pharyngeal secretions, and safety indices were assessed. It was shown that JHG was efficient and safe in treating patients with WHAFS (Li et al., 2013). Japanese doctors have conventionally prescribed TCM to treat influenza. This is based on findings of a randomized controlled trial that compared the efficacy of TCMs with NP inhibitors in treating influenza. It has been established that TCM was effectively tolerated when used to treat influenza. Meanwhile, TCM and NP inhibitors exhibited equivalent clinical efficacies against the influenza virus (Nabeshima et al., 2012). In the US, a randomized, double-blind placebo-controlled study established that *Echinacea angustifolia* DC, a compound used in herbal tea preparations was potent in alleviating influenza symptoms such as stuffiness, scratchy throat and fever (Lindenmuth and Lindenmuth, 2000). In agreement with our meta-analysis, RCTs

demonstrated that TCM abbreviated fever time and showed a satisfactory impact in relieving cough and sore throat. In **Table 1**, we summarized the efficacy of TCMs in treating influenza (**Table 1**).

Retrospective Analysis

Besides meta-analysis RCT, researchers analyzed the duration of viral shedding in influenza patients admitted and administered with TCM in China. A total of 963 patients diagnosed with influenzavirus infection between May and July 2009 were recruited. The study showed that TCM therapy contributed to viral shedding among patients with a temperature of ≥ 38°C (Wang et al., 2012). Overall, these studies demonstrated that, besides alleviating symptoms of influenza patients, such as fever and cough, TCM have been proved to contribute to viral shedding.

Use of TCM in Treating Influenza Among Children and During Pregnancy

Treatment of influenza among children and pregnant women is challenging. However, other than effectively alleviating symptoms, TCM can compensate for deficiencies that cannot be bridged by conventional medicines in pregnant women. Children is the major group affected by influenza virus as they are usually vulnerable to complications. Moreover, the response of children to drug-drug metabolism is profoundly unique from that of adults. Therefore, it is essential to analyze the effects of TCM on children. It is, therefore, essential to analyze the effects of TCM on children. As mentioned above, ma-huang-tang was expansively used in China to manage children diagnosed with influenza. Ma-huang-tang has been widely used in China to manage influenza diagnoses among children. Without exhibiting adverse effects, it has been validated to be clinically useful in neonates, infants, and children with febrile viral symptoms (Nishimura et al., 2009). Additionally, it has been shown that it might potentially be useful in patients aged ≤5 who have a low sensitivity to oseltamivir and experience problems when using zanamivir (Toriumi et al., 2012). Comparison of the efficacies of ma-huang-tang and oseltamivir was evaluated among children with type A influenza. Results showed that ma-huang-tang in combination with oseltamivir was capable of abbreviating fever duration when compared to the group administered with oseltamivir only (Kubo and Nishimura, 2007). Elsewhere, a systematic review focusing on the effects of *Andrographis paniculata (burm.f.) nees* on influenza infections among children reported that this herb minimized the duration of cough, sore throat and morbidity time compared to conventional medicines (Hu et al., 2017). The use of TCM aerosols in treating infantile influenza infections showed an effective rate of 99.03% with a cure rate of 65.38% (Ma et al., 2000). An investigation on the clinical efficacy of a sachet of Chinese herbs in preventing influenza among 239 children from Shanghai Baoshan Xubeihong Art Kindergarten revealed that the sachet alleviated symptoms such as fever, rhinocleisis, runny nose, and throat congestions. Equally, the incidence rates of influenza in the treatment group were low compared to the control group (Liu et al., 2010). Reports indicate that TCM is a valuable option during pregnancy. For instance, when influenza outbreaks occurred in the Middle East, the prevalence in the use of TCM varied between 22.3%–82.3% in pregnant women (John and Shantakumari, 2015). Also, Across-sectional study conducted in the Central Appalachian Region showed that *Trigonella foenum-graecum L.* was regularly used in treating Influenza (Alwhaibi et al., 2017). More and more RCTs are focusing on the efficacy and safety of combination use of TCM and

TABLE 1 | Distribution of influenza article types and outcome indicators.

Study Design	Source	Groups	N	Outcomes							
				Main Outcomes						Secondary Outcomes	
				Fever	Headache	Myalgia	Cough	Sorethroat	Malaise	Hospitalization	Side effects
Meta	Li J. H. et al., 2016	1.Ma Huang Tang plus NAIs vs. NAIs 2. Ma Huang Tang vs. NAIs	30 studies, 3,444 cases	↑	↑	↑			↑	↑	↑
	Yoshino et al., 2019	1.TCM VS oseltamivir 2.TCM + oseltamivir vs. oseltamivir	12 studies, 1,170 cases	↑			↑	↑		↑	
	Hu et al., 2017	Andrographis paniculata vs. placebo	33 studies, 7,175 cases								
Randomized Controlled Trial	Wang et al., 2011	maxingshigan–yinqiaosan vs. Oseltamivir	410 cases	↑	↑		↑	↑			
	Wang et al., 2010	Antiwei vs. placebo	480 cases	↑	↑	↑	↑	↑			
	Li et al., 2013	Echinacea vs. Placebo	136 cases								
	Nabeshima et al., 2012	Jinhua Qinggan Granules vs. Placebo	28 cases	↑	↑	↑	↑	↑			↑
	Lindenmuth et al., 2013	Maoto VS oseltamivir vs. zanamivir	95 cases	↑	↑	↑	↑	↑			↑

The upward arrow represents the relief of symptoms after treatment.

conventional therapy (He et al., 2019). In summary, there is potential value in using TCM to treat influenza among children and pregnant women; nevertheless, more investigations are necessary for clinical validations.

BASIC EXPERIMENTS

Direct Anti-Influenza Virus by Interfering the Invasion Process

In the clinical set-up, we have witnessed the effects of TCM in improving the symptoms of influenza and cutting the course of the disease. However, how TCM act on influenza virus and its effects on the host requires a comprehensive analysis using basic experiments. Recently, researchers have constantly been drawn to investigate the therapeutic effects of TCM. Several types of TCM including, *coptis deltoidea* (*C.Y.Cheng & P.K.Hsiao)*, *Isatis tinctoria L.*, *Lonicera japonica thunb.*, *scutellaria baicalensis* georgi., *cyrtomium fortunei* J.Sm., *Houttuynia cordata thunb.*, *gardenia jasminoides J.Ellis*, and *chrysanthemum indicum L.*, and other TCM prescriptions have been proven to effectively suppress influenza virus (Han et al., 2016).

Single Herbal Medicine

The influenza virus invades the human body in six steps, that is, adsorption, penetration, shelling, biosynthesis, assembly, and release. As its mode of action, TCM targets these six steps. i) The extracts from single herbal medicine: *Lonicera japonica thunb.* HS-encoded atypical microRNA was verified to inhibit influenza viral replication *in vitro* and *in vivo*. Furthermore, HS decoction significantly minimized mice mortalities from influenza virus infection (Zhou et al., 2015). Extracts of *Laggera crispata (vahl) (Hepper & J.R.I.Wood*), a TCM have been shown to inhibit NA activity. It has also been reported that this compound could suppress NF-κB signaling pathways and viral RNP complexes from the nucleus thereby inhibiting viral replication (Guan et al., 2017). Besides blocking viral replication, TCM enhances the prognosis of mice infected by influenza. Yan et al. evaluated the effects of berberine, a natural isoquinoline alkaloid isolated from *coptis chinensis franch.* on influenza virus. Their results showed that berberine suppressed viral replication in A549 cells and the lungs of mice. Compared to conventional medicines, this compound exhibited significant anti-inflammatory effects on the pulmonary system and reduced necrosis in mice. It was also observed that inflammatory cell infiltrations and pulmonary edemas due to viral infections in mice were reduced (Yan Y. Q. et al., 2018). Houttuynia cordata Thunb (HCP), a TCM, plays a pivotal role in the treatment of bacterial and viral respiratory infections. Accompanied by a reduction in virus replication, HCP is reported to increase the overall survival rate of mice infected with influenza. Further studies have proved that it might be associated with the decrease in the concentration of pulmonary proinflammatory cytokines/chemokines and the number of intestinal goblet cells, which resulting in upregulation of sIgA and tight junction protein (ZO-1) in the intestine (Zhu et al., 2018). Researchers at the Kitasato Institute in Japan extracted flavonoids from the roots and leaves of *Astragalus mongholicus bunge* and confirmed their capacity in preventing the growth of influenza virus. It has been reported that glycyrrhizic acid significantly inhibits influenza virus (Pompei et al., 1983; Baltina et al., 2009). Besides, extracts of *Paeonia delavayi* Franch. and *pogostemon cablin (blanco) benth.* were found to efficiently inhibit NP (Li J. et al., 2016; Liu et al., 2016). The roots of *Bupleurum marginatum* var. *stenophyllum* (*H.Wolff*) had inhibitory effects on the replication of influenza (Fang et al., 2017). Importantly, it has been confirmed that *Tetradium ruticarpum* (*A.Juss.*) *T.G.Hartley* effectively hindered viral attachment and penetration into host cells (Lin et al., 2016). ii) Single components: A study by Li et al. addressed that, Dendrobine, extracted from a traditional Chinese herb (*dendrobium nobile lindl.*), interfered with early viral replication and bound to the viral NP thereby restricting nuclear export of viral NP and its oligomerization (Li et al., 2017). HESA-A is a natural ingredient retrieved from marine herbs. This compound blocks viral penetration into the cell (Mehrbod et al., 2014). *Persicaria chinensis (l.) h. gross*, from Vietnam, was shown to target NP, including oseltamivir-resistant ones (Tran et al., 2017). These results show that single herbal medicines inhibit viral proliferation by targeting multiple sites and pathways during replication. These results are presented in **Figure 1**.

Traditional Chinese Herbal Prescription

Besides the single Chinese herbal medicine, traditional Chinese herbal prescription has precariously shaped the academic debate on influenza disease management. Huang-Lian-Jie-Du-Tang (composed of *coptis chinensis Franch.*, *scutellaria baicalensis georgi*, *phellodendron chinense C.K.Schneid.*, and *gardenia jasminoides J.Ellis* at the weight ratio of 3:2:2:3) (HLJDT) is a classical prescription composed of 4 TCM herbs that have been used to treat diverse diseases including influenza. In total, 13 compounds have been isolated from the plasma profile of HLJDT. These compounds include, jatrorrhizine, palmatine, epiberberine, geniposide, oroxylin A, berberine, coptisine, baicalein, wogonoside, phellodendrine, wogonin, oroxylin A-7-O-glucuronide, and baicalin. They have been shown to be potent NA-1 inhibitors (Zhou et al., 2017). Xin-Jia-Xiang-Ru-Yin [(composed of *mosla chinensis* maxim., *lonicera japonica thunb.*, *dolichos lablab* L., *magnolia officinalis rehd. et wils.* and *forsythia suspensa (thunb.) vahl* at the weight ratio of 2:3:3:2:3)], a traditional Chinese prescription used for managing summer influenza in China, has been demonstrated to integrate antiviral therapy and immune modulation effects by lowering the expression of Interferon-γ (IFN-γ) and Signal transducer and activator of transcription-1 (STAT1), resulting to reduced inflammation hence harboring key therapeutic benefits against summer influenza (Li et al., 2018). The Re Du Ping intravenous injection, a TCM can adsorb the virus into host cells and inhibit their proliferation. This injection also has a direct viricidal effect (Jing et al., 2010). Studies into the pharmacodynamics and molecular mechanisms of Qingqi Liangying granules have reported that they participate in Wnt signaling pathways by regulating virus invasions on epithelial cell signaling pathway, thereby, inhibiting viral replication (Wang et al., 2017). Chinese

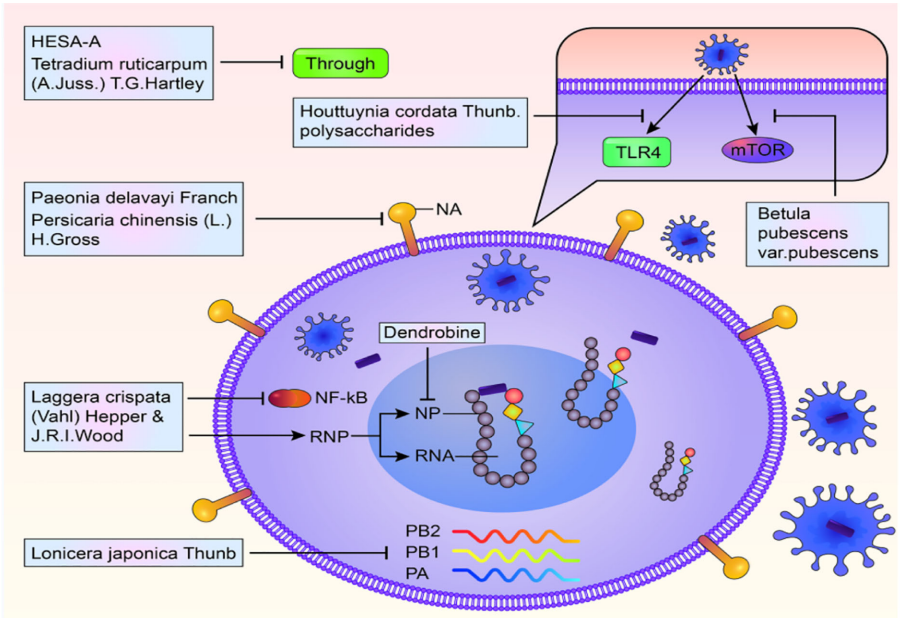

FIGURE 1 | Multiple targets and multiple pathways to inhibit influenza virus.

classical herbal prescription was also used in the prevention of influenza. It was reported to reduce the vulnerability of cells to the invasion of influenza virus and alleviate viral induced lung lesions (Liu et al., 2013).

In-Direct Anti-Influenza Virus by Regulating Host Immune System

In addition to the direct effect on the influenza virus, TCM regulates immune activation and signaling pathways that impact on the influenza virus. The host innate immune response to influenza virus occurs as follows: Infection with influenza virus stimulates the body's innate immune response, which involves multiple effector cells, immune molecules, and factors, such as Interleukin-6 (IL-6) and Interferon-α (IFN-α), to effectively regulate viral replication (Hayden et al., 1998). Several experiments have confirmed that TCM is the most potent anti-inflammatory natural medicine which can modulate all kinds of cytokines and immune molecules.

Traditional Chinese Herbal Prescription

A study conducted on the mechanisms of TCM prescription in the treatment of influenza deduced that anti-inflammatory effects conferred by TCM protect against inflammatory injuries induced by the influenza virus in mice. These herbal medicines significantly reduce the expression of pro-inflammatory cytokines Tumor Necrosis Factor-α (TNF-α) and IL-6 in lung tissues of infected mice (Wang et al., 2005; Xu et al., 2014). Sheng Jiang San (SJS), (*rheum officinale* baill., *bombyx batryticatus*, *cicadae periostracum*, and *curcuma longa L.* in a ratio of 4:2:1:3), a traditional multi-herb prescription, used to treat influenza infections. Research has shown that SJS down-regulates TNF-α and up-regulates IL-2 in influenza infected mice. Equally, lung indices used to evaluate the level of inflammation and viral loads in SJS treated mice were markedly decreased compared to the controls (Zhang et al., 2018). Currently, Yinhuapinggan granule (YHPG), a Chinese drug with patent that originated from ma-huang-tang is used in the treatment of influenza. A study conducted by Du revealed that YHPG markedly inhibited replication of the influenza virus and significantly up-regulated the levels of IFN-β and IFN-stimulated genes (Mx-1, ISG-15, and ISG-56) compared to the control group (Du et al., 2018). The Yinqiao powder [15 g of *forsythia suspensa (thunb.) vahl*, 15 g of *lonicera confusa DC.*, 9 g of *platycodon grandiflorus (jacq.) A.DC.*, 9 g of *mentha canadensis L.*, 6 g of *lophatherum gracile brongn.*, 5 g of *glycyrrhiza uralensis fisch. ex DC.*, 6 g of *nepeta tenuifolia benth.*, 6 g of *glycine max (L.) merr.*, 6 g of *arctium lappa L.*, 10 g of *phragmites australis subsp.* australis]; The Xinjiaxiangruyin concoction [6 g of *mosla chinensis maxim.*, 9 g of *lonicera confusa DC.*, 9 g of *lablab purpureus subsp. purpureus*, 6 g of *magnolia officinalis rehder & E.H.Wilson*, 6 g of *forsythia suspensa (thunb.) vahl*]; and the Guizhi-and-Mahuang decoction [9 g of *ephedra sinica stapf*, 6 g of *cinnamomum cassia (L.) J.Presl*, 9 g of *prunus armeniaca L.*, 6 g of *glycyrrhiza uralensis fisch. ex DC.*, 9 g of *paeonia lactiflora pall.*, 9 g of *zingiber officinale roscoe*, 3 g of *ziziphus jujuba mill.*]

are widely applied in clinical influenza treatment. These compounds reduce the expression levels of TLR7, MyD88, IRAK4, and NF-κB thereby by regulating the Toll-Like Receptor7/Nuclear Factor Kappa-B (TLR7/NF-κB) signaling pathway (Fu et al., 2018). Yi-Zhi-Hao pellet (CYZH) is a popular Chinese prescription used in influenza treatment. Mechanistically, CYZH lacked an inhibitory effect on viral protein HA and IAV RNA-dependent RNA polymerase but inhibited IAV replication by activating the Nrf2/HO-1 pathway (Yin et al., 2017). Lianhuaqingwen, a TCM prescription alleviates viral-induced gene expressions of IL-6, IL-8, TNF-a, IP-10, and MCP-1 (Ding et al., 2017). Furthermore, Lianhuaqingwen treatment resulted in abnormal particle morphology of virion in cells (Runfeng et al., 2020). San Wu Huangqin (SWHD) decoction (*sophora flavescens*, *scutellaria baicalensis*, and *rehmannia glutinosa* at a ratio of 1:1:2) exhibits its anti-viral effects by regulating the immune system (Ma et al., 2018). The Ge Gen Decoction [12 g of *pueraria montana* var. lobata (Willd.) maesen & *S.M.Almeida ex sanjappa & predeep*, 9 g of *ephedra sinica* stapf, 6 g of *cinnamomum cassia (L.) J.Presl*, 6 g of *glycyrrhiza uralensis* fisch. ex *DC*., 6 g of *paeonia lactiflora* pall., 9 g of *zingiber officinale* roscoe, and 22 g of *ziziphus jujuba mill.*] decreased the expression of TNF-α and toll-like receptor 7 signaling pathways in influenza virus infected mice thereby reducing lung inflammation (Geng et al., 2019). Research endorsed that Gui Zhi Ma Huang Ge Ban Tang [9 g of *ephedra sinica* stapf, 6 g of *cinnamomum cassia (L.) J.Presl*, 9 g of *prunus amygdalus batsch*, and 6 g of *glycyrrhiza uralensis fisch. ex DC*., 9 g of *paeonia lactiflora pall*., 9 g of *zingiber officinale roscoe*, and 10 g of *ziziphus jujuba mill.*] exhibit a good ability to reduce the proportion of Helper T cell 1/Helper T cell 2(Th1/Th2) and Helper T cell 1/Regulatory cells (Th17/Treg) cells thus reducing lung inflammation (Qin et al., 2018). *Artemisia scoparia Waldst. & Kit.* is expansively distributed in Xinjiang China and reported to downregulate NF-κB signal pathway thereby inhibiting viral replication (Yan H. et al., 2018). Summarily, TCM regulates signaling pathways like NF-κB and inflammatory factors such as TNF-α and IL-6, that are important in modulating immune responses against the virus.

Single Herbal Medicine

Besides the TCM prescription, single herbal medicine indirectly plays a crucial role in anti-viral activity. i) The extracts from single herbal medicine: As mentioned above, *laggera pterodonta*, demonstrated a wide spectrum of anti-influenza virus activity *via* the NF-κB pathway, COX-2, and p38/MAPK pathway (Wang et al., 2017). Moreover, flavonoids extracted from *Scutellaria baicalensis* Georgi (FESR) could inhibit excessive activations of the complement system, thereby, improving acute lung injuries (Zhi et al., 2020). *Houttuynia cordata* thunb polysaccharide (HCP) aids systemic influenza treatment by locally acting on the intestines and balancing the microbiota (Chen et al., 2019). *Bupleurum falcatum* L., extracted from a traditional Chinese herb, was also found to be an immune modulator (Yao et al., 2018). *Isatis tinctoria* L., attenuates viral-induced NF-κB activation (Li et al., 2015). Research has shown that *Forsythia suspensa (thunb.) vahl* interferes with the budding process of newly formed virions and reduces influenza M1 protein that is necessary for viral spread (Law et al., 2017). ii) Single components: Baicalin, a popularly known herbal medicine ingredient in China for treating Fei-Re syndrome characterized by fever, and cough, can be extracted from *scutellaria baicalensis georgi*, which was reported to induce autophagy so as to inhibit mTOR signaling pathway. Thus, shedding more light on the development of novel anti-influenza drugs (Zhu et al., 2015). Quercetin-7-O-glucoside was discovered in many types of Chinese herb and demonstrated a strong inhibition against influenza A and B viruses by downsizing virus-induced ROS and autophagy formation (Gansukh et al., 2016). The polysaccharides extracted from the roots of *astragalus mongholicus Bunge* species, a famous TCM used for hundreds of years to improve QI with Chinese medicine theory, was ratified to modulate Th1/Th2 balance and secretions of IFN-γ, IL-17A, and IgG2a (Yakuboğulları et al., 2019). These studies testify that different types of TCMs possess remarkable potential in immunomodulation against influenza virus.

SUMMARY

In conclusion, TCM impacts on the prevention and treatment of influenza. It has a potential value in shorting fever durations and alleviating influenza symptoms among children and pregnant women. However, the side effects of TCM in children and pregnant women are still elusive, which needs more clinical trials about the safety and vivo toxicity. These medicines also regulate the immune system. Their modes of action involve inhibiting NA, viral replication, and stopping viral entry into the cell. The synergistic effects of TCM and conventional medicines are encouraging as an avenue for influenza therapy.

AUTHOR CONTRIBUTIONS

YX: Conceptualization, Writing—original draft. ND: Conceptualization. XL: Writing—original draft. BL: Writing—original draft. HZ: Writing—original draft. CZ: Supervision. LL: Supervision. CL: Supervision. LH: Funding acquisition and supervision.

ACKNOWLEDGMENTS

This work was supported by the National Science and Technology Major Project (2018ZX10101001-005) and by the China Academy of Chinese Medical Sciences Project (Nos. Z0656 and Z0606). The authors have no conflicts of interest to declare.

REFERENCES

Alwhaibi, M., Goyat, R., and Kelly, K. M. (2017). The Use of Herbal Remedies among Mothers of Young Children Living in the Central Appalachian Region. *Evid. Based. Complement. Alternat. Med.* 2017:1739740. doi: 10.1155/2017/1739740

Baltina, L. A., Kondratenko, R. M., Baltina, L. A.Jr., Plyasunova, O. A., Pokrovskii, A. G., and Tolstikov, G. A. (2009). Prospects for the creation of new antiviral drugs based on glycyrrhizic acid and its derivatives (a review). *Pharm. Chem. J.* 43 (10), 539–548. doi: 10.1007/s11094-010-0348-2

Birnkrant, D., and Cox, E. (2009). The Emergency Use Authorization of peramivir for treatment of 2009 H1N1 influenza. *N. Engl. J. Med.* 361 (23), 2204–2207. doi: 10.1056/NEJMp0910479

Brody, H. (2019). Influenza. *Nature* 573 (7774), S49. doi: 10.1038/d41586-019-02750-x

Chang, Q., Wo, S., Ngai, K. L., Wang, X., Fok, B., Ngan, T. M., et al. (2014). Bench to bed evidences for pharmacokinetic and pharmacodynamic interactions involving oseltamivir and chinese medicine. *Evid. Based. Complement. Alternat. Med.* 2014:354172. doi: 10.1155/2014/354172

Chen, M. Y., Li, H., Lu, X. X., Ling, L. J., Weng, H. B., Sun, W., et al. (2019). Houttuynia cordata polysaccharide alleviated intestinal injury and modulated intestinal microbiota in H1N1 virus infected mice. *Chin. J. Nat. Med.* 17 (3), 187–197. doi: 10.1016/s1875-5364(19)30021-4

Cox, N. J., and Subbarao, K. (2000). Global epidemiology of influenza: past and present. *Annu. Rev. Med.* 51, 407–421. doi: 10.1146/annurev.med.51.1.407

Ding, Y., Dou, J., Teng, Z., Yu, J., Wang, T., Lu, N., et al. (2014). Antiviral activity of baicalin against influenza A (H1N1/H3N2) virus in cell culture and in mice and its inhibition of neuraminidase. *Arch. Virol.* 159 (12), 3269–3278. doi: 10.1007/s00705-014-2192-2

Ding, Y., Zeng, L., Li, R., Chen, Q., Zhou, B., Chen, Q., et al. (2017). The Chinese prescription lianhuaqingwen capsule exerts anti-influenza activity through the inhibition of viral propagation and impacts immune function. *BMC Complement. Altern. Med.* 17 (1), 130. doi: 10.1186/s12906-017-1585-7

Du, H. X., Zhou, H. F., Wan, H. F., Yang, J. H., Lu, Y. Y., He, Y., et al. (2018). Antiviral effects and mechanisms of Yinhuapinggan granule against H1N1 influenza virus infection in RAW264.7 cells. *Inflammopharmacology* 26 (6), 1455–1467. doi: 10.1007/s10787-018-0457-1

Fang, W., Yang, Y. J., Guo, B. L., and Cen, S. (2017). Anti-influenza triterpenoid saponins (saikosaponins) from the roots of Bupleurum marginatum var. stenophyllum. *Bioorg. Med. Chem. Lett.* 27 (8), 1654–1659. doi: 10.1016/j.bmcl.2017.03.015

Fu, Y. J., Yan, Y. Q., Qin, H. Q., Wu, S., Shi, S. S., Zheng, X., et al. (2018). Effects of different principles of Traditional Chinese Medicine treatment on TLR7/NF-κB signaling pathway in influenza virus infected mice. *Chin. Med.* 13, 42. doi: 10.1186/s13020-018-0199-4

Gaitonde, D. Y., Moore, F. C., and Morgan, M. K. (2019). Influenza: Diagnosis and Treatment. *Am. Fam. Physician* 100 (12), 751–758.

Gansukh, E., Kazibwe, Z., Pandurangan, M., Judy, G., and Kim, D. H. (2016). Probing the impact of quercetin-7-O-glucoside on influenza virus replication influence. *Phytomedicine* 23 (9), 958–967. doi: 10.1016/j.phymed.2016.06.001

Geng, Z. K., Li, Y. Q., Cui, Q. H., Du, R. K., and Tian, J. Z. (2019). Exploration of the mechanisms of Ge Gen Decoction against influenza A virus infection. *Chin. J. Nat. Med.* 17 (9), 650–662. doi: 10.1016/s1875-5364(19)30079-2

Govorkova, E. A., Leneva, I. A., Goloubeva, O. G., Bush, K., and Webster, R. G. (2001). Comparison of efficacies of RWJ-270201, zanamivir, and oseltamivir against H5N1, H9N2, and other avian influenza viruses. *Antimicrob. Agents Chemother.* 45 (10), 2723–2732. doi: 10.1128/aac.45.10.2723-2732.2001

Guan, W., Li, J., Chen, Q., Jiang, Z., Zhang, R., Wang, X., et al. (2017). Pterodontic Acid Isolated from Laggera pterodonta Inhibits Viral Replication and Inflammation Induced by Influenza A Virus. *Molecules* 22 (10), 1738. doi: 10.3390/molecules22101738

Han, X., Zhang, D. K., Guo, Y. M., Feng, W. W., Dong, Q., Zhang, C. E., et al. (2016). Screening and evaluation of commonly-used anti-influenza Chinese herbal medicines based on anti-neuraminidase activity. *Chin. J. Nat. Med.* 14 (10), 794–800. doi: 10.1016/s1875-5364(16)30095-4

Hayden, F. G., Fritz, R., Lobo, M. C., Alvord, W., Strober, W., and Straus, S. E. (1998). Local and systemic cytokine responses during experimental human influenza A virus infection. Relation to symptom formation and host defense. *J. Clin. Invest.* 101 (3), 643–649. doi: 10.1172/jci1355

He, W., Han, H., Wang, W., and Gao, B. (2011). Anti-influenza virus effect of aqueous extracts from dandelion. *Virol. J.* 8:538. doi: 10.1186/1743-422x-8-538

He, J., Li, Z., Huang, W., Guan, W., Ma, H., Yang, Z. F., et al. (2019). Efficacy and safety of Chou-Ling-Dan granules in the treatment of seasonal influenza via combining Western and traditional Chinese medicine: protocol for a multicentre, randomised controlled clinical trial. *BMJ Open* 9 (4), e024800. doi: 10.1136/bmjopen-2018-024800

Hu, X. Y., Wu, R. H., Logue, M., Blondel, C., Lai, L. Y. W., Stuart, B., et al. (2017). Andrographis paniculata (Chuān Xīn Lián) for symptomatic relief of acute respiratory tract infections in adults and children: A systematic review and meta-analysis. *PloS One* 12 (8), e0181780. doi: 10.1371/journal.pone.0181780

Huang, I. C., Li, W., Sui, J., Marasco, W., Choe, H., and Farzan, M. (2008). Influenza A virus neuraminidase limits viral superinfection. *J. Virol.* 82 (10), 4834–4843. doi: 10.1128/jvi.00079-08

Jing, S., Gu, L. G., and Zhou, Y. (2010). [Effect of dureping injection on T-cells function and their function in killing FM1 infected Mphi in vitro]. *Zhongguo Zhong Xi Yi Jie He Za Zhi* 30 (7), 729–732.

JJ, X. (2010). *Traditional Chinese Medicine Treatment of Viral Infectious Diseases* Vol. 2010 (Beijing: Science and Technology Press).

John, L. J., and Shantakumari, N. (2015). Herbal Medicines Use During Pregnancy: A Review from the Middle East. *Oman Med. J.* 30 (4), 229–236. doi: 10.5001/omj.2015.48

Kamali, A., and Holodniy, M. (2013). Influenza treatment and prophylaxis with neuraminidase inhibitors: a review. *Infect. Drug Resist.* 6, 187–198. doi: 10.2147/idr.S36601

Kawaoka, Y. (2006). *Influenza Virology: Current Topics* (England: Caister Academic Press).

Kiso, M., Mitamura, K., Sakai-Tagawa, Y., Shiraishi, K., Kawakami, C., Kimura, K., et al. (2004). Resistant influenza A viruses in children treated with oseltamivir: descriptive study. *Lancet* 364 (9436), 759–765. doi: 10.1016/s0140-6736(04)16934-1

Kubo, T., and Nishimura, H. (2007). Antipyretic effect of Mao-to, a Japanese herbal medicine, for treatment of type A influenza infection in children. *Phytomedicine* 14 (2-3), 96–101. doi: 10.1016/j.phymed.2006.09.015

Law, A. H., Yang, C. L., Lau, A. S., and Chan, G. C. (2017). Antiviral effect of forsythoside A from Forsythia suspensa (Thunb.) Vahl fruit against influenza A virus through reduction of viral M1 protein. *J. Ethnopharmacol.* 209, 236–247. doi: 10.1016/j.jep.2017.07.015

Lee, J., Park, J. H., Jwa, H., and Kim, Y. H. (2017). Comparison of Efficacy of Intravenous Peramivir and Oral Oseltamivir for the Treatment of Influenza: Systematic Review and Meta-Analysis. *Yonsei Med. J.* 58 (4), 778–785. doi: 10.3349/ymj.2017.58.4.778

Li, G. Q., Zhao, J., Tu, Z. T., Li, J. B., Liu, Q. Q., Shi, L. Q., et al. (2013). [Treating influenza patients of wind-heat affecting Fei syndrome by jinhua qinggan granule: a double-blinded randomized control trial]. *Zhongguo Zhong Xi Yi Jie He Za Zhi* 33 (12), 1631–1635.

Li, C., Fang, J. S., Lian, W. W., Pang, X. C., Liu, A. L., and Du, G. H. (2015). In vitro antiviral effects and 3D QSAR study of resveratrol derivatives as potent inhibitors of influenza H1N1 neuraminidase. *Chem. Biol. Drug Des.* 85 (4), 427–438. doi: 10.1111/cbdd.12425

Li, J., Zhou, B., Li, C., Chen, Q., Wang, Y., Li, Z., et al. (2015). Lariciresinol-4-O-β-D-glucopyranoside from the root of Isatis indigotica inhibits influenza A virus-induced pro-inflammatory response. *J. Ethnopharmacol.* 174, 379–386. doi: 10.1016/j.jep.2015.08.037

Li, J. H., Wang, R. Q., Guo, W. J., and Li, J. S. (2016). Efficacy and safety of traditional Chinese medicine for the treatment of influenza A (H1N1): A meta-analysis. *J. Chin. Med. Assoc.* 79 (5), 281–291. doi: 10.1016/j.jcma.2015.10.009

Li, J., Yang, X., and Huang, L. (2016). Anti-Influenza Virus Activity and Constituents. Characterization of Paeonia delavayi Extracts. *Molecules* 21 (9), 1133. doi: 10.3390/molecules21091133

Li, R., Liu, T., Liu, M., Chen, F., Liu, S., and Yang, J. (2017). Anti-influenza A Virus Activity of Dendrobine and Its Mechanism of Action. *J. Agric. Food Chem.* 65 (18), 3665–3674. doi: 10.1021/acs.jafc.7b00276

Li, Q., Pang, P., Zheng, K., Sun, L., Wang, J., and Chen, X. (2018). Xin-Jia-Xiang-Ru-Yin alleviated H1N1-induced acute lung injury and inhibited the IFN-γ-

related regulatory pathway in summer flu. *BioMed. Pharmacother.* 108, 201–207. doi: 10.1016/j.biopha.2018.09.022

Lin, T. J., Lin, C. F., Chiu, C. H., Lee, M. C., and Horng, J. T. (2016). Inhibition of endosomal fusion activity of influenza virus by Rheum tanguticum (da-huang). *Sci. Rep.* 6:27768. doi: 10.1038/srep27768

Lindenmuth, G. F., and Lindenmuth, E. B. (2000). The efficacy of echinacea compound herbal tea preparation on the severity and duration of upper respiratory and flu symptoms: a randomized, double-blind placebo-controlled study. *J. Altern. Complement. Med.* 6 (4), 327–334. doi: 10.1089/10755530050120691

Liu, L., Yue, X. Q., Wang, L. N., Gu, W., Xin, H. L., Zheng, G. Y., et al. (2010). [Preventive effects of a sachet of Chinese herbs on influenza and its immune regulation]. *Zhong Xi Yi Jie He Xue Bao* 8 (10), 949–954. doi: 10.3736/jcim20101006

Liu, Q., Lu, L., Hua, M., Xu, Y., Xiong, H., Hou, W., et al. (2013). Jiawei-Yupingfeng-Tang, a Chinese herbal formula, inhibits respiratory viral infections in vitro and in vivo. *J. Ethnopharmacol.* 150 (2), 521–528. doi: 10.1016/j.jep.2013.08.056

Liu, F., Cao, W., Deng, C., Wu, Z., Zeng, G., and Zhou, Y. (2016). Polyphenolic glycosides isolated from Pogostemon cablin (Blanco) Benth. as novel influenza neuraminidase inhibitors. *Chem. Cent J.* 10, 51. doi: 10.1186/s13065-016-0192-x

Lu, Z. Y. (2008). *ZN. Internal Medicine* (Beijing: People's Medical Publishing House).

Ma, B., Duan, X., and Wang, Z. (2000). [Clinical and experimental study on Shuanghua aerosol in treating infantile upper respiratory tract infection]. *Zhongguo Zhong Xi Yi Jie He Za Zhi* 20 (9), 653–655.

Ma, Q., Yu, Q., Xing, X., Liu, S., Shi, C., and Luo, J. (2018). San Wu Huangqin Decoction, a Chinese Herbal Formula, Inhibits Influenza a/PR/8/34 (H1N1) Virus Infection In Vitro and In Vivo. *Viruses* 10 (3), 117. doi: 10.3390/v10030117

Mehrbod, P., Ideris, A., Omar, A. R., and Hair-Bejo, M. (2014). Prophylactic effect of herbal-marine compound (HESA-A) on influenza A virus infectivity. *BMC Complement. Altern. Med.* 14:131. doi: 10.1186/1472-6882-14-131

Moscona, A. (2004). Oseltamivir-resistant influenza? *Lancet* 364 (9436), 733–734. doi: 10.1016/s0140-6736(04)16947-x

Moscona, A. (2009). Global transmission of oseltamivir-resistant influenza. *N. Engl. J. Med.* 360 (10), 953–956. doi: 10.1056/NEJMp0900648

Nabeshima, S., Kashiwagi, K., Ajisaka, K., Masui, S., Takeoka, H., Ikematsu, H., et al. (2012). A randomized, controlled trial comparing traditional herbal medicine and neuraminidase inhibitors in the treatment of seasonal influenza. *J. Infect. Chemother.* 18 (4), 534–543. doi: 10.1007/s10156-012-0378-7

Nagai, E., Iwai, M., Koketsu, R., Okuno, Y., Suzuki, Y., Morimoto, R., et al. (2019). Anti-Influenza Virus Activity of Adlay Tea Components. *Plant Foods Hum. Nutr.* 74 (4), 538–543. doi: 10.1007/s11130-019-00773-3

Nishimura, N., Doi, N., Uemura, T., Taketani, T., Hayashi, G., Kasai, T., et al. (2009). [Pharmaceutical analysis and clinical efficacy of Kampo medicine, maoto, extract suppository against pediatric febrile symptoms]. *Yakugaku Zasshi* 129 (6), 759–766. doi: 10.1248/yakushi.129.759

Panning, M. (2013). [Influenza today and in the future]. *Pneumol. (Berl)* 10 (5), 314–325. doi: 10.1007/s10405-013-0674-7

Pompei, R., Paghi, L., Ingianni, A., and Uccheddu, P. (1983). Glycyrrhizic acid inhibits influenza virus growth in embryonated eggs. *Microbiologica* 6 (3), 247–250.

Qin, H. Q., Shi, S. S., Fu, Y. J., Yan, Y. Q., Wu, S., Tang, X. L., et al. (2018). Effects of Gui Zhi Ma Huang Ge Ban Tang on the TLR7 Pathway in Influenza Virus Infected Mouse Lungs in a Cold Environment. *Evid. Based. Complement. Alternat. Med.* 2018:5939720. doi: 10.1155/2018/5939720

Rajasekaran, D., Palombo, E. A., Chia Yeo, T., Lim Siok Ley, D., Lee Tu, C., Malherbe, F., et al. (2013). Identification of traditional medicinal plant extracts with novel anti-influenza activity. *PloS One* 8 (11), e79293. doi: 10.1371/journal.pone.0079293

Runfeng, L., Yunlong, H., Jicheng, H., Weiqi, P., Qinhai, M., Yongxia, S., et al. (2020). Lianhuaqingwen exerts anti-viral and anti-inflammatory activity against novel coronavirus (SARS-CoV-2). *Pharmacol. Res.* 156:104761. doi: 10.1016/j.phrs.2020.104761

Shetty, A. K., and Peek, L. A. (2012). Peramivir for the treatment of influenza. *Expert Rev. Anti Infect. Ther.* 10 (2), 123–143. doi: 10.1586/eri.11.174

Tian, L., Wang, Z., Wu, H., Wang, S., Wang, Y., Wang, Y., et al. (2011). Evaluation of the anti-neuraminidase activity of the traditional Chinese medicines and determination of the anti-influenza A virus effects of the neuraminidase inhibitory TCMs in vitro and in vivo. *J. Ethnopharmacol.* 137 (1), 534–542. doi: 10.1016/j.jep.2011.06.002

Toriumi, Y., Kamei, T., Murata, K., Takahashi, I., Suzuki, N., and Mazda, O. (2012). Utility of Maoto in an influenza season where reduced effectiveness of oseltamivir was observed - a clinical, non-randomized study in children. *Forsch Komplementmed.* 19 (4), 179–186. doi: 10.1159/000341547

Tran, T. T., Kim, M., Jang, Y., Lee, H. W., Nguyen, H. T., Nguyen, T. N., et al. (2017). Characterization and mechanisms of anti-influenza virus metabolites isolated from the Vietnamese medicinal plant Polygonum chinense. *BMC Complement. Altern. Med.* 17 (1), 162. doi: 10.1186/s12906-017-1675-6

Wang, X., Yu, S. Y., Shen, P. L., Wang, S. L., Wei, Z. H. , Liu, Z. G., et al. (2017) Analysis of anti-influenza virus pharmacodynamics of QingQiLiangYing granule and its molecular mechanism. *Chin. Pharmacol. Bull.* 33, 719–728. doi: 10.3969/j.issn.1001-1978.2017.05.025

Wang, C. X., Gao, G. X., Wei, S. C., and Xu, H. R. (2005). [The dynamic effect of yiqi qingwen jiedu heji on the protein expressions of cytokine IFN-gamma, TNF-alpha, IL-10 and IL-6 in the lungs of mice infected by IV FM1]. *Zhongguo Zhong Yao Za Zhi* 30 (7), 541–544.

Wang, L., Zhang, R. M., Liu, G. Y., Wei, B. L., Wang, Y., Cai, H. Y., et al. (2010). Chinese herbs in treatment of influenza: a randomized, double-blind, placebo-controlled trial. *Respir. Med.* 104 (9), 1362–1369. doi: 10.1016/j.rmed.2010.05.015

Wang, C., Cao, B., Liu, Q. Q., Zou, Z. Q., Liang, Z. A., Gu, L., et al. (2011). Oseltamivir compared with the Chinese traditional therapy maxingshigan-yinqiaosan in the treatment of H1N1 influenza: a randomized trial. *Ann. Intern Med.* 155 (4), 217–225. doi: 10.7326/0003-4819-155-4-201108160-00005

Wang, Y. G., Jiang, M., Wang, R. B., Zha, Q. L., Zhang, S. J., Zhou, G. Q., et al. (2012). Duration of viral shedding of influenza A (H1N1) virus infection treated with oseltamivir and/or traditional Chinese medicine in China: a retrospective analysis. *J. Tradit. Chin. Med.* 32 (2), 148–155. doi: 10.1016/s0254-6272(13)60004-7

Wang, Y., Zhou, B., Lu, J., Chen, Q., Ti, H., Huang, W., et al. (2017). Inhibition of influenza virus via a sesquiterpene fraction isolated from Laggera pterodonta by targeting the NF-κB and p38 pathways. *BMC Complement. Altern. Med.* 17 (1), 25. doi: 10.1186/s12906-016-1528-8

Webster, R. G., Bean, W. J., Gorman, O. T., Chambers, T. M., and Kawaoka, Y. (1992). Evolution and ecology of influenza A viruses. *Microbiol. Rev.* 56 (1), 152–179. doi: 10.1128/MMBR.56.1.152-179.1992

Xu, H. R., Wang, C. X., Wang, L., Zhou, P. A., Yin, R. Y., Jiang, L. D., et al. (2014). [Mechanism of tonifying Qi traditional Chinese medicines contained in Yiqi Qingwen Jiedu mixture against influenza immune inflammatory injury]. *Zhongguo Zhong Yao Za Zhi* 39 (20), 4020–4026.

Yakuboğulları, N., Genç, R., Çöven, F., Nalbantsoy, A., and Bedir, E. (2019). Development of adjuvant nanocarrier systems for seasonal influenza A (H3N2) vaccine based on Astragaloside VII and gum tragacanth (APS). *Vaccine* 37 (28), 3638–3645. doi: 10.1016/j.vaccine.2019.05.038

Yan, Y. Q., Fu, Y. J., Wu, S., Qin, H. Q., Zhen, X., Song, B. M., et al. (2018). Anti-influenza activity of berberine improves prognosis by reducing viral replication in mice. *Phytother. Res.* 32 (12), 2560–2567. doi: 10.1002/ptr.6196

Yan, H., Wang, H., Ma, L., Ma, X., Yin, J., Wu, S., et al. (2018). Cirsimaritin inhibits influenza A virus replication by downregulating the NF-κB signal transduction pathway. *Virol. J.* 15 (1), 88. doi: 10.1186/s12985-018-0995-6

Yao, J., Zhang, H., Ma, L., Mu, X., Wang, Y., Lu, Y., et al. (2018). Effect of traditional Chinese medicine Bupleurum in the treatment of influenza A (H1N1). *Pak J. Pharm. Sci.* 31 (4(Special), 1713–1717.

Yin, J., Ma, L., Wang, H., Yan, H., Hu, J., Jiang, W., et al. (2017). Chinese herbal medicine compound Yi-Zhi-Hao pellet inhibits replication of influenza virus infection through activation of heme oxygenase-1. *Acta Pharm. Sin. B.* 7 (6), 630–637. doi: 10.1016/j.apsb.2017.05.006

Yoshino, T., Arita, R., Horiba, Y., and Watanabe, K. (2019). The use of maoto (Ma-Huang-Tang), a traditional Japanese Kampo medicine, to alleviate flu symptoms: a systematic review and meta-analysis. *BMC Complement. Altern. Med.* 19 (1), 68. doi: 10.1186/s12906-019-2474-z

Zhang, T., Xiao, M., Wong, C. K., Mok, K. C., Zhao, X., Ti, H., et al. (2018). Sheng Jiang San, a traditional multi-herb formulation, exerts anti-influenza effects in vitro and in vivo via neuraminidase inhibition and immune regulation. *BMC Complement. Altern. Med.* 18 (1), 150. doi: 10.1186/s12906-018-2216-7

Zhi, H., Jin, X., Zhu, H., Li, H., Zhang, Y., Lu, Y., et al. (2020). Exploring the effective materials of flavonoids-enriched extract from Scutellaria baicalensis roots based on the metabolic activation in influenza A virus induced acute lung injury. *J. Pharm. BioMed. Anal.* 177:112876. doi: 10.1016/j.jpba.2019.112876

Zhou, Z., Li, X., Liu, J., Dong, L., Chen, Q., Liu, J., et al. (2015). Honeysuckle-encoded atypical microRNA2911 directly targets influenza A viruses. *Cell Res.* 25 (1), 39–49. doi: 10.1038/cr.2014.130

Zhou, X., Li, H., Shi, Z., Gao, S., Wei, S., Li, K., et al. (2017). Inhibition activity of a traditional Chinese herbal formula Huang-Lian-Jie-Du-Tang and its major components found in its plasma profile on neuraminidase-1. *Sci. Rep.* 7 (1), 15549. doi: 10.1038/s41598-017-15733-7

Zhu, H. Y., Han, L., Shi, X. L., Wang, B. L., Huang, H., Wang, X., et al. (2015). Baicalin inhibits autophagy induced by influenza A virus H3N2. *Antiviral Res.* 113, 62–70. doi: 10.1016/j.antiviral.2014.11.003

Zhu, H., Lu, X., Ling, L., Li, H., Ou, Y., Shi, X., et al. (2018). Houttuynia cordata polysaccharides ameliorate pneumonia severity and intestinal injury in mice with influenza virus infection. *J. Ethnopharmacol.* 218, 90–99. doi: 10.1016/j.jep.2018.02.016

Conflict of Interest: The authors declare that the research was conducted in the absence of any commercial or financial relationships that could be construed as a potential conflict of interest.

The handling editor declared a shared affiliation, though no other collaboration, with the authors at the time of the review.

Copyright © 2020 Xiong, Li, Duan, Liu, Zhu, Zhang, Li, Lu and Huang. This is an open-access article distributed under the terms of the Creative Commons Attribution License (CC BY). The use, distribution or reproduction in other forums is permitted, provided the original author(s) and the copyright owner(s) are credited and that the original publication in this journal is cited, in accordance with accepted academic practice. No use, distribution or reproduction is permitted which does not comply with these terms.

frontiers in Pharmacology

ORIGINAL RESEARCH
published: 23 September 2020
doi: 10.3389/fphar.2020.575772

Veratrilla baillonii Franch Could Alleviate Lipid Accumulation in LO2 Cells by Regulating Oxidative, Inflammatory, and Lipid Metabolic Signaling Pathways

Xian-ju Huang[2†], Cai-jing He[2†], Shuai Liang[2], Jing Wang[2], Jun Li[2], Guang-zhong Yang[2] and Zhang Zhao[1]*

[1] Department of Anesthesiology Union Hospital, Tongji Medical College, Huazhong University of Science and Technology, Wuhan, China, [2] School of Pharmacy, South-Central University for Nationalities, Wuhan, China

OPEN ACCESS

Edited by:
Yan Xu,
Cleveland State University,
United States

Reviewed by:
Walter Wahli,
University of Lausanne, Switzerland
Wei Chen,
Yunnan Agricultural University, China

***Correspondence:**
Zhang Zhao
lyzzaaaa@126.com

[†]These authors have contributed equally to this work

Specialty section:
This article was submitted to Ethnopharmacology, a section of the journal Frontiers in Pharmacology

Received: 24 June 2020
Accepted: 03 September 2020
Published: 23 September 2020

Citation:
Huang X-j, He C-j, Liang S, Wang J, Li J, Yang G-z and Zhao Z (2020) Veratrilla baillonii Franch Could Alleviate Lipid Accumulation in LO2 Cells by Regulating Oxidative, Inflammatory, and Lipid Metabolic Signaling Pathways. Front. Pharmacol. 11:575772. doi: 10.3389/fphar.2020.575772

Based on the pathological theory of lipid metabolism and using network pharmacology, this study was designed to investigate the protective effect of water extract of *Veratrilla baillonii* (WVBF) on non-alcoholic fatty liver disease (NAFLD) model using LO2 cells and to identify the potential mechanism underlying the effect. The components of *V. baillonii* were identified from the public database of traditional Chinese medicine systems pharmacology database (TCMSP). Cytoscape software was used to construct the related composite target network. Then, Gene Ontology (GO) and Kyoto Encyclopedia of Genes and Genomes (KEGG) analysis were carried out for critical nodes. The BioGPS database was used to determine the distribution of the target in tissues and organs. Moreover, the inhibitory effect of *V. baillonii* was further investigated using an *in vitro* hepatocyte NAFLD model. Fourteen active components were then selected from the 27 known compounds of *V. baillonii*. The targets of gene enrichment analysis were mainly distributed in the lipid catabolism-related signaling pathway. Network analysis revealed that five target genes of TNF, MAPK8, mTOR, NF-κB, and SREBP-1c were key nodes and played important roles in this process. Organ localization analysis indicated that one of the core target site of *V. baillonii* was liver tissue. The results of the *in vitro* study revealed that WVBF can alleviate the inflammatory response and lipid accumulation in LO2 hepatocytes by inhibiting oxidative stress and the adipocytokine signaling pathway. Genes and proteins related to the lipid synthesis, such as SREBP-1C, acetyl-CoA carboxylase (ACC), and fatty acid synthase (FASN), were significantly decreased, and PPARα expression is significantly increased with WVBF administration. In conclusion, *V. baillonii* may regulate local lipid metabolism and attenuate oxidative stress and inflammatory factors through the PPARα/SREBP-1c signaling pathway. The present study also indicates that multiple components

of *V. baillonii* regulate multiple targets and pathways in NAFLD. The findings highlight the potential of *V. baillonii* as a promising treatment strategy for nonalcoholic fatty liver injury.

Keywords: nonalcoholic fatty liver, lipid metabolism, amarogentin, network pharmacology, *Veratrilla baillonii Franch*

INTRODUCTION

Non-alcoholic fatty liver disease (NAFLD), the most common chronic liver disease, is a metabolic syndrome characterized by hepatocellular steatosis and fat storage without a history of excessive alcohol consumption (Younossi et al., 2016). Globally, NAFLD accounts for 25.2% of global burden of disease epidemics, with approximately 30% of adults having underlying lipid metabolic disorders (Zobair et al., 2016). NAFLD affects nearly one-third of the world's population and the prevalence of this disorder is increasing every year (Hu et al., 2019). Excessive accumulation of triglyceride (TG) due to an imbalance in fatty acid uptake, synthesis, transportation, and oxidation is the leading cause of liver injury (Du et al., 2016). Based on the underlying pathological conditions, NAFLD can further develop into simple fatty liver, non-alcoholic steatohepatitis (NASH), fatty liver fibrosis, or cirrhosis, which significantly increases the associated mortality (Perumpail et al., 2017; Ipsen et al., 2018). Since no pharmacological therapy has been approved for the treatment of NAFLD so far, there is an urgent necessity to define multiple components, multiple targets and pathways of traditional Chinese medicine (TCM) based strategies of future interventions.

Veratrilla baillonii Franch (*V.* baillonii) belongs to the Gentianaceae family. *V.* baillonii, a traditional folk medicine, has been widely used in the treatment of hepatitis-induced jaundice and drug-induced hepatitis for decades (Olennikov et al., 2015; He et al., 2015). The water extract of *V.* baillonii (WVBF), which contain flavonoids, iridoid glycosides, and other substances (Vaidya et al., 2009; Ge et al., 2016; Yu et al., 2016; Zhang S. R. et al., 2018; Li et al., 2019). WVBF has significant protective effects on oxidative stress-induced liver injury (Dai et al., 2018), diabetic liver injury (Lian et al., 2010), and drug liver toxicity (Huang et al., 2016). However, the effects and underlying mechanism of *V.* baillonii in NAFLD are still unclear.

Therefore, this study explored the main components, key targets, and signaling pathways of *V.* baillonii in NAFLD. Further, the efficacy network and pharmacodynamic mechanism of WVBF were investigated using the network pharmacology method. Additionally, LO2 liver cells were exposed to mixed free fatty acids (FFA), to establish an *in vitro* NAFLD model for investigation of the protective effect of *V.* baillonii on the liver.

MATERIALS AND METHODS

Network Pharmacology Study

Compound Profiling and Disease Target Identification

The following databases were searched to identify the compounds in *V. baillonii*: traditional Chinese medicine systems pharmacology database (TCMSP) (http://lsp.nwu.edu.cn/tcmsp.php), a unique pharmacology platform that captures the relationships between herbal ingredients, targets, and diseases: SymMap (http://www.symmap.org/search/). The components were filtered by integrating oral bioavailability (OB ≥ 30%) and drug-likeness (DL ≥ 0.18), as suggested by the TCMSP and SymMap databases. OB and DL were used for candidate active ingredient screening based on a computer integrated model of absorption, distribution, metabolism, and excretion (ADME) (Xu et al., 2014).

The PubChem (https://pubchem.ncbi.nlm.nih.gov/) and HIT (http://lifecenter.biosino.org/hit/) databases were utilized to identify the verified targets of each active component (Song et al., 2018). In order to identify the potential targets of *V. baillonii*, the molecular similarity match tool was used based on the simplified molecular input line entry specification (SMILES) in the similarity ensemble approach (SEA) (P<0.05) (http://sea.bkslab.org/) and SwissTargetPrediction (P<0.05) (http://www.swisstargetprediction.ch/) (Stork et al., 2019). The UniProt (https://www.uniprot.org/) database was used to standardize the results. An interaction network of component-targets was constructed and visualized by Cytoscape software.

Non-alcoholic fatty liver-related targets were retrieved from the online human Mendelian genetics (OMIM, https://omim.org/), DisGeNET (http://www.disgenet.org/), and GeneCards (https://www.genecards.org/) databases. "Non-alcoholic fatty liver disease" was used as the keyword and duplicate values were deleted. The Bioconductor package in the software package R was used to standardize the disease gene targets obtained (Zeng et al., 2019). Finally, Cytoscape 3.2.1 was used to perform visual network analysis of the "disease-target."

Screening of Candidate Targets for the Treatment of Non-Alcoholic Fatty Liver Disease

Based on the previous steps, two sets of target data files were prepared: drug-related component targets and disease-related targets. Cross genes were screened using the Venn Diagram software package in R. Intersecting protein interactions (PPIs) were analyzed using the String 11.0 database and the common targets were counted using R software. Finally, Cytoscape 3.2.1 was used to perform visual network analysis of the "drug-active ingredient-target-disease" network.

Network Construction and Central Network Topological Analysis

PPIs for each target were generated from a string database that provides experimental and predictive interaction information based on systematic co-expression analysis, shared selection signal detection across genomes, and automated text mining of scientific literature (Liu et al., 2013). The central network analysis was performed according to the topological method. Three

topological parameters, degree centrality (DC), betweenness centrality (BC), and closeness centrality (CC), were calculated to evaluate the central attributes of the nodes in the network (Wang et al., 2015). In the target network of WVBF and NAFLD, DC ≥ 2 × median DC, BC ≥ median BC, and CC ≥ median CC were used as the screening criteria to obtain the key targets. The key target interaction network was also depicted using Cytoscape 3.2.1.

Bioinformatics Annotation Analysis

Bioinformatics annotation using Bioconductor R language was used to evaluate genes with high expression patterns. In this study, the PANTHER classification system (http://www.pantherdb.org/), Gene Ontology (GO) annotation database website (http://www.geneontology.org), Kyoto Encyclopedia of Genes and Genomes (KEGG) pathway enrichment analysis (http://www.genome.jp/kegg/), and PPIs analysis (http://string-db.org/) were used to analyze the effect of potential targets of active ingredients in *V. baillonii* on gene function and signaling pathways.

Prediction of Target Organ Recognition

In order to understand the intervention function of *V. baillonii* in NAFLD, the distribution of targets in tissues and organs was analyzed. To gain information about key targets function, the tissue specific probes of the key targets core were identified using the BioGPS Gene Expression Database (Novartis Research Foundation; http://biogps.org). The tissue distribution of targets was determined, specific methods have been described as the following aspects. Firstly, all the core targets collected above were inputted as keywords into BioGPS for screening, and species of human was selected. Secondly, the detailed information of the core targets was queried and click to retrieve the target to show its expression in different tissues. Finally, the obtained distribution and expression of each target in different tissues were imported into the SPSS, and the gene expression in different tissues was plotted (Pritchard et al., 2012; Wang et al., 2017).

Experimental Cells and Design

Extract Preparation

The dried roots of *V. baillonii* (**Figure 1A**) were bought from Kunming city, Yunnan province in China. The plant materials were authenticated by Dr. Liu Xinqiao, who is affiliated to the School of Pharmaceutical Sciences, South-Central University for Nationalities, China. The voucher specimens (No. S20140710) were deposited at the Herbarium situated in the College of Pharmaceutical Sciences at South-Central University for Nationalities, Wuhan, Hubei, P. R. China. The WVBF was extracted as described previously (Ge et al., 2016; Yu et al., 2016; Li et al., 2019). Briefly, WVBF was prepared by extracting the plant (200 g) crushed into small pieces. The mixture was

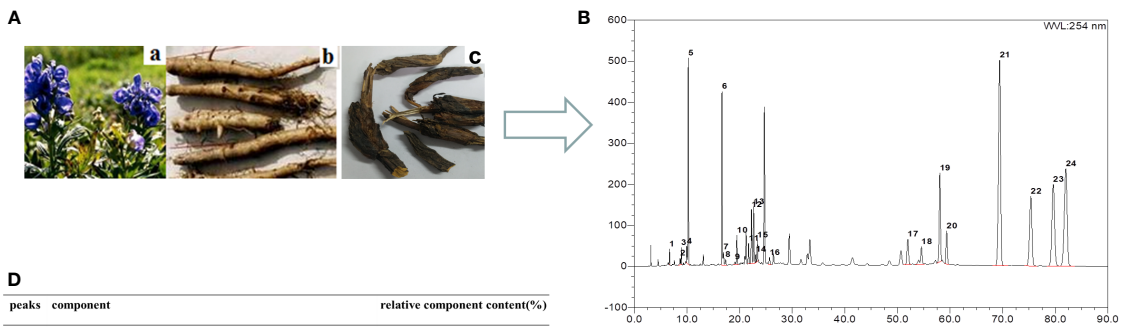

peaks	component	relative component content(%)
1	Tetraswerosides A	0.34
2	Secamonoides B	0.19
3	1-Hydroxy-2,7-dimethoxy-3-O-β-D-glucopyranosylxanthone	0.35
4	2,3,4,7-Tetramethoxy-1-O-primeverosyloxyxanthone	0.41
5	Sweroside	4.96
6	Gentiopicroside	5.27
7	Swertiamarin	0.50
8	1-Hydroxy-3,4-dimethoxy-7-O-β-Dglucopyranosylxanthone	0.19
9	Diisobutyl phthalate	0.89
10	1,7-Dihydroxy-2,3,4-t rimethoxyxanthone	0.18
11	1-Hydroxy-2,3,5 -trimethoxyxanthone	0.69
12	1-Hydroxy-2,3,4,7-tetramethoxy xanthone	2.06
13	Tripteroside	1.95
14	Veratriloside B	0.28
15	2,3,5-Trimethoxy-1-O-primeverosyloxyxanthon	0.88
16	2,3,4,5-Tetramethoxyxanthone-1-O-gentiobioside	0.32
17	Dibutyl fumarate	2.01
18	1,7-Dihydroxy-3,4-dimethoxyxanthone	1.31
19	1,3-Dihydroxy-4,7-dimethoxyxanthone	5.43
20	1 ,7-Dihydroxy-3-methoxyxanthone	2.08
21	1-Hydroxy-2,3,4,5-tetramethoxy xanthone	20.53
22	1-Hydroxy-2,3,7 -trimethoxyxanthone	8.13
23	Deacetylcentapicrin	10.59
24	Amaronitidin	13.27

FIGURE 1 | The chemical structures and the typical high-performance liquid chromatographic (HPLC) chromatographic profile of *V. baillonii*. **(A)** The stems and roots of *Veratrilla baillonii*. **(B)** The HPLC chromatographic profile of *V. baillonii*. **(C)** The chemical structures of glycoside of xanthone and iridoid derivatives from Radix of *V. baillonii*. **(D)** The relative contents of main activate components in *V. baillonii*.

refluxed with water (1:10, w/v) for 2 h. The filtrates were collected and the residues were then refluxed in water (1:10, w/v) for 1.5 h. Two batches of filtrates were combined. Afterwards, the concentrated extract was dried by vacuum concentration to obtain the WVBF extract with a yield of 25.6% (w/w, dried extract/crude herb).

Analysis of Water Extract of *Veratrilla baillonii* by High-Performance Liquid Chromatographic

The multi-components of WVBF were characterized by high-performance liquid chromatographic (HPLC) (**Figure 1**). The samples were analyzed using Phecda C18 column (150 mm×2.1 mm, 3 μm) with the detector wave length set at 215 nm, and the mobile phase consisted of water containing acteonitrile (A) and 0.1% (v/v) aceticacid (B). A gradient program was used as follows: 0–10 min, 32–55% A; 10–20 min, 55–100% A. The flow rate was 0.3 ml/min. HPLC fingerprint analysis method was established to obtain the complete fingerprint of WVBF, and the corresponding 24 compounds were identified (**Figure 1B**). According to the peak area normalization method, the relative contents of WVBF are calculated as follows: gentiopicroside (peak6, 5.27%), tripteroside (peak 13, 1.95%), 1,3-Dihydroxy-4,7-dimethoxyxanthone (peak 19, 5.43%), 1-Hydroxy-2,3,4,5-tetramethoxy xanthone (peak 21, 20.53%), 1-Hydroxy-2,3,7-trimethoxyxanthone (peak 22, 8.13%), Deacetylcentapicrin (peak 23, 10.59%), Amaronitidin (peak 24, 13.27%) (**Figures 1C, D**).

Reagents and Instrument

Fetal bovine serum (FBS) and Dulbecco's modified Eagle's medium (DMEM) were purchased from HyClone. A triglyceride (TG) kit (lot: A110-1-1), lipid peroxides (LPO) kit (lot: A106-1-2), superoxide dismutase (SOD) kit (lot: A001-1-2), and glutathione peroxidase (GSHPx) detection kit (lot: A005), malondialdehyde (MDA) kit (lot: A003-1), alanine aminotransferase (ALT) kit (lot: C009-2-1), aspartate aminotransferase (AST) kit (lot: C010-2-1), reactive oxygen species (ROS) kit (lot: E004) were purchased from Nanjing Jiancheng Bioengineering Institute (Nanjing, China). An Annexin V-FITC Cell Apoptosis Assay Kit (lot: C1062L) and bicinchoninic acid (BCA) protein concentration determination kit (enhanced) (lot: P0010) were purchased from Beyotime Biotechnology (Shanghai, China). Bovine serum albumin (BSA) (98%, Sigma, St. Louis, MO, America), oil red O dye (cell-specific smear), amarogentin (AG) (HPLC≥98%, lot: B20683), gentiopicroside (HPLC≥98%, lot: B20763), sweroside (HPLC≥98%, lot: B21643), and swertiamarin (HPLC≥98%, lot: B21644) were purchased from Shanghai Yuanye Biotechnology Co., LTD. Sodium oleate (OA), palmitic acid sodium (PA), and bezafibrate tablets (BT) (HPLC≥99%) were purchased from Shanghai Macklin Biochemical, China.

A CKX41 inverted microscope (Olympus Corporation, Tokyo, Japan; Spectra Max Plus384), full wavelength marker (Molecular Devices, USA), flow cytometer (BD influx), and an Applied Biosystems 7500 fluorescence quantitative PCR instrument were also used.

Preparation of Sample Solution

The FFA mixture was preparation as reference described (Zhang et al., 2015). Non-fatty acid BSA was dissolved in DMEM medium to prepare a BSA solution with a concentration of 18.4%. OA (9 mmol·L^{-1}) and PA (9 mmol·L^{-1}) were each dissolved in medium containing BSA. An FFA/BSA mixture with mixture of (OA: PA, 2:1) was produced. The FFA/BSA mixture was stirred at 37°C for 6 h and the pH of the medium was adjusted to 7.4 with a pH regulator. The medium was filtered aseptically and stored at −20°C for later use.

Cell Culture and Treatment

Human LO2 cells (obtained from Chinese Academy of Science Committee Type Culture Collection Cell Bank, Shanghai, China) were kept in DMEM containing 10% (v/v) heat-inactivated FBS and 1% (v/v) penicillin/streptomycin (Gibco/BRL, NY) in a 5% CO_2 incubator at 37°C. The cells were exposed to (0.125–2.0 mmol·L^{-1}) FFA mixture (OA: PA, 2:1) for 24 or 48 h to induce steatosis. DMEM medium containing 2% FBS without fatty acids was used as the control. Then, cells were divided into eight groups: 1) normal control group (NC), treated with PBS only as vehicle; 2) NC+ high dose of WVBF group (WVBF 5.0), treated with PBS only as vehicle, 3) FFA group (MC), treated with 0.5 mM FFA mixture for 24 h, 4) FFA+ bezafibrate tablets group (BT), 5) FFA+ amarogentin group (AG), 6) FFA+ gentiopicroside: sweroside: swertiamarin: amarogentin, 5:8:6:80 group (PC), 7) FFA+ high dose of WVBF group (WVBF 5.0), and 8) FFA+ low dose of WVBF group (WVBF2.5) treated with ghrelin and FFA mixture described above (as **Table 1**).

To detect the cell viability, AST and ALT were used as the basis indices for selecting the optimal time and the concentrations of FFA (Mao et al., 2015; Zhang S. R. et al., 2018).

EFFECT OF WATER EXTRACT OF *VERATRILLA BAILLONII* ON NON-ALCOHOLIC FATTY LIVER DISEASE CELL MODEL

Assessment of Cell Viability

Cell viability was evaluated by the methylcyclopentadienyl manganese tricarbonyl (MTT) method. After the indicated treatment, MTT was added at a working concentration of 5 mg·ml^{-1} and the solution was incubated for 4 h. Then, the MTT solution was removed and 150 μl $well^{-1}$ of dimethyl

TABLE 1 | Experimental protocol and group.

Group	0.5 mmol ml^{-1} FFA	Drug concentration
Normal control (NC)	-	-
Model control (MC)	+	-
BT	+	Bezafibrate tablets (5.0 μg.ml^{-1})
AG	+	Amarogentin (5.0 μg.ml^{-1})
PC	+	Sweroside:gentiopicroside: swertiamarin:amarogentin=5:8:6:80 (5.0 μg.ml^{-1})
WVBF2.5	+	WVBF (2.5 μg.ml^{-1})
WVBF5.0	+	WVBF (5.0 μg.ml^{-1})
WVBF5.0	-	WVBF (5.0 μg.ml^{-1})

sulfoxide (DMSO) was added to dissolve the needle-like formazan crystals formed by viable cells. The absorbance was measured at 490 nm, and the percentage of cell viability was calculated.

Flow Cytometry Analysis of Apoptosis

After treatment, the LO2 cells were collected after centrifugation at 2,000 r·min^{-1} for 5 min. The cells were treated according to the instructions of the Annexin V-FITC Cell Apoptosis Assay Kit. Then, a FACSCalibur flow cytometer (BD Biosciences, San Jose, CA, USA) was used to evaluate cell apoptosis and necrosis.

Cell Oil Red O Staining

The levels of lipids were assessed by oil red O stains on cells. Firstly, the cells grown in six-well plates were washed with phosphate buffer saline (PBS) three times, then 4% paraformaldehyde was used to fix the cells for 20 min. Secondly, the cells attached to the coverslip were stained with the oil red O (ORO) fixative for 15 min, and soaked with 60% isopropanol for 5 min. Then, hematoxylin stain was added onto the slides for 1 min after the slides were washed with distilled water according to the manufacturer's instructions. The lipid droplets stained with oil red O were visualized with a CKX41 inverted microscope equipped with a DP72 microscope digital camera. Then 100% isopropanol was used to extract intracellular cholesterol. The liquid absorbance was measured at OD490 with spectrophotometer.

Biochemical Analyses

The cell lysates were homogenized and the total lipids were extracted by a mixture of chloroform and methanol (2:1). The protein concentrations of lysis buffer were measured using an enhanced bicinchoninic acid (BCA) protein assay kit. The concentrations of TG, total cholesterol (TC), total superoxide dismutase (T-SOD), glutathione peroxidase (GSH-Px), MDA, and LPO in cell homogenate were determined with commercial kit. All experimental results were normalized according to total protein levels of the samples. The levels of AST and ALT in cell culture supernatant were also determined using a fully automatic biochemical analyzer (Mindray, BS-600, China), according to the manufacturer's protocol.

Analysis of Intracellular Reactive Oxygen Species Generation

Fluorescent dye 2,7-dichlorofluorescein-diacetate (DCFH-DA, Beyotime, China) was used to detect intracellular ROS generation. After the cells were exposed to FFA for 24 h, and treatment of BT, AG, PC, and WVBF, the LO2 cells were washed with DMEM and stained with 10 μm of DCFH-DA for 30 min at 37°C. Subsequently, cells were harvested, rinsed twice with DMEM, and then resuspended in 0.5 ml of DMEM and analyzed for DCF fluorescence by flow cytometry.

Quantitative Real-Time PCR (qRT-PCR)

Quantitative real-time PCR was used to determine the messenger RNA (mRNA) levels of sterol regulatory element binding proteins-1c (SREBP-1c), peroxisome proliferators activator receptors alpha (PPARα), fatty acid synthase (FASN), acetyl-CoA carboxylase (ACC), nuclear factor-erythroid 2-related factor 2 (Nrf2), nuclear factor kappa-B (NF-κB), and tumor necrosis factor-α (TNF-α) in LO2 cells. Total RNA was extracted from the cells using TRIzol Reagent according to the manufacturer's instruction. Then, total RNA was reverse-transcribed to complementary DNA (cDNA) using an SYBR® PrimeScript® RT-PCR Reagent Kit with genomic DNA (gDNA) Eraser (TaKaRa, Japan). The master mix (10 μl) included: PrimeScript RT Enzyme Mix I (1.0 μl), RT Primer Mix*4 (1.0 μl), 5×PrimeScript Buffer 2 (for real time) (4.0 μl), and RNase Free dH_2O (4.0 μl). PCR amplification was performed as follows: stage 1, preheat denaturation at 95°C for 40 s, stage 2, circulatory system cycled 40 times at 95°C for 15 s, and 58°C for 1 min. The sequence of primers used for this reaction is provided in **Table 2**. Each sample was measured three times. The expression levels of the above genes were normalized to those of glyceraldehyde 3-phosphate dehydrogenase (GAPDH) and measured by the comparative $2^{-\Delta\Delta Ct}$ method.

Western Blotting

Total protein was extracted from frozen LO2 cells by adding protein lysates (Beyotime Biotechnology Co, Ltd, Shanghai, China). Protein was quantified using the Bradford method (Thermo Fisher Scientific Inc, Rockford, IL). Total protein was separated by sodium dodecyl sulfate-polyacrylamide gel electrophoresis (50 μg), and was then transferred to Millipore Corp, Billerica, MA membranes and sealed with 5% skim milk powder at 37°C for 1 h. Subsequently, rabbit anti-mouse monoclonal antibodies against PPARα, SREBP-1c, FASN, Nrf2, and GAPDH (1:1,000; Abcam, Cambridge, MA) were added to the membrane and it was shaken at 4°C overnight. The membrane was washed with phosphate buffered saline with Tween (PBST) three times, for 5 min each time. Then, horseradish peroxidase-labeled goat anti-rabbit secondary antibody (1:4,000; Cell Signaling Technology, Danvers, MA) was added to the membrane and it was incubated at room temperature for 2 h. The membrane was washed twice using tris-buffered saline with Tween (TBST) for 10 min and was then treated with

TABLE 2 | Primers used for real time PCR (RT-PCR).

Gene name	Gene number	Primer sequence
GAPDH	NM-002046.7	Forward 5'-ACCCAGAAGACTGTGGATGG-3'
		Reverse 5'-TCAGCTCAGGGATGACCTTG-3'
SREBP-1C	NM-004176.4	Forward 5'-GAGCTCAAGGATCTGGTGGT-3'
		Reverse 5'-CAGTGCGCAGACTTAGGTTC-3'
FASN	NM-004104.5	Forward 5'-GGCTGCCTACTACATCGACT-3'
		Reverse 5'-CGAACAGGAAGAGGCTGTTG-3'
NF-κB	NM-003998.4	Forward 5'-AGCAAATAGACGAGCTCCGA-3'
		Reverse 5'-TCGGTAAAGCTGAGTTTGCG-3'
ACC	NM-198836.2	Forward 5'-CATGAAGGCTGTGGTGATGGA-3'
		Reverse 5'-CTTGGTGACTTGAGCGTGAG-3'
PPARα	NM_005036.6	Forward 5'-TGCTACTTACCAGCCGCATA-3'
		Reverse 5'-GTCTTAGCTGGGTGCATTGG-3'
TNF-α	NM_000594.4	Forward 5'-TCAATCGGCCCGACTATCTC-3'
		Reverse 5'- ATGTTCGTCCTCCTCACAGG-3'
Nrf2	NM_006164.5	Forward 5'-CGCAGACATTCCCGTTTGTA-3'
		Reverse 5'- AGCAATGAAGACTGGGCTCT-3'

electrochemiluminescence (ECL) photoluminescence solution for imaging. ImageJ software was used to analyze the test results. The ratio of the gray value of the target band to the GAPDH reference band was used as the relative expression level of the protein. Each experiment was repeated three times.

Statistical Analysis

The results are expressed as mean ± standard error (SE). Multiple comparisons were performed using one-way analysis of variance (ANOVA) followed by Tukey's *post hoc* test. For all analyses, P values below 0.05 were considered to indicate statistical significance. Analyses were performed using SPSS 18.0 software for Windows.

RESULTS

Active Ingredient Targets and Disease Targets

As shown in **Table 3**, 14 active ingredients were collected from *V. baillonii* and 496 target proteins were found. Although the number of targets of each compound was different, the targets of the 14 active ingredients significantly overlapped. Topological analysis of protein-interaction network nodes, including screening of key nodes to eliminate duplicates, revealed a total of 287 target proteins. The constructed "composite target" network was used to evaluate the relationships between 287 targets, which had as many as 2,672 nodes. Targets associated with NAFLD were identified in the OMIM, DisGeNET, and GeneCards databases. In this study, 1,200 target genes of disease were retrieved, and 872 key nodes were obtained through screening.

Target Network Analysis

All active compound protein targets and disease-related proteins were classified into two independent groups. The set and its relations were expressed in a closed-loop form with a fixed position to obtain a Venn diagram and 31 interacting proteins, as shown in **Figure 2A**. Proteins were obtained using String 11.0 and topological data analysis was conducted through CytoNCA, a plugin for Cytoscape, to obtain a network PPI of 17 key targets, as shown in **Figure 2B**. Through network prediction, it was found that TNF, MAPK8, mTOR, HRAS, and PTGS2 were important target genes in the first few degrees.

Gene Ontology Function, Kyoto Encyclopedia of Genes and Genomes Pathway, and Localization Analysis of Key Targets

The GO functional analysis revealed that *V. baillonii* affected 17 potential key target genes of five main biological processes, including regulation of lipid metabolic process, positive regulation of nitric oxide biosynthetic process, positive regulation of fever generation, regulation of monooxygenase activity, and regulation of fatty acid metabolic process, as shown in **Figures 3A, B**. In addition, a visual analysis was performed on the top 20 signal pathways enriched by KEGG analysis (**Figure 3C**). KEGG enrichment analysis demonstrated that many target genes of *V. baillonii* were closely related to oxidative stress indices, inflammatory factors, the TNF signaling pathway, lipid metabolism, and other signaling pathways such as

TABLE 3 | Information on 14 compounds of *Veratrilla baillonii*.

NO	Compound	CAS	Molecular formula
M1	1,3-Dihydroxy-4,7-dimethoxyxanthone	23251-54-9	$C_{15}H_{12}O_6$
M2	1,7-Dihydroxy-3-methoxyxanthone	437-50-3	$C_{19}H_{18}O_5$
M3	1-Hydroxy-2,3,4,5-tetramethoxyxanthone	22961-79-1	$C_{17}H_{16}O_7$
M4	1-Hydroxy-2,3,4,7-tetramethoxyxanthone	14103-09-4	$C_{17}H_{16}O_7$
M5	1-Hydroxy-2,3,5-trimethoxyxanthone	22804-49-5	$C_{16}H_{14}O_6$
M6	1-Hydroxy-2,3,7-trimethoxyxanthone	22804-58-6	$C_{16}H_{14}O_6$
M7	Amarogentin	21018-84-8	$C_{29}H_{30}O_{13}$
M8	Dibutyl fumarate	105-75-9	$C_{12}H_{20}O_4$
M9	Diisobutyl phthalate	84-69-5	$C_{16}H_{22}O_4$
M10	Gentiopicrin	20831-76-9	$C_{16}H_{20}O_9$
M11	Loganic acid	22255-40-9	$C_{16}H_{24}O_{10}$
M12	Swertiamarin	20831-76-9	$C_{16}H_{22}O_{10}$
M13	Tripteroside	82855-00-3	$C_{19}H_{18}O_{11}$
M14	Veratriloside B	76907-78-3	$C_{21}H_{22}O_{11}$

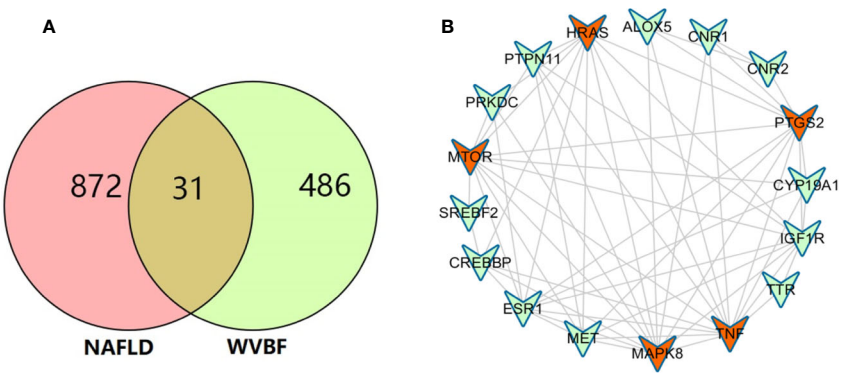

FIGURE 2 | Target network analysis. **(A)** Venn diagram of active ingredient targets and disease proteins. **(B)** Fourteen active ingredients of *Veratrilla baillonii* and cross-critical disease targets. Blue represents the protein at the intersection of the active compound with the disease. Red is the active compound.

the AMPK signaling pathway and PI3K-Akt signaling pathway, among others.

Moreover, to study the relationship between *V. baillonii* and vital organs, the BioGps database was used. The above mentioned 17 key targets were imported in the BioGps database for organ positioning. The network was divided into several tissue modules, including liver (12 targets), heart (11 targets), and kidney (7 targets) (**Figure 3D**). The results of this analysis indicated that the targets of the active components of *V. baillonii* were closely related to lipid metabolism disorder. The majority of targets of *V. baillonii* were located in liver tissues (**Figure 3E**). Lipid metabolic disorders are considered to be one of the vital causes of NAFLD (Ziamajidi et al., 2013). Important target genes of TNF, MAPK8, mTOR, NF-κB, and PPARα were mainly distributed in the "adipocytokine signaling pathway". The AMPK pathway and insulin signaling pathway were the other important pathways. These results suggest that the molecular mechanisms of the most active compounds of *V. baillonii* are related to inflammation and lipid metabolism. Based on these predictions and the available literature, experiment at the cellular level was conducted then to verified our hypothesis.

Free Fatty Acids Reduced Cell Viability and Increased Lipid Accumulation in LO2 Cells

As shown in **Figure 4Aa**, FFA (0.125–2.0 mM) dose-dependently reduced the cell viability of LO2 cells after incubation for 24 or 48 h. A 0.5 mmol·L^{-1} dose of FFA inhibited cell growth by more than 50% after 24 or 48 h. Furthermore, ALT and AST leakage were markedly increased in the FFA group compared with the control group (**Figures 4Ab, Ac**). As the concentration of FFA increased, the accumulation of red-stained lipid droplets in LO2 hepatic cytoplasms increased in a dose-dependent manner (**Figures 4Ad, B**). Then, a low cytotoxic dose of 0.5 mmol·l^{-1} FFA was used and the shorter induction group was exposed for 24 h in the following experiment.

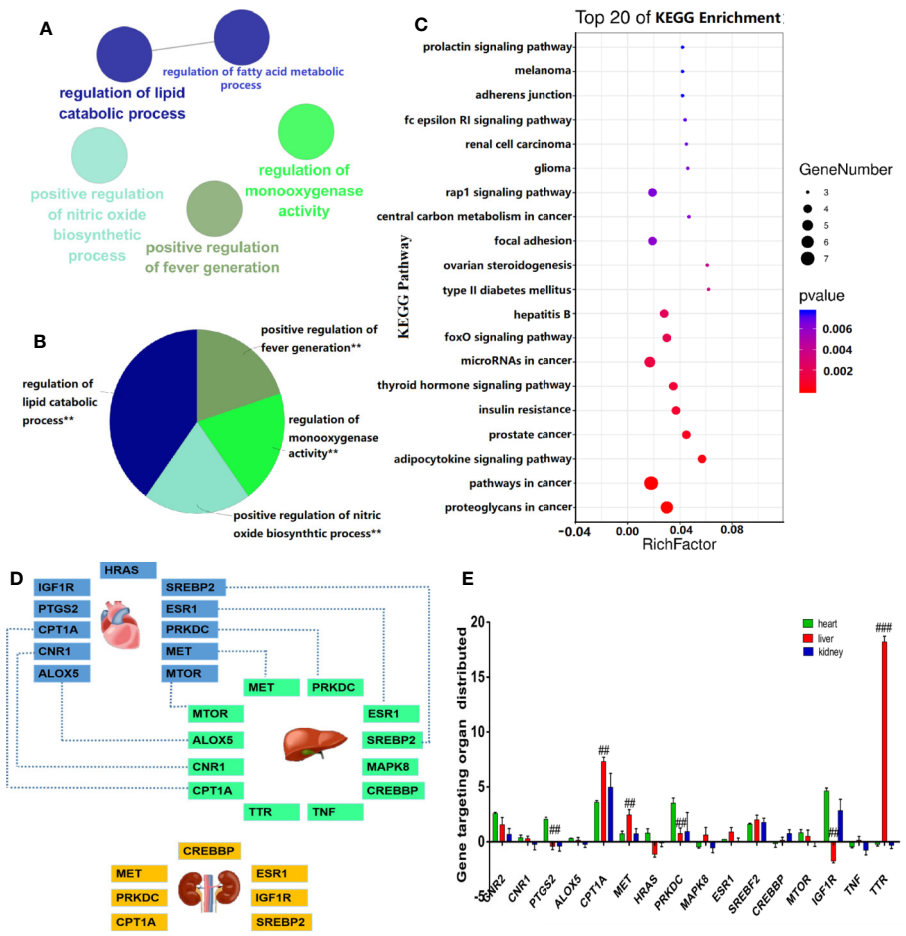

FIGURE 3 | Bioinformatics analysis and localization analysis of key targets. **(A)** Gene ontology (GO) enrichment analysis of the hierarchical network diagram. **(B)** GO biological process enrichment analysis. **(C)** Enrichment analysis of Kyoto Encyclopedia of Genes and Genomes (KEGG) annotation signaling pathway. **(D)** Targeted organ localization analysis network. **(E)** The key gene expression in different tissues and organs ($^{\#\#}P < 0.01$, and $^{\#\#\#}P < 0.001$, liver *vs*. control heart or kidney.)

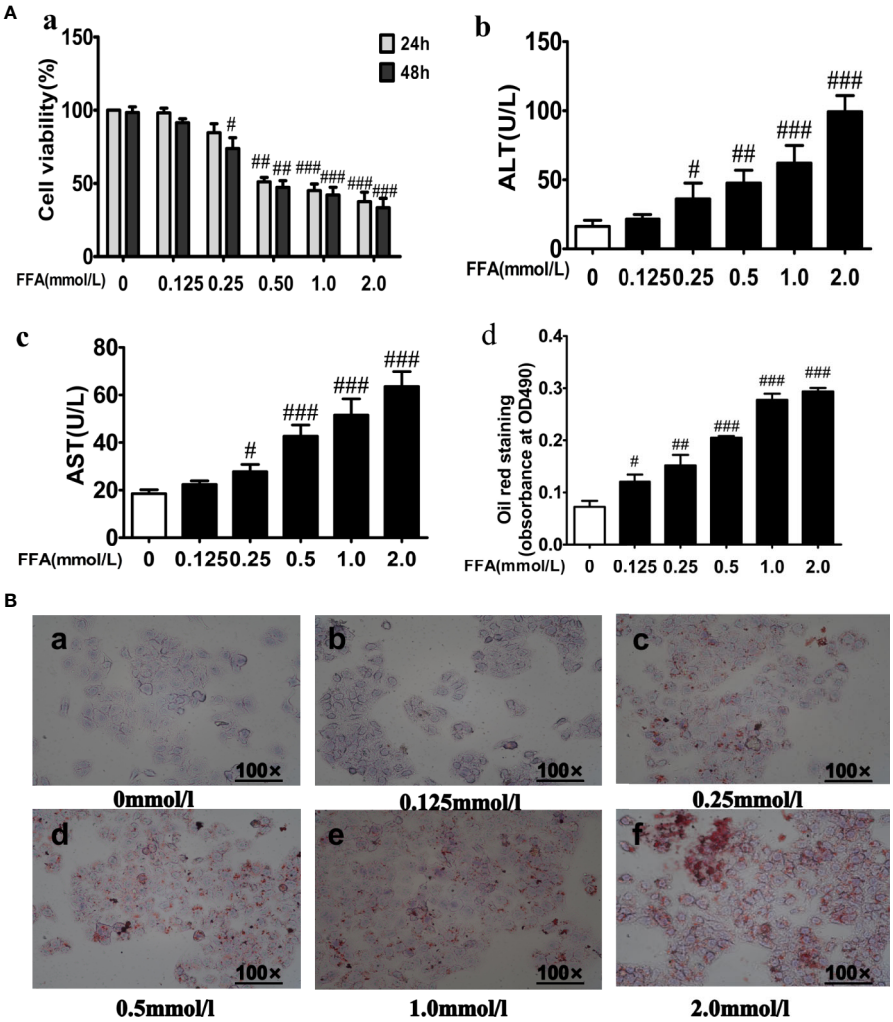

FIGURE 4 | Effects of free fatty acids (FFA) on cell viability and lipid accumulation in LO2 cells. **(A)** LO2 cells were exposure to the different concentrations of FFA for 24 or 48 h, cell viability (a), ALT (b), AST (c) and quantitative results of graph-B detected by spectrophotometer at OD490nm (d). **(B)** The effect of FFA on the lipid accumulation of LO2 cells. n =3 (n, the number of experiment), ($^{\#}P < 0.05$, $^{\#\#}P < 0.01$, and $^{\#\#\#}P < 0.001$ *vs*. control group).

Effects of Water Extract of *Veratrilla baillonii* on Free Fatty Acids-Induced LO2 Cells

Water Extract of *Veratrilla baillonii* Elevated Cell Viability and Reduced Free Fatty Acids-Induced Cell Apoptosis

After 24 h of FFA treatment, ALT, AST levels in LO2 cells were significantly elevated, cell viability were significantly decreased. ALT, AST levels significantly decreased, the cell viability rates significantly increased in cells treated with WVBF, BT, AG, and PC (**Figures 5A, B**). Flow cytometry analysis showed that the increased cell apoptosis and cell necrosis rate induced by FFA could be significantly reduced by WVBF treatment in a dose-dependent manner (**Figure 5C**), indicating the protective effect of WVBF treatment on FFA-induced LO2 liver injury.

Water Extract of *Veratrilla baillonii* Attenuates Lipid Metabolic Risk Factors and Accumulation in Cells

FFA resulted in a steady increase in TG, TC levels in liver cells, and increased accumulation of fat droplets in the cytoplasm after incubated for 24 h. And the TG, TC levels could be significantly attenuated by WVBF, BT, AG, and PC (**Figures 6A, B**). Moreover, WVBF significantly reduced the FFA-induced accumulation of fat droplets in the cytoplasm after incubated for 24 h (**Figure 6B**). The high-dose of WVBF group exhibited the best efficacy and showed a specific dose-dependent enhancement. The above results indicate that WVBF regulate the lipids metabolism in cells, thus remission lipotoxicity induced hepatocyte injury.

Effects of Water Extract of *Veratrilla baillonii* on Free Fatty Acids-Induced Oxidative Injury in LO2 Cells

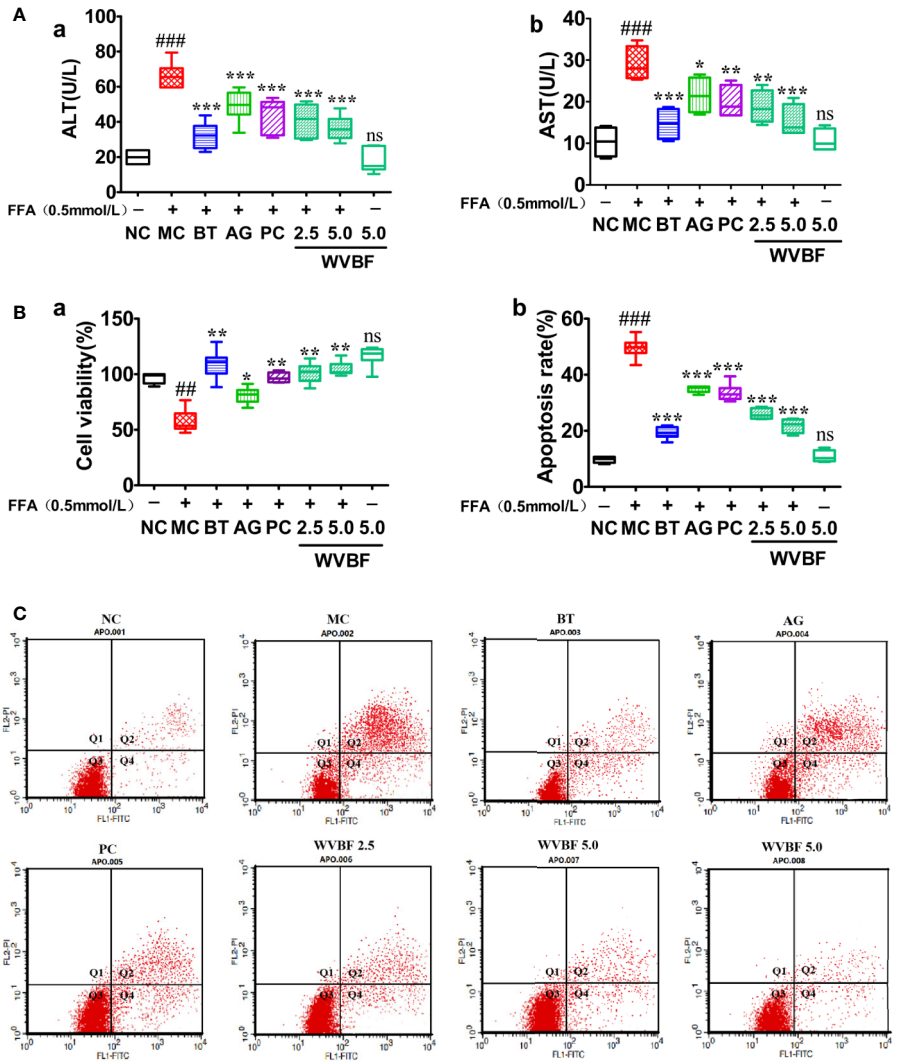

FIGURE 5 | The effect of water extract of *Veratrilla baillonii* (WVBF) on free fatty acids (FFA)-induced apoptosis and injury. **(A)** The cell viability was measured by the methylcyclopentadienyl manganese tricarbonyl (MTT) assay, and the levels of alanine aminotransferase (ALT) and aspartate aminotransferase (AST). **(B)** Annexin V-FITC/PI and analyzed by flow cytometry (the upper right quadrant represents late apoptosis. The lower right quadrant represents early apoptosis). **(C)** Apoptosis rate (a) and necrotic cell rate (b). *n* =3 (*n*, the number of experiment), ($^{\#\#}P < 0.01$, $^{\#\#\#}P < 0.001$ *vs*. control group; $^{*}P < 0.05$, $^{**}P < 0.01$, and $^{***}P < 0.001$ *vs*. FFA group).

The exposure of the cells to FFA resulted in a significant decrease in T-SOD and GSH-PX level, increase in MDA and LPO levels, and produced stronger DCF signals compared to the control group. However, after WVBF, BT, AG, and PC treatment resulted in a marked reduction in DCF fluorescence, indicating an inhibitory effect of WVBF on FFA-induced intracellular ROS production. The above results show that WVBF has certain roles in antioxidation and regulation of oxidation(**Figures 7A, B**).

Water Extract of *Veratrilla baillonii* Regulated the PPARα/SREBP/NF-κB Pathway

The key targets and important signaling pathways, including TNF, MAPK8, mTOR, and NF-κB targets and the adipocytokine signaling pathway, which were obtained from the network pharmacology analysis, were further explored and verified at the cellular level. As shown in **Figure 8A**, FFA significantly up-regulated the mRNA levels of SREBP-1c, FASN, ACC, NF-κB, and TNF-α and down-regulated the mRNA levels of Nrf2 and PPARα. The same trends were observed at the protein level (**Figures 8B, C**). However, those imbalances were significantly recovered by WVBF in a dose-dependent manner. The results were in accordance with the network analysis to some extent and provide evidence to support the view that activation of oxidative, inflammation, and lipid metabolism stress pathways are involved in a NAFLD cell model.

DISCUSSION

Research on the efficacy and mechanism of traditional Chinese medicine (TCM) is critical to the modernization of Chinese

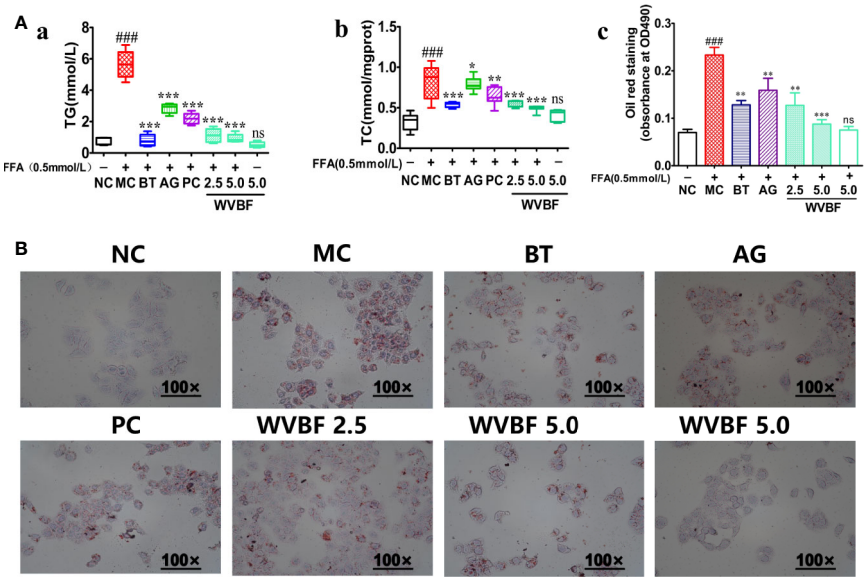

FIGURE 6 | Effect of water extract of *Veratrilla baillonii* (WVBF) on lipid metabolic factors and lipid accumulation in LO2 cells. **(A)** Effect of WVBF on TG (a), TC (b), and quantitative results of graph-B detected by spectrophotometer at OD490nm (c) in LO2 cells. **(B)** Effect of WVBF on lipid accumulation in LO2 cells subjected to free fatty acids (FFA) (the deeper the red oil stain, the more lipid accumulation in the cell). ($^{\#\#}P < 0.01$, $^{\#\#\#}P < 0.001$ *vs*. control groups; $^{*}P < 0.05$, $^{**}P < 0.01$, and $^{***}P < 0.001$ *vs*. FFA group).

medicine (Hopkins, 2008). Many studies have shown that the effectiveness of TCM in the complex diseases depends on the synergistic effects of multiple compounds and their targets. Network pharmacology and system biology can explain the effects of drugs on biological network destruction from the perspective of macro or global regulation and provide new research ideas and technical means for studying the mechanism of ethnic drug compounds (Muhammad et al., 2018; Zhang Y. et al., 2018). In this study, the complexity of the active ingredients in *V. baillonii* and the diversity of potential regulatory targets in diseases were studied through network pharmacology analysis. The results revealed that the main active ingredients of *V. baillonii*, such as amarogentin, 1-hydroxy-2,3,7-trimethoxyxanthone, and 1,7-dihydroxy-3-methoxyxanthone, possess anti-inflammatory, antioxidant, and liver protection effects, among others. These findings are consistent with those reported in the literature. Clinical and pharmacological studies have found that *V. baillonii* has a variety of anti-inflammatory, antioxidant, antiviral, and liver protective effects in autoimmune diseases. It has remarkable efficacy in the treatment of pulmonary fever, enteritis, cholecystitis, hepatitis, and other diseases of the digestive system (Lian et al., 2010).

Based on the present results, a NAFLD cell model establishment by FFA-induced LO2 was preliminarily confirmed (Zhang et al., 2015; Zhang Y. et al., 2018; Mao et al., 2015). There are significant increases in ALT and AST levels in patients with fatty liver disease. In NAFLD patients, the levels of TG, and TC, indicators of blood lipids, are significantly increased (Chavez-Tapia et al., 2011). A previous study (Ge et al., 2016) reported that WVBF can decrease *Aconitum brachypodum*-induced acute toxicity in KM mice and can protect liver tissue by decreasing the release of ALT, AST, and TG in serum. The present study also found that the levels of ALT, AST, TG, and TC in NAFLD model cells were significantly reduced after WVBF treatment, suggesting that WVBF can reduce FFA-induced steatosis injury and the accumulation of lipids in hepatocytes.

Oxidative stress plays an essential role in the regulation of NAFLD from steatosis to steatohepatitis, liver fibrosis, and cirrhosis (Izdebska et al., 2017). Oxidation of fatty acids is considered to be an important source of ROS in fatty liver. ROS can attack a variety of unsaturated fatty acids and induce lipid peroxidation in cells, results in the formation of aldehyde byproducts, such as MDA (Takaki et al., 2013). These molecules can spread inside and outside the cell and accelerating the effects of oxidative stress. Our previous study (Yu et al., 2016) found that WVBF has antioxidant effects which are related to the amarogentin components in WVBF. The current study also confirmed that WVBF has a significant antioxidant effect.

The Nrf2 signaling pathway is an important mechanism of cell resistance to oxidative stress. It can regulate the expression of liver detoxification and antioxidant defense genes (Kathirvel et al., 2010). Preliminary results indicate that WVBF can regulate the NRF2 pathway, WVBF treatment of NAFLD cells increased intracellular Nrf2 expression in a dose-dependent manner, suggesting that the antioxidant potential of WVBF could be an important mechanism for improving liver function of NAFLD cells, which is similar to the results of our previous study (Dai et al., 2018).

PPARα plays an essential role in fat synthesis (Qiao et al., 2013). The SREBP-1c subtype is a key regulatory element in the

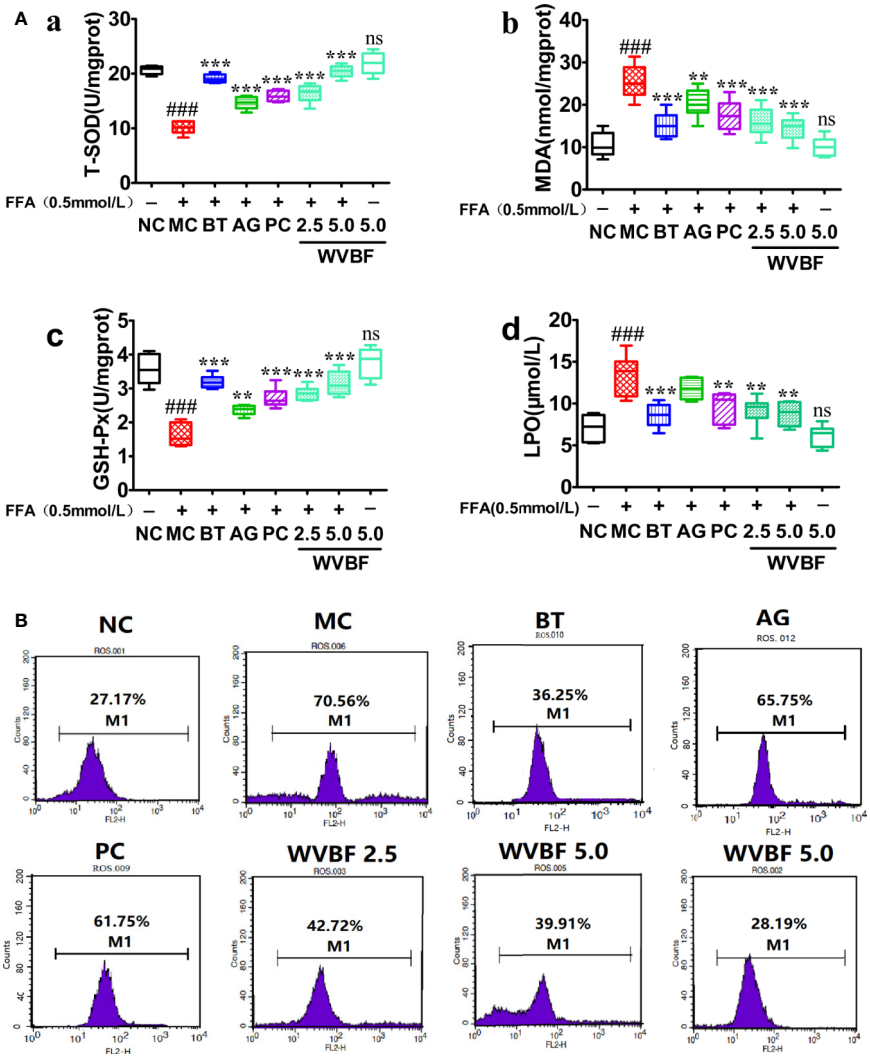

FIGURE 7 | Effects of water extract of *Veratrilla baillonii* (WVBF) on free fatty acids (FFA)-induced oxidative stress and intercellular reactive oxygen species (ROS) production in LO2. **(A)** Effects of WVBF pre-treatment on T-SOD (a), MDA (b), GSH-Px (c), LPO (d) product in LO2. **(B)** Flow cytometry analysis of FFA-induced ROS. n=3 (n, the number of experiments), ($^{\#\#}P < 0.01$, $^{\#\#\#}P < 0.001$ *vs*. control group; $^{*}P < 0.05$, $^{**}P < 0.01$, and $^{***}P < 0.001$ *vs*. FFA group).

process of lipid synthesis. Its downstream factors include acetyl-CoA carboxylase (ACC) and fatty acid synthase (FAS), which are essential enzymes for fat production (Kanuri and Bergheim, 2013). FFA treatment enhanced the expression of PPARα and decreased the expression of SREBP-1c in FFA-exposed NAFLD model cells, indicating that WVBF activated the PPARα pathway and inhibited the expression of the SREBP-1c/ACC/FAS pathway.

Inflammation is another important factor mediating the pathogenesis of NAFLD (Zhou et al., 2018). TNF-α, a pro-inflammatory cytokine, is involved in the pathogenesis of NAFLD (Parafati et al., 2018). Continuous accumulation of fatty acids activates the NF-κB pathway, promoting the release of inflammatory cytokines and causing inflammation (Cheng et al., 2019). In the current study, WVBF inhibited the increased expression of NF-κB and TNF-α induced by FFA, thereby reducing the liver inflammation reaction in the cell.

Together, the above findings indicate that WVBF treatment can significantly reduce FFA-induced lipid metabolism disorder, oxidative stress, and the inflammatory response in LO2 cells by activating PPARα and inhibiting fat synthesis of the SREBP-1c/FASN/ACC pathway. This ameliorates the symptoms of NAFLD and plays a role in protecting the liver (**Figure 9**). These results are consistent with our predicted target and signaling network analysis.

CONCLUSION

This study revealed the potential active compounds and the protective action of *V. baillonii* in a NAFLD cell model. WVBF inhibited oxidative stress and the inflammatory response, and reduced lipid metabolism disorder through various signaling pathways, suggesting that *V. baillonii* may be a candidate drug

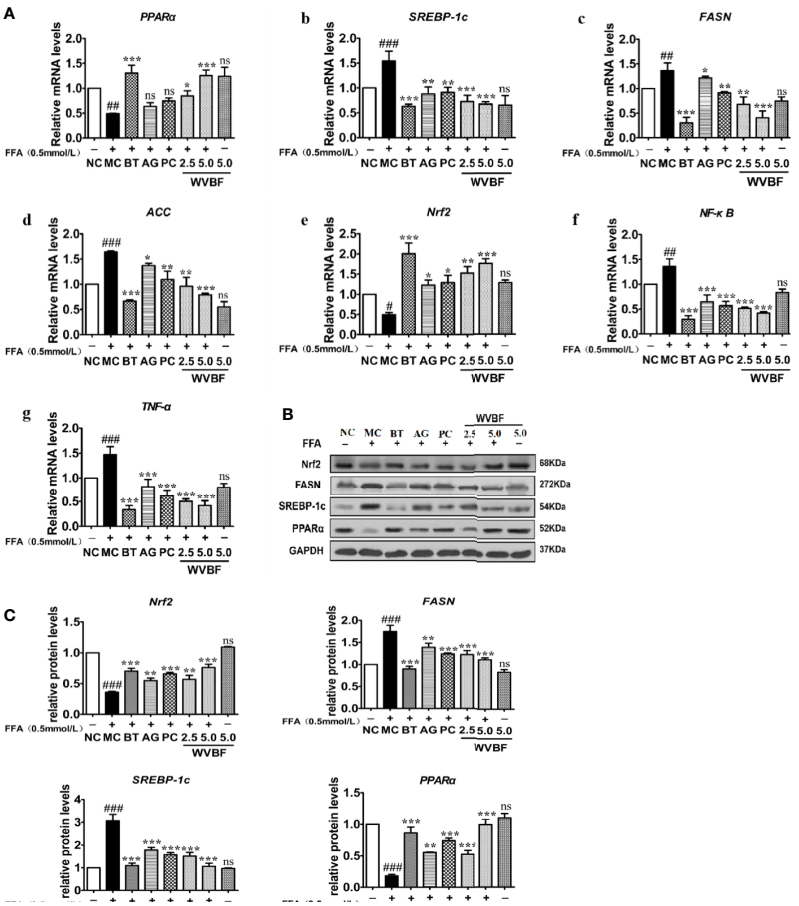

FIGURE 8 | Effect of water extract of *Veratrilla baillonii* (WVBF) on non-alcoholic fatty liver disease (NAFLD) lipid, oxidative stress, and inflammation of free fatty acids (FFA)-induced cell. **(A)** Effect of WVBF on the expression of PPARα (a), SREBP-1c (b), FASN (c), ACC (d), Nrf2 (e), NF-κB (f), and TNF-α (g) messenger RNA (mRNA). **(B)** Protein expression of PPARα, SREBP-1c, fatty acid synthase (FAS), acetyl-CoA carboxylase (ACC), and Nrf2 in FFA-induced LO2 cell was detected by western blot. **(C)** Effect of WVBF on the expression of Nrf2, ACC, FASN, SREBP-1c, and PPARα protein. n =3 (n, the number of experiment), ($^{\#\#}P < 0.01$, $^{\#\#\#}P < 0.001$, *vs*. control group; $^{*}P < 0.05$, $^{**}P < 0.01$, and $^{***}P < 0.001$ *vs*. FFA group).

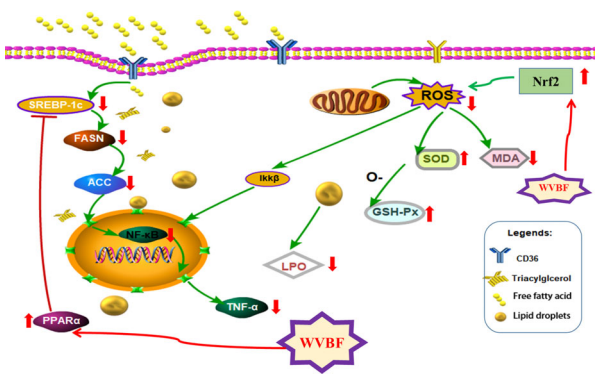

FIGURE 9 | The protective mechanism of water extract of *Veratrilla baillonii* (WVBF) on free fatty acids (FFA)-induced non-alcoholic fatty liver disease (NAFLD) LO2 cells.

for the treatment of NAFLD. Since NAFLD is a very complex condition in which many factors are involved, lipid accumulation in LO2 liver cells induced by fatty acids can only partially represent NAFLD condition. Further studies are needed to determine the regulatory effect and mechanism of WVBF in animal models of NAFLD.

DATA AVAILABILITY STATEMENT

The raw data supporting the conclusions of this article will be made available by the authors, without undue reservation, to any qualified researcher.

AUTHOR CONTRIBUTIONS

X-JH and C-JH conceived the study, participated in its design and coordination, and helped draft the manuscript. C-JH and SL

carried out the experiments and drafted the manuscript. JW carried out the network study. JL and G-ZY carried out the chemical analysis of the WVBF, and ZZ participated in the design of the study and performed the statistical analysis. All authors contributed to the article and approved the submitted version.

FUNDING

This work was supported by grants from the National Natural Science Foundation of China (81873090) and the Fundamental Research Funds for the Central Universitie, South-Central University for Nationalities (CZP20002).

REFERENCES

Chavez-Tapia, N. C., Rosso, N., and Tiribelli, C. (2011). In vitro models for the study of non-alcoholic fatty liver disease. *Med. Chem.* 18 (7), 1079–1084. doi: 10.2174/092986711794940842

Cheng, H., Huang, X. J., Tong, H. Y., Usman, M., Zhang, Z. H., Liu, Z. Y., et al. (2019). Hepatoprotective Activity of Veratrilla baillonii Franch on Tripterygium wilfordii Glycosides-Induced Liver Injury. *Latin Am. J. Pharm.* 38 (7), 1334–1341.

Dai, K., Yi, X. J., Huang, X. J., Muhammadet, A., Li, M., and Li, J. (2018). Hepatoprotective activity of iridoids, seco-iridoids and analog glycosides from Gentianaceae on HepG2 cells via CYP3A4 induction and mitochondrial pathway. *Food and Function* 9 (5), 2673–2683. doi: 10.1039/C8FO00168E

Du, T. T., Sun, X. X., Gang, Y., Zhou, X. R., Lu, H. M., Lin, X., et al. (2016). Lipid phenotypes in patients with nonalcoholic fatty liver disease. *Metab. Clin. And Exp.* 65 (09), 1391–1398. doi: 10.1016/j.metabol.2016.06.006

Ge, Y. B., Jiang, Y., Zhou, H., Zheng, M., Li, J., Huang, X. J., et al. (2016). Antitoxic effect of *Veratrilla baillonii* on the acute toxicity in mice induced by Aconitum brachypodum, one of the genus Aconitum. *J. Ethnopharmacol.* 179, 27–37. doi: 10.1016/j.jep.2015.12.030

He, Y. M., Zhu, S., Ge, Y. W., Kazuma, K., Zou, K., Cai, S. Q., et al. (2015). The anti-inflammatory secoiridoid glycosides from Gentianae Scabrate Radix: the root and rhizome of Gentiana scabra. *J. Nat. Med.* 69 (3), 303–312. doi: 10.1007/s11418-015-0894-8

Hopkins, A. L. (2008). Network pharmacology: the next paradigm in drug discovery. *Nat. Chem. Biol.* 11, 682–690. doi: 10.1038/nchembio.118

Hu, J., Hong, W., Yao, K. N., Zhu, X. H., Chen, Z. Y., and Ye, L. (2019). Ursodeoxycholic acid ameliorates hepatic lipid metabolism in LO2 cells by regulating the AKT/mTOR/SREBP-1 signaling pathway. *World J. Gastroenterol.* 25 (12), 1492–1501. doi: 10.3748/wjg.v25.i12.1492

Huang, X. J., Li, J., Mei, Z. Y., and Chen, G. X. (2016). Gentiopicroside and sweroside from *Veratrilla baillonii* Franch. induce phosphorylation of Akt and suppress Pck1 expression in hepatoma cells. *Biochem. And Cell Biol.* 94 (3), 270–278. doi: 10.1139/bcb-2015-0173

Ipsen, D. H., Lykkesfeldt, J., and Tveden-Nyborg, P. (2018). Molecular mechanisms of hepatic lipid accumulation in non-alcoholic fatty liver disease. *Cell Mol. Life* 75 (18), 3313–3327. doi: 10.1007/s00018-018-2860-6

Izdebska, M., Pitkowska-Chmiel, I., Korolczuk, A., Herbet, M., and Dudka, J. (2017). The beneficial effects of resveratrol on the steatosis and mitochondrial oxidative stress in HepG2 cells. *Can. J. Physiol. Pharmacol.* 95 (12), 1442–1453. doi: 10.1139/cjpp-2016-0561

Kanuri, G., and Bergheim, I. (2013). In vitro and in vivo models of non-alcoholic fatty liver disease (NAFLD). *J. Mol.* 14 (6), 11963–11980. doi: 10.3390/ijms140611963

Kathirvel, E., Chen, P., Morgan, K., French, S. W., and Morgan, T. R. (2010). Oxidative stress and regulation of anti-oxidant enzymes in cytochrome P4502E1 transgenic mouse model of non-alcoholic fatty liver. *J. Gastroenterol. Hepatol.* 25 (6), 1136–1143. doi: 10.1097/MEG.0b013e328328f461

Li, J., Liu, G., Ihsan, A., Yi, X. J., Wang, D. G., Cheng, H., et al. (2019). Effects of Veratrilla baillonii Extract on Hepatic Gene Expression Profiles in Response to Aconitum brachypodum-Induced Liver Toxicity in Mice. *Front. Pharmacol.* 10, 568. doi: 10.3389/fphar.2019.00568

Lian, L. H., Wu, Y. L., Wan, Y., Li, X., Xie, W. X., Nan, J. X., et al. (2010). Anti-apoptotic activity of gentiopicroside in D-galactosamine/lipopolysaccharide-induced murine fulminant hepatic failure. *Chem. Biol. Interact.* 188 (1), 127–133. doi: 10.1016/j.cbi.2010.06.004

Liu, J., Pei, M., Zheng, C., Li, Y., and Yang, L. (2013). A systems-pharmacology analysis of herbal medicines used in health improvement treatment: predicting potential new drugs and targets. *Alternat. Med.* 938764, 17. doi: 10.1155/2013/938764

Mao, Y., Cheng, J., Yu, F., Li, H., Guo, C., and Fan, X. (2015). Ghrelin attenuated lipotoxicity via autophagy induction and nuclear factor-κB inhibition. *Cell. Physiol. Biochem. Pharmacol.* 37 (2), 563–576. doi: 10.1159/000430377

Muhammad, J., Khan, A., Ali, A., Fang, L., Wu, Y. J., and Xu, Q. (2018). Network Pharmacology: Exploring the Resources and Methodologies. *Curr. Top. Med. Chem.* 18 (12), 949–964. doi: 10.2174/1568026618666180330141351

Olennikov, D. N., Kashchenko, N. I., Chirikova, N. K., and Tankhaeva, L. M. (2015). Iridoids and Flavonoids of Four Siberian Gentian: Chemical Profile and Gastric Stimulatory Effect. *Molecules* 20 (10), 19172–19188. doi: 10.3390/molecules201019172

Parafati, M., Kirby, R. J., Khorasanizadeh, S., Rastinejad, F., and Malany, S. (2018). A nonalcoholic fatty liver disease model in human induced pluripotent stem cell-derived hepatocytes, created by endoplasmic reticulum stress-induced steatosis. *Dis. Models Mech.* 11 (09). doi: 10.1242/dmm.033530. UNSP dmm.

Perumpail, B. J., Khan, M. A., Yoo, E. R., George, C., Donghee, K., Aijaz, A., et al. (2017). Clinical epidemiology and disease burden of nonalcoholic fatty liver disease. *World J. Gastroenterol.* 23 (47), 8263–8276. doi: 10.3748/wjg.v23.i47.8263

Pritchard, S., Wick, H. C., Slonim, D. K., Johnson, K. L., and Bianchi, D. W. (2012). Comprehensive Analysis of Genes Expressed by Rare Microchimeric Fetal Cells in the Maternal Mouse Lung. *Biol. Reprod.* 8742 (2), 1–6. doi: 10.1095/biolreprod.112.101147

Qiao, Y., Xiang, Q., Yuan, L., Xu, L., Liu, Z., and Liu, X. (2013). Herbacetin induces apoptosis in HepG2 cells: involvements of ros and PI3K/Akt pathway. *Food Chem. Toxicol.* 51, 426–433. doi: 10.1016/j.fct.2012.09.036

Song, W., Ni, S., Fu, Y., and Wang, Y. (2018). Uncovering the mechanism of Maxing Ganshi Decoction on asthma from a systematic perspective: A network pharmacology study. *Sci. Rep.* 8, 17362. doi: 10.1038/s41598-018-35791-9

Stork, C., Chen, Y., Šícho, M., and Kichmair, J. (2019). Hit dexter 2.0: machine-learning models for the prediction of frequent hitters. *J. Chem. Inf. Model.* 59 (3), 1030–1043. doi: 10.1021/acs.jcim.8b00677

Takaki, A., Kawai, D., and Yamamoto, K. (2013). Multiple hits, including oxidative stress, as pathogenesis and treatment target in non-alcoholic steatohepatitis (NASH). *J. Mol.* 14 (10), 20704–20728. doi: 10.3390/ijms141020704

Vaidya, H., Rajani, M., Sudarsanam, V., Padh, H., and Goyal, R. (2009). Antihyperlipidaemic activity of swertiamarin, a secoiridoid glycoside in poloxamer-407-induced hyperlipidaemic rats. *J. Nat. Med.* 63 (4), 437–442. doi: 10.1007/s11418-009-0350-8

Wang, Y. H., Zheng, C. L., Huang, C., Li, Y., Chen, X. T., Wu, Z. Y., et al. (2015). Systems pharmacology dissecting holistic medicine for treatment of complex diseases: an example using cardiocerebrovascular diseases treated by TCM. *Evid. Based Complement Altern. Med.* 980190, 19. doi: 10.1155/2015/980190

Wang, Y., Li, J., Wu, Z., Zhang, B., Yang, H., Wang, Q., et al. (2017). Insights into the molecular mechanisms of Polygonum multiflorum Thunb-induced liver injury: a computational systems toxicology approach. *Acta Pharmacol. Sin.* 38, 719–732. doi: 10.1038/aps.2016.147

Xu, H. Y., Zhang, Y. Q., Lei, Y., Gao, X. M., Zhai, H. Q., Lin, N., et al. (2014). A systems biology-based approach to uncovering the molecular mechanisms underlying the effects of dragon's blood tablet in colitis, involving the integration of chemical analysis, ADME prediction, and network pharmacology. *PloS One* 9 (7), e101432. doi: 10.1371/journal.pone.0101432

Younossi, Z. M., Koenig, A. B., Abdelatif, D., Fazel, Y., Henry, L., and Wymer, M. (2016). Global epidemiology of nonalcoholic fatty liver disease-meta-analytic assessment of prevalence, incidence, and outcomes. *Hepatology* 64 (4), 1388–1389. doi: 10.1002/hep.28584

Yu, Y., Yi, X. J., Mei, Z. Y., Li, J., Huang, X. J., Yang, G. Z., et al. (2016). The water extract of *Veratrilla baillonii* could attenuate the subacute toxicity induced by *Aconitum* brachypodum. *Phytomedicine* 23, 1591–1598. doi: 10.1016/j.phymed.2016.10.001

Zeng, Q., Li, L., and Siu, W. (2019). A combined molecular biology and network pharmacology approach to investigate the multi-target mechanisms of Chaihu Shugan San on Alzheimer's disease. *Biomed. Pharmacother.* 120, 1–11. doi: 10.1016/j.biopha.2019.109370. UNSP 109370.

Zhang, S. S., Chen, G. Z., Li, N., Dai, M. Y., Chen, C., Wang, P. H., et al. (2015). CYP2J2 overexpression ameliorates hyperlipidemia via increased fatty acid oxidation mediated by the AMPK pathway. *Obes. Soc.* 23 (7), 1401–1413. doi: 10.1002/oby.21115

Zhang, S. R., Mao, Y. Q., and Fan, X. M. (2018). Inhibition of ghrelin o-acyltransferase attenuated lipotoxicity by inducing autophagy via AMPK-mTOR pathway. *Drug Design Dev. Ther.* 12, 873–885. doi: 10.2147/DDDT.S158985

Zhang, Y., Zhang, M., Li, H., Zhao, H., Wang, F., He, Q. Y., et al. (2018). Serum metabonomics study of the hepatoprotective effect of amarogentin on CCl4-induced liver fibrosis in mice by GC-TOF-MS analysis. *J. Of Pharm. And Biomed. Anal.* 149, 120–127. doi: 10.1016/j.jpba.2017.10.029

Zhou, Y., Ding, Y. L., Zhang, J. L., Zhang, P., Wang, J. Q., and Li, Z. H. (2018). Alpinetin improved high fat diet-induced non-alcoholic fatty liver disease (NAFLD) through improving oxidative stress, inflammatory response and lipid metabolism. *Biomed. Pharmacother.* 97, 1397–1408. doi: 10.1016/j.biopha .2017.10.035

Ziamajidi, N., Khaghani, S., Hassanzadeh, G., Vardasbi, S., Ahmadian, S., Nowrouzi, A., et al. (2013). Amelioration by chicory seed extract on diabetes- and oleic acid-induced non-alcoholic fatty liver disease (NAFLD)/ non-alcoholic steatohepatitis (NASH) via modulation of PPARα and SREBP-1. *Food Chem. Toxicol.* 58, 198–209. doi: 10.1016/j.fct.2013.04.018

Zobair, M., Younossi, Z. M., Blissett, D., and Blissett, R. (2016). The economic and clinical burden of nonalcoholic fatty liver disease in the United States and Europe. *Hepatology* 64 (5), 1577–1586. doi: 10.1002/hep.28785

Conflict of Interest: The authors declare that the research was conducted in the absence of any commercial or financial relationships that could be construed as a potential conflict of interest.

Copyright © 2020 Huang, He, Liang, Wang, Li, Yang and Zhao. This is an open-access article distributed under the terms of the Creative Commons Attribution License (CC BY). The use, distribution or reproduction in other forums is permitted, provided the original author(s) and the copyright owner(s) are credited and that the original publication in this journal is cited, in accordance with accepted academic practice. No use, distribution or reproduction is permitted which does not comply with these terms.

frontiers in Pharmacology

ORIGINAL RESEARCH
published: 25 September 2020
doi: 10.3389/fphar.2020.544794

Gastrointestinal Motility, Muscle Relaxation, Antipyretic and Acute Toxicity Screening of Amyrin Type Triterpenoid (Daturaolone) Isolated From *Datura metel* Linnaeus (Angel's Trumpet) Fruits

Saud Bawazeer[1]*, *Abdur Rauf*[2]* and *Sami Bawazeer*[3]

[1] Department of Pharmaceutical Chemistry, Faculty of Pharmacy, Umm Al-Qura University, Makkah, Saudi Arabia, [2] Department of Chemistry, University of Swabi, Swabi, Pakistan, [3] Department of Pharmacognosy, Faculty of Pharmacy, Umm Al-Qura University, Makkah, Saudi Arabia

OPEN ACCESS

Edited by:
Yanqiong Zhang,
China Academy of Chinese Medical Sciences, China

Reviewed by:
Subhalakshmi Ghosh,
Independent Researcher, Kolkata, India
Habib Ur Rehman,
University of Veterinary and Animal Sciences, Pakistan

***Correspondence:**
Abdur Rauf
mashaljcs@yahoo.com
Saud Bawazeer
ssbawazeer@uqu.edu.sa

Specialty section:
This article was submitted to Ethnopharmacology, a section of the journal Frontiers in Pharmacology

Received: 22 March 2020
Accepted: 28 August 2020
Published: 25 September 2020

Citation:
Bawazeer S, Rauf A and Bawazeer S (2020) Gastrointestinal Motility, Muscle Relaxation, Antipyretic and Acute Toxicity Screening of Amyrin Type Triterpenoid (Daturaolone) Isolated From Datura metel Linnaeus (Angel's Trumpet) Fruits. Front. Pharmacol. 11:544794. doi: 10.3389/fphar.2020.544794

Datura metel Linn is used traditionally for the treatment of various diseases including relaxation of smooth muscles, relief of fever, as well as gastrointestinal disorder. This study deals with the bio-guided isolation of an active, amyrin-type triterpenoid, namely 3-oxo-6-β-hydroxy-β-amyrin (daturaolone; **1**), from the chloroform fraction of *Datura metel* L. (Angel's trumpet) fruits and its gastrointestinal motility, antipyretic, and muscle relaxation effects in animal models. The chemical structure of daturaolone (**1**) was elucidated by NMR spectroscopy and crystallography techniques. The chloroform fraction and daturaolone (**1**) were assessed for the GIT motility test. Data exhibited in charcoal meal GI transit test show that chloroform fraction and daturaolone (**1**) significantly reduce GIT motility and increased intestinal transit time, comparable to the standard (atropine), a muscarinic receptor blocking agent. Muscle relaxant potency of the extract and daturaolone (**1**) was assessed in various animal paradigms. In the inclined plane screening test, it produced a significant ($P < 0.05$) muscle relaxation potential in a dose-dependent manner after 30, 60, and 90 min. Likewise, the muscle relaxation potential of the extract and daturaolone (**1**) was strongly complemented by the chimney and traction test, representing a dominant effect after 60 min of sample administration. The chloroform fraction showed good antipyretic activity, and while daturaolone (**1**) exhibited significant activity at a higher dose, the maximum effect (84.64%) was at 20 mg/kg i.p. In acute toxicity screening test, the chloroform extract (100, 250, 500, and 1,000 mg/kg) and daturaolone (**1**) (5, 10, 20, and 50 mg/kg) were found safe. In conclusion, the chloroform extract and daturaolone (**1**) exhibited strong gastrointestinal motility, muscle relaxation, and antipyretic activity in different animal models and intestinally, was found safe at higher tested doses.

Keywords: ***Datura metel*, daturaolone, gastrointestinal motility, antipyretic activity, muscle relaxation activity**

INTRODUCTION

Datura metel is a member of the family Solanaceae and is an erect shrub with spreading branches. The plant has a local name in Bengali called Dhutura. *D. metel* grows throughout the year and is commonly known as Devil's Trumpet in English (Duke and Ayensu, 1985; Dabur et al., 2004). It grows in both hot and humid climate. The plant also has an American origin and is widely distributed in Pakistan, India, South America, and Africa (Sangwan and Camefort, 1983). It has long flowers having purple and white colors which scented up to 6″ (Okwu and Igara, 2009), while the leaves are broad in shape and dark green in color. *D. metel* is 10–20 cm long and 5–18 cm broad. Its fruits are spiny capsules in nature with a thickness of 4–10 cm. *D. metel* is widely used in Bangladeshi herbal medicine (Monira and Munan, 2012). In Chinese traditional system, its flowers are known as baimantuoluo which are used for the treatment of psoriasis and inflammation of the skin (Wang et al., 2008; Monira and Munan, 2012). In Ayurvedic medicinal systems, its seeds are used to cure ulcers, jaundice, diabetes, skin rashes, and bronchitis (Monira and Munan, 2012). Further to these uses, its flowers are involved in cigarette production, while the seeds are used in making tea with potent sedative action in Brazil (Agra et al., 2007). It is also used for the treatment of heart disease, epilepsy, diabetes, insanity, fever, diarrhea, asthmatic anesthetic, hallucinogenic, anti-asthmatic, hypnotic, antitussive, bronchodilator, anodyne narcotic, and skin diseases (Chopra et al., 1956; Chopra et al., 1986; Monira and Munan, 2012). The bioactivities of *D. metel* are due to secondary metabolites present in it. *D. metel* is well documented to contain varieties of potent secondary metabolites including alkaloids, steroids, saponins, flavonoids, triterpenoids, and tannins (Okwu and Igara, 2009). Various types of alkaloids have been detected in different parts of *D. metel*; the numbers of alkaloids increase with the age of the plant (Afsharypuor et al., 1995; Monira and Munan, 2012). The important compounds of *D. metel* are tropane alkaloids including hyoscine, hyoscyamine, littorine, valtropine, acetoxytropine, fastusine, and various withanolides as well as a number of trigloyl ester of tropine (Afsharypuor et al., 1995; Monira and Munan, 2012). An alkaloid known as scopolamine, a major compound isolated from *D. metel*, has been documented for curing various diseases including bronchitis and asthma (Dabur et al., 2004). Other tropane alkaloids isolated from *D. metel* are used as antispasmodic, mydriatic, and sedative agents (Nuhu, 2002). It is also an important source of withanolides, which is used to cure pain and has hallucinogenic potency (Abubakar et al., 2009; Yang et al., 2014; Arjun et al., 2015). The seeds of *D. metel* are used to relieve dental pain. Also, it has wide applications in ayurvedic medication such as the ability to cure hair fall and other skin-related infectious diseases (Soni et al., 2012). The plant extracts of *D. metel* have been documented for antimicrobial and anti-inflammatory properties (Akharaiyi, 2011; Alabri et al., 2014). In this context, atropine isolated from the title plant has been used to dilate the pupil, and it helps in the surgery of the eyes (Satyavati and Raina, 1977). The current study deals with the isolation of a triterpenoid, namely daturaolone (**1**), and the *in vivo* gastrointestinal motility, antipyretic, and muscle relaxation as well as acute toxicity study of the chloroform extract and the isolated daturaolone (**1**).

MATERIAL AND METHODS

Plant Material Collection

Fruits of *Datura metel* (Angel's trumpet) were obtained from the ground of Razagram (Khall, Distt; Dir, KPK, Pakistan. The plant specimen was identified by Dr. Muhammad Ilyas, Head of the Department of Botany, University of Swabi, KPK, Pakistan. The voucher specimen no. Bot (UOS-521) was deposited at the herbarium of the Botany Department, University of Swabi.

Extractions, Fractionation, and Isolation

The fruits (8.2 kg) were dried in a shade at room temperature, ground into powder and then subjected to cold extraction with methanol (×3), which yield 349 g of reddish extract. The extract was suspended in distilled water and then successively extracted with *n*-hexane (52.8 g), chloroform (93.6 g), and ethyl acetate (45.1 g) as per reported methods (Bawazeer et al., 2019). Based on the TLC profile, the chloroform extract (25.0 g) was chromatographed on the silica gel normal phase column. The column was eluted with a mixture of *n*-hexane and ethyl acetate (0:100) of increasing polarity order. One hundred sub-fractions were obtained, which were combined to 12 major sub-fractions (SB-1–SB-12), as per the TLC profile. Based on the TLC profile, SB-7 was subjected to frequent pencil column chromatography (CC), eluting with *n*-hexane and ethyl acetate (14:86), which yielded white crystals. The obtained crystals were washed with *n*-hexane to afford daturaolone (**1**) (2.7 g; 99.87% pure). The chemical structure of daturaolone (**1**) was elucidated by advanced spectroscopic technique. The structure was confirmed by crystallography technique (**Figure 1**), and the spectral data were compared with the reported ones (Wang et al., 2005).

Animals

Balb/c mice of either sex, weighing 18–22 g were used throughout this work. These animals were placed under standard laboratory conditions. All animals were served with standard laboratory diet and *ad libitum* water. Experiment was performed at the Pharmacy Department University of Swabi as per standard procedure. Studies involving human participants were reviewed and approved by the ethical committee UOS/Pharm-649, Department of Pharmacy, University of Swabi, Swabi, Pakistan.

Gastrointestinal Motility Test

The chloroform fraction and daturaolone (**1**) were assessed for gastrointestinal motility screening test. In these tests, mice were divided into six groups ($n = 6$). The 1st group received normal saline (10 ml/kg) and acted as a negative control; the 2nd group was administered with the reference drug (atropine; 10 mg/kg, i.p.). The remaining groups were treated with chloroform fraction at the doses 10, 25, 50, 100, and 200 mg/kg, i.p. and daturaolone (**1**) at the doses 2.5, 5, 10, 20, and 40 mg/kg, i.p. After 15 min of treatment, every animal received a 0.3 ml charcoal meal in the form of a suspension in water with 10% vegetable charcoal and 10% gum acacia. Exactly after 30 min of

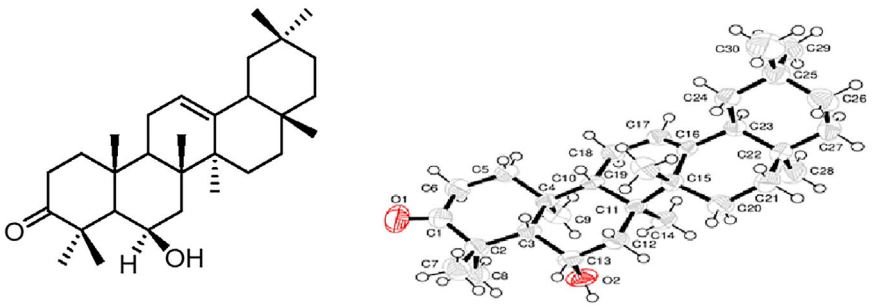

FIGURE 1 | Chemical structure and x-rays' crystallographic image of daturaolone (**1**) isolated from *Datura metel*.

the above administration, all animals were sacrificed by cervical dislocation, and the whole small intestine was detached. Experiments were performed in triplicate, and the percent activity was measured from the distance traveled by charcoal in the small intestine as per our previous methods (Rauf et al., 2016a; Ahmad et al., 2018).

Muscle Relaxation Assay

The muscle relaxation activity of the chloroform fraction and daturaolone (**1**) was performed using the chimney and inclined plane model according to the standard method (Rauf et al., 2018).

Chimney Model

Muscle relaxation potency of chloroform fractions and daturaolone (**1**) was performed according to our reported procedure (Rauf et al., 2018). In this model, a pyrex tube having a diameter of 3 cm and length of 30 cm was used. The design tube was marked 22 cm from the base, and the treated mice were allowed to muscle relaxant traits after 30, 60, and 90 min. The animals were divided into various groups ($n = 6$). Animals in one group were fed with distilled water (10 ml/kg), one group with diazepam (1 mg/kg) as a standard drug, and the remaining animals with chloroform fractions at the doses 10, 25, 50, 100, and 200 mg/kg, i.p. and daturaolone (**1**) at doses 2.5, 5, 10, 20, and 40 mg/kg, i.p. All groups of treated animals were allowed at the one adjacent of the tube and then permitted to move rising from the base to the marked position at 20 cm. When the animals reached the mark then we directly converted the tube to vertical. Those animals which fail to climb to the 20 cm mark of the glass tube in 30 s were counted as animals with muscle relaxation potential.

Traction Model

The muscle relaxation effect of chloroform fractions and daturaolone (**1**) was performed according to our reported traction methods (Rauf et al., 2018). These methods were designed by using a metallic wire coated with rubber, and both sides of the wire were connected with a stand around 60 cm upstairs of the laboratory bench. Different groups of animals ($n = 6$) were fed with distilled water (10 ml/kg), diazepam (1 mg/kg), and the chloroform extract and isolated daturaolone (**1**) (2.5, 5, 10, 20 mg/kg i.p.). Then all the animals were open to traction testing after 30, 60, and 90 min. All groups of animals were suspended by back legs to the attached wire then hanging time was recorded for less than 5 s. Failure of each animal to hang to the wire indicated muscle relaxant potency. The activity was performed again and again to calculate the muscle relaxant potency according to reported methods (Rauf et al., 2018).

Inclined Plane Model

This model was also used to check the muscle relaxation effect of chloroform fractions and daturaolone (**1**) as per the published method (Rauf et al., 2018). The inclined plane used in this method consisted of two plywood boards which were joined in such a pattern that one plywood board was from the base and the other with the base at 65°. Animals were divided into various groups ($n = 6$); each group was administered with distilled water (10 ml/kg), standard drug (1 mg/kg), chloroform fraction at the doses 10, 25, 50, 100, and 200 mg/kg, i.p., and daturaolone (**1**) at the doses 2.5, 5, 10, 20, 40 mg/kg, i.p. After 30, 60, and 90 min of the administration, animals were permitted on the higher portion of the inclined plane for 30 s to hang or fall.

Yeast Induced Antipyretic Activity

The antipyretic effect of chloroform extract and daturaolone (**1**) isolated from the title plant was evaluated using a standard procedure (Muhammad et al., 2012). Animals were distributed into various groups ($n = 6$). All groups of animals were subjected to fasting and allowed free access to drinking water. Among the divided groups, Group I received saline (control), Group II received the standard drug (Paracetamol), while the remaining groups (III–VII) received the fraction at different doses 10, 25, 50, 100, and 200 mg/kg, and daturaolone (**1**) at 2.5, at 10, 15, and 20 mg/kg. The normal temperature was noted with the help of a numerical thermometer, and then pyrexia was induced in all groups of animals by introducing aqueous suspension (20%) of Brewer's yeast (10 ml/kg, s.c.). After 24 h, the rectal temperature was noted and groups (III–VII) were administered with the above doses. After drug administration, the rectal temperature was once more noted periodically at 1, 2, 3, 4, and 5 h of drug administration. The percent effect was calculated using our previous formula (Muhammad et al., 2013).

Toxicological Screening

The acute toxic effect of chloroform fraction and daturaolone (**1**) was performed in mice of both sexes as per our standard method (Rauf et al., 2016a). To find the toxicological profile of the extract and daturaolone (**1**), mice were starved for 16 h earlier to the experiment. All animals were divided into various groups ($n = 6$). Group I (Control group) was fed with normal saline (10 ml/kg). The remaining animals were treated with chloroform fraction in various doses (50, 100, 250, 500, and 1,000 mg/kg, (p.o.) and daturaolone (**1**) at (10, 25, 50, 100, 250, 500 mg/kg, (p.o.). Treated mice were then allowed free access to water and food and were noted for gross behavior change as well as mortality for 24 h.

Statistical Analysis

All results of this biological screening are presented as the mean ± standard error of the mean (SEM). To find the level of significant differences ($p < 0.05$ or 0.01) among the experimental groups, One-way analysis of variance (ANOVA) was achieved by Dunnett's multiple comparison test.

RESULTS AND DISCUSSION

Structure Elucidation

Daturaolone (**1**) was isolated from chloroform fraction and identified as 3-oxo-6β-hydroxy-β-amyrin by different spectroscopic techniques.

Daturaolone (**1**) was isolated as white crystals; IR (KBr, cm^{-1}) ν_{max} = 1599 (C=C), 1699 (C=O), 2,918 (C-H), 3650 (OH). ^{1}H NMR (500 MHz, $CDCl_3$): δ 0.83 (s, 3H, CH_3-28), 0.85 (s, 6H, CH_3-29, CH_3-30), 1.08 (s, 3H, CH_3-27), 1.15 (s, 3H, CH_3-23), 1.22 (t, 2H, CH_2-22), 1.32 (s, 3H, CH_3-26), 1.40 (s, 3H, CH_3-24), 1.49 (s, 3H, CH_3-25), 1.53 (s, 2H, CH_2-7), 1.62 (t, 2H, CH_2-15), 1.64 (d, 1H, CH-5), 1.65 (d, 2H, CH_2-19), 1.67 (t, 1H, CH-18), 1.76 (m, 2H, CH_2-11), 1.98 (t, 2H, CH_2-16), 2.06 (t, 1H, CH-5), 2.22 (3, 2H, CH_2-1), 2.73 (3, 2H, CH_2-2), 4.49 (brs, 1H, CH-6), 5.24 (s, 1H, CH_2-12); ^{13}C NMR (125 Hz, $CDCl_3$): δ 16.5 (CH_3-19), (CH_3-19), 18.6 (CH_3-26), 23.6 (CH_3-11, 24), 23.9 (CH_3-30), 25.8 (CH_3-23), 25.9 (CH_3-27), 26.1 (CH_2-15), 26.9 (CH_2-16), 28.3 (CH_3-28), 31.0 (C-20), 32.8 (C-17), 33.3 (CH_3-29), 34.0 (CH_2-21), 34.4 (CH_2-2), 36.3 (C-10), 37.0 (CH_2-22), 39.0 (C-14), 40.6 (CH_2-1), 41.6 (CH_2-7), 42.5 (C-8), 46.7 (CH_2-19), 47.3 (CH-9, 18), 48.7 (C-4), 56.5 (CH-5), 69.3 (CH-6), 121.2 (CH-12), 144.5 (C-13), 216.6 (C-3), ppm; HRMS (ESI) *m/z*: calcd. for $C_{30}H_{48}O_2$ $[M]^+$ 440.3710, found 440.3700. The spectroscopic data were compared to those published in the literature for the known compound and were found identical (Wang et al., 2005; Rauf et al., 2016b); furthermore, the daturaolone (**1**) was confirmed by X-ray crystallography data (**Figure 1**).

Effect on GIT Motility

Results of the GIT motility test of the extract and daturaolone (**1**) are given in **Figures 2**, **3**. A significant movement of the charcoal meal was recorded in the intestine of mice due to chloroform at a dose of 200 mg/kg; similarly, daturaolone (**1**) exhibited excellent movement of the charcoal meal at a dose of 20 mg/kg. The normal saline was used as a positive control. The tested fraction attenuated the movement of charcoal 60% as compared to normal saline, and the positive control demonstrated 24% motility (**Figure 2**). Multiple comparison screening tests indicated that the extract and daturaolone (**1**) at a dose of 200 and 20 mg/kg significantly reduce the GIT motility (**Figure 3**).

Muscle Relaxant Effect

In both muscle relaxant testing paradigms, the chloroform fraction and tested daturaolone (**1**) demonstrated a significant muscle relaxant effect (**Tables 1**, **2**). Dose- and time-dependent effects were noticed. The effect of chloroform fraction was 49.32% in both tested experimental paradigms. The muscle coordination activity of daturaolone (**1**) was greater than that of chloroform fraction. The isolated daturaolone (**1**) also demonstrated a significant dose- and time-dependent effect. However, the effect of daturaolone (**1**) was highly significant from the start of the experiment as compared to the chloroform fraction.

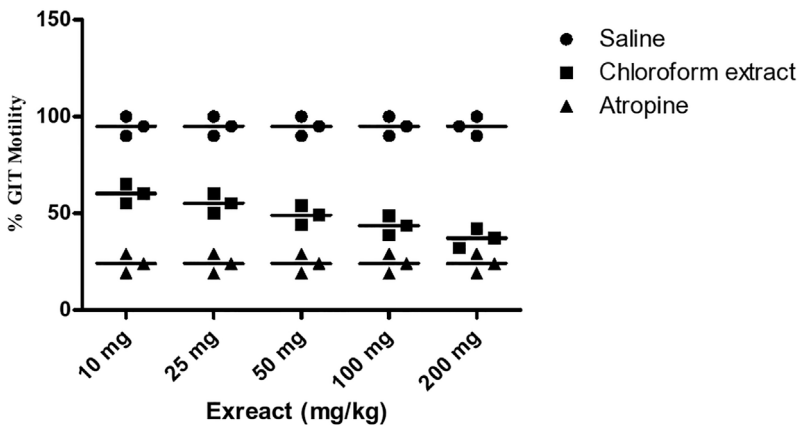

FIGURE 2 | Bar diagram indicated the GIT motility profile of chloroform extract in a dose-dependent manner of charcoal meals through small intestine of mice.

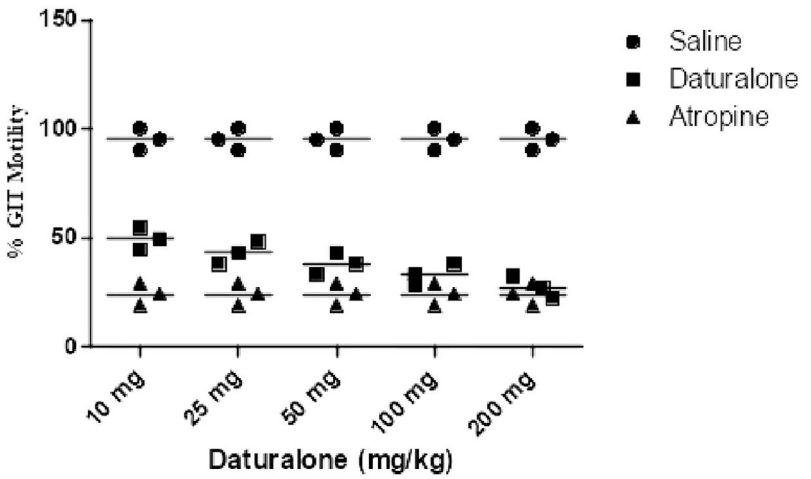

FIGURE 3 | Bar diagram indicated the GIT motility screening profile of daturalone (**1**) in dose-dependent method of charcoal meals through the small intestine of mice.

TABLE 1 | Effect of chloroform fraction and daturaolone (**1**) on relaxation of muscles.

Group	Dose/kg	Chimney test			Traction test		
		30 min	60 min	90 min	30 min	60 min	90 min
Distilled water	10 ml	0.0 ± 0.00	0.0 ± 0.00	0.0 ± 0.00	0.0 ± 0.00	0.0 ± 0.00	0.0 ± 0.00
Diazepam	0.25 mg	100.0 ± 0.0***	100.0 ± 0.0***	100.0 ± 0.0***	100.0 ± 0.0***	100.0 ± 0.0***	100.0 ± 0.0***
Chloroform	10	3.2.64 ± 1.40	9.87 ± 1.28	14.89 ± 1.20	1.99 ± 1.88	5.10 ± 1.70	9.43 ± 1.50
	25	07.09 ± 1.60	12.65 ± 1.66	17.98 ± 1.88	4.8.97 ± 2.00	9.10 ± 1.98	15.00 ± 1.80
	50	12.99 ± 1.99	18.33 ± 1.66	23.45 ± 1.41	9.2.34 ± 2.88	14.98 ± 2.9	19.22 ± 2.00
	100	20.10 ± 1.18	26.35 ± 1.87	31.98 ± 1.98	17.43 ± 1.88	22.12 ± 191	27.44 ± 1.65
	200	42.54 ± 2.00**	49.32 ± 2.12**	55.09 ± 2.19***	33.66 ± 189**	38.98 ± 2.55**	41.23 ± 2.12***
Daturaolone (**1**)	2.5	4.44 ± 1.55	10.981.87	17.98 ± 1.98	2.12 ± 1.44	7.7.60 ± 1.90	11.12 ± 2.00
	5	9.23 ± 1.80	15.12 ± 1.34	21.77 ± 1.98	5.7.23 ± 1.60	11.99 ± 1.20	18.01 ± 1.30
	10	15.23 ± 2.08	22.98 ± 2.11	27.98 ± 1.98	11.99 ± 2.16	17.09 ± 2.28	24.07 ± 2.20
	15	26.91 ± 1.44	31.02 ± 1.56	37.20 ± 1.70	20.09 ± 1.76	27.00 ± 1.63	35.99 ± 1.59
	20	53.88 ± 1.28**	59.98 ± 1.98***	66.32 ± 1.99***	44.10 ± 1.87**	51.16 ± 1.98***	58.07 ± 2.03***

*The data of muscle relaxant effect represented the % activity of mice (n = 6) in both models at 30, 60, and 90 min after administration of samples. The data is represented as the mean ± SEM (n = 6); *p < 0.05, **p < 0.0.01, ***p < 0.001, all values as related with control.*

TABLE 2 | Effect of chloroform fraction and daturaolone (**1**) on muscle relaxation (Inclined plane test).

Group	Dose/kg	Inclined plane test		
		30 min	60 min	90 min
Distilled water	10 ml	0. ± 0.00	0. ± 0.00	0. ± 0.00
Diazepam	0.25 mg	100. ± 0.00***	100. ± 0.00***	100. ± 0.00***
Chloroform	10	2.9. 33 ± 1.49	8.83 ± 1.99	14.00 ± 1.80
	25	8.1.02± 1.60	13.60 ± 1.68	19.92 ± 1.98
	50	16.09± 1.90	20.30 ± 1.80	26.43 ± 1.40
	100	25.98± 1.19	30.30 ± 1.82	37.91 ± 1.90
	200	33.32 ± 2.07*	38.32 ± 2.12**	43.11. ± 2.00**
Daturaolone (**1**)	2.5	3.23.45 ± 1.50	8.2.96.86	15.98 ± 1.92
	5	7.88 ± 1.81	12.10 ± 1.32	17.78 ± 1.96
	10	13.25 ± 2.03	18.90 ± 2.15	13.91 ± 1.90
	15	24.94 ± 1.45	29.09 ± 1.57	35.30 ± 1.79
	20	49.80 ± 1.29**	54.91 ± 1.56***	62.21 ± 1.22***

*The data of muscle relaxant effect represented the % activity of mice (n = 6) in both models, at 30, 60, and 90 min after administration of samples. The data is represented as the mean ± SEM (n = 6); *p < 0.05, **p < 0.0.01, ***p < 0.001; all values as related with control.*

Antipyretic Effect

Post treatment of chloroform fraction and daturaolone (**1**) showed a significant ($p < 0.001$) antipyretic activity in febrile mice during different assessment times (1–5 h). The promising antihyperthermia activity (66.98% was recorded for chloroform fraction at 200 mg/kg i.p., while for daturaolone (**1**) was (78.98%) at 20 mg/kg i.p. after 3 h of sample administration (**Figures 4**, **5**).

Acute Toxicity

The acute toxicity of chloroform fraction was screen in doses, 100, 250, 500, and 1,000 mg/kg. During 24 h assessment no toxicity was observed. Similarly, daturaolone (**1**) in doses of, 5, 10, 20, and 50 mg/kg showed no mortality during 24 h of assessment. Neither gross behavior changes nor mortality was observed for the extract and daturaolone (**1**).

Pretreatment with chloroform fractions and daturaolone (**1**) caused marked ($P < 0.05$) dose-dependent decrease in distance traveled by charcoal meal and showed a remarkable increase in GI transit time. The percent activity exhibited significant effect of extract and daturaolone (**1**) isolated from the title plant. When investigated in charcoal meal gastrointestinal transit, the extract and daturaolone (**1**) caused a dose-dependent decrease in the propulsive association of charcoal and displayed strong GIT motility effects as compared to atropine sulfate, a muscarinic receptor blocking agent. It has been reported that blockage of muscarinic receptors in the GIT has a promising effect on the GIT smooth muscle motility. Normally, tone and propulsive moments are diminished, thus causing an increase in the intestinal transit time (Rauf et al., 2016a). Consequently, it is recommended that anti-GIT motility of chloroform fraction and daturaolone (**1**) may be due to the blockage of muscarinic receptors in the GIT. In short, the chloroform fraction and daturaolone (**1**) isolated from title plant provoked a strong decrease in GIT motility with significant safety in initial studies. More studies are required to ascertain clinical utility.

In vivo traction test, chimney test, and inclined plane screening test are the most widely used tools for evaluation of muscle relaxant activity (Rauf et al., 2014). Results of the current finding indicated a strong potential of title plant fraction and daturaolone (**1**) for muscle relaxation. The muscle relaxation

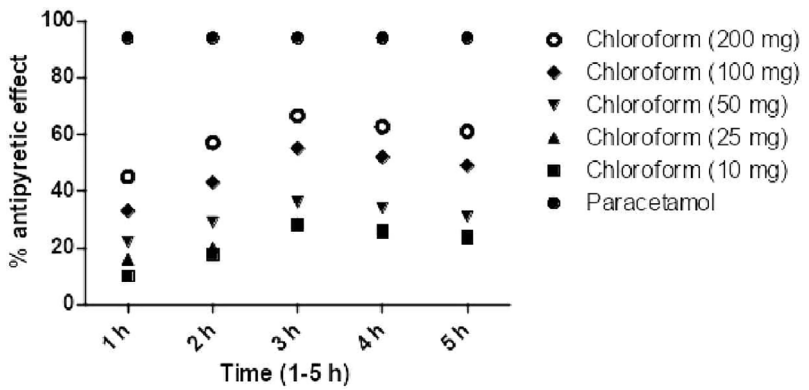

FIGURE 4 | Percent antipyretic effects of chloroform extract in yeast induced test at various doses.

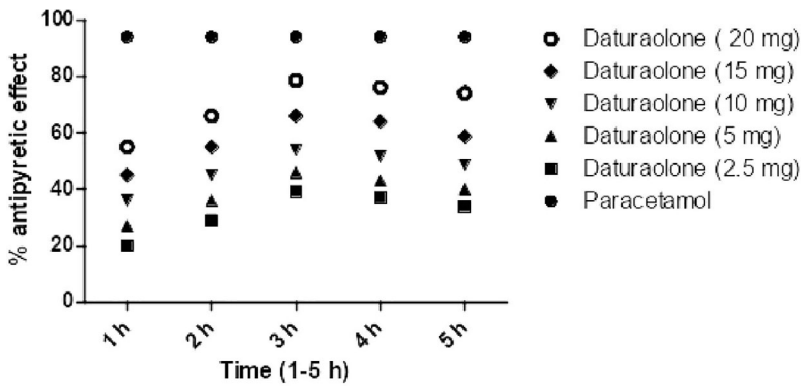

FIGURE 5 | Percent antipyretic effects of daturaolone (**1**) in yeast-induced test at various doses. All values are represented as the mean ± SEM for all groups of six animals.

effect of chloroform fractions and daturaolone (**1**) isolated from the title plant is displayed in **Table 1** and **Figure 1**. The tested fraction and isolated daturaolone (**1**) exhibited marked muscle relaxation in several animal models such as traction test, chimney test, and inclined plane model. Muscle relaxation effect of the extract and isolated daturaolone (**1**) was assessed in several muscle relaxant paradigms including traction test, chimney test, and inclined plan model. In these models, the muscle relaxant efficiency was assessed after 30, 60, and 90 min of treatment of chloroform fractions and daturaolone (**1**). Significant activity was observed after 60 min of chloroform fractions and daturaolone (**1**) administration. In all tested model the maximum muscle relaxation was noted at a higher dose. It is concluded that chloroform extract and daturaolone (**1**) exhibited promising muscle relaxation effects in various *in vivo* protocols. The hypodermic injection of brewer's yeast induced pyrexia by eventually increasing the synthesis of prostaglandin, and this method is considered the most important *in vivo* analysis test for the evaluation of antipyretic activity (Bertram, 2007; Rauf et al., 2014). Yeast-induced pyrexia is known as none pathogenic fever, the etiology of which is the making of prostaglandin (PG). Inhibition of PG synthesis may be the potential mechanism of antipyretic potency; that of paracetamol the inhibition of prostaglandin can be attained by blocking the cyclooxygenase enzyme effect (Rauf et al., 2014; Barkatullah et al., 2016). The promising antipyretic effect of chloroform fractions and daturaolone (**1**) is associated with numerous mediators based on pyrexia, mainly prostaglandins (Islam et al., 2015; Barkatullah et al., 2016). The intraperitoneal administration of chloroform fractions and daturaolone (**1**) remarkably attenuated the rectal temperature of yeast-induced febrile mice. Therefore, it can be concluded that chloroform fractions and daturaolone (**1**) interface with the synthesis/release of PG at any stage. We recommend chloroform extract and daturaolone (**1**) to researchers for further detailed and careful studies as potential plants for the controlling of various diseases. The promising gastrointestinal motility, muscle relaxation, antipyretic effects of chloroform fractions and isolated daturaolone (**1**) provide a strong scientific background to the traditional uses of *Datura metel* in the treatment of fever and muscle relaxation.

CONCLUSIONS

Phytochemicals can afford an excellent pharmacophore template for novel drug discovery which is used for the cure of many diseases. The crude extract/fraction and the isolated compound, daturaolone (**1**) exhibited significant gastrointestinal motility cessation, muscle relaxation, antipyretic effects. The fractions and daturaolone (**1**) were found safe when tested in a wide range of doses for acute toxicity. However, its safety and effect should further be assessed in chronic disease animal models. Thus daturaolone (**1**) could be used as lead compound for new drug development for fever, muscle relaxation, and associated gastrointestinal problems.

DATA AVAILABILITY STATEMENT

The original contributions presented in the study are included in the article/supplementary material; further inquiries can be directed to the corresponding author.

ETHICS STATEMENT

The studies involving human participants were reviewed and approved by ethical committee UOS/Pharm-649, Department of Pharmacy, University of Swabi, Swabi, Pakistan.

AUTHOR CONTRIBUTIONS

SauB supervised this project. AR and SamB were involved in the experimental part and writing of this paper. All authors contributed to the article and approved the submitted version.

FUNDING

The work is funded by grant number 14-MED333-10 from the National Science, Technology and Innovation Plan (MAARIFAH), the King Abdul-Aziz City for Science and Technology (KACST), Kingdom of Saudi Arabia.

ACKNOWLEDGMENTS

We thank the Science and Technology Unit at Umm Al-Qura University for their continued logistic support.

REFERENCES

Abubakar, M., Suleiman, U., Frank, A., and Ukwuani, A. (2009). Hallucinogenic effects of aqueous seeds extract of Datura metel in rats. *Internet J. Pharmacol.* 9 (1).

Afsharypuor, S., Mostajeran, A., and Mokhtary, R. (1995). Variation of scopolamine and atropine in different parts of Datura metel during development. *Planta Med.* 61, 383–384. doi: 10.1055/s-2006-958114

Agra, M. F., Baracho, G. S., Nurit, K., Basilioa, I. J. L. D., and Coelho, V. P. M. (2007). Medicinal and poisonous diversity of the flora of ''Cariri Paraibano'' Brazil. *J. Ethnopharmacol.* 111, 383–395. doi: 10.1016/j.jep.2006.12.007

Ahmad, B., Naz, S., Rauf, A., Bashir, S., Khan, A., Farooq, U., et al. (2018). *In vivo* study on analgesic, gastrointestinal tract (GIT) motility, and anti-termite potential of methanolic extract of Sarcococca saligna (D. Don) Muell. *Fruits. South Afr. J. Bot.* 114, 40–43. doi: 10.1016/j.sajb.2017.10.013

Akharaiyi, F. C. (2011). Antibacterial, Phytochemical and Antioxidant activities of Datura metel. *Int. J. Pharm. Tech. Res.* 3, 478–483.

Alabri, T. H. A., Al Musalami, A. H. S., Hossain, M. A., Weli, A. M., and Al-Riyami, Q. (2014). Comparative study of phytochemical screening, antioxidant and antimicrobial capacities of fresh and dry leaves crude plant extracts of Datura metel L. J. *King Saud Univ. Sci.* 26, 237–243. doi: 10.1016/j.jksus.2013.07.002

Arjun, T. N., Sudhir, H., Saxena, E., Dayma, A., Raghuvanshi, R. S., and Shah, R. (2015). Role of siddha system of medicine in the management of oro-facial diseases. *World J. Pharm. Pharmaceut. Sci.* 4, 1661–1671.

Barkatullah, I. M., Ikram, N., Rauf, A., Hadda, T. B., Bawazeer, S., Khan, H., et al. (2016). *In vivo* antinociceptive and muscle relaxant activity of leaf and bark of *Buddleja asiatica* L. *Pakistan J. Pharm. Sci.* 29 (5), 1509–1512.

Bawazeer, S., Rauf, A., Shah, S. U. A., Ullah, N., Uddin, G., Khan, H., et al. (2019). Antioxidant and Enzyme inhibitory activities of extracts and phytochemicals isolated from Pistacia integerrima. *J. Med. Spice Plants* 23 (2), 55–58.

Bertram, G. (2007). *Basic and Clinical Pharmacology, McGraw-Hill education*. Access Medicine.

Chopra, R. N., Nayar, S. N., and Chopra, I. C. (1956). *Glossary of Indian Medicinal Plants* Vol. Vol. 91 (New Delhi, India: Council of Scientific and Industrial Research).

Chopra, R. N., Nayar, S. L., and Chopra, L. C. (1986). *Glossary of Indian Medicinal Plants* (New Delhi, India: Council of Scientific and Industrial Research), 238–240.

Dabur, R., Ali, M., Singh, H., Gupta, J., and Sharma, G. L. (2004). A novel antifungal pyrrole derivative from Datura metel leaves. *Die Pharmazie: Int. J. Pharmaceut. Sci.* 59, 568–570.

Duke, J. A., and Ayensu, E. S. (1985). *Medicinal Plants of China* Vol. 1 (Algonac, MI., USA.: Reference Publications), 90–91.

Islam, N. U., Khan, I., Rauf, A., Muhammad, N., Shahid, M., and Shah, M. R. (2015). Antinociceptive, muscle relaxant and sedative activities of gold nanoparticles generated by methanolic extract of *Euphorbia milii*. *BMC Complement. Altern. Med.* 29 (15), 160. doi: 10.1186/s12906-015-0691-7

Monira, K. M., and Munan, M. S. (2012). Review on Datura Metel: A potential medicinal plant. *Global J. of Res. Med. Plants Indigenous Med.* 1 (4), 123–132.

Muhammad, N., Saeed, M., and Haroon khan, (2012). Antipyretic, analgesic and anti-inflammatory activity of Viola betonicifolia whole plant. *BMC Complement. Altern. Med.* 12 (1), 59. doi: 10.1186/1472-6882-12-59

Muhammad, N. 1., Saeed, M., Khan, H., Raziq, N., Halimi, S. M., and Abass, M. (2013). Antipyretic and anticonvulsant activity of n-hexane fraction of Viola betonicifolia. *Asian Pacific J. Trop. Biomed.* 3 (4), 280–283. doi: 10.1016/S2221-1691(13)60063-5

Nuhu, H. (2002). Alakaloid content of the leaves of three Nigerian Datura species Nig. *J. Nat. Prod. And Med.* 6, 15–18.

Okwu, D. E., and Igara, E. C. (2009). Isolation, characterization and antibacterial activity of alkaloid from Datura metel Linn leaves. *Afr. J. Pharmacol.* 3, 277–281.

Rauf, A., Uddin, G., Siddiqui, B. S., Khan, A., Khan, H., Arfan, M., et al. (2014). *In-vivo* antinociceptive, anti-inflammatory and antipyretic activity of pistagremic acid isolated from *Pistacia integerrima*. *Phytomedicine* 21 (12), 1509–1515. doi: 10.1016/j.phymed.2014.07.015

Rauf, A., Abu-Izneid, T., Maalik, A., Bawazeer, S., Khan, A., Hadda, T. B., et al. (2016a). Gastrointestinal Motility and Acute Toxicity of Pistagremic acid Isolated from the Galls of *Pistacia integerrim*a. *Med. Chem.* 13 (3), 292–294. doi: 10.2174/1573406412666161007145247

Rauf, A., Maione, F., Uddin, G., Raza, M., Siddiqui, B. S., Muhammad, N., et al. (2016b). Biological evaluation and docking analysis of daturaolone as potential cyclo-1 oxygenase inhibitor. *Evidence-Based Complement. Altern. Med.*, Article ID 4098686, 7 pages. doi: 10.1155/2016/4098686

Rauf, A., Bawazeer, S., Uddin, G., Siddiqui, B. S., Khan, H., Hadda, T. B., et al. (2018). Muscle relaxant activities of pistagremic acid isolated from Pistacia integerrima. *Z. für Naturforschung C.* 27, 413–416. doi: 10.1515/znc-2017-0179

Sangwan, R. S., and Camefort, H. (1983). The tonoplast, a specific marker of embryogenic microspores of Datura cultured in vitro. *Histochemistry* 78, 473–480. doi: 10.1007/BF00496198

Satyavati, G. V., and Raina, M. K. (1977). *Medicinal Plants of India* Vol. vol. 1 (New Delhi, India: Indian Council for Medical Research Publication), 333–334.

Soni, P., Siddiqui, A. A., Dwivedi, J., and Soni, V. (2012). Pharmacological properties of Datura stramonium L. as a potential medicinal tree: An overview. *Asian Pac. J. Trop. Biomed.* 2, 1002–1008. doi: 10.1016/S2221-1691(13)60014-3

Wang, K., Sun, H., Wu, B., and Pan, Y. (2005). Two Novel Olean Triterpenoids from Celastrus hypoleucus. *Helv. Chim. Acta* 88, 990–995. doi: 10.1002/hlca.200590094

Wang, Q. H., Xiao, H. B., Yang, B. Y., Yao, F. Y., and Kuang, H. X. (2008). Studies on pharmacological actions of the effective parts for psoriasis in Flos Daturae (I) Chinese. *J. Exp. Trad. Med. Formulae* 14, 48–51.

Yang, B. Y., Guo, R., Li, T., Wu, J. J., and Zhang, J. (2014). New anti-inflammatory withanolides from the leaves of Datura metel L. *Steroids* 87, 26–34. doi: 10.1016/j.steroids.2014.05.003

Conflict of Interest: The authors declare that the research was conducted in the absence of any commercial or financial relationships that could be construed as a potential conflict of interest.

Copyright © 2020 Bawazeer, Rauf and Bawazeer. This is an open-access article distributed under the terms of the Creative Commons Attribution License (CC BY). The use, distribution or reproduction in other forums is permitted, provided the original author(s) and the copyright owner(s) are credited and that the original publication in this journal is cited, in accordance with accepted academic practice. No use, distribution or reproduction is permitted which does not comply with these terms.

frontiers in Pharmacology

REVIEW
published: 02 October 2020
doi: 10.3389/fphar.2020.583171

Tripterygium Ingredients for Pathogenicity Cells in Rheumatoid Arthritis

Yujun Tang, Qiuping Liu, Yuxiang Feng, Yi Zhang, Zhenghao Xu, Chengping Wen and Yun Zhang**

College of Basic Medical Science, Zhejiang Chinese Medical University, Hangzhou, China

Rheumatoid arthritis (RA) is an autoimmune disease mainly characterized by chronic polyarthritis. Many types of cells play pivotal roles in the pathogenicity of RA, such as T cells, B cells, macrophages, dendritic cells (DCs), osteoclasts (OCs), and fibroblast-like synoviocytes (FLS). Tripterygium wilfordii Hook f. (TwHf) and its ingredients are able to control disease activity by regulating the functions of cells mentioned above, and the clinical studies have highlighted the importance of TwHf ingredients in RA treatment. They have been demonstrated to improve the RA symptoms of animal models and patients. In this review, we discussed the effect of TwHf ingredients on pathogenicity cells, including disease/cell phenotypes and molecular mechanisms. Here, we constructed a cell-cell interaction network to visualize the effect of TwHf ingredients. We found that TwHf ingredients could inhibit the differentiation and proliferation of the pathogenicity cells. Besides, the components could decrease the levels of pathogenicity cytokines [i.e., interleukin-6 (IL-6), interleukin-1β (IL-1β), and tumor necrosis factor-α (TNF-α)]. Many signaling pathways are involved in the underlying mechanisms, such as PI3K, NF-κB, and MAPK signaling pathways.

Keywords: Tripterygium wilfordii Hook f., rheumatoid arthritis, immune cell, mechanism, review

OPEN ACCESS

Edited by:
Yanqiong Zhang,
China Academy of Chinese Medical Sciences, China

Reviewed by:
Jinxia Zhao,
Peking University Third Hospital, China
Ganesan Ramamoorthi,
Moffitt Cancer Center, United States

****Correspondence:***
Chengping Wen
wengcp@163.com
Yun Zhang
zhangyun@zcmu.edu.cn

Specialty section:
This article was submitted to Ethnopharmacology, a section of the journal Frontiers in Pharmacology

Received: *14 July 2020*
Accepted: *03 September 2020*
Published: *02 October 2020*

Citation:
Tang Y, Liu Q, Feng Y, Zhang Y, Xu Z, Wen C and Zhang Y (2020) Tripterygium Ingredients for Pathogenicity Cells in Rheumatoid Arthritis. Front. Pharmacol. 11:583171. doi: 10.3389/fphar.2020.583171

INTRODUCTION

Rheumatoid arthritis (RA) is an autoimmune disease mainly characterized by chronic persistent synovitis, which causes the destruction of articular cartilage and bone, eventually leading to joint deformity and finally loss of function. The incidence of RA in mainland China is about 0.42%, and the disability rate of this disease course over 15 years is 61.3%. The clinical studies have shown that the effectiveness of the anchoring drug methotrexate is only 15%–25% (Lopez-Olivo et al., 2014; Chinese Rheumatology Association, 2018). While the addition of Tripterygium wilfordii Hook. f. (TwHf) or Tripterygium hypoglaucum (Levl.) Hutch is able to control RA disease activity more effectively by regulating immune cell functions (Jun et al., 2016; Xiao-yue et al., 2019). In the separable components of TwHf and Levl. Hutch, there are many similar but different active component, such as Wilforlide, Celastrol (Cel), and Triptolide (TP) (Xianguang and Li, 2006; Chao, 2015; Chen-qiong et al., 2015). These active components can regulate the pathogenicity immune cells and connective tissue cells of RA. For example, they can reduce the secretion of inflammatory cytokines (such as TNF-α, IL-1β, and IL-6) of macrophages, the proliferation, and differentiation of

pathogenic T cells, and the bone destruction which mediated by the fibroblast-like synoviocytes (FLS) and the osteoclasts (Peng et al., 2014; Wang et al., 2014; Te et al., 2019).

Tripterygium genus alleviates disease activity by regulating RA-related cells by multiple targeting approaches. Up to date, there is no literature review for TwHf or its active ingredients on RA-related cell dysfunction. Meanwhile, there are signal transduction interactions between various immune cells and connective tissue cells in the process of RA, which jointly promote the occurrence and development of RA. Therefore, we conducted a literature review (search strategy is available in **Supplementary Materials 1**) to summarize the effects of Tripterygium genus active ingredients on RA-related cells. Furthermore, we constructed signal pathways and cell-cell interaction networks to summarize their molecular mechanisms and to speculate the potential target cells and proteins.

THE FUNCTIONS OF TRIPTERYGIUM INGREDIENTS ON T CELLS AND THE MOLECULE MECHANISMS

T cells play a crucial role in various adaptive immune responses. During RA, T cells received antigens will be activated and proliferate (Smolen et al., 2018). Ho et al. (2013) found that PG27, one of the ingredients of TwHf, inhibited the T cell activation *via* targeting NF-κB and AP-1 pathways. PG27 can inhibit IKKα/IκBα/NF-κB and mitogen-activated protein kinase (MAPK)-AP-1 signaling pathways, while IKKβ activity was less sensitive for the inhibition of PG27. By contrast, the purified component of TwHf, PG490 (triptolide), similarly suppressed the above pathways. Similar results were demonstrated in RA animal models and patients but lacking molecule mechanisms. Triptolide reduced the numbers of CD4+ cells in the periphery and increased the numbers of CD8+ cells in Peyer's patch (Zhou et al., 2006). When triptolide was used to treat T cell isolated from peripheral blood of RA patients, the percentage of CD4+ and CD8+T cells secreting IFN-γ, IL-2, and IL-4 was decreased, and the percentage of CD4+ and CD8+T cells expressing CD69 and CD25 was also reduced (Ming et al., 2014). Besides, Tripterygium active compounds have been demonstrated *in vivo* and *in vitro* to reduce T cell number by promoting T cell apoptosis as well as suppressing T cell proliferation and cytokine secretion, while the mechanism is unknown (Tao et al., 1991; Cascão et al., 2015b; Wang et al., 2018).

CD4+ T cells can activate and polarize into various T helper cell subsets, including T helper 1 (Th1), T helper 2 (Th2), regulatory T (Treg), T helper 9 (Th9), T follicular helper cells (Tfh), T helper 17 (Th17), or T helper 22 (Th22) cells. Th17 cell numbers were increased in the peripheral blood, inflamed synovial tissue, and synovial fluid of RA patients (Leipe et al., 2010; van Hamburg et al., 2011; Penatti et al., 2017). Th17 cells promote the development of RA through the secretion of various inflammatory cytokines and chemokines. TGF-β/SMADs/RORγt and IL-6/STAT3 pathways are involved in mediating Th17 cell differentiation and mediating the expression of IL-17A, IL-17F, and IL-21 (Ivanov et al., 2006; Nishihara et al., 2007; Yang et al., 2008). The Cel, one of the Tripterygium ingredients, has been proved to have anti-arthritic activity by inhibiting IL-6/STAT3 signal and finally reduce the secretion of Th17-related pro-inflammatory cytokines (Venkatesha et al., 2011). Moreover, Cel inhibits the activation of NF- κB, and caspase-1 in macrophages, resulting in the reduced release of IL-1β and TNF-α, and finally decreased the infiltration and proliferation of joint Th17 cells (Cascão et al., 2012) because IL-1β is able to promote the polarization of Th17 cells through inducing the expression of the transcription factors IFR4 and RORγ (Vallières et al., 2019). In addition, TP inhibits the expression of COX2 and the secretion of PGE2 in the co-culture models of RA synovial fibroblasts (RASFs) and RA $CD4^+$ T cells, blocking the differentiation of Th17 cells *in vitro* (Peng et al., 2014).

Similar to Th17, Tfh cells also promote RA progression by secreting IL-21 (Vinuesa et al., 2016). However, there is less research on the effects of TwHf on Tfh. In patients with RA treated with TwHf, the number of tenderness joints, the number of swollen joints, and the evaluation score of overall RA in the experimental group were lower than those in the control group. Consistently, the levels of Tfh cells and IL-21 were lower than those in the control group, and the levels of Tfh cells and IL-21 were positively correlated with DAS28 score (Sun et al., 2016).

Treg cells act as protective cells during RA. Enhancing the function or improving the number of Treg cells has been proved to alleviate the RA activity in varying degrees (Cooles et al., 2013). So far, research focused on the effects of TwHf on Treg cells in RA were limited. In the co-culture system of bone marrow macrophages and Tregs, TP up-regulated IL-10 and TGF-β1 produced by Treg cells, resulting in the inhibition of osteoclast differentiation and bone resorption (Xu et al., 2016).

The role of tripterygium ingredients for T cells and the molecule mechanisms were summarized in **Table 1**. The molecule mechanisms of $CD8^+$ cell and Th17 are available in **Figures 1**, **2** (Th1, Th2, Treg, and Tfh are not available because insufficient study describes their molecule mechanism).

THE EFFECTS OF TRIPTERYGIUM INGREDIENTS ON B CELLS

B cells are also critical in the development of RA. B cells can be used as antigen-presenting cells (APC) to provide synergistic stimulation and then activate T cells. In addition, B cells are able to secrete autoantibodies, such as rheumatoid factor (RF) and anti-citrullinated protein antibody (ACPA) (Scherer et al., 2018; Smolen et al., 2018). ACPAs, RF, or their immune complexes interact with immune cells such as macrophages, neutrophils, and osteoclasts to promote joint inflammation of RA. The differentiation and activation of B cells could be mediated by BAFF/BAFF-R-ATK-mTOR, and TACI-NF-κB (Niiro and Clark, 2002; Schmidlin et al., 2009; Pieper et al., 2013). Many studies have demonstrated that Tripterygium ingredients could inhibit the proliferation and the antibody production of B cells while the molecular mechanisms remained unknown (Tao et al., 1991; Wang and Wu, 1994; Chang et al., 1997; Cascão et al., 2015b). Only one study revealed the molecular mechanisms. Pan etc. found Xinfeng capsule, a proprietary Chinese medicine mainly

TABLE 1 | The effects of Tripterygium ingredients on T cells.

Subtype	Component	Models	Molecular mechanism	Effects	Animal disease phenotype	Ref.
$CD4^+$T cell	TP	CIA rats	NA	Reduce the number of $CD4^+$ T cells in periphery blood	Ameliorate	(Zhou et al., 2006)
$CD8^+$ T cell	TP	CIA rats	NA	Increase the number of $CD8^+$ T cells in Peyer's patch	Ameliorate	(Zhou et al., 2006)
$CD4^+$T cell and $CD8^+$T cell	TP	Peripheral blood T cells in RA patients	NA	Reduce the percentage of $CD4^+$ and $CD8^+$ T cells. Reduce the levels of IFN-γ, IL-2, IL-4. Decrease the expression of CD69 and CD25	NA	(Ming et al., 2014)
Th17	Cel	AIA Lewis rats	Prohibit the phosphorylation of STAT3 and ERK	Inhibit the differentiation of Th17; decrease the levels of cytokines (IL-17, IL-6, and IFN-γ) and antibodies (anti-Bhsp65 and anti-CCP)	Ameliorate	(Venkatesha et al., 2011)
Th17	TP	Synovial fibroblasts from RA patients and Th17 cells co-cultured model	regulating cyclooxygenase-2/prostaglandin E2 axis	Inhibit Th17 differentiation	NA	(Peng et al., 2014)
Th17	Cel	E. coli stimulated THP-1 macrophage-like cell line and AIA Wistar rats	Inhibiting activation of NF-κB and caspase-1	Inhibit the release of IL-1β and TNF from macrophages, reducing joint the infiltration and proliferation of TH17 cells	Ameliorate	(Cascão et al., 2012)
Treg	TP	Co-cultures system of Tregs and BMMs	NA	Up-regulate IL-10 and TGF-β1, secreted by Treg. Inhibit the osteoclast differentiation and bone resorption caused by osteoclast	NA	(Xu et al., 2016)
TfH	Tripterygium glycosides tablets	Peripheral blood in patients with RA	NA	Decrease the numbers of TfH and the levels of IL-21	Ameliorate	(Sun et al., 2016)
T cell	PG27	Human peripheral blood T cells	Inhibiting activation of IKKα and AP-1	Inhibit the activation of T cell	NA	(Ho et al., 2013)
T cell	TP	Human peripheral blood T cells	Inhibiting activation of IKKα, AP-1, and IKKβ	Inhibit the activation of T cell	NA	(Ho et al., 2013)
T cell	Cel	AIA rats	NA	Promote T cell apoptosis	Ameliorate	(Cascão et al., 2015b)
T cell	TP	TNF transgenic mice	NA	Promote T cell apoptosis	Ameliorate	(Wang et al., 2018)
T cell	Triptolide ethanol extraction	Human peripheral blood	NA	Inhibit antigen and mitogen stimulated T cell proliferation and the secretion of IL-2	NA	(Tao et al., 1991)

Cel, Celastrol; TP, Triptolide; STAT3, Signal Transduction and Transcription Activator Protein 3; SOCS, Cytokine Signal Negative Regulator; IL, Interleukin; IKK, IκB Kinase; AP-1, Activin 1; TfH, Follicular helper T cells; OC, Osteoclasts; TNF, Tumor necrosis factor.

composed of TwHf, can up-regulate the PTEN level of B cells while down-regulate PDK1 and BAFF/BAFF-R to suppress the activation of PI3K/AKT/mTORC signal pathway and finally inhibit the proliferation and activation of B cells (Pan, 2018). Besides, the levels of related antibodies such as RF, anti-cyclic citrullinated peptide antibody (anti-CCP Ab), IgG, and IgM, were also inhibited. The effects of Tripterygium ingredients on B cells and the molecule mechanisms are summarized in **Table 2**. The molecule mechanisms of B cell are summarized in **Figure 3**.

THE ROLE OF TRIPTERYGIUM INGREDIENTS ON MACROPHAGE AND THE MOLECULE MECHANISM

Macrophages are mainly divided into classical activated M1 type and selective activated M2 type. The immuno-inflammatory reaction in RA patients directly affects the polarization of macrophages in peripheral blood, synovium, and synovial fluid, resulting in the continuous increase of M1-type macrophages and disrupting the balance of M1/M2 (Laria et al., 2016). Macrophages also promote RA and participate in the bone destruction of RA through antigen presentation. The degree of synovial macrophage infiltration was positively correlated with the bone destruction and clinical symptoms of RA (Gierut et al., 2010).

Tripterygium ingredients have been reported to inhibit the M1 polarization and promote the polarization of M2 type macrophages, resulting in the rebalance of the pro-inflammatory and anti-inflammatory cytokines (Feng, 2015; Liu, 2018). Besides, tripterygium ingredients could alleviate synovial macrophage infiltration. However, the molecular mechanism was not explained (Bao et al., 2007; Cascão et al., 2015a; Cascão et al., 2015b; Feng, 2015; Gan et al., 2015; Liu, 2018; Tong et al., 2018; Wang et al., 2018). M1 polarization is mediated by JAK-STAT1 signaling stimulated with IFNγ and characterized by increased iNOS, IL-1β, and TNF-α. Another M1 activated signaling pathway is the TLR4/NF-κB signaling pathway (Lawrence and Natoli, 2011). In the AIA rat model, Cel exerted the anti-inflammatory properties *via* down-regulating the NF-κB and the caspase-1 activation, leading to a decrease of IL-1β and TNF-α secretion in macrophages.

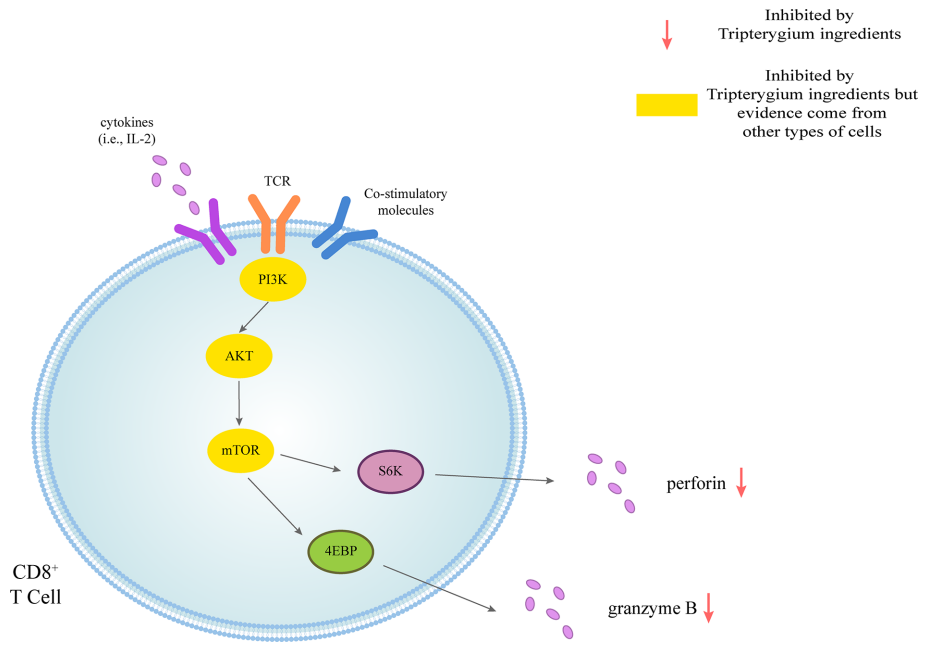

FIGURE 1 | Tripterygium ingredients act on the $CD8^+$ T cell. $CD8^+$ T cells could be activated through three signals. The first signal of T cell activation comes from the specific binding of its receptor TCR to the antigen. The second signal of T cell activation comes from costimulatory molecules. Cytokines promote the full activation of T cells. Perforin and granzyme B are secreted to exert cellular immunity *via* the PI3K signaling pathway. In other cell types, tripterygium ingredients act on the PI3K signaling pathway to prohibit the activation of $CD8^+$ T cells. Note: AKT (also known as PKB), Protein kinase B; PI3K, Phosphoinositide 3-kinase; mTOR, Mechanistic target of rapamycin kinase; S6K, Ribosomal protein S6 kinase; TCR, T-cell receptor; 4EBP, 4E-binding protein.

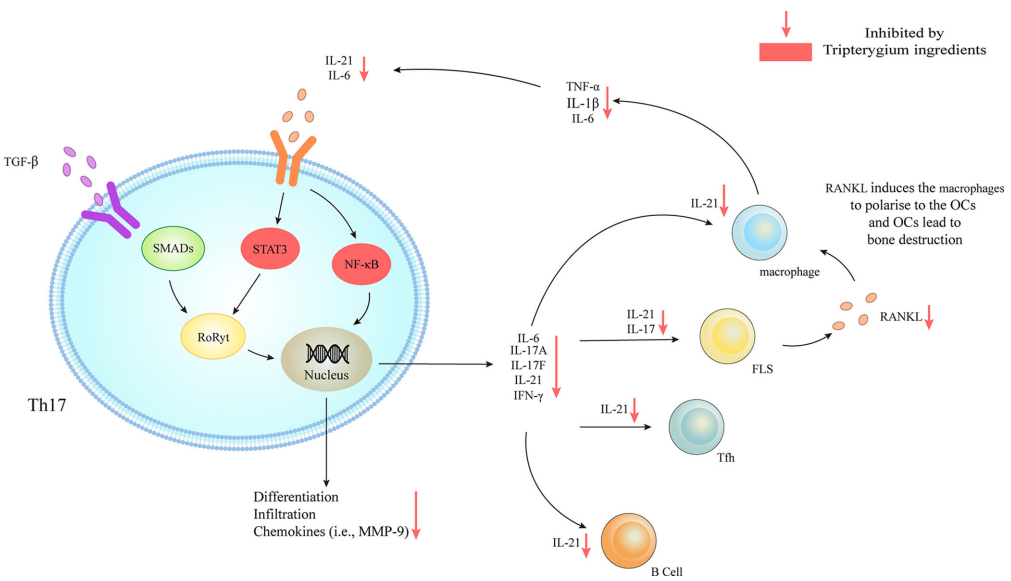

FIGURE 2 | Tripterygium ingredients act on Th17. TGF-β/SMADs/RORγt, IL-6/STAT3/RORγt, and IL-6/NF-κβ signaling pathways are responsible for the differentiation and the secretion of chemokines and cytokines of Th17. The downstream effector cells include B cells, Tfh, FLS, and macrophages. The activation of FLS releases RANKL to promote the secretion of chemokines (i.e., IL-6, IL-1β, and TNF-α) of macrophages, which could target Th17 and further active Th17. Tripterygium ingredients inhibit STAT3 and NF-κβ, resulting in the reduction of many cytokines (i.e., IL-6 and IL-21) to negatively regulates Th17 and downstream effector cells. Note: FLS, Fibroblast-like synoviocytes; IFN-γ, Interferon-gamma; IL, Interleukin; NF-κβ, Nuclear factor-kappa B; RANKL, Receptor activator of nuclear factor-κB ligand; RORγt, Retinoic acid-related orphan receptor gamma t; SMAD, Suppressor of mothers against decapentaplegic; STAT, Signal transducer and activator of transcription; TGF-β, Transforming growth factor-beta; TNF-α, Tumor necrosis factor-alpha.

TABLE 2 | The effects of Tripterygium ingredients on B cells.

Subtype	Component	Models	Molecular mechanism	Effects	Animal disease phenotype	Ref.
$CD19^+$ B cells	Cel	AIA rats	NA	Decrease the numbers of $CD19^+$ cells	Ameliorate	(Cascão et al., 2015a)
$CD19^+CD81^+$ and $CD19^+CD40^+$ B cells	Xinfeng capsule	RA patients	Inhibit PI3K/AKT/mTOR signaling pathway. Up-regulate PTEN; Down-regulate PDK1 and BAFF/BAFF-R	Inhibit B cells proliferation, and activation; Decrease the levels of antibodies, such as RF, anti-CCP Ab, IgG, and IgM	Ameliorate	(Pan, 2018)
B cells	Tripterygium glycosides	B cells	NA	Inhibit the IgG levels secreted by B cell	NA	(Chang et al., 1997)
B cells	Triptolide ethanol extraction	Human peripheral blood	NA	Inhibit B cell proliferation and decrease immunoglobulin levels	Ameliorate	(Tao et al., 1991)
B cells	TwHf	RA patients	NA	Decrease the percentage of B cells	Ameliorate	(Wang and Wu, 1994)

PTEN, Phosphatase and tensin homolog; PDK1, 3-phosphoinositide-dependent protein kinase 1; BAFF, B cell activating factor; BAFF-R, B cell activating factor receptor; PI3K, Phosphatidyl muscle Alcohol-3-kinase; AKT, Serine protein kinase; mTORC, Rapamycin target protein complex; IL, Interleukin; IgG, Immunoglobulin; TwHf, Tripterygium wilfordii Hook f.

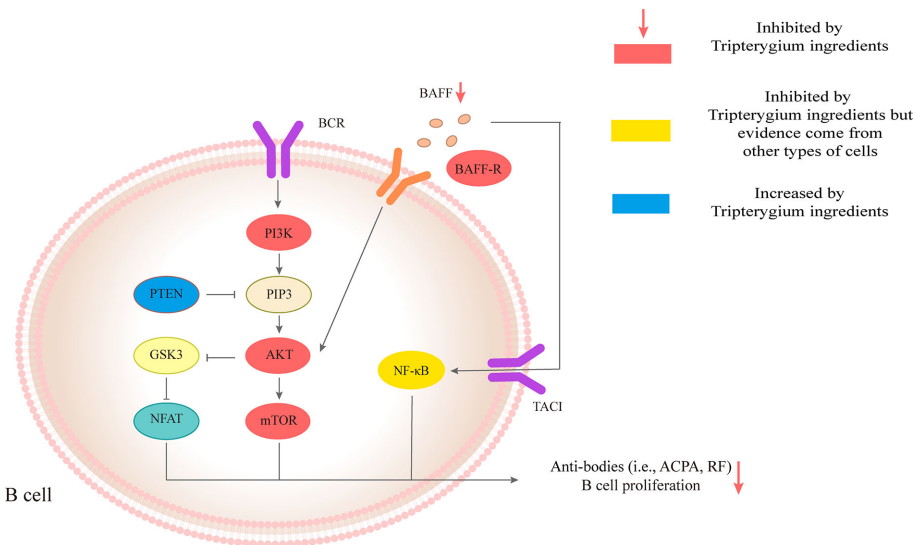

FIGURE 3 | Tripterygium ingredients act on the B cell. The anti-bodies production and proliferation of B cells are associated with BAFF/AKT/mTOR, PI3K/AKT/mTOR, and TACI/NF-κβ signaling pathways. PTEN negatively regulates PI3K/AKT/mTOR signaling pathways through dephosphorylating the lipid signaling intermediate PIP3. Tripterygium ingredients could increase the levels of PTEN and decrease the levels of molecules (red nodes) in the three pathways mentioned above to inhibit the anti-bodies production and proliferation of B cells. Note: AKT (also known as PKB), Protein kinase B; BCR, B cell receptor; BAFF, B cell-activating factor; BAFF-R, B cell-activating factor receptor; GSK3. Glycogen synthase kinase-3; mTOR, Mechanistic target of rapamycin kinase; NF-κβ, Nuclear factor-kappa B; NFAT, Nuclear factor of activated T-cells; PI3K, Phosphoinositide 3-kinase; PIP3, phosphatidylinositol-3,4,5-trisphosphate; PTEN, Phosphatase and tensin homolog.

Furthermore, the proliferation of Th17 was also inhibited because of lacking cytokines stimulation (Cascão et al., 2012). In addition, research has indicated that Cel blocked the binding of lipopolysaccharides (LPS) to a myeloid differentiation factor2 (MD2) and then inhibited the M1 activation, which was measured by the expression of inflammatory cytokines including TNF-α, IL-6, and IL-1β (Lee et al., 2015). Some researchers (Lin et al., 2001; Ping et al., 2015) also found that Tripterygium ingredients decreased the production of TNF-α, IL-1β, and IL-6 *via* inhibiting the expression of the TLR4, NF-κB, and prostaglandin E2 (PGE2). Besides, NO production and iNOS expression in macrophages were significantly inhibited by Tripterygium ingredients (Wang et al., 2004; Chen et al., 2018). Furthermore, TP inhibited the promoter activity of the iNOS gene and the inducible activity of iNOS transcriptional regulator Oct-1 (Wang et al., 2004). Pyroptosis is a unique and newly discovered mode of programmed cell death, which is triggered by the activation of Caspase-1 (Bergsbaken et al., 2009). It has been found that Cel can inhibit the pyroptosis induced by LPS and ATP *via* inhibiting the enzyme activities of cleaved-Caspase1 and Caspase-1, and finally blocking the secretion of IL-1β in macrophages (Xin et al., 2018). The effect of tripterygium ingredients on macrophages and the molecule mechanisms are summarized in **Table 3**. The figure for the molecule mechanism of macrophages is available in **Figure 4**.

TABLE 3 | The role of Tripterygium ingredients on macrophages.

Subtype	Component	Models	Molecular mechanism	Effects	Animal disease phenotype	Ref.
M1, M2 macrophages	Cel	Healthy mice	NA	Inhibit abdominal macrophages to M1 polarization. Promote M2 macrophages polarization	Alleviate	(Liu, 2018)
M1, M2 macrophages	TP	PBMCs, isolated from healthy people, cultured in different pH RPMI-1640	NA	Decrease M1 macrophages level and promote M2 macrophages level	NA	(Feng, 2015)
$CD68^+$ $CD168^+$ synovial macrophage	Cel	AIA rats	NA	Inhibit the infiltration and proliferation of $CD68^+$ $CD168^+$ synovial macrophages in the synovial membrane	Alleviate	(Cascão et al., 2015a)
OCP	TP	TNF transgenic mice	NA	Promote the apoptosis of OCP. Inhibit OC proliferation, bone resorption and pro-inflammatory cytokines levels secreted by macrophages	Alleviate	(Wang et al., 2018)
BMDMs	Cel	LPS-induced BMDMs.	Inhibit TLR4 activation *via* prohibiting the binding of LPS to the TLR4/MD2 complex	Inhibit pro-inflammatory cytokine levels and TLR4 activation in macrophages	NA	(Lee et al., 2015)
Macrophage	Cel	E. coli stimulated THP-1 macrophage-like cell line and AIA Wistar rats	Inhibiting activation of NF-κB and caspase-1	Inhibit the release of IL-1β and TNF from macrophages, reducing joint the infiltration and proliferation of TH17 cells	Alleviate	(Cascão et al., 2012)
Macrophage	TP	RAW 264.7 and U937 macrophage-like cell lines	Induce the degradation of Bcl-2 and the activation of caspase-3	Promote macrophages apoptosis	NA	(Bao et al., 2007)
Macrophage	Cel	CIA DBA/1J mice and RANKL induced RAW264.7 cells	Decrease serum TRAP 5b and the expression of osteoclastic genes (Trap, Ctsk, Ctr, MMP-9) and transcriptional factors (c-Fos, c-Jun and NFATc1); Inhibit NF-κB and MAPK	Decrease the infiltration of osteoclast cells in joints. Decrease serum TRAP 5b and the expression of osteoclastic genes and transcriptional factors	Alleviate	(Gan et al., 2015)
Macrophage	Tripterygium glycosides	CFA-induced arthritis rat and LPS-induced RAW264.7	NA	Ameliorate in paw swelling perimeter, arthritics score, and body weight loss. Reduce the levels of inflammatory cytokine (TNF-α, IL-6, and IL-1β) secreted by macrophages	Alleviate	(Tong et al., 2018)
Macrophage	Tripterygium glycosides	LPS-induced RAW264.7	down-regulate the expression of TLR4and NF-κB p65	Decrease the levels of TNF-α and IL-1β secreted by macrophages	NA	(Ping et al., 2015)
Macrophage	TP	LPS induced J774A.1 macrophage and IL-1α induced human synovial fibroblasts	Inhibit COX-2 in macrophages and pro-MMPs 1 and 3 in synovial fibroblasts. Up-regulate TIMPs 1 and 2 levels in synovial fibroblasts	Decrease PGE2 *via* inhibiting COX-2. Inhibit pro-MMPs and Up-regulate TIMPs	NA	(Lin et al., 2001)
Macrophage	Tripterygium wilfordii extraction	LPS-induced RAW264.7	NA	Reduce the production of NO and iNOS mRNA in macrophages	NA	(Chen et al., 2018)
Macrophage	TP and TwHf ethyl acetate extraction	Peritoneal macrophages isolated from AIA C57BL/6J mice	Inhibit NO production and iNOS mRNA expression in macrophages. Inhibit the promoter activity of iNOS gene to regulate its transcript factor (Oct-1) activity	Inhibit the production of NO, iNOS, and the activity of Oct-1	Alleviate	(Wang et al., 2004)
Macrophage	Cel	RAW264.7	Decrease the expression of cleaved-caspase-1 and inhibit caspase-1 enzyme activity	Ameliorate cell pyroptosis	NA	(Xin et al., 2018)

TP, Triptolide; Cel, Celastrol; OC, Osteoclasts; TLR4, Toll-like receptor 4; NF-κB, Nuclear factor activated B cell kappa light chain enhancer; Caspase, Aspartic acid protease containing cysteine; NO, Nitric oxide; OCP, Osteoclast progenitor cells; MD2, Medullary differentiation factor2; PGE2, Prostaglandin E2: Cox, Cyclooxygenase; TIMPs, Metalloproteinases; proMMP, pro-matrix metalloproteinase; TRAP, Tartrate-resistant acid phosphatase; MAPK, Mitogen-activated protein kinases; BMDMs, Bone marrow-derived primary macrophages.

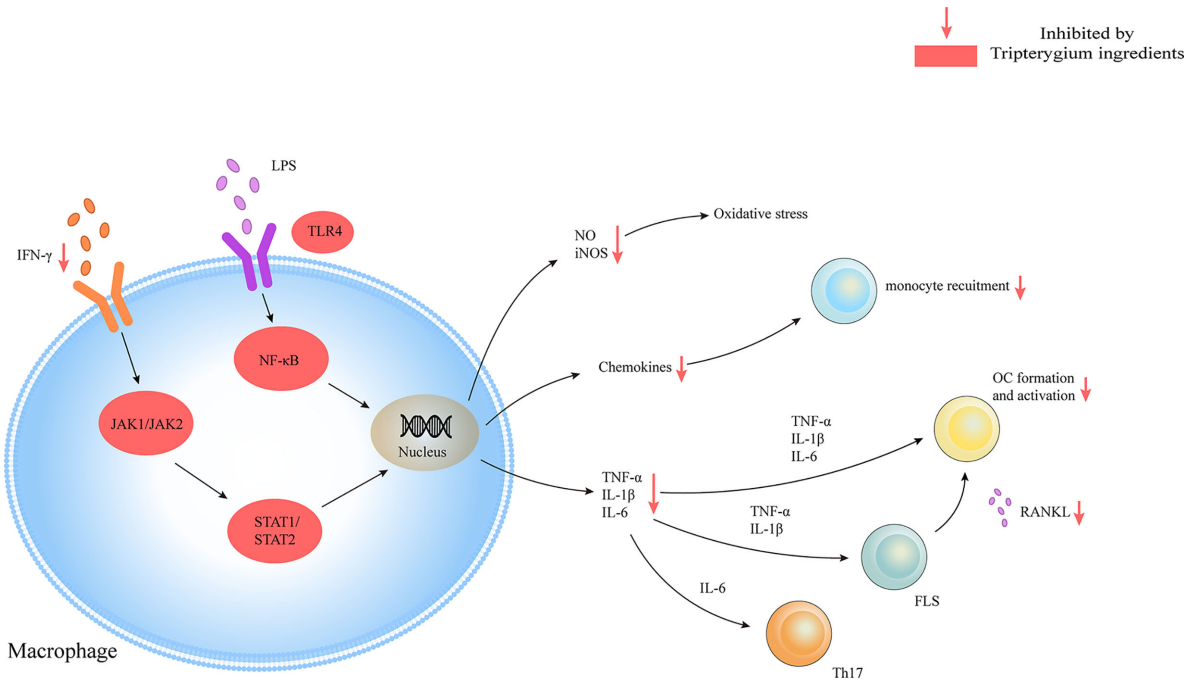

FIGURE 4 | Tripterygium ingredients act on the macrophage. Macrophages play as pro-inflammatory cells in RA with the release of chemokines, cytokines, and oxidative stress molecules through JAK/STAT and TLR/NF-κβ signaling pathways. Tripterygium ingredients block the signaling pathways to lead to the reduction of cytokines, which would inhibit the activation of effector cells. Note: FLS, Fibroblast-like synoviocytes; IFN-γ, Interferon-gamma; IL, Interleukin; JAK, Janus kinase; NF-κβ, Nuclear factor-kappa B; OC, Osteoclast; RANKL, Receptor activator of nuclear factor-κB ligand; STAT, Signal transducer and activator of transcription; TLR, Toll-like receptor; TNF-α, Tumor necrosis factor alpha.

THE EFFECTS OF TRIPTERYGIUM INGREDIENTS ON DENDRITIC CELLS (DCS)

TwHf is reported to inhibit DC development and induce DC apoptosis, finally decreasing the DC number, which resulted in the blocking of the naïve T cell activation and ultimately reduced the differentiation of the autoinflammatory T cells (Wang et al., 2001; Chen et al., 2006; Sun, 2017). Also, TP inhibits DC-related chemokines and reduces the sharing of DCs with MHC molecules and co-stimulatory factors of T and B cells, thereby blockade T and B cell activation. Antigenic peptide on MHC molecules, co-stimulatory molecules (CD80, CD86), and IL-12 of DCs promote the differentiation of Th1 cells, which produce IFN-γ and IL-2, required for cell-mediated immunity. Th1 cells directly modulate B cell differentiation into plasma cells. Besides, DCs also mediate the proliferation of these antibody-producing cells by producing BAFF (Khan et al., 2009). Unfortunately, the specific molecule mechanisms were not involved in these studies. Tripterygium ingredients for DCs are summarized in **Table 4**.

THE FUNCTIONS OF TRIPTERYGIUM INGREDIENTS ON OSTEOCLASTS (OCS) AND THE MOLECULE MECHANISM

OC-mediated bone resorption is one of the typical manifestations of RA. OCs, giant multinucleated cells derived from the monocyte lineage, are the only cells capable of resorbing bone (Teitelbaum and Ross, 2003). Receptor activator of nuclear factor kappa-B (RANK)/Receptor activator of nuclear factor kappa-B ligand (RANKL)/Osteoprotegerin (OPG) is the most crucial pathway of OC differentiation. Leibbrandt A etc. has demonstrated that RANKL is the critical mediator of OC activation and joint destruction; In a rat model of arthritis, osteoblasts and bone marrow stromal cells produce RANKL, which then triggers local development and activation of OCs. This finding has now become the basis for osteoimmunology (Leibbrandt and Penninger, 2009). Multiple studies have confirmed that Tripterygium ingredients can inhibit the expression of RANK and RANKL, thereby increasing the proportion of OPG, which can antagonize the function of RANK and finally inhibit the differentiation of OCs and reduce bone destruction (Nanjundaiah et al., 2012; Feng et al., 2013; Liu et al., 2013; Wang, 2015). Youn-Kwan Jung et al. (Jung et al., 2019) reviewed the roles of inflammatory signal pathways, including IL-1β/Myd88/TRAF6/NF-κB, TNF-α/TRADD/TRAF2/NF-κB, IL-6/STAT3/MAPK, and RANKL/RANK signal transduction. In these inflammatory pathways, TwHf or its active components impaired the release of cytokines/chemokines, reduced osteoclast differentiation, and activation, then finally blocked bone erosion in mice with collagen-induced arthritis through inhibiting the phosphorylation of NF- κB p65, MAPK (ERK, JNK, and p38) and reducing the expression of

TABLE 4 | The role of Tripterygium ingredients for DCs.

Component	Models	Molecular mechanism	Effects	Animal disease phenotype	Ref.
Duantengyimu decoction	GM-CSF and IL-4 stimulate PBMCs isolated from patients with RA	NA	Decrease the expression of CCR5 and CCR7, decrease the secretion of CXCL9 and CXCL10, and inhibit the migration of DC	NA	(Sun, 2017)
Tripterygium Wilfordii Saponins	GM-CSF, TNF-α, and IL-4 stimulate PBMCs	NA	Inhibit the expressions HLA-DR and CD80 on the membrane. Decrease the synthesis of IL-12 p40 subunit	NA	(Wang et al., 2001)
Tripterygium glycosides	DCs isolated from rats	NA	Reduce the expression of MHC-II, CD80, CD86, and CD40 on the membrane of DC	NA	(Chen et al., 2006)

TP, Triptolide; Caspase, Aspartic acid protease containing cysteine; CCR, Chemokine receptor; CXCL, C-X-C motif chemokine ligand; MAP, Mitogen activated protein; MHC, Major histocompatibility complex.

transcription factors c-Fos, c-Jun, and NFATcl (Gan, 2013; Qian et al., 2015). TwHf or its active components can also promote the apoptosis of OCs and osteoclast precursor (OCP) (Wang et al., 2018; Wang S. et al., 2019). The mechanism may be due to the inhibition of cIAP2 (the positive regulatory protein of TNF and NF-κB signaling pathway). Furthermore, TP has been reported to block OC differentiation by down-regulating the receptor for advanced glycation end-products (RAGE) and the high-mobility group box chromosomal protein 1 (HMGB1) (Wang et al., 2017). RAGE and its ligands (i.e., HMGB1) are necessary for the skeletal homeostasis and related-disease onset/progression (Plotkin et al., 2019). The elevated levels of RAGE and HMGB1 induce osteoblast apoptosis and OC differentiation/activity. Tripterygium ingredients on OC and the molecule mechanisms are summarized in **Table 5**. The figures for the molecule mechanism of OCs are available in **Figure 5**.

TABLE 5 | The function of Tripterygium ingredients on OC.

Component	Models	Molecular mechanism	Effects	Animal disease phenotype	Ref.
Cel	CIA mice	Reduce RANKL levels	Inhibiting OC differentiation	Alleviate	(Wang, 2015)
TP	CIA mice	Regulating the RANKL/RANK/OPG signaling pathway	Inhibiting OC differentiation	Alleviate	(Liu et al., 2013)
Cel	AIA Lewis rats and RANKL induced RAW264.7	Decrease RANKL levels and regulate RANKL/OPG ratio	Reduce OC proliferation. Ameliorate bone destruction. Decrease levels of upstream pro-inflammatory cytokine (i.e., IL-6) and downstream effectors (i.e., MMP-9)	Alleviate	(Nanjundaiah et al., 2012)
Cel	IL-1β stimulated MH7A	Decrease RANKL levels and increase OPG levels	Inhibit OC differentiation and activation	NA	(Feng et al., 2013)
Cel	RANKL induced RAW264.7 and CIA mice	Inhibit the protein phosphorylation of RANK downstream signalings, such as NF-κB p65, MAPK (ERK, JNK, p38) and the expression of the relevant transcription factors (i.e., c-Fos, c-Jun, and NFATcl)	Inhibit OC differentiation and bone resorption	Alleviate	(Gan, 2013)
Cel	RANKL induced RAW264.7	NA	Inhibit OC differentiation and chemokine CCl4	NA	(Qian et al., 2015)
TP	C57BL/6 mice bone marrow mesenchymal stem cells induced by RANKL, M-CSF, and HMGB1	Reduce the expression of RAGE mRNA to inhibit HMGB1	Inhibit OC differentiation	NA	(Wang et al., 2017)
TP	Co-cultures system of Tregs and BMMs	NA	Increase the levels of IL-10 and TGF-β1 secreted by Treg to inhibit OC differentiation and bone resorption	NA	(Xu, 2016; Xu et al., 2016)
TP	TNF-Tg mice and spleen cells isolated and induced to differentiate into OCs by M-CSF	Down-regulate the cIAP2	Promote OCP apoptosis and OC reduction	NA	(Wang S. et al., 2019)
TP	TNF-Tg mice	NA	Promote apoptosis rates of OCP and OC. Prohibit the bone erosion	Alleviate	(Wang et al., 2018)

TP, Triptolide; Cel, Celastrol; RANKL, Nuclear factor kappa B ligand receptor activator; RANK, Nuclear factor receptor activator; OPG, Osteoprotegerin; NF-kappa B, Nuclear factor activated B cell κ light chain enhancer; MAPK, Mitogen activated protein kinase; ERK, Extracellular regulatory protein kinase; JNK, Jun N-terminal kinase; NFATcl, Osteoclast activated T nuclear factor 1; CCl4, C-C motif chemokine ligand 4; HMGB1, High mobility group protein B1; RAGE, Receptor for advanced glycation end products; OC, Osteoclasts.

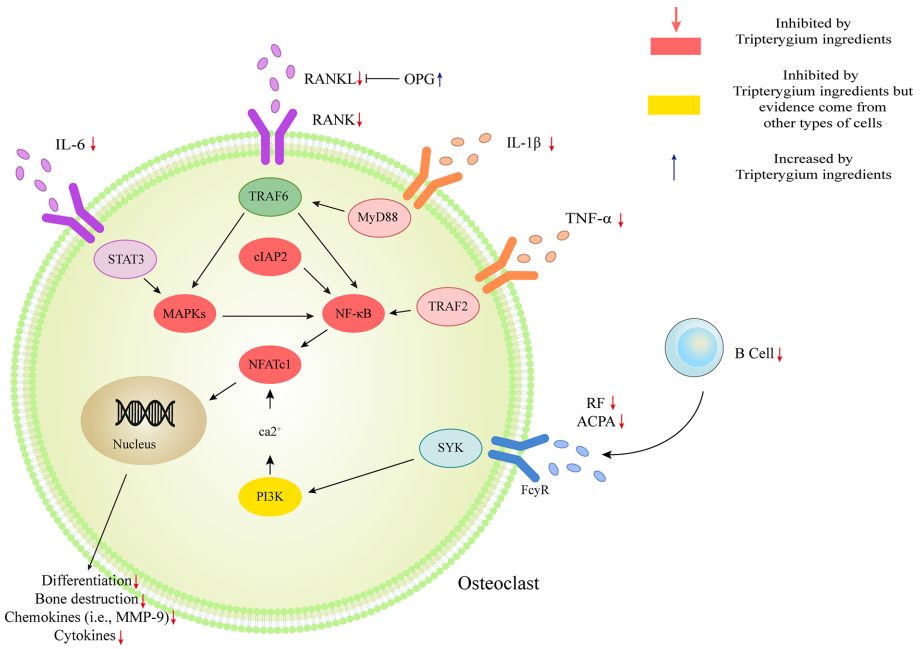

FIGURE 5 | Tripterygium ingredients act on osteoclast. The activation of osteoclast mostly involved IL-1β/Myd88/TRAF6/NF-κB, TNF-α/TRADD/TRAF2/NF-κB, IL-6/STAT3/MAPK, and RANKL/RANK signal transduction. Besides, the anti-bodies released by B cells would promote the activation of osteoclast *via* PI3K signaling. OPG takes part as a decoy receptor for RANKL and inhibiting RANKL-RANK binding. By rebalancing the RANKL and OPG levels, and inhibiting the pathways mentioned above, tripterygium ingredients negatively regulate the differentiation, bone destruction, cytokines and chemokines expression of osteoclast. Note: ACPA, Anti-citrullinated protein antibodies; cIAP2, Cellular inhibitor of apoptosis 2; IL, Interleukin; MAPK, Mitogen-activated protein kinase; MYD88, Myeloid differentiation primary response 88; NFATc1, Nuclear factor of activated T cells 1; RANK, Receptor activator of nuclear factor-κB; RANKL, Receptor activator of nuclear factor-κB ligand; RF, Rheumatoid factor; STAT, Signal transducer and activator of transcription; SYK, Spleen tyrosine kinase; TNF-α, Tumor necrosis factor-alpha; TRAF, Tumor necrosis factor receptor-associated factor.

THE ROLE OF TRIPTERYGIUM INGREDIENTS ON FLS AND THE MOLECULE MECHANISM

Synovial inflammation and synovial cell hyperplasia is a distinctive feature of RA. Synovial cells are composed of two types of cells, including type A and type B. Type A cells have a phagocytic function and are macrophage-like cells; type B cells are fibroblast-like, called FLS (Junqueira and Mescher, 2013). FLS is abundant in the endoplasmic reticulum and can secrete protein complexes (mucin) and hyaluronic acid in synovial fluid. FLS contributes mainly to the exacerbation of RA by attaching to, followed by invading into, and finally degrading cartilage and bone (Lefèvre et al., 2009). FLS are the primary cells leading to joint destruction in RA (Bartok and Firestein, 2010).

The molecular pathologic basis RA-FLS includes the MAPK and NF-κB pathways. These pathways are the most widely studied to mediate the aggressiveness of FLS in RA (Bottini and Firestein, 2013; Ganesan and Rasool, 2017). NF-κB pathway, a significant regulator of pro-inflammatory cytokine production, activates NF-κB kinase (IKK) subunit β (IKKβ) in the cytosol through IL-1β, TNF-α, and TLR signaling. The activation of IKKβ results in the NF-κB family inhibitor proteins (IκB) degradation, promoting NF-κB to migrate freely into the nucleus and initiate gene transcription (Bottini and Firestein, 2013). Cel inhibited the translocation of NF-κβ p65 and reduced the phosphorylation of IKBα and IKK in FLSs from patients with RA, resulting in the decreased expression of several chemokines (i.e., CCR2, CXCR4, CCL2, CXCL10, and CXCL12), cytokines (i.e., IL-6, IL-8, and MCP-1), and matrix metalloproteinase-9 (MMP-9) (Fang et al., 2017). Besides, HIF-1α binding to the CXCR4 promoter would increase the transcriptional activity of CXCR4, consequently leading to FLS migration and invasion. However, it could be reversed by Cel treatment (Li et al., 2013b). Guo et al. (Li et al., 2012) found that Cel inhibited IκBα phosphorylation and nuclear translocation of NF-κB. Cel also has been found to inhibit the expression of MMP-9 by suppressing the binding activity of NF-κB to the MMP-9 promoter (Li et al., 2012; Li et al., 2013a). Furthermore, MMP-9 suppression was also related to the inhibition of the TLR4/MyD88/NF-κB pathway (Li et al., 2013a). As a result, Cel changes the phenotype of FLS migration and invasion *via* the molecule mechanism mentioned above. RA-FLS releases important inflammatory cytokines (TNF-α, IL-1β, IL-6, IL-21, IL-22, and IL-32), chemokines (CXCL1, CXCL5, MCP-1, G-CSF, and IL-8) and Inflammatory mediators (TLR-2, TLR-3, TLR-4, iNOS, and COX-2), which promotes the infiltration of monocytes, macrophages, neutrophils, DCs, T cells, and B cells

into joints and results in chronic inflammation and joint destruction (Bottini and Firestein, 2013; Ganesan and Rasool, 2017). Additionally, TP also was found to reduce the FLS migration and invasion by targeting JNK/MAPK signaling pathway (Yang et al., 2016). Moreover, LLDT-8, a Tripterygium derivative, decreased the secretion of chemokines in FLS (Ping et al., 2016; Jia et al., 2017).

Many studies showed the Tripterygium ingredients have the properties to promote FLS apoptosis and cell cycle arrest and inhibit FLS autophagy (Xu, 2013; Xu et al., 2013; Lei et al., 2015; Su et al., 2017; Wong et al., 2019). It may be relevant to the increased expression of Bax/Bcl-2, Caspase-3, Caspase-9, and regulating by Ca2+/calmodulin-dependent protein kinases beta (CaMKK)-AMPK-mTOR signaling pathway. Tripterygium ingredients for FLS and the molecule mechanism are summarized in **Table 6**. The figures for the molecule mechanism of FLS are available in **Figure 6**.

DISCUSSION

We systematically summarized the role of tripterygium ingredients in the RA treatment as well as explained the therapeutic mechanism (**Figure 7**). The NF-κB pathway is a common pathway involved in TwHf-treated RA. It has been involved in mediating multiple genes, such as the genes of cytokines (i.e., IL-6, IL-17, and TNF-α), chemokines (i.e., CCL2 and CXCL5), growth factors (i.e., GM-CSF and M-CSF),

TABLE 6 | The function of Tripterygium ingredients on FLS.

Component	Models	Molecular mechanism	Effects	Animal disease phenotype	Ref.
Cel	FLSs from patients with RA	Reduce the phosphorylation of IKK and IKBα, and inhibit the translocation of NF-κβ p65 from the cytoplasm to the nucleus	Inhibit FLS proliferation and invasion. Reduce the levels of FLS pro-inflammatory cytokines (i.e., IL-6, IL-8, MCP, and MMP9) and chemokines (i.e., CCL2, CXCL10, CXCL12, CCR2, and CXCR4)	NA	(Fang et al., 2017)
Cel	AIA model	Inhibited the transcriptional activity of MMP-9 by suppression of the binding activity of NF-κB in the MMP-9 promoter, and inhibited IκBα phosphorylation and nuclear translocation of NF-κB	Suppressed the IL-17A-induced migration and invasion abilities of FLS	Alleviate	(Li et al., 2012)
Cel	FLSs isolated from the synovium of active RA patients	Inhibit the transcriptional activity of MMP-9 and TLR4/MyD88/NF-κB signaling pathway	Inhibit FLS invasion and migration	NA	(Li et al., 2013a)
TP	FLSs isolated from active RA patients and CIA DBA/1 mice	Inhibit JNK/MAPK signaling pathway	Inhibit FLS invasion and migration	Alleviate	(Yang et al., 2016)
Cel	FLSs isolated from active RA patients	Inhibit the binding activity of HIF-1α in the CXCR4 promoter to inhibit the transcription activity of CXCR4	Inhibit FLS invasion and migration	NA	(Li et al., 2013b)
TP	MH7A cell line	NA	Promote MH7A cell apoptosis; Decrease the levels of IL-1β, IL-6, and IL-8; Induce membrane ultrastructural changes	NA	(Su et al., 2017)
Cel	Human fibroblast-like synoviocytes-rheumatoid arthritis cells	Increase the expression of Bax/Bcl-2 and promote proteolytic cleavage of Caspase-3, Caspase-9, and PARP	Lead to FLS DNA damage and cycle arrest; Promote FLS apoptosis	NA	(Xu, 2013; Xu et al., 2013)
Cel	Immortalized wild-type and Bax-Bak double-knockout mouse embryonic fibroblasts; RASFs isolated from RA patients; AIA rats	Inhibit SERCA to induce autophagy-dependent cytotoxicity in RASFs/RAFLS *via* $Ca2^{+}$/calmodulin-dependent kinase kinase-β-AMP-activated protein kinase-mTOR pathway	Induce autophagic FLS death in RASFs/RAFLS	Alleviate	(Wong et al., 2019)
TP	MH7A cell line	NA	Inhibit angiogenesis	NA	(Zhang et al., 2008; Mao et al., 2009)
TP	FLSs isolated from RA patients	NA	Lead to FLS cycle arrest and promote FLS apoptosis	NA	(Lei et al., 2015)
LLDT-8	FLSs isolated from RA patients	NA	Inhibit FLS cytokines and chemokines (i.e., IL-6, CCL3, and CCL5)	NA	(Ping et al., 2016; Jia et al., 2017)

TP, Triptolide; Cel, Celastrol; NF-κB, Nuclear factor activated B cell kappa light chain enhancer; Caspase, Aspartic acid protease containing cysteine; TLR4, Toll-like receptor 4; JNK, Jun N-terminal kinase; MAPK, Mitogen activated protein kinase; mTOR, Rapamycin target protein; MMP-9, Matrix metalloproteinase-9; IL, Interleukin; AMPK, AMP-dependent protein kinase.

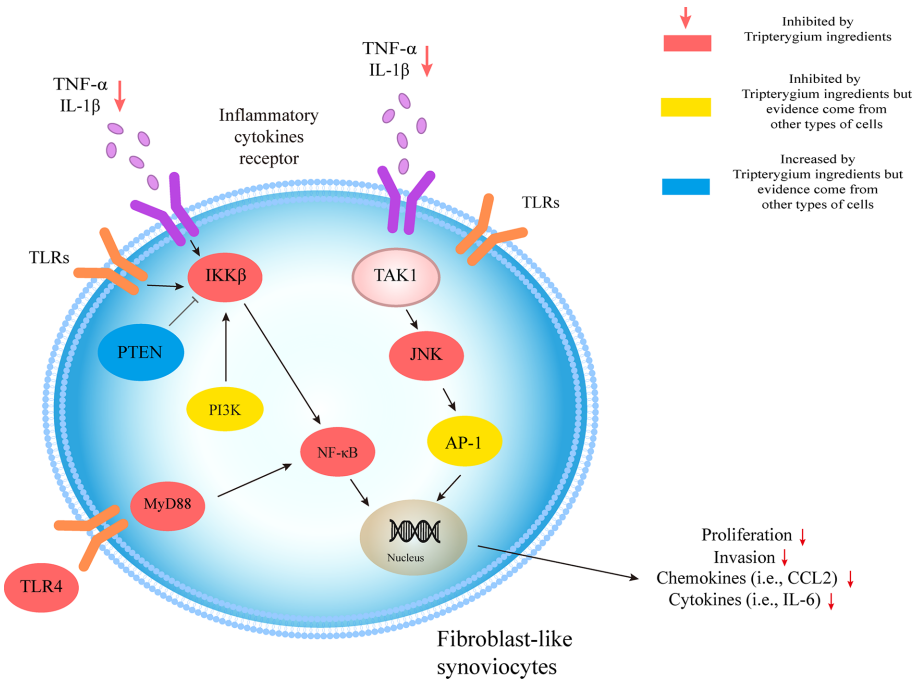

FIGURE 6 | Tripterygium ingredients act on FLS. The molecular pathologic basis FLS includes the MAPK and NF-κB pathways. By prohibiting the signal transduction in the pathways, tripterygium ingredients alleviate the proliferation, invasion of FLS, which would promote bone erosion in RA. PTEN and PI3K, which inhibit and promote the activity of IKKβ, respectively, also are related in the networks of FLS. We suppose tripterygium ingredients could increase PTEN and decrease PI3K to alleviate the pathogenicity of FLS. Note: AP-1, Activator protein 1; FLS, Fibroblast-like synoviocytes; JNK, c-Jun N-terminal kinase; IL, Interleukin; IKKβ, IκB Kinase β; MYD88, Myeloid differentiation primary response 88; NF-κβ, Nuclear factor-kappa B; PI3K, Phosphoinositide 3-kinase; PTEN, Phosphatase and tensin homolog; TNF-α, Tumor necrosis factor-alpha; TLR, Toll-like receptor; TAK1, Transforming growth factor beta-activated kinase 1.

regulators of apoptosis (i.e., Bcl-2) and transcription factors (i.e., HIF-1α), to regulate cell function, cell death and survival, and proliferation (Mitchell and Carmody, 2018). Experimental inhibitors targeted the IKK kinases to inhibit the activation of NF-κB, but they failed due to toxicity in genetic models (Mitchell and Carmody, 2018). The failure indicated that a broad blockade of NF-κB activation maybe an impracticable approach. Thus, some drugs focus on the non-canonical NF-κB pathway in RA, such as BAFF/NF-κB, RANK/NF-κB signaling (Noort et al., 2015). A phase II trial showed that belimumab [a biologics target B lymphocyte stimulator (BLyS)] was efficacy and well-tolerated in patients with RA (Stohl et al., 2013). Denosumab is a monoclonal antibody neutralizing RANKL. Up to date, many clinical studies have demonstrated that denosumab could inhibit the progression of joint destruction and increase bone mineral density, including a double-blind, placebo-controlled phase 3 trial (Deodhar et al., 2010; Dore et al., 2010; Sharp et al., 2010; Takeuchi et al., 2016; Yue et al., 2017; Takeuchi et al., 2019). However, none of the studies reported there is any benefit in improving disease activity. It is also regrettable that none of the studies test the expression of cytokines, chemokines, and RA-related pathogenicity cells. NF-κB pathways, including canonical and non-canonical pathways, are critical targets of tripterygium ingredients. In the experimental and clinical dimensions, these could explain why tripterygium ingredients could reduce the levels of many chemokines, cytokines, and growth factors in different cells to improve disease activity as well as inhibit the progression of joint destruction. TwHf and its ingredients could be regarded as one of DMARDs. Thus, they are widely used in treating RA in China. The last 24 weeks, open-label, multicentre, randomized controlled trial demonstrated MTX+TwHF was better than MTX monotherapy (Lv et al., 2015). Furthermore, three meta-analyses (the trial mentioned above included) showed that MTX+TwHF had advantages in improving the laboratory index (CRP, RF, ESR), clinical symptoms, and clinical efficacy, compared with MTX alone (assessed in ACR20, ACR50, and ACR70) (Li et al., 2019; Wang X. et al., 2019; Chen et al., 2020). Another small sample meta-analyses showed that TwHF could decrease bone destruction scores (Zhu et al., 2019).

Our previous research using a bioinformatics approach demonstrated that Kunxian Capsule (a Traditional Chinese Medicine (TCM) patent prescription mainly comprises Levl. Hutch) could target at PI3K/AKT/mTOR signaling pathway (Tang et al., 2020). Therefore, we speculate that some proteins in the PI3K-AKT-mTOR signal pathway are the most likely direct targets of tripterygium ingredients. The signaling pathway is an intracellular signaling pathway and performs multiple physiological functions, such as regulating the cell cycle, survival, and growth (Yap et al., 2008; Ersahin et al., 2015). By far, no clinical study has reported PI3K inhibitors approved by

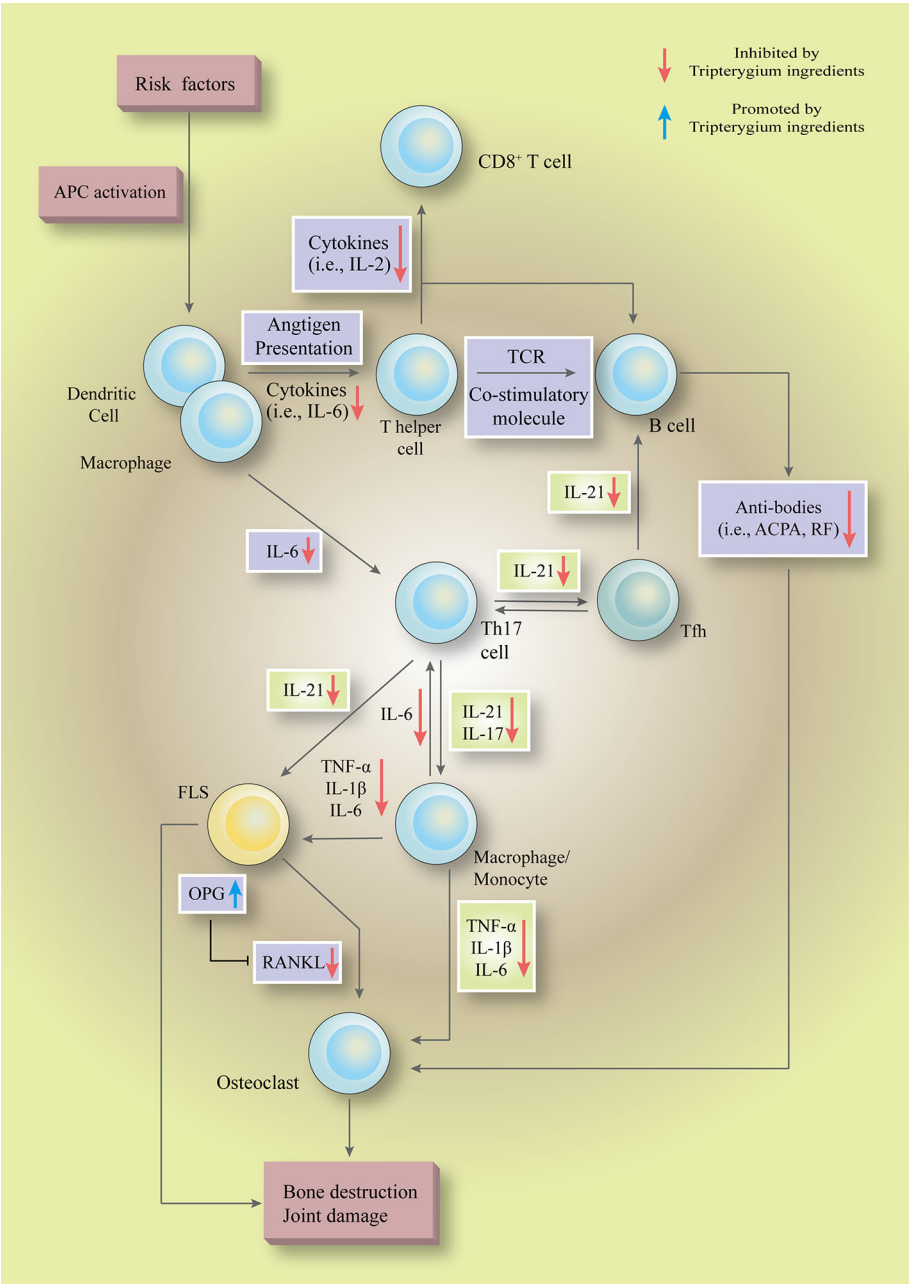

FIGURE 7 | Tripterygium ingredients could inhibit multiple pathways, such as the NF-κB pathway, JAK-STAT pathway, and PI3K-mTOR pathway, to regulate the hyperactive as well as pathogenicity biological functions in a various type of cells (to). In the initial phase, tripterygium ingredients inhibit the immunological recognition functions of APCs to block the pathogenicity signals which are responsible for activating the lymphocytes. In the secondary stage, tripterygium ingredients could inhibit the humoral immunity and cellular immunity of lymphocytes. Meanwhile, the pro-inflammatory signals are amplified by pro-inflammatory cells, such as macrophages. The pro-inflammatory cells release inflammatory cytokines and chemokines to recruit and activate immune cells (i.e., APCs and T cells), connective tissue cells (i.e., macrophages and FLS) and OCs to infiltrate into the joints. Besides, the pro-inflammatory cells lead to a systemic inflammatory response, further promoting the pathogenicity signals of lymphocytes in central and peripheral immune organs. Tripterygium ingredients prohibit the pro-inflammatory signals, alleviate the infiltration and activation of pathogenicity cells in the joint, and finally interrupt the vicious circle which formed by pro-inflammatory cells and immune cells. In the final stage, tripterygium ingredients relieve the joint damage and bone destruction by mediating the expression of OPG and RANKL. Note: APC, Antigen-presenting cell; ACPA, Anti-citrullinated protein antibodies; FLS, Fibroblast-like synoviocytes; IL, Interleukin; OPG, Osteoprotegerin; RANKL, Receptor activator of nuclear factor-κB ligand; RF, Rheumatoid factor; TCR, T-cell receptor; TNF-α, Tumor necrosis factor-alpha.

the FDA (idelalisib, copanlisib, duvelisib, and alpelisib) in treating RA. Some drugs were demonstrated they were effective in treating RA models *via* PI3K signaling pathway *in vivo* and *in vitro*, including one PI3K inhibitor (Boyle et al., 2014; Feng and Qiu, 2018; Qi et al., 2019).

The two pathways mentioned above have a variety of biological functions. Both of them control cell death, survival, and proliferation. We found that the therapeutic effects of tripterygium ingredients are mostly related to the reduction of the absolute number of cells. At the same time, there are some differences in stimulating signals, signal receptors, and transcription factors required for cascade reactions in different cells, which is related to the multi-target of TwHf. Considering the adverse effects (AEs) of these drugs, a variety of healthy cells in multiple systems (i.e., liver cells) are also be affected. Therefore, the AEs of tripterygium ingredients could be due to the inhibition of NF-κB and PI3K pathways. Ameliorating AEs through drug matching may be a feasible strategy (Tang et al., 2020). For example, some Chinese researchers matched the TwHf with *Cistanche deserticola Ma* or *Cuscuta chinensis Lam*, to reduce the reproductive toxicity of TwHf (Dong et al., 2009; Jing and He, 2013). Nevertheless, whether drug matching would impair the curative effect, still needed to be discovered.

There are many deficiencies in this review. The studies on the drugs/ingredients are all indirect mechanism studies, even with only cell phenotypes but no specific molecular mechanism. Besides, most of them are normal phenotypes in this field, such as inhibition of the apoptosis and differentiation of T cells or impaired proliferation, migration, and invasion of FLS. Moreover, none of the studies analyzed the direct interaction between the drugs and proteins *via* bioinformatics and mass spectrometry approaches. For example, computer simulation and electrospray mass spectrometry (ESI-MS) were used to explore the inhibitory effect of paclitaxel and aryl ether ketone on farpentine diphosphate synthetase by binding to isoprene diphosphate site (Liu et al., 2014), and explain the anticancer and anti-infective drug mechanism of paclitaxel and aryl et her ketone in the direct interaction mechanism. Therefore, we could follow the methods which were used in the study, as mentioned above. For example, we could use bioinformatics to identify whether TP and Cel could bind to some sites of PI3K, ATK, and NF-κB. Subsequently, we could use ESI-MS to validate it.

AUTHOR CONTRIBUTIONS

YT: evidence collection, manuscript preparation and write the central part of the manuscript. QL: evidence collection and manuscript editing. FY: evidence collection and write the minor part of the manuscript. YiZ: evidence collection, figures preparation. XZ: gave many professional suggestions and project funding. CW: ideas, reviewed the manuscript, and project funding. YuZ: critically reviewed the manuscript, study initiation, and project funding. All authors contributed to the article and approved the submitted version.

FUNDING

Research was funded by National Key R&D Program of China (2018YFC1705500) to CW, National Natural Science Foundation of Zhejiang Province (No.LY20H270007), TCM Science and Technology Plan of Zhejiang Province (No.2020ZQ012) to YZ, and National Natural Science Foundation of China (81673623) to ZX.

ACKNOWLEDGMENTS

We thank Yujie Tang for the modification of the figures.

SUPPLEMENTARY MATERIAL

The Supplementary Material for this article can be found online at: https://www.frontiersin.org/articles/10.3389/fphar.2020.583171/full#supplementary-material

REFERENCES

Bao, X., Cui, J., Wu, Y., Han, X., Gao, C., Hua, Z., et al. (2007). The roles of endogenous reactive oxygen species and nitric oxide in triptolide-induced apoptotic cell death in macrophages. *J. Mol. Med. (Berl)* 85 (1), 85–98. doi: 10.1007/s00109-006-0113-x

Bartok, B., and Firestein, G. S. (2010). Fibroblast-like synoviocytes: key effector cells in rheumatoid arthritis. *Immunol. Rev.* 233 (1), 233–255. doi: 10.1111/j.0105-2896.2009.00859.x

Bergsbaken, T., Fink, S. L., and Cookson, B. T. (2009). Pyroptosis: host cell death and inflammation. *Nat. Rev. Microbiol.* 7 (2), 99–109. doi: 10.1038/nrmicro2070

Bottini, N., and Firestein, G. S. (2013). Duality of fibroblast-like synoviocytes in RA: passive responders and imprinted aggressors. *Nat. Rev. Rheumatol.* 9 (1), 24. doi: 10.1038/nrrheum.2012.190

Boyle, D. L., Kim, H. R., Topolewski, K., Bartok, B., and Firestein, G. S. (2014). Novel phosphoinositide 3-kinase δ,γ inhibitor: potent anti-inflammatory effects and joint protection in models of rheumatoid arthritis. *J. Pharmacol. Exp. Ther.* 348 (2), 271–280. doi: 10.1124/jpet.113.205955

Cascão, R., Vidal, B., Raquel, H., Neves-Costa, A., Figueiredo, N., Gupta, V., et al. (2012). Effective treatment of rat adjuvant-induced arthritis by celastrol. *Autoimmun. Rev.* 11 (12), 856–862. doi: 10.1016/j.autrev.2012.02.022

Cascão, R., Vidal, B., Lopes, I. P., Paisana, E., Rino, J., Moita, L. F., et al. (2015a). Decrease of CD68 Synovial Macrophages in Celastrol Treated Arthritic Rats. *PloS One* 10 (12), e0142448. doi: 10.1371/journal.pone.0142448

Cascão, R., Vidal, B., Lopes, I. P., Paisana, E., Rino, J., Moita, L. F., et al. (2015b). Decrease of CD68 synovial macrophages in celastrol treated arthritic rats. *PloS One* 10 (12), e0142448. doi: 10.1371/journal.pone.0142448

Chang, D. M., Chang, W. Y., Kuo, S. Y., and Chang, M. L. (1997). The effects of traditional antirheumatic herbal medicines on immune response cells. *J. Rheumatol.* 24 (3), 436–441.

Chao, L. (2015). *Study on the differences between Tripterygium wilfordii Hook.f. and Tripterygium Hypoglaucum (Level) Hutch Based on Genetics and chemical methods* (China Academy of Chinese Medical Sciences: Dissertation).

Chen, T., Xu, H., Wang, H., Ji, M., and Wu, W. (2006). Single and conjoined effects of tripterygium wilfordii and IL-10 on the immuna function of rat dendritic cells in vitro. *Acta Universit. Med. Nanjing (Natural Sci.)* 07), 520–522. doi: 10.1007/s11664-006-0095-z

Chen, X.-L., Liu, F., Xiao, X.-R., Yang, X.-W., and Li, F. (2018). Anti-inflammatory abietanes diterpenoids isolated from Tripterygium hypoglaucum. *Phytochemistry* 156, 167–175. doi: 10.1016/j.phytochem.2018.10.001

Chen, W., Li, T., Wang, X., Xue, Z., Lv, C., Li, H., et al. (2020). Meta-analysis of RCT studies on clinical efficacy of single administration of Tripterygium Glycosides Tablets or combined administration with methotrexate against rheumatoid arthritis. *China J. Chin. Mater. Med.* 45 (04), 791–797. doi: 10.19540/j.cnki.cjcmm.20191115.503

Chen-qiong, X., Ping, Z., Xiang, L., and Jian-wei, C. (2015). Research progress on chemical constituents, pharmacological effects, and clinical application of Tripterygium hypoglaucum. *Chin. Tradit. Herbal Drugs* 46 (13), 1996–2010. doi: 10.7501/j.issn.0253-2670.2015.13.024

Chinese Rheumatology Association (2018). 2018 Chinese rheumatoid arthritis diagnosis and treatment guide. *Clin. Res. Pract.* 57 (4), 242–251. doi: 10.3760/cma.j.issn.0578-1426.2018.04.004

Cooles, F. A., Isaacs, J. D., and Anderson, A. E. (2013). Treg cells in rheumatoid arthritis: an update. *Curr. Rheumatol. Rep.* 15 (9), 352. doi: 10.1007/s11926-013-0352-0

Deodhar, A., Dore, R. K., Mandel, D., Schechtman, J., Shergy, W., Trapp, R., et al. (2010). Denosumab-mediated increase in hand bone mineral density associated with decreased progression of bone erosion in rheumatoid arthritis patients. *Arthritis Care Res. (Hoboken)* 62 (4), 569–574. doi: 10.1002/acr.20004

Dong, F., Li, J., Huang, D., and He, L. (2009). Effects of Glycosides of Tripterygium Wilfordii on Reproduction Capacity and Its Intervention by Caulis Cistanchi in Male Mice. *Shanghai J. Tradit. Chin. Med.* 43 (08), 64–66. doi: 10.16305/j.1007-1334.2009.08.025

Dore, R. K., Cohen, S. B., Lane, N. E., Palmer, W., Shergy, W., Zhou, L., et al. (2010). Effects of denosumab on bone mineral density and bone turnover in patients with rheumatoid arthritis receiving concurrent glucocorticoids or bisphosphonates. *Ann. Rheum Dis.* 69 (5), 872–875. doi: 10.1136/ard.2009.112920

Ersahin, T., Tuncbag, N., and Cetin-Atalay, R. (2015). The PI3K/AKT/mTOR interactive pathway. *Mol. Biosyst.* 11 (7), 1946–1954. doi: 10.1039/c5mb00101c

Fang, Z., He, D., Yu, B., Liu, F., Zuo, J., Li, Y., et al. (2017). High-Throughput Study of the Effects of Celastrol on Activated Fibroblast-Like Synoviocytes from Patients with Rheumatoid Arthritis. *Genes (Basel)* 8 (9), 221. doi: 10.3390/genes8090221

Feng, F. B., and Qiu, H. Y. (2018). Effects of Artesunate on chondrocyte proliferation, apoptosis and autophagy through the PI3K/AKT/mTOR signaling pathway in rat models with rheumatoid arthritis. *BioMed. Pharmacother.* 102, 1209–1220. doi: 10.1016/j.biopha.2018.03.142

Feng, X., Tan, W., Wan, F., Gan, K., Zhang, M., and Zhang, Q. (2013). The effect of Celastrol on the expressions of RANKL, OPG, IL-6, TNF-α and IL-8 in human rheumatoid synoviocyte MH7A. *Acta Universit. Med. Nanjing (Natural Sci.)* 33 (06), 759–765. doi: 10.7655/NYDXBNS20130609

Feng, H. (2015). *Influence of Acid-microenvironment on Monocyte-macrophages, Tca8113 Cells and the Role of Triptolide. dissertation* (Guizhou: Guizhou Medical University).

Gan, K., Xu, L., Feng, X., Zhang, Q., Wang, F., Zhang, M., et al. (2015). Celastrol attenuates bone erosion in collagen-Induced arthritis mice and inhibits osteoclast differentiation and function in RANKL-induced RAW264. 7. *Int. Immunopharmacol.* 24 (2), 239–246. doi: 10.1016/j.intimp.2014.12.012

Gan, K. (2013). *The role of Celastrol on osteoclastogenesis and bone erosion in collagen-induced arthritis doctor* (Nanjing: Nanjing University of Chinese Medicine).

Ganesan, R., and Rasool, M. (2017). Fibroblast-like synoviocytes-dependent effector molecules as a critical mediator for rheumatoid arthritis: Current status and future directions. *Int. Rev. Immunol.* 36 (1), 20–30. doi: 10.1080/08830185.2016.1269175

Gierut, A., Perlman, H., and Pope, R. M. (2010). Innate immunity and rheumatoid arthritis. *Rheumatic Dis. Clinics* 36 (2), 271–296. doi: 10.1016/j.rdc.2010.03.004

Ho, L. J., Chang, W. L., Chen, A., Chao, P., and Lai, J. H. (2013). Differential immunomodulatory effects by Tripterygium wilfordii Hook f-derived refined extract PG27 and its purified component PG490 (triptolide) in human peripheral blood T cells: potential therapeutics for arthritis and possible mechanisms explaining in part Chinese herbal theory "Junn-Chenn-Zuou-SS". *J. Transl. Med.* 11:294. doi: 10.1186/1479-5876-11-294

Ivanov, I. I., McKenzie, B. S., Zhou, L., Tadokoro, C. E., Lepelley, A., Lafaille, J. J., et al. (2006). The orphan nuclear receptor RORγt directs the differentiation program of proinflammatory IL-17+ T helper cells. *Cell* 126 (6), 1121–1133. doi: 10.1016/j.cell.2006.07.035

Jia, L., Ping, T., and Dongyi, H. (2017). Effects of (5R) -5-Hydroxytriptolide (LLDT-8) on Gene Expressions in Fibroblast-like Synoviocytes of Rheumatoid Arthritis. *Acta Universit. Tradit. Med. Sinensis Pharmacol. Shanghai* 31 (06), 70–75. doi: 10.16306/j.1008-861x.2017.06.017

Jing, X., and He, L. (2013). Effects of GTW on expression of EGF and the intervention effect of Tusizi flavones in male juvenile rats. *China J. Tradit. Chin. Med. Pharm.* 28 (06), 1884–1886.

Jun, Z., Wei, X., Rui, W., and Xiaole, S. (2016). Effectiveness and Safety of Kunxian Capsule for Rueumatoid Arthritis:A Systematic Review. *J. Liaoning Univ. Tradit. Chin. Med.* 18 (10), 122–126. doi: 10.13194/j.issn.1673-842x.2016.10.037

Jung, Y.-K., Kang, Y.-M., and Han, S. (2019). Osteoclasts in the inflammatory arthritis: Implications for pathologic osteolysis. *Immune Netw.* 19 (1), e2. doi: 10.4110/in.2019.19.e2

Junqueira, L. C., and Mescher, A. L. (2013). *Junqueira's basic histology: text & atlas/Anthony L. Mescher* (New York [etc.]: McGraw-Hill Medical).

Khan, S., Greenberg, J. D., and Bhardwaj, N. (2009). Dendritic cells as targets for therapy in rheumatoid arthritis. *Nat. Rev. Rheumatol.* 5 (10), 566. doi: 10.1038/nrrheum.2009.185

Laria, A., Lurati, A., Marrazza, M., Mazzocchi, D., Re, K. A., and Scarpellini, M. (2016). The macrophages in rheumatic diseases. *J. Inflammation Res.* 9, 1–11. doi: 10.2147/JIR.S82320

Lawrence, T., and Natoli, G. (2011). Transcriptional regulation of macrophage polarization: enabling diversity with identity. *Nat. Rev. Immunol.* 11 (11), 750–761. doi: 10.1038/nri3088

Lee, J. Y., Lee, B. H., Kim, N. D., and Lee, J. Y. (2015). Celastrol blocks binding of lipopolysaccharides to a Toll-like receptor4/myeloid differentiation factor2 complex in a thiol-dependent manner. *J. Ethnopharmacol.* 172, 254–260. doi: 10.1016/j.jep.2015.06.028

Lefèvre, S., Knedla, A., Tennie, C., Kampmann, A., Wunrau, C., Dinser, R., et al. (2009). Synovial fibroblasts spread rheumatoid arthritis to unaffected joints. *Nat. Med.* 15 (12), 1414–1420. doi: 10.1038/nm.2050

Lei, Y., Shuang, J., and Wenping, P. (2015). Study on Inhibitory Effects of Triptolide on the Proliferation of Fibroblast-like Synovial Cells from Patients with Rheumatoid Arthritis in vitro. *China Pharm.* 26 (31), 4357–4359. doi: 10.6039/j.issn.1001-0408.2015.31.13

Leibbrandt, A., and Penninger, J. M. (2009). RANKL/RANK as key factors for osteoclast development and bone loss in arthropathies. *Adv. Exp. Med. Biol.* 649, 100–113. doi: 10.1007/978-1-4419-0298-6_7

Leipe, J., Grunke, M., Dechant, C., Reindl, C., Kerzendorf, U., Schulze-Koops, H., et al. (2010). Role of Th17 cells in human autoimmune arthritis. *Arthritis Rheumatism* 62 (10), 2876–2885. doi: 10.1002/art.27622

Li, X., and He, L. (2006). Pharmacological Control Study between Tripterygium. *J. Kunming Med. Coll.* 02), 107–110.

Li, G. Q., Zhang, Y., Liu, D., Qian, Y. Y., Zhang, H., Guo, S. Y., et al. (2012). Celastrol inhibits interleukin-17A-stimulated rheumatoid fibroblast-like synoviocyte migration and invasion through suppression of NF-kappaB-mediated matrix metalloproteinase-9 expression. *Int. Immunopharmacol.* 14 (4), 422–431. doi: 10.1016/j.intimp.2012.08.016

Li, G., Liu, D., Zhang, Y., Qian, Y., Zhang, H., Guo, S., et al. (2013a). Celastrol inhibits lipopolysaccharide-stimulated rheumatoid fibroblast-like synoviocyte invasion through suppression of TLR4/NF-kappaB-mediated matrix metalloproteinase-9 expression. *PloS One* 8 (7), e68905. doi: 10.1371/journal.pone.0068905

Li, G. Q., Liu, D., Zhang, Y., Qian, Y. Y., Zhu, Y. D., Guo, S. Y., et al. (2013b). Anti-invasive effects of celastrol in hypoxia-induced fibroblast-like synoviocyte through suppressing of HIF-1alpha/CXCR4 signaling pathway. *Int. Immunopharmacol.* 17 (4), 1028–1036. doi: 10.1016/j.intimp.2013.10.006

Li, T., Wang, X., Xue, Z., Lv, C., Li, H., Fan, Y., et al. (2019). Meta-analysis of laboratory index of Tripterygium Glycosides Tablets in treatment of

rheumatoid arthritis. *China J. Chin. Mater. Med.* 44 (16), 3542–3550. doi: 10.19540/j.cnki.cjcmm.20190612.503

Lin, N., Sato, T., and Ito, A. (2001). Triptolide, a novel diterpenoid triepoxide from Tripterygium wilfordii Hook. f., suppresses the production and gene expression of pro-matrix metalloproteinases 1 and 3 and augments those of tissue inhibitors of metalloproteinases 1 and 2 in human synovial fibroblasts. *Arthritis Rheum* 44 (9), 2193–2200. doi: 10.1002/1529-0131(200109)44:9<2193::aid-art373>3.0.co;2-5

Liu, C., Zhang, Y., Kong, X., Zhu, L., Pang, J., Xu, Y., et al. (2013). Triptolide prevents bone destruction in the collagen-induced arthritis model of rheumatoid arthritis by targeting RANKL/RANK/OPG signal pathway. *Evidence-Based Complement. Altern. Med.* 2013, 626038. doi: 10.1155/2013/626038

Liu, Y. L., Lindert, S., Zhu, W., Wang, K., McCammon, J. A., and Oldfield, E. (2014). Taxodione and arenarone inhibit farnesyl diphosphate synthase by binding to the isopentenyl diphosphate site. *Proc. Natl. Acad. Sci. U.S.A.* 111 (25), E2530–E2539. doi: 10.1073/pnas.1409061111

Liu, X. (2018). Impact of celastrol on polarization of mouse peritoneal macrophage. *Basic Clin. Med.* 38 (05), 643–648. doi: 10.16352/j.issn.1001-6325.2018.05.011

Lopez-Olivo, M. A., Siddhanamatha, H. R., Shea, B., Tugwell, P., Wells, G. A., and Suarez-Almazor, M. E. (2014). Methotrexate for treating rheumatoid arthritis. *Cochrane Database Systemat. Rev.* 2014 (6), CD000957. doi: 10.1002/14651858.CD000957.pub2

Lv, Q. W., Zhang, W., Shi, Q., Zheng, W. J., Li, X., Chen, H., et al. (2015). Comparison of Tripterygium wilfordii Hook F with methotrexate in the treatment of active rheumatoid arthritis (TRIFRA): a randomised, controlled clinical trial. *Ann. Rheum Dis.* 74 (6), 1078–1086. doi: 10.1136/annrheumdis-2013-204807

Mao, X., Sun, S., Pei, Z., and Zhang, L. (2009). Inhibitory effect of triptolide on interleukin-18 and its receptor in rheumatoid arthritis synovial fibroblasts. *Chin. J. Cell. Mol. Immunol.* 25 (07), 606–608+611. doi: 10.1007/s00011-007-7128-9

Ming, Z., Lihua, M., Ying, C., and Jun, X. (2014). Inhibitory Effects of Triptolide on Immune Function of Peripheral Blood T Cells in Rheumatoid Arthritis Patients. *China Pharm.* 25 (47), 4441–4443. doi: 10.6039/j.issn.1001-0408.2014.47.08

Mitchell, J. P., and Carmody, R. J. (2018). NF-κB and the Transcriptional Control of Inflammation. *Int. Rev. Cell Mol. Biol.* 335, 41–84. doi: 10.1016/bs.ircmb.2017.07.007

Nanjundaiah, S. M., Venkatesha, S. H., Yu, H., Tong, L., Stains, J. P., and Moudgil, K. D. (2012). Celastrus and its bioactive celastrol protect against bone damage in autoimmune arthritis by modulating osteoimmune cross-talk. *J. Biol. Chem.* 287 (26), 22216–22226. doi: 10.1074/jbc.M112.356816

Niiro, H., and Clark, E. A. (2002). Regulation of B-cell fate by antigen-receptor signals. *Nat. Rev. Immunol.* 2 (12), 945–956. doi: 10.1038/nri955

Nishihara, M., Ogura, H., Ueda, N., Tsuruoka, M., Kitabayashi, C., Tsuji, F., et al. (2007). IL-6–gp130–STAT3 in T cells directs the development of IL-17+ Th with a minimum effect on that of Treg in the steady state. *Int. Immunol.* 19 (6), 695–702. doi: 10.1093/intimm/dxm045

Noort, A. R., Tak, P. P., and Tas, S. W. (2015). Non-canonical NF-κB signaling in rheumatoid arthritis: Dr Jekyll and Mr Hyde? *Arthritis Res. Ther.* 17 (1):15. doi: 10.1186/s13075-015-0527-3

Pan, H. (2018). *Mechanism Research of Xinfeng Capsule on rheumatoid arthritis by PI3K / AKT / mTOR signal pathway mediated by BAFF / BAFF-R. master* (Hefei: Anhui University of Chinese Medicine).

Penatti, A., Facciotti, F., De Matteis, R., Larghi, P., Paroni, M., Murgo, A., et al. (2017). Differences in serum and synovial CD4+ T cells and cytokine profiles to stratify patients with inflammatory osteoarthritis and rheumatoid arthritis. *Arthritis Res. Ther.* 19 (1), 103. doi: 10.1186/s13075-017-1305-1

Peng, A., Wang, X., and Zhuang, J. (2014). Triptolide inhibites Th17 cell differentiation via regulating cyclooxygenase-2/prostaglandin E2 axis in synovial fibroblasts from rheumatoid arthritis. *China J. Chin. Mater. Med.* 39 (3), 536–539. doi: 10.4268/cjcmm20140334

Pieper, K., Grimbacher, B., and Eibel, H. (2013). B-cell biology and development. *J. Allergy Clin. Immunol.* 131 (4), 959–971. doi: 10.1016/j.jaci.2013.01.046

Ping, Q., Zhou, Y., Zhang, S., Cao, J., Xu, L., Fang, G., et al. (2015). Study on effects of Tripterygium wilfordii polycoride in resisting macrophage inflammation and regulating inflammation via TLR4/NF-κB. *China J. Chin. Mater. Med.* 40 (16), 3256–3261. doi: 10.4268/cjcmm20151626

Ping, T., Jia, L., and Dongyi, H. (2016). Effect of (5R)-5-hydroxytriptolide(LLDT-8) on chemotactic factor in fibroblast-like synoviocytes. *Curr. Immunol.* 36 (06), 448–454.

Plotkin, L. I., Essex, A. L., and Davis, H. M. (2019). RAGE Signaling in Skeletal Biology. *Curr. Osteoporos Rep.* 17 (1), 16–25. doi: 10.1007/s11914-019-00499-w

Qi, W., Lin, C., Fan, K., Chen, Z., Liu, L., Feng, X., et al. (2019). Hesperidin inhibits synovial cell inflammation and macrophage polarization through suppression of the PI3K/AKT pathway in complete Freund's adjuvant-induced arthritis in mice. *Chem. Biol. Interact.* 306, 19–28. doi: 10.1016/j.cbi.2019.04.002

Qian, C., Peng, L., Feng, X., Tan, W., and Zhang, Q. (2015). Celastrol Inhibiting Osteoclast Formation by Reducing Chemokine CCl4. *Liaoning J. Tradit. Chin. Med.* 42 (02), 415–417+447. doi: 10.13192/j.issn.1000-1719.2015.02.078

Scherer, H. U., Huizinga, T. W., Krönke, G., Schett, G., and Toes, R. E. (2018). The B cell response to citrullinated antigens in the development of rheumatoid arthritis. *Nat. Rev. Rheumatol.* 14 (3), 157. doi: 10.1038/nrrheum.2018.10

Schmidlin, H., Diehl, S. A., and Blom, B. (2009). New insights into the regulation of human B-cell differentiation. *Trends Immunol.* 30 (6), 277–285. doi: 10.1016/j.it.2009.03.008

Sharp, J. T., Tsuji, W., Ory, P., Harper-Barek, C., Wang, H., and Newmark, R. (2010). Denosumab prevents metacarpal shaft cortical bone loss in patients with erosive rheumatoid arthritis. *Arthritis Care Res. (Hoboken)* 62 (4), 537–544. doi: 10.1002/acr.20172

Smolen, J. S., Aletaha, D., Barton, A., Burmester, G. R., Emery, P., Firestein, G. S., et al. (2018). Rheumatoid arthritis. *Nat. Rev. Dis. Primers* 4, 18001. doi: 10.1038/nrdp.2018.1

Stohl, W., Merrill, J. T., McKay, J. D., Lisse, J. R., Zhong, Z. J., Freimuth, W. W., et al. (2013). Efficacy and safety of belimumab in patients with rheumatoid arthritis: a phase II, randomized, double-blind, placebo-controlled, dose-ranging Study. *J. Rheumatol.* 40 (5), 579–589. doi: 10.3899/jrheum.120886

Su, Z., Sun, H., Ao, M., and Zhao, C. (2017). Atomic Force Microscopy Study of the Anti-inflammatory Effects of Triptolide on Rheumatoid Arthritis Fibroblast-like Synoviocytes. *Microsc. Microanal.* 23 (5), 1002–1012. doi: 10.1017/s1431927617012399

Sun, F., Jiang, S., Ping, L., Feng, H., and Dai, L. (2016). Effect of Tripterygium Wilfordii on Follicular Helper T Cells and IL-21 of Rheumatoid Arthritis Patients. *Med. Recapitulate* 22 (03), 566–569. doi: 10.3969/j.issn.1006-2084.2016.03.044

Sun, J. (2017). *The effects of Duantengyimu decoction on the expression of chemokine receptor and secretion of chemokine in dendritic cells of patients with rheumatoid arthritis. dissertation* (Guangzhou: Guangzhou University of Chinese Medicine).

Takeuchi, T., Tanaka, Y., Ishiguro, N., Yamanaka, H., Yoneda, T., Ohira, T., et al. (2016). Effect of denosumab on Japanese patients with rheumatoid arthritis: a dose-response study of AMG 162 (Denosumab) in patients with RheumatoId arthritis on methotrexate to Validate inhibitory effect on bone Erosion (DRIVE)-a 12-month, multicentre, randomised, double-blind, placebo-controlled, phase II clinical trial. *Ann. Rheum Dis.* 75 (6), 983–990. doi: 10.1136/annrheumdis-2015-208052

Takeuchi, T., Tanaka, Y., Soen, S., Yamanaka, H., Yoneda, T., Tanaka, S., et al. (2019). Effects of the anti-RANKL antibody denosumab on joint structural damage in patients with rheumatoid arthritis treated with conventional synthetic disease-modifying antirheumatic drugs (DESIRABLE study): a randomised, double-blind, placebo-controlled phase 3 trial. *Ann. Rheum Dis.* 78 (7), 899–907. doi: 10.1136/annrheumdis-2018-214827

Tang, Y., Zhang, Y., Li, L., Xie, Z., Wen, C., and Huang, L. (2020). Kunxian Capsule for Rheumatoid Arthritis: Inhibition of Inflammatory Network and Reducing Adverse Reactions Through Drug Matching. *Front. Pharmacol.* 11, 485. doi: 10.3389/fphar.2020.00485

Tao, X., Davis, L. S., and Lipsky, P. E. (1991). Effect of an extract of the Chinese herbal remedy Tripterygium wilfordii Hook F on human immune responsiveness. *Arthritis Rheum* 34 (10), 1274–1281. doi: 10.1002/art.1780341011

Te, W., Zhao-fu, L., Tao, L., Xiao-you, Y., and Li-ping, Z. (2019). Research Progress on the Mechanism of Kunmingshanhaitang in the Treatment of Rheumatoid Arthritis. *Rheumatism Arthritis* 08), 60–63. doi: 10.3969/j.issn.2095-4174.2019.08.014

Teitelbaum, S. L., and Ross, F. P. (2003). Genetic regulation of osteoclast development and function. *Nat. Rev. Genet.* 4 (8), 638. doi: 10.1038/nrg1122

Tong, Z., Cheng, L., Song, J., Wang, M., Yuan, J., Li, X., et al. (2018). Therapeutic effects of Caesalpinia minax Hance on complete Freund's adjuvant (CFA)-induced arthritis and the anti-inflammatory activity of cassane diterpenes as main active components. *J. Ethnopharmacol.* 226, 90–96. doi: 10.1016/j.jep.2018.08.011

Vallières, F., Durocher, I., and Girard, D. (2019). Biological activities of interleukin (IL)-21 in human monocytes and macrophages. *Cell. Immunol.* 337, 62–70. doi: 10.1016/j.cellimm.2019.02.002

van Hamburg, J. P., Asmawidjaja, P., Davelaar, N., Mus, A., Colin, E., Hazes, J., et al. (2011). Th17 cells, but not Th1 cells, from patients with early rheumatoid arthritis are potent inducers of matrix metalloproteinases and proinflammatory cytokines upon synovial fibroblast interaction, including autocrine interleukin-17A production. *Arthritis Rheumatism* 63 (1), 73–83. doi: 10.1002/art.30093

Venkatesha, S. H., Yu, H., Rajaiah, R., Tong, L., and Moudgil, K. D. (2011). Celastrus-derived celastrol suppresses autoimmune arthritis by modulating antigen-induced cellular and humoral effector responses. *J. Biol. Chem.* 286 (17), 15138–15146. doi: 10.1074/jbc.M111.226365

Vinuesa, C. G., Linterman, M. A., Yu, D., and MacLennan, I. C. (2016). Follicular Helper T Cells. *Annu. Rev. Immunol.* 34, 335–368. doi: 10.1146/annurev-immunol-041015-055605

Wang, G., and Wu, D. (1994). Effect of tripterygium wilfordii on lymphocyte subsets in patients with rheumatoid arthritis. *Chin. J. Internal Med.* 01), 41–42.

Wang, S. J., Yao, K., Xie, F. D., and Ji, X. H. (2001). Effects of Tripterygium wilfordii saponins and interleukin-10 on dendritic cells from human peripheral blood. *Acta Pharmacol. Sin.* 22 (8).

Wang, B., Ma, L., Tao, X., and Lipsky, P. (2004). Triptolide, an active component of the Chinese herbal remedy Tripterygium wilfordii Hook F, inhibits production of nitric oxide by decreasing inducible nitric oxide synthase gene transcription. *Arthritis Rheumatism: Off. J. Am. Coll. Rheumatol.* 50 (9), 2995–3003. doi: 10.1002/art.20459

Wang, X., Zhang, L., Duan, W., Liu, B., Gong, P., Ding, Y., et al. (2014). Anti−inflammatory effects of triptolide by inhibiting the NF−κB signalling pathway in LPS–induced acute lung injury in a murine model. *Mol. Med. Rep.* 10 (1), 447–452. doi: 10.3892/mmr.2014.2191

Wang, G., Guo, M., Xu, H., Huang, J., Lv, S., Zhao, H., et al. (2017). The effect of triptolide on differentiation of osteoclasts induced by HMGB1. *J. China-Japan Friendship Hosp.* 31 (02), 102–106+130. doi: 10.3969/j.issn.1001-0025.2017.02.010

Wang, S., Zuo, S., Liu, Z., Ji, X., Yao, Z., and Wang, X. (2018). Study on the efficacy and mechanism of triptolide on treating TNF transgenic mice with rheumatoid arthritis. *BioMed. Pharmacother.* 106, 813–820. doi: 10.1016/j.biopha.2018.07.021

Wang, S., Liu, Z., Wang, J., Wang, Y., Liu, J., Ji, X., et al. (2019). The triptolide-induced apoptosis of osteoclast precursor by degradation of cIAP2 and treatment of rheumatoid arthritis of TNF-transgenic mice. *Phytother. Res.* 33 (2), 342–349. doi: 10.1002/ptr.6224

Wang, X., Li, T., Xue, Z., Lv, C., Li, H., Fan, Y., et al. (2019). Clinical symptoms effect of Tripterygium Glycosides Tablets alone or combined with methotrexate in treatment of rheumatoid arthritis: a Meta-analysis. *China J. Chin. Mater. Med.* 44 (16), 3533–3541. doi: 10.19540/j.cnki.cjcmm.20190605.501

Wang, X. (2015). *Effects of Triptolide on RANKL Expression in the Epidermal Microenvironment of CIA Mice. dissertation* (Nanjing: Nanjing Medical University).

Wong, V. K. W., Qiu, C., Xu, S. W., Law, B. Y. K., Zeng, W., Wang, H., et al. (2019). Ca(2+) signalling plays a role in celastrol-mediated suppression of synovial fibroblasts of rheumatoid arthritis patients and experimental arthritis in rats. *Br. J. Pharmacol.* 176 (16), 2922–2944. doi: 10.1111/bph.14718

Xiao-yue, W., Tai-xian, L., Zhi-peng, X., Cheng, L., Hui-zhen, L., Yuan-fang, F., et al. (2019). Clinical symptoms effect of Tripterygium Glycosides Tablets Tablets alone or combined with methotrexate in treatment of rheumatoid arthritis: a Meta-analysis. *China J. Chin. Mater. Med.* 44 (16), 3533–3541. doi: 10.19540/j.cnki.cjcmm.20190605.501

Xin, W., Wei, Z., Zhang, Y., Sun, Y., and Zhang, D. (2018). Effect of celastrol on pyroptosis of macrophages RAW264.7. *Chin. Tradit. Herbal Drugs* 49 (05), 1087–1091. doi: 10.7501/j.issn.0253-2670.2018.05.015

Xu, Z., Wu, G., Wei, X., Chen, X., Wang, Y., and Chen, L. (2013). Celastrol induced DNA damage, cell cycle arrest, and apoptosis in human rheumatoid fibroblast-like synovial cells. *Am. J. Chin. Med.* 41 (3), 615–628. doi: 10.1142/s0192415x13500432

Xu, H., Zhao, H., Lu, C., Qiu, Q., Wang, G., Huang, J., et al. (2016). Triptolide Inhibits Osteoclast Differentiation and Bone Resorption In Vitro via Enhancing the Production of IL-10 and TGF-β1 by Regulatory T Cells. *Mediators Inflammation* 2016, 8048170. doi: 10.1155/2016/8048170

Xu, Z. (2013). *Celastrol-Introduced Apoptosis, cell Cycle arrest and DNA Damage in Rheumatoid Arthritis Fibroblast-like synovial dissertation* (Fuzhou: Fujian University of Traditional Chinese Medicine).

Xu, H. (2016). *Effects of Triptolide on OC Differentiation and Bone Resorption in Tregs-OC Co-culture System. dissertation* (Beijing: Beijing University of Chinese Medicine).

Yang, X. O., Pappu, B. P., Nurieva, R., Akimzhanov, A., Kang, H. S., Chung, Y., et al. (2008). T helper 17 lineage differentiation is programmed by orphan nuclear receptors RORα and RORγ. *Immunity* 28 (1), 29–39. doi: 10.1016/j.immuni.2007.11.016

Yang, Y., Ye, Y., Qiu, Q., Xiao, Y., Huang, M., Shi, M., et al. (2016). Triptolide inhibits the migration and invasion of rheumatoid fibroblast-like synoviocytes by blocking the activation of the JNK MAPK pathway. *Int. Immunopharmacol.* 41, 8–16. doi: 10.1016/j.intimp.2016.10.005

Yap, T. A., Garrett, M. D., Walton, M. I., Raynaud, F., de Bono, J. S., and Workman, P. (2008). Targeting the PI3K-AKT-mTOR pathway: progress, pitfalls, and promises. *Curr. Opin. Pharmacol.* 8 (4), 393–412. doi: 10.1016/j.coph.2008.08.004

Yue, J., Griffith, J. F., Xiao, F., Shi, L., Wang, D., Shen, J., et al. (2017). Repair of Bone Erosion in Rheumatoid Arthritis by Denosumab: A High-Resolution Peripheral Quantitative Computed Tomography Study. *Arthritis Care Res. (Hoboken)* 69 (8), 1156–1163. doi: 10.1002/acr.23133

Zhang, Q., Shi, Y., Tan, W., and Wang, F. (2008). Effect of triptolide on the changes of VEGF and MMP-9 levels in the rheumatoid arthritis fibroblast-like synoviocyte line, MH7A. *Acta Universit. Med. Nanjing (Natural Sci.)* 07), 902–905. doi: 10.3724/SP.J.1141.2008.00459

Zhou, J., Xiao, C., Zhao, L., Jia, H., Zhao, N., Lu, C., et al. (2006). The effect of triptolide on CD4+ and CD8+ cells in Peyer's patch of SD rats with collagen induced arthritis. *Int. Immunopharmacol.* 6 (2), 198–203. doi: 10.1016/j.intimp.2005.08.011

Zhu, G., Han, X., Wang, H., Yuzheng, Y., Gao, Y., and Wang, H. (2019). Effect of Tripterygium Glycosides Tablets in treating rheumatoid arthritis:a systematic review and Meta-analysis. *China J. Chin. Mater. Med.* 44 (15), 3358–3364. doi: 10.19540/j.cnki.cjcmm.20190305.004

Conflict of Interest: The authors declare that the research was conducted in the absence of any commercial or financial relationships that could be construed as a potential conflict of interest.

Copyright © 2020 Tang, Liu, Feng, Zhang, Xu, Wen and Zhang. This is an open-access article distributed under the terms of the Creative Commons Attribution License (CC BY). The use, distribution or reproduction in other forums is permitted, provided the original author(s) and the copyright owner(s) are credited and that the original publication in this journal is cited, in accordance with accepted academic practice. No use, distribution or reproduction is permitted which does not comply with these terms.

frontiers in Pharmacology

ORIGINAL RESEARCH
published: 02 October 2020
doi: 10.3389/fphar.2020.551683

Onion Bulb Extract Downregulates EGFR/ERK1/2/AKT Signaling Pathway and Synergizes With Steroids to Inhibit Allergic Inflammation

Ahmed Z. El-Hashim[1], Maitham A. Khajah[1], Khaled Y. Orabi[2], Sowmya Balakrishnan[1], Hanan G. Sary[2] and Ala A. Abdelali[1]*

[1] Department of Pharmacology & Therapeutics, Faculty of Pharmacy, Kuwait University, Kuwait City, Kuwait, [2] Department of Pharmaceutical Chemistry, Faculty of Pharmacy, Kuwait University, Kuwait City, Kuwait

OPEN ACCESS

Edited by:
Takashi Sato, Tokyo University of Pharmacy and Life Sciences, Japan

Reviewed by:
Suresh Kumar Mohankumar, JSS College of Pharmacy, India
You Yun, China Academy of Chinese Medical Sciences, China

***Correspondence:**
Ahmed Z. El-Hashim
ahmed.elhashim@ku.edu.kw

Specialty section:
This article was submitted to Ethnopharmacology, a section of the journal Frontiers in Pharmacology

Received: *14 April 2020*
Accepted: *27 August 2020*
Published: *02 October 2020*

Citation:
El-Hashim AZ, Khajah MA, Orabi KY, Balakrishnan S, Sary HG and Abdelali AA (2020) Onion Bulb Extract Downregulates EGFR/ERK1/2/AKT Signaling Pathway and Synergizes With Steroids to Inhibit Allergic Inflammation. Front. Pharmacol. 11:551683. doi: 10.3389/fphar.2020.551683

The treatment of allergic diseases, such as asthma, with both conventional and novel therapies presents a challenge both in terms of optimal effect and cost. On the other hand, traditional therapies utilizing natural products such as onion have been in use for centuries with demonstrated efficacy and safety but without much knowledge of their mechanims of action. In this study, we investigated if the anti-inflammatory effects of onion bulb extract (OBE) are mediated *via* the modulation of the EGFR/ERK1/2/AKT signaling pathway, and whether OBE can synergise with steroids to produce greater anti-inflammatory actions. Treatment with OBE inhibited the house dust mite (HDM)-induced increased phosphorylation of EGFR, ERK1/2 and AKT which resulted in the inhibition of HDM-induced increase in airway cellular influx, perivascular and peribronchial inflammation, goblet cell hyper/metaplasia, and also inhibited *ex vivo* eosinophil chemotaxis. Moreover, treatment with a combination of a low dose OBE and low dose dexamethasone resulted in a significant inhibition of the HDM-induced cellular influx, perivascular and peribronchial inflammation, goblet cell hyper/metaplasia, and increased the pERK1/2 levels, whereas neither treatment, when given alone, had any discernible effects. This study therefore shows that inhibition of the EGFR/ERK1/2/AKT-dependent signaling pathway is one of the key mechanisms by which OBE can mediate its anti-inflammatory effects in diseases such as asthma. Importantly, this study also demonstrates that combining OBE with steroids results in significantly enhanced anti-inflammatory effects. This action may have important potential implications for future asthma therapy.

Keywords: onion (*Allium cepa* Hysam), asthma, signalling, steroids, synergisctic effects

INTRODUCTION

Natural products have been the cornerstone of therapeutic agents for millennia and more recently an important source of therapeutic drugs with unique structural diversity and pharmacological actions (Newman and Cragg, 2016). Many therapeutic agents currently in use in several therapeutic areas such as cardiovascular, oncology, transplantation are natural products or their derivatives such as digoxin, vincristine, and cyclosporine, respectively. However, their use as pharmaceutical agents has waned over the last few decades in the face of advances in combinatorial chemistry and biopharmaceutical technology, the latter supplying the majority of the top ten block buster drugs in the market in 2018 (Brown et al., 2017). Indeed, more than 70% of the world's population use herb-based medicines for primary healthcare (Newman and Cragg, 2016). A recent study has also reported that approximately 60% of asthma patients in the UK have used herbal remedies for their asthma (Clark et al., 2010). These findings suggest a strong held belief that natural products not only have therapeutic benefit in a wide range conditions, but that they are also safe.

Inflammatory-based diseases, such as asthma, present a global healthcare challenge. Worldwide prevalence of asthma has been estimated to range from 1% to as high as 18% in different populations, affecting up to 300 million people worldwide (Nunes et al., 2017; WHO, 2019) with increasing prevalence particularly among children (GINA, 2019). It is currently the most common chronic respiratory disease in children and costs over a £1 billion per year in some healthcare systems in Europe (Harrison, 2015). There is also good evidence that food allergy and eczema are rising, in parallel to asthma, and have been described as a "second wave" of allergy epidemic particularly in children (Prescott and Allen, 2011). While the mechanisms of asthma still remain unclear, it is well recognized that chronic airway inflammatory disease is central to its pathogenesis and is mediated by inflammatory cells such as mast cells and eosinophils and is driven by specific Th2 and Th17 lymphocytes, cytokines, and chemokines (Massoud et al., 2016; Athari, 2019).

There have been several recent studies demonstrating that pathogenic EGF/EGFR-dependent signaling through EGF and other EGFR ligands, such as amphiregulinin, is increased in asthma (Acciani et al., 2016; Ha and Rogers, 2016). EGFR expression has been reported to be weak or absent in healthy individuals but is significantly increased in the airway epithelium of not only asthmatics (Puddicombe et al., 2000; Takeyama et al., 2001a; Takeyama et al., 2001b; Polosa et al., 2002), but also in patients with COPD (de Boer et al., 2006) and cystic fibrosis patients (CF) (Burgel et al., 2007). Furthermore, in a recent clinical study conducted using *ex vivo* lung tissue from patients with COPD, the EGFR inhibitor BIBW 2948 showed some efficacy in inhibiting EGFR phosphorylation and a tendency toward reducing mucous cell metaplasia. More importantly, a positive correlation between EGFR immunoreactivity and MUC5AC mucin staining was noted when bronchial biopsies from healthy volunteers and subjects with mild-to-moderate asthma were compared, suggesting a causal relationship (Puddicombe et al., 2000). Also, areas of epithelial damage in asthmatic patients exhibited a strong EGFR immunoreactivity suggesting that EGFR activation plays an important role in the epithelial damage/repair process in asthma (Puddicombe et al., 2000). Of interest also is that a positive correlation between mucin and EGFR staining has been shown in the small airway of CF patients (Burgel et al., 2007). Thus, increased EGFR expression is a consistent finding not only in asthma but across several disease states. Moreover, preclinical animal models have also demonstrated a strong role for EGFR in asthma. We and others have shown, using an allergic model of inflammation, that EGFR inhibitors, such as AG1478 or gefitnib, significantly reduce eosinophil recruitment, airway inflammation, airway hyperresponsiveness (AHR), and goblet cell hyper/metaplasia, thus, underscoring the importance of this signaling pathway in asthma pathogenesis (Tamaoka et al., 2008; Le Cras et al., 2011; Song H. N. et al., 2016; El-Hashim et al., 2017). Furthermore, we have also reported that ERK1/2 and AKT are downstream signaling molecules of EGFR activation (El-Hashim et al., 2017). Therefore, both clinical and preclinical studies clearly establish an important role for EGFR-dependent signaling in inflammatory-based diseases.

While the combination of inhaled corticosteroids (ICS) and long-acting beta-agonists (LABA) is a main treatment advocated by most asthma guidelines (O'Byrne et al., 2001; GINA, 2019), a significant number of patients are poorly compliant with inhaled treatments and remain under-controlled (Sherman et al., 2001). Furthermore, severe asthmatics require treatment with moderate to high doses of steroids (Carr and Kraft, 2017). This is associated with a significant side effect profile (Pinto et al., 2013). Therefore, it would be more advantageous if the asthma therapeutic goals can be achieved at lower doses of steroids since the side effects would be minimal. Synergism is a phenomenon whereby combination of drugs produces a greater effect than when each drug is given alone (Jia et al., 2009). This phenomenon is useful when low doses of efficacious drugs are combined as they produce a superior effect but with fewer side effects. Indeed, this has been demonstrated with ICS and several drug classes such as LABA and anti-leukotrienes (Beasley et al., 2019). However, no study has tested if synergism occurs between steroids and natural products within the context of inflammatory based diseases such as asthma.

Novel monoclonal antibody-based therapy, in inflammatory disease management, has made an impact on disease control. For example, the anti-IgE antibody, omalizumab, has been used as a steroid sparing drug in patients with severe asthma, but unfortunately its use is limited (Plosker and Keam, 2008) due to a high frequency of anaphylactic reaction and serum sickness (Harrison et al., 2015) and lack of cost-effectiveness. Similarly, the use of the newly introduced anti-IL5 antibodies such as mepolizumab and benralizumab is limited to severe asthmatics with a high eosinophilic component. However concerns have been raised regarding their cost-effectiveness (Agache et al., 2020). Despite the recent market increase in therapeutic agents that selectively target specific molecules, it is unlikely that the blockade

of individual mediator signaling pathways would result in optimal therapeutic outcomes in asthma, and monoclonal based therapy would certainly be beyond the financial reach of most asthma patients in the developing world due to their high cost.

Allium cepa L. (Family Amaryllidaceae) is one of the most commonly consumed vegetables and has also been used for medicinal purposes for numerous ailments such as ulcer wounds, scars, dysentery, inflammation, hypertension and also in respiratory conditions such as cough, asthma, and bronchitis (Lanzotti, 2006; Upadhyay, 2016; Zeng et al., 2017). Onion bulb extract (OBE) has also been shown to effectively reduce airway inflammation, IL4, and IgE levels and induces oxidation in animal models of asthma (Oliveira et al., 2015; Marefati et al., 2018). Thiosulfinates (TS) and cepaenes (CS), isolated from onions and/or synthesized, were also shown to have dose-dependent inhibitory effects on both cyclooxygenase and 5-lipoxygenase activity (Dorsch et al., 1990; Wagner et al., 1990) and inhibit *in vitro* chemotaxis of human granulocytes induced by formyl-methionine-leucine-phenylalanine (WKYMvm) (Dorsch et al., 1990). In this regard, it is of interest to note that many of the previous studies that assessed the effects of onion extract have used ovalbumin as the allergenic material to induce airway inflammation. However, the use of ovalbumin has recently been questioned on the basis that it is not clincally relevant, and therefore studies using allergens such as house dust mite or *Alternaria alternata*, that simulate clincal asthma more closely (Gorska, 2018), are necessary in order to better assess the effects of onion extract in animal models.

The EGFR/ERK1/2/AKT signaling pathway has been recently shown to be an important signaling pathway, in both clincial and preclinical studies. However, whether the EGFR/ERK1/2/AKT signaling pathway is a target for OBE in a clincially relevant animal model of allergic asthma, is not known. Also whether OBE synergizes with steroids has not been studied previously. In this study, using a clincially relevant allergen (HDM), we investigated 1) whether the EGFR/ERK1/2/AKT signaling pathway is modulated by OBE, and 2) if OBE synergizes with dexamethasone to result in a greater anti-inflammatory action.

METHODS

Acquisition of the Plant Material

Fresh red onion bulbs were bought from the local market. The plant was identified as *Allium cepa*, and a voucher specimen, number KOE-010, was deposited at the herbarium of Kuwait University (KTUH), College of Science, Kuwait.

Extraction of Onion Bulbs

About 20 kg of fresh red onion was peeled, coarsely cut, and percolated three times, each using 10 L of dichloromethane. The dichloromethane layers of the percolates were separated from the aqueous layer, dried over anhydrous sodium sulphate, and then evaporated in *vacuo* till dryness to obtain brownish syrupy residue. This extraction process was repeated as needed. The treatment stock solution was prepared using the residue and PBS as a vehicle.

GC–MS Analysis

Dichloromethane extract of onion bulbs (1 µl sample size) was analyzed on a Thermo high resolution gas chromatography–mass spectrometer Double Focusing Sector system (GC–MS DFS) fitted with a DB-5MS capillary column with 0.25 µm film thickness, 30 m length and 0.25 mm inner diameter, using helium as a carrier gas with a flow rate of 0.8 ml/min. The operating conditions were as follows: splitless injector with port temperature 250°C, detector temperature 280°C, and program temperature from 50 to 250°C at the rate of 6°C/min with 10 min hold time, and from 250 to 300°C at the rate of 10°C/min with 6 min hold time. The MS conditions were as follows: electron impact ionization mode, ionization energy 70 eV, ion source temperature 175°C, scan range *m/z* 40–900 Da. The qualitative identification of the compounds was based on computer matching with NIST MS Search 2.0 library and by comparison with data in the literature (Mondy et al., 2001; Gitin et al., 2014; Abdel-Lateef et al., 2018; Fredotovic et al., 2020).

Animals

Male BALB/c mice (6–8 weeks old, average weight 25 g) were used in this study. All studies involving animals were in accordance with the ARRIVE guidelines for reporting experiments involving animals. All experimental protocols were approved by the Animal Welfare and Use of Laboratory Animals Committee in the Health Sciences Center, Kuwait University and were carried out in accordance with the EU Directive 2010/63/EU for animal experiments and the National Institutes of Health guide for the care and use of Laboratory animals (NIH Publications No. 8023, revised 1978). Animals were maintained under temperature-controlled conditions with an artificial 12 h light/dark cycle and were allowed standard chow and water *ad libitum*.

Immunization and Intranasal Challenge and Drug Treatment Protocols

Protocol for Prophylactic Treatment Experiments

Seven treatment groups (A–G, 9–15 animals per group) were established to determine whether OBE if given prophylactically inhibits the HDM-induced asthma phenotype. All mice were immunized once by intraperitoneal (i.p.) injection of 40 µg HDM in 0.2 ml of alu-Gel-S (Alu-Gel-S; SERVA Electrophoresis GmbH) on day 0. Mice were subsequently challenged for 3 days, days 14, 17, and 18 with HDM or PBS in the case of the control group. Mice in groups A (n = 11) and B (n = 13) were pretreated intraperitoneally with 0.2 ml of the drug vehicle, 1 h before each intranasal challenge with PBS and HDM, respectively. In the same manner, groups C (n = 10), D (n = 9), E (n = 10), and F (n = 15) were pretreated with the same volume of OBE at 10, 30, 60, and 100 mg/kg, respectively, and group G (n = 11) with dexamethasone (3 mg/kg), 1 h before each intranasal challenge with HDM (**Figure 1**).

24 h after the last intranasal challenge, animals were sacrificed with an overdose of halothane; bronchoalveolar lavage (BAL) was performed to obtain BAL fluid, and then the lungs were excised for preparation for histology, Western Blot (WB), and

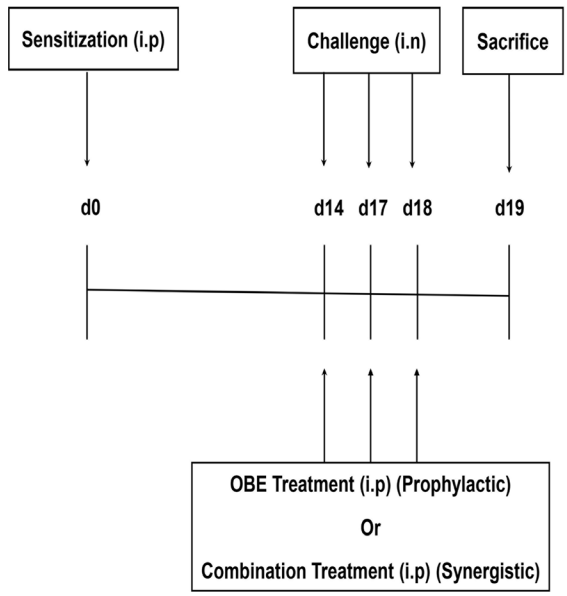

FIGURE 1 | Schematic representation of the immunization and the treatment protocol used for boh the prophylactic and synergistic studies.

immunofluorescence (IF) studies. In another separate group of animals, airway responsiveness was measured. For the histology/WB/IF studies, the OBE dose of 60 mg/kg was selected to represent the prophylactic approach as it gave an optimum effect.

Protocol for Synergistic Treatment Experiments

Six treatment groups (A–F, 9-11 animals per group) were established to determine whether combining OBE and dexamethasone would results in synergistic anti-inflammatory actions. Mice in groups A (n = 9) and B (n = 11) were pretreated intraperitoneally with 0.2 ml of the drug vehicle 1 h before each intranasal challenge with PBS and HDM, respectively. In the same manner, groups C (n = 11), D (n = 7), E (n = 11), and F (n = 9) were pretreated with the same volume of OBE at 30 mg/kg (OBE 30), OBE at 30 mg/kg in combination with dexamethasone (DEX) at 0.5 mg/kg (OBE 30 + DEX 0.5), 0.5 mg/kg (DEX 0.5 mg) and 3 mg/kg (DEX 3 mg), respectively, 1 h before each intranasal challenge with HDM. Treatment with OBE and/or dexamethasone was also repeated on days 14, 17, and 18 (**Figure 1**).

Bronchoalveolar Lavage Fluid Cell Counts and Lung Histology

BAL fluid was collected by cannulating the trachea and washing the lungs with saline solution (0.3 ml × 4 each) after sacrificing the animals with an over dose of halothane. The BAL cells were then counted using a particle-size counter (Z1 Single Threshold; Beckman Coulter), and cytosmears were prepared for differential count. The cells were stained with Diff-Quik, and a differential count of 200 cells was performed using standard morphologic criteria. Results are expressed as total cell count/ml and as total macrophages, lymphocytes, neutrophils, and eosinophils/ml in BAL fluid. For histological assessment, segments of the lung tissue were removed and fixed in 10% buffered formalin, embedded in paraffin wax and sectioned into 5-μm-thick slices. The sections were processed and stained separately with H&E stain and periodic acid–Schiff (PAS) according to standard methods as previously described (El-Hashim et al., 2017). Sections were examined under light microscope and the severity of pathologic changes scored independently by two experienced histologists unfamiliar with the slides. Score coding was as follows: (1 = normal, 2 = mild, 3 = moderate, 4 = severe and 5 = highly severe).

Measurement of Airway Responsiveness

Airway responsiveness was measured 24 h after last HDM or PBS challenge, using a separate set of animals using the Buxco FinePointe series RC site (DSI, Wilmington, NC) as described previously (Queto et al., 2010; Ezeamuzie et al., 2014; Correa et al., 2017). Briefly, mice were anesthetized with an intraperitoneal injection of ketamine/xylazine (1:0.1 mg/kg) cocktail and tracheotomized with a steel 18-gauge cannula. Mice were then mechanically ventilated at a rate of 150 breaths/min and a tidal volume of 0.15 ml using a computerized small animal ventilator (FinePointe site). Following a 5 min period of stabilization and administration of PBS, airway resistance was measured by exposing mice to aerosolized methacholine (6.25–50.0 mg/ml, 5 μl per delivery) delivered by an aerogen nebulizer and reported as total lung resistance (R_L) (cm H_2O per ml/s).

Immunofluorescence

Lung tissues were processed as described above. Immunofluorescence was performed as previously described (Khajah et al., 2016). In short, lung sections were incubated in a blocking solution (5% bovine serum albumin (BSA) + 0.3% Triton X-100 in PBS) for 1 h and were subsequently incubated overnight at 4°C with primary antibodies [p-EGFR (Tyr1068) (Rabbit; Cat. No. 3777S), pAKT (Ser 473) (Rabbit; Cat. No. 9271L) and pERK1/2 (Thr202/Tyr204) (Rabbit; Cat. No. 9101L) (1:25–1:800 dilution) or only 1% BSA (for negative control); Cell Signaling, USA], diluted in 1% blocking solution. 24 h later, sections were washed and incubated with secondary antibody conjugated to Alexa Fluor 555 (Goat anti rabbit SFX kit; Life Technologies, USA, 1:400 dilution) for 2 h at room temperature in the dark. Following several washes in PBS, sections were stained with 4′, 6 diamidino-2-phenylindole and mounted. Images were then captured on a ZEISS LSM 700 confocal microscope and fluorescence intensity estimated in defined fields using Image J software package. The laser setting and photo processing were equal among the different treatment groups for each protein. 40× magnification for the tested molecules was equally modified in terms of sharpness and contrast to show localization of the phospho-proteins in the lung tissue.

Western Blotting

Appropriate lobes from the dissected lungs of the mice were snap-frozen in liquid nitrogen and stored at −80°C. Following

that, the tissue samples were defrosted in ice then transferred to lysis buffer (pH 7.6) containing 50 mM Tris-base, 5 mM EGTA, 150 mM NaCl, 1% Triton 100, 2 mM Na_3VO_4, 50 mM NAF, 1 mM PMSF, 20 μM phenyl arsine, 10 mM sodium molybdate, 10 μg ml^{-1} leupeptin and 8 μg ml^{-1} aprotinin. Using a homogenizer, the tissues were homogenized for 10 s, three times. Samples were allowed to lyse completely by incubation on ice for 30 min. The lysates were then centrifuged at 13,000 rpm for 10 min at 4°C and the supernatants collected, and protein concentrations were estimated by Bio-Rad Bradford Protein Assay (Bio-Rad, Hercules, CA, USA). Aliquots containing equal amounts of protein were subjected to SDS-PAGE and transferred electrophoretically onto nitrocellulose membrane (Schleicher & Schuell, Dassel, Germany). The membranes were blocked with 5% BSA and then incubated with ERK1/2 (137F5) (Rabbit; Cat. No. 4695S), pERK1/2 (Thr202/Tyr204) (Rabbit; Cat. No. 9101L) and β-actin antibody (Cell Signaling Technology, Boston, MA, USA; 1/1,000 dilution) (used as loading control, 1:1,000 in 5% BSA) at 4°C overnight. Membranes were incubated with appropriate secondary antibodies conjugated to horseradish peroxidase (Amersham, Buckinghamshire, UK) to detect phosphorylated form of ERK1/2 (42/44 kDa), or total form of actin (45 kDa). The immunoreactive bands were detected with Super Signal Chemiluminescent Substrate (Immuno Cruz Western blotting luminal reagent SC-20428, Santa Cruz Biotechnology) utilizing a Kodak autoradiography film (Care stream Biomax Xarfil 1660760). Images were then analyzed and quantified and the data were normalized to β-actin levels. The experiment was run twice with lung samples from three different mice in each treatment group (pooled) in each run.

Measurement of Lung Cytokines

Lung tissues from mice were collected and stored at −80°C. The amount of total protein was determined by Bradford analysis using the Bio-Rad Protein Assay reagent. The relative changes of different cytokines and chemokines were detected using Proteome Profiler™ Mouse Cytokine Array Kit (Catalog # ARY006, R&D Systems, Inc., Minneapolis, USA). The procedure was done in line with the manufacturer's protocols and as recently described (Khajah et al., 2019).

Isolation of Human Blood Eosinophils

For this experiment, fresh blood was obtained from healthy individuals with no history of allergic disease and had not taken any medication in the last 72 h after receiving their informed consent. The methods and protocol for these experiments were performed in accordance with and approved by the "Ethical Committee of the Faculty of Medicine, Kuwait University". Granulocytes were isolated from heparinized (10 IU/ml) blood by erythrocyte sedimentation, followed by percoll gradient centrifugation as reported recently (Ezeamuzie et al., 2014). Eosinophils were separated using negative selection with the immunomagnetic method as previously described (Hansel et al., 1991). The eosinophil purity was checked by differential count of a Wright–Giemsa stained cytosmear and was routinely >98%. Viability was determined by Trypan blue exclusion and exceeded 98%.

Boyden Chamber Assay for Eosinophil Chemotaxis

Peripheral blood derived eosinophils were used for chemotaxis assay utilizing a Boyden chamber as previously described (Gomez-Cambronero et al., 2003). Purified naïve eosinophils (2×10^5) were then placed in the upper wells, and 500 μl of BAL fluid derived from mice challenged with PBS (vehicle) or with HDM, pretreated *ex-vivo* with either vehicle or OBE (100 and 1,000 ng/ml), were placed in the lower wells (37 °C/5%CO_2) and eosinophils allowed to migrate for 1 h. The transmigrated eosinophils were determined by counting under the microscope by using a hemocytometer.

Statistical Analyses

All numerical values were expressed as means ± SEM. Total cell counts represent the number of cells/ml of BAL fluid. Differential cell counts represent the absolute number of each cell type/ml of BAL fluid. Absolute R_L values were computed and were used as an index of airway responsiveness. For the histopathological assessment, a semi-quantitative 5-level lung pathology score was used to grade the degree of inflammation in each microscopic field at 20×. All data were initially assessed for normality. One-way analysis of variance (ANOVA) test followed by Bonferroni *post hoc* was used to compare differences between individual groups for both total and differential cell count as well as histopathological data and the immunofluorescence data for both the prophylactic and the synergistic studies. A two-way repeated measure analysis of variance followed by a Bonferroni *post hoc* test was used for the airway responsiveness data. The mean difference was considered as significant at a probability level of less than 0.05. All analyses were performed using GraphPad Prism.

RESULTS

Extraction of Onion Bulbs

The extraction process was repeated four times to afford 7.5 g (0.038% yield) of brownish syrupy residue (**Figure 2**).

GC–MS Analysis of OBE

Dichloromethane extract of *Allium cepa* bulb (OBE) was analyzed to identify different compounds and confirm the identity of the plant. The identified compounds and their mass spectral data are listed in **Table 1**. The major compound identified in the extract was shown to be the sulfur-containing compounds dipropyl disulfide, dipropyl trisulfide, and propylpropane thiosulfonate. Other sulfur compounds were also identified but at lesser quantities. **Figure 2A** shows the TIC of OBE where different 28 peaks are shown. Furthermore, **Figure 2B** shows the fragmentation patterns of some of these compounds. The identity of these compounds was confirmed *via*

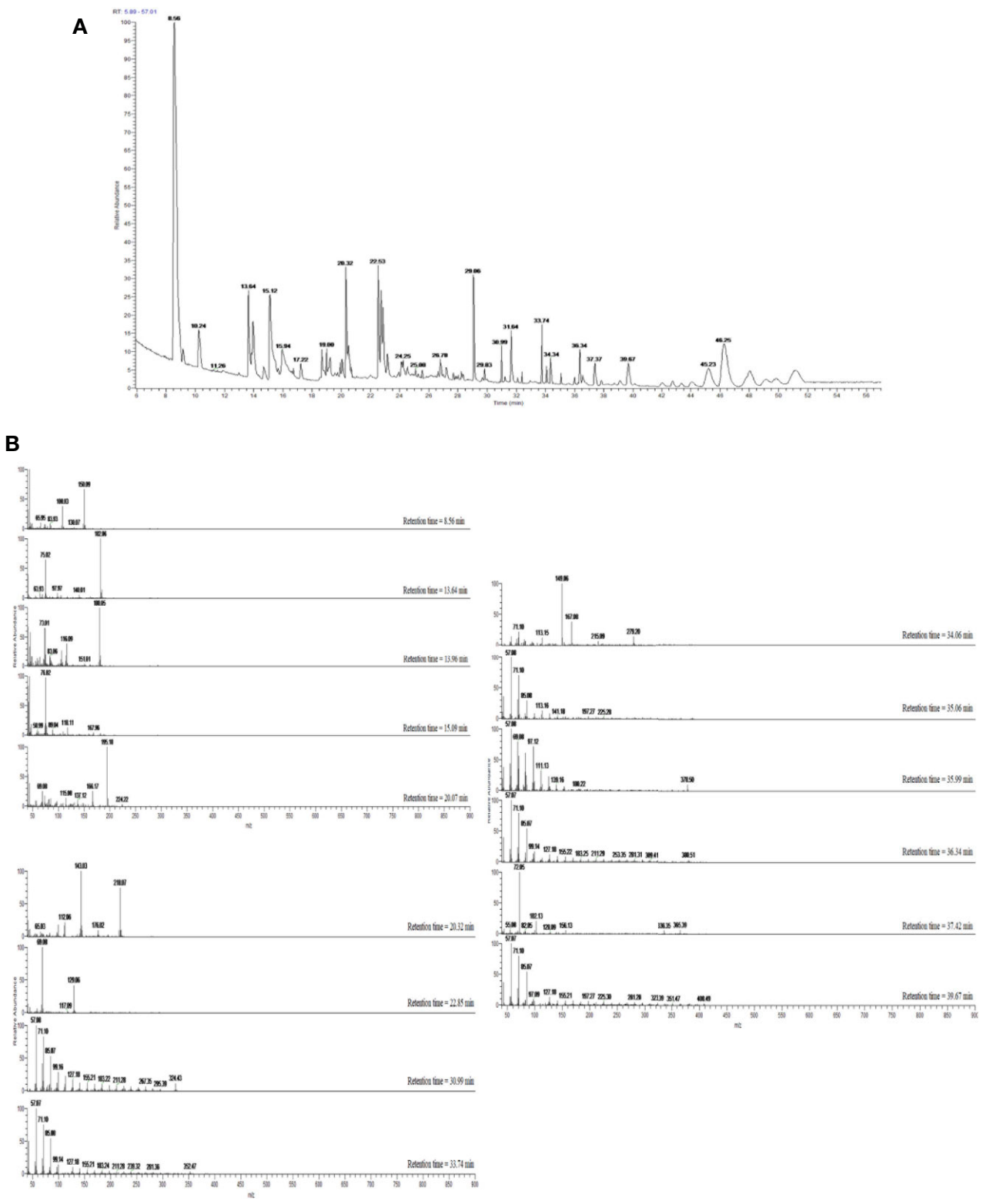

FIGURE 2 | **(A)** GC–MS total ion chromatogram (TIC) of OBE. Peaks were identified through comparison with mass spectral data in the NIST MS Search 2.0 library stored in the GC–MS system and are represented in **Table 1**. **(B)** Mass spectra of compounds eluted with retention times 8.56–46.25 min and presented in **Table 1**.

TABLE 1 | Compounds identified in *Allium cepa* bulb extract.

Identified Compounds[a]	Retention timet$_r$ (min)	Area (%)
Dipropyl disulfide	8.56	45.93
Dipropyl trisulfide	13.64	3.16
3,5-Diethyl-1,2,4-trithiolane	13.96	1.88
Propylpropane thiosulfonate	15.09	5.07
1,5-Dithiaspiro[5.6]dodecan-7-ol	20.32	3.46
Methyl-2,6-anhydro-3,4,7-tridesoxy-1-erythro-hept-2-enulonate	22.85	1.25
Tricosane	30.99	0.63
Pentacosane	33.74	1.37
1,2-Benzenedicarboxylic acid	34.06	0.34
Hexacosane	35.06	0.3
1-Heptacosanol	35.99	0.18
Nonacosane	36.34	1.2
Nonacosane	39.67	1.88
Tetratriacontane	45.23	4.09

[a]*Identified by matching with mass spectral data in the NIST MS Search 2.0 library stored in the GC-MS system, and comparison with data reported in the literature.*

a direct comparison and matching with the stored spectra in the GC–MS system.

Effect of OBE on HDM-Induced Inflammatory Cell Influx

In these experiments, we evaluated the effect of OBE on HDM-induced total and differential cell influx. Our findings show that HDM-sensitized and challenged animals (HDM group) developed a significant increase in total cell count (1.3 ± 0.3 *vs* 11.0 ± 2.0 × 10^5 cells/ml) as well as in lymphocytes (0.03 ± 0.01 *vs* 1.9 ± 0.6 × 10^5 cells/ml) and eosinophils (0.04 ± 0.02 *vs* 4.9 ± 0.6 × 10^5 cells/ml), ($P < 0.05$; **Figures 3A, B**, n = 9–15), 24 h after the last HDM challenge compared to the control group. Prophylactic treatment with OBE (10, 30, 60, and 100 mg/kg) dose-dependently inhibited the HDM-induced increase in the total cells and was significant at the doses of 60 and 100 mg/kg (3.3 ± 0.7 and 2.2 ± 0.4 *vs* 11.0 ± 2.0 × 10^5, respectively, $P < 0.05$; **Figure 3A**, n = 9–15) and were comparable to the dexamethasone (DEX) group (used as a positive control). Moreover, OBE treatment also inhibited the HDM-induced increase in lymphocytes (0.4 ± 0.2 *vs* 1.9 ± 0.6 × 10^5 cells/ml, $P < 0.05$; **Figure 3B**, n = 9–15) and eosinophils (0.6 ± 0.2 *vs* 4.9 ± 0.6 × 10^5 cells/ml, $P < 0.05$; **Figure 3B**, n = 9–15).

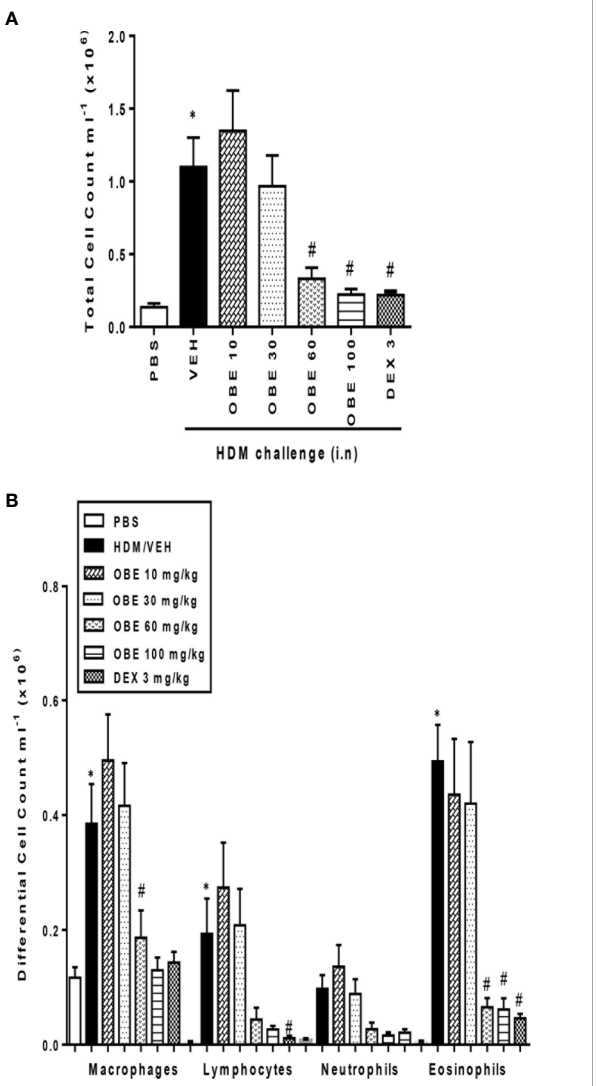

FIGURE 3 | Effect of OBE, 10, 30, 60, and 100 mg/kg (i.p.) on HDM-induced increase in **(A)** total cell and **(B)** differential cell count. OBE treatment resulted in a dose-dependent inhibition of total and eosinophil numbers. Data are expressed as mean ± SEM (*n* = 9–15) *P < 0.05 *vs* PBS group, #P < 0.05 *vs* HDM group.

Effect of OBE on HDM-Induced Histopathological Changes

H&E and PAS stained lung sections from control mice (PBS group) showed normal histology (**Figures 4A, B**). In contrast, lung sections from mice challenged with HDM showed consistently marked and severe perivascular and peribronchial inflammatory cell infiltration (cellular infiltration score, HDM vs PBS, 4.2 ± 0.2 *vs* 1.0 ± 0.07) and increase in bronchial mucus production and goblet cell hyper/metaplasia (mucous intensity score, HDM *vs* PBS, 4.1 ± 0.3 *vs* 1.0 ± 0.02) demonstrating a marked degree in airway remodeling ($P < 0.05$; **Figures 4A–D**, n = 3–6). However, lung sections from OBE-treated mice (60 mg/kg) showed a significantly lower score of the histopathological parameters that were assessed (cellular infiltration score; 2.7 ± 0.3 *vs* 4.2 ± 0.2, and mucous intensity score; 2.3 ± 0.5 *vs* 4.1 ± 0.3), achieving almost normal histological appearance that was very similar to the dexamethasone treatment group ($P < 0.05$; **Figures 4A–D**, n = 3–6).

Effect of OBE on HDM-Induced Phosphorylation of EGFR, ERK1/2, and AKT as Determined by Immunofluorescence

Our findings show that HDM challenge induced a significant increase of about 3.0, 2.3 and 2.4-fold in the phosphorylation of EGFR, ERK1/2, and AKT, respectively, compared to PBS control as detected by immunofluorescence ($P < 0.05$; **Figures 5A–C**, n =

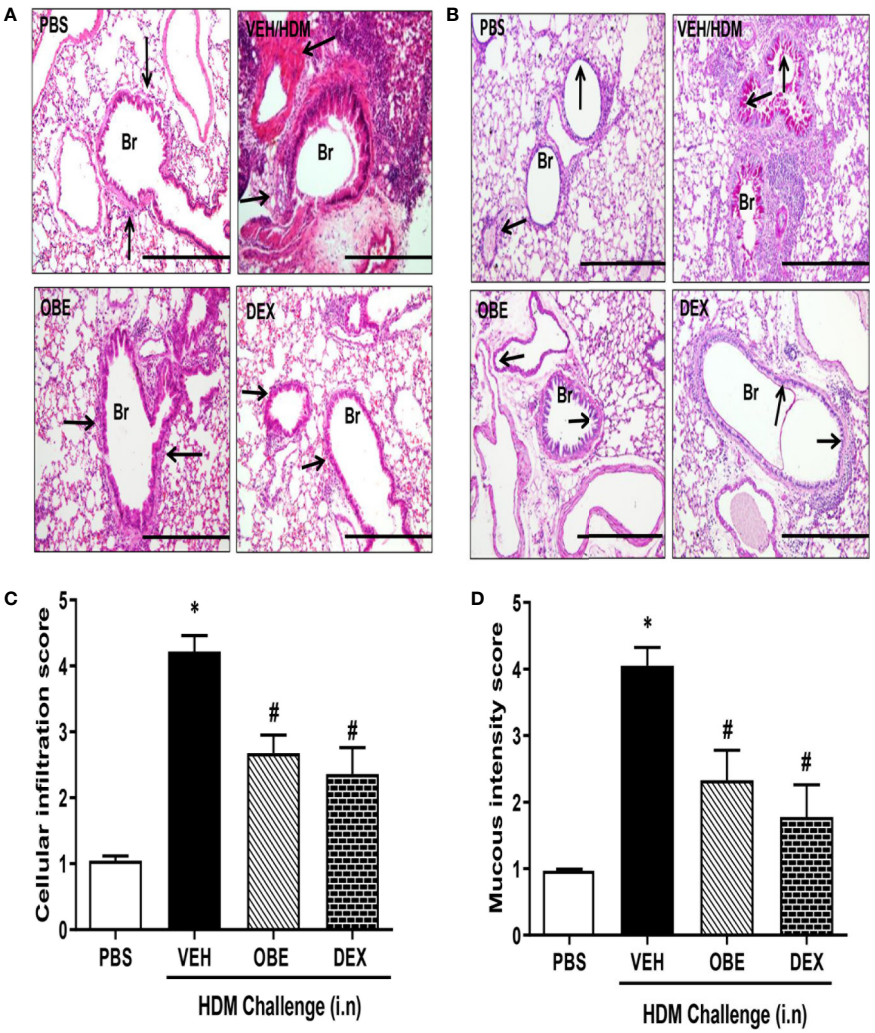

FIGURE 4 | Effect of OBE (60 mg/kg; i.p.) on HDM-induced histopathological changes: **(A)** representative low-magnification light photomicrographs displaying **(A)** H&E and **(B)** PAS staining of whole lung samples from control PBS-challenged mice (PBS), HDM-challenged mice (HDM), HDM-challenged mice pretreated with OBE (60 mg/kg; i.p.) (OBE) and HDM-challenged mice pretreated with dexamethasone (3 mg/kg; i.p.) (DEX), scale bar = 200μm. Graphs shows **(C)** cellular infiltration and **(D)** mucous intensity score for H&E and PAS staining, respectively. OBE treatment resulted in a significant decrease in both peribronchial and perivascular inflammatory cell infiltrations and bronchial mucus production and goblet cell hyper/metaplasia compared with HDM-challenged vehicle treated mice. Data are expressed as mean ± SEM (n = 3–6). *P < 0.05 *vs* PBS group, $^{\#}$P < 0.05 *vs* HDM group.

3–5). Negative control shows no non-specific staining (data not shown). Treatment with OBE (60 mg/kg) significantly inhibited the HDM-induced phosphorylation of all proteins (P < 0.05) and was comparable to the inhibition obtained in the dexamethasone treatment group (P < 0.05, **Figures 5A–C**, n = 3–5).

Effect of OBE on HDM-Induced Phosphorylation of ERK1/2 as Determined by Western Blotting

In this experiment, we assessed the levels of p-ERK1/2 and total ERK1/2 by Western blotting in order to confirm and validate the immunofluorescence data. Western blotting analysis of lung homogenate (**Figure 6A**) confirmed the modulated levels of p-ERK1/2 as seen in the immunofluorescence. HDM challenge resulted in a marked increase in p-ERK1/2 levels compared to PBS-challenged mice (**Figures 6A, B**). Treatment with OBE resulted in a clear inhibition of the p-ERK1/2 and was similar to the dexamethasone-treated group (**Figures 6A, B**, n = 3 for each blot). The effect on HDM and OBE on total ERK1/2 was relatively unchanged.

Effect of OBE on Airway Levels of Various Cytokines Using a Proteome Profiling-Based Technique

The effect of OBE treatment (60 mg/kg) on the airway expression levels of various pro-inflammatory cytokines was determined. HDM challenge significantly enhanced the expression of the following interleukins (IL) by: IL-3 (147.4%), IL-4 (104.6%), IL-5 (5400%), IL-

10 (152.0%), and tumor necrosis factor (TNF-α) (17,200%) ($P < 0.05$; **Figure 7A**, n = 4) compared to PBS-challenged mice. Treatment with OBE significantly reduced the expression of all of the above molecules by approximately 98.2–99.5%, except IL-10 (anti-inflammatory cytokine) which was significantly increased (78.6%) above the HDM levels ($P < 0.05$; **Figure 7A**, n = 4).

Effect of OBE on Eosinophil Chemotaxis *Ex Vivo*

In this experiment, eosinophils showed significant migration towards BAL fluid derived from HDM-challenged mice compared to BAL fluid from PBS-challenged mice (16.5 ± 2.4 *vs* $4.2 \pm 0.6 \times 10^4$/ml, $P < 0.05$; **Figure 7B**). In contrast, pretreatment

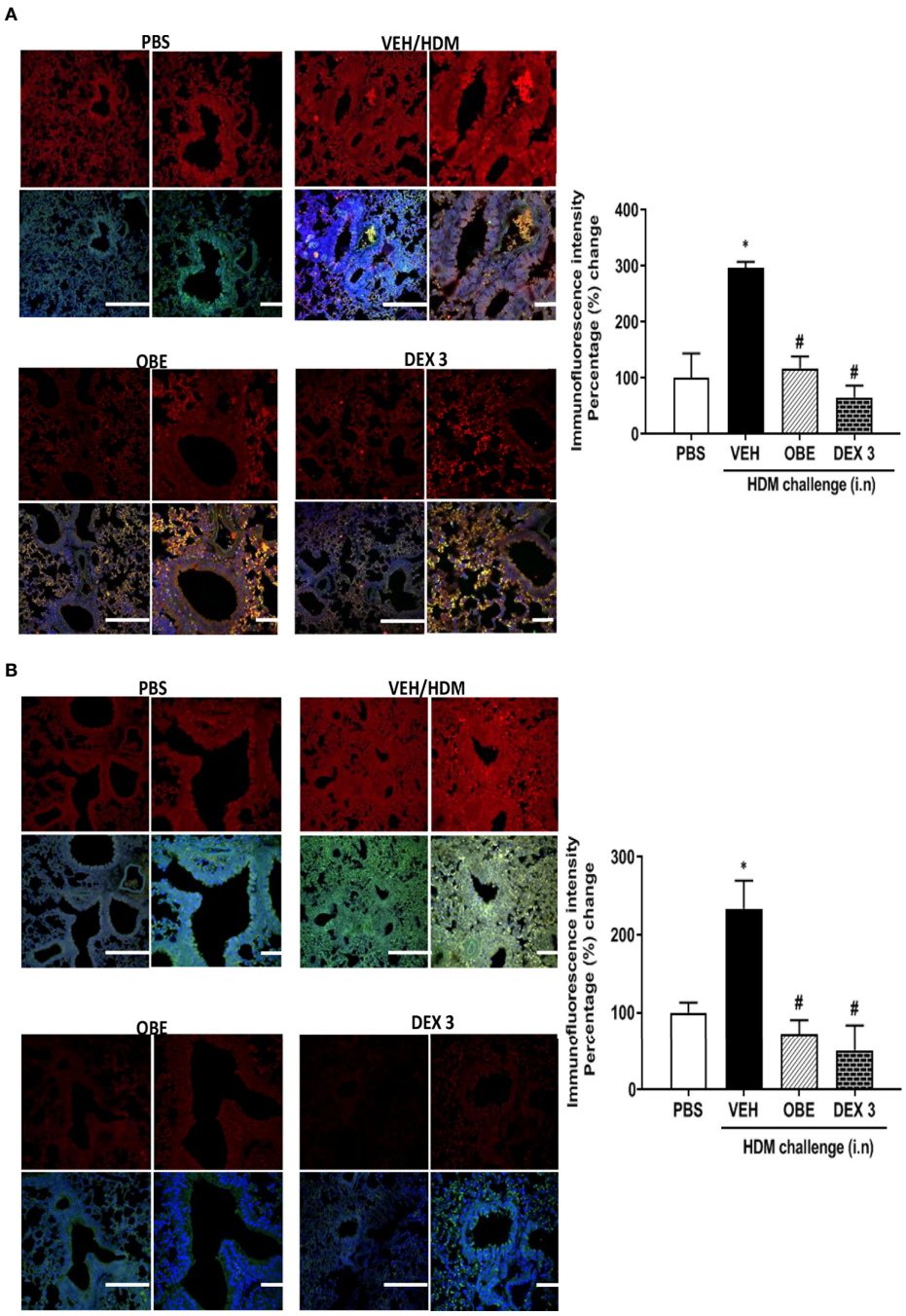

FIGURES 5 | Continued

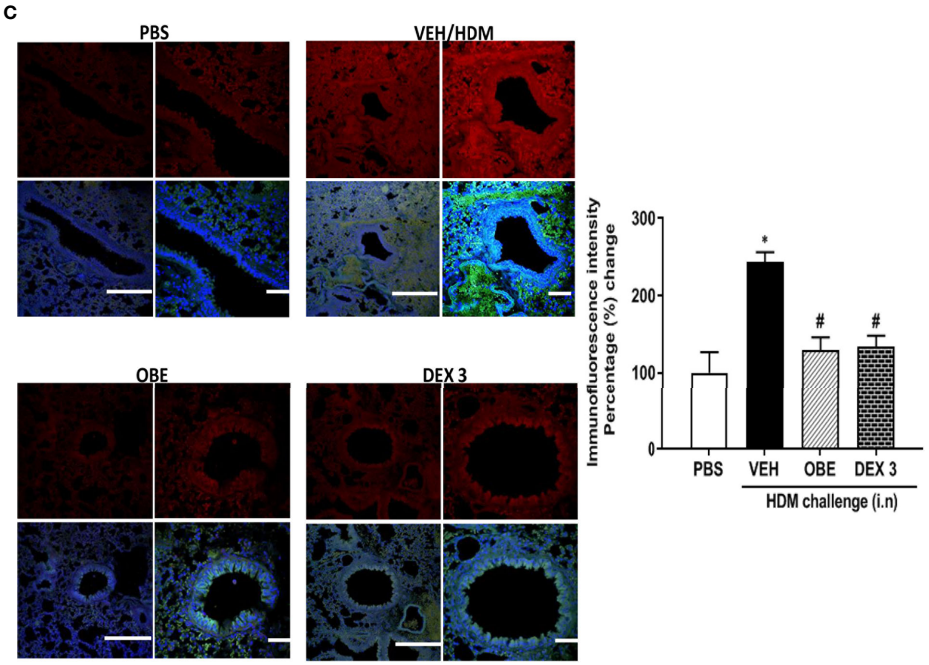

FIGURES 5 | Immunofluorescent (Alexa Fluor) detection of pEGFR **(A)** pERK1/2 **(B)** and pAKT **(C)** shown in the upper panels overlaid with DAPI stain on the lower panel to show lung tissue architecture. Lung sections were taken from different treatment groups: PBS-challenged mice (PBS), HDM-challenged mice pretreated with vehicle (HDM), HDM-challenged mice pretreated with OBE (60 mg/kg; i.p.) (OBE), and HDM-challenged mice pretreated with dexamethasone (DEX) and immunostained for pEGFR, pERK, and pAKT. PBS-treated mice showed minimal pEGFR, pERK1/2, and pAKT expression. HDM challenge resulted in a significant increase in pEGFR, pERK, and pAKT expression, and this was inhibited following treatment with OBE (60 mg/kg; i.p.) and was comparable to the dexamethasone-treated animals, scale bar = 50 μm. Graphs show quantitative assessment of fluorescence intensity of pEGFR, pERK1/2, and pAKT (arbitrary units). Data are expressed as mean ± SEM (n = 3–5). *P < 0.05 *vs* PBS group, $^{\#}$P < 0.05 *vs* HDM group.

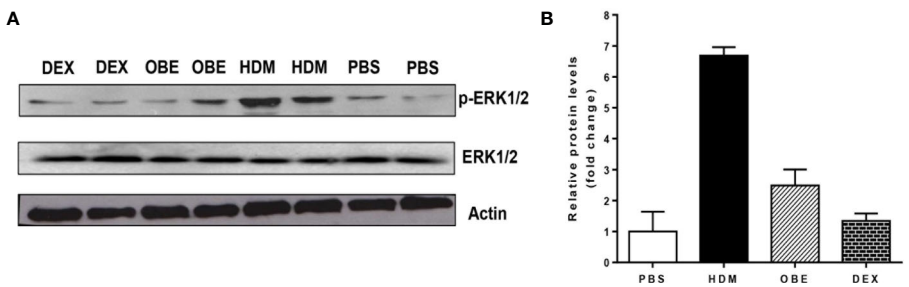

FIGURE 6 | **(A)** Western blot analysis of pERK1/2 and total ERK1/2 protein levels from lungs of PBS-challenged mice pretreated with vehicle (PBS), HDM-challenged mice pretreated with vehicle (HDM), HDM-challenged mice pretreated with OBE (60 mg/kg; i.p.) (OBE) and HDM-challenged mice pretreated with dexamethasone (DEX). The blots are of two pooled lung sample (n = 3, for each). **(B)** Graph b shows relative densitometric quantification levels of pERK1/2 (relative to total ERK1/2, both normalized to β-actin).

with OBE (100 and 1,000 ng/ml) dose-dependently inhibited the HDM/BAL fluid-induced eosinophil chemotaxis (6.4 ± 1.0 and 3.7 ± 0.5 *vs* 16.5 ± 2.4 × 10^4/ml, respectively, P < 0.05; **Figure 7B**, n = 5).

Effect of OBE on HDM-Induced Airway Hyperresponsiveness

In this experiment, we evaluated the effect of OBE treatment on the HDM-induced AHR (n = 6–13). Our data show that there was a significant increase in airway responsiveness 24 h after the last intranasal HDM challenge as demonstrated by a significant increase in lung resistance (R_L) to methacholine in the HDM-challenged mice as compared to the PBS-treated control mice at a dose of 25 mg/ml (5.2 ± 0.2 *vs* 3.9 ± 0.2 cm H_2O per ml/s) and 50 mg/ml (7.9 ± 0.5 *vs* 4.6 ± 0.3 cm H_2O per ml/s) (**Figure 8**; P < 0.05). However, treatment with OBE did not significantly reduce the average R_L in comparison with the HDM-challenged/vehicle-

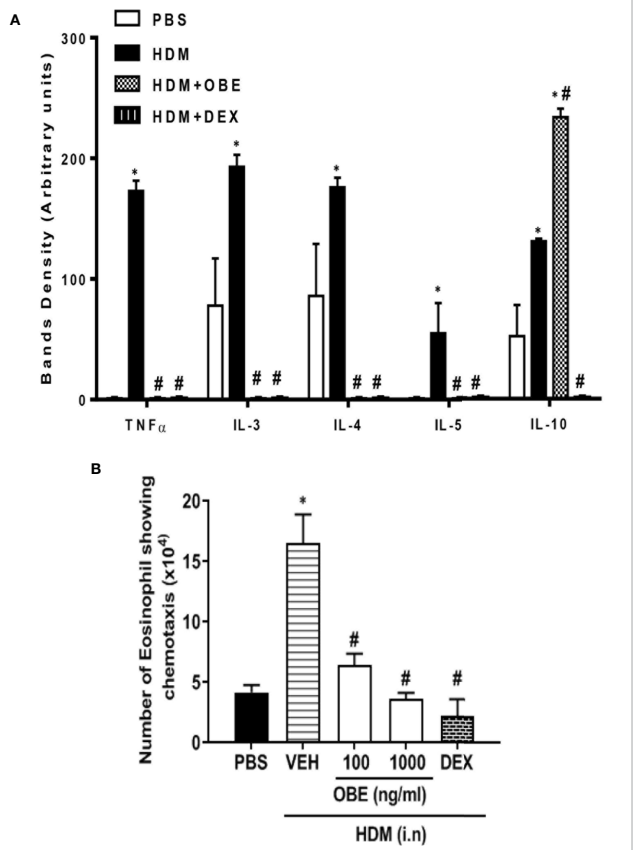

FIGURE 7 | **(A)** Effect of OBE treatment (60 mg/kg; i.p.) on the airway expression of various pro-inflammatory cytokines. HDM challenge significantly enhanced the expression of the following interleukins (IL): IL-3, IL-4, IL-5, IL-10, and tumor necrosis factor (TNF-α). Treatment with OBE significantly reduced the expression of these cytokines except IL-10 which was significantly increased above the HDM levels. Data are expressed as mean ± SEM (n = 4). *P < 0.05 *vs* PBS group, #P < 0.05 *vs* HDM group. **(B)** Effect of OBE (100 and 1,000 ng/ml) on HDM/BALF-induced eosinophil chemotaxis. BALF from HDM-challenged mice induced a significant increase in eosinophil chemotaxis compared to BALF from PBS-challenged mice. Pretreatment with OBE (100 and 1,000 ng/ml) dose-dependently inhibited eosinophil chemotaxis. Data are expressed as mean ± SEM (*n* = 5). *P < 0.05 *vs* PBS group, #P < 0.05 *vs* HDM group.

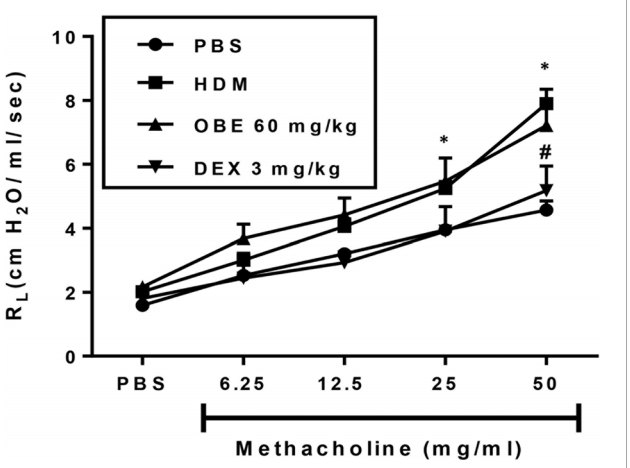

FIGURE 8 | Effect of OBE treatment on HDM-induced AHR to inhaled methacholine. HDM challenged mice demonstrated significant AHR compared to the control group at doses 25 and 50 mg/kg of methacholine. Treatment with dexamethasone (3 mg/kg; i.p.) significantly reduced the HDM-induced AHR. However, treatment with OBE (60 mg/kg; i.p.) did not significantly reduce the average R_L in comparison with the HDM-challenged/vehicle-treated group at any of the doses of methacholine tested (P > 0.05). Data are expressed as mean ± SEM (*n* = 6–13). *P < 0.05 *vs* PBS group, #P < 0.05 for HDM group *vs* DEX group.

treated group at any of the tested doses of methacholine (**Figure 8**; P > 0.05). Treatment with dexamethasone (3 mg/kg) nonetheless resulted in a significant reduction (7.9 ± 0.5 *vs* 5.2 ± 0.8 cm H_2O per ml/s) (P < 0.05; **Figure 8**) of the HDM-induced AHR at the 50 mg/ml of methacholine.

Synergism Between OBE and Dexamethasone on Airway Inflammatory Cell Influx

In this experiment, we evaluated the effect of combining OBE with dexamethasone on the HDM-induced total and differential cell influx. Treatment with either OBE 30 mg/kg or 0.5 mg/kg of dexamethasone had minimal to modest effects on the HDM-induced increase in the total cell count (5.2 ± 0.6 and 4.3 ± 0.2 *vs* 6.4 ± 0.5 × 10^5, respectively, **Figure 9A**, n = 7–11). Furthermore, while treatment with either OBE at 30 mg/kg or dexamethasone at 0.5 mg/kg alone reduced the eosinophil influx, this did not reach statistical significance (OBE 30 and 0.5 mg/kg dexamethasone alone *vs* HDM, 1.9 ± 0.3 and 1.3 ± 0.1 *vs* 3.7 ± 0.3 × 10^5, respectively, P > 0.05; **Figure 9B**). However, when OBE, at 30 mg/kg, was combined with dexamethasone [0.5 mg/kg], the inhibitory effect of this combination was significantly greater compared to either treatment when given alone (2.7 ± 0.2 *vs* 5.2 ± 0.6, 4.3 ± 0.2, 6.4 ± 0.5 × 10^5, respectively, P < 0.05, **Figure 9A**) and was indeed comparable to the high dose dexamethasone (3 mg/kg). Similarly, the combined treatment of both OBE (30 mg/kg) and dexamethasone (0.5 mg/kg), resulted in a significant reduction in the HDM-induced airways eosinophilia (0.4 ± 0.1 *vs* 1.9 ± 0.3, 1.3 ± 0.1, 3.7 ± 0.3 × 10^5, respectively, P < 0.05; **Figure 9B**) compared to either treament when given alone and was comparable to the high dose dexamethasone treatment (3 mg/kg).

Synergism Between OBE and Dexamethasone on HDM-Induced Histopathological Changes

In this experiment, our data show that treatment with either OBE (30 mg/kg) or dexamethasone (0.5 mg/kg) alone resulted in modest but significant reduction in the HDM-induced perivascular and peribronchial inflammation (cellular infiltration score; 3.5 ± 0.2 and 3.1 ± 0.3 *vs* 4.5 ± 0.2, respectively, P < 0.05; **Figures 10A, B**, n = 5). However, when OBE (30 mg/kg) was combined with dexamethasone (0.5 mg/kg), the inhibitory effect on the HDM-induced inflammation was now more marked and significantly greater than each treatment given alone (cellular infiltration score, 2.3 ± 0.1 *vs* 3.5 ± 0.2, 3.1 ±

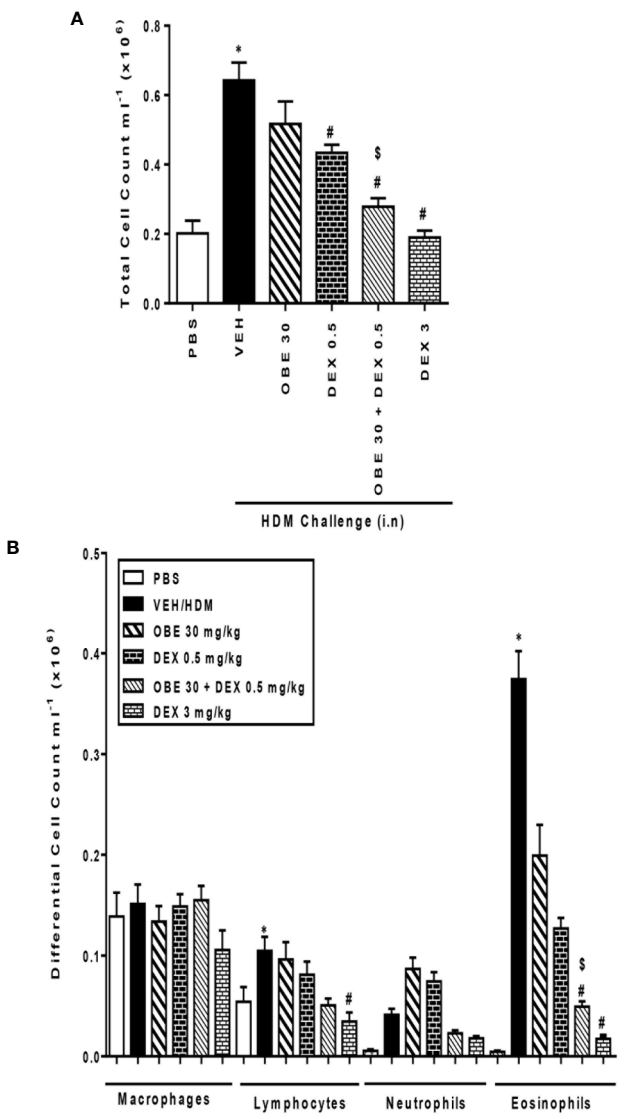

FIGURE 9 | Effect of OBE (30 mg/kg; i.p.) both alone and in combination with low dexamethasone (0.5 mg/kg) on HDM-induced increase in **(A)** total cell and **(B)** differential cell count. Treatment with OBE, in combination with low dose dexamethasone, resulted in a significant inhibition of both total and eosinophil numbers compared to either treatment alone. Data are expressed as mean ± SEM (n = 7–11). *P < 0.05 *vs* PBS group, $^{\#}$P < 0.05 *vs* HDM group and $^{\$}$P < 0.05 *versus* either OBE (30 mg/kg; i.p.) alone or dexamethasone (0.5 mg/kg/i.p.) alone.

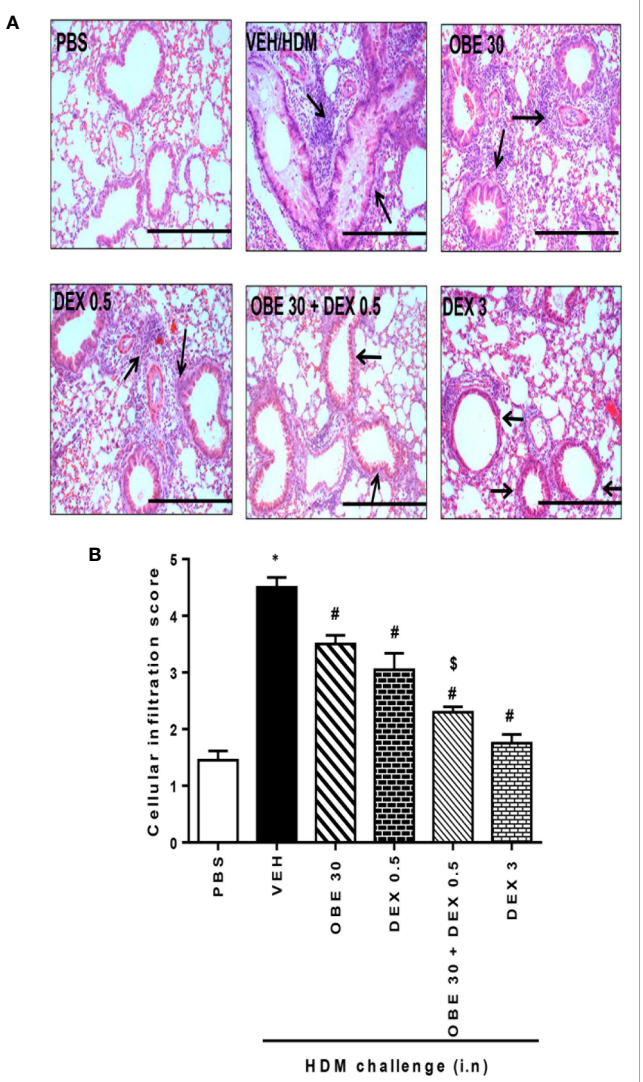

FIGURE 10 | Effect of OBE (30 mg/kg; i.p.) alone and in combination with low dexamethasone (0.5 mg/kg) on HDM-induced peribronchial and perivascular inflammatory cell infiltrations. **(A)** Representative low-magnification light photomicrographs displaying H&E staining of whole lung samples from control PBS-challenged mice (PBS), HDM-challenged mice (HDM), HDM-challenged mice pretreated with OBE (30 mg/kg; i.p.) (OBE 30), HDM-challenged mice pretreated with low dexamethasone treated (0.5 mg/kg; i.p.) (DEX 0.5), HDM-challenged mice pretreated with a combination of OBE (30 mg/kg; i.p.) and low dexamethasone treated (0.5 mg/kg; i.p.) (DEX 30 + DEX 0.5), HDM-challenged mice pretreated with high dose dexamethasone (3 mg/kg; i.p.) (DEX 3), scale bar = 200 μm. Graphs shows **(B)** cellular infiltration score for H&E. OBE treatment in combination with low dose dexamethasone resulted in a significant decrease in both peribronchial and perivascular inflammatory compared to either treatment when give alone. Data are expressed as mean ± SEM (n = 5). *P < 0.05 *vs* PBS, $^{\#}$P < 0.05 *vs* HDM and $^{\$}$P < 0.05 *versus* either OBE (30 mg/kg; i.p.) alone group or dexamethasone (0.5 mg/kg/i.p.) alone group.

0.3, 4.5 ± 0.2, respectively, P < 0.05; **Figures 10A, B**) and was similar to the high dose dexamethasone (3 mg/kg) treatment. Similarly, treatment with either OBE (30 mg/kg) or dexamethasone (0.5 mg/kg) alone resulted in a modest reduction in the HDM-induced goblet cell hyper/metaplasia and increase in bronchial mucus production (mucous intensity score; 3.5 ± 0.2 and 3.0 ± 0.2 *vs* 4.2 ± 0.2, respectively, P < 0.05; **Figures 11A, B**, n = 5). However, the combination treatment of OBE (30 mg/kg) with dexamethasone (0.5 mg) significantly inhibited the HDM-induced goblet cell hyper/metaplasia and increase in bronchial mucus production airway when compared to either OBE (30 mg/kg) or dexamethasone (0.5 mg/kg) given alone (mucous intensity score; 2.2 ± 0.4 *vs* 3.5 ± 0.2, 3.0 ± 0.2, 4.2 ± 0.2, respectively, P < 0.05; **Figures 11A, B**) and was almost as effective as dexamethasone at 3 mg/kg.

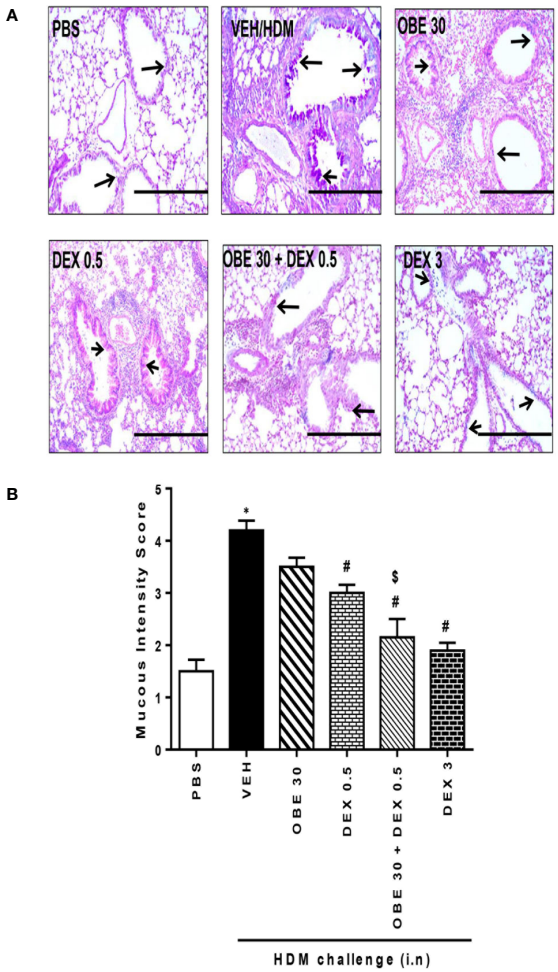

FIGURE 11 | Effect of OBE (30 mg/kg; i.p.) both alone and in combination with low dexamethasone (0.5 mg/kg) on HDM-induced bronchial mucous production and goblet cell hyper/metaplasia. **(A)** Representative low-magnification light photomicrographs displaying PAS staining of whole lung samples from control PBS-challenged mice (PBS), HDM-challenged mice (HDM), HDM-challenged mice pretreated with OBE (30 mg/kg; i.p.) (OBE 30), HDM-challenged mice pretreated with low dose dexamethasone (0.5 mg/kg; i.p.) (DEX 0.5), HDM-challenged mice pretreated with a combination of OBE (30 mg/kg; i.p.) and low dose dexamethasone (0.5 mg/kg; i.p.) (OBE 30 + DEX 0.5), HDM-challenged mice pretreated with high dose dexamethasone (3 mg/kg; i.p.) (DEX 3), scale bar = 200μm. Graphs show **(B)** mucous intensity score. OBE treatment in combination with low dose dexamethasone resulted in a significant decrease in bronchial mucus production and goblet cell hyper/metaplasia compared to either treatment when give alone. Data are expressed as mean ± SEM (n = 5). *P < 0.05 *vs* PBS and $^{\#}$P < 0.05 *vs* HDM and $^{\$}$P < 0.05 *versus* either OBE (30 mg/kg; i.p.) alone group or dexamethasone (0.5 mg/kg/i.p.) alone group.

Synergism Between OBE and Dexamethasone on HDM-Induced pERK1/2 Levels

In this experiment, our data show that treatment with either OBE (30 mg/kg) or the low dose dexamethasone (0.5 mg/kg) did not result in marked inhibition of the HDM-induced phosphorylation of ERK1/2 (267.0 ± 13.8 and 264.8 ± 4.9 *vs* 319.0 ± 10.4%, respectively, P < 0.05; **Figure 12**, n = 4–5). However, when OBE (30 mg/kg) was combined with the low dexamethasone (0.5 mg/kg), there was now a marked and significant reduction in pERK1/2 levels compared to either OBE (30 mg/kg) or the low dose dexamethasone (0.5 mg/kg) alone (80.0 ± 16.0 *vs* 267.0 ± 13.8 and 264.8 ± 4.9, respectively, P < 0.05; **Figure 12**). Of interest, the degree of inhibitory effect on pERK1/2, in the combination treatment, was twofold greater than that were obtained with the high dexamethasone dose (3 mg/kg) (P < 0.05; **Figure 12**).

DISCUSSION

The major finding of this study is that OBE produces anti-inflammatory actions in an established asthma model, partly, *via* inhibition of the EGFR/ERK1/2/AKT pathway. Furthermore, our data show that combined treatment with OBE and a classical steroid (dexamethasone) at sub-maximal doses resulted in an enhanced anti-inflammatory effect at the cellular, histopathological, and molecular levels.

The use of natural products as therapeutic agents has been on the rise, not only due to their demonstrated efficacy (both in humans and in preclinical models of disease) but possibly due to their perceived, and in many instances, real lack of adverse effects, even when consumed in large quantities (Bohlin et al., 2010; Atanasov et al., 2015). Based on this, many studies have been conducted over the past decades in an attempt to understand the scientific basis for the use of many natural products, elucidate their actions, and identify their mechanisms of action in animal models of disease (Fang et al., 2017). To this point, several studies have reported that OBE, or its constituents, have many pharmacological actions in many conditions and diseases such as wounds, scars, dysentery, inflammation, hypertension, and also asthma.

Our data show that OBE dose-dependently decreased the total and differential cell influx into the airways, at both 60 and 100 mg/kg dose, confirming data from recent studies reporting its inhibitory effect on BAL fluid cellularity (Ghorani et al., 2018). In line with this, we found that 60 mg/kg dose of OBE resulted in significant reduction of the HDM-induced perivascular and peribronchial inflammatory cell infiltration and goblet cell hyper/metaplasia. These anti-inflammatory actions were comparable to the action of dexamethasone (3 mg/kg) which indicates that the anti-inflammatory action of OBE is, at least, as effective as that of steroids. Our findings are in agreement with studies showing anti-inflammatory action of OBE in asthma-like models and more recently in a mouse model of colitis (Ghorani et al., 2018; Khajah et al., 2019). It is of interest to note that many of the documented activities for onion extract have been attributed to its polar constituents, particularly the known flavonoid quercetin, where polar solvents were mainly used to prepare the tested extracts (Oliveira et al., 2015). However, in this study, the anti-inflammatory action noted are most likely due to non-polar fat-soluble constituents, such as sulfur-containing compounds, mainly dipropyl disulfide and dipropyl trisulfide, which were found in abundance in the essential oil of onion since dichloromethane was used for the extraction method.

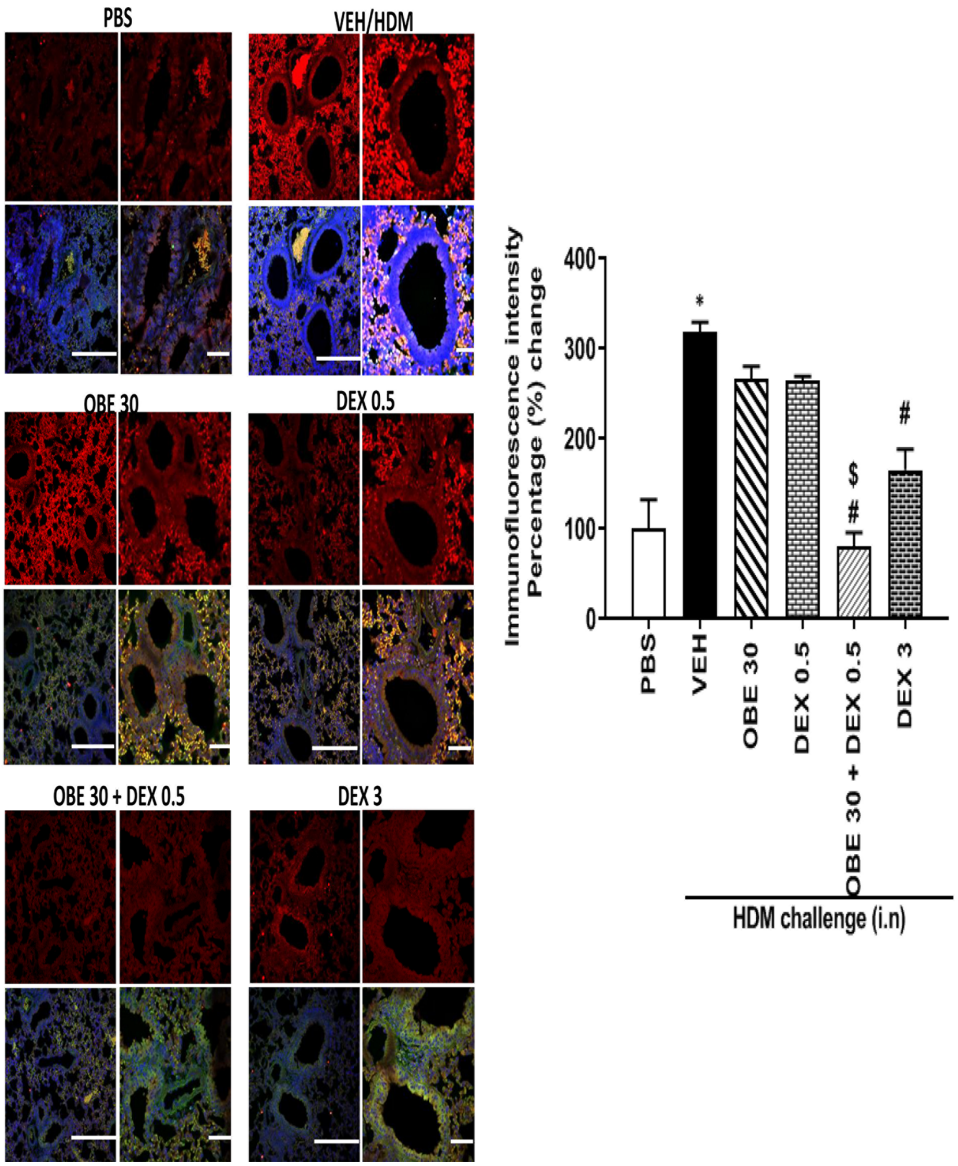

FIGURE 12 | Immunofluorescence (Alexa Fluor) detection of phosphorylated ERK1/2 are shown in the upper panels overlaid with DAPI stain on the lower panel to show lung tissue architecture. Lung sections were taken from different treatment groups, control PBS-challenged mice (PBS), HDM-challenged mice (HDM), HDM-challenged mice pretreated with OBE (30 mg/kg; i.p.) (OBE 30), HDM-challenged mice pretreated with low dose dexamethasone (0.5 mg/kg; i.p.) (DEX 0.5), HDM-challenged mice pretreated with a combination of OBE (30 mg/kg; i.p.) and low dose dexamethasone (0.5 mg/kg; i.p.) (OBE 30 + DEX 0.5), HDM-challenged mice pretreated with high dose dexamethasone (3 mg/kg; i.p.) (DEX 3), scale bar = 50 μm. Graph shows quantitative assessment of fluorescence intensity of ERK (arbitrary units). Data are expressed as mean ± SEM (n = 4–5). *P < 0.05 *vs* PBS and $^{\#}$P < 0.05 *vs* HDM and $^{\$}$P < 0.05 *versus* either OBE (30 mg/kg; i.p.) alone group or dexamethasone (0.5 mg/kg/i.p.) alone group.

The EGF/EGFR is a critical signaling pathway in the pathogenesis of asthma, and both EGF and EGFR levels have been shown to be consistently increased in both human asthma and in animal models of asthma (Amishima et al., 1998; Puddicombe et al., 2000; Song L. et al., 2016). However, other ligands such as heparin-binding EGF-like growth factor (HB-EGF), amphiregulin, and betacellulin can also bind to and activate EGFR (Acciani et al., 2016; Ha and Rogers, 2016). In addition, ERK1/2 and AKT are not only key signaling molecules in asthma but have also been recently shown to be downstream of EGFR activation (El-Hashim et al., 2017). Our data show that treatment with OBE not only inhibited the development of asthma but also reduced pEGFR levels. Of interest and relevance is data from a recent study from our group, and that of others, using a similar model of asthma, has shown that treatment with selective EGFR inhibitors inhibited the EGFR-

dependent signaling pathway and also reduced eosinophil recruitment, airway inflammation, AHR, and goblet cell hyper/metaplasia (Song L. et al., 2016; El-Hashim, 2017). Therefore, our findings would imply that the inhibitory effects of OBE on the asthmatic phenotype may be, at least partly, *via* inhibition of EGFR-dependent signaling perturbation. However, it is also likely that in addition to the EGFR pathway, OBE may inhibit other pro-inflammatory signaling pathways.

Our data also show that HDM-induced increase in pERK1/2 and pAKT were both inhibited following OBE treatment. While it is plausible that the effect of OBE on these signaling molecules represents independent and separate effects, since both ERK1/2 and AKT are ubiquitous signaling molecules, we have previously reported that AG1478, a selective EGFR receptor inhibitor, inhibited not only EGFR activation but also decreased pERK1/2 and pAKT levels, suggesting that both molecules are downstream of EGFR activation (El-Hashim et al., 2017). Therefore, it is very likely that the inhibitory effect of OBE on these two molecules is primarily due to upstream inhibition of EGFR-dependent signaling. This notion is further confirmed by our recent study showing that the effects of the anti-inflammatory endogenous molecule, Ang-(1-7), in asthma, are mediated *via* inhibition of the EGFR/ERK1/2 dependent signaling (El-Hashim et al., 2019). That OBE can inhibit the EGFR-triggered signaling perturbations suggests that it can inhibit a central signaling pathway in asthma.

It is well recognized that asthma is an immune response driven by Th2 and Th17 cells with cytokines such as IL-4, IL-5, IL-9, IL-10, IL-13, and IL-7 playing important roles (Saeki et al., 2019). Moreover, Th1 cytokines such as TNF-α and IFN-γ are also involved in asthma, with pro - and anti-asthma effects, respectively. Our findings show that OBE treatment resulted in a significant reduction of IL-4 and IL-5 consistent with other studies and effects of drugs that mediate an anti-allergic/anti-asthma action (Seo et al., 2019). In addition, OBE treatment decreased the pro-asthma TNF-α but increased the Th2 anti-inflammatory cytokine, IL-10. It is therefore plausible that the OBE-induced increase in IL-10 levels may, in part, explain the anti-inflammatory action of OBE in general and/or the specific decrease in the levels of IL-4 and IL-5, as these cytokines are known to have a reciprocal relationship (Oliveira et al., 2015).

The recent introduction of monoclonal antibodies targeting the eosinophil chemoattractant underscores the importance of eosinophils in asthma (Agache et al., 2020). Our data show that treatment with OBE significantly reduced eosinophil numbers not only in the tissue but also their *ex vivo* chemotaxis towards BAL fluid from HDM challenged mice. Studies have shown that onion constituents, such as thiosulfinates and cepaenes, dose-dependently inhibit both cyclooxygenase and 5-lipoxygenase enzyme activity (Werz, 2007). Furthermore, products of 5-lipoxygenase, namely the cysteinyl leukotrienes LTC_4, LTD_4, and LTE_4, are known to be potent inducers of eosinophil chemotaxis (Werz, 2007). Therefore, inhibition of 5-lipoxygenase may represent one possible mechanism by which OBE inhibits eosinophil chemotaxis.

Our data also show that HDM challenge resulted in the induction of AHR, a characteristic feature of both clinical and preclinical asthma that is not easily amenable to asthma therapy (Busse, 2010; Ezeamuzie et al., 2014). Our findings show that treatment with OBE had no effect on this parameter. Although many studies have reported a causal link between airway inflammation and AHR, others have not been able to confirm this relationship, at least not for all types of AHR (Gozzard et al., 1996; Spina et al., 1998; El-Hashim et al., 1999; Spina and Page, 2009). Indeed, there may be a separation between the two phenomena, as not all agents that inhibit airway inflammation reduce AHR and *vice versa* (Riccio et al., 1997; El-Hashim et al., 2004). Recent studies have also provided good evidence that airway sensory hyper-excitability may also underlie AHR, and hyperactivity of airway nerves is less susceptible to anti-inflammatory agents (Spina and Page, 2009; Delescluse et al., 2012; Lommatzsch, 2012).

Although ICS have been the mainstay treatment for asthma, being effective anti-inflammatory agents, their major limitation is their high side effect profile, particularly with moderate-to-high doses (Hossny et al., 2016). In addition, the high cost of ICS is a real problem in poorer regions of the world (Watson and Lewis, 1997). To test whether OBE and steroids have a synergistic effect, we combined a low dose of OBE, 30 mg/kg and a low dose of dexamethasone, 0.5 mg/kg both of which produced minimal to mild anti-inflammatory effect when given alone. An important and novel finding in this study is that when OBE is combined with a low dose dexamethasone, a more powerful and effective anti-inflammatory effect was produced. Our data also show that the combination treatment resulted in a marked and significant enhancement of the anti-inflammatory effects on the total cell, eosinophil influx, histopathological changes (both perivascular and peribronchial inflammation and goblet cell hyper/metaplasia) when compared to either treatment alone. This combination was at least as effective as the high dose (3 mg/kg) steroid. To determine whether this was being mediated *via* enhanced suppression of the EGFR/ERK1/2/AKT signaling pathway, we assessed p-ERK1/2 expression level as a marker of activation of this signaling pathway. Our results clearly show that whilst neither 0.5 mg/kg dexamethasone nor 30 mg/kg alone had any effect on p-ERK1/2 levels, when both agents are combined, a significant and dramatic decrease in p-ERK1/2 levels was detected. This clearly indicates that the enhanced suppressive effects are being mediated *via* synergistic actions at the molecular level.

In conclusion, our data clearly show that OBE inhibits the asthma phenotype in a clinically relevant murine model of asthma, at least in part, *via* inhibition of Th2 cytokine profile, *via* inhibition of the EGFR/ERK/1/2/AKT signaling pathway. In addition, our data also show that combining OBE with steroids resulted in an enhanced anti-inflammatory effect *via* a synergistic action at the molecular signaling level. Therefore, this study not only identifies an important molecular signaling pathway that is targeted by OBE to inhibit the asthma phenotype, but also shows that OBE synergizes with steroids resulting in a greater anti-inflammatory action. This finding may have important implication for the treatment of asthma as it provides a potential to reduce steroid toxicity while maintaining efficacy.

DATA AVAILABILITY STATEMENT

The raw data supporting the conclusions of this article will be made available by the authors, without undue reservation.

ETHICS STATEMENT

The animal study was reviewed and approved by Animal Welfare and Use of Laboratory Animals Committee in the Health Sciences Center.

AUTHOR CONTRIBUTIONS

Conceived and designed the experiments: AE-H, MK, and KO. Performed the experiments: SB, AA and HS. Analyzed the data: SB, AA, HS, AE-H, KO, and MK. Wrote the paper: AE-H. Edited the paper: KO and MK. All authors contributed to the article and approved the submitted version.

FUNDING

This work was supported by Kuwait Foundation for the Advancement of Sciences, grant number: P11613PT01. Parts of this work were supported by grant SRUL02/13 to the Research Unit for Genomics, Proteomics and Cellomics Studies (OMICS), Kuwait University. GC-MS analyses were done at Research Sector Project Unit (RSPU), Faculty of Science, Kuwait University, supported by Grant numbers GS01/03.

ACKNOWLEDGMENTS

The authors are thankful for the support of Mr. Sunny Ojoko and Mr. Hecktor Velasco from the Animal Resources Center of Health Sciences Center. The authors would also like to thank Mr. Yousef Al-Farahan, Ms Sahar Farag, and Prof Waleed Renno for the early work done with the ovalbumin asthma model. We would also like to thank Prof Samuel Kombian for discussion and proofreading the manuscript.

REFERENCES

Abdel-Lateef, E., Rabia, I., Abdel-Gawad, M., and El-Sayed, M. (2018). In vitro antischistosomal activity of Allium cepa L. (red onion) extracts and identification of the essential oil composition by GC-MS. *J. Microbiol. Biotechnol. Food Sci.* 7, 421–425. doi: 10.15414/jmbfs.2018.7.4.421-425

Acciani, T. H., Suzuki, T., Trapnell, B. C., and Le Cras, T. D. (2016). Epidermal growth factor receptor signalling regulates granulocyte-macrophage colony-stimulating factor production by airway epithelial cells and established allergic airway disease. *Clin. Exp. Allergy* 46 (2), 317–328. doi: 10.1111/cea.12612

Agache, I., Beltran, J., Akdis, C., Akdis, M., Canelo-Aybar, C., Canonica, W., et al. (2020). Efficacy and safety of treatment with biologicals (benralizumab, dupilumab, mepolizumab, omalizumab and reslizumab) for severe eosinophilic asthma. *Allergy* 75 (5), 1023–1042. doi: 10.1111/all.14221

Amishima, M., Munakata, M., Nasuhara, Y., Sato, A., Takahashi, T., Homma, Y., et al. (1998). Expression of epidermal growth factor and epidermal growth factor receptor immunoreactivity in the asthmatic human airway. *Am. J. Respir. Crit. Care Med.* 157 (6 Pt 1), 1907–1912. doi: 10.1164/ajrccm.157.6.9609040

Atanasov, A. G., Waltenberger, B., Pferschy-Wenzig, E. M., Linder, T., Wawrosch, C., Uhrin, P., et al. (2015). Discovery and resupply of pharmacologically active plant-derived natural products: a review. *Biotechnol. Adv.* 33 (8), 1582–1614. doi: 10.1016/j.biotechadv.2015.08.001

Athari, S. S. (2019). Targeting cell signaling in allergic asthma. *Signal Transduct. Target Ther.* 4, 45. doi: 10.1038/s41392-019-0079-0

Aun, M. V., Bonamichi-Santos, R., Arantes-Costa, F. M., Kalil, J., and Giavina-Bianchi, P. (2017). Animal models of asthma: utility and limitations. *J. Asthma Allergy* 10, 293–301. doi: 10.2147/JAA.S121092

Beasley, R., Harper, J., Bird, G., Maijers, I., Weatherall, M., and Pavord, I. D. (2019). Inhaled corticosteroid therapy in adult asthma. Time for a new therapeutic dose terminology. *Am. J. Respirat. Crit. Care Med.* 199 (12), 1471–1477. doi: 10.1164/rccm.201810-1868CI

Bohlin, L., Göransson, U., Alsmark, C., Wedén, C., and Backlund, A. (2010). Natural products in modern life science. *Phytochem. Rev.* 9 (2), 279–301. doi: 10.1007/s11101-009-9160-6

Brown, A., Elmhirst, E., and Gardner, J. (2017). *EP Vantage 2018 Preview*. (Evaluate Ltd.), 1–26.

Burgel, P. R., Montani, D., Danel, C., Dusser, D. J., and Nadel, J. A. (2007). A morphometric study of mucins and small airway plugging in cystic fibrosis. *Thorax* 62 (2), 153–161. doi: 10.1136/thx.2006.062190

Busse, W. W. (2010). The relationship of airway hyperresponsiveness and airway inflammation: airway hyperresponsiveness in asthma: its measurement and clinical significance. *Chest* 138 (2 Suppl), 4S–10S. doi: 10.1378/chest.10-0100

Carr, T. F., and Kraft, M. (2017). Management of severe asthma before referral to the severe asthma specialist. *J. Allergy Clin. Immunol. Pract.* 5 (4), 877–886. doi: 10.1016/j.jaip.2017.04.027

Clark, C. E., Arnold, E., Lasserson, T. J., and Wu, T. X. (2010). Herbal interventions for chronic asthma in adults and children: a systematic review and meta-analysis. *Primary Care Respirat. J.* 19 (4), 307–314. doi: 10.4104/pcrj.2010.00041

Correa, M. F., Barbosa, A. J. R., Teixeira, L. B., Duarte, D. A., Simoes, S. C., Parreiras, E. S. L. T., et al. (2017). Pharmacological Characterization of 5-Substituted 1-[(2,3-dihydro-1-benzofuran-2-yl)methyl]piperazines: novel antagonists for the histamine H3 and H4 receptors with anti-inflammatory potential. *Front. Pharmacol.* 8, 825. doi: 10.3389/fphar.2017.00825

de Boer, W. I., Hau, C. M., van Schadewijk, A., Stolk, J., van Krieken, J. H. J., and Hiemstra, P. S. (2006). Expression of epidermal growth factors and their receptors in the bronchial epithelium of subjects with chronic obstructive pulmonary disease. *Am. J. Clin. Pathol.* 125 (2), 184–192. doi: 10.1309/W1AXKGT7UA37X257

Delescluse, I., Mace, H., and Adcock, J. (2012). Inhibition of airway hyper-responsiveness by TRPV1 antagonists (SB-705498 and PF-04065463) in the unanaesthetized, ovalbumin-sensitized guinea pig. *Br. J. Pharmacol.* 166 (6), 1822–1832. doi: 10.1111/j.1476-5381.2012.01891.x

Dorsch, W., Schneider, E., Bayer, T., Breu, W., and Wagner, H. (1990). Anti-inflammatory effects of onions: inhibition of chemotaxis of human polymorphonuclear leukocytes by thiosulfinates and cepaenes. *Int. Arch. Allergy Appl. Immunol.* 92 (1), 39–42. doi: 10.1159/000235221

El-Hashim, A. Z., Banner, K. H., Paul, W., and Page, C. P. (1999). Effects of dexamethasone on airway hyper-responsiveness to the adenosine A1 receptor agonist cyclo-pentyl adenosine in an allergic rabbit model. *Br. J. Pharmacol.* 126 (6), 1513–1521. doi: 10.1038/sj.bjp.0702455

El-Hashim, A. Z., Buchheit, K. H., Fozard, J., and Page, C. (2004). Effect of the K+(ATP) channel opener, KCO912, on baseline and allergen induced airway hyperresponsiveness in allergic rabbits. *Eur. J. Pharmacol.* 484 (2–3), 351–356. doi: 10.1016/j.ejphar.2003.11.018

El-Hashim, A. Z., Khajah, M. A., Renno, W. M., Babyson, R. S., Uddin, M., Benter, I. F., et al. (2017). Src-dependent EGFR transactivation regulates lung inflammation via downstream signaling involving ERK1/2, PI3Kdelta/Akt and NFkappaB induction in a murine asthma model. *Sci. Rep.* 7 (1), 9919. doi: 10.1038/s41598-017-09349-0

El-Hashim, A. Z., Khajah, M. A., Babyson, R. S., Renno, W. M., Ezeamuzie, C. I., Benter, I. F., et al. (2019). Ang-(1-7)/ MAS1 receptor axis inhibits allergic airway inflammation via blockade of Src-mediated EGFR transactivation in a

murine model of asthma. *PLoS One* 14 (11), e0224163. doi: 10.1371/journal.pone.0224163

Ezeamuzie, C.II, El-Hashim, A. Z., Renno, W. M., and Edafiogho, I. O. (2014). Antiallergic and antiasthmatic effects of a novel enhydrazinone ester (CEE-1): inhibition of activation of both mast cells and eosinophils. *J. Pharmacol. Exp. Ther.* 350 (2), 444–454. doi: 10.1124/jpet.114.213751

Fang, J., Gao, L., Ma, H., Wu, Q., Wu, T., Wu, J., et al. (2017). Quantitative and systems pharmacology 3. network-based identification of new targets for natural products enables potential uses in aging-associated disorders. *Front. Pharmacol.* 8, 747. doi: 10.3389/fphar.2017.00747

Fredotovic, Z., Soldo, B., Sprung, M., Marijanovic, Z., Jerkovic, I., and Puizina, J. (2020). Comparison of organosulfur and amino acid composition between triploid onion Allium Cornutum Clementi ex Visiani 1842, and common onion Allium cepa L., and evidences for antiproliferative activity of their extracts. *Plants (Basel)* 9 (1), 98. doi: 10.3390/plants9010098

Ghorani, V., Marefati, N., Shakeri, F., Rezaee, R., Boskabady, M., and Boskabady, M. H. (2018). The effects of Allium cepa extract on tracheal responsiveness, lung inflammatory cells and phospholipase A2 level in asthmatic rats. *Iranian J. Allergy Asthma Immunol.* 17 (3), 221–231.

GINA (2019). *Global initiative for asthma (GINA): Global strategy for asthma management and prevention*. (Global Initiative for Asthma). Available at: http://www.ginasthma.or (Retrieved January 26, 2020).

Gitin, L., Dinica, R., Neagu, C., and Dumitrascu, L. (2014). Sulfur compounds identification and quantification from Allium spp. fresh leaves. *J. Food Drug Anal.* 22 (4), 425–430. doi: 10.1016/j.jfda.2014.04.002

Gomez-Cambronero, J., Horn, J., Paul, C. C., and Baumann, M. A. (2003). Granulocyte-macrophage colony-stimulating factor is a chemoattractant cytokine for human neutrophils: involvement of the ribosomal p70 S6 kinase signaling pathway. *J. Immunol.* 171 (12), 6846–6855. doi: 10.4049/jimmunol.171.12.6846

Gorska, M. M. (2018). Mouse models of asthma. *Methods Mol. Biol.* 1809, 351–362. doi: 10.1007/978-1-4939-8570-8_23

Gozzard, N., el-Hashim, A. , Herd, C. M., Blake, S. M., Holbrook, M., Hughes, B., et al. (1996). Effect of the glucocorticosteroid budesonide and a novel phosphodiesterase type 4 inhibitor CDP840 on antigen-induced airway responses in neonatally immunised rabbits. *Br. J. Pharmacol.* 118 (5), 1201–1208. doi: 10.1111/j.1476-5381.1996.tb15524.x

Ha, E. V. S., and Rogers, D. F. (2016). Novel therapies to inhibit mucus synthesis and secretion in airway hypersecretory diseases. *Pharmacology* 97 (1–2), 84–100. doi: 10.1159/000442794

Hansel, T. T., De Vries, I. J., Iff, T., Rihs, S., Wandzilak, M., Betz, S., et al. (1991). An improved immunomagnetic procedure for the isolation of highly purified human blood eosinophils. *J. Immunol. Methods* 145 (1–2), 105–110. doi: 10.1016/0022-1759(91)90315-7

Harrison, G. J. (2015). Current controversies in diagnosis, management, and prevention of congenital cytomegalovirus: updates for the pediatric practitioner. *Pediatr. Ann.* 44 (5), E115–E125. doi: 10.3928/00904481-20150512-11

Harrison, R. G., MacRae, M., Karsh, J., Santucci, S., and Yang, W. H. (2015). Anaphylaxis and serum sickness in patients receiving omalizumab: reviewing the data in light of clinical experience. *Ann. Allergy Asthma Immunol.* 115 (1), 77–78. doi: 10.1016/j.anai.2015.04.014

Hossny, E., Rosario, N., Lee, B. W., Singh, M., El-Ghoneimy, D., Soh, J. Y., et al. (2016). The use of inhaled corticosteroids in pediatric asthma: update. *World Allergy Organ J.* 9, 26. doi: 10.1186/s40413-016-0117-0

Jia, J., Zhu, F., Ma, X., Cao, Z. W., Li, Y. X., and Chen, Y. Z. (2009). Mechanisms of drug combinations: interaction and network perspectives. *Nat. Rev. Drug Discov.* 8 (2), 111–128. doi: 10.1038/nrd2683

Khajah, M. A., Fateel, M. M., Ananthalakshmi, K. V., and Luqmani, Y. A. (2016). Anti-inflammatory action of angiotensin 1-7 in experimental colitis. *PLoS One* 11 (3), e0150861. doi: 10.1371/journal.pone.0150861

Khajah, M. A., Orabi, K. Y., Hawai, S., Sary, H. G., and El-Hashim, A. Z. (2019). Onion bulb extract reduces colitis severity in mice via modulation of colonic inflammatory pathways and the apoptotic machinery. *J. Ethnopharmacol.* 241, 112008. doi: 10.1016/j.jep.2019.112008

Lanzotti, V. (2006). The analysis of onion and garlic. *J. Chromatogr. A* 1112 (1-2), 3–22. doi: 10.1016/j.chroma.2005.12.016

Le Cras, T. D., Acciani, T. H., Mushaben, E. M., Kramer, E. L., Pastura, P. A., Hardie, W. D., et al. (2011). Epithelial EGF receptor signaling mediates airway hyperreactivity and remodeling in a mouse model of chronic asthma. *Am. J. Physiol. Lung Cell Mol. Physiol.* 300 (3), L414–L421. doi: 10.1152/ajplung.00346.2010

Lommatzsch, M. (2012). Airway hyperresponsiveness: new insights into the pathogenesis. *Semin. Respir. Crit. Care Med.* 33 (6), 579–587. doi: 10.1055/s-0032-1325617

Marefati, N., Eftekhar, N., Kaveh, M., Boskabadi, J., Beheshti, F., and Boskabady, M. H. (2018). The effect of allium cepa extract on lung oxidant, antioxidant, and immunological biomarkers in ovalbumin-sensitized rats. *Med. Princ. Pract.* 27 (2), 122–128. doi: 10.1159/000487885

Massoud, A. H., Charbonnier, L. M., Lopez, D., Pellegrini, M., Phipatanakul, W., and Chatila, T. A. (2016). An asthma-associated IL4R variant exacerbates airway inflammation by promoting conversion of regulatory T cells to TH17-like cells. *Nat. Med.* 22 (9), 1013–1022. doi: 10.1038/nm.4147

Mondy, N., Naudin, A., Christides, J. P., Mandon, N., and Auger, J. (2001). Comparison of GC-MS and HPLC for the analysis of Allium volatiles. *Chromatographia* 53 (1), S356–S360. doi: 10.1007/BF02490356

Newman, D. J., and Cragg, G. M. (2016). Natural products as sources of new drugs from 1981 to 2014. *J. Nat. Prod.* 79 (3), 629–661. doi: 10.1021/acs.jnatprod.5b01055

Nunes, C., Pereira, A. M., and Morais-Almeida, M. (2017). Asthma costs and social impact. *Asthma Res. Pract.* 3, 1. doi: 10.1186/s40733-016-0029-3

Oliveira, T. T., Campos, K. M., Cerqueira-Lima, A. T., Cana Brasil Carneiro, T., da Silva Velozo, E., Ribeiro Melo, I. C. A., et al. (2015). Potential therapeutic effect of Allium cepa L. and quercetin in a murine model of Blomia tropicalis induced asthma. *Daru* 23 (1), 18. doi: 10.1186/s40199-015-0098-5

O'Byrne, P. M., Barnes, P. J., Rodriguez-Roisin, R., Runnerstrom, E., Sandstrom, T., Svensson, K., et al. (2001). Low dose inhaled budesonide and formoterol in mild persistent asthma: the OPTIMA randomized trial. *Am. J. Respir. Crit. Care Med.* 164 (8 Pt 1), 1392–1397. doi: 10.1164/ajrccm.164.8.2104102

Pinto, C. R., Almeida, N. R., Marques, T. S., Yamamura, L. L., Costa, L. A., and Souza-Machado, A. (2013). Local adverse effects associated with the use of inhaled corticosteroids in patients with moderate or severe asthma. *J. Bras. Pneumol.* 39 (4), 409–417. doi: 10.1590/S1806-37132013000400003

Plosker, G. L., and Keam, S. J. (2008). Omalizumab - a review of its use in the treatment of allergic asthma. *Biodrugs* 22 (3), 189–204. doi: 10.2165/00063030-200822030-00005

Polosa, R., Puddicombe, S. M., Krishna, M. T., Tuck, A. B., Howarth, P. H., Holgate, S. T., et al. (2002). Expression of c-erbB receptors and ligands in the bronchial epithelium of asthmatic subjects. *J. Allergy Clin. Immunol.* 109 (1), 75–81. doi: 10.1067/mai.2002.120274

Prescott, S., and Allen, K. J. (2011). Food allergy: riding the second wave of the allergy epidemic. *Pediatr. Allergy Immunol.* 22 (2), 155–160. doi: 10.1111/j.1399-3038.2011.01145.x

Puddicombe, S. M., Polosa, R., Richter, A., Krishna, M. T., Howarth, P. H., Holgate, S. T., et al. (2000). Involvement of the epidermal growth factor receptor in epithelial repair in asthma. *FASEB J.* 14 (10), 1362–1374. doi: 10.1096/fasebj.14.10.1362

Queto, T., Xavier-Elsas, P., Gardel, M. A., de Luca, B., Barradas, M., Masid, D., et al. (2010). Inducible nitric oxide synthase/CD95L-dependent suppression of pulmonary and bone marrow eosinophilia by diethylcarbamazine. *Am. J. Respir. Crit. Care Med.* 181 (5), 429–437. doi: 10.1164/rccm.200905-0800OC

Riccio, M. M., Matsumoto, T., Adcock, J. J., Douglas, G. J., Spina, D., and Page, C. P. (1997). The effect of 15-HPETE on airway responsiveness and pulmonary cell recruitment in rabbits. *Br. J. Pharmacol.* 122 (2), 249–256. doi: 10.1038/sj.bjp.0701379

Saeki, M., Nishimura, T., Kitamura, N., Hiroi, T., Mori, A., and Kaminuma, O. (2019). Potential mechanisms of T cell-mediated and eosinophil-independent bronchial hyperresponsiveness. *Int. J. Mol. Sci.* 20 (12), 2980. doi: 10.3390/ijms20122980

Seo, M. Y., Kim, K. R., Lee, J. J., Ryu, G., Lee, S. H., Hong, S. D., et al. (2019). Therapeutic effect of topical administration of red onion extract in a murine model of allergic rhinitis. *Sci. Rep.* 9 (1), 2883. doi: 10.1038/s41598-019-39379-9

Sherman, J., Patel, P., Hutson, A., Chesrown, S., and Hendeles, L. (2001). Adherence to oral montelukast and inhaled fluticasone in children with persistent asthma. *Pharmacotherapy* 21 (12), 1464–1467. doi: 10.1592/phco.21.20.1464.34485

Song, H. N., Jung, K. S., Yoo, K. H., Cho, J., Lee, J. Y., Lim, S. H., et al. (2016). Acquired C797S mutation upon treatment with a T790M-specific third-generation EGFR inhibitor (HM61713) in non-small cell lung cancer. *J. Thorac. Oncol.* 11 (4), e45–e47. doi: 10.1016/j.jtho.2015.12.093

Song, L., Tang, H., Liu, D., Song, J., Wu, Y., Qu, S., et al. (2016). The chronic and short-term effects of gefinitib on airway remodeling and inflammation in a mouse model of asthma. *Cell Physiol. Biochem.* 38 (1), 194–206. doi: 10.1159/000438621

Spina, D., and Page, C. (2009). Airway irritability–a burning issue? *Curr. Opin. Pharmacol.* 9 (4), 530–534. doi: 10.1016/j.coph.2009.06.019

Spina, D., Shah, S., and Harrison, S. (1998). Modulation of sensory nerve function in the airways. *Trends Pharmacol. Sci.* 19 (11), 460–466. doi: 10.1016/S0165-6147(98)01261-9

Takeyama, K., Fahy, J. V., and Nadel, J. A. (2001a). Relationship of epidermal growth factor receptors to goblet cell production in human bronchi. *Am. J. Respir. Crit. Care Med.* 163 (2), 511–516. doi: 10.1164/ajrccm.163.2.2001038

Takeyama, K., Jung, B., Shim, J. J., Burgel, P. R., Dao-Pick, T., Ueki, I. F., et al. (2001b). Activation of epidermal growth factor receptors is responsible for mucin synthesis induced by cigarette smoke. *Am. J. Physiol. Lung Cell Mol. Physiol.* 280 (1), L165–L172. doi: 10.1152/ajplung.2001.280.1.L165

Tamaoka, M., Hassan, M., McGovern, T., Ramos-Barbon, D., Jo, T., Yoshizawa, Y., et al. (2008). The epidermal growth factor receptor mediates allergic airway remodelling in the rat. *Eur. Respir. J.* 32 (5), 1213–1223. doi: 10.1183/09031936.00166907

Upadhyay, R. K. (2016). Nutraceutical, pharmaceutical and therapeutic uses of Allium cepa: a review. *Int. J. Green Pharm. (IJGP)* 10 (1), 46–64. doi: 10.22377/ijgp.v10i1.612

Wagner, H., Dorsch, W., Bayer, T., Breu, W., and Willer, F. (1990). Antiasthmatic effects of onions: inhibition of 5-lipoxygenase and cyclooxygenase in vitro by thiosulfinates and "Cepaenes". *Prostagland. Leukot. Essent. Fatty Acids* 39 (1), 59–62. doi: 10.1016/0952-3278(90)90173-I

Watson, J. P., and Lewis, R. A. (1997). Is asthma treatment affordable in developing countries? *Thorax* 52 (7), 605–607. doi: 10.1136/thx.52.7.605

Werz, O. (2007). Inhibition of 5-lipoxygenase product synthesis by natural compounds of plant origin. *Planta Med.* 73 (13), 1331–1357. doi: 10.1055/s-2007-990242

WHO (2019). *Asthma*. from http://www.who.int

Zeng, Y., Li, Y., Yang, J., Pu, X., Du, J., Yang, X., et al. (2017). Therapeutic role of functional components in Alliums for preventive chronic disease in human being. *Evid. Based. Complement. Alternat. Med.* 2017, 9402849. doi: 10.1155/2017/9402849

Conflict of Interest: The authors declare that the research was conducted in the absence of any commercial or financial relationships that could be construed as a potential conflict of interest.

Copyright © 2020 El-Hashim, Khajah, Orabi, Balakrishnan, Sary and Abdelali. This is an open-access article distributed under the terms of the Creative Commons Attribution License (CC BY). The use, distribution or reproduction in other forums is permitted, provided the original author(s) and the copyright owner(s) are credited and that the original publication in this journal is cited, in accordance with accepted academic practice. No use, distribution or reproduction is permitted which does not comply with these terms.

frontiers in Pharmacology

ORIGINAL RESEARCH
published: 02 October 2020
doi: 10.3389/fphar.2020.01261

An Integrative Serum Pharmacology-Based Approach to Study the Anti-Tumor Activity of *B. paniculatum* Aqueous Bulb Extract on the Human Hepatocellular Carcinoma Cell Line BEL-7404

Xuesong Feng[1], *Guangyuan Ma*[1], *Hailong Shi*[1], *Yuewen Wang*[1] *and Xu Chao*[1,2]*

[1] Basic Medical Academy, Shaanxi University of Chinese Medicine, Xianyang, China, [2] The Research Department, The Second Affiliated Hospital of Shaanxi University of Chinese Medicine, Xianyang, China

OPEN ACCESS

Edited by:
Yanqiong Zhang,
China Academy of Chinese Medical Sciences, China

Reviewed by:
Zhenxi Zhang,
Xi'an Jiaotong University, China
Chengcheng Liu,
Xi'an Jiaotong University, China

***Correspondence:**
Xu Chao
Chaoxu2004@126.com

Specialty section:
This article was submitted to Ethnopharmacology, a section of the journal Frontiers in Pharmacology

Received: *19 May 2020*
Accepted: *30 July 2020*
Published: *02 October 2020*

Citation:
Feng X, Ma G, Shi H, Wang Y and Chao X (2020) An Integrative Serum Pharmacology-Based Approach to Study the Anti-Tumor Activity of B. paniculatum Aqueous Bulb Extract on the Human Hepatocellular Carcinoma Cell Line BEL-7404. Front. Pharmacol. 11:01261. doi: 10.3389/fphar.2020.01261

The herb *Bolbostemma paniculatum* (Maxim) *Franquet* (Cucurbitaceae family), also known as Tu-Bei-Mu (TBM) in Chinese, has shown curative effects to treat several types of cancer as an adjunctive therapy. Thereby we intend to find its effect on the human hepatocellular carcinoma (HCC) and to understand the pharmacological mechanism behind it. In this study, an integrative serum pharmacology-based approach linking serum pharmacology and bioinformatics prediction was employed. Firstly, we used the serum taken introgastrically from the rats dministered by TBM aqueous bulb extract to culture the HCC cell line BEL-7404 and detect its anti-tumor effects. Secondly, the TBM putative targets were predicted using the ETCM database and known therapeutic targets of NPC were collected from the OMIM database. Then, a TBM-HCC putative targets network was constructed using the DAVID and STRING databases. Thirdly, key gene targets were obtained based on topological analysis and pathway enrichment analysis. The expression of 4 representative key targets were validated by Western blotting. As a result, 36 TBM targets and 26 known therapeutic targets of HCC were identified. These key targets were found to be frequently involved in 13 KEGG pathways and 4 biological processes. The expression of four representative key targets: TP53, CASP3, BCL2 and BAX further supports the suppression of TBM on HCC. In general, our study shows the curative effects of TBM against HCC. By using this integrative approach, we may find novel potential therapeutic targets to suppress HCC using TBM as an adjunctive therapy. And it could also help us understand the mechanism of HCC treatments in response to TBM.

Keywords: traditional Chinese medicine, *Bolbostemma paniculatum*, Tu Bei Mu, hepatocellular carcinoma, network pharmacology

INTRODUCTION

Hepatocellular carcinoma (HCC) is a globally increased malignant cancer with high death occurrence (Jorge et al.; Elserag, 2011). The major management of HCC includes resection and chemotherapy (Baer et al., 1998; Whittaker et al., 2010). However, many drugs for HCC still have toxic side effects, which limit their usage in the clinic (Cheung et al., 2007; Sak, 2012; Chen et al., 2020; Zingales et al., 2020), and drug resistance of HCC hampers the treatment effects (Xiong et al.; Folmer et al., 2007; Tan et al., 2019; Li et al., 2020; Xu et al., 2020; Yang et al., 2020). Hence, it is urgent to discover new curative compounds with less adverse effects to treat this disease.

Traditional Chinese medicine (TCM) has been used to treat many diseases for more than 2500 years with its comprehensive active compounds and curative therapeutic effects. It has been reported that many herbs show suppressing effects on tumor cells (Wu and Yao; He, 2004; Dorsher and Peng, 2010). People have summarized Chinese herbal medicine's advantages in reducing the side effects of chemo- and radiotherapy (Qi et al., 2010). Several formulas including astragalus, Turmeric (curcumin), and Ginseng have been used to reduce the toxicity as adjunctive therapies. For liver cancer treatment, formulations such as Bojungikki-tang, Kang-Fu-Zhi-Tong, PHY906, Xiao-Chai-Hu-Tang, Huang-Lian-Jie-Du-Tang, and Yin-Chen-Wu-Ling-San, have been reported to protect liver function, reduce cancer-related pain, improve respiratory tract infections and gastrointestinal side effects (Ling et al., 2007; Jeong et al., 2010; M. et al., 2010; Liu et al., 2011). *Bolbostemma paniculatum* (Maxim.) Franquet (Cucurbitaceae family), whose tuber named "Tu-Bei-Mu (TBM)" in Traditional Chinese Medicine, is one such herb (the name of the herb is verified in The Plant List (www.theplantlist.org) and Kew Medicinal Plant Names Services (https://mpns.science.kew.org/mpns-portal/)). Several groups reported the suppressing effects of TBM on several types of cancer (Islam et al.; Yu et al., 1992; Cheng et al., 2010; Xu, 2010; Chao et al., 2019). Thereby, we intend to study the effects of TBM on hepatocellular carcinoma and to decode the pharmacological mechanism of TBM's action on HCC.

In 1987, a Japanese scientist Hiroko used the serum obtained from mice orally treated with the herbs to culture the cells. And the herb-contained serum effectively increased the mitogenic activity of lipopolysaccharide of murine splenic cells (Hiroko et al., 1987). Since then, many groups have been using herb-contained serum to treat the cells in order to study the herbs' effect on diseases (Zhang et al., 2007; Rui et al., 2011). Cells directly treated by the herbs are easily disturbed by the chemical and physical properties of the herbs itself. Using serum from the rats orally treated or introgastrically administered with herbs can mimic the *in vivo* environment of the cell (Wang et al., 1999; Chen X. Z. et al., 2013). A serum complex containing the herb compounds, serum proteins, genes and other molecules takes its effect as a whole to the disease. The curative effects were obvious when cells were cultured with serum, orally treated or introgastrically administered with herbs (Yun-Ming, 2007; Chen L. et al., 2013). Thereby, we used the serum from rats introgastrically administered by TBM aqueous bulb extract to decipher its anti-tumor activity on the HCC cells.

As an alternative medicine remedy, TCM is characterized as multi-compound and multi-target, which hinders our understand the mechanism of the action. To address this problem, network pharmacology has been considered as a promising strategy. It combines experiments with bioinformatics, system biology and pharmacology to reveal the interactions among compounds, genes, proteins and metabolites (Lee; Hopkins, 2007; Da and Pei, 2014). This integrative approach helps us to more deeply understand the drug's action on certain diseases and find potential curative compounds. In recent years, our group has been using this approach to decipher the pharmacological mechanism of the herb *Radix Ophiopogonis* in the treatment of Nasopharyngeal Carcinoma (Feng et al., 2019).

In this study, an integrative pharmacology-based approach was employed to understand the TBM's effects on HCC by integrating experiments with bioinformatics predictions. Our study was implemented in three steps: (1) Lab experiments: Studying the effects of a TBM-contained serum on HCC; (2) Bioinformatics: TBM and HCC target prediction, network analysis and identification of key targets; (3) Validation of representative key targets of TBM against HCC. The workflow was elucidated in **Figure 1**.

MATERIAL AND METHODS

Step 1: Effects of TBM on HCC

Chemicals

RPMI-1640, 3-[4, 5-Dimethylthiazol-2-yl]-2, 5-diphenyltetrazolium bromide (MTT) powder, dimethyl sulfoxide (DMSO) (purity ≧99.7), anti-Bax, Bcl-2, p53, caspase-3 and β-actin primary antibodies were manufactured by Sigma-Aldrich Chemical Co., Ltd.

Preparation of the Fraction

The bulb of the *B. paniculatum* (TBM) was bought from the hospital of Shaanxi University of Chinese Medicine (Voucher number: 20181001). The TBM was cultivated and picked in Shaanxi province of China. The herbs were examined under the protocol of Chinese Pharmacopoeia (2015 vision). The TBM was characterized by Thin-layer chromatography (1.5% impurity, 11.9% H_2O, 13mg/kg CO_2 residue and 1.1% Tubeimuside I). The characterization and inspection were provided by Xing Sheng De pharmaceutical Co., Ltd (Report number: C201810070). The herb was further identified by Dr Bo Li (Shaanxi Collaborative Innovation Center of Chinese Medicinal Resources Industrialization, Shaanxi University of Chinese Medicine, China).200 ml distilled water was added to 60 g of coarsely powdered bulbs in a beaker. The mixture was kept in a water bath for 30min and boiled for 1h. The aqueous extract was then filtered and collected. The remaining powder was mixed with 200ml distilled water, boiled for 40min, filtered, and added to the prior filtrate. After evaporation, the raw concentration of the TBM was 2.5g/ml. The TBM mixture was

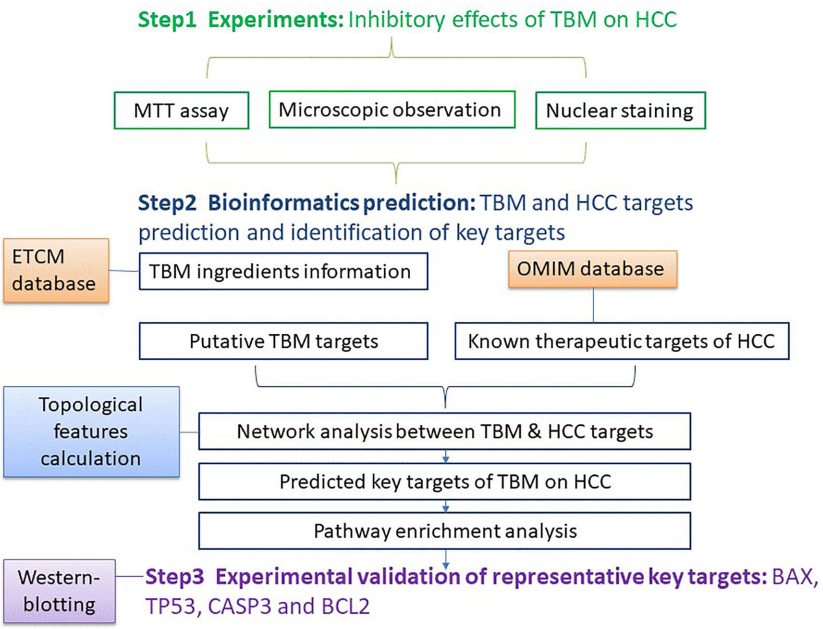

FIGURE 1 | The work flow of studying the TBM's inhibitory effects on HCC using an integrative pharmacology-based approach.

stored at 4°C in labelled sample bottles. We heated the mixture to 37°C when it wass needed to feed the rats.

Animals and Treatments

30 adult female Wistar rats (200–220 g) were purchased from the Experimental Animal Center of Xi'an Jiaotong University (license number: SCXK 2017-003). The animals were housed (5 rats/cage) in the standard rats plexiglass cages in a room maintained under standard conditions of temperature and humidity with an alternating 12-hr light/dark cycle and we provided regular commercial pellet diet and water to the rats. Female Wistar rats were randomly divided into two groups: the control group and the TBM group. Control group (n = 15) received 2ml tap water twice per day for 14 days by intragastric administration. TBM group (n = 15) received the aqueous fraction of TBM with the same frequency. One hour after the last time intragastric administration, all rats were anesthetized with 2% halothane in 100% O_2 blown over the nose through a face mask. Then the blood was collected from the abdominal aorta of the rats. The serum was collected after centrifuging the blood for 10min at 3000r/min and stored at -20°C for use. To ensure the biosecurity, we all follow the standard protocols in each step. All experiments were conducted in accordance with the ethical guidelines of the Declaration of Helsinki, and all experimental procedures were approved and performed in accordance with the guidelines of the local Institutional Animal Experimentation Ethics Committee.

Cell Culture

The human hepatocellular carcinoma cell line BEL-7404 and the human liver cell line L-02 were purchased from the Cell Bank of the Type Culture Collection of the Chinese Academy of Sciences (Shanghai, China) and cultured in the RPMI-1640 containing 10% (v/v) heat-inactivated fetal bovine serum (FBS), 100 μg/ml streptomycin and 100 U/ml penicillin at 37°C in a 5% CO_2 incubator. After the cells were grown into confluency, the HCC BEL-7404 cell line was divided into the following 4 groups: 10% fetal bovine serum (Contro), 25% TBM serum, 12.5% TBM serum and 6.25% TBM serum respectively prior to MTT assay and nuclear staining (The original serum obtained from rats containing TBM was considered as 100% TBM serum). The human liver cell line L-02 were regrouped into 4 groups with the same serum accordingly (Control, 25% TBM, 12.5% TBM and 6.25% TBM respectively.)

MTT Assay

The MTT (3-(4,5-dimethylthiazol-2-yl)-2,5-diphenyltetrazolium bromide) assay was performed with 1×10^4 cells/well in 96-well plates. After culture for 12h, the cells were incubated with serum containing TBM. Then, 20 μl MTT (5 mg/ml) was added for 4 h. After removal of the medium, the formazan crystals were dissolved in 150 μl DMSO. Absorbance was obtained at 570 nm with an ELx-800 Universal Microplate Reader (BioTek, Winooski, VT). Cell Inhibition Ratio (%) (IR) was determined as follows:

Inhibition Ratio (%) = [(ODcontrol − ODtreated)/(ODcontrol − ODblank)] ×100% (The control was 10% FBS serum; the treated cells are HCC cell line BEL-7404 and the human liver cell line L-02 treated by different concentrations of TBM; the blank was DMSO)

Nuclear Staining

BEL-7404 cells treated with the serum containing TBM were fixed with paraformaldehyde at room temperature for 10 min. Then the

cells were incubated with 20 μl DAPI at a concentration of 10 μg/ml (10 min, room temperature). Nuclear morphology was observed using a fluorescence microscope (Olympus FV1000).

Statistical Analysis

We display the data as Mean ± SD from 3 independent experiments. A student's t-test was employed to test the deviation between different batches. Values were only considered to be statistically significant when p-values were less than 0.05.

Step 2: TBM and HCC Target Prediction, Network Analysis and Identification of Key Targets

Compositive Compounds of TBM

The chemical compounds of TBM were obtained from The Encyclopedia of Traditional Chinese Medicine (ETCM) database (Huang et al., 2015; Haiyu et al., 2016; Yu et al., 2017; Xu et al., 2018) (http://www.nrc.ac.cn:9090/ETCM/index.php/Home/, updated on 2018). The chemical compounds contained in the TBM aqueous bulb extract were selected by the criteria "Tanimoto scores > 0.8." This score represents the similarity degree of the certain chemical components to that of known drugs. Tanimoto score ranges from "0 –1", where "0" means the completely different structures between ingredients and known drugs, and "1" means the same structures of two compounds. This Tanimoto score is the criteria to remove redundant compounds. The known compounds with high structural similarity (the structural similarity score is higher than 0.8) were identified as the putative compounds of TBM. The compounds with a similarity score lower than 0.8 were seen as redundant compounds. Under the criteria above, 10 chemical compounds were obtained from TBM. Detailed information of the chemical compounds contained in TBM is provided in **Supplementary Table S1**.

TBM Putative Targets Prediction

The known putative targets of TBM were identified from the ETCM database as described above (Xue et al., 2013). As described above, putative targets of certain chemical components were predicted by comparing the structure of the certain chemical components to that of known drugs. The targets of known drugs with high structural similarity (the structural similarity score is higher than 0.8) were identified as the putative targets of the certain chemical components. After removing redundancy, we found 155 TBM putative gene targets. These targets are also provided in **Supplementary Table S1**.

Known Therapeutic Targets of HCC

Known therapeutic targets for the treatment of HCC were collected from the OMIM database (www.omim.org, last updated October 31, 2013) (Hamosh et al., 2005). Only Food and Drug Administration (FDA) approved drugs used in humans were chosen. In total, 282 therapeutic targets were selected as HCC-related targets. Detailed information on the collected known therapeutic targets is provided in **Supplementary Table S2**.

Pathway Enrichment Analysis of TBM and HCC Putative Targets

Both TBM putative targets and known therapeutic targets of HCC treatments were analyzed through pathway enrichment analysis. We used the Database for Annotation, Visualization and Integrated Discovery (DAVID, http://david.abcc.ncifcrf.gov/home.jsp, version 6.8) and Kyoto Encyclopedia of Genes and Genomes database (KEGG, http://www.genome.jp/kegg/, updated on April 18, 2016) (Kanehisa and Goto, 2000; Dennis et al., 2003) to analyze those targets and involved pathways.

Network Analysis Between TBM Putative Targets and HCC Known Therapeutic Targets

We use the STRING (Search Tool for the Retrieval of Interacting Genes/Proteins, https://string-db.org/, vision 10.5) database to analyze the interaction between TBM putative targets and HCC known therapeutic targets. Interaction confidence of proteins were indicated by scores. We collected the targets when the combined score of those were higher than the medium value. Targets with the combined score lower than the medium value were discarded. Detailed information obtained is provided in **Supplementary Table S3**. Then we use Cytoscape (Vision 3.5.1, Boston, MA, USA) to visualize the networks.

Identification of Key Predicted Targets Based on TBM-HCC Interaction Network

Based on the above network, we further identified the major nodes in the direct protein-protein interactions. We employ the three topological features: "degree", "betweenness" and "closeness" as criteria to screen the putative targets due to their topological importance. "Degree" was defined as the number of links to one node. "Node betweenness" was defined as the number of the shortest paths between pairs of nodes that ran through one node. "Closeness" was defined as the inverse of the farness, which was the sum of the node distances to all other nodes. The closeness centrality can be regarded as a measure of how long it will take to sequentially spread information from the node to all the other nodes. Degree, node betweenness and closeness centralities can be used to measure a protein's topological importance in the network. A larger value of a certain protein's degree/node betweenness/closeness centrality indicates that this protein is more important in the network (Wang et al., 2012). Only nodes with topological features higher than the corresponding median values were identified as the major targets. After screening with the above criteria, 66 candidates were identified as key targets, provided in **Supplementary Table S4**.

Step 3: Validation of Representative Key Targets of TBM Against HCC

Western-Blotting of Key Targets

On the spectrum of key targets' biological and topological significance, we chose caspase-3, p53, Bcl-2 and Bax to detect their expression in TBM-treated cells. As described previously, the HCC cell line BEL-7404 was treated with 10% fetal bovine serum (Contro), 25% TBM serum, 12.5% TBM serum and 6.25%

TBM serum respectively. When the cells were grown into 1×10^6 per plate, we treated the cell line with 2, 4 or 6 μg/ml of peiminine for 24 h. Cell lysates were prepared in RIPA buffer (50 mmol/L Tris-HCl buffer, pH 7.4, 150 mmol/L NaCl, 1% Triton X-100, 1% sodium deoxycholate, and 0.1% sodium dodecyl sulfate) supplemented with a protease inhibitor to prevent the protein degradation. Cell lysates were centrifuged at 12,000×g for 15 min at 4°C. Total protein was extracted from the resulting supernatant and the concentration was quantified by the BCA assay. Proteins were separated on 10-12% sodium dodecyl sulfate-polyacrylamide gel electrophoresis and transferred to PVDF membranes. The membranes were firstly treated overnight at 4°C with rabbit monoclonal anti-human β-actin, caspase-3, p53, Bcl-2 and Bax primary antibodies. And then the membranes were washed with PBS incubated with appropriate horseradish peroxidase (HRP)-conjugated secondary antibodies for 1 hour at room temperature. The chemiluminescence of proteins transferred to PVDF membranes was detected with ECL kit (GE Healthcare Amersham, Piscataway, NJ).

RESULTS

The work-flow of studying the TBM's inhibitory effects on HCC using an integrative pharmacology-based approach was elucidated in **Figure 1**.

Step I: Inhibitory Effects of TBM on HCC

Cytotoxicity of TBM on HCC

The cytotoxicity of the serum containing the TBM aqueous bulb extract upon HCC cell line BEL-7404 and the human liver cell line L-02 was assessed by the MTT assay. We considered the original serum from the rats treated with TCM as 100% TBM serum. We observed the cell viability after 24h and 48hrs. We chose 25%, 12.5% and 6.25% TBM serum to treat the cells. 10% FBS was used as the control medium. As shown in **Table 1A**, the OD values were significantly decreased after the HCC cells were treated with the TBM serum. The 25% TBM serum inhibited the HCC cells with the inhibition ratio 22.8%, indicating that TBM can significantly inhibit the growth of the HCC cells. Meanwhile, the TBM serum has much fewer inhibitory effects on the human liver cell line L-02 as shown in **Table 1B**. The total inhibitory effects were shown in **Figure 2**.

TABLE 1A | The inhibitory effects of the TBM serum on the HCC cell line BEL-7404.

	OD	Inhibition Ratio
Control	0.5891 ± 0.0061	0
25% TBM serum	0.4550 ± 0.0089	22.8%
12.5% TBM serum	0.5278 ± 0.0162	10.4%
6.25% TBM serum	0.5596 ± 0.0158	5.5%

The control was 10% FBS serum. Data are presented as the mean ± SD from three independent experiments($p < 0.05$).

TABLE 1B | The inhibitory effects of the TBM serum on the human liver cell line L-02.

	OD	Inhibition Ratio
Control	0.4891 ± 0.0055	0
25% TBM serum	0.4633 ± 0.0146	5.4%
12.5% TBM serum	0.4775 ± 0.0127	2.5%
6.25% TBM serum	0.4823 ± 0.0166	1.9%

The control was 10% FBS serum. Data are presented as the mean ± SD from three independent experiments($p < 0.05$).

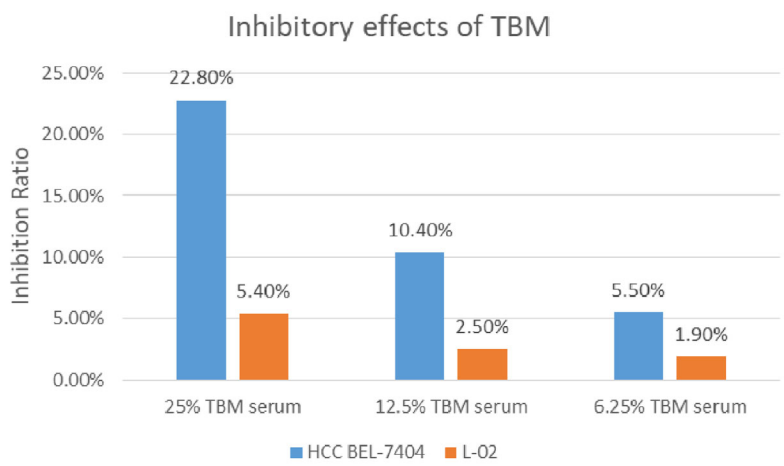

FIGURE 2 | Inhibition of the TBM serum on the HCC cell line BEL-7404 and the human liver cell line L-02. The Inhibition ratio was calculated as follows: Inhibition Ratio (%) = [(ODcontrol – ODtreated)/(ODcontrol – ODblank)] ×100%. The control was 10% FBS serum. The blue bar shows the inhibition ratio of the TBM serum with different concentrations upon HCC BEL-7404 cells and the yellow bar shows the inhibition ratio of the TBM serum upon the human liver cell line L-02.

Microscopic Observation Showing TBM's Inhibition on HCC Cell Line BEL-7404 With Less Cytotoxicity Towards the Human Liver Cell Line L-02

Representative images of the morphological changes observed after 48h are shown in **Figures 3A**, **B**. Compared to the control (FBS-treated cells), the HCC cell line BEL-7404 exposed to the TBM serum was significantly inhibited (**Figure 3A**). And the human liver cell line L-02 showed no obvious difference when they were treated with the TBM serum (**Figure 3B**).

Nuclear Morphology of the HCC Cell Line BEL-7404 Treated With the TBM Serum

The results of nuclear staining further confirmed that TBM could inhibit the growth of HCC cells. After culturing the HCC cell line BEL-7404 with 10% FBS serum (control), 25% TBM, 12.5% TBM and 6.25% TBM respectively for 48h, the cells show different nuclear morphology as elucidated in **Figure 4**. Compared with the control, the nuclear morphology of the cells treated with TBM were damaged obviously. A higher concentration of TBM culture resulted in more cell damage.

Step 2: Bioinformatics Prediction

Chemical Compounds of TBM and Its Potential Gene Targets Prediction

The ETCM database was employed to obtain the chemical compounds of TBM as described previously. As a result, we collected 10 chemical compounds contained in TBM under the criteria "Tanimoto score > 0.8" as described previously in **Supplementary Table S1**. In total, 155 putative TBM gene targets were collected, also shown in **Supplementary Table S1**.

TBM Compositive Compound-Putative Target Network

A TBM compositive compound-putative target network was built to understand the interaction between the TBM's ingredients with its putative targets as indicated in **Figure 5**. The network consists of 166 nodes (1 herb, 10 compositive compounds and 155 putative targets) and 165 edges. 91 genes with a combined score higher than the medium value were selected as the major TBM putative targets. By pathway enrichment analysis, we found these TBM putative targets were frequently involved in 8 pathways and biological processes including the p53 signaling pathway, Adipocytokine signaling pathway, PPAR signaling pathway, AMPK signaling pathway, FoxO signaling pathway, cyclooxygenase pathway, intrinsic apoptotic signaling pathway in response to endoplasmic reticulum stress and regulation of protein heterodimerization activity.

TBM Compositive Compound-Putative Known HCC Target Network

We analyzed the interaction between the TBM compositive compounds' targets and putative known HCC targets to evaluate the effects of TBM on HCC. The interaction data of TBM putative targets and HCC known therapeutic targets was acquired as previously described in the materials and methods section. As shown in **Figure 6**, the network consists of 307 nodes (containing 1 ingredient, 10 compositive compounds of TBM, 155 TBM putative targets, and 282 known therapeutics of HCC) and 1086 edges. As mentioned in material and methods section, three topological features "degree", "betweenness" and "closeness" were employed as criteria to screen the putative targets for topological importance. Only nodes with topological features higher than the corresponding median values were identified as major nodes. As a result, we identified 66 major nodes containing 1 ingredient, 3 compositive compounds in HCC, 36 TBM's putative targets and 26 known therapeutic targets for the treatments of HCC. Details concerning the topological features of the 66 major nodes in this network was shown in **Supplementary Table S4**. Except the ingredient TBM and its three compounds, 62 gene targets (36 TBM's targets and 26 known therapeutic targets of HCC) were considered as the key TBM-HCC predicted targets. According to the pathway enrichment analysis based on the GO annotation system and the KEGG pathway, the key TBM-HCC targets were frequently involved in 4 biological processes and 13 KEGG pathways as shown in **Table 2**. Based on the number of the edges between key targets and pathways, TBM's key targets were found to be strongly connected with Adipocytokine signaling pathway, AMPK signaling pathway, FoxO signaling pathway, Rap1 signaling pathway, mROT signaling pathway, p53 signaling pathway, VEGF signaling pathway, intrinsic apoptotic signaling pathway in response to endoplasmic reticulum stress, PI3K-AKT signaling pathway, TNF signaling pathway, activation of cysteine-type endopeptidase activity involved in apoptotic process by cytochrome c and positive regulation of ERK1 and ERK2 cascade. In the meantime, HCC key gene targets indicate that they are frequently involved in focal adhesion, positive regulation of I-kappaB kinase/NF-kappaB signaling, ErbB signaling pathway, MAPK signaling pathway and Hippo signaling pathway.

Step 3: Expression of Representative Key Targets Validated by Western Blotting

In total, 62 gene targets were selected as key TBM-HCC targets. These targets show an important role potentially during TBM-HCC interactions. Based on the three topological features "degree", "betweenness" and "closeness", the "degree" ranges from 6-61, the "betweenness" ranges from $4.55x10^{-4}$ to 0.1279, the "closeness" ranges from 0.3252 to 0.4287, we chose four key targets averagely distributed on the spectrum of their topological significance to validate their expression by Western blotting. The topological values of these four key targets were as follows: TP53 degree 61, betweenness 0.1278, closeness 0.4129; CASP3 degree 24, betweenness 0.0246, closeness 0.3711; BCL2 degree 12, betweenness 0.0028, closeness 0.3333; BAX degree 8, betweenness 4.55x10-4, closeness 0.3271; The detailed information of the key targets is provided in **Supplementary Table S4**. As shown in **Figure 7**, the expression of TP53, CASP3, and BAX were significantly increased when HCC cells were treated with the aqueous extract of TBM. BCL2 was down-regulated when cells were treated by 12%TBM and 25% TBM. The tumor suppressor TP53, CASP3 and BAX genes were mostly down-regulated in many types of tumors including liver cancer, while BCL2 gene suppresses the apoptosis. The up-

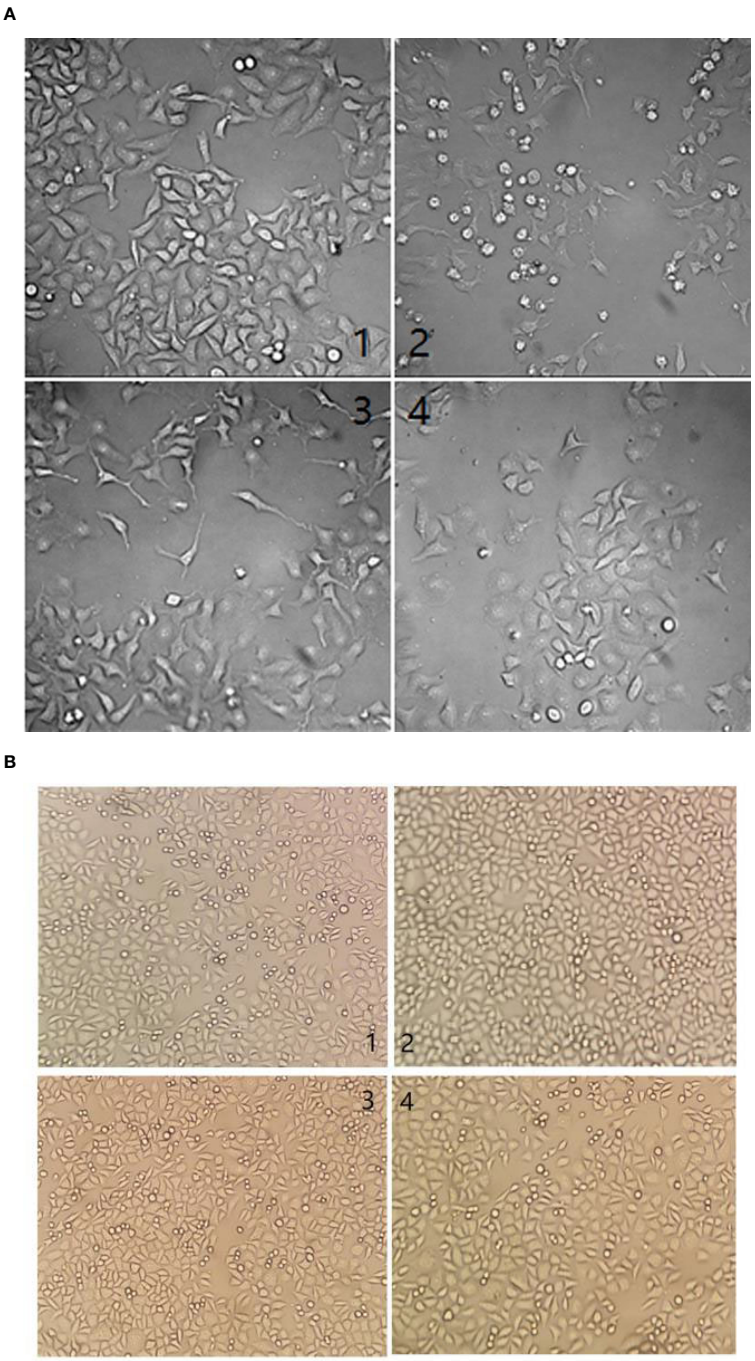

FIGURE 3 | **(A)** Morphological changes by different serum treatments on the HCC cell line BEL-7404 after 48h. (1) cells were cultured with 10% FBS at a concentration of 5.1×10^7 cfu/ml. (2) Cells were cultured with 25% TBM serum at the same concentration. (3) Cells were cultured with 12.5% TBM serum at the same concentration. (4). Cells were cultured with 6.25% TBM serum at the same concentration. **(B)** Morphological changes by different serum treatment on the human liver cell line L-02 after 48h. (1) cells were cultured with 10% FBS at a concentration of 5.1×10^7 cfu/ml. (2) Cells were cultured with 25% TBM serum at the same concentration. (3) Cells were cultured with the 12.5% TBM serum at the same concentration. (4). Cells were cultured with 6.25% TBM serum at the same concentration.

regulation of TP53, CASP3 and BAX and down-regulation of BCL2 supports the TBM's suppression effect on HCC cells. This result further confirms that the TBM's aqueous bulb extract is effective to suppress the growth of HCC cells by regulating these key targets.

DISCUSSION

Traditional Chinese medicine has been proved to treat cancer effectively with its multi-target therapeutics. TBM, characterized

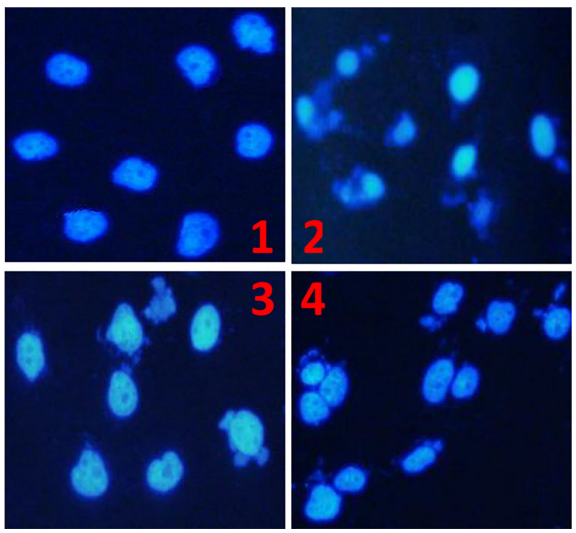

FIGURE 4 | The Morphology of the HCC cell line BEL-7404 by nuclear staining. The HCC BEL-7404 cells were stained using DAPI solution and observed by fluorescence microscopy (×400). (1) The HCC cells cultured with 10% FBS serum for 48h (Control). (2) The HCC cells cultured with 25% TBM. (3) The HCC cells cultured with 12.5% TBM. (4) The HCC cells cultured with 6.25% TBM.

with multi-components and multi-targets, have been used to suppress liver cancer as an adjunctive therapy in recent years. In this study, we develop an integrative pharmacology-based strategy to decipher the mechanism of the TBM's aqueous bulb extract in suppressing HCC. By integrating experiments, bioinformatics prediction and validation, 62 key targets (36 TBM's targets and 26 known therapeutic targets of HCC) were identified after analyzing TBM-HCC interactions. These key targets were frequently involved in 13 KEGG pathways and 4 biological processes. The integrative analysis bridging experiments with bioinformatics prediction provides us novel potential therapeutic targets to treat HCC using TBM. And it could also help us understand the mechanism of HCC treatments in response to TBM.

All 62 key targets have shown their topological and biological significance (**Table 2**). On the topological spectrum of these key targets, we choose 4 representative targets because they are averagely distributed on the topological table (**Supplementary Table S4**). The degree score of TP53, CASP3, BAX and BCL2 are 61, 24, 8 and 12 respectively (the total degree ranges from 6 to 61).

Tumor suppressor protein p53 (TP53) is a suppressor of tumor cells by inducing growth arrest or apoptosis (Moshe et al., 2002). This study revealed that TP53 were frequently involved in the p53 signaling pathway, PI3K-Akt signaling pathway and MAPK signaling pathway in hepatocellular carcinoma. TP53 takes important roles in the signaling pathways of HCC (Sia and Villanueva; Villanueva et al.; Whittaker et al., 2010). Repressed by MDM2, TP53 takes effects on cell survival in PI3K-Akt signaling pathway (Luo et al., 2003; Vara et al., 2004; Gang et al., 2005). the crosstalk between p53 protein and the MKK3/MKK6/p38 MAPK Signaling Pathway in Cancer has also been reported (Lorenzo et al.). The up-regulation of TP53 in the TCM-treated cells indicates TCM's inhibitory effects on tumor cells. And the p53 signaling pathway could act as a significant route when the curative effect of TCM takes place on HCC.

CASP3 encodes a cysteine-aspartic acid protease that plays a central role in the execution-phase of cell apoptosis. We found CASP3 was frequently involved in p53 signaling pathway, TNF

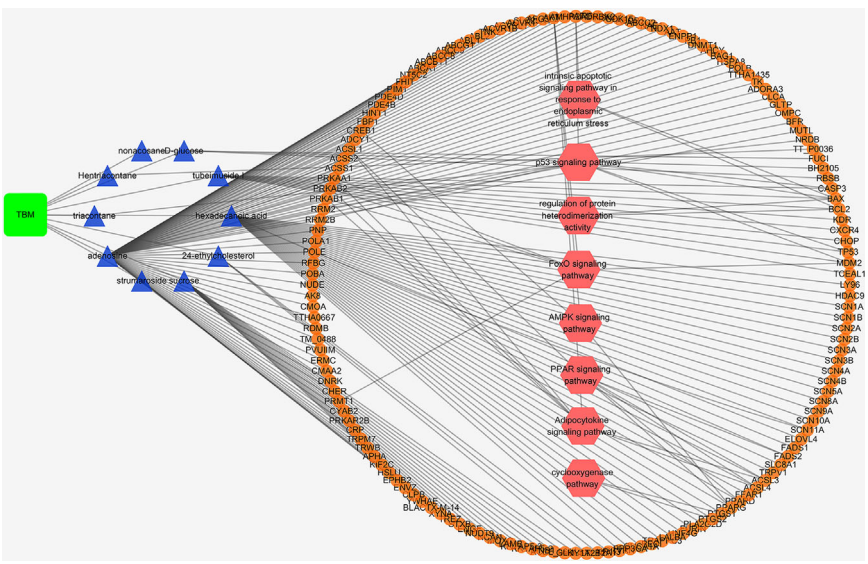

FIGURE 5 | TBM compositive compound-putative target network built and visualized with Cytoscape. Edges: interactions between compositive compounds of TBM and their putative targets; green square node: the herb TBM; blue triangular nodes: compositive compounds of TBM; orange round nodes: putative targets of compositive compounds of TBM; pink hexagonal nodes: the main pathways from enrichment analysis of major targets.

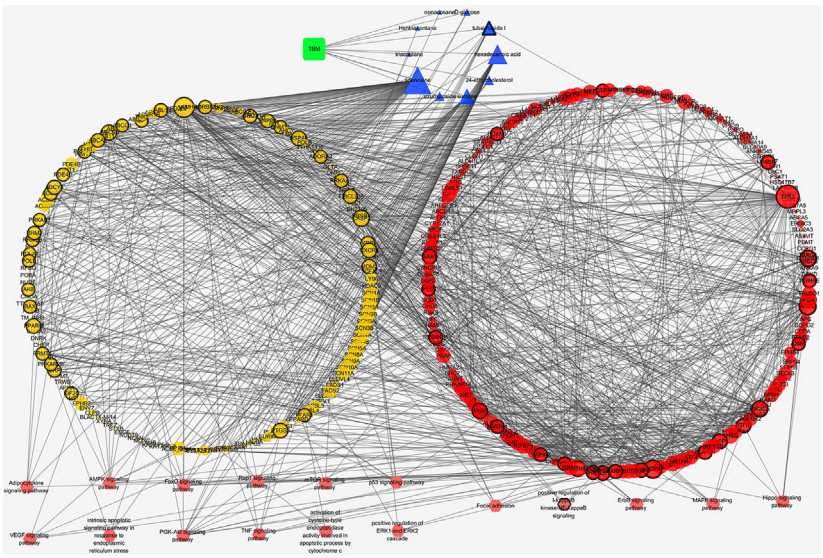

FIGURE 6 | TBM compositive compound-putative known HCC target network visualized with Cytoscape. Edges: Interactions among TBM, compositive compounds, putative targets, and known therapeutic targets of HCC. Green square nodes: the ingredient TBM; blue triangular nodes: compositive compounds of TBM; yellow round nodes: putative targets of TBM compositive compounds; red round nodes: known therapeutic targets for the treatment of HCC; pink hexagonal nodes: the pathways from enrichment analysis of key nodes. Nodes marked with dark rings: key nodes (the "degree," "node betweenness," and "closeness" of which were all larger than the corresponding median values).

TABLE 2 | Major GO biological processes and KEGG pathways with their key targets.

Term	Key targets	P-value
Biological processes		
GO:0070059 intrinsic apoptotic signaling pathway in response to endoplasmic reticulum stress	BCL2, BAX, APAF1	0.0059
GO:0008635 activation of cysteine-type endopeptidase activity involved in apoptotic process by cytochrome c	BAX, APAF1	0.0184
GO:0043123 positive regulation of I-kappaB kinase/NF-kappaB signaling	HMOX1, CASP8, ABL1, CTNNB1	0.0192
GO:0070374 positive regulation of ERK1 and ERK2 cascade	EGFR, ABL1, TGFB1, KDR	0.0209
KEGG pathways		
cfa04152:AMPK signaling pathway	AKT1, CREB1, PPARG, PRKAB2, FBP1, PRKAB1, FASN, PIK3CA, ELAVL1, RPS6KB1, PRKAA1, IRS1	1.71E-09
cfa04068:FoxO signaling pathway	EGFR, AKT1, PRMT1, MAPK14, PRKAB2, PRKAB1, PIK3CA, MDM2, PRKAA1, IRS1, TGFB1	5.16E-08
cfa04115:p53 signaling pathway	CASP3, RRM2, BAX, CASP8, TP53, MDM2, RRM2B, APAF1	6.00E-07
cfa04151:PI3K-Akt signaling pathway	EGFR, AKT1, YWHAZ, BCL2, CREB1, TP53, MDM2, PIK3CA, RPS6KB1, PRKAA1, IRS1, YWHAE, KDR	8.24E-06
cfa04668:TNF signaling pathway	AKT1, CASP3, PTGS2, MAPK14, CREB1, CASP8, PIK3CA	1.40E-04
ptr04151:PI3K-Akt signaling pathway	AKT1, CREB1, VEGFA, TP53	0.0107
cfa04920:Adipocytokine signaling pathway	AKT1, ACSL1, PRKAB2, PRKAB1, PRKAA1, IRS	2.17E-04
cfa04370:VEGF signaling pathway	AKT1, PTGS2, MAPK14, PIK3CA, KDR	0.0011
cfa04150:mTOR signaling pathway	AKT1, PIK3CA, RPS6KB1, PRKAA1, IRS1	0.0011
cfa04012:ErbB signaling pathway	EGFR, AKT1, PIK3CA, RPS6KB1, ABL1	0.0047
cfa04015:Rap1 signaling pathway	EGFR, AKT1, ADCY1, MAPK14, PIK3CA, KDR, CTNNB1	0.0053
cfa04390:Hippo signaling pathway	AFP, YWHAZ, YWHAE, TGFB1, CTNNB1, AXIN1	0.0063
cfa04010:MAPK signaling pathway	EGFR, AKT1, CASP3, MAPK14, TP53, TGFB1, HSPA8	0.0125
cfa04510:Focal adhesion	EGFR, AKT1, BCL2, PIK3CA, KDR, CTNNB1	0.0225

signaling pathway and MAPK signaling pathway in this study. This gene has been recognized for its importance in regulating hepatocellular carcinoma (Aquino et al.; Lu et al.). Our study shows the TBM's action on HCC cells lead to the down-regulation of CASP3, suggesting CASP3's critical role during treating HCC with TBM.

BAX encodes Bax protein which forms a heterodimer with BCL2, and functions as an apoptotic activator. The association

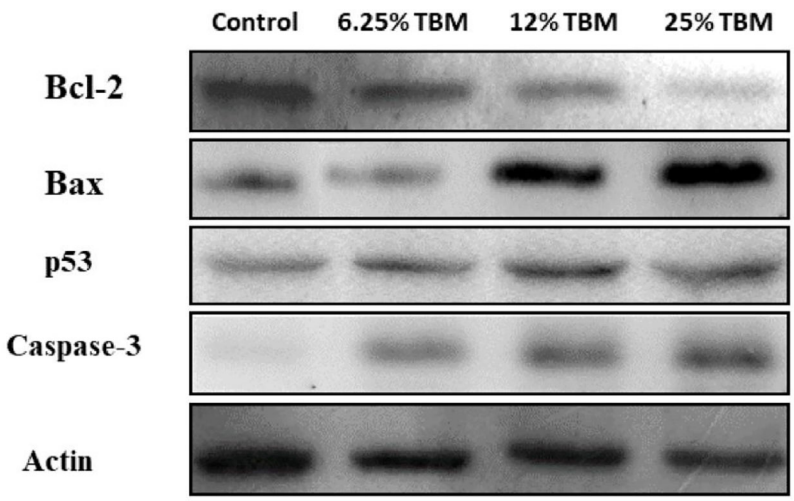

FIGURE 7 | Expression of Bcl-2, Bax, p53 and Caspase-3 in TBM-treated HCC cells validated by Western blotting. The Control group is the expression of representative key targets when cells are cultured with 10% FBS. The other three groups are the expression of these targets when cells are cultured with 6.25%, 12.5% and 25% TBM serum respectively ($p < 0.05$).

and the ratio of BAX to BCL2 also determines survival or death of a cell following an apoptotic stimulus. Compared with normal cells, the tumor cells always show a decreased expression of the Bax/BCL2 ratio (Sakinah et al., 2007; Wei et al., 2008). Our study shows an up-regulation of BAX and a down-regulation of BCL2 after the HCC cells were cultured with the aqueous extract of TBM. This result suggests TBM might take its inhibitory effect on HCC *via* regulating the Bax/BCL2 ratio. Furthermore, the result of Western blotting indicates higher concentration of TBM (12% and 25% TBM) is more effective to increase the expression of BAX and to decrease the expression of BCL2.

CONCLUSION

This study, for the first time, reports that TBM-containing serum could suppress the growth of HCC cells. And we employ an integrative pharmacology-based strategy combining experiments and TCM-HCC network analysis to decipher the mechanism behind. From the results, the inhibitory effects of TBM might be related to its regulation on 62 key targets *via* 13 KEGG pathways and 4 biological processes. Our findings could help us consider novel potential gene targets when treating the hepatocellular carcinoma and understanding the mechanism of curative effect of TBM.

DATA AVAILABILITY STATEMENT

All datasets presented in this study are included in the article/ **Supplementary Material**.

ETHICS STATEMENT

The animal study was reviewed and approved by Shaanxi University of Chinese Medicine Animal Experimentation Ethics Committee.

AUTHOR CONTRIBUTIONS

XF and XC designed the research. XF performed the research and wrote the paper. GM cultured the cells and feed the rats. HS contributed analytic tools. YW carried out the experimental validation. All authors contributed to the article and approved the submitted version.

FUNDING

This study was supported by the fund from the Subject Innovation Team of Shaanxi University of Chinese Medicine (2019YS05) and Basic Scientific Research Project of Shaanxi Province (2020JQ-867).

ACKNOWLEDGMENTS

The authors thank Dr. Li Bo for identifying the herb. We also thank Institute of Chinese Materia Medica, China Academy of Chinese Medical Sciences for providing ETCM database.

SUPPLEMENTARY MATERIAL

The Supplementary Material for this article can be found online at: https://www.frontiersin.org/articles/10.3389/fphar.2020.01261/full#supplementary-material

REFERENCES

Aquino, I., Tsuboy, M. S. F., Marcarini, J. C., Mantovani, M. S., and Perazzo, F. F. E L Maistro Genotoxic evaluation of the antimalarial drugs artemisinin and artesunate in human HepG2 cells and effects on CASP3 and SOD1 gene expressions. *Genet. Mol. Res.* 12, 2517–2527. doi: 10.4238/2013.July.24.6

Baer, H. U., Holzinger, F., Feodorovici, M., and Büchler, M. W. (1998). Diagnosis and treatment of hepatocellular carcinoma. *Therapeut. Umschau Rev. Therapeut.* 55, 127–133. doi: 10.1016/j.medcli.2008.11.024

Chao, X., Wang, G., Tang, Y., Dong, C., Li, H., Wang, B., et al. (2019). The effects and mechanism of peiminine-induced apoptosis in human hepatocellular carcinoma HepG2 cells. *PLoS One* 14 (1), e0201864. doi: 10.1101/377069

Chen, L., Sun, Z., Wang, F., Xu, C., and Duan, D. (2013). Shuyusan-containing serum protects SH-SY5Y cells against corticosterone-induced impairment. *Neural Regeneration Res.* 8, 2060–2068. doi: 10.3969/j.issn.1673-5374.2013.22.005

Chen, X. Z., Cao, Z. Y., Liao, L. M., Liu, Z. Z., and Jian, D. (2013). Application of serum pharmacology in evaluating the antitumor effect of Fuzheng Yiliu Decoction from Chinese medicine. *Chin. J. Integr. Med.* 20, 450. doi: 10.1007/s11655-013-1544-1

Chen, P., Luo, X., Dai, G., Jiang, Y., Luo, Y., Peng, S., et al (2020). Dexmedetomidine promotes the progression of hepatocellular carcinoma through hepatic stellate cell activation. *Exp. Mol. Med.* 52, 1062–1074. doi: 10.1038/s12276-020-0461-6

Cheng, G., Zhang, Y., Zhang, X., Tang, H. F., Cao, W. D., Gao, D. K., et al. (2010). Tubeimoside V (1), a new cyclic bisdesmoside from tubers of Bolbostemma paniculatum, functions by inducing apoptosis in human glioblastoma U87MG cells 37. *Bioorg. Med. Chem. Lett.* 16, 4575–4580. doi: 10.1016/j.bmcl.2006.06.020

Cheung, C. S.-F., Chung, K. K.-W., Lui, J. C.-K., Lau, C.-P., Hon, P.-M., Chan, J. Y.-W., et al. (2007). Leachianone A as a potential anti-cancer drug by induction of apoptosis in human hepatoma HepG2 cells. *Cancer Lett.* 253, 224–235. doi: 10.1016/j.canlet.2007.01.025

Da, C. H., and Pei, G. X. (2014). Network Pharmacology: A Rosetta Stone for Traditional Chinese Medicine. *Drug Dev. Res.* 75, 299–312. doi: 10.1002/ddr.21214

Dennis, G.Jr, Sherman, B. T., Hosack, D. A., Yang, J., Gao, W., Lane, H. C., et al. (2003). DAVID: database for annotation, visualization, and integrated discovery. *Genome Biol.* 4, 3–3. doi: 10.1186/gb-2003-4-5-p3

Dorsher, P., and Peng, Z. (2010). "Chinese Medicinal Herbs Use in Managing Cancer," in *Supportive Cancer Care with Chinese Medicine.* Ed. Cho, W. C. S. (The Netherlands: Springer, Dordrecht), 14, 55–75. doi: 10.1007/978-90-481-3555-4_3

Elserag, H. B. (2011). Hepatocellular Carcinoma. *New Engl. J. Med.* 365 (12), 1118–1127. doi: 10.1056/NEJMra1001683

Feng, X., Shi, H., Chao, X., Zhao, F., Song, L., Wei, M., et al. (2019). Deciphering the Pharmacological Mechanism of the Herb Radix Ophiopogonis in the Treatment of Nasopharyngeal Carcinoma by Integrating iTRAQ-Coupled 2-D LC-MS/MS Analysis and Network Investigation. *Front. Pharmacol.* 10, 253. doi: 10.3389/fphar.2019.00253

Folmer, Y., Schneider, M., Blum, H. E., and Hafkemeyer, P. (2007). Reversal of drug resistance of hepatocellular carcinoma cells by adenoviral delivery of anti-ABCC2 antisense constructs. *Cancer Gene Ther.* 14, 875–884. doi: 10.1038/sj.cgt.7701082

Gang, S., Gaoliang, O., and Shideng, B. (2005). The activation of Akt/PKB signaling pathway and cell survival. *J. Cell. Mol. Med.* 9, 59–71. doi: 10.1111/j.1582-4934.2005.tb00337.x

Haiyu, X., Yang, S., Yanqiong, Z., Qiang, J., Defeng, L., Yi, Z., et al. (2016). Identification of key active constituents of Buchang Naoxintong capsules with therapeutic effects against ischemic stroke by using an integrative pharmacology-based approach. *Mol. Biosyst.* 12, 233–245. doi: 10.1039/C5MB00460H

Hamosh, A., Scott, A. F., Amberger, J. S., Bocchini, C. A., and Mckusick, V. A. (2005). Online Mendelian Inheritance in Man (OMIM), a knowledgebase of human genes and genetic disorders. *Nucleic Acids Res.* 33, D514–D517. doi: 10.1093/nar/gki033

He, Y. (2004). Progress in using combination of Chinese drug with chemotherapy to treat cancer. *J. Tradit. Chin. Med.* 24, 153–157. doi: 10.3969/j.issn.0255-2922.2004.02.024

Hiroko, I., Sakae, A., and Yukio, O. (1987). Effect of shosaikoto, a japanese and chinese traditional herbal medicinal mixture, on the mitogenic activity of lipopolysaccharide: A new pharmacological testing method. *J. Ethnopharmacol.* 21, 45–53. doi: 10.1016/0378-8741(87)90093-6

Hopkins, A. L. (2007). Network pharmacology. *Nat. Biotechnol.* 25, 1110–1111. doi: 10.1038/nbt1007-1110

Huang, L., Lv, Q., Liu, F., Shi, T., and Wen, C. (2015). A Systems Biology-Based Investigation into the Pharmacological Mechanisms of Sheng-ma-bie-jia-tang Acting on Systemic Lupus Erythematosus by Multi-Level Data Integration. *Sci. Rep.* 5, 16401. doi: 10.1038/srep16401

Islam, S., Wang, C., Zheng, J., and Paudyal, N. The potential role of tubeimosides in cancer prevention and treatment. *Eur. J. Med. Chem.* 162, 109–121. doi: 10.1016/j.ejmech.2018.11.001

Jeong, J. S., Ryu, B. H., Kim, J. S., Park, J. W., Choi, W. C., and Yoon, S. W. (2010). Bojungikki-tang for cancer-related fatigue: a pilot randomized clinical trial. *Integr. Cancer Ther.* 9, 331. doi: 10.1177/1534735410383170

Kanehisa, M., and Goto, S. (2000). KEGG: Kyoto Encyclopedia of Genes and Genomes. *Nucleic Acids Res.* 28, 27–30. doi: 10.1093/nar/28.1.27

Lee, S. Systems Biology - A Pivotal Research Methodology for Understanding the Mechanisms of Traditional Medicine. *J. Pharmacopuncture* 18, 11–18. doi: 10.3831/kpi.2015.18.020

Li, D., Wang, T., Sun, F. F., Feng, J. Q., Peng, J. J., Li, H., et al (2020). MicroRNA-375 represses tumor angiogenesis and reverses resistance to sorafenib in hepatocarcinoma. *Cancer Gene Ther.* doi: 10.1038/s41417-020-0191-x

Ling, X., Li, X. L., Ge, A., Shan, Y., Jie, L., and Mansky, P. J. (2007). Chinese Herbal Medicine for Cancer Pain. *Integr. Cancer Ther.* 6, 208–234. doi: 10.1177/1534735407305705

Liu, M., Chien, L., Tai, C., Lin, K., and Tai, C. (2011). Effectiveness of Traditional Chinese Medicine for Liver Protection and Chemotherapy Completion among Cancer Patients. *Evidence-Based Complement. Altern. Med. eCAM* 2011, 291843. doi: 10.1093/ecam/nep185

Lorenzo, S., Angelina, P., and Gianluca, B. Insights of Crosstalk between p53 Protein and the MKK3/MKK6/p38 MAPK Signaling Pathway in Cancer. *Cancers* 10, 131–. doi: 10.3390/cancers10050131

Lu, Y., Wu, L.-Q., Wang, S.-G., Lv, Z.-H., and Han, B. Caspase-3 gene transfected with LIGHT gene: can it be used for therapy of human hepatocellular carcinoma? *Clin. Chem. Lab. Med. Cclm* 46, 470—474. doi: 10.1515/CCLM.2008.094

Luo, J., Manning, B. D., and Cantley, L. C. (2003). Targeting the PI3K-Akt pathway in human cancer. *Cancer Cell* 4, 257–262. doi: 10.1016/S1535-6108(03)00248-4

Marrero, J. A., and Pelletier, S. (2006). Hepatocellular Carcinoma. *Clin. Liver Disease* 10, 339–351. doi: 10.1016/j.cld.2006.05.012

Moshe, O., Alexander, D., Tanya, G., Dan, M., Jan, T., Martinez, L. J. F., et al. (2002). Regulation of p53. *Ann. New Y. Acad. Sci.* 973, 374–383. doi: 10.1111/j.1749-6632.2002.tb04669.x

Qi, F., Li, A., Inagaki, Y., Gao, J., and Tang, W. (2010). Chinese herbal medicines as adjuvant treatment during chemoor radio-therapy for cancer. *Biosci. Trends* 4, 297–307.

Rui, K. E., Hua, D., Ying-Jie, X. U., Gang, H. L., and Wang, Z. G. (2011). Inhibition of Proliferation and Induction of Apoptosis by the Herb Serum Containing HORN LIAN on K562 Leukemia Cells. *Acta Chin. Med. Pharmacol.* 39 (2), 37–40. doi: 10.19664/j .cnki .1002-2392.2011.02.014

Sak, K. (2012). Chemotherapy and Dietary Phytochemical Agents. *Chemother. Res. Pract.* 2012, 282570. doi: 10.1155/2012/282570

Sakinah, S., Handayani, S. T., and Hawariah, L. P. A. (2007). Zerumbone induced apoptosis in liver cancer cells via modulation of Bax/Bcl-2 ratio. *Cancer Cell Int.* 7, 4. doi: 10.1186/1475-2867-7-4

Sia, D., and Villanueva, A. Signaling Pathways in Hepatocellular Carcinoma. *Oncology* 81, 18–23. doi: 10.1159/000333254

Tan, W., Luo, X., Li, W., Zhong, J., Cao, J., Zhu, S., et al. (2019). TNF-α is a potential therapeutic target to overcome sorafenib resistance in hepatocellular carcinoma. *EBioMedicine* 40, 446–456. doi: 10.1016/j.ebiom.2018.12.047

Vara, J. F., Casado, E., De Castro, J., Cejas, P., Belda-Iniesta, C., and González-Barón, M. (2004). PI3K/Akt signalling pathway and cancer. *Cancer Treat Rev.* 30, 193–204. doi: 10.1016/j.ctrv.2003.07.007

Villanueva, A., Newell, P., Chiang, D., Friedman, S., and Llovet, J. Genomics and Signaling Pathways in Hepatocellular Carcinoma. *Semin. Liver Dis.* 27, 055–076. doi: 10.1055/s-2006-960171

Wang, X., Liu, P., Liu, C., Liu, C., and Hong, G. U. (1999). Investigation of Fuzheng Huayu Decoction on Coordination Effect of Anti fibrosis of Liver with Serum Pharmacology. *Chin. J. Exp. Tradit. Med. Formul.* 5 (6), 22–25. doi: 10.1142/4244

Wang, Y., Liu, Z., Li, C., Li, D., Ouyang, Y., Yu, J., et al. (2012). Drug Target Prediction Based on the Herbs Components: The Study on the Multitargets Pharmacological Mechanism of Qishenkeli Acting on the Coronary Heart Disease. *Evidence-Based Complement. Altern. Med.* 2012, 10. doi: 10.1155/2012/698531

Wasif, Saif, M., Lansigan, F., and Ruta, S. (2010). Phase I study of the botanical formulation PHY906 with capecitabine in advanced pancreatic and other gastrointestinal malignancies. *Phytomedicine* 17 (3–4), 161–169. doi: 10.1016/j.phymed.2009.12.016

Wei, F. X., Liu, J. X., Wang, L., Li, H. Z., and Luo, J. B. (2008). Expression of Bcl-2 and Bax Genes in the Liver Cancer Cell Line HepG2 after Apoptosis Induced by Essential Oils from Rosmarinus officinalis. *J. Chin. Med. Mater.* 31, 877–879. doi: 10.13863/j .issn1001-4454.2008.06.053

Whittaker, S., Marais, R., and Zhu, A. X. (2010). The role of signaling pathways in the development and treatment of hepatocellular carcinoma. *Oncogene* 29, 4989–5005. doi: 10.1038/onc.2010.236

Wu, M., and Yao, B. Advances in TCM Treatment of Gastric Cancer and Studies on the Apoptosis. *J. Tradit. Chin. Med.* 22 (4), 303–307. doi: 10.3969/j.issn.0255-2922.2002.04.020

Xiong, Y. Q., Sun, H.-C., Zhang, W., Zhu, X.-D., Zhuang, P.-Y., Zhang, J.-B., et al. Human Hepatocellular Carcinoma Tumor-derived Endothelial Cells Manifest Increased Angiogenesis Capability and Drug Resistance Compared with Normal Endothelial Cells. *Clin. Cancer Res.* 15, 4838–4846. doi: 10.1158/1078-0432.CCR-08-2780

Xu, H.-Y., Zhang, Y.-Q., Liu, Z.-M., Chen, T., Lv, C.-Y., Tang, S.-H., et al. (2018). ETCM: an encyclopaedia of traditional Chinese medicine. *Nucleic Acids Res.* 47 (D1), D976–D982. doi: 10.1093/nar/gky987

Xu, Y., Liu, Y., Li, Z., Li, H., Li, X., Yan, L., et al. (2020). Long non−coding RNA H19 is involved in sorafenib resistance in hepatocellular carcinoma by upregulating miR−675. *Oncol. Rep.* 44, 165–173. doi: 10.3892/or.2020.7608

Xu, Y. (2010). Proteomic and biochemical characterization of the anti-cancer mechanism of tubeimoside-1 extracted from the Chinese herbalmedicine "Tu bei mu". *Hku Theses Online* 4, 775–796. doi: 10.5353/th_b4413596

Xue, R., Fang, Z., Zhang, M., Yi, Z., Wen, C., and Shi, T. (2013). TCMID: traditional Chinese medicine integrative database for herb molecular mechanism analysis. *Nucleic Acids Res.* 41, D1089–D1095. doi: 10.1093/nar/gks1100

Yang, Y., Liao, Y., Gui, Y. P., Zhao, L., and Guo, L. B. (2020). GL-V9 reverses adriamycin resistance in hepatocellular carcinoma cells by affecting JNK2-related autophagy. *Chin. J. Natural Medicines* 18, 491–499. doi: 10.1016/S1875-5364(20)30059-5

Yu, L. J., Ma, R. D., Wang, Y. Q., Nishino, H., and Fan, S. X. (1992). Potent anti-tumorigenic effect of tubeimoside 1 isolated from the bulb of Bolbostemma paniculatum (Maxim) Franquet. *Int. J. Cancer* 50, 635–638. doi: 10.1002/ijc.2910500425

Yu, G., Zhang, Y., Ren, W., Dong, L., Li, J., Geng, Y., et al. (2017). Network pharmacology-based identification of key pharmacological pathways of Yin–Huang–Qing–Fei capsule acting on chronic bronchitis. *Int. J. Chronic Obstruct. Pulmon. Dis.* 12, 85–94. doi: 10.2147/COPD.S121079

Yun-Ming, S. U. (2007). Inhibition of proliferation by herb serum containing LQC on K562 leukemia cells. *J. Harbin Univ. Commerce*. 23 (5), 517–519. doi: 10.19492/j.cnki.1672-0946.2007.05.002

Zhang, Y.-H., Liu, J.-T., Wen, B.-Y., and Xiao, X.-H. (2007). In vitro inhibition of proliferation of vascular smooth muscle cells by serum of rats treated with Dahuang Zhechong pill. *J. Ethnopharmacol.* 112 (2), 0–379. doi: 10.1016/j.jep.2007.03.018

Zingales, V., Fedeli, C., Fernández-Franzón, M., and Ruiz, M.-J. (2020). Cytotoxic effects of individual and combined sterigmatocystin and nivalenol on liver hepatocellular carcinoma cells. *Food Chem. Toxicol.* 143, 111473. doi: 10.1016/j.fct.2020.111473

Conflict of Interest: The authors declare that the research was conducted in the absence of any commercial or financial relationships that could be construed as a potential conflict of interest.

Copyright © 2020 Feng, Ma, Shi, Wang and Chao. This is an open-access article distributed under the terms of the Creative Commons Attribution License (CC BY). The use, distribution or reproduction in other forums is permitted, provided the original author(s) and the copyright owner(s) are credited and that the original publication in this journal is cited, in accordance with accepted academic practice. No use, distribution or reproduction is permitted which does not comply with these terms.

frontiers in Pharmacology

ORIGINAL RESEARCH
published: 14 October 2020
doi: 10.3389/fphar.2020.581991

The Interventional Effects of Tubson-2 Decoction on Ovariectomized Rats as Determined by a Combination of Network Pharmacology and Metabolomics

Fan Yang[1†], Xin Dong[1†], Feixiang Ma[1], Feng Xu[2], Jie Liu[1], Jingkun Lu[1], Chunyan Li[1], Ren Bu[1] and Peifeng Xue[1]*

[1] Department of Pharmacy, Inner Mongolia Medical University, Hohhot, China, [2] State Key Laboratory of Natural and Biomimetic Drugs, School of Pharmaceutical Sciences, Peking University, Beijing, China

OPEN ACCESS

Edited by:
Yan Xu,
Cleveland State University,
United States

Reviewed by:
Man Sau Wong,
Hong Kong Polytechnic University,
Hong Kong
Yun-lun Li,
Shandong University of Traditional Chinese Medicine, China

***Correspondence:**
Peifeng Xue
Xpfdc153@163.com

[†]These authors have contributed equally to this work

Specialty section:
This article was submitted to Ethnopharmacology, a section of the journal Frontiers in Pharmacology

Received: 10 July 2020
Accepted: 09 September 2020
Published: 14 October 2020

Citation:
Yang F, Dong X, Ma F, Xu F, Liu J, Lu J, Li C, Bu R and Xue P (2020) The Interventional Effects of Tubson-2 Decoction on Ovariectomized Rats as Determined by a Combination of Network Pharmacology and Metabolomics. Front. Pharmacol. 11:581991. doi: 10.3389/fphar.2020.581991

Post-menopausal osteoporosis (PMOP) is associated with estrogen deficiency and worldwide, is becoming increasingly more prevalent in aging women. Various anti-PMOP drugs have been developed to reduce the burden of PMOP; generally, these drugs are efficacious, but with some adverse side effects. Tubson-2 decoction (TBD), a popular traditional Mongolian medicine, has been used to treat PMOP for centuries. However, the precise mechanisms underlying the action of TBD on PMOP have yet to be fully elucidated. Herein, we combined network pharmacology with untargeted metabolomics to identify the key targets and metabolic pathways associated with the interventional effects of TBD on ovariectomized (OVX) rats. Furthermore, we investigated the bone histomorphometry of eight different groups of rats to evaluate the therapeutic effect of TBD. First, we established a TBD-target/PMOP network *via* network pharmacology; this network identified three key protein targets—vitamin D receptor (VDR), cytochrome P450 19A1 (CYP19A1), and 11β-hydroxysteroid dehydrogenase type 1 (HSD11B1). Morphological analysis showed that severe impairment of the bone micro-architecture in OVX rats could be improved by TBD administration. The TBD-treated rats had a significantly lower bone surface-to-tissue volume (BS/TV) and a significantly smaller trabecular separation (Tb·Sp.) ($P<0.05$) than the OVX rats; in contrast, bone volume fraction (BVF), trabecular thickness (Tb·Th.), trabecular number (Tb·N.), and bone mineral density (BMD) were significantly higher in the TBD-treated rats ($P<0.05$). Multivariate and univariate analysis showed that OVX resulted in significant alterations in the concentrations of 105 metabolites and 11 metabolic pathways ($P<0.05$); in addition, 26 potential biomarkers were identified to investigate the progression of PMOP. Network pharmacology showed that major alterations in vitamin B6 metabolism were associated with the VDR target. Next, we validated the three crucial targets (VDR [$P<0.01$], HSD11B1 [$P<0.01$], and CYP19A1 [$P<0.05$]) by enzyme-linked immunosorbent assays (ELISAs) and demonstrated that the levels of these targets were elevated in the

OVX group but reduced in the TBD-treatment group. Collectively, our results suggest that the interventional effects of TBD on OVX rats are likely to be associated with the down regulation of VDR. Our findings enhance our molecular understanding of the interventional effects of TBD on PMOP and will allow us to develop further TBD studies.

Keywords: network pharmacology, metabolomics, post-menopausalosteoporosis, ovariectomized, Tubson-2

INTRODUCTION

Osteoporosis is a systemic bone disease that results in alterations in the microscopic architecture of the bone and a reduction in bone mass (Zou et al., 2020); collectively, these effects result in an impairment of bone quality. Post-menopausal osteoporosis (PMOP) is a global public health issue and has become a significant cause for concern for middle-aged and elderly women (Alexandre and Vico, 2011). Estrogen deficiency is known to be one of the most important mechanisms underlying PMOP and usually occurs 5 to 10 years after menopause (Li et al., 2020). Research studies have also shown that osteoclastic activity exceeds osteoblastic activity after menopause, thus leading to an increase in bone resorption. In turn, these events cause an overall reduction in bone mass reduction and a concomitant increase in skeletal fragility (Gambacciani et al., 2019). Over the last few decades, a considerable body of evidence has accumulated in support of the fact that estrogen prevents bone loss by blocking the production of proinflammatory cytokines by the bone marrow and bone cells. Thus, estrogen replacement therapy remains the gold standard for treating PMOP (Jiang, 2018). However, over the long-term, estrogen replacement therapy is associated with a range of side effects, including pain in the ovaries and endometrium and invasive breast cancer (Komm et al., 2015). Consequently, there is an urgent need to identify novel treatment modalities that are effective but with fewer side effects than existing therapies. Traditional Chinese medicine (TCM), along with other forms of ethnic medicines, has emerged as promising candidates for the treatment of complex disease because these forms of medicine contain multiple components that act on multiple targets. Many researchers have highlighted the fact that many herbs, and prescriptions created from these herbs, can exert and estrogen-like action, including *Eucommia ulmoides* Oliver (EC) (Zhang et al., 2012), *Epimedium brevicornu* Maxim (Liu H. et al., 2018), *Achyranthes bidentata* (Zhang M. et al., 2018), and *Echinops latifolius* Tausch (ELT) (Wang et al., 2020). Considering that these herbs, and their prescriptions, are known to have good anti-osteoporosis effects, it follows that TCM (Li et al., 2018), and other ethnic medicines, may represent a natural drug resource for screening new drugs for the treatment of PMOP.

Tubson-2 (TBD), also known as Erwei Duzhong Decoction, is composed of ELT and EC. This is the basic prescription of Mongolian medicine for treating osteoporosis, recorded in Golden Cabinet of Mongolian Medicine (Zhan, 1977). In a previous study, researchers (Liu, 2016) applied this prescription to 60 patients with PMOP and reported a total effective rate of 90%. In addition, the ameliorating effect of TBD on estrogen receptors, inorganic elements, bone density, bone biomechanics, and bone metabolism, in ovariectomized (OVX) rats have also been investigated in previous research studies (Liu, 2016). Interestingly, ELT was shown to be able to prevent PMOP by activating the estrogen receptor (ER)/protein kinase B (AKT)/extracellumar-signal regulated kinase (ERK) pathway in bone marrow derived mesenchymal stem cells (BMSCs) (Liu Y. et al., 2018), and that the main components of ELT (such as chlorogenic acid and its derivatives) were closely related to oxidative balance in femoral tissue (Han et al., 2017). Moreover, the active compound in EC is known to be a powerful inhibitor of adipogenesis and an enhancer of osteoblastogenesis (Tan et al., 2014). Although the substances that make up ELT and EC have been shown to exert good effects against osteoporosis, the specific mechanisms that underlie the effect of TBD on PMOP have yet to be fully elucidated. However, the complexity of TBD makes its very challenging to investigate its specific mechanism of action. Unlike traditional western medicine, it is not possible to use monomers to perform pharmacodynamic tests with TBD.

Network pharmacology is a new discipline that allows researchers to discover the mechanisms underlying the effects of drug combinations based on multidisciplinary theories such as systems biology and multidirectional pharmacology (Hao and Xiao, 2014). Furthermore, network pharmacology allows us to construct a 'disease-targets-drug' network in order to elucidate the mechanisms of action for specific drugs. Metabolomics is considered the latest "omics" science and involves the comprehensive and systematic analysis of small molecular metabolites from tissues, cells, or biological fluids (Johnson et al., 2016). The composition and concentration of metabolites may change with disease progression; this, in turn, will help us to screen potential biomarkers or targeted therapeutic pathways that are closely related to the disease (Lv et al., 2016). Currently, the overall concept of network pharmacology and metabolomics concurs with the 'multi-component and multi-target' theory of traditional herbal medicines that is used widely to discover the mechanisms underlying the action of traditional herbal medicines (Zhang et al., 2020).

In the present study, we used a combination of network pharmacology and non-targeted metabolomics to identity and characterize the key targets and metabolic pathways associated with the interventional effects of TBD on PMOP. To verify the efficacy of TBD on PMOP, we created an OVX rat model to mimic the physiological characteristics of menopausal women. First, we established a TBD-target/PMOP network *via* network pharmacology; this network was then used to identify key

protein targets. Next, we analyzed relevant metabolites and metabolic pathways by performing ultra-high performance liquid chromatography mass spectrometry (UHPLC-MS) on serum samples acquired from treated and non-treated rats. Finally, we validated the crucial targets of shared pathways identified by network pharmacology and metabolomics to identify the main interventional effects of TBD on OVX rats. We believe that this approach could significantly enhance our understanding of the mechanisms underlying the effect of TBD on PMOP and thus help to promote its clinical application.

MATERIALS AND METHODS

Chemicals and Reagents

Echinops latifolius Tausch (ELT) was collected from Wu Chuan (Hohhot, China) and *Eucommia ulmoides* Oliv. (EC) was purchased from Bozhou Pharmaceutical Co. Ltd. (Anhui, China). Chloral hydrate, combined estrogen tablets, Gushukang granules, and saline, were purchased from Ze Sheng Biotechnology Company (Hohhot, China). Methanol and formic acid (MS grade) were acquired from Fisher Scientific Corporation (Loughborough, UK). Ultra-high purity water (18.2 MΩ) was obtained from an ALH-600-U purification system (Chongqing, China). Enzyme-linked immunosorbent assay (ELISA) kits for the vitamin D receptor (VDR), cytochrome P450 19A1 (CYP19A1), 11β-hydroxysteroid dehydrogenase type 1 (HSD11B1) were obtained from Hua Lian Biotechnology Institute (Wuhan, China).

Instrumentation

The research described herein utilized the following equipment: a high resolution *in-vivo* X-ray microtomograph (SkyScan 1176, Bruker, Germany), a digital microscope (MOTICBA210, Motic, China), an ultrapure water system (ALH-600-U, China), a Thermo Scientific Q Exactive Quadrupole-Orbitrap Mass Spectrometer System (Thermo Fisher Scientific Inc, Grand Island, NY, USA), a rotary evaporator (EYELA n-1100, Shanghai Alang Instruments Co., China), and a microplate reader (Beijing Prolong New Technology Co., China).

Plant Materials and Preparation of Tubson-2 Decoction

Herbal materials of ELT were collected from Wu Chuan (Hohhot, China, GPS co-ordinates of the plant collection site is 41.1206962700, 111.4084477500) in early autumn 2019 and identified by Professor PX (Department of Natural Medicinal Chemistry, Inner Mongolia Medical University) with the voucher specimen (#20190715) collected in the herbarium of Inner Mongolia Medical University. EC herbal materials were purchased from Bozhou Pharmaceutical Co. Ltd. (Anhui, China) and morphologically authenticated by PX. The voucher specimens were also deposited in the herbarium of Inner Mongolia Medical University (#20190822).

The final preparation of TBD was carried out as described in our previous paper. In brief, two herbal materials were ground into powder and screened over 50 mm sieve before use. Equal amounts of ELT and EC powders were mixed and then were soaked with ultrapure water at a material-liquid ratio of 1:10 (g/ml) for half an hour before being hot reflux extraction. Subsequently, these powders were refluxed at 100°C twice (for 30 min each time), and then filtered through 180 mm sieve. Following filtration, the filtrate was collected, concentrated, and freeze-dried to obtain a lyophilized TBD powder. Powders were stored in a refrigerator at 4°C and dissolved in an appropriate amount of distilled water prior to use. The chemical profile of TBD was achieved by UPLC-MS/MS (Supporting Information **Figure S1**). The content of sixteen active ingredients in TBD sample was list as **Supporting Information Table S1**.

Establishment of an OVX Rat Model

Twelve-week-old female Wistar rats, 250–270 g in weight, were purchased from the Laboratory Animal Institute of Inner Mongolia Medical University (Hohhot, China). All animal procedures were approved by the Animal Ethics Committee of Inner Mongolia Medical University (Reference: SCXK2015-0001). Rats were kept in a barrier system with controlled temperature (25–28°C) and humidity (50%–60%) and a light-dark cycle of 12 h per day. After 7-day of acclimatization, 48 rats were equally randomized to 8 groups (6 rats per group), including a blank group, a sham group, an OVX group, a positive control drug group (Gushukang-treated group and an estrogen-treated group), a TBD high dose group, a TBD middle dose group, and a TBD low dose group. All rats except those in the blank group were injected with 10% chloral hydrate solution (0.5 ml/100 g body weight) prior to surgery. Bilateral laparotomy was conducted in the sham group (n=6) while bilateral ovariectomy was carried out in the model group (n=36, six rats were regarded as the OVX group, while the remaining rats were allocated to drug-treatment groups). Seven days after surgery, all rats were subjected to keratinization experiments involving the vaginal epithelium; vaginal smears were then performed once a day for 5 consecutive days. The morphology and staining of the cells contained within vaginal smears were observed by optical microscopy at a magnification of 100×. Results showed that the estrus cycle appeared alternately in the blank group (**Figures 1A–C**), while an estrus interval appeared in the model group (**Figure 1D**) five consecutive days of vaginal smear to tips for successful modeling.

The low dose group was given 237.5 $mg{\cdot}kg^{-1}{\cdot}d^{-1}$ of lyophilized TBD (equivalent to 1.05 $g{\cdot}kg^{-1}{\cdot}d^{-1}$ of raw medicine), the middle dose group was given 475 $mg{\cdot}kg^{-1}{\cdot}d^{-1}$ (equivalent to 2.1 $g{\cdot}kg^{-1}{\cdot}d^{-1}$ of raw medicine), and the high dose was given 950 $mg{\cdot}Kg^{-1}{\cdot}d^{-1}$ (equivalent to 4.2 $g{\cdot}kg^{-1}{\cdot}d^{-1}$ of raw medicine). The Gushukang-treated group was given Gushukang granules (105.1 $mg{\cdot}kg^{-1}{\cdot}d^{-1}$) while estrogen-treated group was given combined estrogen tablets (0.065 $mg{\cdot}kg^{-1}{\cdot}d^{-1}$). During the same period, the blank group, sham group, and OVX group, were given the same volume of 0.9% saline daily. After 8 weeks of gavage treatment, we anesthetized all animals with 10% chloral hydrate solution and acquired cardiac blood samples. Serum was separated by centrifugation at 3,500 rpm for 10 min at 4°C and frozen at -80°C to await metabolomics analysis. We also removed the left tibia

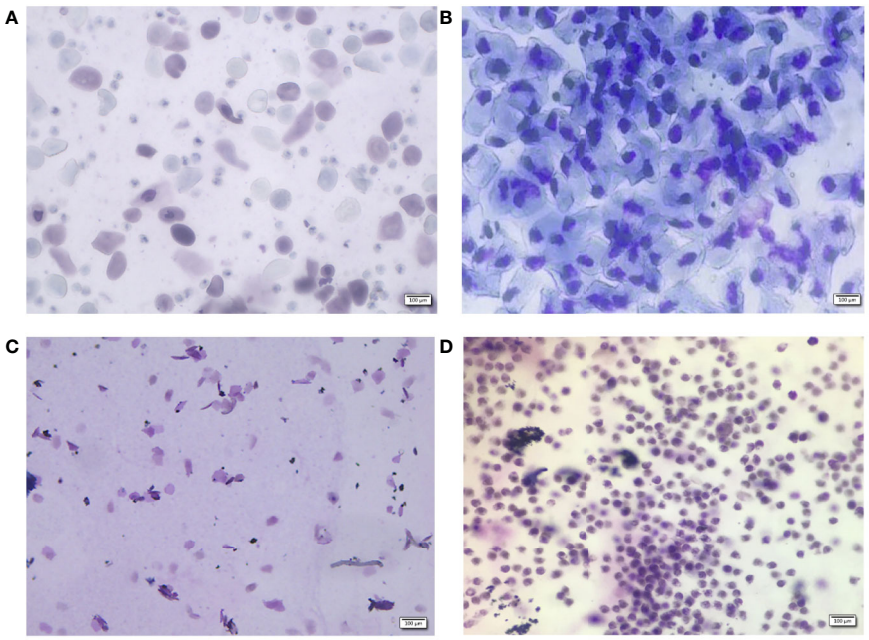

FIGURE 1 | Vaginal morphology in sham-operated **(A–C)** rats and ovariectomized (OVX) rats **(D)**. Methylene blue for 10 min, ×100. Sham group rats had an estrous cycle in general, **(A)**: nucleated epithelial cells, keratinized epithelial cells, and leukocytes appear evenly to show a state of the estrous, **(B)**: a large number of nucleated epithelial cells show the a state of proestrus period, **(C)**: a lot of keratinized epithelial cells show the a state of estrus period, **(D)**: a large number of non-nucleated leukocytes show the a state of diestrus period.

from each animal and fixed these samples in formalin to await analysis.

Analysis of Bone Mineral Density and Trabecular Micro-Architecture

X-ray microtomography was used to analyze bone mineral density and trabecular micro-architecture. All tibias were fixed with 70% ethanol and subjected to X-ray microtomography with an isotropic voxel size of 10 μm. Tomographic images were acquired at an integration time of 250 ms with 500 projections over the full 360° rotation. Three dimensional reconstructions were generated with the following parameters: smoothing was set as 3; ring artifacts reduction was set to 5; and beam hardening correction was set to 30%. Bone volume fraction (BVF), bone surface to tissue volume (BS/TV), trabecular thickness (Tb·Th.), trabecular number (Tb·N.), trabecular separation (Tb·Sp.), and bone mineral density (BMD), were all determined by analyzing a specific region of interest (ROI) that was chosen by setting the same coordinates in the tibial growth plate for each sample.

Network Pharmacology Analysis

Compound Data Acquisition

Details relating to the compounds identified in ELT and EC were obtained by searching the Traditional Chinese Medicine Systems Pharmacology Database and Analysis Platform (TCMSP; http://tcmspw.com/tcmsp.php) (Ru et al., 2014), the Encyclopedia of Traditional Chinese Medicine (ETCM; http://www.nrc.ac.cn:9090/ETCM/) (Xu et al., 2019), and existing literature (Wang et al., 2020). We also added some additional compounds, as determined by the fingerprint we created for TBD in a previous study (Guo et al., 2020).

Target Fishing

We used a systemic approach that was based on information integration and text-mining to identify the targets of TBD. Targets were retrieved from Swiss Target Prediction (http://www.swisstargetprediction.ch) (Gfeller et al., 2014) and Superpred Webserver (http://prediction.charite.de/) (Nickel et al., 2014) software. The SMILE structure of each component was then introduced into Swiss Target Prediction with a probability threshold of 0.6–1. All known and predicted targets were then selected from the Superpred Webserver. Next, the targets that were related to PMOP were acquired from Drugbank (http://www.drugbank.ca/atc) (Wishart et al., 2018). We then constructed a compound-target network and then removed the components of TBD that were not connected with PMOP targets.

Construction of a Protein-Protein Interactions (PPI) Network Related to PMOP

The String database (https://string-db.org/Version 10.5) is a database that is commonly used to analyze known and predicted protein-protein interactions. The common targets of PMOP, along with the active ingredients of TBD, were introduced into the database for protein-protein interaction

(PPI) analysis and the species set to "human." We then imported node 1, node 2, and comprehensive scoring information, into Cytoscape 3.0 software to create a PPI network map.

Determination of Key Targets

By filtering common targets, it was possible to identify the specific pathways of the targets *via* the DAVID database (https://david.ncifcrf.gov/). Next, using the potential targets of TBD for PMOP, we performed enrichment analysis of biological processes using the CLUE GO plugin in Cytoscape software. We then considered this data along with the rankings for biological functions and pathways and identified important pathways. Next, we ranked the genes associated with the identified pathways in terms of frequency and integrated the target data into the PPI network diagram. Finally, we defined the key targets of TBD in PMOP that would be subsequently assayed quantitatively by enzyme-linked immunosorbent assays (ELISAs).

Metabolomics Analysis

Preparation of Serum Samples and Quality Control (QC) Samples

Serum samples were thawed at 4°C prior to analysis. Then, 200 μl of each serum sample was mixed with 600 μl of methanol and vortexed for 3 min. Subsequently, the samples were centrifuged at 15,000 rpm for 10 min at 4°C. Supernatants were then transferred to new microcentrifuge tubes and dried in a vacuum dryer. Finally, the samples were dissolved in 200 μl of methanol for analysis.

Quality control (QC) samples were created by pooling serum samples from each analysis sequence. QC samples were analyzed after every 10 samples. This practice ensured that our analysis was accurate and consistent.

UHPLC-MS Conditions

UHPLC-MS analysis was performed on a Thermo Q-Exactive-MS (Thermo, USA). Chromatographic separations were performed on a Waters ACQUITY UPLC HSS T3 column (2.1×50 mm, 1.8 μm) at 35°C, and the flow rate was set to 0.4 ml/min. The mobile phase was formed by MS-grade methanol (A) and water containing 0.1% formic acid (B). The gradient program was set to the following parameters: 0–1.7 min, 5%–10% A; 1.7–3.0 min, 15%–17% A; 3.0–3.3 min,17% A; 3.3–8.0 min, 17%–25% A; 8.0–9.7 min, 25%–30% A; 9.7–10.6 min, 30%–35% A; 10.6–14.1 min, 35%–55% A, 14.1–14.6 min, 55% A; 14.6–15.1 min, 55%–100% A; 15.1–17.0 min, 100% A; 17.0–18.1 min, 100%–5% A; 18.1–20 min, 5% A. For each sample, we injected 5 μl for analysis.

Q-Exactive-MS analysis was performed in full scan/dd ms^2 mode. Spray voltage was set to 4 kV for positive ion mode and 3.2 kV for negative ion mode. The sheath gas flow rate was 40 L/min for positive ion mode and 35 L/min for negative ion mode. The auxiliary gas flow was 2 L/min for both of the ion mode sat 350°C. The capillary temperature was 300 V for both two ion modes. Data were collected in centroid mode and the mass range was 100–1,100 m/z.

Data Processing and Statistical Analysis

Original data files were independently processed by Compound Discoverer (CD) ^{TM} 2.0 software for peak alignment, peak filter, peak extraction, and automatic integration. The minimum peak intensity for component extraction was 2×10^6 and the mass tolerance was 10 ppm. The retention time window was 1 min and the signal-to-noise ratio was 3. CD software was then used for spectral comparison, grouping, compound detection, and metabolite identification. We were then able to create multi-dimensional peak tables containing prediction formulas, accurate mass data, retention times, peak areas, and mzCloud results. The multi-dimensional peak tables acquired in positive and negative ion mode were processed separately and transferred into a Microsoft Excel file which was subsequently imported into SIMCA-P (version 14.1, Umetrics, Sweden) Performed principal component analysis (PCA) was then performed to identify the overall metabolic profile for each group of samples. Supervised partial least squares discriminant analysis (PLS-DA) was then applied to compare distinguishing markers between the OVX group and the sham group. The fitness and predictive ability of the model were then verified according to R2 and Q2 values in cross-validation and permutation tests, respectively. We then identified potential biomarkers as metabolites with $P < 0.05$ and variable importance plot (VIP) > 1.

Potential biomarkers were then matched with structural data acquired from the Human Metabolome Database (HMDB) (http://www.hmdb.ca/) and mzCloud (https://www.mzcloud.org/). Pathway enrichment analysis was then performed for the identified biomarkers using MetaboAnalyst (http://www.metaboanalyst.ca/).

Analysis of Biochemical Indicators

Blood samples were collected from all rats at sacrifice, as described earlier. The serum levels of VDR, HSD11B1, and CYP19A1, were then determined byenzyme-linked immunosorbent assays (ELISAs) in accordance with the manufacturer's instructions.

Statistical Analysis

Data relating to BVF, BS/TV, Tb·N., Tb·Sp., Tb·Th., BMD, CYP19A1,VDR, and HSD11B1, are described as the mean ± standard deviation (SD). The student's unpaired t test was performed with SPSS 19.0 software and a P value ≤ 0.05 was regarded as statistically significant.

RESULTS

TBD Improved Ovariectomy-Induced Bone Loss and Deleterious Changes in the Trabecular Micro-Architecture

Analysis of vaginal smears from our experimental rats proved that the PMOP model had been successfully established by ovariectomy. Three dimensional microtomographic analyses allowed us to gather additional architectural, cortical, and trabecular, information from the tibias of experimental rats. We found that the OVX group showed significant changes in both BMD and trabecular micro-architecture. As shown in **Figure 2C**, the bone microstructure of the tibia in the OVX group exhibited severe damage. Moreover, the trabecular region in the OVX rats appeared to be small, thin and

sparse. Analysis also revealed that there was a significant reduction in Tb·N. (P=0.003), BVF (P=0.011), BMD (P=0.008), and BS/TV (P=0.001), along with a significant increase in Tb·Sp. (P=0.000) in the OVX group (**Figures 3A–F**).

One striking observation arising from our analysis of bone mineral density and trabecular micro-architecture was the existence of a severe reversion in bone loss in the treatment groups (**Figures 2A–H**). All treatment groups showed a remarkable improvement in trabecular micro-architecture, with a slightly dilated medullary cavity and a slightly disordered trabecular arrangement (**Figures 2D–H**). The trabecular morphological parameters were turned over in these drug-treated groups as shown in **Figures 3A–F**. Compared with the OVX group, the drug-treatment groups showed significant elevations of Tb·N. (P<0.05), BVF (P<0.05), BMD (P<0.05), and BS/TV (P<0.05), and a reduction of Tb·Sp. (P<0.05). There was only a marginal and non-significant difference in the estimated trabecular morphological parameters when compared between different drug-treatment groups. This data demonstrated that TBD has similar effects in OVX rats as the positive drug. However, the effect of TBD on these indicators did not show a dose-dependent effect.

VDR, HSD11B1, and CYP19A1 Were Crucial Targets in the Interventional Effects of TBD on OVX Rats

Following the screening of compound data, we identified 195 compounds in TBD, of which 28 were unique to ELT, 163 were unique to EC, and 4 were common to both herbs. Because the oral bioavailability (OB) and drug-likeness (DL) values for most compounds in EC and ELT were low or unknown, we were not able to apply these values for compound screening. We therefore considered all compounds with known targets as the active ingredients of EC and ELT. In total, 62 compounds had known targets; these were considered as the active ingredients of TBD.

Following the removal of duplicates, we identified a total of 2,251 targets for TBD. In total, we identified 1,412 targets for the active ingredients of EC, 509 targets for the active ingredients of ELT, and 330 targets for the targets shared by EC and ELT. All compound targets were retrieved from Swiss Target Prediction software and the Superpred Webserver. We also identified 581 gene targets that were associated with PMOP *via* the use of Drugbank. After comparing the targets that were associated with both TBD and PMOP, we identified 89 potential targets for TBD against PMOP. These potential targets were entered into the String database (set to human and a high confidence level of 0.7). Node1 and node 2 were then imported into Cytoscape software to allow us to create an interaction network (**Figure 4**). The nodes shown in **Figure 4** graph represent the targets while the edges represent associations between different proteins. The color and size of the nodes reflect the degree value for each protein target: the larger and darker the node, the greater the degree value. As shown in **Figure 4**, the target interaction network featured 89 nodes and 626 edges. According to degree

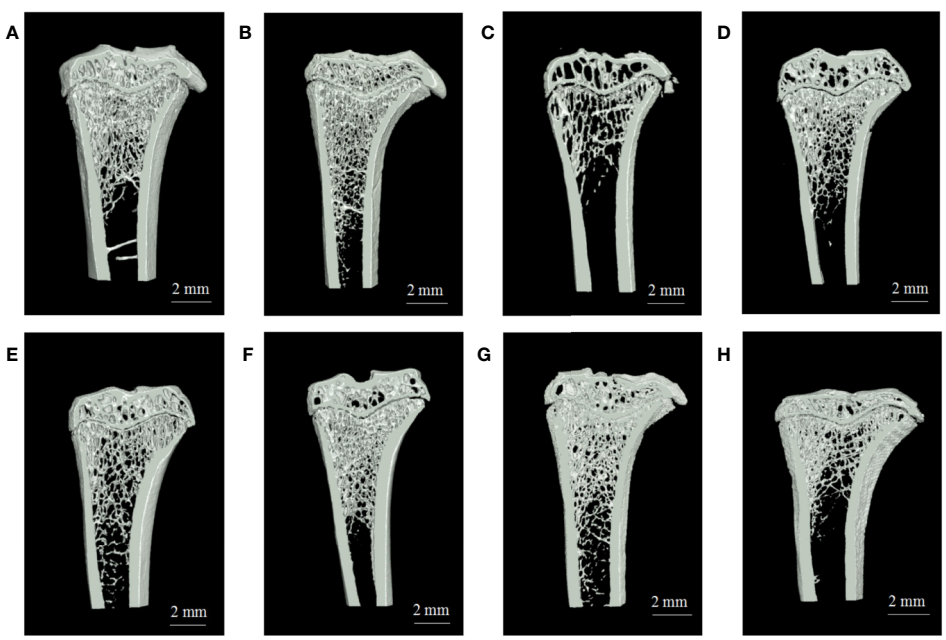

FIGURE 2 | The region of interest (ROI) image and bone parameters analysis in tibia in different rats: **(A)** sham group, **(B)** blank group, **(C)** ovariectomized (OVX) group, **(D)** low dose treated group, **(E)** medium dose treated group, **(F)** high dose treated group, **(G)** gushukang treated group, and **(H)** estrogen treated group.

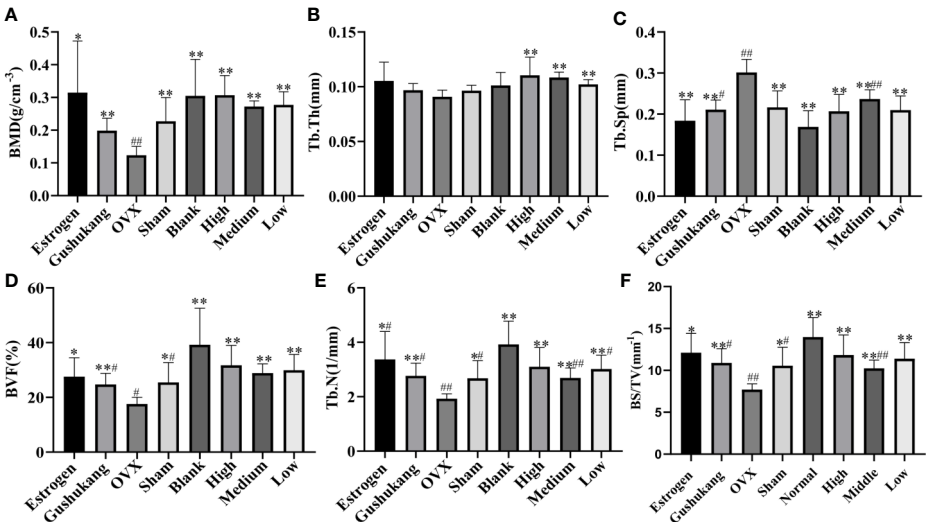

FIGURE 3 | **(A)** Comparison of bone mineral density (BMD) in eight groups; **(B)** Comparison of Tb•Th in eight groups; **(C)** Comparison of Tb•Sp in eight groups; **(D)** Comparison of bone volume fraction (BVF) in eight groups; **(E)** Comparison of Tb•N in eight groups; **(F)** Comparison of BS/TV in eight groups. Values were expressed as the mean ± SD; n = 6. $^{\#}p < 0.05$, $^{\#\#}p < 0.01$ compared with blank group. $^{*}p < 0.05$, $^{**}p < 0.01$ compared with OVX group.

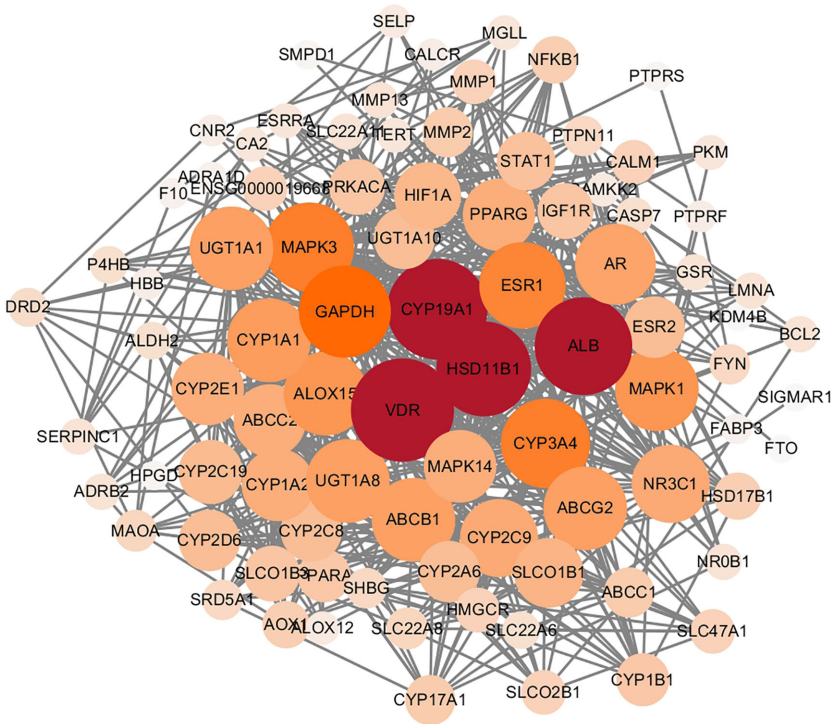

FIGURE 4 | Protein interaction network of Tubson-2 decoction (TBD) against post-menopausal osteoporosis (PMOP). The nodes in the graph represent targets, while the edges represent the association between proteins. And the node size represented degree value. The larger the node, the larger the degree value.

values, the key targets for TBD against PMOP were CYP19A1, HSD11B1, VDR, and albumin (ALB).

GLUE GO analysis identified the top biological features of our interaction network as hormone metabolic process, steroid metabolic process, and oxidoreductase process. We then calculated the gene frequencies for the key target genes in these three biological pathways. Analysis showed that VDR, CYP19A1 and beta-2 adrenergic receptor (ADRB2) appeared eight times; tyrosine-protein phosphatase non-receptor type (PTPN), estradiol 17-beta-dehydrogenase 1 (HSD17B1), and ethylene-responsive transcription factor ESR1 (ESR1) appeared seven times; and HSD11B1 appeared six times. By combining these results with the PPI data, we found that CYP19A1, HSD11B1, and VDR were the most important potential targets for TBD when used to treat PMOP.

Metabolomics Analysis Showed That 26 Potential Biomarkers Were Involved in OVX-Induced Osteoporosis and Regulated by TBD

As shown in the PCA score plot (**Figures 5A, B**), the analysis of QC samples showed good reproducibility and reliability. PCA showed that the dataset derived from the OVX group was separated from the data derived from the other groups. The widespread distribution of data following PCA was likely to be caused by individual differences in rats and/or the timing of sampling. To exclude the effect of potential confounding variables that were not related to the group differences, and to evaluate the statistical significance of these effects, we applied PLS-DA analysis (**Figures 5C, D**). The results of this analysis were highly encouraging as the discrimination model could readily differentiate between the eight groups. Although the distribution of pre-cachexia overlapped with the OVX and estrogen groups, these models showed appropriate goodness-of-fit values with high cross-validation predictability, with cumulative R2Y values of 1.000 and cumulative Q2 values of 0.977 in the positive mode, and R2Y value of 0.959 and a cumulative Q2 value of 0.541 in the negative mode (**Table 1**), indicating reliable differentiation between the groups.

In order to identify distinct biomarkers that may be associated with TBD treat OVX-induced osteoporosis among a dataset featuring thousands of variables, we conducted pairwise comparisons between the OVX and TBD medium-treated groups (**Figures 6A, B**). Validation analysis was satisfactory with regards to group classification, with a cumulative R^2Y value of 0.999 and a cumulative Q^2 value of 0.978 in the positive mode, and a cumulative R^2Y value of 0.997 and a cumulative Q^2 value of 0.935 in the negative mode (**Table 1**). Permutation tests for the TBD medium-treated groups and OVX group are shown in **Figures 6C, D**. After filtering with VIP values, and results arising from the Student's t test, we identified 105 metabolites as potential biomarkers (82 metabolites from the positive ion mode and 23 metabolites from the negative ion mode). Next, we used HMBD and the mzCloud online database to identify these potential biomarkers. By considering the metabolites that overlapped each pairwise comparison, we identified a total of 26 putative biomarkers (**Table 2**). The potential differential metabolites were identified by standard,

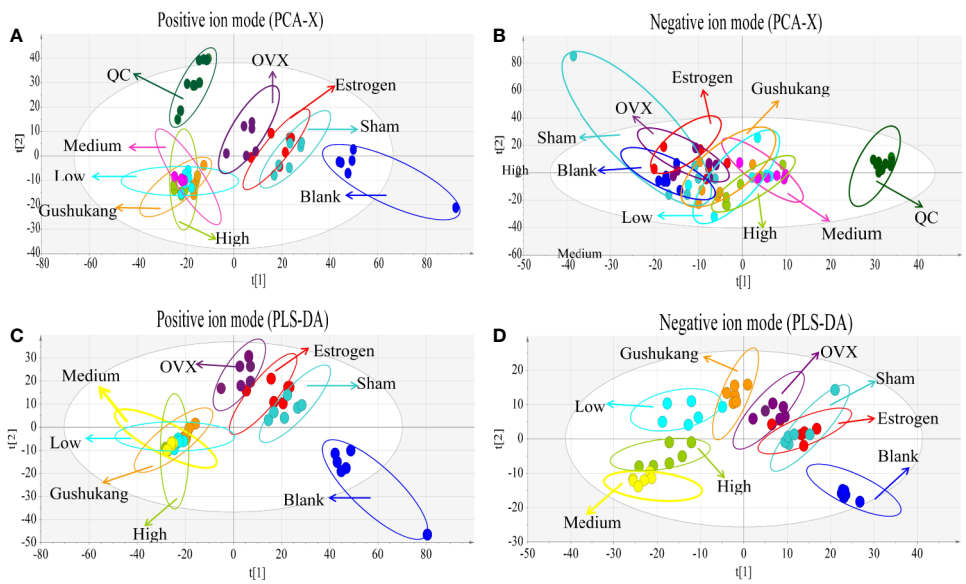

FIGURE 5 | Multivariate analysis based on the UHPLC- Q-Exactive-MS profiling data for samples in the blank, sham, ovariectomized (OVX), low dose treated group, medium dose treated group, high dose treated group, estrogen treated group, and gushukang treated group in positive and negative ion mode (n = 6). **(A)** Principal component analysis (PCA) score plot in positive ion mode; **(B)** PCA score plot in negative ion mode; **(C)** Partial least squares discriminant analysis (PLS-DA) score plot in positive ion mode; **(D)** PLS-DA score plot in negative ion mode.

TABLE 1 | Summary of partial least squares discriminant analysis (PLS-DA) model parameters for evaluating model quality by 200 permutation tests of corresponding validation plots.

	Ion mode	*A*	R2X	R2Y	Q2(cum)	R2 intercepts	Q2 intercepts
OVX vs Sham	Positive mode	2	0.413	0.998	0.939	0.921	-0.237
	Negative mode	2	0.361	0.956	0.517	0.88	-0.0204
OVX vs Mediuim-treated	Positive mode	2	0.620	0.999	0.978	0.802	-0.0681
	Negative mode	2	0.420	0.997	0.935	0.895	-0.0716
OVX VS Estrogen-treated	Positive mode	2	0.552	1.000	0.977	0.868	-0.0496
	Negative mode	2	0.313	0.959	0.541	0.914	-0.0144

A was number of components.

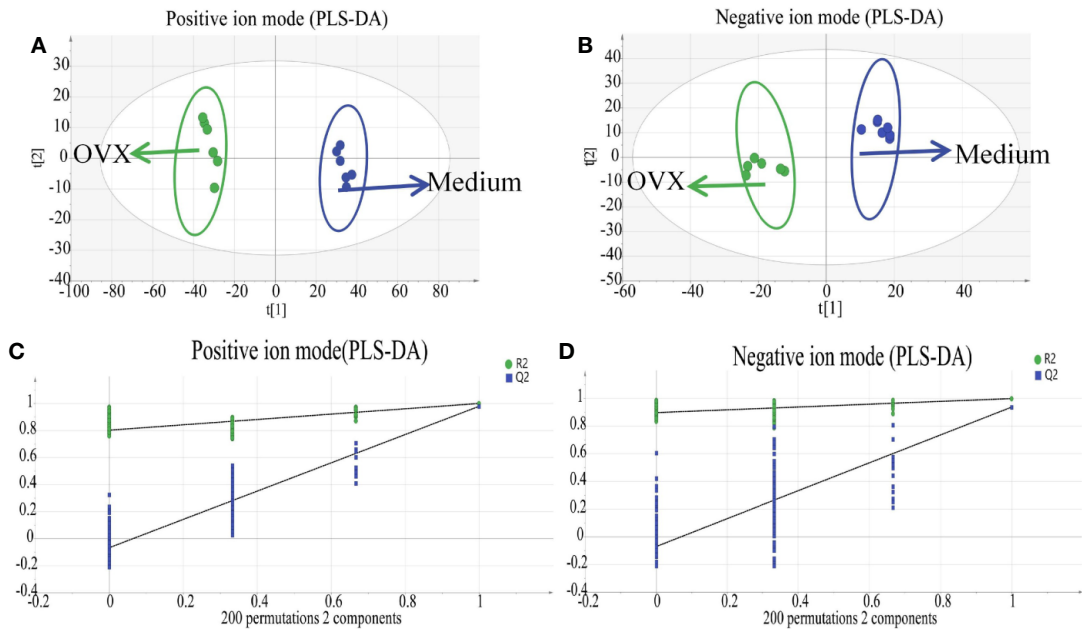

FIGURE 6 | Multivariate analysis based on the UHPLC- Q-Exactive-MS profiling data for samples in the Tubson-2 decoction (TBD) medium-treated and ovariectomized (OVX) group in positive and negative ion mode (n = 6). **(A)** Partial least squares discriminant analysis (PLS-DA) score plot in positive ion mode; **(B)** PLS-DA score plot in negative ion mode. **(C)** permutation test of the TBD medium-treated and OVX group in positive ion mode; **(D)** permutation test of the TBD medium-treated and OVX group in negative ion mode.

ferulic acid, 350 its parent ion is [M-H]-: 193.005063, the main product ion fragments are (m/z): 134.03546, 351 149.06041, 178.00696, and the retention time is 11.45 min. This is consistent with our results and 352 further confirms the reliability of the ferulic acid test results.

Metabolomic Analysis Identified Vitamin B6 Metabolism as the Key Pathway in OVX-Induced Osteoporosis and Could Be Regulated by Tubson-2

Next, we pooled the metabolites that showed alterations in rat serum and identified a total of 26 putative metabolites for analysis. The fold-changes of these metabolites in the OVX, sham, and medium-dose-treated groups are shown in **Table 2**. Pathway analysis, carried out using MetaboAnalyst (http://www.metaboanalyst.ca/), revealed the detailed impacts of OVX-related alterations in metabolic networks (**Figure 7A**). To investigate the most influential metabolic pathway, we set the following threshold values: -log (*P*) values >1.5 and pathway impact >0.1. Three metabolic pathways were defined as being disturbed in the serum profiles of rats with TBD treated OVX-induced osteoporosis: vitamin B6 metabolism, phenylalanine metabolism, phenylalanine, and tyrosine and tryptophan biosynthesis. Based on the biomarkers that were potentially responsible for TBD treatment, we then used the Kyoto Gene and Genome Encyclopedia database (KEGG (http://www.genome.ad.jp/kegg/), and the human metabolism database (http://www.hmdb.ca/), to create a metabolic network for metabolic pathways that were altered by TBD treated OVX (**Figure 7B**).

TABLE 2 | Identification of potential differential metabolites in rats serum in positive and negative mode.

NO.	Metabolite	Formula	Adduct	Accurate Mass (m/z)		Error*(ppm)	RT(min)	VIP	(OVX)/(Sham)	(Medium treated)/(OVX)
				measured	predicted					
1	Monobutyl phthalate	$C_{12}H_{14}O_4$	[M-H]-	223.0964	222.0888	-4.51	1.77	1.80	↑	↓
2	4-Methylhippuric acid	$C_{10}H_{11}NO_3$	[M-H]-	192.0666	193.0724	-5.24	6.60	1.20	↑	↓
3	N-Isovalerylglycine	$C_7H_{13}NO_3$	[M-H]-	158.0822	159.0878	-6.36	4.79	1.48	↑	↓
4	Phenobarbital	$C_{12}H_{12}N_2O_3$	[M-H]-	231.0775	232.0836	-4.35	8.02	1.46	↑	↓
5	Indole-3-acrylic acid	$C_{11}H_9NO_2$	[M+H]-	188.0706	187.0631	5.35	13.48	1.45	↓	↑
6	13S-hydroxyoctadecadienoic acid	$C_{18}H_{32}O_3$	[M-H]-	295.2279	296.2346	-3.41	18.10	1.44	↑	↓
7	N-Formylmethionine	$C_6H_{11}NO_3S$	[M-H]-	176.0387	177.0445	-5.71	1.72	1.42	↑	↓
8	N-Isobutyrylglycine	$C_6H_{11}NO_3$	[M-H]-	144.0666	145.0722	-6.98	1.93	1.38	↑	↓
9	3-Hydroxybutyric acid	$C_4H_8O_3$	[M-H]-	103.0400	104.0456	-9.75	0.82	1.36	↑	↓
10	12-Hydroxydodecanoic acid	$C_{12}H_{24}O_3$	[M-H]-	215.1653	216.1713	-4.68	17.8	1.25	↑	↓
11	Ferulic acid	$C_{10}H_{10}O_4$	[M-H]-	193.0506	194.0558	-5.21	11.46	1.22	↑	↓
12	Testosterone glucuronide	$C_{25}H_{36}O_8$	$[M+H]^+$	465.2483	464.2409	2.17	17.64	1.52	↑	↓
13	1,2-Dipalmitoylphosphatidylglycerol	$C_{38}H_{75}O_{10}P$	$[M+H]^+$	723.5171	744.4980	-2.90	20.67	1.52	↑	↓
14	Kynurenine	$C_{10}H_{12}N_2O_3$	[M+H]+	209.0921	208.0844	4.82	2.84	1.41	↑	↓
15	Spectinomycin	$C_{14}H_{24}N_2O_7$	[M+H]+	333.1656	332.1624	3.01	16.49	1.37	↑	↓
16	DL-Carnitine	$C_7H_{15}NO_3$	$[M+H]^+$	162.1125	161.1047	6.22	1.13	1.35	↓	↑
17	Phenylalanine	$C_9H_{11}NO_2$	$[M+H]^+$	166.0863	165.0786	6.07	3.24	1.34	↑	↓
18	Phenylacetylglycine	$C_{10}H_{11}NO_3$	$[M+H]^+$	194.0812	193.0735	5.19	6.20	1.34	↑	↓
19	Hippuric acid	$C_9H_9NO_3$	[M+H]+	180.0655	179.0582	5.59	5.78	1.32	↑	↓
20	6-Methylquinoline	$C_{10}H_9N$	$[M+H]^+$	142.0662	143.0733	7.09	5.12	1.29	↓	↑
21	Skatole	C_9H_9N	[M+H]+	132.0808	131.0735	7.63	5.12	1.28	↑	↓
22	2-Amino-1,3,4-octadecanetriol	$C_{18}H_{39}NO_3$	[M+H]+	318.3003	317.2921	3.17	18.88	1.10	↓	↑
23	Pyridoxal	$C_8H_9NO_3$	[M+H]+	168.0655	167.0581	5.99	1.78	1.09	↓	↑
24	Pyridoxamine	$C_8H_{12}N_2O_2$	[M+H]+	169.0972	168.0872	5.97	1.45	1.07	↑	↓
25	3-Hydroxyanthranilic acid	$C_7H_7NO_3$	$[M+H]^+$	154.0499	153.0427	6.54	1.13	1.06	↑	↓
26	Creatine	$C_4H_9N_3O_2$	[M+H]+	132.0768	131.0694	7.63	1.77	1.05	↑	↓

**The error between predicted accurate mass and measured accurate mass; RT, retention time; (↓):down-regulated, (↑):up-regulated.*

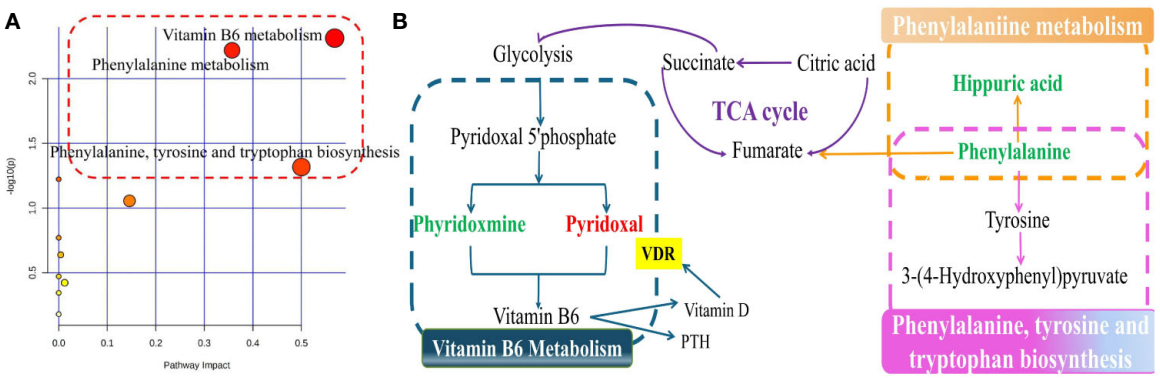

FIGURE 7 | The signaling pathway analysis based on the potential biomarkers **(A)** Summary of ingenuity pathway analysis with MetaboAnalyst. The size and color of each circle were based on pathway impact value and p-value, respectively; **(B)** Construction of the main metabolic pathways related to differential metabolites. (down-regulated in green, up-regulated in red.)

Target Validation Was Performed by ELISA Assay

We used network pharmacology and metabolomics to identify the crucial targets for TBD in the treatment of PMOP; the most important targets were VDR, HSD11B1, and CYP19A1. We then used ELISA kits to validate the levels of these crucial targets in samples of rat sera. As shown in **Figure 8**, the concentrations of VDR, HSD11B1, and CYP19A1 were elevated in the OVX group, thus presenting the inhibition of these cytokines. The serum levels of VDR and CYP19A1 were reduced following the administration of TBD, suggesting that TBD is able to treat OVX-induced osteoporosis by ameliorating the levels of VDR and CYP19A1.

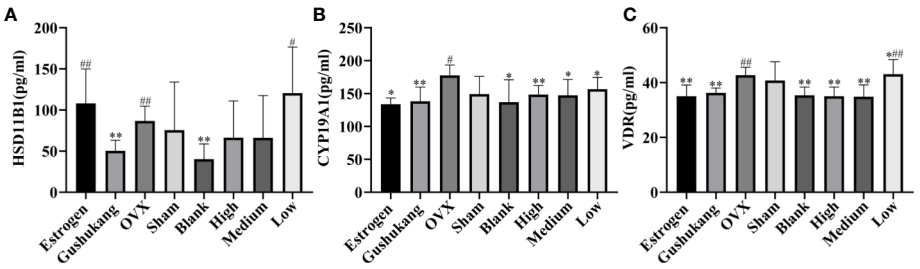

FIGURE 8 | Three targets levels of serum in eight groups: **(A)** HSD11B1; **(B)** CYP19A1; **(C)** VDR. Values were expressed as the mean ± SD; n = 6. $^{\#}p < 0.05$, $^{\#\#}p < 0.01$ compared with blank group. $^{*}p < 0.05$, $^{**}p < 0.01$ compared with OVX group.

DISCUSSION

Previous research (Li et al., 2016) has demonstrated that PMOP is related to estrogen withdrawal and represents the most common metabolic bone disease in females. The use of bilateral ovariectomies in female rats is now well established as the method of choice with which to create an experimental model of osteoporosis (Thompson et al., 1995). Ovariectomy simulates menopause and osteopenia in experimental rats. Although it is well known that ovariectomy induces a menopausal status and 'osteoporotic' bone changes (Saleh et al., 2020), we analyzed vaginal smears and performed X-ray microtomography on each of our ovariectomized rats in order to confirm that the OVX-induced model of osteoporosis had been successfully created (Yousefzadeh et al., 2020). We selected Gushukang granules, as a traditional Chinese medicine (TCM) (Li et al., 2019), for osteoporosis, and estrogen tablets, a common supplement for PMOP patients, as positive control drugs with which to evaluate the efficacy of TBD on PMOP. As illustrated in previous, there was only a marginal and non-significant difference between different drug-treatment groups with respect to several trabecular morphological parameters. This implies that TBD exerts the same effect on OVX rats as the positive control drugs. We also investigated the relative effects of different TBD doses on OVX rats; doses were selected according to the guiding principles laid down by non-clinical pharmacokinetic drug research. The "low-dose" of TBD was the clinical equivalent dose, the "medium-dose" of TBD was double the clinical equivalent dose, and the "high-dose" of TBD was four times the clinical equivalent dose. However, we observed no dose-dependent relationship with regards to the relative effects of TBD on trabecular morphological parameters. It is likely that this observation was related to individual differences among the rats.

Metabolomics analysis revealed that 26 putative metabolites and 11 metabolic pathways were associated with the progression of TBD-treated-PMOP, including vitamin B6 (Hellmann and Mooney, 2010) metabolism, phenylalanine metabolism, phenylalanine, and the biosynthesis of both tyrosine and tryptophan. The metabolites involved in these metabolic pathways were shown to interact with each other to form a complex network. The derivatives of pyridoxal and pyridoxamine are able to form vitamin B6; consequently, these are key metabolites in the vitamin B6 metabolism pathway and were previously reported to be reduced in OVX results. Over recent years, an increasing body of research studies have demonstrated that a low dietary intake of vitamin B6, or low levels of vitamin B6 in the blood, might represent a novel and potentially modifiable risk factor for osteoporosis (Wang et al., 2019). Phenylalanine and hippuric acid are known to be the key biomarkers associated with the metabolic pathway of phenylalanine. Phenylalanine is an essential amino acid in the human body and belongs to the family of aromatic amino acids (Lopansri et al., 2006). Phenylalanine is oxidized by phenylalanine hydroxylase to form tyrosine and a range of brain chemicals, including levodopa, epinephrine, norepinephrine, and thyroid hormones (Fernstrom and Fernstrom, 2007). Therefore, the metabolic status of phenylalanine is closely related to normal physiological function in the body. Previous researchers (Tao et al., 2017) have highlighted that the regulation of metabolic disorders associated with phenylalanine can prevent the occurrence of osteoporosis. Hippuric acid, a glycine conjugate of benzoic acid, is expressed in many disorders associated with enzymatic metabolism, including diabetes, obesity, and osteoporosis. Hippuric acid is mainly excreted *via* glomerular filtration and by an active secretion mechanism in the renal tubules. However, when the kidney is damaged, the content of hippuric acid in the urine decreases; consequently, there is an increase in the serum levels of hippuric acid (Wang and Bao, 2013). Vitamin D needs to be catalyzed by 1α-hydroxylase in the kidney and is then hydroxylated again to become the more active 1,25-(OH)2D3. A reduction in 1,25-(OH) 2D3 content will inevitably lead to the loss of bone mass and induce osteoporosis in the bones (Lin et al., 2008).

CYP19A1, an aromatase-encoding gene, is known to be related to osteoporosis and can influence BMD by altering the levels of estrogen (Sowers et al., 2006). HSD11B1 is known to be expressed by human osteoblasts *in vivo* and could reduce the proliferation of osteoblasts and induce the differentiation of osteoblasts *in vitro*. Gene polymorphism can result in direct changes in the mass of bone and can help to convert androgens and glucocorticoids to estrogen (Hwang et al., 2009). A previous study showed significant associations between a range of HSD11B1 alleles and haplotypes and bone fracture density and BMD in postmenopausal women. VDR is the target receptor that regulates the transcription of vitamin D. Previously, researchers

have focused on the relationship between VDR and PMOP and demonstrated that changes in the VDR genotype were evident in patients with PMOP (Zhang L. et al., 2018). We found that the levels of these indices in the OVX group were much higher than those in the sham group, but were down regulated in the drug-treatment groups, thus suggesting that TBD can treat PMOP by regulating the specific levels of these targets.

Previous literature has reported a clear relationship between vitamin B6 levels, vitamin D, and parathyroid hormone (PTH) (Khundmiri et al., 2016), and a positive correlation between VDR, PTH, and vitamin D. This view makes the results of network pharmacology and metabolomics organically combined. Phyridoxmine and pyridoxal are two forms of vitamin B6, which are important different metabolites in the vitamin B6 metabolic pathway (Saito, 2006). In other words, there is a close connection between the gene VDR and the differential metabolites compound phyridoxmine, pyridoxal, and the vitamin B6 metabolic pathway. We used network pharmacology and metabolomics to integrate the crucial targets, differential metabolite and metabolic pathways to explore the mechanism of TBD to treat PMOP. Our analysis showed that VDR and vitamin B6 metabolism were critical mechanisms underlying the effect of TBD on PMOP. However, we have not been able to identify the specific components of TBD that combine with the target VDR. In our future research, we aim to use online docking software in an attempt to identify the specific compounds in TBD that bind to VDR; such work should provide us with stronger evidence for the wider application of TBD in the clinical treatment of PMOP.

CONCLUSION

By integrating the results derived from network pharmacology and metabolomics, we identified VDR and vitamin B6 metabolism as the key indicator and pathway, respectively, for the action of TBD against PMOP. ELISAs further showed that several crucial targets (VDR, HSD11B1, and CYP19A1) were elevated in the OVX group but were reduced following TBD treatment. From a mechanistic point of view, TBD appears to regulate vitamin B6 metabolism by altering VDR content, thus mitigating the process of PMOP. Our findings enhance our understanding of how TBD could be used to treat PMOP and will help to facilitate the wider clinical use of TBD treatments.

DATA AVAILABILITY STATEMENT

The raw data supporting the conclusions of this article will be made available by the authors, without undue reservation, to any qualified researcher.

ETHICS STATEMENT

The animal study was reviewed and approved by Animal Ethics Committee of Inner Mongolia Medical University (Reference: SCXK2015-0001).

AUTHOR CONTRIBUTIONS

PX conceived of and designed the experiments. FY performed the experiment and carried out the animal experiments. XD performed the data analysis and wrote the paper. FX gave some advices. JL, FM, JKL, CL, and RB collected *Echinops latifolius* Tausch samples outside. FY and XD conducted the data interpretation. All authors contributed to the article and approved the submitted version.

FUNDING

This work was financially supported by National Natural Science Foundation of China (81860756), National Natural Science Foundation of China (81960758), Natural Science Foundation of Inner Mongolia Autonomous Region (2017MS08122), Natural Science Foundation of Inner Mongolia Autonomous Region (2019MS08111), Inner Mongolia Science and Technology Innovation Guide Project (02039001), Inner Mongolia Autonomous Region Higher Education Science Research Project (NJZY19099).

SUPPLEMENTARY MATERIAL

The Supplementary Material for this article can be found online at: https://www.frontiersin.org/articles/10.3389/fphar.2020.581991/full#supplementary-material

REFERENCES

Alexandre, C., and Vico, L. (2011). Pathophysiology of bone loss in disuse osteoporosis. *Joint Bone Spine* 78, 572–576. doi: 10.1016/j.jbspin.2011.04.007

Fernstrom, J. D., and Fernstrom, M. H. (2007). Tyrosine, phenylalanine, and catecholamine synthesis and function in the brain. *J. Nutr.* 137, 1539S–1547S. doi: 10.1093/jn/137.6.1539S

Gambacciani, M., Cagnacci, A., and Lello, S. (2019). Hormone replacement therapy and prevention of chronic conditions. *Climacteric* 22, 303–306. doi: 10.1080/13697137.2018.1551347

Gfeller, D., Grosdidier, A., Wirth, M., Daina, A., Michielin, O., and Zoete, V. (2014). SwissTargetPrediction: a web server for target prediction of bioactive small molecules. *Nucl. Acids Res.* 42, W32–W38. doi: 10.1093/nar/gku293

Guo, S., Liu, J., Li, N., Ma, F. X., Gao, J. P., Xue, P. F., et al. (2020). Evaluation of the Possibility of Eucommia ulmoides Leaves Replacing its Barks by Fingerprint combined with multi-components Quantitive by One Marker Method. *J. Chin. Med. Mater.* 4, 898–904. doi: 10.13863/j.issn1001-4454.2020.04.022

Han, D., Chen, W., Gu, X., Shan, R., Zou, J., Liu, G., et al. (2017). Cytoprotective effect of chlorogenic acid against hydrogen peroxide-induced oxidative stress in MC3T3-E1 cells through PI3K/Akt-mediated Nrf2/HO-1 signaling pathway. *Oncotarget* 8, 14680–14692. doi: 10.18632/oncotarget.14747

Hao, D., and Xiao, P. G. (2014). Network pharmacology: a Rosetta Stone for traditional Chinese medicine. *Drug Dev. Res.* 75, 299–312. doi: 10.1002/ddr.21214

Hellmann, H., and Mooney, S. (2010). Vitamin B6: a molecule for human health? *Molecules* 15, 442–459. doi: 10.3390/molecules15010442

Hwang, J. Y., Lee, S. H., Kim, G. S., Koh, J. M., Go, M. J., Kim, Y. J., et al. (2009). HSD11B1 polymorphisms predicted bone mineral density and fracture risk in postmenopausal women without a clinically apparent hypercortisolemia. *Bone* 45, 1098–1103. doi: 10.1016/j.bone.2009.07.080

Jiang, X. D. (2018). Hormone therapy for the treatment of postmenopausal osteoporosis: will it soon become a lost art in medicine? *Menopause* 25, 723–727. doi: 10.1097/GME.0000000000001124

Johnson, C. H., Ivanisevic, J., and Siuzdak, G. (2016). Metabolomics: beyond biomarkers and towards mechanisms. *Nat. Rev. Mol. Cell. Biol.* 17, 451–459. doi: 10.1038/nrm.2016.25

Khundmiri, S. J., Murray, R. D., and Lederer, E. (2016). PTH and Vitamin D. *Compr. Physiol.* 6, 561–601. doi: 10.1002/cphy.c140071

Komm, B. S., Morgenstern, D., A Yamamoto, L., and Jenkins, S. N. (2015). The safety and tolerability profile of therapies for the prevention and treatment of osteoporosis in postmenopausal women. *Expert. Rev. Clin. Pharmacol.* 8, 769–784. doi: 10.1586/17512433.2015.1099432

Li, F., Yang, X., Bi, J., Yang, Z., and Zhang, C. (2016). Antiosteoporotic activity of Du-Zhong-Wan water extract in ovariectomized rats. *Pharm. Biol.* 54, 1857–1864. doi: 10.3109/13880209.2015.1133657

Li, Y., Li, Y., Lu, W., Li, H., Wang, Y., Luo, H., et al. (2018). Integrated network pharmacology and metabolomics analysis of the therapeutic effects of Zi Dian Fang on immune thrombocytopenic purpura. *Front. Pharmacol.* 9, 597. doi: 10.3389/fphar.2018.00597

Li, X. L., Wang, L., Bi, X. L., Chen, B. B., and Zhang, Y. (2019). Gushukang exerts osteopreserve effects by regulating vitamin D and calcium metabolism in ovariectomized mice. *J. Bone Miner. Metab.* 37, 224–234. doi: 10.1007/s00774-018-0924-1

Li, J., Chen, X., Lu, L., and Yu, X. (2020). The relationship between bone marrow adipose tissue and bone metabolism in postmenopausal osteoporosis. *Cytokine. Growth. Factor. Rev.* 52, 88–98. doi: 10.1016/j.cytogfr.2020.02.003

Lin, Y. P., Guo, S. M., Wu, Y. S., Lin, Y., Lu, T. X., Huang, M. Y., et al. (2008). Study on the correlations between the bone quality and level of u-DPD and serum 1,25-(OH) 2D3 in the ovariectomized osteoporosis rats. *Chin. J. Ortho. Trauma.* 21, 910–913.

Liu, J. (2016). Clinical study of Mongolian medicine Erwei Duzhong Decoction in the treatment of postmenopausal osteoporotic bone pain. *J. Med. Phar. Chin.* 22, 18–19. doi: 10.16041/j.cnki.cn15-1175.2016.08.011

Liu, H., Xiong, Y., Wang, H., Yang, L., Wang, C., Liu, X., et al. (2018). Effects of water extract from epimedium on neuropeptide signaling in an ovariectomized osteoporosis rat model. *J. Ethnopharmacol.* 221, 126–136. doi: 10.1016/j.jep.2018.04.035

Liu, Y., Wang, X., Chang, H., Gao, X., Dong, C., Li, Z., et al. (2018). Mongolian Medicine echinops prevented postmenopausal osteoporosis and induced ER/AKT/ERK pathway in BMSCs. *Biosci. Trends* 12, 275–281. doi: 10.5582/bst.2018.01046

Lopansri, B. K., Anstey, N. M., Stoddard, G. J., Mwaikambo, E. D., Boutlis, C. S., Tjitra, E., et al. (2006). Elevated plasma phenylalanine in severe malaria and implications for pathophysiology of neurological complications. *Infect. Immun.* 74, 3355–3359. doi: 10.1128/IAI.02106-05

Lv, H., Jiang, F., Guan, D., Lu, C., Guo, B., Chan, C., et al. (2016). Metabolomics and Its Application in the Development of Discovering Biomarkers for Osteoporosis Research. *Int. J. Mol. Sci.* 17, 2018. doi: 10.3390/ijms17122018

Nickel, J., Gohlke, B. O., Erehman, J., Banerjee, P., Rong, W. W., Goede, A., et al. (2014). SuperPred: update on drug classification and target prediction. *Nucl. Acids Res.* 42, W26–W31. doi: 10.1093/nar/gku477

Ru, J., Li, P., Wang, J., Zhou, W., Li, B., Huang, C., et al. (2014). TCMSP: a database of systems pharmacology for drug discovery from herbal medicines. *J. Cheminform.* 6:13. doi: 10.1186/1758-2946-6-13

Saito, M. (2006). Elevated plasma concentration of homocysteine, low level of vitamin b6, pyridoxal, and vitamin d insufficiency in patients with hip fracture: a possible explanation for detrimental cross-link pattern in bone collagen. *Clin. Calcium* 16 (12):1974.

Saleh, N., Nassef, N. A., Shawky, M. K., Elshishiny, M.II, and Saleh, H. A. (2020). Novel approach for pathogenesis of osteoporosis in ovariectomized rats as a model of postmenopausal osteoporosis. *Exp. Gerontol.* 137, 110935. doi: 10.1016/j.exger.2020.110935

Sowers, M. R., Wilson, A. L., Kardia, S. R., Chu, J., and Ferrell, R. (2006). Aromatase gene (CYP 19) polymorphisms and endogenous androgen concentrations in a multiracial/multiethnic, multisite study of women at midlife. *Am. J. Med.* 119, S23–S30. doi: 10.1016/j.amjmed.2006.07.003

Tan, X. L., Zhang, Y. H., Cai, J. P., Zhu, L. H., Ge, W. J., and Zhang, X. (2014). 5-(Hydroxymethyl)-2-furaldehyde inhibits adipogenic and enhances osteogenic differentiation of rat bone mesenchymal stem cells. *Nat. Prod. Commun.* 9, 529–532. doi: 10.1177/1934578X1400900427

Tao, Y., Chen, X., Li, W., Cai, B., Di, L., Shi, L., et al. (2017). Global and untargeted metabolomics evidence of the protective effect of different extracts of Dipsacus asper Wall. ex C.B. Clarke on estrogen deficiency after ovariectomia in rats. *J. Ethnopharmacol.* 199, 20–29. doi: 10.1016/j.jep.2017.01.050

Thompson, D. D., Simmons, H. A., Pirie, C. M., and Ke, H. Z. (1995). FDA Guidelines and animal models for osteoporosis. *Bone* 17, 25S–133S. doi: 10.1016/8756-3282(95)00285-l

Wang, Y., and Bao, X. (2013). Effects of uric acid on endothelial dysfunction in early chronic kidney disease and its mechanisms. *Eur. J. Med. Res.* 20, 44. doi: 10.1186/s40001-015-0124-6

Wang, J., Chen, L., Zhang, Y., Li, C. G., Zhang, H., Wang, Q., et al. (2019). Association between serum vitamin B_6 concentration and risk of osteoporosis in the middle-aged and older people in China: a cross-sectional study. *BMJ Open* 9, e028129. doi: 10.1136/bmjopen-2018-028129

Wang, J., Dong, X., Ma, F., Li, C., Bu, R., Lu, J., et al. (2020). Metabolomics profiling reveals Echinops latifolius Tausch improves the trabecular micro-architecture of ovariectomized rats mainly via intervening amino acids and glycerophospholipids metabolism. *J. Ethnopharmacol.* 260, 113018. doi: 10.1016/j.jep.2020.113018

Wishart, D. S., Feunang, Y. D., Guo, A. C., Lo, E. J., Marcu, A., Grant, J. R., et al. (2018). DrugBank 5.0: a major update to the DrugBank database for 2018. *Nucl. Acids Res.* 46, D1074–D1082. doi: 10.1093/nar/gkx1037

Xu, H. Y., Zhang, Y. Q., Liu, Z. M., Chen, T., Lv, C. Y., Tang, S. H., et al. (2019). ETCM: an encyclopaedia of traditional Chinese medicine. *Nucl. Acids Res.* 47, D976–D982. doi: 10.1093/nar/gky987

Yousefzadeh, N., Kashfi, K., Jeddi, S., and Ghasemi, A. (2020). Ovariectomized rat model of osteoporosis: a practical guide. *Excli. J.* 19, 89–107. doi: 10.17179/excli2019-1990

Zhan, B. L. (1977). *Golden Cabinet of Mongolian Medicine* (Hohhot: Inner Mongolia People's Publishing House).

Zhang, W., Fujikawa, T., Mizuno, K., Ishida, T., Ooi, K., Hirata, T., et al. (2012). Eucommia leaf extract (ELE) prevents OVX-induced osteoporosis and obesity in rats. *Am. J. Chin. Med.* 40, 735–752. doi: 10.1142/S0192415X12500553

Zhang, M., Wang, Y., Zhang, Q., Wang, C., Zhang, D., Wan, J. B., et al. (2018). UPLC/Q-TOF-MS-based metabolomics study of the anti-osteoporosis effects of Achyranthes bidentata polysaccharides in ovariectomized rats. *Int. J. Biol. Macromol* 112, 433–441. doi: 10.1016/j.ijbiomac.2018.01.204

Zhang, L., Yin, X., Wang, J., Xu, D., Wang, Y., Yang, J., et al. (2018). Associations between VDR Gene Polymorphisms and Osteoporosis Risk and Bone Mineral Density in Postmenopausal Women: A systematic review and Meta-Analysis. *Sci. Rep.* 8, 981. doi: 10.1038/s41598-017-18670-7

Zhang, Z., Yi, P., Yang, J., Huang, J., Xu, P., Hu, M., et al. (2020). Integrated network pharmacology analysis and serum metabolomics to reveal the cognitive improvement effect of Bushen Tiansui formula on Alzheimer's disease. *J. Ethnopharmacol.* 249:112371. doi: 10.1016/j.jep.2019.112371

Zou, Z., Liu, W., Cao, L., Liu, Y., He, T., Peng, S., et al. (2020). Advances in the occurrence and biotherapy of osteoporosis. *Biochem. Soc Trans.* 6, BST20200005. doi: 10.1042/BST20200005

Conflict of Interest: The authors declare that the research was conducted in the absence of any commercial or financial relationships that could be construed as a potential conflict of interest.

Copyright © 2020 Yang, Dong, Ma, Xu, Liu, Lu, Li, Bu and Xue. This is an open-access article distributed under the terms of the Creative Commons Attribution License (CC BY). The use, distribution or reproduction in other forums is permitted, provided the original author(s) and the copyright owner(s) are credited and that the original publication in this journal is cited, in accordance with accepted academic practice. No use, distribution or reproduction is permitted which does not comply with these terms.

frontiers in Pharmacology

ORIGINAL RESEARCH
published: 15 October 2020
doi: 10.3389/fphar.2020.01320

Regulation of $GABA_A$ and 5-HT Receptors Involved in Anxiolytic Mechanisms of Jujube Seed: A System Biology Study Assisted by UPLC-Q-TOF/MS and RT-qPCR Method

Liang Chen[1†], Xue Zhang[1†], Chun Hu[2], Yi Zhang[1], Lu Zhang[1], Juntao Kan[1], Bo Li[1] and Jun Du[1]*

[1] Nutrilite Health Institute, Amway (China) R&D Center, Shanghai, China, [2] Nutrilite Health Institute, Amway Innovation and Science, Buena Park, CA, United States

OPEN ACCESS

Edited by:
Hai Yu Xu,
China Academy of Chinese Medical Sciences, China

Reviewed by:
Juan Francisco Rodríguez-Landa, University of Veracruz, Mexico
Chunmei Zhang, Shandong Agricultural University, China

***Correspondence:**
Jun Du
eric.du@amway.com

[†]These authors have contributed equally to this work

Specialty section:
This article was submitted to Ethnopharmacology, a section of the journal Frontiers in Pharmacology

Received: 01 April 2020
Accepted: 07 August 2020
Published: 15 October 2020

Citation:
Chen L, Zhang X, Hu C, Zhang Y, Zhang L, Kan J, Li B and Du J (2020) Regulation of $GABA_A$ and 5-HT Receptors Involved in Anxiolytic Mechanisms of Jujube Seed: A System Biology Study Assisted by UPLC-Q-TOF/MS and RT-qPCR Method. Front. Pharmacol. 11:01320. doi: 10.3389/fphar.2020.01320

The increase of the prevalence of anxiety greatly impacts the quality of life in China and globally. As the most popular traditional Chinese medicinal ingredient for nourishing health and tranquilizing mind, Jujube seed (*Ziziphus jujuba* Mill., Rhamnaceae) (SZJ) has been proved to exert anxiolytic effects in previous reports. In this study, a system biology method assisted by UPLC-Q-TOF/MS and RT-qPCR was developed to systematically demonstrate the anxiolytic mechanisms of SZJ. A total of 35 phytochemicals were identified from SZJ extract (*Ziziphus jujuba* Mill. var. spinosa [Bunge] Hu ex H.F. Chow), which interact with 71 anxiolytic targets. Protein-protein interaction, genes cluster, Gene Ontology, and Kyoto Encyclopedia of Genes and Genomes (KEGG) pathways analysis were subsequently conducted, and results demonstrated that regulation of serotonergic and GABAergic synapse pathways were dominantly involved in the anxiolytic mechanisms of SZJ extract. The effects of SZJ extract on mRNA expressions of multiple $GABA_A$ (gamma-aminobutyric acid type A) and 5-HT (serotonin) receptors subtypes were further validated in human neuroblastoma SH-SY5Y cells using RT-qPCR. Results showed that SZJ extract (250 μg/mL) significantly up-regulated the mRNA level of GABRA1 and GABRA3 as well as HTR1A, HTR2A, and HTR2B in non-H_2O_2 treated SH-SY5Y cells. However, it exerted an inhibitive effect on the overexpressed mRNA of GABRA1, GABRA2, HTR1A, and HTR2A in H_2O_2 treated SH-SY5Y cells. Taken together, our findings suggest that anxiolytic mechanisms of SZJ mostly involve the regulation of GABAergic and serotonergic synapse pathways, especially a two-way modulation of GABRA1, HTR1A, and HTR2A. Our current results provide potential direction for future investigation of SZJ as an anxiolytic agent.

Keywords: anxiety, jujube seed, anxiolytic mechanism, system biology, 5-HT receptors, $GABA_A$ receptors

INTRODUCTION

Anxiety is characterized as excessive and persistent worry about the future, which in turn can impact one's ability to carry out activities of daily living. Anxiety can be divided into generalized anxiety disorder, panic disorder, obsessive-compulsive disorder, social anxiety disorder, and posttraumatic stress disorder (Möhler, 2012; Cohen et al., 2015). Physiological anxiety symptoms include pounding heart, difficulty breathing, upset stomach, muscle tension, sweating, and feeling faint or shaky (Teychenne et al., 2015). The global prevalence of anxiety is estimated at 16.6% across the life span, and it becomes a burden of healthcare and quality of life (Somers et al., 2006); therefore, it is important to develop effective and safe solutions for treatment (Starcevic, 2006). Tricyclic antidepressants, serotonin-specific reuptake inhibitors, and benzodiazepines have been developed to mitigate anxiety. While effective, these classes of drugs come with many side effects, such as insomnia, sexual dysfunction, suicidal ideation, and/or drug-dependency (Lakhan and Vieira, 2010). Therefore, the use of complementary and alternative medicines to improve anxiety has received increased attention. Traditional medicinal materials, such as Jujube seed (*Ziziphus jujuba* Mill., Rhamnaceae) (SZJ) (Huang et al., 2008; Wang Y. et al., 2008), saffron (*Crocus sativus* L.) (Lopresti et al., 2018; Milajerdi et al., 2018), valerian root (*Valeriana officinalis* L.), and passion flower (*Passiflora incarnata* L.) (Müller et al., 2003; Cass, 2004; Benke et al., 2009) have shown anti-anxiety benefits.

SZJ, also known as *Suanzaoren* in Chinese, was first recorded in *Shennong Bencao Jing*, the earliest classic treatise of Chinese Materia Medica. SZJ has a long history of use in China as a vital food and/or medicine that traditionally is considered to sustain human health by calming the mind and improving the quality of sleep. In recent years, accumulated evidences have shown that SZJ and/or its preparations exert positive outcome on insomnia (Jiang et al., 2007; Chen et al., 2011; Ni et al., 2015; Shergis et al., 2017; Xiao et al., 2018), anxiety (Peng et al., 2000; Liu et al., 2015), and depression (Liu et al., 2012; Liang et al., 2016), mainly through regulating GABAergic (Chen et al., 2007; Chen, 2008; Shergis et al., 2017) and serotoninergic systems (Wang L.-E. et al., 2008; Wang et al., 2010; Liu et al., 2015). Jujubosides (e.g., jujuboside A, B), C-glycoside flavonoid (e.g., spinosin), and pentacyclic triterpenic acid (e.g., betulinic acid) have been identified from SZJ (Liu et al., 2007; Zhang et al., 2008; Lee et al., 2016) as the potential active phytochemicals contributing to these healthy benefits.

Although previous studies have shown promising anxiolytic effects of SZJ, the underlying mechanism has not been systematically and comprehensively investigated. In our current work, we developed an integrated strategy of system biology assisted by ultra-performance liquid chromatography quadrupole-time of flight mass spectrometer (UPLC-Q-TOF/MS) and real-time quantitative reverse transcription polymerase chain reaction (RT-qPCR) to uncover the active phytochemicals and anxiolytic mechanism of SZJ extract. This approach provides a modern and practical way to study complicated chemical systems with multiple pathways and connected targets, which is otherwise a difficult challenge in mechanistic research of traditional Chinese medicine ingredients.

MATERIAL AND METHOD

Phytochemical Analysis of SZJ Extract Using Ultra-Performance Liquid Chromatography Quadrupole-Time of Flight Mass Spectrometer (UPLC-Q-TOF/MS)

Characteristics of the SZJ Extract

Commercial SZJ extract (batch number HS-180651) was purchased from Honsea Sunshine (Guangzhou, China). Dried seed of *Ziziphus jujuba* Mill. var. spinosa (Bunge) Hu ex H.F. Chow was used for SZJ extract production in Guangzhou, China. SZJ was extracted by supercritical fluid CO_2 to remove lipid fraction, and the residue was further extracted by 50% ethanol, followed by vacuum concentration and vacuum drying. The final extraction ratio is 5:1, and total content of jujuboside A and B was quantitatively detected as 0.20% using HPLC method. A voucher of the batch used has been deposited at -16° refrigerator, sampler chamber of Amway (China) R&D Center (Shanghai, China).

Sample Preparation

Thirty mg of SZJ extract powder was precisely weighted and then transferred to a centrifugal tube, with 1.5 mL of methanol (Mass Pure Grade from MERCK), ultrasonicated for 30 min (KQ-300DB, 300W,40kHZ) at ambient temperature, followed by centrifuge (12000 rpm, 5 min, SIGMA 3K15, SIGMA). The obtained supernatant is filtered through 0.22 μm filter member prior to UPLC-Q-TOF/MS analysis.

UPLC-Q-TOF/MS Conditions

Chemical profiling was performed on an Agilent 1290 UPLC system (Agilent Technologies, Palo Alto, USA) coupled with Sciex TripleTOF 4600® quadrupole-time of flight mass spectrometer (AB Sciex, Darmstadt, Germany) equipped with a DuoSpray source (electrospray ionization, ESI). Agilent SB C18 column (2.1×100 mm i.d., 1.8 μm; Agilent) was used for components separation. The mobile phase consisted of water containing 0.1% formic acid (A) and acetonitrile (B). The following gradient condition was used: 0–2.0 min, 5%–5% B; 2.0–10.0 min, 5%–30% B; 10.0–15.0 min 30%–50% B; 15.0–25.0 min, 50%–95% B; 25.0–27.0 min, 95%–95% B, with the flow rate of 0.3 mL/min. The injection volume was 1 μL, while column oven temperatures was set at 25°C. The mass spectrometer was operated in full-scan TOF-MS at m/z 100–1500 and information-dependent acquisition (IDA) MS/MS modes, with both positive and negative ion modes. The collision energy was -40 ± 20 eV, ion source gas 1 and 2 were set 50 psi, curtain gas was 35 psi. The temperature and ion spray voltage floating were 500°C and 5000/-4500 V, respectively.

Data Analysis

Data recording and processing was performed by Analyst software (Version 1.6, AB Sciex, USA). The compounds were tentatively characterized based on their retention time, mass accuracy of precursor ions, MS/MS spectra, and fragmentation

pathways, referring to the SCIEX natural products HR-MS/MS Spectral Library, standard references, and previous literatures.

System Biology Analysis of SZJ Extract With Anxiolytic Effects

Construction of Anxiety-Related Targets Database

A text mining of National Center for Biotechnology Information (NCBI) (https://www.ncbi.nlm.nih.gov/gene/), Integrative Pharmacology–based Research Platform of Traditional Chinese Medicine (TCMIP, http://www.tcmip.cn/TCMIP/index.php/Home/) (Xu et al., 2019), and Comparative Toxico-genomics Database (CTD, http://www.ctdbase.org/) (Davis et al., 2019) was conducted to retrieve anxiety-related targets with the keywords "anxiety." TCMIP integrates the diseases related genes data of Therapeutic Targets Database (https://db.idrblab.org/ttd/), Human Phenotype Ontology database (HPO, https://hpo.jax.org/app/), and DisGeNET database (https://www.disgenet.org/). The search results of targets from NCBI, TCMIP, and CTD were filtered with "Homo sapiens," and only the targets with direct evidence supported by CTD were selected. All acquired targets were combined and then mapped to UniProt (https://www.uniprot.org/) for normalization and removal of duplicate and erroneous targets (Liu J. et al., 2018). The remaining satisfactory targets constitute the anxiety-related gene targets database.

Acquisition of Potential Targets Regarding Anxiolytic Benefits for Identified Phytochemicals

The targets of identified phytochemicals and their potential metabolisms were acquired from multiple databases. In addition to retrieving candidate targets from TCMIP and CTD platforms, PharmMapper Server (http://www.lilab-ecust.cn/pharmmapper/) (Wang et al., 2017) was employed to fish the potential targets for those phytochemicals of which no available candidate targets were found in TCMIP and CTD. Those targets were excluded if their reliable score was lower than 0.8 from TCMIP, interaction counts less than 5 from CTD, and/or their normalized fit score lower than 0.8 from PharmMapper. After removal of the duplicates, erroneous, and non-Homo sapiens targets, the rest were then mapped to an anxiety-related gene targets database to screen out the intersecting targets.

Protein-Protein-Interaction (PPI) and Clusters Analysis.

The selective target genes of SZJ extract were imported to STRING (Version 11.0, https://string-db.org/) (Szklarczyk et al., 2019) to obtain PPI results. The interaction score set as high confidence (>0.7). The STRING analysed results were then imported into Cytoscape (Version 3.6.1) (Su et al., 2014), and cluster analysis of target genes was conducted using a Molecular Complex Detection (MCODE) plug-in according to the method in the literature (Wang et al., 2020).

Enrichments Analysis Along With Network Construction.

The target genes contained in the MCODE enriched clusters were imported into the database for annotation, visualization, and integrated discovery (DAVID, version 6.8) (https://david.ncifcrf.gov/tools.jsp) (Huang et al., 2009) to conduct Gene Ontology (GO) terms enrichment including biological processes, cell component, and molecular function. ClueGo plug-in (Version 2.5.7) (Bindea et al., 2009) was further employed to analyze and demonstrate their participated biologic process and Kyoto Encyclopedia of Genes and Genomes (KEGG) pathways, respectively. The latest databases of GO-Biologic Process annotation EB1-Uniport and KEGG pathway were selected. Visual style was set as "groups," minimum gene number, and percentage contained in a term set as 5 and 5%. Statistical method of two-sided hypergeometric test and Bonferroni step down p-value correction was used. Cut-off value of kappa score of GO term/pathway network connectivity was set as 0.5, and only term/pathway with p-value < 0.05 was shown.

RT-qPCR Test

Samples Preparation

Gamma-amino butyric acid (GABA) was kindly provided by Toong Yeuan International Group (Shanghai, China). GABA was considered as positive control in this test. SZJ extract and GABA ingredients were dissolved in deionized water and diluted in culture solution before use.

Cell Culture

Human neuroblastoma SH-SY5Y cells were kindly provided by Stem Cell Bank, Chinese Academy of Sciences, and cultured in MEM/F12 (Gibco) supplemented with 10% (v/v) inactivated fetal bovine serum (Gibco), 1% Gluta-max (Gibco), 1% Sodium pyruvate (Gibco), 1% NEAA (Gibco), and 100 U/mL penicillin/streptomycin. The cells were maintained at 37° in 5% CO_2 and 95% humidified air incubator for the indicated time. All experiments were carried out 24 h after cells were seeded.

Samples Concentration Determination

CellTiter-Glo assay was used to evaluate the available concentration of test samples according to the method described in literature (Fallahi-Sichani et al., 2013). The inhibition on SH-SY5Y cell viability of a series of concentrations of SZJ extract and GABA samples, from 3 mg/mL-0.46 μg/mL, were respectively evaluated. The nonlinear fitting curve of logarithm concentration response to cells viability was then simulated by GraphPad Prism 7.0 (GraphPad Software Inc., San Diego, CA, USA). The concentration of SZJ extract for further test referred to the correspondence value of 90% cells viability.

Samples Stimulation and Grouping

A total of 6 group samples were simultaneously tested: control group (deionized water), 250 μg/mL SZJ extract group, 100 μg/mL GABA group, 100 μM H_2O_2 group, 250 μg/mL SZJ extract with 100 μM H_2O_2 group, and 100 μg/mL GABA with 100 μM H_2O_2 group. Stimulation duration of all group samples was 48 h. Duplicates for each group were set as 3.

RNA Isolation and Reverse Transcription

RNA isolation and reverse transcription were conducted following the method reported in the literature (Fuchsova

et al., 2016). Briefly, RNAprep Pure Cell/Bacteria kit (Tiangen, China) was used to extract total RNA according to the manufacturer's instructions. NanoDrop One^C (ThermoFisher, USA) was used to determine RNA yield and purity by absorbance ratios A260/A280 and A260/A230. OD260/OD280 ratios of the RNA of all samples were in the range of 1.8–2.0. 2 μg of total RNA used to synthesize the first strand complementary DNA (cDNA) using high-capacity cDNA reverse transcription kit (ThermoFisher, USA) according to manufacturer's directions. All reverse transcription products were 10-fold dilution.

Oligonucleotide Primers

PrimerBank was applied to search primers for the amplification of human GABRA1, GABRA2, GABRA3, HTR1A, HTR1B, HTR2A, HTR2B, and internal reference genes (GAPDH and ACTB). Nucleotide sequence of primers are listed in **Table 1**.

Real-Time PCR (qPCR).

Levels of mRNA were quantified by conducting qPCR reactions with SsoAdvanced Universal SYBR Green Supermix (Bio-Rad, USA) according to the manufacturer's directions. CFX equipped with software (Bio-Rad, USA) was used to perform measurements. PCR was in the 20 μL reaction system containing 0.5 μM primer, 10 μL Mix, 5 μL cDNA, and 3 μL RNase-free ddH_2O, and the amplification and dissolution curve condition was shown in **Table 2**. qPCR amplification of ACTB (β-actin) and GAPDH (glyceraldehyde-3-phosphate dehydrogenase) transcription were used as the internal control to verify that equal amounts of RNA were used in each reaction. Fold expression was defined as the fold change relative to control cells.

Statistical Analysis

Bio-Rad CFX Manager software (Bio-Rad, USA) was employed to analyze raw expression data (CT values). For further statistical analysis we used values normalized to the normalization factor calculated as a geometric mean of the expression of two reference genes. All data were expressed as the mean ± SD, and a two-way ANOVA followed by Tukey test was applied for statistical analysis using GraphPad Prism 7.0.

TABLE 1 | Nucleotide sequence of the forward and reverse primers, the lengths of the PCR products.

Target mRNA bases	Primer sequences	T_m (°C)	PCR products (bp)
GABRA1	Forward, 5' AGCCGTCATTACAAGATGAACTT 3'	60	95
	Reverse, 5' TGGTCTCAGGCGATTGTCATAA 3'	61.2	
GABRA2	Forward, 5' GCTGGCTAACATCCAAGAAGAT3'	60.1	92
	Reverse, 5' GCCGATTATCGTAACCATCCAGA3'	61.9	
GABRA3	Forward, 5' CAAGGGGAATCAAGACGACAA 3'	60	145
	Reverse, 5' CGTCCAGAAGACGATCCAAGAT 3'	61.5	
HTR1A	Forward, 5' ACCATTAGCAAGGATCATGGC 3'	60.2	94
	Reverse, 5' ATATGCGCCCATAGAGAACCA 3'	60.8	
HTR1B	Forward, 5' GGGTTCCTCAAGCCAACTTATC 3'	60.6	115
	Reverse, 5' GCCAATAGCATAACCAGCAGT 3'	60.8	
HTR2A	Forward, 5' TTAAGGAGGGGAGTTGCTTACT 3'	55.1	156
	Reverse, 5' TGCCAAGATCACTTACACACAAA 3'	54.1	
HTR2B	Forward, 5' TGATTTGCTGGTTGGATTGTTTG 3'	53.9	132
	Reverse, 5' ATGGATGCGGTTGAAAAGAGAA 3'	54.3	
β-actin	Forward, 5' CTTCGCGGGCGACGAT 3'	65.1	104
(ACTB)	Reverse, 5' CCACATAGGAATCCTTCTGACC 3'	63.1	
GAPDH	Forward, 5' GGAAGGTGAAGGTCGGAGTC 3'	64.9	166
	Reverse, 5' TGGAATTTGCCATGGGTGGA3'	65.5	

RESULTS

Phytochemicals Identification of SZJ Extract

Thirty-five phytochemicals were identified from SZJ by using the UPLC-Q-TOF/MS method. The MS chromatogram in negative ion model of SZJ extract is shown in **Figure 1**. The chemical information of identified phytochemicals is seen in **Table 3**. Among them, 11 phytochemicals were identified by comparison with standard references. The rest of the compounds were identified through comparison with literature data. These phytochemicals are mainly classified into four subcategories: (1) saponins including jujuboside A and jujuboside B; (2) flavones and their C-glycosides including catechin, epicatechin, vicenin-2, swertisin, nicotiflorin, isovitexin and its analogues, and spinosin and its analogues; (3) organic acids including triterpenic acid (e.g., alphitolic acid), fatty acid (e.g., linoleic acid), and glycosylated organic acids (pseudolaroside B and oleuropein); and (4) alkaloids including indoleacetic acid derivatives (e.g., N-glc-indoleacetic acid) and isoquinoline alkaloids (zizyphusine).

Potential Metabolic Products by Gut Microbes of C-Glycoside and Jujubosides Phytochemicals

Gut microbes are known to deglycosylize and cleavage ester bond of flavone C-glycosides and their derivates (Kim et al., 2015; Vollmer et al., 2018; Zheng et al., 2019). Similarly, jujuboside A is metabolized to jujubogenin in gastrointestine to exhibit effects on the expression and activation of gamma amino-butyric acid A ($GABA_A$) receptors (Song et al., 2017). Based on the metabolic patterns reported in those literatures, we deduced the metabolic products by gut microbe of flavone C-glycosides and jujubosides of SZJ extracts. As a result, 11 metabolites of these flavone C-glycosides and jujubosides are concluded for further system biology analysis. To be specific, ferulic acid is metabolized from 6'''-feruloyspinosin and 6''-O-feruloylspinosin, para-coumaric acid is from 6'''-para-coumaroylspinosin, phaseic acid is from 6'''-(E)-phaseolspinosin, para-hydroxybenzoic acid is from 6'''-para-hydroxyl-benzoylspinosin, sinapic acid is from 6'''-sinapoylspinosin, vanillic acid is from 6'''-vanilloyl-spinosin,

TABLE 2 | Condition of amplification and dissolution curve.

Stage	Temperature (°C)	Time	Number of cycles
Ding stage	95	30s	1
Cycling stage	95	10s	40
	60	20s	
Melt curve stage	65–95°C 0.5°C increment		1

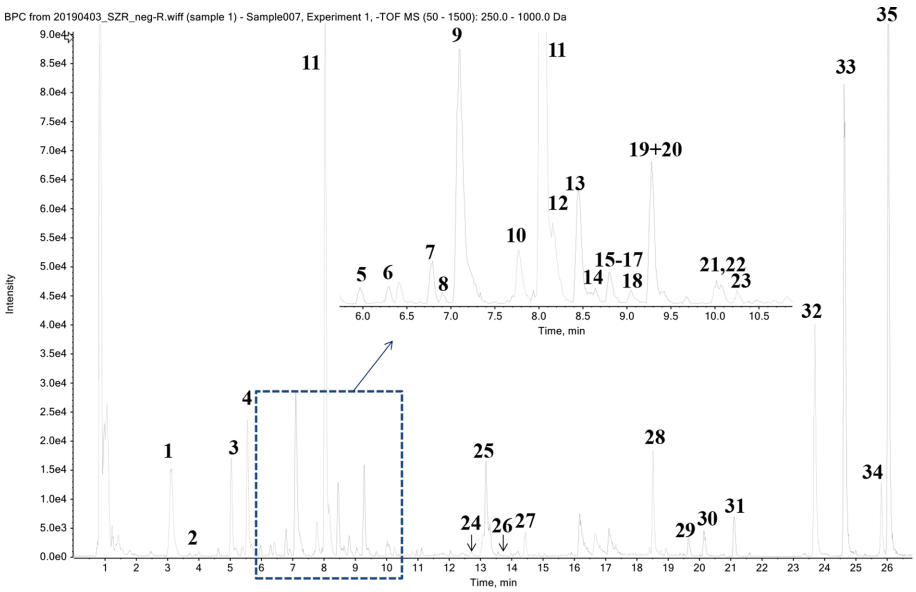

FIGURE 1 | Chromatographic profile of SZJ extract using UPLC-Q-TOF/MS in negative ion mode.

kaempferol is from kaemperol-3-O-rutinoside, genkwanin is from swertisin, naringenin is from 5,7-Dihydroxy-2-(4-hydroxyphenyl)6,8-bis[3,4,5-trihydroxy-6(hydroxymethyl) oxan-2-yl]-2,3dihydrochromen-4-one, apigenin is from spinosin and its analogues, and isovitexin and vicenin-2, jujubogenin is from jujuboside A and jujuboside B.

Anxiolytic Effect-Related Targets of Phytochemicals in SZJ Extract and Their Metabolites

In an integrated search of multiple databases, a total of 476 targets were found to be relevant with anxiety related disorders or diseases, of which 455 targets were acquired for 35 phytochemicals and 11 metabolites. All the interactions among the phytochemicals and targets are listed in **Supplementary Table 1**. After the two clusters were compared and analyzed, 71 target intersects were further determined and are listed in **Table 4**. Among the interactions of phytochemicals and metabolites on those 71 targets (data is not shown), (epi) catechin had the most interactions (degree =22), followed by kaempferol (degree =19), palmitic acid (degree =17), oleic acid (degree =15), betulinic acid (degree =14), apigenin (degree =14), zizyphusine (degree =12), and naringenin (degree =11), etc.

To screen out the core targets, PPI and MCODE cluster analysis was performed on 71 identified targets. As shown in **Figure 2**, 67 nodes plus 260 edges were obtained, in which the clustering coefficient is 0.564 and average number of neighbors is 7.761. With that, MCODE cluster analysis indicated 5 clusters. Specific data of target clusters were exported and are presented in **Table 5**. As a result, 35 core targets were obtained from these 5 clusters, suggesting the core anxiolytic effect targets of SZJ extract. Notably, most of these targets are neuroactive ligand receptors including serotonin (5-HT) receptors (e.g., HTR1A, HTR1B, HTR2A, HTR2B, HTR2C, and HTR1D), $GABA_A$ receptors (e.g., GABRA1, GABRA2, GABRA3, GABRA6, and GABRG2), dopamine receptors (e.g., DRD2, DRD3, and DRD4), cannabinoid signaling (CNR1 and CNR2), and adrenergic (ADRA2A) and glutamate receptor (GRIN2A).

GO and KEGG Pathway Enrichment and Analysis

GO enrichment analysis was conducted on the 35 core targets by using DAVID. All the enriched GO terms are seen in **Supplementary Table 2**. The top 10 significant terms in biological process, molecular function, and cell component categories are shown in **Figure 3**. The results demonstrated that GO terms were mainly concentrated in neurotransmitter receptors signaling, particularly GABA and serotonin receptor signaling. Functions of activating neurotransmitter receptors and ligand-gated ion channel *via* receptor complex, and regulating synaptic transmission were mainly involved. Cytoscape ClueGo plug-in was further applied to visualize the interaction network of biological process, as shown in **Figure 4**. All statistically significant biological processes were listed in **Supplementary Table 3**.

In addition, 35 identified core targets were imported to ClueGo for KEGG pathway enrichment, resulting in 14 statistically significant pathways. The targets-pathway network is shown in **Figure 5**, demonstrating that neuroactive ligand-receptor interaction is the most significant pathway with involvement of 18 targets, followed by serotonergic synapse pathway (8 targets), taste transduction pathway (7 targets), etc. Other nervous system related pathways including GABAergic synapse and retrograde endocannabinoid signaling, signaling transduction related pathways including TNF signaling

TABLE 3 | Identified phytochemicals in SZJ extract.

No	RT (min)	Adducts	Measured *m/z*	Expected *m/z*	Mass error (ppm)	Formula	Molecular weight	Phytochemical name	MS/MS fragment ions	Reference
S1	3.11	$[M-H]^-$	368.0999	368.0987	3.2	$C_{16}H_{19}NO_9$	369.11	3S-N-glc-3-hydroxy-indoleacetic acid	368.0062,204.0059,176.0160,158.0085,143.9957,130.0195,	(Zhang F.-X. et al., 2016)
S2	3.70	$[M-H]^-$	329.0885	329.0878	2.1	$C_{14}H_{18}O_9$	330.29	Pseudolaroside B	166.9794,151.9582	(Zhang F.-X. et al., 2016)
S3	5.04	$[M-H]^-$	352.1050	352.1038	3.4	$C_{16}H_{19}NO_8$	353.11	N-glc-indoleaceticacid	352.0176,308.0360,188.0133,160.0243,146.0105,	(Zhang F.-X. et al., 2016)
S4	5.55	$[M-H]^-$	352.1054	352.1038	4.6	$C_{16}H_{19}NO_8$	353.11	isomer of N-glc-indoleaceticacid	352.0161,308.0324,188.0126,160.0231,146.0103,	(Zhang F.-X. et al., 2016)
S5	5.97	$[M-H]^-$	289.0724	289.0718	2.2	$C_{15}H_{14}O_6$	290.08	catechin	288.9944,245.0123,202.0026,173.8291,122.9996,	a
S6	6.29	$[M-H]^-$	595.1694	595.1668	4.3	$C_{27}H_{32}O_{15}$	596.17	5,7-dihydroxy-2-(4-hydroxyphenyl)6,8-bis[3,4,5-trihydroxy-6(hydroxymethyl)oxan-2-yl]-2,3dihydrochromen-4-one	595.0439,475.0168,385.0004,354.9931	(Khan et al., 2020)
S7	6.78	$[M-H]^-$	593.1544	593.1512	5.4	$C_{27}H_{30}O_{15}$	594.16	vicenin 2	593.0275,473.0027,382.9841,352.9774	a
S8	6.90	$[M-H]^-$	289.0722	289.0718	1.5	$C_{15}H_{14}O_6$	290.08	epicatechin	288.9950,245.0136,203.0092,186.9836,136.9752,108.9860,	a
S9	7.10	$[M-H]^-$	340.1574	340.1554	5.8	$C_{20}H_{23}NO_4$	341.16	zizyphusine	340.0703,325.0486,310.0285,251.9723,223.9819,195.9970,	(Zhang F.-X. et al., 2016)
S10	7.77	$[M-H]^-$	593.1533	593.1512	3.5	$C_{27}H_{30}O_{15}$	594.16	isovitexin-2″-O-glucopyranoside	593.0285,412.9906,310.9741,292.9673,	(Wang et al., 2009)
S11	8.04	$[M-H]^-$	607.1698	607.1727	-4.8	$C_{21}H_{36}O_{20}$	608.18	spinosin	607.0438,445.0129,427.0056,306.9819,	a
S12	8.22	$[M-H]^-$	431.1003	431.0984	4.5	$C_{21}H_{20}O_{10}$	432.11	isovitexin	412.9913,340.9805,310.9738,282.9840,239.0020,	(Niu et al., 2010)
S13	8.45	$[M-H]^-$	445.115	445.114	2.2	$C_{22}H_{22}O_{10}$	446.12	swertisin	445.0127,324.9879,296.9616,281.9768,	(Wang et al., 2009)
S14	8.63	$[M-H]^-$	757.2028	757.1985	1.8	$C_{36}H_{38}O_{18}$	758.21	6‴-vanilloylspinosin	757.0502,427.0029,268.9916,208.9818,	(Zhang F.-X. et al., 2016)
S15	8.81	$[M-H]^-$	593.1542	593.1512	5.1	$C_{27}H_{30}O_{15}$	594.16	nicotiflorin	593.0301,284.9642,254.9591,	a
S16	8.82	$[M-H]^-$	727.1921	727.188	5.7	$C_{35}H_{36}O_{17}$	728.20	6‴-para-hydroxylbenzoylspinosin	727.0437,427.0015,238.9858,178.9772,136.9742,	(Niu et al., 2010)
S17	8.89	$[M-H]^-$	769.1986	769.1985	0.1	$C_{37}H_{38}O_{18}$	770.21	isovitexin-2″-O-(6-feruloy)-glucopyranoside	593.0295,412.9894,292.9667,234.9919,	(Zhang F.-X. et al., 2016)
S18	9.08	$[M-H]^-$	813.2329	813.2246	10	$C_{39}H_{42}O_{19}$	814.23	6‴-sinapoylspinosin	813.0779,607.0452,427.0041,325.0097	(Wang et al., 2009)
S19	9.27	$[M-H]^-$	753.2087	753.2036	6.7	$C_{37}H_{38}O_{17}$	754.21	6‴-para-coumaroylspinosi	753.0614,607.0459,427.0065,306.9802,264.9971,	(Niu et al., 2010)
S20	9.28	$[M-H]^-$	783.2183	783.2142	5.2	$C_{38}H_{40}O_{18}$	784.22	6‴-feruloyspinosin	783.0707,427.0056,234.9936,192.9904,	(Wang et al., 2009)
S21	9.92	$[M-H]^-$	869.2945	869.2874	8.2	$C_{43}H_{50}O_{19}$	870.29	6‴-(-)-phaseoylspinosin	869.1331,839.1245,607.0473,427.0105,	(Zhang F.-X. et al., 2016)
S22	10.04	$[M-H]^-$	539.1786	539.177	2.9	$C_{25}H_{32}O_{13}$	540.51	oleuropein	539.0602,307.0033,275.0163	(Rached et al., 2019)
S23	10.26	$[M-H]^-$	783.2172	783.2142	3.8	$C_{38}H_{40}O_{18}$	784.22	6‴-O-feruloylspinosin	783.0707,607.0454,445.0149,160.9688	(Wang et al., 2009)
S24	12.68	$[M+HCOO]^-$	1251.608	1251.602	4.8	$C_{58}H_{94}O_{26}$	1206.60	jujuboside A	1244.5868,1207.3994,1075.3781,	a
S25	13.12	$[M-H]^-$	329.2349	329.2333	4.7	$C_{18}H_{34}O_5$	330.46	octadecenoic acid	329.1494,229.0779,211.0714,171.0473	
S26	13.47	$[M+HCOO]^-$	1089.555	1089.549	5.9	$C_{52}H_{84}O_{21}$	1044.55	jujuboside B	1043.3670,911.3407,749.3084,	a
S27	14.43	$[M-H]^-$	329.2349	329.2333	4.7	$C_{18}H_{34}O_5$	330.46	octadecenoic acid	329.1487,201.0517,171.0472	
S28	18.51	$[M-H]^-$	485.3305	485.3272	6.7	$C_{30}H_{46}O_5$	486.33	epiceanothic acid	485.2225,423.2285,	(Yang et al., 2013)
S29	19.65	$[M-H]^-$	295.2296	295.2279	5.9	$C_{18}H_{32}O_3$	296.24	octadecenoic acid methyl ester	295.1481,277.1445,195.0798,155.0569,	
S30	20.17	$[M-H]^-$	471.3516	471.348	7.7	$C_{30}H_{48}O_4$	472.36	alphitolic acid	471.2459	(Yang et al., 2013)
S31	21.11	$[M-H]^-$	485.329	485.3272	3.6	$C_{30}H_{46}O_5$	486.33	ceanothic acid	485.2209,423.2296,	(Yang et al., 2013)
S32	23.69	$[M-H]^-$	455.3555	455.3531	5.3	$C_{30}H_{48}O_3$	456.36	betulinic acid	455.2508	a
S33	24.64	$[M-H]^-$	279.2345	279.233	5.5	$C_{18}H_{32}O_2$	280.24	linoleic acid	279.1583	a
S34	25.82	$[M-H]^-$	255.233	255.233	0.2	$C_{16}H_{32}O_2$	256.24	palmitic acid	255.1609	a
S35	26.04	$[M-H]^-$	281.2492	281.2486	2.1	$C_{18}H_{34}O_2$	282.26	oleic acid	281.1739	a

a, identified by standard references.

TABLE 4 | Information of anxiolytic effects related targets of SZJ extract.

Gene Symbol	Full Name
ACSL4	acyl-CoA synthetase long-chain family member 4
ADIPOQ	adiponectin, C1Q and collagen domain containing
ADRA2A	adrenoceptor alpha 2A
AKR1C1	aldo-keto reductase family 1 member C1
AKT1	AKT serine/threonine kinase 1
ALDH2	aldehyde dehydrogenase 2 family (mitochondrial)
ALDH5A1	aldehyde dehydrogenase 5 family member A1
ANG	angiogenin
APP	amyloid beta precursor protein
ATP1A1	ATPase Na+/K+ transporting subunit alpha 1
ATP1A3	ATPase Na+/K+ transporting subunit alpha 3
BCAT2	branched chain amino acid transaminase 2
BDNF	brain derived neurotrophic factor
CAT	catalase
CCL3	C-C motif chemokine ligand 3
CHRNA7	cholinergic receptor nicotinic alpha 7 subunit
CNR1	cannabinoid receptor 1
CNR2	cannabinoid receptor 2
COMT	catechol-O-methyltransferase
COX1	cytochrome c oxidase subunit I
COX2	cytochrome c oxidase subunit II
CREB1	cAMP responsive element binding protein 1
CTNNB1	catenin beta 1
CXCL8	C-X-C motif chemokine ligand 8
CYP2E1	cytochrome P450 family 2 subfamily E member 1
DNMT1	DNA methyltransferase 1
DRD2	dopamine receptor D2
DRD3	dopamine receptor D3
DRD4	dopamine receptor D4
EDN1	endothelin 1
ESR1	estrogen receptor 1
ESR2	estrogen receptor 2
GABRA1	gamma-aminobutyric acid type A receptor alpha1 subunit
GABRA2	gamma-aminobutyric acid type A receptor alpha2 subunit
GABRA3	gamma-aminobutyric acid type A receptor alpha3 subunit
GABRA6	gamma-aminobutyric acid type A receptor alpha6 subunit
GABRG2	gamma-aminobutyric acid type A receptor gamma2 subunit
GLO1	glyoxalase I
GM2A	GM2 ganglioside activator
GPER1	G protein-coupled estrogen receptor 1
GRIN2A	glutamate ionotropic receptor NMDA type subunit 2A
GSK3B	glycogen synthase kinase 3 beta
GSTP1	glutathione S-transferase pi 1
HSD11B2	hydroxysteroid 11-beta dehydrogenase 2
HTR1A	5-hydroxytryptamine receptor 1A
HTR1B	5-hydroxytryptamine receptor 1B
HTR1D	5-hydroxytryptamine receptor 1D
HTR2A	5-hydroxytryptamine receptor 2A
HTR2B	5-hydroxytryptamine receptor 2B
HTR2C	5-hydroxytryptamine receptor 2C
HTR3A	5-hydroxytryptamine receptor 3A
ICAM1	intercellular adhesion molecule 1
IL6	interleukin 6
INS	insulin
MAPK1	mitogen-activated protein kinase 1
MIF	macrophage migration inhibitory factor (glycosylation-inhibiting factor)
ND1	NADH dehydrogenase, subunit 1 (complex I)
NOS2	nitric oxide synthase 2
NR1I2	nuclear receptor subfamily 1 group I member 2
NR3C1	nuclear receptor subfamily 3 group C member 1
PAH	phenylalanine hydroxylase
PON1	paraoxonase 1
SCN1A	sodium voltage-gated channel alpha subunit 1
SHBG	sex hormone binding globulin
SIRT1	sirtuin 1
SOD1	superoxide dismutase 1, soluble
SQSTM1	sequestosome 1
TGFBR2	transforming growth factor beta receptor 2
TNF	tumor necrosis factor
TP53	tumor protein p53
TRPV1	transient receptor potential cation channel subfamily V member 1

pathway, and longevity regulating pathways were also significantly enriched. These results are consistent with the results from GO enrichment analysis. Taken together, these findings suggest that SZJ extract mainly exerts an anxiolytic effect *via* modulation of serotonergic and GABAergic systems.

$GABA_A$ receptors in the central nervous system are known as the major targets for the first line treatment of anxiety (Poisbeau et al., 2018). $GABA_A$ receptors subunits, mainly including GABRA1, GABRA2, and GABRA3, have been reported to mediates anxiolysis (Möhler, 2012). Similarly, preclinical studies have suggested that most 5-HT receptors subtypes participate in anxiety-like processes, and blocking or stimulating individual 5-HT receptor subtypes might cause the anxiolytic-like effect (Żmudzka et al., 2018). HTR1A, HTR1B, HTR2A, and HTR2B were commonly targeted in preclinical studies for the anxiety treatment (Graeff et al., 1996; Clinard et al., 2015; Spiacci et al., 2016; Colangeli et al., 2019) as well as the anxiolytic-like studies of SZJ (Wang et al., 2010; Liu et al., 2015). Hence, among the potential targets acted by SZJ, GABRA1, GABRA2, GABRA3, HTR1A, HTR1B, HTR2A, and HTR2B were preferentially selected for further validation.

Effects of SZJ Extract on mRNA Expression of $GABA_A$ and 5-HT Receptor Subtypes

Based on the findings from system biology analysis, RT-qPCR was employed to evaluate the effects of SZJ extract on mRNA expression of GABRA1, GABRA2, GABRA3, HTR1A, HTR1B, HTR2A, and HTR2B. As shown in **Figure 6**, in the non-H_2O_2 treated cells, GABA 100 μg/mL significantly enhanced the expression of GABRA1 ($p< 0.0001$), GABRA2 ($p< 0.0001$), and HTR1A ($p< 0.001$) comparing with the control group, while it significantly decreased the expression of GABRA3 ($p< 0.01$) and HTR2B ($p< 0.05$). Similar as GABA, SZJ extract 250 μg/mL exhibited significant effect on enhancing expression of GABRA1 ($p< 0.001$) and HTR1A ($p< 0.05$). However, contrast to GABA group, obvious expression enhancement of GABRA3 ($p< 0.01$) and HTR2B ($p< 0.0001$) were observed at 250 μg/mL SZJ extract. These differences in regulating $GABA_A$ receptor subtypes following SZJ and GABA stimulations could help to explain the different mechanisms of anxiolytic effect of the two ingredients.

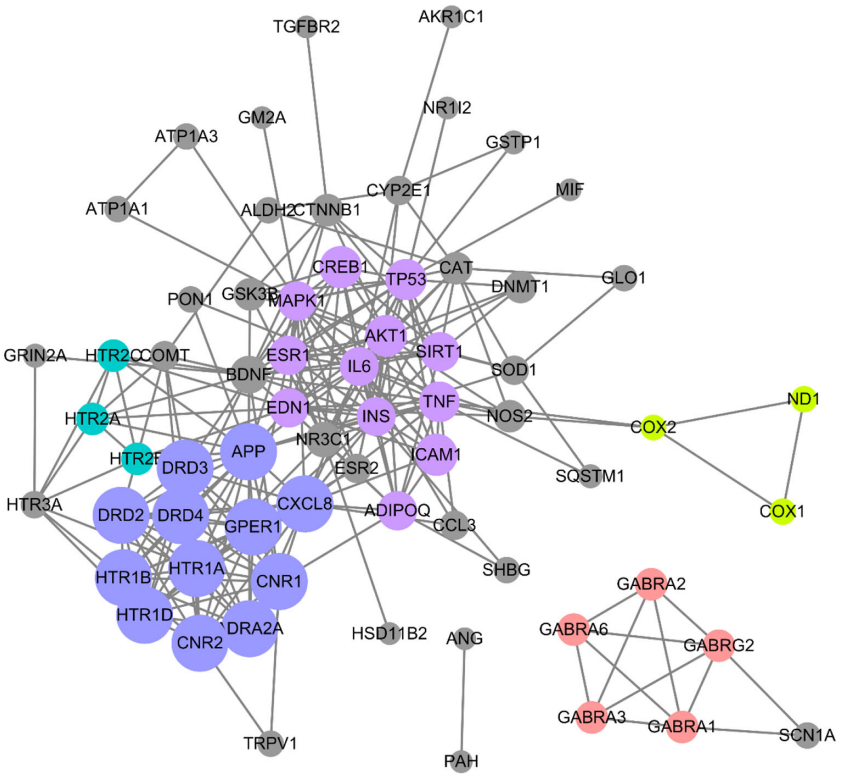

FIGURE 2 | Protein-protein interaction (PPI) network of anxiolytic effects-related targets of SZJ. Cytoscape (Version 3.6.1) was applied to construct the interactions downloaded from the STRING (interaction score set as high confidence >0.7). All the targets are represented by nodes, whereas the interactions between the targets are represented by edges. MCODE plug-in was applied to conduct cluster analysis. Different clusters are noted with different colors. The node size is proportional to its located cluster MCODE score.

TABLE 5 | List of genes clusters information analyzed by MOCDE on the base of PPI data downloaded from the STRING.

Cluster	Score (Density*#Nodes)	Nodes	Edges	Node IDs
1	10.154	12	66	GPER1, ADRA2A, DRD2, CNR2, CNR1, HTR1A, HTR1B, APP, DRD4, HTR1D, DRD3, CXCL8
2	8	12	52	CREB1, AKT1, TNF, SIRT1, TP53, MAPK1, EDN1, ICAM1, ADIPOQ, IL6, ESR1, INS
3	3.333	5	10	GABRA2, GABRG2, GABRA6, GABRA3, GABRA1
4	1.5	3	3	HTR2C, HTR2A, HTR2B
5	1.5	3	3	COX1, COX2, ND1

Furthermore, because oxidative stress mechanisms have been well explored in anxiety disorders (Bouayed et al., 2009; Salim, 2017), the effects of SZJ extract on $GABA_A$ and 5-HT receptors were also evaluated in hydrogen peroxide (H_2O_2) induced oxidative stress condition. As a result, a remarkable increase ($p< 0.0001$) in GABRA1, GABRA2, HTR1A, HTR1B, and HTR2A expression following 100 μM H_2O_2 stimulation was observed. Currently, though the alteration of $GABA_A$ and 5-HT receptors under strong oxidative stimulation is unclear, our result in some extent suggested that overexpression of GABRA1, GABRA2, HTR1A, HTR1B, and HTR2A may be involved in oxidative stress-induced anxiety. Intriguingly, the sharp increase induced by H_2O_2 in GABRA1, GABRA2, HTR1A, and HTR2A were significantly antagonized by both SZJ extract 250 μg/mL and GABA 100 μg/mL. Hence, inhibition of GABRA1, GABRA2, HTR1A, and HTR2A overexpression is also possibly involved in anxiolytic-like mechanisms of SZJ.

DISCUSSION

The identification of phytochemicals in herbal materials is a critical step during the process of system biology analysis. Herbal materials are often subjected to extraction, concentration, and/or purification, resulting in the phytochemical compositions alteration. The phytochemical data from current databases (e.g., TCMSP, http://tcmspw.com/tcmsp.php; TCMID, http://www.megabionet.org/tcmid/) may not be used directly for system biology investigation. Additional methods for phytochemical identification, such as UPLC-Q-TOF/MS, should be a complementary tool to obtain

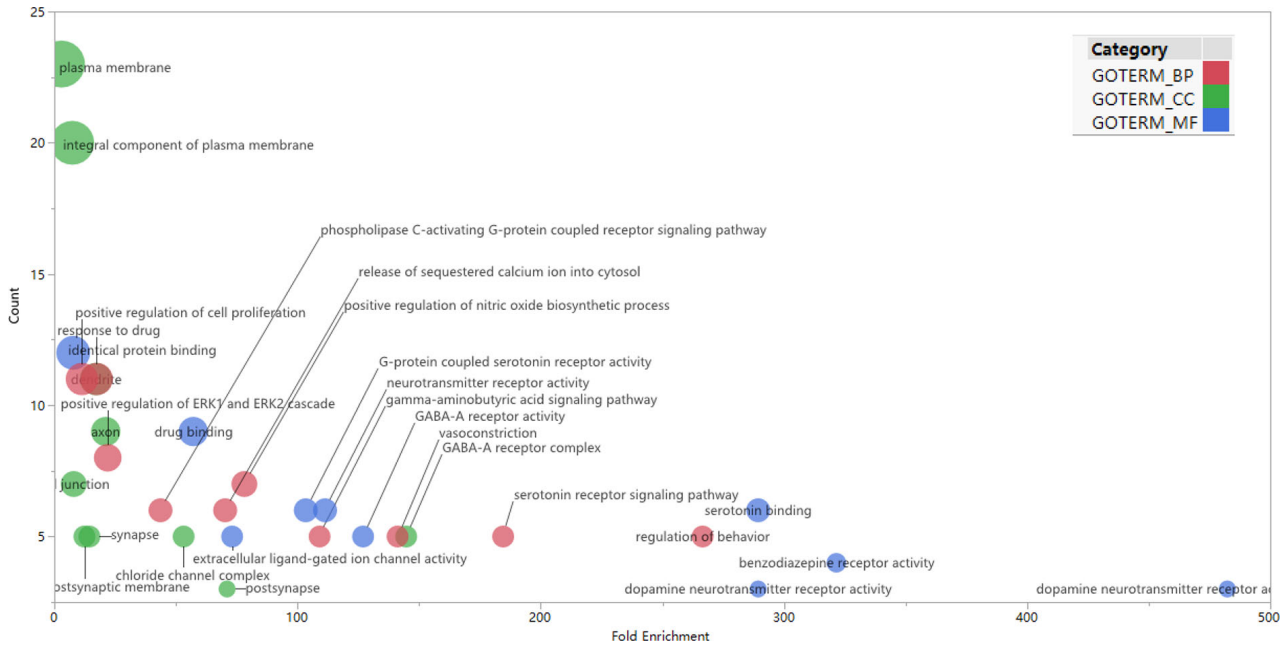

FIGURE 3 | Top 10 significantly enriched GO terms in biologic process (red), cellular components (green), and molecular function (blue) categories. The bubble diagram was made using JMP software 14.2.0 (SAS Institute Inc., USA). The bubble size is proportional to its involved targets percentage in the term.

more accurate results of phytochemical compositions (Shen et al., 2013). In current work, a series of flavonoid glycosides and saponins were identified from SZJ extract, in which the spinosin derivatives including 6'''-vanilloylspinosin, 6'''-para-hydroxylbenzoylspinosin, 6'''-sinapoylspinosin, 6'''-para-coumaroylspinosin, 6'''-feruloyspinosin, 6'''-(-)-phaseoylspinosin, and 6''-O-feruloylspinosin are rare in other plant species. The studies on their bioactivities and effective targets have been so poorly reported that there is not enough data for system biology analysis. In addition, their chemical structures are complicated and contain multi-chiral centers that bring a great challenge to obtain the potential targets through reverse virtual fishing technique. Traditional system biology analysis would take ADME (absorption, distribution, metabolism, and excretion) screening strategy that may exclude these glycosides with low oral bioavailability and low drug-likeness (Yue et al., 2017a; Yue et al., 2017b). For instance, ginsenosides are the dominant phytochemicals in ginseng and are thought to be contributed to its multiple bioactivities (Ru et al., 2015; Kim et al., 2017). However, the above analysis strategy, i.e., ADME screening, would exclude the ginsenosides along with their contributions on efficacy when performing systematic research of ginseng. Therefore, such an analytical strategy is incomplete and not systematic. In fact, it has been well demonstrated that the metabolites of the ginsenosides are responsible for the specific bioactivities (Chen et al., 2018; Kim, 2018). Similarly, the chemoinformatics and pharmacoinformatics approach indicated that jujubogenin was the effective $GABA_A$ agonist, neither jujuboside A nor jujuboside B (Chen, 2009). Gut microbes play an important role in favoring phytochemicals transformation into metabolites endowed with biological activity (Dey, 2019). As a result, the strategy that involves the metabolites of glycosides in gastrointestinal environment (e.g., gut microbes) will be a more reasonable approach to understand the actual efficacy and mechanism of herbal materials in which the glycosides are considered as the main active components.

The $GABA_A$ receptors are chloride channels and are composed of several subunit classes (α, β, γ, δ, and ϵ) (Olsen and Sieghart, 2008). GABAergic neurotransmission plays an important role in anxiety status. Previous studies have shown that deficit of $GABA_A$ receptors and reduction of GABA transmission were observed in people with anxiety-like symptoms (Horowski and Dorow, 2002; Nutt and Malizia, 2004; Hasler et al., 2008). In contrast, positive modulation of $GABA_A$ receptors and enhancement of GABA transmission have shown anxiolytic effects. Classic benzodiazepines reduce anxiety by interacting with the $GABA_A$ receptors *via* the benzodiazepine binding site, which is present at the interface of α1, α2, α3, or α5 subunits and γ subunit of $GABA_A$ receptors (Möhler, 2012). Other classes of compounds, GABA, barbiturates, and alcohol also could act at different benzodiazepine binding sites to increase the opening of the chloride channel resulting in enhancement of inhibitory synaptic transmission (Harris, 1990; Schousboe and Redburn, 1995). The results of our system biology study suggested the $GABA_A$ receptors signaling is a significant pathway involving in anxiolytic effect of SZJ. In fact, pharmacologic study has found that spinosin, a major C-glycoside flavonoid in SZJ, exerted anxiolytic-like effects *via* modulation of $GABA_A$ and 5-HT receptors (Liu et al., 2015). Similarly, 6'''-feruloylspinosin and

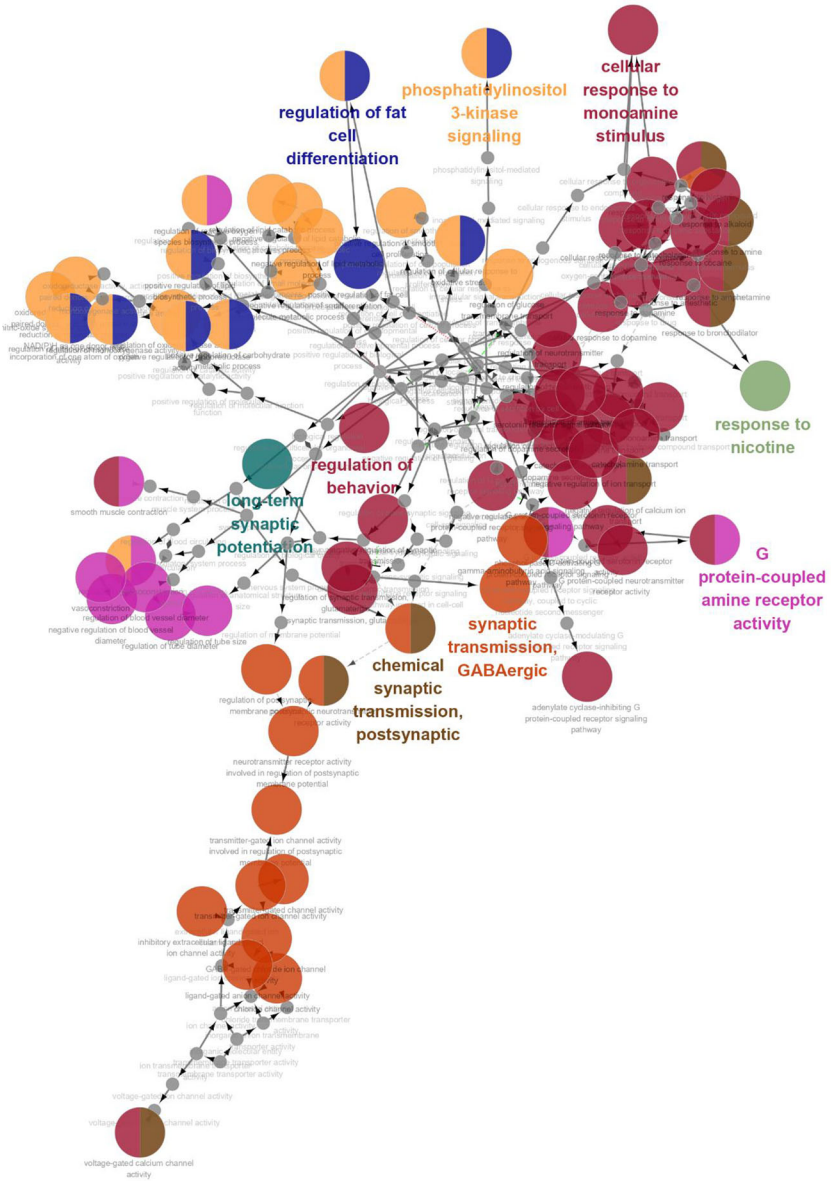

FIGURE 4 | The interaction networks of enriched biological processes. ClueGO was applied to analysis procedure, and multiple color circles indicate that they are involved in multiple biological processes.

spinosin have been reported to significantly enhance the expression of GABRA1 and GABRA5 mRNA in rat hippocampal neurons (Qiao et al., 2016). In addition, it has been found that stimulation of jujuboside A at 50 μg/mL could increase the mRNA transcription levels of GABRA1, GABRA5, GABRB1, and GABRB2 in hippocampal neurons (You et al., 2010; Wang et al., 2015); however, long time stimulation of jujuboside A at a high dose of 100 μg/mL result in the decrease of GABRA1 and GABRB2 mRNAs expression (You et al., 2010). These results suggested a two-way modulatory effect of SZJ on GABRA1 and other $GABA_A$ receptors. Such benefits were similar to what we found in this work, that is, SZJ extract enhanced mRNA level of GABRA1 in non-H_2O_2 treated SH-SY5Y cells, but inhibited the H_2O_2-induced overexpression of GABRA1. Therefore, combining with the results from literatures and our results, it was suggested that SZJ exhibited anxiolytic effects through modulating $GABA_A$ receptors, in which a two-way modulation of GABRA1 may play an important role.

It was well established that the alteration of various behaviors in anxiety disorders including appetite, mood, sleep, and cognitive function have been linked to the serotonergic system (Liu Y. et al., 2018; Liu et al., 2019). Serotonin receptors are

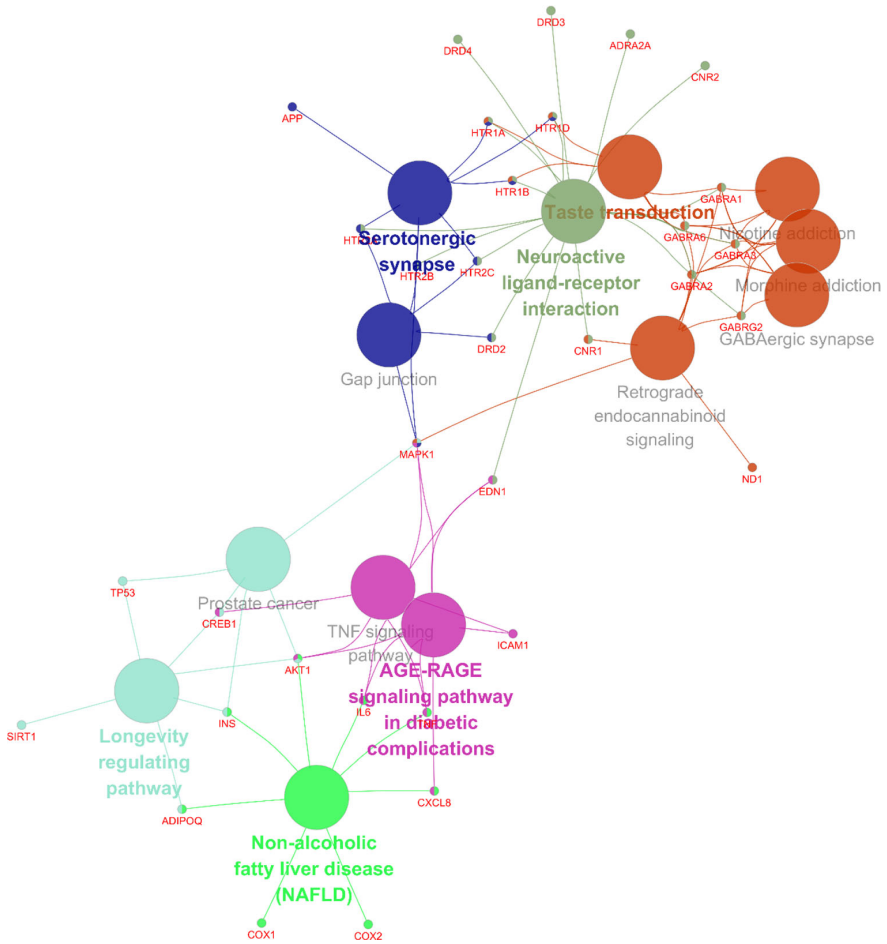

FIGURE 5 | Targets-pathway network associated with anxiolytic effects of SZJ extract. A cytoscape ClueGo plug-in was applied to enrich the pathways and construct the network.

prevalent throughout the nervous system and the periphery, and they potentially control the serotonergic neurotransmission throughout the brain and neuronal activity to alleviate neuropsychiatric disorders (Okazawa et al., 1999). Generally, the activation of HTR1A, HTR2A receptors can produce anxiolytic effects, whereas inactivation of them increases anxiety-like behaviors (Clinard et al., 2015; Spiacci et al., 2016). Involvement of other 5-HT receptors including HTR1B, HTR1B, and HTR2C in the mechanisms of anxiety have also been recognized (Graeff et al., 1996; Griebel et al., 1997; McCorvy and Roth, 2015). Similarly, our system biology analysis found that the serotonergic synapse pathway was dominant in anxiolytic effects mechanism of SZJ extract, in which different subtypes of 5-HT receptors were involved. Notably, as the same effect on GABRA1, SZJ extract also showed a two-way modulation on HTR1A and HTR2A in our RT-qPCR test. Genetic studies in animal models have suggested that anxiety-like behavior can increase when the HTR1A function is eliminated or overexpressed (Overstreet et al., 2003). Hence, these results suggested the involvement of modulating serotonergic synapse pathway, specifically two-way modulation of HTR1A and HTR2A in anxiolytic effects of SZJ.

In addition, the cannabinoid receptors (CNR) are extensively expressed in areas of the nervous system and have been found closely associated with anxiety behavior (Akirav, 2011). It has been well illustrated that endocannabinoid (eCB) reduces the serotonin release in the central nervous system and increases the expression and function of HTR1A in the hippocampus *via* the activation of CNR1 (Haj-Dahmane and Shen, 2011; Patel et al., 2017). Beyond CNR1, eCB system could exert actions on other targets including CNR2, transient receptor potential vanilloid receptor type 1 (TRPV1), or cyclooxygenase-2 (COX2) to participate in improvement of anxiety (Patel et al., 2017). In addition, cyclic AMP-responsive element-binding protein (CREB) has been suggested to be crucial for the role of HTR1A in modulating anxiety-related behaviors *via* mediating hippoacampus structural plasticity (Zhang J. et al., 2016). Intriguingly, this systematic analysis work showed phytochemicals in SZJ extracts potentially

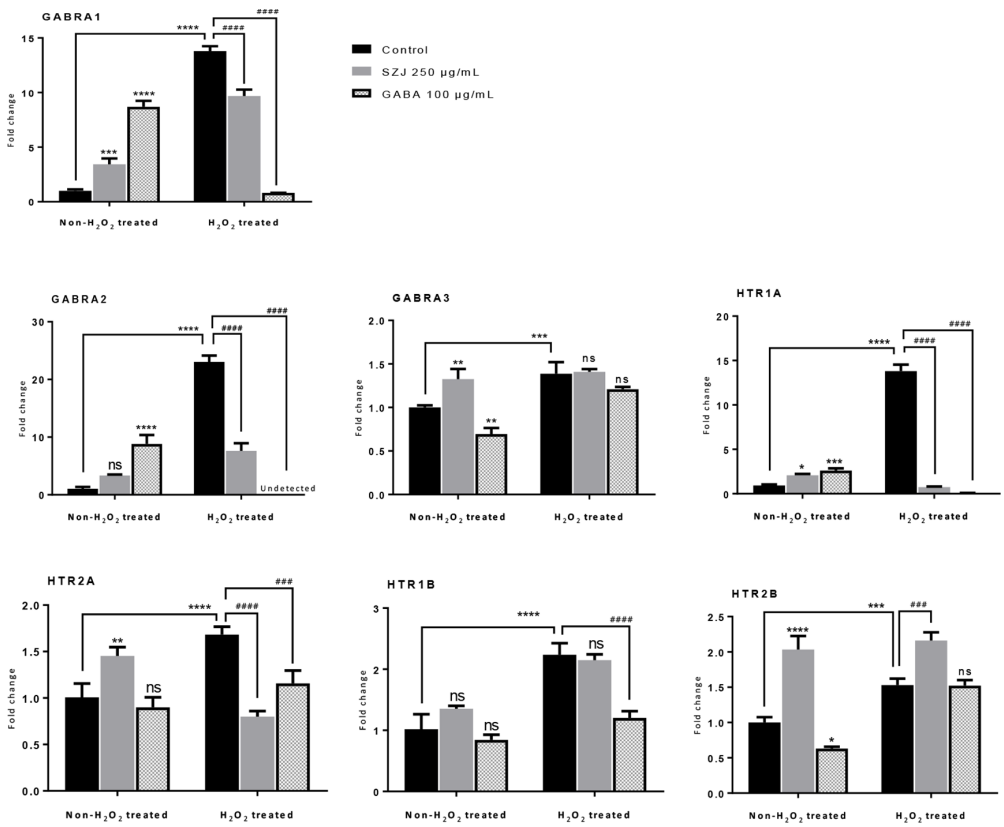

FIGURE 6 | Effects of SZJ extract on mRNA gene expressions of different subtypes of $GABA_A$ and 5-HT receptors. GraphPad Prism 7.0 software was applied for statistical analysis and graphing. All data were expressed as mean ± SD, and a two-way ANOVA followed by Tukey's test was applied. Two-way ANOVA analysis results presented that, GABRA1, F (2, 12) =57.27: $p < 0.0001$; GABRA2, F (2, 12) =112.50: $p < 0.0001$; GABRA3, F (2, 12) =40.10: $p < 0.0001$; HTR1A, F (2, 12) =677.80: $p < 0.0001$; HTR2A, F (2, 12) =13.07: $p = 0.0010$; HTR1B, F (2, 12) =42.99: $p < 0.0001$; HTR2B, F (2, 12) =151.50: $p < 0.0001$. Post hoc Tukey's test results were represented by comparing with non-H_2O_2 treated control group, $^{*}p < 0.05$, $^{**}p < 0.01$, $^{***}p < 0.001$ and $^{****}p < 0.0001$; compared with H_2O_2 treated control group, $^{\#\#\#}p < 0.001$ and $^{\#\#\#\#}p < 0.0001$.

act on the above mentioned targets including CNR1, CNR2, TRPV1, COX2, and CREB. These results, to some extent, suggested that the mechanism of action of SZJ in anti-anxiety may also involve those pathways/targets that indirectly modulate eCB and serotoninergic systems. More attention needs to be paid to those targets/pathways in further experimental studies on anxiolytic effects of SZJ.

The phytochemicals in herbal medicines are the substantial basis for their pharmacologic actions. Those phytochemicals with good bioactivity and high content are considered to be the chemical markers in quality control of the herbal medicines. Jujuboside A and spinosin are used to quality markers of SZJ crude drug in Chinese Pharmacopoeia (Edition 2020). Combining the results from literatures reports (Han et al., 2009; Abdoul-Azize, 2016) and our results, the modulations of GABAergic and serotoninergic systems seem the major mechanisms of SZJ exerting anxiolytic effects, as well as the traditional efficacy of nourishing heart and calming mind. Based on that, we abstracted the phytochemicals-targets-pathway sub-networks of GABAergic and serotoninergic synapse pathways. As shown in **Figure 7**, it demonstrated that metabolites of C-glycosides (spinosin, etc.) and jujubosides (jujuboside A, etc.) including apigenin, kaempferol, naringenin, genkwanin, and jujubogenin were involved in modulation of GABAergic and serotoninergic synapse pathways. The result provides the extra evidence to support that C-glycosides and jujubosides are responsible for the anxiolytic effects of SZJ, and they support jujuboside A and spinosin as chemical markers for quality control of SZJ and its preparations. Beyond the C-glycosides and jujubosides, the involvements of triterpenic acid (e.g., betulinic acid) and alkaloid (zizyphusine) were also observed in modulation of GABAergic and serotoninergic synapse pathways. Specifically, betulinic acid is a function of the modulating GABAergic system *via* multiple subtypes of $GABA_A$ receptors, whereas zizyphusine is a function of the modulating serotoninergic system *via* multiple subtypes of 5-HT receptors. Notably, it has been reported that zizyphusine was identified as one of the principal components in SZJ by principal component

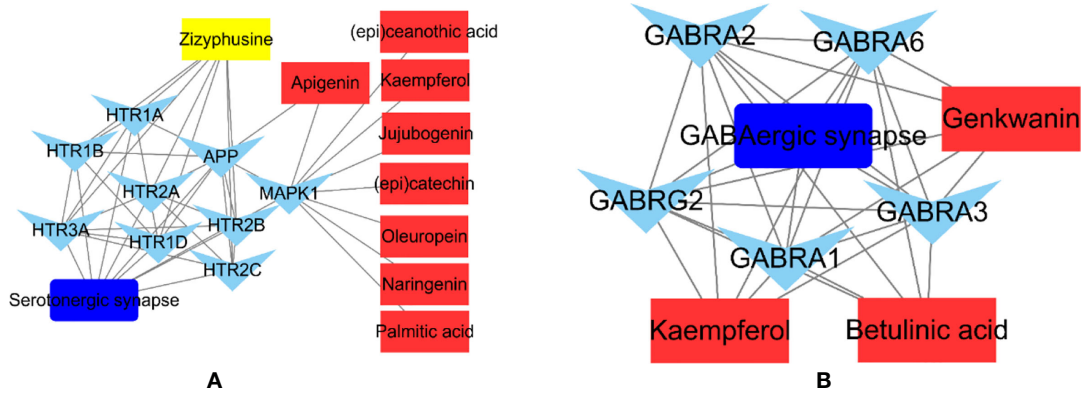

FIGURE 7 | Abstracted phytochemicals-targets-pathway sub-networks of serotoninergic synapse **(A)** and GABAergic pathways **(B)**. Cytoscape (Version 3.6.1) was applied to construct the sub-networks.

analysis (Sun et al., 2014). And according to records in TCMIP, zizyphusine is exclusively derived from *Ziziphus jujube* (fruit or seeds), and its bioavailability and druglikeness is much better than C-glycosides and jujubosides. These findings recommend that the involvement of zizyphusine in quality control of SZJ extract and pharmacologic actions in anxiolytic effect is worth investigating in the future. Because the pharmacologic study of zizyphusine is poor at present, more attention could be paid to research and development of zizyphusine as a potential natural anti-anxiety drug.

There are some limitations of our current research. First, we did not conduct the behavioral test to confirm the anxiolytic-like effect of SZJ. Such benefit of SZJ was concluded on the base of previous pharmacodynamic studies, as well as clinical practice experience of traditional medicine. Our *in vitro* mRNA expression evaluation of $GABA_A$ and 5-HT receptors only used a single concentration of SZJ extract, which corresponds to approximately 90% cell viability in CellTiter-Glo assay. Leveraging the integrated approach of system biology, UPLC-Q-TOF/MS and RT-qPCR, present work contributed to the illustration of potential mechanism of action involved in the anxiolytic-like effect of SZJ. However, further in-depth preclinical studies are warranted to verify the results obtained from the current analysis.

CONCLUSIONS

In conclusion, our results systematically demonstrated that anxiolytic mechanisms of SZJ mainly involved the regulation of serotonergic and GABAergic synapse pathways, in which the two-way modulation of GABRA1, HTR1A, and HTR2A may play an important role. In addition to C-glycosides and jujubosides, triterpenic acids and zizyphusine identified in SZJ also contributed to the regulation of serotonergic and GABAergic synapse pathways. This study provides directional predictions of anxiolytic mechanism of SZJ and insights to improve the quality control of standard extraction.

DATA AVAILABILITY STATEMENT

The raw data supporting the conclusions of this article will be made available by the authors, without undue reservation, to any qualified researcher.

AUTHOR CONTRIBUTIONS

LC, XZ, and JK designed the study. XZ, YZ, LZ, and BL performed the experiments. LC, CH, and JD prepared the manuscript. All authors contributed to the article and approved the submitted version.

FUNDING

The Nutrilite Health Institute fully funded this study.

ACKNOWLEDGMENTS

We would like to thank Dr. Zhou Yang from Shanghai Standard Technology Co., Ltd. for chemical composition analysis and identification in this paper.

SUPPLEMENTARY MATERIAL

The Supplementary Material for this article can be found online at: https://www.frontiersin.org/articles/10.3389/fphar.2020.01320/full#supplementary-material

SUPPLEMENTARY TABLE 1 | Acquired targets for identified phytochemicals in SZJ extract.

SUPPLEMENTARY TABLE 2 | Enrichment results of GO terms including biological process, cellular component, and molecular function. DAVID bioinformatics platform (version 6.8) was used for analysis.

SUPPLEMENTARY TABLE 3 | The information of enriched biological processes.

REFERENCES

Abdoul-Azize, S. (2016). Potential Benefits of Jujube (Zizyphus Lotus L.) Bioactive Compounds for Nutrition and Health. *J. Nutr. Metab.* 2016, 2867470–2867470. doi: 10.1155/2016/2867470

Akirav, I. (2011). The role of cannabinoids in modulating emotional and non-emotional memory processes in the hippocampus. *Front. Behav. Neurosci.* 5, 34–34. doi: 10.3389/fnbeh.2011.00034

Benke, D., Barberis, A., Kopp, S., Altmann, K.-H., Schubiger, M., Vogt, K. E., et al. (2009). GABAA receptors as in vivo substrate for the anxiolytic action of valerenic acid, a major constituent of valerian root extracts. *Neuropharmacology* 56, 174–181. doi: 10.1016/j.neuropharm.2008.06.013

Bindea, G., Mlecnik, B., Hackl, H., Charoentong, P., Tosolini, M., Kirilovsky, A., et al. (2009). ClueGO: a Cytoscape plug-in to decipher functionally grouped gene ontology and pathway annotation networks. *Bioinf. (Oxford Engl.)* 25, 1091–1093. doi: 10.1093/bioinformatics/btp101

Bouayed, J., Rammal, H., and Soulimani, R. (2009). Oxidative stress and anxiety: relationship and cellular pathways. *Oxid. Med. Cell Longev.* 2, 63–67. doi: 10.4161/oxim.2.2.7944

Cass, H. (2004). Herbs for the nervous system: Ginkgo, kava, valerian, passionflower. *Semin. Integr. Med.* 2, 82–88. doi: 10.1016/j.sigm.2004.07.001

Chen, Y. C., Lin, J. L., Chen, K. T., Chen, Y. C., and Jujuboside, A. (2007). and Zolpidem Inhibiting Gamma Aminobutyric Acid Type A Receptor. *J. Biomech.* 40, S556. doi: 10.1016/S0021-9290(07)70546-8

Chen, C.-J., Li, M., Wang, X.-L., Fang, F.-F., and Ling, C.-Q. (2011). "Chapter 123 - Effect of Sour Date (Semen ziziphi spinosae) Seed Extract on Treating Insomnia and Anxiety," in *Nuts and Seeds in Health and Disease Prevention*. Eds. V. R. Preedy, R. R. Watson and V. B. Patel (San Diego: Academic Press), 1037–1043.

Chen, M.-Y., Shao, L., Zhang, W., Wang, C.-Z., Zhou, H.-H., Huang, W.-H., et al. (2018). Metabolic analysis of Panax notoginseng saponins with gut microbiota-mediated biotransformation by HPLC-DAD-Q-TOF-MS/MS. *J. Pharm. Biomed. Anal.* 150, 199–207. doi: 10.1016/j.jpba.2017.12.011

Chen, C. Y.-C. (2008). Insights into the suanzaoren mechanism-From constructing the 3D structure of GABA-A receptor to its binding interaction analysis. *J. Chin. Institute Chem. Engineers* 39, 663–671. doi: 10.1016/j.jcice.2008.03.013

Chen, C. Y.-C. (2009). Chemoinformatics and pharmacoinformatics approach for exploring the GABA-A agonist from Chinese herb suanzaoren. *J. Taiwan Institute Chem. Engineers* 40, 36–47. doi: 10.1016/j.jtice.2008.07.011

Clinard, C. T., Bader, L. R., Sullivan, M. A., and Cooper, M. A. (2015). Activation of 5-HT2a receptors in the basolateral amygdala promotes defeat-induced anxiety and the acquisition of conditioned defeat in Syrian hamsters. *Neuropharmacology* 90, 102–112. doi: 10.1016/j.neuropharm.2014.11.016

Cohen, B. E., Edmondson, D., and Kronish, I. M. (2015). State of the Art Review: Depression, Stress, Anxiety, and Cardiovascular Disease. *Am. J. Hypertens.* 28, 1295–1302. doi: 10.1093/ajh/hpv047

Colangeli, R., Di Maio, R., Pierucci, M., Deidda, G., Casarrubea, M., and Di Giovanni, G. (2019). Synergistic action of CB1 and 5-HT2B receptors in preventing pilocarpine-induced status epilepticus in rats. *Neurobiol. Dis.* 125, 135–145. doi: 10.1016/j.nbd.2019.01.026

Davis, A. P., Grondin, C. J., Johnson, R. J., Sciaky, D., McMorran, R., Wiegers, J., et al. (2019). The Comparative Toxicogenomics Database: update 2019. *Nucleic Acids Res.* 47, D948–D954. doi: 10.1093/nar/gky868

Dey, P. (2019). Gut microbiota in phytopharmacology: A comprehensive overview of concepts, reciprocal interactions, biotransformations and mode of actions. *Pharmacol. Res.* 147, 104367–104367. doi: 10.1016/j.phrs.2019.104367

Fallahi-Sichani, M., Honarnejad, S., Heiser, L. M., Gray, J. W., and Sorger, P. K. (2013). Metrics other than potency reveal systematic variation in responses to cancer drugs. *Nat. Chem. Biol.* 9, 708–714. doi: 10.1038/nchembio.1337

Fuchsova, B., Alvarez Juliá, A., Rizavi, H. S., Frasch, A. C., and Pandey, G. N. (2016). Expression of p21-activated kinases 1 and 3 is altered in the brain of subjects with depression. *Neuroscience* 333, 331–344. doi: 10.1016/j.neuroscience.2016.07.037

Graeff, F. G., Guimarães, F. S., De Andrade, T. G. C. S., and Deakin, J. F. W. (1996). Role of 5-HT in stress, anxiety, and depression. *Pharmacol. Biochem. Behav.* 54, 129–141. doi: 10.1016/0091-3057(95)02135-3

Griebel, G., Perrault, G., and Sanger, D. J. (1997). A Comparative Study of the Effects of Selective and Non-Selective 5-HT2 Receptor Subtype Antagonists in Rat and Mouse Models of Anxiety. *Neuropharmacology* 36, 793–802. doi: 10.1016/S0028-3908(97)00034-8

Haj-Dahmane, S., and Shen, R.-Y. (2011). Modulation of the serotonin system by endocannabinoid signaling. *Neuropharmacology* 61, 414–420. doi: 10.1016/j.neuropharm.2011.02.016

Han, H., Ma, Y., Eun, J. S., Li, R., Hong, J.-T., Lee, M.-K., et al. (2009). Anxiolytic-like effects of sanjoinine A isolated from Zizyphi Spinosi Semen: Possible involvement of GABAergic transmission. *Pharmacol. Biochem. Behav.* 92, 206–213. doi: 10.1016/j.pbb.2008.11.012

Harris, R. A. (1990). Distinct actions of alcohols, barbiturates and benzodiazepines on GABA-activated chloride channels. *Alcohol* 7, 273–275. doi: 10.1016/0741-8329(90)90017-7

Hasler, G., Nugent, A. C., Carlson, P. J., Carson, R. E., Geraci, M., and Drevets, W. C. (2008). Altered Cerebral γ-Aminobutyric Acid Type A–Benzodiazepine Receptor Binding in Panic Disorder Determined by 11C]Flumazenil Positron Emission Tomography. *Arch. Gen. Psychiatry* 65, 1166–1175. doi: 10.1001/archpsyc.65.10.1166

Horowski, R., and Dorow, R. (2002). Anxiogenic, not psychotogenic, properties of the partial inverse benzodiazepine receptor agonist FG 7142 in man. *Psychopharmacology* 162, 223–224. doi: 10.1007/s00213-002-1095-1

Huang, W., Jin, B., Cheng, G., Yang, Y., Feng, B., and Wu, J. (2008). Content Determination of Functional Composition of Semen Ziziphi Spinosae and its Effect on Sleep Improvement of Mice. *Lishizen Med. Mater. Med. Res.* 19, R284.2–R285-5.

Huang, D. W., Sherman, B. T., and Lempicki, R. A. (2009). Systematic and integrative analysis of large gene lists using DAVID bioinformatics resources. *Nat. Protoc.* 4, 44–57. doi: 10.1038/nprot.2008.211

Jiang, J. G., Huang, X. J., Chen, J., and Lin, Q. S. (2007). Comparison of the sedative and hypnotic effects of flavonoids, saponins, and polysaccharides extracted from Semen Ziziphus jujube. *Natural Product Res.* 21, 310–320. doi: 10.1080/14786410701192827

Khan, M. N., Ul Haq, F., Rahman, S., Ali, A., and Musharraf, S. G. (2020). Metabolite distribution and correlation studies of Ziziphus jujuba and Ziziphus nummularia using LC-ESI-MS/MS. *J. Pharm. Biomed. Anal.* 178, 112918–112918. doi: 10.1016/j.jpba.2019.112918

Kim, M., Lee, J., and Han, J. (2015). Deglycosylation of isoflavone C-glycosides by newly isolated human intestinal bacteria. *J. Sci. Food Agric.* 95, 1925–1931. doi: 10.1002/jsfa.6900

Kim, J. H., Yi, Y.-S., Kim, M.-Y., and Cho, J. Y. (2017). Role of ginsenosides, the main active components of Panax ginseng, in inflammatory responses and diseases. *J. Ginseng Res.* 41, 435–443. doi: 10.1016/j.jgr.2016.08.004

Kim, D.-H. (2018). Gut microbiota-mediated pharmacokinetics of ginseng saponins. *J. Ginseng Res.* 42, 255–263. doi: 10.1016/j.jgr.2017.04.011

Lakhan, S. E., and Vieira, K. F. (2010). Nutritional and herbal supplements for anxiety and anxiety-related disorders: systematic review. *Nutr. J.* 9, 42. doi: 10.1186/1475-2891-9-42

Lee, Y., Jeon, S. J., Lee, H. E., Jung, I. H., Jo, Y.-W., Lee, S., et al. (2016). Spinosin, a C-glycoside flavonoid, enhances cognitive performance and adult hippocampal neurogenesis in mice. *Pharmacol. Biochem. Behav.* 145, 9–16. doi: 10.1016/j.pbb.2016.03.007

Liang, Y., Yang, X., Zhang, X., Duan, H., Jin, M., Sun, Y., et al. (2016). Antidepressant-like effect of the saponins part of ethanol extract from SHF. *J. Ethnopharmacol.* 191, 307–314. doi: 10.1016/j.jep.2016.06.044

Liu, J., Chen, B., and Yao, S. (2007). Simultaneous analysis and identification of main bioactive constituents in extract of Zizyphus jujuba var. sapinosa (Zizyphi spinosi semen) by high-performance liquid chromatography–photodiode array detection–electrospray mass spectrometry. *Talanta* 71, 668–675. doi: 10.1016/j.talanta.2006.05.014

Liu, J., Qiao, W., Yang, Y., Ren, L., Sun, Y., and Wang, S. (2012). Antidepressant-like effect of the ethanolic extract from Suanzaorenhehuan Formula in mice models of depression. *J. Ethnopharmacol.* 141, 257–264. doi: 10.1016/j.jep.2012.02.026

Liu, J., Zhai, W.-M., Yang, Y.-X., Shi, J.-L., Liu, Q.-T., Liu, G.-L., et al. (2015). GABA and 5-HT systems are implicated in the anxiolytic-like effect of spinosin in mice. *Pharmacol. Biochem. Behav.* 128, 41–49. doi: 10.1016/j.pbb.2014.11.003

Liu, J., Liu, J., Shen, F., Qin, Z., Jiang, M., Zhu, J., et al. (2018). Systems pharmacology analysis of synergy of TCM: an example using saffron formula. *Sci. Rep.* 8, 380. doi: 10.1038/s41598-017-18764-2

Liu, Y., Zhao, J., and Guo, W. (2018). Emotional Roles of Mono-Aminergic Neurotransmitters in Major Depressive Disorder and Anxiety Disorders. *Front. Psychol.* 9, 2201–2201. doi: 10.3389/fpsyg.2018.02201

Liu, Y., Zhao, J., Fan, X., and Guo, W. (2019). Dysfunction in Serotonergic and Noradrenergic Systems and Somatic Symptoms in Psychiatric Disorders. *Front. Psychiatry* 10, 286–286. doi: 10.3389/fpsyt.2019.00286

Lopresti, A. L., Drummond, P. D., Inarejos-García, A. M., and Prodanov, M. (2018). affron®, a standardised extract from saffron (Crocus sativus L.) for the treatment of youth anxiety and depressive symptoms: A randomised, double-blind, placebo-controlled study. *J. Affect. Disord.* 232, 349–357. doi: 10.1016/j.jad.2018.02.070

McCorvy, J. D., and Roth, B. L. (2015). Structure and function of serotonin G protein-coupled receptors. *Pharmacol. Ther.* 150, 129–142. doi: 10.1016/j.pharmthera.2015.01.009

Milajerdi, A., Jazayeri, S., Shirzadi, E., Hashemzadeh, N., Azizgol, A., Djazayery, A., et al. (2018). The effects of alcoholic extract of saffron (Crocus satious L.) on mild to moderate comorbid depression-anxiety, sleep quality, and life satisfaction in type 2 diabetes mellitus: A double-blind, randomized and placebo-controlled clinical trial. *Complement. Ther. Med.* 41, 196–202. doi: 10.1016/j.ctim.2018.09.023

Möhler, H. (2012). The GABA system in anxiety and depression and its therapeutic potential. *Neuropharmacology* 62, 42–53. doi: 10.1016/j.neuropharm.2011.08.040

Müller, D., Pfeil, T., and von den Driesch, V. (2003). Treating depression comorbid with anxiety – results of an open, practice-oriented study with St John's wort WS® 5572 and valerian extract in high doses. *Phytomedicine* 10, 25–30. doi: 10.1078/1433-187X-00305

Ni, X., Shergis, J. L., Guo, X., Zhang, A. L., Li, Y., Lu, C., et al. (2015). Updated clinical evidence of Chinese herbal medicine for insomnia: a systematic review and meta-analysis of randomized controlled trials. *Sleep Med.* 16, 1462–1481. doi: 10.1016/j.sleep.2015.08.012

Niu, C. Y., Wu, C. S., Sheng, Y. X., and Zhang, J. L. (2010). Identification and characterization of flavonoids from semen zizyphi spinosae by high-performance liquid chromatography/linear ion trap FTICR hybrid mass spectrometry. *J. Asian Nat. Prod. Res.* 12, 300–312. doi: 10.1080/10286021003752284

Nutt, D. J., and Malizia, A. L. (2004). Structural and functional brain changes in posttraumatic stress disorder. *J. Clin. Psychiatry* 65 Suppl 1, 11–17.

Okazawa, H., Yamane, F., Blier, P., and Diksic, M. (1999). Effects of Acute and Chronic Administration of the Serotonin1A Agonist Buspirone on Serotonin Synthesis in the Rat Brain. *J. Neurochem.* 72, 2022–2031. doi: 10.1046/j.1471-4159.1999.0722022.x

Olsen, R. W., and Sieghart, W. (2008). International Union of Pharmacology. LXX. Subtypes of γ-Aminobutyric AcidA Receptors: Classification on the Basis of Subunit Composition, Pharmacology, and Function. Update. *Pharmacol. Rev.* 60, 243. doi: 10.1124/pr.108.00505

Overstreet, D. H., Commissaris, R. C., De La Garza, R., File, S. E., Knapp, D. J., and Seiden, L. S. (2003). Involvement of 5-HT1A receptors in animal tests of anxiety and depression: evidence from genetic models. *Stress* 6, 101–110. doi: 10.1080/1025389031000111311

Patel, S., Hill, M. N., Cheer, J. F., Wotjak, C. T., and Holmes, A. (2017). The endocannabinoid system as a target for novel anxiolytic drugs. *Neurosci. Biobehav. Rev.* 76, 56–66. doi: 10.1016/j.neubiorev.2016.12.033

Peng, W.-H., Hsieh, M.-T., Lee, Y.-S., Lin, Y.-C., and Liao, J. (2000). Anxiolytic effect of seed of Ziziphus jujuba in mouse models of anxiety. *J. Ethnopharmacol.* 72, 435–441. doi: 10.1016/S0378-8741(00)00255-5

Poisbeau, P., Gazzo, G., and Calvel, L. (2018). Anxiolytics targeting GABAA receptors: Insights on etifoxine. *World J. Biol. Psychiatry* 19, S36–S45. doi: 10.1080/15622975.2018.1468030

Qiao, L., Liu, Y., Chen, X., Xie, J., Zhang, Y., Yang, K., et al. (2016). A HPLC-MS/MS method for determination of 6‴-feruloylspinosin in rat plasma and tissues: Pharmacokinetics and tissue distribution study. *J. Pharm. Biomed. Anal.* 121, 77–83. doi: 10.1016/j.jpba.2016.01.005

Rached, W., Barros, L., Ziani, B. E. C., Bennaceur, M., Calhelha, R. C., Heleno, S. A., et al. (2019). HPLC-DAD-ESI-MS/MS screening of phytochemical compounds and the bioactive properties of different plant parts of Zizyphus lotus (L.) Desf. *Food Funct.* 10, 5898–5909. doi: 10.1039/C9FO01423C

Ru, W., Wang, D., Xu, Y., He, X., Sun, Y.-E., Qian, L., et al. (2015). Chemical constituents and bioactivities of Panax ginseng (C. *A Mey.) Drug Discovery Ther.* 9, 23–32. doi: 10.5582/ddt.2015.01004

Salim, S. (2017). Oxidative Stress and the Central Nervous System. *J. Pharmacol. Exp. Ther.* 360, 201. doi: 10.1124/jpet.116.237503

Schousboe, A., and Redburn, D. A. (1995). Modulatory actions of gamma aminobutyric acid (GABA) on GABA type a receptor subunit expression and function. *J. Neurosci. Res.* 41, 1–7. doi: 10.1002/jnr.490410102

Shen, J., Mo, X., Tang, Y., Zhang, L., Pang, H., Qian, Y., et al. (2013). Analysis of herb–herb interaction when decocting together by using ultra-high-performance liquid chromatography–tandem mass spectrometry and fuzzy chemical identification strategy with poly-proportion design. *J. Chromatogr. A* 1297, 168–178. doi: 10.1016/j.chroma.2013.05.001

Shergis, J. L., Ni, X., Sarris, J., Zhang, A. L., Guo, X., Xue, C. C., et al. (2017). Ziziphus spinosa seeds for insomnia: A review of chemistry and psychopharmacology. *Phytomedicine* 34, 38–43. doi: 10.1016/j.phymed.2017.07.004

Somers, J. M., Goldner, E. M., Waraich, P., and Hsu, L. (2006). Prevalence and Incidence Studies of Anxiety Disorders: A Systematic Review of the Literature. *Can. J. Psychiatry* 51, 100–113. doi: 10.1177/070674370605100206

Song, P., Zhang, Y., Ma, G., Zhang, Y., Zhou, A., and Xie, J. (2017). Gastrointestinal Absorption and Metabolic Dynamics of Jujuboside A, A Saponin Derived from the Seed of Ziziphus jujuba. *J. Agric. Food Chem.* 65, 8331–8339. doi: 10.1021/acs.jafc.7b02748

Spiacci, A., Pobbe, R. L. H., Matthiesen, M., and Zangrossi, H. (2016). 5-HT1A receptors of the rat dorsal raphe lateral wings and dorsomedial subnuclei differentially control anxiety- and panic-related defensive responses. *Neuropharmacology* 107, 471–479. doi: 10.1016/j.neuropharm.2015.06.015

Starcevic, V. (2006). Review: worldwide lifetime prevalence of anxiety disorders is 16.6%, with considerable heterogeneity between studies. *Evid. Based Ment. Health* 9, 115. doi: 10.1136/ebmh.9.4.115

Su, G., Morris, J. H., Demchak, B., and Bader, G. D. (2014). Biological Network Exploration with Cytoscape 3. *Curr. Protoc. Bioinf.* 47, 8.13.1–8.13.24. doi: 10.1002/0471250953.bi0813s47

Sun, S., Liu, H., Xu, S., Yan, Y., and Xie, P. (2014). Quality analysis of commercial samples of Ziziphi spinosae semen (suanzaoren) by means of chromatographic fingerprinting assisted by principal component analysis. *J. Pharm. Anal.* 4, 217–222. doi: 10.1016/j.jpha.2014.01.003

Szklarczyk, D., Gable, A. L., Lyon, D., Junge, A., Wyder, S., Huerta-Cepas, J., et al. (2019). Mering, STRING v11: protein–protein association networks with increased coverage, supporting functional discovery in genome-wide experimental datasets. *Nucleic Acids Res.* 47, D607–D613. doi: 10.1093/nar/gky1131

Teychenne, M., Costigan, S. A., and Parker, K. (2015). The association between sedentary behaviour and risk of anxiety: a systematic review. *BMC Public Health* 15, 513. doi: 10.1186/s12889-015-1843-x

Vollmer, M., Esders, S., Farquharson, F. M., Neugart, S., Duncan, S. H., Schreiner, M., et al. (2018). Mutual Interaction of Phenolic Compounds and Microbiota: Metabolism of Complex Phenolic Apigenin-C- and Kaempferol-O-Derivatives by Human Fecal Samples. *J. Agric. Food Chem.* 66, 485–497. doi: 10.1021/acs.jafc.7b04842

Wang, Y., Huang, L., and Li, T. (2008). The Effects of Semen Ziziphi Spinosae decoction on sleeping state in Rats. *Lishizen Med. Mater. Med. Res.* 19, R285.5.

Wang, L.-E., Bai, Y.-J., Shi, X.-R., Cui, X.-Y., Cui, S.-Y., Zhang, F., et al. (2008). Spinosin, a C-glycoside flavonoid from semen Zizhiphi Spinozae, potentiated pentobarbital-induced sleep via the serotonergic system. *Pharmacol. Biochem. Behav.* 90, 399–403. doi: 10.1016/j.pbb.2008.03.022

Wang, W., Luo, J., and Kong, L. (2009). HPLC-ESI-MS(n) analysis of chemical constituents in Semen Ziziphi Spinosae. *Zhongguo Zhongyao Zazhi* 34, 2768–2773.

Wang, L. E., Cui, X. Y., Cui, S. Y., Cao, J. X., Zhang, J., Zhang, Y. H., et al. (2010). Potentiating effect of spinosin, a C-glycoside flavonoid of Semen Ziziphi spinosae, on pentobarbital-induced sleep may be related to postsynaptic 5-HT1A receptors. *Phytomedicine* 17, 404–409. doi: 10.1016/j.phymed.2010.01.014

Wang, X.-X., Ma, G.-I., Xie, J.-B., and Pang, G.-C. (2015). Influence of JuA in evoking communication changes between the small intestines and brain tissues of rats and the GABAA and GABAB receptor transcription levels of hippocampal neurons. *J. Ethnopharmacol.* 159, 215–223. doi: 10.1016/j.jep.2014.11.012

Wang, X., Shen, Y., Wang, S., Li, S., Zhang, W., Liu, X., et al. (2017). PharmMapper 2017 update: a web server for potential drug target identification with a

comprehensive target pharmacophore database. *Nucleic Acids Res.* 45, W356–W360. doi: 10.1093/nar/gkx374

Wang, J., Zhang, Y., Liu, Y.-M., Yang, X.-C., Chen, Y.-Y., Wu, G.-J., et al. (2020). Uncovering the protective mechanism of Huoxue Anxin Recipe against coronary heart disease by network analysis and experimental validation. *Biomed. Pharmacother.* 121, 109655. doi: 10.1016/j.biopha.2019.109655

Xiao, H.-B., Wang, Y.-S., Luo, Z.-F., and Lu, X.-Y. (2018). SZSJ protects against insomnia by a decrease in ADMA level and an improvement in DDAH production in sleep-deprived rats. *Life Sci.* 209, 97–102. doi: 10.1016/j.lfs.2018.07.044

Xu, H.-Y., Zhang, Y.-Q., Liu, Z.-M., Chen, T., Lv, C.-Y., Tang, S.-H., et al. (2019). ETCM: an encyclopaedia of traditional Chinese medicine. *Nucleic Acids Res.* 47, D976–D982. doi: 10.1093/nar/gky987

Yang, B., Yang, H., Chen, F., Hua, Y., and Jiang, Y. (2013). Phytochemical analyses of Ziziphus jujuba Mill. var. spinosa seed by ultrahigh performance liquid chromatography-tandem mass spectrometry and gas chromatography-mass spectrometry. *Analyst* 138, 6881–6888. doi: 10.1039/c3an01478a

You, Z.-L., Xia, Q., Liang, F.-R., Tang, Y.-J., Xu, C.-l., Huang, J., et al. (2010). Effects on the expression of GABAA receptor subunits by jujuboside A treatment in rat hippocampal neurons. *J. Ethnopharmacol.* 128, 419–423. doi: 10.1016/j.jep.2010.01.034

Yue, S.-J., Xin, L.-T., Fan, Y.-C., Li, S.-J., Tang, Y.-P., Duan, J.-A., et al. (2017a). Herb pair Danggui-Honghua: mechanisms underlying blood stasis syndrome by system pharmacology approach. *Sci. Rep.* 7, 40318. doi: 10.1038/srep40318

Yue, S.-J., Liu, J., Feng, W.-W., Zhang, F.-L., Chen, J.-X., Xin, L.-T., et al. (2017b). System Pharmacology-Based Dissection of the Synergistic Mechanism of Huangqi and Huanglian for Diabetes Mellitus. *Front. Pharmacol.* 8, 294. doi: 10.3389/fphar.2017.00694

Zhang, M., Zhang, Y., and Xie, J. (2008). Simultaneous determination of jujuboside A, B and betulinic acid in semen Ziziphi spinosae by high performance liquid chromatography-evaporative light scattering detection. *J. Pharm. Biomed. Anal.* 48, 1467–1470. doi: 10.1016/j.jpba.2008.09.022

Zhang, J., Cai, C.-Y., Wu, H.-Y., Zhu, L.-J., Luo, C.-X., and Zhu, D.-Y. (2016). CREB-mediated synaptogenesis and neurogenesis is crucial for the role of 5-HT1a receptors in modulating anxiety behaviors. *Sci. Rep.* 6, 29551. doi: 10.1038/srep29551

Zhang, F.-X., Li, M., Qiao, L.-R., Yao, Z.-H., Li, C., Shen, X.-Y., et al. (2016). Rapid characterization of Ziziphi Spinosae Semen by UPLC/Qtof MS with novel informatics platform and its application in evaluation of two seeds from Ziziphus species. *J. Pharm. Biomed. Anal.* 122, 59–80. doi: 10.1016/j.jpba.2016.01.047

Zheng, S., Geng, D., Liu, S., Wang, Q., Liu, S., and Wang, R. (2019). A newly isolated human intestinal bacterium strain capable of deglycosylating flavone C-glycosides and its functional properties. *Microb. Cell Fact* 18, 94–94. doi: 10.1186/s12934-019-1144-7

Żmudzka, E., Sałaciak, K., Sapa, J., and Pytka, K. (2018). Serotonin receptors in depression and anxiety: Insights from animal studies. *Life Sci.* 210, 106–124. doi: 10.1016/j.lfs.2018.08.050

Conflict of Interest: The authors declare that the research was conducted in the absence of any commercial or financial relationships that could be construed as a potential conflict of interest.

Copyright © 2020 Chen, Zhang, Hu, Zhang, Zhang, Kan, Li and Du. This is an open-access article distributed under the terms of the Creative Commons Attribution License (CC BY). The use, distribution or reproduction in other forums is permitted, provided the original author(s) and the copyright owner(s) are credited and that the original publication in this journal is cited, in accordance with accepted academic practice. No use, distribution or reproduction is permitted which does not comply with these terms.

frontiers in Pharmacology

ORIGINAL RESEARCH
published: 20 October 2020
doi: 10.3389/fphar.2020.586350

Integrating Pharmacology and Gut Microbiota Analysis to Explore the Mechanism of Citri Reticulatae Pericarpium Against Reserpine-Induced Spleen Deficiency in Rats

*Yuying Zheng, Xuan Zeng, Pan Chen, Tingting Chen, Wei Peng and Weiwei Su**

Guangdong Engineering and Technology Research Center for Quality and Efficacy Re-evaluation of Post-Market Traditional Chinese Medicine, Guangdong Provincial Key Laboratory of Plant Resources, School of Life Sciences, Sun Yat-sen University, Guangzhou, China

OPEN ACCESS

Edited by:
Yanqiong Zhang,
China Academy of Chinese Medical Sciences, China

Reviewed by:
Lei Wang,
Capital Medical University, China
Dinghong Wu,
Guangdong Provincial Academy of Chinese Medical Sciences, China

***Correspondence:**
Weiwei Su
lsssww@126.com

Specialty section:
This article was submitted to Ethnopharmacology, a section of the journal Frontiers in Pharmacology

Received: *23 July 2020*
Accepted: *18 September 2020*
Published: *20 October 2020*

Citation:
Zheng Y, Zeng X, Chen P, Chen T, Peng W and Su W (2020) Integrating Pharmacology and Gut Microbiota Analysis to Explore the Mechanism of Citri Reticulatae Pericarpium Against Reserpine-Induced Spleen Deficiency in Rats. Front. Pharmacol. 11:586350. doi: 10.3389/fphar.2020.586350

Citri Reticulatae Pericarpium (CRP), dried peels of *Citrus reticulata* Blanco and its cultivars, is an important traditional Chinese medicine for the treatment of spleen deficiency-related diseases. To date, the mechanism of CRP alleviating spleen deficiency has not been well investigated. This study aimed to explore corresponding mechanisms with integrating pharmacology and gut microbiota analysis. Firstly, the therapeutic effects of CRP against spleen deficiency were evaluated in reserpine-treated rats. CRP was found to effectively relieve the typical symptoms of spleen deficiency, including poor digestion and absorption capacity, and disorder in gastrointestinal hormones, immune cytokines and oxidative stress. Secondly, high throughput 16S rRNA gene sequencing revealed that CRP could not only up-regulate some short-chain fatty acids producing and anti-inflammatory bacteria but also down-regulate certain spleen deficiency aggravated related bacteria, eventually led to the rebalance of gut microbiota in spleen deficiency rats. In addition, a total of 49 compounds derived from CRP were identified in rat urine using ultra-high performance liquid chromatography-quadrupole- time of flight tandem mass spectrometry. Network pharmacology analysis showed that apigenin, luteolin, naringenin, hesperidin, hesperetin, homoeriodictyol, dihydroxy-tetramethoxyflavone, and monohydroxy-tetramethoxyflavone were the core bioactive components for CRP against spleen deficiency. Further Gene Ontology analysis and pathway enrichment suggested that therapeutic effects of CRP against spleen deficiency involved multiple pathways such as tumor necrosis factor signaling, hypoxia-inducible factor-1 signaling and Toll-like receptor signaling pathway. These results would help to understand the mechanism of CRP alleviating spleen deficiency and provide a reference for further studies.

Keywords: Citri Reticulatae Pericarpium, spleen deficiency, gut microbiota, metabolites, network pharmacology

INTRODUCTION

In the theory of traditional Chinese medicine (TCM), spleen deficiency is a common clinical syndrome and described as symptoms such as emaciation, inappetence, epigastralgia, flatulence, lassitude, wilted complexion, loose stool, *etc*. Modern researches show that the spleen in TCM theory not only refers to the anatomical spleen, but also includes some functions of the pancreas and lymphatic system (Zheng et al., 2014). Spleen deficiency is a comprehensive manifestation of multiple functional declines, involving food digestion, nutrient absorption, energy metabolism, and immune system (Wang et al., 2016). Moreover, recent studies suggested that spleen deficiency is closely related to gut microbiota disorder (Qiu et al., 2017; Lin et al., 2018). Gut microbiota, as the main member of gut microecology, plays an essential role in the host's health and can be deeply influenced by diets (Bibbò et al., 2016), antibiotics (Nogacka et al., 2018) and other environmental factors (Capurso and Lahner, 2017). In turn, the dysbiosis of the gut microbiota will act as a causative factor in gastrointestinal diseases (Feng et al., 2018). Recently, researchers found that some TCMs could exert their therapeutic effects on gastrointestinal diseases through regulating the balance of gut microbiota (Yang et al., 2017).

Citri Reticulatae Pericarpium (CRP), commonly referred to as Chenpi in Chinese, is derived from the pericarp of mature fruits of *Citrus reticulata* Blanco and its cultivars (State Pharmacopoeia Committee of People's Republic of China, 2015). It is an important Chinese medicinal material which has been used for the treatment of respiratory and digestive diseases for thousands of years (Zheng et al., 2018). Long-term and extensive clinical applications have confirmed that CRP could alleviate multiple spleen deficiency related diseases, including indigestion, inappetence, abdominal fullness and distention (Yu et al., 2018). However, the mechanism of CRP alleviating spleen deficiency has not been well investigated. On the one hand, information concerning the bioactive components and potential targets involved in the effects of CRP against spleen deficiency are scarce. On the other hand, given the gut microbiota modulatory potential of CRP (Zeng et al., 2020a), it is meaningful to investigate the role of gut microbiota in the therapeutic efficacy of CRP.

In this study, reserpine-induced spleen deficiency rat model was established and used to evaluate the therapeutic effects of CRP. Reserpine, which was once used in the treatment of hypertension, could inhibit the vesicular monoamine transporter and deplete the brain monoamines such as 5-hydroxytryptamine by interfering with storage capacity, and ultimately lead to similar syndromes of spleen deficiency (Zhao et al., 2011; Maldonado and Maeyama, 2015). Meanwhile, spleen deficiency related disease targets were collected from accessible online databases and then used to explore the bioactive components and potential targets of CRP based on a network pharmacology strategy. Network pharmacology is a new discipline combined systems biology with drug efficacy, which helps to elucidate the inherent multi-component, multi-target, and multi-pathway characteristics of TCM (Ning et al., 2017).

Hereon, the therapeutic efficacy of CRP against spleen deficiency was evaluated in reserpine treated rats based on body signs and biochemical indexes including digestion, absorption, gastrointestinal hormones, immune regulation and oxidative stress. The gut microbiota modulatory properties of CRP in spleen deficiency rats were investigated with high throughput 16S rRNA gene sequencing. Moreover, CRP derived metabolites were identified using ultra-high performance liquid chromatography-quadrupole-time of flight tandem mass spectrometry (UHPLC-Q-TOF-MS/MS) and were further employed in network pharmacology analysis to capture the bioactive components and potential targets of CRP in treating spleen deficiency. This study would be helpful for further understanding of the pharmacological effects and therapeutic benefits of CRP against spleen deficiency related diseases.

MATERIALS AND METHODS

Chemicals and Materials

CRP samples (Batch number: 201712) were acquired from Xinhui Hele Tea Art Co. Ltd. (Jiangmen, China), and were authenticated by Prof. Wenbo Liao from Sun Yat-sen University. Corresponding voucher specimens were kept in our laboratory. Reserpine injection was purchased from Guangdong Bangmin Pharmaceutical Co., Ltd. (Jiangmen, China). The reference standards of hesperidin, naringin, neohesperidin and rutin were obtained from National Institute for Control of Biological and Pharmaceutical Products of China (Beijing, China). Hesperetin, naringenin, nobiletin and mass spectrometry (MS) grade formic acid were purchased from Sigma-Aldrich (St. Louis, MO, United States). MS grade acetonitrile was purchased from Fisher Scientific (Pittsburgh, PA, United States). All water used was distilled and further purified by a Milli-Q system (Millipore, Milford, MA, United States). Other reagents used in the experiment were of analytical grade.

Preparation of Citri Reticulatae Pericarpium Extract

The CRP sample (20 g) was cut into small pieces, and soaked in boiled distilled water for three times (2, 1.5 and 1.5 L of each bulk, respectively; 20, 15 and 15 min of each time, respectively). After filtration, the whole extracts were evaporated to 500 ml with a rotary evaporator (Eyela, Tokyo, Japan) at 60°C, to obtain the CRP extract with a concentration of 0.04 g mL^{-1}.

Animals and Experimental Design

Thirty male Sprague-Dawley rats (weighting 180–220 g) were purchased from Guangdong Medical Laboratory Animal Center, and maintained in standard temperature conditions (20–23°C) and a 12/12-h light-dark cycle, with food and water supplied *ad libitum*. All experimental procedures were approved by the Animal Ethics Committee of the School of Life Sciences in Sun Yat-sen University and carried out in accordance with the National Institutes of Health guide for the care and use of Laboratory animals (NIH Publications No. 8023, revised 1978).

Rats were randomly divided into three groups (control group, model group and CRP group). Rats in model and CRP group were injected subcutaneously with reserpine injection at 0.5 mg kg^{-1} d^{-1}

for 14 days to induce spleen deficiency (Wang et al., 2016). Rats in the control group were injected with the same volume of saline. After that, rats in CRP group were intragastrically given CRP extract (0.04 g ml^{-1}, 15 ml kg^{-1} d^{-1}) for 14 days. Rats in control and model groups received distilled water.

After the last administration, rats were housed individually in metabolic cages (Y-3102, Yuyan Instruments Co. Ltd.; Shanghai, China), with fasting and free access to water. Urine samples were collected within 12 h post-dose for metabolite identification. Subsequently, about 1 ml blood was sampled from retro orbital plexus, and then 5 ml 3% D-xylose solution was intragastrically administered to rats. Exactly 1 h later, rats were anesthetized with 10% chloral hydrate (3 ml kg^{-1}) to collect blood samples from abdominal artery. Serum was obtained after centrifugation. In addition, feces samples for gut microbiota analysis were collected from the rectum, transferred into sterile conical tubes, and then immediately frozen in liquid nitrogen. Obtained samples were stored at −80°C until analysis.

Kits Tests

The activities of superoxide dismutase (SOD) and amylase in serum, as well as the concentrations of D-xylose and malondialdehyde, were determined following protocols of corresponding Kits (Nanjing Jiancheng Bioengineering Institute, Nanjing, China). The concentrations of gastrin, motilin, cholecystokinin-8 (CCK-8), interleukin 6 (IL-6) and tumor necrosis factor-alpha (TNF-α) in serum were detected using commercial ELISA kits (Uscnlife Sciences & Technology Co., Wuhan, China) according to the manufacturer's instructions.

Gut Microbiota Analysis Using 16S rRNA Gene Sequencing

Total bacterial DNA were extracted and amplified as previously described (Zheng et al., 2020). After PCR amplification, sequencing was performed on an Illumina Hiseq 2500 platform by Biomarker Technologies Co. Ltd. (Beijing, China). Bioinformatics analysis was performed based on operational taxonomic units, which were clustered based on a 97% sequence similarity according to UCLUST (Edgar, 2010). For alpha diversity analysis, Chao1, ACE, Shannon index, and Simpson index were calculated in the QIIME program (version 1.8) (Caporaso et al., 2010). For beta diversity analysis, principal coordinate analysis (PCoA) was performed under the Gower algorithm. All processes were performed on the BMKCloud platform (www.biocloud.net). The Spearman's rho non-parametric correlations between gut microbiota (the top 60 genera in relative abundance) and spleen deficiency related indexes were then calculated by using SPSS software (version 22.0) and displayed by R software with a pheatmap package.

Identification of Metabolites Derived From Citri Reticulatae Pericarpium

To identify CRP derived metabolites, an aliquot of 100 μL urine sample was vortex-mixed with 200 μL volume acetonitrile for 3 min, and centrifuged at 15,000 × g for 30 min at 25°C. Finally, 10 μL supernatant was subject to UHPLC-Q-TOF-MS/MS analysis.

Detection of CRP derived metabolites was carried out using an ultra-fast liquid chromatography (Shimadzu Corp., Kyoto, Japan) coupled with quadrupole/time-of-flight mass spectrometry (Triple TOF 5600 plus, AB SCIEX, Foster City, United States). Gradient chromatographic separation was performed on a Kinetex C_{18} column (2.6 μM, 150 mm × 3.0 mm) and maintained at 40°C. The mobile phase consisted of acetonitrile (A) and water containing 0.1% aqueous formic acid (*v*/*v*) (B). The elution was carried out following the program: 5–100% A (0–30 min), 100% A (30–34 min) with the flow rate kept at 0.3 ml/min. The mass spectrometry detector was equipped with an electrospray ionization source and operated under the same parameters with our reported studies (Zeng et al., 2019).

Data acquisition was carried out using Analyst® TF 1.6 software (AB Sciex, Foster City, United States) in information-dependent acquisition mode. Metabolite identification was based on chromatographic elution time, chemical composition, MS/MS fragmentation pattern, and comparisons with available standards and references.

Network Pharmacology Analysis

Collection of Potential Targets for Citri Reticulatae Pericarpium

With the UHPLC-Q-TOF-MS/MS system, a total of 49 metabolites were characterized in rat urine. The associated proteins of CRP were searched in Comparative Toxicogenomics Database (Davis et al., 2019), Encyclopedia of TCM (Xu et al., 2019) and Swiss Target Prediction Database (Gfeller et al., 2014).

Collection of Potential Targets for Spleen Deficiency

As there are no therapeutic targets about spleen deficiency that were available directly in the databases, targets of diseases that have similar pathological features with spleen deficiency were collected as alternatives. Diarrhea, dyspepsia, enteritis and gastritis were chosen out, and the corresponding targets were searched in DisGeNET (Pinero et al., 2020).

Protein-Protein Interaction Analysis

Protein-protein interaction (PPI) data was constructed by inputting official gene symbol to the "Multiple Proteins" search on String website (Szklarczyk et al., 2019), with organism species limited to "Homo sapiens" and a confidence score >0.9. The interaction results were exported as (.tsv) file for further network analysis by using Cytoscape software. The CRP-related target-spleen deficiency target network (CT-ST network) was constructed based on their PPI data and visualized by Cytoscape 3.7.0 software. The CRP-related targets were mapped to the spleen deficiency-related targets for obtaining the common targets of both. Then a network including the common targets and their first neighbors was extracted from the CT-ST network. In the generated networks, nodes represent targets and components, and edges represent the relationship between them. The targets without interaction were excluded

from the network. Afterward, a plugin of Cytoscape (Network Analyzer) was applied to analyze the topological parameters of each node in the network. Among the topological parameters, degree, betweenness centrality and closeness centrality were used as crucial factors to evaluate the most influential nodes in networks. The nodes with "Degree" value greater than twofold the median value of all the network nodes, "Betweenness centrality" and "Closeness centrality" value greater than the median value of all the network nodes were chosen as the key targets.

Gene Ontology Enrichment and Pathway Analysis

The Database for Annotation, Visualization and Integrated Discovery was applied for Gene Ontology (GO) enrichment and pathway analysis (Jiao et al., 2012). The specific operation steps were as following, inputting the protein ID and restricting the species to "Homo sapiens," then utilizing the functional annotation tool to make GO enrichment and pathway analysis.

Statistical Analysis

Data were expressed as mean ± standard deviation (n = 10). The significant differences between the groups were assessed by ANOVA test in SPSS software (version 22.0), and p values less than 0.05 or 0.01 were considered as significant difference. Figures were plotted with GraphPad Prism (Version 7.00).

RESULTS AND DISCUSSION

Therapeutic Effects of Citri Reticulatae Pericarpium Against Spleen Deficiency

TCM clinical syndromes are often difficult to quantify with modern analysis methods. How to use animal models to characterize the syndromes is one of the difficulties in the modern researches on TCM (Meng et al., 2013). In this work, a reserpine-induced spleen deficiency rat model was established to evaluate the therapeutic effects of CRP based on body symptoms and biochemical indexes. Three days after the subcutaneous injection of reserpine, rats showed typical symptoms of spleen deficiency, such as anorexia, weight loss, pasty loose stools, inactiveness, and grouping. As presented in **Figure 1**, reserpine treatment significantly reduced the body weight of rats (p < 0.01). With the administration of CRP for 14 days, above-mentioned symptoms of spleen deficiency in rats were significantly improved. Rat body weights of CRP group were higher than that of model group, although there was no significant difference. These results preliminarily suggested that CRP administration could relieve the symptoms of spleen deficiency induced by reserpine.

Subsequently, we further investigated the effects of CRP on biochemical indexes in reserpine-induced spleen deficiency rats, including the parameters used to characterize digestion, absorption, gastrointestinal hormones, immune regulation and oxidative stress. Obtained results were illustrated in **Figure 2**. Reported studies have observed that patients with spleen deficiency usually showed the symptoms of poor digestion and absorption (Chung et al., 2016). In this study, the activity of amylase and the concentration of D-xylose in serum were used to reflect the digestion and absorption of nutrients in rats (Gao et al., 2009; Li et al., 2020). As shown in **Figure 2**, the level of D-xylose and the activity of amylase in model group were significantly lower than that in control and CRP group (p < 0.01), suggesting that reserpine treatment could significantly reduce the digestion and absorption in rats while CRP administration could effectively reverse these changes.

Gastrointestinal hormones take an important role in regulating secretory and motor functions of the digestive tract (Xie et al., 2006). It has been found that the levels of gastrointestinal

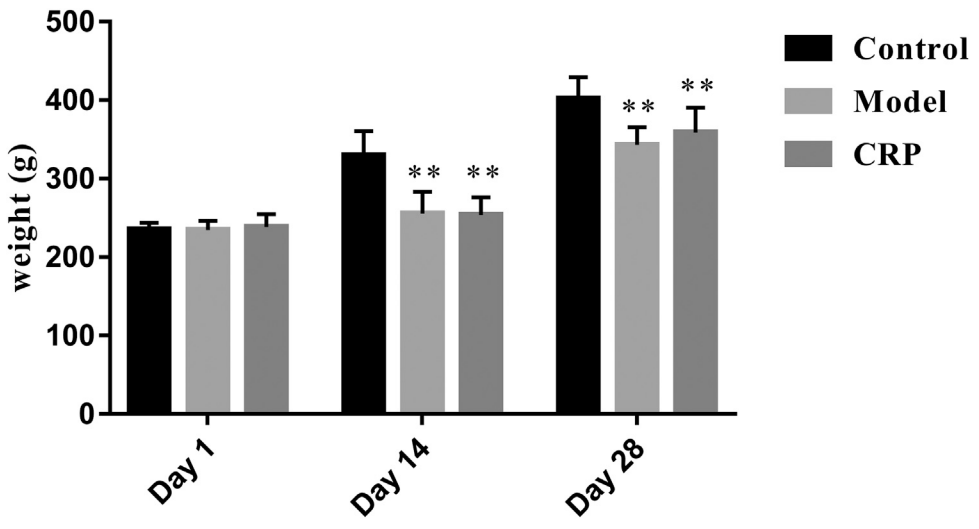

FIGURE 1 | Rat body weights comparison between control, model and CRP treated group. (n = 10, $^{**}p$ < 0.01, vs. control group. Although the body weights of CRP treated group were higher than that of model group after intervention, there existed no significant difference.)

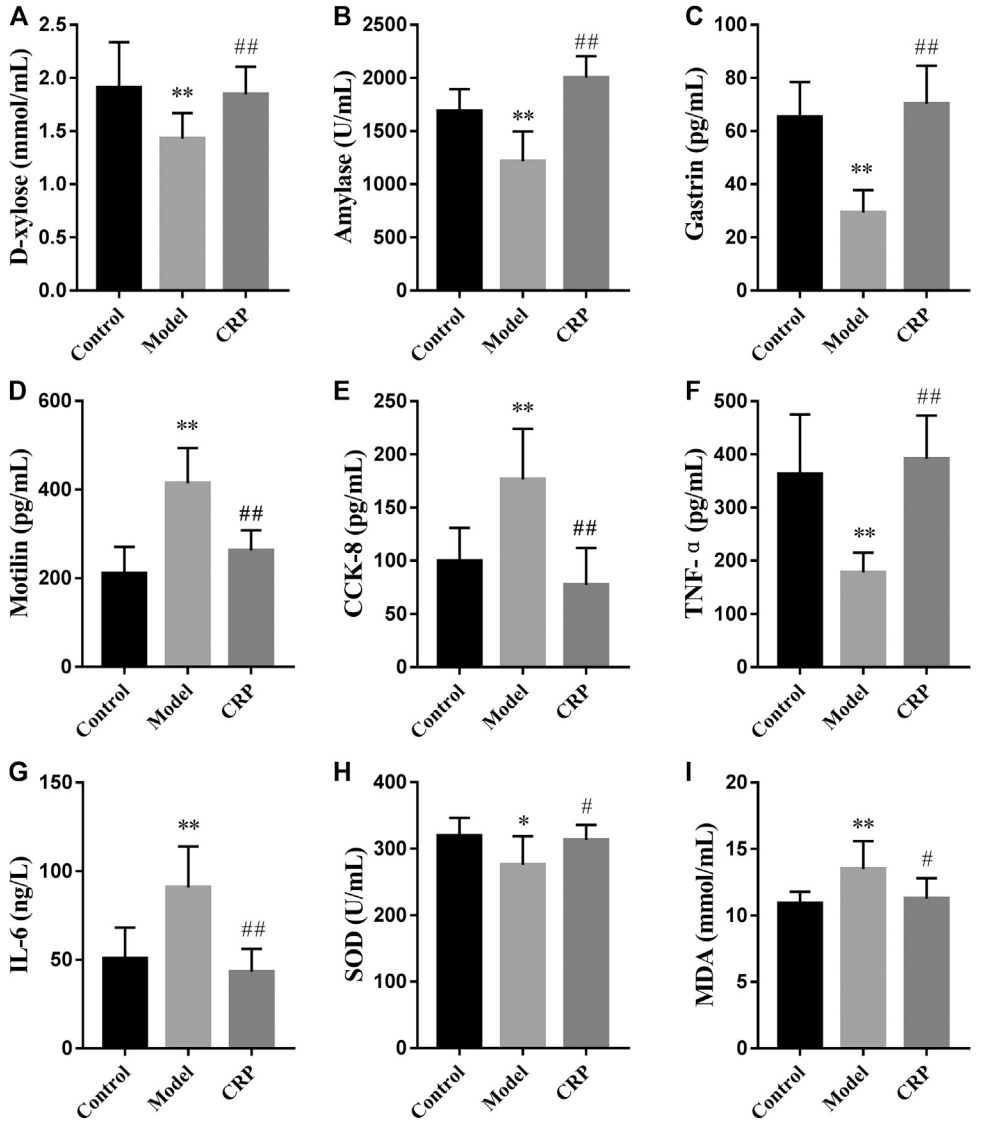

FIGURE 2 | Effects of CRP on biochemical parameters in serum, including the concentrations of **(A)** D-xylose and **(I)** MDA, the activities of **(B)** amylase and **(H)** SOD, the levels of **(C)** gastrin, **(D)** motilin, **(E)** cholecystokinin-8, **(F)** TNF-α and **(G)** IL-6 ($n = 10$; $^{*}p < 0.05$, vs. control group; $^{**}p < 0.01$, vs. control group; $^{\#}p < 0.05$, vs. model group; $^{\#\#}p < 0.01$, vs. model group).

hormones in patients with gastrointestinal diseases were different from those in normal individuals (Wang et al., 2013). Hereon, three representative gastrointestinal hormones (gastrin, motilin, CCK-8) were employed to evaluate the effects of CRP on neuroendocrine in spleen deficiency rats. Gastrin, released from the G cells in antrum and duodenum, could stimulate the secretion of gastric acid, pepsin, bile and improve gastrointestinal movement (Itoh et al., 2005). Motilin is a peptide synthesized by mucosal endocrine cells in the upper segment of small intestine. It could promote gastrointestinal motility and improve the contractility and tension of the gastrointestinal tract and biliary tract (Itoh et al., 2005). CCK-8, a peptide hormone widely distributed in gastrointestinal tract and brain, is experimentally identified as a transmitter involved in multiple physiological activities, such as acting on feeding center, causing satiety and inhibiting feeding (Stengel and Tache, 2011). As illustrated in **Figure 2**, compared with control group, the level of gastrin in model group significantly decreased while the levels of motilin and CCK-8 significantly increased ($p < 0.01$), showing that reserpine treatment led to the disorder of gastrointestinal hormones secretion in rats. Changes in these three gastrointestinal hormones caused by reserpine treatment were up to normal after the administration of CRP for 14 days, revealing the efficiency of CRP in improving digestive dysfunction through regulating neuroendocrine.

The dynamic balance between Th1 and Th2 immune response is important for the immune system (Bashyam, 2007; Fischer et al., 2007). Th1 cytokines are with mediation in cell immunity response and mainly include IFN-γ, TNF-α, IL-1, IL-2, while Th2 cytokines mediate humoral immunity and include IL-4, IL-5,

TABLE 1 | The diversity index of gut microbiota in rats in different groups.

Group	Community richness		Community diversity	
	ACE	Chao1	Shannon	Simpson
Control	516.47 ± 24.71	524.54 ± 26.4	4.51 ± 0.23	0.03 ± 0.01
Model	396.41 ± 38.51**	407.74 ± 39.15**	4.06 ± 0.17**	0.04 ± 0.01
CRP	459.20 ± 37.60##	460.2 ± 34.76##	3.68 ± 0.18	0.07 ± 0.01

Note: n = 10, *vs. Control:* **p < 0.01; *vs. Model:* ##p < 0.01.

IL-6, IL-10 (Mosmann et al., 1986). In the model group, reserpine treatment significantly decreased the level of TNF-α while promoted that of IL-6 in serum ($p < 0.01$). After the intervention with CRP, the level of TNF-α and IL-6 restored to normal, suggesting that CRP could help maintain the balance of Th1 and Th2 immune response.

In addition, the balance between oxidants and antioxidants is necessary in maintaining health, and corresponding imbalance may result in oxidative stress causing functional disorders and certain diseases (Sharma et al., 2015). In this study, rats in model group had lower activity of SOD and higher level of malondialdehyde ($p < 0.05$) than control group, indicating that reserpine treatment resulted in free radical disorder in spleen deficiency rats. CRP administration could improve the activity of antioxidant enzyme and reduce lipid peroxidation damage ($p < 0.05$).

In summary, CRP administration could effectively alleviate the syndromes of spleen deficiency induced by reserpine treatment in rats, including poor digestion and absorption capacity, and disorder in gastrointestinal hormones, immune cytokines and oxidative stress.

Gut Microbiota Modulatory Effects of Citri Reticulatae Pericarpium in Spleen Deficiency Rats

Gut microbiota plays a vital role in maintaining normal intestinal functions, such as food digestion, nutrient absorption, integrity of epithelial barrier, and development of mucosal immunity (Veerappan et al., 2012). Recently, more and more evidence indicated that gut microbiota imbalance is a potential trigger for many diseases such as inflammatory bowel disease (Veerappan et al., 2012), diabetes (Meijnikman et al., 2018) and metabolic syndrome (Zeng et al., 2020a). In this study, the changes of bacterial richness (expressed in ACE and Chao1) and diversity (expressed in Shannon and Simpson index) in response to reserpine treatment and CRP intervention were investigated. As shown in **Table 1**, remarkably lower ACE, Chao1 and Shannon indexes were observed in the model group ($p < 0.01$), which suggested that reserpine treatment disturbed the balance of gut microbiota. By contrast, supplement with CRP gave rise to a higher community richness than that of the model group ($p < 0.01$), indicating that CRP is beneficial to the growth of gut microbiota. Beta diversity analysis among experimental groups was performed with PCoA. As shown in **Figure 3**, the PCoA score plot depicted three clearly

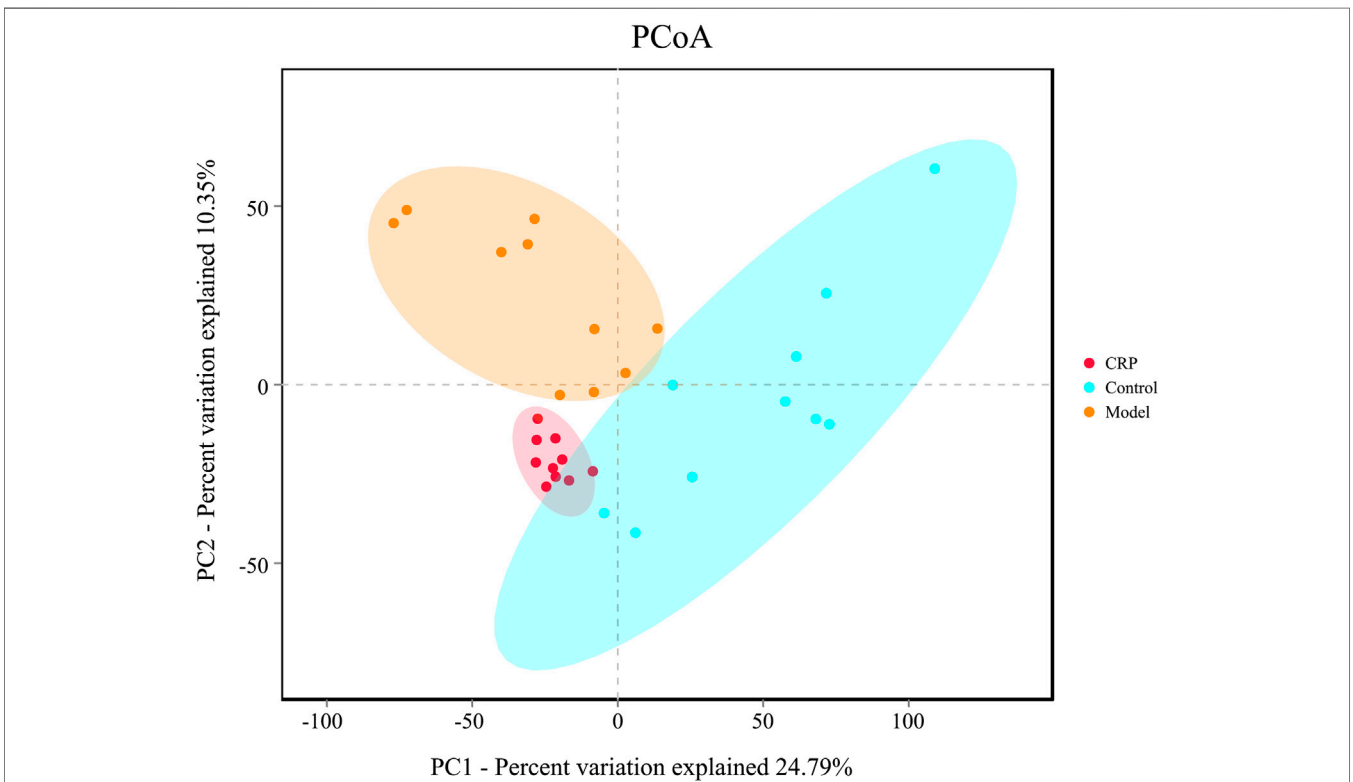

FIGURE 3 | PCoA plot of microbial communities were based on OTU composition, each treatment group is represented by different color. *N* = 10 in each group.

divided groups: samples from the model group gathered in the second quadrant; samples from the control group dispersed in the first, third, and fourth quadrants; and samples from CRP group concentrated in the third quadrant, which were similar to that of control group. These results indicated that CRP intervention could help to restore changes in the richness and diversity of gut microbiota in spleen deficiency rats.

The correlations between gut microbiota (the top 60 genera in relative abundance) and spleen deficiency-related indexes were calculated using Spearman's rho non-parametric correlation analysis (**Figure 4**). The heatmap reflected significant positive correlations between the improvement of spleen deficiency related-indexes and some short-chain fatty acids (SCFAs) producing bacteria, such as *Bifidobacterium*, *Lactobacillus*, *Allobaculum*, *Psychrobacter*, *Prevotellaceae_Ga6A1_group*, *[Eubacterium]_coprostanoligenes_group*, *Parasutterella*, etc. SCFAs (acetate, propionate and butyrate), the end products of gut microbial fermentation of indigestible dietary components, appeared to enhance epithelial barrier function, improve gut permeability, inhibit the inflammation. Among them, *Bifidobacterium* and

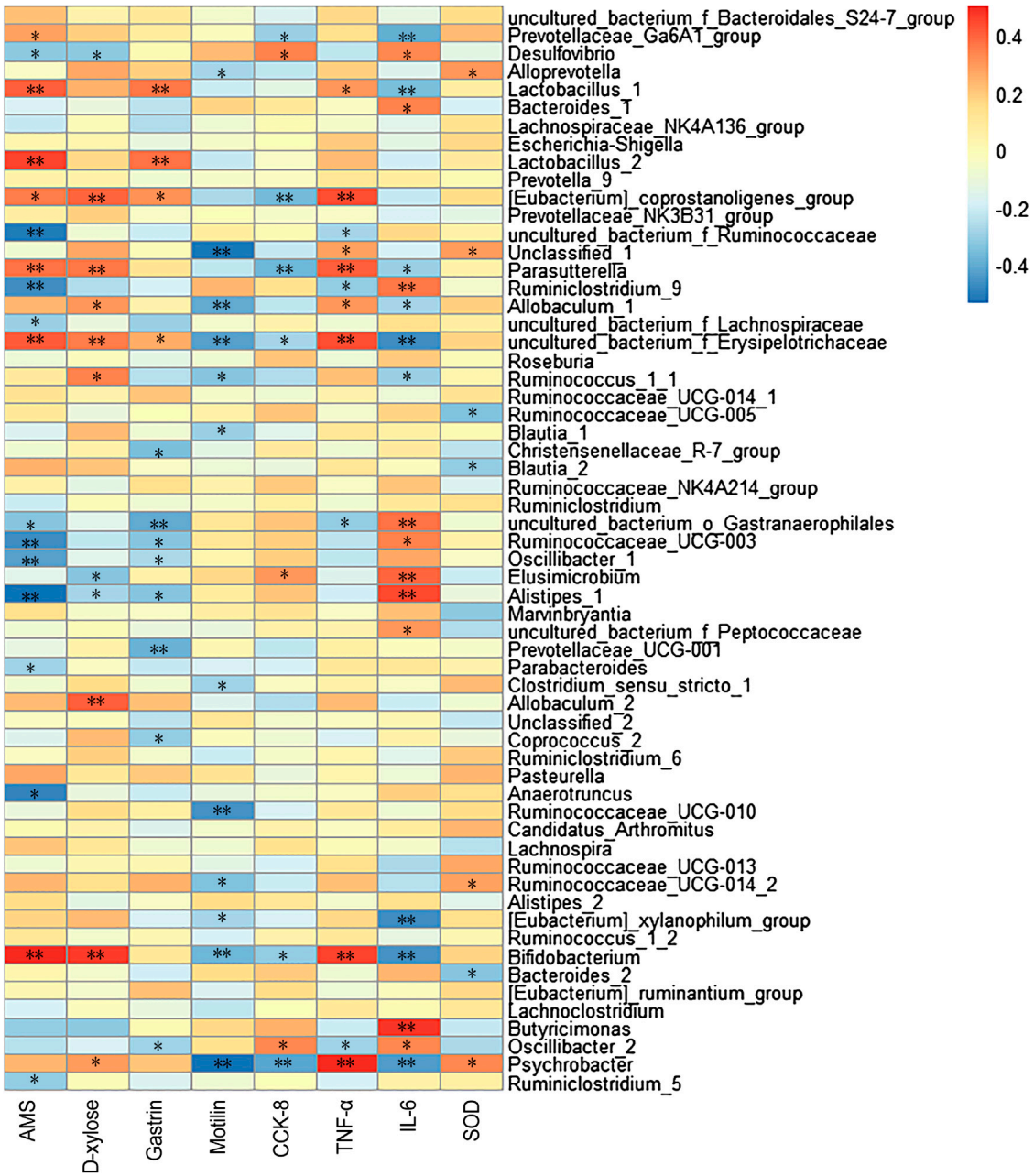

FIGURE 4 | Heatmap of Spearman's correlation between gut microbiota (the relative abundances of top 60 genus) and spleen deficiency related indexes. The colors range from blue (negative correlation) to red (positive correlation). Significant correlations are noted by $*p < 0.05$ and $**p < 0.01$.

Lactobacillus are the most widely used probiotics with many health-promoting properties, such as prevention of enteropathogen colonization (barrier effects) (Candela et al., 2008), anti-inflammatory effects on mucosal surfaces, optimization of the composition of gut microbiota (O'Mahony et al., 2005). There has been growing interest in using probiotics as an adjunct to standard anti-inflammatory and immune suppressing therapy (Veerappan et al., 2012). *Allobaculum*, a butyrate-producing genus, has been reported to be an important functional phylotypes in many researches, its reduction was associated with obesity and diabetes (Zhang et al., 2015; Barouei et al., 2017). *Eubacterium coprostanoligenes group* can convert cholesterol to coprostanol which is poorly absorbed in human intestines and would be excreted, leading to blood cholesterol concentration reduction (Li et al., 1998) In addition, *Alloprevotella* was positively correlated with SOD activity, a genus that fermented carbohydrates and produced acetate and butyrate (Downes et al., 2013). Studies have illustrated that its abundance was negatively correlated with various diseases such as obesity, diabetes and cardiovascular diseases (Wei et al., 2018).

Moreover, significant negative correlations between spleen-deficiency aggravated related indexes and *Alistipes*, *Anaerotruncus*, *Desulfovibrio*, *Oscillibacter*, *Ruminiclostridium_9*, *Ruminococcaceae_UCG-003*, *Parabacteroides*, *Ruminiclostridium_5*, *etc.* Among them, *Desulfovibrio* is the predominant bacteria in human colon sulfate-reducing bacteria, which can reduce sulfate to produce H_2S. Since endogenous H_2S can poison intestinal epithelial cells, clinical studies have inferred that *Desulfovibrio* was associated with intestinal diseases (Gobert et al., 2016). It is reported that *Oscillibacter* was increased in the diet-induced metabolic dysfunctions, and associated with impaired intestinal barrier integrity (Lam et al., 2012).

As described in our preliminary study, flavonoids are the primary components in CRP (Zheng et al., 2019). Flavonoids, as common dietary polyphenols, have been proven to exert potential modulatory effects on gut microbiota by inhibiting the growth of multiple pathogens and promoting beneficial genera. These modulations in turn promote gut health through maintaining gut immune homeostasis, and improving nutrients absorption (Dueñas et al., 2015; Pei et al., 2020). In this work, CRP exerted a significant effect on improving the composition of gut microbiota, especially for SCFAs producing and anti-inflammatory bacteria (**Figure 5**), whose metabolites could enhance epithelial barrier function, improve gut permeability, and inhibit inflammation. Based on these results, it is reasonable to propose that the relief of symptoms in spleen deficiency rats was closely associated with the rebalance of gut microbiota.

Identification of Metabolites Derived From Citri Reticulatae Pericarpium

Generally, ingested exogenous compounds would undergo multi-step *in vivo* biotransformation processes mediated by gut

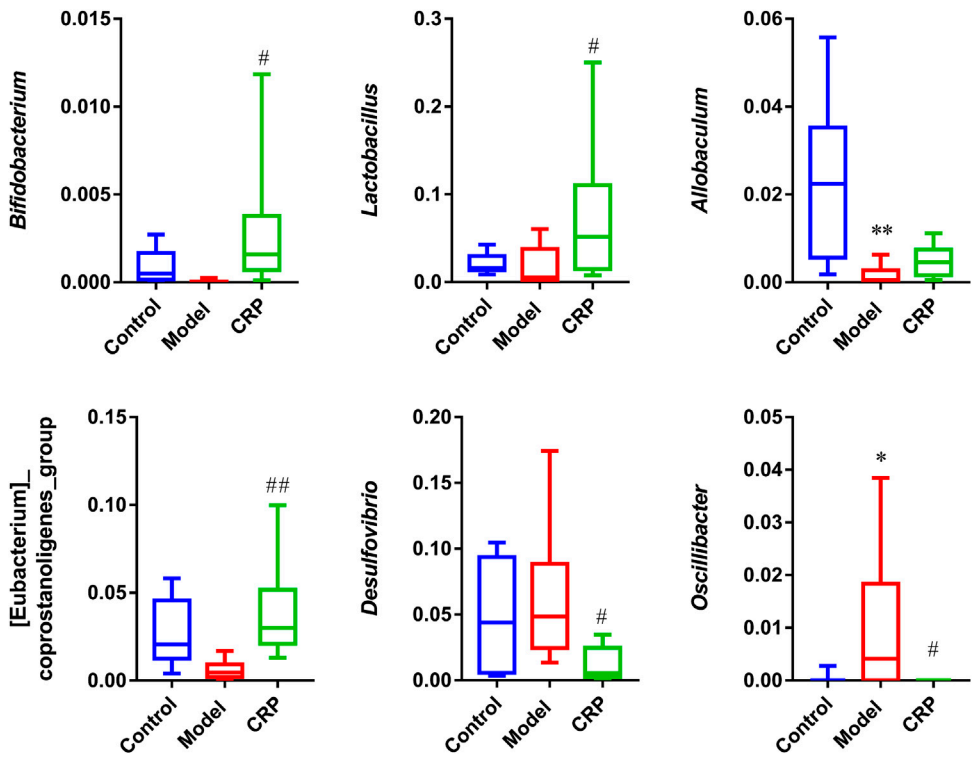

FIGURE 5 | Relative abundances of *Bifidobacterium*, *Lactobacillus*, *Allobaculum*, *[Eubacterium]_coprostanoligenes_group*, *Desulfovibrio*, *Oscillibacter*. (n = 10; $^{*}p < 0.05$, vs. control group; $^{\#}p < 0.05$, vs. model group; $^{\#\#}p < 0.01$, vs. model group.)

microbiota and mammalian metabolic enzymes (Walle, 2004), which mainly comprise phase I and phase II metabolism. Phase I metabolism (hydrolysis, oxidation, demethylation, etc.) would change the skeleton structure of compounds, while phase II metabolism (glucuronidation, sulfation, acetylation, etc.) converts the compound into more water-soluble metabolites for excretion through urine (Gradolatto et al., 2004). Urine is filtered and concentrated from the blood through nephron. Metabolites in the blood are eventually excreted in the urine with higher concentrations, making them easier to be detected in urine by analytical instruments (Gao, 2015; Zhao et al., 2018). In addition, urine can be continuously sampled in a non-invasive way, and will not affect the body's normal physiological processes. Hence, urine is probably a better source for metabolite identification than blood.

In this work, based on our preliminary results of chemical composition analysis (Zheng et al., 2019), a total of 26 prototype compounds and 23 metabolites were detected in rat urine after the ingestion of CRP. Prototype compounds were mainly polymethoxyflavones, as well as hesperetin, naringenin, isoprinol, luteolin and apigenin. Catalyzed by phase I and phase II metabolic enzymes, ingested prototype compounds underwent hydrolysis, demethylation, glucuronidation and sulfation, giving rise to a mass of metabolites. Compound descriptions, molecular formulas, retention times, and fragment ions of these prototype compounds and metabolites were detailed in **Table 2**.

Nobiletin is a hexamethoxyflavone abundant in CRP and has been documented to possess multiple pharmacological activities, such as anti-inflammatory, bacteriostasis and antioxidant (Li et al., 2014). As shown in **Table 2**, nobiletin gave its quasi-molecular ion $[M + H]^+$ at *m/z* 403.1363, yielding the characteristic ions at *m/z* 388.1176, 373.0916, 358.0858 with successive loss of CH_3. Compound 26, 27, 28 all possessed the $[M + H]^+$ ion at *m/z* 389, which was is 14 Da (CH_2) less than protonated nobiletin. Herein compound 26, 27, 28 were tentatively assigned as the mono-demethylated metabolite of nobiletin. Using *in vitro* incubation methods, Koga et al. (Koga et al., 2007) investigated the metabolism of nobiletin in rat liver microsomes. As a result, three mono-demethylated metabolites were identified, which were 4′-OH-, 7-OH-, and 6-OH-nobiletin. Based on the retention time, compound 26, 27, 28 were identified as 6-OH-, 7-OH-, and 4′-OH-nobiletin, respectively. These metabolites could be subsequently demethylated into several dihydroxy-tetramethoxyflavone, while the position of the hydroxyl group needs to be further assigned. These hydroxyl-containing polymethoxyflavones could be further combined with glucuronic acid or sulfuric acid to generate corresponding phase II metabolites.

As presented in **Table 2**, retro Diels-Alder reaction was a characteristic pattern of flavanone and flavone derivates in MS/MS fragmentation (Zeng et al., 2020b). Taking naringenin as an example, in the negative ion mode, the main fragment ions of deprotonated naringenin (*m/z* 271.0613) were *m/z* 151.0043, 119.0508, 107.0154, and 93.0381. Among them, product ions *m/z* 151.0043 ($^{1,3}A^-$) and 119.0508 ($^{1,3}B^-$) were presumed to be produced by retro Diels-Alder reaction on chemical bond 1 and 3, while *m/z* 107.0154 was derived from $^{1,3}A^-$ with the loss of CO_2 (44 Da). The signal at *m/z* 93.0381 was presumed to be yielded by the breaking of chemical bond 5. Above fragmentation schemes were proposed in **Figure 6**.

Oral ingestion is the most common mode of administration used in herbal medicine. Generally speaking, exogenous compounds could only exert its pharmacological activity if it is absorbed into the blood and maintains a certain concentration. Urine is filtered from the blood and accumulated all changes in the body. It contains all metabolites in the blood, and thus comprehensively reflects the metabolic information. In this work, the concentration of prototype compounds detected in urine was much lower than that of the corresponding metabolites, suggesting that flavonoid metabolites may be the primary substance for pharmacological activity of CRP, rather than its prototype compounds. Therefore, identified metabolites were employed in subsequent network pharmacology analysis so as to discover the bioactive components and potential targets of CRP against spleen deficiency.

Network Pharmacology Analysis

On the basis of identified metabolites, a total of 583 potential targets for CRP's efficacy were defined. Meanwhile, a total of 520 spleen deficiency-related disease targets were acquired by integrating data on diarrhea, dyspepsia, enteritis and gastritis from disease databases. Detailed information was presented in **Supplementary Table S1**. The CRP's efficacy-related targets were mapped to the spleen deficiency-related targets, and as a result, 98 common targets were obtained. Then a PPI network (**Supplementary Figure S1**) was constructed using the common targets and further used to construct the CT-ST network. **Figure 7** illustrated the CT-ST network which consists of 111 nodes (17 compounds and 94 candidate targets, compounds with multiple isomers are combined and shared one name) and 662 edges. Among them, several flavonoids including apigenin, luteolin, naringenin, hesperidin, hesperetin, dihydroxy-tetramethoxyflavone, monohydroxy- tetramethoxyflavone and homoeriodictyol were considered to be key compounds for CRP to alleviate spleen deficiency. The primary targets of these compounds included STAT3, IL6, TNF, JUN, AKT1, TP53, MAPK1, MMP9, PIK3R1, PTGS2, VEGFA, EGFR, IL1B, CXCL8, IL4, CCL2, IL10, and FOS. That is to say, CRP may interact with these targets to exert its effects in relieving spleen deficiency.

In order to further reveal the molecular mechanism of CRP against spleen deficiency, GO analysis and pathway enrichment of mentioned 94 common targets were performed with KEGG database. The results of GO analysis were described by biological process (BP), cell component (CC), and molecular function (MF) terms. In GO analysis, 330 of 426 BPs, 58 of 72 MFs, and 26 of 33 CCs enriched for these targets were recognized as $p < 0.05$. Top 5 enriched terms of BP, MF, CC categories in the GO analysis were presented in **Figure 8A**. Moreover, 97 target-related pathways were found in KEGG, top 15 KEEG signaling pathways were constructed in bubble plot based on *P*-Value (**Figure 8B**), and the involved genes were showed in **Supplementary Table S2**. Consistent with the

TABLE 2 | Identification of metabolites in rat urine, and feces samples after the oral administration of Citri Reticulatae Pericarpium extract.

Peak no.	Identification	Molecular formula	Retention time (min)	$[M + H]^+$(*m/z*) (error, ppm)	$[M - H]^-$(*m/z*) (error, ppm)	Fragment ions in the positive ion mode(*m/z*)[a]	Fragment ions in the negative ion mode(*m/z*)[a]
	Polymethoxyflavone derivates						
1	Monohydroxy-trimethoxyflavone	$C_{18}H_{16}O_6$	14.7	329.1033 (2.2)	327.0879 (0.5)	314.0777 $[M+ H\text{-}CH_3]^+$, 299.0558 $[M + H\text{-}2CH_3]^+$, 285.0754 $[M + H\text{-}CH_3\text{-}HCO]^+$, 271.0600 $[M + H\text{-}2CH_3\text{-}CO]^+$, 243.0630, 229.0485, 181.0130, 153.0172	312.0688 $[M - H\text{-}CH_3]^-$, 297.0380 $[M - H\text{-}2CH_3]^-$, 282.2452 $[M - H\text{-}3CH_3]^-$, 177.0194
2	Monohydroxy-trimethoxyflavone	$C_{18}H_{16}O_6$	15.7	329.1031 (2.7)	327.0885 (0.8)	313.0720, 299.0545 $[M + H\text{-}2CH_3]^+$, 285.0783 $[M + H\text{-}CH_3\text{-}HCO]^+$, 271.0609 $[M + H\text{-}2CH_3\text{-}CO]^+$, 268.0725 $[M + H\text{-}2CH_3\text{-}CH_3O]^+$, 239.0696	312.0650 $[M - H\text{-}CH_3]^-$, 297.0430 $[M - H\text{-}2CH_3]^-$, 282.2433 $[M - H\text{-}3CH_3]^-$, 146.9376, 102.9446
3	Dihydroxy-trimethoxyflavone	$C_{18}H_{16}O_7$	13.5	345.0987 (3.3)	343.0806 (1.6)	330.0712 $[M + H\text{-}CH_3]^+$, 315.0500 $[M + H\text{-}2CH_3]^+$, 287.0576 $[M + H\text{-}2CH_3\text{-}CO]^+$	328.0553 $[M - H\text{-}CH_3]^-$, 313.0407 $[M - H\text{-}2CH_3]^-$, 298.2388 $[M - H\text{-}3CH_3]^-$, 297.2190
4	Dihydroxy-trimethoxyflavone	$C_{18}H_{16}O_7$	19.0	345.0963 (2.0)	343.0836 (0.7)	330.0748 $[M + H\text{-}CH_3]^+$, 315.0531 $[M + H\text{-}2CH_3]^+$, 284.0715 $[M + H\text{-}2CH_3\text{-}CH_3O]^+$, 257.1077, 197.0121	328.05384 $[M - H\text{-}CH_3]^-$, 313.0351 $[M - H\text{-}2CH_3]^-$, 298.0067 $[M - H\text{-}3CH_3]^-$, 281.9727 $[M - H\text{-}2CH_3\text{-}CH_3O]^-$, 255.9557, 208.0703, 166.0599
5	Trimethoxyflavone-*O*-glucuronide	$C_{24}H_{24}O_{12}$	11.0	505.1350 (2.0)	503.1162 (–3.4)	329.1009 $[M + H\text{-}GlcUA]^+$, 314.0760 $[M + H\text{-}GlcUA\text{-}CH_3]^+$, 299.0559 $[M + H\text{-}GlcUA\text{-}2CH_3]^+$, 249.0630	ND
6	Trimethoxyflavone-*O*-sulfate	$C_{18}H_{16}O_9S$	12.6	409.0614 (2.6)	407.0434 (–2.1)	329.1041 $[M + H\text{-}SO_3]^+$, 314.0815 $[M + H\text{-}SO_3\text{-}CH_3]^+$, 299.0563 $[M + H\text{-}SO_3\text{-}2CH_3]^+$, 271.0593 $[M + H\text{-}SO_3\text{-}2CH_3\text{-}CO]^+$, 243.0691, 181.0111	327.0869 $[M - H\text{-}SO_3]^-$, 312.0641 $[M - H\text{-}SO_3\text{-}CH_3]^-$, 297.0427 $[M - H\text{-}SO_3\text{-}2CH_3]^-$, 201.0307
7	Trimethoxyflavone-*O*-sulfate	$C_{18}H_{16}O_9S$	13.8	409.0630 (5.8)	407.0477 (4.5)	329.1052 $[M + H\text{-}SO_3]^+$, 313.0761, 268.0755, 257.0416, 239.0620	327.0877 $[M - H\text{-}SO_3]^-$, 312.0682 $[M - H\text{-}SO_3\text{-}CH_3]^-$, 297.0455 $[M - H\text{-}SO_3\text{-}2CH_3]^-$
8	Trimethoxyflavone-*O*-sulfate	$C_{18}H_{16}O_9S$	14.5	409.0721 (1.2)	407.0440 (–0.5)	329.1024 $[M + H\text{-}SO_3]^+$, 299.0566 $[M + H\text{-}SO_3\text{-}2CH_3]^+$, 257.0455	ND
9	Monohydroxy-tetramethoxyflavone	$C_{19}H_{18}O_7$	14.7	359.1133 (1.5)	357.0976 (–0.8)	344.0844 $[M + H\text{-}CH_3]^+$, 329.0648 $[M + H\text{-}2CH_3]^+$, 301.0720 $[M + H\text{-}2CH_3\text{-}CO]^+$, 285.0410	ND
10	Monohydroxy-tetramethoxyflavone	$C_{19}H_{18}O_7$	15.0	359.1137 (3.5)	357.0972 (–1.3)	344.0869 $[M + H\text{-}CH_3]^+$, 329.0664 $[M + H\text{-}2CH_3]^+$, 314.0438 $[M + H\text{-}3CH_3]^+$, 301.0710 $[M + H\text{-}2CH_3\text{-}CO]^+$, 286.0485 $[M + H\text{-}3CH_3\text{-}CO]^+$, 181.0144, 153.0186	342.0704 $[M - H\text{-}CH_3]^-$, 327.0474 $[M - H\text{-}2CH_3]^-$, 312.0306 $[M - H\text{-}3CH_3]^-$, 269.0069
11	Monohydroxy-tetramethoxyflavone	$C_{19}H_{18}O_7$	15.4	359.1111 (2.2)	ND	344.0889 $[M + H\text{-}CH_3]^+$, 326.0789 $[M + H\text{-}CH_3\text{-}H_2O]^+$, 298.0848, 162.0690	ND
12	Monohydroxy-tetramethoxyflavone	$C_{19}H_{18}O_7$	16.1	359.1136 (4.0)	357.0976 (–1.6)	344.0888 $[M + H\text{-}CH_3]^+$, 329.0662 $[M + H\text{-}2CH_3]^+$, 315.0865, 298.0840 $[M + H\text{-}2CH_3\text{-}CH_3O]^+$, 283.0607 $[M + H\text{-}3CH_3\text{-}CH_3O]^+$, 255.0668 $[M + H\text{-}3CH_3\text{-}CH_3O\text{-}CO]^+$, 227.0700, 153.0168	342.0745 $[M - H\text{-}CH_3]^-$, 327.0516 $[M - H\text{-}2CH_3]^-$, 312.0262 $[M - H\text{-}3CH_3]^-$, 297.0033, 269.0098

(Continued on following page)

TABLE 2 | (*Continued*) Identification of metabolites in rat urine, and feces samples after the oral administration of Citri Reticulatae Pericarpium extract.

Peak no.	Identification	Molecular formula	Retention time (min)	$[M + H]^+$(*m/z*) (error, ppm)	$[M - H]^-$(*m/z*) (error, ppm)	Fragment ions in the positive ion mode(*m/z*)[a]	Fragment ions in the negative ion mode(*m/z*)[a]
13	Monohydroxy-tetramethoxyflavone	$C_{19}H_{18}O_7$	16.7	359.1131 (3.3)	357.0977 (–0.8)	344.0898 [M + H-CH_3]$^+$, 329.0663 [M + H-2CH_3]$^+$, 314.0432 [M + H-3CH_3]$^+$, 311.0533, 283.0613 [M + H-3CH_3-CH_3O]$^+$, 257.0453, 211.0240, 183.0297	342.0751 [M – H-CH_3]$^-$, 327.0513 [M – H-2CH_3]$^-$, 312.0276 [M – H-3CH_3]$^-$, 299.0565 [M – H-2CH_3-CO]$^-$, 284.0322 [M – H-3CH_3-CO]$^-$, 269.0095 [M – H-4CH_3-CO]$^-$, 207.0301, 192.0063, 117.0354
14	Monohydroxy-tetramethoxyflavone	$C_{19}H_{18}O_7$	17.9	359.1128 (1.2)	ND	344.0882 [M + H-CH_3]$^+$, 329.0630 [M + H-2CH_3]$^+$, 311.0548, 283.0524 [M + H-3CH_3-CH_3O]$^+$, 261.0190	ND
15	Tetramethoxyflavone-*O*-glucuronide	$C_{25}H_{26}O_{13}$	11.7	535.1423 (2.7)	533.1281 (–3.6)	359.1123 [M + H-GlcUA]$^+$, 344.1085 [M + H-GlcUA-CH_3]$^+$, 329.0631 [M + H-GlcUA-2CH_3]$^+$, 289.0655	ND
16	Tetramethoxyflavone-*O*-glucuronide	$C_{25}H_{26}O_{13}$	12.3	535.1434 (2.9)	533.1299 (–0.6)	359.1135 [M + H-GlcUA]$^+$, 344.0922 [M + H-GlcUA-CH_3]$^+$, 315.0886, 298.0884 [M + H-GlcUA-2CH_3-CH_3O]$^+$	ND
17	Tetramethoxyflavone-*O*-glucuronide	$C_{25}H_{26}O_{13}$	12.6	535.1476 (3.7)	533.1297 (–0.7)	359.1145 [M + H-GlcUA]$^+$, 344.0901 [M + H-GlcUA-CH_3]$^+$, 329.0674 [M + H-GlcUA-2CH_3]$^+$, 311.0534, 298.0843 [M + H-GlcUA-2CH_3-CH_3O]$^+$, 283.0608 [M + H-GlcUA-3CH_3-CH_3O]$^+$	ND
18	Tetramethoxyflavone-*O*-sulfate	$C_{19}H_{18}O_{10}S$	12.7	439.0706 (2.8)	437.0540 (–1.3)	359.1128 [M + H-SO_3]$^+$, 344.0889 [M + H-SO_3-CH_3]$^+$, 329.0664 [M + H-SO_3-2CH_3]$^+$, 271.0532, 153.0228	357.0995 [M – H-SO_3]$^-$, 342.0725 [M – H-SO_3-CH_3]$^-$, 327.0507
19	Tetramethoxyflavone-*O*-sulfate	$C_{19}H_{18}O_{10}S$	14.7	439.0698 (1.9)	437.0543 (–1.1)	359.1133 [M + H-SO_3]$^+$, 344.0938 [M + H-SO_3-CH_3]$^+$, 329.0673 [M + H-SO_3-2CH_3]$^+$, 311.0511, 283.0590 [M + H-SO_3-3CH_3-CH_3O]$^+$, 257.0479	357.0990 [M – H-SO_3]$^-$, 327.0496 [M – H-SO_3-2CH_3]$^-$, 312.0270, 269.0075
20	Dihydroxy-tetramethoxyflavone	$C_{19}H_{18}O_8$	14.0	375.1074 (1.6)	373.032 (–0.9)	360.0832 [M + H-CH_3]$^+$, 345.0588 [M + H-2CH_3]$^+$, 327.0467 [M + H-2CH_3-H_2O]$^+$, 314.0813 [M + H-2CH_3-CH_3O]$^+$, 299.0500 [M + H-3CH_3-CH_3O]$^+$, 271.0566 [M + H-3CH_3-CH_3O-CO]$^+$	ND
21	Dihydroxy-tetramethoxyflavone	$C_{19}H_{18}O_8$	14.5	375.1090 (1.3)	373.0917 (–3.2)	360.0861 [M + H-CH_3]$^+$, 345.0598 [M + H-2CH_3]$^+$, 327.0496 [M + H-2CH_3-H_2O]$^+$, 197.0062	358.0721 [M – H-CH_3]$^-$, 343.0473 [M – H-2CH_3]$^-$
22	Dihydroxy-tetramethoxyflavone	$C_{19}H_{18}O_8$	15.1	375.1080 (3.1)	373.0924 (–0.9)	360.0829 [M + H-CH_3]$^+$, 345.0612 [M + H-2CH_3]$^+$, 327.0456, 273.0403, 256.0380	358.0720 [M – H-CH_3]$^-$, 343.0452 [M – H-CH_3]$^-$, 327.1716 [M – H-CH_3-CH_3O]$^-$, 305.1931, 285.0019, 263.0357
23	Dihydroxy-tetramethoxyflavone	$C_{19}H_{18}O_8$	19.4	375.1095 (2.3)	373.0919 (–2.8)	360.0828 [M + H-CH_3]$^+$, 345.0595 [M + H-2CH_3]$^+$, 327.0488 [M + H-2CH_3-H_2O]$^+$, 313.0704, 197.0084	358.0680 [M – H-CH_3]$^-$, 343.0460 [M – H-2CH_3]$^-$, 328.0226 [M – H-3CH_3]$^-$, 312.9910
24	Monohydroxy-tetramethoxyflavone-*O*-glucuronide	$C_{25}H_{26}O_{14}$	11.8	551.1396 (2.6)	ND	375.1088 [M + H-GlcUA]$^+$, 360.0890 [M + H-GlcUA-CH_3]$^+$, 345.0622 [M + H-GlcUA-2CH_3]$^+$, 327.0489 [M + H-GlcUA-2CH_3-H_2O]$^+$, 305.1602 [M + H-GlcUA-4CH_3]$^+$, 133.0879	ND
25	Nobiletin[b, c]	$C_{21}H_{22}O_8$	19.3	403.1363 (0.5)	ND	388.1176 [M + H-CH_3]$^+$, 373.0916 [M + H-2CH_3]$^+$, 358.0858 [M + H-3CH_3]$^+$, 327.0858	ND

(Continued on following page)

TABLE 2 | (*Continued*) Identification of metabolites in rat urine, and feces samples after the oral administration of Citri Reticulatae Pericarpium extract.

Peak no.	Identification	Molecular formula	Retention time (min)	$[M + H]^+$(*m/z*) (error, ppm)	$[M - H]^-$(*m/z*) (error, ppm)	Fragment ions in the positive ion mode(*m/z*)[a]	Fragment ions in the negative ion mode(*m/z*)[a]
26	Monohydroxy-pentamethoxyflavone	$C_{20}H_{20}O_8$	15.8	389.1255 (3.6)	387.1081 (–1.2)	374.1016 $[M + H\text{-}CH_3]^+$, 359.0770 $[M + H\text{-}2CH_3]^+$, 341.0665 $[M + H\text{-}2CH_3\text{-}H_2O]^+$, 331.0835 $[M + H\text{-}2CH_3\text{-}CO]^+$, 316.0585 $[M + H\text{-}3CH_3\text{-}CO]^+$, 285.0766 $[M + H\text{-}3CH_3\text{-}CO\text{-}CH_3O]^+$	372.0849 $[M - H\text{-}CH_3]^-$, 357.0620 $[M - H\text{-}2CH_3]^-$, 342.0370 $[M - H\text{-}3CH_3]^-$, 299.0162, 271.0243
27	Monohydroxy-pentamethoxyflavone	$C_{20}H_{20}O_8$	16.5	389.1247 (2.7)	ND	374.1012 $[M + H\text{-}CH_3]^+$, 359.0777 $[M + H\text{-}2CH_3]^+$, 344.0658 $[M + H\text{-}3CH_3]^+$, 341.0635 $[M + H\text{-}2CH_3\text{-}H_2O]^+$, 331.0823 $[M + H\text{-}2CH_3\text{-}CO]^+$, 316.0596 $[M + H\text{-}3CH_3\text{-}CO]^+$	ND
28	Monohydroxy-pentamethoxyflavone	$C_{20}H_{20}O_8$	17.1	389.1242 (3.2)	387.1082 (–0.8)	374.1015 $[M + H\text{-}CH_3]^+$, 359.0771 $[M + H\text{-}2CH_3]^+$, 344.0542 $[M + H\text{-}3CH_3]^+$, 341.0665 $[M + H\text{-}2CH_3\text{-}H_2O]^+$, 313.0724 $[M + H\text{-}3CH_3\text{-}H_2O\text{-}CO]^+$, 287.0563, 244.0372, 211.0238	372.0845 $[M - H\text{-}CH_3]^-$, 357.0607 $[M - H\text{-}2CH_3]^-$, 342.0369 $[M - H\text{-}3CH_3]^-$, 327.0136 $[M - H\text{-}4CH_3]^-$, 314.0418 $[M - H\text{-}3CH_3\text{-}CO]^-$, 299.0168 $[M - H\text{-}4CH_3\text{-}CO]^-$
29	Pentamethoxyflavone-*O*-glucuronide	$C_{26}H_{28}O_{14}$	12.8	565.1574 (2.5)	563.1398 (–1.4)	389.1245 $[M + H\text{-}GlcUA]^+$, 374.1042 $[M + H\text{-}GlcUA\text{-}CH_3]^+$, 359.0758 $[M + H\text{-}GlcUA\text{-}2CH_3]^+$	ND
30	Pentamethoxyflavone-*O*-glucuronide	$C_{26}H_{28}O_{14}$	13.1	565.1578 (3.4)	563.1402 (–0.5)	389.1251 $[M + H\text{-}GlcUA]^+$, 374.1002 $[M + H\text{-}GlcUA\text{-}CH_3]^+$, 359.0774 $[M + H\text{-}GlcUA\text{-}2CH_3]^+$, 341.0664 $[M + H\text{-}GlcUA\text{-}2CH_3\text{-}H_2O]^+$, 313.0724 $[M + H\text{-}GlcUA\text{-}2CH_3\text{-}H_2O\text{-}CO]^+$	387.1083 $[M - H\text{-}GlcUA]^-$, 372.0851 $[M - H\text{-}GlcUA\text{-}CH_3]^-$, 357.0587 $[M - H\text{-}GlcUA\text{-}2CH_3]^-$, 342.0357 $[M - H\text{-}GlcUA\text{-}3CH_3]^-$, 175.0211, 113.0255
31	Pentamethoxyflavone-*O*-sulfate	$C_{20}H_{20}O_{11}S$	14.2	469.0743 (1.6)	467.0650 (–0.7)	389.1221 $[M + H\text{-}SO_3]^+$, 374.1044 $[M + H\text{-}SO_3\text{-}CH_3]^+$, 359.0794 $[M + H\text{-}SO_3\text{-}2CH_3]^+$, 341.0606 $[M + H\text{-}SO_3\text{-}2CH_3\text{-}H_2O]^+$	387.1066 $[M - H\text{-}SO_3]^-$, 357.0605 $[M - H\text{-}SO_3\text{-}2CH_3]^-$, 342.0430 $[M - H\text{-}SO_3\text{-}3CH_3]^-$
32	Pentamethoxyflavone-*O*-sulfate	$C_{20}H_{20}O_{11}S$	14.5	469.0788 (1.2)	467.0650 (–1.8)	389.1226 $[M + H\text{-}SO_3]^+$, 374.1020 $[M + H\text{-}SO_3\text{-}CH_3]^+$, 359.0764 $[M + H\text{-}SO_3\text{-}2CH_3]^+$, 341.0676	387.1111 $[M - H\text{-}SO_3]^-$, 372.0868 $[M - H\text{-}SO_3\text{-}CH_3]^-$, 357.0680, 342.0405 $[M - H\text{-}SO_3\text{-}2CH_3]^-$, 327.0110
33	Pentamethoxyflavone-*O*-sulfate	$C_{20}H_{20}O_{11}S$	14.8	469.0814 (2.2)	467.0646 (–1.5)	389.1230 $[M + H\text{-}SO_3]^+$, 374.1010 $[M + H\text{-}SO_3\text{-}CH_3]^+$, 359.0785 $[M + H\text{-}SO_3\text{-}2CH_3]^+$, 345.0986, 285.0794	387.1094 $[M - H\text{-}SO_3]^-$, 372.0843 $[M - H\text{-}SO_3\text{-}CH_3]^-$, 357.0602 $[M - H\text{-}SO_3\text{-}2CH_3]^-$, 342.0352 $[M - H\text{-}SO_3\text{-}3CH_3]^-$, 299.0160, 264.9846, 207.0359
34	Monohydroxy-hexamethoxyflavone	$C_{21}H_{22}O_9$	16.5	419.1342 (0.9)	417.1177 (–2.2)	404.1117 $[M + H\text{-}CH_3]^+$, 389.0872 $[M + H\text{-}2CH_3]^+$, 374.3168 $[M + H\text{-}3CH_3]^+$, 371.0768 $[M + H\text{-}2CH_3\text{-}H_2O]^+$, 343.0765	402.1001 $[M - H\text{-}CH_3]^-$, 387.0742 $[M - H\text{-}2CH_3]^-$, 372.0433 $[M - H\text{-}3CH_3]^-$, 355.2913, 329.0341
35	Monohydroxy-hexamethoxyflavone	$C_{21}H_{22}O_9$	17.1	419.1323 (–0.9)	ND	404.1052 $[M + H\text{-}CH_3]^+$, 389.0895 $[M + H\text{-}2CH_3]^+$, 371.0796 $[M + H\text{-}2CH_3\text{-}H_2O]^+$, 346.0798, 328.0616	ND
36	Monohydroxy-hexamethoxyflavone	$C_{21}H_{22}O_9$	17.8	419.1344 (1.4)	417.1176 (–3.7)	404.1093 $[M + H\text{-}CH_3]^+$, 389.0879 $[M + H\text{-}2CH_3]^+$, 371.0762 $[M + H\text{-}2CH_3\text{-}H_2O]^+$, 346.0686, 311.0574 $[M + H\text{-}6CH_3\text{-}H_2O]^+$, 275.0553, 211.0209, 183.0255, 151.0387	402.1048 $[M - H\text{-}CH_3]^-$, 387.0712 $[M - H\text{-}2CH_3]^-$, 371.3115, 355.2848, 349.2049, 329.0251
37	Hexamethoxyflavone-*O*-glucuronide	$C_{27}H_{30}O_{15}$	13.2	595.1672 (2.4)	ND	419.1361 $[M + H\text{-}GlcUA]^+$, 389.0896 $[M + H\text{-}GlcUA\text{-}3CH_3]^+$, 287.0785	ND

(Continued on following page)

TABLE 2 | (*Continued*) Identification of metabolites in rat urine, and feces samples after the oral administration of Citri Reticulatae Pericarpium extract.

Peak no.	Identification	Molecular formula	Retention time (min)	$[M + H]^+$(*m/z*) (error, ppm)	$[M - H]^-$(*m/z*) (error, ppm)	Fragment ions in the positive ion mode(*m/z*)[a]	Fragment ions in the negative ion mode(*m/z*)[a]
	Flavanone derivates						
38	Homoeriodictyol	$C_{16}H_{14}O_6$	12.2	303.0866 (1.5)	ND	285.0755 $[M + H\text{-}H_2O]^+$, 177.0536, 153.0190 $[M + H\text{-}C_9H_{10}O_2]^+$, 117.0324	ND
39	Hesperidin[b, c]	$C_{28}H_{34}O_{15}$	11.4	611.2039 (3.3)	ND	566.4279, 465.1412, 449.1442, 413.1224, 345.0988 $[M + H\text{-}Rha\text{-}C_4H_8O_4]^+$, 303.0872 $[M + H\text{-}Rha\text{-}Glc]^+$, 285.0762 $[M + H\text{-}Rha\text{-}Glc\text{-}H_2O]^+$, 263.0545, 153.0147 $[M + H\text{-}Rha\text{-}Glc\text{-}C_9H_{10}O_2]^+$	ND
40	Hesperetin[b, c]	$C_{16}H_{14}O_6$	16.0	303.0869 (2.3)	301.0715 (–0.8)	285.0737 $[M + H\text{-}H_2O]^+$, 177.0552, 153.0186 $[M + H\text{-}C_9H_{10}O_2]^+$, 117.0333, 89.0401	286.0488 $[M - CH_3]^-$, 242.0557 $[M - H\text{-}CH_2O\text{-}HCO]^-$, 199.0418, 164.0120 $[M - H\text{-}C_8H_9O_2]^-$, 151.0060 $[M - H\text{-}C_9H_{10}O_2]^-$, 136.0193, 125.0260, 108.0246
41	Hesperetin-*O*-glucuronide/ Homoeriodictyol-*O*-glucuronide	$C_{22}H_{22}O_{12}$	12.2	479.1190 (2.7)	477.1026 (–2.6)	461.1046 $[M + H\text{-}H_2O]^+$, 303.0892 $[M + H\text{-}GlcUA]^+$, 285.0768 $[M + H\text{-}GlcUA\text{-}H_2O]^+$, 231.0244, 177.0540, 153.0180 $[M + H\text{-}GlcUA\text{-}C_9H_{10}O_2]^+$	301.0712 $[M - H\text{-}GlcUA]^-$, 286.0520 $[M - H\text{-}GlcUA\text{-}CH_3]^-$, 227.0294, 175.0213, 113.0242
42	Hesperetin-*O*-sulfate/Homoeriodictyol-*O*-sulfate	$C_{16}H_{14}O_9S$	13.0	383.0463 (1.6)	ND	303.0903 $[M + H\text{-}SO_3]^+$, 153.0204 $[M + H\text{-}SO_3\text{-}C_9H_{10}O_2]^+$	ND
43	Naringenin[b, c]	$C_{15}H_{12}O_5$	15.4	273.0771 (2.2)	271.0613 (0.3)	153.0186 $[M + H\text{-}C_8H_8O]^+$, 119.0492, 91.0606	151.0043 $[M - H\text{-}C_8H_8O]^-$, 119.0508 $[M - H\text{-}C_7H_4O_4]^-$, 107.0154 $[M - H\text{-}C_8H_8O\text{-}CO_2]^-$, 93.0381 $[M - H\text{-}C_9H_6O_4]^-$
44	Isosakuranetin[c]	$C_{16}H_{14}O_5$	19.1	287.0928 (2.4)	285.0767 (–0.6)	246.8594, 167.0341 $[M + H\text{-}C_8H_8O]^+$, 147.0431, 119.0496, 91.05551	270.0544 $[M - CH_3]^-$, 243.0657, 199.0748, 165.0130 $[M - H\text{-}C_8H_8O]^-$, 136.0137, 119.0498
	Flavone derivates						
45	Luteolin	$C_{15}H_{10}O_6$	14.4	287.0547 (–4.4)	ND	153.0169 $[M + H\text{-}C_8H_6O_2]^+$	ND
46	Apigenin[b, c]	$C_{15}H_{10}O_5$	15.5	271.0606 (2.5)	269.0457 (0.8)	253.0497 $[M + H\text{-}H_2O]^+$, 243.0659 $[M + H\text{-}CO]^+$, 215.0708, 197.0603, 153.0183 $[M + H\text{-}C_8H_8O]^+$, 115.0541, 91.0563	241.0494 $[M - H\text{-}CO]^-$, 224.0491, 201.0560, 159.0450, 133.0289, 107.0151
47	Apigenin-*O*-glucuronide	$C_{21}H_{18}O_{11}$	8.3	447.0879 (0.6)	ND	350.1642, 271.0582 $[M + H\text{-}GlcUA]^+$, 215.0660, 153.0222 $[M + H\text{-}GlcUA\text{-}C_8H_8O]^+$	ND
48	Apigenin-*O*-glucuronide	$C_{21}H_{18}O_{11}$	10.8	447.0930 (1.4)	445.0766 (–2.3)	ND	269.0459 $[M - H\text{-}GlcUA]^-$, 113.0269
49	Apigenin-*O*-Sulfate	$C_{15}H_{10}O_8S$	13.0	351.0182 (3.6)	349.0026 (–0.6)	271.0593 $[M + H\text{-}SO_3]^+$, 253.0471 $[M + H\text{-}SO_3\text{-}H_2O]^+$, 243.0619 $[M + H\text{-}SO_3\text{-}CO]^+$, 215.0704, 153.0175 $[M + H\text{-}SO_3\text{-}C_8H_8O]^+$	269.0457 $[M - H\text{-}SO_3]^-$, 241.0487, 225.0567, 213.0518, 151.0048 $[M - H\text{-}SO_3\text{-}C_8H_8O]^-$, 117.0345 $[M - H\text{-}SO_3\text{-}C_7H_4O_4]^-$

[a]*The losses are: Glc, glucose moiety; Rha, rhamnose moiety; ND, not detect.*

[b]*Confirmation in comparison with authentic standards.*

[c]*Confirmation in comparison with mass spectral library (Natural Products HR-MS/MS Spectral Library, Version 1.0; AB Sciex, Foster City, United States).*

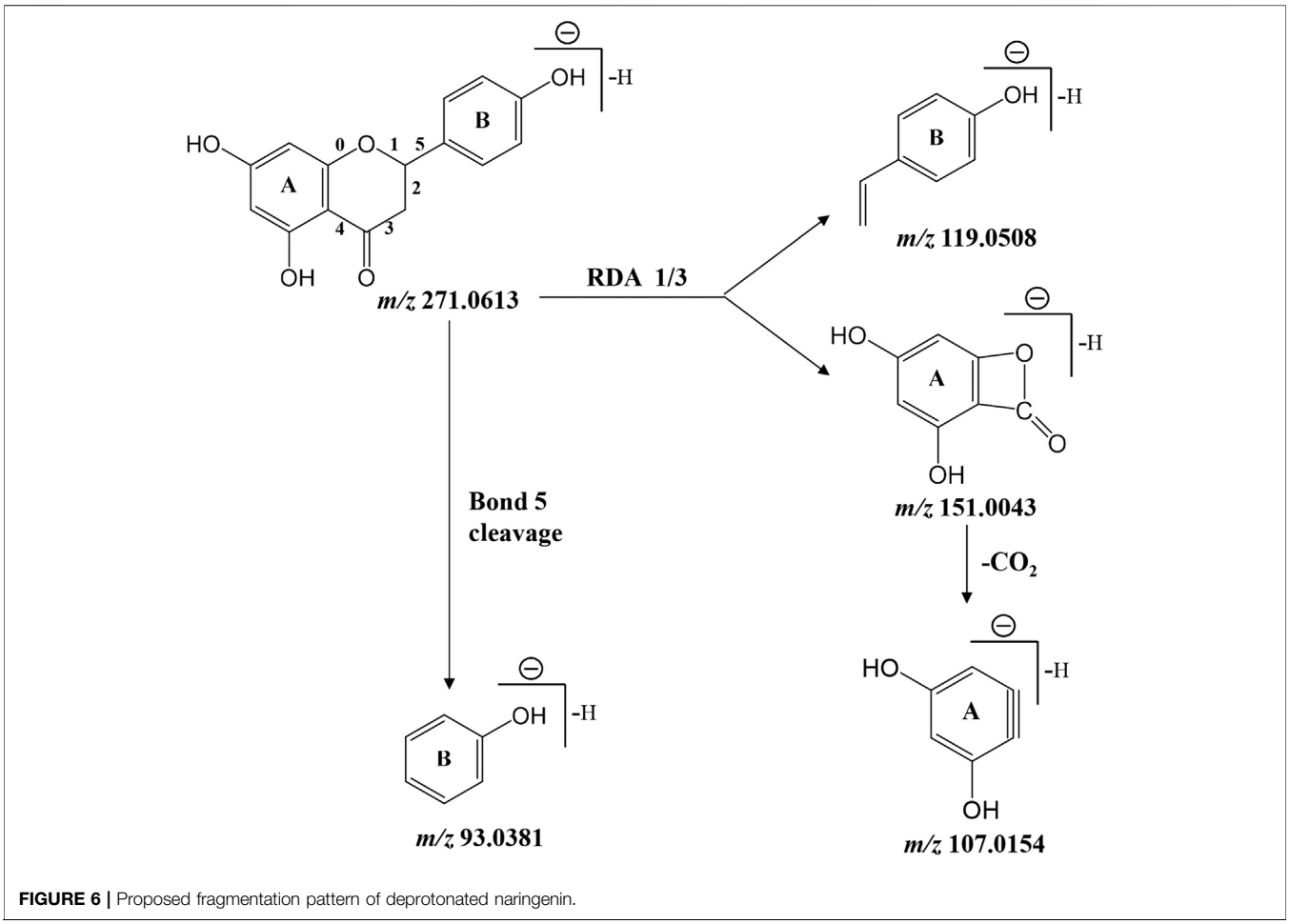

FIGURE 6 | Proposed fragmentation pattern of deprotonated naringenin.

pharmacological activities, network pharmacology analysis revealed that the interaction between CRP and spleen deficiency involved multiple BPs and pathways, including inflammatory responses, immune system, and oxidative stress, mediating by TNF signaling pathway, hypoxia-inducible factor-1 (HIF-1) signaling pathway, Toll-like receptor signaling pathway, *etc*. Reported studies showed that pro-inflammatory and/or oxidative stress mediators are directly interlinked with the pathogenesis of many gastrointestinal diseases (Chung et al., 2016). Among mentioned pathways, TNF signaling is critical to the maintenance of intestinal barrier and epithelial cell tight junctions (Kolodziej et al., 2011). HIF-1 signaling pathway is closely related to stress-responsive gene expression (Surazynski et al., 2008). Toll-like receptor signaling pathway is important for maintaining tolerance to commensal microbiota and inducing inflammation against pathogens, hence playing an essential role in homeostasis of the intestine (Biswas et al., 2011; Kamdar et al., 2013). However, further mechanism studies are necessary to assign the role of these pathway in CRP against spleen deficiency.

As shown in **Figure 7**, a total of 17 compounds (mainly flavonoids) were assigned as the core bioactive components in CRP by network pharmacology analysis. Our preliminary chemical profile analysis suggested that these compounds were abundant in CRP herbs (Zheng et al., 2019). Besides mentioned targets and pathways, these compounds could also interact with gut microbiota after oral administration, which probably contribute to the overall therapeutic effects of CRP against spleen deficiency. Take hesperetin as an example, ingestion of an assigned diet (0.5% hesperetin) for three weeks could significantly affect the structure and activity of gut microbiota in rats (Unno et al., 2015). The richness of *Clostridium subcluster XIVa* in feces was significantly reduced, while the cecal SCFA pool was noticeably increased. Therefore, in the follow-up study to clarify the mechanism of action, we should not only pay attention to identified targets and pathways but also focus on gut microbiota.

CONCLUSION

In this study, the efficacy against spleen deficiency and gut microbiota modulatory properties of CRP were investigated using reserpine treated rats as the animal model. CRP derived metabolites were identified in rat urine and further applied to explore the core bioactive components and potential targets through network pharmacology analysis. As a result, CRP administration could effectively alleviate the typical symptoms of spleen deficiency induced by reserpine treatment, including

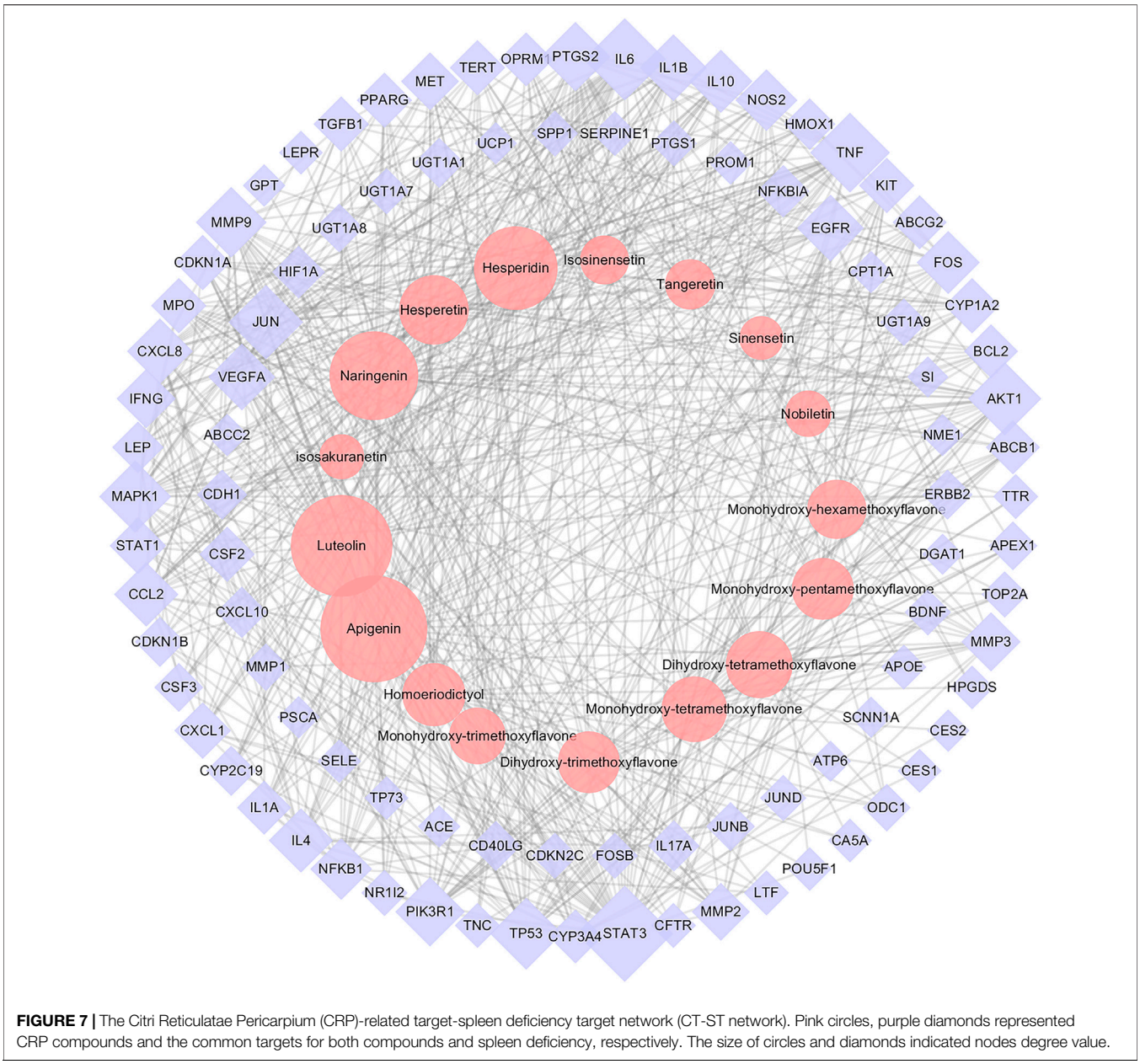

FIGURE 7 | The Citri Reticulatae Pericarpium (CRP)-related target-spleen deficiency target network (CT-ST network). Pink circles, purple diamonds represented CRP compounds and the common targets for both compounds and spleen deficiency, respectively. The size of circles and diamonds indicated nodes degree value.

poor digestion and absorption capacity, and disorder in gastrointestinal hormones, immune cytokines and oxidative stress. Meanwhile, CRP was found to improve the diversity and structure of the gut microbiota in spleen deficiency rats. Compared with model group, some SCFAs producing and anti-inflammatory bacteria including *Bifidobacterium*, *Lactobacillus*, *Allobaculum*, *Psychrobacter*, *[Eubacterium]_ coprostanoligenes_ group*, *Prevotellaceae_Ga6A1_group*, *Parasutterella* were up-regulated, while some spleen deficiency aggravated related bacteria including *Alistipes*, *Anaerotruncus*, *Desulfovibrio*, *Oscillibacter*, *Ruminiclostridium_9*, *Ruminococcaceae_UCG-003*, *Ruminiclostridium_5*, *Parabacteroides* were down-regulated in CRP group rats. Further Spearman's correlation analysis indicated that there existed a close correlation between the profiles of gut microbiota and the spleen-deficiency related biochemical indexes. In addition, a total of 26 prototype compounds and 23 metabolites were detected in rat urine after the ingestion of CRP. Through network pharmacology analysis, apigenin, luteolin, naringenin, hesperidin, hesperetin, dihydroxy-tetramethoxyflavone, monohydroxy-tetramethoxyflavone and homoeriodictyol were assigned as the core bioactive components, while STAT3, IL6, TNF, JUN, AKT1, TP53, MAPK1, MMP9, PIK3R1, PTGS2, VEGFA, EGFR, IL1B, CXCL8, IL4, CCL2, IL10, and FOS were defined as the major potential targets. Further GO analysis and pathway enrichment suggested that therapeutic effects of CRP against spleen deficiency involved multiple BPs, including inflammatory responses, immune system and oxidative stress such as TNF signaling pathway, HIF-1 signaling pathway, and Toll-like receptor signaling pathway. Besides these targets and pathways,

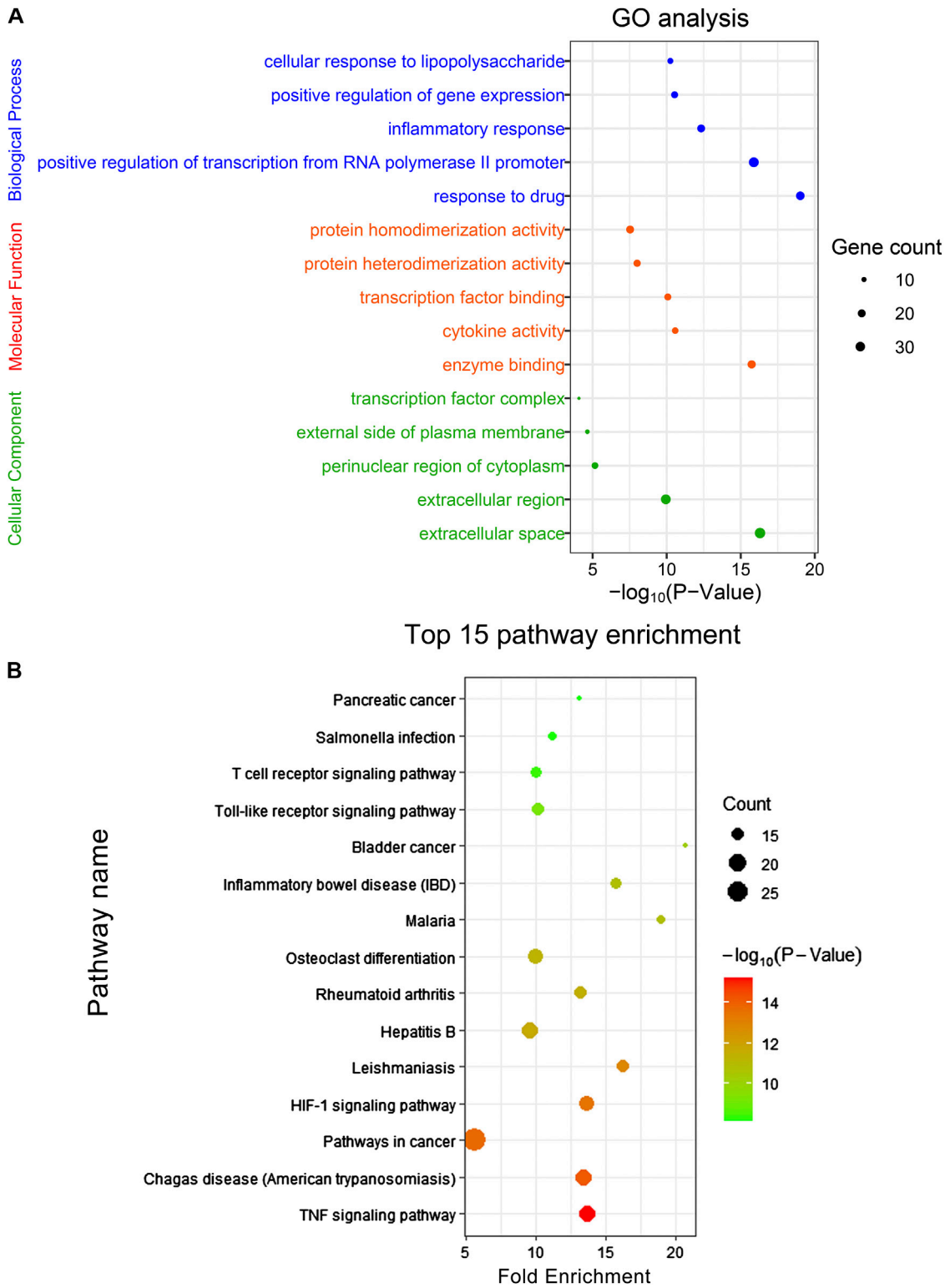

FIGURE 8 | (A) GO analysis and **(B)** KEEG signaling pathway enrichment of the common targets. The size of the dot indicates the number of target genes in the pathway and the color of the dot reflects the *p* values.

identified compounds could also interact with gut microbiota after oral administration, which probably contribute to the overall therapeutic effects of CRP. This work provided systematic insights to understand the mechanism of CRP alleviating spleen deficiency-related diseases.

DATA AVAILABILITY STATEMENT

The datasets generated for this study can be found in GenBank accession numbers (MW015148–MW015742).

ETHICS STATEMENT

The animal study was reviewed and approved by Animal Ethics Committee of the School of Life Sciences in Sun Yat-sen University.

AUTHOR CONTRIBUTIONS

YZ, WP, and WS conceived and designed the study. YZ, XZ, and TC carried out the experiments. YZ, XZ, and PC analyzed the research data and wrote the manuscript.

FUNDING

This research was supported by the Science and Technology Planning Project of Guangdong Province in China (2019B090905002).

SUPPLEMENTARY MATERIAL

The Supplementary Material for this article can be found online at: https://www.frontiersin.org/articles/10.3389/fphar.2020.586350/full#supplementary-material

REFERENCES

Barouei, J., Bendiks, Z., Martinic, A., Mishchuk, D., Heeney, D., Hsieh, Y.-H., et al. (2017). Microbiota, metabolome, and immune alterations in obese mice fed a high-fat diet containing type 2 resistant starch. *Mol. Nutr. Food Res.* 61 (11), 1700184. doi:10.1002/mnfr.201700184

Bashyam, H. (2007). Th1/Th2 cross-regulation and the discovery of IL-10. *J. Exp. Med.* 204 (2), 237. doi:10.1084/jem.2042fta

Bibbò, S., Ianiro, G., Giorgio, V., Scaldaferri, F., Masucci, L., Gasbarrini, A., et al. (2016). The role of diet on gut microbiota composition. *Eur. Rev. Med. Pharmacol. Sci.* 20 (22), 4742–4749.

Biswas, A., Wilmanski, J., Forsman, H., Hrncir, T., Hao, L., Tlaskalova-Hogenova, H., et al. (2011). Negative regulation of Toll-like receptor signaling plays an essential role in homeostasis of the intestine. *Eur. J. Immunol.* 41 (1), 182–194. doi:10.1002/eji.201040479

Candela, M., Perna, F., Carnevali, P., Vitali, B., Ciati, R., Gionchetti, P., et al. (2008). Interaction of probiotic *Lactobacillus* and *Bifidobacterium* strains with human intestinal epithelial cells: adhesion properties, competition against enteropathogens and modulation of IL-8 production. *Int. J. Food Microbiol.* 125 (3), 286–292. doi:10.1016/j.ijfoodmicro.2008.04.012

Capurso, G., and Lahner, E. (2017). The interaction between smoking, alcohol and the gut microbiome. *Best Pract. Res. Clin. Gastroenterol.* 31 (5), 579–588. doi:10.1016/j.bpg.2017.10.006

Caporaso, J. G., Kuczynski, J., Stombaugh, J., Bittinger, K., Bushman, F. D., Costello, E. K., et al. (2010). QIIME allows analysis of high-throughput community sequencing data. *Nat. Methods* 7, 335–336. doi:10.1038/nmeth.f.303

Chung, Y. K., Chen, J., and Ko, K. M. (2016). Spleen function and anxiety in Chinese medicine: a western medicine perspective. *Chinese Med.* 7 (3), 110–123. doi:10.4236/cm.2016.73012

Davis, A. P., Grondin, C. J., Johnson, R. J., Sciaky, D., McMorran, R., Wiegers, J., et al. (2019). The comparative toxicogenomics database: update 2019. *Nucleic Acids Res.* 47 (D1), D948–D954. doi:10.1093/nar/gky868

Downes, J., Dewhirst, F. E., Tanner, A. C. R., and Wade, W. G. (2013). Description of *Alloprevotella rava* gen. nov., sp. nov., isolated from the human oral cavity, and reclassification of *Prevotella tannerae* Moore et al. 1994 as *Alloprevotella tannerae* gen. nov., comb. nov. *Int. J. Syst. Evol. Microbiol.* 63 (Pt 4), 1214–1218. doi:10.1099/ijs.0.041376-0

Dueñas, M., Muñoz-González, I., Cueva, C., Jiménez-Girón, A., Sánchez-Patán, F., Santos-Buelga, C., et al. (2015). A survey of modulation of gut microbiota by dietary polyphenols. *BioMed Res. Int.* 2015, 850902. doi:10.1155/2015/850902

Edgar, R. C. (2010). Search and clustering orders of magnitude faster than BLAST. *Bioinformatics* 26 (19), 2460–2461. doi:10.1093/bioinformatics/btq461

Feng, Q., Chen, W.-D., and Wang, Y.-D. (2018). Gut microbiota: an integral moderator in health and disease. *Front. Microbiol.* 9, 151. doi:10.3389/fmicb.2018.00151

Fischer, R., Tomé, D., McGhee, J. R., and Boyaka, P. N. (2007). Th1 and Th2 cells are required for both eosinophil- and neutrophil-associated airway inflammatory responses in mice. *Biochem. Biophys. Res. Commun.* 357 (1), 44–49. doi:10.1016/j.bbrc.2007.03.058

Gao, X. L., Guo, W. F., Li, R. L., and Chen, W. W. (2009). Effects of Sijunzi Decoction on urine's xylose excretion rate and ATP in mucosa of spleen deficiency rats. *J. Chin. Med. Mater.* 32 (8), 1242–1245.

Gao, Y. (2015). Urine is a better biomarker source than blood especially for kidney diseases. *Adv. Exp. Med. Biol.* 845, 3–12. doi:10.1007/978-94-017-9523-4_1

Gfeller, D., Grosdidier, A., Wirth, M., Daina, A., Michielin, O., and Zoete, V. (2014). SwissTargetPrediction: a web server for target prediction of bioactive small molecules. *Nucleic Acids Res.* 42 (Web Server Issue), W32–W38. doi:10.1093/nar/gku293

Gobert, A. P., Sagrestani, G., Delmas, E., Wilson, K. T., Verriere, T. G., Dapoigny, M., et al. (2016). The human intestinal microbiota of constipated-predominant irritable bowel syndrome patients exhibits anti-inflammatory properties. *Sci. Rep.* 6, 39399. doi:10.1038/srep39399

Gradolatto, A., Canivenc-Lavier, M.-C., Basly, J.-P., Siess, M.-H., and Teyssier, C. (2004). Metabolism of apigenin by rat liver phase I and phase II enzymes and by isolated perfused rat liver. *Drug Metab. Dispos.* 32 (1), 58–65. doi:10.1124/Dmd.32.1.58

Itoh, H., Katagiri, F., Ikawa, K., and Takeyama, M. (2005). Effects of domperidone on human plasma levels of motilin, somatostatin, gastrin, adrenocorticotropic hormone and cortisol. *Biol. Pharm. Bull.* 28 (9), 1752–1756. doi:10.1248/bpb.28.1752

Jiao, X., Sherman, B. T., Huang, D. W., Stephens, R., Baseler, M. W., Lane, H. C., et al. (2012). DAVID-WS: a stateful web service to facilitate gene/protein list analysis. *Bioinformatics* 28 (13), 1805–1806. doi:10.1093/bioinformatics/bts251

Kamdar, K., Nguyen, V., and DePaolo, R. W. (2013). Toll-like receptor signaling and regulation of intestinal immunity. *Virulence* 4 (3), 207–212. doi:10.4161/viru.23354

Koga, N., Matsuo, M., Ohta, C., Haraguchi, K., Matsuoka, M., Kato, Y., et al. (2007). Comparative study on nobiletin metabolism with liver microsomes from rats, Guinea pigs and hamsters and rat cytochrome p450. *Biol. Pharm. Bull.* 30 (12), 2317–2323. doi:10.1248/bpb.30.2317

Kolodziej, L. E., Lodolce, J. P., Chang, J. E., Schneider, J. R., Grimm, W. A., Bartulis, S. J., et al. (2011). TNFAIP3 maintains intestinal barrier function and supports epithelial cell tight junctions. *PLoS One* 6 (10), e26352. doi:10.1371/journal.pone.0026352

Lam, Y. Y., Ha, C. W. Y., Campbell, C. R., Mitchell, A. J., Dinudom, A., Oscarsson, J., et al. (2012). Increased gut permeability and microbiota change associate with mesenteric fat inflammation and metabolic dysfunction in diet-induced obese mice. *PLoS One* 7 (3), e34233. doi:10.1371/journal.pone.0034233

Li, L., Batt, S. M., Wannemuehler, M., Dispirito, A., and Beitz, D. C. (1998). Effect of feeding of a cholesterol-reducing bacterium, Eubacterium coprostanoligenes, to germ-free mice. *Lab. Anim. Sci.* 48 (3), 253–255.

Li, S., Wang, H., Guo, L., Zhao, H., and Ho, C.-T. (2014). Chemistry and bioactivity of nobiletin and its metabolites. *J. Funct. Foods* 6, 2–10. doi:10.1016/j.jff.2013.12.011

Li, X. J., Qiu, W. Q., Da, X. L., Hou, Y. J., Ma, Q. Y., Wang, T. Y., et al. (2020). A combination of depression and liver Qi stagnation and spleen deficiency syndrome using a rat model. *Anat. Rec.* 303 (8), 2154–2167. doi:10.1002/ar.24388

Lin, Z., Ye, W., Zu, X., Xie, H., Li, H., Li, Y., et al. (2018). Integrative metabolic and microbial profiling on patients with Spleen-yang-deficiency syndrome. *Sci. Rep.* 8 (1), 6619. doi:10.1038/s41598-018-24130-7

Maldonado, M., and Maeyama, K. (2015). The metabolism of histamine in rat hypothalamus and cortex after reserpine treatment. *Neurochem. Int.* 85–86, 31–39. doi:10.1016/j.neuint.2015.04.005

Meijnikman, A. S., Gerdes, V. E., Nieuwdorp, M., and Herrema, M. (2018). Evaluating causality of gut microbiota in obesity and diabetes in humans. *Endocr. Rev.* 39 (2), 133–153. doi:10.1210/er.2017-00192

Meng, Q. B., Yin, Y. X., Zhang, D. Z., and Yang, G. P. (2013). Study on syndrome quantification, differentiation and classification of traditional Chinese medicine with data envelopment analysis. *China J. Chin. Mater. Med.* 38 (10), 1631–1642.

Mosmann, T. R., Cherwinski, H., Bond, M. W., Giedlin, M. A., and Coffman, R. L. (1986). Two types of murine helper T cell clone. I. Definition according to profiles of lymphokine activities and secreted proteins. *J. Immunol.* 136 (7), 2348–2357.

Ning, K., Zhao, X., Poetsch, A., Chen, W.-H., and Yang, J. (2017). Computational molecular networks and network pharmacology. *BioMed Res. Int.* 2017, 1. doi:10.1155/2017/7573904

Nogacka, A. M., Salazar, N., Arboleya, S., Suárez, M., Fernández, N., Solís, G., et al. (2018). Early microbiota, antibiotics and health. *Cell. Mol. Life Sci.* 75 (1), 83–91. doi:10.1007/s00018-017-2670-2

O'Mahony, L., McCarthy, J., Kelly, P., Hurley, G., Luo, F., Chen, K., et al. (2005). Lactobacillus and bifidobacterium in irritable bowel syndrome: symptom responses and relationship to cytokine profiles. *Gastroenterology* 128 (3), 541–551. doi:10.1053/j.gastro.2004.11.050

Pei, R., Liu, X., and Bolling, B. (2020). Flavonoids and gut health. *Curr. Opin. Biotechnol.* 61, 153–159. doi:10.1016/j.copbio.2019.12.018

Piñero, J., Ramírez-Anguita, J. M., Saüch-Pitarch, J., Ronzano, F., Centeno, E., Sanz, F., et al. (2020). The DisGeNET knowledge platform for disease genomics: 2019 update. *Nucleic Acids Res.* 48 (D1), D845–D855. doi:10.1093/nar/gkz1021

Qiu, J.-J., Liu, Z., Zhao, P., Wang, X.-J., Li, Y.-C., Sui, H., et al. (2017). Gut microbial diversity analysis using Illumina sequencing for functional dyspepsia with liver depression-spleen deficiency syndrome and the interventional Xiaoyaosan in a rat model. *World J. Gastroenterol.* 23 (5), 810–816. doi:10.3748/wjg.v23.i5.810

Sharma, M., Akhtar, N., Sambhav, K., Shete, G., Bansal, A., and Sharma, S. (2015). Emerging potential of citrus flavanones as an antioxidant in diabetes and its complications. *Curr. Top. Med. Chem.* 15 (2), 187–195. doi:10.2174/1568026615666141209163013

State Pharmacopoeia Committee of People's Republic of China (2015). *Pharmacopoeia of People's Republic of China*. Beijing, China: China Medical Science and Technology Press.

Stengel, A., and Tache, Y. (2011). Interaction between gastric and upper small intestinal hormones in the regulation of hunger and satiety: ghrelin and cholecystokinin take the central stage. *Curr. Protein Pept. Sci.* 12 (4), 293–304. doi:10.2174/138920311795906673

Surazynski, A., Donald, S. P., Cooper, S. K., Whiteside, M. A., Salnikow, K., Liu, Y., et al. (2008). Extracellular matrix and HIF-1 signaling: the role of prolidase. *Int. J. Cancer* 122 (6), 1435–1440. doi:10.1002/ijc.23263

Szklarczyk, D., Gable, A. L., Lyon, D., Junge, A., Wyder, S., Huerta-Cepas, J., et al. (2019). STRING v11: protein-protein association networks with increased coverage, supporting functional discovery in genome-wide experimental datasets. *Nucleic Acids Res.* 47 (D1), D607–D613. doi:10.1093/nar/gky1131

Unno, T., Hisada, T., and Takahashi, S. (2015). Hesperetin modifies the composition of fecal microbiota and increases cecal levels of short-chain fatty acids in rats. *J. Agric. Food Chem.* 63 (36), 7952–7957. doi:10.1021/acs.jafc.5b02649

Veerappan, G. R., Betteridge, J., and Young, P. E. (2012). Probiotics for the treatment of inflammatory bowel disease. *Curr. Gastroenterol. Rep.* 14 (4), 324–333. doi:10.1007/s11894-012-0265-5

Walle, T. (2004). Absorption and metabolism of flavonoids. *Free Radic. Biol. Med.* 36 (7), 829–837. doi:10.1016/j.freeradbiomed.2004.01.002

Wang, H., Huang, Y. K., and Liu, M. (2013). Relationship between gastrointestinal hormones and gastrointestinal tract function and diseases. *Med. Recapitulate* 19 (15), 2735–2738.

Wang, R., Peng, Y., Meng, H., and Li, X. (2016). Protective effect of polysaccharides fractions from Sijunzi decoction in reserpine-induced spleen deficiency rats. *RSC Adv.* 6 (65), 60657–60665. doi:10.1039/c6ra06361f

Wei, X., Tao, J., Xiao, S., Jiang, S., Shang, E., Zhu, Z., et al. (2018). Xiexin Tang improves the symptom of type 2 diabetic rats by modulation of the gut microbiota. *Sci. Rep.* 8 (1), 3685. doi:10.1038/s41598-018-22094-2

Xie, X.-Z., Zhao, Z.-G., Qi, D.-S., and Wang, Z.-M. (2006). Assay of gastrin and somatostatin in gastric antrum tissues of children with chronic gastritis and duodenal ulcer. *World J. Gastroenterol.* 12 (14), 2288–2290. doi:10.3748/wjg.v12.i14.2288

Xu, H.-Y., Zhang, Y.-Q., Liu, Z.-M., Chen, T., Lv, C.-Y., Tang, S.-H., et al. (2019). ETCM: an encyclopaedia of traditional Chinese medicine. *Nucleic Acids Res.* 47 (D1), D976–D982. doi:10.1093/nar/gky987

Yang, Y., Chen, G., Yang, Q., Ye, J., Cai, X., Tsering, P., et al. (2017). Gut microbiota drives the attenuation of dextran sulphate sodium-induced colitis by Huangqin decoction. *Oncotarget* 8 (30), 48863–48874. doi:10.18632/oncotarget.16458

Yu, X., Sun, S., Guo, Y., Liu, Y., Yang, D., Li, G., et al. (2018). Citri Reticulatae Pericarpium (Chenpi): botany, ethnopharmacology, phytochemistry, and pharmacology of a frequently used traditional Chinese medicine. *J. Ethnopharmacol.* 220, 265–282. doi:10.1016/j.jep.2018.03.031

Zeng, S.-L., Li, S.-Z., Xiao, P.-T., Cai, Y.-Y., Chu, C., Chen, B.-Z., et al. (2020a). Citrus polymethoxyflavones attenuate metabolic syndrome by regulating gut microbiome and amino acid metabolism. *Sci. Adv.* 6 (1), eaax6208. doi:10.1126/sciadv.aax6208

Zeng, X., Su, W., Zheng, Y., He, Y., He, Y., Rao, H., et al. (2019). Pharmacokinetics, tissue distribution, metabolism, and excretion of naringin in aged rats. *Front. Pharmacol.* 10, 34. doi:10.3389/fphar.2019.00034

Zeng, X., Yao, H., Zheng, Y., Chen, T., Peng, W., Wu, H., et al. (2020b). Metabolite profiling of naringin in rat urine and feces using stable isotope-labeling-based liquid chromatography-mass spectrometry. *J. Agric. Food Chem.* 68 (1), 409–417. doi:10.1021/acs.jafc.9b06494

Zhang, X., Zhao, Y., Xu, J., Xue, Z., Zhang, M., Pang, X., et al. (2015). Modulation of gut microbiota by berberine and metformin during the treatment of high-fat diet-induced obesity in rats. *Sci. Rep.* 5, 14405. doi:10.1038/srep14405

Zhao, M., Wu, J., Li, X., and Gao, Y. (2018). Urinary candidate biomarkers in an experimental autoimmune myocarditis rat model. *J. Proteomics* 179, 71–79. doi:10.1016/j.jprot.2018.02.032

Zhao, N., Zhang, W., Guo, Y., Jia, H., Zha, Q., Liu, Z., et al. (2011). Effects on neuroendocrinoimmune network of Lizhong Pill in the reserpine induced rats with spleen deficiency in traditional Chinese medicine. *J. Ethnopharmacol.* 133 (2), 454–459. doi:10.1016/j.jep.2010.10.016

Zheng, X.-f., Tian, J.-s., Liu, P., Xing, J., and Qin, X.-m. (2014). Analysis of the restorative effect of Bu-zhong-yi-qi-tang in the spleen-qi deficiency rat model using 1H-NMR-based metabonomics. *J. Ethnopharmacol.* 151 (2), 912–920. doi:10.1016/j.jep.2013.12.001

Zheng, Y., Zeng, X., Chen, T., Peng, W., and Su, W. (2020). Chemical profile, antioxidative, and gut microbiota modulatory properties of Ganpu tea: a derivative of Pu-erh tea. *Nutrients* 12 (1), 224. doi:10.3390/nu12010224

Zheng, Y., Zeng, X., Peng, W., Wu, Z., and Su, W. (2018). Study on the discrimination between Citri Reticulatae Pericarpium varieties based on HS-SPME-GC-MS combined with multivariate statistical analyses. *Molecules* 23 (5), 1235. doi:10.3390/molecules23051235

Zheng, Y. y., Zeng, X., Peng, W., Wu, Z., and Su, W. w. (2019). Characterisation and classification of Citri Reticulatae Pericarpium varieties based on UHPLC-Q-TOF-MS/MS combined with multivariate statistical analyses. *Phytochem. Anal.* 30 (3), 278–291. doi:10.1002/pca.2812

Conflict of Interest: The authors declare that the research was conducted in the absence of any commercial or financial relationships that could be construed as a potential conflict of interest.

Copyright © 2020 Zheng, Zeng, Chen, Chen, Peng and Su. This is an open-access article distributed under the terms of the Creative Commons Attribution License (CC BY). The use, distribution or reproduction in other forums is permitted, provided the original author(s) and the copyright owner(s) are credited and that the original publication in this journal is cited, in accordance with accepted academic practice. No use, distribution or reproduction is permitted which does not comply with these terms.

frontiers in Pharmacology

ORIGINAL RESEARCH
published: 04 December 2020
doi: 10.3389/fphar.2020.567088

A Novel Strategy for Decoding and Validating the Combination Principles of Huanglian Jiedu Decoction From Multi-Scale Perspective

Ke-Xin Wang[1,2†], Yao Gao[1,2†], Wen-Xia Gong[1], Xiao-Feng Ye[2], Liu-Yi Fan[3], Chun Wang[4], Xue-Fei Gao[5], Li Gao[1], Guan-Hua Du[1,6], Xue-Mei Qin[1], Ai-Ping Lu[2]* and Dao-Gang Guan[7,8]**

[1]Modern Research Center for Traditional Chinese Medicine, Shanxi University, Taiyuan, China, [2]Institute of Integrated Bioinformedicine and Translational Science, Hong Kong Baptist University, Hong Kong, China, [3]Department of Orthopaedics and Traumatology, Nanfang Hospital, Southern Medical University, Guangzhou, China, [4]Institute of Basic Theory for Chinese Medicine, China Academy of Chinese Medical Sciences, Beijing, China, [5]Department of Physiology, School of Basic Medical Sciences, Southern Medical University, Guangzhou, China, [6]Institute of Materia Medica, Chinese Academy of Medical Sciences & Peking Union Medical College, Beijing, China, [7]Department of Biochemistry and Molecular Biology, School of Basic Medical Sciences, Southern Medical University, Guangzhou, China, [8]Guangdong Key Laboratory of Biochip Technology, Southern Medical University, Guangzhou, China*

Traditional Chinese medicine (TCM) formulas treat complex diseases through combined botanical drugs which follow specific compatibility rules to reduce toxicity and increase efficiency. "Jun, Chen, Zuo and Shi" is one of most used compatibility rules in the combination of botanical drugs. However, due to the deficiency of traditional research methods, the quantified theoretical basis of herbal compatibility including principles of "Jun, Chen, Zuo and Shi" are still unclear. Network pharmacology is a new strategy based on system biology and multi-disciplines, which can systematically and comprehensively observe the intervention of drugs on disease networks, and is especially suitable for the research of TCM in the treatment of complex diseases. In this study, we systematically decoded the "Jun, Chen, Zuo and Shi" rules of Huanglian Jiedu Decoction (HJD) in the treatment of diseases for the first time. This interpretation method considered three levels of data. The data in the first level mainly depicts the characteristics of each component in single botanical drug of HJD, include the physical and chemical properties of component, ADME properties and functional enrichment analysis of component targets. The second level data is the characterization of component-target-protein (C-T-P) network in the whole protein-protein interaction (PPI) network, mainly include the characterization of degree and key communities in C-T-P network. The third level data is the characterization of intervention propagation properties of HJD in the treatment of different complex diseases, mainly include target coverage of pathogenic genes and propagation coefficient of intervention effect between target proteins and pathogenic genes. Finally, our method was validated by metabolic data, which could be used to detect the components absorbed into blood. This research shows the scientific basis of "Jun-Chen-Zuo-Shi" from a multi-dimensional perspective, and provides a good methodological reference for the subsequent interpretation of key components and speculation mechanism of the formula.

Keywords: system pharmacology, traditional Chinese medicine, compatibility, Dijkstra model, information graph algorithm

OPEN ACCESS

Edited by:
Takashi Sato,
Tokyo University of Pharmacy and Life Sciences, Japan

Reviewed by:
Sayeed Ahmad,
Jamia Hamdard University, India
Haolong Liu,
Peking University Health Science Centre, China

***Correspondence:**
Dao-Gang Guan
guandg0929@hotmail.com
Xue-Mei Qin
qinxm@sxu.edu.cn
Ai-Ping Lu
aipinglu@hkbu.edu.hk

†These authors have contributed equally to this work.

Specialty section:
This article was submitted to Ethnopharmacology, a section of the journal Frontiers in Pharmacology

Received: *29 May 2020*
Accepted: *12 November 2020*
Published: *04 December 2020*

Citation:
Wang K-X, Gao Y, Gong W-X, Ye X-F, Fan L-Y, Wang C, Gao X-F, Gao L, Du G-H, Qin X-M, Lu A-P and Guan D-G (2020) A Novel Strategy for Decoding and Validating the Combination Principles of Huanglian Jiedu Decoction From Multi-Scale Perspective. Front. Pharmacol. 11:567088. doi: 10.3389/fphar.2020.567088

INTRODUCTION

After thousands of years of experience in the treatment of diseases, the effectiveness of traditional Chinese medicine (TCM) is indisputable (Liang et al., 2015). During this process, TCM has also formed unique medication standards and compatibility theories, such as "Jun (emperor), Chen (minister), Zuo (adjuvant) and Shi (messenger)" (Wang et al., 2008; Lin and Yuhang, 2009). The basic and common feature of TCM is that it is consisted in the form of formula by the guidance of compatibility theory, different botanical drugs are orchestrated to form a multi-botanical drug combination of TCM (Lv et al., 2018). The principle of a formula is not just simply to mix botanical drugs, it is a process to increase efficiency and reduce toxicity. During this process, traditional compatibility rules will affect the changes of effective and toxic components of the formula, thus could reflect the advantages of enhancing synergistic effect and reducing toxicity of the formula (Liu et al., 2018). In TCM formula, botanical drugs are divided into "Jun, Chen, Zuo and Shi" according to the therapeutic characteristics of TCM, which are the basis of compatibility of TCM formula. "Jun" botanical drugs play leading roles in the treatment of diseases in the formula. "Chen" botanical drugs are usually worked as assistants to provide help to Jun botanical drugs in treating diseases; "Zuo" botanical drugs are used in combination with Jun and Chen botanical drugs to treat diseases or inhibit the toxic effects of Jun and Chen botanical drugs; "Shi" botanical drugs are widely used to coordinate the above botanical drugs and enhance their functions. It can be seen from this that the "Jun, Chen, Zuo and Shi" of the botanical drugs in the formula are mainly distinguished according to the primary and secondary roles of the medicine in the formula (Yao et al., 2013; Wu et al., 2014). Although "Jun, Chen, Zuo and Shi" is a widely used principle in the compatibility of TCM, the action pattern and underlying mechanisms of the compatibility rule of "Jun, Chen, Zuo and Shi" is still unclear. How to understand the action pattern and underlying mechanisms of compatibility rule is the basic and key step to decode the functional mechanisms of formulas in the treatment of complex diseases and benefit to secondary development of formulas.

A TCM formula generally contains several botanical drugs, and each botanical drug contains numbers of chemical components (Jia et al., 2004). These components are the material basis of the effect and mechanism of action (MOA) of the TCM formula. Studying the chemical composition and differences in efficacy of formula compatibility are helpful to clarify the pharmacological mechanism of TCM formula (Zhang, 2017). The traditional method to study the pharmacological effects of the single or several components in TCM is cell test or animal verify. These experiment-based research methods are divorced from the characteristics of the overall treatment of TCM, not only unable to tap the effective components of TCM, but also have no ability to effectively reveal the mechanism of TCM.

Network pharmacology has been widely used in the research of TCM in the treatment of complex diseases (Gu and Jianfeng, 2017). With the accumulation of omics data and the progress of network pharmacology technologies, increasing models are proposed to decode the therapeutic molecular mechanisms of formulas in treating complex diseases. For example, Wang et al. employed network pharmacology model combined with hypergeometric distribution to identify the enriched significant pathways. These pathways affected by a group of differentially expressed genes in pathway enrichment analysis, and further be used to reveal the mechanism of Wuwei-Ganlu-Yaoyu-Keli in treating rheumatoid arthritis (Wang et al., 2017). Gu et al. established a model for predicting signal transduction effects and extracting sub-networks by using EGS for mechanism analysis based on the data of TCM components and diseases (Gu et al., 2014). However, most models are used to decode the mechanism of TCM in treating complex diseases via networks analysis. Few models considered the compatibility rules and formulation principles of TCM, which are closely related to the effect and toxicity of drugs. He et al. studied the effect of compatibility of *Ginseng trifolium* (L.) Alph. Wood and *Aconitum carmichaeli* Debeaux on cardiac toxicity of rats through metabolomics and found that *Ginseng trifolium* (L.) Alph. Wood compatibility of *Aconitum carmichaeli* Debeaux can reduce its cardiac toxicity and increase its pharmacological effects by affecting the content of citric acid, glutathione, phosphatidyl choline and uric acid (He et al., 2015). In the treatment of rheumatoid arthritis, Zhang et al. observed that total glucosides of paeony combined with Tripteryginum wilfordii polyglycoside has better performance in the treatment of RA by increasing efficiency and reducing toxicity at the clinical applications (Zhang et al., 2019). How to utilize system pharmacology to analyze the principle of formulas in TCM at systemic level through mathematical and quantitative methods could be benefit for truly understanding the mechanisms of formula in the treatment of diseases.

Huanglian Jiedu Decoction (HJD) is composed of four botanical drugs, namely, *Coptis chinensis* Franch (Huanglian), *Scutellaria baicalensis* Georgi (Huangqin), *Phellodendron amurense* Rupr (Huangbo) and *Gardenia jasminoides* J. Ellis (Zhizi), with a compatible dosage of 3:2:2:3 (Ma et al., 2009). HJD is widely used in diabetes, cardiovascular and cerebrovascular diseases, inflammation, alzheimer's disease, etc. in clinical applications (Wang and Xu, 2000; Xin et al., 2011; Zhang et al., 2014). It has a wide range of pharmacological activities such as antibacterial, anti-inflammatory, antioxidant, neuroprotective, etc (Lv et al., 2017). Previous pharmacological studies have shown that HJD could effectively control the weight of diabetic rats and has a good regulating effect on blood lipid and oxygen radical metabolism (Zhang et al., 2011). It has been reported that HJD has a strong lipid-regulating effect on type 2 diabetic rats, which can reduce the increase of pancreatic lipase activity in intestinal tract and inhibit the activity of pancreatic lipase *in vitro* (Zhang et al., 2014). In addition, pharmacological experimental study has found that the inflammatory factors in cerebrospinalfluid of AD rats demonstrated a callback trend after treatment with HJD, indicated that HJD can ameliorate the central inflammatory status of AD rats by regulating the levels of inflammatory factors (Gu et al., 2018). The above experimental results showed that HJD possessed obvious beneficial effects in the treatment of DM and AD.

Four botanical drugs in this formula are used for clearing away heat and toxic materials for thousands of years. In order to compare the effects of HJD and its botanical drugs on C. albicans biofilm formationin *in vitro*, Wang et al. found that the inhibitory effects of Huangqin, Huangbo on C. albicans biofilm were close to that of HJD, and Huanglian was superior to the other agents, Zhizi had no evidently inhibitory effect. Studies have also shown that HJD has obvious protective effect on cerebral ischemia injury (Wang et al., 2008). Wang et al. evaluated the effect of HJD and its botanical drugs on rabbit platelet aggregation and found that the aggregation inhibition rate of HJD was higher than that of each single botanical drug, and in four botanical drugs of HJD the aggregation inhibition rate of Huanglian was higher than that of the other three botanical drugs (Wang et al., 2014). The above applications of "Jun, Chen, Zuo and Shi" of HJD show that the relationship among "Jun, Chen, Zuo and Shi" does exists and has quantitative basis in modern pharmacology and experimental scientific research. How to detect the action pattern and underlying mechanisms of "Jun, Chen, Zuo and Shi" at a systematic and global perspective is the key to understand the mechanisms of formulas in the treatment of complex diseases in TCM.

In this study, the compatibility rules of "Jun, Chen, Zuo and Shi" of HJD in the treatment of diseases are systematically interpreted. Specifically, our new system pharmacology strategy integrated three levels of data including the characteristics of each component in HJD single botanical drug, the characterization of component-target-protein (C-T-P) network in the whole protein-protein interaction (PPI) network and the characterization of intervention propagation properties of HJD in the treatment of different complex diseases. Overall, our study provides a comprehensive systems pharmacology framework to decode the principles of "Jun-Chen-Zuo-Shi" from multi-level perspective, which may give some enlightenment for the subsequent interpretation of key components and hidden mechanism of the formula.

MATERIALS AND METHODS

Chemical Components Collection

All chemical components of HJD and seven important pharmacological related descriptors (MW, ALOGP, HDON, HACC, CACO-2, OB (%) and DL) for each component were collected from Traditional Chinese Medicine Systems Pharmacology (TCMSP) database (Ru et al., 2014) (http://lsp.nwsuaf.edu.cn/tcmsp.php). The chemical identification and concentration of in HJD were collected from the previous reports (Yang et al., 2019). All chemical structures were prepared and converted into canonical SMILES using Open Babel Toolkit (version 2.4.1). The targets of HJD were predicted by using Similarity Ensemble Approach SEA (Keiser et al., 2007) (http://sea.bkslab.org/), hitpick (Liu et al., 2013) (http://mips.helmholtz-muenchen.de/proj/hitpick) and Swiss Target Prediction (David et al., 2014) (http://www.swisstargetprediction.ch/).

Active Components Screening

ADME properties of drugs refer to the Absorption, Distribution, Metabolism and Elimination, which are the key properties of whether small molecules of drugs can be used as medicines. It is estimated that due to low intestinal absorption rate and poor metabolic stability, the oral bioavailability of drugs is low, and finally about 50% of drugs fail in clinical trials (Beaumont et al., 2014). Therefore, ADME predictive screening of drugs is particularly important in drug discovery.

Oral bioavailability (OB) refers to the percentage of oral dose of drugs reaching the blood circulation system, which is the most common pharmacokinetic parameter for drug screening (Chiou, 2001). For specific oral drugs, due to poor intestinal absorption, drug metabolism, efflux and other reasons, the number of drugs that eventually reach the circulatory system is greatly reduced, so the oral availability of drugs ranges from 0 to 100%. As the initial absorption rates of intestinal tract and liver are generally about 43 and 44% respectively, components with OB greater than or equal to 30% are selected as active components.

Drug-like (DL) refers to a class of components that have the same functional group or similar physical characteristics as most known drugs (Han et al., 2011). The drug-like index of a new component is calculated based on Tanimoto similarity. According to the drug-like index, molecules with drug-like properties less than 0.14 are eliminated. Finally, the components screened according to OB and drug-like index take intersection as the active component (Wang et al., 2018).

Network Construction

The C-T-P network of HJD were constructed by using Cytoscape wsoftware (Version 3.7.0) (Lopes et al., 2010). The networks and topological parameters were analyzed using NetworkAnalyzer, which is a plugin of Cytoscape (de Jong et al., 2003). The PPI data were derived from public databases BioGRID, STRING, Dip, HPRD, Intact, Mint and Reactome (Guan et al., 2014).

Detection of Functional Communities Structure in HJD

Community structures in the biomedical network are more important for annotating the biological means. One index *codebook* and *n community codebooks* were defined to character the movements of random walker within and between communities respectively. Community codebook x has one codeword for each node $\alpha \in x$ and one exit codeword. The frequency at which random walkers visit each node in the community is the codeword length, $k_{\alpha \in x}$, and exits the community, $s_{x \curvearrowright}$. The was used to denote the sum of these frequencies, the total use of codewords in community x, and K^x to denote the normalized probability distribution. Consistent with the above, the index codebook has the community entries of codewords. The codeword lengths are derived from the set of frequencies at which the random walker enters each community. The was used to denote the sum of these frequencies, the total use of codewords to move into communities, and S to denote the

normalized probability distribution. We want to express average length of codewords from the index codebook and the community codebooks weighted by their rates of use. Therefore, the map equation is

$$L(\mathrm{N}) = s_{\curvearrowleft} H(S) + \sum_{x=1}^{n} k_{x\circlearrowright} H(k_x) \quad (1)$$

Next, we elaborate on the terms of the map equation in detail and illustrate it with Hoffman code examples.

$L(\mathrm{N})$ represents the per-step description length for community partition N. That is, for community partition N of n nodes into n communities, the lower bound of the average length of the code describing a step of the random walker.

$$s_{\curvearrowleft} = \sum_{x=1}^{n} s_{x\curvearrowleft} \quad (2)$$

The index codebook rate is used. The per-step use rate of the index codebook is given by the total probability that the random walker enters any of them communities. This variable represents the proportion of all codes representing community names in the codes. Where is probability of jumping out of community x.

$$H(S) = -\sum_{x=1}^{n} (s_{\curvearrowleft}/s_{x\curvearrowleft}) \log(s_{x\curvearrowleft}/s_{\curvearrowleft}) \quad (3)$$

This variable represents the average byte length required to encode community names. The frequency-weighted average length of codewords in the index codebook. The entropy of the relative rates to use the motif codebooks measures the smallest average codeword length that is theoretically possible. The heights of individual blocks under *Index codebook* correspond to the relative rates and the codeword lengths approximately correspond to the negative logarithm of the rates in base 2.

$$k_{x\circlearrowright} = \sum_{\alpha \in x} k_{\alpha} + s_{x\curvearrowright} \quad (4)$$

This variable represents the coding proportion of all nodes (including jump-out nodes) belonging to community x in the coding. The rate at which the community codebook x is used, which is given by the total probability that any node in the community is visited, plus the probability that the random walker exits the community and the exit codeword is used.

$$H(k^x) = -(s_{x\curvearrowright}/k_{x\circlearrowright}) \log(s_{x\curvearrowright}/k_{x\circlearrowright}) - \sum_{\alpha \in x} (k_a/k_{x\circlearrowright}) \log(k_a/k_{x\circlearrowright}) \quad (5)$$

This variable represents the average byte length required to encode all nodes in community x. The frequency-weighted average length of codewords in community codebook x. The entropy of the relative rates at which the random walker exits community x and visits each node in community x measures the smallest average codeword length that is theoretically possible. The heights of individual blocks under community codebooks correspond to the relative rates and the codeword lengths approximately correspond to the negative logarithm of the rates in base 2.

Propagation Coefficient Calculation

The role of drug response in the body is a complex process involving different proteins or genes. However, these proteins and genes are regulated by different cellular components, which constitute complex network relationships in the process of disease occurrence and development. These network relations could propagate the therapeutic effects through the network and orchestrate the cascade path of drug response. At present, most network pharmacological models just focus on the direct relationships between drugs and targets, and do not consider the propagation mode and propagation effect of drug intervention. In this study, we use Dijkstra model to detect the shortest distance from the direct target to the pathogenic gene based on C-T-P network, and keep the path with less than or equal to three nodes in the shortest distance. We believe that the initial node is the direct target of components, the final node is the pathogenic gene, which is also defined as the number of reached effector proteins, and the intermediate node is defined as the mode of propagation. Components with more modes of propagation and more effector proteins usually have better intervention effects. Based on the number of reached effector proteins and the mode of propagation, we calculated the propagation coefficient of each single botanical drug in HJD.

We defined the C-T-P network as the graph G (V, E), V and E represents nodes and edges, respectively (u, v) represents edge in E, $W_{u,v}$ stand for the weight of the edge. V is divided into two sets S and T, where the distance from the targets in S to U has been determined and the distance from the target to U contained in T has not been determined. Then, the distance from u to the target x in T is set as $d_{u,x}$, which is defined as the shortest path length from u to the target x in T. The specific formula is as follows:

1) At the beginning, S = {u}, T = V-{u}. For all targets x in t, if there is a path from u to x, then $d_{u,x} = w_{u,v}$; Otherwise, set $d_{u,x} = \infty$.
2) For all targets x in T, find the target T with smallest $d_{u,x}$, i.e.: $d_{u,t} = \min\{d_{u,x} | x \in T|\}$
   $d_{u,t}$ is the shortest distance from target t to effector proteins u. At the same time, target T is also the target closest to u among all targets in set T. Delete target t from T and merge it into S.
3) For all targets x adjacent to t in T, update the values of $d_{u,x}$ with the following formula:
   $d_{u,x} = \min\{d_{u,x}, d_{u,t} + w_{t,x}\}$
4) Continue the above steps until T is an empty set.

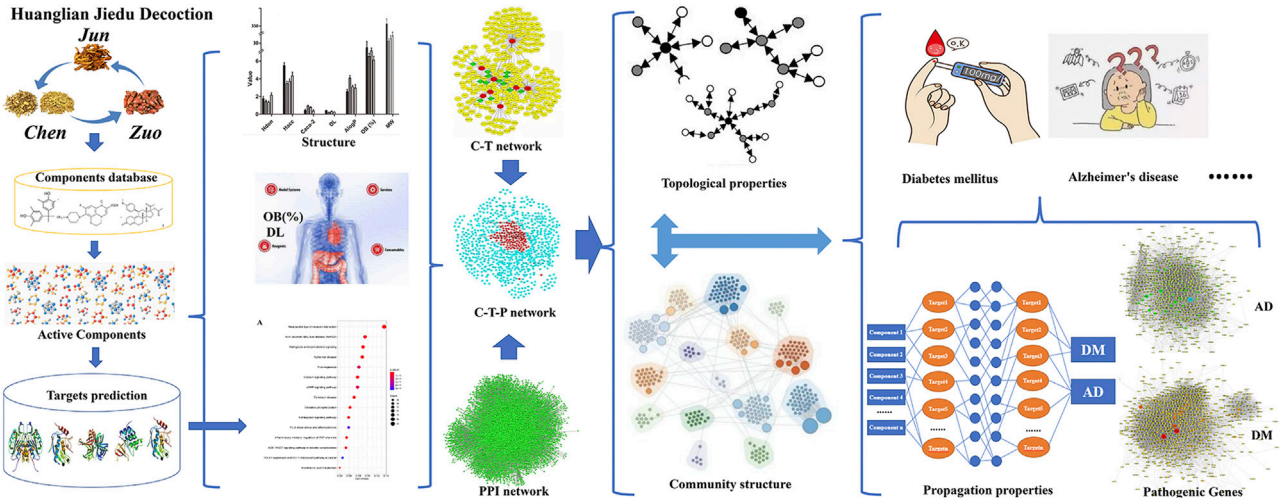

FIGURE 1 | A schematic diagram of network pharmacology-based strategy to decode the principles of "Jun-Chen-Zuo-Shi" in TCM.

5) During calculation of $d_{u,x}$ holding paths less than or equal to 3 nodes as the shortest distance dmin, in a path with three nodes, the first node mean components targets, the second node represent propagation modes, the third node represent effector proteins, the formula for calculating the propagation coefficient of each single botanical drug is:

$$PC_{(botanical\ drug)} = \frac{\sum_i^n dmin/n}{\sum_j^m u/m} \quad (6)$$

The propagation coefficient (PC) represents the strength of intervention ability of a botanical drug. The n represents the number of propagation modes, the m represents the number of effector proteins.

KEGG Pathway

To analyze the main function of botanical drugs in HJD, the latest pathway data were obtained from the Kyoto Encyclopedia of Genes and Genomes (KEGG) database (Draghici et al., 2007) were extracted for KEGG pathway enrichment analyses. *p*-values were set at 0.05 as the cut-off criterion. The results of analysis were annotated by Pathview (Luo and Brouwer, 2013) in the R Bioconductor package (https://www.bioconductor.org/).

Statistical Analysis

To compare the importance of communities in HJD, SPSS22.0 was used for statistical analysis. One-way analysis of variance followed by a Dunnett post-hoc test was used to compare more than two groups. Obtained *p*-values were corrected by Benjamini-Hochberg false discovery rate (FDR). Results were considered as statistically significant if the *p*-value was <0.05.

RESULTS

"Jun-Chen-Zuo-Shi" is one of the widely used compatibility principles of TCM in the treatment of diseases. However, there is still lack researches on the compatibility principle of "Jun-Chen-Zuo-Shi". In this study, we systematically analyze the compatibility principle and mechanism of HJD based on "Jun-Chen-Zuo-Shi" at three levels: the characteristics of each component in single botanical drug of HJD, including the physical and chemical properties of component, ADME properties and functional enrichment analysis of component targets; the characterization of C-T-P network in the whole PPI network, mainly including the characterization of degree and key communities in C-T-P network; the characterization of intervention propagation properties of HJD in the treatment of different complex diseases, mainly including target coverage of pathogenic genes and propagation coefficient of intervention effect between targets and pathogenic genes (**Figure 1**).

Comparison of Chemical Properties of Components

Physical and chemical properties of drugs directly affect the activity of drugs and play important roles in the druggability of TCM. In order to detect the importance of these physical and chemical properties in "Jun-Chen-Zuo-Shi", seven important pharmacologically related descriptors, MW, ALOGP, HDON, HACC, CACO-2, OB (%) and DL, were analyzed from four botanical drugs in HJD. Principal component analysis (PCA) widely used as a pattern recognition method to reflect the most primitive state of data in an unsupervised state. Here, PCA was applied to detect the distribution of the above physical and chemical properties of four botanical drugs in "Jun-Chen-Zuo-Shi". The results showed that Huangqin and Huangbo are closest

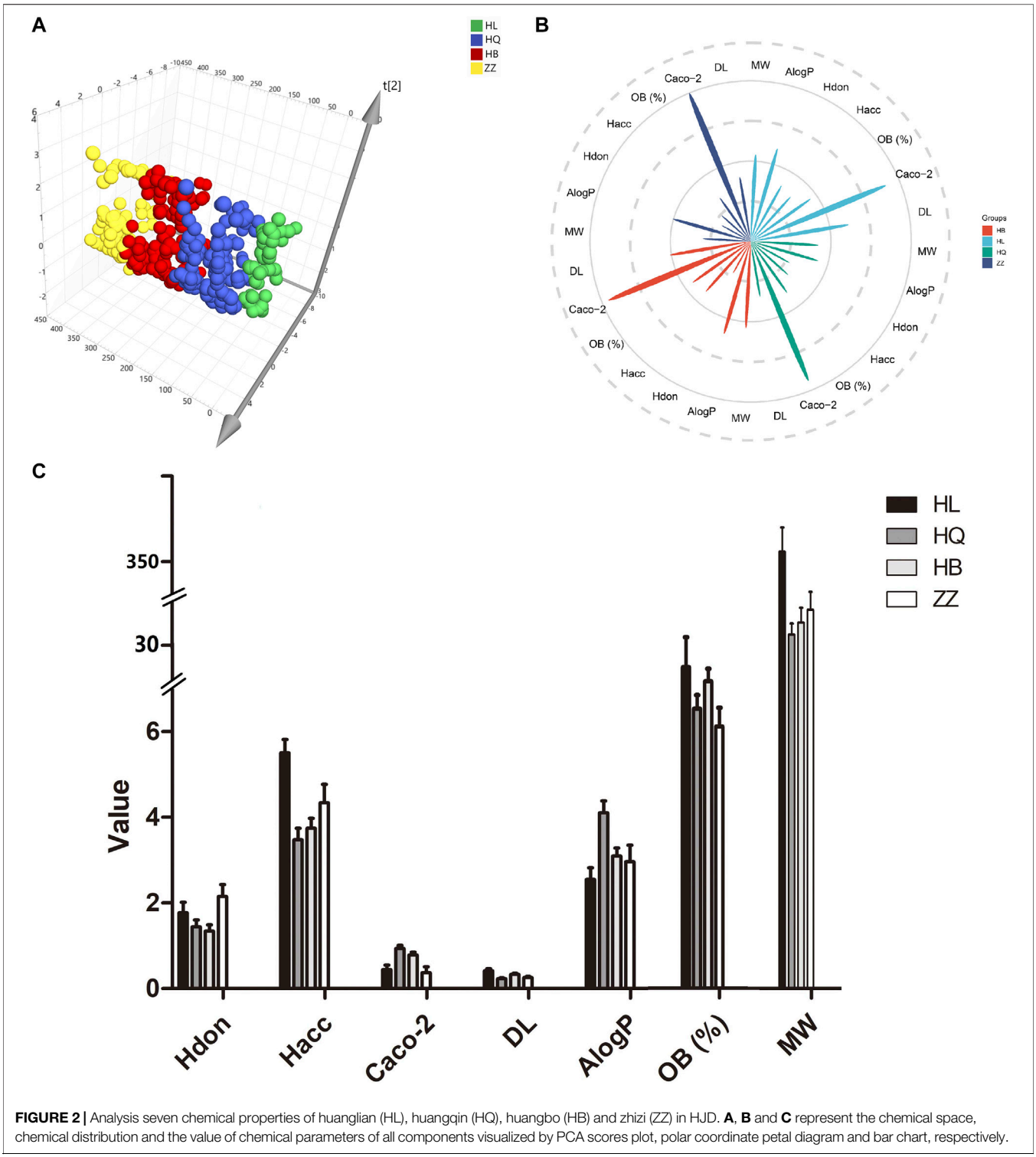

FIGURE 2 | Analysis seven chemical properties of huanglian (HL), huangqin (HQ), huangbo (HB) and zhizi (ZZ) in HJD. **A**, **B** and **C** represent the chemical space, chemical distribution and the value of chemical parameters of all components visualized by PCA scores plot, polar coordinate petal diagram and bar chart, respectively.

to Huanglian, indicating that their physical and chemical properties are close to Huanglian. Zhizi is farthest from Huanglian, which indicates that their physical and chemical properties are quite different in PCA scatter plot (**Figure 2A**). To further describe the specific differences among the four botanical drugs, we have made a detailed analysis of the seven parameters. As shown in **Figures 2B,C**, 1) For MW, the average value of all components in huanglian (342.2) is higher than that of huangqin (277.7), huangbo (287) and zhizi (297). 2) For bioavailability, the average OB value (%) of huanglian (36.09) is also higher than that of huangqin (31.42), huangbo (34.51) and zhizi (29.43). (3) For permeability, the average Caco-2 value of

TABLE 1 | The information on chemical analysis of the botanical drugs from the literature in HJD.

Formula	Method	Component	Concentration (mg/g)	Ref
Huanglian Jiedu decoction (HJD)	HPLC	Phellodendrine	3.8276 ± 0.1158	(Yang et al., 2019)
		Heriguard	1.0800 ± 0.0261	
		Magnoflorine	6.7489 ± 0.0450	
		Geniposide	72.3830 ± 1.0948	
		Coptisine	14.0580 ± 0.1631	
		Epiberberine	8.9056 ± 0.0864	
		Jatrorrizine	9.4028 ± 0.0966	
		Berberine	53.0820 ± 0.5443	
		Palmatine	19.6820 ± 0.1452	
		Baicalin	18.5770 ± 0.0927	
		Oroxindin	17.5360 ± 0.2370	
		Wogonin	2.1689 ± 0.3488	
		Oroxylin A	0.2618 ± 0.0212	

huanglian (0.4423) is lower than that of huangqin (0.9371) and huangbo (0.7851). (4) For DL, like MW and OB, huanglian possessed higher average DL value (0.4165), that is very different from that of huangqin (0.2301), huangbo (0.3303) and zhizi (0.258). (5) Compared with the all components of huanglian (2.551), the ALogP value of huangqin (4.101), huangbo (3.096) and zhizi (2.964) exhibited siginifically higher average ALogP values, which indicates the majority components in huangqin, huangbo and zhizi are hydrotropic, but that in huanglian are hydrophobic. (6) The values of nHAcc in huanglian (5.5) are all higher than those in others (3.476, 3.743, 4.337, respectively). The above analysis results show that the chemical properties of the four botanical drugs are obviously different. Therefore, we can speculate that each botanical drug plays a different role in the compatibility of this TCM. The Jun botanical drug huanglian is distinguished based on the compatibility principle of "Jun-Chen-Zuo-Shi", and has good performance in most physical and chemical properties such as OB (%), DL and MW, which indicated that it may play a leading role at the functional level.

Chemical Analysis in HJD

Chemical analysis plays an important role in the study of the substances basis and mechanism of botanical drugs in the formula. The information on specific chemical identification and concentration of the botanical drugs in HJD were collected by searching from the literature (Yang et al., 2019). The detailed information was shown in **Table 1**. The results suggest that the chemical components of botanical drugs and the concentration of identified components provide an experiment-aided chemical space for the search of active components. This will provide valuable reference for further analysis.

Comparison of Active Components

TCM formula contains a large number of chemical molecules, the traditional methods of exploring the active components in TCM are mainly based on the separation, purification and structure analysis of mass spectrometry (MS) and high-performance liquid chromatography (HPLC). These methods supplied quantitative concentration of components, however, these experiment-based methods cost a lot of manpower, material and financial resources to excavate the effective components in TCM. Therefore, it is particularly important to analyze, explore and optimize the TCM formula by calculating ADME properties, which could be helpful to screen the potential active components of TCM, and further optimize the TCM formula, improve the research and development of new drugs from TCM. In this study, botanical drug components were evaluated by using the two representative ADME parameters, oral bioavailability (OB) and drug-like (DL), to screen the active components of TCM formula.

Our statistic results show that 26.81% (94) of the components in HJD meet OB ≥ 30% and DL ≥ 0.14 (**Table 2**). Specifically, 31.25% of the components in Huanglian satisfy OB ≥ 30% and DL ≥ 0.14. These components are regarded as the active components in Huanglian, which included berberine, coptisine, epiberberine, and palmatine, etc. Studies have shown that berberine could significantly reduce hyperglycemia and glycogen content in liver of diabetic mice, increase the expression of Akt and IRS, and inhibit the expression of GSK-3β (Xie et al., 2011). It has been reported that berberine can reduce the release of neuroamyloid through PI3K/Akt/GSK3 pathway, decrease the number of senile plaques in the brain of AD mice model, and play a therapeutic role in AD (Durairajan et al., 2012). Zhai et al. has reported that coptisine could improve oxidative renal injury in diabetic rats, and the potential mechanisms may be associated to activation of the Nrf2 signaling pathway (Zhai et al., 2019). Jung et al. found that epiberberine has a strong potential of inhibition and prevention of AD mainly through ChEs and beta-amyloids pathways, and additionally through antioxidant capacities (Jung et al., 2009). Previous pharmacological studies have shown that palmatine treatment can alleviate the hyperalgesia, allodynia and depressive behaviors of rats with comorbidity of diabetic neuropathic pain and depression (Shen et al., 2018). 27.27% of the components in Huangqin meet OB ≥ 30% and DL ≥ 0.14, including most common active components such as coptisine, epiberberine, wogonin, and oroxylin A, etc. Khan et al. (2016) found that wogonin administration could suppress hyperglycemia, improve cardiac function, and mitigate cardiac fibrosis in STZ-induced diabetic mice. 29.28% of the molecules in Huangbo meet OB ≥ 30% and DL ≥ 0.14, a total of 41 components meet the threshold selection criteria, such

TABLE 2 | Components in HJD for further analysis after ADME screening.

No	Component	OB (%)	DL	botanical drug	No	Component	OB (%)	DL	botanical drug
HJD1	Quercetin	46.43	0.28	Huanglian Jun	HJD58	Magnograndiolide	63.71	0.19	Huangbo Chen
HJD2	Magnograndiolide	63.71	0.19	Huanglian Jun	HJD59	Oleic acid	33.13	0.14	Huangbo Chen
HJD3	Palmidin A	35.36	0.65	Huanglian Jun	HJD60	Palmidin A	35.36	0.65	Huangbo Chen
HJD4	Corchoroside A_qt	104.95	0.78	Huanglian Jun	HJD61	phellamurin_qt	56.6	0.39	Huangbo Chen
HJD5	Obacunone	43.29	0.77	Huanglian Jun	HJD62	Poriferast-5-en-3beta-ol	36.91	0.75	Huangbo Chen
HJD6	Palmatine	64.6	0.65	Huanglian Jun	HJD63	Kihadalactone A	34.21	0.82	Huangbo Chen
HJD7	Berberine	36.86	0.78	Huanglian Jun	HJD64	Phellavin_qt	35.86	0.44	Huangbo Chen
HJD8	Coptisine	30.67	0.86	Huanglian Jun	HJD65	Delta 7-stigmastenol	37.42	0.75	Huangbo Chen
HJD9	Fagarine	72.23	0.15	Huanglian Jun	HJD66	Phellopterin	40.19	0.28	Huangbo Chen
HJD10	Worenine	45.83	0.87	Huanglian Jun	HJD67	Dehydrotanshinone II A	43.76	0.4	Huangbo Chen
HJD11	Berberrubine	35.74	0.73	Huanglian Jun	HJD68	Dihydroniloticin	36.43	0.81	Huangbo Chen
HJD12	Epiberberine	43.09	0.78	Huanglian Jun	HJD69	Kihadanin A	31.6	0.7	Huangbo Chen
HJD13	(R)-Canadine	55.37	0.77	Huanglian Jun	HJD70	Niloticin	41.41	0.82	Huangbo Chen
HJD14	Berlambine	36.68	0.82	Huanglian Jun	HJD71	Chelerythrine	34.18	0.78	Huangbo Chen
HJD15	Moupinamide	86.71	0.26	Huanglian Jun	HJD72	Candletoxin A	31.81	0.69	Huangbo Chen
HJD16	Ent-Epicatechin	48.96	0.24	Huangqin Chen	HJD73	Hericenone H	39	0.63	Huangbo Chen
HJD17	EIC	41.9	0.14	Huangqin Chen	HJD74	Hispidone	36.18	0.83	Huangbo Chen
HJD18	Wogonin	30.68	0.23	Huangqin Chen	HJD75	Campesterol	37.58	0.71	Huangbo Chen
HJD19	(2 R)-7-hydroxy-5-methoxy-2-phenylchroman-4-one	55.23	0.2	Huangqin Chen	HJD76	Melianone	40.53	0.78	Huangbo Chen
HJD20	Beta-sitosterol	36.91	0.75	Huangqin Chen	HJD77	Phellochin	35.41	0.82	Huangbo Chen
HJD21	Sitosterol	36.91	0.75	Huangqin Chen	HJD78	Obacunone	43.29	0.77	Huangbo Chen
HJD22	Stigmasterol	43.83	0.76	Huangqin Chen	HJD79	Palmatine	64.6	0.65	Huangbo Chen
HJD23	Norwogonin	39.4	0.21	Huangqin Chen	HJD80	Fumarine	59.26	0.83	Huangbo Chen
HJD24	5,2′-dihydroxy-6,7,8-trimethoxyflavone	31.71	0.35	Huangqin Chen	HJD81	Isocorypalmine	35.77	0.59	Huangbo Chen
HJD25	Coptisine	30.67	0.86	Huangqin Chen	HJD82	Berberine	36.86	0.78	Huangbo Chen
HJD26	Supraene	33.55	0.42	Huangqin Chen	HJD83	(S)-Canadine	53.83	0.77	Huangbo Chen
HJD27	Acacetin	34.97	0.24	Huangqin Chen	HJD84	Coptisine	30.67	0.86	Huangbo Chen
HJD28	Methyl linolelaidate	41.93	0.17	Huangqin Chen	HJD85	N-Methylflindersine	32.36	0.18	Huangbo Chen
HJD29	Baicalein	33.52	0.21	Huangqin Chen	HJD86	delta7-dehydrosophoramine	54.45	0.25	Huangbo Chen
HJD30	Diop	43.59	0.39	Huangqin Chen	HJD87	Rutaecarpine	40.3	0.6	Huangbo Chen
HJD31	Epiberberine	43.09	0.78	Huangqin Chen	HJD88	Skimmianin	40.14	0.2	Huangbo Chen
HJD32	5,7,2,5-Tetrahydroxy-8,6-dimethoxyflavone	33.82	0.45	Huangqin Chen	HJD89	Fagarine	72.23	0.15	Huangbo Chen
HJD33	Carthamidin	41.15	0.24	Huangqin Chen	HJD90	Worenine	45.83	0.87	Huangbo Chen
HJD34	2,6,2′,4′-tetrahydroxy-6′-methoxychaleone	69.04	0.22	Huangqin Chen	HJD91	Cavidine	35.64	0.81	Huangbo Chen
HJD35	Dihydrobaicalin_qt	40.04	0.21	Huangqin Chen	HJD92	Berberrubine	35.74	0.73	Huangbo Chen
HJD36	Eriodyctiol (flavanone)	41.35	0.24	Huangqin Chen	HJD93	Ptelein	72.44	0.15	Huangbo Chen
HJD37	Salvigenin	49.07	0.33	Huangqin Chen	HJD94	Thalifendine	44.41	0.73	Huangbo Chen
HJD38	5,2′,6′-trihydroxy-7,8-dimethoxyflavone	45.05	0.33	Huangqin Chen	HJD95	Quercetin	46.43	0.28	Zhizi Zuo
HJD39	5,7,2′,6′-tetrahydroxyflavone	37.01	0.24	Huangqin Chen	HJD96	EIC	41.9	0.14	Zhizi Zuo
HJD40	Dihydrooroxylin A	38.72	0.23	Huangqin Chen	HJD97	Beta-sitosterol	36.91	0.75	Zhizi Zuo
HJD41	Skullcapflavone II	69.51	0.44	Huangqin Chen	HJD98	Kaempferol	41.88	0.24	Zhizi Zuo
HJD42	Oroxylin a	41.37	0.23	Huangqin Chen	HJD99	Stigmasterol	43.83	0.76	Zhizi Zuo
HJD43	Panicolin	76.26	0.29	Huangqin Chen	HJD100	Oleic acid	33.13	0.14	Zhizi Zuo
HJD44	5,7,4′-trihydroxy-8-methoxyflavone	36.56	0.27	Huangqin Chen	HJD101	Crocetin	35.3	0.26	Zhizi Zuo
HJD45	NEOBAICALEIN	104.34	0.44	Huangqin Chen	HJD102	Mandenol	42	0.19	Zhizi Zuo
HJD46	DIHYDROOROXYLIN	66.06	0.23	Huangqin Chen	HJD103	Supraene	33.55	0.42	Zhizi Zuo
HJD47	Moslosooflavone	44.09	0.25	Huangqin Chen	HJD104	METHYL LINOLEATE	41.93	0.17	Zhizi Zuo

(Continued on following page)

TABLE 2 | (*Continued*) Components in HJD for further analysis after ADME screening.

No	Component	OB (%)	DL	botanical drug		No	Component	OB (%)	DL	botanical drug	
HJD48	11,13-Eicosadienoic acid, methyl ester	39.28	0.23	Huangqin	Chen	HJD105	(4aS,6 aR,6aS,6bR,8 aR,10R,12 aR,14bS)-10-hydroxy-2,2,6a,6b,9,9,12a-heptamethyl-1,3,4,5,6,6a,7,8,8a,10,11,12,13,14 b-tetradecahydropicene-4a-carboxylic acid	32.03	0.76	Zhizi	Zuo
HJD49	Linolenic acid methyl ester	46.15	0.17	Huangqin	Chen	HJD106	Methyl vaccenate	31.9	0.17	Zhizi	Zuo
HJD50	5,7,4′-trihydroxy-6-methoxyflavanone	36.63	0.27	Huangqin	Chen	HJD107	Ammidin	34.55	0.22	Zhizi	Zuo
HJD51	5,7,4′-trihydroxy-8-methoxyflavanone	74.24	0.26	Huangqin	Chen	HJD108	Isoimperatorin	45.46	0.23	Zhizi	Zuo
HJD52	Rivularin	37.94	0.37	Huangqin	Chen	HJD109	Exceparl M-OL	31.9	0.16	Zhizi	Zuo
HJD53	bis [(2 S)-2-ethylhexyl] benzene-1,2-dicarboxylate	43.59	0.35	Huangqin	Chen	HJD110	Ethyl oleate (NF)	32.4	0.19	Zhizi	Zuo
HJD54	5,8,2′-trihydroxy-7-methoxyflavone	37.01	0.27	Huangqin	Chen	HJD111	5-Hydroxy-7-methoxy-2-(3,4,5-trimethoxyphenyl) chromone	51.96	0.41	Zhizi	Zuo
HJD55	Quercetin	46.43	0.28	Huangbo	Chen	HJD112	3-Methylkempferol	60.16	0.26	Zhizi	Zuo
HJD56	Beta-sitosterol	36.91	0.75	Huangbo	Chen	HJD113	GBGB	45.58	0.83	Zhizi	Zuo
HJD57	Stigmasterol	43.83	0.76	Huangbo	Chen	HJD114	Sudan III	84.07	0.59	Zhizi	Zuo

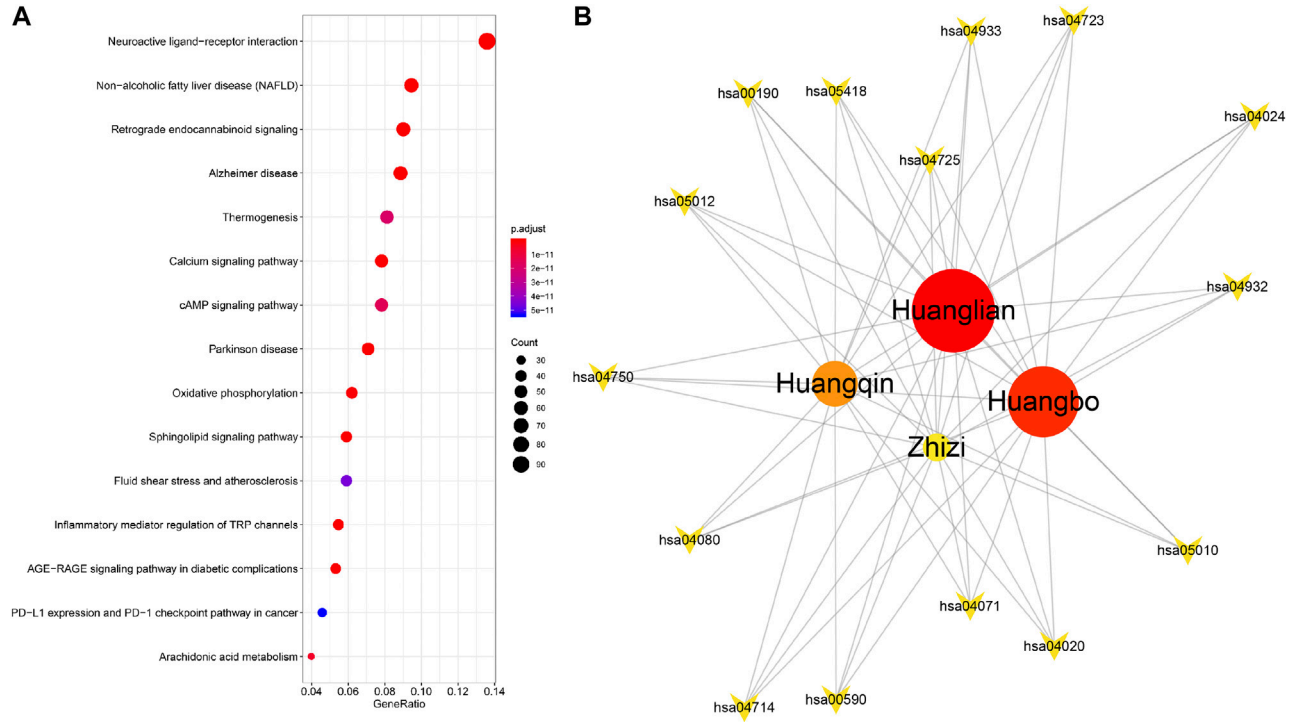

FIGURE 3 | Gene enrichment analysis of all targets from HJD **(A)**. botanical drug-pathway network of HJD **(B)**. The circle nodes represent botanical drugs, and the inverted triangle represents the top 15 pathways of HJD. The size and color of the node represents the importance of the herbal regulation pathway.

as coptisine, berberine, and palmatine, etc. Only 20.41% of the molecules in Zhizi meet OB ≥ 30% and DL ≥ 0.14, including oleic acid, kaempferol and mandenol, etc. The above results suggest that the number of active components retained by Huanglian are the highest compared with those before screening. This shows that more components in Huanglian have better OB and DL properties, and indicates that these components may play a major therapeutic role in the treatment disease. Huangqin and Huangbo have the second highest proportion of active components, and have more overlapping components with Huanglian, which intimates that Huangqin and Huangbo can assist and enhance therapeutic effect of Huanglian. In HJD, Zhizi is the Zuo botanical drug with the lowest content of active components, indicating that it may have auxiliary effect on Jun botanical drugs and/or Chen botanical drugs.

Coverage Rate Based on Functional Pathway

Most complex diseases are not caused by a single pathological change, but a series of physiological reactions caused by abnormal pathways due to disorder of multiple proteins or genes in the cell. In order to further explore the "Jun-Chen-Zuo-Shi" compatibility principle of HJD at the potential molecular mechanism level, we evaluated it through the functional pathway enrichment analysis based on KEGG (**Figure 3A**). Previous reports confirm that HJD has significant therapeutic effects on Alzheimer's disease (AD), Parkinson's disease (PD) and diabetes mellitus (DM) etc. The top 15 enriched pathways were selected for further analysis. The targets of each botanical drug in HJD was mapped to the enriched genes involved in these 15 enriched pathways for enrichment analysis. It was found that 40.54, 33.14, 38.10, and 29.69% of the targets in the Jun (Huanglian), Chen (Huangqin and Huangbo) and Zuo (Zhizi) botanical drug were enriched in the top 15 enriched pathways, respectively (**Figure 3B**). The above analysis show that Huanglian has a higher target contribution rate among all the genes enriched in the top 15 functional pathways, which means that targets of Huanglian could play primary therapeutic roles in the treatment of disease, and the target contribution rate of Chen botanical drugs is slightly lower, which indicates that the relatively low target utilization rate may play a role in assisting Jun botanical drug in the treatment process. Zuo botanical drug have the lowest target contribution rate, indicating that the ability of therapeutic role in the treatment of diseases is slightly weak, and may play an auxiliary role in other aspects. The above results once again confirm the major functional role of the Jun botanical drug Huanglian, the auxiliary effects of the Chen botanical drugs Huangqin and Huangbo, and the supplementary effects of the Zuo botanical drug Zhizi in the functional level of HJD.

C-T-P Network Construction and Analysis

In the process of treating complex diseases, TCM formula usually acts in the form of multi-component and multi-target. These components and targets form the most direct target-protein network, which can reflect some therapeutic effects but cannot reflect the propagation mode of this therapeutic effect. More and

more evidences show that the therapeutic effect of drugs on diseases can be propagated through PPI (Andras et al., 2013). Hormozdiari et al. proposed that identified potential multiple-drug targets in pathogenic PPI networks can help us to better discover the therapeutic effect of drugs (Hormozdiari et al., 2010). Chu et al. applied a nonlinear stochastic model and maximum likelihood parameter estimation to identify the cancer-perturbed PPI involved in apoptosis and to identify potential molecular targets for the development of anti-cancer drugs (Chu and Chen, 2008). How to characterize this propagation effect has not been systematically reported.

In this study, we first constructed the C-T network of HJD, then integrated multiple PPI data to construct a comprehensive PPI network. C-T network and PPI networks were integrated as the C-T-P network. By analyzing the C-T-P network, comprehensive information can be obtained and intricate relationships that manage cellular activities can be revealed. In a network, the number of nodes directly interacting with a node is called degree. Several reports have confirmed that the greater the degree, the more biological functions it participates in, and the stronger its biological importance. Under this concept, we made further analysis of C-T-P network. Our results show that the targets of Jun botanical drug Huanglian has the highest average degree 131.75 in C-T-P network. It indicates that these targets affect more proteins in the C-T-P network and have the possibility to play more important roles. By comparative analysis, we found that the degree of huangqin and huanngbo in C-T-P network are 102.46 and 110.33, respectively. The degree of targets of Huangqin and Huangbo are relatively smaller, which indicate that the number of target protein is not as high as that of Jun botanical drug and may play a supplementary role. Zhizi has the lowest average degree 101.42, while indicates that the number of targeted proteins is smallest, and together with Chen botanical drugs to assist the Jun botanical drug.

Functional Communities Structure Predication and Analysis

In complex life activities such as diseases, development, and drug intervention, etc, a plurality of genes, proteins, and other constituent components in cells are involved, and these genes, proteins, and components form a complex regulation network in cells. In the process of drug intervention, drugs play an intervention regulatory role on the complex network by targeting specific proteins. This intervened regulation and intracellular gene regulation network form a drug-target-pathway complex network at the molecular level. Further research found that the neighbors of drug responding genes in the network tend to be related to the same or similar intervention responses (Li and Zhan, 2006; Zhang et al., 2014).

Genes with the same drug response are often functionally related and form biological network communities (Tari et al., 2005). At the molecular level, the community can be considered as a group of genes, proteins or metabolites that are functionally related, physically interact or jointly response to drug. The molecules in these communities usually jointed together to drive a biological process or respond to the treatment of drugs (Tripathi et al., 2019). For drug intervention in complex diseases, single gene analysis cannot effectively consider the cooperative relationship among genes, and is difficult to explain its biological mechanism. However, community-based analysis can identify response gene sets with cooperative relationships. Revealing the functions of these simple network modules at the molecular level is the key step for understanding the drug response regulation mechanism of more complex networks and even for understanding the mechanism of drug treatment.

In this study, we construct the C-T-P network by integrating C-T network of HJD and PPI network. This extremely complex C-T-P network with 12,324 nodes and 84,138 interactions is difficult to clarify drug MOA, so discovery of functional communities in the C-T-P network is very important for understanding the organization and function units of the HJD under the concept of the compatibility principle "Jun-Chen-Zuo-Shi". The extraction of these community structures can reduce the dimension of complex networks and could be considered as the key factor for further clarify the compatibility principle of HJD's "Jun-Chen-Zuo-Shi", we identify the functional communities in the C-T-P network based on the information graph algorithm combining random walk theory and huffman encoding. The algorithm performs to optimize the discovery of communities in C-T network heuristically by using a reasonable global metric. The results show that 8 significant functional communities are found in the C-T-P network (**Figure 4A**). In order to determine whether communities found in HJD can represent their complete C-T network. We evaluate the importance of communities at the gene functional level based on enrichment pathway analysis. The analysis results showed that genes enriched pathways of HJD communities accounts for 93.4% of genes enriched pathways of the full C-T network in HJD (**Figure 4B**), which indicated that the enriched pathways of genes involved in communities of HJD are highly compatible with enriched pathways of genes in C-T network. Further analysis of the components identified by these functional communities shows that 93.33, 87.5, 84.62, and 75% of the components in the Jun botanical drug Huanglian is covered by functional communities, which once again indicates that Huanglian plays a leading role in the function of C-T-P network (**Figure 5**).

Coverage Rate Based on Pathogenic Genes

In order to better explore how HJD exerts its therapeutic effect based on the compatibility principle of "Jun-Chen-Zuo-Shi", DM and AD were selected for further evaluation. Both of two diseases have been reported with significant therapeutic effects of HJD. Pathogenic genes of both diseases were collected from GeneCards database (Safran et al., 2010). PPI data of both diseases were extracted from STRING database (Szklarczyk et al., 2019). The weighted gene reulatory network of disease was constructed by mapping pathogenic genes to PPI data, the weight was assigned by using relevance scores in GeneCards database (**Figure 6A,B**; **Supplementary Table S1**). The relevance score of genes in GeneCards takes into account three aspects: the frequency of the term in the disease related document would raises the score, while the frequency of the term in disease related documents across the site would lower the score, and the size of the subfield

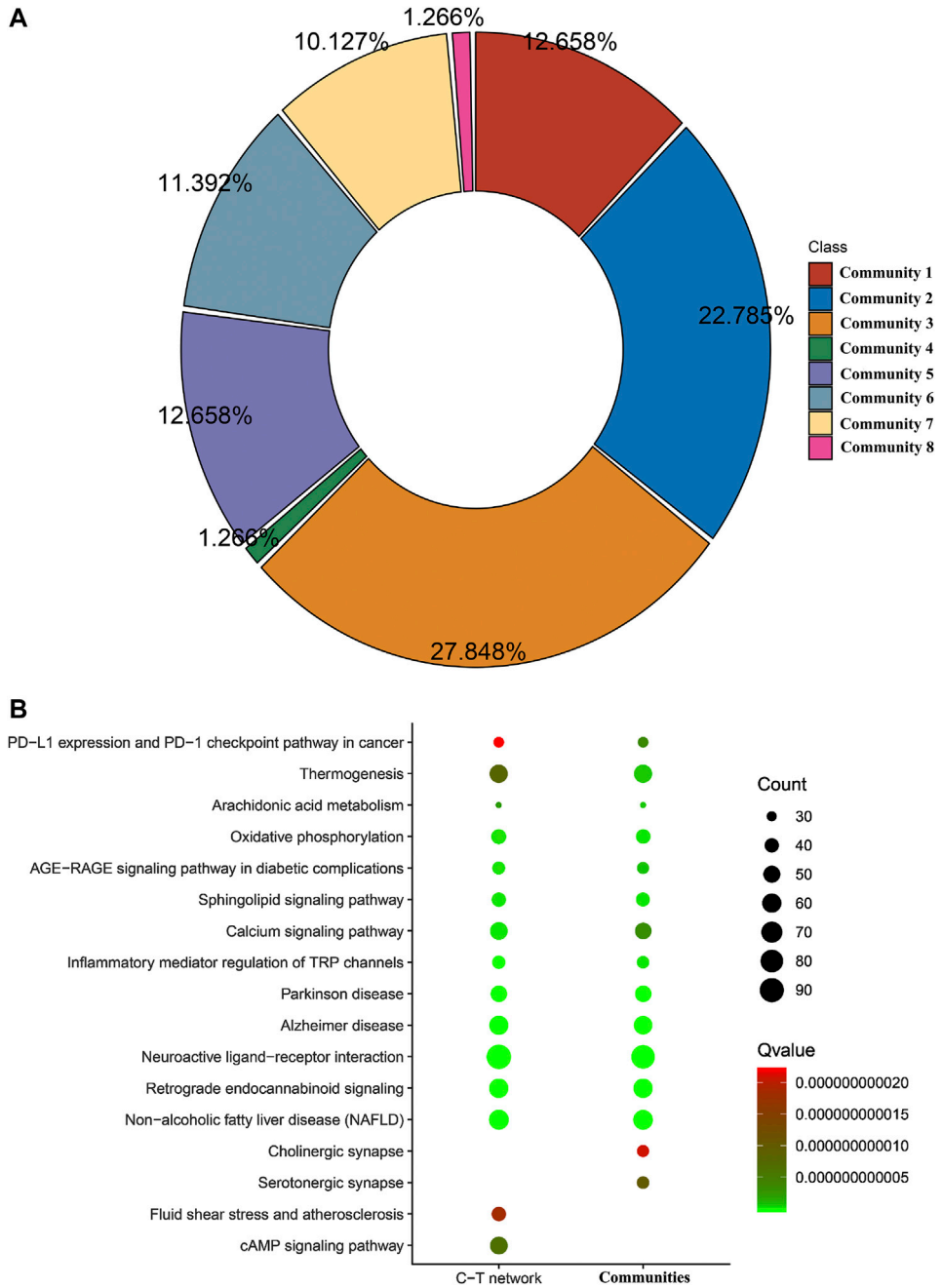

FIGURE 4 | The predicated communities of C-T-P network of HJD **(A)**. Different color represents different communities. The functional similarity analysis between C-T-P network and communities in HJD **(B)**.

containing the term, if the term appears in a smaller field, such as gene name, the score would be increased (Stelzer et al., 2016). This indicates that the higher the relevance score, the more important that the genes are involved in pathogenesis of the disease. For further analyzed the "Jun-Chen-Zuo-Shi" compatibility principle of HJD, we design a pipeline to capture the role of each botanical drug in HJD based on botanical drug targets and their associated pathogenic genes. Firstly, we get common gene datasets by overlapping pathogenic genes of each diseases and component targets of each botanical drug, and then analyze the average relevance score of the common gene datasets, then we calculate the possession rate by compare the common gene datasets to targets genes of each botanical drug in HJD. For DM, 87.91% of the targets in the Jun botanical drug Huanglian overlap with the pathogenic genes with an average relevance score of 6.91, 80.67% and 81.41% of the targets in the

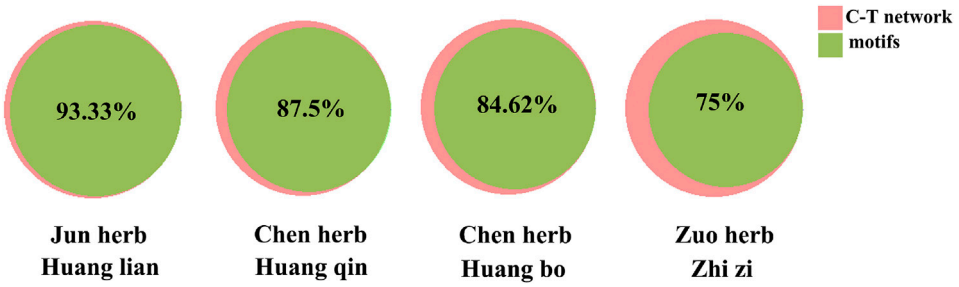

FIGURE 5 | Venn diagram was used to visualize the overlap number between C-T-P network and communities in HJD, the pink represents the C-T-P network, and the green represents communities.

Chen botanical drugs Huangqin and Huangbo overlap with the pathogenic genes with average relevance scores of 5.44 and 6.13, and 82.93% of the targets in the Zuo botanical drug Zhizi overlap with the pathogenic genes with an average relevance score of 6.51. For AD, 73.08% of the targets in the Jun botanical drug Huanglian overlap with the disease genes with an average relevance score of 12.55, 65.83 and 67.80% of the targets in the Chen botanical drugs Huangqin and Huangbo overlap with the pathogenic genes with average relevance scores of 9.74 and 10.52, and 66.11% of the targets in the Zuo botanical drug Zhizi overlap with the pathogenic genes with an average relevance score of 11.02 (**Figure 6**). The above results show that the Jun botanical drug Huanglian has the highest possession rate and average relevance score, which indicate that Huanglian acts on as many important targets as possible in pathogenic genes.

Calculation and Analysis of Propagation Coefficient

The interactions between genes or proteins in cells form complex biological networks. Molecular interactions in biological networks have dynamic and spatiotemporal specific features. At present, protein interaction network and drug regulatory network can only provide static interaction information. In the function analysis of drug targets and pathogenetic genes, the dynamic characteristics of molecular interactions are more significant than static characteristics for understanding the MOA and propagation features of drug intervention in the disease networks. In order to analyze and understand the propagation characteristics of drugs in the disease network more effectively, this study proposed an important monitor which named as propagation coefficient to characterize the drug response network-propagation characteristics by integrating the data of botanical drug targets, PPI, and pathogenic genes. The propagation coefficient contains propagation modes and effector proteins, which could be used to indicate the propagation power of drug. Based on the novel calculate method, the propagation coefficient of single botanical drug in HJD is analyzed, and the scientific basis of the compatibility rule of "Jun-Chen-Zuo-Shi" is revealed from the perspective of propagation characteristics.

The propagation coefficient value of each botanical drug in HJD is calculated and showed in **Figure 7**. According to the calculation results, for DM and AD, the Huanglian with a propagation coefficient of 72.62 and 67.05, the Huangbo with a propagation coefficient of 63.69 and 59.30, the Huangqin with a propagation coefficient of 59.55 and 55.54, and the Zhizi with a propagation coefficient of 59.10 and 54.87, respectively. From the above analysis, Huanglian has highest propagation coefficient both in DM and AD, the propagation coefficient of Haungqin and Huangbo is lower than Huanglian and Zhizi has the lowest propagation coefficient, which indicate that Huanglian plays a major role in disease treatment by spreading the intervention effect at a more powerful level, and Chen botanical drugs and Zuo botanical drugs play a role in assisting Huanglian. This once again confirmed the compatibility rules of "Jun-Chen-Zuo-Shi" in HJD at quantitative level.

Experimental Evaluation

In order to further explore the accuracy and reliability of the above strategies for analyzing the compatibility rules of HJD "Jun-Chen-Zuo-Shi," components absorbed into blood were used to validate our strategy. In the study of complex components system of TCM, it is generally believed that the components which can be absorbed into blood are the active components with therapeutic effect. Analysis of the components in blood after oral administration of TCM is an effective and accurate way to study the substance basis of drug effect of TCM. The absorbed components in rat plasma after oral administration of HJD were collected from the previous reports (Zuo et al., 2014). A total of 22 prototype components were obtained, the detailed information was shown in **Supplementary Table S2**.

For the components obtained by functional communities structure prediction and active components screening in the above strategy, 26.67% of the predicted components in the Jun botanical drug of Huanglian overlap with the components were absorbed into blood; 10.26 and 7.5% of the predicted components in the Chen botanical drugs Huangqin and Huangbo overlap with

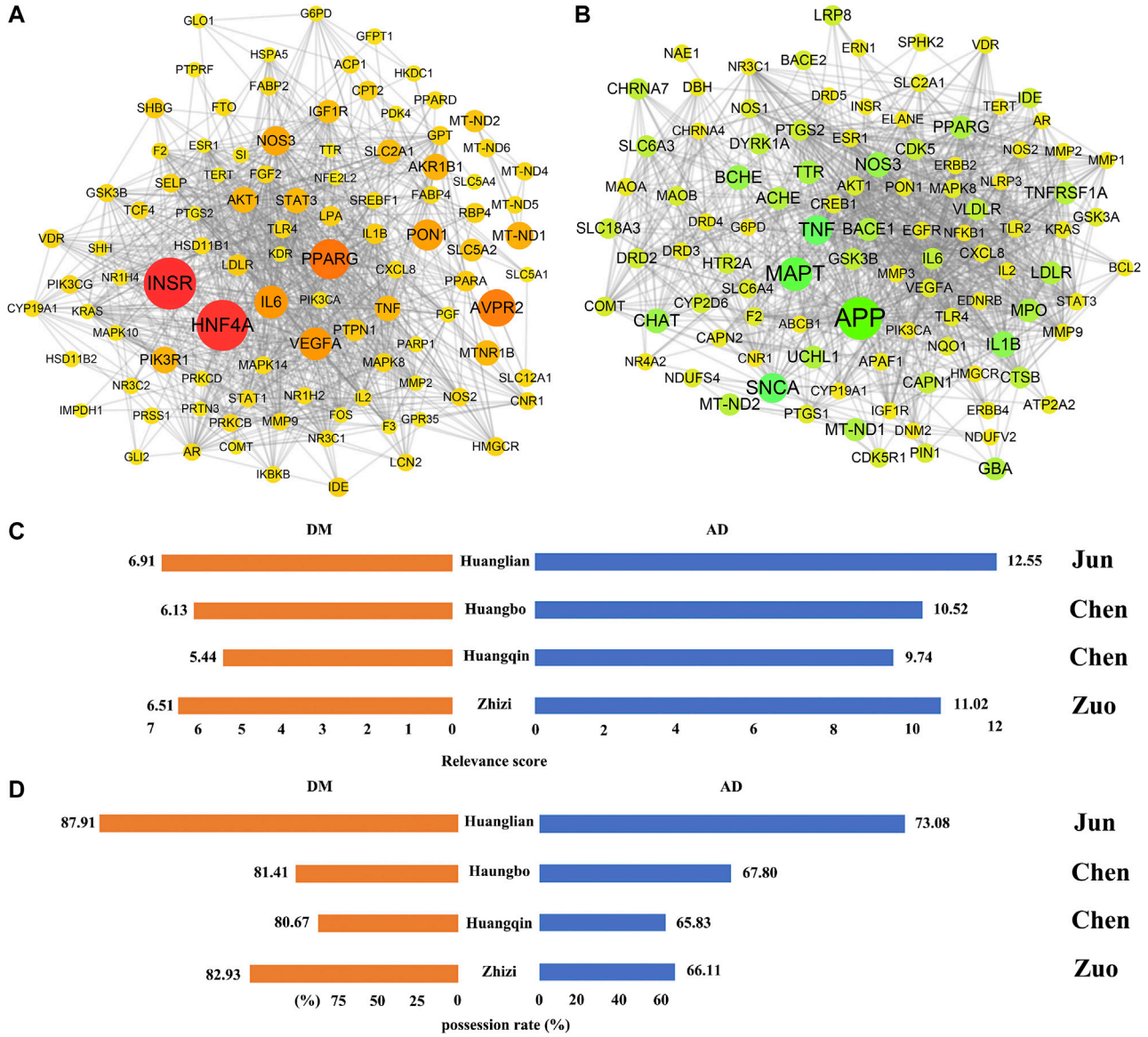

FIGURE 6 | The disease weight gene regulatory network of diabetes mellitus **(A)** and alzheimer's disease **(B)**. The size and color of the node represents the relevance score of herbal therapeutic targets. The bar chart represents the average relevance score **(C)** and possession rate **(D)** of overlap of botanical drug targets and pathogenic genes.

the components were absorbed into blood. There is no overlap between the predicted components and the components were absorbed into blood in the Zuo botanical drug Zhizi. The above results indicate that the proportion of components in Jun botanical drug were absorbed into blood is higher, followed by Chen botanical drugs, which confirm the accuracy and reliable of our analysis strategy. Meanwhile, the results once again confirm the important role of the Jun botanical drug Huanglian through a higher absorbed into blood rate, the auxiliary effects of the Chen botanical drugs Huangqin and Huangbo, and the supplementary effects of the Zuo botanical drug Zhizi.

DISCUSSION

TCM usually exerts its efficacy in the form of formula, which is not only a simple combination of botanical drugs, but follows reasonable compatibility principles to treat complex diseases (Sucher, 2013). The main purpose of these compatibility principles is to enhance efficacy or reduce toxicity, so that different chemical components in botanical drugs can promote, coordinate, and restrict each other, thus ensuring the safety and effectiveness of clinical medication (Sucher, 2013). "Jun-Chen-Zuo-Shi" is one of the most common used rules in the

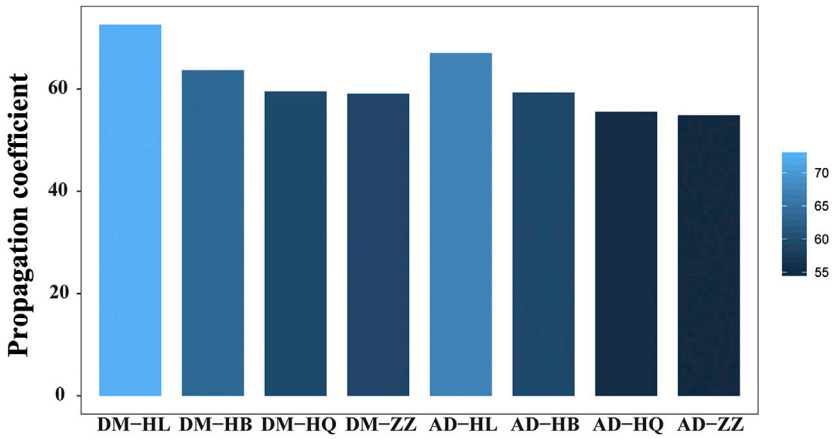

FIGURE 7 | The propagation coefficient of HJD botanical drugs in diabetes mellitus (DM) and alzheimer's disease (AD).

compatibility principles of TCM (Yao et al., 2013; Wu et al., 2014). The botanical drugs in a formula can be divided into "Jun", "Chen", "Zuo" and "Shi" botanical drugs according to their functions. Based on the compatibility principles of "Jun-Chen-Zuo-Shi", the function of each botanical drug and its relationship with other botanical drugs are revealed. For example, Yujinfang is based on the compatibility rules of "Jun-Chen-Zuo-Shi" in the treatment of cardiovascular and cerebrovascular diseases (Li et al., 2014). The "Jun" botanical drug *Curcuma wenyujin* Y.H.Chen and C. Ling accounts for the largest proportion of active ingredients and action targets, and treats diseases by acting on the main targets of cardiovascular and cerebrovascular diseases. "Chen" botanical drug *Gardenia jasminoides* J. Ellis can enhance the effect of *Curcuma wenyujin* Y.H.Chen and C. Ling. The "Zuo" and "Shi" botanical drugs can achieve their auxiliary effects by reducing the toxicity of *Curcuma wenyujin* Y.H.Chen and C. Ling and *Gardenia jasminoides* J. Ellis. Many botanical drugs in TCM have both unique effects and strong toxicity in clinical application. According to the needs of clinical treatment, the effectiveness of these botanical drugs should be utilized as much as possible and the toxic and side effects should be reduced at the greatest extent. Based on the compatibility rules of "Jun-Chen-Zuo-Shi", botanical drugs with toxicity usually are compatible with other botanical drugs to inhibit their toxicity and side effects and to play unique curative effects. This is an important aspect of improving the efficacy of TCM. For example, *Pinellia cordata* N.E.Br. in Xiaobanxia decoction is a commonly used medicine for resolving phlegm and arresting vomiting, but it is toxic. Compatibility with *Zingiber officinale* Roscoe can not only relieve the toxicity of *Pinellia cordata* N.E.Br. but also enhance the anti-vomiting effect of *Pinellia cordata* N.E.Br. to achieve synergistic effect (Gong-Chang et al., 2015).

Recently, more and more attention has been paid to the practice of verifying and explaining the compatibility theory of TCM by using different modern technologies, such as component combination and computer modeling (Wu et al., 2014). However, most of these analysis of compatibility rules of "Jun-Chen-Zuo-Shi" in TCM only focuses on one or several aspects. There is a lack of systematic and multi-dimensional analysis of the compatibility rules of "Jun-Chen-Zuo-Shi." Network pharmacology mainly focus on problems from the perspective of mutual connection, which is exactly consistent with the core idea of TCM (Li and Zhang, 2013). Therefore, the application of network pharmacology in Chinese medicine research has unique advantages and great development potentiality. However, most of the current network pharmacology research focuses on the interpretation of the functional mechanism of formula in the treatment of specific diseases, and does not interpret the compatibility rules of "Jun-Chen-Zuo-Shi" at a systematic level.

In this study, the compatibility rules and possible mechanisms of TCM in treating complex diseases are analyzed through six detail properties, include the physical and chemical properties of each component in single botanical drug of HJD, ADME properties and functional enrichment analysis of component targets, the characterization of degree and key communities in C-T-P network, the characterization of intervention propagation properties in the treatment of different complex diseases. The pharmacological action of drugs depends on the physical and chemical properties of drugs, which can reflect ADMET characteristics of drugs in the body and is also a basic attribute to be considered in interpreting the compatibility rules of TCM. Complex networks are made up of a large number of nodes, of which the important nodes are a few special parts that can deeply influence on the structure and function of the whole network. Node degree in the topological structure can reflect the importance of nodes, and is a key topological parameter to characterize the most influential nodes in the network (Lv et al., 2014). For example, in order to evaluate the influence of components in ZZW on FD treatment, Wang et al. constructed a contribution index model based on the topological parameter degree in the network. By using this algorithm, they selected key component groups for FD treatment and clarified possible cooperative mechanisms (Wang et al., 2018).

Modularity is a very important characteristic of complex networks and a common phenomenon in biological systems (Yang and Leskovec, 2012). Studying the response network

modules of different chemical components in different botanical drugs is very important to analyze the drug mechanism. It is also an important way to systematically validate the rules of "Jun-Chen-Zuo-Shi." The intervention effect of compounds in herbal medicine could propagate through PPI (Comola and Prina, 2013). The propagation of this intervention in the network has specific propagation modes and paths. The propagation coefficient defined based on the propagation method and path is also different in the principle of "Jun-Chen-Zuo-Shi." Enrichment analysis of gene function is a routine method for gene group function analysis, which is of great significance for revealing the molecular mechanism of different Chinese medicines in formula, and is a further explanation for the correlation between compatibility rules and mechanisms of Chinese medicines based on "Jun-Chen-Zuo-Shi". Based on the above-mentioned features, we designed a new system pharmacology strategy, which can systematically interpret the compatibility rule of "Jun-Chen-Zuo-Shi" from structure to function and then to propagation mode at a multi-level perspective.

Taking HJD as an example, we deeply decoded the compatibility rules of TCM. Jun botanical drugs play a leading role in formula, and exert the strongest effect in treating diseases through the best chemical properties, the highest occupancy rate of active components, the highest topological structure of drug action network, the highest occupancy rate of functional communities of drug response network and the highest drug intervention coefficient and potential molecular pathways of action. The Chen botanical drugs can enhance the pharmacological effects of Jun botanical drugs and reduce the dosage required by Jun botanical drugs through slightly lower functional targets. Zuo and Shi botanical drugs could be improved the bioavailability and active component of Jun and Chen botanical drugs. In addition, the C-T-P network proves the multidirectional pharmacological treatment mechanism of TCM, i.e. multiple components, multiple targets and multiple therapeutic effects. The prescription principle of different botanical drugs provides a unique opportunity to explore multiple therapeutic mechanisms according to the efficacy of botanical drugs. The combination of different botanical drugs can not only treat diseases by increasing bioavailability or promoting the synergistic effect of different botanical drugs, but also reduce the toxicity of some botanical drugs. The synergistic mechanism and toxicity-reduced effect embodied by these compatibility rules also indicate that the botanical drug combination is more effective than the use of single botanical drug.

Additionally, HJD was widely used in the treatment of AD and PD, thus, the study of brain tissue distribution of HJD is particularly important. Passing through the blood-brain barrier (BBB) is crucial for drugs to enter the central nervous system and play therapeutic roles. Through the analysis of components absorbed into blood in HJD, we found the components that can be absorbed into blood in the Jun botanical drug of Huanglian have strong permeability of BBB (>0.3), including berberine, palmatine, coptisine, and epiberberine. However, specific components wogonin and oroxylin a absorbed into blood in the Chen botanical drug of Huangqin only have moderate permeability of BBB. This proves once again that Jun botanical drugs are the core of the formulas, and they play a major role in treating diseases.

In this study, the compatibility rule of "Jun-Chen-Zuo-Shi" of HJD was in-depth decoded from multi-scale perspective. At the components and targets level, the Jun botanical drug huanglian plays a leading role at the functional level and has good performance in most physical and chemical properties, ADME properties and functional enrichment analysis of component targets. At the C-T-P interaction level, the leading role of the Jun botanical drug huanglian is also confirmed by having the highest average degree in C-T-P network and targets coverage rate of functional communities. At the intervention propagation level, the Jun botanical drug Huanglian has highest propagation coefficient both in DM and AD, this once again confirmed the Jun botanical drug plays a leading role in a formula for treating diseases. Finally, the results of experimental validation showed that the proportion of components in Jun botanical drug were absorbed into blood is higher than Chen and Zuo botanical drugs, including berberine, palmatine, and coptisine etc. Our approach confirmed the compatibility rules of "Jun-Chen-Zuo-Shi" in HJD at multiple quantitative level. This research shows the scientific basis of "Jun-Chen-Zuo-Shi" from a multi-dimensional perspective, which providing a good methodological reference for the subsequent interpretation of key components and speculation mechanism of the formula.

However, there are still some limitations of this study. This research is a computational pharmacological work based on pharmacological experiment data and public data. Pharmacological calculation is the forerunner and basis of the experiment, which provides a feasible scheme to reduce the verification scale for the experiment. Evidence from pharmacological experiments should be added in future research.

DATA AVAILABILITY STATEMENT

The raw data supporting the conclusions of this article will be made available by the authors, without undue reservation, to any qualified researcher.

AUTHOR CONTRIBUTIONS

K-XW and YG contributed equally to this work. D-GG, A-PL, and X-MQ provided the concept and designed the study. K-W and YG conducted the analyses. K-XW and YG wrote the manuscript. K-XW, YG, W-XG, X-FY, CW, L-YF, and X-FG participated in data analysis. X-MQ, G-HD, LG, and A-PL provided oversight. D-GG and A-PL contributed to revising and proof-reading the manuscript.

FUNDING

This study is financially supported by the Startup fund from Southern Medical University (grant No. G619280010), the Natural Science Foundation Council of China (grant No. 31501080), Hong Kong Baptist University Strategic Development Fund (grant No. SDF13-1209-P01, SDF15-0324-P02(b) and SDF19-0402-P02), the Key

Laboratory of Effective Substances Research and Utilization in TCM of Shanxi Province (No. 201705D111008-21), Hong Kong Baptist University Interdisciplinary Research Matching Scheme (grant No. RC/IRCs/17-18/04), the General Research Fund of Hong Kong Research Grants Council (grant No. 12101018, 12100719, 12102518).

SUPPLEMENTARY MATERIAL

The Supplementary Material for this article can be found online at: https://www.frontiersin.org/articles/10.3389/fphar.2020.567088/full#supplementary-material

REFERENCES

Andras, S., Ruth, N., and Peter, C. (2013). Allo-network drugs: extension of the allosteric drug concept to protein- protein interaction and signaling networks. *Curr. Top. Med. Chem.* 13 (1), 64–77. doi:10.2174/1568026611313010007

Beaumont, C., Young, G. C., Cavalier, T., and Young, M. A. (2014). Human absorption, distribution, metabolism and excretion properties of drug molecules: a plethora of approaches. *Br. J. Clin. Pharmacol.* 78 (6), 1185–1200. doi:10.1111/bcp.12468

Chiou, W. L. (2001). The rate and extent of oral bioavailability versus the rate and extent of oral absorption: clarification and recommendation of terminology. *J. Pharmacokinet. Pharmacodyn.* 28 (1), 3–6. doi:10.1023/a:1011544501243

Chu, L. H., and Chen, B. S. (2008). Construction of a cancer-perturbed protein-protein interaction network for discovery of apoptosis drug targets. *BMC Syst. Biol.* 2 (1), 56. doi:10.1186/1752-0509-2-56

Comola, M., and Prina, S. (2013).Treatment effect accounting for network changes: evidence from a randomized intervention. *Social Science Electronic Publishing*. doi:10.2139/ssrn.2250748

David, G., Aurélien, G., Matthias, W., Antoine, D., Olivier, M., and Vincent, Z. (2014). SwissTargetPrediction: a web server for target prediction of bioactive small molecules. *Nucleic Acids Res.* 42, W32–W38. doi:10.1093/nar/gku293. Web Server issue)

de Jong, H., Geiselmann, J., Hernandez, C., and Page, M. (2003). Genetic Network Analyzer: qualitative simulation of genetic regulatory networks. *Bioinformatics* 19 (3), 336–344. doi:10.1093/bioinformatics/btf851

Draghici, S., Khatri, P., Tarca, A. L., Amin, K., Done, A., Voichita, C., et al. (2007). A systems biology approach for pathway level analysis. *Genome Res.* 17 (10), 1537–1545. doi:10.1101/gr.6202607

Durairajan, S. S. K., Liu, L. F., Lu, J. H., Chen, L. L., Yuan, Q. J., Chung, S. K., et al. (2012). Berberine ameliorates β-amyloid pathology, gliosis, and cognitive impairment in an Alzheimer's disease transgenic mouse model. *Neurobiol. Aging* 33 (12), 2903–2919. doi:10.1016/j.neurobiolaging.2012.02.016

Gong-Chang, Y. U., Zhang, Y., and Nie, K. (2015). Anti-emetic mechanisms of Xiaobanxia Tang decoction on the chemotherapy-induced pica model in rats. *Chin. J. Pharmacol. Toxicol.* 29 (s1), 95–96.doi:CNKI:SUN:YLBS.0.2015-S1-130

Gu, H., Ma, L., Ren, Y., He, W., Wang, Y., and Qiao, Y. (2014). Exploration of the mechanism of pattern-specific treatments in coronary heart disease with network pharmacology approach. *Comput. Biol. Med.* 51, 198–204. doi:10.1016/j.compbiomed.2014.05.003

Gu, S., and Jianfeng, P. (2017). Chinese herbal medicine meets biological networks of complex diseases: a computational perspective. *Evid Based Complement Alternat Med* 2017, 7198645. doi:10.1155/2017/7198645

Gu, X. R., Fang, S. Y., Ren, W., Wang, H. J., Yang, J., Si, N., et al. (2018). Pharmacodynamics of Huanglian Jiedu decoction in Alzheimer's disease (AD) model rats and effect on improvement of inflammation microenvironment in brain. *China J. Chin. Mater. Med.* 43 (14), 3006–3011. doi:10.19540/j.cnki.cjcmm.2018.0092

Guan, D., Shao, J., Zhao, Z., Wang, P., Jing, Q., Deng, Y., et al. (2014). PTHGRN: unraveling post-translational hierarchical gene regulatory networks using PPI, ChIP-seq and gene expression data. *Nucleic Acids Res.* 42, W130–W136. doi:10.1093/nar/gku471.Web Server issue)

Han, C., Zhang, J., Zheng, M., Xiao, Y., Li, Y., and Liu, G. (2011). An integrated drug-likeness study for bicyclic privileged structures: from physicochemical properties to *in vitro* ADME properties. *Mol. Divers.* 15 (4), 857–876. doi:10.1007/s11030-011-9317-2

He, J. L., Zhao, J. W., Ma, Z. C., Liang, Q. D., Wang, Y. G., Tan, H. L., et al. (2015). Cardiotoxicity study of Shenfu compatibility in rats based on metabonomics. *Zhongguo Zhongyao Zazhi* 40 (14), 2743–2747. doi:10.4268/cjcmm20151412

Hormozdiari, F., Salari, R., Bafna, V., and Sahinalp, S. C. (2010). Protein-protein interaction network evaluation for identifying potential drug targets. *J. Comput. Biol.* 17 (5), 669–684. doi:10.1089/cmb.2009.0032

Jia, W., Gao, W. Y., Yan, Y. Q., Wang, J., and Xiao, P. G. (2004). The rediscovery of ancient Chinese herbal formulas. *Phytother Res.* 18 (8), 681–686. doi:10.1002/ptr.1506

Jung, H. A., Min, B. S., Yokozawa, T., Lee, J. H., Kim, Y. S., and Choi, J. S. (2009). Anti-alzheimer and antioxidant activities of coptidis rhizoma alkaloids. *Biol. Pharm. Bull.* 32 (8), 1433–1438. doi:10.1248/bpb.32.1433

Keiser, M. J., Roth, B. L., Armbruster, B. N., Ernsberger, P., Irwin, J. J., and Shoichet, B. K. (2007). Relating protein pharmacology by ligand chemistry. *Nat. Biotechnol.* 25 (2), 197–206. doi:10.1038/nbt1284

Khan, S., Zhang, D., Zhang, Y., Li, M. X., and Wang, C. X. (2016). Wogonin attenuates diabetic cardiomyopathy through its anti-inflammatory and anti-oxidative properties. *Mol. Cell. Endocrinol.* 428, 101–108. doi:10.1016/j.mce.2016.03.025

Li, B., Tao, W., Zheng, C., Shar, P. A., Huang, C., Fu, Y., et al. (2014). Systems pharmacology-based approach for dissecting the addition and subtraction theory of traditional Chinese medicine: an example using Xiao-Chaihu-Decoction and Da-Chaihu-Decoction. *Comput. Biol. Med.* 53, 19–29. doi:10.1016/j.compbiomed.2014.05.007

Li, H., and Zhan, M. (2006). Systematic intervention of transcription for identifying network response to disease and cellular phenotypes. *Bioinformatics* 22 (1), 96–102. doi:10.1093/bioinformatics/bti752

Li, S., and Zhang, B. (2013). Traditional Chinese medicine network pharmacology: theory, methodology and application. *Chin. J. Nat. Med.* 11 (2), 110–120. doi:10.1016/S1875-5364(13)60037-0

Li-hong, Y., Zi-wen, Y., Peng, J., Xiao-song, Z., Yong-li, H., and Yan-ming, W. (2019). Determination of 13 active components in Huanglian Jiedu Decoction by HPLC and screening of its effective fraction. *Chin. Tradit. Herb. Drugs* 50 (16), 3794–3801

Liang, Y., Yin, Z., Wei, B., Wei, W., Zhang, Y., and Ren, X. (2015). Discovering treatment pattern in traditional Chinese medicine clinical cases using topic model and domain knowledge. *J. Biomed. Inf.* 58, 260–267. doi:10.1109/BIBM.2014.6999356

Lin, T., and Yuhang, L. (2009). Discussion on the three levels of the prescription-composition principle of TCM. *Dtsch. Z. Akupunkt.* 52 (3), 27–30. doi:10.1016/j.dza.2009.05.008

Liu, J., Liu, J., Shen, F., Qin, Z., Jiang, M., Zhu, J., et al. (2018). Systems pharmacology analysis of synergy of TCM: an example using saffron formula. *Sci. Rep.* 8 (1), 380. doi:10.1038/s41598-017-18764-2

Liu, X., Vogt, I., Haque, T., and Campillos, M. (2013). HitPick: a web server for hit identification and target prediction of chemical screenings. *Bioinformatics* 29 (15), 1910–1912. doi:10.1093/bioinformatics/btt303

Lopes, C. T., Franz, M., Kazi, F., Donaldson, S. L., Morris, Q., and Bader, G. D. (2010). Cytoscape Web: an interactive web-based network browser. *Bioinformatics* 26 (18), 2347–2348. doi:10.1093/bioinformatics/btq430

Luo, W., and Brouwer, C. (2013). Pathview: an R/Bioconductor package for pathway-based data integration and visualization. *Bioinformatics* 29 (14), 1830–1831. doi:10.1093/bioinformatics/btt285

Lv, C. Y., Lv, S. W., Li, G. Y., and Kuang, H. X. (2018). Pharmacological effect of combined administration of natures, tastes and components of Chinese herbal compounds. *Zhongguo Zhongyao Zazhi* 43 (6), 1099–1103. doi:10.19540/j.cnki.cjcmm.20171226.001

Lv, Y. N., Li, S. X., Zhai, K. F., Kou, J. P., and Yu, B. Y. (2014). Network pharmacology-based prediction and verification of the molecular targets and pathways for schisandrin against cerebrovascular disease. *Chin. J. Nat. Med.* 12 (4), 251–258. doi:10.1016/S1875-5364(14)60051-0

Lv, Y. N., Wang, J., Xu, D., Liao, S., Li, P., Zhang, Q., et al. (2017). Comparative study of single/combination use of Huang-Lian-Jie-Du decoction and berberine

on their protection on sepsis induced acute liver injury by NMR metabolic profiling. *J. Pharmaceut. Biomed. Anal.* 145, 794–804. doi:10.1016/j.jpba.2017.07.062

Ma, Z., Yang, X., and Zhong, G. (2009). A new flavonoid glucoside from Huanglian jiedutang decoction. *Zhongguo Zhongyao Zazhi* 34 (9), 1097–1100

Ru, J., Li, P., Wang, J., Zhou, W., Li, B., Huang, C., et al. (2014). TCMSP: a database of systems pharmacology for drug discovery from herbal medicines. *J. Cheminf.* 6, 13. doi:10.1186/1758-2946-6-13

Safran, M., Dalah, I., Alexander, J., Rosen, N., Iny Stein, T., Shmoish, M., et al. (2010). GeneCards Version 3: the human gene integrator.*Database* 2010, baq020. doi:10.1093/database/baq020

Shen, Y. L., Guan, S., Ge, H. X., Xiong, W., He, L. K., Liu, L. J., et al. (2018). Effects of palmatine on rats with comorbidity of diabetic neuropathic pain and depression. *Brain Res. Bull.* 139, 56–66. doi:10.1016/j.brainresbull.2018.02.005

Stelzer, G., Rosen, N., Plaschkes, I., Zimmerman, S., Twik, M., Fishilevich, S., et al. (2016). The GeneCards suite: from gene data mining to disease genome sequence analyses. *Curr Protoc Bioinformatics* 54. doi:10.1002/cpbi.5

Sucher, N. J. (2013). The application of Chinese medicine to novel drug discovery. *Expet Opin. Drug Discov.* 8 (1), 21–34. doi:10.1517/17460441.2013.739602

Szklarczyk, D., Gable, A. L., Lyon, D., Junge, A., Wyder, S., Huerta-Cepas, J., et al. (2019). STRING v11: protein–protein association networks with increased coverage, supporting functional discovery in genome-wide experimental datasets. *Nucleic Acids Res.* 47 (D1), D607–D613. doi:10.1093/nar/gky1131

Tari, L., Baral, C., and Dasgupta, P. (2005). Understanding the global properties of functionally-related gene networks using the gene ontology. *Pac. Symp. Biocomput.* 2005, 209–220. doi:10.1142/9789812702456_0020

Tripathi, B., Parthasarathy, S., Sinha, H., Raman, K., and Ravindran, B. (2019). Adapting community detection algorithms for disease module identification in heterogeneous biological networks. *Front. Genet.* 10, 164. doi:10.3389/fgene.2019.00164

Wang, C., Ren, Q., Chen, X. T., Song, Z. Q., Ning, Z. C., Gan, J. H., et al. (2018). System pharmacology-based strategy to decode the synergistic mechanism of zhi-zhu wan for functional dyspepsia. *Front. Pharmacol.* 9, 841. doi:10.3389/fphar.2018.00841

Wang, C. Z., Cheng, H. J., Xu, Y., Song, G. D., Guan, Y., and Wang, Y. (2008). Differences in Candida albicans biofilm formation: a comparison between "huanglian Jiedu decoction" and its single components. *Shanghai J. Tradit. Chin. Med.* 42 (2), 63–65

Wang, F. Q., Cen, C., Xia, Z. N., and Yang, F. Q. (2014). Applications of platelets in studies on traditional Chinese medicines promoting blood circulation to remove blood stasis. *Zhongguo Zhongyao Zazhi* 39 (16), 2993–3003. doi:10.4268/cjcmm20141601

Wang, L. J., and Xu, Q. (2000). Mechanism of anti-inflammatory action of Huanglian Jiedu Decoction a traditional Chinese prescription. *Zhongguo Zhongyao ZaZhi* 25 (8), 493–496

Wang, L., Zhou, G. B., Liu, P., Song, J. H., Liang, Y., Yan, X. J., et al. (2008). Dissection of mechanisms of Chinese medicinal formula Realgar-Indigo naturalis as an effective treatment for promyelocytic leukemia. *Proc. Natl. Acad. Sci. USA* 105 (12), 4826–4831. doi:10.1073/pnas.0712365105

Wang, T., Yang, J., Chen, X., Zhao, K., Wang, J., Zhang, Y., et al. (2017). Systems study on the antirheumatic mechanism of Tibetan medicated-bath therapy using wuwei-ganlu-yaoyu-keli. *BioMed. Res. Int.* 2017, 2320932

Wu, L., Wang, Y., Li, Z., Zhang, B., Cheng, Y., and Fan, X. (2014). Identifying roles of "Jun-Chen-Zuo-Shi" component herbs of Qi Shen Yi Qi formula in treating acute myocardial ischemia by network pharmacology. *Chin. Med.* 9 (1), 24. doi:10.1186/1749-8546-9-24

Xie, X., Li, W. Y., Lan, T., LiuPeng, W. H. J., Huang, K. P., et al. (2011). Berberine ameliorates hyperglycemia in alloxan-induced diabetic C57BL/6 mice through activation of Akt signaling pathway. *Endocr. J.* 58 (9), 761–768. doi:10.1507/endocrj.k11e-024

Xin, Q., Chen, G. H., and Tao, W. (2011). Effects of huanglian Jiedu decoction on free radicals metabolism and pathomorphism of the Hippocampus in APP/PS1 double transgenic mice. *Zhongguo Zhong Xi Yi Jie He Za Zhi* 31 (10), 1379–1382. doi:10.1097/MOP.0b013e328341d1da

Yang, J., and Leskovec, J. (2012). Community-affiliation graph model for overlapping network community detection, in Proceedings of the IEEE international conference on data mining. Brussels, Belgium. December 2012. (IEEE) doi:10.1109/ICDM.2012.139.

Yang, L. H., Yuan, Z. W., Peng, J., Zhang, X. S., Hua, Y. L., and Wang, Y. M. (2019). Determination of 13 active components in Huanglian Jiedu Decoction by HPLC and screening of its effective fraction. *Chin. Tradit. Herb. Drugs* 50 (16), 3794–3801.

Yao, Y., Zhang, X., Wang, Z., Zheng, C., Li, P., Huang, C., et al. (2013). Deciphering the combination principles of Traditional Chinese Medicine from a systems pharmacology perspective based on Ma-huang Decoction. *J. Ethnopharmacol.* 150 (2), 619–638. doi:10.1016/j.jep.2013.09.018

Zhai, J. J., Li, Z. P., Zhang, H. F., Ma, L. Y., Ma, Z. Q., Zhang, Y., et al. (2019). Coptisine ameliorates renal injury in diabetic rats through the activation of Nrf2 signaling pathway. *Naunyn-Schmiedeberg's Arch. Pharmacol.* 393 (1), 57–65

Zhang, L., Yu, J., Wang, C., and Wei, W. (2019). The effects of total glucosides of paeony (TGP) and paeoniflorin (Pae) on inflammatory-immune responses in rheumatoid arthritis (RA). *Funct. Plant Biol.* 46 (2), 107–117

Zhang, S. W., Shao, D. D., Zhang, S. Y., and Wang, Y. B. (2014). Prioritization of candidate disease genes by enlarging the seed set and fusing information of the network topology and gene expression. *Mol. Biosyst.* 10 (6), 1400–1408. doi:10.1039/C3MB70588A

Zhang, X. J., Deng, Y. X., Shi, Q. Z., He, M. Y., Chen, B., and Qiu, X. M. (2014). Hypolipidemic effect of the Chinese polyherbal Huanglian Jiedu decoction in type 2 diabetic rats and its possible mechanism. *Phytomedicine* 21 (5), 615–623. doi:10.1016/j.phymed.2013.11.004

Zhang, Y., Jin, J., Zhang, L. Z., Lin, Y., Hu, W. X., Xu, N. N., et al. (2011). Effects of huanglian Jiedu decoction on blood lipid and oxygen radical metabolism in experimental hyperlipidemia rats. *Chinese Journal of Experimental Traditional Medical Formulae* 17 (2), 169–172

Zhang, Y. X. (2017). Pharmacological study on traditional Chinese medicine and natural product in China. *Chin. J. Pharmacol. Toxicol.* 31 (10), 941. doi:10.3867/j.issn.1000-3002.2017.10.001

Zuo, R., Wang, H. J., Si, N., Zhao, H. Y., Yang, J., and Bian, B. L. (2014). LC-FT-ICR-MS analysis of the prototypes and metabolites in rat plasma after administration of Huang-Lian-Jie-Du Decoction. *Acta Pharm. Sin.* 49 (2), 237–243

Conflict of Interest: The authors declare that the research was conducted in the absence of any commercial or financial relationships that could be construed as a potential conflict of interest.

Copyright © Wang, Gao, Gong, Ye, Fan, Wang, Gao, Gao, Du, Qin, Lu and Guan. This is an open-access article distributed under the terms of the Creative Commons Attribution License (CC BY). The use, distribution or reproduction in other forums is permitted, provided the original author(s) and the copyright owner(s) are credited and that the original publication in this journal is cited, in accordance with accepted academic practice. No use, distribution or reproduction is permitted which does not comply with these terms.

frontiers in Pharmacology

REVIEW
published: 11 December 2020
doi: 10.3389/fphar.2020.579332

Hydroxysafflor Yellow A: A Systematical Review on Botanical Resources, Physicochemical Properties, Drug Delivery System, Pharmacokinetics, and Pharmacological Effects

Feng Zhao[1†], *Ping Wang*[1†], *Yuanyuan Jiao*[2], *Xiaoxiao Zhang*[3,4,5], *Daquan Chen*[6] *and Haiyu Xu*[1,7*]

[1]Institute of Chinese Materia Medica, China Academy of Chinese Medical Sciences, Beijing, China, [2]Tianjin University of Traditional Chinese Medicine, Tianjin, China, [3]Resource Center for Chinese Materia Medica, China Academy of Chinese Medical Sciences, Beijing, China, [4]Postdoctoral Management Office, China Academy of Chinese Medical Sciences, Beijing, China, [5]China Association of Chinese Medicine, Beijing, China, [6]School of Pharmacy, Yantai University, Yantai, China, [7]Shaanxi Institute of International Trade and Commerce, Xianyang, China

Hydroxysafflower yellow A (HSYA), as a principal natural ingredient extracted from safflower (*Carthamus tinctorius* L.), has significant pharmacological activities, such as antioxidant, anti-inflammatory, anticoagulant, and anticancer effects. However, chemical instability and low bioavailability have been severely hampering the clinical applications of HSYA during the treatment of cardiovascular and cerebrovascular disease. Therefore, this present review systematically summarized the materials about HSYA, including acquisition methods, extraction and detection methods, pharmacokinetics, pharmacological effects and molecular mechanism, especially focus on the possible causes and resolutions about the chemical instability and low bioavailability of HSYA, in order to provide relatively comprehensive basic data for the related research of HSYA.

Keywords: hydroxysafflor yellow A, bioavailability, biological activity, chemical stability, delivery systems, botanical resources

OPEN ACCESS

Edited by:
Yanqiong Zhang,
Institute of Chinese Materia Medica, China

Reviewed by:
Guibo Sun,
Chinese Academy of Medical Sciences and Peking Union Medical College, China
Tan Loh Teng Hern,
Guangdong University of Technology, China
Shuzhen Guo,
Beijing University of Chinese Medicine, China

***Correspondence:**
Haiyu Xu
hyxu@icmm.ac.cn

[†]*These authors have contributed equally to this work*

Specialty section:
This article was submitted to Ethnopharmacology, a section of the journal Frontiers in Pharmacology

Received: *02 July 2020*
Accepted: *23 October 2020*
Published: *11 December 2020*

Citation:
Zhao F, Wang P, Jiao Y, Zhang X, Chen D and Xu H (2020) Hydroxysafflor Yellow A: A Systematical Review on Botanical Resources, Physicochemical Properties, Drug Delivery System, Pharmacokinetics, and Pharmacological Effects. Front. Pharmacol. 11:579332. doi: 10.3389/fphar.2020.579332

INTRODUCTION

Cardiovascular and cerebrovascular disease (CCD), as one of the leading causes of mortality worldwide, has been increased rapidly and presented younger trend, with high mortality all of the world (Collins et al., 2017; Donahue and Hendrikse, 2017). Although many types of therapeutic strategies were used to treat patients with CCD, such as angiotensin converting enzyme inhibitor (ACEI), β-receptor blocker, and statins, the outcome remains not satisfactory due to the inevitable side effects and high treatment expenditure. To address the problem, more and more studies are trying to seek treatment strategy from Traditional Chinese Medicine (TCM). Characterized by minor side effects, TCM has become an important source of natural product, such as Aspirin, Digoxin, Hydroxysafflor yellow A, which exhibit substantially protective effects against CCD (Eichhorn and Gheorghiade, 2002; Dai and Ge, 2012; Desborough and Keeling 2017; Hu et al., 2020).

Hydroxysafflor yellow A (HSYA) is a primary active product derived from safflower (*Carthamus tinctorius* L.), a plant of the *Compositae* (*Asteraceae*) family, which was used to improve blood circulation, eliminate blood stasis, and relieve menstrual pain as early as recorded in *Kaibao Bencao*. HSYA, as an indicator component to characterize the medical value of safflower recorded in *The Pharmacopoeia of the People's Republic of China* from 2005 edition, possesses a broad spectrum of pharmacological activities, such as antioxidant, anti-inflammatory and anticoagulant effects, which play an important role acting on cardiovascular and cerebrovascular disease (Sun et al., 2010; Wu et al., 2012; Ma et al., 2019a; Zhou et al., 2019; Bacchetti et al., 2020). However, chemical instability and low bioavailability of HSYA severely hamper the clinical applications. It can be easily oxidized, hydrolyzed, polymerized by light, high temperature, and alkaline conditions due to its structural characteristics. The high polarity directly leads to difficulty of transmembrane transport, resulting in low bioavailability. To address these problems, new drug delivery systems were developed to improve the therapeutic efficacies of HSYA based on lipid-based carriers, such as microemulsions, self-emulsifying systems, nanoparticles, chitosan, and the combination of HSYA with other drugs, which may have a good application prospect.

The present review systematically summarized the literatures about HSYA, including botanical resources, extraction and detection methods, pharmacokinetics, pharmacological effects and molecular mechanism, especially focus on the possible causes and resolutions about the chemical instability and low bioavailability of HSYA, in order to provide relatively comprehensive basic data for the related research of HSYA.

ACQUISITION OF HYDROXYSAFFLOWER YELLOW A

HSYA is mainly extracted from safflower, but the amount is not enough to support current clinical applications. Therefore, it is urgent find other ways to obtain HSYA. At present, chemical synthesis and biosynthesis are two promising ways to obtain HSYA. The information was detailed as follows.

Acquisition From Safflower

Safflower, as the natural source of HSYA, is widely planted worldwide. It is said that safflower originated in West Asia (Iran, Nicaragua and Turkey), and were later introduced for cultivation on almost every continent except Antarctica, such as America, Australia, China, Ethiopia, India, Italy, Mexico, Spain, and so on (**Figure 1**). India has developed into the most productive country with the planting areas of over 760,000 hm^2, and the yield of about 460,000 t, accounting for 50% of the total area and yield in the world (Liang et al., 2015).

Safflower is also widely cultivated in China with planting area of about 30,000–58,000 hm^2, and dried flowers yield of about 1,500–2000 t every year. Xinjiang province has become the major safflower production area, covering an area of 16,700–40,000 hm^2, which accounts for more than 3/4 of the total planting areas and provides more than 80% dried flowers and seeds in China. Henan province (*Weihonghua*, 卫红花), Zhejiang province (*Duhonghua*, 杜红花) and Sichuan province (*Chuanhonghua*, 川红花) are described as the authentic product areas of safflower in the history of China.

The content of HSYA containing in safflower were affected by many factors, including geographical origins, color and harvest time. The content of HSYA ranged from 0.05 to 14.99 mg/g by comparing 80 safflower cultivars collected from Africa, America, Asia, and Europe. HSYA in Africa cultivars was higher than that in Asia and Europe, and China cultivars is higher than that in Turkey, India and Kenya. Moreover, color is another factor to influence the content of HSYA. The darker the color of safflower, the higher the content of HSYA (red > orange > yellow > white according to PANEONE) (Tong et al., 2011; Xu et al., 2018). For example, Hebei safflower (red) was richer in HSYA (26.943 mg/g) than that in Wei safflower (white flowers, 0.472 mg/g) in China (Zhao, 2015). The most appropriate time to pick safflower is the

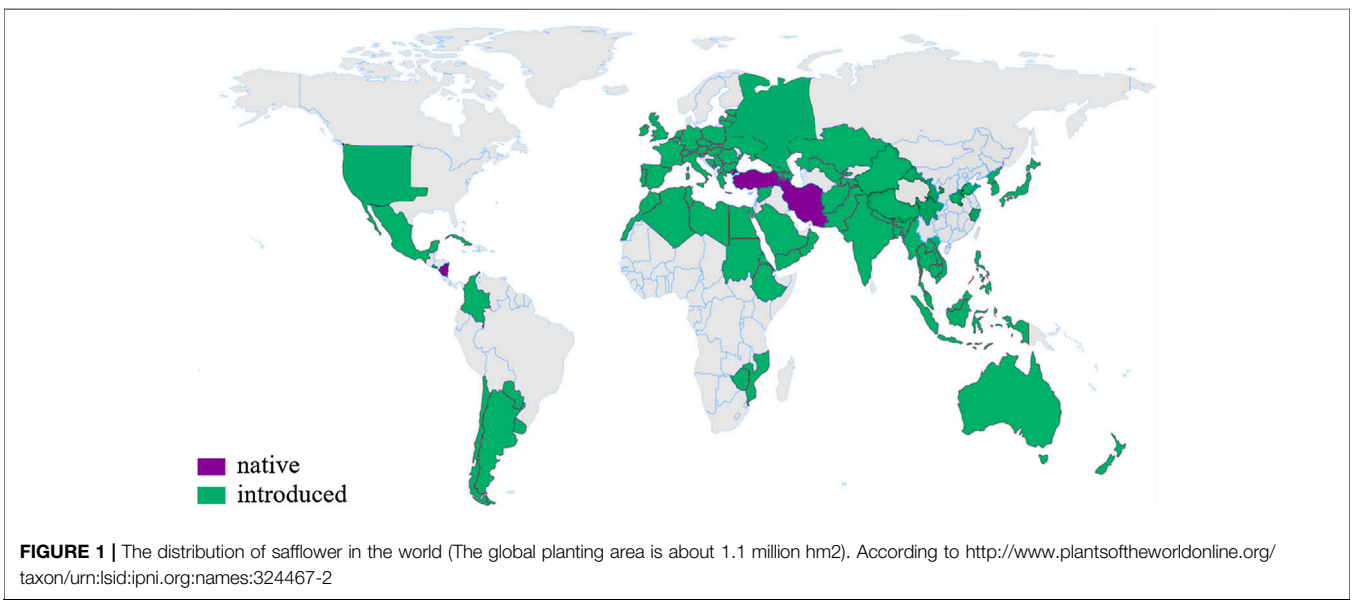

FIGURE 1 | The distribution of safflower in the world (The global planting area is about 1.1 million hm2). According to http://www.plantsoftheworldonline.org/taxon/urn:lsid:ipni.org:names:324467-2

morning of the third or fourth day after flowering (Tian et al., 2007).

Oxidation Synthesis Pathway

Chemical synthesis is an efficient way to obtain the natural or unnatural products within a short time period. Oxidation synthesis for HSYA is a rapid and highly efficient chemical synthesis method, and the synthetic pathway was shown in **Figure 2A**.

According to a retrosynthetic analysis of HSYA, di-C-glucosyl chloroacetophenone (3) transformed into di-C-(per-O-acetylglucosyl) phloroacetophenone (4) with BF_3.2AcOH at room temperature for 5 h. A further oxidation afforded the phenolic hydroxyl-free glycoside (5) with the quinol. Moreover, the two enantiomers of 4-(S)-2-acetyl- 4,5-dihydroxy-4,6-di-C-β-D-glucosyl-3-methoxycyclohexa-2,5-dienone (6) was obtained after diazomethane added to acetic acid solution of product 4 at 0°C. Finally, compound 6 transformed into HSYA (7). Compared the oxidant synthesis pathway mentioned above, di-C-glucosyl chloroacetophenoneoxidation (1) was converted into di-C-glycosylquinol(2) via an oxidation, and then was directly transformed into HSYA (7) with the yield at 18%, suggesting it is worthy promoting in the future (Suzuki et al., 2017).

Biosynthetic Pathway

Biosynthesis is a multi-step enzymatic process, in which a simple product is converted into a more complex desired product in a living organism. Biosynthesis is characterized by continuous and effective production, low-carbon and friendly environment, which provides a great support to the development of natural products (Pang et al., 2015). This production model will be the main source of HSYA in the future. However, the biosynthetic pathway of HSYA in plant remains unclear. According to the vital reaction of chalcone biosynthetic pathway, one molecular of 4-coumaroyl-CoA and three molecules of malonyl-CoA are converted into naringenin chalcone (4,2′,4′,6′-tetrahydroxychalcone) via the intervention of chalcone synthase, and it was transformed into HSYA after glycosylated (Heller and Hahlbrock, 1980; Knogge et al., 1986). The possible biosynthetic pathway of HSYA in phytosomal was shown in **Figure 2B**.

The content of HSYA is controlled by a nuclear gene with two alleles, HSya and hsya gene. HSya gene dominates completely over hsya gene to promote HSYA biosynthesis (Zhang et al., 2009; Yang et al., 2011). *sHSP* is a small heat shock protein and encoded by CTL-*hsyapr,* which might be directly or indirectly disturb HSYA biosynthetic pathway (Tang et al., 2010). When safflower is under external pressure, CT-*wpr* (TDF-11) was activated, which might arouse *sHSP* and inhibit the expression of HSya to some extent, finally leading to the inhibition of biosynthetic pathway of HSYA (Li et al., 2010b).

EXTRACTION AND DETECTION

Extraction Methods

HSYA is highly soluble in water, while hardly dissolve in lipophilic solvents such as ethyl-acetate, ether, benzene, and

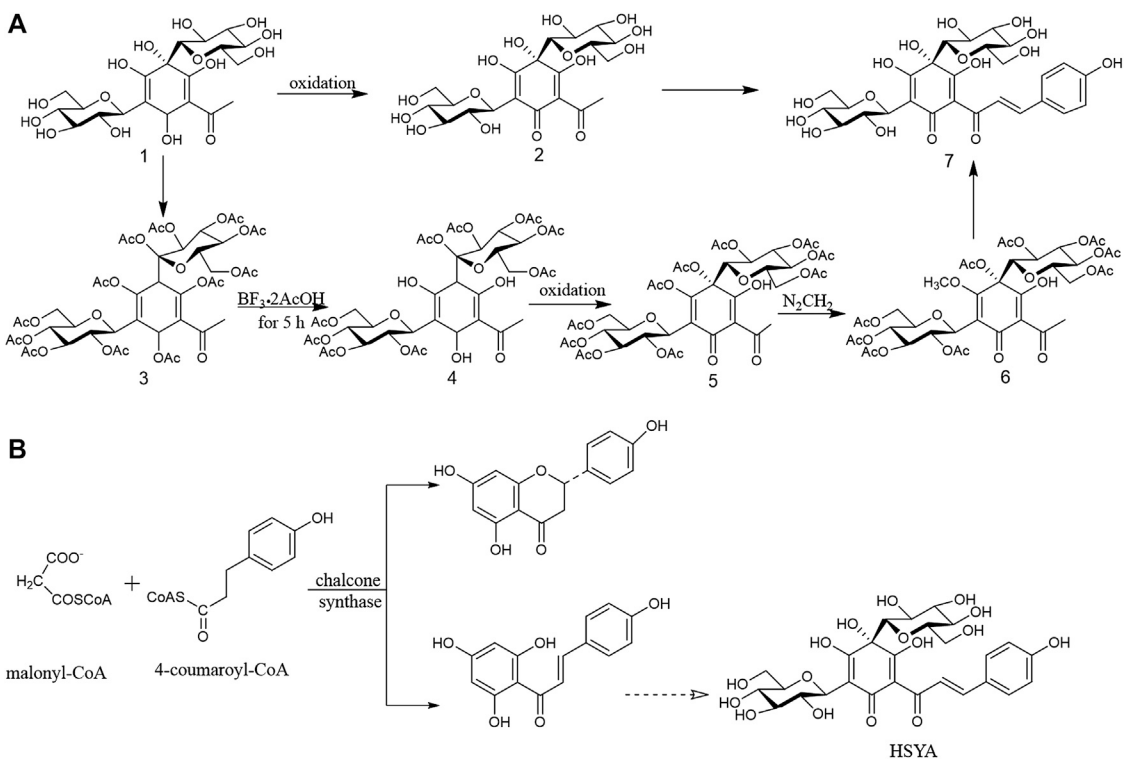

FIGURE 2 | (A) Oxidative synthesis pathway of HSYA; **(B)** The possible biosynthetic pathway of HSYA in phytosomal.

TABLE 1 | Representative examples of the extraction and purification methods of HSYA.

No	Total sample	Method	Pre-treatment	Extraction	Purification	Yield	Additional notes	Referencces
1	800 g	Water immersion	NA	Distilled water (10 L, 80°C, 20 min) for 2 cycles	The extracts were combined, evaporated and filtered	0.023%	NA	Li et al. (2013)
2	2000 g	Water immersion	The fresh flowers were shade dried and powdered	Distilled water (60°C, 30 min, 20 L) for three times	The solvent by evaporation under the reduced pressure, the residue was dissolved in 10% ethanol (1,000 ml), then evaporated to dryness under vacuum to afford a residue	0.066%	NA	Bai et al. (2012)
3	1 g	MAS-I microwave extraction system	NA	Distilled water at 70 °C for 20 min with solid and liquid ratio 100 for 3 cycles, and then the extracts were filtered	NA	6.96%	NA	Yang et al. (2008)
4	0.5 g	UAE extraction system	NA	Ultra-pure water (55°C, 39 min, liquid-to-solid ratio of 16) in ultrasonic (40 kHz, 250 W) for 3 times	The extracts were filtered, and transferred to 100 ml volumetric flask, filtered by a 0.22 μm filter	1.798%	Reflow by cold water during ultrasonic procedure	Sun et al. (2013)
5	20 g	Smashing tissue extraction system	NA	Distilled water with liquid-to-solid ratio of 40, at 2.5 min for 90 V, and filtered	NA	1.359%	NA	Wang et al. (2012)
6	500 g	Alcohol extraction method	NA	75% aqueous ethanol (3,000 ml, 12 h) for 10 cycles	The extracts were concentrated to dryness in *vacuo* at 55°C, re-solved with water, and extracted by petroleum ether and ethyl acetate for five times	0.584%	RP-MPLC was used to isolate and purify	Zong et al. (2013)
7	2. 5 g	DMSO extraction method	Stirred 14 times the amount of DMSO at room temperature to avoid light for 30 min, impurity removal, filtered	The filter residue added DMSO to soaking, heating extraction in seal condition at 80°C for 50 min, filtered. Then residue again added 12 times the amount of DMSO, heating extraction in seal condition at 80°C for 50 min. Filtered and combined the filtrate	The filtrate added 3 times of the amount of butyl acetate, centrifuged. Washed the precipitate with ethanol, dried	14.564%	A comparation of hot, cold and ultrafiltration models	Li et al. (2016)

TABLE 2 | Summary of the detection methods of HSYA.

No	Methods	Sample source	Sample preparation	Chromatographic method details	Advantage	Reference
1	HPLC-DAD and UPLC-Q-TOF-MS	Plant extracts	Dried in the cabinet drier at 35°C for 24 h, crushed and passed through an 80-mesh sieve and stored in a desiccator at room temperature	Waters ACQUITY BEH C18 column (30.0°C), elution solvent: Methanol: Water (1: 3, v: v) And flow-rate of 0.8 ml/min	High-speed separation and structural identification of multiple constituents	Hong et al. (2015)
2	UFLC-Q-TOF/MS	Bile, urine, plasma and feces samples from SD rat	Mixed sample at same time point, loaded onto a SupelClean™ LC-18 SPE tube	Thermo hypersil gold C18 column (35.0°C), elution solvent: Phase gradient, methanol A and 0.5‰ acetic acid in water B, flow rate of 0.2 ml/min	NA	Jin Y.et al. (2016)
3	LC–MS/MS	Human plasma	Mixed with internal standard working solution and vortexed for 30 s	Shim-pack VP-ODS C_{18} column (30.0°C), isocratic elution system: Methanol and 5 mM ammonium acetate (80:20, v/v), flow rate of 0.4 ml/min	High selectivity, wide linear range, short run time (5.5 min per sample), low LOQ and small injection volume	Wen et al. (2008)
4	LC-MS/MS	Human plasma	Added to an internal standard working solution, vortexed and centrifuged, the supernatant loaded to the activated SPE solid phase cartridge, and then washed with water	Agilent ZORBAX SB C18 column (4.6 mm × 150 mm, 5 μm, 35°C), elution solvent: 0. 2 mol L^{-1} ammonium acetate aqueous solution/ methanol (30/70), flow rate of 400 μL/min	NA	Li et al. (2014)
5	UPLC–MS–MS	Human urine	Freeze-dried, added 10% perchloric acid and 1 ml ethyl acetate, centrifuged, and dried under uitrogen gas blower	UPLC BEH C18 column (2.1 × 100 mm, 1.7 μm), elution solvent: Gradient elution, Acetonitrile-0.5% acetic acid (42:58), flow rate of 0.35 ml/min	NA	Zeng et al. (2013)
6	UPLC-DAD–MS	Xue fu zhu yu (XFZY)	Pills and granules of XFZY ground to fine powder, separated by 50% methanol–water solution extraction. Liquids of XFZY, 1 ml was diluted to 50 ml by 50% methanol–water solution	ZORBAX SB-C18 column (4.6 mm × 100 mm, 1.8 m): (50.0°C), mobile phase: 0.1% formic acid–water A and acetonitrile B, gradient program, flow rate of 0.5 ml/min	High-speed detection, excellent peak shapes, and less solvent usage	Zhang et al. (2012)
7	RP-HP LC-UV	Xuebiqing injection	XBJ injection of 1.0 ml was diluted to 10 ml with millipore water and filtered through 0.45 mm membrane filters	Zorbox SB C18 column, elution solvent: Gradient elution, water with 0.2% phosphoric acid A and acetonitrile B, flow rate of 1.0 ml/min	Better biocompatibility, larger specific surface area, good conduction effect and catalytic activity	Wang et al. (2016)
8	Novel multilayered porous silicon-based immunosensor	NA	Synthesized the polyclonal anti-HSYA antibody and HSYA artificial antigen by the immediate coupling method	NA	High surface area, easily preparation, label-free procedures and compatibility with standard microelectronics processing	Lv et al. (2011)

chloroform. So, the most general and traditional extraction method to get HSYA is water immersion. However, water immersion has the characteristic of low yield and high consumption of raw materials (e.g., the yield of 0.023%, 800 g of safflower; the yield of 0.066%, 2000 g of safflower) (Bai et al., 2012; Li et al., 2013a). Simultaneously, high temperature, alkaline conditions, and illumination all accelerate the degradation of HSYA in the traditional procedure.

As shown in **Table1**, many other extraction systems were developed. Smashing tissue extraction holds an absolute advantage in time consumption compared with other extraction systems, with a yield of 1.359% in two minutes (Wang et al., 2012). MAS-I microwave extraction system with a solid and liquid ratio of 100 maintained at 70°C for 3 cycles in 20 min could obtain HSYA with higher yield of 6.96% (Yang et al., 2008). Hong et al. (2015) compared the effectiveness of MSPD, ultrasound extraction, and Soxhlet extraction methods. MSPD system obtained the highest yield at 14.89% compared with ultrasonic (12.25%) and Soxhlet extraction (13.09%), and also achieved the lowest consumption of raw materials.

Solvents also affect the extraction efficiency. Li et al. (2016) developed the DMSO extraction method as follows: Soak 2.0 g safflower with 14 volumes DMSO and stir for 30 min to remove impurities at room temperature in dark environment. Then soak the filter residue with 14 volumes of DMSO at 80°C for 1 h before heating for 50 min in the same environment. Soak the filter residue with another 12 volumes DMSO and repeat the steps above. Then add 3 volumes butyl acetate to the filtrate and centrifuge to obtain crimson precipitates. Finally, wash the precipitates with an appropriate amount of ethanol before drying to obtain light yellow powder with yield at 14.56%. DMSO is a "universal solvent" in areas of pharmaceutical sciences and cell biology, so it is inevitable to dissolve a lot of impurities during the extraction process, and the toxicity of DMSO is difficult to remove. Therefore, this method is not recommended to be extensively promoted.

Detection Methods

Several detectors coupled with a liquid chromatography (LC) system have already been used for HSYA detection, including diode (DAD) (Qi et al., 2007), electrochemical (ECD), mass spectrometer (MS), and ultraviolet (UV). In addition, the novel multilayer porous silicon-based immunosensor has also been applied for HSYA detection. Detailed information is provided in **Table 2**.

MS is the most effective detector for qualitative analysis of HSYA with a high detection sensitivity, selectivity and low-interference. HSYA and its metabolites can be accurately identified, based on mass-to-charge ratio (m/z) and fragmentation patterns.

The content of HSYA in human plasma was determined after oral administration of safflower. LC-MS/MS method with isocratic elution system composing of methanol and 5 mM ammonium acetate (80:20, v/v) was proved with a linear range of 1–1,000 ng/ml, a correlation coefficient ≥0.999 (Wen et al., 2008). Li et al. (2014) optimized the sensitivity and selectivity of this method to be more simplified and effective. The researchers replaced the Thermo syncronis C8 with Agilent ZORBAXSB C18, added ammonium acetate to the mobile phase and increased concentration dilution ratio. The modified method reduced the injection volume, improved the response intensity and peak shape, and shortened the retention time.

UPLC-DAD-MS method had the advantages of fast detection speed, good peak shape and less solvent consumption. Twenty-eight compounds were identified only in 30 min, including HSYA from Xue Fu Zhu Yu decoction, a classic prescription of TCM (Zhang et al., 2012).

UPLC-TOF-MS is the most powerful tool with accurate activity measurement and full spectral sensitivity to determine HSYA using gradient elution with acetonitrile and 0.1% (v/v) formic acid aqueous solution in ESI^+. This method showed good linearity ($r^2 \geq 0.9992$) and precision (RSD ≤3.4%) with the limits of detection (LOD) at 35.2 ng/ml (Hong et al., 2015). Jin et al. (2016b) successfully developed a UFLC-Q-TOF-MS method to detect HSYA and its multiple metabolites in the plasma, bile, urine and feces of SD rats after oral administration with HSYA using the mobile phase consisting of methanol and 0.5‰ acetic acid in water.

The analysis speed of UV detector for HSYA is very fast, but its sensitivity and selectivity are slightly weaker than that of MS system (Chen et al., 2010). Novel multilayer porous silicon-based immunosensor is an easy way to alter the etching current periodically, which fabricated of *p*Si photonic crystal. The linear relationship was ranging from 1 to 3 g/ml and detection limit at 0.78 ng/ml for HSYA detection (Lv et al., 2011).

PHYSICOCHEMICAL PROPERTIES

Physical Properties

HSYA, a C-glucosyl quinochalcone, is a yellow amorphous powder with a molecular formula of $C_{27}H_{32}O_{16}$ (Meselhy et al., 1993). It is usually used as a dye owing to its attractive color. It shows maximum absorption at 403 nm due to *p*-conjugated system coupled with several hydroxyl groups (Ma et al., 2014). The C-glycoside bond, located between the 1,3-diketone on the ring A, is unstable in HSYA. The hydroxyl group located at the C-2 position in the glycoside is easily condensed with the adjacent enol due to the strain effect. The pyranose ring is opened, and then forms an oxyfuran [3,2 days] benzofuran ring by a cyclization reaction (Suzuki et al., 2017). HSYA is easily degraded by light, high temperature, and alkaline conditions. HSYA emits weak fluorescence at 450 nm in aqueous solution owing to the lack of rigid planar configuration in the molecular structure, and borax can significantly increase the HSYA fluorescence intensity by 20 times (Cao et al., 2020). Due to the existence of phenolic hydroxyl groups, HSYA exists in protonated form in natural or alkaline aqueous solutions, which seriously affects its transmembrane ability and leads to low bioavailability.

Chemical Stability

Effect of pH

HSYA is easy to degrade under alkaline conditions. Pu et al. (2017) had illustrated the pH profile (1–14) of HSYA stability in

aqueous solution follows an inverted V curve, and it was most unstable at pH 9. When HSYA was transferred from the aqueous solution to the buffer solution at pH 9.16, the UV absorbance was red-shifted from 404 nm to 426 nm, with the gradually increased absorbance of degradation products at 300 and 380 nm, which indicated that the electron cloud density of the conjugate system increased after rapid ionization under alkaline conditions.

As shown in **Figure 3**, there were two degradation products proposed in HSYA aqueous solution. The hydroxyl group at C-2′ was ionized under the moderate solution (pH 7–9). Intramolecular nucleophilic attacks Cβ and add O_2 to the α, *ß*-unsaturated double bond. The two products are isomers, which obtained after hydrogen migration. There were chalcone, flavones, and carbanion intermediates detected in HSYA acidic neutral and aqueous solution. However, only flavones were found under strong alkaline conditions (pH 13).

Effect of Temperature

When HSYA was incubated in boiling water under dark conditions for 0, 0.5, 1, 2, and 4 h, the degradation rate of HSYA was increased gradually detected by HPLC system. The possible mechanism of HSYA degradation was that the colorless glycoside of HSYA bonded with H_2O to form conjugate system, which reacted with the adjacent enol to transform the chromophore structure under the high temperature (Yue et al., 2003; Li et al., 2009). HSYA can be directly hydrolyzed and transformed into *p*-coumaric acid. And the hydroxyl group at the 2-position of C-glycoside of HSYA can be also condensed with the adjacent enol on A ring, and oxidized by O_2 at pH 8 under the high-temperature condition, then obtained the degradations (**Figure 4**). Due to the instability of the degradations as enols, a mixture of the two degradations were obtained (Fan et al., 2011).

Effect of Light

HSYA degrades when exposed to light, so it is generally stored in dark conditions. When distilled water solution of HSYA was exposed under sunlight, ultraviolet, incandescent light, and the dark environment respectively, the content of HSYA decreased in turn analyzed by HPLC (Li et al., 2011). The content of HSYA in aqueous solution decreased when stored under natural light at room temperature for 20 days (Wang, 2017).

Effect of Fe^{3+}/Fe^{2+}

When HSYA was incubated with Fe^{3+} (0.1 μg/ml) or Fe^{2+} (0.05 μg/ml) at 60°C for 10 h, the multiple nucleophilic hydroxyl groups and carbonyl groups of HSYA combined with Fe^{3+} and Fe^{2+} to form chelate compounds, leading to accelerate degradation of HSYA. Ethylenediaminetetraacetic acid (EDTA) competes with Fe^{3+} or Fe^{2+} to reduce HSYA degradation (Wang, 2017).

DRUG DELIVERY SYSTEM

A drug delivery system is responsible to control the release rate, extend the duration of drug action, and eliminate side effects, which can be divided into 4 types, including lipid-based carriers, polymer nanoparticles, inclusion complexes, and capsulations. At present, the studies on the HYSA drug delivery systems mainly focuses on lipid-based carriers, which can improve the bioavailability by reducing the high-water solubility of HSYA. Moreover, microemulsions, self-emulsifying systems, and nanoparticles can also enhance the transmembrane capacity of HSYA. In this review, we also summarized other drug deliveries, such as chitosan, and the combination of HSYA with other drugs. A detailed description is provided in Ahmed and Aljaeid, 2016, **Figure 5**.

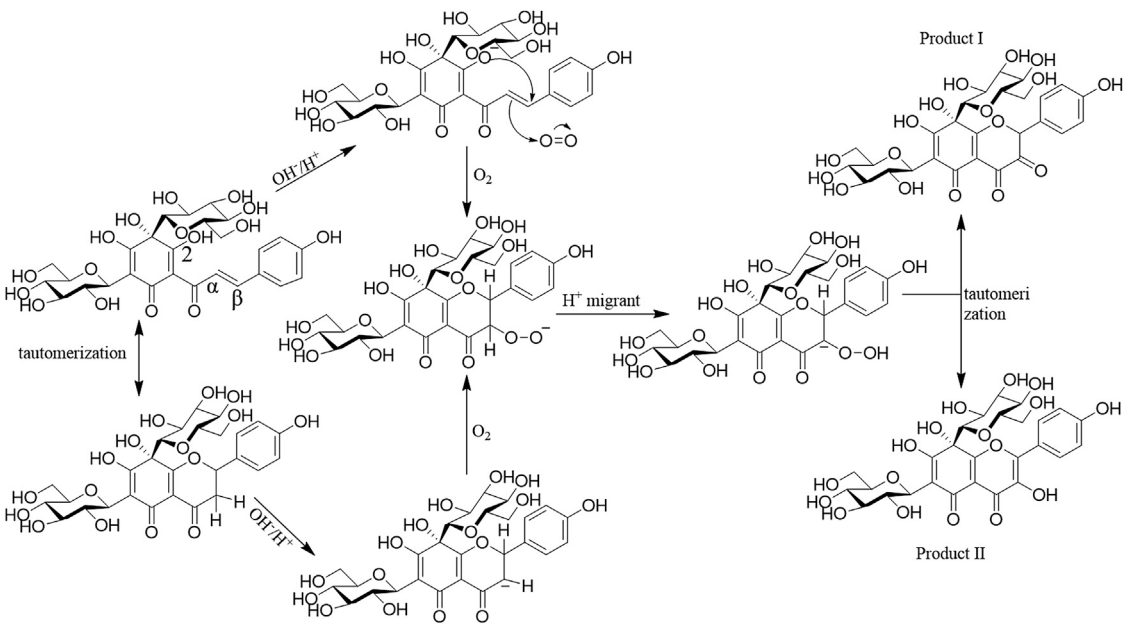

FIGURE 3 | The pathway of HSYA degradation (Pu et al., 2017).

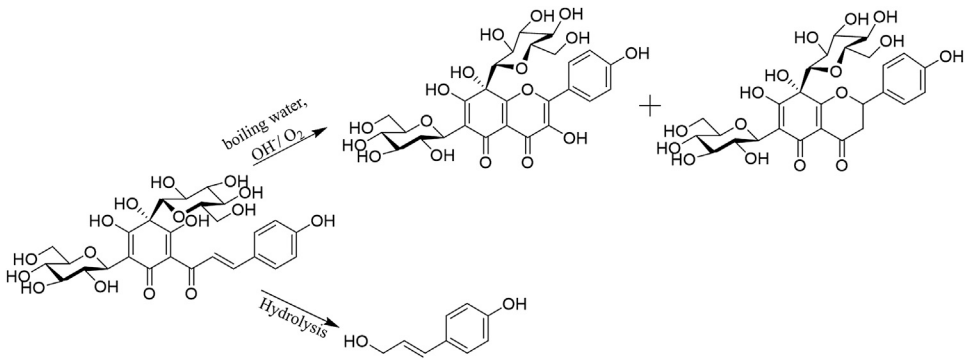

FIGURE 4 | Proposed degradation pathways of HSYA in the buffer solution at pH 8.0 at 100°C.

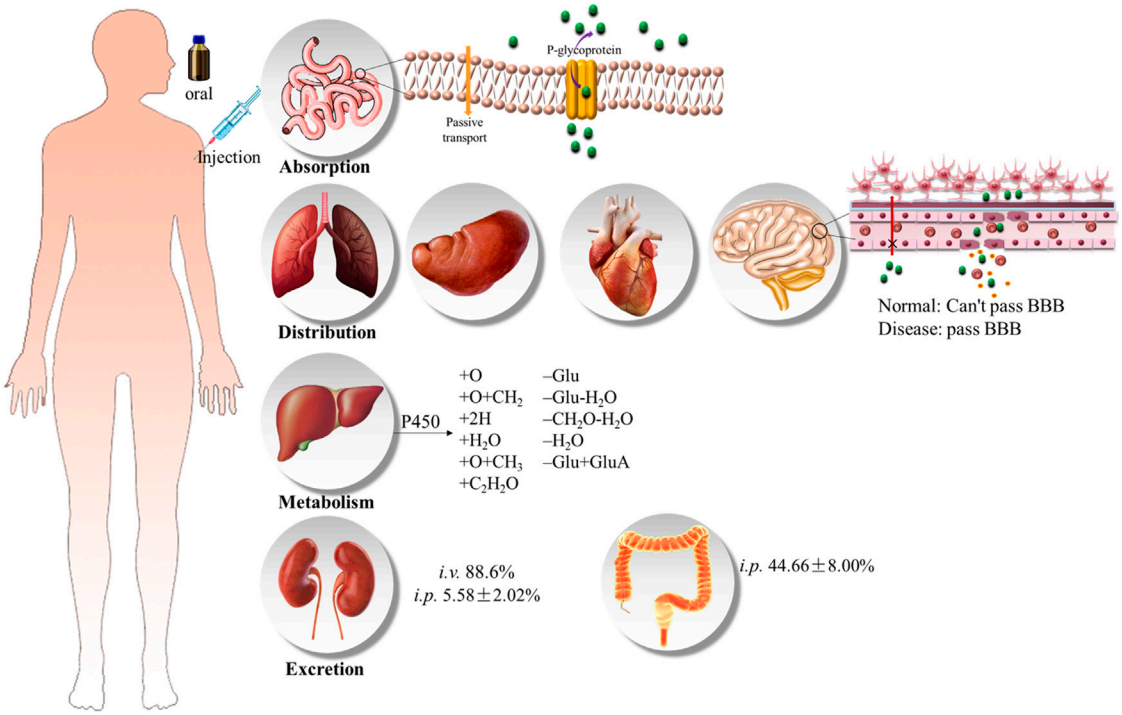

FIGURE 5 | Scheme of the pharmacokinetics of HSYA.

Microemulsions

Microemulsions are stable liquid solution consisted of water, oil, surfactant, and co-surfactant, with the characteristic of isotropic and thermodynamics. They are transparent or translucent with small droplet size, typically up to 150 nm (Lopes et al., 2014; Lv et al., 2018). Microemulsions are used to increase the permeability of hydrophilic peptides by enhancing the fluidity of cell membranes and opening tight connections between cells, which is a potential tool for hydrophilic drug molecules. Qi et al. (2011) investigated the bioavailability of HSYA microemulsion by intraduodenally administration. The microemulsion of HSYA was prepared by mixing Cremophor RH40 (surfactant), ethanol (cosurfactant), and PG (oil phase) together. Compared with HSYA aqueous solution, the bioavailability of HSYA microemulsion was increased by almost 1937%. It is worth noting that bile has a significant effect on the absorptive capacity of microemulsions. The microemulsion showed lower enhanced bioavailability of only 181% in bile duct-ligated rats. Microemulsion digested by pancreatic lipase increased 5.56 times permeability than the diluted microemulsion. The lipids and surfactants in the HSYA microemulsion might increase the fluidity of cell membranes and open the tight junctions between cells, thereby improving the permeability of hydrophilic drug molecules.

Self-emulsifying drug delivery system (SDEDDS) is a kind of the microemulsions. It could rapidly and spontaneously form a microemulsion in the gastrointestinal tract, where the peristalsis of the gastrointestinal tract and small intestine provides the necessary agitation for emulsification. SDEDDS have multiple advantages, including 100% drug entrapment capacity, physically stable formulations, no dissolution required, and submicron droplet sizes (Ghasemiyeh and Mohammadi, 2018). SDEDDS of HSYA were synthesized by inner water phase of 0.5% gelatin solution, and the external oil phase of bean phospholipids, medium chain triglycerides, Tween 80, oleic acid, and labrasol (20/65/7.4/2.5/0.1, in wt%). The study demonstrated that SDEDDS significantly improved the permeability of HSYA through Caco-2 cells monolayers, and plasma concentration increased by 2.17 times. The apparent permeability coefficient (Papp) of HSYA and HSYA-SDEDDS were (3.52 ± 1.41) × 10^{-6} cm/s and (6.62 ± 2.61) × 10^{-6} cm/s at the same concentrate (0.4 mg/ml), which improved to 1.88-fold by SDEDDS (Lv et al., 2012).

Labrafac lipophilic WL1349 (WL1349) is a medium-chain triglyceride that can be digested, absorbed, and hydrolyzed by pancreatic lipase after being emulsified by an endogenous emulsifier (such as bile). Preparation of HSYA-phospholipid complex increased lipophilicity, and dissolved in WL1349 to form a stable oil solution (a lipid-based preparation). Compared with HSYA aqueous solution, the oral bioavailability of HSYA-phospholipid complex WL 1349 oil solution in rats increased by about 37 times (Cmax of 2.79 μg/ml vs. 0.08 μg/ml within 24 h) and reduced the excretion of the drugs (8.80 ± 2.30% vs. 44.66 ± 8.00% in feces within 24 h) (Wang et al., 2008; Li et al., 2010a).

Nanoparticles

Solid lipid nanoparticles (SLN) is the earliest lipid-based nanocarriers formulated from lipids with a submicron size less than 1,000 nm, which are solid at body temperature and stabilized by emulsifiers (Koga et al., 2010). They can protect drugs against harsh environmental and are easy to mass-produce. However, owing to the crystalline structure existed in SLN, the drug-loading efficiency is poor. Some of the main lipids that have been used so far are monostearic acid, stearyl alcohol, stearic acid, glyceryl monostearate, cetyl palmitate, poloxamer 188, Tween 80, and dimethyl octadecyl ammonium bromide (DDAB) (Lee et al., 2016; Tapeinos et al., 2017; Ghasemiyeh and Mohammadi, 2018). As reported by Zhao et al. (2017), 1% Tween 80 was used as an emulsifier. HSYA-SLN with w/o/w structure prepared by micro emulsification procedure significantly improved oral bioavailability. HSYA SLNs is spherical with an average diameter of 174 ± 20 nm, zeta potential of −12.4 ± 1.2 mV, and the encapsulation efficiency is 55%. The SLNs of HSYA were stable within ten days at 4 or 30°C. SLNs of HSYA increased the oral bioavailability of HSYA in rats about 3.97-fold. It also significantly enhanced the C_{max} and AUC by 7.76 and 3.99 folds. The pharmacodynamic evaluation showed that HSYA-SLNs had a better therapeutic effect on the cerebral ischemia rats compared to HSYA aqueous solutions (Zhao et al., 2018).

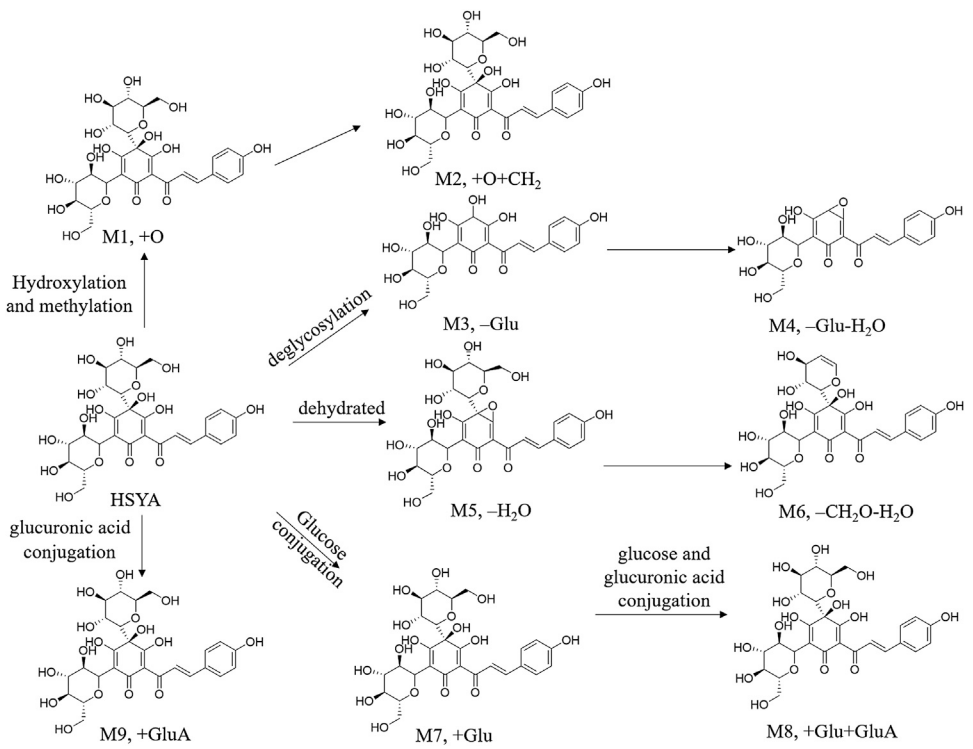

FIGURE 6 | Proposed metabolic pathways of HSYA (Jin et al., 2016; Wu et al., 2018).

Others Delivery System

The combination of *Ligusticum* chuanxiong volatile oil (CVO) and HSYA also improved the bioavailability in rats. When HSYA co-administered with CVO of 0.02 mg/ml, the bioavailability of HSYA in rats was increased by 6.48 folds. The emulsification of CVO increased Papp of HSYA and the paracellular transport by opening the integral tight junction of Caco-2 cells.

Chitosan, a kind of biological polysaccharide, is a molecule usually obtained by deacetylation of chitin with the carbohydrate backbone structure similar to cellulose, which is composed of two kinds of repeating units, N-acetyl-D-glucosamine and D-glucosamine, combined with (1–4)-β-glucoside linkage. It is characterized by the presence of a lot of amino groups on the chain (Ahmed and Aljaeid, 2016; Hong et al., 2017). HSYA-Chitosan complex effectively improved the oral absorption of HSYA, and the bioavailability increased to 476% (Ma et al., 2015).

Drug delivery system has great potential to improve the bioavailability and chemical instability of HSYA. However, there are also some several challenges, such as high preparation cost and poor promotional effect, which need further improvement.

PHARMACOKINETICS

HSYA is one of the representative chemical compounds of biopharmaceutics classification system (BCS) class III drugs. Pharmacokinetic studies showed that HSYA had low bioavailability. The oral bioavailability of HSYA is only 1.2%, and 48% of the prototype drug is excreted in urine, 2.9% in feces, and only 0.062% ± 0.011% in bile (Zhang, 2006). Similarly, 88.6% was directly excreted through urine after intravenous administration (Sun et al., 2009) (Ahmed and Aljaeid 2016, **Figure 6**).

Caco-2 cell monolayer model was usually used to study the transmembrane characteristic of HSYA, and the result prompted that the absorption of HSYA is basically in line with the passive diffusion. P-gp inhibitors (verapamil) and energy metabolism inhibitors (sodium azide) failed to block the intake of HSYA, which demonstrated that the absorption of HSYA is irrelevant to the P-gp protein (Zhou et al., 2014). However, this conclusion needed more evidence to verify owing to the opposite result in another study (Wang et al., 2009). The peak concentration of HSYA generally appeared at 10 min after oral administration (Li et al., 2007). A study has shown that healthy volunteers received intravenous injections of 35, 70, and 140 mg of HSYA, the elimination half-life values ($t_{1/2}$) of HSYA was 3.32 h, and the C_{max} was (2.02 ± 0.18), (7.47 ± 0.67), (14.48 ± 4.70) mg L^{-1}, respectively, (Qiao et al., 2009). HSYA has a low plasma protein binding rate (48%–54.6%, 72 h, *i. v.*), and it has no competitive binding to other drugs. So, HSYA is highly safe *in vivo* (Chu et al., 2006). Yang et al. (2009) suggested that the therapeutic effect of the single-dose HSYA indicated proportional to the dose ranging from 35 to 140 mg/kg, which conformed to first-order kinetics in

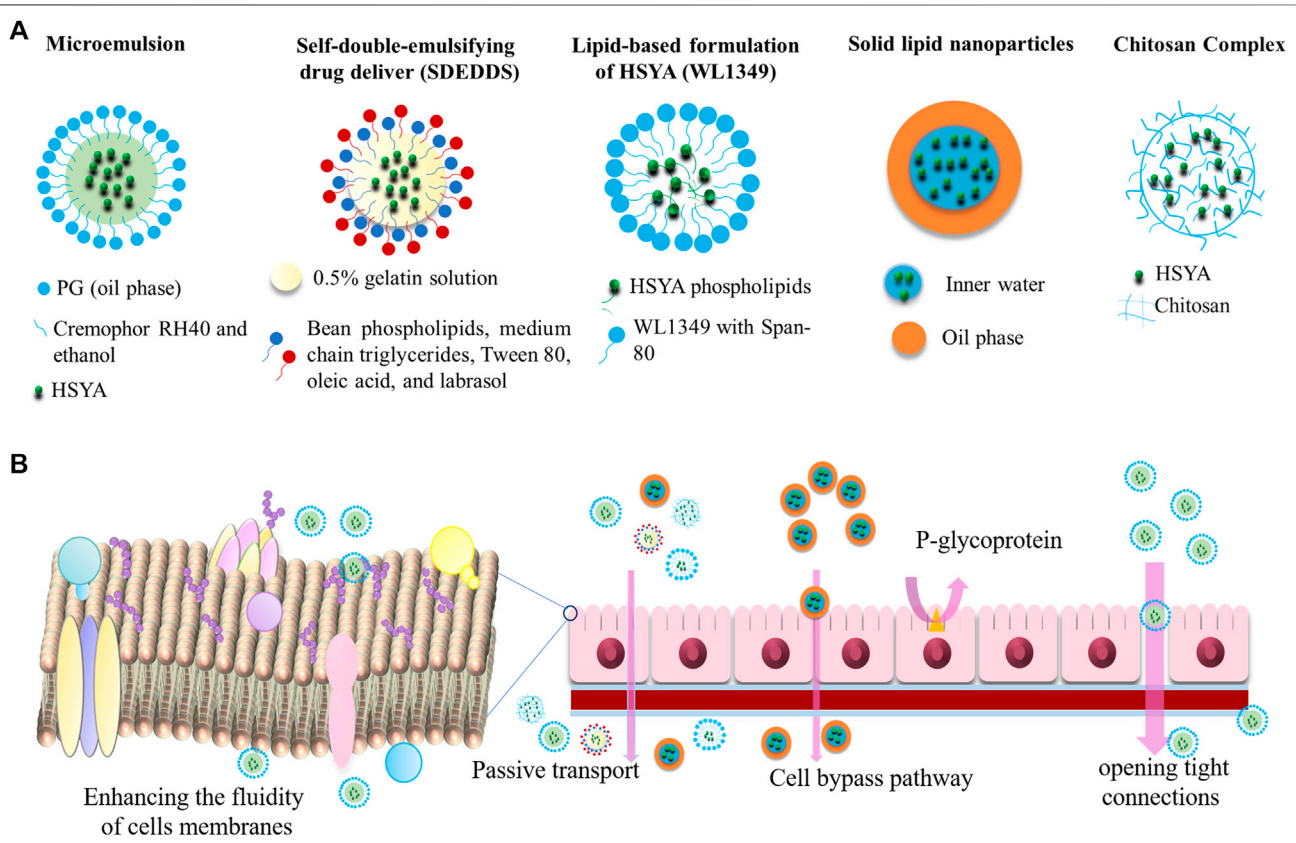

FIGURE 7 | Schematic representation of the different kinds of colloidal delivery systems.

TABLE 3 | Pharmacological effects of HSYA.

Pharmacological effects	Species	Study model	Detail	Effective concentration/dose/pattern	Remark	References
Cardioprotective effects	*In vivo*: SD rats	LAD of the coronary artery ligation	Reduce the myocardial infarct size (MIS), decrease CK-MB, MDA, increase eNOS, SOD, NO	HSYA + NTG (10 mg/kg+0.3 mg/kg)	HSYA combined with NTG	Wang et al. (2017)
	In vivo: SD rats *In vitro*: H9c2 cells	*In vivo*: isoproterenol-induced myocardial injury *in vitro*: Oxygen–glucose deprivation (OGD) model	Reduce the levels of CK-MB, ROS, LDH, inhibit apoptosis, increase PGC-1α and Nrf2	*In vivo*: HSYA + AKBA (50 mg/kg+50 mg/kg) via intragastric tubes. *In vitro*: HSYA + AKBA (5 μM + 5 μM)	HSYA and AKBA	Chen et al. (2016)
	In vitro: Cells from SD rats	Hypoxia/Reoxygenation (H/R)	Enter the cardiac myocyte and able to modulate H/R-induced damage by interacting with the MPTP	200 μM	NA	Huber et al. (2018)
	In vivo: SD rats	Ischemia–reperfusion (I/R) langendorff apparatus model	Inhibit MPTP opening, enhance nitric oxide production	0.05, 0.1 mmol/L	NA	Liu et al. (2008)
	In vivo: Wistar rats, TLR4-knockout C57 mice *in vitro*: NRVMs cells	*In vivo*: Hyperlipidemia combined with MI/R model. *In vitro*: LPS injured	Alleviate myocardial inflammatory injury, decrease MIS, CK-MB, LDH, LPS, TNF-α and IL-1β ability	Wistar rats: 8, 16, 32 mg/kg. TLR4-knockout mice: 16, 32, 64 mg/kg	NA	Han et al. (2016)
	In vivo: SD rats. *In vitro*: H9c2 cells	*In vivo*: LAD of the coronary artery ligation. *In vitro*: H/R model	Decrease apoptosis, improve antioxidant capacity, decrease the releases of cTnI, IL-6. LDH, and JAK2/STAT1 activity, maintain MMP, decrease ROS generation	*In vivo*: 5 mg/kg (*i.p.*). *In vitro*: 20 μM	NA	Zhou et al. (2019)
	In vitro:BV2 cells	OGD model	Decrease 1L-1β, TNF-α, iNOS, COX-2, MCP-1ability, inhibit NF-κB ability, phosphorylation of p38	20, 40, 80, 160, 320, 640, and 1,280 μM	NA	Li et al. (2013)
	In vivo: Male C57 mice. *In vitro*: HUVECs cells	*In vivo*: LAD of the coronary artery ligation	Improve ischemia-induced cardiac hemodynamics, enhance the survival rate, alleviate the myocardial injury, increase the level of CD31, VEGF-A and nucleolin	25 mg/kg (*i.p.*) twice a day for 2 weeks	NA	Zou et al. (2018)
	In vivo: SD rats. *In vitro*: H9c2 cells	*In vivo*: LAD of the coronary artery ligation. *In vitro*: H/R injury	Reduce CK-MB, cTnI, MDA and 8-OHdG, enhance SOD, Nrf2 and HO-1	1, 10, 35, 60, and 80 μM DSS + HSYA	Danshensu (DSS) and HSYA	Hu et al. (2016)
	In vitro: H9c2 cells	*In vitro*: H/R injury	Improve cardiomyocyte viability, maintain mitochondrial membrane potential, reduce apoptotic cardiomyocytes, decrease caspase-3 activity, and inhibit NOD-like receptor 3 (NLRP3) inflammasome activation through the AMPK signaling pathway	12.5 μM for 4 h	NA	Ye et al. (2020)
	In vivo: SD rats	*In vivo*: LAD of the coronary artery ligation	Reduce MIS, inhibit CK-MB and MDA content, increase SOD, eNOS and NO	2, 4, or 8 mg/kg via the tail vein injection	NA	Tu et al. (2009)
Neuroprotective effect	*In vivo*: Male C57BL/6 mice	*In vivo*: MCAO model. *In vitro*: OGD/R model	Reduce ROS, suppress cellular apoptosis, promote mitochondrial function and biogenesis	*In vivo*: 5, 20 mg/kg for 3 days. *In vitro*: 1, 10 μM	NA	Chen et al. (2019)
	In vivo: Wistar rats. *In vitro*: PC12 cells	MCAO/R model	Attenuate pressure overloaded hypertrophy, inhibit platelet aggregation, NF-κB p65 nuclear translocation, p65 binding activity, ICAM-1 and the infiltration of neutrophils	8, 4, 2 mg/kg (*i.v.*)	NA	Sun et al. (2010)
	In vivo: SD rats	MCAO model	Protect cognitive function and synaptic plasticity, promote learning and memory ability	8, 16 mg/kg via common carotid artery (CCA) injection	NA	Yu et al. (2020)
	In vivo: Wistar rats	MCAO model	Decrease neurological deficit scores, reduce the percentage of infarction, attenuate MDA content, increase SOD and the T-AOC activity	2, 4, 8 mg/kg (*i.v.*)	NA	Wei et al. (2005)
	In vivo: C57BL/6J mice	MCAO model	Inhibit TLR4, NF-κB, p-p65 expression, ERE1/2, JNK and p38 phosphorylation, suppressed TNF-α, IL-1β, NO	2 mg/kg via the tail vein injection	NA	Lv et al. (2015)
	In vivo: SD rats	MCAO/R model	Increase GFAP, NGF and Bcl-2 expression, suppress the expression of bax, caspase-3 and ICAM-1, IL-1ß, TNF-α and NF-κB	10 mg/kg HSYA+300 mg/kg acetylglutamine (NAG) once each day for 7 days	HSYA and NAG	Deng et al. (2018)
	In vivo: SD rats. *In vitro*: Cortical neurons cells	*In vivo*: MCAO model. *In vitro*: OGD model	Decrease LDH, TNF-α, IL-1β and IL-6, increase SOD, MDA, GSH-Px, suppress TLR4 and NF-κB expression, enhance Nrf2 and HO-1 expression	*In vivo*: 7.5 mg/kg+3 mg/kg (DSS + HSYA). *In vitro*: 40 μM + 40 μM (DSS + HSYA)	HSYA and DSS	Xu et al. (2018)
	In vivo: Male C57BL/6 mice	NA	Prevent the appearance of motor abnormalities, attenuate the reduction of dopamine (DA), 3,4-dihydroxyphenylacetic acid (DOPAC) and homovanillic acid (HVA) in striatum	2, 8 mg/kg for five days (*i. v.*)	NA	Han and Zhao (2010)
	In vivo: C57/BL6 mice	Rotenone-induced PD model	Increase the expression BDNF, *p*-TrkB/TrkB, DRD3, p-PI3K/PI3K, *p*-AKT/AKT, improve motor dysfunction	20 mg/kg for 28 days	NA	Wang et al. (2017)
	In vivo: SD rats	Unilateral 6-OHDA lesion (PD model)	Increase the levels of dopamine and its metabolites, glial cell line-derived neurotrophic factor and brain-derived neurotrophic factor	2 or 8 mg/kg via caudal vein injection for 4 weeks	NA	Han et al. (2016)
	In vivo: SD rats	Hcy-induced AD model	Attenuate ab accumulation, improve synaptic function, and reversed hcy-induced cognitive impairment	6 mg/kg (*i.v.*) for 2 weeks	NA	Lu et al. (2013)

(Continued on following page)

TABLE 3 | (*Continued*) Pharmacological effects of HSYA.

Pharmacological effects	Species	Study model	Detail	Effective concentration/dose/pattern	Remark	References
	In vivo: Wistar kyoto (WKY) rats	MCAO model	Increase the ratio of 6-keto-PGF1a and TXB2	1.5, 3.0, 6.0 mg/kg via sublingular vein injection	NA	Zhu et al. (2015)
	In vivo: SD rats	MCAO model	Inhibit protein oxidation and nitration, 12/15 lipoxygenase (12/15-lox), oxidative stress, attenuate BBB breakdown, infarct volume, BBB permeability, and brain edema	1, 5 and 10 mg/kg via caudal vein injection	NA	Sun et al. (2012)
	In vivo: Wistar rats	Cervical lymphatic blockade model	Alleviate the neurological deficits, attenuated cell apoptosis, prevent the decrease of eNOS mRNA and protein expression	5 mg/kg, (*i.p.*)	NA	*Pan* et al. (2012)
	In vivo: SD rats	Isolate brain mitochondria of SD rat	Inhibit Ca^{2+}- and H_2O_2-induced swelling of mitochondria, improve mitochondrial energy metabolism, enhance ATP levels and the respiratory control ratio	10–80 μmol/L	NA	Tian et al. (2008)
	In vivo: SD rats	Vascular dementia (VaD) model	Reduce escape latency in the water maze, enhance the LTP at CA3-CA1 synapses, up-regulated both VEGF and NR1, promote angiogenesis and increase synaptic plasticity, improve spatial learning and memory	0.6 mg/100 g via tail-vein injection for two weeks	NA	Zhang et al. (2014)
	In vivo: SD rats	Traumatic brain injury	Increase superoxide dismutase activity, decrease MDA content, enhance the t-PA activity, decrease the PAI-1 activity, decrease the MMP-9 expression	4 mg/kg (*i.v.*)	NA	Bie et al. (2010)
	In vivo: SD rats and balb/c male mice. *In vitro*: PC12 cell line	*In vivo:* MCAO model. *In vivo*: H_2O_2	Reduce the volume of cerebral infarction, improve the histopathological morphology, recruit brain-derived neurotrophic factors, down-regulate NLRP3, ASC, Caspase-1, GSDMD, IL-1β, IL-18, LDH, NF-κB, and p-p56 expression	*In vivo*: 5, 10 and 20 mg/kg (*i.v.*)	HSYA with lexiscan	Tan et al. (2020)
	In vivo: Pregnant C57BL6 mice	LPS-induced neurotoxicity and neuroinflammation	Decrease the content of IL-1β, TNF-α and NO, attenuate the LPS-induced dopaminergic neurons damage, inhibit the expressions of NF-κB, p65 and iNOS, decrease the content of IL-1β, TNF-α and NO	0, 20, 40, 80, 160, 320, 640 μM	NA	Wang et al. (2018)
	In vivo: C57BL6 mice. *In vitro*. SH-SY5Y cells	*In vivo*: PD model (*6-hyroxydopamine*)	Reduce iNOS, COX-2 and NF-κB, attenuate neuronal apoptosis, reduce the levels of p-p38 and *p*-JNK and increase that of *p*-ERK	*In vivo*: 2, 4, or 8 mg/kg (*i.v.*). *In vitro*: 1, 5, or 10×10^{-6} mol/L	NA	Yang et al. (2020a)
	In vivo: Wistar rats. *In vitro*: Primary neuronal cells	*In vivo*: MCAO model. *In vitro*: OGD model	Reduce infarct volume, decrease neurological deficit scores, elevate. GSK3β phosphorylation and inhibite the activation of iNOS, NF-κB, and capase-3	*In vivo*: 2, 4, or 8 mg/kg (*i.v.*)	NA	Yang et al. (2020b)
	In vitro: Human brain microvascular endothelial cells (HBMEC)	Methylglyoxal (MGO)-induced injury	Inhibit MGO-induced cell apoptosis, attenuate AGEs accumulation	10–100 μmol/L	NA	Li et al. (2013)
–	*In vivo*: SD rats	MCAO/R model	Promote neurological and functional recovery, suppress JAK2/STAT3 activation, activate of SOCS3	4, 8 or 16 mg/kg injected via the unilateral common carotid artery of rat	NA	Yu et al., 2020
–	*In vivo*: SD rats	A rat model of vascular dementia	Reduce escape latency in the water maze, promote angiogenesis and increase synaptic plasticity, improve spatial learning and memory, increase VEGF-A expression, protect neurons against hypoxia, increase NR1 expression, promote LTP and increase synaptic plasticity	0.6 mg/100 g for two weeks via tail-vein injection	NA	Zhang et al., 2014
Anticancer effect	*In vivo*: BALB/c mice. *In vitro*: Hepa1-6 murine HCC cells	A mouse model of hepatocellular carcinoma	Inhibit the proliferation of liver cancer cells, reduce the extent of tissue damage induced by cisplatin, increase the thymus index of HCC model mice, reduce the expression of Foxp3 and roryt mRNA, improve the tumor immune microenvironment of HCC model mice	2.25, 1.13 and 0.57 mg/kg twice per day (*i.v.*) for 11 days	NA	Ma et al., 2019a
	In vitro: Human umbilical vein endothelial cell (HUVEC)	High-glucose induced HUVEC injury	Attenuate cells apoptosis, decrease hyperpermeability, inhibit ROS levels	0–50 μM	NA	Chen et al. (2019)
	In vitro: Skov3 cells	NA	Decrease ovarian cancer cell proliferation, decrease ovarian cancer cell viability and sensitizes cells to chemotherapeutic agents, downregulate WSB1 expression	0, 10, 20, 50, 100, and 150 mg/L for 72 h	NA	Ma et al., 2019b
	In vitro: KYSE-30 cells	NA	Suppress proliferation, invasion, and migration, simultaneously induce apoptosis, regulate NF-κB signaling pathway, ICAM1, MMP9, TNF-α, and VCAM1	0.1, 1, 10, 20, 50 μM	NA	Chen et al. (2020)
	In vivo: Kunming mice. *In vitro*: HepG2 cells	H22 liver cancer cells injected into the abdominal cavity of kunming mice	Suppress p38MAPK phosphorylation, decrease HepG2 cell viability, proliferation, and migration, inhibit apoptosis of HepG2 cells	*In vivo*: 1.125 mg/kg, 2.25 mg/kg for 14 days (*i.v.*). *In vitro*: 80 μM	NA	Zhang et al., 2019

(Continued on following page)

TABLE 3 | (*Continued*) Pharmacological effects of HSYA.

Pharmacological effects	Species	Study model	Detail	Effective concentration/dose/pattern	Remark	References
Immunoprotection	*In vivo*: C57BL/6	Bleomycin-induced mice lung injury model	Attenuate the loss in body weight, alleviate bleomycin-induced increase of mRNA level of TNF-α, IL-1β and TGF-β1 in lung homogenates, inhibited NF-κB and phosphorylation of p38 MAPK in lung tissue	26.7, 40, 60 mg/kg/d (*i.v.*) for 1 week	NA	Wu et al., 2012
	In vivo: C57BL/6 mice	LPS-induced acute respiratory distress syndrome	Alleviate expressions of TNF-α, IL-1β, IL-6, TGF-β1, Col-I, col III, *a*-SMA, MD-2, TLR and CD14, inhibit the elevated levels of NF-κB and *a*-SMA, alleviated the slight collagen deposition in pulmonary tissues, attenuated increased levels of p65	14, 28, 56 mg/kg/d for 10 days (*i.v.*)	NA	Zhang et al., 2017
	In vivo: Hep-G2 liver cancer cell line	NA	Increase LC3-II and beclin 1 expression, decrease the level of p62 and phosphorylated-ERK1/2	20 mg HYSA solved in 1.02 ml PBS	NA	Liu et al., (2020)
	In vivo: ICR mice	LPS-induced acute lung injury (ALI)	Attenuate lung vascular permeability and edema, down-regulate myeloperoxidase (MPO), inhibited p38, ERK, JNK, TLR4, MyD88 and TRIF and the phosphorylations of interferon regulatory factor 3 (IRF3)	40, 80, and 120 mg/kg (*i.p.*)	NA	Liu et al., 2014
	In vivo: Specific-pathogen-free mature male hartley Guinea pigs	Ovalbumin (OVA)-induced asthma in Guinea pigs	Reduce airway resistance, improve dynamic lung compliance, attenuate the pathologic changes, inhibit the phosphorylation of JNK, p38, ERK, and IkBa, and inhibited IgE, PAF, IL-1b, IL-6, IL-4, IL-5, and IL-13 and increase in TNF-a, IFN-g, IL-2, and IL-3	50, 75, 112.5 mg/kg once daily from days 2–22 (*i.v.*)	NA	Zheng et al., 2019
	In vitro: Human non-small cell lung cancer cell line (A549)	LPS-mediated inflammatory injury	Suppress the expression of TLR-4, Myd88, ICAM-1, TNFα, IL-1β and IL-6, inhibit the adhesion of leukocytes, decrease NF-κB p65 nuclear translocation, inhibit the phosphorylation of p38 MAPK	1, 4 and 16 μmol/L	NA	Han and Zhao (2010)
	In vitro: A549 and H1299	LPS-mediated inflame matory injury	Suppress proliferation, migration, invasion, and EMT, inhibit the PI3K/Akt/mTOR and ERK/MAPK signaling pathways	5, 10, and 20 μM for two weeks	NA	Jiang et al. (2019)
	In vitro: Human bronchial smooth muscle cells (HBSMCs)	NA	Suppress MLC phosphorylation, inhibit the activation, block asthma-related signal transduction pathways, block the binding of PAF to the PAFR on the target cell membrane	9, 27, 81 μmol/L	NA	Guo et al. (2019)
	In vitro: Eahy926 human endothelium cell	LPS-induced endothelium inflammatory injury	Attenuate ICAM-1 and E-selectin mRNA levels elevation, phosphorylation of p38 MAPK, Jun MAPK, inhibit leukocyte adhesion to EC	1, 10 and 100 μ mol/L	NA	Jin et al. (2016)
	In vitro: Human small airway epithelial cells (HSAECs)	PAF-induced activation of HSAECs	Inhibit PAF-induced inflammatory activation, inhibit the PKC and MAPK signaling pathways, suppress the activities of NF-κB and AP1	9, 27, and 81 μmol/L	NA	Guo et al., 2018
	In vivo: Male NIH mice	Cecal ligation and puncture mouse model of sepsis	Improve sepsis induced immunosuppression via inhibiting $CD4^+$ lymphocytes apoptosis under septic conditions, upregulate the expression of Bcl-2 protein, inhibit protein expression of cytc, bax, cleaved caspase-3, and cleaved caspase-9	120 mg/kg (*i. v.*)	NA	Wang et al., 2017
Vascular dementia	*In vitro*: Mouse 3T3-L1 preadipocytes	NA	Inhibit the proliferation and adipogenesis of 3T3-L1 preadipocytes, increase hormone-sensitive lipase (HSL) mRNA expression and promoter activities, increase HSL promoter activity	1 mg/L	NA	Zhu et al., 2015
	In vivo: Wistar rats	PE (phenylephrine)-induced vascular constriction	Possess vascular relaxation effects, activate the KV channel in pulmonary vascular smooth muscle cells	10^{-9} M, 10^{-8} M, 10^{-7} M, 10^{-6} M, 10^{-5} M	NA	Bai et al., 2012
	in vivo: C57BL/6J mice. *in vitro*: HUVEC cells	Mouse hindlimb ischemia model	Increase the capillary-like tube formation and migration of HUVEC, increase phosphorylation of Tie-2, akt, and extracellular signal-regulated kinase 1/2, promote reperfusion of ischemic hindlimb tissue	*in vivo*: 6 mg/kg for 11 days via the tail vein. *in vitro*: 0, 1, 10, 50, and 100 μM for 24 h	NA	Chen et al. (2016)
	in vivo: Wistar-Kyoto (WKY) rats and spontaneously hypertensive rats (SHR). *in vitro*. HEK293cells	NA	Activate BKCa channels, inhibit Ca-L channels, reduce intracellular free Ca^{2+} level	*In vivo:* 1, 10 mg/kg. *In vitro:* 50 μM, 100 μM, 150 μM	NA	Wang et al. (2020)
	in vivo: Wistar rats. *In vitro:* Rat mesenteric endothelial cells (primary)	NA	Decrease TRPV4-dependent influx of Ca^{2+} in endothelium cells, promote PKA-dependent eNOS phosphorylation and increase NO production mechanism	*In vitro*: 10^{-7}, 10^{-6}, 10^{-5}, 10^{-4} M	NA	Yang et al. (2020)
	In vitro: HUVEC cells	NA	Inhibit the expression of VEGF and KDR, reduce Ras, *p*-raf, *p*-ERK and p-p38MARK, inhibit the expression of c-myc, N-ras, and NF-κB	NA	NA	Wang et al. (2016)

(Continued on following page)

TABLE 3 | (*Continued*) Pharmacological effects of HSYA.

Pharmacological effects	Species	Study model	Detail	Effective concentration/dose/pattern	Remark	References
Hepatoprotective effects	*In vivo:* C57BL/6 mice	D-galactose- (D-gal-) induced aging	Increase SOD, CAT, GSH-Px and MDA, decreased the mRNA and protein level of cyclin-dependent kinase inhibitor p16, increase CDK4/6 protein expression and decrease the phosphorylation of retinoblastoma (pRb)	25 mg/kg HSYA daily (*i.v.*) for 8 weeks	NA	Min et al. (2020)
Pulmonary arterial hypertension	*In vivo*: male wistar rats	A model of monocrotaline (MCT)-induced pulmonary arterial hypertension (PAH)	Reduce hemodynamic changes, right ventricular hypertrophy and morphometric changes; suppressed inflammation and oxidative stress	10 mg/kg (*i.p.*)	NA	Han et al. (2016)
Obesity	*In vivo:* C57BL/6J mice. *In vitro:* HepG2 cells and 3T3-L1 adipocytes	*In vivo:* diet-induced obese (DIO) mice. *In vitro:* H_2O_2-induced oxidative stress	Increase the expression of Nrf2, GCLC and CAT, improve glucose metabolism and liver function, decrease body weight gain	*In vivo*: 200 mg/kg/d for 10 weeks (*i.v. In vitro*: 10, 50, and 100 mg/L	NA	Yan et al. (2020)
Skin photoprotective effect	*In vivo* female KM mice	Photoaged mouse model	Prevent UV-induced macroscopic skin lesions, promote the ability of the skin to regain its initial shape, elevated the activities of skin anti-oxidant enzymes, increased skin collagen content, maintained the structural integrity of the skin	50, 100, and 200 l g/mouse following each UV exposure	NA	Kong et al. (2013)
Anti-anaphylactoid activity	*In vivo:*C57BL/6 mice. *In vitro*: Laboratory of allergic disease 2 (LAD2) human mast cells and mouse peritoneal mast cells	a mouse model of hindpaw extravasation	Attenuate calcium flux, decrease degranulation, attenuated degranulation triggered by endogenous and exogenous substances, decrease the activation of the plcγ-pkc-IP3 signaling pathway regulating calcium fluctuations	*In vivo*: 0, 2.5 mg/kg. 5 mg/kg, 10 mg/kg (*i.v.*). *In vitro*: 0, 50 μM, 100 μM, 200 μM. NA	NA	Liu et al. (2014)
Inhibition of hepatic fibrosis	*In vivo*: SD rats	CCl_4-caused fibrogenesis	Decrease in fibrosis, protein expression of *a*-SMA, and MEF-2C gene expression, decreased expression of Tβ-RI, Tβ-RII, MEKK3, MEK5, and phosphorylation of ERk5	5 mg/kg/d for 12 weeks	NA	Zhang et al. (2012)
Type 1 diabetes	*In vivo*: SD rats. *In vitro*: Human epithelial and keratinocytes (HEKs)	*In vivo*: Type 1 diabetes mellitus (T1DM) model	Accelerate diabetic wound healing through promoting angiogenesis and reducing inflammatory response, enhance angiogenesis by upregulation of hypoxia inducible factor-1 alpha (HIF-1a) expression	2/0.4 mg/ml of HSYA/DFO hydrogel solution for five weeks	Deferoxamine (DFO) and HSYA	Gao et al. (2018)
Type 2 diabetes mellitus	*In vivo*: Wistar rats	*In vivo:* HFD feeding-induced T2DM model	Reduce fasting-blood glucose and insulin resistance, up-regulate of PI3K and AKT, inhibit the apoptosis	120 mg/kg (*i.v.*)	NA	Lee et al. (2020)
Polycystic ovary syndrome (PCOS)	*In vivo*: ICR female mice	*In vivo:* Dehydroepiandrosterone-induced PCOS model	Elevate serum E2, P4, LH and AMH levels, reduce FSH. Level, reverse the expression of steroid hormone secretion-related genes Star, hsd3b1, cyp11a1 and cyp19a1, improve GSH content, enhance the activities of antioxidant enzymes SOD, GSH-Px and CAT	3.5 mg/kg (*i. p.*)	HSYA and ginsenoside Rb1	Luo et al. (2020)

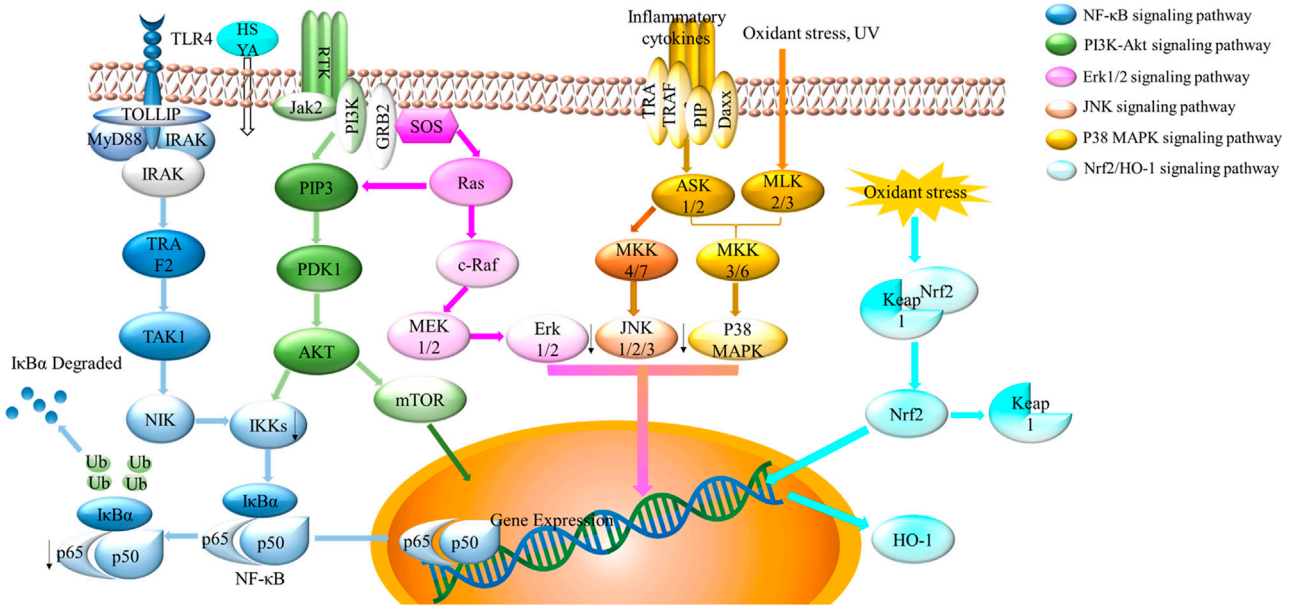

FIGURE 8 | Schematic showing multiple signaling pathways of HSYA. The four crucial signaling pathways were displayed above, including NF-κB signaling pathway, PI3K-Akt signaling pathway, MAPK signaling pathway (Erk1/2, JNK, p38 signaling pathway), and Nrf2/HO-1 signaling pathway.

healthy Chinese female volunteer. The $t_{1/2}$ corresponded to the median of the range from 2.23 to 4.63 h (the average value of 3.17 h) at each dose. But this research had some potential limitations, such as a low-volume sample and only female volunteers, which lack of universality. Moreover, the combination therapy of HSYA and protocatechuic aldehyde greatly promoted the intake of HSYA (Ao et al., 2018).

HYSA is reduced and hydrolyzed, such as hydroxylation, hydroxylation and methylation, dehydration, hydrogenation and hydration, to obtain phase I metabolites under the action of hepatic microsomal drug-metabolizing enzyme in the liver. Phase II metabolism included acetylation and glucuronidation, dehydration, hydrogenation, hydration, hydroxylation with glucuronidation, deglycosylation, methylation and glucuronic acid conjugation reactions (Jin et al., 2016b; Wu et al., 2018). The possible metabolic pathways were summarized in Ahmed and Aljaeid, 2016, **Figure 7**. HSYA and its metabolites are distributed in the heart, liver, spleen, lung, kidney, brain and intestines. In addition, it is almost impossible to cross the healthy blood-brain-barrier (BBB), but easily to penetrate damaged BBB (Sheng et al., 2019).

The low bioavailability of HSYA directly blocks its therapeutic efficiency. It is difficult for HSYA to pass through phospholipid bilayer because of its strong polarity and poor membrane permeability, which is also an important reason for its low bioavailability. Therefore, the design of HSYA delivery systems mainly focused on improving its lipsolubility. Despite, HSYA exists as an undivided molecule in the strong acid environment of the stomach, it cannot be absorbed by the stomach due to its high molecular weight and strong hydrophilicity (Zhang, 2006). Besides, the small intestine actually is the main absorption site of HSYA. However, gastrointestinal metabolism in a weak alkaline environment is not conducive to the absorption of HSYA, on the contrary, it promotes degradation (Wu et al., 2018).

PHARMACOLOGICAL EFFECTS AND MOLECULAR MECHANISM

HSYA shows excellent therapeutic effects on various diseases, such as cardiovascular and cerebrovascular diseases, cancer, and so on. This part provided the biological activity of HSYA in detail (**Table 3**, **Figure 8**).

Cardioprotective Effects

HSYA has been proved to be a superior agent on the cardioprotective system *in vivo* and *in vitro*. HSYA (5 mg/kg, 30 min before ischemia, *i. p.*) was found to improve ischemia/reperfusion (I/R) injury by reducing the releases of cTnI, IL-6. LDH and the myocardial infarction size (Zhou et al., 2019). Similarly, HSYA (4 or 8 mg/kg) could reduce the expression of MIS, CK-MB, and MDA in experimental acute myocardial ischemic model, which induced by left anterior descending coronary artery (LAD) ligation (Tu et al., 2009). Furthermore, HSYA combined with nitroglycerin showed a better therapeutic action on acute myocardial infarction than HSYA alone, which produced a marked increase in SOD, eNOS, and NO content.

The mechanisms of HSYA on cardioprotective effects are related to antioxidant, free radical scavenging abilities, and anti-inflammatory activity. The nuclear factor erythroid 2-related factor 2 (Nrf2) is a transcription factor responsible for the regulation of cellular redox balance and protective antioxidant and phase II detoxification responses in mammals. On basal condition, Nrf2 binding with the chaperon protein Kelch like-ECH-associated

protein 1 (Keap1) located in cytoplasm with inhibition abilities. When facing oxidant stress, Nrf2-Keap1 combination is separated. Nrf2 transports to the nucleus and activates the transcription of genes encoding. Heme oxygenase-1 (HO-1), as one of Nrf2-dependent gene, protects against oxidant stress (Loboda et al., 2016; Reuland et al., 2013). Hu et al. (2016) reported that the combination of HSYA and DSS exerted the markedly antioxidant capacity on increasing the expression of HO-1, the phosphorylation of Akt, and the translocation of Nrf2 (**Figure 8**). Similarly, HSYA attenuated the expression of IL-1β, TNF-α, iNOS, COX-2, MCP-1 on BV2 cells of oxygen and glucose deprivation models (OGD). HSYA also inhibited NF-κB signaling pathway, TLR4 signaling pathway and phosphorylation of p38 (Han et al., 2016; Li et al., 2013). In addition, HSYA decreased the formulation of mitochondrial permeability transition pore in hypoxic cardiac myocytes, thereby inhibiting cardiomyocytes from damage during cardiomyocyte reoxygenation (Huber et al., 2018). In summary, oxidative stress and inflammation related signaling pathways (e.g., Nrf2/OH-1, p38 MAPK, NF-κB signaling pathway and TLR4 signaling pathway all play an important role during the treatment of cardiovascular disease with HSYA.

Neuroprotective Effect

HSYA showed excellent neuroprotective effect. HSYA injection (50 mg/d and 75 mg/d) in patients with acute ischemic stroke of blood stasis syndrome might be to undergo for a phase III clinical trial (Zhu et al., 2020). HSYA (2 mg/kg, tail vein injection) protected the C57BL/6J mice against middle cerebral artery occlusion (MCAO) by decreasing the expression of inflammatory genes factors, including TNF-α, IL-1β, and NO (Lv et al., 2015). HSYA (0.6 mg/100 g, tail vein injection) could also improve spatial learning and memory ability of vascular dementia model rat by promoting angiogenesis and increasing synaptic plasticity (Zhang et al., 2014). Moreover, HSYA (6 mg/kg per day, 2 weeks, *i. v.*) could reduce the accumulation of amyloid precursor protein, improve synaptic function and reverse homocysteine (Hcy) induced cognitive impairment in Alzheimer's disease mice (Lu et al., 2013).

The neuroprotective effect of HSYA might be related to the regulation of TLR4, NF-κB, p-p65, MAPK, PI3K/Akt and Nrf2/HO-1 signaling pathways (Wei et al., 2005; Lv et al., 2015; Deng et al., 2018). NF-κB is a family of dimeric transcription factors central to regulate immune development, immune responses, inflammation, cancer, and other diseases. HSYA inhibited NF-κB to exert neuroprotective effect (Yu et al., 2020). Similarly, HSYA (20 mg/kg for 28 days) could improve motor dysfunction in C57/BL6 mice model of Parkinson by promoting the expression of BDNF, *p*-TrkB/TrkB, DRD3, p-PI3K/PI3K and *p*-AKT/AKT (Wang et al., 2017).

Anticancer Effect

Some studies have found that HSYA exerted anticancer activity in several cancer cells, such as human umbilical vein endothelial cells (HUVEC), HepG2 cells, Skov3 cells, as well as some *in vivo* studies. HSYA could eliminate reactive oxygen species (ROS), prevent apoptosis from membrane permeability, and inhibit proliferation and migration (Ma et al., 2019a; Chen et al., 2019; Zhang et al., 2019). HSYA also increased the thymus index, and effectively down-regulate the mRNA levels of forkhead box P3-positive (Foxp3) and retinoic acid receptor-related orphan receptor-gamma-t ($ROR\gamma t$), which contributed to improve the tumor immune microenvironment-the key points of tumor cell proliferation and invasion (Ma et al., 2019b). What is particularly noteworthy is the anticancer abilities of HSYA might related to the excellent antioxidant effect.

Anticoagulant Effect

PAF, as the most effective platelet activator known so far, has a wide range of biological activities, and can be synthesized by a variety of cells such as platelets, leukocytes, endothelial cells. Anticoagulant effect of HSYA plays a significant mediating role in many pathological processes, such as tissue IR injury, coronary heart disease, atherosclerosis, cerebrovascular disease and many other cardiovascular diseases. HSYA dose-dependently inhibited the specific binding between [^{3}H] PAF and washed rabbit platelet, which is considered as a new generation PAF receptor antagonist in the future (Zang et al., 2002). PAF-activated human small airway epithelial cells model was pretreated with HSYA. Guo et al. (2018) proposed that HSYA could attenuate the PAF-induced inflammatory factors, destruct cell-barrier function, and inhibit the expression of protein kinase C, MAPK, activator protein-1, and NF-κB activation to show anticoagulant effect.

Other Pharmacological Effects

In addition to the biological activities discussed above, HSYA also has other diverse pharmacological effects, such as immunodeficiency, anaphylactoid, hepatic fibrosis, pulmonary arterial hypertension, skin photosensitivity, Type 1 diabetes, vascular dementia, and so on.

HSYA is an immunomodulator that regulates the inflammatory response induced by lipopolysaccharide in various cells, including human non-small lung cancer cell line (A549 cells), H1299 and Eahy926 human endothelium cells. It could inhibit many kinase activities related to inflammatory factors, such as TNFα, IL-1β, and IL-6. HSYA could also inhibit the pro-inflammatory proteins expression, such as NF-κB p65, PI3K/Akt/mTOR, MAPK TLR-4, Myd88 and ICAM-1 (Han and Zhao, 2010; Jin et al., 2016; Jiang et al., 2019. HSYA was also proved to relieve certain respiratory conditions by decreasing mRNA levels of ICAM-1 and E-selectin elevation (Liu et al., 2014; Zhang et al., 2017). Moreover, another study implemented by Zheng et al. (2019) showed that HSYA could attenuate ovalbumin-induced allergic asthma in guinea pigs.

HSYA possesses a strong vascular relaxation effect on pulmonary arterial hypertension (PAH). It reduced the vascular tension by activating the Kv channel in pulmonary vascular smooth muscle cells (PVSMCs) (Bai et al., 2012). HSYA (6 mg/kg for 11 days) promoted angiogenesis in ischemic mice. The therapeutic mechanisms of HSYA might be associated to significantly increase the capillary-like tube formation and migration of HUVEC, enhance the expression of angiopoietin 1 and Tie-2, phosphorylations of Tie2, Akt and extracellular signal-regulated kinase 1/2 (Chen T. et al., 2016).

It is also reported that HSYA could exert protection on macroscopic skin lesions induced by ultraviolet rays (UV). It could promote the skin to regain its initial shape, elevate the activities of skin anti-oxidant enzymes, increase skin collagen content and maintain the structural integrity of the skin (Kong et al., 2013).

The combination of HSYA and deferoxamine (DFO) was discovered to improve type 1 diabetes by accelerating diabetic wound healing, promoting angiogenesis, reducing the inflammatory response, and up-regulating the expression of hypoxia-inducible factor-1 *a* (HIF-1 α) (Gao et al., 2018).

DISCUSSION AND CONCLUSION

In the present review, we systematically summarized the materials about HSYA, including acquisition methods, extraction and detection methods, pharmacokinetics, pharmacological effects and molecular mechanism. HSYA is proved to be an excellent antioxidant, anti-inflammatory and anticoagulant agent, so it plays an exceptional role in the treatment of cardiovascular and cerebrovascular diseases by down-regulating NF-κB signaling pathways, inhibiting MAPK signaling pathways, and attenuating the activation of Nrf-2/HO-1 signaling pathways. However, it is easily to degrade in the process of storage, extraction and separation procedure due to its chemical instability, which brings great challenges to the application of HSYA. Another major challenge is the low bioavailability caused by strong polarity. A large number of studies have been carried out to improve the chemical instability and bioavailability. Microemulsions, self-emulsifying systems, nanoparticles and other drug delivery systems have gradually improved the bioavailability, chemical stability, cellular uptake and biological activity of HSYA, which will be evaluated in clinical trials later.

Although great progress has been made in the research and application of HSYA in the past few decades, there are still many problems and challenges. First of all, chemical instability and low bioavailability of HSYA are still far from being resolved, which is still a key issue of the future research. It is important to continue the development of viable drug delivery systems for HSYA. The crucial aspects will involve in the enhancement of the solubility and bioavailability, as well as methods for selectively targeting these delivery systems to disease sites. Secondly, HSYA has been used to treat cardiovascular and cerebrovascular diseases clinically in China, but the drug target has not been completely revealed at present, which needs in-depth study later. Finally, the approach of obtaining HSYA from plants is cumbersome and complicated, and the yield is unsatisfactory. Chemical synthesis might pollute the environment, so it does not recommend to popularize. Biosynthesis is characterized by high efficiency, energy saving, and environmental protection, and it will transform into the major source of HSYA in the near future.

In short, it is the first time to systematically summarize the basic information about HSYA, which might provide relatively comprehensive basic data for the related research of HSYA.

AUTHOR CONTRIBUTIONS

HX, FZ and PW performed the frame design of the manuscript. FZ collected the data and drafted the manuscript. YJ, XZ and DC helped to organize the data. PW revised the manuscript. All authors read and approved the final manuscript.

FUNDING

This work was supported by grants from National Key Research and Development Program of China (2017YFC1702104, 2017YFC1702303), the National Natural Science Foundation of China (81830111, 81774201), National Science and Technology Major Project of China (2019ZX09201005-001-003), the Youth Innovation Team of Shaanxi Universities and Shaanxi Provincial Science and Technology Department Project (2016SF-378), the Fundamental Research Funds for the Central public welfare research institutes (ZXKT17058). Natural Science Foundation of Shandong Province (ZR2019ZD24, ZR2019YQ30).

The funding agencies had no role in the study design, the collection, analysis, or interpretation of data, the writing of the report, or the decision to submit the article for publication.

REFERENCES

Ahmed, T., and Aljaeid, B. (2016). Preparation, characterization, and potential application of chitosan, chitosan derivatives, and chitosan metal nanoparticles in pharmaceutical drug delivery. *Ddt* 10, 483–507. doi:10.2147/DDDT.S99651

Ao, H., Feng, W., and Peng, C. (2018). Hydroxysafflor yellow A: a promising therapeutic agent for a broad spectrum of diseases. *Evid. base Compl. Alternative Med.* 2018, 1–17. doi:10.1155/2018/8259280

Bacchetti, T., Morresi, C., Bellachioma, L., and Ferretti, G. (2020). Antioxidant and pro-oxidant properties of carthamus tinctorius, hydroxy safflor yellow A, and safflor yellow A. *Antioxidants* 9, 119. doi:10.3390/antiox9020119

Bie, X. D., Han, J., and Dai, H. B. (2010). Effects of hydroxysafflor yellow A on the experimental traumatic brain injury in rats. *J. Asian. Nat. Prod. Res.* 12, 239–247. doi:10.1080/10286020903510636

Bai, Y., Lu, P., Yu, C., Chen, M., He, F., et al. (2012). Hydroxysafflor yellow A (HSYA) from flowers of Carthamus tinctorius L. and its vasodilatation effects on pulmonary artery. *Molecules* 17, 14918–14927. doi:10.3390/molecules171214918

Cao, H. Y., Qin, X. D., Liu, C., Zhao, X. Z., Ma, Y. H., Zhou, J. N., et al. (2020). Establishment of fluorescence sensitization method for Hydroxysafflor yellow A. *Evid. Based. Complement. Alternat, Med.* 2020 (1–13), 3027843. doi:10.1155/2020/3027843

Chen, S., Ma, J., Zhu, H., Deng, S., Gu, M., and Qu, S. (2019). Hydroxysafflor yellow A attenuates high glucose-induced human umbilical vein endothelial cell dysfunction. *Hum. Exp. Toxicol.* 38, 685–693. doi:10.1177/0960327119831065

Chen, X., Wang, Y., Zhang, L., and Gao, Y. (2020a). Hydroxysafflor yellow A of carthamus tinctorius L., represses the malignant development of esophageal cancer cells via regulating NF-κB signaling pathway. *Cell Biochem. Biophys.* 78, 511. doi:10.1007/s12013-020-00934-1

Chen, Y., Li, Y., Chen, X., Wang, L., Sun, C., Yan, W., et al. (2010). Development and validation of a HPLC method for the determination of five bioactive

compounds in the "Xuebijing" injection. *Anal. Lett.* 43, 2456–2464. doi:10.1080/00032711003698739

Chen, T., Chen, N., Pang, N., Xiao, L., Li, Y., Li, R., et al. (2016a). Hydroxysafflor yellow A promotes angiogenesis via the angiopoietin 1/tie-2 signaling pathway. *J. Vasc. Res.* 53, 245–254. doi:10.1159/000452408

Chen, C. P., Pei, J., Wu, Y. Y., Ren, C. X., Chen, J., Liu, W., et al. (2016b). [Cloning,Bioinformatic analysis of chalcone-flavonone isomerase gene(CHI) and relationship between expression of CHI and accumulation of HSYA in Carthamus tinctorius]. *Zhong Yao Cai* 39, 499–503.

Collins, D. R. J., Tompson, A. C., Onakpoya, I. J., Roberts, N., Ward, A. M., and Heneghan, C. J. (2017). Global cardiovascular risk assessment in the primary prevention of cardiovascular disease in adults: systematic review of systematic reviews. *BMJ Open.* 7 (1–13), e013650. doi:10.1136/bmjopen-2016-013650

Chu, D., Liu, W., Huang, Z., Liu, S., Fu, X., and Liu, K. (2006). Pharmacokinetics and excretion of hydroxysafflor yellow A, a potent neuroprotective agent from safflower, in rats and dogs. *Planta Med.* 72, 418–423. doi:10.1055/s-2005-916249

Dai, Y., and Ge, J. (2012). Clinical use of aspirin in treatment and prevention of cardiovascular disease. *Thrombosis* [Epub ahead of print]. doi:10.1109/cis.2012.56

Deng, L., Wan, H., Zhou, H., Yu, L., and He, Y. (2018). Protective effect of hydroxysafflor yellow A alone or in combination with acetylglutamine on cerebral ischemia reperfusion injury in rat: a PET study using 18F-fuorodeoxyglucose. *Eur. J. Pharmacol.* 825, 119–132. doi:10.1016/j.ejphar.2018.02.011

Desborough, M. J. R., and Keeling, D. M. (2017). The aspirin story–from willow to wonder drug. *Br. J. Haematol.* 177, 674–683. doi:10.1111/bjh.14520

Donahue, M. J., and Hendrikse, J. (2018). Improved detection of cerebrovascular disease processes: introduction to the journal of cerebral blood flow and metabolism special issue on cerebrovascular disease. *J. Cerebr. Blood Flow Metabol.* 38, 1387–1390. doi:10.1177/0271678X17739802

Eichhorn, E. J., and Gheorghiade, M. (2002). Digoxin. *Prog. Cardiovasc. Dis.* 44, 251–266. doi:10.1053/pcad.2002.31591

Fan, L., Pu, R., Zhao, H. Y., Liu, X., Ma, C., Wang, B. R., et al. (2011). Stability and degradation of hydroxysafflor yellow A and anhydrosafflor yellow B in the Safflower injection studied by HPLC-DAD-ESI-MSn. *J. Chin. Pharmaceut. Sci.* 20, 47–56. doi:1-47-1010.5246/jcps.2011.01.007

Gao, S.-Q., Chang, C., Li, J.-J., Li, Y., Niu, X.-Q., Zhang, D.-P., et al. (2018). Co-delivery of deferoxamine and hydroxysafflor yellow a to accelerate diabetic wound healing via enhanced angiogenesis. *Drug Deliv.* 25, 1779–1789. doi:10.1080/10717544.2018.1513608

Ghasemiyeh, P., and Mohammadi-Samani, S. (2018). Solid lipid nanoparticles and nanostructured lipid carriers as novel drug delivery systems: applications, advantages and disadvantages. *Res. Pharm. Sci.* 13, 288–303. doi:10.4103/1735-5362.235156

Guo, L. F., Zhang, Y., Hu, Z. H., Hu, X. L., Xu, N. S., Zhang, X. S., et al. (2013). Clustering analysis of safflower (*Carthamuss tinctorius* L.) germplasm resources based on morphological markers. *J. Henan Agric. Sci.* 42, 41–97. doi:10.15933/j.cnki.1004-3268.2013.02.020

Guo, X., Zheng, M., Pan, R., Zang, B., and Jin, M. (2018). Hydroxysafflor yellow a suppresses platelet activating factor-induced activation of human small airway epithelial cells. *Front. Pharmacol.* 9, 859–870. doi:10.3389/fphar.2018.00859

Han, B., and Zhao, H. (2010). Effects of hydroxysafflor yellow a in the attenuation of MPTP neurotoxicity in mice. *Neurochem. Res.* 35, 107–113. doi:10.1007/s11064-009-0035-4

Han, D., Wei, J., Zhang, R., Ma, W., Shen, C., Feng, Y., et al. (2016). Hydroxysafflor yellow a alleviates myocardial ischemia/reperfusion in hyperlipidemic animals through the suppression of TLR4 signaling. *Sci. Rep.* 6, 35319–35332. doi:10.1038/srep35319

Heller, W., and Hahlbrock, K. (1980). Highly purified "flavanone synthase" from parsley catalyzes the formation of naringenin chalcone. *Arch. Biochem. Biophys.* 200, 617–619. doi:10.1016/0003-9861(80)90395-1

Hong, B., Wang, Z., Xu, T., Li, C., and Li, W. (2015). Matrix solid-phase dispersion extraction followed by high performance liquid chromatography-diode array detection and ultra performance liquid chromatography-quadrupole-time of flight-mass spectrometer method for the determination of the main compounds from *Carthamus tinctorius* L. (Hong-hua). *J. Pharmaceut. Biomed. Anal.* 107, 464–472. doi:10.1016/j.jpba.2015.01.040

Hong, S.-C., Yoo, S.-Y., Kim, H., and Lee, J. (2017). Chitosan-based multifunctional platforms for local delivery of therapeutics. *Mar. Drugs* 15 (1–16), 60. doi:10.3390/md15030060

Hu, T., Wei, G., Xi, M., Yan, J., Wu, X., Wang, Y., et al. (2016). Synergistic cardioprotective effects of danshensu and hydroxysafflor yellow a against myocardial ischemia-reperfusion injury are mediated through the Akt/Nrf2/HO-1 pathway. *Int. J. Mol. Med.* 38, 83–94. doi:10.3892/ijmm.2016.2584

Huber, G., Priest, S., and Geisbuhler, T. (2018). Cardioprotective effect of hydroxysafflor yellow A via the cardiac permeability transition pore. *Planta. Med.* 84, 507–518. doi:10.1055/s-0043-122501

Jiang, M., Zhou, L. Y., Xu, N., and An, Q. (2019). Hydroxysafflor yellow A inhibited lipopolysaccharide-induced non-small cell lung cancer cell proliferation, migration, and invasion by suppressing the PI3K/AKT/mTOR and ERK/MAPK signaling pathways. *Thorac. Cancer* 10, 1319–1333. doi:10.1111/1759-7714.13019

Jin, M., Sun, C.-y., and Zang, B.-x. (2016a). Hydroxysafflor yellow A attenuate lipopolysaccharide-induced endothelium inflammatory injury. *Chin. J. Integr. Med.* 22, 36–41. doi:10.1007/s11655-015-1976-x

Jin, Y., Wu, L., Tang, Y., Cao, Y., Li, S., Shen, J., et al. (2016b). UFLC-Q-TOF/MS based screening and identification of the metabolites in plasma, bile, urine and feces of normal and blood stasis rats after oral administration of hydroxysafflor yellow A. *J. Chromatogr. B* 1012–1013, 124–129. doi:10.1016/j.jchromb.2016.01.023

Knogge, W., Schmelzer, E., and Weissenböck, G. (1986). The role of chalcone synthase in the regulation of flavonoid biosynthesis in developing oat primary leaves. *Arch. Biochem. Biophys.* 250, 364–372. doi:10.1016/0003-9861(86)90738-1

Koga, K., Takarada, N., and Takada, K. (2010). Nano-sized water-in-oil-in-water emulsion enhances intestinal absorption of calcein, a high solubility and low permeability compound. *Eur. J. Pharm. Biopharm.* 74, 223–232. doi:10.1016/j.ejpb.2009.09.004

Kong, S.-Z., Shi, X.-G., Feng, X.-X., Li, W.-J., Liu, W.-H., Chen, Z.-W., et al. (2013). Inhibitory effect of hydroxysafflor yellow A on mouse skin photoaging induced by ultraviolet irradiation. *Rejuvenation Res.* 16, 404–413. doi:10.1089/rej.2013.1433

Lee, M., Li, H., Zhao, H., Suo, M., and Liu, D. (2020). Effects of Hydroxysafflor Yellow A on the PI3K/AKT pathway and apoptosis of pancreatic β-Cells in Type 2 diabetes mellitus rats. *Diabetes. Metab. Syndr. Obes* 13, 1097–1107. doi:10.2147/DMSO.S246381

Lee, S.-E., Lee, J.-K., Jang, W.-S., Kim, T.-H., Tunsirikongkon, A., Choi, J.-S., et al. (2016). Enhancement of stability and controlled drug release of lipid nanoparticles by modified solvent-evaporation method. *Colloid. Surface. Physicochem. Eng. Aspect.* 508, 294–300. doi:10.1016/j.actbio.2014.07.032

Li, Y., Zhang, Z., and Zhang, J. (2007). Determination of hydroxysafflor yellow A in rat plasma and tissues by high-performance liquid chromatography after oral administration of safflower extract or safflor yellow. *Biomed. Chromatogr.* 21, 326–334. doi:10.1002/bmc.769

Li, H., Huang, L., Ping, Q., and Zhao, H. (2009). Study on the stability of safflower yellow. *Strait. Pharm. J.* 21, 12–14.

Li, J. R., Sun, M. J., Ping, Q. N., Chen, X. J., Qi, J. P., and Han, D. E. (2010a). Metabolism, excretion and bioavailability of hydroxysafflor yellow A after oral administration of its lipid-based formulation and aqueous solution in rats. *Chin. J. Nat. Med.* 8, 233–240. doi:10.3724/SP.J.1009.2010.00233

Li, S., Kesarla, R., and Omri, A. (2013). Formulation strategies to improve the bioavailability of poorly absorbed drugs with special emphasis on self-emulsifying systems. *ISRN Pharmaceut.* 2013 (1–16), 1. doi:10.1155/2013/848043

Li, L., Yang, Y., Hou, X., Gu, D., Ba, H., Abdulla, R., et al. (2013a). Bioassay-guided separation and purification of water-soluble antioxidants from *Carthamus tinctorius* L. by combination of chromatographic techniques. *Separ. Purif. Technol.* 104, 200–207. doi:10.1016/j.seppur.2012.11.027

Li, J., Zhang, S. Y., Lu, M. R., Chen, Z. B., Chen, C., Han, L. J., et al. (2013b). Hydroxysafflor yellow A suppresses inflammatory responses of BV2 microglia after oxygen–glucose deprivation. *Neurosci. Lett.* 535, 51–56. doi:10.1016/j.neulet.2012.12.056

Li, C. Y., Chu, J. H., Zhang, J., Dai, G. L., Zou, J. D., and Ju, W. Z. (2014). Determination of hydroxysafflor yellow A in human plasma by LC-MS/MS analysis. *Chin. Pharmacol. Bull.*, 1402–1407. doi:10.3969/j.issn.1001-1978.2014.10.016

Li, L. J., Jiang, T. T., and Guo, J. (2016). Preparation of HSYA by organic reagent method. *Strait. Pharm. J.* 28, 30–34.

Li, Y., Wang, Z., Chang, H., Wang, Y., and Guo, M. (2010b). Expression of CT-wpr, screened by cDNA-AFLP approach, associated with hydroxysafflor yellow A in *Carthamus tinctorius* L. *Biochem. Systemat. Ecol.* 38, 1148–1155. doi:10.1016/j.bse.2010.10.010

Li, X., Huang, L., and Fu, Z. (2011). The influence of light on stability of Safflowler Yellow. *Strait. Pharm. J.* 23, 64–66.

Liang, H. Z., Dong, W., Yu, Y. L., Yang, H. Q., Xu, L. J., and Niu, Y. G. (2015). Advances in studies on safflower (*carthamus tinctorius* L.) at home and abroad. *J. Anhui Agri. Sci.* 43, 71–74. doi:10.13989/j.cnki.0517-6611.2015.16.030

Liu, Y. L., Liu, Y. J., Liu, Y., Li, X. S., Liu, S. H., Pan, Y. G., et al. (2014). Hydroxysafflor yellow A ameliorates lipopolysaccharide-induced acute lung injury in mice via modulating toll-like receptor 4 signaling pathways. *Int. Immunopharm.* 23, 649–657. doi:10.1016/j.intimp.2014.10.018

Liu, Z., Liu, L., Liu, Y., Wang, S., Zhang, S., Dong, R., et al. (2020). Hydroxysafflor yellow A induces autophagy in human liver cancer cells by regulating Beclin 1 and ERK expression. *Exp Ther Med.* 9, 2989–2996. doi:10.3892/etm.2020.8552

Loboda, A., Damulewicz, M., Pyza, E., Jozkowicz, A., and Dulak, J. (2016). Role of Nrf2/HO-1 system in development, oxidative stress response and diseases: an evolutionarily conserved mechanism. *Cell. Mol. Life Sci.* 73, 3221–3247. doi:10.1007/s00018-016-2223-0

Lopes, L. B. (2014). Overcoming the cutaneous barrier with microemulsions. *Pharmaceutics* 28, 52–77. doi:10.3390/pharmaceutics6010052

Lu, Y. Q., Luo, Y., He, Z. F., Chen, J., Yan, B., Wang, Y., et al. (2013). Hydroxysafflor yellow A ameliorates homocysteine-induced Alzheimer-like pathologic dysfunction and memory/synaptic disorder. *Rejuvenation Res.* 16, 446–452. doi:10.1089/rej.2013.1451

Luo, M., Huang, J. C., Yang, Z. Q., Wang, Y. S., Guo, B., and Yue, Z. P. (2020). Hydroxysafflor yellow A exerts beneficial effects by restoring hormone secretion and alleviating oxidative stress in polycystic ovary syndrome mice. *Exp. Physiol.* 105, 282–292. doi:10.1113/EP088147

Lv, X. Y., Mo, J. Q., Jiang, T., Zhong, F. R., Jia, Z. H., Li, J. W., et al. (2011). Novel multilayered porous silicon-based immunosensor for determining Hydroxysafflor yellow A. *Appl. Surf. Sci.* 257, 1906–1910. doi:10.1016/j.apsusc.2010.09.024

Lv, L. Z., Tong, C. Q., Lv, Q., Tang, X. J., Li, L. M., Fang, Q. X., et al. (2012). Enhanced absorption of hydroxysafflor yellow A using a self-double-emulsifying drug delivery system: *in vitro* and *in vivo* studies. *Int. J. Nanomed.* 7, 4099–4107. doi:10.2147/IJN.S33398

Lv, Y., Qian, Y., Fu, L., Chen, X., Zhong, H., and Wei, X. (2015). Hydroxysafflor yellow A exerts neuroprotective effects in cerebral ischemia reperfusion-injured mice by suppressing the innate immune TLR4-inducing pathway. *Eur. J. Pharmacol.* 769, 324–332. doi:10.1016/j.ejphar.2015.11.036

Lv, X., Zhang, S. G., Ma, H. P., Dong, P. P., Ma, X. D., Xu, M., et al. (2018). *In situ* monitoring of the structural change of microemulsions in simulated gastrointestinal conditions by SAXS and FRET. *Acta Pharm. Sin. B.* 8, 655–665. doi:10.1016/j.apsb.2018.05.008

Ma, G. N., Yu, F. L., Zhang, H., Li, Z. P., and Mei, X. G. (2014). Pharmacokinetics and biopharmaceutics of hydroxysafflor yellow A: research advances. *J. Int. Pharm. Res.* 41, 195–199. doi:10.13220/j.cnki.jipr.2014.02.012.220

Ma, Y., Feng, C., Wang, J., Chen, Z., Wei, P., Fan, A. R., et al. (2019a). Hydroxyl safflower yellow A regulates the tumor immune microenvironment to produce an anticancer effect in a mouse model of hepatocellular carcinoma. *Oncol. Lett.* 17, 3503–3510. doi:10.3892/ol.2019.9946

Ma, Y. C., Li, M. M., Wu, Q., Xu, W. F., Lin, S., Chen, Z. W., et al. (2019b). Hydroxysafflor yellow A sensitizes ovarian cancer cells to chemotherapeutic agent by decreasing WSB1 expression. *Eur. J. Integr. Med.* 25, 6–12. doi:10.1016/j.eujim.2018.11.007

Meselhy, M. R., Kadota, S., Momose, Y., Hatakeyama, N., Kusai, A., Hattori, M., et al. (1993). Two new quinochalcone yellow pigments from Carthamus tinctorius and Ca^{2+} antagonistic activity of tinctormine. *Chem. Pharm. Bull.* 41, 1796–1802. doi:10.1248/cpb.41.1796

Min, F., Sun, H., Wang, B., Ahmad, N., Guo, H., Gao, H. T., et al. (2020). Hepatoprotective effects of hydroxysafflor yellow A in D-galactose-treated aging mice. *Eur. J. Pharmacol.* 881 (1–36), 173214. doi:10.1016/j.ejphar.2020.173214

Pang, B., Zheng, Q. F., and Liu, W. (2015). Synthetic biology in natural medicine research. *Scientia. Sinica. Vitae.* 45, 1015–1026. doi:10.1360/N052015-00041

Pan, Y., Zheng, D. Y., Liu, S. M., Meng, Y., Xu, H. Y., Zhang, Q., et al. (2012). Hydroxysafflor yellow A attenuates lymphostatic encephalopathy-induced brain injury in rats. *Phytother. Res* 26, 1500–1506. doi:10.1002/ptr.4594

Pu, W., Zhang, H., Wang, M., Liu, Y. N., Sun, L. L., and Ren, X. L. (2017). Superior stability of Hydroxysafflor Yellow A in Xuebijing injection and the associated mechanism. *Molecules* 22 (1–12), 2129. doi:10.3390/molecules22122129

Qi, J., Jin, X., Huang, L., and Ping, Q. (2007). Simultaneous determination of hydroxysafflor yellow A and ferulic acid in rat plasma after oral administration of the co-extractum of *Rhizoma* chuanxiong and *Flos Carthami* by HPLC–diode array detector. *Biomed. Chromatogr.* 21, 816–822. doi:10.1002/bmc.821

Qi, J., Zhuang, J., Wu, W., Lu, Y., Song, Y. M., Zhang, Z. T., et al. (2011). Enhanced effect and mechanism of water-in-oil microemulsion as an oral delivery system of hydroxysafflor yellow A. *Int. J. Nanomed.* 6, 985–991. doi:10.2147/IJN.S18821

Reuland, D. J., McCord, J. M., and Hamilton, K. L. (2013). The role of Nrf2 in the attenuation of cardiovascular disease. *Exerc. Sport Sci. Rev.* 41, 162–168. doi:10.1097/JES.0b013e3182948a1e

Sheng, C., Peng, W., Xia, Z., and Wang, Y. (2019). Plasma and cerebrospinal fluid pharmacokinetics of hydroxysafflor yellow A in patients with traumatic brain injury after intravenous administration of Xuebijing using LC-MS/MS method. *Xenobiotica* 50, 545–551. doi:10.1080/00498254.2019.1668983

Sun, M. J., Chen, X. J., and Ping, Q. N. (2009). HPLC analysis of the hydroxysafflor yellow A in excretion of rat. *Pharm. Clin. Res.* 17, 191–194.

Sun, X., Wei, X., Qu, S., Zhao, Y., and Zhang, X. (2010). Hydroxysafflor Yellow A suppresses thrombin generation and inflammatory responses following focal cerebral ischemia–reperfusion in rats. *Bioorg. Med. Chem. Lett.* 20, 4120–4124. doi:10.1016/j.bmcl.2010.05.076

Sun, Y. W., He, Y., Zhang, R. P., Huang, J. W., and Gu, M. C. (2013). Optimization of ultrasonic extraction conditions of safflower yellow from *Carthamus tinctorius* by response surface methodology. *J. Chin. Med. Mater.* 36, 2018–2022. doi:10.13863/j.issn1001-4454.2013.12.001

Suzuki, T., Ishida, M., Kumazawa, T., and Sato, S. (2017). Oxidation of 3, 5-di-C-(per-O-acetylglucopyranosyl) phloroacetophenone in the synthesis of hydroxysafflor yellow A. *Carbohydr. Res.* 448, 52–56. doi:10.1016/j.carres.2017.05.009

Tan, L., Wang, Y., Jiang, Y., Wang, R., Zu, J., and Tan, R. (2020). Hydroxysafflor Yellow A together with blood-brain barrier regulator Lexiscan for cerebral ischemia reperfusion injury treatment. *ACS Omega* 5, 19151–19164. doi:10.1021/acsomega.0c02502

Tang, J., Lou, Z., Wang, Y., and Guo, M. (2010). Expression of a small heat shock protein (CTL–hsyapr) screened by cDNA-AFLP approach is correlated with hydroxysafflor yellow A in safflower (*Carthamus tinctorius* L.). *Biochem. Systemat. Ecol.* 38, 722–730. doi:10.1016/j.bse.2010.06.001

Tapeinos, C., Battaglini, M., and Ciofani, G. (2017). Advances in the design of solid lipid nanoparticles and nanostructured lipid carriers for targeting brain diseases. *J. Contr. Release* 264, 306–332. doi:10.1016/j.jconrel.2017.08.033

Tian, L., Wu, G. R., and Wang, Y. (2007). Quality assessment of *Carthamus tinctorius* L. In emin country, tacheng prefecture, xinjiang. *China. Pharmaceuticals* 16, 5–7.

Tong, W., Sun, P., Yang, X., Huang, L. L., and Hu, S. Q. (2011). Study on relativity of safflower color and hydroxysafflor yellow A. *South west China. J. Agric. Sci.* 24, 101–104. doi:10.16213/j.cnki.scjas.2011.01.035

Tu, Y. H., Xue, Y. R., Guo, D. D., Sun, L. N., and Guo, M. L. (2009). Hydroxysafflor yellow A reduces myocardial infarction size after coronary artery ligation in rats. *Pharm. Biol.* 47, 458–462. doi:10.1080/13880200902822612

Wang, S., Sun, M., and Ping, Q. (2008). Enhancing effect of labrafac lipophile WL 1349 on oral bioavailability of hydroxysafflor yellow A in rats. *Int. J. Pharm. (Amst.)* 358, 198–204. doi:10.1016/j.ijpharm.2008.03.006

Wang, G., Li, Q. Y., Fang, Q. L., Han, M., and Gao, J. Q. (2009). Uptake and transport of hydroxysafflor yellow A in Caco-2 cells monolayer. *J. Chin. Pharmaceut. Sci.* 44, 353–357.

Wang, H. (2017). *Studies on the extraction and purification and stability of HSYA*. Shanxi, China: Shanxi university.

Wang, J., Wang, J., Wang, X., Liu, L., Hu, J. H., and Yu, X. (2016). Molecular mechanism of inhibition of the abnormal proliferation of human umbilical vein endothelial cells by Hydroxysafflor-yellow A. *Pharm. Biol.* 54, 1800–1807. doi:10.3109/13880209.2015.1129541

Wang, J. P., Wang, P., Gui, S. Q., Li, Y., Chen, R. H., Zeng, R. Q., et al. (2017). Hydroxysafflor yellow A improves motor dysfunction in the rotenone-induced mice model of Parkinson's disease. *Front. Pharmacol.* 8 (1–10), 613. doi:10.1007/s11064-017-2176-1

Wang, N., He, D., Zhou, Y., Wen, J., Liu, X. Q., Li, P, Y., et al. (2019). Hydroxysafflor yellow A actives BKCa channels and inhibits L-type Ca channels to induce vascular relaxation. *Eur. J. Pharmacol.* 870 (1–10), 172873. doi:10.1016/j.ejphar.2019.172873

Wang, Y., Du, S. Y., Wu, Q., Xiao, Y., Wu, H. C., Lu, X. J., et al. (2012). Optimization of smashing tissue extraction of hydroxyl safflor yellow A

from *carthamus tinctorius* L. *Lishizhen Med. Materia. Med. Res.* 9, 2144–2145. doi:10.3969/j.issn.1008-0805.2012.09.013

Wei, X. B., Liu, H. Q., Sun, X., Fu, F. H., Zhang, X. M., Wang, J., et al. (2005). Hydroxysafflor yellow A protects rat brains against ischemia-reperfusion injury by antioxidant action. *Neurosci. Lett.* 386, 58–62. doi:10.1016/j.neulet.2005.05.069

Wen, A. D., Yang, J., Jia, Y. Y., Yang, Z. F., Tian, Y., Wu, Y., et al. (2008). A rapid and sensitive liquid chromatography–tandem mass spectrometry (LC–MS/MS) method for the determination of hydroxysafflor yellow A in human plasma: application to a pharmacokinetic study. *J. Chromatogr. B.* 876, 41–46. doi:10.1016/j.jchromb.2008.10.007

Wu, L., Tang, Y., Shan, C., Chai, C., Zhou, Z., Shi, X. Q., et al. (2018). A comprehensive *in vitro* and *in vivo* metabolism study of hydroxysafflor yellow A. *J. Mass Spectrom.* 53, 99–108. doi:10.1002/jms.4041

Wu, Y., Wang, L., Jin, M., and Zang, B. (2012). Hydroxysafflor yellow A alleviates early inflammatory response of bleomycin-induced mice lung injury. *Biol. Pharm. Bull.* 35, 515–522. doi:10.1248/bpb.35.515

Xiong, Q. M., Min, C., Liu, Y., Pan, M. F., and Liu, Q. H. (2004). Pharmacokinetics of hydroxysafflor yellow A. *Chin. J. Pharm.* 35, 228–230.

Xu, L. J., Liang, H. Z., Yu, Y. L., Tan, Z. W., Yang, H. Q., Dong, W., et al. (2018). *Carthamus tinctorius* L.: evaluation on correlations of hydroxysafflor with flower color and the difference among cultivars. *Chin. Agricu. Sci. Bull.* 34, 41–45.

Yan, K., Wang, X., Pan, H., Wang, L. J., Yang, H. B., Liu, M. J., et al. (2020). Safflower Yellow and its main component HSYA alleviate diet-induced obesity in mice: possible involvement of the increased antioxidant enzymes in liver and adipose tissue. *Front. Pharmacol.* 11 (1–13), 482. doi:10.3389/fphar.2020.00482

Yang, J., Wang, Y., and Guo, M. L. (2011). Identification and mapping of a novel hydroxysafflor yellow A (HSYA) biosynthetic gene in *Carthamus Tinctorius*. *Biochem. Genet.* 49, 410–415. doi:10.1007/s10528-011-9417-9

Yang, Y., Dai, F., Liu, S., and Kuang, C. (2008). Study on extraction technology of yellow pigment from *Carthamus tinctorius* with microwave extraction. *Food Res. Dev.* 29, 190–192.

Yang, X., Chen, L., Li, Y., Gao, F., Yan, Z., Zhang, P., et al. (2020a). Protective effect of Hydroxysafor Yellow A on cerebral ischemia reperfusion-injury by regulating GSK3β-mediated pathways. *Neurosci. Lett.* 736 (1–25), 135258. doi:10.1016/j.neulet.2020.135258

Yang, X., Li, Y., Chen, L., Xu, M. G., Wu, J. B., Zhang, P., et al. (2020b). Protective effect of hydroxysafflor yellow A on dopaminergic neurons against 6-hydroxydopamine, activating anti-apoptotic and anti-neuroinflammatory pathways. *Pharm. Biol.* 58 (1), 686–694. doi:10.1080/13880209.2020.1784237

Yang, Z., Yang, J., Jia, Y., Tian, Y., and Wen, A. (2009). Pharmacokinetic properties of hydroxysafflor yellow A in healthy Chinese female volunteers. *J. Ethnopharmacol.* 124, 635–638. doi:10.1016/j.jep.2009.02.026

Ye, J. X., Wang, M., Wang, R. Y., Liu, H. T., Qi, Y. D., Fu, J. H., et al. (2020). Hydroxysafflor yellow A inhibits hypoxia/reoxygenation-induced cardiomyocyte injury via regulating the AMPK/NLRP3 inflammasome pathway [published online ahead of print, 2020 Feb 19]. *Int. Immunopharm.* 82 (1–7), 106316. doi:10.1016/j.intimp.2020.106316

Yue, M., Zang, B. X., Li, J. R., and Wang, J. F. (2003). Preliminary study on the thermal stability of hydroxysafflor yellow A. *China J. Chin. Mater. Med.* 28, 1197–1198.

Yu, L., Liu, Z., He, W., Chen, H. F., Lai, Z. L., Duan, Y. H., et al. (2020). Hydroxysafflor Yellow A confers neuroprotection from focal cerebral ischemia by modulating the crosstalk between JAK2/STAT3 and SOCS3 signaling pathways [published online ahead of print, 2020 Feb 14]. *Cell. Mol. Neurobiol.* 40 (8), 1271–1281. doi:10.1007/s10571-020-00812-7

Zang, B. X., Jin, M., Si, N., Zhang, Y., Wu, W., and Piao, Y. Z. (2002). Antagonistic effect of hydroxysafflor yellow A on the platelet activating factor receptor. *Yao Xue Xue Bao* 37, 696–699.

Zeng, Q. Y., Huang, X., Wang, Y., Lv, H. Y., Xia, Z., and Ji, H. (2013). Simultaneous determination of three metabolism constituents of Danchuanhong formula in urinein of patients with traumatic brain injury after oral administration by UPLC-ESI-MS/MS. *Pharmacol. Clin. Chin Materia. Med.* 29, 182–185.

Zhang, L., Zhu, L., Wang, Y. F., Jiang, Z. Z., Chai, X., Zhu, Y., et al. (2012). Characterization and quantification of major constituents of Xue Fu Zhu Yu by UPLC-DAD–MS/MS. *J. Pharmaceut. Biomed.* 62, 203–209. doi:10.1016/j.jpba.2011.12.026

Zhang, N., Xing, M. Y., Wang, Y. Y., Liang, H., Yang, Z., Shi, F. D., et al. (2014). Hydroxysafflor yellow A improves learning and memory in a rat model of vascular dementia by increasing VEGF and NR1 in the hippocampus. *Neurosci. Bull.* 30, 417–424. doi:10.1007/s12264-013-1375-2

Zhang, J., Li, J., Song, H., Xiong, Y., Liu, D., and Bai, X. (2019). Hydroxysafflor yellow A suppresses angiogenesis of hepatocellular carcinoma through inhibition of p38 MAPK phosphorylation. *Biomed. Pharmacother.* 109, 806–814. doi:10.1016/j.biopha.2018.09.086

Zhang, H. F. (2006). *Study on absorption mechanism of hydroxysafflor yellow A in gastrointestinal tract*. Beijing, China: Chin Pharmaceutical University.

Zhang, L. L., Tian, K., Tang, Z. H., Chen, X. J., Bian, Z. X., Wang, Y. T., et al. (2016). Phytochemistry and pharmacology of *Carthamus tinctorius* L. *Am. J. Chin. Med.* 44, 197–226. doi:10.1142/S0192415X16500130

Zhang, Y. D., Song, L. J., Pan, R. Y., Gao, J. W., Zang, B. X., and Jin, M. (2017). Hydroxysafflor yellow A alleviates lipopolysaccharide-induced acute respiratory distress syndrome in mice. *Biol. Pharm. Bull.* 40, 135–144. doi:10.1248/bpb.b16-00329

Zhang, Z., Guo, M., and Zhang, J. (2009). Identification of AFLP fragments linked to hydroxysafflor yellow A in *Flos Carthami* and conversion to a SCAR marker for rapid selection. *Mol. Breed.* 23, 229–237. doi:10.1007/s11032-008-9228-9

Zhao, B., Gu, S., Du, Y., Shen, M., Liu, X., and Shen, Y. (2018). Solid lipid nanoparticles as carriers for oral delivery of hydroxysafflor yellow A. *Int. J. Pharm. (Amst.)* 535, 164–171. doi:10.1016/j.ijpharm.2017.10.040

Zhao, X. P. (2015). *The evaluation and breeding selection of Safflower germplasm resources*. Henan, China: Henan Normal University.

Zheng, M., Guo, X. J., Pan, R. Y., Gao, J. W., Zang, B. X., and Jin, M. (2019). Hydroxysafflor yellow A alleviates ovalbumin-induced asthma in a Guinea pig model by attenuateing the expression of inflammatory cytokines and signal transduction. *Front. Pharmacol.* 10, 328. doi:10.3389/fphar.2019.00328

Zhou, P., Zhou, H. F., He, Y., Zhang, Y. Y., Yang, J. H., Dai, L. L., et al. (2014). Transport characteristics of hydroxysafflor yellow A across Caco-2 cell monolayer model. *Chin. Tradit. Herb. Drugs* 45, 2030–2035. doi:10.7501/j.issn.0253-2670.2014.14.014

Zhou, J., Li, M., Jin, W., Li, X., Fan, H., and Zhang, Y. (2018). Pharmacokinetic study on protocatechuic aldehyde and hydroxysafflor yellow A of Danhong injection in rats with hyperlipidemia. *Pharmacology* 102, 154–160. doi:10.1159/000491020

Zhou, D. L., Ding, T. T., Ni, B., Jing, Y. Y., and Liu, S. X. (2019). Hydroxysafflor Yellow A mitigated myocardial ischemia/reperfusion injury by inhibiting the activation of the JAK2/STAT1 pathway. *Int. J. Mol. Med.* 44, 405–416. doi:10.3892/ijmm.2019.4230

Zhu, H. J., Wang, L. J., Wang, X. Q., Pan, H., Li, N. S., Yang, H. B., et al. (2015). Hydroxysafflor yellow A (HYSA) inhibited the proliferation and differentiation of 3T3-L1 preadipocytes. *Cytotechnology* 67, 885–892. doi:10.1007/s10616-014-9783-3

Zhu, M.-Z., Zhou, Z.-Y., Zhou, Z.-Y., Lu, H., Gao, M., Liu, L.-M., et al. (2020). Effect and safety of hydroxysafflor yellow a for injection in patients with acute ischemic stroke of blood stasis syndrome: a phase II, multicenter, randomized, double-blind, multiple-dose, active-controlled clinical trial. *Chin. J. Integr. Med.* 26, 420–427. doi:10.1007/s11655-020-3094-7

Zong, X., Li, L., Zhang, H., Li, B., and Liu, C. (2013). Preparative separation of hydroxyl safflower yellow A and anhydrosafflor yellow B in plant extract of *Carthamus Tinctorius* L. by reverse-phase medium-pressure liquid chromatography. *J. Liq. Chromatogr. Relat. Technol.* 36. doi:10.1080/10826076.2012.704614

Zou, J., Wang, N., Liu, M., Bai, Y., Wang, H., Liu, K., et al. (2018). Nucleolin mediated pro-angiogenic role of Hydroxysafflor Yellow A in ischaemic cardiac dysfunction: Post-transcriptional regulation of VEGF-A and MMP-9. *J. Cell. Mol. Med.* 22. 2692–2705. doi:10.1080/10826076.2012.704614

Conflict of Interest: The authors declare that the research was conducted in the absence of any commercial or financial relationships that could be construed as a potential conflict of interest.

The handling Editor declared a past co-authorship with one of the authors HX.

Copyright © 2020 Zhao, Wang, Jiao, Zhang, Chen and Xu. This is an open-access article distributed under the terms of the Creative Commons Attribution License (CC BY). The use, distribution or reproduction in other forums is permitted, provided the original author(s) and the copyright owner(s) are credited and that the original publication in this journal is cited, in accordance with accepted academic practice. No use, distribution or reproduction is permitted which does not comply with these terms.

GLOSSARY

AUMC the plasma concentration-time curve
BBB the blood-brain barrier
DAD diode
DDAB dimethyl octadecyl ammonium bromide
ECD electrochemical
EDTA ethylenediaminetetraacetic acid
HIF-1 α hypoxia-inducible factor-1 α
HO-1 hemeoxygenase-1
HSYA Hydroxysafflor yellow A
I/R ischemia/reperfusion
LAD left anterior descending coronary artery
LOD the limits of detection
LOQ the limit of quantification
MCAO middle cerebral artery occlusion
MIS myocardial infarction size
Nrf2 nuclear factor erythroid 2-related factor 2
MSPD Matrix solid-phase dispersion
OGD oxygen and glucose deprivation models
PAH pulmonary arterial hypertension
Papp the apparent permeability coefficient
P-gp P-glycoprotein
SDEDDS Self-emulsifying drug delivery system
SLN Solid lipid nanoparticles
SY safflower yellow
TBI traumatic brain injury
UAE ultrasound-assisted treatment.

frontiers in Pharmacology

ORIGINAL RESEARCH
published: 17 December 2020
doi: 10.3389/fphar.2020.587176

Bufei Jianpi Formula Improves Mitochondrial Function and Suppresses Mitophagy in Skeletal Muscle via the Adenosine Monophosphate-Activated Protein Kinase Pathway in Chronic Obstructive Pulmonary Disease

*Jing Mao[1,2†], Ya Li[2,3,4†], Suxiang Feng[1,2,4], Xuefang Liu[2,4], Yange Tian[2,4], Qingqing Bian[2,3,4], Junzi Li[2,4], Yuanyuan Hu[2,4], Lanxi Zhang[2,4], Huige Ji[2,4] and Suyun Li[2,3,4]**

[1]College of Pharmacy, Henan University of Chinese Medicine, Zhengzhou, China, [2]Henan Key Laboratory of Chinese Medicine for Respiratory Disease, Henan University of Chinese Medicine, Zhengzhou, China, [3]Institute for Respiratory Diseases, The First Affiliated Hospital, Henan University of Chinese Medicine, Zhengzhou, China, [4]Co-Construction Collaborative Innovation Center for Chinese Medicine and Respiratory Disease by Henan and Education Ministry of P.R. China, Henan University of Chinese Medicine, Zhengzhou, China

OPEN ACCESS

Edited by:
Yanqiong Zhang,
China Academy of Chinese Medical Sciences, China

Reviewed by:
Yu Chiang Hung,
Kaohsiung Chang Gung Memorial Hospital, Taiwan
Yih-Fung Chen,
Kaohsiung Medical University, Taiwan

***Correspondence:**
Suyun Li
lisuyun2000@126.com

[†]These authors have contributed equally to this work

Specialty section:
This article was submitted to Ethnopharmacology, a section of the journal Frontiers in Pharmacology

Received: 25 July 2020
Accepted: 24 November 2020
Published: 17 December 2020

Citation:
Mao J, Li Y, Feng S, Liu X, Tian Y, Bian Q, Li J, Hu Y, Zhang L, Ji H and Li S (2020) Bufei Jianpi Formula Improves Mitochondrial Function and Suppresses Mitophagy in Skeletal Muscle via the Adenosine Monophosphate-Activated Protein Kinase Pathway in Chronic Obstructive Pulmonary Disease. Front. Pharmacol. 11:587176. doi: 10.3389/fphar.2020.587176

Skeletal muscle dysfunction, a striking systemic comorbidity of chronic obstructive pulmonary disease (COPD), is associated with declines in activities of daily living, reductions in health status and prognosis, and increases in mortality. Bufei Jianpi formula (BJF), a traditional Chinese herbal formulation, has been shown to improve skeletal muscle tension and tolerance via inhibition of cellular apoptosis in COPD rat models. This study aimed to investigate the mechanisms by which BJF regulates the adenosine monophosphate-activated protein kinase (AMPK) pathway to improve mitochondrial function and to suppress mitophagy in skeletal muscle cells. Our study showed that BJF repaired lung function and ameliorated pathological impairment in rat lung and skeletal muscle tissues. BJF also improved mitochondrial function and reduced mitophagy via the AMPK signaling pathway in rat skeletal muscle tissue. *In vitro*, BJF significantly improved cigarette smoke extract-induced mitochondrial functional impairment in L6 skeletal muscle cells through effects on mitochondrial membrane potential, mitochondrial permeability transition pores, adenosine triphosphate production, and mitochondrial respiration. In addition, BJF led to upregulated expression of mitochondrial biogenesis markers, including AMPK-α, PGC-1α, and TFAM and downregulation of mitophagy markers, including LC3B, ULK1, PINK1, and Parkin, with increased expression of downstream markers of the AMPK pathway, including mTOR, PPARγ, and SIRT1. In conclusion, BJF significantly improved skeletal muscle and mitochondrial function in COPD rats and L6 cells by promoting mitochondrial biogenesis and suppressing mitophagy via the AMPK pathway. This study suggests that BJF may

have therapeutic potential for prophylaxis and treatment of skeletal muscle dysfunction in patients with COPD.

Keywords: mitophagy, mitochondrial biogenesis, chronic obstructive pulmonary disease, Bufei Jianpi formula, skeletal muscle dysfunction

INTRODUCTION

Chronic obstructive pulmonary disease (COPD), a common and preventable disease, is characterized by persistent airflow limitations caused by chronic inflammatory responses to noxious particles and gases (Patel et al., 2019). In China, COPD has become the third leading cause of death and the third most prevalent chronic disease (Collaborators, 2015), with an estimated 99.9 million individuals aged 20 years or older with spirometry-defined COPD (Wang et al., 2018a). Skeletal muscle dysfunction (SMD), a serious systemic comorbidity of COPD (Ceco et al., 2017), has been recognized as an early disease feature and an important causative factor in the limited mobility and mortality of patients with this disease (Maltais et al., 2014; Barreiro, 2016). Studies have shown that muscle wasting is experienced in up to 30%–40% of COPD patients, with significant impairments in activities of daily living, health status, and prognosis (Mowery, 2017).

Development of SMD is likely multifactorial, with inflammation and mitochondrial dysfunction playing predominant roles. Other pathophysiological factors, including oxidative stress, imbalance of protein synthesis/degradation, hypoxia, and cellular apoptosis have also been postulated to contribute to the muscle wasting experienced by COPD patients (Barreiro and Gea, 2016). Recent studies have identified major mitochondrial abnormalities in COPD skeletal muscle cells, including decreases in mitochondrial density and biogenesis, reductions in oxidative capacity, impairments in activity and coupling of mitochondrial respiratory chain complexes, increases in production of mitochondrial reactive oxygen species (ROS), and enhancements in autophagy and apoptosis (Meyer et al., 2013; Taivassalo and Hussain, 2016).

Decreased mitochondrial biogenesis and enhanced mitophagy play particularly important roles in mitochondrial impairment. Peroxisome proliferator-activated receptor gamma coactivator (PGC)-1α has been shown to be a master regulator of mitochondrial biogenesis (Tadaishi et al., 2011). PGC-1α acts as a cotranscriptional regulatory factor that induces mitochondrial biogenesis by activating nuclear respiratory factors (NRF) 1 and 2, which then activate mitochondrial transcription factor A (TFAM), an essential factor for replication, maintenance, and transcription of mitochondrial DNA (Grabacka et al., 2016; Yu et al., 2017).

Mitophagy, on the other hand, is closely associated with the AMPK pathway. AMPK directly facilitates phosphorylation of UNC-51-like kinase (ULK1), which stimulates the mitophagic activity of ULK1 (Allavena et al., 2016). The PTEN-induced putative kinase 1 (PINK1)/Parkin pathway has also been implicated as an important molecular mechanism mediating mitophagy. While PINK1 is a protein kinase primarily located in the mitochondrial outer membrane, Parkin is an E3 ubiquitin ligase generally located in the cytoplasm. When mitochondrial damage occurs, PINK1 phosphorylates the Parkin ubiquitin ligase at S65 and initiates its recruitment to the mitochondria. Once activated, Parkin ubiquitinates substrates on the outer mitochondria for two divergent processes, autophagosome recruitment and proteasomal degradation of ubiquitinated mitochondrial substrates. Mitochondrial fission-1 protein (Fis1), a receptor on the outer membrane, governs the developing light chain (LC) 3 isolation membrane to generate an autophagosome around the damaged mitochondria. The autophagosome is then delivered to the lysosome for degradation (Hardie, 2011; Wei et al., 2017).

Traditional Chinese medicine (TCM) has been successfully used to treat COPD for thousands of years. Lung-spleen qi deficiency syndrome is believed to be the main underlying pathologic mechanism for the SMD observed in patients with COPD (Medicine, 2012). Bufei Jianpi formula (BJF), which is composed of 12 medicinal herbs, has been proven to have efficacy in patients with COPD by improving respiratory function, reducing the frequency of acute exacerbations, and enhancing exercise tolerance (Li et al., 2012a). In previous experimental studies, we also found that BJF significantly improved skeletal muscle tension and tolerance in COPD rats, reduced cellular apoptosis, and improved mitochondrial function (Dong et al., 2015; Mao et al., 2019). It remains unclear, however, if mitochondrial dysregulation underlies the SMD observed in COPD.

In this study, we aimed to explore the mechanism by which BJF affects mitochondrial regulation via the AMPK pathway in an *in vivo* COPD rat model and an *in vitro* cigarette smoke extract (CSE)-induced skeletal muscle cell line to identify potential underlying mechanisms and to provide a basis for further research.

MATERIALS AND METHODS

Reagents and Animals

Klebsiella pneumoniae (strain: 46114) was obtained from the National Center for Medical Culture Collections (Beijing, China). HongqiQu® filter cigarettes (tobacco-type of tar: 10 mg, nicotine content: 1.0 mg, carbon monoxide fumes: 12 mg) were purchased from Henan Tobacco Industry (Zhengzhou, China). Aminophylline (APL) tablets were obtained from Shandong Xinhua Pharmaceutical Co., LTD. (lot H37020630) (Shandong, China). 5-Aminoimidazole-4-carboxamide ribonucleotide (AICAR) was purchased from Selleck Chemicals (lot 2627-69-2) (Houston, TX, USA).

TABLE 1 | Components of BJF.

Chinese name	Name for publishing	Amount (g)	Lot. No	Company
Dang Shen	Codonopsis pilosula (Franch.) Nannf.	15	19110102	Zhengzhou Ruilong Pharmaceutical Co. Ltd.
Huang Qi	Astragalus mongholicus Bunge	15	19070102	Zhengzhou Ruilong Pharmaceutical Co. Ltd.
Bai Zhu	Atractylodes macrocephala Koidz	12	19110202	Zhengzhou Ruilong Pharmaceutical Co. Ltd.
Fu Ling	Poria cocos (Schw.) Wolf	12	19100102	Zhengzhou Ruilong Pharmaceutical Co. Ltd.
Huang Jing	Polygonatum kingianum Collett & Hemsl	15	191001	Bozhou Guangyuan Tang Traditional Chinese Medicine Decoction pieces Co. Ltd.
Zhe Bei Mu	Fritillaria thunbergii Miq	9	19060101	Zhengzhou Ruilong Pharmaceutical Co. Ltd.
Di Long	Pheretima aspergillum (E. Perrier)	12	19100102	Zhengzhou Ruilong Pharmaceutical Co. Ltd.
Hou Po	Magnolia officinalis Rehder and E. H. Wilson	9	19100102	Zhengzhou Ruilong Pharmaceutical Co. Ltd.
Chen Pi	Citrus reticulata Blanco	9	19120103	Zhengzhou Ruilong Pharmaceutical Co. Ltd.
Zi Wan	Aster tataricus L.f.	9	CP-427-191101	Bozhou Shenglin Pharmaceutical Co. Ltd.
Ai Di Cha	Ardisia japonica (Thunb.) Blume	15	191201	Anhui Jishun Traditional Chinese Medicine Decoction pieces Co. Ltd.
Yin Yang Huo	Epimedium brevicomu Maxim	6	190201	Hebei Sirui Pharmaceutical Co. Ltd.

Dorsomorphin dihydrochloride (BML-275 dihydrochloride) was purchased from MedChemExpress (lot 1219168-18-9) (Shanghai, China).

Thirty-six male and 36 female Sprague-Dawley (SD) rats with an average body weight of 200 ± 20 g were purchased from the Experimental Animal Center of Henan Province (Zhengzhou, China). The rats were housed in specific pathogen-free cages under standard temperature (25 ± 2°C) and light conditions, with a 12-h light/dark cycle, and free access to food and water. All animal studies were conducted in accordance with the Institute's Guide for the Care and Use of Laboratory Animals and were approved by the Experimental Animal Care and Ethics Committee of the First Affiliated Hospital of the Henan University of Chinese Medicine.

Preparation of Herbal Medicines

BJF, consisting of 12 herbs (**Table 1**), was prepared by the Laboratory of Pharmacology in Henan University of Chinese Medicine. All herbs were prepared in a fluid extract in accordance with the standard operating procedures. The high performance liquid chromatography (HPLC) fingerprint was performed to identify the main chemical constituents in BYF. A highresolution HPLC column (Venusil XBP C18, 4.6 × 250 mm, 5 μm) (Thermo Scientific, United States) were used at a flow rate of 1.0 ml/min at 30°C. Mobile phase A was 0.1% formic acid in water and mobile phase B was acetonitrile. The gradient elution program was 5–30 min, 5–100% B. The UV spectrophotometer detector was set at 270 nm.

Preparation of BJF-Containing Serum

Sixty Sprague-Dawley rats were randomized into control and Bufei Jianpi groups. Rats in the Bufei Jianpi group were administered BJF (4.5 1g/kg/d) intragastrically 10 times once per day for 7 days. Rats in control group were administrated distilled water (2 ml per animal). On day 7, all rats were narcotized with 4% chloral hydrate and blood samples were collected, centrifugated at 3,500 rpm for 15 min, inactivated at 56°C, and stored in a −80°C freezer for further study.

Preparation of COPD Rat Model and Drug Administration

Seventy-two rats were randomly assigned to the following groups: control, model, Bufei Jianpi Formula (BJF), 5-Aminoimidazole-4-carboxamide ribonucleotide (AICAR), Bufei Jianpi Formula + 5-Aminoimidazole-4-carboxamide ribonucleotide (BJF + AICAR), and Aminophylline (APL), with 12 animals in each group. The detailed procedures for creation of the COPD rat model have been described in a previous report (Li et al., 2012b); however, in brief, rats were exposed to cigarette smoke (concentration: 3,000 ± 500 ppm) for 30 min twice per day from week 1 through week 12. In addition, 0.1 ml of *Klebsiella pneumonia* suspension (6×10^8 CFU/mL, 100 μL) was slowly dropped into the nasal cavities of rats every 5 days for the first 8 weeks. The successful generation of a COPD rat model was evaluated based on symptoms, lung function, and pulmonary pathology (Li et al., 2012a).

Starting from week 9, rats in the control and model groups were intragastrically administered normal saline (2 mL/animal). BJF (4.51 g/kg/d) was administered to rats in the BJF and BJF + AICAR groups, while APL (2.7 mg/kg/d) was administered to rats in the APL group twice per day for 12 weeks. AICAR (25 mg/kg/d) was intraperitoneally administered to rats in the AICAR and BJF + AICAR groups once a day during week 20. The equivalent dosages of BJF and APL were calculated using the equation:

$$D_{rat} = D_{human} \times \left(\frac{I_{rat}}{I_{human}}\right) \times \left(\frac{W_{rat}}{W_{human}}\right)^{2/3}$$

in which D represents dose, I represents body shape index, and W represents body weight.

All rats underwent necropsy after intraperitoneal injection of 10% chloral hydrate at 100 mg/kg of body weight at the end of

week 20, and lung and quadriceps muscle tissues were collected for further analysis.

Respiratory Function Analysis in Rat Model

Lung function was measured by a whole-body plethysmography system (Buxco Inc., Wilmington, NC, USA) at weeks 0, 4, 8, 12, 16, and 20. Tidal volume (TV), peak expiratory flow (PEF), and 50% tidal volume expiratory flow (EF50) were evaluated.

Lung and Skeletal Muscle Histopathology in Rat Model

After being fixed in 10% formalin for 72 h, left lung and quadriceps muscle tissues were embedded with paraffin, cut into 4-μm thick sections, and stained with hematoxylin and eosin (HE) for light microscopy.

Skeletal Muscle Ultrastructure Morphology in Rat Model

After being cut into sections with 1-mm thicknesses, fresh quadriceps muscle tissue was fixed in 2.5% glutaraldehyde for 2 h followed by 1% osmium tetroxide. Sections were then stained with uranyl acetate, dehydrated in a methanol series and propylene oxide, and embedded with Epon-812. Ultrathin sections were obtained, and ultrastructural changes and mitophagy of skeletal muscle cells were examined using a JEM-1400 transmission electron microscope (OLYMPUS, Japan).

Measurement of Mitochondrial Function in Skeletal Muscle

Mitochondrial characteristics, including mitochondrial membrane potentials (MMP), ATP production, and opening of mitochondrial permeability transition pores (MPTPs) were measured with a JC-1 kit (Beyotime Biotech Co., Ltd., Shanghai, China), an ATP assay kit (Beyotime Biotech Co., Ltd., Shanghai, China), and an MPTP assay (Genmed Scientifics Inc., DE, USA), respectively, according to the manufacturer's instruction and as previously described (Mao et al., 2019).

Cell Culture and Transfection

Rat L6 myoblasts (obtained from the Cell Bank of Chinese Academy of Sciences, Shanghai) were cultured in Dulbecco's modified Eagle's medium (DMEM) (Solarbio Tech Co., Ltd., Beijing, China) supplemented with 10% fetal bovine serum (FBS) in a 5% CO_2-humidified atmosphere at 37°C. When cells had grown by 70–90%, they were plated on dishes at a density of 1×10^5 cells/mL and incubated in 5% CO_2-95% air for 24 h. On the next day, cells were treated with 10% cigarette smoke extract (CSE), 10% CSE + AICAR (2.5 ng/mL), or 10% CSE +10% BJF-containing serum in DMEM and harvested 24 h later.

Preparation of Cigarette Smoke Extract

CSE was prepared using a modified version of Sheridan's method (Sheridan et al., 2015). Briefly, a filterless HongqiQu cigarette was combusted through a modified 50-ml syringe apparatus, and the smoke was dissolved in 20 ml of DMEM. The pH was adjusted to 7.4 with 1 mol/L sodium hydroxide and 37.5%-concentrated hydrochloric acid, and then diluted with DMEM until the optical density was measured to be 2.0 ± 0.05 using an ultraviolet spectrophotometer (Thermo Fisher Scientific, MA, USA). This solution represented "100%" strength. Smoked medium was then passed through a 0.22-μm filter to sterilize the solution. Finally, smoked medium was diluted in DMEM to the required strength and used for the experiment within 30 min.

Measurement of Mitochondrial Respiration in L6 Cells

Mitochondrial respiration was measured with a Seahorse XF Cell Mito Stress Test Kit (Agilent Technologies, CA, United States) on a Seahorse XF24 Extracellular Flux Analyzer (Seahorse Bioscience, MA, United States) according to the manufacturer's instruction. L6 cells were seeded (10,000 cells/per well) onto Seahorse assay plates in DMEM media and treated with 10% CSE for 24 h. During the experiment, cells were switched to an XF assay medium (HCO3-free modified DMEM) supplemented with 10 mM of L-glutamine, 10 mM of glucose, and 10 mM of pyruvate, while a pH of 7.4 was maintained at 37°C. After baseline measurement of oxygen combustion rate (OCR), a mitochondrial respiration test was performed by sequential additions of 1.0 μM oligomycin, 2.0 μM carbonyl cyanide 4-(trifluoromethoxy) phenylhydrazone, and 0.5 μM rotenone/antimycin A. Several mitochondrial parameters were determined, including basal respiration, maximal respiratory capacity, proton leak, and non-mitochondrial respiration. The results were expressed as OCRs (pmol/min/lg protein).

Measurement of Mitochondrial Membrane Potentials in L6 Cells

For measurement of mitochondrial membrane potentials, L6 cells were seeded in 6-well plates with a density of 1×10^5 cells per well and treated with 10% CSE, 10% CSE + AICAR, or 10% CSE +10% BJF-containing serum for 24 h. Before the experiment, cells were treated with carbonyl cyanide *m*-chlorophenyl hydrazone (CCCP) (100 μM, Sigma) for 1 h as a positive control. Changes in mitochondrial membrane potentials of L6 cells in different groups were then assessed using the JC-1 mitochondrial membrane potential detection kit according to the manufacturer's instruction. Red fluorescence represented JC-1 aggregates, whereas green fluorescence represented the monomeric form of JC-1. Fluorescence intensity was analyzed by a Varioskan® Flash Microplate Reader (Thermo Fisher Scientific, MA, USA). MMPs in each group were calculated as the ratio of red/green fluorescence. In addition, cells were visualized using confocal laser scanning microscopy at a 514-nm excitation and a 529-nm emission for green and a 585-nm excitation and a 590-nm emission for red.

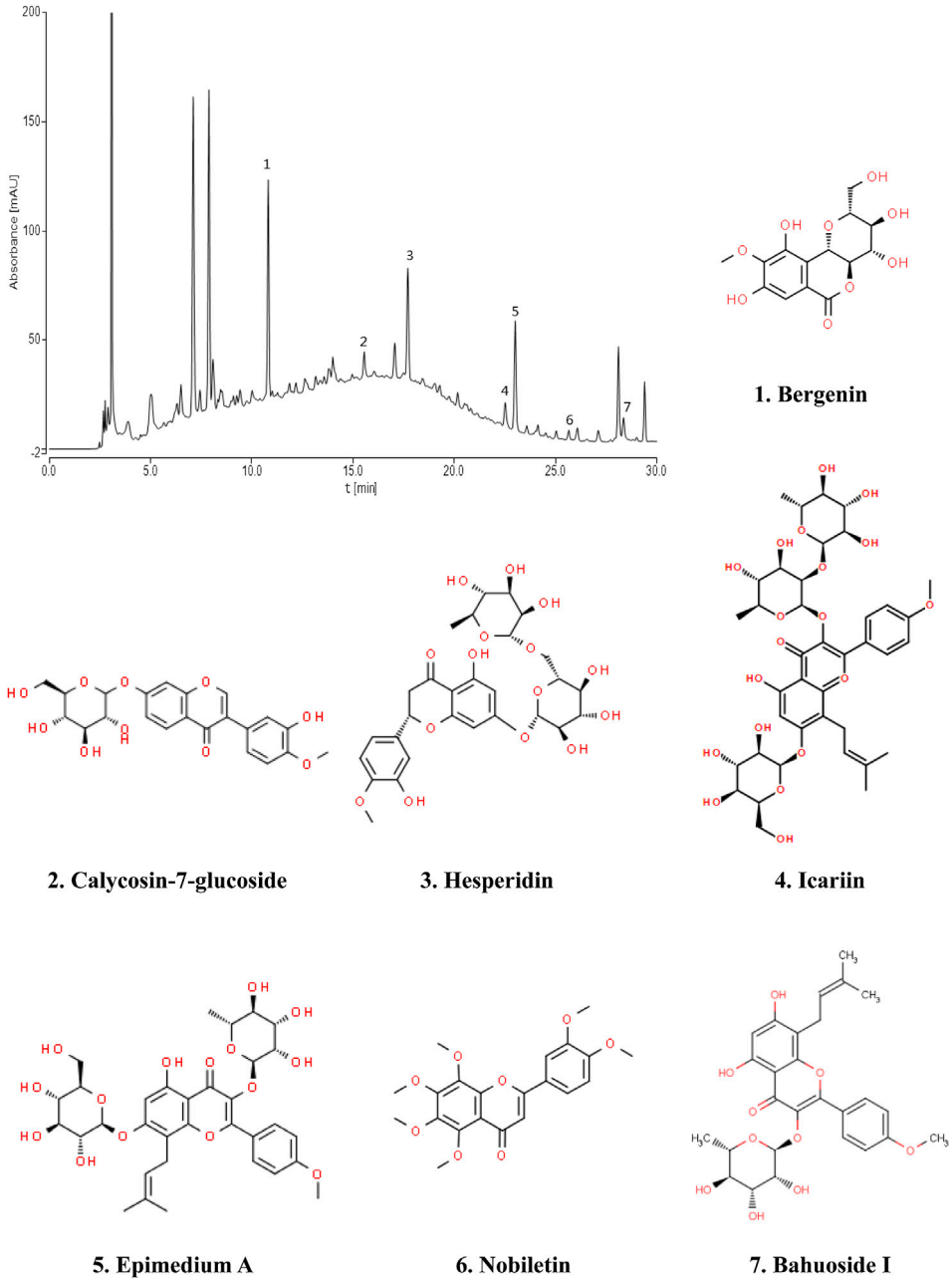

FIGURE 1 | Chromatogram fingerprint of Bufei Jianpi formula (BJF). The 7 compounds were identified in BJF: 1, Bergenin; 2, Calycosin-7-glucoside; 3, Hesperidin; 4, Icariin; 5, Epimedium A; 6, Nobiletin; 7, Baohuoside I.

Measurement of ATP Levels in L6 Cells

For measurement of ATP levels, L6 cells were seeded in 6-well plates with a density of 1 $\times 10^5$ cells per well for 24 h. After treatment with study drugs, cells were lyzed using a cell lysis reagent, and the ATP content in cell lysates was measured using an ATP assay kit (Beyotime Biotech Co., Ltd., Shanghai, China) following the manufacturer's protocol. The total and mitochondrial protein concentrations were determined using a bicinchoninic acid (BCA) protein assay kit (Beyotime Biotech Co., Ltd., Shanghai, China).

RNA Isolation and Real-Time PCR Analysis

Expression levels of mRNA in quadriceps muscle tissuewere analyzed by semiquantitative polymerase chain reactions (qPCR). Total RNA was extracted from the quadriceps muscle using a total RNA isolation kit (Solarbio Tech Co., Ltd., Beijing, China) according to the manufacturer's protocol. Real-time (RT)-qPCR was performed using a reverse transcriptase kit (Solarbio Tech Co., Ltd., Beijing, China) and a SYBR Green Master Mix (Vazyme Biotech Co., Ltd. Nanjing, China). To normalize the amount of total RNA in each reaction, a reference gene (*GAPDH*) was used as an internal standard.

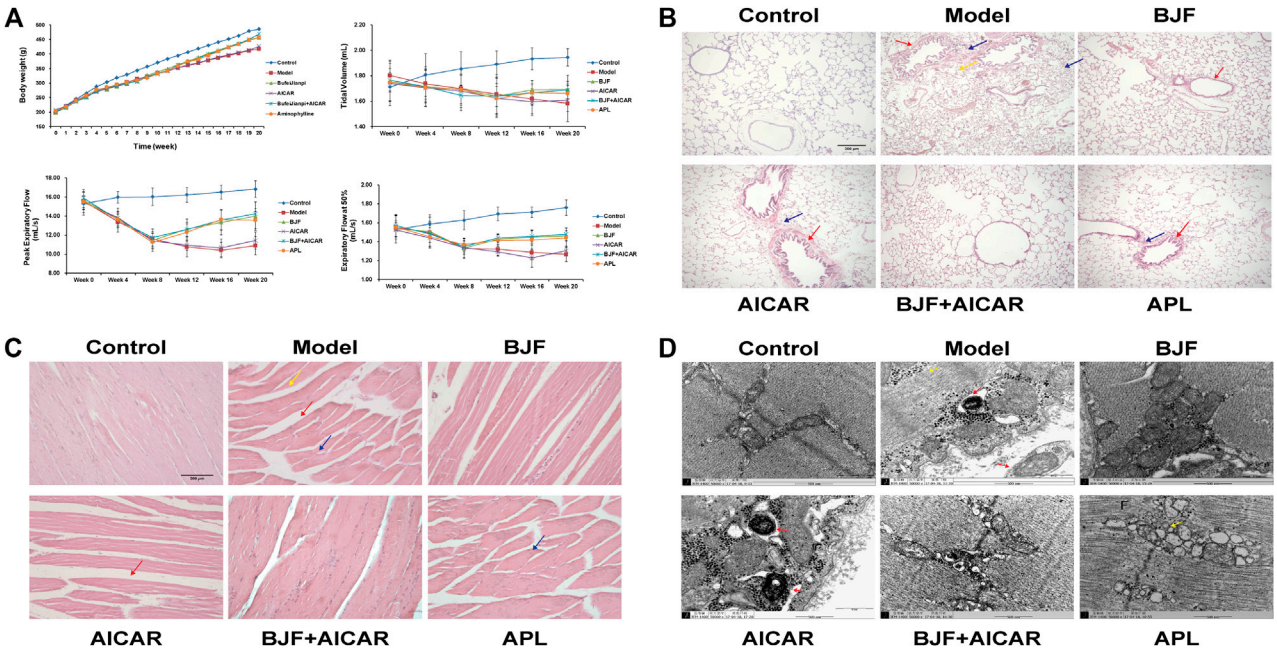

FIGURE 2 | Effects of Bufei Jianpi formula (BJF) on COPD rats. **(A)** Body weight and pulmonary function [data are presented as mean ± SD (n = 6 per group)], **(B)** lung histomorphology, with red arrow indicating airway wall thickening, yellow arrow indicating pulmonary alveoli wall rupture, and blue arrow indicating inflammatory cell infiltration [hematoxylin and eosin (HE) staining, magnification ×100, scale bar = 100 μm], **(C)** skeletal muscle histomorphology, with red arrow indicating the increased intervals between muscle fibers, yellow arrow indicating muscle fiber atrophy and blue arrow indicating muscle fibers disarrangement (HE staining, magnification ×200, scale bar = 200 μm), and **(D)** skeletal muscle ultrastructure, with red arrow indicating mitochondrial autophagosomes fusing with lysosomes and yellow arrow indicating mitochondria complicated with vacuoles (magnification ×50,000). AICAR, 5-aminoimidazole-4-carboxamide ribonucleotide; APL, aminophylline.

Western Blotting

Total proteins from cells or tissue samples were lyzed in a lysis buffer and quantified using a BCA assay. Ten-cell lysates were loaded into each well in 10% sodium dodecyl sulfate polyacrylamide gel electrophoresis (SDS-PAGE) gels and transferred to a polyvinylidene difluoride (PVDF) membrane. Membranes were blocked in 5% nonfat milk in tris-buffered saline and polysorbate 20 (TBST) for 2 h at room temperature and incubated with the indicated primary antibodies, including anti-AMPK-α, anti-*p*-AMPK-α, anti-PGC-1α, anti-TFAM, anti-LC3B, anti-ULK1, anti-PINK1, anti-Parkin, anti-mammalian target of rapamycin (mTOR), anti-sirtuin 1 (SIRT1), anti-peroxisome proliferator-activated receptor (PPAR)γ (Abcam, Cambridge, United Kingdom), or anti-glyceraldehyde 3-phosphate dehydrogenase (GAPDH) (Proteintech, Wuhan, China) at 4°C overnight. After incubation with the HRP-coupled secondary antibody (Proteintech, Wuhan, China) at room temperature for 2 h, signals were detected using a super-enhanced chemiluminescence plus reagent and scanned and quantified by a ChemiDoc MP imaging system (Bio-Rad, CA, USA).

Statistical Analysis

Data are expressed as mean ± SD. Statistical differences between the groups were identified by one-way analysis of variance (ANOVA). Differences were considered to be significant at P-values of < 0.05.

RESULTS

Fingerprint of BJF The retention time values of the identified compounds were compared with that of the reference substances. A representative chromatogram of BJF was shown in **Figure 1**. 7 compounds including Bergenin (1.3456 mg/g), Calycosin-7-glucoside (0.5616 mg/g), Hesperidin (1.1755 mg/g), Epimedium A (0.6869 mg/g), Icariin (1.1195 mg/g), Nobiletin (0.0951 mg/g), Baohuosidl (0.0806 mg/g) were identified and their structures had also been shown.

BJF Attenuated the Severity of Respiratory and Skeletal Muscle Dysfunction in COPD Rats

To assess potential effects on skeletal and lung tissues, BJF was orally administered to COPD rats for 12 weeks using APL as a positive control. We found that BJF attenuated declines in body weight and respiratory function in COPD rats. As shown in **Figure 2A**, the body weight of rats in the model group increased slowly and was significantly lower than the control group at week 8. This decrease in body weight was markedly inhibited by treatment with BJF, APL, and AICAR, with no significant differences between the effects of these substances.

As shown in **Tables 2–4**, respiratory function analysis revealed that the PEF was significantly decreased in the model group at week 4 and that the VT and EF50 declined in the model group at

TABLE 2 | Tidal volume analysis.

Group	Week0	Week4	Week8	Week12	Week16	Week20
Control	1.71 ± 0.11	1.81 ± 0.17	1.86 ± 0.13	1.89 ± 0.11	1.93 ± 0.09	1.94 ± 0.07
COPD	1.80 ± 0.12	1.74 ± 0.14	1.70 ± 0.15**	1.65 ± 0.16**	1.62 ± 0.12**	1.58 ± 0.14**
BJF	1.75 ± 0.14	1.72 ± 0.13	1.69 ± 0.11	1.64 ± 0.15	1.69 ± 0.07	1.69 ± 0.11$^{\#\#}$
AICAR	1.74 ± 0.17	1.70 ± 0.14	1.68 ± 0.13	1.62 ± 0.15	1.59 ± 0.11$^{\Delta}$	1.61 ± 0.08$^{\Delta}$
BJF + AICAR	1.76 ± 0.09	1.72 ± 0.10	1.65 ± 0.08	1.64 ± 0.08	1.67 ± 0.10	1.69 ± 0.07$^{\#\#}$
APL	1.75 ± 0.15	1.71 ± 0.15	1.69 ± 0.17	1.62 ± 0.12	1.67 ± 0.09	1.66 ± 0.07$^{\#}$

Data are presented as mean ± SD (n = 6 per group). $^{**}P < 0.01$, $^{*}P < 0.05$ *vs. control group;* $^{\#\#}P < 0.01$, $^{\#}P < 0.05$ *vs. model group;* $^{\Delta\Delta}P < 0.01$, $^{\Delta}P < 0.05$ *vs. BJF group;* $^{\blacktriangle\blacktriangle}P < 0.01$, $^{\blacktriangle}P < 0.05$ *vs. 5-aminoimidazole-4-carboxamide ribonucleotide (AICAR) group; and* $^{\square\square}P < 0.01$, $^{\square}P < 0.05$ *vs. BJF + AICAR group. APL, aminophylline.*

TABLE 3 | Peak expiratory flow analysis.

Group	Week0	Week4	Week8	Week12	Week16	Week20
Control	15.30 ± 1.18	15.97 ± 0.60	16.02 ± 0.93	16.22 ± 0.77	16.51 ± 0.72	16.83 ± 0.88
COPD	15.55 ± 1.22	13.40 ± 1.09**	11.62 ± 1.00**	10.75 ± 1.04**	10.42 ± 0.78**	10.89 ± 0.97**
BJF	15.63 ± 0.93	13.75 ± 0.58	11.43 ± 0.91	12.64 ± 1.04$^{\#\#}$	13.35 ± 1.33$^{\#\#}$	13.98 ± 1.50$^{\#\#}$
AICAR	15.44 ± 0.70	13.83 ± 0.98	11.39 ± 0.85	10.93 ± 0.49$^{\Delta\Delta}$	10.66 ± 0.92$^{\Delta\Delta}$	11.43 ± 0.88$^{\Delta\Delta}$
BJF + AICAR	15.88 ± 0.60	13.59 ± 0.58	11.74 ± 0.92	12.60 ± 0.77$^{\#\#}$	13.57 ± 1.04$^{\#\#\blacktriangle\blacktriangle}$	14.23 ± 0.56$^{\#\#\blacktriangle\blacktriangle}$
APL	15.50 ± 0.59	13.64 ± 0.85	11.24 ± 0.94	12.29 ± 0.90$^{\#\#}$	13.63 ± 1.08$^{\#\#\blacktriangle\blacktriangle}$	13.57 ± 0.90$^{\#\#}$

Data are presented as mean ± SD (n = 6 per group). $^{**}P < 0.01$, $^{*}P < 0.05$ *vs. control group;*$^{\#\#}P < 0.01$, $^{\#}P < 0.05$ *vs. model group;* $^{\Delta\Delta}P < 0.01$, $^{\Delta}P < 0.05$ *vs. BJF group;* $^{\blacktriangle\blacktriangle}P < 0.01$, $^{\blacktriangle}P < 0.05$ *vs. 5-aminoimidazole-4-carboxamide ribonucleotide (AICAR) group; and* $^{\square\square}P < 0.01$, $^{\square}P < 0.05$ *vs. BJF + AICAR group. APL, aminophylline.*

TABLE 4 | 50% tidal volume expiratory flow analysis.

Group	Week0	Week4	Week8	Week12	Week16	Week20
Control	1.53 ± 0.14	1.59 ± 0.10	1.63 ± 0.10	1.69 ± 0.07	1.71 ± 0.06	1.76 ± 0.08
COPD	1.55 ± 0.12	1.50 ± 0.10	1.33 ± 0.11*	1.32 ± 0.07**	1.29 ± 0.08**	1.27 ± 0.08**
BJF	1.54 ± 0.08	1.51 ± 0.15	1.33 ± 0.10	1.42 ± 0.05$^{\#\#}$	1.45 ± 0.07$^{\#\#}$	1.46 ± 0.06$^{\#\#}$
AICAR	1.53 ± 0.08	1.44 ± 0.11	1.34 ± 0.07	1.29 ± 0.04$^{\Delta\Delta}$	1.23 ± 0.10$^{\Delta\Delta}$	1.30 ± 0.05$^{\Delta\Delta}$
BJF + AICAR	1.57 ± 0.12	1.48 ± 0.14	1.35 ± 0.06	1.44 ± 0.04$^{\#\#\blacktriangle\blacktriangle}$	1.46 ± 0.06$^{\#\#\blacktriangle\blacktriangle}$	1.48 ± 0.07$^{\#\#\blacktriangle\blacktriangle}$
APL	1.55 ± 0.12	1.45 ± 0.12	1.37 ± 0.07	1.41 ± 0.06$^{\#\#\blacktriangle\blacktriangle}$	1.42 ± 0.10$^{\#\#\blacktriangle\blacktriangle}$	1.44 ± 0.10$^{\#\#\blacktriangle\blacktriangle}$

Data are presented as mean ± SD (n = 6 per group). $^{**}P < 0.01$, $^{*}P < 0.05$ *vs. control group;*$^{\#\#}P < 0.01$, $^{\#}P < 0.05$ *vs. model group;* $^{\Delta\Delta}P < 0.01$, $^{\Delta}P < 0.05$ *vs. BJF group;* $^{\blacktriangle\blacktriangle}P < 0.01$, $^{\blacktriangle}P < 0.05$ *vs. 5-aminoimidazole-4-carboxamide ribonucleotide (AICAR) group; and* $^{\square\square}P < 0.01$, $^{\square}P < 0.05$ *vs. BJF + AICAR group. APL, aminophylline.*

week 8. Treatment with BJF, APL, and AICAR resulted in increased VT, PEF, and EF50.

We also found that BJF obviously reduced lung injury identified on histopathological examination. As shown in **Figure 2B**, the structure of the pulmonary alveoli and airways were fully intact in control rats, while marked airway wall thickening, alveolar wall rupture and inflammatory cell infiltration were observed in the lungs of COPD rats. These pulmonary histopathological impairments were significantly improved in rats treated with BJF, APL, and AICAR, with reductions in inflammatory cell infiltration, especially in the BJF and BJF + AICAR groups.

BJF also obviously improved morphological and ultrastructural changes in skeletal muscle of COPD rats. As shown in **Figures 2C,D**, marked morphological changes, including muscle fiber atrophy and disarrangement, increased intervals between muscle fibers, uneven myocyte cytoplasmic staining, and differently sized nuclei were observed in the skeletal muscle of model rats. These changes were improved after treatment with BJF, APL, and AICAR, particularly in the BJF and BJF + AICAR groups. While the model, APL, and AICAR groups showed marked ultrastructural changes, including an abundance of swollen mitochondria with increased number of vacuoles, a fracturecrest of the mitochondria, and increased mitophagy, BJF ameliorated these abnormal mitochondrial findings.

BJF Ameliorated Mitochondrial Function in COPD Rats

To confirm the effect of BJF on mitochondrial function, we measured the levels of mitochondrial functional indicators. As shown in **Figures 3A–C**, MMPs, MPTP openings, and ATP levels in model rats were significantly lower than in control rats, with BJF administration significantly increasing MMPs, MPTP openings, and ATP levels. Meanwhile, AICAR and APL increased levels of MMPs and ATP but had no effect on MPTP openings.

BJF Promoted Expression of Mitochondrial Biogenesis Factors via Regulation of the AMPK Signaling Pathway in COPD Rats

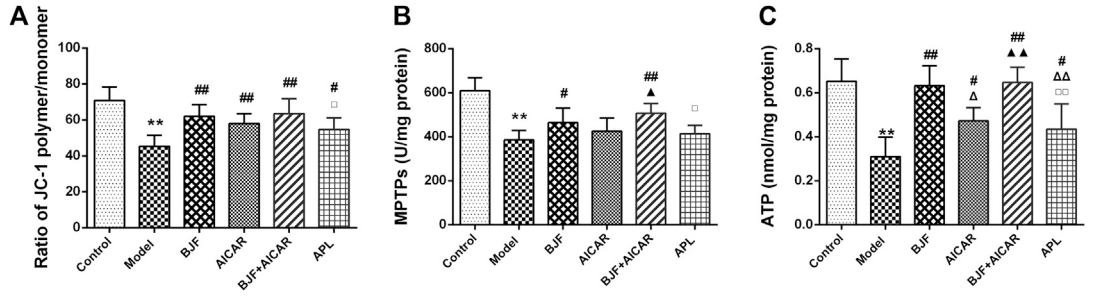

FIGURE 3 | Effects of Bufei Jianpi formula (BJF) on mitochondrial function of COPD rats. **(A)** Mitochondrial membrane potential **(B)** mitochondrial permeability transition pore openings (MPTPs); and **(C)** adenosine triphosphate (ATP) levels. Data are presented as mean ± SD (n = 6 per group). $^{**}p < 0.01$, $^{*}p < 0.05$ vs. control group; $^{\#\#}p < 0.01$, $^{\#}p < 0.05$ vs. model group; $^{\Delta\Delta}P < 0.01$, $^{\Delta}P < 0.05$ vs. BJF group; $^{\blacktriangle\blacktriangle}p < 0.01$, $^{\blacktriangle}p < 0.05$ vs. 5-aminoimidazole-4-carboxamide ribonucleotide (AICAR) group; and $^{\square\square}p < 0.01$, $^{\square}p < 0.05$ vs. BJF + AICAR group. APL, aminophylline.

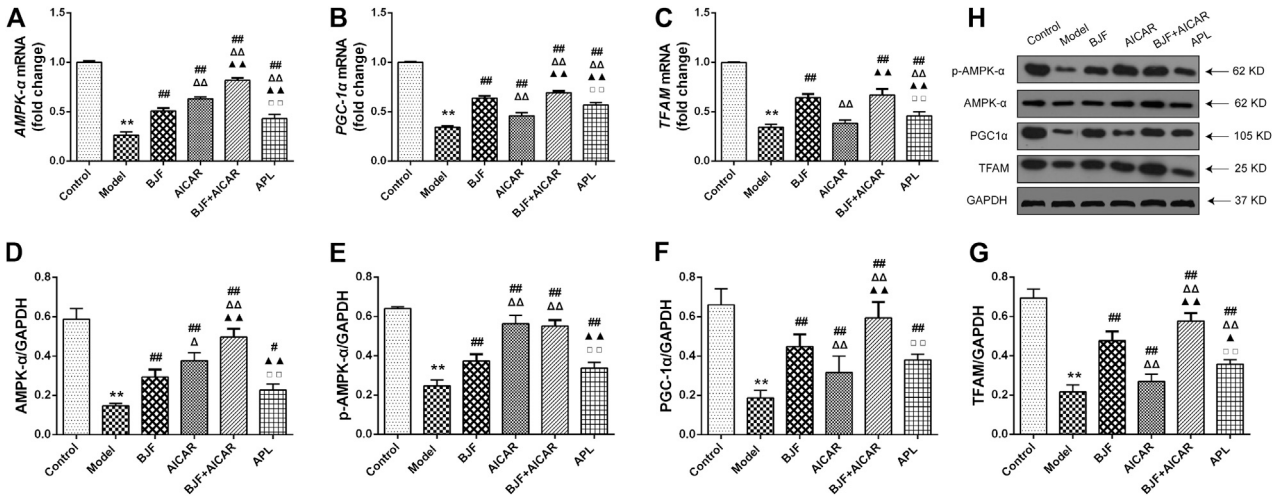

FIGURE 4 | Effects of Bufei Jianpi formula (BJF) on expression of mitochondrial biogenesis factors in COPD rats. **(A–C)** Real-time polymerase chain reaction validation of adenosine monophosphate-activated protein kinase (*AMPK-α*), peroxisome proliferator-activated receptor gamma coactivator (*PGC-α*), and mitochondrial transcription factor A (*TFAM*) mRNA expression changes and **(D–H)** representative Western blot analysis of AMPK-α, *p*-AMPK-α, PGC-α, and TFAM protein expression levels. Data are shown as mean ± SD (n = 6 per group). $^{**}p < 0.01$, $^{*}p < 0.05$ vs. control group; $^{\#\#}p < 0.01$, $^{\#}p < 0.05$ vs. model group; $^{\Delta\Delta}P < 0.01$, $^{\Delta}P < 0.05$ vs. BJF group; $^{\blacktriangle\blacktriangle}p < 0.01$, $^{\blacktriangle}p < 0.05$ vs. 5-aminoimidazole-4-carboxamide ribonucleotide (AICAR) group; $^{\square\square}p < 0.01$, $^{\square}p < 0.05$ vs. BJF + GAPDH, glyceraldehyde 3-phosphate dehydrogenase.

To explore the mitochondrial biogenesis-related mechanisms of BJF, we measured mRNA and protein levels of AMPK-α, PGC-α, and TFAM in skeletal muscle tissues of COPD rats. As shown in **Figures 4A–C**, mRNA levels of *AMPK-α*, *PGC-α*, and *TFAM* were markedly decreased in model rats. While treatment with BJF and APL significantly promoted expression of *AMPK-α*, *PGC-α*, and *TFAM* mRNA, AICAR upregulated levels of *AMPK-α* and *PGC-α* but not TFAM. As shown in **Figures 4D–H**, protein expression of AMPK-α, *p*-AMPK-α, PGC-α, and TFAM were lowered in model rats compared with control rats. BJF, AICAR, and APL treatment resulted in dramatic increases in AMPK-α, *p*-AMPK-α, PGC-α, and TFAM protein expression.

BJF Downregulated Expression of Mitophagic Factors via Regulation of the AMPK Signaling Pathway in COPD Rats

To identify the mitophagy-related mechanisms of BJF, we measured mRNA and protein levels of LC3B, ULK1, PINK1, and Parkin in skeletal muscle tissues of COPD rats. As shown in **Figures 5A–D**, we found that *LC3B*, *ULK1*, *PINK1*, and *Parkin* mRNA levels were significantly upregulated in COPD rats in comparison to control rats. While treatment with BJF, AICAR, and APL downregulated expression of *LC3B*, *ULK1*, *PINK1*, and *Parkin* mRNA, AICAR upregulated levels of all the above-mentioned indicators. Additionally, protein expression of LC3B, ULK1, PINK1, and Parkin were markedly decreased in COPD rats compared with control rats. While BJF and APL treatment

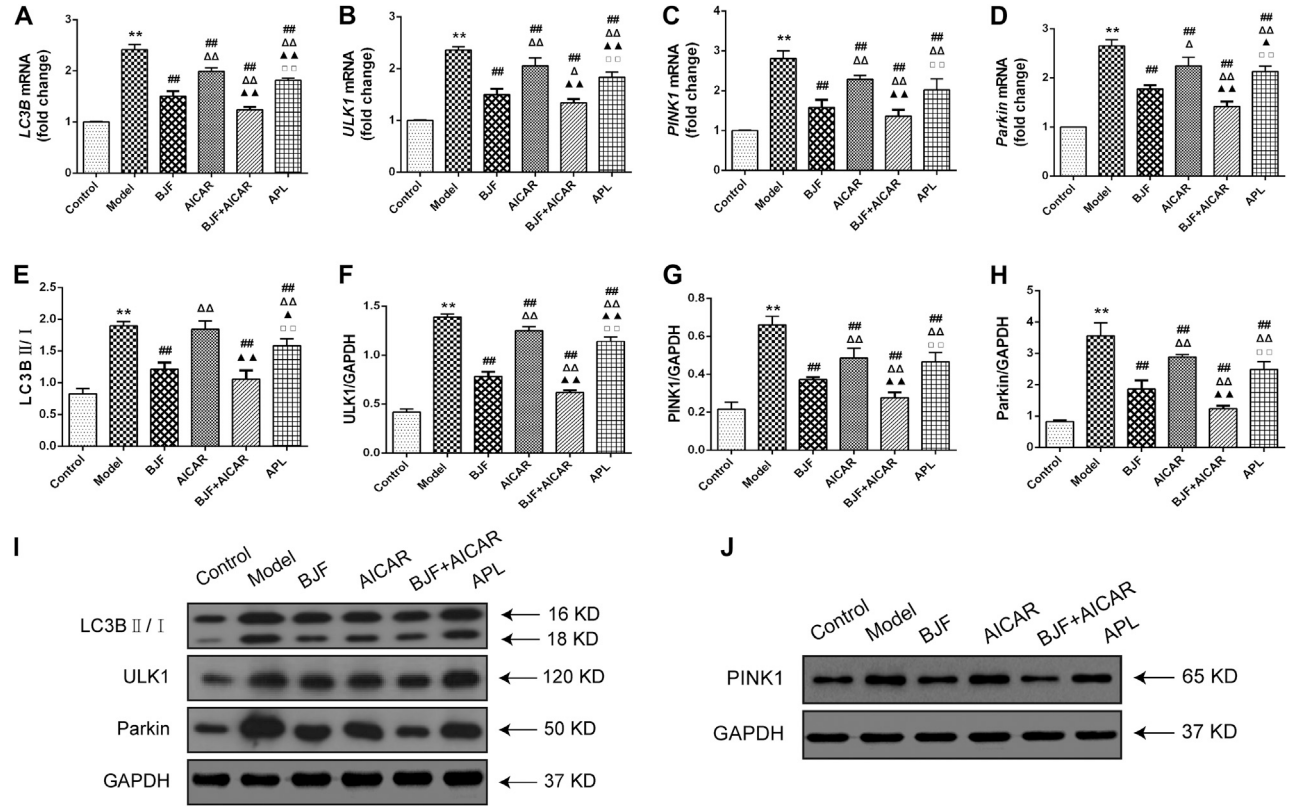

FIGURE 5 | Effects of Bufei Jianpi formula (BJF) on expression of mitophagic factors in COPD rats. **(A–D)** Real-time polymerase chain reaction validation of light chain 3B (*LC3B*), UNC-51-like kinase (*ULK1*), PTEN-induced putative kinase 1 (*PINK1*), and P*arkin* mRNA expression levels. **(E–J)** Representative Western blot analysis of LC3B, ULK1, PINK1, and Parkin protein expression. Data are presented as mean ± SD ($n = 6$ per group). $^{**}p < 0.01$, $^{*}p < 0.05$ vs. control group; $^{\#\#}p < 0.01$, $^{\#}p < 0.05$ vs. model group; $^{\Delta\Delta}P < 0.01$, $^{\Delta}P < 0.05$ vs. BJF group; $^{\blacktriangle\blacktriangle}p < 0.01$, $^{\blacktriangle}p < 0.05$ vs. 5-aminoimidazole-4-carboxamide ribonucleotide (AICAR) group; $^{\square\square}p < 0.01$, $^{\square}p < 0.05$ vs. BJF + AICAR group. GAPDH, glyceraldehyde 3-phosphate dehydrogenase.

upregulated protein expression of LC3B, ULK1, PINK1, and Parkin, AICAR showed no effect on the level of LC3B (**Figures 5E–J**).

BJF Improved CSE-Induced Mitochondrial Injury in L6 Cells

To explore the effects of BJF treatment on mitochondrial membrane potentials, a JC-1 fluorescent probe was measured in rat L6 cells under CSE conditions. The ratio of JC-1 red to green fluorescence was significantly decreased in CSE-exposed L6 cells; however, treatment with BJF and AICAR significantly increased MMPs in L6 cells (**Figures 6A**,**B**). As shown in **Figures 6C,D**, BJF also markedly improved opening of MPTPs and ATP levels in CSE-exposed L6 cells.

BJF Restored Mitochondrial Respiration in CSE-Exposed L6 Cells

To determine the effects of BJF on mitochondrial respiration, L6 cells were treated with a 10% CSE, 10% CSE +10% BJF-containing serum, or a 10% CSE + AICAR for 24 h, and OCRs were measured. As demonstrated in **Figures 7B–F,** significant reductions in basal respiration, ATP production, proton leak, and maximal respiratory capacity were observed in L6 cells after exposure to CSE. BJF treatment markedly reversed these CSE-induced changes.

BJF Regulated Expression of Mitochondrial Biogenesis Factor in CSE-Exposed L6 Cells

To explore the effects of BJF on mitochondrial biogenesis, mRNA and protein levels of AMPK-α, PGC-α, and TFAM were measured in L6 cells exposed to CSE. As shown in **Figures 8A–C**, mRNA expression levels of *AMPK-α*, *PGC-α*, and *TFAM* were markedly lower in L6 cells exposed to CSE than in control cells, and BJF administration markedly reversed these changes. Meanwhile, AICAR upregulated levels of *AMPK-α* and *PGC-α* but had no effect on levels of *TFAM*. As shown in **Figures 8D–H**, protein expression of AMPK-α, *p*-AMPK-α, PGC-α, and TFAM were lowered in L6 cells exposed to CSE compared with control cells. BJF treatment resulted in dramatic increases in these changes,while AICAR upregulated levels of AMPK-α, *p*-AMPK-α and TFAM.

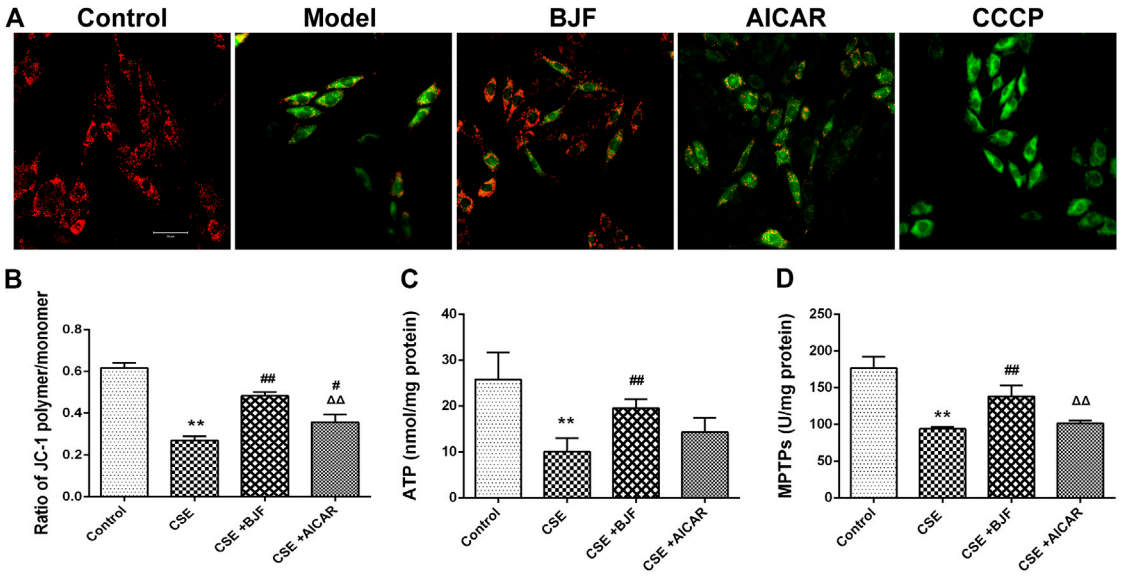

FIGURE 6 | Bufei Jianpi formula (BJF) improved cigarette smoke extract (CSE)-induced mitochondrial injury in L6 cells. **(A)** Effect of BJF on mitochondrial membrane potential. Red fluorescence represents the mitochondrial aggregate form of JC-1, indicating an intact mitochondrial membrane potential. Green fluorescence represents the monomeric form of JC-1, indicating dissipation of ΔΨm (confocal laser scanning microscope, magnification ×200, scale bar = 50 μm), **(B)** mitochondrial membrane potential, **(C)** ATP, and **(D)** mitochondrial permeability transition pore (MPTP) openings. Data are presented as mean ± SD. $^{**}p < 0.01$, $^{*}p < 0.05$ vs. control group; $^{\#\#}p < 0.01$, $^{\#}p < 0.05$ vs. model group; $^{\Delta\Delta}P < 0.01$, $^{\Delta}P < 0.05$ vs. BJF group. AICAR, aminoimidazole-4-carboxamide ribonucleotide; CCCP, carbonyl cyanide *m*-chlorophenyl hydrazone.

BJF Downregulated Expression of Mitophagic Factor in CSE-Exposed L6 Cells

We measured mRNA and protein levels of ULK1, PINK1, and Parkin in L6 cells under CSE conditions. As shown in **Figures 9A–G**, *ULK1*, *PINK1*, and *Parkin* mRNA levels were significantly upregulated in CSE-induced L6 cells in comparison to control cells. Meanwhile, BJF treatment downregulated *ULK1*, *PINK1*, and *Parkin* mRNA and protein expression levels. Similarly, AICAR increased Parkin protein expression.

BJF Regulated the AMPK Signaling Pathway in CSE-Exposed L6 Cells

To further explore the effects of BJF treatment on the AMPK signaling pathway, mRNA and protein levels of factors downstream of AMPK, including mTOR, PPARγ, and SIRT1 were analyzed. As shown in **Figures 10A–G**, mRNA levels of *mTOR*, *PPARγ*, and *SIRT1* were significantly decreased after administration of CSE for 24 h, and treatment with BJF and AICAR inhibited these changes. Similarly, BJF increased protein expression of mTOR, PPARγ, and SIRT1, while AICAR upregulated levels of PPARγ and SIRT1 but had no effect on mTOR levels. BML increased mRNA expression of *PPARγ* , SIRT1and protein expression of PPARγ.

DISCUSSION

TCM has been widely used for treatment of COPD for thousands of years. BJF, a traditional Chinese herbal formula for lung-spleen qi deficiency syndrome, has been shown to have reproducible efficacy for treatment of COPD in previous clinical and experimental studies (Li et al., 2012a; Dong et al., 2015; Mao et al., 2019). In this study, we showed that BJF significantly improved SMD in rats with COPD via regulation of the AMPK pathway which is shown in **Figure 11**. It also improved mitochondrial function and decreased mitophagy in model rats and a myocyte cell line exposed to cigarette smoke extract.

Mitochondria, an important and essential organelle in the skeletal muscle, is involved in metabolic regulation and ATP production, which are two key elements of muscle contractibility and plasticity (Abrigo, 2019). Many evidence has accumulated to support the notion that mitochondrial dysfunction contribute to the poor endurance capacity and atrophy that characterize locomotor muscle dysfunction in patients with COPD (Allaire, 2004). There are several potential therapeutic agents targeted at reducing mitochondrial impairment in skeletal muscle of patients with COPD, including polyunsaturated fatty acids (PUFA), exercise rehabilitation, and mitochondria-targeting antioxidant therapies (Taivassalo and Hussain, 2016). TCM has also been shown to have clinically beneficial effects on mitochondrial impairment. For example, Astragalus polysaccharide has been shown to improve mitochondrial dysfunction via inhibiting the opening of a mitochondrial permeability transition pore, improving synergistic interactions between mitophagy and mitochondrial fusion. (Huang et al., 2016; Sun et al., 2014.). Our previous study also showed that BJF reversed the reductions in mitochondrial density observed in COPD rats and improved skeletal muscle tension and tolerance (Dong et al., 2015). In the present study, we demonstrated that BJF treatment elevated

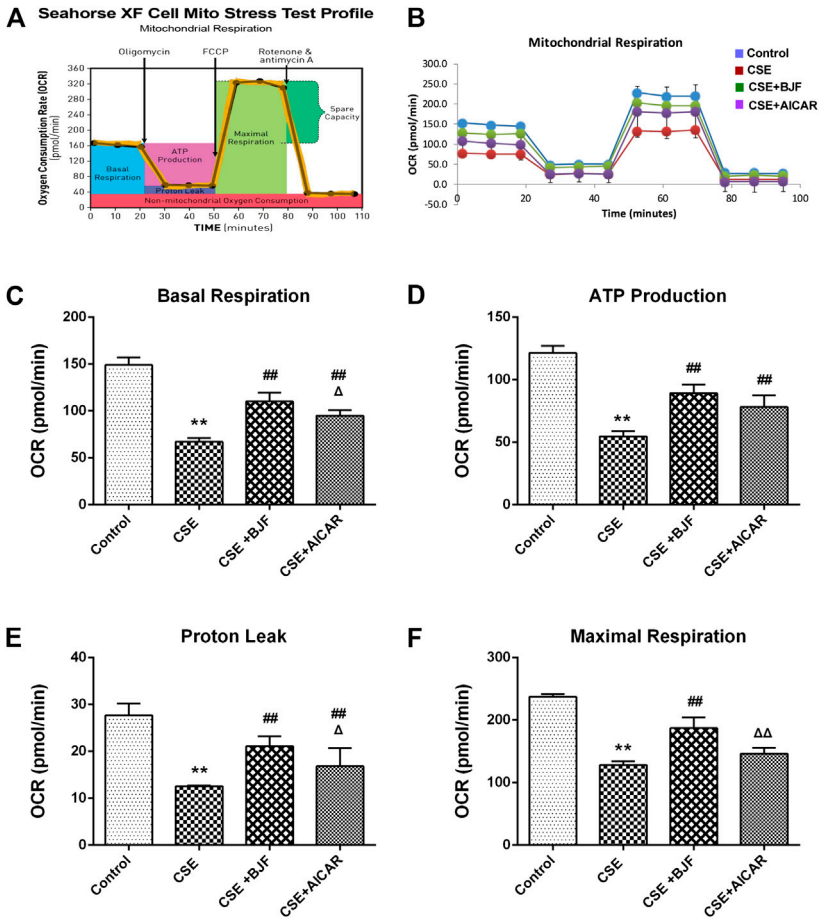

FIGURE 7 | Bufei Jianpi formula (BJF) restored mitochondrial respiration in cigarette smoke extract (CSE)-exposed L6 cells. **(A)** Schematic representation of the mitochondrial functional assay, and **(B)** mitochondrial respiration under CSE conditions. L6 cells were treated with 10% CSE, 10% CSE +10% BJF-containing serum, or 10% CSE + 5-aminoimidazole-4-carboxamide ribonucleotide (AICAR) for 24 h. The cells were then switched to unbuffered Dulbecco's modified Eagle's medium supplemented with pyruvate, followed by real-time analysis of oxygen consumption rate (OCR). Analysis of **(C)** basal respiration, **(D)** adenosine triphosphate (ATP) production, **(E)** proton leak, and **(F)** maximal respiration. Data are presented as mean ± SD. $^{**}p < 0.01$, $^{*}p < 0.05$ vs. control group; $^{\#\#}p < 0.01$, $^{\#}p < 0.05$ vs. model group; $^{\Delta\Delta}P < 0.01$, $^{\Delta}P < 0.05$ vs. BJF group.

indicators of effective mitochondrial functioning, including ATP, MMP, and MPTP openings in COPD rats, as well as restored levels of mitochondrial respiration in CSE-exposed L6 cells.

Mitochondria use oxidative phosphorylation to synthesize ATP, which provides 90% of the energy required for all cellular activities (Zhang L. et al., 2017). Thus, damage to the mitochondria reduces ATP synthesis; this not only directly leads to mitochondrial swelling, disruption of cristae, and uncoupling of oxidative phosphorylation but also exacerbates ion metabolism disorders (Formentini et al., 2017). Repeated vicious cycles ultimately lead to myocyte damage and cause impairment. Several studies have found that the skeletal muscle cells of patients with COPD hold features of mitochondrial dysfunction, such as increased synthesis of ROS and decreased ATP production (Puente-Maestu et al., 2009). A normal mitochondrial membrane potential is a prerequisite for maintaining oxidative phosphorylation and ATP synthesis, to ensure normal mitochondrial activity. The MPTP is located between the outer and inner mitochondrial membranes and is a nonselective complex pore composed of several proteins. The MPTP cyclical opening maintains the calcium ion flow, pH, and charge equilibrium in the mitochondrial matrix, ensuring a stable membrane potential while maintaining mitochondrial homeostasis. Pathological or other factors can stimulate the MPTP and induce its excessive opening, which results in the influx of a large number of protons from the inner membrane to the matrix and, hence, in the loss of mitochondrial membrane potential, uncoupling of oxidative phosphorylation, and ATP synthesis failure. In addition, aberrant opening of the MPTP may allow solute molecules to freely pass through the mitochondrial matrix and trigger significant mitochondrial swelling. Ultimately, mitochondrial swelling can lead to the disruption of the mitochondrial outer membrane and the release of cytochrome C and other pro-apoptotic factors, thereby activating apoptosis or necrosis pathways (Bernardi et al., 2015; Ong et al., 2015; Teixeira et al., 2018). One study

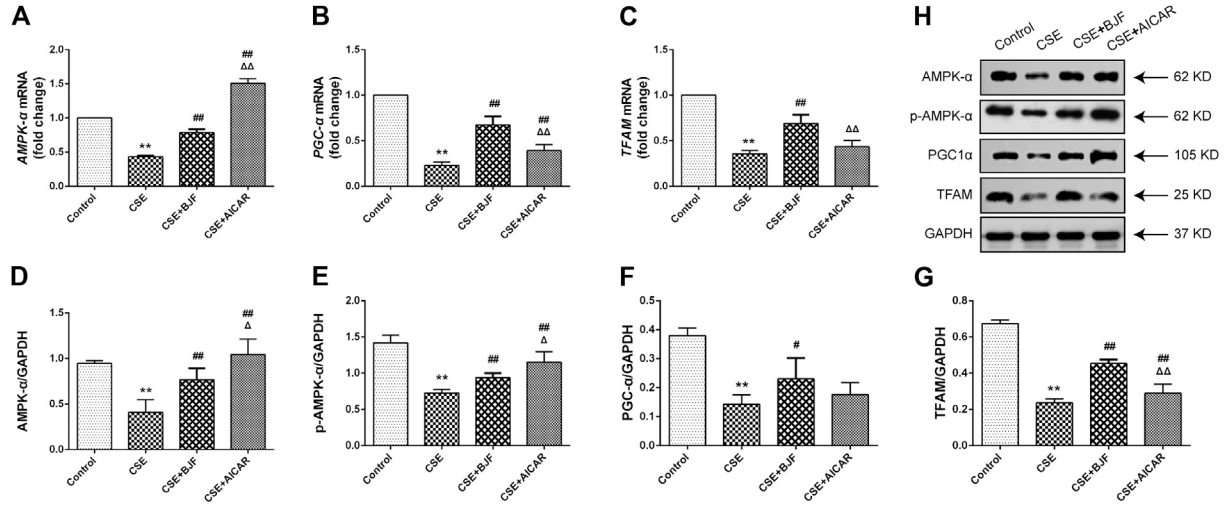

FIGURE 8 | Bufei Jianpi formula (BJF) regulated expression of mitochondrial biogenesis factors in cigarette smoke extract (CSE)-exposed L6 cells. **(A–C)** Real-time polymerase chain reaction validation of adenosine monophosphate-activated protein kinase (*AMPK-α*), peroxisome proliferator-activated receptor gamma coactivator (*PGC-α*), and mitochondrial transcription factor A (*TFAM*) mRNA expression levels and **(D-H)** Representative Western blot analysis of AMPK-α, *p*-AMPK-α, PGC-α, and TFAM protein expression levels. Data are presented as mean ± SD. $^{**}p < 0.01$, $^{*}p < 0.05$ vs. control group; $^{\#\#}p < 0.01$, $^{\#}p < 0.05$ vs. model group; $^{\Delta\Delta}P < 0.01$, $^{\Delta}P < 0.05$ vs. BJF group. GAPDH, glyceraldehyde 3-phosphate dehydrogenase.

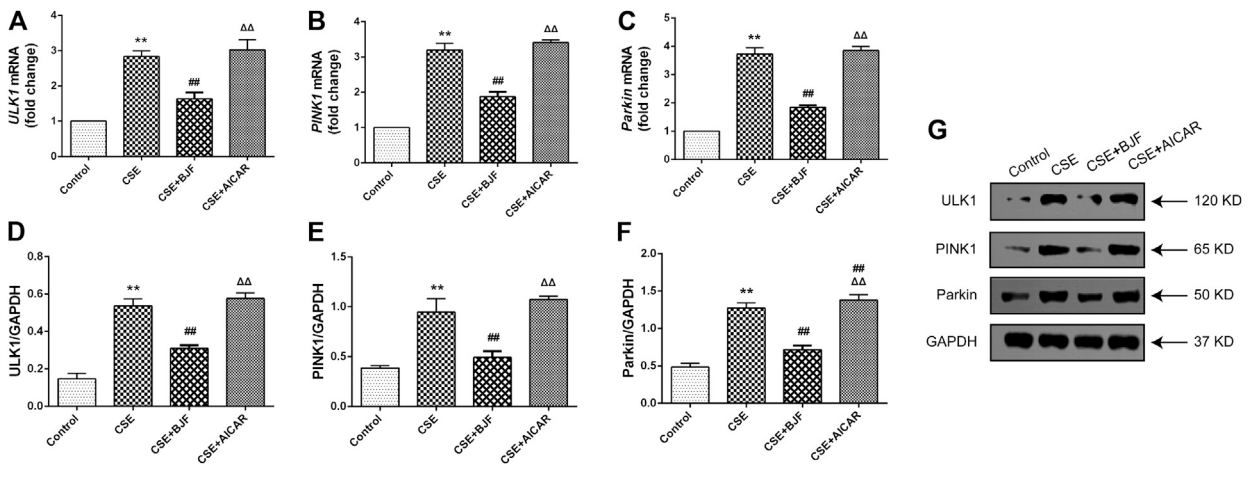

FIGURE 9 | Bufei Jianpi formula (BJF) downregulated expression of mitochondrial autophagic factors in cigarette smoke extract (CSE)-exposed L6 cells. **(A–C)** Real-time polymerase chain reaction validation of UNC-51-like kinase (*ULK1*), PTEN-induced putative kinase 1 (*PINK1*), and *Parkin* mRNA expression levels and **(D–G)** Representative Western blot analysis of ULK1, PINK1, and Parkin protein expression levels. Data are presented as mean ± SD. $^{**}p < 0.01$, $^{*}p < 0.05$ vs. control group; $^{\#\#}p < 0.01$, $^{\#}p < 0.05$ vs. model group; $^{\Delta\Delta}P < 0.01$, $^{\Delta}P < 0.05$ vs. BJF group. GAPDH, glyceraldehyde 3-phosphate dehydrogenase.

found that MPTP opening is aberrant in the skeletal muscles of COPD patients (Puente-Maestu et al., 2009). In contrast, another study reported that COPD patients were less prone to aberrant MPTP opening in the skeletal muscles compared with healthy individuals (Picard et al., 2008). To date, relatively few studies have explored the MMP and MPTP opening in the skeletal muscles of COPD patients; therefore, further research on these factors is warranted. This study showed that ATP synthesis, MMP levels, and MPTP opening were significantly increased in BJF and BJF+AICAR group. These results suggest that "the spleen is the source of qi and blood" and is closely associated with mitochondrial function. In addition, BJF can significantly improve mitochondrial function, thereby ameliorating skeletal muscle atrophy.

The mitochondria are essential for cellular aerobic respiration, partaking in stages 2 and 3 (i.e., Krebs cycle and oxidative phosphorylation). Our study measured the respiratory characteristics of mitochondria under cellular baseline and stress conditions. there is evidence indicated that mitochondrial aerobic

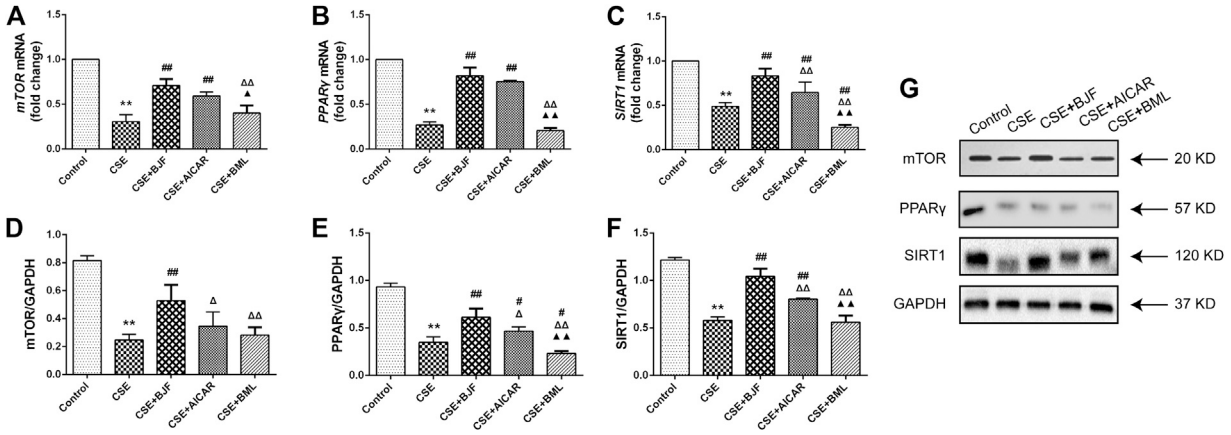

FIGURE 10 | Bufei Jianpi formula (BJF) regulated the adenosine monophosphate-activated protein kinase (AMPK) signaling pathway in cigarette smoke extract (CSE)-exposed L6 cells. **(A–C)** Real-time polymerase chain reaction validation of mammalian target of rapamycin (*mTOR*), *PPARγ*, and *SIRT1* mRNA expression levels and **(D–G)** Representative Western blot analysis of mTOR, peroxisome proliferator-activated receptor (PPAR)-γ, and sirtuin 1 (SIRT1) protein expression levels. Data are presented as mean ± SD. $^{**}p < 0.01$, $^{*}p < 0.05$ vs. control group; $^{\#\#}p < 0.01$, $^{\#}p < 0.05$ vs. model group; $^{\Delta\Delta}P < 0.01$, $^{\Delta}P < 0.05$ vs. BJF group; $^{\blacktriangle\blacktriangle}p < 0.01$, $^{\blacktriangle}p < 0.05$ vs. AICAR group. GAPDH, glyceraldehyde 3-phosphate dehydrogenase.

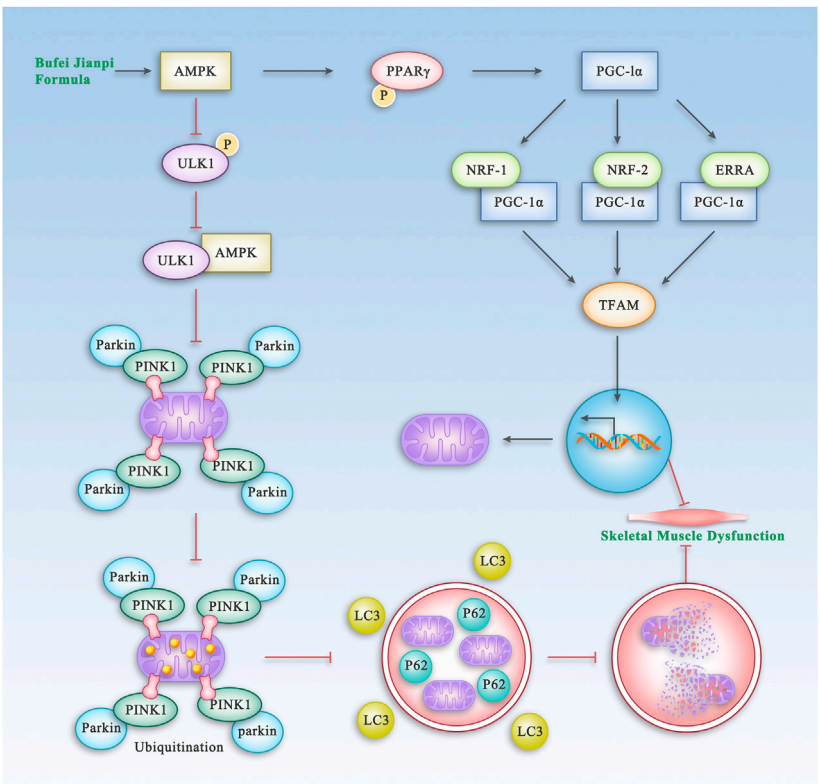

FIGURE 11 | The Proposed Pathway of BJF for the Treatment of Skeletal Muscle Dysfunction in COPD. BJF improves skeletal muscle and mitochondrial function in COPD rats and L6 cells by promoting mitochondrial biogenesis and suppressing mitophagy via the AMPK pathway.

respiration was inhibited in L6 skeletal muscle cells exposed to high-dose fructose, with significantly reduced oxygen consumption rate, basal and maximal respiration, and ATP synthesis (Jaiswal et al., 2015). Nevertheless, another study found that resveratrol could partially overcome dexamethasone-induced impaired mitochondrial respiration in C2C12 myoblasts, thereby preventing

mitochondrial dysfunction. The results of this study showed that treatment with CSE could decrease basal mitochondrial oxygen consumption rate, ATP synthesis, and proton leakage in L6 cells (Liu et al., 2016). Taken together, these results suggest that CSE-induced mitochondrial dysfunction and BJF can significantly increase aerobic respiration in mitochondria.

Different factors related to mitochondrial dysfunction, including abnormalities in mitochondrial biogenesis and mitophagy, may contribute to the loss of skeletal muscle strength that leads to functional declines in patients with COPD (Wiegman et al., 2015). AMPK, a vital regulator of bioenergetic metabolism, is critical for mitochondrial biogenesis and mitophagy in muscle cells (Zhang et al., 2018). AMPK activates TFAM via regulation of PGC-1α and NRF, which contributes to mitochondrial biogenesis when activated by hypoxia and oxidative stress. PGC-1α has been shown to play a central role in enhancing mitochondrial biogenesis (Islam et al., 2018). TFAM is another key molecule in the regulation of mtDNA copy numbers and mitochondrial function (Kang et al., 2018). Emerging evidence indicates that levels of PGC-1α and TFAM are decreased in COPD rats (Remels et al., 2007; Lu et al., 2017; Zhang M. et al., 2017). Meanwhile, other studies have demonstrated that protein expression of PGC-1α is significantly lower in patients with COPD due to decreased numbers of type I fibers (van den Borst et al., 2013; Puente-Maestu et al., 2013). These studies suggest that these factors may serve important regulatory functions in COPD-related mitochondrial dysfunction. In the present study, BJF was shown to effectively upregulate mitochondria biogenesis by increasing expression levels of AMPK-α, PGC-1α, and TFAM.

The PINK1/Parkin pathway is one of the main molecular mechanisms mediating the mitophagic process. A previous study showed that the number of autophagosomes was clearly increased in skeletal muscles of patients with COPD, which was associated with functional impairments in lungs and muscular atrophy. Increased expressions of LC3BII/I and *p*-ULK have also been observed in COPD patients (Kneppers et al., 2017), indicating abnormalities in autophagy. In the present study, we found that the levels of ULK1, PINK1, Parkin, and LC3B were significantly increased in the skeletal muscle of COPD rats, while treatment with BJF or APL could inhibit mitophagy to different degrees. MTOR is a 289-kDa serine/threonine protein involved in multiple cellular processes, including autophagy (Maiese, 2016). AMPK plays an important role in the signaling cascade of mTOR by inhibiting mTORC1 activity, which results in induction of autophagy (Duan et al., 2016). SIRT1 is a downstream target of AMPK and is therefore downregulated when *p*-AMPK is downregulated (Qi et al., 2014). In the present study, we found that BJF upregulated expression of mTOR, PPARγ, and SIRT1 via regulation of the AMPK signaling pathway in CSE-exposed L6 cells. Therefore, these results suggest that BJF can improve mitochondrial dysfunction by suppressing mitophagy and enhancing mitochondrial biogenesis via regulation of the AMPK signaling pathway.

Nevertheless, further study is needed to figure out which chemical components in BJF are responsible for suppressing mitophagy and enhancing mitochondrial biogenesis, maybe other mechanism involve in this process.

CONCLUSION

In conclusion, this study demonstrated that BJF can improve the SMD observed in COPD both *in vitro* and *in vivo* by promotion of mitochondrial biogenesis and by suppression of mitophagy via regulation of the AMPK pathway. The results of this study indicate potential mechanisms for future therapeutic agents and provide a basis for further study of SMD in COPD patients.

DATA AVAILABILITY STATEMENT

The raw data supporting the conclusions of this article will be made available by the authors, without undue reservation, to any qualified researcher.

ETHICS STATEMENT

The animal study was reviewed and approved by the Experimental Animal Care and Ethics Committee of the First Affiliated Hospital of Henan University of Traditional Chinese Medicine.

AUTHOR CONTRIBUTIONS

JM performed the research, analyzed the data, and wrote the manuscript. YL, YT, and SL designed and conceptualized the research and revised the manuscript. QB, JL, YH, LZ, and HJ contributed to animal experiments and cell culture. SF and XL contributed to the preparation of BJF. All authors read and approved the final manuscript.

FUNDING

This work was supported by the General Program of National Natural Science Foundation of China (81573947 and 81904116) and the Scientific Research Fund for doctors of Henan University of Chinese Medicine (RSBSJJ2018-03).

REFERENCES

Abrigo, J., Simon, F., Cabrera, D., Vilos, C., and Cabello-Verrugio, C. (2019). Mitochondrial dysfunction in skeletal muscle pathologies. *Curr. Protein Pept. Sci.* 20, 536–546. doi:10.2174/1389203720666190402100902

Allaire, J., Maltais, F., Doyon, J. F., Noël, M., LeBlanc, P., Carrier, G., et al. (2004). Peripheral muscle endurance and the oxidative profile of the quadriceps in patients with COPD. *Thorax* 59, 673–678. doi:10.1136/thx.2003.0206362004

Allavena, G., Boyd, C., Oo, K. S., Maellaro, E., Zhivotovsky, B., and Kaminsky, V. O. (2016). Suppressed translation and ULK1 degradation as potential mechanisms

of autophagy limitation under prolonged starvation. *Autophagy* 12, 2085–2097. doi:10.1080/15548627.2016.1226733

Barreiro, E. (2016). Role of protein carbonylation in skeletal muscle mass loss associated with chronic conditions. *Proteomes* 4, 18. doi:10.3390/proteomes4020018

Barreiro, E., and Gea, J. (2016). Molecular and biological pathways of skeletal muscle dysfunction in chronic obstructive pulmonary disease. *Chron. Respir. Dis.* 13, 297–311. doi:10.1177/1479972316642366

Bernardi, P., Rasola, A., Forte, M., and Lippe, G. (2015). The mitochondrial permeability transition pore: channel formation by F-ATP synthase, integration in signal transduction, and role in pathophysiology. *Physiol. Rev.* 95, 1111–1155. doi:10.1152/physrev.00001.2015

Ceco, E., Weinberg, S. E., Chandel, N. S., and Sznajder, J. I. (2017). Metabolism and skeletal muscle homeostasis in lung disease. *Am. J. Respir. Cell Mol. Biol.* 57, 28–34. doi:10.1165/rcmb.2016-0355TR

Collaborators, GMaCoD. (2015). Global, regional, and national age-sex specific all-cause and cause-specific mortality for 240 causes of death, 1990–2013: a systematic analysis for the Global Burden of Disease Study 2013. *Lancet* 385, 117–171. doi:10.1016/S0140-6736(14)61682-2

Dong, Y., Li, Y., Sun, Y., Mao, J., Yao, F., Tian, Y., et al. (2015). Bufei Jianpi granules improve skeletal muscle and mitochondrial dysfunction in rats with chronic obstructive pulmonary disease. *BMC Compl. Alternative Med.* 15, 51. doi:10.1186/s12906-015-0559-x

Duan, P., Hu, C., Quan, C., Yu, T., Zhou, W., Yuan, M., et al. (2016). 4-Nonylphenol induces apoptosis, autophagy and necrosis in Sertoli cells: involvement of ROS-mediated AMPK/AKT-mTOR and JNK pathways. *Toxicology* 341–343, 28–40. doi:10.1016/j.tox.2016.01.004

Formentini, L., Ryan, A. J., Gálvez-Santisteban, M., Carter, L., Taub, P., Lapek, J. D., Jr., et al. (2017). Mitochondrial H+-ATP synthase in human skeletal muscle: contribution to dyslipidaemia and insulin resistance. *Diabetologia* 60, 2052–2065. doi:10.1007/s00125-017-4379-z

Grabacka, M., Pierzchalska, M., Dean, M., and Reiss, K. (2016). Regulation of ketone body metabolism and the role of PPARα. *Int. J. Mol. Sci.* 17, 2093. doi:10.3390/ijms17122093

Hardie, D. G. (2011). AMPK and autophagy get connected. *EMBO J.* 30, 634–635. doi:10.1038/emboj.2011.12

Huang, Y. F., Lu, L., Zhu, D. J., Wang, M., Yin, Y., Chen, D. X., et al. (2016). Effects of Astragalus polysaccharides on dysfunction of mitochondrial dynamics induced by oxidative stress. *Oxid. Med. Cell. Longev.* 19, 9573291. doi:10.1155/2016/9573291

Islam, H., Edgett, B. A., and Gurd, B. J. (2018). Coordination of mitochondrial biogenesis by PGC-1α in human skeletal muscle: a re-evaluation. *Metabolism* 79, 42–51. doi:10.1016/j.metabol.2017.11.001

Jaiswal, N., Maurya, C. K., Arha, D., Avisetti, D. R., Prathapan, A., Raj, P. S., et al. (2015). Fructose induces mitochondrial dysfunction and triggers apoptosis in skeletal muscle cells by provoking oxidative stress. *Apoptosis* 20, 930–947. doi:10.1007/s10495-015-1128-y

Kang, I., Chu, C. T., and Kaufman, B. A. (2018). The mitochondrial transcription factor TFAM in neurodegeneration: emerging evidence and mechanisms. *FEBS Lett.* 592, 793–811. doi:10.1002/1873-3468.12989

Kneppers, A. E. M., Langen, R. C. J., Gosker, H. R., Verdijk, L. B., Lipovec, N. C., Leermakers, P. A., et al. (2017). Increased myogenic and protein turnover signaling in skeletal muscle of chronic obstructive pulmonary disease patients with sarcopenia. *J. Am. Med. Dir. Assoc.* 18, 637. doi:10.1016/j.jamda.2017.04.016

Li, S. Y., Li, J. S., Wang, M. H., Xie, Y., Yu, X. Q., Sun, Z. K., et al. (2012a). Effects of comprehensive therapy based on traditional Chinese medicine patterns in stable chronic obstructive pulmonary disease: a four-center, open-label, randomized, controlled study. *BMC Compl. Alternative Med.* 12, 197. doi:10.1186/1472-6882-12-197

Li, Y., Li, S. Y., Li, J. S., Deng, L., Tian, Y. G., Jiang, S. L., et al. (2012b). A rat model for stable chronic obstructive pulmonary disease induced by cigarette smoke inhalation and repetitive bacterial infection. *Biol. Pharm. Bull.* 35, 1752–1760. doi:10.1248/bpb.b12-00407

Liu, J., Peng, Y., Wang, X., Fan, Y., Qin, C., Shi, L., et al. (2016). Mitochondrial dysfunction launches dexamethasone-induced skeletal muscle atrophy via AMPK/FOXO3 signaling. *Mol. Pharm.* 13, 73–84. doi:10.1021/acs.molpharmaceut.5b00516

Lu, J. J., Wang, Q., Xie, L. H., Zhang, Q., and Sun, S. H. (2017). Tumor necrosis factor-like weak inducer of apoptosis regulates quadriceps muscle atrophy and fiber-type alteration in a rat model of chronic obstructive pulmonary disease. *Tob. Induc. Dis.* 15, 43. doi:10.1186/s12971-017-0148-5

Maiese, K. (2016). Novel nervous and multi-system regenerative therapeutic strategies for diabetes mellitus with mTOR. *Neural Regen. Res.* 11, 372–385. doi:10.4103/1673-5374.179032

Maltais, F., Decramer, M., Casaburi, R., Barreiro, E., Burelle, Y., Debigaré, R., et al. (2014). An official American Thoracic Society/European Respiratory Society statement: update on limb muscle dysfunction in chronic obstructive pulmonary disease. *Am. J. Respir. Crit. Care Med.* 189, e15–e62. doi:10.1164/rccm.201402-0373ST

Mao, J., Li, Y., Li, S., Li, J., Tian, Y., Feng, S., et al. (2019). Bufei Jianpi granules reduce quadriceps muscular cell apoptosis by improving mitochondrial function in rats with chronic obstructive pulmonary disease. *Evid. Based Complement. Alternat. Med.* 7, 1216305. doi:10.1155/2019/1216305

Medicine PCoPDoIMBoCAoC (2012). Syndrome diagnostic criteria of traditional Chinese medicine for chronic obstructive pulmonary disease (2011 version). *Zhong Yi Za Zhi* 53, 177–178.

Meyer, A., Zoll, J., Charles, A. L., Charloux, A., de Blay, F., Diemunsch, P., et al. (2013). Skeletal muscle mitochondrial dysfunction during chronic obstructive pulmonary disease: central actor and therapeutic target. *Exp. Physiol.* 98, 1063–1078. doi:10.1113/expphysiol.2012.069468

Mowery, N. T. (2017). Ventilator strategies for chronic obstructive pulmonary disease and acute respiratory distress syndrome. *Surg. Clin.* 97, 1381–1397. doi:10.1016/j.suc.2017.07.006

Ong, S. B., Samangouei, P., Kalkhoran, S. B., and Hausenloy, D. J. (2015). The mitochondrial permeability transition pore and its role in myocardial ischemia reperfusion injury. *J. Mol. Cell. Cardiol.* 78, 23–34. doi:10.1016/j.yjmcc.2014.11.005

Patel, A. R., Patel, A. R., Singh, S., Singh, S., and Khawaja, I. (2019). Global initiative for chronic obstructive lung disease: the changes made. *Cureus* 11, e4985. doi:10.7759/cureus.4985

Picard, M., Godin, R., Sinnreich, M., Baril, J., Bourbeau, J., Perrault, H., et al. (2008). The mitochondrial phenotype of peripheral muscle in chronic obstructive pulmonary disease: disuse or dysfunction?. *Am. J. Respir. Crit. Care Med.* 178, 1040–1047. doi:10.1164/rccm.200807-1005OC

Puente-Maestu, L., Lázaro, A., and Humanes, B. (2013). Metabolic derangements in COPD muscle dysfunction. *J. Appl. Physiol.* 114, 1282–1290. doi:10.1152/japplphysiol.00815.20121985

Puente-Maestu, L., Pérez-Parra, J., Godoy, R., Moreno, N., Tejedor, A., González-Aragoneses, F., et al. (2009). Abnormal mitochondrial function in locomotor and respiratory muscles of COPD patients. *Eur. Respir. J.* 33, 1045–1052. doi:10.1183/09031936.00112408

Qi, Y., Shang, J. Y., Ma, L. J., Sun, B. B., Hu, X. G., Liu, B., et al. (2014). Inhibition of AMPK expression in skeletal muscle by systemic inflammation in COPD rats. *Respir. Res.* 15, 156. doi:10.1186/s12931-014-0156-4

Remels, A. H., Schrauwen, P., Broekhuizen, R., Willems, J., Kersten, S., Gosker, H. R., et al. (2007). Peroxisome proliferator-activated receptor expression is reduced in skeletal muscle in COPD. *Eur. Respir. J.* 30, 245–252. doi:10.1183/09031936.00144106

Sheridan, J. A., Zago, M., Nair, P., Li, P. Z., Bourbeau, J., Tan, W. C., et al. (2015). Decreased expression of the NF-κB family member RelB in lung fibroblasts from Smokers with and without COPD potentiates cigarette smoke-induced COX-2 expression. *Respir. Res.* 16, 54. doi:10.1186/s12931-015-0214-6

Sun, Q., Jia, N., Wang, W., Jin, H., Xu, J., and Hu, H. (2014). Protective effects of astragaloside IV against amyloid beta1-42 neurotoxicity by inhibiting the mitochondrial permeability transition pore opening. *PLoS One* 9, e98866. doi:10.1371/journal.pone.0098866

Tadaishi, M., Miura, S., Kai, Y., Kawasaki, E., Koshinaka, K., Kawanaka, K., et al. (2011). Effect of exercise intensity and AICAR on isoform-specific expressions of murine skeletal muscle PGC-1α mRNA: a role of β2-adrenergic receptor activation. *Am. J. Physiol. Endocrinol. Metab.* 300, E341–E349. doi:10.1152/ajpendo.00400.2010

Taivassalo, T., and Hussain, S. N. (2016). Contribution of the mitochondria to locomotor muscle dysfunction in patients with COPD. *Chest* 149, 1302–1312. doi:10.1016/j.chest.2015.11.021

Teixeira, J., Oliveira, C., Cagide, F., Amorim, R., Garrido, J., Borges, F., et al. (2018). Discovery of a new mitochondria permeability transition pore (mPTP) inhibitor based on gallic acid. *J. Enzym. Inhib. Med. Chem.* 33, 567–576. doi:10.1080/14756366.2018.1442831

van den Borst, B., Slot, I. G., Hellwig, V. A., Vosse, B. A. H., Kelders, M. C. J. M., Barreiro, E., et al. (2013). Loss of quadriceps muscle oxidative phenotype and decreased endurance in patients with mild-to-moderate COPD. *J. Appl. Physiol.* 114, 1319–1328. doi:10.1152/japplphysiol.00508.20121985

Wang, C., Xu, J., Yang, L., Xu, Y., Zhang, X., Bai, C., et al. (2018a). Prevalence and risk factors of chronic obstructive pulmonary disease in China [the China Pulmonary Health (CPH) study]: a national cross-sectional study. *Lancet* 391, 1706–1717. doi:10.1016/S0140-6736(18)30841-9

Wei, L., Wang, J., Chen, A., Liu, J., Feng, X., and Shao, L. (2017). Involvement of PINK1/parkin-mediated mitophagy in ZnO nanoparticle-induced toxicity in BV-2 cells. *Int. J. Nanomed.* 12, 1891–1903. doi:10.2147/IJN.S129375

Wiegman, A., Gidding, S. S., Watts, G. F., Chapman, M. J., Ginsberg, H. N., Cuchel, M., et al. (2015). Familial hypercholesterolaemia in children and adolescents: gaining decades of life by optimizing detection and treatment. *Eur. Heart J.* 36, 2425–2437. doi:10.1093/eurheartj/ehv157

Yu, L., Gong, B., Duan, W., Fan, C., Zhang, J., Li, Z., et al. (2017). Melatonin ameliorates myocardial ischemia/reperfusion injury in type 1 diabetic rats by preserving mitochondrial function: role of AMPK-PGC-1α-SIRT3 signaling. *Sci. Rep.* 7, 41337. doi:10.1038/srep41337

Zhang, L., Wang, W., Zhu, B., and Wang, X. (2017). Epithelial mitochondrial dysfunction in lung disease. *Adv. Exp. Med. Biol.* 1038, 201–217. doi:10.1007/978-981-10-6674-0_14

Zhang, M., Tang, J., Li, Y., Xie, Y., Shan, H., Chen, M., et al. (2017). Curcumin attenuates skeletal muscle mitochondrial impairment in COPD rats: PGC-1α/SIRT3 pathway involved. *Chem. Biol. Interact.* 277, 168–175. doi:10.1016/j.cbi.2017.09.018

Zhang, Z., Cheng, X., Yue, L., Cui, W., Zhou, W., Gao, J., et al. (2018). Molecular pathogenesis in chronic obstructive pulmonary disease and therapeutic potential by targeting AMP-activated protein kinase. *J. Cell. Physiol.* 233, 1999–2006. doi:10.1002/jcp.25844

Conflict of Interest: The authors declare that the research was conducted in the absence of any commercial or financial relationships that could be construed as a potential conflict of interest.

Copyright © 2020 Mao, Li, Feng, Liu, Tian, Bian, Li, Hu, Zhang, Ji and Li. This is an open-access article distributed under the terms of the Creative Commons Attribution License (CC BY). The use, distribution or reproduction in other forums is permitted, provided the original author(s) and the copyright owner(s) are credited and that the original publication in this journal is cited, in accordance with accepted academic practice. No use, distribution or reproduction is permitted which does not comply with these terms.

GLOSSARY

AICAR 5-aminoimidazole-4-carboxamide ribonucleotide
AMPK adenosine monophosphate-activated protein kinase
APL aminophylline
ATP adenosine triphosphate
BCA bicinchoninic acid
BFJ Bufei Jianpi formula
CCCP carbonyl cyanide *m*-chlorophenyl hydrazone
COPD chronic obstructive pulmonary disease
CSE cigarette smoke extract
DMEM Dulbecco's modified Eagle's medium
EF-50 mid-tidal expiratory flow
FBS fetal bovine serum
FCCP carbonyl cyanide 4-(trifluoromethoxy) phenylhydrazone
Fis-1 mitochondrial fission-1 protein
GAPDH glyceraldehyde 3-phosphate dehydrogenase
HE hematoxylin and eosin
LC3B light chain 3B
MMP mitochondrial membrane potential
MPTP mitochondrial permeability transition pores;
mTOR mammalian target of rapamycin
NRF nuclear respiratory factor
OCR oxygen combustion rate
PEF peak expiratory flow
PGC-1α peroxisome proliferator-activated receptor gamma coactivator
PINK-1 PTEN-induced putative kinase 1
PPAR peroxisome proliferator-activated receptor
PVDF polyvinylidene difluoride
ROS reactive oxygen species
SD Sprague–Dawley
SDS-PAGE sodium dodecyl sulfate polyacrylamide gel electrophoresis
SIRT1 (sirtuin 1)
SMD skeletal muscle dysfunction
TCM traditional Chinese medicine
TFAM mitochondrial transcription factor A
TV tidal volume
ULK-1 UNC-51-like kinase

frontiers in Pharmacology

ORIGINAL RESEARCH
published: 18 December 2020
doi: 10.3389/fphar.2020.554777

Quality Markers for Astragali Radix and Its Products Based on Process Analysis

Yuntao Dai[1†], Dongbo Wang[1†], Manjia Zhao[1], Lihua Yan[1], Chao Zhu[2], Pengyue Li[1], Xuemei Qin[3], Rob Verpoorte[4] and Shilin Chen[1*]*

[1]Institute of Chinese Materia Medica, China Academy of Chinese Medical Sciences, Beijing, China, [2]College of Medicine and Nursing, Dezhou University, Shandong, China, [3]China Modern Research Center for Traditional Chinese Medicine, Shanxi University, Shanxi, China, [4]Natural Products Laboratory, Institute of Biology, Leiden University, Leiden, Netherlands

Due to the complex nature of traditional medicines, quality control methods need to cover two aspects: compliance of raw materials with quality standards and process control. Astragali radix (AR), the roots of *Astragalus mongholicus* Bunge, was selected in this study as an example of a widely used traditional medicine in various formulations. Astragaloside IV (AG IV) and calycosin 7-*O*-β-D-glucoside (CG) are used as the markers for the quality control of AR and its products in the Chinese Pharmacopoeia. However, in the raw materials, malic acid esters of the CG and acetate esters of the astragaloside are easily decomposed into CG and AG IV during storage and processing of AR to make extracts for various preparations. The thermal stability of the isoflavonoids and astragalosides in decoction was studied. The level of CG and astragalosides (AG I/AG II/AG IV) was strongly affected by prolonged heat during processing, while calycosin was stable in the conditions. Also the major astragalosides in AR could fully converted into AG IV which eventually reaches a stable level under certain conditions. With calycosin and AG IV as marker components, practical, reproducible, and precise methods were established and applied to the quality analysis of AR from its raw materials to its intermediates and products. This study demonstrates that a full chemical profiles analysis of the whole manufacturing process (from "raw materials—intermediates/extracts—final product") is important to identify quality markers (Q-markers) and even to establish proper analysis methods for traditional Chinese medicine products.

Keywords: astragali radix, quality control, process analysis, quality markers, fingerprint analysis

OPEN ACCESS

Edited by:
Yan Xu,
Cleveland State University,
United States

Reviewed by:
Pei Luo,
Macau University of Science and Technology, Macau
Dingkun Zhang,
Chengdu University of Traditional Chinese Medicine, China

****Correspondence:***
Yuntao Dai
ytdai@icmm.ac.cn
Shilin Chen
slchen@icmm.ac.cn

†These authors share first authorship

Specialty section:
This article was submitted to Ethnopharmacology, a section of the journal Frontiers in Pharmacology

Received: *23 April 2020*
Accepted: *25 November 2020*
Published: *18 December 2020*

Citation:
Dai Y, Wang D, Zhao M, Yan L, Zhu C, Li P, Qin X, Verpoorte R and Chen S (2020) Quality Markers for Astragali Radix and Its Products Based on Process Analysis. Front. Pharmacol. 11:554777. doi: 10.3389/fphar.2020.554777

INTRODUCTION

Astragali radix (AR) (Huang Qi in Chinese) is derived from the dried roots of *Astragalus mongholicus* or *A. membranaceus* (Fisch.) Bge (National Commission of Chinese Pharmacopoeia, 2015). For more than 2,000 years it is one of the most widely used Chinese herbal medicines and also functional food for reinforcing "Qi" (vital energy). It's traditionally used for revitalizing, tonifying, skin reinforcement diuretic, abscess-draining, and tissue-generative purpose (National Commission of Chinese Pharmacopoeia, 2015). Modern pharmacological studies have demonstrated that AR possesses a variety of biological activities, such as immunomodulating (Jin et al., 1994), anti-oxidative (Lee et al., 2005), and cardiovascular protective function in diabetic nephropathy (Fu et al., 2014). AR is widely used in different complex formulations, and there are almost 150 traditional

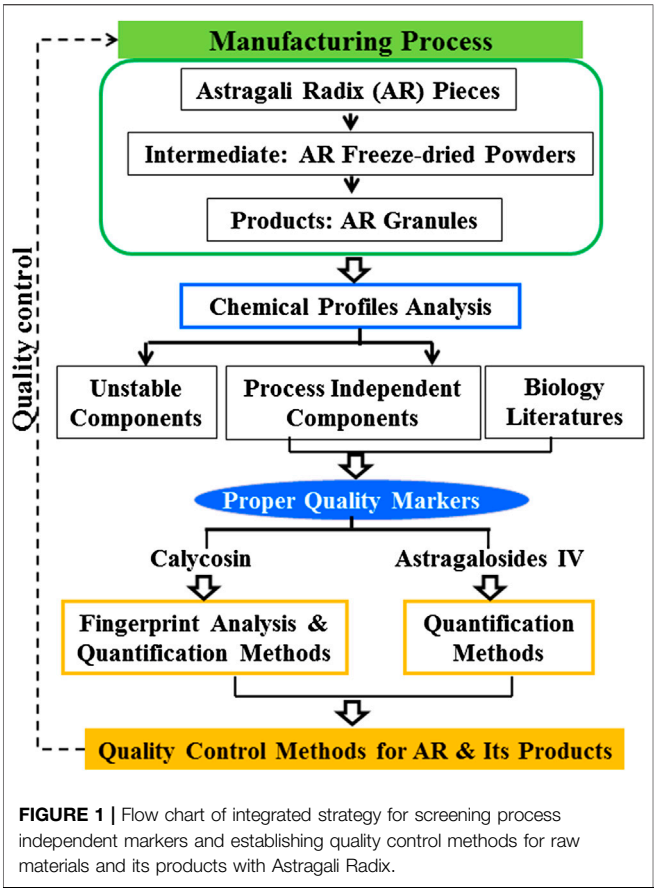

FIGURE 1 | Flow chart of integrated strategy for screening process independent markers and establishing quality control methods for raw materials and its products with Astragali Radix.

Chinese patent medicines (TCPMs) containing AR described in the Chinese Pharmacopoeia (2015 version) (National Commission of Chinese Pharmacopoeia, 2015).

The TCPMs that contain AR include granules, capsules, tablets, syrups, plasters/concentrated decoctions, and so on. The manufacturing processes of these products must at least include the extraction of AR pieces with hot water, followed by concentration of the decoction (National Commission of Chinese Pharmacopoeia, 2015). During the processing, from raw materials to concentrated extract, conversions of constituents may occur due to e.g., high temperature, and prolonged contact with air, pH and water (Lin et al., 2000; Chu et al., 2014). For a proper quality control ensuring reproducible end products, Q-markers are required that have a stable level during the whole production process. The Q-markers should be chemically stable and its levels can be followed during the whole manufacturing process. So whole process (i.e., from "raw materials—intermediates/extracts—final product") analysis is very necessary to identify Q-markers.

Isoflavonoids and triterpene saponins are important active compounds in AR. Astragaloside IV (AG IV) and calycosin 7-*O*-β-D-glucoside (CG) are used as the marker substances for the quality control of AR and its products in the Chinese Pharmacopoeia (National Commission of Chinese Pharmacopoeia, 2015). However, it has been reported that calycosin 7-*O*-β-D-(6″-malonyl) glucoside (CGM) is unstable during sample preparation and may degrade into CG (Lin et al., 2000). Astragaloside I (AG I), isoastragaloside I (iAG I), astragaloside II (AG II), and acetylastragaloside I (acetyl AG I) were also shown to be unstable and to be converted into AG IV under basic conditions (Chu et al., 2014). These observations imply that the CG and AG IV contents detected in AR are the results of chemical transformations during manufacturing process and sample preparation, and thus their levels are affected by the degree of transformation. Therefore, the present quality analysis methods based on AG IV and CG as Q-markers of AR and its products should be reconsidered. Previous studies on AR, have identified the major small molecules and different quantification methods have been developed for AR and its products (Qi et al., 2006; Song et al., 2007; Qi et al., 2008; Song et al., 2008; Zhao et al., 2018). However, the stability of the levels of Q-makers during the whole manufacturing process and sample preparations were neglected. Specific studies on the stability of the levels of these constituents and their possible chemical conversions during manufacturing processes and sample preparation are essential to guarantee the accuracy of the quality control methods.

This study aims to analyze the stability of the major components of AR during the manufacturing process to identify proper Q-markers for AR, and then develop a practical analytical method for the quality control of AR and its preparations based on these markers. The analysis of the stability of the levels of major components of AR was done by following the changes of chemical profiles throughout the manufacturing process (i.e., from "pieces—freeze-dried powders of extracts—granules") (**Figure 1**). To achieve a proper quality control protocol, fingerprint analysis of isoflavonoids including quantitation of calycosin content was established, as well as an optimized method for the determination of AG IV content in AR and its products. This study demonstrates how to develop quality control methods for TCPMs that are independent of processing in the whole production chain from raw materials to its final products. The Q-markers can be accurately detected in raw materials to terminal products, which provides methods for the whole chain analysis of traditional Chinese medicine (TCM) and facilitates the traceability analysis of the quality of TCM.

MATERIALS AND METHODS

Chemicals, Materials and Reagents

Pieces, freeze-dried powders of extracts, and formula particles (the final formulated product in the form of granules, batch NO. 406209L, 1406002, 1506027, 1601057, 6101141, 5090891) of AR were obtained from Tianjiang Yifang Company, China. A voucher specimen (RA-YP-1~RA-YP-12; RA-DGF-1~RA-DGF-12; RA-PFKL-1~RA-PFKL-6) were deposited in the herbarium of the Institute of Chinese Materia Medica, China Academy of Chinese Medical Sciences. The dosage forms and batch numbers used are listed in **Table 1**. Reference compounds, including astragaloside IV (AG IV, S1, CHB170727), calycosin 7-*O*-β-D-glucoside (CG, F1, CHB161105), and calycosin (C, F7,

TABLE 1 | The batch numbers, correlation coefficients to the mean chromatogram of pieces of Astragali Radix, and mean content of quality marker (calycosin and astragaloside IV) for pieces (YP-1–YP-12), freeze-dried powders (DGF-1–DGF-12), and formula granules (PFKL-1–PFKL-6) of Astragali Radix in this study. The mean content was calculated with the weight of target compounds divided by the weight of the samples.

No.	Batch number	Correlation coefficient	Content of quality marker (%) (n = 3)			
			Calycosin	RSD%	Astragaloside IV	RSD%
YP-1	AR-201504	0.980	0.007	3.85	0.06	0.93
YP-2	AR-201505	0.967	0.009	3.84	0.06	0.14
YP-3	AR-201506	0.989	0.015	2.83	0.06	0.71
YP-4	AR-201507	0.894	0.018	0.16	0.05	1.65
YP-5	AR-201508	0.906	0.023	0.24	0.05	0.72
YP-6	AR-201509	0.986	0.035	1.14	0.04	0.42
YP-7	AR-201510	0.969	0.016	0.99	0.05	1.27
YP-8	AR-201511	0.979	0.007	0.17	0.05	0.67
YP-9	AR-201512	0.976	0.007	4.26	0.05	1.92
YP-10	AR-201504	0.983	0.007	2.93	0.04	1.70
YP-11	AR-201505	0.943	0.005	0.00	0.06	1.65
YP-12	AR-201506	0.983	0.009	1.77	0.07	1.27
DGF-1	DG16009015	0.804	0.117	3.90	0.16	0.42
DGF-2	DG1609002	0.861	0.108	0.64	0.14	0.57
DGF-3	DG1609008	0.868	0.102	0.31	0.14	0.18
DGF-4	DG1611006	0.851	0.075	0.04	0.14	0.55
DGF-5	DG1609014	0.848	0.065	0.69	0.19	0.24
DGF-6	DG169011	0.786	0.066	0.27	0.14	0.34
DGF-7	DG1609007	0.768	0.096	1.34	0.12	0.69
DGF-8	DG1611003	0.807	0.065	2.21	0.13	0.34
DGF-9	DG1607007	0.867	0.078	0.95	0.13	0.29
DGF-10	DG1611007	0.795	0.072	3.08	0.15	0.63
DGF-11	DG1611002	0.794	0.174	0.08	0.12	1.36
DGF-12	DG1611001	0.795	0.058	2.21	0.10	2.74
PFKL-1	406209L	0.534	0.013	2.67	0.11	2.66
PFKL-2	1406002	0.591	0.030	1.51	0.13	0.96
PFKL-3	1506027	0.560	0.022	2.02	0.13	1.60
PFKL-4	1601057	0.584	0.028	0.93	0.13	1.68
PFKL-5	6101141	0.557	0.013	0.31	0.12	0.42
PFKL-6	5090891	0.544	0.016	0.71	0.12	2.98

CHB161104) were obtained from the National Institute for the Control of Pharmaceutical and Biological Products. Their purity, as determined by HPLC, was above 98%. The structures of these compounds are shown in **Supplementary Figure S1**. The quality of the AR pieces used met the requirement of the Chinese Pharmacopoeia (2015 version) (National Commission of Chinese Pharmacopoeia, 2015).

HPLC-grade acetonitrile (Fisher Scientific, United States), Optima liquid chromatography–mass spectrometry (LC-MS)-grade formic acid (Fisher Scientific, Czech Republic), and pure water (Wahaha, China) were used as mobile phases. UniElut C_{18}EC column (500 mg/6 ml) were bought from Acchrom Instrument (Beijing) Technologies Co., Ltd. Other reagents and chemicals were of analytical grade. All solvents and samples were filtered through 0.45-μm membrane filters (Jinteng, Tianjin, China) before being injected into the HPLC system.

Preparation of Solutions

Preparation of Standards Solution

Reference compounds, including AG IV, CG, and C, were accurately weighed and dissolved in methanol to form 1 mg/ml stock solutions, and stored at 4°C for further use.

Sample Preparation for Isoflavonoid Analysis

Dried pieces of AR were milled to a homogeneous powder and then sieved through a No. 65 mesh listed in Chinese pharmacopeia. Samples of the powder were accurately weighed to a mass of 1 g, placed in a 50 ml centrifuge tube, and ultrasonicated (40 kHz, 500 W) with 15 ml of methanol for 30 min. After being centrifuged (at 3,000 × g) for 5 min, the methanol solution was collected and filtered. The residue was washed twice with 7.5 ml of methanol, ultrasonicated (40 kHz, 500 W) for 5 min, centrifuged (at 3,000 × g) for 5 min, and filtered again. The filtrates were combined, passed through a membrane filter (0.45 μm), and then a sample was injected into the HPLC system.

Freeze-dried powder and granule sample were accurately weighed to a mass of 0.3 and 0.8 g, respectively, and then placed in a 50 ml centrifuge tube and ultrasonicated (40 kHz, 500 W) with 20 ml of an aqueous solution containing 5% methanol for 10 min. After being allowed to cool, the methanol solution was filtered through a membrane filter (0.45 μm) and injected into the HPLC system for analysis.

Sample Preparation for Astragaloside IV Content Determination

Extraction and preparation of AR pieces was carried out as described in our previous study (Zhao et al., 2018).

Each sample of freeze-dried powder and formula granules was accurately weighed, 0.3 and 0.5 g, respectively, placed in a 50 ml centrifuge tube. After addition of 20 ml of aqueous solution containing 60% methanol, the sample was ultrasonicated (40 kHz, 500 W) 30 min. After adding 10 ml of ammonia, the aqueous methanol solution was centrifuged (at 3,000 × g) for 30 min and filtered. The residue was washed with a mixture of 2 ml of a 60% methanol solution and 1 ml of ammonia, and then centrifuged (at 3,000 × g) for 30 min. The filtrates were combined and loaded onto a solid-phase extraction column (SPE column, UniElut C18EC column, 500 mg/6 ml), which had been activated with 5.0 ml methanol. The SPE column was washed with 5.0 ml of water, and then eluted with 5.0 ml methanol. The methanol eluent was collected and filtered through a membrane filter (0.45 μm), and finally injected into the HPLC system for analysis.

HPLC and MS Analysis Conditions

HPLC-DAD Conditions for Isoflavonoid Analysis

HPLC-DAD analyses were performed using a 1200 Series HPLC (Agilent)-DAD system. A YMC-Triart C18 column (250 × 4.6 mm. 5 μm) was used for the chromatographic separations. The mobile phase consisted of 0.1% formic acid in acetonitrile (A) and water with 0.1% formic acid (B), using a gradient elution of 5–20% A at 0–8 min, 20–25% A at 8–15 min, 25% A at 15–20 min, 25–40% A at 20–30 min, and 40–60% A at 30–40 min. The wavelength was set at 260 nm. The injection volume was 20 μl, and the flow rate was 1 ml/min.

HPLC-ELSD Conditions for Astragaloside Content Determination

HPLC with evaporative light scattering detector (HPLC-ELSD) analyses were performed using a 1200 Series HPLC (Agilent)-ELSD system (Alltech 2000 ES). A YMC-Triart C18 column (250 × 4.6 mm. 5 μm) was used for chromatographic separations. The mobile phase consisted of 0.1% formic acetonitrile (A) and water with 0.1% formic acid (B), using a gradient elution of 5–10% A at 0–5 min, 10–32% A at 5–10 min, 32–45% A at 10–30 min, 45–95% A at 30–35 min, and 95–5% A at 35–40 min. The injection volume was 20 μl, and the flow rate was 1 ml/min. ELSD was performed with nitrogen as the carrier gas at a flow rate of 2.5 L/min, and the nebuliser temperature was set to 100°C.

HPLC-Linear Trap Quadrupole-MS Analysis

To identify the major peaks in the HPLC-UV/ELSD chromatograms, the high-performance liquid chromatography system coupled with a high-resolution linear trap quadrupole Orbitrap mass spectrometry (Thermo Scientific, United States) was used. A full-scan model was employed, and the m/z range was set to 150–1,000. Electrospray ionization was done with the following conditions: a source heater temperature of 400°C, capillary temperature of 350°C, ion spray voltage of 3.5 kV, capillary voltage of 35 eV, gas flow rate of 35 arb, and auxiliary gas flow rate of 10 L/h. A data-dependent scan was used for tandem mass spectrometry (MS/MS).

Method Validation

Calibration Curves and Linearity Range

A series of analyses were conducted to validate the performance of the methods, including determinations of their linearity, precision, repeatability, stability, and accuracy. The relative standard deviation (RSD) was used to evaluate the precision of the developed method. Methanol stock solutions of AG IV and C were prepared and diluted to appropriate concentration ranges for the construction of calibration curves. The calibration curve of C was constructed using its peak areas and its calculated concentrations. The calibration curve of AG IV was constructed by plotting the logarithm of the peak areas vs. the logarithm of its concentrations.

Precision, Repeatability, Stability, and Accuracy

Analyses of intra-day variations among six successive injections were chosen to determine the precision of the developed method. To confirm its repeatability, six different working solutions from the same sample were prepared and analyzed. The sample stability was determined by examining one sample at different times during one day, at 0, 1, 2, 4, 12, and 24 h. Over this period, the solution was stored at room temperature.

The recovery of the marker components was determined by spiking the same amount of reference standards into samples with known contents, and these were then extracted and analyzed as described in *Preparation of Solutions* and *HPLC and MS Analysis Conditions* sections. The recoveries were calculated with the following formulas: recovery (%) = (detected amount − original amount)/added amount × 100%; and RSD (%) = (SD/Mean) × 100.

Stability Test of AR Decoction During Processing

Preparation of AR Decoction

Pieces of AR (100 g) were placed in 800 ml of water for 30 min at room temperature, and then refluxed for 1 h (at 100°C). Each decoction was filtered, and the residue was refluxed for another 30 min in 600 ml of water (at 100°C). The filtrates were combined and evaporated to a final volume of <500 ml under reduced pressure at a temperature not exceeding 50°C, and then the volume of the concentrated solution was adjusted to 500.0 ml in a volumetric flask using water. The solution was centrifuged at 12,000 rpm for 20 min prior to analysis of the supernatant.

Stability Test of AR Decoction in the Heating Process

The final AR decoction was separated into nine Eppendorf (EP) tubes, which were then closed and sealed with sealing film. Three of them were heated for 0, 0.5, and 2 h at 100°C, respectively, and the processed solutions were then cooled to room temperature, centrifuged at 12,000 rpm for 20 min, and analyzed by HPLC with DAD/ELSD.

Stability Tests of Aqueous Solution of Standards

Stability tests were conducted using pure compounds (AG II and AG IV) as representative of astragalosides and an aqueous solution of a mixture of main astragalosides (AG II, iAG II, AG I, and iAG I) in AR. Known amounts (10–50 μl) of the solutions of the target compounds were added to water prior to vortex mixing and centrifugation. The supernatant was divided into six tubes, which were closed and heated at 100°C for 2 h. The samples were then cooled to room temperature, filtered, and analyzed using HPLC-ELSD. These analyses were conducted as described in *HPLC and MS Analysis Conditions* section, and the peaks were identified using pure standard compounds and a high-resolution linear trap quadrupole Orbitrap, as described in *HPLC-Linear Trap Quadrupole-MS Analysis* section.

Data Analysis

The software "Similarity Evaluation System for Chromatographic Fingerprint of TCM" published by GPC (Version 2004A) was employed. This software was used to generate the mean chromatogram as a representative standard fingerprint chromatogram for a group of chromatograms, calculate the correlation coefficients among these, and carry out a similarity analysis to compare the samples with the mean chromatogram based on the peak areas. The relative retention time (RRT) and relative peak area (RPA) of each common peak in the mean chromatogram were calculated, using calycosin (C) as reference within each preparation, respectively, to semi-quantitatively express the different chemical properties in the chromatographic profiles of the samples.

RESULTS AND DISCUSSION

Method Optimization for the Analysis of Isoflavonoids

Optimization of Sample Preparation Methods for AR Pieces

The Chinese Pharmacopeia (National Commission of Chinese Pharmacopoeia, 2015) uses reflux heating for 4 h in methanol for the sample preparation method for the determination of CG and AG IV contents in AR roots. However, such a method is not convenient for analysis of a large number of samples. To shorten the time of sample preparation, we developed an ultrasonic extraction method. Different parameters were investigated, including the amount of MeOH, ultrasonication times, and extraction time, to reach a complete extraction of C. The reason why C instead of the CG was selected as the Q-marker of AR was demonstrated in *The Stability of Isoflavonoids in AR During Manufacturing Process* section. The amount of sample was kept the same as used in the Chinese Pharmacopeia (version 2015) (National Commission of Chinese Pharmacopoeia, 2015). The results indicated that the most efficient dissolution was sonication with methanol for three times (**Supplementary Table S1**), as described in *Sample Preparation for Isoflavonoid Analysis* section.

Optimization of the Sample Preparation Methods for Freeze-Dried Powder and Formula Granules of AR

Different sample preparation methods for freeze-dried powder and formula granules of AR were investigated. The amount of sample was calculated in accordance with the extraction rate (~33.0%) and the proportion of its excipients in granules to ensure that the amount in the sample was consistent with that in the AR pieces. The extraction ability of different solvents (water, 5% methanol, and 50% methanol) and extraction times (10, 30, and 60 min) to extract C were tested. The results indicated that the most efficient solvent was the one using 5% methanol as solvent with sonication for 10 min (**Supplementary Table S1**), as described in *Preparation of Solutions* section.

Optimization of HPLC Separation

An HPLC-DAD fingerprint analysis of the isoflavonoids in AR was established based on the literature (Qi et al., 2008). The chromatographic conditions were further optimized based on the following principles: 1) to be suitable for the analysis of both the alcohol and the aqueous extract of AR; and 2) to be able to detect the main isoflavonoids in the extracts of AR with baseline separation. After optimizing different chromatographic parameters, including the elution gradient, column temperature, and injection volume, were set as described in *HPLC and MS Analysis Conditions* section.

The Stability of Isoflavonoids in AR During Manufacturing Process

Fingerprint Analysis of Isoflavonoids

The fingerprints of 12 batches of AR pieces, 12 batches of freeze-dried AR powders, and six batches of AR formula granules, from the same manufacturer, were analyzed using the established conditions of fingerprint analysis. The mean chromatograms of AR pieces, freeze-dried powders, and formula granules were generated as described in *Data Analysis* section (**Figure 2**), and 10 common peaks were observed for AR among raw materials, intermediates, and final preparations. The common peaks were identified with high-resolution MS by comparisons with our in-house database, and confirmed with analyses of standard compounds. These common constituents included isoflavones [calycosin 7-*O*-β-D-glucoside (CG, F1), calycosin (C, F7), calycosin 7-*O*-β-D-(6″-malonyl)-glucoside (CGM, F2), formononetin-7-*O*-glucoside (FG, F3), formononetin (F, F8), and 6″-*O*-malonylononin (FGM, F6)], pterocarpans [(6α*R*, 11α*R*)-3-hydroxy-9,10-dimethoxypterocarpan-3-*O*-β-D-glucoside (F4) and (6α*R*, 11α*R*)-3-hydroxy-9,10-dimethoxypterocarpan (F9)], and isoflavans [(3*R*)-7,2′-dihydroxy-3′,4′-dimethoxyisoflavan-7-*O*-β-D-glucoside (F5) and (3*R*)-7,2′-dihydroxy-3′,4′-dimethoxyisoflavan (F10)] (Qi et al., 2008; Qi et al., 2009) (**Table 2**). The RRT and RPA of these 10 common peaks were calculated using C (F7) as the reference peak in the mean chromatogram of each respective preparation (**Table 3**).

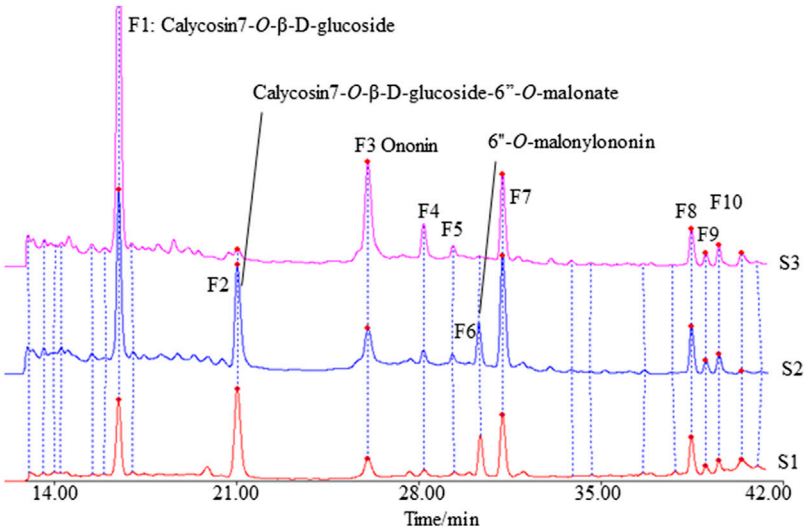

FIGURE 2 | The mean chromatograms of isoflavonoids used as representative fingerprint chromatograms in analyses of the extracts of Astragali radix pieces (S1), freeze-dried powders (S2), and formula granules (S3) by HPLC-DAD at 260 nm [F1: calycosin 7-*O*-β-D-glucoside; F2: calycosin 7-*O*-β-D-glucoside-6″-*O*-malonate; F3: formononetin-7-*O*-glucoside; F4: (6α*R*, 11α*R*)-3-hydroxy-9,10-dimethoxypterocarpan-3-*O*-β-D-glucoside; F5: (3*R*)-7,2′-dihydroxy-3′,4′-dimethoxyisoflavan-7-*O*-β-D-glucoside; F6: 6″-*O*-malonylononin; F7: calycosin; F8: formononetin; F9: (6α*R*, 11α*R*)-3-hydroxy-9,10-dimethoxypterocarpan; F10: (3*R*)-7,2′-dihydroxy-3′,4′-dimethoxyisoflavan].

TABLE 2 | Assignment of identities to isoflavonoids and saponins detected in the HPLC chemical profiles of Astragali radix by high-resolution LC-MS.

No.[a]	Identification	Formula [M]	Experimental	Theoretical
F1	Calycosin 7-*O*-β-D-glucoside (CG)[b]	$C_{22}H_{22}O_{10}$	[M + H, 447.1285]	447.1291
F2	Calycosin 7-*O*-β-D-(6″-malonyl)-glucoside (CGM)	$C_{25}H_{24}O_{13}$	[M + H, 533.1246]	533.1295
F3	Ononin (FG)[b]	$C_{22}H_{22}O_{9}$	[M + H, 431.1328]	431.1342
F4	(6α*R*,11α*R*)-3-hydroxyl-9,10-dimethoxypterocarpan-3-*O*-β-D-glucoside	$C_{23}H_{26}O_{10}$	[M + H, 463.1585]	463.1604
F5	(3*R*)-2′7-dihydroxy-3′,4′-dimethoxyisoflavan-7-*O*-β-D-glucoside	$C_{23}H_{28}O_{10}$	[M + H, 465.1748]	465.176
F6	6″-*O*-malonylononin (FGM)	$C_{25}H_{24}O_{12}$	[M + H, 517.1364]	517.1346
F7	Calycosin (C)[b]	$C_{16}H_{12}O_{5}$	[M + H, 285.07151]	285.0762
F8	Formononetin (F)[b]	$C_{16}H_{12}O_{4}$	[M + H, 269.0886]	269.2812
F9	(6α*R*, 11α*R*)-3-hydroxy-9,10-dimethoxypterocarpan[b]	$C_{17}H_{16}O_{5}$	[M + H, 301.1071]	301.1071
F10	(3*R*)-7,2′-dihydroxy-3′,4′-dimethoxyisoflavan[b]	$C_{17}H_{18}O_{5}$	[M + H, 303.1239]	303.1232
S1	Astragaloside IV (Ag IV)[b]	$C_{41}H_{68}O_{14}$	[M-H + FA-H, 829.4547]	829.4585
S3	Astragaloside II (Ag II)[b]	$C_{43}H_{70}O_{15}$	[M-H + FA, 871.4705]	871.1691
S4	Isoastragaloside II (iAg II)[b]	$C_{43}H_{70}O_{15}$	[M-H + FA, 871.4705]	871.1691
S5	Astragaloside I (Ag I)[b]	$C_{45}H_{72}O_{16}$	[M-H + FA, 913.4780]	913.4796
S6	Isoastragaloside I (iAg I)[b]	$C_{45}H_{72}O_{16}$	[M-H + FA, 913.4780]	913.4796
S7	Acetylastragaloside I (AgA I)	$C_{47}H_{74}O_{17}$	[M-H + FA, 955.4964] [M-H, 911.5013]	955.4902

[a]*Refer to the same numbers in* ***Figures 2***, ***3***.
[b]*Confirmed with standard compounds in HPLC-PDA.*

Difference Between the Fingerprint of Isoflavonoids in Pieces, Freeze-Dried Powder, and Formula Granules of AR

The correlation coefficients between the mean chromatograms of the pieces, freeze-dried powder, and formula granules of AR showed that there were differences in the chemical compositions of the raw materials, intermediates, and final preparations of AR (**Supplementary Table S2**). Compared with AR pieces, the RPA of CG in freeze-dried powder and formula granules was significantly higher, while that of CGM was much lower. In formula granules, the content of CG was four times higher than that in other forms of AR, while the peak of CGM (F2) was almost absent. The same phenomenon was observed for FG and FGM. The chromatographic profiles of the aglycones (F8–F10) in the different preparations were similar.

The Thermal Stability of Isoflavonoids in the Water Decoction of AR

The remarkable increase in the RPA of CG and FG and the significant decrease in the RPA of CGM and FGM from raw

TABLE 3 | Relative retention time and relative peak area of common peaks in the mean chromatograms of pieces, freeze-dried powders, and formula granules of Astragali Radix with peak F7 in each chromatogram as reference.

No.[a]	Relative retention time	Relative peak area		
		Pieces	Freeze-dried powders	Formula granules
F1	0.53	1.14	1.61	4.74
F2	0.68	1.74	1.09	0.22
F3	0.84	0.44	0.54	1.74
F4	0.90	0.12	0.16	0.52
F5	0.94	0.06	0.13	0.28
F6	0.97	0.59	0.36	0.11
F7(s)	1.00	1.00	1.00	1.00
F8	1.23	0.59	0.36	0.38
F9	1.25	0.15	0.10	0.12
F10	1.26	0.25	0.15	0.21

[a]*Refer to the same numbers in* ***Figure 2***.

materials to granules may be related to the instability of CGM and FGM. For further study, a decoction of AR was prepared and its thermal stability was investigated at 100°C. The results showed that the RPA of CGM and FGM decreased significantly after heating for 30 min, and after 4 h heating these peaks were not detectable anymore. Meanwhile, the RPA of CG and FG increased significantly with heating (**Supplementary Figure S2**). The duration of heating seems to be a major reason for the degradation of CGM and FGM into CG and FG in the aqueous decoction of AR. The levels of CG and FG in the final preparations of AR are thus dependent on the exposure time to heat in the manufacturing process. A previous study on FGM and CGM showed that these esters were almost completely converted into their related glycosides when the decoction was refluxed for 16 h in an 80% ethanol extract or stored in an 80% methanol extract at room temperature for 4 weeks (Lin et al., 2000). Apparently the levels of FGM and CGM seems to be good indicators for the processing of the aqueous and alcoholic preparations of AR roots, low levels of these compounds means that the material has been exposed to heat for prolonged time or has been stored for long periods.

At present, CG is used as the index for isoflavonoids in the quality evaluation of AR in the Chinese Pharmacopoeia (version 2015) (National Commission of Chinese Pharmacopoeia, 2015). However, due to the thermal instability of CGM, the content of CG will increase during sample preparation and storage. Therefore, although CG itself is stable during sample preparation, it is not suitable as a Q-marker of AR and its preparations. Our data show that C remains stable during the manufacturing process. A similar observation was reported for F in Hedysari radix (Liu et al., 2006). Calycosin has a variety of pharmacological properties, such as vascular endothelial cell protection, anti-osteoporosis, antioxidant, anti-tumor, and immunomodulating properties (Zhang et al., 2015). In addition, it is a typical phytoestrogen, with estrogen-like effects. Our previous studies found that the estrogen receptor activity of C is greater than that of CG. Therefore, C can be considered as a marker compound for AR because of its chemical properties as well as its activity. The sample preparation and determination methods of C were optimized as descried in *Method Optimization for the Analysis of Isoflavonoids* section and the final established methods were described in *Preparation of Solutions* and *HPLC and MS Analysis Conditions* sections.

The Stability of Saponins in AR During Manufacturing Process

The Chemical Profile of Saponins in AR and Its Preparations

We first analyzed the saponins' profile in AR by HPLC-ELSD (**Figure 3A**). A total of more than seven peaks were found to be in common for the different materials analyzed. By high-resolution MS they were identified as Astragaloside IV (AG IV), astragaloside III (AG III), astragaloside II (AG II), isoastragaloside II (iAG II), astragaloside I (AG I), isoastragaloside I (iAG I), and acetylAG I. A method for the simultaneous determination of the content of different saponins (AG IV, AG II, iAG II, AG I, iAG I, and acetyl AG I) was established using UPLC time-of-flight MS (UPLC-TOF-MS) (Qi et al., 2008). Analyzing the content of astragalosides in different preparations, the following observations were made: 1) in AR pieces, the content of AG I was significantly higher than that of other astragalosides; 2) in formula granules of AR, the content of AG II was significantly higher than that of other astragalosides; and 3) in the oral liquids of AR, AG IV was the main components. The astragalosides (AG I, iAG I, AG II, iAG II, and acetyl AG I) are acetylated derivatives of astragaloside IV, which differ only in the number and positions of the acetyl groups in their β-D-xylose attached at position C-3 (**Supplementary Figure S1**). The differences in the astragalosides' profiles in the different preparations seem to be related to the loss of the acetyl groups of the xylose group during the manufacturing process. Loss of all acetyl groups results in AG IV as final product.

The Stability of Astragalosides in Aqueous Solution at High Temperature

A decoction of AR was prepared and its thermal stability was investigated at 100°C. The results showed that the RPA of AG I, iAG I and iAG II decreased significantly with heating, while the RPA of AG IV increased significantly (data not shown). This result indicates that AG I, iAG I and iAG II in the decoction of AR were unstable and they may be transformed into AG IV during

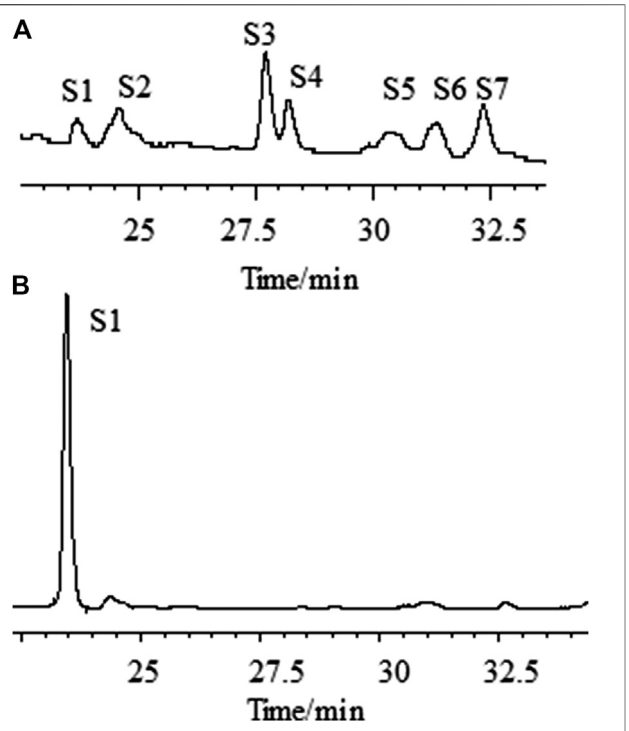

FIGURE 3 | Chromatographic profiles of aqueous extracts of Astragali radix before **(A)** and after **(B)** the addition of ammonia, as determined by HPLC–ELSD. [S1: astragaloside IV (AG IV); S2: astragaloside III (AG III) and formononetin; S3: astragaloside II (AG II); S4: isoastragaloside II (iAG II); S5: astragaloside I (AG I); S6: isoastragaloside I (iAG I); S7: acetylastragaloside I.]

heating. Then, the stability of an aqueous solution of a mixture of astragalosides (AG II, iAG II, AG I, and iAG I) was tested. The HPLC chromatograms of the samples heated for 2 h at 100°C showed that the levels of AG II, iAG II, AG I, and iAG I decreased while the content of AG IV increased (data not shown). Further investigations of the stability of two single standard compounds (AG II and AG IV) showed that in an aqueous solution, at room temperature, AG II was partly transformed into AG IV, and heating at 100°C further promoted the conversion of AG II into AG IV, while AG IV was stable in this condition (**Supplementary Figure S3**). Thus, heating is a major factor promoting the deacetylation reaction, leading to the transformation of astragalosides. The proposed chemical degradations of astragalosides were summarized in **Supplementary Figure S4**. This explains the different saponin profiles of AR preparations. Heat and long term storage lead to preparations with only AG IV, as found in oral liquid samples of AR (Qi et al., 2008). This implies that the saponins' fingerprint for AR gives information about the manufacturing process and storage.

Method Optimization for the Analysis of Astragaloside IV

The sample preparation for the AG IV determination in the Chinese Pharmacopoeia (National Commission of Chinese Pharmacopoeia, 2015) (version 2015) involves reflux extraction, liquid-liquid separation with *n*-butanol, and liquid-liquid separation with ammonia, which may take more than 2 days to complete per sample. Therefore, we optimized and established practical method for the determination of AG IV content in raw materials and pieces of AR (Zhao et al., 2018). This method replaces all of the time-consuming preparation steps with sonication extraction and ammonia hydrolysis, shortening the preparation time from around 2 days to less than 2 h. Sample preparation methods and analysis methods were optimized in this study for freeze-dried powder and formula granules of AR as described below.

Optimization of Extraction Methods for Freeze-Dried Powder and Formula Granules of AR

The sample preparation methods for freeze-dried powder and formula granules of AR were investigated. The extract ability of different solvents [5% methanol (v/v), 60% methanol (v/v), and methanol] and extraction times (10, 30, and 60 min) to extract AG IV were tested. The results indicated that extraction with 60% (v/v) methanol and sonication for 30 min showed the best performance in sample preparation (**Supplementary Table S1**), as described in *Sample Preparation for Isoflavonoid Analysis* section.

Optimization of the Amount of Ammonia

One critical step for the sample preparation of AR in Chinese Pharmacopoeia was reverse extraction with ammonia (National Commission of Chinese Pharmacopoeia, 2015). The purpose of this step was to transform other saponins into AG IV (Zhao et al., 2018). As an important parameter, the amount of ammonia solution needed for the transformation of astragalosides into AG IV was investigated. The fingerprint profiles of the astragalosides of AR extracts before and after adding 10 ml of ammonia solution ammonia were analyzed by HPLC-ELSD and compared (**Figure 3**). The results show that, under the specific conditions, the content of AG IV increased, while the peaks of all other astragalosides disappeared. The peak area of AG IV increased with the increased amount of ammonia solution, reaching its highest amount with 10 ml or more of ammonia solution. This implies that AG II, iAG II, AG I, iAG I, and acetyl AG I can be completely converted into AG IV which was stable under this alkaline conditions. Therefore, 10 ml of ammonia solution was used in this study.

Optimization of the Enrichment Methods of Astragaloside IV

The most practical method for the determination of AG IV content is the HPLC-ELSD. ELSD is a universal detector that gives very strong signals of primary compounds in the water extracts of herbal materials. Therefore it is necessary to remove the major primary metabolites from the aqueous AR extracts and the AR preparations, before the analysis of the saponins. Especially in case of formulated granules, the various excipients may interfere with the analysis. An SPE column separation method was applied to enrich AG IV in samples and remove the primary compounds. The following

parameters were investigated in a step-by-step approach: the amount of ammonia added (1, 5, 10, 12, and 15 ml), the size of the SPE column (1,000 mg/6 ml and 500 mg/3 ml), the volume used in the water elution (3, 5, and 6 ml), and the volume used in the methanol elution (3, 5, and 6 ml). Finally, the content of AG IV was compared among procedures and the optimized methods were described in *HPLC-ELSD Conditions for Astragaloside Content Determination* section.

Optimization of ELSD Conditions for the Determination of Astragaloside IV

The effects of the elution gradient, carrier gas velocity (2.3, 2.4, 2.5, 2.7, and 2.8 L/min), and temperature of the drift tube (100, 105, and 110°C) of ELSD were investigated simultaneously. The largest peak area of AG IV was obtained at the flow rate of 2.4 L/min and the drift tube temperature of 110°C. The analytical method to determine AG IV content was described in *HPLC-ELSD Conditions for Astragaloside Content Determination* section.

Method Validation and Sample Analysis

Method Validation

The calibration curve of C was successfully constructed as follows: Y = 90,909X − 19.877, where Y is the peak area and X is the concentration of C (mg/ml). The calibration curve of AG IV was also constructed, as: ln(Y) = 1.6723ln(X) − 1.8336, where ln(Y) is the natural logarithm of the peak area and ln(X) is the logarithm of the concentration of AG IV (mg/L). The LOD, LOQ, precision, stability, repeatability, and accuracy of the established methods for the determination of C and AG IV content are summarized in **Supplementary Table S3**. All results for the precision, stability, repeatability, and accuracy of these methods confirmed their validity and acceptability.

Sample Analysis

Samples of 12 batches of AR pieces, 12 batches of AR freeze-dried powders, and six batches of AR formula granules from the same manufacturer were analyzed by applying the specific extraction procedure for each type of material and the chromatographic methods for isoflavonoids and saponins. All analyses were repeated three times, and the data were recorded and expressed as the mean contents of C and AG IV (**Table 1**). The results demonstrated that this developed method was suitable for the determination of C and AG IV content in AR, from its raw materials to its final preparations.

CONCLUSION

This study demonstrates that investigating the manufacturing process of traditional medicines from their raw materials to final preparations/products by chemical profile analysis is useful and effective for both the selection of suitable marker components and establishment of proper analytical methods for the quality control of traditional medicines. The quality control of the whole manufacturing process needs the process independent markers from the original raw plant material. For AR roots that is calycosin in case of the isoflavonoids and astragaloside IV in case of saponins. The established fingerprint methods for isoflavonoids and quantification methods for calycosin and AG IV were further validated by the analysis of a large number of samples, ranging from raw materials to final products. The developed methods were found to be simple, robust and reproducible, and thus suited as reliable quality control procedures for AR and its derived products. This work provides a demonstration study on the whole-process quality control of TCM and provides reference for improving the quality control methods of AR in Chinese Pharmacopoeia. The results suggest that it is necessary to reanalyze the quality control methods of other Chinese herbal medicines and their products derived from their water decoctions.

DATA AVAILABILITY STATEMENT

The raw data supporting the conclusions of this article will be made available by the authors, without undue reservation, to any qualified researcher.

AUTHOR CONTRIBUTIONS

YD, XQ, and SC designed the study. DW, MZ, LY, and PL did the experiments. YD, DW, and RV wrote the manuscript. All authors gave approval to the final version.

FUNDING

This work was supported by the Natural Science Foundation (grant numbers: 81473340, 81803734) and Project of China Academy of Chinese Medical Sciences (grant numbers: ZXKT17009, GH201701).

ACKNOWLEDGMENTS

We would like to thank Tianjiang Yifang Company, China, to provide pieces, freeze-dried powders, and formula particles of AR for this study.

SUPPLEMENTARY MATERIAL

The Supplementary Material for this article can be found online at: https://www.frontiersin.org/articles/10.3389/fphar.2020.554777/full#supplementary-material.

REFERENCES

Chu, C., Liu, E. H., Qi, L. W., and Li, P. (2014). Transformation of astragalosides from Radix Astragali under acidic, neutral, and alkaline extraction conditions monitored by LC-ESI-TOF/MS. *Chin. J. Nat. Med.* 12, 314–320. doi:10.1016/S1875-5364(14)60062-5

Fu, J., Wang, Z., Huang, L., Zheng, S., Wang, D., Chen, S., et al. (2014). Review of the botanical characteristics, phytochemistry, and pharmacology of *Astragalus membranaceus* (Huangqi). *Phytother. Res.* 28, 1275–1283. doi:10.1002/ptr.5188

Jin, R., Wan, L. L., Mitsuishi, T., Kodama, K., and Kurashige, S. (1994). [Immunomodulative effects of Chinese herbs in mice treated with anti-tumor agent cyclophosphamide]. *Yakugaku Zasshi* 114, 533–538. doi:10.2974/kmj1951.44.125

Lee, Y. S., Han, O. K., Park, C. W., Yang, C. H., Jeon, T. W., Yoo, W. K., et al. (2005). Pro-inflammatory cytokine gene expression and nitric oxide regulation of aqueous extracted Astragali radix in RAW 264.7 macrophage cells. *J. Ethnopharmacol.* 100, 289–294. doi:10.1016/j.jep.2005.03.009

Li, S., Han, Q., Qiao, C., Song, J., Lung Cheng, C., and Xu, H. (2008). Chemical markers for the quality control of herbal medicines: an overview. *Chin. Med.* 3, 7. doi:10.1186/1749-8546-3-7

Lin, L. Z., He, X. G., Lindenmaier, M., Nolan, G., Yang, J., Cleary, M., et al. (2000). Liquid chromatography-electrospray ionization mass spectrometry study of the flavonoids of the roots of *Astragalus mongholicus* and *A. membranaceus*. *J. Chromatogr. A* 876, 87–95. doi:10.1016/s0021-9673(00)00149-7

Liu, Y., Chen, H. B., Zhao, Y. Y., Wang, B., Zhang, Q. Y., Zhang, L., et al. (2006). Quantification and stability studies on the flavonoids of Radix hedysari. *J. Agr. Food Chem.* 54, 6634–6639. doi:10.1021/jf061335o

National Commission of Chinese Pharmacopoeia (2015). *Pharmacopoeia, Pharmacopoeia of People's Republic of China.* Beijing: Chemical Industry Press, 302–303.

Qi, L. W., Cao, J., Li, P., and Wang, Y. X. (2009). Rapid and sensitive quantitation of major constituents in Danggui Buxue Tang by ultra-fast HPLC-TOF/MS. *J. Pharmaceut. Biomed. Anal.* 49, 502–507. doi:10.1016/j.jpba.2008.10.026

Qi, L. W., Cao, J., Li, P., Yu, Q. T., Wen, X. D., Wang, Y. X., et al. (2008). Qualitative and quantitative analysis of Radix Astragali products by fast high-performance liquid chromatography-diode array detection coupled with time-of-flight mass spectrometry through dynamic adjustment of fragmentor voltage. *J. Chromatogr. A* 1203, 27–35. doi:10.1016/j.chroma.2008.07.019

Qi, L. W., Yu, Q. T., Li, P., Li, S. L., Wang, Y. X., Sheng, L. H., et al. (2006). Quality evaluation of Radix Astragali through a simultaneous determination of six major active isoflavonoids and four main saponins by high-performance liquid chromatography coupled with diode array and evaporative light scattering detectors. *J. Chromatogr. A* 1134, 162–169. doi:10.1016/j.chroma.2006.08.085

Song, J. Z., Mo, S. F., Yip, Y. K., Qiao, C. F., Han, Q. B., and Xu, H. X. (2007). Development of microwave assisted extraction for the simultaneous determination of isoflavonoids and saponins in radix astragali by high performance liquid chromatography. *J. Separ. Sci.* 30, 819–824. doi:10.1002/jssc.200600340

Song, J. Z., Yiu, H. H., Qiao, C. F., Han, Q. B., and Xu, H. X. (2008). Chemical comparison and classification of Radix Astragali by determination of isoflavonoids and astragalosides. *J. Pharmaceut. Biomed. Anal.* 47, 399–406. doi:10.1016/j.jpba.2007.12.036

Zhang, D. Q., Wang, H. B., Wang, S. F., and Wang, D. Q. (2015). [Research achievements on biological activities of calycosin]. *Zhongguo Zhong Yao Za Zhi* 40, 4339–4345. doi:10.4268/cjcmm20152204

Zhao, M., Dai, Y., Li, Q., Li, P., Qin, X. M., and Chen, S. (2018). A practical quality control method for saponins without UV absorption by UPLC-QDA. *Front. Pharmacol.* 9, 1377. doi:10.3389/fphar.2018.01377

Conflict of Interest: The authors declare that the research was conducted in the absence of any commercial or financial relationships that could be construed as a potential conflict of interest.

Copyright © 2020 Dai, Wang, Zhao, Yan, Zhu, Li, Qin, Verpoorte and Chen. This is an open-access article distributed under the terms of the Creative Commons Attribution License (CC BY). The use, distribution or reproduction in other forums is permitted, provided the original author(s) and the copyright owner(s) are credited and that the original publication in this journal is cited, in accordance with accepted academic practice. No use, distribution or reproduction is permitted which does not comply with these terms.

frontiers in Pharmacology

ORIGINAL RESEARCH
published: 11 January 2021
doi: 10.3389/fphar.2020.572624

Network Pharmacology Reveals the Mechanism of Activity of Tongqiao Huoxue Decoction Extract Against Middle Cerebral Artery Occlusion-Induced Cerebral Ischemia-Reperfusion Injury

Si-peng Wu[1,2], *Ning Wang*[1,3,4]* *and Li Zhao*[1,3,4]

[1]*Key Laboratory of Chinese Medicinal Formula of Anhui Province, Anhui University of Chinese Medicine, Hefei, China,* [2]*State Key Laboratory of Cellular Stress Biology, School of Life Sciences, Xiamen University, Xiamen, China,* [3]*Institute for Pharmacodynamics and Safety Evaluation of Chinese Medicine, Anhui Academy of Chinese Medicine, Hefei, China,* [4]*Key Laboratory of Xin'an Medicine, Ministry of Education, Hefei, China*

OPEN ACCESS

Edited by:
Yan Xu,
Cleveland State University, United States

Reviewed by:
Lei Wang,
Capital Medical University, China
Lei Wang,
Guangzhou University of Chinese Medicine, China

***Correspondence:**
Ning Wang
wnsci123@163.com

Specialty section:
This article was submitted to Ethnopharmacology, a section of the journal Frontiers in Pharmacology

Received: *15 June 2020*
Accepted: *13 November 2020*
Published: *11 January 2021*

Citation:
Wu S, Wang N and Zhao L (2021) Network Pharmacology Reveals the Mechanism of Activity of Tongqiao Huoxue Decoction Extract Against Middle Cerebral Artery Occlusion-Induced Cerebral Ischemia-Reperfusion Injury. Front. Pharmacol. 11:572624. doi: 10.3389/fphar.2020.572624

Several clinical therapies such as tissue repair by replacing injured tissues with functional ones have been reported; however, there is great potential for exploring traditional herbal-induced regeneration with good safety. Tongqiao Huoxue Decoction (TQHXD), a well-known classical traditional Chinese medicinal formula, has been widely used for clinical treatment of stroke. However, biological activity and mechanisms of action of its constituents toward conferring protection against cerebral ischemia-reperfusion (I/R) injury remain unclear. In this present study, we evaluated TQHXD quality using HPLC; then, it was screened for its potential active ingredients using a series of indices, such as their drug-likeness and oral bioavailability. Subsequently, we analyzed the potential mechanisms of TQHXD anti-I/R using gene ontology functional enrichment analyses. The network pharmacological approach enabled us to screen 265 common targets associated with I/R, indicating that TQHXD had remarkable protective effects on infarction volume, neurological function scores, and blood-brain barrier (BBB) injury. In addition, TQHXD significantly promoted the recovery of regional cerebral blood flow (rCBF) 7 days after reperfusion compared to rats in the vehicle group. Immunofluorescence results revealed a significantly higher CD34 expression in TQHXD-treated rats 7 days after reperfusion. TQHXD is not merely effective but eventually develops a secretory profile composed of VEGF and cerebral blood flow, a typical signature termed the angiogenesis-associated phenotype. Mechanistically, our data revealed that TQHXD (6 g/kg) treatment resulted in a marked increase in expression of p-focal adhesion kinase (FAK) and p-Paxillin proteins. However, Ki8751-mediated inhibition of VEGFR2 activity repealed its angiogenesis and protective effects and decreased both p-FAK and p-Paxillin protein levels. Taken together, these findings affirmed the potential of TQHXD as a drug for the management of stroke, which might be exerted by increasing the angiogenesis via the VEGF pathway. Therefore, these results provide proof-of-concept evidence that

angiogenesis is a major contributor to TQHXD-treated I/R and that TQHXD is a promising traditional ethnic medicine for the management of this condition.

Keywords: Tongqiao Huoxue Decoction, cerebral ischemia reperfusion injury, angiogenesis, vascular endothelial growth factor, network pharmacology

INTRODUCTION

Stroke is the second leading cause of death in the world owing to its high morbidity, mortality, and disability rates (Benjamin et al., 2018). Approximately four-fifths of all patients with stroke suffer from ischemia stroke, and most of them live with disabilities for a long time (Mozaffarian et al., 2015). One of the principles of clinical treatment of ischemic stroke is to restore blood flow in time. Although this approach is an effective protection measure, long-term accumulation of reperfusion can lead to cerebral ischemia-reperfusion (I/R) injury. Treatment of I/R injury-induced ischemic stroke is challenging. To date, recombinant plasminogen activator is still the only drug approved by the Food and Drug Administration (FDA) for treating stroke. Therefore, the development of novel drugs is necessary to aid in the management of patients with stroke.

Angiogenesis, a basic biological process that aids in the development of new blood vessels from existing capillaries, has been implicated in multiple pathological and physiological processes (Beck and Plate, 2009). Although the connection between the brain and blood is a new focus in scientific researches, theories have linked this connection to traditional Chinese medicine. For example, many studies have shown that angiogenesis plays a pivotal role in many pathological conditions, such as cerebrovascular and cardiovascular diseases and cancer (Ferrara and Kerbel, 2005). These diseases involve actions of multiple growth factors, receptors, and molecules, resulting in diverse signaling pathways that affect the pathogenicity of angiogenesis across different diseases (Carmeliet, 2000). In addition, angiogenesis mediates the production of new blood vessels, thereby contributing to patient recovery after ischemic injury (Liu et al., 2017). Although angiogenesis is elevated during ischemia and hypoxia, this process is too slow to meet the needs of body recovery (Krupinski et al., 1994). Therefore, accelerating angiogenesis during the establishment of collateral circulation has been proposed as an attractive approach for treating cerebral ischemia injury (Liu et al., 2014).

Traditional Chinese medicine (TCM), which has been used for more than 2000 years with the characteristics of multiple pathways and multiple targets, is likely to represent novel therapeutic targets for developing effective treatment against I/R (Wu et al., 2019; Peng et al., 2019). In fact, numerous TCM-based remedies for stroke have been introduced into the market, owing to their unique advantages (Wu et al., 2019; Chen et al., 2009; She et al., 2019). For example, Tongqiao Huoxue Decoction (TQHXD), a classic traditional Chinese herbal formula, has been used to treat stroke. It had subsequently been embodied in Corrections on the Errors of Medical Works prescribed by Qingren Wang, comprising eight Chinese herbs (**Table 1**). Currently, TQHXD is widely used to treat patients with ischemic stroke (Yang and Fan, 2009; Liu et al., 2003). The key active components for this drug include paeoniflorin, ferulic acid, and muscone (Xu et al., 2008; Wu et al., 2018). Collectively, TQHXD controls stroke via various mechanisms. For instance, the drug can module permeability of the blood-brain barrier (BBB) and activity of plasminogen activator inhibitor-1 (Li et al., 2017; Wang et al., 2012; Kim et al., 2016; Wu et al., 2019). However, the mechanisms involved in TQHXD have only partially been unraveled. There is still a thought-provoking question of whether TQHXD can protect against the I/R injury by targeting angiogenesis.

The present study sought to provide new insights into TQHXD's anti-I/R effects in rats. Summarily, we employed network pharmacology, an approach by using high-throughput data from public databases to identify interactions among "compound-target-disease," and gave a holistic cognition of the relationship between formula and diseases (Hopkins, 2008). This approach's systemic and holistic traits are in line with the concept of TCM (Pan et al., 2020; Mou et al., 2020). In this work, the network pharmacology approach was used to provide a new understanding of TQHXD that exert anti-I/R effects, and TQHXD was intragastrically administered to rats with MCAO for 7 days to explore the mechanism.

METHODS AND MATERIALS

Animals

Male healthy Sprague Dawley rats weighing 240–260 g were purchased from the Laboratory Animal Center of Anhui Medical University (Hefei, certificate of quality: No. SXCK 2011-002, China). All rats had free access to standard diet and water. All experimental rats were approved by the Institutional Animal Care and Use Committee at Anhui University of Chinese Medicine. In addition, rats had undergone treatments according to "3 Rs" rules (Reduction, Refinement, and Replacement) in all experiments.

TABLE 1 | The composition of TQHXD.

	Chinese medicine	Family	Weight (g)
1	Taoren (Semen Persicae)	Rosaceae	9
2	Chishao (Radix Paeoniae Rubra)	Ranunculaceae	3
3	Chuanxiong (Rhizoma Ligustici Chuanxiong)	Apiaceae	3
4	Honghua (*Flos carthami*)	Asteraceae	9
5	Dazao (Fructus Jujubae)	Rhamnaceae	5
6	Cong (Scallion)	Liliaceae	3
7	Shexiang (*Moschus*)	Cervidae	0.15
8	Shengjiang (*Zingiber officinale* Roscoe)	Zingiberaceae	9

Herbs and Reagents

Herbs of TQHXD were purchased from Xin He Traditional Chinese Medicines Group Corporation (Hefei, China). Furthermore, each herb was authenticated by the herbal medicinal botanist, Professor Shoujin Liu, at the Anhui University of Chinese Medicine. Nimodipine Tablets (NMDP) were purchased from Bayer (Batch Number: H20003010), and 2% triphenyltetrazolium chloride (TTC) dye solution was purchased from Sigma Chemical. Ki8751 (VEGFR2 special inhibitor) was selected from Selleck Chemicals Co., Ltd. Rabbit primary antibodies for VEGF-A, p-FAK (Tyr576), p-Paxillin (Tyr118), and β-actin were bought from CST (Boston, United States). The mouse antibodies against FAK and Paxillin were bought from Abcam (Cambridge, MA, United States). The secondary horseradish peroxidase- (HRP-) labeled antibodies were acquired from Santa Cruz Biotechnology (Santa Cruz, CA, United States). All of the reagents or herbs were standard and commercially available.

Network Pharmacology

In this section, the intersect target enrichment analysis and protein-protein interaction (PPI) network were utilized to reveal the multitarget, multifunction, and multipathway therapeutic advantages of TQHXD in protecting I/R.

Collection of Potential Active Ingredients and Disease Targets in TQHXD

Three TCM databases were used to collect the active ingredients of TQHXD, including the traditional Chinese medicine systems pharmacology database (TCMSP) (Ru et al., 2014), (TCMSP™, http://lsp.nwsuaf.edu.cn/tcmsp.php), the Traditional Chinese Medicine Integrated Database (Xue et al., 2013) (TCMID, http://www.megabionet.org/tcmid/), and the TCM Database @Taiwan (Chen et al., 2014) (http://tcm.cmu.edu.tw/). Importantly, the interrelated scientific literature databases (PubMed, MEDLINE, and China National Knowledge Infrastructure) were also employed in this work. Subsequently, we set an OB (oral bioavailability) value of ≥30% and DL (drug-like quality) value of ≥0.18 as standard to screen out the potential ingredients of TQHXD. Secondly, the 2D structure of components was transformed into SDF structure format through the PubChem database (https://Pubchem.ncbi.nlm.nih.gov/). Subsequently, the targets were obtained using SwissTargetPrediction (http://new.swisstargetprediction.ch/index.php) and TCMSP, an online tool for predicting targets. In addition, related targets belonging to *Homo sapiens* were renamed retrieved from the UniProt database (https://www.uniprot.org/uniprot/). Finally, the NIMNT database (http://www.idrug.net.cn/NIMNT/) was used to enrich the possible indications of TQHXD.

Disease Target

The keyword "cerebral ischemia reperfusion injury" was used in GeneCards (https://www.genecards.org/), OMIM (Online Mendelian Inheritance in Man, https://omim.org/) and DrugBank databases (https://www.drugbank.ca/) to search for I/R-related targets. These databases (Wishart et al., 2018) are free bioinformatics resources that combine disease data with comprehensive targets. Finally, these targets were intersected with related targets of TQHXD by the online tool (http://bioinfogp.cnb.csic.es/tools/venny/index.html).

Gene Ontology Functional Enrichment Analysis

The Database for Annotation, Visualization, and Integrated Discovery (DAVID; http://david.abcc.ncifcrf.gov/home.jsp, version 6.8), together with pathway data obtained from the KEGG database, was used to find the identification of characteristic biological attributes of the potential target for I/R in TQHXD. Finally, FunRich tool (http://www.funrich.org/) was used to analyze more biological characteristics of a common target.

Protein-Protein Interaction Network

Generally speaking, it is difficult for a single protein to complete a series of complex biological processes. Hence, it is important to find the PPI network. The overlapped components-targets belonging to *Homo sapiens* were imported to the STRING database (https://string-db.org/, version 11.0), and an organism entry was set with the minimum required interaction score = 0.900. Finally, the PPI network was visualized in Cytoscape (https://cytoscape.org/, version 3.7.2). A higher degree value node represented putative crucial targets of herbs in the PPI network.

Experimental Verification of the Protective Effect of Tongqiao Huoxue Decoction Against Ischemia-Reperfusion

Establishment of Ischemia-Reperfusion Model

The cerebral I/R injury model *in vivo* was performed according to Longa's method (E. Z. Longa et al., 1989). Firstly, rats were anesthetized with 4% isoflurane (4% for anesthesia induction; 2% for anesthesia maintenance, 3 ml/kg). Then, the internal carotid artery (ICA), external carotid artery (ECA), and left common carotid artery (CCA) were carefully separated by tweezers. Subsequently, the left CCA and ECA were blocked by microvascular aneurysm clips, followed by occluding the middle cerebral artery (MCA) through inserting a filament (Doccol, United States) coated through the ECA (18 ± 2 mm). Two hours later, the filament was removed to achieve reperfusion. Sham group received the same procedures, but no filament was inserted into the MCA. The temperature of the operation chamber was maintained at 37 ± 0.5 °C throughout the whole surgery. After waking up, the rats were put back into the cages and had free access to water and food.

Preparation of Tongqiao Huoxue Decoction Sample

The ethanol extract of TQHXD was prepared as previously described in (Chao-Liang et al., 2015). *Prunus persica* (L.) Batsch 90 g (Xin He Traditional Chinese Medicines Co., Ltd.,

Hefei, China, product batch number: 1702181), *Paeonia anomala* subsp. *veitchii* (Lynch) D.Y.Hong and K.Y.Pan [Paeoniaceae] 30 g (Xin He Traditional Chinese Medicines Co., Ltd., Hefei, China, product batch number: 1709201), *Conioselinum anthriscoides* "Chuanxiong" [Apiaceae] 30 g (Xin He Traditional Chinese Medicines Co., Ltd., Hefei, China, product batch number: 1701033), *Carthamus tinctorius* L. 90 g (Xin He Traditional Chinese Medicines Co., Ltd., Hefei, China product batch number:1707213) 90 g, *Ziziphus jujuba* Mill. 50 g (Huidu Traditional Chinese Medicines Co., Ltd., Bozhou, China, product batch number: 1707223), *Zingiber officinale* Roscoe 90 g (Zhejiang Chinese Medical University prepared pieces Co., Ltd., Hangzhou, Zhejiang, China, product batch number: 190601), and fresh *Allium fistulosum* L [Amaryllidaceae] 30 g (WalMart Inc. Hefei, China) were extracted in 3200 ml 75% ethanol for 2 h and filtered. After the confluent solutions pump vacuum, 1,600 ml 75% ethanol was added to it and then pump-vacuumed again until there is no alcoholic taste. Finally, 1.5 g *Moschus* (Lasa Chinese Medicines Co., Ltd., Lasa, China, product batch number: 62523635662) was added to the solutions to form the extract solutions with a concentration of 2 g/ml (equivalent to the dry weight of raw materials). The medicinal plant scientific names have been unified using the Kew Science database (https://mpns.science.kew.org/mpns-portal/?_ga=1.111763972.1427522246.1459077346%20or%20http://www.plantsoftheworldonline.org/%20or%20www.theplantlist.org).

High-Performance Liquid Chromatography (HPLC)

The quality control reproducible experiments of TQHXD were conducted using HPLC. The quality control of TQHXD was completed by paeoniflorin (a characteristic pharmaceutically active component of TQHXD) in our work. Firstly, TQHXD solutions were put into the HPLC facilities (Agilent 1100 HPLC system, United States). The separations were carried out on a Phenomenex C18 column (4.6 mm × 250 mm, 5 μm) with the following conditions: temperature, 30 °C; flow rate, 1.0 ml min^{-1}. The mobile phase consisted of methanol (A)-H_2O (0.05% V/V phosphoric acid), and gradient elution was set as follows: 0–15 min, 10% A–28% A; 15–30 min, 28% A–40% A; 30–55 min, 40% A–48% A; 55–70 min, 48% A–54% A. Finally, the detection wavelength and the injection volume were 254 nm and 20 μL, respectively.

Experimental Groups and Drug Administration

Firstly, to investigate whether the protective effects of TQHXD were involved in angiogenesis (experiment 1), rats were randomly divided into six groups: the sham group, vehicle group, TQHXD group (3 g/kg, 6 g/kg, and 12 g/kg), and positive group (NMDP, 0.02 g/kg). Dosages of TQHXD (3, 6, and 12 g/kg) and NMDP (0.02 g/kg) groups were equivalent to the dose of clinical adult patients. Rats in the TQHXD and NMDP groups were treated with respective doses by intragastric administration once a day for 7 days after reperfusion. Rats in sham or vehicle groups were given normal saline.

Secondly, to explore the mechanisms of TQHXD-associated angiogenesis (experiment 2), rats were randomly divided into five groups: the sham group, vehicle group, TQHXD group (6 g/kg), Ki8751 (0.5 mg/kg) group, and combine group (TQHXD + Ki8751). As mentioned in experiment 1, TQHXD and TQHXD + Ki8751 combine groups were treated with TQHXD by intragastric administration for 7 days. Rats in sham, vehicle, and Ki8751 groups were given the same volume of normal saline for 7 days. Tail vein injection Ki8751 (final dose: 0.5 mg/kg (Hou et al., 2015)) was administered to rats 30 min prior to operation (**Figure 1**).

Neurological Score

Neurological recovery was examined at day 1 and day 7 after 24 h reperfusion using Longa's method (Longa et al., 1989): 0, no neurologic deficit; 1, failure to extend forepaw fully; 2, circling to the left; 3, falling to the left or no spontaneous motor activity; 4, not walking spontaneously and experiencing a lowered stage of consciousness. Rats with scores of 0 and 4 were excluded from the experiment.

Monitoring Local Blood Flow Changes by Laser Doppler Flow

The rCBF of the left brain was measured by laser Doppler flow (LDF). Rats were anesthetized with 4% isoflurane; the skin and subcutaneous tissue were cut slowly. The fascia on the skull of rats was separated by nipper to fully expose the area of the skull. The position of assessment was recorded in the following coordinates relative to Bregma: ML: +2.0 mm, AP: +1.0 mm (Schmid-Elsaesser et al., 1998). Routine zero-calibration with front probe and monitoring the blood flow during the operation were performed. Finally, the blood flow was detected through LDF at days 1 and 7.

Triphenyltetrazolium Chloride Staining

Rats were sacrificed at 30 min after the last drug administration; then frozen brains were sliced into coronal sections of 2 mm thickness. The slices were stained with 2% TTC (pH = 7.4, Sigma Chemical Co., United States) at room temperature. The change of cerebral infarct volume in all groups was analyzed by ImageJ. The infarct volume was calculated by infarct size * average slice thickness (2 mm).

Immunofluorescence

Rats were sacrificed after the last drug treatment; brain tissues were isolated after being perfused with 0.9% normal saline followed by 4% cold paraformaldehyde. The brains were quickly frozen after gradient elution with sucrose and cut into 5 μm coronal thick slices. The sections were transparent with 0.5% Triton X-100 for 5 min and then blocked with 10% BSA for 1 h. Slices were incubated with primary anti-CD34 antibody (1:100, Abcam, United States) at 4 °C overnight. Then, the slices were washed with PBST 3 times. Slices were incubated with anti-rabbit secondary antibody (1:1,000, Cell Signal, United States) for 50 min at 37 °C. After counterstaining with 4, 6-diamidino-2-phenylindole (DAPI) and covering slices with anti-fluorescent quenching, the slices were observed and photographed under fluorescent microscopy (Leica, Germany) and then analyzed by Image-Pro 6.0 software.

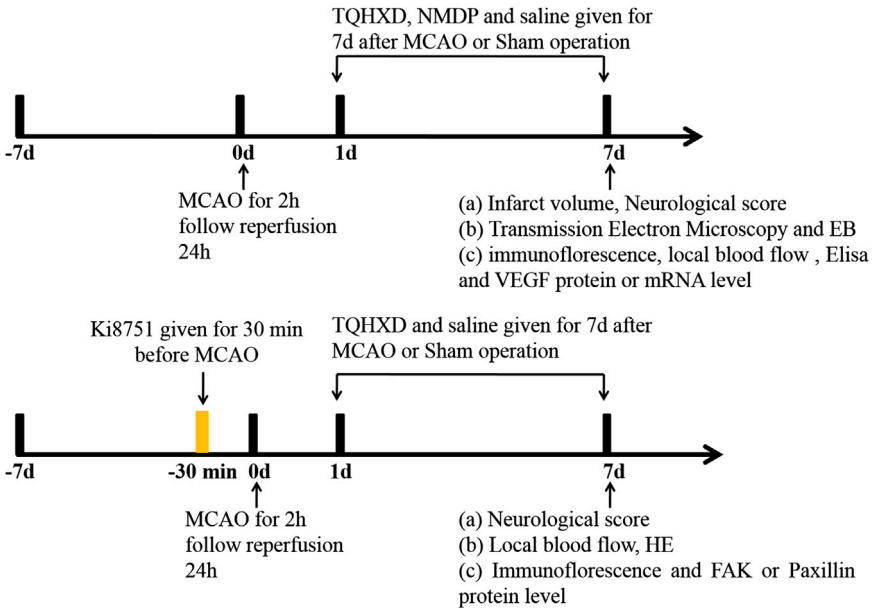

FIGURE 1 | Experimental design and schedules. MCAO: middle cerebral artery occlusion; TQHXD: Tongqiao Huoxue Decoction; EB: Evans blue; ELISA: enzyme-linked immunosorbent assay; HE: hematoxylin-eosin staining; VEGF: vascular endothelial growth factor; FAK: focal adhesion kinase.

Blood-Brain Barrier Permeability

The BBB permeability was determined by measuring the amount of Evans blue (EB). EB dye (2%, 4 ml/kg body weight) was slowly injected by tail vein injection intravenously 30 min after last drug treatment and allowed to circulate for 2 h. Rats were anesthetized with 4% isoflurane and then transcardially perfused with 0.9% normal saline to wash away any remaining dye in the blood vessels. The brain was incubated in 3 ml formamide at 45 °C for 72 h. The solutions were centrifuged for 40 min at 25,000 g. Finally, the absorption of each well was measured at 632 nm with a microplate reader (Thermo Scientific, United States). The content of EB in all groups was expressed as μg/g of the brain according to the standardized curve (Ren et al., 2015).

Hematoxylin and Eosin Staining

At 24 h after reperfusion, rats were anesthetized with 4% isoflurane and perfused transcardially with 0.9% saline and then reperfused with pre-ice cold 4% paraformaldehyde. The brain was embedded in paraffin after being dehydrated in graded ethanol and cleared in xylene. Finally, the slices of 4 μm sections were stained with hematoxylin and eosin (HE) staining following histochemical procedures.

Ultrastructural of Tight Junction Detection Through Transmission Electron Microscopy

In brief, rats were anesthetized with 4% isoflurane and then perfused with 0.9% normal saline, followed by precold 4% paraformaldehyde. The frontoparietal cortex of the ischemia brain was separated into pieces of 1 mm^3 and then blended with 2.5% glutaraldehyde at 4 °C. Then, these pieces were dunked in 2% OsO_4 for 2 h. The pieces were embedded in Epon 812 after being incubated with OsO_4. Finally, ultrathin pieces of cortex were stained with citramalic acid and acetic acid uranium and then scanned by transmission electron microscopy (TEM).

Detection of Vascular Endothelial Growth Factor in Serum by Enzyme-Linked Immunosorbent Assay

At 30 min after the last drug treatment, rats were anesthetized with 4% isoflurane. Blood was collected from the abdominal aorta by a one-time negative pressure tube without anticoagulant. Blood was stood at room temperature for 3 h and then centrifuged at 2000 rpm for 20 min to collected serum. The expression of vascular endothelial growth factors (VEGF) in rats was detected using a VEGF ELSIA kit (RRV00. R&D Systems, Minneapolis, MN, USA). The absorbance of each well was measured at 450 nm through a microplate reader (Thermo Scientific, United States). The content of VEGF-A in the samples was calculated according to the standardized curve.

Western Blot

The protein levels of VEGF-A, FAK, Paxillin, and β-actin were detected using Western blot. Cortex tissues were lyzed with precold RIPA lysis buffer and immediately mixed with phenylmethanesulfonyl fluoride (PMSF, Beyotime, Nanjing, China) centrifuged at 12,000 rpm at 4 °C for 15 min. The concentration of protein was quantified by bicinchoninic acid (BCA) (Beyotime, Nanjing, China). All proteins were run on 12% (*w/v*) or 10% SDS-PAGE gel and then transferred to polyvinylidene difluoride (PVDF) membrane with Bio-Rad electrophoretic transfer system. The membrane was blocked with 5% (*w/v*) nonfat milk for 2 h at 37 °C and incubated with

the primary antibody to VEGF-A (1: 800), p-FAK (1: 1,000), Paxillin (1: 1,000), and β-actin (1: 1,000) at 4 °C overnight, respectively. After washing with Tris-Hcl Buffered Saline containing 0.1% Tween-20 (TBS-T) 3 times, the membrane was incubated with coherent secondary (1:5,000) antibody for 2 h at 37 °C. β-Actin was used as an internal reference. The protein bands were developed using enhanced chemiluminescence (ECL) reagents (Thermo, United States). Finally, images were scanned by an Amersham Imager 600 (GE, United States).

Quantitative Real-Time PCR

In brief, RNA was isolated using a tissue RNA kit (Omega Bio-Tek, GA) and then was reverse-transcribed using a TAKARA reverse transcription kit. Real-time quantitative PCR (qRT-PCR) was performed on the Mx3000P qPCR System (Agilent Technologies, Santa Clara, CA, United States) using SYBR Premix Ex Taq TM (TAKARA). Primer sequences used to amplify fragments were synthesized by Sangon Biotech, Shanghai. The relative mRNA expression was normalized to GAPDH using the relative quantification method $2^{-\Delta\Delta Ct}$. The sequences of primers in this experiment were as follows: GAPDH Forward, 5-GGGTGTGAACCATGAGAAGTATG-3, GAPDH Reverse, 5-GATGGCATGGACTGTGGTCAT-3; VEGF Forward, 5-CTGCCATCCAATCGAGACCC-3, VEGF Reverse, 5-TGCATT CACATTTGTTGTGCTG-3.

Statistical Analysis

The Shapiro–Wilk normality test was used to analyze whether the data were normally distributed. Then, the *t*-test was utilized to analyze the significance of differences. Statistical significance between groups was evaluated by one-way analysis of variance (ANOVA). All data were presented as mean ± standard deviation (SD). Statistical analysis was performed using SPSS (SPSS, Inc., version20.0). A significant difference was accepted at p values lower than 0.05.

RESULTS

Genes Associated with Ischemia-Reperfusion

A total of 929 significant genes were obtained from the GeneCards, OMIM, and DrugBank databases after screening out some targets with low credibility (**Supplementary Table S1**).

Drug Targeting

According to the ADME thresholds of OB ≥ 30% and DL ≥ 0.18, 94 compounds of TQHXD were obtained from the three following databases: TCMSP, TCM Database@Taiwan, and TCMID after eliminating the common compounds, as listed in **Supplementary Table S2**. In addition, we also achieved quality control, that is, the HPLC system of herbs in TQHXD, such as precision, stability, repeatability, and wavelength, as shown in **Supplementary Table S3**. More importantly, some compounds with low OB or HL values but with significant protective effects on I/R injury, such as ligustrazine, muscone, and hydroxysafflor yellow A, were also explored in our work (Wu et al., 2018; Li et al., 2017).

Functional Enrichment Analysis of Intersection Targets of Tongqiao Huoxue Decoction

A total of 265 matching targets as the related targets of I/R and TQHXD are shown in **Figure 2A**. The multiple biological senses of TQHXD on I/R from a systematic level were assessed using the GO enrichment analysis (**Figure 2C**). For biological processes, potential targets of TQHXD were remarkably enriched in "response to hypoxia" (GO: 0001666), protein phosphorylation (GO: 0006468), and inflammatory response (GO: 0006954). For cellular components, mainly, plasma membrane (GO: 0005886), cytosol (GO: 0005829), and extracellular exosome (GO: 0070062) were enriched. Subsequently, the crucial pathways among the 265 potential targets in TQHXD treatment were also elucidated in this work. The threshold of FDR <0.01 was used as an enrichment screening criterion, and the top 24 pathways were screened out (**Figure 2B**), including the VEGF signaling pathway (hsa04370) and TNF signaling pathway (hsa04668).

PPI Network and Disease Analysis of Intersection Targets of Tongqiao Huoxue Decoction

Furthermore, the PPI network of those common targets was found in **Figure 3** (**Figure 3A**). Ultimately, TNF, AKT1, IL-6, VEGF-A, JUN, EGFR, IL1B, IGF1, MMP9, and TGFB1 were identified as major nodes. Similarly, we analyzed the diseases of these targets. For the site of expression, the targets were enriched in the central nervous system and skin, etc. Finally, we used the disease analysis function of the NIMNT database and entered 265 intersection targets of TQHXD to enrich the possible indications of TQHXD. After setting p.adjust <0.001, the top 10 diseases were observed, as shown in **Figure 3**, which mainly include ischemia, urinary system disease, and arteriosclerotic cardiovascular disease (**Figure 3C**).

The Quality Control of Tongqiao Huoxue Decoction by HPLC

As shown in **Figure 4A**, the retention time of paeoniflorin of TQHXD was about 24.2 min. Subsequently, the HPLC method was validated by reproducibility, stability, and precision. It is worth noticing that there was an identical chromatographic pattern in six batches of TQHXD solutions. This suggested a good reproducibility for the HPLC system or TQHXD solutions. Finally, the relative standard deviation (RSD) of the instrument was less than 3%, indicating that the precision of the instrument was good. Similarly, the RSDs of relative retention time and relative peak area of each characteristic peak were less than 5%, indicating that it has good repeatability. The RSDs of relative retention time and relative peak area of characteristic peaks were less than 5% after 0, 2, 4, 8, 12, and 24 h injection, respectively,

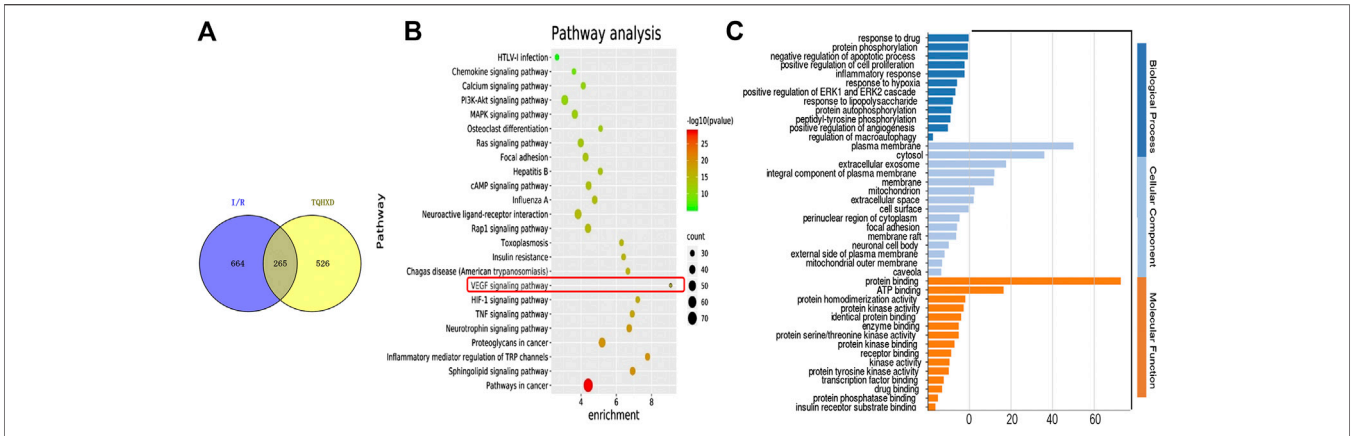

FIGURE 2 | Network pharmacology analysis of the ingredients of TQHXD. **(A)** Common targets between TQHXD and targets associated with I/R. **(B,C)** GO enrichment analysis of 265 common targets.

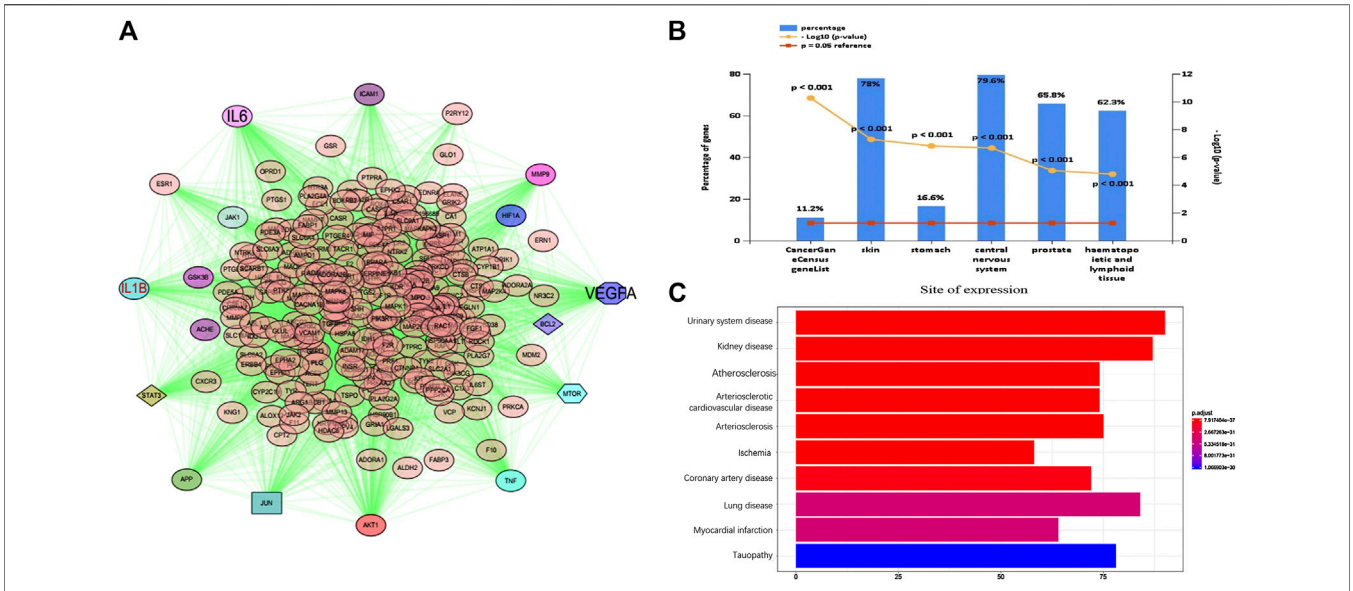

FIGURE 3 | PPI network and disease analysis of intersecting target of TQHXD. **(A)** PPI network of 265 common targets. **(B,C)** Clinical synopsis phenotypic terms.

indicating that the solution of the test sample was stable within 24 h (**Figure 4B–D**, **Supplementary Table S3**).

Tongqiao Huoxue Decoction Ameliorated Ischemia-Reperfusion Injury and Attenuated Blood-Brain Barrier Damage

Neurological scores remarkably increased in the vehicle group compared with the sham group at 7 days. After reperfusion, treatment with TQHXD or NMDP showed significant neurological recovery, characterized by a decrease in neurological scores, compared with that in the vehicle group; however, TQHXD (6 g/kg) reduced the score compared to NMDP. These data showed that TQHXD might exert an effect on improving the neural function of MCAO rats (**Figure 5A**).

Infarct volume was not observed in brain slices of the sham group, whereas a large area of infarct volume (41.10%) was seen in the vehicle group. The infarct volumes in the TQHXD groups were 29.3, 14.83, and 22.20%, respectively. Furthermore, infarct volume in the NMDP group (11.79%) was close to that observed in the TQHXD group at the dose of 6 g/kg, compared with the vehicle group (**Figure 5B**).

The protective effect of TQHXD on the permeability of BBB was quantified by EB dye (**Figure 5C**). On the dye solution, we found that there was a remarkable ($p < 0.01$) increase in BBB permeability in rats from the vehicle group compared to that in

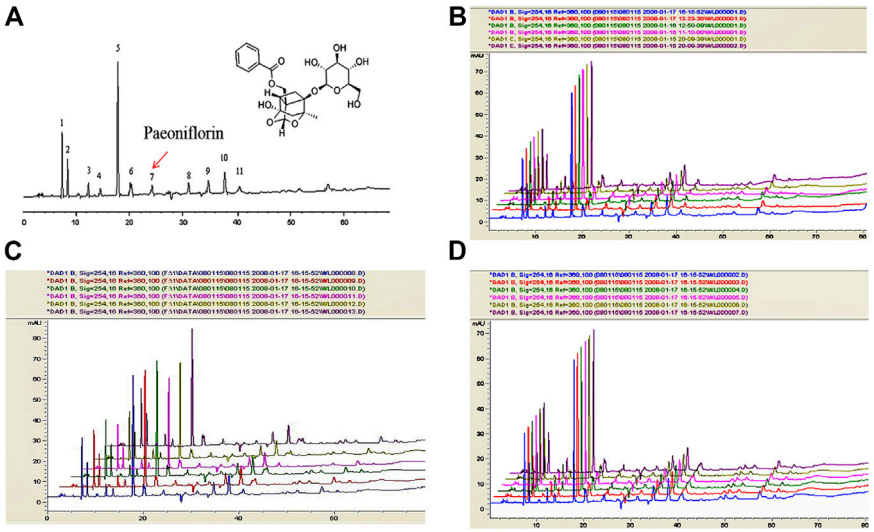

FIGURE 4 | The fingerprints of TQHXD for quality control by HPLC. Conditions: column, C18 column (250 × 4.6 mm, 5 μm); mobile phase, methanol. **(A)** H_2O (0.05% V/V phosphoric acid). Flow rate: 1 ml min^{-1}; column temperature: 25 °C; injection volume: 10 μL. **(A)** Representative HPLC chromatogram of TQHXD. 7, Paeoniflorin. **(B–D)** The quality control of six batches of TQHXD evaluated by HPLC. The TQHXD solution from six separated raw crude extractions was analyzed by the HPLC method. Colors represent different groups of TQHXD test solutions. The *X*-axis represents acquisition time (Min) and the *Y*-axis indicates intensity (mAU).

sham rats. TQHXD (3, 6, and 12 g/kg) or NMDP (0.02 g/kg) reduced the content of EB under I/R. The treatment of TQHXD (6 g/kg) and NMDP made a significant difference to the BBB permeability when compared with the vehicle group ($p < 0.01$). Subsequently, we also detected the situation of tight junctions (TJ) by TEM. The TJ were normal in the sham group, whereas they were in an open state in the vehicle group (**Figure 5D**). However, different degrees of TJ reduction were observed in the TQHXD or NMDP group, indicating that TQHXD might repair the poststroke TJ completeness.

Tongqiao Huoxue Decoction Strengthened Angiogenesis in MCAO/R Rats

The data of Western blot and ELISA demonstrated that an increased expression of VEGF exposed to I/R as compared to the sham group. Then, the TQHXD or NMDP treatment further upregulated the expressions of VEGF-A in both serum and cortex tissue, as compared with the vehicle group, which showed that TQHXD could be involved in angiogenesis. Finally, qPCR analysis of VEGF mRNA expression provided further proof of the effects of TQHXD on angiogenesis (**Figure 6**).

The cerebral blood flow was reduced rapidly to 30% during ischemia after 2 h and then was restored to 80% of the baseline after reperfusion. The rCBF showed that blood flow had no significant difference in the sham group between the time points of 1 and 7 days. The rCBF of the vehicle group or drug groups was lower than that of the sham group at day 1 ($p < 0.01$). Similarly, the rCBF of the vehicle group rats had no significant difference at 7 days, as compared to the sham group. Instead, compared with the vehicle group, TQHXD (6 g/kg) and NMDP groups significantly increased the rCBF at 7 days (**Figure 6D**).

Subsequently, we used CD34 immunofluorescence to mark the MVD at 7 days after TQHXD treatment. In the vehicle group, MVD increased at 7 days after I/R when compared with the sham group. More importantly, the expression of CD34 in the TQHXD group was significantly higher than that in the sham and vehicle groups (**Figure 6E**).

Exogenous VEGFR2 Inhibition Reversed Angiogenesis in Tongqiao Huoxue Decoction

To further explore the molecular mechanisms associated with the phenotype observed upon TQHXD administration, we profiled angiogenesis from rats after being injected with Ki8751 (a specific VEGFR2 inhibitor). Firstly, we investigated whether Ki8751 could reverse the effect of TQHXD on neurological function score and cerebral blood flow. Notably, the neurological and neuronal death and rCBF were substantially protected by the TQHXD treatment in MCAO rats (**Figures 7A,B,D**). Subsequently, as shown in **Figure 7C**, the expression of p-FAK and p-Paxillin proteins in the cortex of brain induced by I/R was greater than that in the sham group ($p < 0.05$). However, TQHXD (6 g/kg) remarkably promoted the expression of p-FAK and p-Paxillin proteins ($p < 0.01$ vs. vehicle group) (**Figure 7C**). Conversely, the treatment of rats with VEGFR2 inhibitors, such as Ki8751, substantially reduced the TQHXD-induced angiogenesis. For example, the

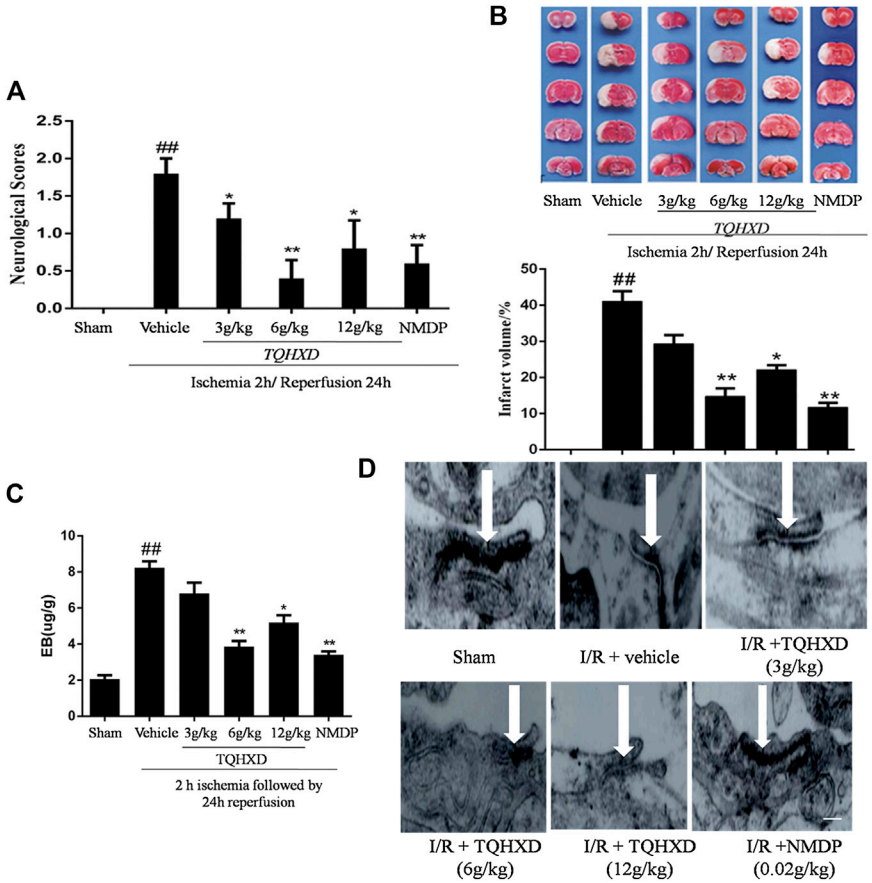

FIGURE 5 | TQHXD ameliorated I/R injury and attenuated blood-brain barrier damage. **(A)** The neurological scores were evaluated by Longa's methods. **(B)** Representative TTC staining **(top)** and quantitative analysis **(bottom)** of brain infarct volumes, $n = 6$. **(C)** Quantitative analysis of the content of EB, $n = 6$. **(D)** Representative TEM images of ultrastructural changes in I/R-induced tight junction ($n = 3$). *Arrows* imply electronically dense bands; the electronically dense bands represent TJ; the open state of electronically dense bands represents the injury degrees of TJ; scale bar = 200 μm (×20,000 magnification). Data are presented as means ± SD. $^{\#\#}p < 0.01$ vs. sham group; $^{*}p < 0.05$, $^{**}p < 0.01$ vs. vehicle group.

upregulating effect of TQHXD on p-FAK or p-Paxillin was impeded by the cotreatment with Ki8751 ($p < 0.05$). Similarly, the expression of CD34 induced by TQHXD was also inhibited by Ki8751. These results demonstrated that TQHXD enhanced angiogenesis in a VEGFR2-FAK-Paxillin-dependent manner.

DISCUSSION

In the present study, a total of 94 potential compounds were screened according to OB and DL. The results revealed that TQHXD regulated the intersection of 265 targets with I/R, including VEGF-A, IL6, JUN, mTOR, TNF, and AKT1. These 265 targets were mainly enriched in cancer, VEGF, and neurotrophin signaling pathways. To ascertain TQHXD's role, our results of the network indicated that TQHXD regulated I/R through the pattern multiple components-multiple targets-multiple pathways. However, given the importance of angiogenesis in I/R, we linked the role of TQHXD with angiogenesis by the results of network pharmacology and enrichment analysis of the KEGG pathway.

A huge percentage of elderly people reportedly suffer from ischemic stroke worldwide. Neurovascular unit (NVU), a conceptual model of stroke depending on the structure of blood vessels and brain, has been proposed by the National Institutes of Neurological Disorders and Stroke (Zhao et al., 2017). Previous studies have shown that angiogenesis is a key process in NVU recovery following ischemia stroke. This process leads to restoration of rCBF after cerebral ischemia and redounds to the neurological recovery of patients with stroke (Liu et al., 2017). In fact, recent research shows that patients with angiogenesis exhibit lower morbidity and mortality rates relative to those without the condition (Ducruet et al., 2010). In the present study, we show that TQHXD is a key mediator of angiogenesis. Specifically, our results show that the amount of blood flow in ischemic brain tissue is the most intuitive indicator for evaluating the maturity of neovascularization. We found no significant increase in rCBF in the MCA and cortical regions in rats from the sham group. In contrast, rats treated with TQHXD

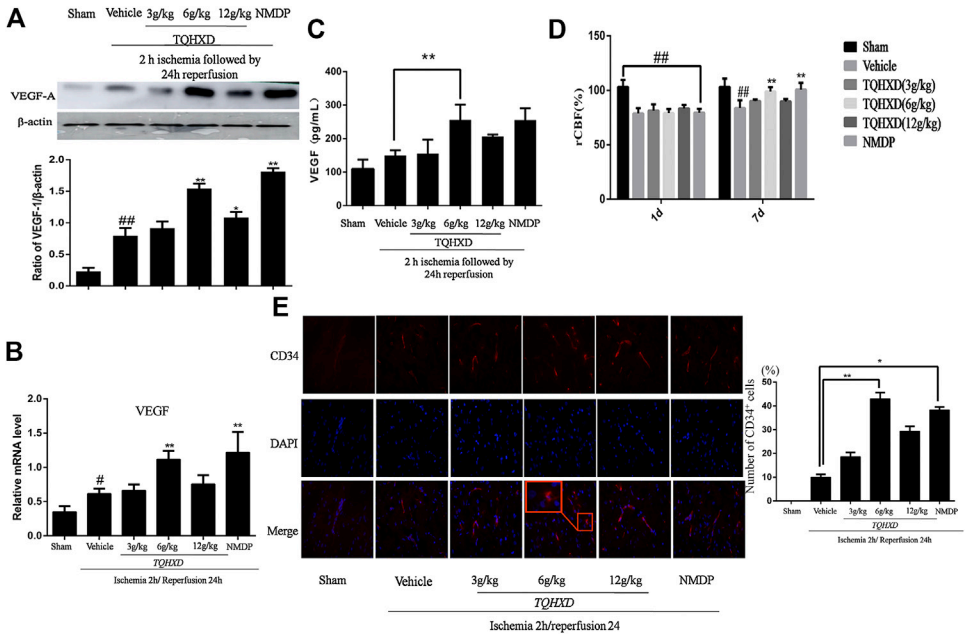

FIGURE 6 | TQHXD strengthened angiogenesis in MCAO rats. **(A)** Representative band image **(top)** and quantitative analysis **(bottom)** of VEGF-A ($n = 3$). **(B)** The mRNA expression of VEGF in cortex detected by qPCR. **(C)** Quantitative analysis for ELISA results of VEGF at 7 days. **(D)** The changes of rCBF for all groups at 1 and 7 d after reperfusion, $n = 3$. **(E)** Immunofluorescence of brain section. Angiogenesis was visualized by CD34 staining (red), and DNA was stained by 4′6,-diamidino-2-phenylindole (DAPI; blue). *Red box* implies zoom-in fluorescence. Right, the histograms indicate the percentages of CD34-expressing cells that were positive for indicated markers. Scale bar = 50 μm (×200 magnification). Data are presented as means ± SD. $^{\#\#}p < 0.01$ vs. sham group; $^{*}p < 0.05$, $^{**}p < 0.01$ vs. vehicle group.

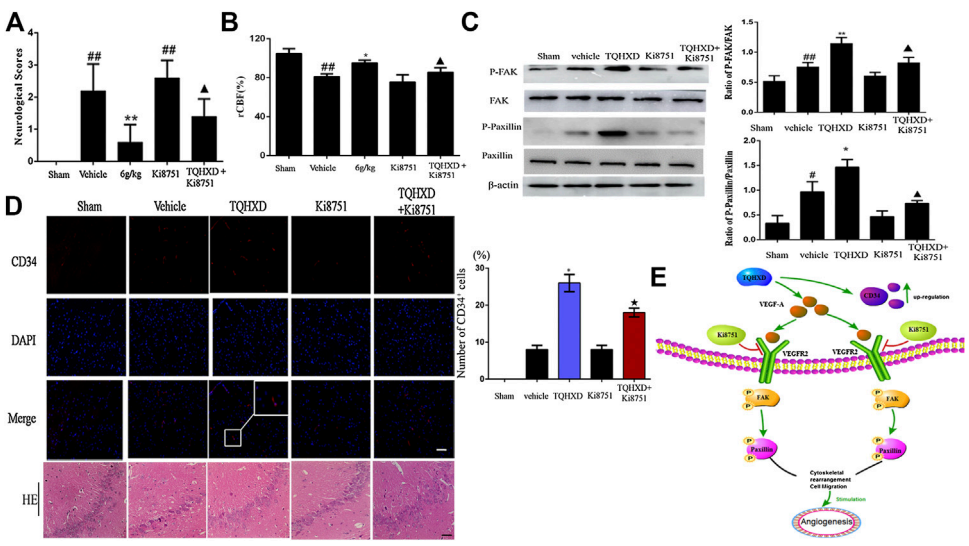

FIGURE 7 | TQHXD enhanced I/R-induced angiogenesis via activation of VEGF-A/VEGFR2-FAK-Paxillin signaling. **(A)** Neurological scores measured by Longa's method ($n = 5$). **(B)** The changes of rCBF for all groups at 7 days after reperfusion, $n = 6$. **(C)** Representative Western blot band **(top)** and quantitative analysis **(bottom)** of the expressions of FAK, p-FAK, Paxillin, and p-Paxillin ($n = 3$). β-Actin was used as an internal reference. **(D)** Left, serial sections of the brain were subjected to hematoxylin and eosin (HE) staining, immunofluorescence for angiogenesis markers (CD34, red), and DNA was stained by 4′6-diamidino-2-phenylindole (DAPI; blue). *White box* implies zoom-in fluorescence. Right, the histograms indicate the percentages of CD34-positive cells. Scale bar = 50 μm (×200 magnification). *White box* implies zoom-in fluorescence. **(E)** The model illustrates the molecular mechanism of TQHXD on angiogenesis in MCAO injury rats. Data were expressed as mean ± SD. $^{\#\#}p < 0.01$ vs. sham group; $^{*}p < 0.05$, $^{**}p < 0.01$ vs. vehicle group; ▲, ★$p < 0.05$ vs. TQHXD (6 g/kg) group.

or NMDP exhibited significantly higher CD34 or rCBF levels 7 days after reperfusion, compared to those in the vehicle group.

Ischemic injury causes endothelial progenitor cells to participate in the repair of new blood vessels. In fact, numerous cytokines reportedly play a critical role in this process, with a combination of these factors found to promote angiogenesis. Previous studies had shown that under specific environmental conditions, brain neurovascular cells produced and oozed VEGF, a central angiogenesis mediator following stroke (Yin et al., 2015). VEGF was upregulated both *in vivo* and *in vitro* during the I/R or oxygen-glucose deprivation induced by ischemia injury and continued 3–14 days poststroke (Zheng et al., 2018; Liu et al., 2018). This expression pattern indicates that ischemic injury induces angiogenesis, which was enhanced by TQHXD, to repair damaged blood vessels after stroke. In the present study, a significantly higher VEGF expression was observed in the TQHXD, compared to the vehicle group ($p < 0.05$), with a concentration of 6 g/kg generating the highest levels. These results strongly indicated that TQHXD protects against I/R injury by upregulating angiogenesis either directly or indirectly.

Compared with NMDP, our results showed the therapeutic effects of TQHXD on the MCAO model. Notably, upon TQHXD administration, remarkably better levels of the neurological score and MVD were observed in the TQHXD group than those in the NMDP groups. These results illustrated that the nerve recovery activity of TQHXD was better than that of NMDP. As we all know, nerve recovery is a complex process involved in multiple-target and multiple-pathway. Compared with a single target drug (NMDP), the multitarget advantage of TQHXD could effectively regulate multiple processes to accelerate nerve recovery, which was also in agreement with our network pharmacology results. More importantly, despite the encouraging progress to apply NMDP in clinical trials, various adverse side-effects associated with NMDP may limit its clinical application. The relevant example is a reduction in blood pressure and a reversible increase in the serum concentrations of liver enzymes during intravenous therapy. On the contrary, compared with chemical medicines, TCMs are considered to be safe, with fewer side-effects. As such, the established safety and drug tolerability are the advantages of TCM over several Western medicines, which is exactly also the biggest benefit of TCM. Interestingly, our results showed that TQHXD's protective effect on I/R was not in a dose-dependent manner. Generally speaking, the effect of drugs may show a dose-dependent manner; previous studies had shown that the protective effect of some classical TCM does not always follow this trend (Yang et al., 2013; Xin-Xin et al., 2015). For example, some chemical and physical reactions may occur during the preparation of the formula, resulting in changes in some active components, which may not reflect dose-dependency (Xu et al., 2008). Herein, in-depth studies are required to elucidate the mechanisms of TQHXD action to provide valuable insights into its effects on I/R.

Previous studies have shown that VEGF combines with its receptors to promote angiogenesis against I/R (Beck and Plate, 2009; Greenberg and Jin, 2005). Specifically, the VEGF signaling pathway plays a fundamental role in angiogenesis response by regulating the release of growth factors. VEGFR2 regulates the expression of vascular endothelial cell receptor proteins, thereby playing a critical role in the development of many diseases mediated by vascular endothelial cells. Notably, FAK is considered the key signaling molecule in cells and has been reported to regulate cell proliferation, migration, spreading, adhesion, and key processes in angiogenesis (You et al., 2014).In addition, Paxillin, a key downstream FAK protein that acts on adhesion plaque, has been found to mediate the formation of adhesion plaque, activate downstream proteins, and promote angiogenesis. Some studies have shown its phosphorylation directly affects the formation of adhesion plaques and ultimately affects the motility of endothelial cells (Blackstone et al., 2015). In addition, blocking FAK phosphorylation can significantly reduce the degree of angiogenesis (Masakazu et al., 2010). To determine whether TQHXD provokes angiogenesis through the VEGF machinery, we evaluated the effect of TQHXD with Ki8751, a potent VEGFR2 inhibitor known to block angiogenesis (Lu et al., 2017). Our results indicated that I/R-induced angiogenesis increased CD34 expression and decreased neuronal death in rats. However, TQHXD treatment promoted this effect. In addition, Ki8751 decreased the levels of FAK and Paxillin expression, with its Ki8751 treatment clearly attenuating TQHXD-induced angiogenesis. Overall, these results indicate that TQHXD confers protection against I/R in rats via angiogenesis by activating the VEGF-A/VEGFR2-FAK-Paxillin signaling pathway.

Although network pharmacology has revealed the effects of TQHXD, there are still some limitations to be addressed. First, the biggest challenge is the results from the database on Chinese herbs. The public database information on herbal medicine remains incomplete to some extent. Subsequently, in order to further substantiate the idea that TQHXD provokes angiogenesis through promoting the VEGF machinery, we could test whether the angiogenesis effect of TQHXD could be blocked by shVEGF or hVEGF-IN-1 (VGEF inhibitor), a potent VEGF interference known to block VEGF. Finally, although our study shows that TQHXD has an impact on angiogenesis, our results are not capable of distinguishing which angiogenesis cell types are responsible. Angiogenesis cells can be labeled in a specific manner, and this issue will be addressed in future research.

CONCLUSION

In conclusion, the present study revealed that TQHXD administration was able to ameliorate the ischemic stroke of MCAO rats through promoting angiogenesis to active the VEGF-A/VEGFR2-FAK-Paxillin pathway.

DATA AVAILABILITY STATEMENT

The raw data supporting the conclusions of this article will be made available by the authors, without undue reservation, to any qualified researcher.

ETHICS STATEMENT

The animal study was reviewed and approved and animal experiments were approved by the Animal Care and Use Committee of Anhui University of Chinese Medicine, China, and implemented in accordance with the Guidelines of the National Institutes of Health on the Care and Use of Animals.

AUTHOR CONTRIBUTIONS

SW and NW conceived the project and designed research. SW and LZ performed the experiments and wrote the manuscript. NW and SW revised the manuscript.

FUNDING

The study was supported by the National Natural Science Foundation of China (Nos. 81773933 and 30973979) and academic assistance program for the top-notch innovative talents from universities in 2017 provided by Anhui Province Office of Education (gxbjZD15).

SUPPLEMENTARY MATERIAL

The Supplementary Material for this article can be found online at: https://www.frontiersin.org/articles/10.3389/fphar.2020.572624/full#supplementary-material.

REFERENCES

Beck, H., and Plate, K. H. (2009). Angiogenesis after cerebral ischemia. *Acta Neuropathol.* 117, 481–496. doi:10.1007/s00401-009-0483-6

Benjamin, E. J., Virani, S. S., Callaway, C. W., Chang, A. R., and Muntner, P. (2018). Heart disease and stroke statistics—2018 update: a report from the American heart association. *Circulation*, 137, e67–e492. doi:10.1161/CIR.0000000000000558

Blackstone, B. N., Li, R., Ackerman, W. E., Ghadiali, S. N., Powell, H. M., and Kniss, D. A. (2015). Myoferlin depletion elevates focal adhesion kinase and paxillin phosphorylation and enhances cell-matrix adhesion in breast cancer cells. *Am. J. Physiol. Cell Physiol.* 308, C642. doi:10.1152/ajpcell.00276.2014

Carmeliet, P. (2000). Mechanisms of angiogenesis and arteriogenesis. *Nat. Med.* 6, 389–395. doi:10.1038/74651

Ge, C.-L., Wang, X.-M., Huang, Z.-G., Xia, Q., Wang, N., and Xu, D.-J. (2015). Tongqiao Huoxue Decoction ameliorates learning and memory defects in rats with vascular dementia by up-regulating the Ca(2+)-CaMKII-CREB pathway. *Chin. J. Nat. Med.* 13, 823–830. doi:10.1016/S1875-5364(15)30086-8

Chen, C., Venketasubramanian, N., Gan, R. N., Lambert, C., Picard, D., Chan, B. P., et al. (2009). Danqi piantang jiaonang (DJ), a traditional Chinese medicine, in poststroke recovery. *Stroke* 40, 859–863. doi:10.1161/STROKEAHA.108.531616

Chen, F. P., Chang, C. M., Hwang, S. J., Chen, Y. C., and Chen, F. J. (2014). Chinese herbal prescriptions for osteoarthritis in Taiwan: analysis of National Health Insurance dataset. *BMC Compl. Alternative Med.* 14, 91. doi:10.1186/1472-6882-14-91

Ducruet, A. F., Gigante, P. R., Hickman, Z. L., Zacharia, B. E., Arias, E. J., Grobelny, B. T., et al. (2010). Genetic determinants of cerebral vasospasm, delayed cerebral ischemia, and outcome after aneurysmal subarachnoid hemorrhage. *J. Cerebr. Blood Flow Metabol.* 30, 676. doi:10.1038/jcbfm.2009.278

Ferrara, N., and Kerbel, R. S. (2005). Angiogenesis as a therapeutic target. *Nature* 438, 967–974. doi:10.1038/nature04483

Greenberg, D. A., and Jin, K. (2005). From angiogenesis to neuropathology. *Nature* 438, 954–959. doi:10.1038/nature04481

Hopkins, A. L. (2008). Network pharmacology: the next paradigm in drug discovery. *Nat. Chem. Biol.* 4, 682–690. doi:10.1038/nchembio.118

Hou, S. T., Nilchi, L., Li, X., Gangaraju, S., Jiang, S. X., Aylsworh, A., et al. (2015). Semaphorin3A elevates vascular permeability and contributes to cerebral ischemia-induced brain damage. *Sci. Rep.* 5, 7890. doi:10.1038/srep07890

Kim, S. H., Park, H. S., Hong, M. J., Yoo, J. Y., Lee, H., Lee, J. A, et al. (2016). Tongqiaohuoxue decoction ameliorates obesity-induced inflammation and the prothrombotic state by regulating adiponectin and plasminogen activator inhibitor-1. *J. Ethnopharmacol.* 192, 201–209. doi:10.1016/j.jep.2016.07.023

Krupinski, J., Kaluza, J., Kumar, P., Kumar, S., and Wang, J. M. (1994). Role of angiogenesis in patients with cerebral ischemic stroke. *Stroke* 25, 1794–1798. doi:10.1161/01.str.25.9.1794

Li, L., Wang, N., Jin, Q., Wu, Q., Liu, Y., and Wang, Y. (2017). Protection of tong-qiao-huo-xue decoction against cerebral ischemic injury through reduction blood-brain barrier permeability. *Chem. Pharm. Bull.* 65, 1004–1010. doi:10.1248/cpb.c17-00267

Liu, C., Zhou, L., and Shui, Z. (2003). Tongqiao huoxue tang and buyang huanwu tang for treatment of vascular dementia—a report of 36 cases. *J. Tradit. Chin. Med.* 23, 243–245.

Liu, J., Li, Q., Zhang, K.-S., Hu, B., Niu, X., Zhou, S.-M., et al. (2017). Downregulation of the long non-coding RNA Meg3 promotes angiogenesis after ischemic brain injury by activating notch signaling. *Mol. Neurobiol.* 54, 8179–8190. doi:10.1007/s12035-016-0270-z

Liu, J., Wang, Y., Akamatsu, Y., Lee, C. C., Stetler, R. A., Lawton, M., et al. (2014). Vascular remodeling after ischemic stroke: mechanisms and therapeutic potentials. *Prog. Neurobiol.* 115, 138–156. doi:10.1016/j.pneurobio.2013.11.004

Liu, Y., Li, Y., Zhan, M., Liu, Y., Li, Z., Li, J., et al. (2018). Astrocytic cytochrome P450 4A/20-hydroxyeicosatetraenoic acid contributes to angiogenesis in the experimental ischemic stroke. *Brain Res.* 1708, 84–70. doi:10.1016/j.brainres.2018.12.023

Longa, E. Z., Weinstein, P. R., Carlson, S., and Cummins, R. (1989). Reversible middle cerebral artery occlusion without craniectomy in rats. *Stroke* 20, 84. doi:10.1161/01.str.20.1.84

Lu, X., Horner, J. W., Paul, E., Shang, X., Troncoso, P., Deng, P., et al. (2017). Effective combinatorial immunotherapy for castration-resistant prostate cancer. *Nature* 543, 728–732. doi:10.1038/nature21676

Masakazu, H., Masahiro, O., Yuji, K., and Yushi, I. (2010). Sequential activation of RhoA and FAK/paxillin leads to ATP release and actin reorganization in human endothelium. *J. Physiol.* 558, 479–488. doi:10.1113/jphysiol.2004.065334

Mou, X., Zhou, D. Y., Zhou, D., Liu, K., Chen, L. J., and Liu, W. H. (2020). A bioinformatics and network pharmacology approach to the mechanisms of action of Shenxiao decoction for the treatment of diabetic nephropathy. *Phytomedicine* 69, 153192. doi:10.1016/j.phymed.2020.153192

Mozaffarian, D., Benjamin, E. J., Go, A. S., Amett, D. K., Blaha, M. J., Cushman, M., et al. (2015). Heart disease and stroke statistics—2015 update: a report from the American heart association. *Circulation* 131, e29–322. doi:10.1161/CIR.0000000000000152

Pan, L., Li, Z., Wang, Y., Zhang, B., Lu, G., and Liu, J. (2020). Network pharmacology and metabolomics study on the intervention of traditional Chinese medicine Huanglian Decoction in rats with type 2 diabetes mellitus. *J. Ethnopharmacol.* 258, 112842. doi:10.1016/j.jep.2020.112842

Peng, T., Jiang, Y., Farhan, M., Lazarovici, P., Chen, L., and Zheng, W. (2019). Anti-inflammatory effects of traditional Chinese medicines on preclinical *in vivo* models of brain ischemia-reperfusion-injury: prospects for neuroprotective drug discovery and therapy. *Front. Pharmacol.* 10, 204. doi:10.3389/fphar.2019.00204

Ren, C., Li, N., Wang, B., Yang, Y., Gao, J., Li, S., et al. (2015). Limb ischemic perconditioning attenuates blood-brain barrier disruption by inhibiting activity of MMP-9 and occludin degradation after focal cerebral ischemia. *Aging Dis.* 6, 406–417. doi:10.14336/AD.2015.0812

Ru, J., Li, P., Wang, J., Zhou, W., Li, B., Huang, C., et al. (2014). TCMSP: a database of systems pharmacology for drug discovery from herbal medicines. *J. Cheminf.* 6, 13. doi:10.1186/1758-2946-6-13

Schmid-Elsaesser, R., Zausinger, S., Hungerhuber, E., Baethmann, A., and Reulen, H. J. (1998). A critical reevaluation of the intraluminal thread model of focal cerebral ischemia: evidence of inadvertent premature reperfusion and subarachnoid hemorrhage in rats by laser-Doppler flowmetry. *Stroke* 29, 2162–2170. doi:10.1161/01.str.29.10.2162

She, Y., Shao, L., Zhang, Y., Hao, Y., Cai, Y., Cheng, Z., et al. (2019). Neuroprotective effect of glycosides in Buyang Huanwu Decoction on pyroptosis following cerebral ischemia-reperfusion injury in rats. *J. Ethnopharmacol*. 242, 112051. doi:10.1016/j.jep.2019.112051

Wang, N., Deng, Y., Wei, W., Song, L., and Wang, Y. (2012). Serum containing Tongqiaohuoxue decoction suppresses glutamate-induced PC12 cell injury. *Neural Regen Res*. 7, 1125–1131. doi:10.3969/j.issn.1673-5374.2012.15.001

Wishart, D. S., Feunang, Y. D., Guo, A. C., Lo, E. J., Marcu, A., Grant, J. R., et al. (2018). DrugBank 5.0: a major update to the DrugBank database for 2018. *Nucleic Acids Res*. 46, D1074–d1082. doi:10.1093/nar/gkx1037

Wu, S., Wang, N., Li, J., Wang, G., Seto, S. W., Chang, D., et al. (2019). Ligustilide ameliorates the permeability of the blood-brain barrier model in vitro during oxygen-glucose deprivation injury through HIF/VEGF pathway. *J. Cardiovasc. Pharmacol*. 73, 316–325. doi:10.1097/FJC.0000000000000664

Wu, S., Wang, N., He, Q., Chang, G., Seto, S. W., Chang, D., et al. (2018). The establishment of the method of cell biochromatograpy and analysis of the active ingredients from TongQiaoHuoXue decoction acting on the neurocytes. *Chem. Pharm. Bull. (Tokyo)*. 66, 983–991. doi:10.1248/cpb.c18-00455

Wu, S. P., Li, D., Wang, N., Hou, J. C., and Zhao, L. (2019). YiQi tongluo granule against cerebral ischemia/reperfusion injury in rats by freezing GluN2B and CaMK II through NMDAR/ERK1/2 signaling. *Chem. Pharm. Bull. (Tokyo)*. 67, 244–252. doi:10.1248/cpb.c18-00806

Xin-Xin, P., Ning, W., Guang-yun, W., Fei-xue, Y., Zi-hua, X., Rong-feng, H., et al. (2015). Effects of naoluo xintong capsules on platelet aggregation and thrombus formation in rats with focal cerebral ischemia/reperfusion. *Chin. J. Exp. Trad. Med. Form*. 24, 1–4. doi:10.13422/j.cnki.syfjx.2015220026

Xu, F. Q., Wang, N., Liu, J. Q., Zhou, A., Duan, J. A., Ding, A. W., et al. (2008). Studies on fingerprints of Tongqiao huoxue decoction by HPLC. *Chin. J. Exp. Trad. Med. Form*. 14, 1–4.

Xue, R., Fang, Z., Zhang, M., Yi, Z., Wen, C., and Shi, T. (2013). TCMID: traditional Chinese Medicine integrative database for herb molecular mechanism analysis. *Nucleic Acids Res*. 41, D1089–D1095. doi:10.1093/nar/gks1100

Yang, H., Wang, F., Wang, Q. L., Zhong, Z. D., Li, B., and Yang, K. (2013). Effects of buyang huanwu decoction on expression of TGF-β_1/Smad3 in pulmonary fibrosis rats. *Chin. J. Exper. Trad. Med*. 19, 240–244. doi:10.11653/syfj2013240240

Yang, J. L., and Fan, Y. P. (2009). Clinical effect observation on nervous tinnitus treated with self-made Huoxue Tongqiao Decoction. *J Tradit Chin Med*. 24, 1476–1477.

Yin, K. J., Hamblin, M., and Chen, Y. E. (2015). Angiogenesis-regulating microRNAs and ischemic stroke. *Curr. Vasc. Pharmacol*. 13, 352. doi:10.2174/15701611113119990016

You, J.-J., Yang, C.-H., Yang, C.-M., and Chen, M.-S. (2014). Cyr61 induces the expression of monocyte chemoattractant protein-1 via the integrin αvβ3, FAK, PI3K/Akt, and NF-κB pathways in retinal vascular endothelial cells. *Cell. Signal*. 26, 133–140. doi:10.1016/j.cellsig.2013.08.026

Zhao, Z., Ong, L. K., Johnson, S., Nilsson, M., and Walker, F. R. (2017). Chronic stress induced disruption of the peri-infarct neurovascular unit following experimentally induced photothrombotic stroke. *J. Cerebr. Blood Flow Metabol*. 37 (12), 3709–3724. doi:10.1177/0271678X17696100

Zheng, X. W., Shan, C. S., Xu, Q. Q., Wang, Y., Shi, Y. H., Wang, Y., et al. (2018). Buyang huanwu decoction targets SIRT1/VEGF pathway to promote angiogenesis after cerebral ischemia/reperfusion injury. *Front. Neurosci*. 12, 911. doi:10.3389/fnins.2018.00911

Conflict of Interest: The authors declare that the research was conducted in the absence of any commercial or financial relationships that could be construed as a potential conflict of interest.

Copyright © 2021 Wu, Wang and Zhao. This is an open-access article distributed under the terms of the Creative Commons Attribution License (CC BY). The use, distribution or reproduction in other forums is permitted, provided the original author(s) and the copyright owner(s) are credited and that the original publication in this journal is cited, in accordance with accepted academic practice. No use, distribution or reproduction is permitted which does not comply with these terms.

frontiers in Pharmacology

ORIGINAL RESEARCH
published: 14 January 2021
doi: 10.3389/fphar.2020.580978

An Integrated Strategy for Effective-Component Discovery of Astragali Radix in the Treatment of Lung Cancer

Bing Yang[1,2,3], *Nan Yang*[1], *Yaping Chen*[1,3], *Maomao Zhu*[1,3], *Yuanpei Lian*[1,3], *Zhiwei Xiong*[1,3], *Bei Wang*[1,3], *Liang Feng*[1,3]* *and Xiaobin Jia*[1,2,3]*

[1]School of Traditional Chinese Pharmacy, China Pharmaceutical University, Nanjing, China, [2]Nanjing University of Chinese Medicine, Nanjing, China, [3]State Key Laboratory of Natural Medicines, China Pharmaceutical University, Nanjing, China

Lung cancer is one of the most devastating diseases worldwide, with high incidence and mortality worldwide, and the anticancer potential of traditional Chinese medicine (TCM) has been gradually recognized by the scientific community. Astragali Radix (AR) is commonly used in traditional Chinese medicine in the treatment of lung cancer and has a certain clinical effect, but effective components and targets are still unclear. In the study, we established an integrated strategy for effective-component discovery of AR in the treatment of lung cancer based on a variety of techniques. First, the effective components and potential targets of AR were deciphered by the "component-target-disease" network using network pharmacology, and potential signal pathways on lung cancer were predicted by Gene Ontology (GO) biological function enrichment analysis and Kyoto Encyclopedia of Genes and Genomes (KEGG) enrichment analyses. Then, the therapeutic effects of AR in the treatment of lung cancer were evaluated *in vivo* using A/J mice, and the potential targets related to autophagy and potential signal pathway were verified by Western blot analysis, immunofluorescence staining, and real-time PCR technology at protein and gene expression level. Finally, metabolism *in vitro* by rat intestinal flora and cell membrane immobilized chromatography technology were used to screen the effective components of AR in the treatment of lung cancer, and remaining components from the cell immobilized chromatography were collected and analyzed by ultra-performance liquid chromatography–electrospray quadrupole time-of-flight mass spectrometry (UPLC-Q-TOF-MS). The screening results of the integrated strategy showed that calycosin-7-O-β-D-glucoside, ononin, calycosin, astragaloside IV, astragaloside II, cycloastragenol, and formononetin may be effective components of AR in the treatment of lung cancer, and they may play a role in the treatment of lung cancer through autophagy and p53/AMPK/mTOR signaling pathway. The integrated

OPEN ACCESS

Edited by:
Hai Yu Xu,
China Academy of Chinese Medical Sciences, China

Reviewed by:
Yonghua Zhao,
University of Macau, China
Wenyi Kang,
Henan University, China

***Correspondence:**
Liang Feng
wenmoxiushi@163.com
Xiaobin Jia
jiaxiaobin2015@163.com

Specialty section:
This article was submitted to Ethnopharmacology, a section of the journal Frontiers in Pharmacology

Received: *07 July 2020*
Accepted: *17 November 2020*
Published: *14 January 2021*

Citation:
Yang B, Yang N, Chen Y, Zhu M, Lian Y, Xiong Z, Wang B, Feng L and Jia X (2021) An Integrated Strategy for Effective-Component Discovery of Astragali Radix in the Treatment of Lung Cancer. Front. Pharmacol. 11:580978. doi: 10.3389/fphar.2020.580978

Abbreviations: AR, astragali radix; TCM, traditional Chinese medicine; DDP, cisplatin; GAPDH, glyceraldehyde-3-phosphate dehydrogenase; p53, protein 53; p-Bcl-2, phosphorylated B-cell lymphoma-2; mTOR, mammalian target of rapamycin; AMPK, AMP-activated protein kinase; PPI, protein–protein interactions; GO, gene Ontology; KEGG, kyoto encyclopedia of genes and genomes; CSE, cigarettes extract; HE, hematoxylin-eosin; IHC, immunohistochemistry; NHBE, primary normal human bronchial epithelial; UPLC-ESI-TO-MS, ultra-performance liquid chromatography–electrospray quadrupole time-of-flight mass spectrometry.

strategy for effective-component discovery provided a valuable reference mode for finding the pharmacodynamic material basis of complex TCM systems. In addition, the prediction for targets and signal pathways laid a foundation for further study on the mechanism of AR in the treatment of lung cancer.

Keywords: key word: effective components, traditional Chinese medicine, astragali radix, lung cancer, autophagy, potential targets, network pharmacology, cell membrane immobilized chromatography

INTRODUCTION

As a global health burden, lung cancer is the highest incidence cancer at present (Torre et al., 2015; Wang et al., 2019). According to relevant statistics, lung cancer accounts for 19.4% of cancer-related deaths with 1.59 million deaths each year, which seriously endangers human health (Ke et al., 2019). As estimated by the International Agency for Research on Cancer, the number of deaths caused by lung cancer will raise to 10 million deaths per year by 2030 (Lou et al., 2016). However, the existing therapies, including radiotherapy, chemotherapy, and the emerging target therapy, are still unsatisfactory to improve the survival of lung cancer patients during the last 30 years (Cheng et al., 2018). So, it is an urgently required issue to achieve a breakthrough in medical treatment of lung cancer.

In recent years, the anticancer potential of traditional Chinese medicine (TCM) has been gradually recognized by the scientific community (Jiang et al., 2017; Zhu et al., 2019). In China, TCM is widely used in the treatment of cancer by preventing tumorigenesis, attenuating the toxicity, enhancing the therapeutic effect of radiotherapy and chemotherapy, reducing tumor recurrence, *etc.* (Wang et al., 2018; Zhang et al., 2018). Astragali Radix (AR), a well-known TCM, is the dried root of *Astragalus membranaceus* (Fisch.) Bge. var. *mongholicus* (Bge.) Hsiao or *Astragalus membranaceus* (Fisch.) Bge. has been used as a common clinical medicine in China for thousands of years. The accumulated data showed that AR was beneficial for the treatment of lung cancer in clinical practice (He et al., 2013; Xiao et al., 2019). However, the effective components and potential targets of AR in the treatment of lung cancer have not been reported.

Network pharmacology is a discipline for investigating pathogenesis of disease through constructing and analyzing biological networks (Chen et al., 2019), and provides a powerful tool for screening effective components and potential targets of TCM by establishing a "component-target-disease" network. Modern pharmacological research has proved that the combination of drugs with the lipid bilayer, receptors, and enzymes on the cell membrane is a main mechanism of drug action. Therefore, the effective components can be screened according to the affinity between the components and the cell membrane. Cell membrane immobilized chromatography, as a kind of cell membrane chromatography, uses active cells as the separation vector, TCM extracts as the object, and the separation was carried out according to whether the ingredients in the extract have specific affinity with the cells. In the study, we established an integrated strategy for effective-component discovery of AR in the treatment of lung cancer based on a variety of techniques, and investigated the relationship between autophagy and the anticancer effect of AR *in vitro* and *in vivo*.

MATERIALS AND METHODS

Materials and Reagents

AR was obtained from Anhui Jingquan Group Herbal Pieces Co., Ltd (Anqing city, Anhui Province, China) and was identified by De-kang Wu (professor of Nanjing University of traditional Chinese medicine) as the dried root of *Astragalus membranaceus* (Fisch.) Bge. var. *mongholicus* (Bge.). Benzopyrene was purchased from Aladdin Reagent Co., Ltd. (Shanghai, China). Cisplatin (DDP, 1 mg/ml, 20 ml) was gained from Nanjing pharmaceutical factory Co., Ltd. (Nanjing, China). 4% paraformaldehyde fixative was purchased from Nanjing Nanao Technology Co., Ltd. (Nanjing, China). Hematoxylin dyeing solution (D005) was purchased from Nanjing Jiancheng Bioengineering Institute (Nanjing, China). Eosin dye solution (KGA231), 0.25% trypsin, 1% Triton X-100, goat serum, 4',6-diamidino-2-phenylindole, and DMEM high glucose medium were purchased from Nanjing KeyGen Biotech logical Co., Ltd. (Nanjing, China). Glyceraldehyde-3-phosphate dehydrogenase (GAPDH, 0802) antibody was purchased from Shanghai Kangcheng Biological Engineering Co., Ltd. (Shanghai, China). The antibodies against protein 53 (p53, ab131442), phosphorylated B-cell lymphoma-2 (p-Bcl-2, ab138406), mammalian target of rapamycin (mTOR, ab2732), AMP-activated protein kinase (AMPK, ab32047) and Beclin1 (ab133357) were obtained from Abcam (Cambridge, United Kingdom). NP-40 lysis buffer (1210600) was purchased from Nanjing Shengxing Biotechnology Co., Ltd. (Nanjing, China). Polyvinylidene fluoride (k8JN62911) was purchased from Millipore Corporation (Bedford, MA, USA). Pre-stained protein marker was purchased from Fermentas (Burlington, Canada).

Astragaloside I (MUST-16012906) and astragaloside II (MUST-16031010) were purchased from manster biotechnology Co., Ltd. (Chengdu, China). Cycloastragenol (HHQC20170921) was purchased from Nanjing Spring and Autumn Biological Engineering Co., Ltd. (Nanjing, China). Astragaloside IV (1107781-201616), calycosin (111920-201304), calycosin-7-O-β-D-glucoside (111920-201505), formononetin (111703-200603), and ononin (111703-200501) were purchased from the National institute for Food and Drug Control of China (Beijing, China). LC-MS grade methanol and acetonitrile were purchased from Merk Company (Darmstadt, Germany). HPLC grade formic acid with a purity of 99% was

purchased from Anaqua chemical supply (ACS, Houston, USA). Purified water was prepared from a Milli-Q water purification system (Millipore Corporation, Bedford, MA, USA). Other chemicals (reagent grade) used were purchased from Nanjing Chemical Reagent Co, Ltd. (Nanjing, China).

Database Construction

All components of AR were obtained and cross-validated from TCMSP (http://lsp.nwu.edu.cn/tcmsp.php) database (Ru et al., 2014), ETCM (http://www.nrc.ac.cn:9090/ETCM/) (Xu et al., 2019), TCMID (http://www.megabionet.org/tcmid/) (Xue et al., 2012), CNKI (https://www.cnki.net/), PubMed (https://www.ncbi.nlm.nih.gov/pubmed), and SciFinder (https://scifinder.cas.org), and saved in SDF and Canonical SMILES structure format. All targets related to components of AR were collected from several databases, including PharmMapper (http://www.lilab-ecust.cn/pharmmapper/) (Wang et al., 2017), similarity ensemble approach (SEA, http://sea.bkslab.org/) (Gu and Lai, 2020), and Swiss Institute of Bioinformatics (SIB, http://www.swisstargetprediction.ch/) (Gfeller et al., 2014), and were limited to homo sapiens. All obtained targets were retrieved from GeneCards (http://www.genecards.org/) (Fishilevich et al., 2016) and Therapeutic Target Database (TTD, http://bidd.nus.edu.sg/group/cjttd) (Li et al., 2018) to explore their function to confirm if related to lung cancer, as only targets related to lung cancer can be used in subsequent studies, and named as potential targets. All components related to lung cancer were obtained by matching targets related to lung cancer with components of AR, and named as potential effective components.

Network Construction

The potential target-effective component network was constructed using Cytoscape software (version 3.6.1). In order to further explain the mechanism of AR in the treatment of lung cancer, the protein–protein interaction (PPI) network of lung cancer–related targets was explored by STRING (version 10.5, https://string-db.org/), and was visualized with Cytoscape software (version 3.6.1). Gene Ontology (GO) and Kyoto Encyclopedia of Genes and Genomes (KEGG) enrichment analyses of potential targets were performed using the plugin ClueGo (version 2.5.4) from Cytoscape software (version 3.6.1). The signal pathways closely related to lung cancer were statistically analyzed, and those with $p < 0.01$ after Benjamin's correction were considered to be significantly changed and selected for further research, named as potential signal pathways. Then, the potential signal pathways were evaluated by occurrence frequency of potential targets.

Preparation of Astragali Radix Sample and Component Characterization

AR sample was gained by reflux extraction twice with ten times (w/v) 70% ethanol (v/v) in thermostatic water bath for 1.5 h. The two parts of extracts were combined, and the solvent was removed by rotary evaporation to obtain dried powder of AR. The dried powder of AR was stored in 4 °C refrigerator before use. The AR sample was analyzed by ultra-performance liquid chromatography–electrospray quadrupole time-of-flight mass spectrometry (UPLC-Q-TOF-MS) to characterize chemical component, and main signals in chromatograph were identified, and compared with the reference substances. Eight components, including calycosin-7-O-β-D-glucoside, ononin, calycosin, formononetin, astragaloside IV, astragaloside II, astragaloside I, and cycloastragenol, were accurately identified. The component information and typical total ion chromatogram (AR and reference substances) were shown in **Supplementary Material S1**.

Cigarettes Extract Preparation

A vacuum pump was used to simulate the human lung; a cigarette with the filter (containing 11 mg tar and 1.1 mg nicotine) was ignited and the end of the cigarette attached to a rubber hose. Smoke emitted from the burnt cigarette was dissolved in the serum-free culture medium through a glass pipette tip by a vacuum pump (**Supplementary Figure S1**). The smoke-solubilized serum-free culture medium was filtered by 0.22 μm sterile microporous membrane to obtain CSE.

Animals and Experiment Design

Forty male A/J mice, weighing 18–20 g, were purchased from Shanghai Experimental Animal Research Center (License number SCKK (HU) 2013-0056, Shanghai, China) and housed under pathogen-free environment with a 12h/12 h light–dark cycle and fed with food and water *ad libitum*. All animal experiments were conducted in accordance with the guidelines of the laboratory animals and approved by the Animal Ethics Committee of Nanjing University of Chinese Medicine.

All the mice were randomly assigned to five groups: control group, model group, DDP group, 5.2 g/kg AR group, and 2.6 g/kg AR group. Except for the control group, the lung cancer model of several groups were created by intraperitoneally injecting with benzopyrene (100 mg/kg body weight dissolved in corn oil) twice a week for 4 weeks; the DDP group were intraperitoneally injected with DDP; mice in the 5.2 g/kg AR group and 2.6 g/kg AR group were orally administrated with AR at the dose of 5.2 g/kg/d and 2.6 g/kg/d (dose conversion according to the Chinese pharmacopoeia 2020 edition part one), respectively, while the control group was given normal saline solution by gavage. After that, all the groups continued to receive different treatments for 28 weeks and once a day. After 28 weeks, all mice were sacrificed, and the lungs were collected. Immediately, a portion of lung tissue was snap-froze in liquid nitrogen and stored at −70 °C for further analysis, and another portion was fixed in 4% paraformaldehyde for histopathological study.

Histopathological Study

The lung tissues were fixed in 4% paraformaldehyde for 24 h, dehydrated and paraffin-embedded. The paraffin-embedded lung tissues were sectioned and stained with hematoxylin-eosin (HE) and immunohistochemistry (IHC). For IHC analysis, the paraffin-embedded lung tissue sections were deparaffinized in xylene and rehydrated through graded alcohol. Then, 3% H_2O_2 was added to block endogenous peroxidase activity. Finally, sections were blocked with normal goat serum for 30 min at

room temperature and then incubated with anti-p-Bcl-2 and anti-p53 antibodies at 4 °C overnight. Sections were counterstained with hematoxylin and observed under light microscopy (Olympus, Tokyo, Japan) using ×400 magnification.

NHBE Cell Culture and Treatments

Primary normal human bronchial epithelial (NHBE) cells were purchased from Beina Chuanglian Biotechnology Co., Ltd. (Beijing, China). NHBE cells were seeded into a plastic culture flask containing DMEM, and then placed in a humidified incubator containing 5% CO_2 at 37 °C. Culture medium was changed every two days, until NHBE cells reached 90% confluence. NHBE cells were digested by 0.25% trypsin and 0.02% EDTA solution, and prepared for the experiment with a density of 1×10^6 cells/mL. An MTT assay was used to assess the viability of NHBE cells exposed to different concentrations of CSE and AR (**Supplementary Figure S2**). According to the screening results, 10% CSE was chosen as the modeling concentration, and 1000 μg/ml and 500 μg/ml were chosen as the AR administration concentration. NHBE cells were divided into five groups (six wells per group): control groups (no treatment), model group (10% CSE), DDP groups (10% CSE+10 μg/ml DDP), 1000 μg/ml AR group (10% CSE + 1000 μg/ml AR), and 500 μg/ml AR group (10% CSE + 500 μg/ml AR). All cells were cultured in an incubator at 37 °C with 5% CO_2 for 24 h.

Transmission Electron Microscope Observation

NHBE cells were digested with 0.25% trypsin to prepare single-cell suspension, centrifuged at 1000 rpm for 10 min, washed twice with prechilled PBS, and then fixed with prechilled 2.5% glutaric acid for 90 min at 4 °C. After washing in PBS, the cells were fixed with 1% osmium tetroxide at 4 °C for 30 min. After fixing, the cells were dehydrated with gradient ethanol and acetone, and then embedded in Epon812 resin (Sigma). The embedded blocks were cut into ultrathin sections using an ultramicrotome, and stained with uranyl acetate and lead citrate for ultrastructural examination under transmission electron microscopy (JEOL, Tokyo, Japan).

Western Blot Analysis

The NHBE cells were collected and used for Western blot analysis. The protein was extracted on ice using NP-40 lysis buffer (1% NP-40, 150 mM NaCl, 50 mM Tris-HCl, pH 8.0). Lysates were centrifuged at 13,000 rpm for 10 min at 4 °C, and the supernatants were collected. Protein concentration was measured by using the DC protein assay (Bio-Rad). The separated protein samples were separated by SDS-polyacrylamide gel electrophoresis and then transferred onto polyvinylidene fluoride membrane (Millipore Corporation, Billerica, MA, USA). Membranes was blocked with 5% nonfat dry milk in Tris-buffered saline with 0.05% Tween-20 (TBST) buffer, and then incubated with primary antibodies against p53 (1:500), p-Bcl-2 (diluted: 1:1000), Beclin 1 (diluted: 1:1000), AMPK (diluted: 1:1000), mTOR (diluted: 1:1000), and GAPDH (1:10,000) overnight at 4 °C. Subsequently, the membranes were incubated for 2 h at room temperature with secondary antibodies (1:10,000). Finally, the antigen–antibody complexes were visualized using enhanced chemiluminescence (Amersham) according to the manufacturer's instructions, and visualized using Azure c600 imaging system (Azure Biosystems, Dublin, CA, USA). The protein levels were expressed as relative integrated intensity and were normalized to that of GAPDH.

Immunofluorescence Staining

The NHBE cells were washed three times with cold PBS and fixed by 4% paraformaldehyde for 15 min at room temperature, followed by permeabilization process with 1% Triton X-100 (Fisher). NHBE cells were subsequently immuno-stained with primary antibody for 2 h at room temperature and followed by fluorescein isothiocyanate-labeled secondary antibodies for 30 min at room temperature. The samples were washed twice, adhered onto coverslips, and mounted with 4',6-diamidino-2-phenylindole–containing mounting medium. Acquisition of images was performed using a fluorescence microscope (Leica Microsystems, Wetzlar, Germany).

Real-Time PCR

Total RNA was extracted using the Trizol reagent (Invitrogen) according to the manufacturer's instructions. The RNA concentrations were determined using a spectrophotometer (ThermoFisher, Waltham, MA, USA). cDNA was synthesized from RNA (2 μg) using First-strand cDNA Synthesis Kit (Thermo Fisher Scientific, Waltham, MA, USA). Real-time PCR analyses were conducted to quantitate p-53, p-Bcl-2, Beclin1, AMPK, and mTOR relative expression using SYBR Green real-time PCR kit (TaKaRa, Dalian, China) with GAPDH as an internal control. The cycle threshold values from all quantitative real-time PCR experiments were analyzed using $2^{-\Delta\Delta CT}$ method, and were automatically determined by the ABI 7500 Real-Time PCR System (Applied Biosystems, USA). The primers used for real-time PCR analysis were as follow: p-53, forward primer 5′-CAG ACAGGCTTTGCAGAATG-3′, reverse primer 5′-GACCCT GGCACCTACAATGA-3'; p-Bcl-2, forward primer 5′-AAG CTGTCACAGAGGGGCTA-3′, reverse primer: 5′-CAGGCTGGA AGGAGAAGATG-3'; Beclin1, forward primer 5′-GTCCACGCTCGACCTTCTTAC-3′, reverse primer 5′-CAC TTGCCAGTCTTAACCTCTG-3'; AMPK, forward primer 5′-TGCGTGTACGAAGGAAGAATCC-3′, reverse primer 5′-TGTGACTTCCAGGTCTTGGAGTT-3′; mTOR, forward primer 5′-CAGTTCGCCAGTGGACTGAAG-3′, reverse primer 5′-GCTGGTCATAGAAGCGAGAC-3′; and GAPDH, forward primer 5′-AGGTCGGTGTGAACGGATTTG-3′, reverse primer 5′-TGTAGACCATGTAGTTGAGGTCA-3′.

Metabolism *in vitro* of Rat Intestinal Flora

Preparation of Anerobic Culture Medium

$CaCl_2$ (0.2 g) and MgSO4.7H_2O (0.2 g) were dissolved on 800 ml of distilled water. After that, $K_2HPO_4{\cdot}3H_2O$ (1.0 g), KH_2PO_4 (1.0 g), $NaHCO_3$ (10.0 g), NaCl (2.0 g), and resazurin solution (10 ml, 2.0 g resazurin dissolved in 10 ml double-distilled water) were added and stirred until dissolving, and then boiled distilled

water was added to 1000 ml, mixed well, and cooled to room temperature. Then, tryptone (10.0 g), yeast extract (10.0 g), L-cysteine (1.0 g), and heme chloride solution (10 ml, 0.05 g heme chloride dissolved in 100 ml of 0.01 N NaOH solution) were supplemented. The pH was adjusted to 7.3 with NaOH test solution. All solution was autoclaved at 121 °C for 20 min and stored at 4 °C after cooling.

Preparation of Intestinal Flora Culture Solution

Six male Sprague–Dawley (SD) rats were provided by Shanghai Laboratory Animal Center (License No. SYXK (HU) 2013-0056, Shanghai China). Fresh intestinal contents (5.0 g) taken from SD rats were placed in a sterilized penicillin vial and mixed with normal saline at a ratio of 1 g:4 ml to make a suspension, and then the filtrate and anaerobic culture solution were mixed in a ratio of 1:9 to obtain enteric bacteria culture solution.

Sample Preparation

AR (1 mg/ml, 200 μL) was added to intestinal flora culture medium (1 ml), which was then filled with nitrogen without oxygen. The reactions were terminated by adding 1 ml n-butanol and 1 ml ethyl acetate after incubation for 0, 4, 8, 12, 24, 48, and 72 h, respectively. Next, the mixtures were vortexed for 5 min after adding 10 μL internal standard solution (nitrendipine, 2 μg/ml) and centrifuged at 14,000 rpm for 5 min. Subsequently, the organic phases were collected and evaporated under nitrogen gas, and 200 μL of methanol was added, vortexed, and centrifuged again at 14,000 rpm for 5 min, respectively. The supernatant was passed through the 0.22 μm millipore filter before injecting into the UPLC-Q-TOF-MS.

Cell Membrane Immobilized Chromatography

A549 cells were purchased from Nanjing Kaiji biology Co., Ltd (Nanjing, China). A549 cells were seeded in a plastic culture flask containing DMEM, and then placed in a humidified incubator containing 5% CO_2 at 37 °C. The medium was replaced every day until A549 cells grew to 80–90% confluence. A549 cells were starved in serum-free medium for 3 h after washing with PBS. AR sample was incubated on intestinal bacteria (2×10^{-4} g/ml) for 0, 4, 8, 12, 24, 48, and 72 h, and then the incubated solution was separately added into the A549 cells for 90 min, and was washed repeatedly with PBS until without detected component. The dissociation solution (10.95 g/L Na_2HPO_4 and 12.91 g/L citric acid aqueous solution) was immediately added into the treated A549 cells, which were incubated at 37 °C and 5% CO_2 for 30 min to inactivate the cell effect target. Finally, the dissociation solution was collected.

A549 cells were digested with pancreatin and suspended into DMEM/high glucose medium. The cell suspension was centrifuged at 3,000 rpm for 2 min at 4 °C; the cell density (1×10^7 cells/mL) was adjusted by PBS and then dissociated at room temperature for 1 h with dissociation solution. The cells were quickly placed at −80 °C for 20 min, and thawed in a thermostatic water bath at 37 °C for 10 min. The freezing–thawing process was repeated for 4 times and centrifuged at 2000 rpm for 20 min. Then, the dissociation solution and intracellular dissociation solution were collected and evaporated under nitrogen gas, and 200 μL of methanol was added, vortexed for 2 min, and centrifuged at 11,000 rpm for 10 min. Finally, the supernatant was passed through the 0.22 μm millipore filter before injecting into the UPLC-Q-TOF-MS.

UPLC-Q-TOF-MS Analysis

Chromatographic analysis was performed on a LC-20AD UPLC system (Shimadzu Corporation, Kyoto, Japan) equipped with hybrid quadrupole time-of-flight tandem mass spectrometry (Triple TOF™ 5,600, AB SCIEX, Foster City, CA, USA) coupled with electrospray ionization (ESI) source. Chromatographic separation was performed on a ACQUITY UPLC HSS T3 column (50 mm × 2.1 mm, 1.8 μm). The flow rate was 0.3 ml/min, and the mobile phase consisted of solvent A (0.1% formic acid in water, v/v) and solvent B (acetonitrile) with the optimized gradient elution: 0~2 min, 2%~8% B; 2~8 min, 8%~20% B; 8~12 min, 20%~35% B; 12~18 min, 35%~60% B; 18~24 min, 60%~70% B; 24~28 min, 70%~80% B; 28~28 min, 80%~2% B; and 28~30 min, 2%~2% B. The column temperature was set at 30 °C. In order to get better analysis results, the mass spectrometer was conducted in electrospray and multiple reaction monitoring scanning mode, in negative ion modes. The optimized parameters for mass spectrometer were as follows: capillary voltage, 0.5 kV; ion source temperature, 100 °C; cone gas flow rate, 50 L/h; desolvation temperature, 400 °C; and desolvation gas flow, 800 L/h. The information-dependent acquisition techniques and dynamic background subtraction were used to reduce the impact of matrix interference.

Statistical Analysis

All data are presented as the mean ± standard deviation. Data from mice and NHBE cells were statistically evaluated using *t*-test for pair-wise comparison. $p < 0.05$ was considered to be a significant difference, $p < 0.01$ was considered to be extremely significant difference, and $p > 0.05$ was considered to be no significant difference. All statistical analyses were performed using SPSS software (version 22.0, IBM, Chicago, IL, USA).

RESULTS

Network Pharmacology Analysis of AR in the Treatment of Lung Cancer

Potential Targets and Components Prediction

In this study, the computer virtual screening technology was used to provide a fast and efficient approach to obtain potential targets. At length, 160 potential targets of AR in the treatment of lung cancer were obtained, and the information of potential targets (degree ≥5) are listed in **Table 1**. As shown in **Figure 1A**, the PPI network consisted of 160 nodes and 3,720 edges (average node degree of 46.5 and average local clustering coefficient of 0.634), and the node represents the potential target; the "degree" value

TABLE 1 | Information of potential targets of AR in the treatment of lung cancer (degree ≥ 5).

No.	Gene Name	Protein Name	Uniprot ID	Degree
1	ESR2	Estrogen receptor beta	Q92731	20
2	CDK1	Cyclin-dependent kinase 1	P06493	19
3	CDK2	Cyclin-dependent kinase 2	P24941	18
4	CYP19A1	Aromatase	P11511	18
5	CAT	Catalase	P04040	18
6	ESR1	Estrogen receptor	P03372	18
7	EGFR	Epidermal growth factor receptor	P00533	17
8	AR	Androgen receptor	P10275	16
9	IL2	Interleukin 2	P60568	16
10	ABCB1	ATP-dependent translocase ABCB1	P08183	15
11	HSP90AA1	Heat shock protein HSP 90-alpha	P07900	15
12	PARP1	Poly(ADP-Ribose) polymerase 1	P09874	15
13	TOP1	DNA topoisomerase I	P11387	14
14	KDR	Vascular endothelial growth factor receptor 2	P25968	14
15	SRC	Proto-oncogene tyrosine-protein kinase Src	P12931	14
16	ABCG2	ATP-binding cassette sub-family G member 2	Q9UNQ0	14
17	MAPK14	Mitogen-activated protein kinase 14	Q16539	13
18	MMP2	72 kDa type IV collagenase	P08253	13
19	MET	Hepatocyte growth factor receptor	P08581	12
20	ALOX5	Arachidonate 5-lipoxygenase	P09917	12
21	MMP3	Stromelysin-1	P08254	11
22	MMP9	Matrix metalloproteinase 9	P14780	11
23	TYMS	Thymidylate synthase	P04818	11
24	IGF1R	Insulin-like growth factor I receptor	P08069	11
25	TERT	Telomerase reverse transcriptase	O14746	11
26	CYP1B1	Cytochrome P450 1B1	Q16678	11
27	CHEK1	Serine/threonine-protein kinase Chk1	O14757	10
28	MCL1	Induced myeloid leukemia cell differentiation protein Mcl-1	Q07820	10
29	PIK3CG	Phosphatidylinositol 4,5-bisphosphate 3-kinase catalytic subunit gamma isoform	P48736	10
30	PRKCA	Protein kinase C alpha type	P17252	10
31	PTGS2	Prostaglandin G/H synthase 2	P35354	10
32	F2	Prothrombin	P00734	10
33	MMP1	Interstitial collagenase	P03956	9
34	ABL1	Tyrosine-protein kinase ABL1	P00519	9
35	ALK	ALK tyrosine kinase receptor	Q9UM73	9
36	FGF2	Fibroblast growth factor 2	P09038	9
37	STAT3	Signal transducer and activator of transcription 3	P40763	9
38	VDR	Vitamin D3 receptor	P11473	9
39	VEGFA	Vascular endothelial growth factor A	P15692	9
40	AKT1	RAC-alpha serine/threonine-protein kinase	P31749	9
41	MTOR	Serine/threonine-protein kinase mTOR	P42345	8
42	PIK3CA	Phosphatidylinositol 4,5-bisphosphate 3-kinase catalytic subunit alpha isoform	P42336	8
43	PLK1	Serine/threonine-protein kinase PLK1	P53350	8
44	HMOX1	Heme oxygenase 1	P09601	8
45	CYP2D6	Cytochrome P450 2D6	P10635	8
46	PPARG	Peroxisome proliferator activated receptor gamma	P37231	8
47	CDK6	Cyclin-dependent kinase 6	Q00534	8
48	ABCC1	Multidrug resistance-associated protein 1	P33527	8
49	AURKA	Aurora kinase A	O14965	7
50	LGALS3	Galectin-3	P17931	7
51	PLG	Plasminogen	P00747	7
52	MPO	Myeloperoxidase	P05164	7
53	PIK3CB	Phosphatidylinositol 4,5-bisphosphate 3-kinase catalytic subunit beta isoform	P42338	6
54	CASP3	Caspase-3	P42574	6
55	PIK3R1	Phosphatidylinositol 3-kinase regulatory subunit alpha	P27986	6
56	SLC2A1	Solute carrier family 2, facilitated glucose transporter member 1	P11166	6
57	BCL2L1	Bcl-2-like protein 1	Q07817	6
58	NTRK1	High affinity nerve growth factor receptor	P04629	6
59	ADRB2	Beta-2 adrenergic receptor	P07550	6
60	TLR9	Toll-like receptor 9	Q9NR96	6
61	TNF	Tumor necrosis factor	P01375	6
62	HDAC1	Histone deacetylase 1	Q13547	5
63	BAD	Bcl2-associated agonist of cell death	Q92934	5
64	MMP7	Matrix metalloproteinase 7	P09237	5

(Continued on following page)

TABLE 1 | (*Continued*) Information of potential targets of AR in the treatment of lung cancer (degree ≥ 5).

No.	Gene Name	Protein Name	Uniprot ID	Degree
65	TYMP	Thymidine phosphorylase	P19971	5
66	JAK2	Tyrosine-protein kinase JAK2	O60674	5
67	ITGB1	Integrin beta-1	P05556	5
68	CDK4	Cyclin-dependent kinase 4	P11802	5
69	MDM2	E3 ubiquitin-protein ligase Mdm2	Q00987	5
70	TOP2A	DNA topoisomerase 2 alpha	P11388	5
71	PGR	Progesterone receptor	P06401	5
72	BRAF	Serine/threonine-protein kinase B-raf	P15056	5
73	PTK2	Focal adhesion kinase 1	Q05397	5
74	AHR	Aryl hydrocarbon receptor	P35869	5
75	DAPK1	Death-associated protein kinase 1	P53355	5

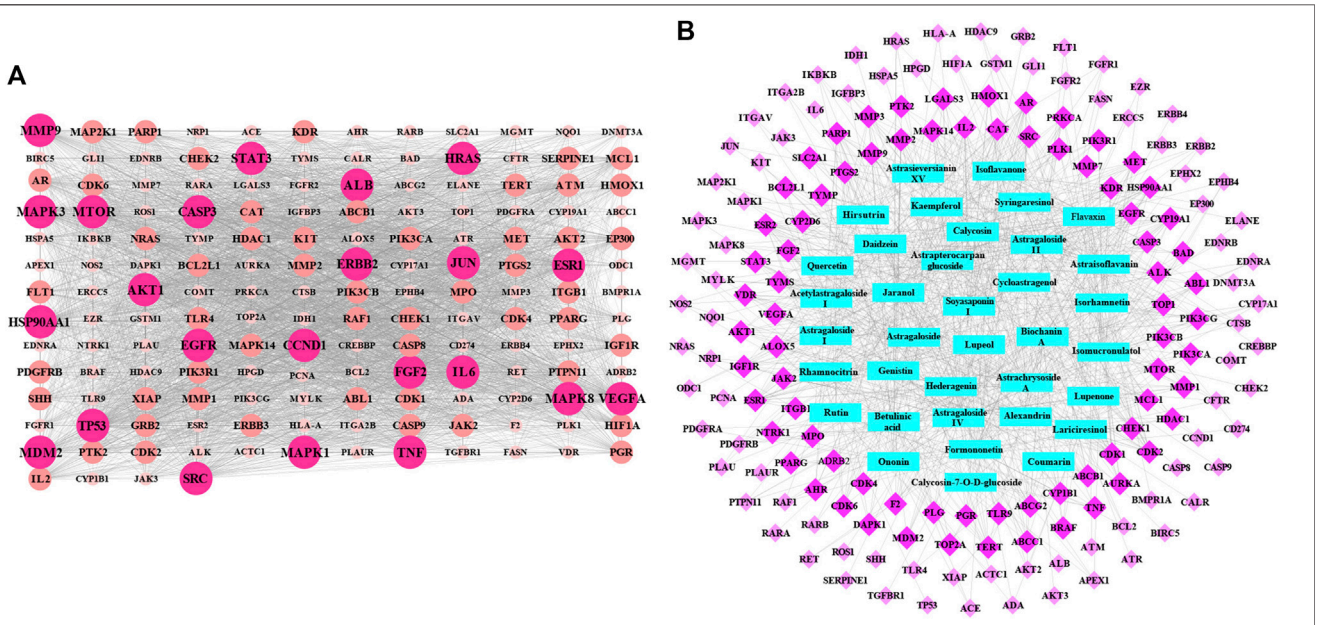

FIGURE 1 | The protein–protein interaction (PPI) network and potential target-effective component network of AR in the treatment of lung cancer. **(A)** The PPI network of 160 potential targets. The node represents the potential target: the larger and brighter the node, the larger the interactions. **(B)** Network of 160 potential targets related to 36 potential effective components. The rose red diamond nodes represent 160 potential targets, blue rectangle nodes represent 36 potential effective components, and the brighter color diamond nodes represent the more important potential targets.

that indicated the strength of the potential target showed the larger the node, the brighter the color, and the larger the value. The results showed that the nodes of TP53, AKT1, VEGFA, EGFR, MAPK3, CCND1, HRAS, CASP3, SRC, ALB, JUN, STAT3, HSP90AA1, IL6, MAPK1, ESR1, ERBB2, TNF, MAPK8, MTOR, FGF2, and MMP9 are larger and brighter, indicating that they play a major role in the treatment of lung cancer. Further analysis found that these potential targets are mainly related to autophagy, apoptosis, and immune-mediated, cell cycle arrest and antioxidation. It is speculated that AR may play a role in the treatment of lung cancer through autophagy, apoptosis, and immune-mediated, cell cycle arrest and antioxidation.

Based on the acquisition of potential targets, 36 potential effective components were obtained by matching potential targets, and their information is listed in **Table 2**. Potential target-effective component network was constructed by Cytoscape 3.6.1 software. As shown in **Figure 1B**, these 160 potential targets were associated with 36 potential effective components, and the blue nodes and rose red nodes represent 160 potential targets and 36 potential effective components, respectively. Potential target-effective component network indicated that the same component could act on multiple targets, and each target is usually associated with multiple components. These results suggested that different components in AR could regulate these same or similar targets to exert effect. So, in the study of TCM, as a complex system with multiple components and multiple targets, synergistic or antagonistic interactions among the different components of TCM should be considered.

TABLE 2 | The summary of potential effective components of AR in the treatment of lung cancer.

Name	Molecular formula	CAS	Degree	Protein targets from effective components
Jaranol	$C_{17}H_{14}O_6$	3301-49-3	42	ABCB1, ABCC1, ABCG2, ACTC1, AHR, AKT1, ALK, ALOX5, APEX1, AR, CAT, CDK1, CDK2, CDK6, CYP19A1, P1B1, DAPK1, EGFR, ESR1, ESR2, F2, IGF1R, KDR, KIT, MCL1, MET, MMP2, MMP3, MMP9, MYLK, NOS2, ODC1, ARP1, PIK3CG, PIK3R1, PLG, PLK1, PTGS2, PTK2, SRC, TERT, TOP2A
Flavaxin	$C_{17}H_{20}N_4O_6$	83-88-5	38	ABCG2, ABL1, ALK, ATM, AURKA, BMPR1A, BRAF, CDK1, CDK2, CDK4, CHEK1, EGFR, EPHB4, F2, HSP90AA1, JAK2, JAK3, JUN, KDR, MAPK1, MAPK14, MAPK8, MMP2, MMP3, MMP9, MTOR, NQO1, NTRK1, PDGFRB, PIK3CA, PIK3CB, PIK3CG, PPARG, PRKCA, PTK2, SRC, TGFBR1, TLR4
Astragaloside IV	$C_{41}H_{68}O_{14}$	84687-43-4	37	ADRB2, AKT1, AKT2, AR, CAT, CDK1, CDK4, CYP2D6, EGFR, ESR1, F2, FGF2, HMOX1, HSP90AA1, IGF1R, IKBKB, IL2, ITGA2B, ITGAV, ITGB1, LGALS3, MDM2, MET, MMP1, MTOR, NRP1, PARP1, PIK3CA, PIK3CG, PLG, PKCA, SRC, STAT3, TOP1, TYMS, VDR, VEGFA
Isorhamnetin	$C_{16}H_{12}O_7$	480-19-3	37	ABCB1, ABCC1, ABCG2, AHR, AKT1, ALK, ALOX5, APEX1, CAT, CDK1, CDK2, CDK6, CYP19A1, CYP1B1, DAPK1, EGFR, ESR1, ESR2, F2, HMOX1, IGF1R, KDR, MET, MMP2, MMP3, MMP9, MPO, MYLK, PARP1, PIK3CG, PIK3R1, PLG, PLK1, PTK2, SRC, TERT, TOP2A
Rhamnocitrin	$C_{16}H_{12}O_6$	569-92-6	37	ABCB1, ABCC1, ABCG2, ADA, AHR, ALK, ALOX5, APEX1, AR, CAT, CDK1, CDK2, CDK6, CFTR, CYP19A1, CYP1B1, DAPK1, EGFR, ESR1, ESR2, F2, GSTM1, IGF1R, KDR, MCL1, MET, MMP2, MMP3, MMP9, MPO, PIK3CG, PI3R1, PLG, PLK1, PTGS2, SRC, TERT
Kaempferol	$C_{15}H_{10}O_6$	520-18-3	35	ABCB1, ABCC1, ABCG2, ADA, AHR, ALK, ALOX5, CAT, CDK1, CDK2, CDK6, CFTR, CYP19A1, CYP1B1, DAPK1, EGFR, ESR1, ESR2, F2, IGF1R, KDR, MET, MMP2, MMP3, MMP9, MPO, PARP1, PIK3R1, PLK1, PTGS2, PTK2, SRC, TERT, TOP1, VEGFA
Quercetin	$C_{15}H_{10}O_7$	117-39-5	35	ABCB1, ABCC1, ABCG2, AHR, AKT1, ALK, ALOX5, APEX1, CALR, CDK1, CDK2, CDK6, CYP19A1, CYP1B1, DAPK1, EGFR, ESR2, F2, IGF1R, KDR, MET, MMP2, MMP3, MMP9, MPO, MYLK, PARP1, PIK3CG, PIK3R1, PLK1, PTK2, SRC, TERT, TOP1, TOP2A
Astrachrysoside A	$C_{47}H_{78}O_{18}$	123914-38-5	33	AR, CAT, CDK1, CDK2, CTSB, CYP2D6, ELANE, ESR1, FGF2, FGF2, FGFR2, HMOX1, HSP90AA1, IKBKB, IL2, ITGA2B, ITGAV, ITGB1, LGALS3, MAPK14, MET, MMP2, MMP9, MTOR, NTRK1, PIK3CA, PIK3CB, PPARG, SLC2A1, STAT3, TYMS, VDR, VEGFA
Astrapterocarpan glucoside	$C_{23}H_{26}O_{10}$	94367-42-7	32	ABL1, AR, CASP3, CASP8, CAT, CDK1, CDK2, CHEK1, CYP19A1, EGFR, ERBB2, HMOX1, HSPA5, IL2, LGALS3, MAP2K1, MAPK1, MAPK14, MCL1, MGMT, MMP1, MMP2, MMP3, MMP9, ODC1, PARP1, PDGFRB, PTGS2, PTPN11, SLC2A1, TOP1, TYMP
Isomucronulatol	$C_{45}H_{72}O_{16}$	84676-88-0	30	ABL1, ALK, AURKA, BAD, CASP3, CCND1, CDK1, CDK2, CHEK1, CYP19A1, EGFR, EP300, EZR, FLT1, HDAC9, HSP90AA1, KDR, MAPK1, MET, MMP1, MMP7, MTOR, PIK3CB, PIK3CG, PIK3R1, PLK1, PRKCA, RAF1, RET, SRC
Calycosin	$C_{16}H_{12}O_5$	20575-57-9	30	ABCB1, ABCC1, ABCG2, ALK, ALOX5, BAD, BCL2, CDK2, CDK6, CHEK1, CYP19A1, CYP1B1, EGFR, ESR1, ESR2, F2, IGF1R, IGFBP3, IL2, KDR, MCL1, MET, PARP1, PLAU, PLAUR, PLG, PLK1, TERT, TLR9, TNF
Cycloastragenol	$C_{30}H_{50}O_5$	84605-18-5	29	AKT1, AKT2, AKT3, ALOX5, AR, ATR, AURKA, BRAF, CDK2, CHEK1, EGFR, EPHX2, ERBB2, ESR1, ESR2, FGFR1, IGF1R, IKBKB, JAK2, KDR, MAPK14, MAPK3, MAPK8, MDM2, MMP3, MTOR, PGR, PLK1, ROS1
Formononetin	$C_{16}H_{12}O_4$	485-72-3	27	ABCB1, ABCG2, AR, BAD, BCL2, CAT, CHEK1, CYP19A1, CYP1B1, EGFR, ERBB2, ERBB3, ERBB4, ERCC5, ESR1, ESR2, EZR, IDH1, IL2, MCL1, MMP2, MMP9, PPARG, RAF1, SRC, TLR9, TOP1
Lariciresinol	$C_{20}H_{24}O_6$	27003-73-2	27	ABL1, ADA, AKT2, ALOX5, AURKA, BRAF, CDK1, CDK2, CDK4, CFTR, CHEK1, EPHB4, HDAC1, HIF1A, JAK2, MAP2K1, MCL1, MMP7, MTOR, NTRK1, PIK3CA, PIK3CB, PIK3CG, SLC2A1, TLR4, TOP1, XIAP
Ononin	$C_{22}H_{22}O_9$	486-62-4	27	ABL1, ACE, CASP3, CD274, CYP19A1, EGFR, HDAC1, HRAS, IL2, KIT, MAPK14, MGMT, MMP1, MMP2, MMP3, MMP7, MMP9, NRAS, NTRK1, PARP1, PDGFRA, PPARG, PRKCA, SRC, TNF, TOP1, TYMP
Biochanin A	$C_{16}H_{12}O_5$	491-80-5	26	ABCB1, ABCC1, ABCG2, ADRB2, BAD, BCL2, BRAF, CCND1, CHEK1, CHEK2, COMT, CYP19A1, CYP1B1, EGFR, ESR1, ESR2, HSP90AA1, IGFBP3, IL2, MCL1, NTRK1, PLAU, PPARG, RAF1, TERT, TLR9
Alexandrin	$C_{35}H_{60}O_6$	474-58-8	25	ABL1, AKT1, ALK, ALOX5, AURKA, BCL2L1, FASN, FGF2, FGFR1, FLT1, HDAC1, HSP90AA1, IGF1R, IL2, JAK2, KIT, MAPK14, MET, PDGFRA, PDGFRB, PTPN11, RET, STAT3, TYMS, VEGFA
Astraisoflavanin	$C_{23}H_{28}O_{10}$	131749-60-5	25	ABL1, BCL2L1, CASP3, CAT, CD274, CDK1, CDK2, CHEK1, ESR1, ESR2, GSTM1, HMOX1, HRAS, HSP90AA1, IGFBP3, MAPK8, MMP1, MMP7, PARP1, PIK3CA, PTGS2, SLC2A1, TOP2A, TYMP, TYMS
Betulinic acid	$C_{30}H_{48}O_3$	472-15-1	25	ACE, AR, CAT, CYP17A1, CYP19A1, EDNRA, ESR2, IKBKB, ITGB1, MDM2, MMP1, MMP2, MMP3, NOS2, PGR, PPARG, PTGS2, PTPN11, RARA, RARB, TERT, TLR9, TOP1, TOP2A, VDR
Daidzein	$C_{15}H_{10}O_4$	486-66-8	25	ABCB1, ABCC1, ABCG2, AR, BAD, BRAF, CAT, CDK6, CFTR, CYP19A1, CYP1B1, EGFR, ESR1, ESR2, HSP90AA1, IGFBP3, IL2, MCL1, NTRK1, PARP1, PLAU, PPARG, PTGS2, RAF1, TLR9
Soyasaponin I	$C_{48}H_{78}O_{18}$	51330-27-9	25	ADRB2, AR, BCL2L1, CASP3, CASP9, CAT, CYP2D6, EDNRA, ESR2, F2, GLI1, GRB2, HLA-A, HMOX1, IGF1R, IL2, ITGB1, JUN, KDR, MMP9, PARP1, SRC, STAT3, TYMS,VDR
Genistin	$C_{21}H_{20}O_{10}$	529-59-9	24	ABCB1, ABCG2, ALB, CDK2, CYP19A1, EGFR, ESR1, ESR2, HRAS, HSP90AA1, IL2, MAPK14, MGMT, MMP1, MMP2, MMP7, NRP1, PRKCA, PTGS2, SLC2A1, SRC, TNF, TOP1, TYMP

(Continued on following page)

TABLE 2 | (*Continued*) The summary of potential effective components of AR in the treatment of lung cancer.

Name	Molecular formula	CAS	Degree	Protein targets from effective components
Astragaloside II	$C_{43}H_{70}O_{15}$	84676-89-1	23	ABCB1, ADRB2, BCL2L1, CDK1, CDK2, CDK4, CTSB, CYP2D6, EGFR, F2, FGF2, HSP90AA1, KDR, LGALS3, MAPK14, MET, PPARG, PRKCA, STAT3, TOP1, TYMS, VDR,VEGFA
Isoflavanone	$C_{15}H_{12}O_2$	4737-27-3	23	ABCG2, ACE, AURKA, CASP3, CAT, CDK1, CDK2, CREBBP, CTSB, CYP19A1, DNMT3A, ELANE, EP300, ESR1, ESR2, HMOX1, MAPK14, MCL1, MPO, PGR, PIK3CA, PIK3CB, TLR9
Astragaloside III	$C_{41}H_{68}O_{14}$	84687-42-3	22	ADRB2, AKT1, AR, CAT, CDK1, CDK2, CDK4, CDK6, CYP2D6, ESR1, ESR2, FGF2, FGFR1, HSP90AA1, IL2, KDR, LGALS3, RARB, STAT3, TYMS, VDR, VEGFA
Astrasieversianin XV	$C_{46}H_{76}O_{17}$	101843-83-8	20	ADRB2, AKT1, AKT2, CDK1, CYP2D6, FGF2, FGFR1, HDAC1, HLA-A, HSP90AA1, IL2, MAPK14, MTOR, PIK3CA, PIK3CG, SLC2A1, STAT3, TOP1, TYMS, VEGFA
Hederagenin	$C_{30}H_{48}O_4$	465-99-6	20	ALOX5, AR, CYP17A1, CYP19A1, EDNRA, EDNRB, ESR1, ESR2, IL6, ITGB1, MAPK3, MDM2, MMP1, MMP2, MMP3, NOS2, PGR, PTPN11, TERT, TOP1
Syringaresinol	$C_{22}H_{26}O_8$	21453-69-0	19	ABCB1, AURKA, CDK1, CDK2, CHEK1, ERBB2, HDAC1, HDAC9, HIF1A, MCL1, MMP1, MTOR, NOS2, PCNA, PIK3CA, PIK3CB, PIK3CG, SERPINE1, TOP1
Acetylastragaloside I	$C_{47}H_{74}O_{17}$	84687-47-8	17	ABCB1, AR, BCL2L1, CAT, CDK1, CYP2D6, ESR2, FGF2, HMOX1, HSP90AA1, LGALS3, PARP1, PRKCA, STAT3, TYMS, VDR, VEGFA
Lupeol	$C_{30}H_{50}O$	545-47-1	16	ABL1, AR, BIRC5, CYP17A1, CYP19A1, ESR1, ESR2, IGF1R, JAK2, KDR, MAPK14, MDM2, MPO, PRKCA, SHH, VDR
Calycosin-7-O-β-D-glucoside	$C_{22}H_{22}O_{10}$	20633-67-4	14	ABCB1, ABL1, HRAS, HSP90AA1, IL2, MAPK14, MET, MGMT, PRKCA, SRC, TNF, TOP1, TYMP, TYMS
Rutin	$C_{27}H_{30}O_{16}$	153-18-4	14	ABCG2, ACTC1, ALOX5, AR, CAT, CYP1B1, ESR2, IL2, PARP1, PLG, PTGS2, TERT, TNF, TP53
Astragaloside I	$C_{43}H_{68}O_{16}$	84680-75-1	12	ABCB1, AR, BCL2L1, CAT, CDK1, CYP2D6, ESR2, FGF2, HMOX1, HSP90AA1, LGALS3, PARP1, PRKCA, STAT3, TYMS, VDR, VEGFA
Hirsutrin	$C_{21}H_{20}O_{12}$	482-35-9	12	ABCG2, ALOX5, CAT, CYP1B1, ESR1, IL2, PARP1, PLG, PTGS2, SRC, TERT, TNF
Lupenone	$C_{30}H_{48}O$	1617-70-5	12	AKT1, AR, CAT, CYP17A1, CYP19A1, EPHB4, HPGD, KDRMAPK14, MPO, PDGFRB, PGR
Coumarin	$C_9H_6O_2$	91-64-5	2	PARP1, TYMS

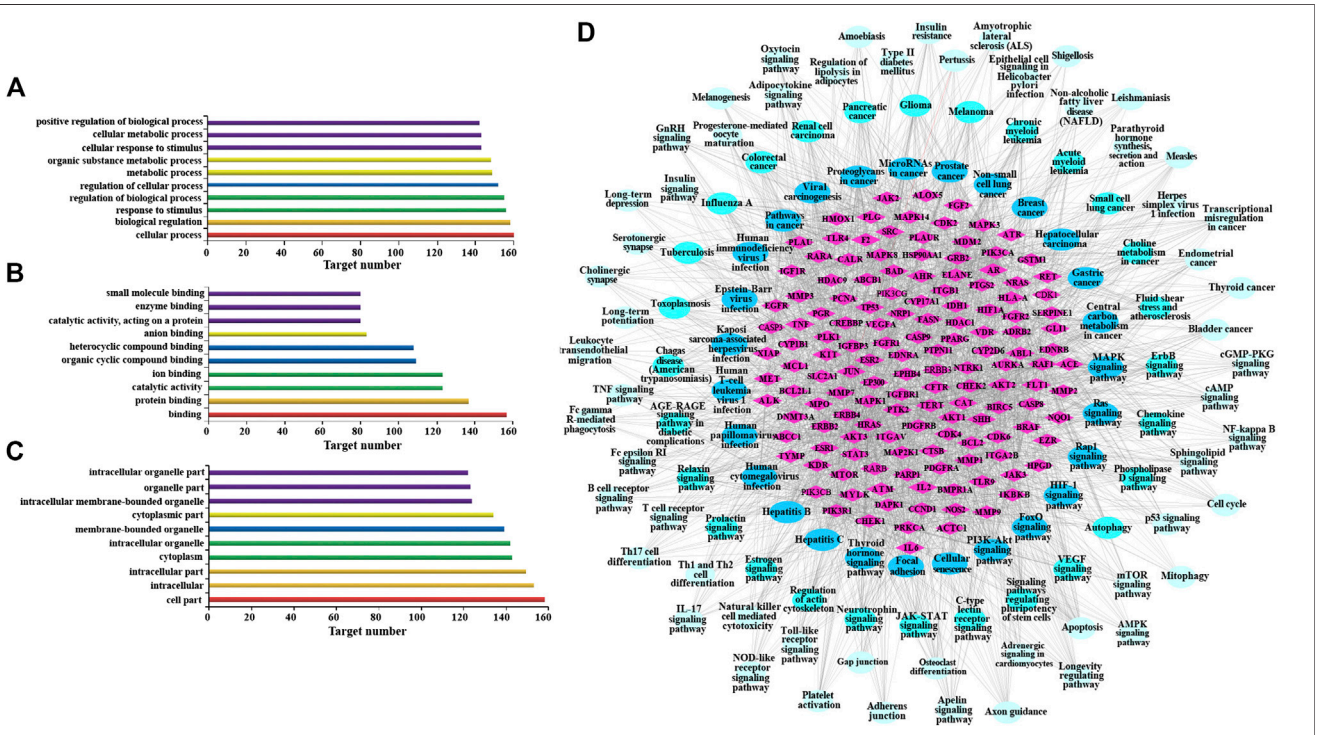

FIGURE 2 | Gene Ontology (GO) enrichment analysis and Kyoto Encyclopedia of Genes and Genomes (KEGG) analysis of AR in the treatment of lung cancer. **(A)** Go enrichment analysis of potential targets in biological process. **(B)** Go enrichment analysis of potential targets in molecular function. **(C)** Go enrichment analysis of potential targets in cell composition. **(D)** The network of potential target-signal pathway by KEGG analysis ($p \leq 0.01$). The diamond nodes represent potential targets, oval nodes represent signal pathways, and the brighter color oval nodes represent the more important the signal pathways.

TABLE 3 | Potential target-pathway enrichment of AR in the treatment of lung cancer.

Potential targets-signal pathway	Genes/ Term%	Nr. Genes	Potential target-signal pathway	Genes/ Term%	Nr. Genes
Pathways in cancer	16.04	85	Progesterone-mediated oocyte maturation	20.20	20
PI3K-Akt signaling pathway	15.25	54	Transcriptional misregulation in cancer	10.75	20
Proteoglycans in cancer	23.38	47	Endometrial cancer	34.48	20
Human papillomavirus infection	12.12	40	Bladder cancer	48.78	20
Hepatitis B	23.93	39	Sphingolipid signaling pathway	15.97	19
MicroRNAs in cancer	13.04	39	mTOR signaling pathway	12.42	19
Human cytomegalovirus infection	16.44	37	T cell receptor signaling pathway	18.81	19
Human T-cell leukemia virus 1 infection	16.89	37	Insulin signaling pathway	13.87	19
Prostate cancer	38.14	37	p53 signaling pathway	25.00	18
MAPK signaling pathway	12.20	36	Axon guidance	9.94	18
Kaposi sarcoma–associated herpesvirus infection	19.35	36	Toll-like receptor signaling pathway	17.31	18
Focal adhesion	17.59	35	Fc epsilon RI signaling pathway	26.47	18
Ras signaling pathway	14.22	33	Measles	13.64	18
Human immunodeficiency virus 1 infection	15.57	33	Cell cycle	13.71	17
Rap1 signaling pathway	14.56	30	Osteoclast differentiation	13.28	17
FoxO signaling pathway	22.73	30	Th17 cell differentiation	15.89	17
Apoptosis	22.06	30	Apelin signaling pathway	11.68	16
Cellular senescence	18.75	30	Natural killer cell mediated cytotoxicity	12.21	16
Hepatocellular carcinoma	17.86	30	Herpes simplex virus 1 infection	8.65	16
Breast cancer	19.73	29	Platelet activation	12.10	15
Gastric cancer	19.46	29	NOD-like receptor signaling pathway	8.43	15
Viral carcinogenesis	13.93	28	IL-17 signaling pathway	16.13	15
HIF-1 signaling pathway	27.00	27	B cell receptor signaling pathway	21.13	15
Thyroid hormone signaling pathway	23.28	27	Cholinergic synapse	13.39	15
Hepatitis C	17.42	27	GnRH signaling pathway	15.05	14
Epstein-Barr virus infection	13.43	27	Oxytocin signaling pathway	9.15	14
Non-small cell lung cancer	40.91	27	Insulin resistance	12.96	14
Central carbon metabolism in cancer	41.54	27	cGMP-PKG signaling pathway	7.83	13
ErbB signaling pathway	30.59	26	Longevity regulating pathway	14.61	13
Relaxin signaling pathway	20.00	26	Gap junction	14.77	13
AGE-RAGE signaling pathway in diabetic complications	26.00	26	Non-alcoholic fatty liver disease (NAFLD)	8.72	13
Colorectal cancer	30.23	26	AMPK signaling pathway	10.00	12
Pancreatic cancer	34.67	26	Longevity regulating pathway	19.35	12
Melanoma	36.11	26	Serotonergic synapse	10.43	12
Chronic myeloid leukemia	34.21	26	Adrenergic signaling in cardiomyocytes	7.59	11
Fluid shear stress and atherosclerosis	18.71	26	Adherens junction	15.28	11
JAK-STAT signaling pathway	15.43	25	Fc gamma R-mediated phagocytosis	12.09	11
Glioma	33.33	25	Leukocyte transendothelial migration	9.82	11
Neurotrophin signaling pathway	20.17	24	Melanogenesis	10.89	11
Regulation of actin cytoskeleton	11.21	24	Adipocytokine signaling pathway	15.94	11
Estrogen signaling pathway	17.39	24	Pertussis	14.47	11
Small cell lung cancer	25.81	24	Thyroid cancer	29.73	11
C-type lectin receptor signaling pathway	22.12	23	NF-kappa B signaling pathway	10.53	10
Chagas disease (American trypanosomiasis)	22.33	23	Long-term potentiation	14.93	10
Toxoplasmosis	20.35	23	Parathyroid hormone synthesis, secretion and action	9.43	10
Tuberculosis	12.85	23	Leishmaniasis	13.51	10
Influenza A	13.45	23	Amebiasis	10.42	10
Renal cell carcinoma	33.33	23	Th1 and Th2 cell differentiation	9.78	9
Chemokine signaling pathway	11.58	22	Long-term depression	15.00	9
Phospholipase D signaling pathway	14.86	22	Type II diabetes mellitus	19.57	9
Signaling pathways regulating pluripotency of stem cells	15.83	22	Amyotrophic lateral sclerosis (ALS)	17.65	9
Prolactin signaling pathway	31.43	22	Epithelial cell signaling in Helicobacter pylori infection	13.24	9
Acute myeloid leukemia	33.33	22	Mitophagy	12.31	8
Autophagy	16.41	21	Apoptosis	24.24	8
VEGF signaling pathway	35.59	21	Regulation of lipolysis in adipocytes	14.55	8
Choline metabolism in cancer	21.21	21	Shigellosis	12.31	8
cAMP signaling pathway	9.43	20	Aldosterone-regulated sodium reabsorption	16.22	6
TNF signaling pathway	18.18	20			

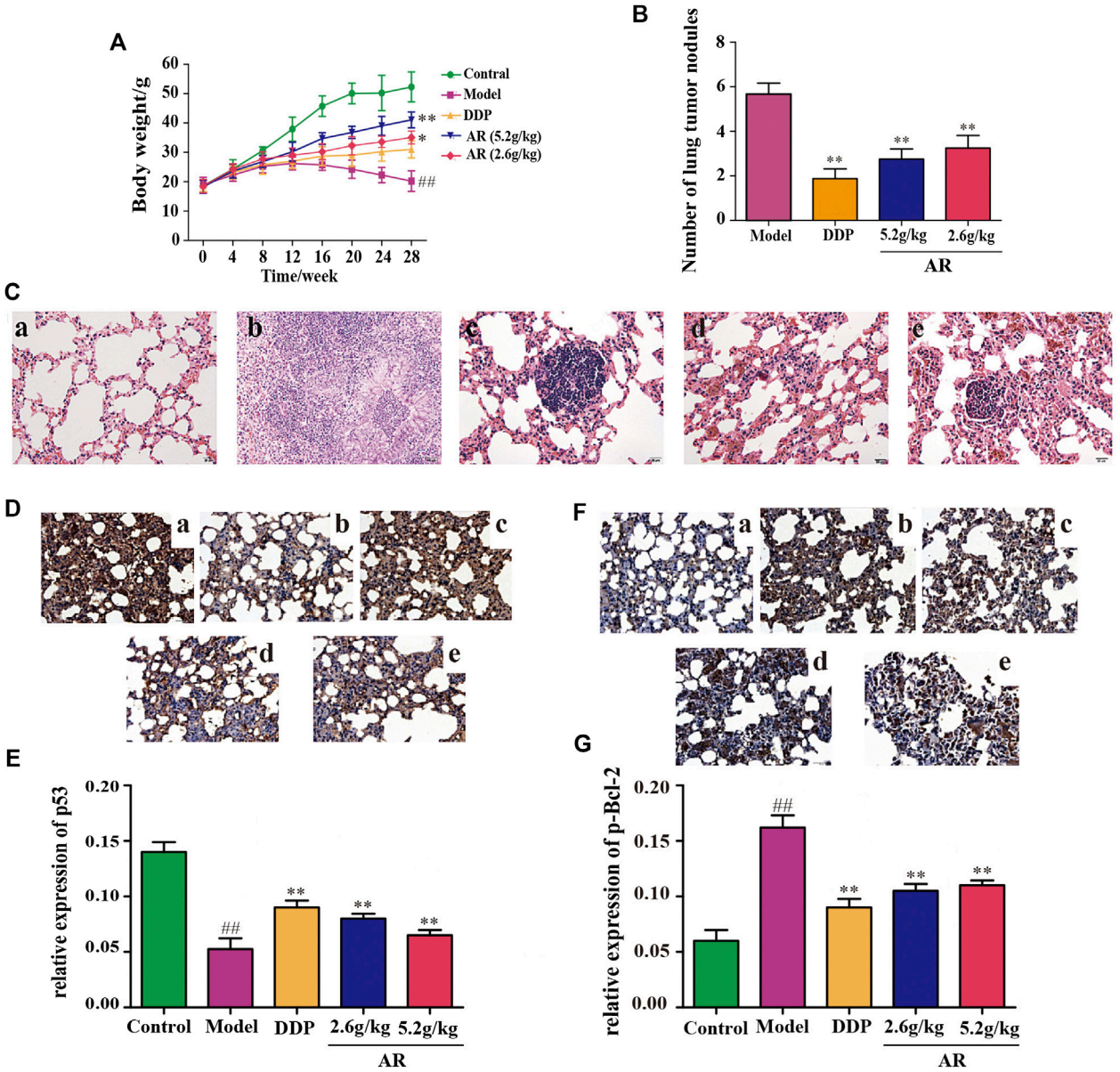

FIGURE 3 | Experimental validation of AR in the treatment of lung cancer *in vivo*. **(A)** Body weight change of A/J mice in different groups. **(B)** The number of lung tumor nodules in different groups. **(C)** The HE staining of lung from A/J mice in different groups. a, control group; b, model group; c, DDP group; d, 5.2 g/kg AR group; e, 2.6 g/kg AR group. **(D)** and **(E)** IHC staining for p53 of lung from A/J mice in different groups. a, control group; b, model group; c, DDP group; d, 5.2 g/kg AR group. e, 2.6 g/kg AR group. **(F)** and **(G)** IHC staining for p-Bcl-2 of lung from A/J mice in different groups. a, control group; b, model group; c, DDP group; d, 5.2 g/kg AR group. e, 2.6 g/kg AR group. Compared with the model group, $^{*}p < 0.05$, $^{**}p < 0.01$; compared with the control group, $\#p < 0.05$, $\#\#p < 0.01$.

Enrichment Analysis and Mechanism Prediction

Go enrichment analysis was performed on 160 potential targets, and limiting annotation was selected to homo sapiens. The top 10 terms of biological process (**Figure 2A**), molecular function (**Figure 2B**), and cell composition (**Figure 2C**) were selected. The results indicated that AR-regulated lung cancer mainly related to cellular process, biological regulation, response to stimulus, regulation of biological process, regulation of cellular process, and metabolic process, and mainly involved binding, protein binding, and catalytic activity in molecular function, and cell part, intracellular, intracellular part, cytoplasm, and intracellular organelle in cell composition.

KEGG analysis was performed using the ClueGO database in Cytoscape 3.6.1, and 115 KEGG pathways with *p*-value less than or equal to 0.01 were obtained (**Table 3**). In order to more intuitively show the relationship among potential targets and signal pathways, the potential target-signal pathway network was

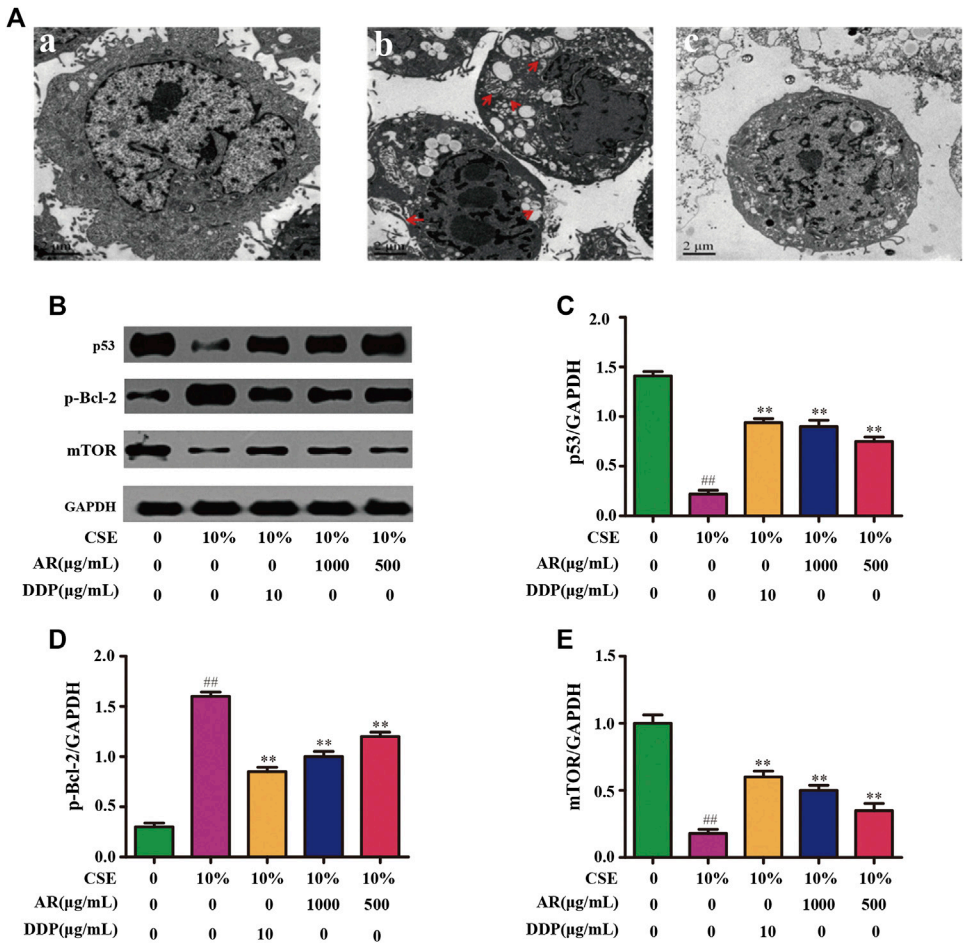

FIGURE 4 | AR on cell autophagy by transmission electron microscope and p53, p-Bcl-2, mTOR expression in NHBE by Western blot analysis. **(A)** AR on cell autophagy by transmission electron microscope. a, control group; b, model group (autophagosomes or autolysosomes were indicated by the red arrows); c, 1000 μg/ml AR group. **(B)** The protein brands of p53, p-Bcl-2, mTOR and GAPDH. **(C)** p53 expression in NHBE by western blot analysis. **(D)** p-Bcl-2 expression in NHBE by western blot analysis. **(E)** mTOR expression in NHBE by western blot analysis. Compared with the model group, $^{*}p < 0.05$, $^{**}p < 0.01$; compared with the control group, $\#p < 0.05$, $\#\#p < 0.01$.

constructed (**Figure 2D**). According to the KEGG analysis, AR in the treatment of lung cancer was related to PI3K-Akt signaling pathway, MAPK signaling pathway, Ras signaling pathway, *etc.*

Experimental Validation of AR in the Treatment of Lung Cancer *In Vivo*

Body Weight Change and Overall Appearance

The body weight changes of the animals in different groups were shown in **Figure 3A**. Compared with the control group, the body weight of mice in other four groups were decreased, and mice in model group had the smallest body weight among these four groups ($p < 0.01$). Besides, compared with the model group, the body weight of 5.2 g/kg AR group and 2.6 g/kg AR group were significantly increased ($p < 0.01$, $p < 0.05$), and the most significant effect was observed in 5.2 g/kg AR group. The appearance of all mice were observations throughout the experimental period, and the results showed that the mice in model group suffered from nose bleeding and sparse neck hair, and no obvious symptoms in other four groups were observed.

Histopathological Study

After 28 weeks, lungs were removed from the mice for analysis. Except for the control group, what were observed in the other groups showed obvious lung lesions, tumor-like proliferation, and tumor nodules. Compared with the model group, the mice by DDP, 5.2 g/kg AR, and 2.6 g/kg AR treatment were able to significantly reduce ($p < 0.01$) the number of lung tumor nodules (**Figure 3B**). The HE staining and IHC staining were used to determine the success of the lung cancer model and the therapeutic effect of AR against lung cancer. As shown in **Figure 3C**, the HE staining results showed that lung tissues of mice in the control group had the intact structure, clear alveolar outline, thin alveolar septum, and no sign of inflammation, while the lung tissues disappear in the model group had serious damage to the alveolar structure, cancerous proliferation, and fibrosis,

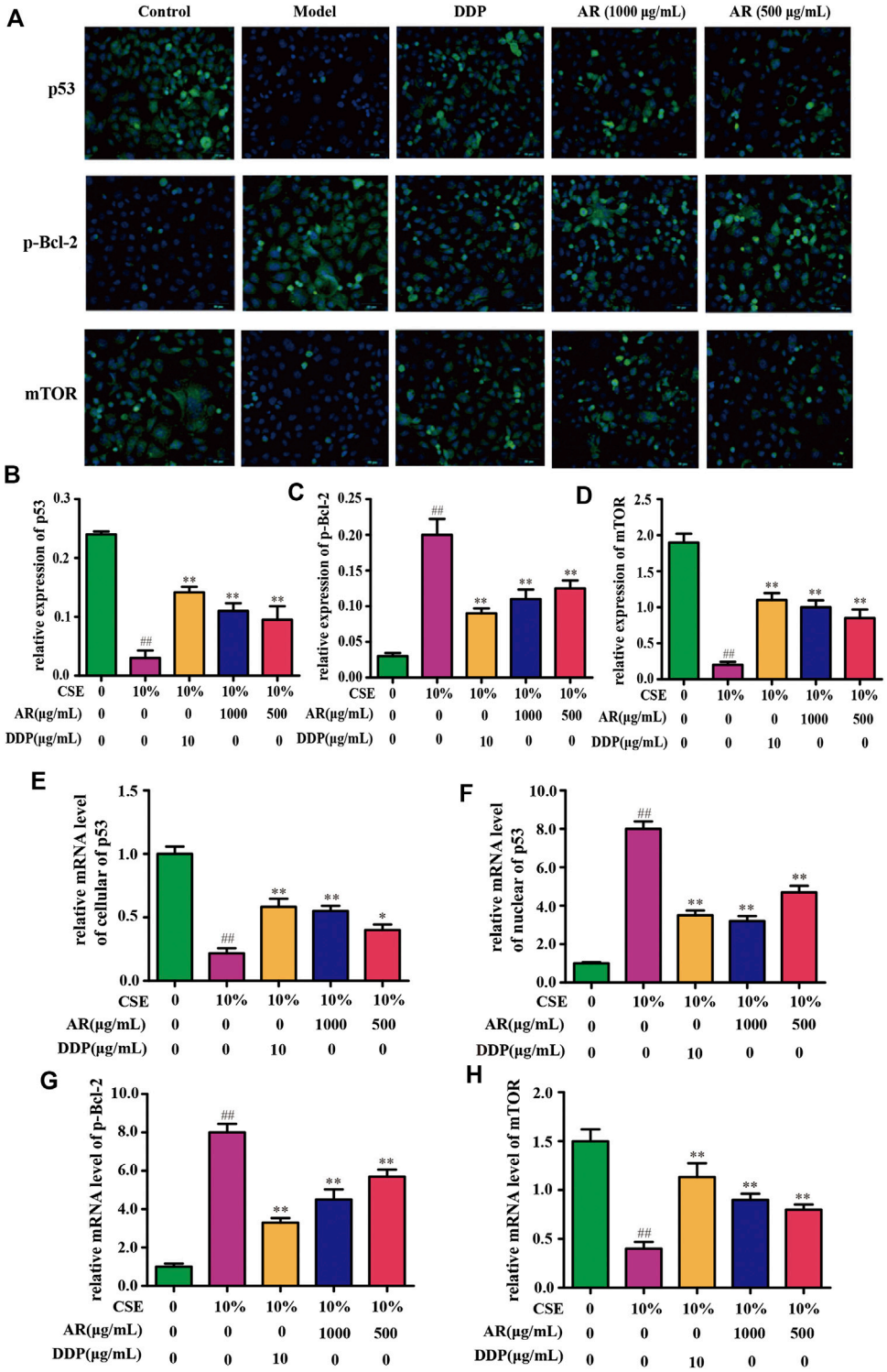

FIGURE 5 | AR on p53, p-Bcl-2, and mTOR expression in NHBE cells by immunofluorescence staining and real-time PCR technology. **(A)** Representative pictures of p53, p-Bcl-2, and mTOR immunofluorescence in different groups. **(B) (C)** and **(D)** Relative p53, p-Bcl-2, and mTOR expression in NHBE by immunofluorescence staining. **(E)** and **(F)** Relative mRNA level of cellular and nuclear p53, respectively. **(G)** and **(H)** Relative mRNA level of p-Bcl-2 and mTOR, respectively. Compared with the model group, $*p < 0.05$, $**p < 0.01$; compared with the control group, $\#p < 0.05$, $\#\#p < 0.01$.

which indicates that the lung cancer model of A/J mice was successfully constructed. In addition, the administration of DDP and AR prevented the structural changes in the lung tissue and the infiltration of inflammatory cell, and improved lung tissue integrity. In addition, the above findings also suggest the effectiveness of AR in the treatment of lung cancer. The results of IHC staining were consistent with the HE staining results. In addition, the IHC staining results indicated that compared with the control group, the p53 expression (**Figures 3D,E**) was significantly decreased ($p < 0.01$), and the p-Bcl-2 expression (**Figure 3F,G**) was significantly increased ($p < 0.01$) in the lung tissue of model group. The administration of AR could upregulate the p53 expression and downregulate the p-Bcl-2 expression in the lung tissue, which indicated that AR can reverse the expression of p53 and p-Bcl-2 in lung cancer mice.

Potential Targets and Mechanism Validation *In Vitro*

Astragali Radix Treatment Inhibited Cell Autophagy Induced by CSE

CSE was used to induce autophagy in NHBE cells. The result showed that a large number of autophagy vacuoles appeared in the cytoplasm. Besides, autophagosome fuse with lysosome to form autolysosome, which decompose and destroy the organelles and damage the normal function of cells. After treatment with AR, the number of autophagosomes and autolysosomes in the cells was significantly reduced, and the structural integrity of the cells was increased, as shown in **Figure 4A**.

Astragali Radix on p53, p-Bcl-2 and Mammalian Target of Rapamycin Expression in NHBE Cells

The potential targets, p53, p-Bcl-2, and mTOR, predicted by network pharmacology technology, were verified at the protein and gene levels. As shown in **Figures 4B,C**, compared with the model group, the p53 expression in NHBE cells was significantly increased in the 1000 μg/ml AR group and 500 μg/ml AR group ($p < 0.01$). As shown in **Figures 5A,B**, immunofluorescence staining analyses showed that 1000 μg/ml AR and 500 μg/ml AR could increase the expression of p53 ($p < 0.01$). RT-PCR results (**Figures 5E,F**) showed that the relative mRNA level of cellular p53 has been increased ($p < 0.01$) and the relative mRNA level of nuclear p53 has been decreased ($p < 0.01$) by the treatment of 1000 μg/ml AR, respectively. The above results indicated that AR could promote p53 expression, thereby inhibiting autophagy and protecting cells from autophagy.

Western blot analysis (**Figures 4B,D**) and immunofluorescence (**Figures 5A,C**) showed that p-Bcl-2 expression was significantly reduced in NHBE cells after treatment with AR ($p < 0.01$). In addition, compared with model group, the relative mRNA level of p-Bcl-2 was significantly reduced ($p < 0.01$) in 1000 μg/ml AR group and 500 μg/ml AR group (**Figure 5G**). The above results indicated that AR could reduce the phosphorylation level of Bcl-2, inhibit autophagy, and protect cells.

As shown in **Figures 4B,E**, compared with the model group, mTOR expression in NHBE cells was significantly increased in the 1000 μg/ml AR group and 500 μg/ml AR group ($p < 0.01$). RT-PCR results (**Figure 5H**) showed that the relative mRNA level of mTOR has also been increased by the treatment of 1000 μg/ml AR and 500 μg/ml AR ($p < 0.01$). Immunofluorescence staining showed increased expression of mTOR expression in AR-treated cells at the concentration of 1000 μg/ml AR and 500 μg/ml AR (**Figures 5A,D**, $p < 0.01$). mTOR is a major negative regulator of autophagy and a key protein for controlling autophagy. The above results showed that AR could increase mTOR expression and regulate cell autophagy to protect cells.

Effect of Astragali Radix on p53/AMPK/Mammalian Target of Rapamycin Signaling Pathway

According to the KEGG analysis, AR in the treatment of lung cancer was mainly related to PI3K-Akt signaling pathway. So, the expression of molecules downstream of the PI3K-Akt signaling pathway was mainly explored. Except for p53, p-Bcl-2, and mTOR (**Figures 4,5**), the expression of AMPK and Beclin1 at the protein and gene levels was also determined. As shown in **Figure 6**, compared with model group, Western blot analysis and immunofluorescence staining showed a significant reduction ($p < 0.01$) on AMPK and Beclin1 expression in NHBE cells after being treated with 1000 μg/ml AR. Besides, the relative mRNA level of AMPK and Beclin1 was significantly reduced ($p < 0.01$) in 1000 μg/ml AR group and 500 μg/ml AR group. It has been documented that p53 mediates autophagy through an AMPK/mTOR-dependent pathway (Tasdemir et al., 2008). AMPK activation leads to autophagy through negative regulation of mTOR and that many other factors involved in the autophagic process govern autophagy through AMPK/mTOR signaling (Jing et al., 2011). Based on the above research results, we speculate that AR in the treatment of lung cancer may through p53/AMPK/mTOR signaling pathway (**Figure 7**), but further validation is still required.

Screening of Effective Components by Metabolism *in vitro* of Rat Intestinal Flora and Cell Membrane–Immobilized Chromatography

The UPLC-Q-TOF-MS analysis results indicated that these components in AR have undergone different degrees of metabolic transformation under the action of intestinal flora, and the typical total ion chromatogram of blank bacterial solution and the intestinal flora incubation solution of AR (2 h) as shown in **Supplementary Figure S3**. Detailed metabolite information was listed in **Table 4**, and the metabolic pathway mainly involves oxidation, reduction, hydrolytic deglycosylation, *etc*. The results of cell membrane–immobilized chromatography are shown in **Figure 8**. The six effective components, such as calycosin-7-O-β-D-glucoside, ononin, calycosin, astragaloside IV, metabolite of astragaloside II (M5), and cycloastragenol, can bind to cell membranes (**Figure 8A**). The three components, that is, reduction product of calycosin (M9), calycosin, and formononetin, can enter into the cell through the cell membrane by passive diffusion (**Figure 8B**).

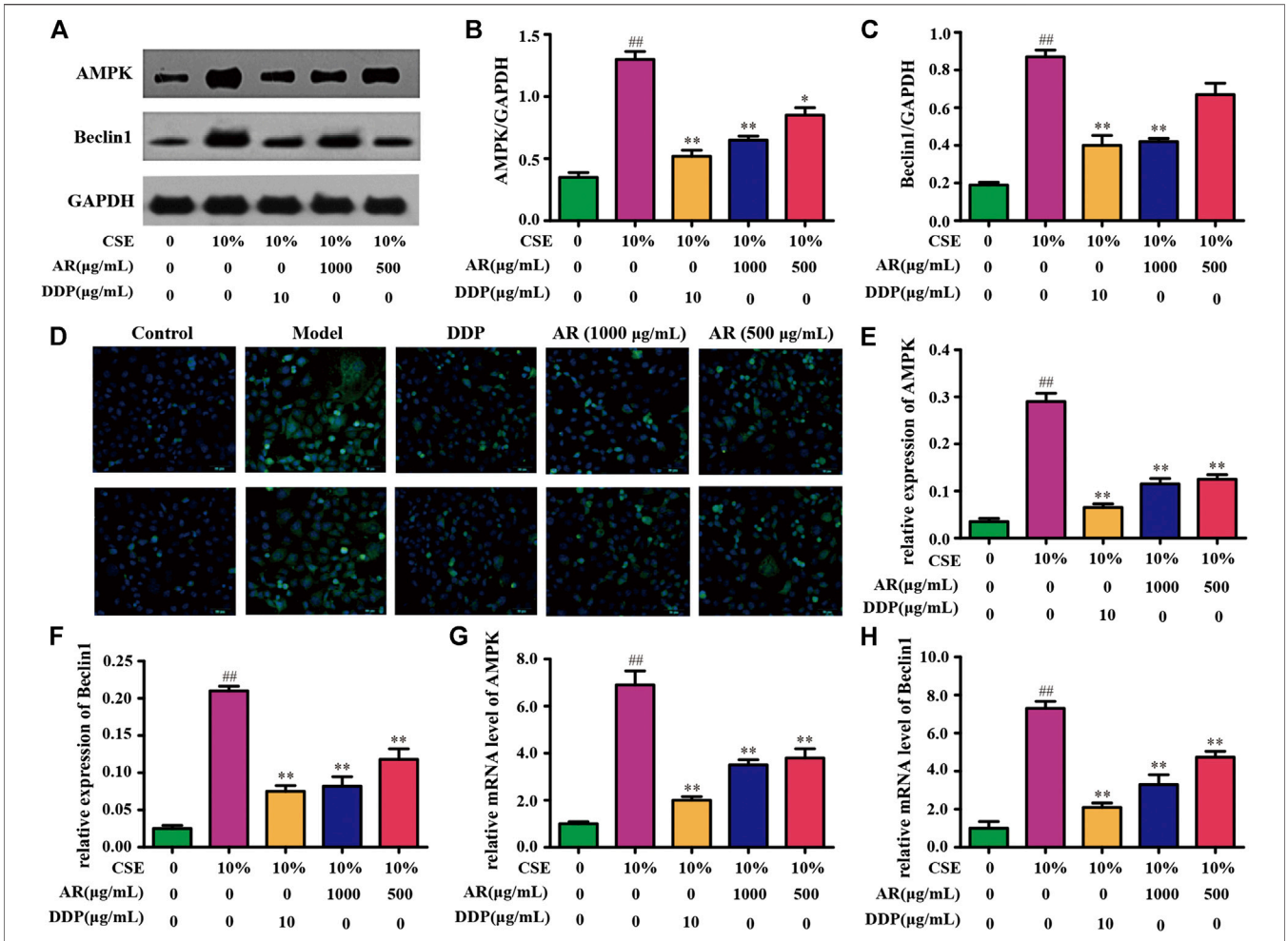

FIGURE 6 | AR on AMPK and Beclin1 expression in NHBE cells. **(A)** The protein brands of AMPK, Beclin1, and GAPDH. **(B)** and **(C)** AMPK and Beclin1 expression in NHBE by Western blot analysis. **(D)** Representative pictures of AMPK and Beclin1 immunofluorescence in different groups. **(E)** and **(F)** Relative AMPK and Beclin1 expression in NHBE by immunofluorescence. **(G)** and **(H)** Relative mRNA level of AMPK and Beclin1, respectively. Compared with the model group, $^{*}p < 0.05$, $^{**}p < 0.01$; compared with the control group, $\#p < 0.05$, $\#\#p < 0.01$.

Ultimately, these effective components, that is, calycosin-7-O-β-D-glucoside, ononin, calycosin, astragaloside IV, astragaloside II, cycloastragenol, and formononetin, together form the material basis of AR for prevention and treatment of lung cancer, and they come from the two-type components, flavone and saponin.

DISCUSSION

In this study, an integrated strategy for effective-component discovery of AR in the treatment of lung cancer was established. The results indicated that the integrated strategy can be applied to the efficiently screen effective components in complex systems. In our research on the bioactivity of AR, we found that the administered doses were high compared with single component drug. Therefore, the screening and confirmation of effective components in this article will help to reduce the dose by removing the ineffective components.

Modern pharmacological studies have shown that the activity of drugs is closely related to their cell membrane affinity and permeability. An important step in the role of TCM is the binding of effective components to cell membranes, specific enzymes, or receptors in cells. In this study, A549 cells were used as the separation carrier, AR was taken as the research object, and the specific affinity between each component in AR and cells was determined by cell membrane–immobilized chromatography. It is worth noting that the screening results show that calycosin-7-O-β-D-glucoside, ononin, calycosin, astragaloside IV, astragaloside II, cycloastragenol, and formononetin may be effective components of AR in the treatment of lung cancer, and which is consistent with the previous research results of AR in the prevention and treatment of cancer (He et al., 2013; Cheng et al., 2016; Xu et al., 2018). Through the ages, TCM have shown good efficacy in treating many and complex diseases (Sreenivasmurthy et al., 2017). The above research on the effective components of AR once again proved that the components of TCM are very complex and diverse, and

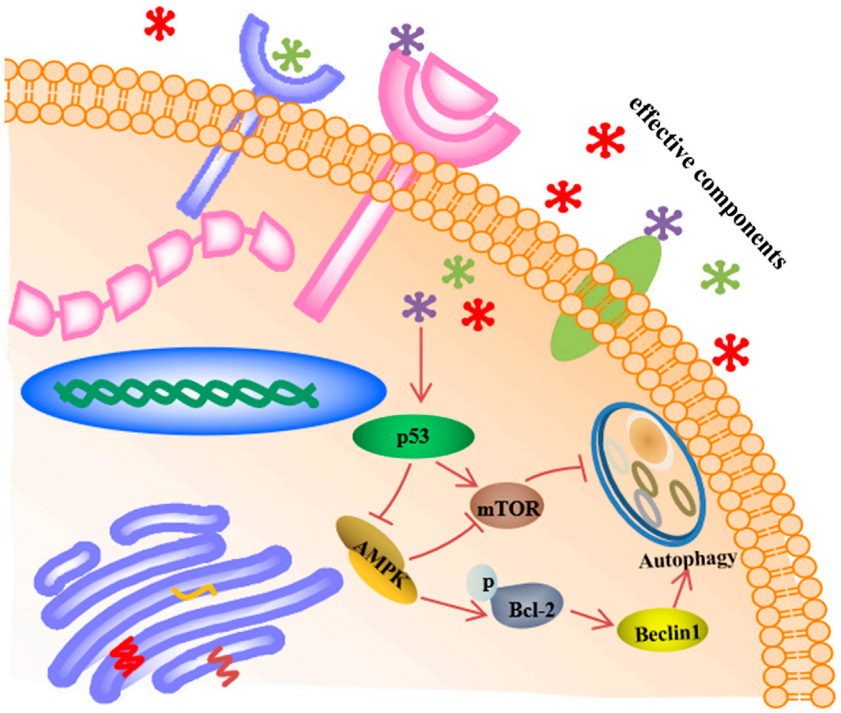

FIGURE 7 | The p53/AMPK/mTOR signaling pathway of AR in the treatment of lung cancer by preliminary prediction.

TABLE 4 | Identification of components in AR by using UPLC-ESI-Q-TOF-MS method in negative ion mode.

No.	RT (min)	Identified compounds	Element composition	Ionization	Prototype	Metabolic way
1	11.09	Astragaloside I	$C_{45}H_{72}O_{16}$	$[M+COOH]^-$	-	-
2	13.52	Astragaloside II	$C_{43}H_{70}O_{15}$	$[M+COOH]^-$	-	-
3	12.78	Astragaloside IV	$C_{41}H_{68}O_{14}$	$[M+COOH]^-$	-	-
4	9.83	Calycosin	$C_{16}H_{12}O_5$	$[M-H]^-$	-	-
5	6.04	Calycosin -7-O-β-D-glucoside	$C_{22}H_{22}O_{10}$	$[M+COOH]^-$	-	-
6	8.72	Ononin	$C_{22}H_{22}O_9$	$[M+COOH]^-$	-	-
7	13.64	M1	$C_{45}H_{68}O_{16}$	$[M-H]^-$	Astragaloside I	dehydrogenation
8	13.46	M2	$C_{36}H_{60}O_{10}$	$[M-H]^-$	Astragaloside I/Astragaloside II/Astragaloside IV	glycosylation
9	13.57	M3	$C_{39}H_{62}O_{11}$	$[M+COOH]^-$	Astragaloside I	glycosylation
10	14.97	M4	$C_{30}H_{50}O_5$	$[M+COOH]^-$	Astragaloside I/Astragaloside II/Astragaloside IV	glycosylation
11	13.89	M5	$C_{37}H_{60}O_9$	$[M+COOH]^-$	Astragaloside II	glycosylation+dehydroxylation
12	13.47	M6	$C_{35}H_{58}O_9$	$[M+COOH]^-$	Astragaloside IV	glycosylation
13	12.14	M7	$C_{16}H_{12}O_4$	$[M-H]^-$	Calycosin/Ononin	dehydroxylation
14	10.68	M8	$C_{16}H_{16}O_5$	$[M-H]^-$	Calycosin	hydrogenation+open loop
15	12.34	M9	$C_{16}H_{16}O_4$	$[M-H]^-$	Calycosin	hydrogenation+deoxidation
16	4.781	M10	$C_{22}H_{22}O_{11}$	$[M+COOH]^-$	Calycosin	hydrogenation+glucuronidation

multicomponent and multi-target may be the characteristic of TCM in treating diseases.

Autophagy has been implicated in a wide range of human diseases, including lung disorders such as lung cancer, chronic obstructive pulmonary disease, and lung infection diseases (Ryter and Choi, 2010; Ryter et al., 2012; Liu, et al., 2017; He et al., 2019). The article mainly investigated the mechanism of AR in the treatment of lung cancer from the perspective of autophagy according to the predictions of network pharmacology. The results suggested that AR may inhibit the development of lung cancer by reducing the p53 expression in the nucleus and promoting p53 expression in the cytoplasm, downregulating the level of p-Bcl-2 and promoting the autophagy inhibitory factor mTOR expression. In order to further explore the mechanism of AR in the treatment of lung cancer, except for the p53, p-Bcl-2 and mTOR, the expression of other molecules downstream of the PI3K-Akt signaling pathway was explored, including AMPK and Beclin1. Under stress, AMPK can promote the dissociation and phosphorylation of autophagy-related gene Bcl-2 (Zhou et al., 2011; He et al., 2012; Meng et al., 2015) and

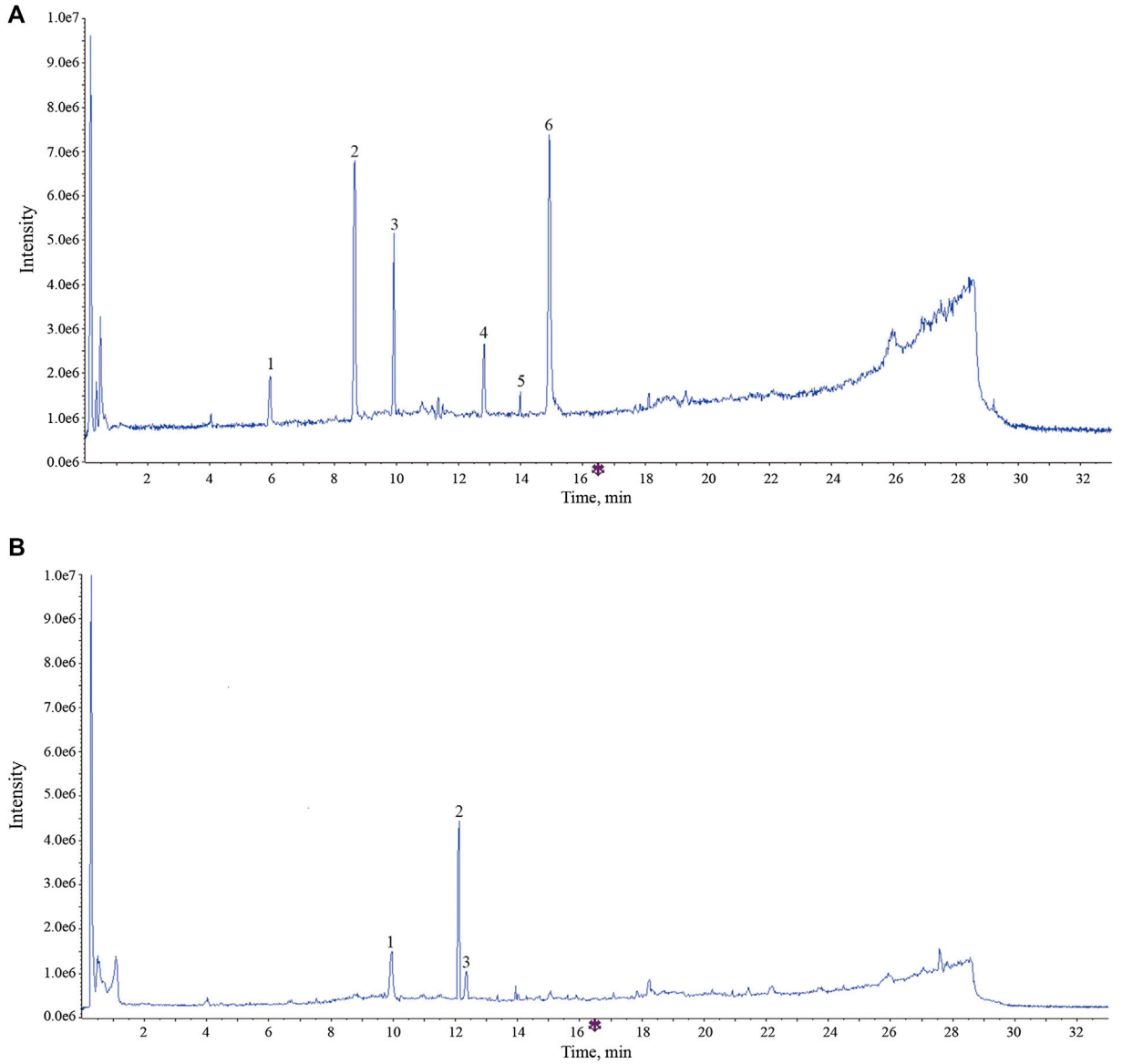

FIGURE 8 | The typical total ion chromatogram of components bound to membrane proteins and intracellular protein. **(A)** Components bound to membrane proteins. 1, calycosin -7-O-β-D-glucoside; 2, ononin; 3, calycosin; 4, astragaloside IV; 5, metabolites of astragaloside II (M5); 6, cycloastragenol. **(B)** Components bound to intracellular protein. 1, calycosin; 2, formononetin; reduction product of calycosin (M9).

inhibit mTOR expression (Chen et al., 2015; Prietodomínguez et al., 2016; Yu et al., 2017), and ultimately promote the occurrence and development of autophagy. Beclin1 is an interacting protein of Bcl-2 (He et al., 2013); binding of Bcl-2 to Beclin1 inhibits Beclin1-mediated autophagy *via* sequestration of Beclin1 away from class III PI3K; and the interaction between Bcl-2 and Beclin1 is related to mTOR kinase-dependent phosphorylation of Bcl-2 (Levine et al., 2008; Pattingre et al., 2008; Chiang et al., 2018; Xu and Qin, 2019). The preliminary research results indicated that the regulation of autophagy may be a useful strategy in the treatment of lung cancer.

In this study, an integrated strategy for effective-component discovery of AR in the treatment of lung cancer was established, which provides a valuable reference mode for finding the effective components of TCM. In addition, preliminary research results indicated that AR in the treatment of lung cancer may through p53/AMPK/mTOR signaling pathway, which laid a foundation for further in-depth study of the mechanism of AR in lung cancer. Despite some promising results were obtained in the study, there are still several potential limitations to improve. First, we have to admit that network pharmacology virtual screening has some limitations, and the predicted effective components and potential targets may need to be further comprehensively verified through a variety of different technologies. Even though the study adopts an integrated research strategy combining network analysis and

in vitro/vivo studies, it still could not avoid some false positives. Moreover, we found that the dosage of AR was very high compared with single-component drug. Therefore, it is necessary to further knock out invalid components of AR to reduce dosage. Finally, the preliminary research results indicated that AR in the treatment of lung cancer may be through p53/AMPK/mTOR signaling pathway; certainly, further experimental validation should be needed to confirm this hypothesis.

DATA AVAILABILITY STATEMENT

The original contributions presented in the study are included in the article/**Supplementary Material**, and further inquiries can be directed to the corresponding authors.

ETHICS STATEMENT

The animal study was reviewed and approved by the Animal Ethics Committee of Nanjing University of Chinese Medicine.

AUTHOR CONTRIBUTIONS

BY and LF conceived the idea of the study and prepared the manuscript. NY, YC, and MZ conducted the experiments and analyzed data. YL, ZX, and BW designed the experiments and participated in the interpretation of experimental results. LF revised the manuscript. XBJ supervised the study. All authors confirmed the final manuscript.

FUNDING

This work was financially supported by the National Key research and development program of China (2018YFC1706900) and "Double First-Class" University project of China Pharmaceutical University (CPU2018GF07; CPU2018GY11).

SUPPLEMENTARY MATERIAL

The Supplementary Material for this article can be found online at: https://www.frontiersin.org/articles/10.3389/fphar.2020.580978/full#supplementary-material.

REFERENCES

Chen, Y. C., Chen, D., Liu, S. J., Yuan, T. Y., Guo, J., Fang, L. H., et al. (2019). Systematic elucidation of the mechanism of genistein against pulmonary hypertension via network pharmacology approach. *Int. J. Mol. Sci* 20 (22), 5569. doi:10.3390/ijms20225569

Chen, Z. T., Zhao, W., Qu, S., Li, L., Lu, X., Su, F., et al. (2015). PARP-1 promotes autophagy via the AMPK/mTOR pathway in CNE-2 human nasopharyngeal carcinoma cells following ionizing radiation, while inhibition of autophagy contributes to the radiation sensitization of CNE-2 cells. *Mol. Med. Rep* 12 (2), 1868–1876. doi:10.3892/mmr.2015.3604

Cheng, H., Ge, X., Zhuo, S., Gao, Y., Zhu, B., Zhang, J., et al. (2018). β-elemene synergizes with gefitinib to inhibit stem-like phenotypes and progression of lung cancer via down-regulating EZH2. *Front. Pharmacol* 9, 1413. doi:10.3389/fphar.2018.01413

Cheng, X. D., Gu, J. F., Yuan, J. R., Feng, L., and Jia, X. B. (2016). Suppression of A549 cell proliferation and metastasis by calycosin via inhibition of the PKC-α/ERK1/2 pathway: an *in vitro* investigation. *Mol. Med. Rep* 13 (6), 3709–3710. doi:10.3892/mmr.2016.4976

Chiang, W. C., Wei, Y., Kuo, Y. C., Wei, S., Zhou, A., Zou, Z., et al. (2018). High-throughput screens to identify autophagy inducers that function by disrupting Beclin 1/Bcl-2 binding. *ACS Chem. Biol* 13 (8), 2247–2260. doi:10.1021/acschembio.8b00421

Fishilevich, S., Zimmerman, S., Kohn, A., Iny Stein, T., Olender, T., Kolker, E., et al. (2016). Genic insights from integrated human proteomics in GeneCards. *Database* 2016, baw030. doi:10.1093/database/baw030

Gfeller, D., Grosdidier, A., Wirth, M., Daina, A., Michielin, O., and Zoete, V. (2014). SwissTargetPrediction: a web server for target prediction of bioactive small molecules. *Nucleic Acids Res* 42, W32–W38. doi:10.1093/nar/gku293

Gu, S., and Lai, L. H. (2020). Associating 197 Chinese herbal medicine with drug targets and diseases using the similarity ensemble approach. *Acta Pharmacol. Sin* 41, 432–438. doi:10.1038/s41401-019-0306-9

He, C., Bassik, M. C., Moresi, V., Sun, K., Wei, Y., Zou, Z., et al. (2012). Exercise-induced BCL2-regulated autophagy is required for muscle glucose homeostasis. *Nature* 481 (7382), 511–515. doi:10.1038/nature10758

He, C., Zhu, H., Li, H., Zou, M., and Xie, Z. (2013). Dissociation of Bcl-2-Beclin1 complex by activated AMPK enhances cardiac autophagy and protects against cardiomyocyte apoptosis in diabetes. *Diabetes* 62 (4), 1270–1281. doi:10.2337/db12-0533

He, H., Zhou, X., Wang, Q., and Zhao, Y. (2013). Does the couse of astragalus-containing Chinese herbal prescriptions and radiotherapy benefit to non-small-cell lung cancer treatment: a meta-analysis of randomized trials. *Evid Based Complement Alternat Med*, 2013, 426207. doi:10.1155/2013/426207

He, Y., Liu, H., Jiang, L., Rui, B., Mei, J., and Xiao, H. (2019). miR-26 Induces apoptosis and inhibits autophagy in non-small cell lung cancer cells by suppressing TGF-β1-JNK signaling pathway. *Front. Pharmacol* 9, 1509. doi:10.3389/fphar.2018.01509

Jiang, L., Wang, W., He, Q., Wu, Y., Lu, Z., Sun, J., et al. (2017). Oleic acid induces apoptosis and autophagy in the treatment of Tongue Squamous cell carcinomas. *Sci. Rep* 7 (1), 11277. doi:10.1038/s41598-017-11842-5

Jing, K., Song, K. S., Shin, S., Kim, N., Jeong, S., Oh, H. R., et al. (2011). Docosahexaenoic acid induces autophagy through p53/AMPK/mTOR signaling and promotes apoptosis in human cancer cells harboring wild-type p53. *Autophagy* 7 (11), 1348–1358. doi:10.4161/auto.7.11.16658

Ke, B., Wu, X., Yang, Q., Huang, Y., Wang, F., Gong, Y., et al. (2019). Yi-qi-yang-yin-tian-sui-fang enhances cisplatin-induced tumor eradication and inhibits interleukin-7 reduction in non-small cell lung cancer. *Biosci. Rep* 39 (6), BSR20190052. doi:10.1042/BSR20190052

Levine, B., Sinha, S., and Kroemer, G. (2008). Bcl-2 family members: dual regulators of apoptosis and autophagy. *Autophagy* 4 (5), 600–606. doi:10.4161/auto.6260

Li, Y. H., Yu, C. Y., Li, X. X., Zhang, P., Tang, J., Yang, Q., et al. (2018). Therapeutic target database update 2018: enriched resource for facilitating bench-to-clinic research of targeted therapeutics. *Nucleic Acids Res* 46 (D1), D1121–D1127. doi:10.1093/nar/gkx1076

Liu, G., Pei, F., Yang, F., Li, L., Amin, A. D., Liu, S., et al. (2017). Role of autophagy and apoptosis in non-small-cell lung cancer. *Int. J. Mol. Sci* 18 (2), 367. doi:10.3390/ijms18020367

Lou, J. S., Yan, L., Bi, C. W., Chan, G. K., Wu, Q., Liu, Y., et al. (2016). Yu Ping Feng San reverses cisplatin-induced multi-drug resistance in lung cancer cells via regulating drug transporters and p62/TRAF6 signalling. *Sci. Rep* 6 (1), 31926. doi:10.1038/srep31926

Meng, F. Y., Ning, H., Sun, Z. X., Huang, F. F., Li, Y. C., Chu, X., et al. (2015). Ursolic acid protects hepatocytes against lipotoxicity through activating

autophagy via an AMPK pathway. *Journal of Functional Foods* 17, 172–182. doi:10.1016/j.jff.2015.05.029

Pattingre, S., Tassa, A., Qu, X., Garuti, R., Liang, X. H., Mizushima, N., et al. (2008). Bcl-2 antiapoptotic proteins inhibit Beclin 1-dependent autophagy. *Cell* 122 (6), 927–939. doi:10.1016/j.cell.2005.07.002

Prietodominguez, N., Ordonez, R., Fernandez, A., Garciapalomo, A., Muntane, J., Gonzalezgallego, J., et al. (2016). Modulation of autophagy by sorafenib: effects on treatment response. *Front. Pharmacol* 7, 151. doi:10.3389/fphar.2016.00151

Ru, J., Li, P., Wang, J., Zhou, W., Li, B., Huang, C., et al. (2014). TCMSP: a database of systems pharmacology for drug discovery from herbal medicines. *J. Cheminf* 6 (1), 13. doi:10.1186/1758-2946-6-13

Ryter, S. W., and Choi, A. M. (2010). Autophagy in the lung. *Proc. Am. Thorac. Soc* 7 (1), 13–21. doi:10.1513/pats.200909-101JS

Ryter, S. W., Nakahira, K., Haspel, J. A., and Choi, A. M. (2012). Autophagy in pulmonary diseases. *Annu. Rev. Physiol* 74 (4), 377–401. doi:10.1164/rccm.201512-2468SO. doi:10.1146/annurev-physiol-020911-153348

Sreenivasmurthy, S. G., Liu, J. Y., Song, J. X., Yang, C. B., Malampati, S., Wang, Z. Y., et al. (2017). Neurogenic traditional Chinese medicine as a promising strategy for the treatment of alzheimer's disease. *Int. J. Mol. Sci* 18 (2), 272. doi:10.3390/ijms18020272

Tasdemir, E., Maiuri, M. C., Galluzzi, L., Vitale, I., Djavaheri-Mergny, M., D'Amelio, M., et al. (2008). Regulation of autophagy by cytoplasmic p53. *Nat. Cell Biol* 10, 676–687. doi:10.1038/ncb1730

Torre, L. A., Bray, F., Siegel, R. L., Ferlay, J., Lortet-Tieulent, J., and Jemal, A. (2015). Global cancer statistics, 2012. *CA A Cancer J. Clin* 65 (2), 87–108. doi:10.3322/caac.21262

Wang, H., Zhang, W. X., Cheng, Y. T., Zhang, X. Y., Xue, N. N., Wu, G. R., et al. (2018). Design, synthesis and biological evaluation of ligustrazine-flavonoid derivatives as potential anti-tumor agents. *Molecules* 23 (9), 2187. doi:10.3390/molecules23092187

Wang, S., Xu, X., Hu, Y., Lei, T., and Liu, T. (2019). Sotetsuflavone induces autophagy in non-small cell lung cancer through blocking PI3K/Akt/mTOR signaling pathway *in vivo* and *in vitro*. *Front. Pharmacol* 10, 1460. doi:10.3389/fphar.2019.01460

Wang, X., Shen, Y., Wang, S., Li, S., Zhang, W., Liu, X., et al. (2017). PharmMapper 2017 update: a web server for potential drug target identification with a comprehensive target pharmacophore database. *Nucleic Acids Res* 45, W356–W360. doi:10.1093/nar/gkx374

Xiao, Z., Wang, C. Q., Zhou, M. H., Hu, S. S., Jiang, Y., Huang, X. R., et al. (2019). Clinical efficacy and safety of Aidi injection plus paclitaxel-based chemotherapy for advanced non-small cell lung cancer: a meta-analysis of 31 randomized controlled trials following the PRISMA guidelines. *J. Ethnopharmacol* 228, 110–122. doi:10.1016/j.jep.2018.09.024

Xu, F., Cui, W. Q., Wei, Y., Cui, J., Qiu, J., Hu, L. L., et al. (2018). Astragaloside IV inhibits lung cancer progression and metastasis by modulating macrophage polarization through AMPK signaling. *J. Exp. Clin. Canc. Res* 37 (1), 207. doi:10.1186/s13046-018-0878-0

Xu, H. D., and Qin, Z. H. (2019). Beclin 1, Bcl-2 and autophagy. *Adv. Exp. Med. Biol* 1206, 109–126. doi:10.1007/978-981-15-0602-4_5

Xu, H. Y., Zhang, Y. Q., Liu, Z. M., Chen, T., Lv, C. Y., Tang, S. H., et al. (2019). ETCM: an encyclopaedia of traditional Chinese medicine. *Nucleic Acids Res* 47 (D1), D976–D982. doi:10.1093/nar/gky987

Xue, R., Fang, Z., Zhang, M., Yi, Z., Wen, C., and Shi, T. (2012). TCMID: traditional Chinese medicine integrative database for herb molecular mechanism analysis. *Nucleic Acids Res* 41, D1089–D1095. doi:10.1093/nar/gks1100

Yu, Y., Hou, L., Song, H., Xu, P., Sun, Y., and Wu, K. (2017). Akt/AMPK/mTOR pathway was involved in the autophagy induced by vitamin E succinate in human gastric cancer SGC-7901 cells. *Mol. Cell. Biochem* 424 (1), 173–183. doi:10.1007/s11010-016-2853-4

Zhang, H. W., Hu, J. J., Fu, R. Q., Liu, X., Zhang, Y. H., Li, J., et al. (2018). Flavonoids inhibit cell proliferation and induce apoptosis and autophagy through downregulation of PI3Kγ mediated PI3K/AKT/mTOR/p70S6K/ULK signaling pathway in human breast cancer cells. *Sci. Rep* 8 (1), 11255. doi:10.1038/s41598-018-29308-7

Zhou, F., Yang, Y., and Xing, D. (2011). Bcl-2 and Bcl-xL play important roles in the crosstalk between autophagy and apoptosis. *FEBS J* 278 (3), 403–413. doi:10.1111/j.1742-4658.2010.07965.x

Zhu, X. Y., Guo, D. W., Lao, Q. C., Xu, Y. Q., Meng, Z. K., Xia, B., et al. (2019). Sensitization and synergistic anti-cancer effects of Furanodiene identified in zebrafish models. *Sci. Rep* 9 (1), 4541. doi:10.1038/s41598-019-40866-2

Conflict of Interest: The authors declare that the research was conducted in the absence of any commercial or financial relationships that could be construed as a potential conflict of interest.

Copyright © 2021 Yang, Yang, Chen, Zhu, Lian, Xiong, Wang, Feng and Jia. This is an open-access article distributed under the terms of the Creative Commons Attribution License (CC BY). The use, distribution or reproduction in other forums is permitted, provided the original author(s) and the copyright owner(s) are credited and that the original publication in this journal is cited, in accordance with accepted academic practice. No use, distribution or reproduction is permitted which does not comply with these terms.

frontiers in Pharmacology

POLICY AND PRACTICE REVIEWS
published: 14 January 2021
doi: 10.3389/fphar.2020.608703

Clinical Practice Guideline for *Tripterygium* Glycosides/*Tripterygium wilfordii* Tablets in the Treatment of Rheumatoid Arthritis

Na Lin[1], Yan-Qiong Zhang[1], Quan Jiang[2], Wei Liu[3], Jian Liu[4], Qing-Chun Huang[5], Kuan-Yu Wu[6], Sheng-Hao Tu[7], Zu-Shan Zhou[8], Wei-Heng Chen[9], Xiao-Xia Li[10], Ying Ding[11], Yong-Fei Fang[12], Jian-Ping Liu[13], Zhen-Bin Li[14], Dong-Yi He[15], Yao-Long Chen[16], Yu-Qian Lou[17], Qing-Wen Tao[18], Qing-Wen Wang[19], Ying-Hui Jin[20], Xing Liao[21], Tai-Xian Li[1] and Xiao-Yue Wang[1]*

[1]*Institute of Chinese Materia Medica, China Academy of Chinese Medical Sciences, Beijing, China,* [2]*Guang'anmen Hospital, China Academy of Chinese Medical Sciences, Beijing, China,* [3]*First Teaching Hospital of Tianjin University of Traditional Chinese Medicine, Tianjin, China,* [4]*First Affiliated Hospital of Anhui University of Traditional Chinese Medicine, Hefei, China,* [5]*Guangdong Provincial Hospital of Traditional Chinese Medicine, Guangzhou, China,* [6]*Second People's Hospital, Fujian University of Traditional Chinese Medicine, Fuzhou, China,* [7]*Tongji Hospital Affiliated to Tongji Medical School, Huazhong University of Science and Technology, Wuhan, China,* [8]*Department of Honghu, Hubei Province Hospital of Traditional Chinese Medicine, Honghu, China,* [9]*Third Affiliated Hospital of Beijing University of Chinese Medicine, Beijing, China,* [10]*Xuanwu Hospital, Capital Medical University, Beijing, China,* [11]*First Affiliated Hospital of the Henan University of Traditional Chinese Medicine, Zhengzhou, China,* [12]*Southwest Hospital, Army Medical University, Chongqing, China,* [13]*Centre for Evidence-Based Chinese Medicine, Beijing University of Chinese Medicine, Beijing, China,* [14]*Bethune International Peace Hospital, People's Liberation Army, Shijiazhuang, China,* [15]*Shanghai Guanghua Hospital of Integrated Traditional and Western Medicine, Shanghai, China,* [16]*Evidence-Based Medicine Center, School of Basic Medical Sciences, Lanzhou University, Lanzhou, China,* [17]*Henan Rheumatism Hospital, Zhengzhou, China,* [18]*China-Japan Friendship Hospital, Beijing, China,* [19]*Shenzhen Hospital, Peking University, Shenzhen, China,* [20]*Center for Evidence-Based and Translational Medicine, Zhongnan Hospital of Wuhan University, Wuhan, China,* [21]*Institute of Basic Research in Clinical Medicine, China Academy of Chinese Medical Sciences, Beijing, China*

OPEN ACCESS

Edited by:
Alejandro Urzua, University of Santiago, Chile

Reviewed by:
Xin Li, Shanghai University of Traditional Chinese Medicine, China
Chi Zhang, China Academy of Chinese Medical Sciences, China
Bin Li, Shanghai University of Traditional Chinese Medicine, China

***Correspondence:**
Na Lin
nlin@icmm.ac.cn

Specialty section:
This article was submitted to Ethnopharmacology, a section of the journal Frontiers in Pharmacology

Received: *21 September 2020*
Accepted: *16 November 2020*
Published: *14 January 2021*

Citation:
Lin N, Zhang Y-Q, Jiang Q, Liu W, Liu J, Huang Q-C, Wu K-Y, Tu S-H, Zhou Z-S, Chen W-H, Li X-X, Ding Y, Fang Y-F, Liu J-P, Li Z-B, He D-Y, Chen Y-L, Lou Y-Q, Tao Q-W, Wang Q-W, Jin Y-H, Liao X, Li T-X and Wang X-Y (2021) Clinical Practice Guideline for Tripterygium *Glycosides/* Tripterygium wilfordii *Tablets in the Treatment of Rheumatoid Arthritis. Front. Pharmacol. 11:608703. doi: 10.3389/fphar.2020.608703*

Tripterygium wilfordii Hook F (*Tw*HF) is one of the most commonly used and effective traditional Chinese herbal medicines against rheumatoid arthritis (RA). Both Tripterygium Glycoside Tablets (TGT) and *Tripterygium wilfordii* Tablets (TWT) are the representative *Tw*HF-based agents enrolled into the 2019 edition of Medicine Catalog for National Basic Medical Insurance, Injury Insurance, and Maternity Insurance. However, individual differences in TGT/TWT response across patients usually exist in the process of treating RA, implying that the clinical application of the two agents may not be standardized leading to the ineffective treatment and the risk of side effects. Growing evidence show that the bioactive constituents of *Tw*HF may often have toxicity, the package insert of TGT and TWT may not be described in detail, and the therapeutic windows of the two agents are narrow. Thus, it is an urgent task to develop a standardized clinical practice guideline for TGT and TWT in the treatment of RA. In the current study, a group of clinical experts of traditional Chinese medicine and Western medicine in the research field of rheumatism diseases, pharmacists, and methodologists of evidence-based medicine were invited to select the clinical questions, to determine the levels of the evidence and the strength of the recommendations, and to develop the recommendations and good practice points. The guideline is formed based on the combination of clinical research evidence and expert experience (evidence-based, consensus, supplemented by

experience). The clinical problems which are supported by clinical evidence may form recommendations, and the clinical problems without clinical evidence may form experts' suggestions. Both recommendations and experts' suggestions in this guideline summarized the clinical indications, usage, dosage, combined medication, and safety of TGT and TWT against RA systematically and comprehensively, which may offer a professional guidance in the context of the clinical application of the two *Tw*HF-based agents.

Keywords: *Tripterygium* glycoside tablet, *Tripterygium wilfordii* tablets, rheumatoid arthritis, clinical practice guideline, rational drug use

INTRODUCTION

Rheumatoid arthritis (RA) is a common chronic autoimmune disorder characterized by synovitis, cartilage damage, and bone erosion (Chimenti et al., 2015). The morbidity of RA is 0.19–0.41% in China. During the progression of the disease, the damage of multiple joints may lead to deformity and disability, which severely influences the patients' quality of life and eventually leads to heavy social and economic burden (Wang et al., 2015). Although various conventional disease-modifying antirheumatic drugs (DMARDs) have been extensively used for the treatment of RA worldwide, the incidence of adverse reactions due to the application of DMARDs has been over 40% (Pavy et al., 2006; Li et al., 2016; Smolen et al., 2017).

Tripterygium wilfordii Hook F (*Tw*HF) is one of the most commonly used medicines and has been widely used as an effective traditional Chinese herbal medicine against RA in China for centuries (Zhang et al., 2010). Both Tripterygium Glycoside Tablets (TGT) and *Tripterygium wilfordii* Tablets (TWT) are the representative *Tw*HF-based agents enrolled into the 2019 edition of Medicine Catalog for National Basic Medical Insurance, Injury Insurance, and Maternity Insurance. Chemically, TGT mainly contains wilforlide A, triptolide, triptonide, wilforine, triptophenolide, tripterine, *etc.* (Wang Y.D. et al., 2019). Similarly, the constituents in TWT include triptolide, tripterine, wilforlide A, wtlfordine, triptophenolide, *etc.* (Gu et al., 2015). Among them, wilforlide A, triptolide, and tripterine have been demonstrated to exert good anti-inflammatory and immune inhibitory effects (Zhu et al., 2009; Xue et al., 2010; Venkatesha et al., 2012), which make both TGT and TWT be commonly used against RA. However, individual differences in TGT/TWT response across patients usually exist in the process of treating RA, implying that the clinical application of the two agents may not be standardized leading to the ineffective treatment and the risk of side effects. Growing evidence shows that the bioactive constituents of *Tw*HF may often have toxicity, the package insert of TGT and TWT may not be described in detail, and the therapeutic windows of the two agents are narrow. Thus, it is an urgent task to develop a standardized clinical practice guideline for TGT and TWT in the treatment of RA.

With the approval and support of the Standardization Office of the Chinese Association of Chinese Medicine, in the current study, we invited a group of clinical experts of traditional Chinese medicine and Western medicine in the research field of rheumatism diseases, pharmacists, and methodologists of evidence-based medicine to select the clinical questions, to determine the levels of the evidence and the strength of the recommendations, and to develop the recommendations and good practice points (GPPs). The guideline is formed based on the combination of clinical evidence and experts' experience (evidence-based, consensus, supplemented by experience). The clinical problems which are supported by clinical evidence may form recommendations, and the clinical problems without clinical evidence may form experts' suggestions. Both recommendations and experts' suggestions in this guideline summarized the clinical indications, usage, dosage, combined medication, and safety of TGT and TWT against RA systematically and comprehensively, which may offer a professional guidance in the context of the clinical application of the two *Tw*HF-based agents (Lin et al., 2020a; Lin et al., 2020b).

METHODS

The "Clinical practice guideline for Tripterygium Glycosides/ *Tripterygium wilfordii* Tablets in the treatment of rheumatoid arthritis" was approved on June 2020 by the Standardization Office of the Chinese Association of Chinese Medicine. To develop an evidence-based and expert-approved Chinese patent medicine treatment guideline for RA, a multidisciplinary guideline development group was established. This guideline was developed according to the Manual for the clinical experts consensus of Chinese patent medicine (Fang et al., 2018). GPP (Liao and Xie, 2008) and the grading of recommendation assessment, development, and evaluation (GRADE) system (Atkins et al., 2004) were used to rate the quality of evidence and the strength of recommendations. Our clinical practice guideline was developed following a six-step plan (**Figure 1**).

Selection of Questions

According to a Delphi prioritization procedure, the following three questions were selected: 1) Whether RA patients without fertility desire may achieve beneficial effects from the treatment of TGT/TWT alone at the active disease stage; 2) whether RA patients without fertility desire may achieve beneficial effects from the treatment of TGT/TWT in combination with Chinese patent medicine at the active disease stage; 3) whether RA

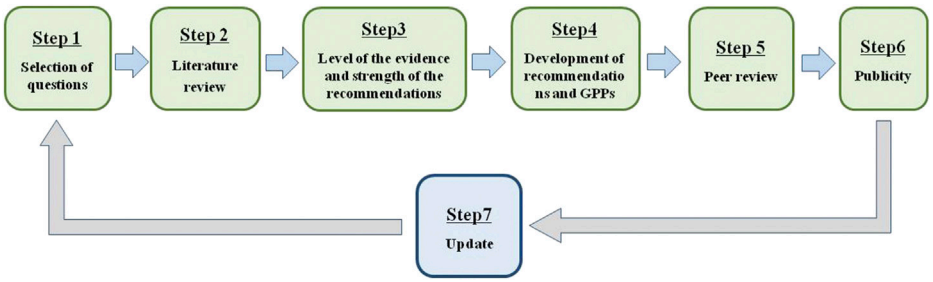

FIGURE 1 | The procedure used to develop the clinical practice guideline.

TABLE 1 | Significance of the four levels of evidence.

Quality level	Definition
High/I	We are very confident that the true effect lies close to that of the estimate of the effect
Moderate/II	We are moderately confident in the effect estimate: The true effect is likely to be close to the estimate of the effect, but there is a possibility that it is substantially different
Low/III	Our confidence in the effect estimate is limited: The true effect may be substantially different from the estimate of the effect
Very low/IV	We have very little confidence in the effect estimate: The true effect is likely to be substantially different from the estimate of effect

TABLE 2 | Significance of the four strengths of recommendations.

Strength of the recommendation	Meaning for clinicians or patients
Strong/A	The panel is highly confident of the balance between desirable and undesirable consequences; they make a strong recommendation for (desirable outweighs undesirable) or against (undesirable outweighs desirable) an intervention
Weak/B	The panel is less confident of the balance between desirable and undesirable consequences; they offer a weak recommendation

patients without fertility desire may achieve beneficial effects from the treatment of TGT/TWT in combination with Western medicine at the active disease stage.

Literature Review

Our literatures were collected from the following databases: 1) Chinese articles: China National Knowledge Infrastructure (CNKI), WanFang Data Resource, Chongqing VIP Information Database, and China BioMedical Literature Service System (SinoMed); 2) English articles: MEDLINE, Embase, and Cochrane Library. Articles published in Chinese or in English before January 2019 were selected. Literature retrieval was run using the keywords related to RA/TGT/TWT. The enrolled articles included the existing guidelines, systematic reviews, meta-analyses, RCTs, nonrandomized controlled trials, and observational studies.

Level of the Evidence and Strength of the Recommendations

The level of the evidence was evaluated according to the guideline of GRADE Working Group (Balshem et al., 2011) (**Table 1**). The evidence-based recommendations were formed based on the strength of recommendations (Andrews et al., 2013) suggested by GRADE Working Group (**Table 2**). The expert-approved GPPs were formed through two rounds of Delphi survey and the consensus development conference (Liao and Xie, 2008).

Development of Recommendations and GPPs

Eight recommendations and seven GPPs on the clinical application of TGT and TWT against RA were developed by taking real-name vote among the experts of the scientific committee and working group based on the following procedures. At first, the articles were carefully reviewed and the level of evidence offered by each article was given. Then, adverse effects, economic considerations, applicability of the recommendation to the target population of each recommendations, and GPPs were also shown in GRADE Evidence to Decision (EtD) framework. After that, GRADE EtD framework of the evidence-based recommendation was using the five-category scale (strongly disagree, disagree, uncertain, weak recommendation, and strong

recommendation). The vote of any strongly disagree, disagree, weak recommendation, strong recommendation over 50% should be deemed to reach a consensus. The vote of any side of "uncertain" over 70% should be deemed to reach a consensus, and the strength of the recommendation should be recognized as weak. GRADE EtD framework of expert-approved GPP was using the three-category scale (consensus, uncertain, and against). The vote of any side of "uncertain" over 50% should be recognized as GPP.

Peer Review

The guideline was assessed twice after the draft was completed by the guideline compiling team. For the first round of assessment, a total of 17 experts were invited to review the first draft of guideline. Following the revision, another 39 experts outside the working group were invited to review draft for the second time. After two rounds of experts' assessment and amendment, the guideline was approved by the Standardization Office of the Chinese Association of Chinese Medicine.

Publicity

The introduction and announcement of this guideline have been published on the official account of the Chinese Association of Chinese Medicine website. The guideline will be publicized in various academic conferences in the future.

Update

The working group will update guideline within three years based on new evidence of TGT and TWT administrations against RA.

DIAGNOSTIC CRITERIA

Diagnosis in Western Medicine

(1) The 1987 American College of Rheumatology (ACR) classification criteria for RA (Arnett et al., 1988).

Seven diagnostic criteria proposed by ACR are as follows: 1) morning stiffness in and around joints lasting at least 1 h before maximal improvement; 2) soft tissue swelling (arthritis) of three or more joint areas observed by a physician; 3) swelling (arthritis) of the proximal interphalangeal, metacarpophalangeal, or wrist joints; 4) symmetric swelling (arthritis); 5) rheumatoid nodules; 6) the presence of rheumatoid factor (RF); 7) radiographic erosions and/or periarticular osteopenia in hand and/or wrist joints. Criteria one through four must have been present for at least 6 weeks. RA is defined by the presence of four or more criteria, and no further qualifications (classic, definite, or probable) or list of exclusions is required.

(2) The 2010 ACR/European League Against Rheumatism (EULAR) classification criteria for RA (Aletaha et al., 2010).

The revised diagnostic criteria issued by ACR and EULAR in 2010 are as follows: 1) Target population (who should be tested?): patients 1) who have at least one joint with definite clinical synovitis (swelling); 2) with the synovitis not better explained by another disease. 2) Classification criteria for RA (score-based algorithm: add score of categories A-D; a score of 6/10 is needed for classification of a patient as having definite RA): A. Joint involvement: 1) large joint calculated as 0; 2) 2–10 large joints calculated as 1; 3) one to three small joints (with or without involvement of large joints) calculated as 2; 4) 4–10 small joints (with or without involvement of large joints) calculated as 3; 5) 10 joints (at least one small joint) calculated as five; B. Serology (at least one test result is needed for classification): 1) negative RF and negative Anti-Citrullinated Protein Antibody (ACPA) calculated as 0; 2) low-positive RF or low-positive ACPA calculated as 2; 3) high-positive RF or high-positive ACPA calculated as three; C. Acute-phase reactants (at least one test result is needed for classification): 1) normal C-reactive protein (CRP) and normal erythrocyte sedimentation rat (ESR) calculated as 0; 2) abnormal CRP or abnormal ESR calculated as one; D. Duration of symptoms: 1) <6 weeks calculated as 0; 2) ≥6 weeks calculated as 1.

Disease Activity Classification

According to Disease Activity Score with 28-joint counts (DAS28) (Anderson et al., 2012), the disease activity of RA could be classified into four stages: clinical remission is defined by DAS28 < 2.6; low/minimal stage of RA is defined by 2.6 ≤ DAS28 < 3.2; moderate stage of RA is defined by 3.2 ≤ DAS28 ≤ 5.1; high/severe stage of RA is defined by DAS28 > 5.1; active stage of RA is defined by DAS28 ≥ 2.6; reaching the target to RA treatment is defined by DAS28 < 2.6.

Diagnosis in Chinese Medicine (CM)

Those with pain and swelling of the small joints and morning stiffness as the chief complaint can be diagnosed with Wang Bi (National Administration of Traditional Chinese Medicine): 1) symmetric pain of the small joints, morning stiffness, and limited mobility are the initial performance of RA; 2) major characteristics of RA are as follows: slow onset, persistent, recurrent, and gradually angular wait; 3) with the progression of the disease, swollen joint, tenderness, and pain that worsens with activity appear gradually and eventually lead to stiffness or deformity of joints, muscular dystrophy, and rheumatoid nodules; 4) obvious changes into the presence of RF, ESR, radiographic erosions, periarticular osteopenia, subluxation and luxation of joint, joint ankylosis, and joint fusion at the active stage of RA appear.

ACTIONABLE RECOMMENDATION

The aim of the administration of both TGT and TWT is to alleviate the disease severity of RA and inflammatory reactions, as well as to slow the progression of erosive osteoclasia.

Suitable Crowd (GPP)

Both TGT and TWT are suitable for RA patients without fertility desire.

Indication (GPP)

Both TGT and TWT are suitable for RA patients at the active stage (DAS28 ≥ 2.6).

Directions (GPP)

TGT: For oral administration, the regular dose is 1 mg for every kilogram of the body weight, and the highest dose is restricted to 1.5 mg for every kilogram of the body weight, three times per day after meals.

TWT: For oral administration, the regular dose is 1–2 pills each time, three times per day after meals.

Course of the Treatment (GPP)

Routine course of the administration of both TGT and TWT is three months. After that, DAS28 should be evaluated to confirm the therapeutic effects of the drugs. If DAS28 < 2.6, the dosage of both TGT and TWT should be reduced gradually.

Combination Therapy (GPP)

If DAS28 is still more than 2.6 at the third month following the administrations of TGT or TWT, the combination therapeutics of TGT/TWT and methotrexate (MTX)/leflunomide (LEF)/total glucosides of white paeony capsules/Zhengqing Fengtongning tablet should be used for the treatment of RA.

Both TGT and TWT are suitable for RA patients with all kinds of TCM syndromes (GPP)

Both "Chinese guideline for the diagnosis and treatment of rheumatoid arthritis (2018 version)" (Chinese Rheumatology Association) and "Guidelines for diagnosis and treatment of rheumatoid arthritis based on the combination of disease and syndrome" (Jiang et al., 2018) recommend TGT and TWT as effective Chinese patent medicine against RA. According to "Guidelines for diagnosis and treatment of rheumatoid arthritis based on the combination of disease and syndrome", both TGT and TWT are suitable for RA patients with all kinds of TCM syndromes.

The single administration of TGT against RA may alleviate the inflammatory reactions (GRADE A, Level III)

A meta-analysis showed that there were four randomized controlled trials (RCTs) that demonstrated ESR and CRP to be the prognostic markers for TGT administration against RA. TGT can significantly decrease CRP and ESR in RA patients, which is similar to MTX, MD_{ESR} = −2.66, 95%CI [−8.17, 2.86], p = 0.35; MD_{CRP} = −2.38, 95%CI [−9.01, 4.24], p = 0.48 (Li et al., 2019).

The combined administration of TGT and MTX against RA may alleviate the inflammatory reactions (GRADE A, Level II)

A meta-analysis showed that there were 24 RCTs that demonstrated ESR, CRP, and RF to be the prognostic markers for the combined administration of TGT and MTX against RA. The combination of TGT with MTX can be more effective in reducing the levels of CRP, ESR, and RF than MTX alone, MD_{ESR} = 8.74, 95%CI [6.72, 10.76], p < 0.000 01; MD_{CRP} = 5.37, 95%CI [3.71, 7.03], p < 0.000 01; SMD_{RF} = 1.05, 95%CI [0.51, 1.60], p = 0.000 1 (Li et al., 2019).

The single administration of TGT against RA may alleviate the symptoms (GRADE A, Level III)

A meta-analysis showed that there were three RCTs that demonstrated swollen joint count (SJC) and tender joint count (TJC) to be the primary outcome of the administration of TGT against RA. The therapeutic effects of TGT on alleviating joint swelling and tenderness in RA patients were similar to MTX, MD_{SJC} = 0.18, 95%CI [-1.06, 1.42], p = 0.78; MD_{TJC} = -0.06, 95% CI [-1.69, 1.56], p = 0.94 (Wang, X. Y et al., 2019).

The combined administration of TGT and MTX against RA may alleviate the symptoms (GRADE A, SJC and TJC: Level II; MS: Level III)

A meta-analysis showed that there were 18 RCTs that demonstrated SJC, TJC, and morning stiffness time (MST) to be the prognostic markers of the combined administration of TGT and MTX against RA. The combination of TGT with MTX can more effective in reducing the levels of SJC, TJC, and MST than MTX alone, MDSJC = 3.01, 95%CI [2.09, 3.39], p < 0.000 01); MDTJC = 2.65, 95%CI [1.85, 3.44], p < 0.000 01; MDMST = 18.24, 95%CI [12.64, 23.84], p < 0.000 01 (Wang, X. Y et al., 2019).

The single administration of TGT against RA may achieve good clinical efficacy (GRADE B, Level III)

A meta-analysis showed that there were three RCTs that demonstrated ACR criteria to be the prognostic criteria of the administration of TGT against RA. The clinical efficacy of TGT administration against RA patients was superior to MTX, RRACR = 1.31, 95%CI [1.15, 1.49], p < 0.000 1 (Chen et al., 2020).

The combined administration of TGT and MTX against RA may achieve good clinical efficacy (GRADE A, Level III)

A meta-analysis showed that there were 10 RCTs that demonstrated ACR criteria to be the prognostic criteria of the combined administration of TGT and MTX against RA. The clinical efficacy of the combination of TGT with MTX was superior to MTX, RRACR = 1.28, 95%CI [1.20, 1.38], p < 0.000 1 (Chen et al., 2020).

The combined administration of TGT and LEF against RA may alleviate the inflammatory reaction (GRADE A, Level II)

There were five RCTs that demonstrated CRP to be the prognostic markers of the combined administration of TGT and LEF against RA. Meta-analysis results showed that the

combined administration of TGT and LEF was more effective in decreasing CRP than LEF alone, SMDCRP = 1.05, 95%CI [0.59, 1.52], $p < 0.000\ 1$ (Zhang et al., 2011; Min et al., 2013; Long and Li, 2014; Cui and Yang, 2016; Sun et al., 2016).

The single administration of TGT against RA may slow the progression of erosive osteoclasia (GRADE B, Level III)

A meta-analysis showed that there were three RCTs that demonstrated the modified Sharp score (including joint erosions, JE; and joint space narrowing, JSN) to be the prognostic marker of the administration of TGT against RA. The therapeutic effects of TGT on slowing the progression of erosive osteoclasia in RA patients were superior to MTX and salazopyridine, RRJE = -1.37, 95% CI [-3.25, 0.51], $p < 0.15$; RRJSN = -1.25, 95%CI [-2.68, 0.18], $p < 0.15$ (Zhu et al., 2019).

Toxic side effects should be monitored during the administration of both TGT and TWT (GPP)

Both the administrations of TGT and TWT may achieve good therapeutic effects in RA patients at the active stage. Because the bioactive constituents of *Tw*HF may often have toxicity, the adverse drug reactions (ADRs) occur occasionally. A meta-analysis (Li et al., 2020) showed that there were 79 studies that reported ADRs of the TGT administration against RA. Of 1,997 cases with ADRs in the experimental group, 792 (39.66%) were reported when TGT was used as the intervention. Of 1,361 cases with ADRs in the control group, 507 (37.25%) were reported when TGT was used as the intervention. The overall incidence of ADRs was 38.68% (1,299/3,358). Meta-analysis results of 49 studies with TGT as intervention in the experimental group showed that the overall incidence of ADRs was 0.23, 95%CI [0.22, 0.24], $p = 0$. ADRs mainly result in the damage of the reproductive, gastrointestinal, skin and accessories, blood, and hepatobiliary systems.

CONCLUSION

Collectively, the development of clinical practice guideline for TGT/TWT in the treatment of RA may offer a clinical decision support for healthcare professionals according to the available evidence and expert opinions, which enables optimal patient care. Furthermore, this will also identify limitations in existing research and knowledge in *Tw*HF-based therapy that will form a research agenda for future investigations.

AUTHOR CONTRIBUTIONS

All authors listed have made a substantial, direct, and intellectual contribution to the work and approved it for publication.

FUNDING

This study was supported by National Natural Science Foundation of China (81974526, 81974529, 81974537, and 81873068), Beijing Municipal Natural Science Foundation (7192139), and Fundamental Research Funds for the central public welfare research institutes (Z2017082 and ZXKT19013).

ACKNOWLEDGMENTS

This study was supported by the Standardization Office of the Chinese Association of Chinese Medicine and China Association of Traditional Chinese Medicine. The authors are grateful to Liang Liu, Xiao-ping Yan, Xiao-he Xiao, Ai-ping Lv, Shuang-cheng Ma, Zu-guang Ye, Lu-yong Zhang, Bing Zhang, Yan-ming Xie, Xiao-xin Guo, and other coworkers for their support.

REFERENCES

Aletaha, D., Neogi, T., Silman, A. J., Funovits, J., Felson, D. T., Bingham, C. O., et al. (2010). 2010 rheumatoid arthritis classification criteria : an american college of rheumatology/european league against rheumatism collaborative initiative. *Ann. Rheum. Dis.* 69, 1580–1588. doi:10.1136/ard.2010.138461

Anderson, J., Caplan, L., Yazdany, J., Robbins, M. L., Neogi, T., Michaud, K., et al. (2012). Rheumatoid arthritis disease activity measures: american college of rheumatology recommendations for use in clinical practice. *Arthritis Care Res.* 64, 640–647. doi:10.1002/acr.21649

Andrews, J., Guyatt, G., Oxman, A. D., Alderson, P., Dahm, P., Falckytter, Y., et al. (2013). Grade guidelines: 14. going from evidence to recommendations: the significance and presentation of recommendations. *J. Clin. Epidemiol.* 66, 719–725. doi:10.1016/j.jclinepi.2012.03.013

Arnett, F. C., Edworthy, S. M., Bloch, D. A., Mcshane, D. J., Fries, J. F., Cooper, N. S., et al. (1988). The American Rheumatism Assotiation 1987 revised criteria for the classification of rheumatoid arthritis. *Arthritis Rheum.* 31, 315–324. doi:10.1016/j.bmc.2012.06.050

Atkins, D., Best, D., Briss, P. A., Eccles, M., and Zaza, S. S. (2004). Grading quality of evidence and strength of recommendations. *BMJ.* 328, 1490. doi:10.1136/bmj.328.7454.1490

Balshem, H., Helfand, M., Holger, J. S., Oxman, A. D., Kunz, R., Brozek, J., et al. (2011). Grade guidelines: 3. rating the quality of evidence. *J. Clin. Epidemiol.* 64, 401–406. doi:10.1016/j.jclinepi.2010.07.015

Chen, W. J., Li, T. X., Wang, X. Y., Xue, Z. P., Lyu, C., Li, H. Z., et al. (2020). Meta-analysis of RCT studies on clinical efficacy of single administration of Tripterygium Glycosides Tablets or combined administration with methotrexate against rheumatoid arthritis. *China J. Chin. Mater. Med.* 45, 791–797. doi:10.19540/j.cnki.cjcmm.20191115.503

Chimenti, M. S., Triggianese, P., Conigliaro, P., Candi, E., Melino, G., and Perricone, R. (2015). The interplay between inflammation and metabolism in rheumatoid arthritis. *Cell Death Dis.* 6, e1887. doi:10.1038/cddis.2015.246

Chinese Rheumatology Association (2018). 2018 Chinese guideline for the diagnosis and treatment of rheumatoid arthritis. *Chin. J. Intern. Med.* 57, 242–251. doi:10.3760/cma.j.issn.0578-1426.2018.04.004

Cui, Y. X., and Yang, N. (2016). The effect of C reactive protein, interleukin-10, Soluble cell adhesion molecule 1 level of Tripterygium Glycosides Tablets combined therapy with Leflunomide to treat elderly patients with active

rheumatoid arthritis. *Chin. J. Gerontol.* 36, 4878–4880. doi:10.3969/j.issn.1005-9202.2016.19.095

Fang, S. N., Guo, Y. B., Liu, J. P., Liao, X., Zhang, X. X., Mo, M., et al. (2018). Manual for the clinical experts consensus of Chinese patent medicine. *China J. Chin. Mater. Med.* 43, 4786–4791. doi:10.19540/j.cnki.cjcmm.20181009.007

Gu, S. P., Fu, S. J., Ally, M., Xun, M. J., Sheng, Y., and He, X. (2015). Quantitative and quality evaluation research of 5 active components in triperygium wilfordii tablets. *Tianjin J. Tradit Chin. Med.* 32, 38–41. doi:10.11656/j.issn.1672-1519.2015.01.11

Jiang, Q., Wang, H. L., Gong, X., and Luo, G. C. (2018). Guidelines for diagnosis and treatment of rheumatoid arthritis based on combination of disease and syndrome. *J. Tradit. Chin. Med.* 59, 1794–1800. doi:10.13288/j.11-2166/r.2018.20.018

Li, R., Zhao, J. X., Su, Y., He, J., Chen, L. N., Gu, F., et al. (2016). High remission and low relapse with prolonged intensive DMARD therapy in rheumatoid arthritis (PRINT): a multicenter randomized clinical trial. *Medicine.* 95, e3968. doi:10.1097/MD.0000000000003968

Li, T. X., Wang, X. Y., Xue, Z. P., Lyu, C., Li, H. Z., Fan, Y. F., et al. (2019). Meta-analysis of laboratory index of Tripterygium Glycosides Tablets in treatment of rheumatoid arthritis. *China J. Chin. Mater. Med.* 44, 3542–3550. doi:10.19540/j.cnki.cjcmm.20190612.503

Li, Y. Q., Hu, R. X., Jia, K., Wang, J. X., Xu, T. T., Cui, R. Z., et al. (2020). Meta-analysis on safety of Tripterygium Glycosides Tablets in treatment of rheumatoid arthritis. *China J. Chin. Mater. Med.* 45, 775–790. doi:10.19540/j.cnki.cjcmm.20191225.501

Liao, X., and Xie, Y. M. (2008). Application of consensus methods in making clinical practice guidelines of traditional medicine. *J. Chin. Integr. Med.* 6, 555–560. doi:10.3736/jcim20080602

Lin, N., Jiang, Q., Liu, J., Huang, Q. C., Wu, K. Y., Tu, S. H., et al. (2020a). Clinical practice guideline for Tripterygium Glycosides/Tripterygium Wilfordii Tablets in treatment of rheumatoid arthritis. *Chin. J. Chin. Mater. Med.* 45, 4149–4153. doi:10.19540/j.cnki.cjcmm.20200710.501

Lin, N., Jiang, Q., Liu, J., Huang, Q. C., Wu, K. Y., Tu, S. H., et al. (2020b). Editorial explanation for Clinical practice guideline for Tripterygium Glycosides/Tripterygium wilfordii Tablets in treatment of rheumatoid arthritis. *Chin. J. Chin. Mater. Med.* 45, 4154–4157. doi:10.19540/j.cnki.cjcmm.20200709.405

Long, H., and Li, R. (2014). Tripterygium Glycosides Tablets combined therapy with Leflunomide to treat elderly active rheumatoid arthritis, 48 cases curative effect study. *Contemp. Med.* 16, 152–153. doi:10.3969/j.issn.1009-4393.2014.16.107

Min, J., Jing, Y., and Gu, Z. H. (2013). Tripterygium Glycosides Tablets combined therapy with Leflunomide to treat the elderly rheumatoid arthritis and the effect on interleukin-1, IL-1, interleukin-6, IL-6 and tumor necrosis factor-α. *Pharm. Clin. Chin. Mater. Med.* 29, 185–186.

National Administration of Traditional Chinese Medicine (1994). Standards for diagnosis and curative effect of Chinese medical symptom. Available at: http://www.360doc.com/document/17/0616/18/363181_663710983.shtml (Accessed November 6, 2018).

Pavy, S., Constantin, A., Pham, T., Gossec, l., Maillefert, J. F., Cantagrel, A., et al. (2006). Methotrexate therapy for rheumatoid arthritis: clinical practice guidelines based on published evidence and expert opinion. *Joint Bone Spine.* 73, 388–395. doi:10.1016/j.jbspin.2006.01.007

Smolen, J. S., Landewé, R., Bijlsma, J., Burmester, G., Chatzidionysiou, K., Dougados, M., et al. (2017). EULAR recommendations for the management of rheumatoid arthritis with synthetic and biological disease-modifying antirheumatic drugs: 2016 update. *Ann. Rheum. Dis.* 76, 960–977. doi:10.1136/annrheumdis-2016-211005

Sun, F. Y., Feng, H. W., Dai, L. Y., and Jiang, S. H. (2016). Curative effect observation of Tripterygium Glycosides Tablets combined therapy with Leflunomide to treat rheumatoid arthritis. *J. Med. Thor. Prac.* 29, 1059–1060. doi:10.19381/j.issn.1001-7585.2016.08.044

Venkatesha, S. H., Astry, B., Nanjundaiah, S. M., Yu, H., and Moudgil, K. D. (2012). Suppression of autoimmune arthritis by celastrus-derived celastrol through modulation of pro-inflammatory chemokines. *Bioorg. Med. Chem.* 20, 5229–5234. doi:10.1016/j.bmc.2012.06.050

Wang, G., Mu, R., and Xu, H. (2015). Management of rheumatoid arthritis in People's Republic of China–focus on tocilizumab and patient considerations. *Int. J. Gen. Med.* 8, 187–194. doi:10.2147/IJGM.S81633

Wang, X. Y., Li, T. X., Xue, Z. P., Lyu, C., Li, H. Z., Fan, Y. F., et al. (2019). Clinical symptoms effect of tripterygium glycosides tablets alone or combined with methotrexate in treatment of rheumatoid arthritis: a meta-analysis. *China J. Chin. Mater. Med.* 44, 3533–3541. doi:10.19540/j.cnki.cjcmm.20190605.501

Wang, Y. D., Wang, Q., Zhang, J. B., Dai, Z., Lin, N., Wu, X. F., et al. (2019). Research progress on chemical constituents and quality control of tripterygium wilfordii preparations. *China J. Chin. Mater. Med.* 44, 3368–3373. doi:10.19540/j.cnki.cjcmm.20190606.501

Xue, M., Jiang, Z. Z., Liu, J. P., Zhang, L. Y., Wang, T., Wang, H., et al. (2010). Comparative study on the anti-inflammatory and immune suppressive effect of wilforlide a. *Fitoterapia.* 81, 1109–1112. doi:10.1016/j.fitote.2010.07.007

Zhang, R., Wu, C. L., Li, S. F., Hou, P., and Xiao, W. G. (2011). The effect of Tripterygium Glycosides Tablets combined therapy with Leflunomide to treat elderly active rheumatoid arthritis. *Chin. J. Gerontol.* 31, 2194–2196. doi:10.3969/j.issn.1005-9202.2011.12.015

Zhang, W., Shi, Q., Zhao, L. D., Li, Y., Tang, F. L., Zhang, F. C., et al. (2010). The safety and effectiveness of a chloroform/methanol extract of tripterygium wilfordii hook f (t2) plus methotrexate in treating rheumatoid arthritis. *J. Clin. Rheumatol.* 16, 375–378. doi:10.1097/RHU.0b013e3181fe8ad1

Zhu, S. G., Han, S. C., Wang, H. Z., Yang, Y. Z., Gao, Y., and Wang, H. L. (2019). Effect of tripterygium glycosides tablets in treating rheumatoid arthritis: a systematic review and meta-analysis. *China J. Chin. Mater. Med.* 44, 3358–3364. doi:10.19540/j.cnki.cjcmm.20190305.004

Zhu, W. B., Hu, H. Y., Qiu, P. X., and Yan, G. M. (2009). Triptolide induces apoptosis in human anaplastic thyroid carcinoma cells by a p53-independent but nf-kappab-related mechanism. *Oncol. Rep.* 22, 1397. doi:10.3892/or_00000580

Conflict of Interest: The authors declare that the research was conducted in the absence of any commercial or financial relationships that could be construed as a potential conflict of interest.

Copyright © 2021 Lin, Zhang, Jiang, Liu, Liu, Huang, Wu, Tu, Zhou, Chen, Li, Ding, Fang, Liu, Li, He, Chen, Lou, Tao, Wang, Jin, Liao, Li and Wang. This is an open-access article distributed under the terms of the Creative Commons Attribution License (CC BY). The use, distribution or reproduction in other forums is permitted, provided the original author(s) and the copyright owner(s) are credited and that the original publication in this journal is cited, in accordance with accepted academic practice. No use, distribution or reproduction is permitted which does not comply with these terms.

frontiers in Pharmacology

STUDY PROTOCOL
published: 14 January 2021
doi: 10.3389/fphar.2020.571106

Effects of *Guanxinshutong* Capsules as Complementary Treatment in Patients With Chronic Heart Failure: Study Protocol for a Randomized Controlled Trial

Yu Wang[1†], Jiaping Xu[1†], Jiehong Yang[2], Ling Zhang[1], Yuanjiang Pan[3], Liping Dou[4], Peng Zhou[5], Yizhou Xu[6], Chang Li[1], Yu He[7], Huifen Zhou[1], Li Yu[1], Jingwen Chen[4], Shuwei Huang[4], Wei Fu[8]* and Haitong Wan[1]**

[1]Institute of Cardio-cerebrovascular Disease, Zhejiang Chinese Medical University, Hangzhou, China, [2]School of Basic Medicine and Public Health, Zhejiang Chinese Medical University, Hangzhou, China, [3]Department of Chemistry, Zhejiang University, Hangzhou, China, [4]Department of Cardiology, Second Affiliated Hospital of Zhejiang Chinese Medical University, Hangzhou, China, [5]Institute of Brain and Heart CO Treatment, Zhejiang Chinese Medical University, Hangzhou, China, [6]Department of Cardiology, Hangzhou First People's Hospital, Hangzhou, China, [7]School of Pharmacy, Zhejiang Chinese Medical University, Hangzhou, China, [8]Department of Cardiac-Cerebral Diseases, Yinchuan Cardiac-Cerebral Treatment Internet Hospital, Yinchuan, China

OPEN ACCESS

Edited by:
Yanqiong Zhang,
China Academy of Chinese Medical Sciences, China

Reviewed by:
Jianxin Chen,
Beijing University of Chinese Medicine, China
Xinli Li,
Nanjing Medical School, China

***Correspondence:**
Shuwei Huang
shuweih@hotmail.com
Wei Fu
fuwei@taoyiboo.com
Haitong Wan
haitongw@163.com

[†]These authors have contributed equally to this study

Specialty section:
This article was submitted to Ethnopharmacology, a section of the journal Frontiers in Pharmacology

Received: 09 June 2020
Accepted: 30 October 2020
Published: 14 January 2021

Citation:
Wang Y, Xu J, Yang J, Zhang L, Pan Y, Dou L, Zhou P, Xu Y, Li C, He Y, Zhou H, Yu L, Chen J, Huang S, Fu W and Wan H (2021) Effects of Guanxinshutong *Capsules as Complementary Treatment in Patients With Chronic Heart Failure: Study Protocol for a Randomized Controlled Trial.* Front. Pharmacol. 11:571106. doi: 10.3389/fphar.2020.571106

Chronic heart failure (CHF) is a common cardiovascular disease with high mortality and a poor prognosis, which places heavy burdens upon society and families. Traditional Chinese medicine (TCM) has been used extensively as complementary treatment for CHF. *Guanxinshutong* (GXST) capsules are used commonly for the treatment of coronary heart disease (CHD). Experimental research and small-sample clinical trials have shown that GXST can attenuate CHF. However, the effects of GXST as complementary medicine in CHF treatment lack high-quality clinical evidence. We have designed a multicenter, randomized, double-blind, placebo-controlled clinical trial that explores the efficacy and safety of using GXST compared with placebo for patients with CHF with reduced left ventricular ejection fraction (LVEF). A total of 480 participants will be assigned randomly to the GXST group or placebo group at a 2:1 ratio. GXST and placebo will be added to standard treatment for 12 weeks, and then followed up for another 40 weeks. The primary outcome is the improvement value of 6-min walk distance, and the secondary outcomes include plasma levels of N-terminal pro-B-type natriuretic peptide, New York Heart Association classification, Minnesota Living with Heart Failure Questionnaire scores, echocardiographic parameters, and clinical endpoint events. Adverse events will be monitored throughout the trial. Data will be analyzed following a predefined statistical analysis plan. This study will show the effects of the specific use of GXST in CHF patients

Abbreviations: ARNI: angiotensin receptor neprilysin inhibitor; CHF: chronic heart failure; TCM: traditional Chinese medicine; CHD: coronary heart disease; GXST: Guanxinshutong; LVEF: left ventricular ejection fraction; ACEI: angiotensin-converting enzyme inhibitor; CFDA: China Food and Drug Administration; NT-proBNP: N-terminal pro-B-type natriuretic peptide; CONSORT: Consolidated Standards of Reporting Trials; FAS, full analysis set; PPS, per protocol analysis set; NYHA: New York Heart Association; eCRF: electronic case report forms; AEs: adverse events; SAE: serious adverse events; 6MWD: 6 min walk distance; SD: standard deviation; SAP: statistical analysis plan; ITT: intention to treat.

with reduced LVEF. The Research Ethics Committee of the Second Affiliated Hospital of Zhejiang Chinese Medical University has approved this study (2019-Y-003-02). Written informed consent of patients will be required. This trial is registered in the Chinese Clinical Trial Registry (ChiCTR1900023877). Our results will be disseminated to the public through peer-reviewed journals, academic conferences, and the Internet.

Keywords: Guanxinshutong (GXST), traditional Chinese medicine (TCM), heart failure, complementary medicine, clinical trial

INTRODUCTION

Chronic heart failure (CHF) is a complex clinical syndrome characterized by reduced cardiac output, insufficient organ perfusion, and venous congestion due to cardiac dysfunction (Coronel et al., 2001; Tan et al., 2010). CHF affects about 26 million people worldwide, with more than one million people hospitalized in the USA and Europe each year (Ambrosy et al., 2014). In China, it is estimated that 4.5 million aged 35–74 years suffer from CHF, and, with an increasingly aging population, the incidence of common cardiovascular diseases, such as hypertension, coronary heart disease (CHD), and CHF, continues to rise (Guo et al., 2003; Huo et al., 2019). CHF brings a heavy economic burden to society, families, and individuals, so new therapies and prevention strategies are needed.

According to guidelines for the diagnosis and treatment of heart failure set by the Chinese government in 2018, angiotensin-converting enzyme inhibitors (ACEIs), β-receptor blockers, and aldosterone receptor antagonists are recommended as "the golden triangle treatment" for patients suffering from CHF with reduced ejection fraction (Heart Failure Group of Chinese Society of Cardiology and Editorial Board of Chinese Journal of Cardiology, 2018). Although the use of the golden triangle treatment has improved the curative effect, this treatment plan is associated with hyperkalemia, deterioration of renal function (Heart Failure Group of Chinese Society of Cardiology and Editorial Board of Chinese Journal of Cardiology, 2018), limited improvement of symptoms, and unsatisfactory improvement in long-term survival (Pitt et al., 2014; Maisel et al., 2018). In recent years, the use of angiotensin receptor neprilysin inhibitors (ARNIs) has been considered as a therapeutic strategy in heart failure (McMurray et al., 2014). The PARADIGM-HF trial provided evidence that combined inhibition of the angiotensin receptor and neprilysin is superior to inhibition of the renin–angiotensin system alone in patients with CHF (McMurray et al., 2014). However, the ARNIs (tablets of sacubitril valsartan sodium) are not widely used in China currently.

Traditional Chinese medicine (TCM) is a popular type of supplementary and complementary medicine. TCM formulations have been employed widely and successfully for CHF treatment in China for more than 2000 years. Currently, the integration of Chinese and Western medicine has shown promising benefits in controlling symptoms, reducing mortality, improving cardiac function, and promoting quality of life in patients with CHF (Xu and Xu, 2011). In TCM, all the related symptoms, signs, tongue appearances, and pulse feelings at a certain stage of disease are summarized as a syndrome ("*Zheng*" in TCM) (Jiang et al., 2012). The syndrome is not only the core of TCM theory but also the base of the definitive diagnosis and efficacious therapies (Xu and Chen, 2008). According to Cui and colleagues, the basic syndrome type of CHF is "blood stasis syndrome" (Cui et al., 2009). The symptoms of CHF with blood stasis syndrome are palpitation, pain in the chest and hypochondrium, prominent blue veins in the neck, dark and purple complexion, cyanotic lips and nails, and edema of the lower extremities combined with a purple tongue, knotted/intermittent/uneven pulses.

Guanxinshutong (GXST) capsules have been developed by Shaanxi Buchang Pharmaceutical Co., Ltd. (Shaanxi, China) and gained approval by the China Food and Drug Administration (CFDA) for CHD treatment (approval number: Z20020055) in 2002. GXST consists of five herbal medicines (**Table 1**), and promotes blood circulation, removes blood stasis, and relieves pain (Zhang et al., 2016). Experimental studies have shown that GXST can inhibit ventricular remodeling through increasing mitochondrial productivity (Zhang et al., 2015; Zhang et al., 2016), repressing the expression of matrix metalloprotein-9, angiotensin receptors-1 and extracellular regulated protein kinases-2 (Zhang et al., 2012; Zhang et al., 2013), and the transforming growth factor-β/Smad signaling pathway (Fang et al., 2019) in myocardial tissue to improve CHF. A clinical trial with 61 patients reported that, compared with conventional treatment, combination with GXST could significantly increase left ventricular ejection fraction (LVEF) and cardiac output, and reduce the end-systolic, diastolic volume in patients with acute myocardial infarction with CHF (Li, 2019). Meanwhile, in our previous clinical study, GXST exerted a therapeutic effect on CHF (unpublished data), which implied that it might be a potential Chinese-patent medicine for CHF treatment. However, the current clinical data of GXST as a complementary therapy in CHF are lack of high quality, and limited in terms of methodology and sample size. Therefore, we designed a large-scale, multicenter, double-blinded clinical trial to investigate the efficacy and safety of GXST in CHF patients with reduced LVEF. The primary hypothesis of this study is as follows: combined with routine standard treatment, GXST is superior to placebo in patients with reduced LVEF caused by CHD.

TABLE 1 | Components of GXST (intervention drug).

Scientific name	Chinese Pinyin	Latin scientific name	Parts & form used
Choerospondias axillaris (Roxb.) B. L. Burtt & A.W. Hill.	Guang Zao	*Choerospondiatis Fructus*	Dried ripe fruit
Salvia miltiorrhiza Bunge	Dan Shen	*Salvia miltiorrhiza Bunge*	Dried root and rhizome
Syzygium aromaticum (L.) Merr. & L. M. Perry.	Ding Xiang	*Caryophylli Flos*	Dried flower bud
Cinnamomum camphora (L.) J. Presl.	Bing Pian	*Borneolum Syntheticum*	Essential oil
Bambusa textilis McClure	Tian Zhu Huang	*Concretio Silicea Bambusae*	Dried mass of secretion

METHODS AND ANALYSES

Design and Settings

This study is a multicenter, prospective, randomized, double-blind, placebo-controlled, superiority trial. The trial will be conducted by 11 centers throughout China (**Table 2**), and a total of 480 participants will be recruited. After the participants have been enrolled and provided written informed consent, they will be assigned randomly to the GXST group or placebo group in a 2:1 ratio. This trial consists of a 1-week baseline period, a 12-week intervention period, and a 40-week follow-up period. A flow diagram of the study procedures is illustrated in **Figure 1**. Participants will be monitored and assessed by the investigators at each study visit. The design follows the rules for Standard Protocol Items Recommendations for Interventional Trials (Chan et al., 2013) and Consolidated Standards of Reporting Trials (CONSORT) (Schulz et al., 2010).

Recruitment

Recruitment strategies will include publishing recruitment advertisements on social media (e.g., QQ™, and We Chat™ in China, which are similar to Facebook™), online publications, and community centers. Patients who consent to participate will be examined and diagnosed by associate chief physicians to confirm their inclusion and will be registered on an online allocation system after written informed consent has been obtained.

Study Population

The inclusion criteria and exclusion criteria are shown in **Tables 3** and **4**, respectively.

Criteria for Withdrawal, Removal, Dropout, and Termination

The withdrawal criteria will be 1) exacerbation or deterioration that is clearly related to intake of the study drug; 2) an allergic reaction that is clearly associated with the study drug; 3) comorbidities, complications, adverse events (AEs), or serious adverse events (SAEs) during the trial, such as the necessity of long-term intravenous medication, repeated hospitalization for heart failure, or New York Heart Association (NYHA) class-IV symptoms; 4) the use of forbidden drugs or receipt of prohibited treatment affect the measures of efficacy and safety; 5) poor compliance by participants, or the amount of drug used does not meet the regulations (<80% or >120%); 6) participants request to withdraw from the study; 7) the blinding is uncovered or emergency unblinding is required.

TABLE 2 | Research setting.

Second Affiliated Hospital of Zhejiang Chinese Medical University
The Affiliated Hospital of Hangzhou Normal University
Pingdingshan First People's Hospital
Hangzhou First People's Hospital
Fenyang Hospital of Shanxi Province
The Affiliated Hospital of Liaoning University of Traditional Chinese Medicine
Tongxiang Traditional Chinese Medicine Hospital
Shaoxing People's Hospital
Pizhou Traditional Chinese Medicine Hospital
Lishui Central Hospital
First Affiliated Hospital of Xinxiang Medical University

Participants who fail to complete the observational period proposed in the trial, regardless of time and reasons, will be considered to be "dropout" cases. Reasons for dropout will be recorded in electronic case report forms (eCRFs), and the last data recorded will be included in data analyses. During the trial, a participant may be removed if he/she 1) is included mistakenly due to a misdiagnosis, 2) has not taken medication after study inclusion, 3) is participating in other clinical trials, and 4) has incomplete data and no evaluable records after inclusion. Another reason for removal is if the combined use of drugs has a great influence on the efficacy and safety of the study drug. Removal cases will not be included in analyses of the intention-to-treat (ITT) population.

The entire research study will be terminated if 1) there is a poor clinical effect of the test drug, and there is no need to continue the trial; 2) there are major defects in the trial; and 3) administrative authorities terminate the trial.

Randomization, Allocation Concealment Mechanism, and Blinding

Participants will be randomized to the GXST group or placebo group in a 2:1 ratio using the Central Randomization System to achieve computerized randomization in blocks of six, stratified by center. The random sequence will be retained in an envelope and sealed subsequently. According to the randomization number, a statistician will send the envelope directly to Shaanxi Buchang Pharmaceutical Co., Ltd. for labeling of the intervention drug and placebo drug. All researchers, participants, physicians, drug administrators, and dispensing nurses will be blinded to the type of treatment until the study is completed. Unblinding will be available if participants experience an SAE or need to be rescued in an emergency situation. Once unblinded, the participant will withdraw from the study. Researchers should

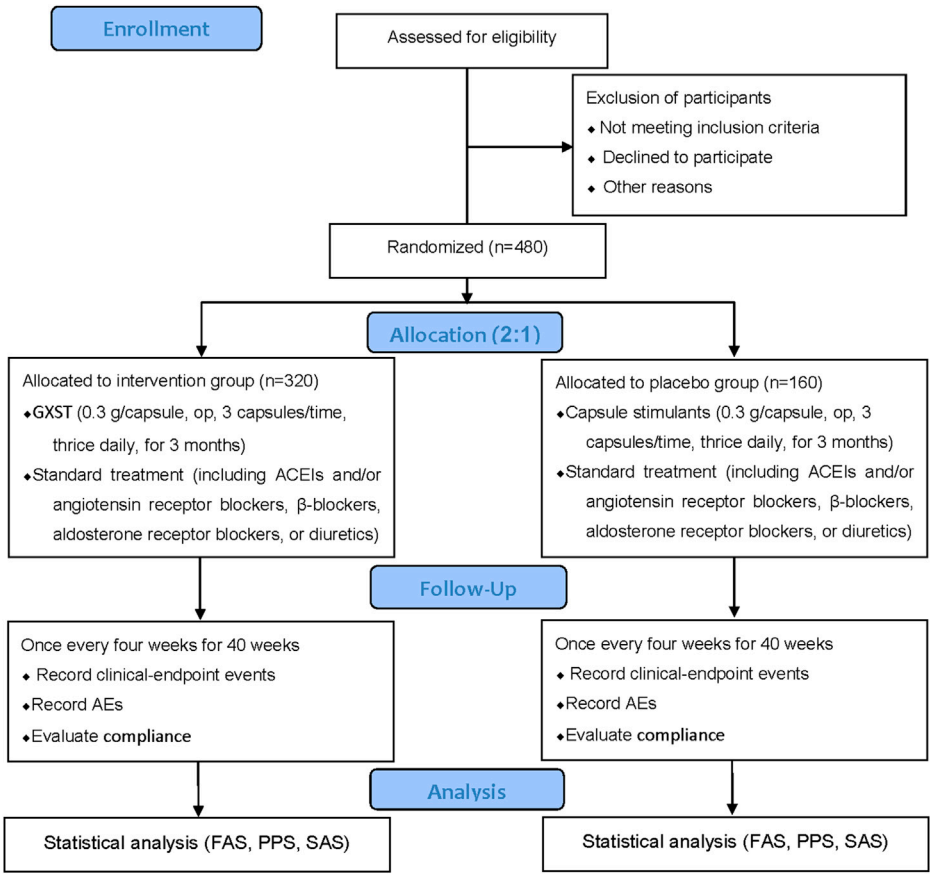

FIGURE 1 | Flowchart of the clinical trial design. The template is from the CONSORT 2010 flowchart. GXST, Guanxinshutong; ACEI, angiotensin-converting enzyme inhibitor; AEs, adverse events; FAS, full analysis set; PPS, per protocol analysis set; SAS, safety assessment set.

report the reasons to the inspector within 24 h. The precise cause of unblinding, date of the AE, the treatment situation, and the results must be recorded in eCRFs.

Interventions

Eligible participants will be allocated randomly to the GXST group or placebo group. If GXST have been used before randomized, a 2-week drug washout period should be implemented to avoid any potential complication from GXST. All participants will receive standard treatment.

The GXST group will receive GXST (batch number: 190214, 0.3 g per capsule, op, 3 capsules per time, thrice daily). The placebo group will receive capsule stimulants (batch number: 190215, 0.3 g per capsule, op, 3 capsules per time, thrice daily).

Concerning standard treatment, during the intervention period, according to the guidelines for CHF treatment (Ponikowski et al., 2016; Chinese Society of Cardiology and Chinese Medical Doctor Association, 2018), ACEIs, and/or angiotensin receptor blockers, β-blockers, aldosterone receptor blockers, or diuretics should be used. TCM formulations with a similar composition and efficacy to those of GXST will not be allowed to be used. Concomitant treatments for comorbidities (e.g., hypertension, diabetes mellitus, hyperlipidemia, and other chronic conditions) are permitted during the intervention. Researchers should record the concomitant medication truthfully and maintain dose stability during the trial.

Concerning emergency treatment, in the event of an SAE or acute exacerbation of the disease during treatment (e.g., acute heart failure and acute coronary syndrome), participants should be treated first, and the treatment status should be recorded as an AE record form and combined medication record form. If the participant's condition deteriorates during treatment and it is not advisable to continue the trial (e.g., long-term intravenous medication, repeated heart failure that necessitates hospital admission, or NYHA class-IV symptoms), one should consider terminating the trial and switching to surgery or another type of clinical treatment. Patients will be classified in the analysis as "treatment ineffective."

GXST and capsule simulants will be provided by Shaanxi Buchang Pharmaceutical Co. Ltd. The quality control of GXST is important. The method of determination of GXST components is based on the general principles of the 2018 edition of the *Chinese Pharmacopoeia*. Using gas chromatography (General Principle 0521), each GXST capsule should contain eugenol ≥2.0 mg and borneol ≥14.0 mg, and the total amount of borneol and isoborneol should be 25.5–34.5 mg. Using liquid chromatography (General Principle 0512), each GXST capsule

TABLE 3 | Inclusion criteria.

Meet all the diagnosis of CHD (Chinese Society of Cardiology and Chinese Medical Doctor Association, 2018), CHF (Ponikowski et al., 2016; Heart Failure Group of Chinese Society of Cardiology and Editorial Board of Chinese Journal of Cardiology, 2018), and TCM diagnosis of blood stasis syndrome according to the *Guidelines for Clinical Research of New TCM Drugs* (Zheng, 2002)
Aged 40–80 years, of both sexes
New York Heart Association class II–III (Hunt et al., 2005)
Left ventricular ejection fraction <50% (using two-dimensional echocardiographic Simpson's method)
Clinical findings of CHF for ≥3 months before screening
Clinically stable in the last 1 month or receiving standardized treatment for ≥1 month, and no modification of dosage or intravenous administration has been given. Standardized treatment includes ACEIs and/or angiotensin receptor blockers, β-blockers, aldosterone receptor blockers, or diuretics
Plasma level of NT-proB-type natriuretic peptide ≥125 ng/L
Volunteer, understand, and provide written informed consent

TABLE 4 | Exclusion criteria.

Acute coronary syndrome within the past 1 month
Plan to have cardiac surgery during the trial
Patients with cardiogenic shock, acute myocarditis, uncontrollable malignant arrhythmia, hypertrophic obstructive cardiomyopathy, pulmonary embolism, or severe valvular disease necessitating surgery
Uncontrolled hypertension, systolic blood pressure (SBP) ≥180 mmHg, and/or diastolic blood pressure (DBP) >110 mmHg; or SBP <90 mmHg and/or DBP <50 mmHg
Combined with severe liver or kidney dysfunction or active liver disease, and/or aspartate transaminase, alanine aminotransferase ≥3 times the upper limit of normal
Patients with diseases affecting walking ability, such as vascular disease of lower extremities
Combined with psychiatric manifestations
Patients with alcohol addiction or history of substance abuse
Females who are pregnant or lactating, preparing for pregnancy during the trial, or have a positive pregnancy test at the time of hospital admission
Have severe allergies, or allergic to research drugs and its ingredients
Patients with a history of previous or present malignancy, or precancerous lesions confirmed by pathology
Participation in other clinical studies within 3 months
Researchers estimate that the patient unable to complete the study

should contain tanshinone II-A ≥0.15 mg and salvianolic acid B ≥2.9 mg. The primary content of capsule simulants is corn starch, silica, caramel (liquid), and sunset yellow. We have added 2% GXST powder to the capsule simulants to achieve smell, color, taste, and texture comparable with that of GXST. After treatment, the package will be returned to the researchers.

OUTCOMES

Primary and Secondary Outcomes

The details of items to be measured and the time window of data collection are shown in **Table 5**. The primary outcome is the improvement in 6-min walk distance (6MWD) (Holland et al., 2014). 6MWD will be measured within 24 h after enrollment and 12 weeks after treatment to evaluate the change in exercise tolerance. Improvement will be calculated using the following formula:

Improvement in exercise tolerance = 6MWD value after treatment − 6MWD value before treatment

The secondary outcomes are 1) changes in plasma levels of N-terminal pro-B-type natriuretic peptide (NT-proBNP) (Booth et al., 2014; Roberts et al., 2015). NT-proBNP will be detected centrally by Zhejiang Chinese Medical University using a standard kit and fixed operating procedures; 2) improvement in NYHA functional class (The Criteria Committee of the New York Heart Association, 1994); 3) improvement in the Minnesota Living with Heart Failure Questionnaire score (Rector and Cohn, 1992); 4) improvement in echocardiographic measurements of left ventricular end-diastolic diameter and LVEF; 5) the incidence rate of clinical endpoint events (rehospitalization for acute aggravation of CHF, cardiogenic death, and all-cause death).

Safety Outcomes

Safety outcomes comprise vital signs (body temperature, heart rate, breathing, and blood pressure), imaging (radiographs or computed tomography), laboratory examinations (routine blood test, routine urinalysis, serum biochemistry, myocardial zymogram, and troponin test), and AEs (which will be recorded throughout the trial).

Metabolomics and Proteomics Analyses

Fifty participants per group will be selected randomly for metabolomics and proteomics analyses to explore the biomarkers of GXST for treating CHF.

Metabolomics analyses will be on blood and urine samples. Gas chromatography–mass spectrometry and liquid chromatography–mass spectrometry will be used to detect chemical and biological "fingerprints," describe the possible metabolic pathways, and identify biomarkers of GXST for CHF treatment.

Proteomics analyses will be of blood samples. Two-dimensional difference gel electrophoresis will be used to establish the proteome of each group before and after the intervention. Matrix-assisted laser desorption/ionization time-of-flight/time-of-flight mass spectrometry will be applied to identify differentially expressed proteins. Bioinformatic analyses are used to assess the biological functions of differentially expressed proteins. The Search Tool for the Retrieval of Interacting Genes/Proteins database and Ingenuity Pathway Analysis (IPA) are employed to establish a protein network affected by GXST.

Concerning the collection of blood samples, participants will fast for 10 h before each collection. Then, 5 ml of blood will be drawn and centrifuged, and serum stored in Eppendorf™ tubes at −70°C. Concerning the collection of urine samples, participants will fast for 10 h before taking the medication (and be allowed to drink water). They will fast, and water consumption will be prohibited 1 h before urine collection to 2 h after taking the medication. Water will be rationed to 200 ml/h for 2–8 h after taking the medication, and a low-fat meal can be consumed 4 h after taking the medication. Urine samples will be collected at

TABLE 5 | Study schedule.

Study phase time	Baseline period	Intervention period			Follow-up
	Visit 1	Visit 2	Visit 3	Visit 4	Every 4 weeks
	−7 to 0 days	4 weeks	8 weeks	12 weeks	Until 52 weeks
Data collection at baseline					
Informed consent	×				
Inclusion/exclusion criteria	×				
Demographic data	×				
Obtain the central random number	×				
Previous history, medical history, and allergies	×				
Comorbidities and co-medications	×				
Safety evaluation					
Vital signs	×	×	×	×	
Physical examination	×	×	×	×	
Blood routine	×			×	
Urine routine	×			×	
Blood biochemistry	×			×	
Myocardial zymogram and troponin	×			×	
ECG	×			×	
Chest radiograph or CT	×			×	
Urine pregnancy test	×			×	
Efficiency evaluation					
6MWD	×			×	
NT-proBNP	×			×	
NYHA class	×	×	×	×	
MLHFQscore	×	×	×	×	
Echocardiographic parameters	×			×	
Clinical-endpoint events		×	×	×	×
Other work					
Dispense drug	×	×	×		
Recovery and record of study drug		×	×	×	
Metabolomics and proteomics	×			×	
Record AEs		×	×	×	×
Complications due to medications		×	×	×	
Evaluate compliance		×	×	×	×

CT, computed tomography; 6MWD, 6-min walk distance; NYHA, New York Heart Association; MLHFQ, Minnesota Living with Heart Failure Questionnaire; TCM, traditional Chinese medicine; AE, adverse event.

baseline and after treatment (28 days) and stored in Eppendorf tubes at −70°C.

Collection and Management of Data

According to the requirements of Good Clinical Practice and our research plan, the investigator shall input data to eCRFs accurately, completely, normatively, and in a timely fashion based on the original observations of participants. To ensure the accuracy of the data, two personnel specializing in data entry should undertake double-entry and proofreading independently. The auditor shall monitor whether the research is conducted following the research plan, ascertain whether all eCRFs have been completed correctly and are consistent with the original data, and issue questions at any time in case of any problem. If errors and omissions are made, the researcher shall be corrected promptly.

After inspection by the auditor, eCRFs must be transmitted to the department of data management in time. In this study, data management will be carried out with an electronic data-capture system by the Department of Medical Statistics within the First Hospital of Peking University (Beijing, China). The data administrator shall adopt system-automatic and manual-logic verification to check the consistency of eCRF data and source data. For questions in the eCRFs, the data administrator will generate a question–answer form and send an inquiry to the investigator through the clinical monitor. The investigator should answer the question as soon as possible, and the data administrator will modify the data according to the investigator's answer. If necessary, a question–answer form can be issued again. After being reviewed and confirmed by the primary researcher, sponsor, statistical analyst, and data administrator, the data will be locked and submitted to the statistician for analyses.

Personal information about potential and enrolled participants will be protected confidentially throughout the trial, and researchers should maintain data secrecy for five years after termination of the trial.

Sample Size

The formula for calculating the sample size is based on the superior clinical trial sample size estimation (Wan et al., 2017). The sample size is driven by the expected improvement

in 6MWD. Referring to clinical studies (Fan and Zhang, 2012; Guo and Li, 2013; Du, 2014; Wu et al., 2015), we assumed that the improvement in 6MWD is 30 m, and the combined standard deviation (SD) is 100 m in the present study. Given a rate of type-I error of $\alpha = 0.025$, a power of 80% (rate of type-II error of $\beta = 0.2$), and, considering a possible dropout rate of 20%, 470 patients will need to be allocated. For the convenience of randomization, the final sample size was 320 cases in the intervention group and 160 cases in the placebo group, a total of 480 cases.

$$n_1 = \left[\frac{(\mu_\alpha + \mu_\beta)\sigma}{\delta}\right]^2 \frac{(1+k)}{k}, \quad n_2 = k\, n_1.$$

In this formula, k is the ratio between two sample cases, δ is the expected improvement in 6MWD, and σ is the combined SD.

Trial Completion

The trial will end once 480 patients have been randomized and all patients have completed 52 weeks of treatment and follow-up.

Statistical Analyses

The statistical analysis plan will be specified before data analyses. The statistical analyses will be undertaken *via* Statistical Analysis System v9.4 (or higher version) by the Department of Medical Statistics, Peking University First Hospital. Professional statisticians who are independent of all other processes of our study will carry out analyses. Consistent with the CONSORT statement and ITT principle, and the last observation, carried forward method will be used for missing values. Cases in the per protocol set (PPS) will be those who adhere to the protocol closely without the absence of baseline characteristics. Analyses of primary outcome and curative effect will be carried out using a full-analysis-set approach and PPS approach. The safety analysis set will include all randomized patients who have accomplished at least one study visit. Participating centers will be required to sum-up participant numbers in each center and list participants who have been removed from PPS.

For continuous variables, we will calculate the mean, SD, median, minimum, maximum, and interquartile range. For categorical variables, we will describe various frequencies or percentages. The chi-square test or Fisher's exact test will be used for categorical variables. The Student's *t*-test will be used for continuous variables with a normal distribution. For data that do not have a normal distribution, intragroup or intergroup differences before and after treatment will be analyzed by the Wilcoxon rank-sum test. The proportion of patients with AEs in two groups will be compared using the chi-square test or Fisher's exact test. Because patients who had use of ARNIs before the recruitment may constitute a specific population, we will run sensitivity analyses of the outcomes with patients used ARNIs as basic treatment, and adjusted for the effect of ARNIs. Significance will be assumed at a two-sided *p*-value less than 5%. The relative risk with corresponding 95% confidence interval to compare dichotomous variables will be calculated. **Table 6** shows the method of analysis for specific outcomes.

Adverse Events

AEs that occur during the observation period will be monitored, reported to a research assistant, causality with the intervention will be evaluated, and the severity of AEs will be analyzed. SAEs will be reported to the ethics committee within 24 h. The classification and coding of AEs are formulated concerning Common Terminology Criteria for AEs version 4.03.

Quality Control of the Intervention

To further ensure the quality of this trial, a multicenter trial coordination committee and general director will be set up for the implementation and solution of the problems related to this trial. The leaders of each center and the sponsor are the members of the coordination committee. Before each center recruits subjects, the sponsor will conduct unified preclinical trial training for all staff. Through such training, all staff (operators, investigators, physicians, data collectors, and analyzers) will fully understand the purpose and content of the trial, and standardize the process of data collection and CRF completion. This trial will be inspected by the CFDA, sponsor, and clinical research organization throughout the trial.

Trial Status

This is an ongoing trial. The first participant was recruited on September 16, 2019. This study is recruiting participants currently.

DISCUSSION

CHF continues to be a major cause of mortality, initial and recurrent hospitalizations, and suboptimal quality of life (Yao et al., 2020). Despite advances in management and treatment of CHF, many CHF patients continue to suffer from exercise intolerance and dyspnea (Simpson et al., 2015). An increasing volume of evidence demonstrates that the combination of TCM with Western medicine could be an optimal approach for achieving greater treatment efficacy in patients with CHF (Gao et al., 2017; Jia et al., 2020).

GXST is a widely used TCM formulation for the treatment of cardiovascular disease in China. Pharmacology results have shown the effects of GXST in multiple mechanism pathways to treat CHF, such as improving hemorheology (Liang et al., 2012); enhancing mitochondrial capacity, and improving myocardial energy metabolism (Zhang et al., 2015; Zhang et al., 2016); and reversing ventricular remodeling (Zhang et al., 2012; Zhang et al., 2013). However, whether GXST is efficacious in patients with CHF requires confirmation by large-sample, multicenter, randomized controlled clinical trials. Therefore, we designed a multicenter, double-blinded, placebo-controlled clinical trial with the hope of verifying the efficacy and safety of GXST for the treatment of CHF with reduced LVEF. The results could provide a strategy for combining TCM and Western medicine in CHF patients.

TABLE 6 | Outcomes and methods of analyses.

Outcome/variable	Hypothesis	Measures	Methods of analyses
Baseline balance test			
		Quantitative outcomes (age, temperature, heart rate, respiratory rate, and blood pressure)	*t*-test/Wilcoxon rank-sum test
		Qualitative outcomes (sex, marriage, and previous treatment)	Chi-squared test/Fisher's exact test/rank-sum test
Adherence at post-intervention		Percent and cases of adherence <80% and ≥80%	Chi-squared test/Fisher's exact test
Concomitant treatments		Percent and cases of concomitant treatments	Chi-squared test/Fisher's exact test
Primary outcome			
6MWD	Improvement occurred		*t*-test/Wilcoxon rank-sum test Covariance analysis
Secondary outcomes			
NT-proBNP	Improvement occurred		*t*-test/Wilcoxon rank-sum test
NYHA classification	Improvement occurred		Wilcoxon rank-sum test
MLHFQ	Improvement occurred	Questionnaire	*t*-test/Wilcoxon rank-sum test
Echocardiographic parameters	Improvement occurred	Left ventricular end-diastolic diameter and LVEF	*t*-test/Wilcoxon rank-sum test
Clinical endpoint events	Improvement occurred	Clinical-endpoint event rate	Log-rank test
Safety outcomes			
AEs, SAE		Percent and cases of AEs and SAEs	Chi-squared test/Fisher's exact test
Vital signs		Change value relative to baseline	*t*-test/Wilcoxon rank-sum test

6MWD, 6-min walk distance; NT-proBNP: N-terminal pro-B-type natriuretic peptide; NYHA, New York Heart Association; MLHFQ, Minnesota Living with Heart Failure Questionnaire; LVEF: left ventricular ejection fraction; AE, adverse event; SAE: serious adverse events.

We chose the 6MWD test to assess the functional capacity and exercise tolerance in patients with CHF. The 6MWD test is a simple and convenient test that requires no special equipment or advanced training for physicians and is well tolerated by patients. Although the plasma level of NT-proBNP is used widely in the differential diagnosis, risk stratification, and prognostic evaluation of CHF, use of ARNIs can affect the NT-proBNP level significantly (Yancy et al., 2017). Therefore, we chose the plasma level of NT-proBNP as a secondary outcome, and use sensitivity analyses to adjust the effect of ARNI on the outcomes. Furthermore, we have applied metabolomics and proteomics analyses to explore the therapeutic biomarkers of GXST in treating CHF, and to improve CHF therapy by providing an objective basis for precise treatment.

Our trial has three main limitations. First, this trial will be conducted in five provinces of China, and whether similar effects are obtainable in other regions and ethnic groups are unknown. Second, the treatment period will be 12 weeks with 40 weeks of follow-up, which is relatively short. Due to the limited time frame, the potential roles of GXST in reducing overall mortality and major vascular events over the long-term are uncertain, and further data on long-term clinical effect and safety will be needed. Third, GXST used in this trial is designed for the treatment of CHF with blood stasis syndrome, so the findings may not apply to other CHF syndromes.

Ethics and Dissemination

The Research Ethics Committee of the Second Affiliated Hospital of Zhejiang Chinese Medical University (Hangzhou, China) has approved the study protocol (2019-Y-003-02). All participating centers have received study approval from their local ethics committee. All participants will provide voluntary written informed consent after a full discussion about the potential benefits and risks before participation. This study will be published in scientific journals to target a wide range of groups, and presented at national conferences in the field of CHF. Study results will also be sent to study participants and disseminated to researchers, as well as the general public through courses, presentations, and the Internet, regardless of the magnitude or direction of influence.

ETHICS STATEMENT

The Research Ethics Committee of the Second Affiliated Hospital of Zhejiang Chinese Medical University has approved this study (No. 2019-Y-003-02). The patients/participants provided their written informed consent to participate in this study.

AUTHOR CONTRIBUTIONS

HW, SH, and FW designed the study. YW and JX contributed equally to the study, and conceptualized the study design and wrote the manuscript. LZ and JY modified the manuscript. YP, YH, and CL are responsible for the quality control of the test drug. LD, YX, JC, HZ, and LY participated in the modification of the study protocol. PZ and JY designed the method for statistical analyses. All authors read and approved the final version of the manuscript.

FUNDING

This project is supported by the National Key R&D Program of China (2017YFC1700400, 2017YFC1700403) and the National Natural Science Foundation of China (81630105).

ACKNOWLEDGMENTS

We acknowledge the help and contributions of the research assistants, cardiologists, experts, and investigators in each participating center. We thank the patients with CHF for participating in this trial. This manuscript has been released as a preprint at Research Square (www.researchsquare.com) (Wang et al., 2020).

SUPPLEMENTARY MATERIAL

The Supplementary Material for this article can be found online at: https://www.frontiersin.org/articles/10.3389/fphar.2020.571106/full#supplementary-material.

REFERENCES

Ambrosy, A. P., Fonarow, G. C., Butler, J., Chioncel, O., Greene, S. J., Vaduganathan, M., et al. (2014). The global health and economic burden of hospitalizations for heart failure: lessons learned from hospitalized heart failure registries. *J. Am. Coll. Cardiol.* 63 (12), 1123–1133. doi:10.1016/j.jacc.2013.11.053

Booth, R. A., Hill, S. A., Don-Wauchope, A., Santaguida, P. L., Oremus, M., McKelvie, R., et al. (2014). Performance of BNP and NT-proBNP for diagnosis of heart failure in primary care patients: a systematic review. *Heart Fail. Rev.* 19 (4), 439–451. doi:10.1007/s10741-014-9445-8

Chan, A., Tetzlaff, J. M., Altman, D. G., Laupacis, A., Gøtzsche, P. C., Krleža-Jerić, K., et al. (2013). SPIRIT 2013 statement: defining standard protocol items for clinical trials. *Ann. Intern. Med.* 158, 200–207. doi:10.7326/0003-4819-158-3-201302050-00583

Chinese Society of Cardiology and Chinese Medical Doctor Association (2018). Interventional cardiology, atherosclerosis and coronary heart disease group of Chinese Society of Cardiology, Thrombus prevention and treatment Committee of cardiovascular physician branch of Chinese Medical Doctor Association. Guidelines for diagnosis and treatment of stable coronary heart disease. *Chin. J. Cardiol.* 46 (9), 680–694. doi:10.3760/cma.j.issn.0253-3758.2018.09.004

Coronel, R., de Groot, J. R., and van Lieshout, J. J. (2001). Defining heart failure. *Cardiovasc. Res.* 50 (3), 419–422. doi:10.1016/S0008-6363(01)00284-X

Cui, X., Mao, J., Wang, X., Wang, H., Li, G., Liu, H., et al. (2009). Expert investigation and analysis of Traditional Chinese Medicine Syndromes of heart failure. *J. Shanghai Univ. Tradi Chin Med.* 23 (02), 31–33. doi:10.2174/138161282366170925163427

Du, X. (2014). Clinical effect of guanxinshutong capsule combined with conventional Western Medicine on patients with acute coronary syndrome. *J. Jilin Med.* 35 (34), 7653–7654. doi:10.1016/j.jacc.2014.09.017

Fan, L., and Zhang, G. (2012). Clinical observation on 45 cases of acute coronary syndrome treated by guanxinshutong capsule combined with conventional Western Medicine. *J.Tradi Chin. Med. Pharm.* 18 (11), 33–35. doi:10.3389/fphar.2020.01260

Fang, H., Liu, F., Han, N., Niu, R., Zhao, M., and Chen, Y. (2019). The study of the mechanism of guanxinshutong capsule inhibits TGF-β/Smad signal pathway and improves the isoproterenol induced cardiac remodeling in rats. *Tradi Chin. Drug Res. Clin. Pharm.* 5, 516–522. doi:10.3390/molecules23123322

Gao, K., Zhao, H., Gao, J., Wen, B., Jia, C., Wang, Z., et al. (2017). Mechanism of Chinese Medicine herbs effects on Chronic Heart Failure based on Metabolic profiling. *Front. Pharmacol.* 8, 864. doi:10.3389/fphar.2017.00864

Guo, D., Huang, G., Wu, X., Duan, X., He, J., Whelton, P. K., et al. (2003). Epidemiological survey and prevalence of heart failure in China. *Chin. J. Cardiol.* 23 (12), 868–879. doi:10.1016/j.cardfail.2017.09.014

Guo, D., and Li, P. (2013). Clinical observation of guanxinshutong capsule in the treatment of unstable angina pectoris. *Chin. J. Clinic.* 41 (12), 37–38. doi:10.1016/j.jclinepi.2020.01.020

Heart Failure Group of Chinese Society of Cardiology, Editorial Board of Chinese Journal of Cardiology. (2018). Guidelines for diagnosis and treatment of heart failure in China. *Chin. J. Cardiol.* 46(10), 760. doi:10.3760/cma.j.issn.0253-3758.2018

Holland, A. E., Spruit, M. A., Troosters, T., Puhan, M. A., Pepin, V., Saey, D., et al. (2014). An official European Respiratory Society/American Thoracic Society technical standard: field walking tests in chronic respiratory disease. *Eur. Respir. J.* 44 (6), 1428–1446. doi:10.1183/09031936.00150314

Hunt, S. A., Abraham, W. T., Chin, M. H., Feldman, A. M., Francis, G. S., Ganiats, T. G., et al. (2005). ACC/AHA 2005 Guideline update for the diagnosis and Management of Chronic Heart Failure in the adult: a report of the American College of Cardiology/American Heart Association Task Force on Practice Guidelines (Writing Committee to update the 2001 Guidelines for the evaluation and Management of Heart Failure): developed in collaboration with the American College of Chest Physicians and the International Society for Heart and lung Transplantation: endorsed by the Heart rhythm Society. *Circulation* 112 (12), e154–235. doi:10.1161/CIRCULATIONAHA.105.167586

Huo, S., Gao, R., Liu, L., Zhu, M., Wang, W., Wang, Y., et al. (2019). Summary of China cardiovascular disease report 2018. *Chin. Circul J.* 34 (03), 209–220. doi:10.11909/j.issn.1671-5411.2020.01.001

Jia, Q., Wang, L., Zhang, X., Ding, Y., Li, H., Yang, Y., et al. (2020). Prevention and treatment of chronic heart failure through traditional Chinese medicine: role of the gut microbiota. *Pharmacol. Res.* 151, 104552. doi:10.1016/j.phrs.2019.104552

Jiang, M., Zhang, C., Zheng, G., Guo, H., Li, L., Yang, J., et al. (2012). Traditional Chinese medicine zheng in the era of evidence-based medicine: a literature analysis. *Evid. Based Complem. Alternat. Med.* 2012, 409568. doi:10.1155/2012/409568

Li, F. (2019). The therapeutic effect of guanxinshutong capsule combined with clopidogrel on patients with acute myocardial infarction and heart failure. *J. Med. Theor. Pract.* 32 (08), 1150–1151. doi:10.12669/pjms.35.2.87

Liang, Z., Liu, L., Yao, T., Huo, Y., and Han, Y. (2012). Cardioprotective effects of Guanxinshutong (GXST) against myocardial ischemia/reperfusion injury in rats. *J. Geriatr. Cardiol.* 9 (2), 130–136. doi:10.3724/SP.J.1263.2011.11261

Maisel, A. S., Daniels, L. B., Anand, I. S., McCullough, P. A., and Chow, S. L. (2018). Utility of natriuretic peptides to assess and manage patients with heart failure receiving angiotensin receptor blocker/neprilysin inhibitor therapy. *Postgrad. Med.* 130 (3), 299–307. doi:10.1080/00325481.2018.1440873

McMurray, J. J., Packer, M., Desai, A. S., Gong, J., Lefkowitz, M. P., Rizkala, A. R., et al. (2014). Angiotensin-neprilysin inhibition versus enalapril in heart failure. *N. Engl. J. Med.* 371 (11), 993–1004. doi:10.1056/NEJMoa1409077

Pitt, B., Pfeffer, M. A., Assmann, S. F., Boineau, R., Anand, I. S., Claggett, B., et al. (2014). Spironolactone for heart failure with preserved ejection fraction. *N. Engl. J. Med.* 370 (15), 1383–1392. doi:10.1056/NEJMoa1313731

Ponikowski, P., Voors, A. A., Anker, S. D., Bueno, H., Cleland, J. G., Coats, A. J., et al. (2016). 2016 ESC Guidelines for the diagnosis and treatment of acute and chronic heart failure: the Task Force for the diagnosis and treatment of acute and chronic heart failure of the European Society of Cardiology (ESC) Developed with the special contribution of the Heart Failure Association (HFA) of the ESC. *Eur. Heart J.* 37, 2129–2200. doi:10.1093/eurheartj/ehw128

Rector, T. S., and Cohn, J. N. (1992). Assessment of patient outcome with the minnesota living with heart failure questionnaire: reliability and validity during a randomized, double-blind, placebo-controlled trial of pimobendan.

Pimobendan multicenter research group. *Am. Heart J.* 124 (4), 1017–1025. doi:10.1016/0002-8703(92)90986-6

Roberts, E., Ludman, A. J., Dworzynski, K., Al-Mohammad, A., Cowie, M. R., McMurray, J. J., et al. (2015). The diagnostic accuracy of the natriuretic peptides in heart failure: systematic review and diagnostic meta-analysis in the acute care setting. *BMJ.* 350, h910. doi:10.1136/bmj.h910

Schulz, K. F., Altman, D. G., and Moher, D. (2010). CONSORT 2010 statement: updated guidelines for reporting parallel group randomised trials. *PLoS Med.* 7, e1000251–2. doi:10.1371/journal.pmed.1000251

Simpson, J., Jhund, P. S., Silva Cardoso, J., Martinez, F., Mosterd, A., Ramires, F., et al. (2015). Comparing LCZ696 with enalapril according to baseline risk using the MAGGIC and EMPHASIS-HF risk scores: an analysis of mortality and morbidity in PARADIGM-HF. *J. Am. Coll. Cardiol.* 66 (19), 2059–2071. doi:10.1016/j.jacc.2015.08.878

Tan, L. B., Williams, S. G., Tan, D. K., and Cohen-Solal, A. (2010). So many definitions of heart failure: Are they all universally valid? A critical appraisal. *Expert Rev. Cardiovasc Ther.* 8 (2), 217. doi:10.1586/erc.09.187

The Criteria Committee of the New York Heart Association (1994). *Nomenclature and criteria for diagnosis of diseases of the heart and great vessels*. 9th Edn. Boston: MassLittle, Brown and Co.

Wan, X., Zhang, L., and Liu, J. (2017). Estimation of sample size in clinical studies: (1) clinical trials. *J. Tradit. Chin. Med.* 48, 504–507. doi:10.3390/molecules25225319

Wang, Y., Xu, J. P., Yang, J. H., Zhang, L., Pan, Y. J., Dou, L. P., et al. (2020). Efficacy and safety of Chinese herbal medicine Guanxinshutong capsule for the treatment of chronic heart failure with ejection fraction decrease (<50%) caused by coronary heart disease: study protocol for a randomized controlled trial, *PREPRINT (Version 1) available at Research Square*. doi:10.21203/rs.2.22735/v1

Wu, Z., Huang, X., and Chen, J. (2015). Clinical observation of Guanxinshutong capsules combined with Western Medicine in the treatment of angina pectoris of coronary heart disease. *J. New Chin Med.* 47 (01), 43–44. doi:10.1186/s12906-015-0586-7

Xu, B., and Xu, X. (2011). Clinical research progress of chronic heart failure treated by traditional Chinese Medicine. *Clin J. Chin Med.* 3 (23), 27–28. doi:10.7150/ijms.5779

Xu, H., and Chen, K. (2008). Integrative medicine: the experience from china. *J. Altern. Compl. Med.* 14 (1), 3–7. doi:10.1089/acm.2006.6329

Yancy, C. W., Jessup, M., Bozkurt, B., Butler, J., Casey, D. E., Colvin, M. M., et al. (2017). 2017 ACC/AHA/HFSA focused update of the 2013 ACCF/AHA guideline for the Management of Heart Failure: a report of the American College of Cardiology/American Heart Association task force on clinical practice guidelines and the Heart Failure Society of America. *J. Card. Fail.* 23 (6), 628–651. doi:10.1016/j.cardfail.2017.04.014

Yao, W., Cheang, I., Liao, S., Zhou, Y., Zhou, F., Xu, D., et al. (2020). Study protocol for a randomized controlled trial: Qiliqiangxin in heart failUre: assESsment of reduction in morTality (QUEST). *BMC Complement. Med. Ther.* 20 (1), 38. doi:10.1186/s12906-020-2821-0

Zhang, Y., Liao, J., Wang, C., Liu, Y., Gong, L., and Gao, S. (2012). Effect of Guanxinshutong capsules on MMP-9 in myocardium of rats with chronic heart failure. *J. Shanghai Univ. Tradi Chin. Med.* 28 (6), 83–85. doi:10.3390/jcm9020472

Zhang, Y., Liu, X., Wang, Y., Wang, S., and Gong, L. (2015). Effect of Guanxinshutong capsules on myocardial energy metabolism in rats with chronic heart failure. *J. Tradit. Chin. Med.* 56 (23), 2054–2057. doi:10.1186/s13020-020-0299-9

Zhang, Y., Wang, C., Gong, L., Liao, J., and Gao, S. (2013). Effect of Guanxinshutong capsule on at 1 and erk 2 in chronic heart failure rats. *Int. J. Tradi Chin. Med.* 35 (1), 37–39. doi:10.1177/147323001003800320

Zhang, Y., Wang, Y., Li, H., Wang, S., Tian, M., and Gong, L. (2016). Effect of Guanxinshutong capsules on ATP metabolism in rats with heart failure. *Word J. Integ Tradi & West Med.* 54 (11), 1523–1525. doi:10.1155/2013/378298

Zheng, X. (2002). *Guidelines for clinical research of new drugs in TCM*. Beijing, China: China Medical Science Press.

Conflict of Interest: The authors declare that the research was conducted in the absence of any commercial or financial relationships that could be construed as a potential conflict of interest.

Copyright © 2021 Wang, Xu, Yang, Zhang, Pan, Dou, Zhou, Xu, Li, He, Zhou, Yu, Chen, Huang, Fu and Wan. This is an open-access article distributed under the terms of the Creative Commons Attribution License (CC BY). The use, distribution or reproduction in other forums is permitted, provided the original author(s) and the copyright owner(s) are credited and that the original publication in this journal is cited, in accordance with accepted academic practice. No use, distribution or reproduction is permitted which does not comply with these terms.

frontiers in Pharmacology

ORIGINAL RESEARCH
published: 20 January 2021
doi: 10.3389/fphar.2020.590824

Network Patterns of Herbal Combinations in Traditional Chinese Clinical Prescriptions

Ning Wang[1†], Ninglin Du[1†], Yonghong Peng[2], Kuo Yang[1], Zixin Shu[1], Kai Chang[1], Di Wu[3,4], Jian Yu[1], Caiyan Jia[1], Yana Zhou[5], Xiaodong Li[5], Baoyan Liu[6], Zhuye Gao[7,8], Runshun Zhang[8,9]* and Xuezhong Zhou[1]**

[1]Medical Intelligence Institute, School of Computer and Information Technology, Beijing Jiaotong University, Beijing, China, [2]Department of Computing and Mathematics, Manchester Metropolitan University, Manchester, United Kingdom, [3]Adams School of Dentistry, University of North Carolina, Chapel Hill, NC, United States, [4]Department of Biostatistics, UNC Gillings School of Global Public Health, University of North Carolina, Chapel Hill, NC, United States, [5]Hubei Provincial Hospital of Traditional Chinese Medicine, Wuhan, China, [6]China Academy of Chinese Medical Sciences, Beijing, China, [7]National Clinical Research Center for Chinese Medicine Cardiology, Beijing, China, [8]Xiyuan Hospital, China Academy of Chinese Medical Sciences, Beijing, China, [9]Guanganmen Hospital, China Academy of Chinese Medical Sciences, Beijing, China

As a well-established multidrug combinations schema, traditional Chinese medicine (herbal prescription) has been used for thousands of years in real-world clinical settings. This paper uses a complex network approach to investigate the regularities underlying multidrug combinations in herbal prescriptions. Using five collected large-scale real-world clinical herbal prescription datasets, we construct five weighted herbal combination networks with herb as nodes and herbal combinational use in herbal prescription as links. We found that the weight distribution of herbal combinations displays a clear power law, which means that most herb pairs were used in low frequency and some herb pairs were used in very high frequency. Furthermore, we found that it displays a clear linear negative correlation between the clustering coefficients and the degree of nodes in the herbal combination network (HCNet). This indicates that hierarchical properties exist in the HCNet. Finally, we investigate the molecular network interaction patterns between herb related target modules (i.e., subnetworks) in herbal prescriptions using a network-based approach and further explore the correlation between the distribution of herb combinations and prescriptions. We found that the more the hierarchical prescription, the better the corresponding effect. The results also reflected a well-recognized principle called "*Jun-Chen-Zuo-Shi*" in TCM formula theories. This also gives references for multidrug combination development in the field of network pharmacology and provides the guideline for the clinical use of combination therapy for chronic diseases.

Keywords: network pharmacology, complex network, herb combination network, clinical prescription, network pattern

OPEN ACCESS

Edited by:
Hai Yu Xu,
China Academy of Chinese Medical Sciences, China

Reviewed by:
Li Peng,
Shanxi Agricultural University, China
GuoZheng Li,
China Academy of Chinese Medical Sciences, China

***Correspondence:**
Zhuye Gao
zhuyegao@126.com
Runshun Zhang
runshunzhang@139.com
Xuezhong Zhou
xzzhou@bjtu.edu.cn

†These authors have contributed equally to this work

Specialty section:
This article was submitted to Ethnopharmacology, a section of the journal Frontiers in Pharmacology

Received: *03 August 2020*
Accepted: *15 December 2020*
Published: *20 January 2021*

Citation:
Wang N, Du N, Peng Y, Yang K, Shu Z, Chang K, Wu D, Yu J, Jia C, Zhou Y, Li X, Liu B, Gao Z, Zhang R and Zhou X (2021) Network Patterns of Herbal Combinations in Traditional Chinese Clinical Prescriptions. Front. Pharmacol. 11:590824. doi: 10.3389/fphar.2020.590824

INTRODUCTION

Human disease phenomenon is complicated due to its roots from the disturbance of diverse pathogens on the hierarchical organization of the human life system interacting with the complex natural and social environment. Therefore, finding effective clinical treatments for chronic complex diseases such as diabetes, heart disease, stroke, and cancer is extremely difficult. Furthermore, due to the individualized phenotypes and genotypes incorporated in distinct persons, adverse drug reactions (ADRs) or drug side effects have increasingly become a major health issue when using targeted drugs for patients in real-world clinical settings (Duke et al., 2011; Smyth et al., 2012; Aagaard and Hansen, 2013). For example, there are 106,000 deaths and 2.2 million serious events caused by ADRs in the United States each year (Lazarou et al., 1998), which were once considered as a leading cause of death in the United States (Lazarou et al., 1998). For elderly patients, the ADR is even serious due to the need for multiple prescribed drugs for chronic disease comorbidities (Routledge et al., 2004). However, this problem cannot be well addressed since, for modern drug discovery, the safety of new agents only can be known with certainty if a drug has been on the market for many years. Drugs were only used for selected populations and in limited periods (Lasser et al., 2002) before knowing their safety with great certainty.

To improve the effectiveness of treatment for patients with chronic diseases and comorbidities and the prevention of the emergence of resistance to individual drugs, combination therapy is a new trend in real-world clinical research (Luzuriaga et al., 1997; Mottonen et al., 1999; Wald et al., 2009; Ascierto and Marincola, 2011; Yardley, 2013), which has been effective in the treatment of HIV as well as certain forms of leukemia. Simultaneous combination therapy like two-drug therapy and triple therapy holds huge promise for cancer treatment from the point of cancer cell evolutionary dynamics (Bozic et al., 2013). However, the mechanism and principle underlying effective combination therapy is still a mystery waiting to be investigated (Pritchard et al., 2013).

As a kind of classical combination therapy, traditional Chinese medicine (TCM), which includes multiple herbal ingredients, has been used by Chinese practitioners for thousands of years in real-world clinical settings. Pioneer research (Wang et al., 2008) has already shown that TCM clinical herbal prescription, called formula, consists of both principal and adjuvant components to yield synergy for disease treatment. This demonstrates the molecular mechanism of a well-recognized principle called "*Jun-Chen-Zuo-Shi*" (JCZS) (He et al., 2015; Duan et al., 2018) in TCM formula theories, which illustrates that a well-organized formula should consist of multiple herbal ingredients with differentiated roles like principal role and adjuvant role. Some adjuvant components should be considered to facilitate the delivery of the principal element to the disease site in the body. In real-world clinical herbal prescriptions, some of these have a good therapeutic effect, while others have a poor therapeutic effect. However, the reason why some prescriptions are more effective than others remains to be studied, and there is still a lack of appropriate method to evaluate whether many herbs grouped in certain formulae are suitable for the treatment of specific disease conditions. Therefore, investigation of herbal combination regularities in herbal prescription will benefit the pharmacological understanding of TCM treatment and discovery of novel combination drugs (Li et al., 2010b). In this study, we proposed a network-based approach to investigate the clinical principle of herbal prescribing and quantify the molecular network interactions between herb target modules of a given clinical prescription in the context of the human protein-protein interaction (PPI) network. In addition, we further investigate the correlation between the organization degree of herbal combinations in clinical prescription and their underlying molecular network interaction closeness, which might partially elucidate the organization principle of JCZS in TCM formula theories.

MATERIALS AND METHODS

Herbal Prescription Dataset

To investigate the regularities of herbal combinations in TCM clinical herbal prescriptions, we collected five different datasets from real-world TCM clinical encounters. These five datasets are described in brief in **Table 1**.

Outpatient formula data was extracted from the outpatient encounters with one and a half years in one well-recognized general TC hospitals in Beijing, China. The data includes 531,284 different clinical formulae that were used by hundreds of TCM physicians for the management of various diseases (e.g., diabetes, CHD (coronary heart disease), stroke, cancer, chronic gastritis, insomnia, and menopause syndrome) in outpatient encounters. The other four datasets are from inpatient clinical cases, which particularly were prescribed for the patients with type 2 diabetes, CHD, qi deficiency, and blood stasis, respectively. The above-mentioned two diseases (i.e., type 2 diabetes and CHD) are major chronic diseases (He et al., 2019) treated by TCM in real-world clinical settings. The other two syndromes, namely, qi deficiency and blood stasis, are two popular TCM diagnoses for various diseases (Wang et al., 2017). These four inpatient datasets are from a TCM clinical data warehouse (Zhou et al., 2010), which collected structured electronic medical record data from real-world clinical settings in about ten top-level TCM hospitals or wards mostly located in Beijing, China. We calculated the distribution of the number of herbs in one formula for each of the five datasets that represent five clinical prescriptions. The average number in each of the five clinical prescription datasets is 13.43 (outpatient), 9.66 (qi deficiency), 11.6 (diabetes), 12.03 (CHD), and 10.13 (blood stasis). We see that most clinical herbal prescriptions have 5–20 different herbs (over 95% of the five clinical formula datasets have 5–20 herbs) and have more than ten herbs averagely, which showed that clinical herbal prescription is a kind of particular multi-ingredients or drug therapy.

Construction of Herbal Combination Network

Considering a clinical formula with multiple herbal ingredients, we can construct a bipartile graph (**Figure 1**) which has clinical formulae and herbs as two types of nodes. The herbal

TABLE 1 | The outline information of five different data sets (in columns) used for analysis.

	Outpatient	Diabetes	CHD	Blood stasis	Qi deficiency
Total number of formulae	531,284	21,626	9,054	2,802	2,393
Distinct number of herbs	576	492	436	439	422
Average frequency of herbs	14,230.02	551.57	270.51	70.65	59.98
Average number of herbs in one formula	15.43	12.55	13.03	11.07	10.58

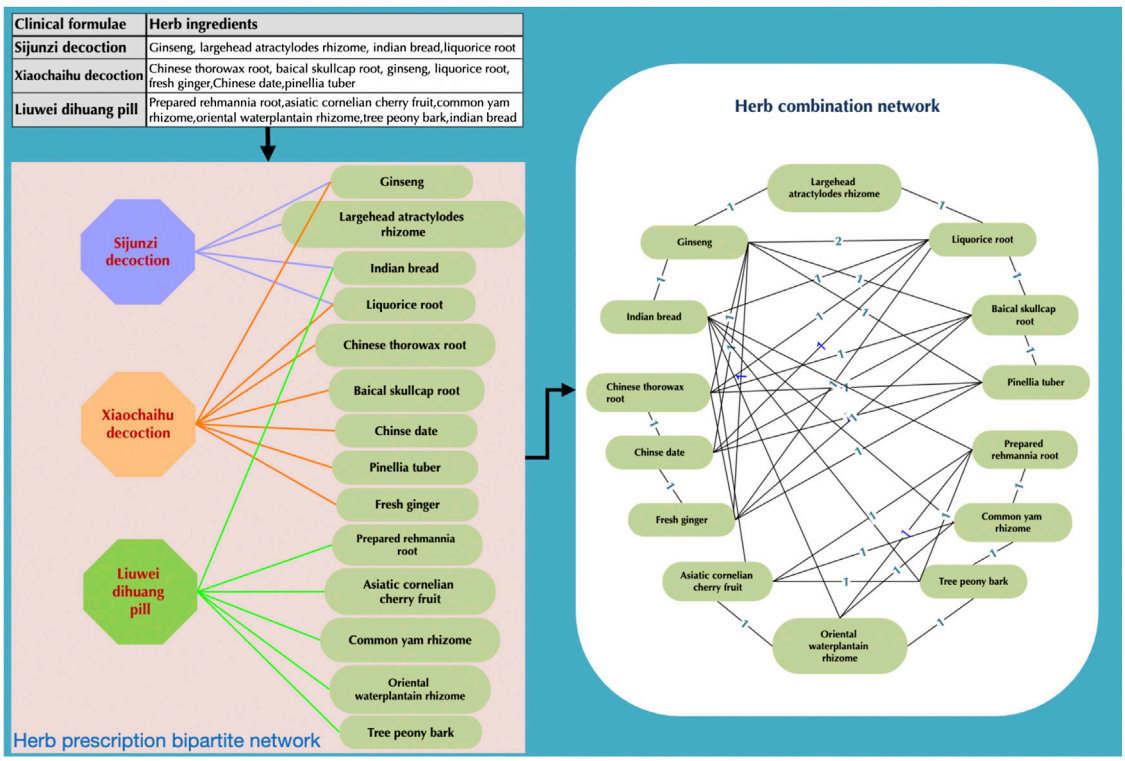

FIGURE 1 | Construction of the bipartite network of TCM clinical formulae. (Table in the left) Three records of clinical formulae, for instance, which include their corresponding herbs. (Left graph) The corresponding bipartite graph of these three clinical formulae, where octagons and oval rectangles correspond to clinical formulae and herbs, respectively. (Right) The herbal combination network where two herbs are connected if they are involved in the same clinical formula. Moreover, the link weight of two herbs corresponds to the number of clinical formulae cooccurring in both herbs.

combination network was constructed by considering herb pairs used in one specific clinical formula if they have been prescribed in more than one clinical formula. Then we would generate links (edges) between these herb pairs. This also means that we would generate a complete graph with each herb in one clinical formula. While a large number of clinical formulae are considered, we can generate a herbal combination network (HCNet, see **Figure 1**) with nodes representing herbs (herbal ingredients) and edges with a weight representing prescribing cooccurrence in clinical formulae. If two herb pairs are used more frequently than other herb pairs, they would be having a higher weight than other pairs. Furthermore, to compare the patterns of real-world data to those of randomly generated data, we generated the corresponding simulation data with random permutation by using Fisher shuffling (Fisher and Yates, 1948) to get random herb ingredients from herb dictionary to a clinical formula.

Network Topological Measurements

To investigate the topological properties of HCNet, we use node degree, clustering coefficient, and link weight distribution measurements, which have been widely used in complex network-related studies. The degree of a node is the number of edges incident to the node, which also means the number of herbs combined with an herb in the HCNet. Clustering coefficient evaluates the link density of the neighborhood of a node, which would be near one if most of the nodes were linked in the neighborhood of a node. We used local clustering coefficient of the undirected network to

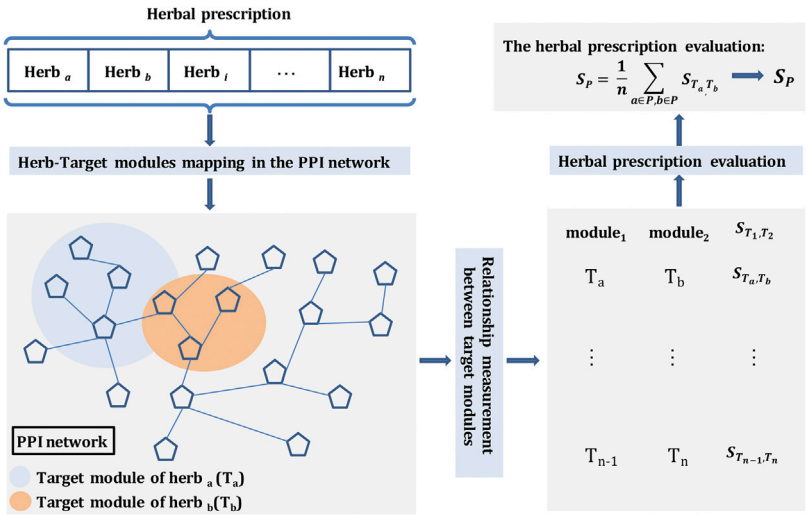

FIGURE 2 | Network-based evaluation measure of herbal prescriptions. A herbal prescription consists of multiple herbs, and herb target modules can be found in the PPI network based on herb-target interactions. Then the relationships between two herb target modules can be measured using the introduced separation measure. Finally, the prescription can be quantified using the relationship of any two herb target modules in the prescription.

calculate for each node in HCNet, which is calculated as follows:

$$C_i = \frac{2\left|e_{jk} : v_j, v_k \in N_i, e_{jk} \in E\right|}{k_i\left(k_i - 1\right)} \quad (1)$$

in which N_i is the node set of the neighborhood of a node v_i in a graph $G(V, E)$ and k_i is the degree of the node v_i. As a weighted network, HCNet has weight w_{ij} between nodes v_i and v_j, which represents the combination occurrence of herb pairs. We use link weight distribution $P(w)$, which denotes the possibility of a link to have a weight w, to investigate the herbal combination behaviors in HCNet and a given single clinical formula.

Network-Based Measures of Molecular Interactions Among Herbs in Prescriptions

As a kind of classical combination therapy, the herbal prescription consists of multiple herbs to treat clinical diseases. Therefore, we adopted a molecular network-based measurement (Menche et al., 2015; Cheng et al., 2019) to quantify the degree of molecular interactions of herbal combinations in each prescription through calculating the average shortest path length between herb target modules (molecular subnetwork of targets) in the context of human PPI network (**Figure 2**).

Firstly, we measured the network relationship of herb target modules T_a and T_b in the prescription using the recently introduced separation measure (Menche et al., 2015) to reflect their target localization (**Eq. 2**):

$$S_{T_a,T_b} = \langle d_{T_a,T_b} \rangle - \frac{\langle d_{T_a,T_a} \rangle + \langle d_{T_b,T_b} \rangle}{2} \quad (2)$$

in which T_a and T_b represent the target modules of herb a and herb b, respectively. S_{T_a,T_b} compares the mean shortest distances between proteins within each herb, d_{T_a,T_a} and d_{T_b,T_b}, to the shortest distances d_{T_a,T_b} between herb a and herb b target pairs. If proteins are associated with both a and b, $d_{T_a,T_b} = 0$. For $S_{T_a,T_b} < 0$, the targets of the herb a and herb b are located in the same network neighborhood, while for $S_{T_a,T_b} \geq 0$, the two herb targets are topologically separated.

Then, we quantified the herbal prescription using the average of S value between any two herb target modules in the prescription (**Eq. 3**):

$$S_P = \frac{1}{n} \sum_{a \in P, b \in P} S_{T_a,T_b} \quad (3)$$

in which S_P represents the herbal prescription score and n is the number of herbs in the prescription.

Hierarchical Organization Measure of Clinical Prescriptions

To further explore the associations between the hierarchical property of prescriptions and the molecular network correlations of the herb ingredients in prescriptions. We use entropy to measure the hierarchical organizing degree of a given prescription in terms of the distribution of herbal combinations.

After we obtained the herbal combinations of each prescription and all the prescription groups in our study (i.e., four types of clinical prescriptions), we could record each herbal combination with its weight and compute the distribution of the weight of herbal combinations for each prescription with regard to the global distribution of herbal combinations of each type of clinical prescriptions. Specifically, according to the weight distribution of herbal combinations of a given clinical prescription dataset, we divided the weight range (e.g., from 1

TABLE 2 | The basic information of five different HCNets used for analysis.

	Outpatient	Diabetes	CHD	Blood stasis	Qi deficiency
Total number of nodes	576	492	436	439	422
Total number of edges	120,619	34,824	29,381	19,323	18,186
Average degree in network	419.82	142.56	135.78	89.64	87.39
Edge density	0.73	0.29	0.31	0.20	0.21
Average clustering coefficient	0.85	0.61	0.63	0.51	0.51

to 3,000) into four intervals of some specific value (i.e., 300 in our study). Then using the list of herbal combinations and their weights, we could further calculate the probability of herbal combinations belonging to each interval of the corresponding prescription group for a given prescription. Next, we quantified the hierarchical degree of a prescription based on the entropy measure (Shannon, 1948; Wallace et al., 2019) as follows (**Eq. 4**). The larger the entropy value, the stronger the hierarchical organization degree for a given prescription, which would medically mean a more systemically organized herbal prescription with hierarchical roles (i.e., tend to prescribe herbal combinations in one formula with diverse global weight ranges in each group). The higher the entropy value, the more the hierarchical organization of the prescription in terms of diverse roles.

$$E = -\sum_{i=1}^{n} p_i \log p_i \tag{4}$$

where n represents the number of weight intervals and is set to four in our analysis and p_i represents the probability of the herbal combinations in each interval and is calculated as follows (**Eq. 5**):

$$p_i = \frac{N_i}{\sum_{i=1}^{n} N_i} \tag{5}$$

in which N_i represents the number of herbal combinations in weight interval i.

Therefore, we could calculate entropy for all prescriptions for each type of the clinical prescriptions. Next, for each type of the clinical prescriptions, we calculate the Pearson Correlations Coefficient (PCC) between its entropy value and S_p score to evaluate the statistical correlation between hierarchical degree and molecular network interactions of the herbal combinations for each prescription group.

RESULTS

Herbal Combination Networks

According to the clinical formulae-herb relationships in outpatient, type 2 diabetes, CHD, qi deficiency, and blood stasis, we constructed five types of herbal combination networks in which nodes represented the herbs and edges represented the cooccurrence of herbs in clinical formulae. These five HCNets were described in brief in **Table 2**.

Hierarchical Organization of Herbal Combinations in Clinical Prescriptions

To investigate the hierarchical properties of herbal combination networks, we evaluate the relationship between the clustering coefficient and node degree in the network. We performed experiments on four types of clinical prescriptions, and the results were shown in **Figure 3**.

We found that it displays a clear linear negative correlation between the clustering coefficients and the degree of nodes. It was found that, in real networks, clustering coefficients decrease with the vertex degree, which has been taken as a signature of the network hierarchical structure (Soffer and Vazquez, 2005). Therefore, this indicates that hierarchical properties exist in the herbal combination networks. Next, we would further investigate the scaling properties of HCNet according to node degree and weight distribution.

Scaling Heterogeneity of Degree and Weight Distribution

To investigate the scaling properties of HCNet, we evaluate the node degree distribution and link weight distribution in the network. It showed that herbal combinations in clinical formulae are obeying a scaling property, which has significantly departed from Poisson distribution (**Figure 4**). Although the node degree distribution in HCNet is not power law (this is obviously rational because the capacity of herb dictionary is fixed and thus increase of nodes is not met in HCNet), it showed a significant heterogeneous scaling for different nodes. The degrees of herb nodes scale from less than ten (e.g., 5) to several hundred (e.g., 550), whose range is much wider than the corresponding Poisson distribution.

Furthermore, it is interesting that the link weight distribution of HCNet is a clear power law, in which several herbal combinations are prescribed in high frequency while most of the other herbal combinations have very low frequency (**Figure 5**). This means that, in clinical practice, the prescription of herbal combinations for treatment is nonrandomly chosen and preferentially used by TCM physicians for the disease management of individualized patients.

We find that herbal combinations in four clinical formulae are obeying a scaling property (**Figure 5**), and it also means that the distribution of herbal combination has a hierarchical property. Next, we will calculate the degree of interaction between the targets in the context molecular network in herbal combinations and investigate whether frequently used herbal combinations hold close pharmacological effects.

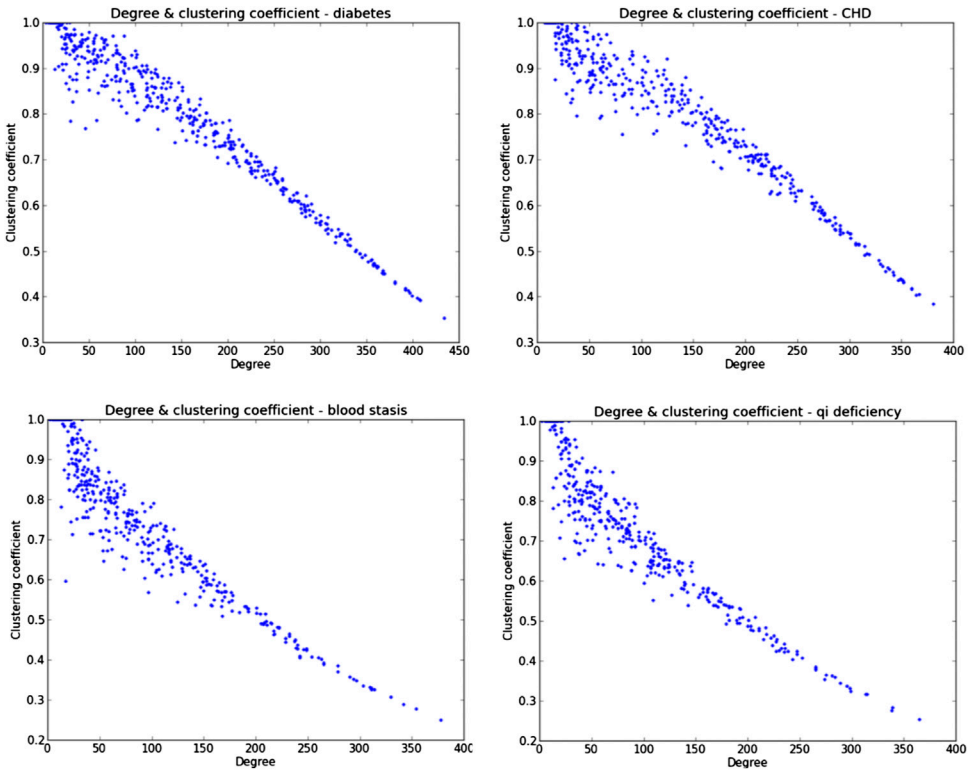

FIGURE 3 | The relationship between clustering coefficient and node degree in HCNets. It indicated a clear linear negative correlation between the clustering coefficients and the degree of nodes.

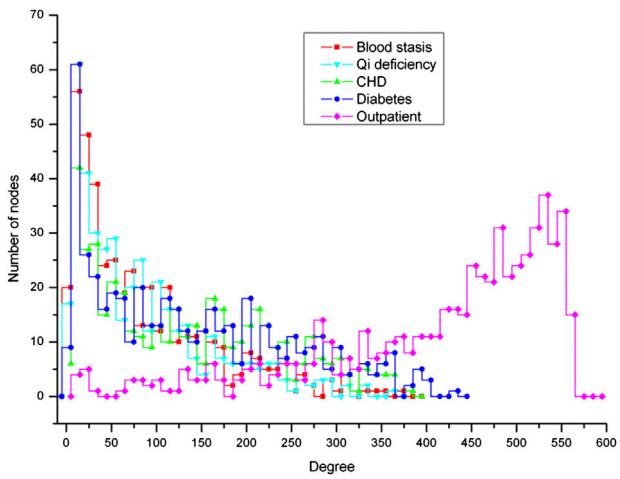

FIGURE 4 | The degree distribution of herb in five HCNets. Four HCNets, namely, blood stasis, qi deficiency, CHD, and diabetes, have a similar distribution. However, the degree of outpatient HCNet obviously has a different distribution, of which most nodes have very high degrees (e.g., 500 more connections) while few nodes have low degrees (e.g., less than 20). In contrast to the real data, the node degrees in the networks derived from randomly shuffled data have a Poisson distribution for qi deficiency and blood stasis datasets, which have comparatively less clinical prescription samples.

Molecular Network Interaction Patterns of Herbal Combinations

To evaluate the underlying pharmacological mechanisms of herbal combinations in clinical prescriptions, we quantified the network correlations between the targets of the herbal ingredients of the four types of clinical prescriptions for diabetes, CHD, qi deficiency, and blood stasis (see Methods section, *Network-Based Measures of Molecular Interactions Among Herbs in Prescriptions*).

We collected the protein targets of herbs in prescriptions from HIT database (Ye et al., 2011), which is a comprehensive and fully curated database of herbs and their corresponding protein targets. Due to the lack of target information for some herbs according to HIT database, at the same time, to assure each prescription should contain at least two herbs in the analysis. Finally, we quantified the molecular network correlations of those herbs in 21,566, 9,051, 2,392, and 2,801 prescriptions from diabetes, CHD, qi deficiency, and blood stasis, respectively, in which the number of herbs containing known targets is greater than or equal to two. The mean and standard deviation (std) of S_p scores of four types of prescriptions were shown in **Table 3**.

In order to give a benchmark reference for the four types of clinical prescriptions, we selected the classical prescriptions of TCM, Treatise on Exogenous Febrile Disease (TEFD), for comparative experiments. The TEFD contained 113 classical prescriptions in total, of which 85

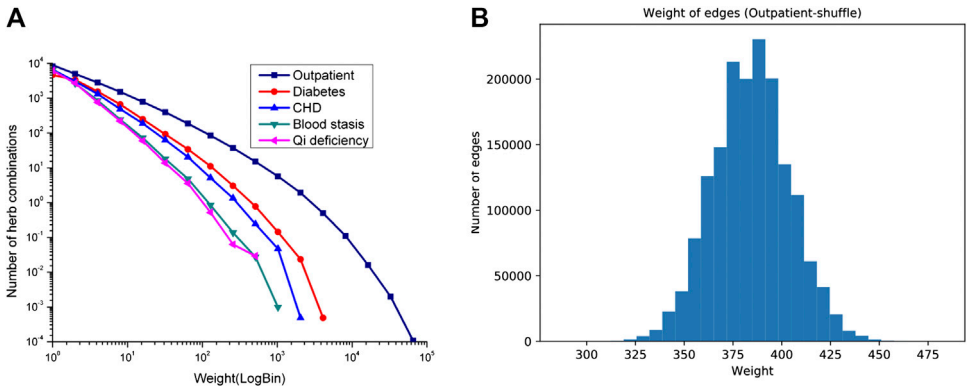

FIGURE 5 | Link weight distributions in HCNets. **(A)** The empirical distribution of five clinical datasets. **(B)** The distribution of random permutated samples of outpatient dataset. The empirical distributions of five real-world clinical formulae display mainly a power law. The weights of links scale from one to tens of thousands that form a wide range. However, the link weight of the corresponding random dataset of outpatient case obeys Poisson distribution with a mean weight, not more than 400. In addition, we also analyzed the random cases of the other four diseases (**Supplementary Figure S1**), the link weight of the corresponding random dataset of diabetes and CHD case obeys Poisson distribution with mean weight not more than 15, and the link weight of the corresponding random dataset of qi deficiency and blood stasis case obeys seminormal distribution with a narrow weight scale.

TABLE 3 | The mean and standard deviation of S_p scores of four types of clinical prescriptions and TEFD.

Type	Diabetes	CHD	Qi deficiency	Blood stasis	TEFD	Random
Mean	−0.03	−0.05	−0.09	−0.11	−0.09	0.16
Std	0.32	0.33	0.28	0.28	0.15	0.08

prescriptions with associated targets were selected for quantification. The number of herbs containing known targets is greater than or equal to two in 85 prescriptions. We collected the classical prescriptions from TEFD as a representative prescription benchmark with high-quality herbal combinations because most prescriptions in TEFD have been widely used in TCM clinical practice for thousands of years (Li et al., 2010a; Wang and Xiao, 2010; Zhang et al., 2010). Therefore, in general, we will consider that the herbal combinations held in the prescriptions from TEFD give a better example than those from the above four types of clinical prescriptions.

Next, we quantified the degree of interactions between the herbal combinations in 85 prescriptions from TEFD in the context of the human PPI network (**Figure 6**). For comparison of random expectations, we reshuffled (1,000 random permutations) the herbs in each prescription by using the Fisher-Yates method (Fisher and Yates, 1948). Finally, we found that the S_p scores of prescriptions in TEFD were significantly lower than those of random prescriptions (p = 2.46718e-27). We found that 92% of real prescriptions in TEFD had lower S_p scores compared to random prescriptions, and S_p scores of 79% of real prescriptions were less than 0, but S_p scores of all random prescriptions were greater than 0. And we found that the mean S_p score in TEFD was -0.09, but the random was 0.16, indicating that the target modules of herbs in a prescription were closely related

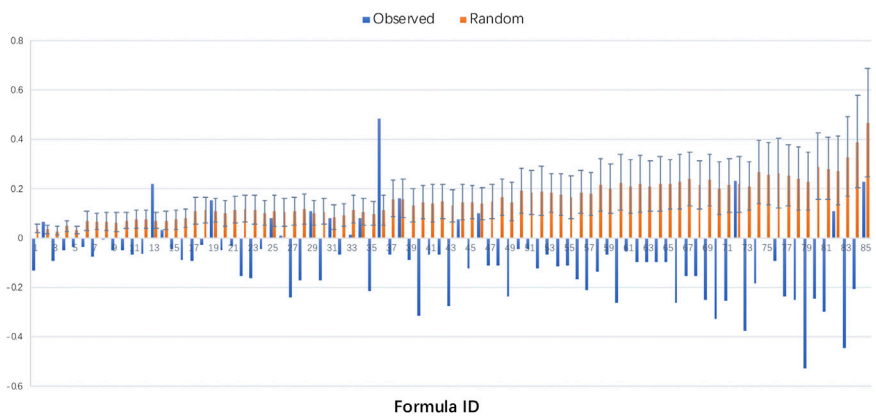

FIGURE 6 | The S_p scores of prescriptions in Treatise on Exogenous Febrile Disease. We ranked the prescriptions in descending order according to the number of herbs and compared the S_p score distribution between prescriptions in TEFD and random prescriptions. The S_p scores of prescriptions in TEFD were shown as blue columnar and random prescriptions were shown as orange columnar.

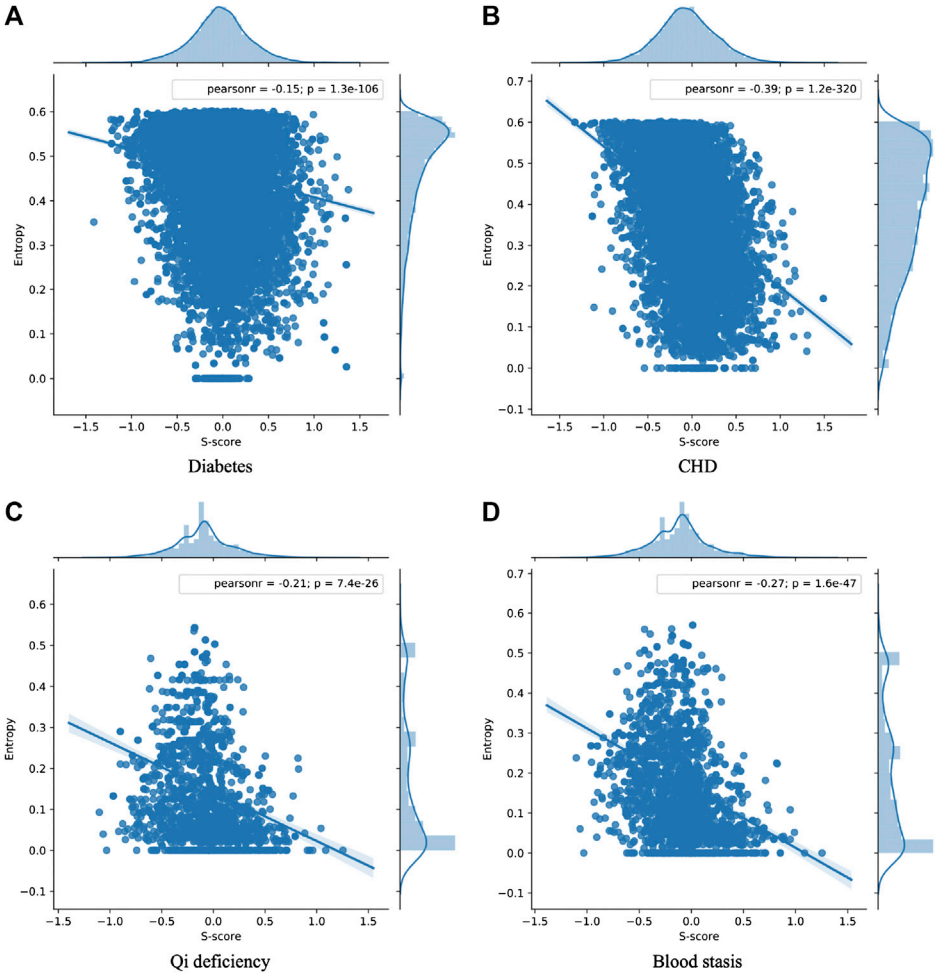

FIGURE 7 | The Pearson correlation coefficient for four types of clinical prescriptions. We could find that entropy value and S score of diabetes **(A)**, CHD **(B)**, qi deficiency **(C),** and blood stasis **(D)** were negatively correlated.

to each other in the context of the molecular network. To further evaluate the quality of herbal combinations of current clinical prescriptions, with similar calculation methods, we obtained the S_p scores of each prescription in the four clinical prescriptions datasets. The results showed that the mean of S_p scores of all four clinical prescriptions was less than 0. This means that most real-world clinical prescriptions would tend to have a high degree of herbal combinations as good as those of TEFD prescriptions. It is practical and reasonable that, in TCM clinical settings, most practitioners would directly adopt the classical prescriptions or use the classical prescriptions as a basic therapeutic framework for clinical treatments (Duan et al., 2018; Chen et al., 2019).

Molecular Correlations of Hierarchical Herbal Combinations in Clinical Prescriptions

We have found that the weights of herbal combinations scale from one to tens of thousands that form a wide range and the distribution of herbal combinations has a hierarchical organization property in our previous analysis. Meanwhile, we also obtained the molecular measures of herbal combinations in prescriptions in terms of their molecular interactions. Next, we would expect the potential associations between these two indexes for a given prescription (see Methods section, *Hierarchical Organization Measure of Clinical Prescriptions*).

To test the assumption, we performed a Pearson correlation analysis on its entropy value and S_p score. The PCC and p-value were shown in **Figure 7**. We could find that entropy value and S_p score of clinical prescriptions were negatively correlated with PCC ranging from −0.15 to −0.39 (**Figure 7A**, p = 1.3e−106; **Figure 7B**, p = 1.2e−320; **Figure 7C**, p = 7.4e−26; **Figure 7D**, p = 1.6e−47) for the four clinical herbal prescriptions. This indicated that the larger the entropy value of a given prescription, the smaller the S_p score of the prescription. Therefore, it indicated that the more the hierarchical herbal combinations were involved in a prescription, the more the connected molecular networks would be found between the targets of the herbal ingredients in a given prescription. The results also reflected exactly a well-recognized principle called JCZS in TCM formula theories,

which illustrates that a well-organized formula should consist of multiple herbal ingredients with differentiated therapeutic roles for targeted disease conditions.

DISCUSSION AND CONCLUSION

TCM herbal prescription which usually includes tens of different herbal ingredients as a single therapeutic formula is the main kind of intervention for chronic disease treatment in China (Qi et al., 2013). Typically, it is a kind of combination therapies with complicated underlying molecular pharmacological mechanisms (Chan et al., 2012). Combination therapies offer promising therapeutic solutions for complex disease treatments, from hypertension, COPD, and cancer with potential high efficacies and lower adverse effects (Yki-Jarvinen, 2001; Margulies and Hicks, 2009). However, the clinical organization principle and its underlying network mechanisms still need to be elucidated. TCM herbal prescription has been widely used as a combination therapy in clinical settings (He et al., 2012; Liu et al., 2013; Duan et al., 2018) by adhering to empirical clinical regularities, such as JCZS (He et al., 2015; Duan et al., 2018), and frequently used herbal combinations. Connecting those clinical regularities with the molecular network patterns related to the targets of herbal ingredients would potentially improve the pharmacological understanding of the empirical rules to develop more effective combination therapies.

The well-recognized principle called JCZS in TCM formula theories means that a well-organized formula should consist of multiple herbal ingredients with different therapeutic roles (Wang et al., 2008). This would imply the existence of a hierarchical organization of herbal combinations and the underlying network mechanisms of herbal ingredients for a well-established set of clinical prescriptions (e.g., the herbal prescriptions in TEFD). Here, we investigated the clinical regularities of herbal combinations involved in each prescription in terms of network topological patterns and applied a network-based measurement (Cheng et al., 2019) to quantify the molecular network interactions between herb target modules in a given herbal prescription. Our results indicate that there do exist clinical prescription rules to choose herbal combinations in a clinical prescription, which can be displayed by the scaling and hierarchical topological properties of the herbal combination network. Specifically, a clinical prescription would tend to consist of both highly used herbs or herbal combinations and less used herbs or herbal combinations as a whole formula for disease treatment. This might resemble to the well-established prescription principle (i.e., JCZS) for TCM herbal prescriptions, which implies a good prescription need include herbs with different pharmacological effects. Furthermore, we found that the network-based measure of high-quality drug combinations (Cheng et al., 2019) could be used for evaluating the molecular interaction closeness of both herbal combinations and prescriptions. For example, a classical formula in TEFD, "Shaoyao Gancao decoction" (SGD), contains two herbs: Radix Paeoniae Alba (hRPA) and Radix Glycyrrhizae Preparata (hRGP), which has been further prescribed as core herbal combinations in many classical formulae [e.g., Mahuang Shengma decoction (Fan et al., 2011), Xiaoqinglong decoction (Wang et al., 2018), Gegen decoction (Chai et al., 2020), Chaihu Guizhi decoction (Li et al., 2019), and HuangQin decoction (Dai et al., 2018)]. According to the molecular network-based measurement, we found that the S_p score of SGD was -0.03 (the random expectation was 0.03). This means that close interactions are involved between the target modules of the two-member herbs in SGD. Actually, by identifying the herb-target associations from HIT database, we found that there are 47 and 24 potential targets of hRPA and hRGP, respectively. These two target sets each form a rather dense PPI subnetwork (we call it a module, **Figure 8A**). There are eight common targets shared by hRPA and hRGP, such as TNF, CASP3, RELA, and NOS2. Meanwhile, 75 interactions exist between the target modules of hRPA and hRGP (with 0.113 network density). We further used DAVID (Huang Da et al., 2009) to obtain the enriched GO and KEGG pathways (**Figure 8B**). The results showed that SGD enriched the inflammation-related pathways such as Hepatitis B, NF-kB, and TLRs (Mantovani, 2010) and liver-related GO annotations such as liver regeneration, which could partially explain the clinical effects of SGD for treating liver disorders and anti-inflammatory in clinic settings (Bi et al., 2014).

Overall, we have been working to investigate the network topological regularities and the underlying molecular network mechanisms of herbal prescriptions, and we hope that our work and findings for clinical prescriptions would give references for understanding of the principles and molecular mechanisms of multidrug combinations (Dawson and Carragher, 2014; Cheng et al., 2019; Zhang et al., 2019) after fully digging the hidden knowledge underlying the effective multiple therapies (e.g., Chinese herbal prescriptions).

This study has several limitations. First, since it is not aiming to predict the specific knowledge on pharmacological effects of specific prescriptions or drugs, unlike the study on pharmacological research of a given herbal prescription or predicting a novel target, it would be difficult for us to design a straightforward wet-lab experiment to validate the rationality of organizing herb combinations in a good clinical prescription. However, large-scale wet-lab experiments on validating the differentiated molecular patterns between high frequently used herbal combinations and rarely used herbal combinations should be designed and performed in further research to improve the reliability of the network analysis results. Second, currently, we only used HIT database as the herb-target associations for molecular network-related analysis, which would limit the number of herb-target associations and thus influence the generalization of our analysis. We would integrate other well-established network pharmacological databases, such as ETCM (Xu et al., 2019) and SymMap (Wu et al., 2019) to further validate the underlying molecular network regularities of herbal prescriptions. Third, due to the complexity of clinical conditions of individualized patients, it is important that the prescribed herbal treatments for specific patients should be evaluated by the outcomes and finally help figure out the true high-quality clinical herbal prescriptions from a large-scale clinical dataset. Therefore, we would extend the evaluation measure together with disease conditions to find good herbal prescriptions with potential effectiveness. However, without the related in vitro or in vivo experimental validations, we believe that

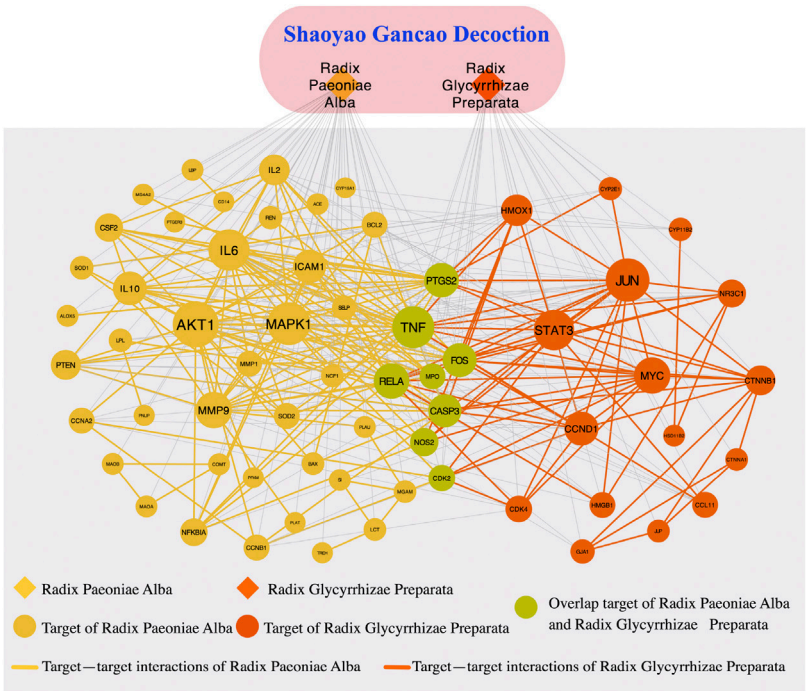

GO/Pathway

Category	Term	Pvalue	Genes	FDR
KEGG_PATHWAY	hsa05161:Hepatitis B	2.75E-15	IL6, TNF, MMP9, RELA, NFKBIA, CDK4, PTEN, CDK2, STAT3, AKT1, MAPK1, FOS, CASP3, CCND1, JUN, BCL2, BAX, MYC, CCNA2	3.45E-12
KEGG_PATHWAY	hsa04620:Toll-like receptor signaling pathway	1.17E-06	AKT1, MAPK1, FOS, IL6, TNF, JUN, RELA, NFKBIA, LBP, CD14	1.45E-03
KEGG_PATHWAY	hsa04064:NF-kappa B signaling pathway	2.63E-06	ICAM1, TNF, PTGS2, RELA, BCL2, NFKBIA, LBP, CD14, PLAU	3.27E-03
GOTERM_BP_DIRECT	GO:0006954~inflammatory response	9.69E-09	SELP, HMGB1, IL6, TNF, PTGER3, PTGS2, RELA, IL10, AKT1, CCL11, FOS, GGT5, MS4A2, CD14	1.61E-05
GOTERM_BP_DIRECT	GO:0097421~liver regeneration	7.59E-06	CCND1, HMOX1, NFKBIA, MYC, IL10	1.26E-02

FIGURE 8 | The network molecular associations for the only two herbs, namely, Radix Paeoniae Alba and Radix Glycyrrhizae Preparata in the Shaoyao Gancao decoction, (SGD). **(A)** Target modules of the two herbs and their interactions. Yellow nodes represent the targets of Radix Paeoniae Alba, and red nodes represent the targets of Radix Glycyrrhizae Preparata, while the edges represent the interactions between the targets in the PPI network. Nodes with green color represent overlapping targets of two herbs. **(B)** The related gene ontology and pathways of target modules of the two herbs.

our current research could deliver certain potential insights for the field of network pharmacology and combination drug development. By evaluating the underlying molecular network patterns of the herbal combinations in herbal prescriptions, it would be promising to propose a novel network pharmacological approach to investigate the inherent network mechanisms (e.g., organizing of herbal combinations) of a given clinical prescription and thus help design combination therapies with better effectiveness for disease treatment.

DATA AVAILABILITY STATEMENT

All datasets presented in this study are included in the article/ **Supplementary Material**.

AUTHOR CONTRIBUTIONS

XZ, ZG, RZ, and BL conceived and designed the study. NW and ND analyzed data and wrote the draft manuscript; KY, ZS, and KC collected related data; YP, RZ, DW, JY, CJ, YZ, and XL reviewed the methods and the results. All authors have reviewed the manuscript; in particular, XZ and DW have revised the manuscript with the help of other coauthors.

FUNDING

The work is supported by the National Key Research and Development Program (2017YFC1703506), the Special

Programs of Traditional Chinese Medicine (201407001, JDZX2015170, and JDZX2015171), National Major Scientific and Technological Special Project for "Significant New Drugs Development" (2019ZX09201005-002-006) and the National Key Technology R&D Program (2013BAI02B01 and 2013BAI13B04).

SUPPLEMENTARY MATERIAL

The Supplementary Material for this article can be found online at: https://www.frontiersin.org/articles/10.3389/fphar.2020.590824/full#supplementary-material.

REFERENCES

Aagaard, L., and Hansen, E. H. (2013). Adverse drug reactions reported by consumers for nervous system medications in Europe 2007 to 2011. *BMC Pharmacol. Toxicol.* 14, 30. doi:10.1186/2050-6511-14-30

Ascierto, P. A., and Marincola, F. M. (2011). Combination therapy: the next opportunity and challenge of medicine. *J. Transl. Med.* 9, 115. doi:10.1186/1479-5876-9-115

Bi, X., Gong, M., and Di, L. (2014). Review on prescription compatibility of shaoyao gancao decoction and reflection on pharmacokinetic compatibility mechanism of traditional Chinese medicine prescription based on *in vivo* drug interaction of main efficacious components. *Evid. Based Complement Alternat. Med.* 2014, 208129. doi:10.1155/2014/208129

Bozic, I., Reiter, J. G., Allen, B., Antal, T., Chatterjee, K., Shah, P., et al. (2013). Evolutionary dynamics of cancer in response to targeted combination therapy. *Elife.* 2, e00747. doi:10.7554/eLife.00747

Chai, C., Hong, F., Yan, Y., Yang, L., Zong, H., Wang, C., et al. (2020). Effect of traditional Chinese medicine formula GeGen decoction on primary dysmenorrhea: a randomized controlled trial study. *J. Ethnopharmacol.* 261, 113053. doi:10.1016/j.jep.2020.113053

Chan, K., Shaw, D., Simmonds, M. S., Leon, C. J., Xu, Q., Lu, A., et al. (2012). Good practice in reviewing and publishing studies on herbal medicine, with special emphasis on traditional Chinese medicine and Chinese materia medica. *J. Ethnopharmacol.* 140, 469–475. doi:10.1016/j.jep.2012.01.038

Chen, Z. K., Wang, X. N., Li, Y. Y., Wang, Y. H., Tang, K. L., Wu, D. F., et al. (2019). Comparative network pharmacology analysis of classical TCM prescriptions for chronic liver disease. *Front. Pharmacol.* 10, 1353. doi:10.3389/fphar.2019.01353

Cheng, F. X., Kovacs, I. A., and Barabasi, A. L. (2019). Network-based prediction of drug combinations. *Nat. Commun.* 10, 1197. doi:10.1038/s41467-019-09186-x

Dai, X. M., Cui, D. N., Wang, J., Zhang, W., Zhang, Z. J., and Xu, F. G. (2018). Systems pharmacology based strategy for Q-markers discovery of HuangQin decoction to attenuate intestinal damage. *Front. Pharmacol.* 9, 236. doi:10.3389/fphar.2018.00236

Dawson, J. C., and Carragher, N. O. (2014). Quantitative phenotypic and pathway profiling guides rational drug combination strategies. *Front. Pharmacol.* 5, 118. doi:10.3389/fphar.2014.00118

Duan, D. D., Wang, Z., and Wang, Y. Y. (2018). New omic and network paradigms for deep understanding of therapeutic mechanisms for Fangji of traditional Chinese medicine. *Acta Pharmacol. Sin.* 39, 903–905. doi:10.1038/aps.2018.42

Duke, J., Friedlin, J., and Ryan, P. (2011). A quantitative analysis of adverse events and "overwarning" in drug labeling. *Arch. Intern. Med.* 171, 944–946. doi:10.1001/archinternmed.2011.182

Fan, F. J., Hong, W. X., Li, X., Zhang, T., Liu, X. L., Chen, W. D., et al. (2011). "Research on compatibility of prescription of TCP based on the principle of attribute partial order chart," in Proceedings of the 2011 first international conference on instrumentation, measurement, computer, communication and control, Beijing, China, October 21–23, 2011, 82–86. doi:10.1109/IMCCC.2011.30

Fisher, R. A., and Yates, F. (1948). *Statistical tables for biological, agricultural and medical research*. London, United Kingdom: Oliver & Boyd.

He, Y. H., Zheng, X., Sit, C., Loo, W. T., Wang, Z. Y., Xie, T., et al. (2012). Using association rules mining to explore pattern of Chinese medicinal formulae (prescription) in treating and preventing breast cancer recurrence and metastasis. *J. Transl. Med.* 10, S12. doi:10.1186/1479-5876-10-S1-S12

He, B., Lu, C., Wang, M. L., Zheng, G., Chen, G., Jiang, M., et al. (2015). Drug discovery in traditional Chinese medicine: from herbal fufang to combinatory drugs. *Science.* 350, S74–S76.

He, D., Huang, J. H., Zhang, Z. Y., Du, Q., Peng, W. J., Yu, R., et al. (2019). A network pharmacology-based strategy for predicting active ingredients and potential targets of LiuWei DiHuang pill in treating type 2 diabetes mellitus. *Drug Des. Dev. Ther.* 13, 3989–4005. doi:10.2147/Dddt.S216644

Huang Da, W., Sherman, B. T., and Lempicki, R. A. (2009). Bioinformatics enrichment tools: paths toward the comprehensive functional analysis of large gene lists. *Nucleic Acids Res.* 37, 1–13. doi:10.1093/nar/gkn923

Lasser, K. E., Allen, P. D., Woolhandler, S. J., Himmelstein, D. U., Wolfe, S. M., and Bor, D. H. (2002). Timing of new black box warnings and withdrawals for prescription medications. *J. Am. Med. Assoc.* 287, 2215–2220. doi:10.1001/jama.287.17.2215

Lazarou, J., Pomeranz, B. H., and Corey, P. N. (1998). Incidence of adverse drug reactions in hospitalized patients: a meta-analysis of prospective studies. *J. Am. Med. Assoc.* 279, 1200–1205. doi:10.1001/jama.279.15.1200

Li, J., Liu, B. X., Zhang, S. G., Ma, H., X., Zhang, Q. N., Lu, Z. Y., et al. (2010a). Study on effective powers of familiar herbs in treatise on exogenous febrile disease of shanghan lun. *J. of Liaoning Univ. of Trad. Chinese Med.* 02, 47–48. doi:10.13194/j.jlunivtcm.2010.02.49.lij.023

Li, S., Zhang, B., Jiang, D., Wei, Y. Y., and Zhang, N. B. (2010b). Herb network construction and co-module analysis for uncovering the combination rule of traditional Chinese herbal formulae. *BMC Bioinf.* 11, S6. doi:10.1186/1471-2105-11-S11-S6

Li, Z., Wen, R., Du, Y., Zhao, S., Zhao, P., Jiang, H., et al. (2019). Simultaneous quantification of fifteen compounds in rat plasma by LC-MS/MS and its application to a pharmacokinetic study of Chaihu-Guizhi decoction. *J. Chromatogr. B Analyt. Technol. Biomed. Life Sci.* 1105, 15–25. doi:10.1016/j.jchromb.2018.12.006

Liu, Z., Chen, S., Cai, J., Zhang, E., Lan, L., Zheng, J., et al. (2013). Traditional Chinese medicine syndrome-related herbal prescriptions in treatment of malignant tumors. *J. Tradit. Chin. Med.* 33, 19–26. doi:10.1016/s0254-6272(13)60095-3

Luzuriaga, K., Bryson, Y., Krogstad, P., Robinson, J., Stechenberg, B., Lamson, M., et al. (1997). Combination treatment with zidovudine, didanosine, and nevirapine in infants with human immunodeficiency virus type 1 infection. *N. Engl. J. Med.* 336, 1343–1349. doi:10.1056/NEJM199705083361902

Mantovani, A. (2010). Molecular pathways linking inflammation and cancer. *Curr. Mol. Med.* 10, 369–373. doi:10.2174/156652410791316968

Margulies, S., and Hicks, R. (2009). Combination therapies for traumatic brain injury: prospective considerations. *J. Neurotrauma.* 26, 925–939. doi:10.1089/neu.2008-0794

Menche, J., Sharma, A., Kitsak, M., Ghiassian, S. D., Vidal, M., Loscalzo, J., et al. (2015). Disease networks. Uncovering disease-disease relationships through the incomplete interactome. *Science.* 347, 1257601. doi:10.1126/science.1257601

Mottonen, T., Hannonen, P., Leirisalo-Repo, M., Nissila, M., Kautiainen, H., Korpela, M., et al. (1999). Comparison of combination therapy with single-drug therapy in early rheumatoid arthritis: a randomised trial. FIN-RACo trial group. *Lancet.* 353, 1568–1573. doi:10.1016/s0140-6736(98)08513-4

Pritchard, J. R., Bruno, P. M., Gilbert, L. A., Capron, K. L., Lauffenburger, D. A., and Hemann, M. T. (2013). Defining principles of combination drug mechanisms of action. *Proc. Natl. Acad. Sci. U.S.A.* 110, E170–E179. doi:10.1073/pnas.1210419110

Qi, F. H., Wang, Z. X., Cai, P. P., Zhao, L., Gao, J. J., Kokudo, N., et al. (2013). Traditional Chinese medicine and related active compounds: a review of their role on hepatitis B virus infection. *Drug Discov Ther.* 7, 212–224. doi:10.5582/ddt.2013.v7.6.212

Routledge, P. A., O'mahony, M. S., and Woodhouse, K. W. (2004). Adverse drug reactions in elderly patients. *Br. J. Clin. Pharmacol.* 57, 121–126. doi:10.1046/j.1365-2125.2003.01875.x

Shannon, C. E. (1948). A mathematical theory of communication. *Bell Syst. Tech.* 27, 379–423. doi:10.1002/j.1538-7305.1948.tb01338.x

Smyth, R. M., Gargon, E., Kirkham, J., Cresswell, L., Golder, S., Smyth, R., et al. (2012). Adverse drug reactions in children--a systematic review. *PLoS One.* 7, e24061. doi:10.1371/journal.pone.0024061

Soffer, S. N., and Vazquez, A. (2005). Network clustering coefficient without degree-correlation biases. *Phys. Rev. E—Stat. Nonlinear Soft Matter Phys*. 71, 057101. doi:10.1103/PhysRevE.71.057101

Wald, D. S., Law, M., Morris, J. K., Bestwick, J. P., and Wald, N. J. (2009). Combination therapy versus monotherapy in reducing blood pressure: meta-analysis on 11,000 participants from 42 trials. *Am. J. Med*. 122, 290–300. doi:10.1016/j.amjmed.2008.09.038

Wallace, Z. S., Rosenthal, S. B., Fisch, K. M., Ideker, T., and Sasik, R. (2019). On entropy and information in gene interaction networks. *Bioinformatics*. 35, 815–822. doi:10.1093/bioinformatics/bty691

Wang, Z. L., and Xiao, X. R. (2010). Relationship between the amount of water added and the weight of drugs for decoction in Treatise on exogenous febrile diseases. *Liaoning J. of Trad. Chinese Med*. 3, 433–435. doi:10.13192/j.ljtcm.2010.03.54.wangzhl.019

Wang, L., Zhou, G. B., Liu, P., Song, J. H., Liang, Y., Yan, X. J., et al. (2008). Dissection of mechanisms of Chinese medicinal formula Realgar-Indigo naturalis as an effective treatment for promyelocytic leukemia. *Proc. Natl. Acad. Sci. U.S.A*. 105, 4826–4831. doi:10.1073/pnas.0712365105

Wang, Q., Yao, G. Z., Pan, G. M., Huang, J. Y., An, Y. P., and Zou, X. (2017). [Analysis of on medication rules for Qi-deficiency and blood-stasis syndrome of chronic heart failure based on data mining technology]. *Zhongguo Zhongyao Zazhi*. 42, 182–186. doi:10.19540/j.cnki.cjcmm.20161222.040

Wang, H., Mao, B., and Chen, C. (2018). Xiaoqinglong decoction attenuates chronic obstructive pulmonary disease in rats via inhibition of autophagy. *Evid. Based Complement. Alternat. Med*. 2018, 6705871. doi:10.1155/2018/6705871

Wu, Y., Zhang, F., Yang, K., Fang, S., Bu, D., Li, H., et al. (2019). SymMap: an integrative database of traditional Chinese medicine enhanced by symptom mapping. *Nucleic Acids Res*. 47, D1110–D1117. doi:10.1093/nar/gky1021

Xu, H. Y., Zhang, Y. Q., Liu, Z. M., Chen, T., Lv, C. Y., Tang, S. H., et al. (2019). ETCM: an encyclopaedia of traditional Chinese medicine. *Nucleic Acids Res*. 47, D976–D982. doi:10.1093/nar/gky987

Yardley, D. A. (2013). Drug resistance and the role of combination chemotherapy in improving patient outcomes. *Int J Breast Cancer*. 2013, 137414. doi:10.1155/2013/137414

Ye, H., Ye, L., Kang, H., Zhang, D. F., Tao, L., Tang, K. L., et al. (2011). HIT: linking herbal active ingredients to targets. *Nucleic Acids Res*. 39, D1055–D1059. doi:10.1093/nar/gkq1165

Yki-Jarvinen, H. (2001). Combination therapies with insulin in type 2 diabetes. *Diabetes Care*. 24, 758–767. doi:10.2337/diacare.24.4.758

Zhang, G. J., Liu, E. S., Wang, D. Q., and Liu, C. X. (2010). Discussing relevance of lung and large intestine from Treatise on exogenous febrile diseases. *Tianjin Journal of Traditional Chinese Medicine*. 4, 299–300.

Zhang, M., Lee, S., Yao, B., Xiao, G., Xu, L., and Xie, Y. (2019). DIGREM: an integrated web-based platform for detecting effective multi-drug combinations. *Bioinformatics*. 35, 1792–1794. doi:10.1093/bioinformatics/bty860

Zhou, X. Z., Chen, S. B., Liu, B. Y., Zhang, R. S., Wang, Y. H., Li, P., et al. (2010). Development of traditional Chinese medicine clinical data warehouse for medical knowledge discovery and decision support. *Artif. Intell. Med*. 48, 139–152. doi:10.1016/j.artmed.2009.07.012

Conflict of Interest: The authors declare that the research was conducted in the absence of any commercial or financial relationships that could be construed as a potential conflict of interest.

Copyright © 2021 Zhou, Wang, Du, Peng, Yang, Shu, Chang, Wu, Yu, Jia, Zhou, Li, Liu, Ye and Zhang. This is an open-access article distributed under the terms of the Creative Commons Attribution License (CC BY). The use, distribution or reproduction in other forums is permitted, provided the original author(s) and the copyright owner(s) are credited and that the original publication in this journal is cited, in accordance with accepted academic practice. No use, distribution or reproduction is permitted which does not comply with these terms.

frontiers in Pharmacology

ORIGINAL RESEARCH
published: 21 January 2021
doi: 10.3389/fphar.2020.596525

The Traditional Chinese Medicine Fuyou Formula Alleviates Precocious Puberty by Inhibiting GPR54/GnRH in the Hypothalamus

Guo-liang Bai[1,2], Kai-li Hu[3], Yi Huan[2], Xing Wang[2], Lei Lei[2], Meng Zhang[1], Chun-yan Guo[1], Hong-sheng Chang[3], Li-bo Zhao[1], Jing Liu[1], Zhu-fang Shen[2], Xiao-ling Wang[1]* and Xin Ni[1]**

[1]Clinical Research Center, Beijing Children's Hospital, National Center for Children's Health, Capital Medical University, Beijing, China, [2]State Key Laboratory of Bioactive Substances and Functions of Natural Medicines, Key Laboratory of Polymorphic Drugs of Beijing, Institute of Materia Medica, Chinese Academy of Medical Sciences, Peking Union Medical College, Beijing, China, [3]Department of Pharmacology, School of Chinese Materia Medica, Beijing University of Chinese Medicine, Beijing, China

OPEN ACCESS

Edited by:
Hai Yu Xu,
China Academy of Chinese Medical Sciences, China

Reviewed by:
Haiyu Zhao,
China Academy of Chinese Medical Sciences, China
Amit Krishna De,
Indian Science Congress Association (ISCA), India

***Correspondence:**
Zhu-fang Shen
shenzhf@imm.ac.cn
Xiao-ling Wang
eyjdb6380@163.com
Xin Ni
nixin@bch.com.cn

Specialty section:
This article was submitted to Ethnopharmacology, a section of the journal Frontiers in Pharmacology

Received: 19 August 2020
Accepted: 10 December 2020
Published: 21 January 2021

Citation:
Bai G-l, Hu K-l, Huan Y, Wang X, Lei L, Zhang M, Guo C-y, Chang H-s, Zhao L-b, Liu J, Shen Z-f, Wang X-l and Ni X (2021) The Traditional Chinese Medicine Fuyou Formula Alleviates Precocious Puberty by Inhibiting GPR54/GnRH in the Hypothalamus. Front. Pharmacol. 11:596525. doi: 10.3389/fphar.2020.596525

The purpose of this study was to explore the effect of the traditional Chinese medicine Fuyou formula on precocious puberty (PP). The Fy formula may exert an effect in female rats with PP and GT-7 cells through the GPR54/GnRH signaling pathway. To confirm the effect of the Fy formula on PP through the GPR54/GnRH signaling pathway, we first treated GT1-7 cells with the Fy formula and observed changes in the expression of related genes and proteins and in GnRH secretion. Then, we randomly divided young female Sprague-Dawley rats into the control group, model group, leuprorelin group and the Fy formula group. A PP model was established by injection of danazol on postnatal day 5, and the Fy formula was administered on PND15. The time of vaginal opening, the wet weights of the ovary and uterus, serum hormone levels and the expression of hypothalamic-related genes were observed. We found that the Fy formula delayed vaginal opening, decreased the wet weights and coefficients of the ovary and uterus, decreased the levels of serum hormones (E2, follicle-stimulating hormone and luteinizing hormone) and the cellular GnRH level, and downregulated the gene expression of Kiss1, GPR54 and GnRH in the hypothalamus and the gene and protein expression of GPR54 and GnRH in GT1-7 cells. In conclusion, the Fy formula may alleviate PP via the GPR54/GnRH signaling pathway.

Keywords: traditional Chinese medicine, Fy formula, precocious puberty, GPR54/GnRH, hypothalamic

INTRODUCTION

Precocious puberty (PP) is one of the most common endocrine diseases in children. PP is commonly defined as puberty that starts before age eight in Chinese girls and age nine in Chinese boys (Bradley et al., 2020), before age 7.5 in African-American and Hispanic girls, and before age eight in Caucasian girls (Herman-Giddens, 2006). The age of pubertal onset based on thelarche has decreased by almost 3 months per decade from 1977 to 2013 (Eckert-Lind et al., 2020). PP is characterized by early onset of puberty, such as early development of secondary sexual characteristics, rapid maturation of bones and acceleration of growth, and early menarche, early closure of the epiphyses, which may lead to poor social adaptability, psychological stress, emotional disorders, risky behaviors, a shorter adult height and future breast and ovarian cancer

(Abbasi, 2019; Fu et al., 2020). PP can be divided into central precocious puberty [CPP, gonadotropin-releasing hormone (GnRH)-dependent] and peripheral precocious puberty (PPP, GnRH-independent). The incidence of CPP in China is approximately 1% (Luan et al., 2007). The male to female ratio of patients with PP is approximately 1:5–10 (Teilmann et al., 2005; Dong et al., 2020), and 74% of the cases in girls with CPP are idiopathic (Bradley et al., 2020; Tao et al., 2020). Although the incidence of PP in boys is low, the disorder may be caused by certain serious diseases and should be given attention (Kaplowitz and Bloch, 2016). The onset of puberty is a complex biological process involving numerous factors under the control of neuroendocrine pathways that are regulated by the hypothalamus-pituitary-gonadal (HPG) axis. Tanner stages are used to evaluate pubertal development (Carel and Léger, 2008; Tena-Sempere, 2012). The key step in puberty onset is the early activation of pulsatile GnRH secretion (Ojeda et al., 2006; Latronico et al., 2016). The timing of PP onset depends on genetic and environmental factors, and numerous studies worldwide have shown that the onset of pubertal characteristics varies with race and ethnicity, genetics, environmental conditions, exposure to certain chemicals, geographical location and nutrition (Herman-Giddens et al., 2001; Latronico et al., 2016; Abbasi, 2019). Concerns about PP in girls are extremely common and are frequently raised by parents and other guardians.

Clinical strategies for the treatment of PP in children include a gonadotropin-releasing hormone analog (GnRHa), progesterone and traditional Chinese medicines (TCMs). GnRHa, which has been used clinically for the treatment of CPP treatment for 40 years, mainly contains triptorelin and leuprorelin, which can inhibit early initiation of the hypothalamus-pituitary-gonadal (HPG) axis, delay gonadal and bone development, delay epiphyseal closure and improve adult height (Kletter and Kelch, 1994; Mul and Hughes, 2008; Guaraldi et al., 2016; Fu et al., 2020). However, side effects, such as local hyperlipidemia, erythema, temporary vaginal bleeding, central obesity, body weight and bone mineral density loss, have been reported (Yu et al., 2014). Additionally, some patients require a combination of GnRHa and recombinant growth hormone (rhGH) to achieve the desired effect. However, not all patients who received combination treatment achieved satisfactory height gains (Kohn et al., 1999; Cisternino et al., 2002; Weise et al., 2004; Fu et al., 2020). CPP is diagnosed based on the GnRHa stimulation test (Carel et al., 2009). The assessment and management of this disease remain a challenge for pediatric endocrinologists (Latronico et al., 2016), and the Pediatric Endocrinology Society has suggested that the combination of GnRHa and rhGH should not be recommended as routine treatment because of its high cost and the lack of large-scale randomized clinical trials evaluating the safety and effectiveness of this combination therapy (Carel et al., 2009).

TCM formulas have played an important role in the modernization of TCM. However, there are many TCM compound preparations, which ingredients of which are complex, and most of them contain many minerals and animal medicinal materials. Some drugs have various bad tastes and smells, such as a bitter taste, astringent taste or sour taste. Therefore, the chemical composition of TCM formulas is more complex than that of a single herbal medicine.

TCM practitioners in China have used oral herbs to treat many pediatric diseases for thousands of years. CPP is rarely reported in ancient literature, probably because it is not very common. However, some Chinese herbal formulas, such as the Nourishing (Yin) Removing (Fire) Chinese herbal mixture (Sun et al., 2010; Wang et al., 2014b; He et al., 2018), Zhi Bai Di Huang Wan (Anemarrhena, Phellodendron, and Rehmannia Pill) (Cheng et al., 2013), Jia Wei Xiao Yao San (Supplemented Free Wanderer Powder) (Yamada and Kanba, 2002), Long Dan Xie Gan Tang (Gentian Liver Draining Decoction) (He et al., 2015), Xiang Sha Liu Jun Zi Tang (Costustoot and Amonum Six Gentlemen Decoction) (Xiao et al., 2012), Cang Er Zi San (Xanthium Powder) (Yang and Yu, 2008), Wen Dan Tang (Gallbladder-Warming Decoction) (Wang et al., 2014a), and Ma Zi Ren Wan (Hemp Seed Pill) (Hu et al., 2015), have been reported to alleviate PP.

Fuyou (Fy) formula is an in-hospital preparation that clears the liver, nourishes yin and removes fire, as described by pediatric gynecologists at Beijing Children's Hospital on the basis of TCM pathogene-sis and the physical characteristics of PP. The salt Anemarrhena and Radix Rehmanniae are the primary components of the Fy formula, which contains 11 TCMs that act together to clear the liver and disperse kont, nourish yin and remove fire. Our team found that clinical application over the past 20 years has suggested that the formula can control the early symptoms of PP in girls, reduce the size of the mammary glands, decrease the level of estrogen and delay the rate of bone maturation without obvious adverse reactions (Huili Liu and Liu, 2009; Pan Yu-chen and Liu, 2019).

In the present paper, we treated GT1-7 cells and young Sprague-Dawley (SD) rats with danazol-induced PP with the Fy formula and analyzed clinical data from a 1-year period. We confirmed the efficacy of the Fy formula for the treatment of PP and preliminarily identified the underlying mechanism. As children are a vulnerable group, it is not feasible to conduct randomized placebo-controlled clinical trials on these patients. Therefore, we compared clinical data before and after treatment.

MATERIALS AND METHODS

Chemicals and Reagents

Dulbecco's modified Eagle's medium (DMEM, 10–013-CV) and fetal bovine serum (FBS, 35–081-CVR) were obtained from Corning (NY, United States). Trypsin (0.25%) was purchased from Gibco (Grand Island, NY, United States). Isopropanol and chloroform were purchased from Sinopharm Chemical Reagent Co., Ltd. (Shanghai, China). Penicillin/streptomycin were obtained from Sigma-Aldrich (St. Louis, MO, United States). The other reagents were of analytical grade and had a purity of 99.5% or higher. Kisspeptin-10 (kp-10, 45–54) was purchased

TABLE 1 | Composition of the Fy formula.

Chinese name	Scientific name	Family	Lot No	Place of origin	Parts of plant used (voucher numbers)
Sheng Di Huang	*Rehmannia glutinosa* (Gaertn.) DC	Plantaginaceae	20181101	Henan, China	Dried root tuber (C18–11001)
Yan Zhi Mu	*Anemarrhena asphodeloides* Bunge	Asparagaceae	20180915	Hebei, China	Dried rhizome (C18–09358)
Cu Bie Jia	*Carapax Trionycis*	Trionyxsinensis Wiegmann	20180903	Hubei, China	Carapace (C18–09047)
Xia Ku Cao	*Prunella vulgaris L*	Lamiaceae	20181006	Jiangsu, China	Dried aerial parts (C18–10063)
Mu Dan Pi	*Paeonia x suffruticosa Andrews*	Paeoniaceae	20181008	Anhui, China	Dried root bark (C18–10127)
Chao Mai Ya	*Hordeum vulgare* L	Poaceae	20180912	Hebei, China	Fruit (C18–09270)
Xuan Shen	*Scrophularia ningpoensis* Hemsl	Scrophulariaceae	20180907	Zhejiang, China	Dried root tuber (C18–09126)
Di Gu Pi	*Lycium chinense* Mill	Solanaceae	20181112	Henan, China	Dried root bark (C18–11315)
Long Dan Cao	*Gentiana* scabra Bunge	Gentianaceae	20180514	Yunnan, China	Dried roots and rhizomes (C18–05490)
Ze Xie	*Alisma plantago-aquatica* L	Alismataceae	20181005	Fujian, China	Dried tuber (C18–10036)
Huang Bai	*Phellodendron chinense* C.K.Schneid	Rutaceae	20181027	Heilongjiang, China	Dried bark (C18–10661)

from Anaspec (San Jose, United States). Danazol was obtained from A&D Technology Corporation (Beijing, China). Leuprorelin acetate microspheres for injection were purchased from Livzon (Zhuhai, China). Leuprolide acetate was purchased from TargetMol (MA, United States). Rabbit anti-GPR54, rabbit anti-kiss1, and rabbit anti-HSP90A antibodies were all purchased from Absin Bioscience Inc. An anti-GnRH antibody was purchased from Lifespan (LS-C294315). Rabbit anti-Erk1/2 (4,695) and anti-pErk1/2 antibodies (4,370) were purchased from CST. ELISA kits for follicle-stimulating hormone (FSH), luteinizing hormone (LH), and estradiol (E2) were obtained from Cloud-Clone Corp. A mouse GnRH ELISA kit was obtained from mIbio (mI701852). The TCM standards Mangiferin (serial number: 111607, purity: 98.1%), Paeoniflorin (serial number: 110736, purity: 97.4%) and Gentiopicrin (serial number: 110770, purity: 98.2%) were purchased from the National Institutes for Food and Drug Control.

Preparation of the Traditional Chinese Medicine Fuyou Formula

The Fy formula was prepared by combining the following 11 medicinal plants: 10 g each of Sheng Di Huang [*Rehmannia glutinosa* (Gaertn.) DC, *Orobanchaceae*], Yan Zhi Mu [*Anemarrhena asphodeloides* Bunge, *Asparagaceae*], Cu Bie Jia (*Trionycis carapax*, *Trionyx sinensis* wiegmann), Xia Ku Cao (*Prunellae spica*, *Prunella vulgaris* L.), Mu Dan Pi (*Paeonia* × *suffruticosa* Andrews, *Paeoniaceae*), and Chao Mai Ya [*Hordeum vulgare* L. (*Poaceae*), *Poaceae*]; 6 g each of Xuan Shen (*Scrophularia ningpoensis* Hemsl, *Scrophulariaceae*), Di Gu Pi (*Lycium chinense* Mill, *Solanaceae*), Long Dan Cao (*Gentiana scabra* Bunge, *Gentianaceae*), and Ze Xie [*Alisma plantago-aquatica* subsp. Orientale (Sam.) Sam, *Alismataceae*]; and 3 g of Huang Bai (*Phellodendron chinense* C.K.Schneid, *Rutaceae*). The TCM compounds are listed in **Table 1**. The Fy formula dry paste powder was provided by Professor Ni Jian from Beijing University of Chinese Medicine after process optimization. The optimized process was as follows: 10 times the amount of water in the whole formulation was added, vinegar turtle was added for 30 min, the remaining 10 TCMs were added, the solution was extracted 3 times for 1 h each, the three decoctions were combined, and the extract was concentrated (at 60 °C) to obtain a dry paste powder. Powdered Fy (40 mg) was dissolved in 1 ml of distilled water and subjected to for ultrasonic treatment for 30 min (power: 250 W, frequency: 40 KHz). The solution was filtered with a 0.22 μm microporous filter membrane, and a sample was used to treated cells. The main components of the Fy formula were determined by high performance liquid chromatography (HPLC).

Animals

At postnatal day (PND)3, female SD rats and their mothers were obtained from SPF Biotechnology Co., Ltd. [Beijing, license no: SYXK (Beijing) 2016–0038]. The SD rats were housed at a constant temperature (23 ± 2°C) on a 12-h light:12-h dark cycle in an SPF animal room. The animals were provided food and water ad libitum and acclimated for three days before the experiment. All animal experiments were performed in strict compliance with Chinese guidelines, including the standards for Laboratory Animals (GB14925–2001) and the Guideline on the Humane Treatment of Laboratory Animals (MOST 2006), and all animal procedures were approved by the Beijing Administration Office for Laboratory Animals (approval number: SCXK-Beijing-2014-0004).

Animal Grouping and Drug Administration

The animals were randomly divided into four groups: the control group, model group, positive control (leuprorelin) group, and Fy formula (Fy) group. At PND5, the rats in the three groups were given a single subcutaneous injection of 300 μg/25 μL danazol (ethylene glycol: ethanol = 1:1, v/v) except the rats in the control group, which were given a subcutaneous injection of 25 μL of glycol/ethanol (Morishita et al., 1993; Ju et al., 2019). The rats in the leuprorelin group were subcutaneously injected with 100 μg/kg leuprorelin. The rats in the Fy group were given dry ointment powder solution by intragastric administration every day, and the rats in the control and model groups were given the same amount of normal saline. The vaginal opening was observed at PND20, and the vaginal exfoliated cells of the rats that exhibited vaginal opening were examined by smear. The rats that exhibited vaginal opening were sacrificed at diestrus after a complete estrous cycle, while the remaining rats were sacrificed at

the same time point. All rats were anesthetized by intraperitoneal injection of 2% pentobarbital sodium. Blood samples were collected from the abdominal aorta before execution, and the serum was separated after centrifugation (3,500 rpm, 20 min, 4°C) and preserved at −80°C for analysis of the serum hormone level. After the rats were sacrificed, the hypothalamus was removed, frozen in liquid nitrogen and stored at −80°C for further analysis. The uterus and ovaries were weighed to assess the organ coefficients (expressed as mg/100 g body weight) and fixed in formalin for hematoxylin and eosin (H&E) staining.

The Fy formula dose was calculated according to the clinical dosage administered to 6-year-old girls according to the following formula:

$$d_B = d_A \times R_B / R_A \times (W_A/W_B)^{1/3}$$

with d_B representing the animal/human body weight dose, d_A representing the known human/animal body weight dose, W_A and W_B representing known human and animal weights, respectively, and R_A and R_B representing known human/animal body shape coefficients, respectively. Every two days, the animals were weight, and the dose was recalculated.

Hormone Assay

The serum concentrations of FSH, LH and E2 were measured by kits for ELISA, which is a competitive inhibition enzyme immunoassay technique, purchased from Cloud-Clone Corp. (Wuhan, China). The samples were measured in duplicate, and all the samples were measured together. The minimum detectable concentration of FSH was less than 1.11 ng/ml, and the intra-assay and inter-assay coefficients were less than 10 and 12%, respectively. The minimum detectable concentration of LH was less than 37.59 pg/ml, and the intra-assay and inter-assay coefficients were less than 10 and 12%, respectively. The minimum detectable concentration of E2 was less than 4.45 pg/ml, and the intra-assay and inter-assay coefficients were less than 10 and 12%, respectively.

GT1-7 Cell Culture and Maintenance

Mouse GnRH-producing hypothalamic GT1-7 neurons (provided by Pamela L. Mellon, University of California San Diego) were cultured in complete fresh DMEM (Corning) containing 10% (v/v) heated-inactivated FBS and 1% antibiotics (100 U/ml penicillin/streptomycin) (Liu et al., 2018) under humidified conditions at 37°C in a 5% CO_2-containing atmosphere. The medium was changed every 3 days, and the cells were passaged at 90% confluency for subsequent experiments. The cell line was confirmed to be free of *mycoplasma* contamination by PCR and culture. When the cells reached approximately 85% confluence, they were washed twice with PBS, digested with 0.25% trypsin-EDTA and resuspended in a single-cell suspension. Then, 1.0×10^6 cells were seeded in a 6-well plate in 2 ml of medium containing 10% FBS for 24 h, and 2.0×10^4 cells were seeded in a 96-well Corning plate in 100 μL of medium containing 10% FBS for 24 h. Then, the cells were administered different treatments in serum-free medium (SFM) for 24 h depending on the experiment.

Cell Counting Kit-8 Assay

Cell counting kit-8 (CCK-8) was purchased from MCE. To assess the toxicity of the Fy formula, GT1-7 cells were seeded in 96-well tissue culture plates at a density of 2.0×10^4 cells per well in 100 μL of medium. After overnight incubation, the cells were incubated with 1.25, 2.5, 5, 10, 20, or 40 μg/ml Fy formula in SFM for 24 h at 37°C, and then 10 μL of CCK-8 solution (MCE, HY-K0301) was added to the cells. Following an incubation period of 1–4 h, the optical density (OD) was measured at 450 nm using an ELISA plate reader.

RNA Extraction and Quantification

Total RNA was extracted from frozen GT1-7 cells and hypothalamic tissue using TRIzol reagent (Invitrogen, United States). Purified total RNA was solubilized in diethylpyrocarbonate (DEPC)-treated water (Beyotime, China), and the concentration was determined using a Biodropsis BD-2000 spectrophotometer (OSTD Beijing Co., Ltd., China) at 260/280 or 260/230 nm. Two micrograms of total RNA was used as a template for reverse transcription using a cDNA synthesis kit (TransGen Biotech, AT311, TransScript One-Step gDNA Removal and cDNA Synthesis SuperMix), and the synthesized first-strand cDNA was stored at −80°C until use. The expression of each gene was quantified by real-time PCR (TransGen Biotech, AQ141, TransScript Tip Green qPCR SuperMix) using the following protocol: 1 cycle at 94°C for 30 s followed by 45 cycles at 94°C for 5 s, 60°C for 15 s and 72°C for 10 s. Briefly, the ΔCt value of each sample normalized to the internal control was calculated using the following equation: ΔCt = Ct (gene) − Ct (β-actin). To assess differences in expression between experimental and control conditions ΔΔCt was calculated with the following formula: ΔΔCt = ΔCt (sample) − ΔCt (control). The results are expressed as fold change in expression calculated by the $2^{\Delta\Delta Ct}$ method, and the levels of the of transcripts were normalized to the level of β-actin.

Single-stranded oligodeoxynucleotide primers for amplification of each gene were designed based on PubMed searches and were synthesized by Invitrogen (Beijing, China). The sequences of these primers are listed in **Table 2**.

GnRH mRNA Expression

GT1-7 cells were plated in 6-well plates at a density of 1.0×10^6 cells per well in 2 ml of complete medium and incubated overnight. Then, the medium was replaced with SFM, and the cells were treated with kp-10 at final concentrations of 10^{-11}, 10^{-9}, 10^{-8}, 10^{-7}, 10^{-6} or 10^{-5} M for four or 24 h. The optimal concentration and duration for GnRH activation were determined. Cells were co-incubated with the Fy formula and the optimal concentration of kp-10, and the effect of the Fy formula on the GnRH gene was investigated.

GnRH Secretion

GT1-7 cells were plated into 96-well plates, and after 24 h, the cells were treated with kp-10 at final concentrations of 10^{-11} to

TABLE 2 | Primer sequences for quantitative real-time polymerase chain reaction.

Gene	Forward primer (5′-3′)	Reverse primer (5′-3′)
β-actin (mouse and rat)	ACTCTTCCAGCCTTC CTTC	ATCTCCTTCTGCATCCTGTC
GnRH (mouse)	GGGAAGACATCAGTG TCCCAG	CTCGAGCTTCCGTTG GTAGG
GPR54 (mouse)	CTGTCAGCCTCAGCA TCTGG	AGCAGCGGCAGCAGA TATAG
Erα (mouse)	AAGACGCTCTTGAAC CAGCA	CGAGTTACAGACTGG CTCCC
Erβ (mouse)	AAGACGCTCTTGAAC CAGCA	CGAGTTACAGACTGG CTCCC
GnRH (rat)	TGGTATCCCTTTGGC TTTCACA	TGATCCTCCTCCTTGCCCAT
Kiss1 (rat)	CAATGGTCTGAACTG CCCAC	CACAGGTGCCATTTT TGCCA
GPR54 (rat)	CAACCTGCTGGCCCT ATACC	CTAGCAGCTGCAGGGCG

GnRH, gonadotropin-releasing hormone; Kiss1, Kiss-1 metastasis suppressor; GPR54, G-protein coupled receptor 54; Erα, estrogen receptor alpha; Erβ, estrogen receptor beta.

10^{-5} M for four or 24 h. To study the effects of the Fy formula in the presence of kp-10, cells were treated with 5 or 10 μg/ml Fy formula and 10^{-9} M kp-10 for 24 h. Then, the 96-well plate was centrifuged (1,000 rpm, 10 min), and the supernatant was transferred to a new 96-well plate for the determination of GnRH levels. RIPA lysis was added to the cells to adjust the protein concentration.

Protein Extraction and Western Blot Analysis

Western blot analysis was performed as previously described (Wang et al., 2017). To assess protein levels, GT1-7 cells were plated into 6-well culture plates at a density of 1.0×10^6 cells per well in 2 ml of SFM and incubated overnight. Then, the GT1-7 cells were incubated with noncytotoxic Fy formula concentrations for 24 h. Then, they were lysed in RIPA lysis buffer supplemented with protease and phosphatase inhibitor cocktail (Applygen Technologies, Inc., China), and the BCA assay was used for quantitative analysis. Equal amounts of protein samples were separated by electrophoresis on 10% sodium dodecyl sulfate polyacrylamide gels and transferred to polyvinylidene fluoride membranes. The membranes were blocked with 5% BSA in Tris-buffered saline containing 0.05% Tween 20 (TBS) for 1 h at room temperature and then incubated with primary antibody at 4°C in blocking buffer. The membranes were washed three times for 10 min with TBST and then incubated for 1 h at room temperature with a horseradish peroxidase-labeled secondary antibody (1:2,000, ZSGB-BIO, Inc., China). An enhanced chemiluminescence detection system was used to visualize the signal. Protein band densities were analyzed by Gel-Pro Analyzer 3.1 software, and the protein expression of β-actin was used as an internal standard.

Histopathological Evaluation of the Uterus

Uteri harvested from female rats were fixed in 4% paraformaldehyde, embedded in paraffin, and cut into 4-mm slices using a slicing machine. The degree of pathological improvement in the uterus was evaluated by H&E staining.

Statistical Analysis

All results are presented as the means ± SDs. Differences were analyzed by one-way ANOVA, and the data were plotted with GraphPad 7 (GraphPad Software, San Diego, CA). Differences were considered statistically significant when $p < 0.05$.

RESULTS

Multicomponent Quantification of the Fuyou Formula High Performance Liquid Chromatography

Analyses were performed using the LC Solution Chromatography workstation (Shimadzu Corporation, Kyoto, Japan). Chromatography was carried out at 30°C on an Angilent Zorbax C18 column (4.6 mm × 150 mm, 5 μm; Agilent Technologies, Santa Clara, CA, United States). The mobile phase consisted of acetonitrile and 0.2% (v/v) acetic acid-water solution (v/v = 9:91) for isocratic elution at a flow rate of 1.0 ml/min. The signal was monitored at wavelengths of 258 and 230 nm. The chromatograms of the standard mixture and Fy formula are presented in **Figure 1**.

The Fuyou Formula Delays Vaginal Opening in Female Rats With Precocious Puberty

In the model group, vaginal opening was observed at PND21 and was completed vaginal opening by PND26. Vaginal opening occurred at PND25 and PND23 in the leuprorelin and Fy groups, respectively. Complete vaginal opening occurred in six rats in the leuprorelin group, six rats in the Fy group, one rat in the control group and all rats in the model group. The mean time of vaginal opening in the Fy group (25.7 ± 2.1) was obviously delayed compared to that in the model group (22.9 ± 1.7, $p < 0.05$, **Figure 2A**).

The Fuyou Formula Inhibits Sex Organ Development in Rats with Danazol-Induced Precocious Puberty

As shown in **Table 3**, the wet weights of the uterus and ovaries, organ coefficients and uterine wall thickness in the model group were obviously lower than those in the control group, while the wet weights of the organs, organ coefficients and uterine wall thickness were significantly lower in the leuprorelin and Fy groups than the model group (**Figure 3**). We found that the fallopian tubes of the model group were obviously thicker than those of the control group and that the thickness of the fallopian tubes became more similar to that of the control group after administration of the Fy formula. The fallopian tubes of the leuprorelin group were thinner than those of the model group

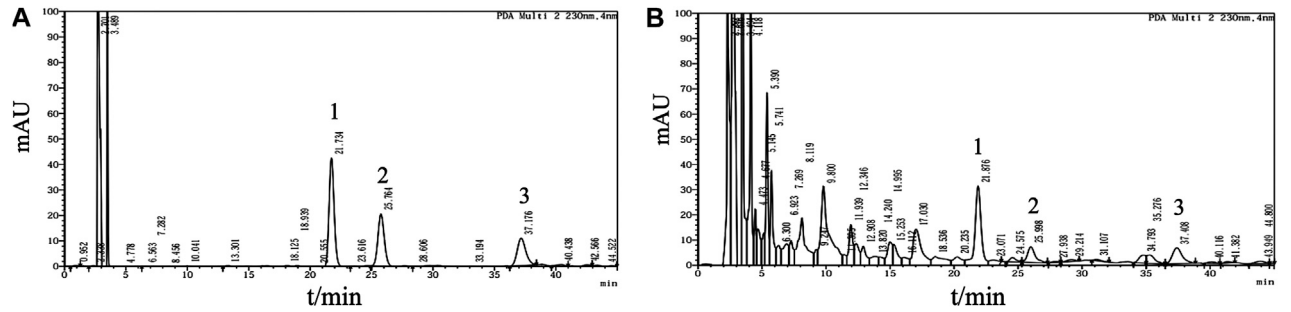

FIGURE 1 | Multicomponent quantification of the Fy formula. **(A)** Chromatogram of the mangiferin, paeoniflorin and gentiopicrin standard mixture. Peak one corresponds to gentiopicrin, peak two corresponds to mangiferin, and peak three corresponds to paeoniflorin. Mangiferin (1.5 mg), paeoniflorin (3 mg) and gentiopicrin (9 mg) were accurately weighed and placed in a 20 ml volumetric flask. The mixture was diluted with methanol to the mark on the flask and shaken to obtain a mixed standard mother liquor. Then, 1.5 ml of the mixed standard mother solution was added to a 5 ml volumetric flask and diluted with methanol to the mark on the flask to obtain the reference solution. **(B)** HPLC profile of the Fy formula. The powered compound extract (0.5 g) was accurately weighed and placed in a stoppered conical flask. Then, 25 ml of methanol was added, and the flask was tightly stoppered and weighed. The compound was subjected to ultrasonic treatment for 30 min, methanol was added until the original weight was obtained, and the compound was shaken well and filtered.

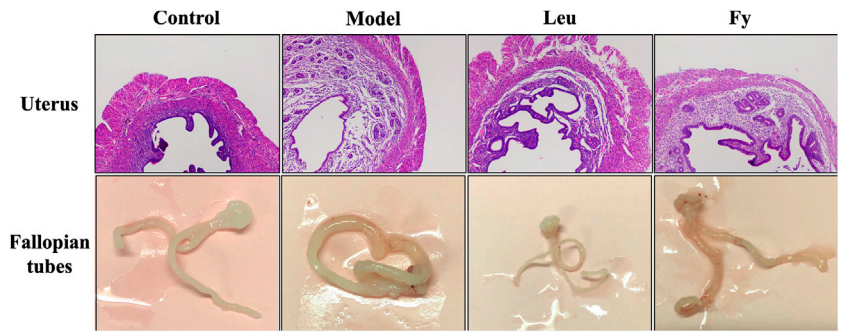

FIGURE 2 | Effects of the Fy formula on uterine wall thickness and fallopian tubes. The uterine wall was thicker in the model group than the control group and returned to normal thickness after administration of the Fy formula. The fallopian tubes of the model were thicker than those of the control group, and the fallopian tubes returned to normal thickness after administration of the Fy formula. However, in the leuprorelin group, the fallopian tubes were significantly thinner than those in the model group.

TABLE 3 | Uterine and ovarian wet weights, organ coefficients and uterine wall thickness (n = 8–10).

Group	Wet weight of the uterus (g)	Organ coefficient of the uterus (10^{-4})	Wet weight of the ovary (g)	Organ coefficient of the ovary (10^{-4})	Uterine wall thickness (mm)
Control	0.0962 ± 0.0230	10.81 ± 2.62	0.0406 ± 0.0053	4.58 ± 0.66	4.62 ± 2.10
Model	0.1841 ± 0.0496$^{\#\#\#}$	19.88 ± 5.21$^{\#\#\#}$	0.0508 ± 0.0069$^{\#\#}$	5.53 ± 1.08$^{\#}$	7.35 ± 1.98$^{\#}$
Leu	0.0402 ± 0.0083***	4.33 ± 0.67***	0.0149 ± 0.0023***	1.62 ± 0.26***	3.28 ± 1.90***
Fy	0.1363 ± 0.0253*	15.00 ± 3.09*	0.0391 ± 0.0059**	4.30 ± 0.66*	4.84 ± 1.27*

(**Figure 3**), indicating that leuprorelin affects the normal development of rats and should be combined with growth hormone, as described in the literature (Weise et al., 2004).

The Fuyou Formula Decreases Blood Hormone Levels and Inhibits GPR54 Expression in Rats with Danazol-Induced Precocious Puberty

ELISA was employed to evaluate the serum levels of the hormones E2, LH and FSH in PP rats. The results suggested that the levels of hormones E2, LH and FSH were higher in the model group than in the control group ($p < 0.001$). However, the levels of E2, LH and FSH in the leuprorelin and Fy formula groups were obviously lower than those in the model group (**Figures 2B–D**).

We observed that the gene expression of kiss1, GPR54 and GnRH was obviously lower in the hypothalamic of SD rats with danazol-induced PP than in the hypothalamic of control rats and that the Fy formula and leuprorelin significantly reduced the expression of kiss1, GPR54 and GnRH genes compared with that in the model group (**Figures 2E–G**). However, there was no significant difference in GPR54 gene expression between the control and model groups.

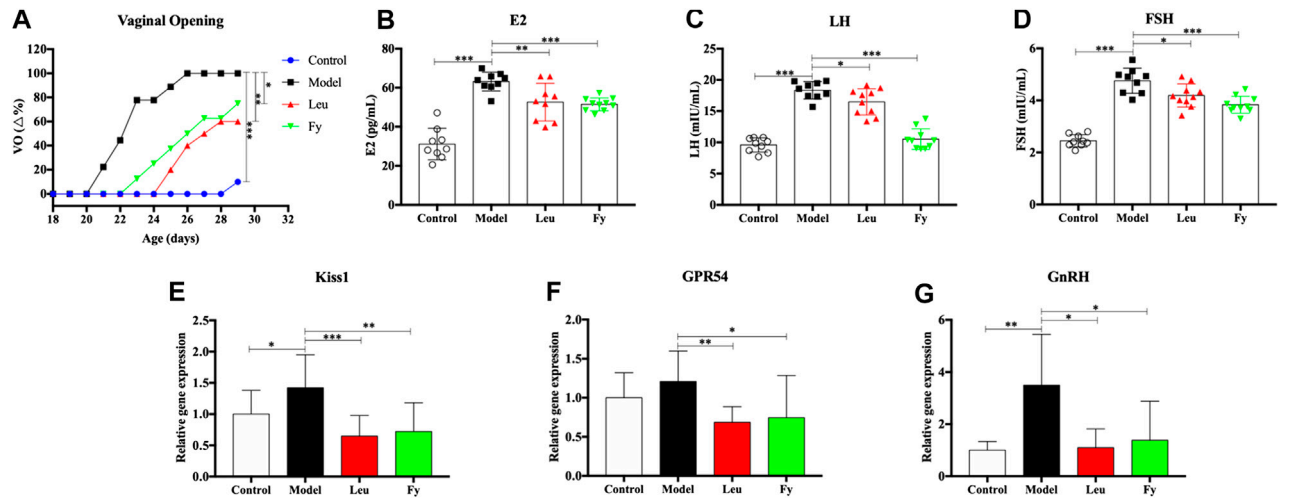

FIGURE 3 | Effects of the Fy formula on vaginal opening **(A)**, serum levels of the hormones E2, LH and FSH **(B–D)** and gene expression in the hypothalamus **(E–G)** in female rats with PP. **(A)** The day of vaginal opening was earlier in the model group than in the control group and was significantly delayed by leuprorelin and the Fy formula. **(B–D)** The serum levels of the hormones E2, LH and FSH were significantly higher in the model group than the control group and lower in the leuprorelin and Fy formula groups than the model group. **(E–G)** The gene expression of Kiss1 and GnRH, but not GPR54, in the hypothalamus was higher in the model group than the control group, and the expression of all three genes was decreased after administration of leuprorelin and the Fy formula. $^{*}p < 0.05$, $^{**}p < 0.01$, $^{***}p < 0.001$ vs the model group.

The Fuyou Formula Downregulates the Expression and Secretion of GnRH in Hypothalamic GT1-7 Neurons

The effect of the Fy formula on the viability of GT1-7 cells was compared with that of vehicle treatment. The maximum noncytotoxic concentration of the Fy formula was 10 μg/ml (**Supplementary Figure S1**). To ensure that the Fy formula was administered at a sufficient concentration to exerts the desired effects, the final treatment concentrations for all subsequent experiments in GT1-7 cells were 5 and 10 μg/ml. Changes in GnRH mRNA expression in GT1-7 cells after treatment with different concentrations of kp-10 for 4 or 24 h were evaluated by RT-PCR. The expression of GnRH mRNA was the highest when GT1-7 cells were treated with kp-10 at a concentration of 10^{-9} M for 24 h (**Supplementary Figure S2**).

To further evaluate the mechanism by which the Fy formula affects the release of GnRH in GT1-7 cells via the GPR54/GnRH signaling pathway, the gene expression of GPR54, GnRH, estrogen receptor α (Erα) and estrogen receptor β (Erβ) in GT1-7 cells treated with kp-10 was detected by RT-PCR. The RT-PCR results showed that compared with vehicle treatment, treatment with 10^{-9} M kp-10 for 24 h significantly upregulated the gene expression of GPR54, GnRH, Erα and Erβ (**Figures 4A–D**) in GT1-7 cells. Additionally, the expression of GnRH, GPR54, and Erβ in the Fy + kp-10 groups, except for Erα expression in the Fy5 + kp-10 group, was significantly lower that than in the kp-10 group.

To evaluate the effect of the Fy formula on GnRH secretion, GT1-7 cells were treated with five or 10 μg/ml Fy formula. Kp-10 significantly elevated GnRH secretion; however, compared with kp-10, the Fy formula significantly decreased GnRH secretion in a concentration-dependent manner (**Figure 4E**).

The Fuyou Formula Inhibits the GPR54/GnRH Pathway in GT1-7 Hypothalamic Neuronal Cells

To additionally investigate the potential molecular mechanism underlying the effect of the Fy formula on the release of GnRH via the GPR54/GnRH signaling pathway, western blot analysis of the protein expression of GPR54, GnRH, PKC and pErk1/2 was conducted in GT1-7 cells treated with the Fy formula (5 or 10 μg/ml). GT1-7 cells expressed the GPR54 protein, as previously reported (Novaira et al., 2009b). We also performed western blot analysis of total and phosphorylated PKC and pErk1/2, as phosphorylation of these proteins is considered to be the main cellular signaling event in GPR54/GnRH activation. The protein levels of GnRH and PKC and the phosphorylation of Erk were decreased by incubation with Fy (10 μg/ml), as shown in **Figures 5C–E**. Compared with the vehicle, Fy formula at concentrations of 5 and 10 μg/ml decreased the protein expression of GPR54 (**Figure 5B**).

DISCUSSION

PP is defined as puberty that occurs before the age of 8 years in girls and before the age of 9 years in boys. PP has a far-reaching influence on children's growth, development and mental health. Chinese herbal medicines have been proven to be effective in regulating the development of puberty, but their mechanisms are still unclear (Wang et al., 2014b; Yu et al., 2014). The GPR54/

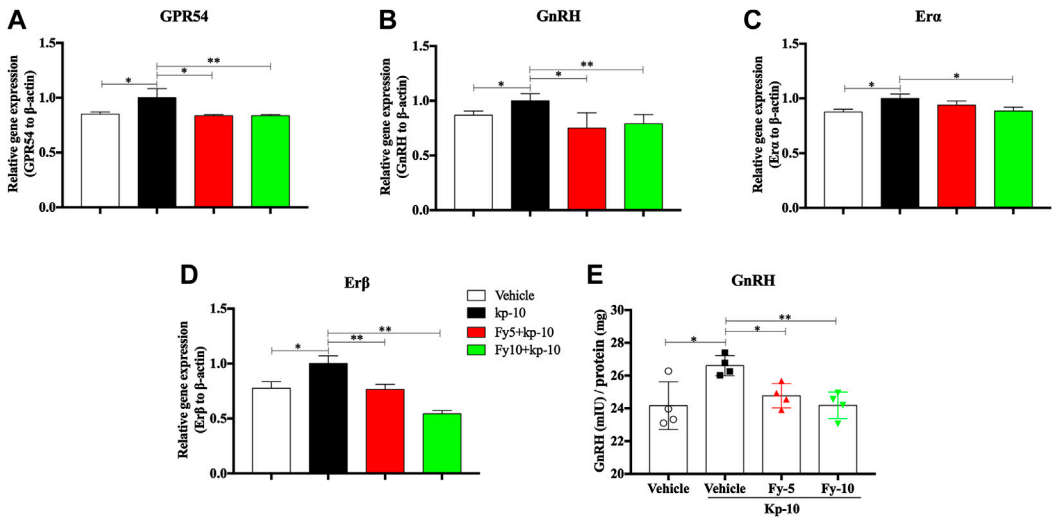

FIGURE 4 | Effects of the Fy formula on GnRH mRNA expression **(A–D)** and secretion in GT1-7 cells **(E)**. GT1-7 cells were divided into the vehicle group (untreated GT1-7 cells), kp-10 group (GT1-7 cells treated with kp-10), and Fy + kp-10 group (GT1-7 cells treated with 5 or 10 μg/ml Fy formula and kp-10 for 24 h). **(A–D)** The gene expression of GPR54, GnRH, Erα and Erβ was higher in the kp-10 group than the vehicle group and lower in the Fy formula group than the vehicle group. **(E)** Cells treated with kp-10 (24 h) exhibited increased secretion of GnRH and decreased secretion when coincubated with the Fy formula. *$p < 0.05$, **$p < 0.01$, ***$p < 0.001$ vs. the kp-10 group.

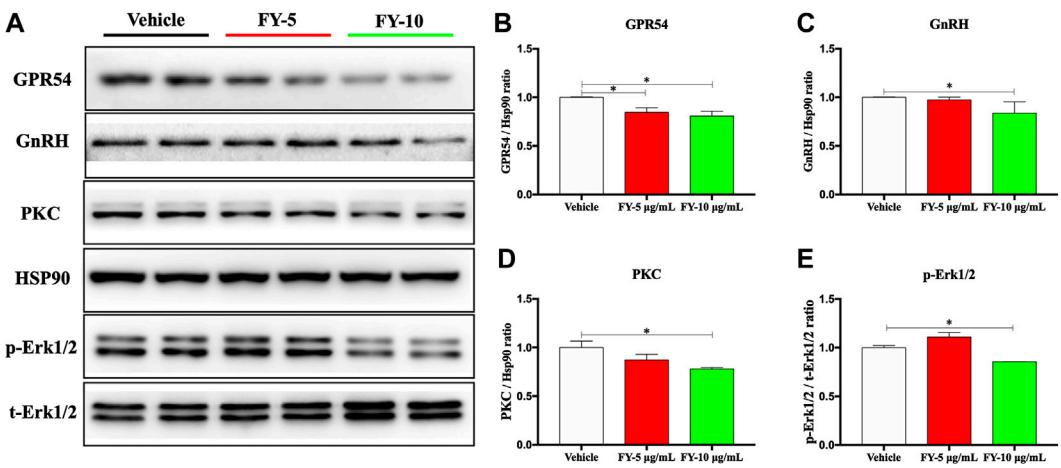

FIGURE 5 | Effects of the Fy formula on GPR54, GnRH, PKC and pErk1/2 expression. **(A)** Representative images of western blots for GPR54, GnRH, PKC and pErk expression in GT1-7 cells after treatment with the Fy formula (5 or 10 μg/ml) for 24 h **(B–E)** Statistical analysis of GPR54, GnRH, PKC and pErk1/2 expression. *$p <$ 0.05 vs. the vehicle group.

GnRH signaling pathway plays an important role in puberty development. The purpose of this study was to investigate the effects of the Fy formula on the GPR54/GnRH signaling pathway in GT1-7 cells and female rats with PP.

Danazol, an isoxazole derivative of 17α-ethynyl testosterone, has a variety of effects on the reproductive system, high affinity for androgen receptors, moderate affinity for glucocorticoid receptors and poor affinity for estrogen receptors. This study showed that subcutaneous injection of 300 μg of danazol into PND5 female rats accelerated the onset of sexual development, increased the weights of the uterus and ovary, increased the release of GnRH from the hypothalamus and accelerated HPG axis activation in rats, thus hastening sexual maturity without increasing the body of the rats (Morishita et al., 1993; Sun et al., 2010). These findings suggest that the rat hypothalamus is immature at birth, hypothalamic maturation may occur from 1 to 10 days after birth, and subcutaneous injection of danazol into newborn rats may quicken the maturation of the hypothalamus-pituitary axis and induce true PP (Sun et al., 2007).

Vaginal opening is a sign of puberty in female rats (Sun et al., 2007). Our experiment showed that the time of vaginal opening was significantly advanced in the model group compared with the control group ($p < 0.001$). After administration of leuprorelin and the Fy formula, vaginal opening was significantly delayed

compared with that in the model group ($p < 0.05$, **Figure 2A**). The wet weights and organ coefficients of the uterus and ovary in the model group were significantly higher than those in the control group ($p < 0.05$) and were decreased after leuprorelin and Fy formula treatment ($p < 0.05$, **Table 3**). The fallopian tubes were thicker in the model group than the control group and returned to normal thickness after administration of the Fy formula. However, the fallopian tubes were significantly thinner in the leuprorelin group than the model group (**Supplementary Figure S2**), suggesting that leuprorelin affects the normal development of sex organs and should be combined with growth hormone (Benabbad et al., 2018). The Fy formula and leuprorelin decreased the serum levels of the hormones E2, LH and FSH compared with those in the model group, suggesting that the Fy formula can significantly delay puberty onset in female rats.

Although the physiological structure of humans is different from that of rodents, the Fy formula was shown to have therapeutic effects in both PP patients and a rat model of danazol-induced PP. As an in-hospital formula of Beijing Children's Hospital, the Fy formula has been used for the management of PP for more than twenty years. These findings confirm the clinical benefits of the Fy formula, which is an advantageous therapeutic approach in our country due to its low cost. We enrolled patients who were treated for more than one year. The clinical data revealed that the Fy formula markedly reduced the serum levels of estrogen in patients, significantly decreased mammary gland size, and delayed bone maturation in girls with PP (**Supplementary Table S1**). Moreover, several Chinese reports also indicated that the Fy formula of Chinese herbs has a good intervention effect on girl's ovarian cysts complicated with PP, causing most ovarian cysts to disappear (Pan Yu-chen and Liu, 2019). The clear clinical efficacy of the Fy formula is enough to prove its effective role in the treatment of PP in children. However, the physiological structure and function of humans and rats are different, so more evidence is needed to prove the mechanism of the Fy formula.

The research in humans and mice has shown that mutations or deletions in GPR54 lead to puberty failure and infertility, which suggests that the kisspeptin-GPR54 signaling pathway is absolutely essential for fertility (De Roux et al., 2003; Seminara et al., 2003; Clarkson, 2013). Subsequent research has shown that the loss of Kiss1 gene function in mice and humans results in pubertal disorders and infertility symptoms similar to GPR54 knockout (Topaloglu et al., 2012). Studies in the last decade have shown that kisspeptin and GPR54 are important regulators of GnRH activity. During puberty maturation, the increased expression of kiss1 mRNA and kisspeptin peptide in the hypothalamus is an important in promoting the full activation of GnRH nerve cells, and plays an important role in adolescent maturation and adult reproductive physiology (Clarkson, 2013), Therefore, kisspeptin mainly regulates reproductive events, such as precocious puberty, primarily by activating the GPR54 receptor indicated by GnRH neurons in the hypothalamus.

To further explore the role of GPR54/GnRH in the effects of the Fy formula on PP, gene expression was analyzed. Our results showed that kiss1, GPR54 and GnRH mRNA expression was higher in the model group than in the control group. One of our most obvious findings was that compared to vehicle, the Fy formula significantly downregulated the gene expression of the Kiss1, GPR54 and GnRH in the hypothalamus of female rats with PP (**Figures 2E–G**). Previous studies have shown that the Kiss1 gene is involved in the development of sexual maturity during early puberty in normal female rats (Sun et al., 2007; Sun et al., 2010) and that kisspeptin administration into the hypothalamus of immature female rats can significantly advance vaginal opening, significantly increase uterine weight (Navarro et al., 2004), and induce precocious activation of the HPG axis and PP development (Plant et al., 2006; Trevisan et al., 2018). These findings suggest that the Fy formula may inhibit the expression of the kiss1 gene, weaken the binding between kisspeptin and GPR54, and ultimately reduce the pulsed secretion of GnRH, weakening the activation of downstream pituitary and gonadal development and thus alleviating PP.

Kisspeptin and its cognate receptor GPR54 are major regulators of the HPG axis (Szereszewski et al., 2010). Kisspeptin is a neuropeptide encoded by the kiss1 gene and secreted in the hypothalamus. Kisspeptin has a highly conservative region at the C-terminal sequence, consisting of 10 amino acids, named kisspeptin-10 (Pasquier et al., 2014). GPR54 couples to the $G_{q/11}$ protein when kisspeptin-10 stimulates GPR54, and $G_{q/11}$ activates phospholipase C and hydrolyzes PIP2 to produce the second messengers IP3 and DAG. IP3 stimulates the endoplasmic reticulum (ER), increasing the levels of intracellular Ca^{2+} and activating Ca-dependent signaling pathways in GnRH neurons, and DAG activates protein kinase C (PKC), activates extracellular signal-regulated kinases one and two in GnRH neurons, and promotes hypothalamic secretion of GnRH (Kotani et al., 2001; Harter et al., 2018; Trevisan et al., 2018). The function of kisspeptin in GnRH neurons also requires the activation of additional signaling mechanisms in the family of MAPKs, which have a strong continuous stimulation effect on the phosphorylation of MAPK extracellular signal-regulating kinases Erk1 and Erk2 (Chianese et al., 2016). Kisspeptin is produced by two main groups of neurons located in the hypothalamus, namely, neurons in the rostral periventricular area of the third ventricle (RP3V) and neurons in the arcuate nucleus (ARC). Kisspeptin produced in the ARC is generally considered to be the generator of GnRH. GPR54 is mainly expressed in the hypothalamus, specifically the POA (Herbison et al., 2010), and is expressed by most GnRH-secreting neurons. Human GPR54 is highly expressed in the placenta, anterior pituitary, pancreas, liver, adipose tissue and spinal cord, suggesting that it plays a role in the regulation of endocrine function (Kotani et al., 2001; Ohtaki et al., 2001). In humans and rats, the onset of puberty is caused by an increase in GnRH pulsed secretion. True PP is mediated by a premature increase in GnRH secretion and should be treated with a potent GnRHa (Tian et al., 2005). The administration of exogenous kisspeptin can advance the puberty of immature rodent (rats) and primates (monkeys) (Plant et al., 2006), on the contrary, administration of kisspeptin antagonist delayed puberty in rats and monkeys (Skorupskaite et al., 2014; Li et al., 2020). These findings show that kisspeptin plays an important role in the regulation of HPG axis.

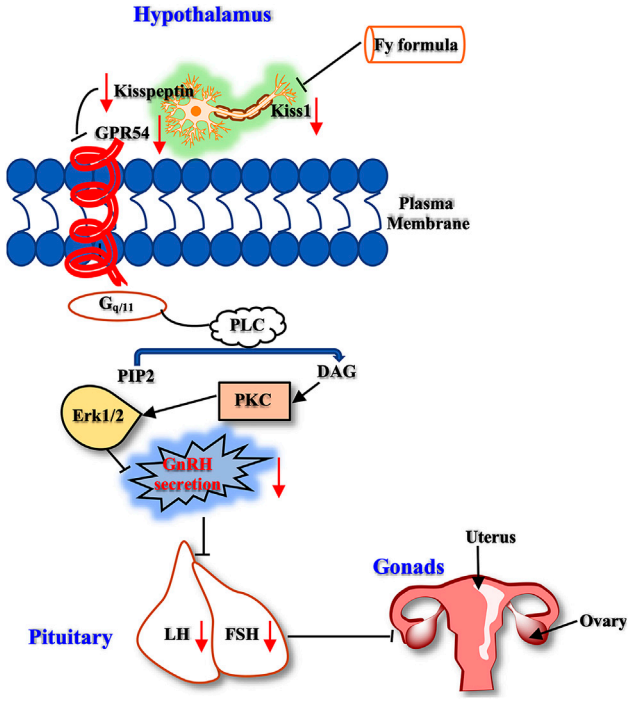

FIGURE 6 | The GPR54/GnRH signaling pathway in the HPG axis. The Fy formula inhibits the gene expression of Kiss1, decreases the secretion of kisspeptin, and weakens the stimulating effect on the kisspeptin receptor GPR54. Gq/11 inhibits PLC, which reduces the hydrolysis of PIP2. This process leads to a decrease in the production of the second messenger DAG, which inhibits the downstream Erk1/2 signaling pathway, resulting in a decrease in GnRH secretion, weakening the stimulatory effect on the pituitary gland, reducing the secretion of LH and FSH, and inhibiting gonadal development.

Therefore, kisspeptin mainly regulates reproductive events, such as precocious puberty, primarily by activating the GPR54 receptor indicated by GnRH neurons in the hypothalamus. In the present study, we designed a series of experiments to investigate the mechanism of the Fy formula. First, we determined that kisspeptin at a concentration of 10^{-9} M had a direct effect on GT1-7 cells and upregulated the expression of the GPR54, GnRH, Erα and Erβ genes (**Figure 4**; **Supplementary Figure S2**). These results are consistent with previous reports showing that which kisspeptin can promote the GnRH system (Clarkson et al., 2008; Novaira et al., 2009a). Kisspeptin binds to GPR54 and stimulates hypothalamic neurons to release GnRH, leading to the secretion of gonadotropins (LH and FSH) and sex steroids, which in turn act on the gonads to produce gametes, by the pituitary gland (Trevisan et al., 2018). The Fy formula (10 μg/ml) decreased the gene expression of GPR54, GnRH, Erα and Erβ, which was increased by kisspeptin in GT1-7 cells (**Figures 4A–D**). Kisspeptin-10 not only upregulated the expression of the GnRH gene but also increased the secretion of GnRH in GT1-7 cells (**Figure 4E**), which is consistent with previous results (Lehnert and Khadra, 2019). However, after administration of the Fy formula, the secretion of GnRH was significantly decreased (**Figure 4E**). To confirm the effect of the Fy formula on the GPR54/GnRH signaling pathway in GT1-7 cells, we investigated its effects on related proteins and found that the Fy formula significantly downregulated the protein expression of GPR54, PKC and GnRH and the phosphorylation of Erk1/2 (**Figure 5**). These results indicate that the Fy formula inhibits Kiss1 gene expression, reduces the expression of kisspeptin, reduces the binding of GPR54 to Gq/11, inhibits the hydrolysis of PIP2 and the Erk1/2 signaling pathway, decreases the secretion of hypothalamic GnRH, weakens the stimulation of the pituitary gland, reduces the secretion of the gonadotropins LH and FSH and sex steroids, inhibits gonadal gamete production and alleviates the symptoms of PP (**Figure 6**) (Roseweir and Millar, 2009; Trevisan et al., 2018).

In this study, the therapeutic effect of the Fy formula on PP was studied in GT1-7 cells and in a rodent model. Additionally, it has also been observed clinically that the Fy formula can reduce the estrogen level in girls with PP, significantly decreased mammary gland size, and delayed bone maturation. However, because the clinical sample size in this study was small, the data may have been slightly skewed. Therefore, it is necessary to increase the clinical sample size and evaluate clinical indicators at a later stage to more comprehensively assess the curative effect of the Fy formula.

CONCLUSION

In summary, the Fy formula reduced blood hormone levels, downregulated the gene expression of kiss1, GPR54 and GnRH in female rats with danazol-induced PP and downregulated GnRH gene and protein expression and hormone secretion induced by kp-10 in GT1-7 cells. The GPR54/GnRH signaling pathway may be involved in the effects of the Fy formula on PP. The potential mechanism of action of the Fy formula needs to be further revealed to provide support for its clinical application.

DATA AVAILABILITY STATEMENT

The original contributions presented in the study are included in the article/**Supplementary Material**, further inquiries can be directed to the corresponding authors.

ETHICS STATEMENT

The studies involving human participants were reviewed and approved by Ethics Committee of Beijing Children's Hospital (IEC-C-008-A08-V.05.1). Written informed consent to participate in this study was provided by the participants' legal guardian/next of kin. The animal study was reviewed and approved by Animal Ethics Committee of Capital Medical University (AEEI-2020-084). Written informed consent was

obtained from the individual(s), and minor(s)' legal guardian/ next of kin, for the publication of any potentially identifiable images or data included in this article.

AUTHOR CONTRIBUTIONS

GB performed the investigation and wrote the paper. KH, YH, XW, LL and HC participated in the collection and preparation of rat samples. MZ, CG and JL participated in the collection of patients data. LZ, ZS, XW, and XN designed the study and revised the paper. All authors reviewed and approved the final manuscript.

FUNDING

This work was supported by the National Major Science and Technology Projects of China, China (grant no. 2018ZX09721003) and the Capital Special Health Development Research (grant no. 2018-2-2097).

SUPPLEMENTARY MATERIAL

The Supplementary Material for this article can be found online at: https://www.frontiersin.org/articles/10.3389/fphar.2020.596525/full#supplementary-material.

REFERENCES

Abbasi, J. (2019). Chemicals in consumer products associated with early puberty. *JAMA*. 321 (16), 1556. doi:10.1001/jama.2019.1111

Benabbad, I., Rosilio, M., Tauber, M., Paris, E., Paulsen, A., Berggren, L., et al. (2018). Growth hormone in combination with leuprorelin in pubertal children with idiopathic short stature. *Endocr. Connect*. 7 (5), 708–718. doi:10.1530/ec-18-0137

Bradley, S. H., Lawrence, N., Steele, C., and Mohamed, Z. (2020). Precocious puberty. *BMJ*. 368, l6597. doi:10.1136/bmj.l6597

Carel, J. C., and Léger, J. (2008). Clinical practice. Precocious puberty. *N. Engl. J. Med*. 358 (22), 2366–2377. doi:10.1056/NEJMcp0800459

Carel, J. C., Eugster, E. A., Rogol, A., Ghizzoni, L., Palmert, M. R., Antoniazzi, F., et al. (2009). Consensus statement on the use of gonadotropin-releasing hormone analogs in children. *Pediatrics*. 123 (4), e752–62. doi:10.1542/peds.2008-1783

Cheng, M., Ye, X. D., Miao, Y. P., Chen, A. Y., and Zheng, G. L. (2013). Experimental study on therapeutic effect of Dabuyin Wan on true precocious puberty in female rats. *Zhongguo Zhong Yao Za Zhi*. 38 (3), 386–390. doi:10.4268/cjcmm20130319

Chianese, R., Cobellis, G., Chioccarelli, T., Ciaramella, V., Migliaccio, M., Fasano, S., et al. (2016). Kisspeptins, estrogens and male fertility. *Curr. Med. Chem*. 23 (36), 4070–4091. doi:10.2174/0929867323666160902155434

Cisternino, M., Draghi, M., Lauriola, S., Scarcella, D., Bernasconi, S., Cavallo, L., et al. (2002). The acid-labile subunit of human ternary insulin-like growth factor-binding protein complex in girls with central precocious puberty before and during gonadotropin-releasing hormone analog therapy. *J. Clin. Endocrinol. Metab*. 87 (10), 4629–4633. doi:10.1210/jc.2002-020308

Clarkson, J., D'anglemont De Tassigny, X., Moreno, A. S., Colledge, W. H., and Herbison, A. E. (2008). Kisspeptin-GPR54 signaling is essential for preovulatory gonadotropin-releasing hormone neuron activation and the luteinizing hormone surge. *J. Neurosci*. 28 (35), 8691–8697. doi:10.1523/jneurosci.1775-08.2008

Clarkson, J. (2013). Effects of estradiol on kisspeptin neurons during puberty. *Front. Neuroendocrinol*. 34 (2), 120–131. doi:10.1016/j.yfrne.2013.02.002

De Roux, N., Genin, E., Carel, J. C., Matsuda, F., Chaussain, J. L., and Milgrom, E. (2003). Hypogonadotropic hypogonadism due to loss of function of the KiSS1-derived peptide receptor GPR54. *Proc. Natl. Acad. Sci. U.S.A*. 100 (19), 10972–10976. doi:10.1073/pnas.1834399100

Dong, G., Zhang, J., Yang, Z., Feng, X., Li, J., Li, D., et al. (2019). The association of gut microbiota with idiopathic central precocious puberty in girls. *Front. Endocrinol*. 10, 941. doi:10.3389/fendo.2019.00941

Eckert-Lind, C., Busch, A. S., Petersen, J. H., Biro, F. M., Butler, G., Bräuner, E. V., et al. (2020). Worldwide secular trends in age at pubertal onset assessed by breast development among girls: a systematic review and meta-analysis. *JAMA Pediatr*. 174 (4), e195881. doi:10.1001/jamapediatrics.2019.5881

Juul, J., Zhang, J., Chen, R., Ma, X., Wang, C., Chen, L., et al. (2020). Long-Term outcomes of treatments for central precocious puberty or early and fast puberty in Chinese girls. *J. Clin. Endocrinol. Metab*. 105 (3). doi:10.1210/clinem/dgz027

Guaraldi, F., Beccuti, G., Gori, D., and Ghizzoni, L. (2016). Management of endocrine disease: long-term outcomes of the treatment of central precocious puberty. *Eur. J. Endocrinol*. 174 (3), R79–R87. doi:10.1530/eje-15-0590

Harter, C. J. L., Kavanagh, G. S., and Smith, J. T. (2018). The role of kisspeptin neurons in reproduction and metabolism. *J. Endocrinol*. 238 (3), R173–R183. doi:10.1530/joe-18-0108

He, Y. M., Zhu, S., Ge, Y. W., Kazuma, K., Zou, K., Cai, S. Q., et al. (2015). The anti-inflammatory secoiridoid glycosides from gentianae scabrae radix: the root and rhizome of Gentiana scabra. *J. Nat. Med*. 69 (3), 303–312. doi:10.1007/s11418-015-0894-8

He, Y., Han, X., Sun, W., Yu, J., and Tamadon, A. (2018). Precocious puberty and the Lin28/Let7 pathway: the therapeutic effect of the nourishing "yin" and purging "fire" traditional Chinese medicine mixture in a rat model. *Evid. Based Complement. Alternat. Med*., 2018, 4868045. doi:10.1155/2018/4868045

Herbison, A. E., De Tassigny, X., Doran, J., and Colledge, W. H. (2010). Distribution and postnatal development of Gpr54 gene expression in mouse brain and gonadotropin-releasing hormone neurons. *Endocrinology*. 151 (1), 312–321. doi:10.1210/en.2009-0552

Herman-Giddens, M. E., Wang, L., and Koch, G. (2001). Secondary sexual characteristics in boys: estimates from the national health and nutrition examination survey III, 1988–1994. *Arch. Pediatr. Adolesc. Med*. 155 (9), 1022–1028. doi:10.1001/archpedi.155.9.1022

Herman-Giddens, M. E. (2006). Recent data on pubertal milestones in United States children: the secular trend toward earlier development. *Int. J. Androl*. 29 (1), 241–290. Discussion 286–290. doi:10.1111/j.1365-2605.2005.00575.x

Hu, D. D., Han, Q. B., Zhong, L. L., Li, Y. H., Lin, C. Y., Ho, H. M., et al. (2015). Simultaneous determination of ten compounds in rat plasma by UPLC-MS/MS: application in the pharmacokinetic study of Ma-Zi-Ren-Wan. *J. Chromatogr. B. Analyt. Technol. Biomed. Life Sci*. 1000, 136–146. doi:10.1016/j.jchromb.2015.07.003

Huili Liu, J. L., and Liu, G. (2009). Clinical study on 60 cases of girls with true precocious puberty treated with Fuyou mixture. *Beijing J. Tradit. Chin. Med*. 28 (8), 588–589. doi:10.13288/j.11-2166/r.1998.10.011

Ju, M., Yang, L., Zhu, J., Chen, Z., Zhang, M., Yu, J., et al. (2019). MiR-664-2 impacts pubertal development in a precocious-puberty rat model through targeting the NMDA receptor-1. *Biol. Reprod*. 100 (6), 1536–1548. doi:10.1093/biolre/ioz044

Kaplowitz, P., and Bloch, C. (2016). Evaluation and referral of children with signs of early puberty. *Pediatrics*. 137 (1). doi:10.1542/peds.2015-3732

Kletter, G. B., and Kelch, R. P. (1994). Clinical review 60: effects of gonadotropin-releasing hormone analog therapy on adult stature in precocious puberty. *J. Clin. Endocrinol. Metab*. 79 (2), 331–334. doi:10.1210/jcem.79.2.8045943

Kohn, B., Julius, J. R., and Blethen, S. L. (1999). Combined use of growth hormone and gonadotropin-releasing hormone analogues: the national cooperative growth study experience. *Pediatrics*. 104 (4 Pt 2), 1014–1018. doi:10.1542/peds.104.4.998

Kotani, M., Detheux, M., Vandenbogaerde, A., Communi, D., Vanderwinden, J. M., Le Poul, E., et al. (2001). The metastasis suppressor gene KiSS-1 encodes

kisspeptins, the natural ligands of the orphan G protein-coupled receptor GPR54. *J. Biol. Chem*. 276 (37), 34631–34636. doi:10.1074/jbc.M104847200

Latronico, A. C., Brito, V. N., and Carel, J. C. (2016). Causes, diagnosis, and treatment of central precocious puberty. *Lancet Diabetes Endocrinol*. 4 (3), 265–274. doi:10.1016/S2213-8587(15)00380-0

Lehnert, J., and Khadra, A. (2019). How pulsatile kisspeptin stimulation and GnRH autocrine feedback can drive GnRH secretion: a modeling investigation. *Endocrinology*. 160 (5), 1289–1306. doi:10.1210/en.2018-00947

Li, D., Wu, Y., Cheng, J., Liu, L., Li, X., Chen, D., et al. (2020). Association of polymorphisms in the kisspeptin/GPR54 pathway genes with risk of early puberty in Chinese girls. *J. Clin. Endocrinol. Metab*. 105 (4). doi:10.1210/clinem/dgz229

Liu, Y., Bai, J. H., Xu, X. L., Chen, Z. L., Spicer, L. J., Feng, T., et al. (2018). Effects of N-carbamylglutamate and L-arginine on gonadotrophin-releasing hormone (GnRH) gene expression and secretion in GT1-7 cells. *Reprod. Fertil. Dev*. 30 (5), 759–765. doi:10.1071/RD17265

Luan, X., Yu, H., Wei, X., Zhou, Y., Wang, W., Li, P., et al. (2007). GPR54 polymorphisms in Chinese girls with central precocious puberty. *Neuroendocrinology*. 86 (2), 77–83. doi:10.1159/000107511

Morishita, H., Takemoto, M., Kondo, H., Higuchi, K., and Aono, T. (1993). Induction of true precocious puberty by neonatal treatment with danazol in female rats. *Neurosci. Lett*. 157 (1), 33–36. doi:10.1016/0304-3940(93)90636-y

Mul, D., and Hughes, I. A. (2008). The use of GnRH agonists in precocious puberty. *Eur. J. Endocrinol*. 159 (Suppl. 1), S3–S8. doi:10.1530/eje-08-0814

Navarro, V. M., Fernández-Fernández, R., Castellano, J. M., Roa, J., Mayen, A., Barreiro, M. L., et al. (2004). Advanced vaginal opening and precocious activation of the reproductive axis by KiSS-1 peptide, the endogenous ligand of GPR54. *J. Physiol*. 561 (Pt 2), 379–386. doi:10.1113/jphysiol.2004.072298

Novaira, H. J., Ng, Y., Wolfe, A., and Radovick, S. (2009a). Kisspeptin increases GnRH mRNA expression and secretion in GnRH secreting neuronal cell lines. *Mol. Cell. Endocrinol*. 311 (1–2), 126–134. doi:10.1016/j.mce.2009.06.011

Novaira, H. J., Ng, Y., Wolfe, A., and Radovick, S. (2009b). Kisspeptin increases GnRH mRNA expression and secretion in GnRH secreting neuronal cell lines. *Mol. Cell. Endocrinol*. 311 (1–2), 126–134. doi:10.1016/j.mce.2009.06.011

Ohtaki, T., Shintani, Y., Honda, S., Matsumoto, H., Hori, A., Kanehashi, K., et al. (2001). Metastasis suppressor gene KiSS-1 encodes peptide ligand of a G-protein-coupled receptor. *Nature*. 411 (6837), 613–617. doi:10.1038/35079135

Ojeda, S. R., Lomniczi, A., Mastronardi, C., Heger, S., Roth, C., Parent, A. S., et al. (2006). Minireview: the neuroendocrine regulation of puberty: is the time ripe for a systems biology approach? *Endocrinology*. 147 (3), 1166–1174. doi:10.1210/en.2005-1136

Pan Yu-Chen, L. J., and Liu, H. L. (2019). Clinical observation on treatment of ovarian cyst complicated with precocious puberty in girls with Chinese herbal medicine Fuyou Mixture. *Beijing J. Trad. Chin. Med*. 38 (07), 700–703. doi:10.16025/j.1674-1307.2019.07.021

Pasquier, J., Kamech, N., Lafont, A. G., Vaudry, H., Rousseau, K., and Dufour, S. (2014). Molecular evolution of GPCRs: kisspeptin/kisspeptin receptors. *J. Mol. Endocrinol*. 52 (3), T101–T117. doi:10.1530/jme-13-0224

Plant, T. M., Ramaswamy, S., and Dipietro, M. J. (2006). Repetitive activation of hypothalamic G protein-coupled receptor 54 with intravenous pulses of kisspeptin in the juvenile monkey (*Macaca mulatta*) elicits a sustained train of gonadotropin-releasing hormone discharges. *Endocrinology*. 147 (2), 1007–1013. doi:10.1210/en.2005-1261

Roseweir, A. K., and Millar, R. P. (2009). The role of kisspeptin in the control of gonadotrophin secretion. *Hum. Reprod. Update*. 15 (2), 203–212. doi:10.1093/humupd/dmn058

Seminara, S. B., Messager, S., Chatzidaki, E. E., Thresher, R. R., Acierno, J. S., Jr., Shagoury, J. K., et al. (2003). The GPR54 gene as a regulator of puberty. *N. Engl. J. Med*. 349 (17), 1614–1627. doi:10.1056/NEJMoa035322.

Colledge, K., George, J. T., and Anderson, R. A. (2014). The kisspeptin-GnRH pathway in human reproductive health and disease. *Hum. Reprod. Update*. 20 (4), 485–500. doi:10.1093/humupd/dmu009

Sun, Y., Tian, Z., Zhao, H., Wong, S. T., and Chen, B. (2007). Characteristic of hypothalamic kisspeptin expression in the pubertal development of precocious female rats. *Neurosci. Lett*. 420 (1), 12–17. doi:10.1016/j.neulet.2007.04.003

Sun, Y., Perry, G. N., Yu, J., Chen, B., and Tian, Z. (2010). Effect of nourishing "Yin"-removing "Fire" Chinese herbal mixture on hypothalamic kisspeptin expression in female precocious rats. *J. Ethnopharmacol*. 127 (2), 274–279. doi:10.1016/j.jep.2009.11.009

Szereszewski, J. M., Pampillo, M., Ahow, M. R., Offermanns, S., Bhattacharya, M., Babwah, A. V., et al. (2010). GPR54 regulates ERK1/2 activity and hypothalamic gene expression in a Gα(q/11) and β-arrestin-dependent manner. *PLoS One*. 5 (9), e12964. doi:10.1371/journal.pone.0012964

Tao, Y., Si, C., Li, H., Han, J., Hou, H., Yang, M., et al. (2020). Effect of gonadotropin-releasing hormone analog on ovarian reserve in children with central precocious puberty. *Ann. Palliat. Med*. 9 (1), 53–62. doi:10.21037/apm.2020.01.04

Teilmann, G., Pedersen, C. B., Jensen, T. K., Skakkebaek, N. E., Juul, A., et al. (2005). Prevalence and incidence of precocious pubertal development in Denmark: an epidemiologic study based on national registries. *Pediatrics*. 116 (6), 1323–1328. doi:10.1542/peds.2005-0012

Tena-Sempere, M. (2012). Deciphering puberty: novel partners, novel mechanisms. *Eur. J. Endocrinol*. 167 (6), 733–747. doi:10.1530/eje-12-0669

Tian, Z., Zhao, H., Sun, Y., Cai, D., and Chen, B. (2005). Evaluation of the true precocious puberty rats induced by neonatal administration of Danazol: therapeutic effects of nourishing "Yin"-Removing "Fire" Chinese herb mixture. *Reprod. Biol. Endocrinol*. 3, 38. doi:10.1186/1477-7827-3-38

Topaloglu, A. K., Tello, J. A., Kotan, L. D., Ozbek, M. N., Yilmaz, M. B., Erdogan, S., et al. (2012). Inactivating KISS1 mutation and hypogonadotropic hypogonadism. *N. Engl. J. Med*. 366 (7), 629–635. doi:10.1056/NEJMoa1111184

Trevisan, C. M., Montagna, E., De Oliveira, R., Christofolini, D. M., Barbosa, C. P., Crandall, K. A., et al. (2018). Kisspeptin/GPR54 system: what do we know about its role in human reproduction? *Cell. Physiol. Biochem*. 49 (4), 1259–1276. doi:10.1159/000493406

Wang, L., Song, Y., Li, F., Liu, Y., Ma, J., Mao, M., et al. (2014a). Effects of Wen Dan Tang on insomnia-related anxiety and levels of the brain-gut peptide Ghrelin. *Neural. Regen. Res*. 9 (2), 205–212. doi:10.4103/1673-5374.125351

Wang, L., Zhu, L., Yu, J., and Tian, Z. (2014b). Effect of nourishing "Yin"-Removing "fire" Chinese herbal mixture on hypothalamic NKB/NK3R expression in female precocious rats. *Evid. Based Complement. Alternat. Med*., 2014, 217424. doi:10.1155/2014/217424

Wang, A., Wang, J., Zhang, S., Zhang, H., Xu, Z., Li, X., et al. (2017). Curcumin inhibits the development of non-small cell lung cancer by inhibiting autophagy and apoptosis. *Exp. Ther. Med*. 14 (5), 5075–5080. doi:10.3892/etm.2017.5172

Weise, M., Flor, A., Barnes, K. M., Cutler, G. B., Jr., and Baron, J. (2004). Determinants of growth during gonadotropin-releasing hormone analog therapy for precocious puberty. *J. Clin. Endocrinol. Metab*. 89 (1), 103–107. doi:10.1210/jc.2002-021999

Xiao, Y., Liu, Y. Y., Yu, K. Q., Ouyang, M. Z., Luo, R., and Zhao, X. S. (2012). Chinese herbal medicine Liu Jun Zi Tang and Xiang Sha Liu Jun Zi Tang for functional dyspepsia: meta-analysis of randomized controlled trials. *Evid. Based Complement. Alternat. Med*. 2012, 936459. doi:10.1155/2012/936459

Yamada, K., and Kanba, S. (2002). Herbal medicine (kami-shoyo-san) in the treatment of premenstrual dysphoric disorder. *J. Clin. Psychopharmacol*. 22 (4), 442. doi:10.1097/00004714-200208000-00023

Yang, S. H., and Yu, C. L. (2008). Anti-inflammatory effects of Bu-Zhong-Yi-Qi-Tang in patients with perennial allergic rhinitis. *J. Ethnopharmacol*. 115 (1), 104–109. doi:10.1016/j.jep.2007.09.011

Yu, C. H., Liu, P. H., Van, Y. H., Lien, A. S., Huang, T. P., Yen, H. R., et al. (2014). Traditional Chinese medicine for idiopathic precocious puberty: a hospital-based retrospective observational study. *Compl. Ther. Med*. 22 (2), 258–265. doi:10.1016/j.ctim.2014.01.002

Conflict of Interest: The authors declare that the research was conducted in the absence of any commercial or financial relationships that could be construed as a potential conflict of interest.

The reviewer PZ declared a shared affiliation with the authors to the handling editor at the time of the review.

Copyright © 2021 Bai, Hu, Huan, Wang, Lei, Zhang, Guo, Chang, Zhao, Liu, Shen, Wang and Ni. This is an open-access article distributed under the terms of the Creative Commons Attribution License (CC BY). The use, distribution or reproduction in other forums is permitted, provided the original author(s) and the copyright owner(s) are credited and that the original publication in this journal is cited, in accordance with accepted academic practice. No use, distribution or reproduction is permitted which does not comply with these terms.

frontiers in Pharmacology

ORIGINAL RESEARCH
published: 21 January 2021
doi: 10.3389/fphar.2020.586498

Paeonol Protects Against Myocardial Ischemia/Reperfusion-Induced Injury by Mediating Apoptosis and Autophagy Crosstalk

Chin-Feng Tsai[1,2], Hsing-Hui Su[3], Ke-Min Chen[4], Jiuan-Miaw Liao[5], Yi-Ting Yao[2], Yi-Hung Chen[6,7,8], Meilin Wang[9], Ya-Chun Chu[10], Yi-Hsin Wang[2,3]* and Shiang-Suo Huang[2,3,11]**

[1]Division of Cardiology, Department of Internal Medicine, Chung Shan Medical University Hospital, Taichung, Taiwan, [2]School of Medicine, Institute of Medicine, Chung Shan Medical University, Taichung, Taiwan, [3]Department of Pharmacology, Chung Shan Medical University, Taichung, Taiwan, [4]Department of Parasitology, Chung Shan Medical University, Taichung, Taiwan, [5]Department of Physiology, Chung Shan Medical University and Chung Shan Medical University Hospital, Taichung, Taiwan, [6]Graduate Institute of Acupuncture Science, China Medical University, Taichung, Taiwan, [7]Research Center for Chinese Medicine and Acupuncture, China Medical University, Taichung, Taiwan, [8]Department of Photonics and Communication Engineering, Asia University, Taichung, Taiwan, [9]Department of Microbiology and Immunology, School of Medicine, Chung-Shan Medical University, Taichung, Taiwan, [10]Department of Anesthesiology, Taipei Veterans General Hospital and National Yang-Ming University, Taipei, Taiwan, [11]Department of Pharmacy, Chung Shan Medical University Hospital, Taichung, Taiwan*

OPEN ACCESS

Edited by:
Yanqiong Zhang,
China Academy of Chinese Medical Sciences, China

Reviewed by:
Haolong Liu,
Peking University Health Science Center, China
Yujie Li,
China Academy of Chinese Medical Sciences, China

***Correspondence:**
Ya-Chun Chu
yachunchu@gmail.com
Yi-Hsin Wang
dolphin11298@gmail.com
Shiang-Suo Huang
sshuang@csmu.edu.tw

Specialty section:
This article was submitted to Ethnopharmacology, a section of the journal Frontiers in Pharmacology

Received: 23 July 2020
Accepted: 30 November 2020
Published: 21 January 2021

Citation:
Tsai C-F, Su H-H, Chen K-M, Liao J-M, Yao Y-T, Chen Y-H, Wang M, Chu Y-C, Wang Y-H and Huang S-S (2021) Paeonol Protects Against Myocardial Ischemia/Reperfusion-Induced Injury by Mediating Apoptosis and Autophagy Crosstalk. Front. Pharmacol. 11:586498. doi: 10.3389/fphar.2020.586498

Many studies have shown that crosstalk exists between apoptosis and autophagy, despite differences in mechanisms between these processes. Paeonol, a major phenolic compound isolated from Moutan *Cortex Radicis*, the root bark of *Paeonia* × *suffruticosa* Andrews (Paeoniaceae), is widely used in traditional Chinese medicine as an antipyretic, analgesic and anti-inflammatory agent. In this study, we investigated the detailed molecular mechanisms of the crosstalk between apoptosis and autophagy underlying the cardioprotective effects of paeonol in rats subjected to myocardial ischemia/reperfusion (I/R) injury. Myocardial I/R injury was induced by occlusion of the left anterior descending coronary artery (LAD) for 1 h followed by 3 h of reperfusion. Paeonol was intravenously administered 15 min before LAD ligation. We found that paeonol significantly improved cardiac function after myocardial I/R injury and significantly decreased myocardial I/R-induced arrhythmia and mortality. Paeonol also significantly decreased myocardial infarction and plasma LDH activity and Troponin-I levels in carotid blood after I/R. Compared with vehicle treatment, paeonol significantly upregulated Bcl-2 protein expression and significantly downregulated the cleaved forms of caspase-8, caspase-9, caspase-3 and PARP protein expression in the I/R injured myocardium. Myocardial I/R-induced autophagy, including the increase of Beclin-1, p62, LC3-I, and LC3-II protein expression in the myocardium was significantly reversed by paeonol treatment. Paeonol also significantly increased the Bcl-2/Bax and Bcl-2/Beclin-1

Abbreviations: ±dp/dtmax, the maximal rate of left ventricular pressure increase and decrease; AAR, Area at risk; Bax, B-cell lymphoma-2-associated X protein; Bcl-2, B-cell lymphoma-2; BP, arterial blood pressure; HR, heart rate; I/R, ischemia/reperfusion; LAD, left anterior descending coronary artery; LC3, light chain 3; LDH, lactate dehydrogenase; LVSP, left ventricular systolic pressure; mTOR, mammalian target of rapamycin; PARP, poly (ADP-ribose) polymerase; VT, ventricular tachycardia; VF, ventricular fibrillation.

ratios in the myocardium after I/R injury. The cardioprotective role of paeonol during I/R injury may be due to its mediation of crosstalk between apoptotic and autophagic signaling pathways, which inhibits apoptosis and autophagic cell death.

Keywords: apoptosis, autophagy, paeonol, myocardial ischemia/reperfusion injury, crosstalk

INTRODUCTION

Recent studies have shown that cardiomyocyte death is the main reason for the poor prognosis of patients with ischemic heart disease (Chiong et al., 2011; Teringova and Tousek, 2017). The most appropriate clinical strategy to limit myocardial infarct size, preserve cardiac function and improve both quality of life and survival in patients with ischemic heart disease is to minimize myocardial ischemia/reperfusion (I/R) injury-induced cardiomyocyte death, such as necrosis, apoptosis, or autophagy (Tian et al., 2013). Necrosis is marked by defective plasma membrane integrity, cellular and organellar swelling, and marked inflammation. Apoptosis and autophagy differ from necrosis, in that neither apoptosis nor autophagy exhibit myocardial inflammation and they share many death signals that regulate cell death, which may be important signaling pathways in myocardial I/R injury (Oerlemans et al., 2013). Apoptosis, characterized by chromatin condensation, nuclear fragmentation, cell shrinkage and production of apoptotic bodies, is a major mechanism of regulated cell death during myocardial I/R injury (Xia et al., 2016). Autophagy is activated in order to remove damaged organelles and stimulate phagocytic clearance of apoptotic cells (Zou et al., 2012). Evidence suggests that autophagy is beneficial during ischemia, functioning as a protein quality controller and cellular homeostasis keeper; however, excessive autophagic activity degrades essential proteins and organelles, leading to progressive consumption of proteins or organelles and autophagic cell death during I/R (Zeng et al., 2016). Even if the mechanisms differ between autophagy and apoptosis, some proteins modulate both autophagy and apoptosis. It is well documented that the crosstalk between autophagy and apoptosis is mediated by the functional and structural interactions between Beclin-1 and Bcl-2. Beclin-1, the mammalian orthologue of yeast Atg6, is part of the class III phosphatidylinositol 3-kinase (PI3K) complex that induces autophagy. Bcl-2 is not only an important regulator in apoptosis, but also an anti-autophagic protein via its inhibitory interaction with Beclin-1 (Pattingre et al., 2005). Notably, after interacting with Bcl-2, Beclin-1 is sequestrated away from the Vps34/class III PI3K complex and autophagy is inhibited, whereas Bcl-2 maintains anti-apoptotic potential (Levine et al., 2008; Ciechomska et al., 2009). Evidence has shown that the interplay between autophagy and apoptosis is closely related to I/R injury, so recent studies have therefore focused on the crosstalk between these cell death processes (Li M. et al., 2016; Dong et al., 2019).

Paeonol, a major phenolic constituent extracted from Moutan *Cortex Radicus*, the root bark of *Paeonia* × *suffruticosa* Andrews (Paeoniaceae), and the root of *Paeonia lactiflora Pall*, is widely used as a nutrient supplement and as an antipyretic, analgesic and anti-inflammatory agent in traditional Chinese medicine. Paeonol is associated with a wide range of biological effects, including antiplatelet aggregation (Koo et al., 2010), antioxidative (Ding et al., 2016) and anti-inflammatory activity (Lei et al., 2016). Paeonol also demonstrates antiatherosclerotic activity via the upregulation of autophagy and inhibition of vascular smooth muscle cell proliferation (Wu et al., 2017), and prevents oxidized low-density lipoprotein (ox-LDL)-induced injury to vascular endothelial cells by inhibiting excessive autophagy, increasing miR-30a levels and reducing Beclin-1 protein expression (Li et al., 2018). Furthermore, paeonol decreases cerebral infarction and neurological deficits in rats subjected to focal cerebral I/R injury (Hsieh et al., 2006; Liao et al., 2016) and has proven cardioprotective effects in rats subjected to myocardial I/R injury, improving hemorrheology indexes, decreasing oxidative injury and repairing endothelial function (Yang et al., 2010). Paeonol has also demonstrated activity against cardiotoxicity induced by epirubicin, a chemotherapeutic agent, by upregulating epirubicin-induced reductions in miR-1 expression and suppressing the phosphatidylinositol 3-kinase (PI3K)/AKT and the mammalian target of rapamycin (mTOR) signaling pathways, and NF-κB signaling pathways (Wu et al., 2018).

None of these previous reports has determined whether the crosstalk between apoptosis and autophagy may play a role in the cardioprotective effect of paeonol. Our investigation is the first to examine the molecular mechanisms involved in the crosstalk between apoptosis and autophagy that underlie the cardioprotective effects of paeonol in rats subjected to myocardial I/R injury.

MATERIALS AND METHODS

Methods

All study protocols were performed in accordance with those in the *Guide for the Care and Use of Laboratory Animals* published by the National Research Council (United States) Committee (National Academies of Sciences, 2011). All efforts were taken to reduce the numbers of sacrificed animals and to minimize animal suffering.

Animals

All experiments and postoperative animal care were reviewed and approved by the Institutional Animal Care and Use Committee of Chung Shan Medical University (IACUC-1772). We used male Sprague-Dawley rats (LASCO Co., Charles River Technology, Taipei, Taiwan) weighing 250–350 g. The animals were housed in a room under controlled temperature (24 ± 1 °C) and humidity

(55 ± 5%) conditions and subjected to a 12:12 h light-dark cycle. They were allowed free access to food and water.

Surgical Procedure

Myocardial I/R injury was induced by temporary occlusion of the left anterior descending coronary artery (LAD), as per previously described procedures (Wang et al., 2016). Briefly, the rats were anesthetized with a single intraperitoneal injection of urethane (1.25 g/kg) and then placed on a heated, small animal operating table. After tracheotomy, the intubated animals were ventilated with room air through a respirator for small rodents (Model 131, NEMI, United States) with a stroke volume of 15 ml/kg body weight and rate of 60 strokes/min. The jugular vein was cannulated to administer drugs and polyethylene catheters (PE-50) were inserted into the common carotid artery with a Statham P23 XL transducer to continuously monitor heart rate (HR) and arterial blood pressure (BP). A standard 1-lead ECG recorded heart rhythm via silver electrodes attached to the extremities and the adequacy of anesthetic depth. Data were acquired with a MP35 physiological recorder (BIOPAC Systems, Inc., United States).

The heart was exposed via left thoracotomy and the fourth and fifth ribs were sectioned approximately 2 mm to the left of the sternum. The heart was rapidly externalized and inverted. A 6/0 silk ligature was then placed around the left main coronary artery. The heart was repositioned in the chest and the animal was allowed to recover for 15 mins. Animals that developed arrhythmia or sustained a decrease in mean BP to less than 70 mmHg during the procedure were not included in the study. A small plastic snare from a Portex P-270 cannula was threaded through the ligature and placed in contact with the heart. The left coronary artery was then occluded by tightening the ligature and reperfusion was achieved by releasing the tension applied to the ligature (operated groups). Successful ligation of the coronary artery was validated by decreased arterial pressure and ECG changes (increase in R wave and ST segment elevation), which are indicators of ischemia. Sham-operated animals underwent the same surgical procedure, except that the silk ligature that was placed around the left coronary artery was not tied. Changes in HR, BP, and ECG were simultaneously recorded using a personal computer with waveform analysis software (AcqKnowledge, Biopac System, Goleta, CA, United States) before and during the ischemia and reperfusion periods. To evaluate antiarrhythmic effects of paeonol during myocardial I/R injury, we occluded the coronary artery for 1 h and then subjected it to reperfusion for 3 h. The ventricular ectopic activity was evaluated according to the diagnostic criteria advocated by the Lambeth Conventions (Curtis et al., 2013). Incidence and duration of ventricular tachyarrhythmias, including ventricular tachycardia (VT) and ventricular fibrillation (VF), were determined in the surviving rats and in the rats that eventually died. In rats with irreversible VF, the duration of VF was recorded until mean BP was <15 mmHg. To evaluate the effect of paeonol on cardiac function during myocardial I/R injury, a Millar catheter was inserted into the left ventricular cavity via the right common carotid artery and changes in the left ventricular systolic pressure (LVSP), left ventricular diastolic pressure (LVDP), maximal slope of systolic pressure increment (max dP/dt) and diastolic decrement (min dP/dt) were continuously recorded using a Transonic Scisense Pressure Measurement system (SP200, Transonic Scisense Inc., Ontario, Canada).

Experimental Groups

Most research has shown that the effective dose range for paeonol cardioprotection is 2.5–100 mg/kg by intragastric or intraperitoneal administration (Yang et al., 2010; Li et al., 2012; Ma et al., 2015; Li H. et al., 2016; Wu et al., 2018). However, recent data indicate that paeonol has higher bioavailability by intranasal and intravenous administration routes in rats compared with the intragastric route (Chen et al., 2010; Adki and Kulkarni, 2020). We therefore investigated the cardioprotective effects of 0.1 and 1 mg/kg paeonol by intravenous administration in rats subjected to myocardial I/R injury. In this study, the solution of paeonol (purity ≧ 98%, Cat. sc-205787, Santa Cruz, Dallas, TX, United States) was freshly prepared and intravenously administered 15 mins before LAD ligation. The rats were randomly assigned to one of five groups: 1) Sham-vehicle: rats underwent all surgical procedures except LAD occlusion and were treated with vehicle (0.1% dimethyl sulfoxide [DMSO] in normal saline); 2) Sham-P-1: rats underwent all surgical procedures except LAD occlusion and were treated with paeonol (1 mg/kg); 3) I/R-Control: rats were treated with vehicle and underwent myocardial I/R injury; 4) I/R-P-0.1: rats were treated with paeonol (0.1 mg/kg) and underwent myocardial I/R injury; or 5) I/R-P-1: rats were treated with paeonol (1 mg/kg) and underwent myocardial I/R injury.

Estimation of Myocardial Infarct Size and Myocardial Damage

The sizes of both the ischemic zone and infarct zone in the rats' hearts were determined by previously described procedures (Wang et al., 2016). Evaluation of the infarct zone and collection of myocardium samples for further analyses were carried out in rats that survived 1 h of ischemia and 3 h of reperfusion. At the end of the experiment, the coronary artery was reoccluded, and 2.0 ml of 0.1% Evans blue solution was intravenously injected to stain non-ischemic myocardium and determine the area at risk. The heart was then excised and the atria were removed. Ventricular tissues were sliced into 2 mm sections and incubated in tetrazolium dye (2% 2,3,5-triphenyltetrazolium chloride [Sigma, United States] in normal saline) at 37 °C for 30 mins in darkness. The sections were placed in a solution of 10% formaldehyde in saline for 1 day before excision of infarcted (white) tissues. The weight of the infarcted tissues is expressed as a percentage of the total ventricle or the area at risk. In addition, arterial blood collected from the carotid catheter in rats that survived after 1 h of ischemia and 3 h of reperfusion was centrifuged at 3,000 g for 10 mins to isolate plasma and determine *in vivo* heart injury. Myocardial cellular damage was determined using automated clinical analyzers to measure plasma activities of lactate dehydrogenase (LDH) (ADVIA 1800; Siemens Healthcare Diagnostics Inc., NY,

United States) and the levels of Troponin-I (Centaur, Siemens Healthcare Diagnostics Inc., NY, United States).

Western Blot

For reducing the number of animal sacrifices in this study, the effective dose of paeonol 1 mg/kg was applied to investigate the underlying mechanism involved in the cardioprotective effect of paeonol. Protein expression was evaluated by Western blot, as per previously described procedures (Su et al., 2019). The hearts of rats with myocardial I/R injury were homogenized in T-PER Tissue Protein Extraction Reagent (Thermo Scientific, United States) containing protease Inhibitor Cocktail (Thermo Scientific, United States). The homogenates were centrifuged at 10,000 g for 10 mins at 4 °C. Protein concentration was determined with protein assay kits (BioRad, United States) using bovine serum albumin (BSA) as the standard. Samples were mixed with an equal volume of loading buffer (62.5 mM Tris-HCl, pH 6.8, 10% [v/v] glycerol, 2% SDS, 5% [v/v] 2-mercaptoethanol and 0.05% [w/v] bromophenol blue) and heated for 10 min at 95 °C. The mixture was subjected to SDS-PAGE and transferred electrophoretically to nitrocellulose membranes at a constant current of 70 V for 120 mins. Membranes were blocked with 5% (w/v) non-fat milk in PBS containing 0.1% (v/v) Tween 20 (PBST) for 1 h at room temperature. Membranes were reacted with primary antibodies at 37 °C for 1 h. Membranes were washed three times with PBST and HRP-conjugated secondary antibody (1:10,000 dilution) was added and incubated at 37 °C for 1 h to detect primary bound antibody. Reactive proteins were detected by enhanced chemiluminescence (T-Pro Biotechnology, Taiwan R.O.C.) and the density of specific immunoreactive bands was quantified by densitometric scanning.

Antibodies

Primary Antibodies

Anti-caspase 3, anti-caspase 9, anti-caspase 8, anti-PARP (Cell Signaling, Danvers, MA, United States), anti-mTOR (Spring Bioscience, Pleasanton, CA, United States), anti-phospho mTOR (Santa Cruz, Dallas, TX, United States), anti-Bcl-2, anti-Bax (Abcam, Cambridge, MA, United States), anti-p62, anti-Beclin-1, anti-light chain 3 (LC3) and anti-GAPDH (Novus Biologicals, Littleton, CO, United States).

Secondary Antibodies

HRP-conjugated goat anti-mouse IgG (H + L) antibody and HRP-conjugated goat anti-rabbit IgG (H + L) antibody (Jackson ImmunoResearch Laboratories, United States).

Statistical Analysis

All results are presented as the mean ± the standard error of the mean (S.E.M.). Statistical analyses of differences were assessed by analysis of variance (ANOVA) for combined data and followed by the Student-Newman-Keuls test. The difference in the percentage incidence of VT, VF and mortality was analyzed with a $\chi 2$ test. $p < 0.05$ was considered to be statistically significant.

RESULTS

Hemodynamic Changes

The hemodynamic parameters did not significantly differ among the four experimental groups in the pre-ischemic period. Intravenous injection of paeonol did not change HR (**Figure 1A**) or mean BP (**Figure 1B**) in rats before and during myocardial I/R injury. No significant differences were recorded in LVSP, $+dp/dt_{max}$ or $-dp/dt_{max}$ values before the LAD ligation, amongst the sham, control and paeonol-treated groups. However, the administration of 1 mg/kg paeonol ameliorated the myocardial function of rats, as reflected by the increase in LVSP (**Figure 1C**) and $\pm dp/dt_{max}$ (**Figures 1D,E**) during myocardial I/R injury and significantly increased $+dp/dt_{max}$ (**Figure 1D**) after myocardial I/R injury.

Myocardial I/R Injury-Induced Rhythm Disturbances

The effects of paeonol on arrhythmias and mortality elicited by myocardial I/R injury in anesthetzed rats are shown in **Supplementary Table S1**. Jugular vein injection of vehicle or paeonol had no induced VT and VF, and none of them died in sham-operated animals. In the control group, severe ventricular arrhythmias occurred at 6–7 mins and peaked at 8–12 mins after LAD ligation. Among the 12 rats in the control group, all animals (100%) exhibited VT (75.44 ± 12.80 s in duration) and 11 rats (92%) exhibited VF (134.36 ± 27.66 s in duration). Administration of paeonol at the dose of 1 mg/kg significantly decreased the incidence of VF (17%), as well as the duration of each (VT: 13.33 ± 6.06 s; VF: 2.00 ± 1.60 s). The mortality rate from myocardial I/R injury was significantly rescued from 50% to 0% in rats treated with paeonol 1 mg/kg.

Myocardial Infarct Size and Myocardial Damage

The effects of paeonol on myocardial infarct size are shown in **Figures 2A–C**. There was no significant difference in the AAR between the control and paeonol-treated groups, indicating that in each group, a similar amount of tissue was at risk from myocardial ischemia (**Figure 2B**). In the control group, the infarct size was 25.20 ± 1.12% of the AAR. Paeonol 1 mg/kg significantly rescued the infarct size to 18.92 ± 0.76% of the AAR (**Figure 2C**).

Plasma LDH activity and Troponin-I levels were used as diagnostic biomarkers for acute myocardial infarction. The effects of paeonol on LDH activity and Troponin-I levels after myocardial I/R injury are shown in **Figures 2D,E**. Low LDH activity and Troponin-I levels in the plasma were recorded in the sham-operated animals, whereas both biomarkers were dramatically increased in the control group after myocardial I/R injury. Paeonol 1 mg/kg significantly reduced plasma LDH activity (**Figure 2D**) and Troponin-I levels (**Figure 2E**) compared with values in the control group during the same period. These results are consistent with the findings of myocardial infarction.

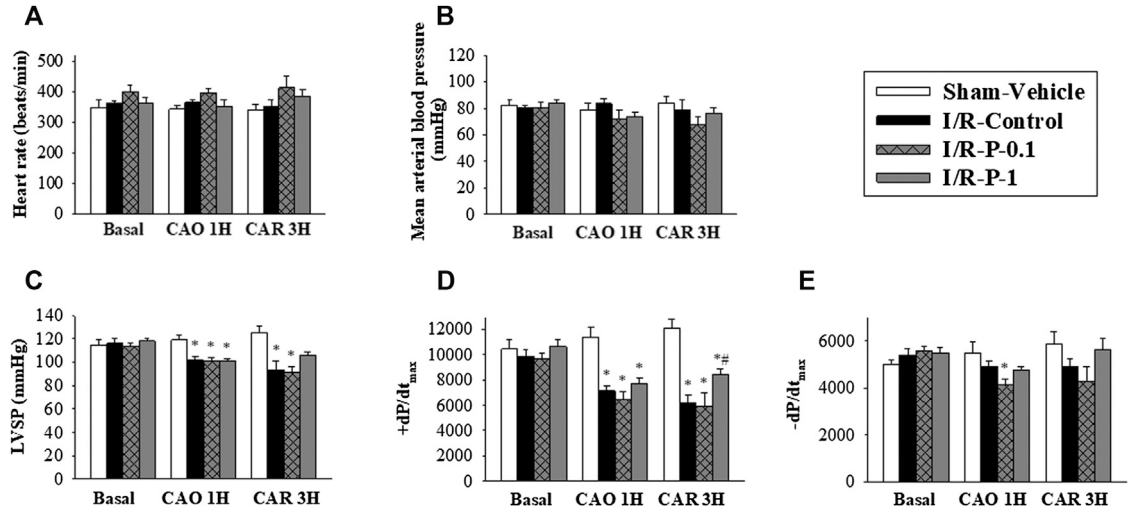

FIGURE 1 | Effect of paeonol on hemodynamic parameters in rats subjected to myocardial I/R injury. **(A)** heart rate, **(B)** mean arterial blood pressure, **(C)** left ventricular systolic pressure (LVSP) **(D)** maximum rates of pressure change in the LV (+dP/dt_{max}) and **(E)** minimum rates of pressure change in the LV (–dP/dt_{max}) were recorded by physiological parameters during myocardial I-R injury (Basal, pre-ischemic period; CAO1H, 1 h after LAD coronary arterial occlusion; CAR3H, 3 h after LAD coronary arterial reperfusion). Values are means ± S.E.M.; (n = 10–11 per group); *p < 0.05 compared with the sham vehicle-treated group; #p < 0.05 compared with the I/R-control group.

Apoptosis and Autophagy Protein Expression

Under the sham-operated non-I/R condition, Bcl-2, the cleaved forms of caspase-3, caspase-8, caspase-9 and PARP protein expression in the myocardium did not differ significantly between the groups. Myocardial I/R injury often leads to apoptosis of cardiomyocytes. In this study, we found that myocardial I/R injury significantly reduced the protein expression of Bcl-2 and the ratio of Bcl-2 to Bax, and significantly increased the cleaved forms of caspase-8, caspase-9, caspase-3 and PARP protein expression in the myocardium, compared with the sham-vehicle-treated group. Paeonol treatment significantly reversed changes in protein expression induced by myocardial I/R injury (**Figure 3**). These results indicate that paeonol attenuates apoptotic cell death in I/R-injured myocardium.

We also investigated the role of autophagy in the cardioprotective effects of paeonol in rats subjected to myocardial I/R injury (**Figure 4**). We found that myocardial I/R injury significantly increased the levels of Beclin-1, p62, LC3-I and LC3-II protein expression in the myocardium in the control group compared with the sham-vehicle-treated group. Paeonol treatment significantly reversed the changes in protein expression induced by myocardial I/R injury. This suggests that paeonol reduced autophagy in the myocardium after I/R injury.

The autophagy induction pathway of Beclin-1 is considered harmful during myocardial I/R injury (Ma et al., 2015). In this study, we found that myocardial I/R injury significantly decreased the ratio of Bcl-2 to Beclin-1 protein expression and significantly increased the ratio of cleaved form of caspase-3 to Beclin-1 protein expression in the control group compared with the sham-vehicle-treated group. Paeonol treatment reversed the protein expression ratio changes induced by myocardial I/R injury. We found that paeonol significantly increased the ratio of Bcl-2 to Beclin-1 protein expression, but without changing the ratio of cleaved-caspase 8 and cleaved-caspase 3 to Beclin-1 protein expression after myocardial I/R injury compared with the control group (**Figure 5**). Finally, paeonol significantly decreased the expression of Beclin-1 protein in the myocardium in the paeonol-treated group compared with the control group.

DISCUSSION

In this study, we provide evidence showing that paeonol protects the heart against myocardial I/R injury by improving cardiac function, reducing myocardial extrinsic and intrinsic apoptosis and attenuating autophagy.

Paeonol is a major phenolic compound of Moutan *Cortex Radicis* that is widely used as a nutrient supplement and in traditional Chinese medicine to regulate human disorders by removing blood stasis, promoting blood flow, attenuating inflammatory responses, relieving pain and eliminating heat (Fu et al., 2012). Yang et al. reported that paeonol improves blood hemorrheology, reduces oxidative injury and repairs endothelial function, and acts as an effective cardioprotective agent in a rabbit model of myocardial ischemia induced by intravenous administration of pituitrin (Yang et al., 2010). Our results suggest that administration of paeonol 1 mg/kg significantly suppressed the incidence of VF, shortened the durations of VT and VF, and completely prevented mortality during myocardial I/R injury. In addition, pretreatment with paeonol significantly reduced cardiac infarction size and protected against cardiomyocyte injury, as indicated by the

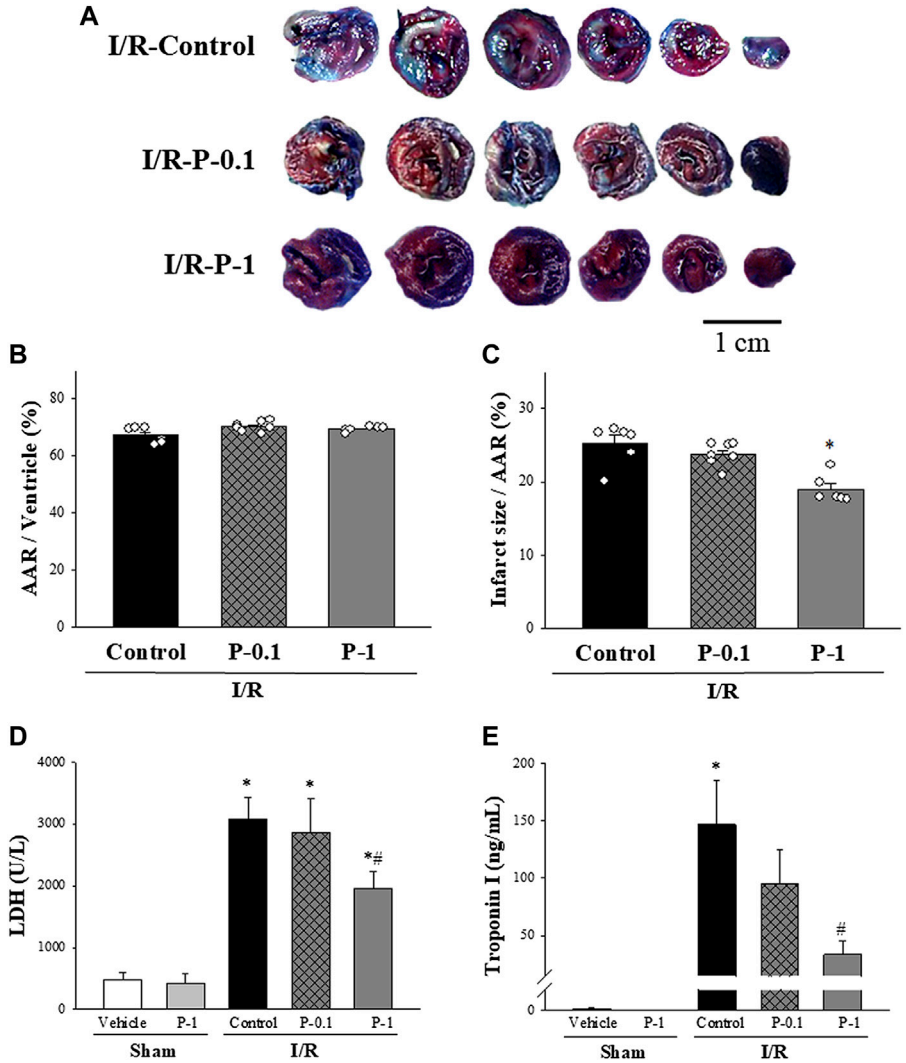

FIGURE 2 | Effect of paeonol on I/R induced myocardial damage in rats. **(A)** Representative Evans blue/TTC staining of heart sections from the control group and different paeonol dose groups (0.1 and 1 mg/kg) after 1 h of ischemia and 3 h of reperfusion. The perfused area is seen in blue; the area at risk (AAR) is seen in red and white. Infarction is seen in white. Quantitative analysis of the AAR/Ventricle % (ratio of non-blue area to total area) (B), and the risk zone infarcted % (ratio of white area to AAR) **(C)** in control and paeonol-treated rats, plasma lactate dehydrogenase (LDH) activity **(D)**, and plasma Troponin-I levels **(E)** in the sham-operated and I/R-operated groups. The results are shown as means ± S.E.M. (n = 10–11 per group); *$p < 0.05$ compared with the sham vehicle-treated group; #$p < 0.05$ compared with the I/R-control group.

decreasing carotid blood Troponin-I levels and LDH activity, which serve as indicators of cellular damage, in rats subjected to cardiac ischemia for 1 h and reperfusion for 3 h. Our results indicate that paeonol is a potent cardioprotective agent in rats with myocardial I/R injury.

Among the many underlying mechanisms of myocardial I/R injury, apoptosis is one of the most important (Xia et al., 2016). Apoptosis is a form of programmed cell death that is positively and negatively regulated by the Bcl-2 family, which includes both pro- and antiapoptotic proteins. The ratio of proapoptotic to antiapoptotic molecules helps determine the susceptibility of cells to a death signal (Gross et al., 1999). In this study, we found that compared with vehicle treatment, paeonol significantly increased the ratio of Bcl-2 to Bax in the myocardium after ischemia for 1 h and reperfusion for 3 h. Much evidence suggests that suppressing apoptosis may protect the heart against myocardial I/R injury (Wang et al., 2015; Wu et al., 2015). We found that paeonol treatment significantly reduced the protein expression levels of cleaved forms of caspase-8, caspase-9, caspase 3 and PARP, when compared with vehicle treatment. These results illustrate that paeonol upregulates Bcl-2 levels and suppresses apoptosis to protect the heart from I/R injury in rats through inhibition of both intrinsic and extrinsic apoptotic pathways.

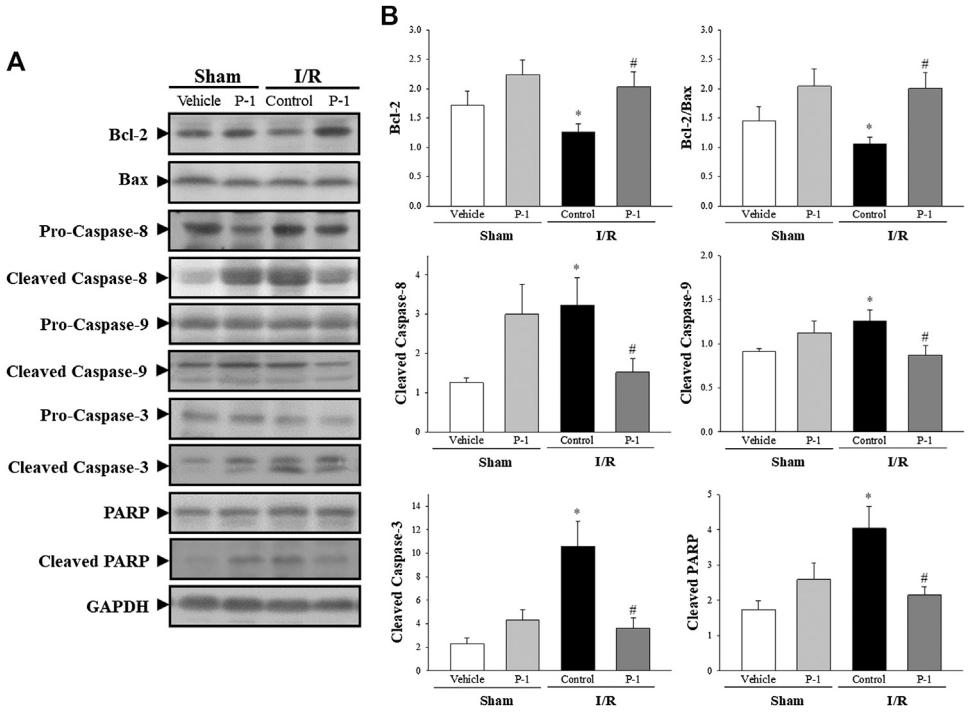

FIGURE 3 | Paeonol decreased apoptosis after myocardial I/R injury**. (A)** Representative images of Western blot results in heart tissue. **(B)** Graphs represent the quantitative differences between vehicle- and paeonol-treated groups in sham- and myocardial I/R-operated animals. GAPDH was used as a loading control for the blots. Data are normalized with the mean expression from the sham vehicle-treated group. *$p < 0.05$ compared with the sham vehicle-treated group; #$p < 0.05$ compared with the I/R-control group. Values are expressed as means ± S.E.M. ($n = 6$).

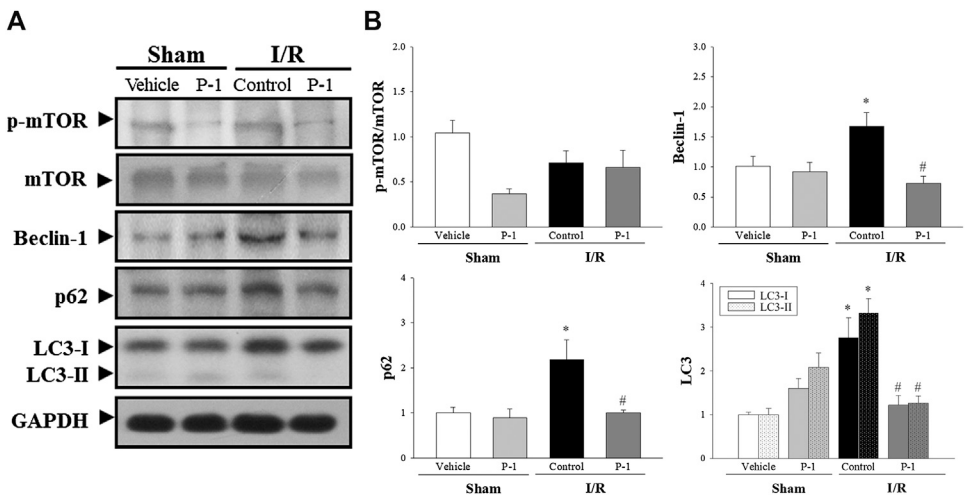

FIGURE 4 | Paeonol decreased autophagy after myocardial I/R injury**. (A)** Representative Western blot images show the expression levels of *p*-mTOR, mTOR, Beclin-1, p62, LC3-I, LC3-II and GAPDH in heart tissue. **(B)** Graphs represent the quantitative differences between vehicle and paeonol-treated groups in sham and myocardial I/R-operated animals. GAPDH was used as a loading control for the blots. Data are normalized with the mean expression from the sham vehicle-treated group. *$p < 0.05$ compared with the sham-vehicle group; #$p < 0.05$ compared with the I/R-control group. Values are expressed as mean ± S.E.M. ($n = 6$).

Besides apoptosis, autophagy may also contribute to myocardial I/R injury (Matsui et al., 2007). Evidence indicates that autophagy plays dual roles in myocardial I/R injury; at low levels, autophagy is protective, by degrading damaged mitochondria and protein aggregates, whereas excessive autophagy such as during myocardial I/R may be deleterious

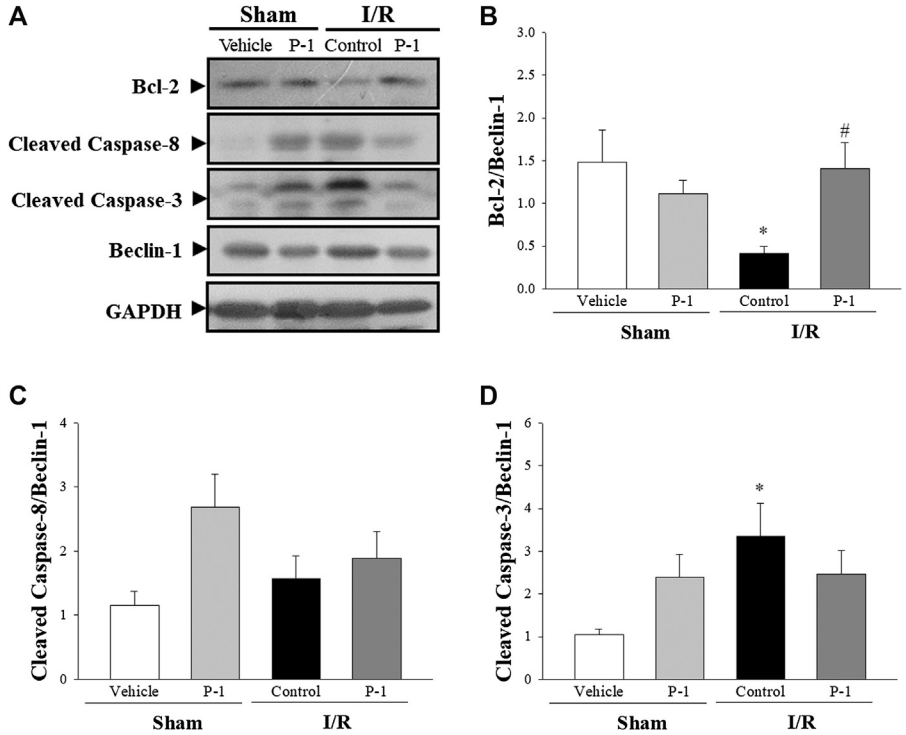

FIGURE 5 | Effect of paeonol on crosstalk between apoptosis and autophagy after myocardial I/R injury in rats**. (A)** Representative images of the Western blots results in heart tissue. Graphs represent the quantitative differences of **(B)** the ratio of Bcl-2 to Beclin-1 **(C)** the ratio of cleaved caspase-8 to Beclin-1 **(D)** the ratio of cleaved caspase-3 to Beclin-1 between vehicle and paeonol-treated groups in sham- and myocardial I/R-operated animals. GAPDH was used as a loading control for the blots. Data are normalized with the mean expression from the sham-vehicle-treated group. *$p < 0.05$ compared with the sham-vehicle group; #$p < 0.05$ compared with the I/R-control group. Values are expressed as means ± S.E.M. ($n = 6$).

for cardiac function, due to overwhelming degradation of essential proteins and organelles (Li M. et al., 2016; Wang et al., 2017). It is known that Beclin-1-dependent autophagy mediates autophagic cell death during myocardial I/R injury (Peng et al., 2013). Beclin-1 is a key autophagic protein that plays a vital role in autophagy in myocardial I/R and therefore serves as a marker for autophagy. Elevated Beclin-1 protein expression induces high levels of autophagy, while inhibition of Beclin-1 protein expression correlates with decreased autophagy and reduced cardiac myocyte death induced by myocardial I/R injury (Matsui et al., 2007). In our studies, we found that paeonol significantly decreased Beclin-1 expression in the occluded zone of rats subjected to myocardial I/R injury. In addition to inhibiting Beclin-1 expression, paeonol also attenuated myocardial I/R injury by dramatically reducing p62, LC3-I and LC3-II expression. Both LC3 and p62 are routinely used as biomarkers to monitor autophagic levels. During autophagy initiation, cytosolic-associated protein LC3-I is converted to the membrane-bound LC3-II form and then binds to the adaptor protein p62, facilitating the autophagic degradation of ubiquitinated protein aggregates in autolysosomes (Aghaei et al., 2019). Our results suggest that paeonol decreases autophagic cell death during myocardial I/R injury.

In this study, we focused on investigating the underlying mechanisms through which the crosstalk between apoptosis and autophagy was involved in the cardioprotective effect of paeonol on rats subjected to myocardial I/R injury. Both apoptosis and autophagy are two highly regulated biological processes with complex protein networks that play a vital role in tissue homeostasis, development, and disease. Autophagy is inhibited downstream of apoptosis induction due to Beclin-1 cleavage by caspases, most prominently caspase-3 (Fairlie et al., 2020). Recent evidence indicates that active caspase-8, a death receptor effector, can be degraded by autophagy, suggesting the existence of a feedback mechanism that cross-regulates autophagy and apoptosis (Hou et al., 2010). However, we found that paeonol did not affect the ratios of cleaved-caspase 8 and cleaved-caspase 3 to Beclin-1 protein expression after myocardial I/R injury compared with those ratios in the control group. It also appears that several inducers of apoptosis, such as p53 and Bcl-2, can activate autophagy. Phosphorylation of p53 is known to inhibit the activity of mTOR through AMPK activation (Mendieta et al., 2019). In this study, we found that paeonol treatment did not change the protein expression of mTOR in rats after myocardial I/R injury, which means that p53 phosphorylation is not involved in the cardioprotective effects of paeonol. Mitochondria-associated

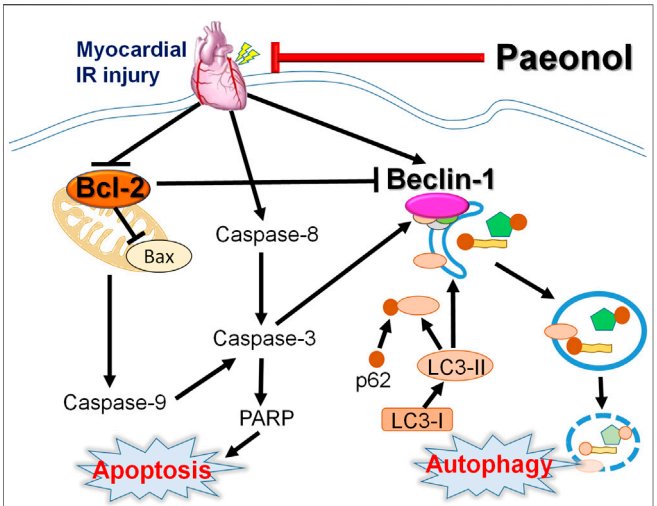

FIGURE 6 | Schematic diagram of paeonol mediating apoptosis and autophagy crosstalk in myocardial I/R injury.

proteins are responsible for interactions between autophagy and apoptosis. Bcl-2 is an anti-apoptotic protein that interferes with Beclin-1 at the mitochondrial outer membrane, resulting in dual regulation of apoptosis and autophagy. In this study, we found that paeonol (1 mM) significantly increased cell viability against OGD/R insult in H9c2 cells, and the protective effect is reversed by Bcl-2-selective inhibitor ABT199 (**Supplementary Figure S2**). The specific Bcl-2 inhibitor, ABT199, is a selective small-molecule B-cell lymphoma 2 Homology 3 (BH3) mimetic, has been shown to disrupt the BH3 dependent Bcl-2/Beclin-1 interaction, thereby induce apoptosis and autophagy (Chiang et al., 2018; Folkerts et al., 2019). Therefore, we suggest that the cardioprotective effects of paeonol against I/R injury may mediated by Bcl-2/Beclin-1 interaction. It is generally believed that Beclin-1-mediated autophagy is not only regulated by its own expression, but is also promoted by the binding of Beclin-1 and Bcl-2 (Marquez and Xu, 2012). Previous studies have shown that the balance between Bcl-2 and Beclin-1 protein expression affects the levels of autophagy (Yi et al., 2020). We therefore explored the association between Bcl-2 and Beclin-1 protein expression in the crosstalk between apoptosis and autophagy in rat heart after I/R injury. Our data verified that compared with vehicle treatment, treatment with paeonol significantly upregulates the expression of Bcl-2 and downregulates the expression of Beclin-1, increasing the ratio of Bcl-2 to Beclin-1 in the I/R-injured myocardium. Upregulation of Bcl-2 and downregulation of Bax, Beclin-1, LC3, and p62 following paeonol treatment suggests that crosstalk exists between apoptosis and autophagy processes during myocardial I/R. Thus, the cardioprotective effects of paeonol against I/R injury may involve upregulation of Bcl-2 that inhibits apoptosis and prevents autophagic cell death.

CONCLUSION

Our results provide valuable insights into the signaling pathways involved in programmed cell death, including crosstalk between apoptosis and autophagy, in paeonol-induced amelioration of myocardial I/R injury in rats (**Figure 6**). Paeonol shows potential as a preventive treatment for ischemic heart diseases or post-coronary revascularization.

DATA AVAILABILITY STATEMENT

The raw data supporting the conclusions of this article will be made available by the authors, without undue reservation, to any qualified researcher.

ETHICS STATEMENT

The animal study was reviewed and approved by The Institutional Animal Care and Use Committee of Chung Shan Medical University.

AUTHOR CONTRIBUTIONS

C-FT and S-SH designed research and provided funding. K-MC, H-HS, J-ML, Y-TY, Y-HW, Y-HC, MW, Y-CC, and S-SH completed animal experiments, conducted molecular biology experiments and analyzed data. C-FT, Y-CC, Y-HW, and S-SH wrote the paper. All authors read and approved the final manuscript.

FUNDING

This work was supported financially by research grants from Chung Shan Medical University Hospital (CSH-2017-C-021 and CSH-2018-C-031), and the Ministry of Science and Technology (MOST 107-2320-B-040-025) of Taiwan to C-FT and S-SH.

ACKNOWLEDGMENTS

We would like to thank Iona J. MacDonald from China Medical University for her English language revision of this manuscript.

SUPPLEMENTARY MATERIAL

The Supplementary Material for this article can be found online at: https://www.frontiersin.org/articles/10.3389/fphar.2020.586498/full#supplementary-material.

REFERENCES

Adki, K. M., and Kulkarni, Y. A. (2020). Chemistry, pharmacokinetics, pharmacology and recent novel drug delivery systems of paeonol. *Life Sci.* 250, 117544. doi:10.1016/j.lfs.2020.117544

Aghaei, M., Motallebnezhad, M., Ghorghanlu, S., Jabbari, A., Enayati, A., Rajaei, M., et al. (2019). Targeting autophagy in cardiac ischemia/reperfusion injury: a novel therapeutic strategy. *J. Cell. Physiol.* 234, 16768–16778. doi:10.1002/jcp.28345

Chen, X., Lu, Y., Du, S., Xu, B., Wang, S., Zhai, Y., et al. (2010). *In situ* and *in vivo* study of nasal absorption of paeonol in rats. *Int. J. Mol. Sci.* 11, 4882–4890. doi:10.3390/ijms11124882

Chiang, W. C., Wei, Y., Kuo, Y. C., Wei, S., Zhou, A., Zou, Z., et al. (2018). High-throughput screens to identify autophagy inducers that function by disrupting Beclin 1/Bcl-2 binding. *ACS Chem. Biol.* 13, 2247–2260. doi:10.1021/acschembio.8b00421

Chiong, M., Wang, Z. V., Pedrozo, Z., Cao, D. J., Troncoso, R., Ibacache, M., et al. (2011). Cardiomyocyte death: mechanisms and translational implications. *Cell Death Dis.* 2, e244. doi:10.1038/cddis.2011.130

Ciechomska, I. A., Goemans, G. C., Skepper, J. N., and Tolkovsky, A. M. (2009). Bcl-2 complexed with Beclin-1 maintains full anti-apoptotic function. *Oncogene*. 28, 2128–2141. doi:10.1038/onc.2009.60

Curtis, M. J., Hancox, J. C., Farkas, A., Wainwright, C. L., Stables, C. L., Saint, D. A., et al. (2013). The Lambeth Conventions (II): guidelines for the study of animal and human ventricular and supraventricular arrhythmias. *Pharmacol. Ther.* 139, 213–248. doi:10.1016/j.pharmthera.2013.04.008

Ding, Y., Li, Q., Xu, Y., Chen, Y., Deng, Y., Zhi, F., et al. (2016). Attenuating oxidative stress by paeonol protected against Acetaminophen-induced hepatotoxicity in mice. *PLoS One*. 11, e0154375. doi:10.1371/journal.pone.0154375

Dong, Y., Chen, H., Gao, J., Liu, Y., Li, J., and Wang, J. (2019). Molecular machinery and interplay of apoptosis and autophagy in coronary heart disease. *J. Mol. Cell. Cardiol.* 136, 27–41. doi:10.1016/j.yjmcc.2019.09.001

Fairlie, W. D., Tran, S., and Lee, E. F. (2020). Crosstalk between apoptosis and autophagy signaling pathways. *Int. Rev. Cell Mol. Biol.* 352, 115–158. doi:10.1016/bs.ircmb.2020.01.003

Folkerts, H., Wierenga, A. T., Van Den Heuvel, F. A., Woldhuis, R. R., Kluit, D. S., Jaques, J., et al. (2019). Elevated VMP1 expression in acute myeloid leukemia amplifies autophagy and is protective against venetoclax-induced apoptosis. *Cell Death Dis.* 10, 421. doi:10.1038/s41419-019-1648-4

Fu, P. K., Wu, C. L., Tsai, T. H., and Hsieh, C. L. (2012). Anti-inflammatory and anticoagulative effects of paeonol on LPS-induced acute lung injury in rats. *Evid. Based Complement Alternat. Med.* 2012, 837513. doi:10.1155/2012/837513

Gross, A., Mcdonnell, J. M., and Korsmeyer, S. J. (1999). BCL-2 family members and the mitochondria in apoptosis. *Genes Dev.* 13, 1899–1911. doi:10.1101/gad.13.15.1899

Hou, W., Han, J., Lu, C., Goldstein, L. A., and Rabinowich, H. (2010). Autophagic degradation of active caspase-8: a crosstalk mechanism between autophagy and apoptosis. *Autophagy*. 6, 891–900. doi:10.4161/auto.6.7.13038

Hsieh, C. L., Cheng, C. Y., Tsai, T. H., Lin, I. H., Liu, C. H., Chiang, S. Y., et al. (2006). Paeonol reduced cerebral infarction involving the superoxide anion and microglia activation in ischemia-reperfusion injured rats. *J. Ethnopharmacol.* 106, 208–215. doi:10.1016/j.jep.2005.12.027

Koo, Y. K., Kim, J. M., Koo, J. Y., Kang, S. S., Bae, K., Kim, Y. S., et al. (2010). Platelet anti-aggregatory and blood anti-coagulant effects of compounds isolated from Paeonia lactiflora and Paeonia suffruticosa. *Pharmazie*. 65, 624–628. doi:10.1691/ph.2010.9870

Lei, H., Wen, Q., Li, H., Du, S., Wu, J. J., Chen, J., et al. (2016). Paeonol inhibits lipopolysaccharide-induced HMGB1 translocation from the nucleus to the cytoplasm in RAW264.7 cells. *Inflammation*. 39, 1177–1187. doi:10.1007/s10753-016-0353-z

Levine, B., Sinha, S. C., and Kroemer, G. (2008). Bcl-2 family members: dual regulators of apoptosis and autophagy. *Autophagy*. 4, 600–606. doi:10.4161/auto.6260

Li, C., Yang, L., Wu, H., and Dai, M. (2018). Paeonol inhibits oxidized low-density lipoprotein-induced vascular endothelial cells autophagy by upregulating the expression of miRNA-30a. *Front. Pharmacol.* 9, 95. doi:10.3389/fphar.2018.00095

Li, H., Song, F., Duan, L. R., Sheng, J. J., Xie, Y. H., Yang, Q., et al. (2016). Paeonol and danshensu combination attenuates apoptosis in myocardial infarcted rats by inhibiting oxidative stress: roles of Nrf2/HO-1 and PI3K/Akt pathway. *Sci. Rep.* 6, 23693. doi:10.1038/srep23693

Li, H., Xie, Y. H., Yang, Q., Wang, S. W., Zhang, B. L., Wang, J. B., et al. (2012). Cardioprotective effect of paeonol and danshensu combination on isoproterenol-induced myocardial injury in rats. *PLoS One* 7 (11), e48872. doi:10.1371/journal.pone.0048872

Li, M., Gao, P., and Zhang, J. (2016). Crosstalk between autophagy and apoptosis: potential and emerging therapeutic targets for cardiac diseases. *Int. J. Mol. Sci.* 17, 332. doi:10.3390/ijms17030332

Liao, W. Y., Tsai, T. H., Ho, T. Y., Lin, Y. W., Cheng, C. Y., and Hsieh, C. L. (2016). Neuroprotective effect of paeonol mediates anti-inflammation via suppressing toll-like receptor 2 and toll-like receptor 4 signaling pathways in cerebral ischemia-reperfusion injured rats. *Evid. Based Complement Alternat. Med.* 2016, 3704647, 1-12. doi:10.1155/2016/3704647

Ma, S., Wang, Y., Chen, Y., and Cao, F. (2015). The role of the autophagy in myocardial ischemia/reperfusion injury. *Biochim. Biophys. Acta*. 1852, 271–276. doi:10.1016/j.bbadis.2014.05.010

Marquez, R. T., and Xu, L. (2012). Bcl-2: Beclin 1 complex: multiple, mechanisms regulating autophagy/apoptosis toggle switch. *Am. J. Cancer Res.* 2, 214–221.

Matsui, Y., Takagi, H., Qu, X., Abdellatif, M., Sakoda, H., Asano, T., et al. (2007). Distinct roles of autophagy in the heart during ischemia and reperfusion: roles of AMP-activated protein kinase and Beclin 1 in mediating autophagy. *Circ. Res.* 100, 914–922. doi:10.1161/01.RES.0000261924.76669.36

Mendieta, G., Ben-Aicha, S., Casani, L., Badimon, L., Sabate, M., and Vilahur, G. (2019). Molecular pathways involved in the cardioprotective effects of intravenous statin administration during ischemia. *Basic Res. Cardiol.* 115, 2. doi:10.1007/s00395-019-0760-z

Oerlemans, M. I., Koudstaal, S., Chamuleau, S. A., De Kleijn, D. P., Doevendans, P. A., and Sluijter, J. P. (2013). Targeting cell death in the reperfused heart: pharmacological approaches for cardioprotection. *Int. J. Cardiol.* 165, 410–422. doi:10.1016/j.ijcard.2012.03.055

Pattingre, S., Tassa, A., Qu, X., Garuti, R., Liang, X. H., Mizushima, N., et al. (2005). Bcl-2 antiapoptotic proteins inhibit Beclin 1-dependent autophagy. *Cell* 122, 927–939. doi:10.1016/j.cell.2005.07.002

Peng, W., Liu, Y., Xu, W. J., and Xia, Q. H. (2013). Role of Beclin 1-dependent autophagy in cardioprotection of ischemic preconditioning. *J. Huazhong Univ. Sci. Technol.—Med. Sci.* 33, 51–56. doi:10.1007/s11596-013-1070-6

Su, H. H., Liao, J. M., Wang, Y. H., Chen, K. M., Lin, C. W., Lee, I. H., et al. (2019). Exogenous GDF11 attenuates non-canonical TGF-β signaling to protect the heart from acute myocardial ischemia-reperfusion injury. *Basic Res. Cardiol.* 114, 20. doi:10.1007/s00395-019-0728-z

Teringova, E., and Tousek, P. (2017). Apoptosis in ischemic heart disease. *J. Transl. Med.* 15, 87. doi:10.1186/s12967-017-1191-y

Tian, X. F., Cui, M. X., Yang, S. W., Zhou, Y. J., and Hu, D. Y. (2013). Cell death, dysglycemia and myocardial infarction. *Biomed. Rep.* 1, 341–346. doi:10.3892/br.2013.67

Wang, D., Yu, W., Liu, Y., Zhong, G., Zhao, Z., Yan, X., et al. (2017). Roles of autophagy in ischemic heart diseases and the modulatory effects of Chinese herbal medicine. *Am. J. Chin. Med.* 45, 1401–1419. doi:10.1142/S0192415X17500768

Wang, Y., Liu, J., Ma, A., and Chen, Y. (2015). Cardioprotective effect of berberine against myocardial ischemia/reperfusion injury via attenuating mitochondrial dysfunction and apoptosis. *Int. J. Clin. Exp. Med.* 8, 14513–14519.

Wang, Y. H., Chen, K. M., Chiu, P. S., Lai, S. C., Su, H. H., Jan, M. S., et al. (2016). Lumbrokinase attenuates myocardial ischemia-reperfusion injury by inhibiting TLR4 signaling. *J. Mol. Cell. Cardiol.* 99, 113–122. doi:10.1016/j.yjmcc.2016.08.004

Wu, H., Song, A., Hu, W., and Dai, M. (2017). The anti-atherosclerotic effect of paeonol against vascular smooth muscle cell proliferation by up-regulation of autophagy via the AMPK/mTOR signaling pathway. *Front. Pharmacol.* 8, 948. doi:10.3389/fphar.2017.00948

Wu, H., Ye, M., Yang, J., Ding, J., Yang, J., Dong, W., et al. (2015). Nicorandil protects the heart from ischemia/reperfusion injury by attenuating endoplasmic

reticulum response-induced apoptosis through PI3K/Akt signaling pathway. *Cell. Physiol. Biochem*. 35, 2320–2332. doi:10.1159/000374035

Wu, J., Sun, C., Wang, R., Li, J., Zhou, M., Yan, M., et al. (2018). Cardioprotective effect of paeonol against epirubicin-induced heart injury via regulating miR-1 and PI3K/AKT pathway. *Chem. Biol. Interact*. 286, 17–25. doi:10.1016/j.cbi.2018.02.035

Xia, P., Liu, Y., and Cheng, Z. (2016). Signaling pathways in cardiac myocyte apoptosis. *BioMed Res. Int*. 2016, 9583268. doi:10.1155/2016/9583268

Yang, Q., Wang, S., Xie, Y., Wang, J., Li, H., Zhou, X., et al. (2010). Effect of salvianolic acid B and paeonol on blood lipid metabolism and hemorrheology in myocardial ischemia rabbits induced by pituitruin. *Int. J. Mol. Sci*. 11, 3696–3704. doi:10.3390/ijms11103696

Yi, C., Si, L., Xu, J., Yang, J., Wang, Q., and Wang, X. (2020). Effect and mechanism of asiatic acid on autophagy in myocardial ischemia-reperfusion injury *in vivo* and *in vitro*. *Exp. Ther. Med*. 20, 54. doi:10.3892/etm.2020.9182

Zeng, M., Wei, X., Wu, Z., Li, W., Zheng, Y., Li, B., et al. (2016). Simulated ischemia/reperfusion-induced p65-Beclin 1-dependent autophagic cell death in human umbilical vein endothelial cells. *Sci. Rep*. 6, 37448. doi:10.1038/srep37448

Zou, W., Wang, X., Vale, R. D., and Ou, G. (2012). Autophagy genes promote apoptotic cell corpse clearance. *Autophagy*. 8, 1267–1268. doi:10.4161/auto.20786

Conflict of Interest: The authors declare that the research was conducted in the absence of any commercial or financial relationships that could be construed as a potential conflict of interest.

Copyright © 2021 Tsai, Su, Chen, Liao, Yao, Chen, Wang, Chu, Wang and Huang. This is an open-access article distributed under the terms of the Creative Commons Attribution License (CC BY). The use, distribution or reproduction in other forums is permitted, provided the original author(s) and the copyright owner(s) are credited and that the original publication in this journal is cited, in accordance with accepted academic practice. No use, distribution or reproduction is permitted which does not comply with these terms.

frontiers in Pharmacology

ORIGINAL RESEARCH
published: 22 January 2021
doi: 10.3389/fphar.2020.618262

Integrating Network Pharmacology and Experimental Validation to Investigate the Effects and Mechanism of *Astragalus* Flavonoids Against Hepatic Fibrosis

Lin An, Yuefang Lin, Leyan Li, Muyan Kong, Yanmei Lou, Jinjun Wu and Zhongqiu Liu**

Joint Laboratory for Translational Cancer Research of Chinese Medicine of the Ministry of Education of the People's Republic of China, International Institute for Translational Chinese Medicine, School of Pharmaceutical Science, Guangzhou University of Chinese Medicine, Guangzhou, China

OPEN ACCESS

Edited by:
Yanqiong Zhang,
China Academy of Chinese Medical Sciences, China

Reviewed by:
Gangjun Du,
Henan University, China
Liang Feng,
China Pharmaceutical University, China

***Correspondence:**
Jinjun Wu
wujinjun@gzucm.edu.cn
Zhongqiu Liu
liuzq@gzucm.edu.cn

Specialty section:
This article was submitted to Ethnopharmacology, a section of the journal Frontiers in Pharmacology

Received: *16 October 2020*
Accepted: *14 December 2020*
Published: *22 January 2021*

Citation:
An L, Lin Y, Li L, Kong M, Lou Y, Wu J and Liu Z (2021) Integrating Network Pharmacology and Experimental Validation to Investigate the Effects and Mechanism of Astragalus *Flavonoids Against Hepatic Fibrosis. Front. Pharmacol. 11:618262. doi: 10.3389/fphar.2020.618262*

Hepatic fibrosis (HF) represents the excessive wound healing where an excess amount of connective tissues is formed within the liver, finally resulting in cirrhosis or even hepatocellular carcinoma (HCC). Therefore, it is significant to discover the efficient agents and components to treat HF, thus restraining the further progression of hepatopathy. *Astragalus membranaceus* (Fisch.) Bunge [also called *Astragali* Radix (AR)] is a famous herb in traditional Chinese medicine (TCM), which possesses a variety of biological activities and exerts good therapeutic effects in the treatment of HF. Flavonoids account for the major active ingredients related to the AR pharmacological effects. Total AR flavonoids have been proved to exert inhibitory effects on hepatic fibrosis. This study aimed to further undertake network pharmacology analysis coupled with experimental validation and molecular docking to investigate the effects and mechanism of multiple flavonoid components from AR against liver fibrosis. The results of the network pharmacology analysis showed that the flavonoids from AR exerted their pharmacological effects against liver fibrosis by modulating multiple targets and pathways. The experimental validation data showed that the flavonoids from AR were able to suppress transforming growth factor beta 1 (TGF-β1)-mediated activation of hepatic stellate cells (HSCs) and reduce extracellular matrix deposition in HSC-T6 cells via regulating the nuclear factor kappa B (NF-κB) signal transduction pathway. The results of the molecular docking study further showed that the flavonoids had a strong binding affinity for IκB kinase (IKKβ) after docking into the crystal structure. The above results indicated that, flavonoids possibly exerted the anti-inflammatory effect on treating HF by mediating inflammatory signaling pathways. The potential mechanism of these flavonoids against liver fibrosis may be related to suppression of the NF-κB pathway through effective inhibition of IKKβ. This study not only provides a scientific basis for clarifying the effects and mechanism of AR flavonoids against liver fibrosis but also suggests a novel promising therapeutic strategy for the treatment of liver fibrosis.

Keywords: flavonoids, *Astragalus membranaceus* (fisch) bunge, liver fibrosis, anti-inflammation, network pharmacology

INTRODUCTION

Hepatic fibrosis (HF) is a pathological event where connective tissues abnormally proliferate in liver, which is associated with a variety of factors, causing excess extracellular matrix (ECM) deposition within liver (Trautwein et al., 2015). When there is acute injury, liver can recover the structural integrity of liver, in the meantime of sustaining the unfavorable chronic injury-derived stimuli, resulting in liver parenchymal distortion (Parola and Pinzani, 2019). For HF, its pathogenic mechanisms are chronic virus infection, nonalcoholic steatohepatitis (NASH), alcoholic liver disease (ALD), together with toxin-related stimuli (such as drugs and alcohol), autoimmune hepatitis, hereditary metabolic disease and cholestatic diseases (Fan et al., 2019). Such injury to liver parenchyma will activate the hepatic stellate cells (HSCs), the cells responsible for storing vitamin A and are involved in HF occurrence (Huang et al., 2017). Upon activation, HSCs gradually transform into myofibroblasts, a heterogeneous cell population with proliferating, migrating, and fibrotic characteristics. This transformation causes a continuous accumulation of alpha smooth muscle actin (α-SMA), ECM, and a large amount of type I and type III collagen, leading to scar deposition (Parola and Pinzani, 2019). In addition, HSCs can produce the transforming growth factor beta 1 (TGF-β1) to induce a fibrotic response, as well as the subsequent connective tissue proliferation (Xu et al., 2020). Cirrhosis is the end-stage disease of HF, and it stands for a major reason for the morbidity and mortality in the world (Scaglione et al., 2015). At present, liver transplantation (LT) remains the unique effective way to treat cirrhosis patients; as a result, it is significant to discover the efficient agents and components to treat HF, thus restraining the further progression of hepatopathy and preventing death. HF or even the early cirrhosis, is suggested to be reversible (Friedman et al., 2000). Certain herbs in the traditional Chinese medicine (TCM) are utilized in clinical treatments for a long history due to the efficient therapeutic effect and usability, particularly in treating hepatopathy (Xie et al., 2013). As a result, applying TCM herbs may serve as the efficient way to prevent and treat HF.

Astragalus membranaceus (Fisch.) Bunge is also called *Astragali* Radix (AR), and it accounts for an extensively used TCM herb in China, with a usage history of more than 2,000 years. Traditionally, AR is frequently applied to treat various diseases, including weakness, anemia, fever, chronic fatigue, wounds, loss of appetite, multiple allergies, and uterine bleeding (Guo et al., 2019). For these bioactive functions, AR has been widely used as a kind of health food additive supplemented in various drinks or in additional food forms for the effective body immunity reinforcement (Bai et al., 2018). Modern pharmacological experiments have indicated that AR has different biological activities, like antioxidation, immunomodulation, anticancer and anti-inflammation, which has been extensively utilized in treating nephritis, diabetes and cancers (Xu et al., 2006; Guo et al., 2019). AR has also been recognized to significantly protect from injuries to intestine, heart, liver, lung, kidney, and brain (Shahzad et al., 2016). Beyond that, AR is commonly used in Chinese herb prescription to treat HF in Chinese clinical practice (Ding et al., 2011; Xu et al., 2015). Modern pharmacological studies has also confirmed that AR can effectively suppress HF (Liang and Yuan, 2013; Zhou et al., 2016; Wang et al., 2019). So far, over 200 components are separated in AR. Typically, flavonoids represent the leading ingredients related to the efficacy and pharmacological effects (Guo et al., 2019). The total flavonoids from AR have been proved to exert inhibitory effects on HF (Liu et al., 2005; Li et al., 2019). However, the specific AR flavonoid components responsible for inhibition on HF, as well as the precise molecular mechanisms, are not completely understood.

TCM herbs are the effective herbal medicines adopted for treating a variety of disorders, which exert pivotal parts in healthcare in the history of China or even numerous other countries. However, it is difficult to elucidate the effects of TCMs because of their multiple targets, multiple pathways, and multiple mechanisms of action. The above features have severely restricted the internationalization and modernization of herbal medicines (Gan et al., 2019). Recently, network pharmacology has been developed to be the effective approach for observing the interactions and impacts of different drugs on disease network (Li and Zhang, 2013; Hao and Xiao, 2014). It integrates chemoinformatics, bioinformatics, network biology, network analysis, and traditional pharmacology (Berger and Iyengar, 2009). Therefore, network pharmacology provides a novel and effective tool that can combine the TCM target database in a variety of disorders and verify at molecular level, thus providing evidence regarding the molecular targets as well as possible underlying mechanisms of herbal medicines (Gan et al., 2019).

Therefore, the present work applied network pharmacology in combination with experimental validation for clarifying the activities and possible mechanisms of flavonoids derived from AR to treat HF (**Figure 1**). The main objectives of the present study were 1) to screen the active flavonoid compounds of AR, to predict the potential targets of these flavonoids against liver fibrosis, and to analyze the potential mechanism of the flavonoids against liver fibrosis by using network pharmacology; 2) to employ TGF-β1 to stimulate HSC transdifferentiation into myofibroblasts to investigate the antifibrotic activity of the flavonoids; 3) to elucidate the potential influence of the flavonoids on HSC activation from the aspect of the inflammatory signaling pathway; and 4) to study the binding ability between flavonoids and key target genes by using molecular docking. Our results may help to understand the mechanisms of AR against liver fibrosis and suggest a novel promising therapeutic strategy for its treatment.

MATERIALS AND METHODS

Screening for Active Flavonoid Compounds in AR

According to ADME (absorption, distribution, metabolism, excretion) parameters (Xu et al., 2012), the active flavonoid compounds of AR were screened by searching the Traditional Chinese Medicine Systems Pharmacology

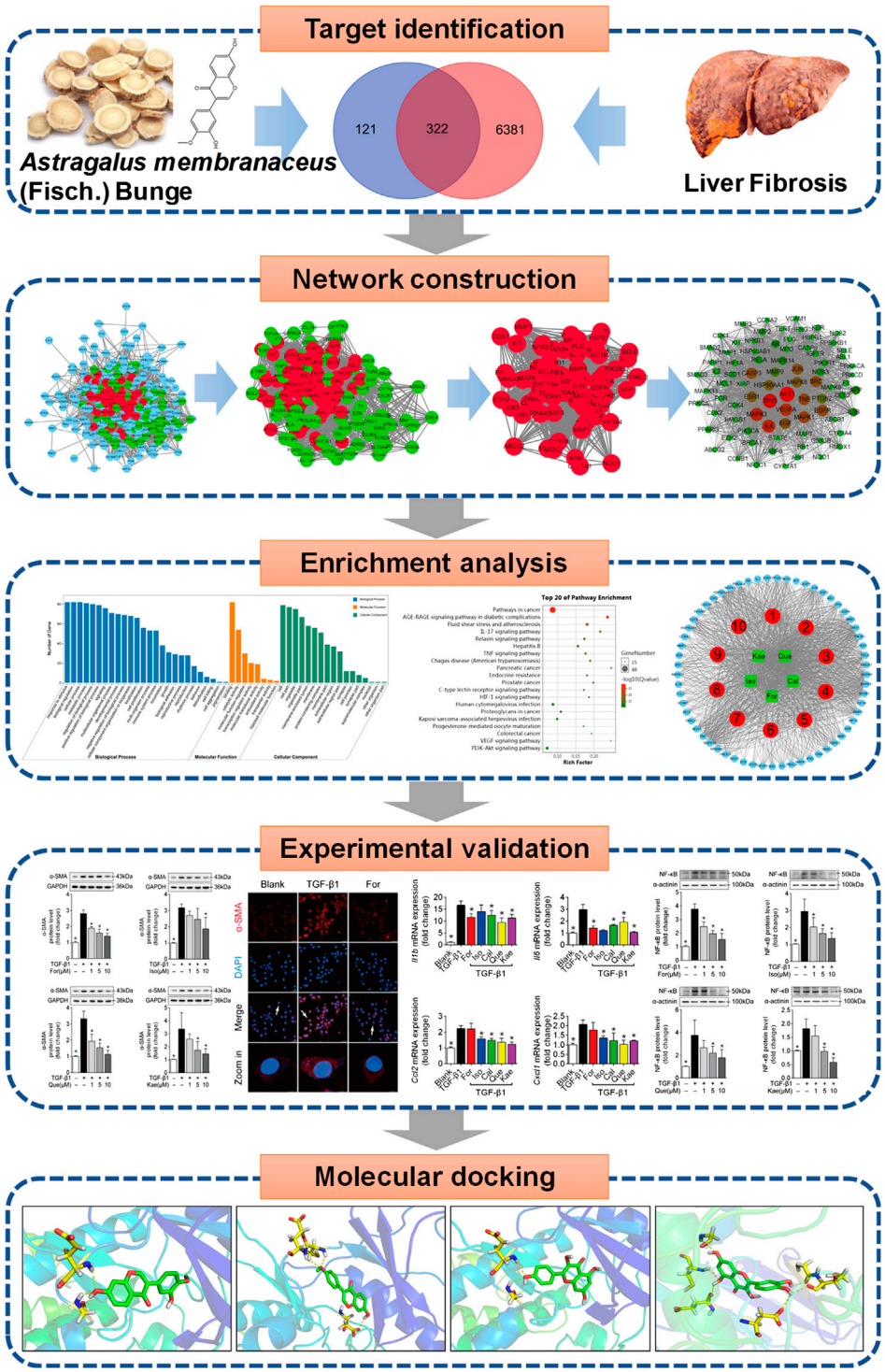

FIGURE 1 | Flowchart showing the systems pharmacology approach for determining the pharmacological effects and mechanism of *Astragali* Radix (AR) in the treatment of liver fibrosis by integrating target identification, network construction, enrichment analysis, experimental validation and a molecular docking study.

(TCMSP, https://tcmspw.com/tcmspsearch.php) (Ru et al., 2014), the Encyclopedia of Traditional Chinese Medicine (ETCM, http://www.ehbio.com/ETCM), and the Integrative Pharmacology-based Research Platform of Traditional Chinese Medicine (TCMIP, http://www.tcmip.cn) databases (Xu et al., 2019). Oral bioavailability (OB) > 30%, along with drug similarity (DL) > 0.18, was used for screening (Li et al., 2015).

Prediction of the Targets of the Active Ingredients in AR

The target prediction for the main active compounds was performed by searching the TCMSP (Ru et al., 2014), PubChem (https://pubchem.ncbi.nlm.nih.gov/) (Zhu et al., 2019), STITCH (http://stitch.embl.de/) (Zhu et al., 2019), SuperPred (http://prediction.charite.de/) (Nickel et al., 2014) and Swiss Target Prediction (http://www.swisstargetprediction.ch/) (Gan et al., 2019) databases with the "*Homo sapiens*" species setting. All targets were combined and identified using the UniProt database (https://www.uniprot.org/) (Gan et al., 2019). Duplicates of the validated and predicted targets were eliminated, and the targets of the active ingredients were screened. Finally, a visual compound-target network was established with Cytoscape v3.7.2, the open-source software utilized to visualize the complicated networks and integrate all attribute data (Shannon et al., 2003).

Screening of Potential Targets for Liver Fibrosis

The GeneCards (https://www.gene-(cards.org/) (Safran et al., 2003) and DisGeNET (http://www.disgenet.org/web/DisGeNET/menu/home) (Ren et al., 2019) databases were searched with the keywords "HF" or "liver fibrosis" to identify targets related to HF.

Network Construction

The common targets of the flavonoid ingredients and liver fibrosis were collected. The STRING database (https://string-db.org/) was utilized to construct the measureable targets of the protein-protein interaction (PPI) network for those main components to treat HF (Szklarczyk et al., 2015). Additionally, Cytoscape was adopted for visualizing and integrating those topological parameters in PPI network regarding the main components to treat HF. The key biological targets were acquired based on the Cytoscape degree.

Enrichment Analysis

OmicShare tools (http://www.omicshare.com/tools), the freely accessible online platform to analyze data, was utilized for Gene Ontology (GO) as well as Kyoto Encyclopedia of Genes and Genomes (KEGG) pathway enrichment analysis for the key targets. GO annotation was classified into three distinct categories, namely, biological process (BP), cell component (CC), and molecular function (MF), and such method was adopted for identifying those potential mechanisms based on the high-throughput transcriptome and genome data (Ashburner et al., 2000). In addition, the KEGG database (https://www.kegg.jp/) was used to identify the systematic functions and biological relevance of candidate targets (Chen et al., 2015). In the current study, the top 20 enriched KEGG pathways were displayed, and only terms with an FDR < 0.05 were selected for analysis. Finally, according to results of KEGG analysis, Cytoscape v3.7.2 was applied in constructing a compound-target-pathway network. The characteristics of multiple components, multiple targets and multiple pathways of the active ingredients against liver fibrosis were revealed through the construction of a network.

Chemicals and Reagents

Formononetin (For, A0232), isorhamnetin (Iso, A0514), kaempferol (Kae, A0129), calycosin (Cal, A0190), and quercetin (Que, A0083) (purity ≥ 98%) were provided by Chengdu Must Biotechnology Co., Ltd. (Chengdu, China), which were mixed with dimethyl sulfoxide (DMSO, 0.1%, v/v; Sigma, St. Louis, MO, United States). In the meantime, the HEK293-derived recombinant human TGF-β1 (100-21) was purchased from PeproTech (New Jersey, United States). The anti-α-SMA (14395-1-AP) and anti-GAPDH (6004-1-lg) antibodies, together with the HRP-labeled AffiniPure goat anti-mouse IgG antibody (H + L) (SA00001-1), were provided by Proteintech (Wuhan, China). The HRP-labeled goat anti-rabbit IgG antibody (H + L) (BS13278) was provided by Bioworld Technology (St. Paul, MN, United States). The Alexa fluor 568-conjugated goat anti-rabbit IgG (H + L) antibody was purchased from Abcam (Cambridge, MA, United States). The enhanced BCA protein assay kit (P0010), RIPA lysis buffer (P0013) and DAPI staining solution (C1005) were provided by Beyotime Institute of Biotechnology (Shanghai, China).

Cell Culture and Treatment

HSC-T6, a rat HSC line, was kindly presented by Zhejiang Cancer Hospital (Zhejiang, China) and cultured in DMEM (Thermo Fisher Scientific, MA, United States) containing 10% fetal bovine serum (FBS, Thermo Fisher Scientific, MA, United States), 100 μg/ml streptomycin and 100 U/ml penicillin. Afterward, cells were subjected to incubation under 37°C and 5% CO_2 conditions. When cells reached confluence, PBS was used to wash cells for two times and the serum-free medium was used for further cell culture prior to subsequent experiment.

Cell Viability Assay

Cellular viability was detected with a CCK-8 assay kit (GLPBIO, California, United States). The HSC-T6 cell line was planted into the 96-well culture plate, followed by 24 h of exposure to various doses of For, Iso, Cal, Que and Kae (0.1–200 μM). Thereafter, 10 μl CCK-8 solution was placed into all wells to incubate for 1 h, and the microplate reader (Thermo Varioskan LUX, MA, United States) was used to measure the absorbance (OD) value at 450 nm.

Quantitative Real-Time Polymerase Chain Reaction (RT-qPCR)

The total pulmonary or cellular RNA was extracted using the TRIzol reagent (Accurate Biotechnology, Human, China) in accordance with specific instructions. Then, 1 ng RNA was used to synthesize cDNA *via* the *Evo M-MLV* RT Kit as well as the gDNA Clean to carry out RT-qPCR (Accurate Biotechnology, Human, China). We performed RT-qPCR for each cDNA sample in triplicate using the SYBR Green Premix *Pro Taq* HS qPCR kit (Accurate Biotechnology, Human, China) and gene-specific primer pairs for *Gapdh*, *Acta2*, *Fn1*, *Col1a1*, *Col3a1*,

TABLE 1 | Nucleotide sequences of the gene-specific primers used for RT-qPCR.

Species	Primers	Sequences
Rattus norvegicus	Gapdh-forward	AGTGCCAGCCTCGTCTCATA
	Gapdh-reverse	GATGGTGATGGGTTTCCCGT
	Acta2-forward	CATCCGACCTTGCTAACGGA
	Acta2-reverse	GTCCAGAGCGACATAGCACA
	Fn1-forward	CACCGAAACCGGGAAGAG
	Fn1-reverse	TTGCCTAGGTAGGTCCGTTC
	Col1a1-forward	GTGCGATGGCGTGCTATG
	Col1a1-reverse	ACTTCTGCGTCTGGTGATACA
	Col3a1-forward	AGATGCTGGTGCTGAGAAGAAAC
	Col3a1-reverse	GCTGGAAAGAAGTCTGAGGAAGG
	Rela-forward	CTGGCCATGGACGATCTGTT
	Rela-reverse	TCCACATATGGCCCAGAAGC
	Jun-forward	TGTCTGTATGCTGGGGTGA
	Jun-reverse	GGTTGCTGGGGAGAGAGA
	Il1β-forward	TGCAGGCTTCGAGATGAAC
	Il1β-reverse	GGGATTTTGTCGTTGCTTGTC
	Il6-forward	CATTCTGTCTCGAGCCCACC
	Il6-reverse	GCAACTGGCTGGAAGTCTCT
	Tnfa-forward	CTTCTGTCTACTGAACTTCGGG
	Tnfa-reverse	CTACGGGCTTGTCACTCG
	Ifng-forward	CATGAGCATCGCCAAGT
	Ifng-reverse	CTCTACCCCAGAATCAGCA
	Ccl2-forward	TTAAGCCCCACTCACCTG
	Ccl2-reverse	CTCTTGAGCTTGGTGACAAATAC
	Cxcl1-forward	TCCAGAGTTTGAAGGTGATGC
	Cxcl1-reverse	GGACACCCTTTAGCATCTTTTG
	Cox2-forward	GATGACGAGCGACTGTTCCA
	Cox2-reverse	TGGTAACCGCTCAGGTGTTG
	Mmp1-forward	AGCTCATACAGTTTCCCCGTG
	Mmp1-reverse	CCTCCTTGGCATCCACGTTT
	Mmp2-forward	TTTGGCCGTCTCTTCCATCC
	Mmp2-reverse	GCATCGATCTTCTGGACGGT
	Mmp9-forward	GATCCCCAGAGCGTTACTCG
	Mmp9-reverse	GTTGTGGAAACTCACACGCC

Rela, *Jun*, *Il1β*, *Il6*, *Tnfa*, *Ifng*, *Ccl2*, *Cxcl2*, *Cox2*, *Mmp1*, *Mmp2*, and *Mmp9* (**Table 1**). A QuantStudio 5 Real-Time PCR instrument (Thermo Fisher Scientific, MA, United States) was applied in PCR amplification under the conditions below: 30 s of enzyme activation under 95°C, 5 s of denaturation under 95°C, followed by 40 cycles of 30 s of annealing and extending under 60°C. In this study, those semi-quantitative RT-qPCR data of every target gene were expressed as $2^{-\Delta\Delta Ct}$ relative expression compared with endogenous GAPDH, and the error bar represented standard error of the mean (SEM) from three independent experiments.

Western Blot Analysis

Cell lysates were produced within the RIPA buffer that contained the fresh phosphatase and protease inhibitors. Following 15 min of centrifugation at 13,000 rpm and 4°C, we collected supernatants to a new tube, followed by boiling within the 1% SDS loading buffer for obtaining samples. Afterward, the resultant samples were added onto the 10% SDS-PAGE, and the protein were transferred onto the NC membranes, followed by 2 h of incubation with 5% nonfat skim milk (FUJIFILM Wako Pure Chemical Corporation, Fuji, Japan) supplemented within the Tris-buffered saline that contained 0.1% Tween. Later, the membranes were incubated with anti-α-SMA and anti-p50 antibodies (1:800) overnight, washed, and further incubated by the HRP-labeled anti-rabbit or anti-mouse IgG secondary antibodies (1:10,000). ECL-enhanced chemiluminescence (Yeasen, Shanghai, China) was used to develop bands, whereas Image-ProPlus 6.0 (Rockville, MD, United States) was utilized for visualization.

Immunofluorescence Assay

The HSC-T6 cell line was exposed to 10 ng/ml TGF-β1 for 24 h in the presence or absence of 10 μM diverse compounds. Thereafter, all cells were rinsed by the cold PBS, followed by 20 min of 4% paraformaldehyde fixation. Later, 0.2% Triton X 100 was used to permeabilize cells, followed by 5% BSA incubation for blocking the nonspecific staining as well as incubation using α-SMA antibody staining under 4°C overnight within the humid chamber. Then, cells were rinsed repeatedly before further 1 h of incubation using Alexa fluor 568-conjugated goat anti-rabbit IgG (H + L) antibody (1:200) under 37°C. Finally, PBS was used to rinse cells for two times, followed by 15 min of incubation with DAPI under 37°C. Images were viewed by confocal scanning microscopy (Leica TCS SP8, Leica, Germany) at an excitation wavelength of 568 nm.

Molecular Docking

Nuclear factor kappa B (NF-κB) proteins are a crucial family of transcription factors in the signal transduction cascade of inflammatory signaling (Hoesel and Schmid, 2013). NF-κB activation is determined by IκB kinase (IKKβ)-mediated IκBα phosphorylation, as well as the later p50–p65 subunit nuclear translocation of NF-κB, finally inducing the expression of pro-inflammatory cytokines (Hoesel and Schmid, 2013). Therefore, the IKKβ selective inhibitor might be used as the candidate drug to resist inflammation. Accordingly, to further analyze the way in which the flavonoids of AR inhibit the inflammatory NF-κB pathway, the interactions between the flavonoids and IKKβ were further measured by AutoDock Vina software. The X-ray crystallographic structure of IKKβ was retrieved from the Protein Data Bank (PDB ID: 3RZF) (Xu et al., 2011). The 3D structures of the AR flavonoids taken as ligands were retrieved from the PubChem database. The grid box for IKKβ used centers of 92.23, −25.49, and 53.01 Å with corresponding sizes of 60, 60, and 60 (x, y, and z positions, respectively) for comprising each amino acid residue of the protein simulated. The other detailed docking procedures were performed as previously described (Ruan et al., 2020). After docking, the flavonoid ligands with the lowest affinity score for the receptor IKKβ were selected for further analysis. All the structure-based features were visualized by using PyMOL software.

Data Analysis

Values were presented in the manner of mean ± SD from three independent replicates. GraphPad Prism 7.0 (San Diego, CA, United States) was used for all statistical analyses. Significant differences were analyzed by single-factor ANOVA and two-tailed Student's *t*-test between the samples and their respective

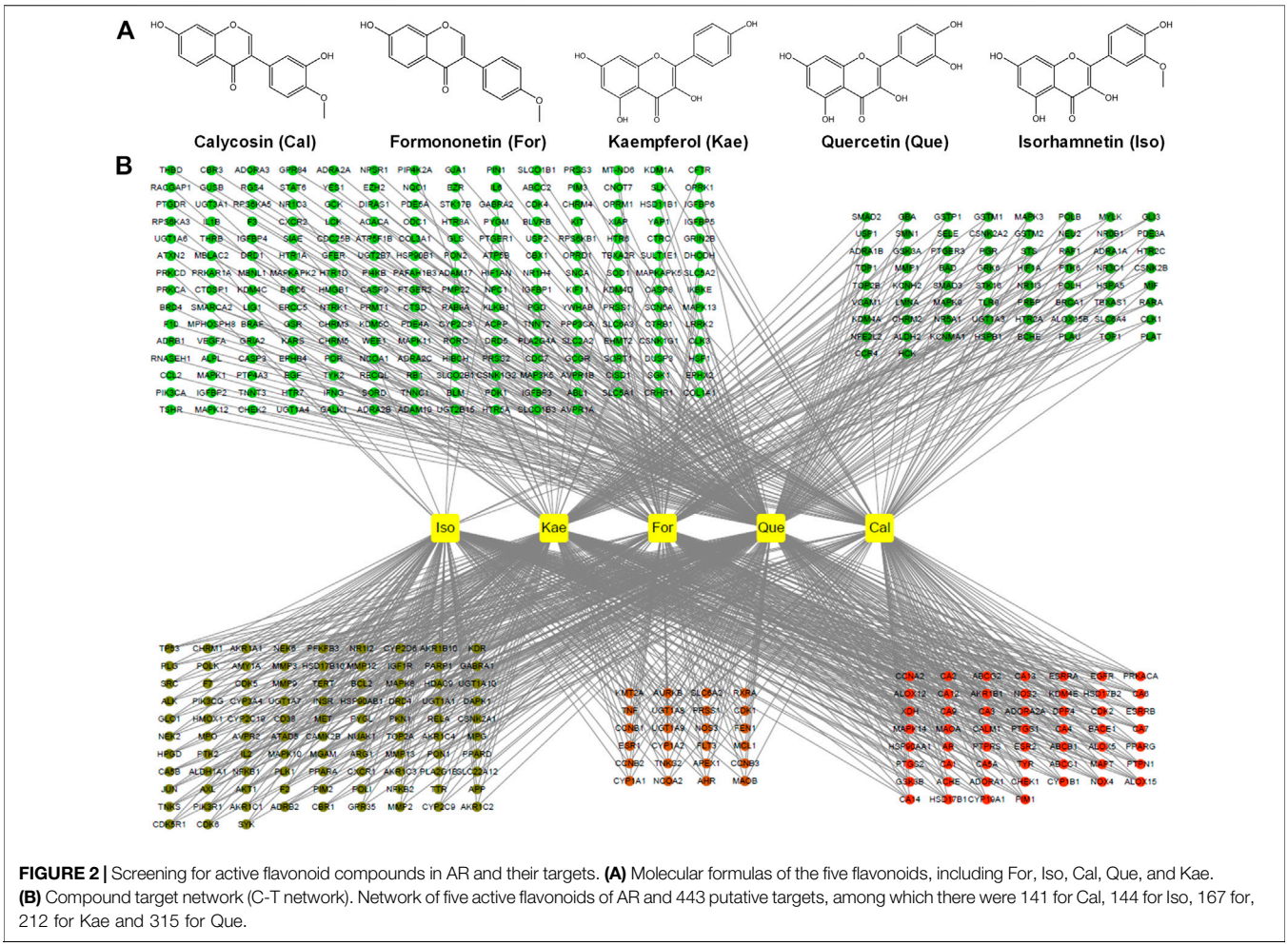

FIGURE 2 | Screening for active flavonoid compounds in AR and their targets. **(A)** Molecular formulas of the five flavonoids, including For, Iso, Cal, Que, and Kae. **(B)** Compound target network (C-T network). Network of five active flavonoids of AR and 443 putative targets, among which there were 141 for Cal, 144 for Iso, 167 for, 212 for Kae and 315 for Que.

controls. Differences were considered statistically significant at p-values of <0.05.

RESULTS

Active AR Flavonoid Compounds

A total of 87 reported active ingredients of AR were retrieved by searching the TCMSP database. A total of 27 reported active ingredients of AR were retrieved by searching the ETCM and TCMIP databases. In this study, we mainly focused on the active flavonoid compounds, and in line with the OB ≥ 30% and DL ≥ 0.18 thresholds, five active flavonoids were selected: For, Iso, Cal, Que, and Kae (**Figure 2A**; **Supplementary Table S1**). These five flavonoids were used for the subsequent network pharmacology analysis and experimental validation.

Target Prediction and Analysis

In this process, we conducted target fishing on the five flavonoids based on the TCMSP, PubChem, STITCH, SuperPred and Swiss Target Prediction databases, obtaining 443 related targets, among which there were 141 for Cal, 144 for Iso, 167 for For, 212 for Kae and 315 for Que (**Figure 2B**). All of these targets were combined and identified using the UniProt database. By searching the GeneCards and DisGeNET databases for related research reports, 6,703 targets were obtained, which are closely related to the occurrence and development of "HF" or "liver fibrosis." Three hundred and twenty-two targets that matched the related targets of the five flavonoids and HF were then collected as the potential targets of the five flavonoids against HF (**Figure 3A**). Then, the PPI network of those 322 targets was established in the database String. There were 320 nodes and 5,476 edges in total.

Afterward, the topological feature analysis of the PPI network was conducted with the Cytoscape software platform based on three major parameters: degree, betweenness, and closeness. Those targets greater than the median were chosen to be key targets, then, hub nodes were established from those five anti-HF flavonoids. In the initial screening, the thresholds were set at degree ≥ 28, betweenness ≥ 0.00115124, and closeness ≥ 0.47399703. At last, 3,473 edges and 161 hub nodes were screened. Thereafter, those 161 key targets were subjected to secondary screening, at the thresholds of degree ≥ 43, betweenness ≥ 0.00312659, and closeness ≥ 0.51203852. The second screening ended with 82 large hub nodes and 1,776 edges (**Figure 3B**). Then, Cytoscape was adopted for visualizing and integrating those PPI network-involved

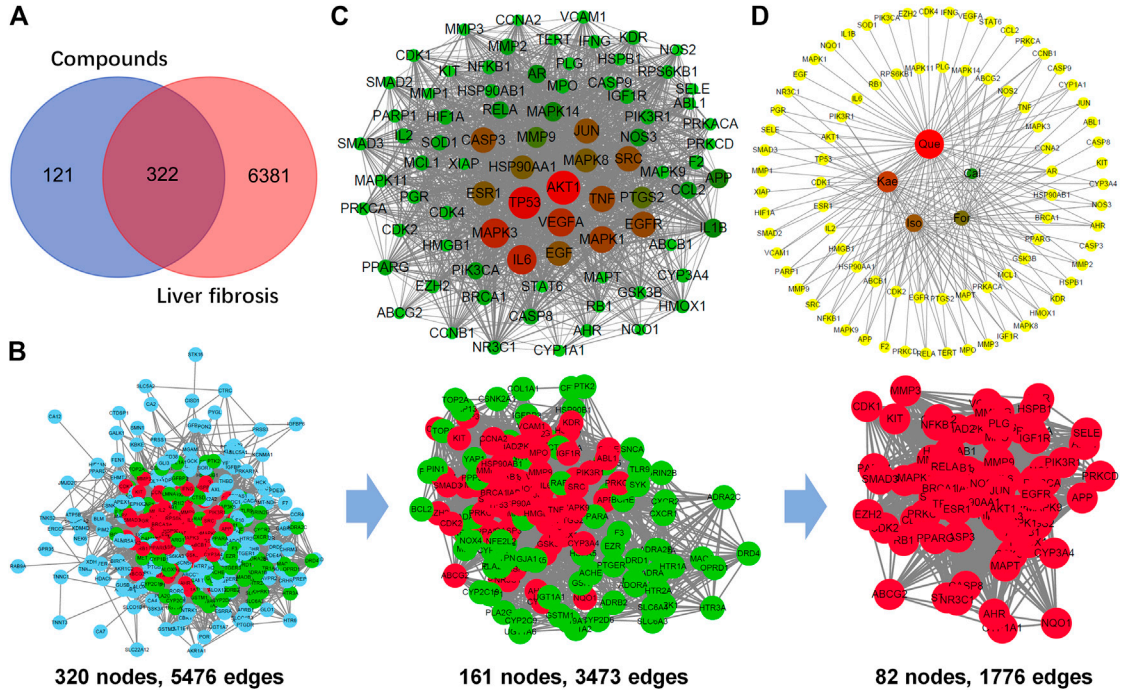

FIGURE 3 | Analysis of the key targets of the flavonoids for the treatment of liver fibrosis. **(A)** Venn diagram summarizing the differential targets of the flavonoids and liver fibrosis. **(B)** The process of topological screening for the protein-protein interaction (PPI) network. Finally, 82 candidate targets were predicted. **(C)** The PPI network of the 82 nodes. Different colors represent nodes of different sizes. The red nodes represent the large hub nodes and the green nodes represent the small hub nodes. The node size is proportional to the target degree in the network. **(D)** Compound target network (C-T network) of the flavonoids and 82 key targets.

topological parameters for those 82 screened key targets. The crucial biotargets were obtained and visualized, which included AKT1, TP53, MAPK3, IL6, TNF, JUN, MAPK1, and EGFR, etc (**Figure 3C**). Finally, based on 82 key targets, a large hub node-compound network was further constructed according to the five flavonoids. It was observed that Cal held relevancy to 23 key targets, For was related to 34 key targets, Iso was connected to 41 key targets, Kae was related to 50 key targets, whereas Que was associated with 72 key targets (**Figure 3D**).

GO Biological Process and KEGG Pathway Enrichment Analysis

The top significant (cutoff criterion with a significant difference of $p < 0.05$) GO categories are shown in **Figure 4A**. In biological processes (BPs), the common targets were mainly enriched in cellular response to chemical stimuli (GO: 0070887), response to oxygen-containing compounds (GO: 1901700), response to organic substances (GO: 0010033), cellular response to oxygen-containing compounds (GO: 1901701), cellular response to organic substances (GO: 0071310), etc. In molecular functions (MFs), the common targets were mainly associated with enzyme binding (GO: 0019899), identical protein binding (GO: 0042802), protein kinase activity (GO: 0004672), kinase binding (GO: 0019900), and protein kinase binding (GO: 0019901), etc. In addition, cellular component (CC) analysis showed that the common targets were the membrane-enclosed lumen (GO: 0031974), organelle lumen (GO: 0043233), intracellular lumen (GO: 0070013), nucleoplasm (GO: 0005654), and cytoplasmic part (GO: 0044444), etc.

To further reveal the potential mechanism of the five flavonoids against HF, KEGG analysis was carried out on those 82 key targets. The top 20 KEGG pathway enrichments were displayed based on the threshold of FDR < 0.01; for instance, AGE-RAGE signal transduction pathway in diabetes-related complications (ko04933), pathways in cancer (ko05200), fluid shear stress and atherosclerosis (ko05418), pancreatic cancer (ko05212), IL-17 signal transduction pathway (ko04657), hepatitis B (ko05161), relaxin signal transduction pathway (ko04926), TNF signaling pathway (ko04668), Chagas disease (American trypanosomiasis) (ko05142), and endocrine resistance (ko01522), etc (**Figure 4B**). Moreover, those 10 most significant KEGG pathways were used to construct the compound-target-pathway network (**Figure 4C**). The characteristics of multiple components, multiple targets and multiple pathways of the active ingredients against liver fibrosis were revealed through the construction of a network. Further analysis revealed that the molecular mechanisms were mainly concentrated in immune and inflammatory pathways, with the main pathway being the classical IL-17 signaling pathway (**Supplementary Figure S1**). The key targets of the IL-17 signaling pathway mainly include NF-κB, AP-1, IL-6, IL-1β, TNFα, IFN-γ, CCL2, COX2, MMP1, MMP3, and MMP9.

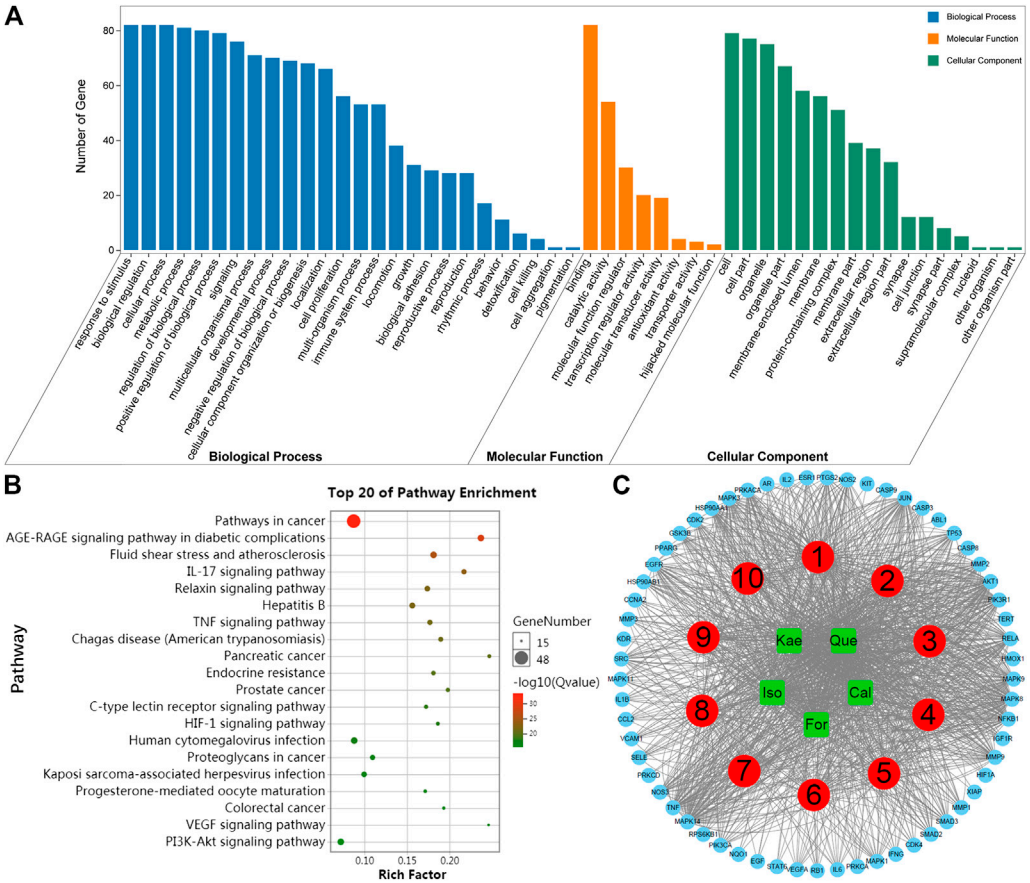

FIGURE 4 | Enrichment analysis of the key targets of the flavonoids against liver fibrosis. **(A)** GO enrichment analysis of the 82 key targets. Biological processes, cellular components, and molecular function terms were performed on the targets. The top significant (the cutoff criterion for a significant difference was $p < 0.05$) GO categories are shown. **(B)** KEGG enrichment analysis of the 82 key targets. The top 20 KEGG pathway enrichments are displayed, and only terms with FDR < 0.05 were selected for analysis. **(C)** Compound-target-pathway network. The red round nodes represent the top ten pathways, the green round nodes represent the flavonoids, and the blue triangles represent the related targets.

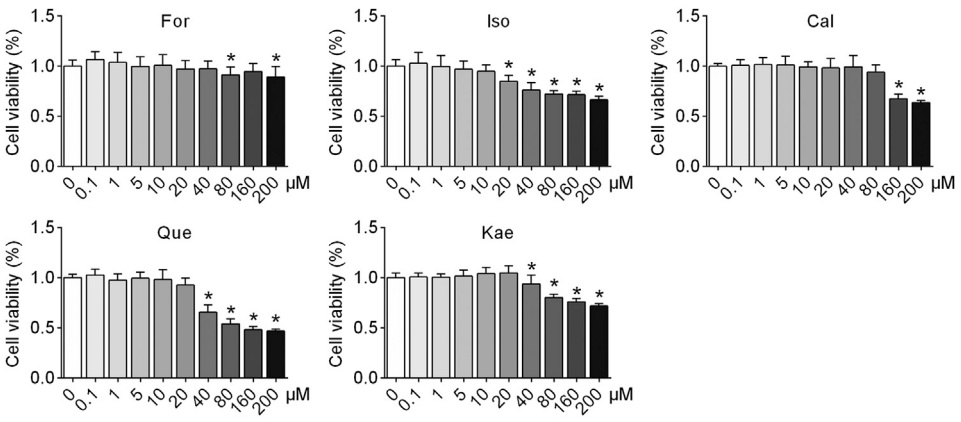

FIGURE 5 | The five flavonoids of AR had no cellular toxicity in HSCs at concentrations of 1, 5, and 10 μM. HSC-T6 cells were treated with For, Iso, Cal, Que, and Kae at concentrations ranging from 0.1 to 200 μM for 24 h. Cell viability was detected by performing a CCK-8 assay ($n = 3$). Data are expressed as the mean ± SD. *$p < 0.05$ vs. the blank control.

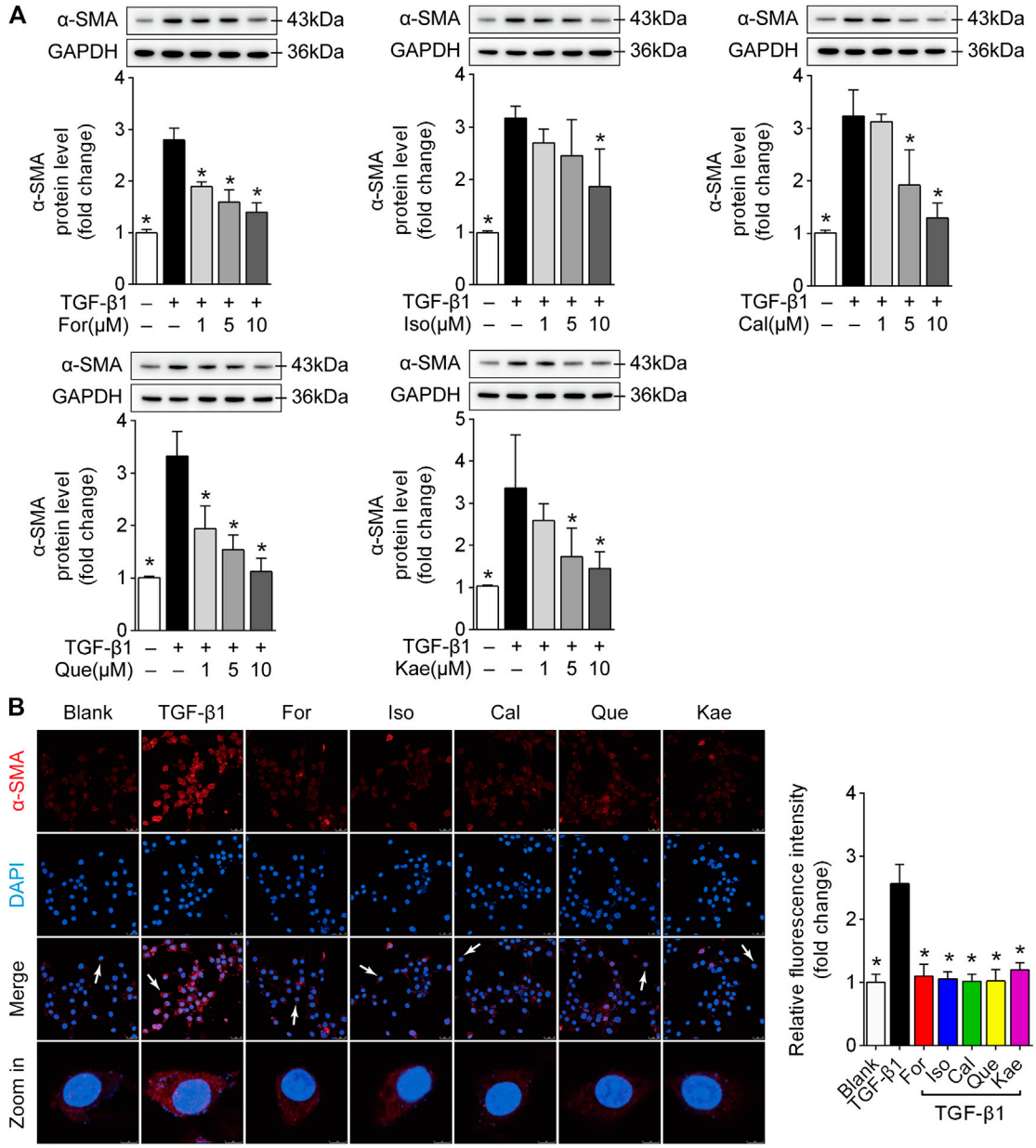

FIGURE 6 | The five flavonoids were able to suppress HSC activation. HSC-T6 cells were stimulated with TGF-β1 (10 ng/ml) for 24 h and prepared for further experiments. **(A)** Alpha-SMA protein expression in TGF-β1-induced HSC-T6 cells (n = 3). **(B)** Confocal scanning images and quantified data of α-SMA in HSC-T6 cells stimulated with TGF-β1 (10 ng/ml) for 24 h (n = 3), scale bar = 50 μm for 400×. Data are expressed as the mean ± SD. *p < 0.05 vs. TGF-β1 treatment.

The Five Flavonoids of AR Did Not Show Cytotoxicity to HSCs

To elucidate the efficacy of the five flavonoids against HF, the first step should be to investigate the cellular toxicity of these compounds against HSCs. The results showed that in resting cells, a concentration of 20 μM Iso produced a significant effect on cell viability in HSC-T6 cells ($p < 0.05$), whereas 0.1–10 μM flavonoids had no toxicity. Thus, the five flavonoids at concentrations of 1, 5, and 10 μM were chosen for the following experiments, excluding the possibility that these five flavonoids inhibited HSC activation *via* cytotoxicity (**Figure 5**).

The Five Flavonoids Were Able to Suppress HSC Activation

In order to further study the effects of the five flavonoids on HSC transdifferentiation, the expression of α-SMA, a hallmark in the process of HSC activation (31258636), was detected in

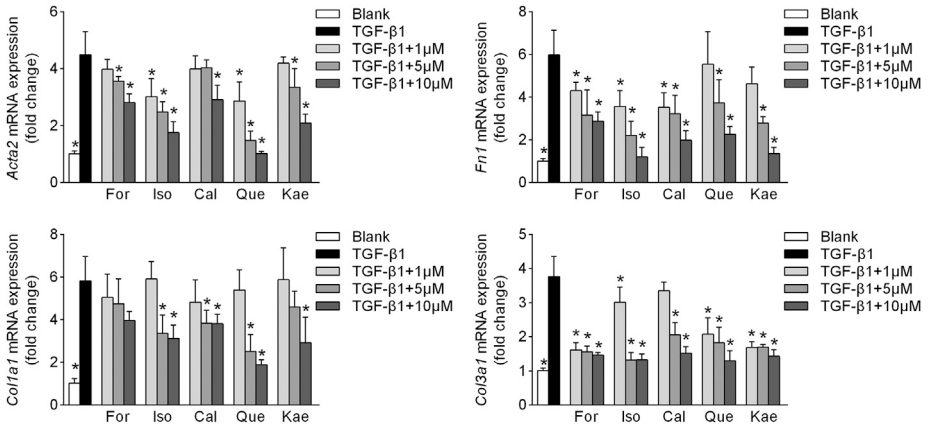

FIGURE 7 | HF phenotypes were improved by the five flavonoids of AR. HSCs were stimulated with TGF-β1 (10 ng/ml) for 24 h and prepared for RT-qPCR experiments. Illustrations are shown for the HF phenotypes of *Acta2* (upper left panel, $n = 4$), *Fn1* (upper right panel, $n = 4$), *Col1a1* (lower left panel, $n = 4$), and *Col3a1* (lower right panel, $n = 4$). Data are expressed as the mean ± SD. *$p < 0.05$ vs. TGF-β1 treatment.

TGF-β1-challenged HSC-T6 cells. As suggested by Western blotting, those five flavonoids significantly decreased α-SMA protein level within HSC-T6 cells induced by TGF-β1 (**Figure 6A**; $p < 0.05$). Additionally, visualization by confocal microscopy and the quantified data confirmed the functional role of the five flavonoids in reducing α-SMA overexpression induced by TGF-β1 (**Figure 6B**; $p < 0.05$). These data revealed that the five flavonoids of AR impeded HSC activation, possibly contributing to the prevention of liver fibrosis.

The Five Flavonoids Regulated the Phenotypes of HF

In the process of HSC transdifferentiation into myofibroblasts, increasing amounts of α-SMA, collagen, fibronectin, and other ECM proteins induced by TGF-β1 eventually give rise to HF (Parola and Pinzani, 2019). The results showed that TGF-β1 stimulation remarkedly increased *Acta2*, *Fn1*, *Col1a1* and *Col3a1* mRNA expression approximately 4~6-fold ($p < 0.001$) in HSC-T6 cells, whereas these effects were significantly reversed by For in a dose-dependent manner (**Figure 7**; $p < 0.05$). Similar results were noted for other flavonoid treatments ($p < 0.05$). These results demonstrated that the five flavonoid interventions increased the resistance of liver stellate cells to TGF-β1-induced fibrogenic responses.

The Inflammatory Pathway Might Be Involved in the Antifibrotic Effects of the Five Flavonoids

Based on the enrichment analysis by using network pharmacology, we noted a number of differentially expressed genes and proteins associated with the inflammatory process, including the inflammatory cytokines IL-1β, IL-6, tumor necrosis factor alpha (TNF-α), and interferon gamma (IFNγ); chemokines CCL2 and CXCL1; the enzyme COX2; and matrix metalloproteinases (MMPs) MMP1, MMP2, and MMP9. We detected these factors by utilizing the RT-qPCR method. The results showed that TGF-β1 stimulation increased the mRNA expression of *Rela*, *Jun*, cytokines *Il1b*, *Il6*, *Tnfa*, and *Ifng*, chemokines *Ccl2*, and *Cxcl1*, the related enzyme *Cox2*, and MMP family members *Mmp2*, and *Mmp9* from ~2 to ~17-fold ($p < 0.05$), whereas the five flavonoids could effectively reverse these effects in HSC-T6 cells ($p < 0.05$). The protein MMP1 was able to degrade ECM in HSCs, especially type I and type III collagen. As **Figure 8** shows, the five flavonoids could effectively elevate *Mmp1* expression ($p < 0.05$); however, there was no significant difference after treatment with For, Que, or Kae. Collectively, these compounds were shown to significantly suppress the inflammatory process (**Figure 8**).

The Five Flavonoids of AR Exhibited Anti-Inflammatory Effects *via* the NF-κB Signaling Pathway

The results from KEGG enrichment showed that the IL-17 pathway, mainly including NF-κB, AP-1 and various related inflammatory factors, might be involved in the treatment of the five flavonoids against liver cirrhosis. Accordingly, it needs to be confirmed whether these flavonoids exhibit antifibrotic effects *via* the regulation of NF-κB or AP-1. Although the five flavonoids showed regulation in AP-1 at the transcriptional level to a certain extent (**Figure 8**), the protein level had no marked change. Moreover, it was found that there were higher protein levels of NF-κB after TGF-β1 treatment than in the flavonoid treatment groups. Moreover, Western blot analysis and the semiquantitative illustration demonstrated that all five flavonoids could decrease NF-κB protein levels in a dose-dependent manner (**Figure 9**; $p < 0.05$). These data suggested that the anti-inflammatory effects of the flavonoids involved NF-κB, indicating that these active flavonoids repressed HSC activation *via* the NF-κB signaling pathway.

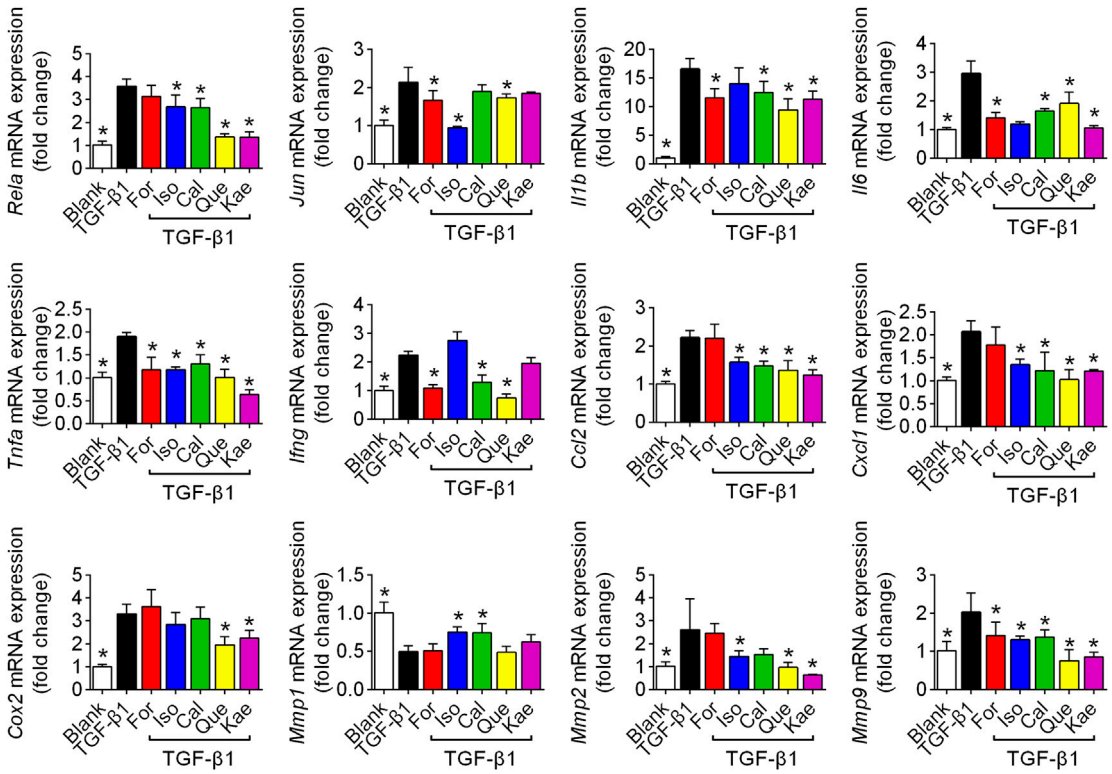

FIGURE 8 | Inflammatory factors were involved in the process of flavonoid inhibition of HSC activation. HSCs were stimulated with TGF-β1 (10 ng/ml) for 24 h and prepared for RT-qPCR experiments. The figures show the mRNA expression of different inflammatory factors with or without interference with For, Iso, Cal, Que, or Kae in TGF-β1-induced HSC-T6 cells (n = 4). Data includes *Rela*, *Jun*, *Il1b*, *Il6*, *Tnfa*, *Ifng*, *Ccl2*, *Cxcl1*, *Cox2*, *Mmp1*, *Mmp2*, and *Mmp9*. Data are expressed as the mean ± SD. *p < 0.05 vs. TGF-β1 treatment.

Analysis of Molecular Docking Results

The docking results of the five flavonoids with the target protein IKKβ are shown in **Figure 10**. The residues docked with the molecular ligands are shown as yellow sticks. Amino acid residues Glu100 and Gly102 in the crystal structure of IKKβ formed hydrogen bonds with Cal (**Figure 10A**). For could bind to the residues Cys99, Glu100, and Asp166 in the IKKβ crystal structure by hydrogen bonds (**Figure 10B**). Both Iso and Kae could bind to the residues Glu100 and Gly102 of the IKKβ crystal structure by hydrogen bonds (**Figures 10C,D**). Amino acid residues Gly22, Thr23, Glu97, Cys99, and Gly102 in the crystal structure of IKKβ formed hydrogen bonds with Que (**Figure 10E**). The docking scores for the five flavonoids (Cal, For, Iso, Kae, and Que) with the IKKβ crystal structure were −8.5, −8.7, −8.4, −8.4 and −8.2 kcal/mol, respectively (**Figure 10F**). The docking score represents the binding affinity, and when the score is lower, the binding affinity is stronger. An affinity <−7 indicates strong binding activity (19,499,576). Our results indicate that the flavonoids have a strong binding affinity for IKKβ.

DISCUSSION

Liver cirrhosis severely decreases the quality of life of patients. It is of great significance to seek an effective therapeutic strategy to restrain liver disease deterioration. AR, a well-known traditional Chinese medicine, has been reported to be therapeutically effective against liver cirrhosis. However, the molecular mechanism has yet to be completely deciphered. Flavonoids are the main bioactive compounds involved in the functions of AR. Thus, in the current study, investigation into the effects and mechanism of the flavonoids from AR against liver fibrosis was conducted based on a network pharmacology approach coupled with experimental validation and molecular docking analysis. These results expand our knowledge pertaining to the basis of the effects and mechanism of AR-induced anti-liver fibrosis.

The use of TCMs, including AR, in the prevention and treatment of liver fibrosis has increased worldwide due to their privileged properties. However, it is difficult to elucidate the effects of AR because of its multiple compounds, multiple targets, multiple pathways, and multiple mechanisms of action (Guo et al., 2019), which greatly restrict the processes of modernization and internationalization of AR. In recent years, along with the generalization of systems biology, network pharmacology, which integrates chemoinformatics, bioinformatics, network biology, network analysis and traditional pharmacology, has emerged as a powerful tool to analyze the mechanism of the complex components of TCMs (Berger and Iyengar, 2009; Li and Zhang, 2013; Hao and Xiao, 2014). Thus, this study is the first to comprehensively screen the

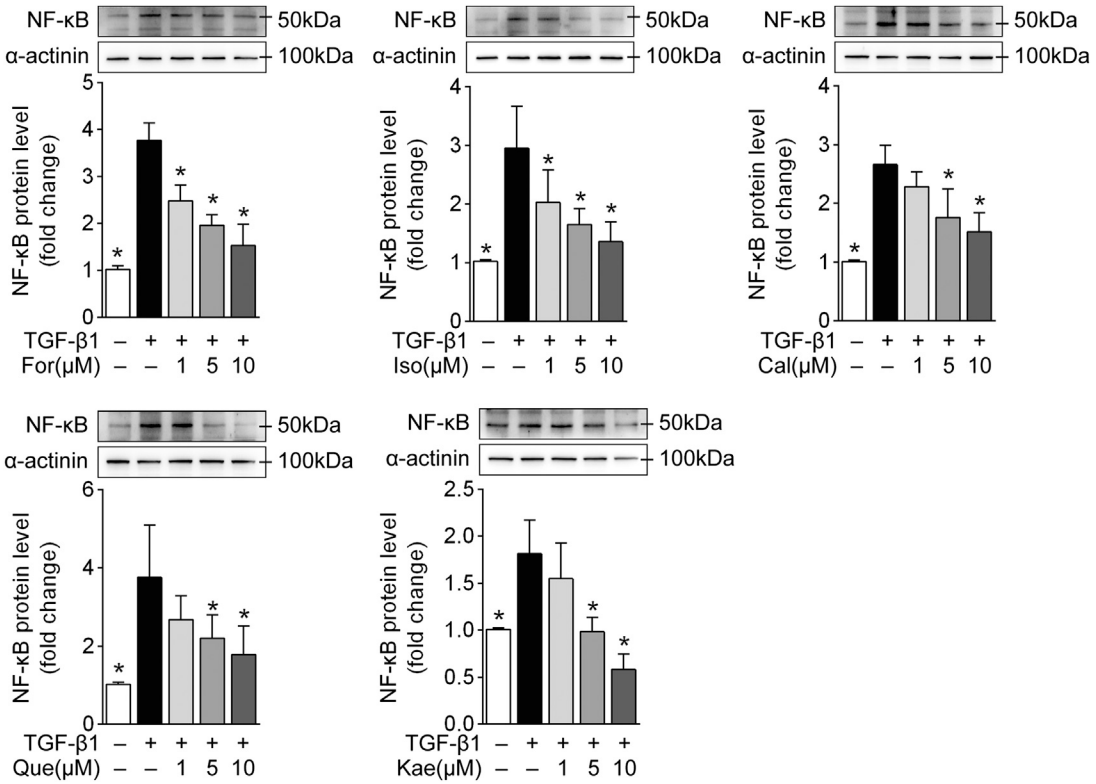

FIGURE 9 | The five flavonoids might exhibit antifibrotic effects *via* the NF-κB signaling pathway. HSC-T6 cells were stimulated with TGF-β1 (10 ng/ml) for 24 h and prepared for protein level analysis. The diagrams show the NF-κB protein level with or without interference with For, Iso, Cal, Que, and Kae in TGF-β1-induced HSC-T6 cells (n = 3). Data are expressed as the mean ± SD. *p < 0.05 vs. TGF-β1 treatment.

active ingredients of AR, predict the targets of these active ingredients and the genes related to liver fibrosis and analyze the potential mechanism of AR against liver fibrosis by using a network pharmacology approach.

After screening AR for OB ≥ 30% and DL ≥ 0.18, a total of 87 reported active ingredients of AR were retrieved by searching the TCMSP database. Modern pharmacological studies indicate that flavonoids are the leading favorable compounds related to different AR pharmacological effects and efficacy (Guo et al., 2019). However, whether the flavonoids of AR can exert inhibitory effects on HF is not yet completely understood. There is little information regarding how flavonoids contribute to the treatment of HF by AR. There is an urgent need for systematic evaluation of the flavonoid components in AR to determine the definite bioactive component responsible for the activity of AR against HF. Thus, five potential bioactive flavonoids were selected: For, Iso, Cal, Que, and Kae (**Figure 2A**; **Supplementary Table S1**), for subsequent network pharmacology analysis and experimental validation. Then, the PPI network of candidate targets for flavonoids in the treatment of liver fibrosis was established based on the flavonoid and liver fibrosis target networks with 322 overlapping genes (**Figures 2B**,**3A**).

Afterward, the topological feature analysis of the PPI network was conducted according those three main parameters, namely, degree, closeness and betweenness. A total of 82 targets greater than the median were screened to be the key targets for those five anti-HF flavonoids (**Figures 3B,C**). It was apparent that most of these targets, including AKT1, TP53, MAPK3, IL6, TNF, JUN, MAPK1, EGFR, and many other inflammation-related proteins, were closely involved in the inflammation process. It was also observed that Que was linked to the greatest number of key targets, followed by Kae, Iso, For, and Cal (**Figure 3D**), suggesting that Que could be the most significant compound in AR against liver fibrosis.

Next, crucial target-related enrichment analyses of the GO and KEGG pathways were performed. GO enrichment analysis, which was based on three different terms, including BP, CC, and MF terms, was used to identify the biological mechanisms of key targets in disease (Ashburner et al., 2000). Based on the GO terms, it was proposed that the pharmacological effects of AR against liver fibrosis occurred by simultaneously activating various biological processes, cellular components, and molecular functions (**Figure 4A**). KEGG database can be adopted to identify potential target biological relevance and systematic functions (Chen et al., 2015). After KEGG enrichment analysis, it was found that the five flavonoids could potentially suppress liver fibrosis through multiple pathways, including pathways in cancer, the AGE-RAGE signal transduction pathway in diabetes-related complications, fluid shear stress

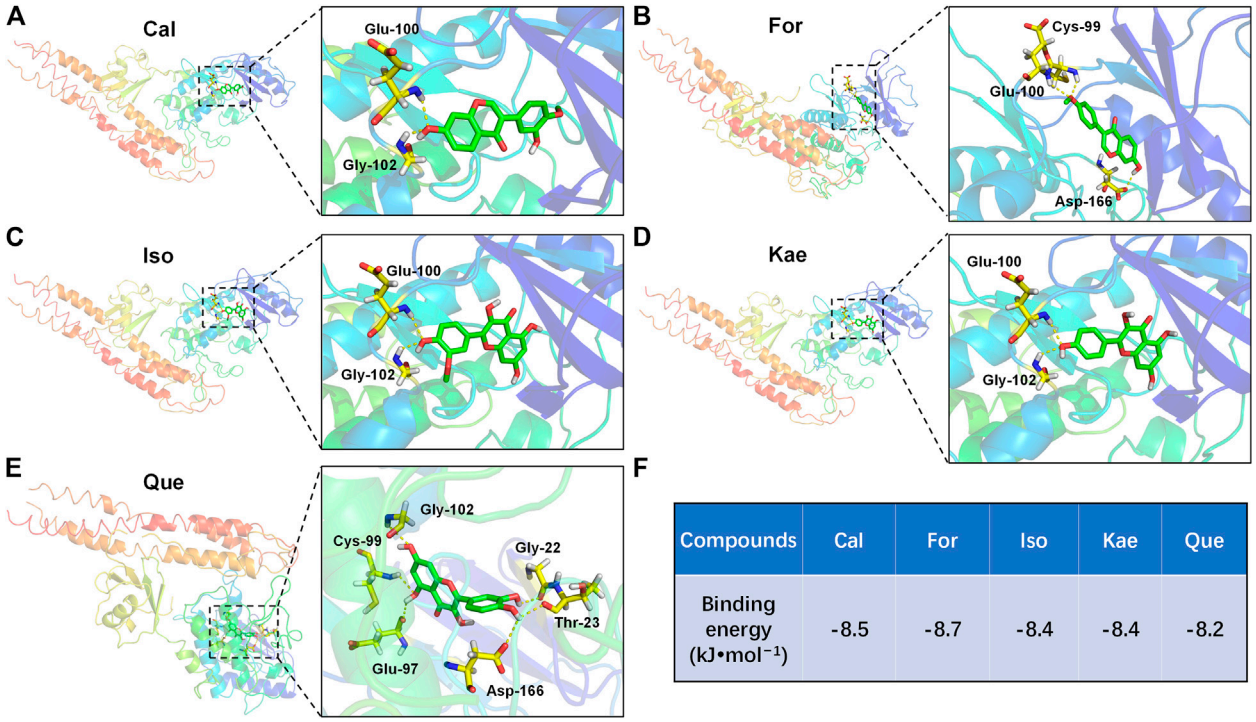

Compounds	Cal	For	Iso	Kae	Que
Binding energy (kJ•mol^{-1})	-8.5	-8.7	-8.4	-8.4	-8.2

FIGURE 10 | Molecular docking diagrams of IKKβ with **(A)** Cal, **(B)** For **(C)** Iso, **(D)** Kae, and **(E)** Que. **(F)** The binding energies for the five flavonoids docked into the IKKβ crystal structure. The yellow dashed lines show H-bonds.

and atherosclerosis, the IL-17 signal transduction pathway, the relaxin signal transduction pathway, hepatitis B, and the TNF signaling pathway, etc (**Figures 4B,C**). Further analysis revealed that the molecular mechanisms were mainly concentrated in the immune and inflammatory pathways, with the main pathway being the classical IL-17 signaling pathway (**Supplementary Figure S1**). The key targets of the IL-17 signaling pathway include NF-κB, AP-1, IL-6, IL-1β, TNFα, IFN-γ, CCL2, COX2, MMP1, MMP3, and MMP9, which all exert vital parts in HF development (Tan et al., 2020; Zhou et al., 2020). Accordingly, in addition to the network pharmacology analysis, we next performed experimental validation to clarify the potential inflammatory mechanism of the flavonoids against liver fibrosis.

HSCs are pericytes found in the perisinusoidal space of the liver. Stellate cells are the major cell type involved in liver fibrosis, which is the formation of scar tissue in response to liver damage (Tsuchida and Friedman, 2017). Based on this, we used HSCs for subsequent biological verification experiments. To determine the effects of the five flavonoid compounds screened by network pharmacology on HSCs, the first step was to explore whether these compounds had cellular toxicity. **Figure 5** shows that except for the Que panel, the cell survival rate of all treatments was higher than 70% in the concentration range of 0.1–200 μM. The cell viability was greater than 70% in the 40 μM group of HSCs treated with Que. However, in all flavonoid intervention groups, a concentration less than or equal to 10 μM compound did not decrease the survival rate of HSCs, indicative of the nontoxicity of the five flavonoids for further experiments.

Liver fibrogenic responses are characterized by the differentiation of HSCs into myofibroblasts, and excessive ECM deposition is a major consequence of myofibroblast activation. HSCs activation to the proliferating fibrogenic myofibroblasts has been extensively recognized to be a pivotal factor of HF in human or experimental liver damage (Parola and Pinzani, 2019). Myofibroblasts are important but transient mediators of normal wound contraction and are characterized phenotypically by their high levels of α-SMA. Therefore, α-SMA is often used as a marker of myofibroblast formation (Peng et al., 2019). In the present study, we applied multiple biological methods for evaluating those flavonoid effects on α-SMA expression within the HSC-T6 cells treated with TGF-β1. As indicated, the five flavonoids had a remarkable inhibitory effect on the transdifferentiation of HSCs (**Figure 6**). Upon HSC activation, formative myofibroblasts secrete large amounts of ECM. Once secreted, the formative myofibroblasts then aggregate with the existing matrix, which eventually leads to liver fibrosis. Collagens are the most abundant protein in the ECM, especially type I collagen (Col-I) and type III collagen (Col-III). Collagen fibers are connected to cells by fibronectins in the ECM (Ricard-Blum, 2011). Hence, these fibrogenic factors are good indicators of the severity of HF. In **Figure 7**, we detected all of these related HF phenotypes, and the RT-qPCR analysis showed that the main flavonoids of AR could counteract the effects induced by TGF-β1 in HSC-T6 cells. Given the critical role of α-SMA and ECM deposition in HSC activation and differentiation, these results indicated that the main flavonoids from AR restrained HF by inhibiting HSC activation, an effect

likely resulting from interference with the inflammatory process when the KEGG map was taken into account.

Inflammatory pathways are associated with numerous diseases. The scientific evidence and KEGG results from our work suggested that the IL-17 pathway, mainly NF-κB and its associated inflammatory factors, accounts for an evolutionarily conservative pathway that can regulate HF (Luedde and Schwabe, 2011). NF-κB is suggested to regulate the liver fibrogenesis mainly in three diverse cell fractions, including regulating hepatocyte injury, inflammatory signals, and fibrogenic responses of HSCs. Among these, there is growing evidence that NF-κB acts as a key mediator of fibrosis in the transdifferentiation of HSCs to myofibroblasts (Friedman, 2004). The potential mechanisms appear through direct fibrogenic effects, anti-apoptotic effects, and secretion of macrophage-recruiting chemokines. NF-κB participates in down-regulating members of the miR-29 family within HSCs, thereby increasing the levels of all collagens together with additional ECM proteins within HSCs (Roderburg et al., 2011). Since NF-κB is primarily composed of the p50 and p65 subunits, we investigated different subunits at different biological levels. In this study, we confirmed that there was a remarkable elevation in NF-κB mRNA (*Rela*) and protein (p50) levels in the process of HSC activation, and all five flavonoids reversed these effects in response to TGF-β1 stimulation in HSC-T6 cells. As shown in **Figures 8**, **9**, Que demonstrated the optimal effect among the five flavonoids.

Activation of NF-κB also promotes the secretion of various inflammatory mediators. Indeed, in the network pharmacology study, we identified several related inflammatory factors, including cytokines, chemokines, enzymes, and the MMP family. Cytokines, the small proteins with the molecular weight of 5–20 kDa, play vital roles in cell signaling. Of these cytokines, IL-1β can directly trigger the synthesis of collagen together with the proliferation of myofibroblasts (Kähäri et al., 1987). IL-6, IFN-γ, and TNF-α are secreted by T cells, biliary cells, and Kupffer cells, respectively, which contributes to HSC activation (Bataller and Brenner, 2005). As **Figure 8** shows, Que and Kae might have better inhibitory effects on these cytokines than the other flavonoids. In addition to cytokines, the increased secretion of chemokines such as CCL2 and CXCL1 results in inflammatory cell influx, like the macrophages, and they show interactions with HSCs and have certain effect on HSC activation as well as wound healing (Seki et al., 2007). In this study, we found that all five flavonoids could downregulate chemokine expression induced by TGF-β1.

Furthermore, we analyzed a vital inducible sensor, COX-2, which exerts a vital part in liver fibrogenesis development. COX-2 is a rate-limiting enzyme responsible for catalyzing arachidonic acid in converting to thromboxane and inflammatory prostaglandins (Yang et al., 2020). Despite the controversial relationship between COX-2 and TGF-β1, we observed a marked increase in *Cox2* mRNA expression after TGF-β1 induction, and this elevation was reversed after flavonoid treatment. Accompanying cellular activation, ECM constituents change from the matrix with abundant laminin and collagen IV to the concentrated interstitial ECM, which suggested the possible occurrence of proteolytic degradation for altering sinusoid microenvironment and HSCs fate (Han, 2006). As a matter of fact, members in MMP family are rapidly expressed via HSCs to respond to a variety of hepatic toxins. Depending on timing and other reasons, MMPs play dual roles in liver fibrosis. It has been reported that MMP2 and MMP9 are expressed in human fibrotic injury, while MMP1 can degrade ECM in HF (Takahara et al., 1997; Iimuro et al., 2003). Our work not only confirmed this phenomenon but also noted that Kae showed better MMP family regulatory ability than the other flavonoids. However, MMPs have different functions during the different processes of HF, and more in-depth experiments are needed. Besides, the antifibrotic effects of the five flavonoids should be further demonstrated using pathway inhibitors *in vitro* and animal model *in vivo*. Transgenic animal experiments have been conducted to clarify the exact mechanism(s).

Finally, the potential mechanism of AR flavonoids against liver fibrosis was further validated by using molecular docking. Molecular docking is a quick and effective method of predicting the binding affinity between TCM ingredients and their targets based on the spatial structure of ligands and receptors (Gan et al., 2019). Molecular docking analysis was conducted by using AutoDock Vina software, which may serve as the AutoDock successor docking analysis, due to its effect on apparently improving performance and accuracy in comparison with those of Lamarckian Genetic Algorithm (Kist et al., 2018). Based on results of network pharmacology, it was known that flavonoids can possibly suppress liver fibrosis by inhibiting the IL-17 signaling pathway, which includes NF-κB, AP-1, IL-6, IL-1β, TNFα, IFN-γ, CCL2, COX2, MMP1, MMP3, and MMP9. The experimental validation results further confirmed that the flavonoids could exhibit potent inhibitory activity against liver fibrosis *via* suppression of NF-κB and its various downstream inflammatory factors. NF-κB represents the key transcription factor related to the inflammatory signaling cascade (Hoesel and Schmid, 2013). Normally, NF-κB can be found in cytoplasm, which can be inactivated by the IκB inhibitors. The NF-κB inflammatory activation is dependent on the IKKβ-mediated IκB protein phosphorylation, as well as p50–p65 subunit nuclear translocation in NF-κB, thus inducing the expression of proinflammatory cytokines (Hoesel and Schmid, 2013). As a result, specifically inhibiting IKKβ is a reasonable way to more effectively treat inflammatory disorders, like HF (Baig et al., 2018). The results of molecular docking showed that the flavonoids had high affinity for IKKβ (**Figure 10**), suggesting that the mechanism of the flavonoids against liver fibrosis may be related to suppression of the NF-κB pathway through effective inhibition of IKKβ.

CONCLUSION

This study aimed to undertake network pharmacology analysis coupled with experimental validation and molecular docking to investigate the effects and mechanism of AR flavonoids against liver fibrosis. The network pharmacology analysis findings showed that the flavonoids from AR exerted their pharmacological effects against liver fibrosis by modulating

multiple targets and pathways. The experimental validation results suggested that flavonoids might play an anti-inflammatory role in the treatment of liver fibrosis by mediating inflammation signaling pathways. Our molecular docking study results also indicated that the mechanism of the flavonoids against liver fibrosis may be related to suppression of the NF-κB pathway through effective inhibition of IKKβ. These findings not only provide a scientific basis for clarifying the mechanism of action of AR in the treatment of liver fibrosis but also suggest a novel promising therapeutic strategy for the treatment of liver fibrosis. However, as this study was based on data mining and experimental validation, further clinical validation studies should be undertaken to determine the role of AR in liver fibrosis.

DATA AVAILABILITY STATEMENT

The original contributions presented in the study are included in the article/**Supplementary Material**, further inquiries can be directed to the corresponding authors.

AUTHOR CONTRIBUTIONS

JW and LA designed the experiments and wrote the manuscript. LA, YFL, MK, LL and YML carried out the experiments and analyzed the data. JW and ZL supervised and corrected the manuscript.

FUNDING

This work was supported by grants from the National Natural Science Foundation of China (81703803, 81930114), the Natural Science Foundation of Guangdong Province (2017A030310464), the Project of Guangzhou University of Chinese Medicine (QNYC20190103), the Basic and Applied Basic Research Fund Project of Guangdong Province (2019A1515110202), the China Postdoctoral Science Foundation (2020M672604), Guangdong Key Laboratory for translational Cancer research of Chinese Medicine (2018B030322011), and Key-Area Research and Development Program of Guangdong Province (No. 2020B1111100004).

ACKNOWLEDGMENTS

We thank the International Institute for Translational Chinese Medicine of Guangzhou University of Chinese Medicine for technical assistance.

SUPPLEMENTARY MATERIAL

The Supplementary Material for this article can be found online at: https://www.frontiersin.org/articles/10.3389/fphar.2020.618262/full#supplementary-material.

REFERENCES

Ashburner, M., Ball, C. A., Blake, J. A., Botstein, D., Butler, H., Cherry, J. M., et al. (2000). Gene ontology: tool for the unification of biology. The gene ontology consortium. *Nat. Genet*. 25, 25–29. doi:10.1038/75556

Bai, C. Z., Hao, J. Q., Hao, X. L., and Feng, M. L. (2018). Preparation of lectin and evaluation of its biological function. *Biomed. Rep*. 9, 345–349. doi:10.3892/br.2018.1132

Baig, M. S. A., Roy, U., Rajpoot, S., Srivastava, M., Naim, A., Liu, D., et al. (2018). Repurposing Thioridazine (TDZ) as an anti-inflammatory agent. *Sci. Rep*. 8, 12471. doi:10.1038/s41598-018-30763-5

Bataller, R., and Brenner, D. A. (2005). Liver fibrosis. *J. Clin. Invest*. 115, 209–218. doi:10.1172/JCI24282

Berger, S. I., and Iyengar, R. (2009). Network analyses in systems pharmacology. *Bioinformatics* 25, 2466–2472. doi:10.1093/bioinformatics/btp465

Chen, J., Li, C., Zhu, Y., Sun, L., Sun, H., Liu, Y., et al. (2015). Integrating GO and KEGG terms to characterize and predict acute myeloid leukemia-related genes. *Hematology* 20, 336–342. doi:10.1179/1607845414Y.0000000209

Ding, Z., Luo, C., Zhang, Z., Chen, J., Wen, B., and Wang, Z. (2011). Clinical research on treatment of liver fibrosis in patients with chronic hepatitis B by Ruangan Jianpi pill. *Chin. J. Integr. Tradit. West. Med. Liver Dis*. 6, 337–339. doi:10.3969/j.issn.1005-0264.2011.06.006

Fan, W., Liu, T., Chen, W., Hammad, S., Longerich, T., Hausser, I., et al. (2019). ECM1 prevents activation of transforming growth factor β, hepatic stellate cells, and fibrogenesis in mice. *Gastroenterology* 157, 1352–1367.e12. doi:10.1053/j.gastro.2019.07.036

Friedman, S. L. (2004). Mechanisms of disease: mechanisms of hepatic fibrosis and therapeutic implications. *Nat. Clin. Pract. Gastroenterol. Hepatol*. 1, 98–105. doi:10.1038/ncpgasthep0055

Friedman, S. L., Maher, J. J., and Bissell, D. M. (2000). Mechanisms and therapy of hepatic fibrosis: report of the AASLD single topic basic research conference. *Hepatology* 32, 1403–1408. doi:10.1053/jhep.2000.20243

Gan, D., Xu, X., Chen, D., Feng, P., and Xu, Z. (2019). Network pharmacology-based pharmacological mechanism of the Chinese medicine rhizoma drynariae against osteoporosis. *Med. Sci. Monit*. 25, 5700–5716. doi:10.12659/MSM.915170

Guo, Z., Lou, Y., Kong, M., Luo, Q., Liu, Z., and Wu, J. (2019). A systematic review of phytochemistry, pharmacology and pharmacokinetics on Radix: implications for radix as a personalized medicine. *Int. J. Mol. Sci*. 20, 1463. doi:10.3390/ijms20061463

Han, Y.-P. (2006). Matrix metalloproteinases, the pros and cons, in liver fibrosis. *J. Gastroenterol. Hepatol*. 21 (Suppl. 3), S88–S91. doi:10.1111/j.1440-1746.2006.04586.x

Hao, da. C., and Xiao, P. G. (2014). Network pharmacology: a Rosetta Stone for traditional Chinese medicine. *Drug Dev. Res*. 75, 299–312. doi:10.1002/ddr.21214

Hoesel, B., and Schmid, J. A. (2013). The complexity of NF-κB signaling in inflammation and cancer. *Mol. Cancer*. 12, 86. doi:10.1186/1476-4598-12-86

Huang, Y., Deng, X., and Liang, J. (2017). Modulation of hepatic stellate cells and reversibility of hepatic fibrosis. *Exp. Cell Res*. 352, 420–426. doi:10.1016/j.yexcr.2017.02.038

Iimuro, Y., Nishio, T., Morimoto, T., Nitta, T., Stefanovic, B., Choi, S. K., et al. (2003). Delivery of matrix metalloproteinase-1 attenuates established liver fibrosis in the rat. *Gastroenterology* 124, 445–458. doi:10.1053/gast.2003.50063

Kähäri, V. M., Heino, J., and Vuorio, E. (1987). Interleukin-1 increases collagen production and mRNA levels in cultured skin fibroblasts. *Biochim. Biophys. Acta*. 929, 142–147. doi:10.1016/0167-4889(87)90169-8

Kist, R., Timmers, L. F. S. M., and Caceres, R. A. (2018). Searching for potential mTOR inhibitors: ligand-based drug design, docking and molecular dynamics studies of rapamycin binding site. *J. Mol. Graph. Model*. 80, 251–263. doi:10.1016/j.jmgm.2017.12.015

Li, J., Zhao, P., Li, Y., Tian, Y., and Wang, Y. (2015). Systems pharmacology-based dissection of mechanisms of Chinese medicinal formula Bufei Yishen as an effective treatment for chronic obstructive pulmonary disease. *Sci. Rep*. 5, 15290. doi:10.1038/srep15290

Li, S., and Zhang, B. (2013). Traditional Chinese medicine network pharmacology: theory, methodology and application. *Chin. J. Nat. Med*. 11, 110–120. doi:10.1016/S1875-5364(13)60037-0

Li, Y., Yi, H., Cai, Y., Lin, H., and Liu, H. (2019). Effect of total flavonoids of *Astragalus* on liver fibrosis induced by carbon tetrachloride in rats. *Chin. Tradit. Patent Med*. 41, 1710–1713. doi:10.3969/j.issn.1673-7202.2015.06.022

Liang, X. L., and Yuan, J. Y. (2013). Effect of Chinese herbal compound on liver fibrosis in rabbits with schistosomiasis by B-ultrasound. *Asian Pac. J. Trop. Med*. 6, 658–662. doi:10.1016/S1995-7645(13)60114-5

Liu, C., Gu, Z., Zhou, W., and Guo, C. (2005). Effect of *Astragalus* complanatus flavonoid on anti-liver fibrosis in rats. *World J. Gastroenterol*. 11, 5782–5786. doi:10.3748/wjg.v11.i37.5782

Luedde, T., and Schwabe, R. F. (2011). NF-κB in the liver—linking injury, fibrosis and hepatocellular carcinoma. *Nat. Rev. Gastroenterol. Hepatol*. 8, 108–118. doi:10.1038/nrgastro.2010.213

Nickel, J., Gohlke, B. O., Erehman, J., Banerjee, P., Rong, W. W., Goede, A., et al. (2014). SuperPred: update on drug classification and target prediction. *Nucl. Acids Res*. 42, W26–W31. doi:10.1093/nar/gku477

Parola, M., and Pinzani, M. (2019). Liver fibrosis: pathophysiology, pathogenetic targets and clinical issues. *Mol. Aspect. Med*. 65, 37–55. doi:10.1016/j.mam.2018.09.002

Peng, Y., Li, L., Zhang, X., Xie, M., Yang, C., Tu, S., et al. (2019). Fluorofenidone affects hepatic stellate cell activation in hepatic fibrosis by targeting the TGF-β1/Smad and MAPK signaling pathways. *Exp. Ther. Med*. 18, 41–48. doi:10.3892/etm.2019.7548

Ren, G., Zhong, Y., Ke, G., Liu, X., Li, H., Li, X., et al. (2019). The mechanism of compound anshen essential oil in the treatment of insomnia was examined by network pharmacology. *Evid. Based Complement. Alternat. Med*. 2019, 9241403. doi:10.1155/2019/9241403

Ricard-Blum, S. (2011). The collagen family. *Cold Spring Harb. Perspect. Biol*. 3, a004978. doi:10.1101/cshperspect.a004978

Roderburg, C., Urban, G. W., Bettermann, K., Vucur, M., Zimmermann, H., Schmidt, S., et al. (2011). Micro-RNA profiling reveals a role for miR-29 in human and murine liver fibrosis. *Hepatology* 53, 209–218. doi:10.1002/hep.23922

Ru, J., Li, P., Wang, J., Zhou, W., Li, B., Huang, C., et al. (2014). TCMSP: a database of systems pharmacology for drug discovery from herbal medicines. *J. Cheminf*. 6, 13. doi:10.1186/1758-2946-6-13

Ruan, X., Du, P., Zhao, K., Huang, J., Xia, H., Dai, D., et al. (2020). Mechanism of Dayuanyin in the treatment of coronavirus disease 2019 based on network pharmacology and molecular docking. *Chin. Med*. 15, 62. doi:10.1186/s13020-020-00346-6

Safran, M., Chalifa-Caspi, V., Shmueli, O., Olender, T., Lapidot, M., Rosen, N., et al. (2003). Human gene-centric databases at the Weizmann Institute of Science: GeneCards, UDB, CroW 21 and HORDE. *Nucl. Acids Res*. 31, 142–146. doi:10.1093/nar/gkg050

Scaglione, S., Kliethermes, S., Cao, G., Shoham, D., Durazo, R., Luke, A., et al. (2015). The epidemiology of cirrhosis in the United States: a population-based study. *J. Clin. Gastroenterol*. 49, 690–696. doi:10.1097/MCG.0000000000000208

Seki, E., De Minicis, S., Osterreicher, C. H., Kluwe, J., Osawa, Y., Brenner, D. A., et al. (2007). TLR4 enhances TGF-beta signaling and hepatic fibrosis. *Nat. Med*. 13, 1324–1332. doi:10.1038/nm1663

Shahzad, M., Shabbir, A., Wojcikowski, K., Wohlmuth, H., and Gobe, G. C. (2016). The antioxidant effects of Radix *Astragali* (*Astragalus membranaceus* and related species) in protecting tissues from injury and disease. *Curr. Drug Targets* 17, 1331–1340. doi:10.2174/1389450116666150907104742

Shannon, P., Markiel, A., Ozier, O., Baliga, N. S., Wang, J. T., Ramage, D., et al. (2003). Cytoscape: a software environment for integrated models of biomolecular interaction networks. *Genome Res*. 13, 2498–2504. doi:10.1101/gr.1239303

Szklarczyk, D., Franceschini, A., Wyder, S., Forslund, K., Heller, D., Huerta-Cepas, J., et al. (2015). STRING v10: protein-protein interaction networks, integrated over the tree of life. *Nucl. Acids Res*. 43, D447–D452. doi:10.1093/nar/gku1003

Takahara, T., Furui, K., Yata, Y., Jin, B., Zhang, L. P., Nambu, S., et al. (1997). Dual expression of matrix metalloproteinase-2 and membrane-type 1-matrix metalloproteinase in fibrotic human livers. *Hepatology* 26, 1521–1529. doi:10.1002/hep.510260620

Tan, E. E. K., Hopkins, A. R., Lim, C. K., Jamuar, S. S., Ong, C., Thoon, K. C., et al. (2020). Dominant-negative NFKBIA mutation promotes IL-1β production causing hepatic disease with severe immunodeficiency. *J. Clin. Invest*. 130 (11), 5817–5832. doi:10.1172/JCI98882

Trautwein, C., Friedman, S. L., Schuppan, D., and Pinzani, M. (2015). Hepatic fibrosis: concept to treatment. *J. Hepatol*. 62, S15–S24. doi:10.1016/j.jhep.2015.02.039

Tsuchida, T., and Friedman, S. L. (2017). Mechanisms of hepatic stellate cell activation. *Nat. Rev. Gastroenterol. Hepatol*. 14, 397–411. doi:10.1038/nrgastro.2017.38

Wang, D., Li, R., Wei, S., Gao, S., Xu, Z., Liu, H., et al. (2019). Metabolomics combined with network pharmacology exploration reveals the modulatory properties of extract in the treatment of liver fibrosis. *Chin. Med*. 14, 30. doi:10.1186/s13020-019-0251-z

Xie, F., Tao, Y., Lv, J., Liu, P., and Liu, C. (2013). Proteomic analysis of the effect of Fuzheng Huayu recipe on fibrotic liver in rats. *Evid. Based Complement. Alternat. Med*. 2013, 972863. doi:10.1155/2013/972863

Xu, G., Zhang, Y. C., Xiao, Q., Lu, G., Yang, X., Yang, X., et al. (2006). Crystal structure of inhibitor of κB kinase β. *Drug Metab. Dispos*. 34, 913–930. doi:10.1124/dmd.105.008300

Xu, G., Lo, Y. C., Li, Q., Napolitano, T., Wu, X., Jiang, X., et al. (2011). Crystal structure of inhibitor of κB kinase β. *Nature* 472, 325–330. doi:10.1038/nature09853

Xu, H., Sun, Y., Zhang, W., Cao, X., Cai, S. Y., Boyer, J. L., et al. (2020). A positive feedback loop of TET3 and TGF-β1 promotes liver fibrosis. *Cell Rep*. 30, 1310–1318.e5. doi:10.1016/j.celrep.2019.12.092

Xu, H., Zhang, Y., Liu, Z., Chen, T., Lv, C., Tang, S., et al. (2019). ETCM: an encyclopaedia of traditional Chinese medicine. *Nucl. Acids Res*. 47, D976–D982. doi:10.1093/nar/gky987

Xu, X., Huang, W., and Huang, C. (2015). Yiqi Huoxue Jiedu decoction in the treatment of chronic viral hepatitis B fibrosis. *Shanxi J. Tradit. Chin. Med*. 36, 1450–1482. doi:10.3969/j.issn.1000-7369.2015.11.004

Xu, X., Zhang, W., Huang, C., Li, Y., Yu, H., Wang, Y., et al. (2012). A novel chemometric method for the prediction of human oral bioavailability. *Int. J. Mol. Sci*. 13, 6964–6982. doi:10.3390/ijms13066964

Yang, H., Xuefeng, Y., Shandong, W., and Jianhua, X. (2020). COX-2 in liver fibrosis. *Clin. Chim. Acta*. 506, 196–203. doi:10.1016/j.cca.2020.03.024

Zhou, Y., Tong, X., Ren, S., Wang, X., Chen, J., Mu, Y., et al. (2016). Synergistic anti-liver fibrosis actions of total astragalus saponins and glycyrrhizic acid via TGF-β1/Smads signaling pathway modulation. *J. Ethnopharmacol*. 190, 83–90. doi:10.1016/j.jep.2016.06.011

Zhou, J., Liu, X., Chen, T., Cheng, G., and Cai, S. (2020). Synergistic anti-liver fibrosis actions of total astragalus saponins and glycyrrhizic acid via TGF-β1/Smads signaling pathway modulation. *Food Funct*. 11, 7061–7072. doi:10.1039/d0fo00548g

Zhu, N., Hou, J., Ma, G., and Liu, J. (2019). Network pharmacology identifies the mechanisms of action of Shaoyao Gancao decoction in the treatment of osteoarthritis. *Med. Sci. Monit*. 25, 6051–6073. doi:10.12659/MSM.915821

Conflict of Interest: The authors declare that the research was conducted in the absence of any commercial or financial relationships that could be construed as a potential conflict of interest

Copyright © 2021 An, Lin, Li, Kong, Lou, Wu and Liu. This is an open-access article distributed under the terms of the Creative Commons Attribution License (CC BY). The use, distribution or reproduction in other forums is permitted, provided the original author(s) and the copyright owner(s) are credited and that the original publication in this journal is cited, in accordance with accepted academic practice. No use, distribution or reproduction is permitted which does not comply with these terms.

GLOSSARY

Acta2 alpha smooth muscle actin
α-SMA alpha smooth muscle actin
AR *Astragalus membranaceus* (Fisch.) Bunge
BP biological process
Cal calycosin
CC cellular component
Ccl2 C-C motif chemokine two
Col-I type I collagen
Col-III type III collagen
Col1a1 type I collagen
Col3a1 type III collagen
Cox2 prostaglandin G/H synthase two
Cxcl1 growth-regulated alpha protein
DL drug similarity
ECM extracellular matrix
Fn1 fibronectin
For formononetin
Gapdh glyceraldehyde-3-phosphate dehydrogenase
GO gene ontology
HF hepatic fibrosis
HSCs Hepatic stellate cells
Ifng interferon gamma
Il1β interleukin-1 beta
Il6 interleukin-6
Iso isorhamnetin
Jun transcription factor AP-1
Kae kaempferol
KEGG encyclopedia of genes and genomes
MF molecular function
Mmp1 matrix metalloproteinase one
Mmp2 matrix metalloproteinase two
Mmp9 matrix metalloproteinase nine
NF-κB nuclear factor kappa B
OB oral bioavailability
PPI protein to protein interaction
Que quercetin
Rela nuclear factor kappa B subunit p65
TCMs traditional Chinese medicines
TCMSP traditional Chinese medicine systems pharmacology
TGF-β1 transforming growth factor beta one
Tnfa tumor necrosis factor

frontiers in Pharmacology

SYSTEMATIC REVIEW
published: 25 January 2021
doi: 10.3389/fphar.2020.578318

The Efficacy and Mechanism of Chinese Herbal Medicines in Lowering Serum Uric Acid Levels: A Systematic Review

Liqian Chen[1,2†], Zhengmao Luo[3†], Ming Wang[1†], Jingru Cheng[4], Fei Li[5], Hanqi Lu[1,2], Qiuxing He[2], Yanting You[2], Xinghong Zhou[2], Hiu Yee Kwan[6], Xiaoshan Zhao[2] and Lin Zhou[7]**

[1]Department of Traditional Chinese Medicine, Zhujiang Hospital of Southern Medical University, Guangzhou, China, [2]Syndrome Laboratory of Integrated Chinese and Western Medicine, School of Chinese Medicine, Southern Medical University, Guangzhou, China, [3]Department of Nephrology, General Hospital of Southern Theatre Command, PLA, Guangzhou, China, [4]Department of Nephrology, The First Affiliated Hospital of Zhengzhou University, Zhengzhou, China, [5]Department of Traditional Chinese Medicine, The Affiliated Ganzhou Hospital of Nanchang University, Ganzhou, China, [6]School of Chinese Medicine, Hong Kong Baptist University, Hong Kong, China, [7]Endocrinology Department, Nanfang Hospital, Southern Medical University, Guangzhou, China

OPEN ACCESS

Edited by:
Hai Yu Xu,
Institute of Chinese Materia Medica, China Academy of Chinese Medical Sciences, China

Reviewed by:
Souad Skalli,
Mohammed V University, Morocco
Bagher Larijani,
Tehran University of Medical Sciences, Iran

***Correspondence:**
Xiaoshan Zhao
zhaoxs0609@163.com
Lin Zhou
zlecho@163.com

†*These authors have contributed equally to this work*

Specialty section:
This article was submitted to Ethnopharmacology, a section of the journal Frontiers in Pharmacology

Received: *30 June 2020*
Accepted: *21 December 2020*
Published: *25 January 2021*

Citation:
Chen L, Luo Z, Wang M, Cheng J, Li F, Lu H, He Q, You Y, Zhou X, Kwan HY, Zhao X and Zhou L (2021) The Efficacy and Mechanism of Chinese Herbal Medicines in Lowering Serum Uric Acid Levels: A Systematic Review. Front. Pharmacol. 11:578318. doi: 10.3389/fphar.2020.578318

Background. Chinese herbal medicines are widely used to lower serum uric acid levels. However, no systemic review summarizes and evaluates their efficacies and the underlying mechanisms of action. *Objectives.* To evaluate the clinical and experimental evidences for the effectiveness and the potential mechanism of Chinese herbal medicines in lowering serum uric acid levels. *Methods.* Four electronic databases PubMed, Wed of Science, the Cochrane Library and Embase were used to search for Chinese herbal medicines for their effects in lowering serum uric acid levels, dated from 1 January 2009 to 19 August 2020. For clinical trials, randomized controlled trials (RCTs) were included; and for experimental studies, original articles were included. The methodological quality of RCTs was assessed according to the Cochrane criteria. For clinical trials, a meta-analysis of continuous variables was used to obtain pooled effects. For experimental studies, lists were used to summarize and integrate the mechanisms involved. *Results.* A total of 10 clinical trials and 184 experimental studies were included. Current data showed that Chinese herbal medicines have promising clinical efficacies in patients with elevated serum uric acid levels (SMD: −1.65, 95% CI: −3.09 to −0.22; $p = 0.024$). There was no significant difference in serum uric acid levels between Chinese herbal medicine treatments and Western medicine treatments (SMD: −0.13, 95% CI: −0.99 to 0.74; $p = 0.772$). Experimental studies revealed that the mechanistic signaling pathways involved in the serum uric acid lowering effects include uric acid synthesis, uric acid transport, inflammation, renal fibrosis and oxidative stress. *Conclusions.* The clinical studies indicate that Chinese herbal medicines lower serum uric acid levels. Further studies with sophisticated research design can further demonstrate the efficacy and safety of these Chinese herbal medicines in lowering serum uric acid levels and reveal a comprehensive picture of the underlying mechanisms of action.

Keywords: Chinese herbal medicine, serum uric acid, serum urate, efficacy, mechanism

Abbreviations: Abbreviations can be referred to **Tables 3**, **4**. FABP1, fatty acid-binding protein; HPRT1, hypoxanthine-guanine phosphoribosyl transferase; APOB, apolipoprotein B; FOS, one subunit of activator protien-1; FN1, fibronectin1; MIP-1α, MIP-1 β, serum proinflammatory cytokines; TXNIP, thioredoxin interacting proteins; PTEN, phosphate and tension homology deleted on chromsome ten; NALP1/6, NACHT, LRR and PYD domains-containing protein one and six; ADAMTs, a family of metalloproteinases with thrombospondin motifs; TIMP, tissue inhibitor of metalloproteinase; CD2AP, CD2-associated protein.

INTRODUCTION

Hyperuricemia refers to an abnormally high concentration of serum uric acid (sUA), typically defined as >7 mg/dL in men and >6 mg/dL in women. The data from the National Health and Nutrition Examination Survey (NHANES) 2007–2016 showed that the prevalence rates of hyperuricemia were 20.2% among men and 20.0% among women between 2015 and 2016 in the United States (Chen-Xu et al., 2019). A cross-sectional survey in China showed that the prevalence of hyperuricemia was 8.4% among Chinese adults from 2009 to 2010 (Liu et al., 2014a). Hyperuricemia and gout remain as a considerable burden, which not only adversely affect patients' health and quality of life (Burke et al., 2015; Gamala and Jacobs, 2019), but also cast an economic burden in the society (Rai et al., 2015). SUA is associated with cardiovascular diseases, such as hypertension (Kuwabara et al., 2018) and atrial fibrillation (Tang et al., 2014). Elevated sUA can lead to decreased renal function, which in turn reduces the excretion of UA in urine, resulting in an increased risk of hyperuricemia or gout (Sato et al., 2019). Elevated sUA may also contribute to the pathogenesis of metabolic syndrome (Battelli et al., 2018; Battelli et al., 2019), non-alcoholic fatty liver disease (Xu et al., 2015), diabetes (Kim et al., 2015). Urate-lowering therapy is a therapeutic strategy for controlling gout, chronic kidney disease, metabolic syndrome and many other diseases. Current interventions for elevated sUA include xanthine oxidase inhibitors, uricosuric agents and anti-inflammatory drugs. Although both febuxostat and allopurinol are effective in reducing sUA, allopurinol may produce a mild skin rash and severe cutaneous reactions (Strilchuk et al., 2019), while febuxostat has a higher risk of all-cause and cardiovascular mortality (White et al., 2018). Benzbromarone is a uricosuric drug which is widely used, but studies have reported possible complications such as hepatotoxicity (Strilchuk et al., 2019). Although these drugs are clinically used, their efficacies are unsatisfactory, and are usually coupled with adverse side effects in the long-term use (Dalbeth et al., 2016).

Hyperuricemia belongs to the arthromyodynia disease category in traditional Chinese medicine. Chinese herbal medicine has been used to treat hyperuricemia for a long time and has significant clinical efficacy (Lin et al., 2016). Chinese herbal medicines with high efficacy and low incidence of adverse reactions have drawn increasing attention from scholars. Studies have compared Chinese herbal medicine with Western medicine for their efficacies in lowering sUA levels. However, these studies differ in their treatment protocols and evaluation methodologies, which greatly limit their clinical applicability. In addition, the mechanism of Chinese herbal medicine in lowering sUA levels is still being explored. Some herbs such as *Phellodendri Chinrnsis* Cortex, *Atractylodes Lancea* (Thunb.)Dc. (Chen et al., 2015b), *Smilacis Glabrae Rhixoma* (Liu et al., 2015), reduce UA intake and/or increase UA excretion by regulating various physiological and cellular pathways. Some herbs like bergenin (Chen et al., 2020a), *alpinia oxyphylla* seed extract (Lee et al., 2019b) and *rhizoma smilacis glabrae* extracts (Liang et al., 2019), promote renal and gut uric acid excretion in hyperuricemia models and also decrease the serum levels of inflammatory cytokines. Most Chinese herbal medicines act on multiple targets to achieve their sUA lowering effects. Therefore, the aim of this systematic review is to evaluate the evidence for the efficacy of Chinese herbal medicines in lowering sUA levels in patients with hyperuricemia, compared to no intervention, placebo or urate-lowering agents, and to comprehensively summarize the mechanisms underlying the sUA lowering effects reported from experimental studies.

MATERIALS AND METHODS

Data Source and Search Strategy

Preferred Reporting Items for Systematic Reviews and Meta-Analyses (PRISMA) (Moher et al., 2009) was used to construct the report of the current study and the completed checklist is provided in Supplementary material, **Supplementary Table S1**. The electronic databases PubMed, Wed of Science, the Cochrane Library and Embase were systematically searched by three researchers (Liqian Chen, Zhengmao Luo and Ming Wang). For any discrepancies between researchers, consensus was reached through discussion. We reviewed literatures published from 1 January 2009 to 19 August 2020 on elevated sUA that had been treated with Chinese herbal medicines. The following combination of terms were used as search keywords: (Traditional Chinese Medicine OR Herbal Medicine OR Chinese Herbal Drugs OR Chinese Plant Extracts OR (Plants, Medicinal) OR Phytochemicals OR herb* OR natural product) combined with (gout OR pain paralysis OR hyperuricemia OR uric acid). The full search strategy in PubMed was provided in Supplementary material, **Supplementary Table S2**. The search did not exclude articles based on language. To look for additional relevant studies, references of all potentially relevant articles were also retrieved, and authors of studies that met the inclusion criteria but lacked data would be contacted. Abstracts, meeting proceedings, and personal communications were not used for the purpose of this study.

Study Selection

The articles in this review included clinical trials and *in vivo* and *in vitro* studies. When screening clinical trials, the followings are the inclusion criteria:

A). Types of trials: All randomized controlled trials (RCTs) investigating the use of Chinese herbal medicine in lowering sUA will be eligible for inclusion.

B). Types of participants: In accordance with the NHANES-III laboratory definition, hyperuricemia is typically defined as >7 mg/dL in men and >6 mg/dL in women (Choi et al., 2020). All adult patients (18 years and older, no upper age limit) with a diagnosis of hyperuricemia will be considered for this review.

C). Types of interventions: According the General guidelines for methodologies on research and evaluation of traditional medicine from WHO, herbal medicines are defined as materials or products derived from plants that have medical or other beneficial effects on human health, including herbs, herbal materials, herbal products,

finished herbal products that contain parts of plants or other plant materials or compositions as active ingredients, as well as materials of inorganic or animal sources. The interventions included in this study include Chinese herbal medicine in various prescriptions, such as herbal formulas, herbal extracts, active ingredients of herbs. Clinical trials comparing Chinese herbal medicine with no intervention, placebo or urate-lowering agents were included in our study. Chinese herbal medicine plus placebo or combined with urate-lowering agents compared to the same medications was also included. We do not limit the formulations or administration of herbal preparations for clinical use.

D). Types of outcome measures: Outcome measures should include at least one essential outcome, such as change in sUA levels after treatment and the overall efficacy.

When screening *in vivo* or vitro experimental studies using the herbs, the following conditions should be met before inclusion: A) Original article investigating the use of Chinese herbal medicine in lowering sUA will be eligible for inclusion. B) Studies using experimental models of mice, rats, rabbits or cell cultures will be considered. All models used should present corresponding pathological symptoms. C) The model should only be treated with Chinese herbal medicine before or after intervention. If medication other than herbs were being used, both the treatment group and the control group must be administered. D) Outcome measures should include change in sUA after treatment.

Data extraction

The data were extracted by three researchers (Jingru Cheng, Fei Li and Hanqi Lu) independently to obtain the following information: A) the design of study; B) characteristics of trial participants (including sample size, age, period); C) type of intervention (including dose regimen, duration); D) type of outcome measure (including the level of sUA). The reported mean (standard deviation [SD]) or risk estimates and 95% confidence intervals (CIs) of sUA were also extracted.

Quality Assessment

The quality assessment of the studies was performed independently by three researchers (Qiuxing He, Yanting You and Xinghong Zhou), and all discrepancies between researchers were resolved through discussion. The methodological quality of RCTs was assessed according to the Cochrane Handbook for Systematic reviews of Interventions. The scores for each bias domain and the final score of risk of systematic bias were graded as low, high or unclear risk. The overall level of evidence was considered "strong" if there were consistent findings among multiple high quality RCTs, and "moderate" if findings were consistent among multiple low-quality RCTs and/or one high-quality RCT. Level of evidence was "conflicting" if findings were inconsistent across the studies, and "no evidence from trials," if there were no RCTs.

Statistical Analysis

Statistical analysis was performed with the software STATA version 16.0. The d index and the standard deviation (SD_d) values of sUA for each RCT were calculated before using STATA. The d index and SD_d values of sUA were continuous, standard mean difference (SMD) with 95% confidence interval (95% CI) was calculated. The overall effect was calculated by a Z-test, and $p < 0.05$ (2-tailed) was deemed statistically significant. Potential heterogeneity was assessed by I^2 statistics. A fixed effects model was chosen if $I^2 \leq 50\%$, otherwise, a random effects model was applied. Subgroup analysis was performed to illuminate the heterogeneity according to the study characteristics, such as interventions other than Chinese herbal medicine. A 'leave-one-out' sensitivity analysis was carried out to test the reliability of the results. Potential publication bias was evaluated by the Egger's test and Begg's test. When the geometric mean and CIs were reported, tools provided in the Cochrane Handbook were used to convert the geometric mean and CIs to arithmetic mean and SD of the raw data.

RESULTS

Literature Flow

The initial electronic search of the literature yielded 4981 potentially relevant citations. After duplicate removal and title/abstract screening, 374 full-text articles were retrieved for detailed assessment. Of these studies, 180 articles did not meet the inclusion criteria. Finally, 194 articles were included in the review with 10 clinical trials, 169 *in vivo* experiments, 0 *in vitro* experiments, and 15 that were a combination of both *in vitro* and *in vivo* experiments (**Figure 1**).

Results of clinical trials

Study Characteristics

The specified characteristics of the included clinical trials as well as their study populations were summarized in **Table 1**. All clinical trials included were RCTs which mainly explored the effects of Chinese herbal medicine on patients with elevated sUA levels such as hyperuricemia and gout. In order to objectively observe the therapeutic effects of herbs on lowering sUA levels, the changes of sUA levels before and after treatment in 10 clinical trials were listed in Supplementary material, **Supplementary Table S3**. Of the 10 included trials, nine were treated with herbal formula, and the remaining one was treated with a combination of herbal extracts and active ingredients. In the subgroup analyses of intervention, two studies compared the therapeutic effects of Chinese herbal medicine and placebo (Rozza et al., 2016; Xie et al., 2017), three studies compared Chinese herbal medicine and Western medicine (Zhang et al., 2009; Zhou et al., 2013; Wang et al., 2014), two studies compared Chinese herbal medicine, Western medicine and placebo or no intervention (Zhang et al., 2011; Wang et al., 2019b), one compared two kinds of Chinese herbal medicine and Western medicine (Yu et al., 2018), and two compared Chinese herbal medicine combined Western medicine and Western medicine (Chen et al., 2009; Xiang et al., 2009).

Meta-Analysis

In order to investigate the efficacy of Chinese herbal medicine in lowering sUA, we performed a subgroup analysis based on

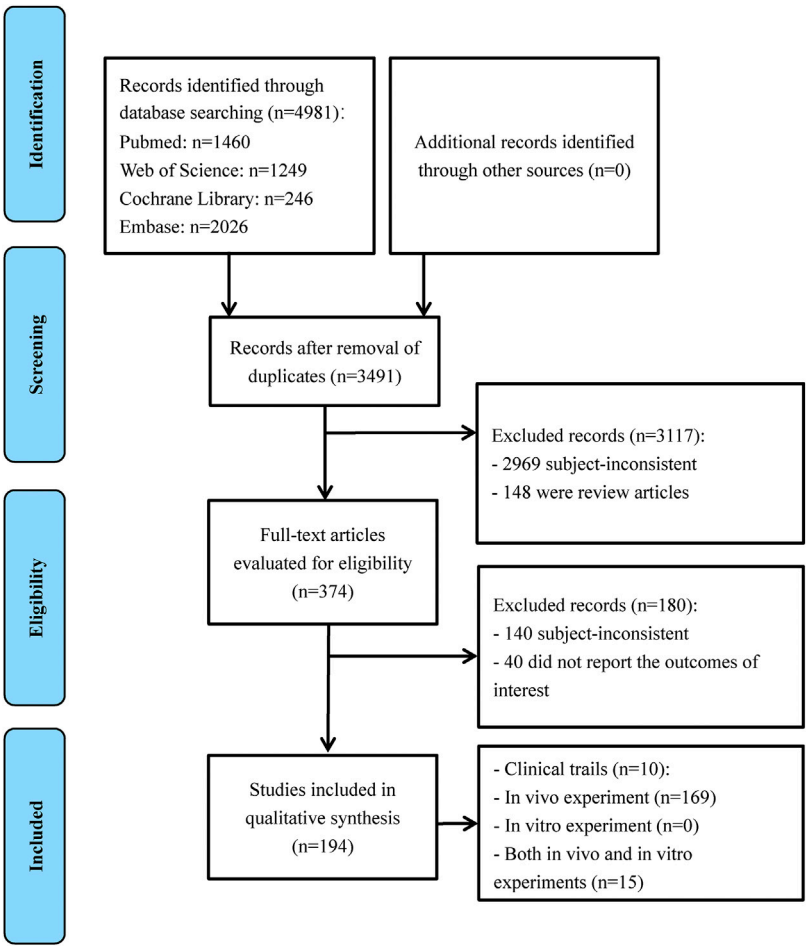

Figure 1 | Flowchart of study selection for the systematic review.

interventions. A random effects model was used for the analysis because I^2 = 96.4%.

Chinese Herbal Medicine vs Placebo or No Intervention

Four RCTs were analyzed. The subgroup meta-analysis showed that all of them were statistically significant differences between Chinese herbal medicine and placebo or no intervention. The combined SMD was −1.65 with a 95% CI of −3.09 to −0.22 (p = 0.024). Therefore, there was a significant difference between the Chinese herbal medicine and placebo or no intervention in the reduction of sUA (**Figure 2**).

Chinese Herbal Medicine vs Western Medicine

Seven RCTs were analyzed. On subgroup meta-analysis, the combined SMD was −0.13 with a 95% CI of −0.99 to 0.74 (p = 0.772), indicating no significant difference between the Chinese herbal medicine and Western medicine in the reduction of sUA (**Figure 2**).

Chinese Herbal Medicine Plus Western Medicine vs Western Medicine

Two RCTs were analyzed. Subgroup meta-analysis (**Figure 2**) showed no statistical significance between the Chinese herbal medicine plus Western medicine and Western medicine in the reduction of sUA (SMD −2.27, 95% CI: −5.84 to 1.31, p = 0.214).

Meta-regression Analyses

The meta-regression showed that samples size, duration of treatment, type of diseases and intervention other than Chinese herbal medicine did not influence these results (all p values >0.05) (**Supplementary Figure S1**).

Quality Assessment

RCT was assessed according to the Cochrane Handbook for Systematic reviews of Interventions (**Table 2**). Generally, the methodological quality was assessed to be moderate. Most of the studies (8/10, 80%) have details on the random grouping of patients, but only half of the studies (5/10, 50%) fully reported the scheme of concealment allocation. Only four trials (4/10, 40%) had their subjects and investigators blinded during the study, and four trials (4/10, 40%) had all the subjects, investigators and outcome evaluators blinded.

Sensitivity Analysis

Sensitivity analysis was conducted to confirm the efficacy Chinese herbal medicine in lowering sUA. The pooled SMDs were

TABLE 1 | Clinical trials for herbs lowering serum uric acid.

Compounds/ formula	Design	Disease	Sample size	T/C	Age (years)		Course of disease		Period	Dose regimen	Duration	Outcome	Side effect	References
					T	C	T	C						
Chuanhutongfeng mixture	RCT	Chronic gouty arthritis	165	58/55	51.10 ± 9.10	50.50 ± 8.90	9.87 ± 5.50	9.91 ± 5.42	2014.05–2015.02	125 ml, po, bid	8 weeks	sUA↓	Diarrhea	Wang et al. (2019b)
Yellow-dragon wonderful-seed formula	RCT	Gout	72	24/24	45.33 ± 9.86	49.21 ± 9.47	39.42 ± 29.00 months	42.96 ± 32.38 months	2012.03.12–2014.12.15	100 ml, po, tid	4 weeks	sUA↓	No side effect is found	Yu et al. (2018)
Yellow-dragon wonderful-seed formula + Gypsum Fibrosum	RCT	Gout	72	24/24	46.13 ± 10.75	49.21 ± 9.47	55.25 ± 36.58 months	42.96 ± 32.38 months	2012.03.12–2014.12.15	100 ml, po, tid	4 weeks	sUA↓	No side effect is found	Yu et al.(2018)
Compound tufuling oral-liquid	RCT	Gout	210	139/71	46.00 (21.00)	49.00 (19.00)	7.00 (9.00) years	5.00 (9.00) years	2012.06.09–2013.05.31	250 ml, po, bid	12 weeks	sUA↓	Leukopenia	Xie et al. (2017)
ZinutriK	RCT	HUA	16	16/16	59.00 ± 11.90		N/A	N/A	N/A	po	4 weeks	sUA↓	No side effect is found	Rozza et al. (2016)
The Chuanhu anti-gout mixture	RCT	Acute gouty arthritis	176	88/88	51.76 ± 13.21	53.82 ± 14.19	N/A	N/A	2011.09–2012.09	250 ml, po, qd	10 days	sUA↓	Diarrhea, nausea	Wang et al. (2014)
A series of tongfeng granule	RCT	Gout	90	60/30	54.10 ± 13.10	49.90 ± 14.20	55.30 ± 47.70 months	53.00 ± 47.30 months	2010.05–2011.12	Huzhang tongfeng granule: 12 g, po, bid; Yinlian tongfeng granule: 10 g, po, bid; Jinhuang Ointment: Ad us.ext, qd	12 weeks	sUA↓	Indigestion, change in frequency of urination and defecation	Zhou et al. (2013)
Xiezhuo chubi recipe	RCT	HUA	99	28/28	56.07 ± 17.62	53. 18 ± 16. 40	N/A	N/A	2009.05.01–2010.03.01	0.5 package, po, bid	20 days	sUA↓	No side effect is found	Zhang et al. (2011)
Retention enema of Chinese herbal medicine	RCT	HUA	78	40/38	51.50 ± 3.40	51.60 ± 3.30	5.40 ± 1.70 years	5.20 ± 1.90 years	2006.10–2007.12	150 ml for high enema for over 60 min, qd	6 weeks	sUA↓	No side effect is found	Chen et al. (2009)
Modified sanmiao powder	RCT	Chronic uric acid nephropathy	94	47/47	42.36 ± 15.11	44.76 ± 14.98	13.28 ± 10.63 years	14.32 ± 12.68 years	2002.06–2008.06	1 package, po, qd	12 weeks	sUA↓	ALT↑	Xiang et al. (2009)
Serial gout granules	RCT	Gout	60	30/30	52.67 ± 10.59	51.10 ± 8.43	6.49 ± 4.78 years	7.02 ± 4.86 years	2007.03–2008.03	Huzhang tongfeng granule: 12 g/package, po, bid; Yinlian tongfeng granule: 10 g/package, po,bid	12 weeks	sUA↓	Not mentioned	Zhang et al. (2009)

Data are presented a mean ± SD or a median (QR) for continuous variables and number for categorical variables. T, treatment group; C, control group; N/A: not available; sUA, serum uric acid, HUA, hyperuricemia.

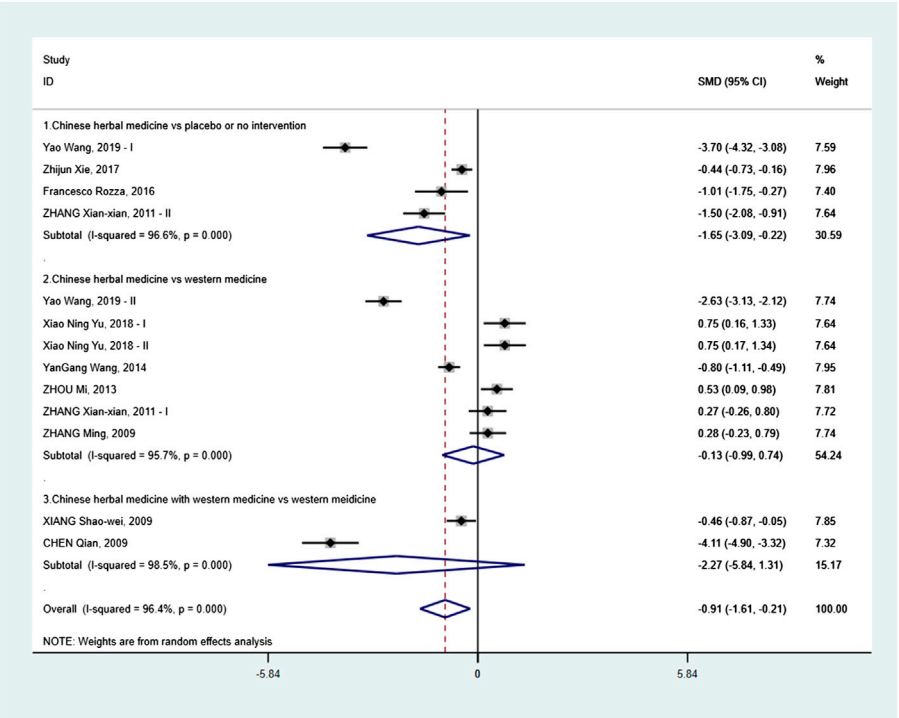

Figure 2 | Effects of Chinese herbal medicine on serum uric acid in patients with elevated serum uric acid.

TABLE 2 | Methodological quality assessment of randomized controlled trials according to the Cochrane Handbook.

Compounds/formula	A	B	C	D	E	F	G	H	References
Chuanhutongfeng mixture	+	+	+	+	+	+	+	?	Wang et al. (2019b)
Yellow-dragon wonderful-seed formula	+	+	–	–	+	+	+	?	Yu et al. (2018)
Compound tufuling oral-liquid	+	+	+	+	+	+	+	?	Xie et al. (2017)
ZinutriK	–	?	+	+	+	+	+	?	Rozza et al. (2016)
The Chuanhu anti-gout mixture	+	+	+	+	+	+	+	?	Wang et al. (2014)
A series of tongfeng granule	+	?	–	–	–	+	+	?	Zhou et al. (2013)
Xiezhuo chubi recipe	+	+	–	?	?	–	?	?	Zhang et al. (2011)
Retention enema of Chinese herbal medicine	–	–	–	–	?	+	+	?	Chen et al. (2009)
Modified sanmiao powder	+	?	–	–	?	+	+	?	Xiang et al. (2009)
Serial gout granules	+	?	–	?	?	+	+	?	Zhang et al. (2009)

A, Adequate sequence generation; B, Allocation concealment; C, Blinding (patient); D, Blinding (investigator); E, Blinding (assessor); F, Incomplete outcome data addressed; G, Selecting reporting; H, Free of other bias; +, Low risk; -, High risk; ?, Unclear.

repeated by sequentially removing one of the included studies with a random-effects model (**Supplementary Figure S2**). None of the studies changed the overall effect.

Publication Bias

There was no evidence of publication bias according to the Begg's test ($p = 0.428$) and Egger's test ($p = 0.344$) for the meta-analysis of Chinese herbal medicine on lowering sUA (**Supplementary Figure S3**).

Results of experimental studies

We categorized 184 *in vivo* and *in vitro* experiments into three groups: 56 active ingredients (**Table 3**), 78 natural products (**Table 4**), and 52 herbal formulas (**Table 5**). Among them, one article described two active ingredients (Lin et al., 2018), and one article (Su et al., 2014) studied one active ingredient and one natural product concurrently. To assure the quality of the studies included, detailed information on herbs (including source, concentration, quality assessment, chemical analysis, and compound purity) was summarized in Supplementary material, **Supplementary Tables S4–S6**.

Active Ingredients That Lower Serum Urate *in vivo* and *in vitro* Studies

Active ingredient is a single ingredient and studies have shown that it plays an important therapeutic role in

TABLE 3 | Active ingredients on lowering serum uric acid based on *in vivo* and *in vitro* studies.

Type	Model	Active ingredients	Inducer	Animal/cell	Major findings	References
In vivo	HUA	Bergenin	Yeast, PO	Mice	SLC2A9, ABCG2, PPAR-γ, IL-6, IL-1β, TNF-α	Chen et al. (2020a)
In vivo	HUA	Phloretin	Adenine and PO	Mice	α-SMA, TGF-β, IL-1β, NLRP3, caspase-1, IL-18, XOD, URAT1, GLUT9	Cui et al. (2020)
In vivo	HUA	Polydatin	PO	SD rats	N/A	Han et al. (2020)
In vivo	HUA	Total glucosides of herbaceous peony (*Paeonia lactiflora* Pall.) flower	Adenine, ethambutol	Rats	XOD, URAT1, OAT1, GLUT9	Kang et al. (2020)
In vivo	HUA and hyperlipidemia	Total flavonoids of *Mori Cortex*	High fat diet, adenine, ethylamine butanol	SD rats	URAT1, IL-6, TNF-α, OAT1	Dang et al. (2019)
In vivo	Gouty arthritis	Pulchinenoside b4	MSU	SD rats	N/A	Lyu et al. (2019)
In vivo	Hyperuricemic nephropathy	Pterostilbene	Adenine and PO	Mice	Fibronectin, collagen I, α-SMA, TGF-β1, Smad3, Src, STAT3	Pan et al. (2019)
In vivo and *in vitro*	HUA	Liquiritigenin	PO, xanthine	Mice, MDCK-hOAT4, HEK293-hURAT1	OAT4, URAT1	Wang et al. (2019e)
In vivo	Nonalcoholic fatty liver disease and HUA	Resveratrol	PO and yeast	Rats	FOXO3a, SIRT1, NF-κB	Xu et al. (2019)
In vivo	Diabetic nephropathy	Total flavonoids from *Oxytropis falcata* Bunge	High-fat diet	Mice	MCP-1, NF-κB, IL-6, TGF-β1, JAK 1, STAT3, STAT 4, SOCS-1, SOCS-3	Yang et al. (2019b)
In vivo	Intestinal injury	*Ganoderma atrum* polysaccharide	Acrylamide	SD rats	MDA, catalase, SOD, glutathione, IL-2, IL-1β, TNF-α, IL-4, IL-10, ALP, endothelin-1	Yang et al. (2019d)
In vivo	HUA and acute gouty arthritis	Luteolin	PO and MSU	Mice	XO, URAT1, GLUT9, IL-1β, TNF-α	Lin et al. (2018)
In vivo	HUA and acute gouty arthritis	Luteolin-4′-O-glucoside	PO and MSU	Mice	XO	Lin et al. (2018)
In vivo	HUA and gouty arthritis	Hirudin	Hypoxanthine, sodium uric	Mice, wistar rats	XOD, GLUT9	Liu et al. (2018)
In vivo	HUA	Arctiin	Adenine and ethambutanol	Rats	XOD, MCP-1, TNF-α	Louxin et al. (2018)
In vivo	HUA	Mangiferin aglycon derivative J99745	PO	Mice	XO, URAT1, GLUT9, OAT1, ABCG2	Qin et al. (2018)
In vivo	HUA and gouty arthritis	[6]—shogaol	PO, MSU and hypoxanthine	SD rats	IL-1β, TNF-α	Wang et al. (2018)
In vivo and *in vitro*	HUA	Dioscin	PO	Mice, HCT116 cells	URAT1, GLUT9	Zhang et al. (2018b)
In vivo	HUA	Epigallocatechin-3-gallate	PO and yeast	Mice	URAT1, GLUT9, XO	Zhu et al. (2018)
In vivo and *in vitro*	HUA	Taxifolin	Mice: GMP and IMP, cells: Guanosine and inosine	Mice, AML12 cells	XO	Adachi et al. (2017)
In vivo	HUA	Vaticaffinol	PO	Mice	XDH, XO, GLUT9, URAT1, OAT1, OCT1, OCT2, OCTN1, NLRP3	Chen et al. (2017b)
In vivo	HUA	Caffeoylquinic acid	PO	Mice	XO, GLUT9, OAT1, URAT1, IL-1β, TNF-α	Jiang et al. (2017)
In vivo and *in vitro*	Gout	Procyanidins	Mice: MSU, cells: LPS and MSU	Mice, raw 264.7 cells	NLRP3, IL-1β, caspase-1, ROS, NR 1, p38, ERK	Liu et al. (2017)
In vivo	HUA	Gypenosides	Lipid emulsion	Rats	ADA, XDH, URAT1, GLUT9, OAT1	Pang et al. (2017)
In vivo	Gouty arthritis	Total saponin fraction from dioscorea nipponica makino	MSU	Rats	TLR2, TLR4, IRAK1, TRAF6, NF-κB, IκBα, IKKα, TAK1, IL-1β, IL-6, TNF-α	Zhou et al. (2017)
In vivo	HUA	Saponins extracted from dioscorea collettii	Adenine and ethambutol	SD rats	URAT1, GLUT9, OAT1, OAT3	Zhu et al. (2017)
In vivo	HUA	Total saponins from dioscorea septemloba thunb	Adenine	SD rats	OATP1A1	Chen et al. (2016b)
In vivo	HUA with renal dysfunction	Emodinol	PO	Mice	XOD, GLUT9, URAT1, ABCG2, OAT1, OCT1, OCT2, OCTN1, OCTN2, OIT3	Hui et al. (2016)
In vivo and *in vitro*	HUA	Pallidifloside D	PO	Mice, PC12	PRPS, HGPRT, PRPPAT	Li et al. (2016)
In vivo	HUA	Mangiferin	PO	Mice	XOD	Niu et al. (2016)
In vivo	HUA	Salvianolic acid C	PO	Mice	XOD	Tang et al. (2016)
In vivo	HUA	Green tea polyphenols	PO	Mice	XO, URAT1, OAT1, OAT3	Chen et al. (2015a)
In vivo	HUA	Flavonoids and phenylethanoid glycosides from Lippia nodiflora	PO and hypoxanthine	SD rats	XO	Cheng et al. (2015)

(Continued on following page)

TABLE 3 | (*Continued*) Active ingredients on lowering serum uric acid based on *in vivo* and *in vitro* studies.

Type	Model	Active ingredients	Inducer	Animal/cell	Major findings	References
In vivo	HUA	Pallidifloside D	PO	Mice	XO, URAT1, GLUT9, OAT1	Hou et al. (2015)
In vivo	Gout	Lemnalol	MSU	Rats	TGF-β1, MMP-9, cathepsin K, TRAP	Lee et al. (2015)
In vivo	HUA and nephropathy	Rhein	Adenine and ethambutol	Mice	IL-1β, TNF-α, PGE2	Meng et al. (2015)
In vivo	HUA	Nuciferine	PO	Mice	URAT1, GLUT9, ABCG2, OAT1, OCT1, OCTN1, OCTN2, IL-1β, TLR2, TLR4, NF-κB, NLRP3, ASC, caspase1	Wang et al. (2015)
In vivo	HUA	Anthocyanins from purple sweet potato	PO	Mice	XO, URAT1, GLUT9, OAT1, OCTN2	Zhang et al. (2015)
In vivo	HUA	Total saponin of dioscorea	PO, ethambutol	SD rats	N/A	Chen et al. (2014b)
In vivo	HUA	*Chrysanthemum* flower oil	PO	Rats	XO	Honda et al. (2014)
In vivo	HUA	Exopolysaccharide produced by Cordyceps militaris	PO	Mice	XO	Ma et al. (2014)
In vivo	HUA	Dioscin	PO	Mice	OAT1, URAT1, OCT2, XO	Su et al. (2014)
In vivo	HUA	Pallidifloside D	PO	Mice	URAT1, GLUT9, OAT1	Wu et al. (2014a)
In vivo	HUA	Smilaxchinoside A, Smilaxchinoside C	PO	Mice	URAT1, GLUT9, OAT1	Wu et al. (2014b)
In vivo	HUA	Riparoside B, timosaponin J	PO	Mice	XO, URAT1, GLUT9, OTA1	Wu et al. (2014d)
In vivo and *in vitro*	HUA	Total saponins from Discorea nipponica	Mice: PO, cells: IL-1β	Mice, synovial cells	URAT1, GLUT9, OAT1, OAT3	Zhou et al. (2014)
In vivo	Uric acid nephropathy	Quercetin	Adenine and ethambutol	SD rats	NLRP3, ASC, Caspase-1, TLR2, TLR4	Hu et al. (2013a)
In vivo	HUA	Aspalathin	IMP	Mice	XO	Kondo et al. (2013)
In vivo	Gouty arthritis	Quercetin	MSU	SD rats	IL–1β, TNF–α, COX-2, PGE2, NO, MDA, SOD, glutathione peroxidase	Huang et al. (2012)
In vivo	HUA	Mangiferin	PO	Mice	XDH, XOD	Niu et al. (2012)
In vivo	Hyperuricemic nephropathy	Tanshinone IIA	Adenine	SD rats	NF-κB, MCP-1, IL-10	Wu et al. (2012a)
In vivo	Uric acid nephropathy	Tanshinone IIA	Adenine	SD rats	NF-κB, MCP-1, IL-10	Wu et al. (2012b)
In vivo	HUA	Curcumin	Fructose	SD rats	NO, GLUT9, RST, OAT1, MRP4, OCT1, JAK2, STAT3, SOCS3, TGF-β1	Zhang et al. (2012)
In vivo	HUA	Iridoid glycosides of Paederia scandens	PO and adenine	SD rats	MCP-1, α-SMA, NF-κB	Zhu et al. (2012)
In vivo	HUA	Mulberroside a	PO	Mice	GLUT9, URAT1, OAT1, OCT1, OCT2, OCTN1, OCTN2	Wang et al. (2011)
In vivo	HUA	Morin	PO	Mice	URAT1, GLUT9, OAT1, OAT3, OCT1, OCT2, OCTN1, OCTN2,	Wang et al. (2010a)

HUA, hyperuricemia; PO, potassium oxonate; MSU, monosodium urate; SLC2A9, solute carrier family 2, facilitated glucose transporter member; PPAR-γ, peroxisome proliferator-activated receptor γ; IL, interleukin; TNF-α, tumor necrosis factor; α-SMA, alpha-smooth muscle actin; TGF-β, transforming growth factor beta-1; NLRP3, the NOD-like receptor P3 inflammasome; XO/XOD, xanthine oxidase; URAT1, urate transporter one; GLUT9, glucose transporter nine; OAT1/3, organic anion transporter one and three; Smad3, mothers against decapentaplegic homolog three; Src, proto-oncogene tyrosine-protein kinase Src; STAT3, signal transducer and activator of transcription three; FOXO3α, forkhead box O3 alpha; SIRT1, silent information regulator one; NF-κB, nuclear factor-kappa B; MCP-1, monocyte chemoattractant protein-1; JAK2, Janus kinase two; SOCS-1/3, suppressor of cytokine signaling 1/3; MDA, malondialdehyde; SOD, superoxide dismutase; ABCG2, adenosine triphosphate (ATP)-binding cassette transporter two; XDH, xanthine dehydrogenase; OCT1/2, organic cation transporter; ALP: alkaline phosphatase; OCTN1/2, organic cation/carnitine transporter one and two; ROS, reactive oxygen species; NR-1, N-methyl-D-aspartic acid receptor one; p38, phosphorylated p38 mitogen-activated protein kinase; ERK, phosphorylated extracellular regulated protein kinase; ADA, adenosine deaminase; TLRs, toll-like receptors; IRAK, IL-1R-associated kinase; TRAF6, TNF receptor associated factor 6; IκB, inhibitor of NF-κB; IKKα, inhibitor of nuclear factor kappa-B kinase; TAK1, transforming growth factor beta-activated kinase one; OATP1A1, organic anion transporting polypeptide 1A1; OIT3, oncoprotein-induced transcript 3; PRPS, phosphoribosyl pyrophosphate synthetase; HGPRT, hypoxanthine-guanine phosphoribosyl transferase; PRPPAT, phosphoribosyl pyrophosphate amino-transferase; MMP-9, matrix metalloproteinase nine; TRAP, tartrate-resistant acid phosphatase; COX-2, cyclooxygenase-2; PGE2, prostaglandin E2; NO, nitric oxide; ASC, the apoptosis-associated speck-like protein containing a caspase recruitment domain; RST, renal-specific transporter; MRP4, multidrug resistance protein 4. N/A, not available.

reducing sUA. Among the active ingredients with potential of lowering sUA (**Table 3**), 25 of which act on uric acid synthesis, 28 target uric acid transporter, 19 resolve inflammation, nine possess kidney protective function, and four regulate the oxidative stress.

Natural Products That Lower Serum Urate *in vivo* and *in vitro* Studies

Natural products include herbs and relatively complex extracts derived from herbs. Among the natural products with potential of lowering sUA (**Table 4**), 40 of which act on uric acid synthesis, 29 target uric acid transporter, 17 resolve inflammation, eight possess kidney protective functions, and three regulate the oxidative stress.

Herbal Formulas That Lower Serum Urate *in vivo* and *in vitro* Studies

Herbal formula is a combination of a variety of herbs. The composition of the herbal formula included in the current study were listed in Supplementary material, **Supplementary Table S7**. Among the herbal formula with lowering sUA effects (**Table 5**), 18 of which act on uric acid synthesis, 15 target uric acid transporter, 15 resolve inflammation, seven possess kidney protective functions, and five regulate the oxidative stress.

TABLE 4 | Natural products that lower serum uric acid based on *in vivo* and *in vitro* studies.

Type	Model	Natural product	Inducer	Animal/cell	Major findings	References
In vivo	HUA	*Clerodendranthus spicatus*	Oteracil potassium	Mice	N/A	Chen et al. (2020b)
In vivo	HUA	Sunflower head enzymatic hydrolysate	PO, yeast	Mice	XOD, ADA, URAT1	Liu et al. (2020)
In vivo	HUA	Macroporous Resin extract of *Dendrobium candidum* leaves	PO, adenine, yeast	SD rats	XOD, ADA, TLR4, NF-κB	Lou et al. (2020)
In vivo	Hyperuricemic nephropathy	Ethanol extract of *Liriodendron chinense (Hemsl.) Sarg* barks	Adenine and PO	Mice	OAT1, OAT3, ABCG2	Pan et al. (2020)
In vivo	HUA	Eucommia ulmoides Oliver	Mice: Oxonic acid potassium salt, rats: hypoxanthine	Mice, rats	URAT1, OAT1, OAT3, GLUT9	Fang et al. (2019)
In vivo	HUA	Smilax glabra extracts	PO	Mice	XOD, OAT1, OCTN2	Huang et al. (2019b)
In vivo and *in vitro*	HUA	*Alpinia oxyphylla* seed extract	PO	Rats, oocytes	XO, URAT1, OAT1, IL-1β, IL-6, TNF-α	Lee et al. (2019b)
In vivo	Chronic HUA and gout	*Rhizoma smilacis glabrae* extracts	PO and MSU	Mice	XO, IL-6, IL-12, IL-1β, IL-10, TNF-α	Liang et al. (2019)
In vivo	HUA	The extract of O. Sativa	PO	SD rats	XO	Liu et al. (2019)
In vivo	Acute gouty arthritis	Ethanolic extract of Polygonum cuspidatum	MSU	Mice	IL-1β, IL-6, TNF-α, NLRP3, ASC, caspase-1	Ma et al. (2019a)
In vivo	Uric acid-induced renal damage	Polygonum cuspidatum	Adenine administering and yeast feeding	SD rats	AMPK, FOXO3α, TLR4, NLRP3, MCP-1	Ma et al. (2019b)
In vivo	Uric acid-induced renal damage	*Polygonum cuspidatum*	Adenine, yeast	SD rats	AMPK, FOXO3α, TLR4, NLRP3, MCP1	Ma et al. (2019c)
In vivo	HUA	*Chrysanthemum* extract	PO	SD rats	XOD, ABCG2, URAT1, GLUT9, IL-1β, TNF-α	Peng et al. (2019)
In vivo	HUA	The flavonoid-rich fraction from rhizomes of Smilax glabra Roxb.	Yeast pellets and adenine	SD rats	ABCG2, OAT1, OCT2, OCTN2, URAT1, GLUT9	Wang et al. (2019a)
In vivo	HUA	Chicory (*Cichorium intybus L.*)	Fructose	SD rats	URAT1, GLUT9, OAT1, OAT3	Wang et al. (2019d)
In vivo	HUA and acute gouty arthritis	Terminthia paniculata extract	PO and MSU	Mice	XO	Yang et al. (2019c)
In vivo	HUA	Highly acylated anthocyanins from purple sweet potato	PO	Mice	TNF-α, IL-6, IL-1β, TGF-β1, ICAM1, COX-2, NF-κB	Zhang et al. (2019c)
In vivo	HUA	Ethanol extract of Dendropanax morbifera leaf	PO	Mice	XO	Cho et al. (2018)
In vivo	Diabetic kidney disease	*Codonopsis tangshen* Oliv.	Unilateral nephrectomy, high fat diet feeding	SD rats	IL-1β, TNF-α, IL-6	Lu et al. (2018)
In vivo	HUA	Ethanol extract of Cudrania tricuspidata leaf	PO	Mice	XO	Song et al. (2018)
In vivo	Hypouricemic and nephroprotective	*Polyrhachis Vicina Roger*	PO	SD rats	IL-1β, IL-6, TNF-α, SOD, MDA, XOD, URAT1, GLUT9, OAT1	Su et al. (2018)
In vivo	HUA	*Lagotis brachystachys Maxim* extract	PO	Mice	URAT1, GLUT9, OAT1	Xiong et al. (2018)
In vivo	HUA	Toona sinensis leaf extract	PO	Rats	XO	Yuk et al. (2018)
In vivo	HUA	Chaenomeles sinensis fruit extract	PO	Mice	URAT1, OAT1	Zhang et al. (2018a)
In vivo	HUA	Fraxini cortex	Hypoxanthine and PO	SD rats	URAT1,GLUT9	Zhou et al. (2018a)
In vivo	HUA	Selaginella tamariscina	Xanthine, PO and MSU	Rats	N/A	Chen et al. (2017a)
In vivo	HUA	Rhizoma Polygoni Cuspidati and Ramulus Cinnamomi	Hypoxanthine, ethambutol and PO	SD rats	XO	Han et al. (2017)
In vivo	HUA	Salvia plebeia extract	PO	Mice	XO	Kim et al. (2017)
In vivo	Gouty arthritis	Mollugo pentaphylla extract	MSU	Mice	TNF-α, IL-1β, NLRP3, ASC, caspase-1, NF-κB	Lee et al. (2017)
In vivo	HUA and gout	Sunflower head extract	PO and MSU	Mice	XO	Li et al. (2017a)
In vivo	HUA	Aristolochia bracteolata extracts	PO	Rats	XO	Li et al. (2017b)
In vivo	HUA	Total flavonoids of Humulus lupulus	PO	Mice	XO	Li et al. (2017c)
In vivo	HUA	Chicory	D-fructose	SD rats	ABCG2	Wang et al. (2017a)
In vivo	HUA	Chicory extract	Fructose	SD rats	GLUT9	Wang et al. (2017b)
In vivo	HUA and gout	Cortex fraxini	PO, yeast and adenine	SD rats	N/A	Wang et al. (2017c)
In vivo	HUA	*Plantago depressa Willd* extract	PO	SD rats	XOD	Xia et al. (2017)
In vivo	HUA	Ganoderma applanatum extracts	Hypoxanthine and PO	Mice	XO, URAT1, GLUT9, OAT1	Yong et al. (2017)
In vivo	HUA	Quercus acuta Thunb. extract	PO	Mice	XO	Yoon et al. (2017a)

(Continued on following page)

TABLE 4 | (*Continued*) Natural products that lower serum uric acid based on *in vivo* and *in vitro* studies.

Type	Model	Natural product	Inducer	Animal/cell	Major findings	References
In vivo	HUA	Ethanol extracts of Camellia japonica leaf	PO	Mice	XO	Yoon et al. (2017b)
In vivo	HUA and acute gouty arthritis	*Gnaphalium* affine D. Don extract	PO and MSU	Mice	XO, GLUT9, URAT1	Zhang et al. (2017a)
In vivo	HUA	Ginkgo folium	Fructose	SD rats	N/A	Zhang et al. (2017b)
In vivo	HUA	*Selaginella moellendorffii* Hieron.	PO	SD rats	XOD, MDA, SOD, TNF-α, IL-1β	Zhao et al. (2017)
In vivo	HUA	*Dioscorea tokoro Makino* extract	PO	Mice	XOD, URAT1, OAT1	Fei et al. (2016)
In vivo and *in vitro*	HUA	Mesona procumbens extracts	THP-1 cells: MSU, mice: PO, SD rats: streptozocin	THP-1 cells, mice, rats	XO, OAT1, GLUT9	Jhang et al. (2016)
In vivo	HUA	Ethyl acetate fraction of Dimocarpus longan Lour. extracts	PO	Mice	XO	Sheu et al. (2016)
In vivo and *in vitro*	HUA	Synsepalum dulcificum	Mice: PO, cells: MSU	Mice, RAW264.7 cells	XO	Shi et al. (2016b)
In vivo	HUA	*Dendropanaxchevalieri* extracts	PO	Mice	XOD, URAT1, GLUT9	Wang et al. (2016a)
In vivo	HUA	Tradescantia albiflora Kunth extracts	PO	Rats	XO	Wang et al. (2016c)
In vivo	HUA	Cortex fraxini	PO, yeast and adenine	Rats	N/A	Wang et al. (2016e)
In vivo	HUA	Cordyceps militaris	PO and hypoxanthine	Mice	XO, URAT1	Yong et al. (2016)
In vivo	HUA	The ethanolic extracts of Corylopsis coreana Uyeki	PO	Mice	XO	Yoon et al. (2016)
In vivo	HUA	Leaves of Perilla frutescens	PO	Mice	XO	Huo et al. (2015)
In vivo	HUA	Ethanol extracts from Dioscoreae nipponicae rhizoma	Hypoxanthine and PO	Mice	N/A	Shan et al. (2015)
In vivo	HUA	*Rhododendron* oldhamii maxim. Leaf extracts	PO	Mice	N/A	Tung et al. (2015)
In vivo	HUA	Smilax riparia	PO	Mice	URAT1, GLUT9, OAT1	Wu et al. (2015)
In vivo	HUA	*Lagotis brevituba Maxim*. extract	PO	Mice	XOD, OAT1, URAT1, GLUT9	Zeng et al. (2015)
In vivo	HUA	Total saponins from *Discorea nipponica* makino	Adenine and ethambutol	Rats	OAT1, OAT3, URAT1	Zhou et al. (2015)
In vivo	HUA	Phytochemicals from Davallia formosana	PO	Mice	XO	Chen et al. (2014a)
In vivo and *in vitro*	HUA	Smilacis glabrae rhizoma	PO and uric acid	SD rats, HUVECs	Catalase	Hong et al. (2014)
In vivo	HUA	*Poecilobdella manillensis*	Hypoxanthine	Mice	N/A	Liu et al. (2014b)
In vivo	Gouty arthritis	Rhizoma Dioscoreae nipponicae	MSU	Rats	SDF-1, CXCR4, p38, IL-1β, MKK 3/6	Lu et al. (2014)
In vivo	HUA	Rhizoma Dioscoreae septemlobae extracts	PO	Mice	OAT1, URAT1, OCT2, XO	Su et al. (2014)
In vivo	HUA	Smilax riparia	PO	Mice	URAT1	Wu et al. (2014c)
In vivo	HUA	Leonurus	PO	SD rats	URAT1, GLUT9, OCT, OCTN	Yan et al. (2014)
In vivo and *in vitro*	Gouty arthritis	Dolichos falcata Klein	MSU	SD rats, raw 264.7 cells	IL-1β, IL-6, TNF-α	Chen et al. (2013b)
In vivo	HUA	Ethanol extract of Fructus Gardenia	PO	Mice	URAT1, ABCG2, GLUT9, OAT1, OAT3, OIT3, OCT1, OCT2, OCTN1, OCTN2	Hu et al. (2013b)
In vivo	HUA and gout	The crude extract of Jatropha isabellei	PO and MSU	Rats	XO	Silva et al. (2013)
In vivo	HUA	Petroleum ether fraction of *Polyrhachis vicina* Roger	Hypoxanthine	Mice	XOD	Wei et al. (2013)
In vivo	HUA	Rhizoma smilacis glabrae	Hypoxanthine	SD rats	N/A	Xu et al. (2013)
In vivo	HUA	*Balanophora* laxiflora extracts and derived phytochemicals	PO	Mice	XO	Ho et al. (2012)
In vivo	HUA	Longan seed extract	PO and hypoxanthine	SD rats	GLUT1, GLUT9, XO	Hou et al. (2012)
In vivo	Gouty arthritis	Ethanol extract from *Mangifera indica*	MSU	SD rats	TNF-α, IL-1β	Jiang et al. (2012)
In vivo	HUA	*Hibiscus sabdariffa L.* extracts	PO	SD rats	XOD	Kuo et al. (2012)
In vivo	HUA	Ramulus Mori ethanol extract	PO	Mice	URAT1, GLUT9, OAT1, OCT1, OCT2, OCTN1, OCTN2	Shi et al. (2012)

(Continued on following page)

TABLE 4 | (*Continued*) Natural products that lower serum uric acid based on *in vivo* and *in vitro* studies.

Type	Model	Natural product	Inducer	Animal/cell	Major findings	References
In vivo	Acute gouty arthritis	Rhizoma Dioscoreae nipponicae	MSU and hypoxanthine	Rats	TRAIL, Neuropilin-2, MMP-13	Yao et al. (2012)
In vivo	HUA	The methanol extract from Prunus mume fruit	PO	Mice	XO	Yi et al. (2012)
In vivo	HUA	Casein or soya protein combined with palm or safflower-seed oil	PO and uric acid	Rats	NO, TNF-α, IFN-γ, Nitrotyrosine	Lo et al. (2010)
In vivo	Gouty arthritis	Extract of Paederia scandens (LOUR.) MERRILL (Rubiaceae)	MSU	SD rats	TNF-α, IL-1β, NF-κB	Ma et al. (2009)

Abbreviations can be referred to ***Table 3****. ICAM1, intercellular adhesion molecule one; IFN, interferon; AMPK, adenosine 5′-monophosphate-activated protein kinase; FOXO3α, forkhead box O3 alpha; SDF-1, stromal cell-derived factor 1; CXCR4, SDF-1 receptor; MKK, mitogen-activated kinase; TRAIL, the tumor necrosis factor-related apoptosis-inducing ligand.*

DISCUSSION

The efficacies of Chinese herbal medicines lowering Serum uric Acid levels

This systematic review compares the efficacies of the Chinese herbal medicines and the Western medicine in lowering sUA levels by analysing10 RCTs with a total of 1,060 patients. The meta-analysis has three important findings. First, there is a significant difference between the Chinese herbal medicine, placebo or no intervention in the reduction of sUA levels. Second, the efficacies of Chinese herbal medicines in lowering sUA levels are comparable to that of Western medicine. Third, the efficacies of Chinese herbal medicines plus Western medicine in lowering sUA levels are comparable to that of Western medicine. The heterogeneity of the meta-analysis was high. To investigate the source of heterogeneity in our analysis, we conducted a sensitivity analysis, removing one study at one time from the primary analysis did not change the main finding. In addition, our findings were confirmed by the lack of publication bias and effect modifiers according to the Begg's test, Egger's test and meta-regression analysis.

The results indicate that the efficacies of Chinese herbal medicines in lowering sUA levels are comparable to that of Western medicine, which is consistent with the analysis result of Lin et al. (Lin et al., 2016). Compared with the study of Lin et al., our study is more comprehensive, because we also compared the sUA lowering efficacy between Chinese herbal medicine and placebo or no intervention, and between Chinese herbal medicine plus western medicine and western medicine. In addition, we have summarized the underlying mechanisms of herbs in lowering sUA. It should be noted that among the 10 RCTs included, a total of six RCTs used one or several components of Simiao Pills, which is a famous formula in traditional Chinese medicine, including *Cortex Phellodendri Chinensis*, *Atractylodes Lancea* (*Thunb.*) DC., *Coix lacryma-jobi L.var.ma-yuen* (*Roman.*) Stapf (*Yi Yi*), *Cyathula officinalis Kuan* (Xiang et al., 2009; Zhang et al., 2009; Zhang et al., 2011; Zhou et al., 2013; Xie et al., 2017; Yu et al., 2018). The specific doses of herbs in each study have been listed in the **Supplementary Tables S4–S6**. According to the Pharmacopoeia of the People's Republic of China revised by the Food and Drug Administration in 2015, except for the use of *Cortex Phellodendri Chinensis*, *Atractylodes Lancea* (*Thunb.*) DC., *Cyathula officinalis Kuan* in one RCT (Xiang et al., 2009) exceeded the recommended dosage, the dosages of these four herbs in the remaining five RCTs were within the recommended dosage range. Except for the RCT in which the dosage exceeded the recommended dosage (Xiang et al., 2009), the dosage of these four herbs in the remaining five RCTs were all at the high level or even reached the critical value within the recommended range. Despite the high dosage, the three RCTs describing the adverse reactions in the six RCTs showed that the incidence of adverse reactions was either lower than that of the placebo group or was not statistically significant compared with the control group.

In addition to clinical studies, experimental studies have also suggested the urate lowering effects of Simiao Pills, which act on xanthine oxidase (XO), uric acid transport-related proteins urate anion transporter 1 (URAT1) and glucose transporter 9 (GLUT9), and also modulate the inflammation, oxidative stress and other processes (Hu et al., 2010; Hua et al., 2012; Shi et al., 2013; Pan et al., 2014; Ma et al., 2015; Lin et al., 2020). The finding suggests that Chinese herbal medicines are mostly multi-targeted or have interplay with other signaling pathways to lower sUA levels. In contrast, conventional Western medicines used to lower sUA levels include allopurinol, probenecid and benzbromarone, which generally act on specific targets. Allopurinol competitively inhibits xanthine oxidase (Strilchuk et al., 2019). Probenecid and benzbromarone are typical urate-promoting drugs target at URAT1 (Azevedo et al., 2019). These may partly explain why the combination of Chinese and Western medicine can improve the index of renal function while lowering sUA levels in patients with hyperuricemia (Chen et al., 2009; Xiang et al., 2009).

Nevertheless, several limitations of the meta-analysis are worth considering. Due to limited reports, participants with elevated sUA levels in this meta-analysis included patients with hyperuricemia and gout, and most participants were from China. These facts indicate that the current meta-analysis could have potential bias. Further trials need to be carried out in a larger comprehensive population to demonstrate the efficacy of Chinese herbal medicines in lowering sUA. In addition, long-term tracking of sUA is necessary to determine whether Chinese herbal medicine can effectively control sUA. However, long-term follow-ups were not available in the current included studies. The incidence of adverse reactions is an important indicator to compare the efficacy and

TABLE 5 | Herbal formulas that lower serum uric acid based on *in vivo* and *in vitro* studies.

Type	Model	Herbal formula	Inducer	Animal/cell	Major findings	References
In vivo	HUA and hyperlipidemia	*Dendrobium officinalis* Six Nostrum	PO and hihg-fat sorghum feed	SD rats	XOD, ADA, LPL, FABP1, HPRT1, NLRP3, Caspase-1, TLR4	Guo et al. (2020)
In vivo	Gouty arthritis	Simiao decoction	Yeast, MSU	Mice	NLRP3, ACS, caspase1, XOD, ADA, IL- 1α, IL-6, IL-1β, IL-9, IL-12, granulocyte colony stimulating factor; MCP-1, TNF-α, STAT3, APOB, caspase 8, c-FOS, PPARα, FN1, LPL, MIP-1α, MIP-1β	Lin et al. (2020)
In vivo	Acute gouty arthritis with HUA	Tu-Teng-Cao	PO, MSU	SD rats	TNF-α, IL-6, IL-1β	Yao et al. (2020)
In vivo	HUA	Erding granules	PO	Mice	N/A	Zuo et al. (2020)
In vivo	HUA	TongFengTangSan	PO	SD rats	XOD	Chen et al. (2019b)
In vivo	HUA	*Alismatis Rhizoma and Rhizoma Smilacis Glabrae* decotion	PO, adenine	SD rats	XOD, URAT1	Cheng et al. (2019)
In vivo	HUA	Er Miao wan	Fructose	SD rats	N/A	Huang et al. (2019a)
In vivo	Renal stones	Huashi pill	Ethylene glycol, ammonium chloride, calcium gluconate	SD rats	Osteopontin	Yang et al. (2019a)
In vivo	HUA	Modified Chuanhu anti-gout mixture	PO	Mice	XOD, URAT1	You et al. (2019)
In vivo	Acute gouty arthritis	Jia-Wei-Si-Miao-Wan	Monosodium urate	Rats	TLR4, NLRP3, ASC, caspase-1, NF-κB, IL-1β, IL-18	Yuan et al. (2019)
In vivo	HUA	Erding granule	PO	Mice, SD rats	GLUT9, OAT1, URAT1	Zhang et al. (2019a)
In vivo and *in vitro*	HUA and acute gouty arthritis	The *Selaginella moellendorffii* prescription	PO, adenine, MSU, LPS	Mice, rats, RAW264.7 cells	NO, NF-κB, NLRP3, IL-1β, PGE-2, IL-8	Zhang et al. (2019b)
In vivo	Acute gouty arthritis	Tongfengning capsule	MSU	Rats	TNF-α, IL-1β	Fan et al. (2018)
In vivo	T2DM	Spleen-kidney supplementing formula	High-fat diet, low-dose streptozotocin	Wistar rats	TGF-β1, miR-21, PTEN	Tian et al. (2018)
In vivo	HUA	Ermiaowan	Xanthine and oxonic acid potassium salt	Rats	N/A	Wei et al. (2018)
In vivo	HUA	Compound tufuling granules		Rats	TNF-α, IL-1β	Wu et al. (2018a)
In vivo	HUA	ShiZhiFang	PO	SD rats	XOD, OAT1, OAT3	Wu et al. (2018b)
In vivo	HUA	Erding formula	Hypoxanthine and PO	Mice	URAT1, OAT3	Zuo et al. (2018)
In vivo	HUA	Qi-Zhu-Xie-Zhuo-Fang	Adenine and PO	Rats	XO, E-cadherin, α-SMA	Huijuan et al. (2017)
In vivo	HUA	Shizhifang	PO	SD rats	TXNIP, NLRP3, ASC, caspase-1, IL-1β, IL-18, ROS	Wu et al. (2017)
In vivo	HUA	Quzhuotongbi decoction	Yeast	SD rats	N/A	Chen et al. (2016a)
In vivo	Gouty arthritis	Zisheng Shenqi decoction	MSU	Rats	IL-1β, TNF-α, IκB, NF-κB, NALP1, NALP6, ROS	Han et al. (2016)
In vivo	HUA	RuPeng15 powder	PO	SD rats	XO	Kou et al. (2016)
In vivo	Gouty arthritis	Xiaofeng granules	MSU	SD rats, rabbits	IL-1β, IL-6, TNF-α, iNOS, ADAMTS-4, TIMP-3	Shi et al. (2016a)
In vivo	HUA	Siwu decoction	PO	Mice	XO, URAT1, GLUT9, OAT1, ABCG2, OCT1, OCT2, OCTN1, OCTN2, NLRP3, ASC, caspase-1, IL-1β	Wang et al. (2016b)
In vivo	HUA	Jianpi Huashi decoction	PO	Rats	XO	Wang et al. (2016d)
In vivo and *in vitro*	Gout	Sanmiao formula	Animals: PO and cold bath, cells: MSU	SD rats, rabbits, primary chondrocyte	IL-1β, TNF-α, MMP-3, TIMP-1, ADAMTS-4, TIMP-3	Zhu et al. (2016)
In vivo	HUA	Karapxa decoction	Yeast and PO	Mice	XO	Amat et al. (2015)
In vivo	HUA	Ermiao pill	PO	SD rats	XO	Chen et al. (2015b)
In vivo	HUA	Si-Wu-Tang and Er-Miao-San	PO and adenine	SD rats	XO, OAT1, OAT3	Guo et al. (2015)
In vivo	HUA	Shuang-Qi gout capsule	PO	Mice	URAT1, OAT1, OCT1, OCT2, ABCG2, OCTN1, OCTN2, GLUT9	Kodithuwakku et al. (2015)
In vivo	Gouty arthritis	RuPeng15 powder	MSU	SD rats	NF-κB, TNF-α, IL-1β, IL-8	Kou et al. (2015)
In vivo	HUA	Compound tufuling granules	Yeast and PO	Mice	GLUT9	Liu et al. (2015)
In vivo	HUA and metabolic syndrome	Simiao pill	Fructose	SD rats	Nephrin, podocin, CD2AP, Sirt1, NF-κB, IL-1β, NLRP3, ACS, caspase1	Ma et al. (2015)

(Continued on following page)

TABLE 5 | (*Continued*) Herbal formulas that lower serum uric acid based on *in vivo* and *in vitro* studies.

Type	Model	Herbal formula	Inducer	Animal/cell	Major findings	References
In vivo	HUA	Xie-Zhuo-Chu-Bi-Fang	Adenine and PO	Mice	URAT1, miR-34a	Sun et al. (2015)
In vivo	HUA	Wuling san	Fructose	Mice	URAT1, GLUT9, ABCG2, OAT1, OCT1, OCT2	Yang et al. (2015)
In vivo	Urate nephropathy	Compound qingqin liquid	Adenine and PO	SD rats	TLR2, TLR4	Chen et al. (2014c)
In vivo	HUA	Modified Simiao wan	Oxonic acid potassium salt, hypoxanthine	SD rats	XOD	Pan et al. (2014)
In vivo	HUA	Compound qingqin liquid	Adenine and PO	SD rats	COX-2	Shang et al. (2014)
In vivo	HUA	Jianpihuashi decoction	PO	SD rats	XO	Chen et al. (2013a)
In vivo	HUA	Wuling san	PO	Mice	URAT1, GLUT9, OAT1, OCT1, OCT2, OCTN2	Ding et al. (2013)
In vivo and *in vitro*	Gout arthritis	Shuang-Qi gout capsule	MSU	Mice, SD rats, HUVECs	TNF-α, IL-1β	Kodithuwakku et al. (2013)
In vivo	HUA	Tongfeng granule	Adenine and ethambutol	Rats	N/A	Liu et al. (2013)
In vivo	HUA	Jieduxiezhuo decoction	Uric acid	Mice	N/A	Pan et al. (2013)
In vivo and *in vitro*	MSU-induced inflammation	Modified Simiaowan	MSU	Mice, HUVECs	ICAM-1	Shi et al. (2013)
In vivo	HUA	Tongxi powder	Uric acid	Mice	N/A	Yang et al. (2013)
In vivo	HUA	Modified Simiao decoction	PO	Mice	XO, URAT1, OAT1, SOD, MDA	Hua et al. (2012)
In vivo	Acute gouty arthritis	Compound Shuiniujiao	MSU	SD rats	N/A	Cao et al. (2011)
In vivo	HUA	Simiao pill	PO	Mice	URAT1, GLUT9, OAT1, OCT1, OCT2, OCTN1, OCTN2	Hu et al. (2010)
In vivo	HUA	Danggui Buxue Tang	Adenine, ethambutol	Rats	NO, NOS, SOD, MDA	Li et al. (2010)
In vivo	HUA	Ermiao pill	Oxygen hydrochloride acid potassium salt	Mice	XOD, URAT1	Lü et al. (2010)
In vivo	HUA	Sanmiao wan	PO	Mice	XOD, URAT1	Wang et al. (2010b)

*Abbreviations can be referred to **Tables 3**, **4**. FABP1, fatty acid-binding protein; HPRT1, hypoxanthine-guanine phosphoribosyl transferase; APOB, apolipoprotein B; FOS, one subunit of activator protien-1; FN1, fibronectin1; MIP-1α, MIP-1 β, serum proinflammatory cytokines; TXNIP, thioredoxin interacting proteins; PTEN, phosphate and tension homology deleted on chromsome ten; NALP1/6, NACHT, LRR and PYD domains-containing protein one and six; ADAMTs, a family of metalloproteinases with thrombospondin motifs; TIMP, tissue inhibitor of metalloproteinase; CD2AP, CD2-associated protein.*

safety of Chinese herbal medicine and Western medicine in lowering sUA levels. However, of the six included studies comparing Chinese herbal medicine and Western medicine, only 2 has reported the adverse reaction events in details. Thus, we cannot evaluate the safety of Chinese herbal medicine vs. western medicine in lowering sUA levels. Moreover, the standardization of the methodologies and the small number of the included trials may lead to an overestimation of the overall efficacy of Chinese herbal medicine. Therefore, studies with high quality are needed to confirm the efficacy and safety of Chinese herbal medicine in lowering sUA levels.

The mechanisms of Chinese herbal medicines in lowering Serum uric Acid

In current review, 186 *in vivo* and *in vitro* experiments with 56 active ingredients (**Table 3**), 78 natural products (**Table 4**), and 52 herbal formulas (**Table 5**) are included to explore the common mechanism of Chinese herbal medicine in lowering sUA levels. According to the summary of the targets of Chinese herbal medicine in lowering sUA, it is clearly revealed that most Chinese herbal medicine lowers sUA by acting on multiple targets or multiple pathways. The therapeutic mechanism of Chinese herbal medicine included in this study mainly involved the UA synthesis, UA transport, inflammation, renal fibrosis and oxidative stress.

Uric acid, produced primarily in the liver, is the final product of diet and endogenous purine metabolism. Problems with key enzymes involved in UA production can cause abnormal UA levels, including phosphoribosyl pyrophosphate (PRPP) synthetase, purine nucleoside phosphorylase, xanthine oxidase, hypoxanthine-guanine phosphoribosyl transferase (HGPRT) (Cammalleri and Malaguarnera, 2007; Maiuolo et al., 2016). In the circulation, UA exists mainly in the form of urate anion under physiologic pH. The saturation level of monosodium urate in human plasma is limited. Hence, UA must be excreted continuously to prevent its accumulation and reduce the toxicity. The primary scavenger of urate is the kidney, which expels about 75% of urate every day (Chaudhary et al., 2013). In recent years, studies have revealed the complex interaction of transporters involved in urate metabolism (Wright et al., 2010). Several transporters involved in urate metabolism have been identified, including URAT1, GLUT9, organic anion transporters (OAT1/3), and adenosine triphosphate (ATP)-binding cassette transporter 2 (ABCG2) (Enomoto et al., 2002; Lipkowitz, 2012; Mandal and Mount, 2015). Previous studies have found that inflammation, oxidative stress, mitochondrial

dysfunction and other factors cause abnormalities in these critical proteins, and thus lead to the disorders in UA metabolism (Lanaspa et al., 2012; Zhou et al., 2018b). On the contrary, abnormal UA levels can also lead to the release of some cytokines, such as tumor necrosis factor-α (TNF-α), nuclear factor-kappa B (NF-*κB*), the NOD-like receptor P3 (NLRP3) inflammasome, interleukin-6 (IL-6), interleukin-1β (IL-1β), and so on (Major et al., 2018; Singh et al., 2019).

Herbs Lower Serum Uric Acid by Targeting Uric Acid Synthesis

The substrate for UA synthesis is ribose-5-phosphate which can be converted to PRPP via PRPP synthase and then to inosine monophosphate. This intermediate compound produces adenosine monophosphate and guanosine monophosphate, which subsequently release adenosine and guanosine molecules, respectively. Adenosine deaminase converts adenosine to inosine, while guanosine to free guanine. Inosine is degraded to hypoxanthine via purine nucleoside phosphorylase. Xanthine oxidase, one of the key enzymes involved in UA synthesis, converts hypoxanthine to xanthine which then converts to UA. Guanine is directly converted to xanthine, which subsequently to UA by XO. On the other hand, hypoxanthine and guanine enter a salvage pathway through the activity of HGPRT, which converts these purine into their respective nucleotides (Lipkowitz, 2012; Lima et al., 2015; Maiuolo et al., 2016). Thus, PRPP synthase, XO and HGPRT are all key enzymes that can cause abnormal sUA levels. PRPP gene mutations have been implicated in a number of human diseases. Overexpression of PRPP results in the enhanced activity of phosphoribosyl pyrophosphate synthetase-I, which can lead to excessive production of purine. Patients with active phosphoribosyl pyrophosphate synthetase-I may result in UA over production (Mittal et al., 2015). Lesch-Nyhan disease is caused by a wide variety of mutations in the HGPRT gene and is one of the models of gout caused by the increased production of UA (Fu et al., 2014; Harris, 2018). Lack of HGPRT can lead to Kelley-Seegmiller syndrome, which is characterized by hyperuricemia, hyperuricosuria, gouty arthritis and urolithiasis (Chavarriaga et al., 2019). Among these key enzymes, XO is the most commonly studied enzyme. 3,5,2′,4′-tetrahydroxychalcone significantly inhibits the activities of XO in liver, and the decreased content of PRPP in liver will suppresse the UA production (Niu et al., 2018). In our review, nearly half of the studies (83/186, 45%) confirm that herbs regulate XO synthesis and activity. For example, pallidifloside D, a saponin glycoside constituent from the total saponins of Smilax riparia, enhances the hypouricemic effect of allopurinol by regulating XO activity. The combination of allopurinol and Pallidifloside D significantly up-regulates HGPRT expression and down-regulates the expressions of PRPP in PC12 cells (Li et al., 2016).

Herbs Lower Serum Uric Acid by Targeting Uric Acid Transporter

About two-thirds of UA is excreted by the kidneys, and the remaining is excreted via the gastrointestinal tract. Renal excretion of UA consists of four steps: 1) glomerular filtration, 2) presecretory reabsorption, 3) secretion and 4) post-secretory reabsorption (Maiuolo et al., 2016). Urate is filtered through the glomerulus, so the reabsorption and secretion of UA after glomerulus play an important role in regulating the excretion of UA. Most of the urate (99%) filtered through the glomerulus is reabsorbed in the early S1 segment of the proximal tubule (presecretory reabsorption). Uric acid is then secreted in the S2 segment of the proximal tubule to return approximately 50% of the filtered urate into the tubule lumen. Post-secretory reabsorption occurs primarily in the distal S3 segment of the proximal tubule, followed by about 10% of the secreted urate in the urine (Diamond and Paolino, 1973; Mandal and Mount, 2015). Urate transporters such as URAT1, OAT1, OAT3, GLUT9, ABCG2 play important roles in regulating sUA, and their dysfunction may cause abnormal urate transport. URAT1, the main urate-anion exchanger in the luminal membrane of the proximal tubules, can be inhibited by the uricosuric agents, likes probenecid, benzbromarone and losartan (Enomoto et al., 2002). URAT1 mutations have been found in patients with familial hypouricemia and UA levels below 1 mg/dL, and the UA transport is inactivated when this mutant transporter is expressed in *xenopus* oocytes (Dinour et al., 2011). Clinical studies have shown that inhibition of URAT1 effectively reduces sUA levels and resolves the gout symptoms (Lee et al., 2019a). URAT1 is a branch of the organic anion transporter (OAT). OAT1 and OAT3 exchange urate with bivalent anions, suggesting that they are suitable for basolateral entry of urate during urate secretion (Mandal and Mount, 2015). Among the 14 members of the GLUT family transport glucose or other monosaccharides, GLUT9 does transport essentially urate (Caulfield et al., 2008). GLUT9 mediates urate transport, which is independent of sodium, chlorine and anions, but voltage-dependent (Anzai et al., 2008). Compared with the mutation in URAT1, the complete loss of GLUT9 results in the net secretion of urate (Preitner et al., 2009). ABCG2 is a multidrug resistance transporter that is also implicated as an important urate transporter. Its gene variation has become the main cause of elevated sUA levels (Dehghan et al., 2008). ABCG2-mediated loss or reduction of renal urate secretion will lead to increased renal urate reabsorption (Woodward et al., 2009).

In our review, more than one-third of the studies (72/186, 39%) show that Chinese herbal medicines target uric acid transporters. *Alpinia oxyphylla* seed extract enhances UA excretion in the kidney by reducing URAT1 and up-regulating OTA1 (Lee et al., 2019b). Wuling San down-regulates mRNA and protein levels of URAT1 and GLUT9, as well as up-regulates OAT1 in the kidney of hyperuricemic mice. Moreover, Wuling San also up-regulates organic cation/carnitine transporters which are associated with impaired renal function, leading to kidney protection (Ding et al., 2013). Gypenosides, natural saponins extracted from Gynostemma pentaphyllum, significantly lower sUA levels by reducing XO and increasing in urate excretion through regulating URAT1, GLUT9, and OAT1 (Pang et al., 2017).

Herbs Lowering Serum Uric Acid Resolve Inflammation

Uric acid belongs to the damage-associated molecular patterns, altered metabolites of necrotic or stressed cells that the innate immune system sees as an alarm signal (Patel, 2018). Elevated UA levels alters the physiology, boosting the expressions of inflammatory proteins by triggering complex pro-inflammatory cascades that damage cells and tissues (Chen and Lan, 2017). Clinical trials have shown that serum levels of IL-6 and TNF-α are significantly higher in hyperuricemia patients than in healthy people, and that of IL-6 and TNF-α are significantly increased as sUA levels increase (Zhou et al., 2018b). SUA above 9 mg/dl is associated with a gouty arthritis incidence of 4.9%. The accumulation of monosodium urate (MSU) crystals induce a mass of inflammatory cells (such as neutrophils and monocytes) to infiltrate into the site of MSU crystal deposits in patients, resulting in an acute inflammatory response, manifested as acute gout flares (Dalbeth et al., 2016). IL-1 released from these immune cells further triggers the release of various pro-inflammatory cytokines and chemokines, such as IL-8, IL-6 and TNF-α, which can further enhance neutrophil recruitment (El Ridi and Tallima, 2017). Inflammatory cytokines, especially IL-1β, are the key mediators of gouty inflammation. A phase III, international safety study of patients with acute gout arthritis treated with rilonacept (an IL-1 blocker) for 16 weeks shows that rilonacept significantly reduces the risk of gout attacks by 70.3% (Sundy et al., 2014). In experimental studies included in this review, 37 articles (11 active ingredients, 13 natural products, and 13 herbal formulas) describe the effects of these herbs on IL-1. It is worth mentioning that these herbs not only act on IL-1, but also as XO, UA transporter, other inflammatory factors such as IL-6, IL-8, TNF-α, NF-κB, NLRP3, caspase 1, etc.

There are 16 herbs included in this review that interfere with the NLRP3 inflammasome. Consistent with reported studies, elevated UA can be effectively reduced by regulating NLRP3 inflammasome - IL-1 pathway (Dhanasekar and Rasool, 2016; Szekanecz et al., 2019). Acute gout is an inflammatory response to MSU crystals. Innate immune pathways are essential in the pathogenesis of gout, particularly the activation of NLRP3 inflammasome, which leads to the release of IL-1β and other pro-inflammatory cytokines (So and Martinon, 2017). MSU crystals must first be coated with serum proteins and then interact with articular cell's surface membrane directly or via receptors, to stimulate a cytosolic molecular platform involved in innate immunity and promote the assembly and activation of the NLRP3 inflammasome (El Ridi and Tallima, 2017). NLRP3 inflammasomes are formed by the recruitment of the apoptosis-associated speck-like protein containing a caspase recruitment domain (ASC), and subsequent recruitment of caspase-1. Caspase-1 activates pro-inflammatory cytokines IL-1β and IL-18 by cleaving their respective precursor proteins, pro-IL-1β and pro-IL-18 (So and Martinon, 2017). Neutrophils are recruited and activated in response to the spillover of IL-1, producing ROS, proteolytic enzymes, pro-inflammatory chemokines, cytokines and so on, which recruit and activate macrophages (El Ridi and Tallima, 2017). Thus, the release of IL-1β mediated by inflammasome and the rapid recruitment of neutrophils lead to acute inflammatory episodes in gout patients. It is noteworthy that hyperuricemia may stimulate inflammatory leukocytes through epigenetic modification such as histone methylation, even without MSU crystals, thereby increasing production of IL-1β, IL-6, and TNF-α (Wasilewska et al., 2012; Zhou et al., 2018b).

The activation and maturation of IL-1β in response to endogenous and exogenous stimuli are also involved in the NF-κB pathway (Chen and Lan, 2017). In our review, there are 13 articles focused on NF-κB signaling pathway, showing the inhibitory effect of herbs on NF-κB activation under elevated sUA levels. It has been proved that NF-κB can be activated by UA (Spiga et al., 2017). Its activation transcribes a large number of pro-inflammatory genes. In a resting state, NF-κB combines with IκBα (inhibitor of NF-κB kinase subunit α) form a dimer in the cytoplasm, after IκBα kinase is activated, it phosphorylates IκBα. Subsequently, NF-κB is transferred from the cytoplasm to the nucleus, leading to the transcription and expression of genes related to inflammation. Studies have shown that inhibition of NF-κB restrains inflammation and improves hyperuricemia or gout conditions (Chen et al., 2019a; Wang et al., 2019c). Interestingly, studies focused on NF-κB activity is also related to NLRP3. NF-κB is essential for the initiation, assembly and activation of NLRP3 inflammasome, which is also a key step in the release of inflammatory cytokines in MSU crystal-induced inflammation (So and Martinon, 2017). P38 mitogen-activated protein kinase (MAPK) is also involved in the inflammatory cascade of NF-κB. Uric acid activates NF-κB through MAPK signal pathway, thus leading to the release of inflammatory factors such as TNF-α (Tang et al., 2017).

Herbs Lowering Serum Uric Acid Protect Against Renal Fibrosis

Evidence suggests that UA levels can be used to predict the prognosis of chronic kidney disease and end-stage kidney disease. Elevated sUA level is an independent risk factor for kidney disease and lead to renal fibrosis (Fan et al., 2019). Mice with systemic GLUT9 knockout showed moderate hyperuricemia, excessive hyperaciduria and obstructive nephropathy, along with progressive inflammatory fibrosis (Preitner et al., 2009). Once UA exceeds the maximum amount the kidneys can excrete, it gets deposit in the kidney and firstly causes direct pathological damage to the kidney. Secondly, the deposition of UA in the kidney results in the accumulation of neutrophils and monocytes as well as the release of inflammatory factors, which lead to glomerulosclerosis and interstitial fibrosis and aggravate renal injury (Ye et al., 2018). Prevention and treatment of renal fibrosis is the best treatment for kidney diseases caused by elevated sUA. However, at present, modern medical treatments are not effective in reducing renal fibrosis and preventing the progression of diseases.

A total of 24 studies included in this review are focused on hyperuricemic nephropathy, suggesting that herbal medicines improve renal injury induced by elevated sUA levels by regulating renal fibrosis-related signal pathways. Fibrosis is

usually associated with strong inflammatory reactions and immunocyte infiltration. Therefore, inhibition of inflammatory cytokines might be a potential method to prevent fibrosis. Vaticaffinol, one of the herbs included in this review, markedly down-regulates NLRP3, ASC, caspase-1, IL-1β, IL-18, IL-6 and TNF-α in hyperuricemic mice, thus significantly decreases sUA levels and improves kidney function (Chen et al., 2017b). Transforming growth factor-*β*1/Mothers against decapentaplegic homolog 3 (TGF-β1/Smad3) signaling is the most potent fibrogenic factor in the regulation of renal interstitial fibrosis process (Loeffler and Wolf, 2015). Pterostilbene, also mentioned in this review, suppresses the activation of TGF-β1/Smad3 and proto-oncogene tyrosine-protein kinase Src/Signal transducer and activator of transcription 3 (Src/STAT3) signaling pathway as to decrease sUA level and alleviate renal fibrosis in hyperuricemic mice (Pan et al., 2019). These findings highlight the fact that herbal medicines may be the potential antifibrotic therapeutics for hyperuricemic nephropathy treatment.

Herbs Lowering Serum Uric Acid Modulate Oxidative Stress

In addition to the inflammatory process, oxidative stress is one of the early events related to the elevated sUA. Uric acid entering cells can rapidly induce oxidative stress (Ko et al., 2019; Yin et al., 2019). This state of oxidative stress is governed by the balance between ROS production and their elimination by antioxidants. Since the cell membrane is impermeable to urate anion, cellular concentration of urate depends on the specific transporter of urate and xanthine oxidoreductase (XOR). In mammals, this enzyme exists in two forms, xanthine dehydrogenase (XDH) and XO. XDH transfers electron to NAD^+ and generates NADH, and XO transfers electron to O_2 and generates oxidative stress (Isaka et al., 2016). In addition, XOR may lead to the production of the superoxide anion and nitric oxide, especially under low pH or hypoxia conditions (Godber et al., 2000; Battelli et al., 2019). It can be seen that the generation of UA mediated by XO is closely related to the production of ROS. On the other hand, antioxidant enzymes that scavenge ROS are ubiquitous, including superoxide dismutase, glutathione peroxidase and catalase, the changes of these enzymatic activities may lead to oxidative stress. However, in inflammatory diseases including hyperuricemia, the production of the superoxide anion is often faster than its removal by superoxide dismutase (Zamudio-Cuevas et al., 2015).

There is an increasing interest in using herbs to resolve the inflammatory conditions, including hyperuricemia, because they play an anti-inflammatory role by inhibiting the production of ROS, such as procyanidins, Shizhifang, Zisheng Shenqi decoction, quercetin, Modified Simiao decoction and other herbs included in this review. Antioxidants like quercetin inhibits inflammation in rat models of chronic MSU-induced arthritis by decreasing inflammatory mediators such as IL-1β (Huang et al., 2012). Other herbs mentioned above also show significant antioxidant effects. For example, Shizhifang effectively suppresses the NLRP3-ASC-caspase-1 axis through accommodating the ROS pathway, thereby alleviates potassium oxonate - induced hyperuricemia (Wu et al., 2017). In summary, the herbs that possess anti-oxidant effects may be developed as anti-inflammatory agents to treat inflammatory diseases such as gout and hyperuricemia.

Limitations and Perspectives From the Experimental Studies

As shown in **Tables 3–5**, there are fewer studies on the active ingredients of herbs than on the herbal extracts and herbal formulas. Aside from herbal formula, there can be hundreds of active ingredients in a single-flavored herb, making it difficult to identify the ones that actually mediate the therapeutic effects. This partly explains why multiple signaling pathways are involved in herbal treatments. Extraction of components that mediate the therapeutic effects is difficult. In general, safe and effective single-flavored herb can be screened out from literatures or experimental studies, and its effective active ingredients can be separated by pharmacological methods. Then, the mechanism of action of the drug can be explored based on the identified active ingredients from the herbs. In recent years, there are new approaches to identify the active ingredients of herbs and predict their targets, such as Systems Pharmacology. Researchers used Systems Pharmacology as a basis to screen out active ingredients from herbal formulas or herbs, and predict the targets of active ingredients, and finally verify them through *in vivo* and *in vitro* experimental studies (Zhou et al., 2016; Hong et al., 2017; Zhao et al., 2019). It really opens up new ideas for the studies of herbs and shortens the time to find out the mechanisms of action underlying the therapeutic effects of the herbs. However, with the increasing number of herbal studies using Systems Pharmacology, we can find that it also has disadvantages, such as limited Systems Pharmacology databases, data not updated, limited prediction results and so on. In view of this, it is still necessary to explore how to efficiently screen out the active ingredients of the herbs and identify their molecular targets.

CONCLUSION

In conclusion, the results of meta-analysis indicate that Chinese herbal medicines have potent therapeutic effects in lowering sUA levels. The signaling pathways involved in the sUA lowering effects include UA synthesis, UA transport, inflammation, renal fibrosis and oxidative stress. Further studies with sophisticated research design can further demonstrate the efficacy and safety of these Chinese herbal medicines in lowering sUA levels. Identification of the active ingredients and delineation of the underlying mechanisms of action can facilitate the clinical translation and application of these ingredients.

AUTHOR CONTRIBUTIONS

All the authors contributed sufficiently for their participation in the study, as follows: XZ and LZ conceived, designed, and

supervised the study; LC, ZL, MW, JC, FL, and HL conducted the literature search, data extraction, data analysis and interpretation; QH, YY, and XZ appraised the articles; LC, ZL, and MW wrote the paper, HK modified the paper. All authors have read and approved the final manuscript.

FUNDING

This work was supported by the Key Project of National Natural Science Foundation of China (No. 81830117), the National Science Foundation of China (Nos. 81774212, 81760821, 81703952), the Natural Science Foundation of Guangdong Province, China (Nos. 2017A030313722, 2018A030313375, 2019A1515010400), and the Science & Technical Plan of Guangzhou, Guangdong, China (No.201903010069).

SUPPLEMENTARY MATERIAL

The Supplementary Material for this article can be found online at: https://www.frontiersin.org/articles/10.3389/fphar.2020.578318/full#supplementary-material.

REFERENCES

Adachi, S. I., Nihei, K. I., Ishihara, Y., Yoshizawa, F., and Yagasaki, K. (2017). Anti-hyperuricemic effect of taxifolin in cultured hepatocytes and model mice. *Cytotechnology.* 69 (2), 329–336. doi:10.1007/s10616-016-0061-4

Amat, N., Umar, A., Hoxur, P., Anaydulla, M., Imam, G., Aziz, R., et al. (2015). Traditional Uighur Medicine Karapxa decoction, inhibits liver xanthine oxidase and reduces serum uric acid concentrations in hyperuricemic mice and scavenges free radicals *in vitro*. *BMC Compl. Alternative Med.* 15, 131. doi:10.1186/s12906-015-0644-1

Anzai, N., Ichida, K., Jutabha, P., Kimura, T., Babu, E., Jin, C. J., et al. (2008). Plasma urate level is directly regulated by a voltage-driven urate efflux transporter URATv1 (SLC2A9) in humans. *J. Biol. Chem.* 283 (40), 26834–26838. doi:10.1074/jbc.C800156200

Azevedo, V. F., Kos, I. A., Vargas-Santos, A. B., da Rocha Castelar Pinheiro, G., and Dos Santos Paiva, E. (2019). Benzbromarone in the treatment of gout. *Adv Rheumatol.* 59 (1), 37. doi:10.1186/s42358-019-0080-x

Battelli, M. G., Bortolotti, M., Polito, L., and Bolognesi, A. (2018). The role of xanthine oxidoreductase and uric acid in metabolic syndrome. *Biochim. Biophys. Acta (BBA) - Mol. Basis Dis.* 1864 (8), 2557–2565. doi:10.1016/j.bbadis.2018.05.003

Battelli, M. G., Bortolotti, M., Polito, L., and Bolognesi, A. (2019). Metabolic syndrome and cancer risk: the role of xanthine oxidoreductase. *Redox Biol.* 21, 101070. doi:10.1016/j.redox.2018.101070

Burke, B. T., Kottgen, A., Law, A., Windham, B. G., Segev, D., Baer, A. N., et al. (2015). Physical function, hyperuricemia, and gout in older adults. *Arthritis Care Res.* 67 (12), 1730–1738. doi:10.1002/acr.22648

Cammalleri, L., and Malaguarnera, M. (2007). Rasburicase represents a new tool for hyperuricemia in tumor lysis syndrome and in gout. *Int. J. Med. Sci.* 4 (2), 83–93. doi:10.7150/ijms.4.83

Cao, W., Xu, D., Wu, W., Xu, T., and Li, T. (2011). Experimental study on anti-inflammation and analgesic effects of extracts of compound Shuiniujiao. *Pharmaceut. Care Res.* 11 (2), 103–106. doi:10.5428/pcar20110209

Caulfield, M. J., Munroe, P. B., O'Neill, D., Witkowska, K., Charchar, F. J., Doblado, M., et al. (2008). SLC2A9 is a high-capacity urate transporter in humans. *PLoS Med.* 5 (10), e197. doi:10.1371/journal.pmed.0050197

Chaudhary, K., Malhotra, K., Sowers, J., and Aroor, A. (2013). Uric Acid - key ingredient in the recipe for cardiorenal metabolic syndrome. *Cardiorenal Med.* 3 (3), 208–220. doi:10.1159/000355405

Chavarriaga, J., Ocampo, M., Fakih, N., and Silva Herrera, J. (2019). Kelley-seegmiller syndrome: urolithiasis, renal uric acid deposits, and gout: what is the role of the urologist?. *Urol. Int.* 102 (2), 233–237. doi:10.1159/000494360

Chen, Q., Ma, L., and Akebaier, W. (2009). Clinical study on treatment of hyperuricaemia by retention enema of Chinese herbal medicine combined with allopurinol. *Chin. J. Integr. Med.* 15 (6), 431–434. doi:10.1007/s11655-009-0431-2

Chen, J. W., Zhou, Y., Xue, Z. Y., Li, C., Guo, J., Zhou, L. Y., et al. (2013a). [Effect of jianpihuashi decoction on rats with hyperuricemia]. *Zhong Yao Cai.* 36 (9), 1486–1489

Chen, L., Mola, M., Deng, X., Mei, Z., Huang, X., Shu, G., et al. (2013b). Dolichos falcata Klein attenuated the inflammation induced by monosodium urate crystals *in vivo* and *in vitro*. *J. Ethnopharmacol.* 150 (2), 545–552. doi:10.1016/j.jep.2013.08.063

Chen, C. Y., Huang, C. C., Tsai, K. C., Huang, W. J., Huang, W. C., Hsu, Y. C., et al. (2014a). Evaluation of the antihyperuricemic activity of phytochemicals from Davallia formosana by enzyme assay and hyperuricemic mice model. *Evid Based Complement Alternat Med.* 2014, 873607. doi:10.1155/2014/873607

Chen, G. L., Wu, S., Na, S., and Li, L. (2014b). [Effect of total saponin of dioscorea on uric acid excretion indicators in chronic hyperuricemia rats]. *Zhongguo Zhong Xi Yi Jie He Za Zhi.* 34 (1), 75–80

Chen, Y., Lu, Y., Wang, Y. N., Lin, Z. C., Gu, W., Tan, L., et al. (2014c). [Effect of compound qingqin liquid on the expression of toll-like receptor in the renal tissue of rats with urate nephropathy]. *Zhongguo Zhong Xi Yi Jie He Za Zhi.* 34 (6), 722–727

Chen, G., Tan, M. L., Li, K. K., Leung, P. C., and Ko, C. H. (2015a). Green tea polyphenols decreases uric acid level through xanthine oxidase and renal urate transporters in hyperuricemic mice. *J. Ethnopharmacol.* 175, 14–20. doi:10.1016/j.jep.2015.08.043

Chen, W. J., Wu, Y., Xu, C., Liu, S., Wang, W. Z., Song, F. R., et al. (2015b). [Study on therapeutic effects of ermiao pill and ermiao pill categorized formula in hyperuricemic rats using spectroscopic methods]. *Guang Pu Xue Yu Guang Pu Fen Xi.* 35 (4), 956–960

Chen, J., Zhou, J., Wei, S., Xie, Z., Wen, C., and Xu, G. (2016a). Effect of a traditional Chinese medicine prescription Quzhuotongbi decoction on hyperuricemia model rats studied by using serum metabolomics based on gas chromatography-mass spectrometry. *J Chromatogr B Analyt Technol Biomed Life Sci.* 1026, 272–278. doi:10.1016/j.jchromb.2015.10.031

Chen, Y., Chen, X. L., Xiang, T., Sun, B. G., Luo, H. X., Liu, M. T., et al. (2016b). Total saponins from dioscorea septemloba thunb reduce serum uric acid levels in rats with hyperuricemia through OATP1A1 up-regulation. *J Huazhong Univ Sci Technolog Med Sci.* 36 (2), 237–242. doi:10.1007/s11596-016-1573-z

Chen, W. J., Wu, Y., Bi, R. B., Liu, S., Liu, Z. Y., Liu, Z. Q., et al. (2017a). Therapeutic effects of selaginella tamariscina on the model of acute gout with hyperuricemia in rats based on metabolomics analysis. *Chin. J. Chem.* 35 (7), 1117–1124. doi:10.1002/cjoc.201600810

Chen, Y. S., Chen, C. J., Yan, W., Ge, H. M., and Kong, L. D. (2017b). Anti-hyperuricemic and anti-inflammatory actions of vaticaffinol isolated from Dipterocarpus alatus in hyperuricemic mice. *Chin. J. Nat. Med.* 15 (5), 330–340. doi:10.1016/s1875-5364(17)30053-5

Chen, B., Li, H., Ou, G., Ren, L., Yang, X., and Zeng, M. (2019a). Curcumin attenuates MSU crystal-induced inflammation by inhibiting the degradation of IkappaBalpha and blocking mitochondrial damage. *Arthritis Res. Ther.* 21 (1), 193. doi:10.1186/s13075-019-1974-z

Chen, H.-f., Zhang, C., Yao, Y., Li, J.-m., Du, W.-d., Li, M.-l., et al. (2019b). Study on anti-hyperuricemia effects and active ingredients of traditional Tibetan medicine TongFengTangSan (TFTS) by ultra-high-performance liquid chromatography coupled with quadrupole time-of-flight mass spectrometry. *J. Pharmaceut. Biomed. Anal.* 165, 213–223. doi:10.1016/j.jpba.2018.11.038

Chen, M., Ye, C., Zhu, J., Zhang, P., Jiang, Y., Lu, X., et al. (2020a). Bergenin as a novel urate-lowering therapeutic strategy for hyperuricemia. *Frontiers in Cell and Developmental Biology.* 8. doi:10.3389/fcell.2020.00703

Chen, W. D., Zhao, Y. L., Sun, W. J., He, Y. J., Liu, Y. P., Jin, Q., et al. (2020b). Kidney tea" and its bioactive secondary metabolites for treatment of gout. *J. Agric. Food Chem.* doi:10.1021/acs.jafc.0c03848

Chen, L., and Lan, Z. (2017). Polydatin attenuates potassium oxonate-induced hyperuricemia and kidney inflammation by inhibiting NF-kappaB/NLRP3 inflammasome activation via the AMPK/SIRT1 pathway. *Food Funct.* 8 (5), 1785–1792. doi:10.1039/c6fo01561a

Chen-Xu, M., Yokose, C., Rai, S. K., Pillinger, M. H., and Choi, H. K. (2019). Contemporary prevalence of gout and hyperuricemia in the United States and decadal trends: the national health and nutrition examination survey, 2007-2016. *Arthritis Rheum* 71 (6), 991–999. doi:10.1002/art.40807

Cheng, L. C., Murugaiyah, V., and Chan, K. L. (2015). Flavonoids and phenylethanoid glycosides from Lippia nodiflora as promising antihyperuricemic agents and elucidation of their mechanism of action. *J. Ethnopharmacol.* 176, 485–493. doi:10.1016/j.jep.2015.11.025

Cheng, S., Sun, H., Li, X., Yan, J., Peng, Z., You, Y., et al. (2019). Effects of alismatis rhizoma and rhizoma smilacis glabrae decoction on hyperuricemia in rats. *Evid. base Compl. Alternative Med.* 2019, 1–12. doi:10.1155/2019/4541609

Cho, S. S., Song, S. H., Choi, C. Y., Park, K. M., Shim, J. H., and Park, D. H. (2018). Optimization of the extraction conditions and biological evaluation of dendropanax morbifera H. Lev as an anti-hyperuricemic source. *Molecules.* 23 (12), 3313. doi:10.3390/molecules23123313

Choi, H. K., McCormick, N., Lu, N., Rai, S. K., Yokose, C., and Zhang, Y. (2020). Population impact attributable to modifiable risk factors for hyperuricemia. *Arthritis Rheum* 72 (1), 157–165. doi:10.1002/art.41067

Cui, D., Liu, S., Tang, M., Lu, Y., Zhao, M., Mao, R., et al. (2020). Phloretin ameliorates hyperuricemia-induced chronic renal dysfunction through inhibiting NLRP3 inflammasome and uric acid reabsorption. *Phytomedicine.* 66, 153111. doi:10.1016/j.phymed.2019.153111

Dalbeth, N., Merriman, T. R., and Stamp, L. K. (2016). *Gout. Lancet.* 388 (10055), 2039–2052. doi:10.1016/s0140-6736(16)00346-9

Dang, Y. X., Liang, D. L., Zhou, X. X., Qin, Y., Gao, Y., and Li, W. M. (2019). Protective effect of Mori Cortex on kidney in rats with hyperlipidemia and hyperuricemia based on molecular docking technique. *Chin. Tradit. Herb. Drugs.* 50 (5), 1175–1181. doi:10.7501/j.issn.0253-2670.2019.05.022

Dehghan, A., Kottgen, A., Yang, Q., Hwang, S. J., Kao, W. L., Rivadeneira, F., et al. (2008). Association of three genetic loci with uric acid concentration and risk of gout: a genome-wide association study. *Lancet.* 372 (9654), 1953–1961. doi:10.1016/s0140-6736(08)61343-4

Dhanasekar, C., and Rasool, M. (2016). Morin, a dietary bioflavonol suppresses monosodium urate crystal-induced inflammation in an animal model of acute gouty arthritis with reference to NLRP3 inflammasome, hypo-xanthine phospho-ribosyl transferase, and inflammatory mediators. *Eur. J. Pharmacol.* 786, 116–127. doi:10.1016/j.ejphar.2016.06.005

Diamond, H. S., and Paolino, J. S. (1973). Evidence for a postsecretory reabsorptive site for uric acid in man. *J. Clin. Invest.* 52 (6), 1491–1499. doi:10.1172/jci107323

Ding, X. Q., Pan, Y., Wang, X., Ma, Y. X., and Kong, L. D. (2013). Wuling san ameliorates urate under-excretion and renal dysfunction in hyperuricemic mice. *Chin. J. Nat. Med.* 11 (3), 214–221. doi:10.1016/s1875-5364(13)60019-9

Dinour, D., Bahn, A., Ganon, L., Ron, R., Geifman-Holtzman, O., Knecht, A., et al. (2011). URAT1 mutations cause renal hypouricemia type 1 in Iraqi Jews. *Nephrol. Dial. Transplant.* 26 (7), 2175–2181. doi:10.1093/ndt/gfq722

El Ridi, R., and Tallima, H. (2017). Physiological functions and pathogenic potential of uric acid: a review. *J. Adv. Res.* 8 (5), 487–493. doi:10.1016/j.jare.2017.03.003

Enomoto, A., Kimura, H., Chairoungdua, A., Shigeta, Y., Jutabha, P., Cha, S. H., et al. (2002). Molecular identification of a renal urate anion exchanger that regulates blood urate levels. *Nature.* 417 (6887), 447–452. doi:10.1038/nature742

Fan, H., Zhao, Y., Fu, J., Zhang, H., Wang, D., Gao, Y., et al. (2018). Anti-inflammatory effect of Tongfengning Capsule in rats with acute gouty arthritis and its mechanism. *J. Jilin Univ. - Med. Ed.* 44 (2), 270–274. doi:10.13481/j.1671-587x.20180212

Fan, S., Zhang, P., Wang, A. Y., Wang, X., Wang, L., Li, G., et al. (2019). Hyperuricemia and its related histopathological features on renal biopsy. *BMC Nephrol.* 20 (1), 95. doi:10.1186/s12882-019-1275-4

Fang, C., Chen, L., He, M., Luo, Y., Zhou, M., Zhang, N., et al. (2019). Molecular mechanistic insight into the anti-hyperuricemic effect of Eucommia ulmoides in mice and rats. *Pharm. Biol.* 57 (1), 112–119. doi:10.1080/13880209.2019.1568510

Fei, Y., Ye, D., Fan, X. F., and Dong, F. Q. (2016). Effect of Dioscorea tokoro Makino extract on hyperuricemia in mice. *Trop. J. Pharmaceut. Res.* 15 (9), 1883–1887. doi:10.4314/tjpr.v15i9.10

Fu, R., Ceballos-Picot, I., Torres, R. J., Larovere, L. E., Yamada, Y., Nguyen, K. V., et al. (2014). Genotype-phenotype correlations in neurogenetics: lesch-Nyhan disease as a model disorder. *Brain.* 137 (Pt 5), 1282–1303. doi:10.1093/brain/awt202

Gamala, M., and Jacobs, J. W. G. (2019). Gout and hyperuricaemia: a worldwide health issue of joints and beyond. *Rheumatology.*. doi:10.1093/rheumatology/kez272

Godber, B. L., Doel, J. J., Sapkota, G. P., Blake, D. R., Stevens, C. R., Eisenthal, R., et al. (2000). Reduction of nitrite to nitric oxide catalyzed by xanthine oxidoreductase. *J. Biol. Chem.* 275 (11), 7757–7763. doi:10.1074/jbc.275.11.7757

Guo, Y., Jiang, Q., Gui, D., and Wang, N. (2015). Chinese herbal formulas Si-Wu-tang and Er-Miao-San synergistically ameliorated hyperuricemia and renal impairment in rats induced by adenine and potassium oxonate. *Cell. Physiol. Biochem.* 37 (4), 1491–1502. doi:10.1159/000438517

Guo, L. F., Chen, X., Lei, S. S., Li, B., Zhang, N. Y., Ge, H. Z., et al. (2020). Effects and mechanisms of dendrobium officinalis six nostrum for treatment of hyperuricemia with hyperlipidemia. *Evid Based Complement Alternat Med.* 2020, 2914019. doi:10.1155/2020/2914019

Han, J., Xie, Y., Sui, F., Liu, C., Du, X., Liu, C., et al. (2016). Zisheng Shenqi decoction ameliorates monosodium urate crystal-induced gouty arthritis in rats through anti-inflammatory and anti-oxidative effects. *Mol. Med. Rep.* 14 (3), 2589–2597. doi:10.3892/mmr.2016.5526

Han, B., Zhu, C. X., Shi, W., Huang, H. Z., Hu, X. G., Zhou, X. M., et al. (2017). Effect of Rhizoma Polygoni Cuspidati and Ramulus Cinnamomi compatibility on uric acid metabolism and urinary neutrophil gelatinase-associated lipocalin and kidney injury molecule-1 in rats with hyperuricemia. *Chin. J. Integr. Med.* 23 (7), 535–542. doi:10.1007/s11655-016-2649-0

Han, B., Gong, M., Li, Z., Qiu, Y., and Zou, Z. (2020). NMR-based metabonomic study reveals intervention effects of polydatin on potassium oxonate-induced hyperuricemia in rats. *Oxid Med Cell Longev.* 2020, 6943860. doi:10.1155/2020/6943860

Harris, J. C. (2018). Lesch-Nyhan syndrome and its variants: examining the behavioral and neurocognitive phenotype. *Curr. Opin. Psychiatr.* 31 (2), 96–102. doi:10.1097/yco.0000000000000388

Ho, S. T., Tung, Y. T., Huang, C. C., Kuo, C. L., Lin, C. C., Yang, S. C., et al. (2012). The hypouricemic effect of Balanophora laxiflora extracts and derived phytochemicals in hyperuricemic mice. *Evid Based Complement Alternat Med.* 2012, 910152. doi:10.1155/2012/910152

Honda, S., Kawamoto, S., Tanaka, H., Kishida, H., Kitagawa, M., Nakai, Y., et al. (2014). Administered chrysanthemum flower oil attenuates hyperuricemia: mechanism of action as revealed by DNA microarray analysis. *Biosci. Biotechnol. Biochem.* 78 (4), 655–661. doi:10.1080/09168451.2014.890028

Hong, Q., Yu, S., Mei, Y., Lv, Y., Chen, D., Wang, Y., et al. (2014). Smilacis Glabrae Rhizoma reduces oxidative stress caused by hyperuricemia via upregulation of catalase. *Cell. Physiol. Biochem.* 34 (5), 1675–1685. doi:10.1159/000366369

Hong, M., Li, S., Wang, N., Tan, H. Y., Cheung, F., and Feng, Y. (2017). A biomedical investigation of the hepatoprotective effect of radix salviae miltiorrhizae and network pharmacology-based prediction of the active compounds and molecular targets. *Int. J. Mol. Sci.* 18 (3). doi:10.3390/ijms18030620

Hou, C. W., Lee, Y. C., Hung, H. F., Fu, H. W., and Jeng, K. C. (2012). Longan seed extract reduces hyperuricemia via modulating urate transporters and suppressing xanthine oxidase activity. *Am. J. Chin. Med.* 40 (5), 979–991. doi:10.1142/s0192415x12500723

Hou, P. Y., Mi, C., He, Y., Zhang, J., Wang, S. Q., Yu, F., et al. (2015). Pallidifloside D from Smilax riparia enhanced allopurinol effects in hyperuricemia mice. *Fitoterapia.* 105, 43–48. doi:10.1016/j.fitote.2015.06.002

Hu, Q. H., Jiao, R. Q., Wang, X., Lv, Y. Z., and Kong, L. D. (2010). Simiao pill ameliorates urate underexcretion and renal dysfunction in

hyperuricemic mice. *J. Ethnopharmacol.* 128 (3), 685–692. doi:10.1016/j.jep.2010.02.012

Hua, J., Huang, P., Zhu, C. M., Yuan, X., and Yu, C. H. (2012). Anti-hyperuricemic and nephroprotective effects of Modified Simiao Decoction in hyperuricemic mice. *J. Ethnopharmacol.* 142 (1), 248–252. doi:10.1016/j.jep.2012.04.052

Hu, Q. H., Miao, M. X., Lu, G., and Ji, H. (2013a). Effects of quercetin on expression of renal NLRP3 and TLRs in rats with uric acid nephtopathy. *Chin. Tradit. Herb. Drugs.* 44 (24), 3496–3502. doi:10.7501/j.issn.0253-2670.2013.24.013

Hu, Q. H., Zhu, J. X., Ji, J., Wei, L. L., Miao, M. X., and Ji, H. (2013b). Fructus Gardenia Extract ameliorates oxonate-induced hyperuricemia with renal dysfunction in mice by regulating organic ion transporters and mOIT3. *Molecules.* 18 (8), 8976–8993. doi:10.3390/molecules18088976

Huang, J., Zhu, M., Tao, Y., Wang, S., Chen, J., Sun, W., et al. (2012). Therapeutic properties of quercetin on monosodium urate crystal-induced inflammation in rat. *J. Pharm. Pharmacol.* 64 (8), 1119–1127. doi:10.1111/j.2042-7158.2012.01504.x

Huang, B., Hu, X., Wang, J., Li, P., and Chen, J. (2019a). Study on chemical constituents of herbal formula Er Miao Wan and GC-MS based metabolomics approach to evaluate its therapeutic effects on hyperuricemic rats. *J Chromatogr B Analyt Technol Biomed Life Sci.* 1118–1119, 101–108. doi:10.1016/j.jchromb.2019.04.032

Huang, L., Deng, J., Chen, G., Zhou, M., Liang, J., Yan, B., et al. (2019b). The anti-hyperuricemic effect of four astilbin stereoisomers in Smilax glabra on hyperuricemic mice. *J. Ethnopharmacol.* 238, 111777. doi:10.1016/j.jep.2019.03.004

Hui, W., Yongliang, Y., Yongde, C., Guo, L., Li, L., Zhonglin, Y., et al. (2016). Hypouricemic and nephroprotective effects of emodinol in oxonate-induced hyperuricemic mice are mediated by organic ion transporters and OIT3. *Planta Med.* 82 (4), 289–297. doi:10.1055/s-0035-1558212

Huijuan, W., Xiaoxu, C., Rui, S., Xinghui, L., Beibei, T., and Jianchun, M. (2017). Qi-Zhu-Xie-Zhuo-Fang reduces serum uric acid levels and ameliorates renal fibrosis in hyperuricemic nephropathy rats. *Biomed. Pharmacother.* 91, 358–365. doi:10.1016/j.biopha.2017.04.031

Huo, L. N., Wang, W., Zhang, C. Y., Shi, H. B., Liu, Y., Liu, X. H., et al. (2015). Bioassay-guided isolation and identification of xanthine oxidase inhibitory constituents from the leaves of perilla frutescens. *Molecules.* 20 (10), 17848–17859. doi:10.3390/molecules201017848

Isaka, Y., Takabatake, Y., Takahashi, A., Saitoh, T., and Yoshimori, T. (2016). Hyperuricemia-induced inflammasome and kidney diseases. *Nephrol. Dial. Transplant.* 31 (6), 890–896. doi:10.1093/ndt/gfv024

Jhang, J. J., Ong, J. W., Lu, C. C., Hsu, C. L., Lin, J. H., Liao, J. W., et al. (2016). Hypouricemic effects of Mesona procumbens Hemsl. through modulating xanthine oxidase activity *in vitro* and *in vivo*. *Food Funct.* 7 (10), 4239–4246. doi:10.1039/c6fo00822d

Jiang, Y., You, X. Y., Fu, K. L., and Yin, W. L. (2012). Effects of extract from mangifera indica leaf on monosodium urate crystal-induced gouty arthritis in rats. *Evid Based Complement Alternat Med.* 2012, 967573. doi:10.1155/2012/967573

Jiang, Y., Lin, Y., Hu, Y. J., Song, X. J., Pan, H. H., and Zhang, H. J. (2017). Caffeoylquinic acid derivatives rich extract from Gnaphalium pensylvanicum willd. Ameliorates hyperuricemia and acute gouty arthritis in animal model. *BMC Compl. Alternative Med.* 17 (1), 320. doi:10.1186/s12906-017-1834-9

Kang, L., Miao, J. X., Cao, L. H., Miao, Y. Y., Miao, M. S., Liu, H. J., et al. (2020). Total glucosides of herbaceous peony (Paeonia lactiflora Pall.) flower attenuate adenine- and ethambutol-induced hyperuricaemia in rats. *J. Ethnopharmacol.* 261, 113054. doi:10.1016/j.jep.2020.113054

Kim, S. C., Liu, J., and Solomon, D. H. (2015). Risk of incident diabetes in patients with gout: a cohort study. *Arthritis Rheum* 67 (1), 273–280. doi:10.1002/art.38918

Kim, J. K., Kim, W. J., Hyun, J. M., Lee, J. S., Kwon, J. G., Seo, C., et al. (2017). Salvia plebeia extract inhibits xanthine oxidase activity in vitro and reduces serum uric acid in an animal model of hyperuricemia. *Planta Med.* 83 (17), 1335–1341. doi:10.1055/s-0043-111012

Ko, J., Kang, H. J., Kim, D. A., Kim, M. J., Ryu, E. S., Lee, S., et al. (2019). Uric acid induced the phenotype transition of vascular endothelial cells via induction of oxidative stress and glycocalyx shedding. *Faseb. J.*, fj201901148R. doi:10.1096/fj.201901148R

Kodithuwakku, N. D., Pan, M., Zhu, Y. L., Zhang, Y. Y., Feng, Y. D., Fang, W. R., et al. (2013). Anti-inflammatory and antinociceptive effects of Chinese medicine SQ gout capsules and its modulation of pro-inflammatory cytokines focusing on gout arthritis. *J. Ethnopharmacol.* 150 (3), 1071–1079. doi:10.1016/j.jep.2013.10.016

Kodithuwakku, N. D., Feng, Y. D., Zhang, Y. Y., Pan, M., Fang, W. R., and Li, Y. M. (2015). The molecular insight into the antihyperuricemic and renoprotective effect of Shuang Qi gout capsule in mice. *J. Ethnopharmacol.* 163, 278–289. doi:10.1016/j.jep.2015.01.013

Kondo, M., Hirano, Y., Nishio, M., Furuya, Y., Nakamura, H., and Watanabe, T. (2013). Xanthine oxidase inhibitory activity and hypouricemic effect of aspalathin from unfermented rooibos. *J. Food Sci.* 78 (12), H1935–H1939. doi:10.1111/1750-3841.12304

Kuo, C.-Y., Kao, E.-S., Chan, K.-C., Lee, H.-J., Huang, T.-F., and Wang, C.-J. (2012). Hibiscus sabdariffa L. extracts reduce serum uric acid levels in oxonate-induced rats. *Journal of Functional Foods.* 4 (1), 375–381. doi:10.1016/j.jff.2012.01.007

Kou, Y. Y., Li, Y. F., Xu, M., Li, W. Y., Yang, M., and Li, R. L. (2015). Effects of RuPeng15 powder (RPP15) on monosodium urate crystal-induced gouty arthritis in rats. *Evid Based Complement Alternat Med.* 2015, 527019. doi:10.1155/2015/527019

Kou, Y., Li, Y., Ma, H., Li, W., Li, R., and Dang, Z. (2016). Uric acid lowering effect of Tibetan Medicine RuPeng15 powder in animal models of hyperuricemia. *J. Tradit. Chin. Med.* 36 (2), 205–210

Kuwabara, M., Hisatome, I., Niwa, K., Hara, S., Roncal-Jimenez, C. A., Bjornstad, P., et al. (2018). Uric acid is a strong risk marker for developing hypertension from prehypertension: a 5-year Japanese cohort study. *Hypertension.* 71 (1), 78–86. doi:10.1161/hypertensionaha.117.10370

Lanaspa, M. A., Sanchez-Lozada, L. G., Choi, Y. J., Cicerchi, C., Kanbay, M., Roncal-Jimenez, C. A., et al. (2012). Uric acid induces hepatic steatosis by generation of mitochondrial oxidative stress: potential role in fructose-dependent and -independent fatty liver. *J. Biol. Chem.* 287 (48), 40732–40744. doi:10.1074/jbc.M112.399899

Lee, H. P., Lin, Y. Y., Duh, C. Y., Huang, S. Y., Wang, H. M., Wu, S. F., et al. (2015). Lemnalol attenuates mast cell activation and osteoclast activity in a gouty arthritis model. *J. Pharm. Pharmacol.* 67 (2), 274–285. doi:10.1111/jphp.12331

Lee, Y. M., Shon, E. J., Kim, O. S., and Kim, D. S. (2017). Effects of Mollugo pentaphylla extract on monosodium urate crystal-induced gouty arthritis in mice. *BMC Compl. Alternative Med.* 17 (1), 447. doi:10.1186/s12906-017-1955-1

Lee, H. A., Yu, K. S., Park, S. I., Yoon, S., Onohara, M., Ahn, Y., et al. (2019a). URC102, a potent and selective inhibitor of hURAT1, reduced serum uric acid in healthy volunteers. *Rheumatology.*. doi:10.1093/rheumatology/kez140

Lee, Y. S., Sung, Y. Y., Yuk, H. J., Son, E., Lee, S., Kim, J. S., et al. (2019b). Anti-hyperuricemic effect of Alpinia oxyphylla seed extract by enhancing uric acid excretion in the kidney. *Phytomedicine.* 62, 152975. doi:10.1016/j.phymed.2019.152975

Li, Y. Q., Wei, Y. H., and Han, X. (2010). Effects of Danggui Buxue Tang on heart muscle function in hyperuricemic rats. *Chin. Pharmaceut. J.* 45 (7), 524–526

Li, H. G., Hou, P. Y., Zhang, X., He, Y., Zhang, J., Wang, S. Q., et al. (2016). Hypouricemic effect of allopurinol are improved by Pallidifloside D based on the uric acid metabolism enzymes PRPS, HGPRT and PRPPAT. *Fitoterapia.* 113, 1–5. doi:10.1016/j.fitote.2016.06.015

Li, L., Teng, M., Liu, Y., Qu, Y., Zhang, Y., Lin, F., et al. (2017a). Anti-Gouty arthritis and antihyperuricemia effects of sunflower (helianthus annuus) head extract in gouty and hyperuricemia animal models. *BioMed Res. Int.* 2017, 5852076. doi:10.1155/2017/5852076

Li, Y. P., Wu, S., Ran, A., Xu, D. Y., Wei, J. M., and Zhao, Z. L. (2017b). Aristolochia bracteolate retz. Attenuates hyperuricemia IN a metabolic arthritis rat model. *Afr. J. Tradit., Complementary Altern. Med.* 14 (4), 180–187. doi:10.21010/ajtcam.v14i4.21

Li, Z. J., Li, Z., Dong, X. Y., Lu, L. F., and Wang, C. L. (2017c). Hypouricemic and nephroprotective effects of total flavonoids from the residue of supercritical CO2 extraction of Humulus lupulus in potassium oxonate-induced mice. *Pak. J. Pharm. Sci.* 30 (2), 493–497

Liang, G., Nie, Y., Chang, Y., Zeng, S., Liang, C., Zheng, X., et al. (2019). Protective effects of Rhizoma smilacis glabrae extracts on potassium oxonate- and

monosodium urate-induced hyperuricemia and gout in mice. *Phytomedicine.* 59, 152772. doi:10.1016/j.phymed.2018.11.032

Lima, W. G., Martins-Santos, M. E., and Chaves, V. E. (2015). Uric acid as a modulator of glucose and lipid metabolism. *Biochimie.* 116, 17–23. doi:10.1016/j.biochi.2015.06.025

Lin, J., Chen, S., Li, S., Lu, M., Li, Y., and Su, Y. (2016). Efficacy and safety of Chinese medicinal herbs for the treatment of hyperuricemia: a systematic review and meta-analysis. *Evid Based Complement Alternat Med.* 2016, 2146204. doi:10.1155/2016/2146204

Lin, Y., Liu, P. G., Liang, W. Q., Hu, Y. J., Xu, P., Zhou, J., et al. (2018). Luteolin-4'-O-glucoside and its aglycone, two major flavones of Gnaphalium affine D. Don, resist hyperuricemia and acute gouty arthritis activity in animal models. *Phytomedicine.* 41, 54–61. doi:10.1016/j.phymed.2018.02.002

Lin, X., Shao, T., Huang, L., Wen, X., Wang, M., Wen, C., et al. (2020). Simiao decoction alleviates gouty arthritis by modulating proinflammatory cytokines and the gut ecosystem. *Front. Pharmacol.* 11, 955. doi:10.3389/fphar.2020.00955

Lipkowitz, M. S. (2012). Regulation of uric acid excretion by the kidney. *Curr. Rheumatol. Rep.* 14 (2), 179–188. doi:10.1007/s11926-012-0240-z

Liu, J., Xu, L. L., and Xu, Y. (2013). Antigout active fractions in tongfeng granule. *Chin. Tradit. Herb. Drugs.* 44 (5), 590–594. doi:10.7501/j.issn.0253-2670.2013.05.018

Liu, H., Zhang, X. M., Wang, Y. L., and Liu, B. C. (2014a). Prevalence of hyperuricemia among Chinese adults: a national cross-sectional survey using multistage, stratified sampling. *J. Nephrol.* 27 (6), 653–658. doi:10.1007/s40620-014-0082-z

Liu, X. H., Huang, M. Q., Lin, Z. W., Zhen, H. S., Liu, A. T., and Zhang, K. Y. (2014b). Anti-gout effect of Poecilobdella manillensis. *Chin. Tradit. Herb. Drugs.* 45 (12), 1747–1750. doi:10.7501/j.issn.0253-2670.2014.12.018

Liu, Y. W., Sun, W. F., Zhang, X. X., Li, J., and Zhang, H. H. (2015). Compound Tufuling Granules ([characters: see text]) regulate glucose transporter 9 expression in kidney to influence serum uric acid level in hyperuricemia mice. *Chin. J. Integr. Med.* 21 (11), 823–829. doi:10.1007/s11655-015-2052-2

Liu, H. J., Pan, X. X., Liu, B. Q., Gui, X., Hu, L., Jiang, C. Y., et al. (2017). Grape seed-derived procyanidins alleviate gout pain via NLRP3 inflammasome suppression. *J. Neuroinflammation.* 14 (1), 74. doi:10.1186/s12974-017-0849-y

Liu, X. H., Zhao, Y. X., Zhou, Y. M., Huang, M. Q., Huang, S. S., Zhen, H. S., et al. (2018). Anti-gout effect of hirudin and its mechanism. *Chin. Tradit. Herb. Drugs.* 49 (6), 1365–1370. doi:10.7501/j.issn.0253-2670.2018.06.020

Liu, N., Wang, Y., Yang, M., Bian, W., Zeng, L., Yin, S., et al. (2019). New rice-derived short peptide potently alleviated hyperuricemia induced by potassium oxonate in rats. *J. Agric. Food Chem.* 67 (1), 220–228. doi:10.1021/acs.jafc.8b05879

Liu, G., Chen, X., Lu, X., Zhao, J., and Li, X. (2020). Sunflower head enzymatic hydrolysate relives hyperuricemia by inhibiting crucial proteins (xanthine oxidase, adenosine deaminase, uric acid transporter1) and restoring gut microbiota in mice. *Journal of Functional Foods.* 72. doi:10.1016/j.jff.2020.104055

Lo, H. C., Wang, Y. H., Chiou, H. Y., Lai, S. H., and Yang, Y. (2010). Relative efficacy of casein or soya protein combined with palm or safflower-seed oil on hyperuricaemia in rats. *Br. J. Nutr.* 104 (1), 67–75. doi:10.1017/s0007114510000310

Loeffler, I., and Wolf, G. (2015). Epithelial-to-Mesenchymal transition in diabetic nephropathy: fact or fiction?. *Cells.* 4 (4), 631–652. doi:10.3390/cells4040631

Lou, X. J., Wang, Y. Z., Lei, S. S., He, X., Lu, T. T., Zhan, L. H., et al. (2020). Beneficial effects of macroporous resin extract of dendrobium candidum leaves in rats with hyperuricemia induced by a high-purine diet. *Evid Based Complement Alternat Med.* 2020, 3086106. doi:10.1155/2020/3086106

Louxin, B., Miaoyanyan, F., and Miaomingsan (2018). Effect of arctiin on rat hyperuricemia model. *Acta Med. Mediterr.* 34 (6), 1739–1742. doi:10.19193/0393-6384_2018_6_266

Lü, Y. Z., Hu, Q. H., Wang, X., Ouyang, Z., and Kong, L. D. (2010). Effects of Ermiao Pill water extracts on imbalance of urate levels and its related genes and protein levels in hyperuricemic mice. *Chin. Tradit. Herb. Drugs.* 41 (3), 418–423

Lu, F., Liu, L., Yu, D. H., Li, X. Z., Zhou, Q., and Liu, S. M. (2014). Therapeutic effect of Rhizoma Dioscoreae Nipponicae on gouty arthritis based on the SDF-1/CXCR 4 and p38 MAPK pathway: an *in vivo* and *in vitro* study. *Phytother Res.* 28 (2), 280–288. doi:10.1002/ptr.4997

Lu, X. Y., Zhou, F. H., Dong, Y. Q., Gong, L. N., Li, Q. Y., Tang, L., et al. (2018). Codonopsis tangshen oliv. Amelioration effect on diabetic kidney disease rats induced by high fat diet feeding combined with streptozotocin. *Nat Prod Bioprospect.* 8 (6), 441–451. doi:10.1007/s13659-018-0187-5

Lyu, S., Ding, R., Liu, P., OuYang, H., Feng, Y., Rao, Y., et al. (2019). LC-MS analysis of serum for the metabolomic investigation of the effects of pulchinenoside b4 administration in monosodium urate crystal-induced gouty arthritis rat model. *Molecules.* 24 (17). doi:10.3390/molecules24173161

Ma, Y., Zhou, L. L., Yan, H. Y., and Liu, M. (2009). Effects of extracts from Paederia scandens (LOUR.) MERRILL (Rubiaceae) on MSU crystal-induced rats gouty arthritis. *Am. J. Chin. Med.* 37 (4), 669–683. doi:10.1142/s0192415x09007156

Ma, L., Zhang, S., Yuan, Y., and Gao, J. (2014). Hypouricemic actions of exopolysaccharide produced by Cordyceps militaris in potassium oxonate-induced hyperuricemic mice. *Curr. Microbiol.* 69 (6), 852–857. doi:10.1007/s00284-014-0666-9

Ma, C. H., Kang, L. L., Ren, H. M., Zhang, D. M., and Kong, L. D. (2015). Simiao pill ameliorates renal glomerular injury via increasing Sirt1 expression and suppressing NF-κB/NLRP3 inflammasome activation in high fructose-fed rats. *J. Ethnopharmacol.* 172, 108–117. doi:10.1016/j.jep.2015.06.015

Ma, T. H., Sheng, T., Tian, C. M., Xing, M. Y., Yan, L. J., and Xia, D. Z. (2019a). [Effect of ethanolic extract of Polygonum cuspidatum on acute gouty arthritis in mice through NLRP3/ASC/caspase-1 axis]. *Zhongguo Zhongyao Zazhi.* 44 (3), 546–552. doi:10.19540/j.cnki.cjcmm.20180925.001

Ma, W. G., Wang, J., Bu, X. W., Zhang, H. H., Zhang, J. P., Zhang, X. X., et al. (2019b). Effects of polygonum cuspidatum on AMPK-FOXO3alpha signaling pathway in rat model of uric acid-induced renal damage. *Chin. J. Integr. Med.* 25 (3), 182–189. doi:10.1007/s11655-017-2979-6

Ma, W. G., Wang, J., Bu, X. W., Zhang, H. H., Zhang, J. P., Zhang, X. X., et al. (2019c). Effects of polygonum cuspidatum on AMPK-FOXO3α signaling pathway in rat model of uric acid-induced renal damage. *Chin. J. Integr. Med.* 25 (3), 182–189. doi:10.1007/s11655-017-2979-6

Maiuolo, J., Oppedisano, F., Gratteri, S., Muscoli, C., and Mollace, V. (2016). Regulation of uric acid metabolism and excretion. *Int. J. Cardiol.* 213, 8–14. doi:10.1016/j.ijcard.2015.08.109

Major, T. J., Dalbeth, N., Stahl, E. A., and Merriman, T. R. (2018). An update on the genetics of hyperuricaemia and gout. *Nat. Rev. Rheumatol.* 14 (6), 341–353. doi:10.1038/s41584-018-0004-x

Mandal, A. K., and Mount, D. B. (2015). The molecular physiology of uric acid homeostasis. *Annu. Rev. Physiol.* 77, 323–345. doi:10.1146/annurev-physiol-021113-170343

Meng, Z., Yan, Y., Tang, Z., Guo, C., Li, N., Huang, W., et al. (2015). Anti-hyperuricemic and nephroprotective effects of rhein in hyperuricemic mice. *Planta Med.* 81 (4), 279–285. doi:10.1055/s-0034-1396241

Mittal, R., Patel, K., Mittal, J., Chan, B., Yan, D., Grati, M., et al. (2015). Association of PRPS1 mutations with disease phenotypes. *Dis. Markers.* 2015, 127013. doi:10.1155/2015/127013

Moher, D., Liberati, A., Tetzlaff, J., and Altman, D. G. (2009). Preferred reporting items for systematic reviews and meta-analyses: the PRISMA statement. *Ann. Intern. Med.* 151 (4), 264–269. doi:10.7326/0003-4819-151-4-200908180-00135

Niu, Y., Lu, W., Gao, L., Lin, H., Liu, X., and Li, L. (2012). Reducing effect of mangiferin on serum uric acid levels in mice. *Pharm. Biol.* 50 (9), 1177–1182. doi:10.3109/13880209.2012.663763

Niu, Y., Liu, J., Liu, H. Y., Gao, L. H., Feng, G. H., Liu, X., et al. (2016). Hypouricaemic action of mangiferin results from metabolite norathyriol via inhibiting xanthine oxidase activity. *Pharm. Biol.* 54 (9), 1680–1686. doi:10.3109/13880209.2015.1120322

Niu, Y., Zhou, Y., Lin, H., Gao, L. H., Xiong, W., Zhu, H., et al. (2018). Inhibition of 3,5,2',4'-tetrahydroxychalcone on production of uric acid in hypoxanthine-induced hyperuricemic mice. *Biol. Pharm. Bull.* 41 (1), 99–105. doi:10.1248/bpb.b17-00655

Pan, Y., Chu, Z., Wang, W., and Yang, B. (2013). Pretreatment with Jieduxiezhuo decoction impedes elevations in serum uric acid levels in mice. *J. Tradit. Chin. Med.* 33 (6), 794–797. doi:10.1016/s0254-6272(14)60014-5

Pan, H. Y., Shi, L., Xu, L., Yin, L., Zeng, W. P., Zhang, G. J., et al. (2014). Effect of active fractions from modified Simiao Wan on hyperuricemia and its mechanism. *Chin. J. Pharmacol. Toxicol.* 28 (3), 380–385. doi:10.3867/j.issn.1000-3002.2014.03.012

Pan, J., Shi, M., Li, L., Liu, J., Guo, F., Feng, Y., et al. (2019). Pterostilbene, a bioactive component of blueberries, alleviates renal fibrosis in a severe mouse model of hyperuricemic nephropathy. *Biomed. Pharmacother.* 109, 1802–1808. doi:10.1016/j.biopha.2018.11.022

Pan, J., Zhang, C., Shi, M., Guo, F., Liu, J., Li, L., et al. (2020). Ethanol extract of Liriodendron chinense (Hemsl.) Sarg barks attenuates hyperuricemic nephropathy by inhibiting renal fibrosis and inflammation in mice. *J. Ethnopharmacol.* 113278. doi:10.1016/j.jep.2020.113278

Pang, M., Fang, Y., Chen, S., Zhu, X., Shan, C., Su, J., et al. (2017). Gypenosides inhibits xanthine oxidoreductase and ameliorates urate excretion in hyperuricemic rats induced by high cholesterol and high fat food (lipid emulsion). *Med. Sci. Mon. Int. Med. J. Exp. Clin. Res.* 23, 1129–1140. doi:10.12659/msm.903217

Patel, S. (2018). Danger-Associated molecular patterns (DAMPs): the derivatives and triggers of inflammation. *Curr. Allergy Asthma Rep.* 18 (11), 63. doi:10.1007/s11882-018-0817-3

Peng, A., Lin, L., Zhao, M., and Sun, B. (2019). Identifying mechanisms underlying the amelioration effect of Chrysanthemum morifolium Ramat. 'Boju' extract on hyperuricemia using biochemical characterization and UPLC-ESI-QTOF/MS-based metabolomics. *Food Funct.* 10 (12), 8042–8055. doi:10.1039/c9fo01821b

Preitner, F., Bonny, O., Laverriere, A., Rotman, S., Firsov, D., Da Costa, A., et al. (2009). Glut9 is a major regulator of urate homeostasis and its genetic inactivation induces hyperuricosuria and urate nephropathy. *Proc. Natl. Acad. Sci. U. S. A.* 106 (36), 15501–15506. doi:10.1073/pnas.0904411106

Qin, Z., Wang, S., Lin, Y., Zhao, Y., Yang, S., Song, J., et al. (2018). Antihyperuricemic effect of mangiferin aglycon derivative J99745 by inhibiting xanthine oxidase activity and urate transporter 1 expression in mice. *Acta Pharm. Sin. B.* 8 (2), 306–315. doi:10.1016/j.apsb.2017.05.004

Rai, S. K., Burns, L. C., De Vera, M. A., Haji, A., Giustini, D., and Choi, H. K. (2015). The economic burden of gout: a systematic review. *Semin. Arthritis Rheum* 45 (1), 75–80. doi:10.1016/j.semarthrit.2015.02.004

Rozza, F., Trimarco, V., Izzo, R., Grassi, D., and Ferri, C. (2016). Effects of a novel fixed combination of nutraceuticals on serum uric acid concentrations and the lipid profile in asymptomatic hyperuricemic patients : results from the PICONZ-UA study. *High Blood Pres. Cardiovasc. Prev.* 23 (4), 381–386. doi:10.1007/s40292-016-0168-x

Sato, Y., Feig, D. I., Stack, A. G., Kang, D. H., Lanaspa, M. A., Ejaz, A. A., et al. (2019). The case for uric acid-lowering treatment in patients with hyperuricaemia and CKD. *Nat. Rev. Nephrol.* doi:10.1038/s41581-019-0174-z

Shan, H. L., Shan, R. P., and Fu, X. C. (2015). [Hypouricemic effect of ethanol extracts from dioscoreae nipponicae rhizoma]. *Zhejiang Da Xue Xue Bao Yi Xue Ban.* 44 (1), 49–53

Shang, X. Z., Ma, W. G., Chen, Y., Lu, Y., Wang, Y. N., Xu, Y. M., et al. (2014). [Effect of compound qingqin liquid on the expression levels of ang II and COX-2 mRNA transcription and protein expression in the renal tissue of uric acid nephropathy rats: an experimental study]. *Zhongguo Zhong Xi Yi Jie He Za Zhi.* 34 (7), 819–825

Sheu, S. Y., Fu, Y. T., Huang, W. D., Chen, Y. A., Lei, Y. C., Yao, C. H., et al. (2016). Evaluation of xanthine oxidase inhibitory potential and in vivo hypouricemic activity of dimocarpus longan lour. Extracts. *Phcog. Mag.* 12 (Suppl. 2), S206–S212. doi:10.4103/0973-1296.182176

Shi, Y. W., Wang, C. P., Wang, X., Zhang, Y. L., Liu, L., Wang, R. W., et al. (2012). Uricosuric and nephroprotective properties of Ramulus Mori ethanol extract in hyperuricemic mice. *J. Ethnopharmacol.* 143 (3), 896–904. doi:10.1016/j.jep.2012.08.023

Shi, L., Xu, L., Yang, Y., Song, H., Pan, H., and Yin, L. (2013). Suppressive effect of modified Simiaowan on experimental gouty arthritis: an *in vivo* and *in vitro* study. *J. Ethnopharmacol.* 150 (3), 1038–1044. doi:10.1016/j.jep.2013.10.023

Shi, L., Zhao, F., Zhu, F., Liang, Y., Yang, F., Zhang, G., et al. (2016a). Traditional Chinese Medicine Formula "Xiaofeng granules" suppressed gouty arthritis animal models and inhibited the proteoglycan degradation on chondrocytes induced by monosodium urate. *J. Ethnopharmacol.* 191, 254–263. doi:10.1016/j.jep.2016.06.008

Shi, Y. C., Lin, K. S., Jhai, Y. F., Lee, B. H., Han, Y., Cui, Z., et al. (2016b). Miracle fruit (synsepalum dulcificum) exhibits as a novel anti-hyperuricaemia agent. *Molecules.* 21 (2), 140. doi:10.3390/molecules21020140

Silva, C. R., Frohlich, J. K., Oliveira, S. M., Cabreira, T. N., Rossato, M. F., Trevisan, G., et al. (2013). The antinociceptive and anti-inflammatory effects of the crude extract of Jatropha isabellei in a rat gout model. *J. Ethnopharmacol.* 145 (1), 205–213. doi:10.1016/j.jep.2012.10.054

Singh, A. K., Haque, M., O'Sullivan, K., Chourasia, M., Ouseph, M. M., and Ahmed, S. (2019). Suppression of monosodium urate crystal-induced inflammation by inhibiting TGF-beta-activated kinase 1-dependent signaling: role of the ubiquitin proteasome system. *Cell. Mol. Immunol.* doi:10.1038/s41423-019-0284-3

So, A. K., and Martinon, F. (2017). Inflammation in gout: mechanisms and therapeutic targets. *Nat. Rev. Rheumatol.* 13 (11), 639–647. doi:10.1038/nrrheum.2017.155

Song, S. H., Park, D. H., Bae, M. S., Choi, C. Y., Shim, J. H., Yoon, G., et al. (2018). Ethanol extract of cudrania tricuspidata leaf ameliorates hyperuricemia in mice via inhibition of hepatic and serum xanthine oxidase activity. *Evid Based Complement Alternat Med.* 2018, 8037925. doi:10.1155/2018/8037925

Spiga, R., Marini, M. A., Mancuso, E., Di Fatta, C., Fuoco, A., Perticone, F., et al. (2017). Uric acid is associated with inflammatory biomarkers and induces inflammation via activating the NF-kappaB signaling pathway in HepG2 cells. *Arterioscler. Thromb. Vasc. Biol.* 37 (6), 1241–1249. doi:10.1161/atvbaha.117.309128

Strilchuk, L., Fogacci, F., and Cicero, A. F. (2019). Safety and tolerability of available urate-lowering drugs: a critical review. *Expet Opin. Drug Saf.* 18 (4), 261–271. doi:10.1080/14740338.2019.1594771

Su, J., Wei, Y., Liu, M., Liu, T., Li, J., Ji, Y., et al. (2014). Anti-hyperuricemic and nephroprotective effects of Rhizoma Dioscoreae septemlobae extracts and its main component dioscin via regulation of mOAT1, mURAT1 and mOCT2 in hypertensive mice. *Arch Pharm. Res. (Seoul).* 37 (10), 1336–1344. doi:10.1007/s12272-014-0413-6

Su, Q., Su, H., Nong, Z., Li, D., Wang, L., Chu, S., et al. (2018). Hypouricemic and nephroprotective effects of an active fraction from polyrhachis vicina roger on potassium oxonate-induced hyperuricemia in rats. *Kidney Blood Press. Res.* 43 (1), 220–233. doi:10.1159/000487675

Sun, W. F., Zhu, M. M., Li, J., Zhang, X. X., Liu, Y. W., Wu, X. R., et al. (2015). Effects of Xie-Zhuo-Chu-Bi-Fang on miR-34a and URAT1 and their relationship in hyperuricemic mice. *J. Ethnopharmacol.* 161, 163–169. doi:10.1016/j.jep.2014.12.001

Sundy, J. S., Schumacher, H. R., Kivitz, A., Weinstein, S. P., Wu, R., King-Davis, S., et al. (2014). Rilonacept for gout flare prevention in patients receiving uric acid-lowering therapy: results of RESURGE, a phase III, international safety study. *J. Rheumatol.* 41 (8), 1703–1711. doi:10.3899/jrheum.131226

Szekanecz, Z., Szamosi, S., Kovacs, G. E., Kocsis, E., and Benko, S. (2019). The NLRP3 inflammasome - interleukin 1 pathway as a therapeutic target in gout. *Arch. Biochem. Biophys.* 670, 82–93. doi:10.1016/j.abb.2019.01.031

Tang, R. B., Dong, J. Z., Yan, X. L., Du, X., Kang, J. P., Wu, J. H., et al. (2014). Serum uric acid and risk of left atrial thrombus in patients with nonvalvular atrial fibrillation. *Can. J. Cardiol.* 30 (11), 1415–1421. doi:10.1016/j.cjca.2014.06.009

Tang, H., Yang, L., Li, W., Li, J., and Chen, J. (2016). Exploring the interaction between Salvia miltiorrhiza and xanthine oxidase: insights from computational analysis and experimental studies combined with enzyme channel blocking. *RSC Adv.* 6 (114), 113527–113537. doi:10.1039/c6ra24396g

Tang, L., Xu, Y., Wei, Y., and He, X. (2017). Uric acid induces the expression of TNFalpha via the ROSMAPKNFkappaB signaling pathway in rat vascular smooth muscle cells. *Mol. Med. Rep.* 16 (5), 6928–6933. doi:10.3892/mmr.2017.7405

Tian, C., Wang, Y., Chang, H., Li, J., and La, X. (2018). Spleen-kidney supplementing formula alleviates renal fibrosis in diabetic rats via TGF-β 1-miR-21-PTEN signaling pathway. *Evid. base Compl. Alternative Med.* 2018, 1–9. doi:10.1155/2018/3824357

Tung, Y. T., Lin, L. C., Liu, Y. L., Ho, S. T., Lin, C. Y., Chuang, H. L., et al. (2015). Antioxidative phytochemicals from Rhododendron oldhamii Maxim. leaf extracts reduce serum uric acid levels in potassium oxonate-induced hyperuricemic mice. *BMC Compl. Alternative Med.* 15, 423. doi:10.1186/s12906-015-0950-7

Wang, C. P., Wang, X., Zhang, X., Shi, Y. W., Liu, L., and Kong, L. D. (2010a). Morin improves urate excretion and kidney function through regulation of renal organic ion transporters in hyperuricemic mice. *J. Pharm. Pharmaceut. Sci.* 13 (3), 411–427. doi:10.18433/j3q30h

Wang, X., Wang, C. P., Hu, Q. H., Lv, Y. Z., Zhang, X., Ouyang, Z., et al. (2010b). The dual actions of Sanmiao wan as a hypouricemic agent: down-regulation of

hepatic XOD and renal mURAT1 in hyperuricemic mice. *J. Ethnopharmacol.* 128 (1), 107–115. doi:10.1016/j.jep.2009.12.035

Wang, C. P., Wang, Y., Wang, X., Zhang, X., Ye, J. F., Hu, L. S., et al. (2011). Mulberroside a possesses potent uricosuric and nephroprotective effects in hyperuricemic mice. *Planta Med.* 77 (8), 786–794. doi:10.1055/s-0030-1250599

Wang, Y., Wang, L., Li, E., Li, Y., Wang, Z., Sun, X., et al. (2014). Chuanhu anti-gout mixture versus colchicine for acute gouty arthritis: a randomized, double-blind, double-dummy, non-inferiority trial. *Int. J. Med. Sci.* 11 (9), 880–885. doi:10.7150/ijms.9165

Wang, M. X., Liu, Y. L., Yang, Y., Zhang, D. M., and Kong, L. D. (2015). Nuciferine restores potassium oxonate-induced hyperuricemia and kidney inflammation in mice. *Eur. J. Pharmacol.* 747, 59–70. doi:10.1016/j.ejphar.2014.11.035

Wang, J., Xu, B. B., Zeng, J. X., Zhu, J. X., Wang, X. Y., Ren, G., et al. (2016a). Effect of Dendropanaxchevalieri extracts on uric acid level in hyperuricemic mice and the possible mechanism. *Chinese Journal of New Drugs.* 25 (3), 334–338

Wang, R., Ma, C. H., Zhou, F., and Kong, L. D. (2016b). Siwu decoction attenuates oxonate-induced hyperuricemia and kidney inflammation in mice. *Chin. J. Nat. Med.* 14 (7), 499–507. doi:10.1016/s1875-5364(16)30059-0

Wang, W. L., Sheu, S. Y., Huang, W. D., Chuang, Y. L., Tseng, H. C., Hwang, T. S., et al. (2016c). Phytochemicals from tradescantia albiflora kunth extracts reduce serum uric acid levels in oxonate-induced rats. *Phcog. Mag.* 12 (Suppl. 2), S223–S227. doi:10.4103/0973-1296.182171

Wang, X. Y., Zhou, J. B., Shi, B., Guo, X. L., and Yan, Q. C. (2016d). Hypouricemic and nephroprotective effects of Jianpi Huashi decoction in a rat model of hyperuricemia. *Int. J. Clin. Exp. Med.* 9 (1), 455–465

Wang, Y., Zhao, M., Xin, Y., Liu, J., Wang, M., and Zhao, C. (2016e). (1)H NMR and MS based metabolomics study of the therapeutic effect of Cortex Fraxini on hyperuricemic rats. *J. Ethnopharmacol.* 185, 272–281. doi:10.1016/j.jep.2016.03.043

Wang, Y., Lin, Z., Zhang, B., Nie, A., and Bian, M. (2017a). Cichorium intybus L. promotes intestinal uric acid excretion by modulating ABCG2 in experimental hyperuricemia. *Nutr. Metab.* 14, 38. doi:10.1186/s12986-017-0190-6

Wang, Y., Lin, Z. J., Nie, A. Z., Li, L. Y., and Zhang, B. (2017b). [Effect of Chinese herb chicory extract on expression of renal transporter Glut9 in rats with hyperuricemia]. *Zhongguo Zhongyao Zazhi.* 42 (5), 958–963. doi:10.19540/j.cnki.cjcmm.2017.0029

Wang, Y., Zhao, M., Ye, H., Shao, Y., Yu, Y., Wang, M., et al. (2017c). Comparative pharmacokinetic study of the main components of cortex fraxini after oral administration in normal and hyperuricemic rats. *Biomed. Chromatogr.* 31 (8), e3934. doi:10.1002/bmc.3934

Wang, Q., Yang, Q., Cao, X., Wei, Q., Firempong, C. K., Guo, M., et al. (2018). Enhanced oral bioavailability and anti-gout activity of [6]-shogaol-loaded solid lipid nanoparticles. *Int. J. Pharm.* 550 (1-2), 24–34. doi:10.1016/j.ijpharm.2018.08.028

Wang, S., Fang, Y., Yu, X., Guo, L., Zhang, X., and Xia, D. (2019a). The flavonoid-rich fraction from rhizomes of Smilax glabra Roxb. ameliorates renal oxidative stress and inflammation in uric acid nephropathy rats through promoting uric acid excretion. *Biomed. Pharmacother.* 111, 162–168. doi:10.1016/j.biopha.2018.12.050

Wang, Y., Dong, L., Liu, P., Chen, Y., Jia, S., and Wang, Y. (2019b). A randomized controlled trial of chuanhutongfeng mixture for the treatment of chronic gouty arthritis by regulating miRNAs. *Evid Based Complement Alternat Med.* 2019, 5917269. doi:10.1155/2019/5917269

Wang, Y., Lin, Z., Zhang, B., Jiang, Z., Guo, F., and Yang, T. (2019c). Cichorium intybus L. Extract suppresses experimental gout by inhibiting the NF-kappaB and NLRP3 signaling pathways. *Int. J. Mol. Sci.* 20 (19). doi:10.3390/ijms20194921

Wang, Y., Lin, Z., Zhang, B., Wang, X., and Chu, M. (2019d). Chicory (Cichorium intybus L.) inhibits renal reabsorption by regulating expression of urate transporters in fructose-induced hyperuricemia. *Journal of Traditional Chinese Medical Sciences.* 6 (1), 84–94. doi:10.1016/j.jtcms.2019.01.001

Wang, Z., Ci, X. Y., Cui, T., Wei, Z. H., Zhang, H. B., Liu, R., et al. (2019e). Effects of Chinese herb ingredients with different properties on OAT4, URAT1 and serum uric acid level in acute hyperuricemia mice. *Chin. Tradit. Herb. Drugs.* 50 (5), 1157–1163. doi:10.7501/j.issn.0253-2670.2019.05.020

Wasilewska, A., Tenderenda, E., Taranta-Janusz, K., Tobolczyk, J., and Stypulkowska, J. (2012). Markers of systemic inflammation in children with hyperuricemia. *Acta Paediatr.* 101 (5), 497–500. doi:10.1111/j.1651-2227.2011.02582.x

Wei, G. N., Su, Q. B., He, F., Zeng, X. B., Ya, Q. K., Lü, J. H., et al. (2013). Screening and chemical component analysis of anti-hyperuricemic active fraction of ethanol extract from Polyrhachis vicina Roger in hyperuricemia model mice. *Chin. J. Pharmacol. Toxicol.* 27 (4), 673–677. doi:10.3867/j.issn.1000-3002.2013.04.012

Wei, Z., Xu, C., Liu, S., Song, F., Liu, Z., and Qu, X. (2018). Metabonomics study of the effects of traditional Chinese medicine formula Ermiaowan on hyperuricemic rats. *J. Separ. Sci.* 41 (2), 560–570. doi:10.1002/jssc.201700985

White, W. B., Saag, K. G., Becker, M. A., Borer, J. S., Gorelick, P. B., Whelton, A., et al. (2018). Cardiovascular safety of febuxostat or allopurinol in patients with gout. *N. Engl. J. Med.* 378 (13), 1200–1210. doi:10.1056/NEJMoa1710895

Woodward, O. M., Kottgen, A., Coresh, J., Boerwinkle, E., Guggino, W. B., and Kottgen, M. (2009). Identification of a urate transporter, ABCG2, with a common functional polymorphism causing gout. *Proc. Natl. Acad. Sci. U. S. A.* 106 (25), 10338–10342. doi:10.1073/pnas.0901249106

Wright, A. F., Rudan, I., Hastie, N. D., and Campbell, H. (2010). A 'complexity' of urate transporters. *Kidney Int.* 78 (5), 446–452. doi:10.1038/ki.2010.206

Wu, X., Liu, L., Xie, H., Liao, J., Zhou, X., Wan, J., et al. (2012a). Tanshinone IIA prevents uric acid nephropathy in rats through NF-kappaB inhibition. *Planta Med.* 78 (9), 866–873. doi:10.1055/s-0031-1298487

Wu, X., Liu, L., Xie, H., Liao, J., Zhou, X., Wan, J., et al. (2012b). Tanshinone IIA prevents uric acid nephropathy in rats through NF-κB inhibition. *Planta Med.* 78 (9), 866–873. doi:10.1055/s-0031-1298487

Wu, X. H., Ruan, J. L., Zhang, J., Wang, S. Q., and Zhang, Y. W. (2014a). Pallidifloside D, a saponin glycoside constituent from Smilax riparia, resist to hyperuricemia based on URAT1 and GLUT9 in hyperuricemic mice. *J. Ethnopharmacol.* 157, 201–205. doi:10.1016/j.jep.2014.09.034

Wu, X. H., Wang, C. Z., Zhang, J., Wang, S. Q., Han, L., Zhang, Y. W., et al. (2014b). Effects of Smilaxchinoside A and Smilaxchinoside C, two steroidal glycosides from Smilax riparia, on hyperuricemia in a mouse model. *Phytother Res.* 28 (12), 1822–1828. doi:10.1002/ptr.5207

Wu, X. H., Yu, C. H., Zhang, C. F., Anderson, S., and Zhang, Y. W. (2014c). Smilax riparia reduces hyperuricemia in mice as a potential treatment of gout. *Am. J. Chin. Med.* 42 (1), 257–259. doi:10.1142/s0192415x14200018

Wu, X. H., Zhang, J., Wang, S. Q., Yang, V. C., Anderson, S., and Zhang, Y. W. (2014d). Riparoside B and timosaponin J, two steroidal glycosides from Smilax riparia, resist to hyperuricemia based on URAT1 in hyperuricemic mice. *Phytomedicine.* 21 (10), 1196–1201. doi:10.1016/j.phymed.2014.03.009

Wu, X. H., Wang, C. Z., Wang, S. Q., Mi, C., He, Y., Zhang, J., et al. (2015). Anti-hyperuricemia effects of allopurinol are improved by Smilax riparia, a traditional Chinese herbal medicine. *J. Ethnopharmacol.* 162, 362–368. doi:10.1016/j.jep.2015.01.012

Wu, Y., He, F., Li, Y., Wang, H., Shi, L., Wan, Q., et al. (2017). Effects of shizhifang on NLRP3 inflammasome activation and renal tubular injury in hyperuricemic rats. *Evid Based Complement Alternat Med.* 2017, 7674240. doi:10.1155/2017/7674240

Wu, P., Li, J., Zhang, X., Zeng, F., Liu, Y., and Sun, W. (2018a). Study of the treatment effects of compound tufuling granules in hyperuricemic rats using serum metabolomics. *Evid Based Complement Alternat Med.* 2018, 3458185. doi:10.1155/2018/3458185

Wu, Y., Wang, Y., Ou, J., Wan, Q., Shi, L., Li, Y., et al. (2018b). Effect and mechanism of ShiZhiFang on uric acid metabolism in hyperuricemic rats. *Evid Based Complement Alternat Med.* 2018, 6821387. doi:10.1155/2018/6821387

Xia, N., Li, B. A., Liu, H. J., Fan, J. B., Shen, W., and He, X. G. (2017). Anti-hyperuricemic effect of Plantago depressa Willd extract in rats. *Trop. J. Pharmaceut. Res.* 16 (6), 1365–1368. doi:10.4314/tjpr.v16i6.21

Xiang, S. W., Lai, S. C., and Meng, Y. H. (2009). [Clinical study on modified sanmiao powder in treating chronic uric acid nephropathy]. *Zhongguo Zhong Xi Yi Jie He Za Zhi.* 29 (11), 979–981

Xie, Z., Wu, H., Jing, X., Li, X., Li, Y., Han, Y., et al. (2017). Hypouricemic and arthritis relapse-reducing effects of compound tufuling oral-liquid in intercritical and chronic gout: a double-blind, placebo-controlled, multicenter randomized trial. *Medicine (Baltim.).* 96 (11), e6315. doi:10.1097/MD.0000000000006315

Xiong, W. W., Zhang, H. Y., Wen, L., Wang, X. Y., Zhong, G. Y., Shi, Y. F., et al. (2018). Effect of Lagotis brachystachys Maxim extract on xanthine oxidase and

renal urate transporters in hyperuricemia mice. *Chinese Journal of New Drugs.* 27 (13), 1538–1543

Xu, W. A., Yin, L., Pan, H. Y., Shi, L., Xu, L., Zhang, X., et al. (2013). Study on the correlation between constituents detected in serum from Rhizoma Smilacis Glabrae and the reduction of uric acid levels in hyperuricemia. *J. Ethnopharmacol.* 150 (2), 747–754. doi:10.1016/j.jep.2013.09.024

Xu, C., Wan, X., Xu, L., Weng, H., Yan, M., Miao, M., et al. (2015). Xanthine oxidase in non-alcoholic fatty liver disease and hyperuricemia: one stone hits two birds. *J. Hepatol.* 62 (6), 1412–1419. doi:10.1016/j.jhep.2015.01.019

Xu, K., Liu, S., Zhao, X., Zhang, X., Fu, X., Zhou, Y., et al. (2019). Treating hyperuricemia related non-alcoholic fatty liver disease in rats with resveratrol. *Biomed. Pharmacother.* 110, 844–849. doi:10.1016/j.biopha.2018.12.039

Yan, M., An, Y. T., Li, J., Wu, Z. Z., and Wang, T. (2014). [Regulatory effect of leonurus extracts on hyperuricemia in rats]. *Zhongguo Zhongyao Zazhi.* 39 (24), 4856–4859

Yang, H. X., Su, J. X., Jiang, G. Q., and Chen, X. P. (2013). Effect of Tongxi Powder on blood uric acid of mice with acute hyperuricemia. *Chin. Tradit. Herb. Drugs.* 44 (12), 1635–1637. doi:10.7501/j.issn.0253-2670.2013.12.021

Yang, Y., Zhang, D. M., Liu, J. H., Hu, L. S., Xue, Q. C., Ding, X. Q., et al. (2015). Wuling San protects kidney dysfunction by inhibiting renal TLR4/MyD88 signaling and NLRP3 inflammasome activation in high fructose-induced hyperuricemic mice. *J. Ethnopharmacol.* 169, 49–59. doi:10.1016/j.jep.2015.04.011

Yang, A., Guo, H., Fu, M., and Liu, M. (2019a). Inhibitive effects of huashi pill on formation of renal stones by modulating urine biochemical indexes and osteopontin in renal stone rat models. *Med. Sci. Mon. Int. Med. J. Exp. Clin. Res.* 25, 8335–8344. doi:10.12659/msm.916247

Yang, L. X., Xue, J. J., Meng, X. Y., Wang, Y. S., Wu, L. L., Lv, C. Y., et al. (2019b). Effects of total flavonoids from Oxytropis falcata Bunge on the SOCS/JAK/STAT inflammatory signaling pathway in the kidneys of diabetic nephropathy model mice. *Eur. J. Inflamm.* 17. doi:10.1177/2058739219861877

Yang, T. H., Yan, D. X., Huang, X. Y., Hou, B., Ma, Y. B., Peng, H., et al. (2019c). Termipaniculatones A-F, chalcone-flavonone heterodimers from Terminthia paniculata, and their protective effects on hyperuricemia and acute gouty arthritis. *Phytochemistry.* 164, 228–235. doi:10.1016/j.phytochem.2019.05.019

Yang, Y., Zhang, L., Jiang, G., Lei, A., Yu, Q., Xie, J., et al. (2019d). Evaluation of the protective effects of Ganoderma atrum polysaccharide on acrylamide-induced injury in small intestine tissue of rats. *Food Funct.* 10 (9), 5863–5872. doi:10.1039/c9fo01452g

Yao, L., Dong, W., Lu, F., and Liu, S. (2012). An improved acute gouty arthritis rat model and therapeutic effect of rhizoma Dioscoreae nipponicae on acute gouty arthritis based on the protein-chip methods. *Am. J. Chin. Med.* 40 (1), 121–134. doi:10.1142/s0192415x12500103

Yao, R., Geng, Z., Mao, X., Bao, Y., Guo, S., Bao, L., et al. (2020). Tu-teng-cao extract alleviates monosodium urate-induced acute gouty arthritis in rats by inhibiting uric acid and inflammation. *Evid Based Complement Alternat Med.* 2020, 3095624. doi:10.1155/2020/3095624

Ye, Y., Zhang, Y., Wang, B., Walana, W., Wei, J., Gordon, J. R., et al. (2018). CXCR1/CXCR2 antagonist G31P inhibits nephritis in a mouse model of uric acid nephropathy. *Biomed. Pharmacother.* 107, 1142–1150. doi:10.1016/j.biopha.2018.07.077

Yi, L. T., Li, J., Su, D. X., Dong, J. F., and Li, C. F. (2012). Hypouricemic effect of the methanol extract from Prunus mume fruit in mice. *Pharm. Biol.* 50 (11), 1423–1427. doi:10.3109/13880209.2012.683115

Yin, W., Zhou, Q. L., OuYang, S. X., Chen, Y., Gong, Y. T., and Liang, Y. M. (2019). Uric acid regulates NLRP3/IL-1beta signaling pathway and further induces vascular endothelial cells injury in early CKD through ROS activation and K(+) efflux. *BMC Nephrol.* 20 (1), 319. doi:10.1186/s12882-019-1506-8

Yong, T., Zhang, M., Chen, D., Shuai, O., Chen, S., Su, J., et al. (2016). Actions of water extract from Cordyceps militaris in hyperuricemic mice induced by potassium oxonate combined with hypoxanthine. *J. Ethnopharmacol.* 194, 403–411. doi:10.1016/j.jep.2016.10.001

Yong, T., Chen, S., Xie, Y., Chen, D., Su, J., Shuai, O., et al. (2017). Hypouricemic effects of ganoderma applanatum in hyperuricemia mice through OAT1 and GLUT9. *Front. Pharmacol.* 8, 996. doi:10.3389/fphar.2017.00996

Yoon, I. S., Park, D. H., Ki, S. H., and Cho, S. S. (2016). Effects of extracts from Corylopsis coreana Uyeki (Hamamelidaceae) flos on xanthine oxidase activity and hyperuricemia. *J. Pharm. Pharmacol.* 68 (12), 1597–1603. doi:10.1111/jphp.12626

Yoon, I. S., Park, D. H., Bae, M. S., Oh, D. S., Kwon, N. H., Kim, J. E., et al. (2017a). In Vitro and in vivo studies on quercus acuta thunb. (Fagaceae) extract: active constituents, serum uric acid suppression, and xanthine oxidase inhibitory activity, *Evid. Based Complement. Alternat. Med.* 2017, 4097195. doi:10.1155/2017/4097195

Yoon, I. S., Park, D. H., Kim, J. E., Yoo, J. C., Bae, M. S., Oh, D. S., et al. (2017b). Identification of the biologically active constituents of Camellia japonica leaf and anti-hyperuricemic effect *in vitro* and *in vivo*. *Int. J. Mol. Med.* 39 (6), 1613–1620. doi:10.3892/ijmm.2017.2973

You, W., Wang, J., Zou, Y., Che, K., Hou, X., Fei, H., et al. (2019). Modified Chuanhu anti-gout mixture, a traditional Chinese medicine, protects against potassium oxonate-induced hyperuricemia and renal dysfunction in mice. *J. Int. Med. Res.* 47 (5), 1927–1935. doi:10.1177/0300060519831182

Yu, X. N., Wu, H. Y., Deng, Y. P., Zhuang, G. T., Tan, B. H., Huang, Y. Z., et al. (2018). Yellow-dragon Wonderful-seed Formula" for hyperuricemia in gout patients with dampness-heat pouring downward pattern: a pilot randomized controlled trial. *Trials.* 19 (1), 551. doi:10.1186/s13063-018-2917-8

Yuan, X., Fan, Y. S., Xu, L., Xie, G. Q., Feng, X. H., and Qian, K. (2019). Jia-Wei-Si-Miao-Wan alleviates acute gouty arthritis by targeting NLRP3 inflammasome. *J. Biol. Regul. Homeost. Agents.* 33 (1), 63–71

Yuk, H. J., Lee, Y. S., Ryu, H. W., Kim, S. H., and Kim, D. S. (2018). Effects of toona sinensis leaf extract and its chemical constituents on xanthine oxidase activity and serum uric acid levels in potassium oxonate-induced hyperuricemic rats. *Molecules.* 23 (12). doi:10.3390/molecules23123254

Zamudio-Cuevas, Y., Hernandez-Diaz, C., Pineda, C., Reginato, A. M., Cerna-Cortes, J. F., Ventura-Rios, L., et al. (2015). Molecular basis of oxidative stress in gouty arthropathy. *Clin. Rheumatol.* 34 (10), 1667–1672. doi:10.1007/s10067-015-2933-y

Zeng, J. X., Xu, B. B., Li, M., Li, X. W., Zhu, J. X., Wang, X. Y., et al. (2015). Effect of Lagotis brevituba Maxim. extract in reducing uric acid level in hyperuricemia mice and it's mechanism. *Chinese Journal of New Drugs.* 24 (21), 2489–2493

Zhang, M., Wang, J. F., and Wang, Y. F. (2009). [Effects of serial gout granules on insulin-resistance in primary gout patients]. *Zhongguo Zhong Xi Yi Jie He Za Zhi.* 29 (12), 1068–1072

Zhang, X. X., Sun, W. F., and Xu, W. (2011). [Assessment on the clinical efficacy and safety of xiezhuo chubi recipe in treating hyperuricemia]. *Zhongguo Zhong Xi Yi Jie He Za Zhi.* 31 (9), 1216–1219

Zhang, D. M., Li, Y. C., Xu, D., Ding, X. Q., and Kong, L. D. (2012). Protection of curcumin against fructose-induced hyperuricaemia and renal endothelial dysfunction involves NO-mediated JAK-STAT signalling in rats. *Food Chem.* 134 (4), 2184–2193. doi:10.1016/j.foodchem.2012.04.026

Zhang, Z. C., Su, G. H., Luo, C. L., Pang, Y. L., Wang, L., Li, X., et al. (2015). Effects of anthocyanins from purple sweet potato (Ipomoea batatas L. cultivar Eshu No. 8) on the serum uric acid level and xanthine oxidase activity in hyperuricemic mice. *Food Funct.* 6 (9), 3045–3055. doi:10.1039/c5fo00499c

Zhang, H. J., Li, L. N., Zhou, J., Yang, Q. Q., Liu, P. G., Xu, P., et al. (2017a). Effects of Gnaphalium affine D. Don on hyperuricemia and acute gouty arthritis. *J. Ethnopharmacol.* 203, 304–311. doi:10.1016/j.jep.2017.03.057

Zhang, S., Zhuang, J., Yue, G., Wang, Y., Liu, M., Zhang, B., et al. (2017b). Lipidomics to investigate the pharmacologic mechanisms of ginkgo folium in the hyperuricemic rat model. *J Chromatogr B Analyt Technol Biomed Life Sci.* 1060, 407–415. doi:10.1016/j.jchromb.2017.06.037

Zhang, R., Zhan, S., Li, S., Zhu, Z., He, J., Lorenzo, J. M., et al. (2018a). Anti-hyperuricemic and nephroprotective effects of extracts from Chaenomeles sinensis (Thouin) Koehne in hyperuricemic mice. *Food Funct.* 9 (11), 5778–5790. doi:10.1039/c8fo01480a

Zhang, Y., Jin, L., Liu, J., Wang, W., Yu, H., Li, J., et al. (2018b). Effect and mechanism of dioscin from Dioscorea spongiosa on uric acid excretion in animal model of hyperuricemia. *J. Ethnopharmacol.* 214, 29–36. doi:10.1016/j.jep.2017.12.004

Zhang, W., Du, W., Li, G., Zhang, C., Yang, W., Yang, S., et al. (2019a). Constituents and anti-hyperuricemia mechanism of traditional Chinese herbal formulae erding granule. *Molecules.* 24 (18). doi:10.3390/molecules24183248

Zhang, X. Y., Cheng, J., Zhao, P., Chen, K. L., and Li, J. (2019b). Screening the best compatibility of selaginella moellendorffii prescription on hyperuricemia and gouty arthritis and its mechanism. *Evid Based Complement Alternat Med.* 2019, 7263034. doi:10.1155/2019/7263034

Zhang, Z. C., Zhou, Q., Yang, Y., Wang, Y., and Zhang, J. L. (2019c). Highly acylated anthocyanins from purple sweet potato (Ipomoea batatas L.) alleviate hyperuricemia and kidney inflammation in hyperuricemic mice: possible attenuation effects on allopurinol. *J. Agric. Food Chem.* 67 (22), 6202–6211. doi:10.1021/acs.jafc.9b01810

Zhao, P., Chen, K. L., Zhang, G. L., Deng, G. R., and Li, J. (2017). Pharmacological basis for use of selaginella moellendorffii in gouty arthritis: antihyperuricemic, anti-inflammatory, and xanthine oxidase inhibition. *Evid Based Complement Alternat Med.* 2017, 2103254. doi:10.1155/2017/2103254

Zhao, J., Lv, C., Wu, Q., Zeng, H., Guo, X., Yang, J., et al. (2019). Computational systems pharmacology reveals an antiplatelet and neuroprotective mechanism of Deng-Zhan-Xi-Xin injection in the treatment of ischemic stroke. *Pharmacol. Res.* 147, 104365. doi:10.1016/j.phrs.2019.104365

Zhou, M., Wang, Y. F., Zhou, R., Zhang, M., and Li, B. (2013). [Treatment of gouty arthritis in different phases by a series of tongfeng granule: an efficacy observation]. *Zhongguo Zhong Xi Yi Jie He Za Zhi.* 33 (12), 1603–1607

Zhou, Q., Yu, D. H., Zhang, C., Liu, S. M., and Lu, F. (2014). Total saponins from Discorea nipponica ameliorate urate excretion in hyperuricemic mice. *Planta Med.* 80 (15), 1259–1268. doi:10.1055/s-0034-1383048

Zhou, Q., Yu, D. H., Liu, S. M., and Liu, Y. (2015). Total saponins from Discorea nipponica makino ameliorate urate excretion in hyperuricemic rats. *Phcog. Mag.* 11 (43), 567–573. doi:10.4103/0973-1296.160442

Zhou, W., Wang, J., Wu, Z., Huang, C., Lu, A., and Wang, Y. (2016). Systems pharmacology exploration of botanic drug pairs reveals the mechanism for treating different diseases. *Sci. Rep.* 6, 36985. doi:10.1038/srep36985

Zhou, Q., Lin, F. F., Liu, S. M., and Sui, X. F. (2017). Influence of the total saponin fraction from Dioscorea nipponica Makino on TLR2/4-IL1R receptor singnal pathway in rats of gouty arthritis. *J. Ethnopharmacol.* 206, 274–282. doi:10.1016/j.jep.2017.04.024

Zhou, Y., Zhang, X., Li, C., Yuan, X., Han, L., Li, Z., et al. (2018a). Research on the pharmacodynamics and mechanism of Fraxini Cortex on hyperuricemia based on the regulation of URAT1 and GLUT9. *Biomed. Pharmacother.* 106, 434–442. doi:10.1016/j.biopha.2018.06.163

Zhou, Y., Zhao, M., Pu, Z., Xu, G., and Li, X. (2018b). Relationship between oxidative stress and inflammation in hyperuricemia: analysis based on asymptomatic young patients with primary hyperuricemia. *Medicine (Baltim.).* 97 (49), e13108. doi:10.1097/md.0000000000013108

Zhu, W., Pang, M., Dong, L., Huang, X., Wang, S., and Zhou, L. (2012). Anti-inflammatory and immunomodulatory effects of iridoid glycosides from Paederia scandens (LOUR.) MERRILL (Rubiaceae) on uric acid nephropathy rats. *Life Sci.* 91 (11-12), 369–376. doi:10.1016/j.lfs.2012.08.013

Zhu, F., Yin, L., Ji, L., Yang, F., Zhang, G., Shi, L., et al. (2016). Suppressive effect of Sanmiao formula on experimental gouty arthritis by inhibiting cartilage matrix degradation: an *in vivo* and *in vitro* study. *Int. Immunopharm.* 30, 36–42. doi:10.1016/j.intimp.2015.11.010

Zhu, L., Dong, Y., Na, S., Han, R., Wei, C., and Chen, G. (2017). Saponins extracted from Dioscorea collettii rhizomes regulate the expression of urate transporters in chronic hyperuricemia rats. *Biomed. Pharmacother.* 93, 88–94. doi:10.1016/j.biopha.2017.06.022

Zhu, C., Xu, Y., Liu, Z. H., Wan, X. C., Li, D. X., and Tai, L. L. (2018). The anti-hyperuricemic effect of epigallocatechin-3-gallate (EGCG) on hyperuricemic mice. *Biomed. Pharmacother.* 97, 168–173. doi:10.1016/j.biopha.2017.10.013

Zuo, J., He, H., Zuo, Z., Bou-Chacra, N., and Lobenberg, R. (2018). Erding Formula in hyperuricaemia treatment: unfolding traditional Chinese herbal compatibility using modern pharmaceutical approaches. *J. Pharm. Pharmacol.* 70 (1), 124–132. doi:10.1111/jphp.12840

Zuo, J., Zhang, W., Jian, H., Bou-Chacra, N., and Löbenberg, R. (2020). Esculetin as bioactive marker: towards a rational scientific approach for the treatment of hyperuricemia using traditional Chinese medicine. *Brazilian Journal of Pharmaceutical Sciences.* 56. doi:10.1590/s2175-97902019000417827

Conflict of Interest: The authors declare that the research was conducted in the absence of any commercial or financial relationships that could be construed as a potential conflict of interest.

Copyright © 2021 Chen, Luo, Wang, Cheng, Li, Lu, He, You, Zhou, Kwan, Zhao and Zhou. This is an open-access article distributed under the terms of the Creative Commons Attribution License (CC BY). The use, distribution or reproduction in other forums is permitted, provided the original author(s) and the copyright owner(s) are credited and that the original publication in this journal is cited, in accordance with accepted academic practice. No use, distribution or reproduction is permitted which does not comply with these terms.

frontiers in Pharmacology

ORIGINAL RESEARCH
published: 29 January 2021
doi: 10.3389/fphar.2020.609378

Epigallocatechin Gallate During Dietary Restriction — Potential Mechanisms of Enhanced Liver Injury

Zhuo Shi[1,2†], Jing-xiao Zhu[2,3†], Yu-ming Guo[2†], Ming Niu[2], Le Zhang[4], Can Tu[5], Ying Huang[2,3], Peng-yan Li[2], Xu Zhao[2], Zi-teng Zhang[2], Zhao-fang Bai[2], Guang-qin Zhang[1], Yang Lu[1]*, Xiao-he Xiao[6]* and Jia-bo Wang[2,7]**

[1]School of Basic Medicine and Clinical Pharmacy, China Pharmaceutical University, Nanjing, China, [2]China Military Institute of Chinese Medicine, Fifth Medical Center of Chinese PLA General Hospital, Beijing, China, [3]Hunan University of Chinese Medicine, Changsha, China, [4]College of Pharmacy, Southwest Minzu University, Chengdu, China, [5]Beijing Research Institute of Chinese Medicine, Beijing University of Chinese Medicine, Beijing, China, [6]Integrative Medical Center, Fifth Medical Center of Chinese PLA General Hospital, Beijing, China, [7]School of Traditional Chinese Medicine, Capital Medical University, Beijing, China

Green tea extract (GTE) is popular in weight loss, and epigallocatechin gallate (EGCG) is considered as the main active component. However, GTE is the primary cause of herbal and dietary supplement-induced liver injury in the United States. Whether there is a greater risk of liver injury when EGCG is consumed during dieting for weight loss has not been previously reported. This study found for the first time that EGCG could induce enhanced lipid metabolism pathways, suggesting that EGCG had the so-called "fat burning" effect, although EGCG did not cause liver injury at doses of 400 or 800 mg/kg in normal mice. Intriguingly, we found that EGCG caused dose-dependent hepatotoxicity on mice under dietary restriction, suggesting the potential combination effects of dietary restriction and EGCG. The combination effect between EGCG and dietary restriction led to overactivation of linoleic acid and arachidonic acid oxidation pathways, significantly increasing the accumulation of pro-inflammatory lipid metabolites and thus mediating liver injury. We also found that the disruption of Lands' cycle and sphingomyelin-ceramides cycle and the high expression of taurine-conjugated bile acids were important metabolomic characteristics in EGCG-induced liver injury under dietary restriction. This original discovery suggests that people should not go on a diet while consuming EGCG for weight loss; otherwise the risk of liver injury will be significantly increased. This discovery provides new evidence for understanding the "drug-host" interaction hypothesis of drug hepatotoxicity and provides experimental reference for clinical safe use of green tea-related dietary supplements.

Keywords: green tea extract, epigallocatechin gallate, hepatotoxicity, combination effect, lipid metabolism, metabolomics, herbal and dietary supplements

OPEN ACCESS

Edited by:
Hai Yu Xu,
China Academy of Chinese Medical Sciences, China

Reviewed by:
Yijun Wang,
Anhui Agricultural University, China
Suresh Kumar Mohankumar,
JSS College of Pharmacy, India

***Correspondence:**
Jia-bo Wang
pharm_sci@126.com
Xiao-he Xiao
pharmacy302xxh@126.com
Yang Lu
luyangcpu@hotmail.com
Guang-qin Zhang
njzhanggq@163.com

†These authors have contributed equally to this work

Specialty section:
This article was submitted to Ethnopharmacology, a section of the journal Frontiers in Pharmacology.

Received: *23 September 2020*
Accepted: *24 December 2020*
Published: *29 January 2021*

Citation:
Shi Z, Zhu J, Guo Y, Niu M, Zhang L, Tu C, Huang Y, Li P, Zhao X, Zhang Z, Bai Z, Zhang G, Lu Y, Xiao X and Wang J (2021) Epigallocatechin Gallate During Dietary Restriction — Potential Mechanisms of Enhanced Liver Injury. Front. Pharmacol. 11:609378. doi: 10.3389/fphar.2020.609378

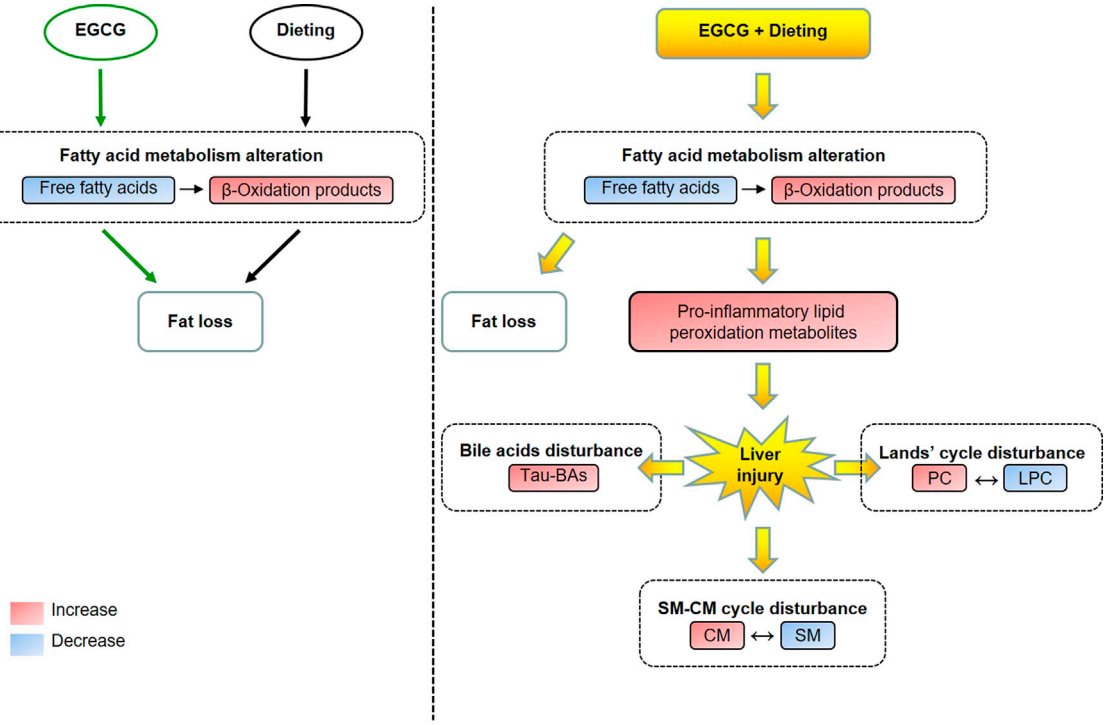

GRAPHICAL ABSTARCT | The metabolic alteration induced by EGCG in normal state and the metabolic homeostasis disturbance induced by EGCG during dieting. Tau-BAs, taurine-conjugated bile acids; PC, phosphatidylcholine; LPC, lysophosphatidylcholine; CM, ceramides; SM, sphingomyelin.

INTRODUCTION

Green tea is a beverage that has been brewed for thousands of years and has been widely popular across the world for hundreds of years. It is rich in catechin compounds with antioxidant effect, and epigallocatechin gallate (EGCG) is the most important component of green tea extract (GTE). It is popularly believed to have a wide range of health benefits, including preventing cancer, lowering cholesterol, reducing inflammation, and delaying aging (Li et al., 2019). In recent years, GTE and its principal component EGCG have been reported to have the so-called "fat-burning" weight loss effect (Chen et al., 2016), which makes it one of the most popular herbal and dietary supplement (HDS) in the world. However, in contrast to these health benefits, the number of drug-induced liver injury (DILI) cases when GTE is used for weight loss has consistently increased, with GTE being the leading cause of HDS-DILI in the United States (Navarro et al., 2017). GTE accounts for more than 50% of the suspected HDS products that cause DILI (Navarro et al., 2013). In severe cases, there is risk of acute liver failure or mortality. According to clinical observational research results, individuals who fasted or lost significant weight seemed to be more prone to liver injury, or liver injury was more severe when consuming GTE (Pillukat et al., 2014; Zheng et al., 2016). Although the hepatotoxicity of GTE and its main component EGCG has been reported (Emoto et al., 2014; Wang et al., 2015), it is not clear why there are more reports of liver injury when GTE is used for weight loss.

The "fat-burning" functions of EGCG were considered to include promoting energy consumption and fatty acid oxidation, inhibiting fatty acid synthesis, and reducing nutrition absorption (Wolfram et al., 2006; Rains et al., 2011; Yamashita et al., 2018). Some studies have shown that the process of weight loss through dieting (calorie restriction) is also accompanied by the remodeling of fatty acid metabolic pathways, such as decomposing more fatty acids to provide calories, thus achieving the effect of fat loss (Bruss et al., 2010; Lee et al., 2015; Collet et al., 2017; Green et al., 2019). Dieting while consuming EGCG can enhance the catabolism of fatty acids, which may increase the effect of fat loss. However, there is no experimental evidence as to whether this superposition of fatty acid metabolism regulation may be involved in the occurrence process of EGCG liver injury, thereby increasing the risk of EGCG-induced liver injury. In this regard, we try to characterize the metabolic alterations induced by EGCG and the dietary restriction in mice plasma using metabolomics approach and investigate the potential liver injury due to EGCG and dietary restriction alone or in combination, so as to provide experimental reference for rational use of GTE products for weight loss.

MATERIALS AND METHODS

Animal Grouping and Administration

Healthy female C57BL/6J mice, SPF grade, weighing 22–24 g, were purchased from SPF Experimental Technology Co., Ltd (License No.: SCXK (BJ) 2018-0010). Mice were provided with

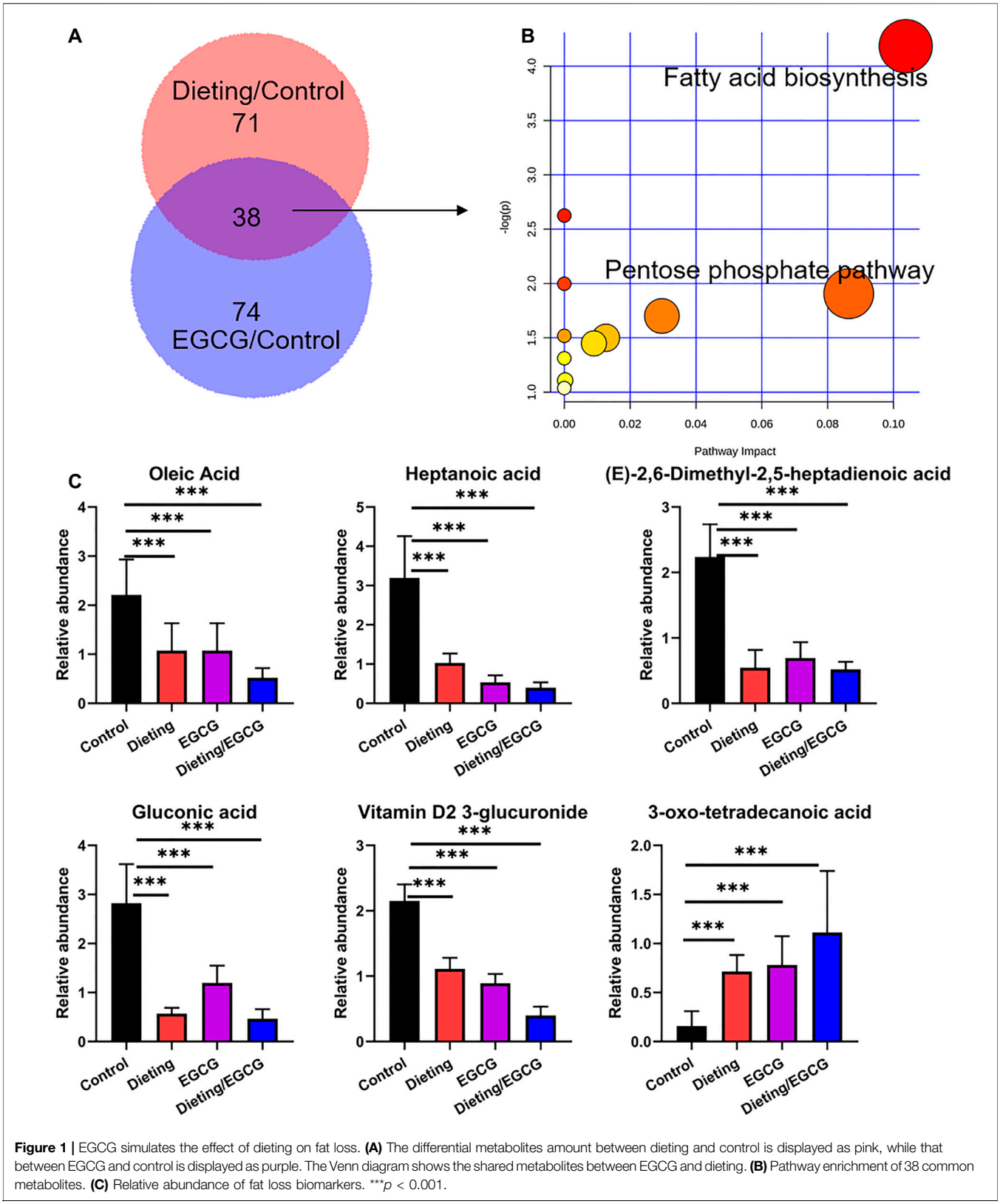

Figure 1 | EGCG simulates the effect of dieting on fat loss. **(A)** The differential metabolites amount between dieting and control is displayed as pink, while that between EGCG and control is displayed as purple. The Venn diagram shows the shared metabolites between EGCG and dieting. **(B)** Pathway enrichment of 38 common metabolites. **(C)** Relative abundance of fat loss biomarkers. ***$p < 0.001$.

food and water and kept at 25 ± 2°C, 50–60% humidity, with 12 h/12 h light and dark cycles, in separate cages in the experimental animal center of the Fifth Medical Center of the Chinese PLA General Hospital. All animal experiments were approved by the Center for Laboratory Animal Welfare and Ethics of the Fifth Medical Center of the Chinese PLA General Hospital and followed the Animal Research

Guidelines of National Institutes of Health. Epigallocatechin gallate (EGCG, purity ≥ 98%) was purchased from Chengdu Preferred Biotech Co., Ltd.

The mice were adaptively fed for 7 days, during which their food intake was monitored to obtain the average daily food intake per cage. The basic feed composition has crude protein (≥180 g/kg), crude fat (≥40 g/kg), total amino acids (≥76.6 g/kg), and various vitamins and micronutrients. The mice were then fed in the following two ways at 17:00 every day for 6 days: 1) free diet and 2) fixed diet, that is, 50% of the average daily food intake (limited less than 2 g each mouse 1 day). On the sixth day, the mice on the free diet were randomly divided into a control group (control), low-dose EGCG group (400 mg/kg), and high-dose EGCG group (800 mg/kg). Meanwhile, the mice on the fixed diet were randomly divided into three groups: dieting group, dieting/low-dose EGCG group (400 mg/kg), and dieting/high-dose EGCG group (800 mg/kg). The four administration groups were treated with intragastric EGCG of the corresponding dose at the same time. The control group and the dieting group were given equal volume of normal saline through intragastric means. There were eight mice in each group. After 24 h, the animals were sacrificed, blood was collected, and plasma was centrifuged at 4°C and frozen at −80°C. Fresh mice liver tissues were washed with normal saline and soaked in 4% neutral paraformaldehyde solution.

Evaluation of Blood Biochemistry and Liver Histology

The frozen plasma was returned to room temperature, and alanine aminotransferase (ALT) and aspartate aminotransferase (AST), glutathione S-transferase (GST) activity, and total bile acid (TBA) concentration were measured and calculated according to the kit instructions. ALT kit (No.: C009-2), AST kit (No.: C010-2), GST kit (No.: A004), and TBA kit (No.: E003-2-1) were purchased from Nanjing Jiancheng Bioengineering Institute.

The liver tissues of mice were collected, and routine histological sections were stained with hematoxylin and eosin (HE). Then, the pathological sections were photographed under a microscope. Terminal deoxynucleotidyl transferase dUTP nick end labeling (TUNEL) was used to detect and analyze the apoptosis of hepatocytes. Image-Pro Plus 6.0 software was used to label and calculate the apoptosis rate.

Metabolomics Analysis

We selected plasma from the control, dieting, high-dose EGCG (800 mg/kg), and dieting/high-dose EGCG (800 mg/kg) groups as metabolomics test samples. The mice samples stored at −80°C refrigeration were thawed to 4°C, and 50 μl of each sample was pipetted into the 1.5 ml EP tube; three times the volume of precooled methanol was added, vortexed for 30 s, and kept standing at 4°C for 30 min. It was then centrifuged at 14,000 rpm for 15 min in a precooled 4°C centrifuge; 100 μl of supernatant was pipetted and dried with nitrogen. 75% methanol of the same volume was added to reconstitute the sample to be tested. Meanwhile, 10 μl of each sample was taken and mixed evenly and used as the quality control (QC) sample. For plasma metabolite chromatographic separation conditions and non-targeted metabolomics mass spectrometry detection conditions, please see the **Supplementary Material**.

Using MassHunter Qualitative Analysis software (version B06.00, Agilent, United States), LC-MS raw data was converted into visual data. MZmine software (version 2.5) was used for peak extraction, data correction, chromatographic deconvolution, and comparison. The raw data was displayed on the MetaboAnalyst webpage (https://www.metaboanalyst.ca/) and normalized and compared between groups, and metabolites with group differences were screened by calculating the fold change (FC) values and significant differences (p value) between groups. The criteria for differences between groups were as follows: FC was greater than 1.5 or less than 0.67, and p value was less than 0.05. At the same time, the obtained data matrix was imported into SIMCA-P software (version 14.1, Umetrics AB, Umea, Sweden) for principal component analysis (PCA) and orthogonal partial least squares discriminant analysis (OPLS-DA). Under the OPLS-DA model, the important variable (VIP) > 0.5 and $|p\ (corr)| \geq 0.5$ were used as the screening criteria for metabolites with inter-group differences. These metabolites were then identified using the Metlin database (http://www.metlin.scipps.edu/) and HMDB (http://www.hmdb.ca/) (mass error limited to 30 ppm). Pathway analysis based on the identified metabolites was conducted using MetaboAnalyst according to the Kyoto Encyclopedia of Genes and Genomes (KEGG) pathway database (www.genome.jp/kegg/). MS/MS spectra of mainly representative metabolites were in **Supplementary Figure S4**.

Statistical Analysis

The experimental data was expressed as mean ± SD. GraphPad Prism software version 8 was used for statistical analysis, Student's t-test was used for inter-group comparison, and analysis of variance (ANOVA) was used for one-way ANOVA. $p < 0.05$, $p < 0.01$, and $p < 0.001$ were considered to be statistically significant.

RESULTS

EGCG Simulates Dieting Effects for Lipid Metabolism

We screened and identified differential metabolites to study the metabolic changes caused by EGCG and diet on the mice. EGCG and diet coregulated metabolites as shown in the Venn diagram in **Figure 1A**. The pathways altered by EGCG and dieting mainly focused on fatty acid biosynthesis and pentose phosphate pathway (**Figure 1B**). Biomarkers included gluconic acid, oleic acid, heptanoic acid, (E)-2, 6-dimethyl-2, 5-heptadienoic acid, vitamin D2 3-glucuronide, and 3-oxo-tetradecanoic acid. The corresponding abundance changes were shown in **Figure 1C**, and the specific identification information was shown in **Supplementary Table S1**. We found that dietary restriction could slow down fatty acid synthesis, which could explain the fat loss effect caused by dieting. EGCG could also slow down fatty acid synthesis, which was consistent with its claimed weight loss effect. At

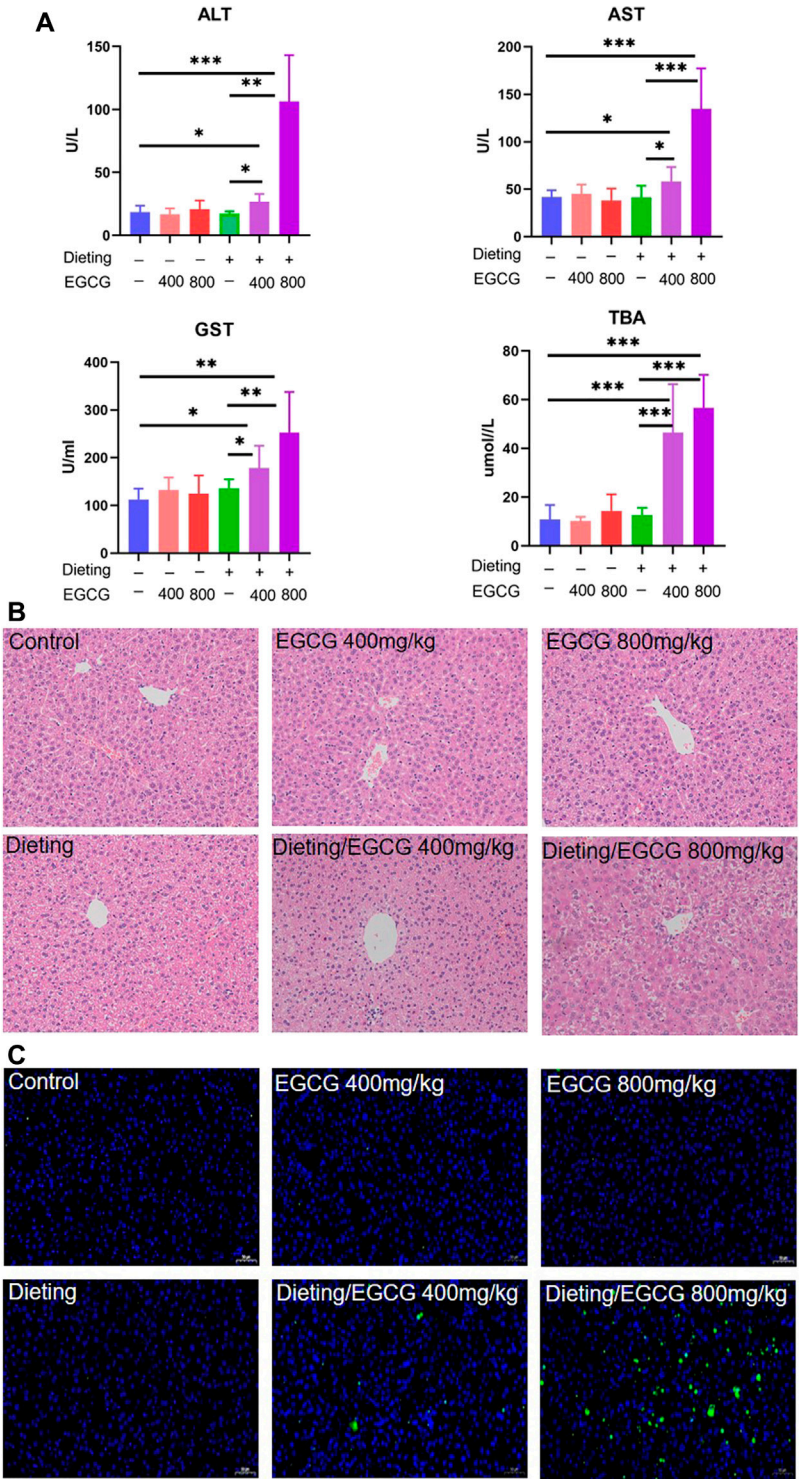

Figure 2 | Dieting exacerbates EGCG hepatotoxicity in mice. **(A)** Plasma ALT; AST; GST; TBA. The data were expressed as mean ± SD. **(B)** Histological assessment of mice liver (HE staining ×200 magnification). **(C)** Hepatocyte apoptosis determination in mice liver using TUNEL assay (×200 magnification). $^{*}p < 0.05$, $^{**}p < 0.01$, and $^{***}p < 0.001$.

the same time, we found that, in the dieting/EGCG group, the content of related biomarkers decreased further, but the excessive metabolic changes brought about by this combination may also cause adverse results. Therefore, we compared the liver injury induced by EGCG with that induced by EGCG under dietary restriction *in vitro* and *in vivo*.

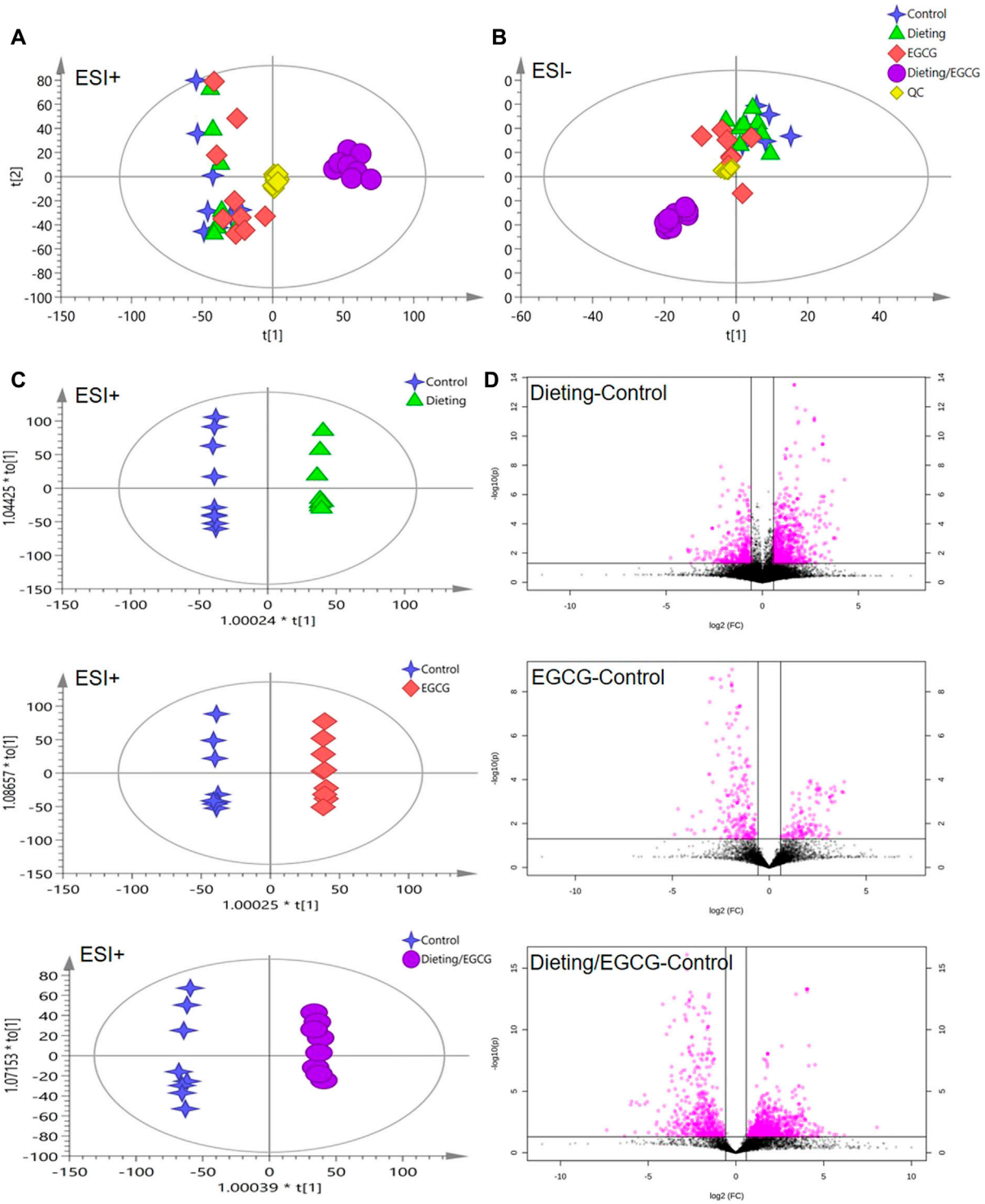

Figure 3 | Metabolomic analysis of mice plasma. **(A)** The principal component analysis (PCA) score plot in positive ESI model. **(B)** The PCA score plot in negative ESI model. **(C)** The orthogonal projection to latent structures discriminant analysis (OPLS-DA) score plots in positive ESI model between dieting, EGCG, dieting/EGCG, and control. **(D)** The volcano plots in positive ESI model between dieting, EGCG, dieting/EGCG, and control.

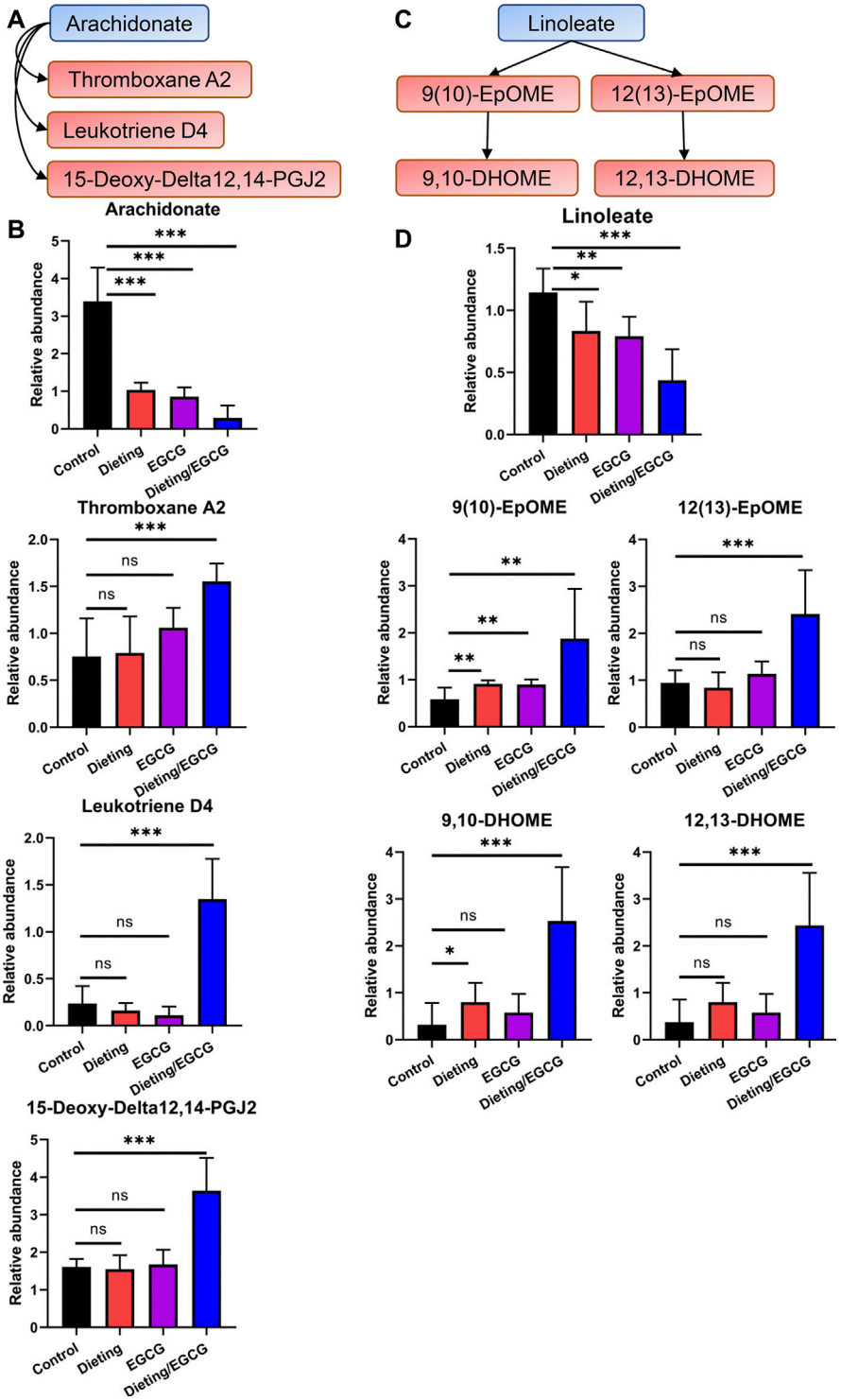

Figure 4 | Dieting exacerbating EGCG hepatotoxicity promotes arachidonic acid and linoleate metabolism. **(A)** Alteration of arachidonic acid metabolism. Blue represents downregulation and red represents upregulation. **(B)** Relative abundance of arachidonate, 15-deoxy-delta12, 14-PGJ2, leukotriene D4, and thromboxane A2. **(C)** Alteration of linoleate metabolism. **(D)** Relative abundance of linoleate, 9 (10)-EpOME, 9,10-DHOME, 12 (13)-EpOME, 12,13-DHOME. $^{*}p < 0.05$, $^{**}p < 0.01$, and $^{***}p < 0.001$; ns, no significance.

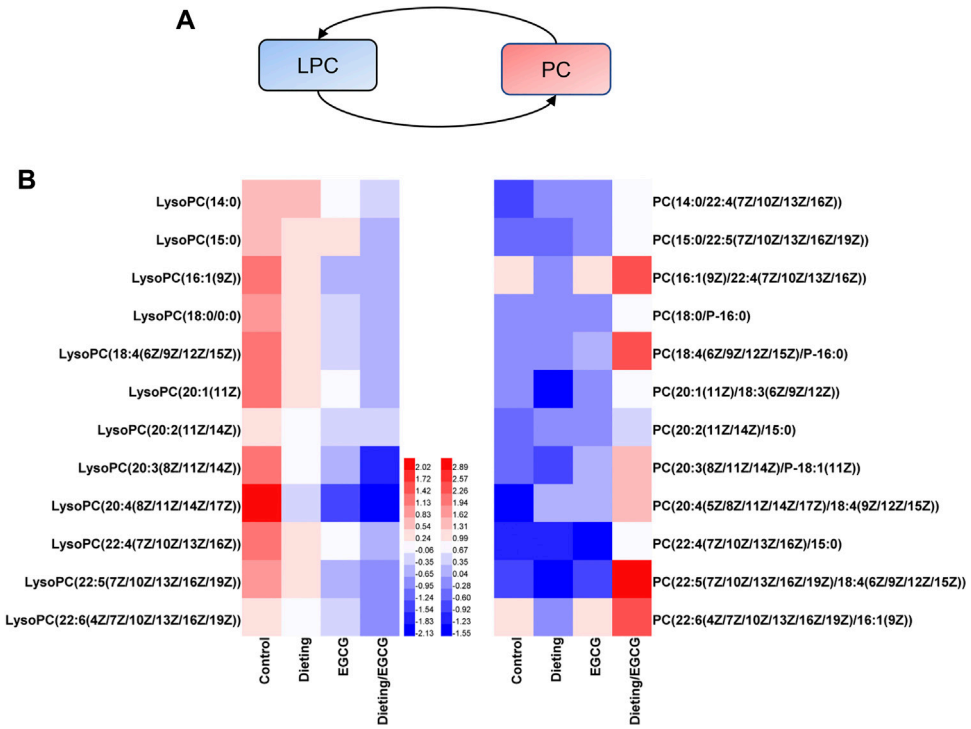

Figure 5 | Dieting exacerbating EGCG hepatotoxicity disrupts Lands' cycle. **(A)** Lands' cycle. Blue represents downregulation and red represents upregulation. **(B)** Heatmap analysis of the identified Lands' cycle biomarkers. PC is synthesized by LPC on the same line. The values are based on Log2FCs of biomarkers relative peak intensity compared to the control. PC, phosphatidylcholine; LPC, lysophosphatidylcholine.

Dietary Restriction Exacerbates EGCG Hepatotoxicity *In Vivo*

The experimental animal results (**Figure 2A**) showed that, compared with the control group, there were no statistical differences in biochemical indexes between dieting group and each EGCG single administration group ($p > 0.05$). However, there were significant increases on ALT, AST, GST, and TBA in the combination groups of dieting with EGCG ($p < 0.01$). The liver injury indicators in the high-dose (800 mg/kg) EGCG with dieting group were higher than those of the low-dose combination group (400 mg/kg).

The results of HE staining (**Figure 2B**) showed that the hepatocytes in the control, EGCG, and dieting groups represented with normal morphology. By contrast, obvious histological changes occurred in the diet combined with EGCG treatment group, including a decrease in the number of hepatocytes and some vacuolar degeneration, accompanied by infiltration of inflammatory cells. In the TUNEL staining results (**Figure 2C**), there were basically no green fluorescence positive cells in the visual field of the single administration group compared with the control group, and there was no statistical difference in the calculated apoptosis rate. Under dietary restriction conditions, green fluorescence positive cells were scattered in the visual field of 400 mg/kg EGCG administration group, and the apoptosis rate was significantly different from that of the control group ($p < 0.05$). There was more hepatocyte apoptosis in the visual field of 800 mg/kg EGCG combined with diet, and the apoptosis rate was significantly different from that in the control group ($p < 0.01$) (**Supplementary Figure S1**). The above results indicate that EGCG can cause increased hepatocyte apoptosis under dietary restriction.

Metabolomics Analysis of Dietary Restriction Exacerbating EGCG Hepatotoxicity

PCA and OPLS-DA analysis were carried out on the data in positive and negative ion modes using SIMCA-P. **Figures 3A,B** displayed the scattered point plots of PCA of all samples in positive ion and negative ion modes. It could be seen that QC samples were concentrated in the middle of the score matrix projection plot, which indicated that the instrument remained stable during the analysis process. In addition, in positive ion mode, control, EGCG, and dieting groups were distributed on the left side of the first principal component, while dieting/EGCG group was located on the right side of the first principal component and was far away from control, EGCG, and dieting groups, suggesting that the metabolic profile of the dieting/EGCG group had obviously changed, which was consistent with the experimental phenotype of liver injury caused by EGCG under dietary restriction.

In order to further obtain the differences between groups and different compounds, OPLS-DA modeling and analysis were carried out. In the positive ion mode, dieting and control,

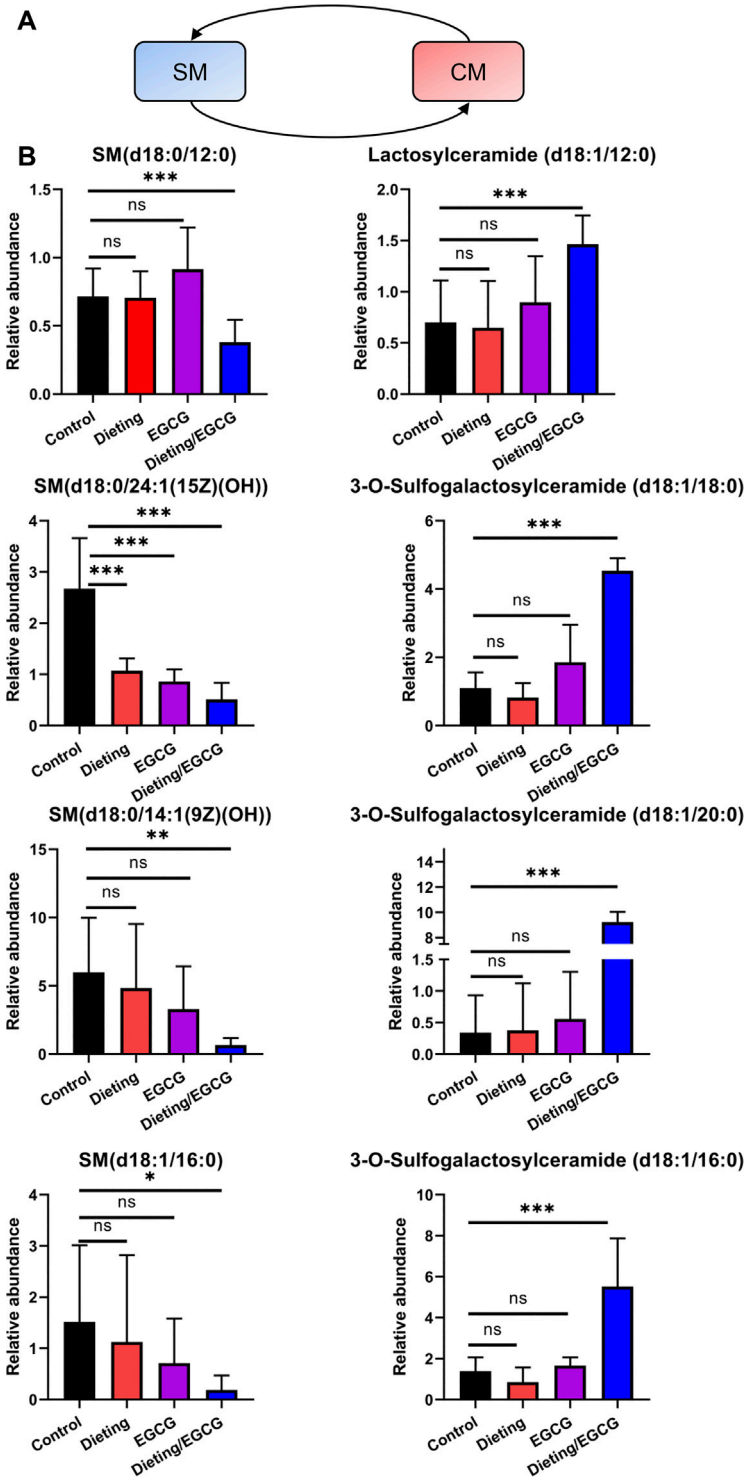

Figure 6 | Dieting exacerbating EGCG hepatotoxicity disrupts SM-CM cycle. **(A)** SM-CM cycle. Blue represents downregulation and red represents upregulation. **(B)** Relative abundance of metabolites in SM-CM cycle. *$p < 0.05$, **$p < 0.01$, and ***$p < 0.001$; CM, ceramides; ns, no significance; SM, sphingomyelin.

EGCG and control, dieting/EGCG and control groups were located on both sides of the ordinate and were completely separated. Volcanic plots showed the metabolic changes in mice induced by dieting, EGCG, or dieting/EGCG (**Figures 3C,D** for positive ion and **Supplementary Figure S2** for negative ion). Further, we used dieting/EGCG and control to screen the metabolic pathways related to liver injury. We found that some important pathways were alteration, including linoleic acid metabolism,

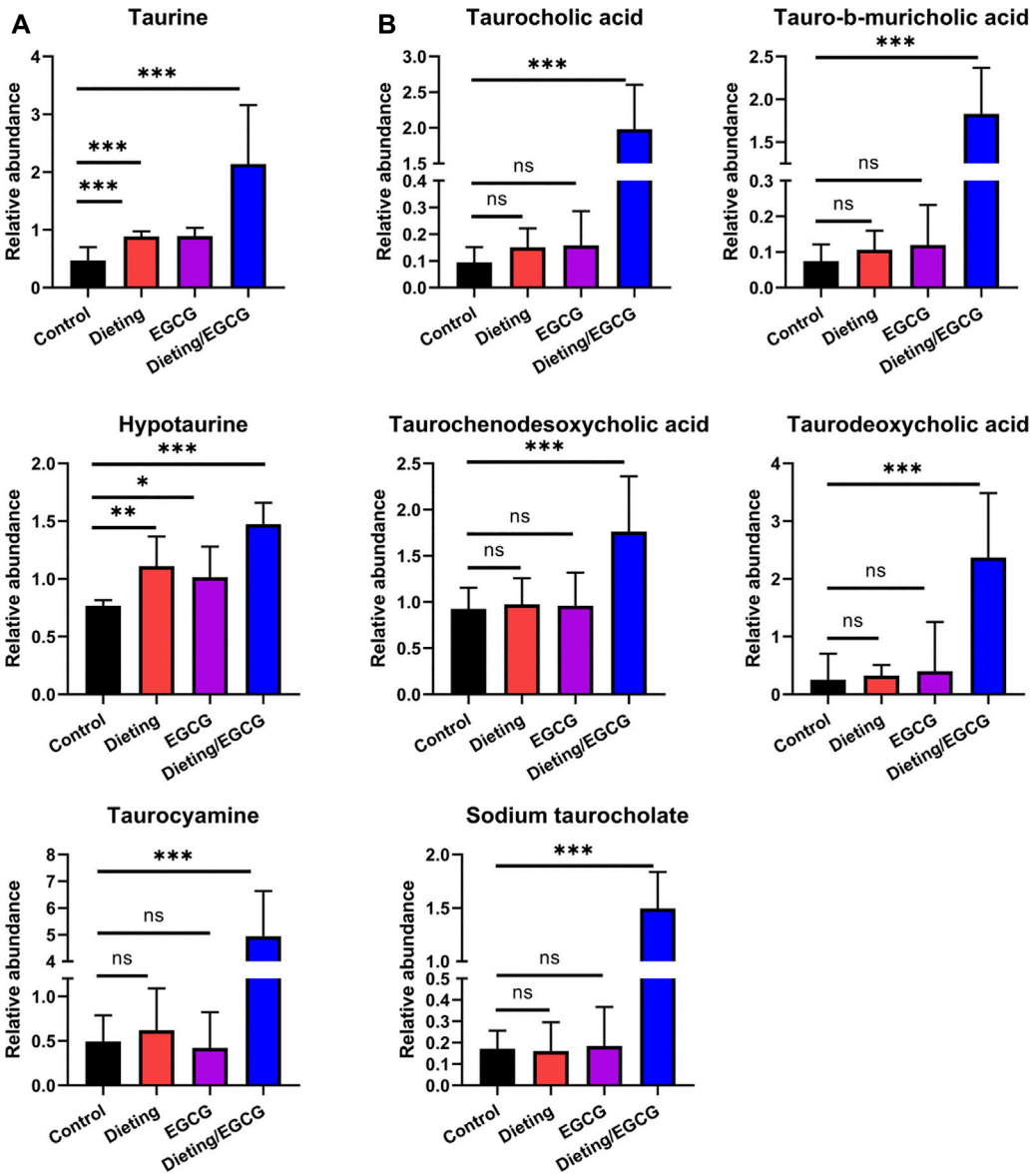

Figure 7 | Dieting exacerbating EGCG hepatotoxicity increases taurine metabolites and taurine-conjugated bile acids. **(A)** Relative abundance of taurine, hypotaurine, taurocyamine. **(B)** Relative abundance of taurine-conjugated bile acids. *$p < 0.05$, **$p < 0.01$, and ***$p < 0.001$; ns, no significance.

glycerophospholipid metabolism, sphingolipid metabolism, taurine, and hypotaurine metabolism (**Supplementary Figure S3**).

Dietary Restriction Exacerbating EGCG Hepatotoxicity Was Associated With Increased Production of Pro-Inflammatory Metabolites Through Arachidonic Acid and Linoleic Acid Metabolism

Unsaturated fatty acid catabolism was significantly enhanced, which may be an important marker of lipid peroxidation; the plasma levels of arachidonic acid (**Figure 4A**) decreased significantly in the dieting/EGCG group, while the levels of its derived eicosanoid acids including 15-deoxy-delta12, 14-PGJ2, leukotriene D4, and thromboxane A2 significantly increased (**Figure 4B**). We also found that linoleic acid metabolism (**Figure 4C**) was disrupted, and the level of linoleate in dieting/EGCG group was significantly reduced. Its downstream metabolites including 9(10)-EpOME, 9,10-DHOME, 12(13)-EpOME, 12,13-DHOME showed different degrees of upregulation in the combined treatment group (**Figure 4D**). The above specific identification information is shown in **Supplementary Tables S2, S3**.

Dietary Restriction Exacerbating EGCG Hepatotoxicity Disrupts Lands' Cycle

Metabolic remodeling is an important manifestation of the liver's stress response, wherein the dynamic transition between phosphatidylcholine (PC) and lysophosphatidylcholine (LPC)

(Lands' cycle) is the key regulatory pathway (**Figure 5A**). We found that dieting/EGCG group significantly upregulated PC, while LPC, a precursor for synthesizing PC, significantly decreased; for example, LPC (20:3) is converted to PC (20:3/18:1) by lysophosphatidylcholine acyltransferases (LPCAT) using oleoyl-CoA (18:1-CoA). We identified 12 groups of LPC to PC transformations (**Figure 5B**) and eight phospholipid metabolites with no corresponding relationship. The specific identification information was shown in **Supplementary Table S4**. As can be clearly seen from **Figure 5B**, the LPCs tended to decrease in the EGCG and dieting groups and further decreased in the dieting/EGCG group. We could see that the length of the carbon chain affected by liver injury ranged from 14 to 22, including both saturated and unsaturated chains, indicating that this metabolic change did not have anything to do with the length of fatty acid side chain and the number of double bonds, but was only related to the formation of PC corresponding to the addition of a fatty acid side chain on LPC. It could be seen that the changes in phospholipid component were extensive and not specific to a specific phospholipid component. The changes of these biomarkers showed that dietary restriction exacerbating liver injury induced by EGCG could cause metabolic abnormalities in Lands' cycle.

Dietary Restriction Exacerbating EGCG Hepatotoxicity Disrupts SM-CM Cycle

The dynamic conversion between sphingomyelin (SM) and ceramides (CM) is another crucial regulatory pathway in the process of liver's stress response (**Figure 6A**). Through metabolomics analysis, we found that the SM-CM cycle was broken during liver injury, which is manifested in the following: multiple sphingomyelins, including SM (d18:0/24:1 (15Z) (OH)), SM (d18:0/14:1 (9Z) (OH)), SM (d18:1/16:0), and SM (d18:0/12:0), were significantly downregulated in the dieting/EGCG group; at the same time, several ceramide metabolites, including lactosylceramide (d18:1/12:0), 3-O-sulfogalactosylceramide (d18:1/18:0), 3-O-sulfogalactosylceramide (d18:1/20:0), and 3-O-sulfogalactosylceramide (d18:1/16:0), were significantly upregulated in the dieting/EGCG group (**Figure 6B**). The specific identification information is shown in **Supplementary Table S5**. These results showed that the metabolic transition from SM to CM was one of the important characteristics of dieting exacerbating liver injury induced by EGCG.

Dietary Restriction Exacerbating EGCG Hepatotoxicity Increases Taurine Metabolites and Taurine-Conjugated Bile Acids Levels

In addition to the above metabolic characteristics, we also found that the levels of taurine and taurine-conjugated bile acids increased significantly. Taurine and its metabolites, hypotaurine and taurocyamine, were significantly higher in the dieting/EGCG group than in the dieting or EGCG group (**Figure 7A**). Taurine-conjugated bile acids, including taurodeoxycholic acid, tauro-b-muricholic acid, taurocholic acid, sodium taurocholate, and taurochenodesoxycholic acid, were not significantly different between the dieting and EGCG groups but increased more than three times in the dieting/EGCG group (**Figure 7B**). Specific identification information is shown in **Supplementary Table S6**.

DISCUSSION

With increasing obesity globally, there has been a steady increase in the consumption of GTE for weight loss. EGCG is the main component of GTE, and its big selling point is fat burning. However, the potential mechanism of such claimed weight loss effect of EGCG has not been fully characterized. Thus, we used metabolomics to reveal the effects between EGCG and dietary restriction on mice. The results showed that either EGCG treatment or dieting could regulate lipid metabolism, pentose phosphate pathway and other metabolic pathways, to inhibit fatty acid synthesis and to enhance the oxidation of fatty acid in mice. In addition, either EGCG or dietary restriction could reduce gluconic acid, indicating that pentose phosphate pathway may be inhibited, and nicotinamide adenine dinucleotide phosphate (NADPH), an important raw material for fatty acid elongation, could be reduced, which in turn would lead to the slowdown of fatty acid synthesis. These results suggested that EGCG could simulate the fatty acid consumption effect caused by dieting and had the so-called "fat-burning" effect.

However, the reports of adverse reactions related to HDS for weight loss, especially the liver injury caused by GTE, have increased significantly to a leading cause of HDS-DILI in recent years. It has been shown that a single large dose of EGCG (1,500 mg/kg) can cause liver injury in normal mice (Lambert et al., 2010). As known, drug-induced liver injury is affected by drugs, the host and the environment, of which the host's state could be an important risk factor (Fontana, 2014). In this study, we observed for the first time that 400 mg/kg EGCG (equivalent to four times the common daily dose) could cause significant increase of transaminase and hepatocyte damage on a dietary restriction mice model; however, in normal mice, the same dose of EGCG did not cause liver injury. The above results suggested that dieting could increase the risk of EGCG-induced liver injury, with the characterization of combined toxicity potentiation. This is the first time that dieting has been proved to be a risk factor for EGCG hepatotoxicity by experimental evidence.

We further investigated the metabolic underlying mechanism wherein dietary restriction could increase the risk of EGCG-induced liver injury. We found that enhancement of fatty acid peroxidation pathway was caused by combining EGCG treatment and dietary restriction. It generated excessive oxidative pro-inflammatory lipid metabolites (9(10)-EpOME, 9,10-DHOME, 12(13)-EpOME, 12,13-DHOME) of linoleic acid. Moreover, the levels of eicosanoid oxidative metabolites (15-deoxy-delta12, 14-PGJ2, leukotriene D4, and thromboxane A2) in the downstream of arachidonic acid increased, which have been shown to promote inflammation and cell damage (Hall et al., 2017). It could be seen that liver injury caused by EGCG and dieting may be related to the increase of pro-inflammatory lipid peroxidation products,

which further mediates tissue inflammation and injury. Except for the overlap of metabolic pathways regulation, other mechanisms could lead to the rising risks of EGCG administration during diet. For example, the blood concentration of EGCG increased more than 3.5-fold in the fasting condition that the EGCG exposure of liver tissue lifted in Beagle dogs, thus exacerbating the risk of liver injury (Kapetanovic et al., 2009).

We also characterized some metabolic features related to EGCG treatment plus dietary restriction-induced liver injury. Among them, the disturbances of Lands' cycle, SM-CM cycle, and bile acids are crucial. Firstly, we observed the significant decrease of LPC and increase of its corresponding PC components in dieting/EGCG group. This feature of disturbance in Lands' cycle has been reported as an important metabolic feature of various liver injuries such as steatohepatitis or alcoholic liver disease (Matsubara et al., 2011), which illustrated the liver injury phenotype found in our experiment. Similarly, the second metabolic feature—SM level decrease and CM level increase—reflects the disturbance of SM-CM cycle. Notably, the conversation of LPC-PC cycle and SM-CM cycle is controlled by LPCAT and sphingomyelin phosphodiesterase (SMPD, also known as sphingomyelinase), respectively. Such two key metabolic enzymes' overexpression has been demonstrated as important features of hepatocytes in response to chemical toxin-induced liver injury (Liu et al., 2014). In addition, due to the combined inhibition of EGCG and dietary restriction on fatty acid synthase (FASN) and carnitine palmitoyl transferase-1 (CPT-1), cytoplasmic fatty acyl CoA accumulates and condenses with serine to produce 3-ketosphinganin and is then metabolized by ceramide synthetase to produce CM (Khiewkamrop et al., 2018). CM is a functional sphingolipid, and the upregulation of CM is an important signal for the activation of apoptosis cascade increasing the expression of pro-apoptotic protein Bcl2 and inducing apoptosis of various cells (Siskind et al., 2010). The high abundance of CM could promote ROS production by directly acting on mitochondrial respiratory electron chains (Abadie et al., 2001). It was indicated that increased CM may not only be a metabolomic characteristic of EGCG liver injury, but also participate in the process of liver injury. Last but not least, dysregulated taurine-conjugated bile acids are suggested to play roles in several diseases, which may be related to the high expression of bile acid transporter induced by hepatocyte injury signal.

Taken together, the disturbances of Lands' cycle, SM-CM cycle, and taurine-conjugated bile acids may be the metabolomic characteristics of EGCG and dieting-induced liver injury, and some active metabolites may also be partially involved in the liver injury process. These metabolic characteristics could be utilized in clinical monitoring of the incidence risk of EGCG hepatotoxicity. Though this paper fully characterizes the metabolic alteration reflecting *in vivo* biological processes, further causality relationship and mechanism researches are worthy explored.

It is worth pointing out that few reports of liver injury were a result of the consumption of green tea in China, which is significantly different from the situation in the United States. Green tea is mainly used as a beverage in China, with 2–3 g of natural tea leaves soaked in water each time, where the average EGCG content is 0.7% in the natural tea beverage (James et al., 2018). However, in the United States, HDS products using GTEs are made up of complete polyphenols extracted from tea leaves with further purified EGCG or artificially added EGCG, and the EGCG content in some GTE products exceeds 90% (Hopley, 2005). The dose of tea polyphenols ingested when consuming tea is very low and obviously lower than that of GTE products in the United States, which means that we take the daily GTE product containing 800 mg of EGCG as the dosage comparable to drinking 114 g of green tea in one day. In addition, tea is traditionally consumed as a beverage in China; its extracts are not concentrated and used for weight loss, nor is it used for dieting, and people often drink tea before or after meals, so it can be explained from one aspect that green tea does not cause liver injury in China.

CONCLUSION

To summarize, low dose of EGCG can increase fatty acid decomposition and inhibit fatty acid synthesis to a certain extent, which simulates the effect of dietary restriction on fatty acid metabolism and has certain fat loss effect. However, consuming EGCG while dieting could excessively disturb lipid metabolic pathways and lead to liver injury in mice, which indicates that dietary restriction could increase the risk of liver injury caused by EGCG. This happens to be a dilemma for people who plan to lose weight, as dieting and consuming EGCG concurrently may speed up weight loss, but it also leads to a higher risk of liver injury.

DATA AVAILABILITY STATEMENT

The original contributions presented in the study are included in the article/**Supplementary Material**. Further inquiries can be directed to the corresponding authors.

ETHICS STATEMENT

The animal study was reviewed and approved by the Center for Laboratory Animal Welfare and Ethics of the Fifth Medical Center of the Chinese PLA General Hospital.

AUTHOR CONTRIBUTIONS

All authors contributed to the study conception and design. ZS, JZ, and YG wrote the manuscript. XX, YL, GZ, and JW designed this research. JZ, ZS, LZ, CT, YH, and PL conducted the research. ZS, YG, JZ, XZ, ZZ, and ZB analyzed the data. MN contributed to new reagents/analytical tools. All authors commented on previous versions of the manuscript. All authors read and approved the final manuscript.

FUNDING

This work was supported by a grant from the National Natural Science Foundation of China (Grant Nos.: 81630100 and 81721002).

SUPPLEMENTARY MATERIAL

The Supplementary Material for this article can be found online at: https://www.frontiersin.org/articles/10.3389/fphar.2020.609378/full#supplementary-material.

REFERENCES

Abadie, N. A., Gouazé, V., Salvayre, R., and Levade, T. (2001). Ceramide in apoptosis signaling: relationship with oxidative stress. *Free Radic. Biol. Med.* 31 (6), 717–728. doi:10.1016/s0891-5849(01)00655-4

Bruss, M. D., Khambatta, C. F., Ruby, M. A., Aggarwal, I., and Hellerstein, M. K. (2010). Calorie restriction increases fatty acid synthesis and whole body fat oxidation rates. *Am. J. Physiol. Endocrinol. Metab.* 298 (1), E108–E116. doi:10.1152/ajpendo.00524.2009

Chen, I., Liu, C. Y., Chiu, J. P., and Hsu, C. H. (2016). Therapeutic effect of high-dose green tea extract on weight reduction: a randomized, double-blind, placebo-controlled clinical trial. *Clin. Nutr.* 35 (3), 592–599. doi:10.1016/j.clnu.2015.05.003

Collet, T. H., Sonoyama, T., Henning, E., Keogh, J. M., Ingram, B., Kelway, S., et al. (2017). A metabolomic signature of acute caloric restriction. *J. Clin. Endocrinol. Metab.* 12, 4486–4495. doi:10.1210/jc.2017-01020

Emoto, Y., Yoshizawa, K., Kinoshita, Y., Yuki, M., Yuri, T., Yoshikawa, Y., et al. 2014). Green tea extract-induced acute hepatotoxicity in rats. *J. Toxicol. Pathol.* 27 (3-4), 163–174. doi:10.1293/tox.2014-0007

Fontana, R. J. (2014). Pathogenesis of idiosyncratic drug-induced liver injury and clinical perspectives. *Gastroenterology* 146 (4), 914–928. doi:10.1053/j.gastro.2013.12.032

Green, C. L., Soltow, Q. A., Mitchell, S. E., Derous, D., Wang, Y., Chen, L., et al. (2019). The effects of graded levels of calorie restriction: XIII. Global metabolomics screen reveals graded changes in circulating amino acids, vitamins, and bile acids in the plasma of C57BL/6 mice. *J. Gerontol. A Biol. Sci. Med. Sci.* 74 (1), 16–26. doi:10.1093/gerona/gly058

Hall, Z., Bond, N. J., Ashmore, T., Sanders, F., Ament, Z., Wang, X., et al. (2017). Lipid zonation and phospholipid remodeling in nonalcoholic fatty liver disease. *Hepatology* 65 (4), 1165–1180. doi:10.1002/hep.28953

Hopley, C. (2005). The empire of tea: the remarkable history of the plant that took over the world. *Gastronomica*. 5 (3), 136–137. doi:10.1525/gfc.2005.5.3.136

James, K. D., Kennett, M. J., and Lamberta, J. D. (2018). Potential role of the mitochondria as a target for the hepatotoxic effects of (-)-epigallocatechin-3-gallate in mice. *Food Chem. Toxicol.* 111, 302–309. doi:10.1016/j.fct.2017.11.029

Kapetanovic, I. M., Crowell, J. A., Krishnaraj, R., Zakharov, A., Lindeblad, M., and Lyubimov, A. (2009). Exposure and toxicity of green tea polyphenols in fasted and non-fasted dogs. *Toxicology* 260 (1-3), 28–36. doi:10.1053/j.gastro.2013.12.032

Khiewkamrop, P., Phunsomboon, P., Richert, L., Pekthong, D., and Srisawang, P. 2018). Epistructured catechins, EGCG and EC facilitate apoptosis induction through targeting de novo lipogenesis pathway in HepG2 cells. *Cancer Cell. Int.* 18, 46. doi:10.1186/s12935-018-0539-6

Lambert, J. D., Kennett, M. J., Sang, S., Reuhl, K. R., Ju, J., and Yang, C. S. (2010). Hepatotoxicity of high oral dose (-)-epigallocatechin-3-gallate in mice. *Food Chem. Toxicol.* 48 (1), 409–416. doi:10.1016/j.fct.2009.10.030

Lee, H.-C., Cheng, W.-Y., Hsu, Y.-H., Su, H.-Y., Huang, B. E. T.-G., Lin, Y.-K., et al. (2015). Effects of calorie restriction with n-3 long-chain polyunsaturated fatty acids on metabolic syndrome severity in obese subjects: a randomize-controlled trial. *J. Funct. Foods* 19, 929–940. doi:10.1016/j.jff.2015.01.040

Li, K., Xiao, G., Richardson, J. J., Tardy, B. L., Ejima, H., Huang, W., et al. (2019). Targeted therapy against metastatic melanoma based on self-assembled metal-phenolic nanocomplexes comprised of green tea catechin. *Adv. Sci.* 6 (5), 180–188. doi:10.1002/advs.201970028

Liu, A., Krausz, K. W., Fang, Z.-Z., Brocker, C., Qu, A., and Gonzalez, F. J. (2014). Gemfibrozil disrupts lysophosphatidylcholine and bile acid homeostasis *via* PPARα and its relevance to hepatotoxicity. *Arch. Toxicol.* 88 (4), 983–996. doi:10.1007/s00204-013-1188-0

Matsubara, T., Tanaka, N., Patterson, A. D., Cho, J. Y., Krausz, K. W., and Gonzalez, F. J. 2011). Lithocholic acid disrupts phospholipid and sphingolipid homeostasis leading to cholestasis in mice. *Hepatology* 53 (4), 1282–1293. doi:10.1002/hep.24193

Navarro, V. J., Bonkovsky, H. L., Hwang, S. I., Vega, M., Barnhart, H., and Serrano, J. 2013). Catechins in dietary supplements and hepatotoxicity. *Dig. Dis. Sci.* 58 (9), 2682–2690. doi:10.1007/s10620-013-2687-9

Navarro, V. J., Khan, I., Björnsson, E., Seeff, L. B., Serrano, J., and Hoofnagle, J. H. 2017). Liver injury from herbal and dietary supplements. *Hepatology* 65 (1), 363–373. doi:10.1002/hep.28813

Pillukat, M. H., Bester, C., Hensel, A., Lechtenberg, M., Petereit, F., Beckebaum, S., et al. (2014). Concentrated green tea extract induces severe acute hepatitis in a 63-year-old woman—a case report with pharmaceutical analysis. *J. Ethnopharmacol.* 155 (1), 165–170. doi:10.1016/j.jep.2014.05.015

Rains, T. M., Agarwal, S., and Maki, K. C. (2011). Antiobesity effects of green tea catechins: a mechanistic review. *J. Nutr. Biochem.* 22 (1), 1–7. doi:10.1016/j.jnutbio.2010.06.006

Siskind, L. J., Mullen, T. D., Romero Rosales, K., Clarke, C. J., Hernandez-Corbacho, M. J., Edinger, A. L., et al. (2010). The BCL-2 protein BAK is required for long-chain ceramide generation during apoptosis. *J. Biol. Chem.* 285(16), 11818–11826. doi:10.1074/jbc.M109.078121

Wang, D., Wei, Y., Wang, T., Wan, X., Yang, C. S., Reiter, R. J., et al. (2015). Melatonin attenuates (-)-epigallocatehin-3-gallate-triggered hepatotoxicity without compromising its downregulation of hepatic gluconeogenic and lipogenic genes in mice. *J. Pineal Res.* 59 (4), 497–507. doi:10.1111/jpi.12281

Wolfram, S., Wang, Y., and Thielecke, F. (2006). Anti-obesity effects of green tea: from bedside to bench. *Mol. Nutr. Food Res.* 50 (2), 176–187. doi:10.1002/mnfr.200500102

Yamashita, S., Hirashima, A., Lin, I. C., Bae, J., Nakahara, K., Murata, M., et al. (2018). Saturated fatty acid attenuates anti-obesity effect of green tea. *Sci. Rep.* 8 (1), 10023. doi:10.1038/s41598-018-28338-5

Zheng, E. X., Rossi, S., Fontana, R. J., Vuppalanchi, R., Hoofnagle, J. H., Khan, I., et al. (2016). Risk of liver injury associated with green tea extract in SLIMQUICK(®) weight loss products: results from the DILIN prospective study. *Drug Saf.* 39 (8), 749–754. doi:10.1007/s40264-016-0428-7

Conflict of Interest: The authors declare that the research was conducted in the absence of any commercial or financial relationships that could be construed as a potential conflict of interest.

Copyright © 2021 Shi, Zhu, Guo, Niu, Zhang, Tu, Huang, Li, Zhao, Zhang, Bai, Zhang, Lu, Xiao and Wang. This is an open-access article distributed under the terms of the Creative Commons Attribution License (CC BY). The use, distribution or reproduction in other forums is permitted, provided the original author(s) and the copyright owner(s) are credited and that the original publication in this journal is cited, in accordance with accepted academic practice. No use, distribution or reproduction is permitted which does not comply with these terms.

frontiers in Pharmacology

ORIGINAL RESEARCH
published: 02 February 2021
doi: 10.3389/fphar.2020.593693

An Integrative Pharmacology-Based Approach for Evaluating the Potential Effects of Purslane Seed in Diabetes Mellitus Treatment Using UHPLC-LTQ-Orbitrap and TCMIP V2.0

Jinli Hou[1,3†], Xiang Zhou[4†], Ping Wang[1], Chunhui Zhao[1], Yuewen Qin[1], Feng Liu[2], Liping Yu[5] and Haiyu Xu[1,2]*

[1]Institute of Chinese Materia Medica, China Academy of Chinese Medical Sciences, Beijing, China, [2]Medical College, Shaanxi Institute of International Trade and Commerce, Xianyang, China, [3]College of Traditional Chinese Medicine, Yunnan University of Chinese Medicine, Kunming, China, [4]State Key Laboratory of Innovative Drug and Efficient Energy-Saving Pharmaceutical Equipment, Jiangxi University of Traditional Chinese Medicine, Nanchang, China, [5]Guangzhou Zhongda Pharmaceutical Development Co. Ltd., Guangzhou, China

Portulaca oleracea L., known as the "vegetable for long life," is an annual succulent herb that is widely distributed worldwide. Many clinical and experimental studies have demonstrated that purslane seed (MCXZ) can be used as an adjunctive and alternative therapy for the treatment of diabetes mellitus (DM). However, the underlying active constituents and pharmacological mechanisms through which MCXZ exerts effects in DM remain unclear. In the present study, we confirmed that MCXZ treatment resulted in hypoglycemic activity, lowering the fasting blood glucose and glycated hemoglobin levels in streptozotocin-induced diabetic mice. Then, ultra-high-pressure liquid chromatography coupled with linear ion trap-Orbitrap tandem mass spectrometry was used to systematically analyze the chemical profile of MCXZ, resulting in the identification of 84 constituents, including 31 organic acids and nine flavonoids. Finally, the Integrative Pharmacology-based Research Platform of Traditional Chinese Medicine was employed to analyze the key active components of MCXZ and the molecular mechanisms through which these components acted in DM. Ten key active compounds were identified based on the topological importance of their corresponding putative targets within the known DM-associated therapeutic target network of known MCXZ putative targets. Functionally, these candidate targets play critical anti-hyperlipidemia, anti-hyperglycemia, immunity regulation, and inflammatory roles involving DM-related pathways, such as the vascular endothelial growth factor (VEGF) signaling pathway and Fc gamma R-mediated phagocytosis, which indicated that MCXZ exhibited anti-diabetic activity through multi-faced actions.

Keywords: purslane seed, diabetes mellitus, UHPLC-LTQ-orbitrap, TCMIP v20, molecular network

OPEN ACCESS

Edited by:
Javier Echeverria, University of Santiago, Chile

Reviewed by:
Jianping Chen, The Fourth Clinical Medical College of Guangzhou University of Chinese Medicine, China
Cheng LU, Chinese Academy of Medical Sciences and Peking Union Medical College, China

***Correspondence:**
Haiyu Xu
hyxu@icmm.ac.cn

†These authors have contributed equally to this work

Specialty section:
This article was submitted to Ethnopharmacology, a section of the journal Frontiers in Pharmacology

Received: *11 August 2020*
Accepted: *09 December 2020*
Published: *02 February 2021*

Citation:
Hou J, Zhou X, Wang P, Zhao C, Qin Y, Liu F, Yu L and Xu H (2021) An Integrative Pharmacology-Based Approach for Evaluating the Potential Effects of Purslane Seed in Diabetes Mellitus Treatment Using UHPLC-LTQ-Orbitrap and TCMIP V2.0. Front. Pharmacol. 11:593693. doi: 10.3389/fphar.2020.593693

INTRODUCTION

Diabetes mellitus (DM) represents a major public health issue, causing serious economic burdens for both developed and developing countries (Papatheodorou et al., 2018). The International Diabetes Federation (IDF) reported that approximately 463 million individuals had diabetes worldwide in 2019, including 116 million patients in China, which was ranked first in the world (International Diabetes Federation (IDF), 2019). Persistent hyperglycemia and long-term metabolic disorders may lead to the development of nephropathy, retinopathy, neuropathy, and cardiovascular disease (Zhang H. et al., 2018). Currently, the drugs used to treat DM include biguanide, sulfonylureas, α-glycosidase inhibitors, benzoin acid, and derivative secretagogues, most of which aim to control blood glucose levels and must be used long-term. Gradual increases in the required doses of these drugs can lead to liver and kidney dysfunction, which can be associated with various complications, in addition to those resulting from the disease process (Moukette et al., 2017). Therefore, the development of safer, more effective drugs, especially those derived from natural products, which can provide improved management for blood glucose and diabetes-associated complications, has long been the focus of DM studies.

Traditional Chinese medicine (TCM) is practiced as a form of holistic and personalized medicine and has been shown to effectively lower blood glucose levels, control diabetic complications, and cause fewer side-effects than western medicines, based on syndrome differentiation and treatments (Zhang, 2014) that are multi-component, multi-pattern, and multi-target. As a result, increasing research has focused on the TCM-based treatment of DM. In TCM theory, DM belongs to the category of "Xiao-Ke-Zheng," which was first recorded in the classical medical text "Huangdi Neijing" over a thousand years ago. Purslane is an annual succulent herb best known as the "vegetable for long life" and is distributed throughout diverse geographical environments worldwide. Purslane seed (MCXZ) has been used as both food and medicine for thousands of years in China (Aberoumand, 2009). Clinically, MCXZ, as an adjuvant combined with other treatments, has been shown to alleviate DM symptoms, including reduced inflammation and improved liver function (El-Sayed, 2011; Dehghan et al., 2016). Chemically, a wide variety of compounds have been identified in MCXZ, including flavonoids, polysaccharides, fatty acids, proteins, glutathione, antioxidants, and vitamins (El-Sayed, 2011). Pharmacologically, MCXZ has been associated with various biological activities, including hypoglycemic (A. Mohamed et al., 2019), hypocholesterolemic (Movahedian et al., 2007), anti-oxidative (Guo et al., 2016), diuretic, antipyretic, analgesic, and anti-inflammatory (Daniel, 2006) processes. Currently, MCXZ is used as an adjuvant treatment for DM to improve glucose tolerance, lipid metabolism disorders, liver functions, and insulin sensitivity and reduce hyperinsulinemia (Mohanapriya et al., 2006; El-Sayed, 2011). However, the potential active components and molecular mechanisms through which MCXZ acts and that may be applied to the direct treatment of DM remain unclear, which limits the clinical applications of MCXZ.

In the current study, an integrative pharmacology approach was used to investigate the active constituents and the underlying pharmacological mechanisms through which MCXZ acts during the treatment of DM. This study combined high-throughput chemical analysis, target prediction, and network construction and analysis, which was performed by following a three-step analytical process (**Figure 1**). 1) Chemical information databases, including the Encyclopedia of Traditional Chinese Medicine (ETCM) and other electronic databases, were searched for the constituents of purslane. 2) Ultra-high-pressure liquid chromatography coupled with linear ion trap-Orbitrap tandem mass spectrometry (UHPLC-LTQ-Orbitrap) was performed to rapidly characterize the preliminary chemical profile of MCXZ. 3) The TCMIP V2.0 platform was utilized to predict MCXZ putative targets, construct a drug target-disease-gene network based on predicted interactions among MCXZ putative targets and known therapeutic targets associated with DM-related diseases, and identify potential active constituents correlated with the candidate MCXZ targets during the treatment of DM.

MATERIALS AND METHODS

Chemicals and Materials

Mass spectrometry-grade methanol, acetonitrile, and formic acid were acquired from Fisher Scientific Co. (Loughborough, United Kingdom). Purified water was prepared by a Milli-Q system (Millipore, Billerica, MA, United States). Other reagents used in the experiment were of analytical grade. MCXZ was supplied by Guangzhou Zhongda Pharmaceutical Development Co., Ltd. (Batch NO. 180201; Guangzhou, China). This drug was identified as a dry, mature seed from *Portulaca oleracea* by the pharmacist Yan Jin (research assistant at the China Academy of Chinese Medical Sciences).

Animals and Experimental Design

Healthy specific-pathogen-free (SPF)-grade male Balb/c mice (body weight: 18.0–21.0 g) were purchased from the Department of Experimental Animal Science, Department of Medicine, Peking University (Beijing, China). The project identification code was 20160010. All animal experiments were approved by the Committee on Animal Care and Use of the Institute of Chinese Materia Medica, China Academy of Chinese Medical Sciences. Before the experiment began, all animals were placed in a standard laboratory environment, during which they were provided free access to food and water. The experiment did not begin until the animals had adapted to the environment for 3 days.

Dried MCXZ was ground into a powder with 80 mesh by a high-speed multi-function grinder (JP-500C, Yongkang Jiupin Industry and Trade Co., Ltd.). Before administration, the powder was dissolved in normal saline containing 0.5% carboxymethyl cellulose sodium to prepare 54.17, 108.33, and 216.67 mg/ml suspensions (Liu, 2018).

Streptozotocin (STZ, 60 mg/kg, dissolved in 0.1 M sodium citrate buffer, pH 4.5) was injected intraperitoneally, continuously for 5 days to induce DM in mice (Goodarzi

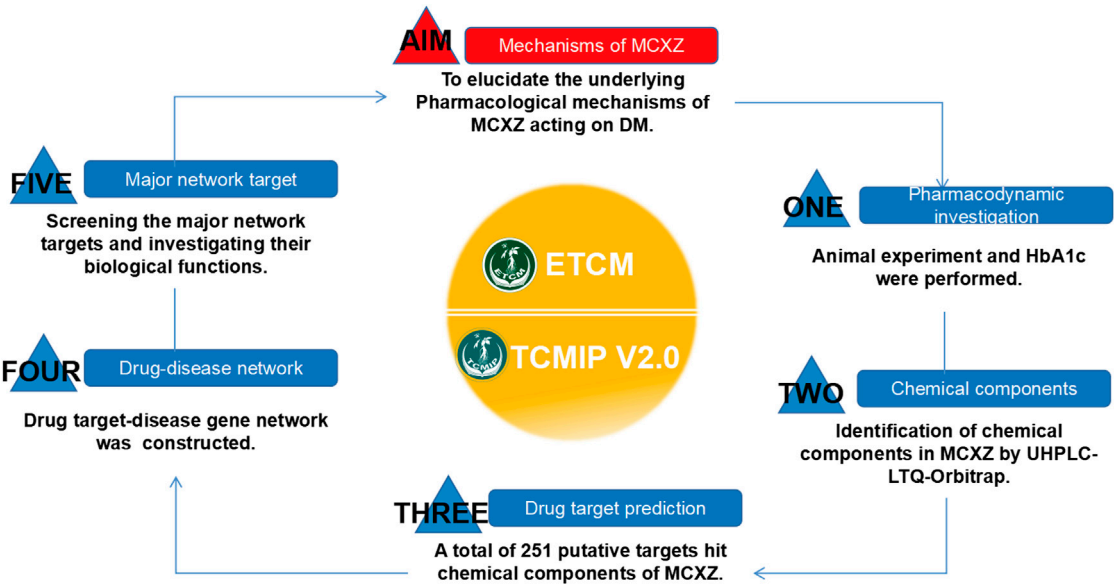

FIGURE 1 | Schematic diagram for revealing the active constituents and the underlying pharmacological mechanisms of MCXZ in the treatment of DM by combining high-throughput technology and integrative pharmacology method.

et al., 2019). To establish the normal control group, 12 healthy mice were injected intraperitoneally with an equal volume of sodium citrate buffer. One week after the last injections, the mice were fasted for 5 h, after which blood was collected from the tail vein, and the fasting blood glucose (FBG) levels were measured using a blood glucose monitor (GT-1980. Aikelai Medical Electronics (Pinghu) Co., Ltd.). Mice with FBG levels greater than 11.1 mmol·L^{-1} were considered to be successful DM model mice. All successfully modeled DM mice were randomly divided into five groups according to body weight and FBG: Model (STZ) group, Met (metformin hydrochloride) group, and MCXZ low-, medium-, and high-dose groups (n = 12 for each group). The dose of metformin hydrochloride used was 130 mg/kg body weight (BW)/day; the low, medium, and high doses of MCXZ powder were 812.5, 1,625, and 3,250 mg/kg BW/day, respectively. The normal control group and model group were administered an equivalent volume of 0.9% NaCl. All groups were treated through intragastric administration for four consecutive weeks.

FBG (fasted for 5 h) was detected every 2 weeks for 4 weeks. At the end of the experiment, the mice were fasted for more than 12 h, and then eye blood samples were collected. Blood samples were collected in blank sterile tubes and allowed to coagulate at room temperature for 1 h. Then, whole blood was centrifuged at 3,500 rpm for 15 min. The serum was separated and stored at −80°C for further studies.

Measurement of Glycated Hemoglobin (HbAlc)

A specific enzyme-linked immunosorbent assay (ELISA) kit (Cusabio, batch number: M03033575) was used to quantify HbAlc from serum samples. This assay employs the competitive inhibition enzyme immunoassay technique. The experiment was performed according to the manufacturer's instructions.

Histopathological Evaluation of Liver and Kidney Tissues

The liver and kidney tissues were removed and immersed in 4% formalin for 72 h at 4°C. To analyze the histopathological changes that occurred in the liver and kidney, sections from paraffin-embedded tissues were stained with hematoxylin and eosin and captured under a light microscope (Olympus, BX51, Japan).

Chemical Information Database for the Compounds Found in Purslane

The chemical compound database information associated with purslane primarily included chemical name, molecular formula, molecular weight, structural formula, and other information. The chemical components associated with purslane were collected from existing databases, using "*Portulaca oleracea*" as the keyword. These databases included the Encyclopedia of Traditional Chinese Medicine (ETCM, http://www.nrc.ac.cn:9090/ETCM/), which contains information about a total of 7,274 herbal ingredients (Xu et al., 2019). Other resources included electronic databases such as PubMed (https://pubmed.ncbi.nlm.nih.gov/, update on 2019) and CNKI (China Journals of Full-text database; https://www.cnki.net/, update on 2019). Detailed information regarding the identified compounds in purslane is presented in **Supplementary Table S1**.

Preparation of Sample Solutions

MCXZ was ground into a powder with 40 mesh, and 1 g of powder was accurately weighed. The powder was dissolved in 10 ml 70% methanol and submitted to ultrasonic extraction for 40 min. The extracts were centrifuged for 12 min (at 12,000 rpm), and the supernatant was separated. The sample solution was subjected to 0.22-mm nylon membrane filtration and analyzed directly by UHPLC-LTQ-Orbitrap.

LC System

Sample analysis was performed using the Thermo Accela UHPLC system (Thermo Fisher Scientific, San Jose, California, United States). Chromatographic separation was performed on a maintained reverse-phase column Waters HSS T3-C18 (2.1 × 100 mm, 1.8 μm). The mobile phase was a mixture of methanol (A) and 0.1% formic acid in water (B). The following elution gradient was used: 0–5 min, 3%–10% A; 5–25 min, 10%–40% A; 25–35 min, 40%–60% A; 35–45 min, 60%–80% A; 45–50 min, 80%–95% A; 50–60 min, 95% A. The flow rate was set to 0.3 ml/min, and the injection volume was 1 μL.

Mass Spectrometry and Data Processing

For LC-ESI-MS^n experiments, the samples were detected in the positive and negative ion modes by electrospray ionization (ESI) source and were scanned in one-stage and multi-stage modes separately. The parameters for the ESI source were as follows: ion source voltage, 3.5 kV; capillary temperature, 350°C; sheath and auxiliary gas pressure, 0.24 and 0.07 MPa, respectively; ion source temperature, 350°C. The sheath and auxiliary gas was nitrogen in both cases. The mass axis of MS was calibrated using an external standard method (the mass error was less than 5 ppm); mass calibration positive ion selection: 74.09643, 3.06037, 195.08465, 262.63612, 524.26496, and 1,022.00341; negative ion selection: 230.10174, 249.15299, and 407.28030. The MS^1 was fully scanned and acquired in the range of 50–1,500 m/z, with a resolution of 30,000. The MS^2 uses a data-dependent scan (DDS). The three peaks with the highest abundance were selected for collision-induced dissociation to obtain MS^2 data.

Mass Frontier 6.0 (Thermo Fisher Scientific) software and Xcalibur 2.1 (Thermo Fisher Scientific) software were employed for data analysis. The accuracy error threshold was fixed at 10 ppm.

Prediction of Putative MCXZ Targets

According to the results of MCXZ component recognition, the corresponding targets were obtained through target prediction and functional analyses of TCM (including prescriptions) using the Integrative Pharmacology-based Research Platform of Traditional Chinese Medicine (TCMIP V2.0 http://www.tcmip.cn/TCMIP/index.php) (Xu H. Y. et al., 2017). The principle underlying target prediction is the use of MedChem Studio (version 3.0) software to search DrugBank for the structural similarities between the two-dimensional structures of chemical components and the certified drug (Approved), followed by scoring the similarity using the Tanimoto coefficient. When the similarity score was ≥0.8 (moderate-high similarity), the potential targets for the MCXZ chemical components were obtained.

Prediction of Known Therapeutic Genes Acting on DM

The candidate therapeutic genes associated with DM were collected from the TCMIP V2.0 database using "Diabetes Mellitus" as the keyword. The platform integrates HPO, OMIM, TTD, Drugbank, DisGeNET, ORPHANET, and other drug, biological, and symptom databases.

Protein–Protein Interaction Data

Protein–protein interactions (PPIs) were obtained by importing putative MCXZ targets and DM-related genes into the STRING database (http://string-db.org/, version 11.0). To ensure the accuracy of the results, the species was set to "Homo sapiens," and the confidence was set to 0.4.

Network Analysis and Visualization

To scientifically explain the complex relationships between putative MCXZ targets and known DM-related genes and to identify key nodes, Cytoscape software (version 3.7.1, Boston, MA, United States) was used to create an interaction network between identified components, putative targets, and known DM-related genes. This complex network analysis method includes data integration, analysis, and visualization. The Network Analyzer in Cytoscape software was then used to calculate the three topological parameters of each node gene, including "degree," "betweenness," and "closeness." The core nodes of the interaction network between MCXZ and DM-related targets were obtained by selecting those targets with degree values greater than 2-fold the median value and the key core target network through which MCXZ acts on DM was acquired by selecting nodes that meet all three topological parameters simultaneously. These three topological parameters are typically used to evaluate the topological importance of nodes in molecular interaction networks. The higher the center of a node, the more important that the node was to the network (Mao et al., 2019).

Pathway Enrichment Analysis

To elucidate the biological functions of putative MCXZ targets, the targets were introduced into DAVID (https://david-d.ncifcrf.gov/, version 6.7), and pathway enrichment analysis was conducted on targets within the network using the Kyoto Encyclopedia of Genes and Genomes database (KEGG, http://www.genome.jp/kegg/). Relevant pathways with p-values < 0.05 were selected as significant pathways.

Quantitative Real-Time Reverse Transcriptase-Polymerase Chain Reaction (qRT-PCR)

Total RNA was isolated from pancreatic tissue using RNAiso Plus (TaKaRa, Tokyo, Japan). The PCR reaction procedures were performed as follows. Stage 1: Pre-denaturation, one cycle at 95°C for 5s. Stage 2: PCR reaction, 40 cycles at 95°C for 10s and 60°C for 30s. Stage 3: 1 cycle heating from 60°C–95°C, at 0.05°C/s. The relative expression levels of vascular endothelial growth

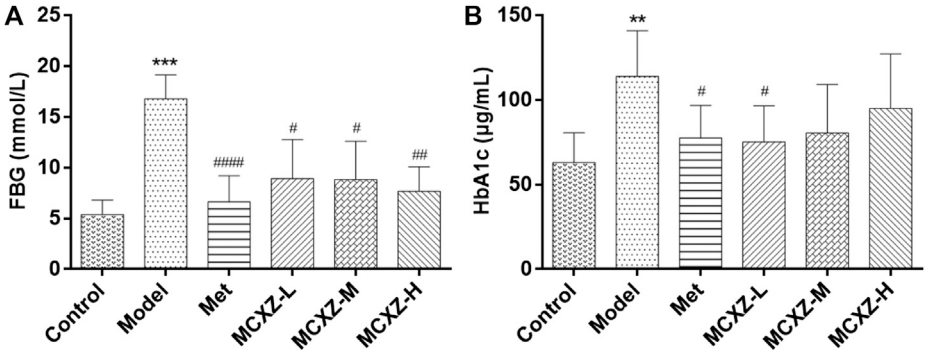

FIGURE 2 | MCXZ alleviates the symptoms of the mice with DM. **(A)** MCXZ reduce the FBG of the mice with DM. **(B)** MCXZ downregulated the level of HbA1c in the serum of mice with DM. MCXZ-L, MCXZ low dose group 812.5 mg/kg; MCXZ-M, MCXZ middle dose group 1625 mg/kg; MCXZ-H, MCXZ high dose group 3250 mg/kg. Data are mean ± SD.$^{***}p < 0.001$, $^{**}p < 0.01$ vs. Control; $^{\#\#\#\#}p < 0.0001$, $^{\#\#}p < 0.01$, $^{\#}p < 0.05$ vs. the modle group; n = 8–12 animals per group.

factor (*VEGF*), erb-b2 receptor tyrosine kinase 2 (*ErbB2*), androgen receptor (*AR*), and protein kinase B (*Akt1*) were calculated using the $2^{-\Delta\Delta Ct}$ method. β-actin (*ACTB*) was used as the internal control. All quantitative real-time reverse transcriptase-polymerase chain reaction (qRT-PCR) experiments were repeated three times. The primer sequences used in this study were as follows: VEGF-F, 5′-CCT GGG AAA TGT GCC TGT GA-3′ and VEGF-R, 5′-ATT CGC ACA CGG TCT GT-3’; ErbB2-F, 5′-ATT GGC TCT CAT TCA CCG CA-3′ and ErbB2-R, 5′-CCA AGC CCT CAA GAC CAC AT-3’; Akt1-F, 5′-GAT AAC GGA CTT CGG GCT GT-3′ and Akt1-R, 5′-CGG CCA CAC ATC TCG TA-3’; androgen receptor (AR)-F, 5′-GCC CGA ATG CAA AGG TCT TC-3′ and AR-R, 5′-CCC AGA GCT ACC TGC TTC AC-3’; ACTB-F, 5′-AGG GAA ATC GTG CGT GAC AT-3′ and ACTB-R, 5′-AAC CGC TCG TTG CCA ATA GT-3’.

Statistical Analysis

All data were analyzed by SPSS 25.0 software (SPSS Inc., Chicago, IL, United States). Data were expressed as the mean ± standard error of the mean (SEM). The results were presented using GraphPad Prism 7.0 software (GraphPad Software, San Diego, CA, United States). Significant differences between normally distributed gene expression data were determined by one-way analysis of variance (ANOVA). The FBG and HbA1c data, which were not normally distributed, were analyzed using the nonparametric Kruskal-Wallis test. $p < 0.05$ was considered significant.

RESULTS

Effects of MCXZ on FBG and HbAlc Levels in DM Model Mice

As shown in **Figure 2A**, the FBG concentrations were significantly increased in diabetic model mice (model group) compared with those in normal mice (control group), whereas the MCXZ and Met groups showed significantly reduced FBG concentrations compared with that in the model group.

Meanwhile, to further examine the effects of MCXZ on DM, HbAlc levels were detected using an ELISA kit. HbA1c is currently considered the gold standard for glucose monitoring in patients with DM and has been increasingly adopted as a criterion for DM diagnosis. HbA1c levels were substantially increased in the diabetic model mice (model group) compared with those in normal animals (control group). Compared with the model group, mice treated with MCXZ showed significantly decreased HbA1c levels (**Figure 2B**). Surprisingly, the hypoglycemic effect observed in the low-dose MCXZ group was better than those observed in the medium- and high-dose groups.

Effects on Liver and Kidney Tissue Histopathology

As shown in **Figure 3**, compared with the control group, the structures of the liver and kidney tissues were not significantly altered in any of the experimental groups, including the Model, Met, MCXZ-L, MCXZ-M, and MCXZ-H groups.

Identifification of the Primary Compounds Found in MCXZ Using UHPLC-LTQ-Orbitrap

The systemic characterization of chemical profiles is an important precondition for determining the pharmacological mechanisms through which TCM agents exert their effects. To perform this characterization in MCXZ, the UHPLC-LTQ-Orbitrap method, together with the ETCM database, was initially applied for the rapid and high-throughput identification of MCXZ compounds (both known and unknown) in the present study. The UHPLC-LTQ-Orbitrap method combines efficient separation and strong structural characterization abilities to achieve the high-resolution acquisition of parent and daughter ion data, both quickly and simultaneously, to obtain multi-stage mass spectrometry fragment information, which can significantly improve the ability to rapidly identify and analyze the chemical components of complex systems, such as those used in TCM (Wang et al., 2015). The ETCM contains 7,274 herbal ingredients. Any identified molecular formulas that are not included in the

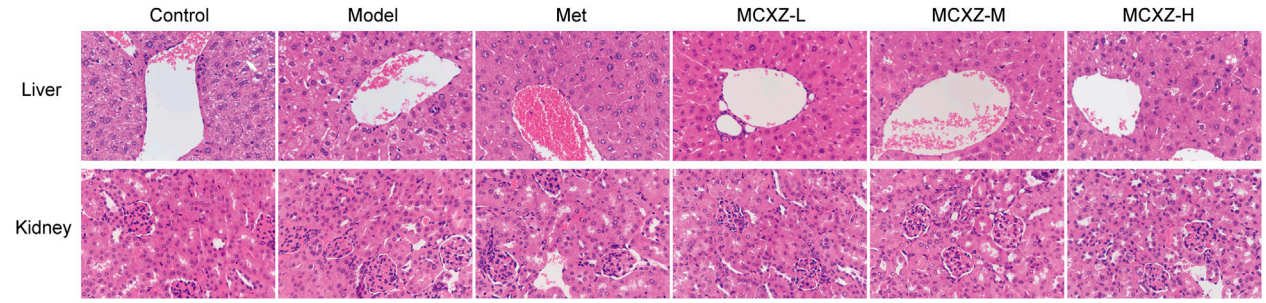

FIGURE 3 | The effects of MCXZ on liver and kidney histopathological injury (× 40).

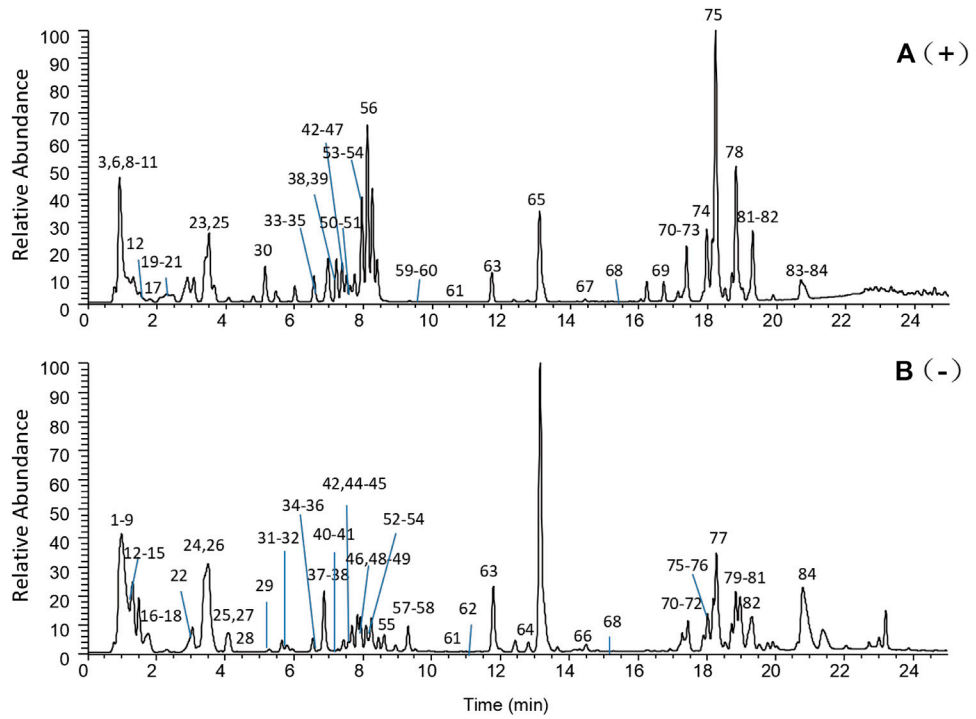

FIGURE 4 | Total ion chromatogram of MCXZ detected by UHPLC-LTQ-Orbitrap. **(A)**: Positive ion detection mode; **(B)**: Negative ion detection mode.

purslane chemical components database may represent either known compounds that have not previously been associated with purslane or new compounds; compounds can be searched in his database and confirmed against various types of information. The total ion chromatograms (TIC) of MCXZ were presented in **Figure 4**, corresponding to the positive and negative signals.

During the identification process, the compounds were first analyzed and identified in positive ion mode, and then further analyzed and verified in negative ion mode. Compounds in MCXZ were identified or tentatively characterized according to their retention times and MS^n data, which are summarized in **Table 1**. The specific method used Xcalibur 2.1 to extract molecular ion peaks from first-order, high-resolution, mass spectrometry data, which were then matched with the high-precision excimer ions in the purslane chemical compound database (the collected compounds were calculated by $[M\text{-}H]^-$, $[M + CH3COO]^-$, $[M]^+$, $[M + H]^+$, and $[M + Na]^+$]. All possible compounds were obtained with a mass error of 5.0 ppm. The MS^n information could also be compared against the precise relative molecular mass, fragmentation patterns, and pathways reported in the related literature to identify compounds (Sun et al., 2014; Yu et al., 2016). Using the described sample treatment methods and analytical conditions, a total of 84 compounds were analyzed and identified in MCXZ using both positive and negative ion modes, including 31 organic acids, 22 alkaloids, nine flavonoids, eight coumarins, et al.

For example, flavonoids respond in both positive and negative ion modes, and molecular ions exist in $(M + H)^+$, $(M + Na)^+$, and $(M\text{-}H)^-$ form during primary mass spectrometry. High-precision quasi-molecular ions for Compound 68 were obtained in both

TABLE 1 | Identification of chemical compounds in MCXZ by UHPLC-LTQ-Orbitrap.

Peak no	tR min	Measured mass m/z	MS2	Formula	Compound Name	References	Error ppm
1	0.88	259.0218[M + HCOO]$^-$	NO	$C_{13}H_{26}O_2$	Tridecylic acid	Jin et al. (2015)	0.772
2	0.89	214.0480[M-H]$^-$	NO	$C_{12}H_9NO_3$	Robustine	Xiang et al. (2007)	1.215
3	0.92	146.0458[M-H]$^-$	119.0446[M-C_2H_3-H]$^-$, 102.0350 [M-C_2H_3-NH_3-H]$^-$	$C_5H_9NO_4$	L-Glutamic acid	Jin et al. (2016)	0.137
	0.94	148.0610[M + H]$^+$	NO				−0.270
4	0.93	193.0352[M + HCOO]$^-$	NO	$C_5H_8O_5$	Malicacid 1-Meester/Malicacid 4-Meester	Jin et al. (2016)	−0.052
5	0.95	185.0220[M + HCOO]$^-$	NO	$C_6H_4O_4$	Coumalic acid	Xiang et al. (2007)	−0.378
6	0.91	116.0346[M + H]$^+$	NO	$C_4H_5NO_3$	5-Hydroxy-2-pyridinecarboxylicacid	Ding et al. (2009)	−0.172
	0.96	114.0310[M-H]$^-$	NO				−1.228
7	0.98	205.0348[M-H]$^-$	NO	$C_7H_{10}O_7$	L-6-citric acid acetate/L-methyl citrate	Jin et al. (2015)	2.341
8	0.98	218.0672[M-H]$^-$	NO	$C_{12}H_{13}NO_3$	Oleracein E	Xiang et al. (2005)	0.780
	0.99	242.0783[M + Na]$^+$	NO				−0.041
9	0.99	157.0368[M-H]$^-$	NO	$C_4H_6N_4O_3$	Allantoin	Xiang et al. (2007)	−0.764
		159.0518[M + H]$^+$	NO				−0.189
10	0.99	170.0816[M + H]$^+$	NO	$C_8H_{11}NO_3$	Noradrenaline	Chen et al. (2003)	0.176
11	1.01	163.0605[M + H]$^+$	132.0815[M-CH_2OH+H]$^+$, 106.0655[M-CH_2OH-C_2H_2+H]$^+$	$C_6H_{10}O_5$	Dimethyl malate	Jin et al. (2016)	0.184
12	1.00	133.0142[M-H]$^-$	NO	$C_4H_6O_5$	Malic acid	Oliveira et al. (2009)	1.729
	1.56	135.0281[M + H]$^+$	NO				−1.555
13	1.01	115.0035[M-H]$^-$	NO	$C_4H_4O_4$	Fumaric acid	Jin et al. (2015)	2.696
14	1.02	664.2009[M-H]$^-$	NO	$C_{30}H_{35}NO_{16}$	Oleracein C	Xiang et al. (2005)	2.710
15	1.06	191.0193[M-H]$^-$	NO	$C_6H_8O_7$	Citric acid	Jin et al. (2016)	2.513
16	1.60	306.0758[M-H]$^-$	NO	$C_{10}H_{17}N_3O_6S$	Glutathiose	Ying et al. (2018)	0.229
17	1.77	196.0616[M-H]$^-$	NO	$C_9H_{11}NO_4$	Levodopa	Chen et al. (2003)	−2.040
	1.81	198.0768[M + H]$^+$	NO				0.353
18	1.85	279.0692[M + HCOO]$^-$	261.0921[M-H_2O + HCOO]$^-$, 233.0973[M-H_2O-CO + HCOO]$^-$, 210.0386[M-H_2O-CO-Na + HCOO]$^-$	$C_9H_{14}O_7$	L-1,5-Dimethyl citric acid	Jin et al. (2016)	1.792
19	2.20	138.0195[M + H]$^+$	NO	$C_8H_{11}NO$	Tyramin	Xin et al. (2009)	−0.072
20	2.27	117.0192[M-H]$^-$	NO	$C_4H_6O_4$	Butanedioic acid	Xiang et al. (2007)	−0.085
21	2.29	132.1024[M + H]$^+$	NO	$C_6H_{13}NO_2$	L-Isoleucine	Jin et al. (2016)	0.151
22	3.07	870.2463[M-H]$^-$	NO	$C_{41}H_{45}NO_{20}$	Oleracein O	Jiao et al. (2015)	0.954
23	3.47	153.0412[M + H]$^+$	NO	$C_8H_{11}NO_2$	Dopamine	Chen et al. (2003)	1.111
24	3.51	151.0398[M-H]$^-$	NO	$C_8H_8O_3$	4-Hydroxyphenyl acetate/Vanillin	Yue et al. (2015)	−0.265
25	3.52	133.0501[M + H]$^+$	NO	$C_5H_8O_4$	Mono-Methyl succinate	Jin et al. (2016)	0.075
	3.94	131.0349[M-H]$^-$	113.9263[M-H_2O-H]$^-$, 104.0254 [M-C_2H_3-H]$^-$, 87.0451[M-C_2H_3-NH_3-H]$^-$, 77.0145[M-C_2H_3-C_2H_3-H]$^-$				−0.839
26	3.52	567.1428[M-H]$^-$	521.1512[M-C_2H_5OH-H]$^-$, 506.3255[M-C_2H_5OH-CH_3-H]$^-$	$C_{25}H_{28}O_{15}$	Portuloside B	Seo et al. (2004)	0.141
27	4.10	218.1029[M-H]$^-$	NO	$C_{12}H_{13}NO_3$	Trollisine	Yao et al. (2007)	0.504
28	4.67	153.0190[M-H]$^-$	109.0296[M-COO-H]$^-$	$C_7H_6O_4$	Protocatechuate	Jiang et al. (2012)	0.850
29	5.21	261.0404[M + HCOO]$^-$	NO	$C_{12}H_8O_4$	5-Methoxypsoralen	Xiang et al. (2007)	−0.115
30	5.52	162.0555[M + H]$^+$	NO	$C_9H_7NO_2$	Indole-3-carboxylic acid	Yan et al. (2012)	0.370
31	5.72	609.2019[M-H]$^-$	NO	$C_{28}H_{34}O_{15}$	Hesperidin	Yang et al. (2007)	−0.295
32	5.80	137.0242[M-H]$^-$	93.0345[M-CO_2-H]$^-$	$C_7H_6O_3$	Salicylic acid	Gao et al. (2019)	0.438
33	6.37	261.1585[M + H]$^+$	243.2121[M-H_2O + H]$^+$, 217.1053 [M-H_2O-C_2H_2+H]$^+$	$C_{15}H_{20}N_2O_2$	3-(2-Methylpropyl)-6-benzyl-2,5-diketopiperazine	Ding et al. (2009)	0.038
34	6.43	327.0091[M + Na]$^+$	NO	$C_{18}H_{28}N_2O_2$	Oleracone A	Li et al. (2016)	2.049
		349.1129[M + HCOO]$^-$	331.1892[M-H_2O + HCOO]$^-$, 313.0924[M-2H_2O + HCOO]$^-$, 267.0722[M-2H_2O-NO_2+HCOO]$^-$, 249.0616[M-3H_2O-NO_2+HCOO]$^-$				−0.057
35	6.59	165.0553[M + H]$^+$	NO	$C_9H_8O_3$	P-Coumaric acid	Xin et al. (2009)	−0.848
	6.74	163.0430[M-H]$^-$	136.0516[M-C_2H_3-H]$^-$, 121.0520 [M-C_2H_3-CH_3-H]$^-$, 106.0413[M-C_2H_3-2CH_3-H]$^-$				0.368
36	6.85	199.0607[M + HCOO]$^-$	NO	$C_8H_{10}O_3$	3,4-Dihydroxyphenylethanol	Jin et al. (2016)	−0.603

(Continued on following page)

TABLE 1 | (*Continued*) Identification of chemical compounds in MCXZ by UHPLC-LTQ-Orbitrap.

Peak no	tR min	Measured mass m/z	MS2	Formula	Compound Name	References	Error ppm
37	6.94	141.0190[M-H]$^-$	NO	$C_6H_6O_4$	3-Hydroxy-5-methylfuran-3-carboxylic acid/5-Hydroxymethyl-2-furoic acid	Jin et al. (2016)	1.276
38	7.13	123.0446[M + H]$^+$	95.0494[M-CO+H]$^+$, 79.0543[M-CO-O+H]$^+$	$C_7H_6O_2$	P-Hydroxybenzaldehyde	Shan et al. (2015)	−1.057
		121.0294[M-H]$^-$	93.0301[M-CO-H]$^-$, 77.0396[M-CO-O-H]$^-$				−0.165
39	7.22	476.3088[M + Na]$^+$	459.2825[M-NH_3+Na]$^+$, 335.2599 [M-NH_3-6H_2O-NH_2+Na]$^+$	$C_{24}H_{39}NO_7$	Oleraciamide C	Xu L. et al. (2017)	0.336
40	7.22	321.1542[M + HCOO]$^-$	NO	$C_{15}H_{20}N_2O_3$	Cyclotyrosine-leucine	Jin et al. (2016)	0.685
41	7.22	177.0191[M-H]$^-$	NO	$C_9H_6O_4$	6,7-Dihydroxycoumarin	Xiang et al. (2007)	−0.565
42	7.51	548.3380[M + H]$^+$	NO	$C_{26}H_{29}NO_{12}$	Oleracein F	Liu et al. (2011)	1.240
	7.54	546.1013[M-H]$^-$	NO				−4.669
43	7.60	534.2263[M + H]$^+$	NO	$C_{25}H_{27}NO_{12}$	Oleracein B	Xiang et al. (2005)	−0.431
44	7.59	502.1347[M-H]$^-$	NO	$C_{24}H_{25}NO_{11}$	Oleracein A	Xiang et al. (2005)	−0.956
	7.62	504.1519[M + H]$^+$	NO				0.754
45	7.64	139.1122[M + H]$^+$	NO	$C_9H_{14}O$	2,4-Nonadienal	Zhao et al. (2014)	0.719
		183.1022[M + HCOO]$^-$	NO				0.928
46	7.64	287.0562[M + H]$^+$	258.0768[M-CO]$^+$, 153.0413[M-$C_8H_6O_2$+H]$^+$, 93.9636[M-$C_8H_6O_4$+H]$^+$	$C_{15}H_{10}O_6$	Kaempferol	Yang (2016): Wu et al. (2019a)	0.348
	7.83	285.0409[M-H]$^-$	267.1966[M-H_2O-CO-H]$^-$, 239.2017[M-H_2O-CO-H]$^-$, 221.1911[M-2H_2O-H]$^-$				0.070
47	7.73	174.1281[M + H]$^+$	NO	$C_{10}H_7NO_2$	3-Quinoline carboxylic acid	Yan et al. (2012)	1.321
		172.0227[M-H]$^-$	NO				1.337
48	7.83	274.0694[M + HCOO]$^-$	255.1966[M -H_2O + HCOO]$^-$, 227.2016[M -H_2O-CO + HCOO]$^-$	$C_{13}H_{11}NO_3$	5,6-Dihydro-8,9-dihydroxy-11H-pyrrolo[2,1-b]benzazepin-11-one	Yue et al. (2015)	−0.109
49	7.92	179.0345[M-H]$^-$	135.0452[M-CO_2-H]$^-$, 107.0145 [M-CO_2-H]$^-$	$C_9H_8O_4$	Caffeicacid	Qin et al. (2018); Zhang X. et al. (2018)	−0.114
50	7.92	197.1178[M + H]$^+$	219.1754[M + Na]$^+$	$C_{11}H_{16}O_3$	Epiloliolide	Jin et al. (2016)	1.979
51	7.94	169.0503[M + H]$^+$	141.9829[M-CO+H]$^+$, 110.0603 [M-CH_3-COO+H]$^+$	$C_8H_8O_4$	Vanillic acid	Xiang et al. (2007)	−0.237
52	7.97	245.0928[M-H]$^-$	NO	$C_{13}H_{10}O_5$	Isopimpinellin	Xiang et al. (2007)	0.898
53	8.00	195.0660[M + H]$^+$	177.1284[M-H_2O + H]$^+$, 159.1178 [M-2H_2O + H]$^+$, 149.1333[M-H_2O-CO + H]$^+$	$C_{10}H_{10}O_4$	Ferulic Acid	Qin et al. (2018); Zhang X. et al. (2018)	−0.205
		193.0503[M-H]-	178.0635[M-CH_3-H]$^-$, 149.0608 [M-COO-H]$^-$, 134.0376[M-COO-CH_3-H]$^-$				0.673
54	8.01	193.0501[M + H]$^+$	NO	$C_{10}H_8O_4$	Scopoletin	Xiang et al. (2007)	0.622
		237.0800[M + HCOO]$^-$	NO				−0.127
55	8.11	396.8029[M + H]$^+$	381.0306[M-CH_3+H]$^+$ 368.2269[M-CO_2+H]$^+$	$C_{26}H_{52}O_2$	Cerotic acid	Zheng et al. (2010)	0.126
56	8.35	197.1182[M + Na]$^+$	NO	$C_9H_{18}O_3$	9-Hydroxynonanoic acid	Zhao et al. (2014)	2.384
57	8.46	479.1186[M + HCOO]$^-$	NO	$C_{26}H_{26}O_6$	Lonchocarpicacid	Xiang et al. (2007)	0.167
58	8.97	137.0244[M-H]$^-$	108.0452[M-CHO-H]$^-$, 92.0268 [M-O-H]$^-$	$C_7H_6O_3$	Protocatechualdehyde	Jiang et al. (2012)	−1.241
59	9.54	314.1399[M + H]$^+$	NO	$C_{18}H_{19}NO_4$	N-Trans-Feruloyltyramine	Yan et al. (2012)	−0.032
60	9.54	137.1330[M + H]$^+$	NO	$C_{10}H_{16}$	7-Propylidene-bicyclo[4,1,0] heptane	Zhao et al., 2014	−0.802
61	10.63	333.2284[M + H]$^+$	315.2539[M-H_2O + H]$^+$, 297.2432 [M-2H_2O + H]$^+$, 279.2326[M-3H_2O + H]$^+$	$C_{17}H_{32}O_6$	3s-3-O-β-D-Glucopyranosyl-3,7-dimethyl-octyl-1,6-diene-3-ol	Seo et al. (2004)	−0.030
	10.70	331.2115[M-H]$^-$	313.2018[M-H_2O-H]$^-$, 295.1917 [M-2H_2O-H]$^-$, 277.1807[M-3H_2O-H]$^-$				−0.030
62	11.04	347.2430[M + HCOO]$^-$	NO	$C_{17}H_{18}O_5$	Portulacanone D	Yan et al. (2012)	0.115

(Continued on following page)

TABLE 1 | (*Continued*) Identification of chemical compounds in MCXZ by UHPLC-LTQ-Orbitrap.

Peak no	tR min	Measured mass m/z	MS2	Formula	Compound Name	References	Error ppm
63	11.74	351.2155[M + Na]$^+$	333.2048[M-H_2O + Na]$^+$	$C_{22}H_{32}O_2$	4,7,10,13,16,19-Docosahexe-noic acid(DHA)	Zou (2004)	0.399
	11.80	327.2167[M-H]$^-$	309.2075[M-H_2O-H]$^-$, 291.1973 [M-2H_2O-H]$^-$, 265.2177[M-2H_2O-C_2H_2-H]$^-$, 247.2073[M-3H_2O-C_2H_2-H]$^-$				–0.275
64	12.82	331.2480[M-H]$^-$	313.2385[M-H_2O-H]$^-$	$C_{18}H_{20}O_6$	Portulacanone C	Yan et al. (2012)	–0.604
65	13.11	395.3155[M + Na]$^+$	NO	$C_{17}H_{24}O_9$	Syringin	Gao et al. (2012)	–0.025
66	14.53	269.1303[M-H]$^-$	241.0504[M-CO-H]$^-$, 240.0434[M-CHO-H]$^-$, 225.0555[M-CO_2-H]$^-$, 197.1915[M-CO_2-CO-H]$^-$	$C_{15}H_{10}O_5$	Genistein	Zhao et al. (2019)	–0.047
67	14.69	228.1967[M]$^+$	199.1488[M-C_2H_5]$^+$, 171.1023[M-C_2H_5-CO]$^+$	$C_{14}H_{28}O_2$	Myristic acid	Li et al. (2008)	–0.131
68	15.67	255.0659[M + H]$^+$	227.1804[M-CO+H]$^+$, 199.1702 [M-2CO+H]$^+$	$C_{15}H_{10}O_4$	Daidzein	Fang et al. (2013)	–0.118
	15.17	253.0862[M-H]$^-$	209.8848[M-CO_2-H]$^-$, 197.0606 [M-2CO-H]$^-$				–0.198
69	16.79	303.3095[M + H]$^+$	NO	$C_{20}H_{30}O_2$	5,8,11,14,17-Eicosapentaenoic acid (EPA)	Zou (2004)	0.824
70	17.22	433.3270[M + H]$^+$	NO	$C_{21}H_{20}O_{10}$	Genistin	Fang et al. (2013)	–0.231
	17.26	431.3099[M-H]$^-$	269.0879[M-Glu-H]$^-$				0.023
71	17.39	518.3262[M + H]$^+$	NO	$C_{25}H_{27}NO_{11}$	Oleracein G	Liu et al. (2011)	0.058
	17.46	562.3136[M + HCOO]$^-$	NO				0.000
72	17.54	301.1071[M + H]$^+$	283.0696[M-H_2O + H]$^+$, 255.1755 [M-H_2O-CO + H]$^+$, 239.0800[M-H_2O-CO-NH_2+H]$^+$	$C_{17}H_{16}O_5$	2,2′-Dihydroxy-4′,6′-dimethoxychalcone	Yan et al. (2012)	3.387
	17.60	299.0764[M-H]$^-$	281.2491[M-H_2O-H]$^-$, 253.2541 [M-H_2O-CO-H]$^-$				–0.167
73	17.64	330.3014[M + H]$^+$	NO	$C_{18}H_{19}NO_5$	N-Trans-Feruloyloctopamine/ N-Cis-Feruloyloctopamine	Yan et al. (2012)	0.061
74	17.90	696.2141[M + H]$^+$	NO	$C_{31}H_{37}NO_{17}$	Oleracein D	Xiang et al. (2005)	–1.030
75	17.95	577.2679[M-H]$^-$	NO	$C_{27}H_{30}O_{14}$	Apigenin-4′-O-α-L-rhamnopyranoside	Jin et al. (2015)	–0.987
	18.25	579.3233[M + H]$^+$	NO				1.484
76	18.19	279.2328[M-H]$^-$	261.2222[M-H_2O-H]$^-$, 243.0621 [M-2H_2O-H]$^-$	$C_{18}H_{32}O_2$	Linoleic acid	Dong et al. (2020)	–1.361
77	18.64	391.2594[M + HCOO]$^-$	373.2502[M-H_2O + HCOO]$^-$	$C_{19}H_{22}O_6$	Portulacanone B	Yan et al. (2012)	0.077
78	18.70	449.2000[M + H]$^+$	NO	$C_{27}H_{28}O_6$	Lonchocarpenin	Xiang et al. (2007)	–0.111
79	18.97	255.2322[M-H]$^-$	NO	$C_{16}H_{32}O_2$	Palmitic acid	Dong et al. (2020)	0.627
80	18.98	329.2689[M-H]$^-$	311.223[M-H_2O-H]$^-$, 293.2122[M-2H_2O-H]$^-$, 275.2015[M-3H_2O-H]$^-$, 229.1449[M-3H_2O-NO_2-H]$^-$, 211.1344[M-4H_2O-NO_2-H]$^-$	$C_{19}H_{38}O_4$	Monopalmitin	Qiao et al. (2012)	0.061
81	18.93	307.2639[M + Na]$^+$	NO	$C_{18}H_{36}O_2$	Stearic acid	Jin et al. (2016);	0.456
	18.98	329.2689[M + HCOO]$^-$	311.223[M-H_2O + HCOO]$^-$, 293.2122[M-2H_2O + HCOO]$^-$, 275.2015[M-3H_2O + HCOO]$^-$			Zhao et al. (2014)	0.061
82	19.26	279.2328[M + H]$^+$	261.2225[M-H_2O + H]$^+$, 243.2116 [M-2H_2O + H]$^+$	$C_{18}H_{30}O_2$	α-Linolenic acid	Xin et al. (2008)	0.072
	19.30	323.2216[M + HCOO]$^-$	NO				0.062
83	20.36	427.3901[M + H]$^+$	408.211[M-H_2O]$^+$	$C_{30}H_{50}O$	Lupeol	Li et al. (2014)	0.374
84	20.69	281.2479[M-H]$^-$	NO	$C_{18}H_{34}O_2$	Oleic acid/14-Octadecenoic acid	Zhao et al. (2014)	0.533
	20.73	283.2643[M + H]$^+$	265.2537[M-H_2O + H]$^+$, 247.2429 [M-2H_2O + H]$^+$				–0.282

positive and negative ion modes, at m/z 255.0659 and 253.0862, respectively, which was identified as daidzein ($C_{15}H_{10}O_4$) based on comparisons with the chemical composition database. Meanwhile, in positive ion mode, the MS^n information showed that the $(M + H)^+$ ion of daidzein at m/z 255 was fragmented by the continuous loss of 28 Da (-CO) at m/z 227 and 56 Da (-2CO) at m/z 199 (**Figures 5A,B**). In negative ion mode, the MS^n information showed that the $(M-H)^-$ ion of daidzein at m/z 253 was fragmented by the loss of 44 Da (-CO_2)at m/z 209 and 56 Da (-2CO) at m/z 197 (**Figures 5C** and **5D**), which was consistent with the results of previous studies (Fang et al., 2013). The above fragmentation pathways provide insights that enable us to speculate on the structures of other flavonoids and their derivatives, such as genistein and kaempferol.

Putative Targets and the Potential Molecular Basis of the Traditional Efficacy Observed During MCXZ Treatment

The TCMIP V2.0 integrated the ETCM database with a series of authoritative algorithms, including the calculation of physicochemical properties, target prediction, network analysis, and visualization. The TCMIP V2.0 had been used as a powerful platform to construct multi-dimensional correlations for in-depth studies of the molecular mechanisms of TCM (Xu H. Y. et al., 2017). In this study, TCMIP V2.0 was used to perform target prediction for MCXZ.

A total of 84 compounds were identified in MCXZ, which were introduced into TCMIP V2.0 to perform target prediction, resulting in a total of 251 putative predicted targets. Detailed information regarding the identified putative MCXZ targets can be found in **Supplementary Table S2**. The functional enrichment analysis of the predicted MCXZ targets was performed using the KEGG database, the pharmacological effects of the pathways were determined by consulting the literature, and the relationships between pharmacological effects and traditional efficacy were analyzed. Network analysis and visualization were performed using Cytoscape software (**Figure 6**).

According to the functional analyses performed for the putative targets and associated pathways affected by MCXZ, combined with the known therapeutic effects of MCXZ in TCM theory, the functional effects of MCXZ could be divided into two modules. The first module includes clearing the liver and improving vision, which is associated with improving endocrine/metabolic system functions (Guan et al., 2019). The second module resolves dampness, which has anti-cancer (Chen and Wang, 2010), antidiuretic (Liu et al., 2012), and sedative (Zhang, 2016) effects. Surprisingly, both functions include anti-inflammatory, anti-microbial, immunomodulatory (Shi et al., 2019), antihyperlipidemic, hypoglycemic (Feng, 2011; Guan et al., 2019), antioxidant (Qi and Li 2018; Chen, 2020), and apoptotic effects.

Underlying Mechanisms Through Which MCXZ Acts on DM

According to the disease-related gene database in TCMIP V2.0, 239, the present study identified DM-related genes, shown in **Supplementary Table S3**. To explore the potential mechanisms through which MCXZ acts on DM, an interaction network, based on the STRING database and the putative MCXZ target-DM-related gene interactions (**Figure 7**) was constructed, and the topological network parameters were calculated. **Supplementary Table S4** provides detailed information regarding the proposed interactions between putative MCXZ targets and DM-related genes. The network consists of 420 nodes and 4,793 edges.

To determine the hub nodes, which may have high value and perform important functions, we calculated the values of the nodes within the putative MCXZ target-DM-related gene interaction network. Consequently, 78 nodes were selected as hubs due to degree values that were greater than 2-fold the median value of all nodes in the network. Based on the direct connections between hubs, an interaction network composed of 78 hubs and 1,079 edges was established (**Supplementary Table S5**). After calculating the topological parameters (degree, betweenness, and closeness) of each hub, 75 major hub nodes were selected as key targets because the three topological parameters for them exceeded the corresponding median values. Among these hubs, 35 major hub nodes were known DM-related genes, of which 44 were putative targets of MCXZ and were considered to be candidate MCXZ targets for the treatment of DM. **Supplementary Table S6** provides details for the 44 targets presumed to be targeted by MCXZ.

The biological functions and pathways of MCXZ target candidates for DM therapy were studied using enrichment analysis, based on the KEGG database. MCXZ appears to treat DM primarily by improving the endocrine/metabolic system, in addition to exerting anti-inflammatory, anti-microbial, immunomodulatory, antihyperlipidemic, hypoglycemic, apoptotic, and other pharmacological effects. The key DM-associated KEGG pathways involved in these pharmacological activities included Type II diabetes mellitus and inflammatory and immune-related pathways such as the Fc epsilon RI signaling pathway, Fc gamma R-mediated phagocytosis, VEGF signaling pathway, T cell receptor signaling pathway, Toll-like receptor signaling pathway, and Calcium signaling pathway. It also involved multiple endocrine/metabolic system-related pathways, including Glutathione metabolism, Metabolism of xenobiotics by cytochrome P 450, Drug metabolism, and Arachidonic acid metabolism, as well as Apoptosis-related pathways, such as ErbB signaling pathway and Apoptosis (**Figure 7**).

Expression of *Akt1*, *VEGF*, *ErbB2*, and *AR* mRNA

The accuracy of network pharmacology prediction results was verified by detecting the expression levels of key genes, including *Akt1*, *VEGF*, *ErbB2,* and *AR,* which are involved in the VEGF and ErbB signaling pathway.

In the pancreatic tissue of diabetic model mice (model group), the expression levels of *Akt1*, *VEGF*, *ErbB2,* and *AR* mRNA were significantly increased ($p < 0.05$) compared with those in normal mice (control group). In contrast, after 4 weeks of treatment with MCXZ, the expression levels of *Akt1*, *VEGF*, *ErbB2,* and *AR* mRNA significantly decreased compared with those in the model group ($p < 0.05$, **Figure 8**).

DISCUSSION

DM has become a common and high-risk disease in modern times. Due to unhealthy lifestyles (e.g., poor diet, low physical activity, and sedentary behavior) (Mozzillo et al., 2017), patients with DM tend to be younger. According to the IDF, currently, 463 million individuals suffer from DM, a number that is expected to reach 592 million by 2035 (Liu et al., 2019). At present, the drugs

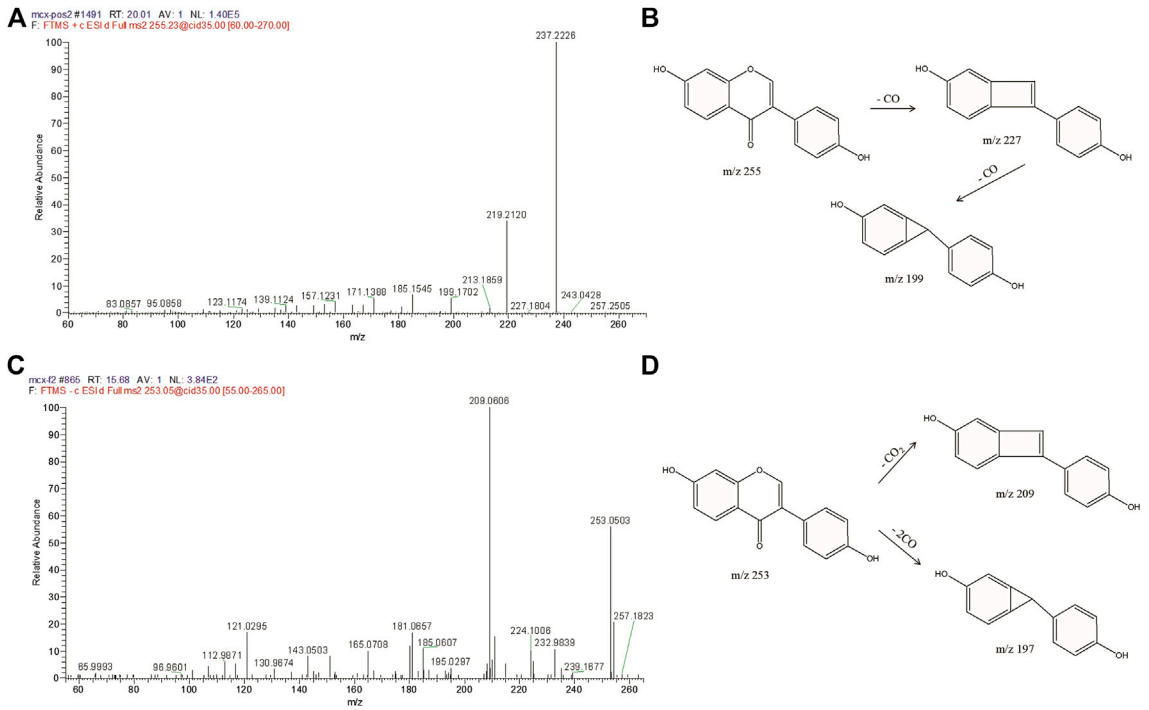

FIGURE 5 | MS^2 spectrum of Flavonoids and main mass spectrometry fragmentation pathways. MS^2 spectrum and fragmentation pathways of daidzein in positive ion mode **(A) (B)**. MS^2 spectrum and fragmentation pathways of daidzein in negative ion mode **(C) (D)**.

used to treat DM typically aim to control blood glucose levels, and most of these drugs lack the sufficient ability to prevent and control disease symptoms, with reduced efficacy over time (Moukette et al., 2017). Therefore, researchers have begun to search for new compounds, especially among natural products, to better control blood glucose levels and associated complications.

MCXZ is widely distributed in tropical, subtropical, and temperate regions. Due to strong adaptability to changes in environmental conditions, the germplasm resources of MCXZ are relatively abundant. Studies have shown that MCXZ could be used as an effective and safe adjuvant therapy among DM subjects (El-Sayed, 2011). In this study, we found that MCXZ alone was able to directly reduce the levels of FBG and HbA1c in STZ-induced DM model mice, and the hypoglycemic effect of the low-dose MCXZ group was found to be better than the middle- and high-dose groups, which may be attributed to lower drug concentrations being more beneficial to digestion and absorption by the gastrointestinal tract.

All experimental data indicated that MCXZ induced anti-hyperglycemic effects and no histopathological damage was observed in the liver or kidney of mice after MCXZ administration, which is consistent with the literature. Chavalittumrong et al. studied the toxicity of purslane and found no histopathological damage to the brain, heart, kidney, liver, spleen, lung, kidney, or other tissues, indicating that purslane had no obvious toxic effects on the examined internal organs (Chavalittumrong et al., 2004).

To explain the material basis and molecular mechanisms of MCXZ treatment in DM, high-throughput technology (UHPLC-LTQ-Orbitrap) and the ETCM database were used to characterize the chemical components of MCXZ quickly and systematically. A total of 84 chemical components were identified, including 34 organic acids, 21 alkaloids, nine flavonoids, and seven coumarins. Some of these compounds have previously been used in the treatment of DM, such as genistein, levodopa, daidzein, 2,4-nonadienal, syringin, glutathione, kaempferol, dopamine, lupeol, and noradrenaline. Several studies have shown that genistein was able to improve dysfunctional hepatic gluconeogenesis in DM (Dkhar et al., 2018). Diabetic retinopathy is a common complication of DM, and clinical studies have also shown that the combined use of levodopa and carbidopa can reverse retinal dysfunction (Motz et al., 2020). Noradrenaline can promote insulin secretion by islet glands and regulate glucose metabolism, reducing and maintaining the stability of blood glucose levels (Zhang and Sun, 1991). Studies have shown that daidzein improved insulin resistance, dyslipidemia, and inflammation and was able to prevent DM and its related complications (Das et al., 2018). The anti-diabetic mechanism of kaempferol may be related to the ability of this substance to promote glucose metabolism and inhibit hepatic gluconeogenesis. (Alkhalidy et al., 2018). Syringin has been shown to treat DM by increasing glucose utilization and reducing plasma glucose levels in rats with insulin deficiency (Niu et al., 2008). Lupeol significantly reduced the level of blood glucose and oxidative stress in DM model rats, indicating that lupeol might have hypoglycemic activity and be useful for the treatment of DM (Malik et al., 2019).

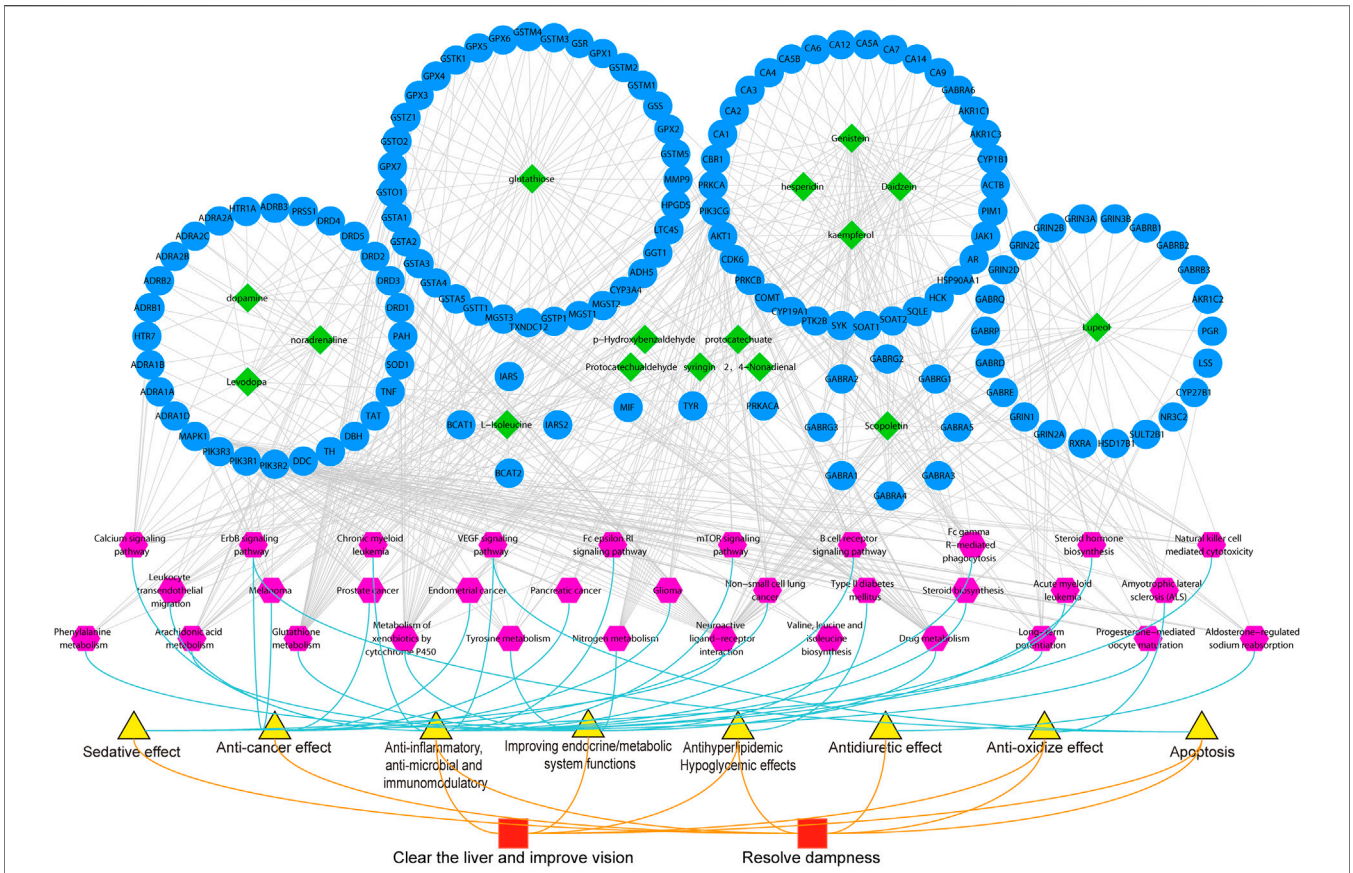

FIGURE 6 | Explain the correlation among the chemical components of MCXZ and the therapeutic efficacy of TCM theory was analyzed based on network pharmacology. Green node indicates the chemical components contained in MCXZ; Blue node refer to the targets of MCXZ; Purple node refers to the pathways involved by MCXZ putative targets; the yellow node refers to the pharmacological action of MCXZ; Red node refers to the therapeutic effect of MCXZ according to the theory of TCM.

A total of 251 putative MCXZ targets were identified using the TCMIP V2.0 database, and the relationships between the putative MCXZ targets and traditional efficacy were analyzed. The pharmacological effects of the predicted MCXZ targets and pathways are closely related to traditional efficacy. MCXZ exerts a hypoglycemic effect through the "clear the liver and improve vision" and "resolve dampness" functions, according to TCM theory, and the possible use of MCXZ in the treatment of DM was preliminarily analyzed (Ren et al., 2017). Furthermore, the interactions between potential MCXZ targets and DM targets were analyzed, and relevant pathways were identified by performing KEGG pathway enrichment analysis. A multi-level association network diagram, showing the "TCM–key active ingredients–core target–key pathways–pharmacological actions–disease effects" relationships were drawn to clarify the pharmacological basis and potential molecular mechanisms through which MCXZ exerts its effects in the treatment of DM.

After combining data from previous publications and performing a multi-dimensional network analysis, we preliminarily determined the potential pathways and targets through which MCXZ is likely to act for the treatment of DM (**Figure 7**). In summary, even after excluding Type II diabetes mellitus as a direct DM pathway, several pathways were identified that could indirectly affect DM and DM-associated complications. VEGF promotes angiogenesis, and an increasing number of studies have shown that VEGF plays an important role in the development of diabetic microvascular complications, such as diabetic retinopathy, skin ulcers, and kidney disease. The inhibition of VEGF expression, the prevention of VEGF receptor binding, and the inhibition of downstream signaling pathways can successfully inhibit the development of diabetic microvascular complications (Li et al., 2017; Zhou et al., 2017).

Fc gamma R-mediated phagocytosis, which is a classical immune regulatory process, may represent a key pathway for the prevention and treatment of DM. Experiments have shown that the activation of Fc gamma R-mediated phagocytosis affects the balance of glucose metabolism. Blocking Fc gamma R-mediated phagocytosis was shown to reduce DM occurrence (Feng et al., 2019).

DM has been associated with a high risk of developing cognitive impairment, and studies have shown that the Calcium signaling pathway affected gut microbiota, which improved cognitive impairment in patients with DM (Zhang

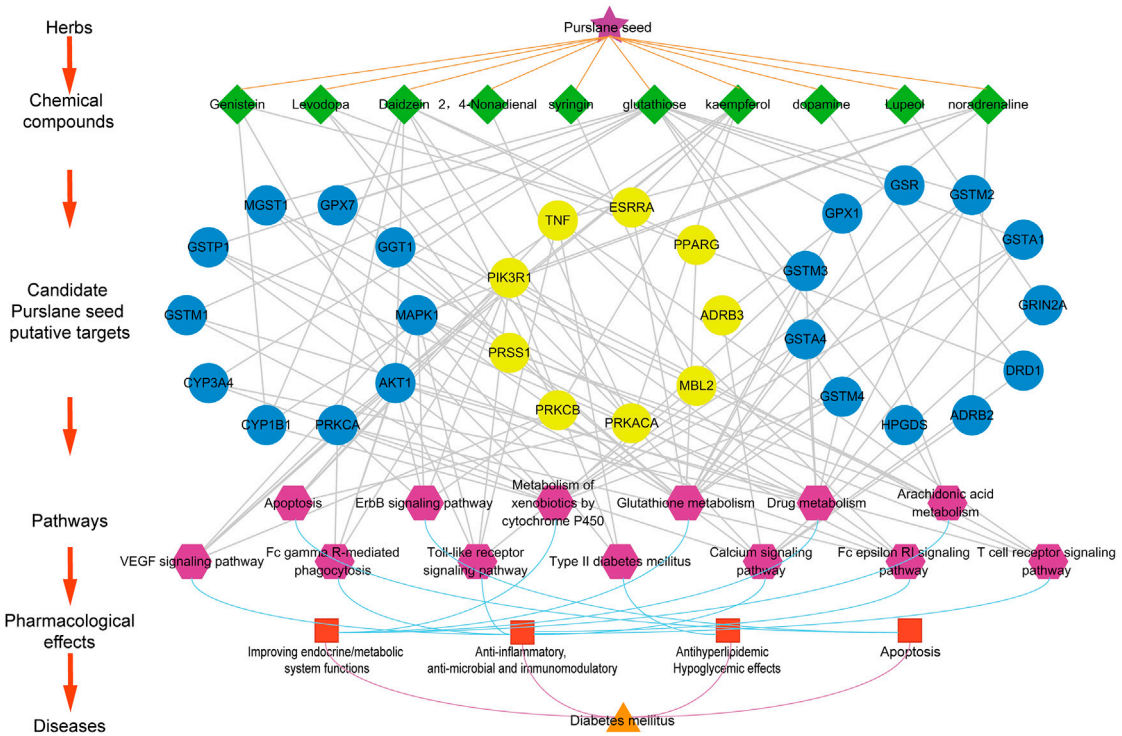

FIGURE 7 | Shows the correlation among the chemical components, candidate targets, involved pathways, and corresponding pharmacological effects of MCXZ. The green node represents the chemical components contained in the MCXZ; the Blue node refers to the candidate targets of MCXZ; the Yellow node refers to the known DM-related genes; the Purple nodes refer to the regulatory pathways of MCXZ candidate targets; the Red node refers to the corresponding pharmacological effects of the main pathways of MCXZ in the treatment of DM.

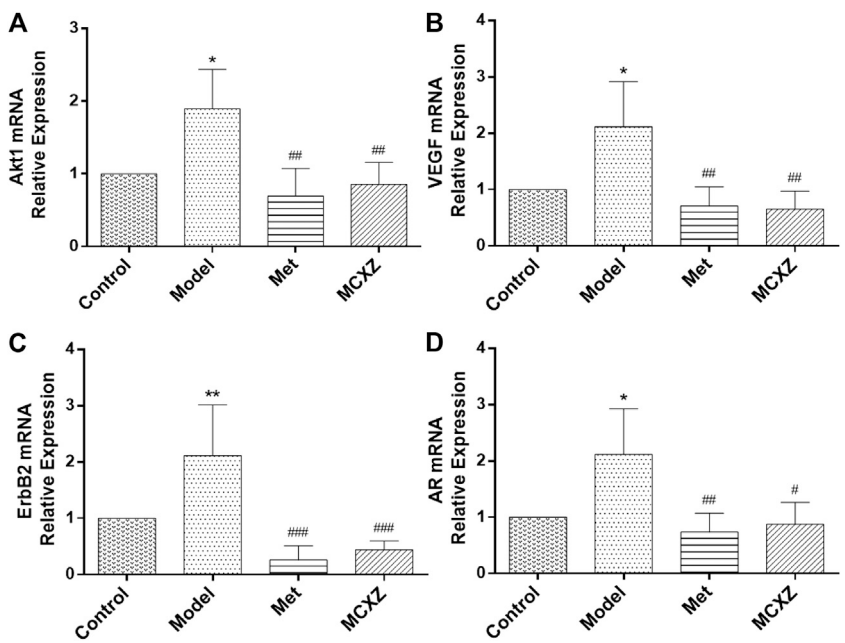

FIGURE 8 | The genes expressions of *Akt1* **(A)**, *VEGF* **(B)**, *ErbB2* **(C)** and *AR* **(D)** in Control, DM, Met and MCXZ treated groups. Data are mean ± SD. $^{*}p < 0.05$ vs. Control; $^{###}p < 0.001$, $^{##}p < 0.01$, $^{#}p < 0.05$ vs. the modle group; n = 3 animals per group.

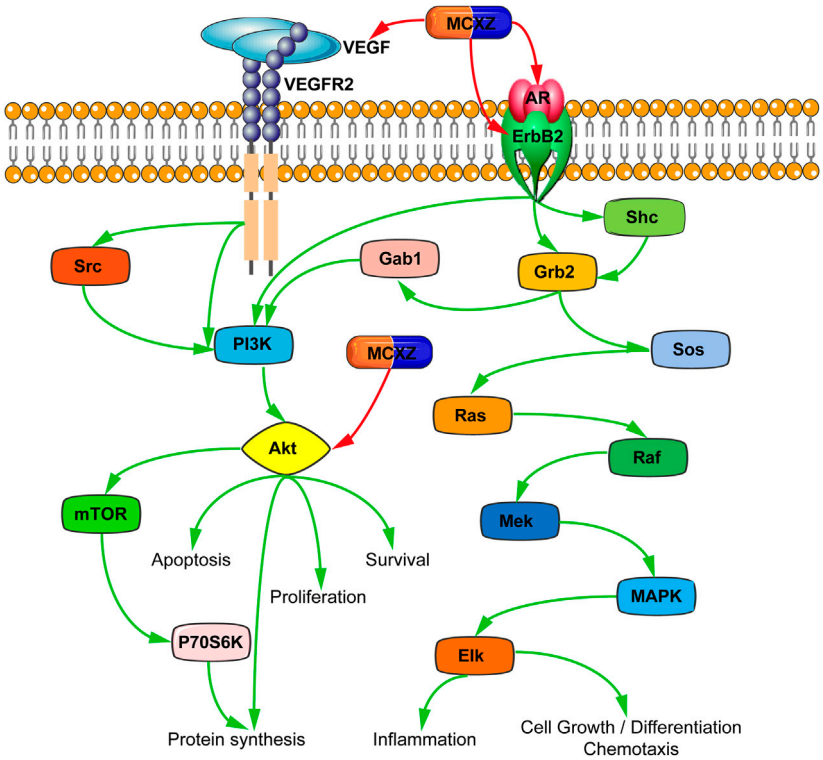

FIGURE 9 | Schematic Illustration of the main pathways of MCXZ in the treatment of DM.

et al., 2020). The primary functions of toll-like receptors include the induction of inflammatory responses and the establishment of adaptive immunity. Studies have shown that toll-like receptors play major roles in the pathogenesis of inflammation-mediated insulin resistance. Taha et al. analyzed 30 DM patients with impaired glucose tolerance and 30 healthy individuals and found a correlation between high levels of toll-like receptor four expression and DM occurrence (Taha et al., 2018).

The glutathione metabolism signaling pathway serves to present oxidative stress-induced injuries and is involved in glucose-induced insulin secretion. Increasing the glutathione concentration in plasma can improve peripheral insulin levels, reduce oxidative damage, and increase insulin sensitivity in diabetic patients (Yang, 2019). The ErbB signaling pathway functions to protect the myocardium, inhibit myocardial fibrosis, and promote angiogenesis. The activation of this pathway might be able to protect against the development of diabetic cardiomyopathy (Han et al., 2019). Other studies have shown that blocking the activation of epidermal growth factor receptor (*EGFR*) can inhibit the infiltration and oxidative stress of kidney immune cells, increase islet autophagy activity, and improve diabetic nephropathy (Li et al., 2018).

The core targets involved in these pathways include phosphoinositide-3-kinase regulatory subunit 1 (*PIK3R1*), serine protease 1 (*PRSS1*), peroxisome proliferator-activated receptor gamma (*PPARG*), protein kinase C beta (*PRKCB*), mannose-binding lectin 2 (*MBL2*), adrenoceptor beta 3 (*ADRB3*), tumor necrosis factor (*TNF*), protein kinase cAMP-activated catalytic subunit alpha (*PRKACA*), and estrogen-related receptor alpha (*ESRRA*) (**Figure 7**). Notably, these nine core target proteins are all known DM candidate targets, and studies have confirmed that they play key roles in relieving major DM symptoms. Studies have demonstrated a critical role for *PIK3R1* in insulin signal transduction, which is closely related to the occurrence of insulin resistance (Karadoğan et al., 2018). Studies have confirmed that activating *PPARG* could significantly improve systemic insulin sensitivity and glucose metabolism (Yang and Chan 2016). PPAR-γ, which is encoded by *PPARG,* is a transcription factor that can be activated by multiple ligands and is widely distributed in adipocytes and immune cells, where it has been shown to promote the differentiation of white adipocytes, increase the number of insulin receptors, promote the transcription of genes associated with insulin signal transduction, and enhance insulin signal transduction. Therefore, the effects of DM can be attenuated by activating PPAR-γ (Gao et al., 2016). *PRKCB* is involved in the regulation of the B cell receptor signaling pathway, apoptosis induced by oxidative stress, insulin signaling transduction, and endothelial cell proliferation (Wu et al., 2019b).

MBL2 is a member of the lectin family, which has been associated with immune dysfunction and is commonly expressed in immune

disorder-related diseases. Recently, *MBL2* has been found to play a role in the development of insulin resistance and gestational DM, and functional variations in *MBL2* can increase DM susceptibility (Muller et al., 2010). *ADRB3* is an obesity-associated gene that plays a key role in the regulation of energy balance. In many ethnic groups, the Arg64 allele in *ADRB3* is associated with the early onset of abdominal obesity and non-insulin-dependent DM (Takenaka et al., 2012). Adipose tissue is an enormously active endocrine organ that secretes various hormones and classical cytokines, such as TNF-α and interleukin (IL)-6. Studies have shown that the upregulation of TNF-α plays an important role in the induction of insulin resistance, which is associated with obesity and DM (Jaganathan et al., 2018). *PRKACA* is involved in the regulation of lipid and glucose metabolism in addition to the insulin signaling pathway (Chi et al., 2019). *ESRRA* is a key regulator of mitochondrial metabolism, able to regulate the absorption of energetic substances, the production and transport of ATP on the mitochondrial membrane, and the response of the body to energy (Dufour et al., 2007). Increased *ESRRA*-activated oxidative phosphorylation in the skeletal muscle of DM patients has been shown to improve blood glucose regulation in DM patients (Mootha et al., 2004).

To verify the accuracy of the predicted network pharmacology results, we detected the expression levels of the key genes *Akt1*, *VEGF*, *ErbB2,* and *AR,* which are members of the VEGF and ErbB signaling pathways. We found that DM upregulated the expression levels of *Akt1*, *VEGF*, *ErbB2,* and *AR* in pancreatic tissue, which is consistent with other literature (Li et al., 2019; Momeny et al., 2019; Srivastava et al., 2019; Zhang et al., 2019).

The results of the present study provide mechanistic insights into the effects of MCXZ in the treatment of DM (**Figure 9**). Our findings indicated that MCXZ might play a role in the treatment of DM in a multi-component, multi-target, and multi-pathway manner, which reflects the therapeutic characteristics of TCM.

CONCLUSION

In conclusion, this study provides evidence to support MCXZ as a promising TCM agent, which can lower blood glucose levels without being associated with negative side effects. MCXZ likely acts in DM by affecting *PIK3R1*, *TNF*, *PRKACA,* and other targets associated with insulin resistance and inflammation through the actions of various chemical components, including genistein, levodopa, and daidzein, which regulate multiple pathways, such as Type II diabetes mellitus, VEGF signaling pathway, Toll-like receptor signaling pathway, and Calcium signaling pathway. These findings were consistent with the existing literature on DM, which was able to describe the molecular mechanisms through which MCXZ acts to treat DM and its complications. This study not only elucidates the effective application of TCM from a macro point of view, but the potential molecular mechanisms of action were also able to be identified from a micro perspective, combining the advantages of TCM theory with modern medical research. However, this study was based on predictions associated with existing research results, and these potential effects must be verified and confirmed through further research.

DATA AVAILABILITY STATEMENT

The raw data supporting the conclusions of this article will be made available by the authors, without undue reservation, to any qualified researcher.

ETHICS STATEMENT

The animal study was reviewed and approved by All animal experiments were approved by the Committee on Animal Care and Use of the Institute of Chinese Materia Medica, China Academy of Chinese Medical Sciences.

AUTHOR CONTRIBUTIONS

JH, XZ, PW, and YQ collected the data and drafted the manuscript. LY proposed the research goal of MCXZ and provided MCXZ. JH, HX, and FL conceived of the study, participated in its design and coordination, and helped to draft the manuscript. The other authors participated in the design of the study and performed the statistical analysis. All authors read and approved the final manuscript.

FUNDING

This work was supported by grants from the National Key Research and Development Program of China (2017YFC1702104, 2017YFC1702303), the National Natural Science Foundation of China (Grant No. 81830111 and 81774201), the Youth Innovation Team of Shaanxi Universities, and Shaanxi Provincial Science and Technology Department Project (No. 2016SF-378), the Fundamental Research Funds for the Central public welfare research institutes (ZXKT17058). The funding agencies had no role in the study design, the collection, analysis, or interpretation of data, the writing of the report, or the decision to submit the article for publication.

SUPPLEMENTARY MATERIAL

The Supplementary Material for this article can be found online at: https://www.frontiersin.org/articles/10.3389/fphar.2020.593693/full#supplementary-material.

REFERENCES

Aberoumand, A. (2009). Preliminary assessment of nutritional value of plant-based diets in relation to human nutrients. *Int. J. Food Sci. Nutr.* 60 (4), 155–162. doi:10.1080/09637480802691044

Alkhalidy, H., Moore, W., and Wang, Y. (2018). The flavonoid kaempferol ameliorates streptozotocin-induced diabetes by suppressing hepatic glucose production. *Molecules*. 23 (9), 2338. doi:10.3390/molecules23092338

Chavalittumrong, P., Chivapat, S., Attawish, A., Bansiddhi, J., Phadungpat, S., Chaorai, B., et al. (2004). Chronic toxicity study of Portulaca grandiflora Hook. *J. Ethnopharmacol.* 90 (2-3), 375–380. doi:10.1016/j.jep.2003.10.018

Chen, J., Shi, Y. P., and Liu, J. Y. (2003). Determination of noradrenaline and dopamine in Chinese herbal extracts from Portulaca oleracea L. by high-performance liquid chromatography. *J. Chromatogr. A*. 1003 (1-2), 127–132. doi:10.1016/s0021-9673(03)00786-6

Chen, P. Y. (2020). Effect of self-made jianpi huashi recipe on rheumatoid factors and oxidative stress indexes for patients with rheumatoid arthritis. *Journal of Sichuan of Traditional Chinese Medicine*. 38 (3), 99–102.

Chen, Y. J., and Wang, J. (2010). Research progress on the molecular mechanism of traditional Chinese medicine against tumor metastasis. *Shaanxi J. Tradit. Chin. Med*. 31 (6), 762–764. doi:10.3969/j.issn.1000-7369.2010.06.082

Chi, L. M., Wang, L. P., and Jiao, D. (2019). Identification of differentially expressed genes and long noncoding RNAs associated with Parkinson's disease. *Parkinsons Dis*. 2019, 6078251. doi:10.1155/2019/6078251

Daniel, M. (2006). *Medicinal Plants: Chemistry and Properties*. Enfield, United Kingdom: Science Publishers.

Das, D., Sarkar, S., Bordoloi, J., Wann, S. B., Kalita, J., and Manna, P. (2018). Daidzein, its effects on impaired glucose and lipid metabolism and vascular inflammation associated with type 2 diabetes. *Biofactors*. 44 (5), 407–417. doi:10.1002/biof.1439

Dehghan, F., Soori, R., Gholami, K., Abolmaesoomi, M., Yusof, A., Muniandy, S., et al. (2016). Purslane (Portulaca oleracea) seed consumption and aerobic training improves biomarkers associated with atherosclerosis in women with type 2 diabetes (T2D). *Sci. Rep*. 6, 37819. doi:10.1038/srep37819

Ding, H. W., Li, F. F., and Song, S. J. (2009). Chemical constituents from Portulaca oleracea L. *J. Shenyang Pharm. Univ.* 26 (11), 38–41. doi:10.14066/j.cnki.cn21-1349/r.2009.11.005

Dkhar, B., Khongsti, K., Thabah, D., Syiem, D., Satyamoorthy, K., and Das, B. (2018). Genistein represses PEPCK-C expression in an insulin-independent manner in HepG2 cells and in alloxan-induced diabetic mice. *J. Cell. Biochem*. 119 (2), 1953–1970. doi:10.1002/jcb.26356

Dong, H. Y., Li, Y. L., Ma, J. S., and Yan, F. L. (2020). Analysis of chemical constituents of Achyranthes bidentata leaf. *J. Xinxiang Med. Univ*. 37 (1), 12–14. doi:10.7683/xxyxyxb.2020.01.004

Dufour, C. R., Wilson, B. J., Huss, J. M., Kelly, D. P., Alaynick, W. A., Downes, M., et al. (2007). Genome-wide orchestration of cardiac functions by the orphan nuclear receptors ERRalpha and gamma. *Cell Metabol.* 5 (5), 345–356. doi:10.1016/j.cmet.2007.03.007

El-Sayed, M. I. (2011). Effects of Portulaca oleracea L. seeds in treatment of type-2 diabetes mellitus patients as adjunctive and alternative therapy. *J. Ethnopharmacol.* 137 (1), 643–651. doi:10.1016/j.jep.2011.06.020

Fang, G., Zhang, P., Ye, X. L., Zhu, X., Zhao, X., and Fang, G. R. (2013). Electron spray ion trap mass spectrometry of isoflavones and isoflavone aglycones of Semen Sojae Praeparatum. *Academic Journal of Second Military Medical University*. 34, 1108–1115. doi:10.3724/SP.J.1008.2013.01108

Feng, T. Y., Li, K. X., Zheng, P. P., Wang, Y. J., Lv, Y. G., Shen, L., et al. (2019). Weighted gene coexpression network analysis identified MicroRNA coexpression modules and related pathways in type 2 diabetes mellitus. *Oxid Med Cell Longev*. 2019, 9567641. doi:10.1155/2019/9567641

Feng, Y. P. (2011). Clinical observation on treatment of 30 cases of damp-heat diabetes with jianpi huashi qingre decoction. *Chinese Journal of Basic Medicine in Traditional Chinese Medicine*. 17 (4), 436–438

Gao, D., Zhang, Y., Yang, F., Lin, Y., Zhang, Q., and Xia, Z. (2016). *In vitro* screening and evaluation of 37 traditional Chinese medicines for their potential to activate peroxisome proliferator-activated receptors-γ. *Phcog. Mag.* 12 (46), 120–127. doi:10.4103/0973-1296.177909

Gao, H. M., Zhao, A. N., and Yu, X. H. (2012). Isolation and identification of chemical constituents from Portulaca oleracea. *China Pharmacy*. 23 (47), 4480–4481. doi:10.6039/j.issn.1001-0408.2012.47.24

Gao, W. Y., Gu, X. R., Zhao, L. J., Zhou, Y. Y., Bian, B. L., and Zhao, H. Y. (2019). Simultaneous determination of 12 components in pudilan xiaoyan oral liquid by ultra-high performance liquid chromatography coupled with triple quadrupole mass spectrometry. *Chinese Journal of Experimental Traditional Medical Formulae*. 25 (18), 150–154. doi:10.13422/j.cnki.syfjx.20191415

Goodarzi, G., Shirgir, A., Alavi, S., and Khoshi, A. (2019). Effect of insulin-glucose metabolism compared with obesity on adipose omentin gene expression in different models of diabetic C57BL/6 mice. *Diabetol. Metab. Syndrome*. 11, 65. doi:10.1186/s13098-019-0460-8

Guan, Z. T., Wang, X. Y., Li, J. A., and Dong, Y. S. (2019). Clinical observation on treating diabetic retinopathy with Qingganmingmu decoction. *Journal of North China University of Science and Technology(Health Sciences Edition)*. 21 (3), 242–246. doi:10.19539/j.cnki.2095-2694.2019.03.016

Guo, G., Yue, L., Fan, S., Jing, S., and Yan, L. J. (2016). Antioxidant and antiproliferative activities of purslane seed oil. *J. Hypertens*. 5 (2), 218. doi:10.4172/2167-1095.1000218

Han, L., Zhang, J., and Qin, L. (2019). Effect of ginsenoside Rb3 on the expression of VE-cadherin, NRG-1, ErbB2 and ErbB4 in rats with myocardial infarction by Neuregulin-1/ErbB signaling pathway. *Chin. J. Evi.-Bas. Cardiova. Med*. 11 (2), 195–199. doi:10.3969/j.issn.1674-4055.2019.02.17

International Diabetes Federation (IDF) (2019). IDF diabetes atlas. Available at: http://www.diabetesatlas.org (Accessed September 15, 2019).

Jaganathan, R., Ravindran, R., and Dhanasekaran, S. (2018). Emerging role of adipocytokines in type 2 diabetes as mediators of insulin resistance and cardiovascular disease. *Can. J. Diabetes*. 42 (4), 446–451. doi:10.1016/j.jcjd.2017.10.040

Jiang, X., Jin, Y., Yuan, B., Sun, S. T., Xu, P. W., and Xu, H. Y. (2012). Analysis on the metabolites of compound prescription salvia miltiorrhiza drop pill *in vivo* of rats. *J. Shenyang Pharm. Univ*. 29 (02), 126–131+142. doi:10.14066/j.cnki.cn21-1349/r.2012.02.003

Jiao, Z. Z., Yue, S., Sun, H. X., Jin, T. Y., Wang, H. N., Zhu, R. X., et al. (2015). Indoline amide glucosides from Portulaca oleracea: isolation, structure, and DPPH radical scavenging activity. *J Nat Prod*. 78 (11), 2588–2597. doi:10.1021/acs.jnatprod.5b00524

Jin, T., Shen, T., Zhou, M., Li, A., Feng, D., Zheng, B., et al. (2016). Chemical constituents from Portulaca oleracea and their bioactivities. *J. Chin. Pharmaceut. Sci*. 25 (12), 898–905. doi:10.5246/jcps.2016.12.101

Jin, Y., Xu, H. Y., and Chen, C. (2015). Anti-diabetic constituents of Portulaca oleracea L. *Chinese Traditional Patent Medicine*. 37 (1), 124–128. doi:10.3969/j.issn.1001-1528.2015.01.025

Karadoğan, A. H., Arikoglu, H., Göktürk, F., İşçioğlu, F., and İpekçi, S. H. (2018). PIK3R1 gene polymorphisms are associated with type 2 diabetes and related features in the Turkish population. *Adv. Clin. Exp. Med*. 27 (7), 921–927. doi:10.17219/acem/68985

Li, C. L., Ding, W. J., and Qu, G. R. (2008). Chemical constituents of galla chinensis. *Chin. Tradit. Herb. Drugs*. 39 (8), 1129–1132.

Li, C. Y., Meng, Y. H., Ying, Z. M., Xu, N., Hao, D., Gao, M. Z., et al. (2016). Three novel alkaloids from Portulaca oleracea L. And their anti-inflammatory effects. *J. Agric. Food Chem*. 64 (29), 5837–5844. doi:10.1021/acs.jafc.6b02673

Li, L., Wang, Y. X., Wang, X. H., Bi, Y. A., and Wu, Y. (2017). Research progress on mechanism of pheretima and compound on diabetic nephropathy. *Chin. J. Experimental. Tradit. Med. Formulae*. 23 (7), 227–234. doi:10.13422/j.cnki.syfjx.2017070227

Li, W., Chang, M., Qiu, M., Chen, Y., Zhang, X., Li, Q., et al. (2019). Exogenous obestatin decreases beta-cell apoptosis and alfa-cell proliferation in high fat diet and streptozotocin induced type 2 diabetic rats. *Eur. J. Pharmacol*. 15 (851), 36–42. doi:10.1016/j.ejphar.2019.02.028

Li, Y., Makabel, B., Ding, G., Zhang, H., Jia, X., and Zou, Z. (2014). Chemical constituents from the roots of echinops sphaerocephalus linn. *Chin. Pharmaceut. J.* 49 (2), 99–101. doi:10.11669/cpj.2014.02.003

Li, Z. L., Li, Y., Overstreet, J. M., Chung, S. J., Niu, A., Fan, X. F., et al. (2018). Inhibition of epidermal growth factor receptor activation is associated with improved diabetic nephropathy and insulin resistance in type 2 diabetes. *Diabetes*. 67 (9), 1847–1857. doi:10.2337/db17-1513

Liu, D. Y., Shen, T., and Xiang, L. (2011). Two antioxidant alkaloids from Portulaca oleracea L. *Helv. Chim. Acta*. 94 (3), 497–501. doi:10.1002/hlca.201000250

Liu, J. Y. (2018). Study on the quality standard of bletilla striata powder. Master's thesis. Chengdu (China): Chengdu University of Tradition Chinese Medicine

Liu, P., Wang, P. F., Wang, K., Ye, H., Dong, C. H., Guo, Y. H., et al. (2019). Research progress of traditional Chinese medicine in treating diabetes mellitus based on PI3K/Akt pathway. *Chin. J. Experi. Tradi. Med. Formulae*. 25 (5), 220–228. doi:10.13422/j.cnki.syfjx.20190537

Liu, X. Q., Zhang, Z. Y., and Guan, Y. (2012). Treatment of 20 cases of chronic nephritis with yishen huashi granules. *The Journal of Practical Medicine*. 28 (5), 840. doi:10.3969/j.issn.1006-5725.2012.05.062

Malik, A., Jamil, U., Butt, T. T., Waquar, S., Gan, S. H., Shafique, H., et al. (2019). In silico and *in vitro* studies of lupeol and iso-orientin as potential antidiabetic agents in a rat model. *Drug Des. Dev. Ther*. 13, 1501–1513. doi:10.2147/DDDT.S176698

Mao, X., Xu, H. Y., Li, S., Su, J., Li, W. J., Guo, Q. Y., et al. (2019). Exploring pharmacological mechanisms of Xueshuan-Xinmai-Ning tablets acting on coronary heart disease based on drug target-disease gene interaction network. *Phytomedicine*. 54, 159–168. doi:10.1016/j.phymed.2018.09.018

Mohamed, A., Abdelgayed, D., S., Essa, S., A., and Mohamed, H., S. R. (2019). Preparation and evaluation of functional foods for prevention of non-alcoholic fatty liver disease. *Pakistan J. Biol. Sci*. 21 (9), 454–462. doi:10.3923/pjbs.2018.454.462

Mohanapriya, S., Senthilkumar, P., Sivakumar, S., Dineshkumar, M., and Subbhuraam, C. V. (2006). Effects of copper sulfate and copper nitrate in aquatic medium on the restoration potential and accumulation of copper in stem cuttings of the terrestrial medicinal plant, Portulaca oleracea linn. *Environ. Monit. Assess*. 121 (1-3), 233–244. doi:10.1007/s10661-005-9117-1

Momeny, M., Esmaeili, F., Hamzehlou, S., Yousefi, H., Javadikooshesh, S., Vahdatirad, V., et al. (2019). The ERBB receptor inhibitor dacomitinib suppresses proliferation and invasion of pancreatic ductal adenocarcinoma cells. *Cell. Oncol*. 42 (4), 491–504. doi:10.1007/s13402-019-00448-w

Mootha, V. K., Handschin, C., Arlow, D., Xie, X. H., Pierre, J. S., Sihag, S., et al. (2004). Erralpha and Gabpa/b specify PGC-1alpha-dependent oxidative phosphorylation gene expression that is altered in diabetic muscle. *Proc. Natl. Acad. Sci. U.S.A*. 101 (17), 6570–6575. doi:10.1073/pnas.0401401101

Motz, C. T., Chesler, K. C., and Allen, R. S. (2020). Novel detection and restorative levodopa treatment for preclinical diabetic retinopathy. *Diabetes*. 69 (7), 1518–1527. doi:10.2337/db19-0869

Movahedian, A., Ghannadi, A., and Vashirnia, M. (2007). Hypocholesterolemic effects of purslane extract on serum lipids in rabbits fed with high cholesterol levels. *Int. J. Pharmacol*. 3 (3). doi:10.3923/ijp.2007.285.289

Mozzillo, E., Zito, E., Maffeis, C., De. Nitto, E., Maltoni, G., Marigliano, M., et al. (2017). Unhealthy lifestyle habits and diabetes-specific health-related quality of life in youths with type 1 diabetes. *Acta Diabetol*. 54 (12), 1073–1080. doi:doi:10.1007/s00592-017-1051-5

Muller, Y. L., Hanson, R. L., Bian, L., Mack, J., Shi, X. L., Pakyz, P., et al. (2010). Functional variants in MBL2 are associated with type 2 diabetes and pre-diabetes traits in Pima Indians and the old order Amish. *Diabetes*. 59 (8), 2080–2085. doi:10.2337/db09-1593

Niu, H. S., Liu, I. M., Cheng, J. T., Lin, C. L., and Hsu, F. L. (2008). Hypoglycemic effect of syringin from Eleutherococcus senticosus in streptozotocin-induced diabetic rats. *Planta Med*. 74 (2), 109–113. doi:10.1055/s-2008-1034275

Oliveira, I., Patrícia, V., Rosário, L., Andrade, P., Bento, A., and Pereria, J. (2009). Phytochemical characterization and radical scavenging activity of Portulaca oleraceae L. leaves and stems. *Microchem. J*. 92 (2), 129–134. doi:10.1016/j.microc.2009.02.006

Papatheodorou, K., Banach, M., Bekiari, E., Rizzo, M., and Edmonds, M. (2018). Complications of diabetes 2017. *J Diabetes Res*. 2018, 3086167. doi:10.1155/2018/3086167

Pardue, B. M., Ama. Moor, V. J., Biapa. Nya, C. P., Nanfack, P., Nzufo, F. T., Kenfack, M. A., et al. (2017). Antioxidant and synergistic antidiabetic activities of a three-plant preparation used in Cameroon folk medicine. *Int Sch Res Notices*. 2017, 9501675. doi:10.1155/2017/9501675

Qi, X., and Li, H. Q. (2018). Protective effects of Qinggan-27 Pills on mouse models of alcoholic liver damage. *Chin. Tradi. Patent Med*. 40 (2), 260–265. doi:10.3969/j.issn.1001-1528.2018.02.003

Qiao, Z. W., Yao, X. Y., Shan, X. C., and Wang, J. L. (2012). Study on chemical constituents of Portulaca oleracea L. *J. Qiqihar Univ. (Natural Science Edition)*. 28 (1), 58–60. doi:10.3969/j.issn.1007-984X.2012.01.020

Qin, W. H., Ren, J. C., Ye, L., Hua, L. H., Wang, Y. H., Guo, Y. L., et al. (2018). UPLC-Q/TOF method for simultaneous qualitative and quantitative analysis of main chemical constituents in medicinal materials of Sinodielsia yunnanensis. *Chin. Tradit. Herb. Drugs*. 49 (15), 3576–3582. doi:10.7501/j.issn.0253-2670.2018.15.016

Ren, J. G., Wang, D. Z., Lei, L., Kang, L., and Liu, J. X. (2017). (Preliminary analysis on relationship between traditional efficacy of Chinese medicine and modern pharmacological action). *Zhongguo Zhongyao Zazhi*. 42 (10), 1979–1983. doi:10.19540/j.cnki.cjcmm.20170307.002

Seo, Y. W., Shin, J. H., Cha, H. J., Kim, Y. A., Ahn, J. W., Lee, B. J., et al. (2004). A new monoterpene glucoside from Portulaca oleracea. *Cheminform*. 35 (10), 1475–1477. doi:10.1002/chin.200410167

Shan, M. Q., Zhang, L., Yu, S., Qian, Y., Wang, J. Y., and Ding, A. W. (2015). Simultaneous determination of eight active components in Gastrodiae Rhizoma by HPLC-MS. *Chin. Tradit. Herb. Drugs*. 46 (14), 2087–2091. doi:10.7501/j.issn.0253-2670.2015.14.012

Shi, M. J., He, K. L., Li, B., Gan, X. F., Yuan, Q. Z., Ren, X., et al. (2019). Study on anti-inflammatory and antibacterial effects of Qinggan Mingmu pellets. *Shaanxi J. Tradit. Chin. Med*. 40 (9), 1158–1161. doi:10.3969/j.issn.1000-7369.2019.09.002

Srivastava, S., Pandey, H., Singh, S. K., and Tripathi, Y. B. (2019). Anti-oxidant, anti-apoptotic, anti-hypoxic and anti-inflammatory conditions induced by PTY-2 against STZ-induced stress in islets. *Biosci Trends*. 13 (5), 382–393. doi:10.5582/bst.2019.01181

Sun, S., Xie, Z. S., Liu, E. H., Yan, Y. T., Xu, X. J., and Li, P. (2014). Chemical profiling of jinqi jiangtang tablets by HPLC-ESI-Q-TOF/MS. *Chin. J. Nat. Med*. 12 (3), 229. doi:10.1016/S1875-5364(14)60039-X

Taha, I. M., Abdu Allah, A. M., and Abd El Gayed, E. M. (2018). Expression of toll-like receptor 4 and its connection with type 2 diabetes mellitus. *Cell Mol Biol (Noisy-le-grand)*. 64 (13), 15–20. doi:10.14715/cmb/2018.64.13.4

Takenaka, A., Nakamura, S., Mitsunaga, F., Inoue-Murayama, M., Udono, T., and Suryobroto, B. (2012). Human-specific SNP in obesity genes, adrenergic receptor beta2 (ADRB2), Beta3 (ADRB3), and PPAR γ2 (PPARG), during primate evolution. *PloS One*. 7 (8), e43461. doi:10.1371/journal.pone.0043461

Wang, S. S., Xu, H. X., Ma, Y., Wang, X. G., Shi, Y., Huang, B., et al. (2015). Characterization and rapid identification of chemical constituents of NaoXinTong capsules by UHPLC-linear ion trap/Orbitrap mass spectrometry. *J. Pharmaceut. Biomed. Anal*. 111, 104–118. doi:10.1016/j.jpba.2015.01.020

Wu, D., Gao, Y., Xiang, H., Xing, J., Han, Y. M., Qin, X. M., et al. (2019a). An exploration on mechanisms of "treating different diseases with same method" of Xiaoyao Powder in treating depression and diabetes based on network pharmacology. *Chin. Tradit. Herb. Drugs*. 50 (08), 1818–1827. doi:10.7501/j.issn.0253-2670.2019.08.009

Wu, D., Wang, J., Huang, B. Y., Wang, Y., and Liu, L. (2019b). Simultaneous determination of six components in Bidens parviflora Willd. by UPLC-MS/MS. *Shandong Sci*. 32 (3), 16–22. doi:10.3976/j.issn.1002-4026.2019.03.003

Xiang, L., Xing, D., Wang, W., Wang, R., Ding, Y., and Du, L. (2005). Alkaloids from Portulaca oleracea L. *Phytochemistry*. 66 (21), 2595–2601. doi:10.1016/j.phytochem.2005.08.011

Xiang, L., Guo, D. X., Ju, R., Ma, B., Lei, F., and Du, L. J. (2007). Cyclic dipeptides from Portulaca oleracea. *Chin. Tradit. Herb. Drugs*. 38 (11), 1622–1625. doi:10.3321/j.issn:0253-2670.2007.11.007

Xin, H. L., Hou, Y. H., Yue, X. Q., Sheng, X., Li, M., Lu, J., et al. (2009). Screening of anti-hypoxic active parts of Portulaca oleracea and its chemical composition. *Chin. Tradit. Herb. Drugs*. 40 (1), 114–116.

Xin, H. L., Xu, Y. F., Yue, X. Q., Hou, Y. H., Li, M., and Yin, C. Q. (2008). Analysis of chemical constituents in extract from Portulaca oleracea L. With GC-MS method. *Pharmaceutical Journal of Chinese People's Liberation Army*. 24 (2), 133–136.

Xu, H. Y., Liu, Z. M., Fu, Y., Zhang, Y. Q., Yu, J. J., Guo, F. F., et al. (2017). Exploiture and application of an internet-based computation platform for integrative pharmacology of traditional Chinese medicine. *Zhongguo Zhong Yao Za Zhi*. 42 (18), 3633–3638. doi:10.19540/j.cnki.cjcmm.2017.0141

Xu, L., Ying, Z., Wei, W., Hao, D., Wang, H., Zhang, W., et al. (2017). A novel alkaloid from Portulaca oleracea L. *Nat. Prod. Res*. 31 (8), 902–908. doi:10.1080/14786419.2016.1253081

Xu, H. Y., Zhang, Y. Q., Liu, Z. M., Chen, T., Lv, C. Y., Tang, S. H., et al. (2019). ETCM: an encyclopaedia of traditional Chinese medicine. *Nucleic Acids Res*. 47 (D1), D976–D982. doi:10.1093/nar/gky987

Yang, C. (2019). The application of jiaotai pill in diabetesmellitus and network pharmacological analysis of its mechanisms. Master's thesis. Yichun (China): Yichun University.

Yang, T. (2016). Studies on characteristic and analysis of chemical components of Aster tataricus and inhibitory effect of friedelan-3beta-ol on cytochrome P450s in human liver microsome. Master's thesis. Shijiazhuang (China): Hebei Medical University.

Yang, Y., and Chan, L. (2016). Monogenic diabetes: what it teaches us on the common forms of type 1 and type 2 diabetes. *Endocr. Rev*. 37 (3), 190–222. doi:10.1210/er.2015-1116

Yang, Z. J., Zheng, Y. N., and Xiang, L. (2007). Study on chemical constituents of Portulaca oleracea. *J. Chin. Med. Mater*. 30 (10), 1248–1250. doi:10.3321/j.issn:1001-4454.2007.10.018

Yan, J., Sun, L. R., Zhou, Z. Y., Chen, Y., Zhang, W., Dai, H., et al. (2012). Homoisoflavonoids from the medicinal plant Portulaca oleracea. *Phytochemistry*. 80, 37–41. doi:10.1016/j.phytochem.2012.05.014

Yao, J. Q., Song, S. J., Meng, N., and Ding, H. W. (2007). Chemical constituents from the Portulaca oleracea L. *J. Shenyang Pharm. Univ*. 24 (12), 751–753. doi:10.3969/j.issn.1006-2858.2007.12.007

Ying, Z. M., Li, C. Y., Gao, M. Z., Ying, X. X., and Yang, G. L. (2018). Pharmacokinetics and metabolism of olerciamide A from Portulaca oleracea L. in rats by UHPLC-UV and UHPLC-ESI-Q-TOF/MS. *Biomed. Chromatogr*. 32 (2), e4061. doi:10.1002/bmc.406110.1002/bmc.4061

Yu, G. H., Yang, H. J., Li, J. F., Geng, Y., Dong, L., and Xu, H. Y. (2016). Analysis of chemical constituents from Citrus aurantium by UHPLC-LTQ-Orbitrap-MS/MS. *Zhongguo Zhongyao Zazhi*. 41 (18), 3371. doi:10.4268/cjcmm20161811

Yue, S., Jiao, Z. Z., and Sun, H. X. (2015). A new tricyclic alkaloid fromPortulaca oleraceaL. *Helv. Chim. Acta*. 98, 961–966. doi:10.1002/hlca.201400374

Zhang, H., Nie, X. Q., Shi, X. J., Zhao, J. F., Chen, Y., Yao, Q. Y., et al. (2018). Regulatory mechanisms of the wnt/β-catenin pathway in diabetic cutaneous ulcers. *Front. Pharmacol*. 9, 1114. doi:10.3389/fphar.2018.01114

Zhang, X., Liang, C., Li, C., Bu, M., Bu, L., Xiao, Y. D., et al. (2018). Simultaneous qualitative and quantitative study of main compounds in Commelina communis linn. By UHPLC-Q-TOF-MS-MS and HPLC-ESI-MS-MS. *J. Chromatogr. Sci*. 56 (7), 582–594. doi:10.1093/chromsci/bmy030

Zhang, H., and Sun, R. (1991). Health plant-portulaca oleracea. *J. Biol*. 18 (1), 26–27.

Zhang, M., Li, C. X., Wei, F., and Qin, Y. (2019). Protective effect of gigantolon human retinal microvascular endothelial cells induced by high glucose. *International Eye Science*. 19 (2), 209–213. doi:10.3980/j.issn.1672-5123.2019.2.06

Zhang, M. X. (2016). The studies on the anti-alzheimer's disease fraction of acorus tatarinowii and its preliminary material basis. MS dissertation. Shanghai (China): China State Institute of Pharmaceutical Industry.

Zhang, Y. Y., Lu, S. R., Yang, Y., Wang, Z., Wang, B., Zhang, B. S., et al. (2020). The diversity of gut microbiota in type 2 diabetes with or without cognitive impairment. *Aging Clin. Exp. Res*. 2020, 1–13. doi:10.1007/s40520-020-01553-9

Zhang, Z. J. (2014). Analysis of TCM treatment principles of chronic complications of diabetes. *Diabetes New World*. 34 (17), 37–38. doi:10.16658/j.cnki.1672-4062.2014.17.004

Zhao, W. J., Liang, Y. Y., Wang, Z. J., Hou, J. Z., Zhang, L. Z., Wang, Z. B., et al. (2019). Structural elucidation of genistein metabolites in rats based on UHPLC-LTQ-orbitrap mass spectrometry. *J. Chin. Mass Spectrom. Soc*. 40 (2), 109–122. doi:10.7538/zpxb.2018.0058

Zhao, X. T., Zhao, R. H., Wang, L. X., He, S. W., Zhao, F. Y., and Hou, L. L. (2014). Isolation and identification of chemical constituents in Purslane fatty acids. *China Medical Herald*. 11 (7), 94–96. doi:10.15406/mojfpt.2016.02.00047

Zheng, S. L., Li, K. T., Yang, S., Zhang, Y. X., and Shi, Y. (2010). Chemical constituents of qingluo prescription. *Chin. Tradit. Patent Med*. 32 (10), 1753–1757. doi:10.3969/j.issn.1001-1528.2010.10.029

Zhou, W. Y., Wang, H. Y., Du, X. J., and Dong, W. H. (2017). Effects of PGMS on the expression of vascular endothelial growth factor in the rat of diabetic retinopathy. *J. Otolaryngol. Ophthalmol. Shandong Univ*. 31 (2), 90–95. doi:10.6040/j.issn.1673-3770.0.2016.146

Zou, Y. H. (2004). Analysis of fatty acids from purslane by gas chromatography-mass spectrometry with 2-amino-2-methylpropanol chemical modifying. *Food Sci. (N. Y.)*. 25 (5), 154–158. doi:10.3321/j.issn:1002-6630.2004.05.036

Conflict of Interest: Author LY was employed by the Guangzhou Zhongda Pharmaceutical Development Co. Ltd.

The remaining authors declare that the research was conducted in the absence of any commercial or financial relationships that could be construed as a potential conflict of interest.

Copyright © 2021 Hou, Zhou, Wang, Zhao, Qin, Liu, Yu and Xu. This is an open-access article distributed under the terms of the Creative Commons Attribution License (CC BY). The use, distribution or reproduction in other forums is permitted, provided the original author(s) and the copyright owner(s) are credited and that the original publication in this journal is cited, in accordance with accepted academic practice. No use, distribution or reproduction is permitted which does not comply with these terms.

frontiers in Pharmacology

ORIGINAL RESEARCH
published: 12 February 2021
doi: 10.3389/fphar.2020.609825

Chemical Characteristics of *Platycodon grandiflorum* and its Mechanism in Lung Cancer Treatment

Yaling Deng[1†], Xianwen Ye[1†], Yufan Chen[2†], Hongmin Ren[1], Lanting Xia[1], Ying Liu[1], Minmin Liu[1], Haiping Liu[3], Huangang Zhang[1], Kairui Wang[1], Jinlian Zhang[1] and Zhongwei Zhang[4]**

[1]School of Pharmacy, Jiangxi University of Traditional Chinese Medicine, Nanchang, China, [2]Patient Service Center, Ganzhou People's Hospital, Ganzhou, China, [3]School of Pharmacy, Guilin Medical University, Guilin, China, [4]School of Pharmacy, Youjiang Medical University for Nationalities, Guangxi, China

OPEN ACCESS

Edited by:
Yan Xu,
Cleveland State University,
United States

Reviewed by:
Shaojie Huang,
Fourth Military Medical University,
China
Swapan Kumar Roy,
Chungbuk National University,
South Korea

***Correspondence:**
Jinlian Zhang
jxjzzjl@163.com
Zhongwei Zhang
zhangzhongwei@ymcn.edu.cn

[†]These authors have contributed equally to this work and share first authorship

Specialty section:
This article was submitted to Ethnopharmacology, a section of the journal Frontiers in Pharmacology

Received: 24 September 2020
Accepted: 10 December 2020
Published: 12 February 2021

Citation:
Deng Y, Ye X, Chen Y, Ren H, Xia L, Liu Y, Liu M, Liu H, Zhang H, Wang K, Zhang J and Zhang Z (2021) Chemical Characteristics of Platycodon grandiflorum and its Mechanism in Lung Cancer Treatment. Front. Pharmacol. 11:609825. doi: 10.3389/fphar.2020.609825

Objective: The technology, network pharmacology and molecular docking technology of the ultra performance liquid chromatography-quadrupole time-of-flight tandem mass spectrometry (UPLC-Q-TOF-MS/MS) were used to explore the potential molecular mechanism of *Platycodon grandiflorum* (PG) in the treatment of lung cancer (LC).

Methods: UPLC-Q-TOF-MS/MS technology was used to analyze the ingredients of PG and the potential LC targets were obtained from the Traditional Chinese Medicine Systems Pharmacology database, and the Analysis Platform (TCMSP), GeneCards and other databases. The interaction network of the drug-disease targets was constructed with the additional use of STRING 11.0. The pathway enrichment analysis was carried out using Gene ontology (GO) and Kyoto Encyclopedia of Genes and Genomes (KEGG) in Metascape, and then the "Drug-Ingredients-Targets-Pathways-Disease" (D-I-T-P-D) network was constructed using Cytoscape v3.7.1. Finally, the Discovery Studio 2016 (DS) software was used to evaluate the molecular docking.

Results: Forty-seven compounds in PG, including triterpenoid saponins, steroidal saponins and flavonoids, were identified and nine main bioactive components including platycodin D were screened. According to the method of data mining, 545 potential drug targets and 2,664 disease-related targets were collected. The results of topological analysis revealed 20 core targets including caspase 3 (CASP3) and prostaglandin-endoperoxide synthase 2 (PTGS2) suggesting that the potential signaling pathway potentially involved in the treatment of LC included MAPK signaling pathway and P13K-AKT signaling pathway. The results of molecular docking proved that the bound of the ingredients with potential key targets was excellent.

Conclusion: The results in this study provided a novel insight in the exploration of the mechanism of action of PG against LC.

Keywords: lung cancer, molecular mechanism, network pharmacology, Platycodon grandiflorum, ultra performance liquid chromatography-quadrupole time-of-flight tandem mass spectrometry

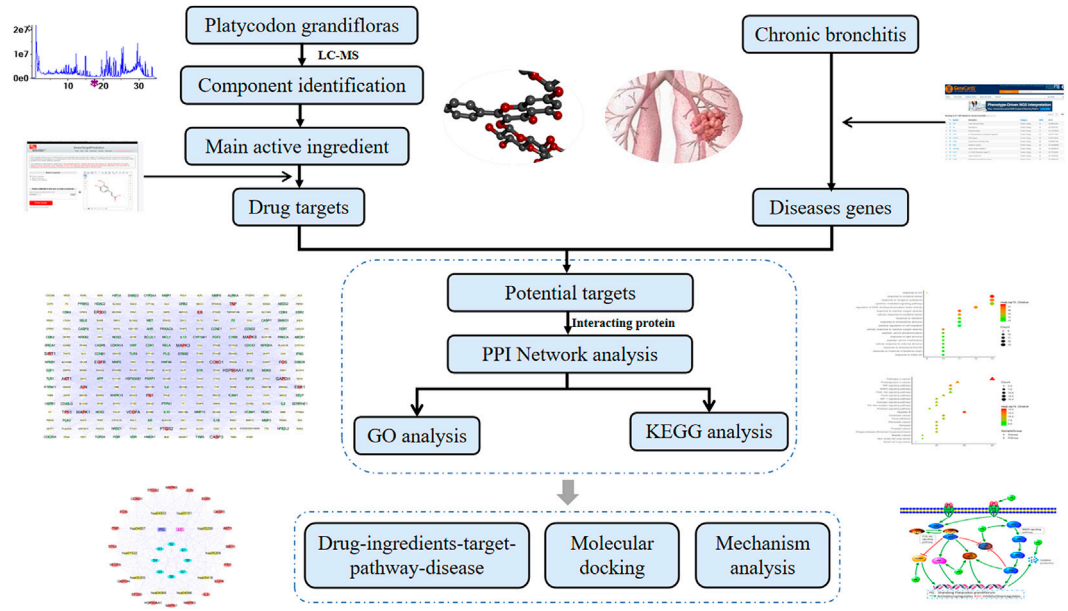

FIGURE 1 | A comprehensive strategy diagram the chemical ingredients analysis, targets prediction, and network calculation for investigation the mechanism of action of *Platycodon grandiflorum* on lung cancer.

INTRODUCTION

Lung cancer (LC) is a malignant tumor with the highest morbidity and mortality worldwide, mostly in male than in female, indeed known as "the king of cancer" (Shao and Zhang, 2020). At present, surgery, chemotherapy and radiotherapy are the main treatments to combat LC, but their side effects are numerous and unavoidable and the clinical prognosis is not ideal. The development of traditional Chinese medicine (TCM) included the discovery and used of anti-cancer drugs; thus, it has attracted more and more attention. TCM adopts syndrome specific treatments, TCM combined with chemotherapy and other methods, with less toxic side effects. For this reason, TCM prescriptions achieved good results in clinical practice (Bai et al., 2017; Wang and Li, 2019). Therefore, the research and development of new TCM to combat LC would be of great significance.

Platycodon grandiflorum (PG) is a plant belonging to the family of campanulaceae, and the dried root is used in TCM to regulate the lung meridian. PG exerts the effect of smoothing lung, dispelling the phlegm, and expelling the pus, and represents the main treatment to cure sore throat, vomiting due to a purulent carbuncle infection in the lung, hypochondriac pain in the chest and other syndromes (Chinese Pharmacopoeia Commission, 2020). The properties of PG were first published in Shennong Materia Medica Classic. PG is mainly growing in the Northeast China, Central China and Guangdong, and the components of PG are different in different areas. Shandong is one of the authentic areas cultivating PG. The roots of PG from Shandong are longer, less bifurcated and with a high content of active components (Zhu et al., 2013). According to the TCM, PG mainly acts on the lung and its related parts, with an antitussive and expectorant effect, and good therapeutic effect on LC (Yim et al., 2016; Li et al., 2019; Deng et al., 2020). However, its mechanism of action in the treatment of LC is not clear.

UPLC-Q-TOF-MS/MS is a high-throughput analytical technology rapidly developed in the past decade, which is widely used in medicine, drug research and other fields (Jin et al., 2018; Ren et al., 2020). Network pharmacology is a theory based on systems biology, which emphasizes the multi-pathway regulation of signaling pathways, thus in agreement with the multi-component-multi-target characteristics of TCM (Yang et al., 2019; Zhang et al., 2019; Ye et al., 2020). Therefore, in this study, the components of the PG roots cultivated in the Shandong Province were analyzed, and then the "Drug-Ingredients-Targets-Pathways-Disease" (D-I-T-P-D) network was constructed according to the relevant principles and methods of network pharmacology to explore the potential molecular mechanism used by PG to treat LC. Our aim was to identify a new drug through the development of the potential of PG to provide a theoretical basis for its clinical application. The flow chart of the approach used in this study is shown in **Figure 1**.

MATERIALS AND METHODS

Chemicals and Materials

Methanol, acetonitrile, and formic acid used for high performance liquid chromatography (HPLC) were purchased from ACS (Washington D.C., MD, United States). Methanol for herb extraction was purchased from Xilong Scientific Co., Ltd (Guangdong, China). Ultrapure water was obtained from a Milli-QB system (Bedford, MA, United States). PG root pieces (simply

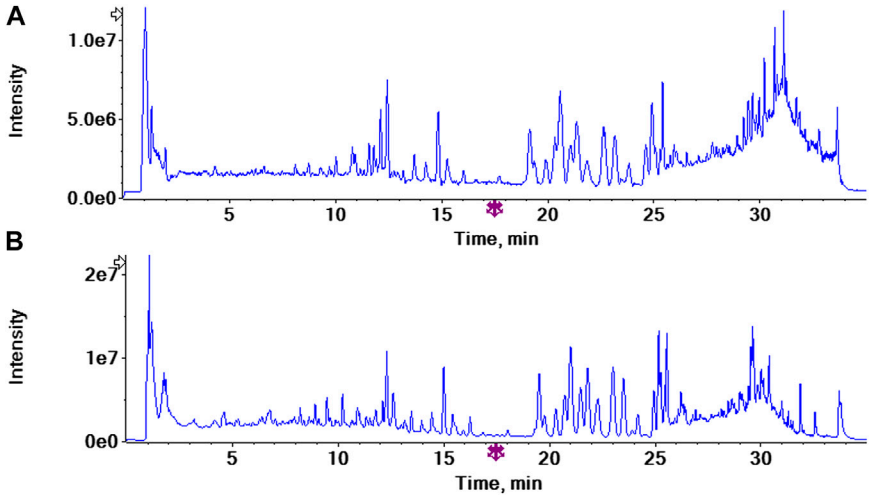

FIGURE 2 | The total ion chromatograms (TICs) of *Platycodon grandiflorum* by UPLC/Q-TOF-MS/MS **(A)** TIC of *Platycodon grandiflorum* in positive ion mode **(B)** TIC of *Platycodon grandiflorum* in negative ion mode.

defined as PG pieces according to the Chinese Pharmacopoeia 2015 edition that assumes that PG is the root) were purchased from Jiangxi Jiangzhong Herbal Pieces Co., Ltd (Jiangxi, China; batch number: 181024). The original PG medicinal material was purchased from Yiyuan, Shandong province, and was identified as the dried root of *Platycodon grandiflorum* (Jacq.) A. DC. Campanulaceae from Professor Fu Xiaomei. PG decoction pieces were processed by Jiangxi Jiangzhong TCM Decoction Co., Ltd. according to the processing method of the Chinese Pharmacopoeia 2015 edition. Next, dried PG pieces were crushed into a 40 mesh powder and stored in the laboratory of the Jiangxi University of TCM.

A total of 15 pure compounds were used as reference standards (purity≥98%). Among them, deapio-platycodin D, platycodin D, polygonatoside C1, rubinin, luteolin, kaempferol, apigenin, caffeic acid, ferulic acid, adenosine, and lobetyolin were purchased from Chengdu Chroma-Biotechnology Co., Ltd (Sichuan, China). 3-O-β-D-glucopyranosyl platycodigenin, rutin, chlorogenic acid, and linoleic acid were purchased from Sichuan Vicky Biotechnology Co., Ltd (Sichuan, China).

Ultra-Performance Liquid Chromatography-Quadrupole-Time-Of-Flight Tandem Mass (UPLC-Q-TOF-MS/MS) Analysis

Preparation of Standard and Sample Solutions

Ten milligrams of each reference compound (deapio-platycodin D, platycodin D, polygonatoside C1, adenosine, ferulic acid, apigenin, luteolin, chlorogenic acid, caffeic acid, kaempferol, robinin, lobetyolin, rutin, 3-O-β-D-glucopyranosyl platycodigenin and linoleic acid) were weighed and transferred into a 10-ml volumetric flask. Methanol was added to reach the volumetric mark, and the solution was shaken well, stored at 4 °C and used as a stock solution. Then, the appropriate amount of stock solution was transferred into a 5 ml volumetric flask, and methanol was added to reach the volumetric mark. The solutions were filtered using a 0.22 μm microporous membrane to obtain the standard solutions.

A total of 2.0 g PG powder was accurately weighed and transferred into a round bottom flask with 50 ml 50% methanol. The solution was mixed well, incubated for 0.5 h at room temperature, and ultrasonically treated for 30 min using an ultrasonic cleaning instrument (Jiangsu, China). The extracted solution was centrifuged at 14,000 rpm for 15 min at room temperature, and filtered using a 0.22 μm microporous membrane before qualitative analysis.

UPLC-Q-TOF-MS/MS Conditions

The chemical analysis was performed on a connected UPLC system (Nexera X2 LC-30A, Shimadzu Corp., Japan) -hybrid triple quadruple time-of-flight mass spectrometer (Triple TOF™ 5600$^+$, AB Sciex, Forster City, CA, United States) with an electrospray ionization source (ESI). Acquity UPLC BEH C_{18} column (2.1 × 100 mm × 1.7 μm) was used to perform chromatographic separation with a flow rate of 0.25 ml/min at 40 °C. The linear gradient program used in this work was composed of a mobile phase system including solvent A (100% acetonitrile, v/v) and solvent B (0.01% formic acid in water, v/v) according to this detailed composition: solvent A at 5–23% for 10 min, 23–25% for 6 min, 25% for 4 min, 25–29% for 3 min, 29–95% for 7 min, 95–5% for 2.1 min, isocratic eluted at 5% for 2.9 min.

The settings of Q-TOF-MS/MS parameters were as follows: ion source gas 1 (GSI) and gas 2 (GS2) were both set at 50 psi, curtain gas (CUR) was set at 40 psi, ion spray voltage floating (ISVF) was set at 5500 V in the positive mode while 4500 V was set in the negative mode, ion source temperature (TEM) was set at 500 °C, collision energy (CE) was set at 60 V, collision energy spread (CES) was set at 15 V, declustering potential (DP) was set

TABLE 1 | Information on chemical ingredients in *Platycodon grandiflorum*.

NO	t_R/ min	Molecular Formula	ESI-MS	Error (ppm)	Fragment ions m/s	Identity	Sort
1	11.99	$C_{42}H_{68}O_{16}$	**827.4435** $[M-H]^-$	−2	707.3943,**665.3866**,647.3830,503.3403,441.2817	platycodon A	triterpene saponins
2	11.99	$C_{42}H_{68}O_{16}$	**827.4435** $[M-H]^-$	−2	707.3943,**665.3866**,647.3830,503.3403,441.2817	platycosaponin A	triterpene saponins
3	13.04	$C_{41}H_{66}O_{15}$	797.4329 $[M-H]^-$	−2.1	**665.3987**,647.3789,**635.3509**,617.3651,485.3600,469.1602	platycodon B	triterpene saponins
4	14.09	$C_{52}H_{84}O_{23}$	**1075.5331** $[M-H]^-$	−2.7	925.4664,**665.3873**,647.3716,485.3034,441.3356,337.1133	platycoside J	triterpene saponins
5	14.55	$C_{36}H_{54}O_{12}$	677.3543 $[M-H]^-$	−3.3	615.3600,515.2936,453.3113	platycoside M1	triterpene saponins
6[a]	19.51	$C_{52}H_{84}O_{24}$	1091.5280 $[M-H]^-$	−2.5	**681.3853**,663.3734,619.3120,**635.3797**,519.3297,501.3211,471.3097,457.3321,337.1140	deapio-platycodin D	triterpene saponins
7	19.99	$C_{58}H_{94}O_{28}$	1237.5859 $[M-H]^-$	−2.1	**827.4311**,503.3298,483.1761,471.3029,483.1761	platycoside H	triterpene saponins
8	20.73	$C_{57}H_{92}O_{28}$	1223.5702 $[M-H]^-$	−3.7	663.3602,**635.3793**,619.3788,501.3227,471.3065,457.3240,441.3025	2′-*O*-polygalacin D	triterpene saponins
9[a]	20.73	$C_{57}H_{92}O_{28}$	1223.5702 $[M-H]^-$	−3.7	**1133.5309,681.3789**,541.1729,501.3189,469.1518,451.3297,409.1329	platycodin D	triterpene saponins
10	20.73	$C_{57}H_{92}O_{28}$	1223.5702 $[M-H]^-$	−3.7	**1133.5309,681.3789**,541.1729,501.3189,469.1518,451.3297,409.1329	3′-*α*-*O*-polygalacin D	triterpene saponins
11	21.27	$C_{52}H_{82}O_{25}$	1105.5072 $[M-H]^-$	−2.8	**1075.4941**,895.4301,485.2880	platyconic acid C	triterpene saponins
12	21.95	$C_{57}H_{92}O_{27}$	**1207.5753** $[M-H]^-$	−3.2	**665.3907**,541.1756,469.1544	polygalacin D	triterpene saponins
13	22.74	$C_{57}H_{90}O_{29}$	1237.5495 $[M-H]^-$	−2.2	**1207.5346**,1027.4720	platycodin J	triterpene saponins
14	22.74	$C_{57}H_{90}O_{29}$	1237.5495 $[M-H]^-$	−2.2	**1207.5346**,1027.4720	platyconic acid A	triterpene saponins
15	23.73	$C_{54}H_{86}O_{25}$	**1133.5385** $[M-H]^-$	−2.4	1091.5274,723.3920,691.3822,663.3695,501.3229,337.1144	platycoside B	triterpene saponins
16	23.73	$C_{54}H_{86}O_{25}$	**1133.5385** $[M-H]^-$	−2.4	1091.5274,723.3920,691.3822,663.3695,501.3229,337.1144	platycoside C	triterpene saponins
17	24.79	$C_{57}H_{90}O_{28}$	1221.5546 $[M-H]^-$	−2.5	469.1542	16-*OXO*-platycodin D	triterpene saponins
18	25.11	$C_{54}H_{84}O_{26}$	1147.5178 $[M-H]^-$	−2.2	1117.5032,937.1142,485.2896	platyconic acid D	triterpene saponins
19[a]	25.84	$C_{36}H_{58}O_{12}$	**681.3856** $[M-H]^-$	−4.3	**635.3761**,471.3072,457.3307,379.2971	3-*O*-*β*-*D*-glucopyranosyl platycodigenin	triterpene saponins
20	26.14	$C_{36}H_{58}O_{11}$	**665.3906** $[M-H]^-$	−3.4	619.3991,503.3352,441.3325,101.0291	3-*O*-*β*-*D*-glucopyranosyl polygalacic acid	triterpene saponins
21	26.92	$C_{30}H_{46}O_8$	533.3120 $[M-H]^-$	−3.6	469.2915	platycogenic acid B	triterpene saponins
22	26.92	$C_{30}H_{46}O_8$	533.3120 $[M-H]^-$	−3.6	485.2892,469.2915,441.3001,377.2838	platycogenic acid A	triterpene saponins
23	27.81	$C_{35}H_{56}O_{10}$	**635.3801** $[M-H]^-$	−4	473.3247,443.3125,425.3030,423.2874,379.2631,217.1586,119.0367	platycodonoids B	triterpene saponins
24	28.61	$C_{18}H_{34}O_4$	313.2382 $[M-H]^-$	−0.8	212.9942,210.1123,199.0968,171.1025,165.0937,155.1079,137.0994,127.1165	dibutyl sebacate	triterpene saponins
25[a]	13.02	$C_{44}H_{70}O_{17}$	869.4540 $[M-H]^-$	−0.4	809.3746,707.3538	polygonatoside C1	steroidal saponins

(Continued on following page)

TABLE 1 | (*Continued*) Information on chemical ingredients in *Platycodon grandiflorum*.

NO	t_R/ min	Molecular Formula	ESI-MS	Error (ppm)	Fragment ions m/s	Identity	Sort
26	25.88	$C_{51}H_{80}O_{24}$	1075.4967 $[M-H]^-$	−1.2	**665.4041,503.2971**,485.1902,409.1317	cyrtonemoside A	steroidal saponins
27	25.88	$C_{51}H_{80}O_{24}$	1075.4967 $[M-H]^-$	−1.2	**665.3867**,619.3991,503.3352,441.3325,101.0291	(25*S*) spirostan-5-en-12-one-3-*O*-**β**-*D*-glucopyranosyl- (1→2) -*O*-[**β**-*D*-*g*lucopyranosyl- (1→3)]-**β**-*D*-glucopyranosyl-(1→4) -**β**-*D*-galactopyranoside	steroidal saponins
28[a]	7.32	$C_{27}H_{30}O_{16}$	611.1607 $[M+H]^+$	−0.8	**449.0946**,315.0935,287.0541,**269.0503**	rutin	flavonoids
29	9.54	$C_{21}H_{20}O_{11}$	**449.1078** $[M+H]^+$	−3.3	287.0546,**269.0432**,203.0322,135.0441,161.0245	luteolin-7-*O*-glucoside	flavonoids
30[a]	11.65	$C_{33}H_{40}O_{19}$	739.2091 $[M-H]^-$	−3	221.0714,179.0589,161.0497	robinin	flavonoids
31[a]	14.61	$C_{15}H_{10}O_6$	285.0405 $[M-H]^-$	−0.6	267.0299,201.0132,175.0421,151.0087,133.0303,107.0166	luteolin	flavonoids
32[a]	14.65	$C_{15}H_{10}O_6$	285.0405 $[M-H]^-$	−0.3	267.0299,217.0512,175.0421,151.0087,133.0308,107.0166	kaempferol	flavonoids
33[a]	18.55	$C_{15}H_{10}O_5$	**269.0456** $[M-H]^-$	−0.8	159.0449,117.0384,115.0085,107.0149	apigenin	flavonoids
34[a]	5.10	$C_{16}H_{18}O_9$	353.0878 $[M-H]^-$	−3.6	191.0569,189.0419,173.0479,171.0325,155.0334,135.0471,107.0499	chlorogenic acid	phenolic acid
35[a]	5.97	$C_9H_8O_4$	179.0350 $[M-H]^-$	3.9	135.0502,133.0340,117.0441,107.0578	caffeic acid	phenolic acid
36[a]	10.00	$C_{10}H_{10}O_4$	193.0506 $[M-H]^-$	0.9	133.0344	ferulic acid	phenolic acid
37	7.03	$C_{12}H_{14}O_5$	239.0914 $[M+H]^+$	−3	147.0456,119.0505	1-*O*-*p*-coumaroylglycerol	organic acid
38	26.23	$C_{18}H_{34}O_5$	329.2334 $[M-H]^-$	−0.9	311.2160,293.2189,211.1344,185.1110,171.1036,129.0907	sanleng acid	organic acid
39	30.76	$C_{19}H_{32}O_2$	293.2475 [M+H]+	−3.8	135.1172,115.0549,109.1014,105.0720	methyl linolenate	organic acid
40[a]	31.87	$C_{18}H_{32}O_2$	279.2330 $[M-H]^-$	0.8	261.2150	linoleic acid	organic acid
41[a]	1.35	$C_{10}H_{13}N_5O_4$	268.1040 [M+H]+	−0.5	136.0621,119.0354	adenosine	others
42	30.13	$C_{28}H_{42}N_4O_6$	529.3008 $[M-H]^-$	−4.5	279.2337,246.0625	kukoamine A	others
43	30.28	$C_{20}H_{34}O_2$	307.2632 $[M+H]^+$	−3.2	217.1018,153.0783,131.0854,119.0864,107.0861	(9*Z*,12*Z*,15*Z*)-ethyl octadeca-9,12,15-trienoate	others
44	31.78	$C_{18}H_{35}NO$	282.2792 $[M+H]^+$	−2.9	114.0931	oleamide	others
45[a]	10.72	$C_{20}H_{28}O_8$	397.1857 $[M+H]^+$	−2	153.0670,127.0592,115.0598,105.0346	lobetyolin	others
46	8.22	$C_{29}H_{42}O_{18}$	677.2298 $[M-H]^-$	−1.4	261.1000,161.0471,153.0584,143.0577,125.0275	tangshenoside **I**	others
47	4.58	$C_{11}H_{12}N_2O_2$	203.0830 $[M-H]^-$	1.8	142.0664,130.0694,116.0542	tryptophan	others

[a] *Structures confirmed by comparison with reference standards*

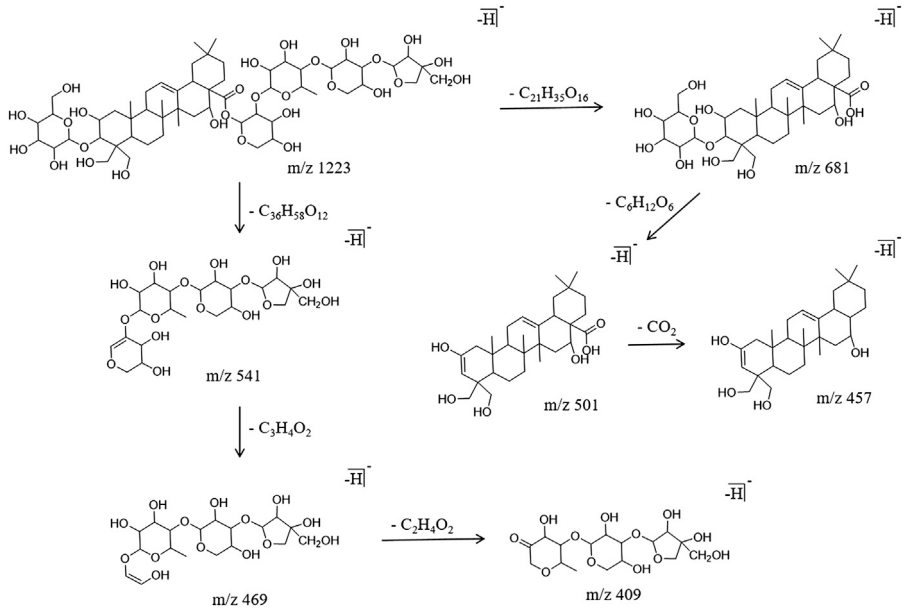

FIGURE 3 | Cracking pathway of triterpenoid saponins.

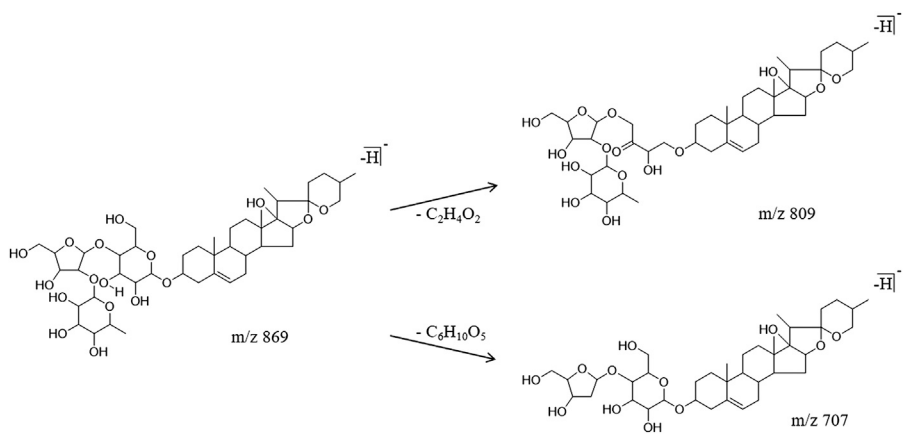

FIGURE 4 | Cracking pathway of steroidal saponins.

at 100 V, and nitrogen was used as a nebulizer and auxiliary gas. Samples were analyzed in both positive and negative ionization modes with a scanning mas-to-charge (m/z) range from 100 to 1,250. Data were collected in the information-dependent acquisition (IDA) mode and analyzed by PeakView®1.2 software (AB Sciex, Foster City, CA, United States).

Identification of the Ingredients

The chemical PG ingredients were collected from existing databases, such as SciFinder (https://scifinder.cas.org), the Traditional Chinese Medicine Systems Pharmacology database, and the Analysis Platform (TCMSP, http://lsp.nwu.edu.cn/tcmsp.php) database. Then, a PG ingredients database was established, containing the basic information, such as ingredient name and molecular formula. A total of 161 ingredients in PG were collected, and the specific information is listed in the **Schedule 1**. MS data were imported into PeakView® 1.2 to perform the ingredient analysis. Chemicals were identified according to the reference standards, chromatographic elution behavior, mass fragment pattern, and mass spectral library (Natural Products HR-MS/MS Spectral Library, Version 1.0, AB Sciex, Forster City, United States).

Predicted and Screened Potential Targets

The prediction targets of the active PG components were obtained using the following databases: Swiss Target

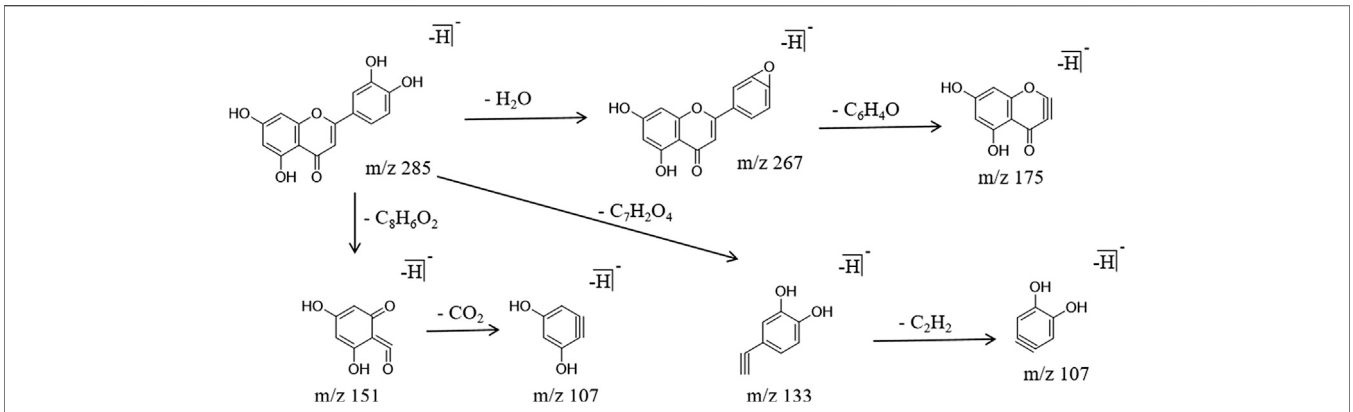

FIGURE 5 | Cracking pathway of flavonoids.

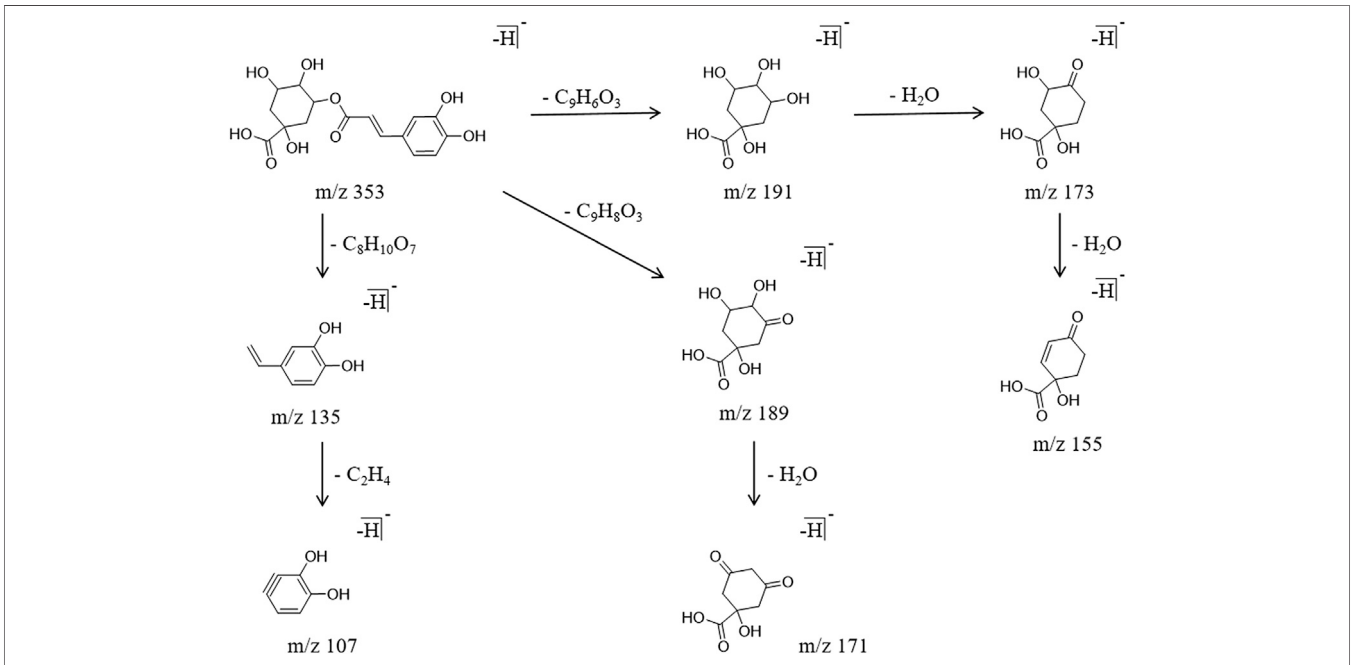

FIGURE 6 | Cracking pathway of phenolic acids.

Prediction (http://www.swisstargetprediction.ch/) (Xu et al., 2018), Pharmmapper (http://www.lilab-ecust.cn/pharmmapper/) (Shen et al., 2019), Pubchem (https://pubchem.ncbi.nlm.nih.gov/) (Xu et al., 2018) and TCMSP (http://lsp.nwu.edu.cn/tcmsp.php) (Ye et al., 2020). The protein name was standardized using Uniprot (http://www.uniprot.org/), and the library of the targets of the active components was obtained. The known disease targets were searched in the databases of GeneCards (https://www.genecards.org/) (Ye et al., 2020) and DisGenet (http://www.disgenet.org/) (Gao et al., 2020) using "Lung cancer" as the keyword, and the LC-target database was obtained.

Protein-Protein Interaction (PPI) Network Construction

R software was used to intersect PG related targets and LC related targets, and the overlapping targets were uploaded into STRING 11.0 (https://string-db.org/). The protein type was set to "*Homo sapiens*" and the minimum interaction score was 0.4. The PPI network diagram was obtained, imported into Cytoscape v3.7.1 software, and CentiScape was used to calculate the degree centrality (DC) to filter PPI network core targets.

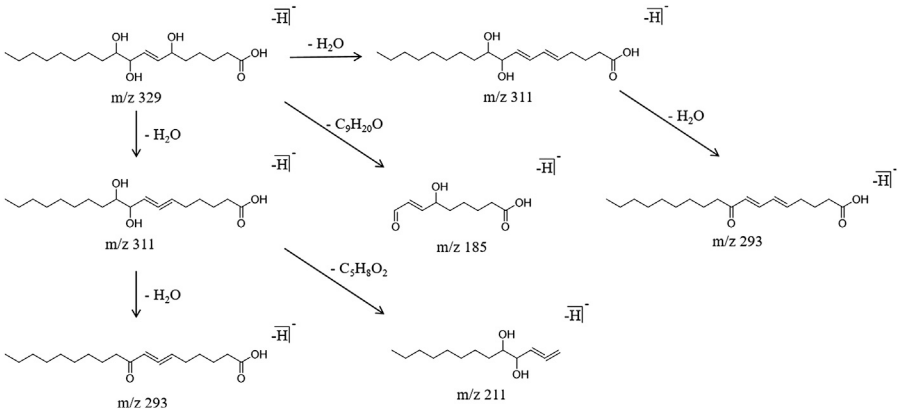

FIGURE 7 | Cracking pathway of organic acids.

Gene Ontology (GO) and Kyoto Encyclopedia of Genes and Genomes (KEGG) Pathway Enrichment Analysis

Metascape (http://www.metascape.org/) is a gene annotation tool that integrates many authoritative databases such as GO, KEGG, UniProt and DrugBank. It allows the completion of pathway enrichment analysis and biological process annotation and performs gene-related protein network analysis and drug analysis, providing comprehensive and detailed information regarding each gene (Zhou et al., 2019). Metascape perfectly fills the gap of DAVID while maintaining its advantages, and its data is frequently updated (the last update was August 14, 2019), greatly guaranteeing the timeliness and credibility of the data.

The gene symbols of the core targets were introduced into Metascape, "*Homo sapiens*" was selected to perform the enrichment analysis, which was annotated and analyzed using the KEGG database (https://www.kegg.jp/) and PathwayBuilderTool_2.0 software to further explain the role of the core targets in gene function and signaling pathway.

D-I-T-P-D Network Construction

The files related to "drug-core ingredient," "core ingredient-core target," "pathway-core target," and "disease-core target" were established, and the D-I-T-P-D network was constructed using Cytoscape v 3.7.1 to explain the multi-effect synergistic mechanism of PG.

Molecular Docking Evaluation

Discovery Studio 2016 software (DS) is a commonly used molecular modeling and simulation software widely used in the field of drug design and optimization, protein structure and function (Zhang and Mao, 2018). The PDB format of the core target is obtained in the Uniprot database, and the X-ray crystal structure of the core target is downloaded from the RCSB database (https://www.rcsb.org/). Then the molecular docking function of DS software is used to perform component-target molecular docking in the LibDock module.

RESULTS

Composition Analysis and Identification

The typical total ion chromatogram of the non-volatile components extracted from PG, shown in **Figure 2**, of positive and negative ions was analyzed by Peakview® 1.2, and the composition was screened by "XIC manager". The structural formula of the target compound was matched with the secondary fragment ion, and the compounds were further identified according to the matching degree and the law of ion bond breaking. The compounds with a matching degree greater than

TABLE 2 | Information on the 9 active ingredients in *Platycodon grandiflorum*.

Note	CAS	Molecular formula	Molecular weight	Compound
S1	1135-24-6	$C_{10}H_{10}O_4$	194.058	ferulic acid
S2	520-36-5	$C_{15}H_{10}O_5$	270.053	apigenin
S3	520-18-3	$C_{15}H_{10}O_6$	286.048	kaempferol
S4	331-39-5	$C_9H_8O_4$	180.042	caffeic acid
S5	7361-80-0	$C_{19}H_{32}O_2$	292.240	methyl linolenate
S6	60-33-3	$C_{18}H_{32}O_2$	280.240	linoleic acid
S7	491-70-3	$C_{15}H_{10}O_6$	286.048	luteolin
S8	301-19-9	$C_{33}H_{40}O_{19}$	740.216	robinin
S9	58479-68-8	$C_{57}H_{92}O_{28}$	1224.578	platycodin D

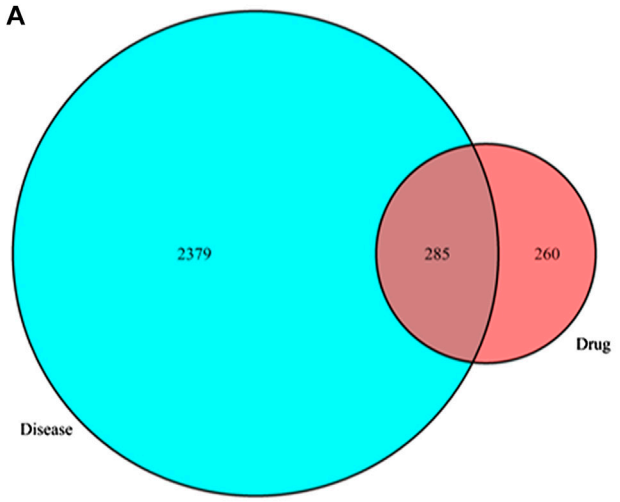

FIGURE 8 | (A) Venny diagram of related targets of drug and disease **(B)** PPI network of 285 overlapping targets between drug and disease.

80% and in accordance with the law of bond breaking were considered. According to the reference (Wang et al., 2017a; 2017b) and the data of the control quality spectrum, 47 chemical constituents were identified in the alcohol extract of PG (**Table 1**). Among them, deapio-platycodin D, platycodin D, polygonatoside C1, adenosine, ferulic acid, apigenin, luteolin, chlorogenic acid, caffeic acid, kaempferol, robinin, lobetyolin, rutin, 3-O-β-D-glucopyranosyl platycodigenin and linoleic acid were compared with the reference standards. Among these 47, 24 were triterpenoid saponins, three were steroidal saponins, six were flavonoids, three were phenolic acids, four were organic acids and seven were other components.

Analysis of the Cracking Law of the Components

Triterpene Saponins

Triterpenoid saponins are the largest number of components and the main components identified from PG. The main approach to cleave triterpenoid saponins is a continuous intramolecular

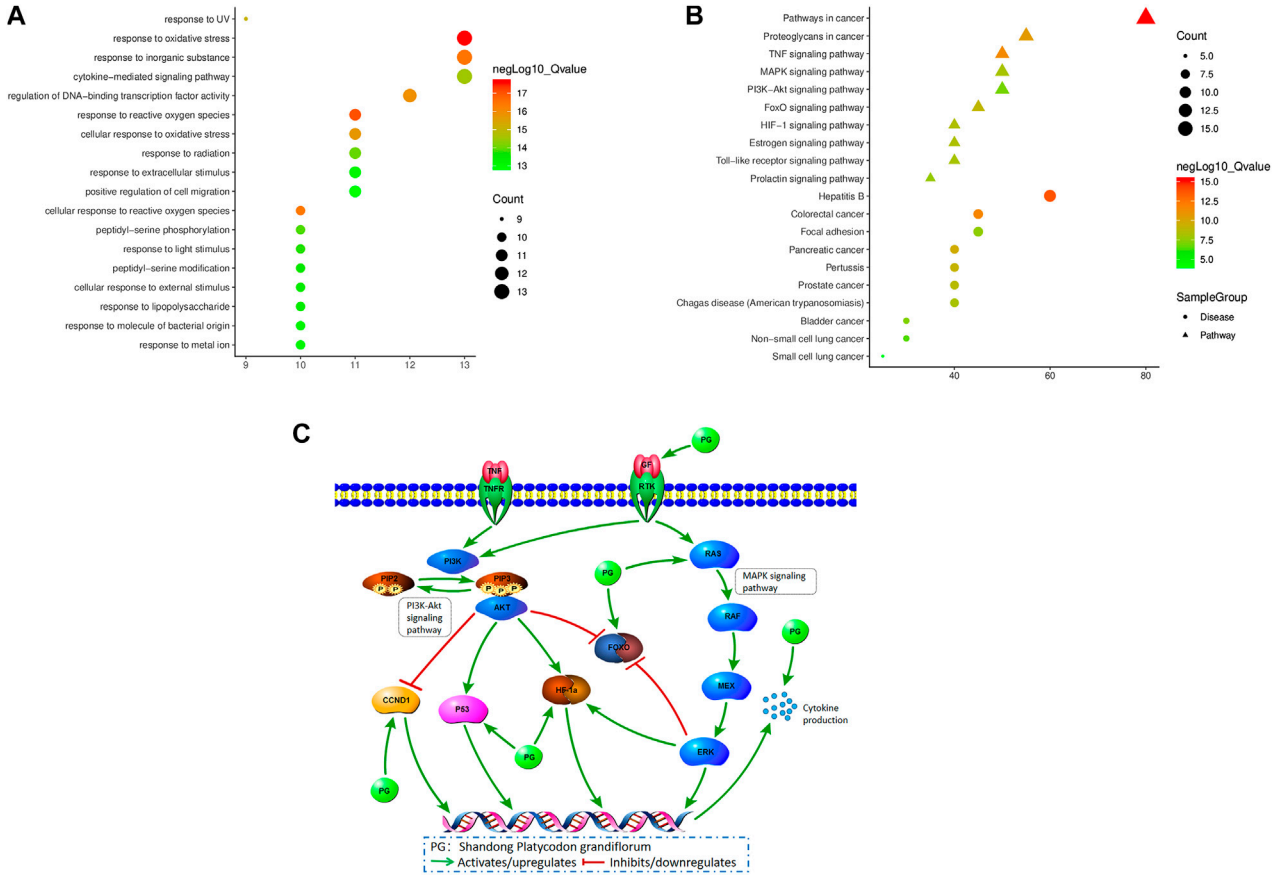

FIGURE 9 | (A) Bubble chart of GO function enrichment of core targets **(B)** Bubble chart of KEGG enrichment of core targets **(C)** Potential mechanisms of *Platycodon grandiflorum* treatment for lung cancer.

deglycosylation and interchain cleavage to obtain the characteristic fragment ions. In this experiment, 24 triterpenoid saponins, including platycodin D, polygalacin D and deapio-platycodin D were identified from PG. Using platycodin D as an example for the analysis, they all behave similarly by producing a molecular ion peak m/z 1,223.5702 in the anion mode, and the retention time was 20.73 min. The glycosidic bond was broken under a high energy bombardment, the fragment ions m/z 681.3789 $[M-H]^-$, m/z 541.1729 $[M-H]^-$, m/z 681.3789 $[M-H]^-$ were further removed, and the fragment ion m/z 501.3189 $[M-H]^-$ was obtained. In addition, the interchain cleavage produced the fragment ions m/z 469.1518 $[M-H]^-$ and m/z 409.1329 $[M-H]^-$. The specific cracking pathway of the triterpenoid saponins is shown in **Figure 3**.

Steroidal Saponins

Three steroidal saponins were identified and their cleavage rules were similar to the ones to cleave triterpenoid saponins. The characteristic fragment ions were obtained by the cleavage of their sugar chains. Using polygonatoside C1 as an example for the analysis, the molecular ion peak m/z 869.4540 was produced in the negative ion mode, and the retention time was 13.02 min. The cleavage of the sugar chain produced the fragment ions m/z 809.3746 $[M-H]^-$ and m/z 707.3538 $[M-H]^-$. The specific cracking pathway of the steroidal saponins is shown in **Figure 4**.

Flavonoids

It is already known that flavonoids are the main components in PG (Wang et al., 2017b; Deng et al., 2020). The main components identified were flavonoids and flavonoid glycosides, and the characteristic cleavage mode was the R-DA cleavage, while glycosides followed the glycosyl cleavage. Using luteolin as an example for the analysis, the molecular ion peak m/z 285.0405 was produced in the negative ion mode, and the retention time was 14.61 min the characteristic fragment ions m/z 151.0087 $[M-H]^-$, m/z 133.0303 $[M-H]^-$, and m/z 107.0166 $[M-H]^-$ were obtained, respectively, by R-DA cleavage at two different positions. In addition, the fragment ion m/z 267.0299 $[M-H]^-$ was obtained by removing one molecule of H_2O, and the fragment ion m/z 175.0421 $[M-H]^-$ was also obtained by alpha cracking. The specific cracking pathway of the flavonoids is shown in **Figure 5**.

TABLE 3 | Top 20 clusters with their representative KEGG enrichment pathways.

ID	Term	Count	LogP	Gene
hsa05200	Pathways in cancer	16	−25.05	AKT1、CCND1、CASP3、EGFR、EP300、FN1、FOS、HSP90AA1、IL6、JUN、MAPK1、MAPK3、MAPK8、PTGS2、TP53、VEGFA
hsa05205	Proteoglycans in cancer	11	−17.75	AKT1、CCND1、CASP3、EGFR、ESR1、FN1、MAPK1、MAPK3、TNF、TP53、VEGFA
hsa04668	TNF signaling pathway	10	−18.43	AKT1、CASP3、FOS、IL6、JUN、MAPK1、MAPK3、MAPK8、PTGS2、TNF
hsa04010	MAPK signaling pathway	10	−14.62	AKT1、CASP3、EGFR、FOS、JUN、MAPK1、MAPK3、MAPK8、TNF、TP53
hsa04151	PI3K-Akt signaling pathway	10	−13.33	AKT1、CCND1、EGFR、FN1、HSP90AA1、IL6、MAPK1、MAPK3、TP53、VEGFA
hsa04068	FoxO signaling pathway	9	−15.28	AKT1、CCND1、EGFR、EP300、IL6、MAPK1、MAPK3、MAPK8、SIRT1
hsa04915	Estrogen signaling pathway	8	−14.18	AKT1、EGFR、ESR1、FOS、HSP90AA1、JUN、MAPK1、MAPK3
hsa04066	HIF-1 signaling pathway	8	−14.07	AKT1、EGFR、EP300、GAPDH、IL6、MAPK1、MAPK3、VEGFA
hsa04620	Toll-like receptor signaling pathway	8	−13.97	AKT1、FOS、IL6、JUN、MAPK1、MAPK3、MAPK8、TNF
hsa04917	Prolactin signaling pathway	7	−13.02	AKT1、CCND1、ESR1、FOS、MAPK1、MAPK3、MAPK8
hsa04919	Thyroid hormone signaling pathway	7	−11.44	AKT1、CCND1、EP300、ESR1、MAPK1、MAPK3、TP53
hsa04921	Oxytocin signaling pathway	7	−10.61	CCND1、EGFR、FOS、JUN、MAPK1、MAPK3、PTGS2
hsa04621	NOD-like receptor signaling pathway	7	−10.27	HSP90AA1、IL6、JUN、MAPK1、MAPK3、MAPK8、TNF
hsa04024	cAMP signaling pathway	7	−9.80	AKT1、EP300、FOS、JUN、MAPK1、MAPK3、MAPK8
hsa04012	ErbB signaling pathway	6	−10.20	AKT1、EGFR、JUN、MAPK1、MAPK3、MAPK8
hsa04660	T cell receptor signaling pathway	6	−9.72	AKT1、FOS、JUN、MAPK1、MAPK3、TNF
hsa04071	Sphingolipid signaling pathway	6	−9.36	AKT1、MAPK1、MAPK3、MAPK8、TNF、TP53
hsa04722	Neurotrophin signaling pathway	6	−9.34	AKT1、JUN、MAPK1、MAPK3、MAPK8、TP53
hsa04014	Ras signaling pathway	6	−7.65	AKT1、EGFR、MAPK1、MAPK3、MAPK8、VEGFA
hsa04370	VEGF signaling pathway	5	−8.96	AKT1、MAPK1、MAPK3、PTGS2、VEGFA

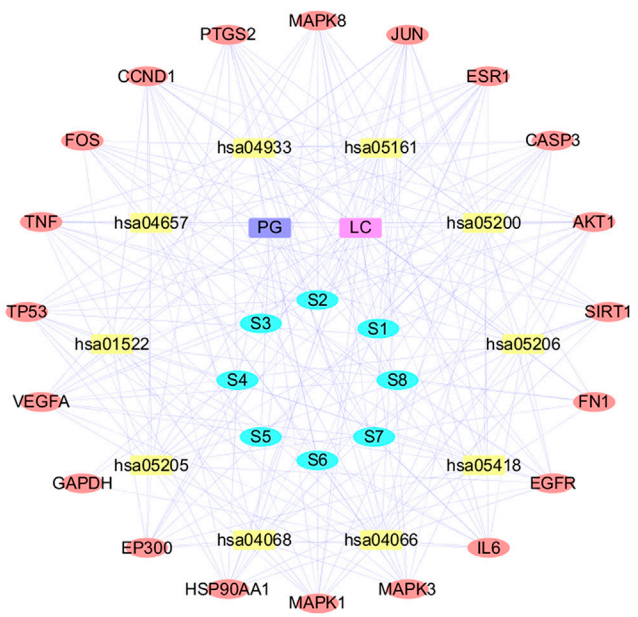

FIGURE 10 | The Drug-Ingredients-Targets-Pathway-Disease Network. S1: ferulic acid; S2: apigenin; S3: kaempferol; S4: caffeic acid; S5: methyl linolenate; S6: linoleic acid; S7: luteolin; S8: robinin; PG: *Platycodon grandiflorum*; LC: lung cancer.

Phenolic Acids

Three phenolic acid components were identified from PG. The main cracking methods were alpha cracking, Michael rearrangement cracking, and neutral H_2O molecule detachment. Using the chlorogenic acid as an example for the analysis, it generated a molecular ion peak m/z 353.0878 in the negative ion mode, with a retention time of 5.10 min. There are three main cracking methods: first, the alpha cleavage produced the fragment ion m/z 191.0569 $[M-H]^-$, and two molecules of H_2O were removed to obtain the fragment ion m/z 173.0479 $[M-H]^-$ and m/z 155.0334 $[M-H]^-$. Second, the cleavage by Michael rearrangement produced the fragment ion m/z 189.0419 $[M-H]^-$, and then a molecule of H_2O

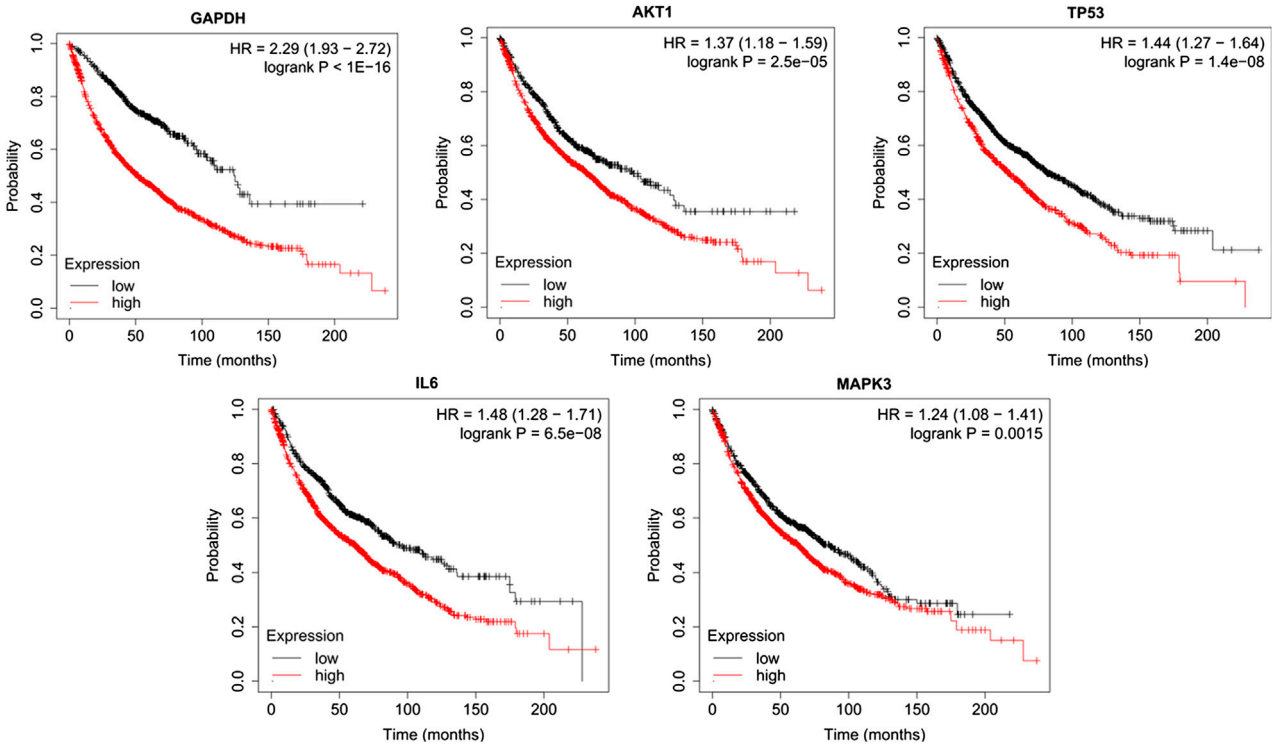

FIGURE 11 | Survival curve of the relationship between high and low expression and overall survival of patients.

was removed to obtain the fragment ion m/z 171.0325 $[M-H]^-$. Third, the alpha fragmentation produced the fragment ion m/z 135.0471 $[M-H]^-$ and m/z 107.0499 $[M-H]^-$. The specific cracking pathway of the phenolic acids is shown in **Figure 6**.

Organic Acids

The organic acid components identified in this work were mainly long-chain carboxylic acids with multiple unsaturated bonds. The characteristic cleavage method involved the Michael rearrangement cracking, alpha cracking and neutral molecule removal. Using the sanleng acid as an example for the analysis, it generated a molecular ion peak m/z 329.2334 in the negative ion mode with a retention time of 26.23 min. Michel rearrangement fragmentation produced the characteristic fragment ion m/z 185.1110 $[M-H]^-$. The fragment ion m/z 311.2160 $[M-H]^-$ was obtained by removing one molecule of H_2O. Another molecule of H_2O was removed from m/z 311.2160 $[M-H]^-$ to obtain the fragment ion m/z 293.2189 $[M-H]^-$; in addition, m/z 311.2160 $[M-H]^-$ underwent alpha cracking to obtain the fragment ion m/z 211.1344 $[M-H]^-$. The specific cracking pathway of the organic acids is shown in **Figure 7**.

Screening of the Active Ingredients

The absorption-distribution-metabolism-excretion-toxicity (ADMET) properties of the chemical constituents were predicted by DS, and apigenin, caffeic acid, kaempferol, linoleic acid, methyl linolenic acid, and ferulic acid were selected. Although some components do not meet the DS screening criteria, they are still considered as active components in order to select the active components of PG more comprehensively. For example, luteolin and robinin were obtained from TCMSP, with oral bioavailability greater than 30% and drug-likeness greater than 0.18 despite they did not meet the DS screening criteria, so they are considered as active ingredients. Recent studies showed that platycodin D is one of the main components of PG, and has a certain preventive and therapeutic effect on LC (Zhao et al., 2015; Zhang, 2016b; Deng et al., 2020), thus platycodin D is also retained as the active ingredient. To sum up, a total of nine ingredients were selected as the active components of PG, and their detailed characteristics are listed in **Table 2**.

PPI Network Analysis

A total of 545 targets of the selected nine active components in PG were obtained using the Swiss Target Prediction, Pubchem, TCMSP and pharmmapper databases. A total of 2664 LC related targets were collected using GeneCards and DisGenet databases using "Lung cancer" as the keyword (**Schedules 2,3**).

The Venn diagram of drug-disease overlapping targets was obtained using the R software to intersect PG related targets and LC related targets (**Figure 8A**), revealing the existence of 285 common targets (**Schedule 4**). The interactive PPI network of common targets was obtained by introducing the 285 drug-disease common targets into STRING and the obtained

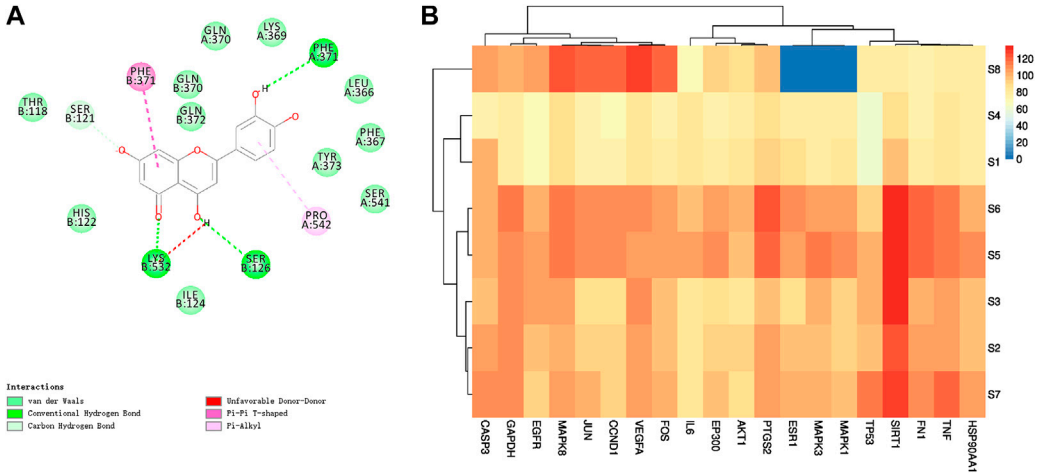

FIGURE 12 | (A) 2D graph of luteolin and PTGS2 molecular docking results **(B)** Heatmap of molecular docking scores of core ingredients and core targets. S1: ferulic acid; S2: apigenin; S3: kaempferol; S4: caffeic acid; S5: methyl linolenate; S6: linoleic acid; S7: luteolin; S8: robinin.

network was imported into the Cytoscape software for visualization (**Figure 8B**). No interaction was found between the target S100P and other targets, but the other 284 common targets had an interaction. The average value of DC calculated by CentiScape was 39.775, and 108 potential targets with DC values greater than 39.775 were selected. The higher the DC value, the more important the role in the network. In this study, the targets with the top 20 DC values were selected as the core targets. The red dot in **Figure 8B** represents the core target, the light green dot represents the potential target, the yellow dot represents the interactive target, and the connection between the nodes represents the interaction between the two proteins.

GO and KEGG Pathway Enrichment Analysis

The pathway enrichment analysis of the 20 core targets was carried out using Metascape. The enrichment results were selected under the conditions of $p < 0.01$, minimum count 3, and enrichment factor>1.5. A total of 849 GO biological functions and 116 KEGG enrichment items were obtained. The GO functions related to the treatment of LC included oxidative stress response (GO:0006979), active regulation of cell migration (GO:0030335), regulation of DNA binding transcription factor activity (GO:0051090), and regulation of cytokine-mediated signaling pathway (GO:0019221) (**Figure 9A**), mostly related to apoptosis, oxidative stress and energy metabolism. The 20 core targets were closely related to cancer pathway (hsa05200), TNF signaling pathway (hsa04668), MAPK signaling pathway (hsa04010) and P13K-AKT signaling pathway (hsa04151), and are related to diseases such as hepatitis B, colorectal cancer, non-small cell LC and small cell LC (**Figure 9B**). The first 20 representative signaling pathways are listed in **Table 3**, which might represent the key pathways in the treatment of LC. It is also suggested that PG can be used in the treatment of LC. The top 10 pathways were determined in the KEGG database and annotated using the PathwayBuilderTool_2.0 software to integrate the potential pathways of PG in the treatment of LC (**Figure 9C**). This analysis provided a new research method for the limitations in treating LC.

D-I-T-P-D Network Analysis

In order to explain the complex mechanism of multi-ingredient-multi-target-multi-pathway of PG in the treatment of LC, this study selected the top 10 pathways and used Ctyoscape v 3.7.1 to construct a D-I-T-P-D network, as shown in **Figure 10**. In this network, the purple node represents the drug, the green node represents the core ingredient of PG, the yellow node represents the core target of PG in the treatment of LC, the red node represents the pathway, the blue node represents the disease, and the edge represents thee interaction among nodes. The network consists of 40 nodes (1 drug, eight core components, 20 core targets, 10 pathways and one disease), with a total of 277 edges, which fully showed that the targets of the core ingredients of PG were distributed in different pathways, and the ingredients coordinated with each other in the body.

Subsistence Analysis

The relationship between the top five core targets in the PPI network and the prognosis of LC patients was analyzed using the Kaplan-Meier Plotter database. The results revealed that the overall survival of LC patients with high expression of GAPDG, AKT1, TP53, IL6 and MPKA3 was significantly lower than that in patients with their low expression ($p < 0.01$) (**Figure 11**).

Molecular Docking Verification Results

The analysis of the D-I-T-P-D network showed that each core component interacted with multiple targets. Thus, the DS software was used to dock the core components with the core target molecules in order to verify the interaction among them. It is generally accepted that the higher the score of the ligand binding to the receptor, the greater the possibility of

interaction. The docking results of luteolin and protein PTGS2 docking are shown in **Figure 12A**, which might bond by hydrogen bonds, van der Waals forces and other forces. The docking score was sorted out, the highest score was obtained (**Schedule 5**), and then ImageGP was used for visual processing (**Figure 12B**). The redder the color, the better the affinity of the component to the target. The relationship between the above-mentioned core components and core targets was consistent according to the analysis of the docking scoring results.

The cluster analysis revealed that GAPDH, VEGFA, EGFR, JUN, CCND1, MAPK8, FOS and CASP3 could be included into one group, while EP300, AKT1, HSP90AA1, MAPK3, TNF, SIRT1, ESR1, PTGS2, TP53, FN1, MAPK1 and IL6 could be included in one category. SIRT1, PTGS2, CASP3, VEGFA, MAPK8 and GAPDH were the targets with strong binding ability according to the molecular docking. Linoleic acid, methyl linolenate, luteolin, apigenin and kaempferol were the core components with strong binding ability according to the molecular docking, and the docking scores of these five components with SIRT1 were greater than 120, followed by methyl linolenate, kaempferol, linoleic acid, luteolin and apigenin. This result suggested that these five components have a good binding activity with SIRT1 and might play a key role in the treatment of LC using PG.

DISCUSSION

The etiology of LC is complex and so far, no final conclusion was obtained. It is related to smoking, air pollution, dietary factors, decreased immune function and genetic factors (Li and Wang, 2019), while TCM believes that the main cause in the development of LC is the lack of "vital qi", since the "deficiency of vital qi" is "evil". Professor Jia Yingjie claims that the "deficiency of vital qi and coexistence of toxin and blood stasis" is the key of the pathogenesis of LC (Yu et al., 2020). PG exerts the effect of smoothing the lung, dispelling the phlegm, and expelling the pus, which is consistent with the pathogenesis of LC. However, the mechanism of PG in the treatment of LC is still unclear due to the multi-ingredient and multi-target characteristics of TCM. Therefore, it is imperative to analyze the ingredients of PG and explore the mechanism used by PG in the treatment of LC.

In this study, 47 non-volatile ingredients were identified from the alcohol extract of PG by the UPLC-Q-TOF-MS/MS technique. According to the ADMET parameters and other basic properties of the ingredients, and combined with the results in the literature, nine main active ingredients including platycodin D and apigenin were selected. The results showed that they play an important role by affecting 285 overlapping genes involved in the treatment of LC. The PPI network showed that the DC values of GAPDH, AKT1 and TP53 were greater than 175, and they were predicted as the most relevant targets. The enrichment analysis of the GO pathway and KEGG pathway in the 20 core targets showed that most of the functional enrichment results of GO were apoptosis, oxidative stress and energy metabolism. Our hypothesis was that oxidative stress response might be the most important biological process managed by PG in the treatment of LC. The results of the KEGG pathway enrichment analysis showed that the top 10 pathways included cancer pathway, TNF signaling pathway, MAPK signaling pathway, P13K-AKT signaling pathway and FoxO signaling pathway. Among them, MAPK signaling pathway, PI3K-AKT signaling pathway, FoxO signaling pathway and HIF-1 signaling pathway were related to cell proliferation and apoptosis, oxidative stress and inflammation. MAPK signaling pathway is one of the most important pathways regulated by PG in the treatment of LC. Related studies showed that the MAPK signaling pathway participates in the regulation of cell cycle, apoptosis and proliferation of NSCLC cells, and inhibits the expression of P-glycoprotein (P-gp), multidrug resistance gene 1 (MDR1), TP53 and other proteins, thus inhibiting the growth of NSCLC cells, blocking cell cycle and inducing apoptosis (Liao et al., 2020; Qiao et al., 2020; Wang et al., 2020). PI3K-AKT signaling pathway is considered as the primary pathway for cancer cell survival, since it promotes tumor cell proliferation and metastasis, and inhibits apoptosis and angiogenesis. If this pathway is abnormal, it directly leads to the abnormal proliferation of cells (Ma et al., 2014; Sui et al., 2018). Therefore, the activation of the MAPK signaling pathway and the inhibition of the PI3K-AKT signaling pathway are crucial in the treatment of LC.

The D-I-T-P-D network showed that the same target could interact with many ingredients. For example, PTGS2 could bind ferulic acid, luteolin, linoleic acid, apigenin and sophorin, while CASP3 can bind methyl linolenic acid, apigenin, ferulic acid and robinin, indicating that multiple active ingredients in PG might act on the same target. In addition, our results showed that apigenin was related to CASP3, AKT1, FOS, JUN, MAPK8, TNF, VEGFA, and CCND1, and linoleic acid was related to PTGS2, TP53, ESR1, MAPK1, MAPK8 and IL6, which was consistent with the results obtained by molecular docking, suggesting that PG could act on multiple targets through the same active component. This result also explained the characteristics of multi-ingredient and multi-target synergism of PG, providing a basis in the mechanism of PG to treat LC. Our hypothesis was that PG was closely related to cell proliferation and apoptosis in the treatment of LC according to the GO pathway and KEGG pathway enrichment analysis. Several core components of PG could interact with PTGS2 and CASP3, potentially promoting cancer cell apoptosis through specific signaling pathways such as MAPK signaling pathway and P13K-AKT signaling pathway in order to cure LC.

The survival analysis results showed that the top five core targets (GAPDG, AKT1, TP53, IL6, and MPKA3) in the PPI network were closely related to the survival of LC patients. The overall survival of LC patients with a high expression of these genes was significantly lower than that of patients with their low expression, suggesting that its overexpression is related to a poor prognosis in LC patients. Thus, they could be used as biomarkers to evaluate LC prognosis.

The results of molecular docking showed that apigenin, luteolin, linoleic acid, kaempferol and methyl linolenate might be the potential active ingredients. Some studies showed that apigenin has a cytotoxic effect on human LC cisplatin-resistant cell line A549/DDP, and indeed it effectively inhibits its growth and reverse its drug resistance (Zhao et al., 2017; Mo et al., 2020). Zhou Liang et al. found that luteolin inhibits the metastasis and proliferation of LC through the down-regulation of the PI3K/AKT signaling pathway and the improvement of the immune function in the body (Zhou et al., 2017). In addition, Li Xiaolin et al. demonstrated that luteolin effectively blocks A549/DDP cell cycle and even promotes apoptosis, and that TP53 protein is involved in this process (Li et al., 2009). In addition, some scientists found that kaempferol weakens the invasion and migration ability of NSCLC A549 cells by inhibiting the expression of estrogen-related receptor α (ERRα), thus providing a strong support in the study of the anti-cancer mechanism of kaempferol (Zhang et al., 2018). However, Mouradian and other scientists found that linoleic acid increases the activity of PI3K/AKT signaling pathway, promotes the proliferation of LC cells, and leads to tumor formation, with GAB1 as the main target of linoleic acid (Mouradian et al., 2014). Apigenin, luteolin, linoleic acid, kaempferol, and methyl linolenate are widely found in plants, but plants that contain all these five components are rare. Besides PG, Panax notoginseng (Liu, 2019) and peony seed (Zhang, 2016a) also contain these five components. However, so far, no reports are available regarding Panax notoginseng and peony seed anti-LC effect. Therefore, our analysis of the effect and mechanism of PG in the treatment of LC is of great significance.

CONCLUSION

PG is one of the most commonly used TCM in clinical practice, since it has a significant therapeutic effect on lung-related diseases and has been used in China for thousands of years. In this study, the chemical constituents of PG were analyzed and identified. A total of nine active PG components and 285 overlapping targets of PG and LC were screened. PPI network, GO and KEGG enrichment analysis showed that the mechanism of PG in the treatment of LC might be related to its involvement in cancer cell apoptosis, inflammation and oxidative stress through the MAPK signaling pathway and P13K-AKT signaling pathway. The network pharmacological method developed in this study provided another strategy for a comprehensive understanding of the mechanism of PG in the treatment of LC.

DATA AVAILABILITY STATEMENT

All datasets presented in this study are included in the article/ **Supplementary Material**.

AUTHOR CONTRIBUTIONS

YD integrated the data and wrote the manuscript; ML, YL, and KW performed the literature search; XY and YC completed the ingredient identification; HR and LX collected the prediction targets; HL and HZ completed the network analysis; ZZ improved the manuscript writing; JZ conceptualized and designed the experimental plan.

FUNDING

This study was supported by the National Key R and D Program—Special Topics for Modernization of TCM (No. 2018YFC1707206), Key R and D Program of Jiangxi Province (No. 20192BBG70073), National Natural Science foundation of China (No. 81560651), Jiangxi Province's double first-class discipline (TCM) construction project (No. JXSYLXK-ZHYAO039/ 141), and Doctoral Research start-up Fund (No. 2018WBZR009).

ACKNOWLEDGMENTS

The authors thank the Jiangxi University of TCM for the assistance in performing this study.

SUPPLEMENTARY MATERIAL

The Supplementary Material for this article can be found online at: https://www.frontiersin.org/articles/10.3389/fphar.2020.609825/ full#supplementary-material.

REFERENCES

Bai, W., Han, Y. B., Zhu, D. M., Jiang, Y. M., and Ling, J. H. (2017). Analysis of TCM drug use in treatment of lung cancer. *Acta Chin Med.* 32 (3), 335–338. doi:10.16368/j.issn.1674-8999.2017.03.086

Chinese Pharmacopoeia Commission (2020). Chinese pharmacopoeia of the People's Republic of China. vol. 1. Beijing, China: Chin Med Sci Tech Press, 277

Deng, Y. L., Ren, H. M., Ye, X. W., Xia, L. T., Zhu, J., Yu, H., et al. (2020). Historical evolution of the processing and progress in modern research of *Platycodonis radix*. *Chin J Exp Tradit Med Form* 26 (2), 190–202. doi:10.13422/j.cnki.syfjx. 20191946

Gao, F. F., Pei, Y. L., Ren, Y., Chen, Z. J., Lu, J. Q., and Zhang, Y. L. (2020). Possible mechanisms by which *Polygonatum sibiricum* opposes atherosclerosis based on network pharmacology and molecular docking analyses. *Acta Pharm. Sin.* 55 (11), 2642–2650. doi:10.16438/j.0513-4870.2020-0299

Jin, M. M., Zhang, W. D., Jiang, H. H., Du, Y. F., Guo, W., Cao, L., et al. (2018). UPLC-Q-TOF-MS/MS-guided dereplication of Pulsatilla chinensis to identify triterpenoid saponins. *Phytochem. Anal.* 29 (5), 516–527. doi:10. 1002/pca.2762

Li, X. L., Xu, Y. Y., Sun, X. Y., Zheng, Y. F., Shen, H. M., and Zhu, X. Q. (2009). Luteolin enhances cisplatin-induced apoptosis of human lung cancer cell A549. *Chin. Tradit. Herb. Drugs* 40 (3), 431–433. doi:10.3321/j.issn:0253-2670.2009. 03.029

Li, B., and Wang, A. H. (2019). Advances in research on risk factors for lung cancer in women. *Med. Recapitulate* 25 (18), 3611–3616 + 3621. doi:10.3969/j.issn.1006-2084.2019.18.015

Li, Y., Wu, Y., Xia, Q., Zhao, Y., Zhao, R., and Deng, S. (2019). *Platycodon grandiflorus* enhances the effect of DDP against lung cancer by down regulating PI3K/Akt signaling pathway. *Biomed. Pharmacother.* 120 (undefined), 109496. doi:10.1016/j.biopha.2019.109496

Liao, X. Z., Gao, Y., Sun, L. L., Liu, J. H., Chen, H. R., Yu, L., et al. (2020). Rosmarinic acid reverses non-small cell lung cancer cisplatin resistance by activating the MAPK signaling pathway. *Phytother Res.* 34, 1142–1153. doi:10.1002/ptr.6584

Liu, M. (2019). Study on the medicinal substances and mechanism of action of Gynura procumbens (Lour.) Merr. on the Improvement of Type 2 diabetes mellitus based on liquid chromatography-mass spectrometry and metabolomics. *Jiangxi Univ Tradit Chin Med*. doi:10.1002/bmc.4635

Ma, N., Guo, R. Z., Ruan, Y., Zhang, S. S., Wang, Z. Q., and Yang, Y. F. (2014). Correlation investigate PI3K-AKT-Bcl-2 anti-apoptotic pathway with scar carcinoma cells apoptosis. *Chin. J. Cancer Prev. Treat.* 21 (8), 599–604. doi:10.16073/j.cnki.cjcpt.2014.08.016

Mo, L., Liu, X., Yang, H. M., He, X. R., Wang, X. L., and Tang, C. H. (2020). Study on RAD51 gene regulatory mechanism of apigenin affecting cisplatin sensitivity to NSCLC A549 cells. *J China Pharm* 31 (6), 708–714. doi:CNKI:SUN:ZGYA.0.2020-06-014

Mouradian, M., Kikawa, K. D., Johnson, E. D., Beck, K. L., and Pardini, R. S. (2014). Key roles for GRB2-associated-binding protein 1, phosphatidylinositol-3-kinase, cyclooxygenase 2, prostaglandin E2 and transforming growth factor alpha in linoleic acid-induced upregulation of lung and breast cancer cell growth. *Prostaglandins Leukot. Essent. Fatty Acids* 90 (4), 105–115. doi:10.1016/j.plefa.2013.12.001

Qiang, Y. W., Ma, F., Wang, Z. R., Nie, Z. C., Xu, L. F., Ding, P. S., et al. (2020). LukS-PV induces cell cycle arrest and apoptosis through p38/ERK MAPK signaling pathway in NSCLC cells. *Biochem. Biophys. Res. Commun.* 521 (4), 846–852. doi:10.1016/j.bbrc.2019.10.181

Ren, H. M., Luo, X., Wan, C., Liu, M., Li, N., Xia, L., et al. (2020). Characterization of the active components of Aurantii fructus causing dry mouth by analysis of aquaporin 5 expression. *Rev. Bras. Farmacogn.* 30 (1), 80–89. doi:10.1007/s43450-020-00001-z

Shao, L., and Zhang, Y. P. (2020). Efficacy and influencing factors of osimertinib in treating patients with advanced non-small cell lung cancer. *Chin. J. New Drugs Clin. Remedies* 39 (3), 155–161. doi:10.14109/j.cnki.xyylc.2020.03.06

Shen, H. B., Zhou, Y. N., Zheng, J., and Zhu, R. H. (2019). Multi-component-multi-target-multi-pathway mechanism of Kuihua Hugan Tablets based on network pharmacology. *China J. Chin. Mater. Med.* 44 (7), 1464–1474. doi:10.19540/j.cnki.cjcmm.20181214.003

Sui, Y. T., Chi, W. C., and Jiang, J. K. (2018). Influence of Qishan Fang combined with cisplatin on PI3K/AKt signal pathway of lung cancer A549 cells. *J Beijing Univ Tradit Chin Med.* 41 (7), 553–558. doi:CNKI:SUN:JZYB.0.2018-07-007

Wang, C. Z., Zhang, N. Q., Wang, Z. Z., Qi, Z., Zheng, B. Z., Li, P. Y., et al. (2017a). Rapid characterization of chemical constituents of *Platycodon grandiflorum* and its adulterant Adenophora stricta by UPLC-QTOF-MS/MS. *J. Mass Spectrom.* 52 (10), 643–656. doi:10.1002/jms.3967

Wang, C. Z., Zhang, N. Q., Wang, Z. Z., Qi, Z., Zhu, H. L., Zheng, B. Z., et al. (2017b). Nontargeted metabolomic analysis of four different parts of *Platycodon grandiflorum* grown in northeast China. *Molecules*. 22 (8), 1280. doi:10.3390/molecules22081280

Wang, C., and Li, Y. B. (2019). Multi-drug resistance mechanisms of lung cancer multi-target reversing by Chinese herbal compound prescription. *China J Tradit Chin Med. Pharm* 34 (2), 688–691. doi:CNKI:SUN:BXYY.0.2019-02-071

Wang, B., Zhu, X. X., Pan, L. Y., Chen, H. F., and Shen, X. Y. (2020). PP4C facilitates lung cancer proliferation and inhibits apoptosis via activating MAPK/ERK pathway. *Pathol. Res. Pract.* 216, 152910. doi:10.1016/j.prp.2020.152910

Xu, T., Ma, C. Y., Fan, S. N., Deng, N., Lian, Y. J., Tan, L., et al. (2018). Systematic understanding of the mechanism of baicalin against ischemic stroke through a network pharmacology approach. *Evid Based Complement Alternat Med*. 2018, 2582843. doi:10.1155/2018/2582843

Yang, S. H., Zhang, J. L., Yan, Y. Q., Yang, M., Li, C., Li, J. M., et al. (2019). Network pharmacology-based strategy to investigate the pharmacologic mechanisms of Atractylodes macrocephala Koidz. for the treatment of chronic gastritis. *Front. Pharmacol.* 10 (undefined), 1629. doi:10.3389/fphar.2019.01629

Yim, N. H., Hwang, Y. H., Liang, C., and Ma, J. Y. (2016). A platycoside-rich fraction from the root of *Platycodon grandiflorum* enhances cell death in A549 human lung carcinoma cells via mainly AMPK/mTOR/AKT signal-mediated autophagy induction. *J. Ethnopharmacol.* 194 (undefined), 1060–1068. doi:10.1016/j.jep.2016.10.078

Ye, X. W., Deng, Y. L., Xia, L. T., Ren, H. M., and Zhang, J. L. (2020). Uncovering the mechanism of the effects of *Paeoniae Radix* Alba on iron-deficiency anaemia through a network pharmacology-based strategy. *BMC Complement Med Ther.* 20, 130. doi:10.1186/s12906-020-02925-4

Yu, X. Y., Xu, Y. L., Li, X. J., Yang, P. Y., Zhang, X., and Jia, Y. J. (2020). Analysis of prevention and control measures of traditional Chinese medicine for patients with lung cancer under the epidemic situation of new coronavirus pneumonia. *Tianjin J Tradit Chin Med.* 37 (11), 1213–1216

Zhang, H. Y. (2016a). *Separation and anyibacterial activity research of the extract from oil peony seed*. Beijing, China: Chinese Academy of Forestry

Zhang, Y. P. (2016b). Platycodin-D promotes TRAIL-induced apoptosis in lung cancer. *Zhejiang J Int Tradit Chin West Med.* 26 (08), 706–709

Zhang, J., Shi, X. Y., Meng, W., Ma, F., Zhao, L. X., and Zhao, J. F. (2018). Kaempferol inhibits invasion and migration of non-small cell lung cancer A549 cells by down-regulating ERRα expression. *Chin J Cancer Biother.* 25 (12), 1230–1236. doi:10.3872/j.issn.1007-385x.2018.12.004

Zhang, X. Y., and Mao, X. S. (2018). The steered molecular dynamics based on molecular simulation drug design software discovery studio. *Smart Healthcare* 4 (7), 74–76. doi:10.19335/j.cnki.2096-1219.2018.07.029

Zhang, J. Y., Liang, R. X., Wang, L., and Yang, B. (2019). Effects and mechanisms of danshen-shanzha herb-pair for atherosclerosis treatment using network pharmacology and experimental pharmacology. *J. Ethnopharmacol.* 229, 104–114. doi:10.1016/j.jep.2018.10.004

Zhao, R. L., Zhou, K. F., Zhang, X., and Chen, M. J. (2015). Research on mechanisms of PD-induced inhibition of adhesion, invasion and migration in non-small cell lung cancer H460 and A549 cells. *Chin. Pharmacol. Bull.* 31 (02), 241–247

Zhao, Y. X., Liu, J. F., and Qian, H. X. (2017). The effect and mechanism of apigenin reverse drugs resistance on A549/DDP cells. *Acta Univ. Med. Nanjing* 37 (11), 1385–1388 + 1394. doi:CNKI:SUN:NJYK.0.2017-11-003

Zhou, L., Qiao, Y. L., Wang, L., Zhu, L., and Zhang, J. Y. (2017). Effects of luteolin on the expression of PTEN PI3K-AKT signaling pathway and immune function in lung cancer model rats. *Nat Prod Res Dev.* 29 (12), 2128–2133 + 2140. doi:10.16333/j.1001-6880.2017.12.022

Zhou, Y. Y., Zhou, B., Pache, L., Chang, M., Khodabakhshi, A. H., Tanaseichuk, O., et al. (2019). Metascape provides a biologist-oriented resource for the analysis of systems-level datasets. *Nat. Commun.* 10 (1), 1523. doi:10.1038/s41467-019-09234-6

Zhu, L. X., Huo, X. H., Sun, H. X., Bi, S., and Ma, W. W. (2013). Effects of continuous cropping of *platycodon grandiflorus* on the soil physical-chemical effects of continuous cropping of *platycodon grandiflorus* on the soil physical-chemical. *J. Soil Water Conserv.* 27 (6), 177–181. doi:10.13870/j.cnki.stbcxb.2013.06.035

Conflict of Interest: The authors declare that the research was conducted in the absence of any commercial or financial relationships that could be construed as a potential conflict of interest.

Copyright © 2021 Deng, Ye, Chen, Ren, Xia, Liu, Liu, Liu, Zhang, Wang, Zhang and Zhang. This is an open-access article distributed under the terms of the Creative Commons Attribution License (CC BY). The use, distribution or reproduction in other forums is permitted, provided the original author(s) and the copyright owner(s) are credited and that the original publication in this journal is cited, in accordance with accepted academic practice. No use, distribution or reproduction is permitted which does not comply with these terms.

frontiers in Pharmacology

REVIEW
published: 15 February 2021
doi: 10.3389/fphar.2021.617559

Review of the Efficacy and Mechanisms of Traditional Chinese Medicines as a Therapeutic Option for Ionizing Radiation Induced Damage

*Xiaomeng Zhang[1], Xiaoying Chen[1], Lei Wang[1], Changhao He[1], Zhongyu Shi[1], Qian Fu[1], Wenhui Xu[2], Shujing Zhang[1] and Sumin Hu[1]**

[1]School of Traditional Chinese Medicine, Beijing University of Chinese Medicine, Beijing, China, [2]Beijing Academy of Traditional Chinese Medicine, Beijing University of Chinese Medicine, Beijing, China

Ionizing radiation damage refers to acute, delayed, or chronic tissue damage associated with ionizing radiation. Specific or effective therapeutic options for systemic injuries induced by ionizing radiation have not been developed. Studies have shown that Chinese herbal Medicine or Chinese Herbal Prescription exhibit preventive properties against radiation damage. These medicines inhibit tissue injuries and promote repair with very minimal side effects. This study reviews traditional Chinese herbal medicines and prescriptions with radiation protective effects as well as their mechanisms of action. The information obtained will guide the development of alternative radioprotectants.

Keywords: ionizing radiation, oxidative damage, Chinese herbal medicines, Chinese herbal prescriptions, anti-radiation, radiation protective drugs

OPEN ACCESS

Edited by:
Hai Yu Xu,
China Academy of Chinese Medical Sciences, China

Reviewed by:
Amit Krishna De,
Indian Science Congress Association (ISCA), India
Tusty-Jiuan Hsieh, Kaohsiung Medical University, Taiwan

****Correspondence:***
Sumin Hu
husm@bucm.edu.cn

Specialty section:
This article was submitted to Ethnopharmacology, a section of the journal Frontiers in Pharmacology

Received: *15 October 2020*
Accepted: *11 January 2021*
Published: *15 February 2021*

Citation:
Zhang X, Chen X, Wang L, He C, Shi Z, Fu Q, Xu W, Zhang S and Hu S (2021) Review of the Efficacy and Mechanisms of Traditional Chinese Medicines as a Therapeutic Option for Ionizing Radiation Induced Damage. Front. Pharmacol. 12:617559. doi: 10.3389/fphar.2021.617559

INTRODUCTION

Ionizing radiation is essential in clinical diagnoses and treatment. It is an effective therapeutic strategy for cancer treatment. Approximately 50% of cancer patients are administered with radiotherapy to inhibit metastasis (Begg et al., 2011). Ionizing radiation causes clustered DNA damage and leads to persistent oxidative stress injuries to cellular macromolecules (Shuryak, 2019). Radiotherapy inhibits metastasis by inducing DNA damage. However, it causes unintended damage to normal cells by enhancing DNA double-strand breaks (DSBs). Double-strand breaks can be repaired through two major pathways: the non-homologous end-joining (NHEJ) and homologous recombination (HR). The NHEJ pathway occurs during the G0/G1 phase, while the HR repair pathway is only active in the late S and G2 phases (Shibata, 2017). Severe genetic changes such as chromosomal deletions and translocations in the repair process can stimulate tumorigenesis (Shrivastav et al., 2008; Gerelchuluun et al., 2015). According to the United Nations Scientific Committee, the effects of atomic radiation include mutations due to DNA deletions (Sankaranarayanan and Wassom, 2005), and epigenetic transmissions that affect generations (Horemans et al., 2019). Oxidative damage after exposure to ionizing radiation is a crucial reason for sustained injuries (Einor et al., 2016). Approximately 70% of cellular radiation damage is indirectly caused by water dissociation and reactive oxygen species (ROS). Free radicals are triggers for a state of constant oxidative stress (Anuranjani and Bala, 2014). Inflammation, immunity, and other associated signaling pathways are involved in the regulation of cellular damage by inducing cell senescence, apoptosis, and other cell fates (Santivasi and Xia, 2014). The pathological process is as shown in **Figure 1**. Ferroptosis is a novel form of cell death that

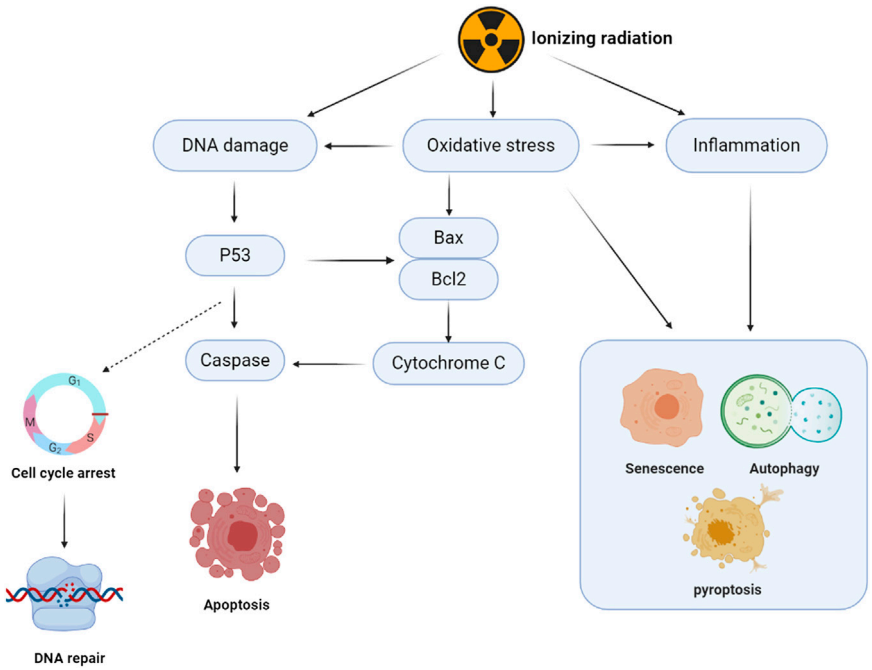

FIGURE 1 | Schematic diagram of ionizing radiation damage mechanism. The damage of ionizing radiation to cell structure mainly has two ways: the direct damage to DNA and the indirect damage from accumulated ROS. DNA damage response and repair induced by ionizing radiation can lead to cell cycle arrest and activate DNA homologous recombination (HR) or non-homologous end joining (NHEJ) repair. DNA damage induces the phosphorylation of P53, promotes the expression of Bax and other apoptotic proteins, promotes the release of Cytochrome C from mitochondria, and activates Caspase from the intrinsic apoptosis pathway. P53 can induce the expression of downstream death receptors and death ligands, which triggers the extrinsic apoptosis pathway. Oxidative stress caused by ROS overproduction triggers DNA double-strand breaks that continue and exacerbate DNA damage. It also induces mitochondrial dysfunction and intrinsic apoptotic cascade reaction. Ionizing radiation increases the secretion of inflammatory factors and induces immune responses. Inflammatory factors and oxidative damage are involved in regulating cell fate, including autophagy, pyroptosis and senescence.

is involved in pathological damage after irradiation (Lei et al., 2020). There is a need for the development of drugs that inhibit or repair pathological damages associated with radiation.

Current therapeutic strategies for radiation damage focus on minimizing DNA breaks, generation of antioxidants, scavenging free radicals, and inhibiting lipid peroxidation (Weiss and Landauer, 2003; Johnke et al., 2014; Smith et al., 2017). However, clinical applications of radioprotectants are limited because of its limited efficacies and severe side effects (Brizel, 2007; Citrin et al., 2010; Singh and Seed, 2019). Chinese herbal medicines have been used for thousands of years. They are widely used in clinical settings to treat various diseases, or are used in combination with western medicines to improve clinical efficacies (Li and Xu, 2011; Hao et al., 2017; Takayama and Iwasaki, 2017; Wang and Zhang, 2017; Yeh et al., 2017; Lei et al., 2019). As early as the 1960s, Chinese researchers had extended the research focused on the anti-radiation effects of Chinese herbal medicines. It has been found that *Panax ginseng C.A.Mey.*, *Ganoderma Lucidum Karst*, *Angelica sinensis (Oliv.) Diels*, and other medicinal herbs exhibit varying degrees of anti-radiation effects. In addition, Chinese Herbal Prescriptions have been shown to facilitate physical recovery. Traditional Chinese medicinal herbs have complex chemical structures and biological activities. The Chinese Herbal Prescription, which is composed of more than one medicinal herb, is the embodiment of traditional Chinese medicine's clinical applications. The Chinese Herbal Prescriptions can enhance the efficacy of a drug, reduce or neutralize the adverse effects of individual drugs and improve their therapeutic efficacies (Shen et al., 2017; Li et al., 2019b; Shi et al., 2019b). In recent years, researches on the treatment of ionizing radiation damage with Traditional Chinese Medicine are regularly emerging. The active compounds in Chinese medicinal herbs and Chinese Herbal Prescriptions exhibit significant effects on the reduction of oxidative stress and promote DNA repair. Their biological mechanisms involve the regulation of multiple signaling pathways.

In this review, we summarized recent advances that have been aimed at elucidating the functions and mechanisms of effective active ingredients of Chinese herbal medicines and prescriptions in preventing ionizing radiation associated damage. We aimed at establishing novel therapeutic avenues for the development and clinical applications of radiation protective drugs.

ANTI-RADIATION ACTIVE COMPOUNDS OF CHINESE HERBAL MEDICINES

Active compounds in Chinese herbal medicines can scavenge for free radicals, reduce DNA damage, promote post-injury repair, and reduce cell apoptosis. Therefore, these herbs prevent

TABLE 1 | Effects and Mechanisms of active compounds of Chinese Herbal Medicines in ionizing radiation damage.

Names	Category	Origins	Objects (model inducer,dose)	Pharmacological action/Mechanisms	References
Ginsenoside Rb(1), Rb(2), Rc, Rd, Re and Rg(1)	Saponins	*Panax ginseng C.A.Mey.*	ICR mice (12 Gy, 6.5 Gy ^{60}Co γ rays)	Reduce intestinal crypt cells apoptosis	Lee et al. (2006)
Gypenosides	Saponins	*Gynostemma pentaphyllum*	Male Balb/c mice (5 Gy ^{60}Co γ rays)	Increase the activity of SOD and CAT in serum, interference with Nrf2 signaling pathways	Ying et al. (2018)
Eleutheroside	Saponins	*Eleutherococcus senticosus (Rupr. & Maxim.) Maxim.*	Male mice (2 Gy x rays)	Improve peripheral blood cell radiation injury	Yue et al. (2005)
Acidic polysaccharide of ginseng	Polysaccharides	*Panax ginseng C.A.Mey.*	Bms (1 Gy ^{60}Co γ rays) Balb/c mice (5 Gy ^{60}Co γ rays)	Alter the phenotype of bms, increase the viability and alloreactivity of bms	Kim et al. (2007)
Acidic polysaccharide of ginseng	Polysaccharides	*Panax ginseng C.A.Mey.*	C57BL/6 mice(7 Gy ^{60}Co γ rays)	Inhibit p53 dependent pathway and mitochondrial apoptosis pathway activation	Park et al. (2011) and Bing et al. (2014)
Lycium Barbarum Polysaccharide	Polysaccharides	*Lycium barbarum L.*	Wistar rats (2.3 Gy ^{60}Co γ rays)	Elevate SOD levels, suppress MDA levels and restores testosterone levels	Luo et al. (2011)
Lycium Barbarum Polysaccharide	Polysaccharides	*Lycium barbarum L.*	Kunming mice (4 Gy X-rays)	Improve antioxidant capacity and cell cycle	Zhou et al. (2016)
Lycium Barbarum Polysaccharide	Polysaccharides	*Lycium barbarum L.*	Wistar rats (2.3 Gy ^{60}Co γ rays)	Inhibit mitochondrial apoptosis	Luo et al. (2014)
Astragalus Polysaccharide	Polysaccharides	*Astragalus mongholicus Bunge*	Balb/c mice (5 Gy ^{60}Co γ rays)	Inhibit the secretion of pro-inflammatory factors, reduce the damage of pulmonary fibrosis caused by peroxide	Liu et al. (2014)
Astragalus Polysaccharide	Polysaccharides	*Astragalus mongholicus Bunge*	Bmscs A549 cells (2 Gy X-rays)	Improve the ROS - mediated side effects of ionizing radiation via MAPK/NF-κB signaling pathway	Zhang et al. (2018c)
Astragalus Polysaccharide	Polysaccharides	*Astragalus mongholicus Bunge*	Human bone marrow mesenchymal stem cells (2 Gy X-rays)	Promote the self-renewal and proliferation of cells	Kongxi et al. (2020)
Astragalus Polysaccharide	Polysaccharides	*Astragalus mongholicus Bunge*	Human bone marrow mesenchymal stem cells (2 Gy $^{12}C^{6+}$)	Down-regulates NF-κB signaling pathway to maintain cell DNA stability	Li-ying et al. (2018)
Ganoderma Polysaccharides	Polysaccharides	*Ganoderma Lucidum Karst*	Mice (5 Gy X-rays)	Improves the expression of biomarkers in the thymus	Kunmu et al. (2020)
Ganoderma Polysaccharides	Polysaccharides	*Ganoderma Lucidum Karst*	Kunming mice (7.5 Gy ^{60}Co γ rays)	Increase the survival rate, improve the phagocytosis of mononuclear macrophages and NK cell activity	Guohui et al. (2004)
Angelica sinensis polysaccharide	Polysaccharides	*Angelica sinensis (Oliv.) Diels*	Balb/c male mice (3 Gy ^{60}Co γ rays)	Increase the number of bone marrow cell and protect hematopoietic system	Zhao et al. (2012)
Gingko flavonoids	Flavonoid	*Ginkgo biloba L.*	SD rats (800 cgy X-rays)	Inhibit lipid peroxidation and reduce the secretion of LDH and TNF-α	Sener et al. (2006)
Houttuynia Cordata	Flavonoid	*Houttuynia cordata Thunb.*	Kunming mice (3 Gy ^{60}Co γ rays)	Improve peripheral blood cell injury	Jun and Zhenghai (2010)
Paeoniflorin	Glycosides	*Paeonia lactiflora Pall.*	EA.hy926 cell line (10 Gy ^{60}Co γ rays)	Interfere with Nrf2/HO-1 pathway to reduce oxidative stress response	Yu et al. (2013)
Paeoniflorin	Glycosides	*Paeonia lactiflora Pall.*	Thymocytes (0–8 Gy ^{60}Co γ rays)	Act on the expression of Bcl-2, Bax and Caspase-3, and reduce mitochondrial apoptosis	Li et al. (2007)
Paeoniflorin	Glycosides	*Paeonia lactiflora Pall.*	HSF cell line (16 Gy X-rays)	Inhibits MAPK signal pathway to revers DNA damage	Yang et al. (2015)
Astragaloside IV	Glycosides	*Astragalus mongholicus Bunge*	Balb/c mice (6 Gy ^{60}Co γ rays)	Regulates cell apoptosis or cell cycle, down-regulates Bax/Bcl-2 ratio, and reduces cell cycle arrest in G0/G1 phase	Li et al. (2011)
Rhodioloside	Glycosides	*Rhodiola rosea L.*	AHH-1 cells (4, 6, 8, 10 Gy ^{60}Co γ rays)	Increases the proliferative activity of lymphocytes	Tianxiang et al. (2013)
Ferulic Acid	Phenolic acids	*Angelica sinensis (Oliv.) Diels*	Swiss albino mice (10 Gy ^{60}Co γ rays)	Promotes Nrf2 nuclear translocation and activates the NHEJ repair pathway	Das et al. (2017a)
Ferulic Acid	Phenolic acids	*Angelica sinensis (Oliv.) Diels*	Swiss mice (4, 6, 8, 10 Gy ^{60}Co γ rays)	Reduces DNA strand break in leukocytes and bone marrow cells and promotes the recovery of bone marrow hematopoietic functions	Maurya and Devasagayam (2013)

(Continued on following page)

TABLE 1 | (*Continued*) Effects and Mechanisms of active compounds of Chinese Herbal Medicines in ionizing radiation damage.

Names	Category	Origins	Objects (model inducer,dose)	Pharmacological action/Mechanisms	References
Ferulic Acid	Phenolic acids	*Angelica sinensis (Oliv.) Diels*	Swiss albino mice (10 Gy ^{60}Co γ rays)	Reduces IκBα phosphorylation, and NF-κB nuclear translocation, improves radiation-induced inflammation	Das et al. (2014)
Ferulic Acid	Phenolic acids	*Angelica sinensis (Oliv.) Diels*	Swiss albino mice (10 Gy ^{60}Co γ rays)	Reduces lipid peroxidation and increases the activity of SOD and catalase, increases PI3K phosphorylation levels, reduces cell cycle arrest	Das et al. (2016)
Ferulic Acid	Phenolic acids	*Angelica sinensis (Oliv.) Diels*	Swiss albino mice (2.5, 5, 10 Gy ^{60}Co γ rays)	Inhibits peroxide and downstream mitochondrial apoptosis pathway activation	Das et al. (2017b)
Ferulic Acid	Phenolic acids	*Angelica sinensis (Oliv.) Diels*	SD rats (5 Gy ^{60}Co γ rays)	Increases SIRT1 activity and testosterone levels in testis, and decreases oxidative stress response	El-Mesallamy et al. (2018)
Salvianic acid A	Phenolic acids	*Salvia miltiorrhiza Bunge*	L-02 cells (4 Gy ^{60}Co γ rays)	Reduces apoptosis and DNA damage	Juan et al. (2012)
Salvianic acid A	Phenolic acids	*Salvia miltiorrhiza Bunge*	Balb/c mice (4, 8 Gy ^{60}Co γ rays)	Protects hematopoietic system	Juan et al. (2015)
Resveratrol	Polyphenols	*Red grapes*	Female SD rats (3.2 Gy ^{137} Cs γ rays)	Inhibits NF-κB - activated inflammatory cytokines	Said et al. (2016)
Resveratrol	Polyphenols	*Red grapes*	Lymphocyte (0.5, 1 Gy X-rays)	Inhibits DNA damage	Basso et al. (2016)
Resveratrol	Polyphenols	*Red grapes*	Male C57BL/6 N mice (7 Gy ^{137} Cs γ rays)	Improves intestinal morphology, reduce crypt cell apoptosis, and regulates the expression of Sirt1 and p53	Zhang et al. (2017a)
Resveratrol	Polyphenols	*Red grapes*	Male C57BL/6 mice (6 Gy ^{137} Cs γ rays)	Ameliorates thymus and spleen atrophy, reduce lymphocyte count, Modulates immunosuppression	Zhang et al. (2018a)
Tea Polyphenols	Polyphenols	*Green tea*	Kunming mice (738 cGy ^{60}Co γ rays)	Recovery the haematopoietic system, antioxidant potential activity and reduce inflammatory cytokines	Hu et al. (2011)
Tea Polyphenols	Polyphenols	*Green tea*	Male C57BL/6 mice (2 Gy X-rays)	Inhibits oxidative stress and mitochondrial apoptosis	Ding et al. (2015)
Ginseng oligopeptide	Oligopeptides	*Panax ginseng C.A.Mey.*	Caco-2 (2 Gy X-rays) Balb/c mice (3.5 Gy X-rays)	Attenuates immune dysfunction	He et al. (2017)
Ginseng oligopeptide	Oligopeptides	*Panax ginseng C.A.Mey.*	BALB/c mice (3.5, 8Gy ^{60}Co γ rays)	Decreases inflammatory and oxidative stress	He et al. (2018)

radiation damage through different mechanisms. Below, we highlight a few representative active compounds and highlight their potential mechanisms and pharmacological activities in radioprotection (As shown in **Table 1**).

Saponins

Saponins are the main active compounds in many Chinese herbal medicines (Yang et al., 2014), especially in *Panax ginseng C.A.Mey*. Lee et al. established that the active ingredients in *Panax ginseng C.A.Mey* such as Ginsenoside Rc, Ginsenoside Rd, and Ginsenoside Re are radioprotective (Lee et al., 2006). The administration of Ginsenoside Rd and Ginsenoside Re in mice before irradiation enhanced the formation of endogenous splenic colonies and inhibited radiation-induced apoptosis of the intestinal crypt cells (Lee et al., 2006). Ginsenosides have a wide range of biological and pharmacological properties. They have been shown to be effective against neurological diseases, infectious diseases, and tumors (Rokot et al., 2016; Arring et al., 2018; Nguyen and Nguyen, 2019). Through intestinal biotransformation, *Panax ginseng C.A.Mey.* can be transformed into high pharmacological activity metabolites that act on multiple human tissues (Mancuso and Santangelo, 2017).

Other medicinal herbs have also been shown to contain saponins that play a role in radioprotection. Administration of Gypenoside before irradiation effectively increased serum superoxide dismutase (SOD) and CAT levels that inhibit the expression of Nrf2 and HO-1 (Ying et al., 2018). Saponins from *Eleutherococcus senticosus (Rupr. & Maxim.) Maxim.* ameliorate peripheral blood cell damage associated with radiation (Yue et al., 2005).

Polysaccharides

Polysaccharides are widespread in animals, plants, and microorganisms. They from part of the primary substances that make up living things (Chen and Huang, 2018). *Panax ginseng C.A.Mey.* contains polysaccharides. The acidic polysaccharide of ginseng (APG) has been shown to increase IL-12 levels in bone marrow cells (BMs) of irradiated mice. Kim et al. speculated that APG contribute to the proliferation of CD4 (+) T lymphocytes and facilitate viability as well as

TABLE 2 | Effects and Mechanisms of Chinese Herbal Medicines in ionizing radiation damage.

Names	Familia	Objects (model inducer,dose)	Pharmacological action/Mechanisms	References
Panax ginseng C.A.Mey.	Araliaceae	Outbred albino rats (4 Gy ^{60}Co γ rays)	Inhibits carcinogenesis	Bespalov et al. (2014)
Panax ginseng C.A.Mey.	Araliaceae	Balb/c mice (8 Gy ^{60}Co γ rays)	Protects the bone marrow and increases inflammatory factor	Song et al. (2003)
Panax ginseng C.A.Mey.	Araliaceae	Swiss albino mice (6 Gy ^{60}Co γ rays)	Protects against radiation-induced hematological and biochemical alterations	Verma et al. (2011)
Panax ginseng C.A.Mey.	Araliaceae	Splenocytes (5 Gy ^{60}Co γ rays) Balb/c mice (4.5 Gy ^{60}Co γ rays)	Inhibits immunosuppression	Han et al. (2005)
Panax ginseng C.A.Mey.	Araliaceae	Wistar rats (6 Gy ^{60}Co γ rays)	Protects against cardio-nephrotoxicity through enhancing the antioxidant activity and inhibition of endothelial dysfunction	Mansour (2013)
Panax ginseng C.A.Mey.	Araliaceae	C57BL/6 mice (15 Gy X-rays)	Prevents the manifestations of oxidative stress, protects against RILI	Jang et al. (2015)
Panax ginseng C.A.Mey.	Araliaceae	C57BL/6 mice(6.5 Gy ^{60}Co γ rays)	Protects against radiation-induced inflammation and cancer	Koo et al. (2013)
Panax ginseng C.A.Mey.	Araliaceae	RAW264.7 cells (10 Gy ^{60}Co γ rays)	Inhibits proinflammatory responses	Lee et al. (2014)
Panax ginseng C.A.Mey.	Araliaceae	RBL-2H3 cells (10, 30, 50, 70, 100 kGy ^{60}Co γ rays) Balb/c mice (100 kGy ^{60}Co γ rays)	Suppresses the release of β-hexosaminidase, histamine, intracellular ROS and Ca2 + influx induced by IgE-antigen complex, inhibits mast cell-mediated signal transduction activity, and reduces IL- 4 serum levels	Kang et al. (2018)
Panax quinquefolius L.	Araliaceae	Human (1, 2 Gy X-rays)	Inhibits lymphocytic DNA damage after radiotherapy, Increases total antioxidant capacity	Lee et al. (2010)
Zingiber officinale roscoe	Zingiberaceae	Swiss albino mice (6–12 Gy ^{60}Co γ rays)	Inhibits lipid peroxidation	Jagetia et al. (2003)
Zingiber officinale roscoe	Zingiberaceae	Human mesenchymal stem cells (4 Gy ^{60}Co γ rays)	Induces Nrf2 nuclear translocation	Ji et al. (2017)
Zingiber officinale roscoe	Zingiberaceae	SD rats (2 Gy ^{60}Co γ rays)	Improves taste, vomiting symptoms	Sharma et al. (2005)
Zingiber officinale roscoe	Zingiberaceae	Albino rats (6 Gy ^{60}Co γ rays)	Regulates inflammatory signaling pathways	Mohamed and Badawy (2019)
Zingiber officinale roscoe	Zingiberaceae	Albino rats (6 Gy ^{60}Co γ rays)	Suppresses inflammatory factors, enhances mitochondrial complex activity	Soliman et al. (2018)
Angelica sinensis (Oliv.) Diels	Apiaceae	Wistar rats (8 Gy X-rays)	Inhibits OPN, C-Jun, miRna-21 expressions, reduces TGF-1 release and Tn-I levels, resistance to radiation-induced cardiac fibrosis	Ma et al. (2019)
Ginkgo biloba L.	Ginkgoaceae	Wistar rats (6 Gy ^{60}Co γ rays)	Inhibits lipid peroxidation and prevents DNA damage	Ismail and El-Sonbaty (2016)
Ginkgo biloba L.	Ginkgoaceae	Wistar rats(1 mci of (99 m)Tc)	Anti-lipid peroxidation and anti-apoptotic	Raafat et al. (2013)
Portulaca oleracea L.	Portulacaceae	Albino rats (6 Gy ^{60}Co γ rays)	Relieves lipid peroxidation in liver and kidney	Abd El-Azime et al. (2014)
Lycium barbarum L.	Solanaceae	Kunming mice (5 Gy X-rays)	Inhibits the expression of P53, caspase-3 and caspase-6, and accelerates the recovery of splenic functions	Duan et al. (2015)
Crataegus pinnatifida Bunge	Rosaceae	Lymphocytes (150 cGy ^{60}Co γ rays)	Reduces micronucleus in lymphocytes	Hosseinimehr et al. (2009)
Hippophae rhamnoides L.	Elaeagnaceae	Swiss albino strain 'A'Male mice (10 Gy ^{60}Co γ rays)	Protects mitochondria and chromatin	Shukla et al. (2006)
Hippophae rhamnoides L.	Elaeagnaceae	Swiss albino mice (5Gy, 10 Gy ^{60}Co γ rays)	Enhances spermatogonial proliferation, stem cell survival and reduces sperm abnormalities	Goel et al. (2006)

alloreactivity by inducing phenotypic changes in BMs (Kim et al., 2007). APG inhibits the activation of the p53-dependent pathway and the mitochondrial apoptosis pathway. It down-regulates pro-apoptotic proteins (p53, BAX, cytochrome-c, and caspase-3), thereby, promoting the proliferation of crypt cells. These effects were shown to protect the small intestines of mice from radiation damage (Park et al., 2011; Bing et al., 2014).

Lycium barbarum L. is commonly used in traditional medicine to nourish the liver and kidney. Its active ingredient, the Lycium barbarum polysaccharide (LBP), exhibits significant antioxidant effects. Studies have reported that after multiple consecutive local ^{60}Co γ-rays irradiation of rats' testis, LBP enhanced testicular SOD activity, inhibited malondialdehyde (MDA) levels, promoted redox balance recovery, and restored the secretion of testosterone (Luo et al., 2011). In the hematopoietic system, LBP was shown to increase the antioxidant capacity of bone marrow mononuclear cells and mitigated cell cycle arrest by interfering with adhesion molecules CD44 and CD49d (Zhou et al., 2016). In addition, by acting on on Bcl-2 and Bax, LBP inhibits spermatogenic cell apoptosis by regulating mitochondrial membrane potential and inhibiting mitochondrial apoptosis (Luo et al., 2014).

TABLE 3 | Effects and Mechanisms of Chinese Herbal Prescription in ionizing radiation damage.

Chinese Herbal Prescription	Content	Objects (model inducer,dose)	Pharmacological action/Mechanisms	References
Siwu Tang	*Rehmannia glutinosa (Gaertn.) DC., Angelica sinensis (Oliv.) Diels, Conioselinum anthriscoides 'Chuanxiong', Paeonia lactiflora Pall.*	Female C57BL/6 mice (3.5 Gy ^{60}Co γ rays))	Promotes hematopoietic and immune system recovery	Liang et al. (2006) and Liu et al. (2017)
BuzhongYiqi Tang	*Astragalus mongholicus Bunge, Codonopsis pilosula (Franch.) Nannf., Atractylodes lancea (Thunb.) DC., Bupleurum chinense DC., Actaea cimicifuga L., CCitrus reticulata Blanco, Angelica sinensis (Oliv.) Diels, Glycyrrhiza glabra L.*	ICR mice (3 Gy ^{60}Co γ rays)	Increases the peripheral white blood cell count, relieves platelet damage, reduces lipid peroxides and improves the hematopoietic microenvironment	Xiao-fang et al. (2013) and Xiaoling et al. (2006)
Xuebijing (XBJ) injection	*Carthamus tinctorius L., Paeonia lactiflora Pall., Conioselinum anthriscoides 'Chuanxiong', Salvia miltiorrhiza Bunge, and Angelica sinensis (Oliv.) Diels*	ICR mice (2 Gy, 7.5Gy ^{60}Co γ rays) Bone marrow mononucleated cells (1 Gy, 4Gy ^{60}Co γ rays)	Reduces ROS in bone marrow cells	Li et al. (2014a)
Yiqi Yangyin Fang (YYF)	*Astragalus mongholicus Bunge, Panax ginseng C.A.Mey., Ligustrum lucidum W.T.Aiton, Eclipta prostrata (L.) L., Angelica sinensis (Oliv.) Diels, Atractylodes macrocephala Koidz., Poria cocos (Schw.) Wolf, Glycyrrhiza glabra L.*	ICR mice (2 Gy, 4Gy ^{137} Cs γ rays)	Increases the number of bone marrow cells, hematopoietic progenitor cells, and hematopoietic stem cells, inhibits bone marrow suppression by reducing intracellular ROS levels	Zhang et al. (2017b)
HemoHIM	*Angelica sinensis (Oliv.) Diels, Ligusticum officinale (Makino) Kitag., Paeonia lactiflora Pall.*	Female C57BL/6 mice (5 Gy ^{137} Cs γ rays)	Regulates IL-12 p70/pSTAT4 signaling pathway, accelerates the recovery of immune cells	Park et al. (2012) Park et al. (2014)
Bushen Jiedu Recipe	*Schisandra chinensis (Turcz.) Baill., Ophiopogon japonicus (Thunb.) Ker Gawl., Codonopsis pilosula (Franch.) Nannf., Astragalus mongholicus Bunge*	Knockout mice (6 Gy ^{60}Co γ rays)	Regulates TLR4 signaling pathway, reduces white blood cell damage, and protects immune organs	Yunjing et al. (2015) and Lidan et al. (2016)
Wumai Danghuang Oral Liquid	*Schisandra chinensis (Turcz.) Baill., Ophiopogon japonicus (Thunb.) Ker Gawl., Codonopsis pilosula (Franch.) Nannf., Astragalus mongholicus Bunge*	Kunming mice (2 Gy, 3 Gy ^{60}Co γ rays)	Increases SOD activity, degrades MDA content, repairs the immune system	Chunhong et al. (2014) and Hang et al. (2013)
Co-Herba Houttuyniae Oral Liquid	*Houttuynia cordata Thunb., Panax ginseng C.A.Mey., Lycium barbarum L.*	Kunming mice (1.5 Gy, 3 Gy ^{60}Co γ rays)	Reduces the rate of chromosomal aberrations, enhances immune functions and the anti-stress ability	Lin et al. (2001) and Lin et al. (2002)
Radioprotection Formula	*Astragalus mongholicus Bunge,Ganoderma Lucidum Karst, Lycium barbarum L., Poria cocos (Schw.) Wolf*	Kunming mice (3 Gy, 7.5 Gy ^{60}Co γ rays)	Increases the survival rate, white blood cell count, thymus index, spleen index and bone marrow cell DNA content	Liming et al. (2011)
STW 5	*Iberis amara L., Melissa officinalis L., Matricaria chamomilla L., Carum carvi L., Mentha aquatica L., Angelica archangelica L., Silybum marianum (L.) Gaertn., Chelidonium majus L., Glycyrrhiza glabra L.*	Male Wistar rats (6 Gy ^{60}Co γ rays)	Inhibita oxidative stress responses, lowers inflammatory factors and intestinal damage index, regulates apoptosis-related factors	Khayyal et al. (2014) and El-Ghazaly et al. (2015)
Astragalus immortal prescription	*Rehmannia glutinosa (Gaertn.) DC., Ophiopogon japonicus (Thunb.) Ker Gawl. and Equus asinus L., Astragalus mongholicus Bunge*	Kunming mice (8 Gy X rays)	Increases the activities of GSH-Px, SOD and reduces MDA content in the liver	Cai-qin et al. (2017)
Wuzi Yanzong Pill (WZYZ)	*Lycium barbarum L., Cuscuta chinensis Lam., Schisandra chinensis (Turcz.) Baill., Plantago asiatica L., Rubus chingii Hu*	Male Kunming mice (4 Gy X rays)	Increases serum testosterone and reduces MDA and oxidative stress index (OSI)	Ji et al. (2016)
Yiqi Jiedu Decoction (YQJD)	*Astragalus mongholicus Bunge, Angelica sinensis (Oliv.) Diels, Lycium barbarum L., Panax quinquefolius L., Paeonia lactiflora Pall., Crataegus pinnatifida Bunge, Poria cocos(Schw.)Wolf, Portulaca oleracea L.*	Male Balb/c mice (2 Gy ^{60}Co γ rays)	Promotes testicular index and testicular structure recovery, decreases spermatogenic cell apoptosis, and protects spermatogenic functions by intervening in TLR5 signaling pathways	Wang et al. (2020)

Astragalus mongholicus Bunge is a qi-tonifying medicinal herb that is often used in qi deficiency syndromes (Li et al., 2014b). Radiation-induced lung injury is one of the most common and fatal complications of chest radiotherapy (Klein et al., 2016). After ionizing irradiation, alveolar epithelial cells in the lung exhibit a senescence phenotype and up-regulates the transcription of pro-inflammatory factors that induce pulmonary fibrosis (Beach et al., 2017). This condition manifests itself as breathlessness. The

Astragalus polysaccharide is the active ingredient in *Astragalus mongholicus Bunge*. It inhibits thiobarbituric acid reactive substances and pro-inflammatory factors, but also activates SOD, catalase and glutathione. In addition, it reduces the damage of pulmonary fibrosis caused by peroxidation. Its mechanism of action is correlated with the expression of NF-κB, and this mechanism applys to radiation-induced liver injury (Liu et al., 2014).

Astragalus polysaccharide inhibits p38 phosphorylation, JNK, ERK1/2, NF-κB P65, and COX-2 protein expression levels. Evidence shows that it inhibits ionizing radiation-induced side effects through the ROS-mediated MAPK/NF-κB signaling pathway (Zhang et al., 2018c). Ionizing radiation decreases the capacity for cell proliferation. The Astragalus polysaccharide has been documented to promote self-renewal and proliferation of cells by elevating the expressions of peroxisome proliferator-activated receptor-γ (PPAR-γ), CCAAT/enhancer-binding protein α (C/EBPα) and protecting adipogenic differentiation functions (Kongxi et al., 2020). *In vitro* studies have also revealed that Astragalus polysaccharides enhance bone marrow mesenchymal stem cell proliferation by downregulating NF-κB signaling pathway-related proteins and maintaining DNA stability (Li-ying et al., 2018).

Ganoderma Lucidum Karst has qi replenishment and nerve soothing properties. It contains various biologically active components and pharmacological activities that are important in the control of multiple diseases (Jin et al., 2016; Ahmad, 2018). The Ganoderma lucidum polysaccharide is the main biologically active component of *Ganoderma Lucidum Karst*. Studies have shown that Ganoderma lucidum polysaccharide regulates the metabolism of endogenous substances (such as L-glutamic acid, taurine, and glycerophospholipid) that enhance the expression of relevant biomarkers in mice thymus and exert radioprotective effects (Kunmu et al., 2020). Guohui et al. reported that after exposing mice to radiation, *Ganoderma Lucidum Karst* increased mice survival rates and improved the phagocytic abilities of mononuclear macrophages and NK cells (Guohui et al., 2004).

The polysaccharides of *Angelica sinensis (Oliv.) Diels* have been documented to exhibit thymus and spleen protective indices, increase the number of red blood cells (RBC), white blood cells (WBC), and bone marrow cells of mice after irradiation. Therefore, they play a role in protecting the hematopoietic system (Zhao et al., 2012).

Flavonoids

Flavonoids are widely distributed in plants and exhibit health promoting properties (Mukai, 2018). *Ginkgo biloba L.* contains flavonols and other active compounds (Mei et al., 2017) that are responsible for its free radical scavenging ability and antioxidant properties (Evans, 2013). Therefore, *Ginkgo biloba L.* prevents ionizing radiation mediated injuries by inhibiting oxidative stress. Sener et al. have detected rat lung, liver, kidney, and ileum. They reported that the administration of *Ginkgo biloba L.* before and after irradiation attenuated malondialdehyde (MDA) content and reduced DNA damage by inhibiting lipid peroxidation (Sener et al., 2006). *Houttuynia cordata Thunb.* has shown to clearing heat and removing toxicity, reducing swelling and draining pus (Ma et al., 2017). The flavonoid contents of *Houttuynia cordata Thunb.* have been shown to improve the state of peripheral blood cells after radiation, thereby reducing injury (Jun and Zhenghai, 2010).

Glycosides

Paeonia lactiflora Pall. is an herb that nourishes the blood, restrains yin, softens the liver, and relieves pain. Paeoniflorin is a component of *Paeonia lactiflora Pall.*. Paeoniflorin increased glutathione (GSH), SOD, and reduced MDA and lactate dehydrogenase (LDH) content in an endothelial cell model. In addition, it was shown to reduce oxidative stress responses by interfering with the Nrf2/HO-1 pathway (Yu et al., 2013). Another study showed that it inhibited ROS-mediated mitochondrial apoptosis and reduced ROS accumulation as well as intracellular cytosolic Ca2 + concentrations. Other than inhibiting the mitochondrial apoptotic pathway by acting on Bcl-2, Bax, and caspase-3 (Li et al., 2007), paeoniflorin also inhibited MAPK signaling pathway activation and reversed radiation-induced DNA damage (Yang et al., 2015).

Astragaloside IV is an active ingredient in *Astragalus mongholicus Bunge* that is involved in controlling apoptosis or cell cycle, down-regulation of the Bax/Bcl-2 ratio, inhibition of G0/G1 cell-cycle arrest, increasing the proliferative ability of bone marrow cells, and in protection against radiation induced damage to the hematopoietic system (Li et al., 2011).

Rhodiola rosea L. contains a variety of biologically active compounds with antioxidant, anti-inflammatory, and stress response properties (Amsterdam and Panossian, 2016; Nabavi et al., 2016). Glycosides in *Rhodiola rosea L.* were shown to stimulate lymphocytic cell proliferation after radiation (Tianxiang et al., 2013).

Phenolic Acids

Angelica sinensis (Oliv.) Diels promotes blood nourishment and circulation and is often used to treat blood deficiency syndromes. Ferulic acid (FA) is a bioactive component of *Angelica sinensis (Oliv.) Diels* that reduces DNA damage. Studies have shown that administration of FA to mice 1 h before or after irradiation inhibited micronuclei formation in peripheral blood. FA promotes hematopoietic recovery by attenuating DSBs in white blood cells and bone marrow cells (Maurya and Devasagayam, 2013). After DNA damage, the PARPI repair mechanism is activated and regulates inflammatory mediators (such as cytokines, chemokines, and inducible Nitric Oxide synthase) (Bai and Virag, 2012), while SIRT1 negatively regulates PARP1 (Caito et al., 2010). After the exposure of mice to ionizing radiation, it was found that PARP1 activities and intracellular calcium concentrations increased in the testis, while SIRT1 activities and expression significantly decreased. FA reversed the expression of SIRT1, maintained testosterone levels, and reduced oxidative stress, while regulating PARP1 and cytosolic calcium concentrations to ameliorate spermatogenesis disorders (El-Mesallamy et al., 2018). Accumulated ROS enhances p53 nuclear transport, expands ataxia capillaries, and activates mutant protein (ATM). Using a radiation damage mice model, Das et al. showed that FA enhanced the nuclear

translocation of nuclear factor Nrf2 and activated the NHEJ repair pathway in response to ROS-mediated oxidative stress and DNA damage (Das et al., 2017a). In addition to inhibiting DNA damage and promoting DNA repair, FA was also involved in the regulation of inflammatory pathways and related factors. It was shown to inhibit the expression of Cox-2 and inducible nitric oxide synthase 2 (iNOS-2) after irradiation, control the phosphorylation/activation of IKKα/β and IκBα pathways, and regulate the downstream NF-κB nuclear translocation, thus ameliorating radiation-induced inflammation (Das et al., 2014).

In the intestines, FA was shown to interfere with the ROS/NF-κB/Nrf2/p53-caspase 3-PARP axis. In this processes, it enhanced the expression of Mn-SOD and Heme oxygenase-1 (HO-1) that inhibited peroxidation, regulated phosphatidylserine and mitochondrial membrane potential, and suppressed the activation of downstream mitochondrial apoptotic pathways (Das et al., 2017b). Therefore, FA can regulate cell cycle while inhibiting lipid peroxidation and radiation-induced cell apoptosis. Ionizing radiation activates stress marker cyclin (Cdc42) and down-regulates the activation of survival pathways by inhibiting the phosphorylation of phosphatidylinositol 3-kinase (PI3K) and serine/threonine kinase (Akt). The phosphatase gene (PTEN) is a critical molecule that regulates the survival pathway of PI3K/Akt. Ionizing radiation significantly increases the expression of PTEN that promotes cell cycle arrest and inhibits survival-related pathways. It has been demonstrated that FA lowers the overexpression of Cdc42, apoptotic proteins (p53, p21, Bax, and PTEN), and increases PI3K phosphorylation. Moreover, reduced cell cycle arrest inhibits lipid peroxidation while increasing SOD and catalase activities (Das et al., 2016). After radiation, the senescence phenotype of normal cells can be observed with the cells undergoing inflammation and fibrosis (Li et al., 2018b). Due to its antioxidant and anti-inflammatory aspects, FA has been shown to ameliorate these conditions.

Salvia miltiorrhiza Bunge is an alternative therapeutic option for cardiovascular and cerebrovascular diseases. It has anti-inflammatory, antioxidant, and anti-cancer biologic properties (Shi et al., 2019a). Salvianic acid A is the active compound in *Salvia miltiorrhiza Bunge* that has been shown to inhibit apoptosis and reduce ionizing radiation associated DNA damage (Juan et al., 2012). An *in vivo* assay established that salvianic acid A protects the hematopoietic system and improves survival after radiation (Juan et al., 2015).

Polyphenols

Polyphenols exhibit antioxidant properties that inhibit DNA damage caused by peroxide free radicals (Fraga et al., 2019). Resveratrol is a vital plant antitoxin that possesses antioxidant and anti-inflammatory effects. Resveratrol inhibits NF-κB -activated inflammatory cytokine secretion by up-regulating the expression of peroxisome proliferation-activated receptor (PPAR-4) and SIRT1. These effects prevent ionizing radiation-induced premature ovarian failure (Said et al., 2016). *In vitro* experiments, Basso et al. demonstrated that resveratrol is involved in inhibiting DNA damage after radiation through the assessment of human lymphocyte DNA damage, repair kinetics, and histone deacetylase activity (Basso et al., 2016). It also improves the morphology of the small intestine, reduces crypt cell apoptosis, regulates Sirt1 and acetylated p53, and has a radioprotective role (Zhang et al., 2017a). Resveratrol improves thymic and spleen atrophy, lymphocyte counts, and proliferation caused by ionizing radiation. Moreover, it inhibits serum levels of IL-2, IL-4, IL-7, and IFN-γ thereby regulating immune functions (Zhang et al., 2018a). Green tea is also rich in polyphenols. Tea polyphenols can improve hematopoietic functions after irradiation (Hu et al., 2011), inhibit oxidative stress and mitochondrial apoptosis as well as prevent radiation induced spermatogenic cell death (Ding et al., 2015).

Oligopeptides

The Ginseng oligopeptide (GOP) reduces the concentration of plasma diamine oxidase and LPS, and inhibits the secretion of IL-1 as well as TNF-α. It also protects the intestinal epithelial barrier by up-regulating the expression of tight junction proteins (ZO-1 and Occludin). It promotes intestinal repairs by suppressing the expression of apoptosis-related proteins (Bax and Caspase-3) and elevating lymphocyte (CD3 +, CD4 +, CD8 +) concentrations (He et al., 2017; He et al., 2018). He et al. reported that prophylactic administration of GOP exhibited radioprotective effects while post-treatment was beneficial for the quick repair of irradiation-induced injuries (He et al., 2017).

In summary, various radioprotective compounds occur in traditional Chinese medicines. This implies that the anti-radiation mechanisms of Chinese herbal medicines are multi-faceted. However, Chinese herbal contains sophisticated compounds. If only an active compound is used to explore the effect mechanism, there may be limitations.

CHINESE HERBAL MEDICINES AND THE ANTI-RADIATION EFFECTS

Extracts from Chinese herbal medicines have been used to comprehensively elucidate on the anti-radiation mechanisms of Chinese Herbal Medicines (**Table 2**).

Roots and Rhizomes of Chinese Herbal Medicine

Studies have confirmed that *Panax ginseng C.A.Mey.* reduces the overall or local cancer rates induced by long-term exposures to radiation (Bespalov et al., 2014). Ionizing radiation causes acute myelosuppression and leads to the apoptosis of hematopoietic stem cells as well as hematopoietic progenitor cells. These pathological changes are the primary causes of death after exposure to moderate-to-high radiation doses (Shao et al., 2014). The extract of *Panax ginseng C.A.Mey.* was shown to increase bone marrow cells, spleen cells, and granulocyte-macrophage colony-forming units (CFU-GM) in mice while promoting the secretion of endogenous cytokines (IL-1, IL-6, and IL-12) to rejuvenate hematopoietic functions (Song et al., 2003). In addition, the extract inhibited the decrease in red blood cell counts, hemoglobin and hematocrit, as well as

prevented radiation induced anemic symptoms (Verma et al., 2011). The extract of *Panax ginseng C.A.Mey.* has been reported to protect the hematopoietic system from ionizing radiation by inhibiting cyclooxygenase 2 (COX-2) and down-regulating activated p38 MAPK and PI3K/Akt pathways (Koo et al., 2013). Ionizing radiation-induced changes in the cellular microenvironment affect the immune system (Frey et al., 2017). *Panax ginseng C.A.Mey.* has immune regulation properties (Lee et al., 2005). Studies have shown that *Panax ginseng C.A.Mey.* elevates the mRNA expression of Th1 and Th2 cytokines and inhibits immunosuppression after radiation by stimulating normal spleen cells in mice (Han et al., 2005). *Panax ginseng C.A.Mey.* also exerts its radioprotective effects by inhibiting the expression of IL-1β in macrophages while simultaneously preventing the signal cascade of CHK2 and nuclear factor kappa B (NF-κB) (Lee et al., 2014). By destroying the intestinal epithelial barrier, radiation therapy enhances intestinal permeability and mucosal injury. Intestinal injuries lead to high plasma lipopolysaccharide (LPS) levels and elevated pro-inflammatory cytokine secretions that trigger a series of inflammatory reactions and bowel syndrome (Romesser et al., 2019). Moreover, *Panax ginseng C.A.Mey.* was shown to improve appetite in rats and reduced anorexic symptoms after radiation (Balaji Raghavendran et al., 2012). Ionizing radiation also causes damage to other tissues and organs. Oral administration of the extract of *Panax ginseng C.A.Mey.* before irradiation inhibited the suppression of serum creatine kinase and lactate dehydrogenase levels, suppressed urea and creatinine levels and further protected against irradiation-induced cardio-nephrotoxicity by enhancing antioxidant activities and inhibiting endothelial dysfunctions (Mansour, 2013). Through its antioxidant mechanisms, *Panax ginseng C.A.Mey.* can inhibit catalase activity, increase glutathione content, suppress the expression of IL-1β, TNF-α, and alleviates inflammation in radiation-induced lung injuries (Jang et al., 2015). Ionizing radiation leads acute skin damage (Park et al., 2018). The extract of *Panax ginseng C.A.Mey.* was shown to suppress the secretion of β-hexosaminidase, histamine, intracellular ROS, and internal Ca2+. It was also revealed that Black *Panax ginseng C.A.Mey.* inhibited mastocyte-mediated signaling activities, suppressed IL-4 serum levels, and ameliorated the symptoms and clinical signs of post-radiation allergic dermatitis (Kang et al., 2018). These studies suggest that *Panax ginseng C.A.Mey.* may be a useful herb against radiation associated damage.

Panax quinquefolius L. belongs to the Araliaceae family and has yin nourishment as well as heat clearing properties. From a clinical observation study, it was suggested that *Panax quinquefolius L.* ameliorated lymphocytic DNA damage after radiotherapy, suppressed micronucleus ratios in human lymphocytes, and enhanced total antioxidant capacities after exposure to radiation (Lee et al., 2010). In addition, this herb protects genes from acute damage in a short period. Studies have established that *Panax quinquefolius L.* tea protects cellular DNA from oxidative stress damage for at least 2 h (Szeto et al., 2015).

A fresh rhizome of *Zingiber officinale Roscoe* has been reported as being able to inhibit lipid peroxidation and excessive glutathione consumption (Jagetia et al., 2003), and improve mice survival after irradiation (Jagetia et al., 2004). Ji et al. demonstrated that the extract of *Zingiber officinale Roscoe* suppresses ionizing radiation-induced overproduction of ROS and DSBs in human mesenchymal stem cells. Its antioxidant mechanisms involve the induction of NRF2 nuclear translocation and activation of its downstream cell protection genes (HO- 1 and NQO-1) (Ji et al., 2017). Radiotherapy confers adverse side effects such as vomiting and nausea. These side effects have been attributed to ionizing radiation associated damage of the gastrointestinal, viscera and the vagus nerve to release serotonin that activates the brains vomiting center through serotonin receptors. Furthermore, radiation affects neural activity in the brain and activates specific sensory receptors. *Zingiber officinale Roscoe* can ameliorate nausea and vomiting. *Zingiber officinale Roscoe* inhibits the activation of related receptors, promotes neurobehavioral functions, and alleviates radiation-induced taste aversion and vomiting (Sharma et al., 2005). Besides, *Zingiber officinale Roscoe* plays a role in the regulation of inflammatory signaling pathways. Zingerone suppresses the MAPK signaling pathway, inhibits cytochrome P4502E1 as well as nicotinamide adenine dinucleotide phosphate (NADPH) oxidase, and downregulates liver enzyme activities. Further, it has been shown to regulate the expression of inflammatory markers such as TLR4, iNOS, COX-2, and MPO (Mohamed and Badawy, 2019). Negative regulation of the TLR4 pathway by zingerone alleviates radiation-induced hepatic injury (Lee et al., 2018). Epidemiological studies have indicated that adults with congenital heart diseases are exposed to low-dose ionizing radiations during cardiac surgeries. These patients have an increased risk for cancer when compared to the general population (Cohen et al., 2018). Studies have shown that prophylactic administration of zingerone regulates serum lactate dehydrogenase, creatine kinase-MB activity and suppresses the expression of TNF-α as well as COX-2. It also inhibits DNA fragmentation, enhances mitochondrial complex activity, and interferes with the aggravation of ionizing radiation induced heart damage (Soliman et al., 2018). The antioxidant and anti-inflammatory effects of *Zingiber officinale Roscoe* in other tissue damage models have not been established.

Chest radiotherapy induces myocardial fibrosis (Curigliano et al., 2016) while whole-body radiation can lead to osteopontin (OPN) activation. OPN is a cytokine involved in myocardial fibrosis. The extract of *Angelica sinensis (Oliv.) Diels* inhibits radiation induced cardiac fibrosis by suppressing the expression of OPN, c-jun, and miRNA-21 as well as suppressing Troponin-I (Tn-I) levels (Ma et al., 2019). The main active components in *Paeonia lactiflora Pall.* have been shown to have radioprotective properties.

Leafy Chinese Herbal Medicines

Different parts of *Ginkgo biloba L.* in the Ginkgo family can be used as alternative medicine. *Ginkgo biloba L. leaves* have been utilized in studies of radiation-associated injuries. Ionizing

radiation induces permanent nervus cerebral defects, chronic microangiopathy, and blood-brain barrier dysfunctions. Radiation associated brain damage results in cerebrovascular abnormalities, demyelination, white matter necrosis, and cognitive impairment (Lumniczky et al., 2017). Abnormally elevated levels of catecholamine, epinephrine, norepinephrine, dopamine, and inflammatory factors are the major causes of radiation-induced brain injuries. Ismail et al. confirmed that the extract of *Ginkgo biloba L.* regulated the above mentioned indicators by suppressing lipid peroxidation (Ismail and El-Sonbaty, 2016). In addition, that the extract of *Ginkgo biloba L.* was shown to suppress the expressions of P53, Bcl-2 and inhibited apoptosis after radiation (Raafat et al., 2013).

Whole Chinese Herbal Medicines

Biologically active compounds in *Portulaca oleracea L.* include flavonoids, alkaloids, terpenoids, and sterols. These compounds have been shown to have antioxidant, anti-bacterial, and anti-inflammatory properties. *Portulaca oleracea L.* extracts alleviated lipid peroxidation in the liver and kidney of irradiated rats. It also suppressed MDA levels in tissues and inhibited total cholesterol (TC), triglyceride (TG), low-density lipoprotein cholesterol (LDL-c), and maintained atherosclerosis indices (Abd El-Azime et al., 2014). From the mechanism perspective, *Portulaca oleracea L.* may also play an anti-inflammatory role by inhibiting TNF-α secretion, thereby preventing NF-κB nuclear translocation. This herb also plays an important role in regulating peroxidation (Zhou et al., 2015). *Mentha canadensis L.* from the Labiatae family inhibits radiation induced damage by scavenging for free radicals, its antioxidant, anti-inflammatory, anti-mutation activities, and enhancing DNA repair (Baliga and Rao, 2010).

Fructus of Chinese Herbal Medicines

The antioxidant properties of the Solanaceae *Lycium barbarum L.* are important in antagonizing mitochondrial apoptosis and inhibiting DNA damage. Duan et al. documented that *Lycium barbarum L.* increases the DNA content of red blood cells and hemoglobin, effectively inhibits P53, caspase-3, and caspase-6 while accelerating the recovery of splenic functions (Duan et al., 2015). *Crataegus pinnatifida Bunge* is rich in polyphenols and total flavonoids. An extract of *Crataegus pinnatifida Bunge* has been established to reduce lymphocytic micronucleus and lowers the effects of radiation (Hosseinimehr et al., 2009). While an extract of *Hippophae rhamnoides L.* scavenges for free radicals, prevents cell cycle arrest in the G2-M phase (Goel et al., 2003), and protects mitochondria and chromatin from radiation-induced damage (Shukla et al., 2006). Moreover, *Hippophae rhamnoides L.* protects against radiation-induced sperm injuries (Goel et al., 2006).

In conclusion, the above reviews show that a single Chinese herbal medicine can ameliorate radiation-induced damage in a variety of ways. These herbs have considerable potential as radioprotectants.

Chinese Herbal Prescriptions in the Prevention of Radiation Damage

Traditional Chinese Medicine's clinical efficacy exerted in the form of Chinese herbal prescriptions, is based on clinical symptoms and purposefully matched different Chinese medicines. Experimental and clinical studies have verified the therapeutic effect of Chinese Herbal Prescriptions (Zhang et al., 2016; Gao et al., 2017). Compared to a single herb or active compound, Chinese Herbal Prescription contains many active compounds with multiple therapeutic targets. These Prescriptions are suitable for the prevention and treatment of multiple ionizing radiation induced systemic damage. Synergism between the different herbs enhance therapeutic effects with reduced toxicity (Zhang et al., 2018b) (**Table 3**).

Hematopoietic System

The hematopoietic system is highly sensitive to radiation. Hematopoietic cells exposed to ionizing radiation degenerate quickly, and undergo necrosis as well as apoptosis. In addition, ionizing radiation decreases the number of peripheral blood cells, especially neutrophils, lymphocytes, and platelets, leading to bleeding and anemia.

Siwu Tang is a classical Chinese herbal prescription that reinforces qi and nourishes the blood. It is comprised of four Chinese herbal medicines (*Rehmannia glutinosa (Gaertn.) DC.*, *Angelica sinensis (Oliv.) Diels*, *Conioselinum anthriscoides 'Chuanxiong'*, and *Paeonia lactiflora Pall.*) (Sun et al., 2016). The active compounds in this prescription include fructose, paeoniflorin, and ferulic acid, among others. This Prescription promotes hematopoietic and immune system recovery after irradiation by increasing the number of peripheral white blood cells and bone marrow colony-forming units (Liang et al., 2006). Studies revealed that Siwu Tang induces the antioxidant Nrf2 pathway, partially inhibits DNA damage, prevents the activation of nuclear transcription factor activating protein-1 (AP-1) and NF-κB, thereby, inhibiting ionizing radiation-induced damage and oncogenesis (Liu et al., 2017).

Buzhong Yiqi Tang is a well-known Chinese herbal prescription with nearly 800 years of application. It is widely used a therapeutic option for spleen-qi deficiencies and post-illness symptoms (Hu et al., 2019; Liu et al., 2019). This prescription is composed of *Astragalus mongholicus Bunge*, *Codonopsis pilosula (Franch.) Nannf.*, *Atractylodes lancea (Thunb.) DC.*, *Bupleurum chinense DC.*, *Actaea cimicifuga L.*, *Citrus reticulata Blanco*, *Angelica sinensis (Oliv.) Diels*, and *Glycyrrhiza glabra L.*. This prescription has been shown to significantly elevate peripheral white blood cell counts in mice after irradiation and relieves platelet damage (Xiao-fang et al., 2013). Further, it suppresses lipid peroxides generated by the accumulation of free radicals and improves the hematopoietic microenvironment (Xiaoling et al., 2006).

Xuebijing (XBJ) is an injection of Chinese herbal prescription. It was approved by the National Medical Products Administration for the clinical management of septicemia. It contains *Carthamus tinctorius L.*, *Paeonia lactiflora Pall.*, *Conioselinum anthriscoides 'Chuanxiong'*, *Salvia miltiorrhiza*

Bunge, and *Angelica sinensis (Oliv.) Diels*. A previous study documented that XBJ improved the survival rate of irradiated mice by suppressing ROS production in bone marrow cells and alleviated radiation induced hematopoietic cell injury (Li et al., 2014a).

In the study of Yiqi Yangyin Fang (YYF: *Astragalus mongholicus Bunge*, *Panax ginseng C.A.Mey.*, *Ligustrum lucidum W.T.Aiton*, *Eclipta prostrata (L.) L.*, *Angelica sinensis (Oliv.) Diels*, *Atractylodes macrocephala Koidz.*, *Poria cocos (Schw.) Wolf*, *Glycyrrhiza glabra L.*), Junling Zhang et al. indicated that this prescription increased the number of bone marrow cells, hematopoietic progenitor cells, and hematopoietic stem cells. It also improved bone marrow suppression after radiation by suppressing intracellular ROS levels (Zhang et al., 2017b).

Immune System

Ionizing radiation damages the hematopoietic system, the thymus and the spleen. Radiation inhibits tissue and cell repair after injury and induces immunosuppression. Inhibition is proportional to the radiation dose. Hematopoietic and immune dysfunctions associated with ionizing radiation elevate tissue permeability, weaken body resistance, and predisposes the body to endogenous or exogenous infections.

HemoHIM is a prescription composed of three herbs with various biological and immunological activities. HemoHIM inhibits the continuous down-regulation of Th1 immune responses after radiation by regulating the IL-12 p70/pSTAT4 signaling pathway (Park et al., 2012). This prescription has also been shown to protect hematopoietic stem cells and speeds up the recovery of immune cells (Park et al., 2014).

Bushen Jiedu Recipe is an optimized combination of Liuwei Dihuang Pills. This prescription maintains kidney tone, nourishes yin, tonifies Qi and blood, clears heat and removes toxin. Yunjing et al. documented that Bushen Jiedu Recipe interfered with the expression of NF-κBp65 by regulating the TLR4 signaling pathway, suppressed white blood cell damage and protected the thymus and spleen (Yunjing et al., 2015; Lidan et al., 2016).

The Wumai Danghuang Oral Liquid is composed of *Schisandra chinensis (Turcz.) Baill.*, *Ophiopogon japonicus (Thunb.) Ker Gawl.*, *Codonopsis pilosula (Franch.) Nannf.*, and *Astragalus mongholicus Bunge*. This prescription exhibits its anti-radiation effects by elevating SOD, degrading MDA and inhibiting the generation of free radicals (Chunhong et al., 2014). In addition, Wumai Danghuang Oral Liquid exhibits protective and repair effect on radiation induced immune injuries (Hang et al., 2013).

Houttuynia cordata Thunb. and its bioactive molecules have anti-inflammatory and antioxidant properties (Shingnaisui et al., 2018). Co-Herba Houttuyniae Oral Liquid contains *Houttuynia cordata Thunb.*, *Panax ginseng C.A.Mey.*, *Lycium barbarum L.*. This liquid suppresses the rate of radiation induced chromosomal aberrations (Lin et al., 2001). It also enhances the anti-stress ability of mice by improving immune functions. Moreover, *Panax ginseng C.A.Mey.* and *Lycium barbarum L.* improve immune functions and inhibit radiation effects by promoting the repair of damaged cells and tissues (Lin et al., 2002).

The radioprotective prescription (*Astragalus mongholicus Bunge*, *Ganoderma Lucidum Karst*, *Lycium barbarum L.,* and *Poria cocos (Schw.)Wolf*) has been shown to improve the survival rate, white blood cell count, thymus index, spleen index, and the DNA content of bone marrow cells thereby reducing radiation induced immune damage in mice models (Liming et al., 2011).

Digestive System

Ionizing radiation severely damages the digestive system and causes pathological changes such as intestinal mucosal damage and liver fibrosis. These damages lead to digestive and absorptive dysfunctions, resulting in a series of clinical symptoms like diarrhea, nausea, and vomiting.

STW 5 is a herbal prescription with anti-inflammatory and antioxidant properties. This prescription inhibits oxidative stress responses, suppresses the levels of inflammation factors, and intestinal damage indices by regulating apoptosis-related factors to prevent intestinal mucosal damage after radiation (Khayyal et al., 2014). Prophylactic administration of STW 5 reduces the severity of radiation mucositis (El-Ghazaly et al., 2015).

Astragalus immortal prescription is composed of *Rehmannia glutinosa (Gaertn.) DC.*, *Ophiopogon japonicus (Thunb.) Ker Gawl.* and *Equus asinus L.*. It is derived from Dunhuang medical papers (now stored in France, code: P.4038), and *Astragalus mongholicus Bunge*. This prescription has been shown to elevate the activities of GSH-Px and SOD while suppressing MDA levels in the liver. Furthermore, it protects the liver from radiation induced oxidative damage (Cai-qin et al., 2017).

Reproductive System

The male reproductive system is very sensitive to ionizing radiation as it can damage the seminiferous epithelium and spermatogenic cells at all levels. These radiations can confer injuries to the reproductive system, and cause male infertility (Bates et al., 2016; Kesari et al., 2018). Radiation also causes DNA damage in spermatogenic cells, increases embryonic mortality, and offspring cancer susceptibility. It may induce hereditary changes.

Wuzi Yanzong Pill (WZYZ) is a Chinese herbal prescription that is used as a therapeutic option for male infertility. Clinically, it has significant therapeutic effects on oligospermia and asthenozoospermia. WZYZ improves sperm quality by suppressing DNA damage (Zhao et al., 2018). A double-blind randomized controlled trial confirmed that WZYZ is an excellent therapeutic option for men with low fertility who cannot be cured by conventional western medicines (Zhao et al., 2019). Pelvic exposure to radiation reduces testicular weight, sperm quality and leads to testicular oxidative stress and abnormal testicular structure. WZYZ protects against suppressed serum testosterone levels, reduces MDA levels and oxidative stress indices (OSI) in the testis. Its mechanism may be associated with up-regulation of PCNA (Ji et al., 2016).

The Yiqi Jiedu Decoction (YQJD) enhances testicular index, structural recovery of the testis, decreases the apoptotic rate of spermatogenic cells, and maintains spermatogenic functions after

irradiation. These results suggest that YQJD plays a protective role by intervening in TLR5 downstream signaling pathways (Wang et al., 2020).

ANTI-RADIATION MECHANISMS OF CHINESE HERBAL MEDICINES

Mitochondrial Apoptosis Pathway

Oxidative stress leads to the pathogenesis of various human diseases and the aging process. Mitochondria is the energy center in cell metabolism, it regulates redox homeostasis, and plays a central role in diseases pathogenesis (Li et al., 2019a). Oxidative stress damages the mitochondria, accelerates excessive ROS production, activates the mitochondrial apoptotic pathway and induces apoptosis (Kim and Kim, 2018). Ionizing radiation mediated overproduction of ROS is associated with mitochondrial dysfunctions. ROS acts as a signaling molecule that initiates a series of cascade reactions (Wu et al., 2019). Changes in the mitochondrial membrane potential elevates the expressions of pro-apoptotic proteins and suppresses the expression of anti-apoptotic proteins (Sun et al., 2018). These events trigger the activation of caspase-3, and initiates the mitochondrial-dependent pathway (Li et al., 2018a). As previously stated, Chinese Herbal Medicines inhibit mitochondrial apoptosis by: i. inhibiting oxidative stress responses and suppressing the generation of ROS, and ii. Interfering with the expression of pathway associated factors, regulating the pro-apoptotic protein and anti-apoptotic protein ratios, as well as by suppressing Cytochrome C and caspase-3.

MAPK Signaling Pathway and PI3K/AKT Signaling Pathway

Mitogen-activated protein kinases (MAPK) family, including three significant members of extracellular signal-regulated kinases (ERK), p38 kinase, and c-Jun N-terminal kinase (JNK), participate in various physiological processes such as morphogenesis, cell growth, proliferation, apoptosis, and differentiation (Fang and Richardson, 2005; Lu et al., 2019). Ionizing radiation activates the classic MAPK signaling pathway, JNK, and P38 MAPK pathways. In addition, radiation-induced secreted cytokines enhance MAPK pathway responses in cells (Dent et al., 2003). Enhancement of the MAPK signal upregulates telomerase activity, initiates changes in chromatin distribution, and regulates the cell cycle (Shain et al., 2018). Activated p38 and JNK signaling pathways are involved in immune regulation (Wang et al., 2019a). After p38 activation, a mitochondrial apoptotic pathway is initiated (Choi et al., 2006; Niaudet et al., 2017). The PI3K/AKT signaling pathway is essential in the regulation of cell growth, migration, proliferation, and metabolism in mammals (Pompura and Dominguez-Villar, 2018). Activated PI3K/Akt pathway accelerates DSB repair. Ionizing radiation inhibits its activation (Toulany and Rodemann, 2015). This pathway is also involved in cell cycle and apoptosis regulation after exposure to ionizing radiation (Chen et al., 2018). Because of the wide reach of the MAPK and PI3K/AKT signaling pathways, Chinese Herbal Medicines regulate them through multiple targets.

Nrf2/HO1 Signaling Pathway

The Nrf2/HO-1 signaling pathway antagonizes tissue and organ oxidative stress injuries by regulating antioxidant, anti-inflammatory, apoptosis, pyroptosis, ferroptosis, and autophagy processes. Nrf2 is a transcription factor and the core regulator of cellular redox. It stimulates gene expression through antioxidant response elements in gene promoters and protects cells against ROS induced DNA damage (Zimta et al., 2019). When exposure to ionizing radiation occurs, Nrf2 acts as a critical transcription factor that regulates antioxidant enzymes and protects tissues from oxidative stress damage. HO-1 regulates the expression of apoptotic and inflammatory factors. In addition, it also promotes angiogenesis by preventing oxidative damage (Loboda et al., 2016). Chinese Herbal Medicines trigger Nrf2 and enhances mRNA and protein expressions of HO-1. These events trigger the antioxidant pathway and inhibits ionizing radiation induced oxidative damage.

Inflammatory Signaling Pathway

Ionizing radiation-induced DNA damage results in phosphorylation and activation of multiple transcription factors (such as NF-κB, p53, and MAPK) by stimulated ATM kinases. ROS is also involved in these processes (Purbey et al., 2017). After exposure to ionizing radiation, the secretion of various inflammatory cytokines (IL-1, IL-6, TNF-α, IFN-γ, COX-2) is elevated. Inflammatory cytokines recruit immune cells that regulate cell microenvironment with a crucial impact on local or systemic tissues (Harding et al., 2017). Chinese Herbal Medicines exhibit a two-way regulation effect on inflammatory factors. The first one is by inhibiting the secretion of inflammatory factors, preventing fibrosis and inflammatory lesions after irradiation. The second strategy is that it plays an immunomodulatory role by regulating signaling pathways such as TLRs and NF-κB to reduce apoptosis (Scholch et al., 2015; Liu et al., 2018).

Traditional Chinese Medicine exhibits its curative effects on multiple body systems (such as hematopoiesis, immunity, reproduction, respiration, and circulation) by inhibiting oxidative stress, reducing DNA damage, and regulating abnormally activated signaling pathways. The Mechanism is as shown in **Figure 2**. It is worth noting that Chinese Herbal Medicines are particularly useful in anti-lipid peroxidation. Recently, a new regulatory cell death method (ferroptosis) has attracted considerable attention. Excessive ROS results in membrane lipid peroxidation. The accumulation of iron-dependent lipid peroxides leads to ferroptosis. Radiation induced damage to the hematological system and the lungs can be relieved by intervening in ferroptosis-related pathways (Li et al., 2019c; Zhang et al., 2020). This is an avenue for Traditional Chinese Medicine research in future.

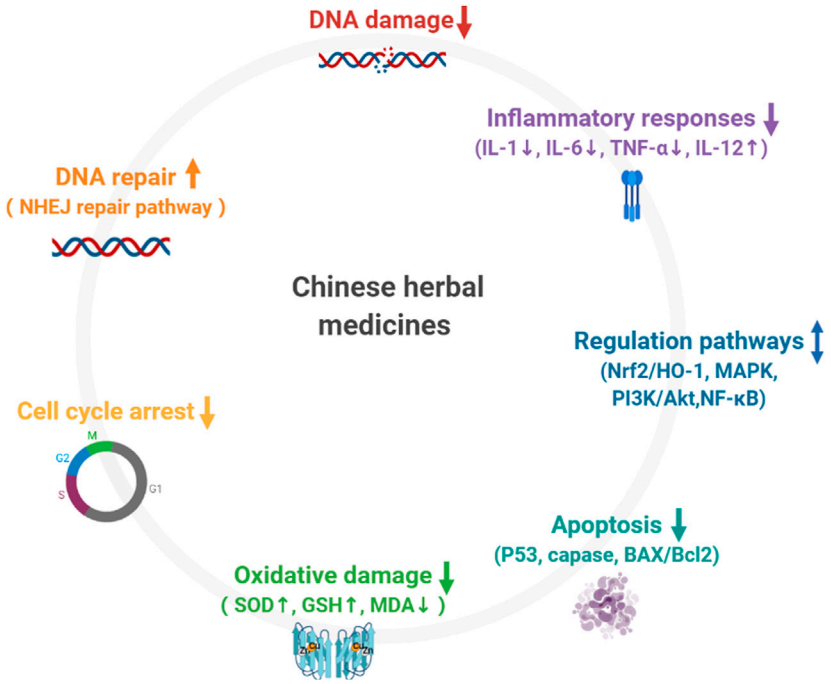

FIGURE 2 | Mechanism of Chinese herbal medicines in preventing radiation injury. 1) Chinese herbal medicines reduce DNA damage; 2) Chinese herbal medicine promote DNA repair; 3) Chinese herbal medicines regulate cell cycle arrest; 4) Chinese herbal medicines prevent excessive accumulation of ROS and inhibits oxidative damage; 5) Chinese herbal medicine suppress extrinsic and intrinsic apoptotic pathways via reduction of P53, caspase, BAX/Bcl2 activation; 6) Chinese herbal medicines are involved in the regulation of inflammatory response; 7) Chinese herbal medicines participate in the regulation of multiple abnormally activated signaling pathways.

CONCLUSION

Ionizing radiation injuries are systemic damages that affect multiple organs and tissues. The Traditional Chinese Medicine characteristic theory lies in its holistic view: man and nature as a harmonious and unified whole, emphasizing the interactions between man and the environment, achieving a balance between the two. Simultaneously, various systems of the human body as a whole are connected physiologically and pathologically influence each other. Based on this holistic view, Chinese medicines and Chinese Herbal Prescriptions are suitable for use as therapeutic options for multi-system damages caused by ionizing radiation.

Compared to a single herb, the composition of Chinese Herbal Prescription is more complex and exhibits its therapeutic effects by having multiple targets (Yang et al., 2017; Wang et al., 2019b). The synergy between the Chinese medicines in the Chinese Herbal Prescriptions improves its efficacy while inhibiting toxic and side effects. A rationally designed Chinese Herbal Prescription will exhibit a better protective effect.

Chinese medicine has favorable economic benefits and is an economical option for the development of safe and effective radioprotectors. With positive effects, many Chinese Herbal Prescriptions have been used in clinical settings to reduce radiation induced damage. Studies on the anti-radiation activities and mechanisms of single Chinese medicines and their active compounds are limited. However, due to their sophisticated active compounds, it is difficult to elucidate on their potential radio-protective mechanisms. More studies are needed to evaluate the efficacy of these medicines. Systemic biology and network pharmacology applications may provide alternative methods and strategies for the applications of Chinese Herbal Prescriptions (Boezio et al., 2017; Tavassoly et al., 2018), and may, therefore, help in the development of innovative drugs for radiation protection.

AUTHOR CONTRIBUTIONS

XZ conceived the topic and wrote the manuscript. SH revised and modified the manuscript. XC, LW, CH, and ZS helped to revise the manuscript and draw the figures. QF, WX and SZ consulted the references.

FUNDING

This work was supported by the National Natural Science Foundation of China (No. 11675027, 12075035).

REFERENCES

Abd El-Azime, A. S., Hussein, E. M., and Ashry, O. M. (2014). Synergestic effect of aqueous purslane (Portulaca oleracea L.) extract and fish oil on radiation-induced damage in rats. *Int. J. Radiat. Biol.* 90 (12), 1184–1190. doi:10.3109/09553002.2014.926040

Ahmad, M. F. (2018). Ganoderma lucidum: persuasive biologically active constituents and their health endorsement. *Biomed. Pharmacother.* 107, 507–519. doi:10.1016/j.biopha.2018.08.036

Amsterdam, J. D., and Panossian, A. G. (2016). Rhodiola rosea L. as a putative botanical antidepressant. *Phytomedicine* 23 (7), 770–783. doi:10.1016/j.phymed.2016.02.009

Anuranjaniand Bala, M. (2014). Concerted action of Nrf2-ARE pathway, MRN complex, HMGB1 and inflammatory cytokines - implication in modification of radiation damage. *Redox. Biol.* 2, 832–846. doi:10.1016/j.redox.2014.02.008

Arring, N. M., Millstine, D., Marks, L. A., and Nail, L. M. (2018). Ginseng as a treatment for fatigue: a systematic review. *J. Alternative Compl. Med.* 24 (7), 624–633. doi:10.1089/acm.2017.0361

Bai, P., and Virag, L. (2012). Role of poly(ADP-ribose) polymerases in the regulation of inflammatory processes. *FEBS Lett.* 586 (21), 3771–3777. doi:10.1016/j.febslet.2012.09.026

Balaji Raghavendran, H. R., Rekha, S., Cho, H. K., Jang, S. S., and Son, C. G. (2012). Ginsenoside rich fraction of Panax ginseng C.A. Meyer improve feeding behavior following radiation-induced pica in rats. *Fitoterapia* 83 (6), 1144–1150. doi:10.1016/j.fitote.2012.04.008

Baliga, M. S., and Rao, S. (2010). Radioprotective potential of mint: a brief review. *J. Canc. Res. Therapeut.* 6 (3), 255–262. doi:10.4103/0973-1482.73336

Basso, E., Regazzo, G., Fiore, M., Palma, V., Traversi, G., and Testa, A., et al. (2016). Resveratrol affects DNA damage induced by ionizing radiation in human lymphocytes *in vitro*. *Mutat. Res. Genet. Toxicol. Environ. Mutagen* 806, 40–46. doi:10.1016/j.mrgentox.2016.07.005

Bates, G. E., Taub, R. N., and West, H. (2016). Fertility and cancer treatment. *JAMA Oncol.* 2 (2), 284. doi:10.1001/jamaoncol.2015.4143

Beach, T. A., Johnston, C. J., Groves, A. M., Williams, J. P., and Finkelstein, J. N. (2017). Radiation induced pulmonary fibrosis as a model of progressive fibrosis: contributions of DNA damage, inflammatory response and cellular senescence genes. *Exp. Lung Res.* 43 (3), 134–149. doi:10.1080/01902148.2017.1318975

Begg, A. C., Stewart, F. A., and Vens, C. (2011). Strategies to improve radiotherapy with targeted drugs. *Nat. Rev. Canc.* 11 (4), 239–253. doi:10.1038/nrc3007

Bespalov, V. G., Alexandrov, V. A., Semenov, A. L., Kovan'Ko, E. G., and Ivanov, S. D. (2014). Anticarcinogenic activity of alpha-difluoromethylornithine, ginseng, eleutherococcus, and leuzea on radiation-induced carcinogenesis in female rats. *Int. J. Radiat. Biol.* 90 (12), 1191–1200. doi:10.3109/09553002.2014.932937

Bing, S. J., Kim, M. J., Ahn, G., Im, J., Kim, D. S., and Ha, D., et al. (2014). Acidic polysaccharide of Panax ginseng regulates the mitochondria/caspase-dependent apoptotic pathway in radiation-induced damage to the jejunum in mice. *Acta Histochem.* 116 (3), 514–521. doi:10.1016/j.acthis.2013.11.012

Boezio, B., Audouze, K., Ducrot, P., and Taboureau, O. (2017). Network-based approaches in pharmacology. *Mol. Inform.* 36 (10), 1–11. doi:10.1002/minf.201700048

Brizel, D. M. (2007). Pharmacologic approaches to radiation protection. *J. Clin. Oncol.* 25 (26), 4084–4089. doi:10.1200/JCO.2007.11.5816

Cai-qin, F., Yong-qi, L., Li-ying, Z., Xiao-ming, X., Tong-tong, Z., Juan, L., et al. (2017). Protective effects of *Astragalus* immortal prescription against liver oxidative stress in irradiated mice. *Med. J. Chin. Peoples Lib. Army* 42 (12), 1061–1065. doi:10.11855/j.issn.0577-7402.2017.12.07

Caito, S., Hwang, J. W., Chung, S., Yao, H., Sundar, I. K., and Rahman, I. (2010). PARP-1 inhibition does not restore oxidant-mediated reduction in SIRT1 activity. *Biochem. Biophys. Res. Commun.* 392 (3), 264–270. doi:10.1016/j.bbrc.2009.12.161

Chen, L., and Huang, G. (2018). Antitumor activity of polysaccharides: an overview. *Curr. Drug Targets* 19 (1), 89–96. doi:10.2174/1389450118666170704143018.

Chen, Y. A., Tzeng, D. T. W., Huang, Y. P., Lin, C. J., Lo, U. G., and Wu, C. L., et al. (2018). Antrocin sensitizes prostate cancer cells to radiotherapy through inhibiting PI3K/AKT and MAPK signaling pathways. *Cancers* 11 (1), 34. doi:10.3390/cancers11010034

Choi, S. Y., Kim, M. J., Kang, C. M., Bae, S., Cho, C. K., and Soh, J. W., et al. (2006). Activation of Bak and Bax through c-abl-protein kinase Cdelta-p38 MAPK signaling in response to ionizing radiation in human non-small cell lung cancer cells. *J. Biol. Chem.* 281 (11), 7049–7059. doi:10.1074/jbc.M512000200

Chunhong, X., Peng, L., Haibo, L., Mei, X., and Xia, Y. (2014). Influence of wumaidanghuang oral liquid on free radicals scavenging capacity in visceral organs of radiation injured mice. *Chin. Pharm.* 23 (7), 20–21.

Citrin, D., Cotrim, A. P., Hyodo, F., Baum, B. J., Krishna, M. C., and Mitchell, J. B. (2010). Radioprotectors and mitigators of radiation-induced normal tissue injury. *Oncol.* 15 (4), 360–371. doi:10.1634/theoncologist.2009-S104

Cohen, S., Liu, A., Gurvitz, M., Guo, L., Therrien, J., Laprise, C., et al. (2018). Exposure to low-dose ionizing radiation from cardiac procedures and malignancy risk in adults with congenital heart disease. *Circulation* 137 (13), 1334–1345. doi:10.1161/CIRCULATIONAHA.117.029138

Curigliano, G., Cardinale, D., Dent, S., Criscitiello, C., Aseyev, O., and Lenihan, D., et al. (2016). Cardiotoxicity of anticancer treatments: epidemiology, detection, and management. *CA A Cancer J. Clin.* 66 (4), 309–325. doi:10.3322/caac.21341

Das, U., Biswas, S., Sengupta, A., Manna, K., Chakraborty, A., and Dey, S. (2016). Ferulic acid (FA) abrogates ionizing radiation-induced oxidative damage in murine spleen. *Int. J. Radiat. Biol.* 92 (12), 806–818. doi:10.1080/09553002.2016.1230241

Das, U., Manna, K., Khan, A., Sinha, M., Biswas, S., and Sengupta, A., et al. (2017a). Ferulic acid (FA) abrogates γ-radiation induced oxidative stress and DNA damage by up-regulating nuclear translocation of Nrf2 and activation of NHEJ pathway. *Free Radic. Res.* 51 (1), 47–63. doi:10.1080/10715762.2016.1267345

Das, U., Manna, K., Sinha, M., Datta, S., Das, D. K., and Chakraborty, A., et al. (2014). Role of ferulic acid in the amelioration of ionizing radiation induced inflammation: a murine model. *PloS One* 9 (5), e97599. doi:10.1371/journal.pone.0097599

Das, U., Sengupta, A., Biswas, S., Adhikary, A., Dey Sharma, R., and Chakraborty, A., et al. (2017b). Alteration of murine duodenal morphology and redox signalling events by reactive oxygen species generated after whole body γ-irradiation and its prevention by ferulic acid. *Free Radic. Res.* 51 (11-12), 1–25. doi:10.1080/10715762.2017.1388916

Dent, P., Yacoub, A., Fisher, P. B., Hagan, M. P., and Grant, S. (2003). MAPK pathways in radiation responses. *Oncogene* 22 (37), 5885–5896. doi:10.1038/sj.onc.1206701

Ding, J., Wang, H., Wu, Z. B., Zhao, J., Zhang, S., and Li, W. (2015). Protection of murine spermatogenesis against ionizing radiation-induced testicular injury by a green tea polyphenol. *Biol. Reprod.* 92 (1), 6. doi:10.1095/biolreprod.114.122333

Duan, Y., Chen, F., Yao, X., Zhu, J., Wang, C., and Zhang, J., et al. (2015). Protective effect of Lycium ruthenicum murr. Against radiation injury in mice. *Int. J. Environ. Res. Publ. Health* 12 (7), 8332–8347. doi:10.3390/ijerph120708332

Einor, D., Bonisoli-Alquati, A., Costantini, D., Mousseau, T. A., and Moller, A. P. (2016). Ionizing radiation, antioxidant response and oxidative damage: a meta-analysis. *Sci. Total Environ.* 548-549, 463–471. doi:10.1016/j.scitotenv.2016.01.027

El-Ghazaly, M. A., El-Hazek, R. M., and Khayyal, M. T. (2015). Protective effect of the herbal preparation, STW 5, against intestinal damage induced by gamma radiation in rats. *Int. J. Radiat. Biol.* 91 (2), 150–156. doi:10.3109/09553002.2014.954059

El-Mesallamy, H. O., Gawish, R. A., Sallam, A. M., Fahmy, H. A., and Nada, A. S. (2018). Ferulic acid protects against radiation-induced testicular damage in male rats: impact on SIRT1 and PARP1. *Environ. Sci. Pollut. Res. Int.* 25 (7), 6218–6227. doi:10.1007/s11356-017-0873-6

Evans, J. R. (2013). Ginkgo biloba extract for age-related macular degeneration. *Cochrane Database Syst. Rev.* (1), CD001775. doi:10.1002/14651858.CD001775.pub2

Fang, J. Y., and Richardson, B. C. (2005). The MAPK signalling pathways and colorectal cancer. *Lancet Oncol.* 6 (5), 322–327. doi:10.1016/S1470-2045(05)70168-6

Fraga, C. G., Croft, K. D., Kennedy, D. O., and Tomas-Barberan, F. A. (2019). The effects of polyphenols and other bioactives on human health. *Food Funct.* 10 (2), 514–528. doi:10.1039/c8fo01997e

Frey, B., Ruckert, M., Deloch, L., Ruhle, P. F., Derer, A., and Fietkau, R., et al. (2017). Immunomodulation by ionizing radiation-impact for design of radio-

immunotherapies and for treatment of inflammatory diseases. *Immunol. Rev.* 280 (1), 231–248. doi:10.1111/imr.12572

Gao, L., Jia, C., Zhang, H., and Ma, C. (2017). Wenjing decoction (herbal medicine) for the treatment of primary dysmenorrhea: a systematic review and meta-analysis. *Arch. Gynecol. Obstet.* 296 (4), 679–689. doi:10.1007/s00404-017-4485-7

Gerelchuluun, A., Manabe, E., Ishikawa, T., Sun, L., Itoh, K., and Sakae, T., et al. (2015). The major DNA repair pathway after both proton and carbon-ion radiation is NHEJ, but the HR pathway is more relevant in carbon ions. *Radiat. Res.* 183 (3), 345–356. doi:10.1667/RR13904.1

Goel, H. C., Kumar, I. P., Samanta, N., and Rana, S. V. (2003). Induction of DNA-protein cross-links by Hippophae rhamnoides: implications in radioprotection and cytotoxicity. *Mol. Cell. Biochem.* 245 (1-2), 57–67. doi:10.1023/a:1022809625826

Goel, H. C., Samanta, N., Kannan, K., Kumar, I. P., and Bala, M. (2006). Protection of spermatogenesis in mice against gamma ray induced damage by Hippophae rhamnoides. *Andrologia* 38 (6), 199–207. doi:10.1111/j.1439-0272.2006.00740.x

Guohui, T., Ling, M., and Hongmei, W. (2004). Studies of G .lucidum spores powcder on the immunoregulation and antiradiation. *Chinese Journal of Food Hygiene* 16 (2), 132–134. doi:10.13590/j.cjfh.2004.02.009

Han, S. K., Song, J. Y., Yun, Y. S., and Yi, S. Y. (2005). Ginsan improved Th1 immune response inhibited by gamma radiation. *Arch Pharm. Res. (Seoul)* 28 (3), 343–350. doi:10.1007/BF02977803

Hang, L., Peng, L., Mei, X., and Haibo, L. (2013). Effects of Wumai Danghuang oral liquid on immune function of radiation damage model mice. *China. Pharm.* 24 (47), 4442–4444. doi:10.6039/j.issn.1001-0408.2013.47.08

Hao, P., Jiang, F., Cheng, J., Ma, L., Zhang, Y., and Zhao, Y. (2017). Traditional Chinese medicine for cardiovascular disease: evidence and potential mechanisms. *J. Am. Coll. Cardiol.* 69 (24), 2952–2966. doi:10.1016/j.jacc.2017.04.041

Harding, S. M., Benci, J. L., Irianto, J., Discher, D. E., Minn, A. J., and Greenberg, R. A. (2017). Mitotic progression following DNA damage enables pattern recognition within micronuclei. *Nature* 548 (7668), 466–470. doi:10.1038/nature23470

He, L. X., Wang, J. B., Sun, B., Zhao, J., Li, L., and Xu, T., et al. (2017). Suppression of TNF-α and free radicals reduces systematic inflammatory and metabolic disorders: radioprotective effects of ginseng oligopeptides on intestinal barrier function and antioxidant defense. *J. Nutr. Biochem.* 40, 53–61. doi:10.1016/j.jnutbio.2016.09.019

He, L. X., Zhang, Z. F., Zhao, J., Li, L., Xu, T., and Bin, S., et al. (2018). Ginseng oligopeptides protect against irradiation-induced immune dysfunction and intestinal injury. *Sci. Rep.* 8 (1), 13916. doi:10.1038/s41598-018-32188-6

Horemans, N., Spurgeon, D. J., Lecomte-Pradines, C., Saenen, E., Bradshaw, C., and Oughton, D., et al. (2019). Current evidence for a role of epigenetic mechanisms in response to ionizing radiation in an ecotoxicological context. *Environ. Pollut.* 251, 469–483. doi:10.1016/j.envpol.2019.04.125

Hosseinimehr, S. J., Mahmoudzadeh, A., Azadbakht, M., and Akhlaghpoor, S. (2009). Radioprotective effects of Hawthorn against genotoxicity induced by gamma irradiation in human blood lymphocytes. *Radiat. Environ. Biophys.* 48 (1), 95–98. doi:10.1007/s00411-008-0190-z

Hu, L., Yao, Z., Qin, Z., Liu, L., Song, X., and Dai, Y., et al. (2019). *In vivo* metabolic profiles of Bu-Zhong-Yi-Qi-Tang, a famous traditional Chinese medicine prescription, in rats by ultra-high-performance liquid chromatography coupled with quadrupole time-of-flight tandem mass spectrometry. *J. Pharm. Biomed. Anal.* 171, 81–98. doi:10.1016/j.jpba.2019.04.001

Hu, Y., Cao, J. J., Liu, P., Guo, D. H., Wang, Y. P., and Yin, J., et al. (2011). Protective role of tea polyphenols in combination against radiation-induced haematopoietic and biochemical alterations in mice. *Phytother Res.* 25 (12), 1761–1769. doi:10.1002/ptr.3483

Ismail, A. F., and El-Sonbaty, S. M. (2016). Fermentation enhances Ginkgo biloba protective role on gamma-irradiation induced neuroinflammatory gene expression and stress hormones in rat brain. *J. Photochem. Photobiol. B Biol.* 158, 154–163. doi:10.1016/j.jphotobiol.2016.02.039

Jagetia, G., Baliga, M., and Venkatesh, P. (2004). Ginger (Zingiber officinale Rosc.), a dietary supplement, protects mice against radiation-induced lethality: mechanism of action. *Cancer Biother. Radiopharm.* 19 (4), 422–435. doi:10.1089/cbr.2004.19.422

Jagetia, G. C., Baliga, M. S., Venkatesh, P., and Ulloor, J. N. (2003). Influence of ginger rhizome (Zingiber officinale Rosc) on survival, glutathione and lipid peroxidation in mice after whole-body exposure to gamma radiation. *Radiat. Res.* 160 (5), 584–592. doi:10.1667/rr3057

Jang, S. S., Kim, H. G., Han, J. M., Lee, J. S., Choi, M. K., and Huh, G. J., et al. (2015). Modulation of radiation-induced alterations in oxidative stress and cytokine expression in lung tissue by Panax ginseng extract. *Phytother Res.* 29 (2), 201–209. doi:10.1002/ptr.5223

Ji, H. J., Wang, D. M., Wu, Y. P., Niu, Y. Y., Jia, L. L., and Liu, B. W., et al. (2016). Wuzi Yanzong pill, a Chinese polyherbal formula, alleviates testicular damage in mice induced by ionizing radiation. *BMC Compl. Alternative Med.* 16 (1), 509. doi:10.1186/s12906-016-1481-6

Ji, K., Fang, L., Zhao, H., Li, Q., Shi, Y., and Xu, C., et al. (2017). Ginger oleoresin alleviated γ-ray irradiation-induced reactive oxygen species via the Nrf2 protective response in human mesenchymal stem cells. *Oxid. Med. Cell Longev.* 2017, 1480294. doi:10.1155/2017/1480294

Jin, X., Ruiz Beguerie, J., Sze, D. M., and Chan, G. C. (2016). Ganoderma lucidum (Reishi mushroom) for cancer treatment. *Cochrane Database Syst. Rev.* 4, CD007731. doi:10.1002/14651858.CD007731.pub2

Johnke, R. M., Sattler, J. A., and Allison, R. R. (2014). Radioprotective agents for radiation therapy: future trends. *Future Oncol.* 10 (15), 2345–2357. doi:10.2217/fon.14.175

Juan, G., Yanjun, Z., Guangzhou, A., Guozhen, G., and Junye, L. (2015). Protective-effects of salvianic acid A on ionizing irradiated mice. *Lishizhen Medicine and Materia Medica Research* 26 (8), 1811–1813. doi:10.3969/j.issn.1008-0805.2015.08.007

Juan, G., Yanjun, Z., Lihua, Z., and Guozhen, G. (2012). Protective effect of salvianic acid A on L-02DNA of human embryonic liver cells damaged by ionizing radiation. *Lishizhen Medicine and Materia Medica Research* 23 (2), 499–500.

Jun, B., and Zhenghai, L. (2010). The study on radioprotective effect of flavonoids from Houttuyniae cordata *Chin. Arch. of Traditional Chinese Med.* 28 (8), 1747–1748.

Kang, J. A., Song, H. Y., Byun, E. H., Ahn, N. G., Kim, H. M., and Nam, Y. R., et al. (2018). Gamma-irradiated black ginseng extract inhibits mast cell degranulation and suppresses atopic dermatitis-like skin lesions in mice. *Food Chem. Toxicol.* 111, 133–143. doi:10.1016/j.fct.2017.11.006

Kesari, K. K., Agarwal, A., and Henkel, R. (2018). Radiations and male fertility. *Reprod. Biol. Endocrinol.* 16 (1), 118. doi:10.1186/s12958-018-0431-1

Khayyal, M. T., Abdel-Naby, D. H., Abdel-Aziz, H., and El-Ghazaly, M. A. (2014). A multi-component herbal preparation, STW 5, shows anti-apoptotic effects in radiation induced intestinal mucositis in rats. *Phytomedicine* 21 (11), 1390–1399. doi:10.1016/j.phymed.2014.04.030

Kim, H. J., Kim, M. H., Byon, Y. Y., Park, J. W., Jee, Y., and Joo, H. G. (2007). Radioprotective effects of an acidic polysaccharide of Panax ginseng on bone marrow cells. *J. Vet. Sci.* 8 (1), 39–44. doi:10.4142/jvs.2007.8.1.39

Kim, S. H., and Kim, H. (2018). Inhibitory effect of astaxanthin on oxidative stress-induced mitochondrial dysfunction-A mini-review. *Nutrients* 10 (9). doi:10.3390/nu10091137

Klein, D., Schmetter, A., Imsak, R., Wirsdorfer, F., Unger, K., and Jastrow, H., et al. (2016). Therapy with multipotent mesenchymal stromal cells protects lungs from radiation-induced injury and reduces the risk of lung metastasis. *Antioxid Redox Signal* 24 (2), 53–69. doi:10.1089/ars.2014.6183

Kongxi, W., Yongqi, L., Yangyang, L., Liying, Z., Xiu, F., Wenjun, W., et al. (2020). Effects of astragalus polysaccharide on radiation-induced adipogenic differentiation of bonemarrow mesenchymal stem cells. *J. Xi'an Jiaot. Univ.* 41 (2), 304–308.

Koo, H. J., Jang, S. A., Yang, K. H., Kang, S. C., Namkoong, S., and Kim, T. H., et al. (2013). Effects of red ginseng on the regulation of cyclooxygenase-2 of spleen cells in whole-body gamma irradiated mice. *Food Chem. Toxicol.* 62, 839–846. doi:10.1016/j.fct.2013.10.009

Kunmu, D. L. Y., Jia-qi, F., Dong-hua, Y., and Chun-miao, Y. (2020). Thymic metabolomics for effect of Ganoderma polysaccharides on radiation-injured mice. *Chinese Journal of Experimental Traditional Medical Formulae* 26 (3), 102–109. doi:10.13422/j.cnki.syfjx.20191952

Lee, H. J., Kim, S. R., Kim, J. C., Kang, C. M., Lee, Y. S., and Jo, S. K., et al. (2006). *In Vivo* radioprotective effect of Panax ginseng C.A. Meyer and identification of active ginsenosides. *Phytother Res.* 20 (5), 392–395. doi:10.1002/ptr.1867

Lee, T. K., Johnke, R. M., Allison, R. R., O'Brien, K. F., and Dobbs, L. J., Jr. (2005). Radioprotective potential of ginseng. *Mutagenesis* 20 (4), 237–243. doi:10.1093/mutage/gei041

Lee, T. K., O'Brien, K. F., Wang, W., Johnke, R. M., Sheng, C., and Benhabib, S. M., et al. (2010). Radioprotective effect of American ginseng on human lymphocytes at 90 minutes postirradiation: a study of 40 cases. *J. Alternative Compl. Med.* 16 (5), 561–567. doi:10.1089/acm.2009.0590

Lee, W., Hwang, M. H., Lee, Y., and Bae, J. S. (2018). Protective effects of zingerone on lipopolysaccharide-induced hepatic failure through the modulation of inflammatory pathways. *Chem. Biol. Interact.* 281, 106–110. doi:10.1016/j.cbi.2017.12.031

Lee, Y. J., Han, J. Y., Lee, C. G., Heo, K., Park, S. I., and Park, Y. S., et al. (2014). Korean Red Ginseng saponin fraction modulates radiation effects on lipopolysaccharide-stimulated nitric oxide production in RAW264.7 macrophage cells. *J. Ginseng. Res.* 38 (3), 208–214. doi:10.1016/j.jgr.2014.02.001

Lei, G., Zhang, Y., Koppula, P., Liu, X., Zhang, J., and Lin, S. H., et al. (2020). The role of ferroptosis in ionizing radiation-induced cell death and tumor suppression. *Cell Res.* 30 (2), 146–162. doi:10.1038/s41422-019-0263-3

Lei, Y., Yang, J., Li, Y., Yu, X., Deng, S., Xue, C., et al. (2019). Traditional Chinese medicine on treating epididymitis: a systematic review and meta-analysis protocol. *Medicine (Baltim.)* 98 (24), e15975. doi:10.1097/MD.0000000000015975

Li, C. R., Zhou, Z., Zhu, D., Sun, Y. N., Dai, J. M., and Wang, S. Q. (2007). Protective effect of paeoniflorin on irradiation-induced cell damage involved in modulation of reactive oxygen species and the mitogen-activated protein kinases. *Int. J. Biochem. Cell Biol.* 39 (2), 426–438. doi:10.1016/j.biocel.2006.09.011

Li, D. D., Luo, Z., Ling, S. C., Wu, K., Chen, G. H., and Cheng, J. (2018a). Mitochondrial apoptotic pathway mediated the Zn-induced lipolysis in yellow catfish Peteobagrus fulvidraco. *Chemosphere* 208, 907–915. doi:10.1016/j.chemosphere.2018.05.200

Li, D., Lu, L., Zhang, J., Wang, X., Xing, Y., and Wu, H., et al. (2014a). Mitigating the effects of Xuebijing injection on hematopoietic cell injury induced by total body irradiation with γ rays by decreasing reactive oxygen species levels. *Int. J. Mol. Sci.* 15 (6), 10541–10553. doi:10.3390/ijms150610541

Li, M., You, L., Xue, J., and Lu, Y. (2018b). Ionizing radiation-induced cellular senescence in normal, non-transformed cells and the involved DNA damage response: a mini review. *Front. Pharmacol.* 9, 522. doi:10.3389/fphar.2018.00522

Li, Q., Dong, Z., Lian, W., Cui, J., Wang, J., and Shen, H., et al. (2019a). Ochratoxin A causes mitochondrial dysfunction, apoptotic and autophagic cell death and also induces mitochondrial biogenesis in human gastric epithelium cells. *Arch. Toxicol.* 93 (4), 1141–1155. doi:10.1007/s00204-019-02433-6

Li, T. T., Wang, Z. B., Li, Y., Cao, F., Yang, B. Y., and Kuang, H. X. (2019b). The mechanisms of traditional Chinese medicine underlying the prevention and treatment of atherosclerosis. *Chin. J. Nat. Med.* 17 (6), 401–412. doi:10.1016/S1875-5364(19)30048-2

Li, X., Qu, L., Dong, Y., Han, L., Liu, E., and Fang, S., et al. (2014b). A review of recent research progress on the astragalus genus. *Molecules* 19 (11), 18850–18880. doi:10.3390/molecules191118850

Li, X., Zhuang, X., and Qiao, T. (2019c). Role of ferroptosis in the process of acute radiation-induced lung injury in mice. *Biochem. Biophys. Res. Commun.* 519 (2), 240–245. doi:10.1016/j.bbrc.2019.08.165

Li, Y. R., Cao, W., Guo, J., Miao, S., Ding, G. R., and Li, K. C., et al. (2011). Comparative investigations on the protective effects of rhodioside, ciwujianoside-B and astragaloside IV on radiation injuries of the hematopoietic system in mice. *Phytother Res.* 25 (5), 644–653. doi:10.1002/ptr.3313

Li, Z., and Xu, C. (2011). The fundamental theory of traditional Chinese medicine and the consideration in its research strategy. *Front. Med.* 5 (2), 208–211. doi:10.1007/s11684-011-0126-x

Li-ying, Z., Lei, W., Li-xin, Z., Yi-ming, Z., Xiao-min, X., Nan, D., et al. (2018). Protective effect of *Astragalus* Polysaccharide on heavy ionizing radiation on BMSCs and its mechanism related with NF-κB. *Chin. J. Traditional Chin. Med. Pharm.* 33 (12), 5576–5580.

Liang, Q. D., Gao, Y., Tan, H. L., Guo, P., Li, Y. F., and Zhou, Z., et al. (2006). Effects of four Si-Wu-Tang's constituents and their combination on irradiated mice. *Biol. Pharm. Bull.* 29 (7), 1378–1382. doi:10.1248/bpb.29.1378

Lidan, Y., Yunshuang, Y., Lei, G., Changpei, L., Xiaoyue, Z., Yunjing, Z., et al. (2016). The effect of bushen Jiedu fang on thymus and spleen of mice with radiation injury. *J. Tradit. Chin. Med.* 57 (1), 67–70. doi:10.13288/j.11-2166/r.2016.01.017

Liming, H., Peng, S., Linjing, Z., and Chengrong, S. (2011). Effects of radioprotection formula of TCM on acute injury induced by(60)Co γ-rays in mice. *Chin. Pharm. Aff.* 25 (2), 132–134.

Lin, H., Weiai, L., Xianjie, Z., and Rong, W. (2001). Effects of Co-herba Houttuyniae oral liquid on the immunological function and the cytogenetics of radiation injuries mice. *Pharmaceutical J. of Chin. People's Liberation Army* 17 (3), 160–161. doi:10.3969/j.issn.1008-9926.2001.03.015

Lin, H., Zhengsheng, S., Romg, W., and Weiai, L. (2002). Effect of Co-herba Houttuyniae oral liquid to the stress function of R adiation injured mice. *Pharmaceutical J. of Chin. People's Liberation Army* 18 (1), 44–45. doi:10.3969/j.issn.1008-9926.2002.01.016

Liu, L., Hu, L., Yao, Z., Qin, Z., Idehara, M., and Dai, Y., et al. (2019). Mucosal immunomodulatory evaluation and chemical profile elucidation of a classical traditional Chinese formula, Bu-Zhong-Yi-Qi-Tang. *J. Ethnopharmacol.* 228, 188–199. doi:10.1016/j.jep.2018.08.003

Liu, M. M., Huang, K. M., Yeung, S., Chang, A., Zhang, S., and Mei, N., et al. (2017). Inhibition of neoplastic transformation and chemically-induced skin hyperplasia in mice by traditional Chinese medicinal formula Si-Wu-Tang. *Nutrients* 9 (3). doi:10.3390/nu9030300

Liu, Y., Liu, F., Yang, Y., Li, D., Lv, J., and Ou, Y., et al. (2014). *Astragalus* polysaccharide ameliorates ionizing radiation-induced oxidative stress in mice. *Int. J. Biol. Macromol.* 68, 209–214. doi:10.1016/j.ijbiomac.2014.05.001

Liu, Z., Lei, X., Li, X., Cai, J. M., Gao, F., and Yang, Y. Y. (2018). Toll-like receptors and radiation protection. *Eur. Rev. Med. Pharmacol. Sci.* 22 (1), 31–39. doi:10.26355/eurrev_201801_14097

Loboda, A., Damulewicz, M., Pyza, E., Jozkowicz, A., and Dulak, J. (2016). Role of Nrf2/HO-1 system in development, oxidative stress response and diseases: an evolutionarily conserved mechanism. *Cell. Mol. Life Sci.* 73 (17), 3221–3247. doi:10.1007/s00018-016-2223-0

Lu, M., Wang, Y., and Zhan, X. (2019). The MAPK pathway-based drug therapeutic targets in pituitary adenomas. *Front. Endocrinol.* 10, 330. doi:10.3389/fendo.2019.00330

Lumniczky, K., Szatmari, T., and Safrany, G. (2017). Ionizing radiation-induced immune and inflammatory reactions in the brain. *Front. Immunol.* 8, 517. doi:10.3389/fimmu.2017.00517

Luo, Q., Cui, X., Yan, J., Yang, M., Liu, J., and Jiang, Y., et al. (2011). Antagonistic effects of Lycium barbarum polysaccharides on the impaired reproductive system of male rats induced by local subchronic exposure to 60Co-γ irradiation. *Phytother Res.* 25 (5), 694–701. doi:10.1002/ptr.3314

Luo, Q., Li, J., Cui, X., Yan, J., Zhao, Q., and Xiang, C. (2014). The effect of Lycium barbarum polysaccharides on the male rats reproductive system and spermatogenic cell apoptosis exposed to low-dose ionizing irradiation. *J. Ethnopharmacol.* 154 (1), 249–258. doi:10.1016/j.jep.2014.04.013

Ma, C., Fu, Z., Guo, H., Wei, H., Zhao, X., and Li, Y. (2019). The effects of Radix Angelica Sinensis and Radix Hedysari ultrafiltration extract on X-irradiation-induced myocardial fibrosis in rats. *Biomed. Pharmacother.* 112, 108596. doi:10.1016/j.biopha.2019.01.057

Ma, Q., Wei, R., Wang, Z., Liu, W., Sang, Z., and Li, Y., et al. (2017). Bioactive alkaloids from the aerial parts of Houttuynia cordata. *J. Ethnopharmacol.* 195, 166–172. doi:10.1016/j.jep.2016.11.013

Mancuso, C., and Santangelo, R. (2017). Panax ginseng and Panax quinquefolius: from pharmacology to toxicology. *Food Chem. Toxicol.* 107 (Pt A), 362–372. doi:10.1016/j.fct.2017.07.019

Mansour, H. H. (2013). Protective effect of ginseng against gamma-irradiation-induced oxidative stress and endothelial dysfunction in rats. *EXCLI J.* 12, 766–777.

Maurya, D. K., and Devasagayam, T. P. (2013). Ferulic acid inhibits gamma radiation-induced DNA strand breaks and enhances the survival of mice. *Cancer Biother. Radiopharm.* 28 (1), 51–57. doi:10.1089/cbr.2012.1263

Mei, N., Guo, X., Ren, Z., Kobayashi, D., Wada, K., and Guo, L. (2017). Review of Ginkgo biloba-induced toxicity, from experimental studies to human case reports. *J. Environ. Sci. Health C Environ. Carcinog. Ecotoxicol. Rev.* 35 (1), 1–28. doi:10.1080/10590501.2016.1278298

Mohamed, H. E., and Badawy, M. M. M. (2019). Modulatory effect of zingerone against cisplatin or γ-irradiation induced hepatotoxicity by molecular targeting regulation. *Appl. Radiat. Isot.* 154, 108891. doi:10.1016/j.apradiso.2019.108891

Mukai, R. (2018). Prenylation enhances the biological activity of dietary flavonoids by altering their bioavailability. *Biosci. Biotechnol. Biochem.* 82 (2), 207–215. doi:10.1080/09168451.2017.1415750

Nabavi, S. F., Braidy, N., Orhan, I. E., Badiee, A., Daglia, M., and Nabavi, S. M. (2016). Rhodiola rosea L. And alzheimer's disease: from farm to pharmacy. *Phytother Res.* 30 (4), 532–539. doi:10.1002/ptr.5569

Nguyen, N. H., and Nguyen, C. T. (2019). Pharmacological effects of ginseng on infectious diseases. *Inflammopharmacology* 27 (5), 871–883. doi:10.1007/s10787-019-00630-4

Niaudet, C., Bonnaud, S., Guillonneau, M., Gouard, S., Gaugler, M. H., and Dutoit, S.et al. (2017). Plasma membrane reorganization links acid sphingomyelinase/ceramide to p38 MAPK pathways in endothelial cells apoptosis. *Cell. Signal.* 33, 10–21. doi:10.1016/j.cellsig.2017.02.001

Park, E., Hwang, I., Song, J. Y., and Jee, Y. (2011). Acidic polysaccharide of Panax ginseng as a defense against small intestinal damage by whole-body gamma irradiation of mice. *Acta Histochem.* 113 (1), 19–23. doi:10.1016/j.acthis.2009.07.003

Park, H. R., Jo, S. K., Choi, N. H., and Jung, U. (2012). HemoHIM ameliorates the persistent down-regulation of Th1-like immune responses in fractionated γ-irradiated mice by modulating the IL-12p70-STAT4 signaling pathway. *Radiat. Res.* 177 (5), 676–684. doi:10.1667/rr2768.1

Park, H. R., Jo, S. K., Jung, U., Yee, S. T., and Kim, S. H. (2014). Protective effects of HemoHIM on immune and hematopoietic systems against γ-irradiation. *Phytother Res.* 28 (2), 245–251. doi:10.1002/ptr.4982

Park, S. J., Cho, W., Kim, M. S., Gu, B. K., Kang, C. M., and Khang, G., et al. (2018). Substance-P and transforming growth factor-β in chitosan microparticle-pluronic hydrogel accelerates regenerative wound repair of skin injury by local ionizing radiation. *J. Tissue. Eng. Regen. Med.* 12 (4), 890–896. doi:10.1002/term.2445

Pompura, S. L., and Dominguez-Villar, M. (2018). The PI3K/AKT signaling pathway in regulatory T-cell development, stability, and function. *J. Leukoc. Biol*. doi:10.1002/JLB.2MIR0817-349R

Purbey, P. K., Scumpia, P. O., Kim, P. J., Tong, A. J., Iwamoto, K. S., and McBride, W. H., et al. (2017). Defined sensing mechanisms and signaling pathways contribute to the global inflammatory gene expression output elicited by ionizing radiation. *Immunity* 47 (3), e421–e423. doi:10.1016/j.immuni.2017.08.017

Raafat, B. M., Saleh, A., Shafaa, M. W., Khedr, M., and Ghafaar, A. A. (2013). Ginkgo biloba and Angelica archangelica bring back an impartial hepatic apoptotic to anti-apoptotic protein ratio after exposure to technetium 99mTc. *Toxicol. Ind. Health* 29 (1), 14–22. doi:10.1177/0748233711433938

Rokot, N. T., Kairupan, T. S., Cheng, K. C., Runtuwene, J., Kapantow, N. H., and Amitani, M., et al. (2016). A role of ginseng and its constituents in the treatment of central nervous system disorders. *Evid. Based Complement Alternat. Evid. Based Complement Alternat. Med.* 2016, 2614742. doi:10.1155/2016/2614742

Romesser, P. B., Kim, A. S., Jeong, J., Mayle, A., Dow, L. E., and Lowe, S. W. (2019). Preclinical murine platform to evaluate therapeutic countermeasures against radiation-induced gastrointestinal syndrome. *Proc. Natl. Acad. Sci. U. S. A.* 116 (41), 20672–20678. doi:10.1073/pnas.1906611116

Said, R. S., El-Demerdash, E., Nada, A. S., and Kamal, M. M. (2016). Resveratrol inhibits inflammatory signaling implicated in ionizing radiation-induced premature ovarian failure through antagonistic crosstalk between silencing information regulator 1 (SIRT1) and poly(ADP-ribose) polymerase 1 (PARP-1). *Biochem. Pharmacol.* 103, 140–150. doi:10.1016/j.bcp.2016.01.019

Sankaranarayanan, K., and Wassom, J. S. (2005). Ionizing radiation and genetic risks XIV. Potential research directions in the post-genome era based on knowledge of repair of radiation-induced DNA double-strand breaks in mammalian somatic cells and the origin of deletions associated with human genomic disorders. *Mutat. Res.* 578 (1-2), 333–370. doi:10.1016/j.mrfmmm.2005.06.020

Santivasi, W. L., and Xia, F. (2014). Ionizing radiation-induced DNA damage, response, and repair. *Antioxid Redox Signal* 21 (2), 251–259. doi:10.1089/ars.2013.5668

Scholch, S., Rauber, C., Weitz, J., Koch, M., and Huber, P. E. (2015). TLR activation and ionizing radiation induce strong immune responses against multiple tumor entities. *OncoImmunology* 4 (11), e1042201. doi:10.1080/2162402X.2015.1042201

Sener, G., Kabasakal, L., Atasoy, B. M., Erzik, C., Velioglu-Ogunc, A., and Cetinel, S., et al. (2006). Ginkgo biloba extract protects against ionizing radiation-induced oxidative organ damage in rats. *Pharmacol. Res.* 53 (3), 241–252. doi:10.1016/j.phrs.2005.11.006

Shain, A. H., Joseph, N. M., Yu, R., Benhamida, J., Liu, S., and Prow, T., et al. (2018). Genomic and transcriptomic analysis reveals incremental disruption of key signaling pathways during melanoma evolution. *Canc. Cell* 34 (1), 45–55, e44. doi:10.1016/j.ccell.2018.06.005

Shao, L., Luo, Y., and Zhou, D. (2014). Hematopoietic stem cell injury induced by ionizing radiation. *Antioxid Redox Signal* 20 (9), 1447–1462. doi:10.1089/ars.2013.5635

Sharma, A., Haksar, A., Chawla, R., Kumar, R., Arora, R., and Singh, S., et al. (2005). Zingiber officinale Rosc. modulates gamma radiation-induced conditioned taste aversion. *Pharmacol. Biochem. Behav.* 81 (4), 864–870. doi:10.1016/j.pbb.2005.06.012

Shen, C. Y., Jiang, J. G., Yang, L., Wang, D. W., and Zhu, W. (2017). Anti-ageing active ingredients from herbs and nutraceuticals used in traditional Chinese medicine: pharmacological mechanisms and implications for drug discovery. *Br. J. Pharmacol.* 174 (11), 1395–1425. doi:10.1111/bph.13631

Shi, M., Huang, F., Deng, C., Wang, Y., and Kai, G. (2019a). Bioactivities, biosynthesis and biotechnological production of phenolic acids in Salvia miltiorrhiza. *Crit. Rev. Food Sci. Nutr.* 59 (6), 953–964. doi:10.1080/10408398.2018.1474170

Shi, Q., Si, D., Bao, H., Yan, Y., Kong, Y., Li, C., et al. (2019b). Efficacy and safety of Chinese medicines for asthma: a systematic review protocol. *Medicine (Baltim.)* 98 (34), e16958. doi:10.1097/MD.0000000000016958

Shibata, A. (2017). Regulation of repair pathway choice at two-ended DNA double-strand breaks. *Mutat. Res.* 803-805, 51–55. doi:10.1016/j.mrfmmm.2017.07.011

Shingnaisui, K., Dey, T., Manna, P., and Kalita, J. (2018). Therapeutic potentials of Houttuynia cordata Thunb. against inflammation and oxidative stress: a review. *J. Ethnopharmacol.* 220, 35–43. doi:10.1016/j.jep.2018.03.038

Shrivastav, M., De Haro, L. P., and Nickoloff, J. A. (2008). Regulation of DNA double-strand break repair pathway choice. *Cell Res.* 18 (1), 134–147. doi:10.1038/cr.2007.111

Shukla, S. K., Chaudhary, P., Kumar, I. P., Samanta, N., Afrin, F., and Gupta, M. L., et al. (2006). Protection from radiation-induced mitochondrial and genomic DNA damage by an extract of Hippophae rhamnoides. *Environ. Mol. Mutagen.* 47 (9), 647–656. doi:10.1002/em.20251

Shuryak, I. (2019). Review of microbial resistance to chronic ionizing radiation exposure under environmental conditions. *J. Environ. Radioact.* 196, 50–63. doi:10.1016/j.jenvrad.2018.10.012

Singh, V. K., and Seed, T. M. (2019). The efficacy and safety of amifostine for the acute radiation syndrome. *Expert Opin. Drug. Saf.* 18 (11), 1077–1090. doi:10.1080/14740338.2019.1666104

Smith, T. A., Kirkpatrick, D. R., Smith, S., Smith, T. K., Pearson, T., and Kailasam, A., et al. (2017). Radioprotective agents to prevent cellular damage due to ionizing radiation. *J. Transl. Med.* 15 (1), 232. doi:10.1186/s12967-017-1338-x

Soliman, A. F., Anees, L. M., and Ibrahim, D. M. (2018). Cardioprotective effect of zingerone against oxidative stress, inflammation, and apoptosis induced by cisplatin or gamma radiation in rats. *Naunyn-Schmiedeberg's Arch. Pharmacol.* 391 (8), 819–832. doi:10.1007/s00210-018-1506-4

Song, J. Y., Han, S. K., Bae, K. G., Lim, D. S., Son, S. J., and Jung, I. S., et al. (2003). Radioprotective effects of ginsan, an immunomodulator. *Radiat. Res.* 159 (6), 768–774. doi:10.1667/0033-7587(2003)159[0768:reogai]2.0.co;2

Sun, J., Zhang, L., He, Y., Zhang, K., Wu, L., and Fan, Y., et al. (2016). To unveil the molecular mechanisms of qi and blood through systems biology-based investigation into Si-Jun-Zi-Tang and Si-Wu-Tang formulae. *Sci. Rep.* 6, 34328. doi:10.1038/srep34328

Sun, X., Zhang, H., Zhang, Y., Yang, Q., and Zhao, S. (2018). Caspase-dependent mitochondrial apoptotic pathway is involved in astilbin-mediated cytotoxicity in breast carcinoma cells. *Oncol. Rep.* 40 (4), 2278–2286. doi:10.3892/or.2018.6602

Szeto, Y. T., Sin, Y. S., Pak, S. C., and Kalle, W. (2015). American ginseng tea protects cellular DNA within 2 h from consumption: results of a pilot study in healthy human volunteers. *Int. J. Food Sci. Nutr.* 66 (7), 815–818. doi:10.3109/09637486.2015.1088937

Takayama, S., and Iwasaki, K. (2017). Systematic review of traditional Chinese medicine for geriatrics. *Geriatr. Gerontol. Int.* 17 (5), 679–688. doi:10.1111/ggi.12803

Tavassoly, I., Goldfarb, J., and Iyengar, R. (2018). Systems biology primer: the basic methods and approaches. *Essays Biochem.* 62 (4), 487–500. doi:10.1042/EBC20180003

Tianxiang, M., Jiuhong, W., Ning, S., and Hongzhu, G. (2013). Screening for radioprotective components of glycosides and alcohols from Rhodiola *in vitro*. *Pharmaceutical Journal of Chinese People's Liberation Army* 29 (3), 203–205.

Toulany, M., and Rodemann, H. P. (2015). Phosphatidylinositol 3-kinase/Akt signaling as a key mediator of tumor cell responsiveness to radiation. *Semin. Canc. Biol.* 35, 180–190. doi:10.1016/j.semcancer.2015.07.003

Verma, P., Sharma, P., Parmar, J., Sharma, P., Agrawal, A., and Goyal, P. K. (2011). Amelioration of radiation-induced hematological and biochemical alterations in Swiss albino mice by Panax ginseng extract. *Integr. Canc. Ther.* 10 (1), 77–84. doi:10.1177/1534735410375098

Wang, A., Wang, L., Lu, X., Wang, Y., Chen, X., and Shi, Z., et al. (2020). A Chinese herbal prescription Yiqi Jiedu decoction attenuates irradiation induced testis injury in mice. *Biomed. Pharmacother.* 123, 109804. doi:10.1016/j.biopha.2019.109804

Wang, J., Shao, W., Niu, H., Yang, T., Wang, Y., and Cai, Y. (2019a). Immunomodulatory effects of colistin on macrophages in rats by activating the p38/MAPK pathway. *Front. Pharmacol.* 10, 729. doi:10.3389/fphar.2019.00729

Wang, W. J., and Zhang, T. (2017). Integration of traditional Chinese medicine and Western medicine in the era of precision medicine. *J. Integr. Med.* 15 (1), 1–7. doi:10.1016/S2095-4964(17)60314-5

Wang, Z., Lin, H. H., Linghu, K., Huang, R. Y., Li, G., and Zuo, H., et al. (2019b). Novel compound-target interactions prediction for the herbal formula hua-yu-qiang-shen-tong-Bi-fang. *Chem. Pharm. Bull. (Tokyo)* 67 (8), 778–785. doi:10.1248/cpb.c18-00808

Weiss, J. F., and Landauer, M. R. (2003). Protection against ionizing radiation by antioxidant nutrients and phytochemicals. *Toxicology* 189 (1-2), 1–20. doi:10.1016/s0300-483x(03)00149-5

Wu, Y., Chen, M., and Jiang, J. (2019). Mitochondrial dysfunction in neurodegenerative diseases and drug targets via apoptotic signaling. *Mitochondrion* 49, 35–45. doi:10.1016/j.mito.2019.07.003

Xiao-fang, Y., Ya-nan, W., Zhe, Z., and Sheng-qi, W. (2013). Experimental research on the protection of buzhong Yiqi pills in low-dose radiation. *World J. Integ. Traditional and Western Med.* 8 (6), 560–562. doi:10.3969/j.issn.1673-6613.2013.06.007

Xiaoling, H., Qiujun, L., zhe, Z., Aidong, M., Xuejun, W., Mingsan, M., et al. (2006). Radiation protection effect of buzhong Yiqi pill and other proprietary Chinese medicines. *Chin. J. Radio. Med. Protection* 26 (4), 366–369. doi:10.3760/cma.j.issn.0254-5098.2006.04.017

Yang, J., Yan, Y., Liu, H., Wang, J., and Hu, J. (2015). Protective effects of acteoside against X-ray induced damage in human skin fibroblasts. *Mol. Med. Rep.* 12 (2), 2301–2306. doi:10.3892/mmr.2015.3630

Yang, Y., Laval, S., and Yu, B. (2014). Chemical synthesis of saponins. *Adv. Carbohydr. Chem. Biochem.* 71, 137–226. doi:10.1016/B978-0-12-800128-8.00002-9

Yang, Y., Zhang, G., Sun, Q., Liu, L., Peng, H., and Wang, J., et al. (2017). Simultaneous determination of 8 compounds in gancao-ganjiang-tang by HPLC-DAD and analysis of the relations between compatibility, dosage, and contents of medicines. *Evid. Based Complement Alternat. Med.* 2017, 4703632. doi:10.1155/2017/4703632

Yeh, M. L., Chiu, W. L., Wang, Y. J., and Lo, C. (2017). An investigation of the use of traditional Chinese medicine and complementary and alternative medicine in stroke patients. *Holist. Nurs. Pract.* 31 (6), 400–407. doi:10.1097/HNP.0000000000000238

Ying, N., Mei-na, Z., Jin-rui, C., Jian, C., and Wei, Z. (2018). Protection and mechanism of gypenosides on the oxidative injury induced by irradiation in mice. *Central South Pharmacy* 16 (7), 935–938. doi:10.7539/j.issn.1672-2981.2018.07.009

Yu, J., Zhu, X., Qi, X., Che, J., and Cao, B. (2013). Paeoniflorin protects human EA.hy926 endothelial cells against gamma-radiation induced oxidative injury by activating the NF-E2-related factor 2/heme oxygenase-1 pathway. *Toxicol. Lett.* 218 (3), 224–234. doi:10.1016/j.toxlet.2013.01.028

Yue, C., Bao-gui, W., Gui-ying, Z., and Wei-qun, Y. (2005). Protective effects of acanthopanax senticosus saponins on mice with irradiation damage induced by X-rays. *J. Jilin Univ. (Med. Ed.)* 31 (3), 423–425. doi:10.3969/j.issn.1671-587X.2005.03.031

Yunjing, Z., Yunshuang, Y., Lidan, Y., Xiaoyue, Z., Lei, D., and Rong, Z. (2015). Effect of BushenJiedu recipe on peripheral blood leukocytes and spleen NF-κBp65 of mice after radiation. *J. Jinan Univ. (Nat. Sci. Med. Ed.)* (6), 490–495. doi:10.11778/j.jdxb.2015.06.009

Zhang, H. P., Wang, L., Wang, Z., Xu, X. R., Zhou, X. M., and Liu, G., et al. (2018b). Chinese herbal medicine formula for acute asthma: a multi-center, randomized, double-blind, proof-of-concept trial. *Respir. Med.* 140, 42–49. doi:10.1016/j.rmed.2018.05.014

Zhang, H., Yan, H., Ying, J., Du, L., Zhang, C., and Yang, Y., et al. (2018a). Resveratrol ameliorates ionizing irradiation-induced long-term immunosuppression in mice. *Int. J. Radiat. Biol.* 94 (1), 28–36. doi:10.1080/09553002.2018.1408976

Zhang, H., Yan, H., Zhou, X., Wang, H., Yang, Y., and Zhang, J., et al. (2017a). The protective effects of Resveratrol against radiation-induced intestinal injury. *BMC Compl. Alternative Med.* 17 (1), 410. doi:10.1186/s12906-017-1915-9

Zhang, J., Li, H., Lu, L., Yan, L., Yang, X., and Shi, Z., et al. (2017b). The Yiqi and Yangyin Formula ameliorates injury to the hematopoietic system induced by total body irradiation. *J. Radiat. Res.* 58 (1), 1–7. doi:10.1093/jrr/rrw056

Zhang, L., Luo, Y., Lu, Z., He, J., Wang, L., and Zhang, L., et al. (2018c). *Astragalus* polysaccharide inhibits ionizing radiation-induced bystander effects by regulating MAPK/NF-kB signaling pathway in bone mesenchymal stem cells (BMSCs). *Med. Sci. Mon. Int. Med. J. Exp. Clin. Res.* 24, 4649–4658. doi:10.12659/MSM.909153

Zhang, W., Wang, S., Zhang, R., Zhang, Y., Li, X., and Lin, Y., et al. (2016). Evidence of Chinese herbal medicine Duhuo Jisheng decoction for knee osteoarthritis: a systematic review of randomised clinical trials. *BMJ Open* 6 (1), e008973. doi:10.1136/bmjopen-2015-008973

Zhang, X., Xing, X., Liu, H., Feng, J., Tian, M., and Chang, S., et al. (2020). Ionizing radiation induces ferroptosis in granulocyte-macrophage hematopoietic progenitor cells of murine bone marrow. *Int. J. Radiat. Biol.* 96 (5), 584–595. doi:10.1080/09553002.2020.1708993

Zhao, L., Wang, Y., Shen, H. L., Shen, X. D., Nie, Y., and Wang, Y., et al. (2012). Structural characterization and radioprotection of bone marrow hematopoiesis of two novel polysaccharides from the root of Angelica sinensis (Oliv.) Diels. *Fitoterapia* 83 (8), 1712–1720. doi:10.1016/j.fitote.2012.09.029

Zhao, M., Chan, C. P. S., Cheung, C. W. C., Alqawasmeh, O., Wang, R. C. C., and Wu, J. C. Y., et al. (2019). A double-blinded, randomized placebo-controlled trial on the effect of traditional Chinese medicine formula Wuzi Yanzong pill on improving semen qualities in men with suboptimal parameters. *Trials* 20 (1), 540. doi:10.1186/s13063-019-3647-2

Zhao, M. P., Shi, X., Kong, G. W. S., Wang, C. C., Wu, J. C. Y., Lin, Z. X., et al. (2018). The therapeutic effects of a traditional Chinese medicine formula wuzi Yanzong pill for the treatment of oligoasthenozoospermia: a meta-analysis of randomized controlled trials. *Evid. Based Complement Alternat. Evid. Based Complement Alternat. Med.* 2018, 2968025. doi:10.1155/2018/2968025

Zhou, J., Pang, H., Li, W., Liu, Q., Xu, L., and Liu, Q., et al. (2016). Effects of Lycium barbarum polysaccharides on apoptosis, cellular adhesion, and oxidative damage in bone marrow mononuclear cells of mice exposed to ionizing radiation injury. *BioMed. Res. Int.* 2016, 4147879. doi:10.1155/2016/4147879

Zhou, Y. X., Xin, H. L., Rahman, K., Wang, S. J., Peng, C., and Zhang, H. (2015). Portulaca oleracea L.: a review of phytochemistry and pharmacological effects. *BioMed. Res. Int.* 2015, 925631. doi:10.1155/2015/925631

Zimta, A. A., Cenariu, D., Irimie, A., Magdo, L., Nabavi, S. M., and Atanasov, A. G., et al. (2019). The role of Nrf2 activity in cancer development and progression. *Cancers* 11 (11), 1755. doi:10.3390/cancers11111755

Conflict of Interest: The authors declare that the research was conducted in the absence of any commercial or financial relationships that could be construed as a potential conflict of interest.

Copyright © 2021 Zhang, Chen, Wang, He, Shi, Fu, Xu, Zhang and Hu. This is an open-access article distributed under the terms of the Creative Commons Attribution License (CC BY). The use, distribution or reproduction in other forums is permitted, provided the original author(s) and the copyright owner(s) are credited and that the original publication in this journal is cited, in accordance with accepted academic practice. No use, distribution or reproduction is permitted which does not comply with these terms.

frontiers in Pharmacology

ORIGINAL RESEARCH
published: 15 February 2021
doi: 10.3389/fphar.2020.590457

An Integrative Pharmacology-Based Pattern to Uncover the Pharmacological Mechanism of Ginsenoside H Dripping Pills in the Treatment of Depression

Libin Zhao[1,2], Rui Guo[3], Ningning Cao[1], Yingxian Lin[1], Wenjing Yang[4], Shuai Pei[1], Xiaowei Ma[5], Yu Zhang[1], Yingpeng Li[1], Zhaohui Song[4], Wuxun Du[1], Xuefeng Xiao[1]* and Changxiao Liu[6]**

[1]School of Graduate, Tianjin University of Traditional Chinese Medicine, Tianjin, China, [2]Zhendong Research Institute, Shanxi Zhendong Pharmaceutical Co., Ltd, Beijing, China, [3]School of Life Sciences, Beijing University of Chinese Medicine, Beijing, China, [4]State Key Laboratory of Critical Technology in Innovative Chinese Medicine, TCM Research Center, Tianjin Tasly Pharmaceutical CO., LTD., Tianjin, China, [5]Shandong Huayu University of Technology, Shandong, China, [6]State Key Laboratory of Drug Delivery Technology and Pharmacokinetics, Tianjin Institute of Pharmaceutical Research, Tianjin, China

OPEN ACCESS

Edited by:
Hai Yu Xu,
China Academy of Chinese Medical Sciences, China

Reviewed by:
Gang Bai,
Nankai University, China
Shao Li,
Tsinghua University, China

***Correspondence:**
Wuxun Du
cnduwux@163.com
Xuefeng Xiao
kai1219@163.com
Changxiao Liu
liuchangxiao@163.com

Specialty section:
This article was submitted to Ethnopharmacology, a section of the journal Frontiers in Pharmacology

Received: 01 August 2020
Accepted: 30 September 2020
Published: 15 February 2021

Citation:
Zhao L, Guo R, Cao N, Lin Y, Yang W, Pei S, Ma X, Zhang Y, Li Y, Song Z, Du W, Xiao X and Liu C (2021) An Integrative Pharmacology-Based Pattern to Uncover the Pharmacological Mechanism of Ginsenoside H Dripping Pills in the Treatment of Depression. Front. Pharmacol. 11:590457. doi: 10.3389/fphar.2020.590457

Objectives: To evaluate the pharmacodynamical effects and pharmacological mechanism of Ginsenoside H dripping pills (GH) in chronic unpredictable mild stress (CUMS) model rats.

Methods: First, the CUMS-induced rat model was established to assess the anti-depressant effects of GH (28, 56, and 112 mg/kg) by the changes of the behavioral indexes (sucrose preference, crossing score, rearing score) and biochemical indexes (serotonin, dopamine, norepinephrine) in Hippocampus. Then, the components of GH were identified by ultra-performance liquid chromatography-iron trap-time of flight-mass spectrometry (UPLC/IT-TOF MS). After network pharmacology analysis, the active ingredients of GH were further screened out based on OB and DL, and the PPI network of putative targets of active ingredients of GH and depression candidate targets was established based on STRING database. The PPI network was analyzed topologically to obtain key targets, so as to predict the potential pharmacological mechanism of GH acting on depression. Finally, some major target proteins involved in the predictive signaling pathway were validated experimentally.

Results: The establishment of CUMS depression model was successful and GH has antidepressant effects, and the middle dose of GH (56 mg/kg) showed the best inhibitory effects on rats with depressant-like behavior induced by CUMS. Twenty-eight chemical components of GH were identified by UPLC/IT-TOF MS. Subsequently, 20(*S*)-ginsenoside Rh2 was selected as active ingredient and the PPI network of the 43 putative targets of 20(*S*)-ginsenoside Rh2 containing in GH and the 230 depression candidate targets, was established based on STRING database, and 47 major targets were extracted. Further network pharmacological analysis indicated that the cAMP signaling pathway may be potential pharmacological mechanism regulated by GH acting on depression. Among the

cAMP signaling pathway, the major target proteins, namely, cAMP, PKA, CREB, *p*-CREB, BDNF, were used to verify in the CUMS model rats. The results showed that GH could activate the cAMP-PKA-CREB-BDNF signaling pathway to exert antidepressant effects.

Conclusions: An integrative pharmacology-based pattern was used to uncover that GH could increase the contents of DA, NE and 5-HT, activate cAMP-PKA-CREB-BDNF signaling pathway exert antidepressant effects.

Keywords: ginsenoside H dripping pills, depression, network pharmacology, chronic unpredictable mild stress, cAMP signaling pathway

INTRODUCTION

Depression is a mental disorder illness with a high disability, morbidity and recurrence rate (Chen et al., 2008). The main clinical features are decreased food-intake, low mood, anhedonia, activity decrease, irritability and other symptoms (Yang et al., 2018). In severe cases, they may have suicidal tendency (Zhu et al., 2020). An epidemiological multicenter study showed the odds of being depressed among cancer patients were more than five times higher than in the general population (Götze et al., 2020). Remarkably, comorbid depression in patients with cancer was compellingly established as a risk factor for suicide as well as rapid cancer progression (Shoval et al., 2019). There is no specific drug for the treatment of depression in cancer patients, and antidepressants are generally used. At present, the commonly used chemical antidepressants are mainly divided into four classes according to the chemical formula and the mechanism, including selective serotonin-re-uptake inhibitors (SSRI) such as sertraline and fluoxetine, serotonin and norepinephrine reuptake inhibitors (SNRI) like duloxetine and milnacipran, tricyclic antidepressants (TCA) such as amitriptyline and imipramine, monoamine oxidase inhibitors (MAOI) like moclobemide and phenelzine (Zhao et al., 2015; Ostuzzi et al., 2018). There are several Chinese herbal formulae for the treatment of depression including Chaihu Shugan powder, Xiaoyao Pill and Shugan Jieyu capsule (Du et al., 2014; Fu et al., 2014; Wang et al., 2014). Clinically, although chemical antidepressants are widely used, their side effects are common, such as hepatotoxicity, drowsiness, sexual dysfunction, nausea, irritability and psychomotor impairment (Dai et al., 2010; Gorzalka and Hill, 2011; Zhu et al., 2020). Compared with chemical drugs, traditional Chinese medicine (TCM) are attracting more and more attention due to its advantages such as low toxicity and side effects, high safety, and high efficacy and toxicity reduction (Xie et al., 2018). Therefore, the research on the treatment of depression with TCM has certain clinical value.

Ginsenoside H dripping pills (GH), originated from Tasly Group, is the class 5 new traditional Chinese medicine which obtained from leaves of Panax Quinquefolium Linn by extracting, chemical degrading and chromatography separating (Chen et al., 2018). It is designed to be used for replenishing qi and blood, and is used as an adjuvant drug for treating cancer. The main ingredient of the drug is ginsenoside Rh2 and the content of ginsenoside Rh2 is about 30% (Ma et al., 2018). Early studies have indicated that ginsenoside Rh2 could significantly inhibit the growth of U14 cervical cancer bearing mouse (Zhang et al., 2013). Besides, ginsenoside Rh2 can significantly improve the depressive behavior of depressing mice (Wang et al., 2016). It can be said that GH not only has significant anti-tumor effects, but also has antidepressant effects, which provides exclusive drugs for the treatment of depression in cancer patients and has research value. However, it is still unclear that antidepressant effects and mechanism of GH. Therefore, the study adopted the integrated pattern of "pharmacodynamics - network pharmacological analysis - mechanism verification" to deeply study the antidepressant effects and potential mechanism of GH.

Chronic unpredictable mild stress (CUMS) model in rats was the closest animal model to clinical depression (Su et al., 2017). During the modeling process, rats which were subjected to different kinds of chronic unpredictable mild stress, fully simulated the social living environment of depressive patients and induced rats to produce many behavioral abnormal symptoms similar to those of depressive patients (Antoniuk et al., 2019; Li et al., 2019). For example, the reducing the sucrose preference in rats simulated the symptoms of anhedonia in depressive patients; the reducing the score of Open field exercise simulated the symptoms of low ability of autonomic movement in depressive patients (Tan et al., 2015; Liu et al., 2018). Therefore, the decrease of behavioral indexes (sucrose preference and open field exercise score) showed that CUMS depression model in rats were successfully established. In addition, the pathogenesis of depression is complex. Although several hypotheses about depression have been proposed, the monoamine hypothesis is still the most common hypothesis for depression, because most of the current antidepressants act on monoamine transporters or receptors (Auclair et al., 2013; Liu et al., 2020). The hypothesis believes that the occurrence of depression is mainly due to the lack of major monoamine neurotransmitters such as 5-hydroxytryptamine (5-HT), dopamine (DA) and norepinephrine (NE) in the central nervous system of the brain (Jesulola et al., 2018). Hence, the contents of 5-HT, DA and NE in hippocampus were decreased, which indicated that CUMS depression model in rats was successfully established. In conclusion, the antidepressant effects of GH were evaluated from the behavioral and biochemical indexes of depression model rats.

Network pharmacology was first proposed by Hopkins in 2007, which is based on disease-gene-target-drug interaction network to predict the material basis and mechanism of drug intervention in diseases (Li and Zhang, 2013). With the

establishment of TCM database systems such as Encyclopedia of Traditional Chinese Medicine and Traditional Chinese Medicine Systems Pharmacology Database (Ru et al., 2014; Xu et al., 2019), network pharmacology has been widely used in TCM (Xu et al., 2014; Yu et al., 2017; Zhang et al., 2017; Li et al., 2018). Interestingly, the holistic philosophy of TCM is consistent with the key idea of emerging network pharmacology (Li et al., 2014). Our group had previously predicted the underlying pharmacological mechanism of Xueshuan-Xinmai-Ning (XXNT) acting on coronary heart disease (CHD) through network pharmacology method, and found that the XXNT in the treatment of CHD might be involved into the signal transduction in nervous-endocrine-immune-cardiovascular-metabolic system, and it is verified by experiments that XXNT plays a role in treating CHD via VEGF signal pathway (Mao et al., 2019). In addition, through network pharmacology analysis, it is found that Zhile alleviated depression-like behaviors by upregulating the cAMP-CREB-BDNF signaling pathway (Wu et al., 2019). Therefore, the pharmacological mechanism of the anti-depressant effects of GH could be evaluated by network pharmacology analysis.

In this study, the integrated pharmacology-based pattern, which adopted pharmacodynamics-network pharmacology-mechanism verification, was used to elucidate the pharmacological mechanism of GH in treatment of depression. The antidepressant effects of GH were first confirmed by using chronic unpredictable mild stress model rats. The chemical components containing in GH were then identified by UPLC/IT-TOF MS, and the active ingredients of GH were further screened out based on OB and DL. Network pharmacology analysis was conducted to predict the potential pharmacological mechanism of GH in treatment of depression. At last, the results predicted by network pharmacology were further validated by western blotting and enzyme-linked immunosorbent assay. A flowchart of this study is illustrated in **Figure 1**.

MATERIALS AND METHODS

Reagents and Materials

Bulk substance of Ginsenoside H dripping pills (GH) and GH (specification: 30 mg/pill, the total saponin content: 3.12 mg) were obtained from Tianjin Tasly Pharmaceutical Co., Ltd. (Batch NO. 20120606-16, 20160309, respectively, Tianjin, China). Fluoxetine hydrochloride (Flu) was provided by Suzhou Eli Lilly and Company (Suzhou, China). Chromatographic grade methanol and acetonitrile were obtained from Fisher Scientific Co. (Loughborough, United Kingdom). Pseudoginsenoside RT5, 20(*S*)-ginsenoside Rh1, 20(*R*)-ginsenoside Rh1, 20(*S*)-ginsenoside F1, ginsenoside Rh4, ginsenoside CK, 20(*S*)-ginsenoside Rh2, 20(*R*)-ginsenoside Rh2, isoginsenoside Rh3 standards were obtained from China National Institute for the Control of Pharmaceutical and Biological Products (Beijing, China). ginsenosides Rk2 standard was purchased from Chengdu Mansite Pharmaceutical Co., Ltd. (Chengdu, China). All standards were of at least 98% purity and were suitable for UPLC/IT-TOF analysis. The enzyme-linked immunosorbent assay (ELISA) kits, including serotonin (5-HT), dopamine (DA), norepinephrine (NE) and cyclic Adenosine monophosphate (cAMP) were supplied by Shanghai Lianshuo Biological Technology Co., Ltd. (Shanghai, China). The radioactive cyclic-AMP dependent protein kinase A (PKA) assay kit was purchased from Promega Corporation (Madison, Wisconsin, United States). The primary antibodies against brain derived neurotrophic factor (BDNF), cAMP-response element binding protein (CREB), phosphorylated cAMP-response element binding protein (*p*-CREB) and the secondary antibodies goat anti-rabbit IgG-HRP were purchased from Affinity Biosciences (Cincinnati, OH, United States). Bicinchoninic acid assay (BCA) kits was produced by Beyotime Institute of Biotechnology Co., Ltd. (Nanjing, China).

Animals

A total of 80 Specific-pathogen free (SPF) male Sprague Dawley rats (180–220 g) were obtained from the China National Institutes for Food and Drug Control (SCXK (jing) 2017-0005). The rats were kept in an environmentally controlled room (temperature 22 ± 2°C, humidity 50 ± 10%, 12 h/12 h light/dark cycle) and were allowed to eat and drink freely. The laboratory animals were used according to requirements of the Ethics Committee of Tianjin University of Traditional Chinese Medicine (Tianjin, China), and the experimental methods were in line with the principles for protection of laboratory animals.

Animal Grouping

After 7 days habituation, the rats were randomly divided into six groups (n = 10) according to the similar sucrose preference, crossing score and rearing score: the control group, CUMS group, low dose group of GH (28 mg/kg), middle dose group of GH (56 mg/kg), high dose group of GH (112 mg/kg), and Flu group (10 mg/kg).

Establishment of Chronic Unpredictable Mild Stress (CUMS) Model and Drug Treatment

The CUMS procedure was carried out as described in the existing literatures (Zhong et al., 2018; Lu et al., 2019). The animals, except the control group, were separately placed and repeatedly exposed to a set of CUMS as follows: restraint stress (4 h), noise environment (110 dB, 1 h), electric shock to the foot (3 mA, one shock/5 s), tail clamp (tail nipped at 1 cm from the tip of the tail for 3 min), damp bedding (24 h), reversed light/dark cycle (24 h), high temperature stress (40°C, 20 min), ice-cold swimming (4°C, 5 min), 45° tilted cage (12 h), cage shaking (15 min), fasting food (24 h), water deprivation (24 h). Two stressors were applied every day and the whole stress procedure lasted for 5 weeks in a completely random order. During the modeling period, rats in the GH group and the Flu group were administrated with corresponding drugs; rats in the control group and the CUMS group were administrated with

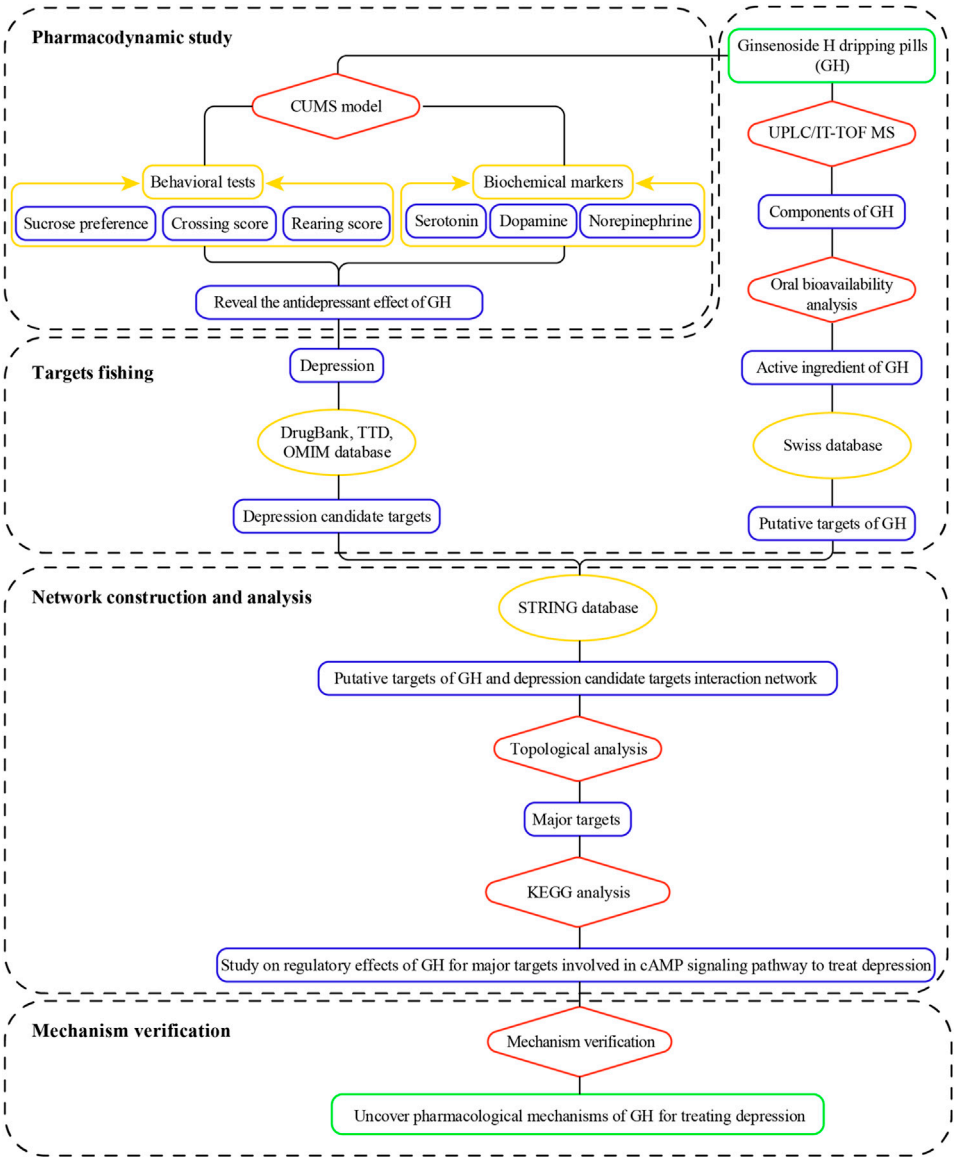

FIGURE 1 | Flowchart of the study.

saline. Rats in all group were injected via gastric gavage at 10 ml/kg once daily.

Behavioral Tests

Sucrose Preference Test

Sucrose preference test (SPT) was conducted at the day 0 and day 35 in accordance with previously described methods (Zhu et al., 2017). Briefly, 72 h before the test, the rats were bred individually two bottles 1% sucrose solution for 24 h, which were aimed to adapt to sucrose solution. Then, rats were exposed to one bottle of 1% sucrose solution and one bottle of water for 24 h. Finally, water and food were deprived for another 24 h. Sucrose preference test was conducted, in which rats were placed in separate cages and were freely access to two bottles containing sucrose solution (1%, w/v) and water, respectively. After 24 h, the weight of solution in every bottle was measured, and the rate of sucrose preference was calculated by the following formula:

$$Sucrose\ preference = \frac{sucrose\ consumtion}{water\ consumption + sucrose\ consumtion} \times 100\%$$

Open Field Test

The open field test (OFT) was carried out at day 0 and day 35 according to previously described methods (Dai et al., 2010). The activity of rats in each group were measured in a 100 cm × 100 cm × 50 cm box without ceiling, the inner wall and floor of which were

coated with black paint. A video camera was used to record the rat behavior. The rats were released from the center of the arena, and were observed for 3 min. The following behavioral parameters were taken into the account: the crossing score (grid lines it crossed with at least three paws) and the rearing score (defined as standing upright with hind legs). To avoid the possible disturbance, the 75% alcohol was used to clean the floor box before each test.

Hippocampus Sampling

The rats were sacrificed, 24 h after the behavioral tests. The whole brain was quickly dissected from the rats in ice-cold saline. The hippocampi were isolated on ice bath and immediately stored in liquid nitrogen for enzyme-linked immunosorbent assay and western blot analysis. All samples were stored at −80°C until assays.

Preparation of Samples and Standard Solution

Bulk substance of GH was weighed 100 mg precisely. The powder was soaked in 20 ml methanol, extracted by ultrasonic at room temperature for 30 min, and precipitated to 25 ml volume. A stock solution containing ten standards (pseudoginsenoside RT5, 20(*S*)-ginsenoside Rh1, 20(*R*)-ginsenoside Rh1, 20(*S*)-ginsenoside F1, ginsenoside Rh4, ginsenoside CK, 20(*S*)-ginsenoside Rh2, 20(*R*)-ginsenoside Rh2, isoginsenoside Rh3 and ginsenoside Rk2) was prepared in methanol. All samples were filtered through 0.22 μm nylon membrane filters and the filtrate was analyzed directly by UPLC/IT-TOF.

UPLC/IT-TOF Conditions

The UPLC analysis was performed on a Shimadzu LC-20A (Shimadzu, Kyoto, Japan) with a Waters Acquity UPLC HSS T3 column (2.1 × 100 mm, 1.8 μm). The column temperature was set at 35°C. The flow rate was set at 0.44 ml/min. The target sample temperature is set at 10°C and 5 μL of each sample was injected onto the column. The solvent system composed of mobile phase A (water) and mobile phase B (acetonitrile) in the following gradient: 0–9 min, 28–47%B; 9–17 min, 47–55%B; 17–22 min, 55–90%B; 22–24 min, 90–28%B; 24–25 min, 28–28% B. The experiment was performed on both ESI (+) ionization mode. The desolvation temperature was set at 200°C with desolvation gas flow set at 1.5 L/min. The capillary voltage was sat at 4.5 KV for ESI (+). The full scan data acquisition range was 100–1,300 Da. The LabSolutions-LCMS software (Shimadzu, Kyoto, Japan) were employed for data analysis and the chemical components of GH was identified.

Targets Fishing

The chemical components containing in GH identified by UPLC/IT-TOF were filtered by integrating oral bioavailability (OB), drug similarity (DL) from Traditional Chinese Medicine Systems Pharmacology Database (TCMSP).[1] The chemical components that meet both of the requirements OB ≥ 30%, DL ≥ 0.18, were retained as candidate active ingredients (Tao et al., 2013). The targets of candidate active ingredients were obtained from Swiss Target Prediction[2,] (Daina and Zoete, 2019). Species were selected as "Homo sapiens" and the targets with probability greater than 0 were predicted as the putative targets.

Known therapeutic targets acting on depression were collected from the DrugBank[3] (Knox et al., 2011). Therapeutic Target Database (TTD)[4] (Li et al., 2018) and Online Mendelian Inheritance in Man (OMIM) database[5] (Hamosh et al., 2005) with the keyword "depression". All targets enrolled in this research were human genes/proteins.

Network Construction and Topological Analysis

Protein-protein interaction (PPI) data were obtained from STRING database[6] (Szklarczyk et al., 2017) with setting species as "Homo sapiens" and the results were imported into the Cytoscape software (version 3.7.1, Boston, MA, United States) where the interaction network was constructed and analyzed. The topological features were calculated using Network Analyzer and the nodes with degree greater than twice the median degree of all nodes will be defined as major targets (Guo et al., 2020).

Pathway Enrichment Analysis

To explore potential mechanism of predicted major targets, the Kyoto Encyclopedia of Genes and Genomes (KEGG) pathway enrichment analysis (Kanehisa et al., 2017) was performed using the Database Visualization and Integrated Discovery (DAVID)[7] (Huang et al., 2007). KEGG pathways with enrichment p value less than 0.05 were employed for further study.

Enzyme-Linked Immunoassay

Tissues from the rat hippocampus were homogenized by adding phosphate buffered saline (PBS) at pH 7.4 (Solarbio Science &Technology Co., Ltd., Beijing, China). Homogenate was centrifuged at 4°C for 10 min at 12,000 rpm to obtain the supernatant. The supernatant was separated and stored at −20°C until analysis. The concentration of 5-HT, DA, NE and cAMP were measured using commercially available ELISA kits in accordance with the manufacturer's instructions. The absorbance at 450 nm was measured with a GloMax microplate reader (Promega, Madison, WI, United States), and the measured OD values were used to quantify the expression of the 5-HT, DA, NE and cAMP. All samples were determined three times repeatedly in the same assay to minimize inter-assay differences.

Assay of PKA Activity

PKA activity was assayed using a radioactive PKA assay kit in accordance with the manufacturer's instructions.

[1]http://lsp.nwu.edu.cn/tcmspsearch.php

[2]http://www.swisstargetprediction.ch/
[3]http://www.drugbank.ca/
[4]http://db.idrblab.net/ttd/
[5]http://www.omim.org/
[6]https://string-db.org/
[7]https://david-d.ncifcrf.gov/

Western Blot

Hippocampus tissue (approximately 50 mg) was solubilized by radio immunoprecipitation assay lysis buffer (Beijing, China) for 30 min on ice. The buffer contained 1% phenylmethylsulphonyl fluoride (Beyotime, China) and/or 1% phosphatase inhibitor. The pyrolysis products were clarified by centrifuging at 4°C for 15 min at 12,000 rpm. The supernatant was collected and the protein concentration was measured with the bicinchoninic acid protein assay kit. Proteins were separated by 10% sodium dodecyl sulfate polyacrylamide gel electrophoresis (SDS-PAGE) and then were transferred to polyvinylidene difluoride (PVDF) membranes, which were blocked in 5% nonfat milk or 5% BSA for 2 h and then washed three times with Tris Buffer Saline supplemented with 0.1% Tween-20 (TBST) buffer for 10 min each time. The membranes were incubated overnight at 4°C with primary antibodies BDNF (1:1,000 dilution), CREB (1:1,000 dilution), *p*-CREB (1:1,000 dilution), and rat polyclonal antibody GAPDH (1:1,000 dilution). Subsequently, the membranes were washed three times with TBST and were incubated for 2 h at room temperature with suitable goat anti-rabbit immunoglobulin G-horseradish peroxidase (IgG-HRP) secondary antibody (1: 5,000 dilution). After rewashing with TBST, the immunoreactivity was observed using ECL reagent. The membranes were scanned by using an imaging system (Bio-Rad, Hercules, CA, United States) and the band strength was analyzed by using ImageJ software (National Institutes of Health, Bethesda, MD, United States).

Statistical Analysis

Date were expressed using the mean ± the standard deviation (SD). SPSS version 21.0 software (IBM, Chicago, IL, United States) was used for statistical analysis. One-way analysis of variance (ANOVA) was used, and p value <0.05 was considered to be statistically significant.

RESULTS

Establishment of CUMS Model and Antidepressant Effects of GH

In the study, CUMS rat model was established according to materials and methods. At the same time, the rats were intragastric administration. The antidepressant effects of GH were evaluated by the behavioral and biochemical indexes.

The results of behavioral indexes of rats in each group were shown in **Figures 2A–F**, the sucrose preference, the crossing score and the rearing score of rats in all groups were basically same at day 0 ($p > 0.05$, $p > 0.05$, $p > 0.05$, respectively). However, the sucrose preference, the crossing score and the rearing score of the CUMS group had a significant decrease compared with the control group at day 35 ($p < 0.01$, $p < 0.01$, $p < 0.01$, respectively). The changes of the sucrose preference, the crossing score and the rearing score of rats are typical characteristics of depression, which indicated that the establishment of depression model was successful. The sucrose preference of rats in low dose group of GH, middle dose group of GH, high dose group of GH, and Flu group were obviously higher than the CUMS group ($p < 0.05$, $p < 0.01$, $p < 0.01$, $p < 0.01$, respectively), showing the significant remission of depression symptoms. In the open field test, the crossing score and the rearing score of CUMS rat treated with middle dose of GH, high dose of GH, and Flu were markedly increased compared with the CUMS group ($p < 0.01$, $p < 0.05$, $p < 0.01$, respectively). However, there was no significant difference in crossing score and rearing score between low dose group of GH and the CUMS group ($p > 0.05$). Taken these results together, GH has antidepressant effects, and the middle dose of GH showed powerfully inhibitory effects on rats with depressant-like behavior induced by CUMS.

The results of biochemical indexes of rats in each group were demonstrated in **Figures 2G–I**. CUMS exposure significantly reduced the concentration of 5-HT, DA and NE ($p < 0.01$, $p < 0.01$, $p < 0.01$, respectively) compared with the control group, which indicated that the establishment of depression model was successful. The treatments with middle dose of GH, high dose of GH, and Flu significantly increased the concentration of 5-HT ($p < 0.01$, $p < 0.05$, $p < 0.01$, respectively), DA ($p < 0.01$, $p < 0.05$, $p < 0.01$, respectively) and NE ($p < 0.01$, $p < 0.05$, $p < 0.01$, respectively) compared with the CUMS group. Meanwhile, the treatments with low dose of GH significantly increased the DA ($p < 0.05$) and NE ($p < 0.05$) concentration compared to the CUMS group. However, low dose of GH had no significant effects on the 5-HT concentration in the CUMS-exposed rats ($p > 0.05$). Overall, the results indicated that middle dose of GH had better antidepressant effects. In the following mechanism verification experiment, the study mainly focused on the treatment group of GH at the middle dose (56 mg/kg).

Identification of Chemical Components in GH by UPLC/IT-TOF MS

The UPLC/IT-TOF conditions was systemically optimized to receive good chromatographic separation and appropriate ionization. The total ion chromatogram (TIC) of the GH sample and mixed standard sample in the positive ion modes are, respectively, presented in **Figures 3A,B**. The 10 chemical components (component 3, 5, 6, 9, 15, 21, 23, 24, 27, 28) were identified as pseudoginsenoside RT5, 20(*S*)-ginsenoside Rh1, 20(*R*)-ginsenoside Rh1, 20(*S*)-ginsenoside F1, ginsenoside Rh4, ginsenoside CK, 20(*S*)-ginsenoside, 20(*R*)-ginsenoside Rh2, ginsenoside Rk2, isoginsenoside Rh3 by comparing the retention time, accurate and high-resolution mass and tandem mass spectra with chemical standards respectively. For the components without chemical standards, the molecular formula was established based on high precision quasi molecular ion such as $[M+H]^+$, $[2M+H]^+$or $[M+Na]^+$ within a mass error of 5.0 ppm. Moreover, the MS^2 information was used for confirming the structures of components by comparing the fragmentation regularity with ten standards or the related literatures (Patel et al., 2012; Zhu et al., 2018). Overall, a total of 28 chemical components were identified in GH and the related information of retention times and MS data was summarized in **Table 1**. The structures of 16 compounds related to 28 chemical components are displayed in **Figure 4**.

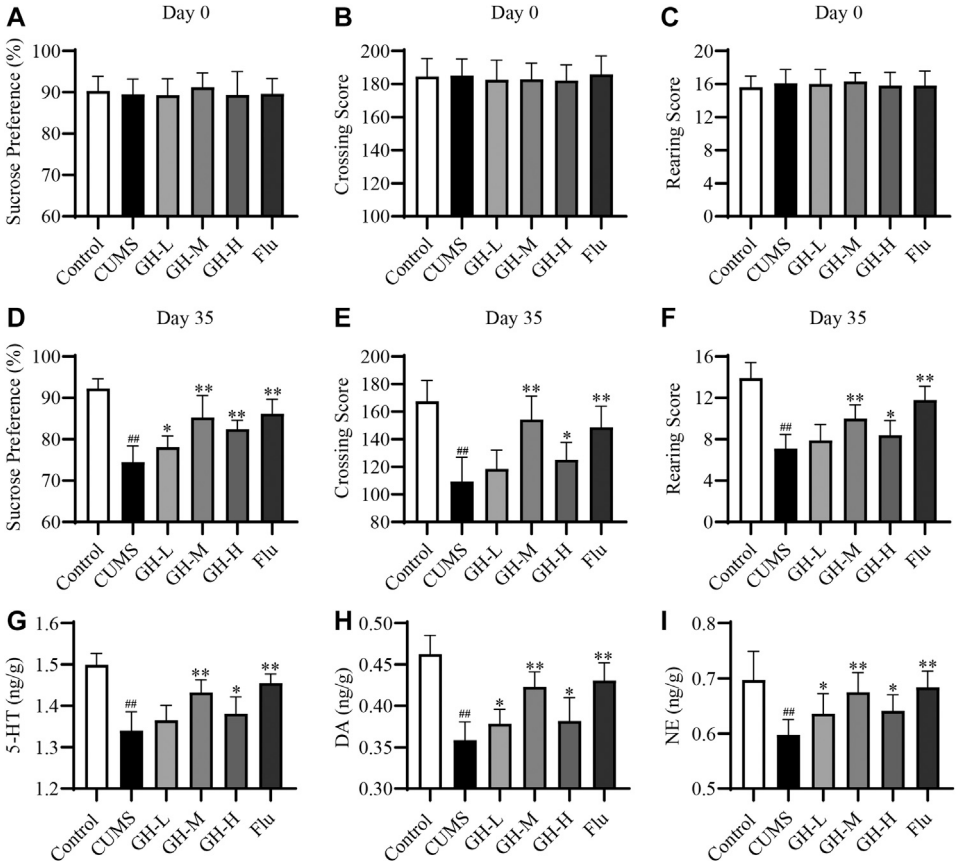

FIGURE 2 | Effect of GH on CUMS rats in SPT, OET and neurotransmitters levels in hippocampus. **(A)** Sucrose preference of rats in each group at day 0. **(B)** Crossing score of rats in each group at day 0. **(C)** Rearing score of rats in each group at day 0. **(D)** Sucrose preference of rats in each group at day 35. **(E)** Crossing score of rats in each group at day 35. **(F)** Rearing score of rats in each group at day 35. **(G)** The concentration of 5-HT in each group. **(H)** The concentration of DA in each group. **(I)** The concentration of NE in each group. All data were expressed as mean ± standard error of mean ($n = 10$). ##$p < 0.01$ versus control group; *$p < 0.05$, *$p < 0.01$ versus CUMS group. GH-L (low dose group of GH), GH-M (middle dose group of GH), GH-H (high dose group of GH).

PPI Network Construction

Among the 16 compounds, only 20(*S*)-ginsenoside Rh2 satisfied the screening rules, OB ≥ 30% and DL ≥ 0.18. So, 20(*S*)-ginsenoside Rh2 was selected as active ingredient. Detailed information about OB and DL of 16 compounds was shown in **Supplementary Table S1**. The structure of 20(*S*)-ginsenoside Rh2 was used for predicting the putative targets in Swiss Target Prediction database. Totally, 43 putative targets of 20(*S*)-ginsenoside Rh2 containing in GH were predicted. Detailed target information about putative targets was shown in **Supplementary Table S2**. A total of 5 and 43 known therapeutic targets for depression were collected from DrugBank and Therapeutic Target Database (TTD) database, respectively, and 184 known targets of depression were obtained from OMIM database. In total, 230 depression candidate targets were enrolled after removing redundant entries. The detailed information is supplemented in **Supplementary Table S3**. The PPI network of the 43 putative targets of 20(*S*)-ginsenoside Rh2 containing in GH and the 230 depression candidate targets, was established based on STRING database, consisting of 184 nodes and 1,392 edges. Detailed information about this network was reflected in **Supplementary Table S4**.

Network and Pathway Analysis

Network analyzer was employed to calculate the topological feature degree of the nodes in the PPI network. Nodes with degrees higher than two-fold median value of all nodes in the network (degree >23) were identified as the major targets. Consequently, 47 major targets were extracted. Among them, 29 targets were putative targets of 20(*S*)-ginsenoside Rh2 containing in GH, 32 targets were depression candidate targets, 15 targets were common targets, which were between putative targets of GH and depression candidate targets. The details were shown in **Supplementary Table S5**.

In order to analyze the representative pathways related to the major targets, KEGG pathway analysis was performed to explore the potential pathways effected by GH and totally 45 significant pathways (p value <0.05) were obtained. The top 10 signal pathways were selected by p value for further study and were as shown in **Figure 5A**. The top 10 significant pathways could be

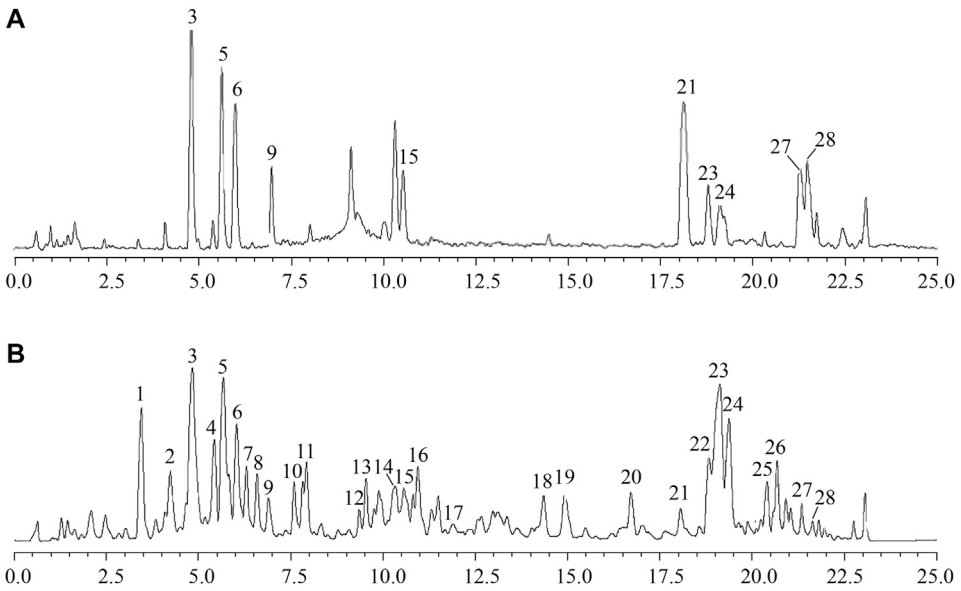

FIGURE 3 | Total ion chromatogram (TIC) of GH sample **(A)** and mixed standard sample **(B)** in positive ion mode using UPLC/IT-TOF MS.

divided into three functional modules, which were related to dopamine, hypothalamic-pituitary-adrenal (HPA) axis and neural plasticity respectively. Detailed information about results of pathways analysis was provided in **Supplementary Table S6**. Afterward a network consisted of the interactions between the active ingredient of GH, major targets, and top 10 significant pathways was constructed to illustrate the potential mechanism (**Figure 5B**). This network illustrated that GH may indirectly influence or directly interact with major targets which are involved in pathways related to HPA axis (such as pathways in cancer, proteoglycans in cancer), dopamine (such as neuroactive ligand-receptor interaction, cocaine addiction, dopaminergic synapse) and neural plasticity (such as cAMP signaling pathway, glutamatergic synapse, gap junction, PI3K-Akt signaling pathway and estrogen signaling pathway) to achieve the antidepressant effects.

Experimental Validation of Major Targets and Pathway

To explore the effects of GH on the cAMP pathway, we examined the concentration of cAMP via ELISA, PKA activity using a radioactive PKA assay kit, and protein expression levels of BDNF, CREB, *p*-CREB in the hippocampus of each group rats by Western blot (**Figure 6**). Compared with the control group, a significant decrease in cAMP concentration and PKA activity was observed in the hippocampus of the CUMS group ($p < 0.01$, $p < 0.01$, respectively), but daily administration of GH (56 mg/kg) or fluoxetine (10 mg/kg) obviously increased cAMP concentration and PKA activity in the hippocampus ($p < 0.01$, $p < 0.01$, respectively) compared with the CUMS rats. Meanwhile, BDNF expression levels and the *p*-CREB/CREB ratio in the hippocampus of the CUMS group were decreased ($p < 0.01$, $p < 0.01$, respectively). Following treatment with GH (56 mg/kg) or fluoxetine (10 mg/kg), BDNF expression levels and the *p*-CREB/CREB ratio in the GH and Flu groups were significantly higher than the CUMS group ($p < 0.01$, $p < 0.01$, respectively), suggesting that GH may regulate the cAMP-PKA-CREB-BDNF signal pathway to play an antidepressant role.

DISCUSSION

Depression is a mental disease characterized by constant low mood, loss of interest, anhedonia, unresponsiveness and sleeplessness (Wang et al., 2017). The causes of depression are complex, among which the increasing competitive pressure, unreasonable living habits and weak adaptability to the social environment are more crucial inducing factors (Wang et al., 2020). The CUMS is a mature animal model of depression that can simulate the chronic stress encountered by depressed patients in clinical observation (Yang et al., 2018). Currently, the widely used assays for depressive-like behaviors include the Sucrose preference test (SPT) and the Open field test (OFT). The SPT could mimic anhedonia-like behavior, a core symptom of depression in human (Sideromenos et al., 2020), and the OFT was used to determine general activity and exploratory behavior, signs of depression (Adelöf et al., 2018). Thus, the study established CUMS rat model and conducted a series of behavioral tests, including SPT and OFT, to study the effects of GH on antidepressant-like behaviors. The results of behavioral indexes of rats in each group indicated that GH has antidepressant effects, and the middle dose of GH showed powerfully inhibitory effects on rats with depressant-like behavior induced by CUMS.

TABLE 1 | Identification of chemical components in GH sample by UPLC/IT-TOF in positive ion mode.

No	tR (min)	Formula	Ion model	Theoretical mass	Measured mass	Error (ppm)	MS^2	Components
1	3.429	$C_{30}H_{54}O_6$	$[M+H]^+$ $[M+Na]^+$	511.3993,533.3813	511.3958,533.3778	−3.5–3.5	493.3876 $[M+H-H_2O]^+$ 475.3807 $[M+H-2H_2O]^+$ 457.3691 $[M+H-3H_2O]^+$ 439.3573 $[M+H-4H_2O]^+$ 421.3460 $[M+H-5H_2O]^+$	Unknown
2	4.206	$C_{36}H_{62}O_{10}$	$[M+H]^+$	655.4416	655.4391	−2.5	637.4292 $[M+H-H_2O]^+$ 619.4224 $[M+H-2H_2O]^+$ 475.3783 $[M+H-H_2O\text{-glc}]^+$ 457.3664 $[M+H-2H_2O\text{-glc}]^+$ 439.3567 $[M+H-3H_2O\text{-glc}]^+$ 421.3459 $[M+H-4H_2O\text{-glc}]^+$	Pseudoginsenoside RT_4
3[a]	4.838	$C_{36}H_{62}O_{10}$	$[M+H]^+$ $[M+Na]^+$	655.4416,677.4235	655.4390,677.4200	−2.6–3.5	457.3648 $[M+H-2H_2O\text{-glc}]^+$ 439.3565 $[M+H-3H_2O\text{-glc}]^+$ 421.3458 $[M+H-4H_2O\text{-glc}]^+$	Pseudoginsenoside RT_5
4	5.402	$C_{36}H_{62}O_9$	$[M+H]^+$	639.4467	639.4463	−0.4	603.4249 $[M+H-2H_2O]^+$ 441.3694 $[M+H-2H_2O\text{-glc}]^+$ 423.3608 $[M+H-3H_2O\text{-glc}]^+$ 405.3521 $[M+H-4H_2O\text{-glc}]^+$	Isomer of ginsenoside Rh_1
5[a]	5.655	$C_{36}H_{62}O_9$	$[M+Na]^+$	661.4286	661.4274	−1.2	621.4345 $[M+H-H_2O]^+$ 603.4256 $[M+H-2H_2O]^+$ 477.3926 $[M+H\text{-glc}]^+$ 441.3687 $[M+H-2H_2O\text{-glc}]^+$ 423.3604 $[M+H-3H_2O\text{-glc}]^+$ 405.3518 $[M+H-4H_2O\text{-glc}]^+$	20(*S*)-ginsenoside Rh_1
6[a]	5.799	$C_{36}H_{62}O_9$	$[M+Na]^+$	661.4286	661.4273	−1.3	621.4348 $[M+H-H_2O]^+$ 603.4248 $[M+H-2H_2O]^+$ 477.3911 $[M+H\text{-glc}]^+$ 441.3699 $[M+H-2H_2O\text{-glc}]^+$ 423.3612 $[M+H-3H_2O\text{-glc}]^+$ 405.3519 $[M+H-4H_2O\text{-glc}]^+$	20(*R*)- ginsenoside Rh_1
7	6.268	$C_{36}H_{62}O_9$	$[M+Na]^+$	661.4286	661.4275	−1.1	621.4347 $[M+H-H_2O]^+$ 603.4254 $[M+H-2H_2O]^+$ 441.3694 $[M+H-2H_2O\text{-glc}]^+$ 423.3606 $[M+H-3H_2O\text{-glc}]^+$ 405.3512 $[M+H-4H_2O\text{-glc}]^+$	Isomer of ginsenoside Rh_1
8	6.566	$C_{36}H_{60}O_9$	$[M+H]^+$	637.4310	637.4283	−2.7	619.4206 $[M+H-H_2O]^+$ 457.3651 $[M+H-H_2O\text{-glc}]^+$ 439.3557 $[M+H-2H_2O\text{-glc}]^+$ 421.3463 $[M+H-3H_2O\text{-glc}]^+$ 403.3338 $[M+H-4H_2O\text{-glc}]^+$	Ginsenoside Rh_5
9[a]	6.875	$C_{36}H_{62}O_9$	$[M+H]^+$	639.4467	639.4446	−2.1	621.4326 $[M+H-H_2O]^+$ 441.3684 $[M+H-2H_2O\text{-glc}]^+$ 423.3609 $[M+H-3H_2O\text{-glc}]^+$	20(*S*)- ginsenoside F_1
10	7.562	$C_{36}H_{60}O_9$	$[M+H]^+$	637.4310	637.4297	−1.3	619.4240 $[M+H-H_2O]^+$ 457.3703 $[M+H-H_2O\text{-glc}]^+$ 439.3581 $[M+H-2H_2O\text{-glc}]^+$ 421.3461 $[M+H-3H_2O\text{-glc}]^+$	Ginsenoside Rh_7/Rh_8/Rh_9
11	7.793	$C_{36}H_{60}O_9$	$[M+H]^+$	637.4310	637.4292	−1.8	619.4221 $[M+H-H_2O]^+$ 457.3666 $[M+H-H_2O\text{-glc}]^+$ 439.3565 $[M+H-2H_2O\text{-glc}]^+$ 421.3457 $[M+H-3H_2O\text{-glc}]^+$	Ginsenoside Rh_7/Rh_8/Rh_9
12	9.327	$C_{36}H_{60}O_8$	$[M+H]^+$	621.4361	621.4349	−1.2	603.4246 $[M+H-H_2O]^+$ 441.3687 $[M+H-H_2O\text{-glc}]^+$ 423.3622 $[M+H-2H_2O\text{-glc}]^+$ 405.3535 $[M+H-3H_2O\text{-glc}]^+$	Ginsenoside Rh_4/Rk_3 or its isomer
13	9.517	$C_{36}H_{60}O_8$	$[M+Na]^+$	643.4180	643.4183	0.3	603.4253 $[M+H-H_2O]^+$ 441.3695 $[M+H-H_2O\text{-glc}]^+$ 423.3614 $[M+H-2H_2O\text{-glc}]^+$ 405.3521 $[M+H-3H_2O\text{-glc}]^+$	Ginsenoside Rh_4/Rk_3 or its isomer
14	10.321	$C_{36}H_{60}O_8$	$[M+H]^+$	621.4361	621.4380	1.9	441.3703 $[M+H-H_2O\text{-glc}]^+$ 423.3613 $[M+H-2H_2O\text{-glc}]^+$ 405.3521 $[M+H-3H_2O\text{-glc}]^+$	Ginsenoside Rh_4/Rk_3 or its isomer
15[a]	10.547	$C_{36}H_{60}O_8$	$[M+H]^+$	621.4361	621.4326	−3.5	603.4245 $[M+H-H_2O]^+$ 441.3698 $[M+H-H_2O\text{-glc}]^+$ 423.3612 $[M+H-2H_2O\text{-glc}]^+$ 405.3515 $[M+H-3H_2O\text{-glc}]^+$ 341.2817 $[2glc+H_2O-H]^+$	Ginsenoside Rh_4
16	10.924	$C_{36}H_{60}O_8$	$[M+H]^+$	621.4361	621.4342	−1.9	603.4233 $[M+H-H_2O]^+$ 441.3699 $[M+H-H_2O\text{-glc}]^+$ 423.3612 $[M+H-2H_2O\text{-glc}]^+$ 405.3510 $[M+H-3H_2O\text{-glc}]^+$ 343.2977 $[2glc+H_2O+H]^+$ 325.2893 $[2glc+H]^+$	Ginsenoside Rh_4/Rk_3 or its isomer
17	11.866	$C_{36}H_{62}O_8$	$[M+H]^+$	623.4517	623.4485	−3.2	605.4379 $[M+H-H_2O]^+$ 587.4325 $[M+H-2H_2O]^+$ 443.3880 $[M+H-H_2O\text{-glc}]^+$ 425.3761 $[M+H-2H_2O\text{-glc}]^+$ 407.3653 $[M+H-3H_2O\text{-glc}]^+$	Isomer of ginsenoside Rh_2
18	14.333	$C_{36}H_{62}O_8$	$[M+H]^+$	623.4517	623.4484	−3.3	605.4428 $[M+H-H_2O]^+$ 587.4309 $[M+H-2H_2O]^+$ 425.3758 $[M+H-2H_2O\text{-glc}]^+$	Isomer of ginsenoside Rh_2

(Continued on following page)

TABLE 1 | (*Continued*) Identification of chemical components in GH sample by UPLC/IT-TOF in positive ion mode.

No	tR (min)	Formula	Ion model	Theoretical mass	Measured mass	Error (ppm)	MS^2	Components
19	14.912	$C_{36}H_{60}O_8$	$[M+H]^+$	621.4361	621.4331	−3.0	603.4266 $[M+H-H_2O]^+$ 585.4148 $[M+H-2H_2O]^+$ 441.3716 $[M+H-H_2O\text{-glc}]^+$ 423.3611 $[M+H-2H_2O\text{-glc}]^+$ 405.3511 $[M+H-3H_2O\text{-glc}]^+$	Ginsenoside Rh_4/Rk_3 or its isomer
20	16.699	$C_{36}H_{60}O_8$	$[M+H]^+$	621.4361	621.4345	−1.6	603.4254 $[M+H-H_2O]^+$ 585.4178 $[M+H-2H_2O]^+$ 441.3703 $[M+H-H_2O\text{-glc}]^+$ 423.3614 $[M+H-2H_2O\text{-glc}]^+$ 405.3509 $[M+H-3H_2O\text{-glc}]^+$	Ginsenoside Rh_4/Rk_3 or its isomer
21[a]	18.035	$C_{36}H_{62}O_8$	$[M+H]^+$ $[M+Na]^+$	623.4517,645.4337	623.4482,645.4407	−3.5 7.0	605.4400 $[M+H-H_2O]^+$ 587.4305 $[M+H-2H_2O]^+$ 443.3866 $[M+H-H_2O\text{-glc}]^+$ 425.3755 $[M+H-2H_2O\text{-glc}]^+$ 407.3670 $[M+H-3H_2O\text{-glc}]^+$	Ginsenoside CK
22	18.809	$C_{36}H_{62}O_8$	$[2M+H]^+$	1,245.8962	1,245.8940	−2.2	587.4286 $[M+H-2H_2O]^+$ 425.3749 $[M+H-2H_2O\text{-glc}]^+$ 407.3656 $[M+H-3H_2O\text{-glc}]^+$	Isomer of ginsenoside Rh_2
23[a]	19.127	$C_{36}H_{62}O_8$	$[M+Na]^+$ $[2M+H]^+$	645.4337 1,245.8962	645.4323 1,245.8922	−1.4–4.0	605.4396 $[M+H-H_2O]^+$ 587.4279 $[M+H-2H_2O]^+$ 425.3741 $[M+H-2H_2O\text{-glc}]^+$ 407.3661 $[M+H-3H_2O\text{-glc}]^+$	20(*S*)-ginsenoside Rh_2
24[a]	19.367	$C_{36}H_{62}O_8$	$[M+Na]^+$ $[2M+H]^+$	645.4337 1,245.8962	645.4333 1,245.8895	−0.4–6.7	605.4403 $[M+H-H_2O]^+$ 587.4296 $[M+H-2H_2O]^+$ 425.3751 $[M+H-2H_2O\text{-glc}]^+$ 407.3652 $[M+H-3H_2O\text{-glc}]^+$	20(*R*)-ginsenoside Rh_2
25	20.349	$C_{36}H_{62}O_8$	$[M+Na]^+$	645.4337	645.4316	−2.1	605.4405 $[M+H-H_2O]^+$ 587.4301 $[M+H-2H_2O]^+$ 443.3876 $[M+H-H_2O\text{-glc}]^+$ 425.3750 $[M+H-2H_2O\text{-glc}]^+$ 407.3667 $[M+H-3H_2O\text{-glc}]^+$	Isomer of ginsenoside Rh_2
26	20.659	$C_{36}H_{62}O_8$	$[2M+H]^+$	1,245.8962	1,245.8914	−4.8	587.4309 $[M+H-2H_2O]^+$ 443.3858 $[M+H-H_2O\text{-glc}]^+$ 425.3751 $[M+H-2H_2O\text{-glc}]^+$ 407.3648 $[M+H-3H_2O\text{-glc}]^+$	Isomer of ginsenoside Rh_2
27[a]	21.328	$C_{36}H_{60}O_7$	$[M+H]^+$	605.4412	605.4398	−1.4	587.4308 $[M+H-H_2O]^+$ 543.4216 $[M+H-H_2O\text{-}CO_2]^+$ 443.3841 $[M+H\text{-glc}]^+$ 425.3750 $[M+H-H_2O\text{-glc}]^+$ 407.3655 $[M+H-2H_2O\text{-glc}]^+$	Ginsenoside Rk_2
28[a]	21.547	$C_{36}H_{60}O_7$	$[M+Na]^+$	605.4412	605.4426	1.4	587.4328 $[M+H-H_2O]^+$ 425.3748 $[M+H-H_2O\text{-glc}]^+$ 407.3657 $[M+H-2H_2O\text{-glc}]^+$	Isoginsenoside Rh_3

[a]*Accurately identified with reference standards.*

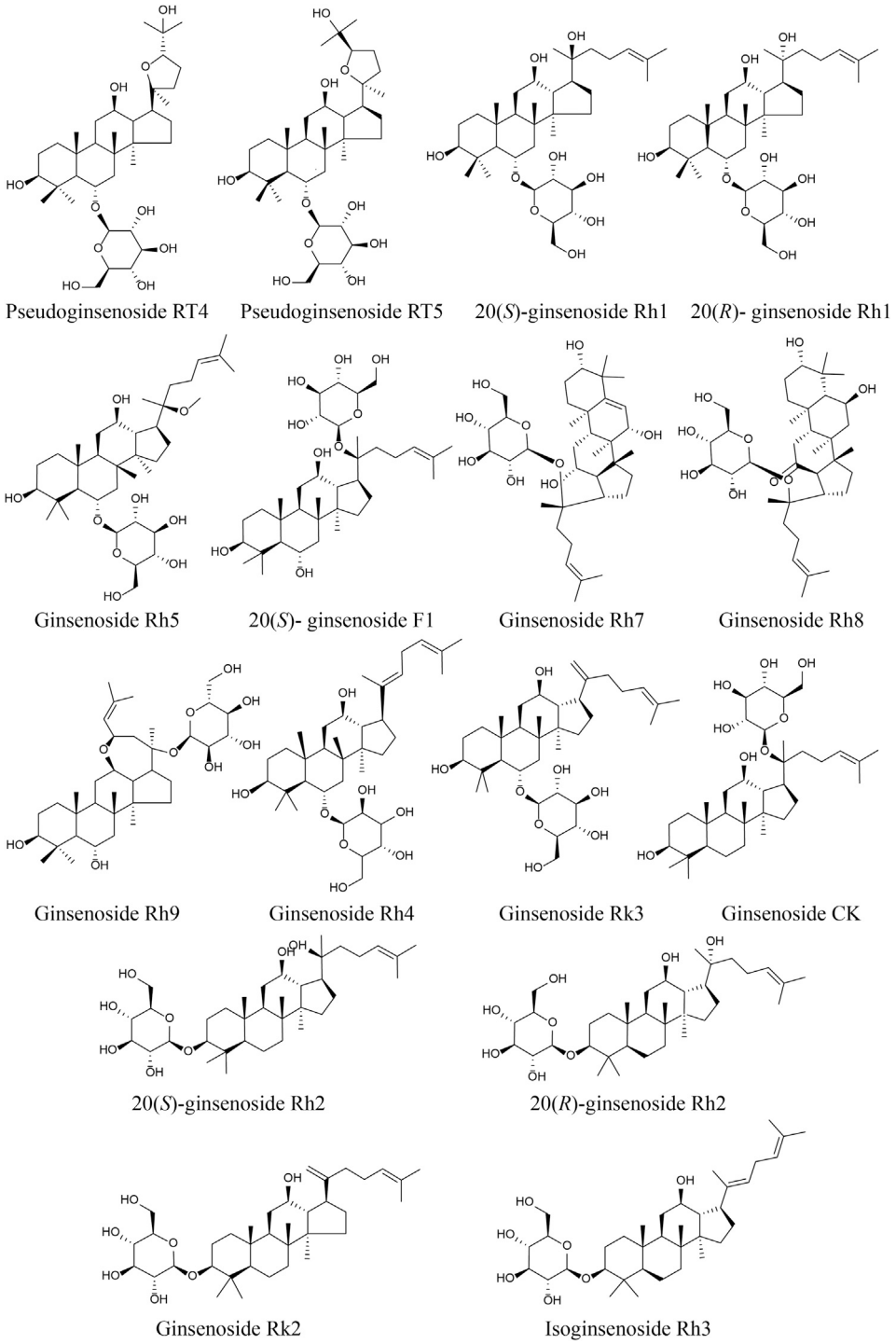

FIGURE 4 | Structures of compounds in GH.

Based on the characteristics of multi-channel and multi-target effects of Chinese herbal compound, the monoamine neurotransmitters such as DA, NE and 5-HT were regarded as the biochemical indexes to further study the antidepressant effects of GH (Gu et al., 2018). The monoamine hypothesis believes that the deficiency of major monoamine neurotransmitters (5-HT, DA, and NE) will lead to decrease of neurotransmission in the brain and the impairment of cognitive

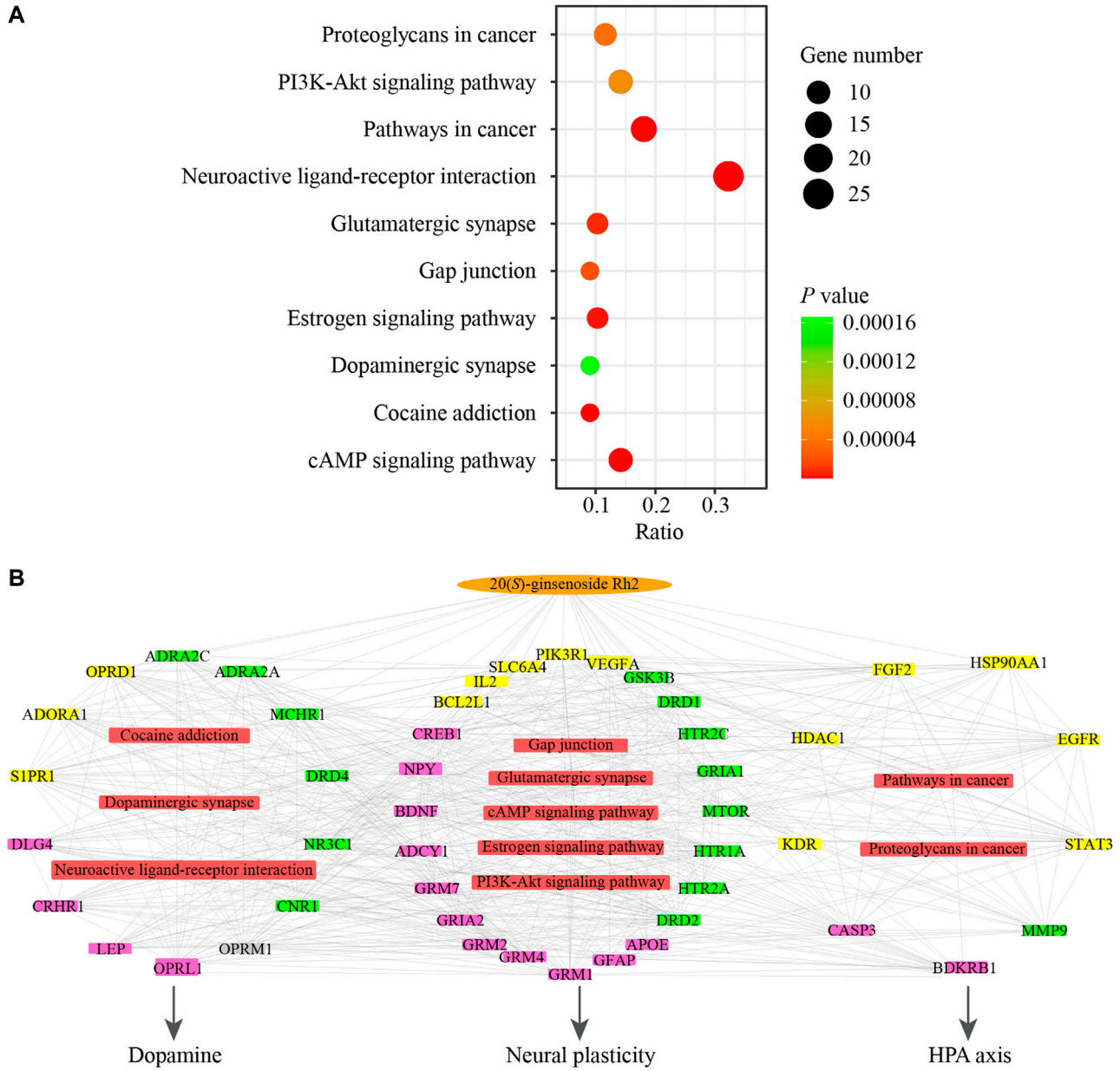

FIGURE 5 | The network pharmacological results associating with GH in the treatment of depression. **(A)** KEGG pathway analysis of major targets. X-axis shows ratio and Y-axis shows involved pathways. Count and P value are shown on right. **(B)** Network of active ingredient in GH, major targets, the corresponding pathways and pharmagological effects. Orange oval nodes represent active ingredient in GH, yellow rectangle nodes represent related major targets of active ingredient in GH, pink rectangle nodes represent related major targets of depression, green rectangle nodes represent common major targets for both GH and depression, grey rectangle node represents other target, red rectangle nodes represent involved pathways from enrichment analysis of major targets, edges represent interactions among them.

performance which may lead to depression (Kofler et al., 2019). Therefore, this study established a CUMS rat model for five weeks to observe the effects of GH intervention on the depressive-like behaviors and the changes of the monoamine neurotransmitters levels in the hypothalamus. The results of biochemical indexes of rats in each group indicated that GH has antidepressant effects, and middle dose of GH had stronger antidepressant effect. In the following mechanism verification experiment, the study mainly focused on the treatment group of GH at the middle dose (56 mg/kg).

Chromatographic techniques coupled with mass spectrometry has been an available method for rapid identification of components in Chinese medicine (Guo et al., 2018). UPLC/IT-TOF MS analysis was performed to identify the chemical components in GH. In this study, the 28 chemical components of GH were identified. Among the chemical

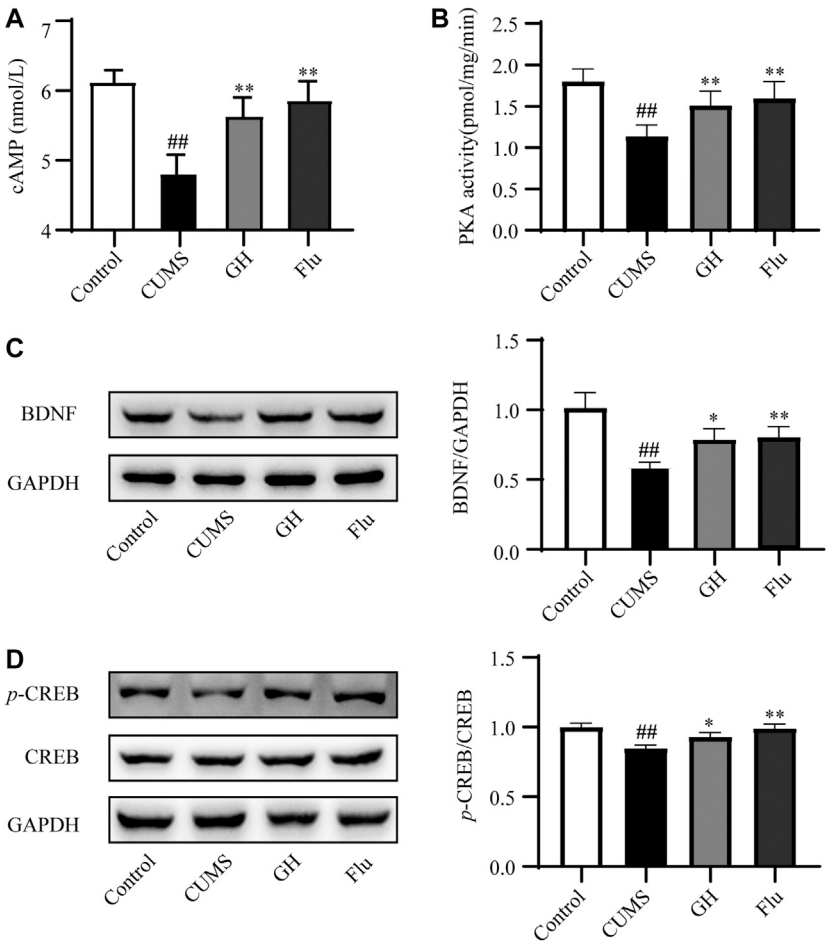

FIGURE 6 | Experimental validation of target proteins involved in cAMP signaling pathway in the hippocampus of CUMS-induced rats. **(A)** Effect of GH treatment on cAMP concentrations (n = 10). **(B)** Effect of GH treatment on PKA activity (n = 10). **(C)** Effect of GH treatment on BDNF expression. **(D)** Effect of GH treatment on p-CREB/CREB ratio. All data were expressed as mean ± standard error of mean. ##p < 0.01 versus control group; *p < 0.05, **p < 0.01 versus CUMS group.

components, only 20(*S*)-ginsenoside Rh2 was selected as active ingredient which satisfied the screening rules, OB ≥ 30% and DL ≥ 0.18. It is consistent with previous studies that ginsenoside Rh2, a main component in GH (Zhou et al., 2014), was a detectable compound in human plasma (Yue et al., 2019), and it can be filtered out by cell membrane chromatography (Ma et al., 2018).

To investigate the pharmacological mechanism of antidepressant effects of GH, 20(*S*)- ginsenoside Rh2, the active ingredient of GH, was used for network pharmacological analysis, and the top 10 significant signaling pathways were enriched by KEGG according to the *p* value. Based on literature search, the top 10 significant signaling pathways could involve in the occurrence of depression in varying degrees. For example, pathways in cancer and proteoglycans in cancer indirectly change the probability of depression by influencing HPA axis function (Young and Singh, 2018); Neuroactive ligand-receptor interaction, cocaine addiction and dopaminergic synapse could affect the occurrence of depression through regulating dopamine levels, emotion, learning and memory functions (Haile et al., 2007; Yang et al., 2017; Sun et al., 2018); cAMP signaling pathway, PI3K-Akt signaling pathway, estrogen signaling pathway, glutamatergic synapse and gap junction could intervene the occurrence of depression by mediating neural plasticity (Hennebelle et al., 2014; Crider and Pillai, 2017; Peng et al., 2018; Ren et al., 2018; Wu et al., 2018).

At present, the antidepressant mechanism of GH is unknown. Among the top 10 signaling pathways predicted by network pharmacological, the signaling pathway ranking at the top had strong correlation with the antidepressant effects of GH, which is the main signaling pathway of the antidepressant mechanism of GH. Therefore, the signaling pathway ranking at the top has more research value (Xiong et al., 2020). The first signaling pathway is neuroactive ligand-receptor interaction, which was related to all receptors and ligands associated with intracellular and extracellular signaling pathways in the plasma membrane (Pan et al., 2011). However, the neuroactive ligand-receptor interaction signaling pathway was related to the occurrence of various diseases, the mechanism of action on depression is not

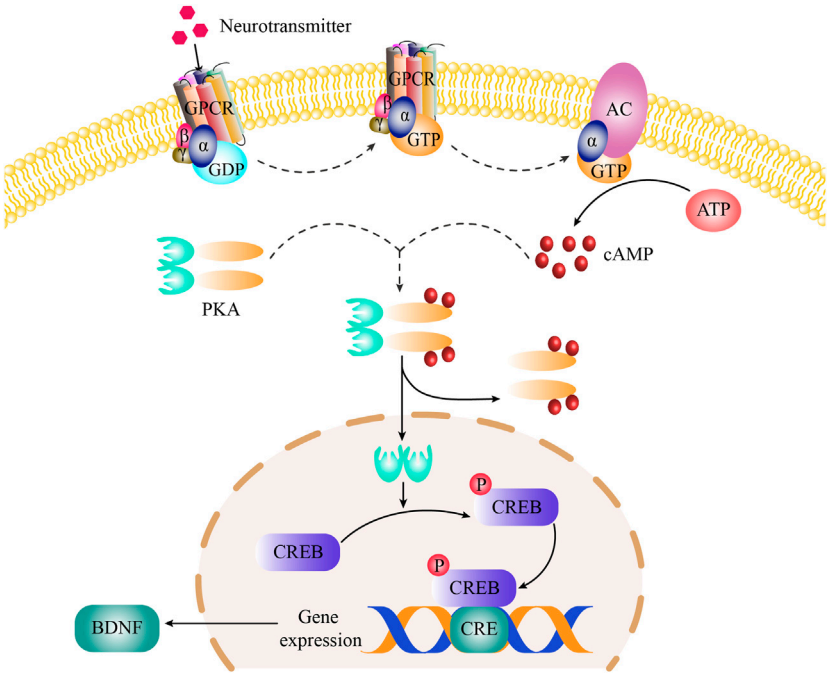

FIGURE 7 | The cAMP-PKA-CREB-BDNF signaling pathway.

specific, and there are only two targets of receptor and ligand. Consequently, the first signaling pathway was not selected to further research. The second signaling pathway is cAMP signaling pathway, which was the most widely studied signaling pathway in the mechanism of antidepressant effects. In the cAMP signaling pathway, BDNF, the terminal downstream protein neurotrophic factor, could resist the damage of neurons, promote the repair and regeneration of neurons, and increased the secretion of monoamine neurotransmitters. Hence, Stress events compromise neuroplasticity via reduction of BDNF and lead to the occurrence of depression (Schmitt et al., 2016). According to the literature, neuroimaging and post-mortem studies have revealed impaired cAMP signaling in depressive patients, indicating cAMP signaling pathway was significantly associated with depression (Plattner et al., 2015). Thus, cAMP signaling pathway is selected to study the antidepressant mechanism of GH.

It is extremely clear that the mechanism of the cAMP signal pathway on depression. Under normal physiological conditions, monoamine neurotransmitters (such as 5-HT, DA, NE) interacts with specific G protein-coupled receptors (including 5-HT receptors, DA receptors, NE receptors) on the cell membrane to activate G protein (Cabrera-Vera et al., 2003; Fredriksson et al., 2003). The G-protein binds to Guanosine triphosphate (GTP) and subsequently GTP-G protein binds to the C2 domain and activates the adenylate cyclase (AC) enzyme. Activated AC catalyzes the biosynthesis of cAMP from adenosine triphosphate (ATP) (Frezza et al., 2018). The cAMP binds to the regulatory subunits of PKA (a tetramer consists of two regulatory subunits and two catalytic subunits), which resulted in the dissociation of catalytic subunit of PKA and enter to the cell nucleus (Wang et al., 2018). In the nucleus, the catalytic subunit of PKA binds to the Ser-133 site of CREB and phosphorylates CREB (Tu et al., 2019). Phosphorylated CREB (*p*-CREB) combines with the cAMP responsive elements (CRE) in the promoter region of BDNF, which can regulate BDNF transcription (Björkholm and Monteggia, 2016). Under the pathological conditions, continuous mental stress and stimulation would lead to the decrease in the content of monoamine neurotransmitters in the patient's body and weaken the transduction of cAMP signaling pathway, which cause the decrease of BDNF expression (Zhang et al., 2012). Lower expression of BDNF is difficult to resist the injury of neurons under stress, which could lead to depression (van den Buuse et al., 2020).

In cAMP signaling pathway, 11 target proteins, such as BDNF, GRIA1, CREB1, ADORA1 and so on, were enriched. The high-degree target proteins in the network may account for the essential therapeutic effects of GH on depression (Guo et al., 2019). The degree value of BDNF is the largest, indicating that BDNF is the most important in cAMP signaling pathway. BDNF is related to the survival, growth, and differentiation of neurons, and plays an important role in the signal transduction of depression (Wang et al., 2017). As the upstream protein of BDNF, *p*-CREB could regulate the expression of BDNF. At the same time, CREB has been confirmed to be related to the pathogenesis of depression and is one of the transcription factors with the most research on antidepressant effects (Wang et al., 2018). Therefore, Western blot was used to determine the expression level of BDNF and the ratio of *p*-CREB/CREB to study the antidepressant mechanism of GH. The results showed that GH significantly increased the expression level of BDNF and the

ratio of *p*-CREB/CREB in the hippocampus of CUMS model rats. In order to further study the antidepressant mechanism of GH, the radioactive PKA assay kit was used to assay the activity of PKA which is the upstream protein of CREB. ELISA was used to detect the contents of cAMP which is the activator of PKA. As shown in our results, GH significantly upregulated the activity of PKA and the content of cAMP in hippocampus of CUMS model rats. Therefore, GH may play an antidepressant effects by regulating cAMP-PKA-CREB-BDNF signaling transduction. The cAMP-PKA-CREB-BDNF signaling pathway was presented in **Figure 7**.

Fluoxetine, a serotonin reuptake inhibitor (SSRI), is mainly used in the treatment of depression in clinic, which can improve the content of 5-HT. The 5-HT combined with its receptors, which resulted in that the cAMP signal pathway is activated and the levels of cAMP, PKA and the ratio of *p*-CREB/CREB were increased (Mato et al., 2010; Zhang et al., 2018). Then the expression level of BDNF is increased, which resisted the injury of neurons under stress, and exert antidepressant effects (Xie et al., 2019). During this process, BDNF increased the content of monoamine neurotransmitters by improving the activity of dopaminergic neurons and noradrenergic neurons, which is more conducive to play an antidepressant effects (Siuciak et al., 1996; Zhang et al., 2007), Therefore, fluoxetine was selected as a positive drug to explore whether GH exerts antidepressant effects by activating the cAMP signal pathway. The results indicated that GH could activate cAMP signaling pathway to play an antidepressant role, but whether it has the same antidepressant mechanism as fluoxetine through increasing 5-HT content and activating cAMP signaling pathway remains to be further studied.

CONCLUSION

In the present study, an integrative pharmacology-based pattern, which adopted pharmacodynamics-network pharmacology-mechanism verification, was used to uncover the pharmacological mechanism of GH against depression. Firstly, it was found that GH at the middle dose (56 mg/kg) obviously alleviated depression-like behaviors induced by CUMS and showed powerful antidepressant effects. Then, we identified 28 main chemical components of GH by UPLC/IT-TOF MS. Furthermore, network pharmacology analysis predicted that cAMP signaling pathway may be the potential pharmacological mechanism regulated by GH acting on depression. Finally, the cAMP signaling pathway was verified as the mechanism of GH against depression through experimental validation of the target proteins (cAMP, PKA, *p*-CREB, and BDNF). Taken together, the current study suggested that GH could exert antidepressant effects by activating the cAMP-PKA-CREB-BDNF signaling pathway in hippocampus, which provided an effective method to uncover the pharmacological mechanism of traditional Chinese medicine.

DATA AVAILABILITY STATEMENT

The raw data supporting the conclusions of this article will be made available by the authors, without undue reservation, to any qualified researcher.

ETHICS STATEMENT

The animal study was reviewed and approved by Tianjin University of Traditional Chinese Medicine Animal Care Committee.

AUTHOR CONTRIBUTIONS

LZ performed the experiments, drafted and modified the manuscript. RG, NC, YL, and XM analyzed the data and modified the manuscript. SP and WY prepared the materials of the paper. YZ, YL, and ZS conceived or designed the studies. WD, XX, and CL contributed to research design, experimental setup, results monitoring, and manuscript correction. All the authors read and approved the final manuscript.

FUNDING

The research was supported by the National Natural Science Foundation of China (81973557), Natural Science Fund of Tianjin City (20JCZDJC00010), and the National Major Scientific and Technological Special Project of China (2018ZX09303-024, 2018ZX09737-019).

ACKNOWLEDGMENTS

The authors would like to acknowledge the technical supports to Pengwei Zhuang from Tianjin University of Traditional Chinese Medicine.

SUPPLEMENTARY MATERIAL

The Supplementary Material for this article can be found online at: https://www.frontiersin.org/articles/10.3389/fphar.2020.590457/full#supplementary-material.

REFERENCES

Adelöf, J., Andersson, M., Porritt, M., Petersen, A., Zetterberg, M., Wiseman, J., et al. (2018). PA28αβ overexpression enhances learning and memory of female mice without inducing 20S proteasome activity. *BMC Neurosci.* 19, 70. doi:10.1186/s12868-018-0468-2

Antoniuk, S., Bijata, M., Ponimaskin, E., and Wlodarczyk, J. (2019). Chronic unpredictable mild stress for modeling depression in rodents: meta-analysis of

model reliability. *Neurosci. Biobehav. Rev.* 99, 101–116. doi:10.1016/j.neubiorev.2018.12.002

Auclair, A. L., Martel, J. C., Assié, M. B., Bardin, L., Heusler, P., Cussac, D., et al. (2013). Levomilnacipran (F2695), a norepinephrine-preferring SNRI: profile *in vitro* and in models of depression and anxiety. *Neuropharmacology* 70, 338–347. doi:10.1016/j.neuropharm.2013.02.024

Björkholm, C., and Monteggia, L. M. (2016). BDNF–a key transducer of antidepressant effects. *Neuropharmacology* 102, 72–79. doi:10.1016/j.neuropharm.2015.10.034

Cabrera-Vera, T. M., Vanhauwe, J., Thomas, T. O., Medkova, M., Preininger, A., Mazzoni, M. R., et al. (2003). Insights into G protein structure, function, and regulation. *Endocr. Rev.* 24, 765–781. doi:10.1210/er.2000-0026

Chen, F., Li, X., Wang, J., Ma, X., Song, Z., Sun, L., et al. (2018). Combination of Ginsenoside H dripping pills and cyclophosphamide improve paraneoplastic syndrome and inhibit postoperative recurrence via the reversion of Th1/Th2 shift. *Biomed. Pharmacother.* 108, 865–875. doi:10.1016/j.biopha.2018.09.085

Chen, P.-J., Hsieh, C.-L., Su, K.-P., Hou, Y.-C., Chiang, H.-M., Lin, I.-H., et al. (2008). The antidepressant effect of Gastrodia elata Bl. on the forced-swimming test in rats. *Am. J. Chin. Med.* 36, 95–106. doi:10.1142/s0192415x08005618

Crider, A., and Pillai, A. (2017). Estrogen signaling as a therapeutic target in neurodevelopmental disorders. *J. Pharmacol. Exp. Therapeut.* 360, 48–58. doi:10.1124/jpet.116.237412

Dai, Y., Li, Z., Xue, L., Dou, C., Zhou, Y., Zhang, L., et al. (2010). Metabolomics study on the anti-depression effect of xiaoyaosan on rat model of chronic unpredictable mild stress. *J. Ethnopharmacol.* 128, 482–489. doi:10.1016/j.jep.2010.01.016

Daina, A., and Zoete, V. (2019). Application of the SwissDrugDesign online resources in virtual screening. *Int. J. Mol. Sci.* 20, 4612. doi:10.3390/ijms20184612

Du, H.-G., Ming, L., Chen, S. J., and Li, C. D. (2014). Xiaoyao pill for treatment of functional dyspepsia in perimenopausal women with depression. *World J. Gastroenterol.* 20, 16739–16744. doi:10.3748/wjg.v20.i44.16739

Fredriksson, R., Lagerström, M. C., Lundin, L.-G., and Schiöth, H. B. (2003). The G-protein-coupled receptors in the human genome form five main families. phylogenetic analysis, paralogon groups, and fingerprints. *Mol. Pharmacol.* 63, 1256–1272. doi:10.1124/mol.63.6.1256

Frezza, E., Martin, J., and Lavery, R. (2018). A molecular dynamics study of adenylyl cyclase: the impact of ATP and G-protein binding. *PLoS One* 13, e0196207. doi:10.1371/journal.pone.0196207

Fu, J., Zhang, Y., Wu, R., Zheng, Y., Zhang, X., Yang, M., et al. (2014). Shuganjieyu capsule increases neurotrophic factor expression in a rat model of depression. *Neural Regen. Res.* 9, 489–497. doi:10.4103/1673-5374.130067

Götze, H., Friedrich, M., Taubenheim, S., Dietz, A., Lordick, F., and Mehnert, A. (2020). Depression and anxiety in long-term survivors 5 and 10 years after cancer diagnosis. *Support. Care Canc.* 28, 211–220. doi:10.1007/s00520-019-04805-1

Gorzalka, B. B., and Hill, M. N. (2011). Putative role of endocannabinoid signaling in the etiology of depression and actions of antidepressants. *Prog. Neuro Psychopharmacol. Biol. Psychiatr.* 35, 1575–1585. doi:10.1016/j.pnpbp.2010.11.021

Gu, S., Jing, L., Li, Y., Huang, J. H., and Wang, F. (2018). Stress induced hormone and neuromodulator changes in menopausal depressive rats. *Front. Psychiatr.* 9, 253. doi:10.3389/fpsyt.2018.00253

Guo, M.-F., Dai, Y.-J., Gao, J.-R., and Chen, P.-J. (2020). Uncovering the mechanism of Astragalus membranaceus in the treatment of diabetic nephropathy based on network pharmacology. *J. Diabetes Res.* 2020, 5947304. doi:10.1155/2020/5947304

Guo, R., Zhang, X., Su, J., Xu, H., Zhang, Y., Zhang, F., et al. (2018). Identifying potential quality markers of Xin-Su-Ning capsules acting on arrhythmia by integrating UHPLC-LTQ-Orbitrap, ADME prediction and network target analysis. *Phytomedicine* 44, 117–128. doi:10.1016/j.phymed.2018.01.019

Guo, W., Huang, J., Wang, N., Tan, H.-Y., Cheung, F., Chen, F., et al. (2019). Integrating network pharmacology and pharmacological evaluation for deciphering the action mechanism of herbal formula Zuojin pill in suppressing hepatocellular carcinoma. *Front. Pharmacol.* 10, 1185. doi:10.3389/fphar.2019.01185

Haile, C. N., Kosten, T. R., and Kosten, T. A. (2007). Genetics of dopamine and its contribution to cocaine addiction. *Behav. Genet.* 37, 119–145. doi:10.1007/s10519-006-9115-2

Hamosh, A., Scott, A. F., Amberger, J. S., Bocchini, C. A., and McKusick, V. A. (2004). Online Mendelian Inheritance in Man (OMIM), a knowledgebase of human genes and genetic disorders. *Nucleic Acids Res.* 33, D514–D517. doi:10.1093/nar/gki033

Hennebelle, M., Champeil-Potokar, G., Lavialle, M., Vancassel, S., and Denis, I. (2014). Omega-3 polyunsaturated fatty acids and chronic stress-induced modulations of glutamatergic neurotransmission in the hippocampus. *Nutr. Rev.* 72, 99–112. doi:10.1111/nure.12088

Huang, D. W., Sherman, B. T., Tan, Q., Kir, J., Liu, D., Bryant, D., et al. (2007). DAVID Bioinformatics Resources: expanded annotation database and novel algorithms to better extract biology from large gene lists. *Nucleic Acids Res.* 35, W169–W175. doi:10.1093/nar/gkm415

Jesulola, E., Micalos, P., and Baguley, I. J. (2018). Understanding the pathophysiology of depression: from monoamines to the neurogenesis hypothesis model-are we there yet? *Behav. Brain Res.* 341, 79–90. doi:10.1016/j.bbr.2017.12.025

Kanehisa, M., Furumichi, M., Tanabe, M., Sato, Y., and Morishima, K. (2017). KEGG: new perspectives on genomes, pathways, diseases and drugs. *Nucleic Acids Res.* 45, D353–D361. doi:10.1093/nar/gkw1092

Knox, C., Law, V., Jewison, T., Liu, P., Ly, S., Frolkis, A., et al. (2011). DrugBank 3.0: a comprehensive resource for 'omics' research on drugs. *Nucleic Acids Res.* 39, D1035–D1041. doi:10.1093/nar/gkq1126

Kofler, M., Schiefecker, A. J., Gaasch, M., Sperner-Unterweger, B., Fuchs, D., Beer, R., et al. (2019). A reduced concentration of brain interstitial amino acids is associated with depression in subarachnoid hemorrhage patients. *Sci. Rep.* 9, 2811. doi:10.1038/s41598-019-39569-5

Li, H., Zhao, L., Zhang, B., Jiang, Y., Wang, X., Guo, Y., et al. (2014). A network pharmacology approach to determine active compounds and action mechanisms of Ge-Gen-Qin-Lian decoction for treatment of type 2 diabetes. *Evid. base Compl. Alternative Med.* 2014, 495840. doi:10.1155/2014/495840

Li, K., Li, J., Su, J., Xiao, X., Peng, X., Liu, F., et al. (2018). Identification of quality markers of Yuanhu Zhitong tablets based on integrative pharmacology and data mining. *Phytomedicine* 44, 212–219. doi:10.1016/j.phymed.2018.03.002

Li, S., and Zhang, B. (2013). Traditional Chinese medicine network pharmacology: theory, methodology and application. *Chin. J. Nat. Med.* 11, 110–120. doi:10.1016/s1875-5364(13)60037-0

Li, X.-Y., Qi, W.-W., Zhang, Y.-X., Jiang, S.-Y., Yang, B., Xiong, L., et al. (2019). Helicid ameliorates learning and cognitive ability and activities cAMP/PKA/CREB signaling in chronic unpredictable mild stress rats. *Biol. Pharm. Bull.* 42, 1146–1154. doi:10.1248/bpb.b19-00012

Li, Y. H., Yu, C. Y., Li, X. X., Zhang, P., Tang, J., Yang, Q., et al. (2018). Therapeutic target database update 2018: enriched resource for facilitating bench-to-clinic research of targeted therapeutics. *Nucleic Acids Res.* 46, D1121–D1127. doi:10.1093/nar/gkx1076

Liu, S., Guo, R., Liu, F., Yuan, Q., Yu, Y., and Ren, F. (2020). Gut microbiota regulates depression-like behavior in rats through the neuroendocrine-immune-mitochondrial pathway. *Neuropsychiatr. Dis. Treat.* 16, 859–869. doi:10.2147/ndt.S243551

Liu, W., Xue, X., Xia, J., Liu, J., and Qi, Z. (2018). Swimming exercise reverses CUMS-induced changes in depression-like behaviors and hippocampal plasticity-related proteins. *J. Affect. Disord.* 227, 126–135. doi:10.1016/j.jad.2017.10.019

Lu, Q., Mouri, A., Yang, Y., Kunisawa, K., Teshigawara, T., Hirakawa, M., et al. (2019). Chronic unpredictable mild stress-induced behavioral changes are coupled with dopaminergic hyperfunction and serotonergic hypofunction in mouse models of depression. *Behav. Brain Res.* 372, 112053. doi:10.1016/j.bbr.2019.112053

Ma, X. W., Yu, M. M., Jin, X. H., He, J. H., Xu, L., He, Y., et al. (2018). Active ingredients screening by cell membrane chromatography and simultaneous quantitation of ginsenosides in bulk drug of secondary ginsenoside H dripping pills. *Chin. Tradit. Herb. Drugs* 49, 2545–2550. doi:10.7501/j.issn.0253-2670.2018.11.009

Mao, X., Xu, H., Li, S., Su, J., Li, W., Guo, Q., et al. (2019). Exploring pharmacological mechanisms of Xueshuan-Xinmai-Ning tablets acting on coronary heart disease based on drug target-disease gene interaction network. *Phytomedicine* 54, 159–168. doi:10.1016/j.phymed.2018.09.018

Mato, S., Vidal, R., Castro, E., Díaz, Á., Pazos, Á., and Valdizán, E. M. (2010). Long-term fluoxetine treatment modulates cannabinoid type 1 receptor-mediated

inhibition of adenylyl cyclase in the rat prefrontal cortex through 5-Hydroxytryptamine1A receptor-dependent mechanisms. *Mol. Pharmacol.* 77, 424–434. doi:10.1124/mol.109.060079

Ostuzzi, G., Matcham, F., Dauchy, S., Barbui, C., and Hotopf, M. (2018). Antidepressants for the treatment of depression in people with cancer. *Cochrane Database Syst. Rev.* 4, CD011006. doi:10.1002/14651858.CD011006.pub3

Pan, Z. L., Yan, Z. Y., Zuo, C. Y., Chen, C., and Li, S. H. (2011). Influence of long-term usage of diazepam on neuroactive ligand-receptor interaction signaling pathway. *J. China Pharm. Univ.* 42, 443–446. doi:10.1002/chin.201109202

Patel, D. N., Lin, H.-S., and Koh, H.-L. (2012). Quantification of ginsenosides Rh4 and Rk3 in rat plasma by liquid chromatography-tandem mass spectrometry: application to a pre-clinical pharmacokinetic study. *J. Mass Spectrom.* 47, 1510–1517. doi:10.1002/jms.3095

Peng, Y., Zhang, C., Su, Y., Wang, Z., and Jiang, Y. (2018). Activation of the hippocampal AC-cAMP-PKA-CREB-BDNF signaling pathway using WTKYR in depression model rats. *Electrophoresis* 40, 1245–1250. doi:10.1002/elps.201800381

Plattner, F., Hayashi, K., Hernández, A., Benavides, D. R., Tassin, T. C., Tan, C., et al. (2015). The role of ventral striatal cAMP signaling in stress-induced behaviors. *Nat. Neurosci.* 18, 1094–1100. doi:10.1038/nn.4066

Ren, Q., Wang, Z.-Z., Chu, S.-F., Xia, C.-Y., and Chen, N.-H. (2018). Gap junction channels as potential targets for the treatment of major depressive disorder. *Psychopharmacology* 235, 1–12. doi:10.1007/s00213-017-4782-7

Ru, J., Li, P., Wang, J., Zhou, W., Li, B., Huang, C., et al. (2014). TCMSP: a database of systems pharmacology for drug discovery from herbal medicines. *J. Cheminf.* 6, 13. doi:10.1186/1758-2946-6-13

Schmitt, K., Holsboer-Trachsler, E., and Eckert, A. (2016). BDNF in sleep, insomnia, and sleep deprivation. *Ann. Med.* 48, 42–51. doi:10.3109/07853890.2015.1131327

Shoval, G., Balicer, R. D., Feldman, B., Hoshen, M., Eger, G., Weizman, A., et al. (2019). Adherence to antidepressant medications is associated with reduced premature mortality in patients with cancer: a nationwide cohort study. *Depress. Anxiety* 36, 921–929. doi:10.1002/da.22938

Sideromenos, S., Lindtner, C., Zambon, A., Horvath, O., Berger, A., and Pollak, D. D. (2020). VEGF treatment ameliorates depression-like behavior in adult offspring after maternal immune activation. *Cells* 9, 1048. doi:10.3390/cells9041048

Siuciak, J. A., Boylan, C., Fritsche, M., Altar, C. A., and Lindsay, R. M. (1996). BDNF increases monoaminergic activity in rat brain following intracerebroventricular or intraparenchymal administration. *Brain Res.* 710, 11–20. doi:10.1016/0006-8993(95)01289-3

Su, W.-J., Zhang, Y., Chen, Y., Gong, H., Lian, Y.-J., Peng, W., et al. (2017). NLRP3 gene knockout blocks NF-κB and MAPK signaling pathway in CUMS-induced depression mouse model. *Behav. Brain Res.* 322, 1–8. doi:10.1016/j.bbr.2017.01.018

Sun, X., Song, Z., Si, Y., and Wang, J.-H. (2018). microRNA and mRNA profiles in ventral tegmental area relevant to stress-induced depression and resilience. *Prog. Neuro Psychopharmacol. Biol. Psychiatr.* 86, 150–165. doi:10.1016/j.pnpbp.2018.05.023

Szklarczyk, D., Morris, J. H., Cook, H., Kuhn, M., Wyder, S., Simonovic, M., et al. (2017). The STRING database in 2017: quality-controlled protein-protein association networks, made broadly accessible. *Nucleic Acids Res.* 45, D362–D368. doi:10.1093/nar/gkw937

Tan, H., Zou, W., Jiang, J., Tian, Y., Xiao, Z., Bi, L., et al. (2015). Disturbance of hippocampal H2S generation contributes to CUMS-induced depression-like behavior: involvement in endoplasmic reticulum stress of hippocampus. *Acta Biochim. Biophys. Sin.* 47, 285–291. doi:10.1093/abbs/gmv009

Tao, W., Xu, X., Wang, X., Li, B., Wang, Y., Li, Y., et al. (2013). Network pharmacology-based prediction of the active ingredients and potential targets of Chinese herbal Radix Curcumae formula for application to cardiovascular disease. *J. Ethnopharmacol.* 145, 1–10. doi:10.1016/j.jep.2012.09.051

Tu, Y., Liang, Y., Xiao, Y., Lv, J., Guan, R., Xiao, F., et al. (2019). Dexmedetomidine attenuates the neurotoxicity of propofol toward primary hippocampal neurons *in vitro* via Erk1/2/CREB/BDNF signaling pathways. *Drug Des. Devel. Ther.* 13, 695–706. doi:10.2147/dddt.S188436

van den Buuse, M., Buret, L., and Hill, R. (2020). Involvement of brain-derived neurotrophic factor (BDNF) in the long-term memory effects of glucocorticoid stimulation during adolescence/young adulthood. *Behav. Brain Res.* 377, 112223. doi:10.1016/j.bbr.2019.112223

Wang, C., Guo, J., and Guo, R. (2017). Effect of XingPiJieYu decoction on spatial learning and memory and cAMP-PKA-CREB-BDNF pathway in rat model of depression through chronic unpredictable stress. *BMC Compl. Alternative Med.* 17, 73. doi:10.1186/s12906-016-1543-9

Wang, H., Xu, J., Lazarovici, P., Quirion, R., and Zheng, W. (2018). cAMP response element-binding protein (CREB): a possible signaling molecule link in the pathophysiology of schizophrenia. *Front. Mol. Neurosci.* 11, 255. doi:10.3389/fnmol.2018.00255

Wang, J., Chen, Y., Dai, C., Shang, Y., and Xie, J. (2016). Ginsenoside Rh2 alleviates tumor-associated depression in a mouse model of colorectal carcinoma. *Am. J. Transl. Res.* 8, 2189–2195.

Wang, S., Hu, S., Zhang, C., Qiu, J., and Li, Y. (2014). Antidepressant-like activity of Chaihu-Shugan-San aqueous extract in rats and its possible mechanism. *Phcog. Mag.* 10, 50–56. doi:10.4103/0973-1296.127342

Wang, T., Yan, Y.-F., Yang, L., Huang, Y.-Z., Duan, X.-H., Su, K.-H., et al. (2020). Effects of Zuojin pill on depressive behavior and gastrointestinal function in rats with chronic unpredictable mild stress: role of the brain-gut axis. *J. Ethnopharmacol.* 254, 112713. doi:10.1016/j.jep.2020.112713

Wu, J., Zhang, T., Yu, L., Huang, S., Yang, Y., Yu, S., et al. (2019). Zhile capsule exerts antidepressant-like effects through upregulation of the BDNF signaling pathway and neuroprotection. *Int. J. Mol. Sci.* 20, 195. doi:10.3390/ijms20010195

Wu, Z., Wang, G., Wei, Y., Xiao, L., and Wang, H. (2018). PI3K/AKT/GSK3β/CRMP-2-mediated neuroplasticity in depression induced by stress. *Neuroreport* 29, 1256–1263. doi:10.1097/wnr.0000000000001096

Xie, W., Meng, X., Zhai, Y., Ye, T., Zhou, P., Nan, F., et al. (2019). Antidepressant-like effects of the Guanxin Danshen formula via mediation of the CaMK II-CREB-BDNF signalling pathway in chronic unpredictable mild stress-induced depressive rats. *Ann. Transl. Med.* 7, 564. doi:10.21037/atm.2019.09.39

Xie, W., Meng, X., Zhai, Y., Zhou, P., Ye, T., Wang, Z., et al. (2018). Panax notoginseng saponins: a review of its mechanisms of antidepressant or anxiolytic effects and network analysis on phytochemistry and pharmacology. *Molecules* 23, 940. doi:10.3390/molecules23040940

Xiong, W.-C., Wu, H.-Z., Xiong, Y.-Y., Liu, B., Xie, Z.-T., Wu, S.-T., et al. (2020). Network pharmacology-based research of active components of albiziae flos and mechanisms of its antidepressant effect. *Curr. Med. Sci.* 40, 123–129. doi:10.1007/s11596-020-2155-7

Xu, H.-Y., Zhang, Y.-Q., Liu, Z.-M., Chen, T., Lv, C.-Y., Tang, S.-H., et al. (2019). ETCM: an encyclopaedia of traditional Chinese medicine. *Nucleic Acids Res.* 47, D976–D982. doi:10.1093/nar/gky987

Xu, H., Zhang, Y., Lei, Y., Gao, X., Zhai, H., Lin, N., et al. (2014). A systems biology-based approach to uncovering the molecular mechanisms underlying the effects of dragon's blood tablet in colitis, involving the integration of chemical analysis, ADME prediction, and network pharmacology. *PLoS One* 9, e101432. doi:10.1371/journal.pone.0101432

Yang, B., Liu, Z., Wang, Q., Chai, Y., and Xia, P. (2018). Pharmacokinetic comparison of seven major bioactive components in normal and depression model rats after oral administration of Baihe Zhimu decoction by liquid chromatography-tandem mass spectrometry. *J. Pharmaceut. Biomed. Anal.* 148, 119–127. doi:10.1016/j.jpba.2017.09.031

Yang, L., Zheng, L., Wan, Y., Chen, Z., Li, P., and Wang, Y. (2018). Metoprolol, N-acetylcysteine, and escitalopram prevents chronic unpredictable mild stress-induced depression by inhibition of endoplasmic reticulum stress. *Front. Psychiatr.* 9, 696. doi:10.3389/fpsyt.2018.00696

Yang, X., Guo, Z., Lu, J., Zhao, B., Fei, Y., Li, J., et al. (2017). The role of MAPK and dopaminergic synapse signaling pathways in antidepressant effect of electroacupuncture pretreatment in chronic restraint stress rats. *Evid. base Compl. Alternative Med.* 2017, 2357653. doi:10.1155/2017/2357653

Young, K., and Singh, G. (2018). Biological mechanisms of cancer-induced depression. *Front. Psychiatr.* 9, 299. doi:10.3389/fpsyt.2018.00299

Yu, G., Zhang, Y., Ren, W., Dong, L., Li, J., Geng, Y., et al. (2017). Network pharmacology-based identification of key pharmacological pathways of Yin–Huang–Qing–Fei capsule acting on chronic bronchitis. *Int. J. Chron. Obstruct. Pulmon. Dis.* 12, 85–94. doi:10.2147/copd.S121079

Yue, J., Wang, Z. L., Li, Y. L., Xia, B. S., Nan, F., Xiang, J., et al. (2019). Determination of ginsenoside-Rh2 in human plasma by HPLC-MS/MS. *Chin. J. New Drugs* 28, 1214–1220.

Zhang, G., Zhang, Y., Yang, J., Hu, M., Zhang, Y., and Liang, X. (2012). Altered serous levels of monoamine neurotransmitter metabolites in patients with refractory and non-refractory depression. *Neural Regen. Res.* 7, 1113–1118. doi:10.3969/j.issn.1673-5374.2012.14.011

Zhang, L. L., Gao, W. Y., Ma, X. H., Song, Z. H., Liu, J. Y., and Zhou, S. P. (2013). Effect of ginsenoside-Rh2 on U14 cervical cancer bearing mouse. *Chin. Tradit. Pat. Med.* 35, 215–219. doi:10.3969/j.issn.1001-1528.2013.02.002

Zhang, R., Guo, L., Ji, Z., Li, X., Zhang, C., Ma, Z., et al. (2018). Radix scutellariae attenuates CUMS-induced depressive-like behavior by promoting neurogenesis via cAMP/PKA pathway. *Neurochem. Res.* 43, 2111–2120. doi:10.1007/s11064-018-2635-3

Zhang, W. J., Chen, M., and Qiu, T. (2007). The investigation of the expression of BDNF in the hippocampi in PSD rat treatment by Huoxue Quyu Jieyu method. *Chin. Arch. Tradit. Chin. Med.*, 1410–1411. doi:10.3969/j.issn.1673-7717.2007.07.041

Zhang, Y., Mao, X., Su, J., Geng, Y., Guo, R., Tang, S., et al. (2017). A network pharmacology-based strategy deciphers the underlying molecular mechanisms of Qixuehe Capsule in the treatment of menstrual disorders. *Chin. Med.* 12, 23. doi:10.1186/s13020-017-0145-x

Zhao, J., Jung, Y.-H., Jang, C.-G., Chun, K.-H., Kwon, S. W., and Lee, J. (2015). Metabolomic identification of biochemical changes induced by fluoxetine and imipramine in a chronic mild stress mouse model of depression. *Sci. Rep.* 5, 8890. doi:10.1038/srep08890

Zhong, X., Li, G., Qiu, F., and Huang, Z. (2018). Paeoniflorin ameliorates chronic stress-induced depression-like behaviors and neuronal damages in rats via activation of the ERK-CREB pathway. *Front. Psychiatr.* 9, 772. doi:10.3389/fpsyt.2018.00772

Zhou, H. Y., Wang, Y., Song, Z. H., Zhang, L. L., Zhou, S. P., and Feng, F. (2014). UPLC determination of ginsenoside Rh1 and Rh2 in secondary ginsenoside H dripping pill. *Chin. J. New Drugs* 23, 1497–1500.

Zhu, H., Lin, H., Tan, J., Wang, C., Wang, H., Wu, F., et al. (2018). UPLC-QTOF/MS-Based nontargeted metabolomic analysis of mountain- and garden-cultivated ginseng of different ages in northeast China. *Molecules* 24, 33. doi:10.3390/molecules24010033

Zhu, Y.-l., Li, S.-l., Zhu, C.-y., Wang, W., Zuo, W.-f., and Qiu, X.-j. (2020). Metabolomics analysis of the antidepressant prescription Danzhi Xiaoyao powder in a rat model of chronic unpredictable mild stress (CUMS). *J. Ethnopharmacol.* 260, 112832. doi:10.1016/j.jep.2020.112832

Zhu, Y., Chao, C., Duan, X., Cheng, X., Liu, P., Su, S., et al. (2017). Kai-Xin-San series formulae alleviate depressive-like behaviors on chronic mild stressed mice via regulating neurotrophic factor system on hippocampus. *Sci. Rep.* 7, 1467. doi:10.1038/s41598-017-01561-2

Conflict of Interest: The authors declare that the research was conducted in the absence of any commercial or financial relationships that could be construed as a potential conflict of interest.

Copyright © 2021 Zhao, Guo, Cao, Lin, Yang, Pei, Ma, Zhang, Li, Song, Du, Xiao and Liu. This is an open-access article distributed under the terms of the Creative Commons Attribution License (CC BY). The use, distribution or reproduction in other forums is permitted, provided the original author(s) and the copyright owner(s) are credited and that the original publication in this journal is cited, in accordance with accepted academic practice. No use, distribution or reproduction is permitted which does not comply with these terms.

frontiers in Pharmacology

ORIGINAL RESEARCH
published: 03 March 2021
doi: 10.3389/fphar.2021.613104

Deciphering the Pharmacological Mechanisms of Guizhi-Fuling Capsule on Primary Dysmenorrhea Through Network Pharmacology

Siqin Zhang[1†], Xinxing Lai[1,2†], Xin Wang[1], Gang Liu[3], Zhenzhong Wang[4], Liang Cao[4], Xinzhuang Zhang[4], Wei Xiao[4] and Shao Li[1]**

[1]Department of Automation, Institute for TCM-X, MOE Key Laboratory of Bioinformatics/Bioinformatics Division, BNRIST, Tsinghua University, Beijing, China, [2]Institute for Brain Disorders, Dongzhimen Hospital, Beijing University of Chinese Medicine, Beijing, China, [3]School of Pharmaceutical Sciences, Tsinghua University, Beijing, China, [4]State Key Laboratory of New-tech for Chinese Medicine Pharmaceutical Process/Key Laboratory for the New Technique Research of TCM Extraction and Purification/ Jiangsu Kanion Pharmaceutical Co., Ltd., Jiangsu, China

Guizhi-Fuling capsule (GZFLC), originated from a classical traditional Chinese herbal formula Guizhi-Fuling Wan, has been clinically used for primary dysmenorrhea in China. Nonetheless, the underlying pharmacological mechanisms of GZFLC remain unclear. The integration of computational and experimental methods of network pharmacology might be a promising way to decipher the mechanisms. In this study, the target profiles of 51 representative compounds of GZFLC were first predicted by a high-accuracy algorithm, drugCIPHER-CS, and the network target of GZFLC was identified. Then, potential functional modules of GZFLC on primary dysmenorrhea were investigated using functional enrichment analysis. Potential bioactive compounds were recognized by hierarchical clustering analysis of GZFLC compounds and first-line anti-dysmenorrhea drugs. Furthermore, the potential anti-dysmenorrhea mechanisms of GZFLC were verified through enzyme activity assays and immunofluorescence tests. Moreover, effects of GZFLC on primary dysmenorrhea were evaluated in oxytocin-induced dysmenorrhea murine model. In the network target analysis, GZFLC may act on five functional modules of pain, inflammation, endocrine, blood circulation and energy metabolism. Integrating computational and experimental approaches, we found that GZFLC significantly inhibited the writhing response and reduced the degree of uterine lesions in oxytocin-induced dysmenorrhea murine model. Furthermore, GZFLC may partially alleviate primary dysmenorrhea by inhibiting cyclooxygenase 2 (COX2) and downregulating MAPK signaling pathway. Consequently, GZFLC presented pain relief and sustained benefits for primary dysmenorrhea. This study could provide a scientific approach for deciphering pharmacological mechanisms of herbal formulae through network pharmacology.

Keywords: primary dysmenorrhea, network target, network pharmacology, pharmacological mechanisms, Guizhi-Fuling capsule

OPEN ACCESS

Edited by:
Hai Yu Xu,
China Academy of Chinese Medical Sciences, China

Reviewed by:
Shi-Bing Su,
Shanghai University of Traditional Chinese Medicine, China
Jianxin Chen,
Beijing University of Chinese Medicine, China

****Correspondence:***
Shao Li
shaoli@mail.tsinghua.edu.cn
Wei Xiao
xw_kanion@163.com

[†]These authors have contributed equally to this work

Specialty section:
This article was submitted to Ethnopharmacology, a section of the journal Frontiers in Pharmacology

Received: *01 October 2020*
Accepted: *13 January 2021*
Published: *03 March 2021*

Citation:
Zhang S, Lai X, Wang X, Liu G, Wang Z, Cao L, Zhang X, Xiao W and Li S (2021) Deciphering the Pharmacological Mechanisms of Guizhi-Fuling Capsule on Primary Dysmenorrhea Through Network Pharmacology. Front. Pharmacol. 12:613104. doi: 10.3389/fphar.2021.613104

INTRODUCTION

Primary dysmenorrhea (PD) is defined as abnormally painful menstruation in the absence of any evident underlying pelvic pathology (Kho and Shields, 2020). Characterized by recurrent, painful, spasmodic cramping in the lower abdomen during menstruation, primary dysmenorrhea is the most common menstrual symptom among adolescent girls and young women, with the prevalence rate ranging from 41.7% to 90% (ACOG, 2018; Hu et al., 2020). As one of the most common gynecologic disorders, primary dysmenorrhea has significant effects on patients' normal school or work, as well as quality of life (Burnett et al., 2005; Wong 2018). The pathogenesis of primary dysmenorrhea is most widely accepted and considered to be the overproduction of uterine prostaglandins (PGs) (Iacovides et al., 2015). Owing to the PGs-based etiology of primary dysmenorrhea, the current first-line pharmacological agents for primary dysmenorrhea include non-steroidal anti-inflammatory drugs (NSAIDs) and hormonal contraceptives (Kho and Shields 2020).

Despite the sufficient evidence supporting the efficacy of NSAIDs in pain relief for patients with primary dysmenorrhea, there are approximately 15% of patients not responding to, or being intolerant to NSAIDs due to many side effects (Campbell and McGrath 1999; Marjoribanks et al., 2010). Oral hormonal contraceptives are also effective for primary dysmenorrhea, however, a meta-analysis has demonstrated the long-suspected association between oral contraceptive use and the risk of venous thromboembolism (Manzoli et al., 2012). Given these disadvantages of NSAIDs and hormonal contraceptives, effective and safe alternative treatments, such as Traditional Chinese Medicine (TCM), are receiving increasing attention worldwide. TCM characterized as holistic thinking emphasizes on regulating the integrity of the human body (Li et al., 2007) and intervenes multiple aspects related to etiological factors and pathogenesis simultaneously, which has accumulated numerous valuable clinical experiences and herbal formulae through long history of development.

Guizhi-Fuling capsule (GZFLC), a Chinese patent medicine approved by China Food and Drug Administration (CFDA), is clinically used for blood stasis syndromes in gynecological diseases including primary dysmenorrhea. It originated from a classical traditional Chinese herbal formula Guizhi-Fuling Wan which was first described in a classics named the Essential Prescriptions from the Golden Cabinet (Jin Kui Yao Lue) documented in 150–219 A.D. Guizhi-Fuling capsule is the modern dosage form of Guizhi-Fuling Wan, and the dosage and ratio of each Chinese herbal medicine in Guizhi-Fuling capsule is the same as Guizhi-Fuling Wan, consisting of five herbs: *Cinnamomum cassia (L.) J. Presl* (Guizhi), *Poria cocos* (Fuling), *Paeonia lactiflora Pall* (Baishao), *Paeonia × suffruticosa Andrews* (Mudanpi) and *Prunus persica (L.) Batsch* (Taoren). Pharmacokinetic-pharmacodynamic modeling study has demonstrated that GZFLC exhibited significant therapeutic effect on primary dysmenorrhea in rat model (Cheng et al., 2018). Moreover, a randomized controlled trial showed that GZFLC significantly relieved pain and reduced the duration of pain compared with placebo during the 3-months treatment period, as well as in the 3-months follow up period, demonstrating a sustained benefit for patients with primary dysmenorrhea (Liu et al., 2013). However, the underlying comprehensive pharmacological mechanisms of GZFLC on primary dysmenorrhea remain unclear.

There are several substantial challenges in terms of deciphering pharmacological mechanisms of herbal formulae. Firstly, herbal formulae are complex chemical systems usually composed of numerous chemical compounds. Secondly, a great majority of bioactive compounds in herbs may have weak or moderate effects on multiple biological molecules, different from most western drugs designed to act on a single target selectively (Ji et al., 2009). Thus, routine pharmacologic analysis methods are difficult to systematically elucidate the mechanisms of herbal formulae. Network pharmacology, a newly developed cross-discipline, is preferable in investigation and elucidation of comprehensive mechanisms of TCM (Li et al., 2007; Hopkins 2008). The key ideas of Network pharmacology share much with the holistic philosophy of TCM (Li and Zhang 2013). TCM network pharmacology highlights a "network target, multicomponent therapeutics" approach (Li et al., 2011; Li 2015) to help elucidate the complex molecular mechanisms of traditional herbal formulae. The core theory of network pharmacology is "network target" distinct from "one target, one drug" paradigm (Li 2011; Li et al., 2011). More specifically, the core principle of network target is constructing a disease-specific biological network as the therapeutic target that herbal formulae are applied to (Li 2015). TCM network pharmacology has been successfully applied in many researches such as molecular mechanism elucidation of herbal formulae (Liang et al., 2014; Zuo et al., 2018), new bioactive compounds discovery (Qi et al., 2016), comprehensive pharmacological function of natural products identification (Zhang et al., 2018) and mechanism of action of toxic components in traditional Chinese medicines (Li et al., 2019).

In this study, we proposed an approach to investigate the underlying pharmacological mechanisms of GZFLC on primary dysmenorrhea based on network pharmacology as shown in **Figure 1**. First, we collected important phytochemistry and absorbed compounds of GZFLC. Second, we predicted the potential targets of GZFLC compounds utilizing a high-accuracy target prediction algorithm, and then validated the potential targets in literatures to ensure the reliability of predictions. Third, we made the network target analysis of GZFLC to investigate the pharmacological mechanisms and bioactive compounds of GZFLC on primary dysmenorrhea, including functional enrichment analysis and hierarchical clustering analysis. These network target analysis results were verified *in vitro* and *in vivo*.

MATERIALS AND METHODS

Representative Compounds in GZFLC Collection

The dosages and ratios of GZFLC compounds could influence their intervention intensity on targets. Considering the influence of GZFLC compounds' dosages and ratios, we selected major

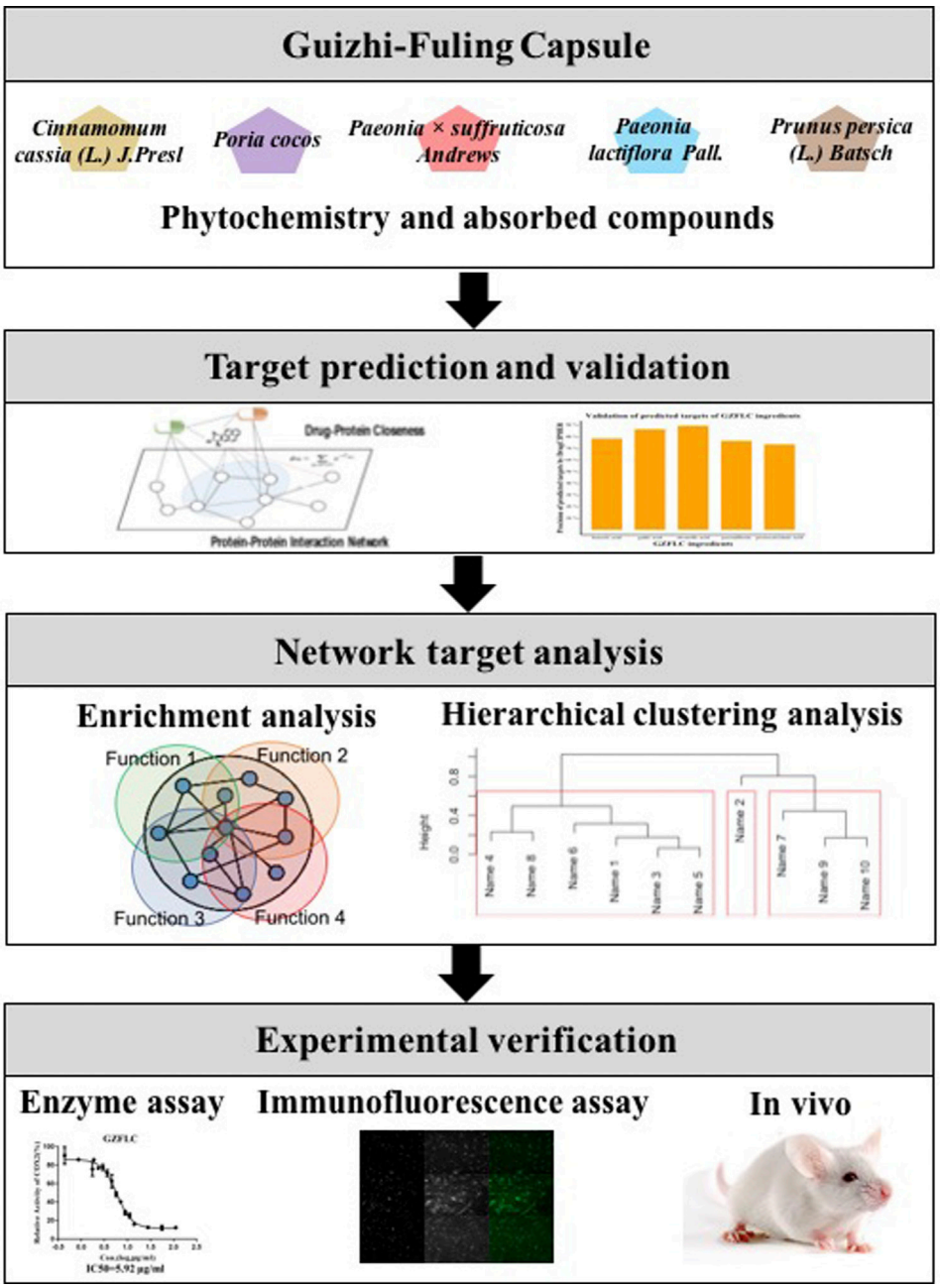

FIGURE 1 | Network pharmacology analysis workflow.

phytochemistry compounds and absorbed compounds of GZFLC as representative compounds to analyze GZFLC's pharmacological mechanisms through network pharmacology. We have investigated phytochemistry compounds of GZFLC and absorbed compounds of GZFLC in plasma previously (Zhong et al., 2016a; Yin et al., 2016; Zhang et al., 2017; Yang et al., 2020). In total, 51 compounds were selected from our previous investigations of phytochemistry and absorbed compounds of GZFLC based on the following criteria: 1) the characteristic compounds were accounted for the major proportion and verified with reference substances; 2) the compounds were quantificationally recorded in each herb from Chinese Pharmacopoeia (2015) (Committee 2015); 3) each compound had specified chemical structure and Pubchem CID.

Preparation and Analysis of GZFLC

GZFLC was provided by the company Jiangsu Kanion Pharmaceutical Co., Ltd., composed of *Cinnamomum cassia (L.) J. Presl* (20%), *Poria cocos* (20%), *Paeonia × suffruticosa Andrews* (20%), *Paeonia lactiflora Pall* (20%), *Prunus persica (L.).*

Batsch (20%). The full taxonomic names of all herbs included have been fully validated using the Kew Medicinal Plant Names Service. Guizhi-Fuling capsules have established fingerprints (Wang et al., 2009; Li et al., 2012) from herb to preparation to make sure that the quality of the preparation is uniform and stable (Li et al., 2015). Guizhi-Fuling capsule is a Chinese patent medicine approved and supervised by CFDA under the same strict quality control standards. Meanwhile, Guizhi-Fuling capsules in our study have come from the same preparation. The chemical constituents analysis of GZFLC has been reported in the literature (Yang et al., 2020). The UPLC analysis of GZFLC (Jiangsu Kanion Pharmaceutical Co., Ltd. Jiangsu, China, No. 20160319) was performed on Agilent SB-RRHD C18 (100 mm × 2.1 mm, 1.8 μm) column at 30°C with a mobile phase consisting of acetonitrile and 0.02% trifluoroacetic acid for gradient elution and the flow rate of 0.2 ml/min. The detection wavelength was set at 230 nm. The representative UPLC fingerprints of GZFLC were shown in **Supplementary Figure S1** in the Supplementary Materials.

Target Predication and Validation for Compounds in GZFLC

To explore the relativity of representative GZFLC compounds and targets, the potential target profiles of compounds in GZFLC were predicted by drugCIPHER-CS (Zhao and Li, 2010), a high-accuracy algorithm developed for global prediction of compound targets. In principle, drugCIPHER-CS used a linear regression model which related chemical similarity vector between compounds in GZFLC and drugs in DrugBank (Wishart et al., 2008) to the drug-protein closeness vector based on a protein–protein interaction network to calculate the concordance score of each compound-protein pair. The concordance score was treated as the likelihood of the compound targeting the protein. Thus, the candidate proteins with high concordance scores were prioritized to be potential targets of the compound. Top 100 ranking predicted proteins of each compound were kept as potential target profiles.

To validate the target prediction of compounds, literature mining method was used to obtain the co-occurrence results of biomolecules and each compound. The biomolecules related to each compound from literature mining were manually examined to delete the false positive results and then considered as the reported targets. Comparing the reported targets with the predicted targets via direct mapping and indirect link, the reliability of target prediction was measured by $\frac{|\text{The predicted targets related to the reported targets}|}{|\text{The predicted targets}|} * 100\%$.

Holistic Target Prediction for GZFLC and Each Herb

To identify potential targets regulated by GZFLC or herbs, predicted proteins ranking top or appearing in the target profiles of many compounds in GZFLC or herbs were hypothesized to be important in the pharmacological effects of GZFLC or herbs. Based on this hypothesis, the potential targets of GZFLC or herbs were considered as significantly frequently occurring targets ($p < 0.05$) by comparing the number of occurrences of a target protein in the target profiles of all compounds in GZFLC or herbs to that in random background (Liang et al., 2014). A Poisson binomial statistical model was used to obtain the random background distribution and represented as:

$$P(K = k) = \sum_{A \in F_k j \in A} \prod p_i \prod_{j \in A^c} (1 - p_j).$$

$P(K = k)$ is the probability of a certain target in k compounds' target profiles, F_k is the set including all sets containing k compounds, A is an element of F_k, and A^c is the complement of A. p_i and p_j are the probabilities of a certain target in i and j compound's target profiles respectively.

Functional Enrichment Analysis and Biological Network Construction

To investigate the potential signaling pathways or biological processes regulated by GZFLC and each herb, functional enrichment analysis was carried out in Comparative Toxicogenomics database (Davis et al., 2019) to obtain the over represented Gene Ontology (GO) biological processes (BP)/KEGG signaling pathways based on the potential targets of GZFLC and each herb. The significantly enriched GO BP/KEGG signaling pathways with $p < 0.05$ after Benjamin's correction were selected for further study. All significantly enriched GO BP/KEGG signaling pathways were categorized by means of key words mapping.

The herbs-compounds-biological functional modules-biological molecules network of GZFLC was constructed to elucidate its putative anti-primary dysmenorrhea mechanisms by considering protein–protein interactions and crosstalk among pathways. First, herbs were connected to their representative compounds. Second, the potential targets of GZFLC were mapped into protein–protein interaction network and the targets were annotated by its biological functions. Third, an edge was added between herbs and biological functional modules if potential targets of a certain herb were significantly enriched in biological functional modules related GO BP or KEGG signaling pathways ($p < 0.05$). The herbs-compounds-biological functional modules-biological molecules network was visualized using Cytoscape v3.7.2 (Shannon et al., 2003).

Hierarchical Clustering Analysis of Anti-Primary Dysmenorrhea Drugs and Compounds in GZFLC

We hypothesized that the drugs with similar target profiles predicted by drugCIPHER-CS may have similar biological activities. The resemblance of compounds' and drugs' biological activities could be further defined on the basis of the similarity between concordance scores of their target profiles. Hierarchical clustering analysis of target profiles was applied to measure the biological activity resemblance of compounds and drugs. Thus, to identify anti-primary dysmenorrhea candidate compounds, hierarchical clustering analysis was conducted using R statistic software (R version 3.6.3) based on target profiles of FDA-approved anti-primary dysmenorrhea drugs and 51 compounds of GZFLC.

COX2 Activity Assay

As GZFLC had multiple compounds and targets, we first qualitatively explored the relativity of representative GZFLC compounds and targets. And then we selected predicted compounds and a specific target for preliminary analysis of their dosages and ratios as a starting point. *In vitro* enzyme activity assays were used to analyze the relationship between predicted GZFLC compounds' different dosages and their intervention intensity on a specific target COX2, and to investigate GZFLC's intervention intensity on COX2 under the specific ratio of GZFLC compounds which is relatively fixed in GZFLC. The content in the GZFLC (Jiangsu Kanion Pharmaceutical Co., Ltd. Jiangsu, China, No. 170601) was weighed and extracted with dimethyl sulfoxide (DMSO, 32.308:1, W/V, mg/ml) at 37°C for 30 min. The liquid was collected by centrifugation, and the supernatant was filtered through a 0.22 μ filter. The effect of GZFLC or pure chemicals including 1,2,3,4,6-penta-O-galloyl-beta-D-glucopyranose (purity (%) ≥98%, CAS: 14,937–32–7, Pubchem CID: 65238, Nanjing SenBeiJia Biological Technology Co., Ltd.), galloylpaeoniflorin (purity (%) ≥98%, CAS: 122,965–41–7, Pubchem CID: 46882879, Nanjing SenBeiJia Biological Technology Co., Ltd.), ethyl gallate (purity (%)≥98%, CAS: 831–61–8, Pubchem CID: 13250, Nanjing SenBeiJia Biological Technology Co., Ltd.) and gallic acid (purity (%)≥98%, CAS: 149–91–7, Pubchem CID: 370, Nanjing SenBeiJia Biological Technology Co., Ltd.) on COX2 activity was measured using cyclooxygenase-2 inhibitor screening kit (Beyotime, Cat. No. #S0168). Briefly, the recombinant human COX2 assay mixture (total volume = 90μL/well) consisting of assay buffer, cofactor, COX2 enzyme, and test compound (diluted in DMSO, 5.56% DMSO finally in assay) was incubated at 25°C for 5 min. Detection of the product was performed by adding probe (5μL/well). Arachidonic acid was added and the reaction was allowed to proceed for 15 min at 37°C. The fluorescence of the resulting solution was measured using SpectraMax M2e multilabel plate reader (Molecular Devices, United Kingdom). COX2 specific inhibitor ibuprofen (98.82% purity, AbMole, Cat. No. M3359) was included as a positive control. Data was represented as $\overline{X} \pm SD$ of duplicated samples. The effect of the samples on COX2 was calculated using the following equation:

$$\text{Relative activity of COX2}\,(\%) = \left(\frac{RFU_{\text{sample}} - RFU_{BW}}{RFU_A - RFU_{BW}}\right) \times 100\%.$$

Animals

Female ICR mice (18–22 g of weight, SPF, license number: SCXK (SU) 2012–0004) were provided by the comparative medicine center of Yangzhou University. All animal experimental procedures were performed in accordance with the Guide for the Care and Use of Laboratory Animals and were approved by the animal ethics committee of the Institutional Animal Care and Use Committee (IACUC) of Kanion Pharmaceutical Co., Ltd.

Uterine Myometrial Cells Culture

Isolation and culture of primary myometrial cells were prepared as previously reported (Mosher et al., 2013; Sun et al., 2017). Briefly, Uterine were removed from adult female ICR mice (7–8 weeks old, purchased from Nanjing Branch of Beijing Weitong Lihua Laboratory Animal Technology Co., Ltd., license number: SCXK (SU) 2016–0003). Uterine were cut longitudinally, and endometria were scraped gently. The myometrial cells were digested in 2 ml collagenase II (GIBCO, Cat. No. 1797319) (0.025 g L^{-1}), then cells were plated onto 25 cm^2 culture bottle (Costar, US) and were cultured in complete DMEM (GIBCO, Cat. No. 11330032) at 37°C with 5%CO_2.

Immunofluorescence Assay

Myometrial cells were seeded in 96 well black-walled clear-bottom plates (Costar, US) (4×10^4/ml density), and incubated overnight at 37°C in air containing 5%CO_2. The blank group and model group were added with 100 μL serum-free medium, and the GZFLC group was added with GZFLC (Jiangsu Kanion Pharmaceutical Co., Ltd. Jiangsu, China, No. 20160319) solution prepared with serum-free medium (25 g·L^{-1}) for 1 h. The supernatant was discarded, 100 μL serum-free medium was added to the control group, and 100 μL oxytocin (Cayman, 11,799) (final concentration of 28 μM) was added to the model group and GZFLC group for 15 min respectively. The supernatant was discarded, fixed with paraformaldehyde (Amresco, Cat. No. J531) (0.4 g·L^{-1}) for 15 min, washed with PBS for 5 min 3 times, and blocked with 5% goat serum (Boster, Cat. No. 10E12B09)/0.3% tritonx-100 for 1 h. Then cells were incubated with primary antibody against p-SAPK/JNK(CST), p-p44/42 MAPK(Erk1/2) (CST), p-p38(CST) (1:150, 1:150, 1:2000) at 4°C overnight. The next day, it was equilibrated to room temperature, followed by 1 h incubation with Alexa Fluor® 488 Conjugate (1:1000, Invitrogen, United States) at room temperature, washed 3 times with PBS, counterstained with DRAQ5® for 5 min, washed once with PBS, and imaged with a high-content instrument (Thermo, ArrayScanVII).

Oxytocin-Induced Dysmenorrhea in Mice

Oxytocin-induced dysmenorrhea in mice was performed according to the method previously reported (Sun et al., 2002). Fifty female ICR mice (license number: SCXK (SU) 2012–0004) were evenly divided into five groups as follows: normal group, model group, ibuprofen group and the GZFLC groups of different doses (0.54 g/kg and 1.08 g/kg). Except for the normal group (subcutaneous injection of saline), the other groups were administrated by subcutaneous estradiol benzoate injection (0.05 ml/mouse on the first and 10th day, and 0.025 ml/mouse on the remaining days) for ten consecutive days. The model group, GZFLC groups, and Ibuprofen group were orally administrated on the fourth day with 0.5% CMC-Na of the same volume (20 ml/kg), GZFLC (0.54 g/kg and 1.08 g/kg) and ibuprofen (0.1 g/kg) for seven days (once a day) in the period, respectively. On the 10th day, oxytocin (0.2 ml/2 IU/mouse) was administered by peritoneal injection 1 h after the last administration. The number of animal writhing times was

observed and recorded within 30 min after injection of oxytocin. The number of writhing inhibition rate (IR %) was calculated according to the formula (inhibition rate% = (number of writhing times in the model group-number of writhing times in the medication group)/number of writhing times in the model group) × 100%). The mice were sacrificed immediately. The uterus tissues were fixed with 10% formalin for further study.

Pathological Examination

The uterus tissues were fixed in 10% formalin and stained with hematoxylin and eosin (H&E). Histopathological changes were observed by optical microscope (OLYMPUS DX45, Japan) including degeneration and necrosis in the endometrial epithelial cells, congestion, edema, inflammatory cell infiltration in the lamina propria, the number of glands (increased or decreased), secretion in the gland cavity, and lesions in the muscle layer and serosal layer. According to the severity of the lesion, it was recorded as one point (mild), two points (moderate), three points (severe), four points (extremely severe), no lesion was recorded as 0 point. All scores were accumulated and the average score ($\overline{X} \pm SD$) of each animal in each group was calculated.

Statistical Analysis

The Fisher's exact test was used to identify significantly enriched KEGG signaling pathways and GO biological processes. The immunofluorescence assay results were analyzed by SPSS 13.0 software. One-way and two-way analysis of variance (ANOVA) were used to calculate statistical levels between groups. The enzyme activity assay results were analyzed using Graphpad Prism software (Graph Pad, United States) presented as $\overline{X} \pm SD$ of duplicated samples. The animal assay results were analyzed using Graphpad Prism software (Graph Pad, United States) presented as $\overline{X} \pm SEM$ or $\overline{X} \pm SD$ of duplicated samples. p-value less than 0.05 was considered to be statistically significant.

RESULTS

Targets Prediction and Validation of GZFLC Compounds

We selected 51 representative compounds of GZFLC according to our previous investigations to further study. It has been known that bioactive natural compounds may have multiple targets to exert certain therapeutic effects. To reveal the pharmacological mechanisms of GZFLC for treating primary dysmenorrhea, potential targets of 51 representative compounds were predicted by our state-of-art network-based algorithm drugCIPHER-CS due to the lack of these compounds' known target records. The top 100 predicted targets of each compound were selected as its potential targets for high precision in this algorithm, called target profiles of each compound. Moreover, the reliability of the predicted targets was verified making use of literature mining method based on text searching. The predicted targets were validated by the reported targets with literature evidence via direct mapping or indirect link as shown in **Figure 2A**. The precision of predicted targets was used to measure the reliability, which stands for the percentage of the predicted targets supported by literatures. Greater than 73% of the predicted targets of compounds could be supported with literature evidence in **Figure 2B**, while the others could be novel targets which would be investigated in the future study. These results indicated the reliability of our predicted targets of GZFLC compounds used for further investigation of pharmacological mechanisms.

Network Target Analysis of Anti-Primary Dysmenorrhea Mechanisms of GZFLC

At first, there was a hypothesis that if a biological molecule was an important target in the pharmacological effects of GZFLC, it may rank top or appear in the target profiles of many compounds in GZFLC. Then, based on this hypothesis, we selected the most representative targets of GZFLC compared to the null model with Poisson binomial statistics as potential targets regulated by GZFLC to uncover its therapeutic mechanisms for primary dysmenorrhea. Finally, we got 240 potential targets as GZFLC network target and made functional enrichment analysis on these targets. The significantly enriched biological processes and signaling pathways were achieved as listed in **Table 1**. According to key words mapping, the network target of GZFLC significantly enriched in some pain, inflammation, endocrine, blood circulation and energy metabolism related biological processes and signaling pathways ($p < 0.05$). Hence, potential functional modules regulated by GZFLC on primary dysmenorrhea could be related to pain, inflammation, endocrine, blood circulation and energy metabolism.

We also got the potential targets of each herb in GZFLC respectively and conducted the functional enrichment analysis for these targets of each herb with the significantly enriched biological processes and signaling pathways of GZFLC as shown in **Figure 3A**. Those results could help us to better elucidate effects of GZFLC for treating primary dysmenorrhea. *Cinnamomum cassia (L.) J. Presl*, *Prunus persica (L.) Batsch* mainly regulated pain, inflammation, endocrine, blood circulation modules. *Paeonia lactiflora Pall.* and *Paeonia* × *suffruticosa Andrews* mainly regulated pain, inflammation, endocrine, blood circulation and energy metabolism modules. *Poria cocos* mainly regulated inflammation, endocrine and energy metabolism modules. To further elucidate the underlying molecular mechanisms of GZFLC, the biological molecular network targeted by GZFLC was constructed to uncover the relationships among herbs, compounds, biological functional modules and targets in **Figure 3B**. These results suggested that GZFLC could reduce pain and inflammation, and improve endocrine, blood circulation and energy metabolism, which was supported by evidences from the following *in vitro* and *in vivo* experiments.

Moreover, the hierarchical clustering analysis of GZFLC compounds and first-line drugs for primary dysmenorrhea was performed to further investigate the anti-primary dysmenorrhea activities of GZFLC compounds. The therapeutic effects of first-line drugs might suggest hypothetical effects for several compounds in GZFLC within the same cluster. The target profiles of GZFLC compounds and nine FDA-approved anti-primary dysmenorrhea drugs including non-steroidal anti-inflammatory drugs (NSAIDs: Ibuprofen, Naproxen sodium,

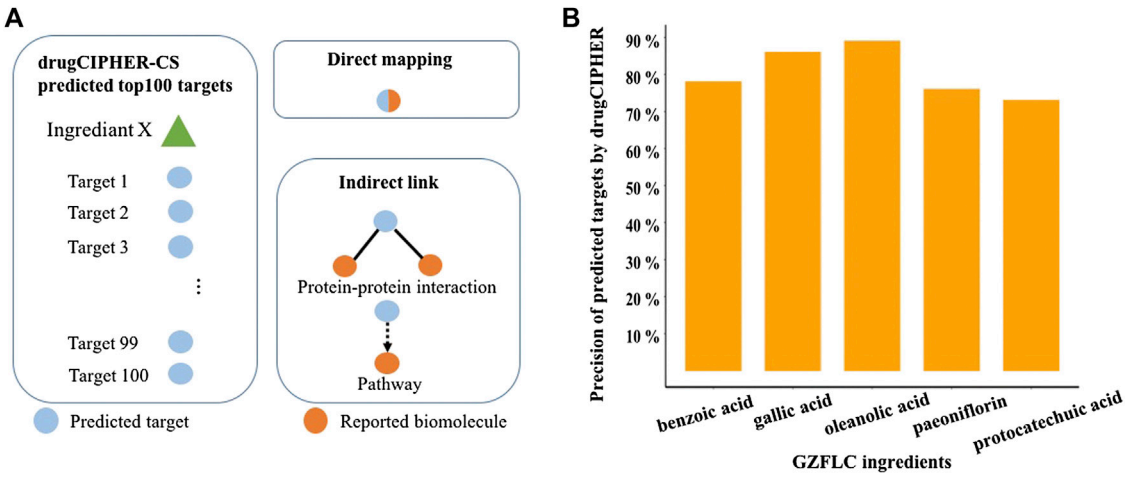

FIGURE 2 | Target prediction of GZFLC compounds and literature validation (A) Top 100 predicted targets were considered as the target profile of each compound. Direct mapping represents that the predicted targets are the same as reported biomolecules. Indirect link represents that the predicted targets are connected to reported biomolecules through protein–protein interactions or pathways **(B)** Reliability validation of predicted targets of representative compounds in GZFLC.

Mefenamic acid and celecoxib) and oral contraceptives (OCs: Norgestimate, Ethynodiol diacetate, Drospirenone, Mestranol and Norethisterone) were predicted by drugCIPHER-CS firstly. Then, hierarchical clustering analysis was performed based on target profiles of GZFLC compounds, NSAIDs and OCs. These two kinds of first-line drugs have different mechanisms on primary dysmenorrhea. First, NSAIDs are often taken to exert analgesic effects via inhibition of cyclooxygenase (Brune and Patrignani, 2015). The compounds of GZFLC in the same cluster with the NSAIDs might be potential active compounds to exert analgesic effects. As shown in **Figure 3C**, the four NSAIDs were clustered into two major groups including 36 compounds of GZFLC, indicating that these compounds might have a similar mechanism of analgesic effects to relieve primary dysmenorrhea with NSAIDs. Second, the OCs were used to regulate hormone levels to suppress ovulation, thereby reducing dysmenorrhea (Proctor et al., 2001). The compounds in GZFLC in the same cluster with OCs were considered to have a similar therapeutic mechanism on primary dysmenorrhea with OCs. As shown in **Figure 3C**, the five oral contraceptives were clustered with 23 compounds from GZFLC, which mainly derived from *Paeonia lactiflora Pall.* and *Paeonia* × *suffruticosa Andrews*, suggesting that these compounds might have the bioactivity of regulating hormone levels to improve endocrine, thereby relieving primary dysmenorrhea.

The Underlying Mechanisms of GZFLC on Primary Dysmenorrhea

Recent studies have demonstrated that hyper-secretion of prostaglandins and an increased uterine contractility are two causes of pain associated with dysmenorrhea (Bernardi et al., 2017). NSAIDs exert analgesia effects to effectively alleviate primary dysmenorrhea through decreasing prostaglandin levels via inhibition of cyclooxygenase-mediated production (Marjoribanks et al., 2010). COX2 is an important cyclooxygenase that catalyzes arachidonic acid conversion to prostaglandins, which is a major target of NSAIDs. Meanwhile, COX2 was predicted as an important biomolecule regulated by GZFLC from our network target analysis. We therefore examined whether GZFLC and its potential bioactive compounds above could affect COX2 activity. We found that GZFLC and four predicted main compounds, including 1,2,3,4,6-penta-O-galloyl-beta-D-glucopyranose, galloylpaeoniflorin, ethyl gallate and gallic acid, could inhibit the activity of COX2 *in vitro*. As shown in **Figure 4A**, GZFLC inhibited the activity of COX2 *in vitro* with an IC50 value of 5.92 μg/ml 1,2,3,4,6-penta-O-galloyl-beta-D-glucopyranose, galloylpaeoniflorin, ethyl gallate and gallic acid inhibited the activity of COX2 *in vitro* with IC50 values of 0.38 μM (0.36 μg/ml), 0.74 μM (0.47 μg/ml), 1.11 μM (0.22 μg/ml) and 1.95 μM (0.33 μg/ml) respectively. Ibuprofen was selected as the positive control in our study and the results showed that ibuprofen potently inhibited the activity of COX2 with an IC50 value of 50.09 μM (10.33 μg/ml).

As a result, the network target of GZFLC was significantly enriched in MAPK signaling pathway. MAPKs could increase cPLA2 activity and hence result in prostaglandin production and myometrial contraction (Lin et al., 1993). Therefore, we used the immunofluorescence assay to determine whether GZFLC could affect MAPK signaling pathway to reduce myometrial contraction. We found that uterine smooth muscle cells in oxytocin-induced dysmenorrhea murine model displayed the increase of p-SAPK/JNK, p-p44/42 MAPK (Erk1/2) and p-p38 protein levels, and this effect was attenuated in cells pre-treated with GZFLC (25 $g \cdot L^{-1}$) as shown in **Figure 4B**, which suggested that GZFLC could downregulate the MAPK signaling pathway.

Integrating network target analysis and *in vitro* experiments, as shown in **Figure 4C**, GZFLC could inhibit the activity of COX2 and

TABLE 1 | Several enriched biological processes and signaling pathways predicted to be regulated by GZFLC using functional enrichment analysis.

Class	Biological processes and signaling pathways	*p*-value
Pain	cAMP signaling pathway	8.80E-14
	MAPK signaling pathway	1.12E-10
	cGMP-PKG signaling pathway	5.75E-10
	HIF-1 signaling pathway	1.42E-08
	Sensory perception of pain	4.37E-05
	Muscle contraction	7.28E-05
	Regulation of neurotransmitter levels	2.74E-03
	Regulation of cytosolic calcium ion concentration	5.64E-03
Inflammation	Cytokine-mediated signaling pathway	8.65E-20
	Inflammatory response	4.43E-14
	Inflammatory mediator regulation of TRP channels	8.90E-05
	NF-kappa B signaling pathway	1.20E-03
Endocrine	Steroid hormone mediated signaling pathway	1.39E-23
	Estrogen signaling pathway	8.25E-18
	Regulation of hormone levels	1.34E-17
	Prolactin signaling pathway	1.36E-13
	Oxytocin signaling pathway	1.79E-05
	GnRH signaling pathway	1.58E-02
	Steroid hormone biosynthesis	2.21E-02
Blood circulation	Blood circulation	9.66E-18
	VEGF signaling pathway	1.63E-06
	Platelet activation	3.01E-06
	Blood coagulation	3.26E-06
	Regulation of blood pressure	1.73E-05
	Blood vessel development	4.37E-04
Energy metabolism	PPAR signaling pathway	2.01E-13
	ATP metabolic process	8.81E-09
	AMPK signaling pathway	4.53E-09

downregulate MAPK signaling pathway to reduce the production of PGs and myometrial contraction to exert analgesia effects for treating primary dysmenorrhea. In addition, GZFLC could regulate cytosolic calcium ion concentration, intervene oxytocin receptor (OTR) to reduce myometiral contraction and decrease inflammation, which was validated in literatures (Sun et al., 2016a; Zhong et al., 2016b) and subsequent *in vivo* experiments.

Primary dysmenorrhea is also related to imbalances in women's endocrine system during the menstrual cycle (Britannica, The Editors of Encyclopedia, 2016). And a color Doppler study (Altunyurt et al., 2005) has found that there was increased impedance to blood flow within the uterus of patients with primary dysmenorrhea on the first day of the menstrual cycle, suggesting the disturbance of blood circulation in primary dysmenorrhea patients. Meanwhile, a previous study (Xiong et al., 2019) has found that there were disorders of energy metabolism in primary dysmenorrhea rats. Thus, Blood circulation, endocrine and energy metabolism may be three important functional modules to be regulated to gain sustained beneficial effects. According to the network target analysis, GZFLC was predicted to regulate blood circulation, endocrine and energy metabolism-related biological processes and signaling pathways, which may contribute to the sustained beneficial effects of GZFLC on primary dysmenorrhea. The effect of GZFLC on blood circulation, endocrine and energy metabolism have been verified in literatures (Su et al., 2015; Sun et al., 2016a; Xiong et al., 2019).

Effects of GZFLC on Primary Dysmenorrhea in Oxytocin-Induced Murine Model

We have investigated the effect of GZFLC on the writhing response in oxytocin-induced dysmenorrhea murine model to study its analgesic activity. Analgesic activity was determined by observed decreases of writhing times in oxytocin-induced murine model, which was a method for quantitative evaluation of pain. As shown in **Figure 5**, GZFLC significantly inhibited the oxytocin-induced writhing response. The inhibition percentages of writhing times were 43.3% and 52.8% after oral administration of GZFLC (0.54 g/kg and 1.08 g/kg) respectively while 85.5% after oral administration of ibuprofen. The numbers of writhing times at GZFLC groups (0.54 g/kg and 1.08 g/kg) and ibuprofen group (0.1 g/kg) were 18.5 ± 4.5, 15.4 ± 4.6 and 5.9 ± 2.1 respectively, significantly lower than that of the model group (32.6 ± 8.5). Each herbal medicine in GZFLC was of the same amount and their dosages and ratios were the same as the traditional dosages and ratios in Guizhi Fuling Wan (Committee 2015). Next, we have investigated effect of GZFLC on uterine histopathology in oxytocin-induced dysmenorrhea murine model. As shown in **Figures 6A,B**, the histopathological results showed that compared with the normal group, the model group mainly showed degeneration and necrosis of endometrial epithelial cells, lamina propria edema, a small amount of inflammatory cell infiltration, reduced number of glands in the lamina propria, secretions in the gland cavity, and the disordered arrangement of smooth muscle cells in the muscle layer. There was a significant difference between the model group and the normal group, indicating that the oxytocin-induced dysmenorrhea murine model was successfully constructed. Meanwhile, ibuprofen and GZFLC had the effect on reducing the degree of uterine lesions as shown in **Figures 6C–E**. Moreover, there was a significant difference in 1.08 g/kg of GZFLC group compared with the model group ($p < 0.05$) as shown in **Figure 6F**.

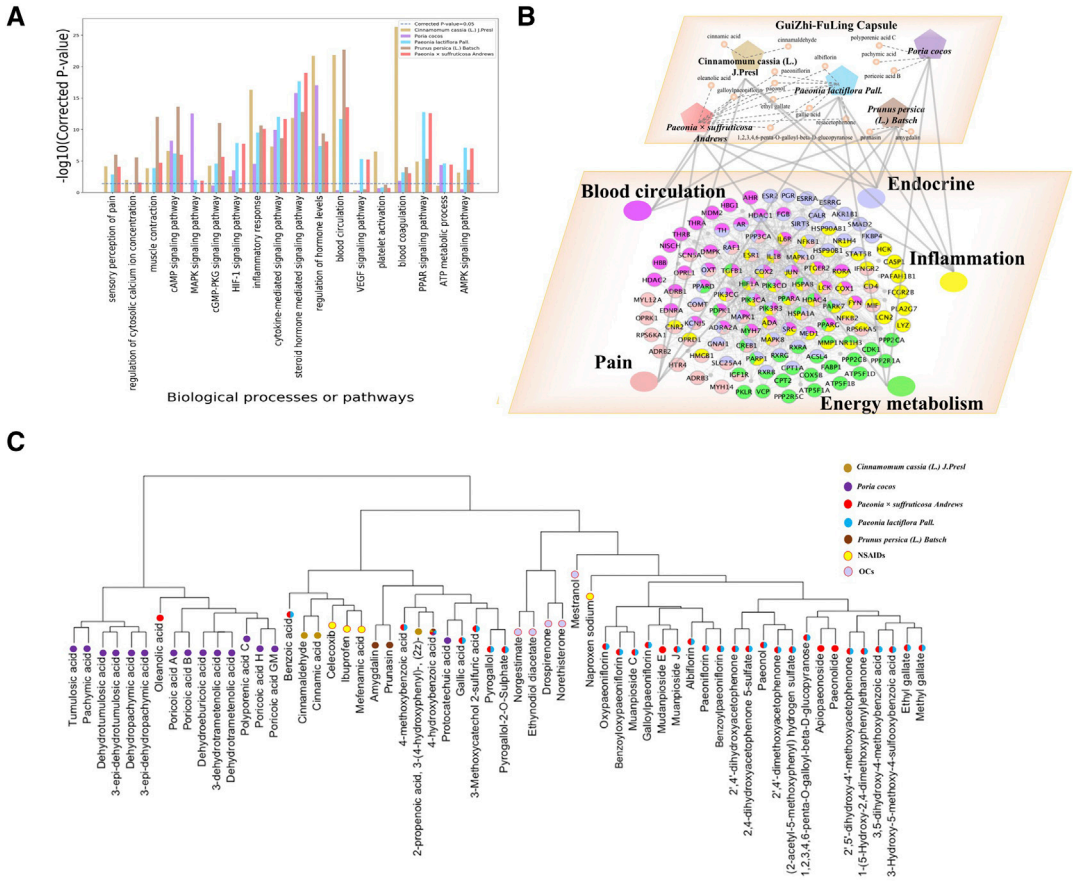

FIGURE 3 | (A)Functional enrichment analysis of each herb's potential targets (B)Herbs-compounds-biological functional modules-biological molecules network to depict the underlying biological mechanisms of GZFLC (Different color nodes represent different function module and its related biomolecules, namely, fuchsia nodes: Blood circulation function module and its related biomolecules; lavender nodes: Endocrine function module and its related biomolecules; yellow nodes: Inflammation function module and its related biomolecules; green nodes: Energy metabolism function module and its related biomolecules; pink nodes: Pain function module and its related biomolecules.) **(C)Hierarchical clustering tree of GZFLC compounds and current anti-primary dysmenorrhea drugs.**

DISCUSSION AND CONCLUSION

Guizhi-Fuling capsule, derived from a classic herbal formula, has been used for the therapy of primary dysmenorrhea for a long time in China. The clinical data has shown the analgesic and sustained beneficial effects of GZFLC on menstruating women with primary dysmenorrhea. However, the pharmacological mechanisms of GZFLC on primary dysmenorrhea are less characterized from a holistic perspective. In this study, we analyzed underlying pharmacological mechanisms of GZFLC in terms of two major clinical effects of GZFLC on primary dysmenorrhea. Generally, the network target analysis of GZFLC indicated that GZFLC may exert analgesic and sustained beneficial effects on primary dysmenorrhea through these five biological functional modules including pain, inflammation, endocrine, blood circulation, and energy metabolism.

GZFLC exerted therapeutic effects on basis of its compounds and their intervention on targets. For analgesic effect, GZFLC and four predicted compounds, including 1,2,3,4,6-penta-O-galloyl-beta-D-glucopyranose, galloylpaeoniflorin, ethyl gallate and gallic acid, were verified to inhibit COX2 activity *in vitro* through COX2 activity assays, which gave hints that 1,2,3,4,6-penta-O-galloyl-beta-D-glucopyranose, galloylpaeoniflorin, ethyl gallate and gallic acid could be used as quality control markers of GZFLC in the treatment of primary dysmenorrhea. In the meanwhile, COX2 and its production PGF2α could be used as optimizing objective and quantitative surrogate outcomes of GZFLC for primary dysmenorrhea. In addition, GZFLC was verified to downregulate MAPK signaling pathway in uterine smooth muscle cells to reduce uterine smooth muscle contraction via an immunofluorescence assay.

From perspectives of TCM, GZFLC is mainly used to treat blood stasis syndromes, and a meta-analysis of randomized clinical trials for GZFLC in the treatment of primary dysmenorrhea (Xing et al., 2019) suggested that GZFLC may be more effective on primary dysmenorrhea in a subgroup of patients with cold blood stasis syndrome, which is one of the common cold syndromes. According to our previous research (Ma et al., 2010), cold syndromes related genes acted as a pivotal part in

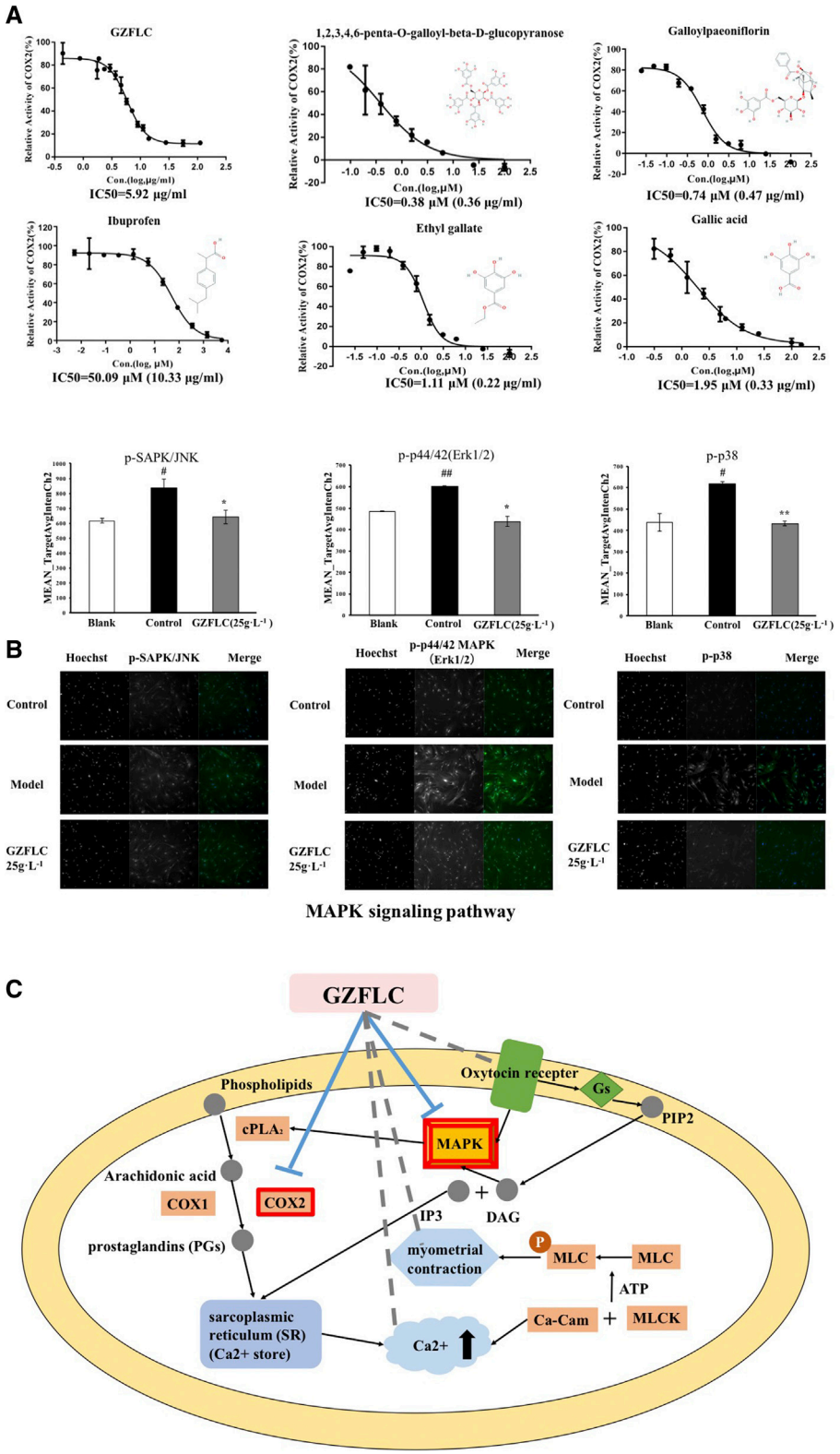

FIGURE 4 | The potential molecular mechanisms of analgesia effects of GZFLC on primary dysmenorrhea (A) GZFLC and four of its compounds were verified to inhibit COX2 *in vitro*, ibuprofen was selected as a positive control **(B)** GZFLC was verified to downregulate predicted MAPK signaling pathway in uterine smooth muscle cells. *$p < 0.05$, **$p < 0.01$, GZFLC group compared with Model group. #$p < 0.05$, ##$p < 0.01$, Model group compared with blank group. Data was

(*Continued*)

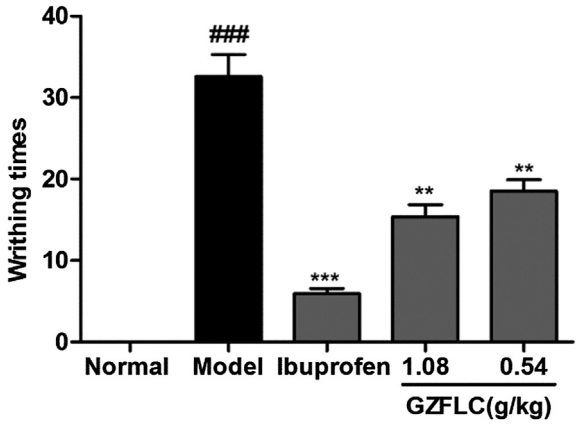

FIGURE 5 | Effects of GZFLC on writhing response in oxytocin-induced dysmenorrhea murine model. ICR mice were divided into five groups as follows: normal group, model group (0.5% CMC-Na, 20 ml/kg), ibuprofen (0.1 g/kg) and the GZFLC groups of different doses (0.54 g/kg and 1.08 g/kg). The number of animal writhing times was observed and recorded within 30 min after injection of oxytocin. $^{**}p < 0.01$, $^{***}p < 0.001$, GZFLC group compared with Model group. $^{###}p < 0.001$, Model group compared with normal group. Data was represented as $\overline{X} \pm SEM$ (n = 10).

energy metabolism, which were tightly connected with the genes of neurotransmitters, hormones and cytokines in the neuro-endocrine-immune interaction network. Interestingly, the network target analysis has found that GZFLC could reduce pain and inflammation, improve endocrine, blood circulation and energy metabolism, which were consistent with the cold syndrome related biological modules. Hence, our study about the pharmacological mechanisms of GZFLC on primary dysmenorrhea could give a potential explanation to the underlying biological basis of the subgroup results in clinical trials.

Oxytocin-induced murine model is a commonly used animal model for primary dysmenorrhea. Our study has investigated the effect of GZFLC on the writhing response, uterine histopathology in oxytocin-induced dysmenorrhea murine model. The results showed that GZFLC could significantly inhibit the writhing response in oxytocin-induced dysmenorrhea murine model. Our network target analysis results about mechanisms of anti-primary dysmenorrhea of GZFLC were partially validated by *in vivo* experiments. The pathological assay showed that high dose of GZFLC had a significant effect on reducing the degree of uterine lesions, indicating that GZFLC could decrease inflammation. These results gave support to efficacy of GZFLC on primary dysmenorrhea. Moreover, The experiment in the early study showed GZFLC markedly reduced the expression of COX2 in uterus tissue of the experimental murine models induced by oxytocin (Sun et al., 2016a). Meanwhile, the previous study showed GZFLC suppressed P42/44 MAPK phosphorylation level in the uterus tissue in PGF2α-induced model animals (Sun et al., 2016b).

In total, GZFLC could treat primary dysmenorrhea through "multi-compound, multi-target, multi-pathway" mode, which distinguished it from two kinds of first-line drugs with few targets to selectively act on. Network target derived from the multi-target nature of TCM could be preferable to analyze and reflect complicated interactions between biological molecules of the human body and chemical compounds in TCM formulae from the perspective of network (Li and Zhang 2013). There are also some limitations in this study. Firstly, some compounds in GZFLC have been ignored which may lead to bias in our study. However, we have selected important phytochemistry and absorbed compounds of GZFLC as representatives. Secondly, the exploration about relationship between the predicted compounds, targets and functional interpretation and dosages and ratios of GZFLC compounds was limited. The analysis about dosages and ratios of compounds in TCM formulae is of great significance, which has addressed lots of researchers' attention. There also have been several research methods developed for this issue (Zhou and Su 2019), and it is urgent to develop more appropriate methods in network pharmacology to investigate this issue. We would explore this issue in more depth in the further study. Briefly, we would first clarify the dosages and ratios of GZFLC's representative compounds using component analysis technology such as liquid chromatography-mass spectrometry (LC-MS), then we would predict those compounds' intervention intensity on targets and integrate their comprehensive effects on interacting targets of different biological functions within the primary dysmenorrhea related biological molecular network based on quantitative network pharmacology analysis in silico.

In summary, this work adopted combination of computational and experimental methods to reveal the underlying pharmacological mechanisms of GZFLC on primary dysmenorrhea. In the network target analysis, GZFLC may act on five functional modules of pain, inflammation, endocrine, blood circulation and energy metabolism. Next, we found that GZFLC significantly inhibited the writhing response and reduced the degree of uterine lesions in oxytocin-induced murine dysmenorrhea model. Furthermore, GZFLC may partially alleviate primary dysmenorrhea by inhibiting COX2 and downregulating MAPK signaling pathway *in vitro*. Thus, GZFLC presented pain relief and sustained benefits for primary dysmenorrhea. The results of this study showed that integrating TCM Network pharmacology and several different experimental methods could effectively elucidate underlying biological molecular mechanisms of GZFLC and identify part of the bioactive compounds. This study could provide a scientific approach for deciphering the pharmacological mechanisms of TCM herbal formulae and developing potential optimizing objective and quantitative surrogate outcomes of GZFLC for primary dysmenorrhea through network pharmacology.

FIGURE 4 | represented as $\overline{X} \pm SD$ (n = 3) **(C)**The regulatory mechanisms of analgesia effects induced by a group of compounds from GZFLC (red rectangle represents that GZFLC-targeted pathways and biological molecules are from network target analysis and have been verified by bioassays. Gray dotted line represents that GZFLC could regulate biological molecules or processes from network target analysis which were verified in literatures.)

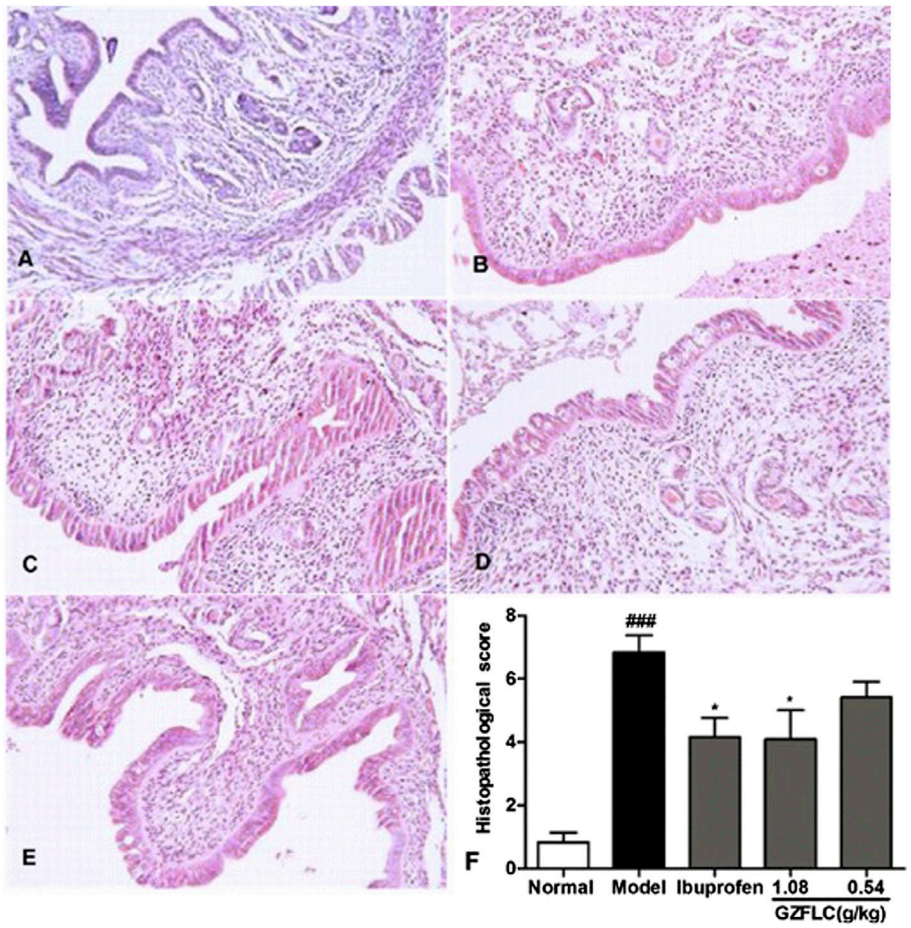

FIGURE 6 | (A-E) Photomicrography of the uterine tissues with H&E staining in normal group, model group, ibuprofen (0.1 g/kg), GZFLC groups (1.08 g/kg and 0.54 g/kg) respectively (F) Effects of GZFLC on uterine histopathology in oxytocin-induced dysmenorrhea murine model. *$p < 0.05$, GZFLC group compared with Model group. ###$p < 0.001$, Model group compared with normal group. Data was represented as $\overline{X} \pm SD$ (n = 6).

DATA AVAILABILITY STATEMENT

The raw data supporting the conclusions of this article will be made available by the authors, without undue reservation.

ETHICS STATEMENT

The animal study was reviewed and approved by the Animal Ethics Committee of the Institutional Animal Care and Use Committee (IACUC) of Kanion Pharmaceutical Co., Ltd.

AUTHOR CONTRIBUTIONS

SL designed and supervised the study. SZ, XW, and SL performed the computational analysis. XL, GL, ZW, LC, XZ, and WX performed the experimental analysis. All authors discussed the results and wrote the manuscript.

FUNDING

This study was supported by the National Natural Science Foundation of China (6201101081, 81630103, and 81225025), Tsinghua University Spring Breeze Fund (2020Z99CFY040) and Beijing National Research Center for Information Science and Technology (BNR2019TD01020 and BNR2019RC01012).

SUPPLEMENTARY MATERIAL

The Supplementary Material for this article can be found online at: https://www.frontiersin.org/articles/10.3389/fphar.2021.613104/full#supplementary-material.

REFERENCES

ACOG (2018). ACOG committee opinion No. 760: dysmenorrhea and endometriosis in the adolescent. *Obstet. Gynecol.* 132 (6), e249–e258. doi:10.1097/AOG.0000000000002978

Altunyurt, S., Göl, M., Altunyurt, S., Sezer, O., and Demir, N. (2005). Primary dysmenorrhea and uterine blood flow: a color Doppler study. *J. Reprod. Med.* 50 (4), 251–255.

Bernardi, M., Lazzeri, L., Perelli, F., Reis, F. M., and Petraglia, F. (2017). Dysmenorrhea and related disorders. *F1000Res.* 6, 1645. doi:10.12688/f1000research.11682.1

Britannica, The Editors of Encyclopaedia (2016). Dysmenorrhea. Edinburgh, Scotland: Encyclopaedia Britannica

Brune, K., and Patrignani, P. (2015). New insights into the use of currently available non-steroidal anti-inflammatory drugs. *J. Pain Res.* 8, 105–118. doi:10.2147/JPR.S75160

Burnett, M. A., Antao, V., Black, A., Feldman, K., Grenville, A., Lea, R., et al. (2005). Prevalence of primary dysmenorrhea in Canada. *J. Obstet. Gynaecol. Can.* 27 (8), 765–770. doi:10.1016/s1701-2163(16)30728-9

Campbell, M. A., and McGrath, P. J. (1999). Non-pharmacologic strategies used by adolescents for the management of menstrual discomfort. *Clin. J. Pain.* 15 (4), 313–320. doi:10.1097/00002508-199912000-00008

Cheng, Y., Chu, Y., Su, X., Zhang, K., Zhang, Y., Wang, Z., et al. (2018). Pharmacokinetic-Pharmacodynamic modeling to study the anti-dysmenorrhea effect of Guizhi Fuling capsule on primary dysmenorrhea rats. *J. Phymed.* 48, 141–151. doi:10.1016/j.phymed.2018.04.041

Committee, N. P. (2015). *Pharmacopoeia of the people's Republic of China*. Beijing, China: China Medical Science and Technology Press

Davis, A. P., Grondin, C. J., Johnson, R. J., Sciaky, D., McMorran, R., Wiegers, J., et al. (2019). The comparative Toxicogenomics Database: update 2019. *Nucleic Acids Res.* 47 (D1), D948–D954. doi:10.1093/nar/gky868

Hopkins, A. L. (2008). Network pharmacology: the next paradigm in drug discovery. *Nat. Chem. Biol.* 4 (11), 682–690. doi:10.1038/nchembio.118

Hu, Z., Tang, L., Chen, L., Kaminga, A. C., and Xu, H. (2020). Prevalence and risk factors associated with primary dysmenorrhea among Chinese female university students: a cross-sectional study. *J. Pediatr. Adolesc. Gynecol.* 33 (1), 15–22. doi:10.1016/j.jpag.2019.09.004

Iacovides, S., Avidon, I., and Baker, F. C. (2015). What we know about primary dysmenorrhea today: a critical review. *Hum. Reprod. Update.* 21 (6), 762–778. doi:10.1093/humupd/dmv039

Ji, H., Li, X., and Zhang, H. (2009). Natural products and drug discovery. Can thousands of years of ancient medical knowledge lead us to new and powerful drug combinations in the fight against cancer and dementia?. *EMBO Rep.* 10 (3), 194–200. doi:10.1038/embor.2009.12

Kho, K. A., and Shields, J. K. (2020). Diagnosis and management of primary dysmenorrhea. *JAMA.* 323 (3), 268–269. doi:10.1001/jama.2019.16921

Li, J., Sun, L., Li, H., Xiao, W., Bi, Y., and Wang, Z. (2012). HPLC fingerprint of guizhi fuling capsule. *Chin. Traditional Herbal Drugs.* 43 (7), 1333–1335. CNKI:SUN:ZCYO.0.2012-07-024

Li, J., Wang, J., Wu, J., Huang, W., Wang, Z., and Xiao, W. (2015). [Quality analysis of Guizhi Fuling capsule before and after application of in-process quality control in pharmaceutical production]. *Zhongguo Zhong Yao Za Zhi.* 40 (6), 1017–1022. doi:10.4268/cjcmm20150606

Li, S., and Zhang, B. (2013). Traditional Chinese medicine network pharmacology: theory, methodology and application. *Chin. J. Nat. Med.* 11 (2), 110–120. doi:10.1016/S1875-5364(13)60037-0

Li, S., Zhang, B., and Zhang, N. (2011). Network target for screening synergistic drug combinations with application to traditional Chinese medicine. *BMC Syst. Biol.* 5(Suppl. 1), S10. doi:10.1186/1752-0509-5-S1-S10

Li, S., Zhang, Z., Wu, L., Zhang, X., Li, Y., and Wang, Y. (2007). Understanding ZHENG in traditional Chinese medicine in the context of neuro-endocrine-immune network. *IET Syst. Biol.* 1 (1), 51–60. doi:10.1049/iet-syb:20060032

Li, S. (2015). Mapping ancient remedies: applying a network approach to traditional Chinese medicine. *Science* 350 (6262), S72–S74. doi:10.1126/science.350.6262.871-c

Li, S. (2011). [Network target: a starting point for traditional Chinese medicine network pharmacology]. *Zhongguo Zhong Yao Za Zhi* 36 (15), 2017–2020. doi:10.4268/cjcmm20111502

Li, X.-y., Jin, X., Li, Y.-z., Gao, D.-d., Liu, R., and Liu, C.-x. (2019). Network toxicology and LC-MS-based metabolomics: new approaches for mechanism of action of toxic components in traditional Chinese medicines. *Chin. Herbal Medicines.* 11, 357–363. doi:10.1016/j.chmed.2019.02.002

Liang, X., Li, H., and Li, S. (2014). A novel network pharmacology approach to analyse traditional herbal formulae: the Liu-Wei-Di-Huang pill as a case study. *Mol. Biosyst.* 10 (5), 1014–1022. doi:10.1039/c3mb70507b

Lin, L. L., Wartmann, M., Lin, A. Y., Knopf, J. L., Seth, A., and Davis, R. J. (1993). cPLA2 is phosphorylated and activated by MAP kinase. *Cell.* 72 (2), 269–278. doi:10.1016/0092-8674(93)90666-e

Liu, Y., Xiao, W., Wang, Z., Zhao, B., Zhou, Z., Jiang, H., et al. (2013). [Effects and safety of varying doses of guizhi fuling capsule in patients with primary dysmenorrhea: a multi-center, randomized, double-blind, placebo-controlled clinical study]. *Zhongguo Zhong Yao Za Zhi.* 38 (12), 2019–2022. doi:10.4268/cjcmm20131235

Ma, T., Tan, C., Zhang, H., Wang, M., Ding, W., and Li, S. (2010). Bridging the gap between traditional Chinese medicine and systems biology: the connection of Cold Syndrome and NEI network. *Mol. Biosyst.* 6 (4), 613–619. doi:10.1039/b914024g

Manzoli, L., De Vito, C., Marzuillo, C., Boccia, A., and Villari, P. (2012). Oral contraceptives and venous thromboembolism: a systematic review and meta-analysis. *Drug Saf.* 35 (3), 191–205. doi:10.2165/11598050-000000000-00000

Marjoribanks, J., Proctor, M., Farquhar, C., and Derks, R. S. (2010). Nonsteroidal anti-inflammatory drugs for dysmenorrhoea. *Cochrane Database Syst. Rev.* 2015(7), CD001751. doi:10.1002/14651858.CD001751.pub3

Mosher, A. A., Rainey, K. J., Bolstad, S. S., Lye, S. J., Mitchell, B. F., Olson, D. M., et al. (2013). Development and validation of primary human myometrial cell culture models to study pregnancy and labour. *BMC Pregnancy Childbirth.* 13 (Suppl. 1), S7. doi:10.1186/1471-2393-13-S1-S7

Proctor, M. L., Roberts, H., and Farquhar, C. M. (2001). Combined oral contraceptive pill (OCP) as treatment for primary dysmenorrhoea. *Cochrane Database Syst. Rev.* (4), CD002120. doi:10.1002/14651858.CD002120

Qi, Q., Li, R., Li, H., Cao, Y., Bai, M., Fan, X., et al. (2016). Identification of the anti-tumor activity and mechanisms of nuciferine through a network pharmacology approach. *Acta Pharmacol. Sin.* 37 (7), 963–972. doi:10.1038/aps.2016.53

Shannon, P., Markiel, A., Ozier, O., Baliga, N. S., Wang, J. T., Ramage, D., et al. (2003). Cytoscape: a software environment for integrated models of biomolecular interaction networks. *Genome Res.* 13 (11), 2498–2504. doi:10.1101/gr.1239303

Su, Z., Li, N., Cao, L., Wang, T., Zhang, C., Ding, G., et al. (2015). [Main progress on studies of pharmacological activities and clinical applications of Guizhi Fuling capsule]. *Zhongguo Zhong Yao Za Zhi.* 40 (6), 989–992. CNKI:SUN:ZGZY.0.2015-06-001

Sun, H., Cao, Y., Liu, J., Gao, J., and Ma, M. (2002). The establishment of the dysmenorrhea model in mice. *Chin. Pharmacol. Bull.* 18 (2), 233–236. doi:10.3321/j.issn:1001-1978.2002.02.032

Sun, L., Liu, L., Zong, S., Wang, Z., Zhou, J., Xu, Z., et al. (2016a). Traditional Chinese medicine Guizhi Fuling capsule used for therapy of dysmenorrhea via attenuating uterus contraction. *J. Ethnopharmacol.* 191, 273–279. doi:10.1016/j.jep.2016.06.042

Sun, L., Liu, L., Li, J., Lv, Y., Zong, S., Zhou, J., et al. (2017). The essential oil from the twigs of Cinnamomum cassia Presl inhibits oxytocin-induced uterine contraction *in vitro* and *in vivo*. *J. Ethnopharmacol.* 206, 107–114. doi:10.1016/j.jep.2017.05.023

Sun, L., Zhou, J., Zong, S., Ding, G., Wang, Z., Xiao, W., et al. (2016b). Inhibition effects and mechanism of guizhi fuling capsule and its containing active ingredients on uterine contraction. *World science and technology/modernization of traditional Chinese medicine and Materia Medica* 18 (2), 274–278. doi:10.11842/wst.2016.02.021

Wang, Z., Li, J., Dou, X., Zhao, Y., Bi, Y., Xiao, W., et al. (2009). Combined use of liquid chromatogram-massspectrometry in identification of characteristic peak in fingerprint of guizhi fuling capsule. *J. Nanjing Univ. Traditional Chin. Med* 25 (3), 194–196. doi:10.3969/j.issn.1000-5005.2009.03.012

Wishart, D. S., Knox, C., Guo, A. C., Cheng, D., Shrivastava, S., Tzur, D., et al. (2008). DrugBank: a knowledgebase for drugs, drug actions and drug targets. *Nucleic Acids Res*. 36, D901–D906. doi:10.1093/nar/gkm958

Wong, C. L. (2018). "Health-related quality of life among Chinese adolescent girls with Dysmenorrhoea." *Reprod. Health* 15, 80. doi:10.1186/s12978-018-0540-5

Xing, J., Song, D., Zhang, W., Guo, J., Wei, L., Lin, K., et al. (2019). Meta analysis of the effect of Guizhi Fuling Capsule on primary dysmenorrhea. *Hunan J. Traditional Chin. Med*. 35 (8), 126–131. doi:10.16808/j.cnki.issn1003-7705.2019.08.059

Xiong, Z., Lang, L., Gao, X., Xiao, W., Wang, Z., and Zhao, L. (2019). An integrative urinary metabolomic study of the therapeutic effect of Guizhi Fuling capsule on primary dysmenorrheal rats based 1H NMR and UPLC-MS. *J. Pharm. Biomed. Anal*. 164, 750–758. doi:10.1016/j.jpba.2018.11.039

Yang, H., Yang, B., Hu, Y., Cao, L., Wang, Z. Z., Zhu, K. J., et al. (2020). [Identification of chemical constituents in guizhi fuling capsules by UPLC-Q-TOF-MS/MS]. *Zhongguo Zhong Yao Za Zhi* 45 (4), 861–877. doi:10.19540/j.cnki.cjcmm.20191002.309

Yin, Q., Li, J., Qin, J., Huang, W., and Wang, Z. (2016). UPLC/Q-TOF-MS rapid analysis of components in plasma from guizhi fuling capsules. *Chin. J. Exp. Traditional Med. Formulae*. 22 (21), 83–86. doi:10.13422/j.cnki.syfjx.2016210083

Zhang, B., Wang, X., Li, Y., Wu, M., Wang, S., and Li, S. (2018). Matrine is identified as a novel macropinocytosis inducer by a network target approach. *Front. Pharmacol*. 9, 10. doi:10.3389/fphar.2018.00010

Zhang, Y., Cheng, Y., Liu, Z., Ding, L., Qiu, T., Chai, L., et al. (2017). Corrigendum to "Systematic screening and characterization of multiple constituents in Guizhi Fuling capsule and metabolic profiling of bioactive components in rats using ultra-high-performance liquid chromatography/quadrupole-time-of-flight mass spectrometry" [J. Chromatogr. B 1061-1062 (2017) 474-486]. *J. Chromatogr. B Analyt Technol. Biomed. Life Sci*. 1064, 160–161. doi:10.1016/j.jchromb.2017.09.016

Zhao, S., and Li, S. (2010). Network-based relating pharmacological and genomic spaces for drug target identification. *PLoS One* 5 (7), e11764. doi:10.1371/journal.pone.0011764

Zhong, Y., Jin, X., Gu, S., Peng, Y., Zhang, K., Ou-Yang, B., et al. (2016b). Integrated identification, qualification and quantification strategy for pharmacokinetic profile study of Guizhi Fuling capsule in healthy volunteers. *Sci. Rep*. 6, 31364. doi:10.1038/srep31364

Zhong, Y., Jin, X., Gu, S., Peng, Y., Xiao, W., Wang, Z., et al. (2016a). Anti-dysmenorrhea mechanism of Guizhifuling capsule based on its anti-inflammation effect. *Chin. J. Clin. Pharmacol. Ther*. 21 (10), 1095–1102.

Zhou, Y., and Su, S. (2019). Research methods of compatibility of traditional Chinese medicine formulas and its advances. *Chin. J. Exp. Traditional Med. Formulae*, 25, 202–208. doi:10.13422/j.cnki.syfjx.20191550

Zuo, J., Wang, X., Liu, Y., Ye, J., Liu, Q., Li, Y., et al. (2018). Integrating network pharmacology and metabolomics study on anti-rheumatic mechanisms and antagonistic effects against methotrexate-induced toxicity of qing-Luo-Yin. *Front. Pharmacol*. 9, 1472. doi:10.3389/fphar.2018.01472

Conflict of Interest: ZW, LC, and XZ, and WX were employed by State Key Laboratory of New-tech for Chinese Medicine Pharmaceutical Process/Key Laboratory for the New Technique Research of TCM Extraction and Purification/Jiangsu Kanion Pharmaceutical Co., Ltd.

The remaining authors declare that the research was conducted in the absence of any commercial or financial relationships that could be construed as a potential conflict of interest.

Copyright © 2021 Zhang, Lai, Wang, Liu, Wang, Cao, Zhang, Xiao and Li. This is an open-access article distributed under the terms of the Creative Commons Attribution License (CC BY). The use, distribution or reproduction in other forums is permitted, provided the original author(s) and the copyright owner(s) are credited and that the original publication in this journal is cited, in accordance with accepted academic practice. No use, distribution or reproduction is permitted which does not comply with these terms.

frontiers in Pharmacology

ORIGINAL RESEARCH
published: 08 March 2021
doi: 10.3389/fphar.2021.619311

The Protective Effects of Shengmai Formula Against Myocardial Injury Induced by Ultrafine Particulate Matter Exposure and Myocardial Ischemia are Mediated by the PI3K/AKT/p38 MAPK/Nrf2 Pathway

Lina Chen[1,2†], *Yuan Guo*[1,2†], *Shuiqing Qu*[1,2], *Kai Li*[1,2], *Ting Yang*[1,2], *Yuanmin Yang*[1,2], *Zhongyuan Zheng*[1,2], *Hui Liu*[1,2], *Xi Wang*[1,2], *Shuoqiu Deng*[1,2], *Yu Zhang*[1,2], *Xiaoxin Zhu*[1,2*] *and Yujie Li*[1,2*]

[1]*Artemisinin Research Center, China Academy of Chinese Medical Sciences, Beijing, China,* [2]*Institute of Chinese Materia Medica, China Academy of Chinese Medical Sciences, Beijing, China*

Background and Purpose: Ultrafine particulate matter (UFPM) induces oxidative stress (OS) and is considered to be a risk factor of myocardial ischemia (MI). Shengmai formula (SMF) is a traditional Chinese medicine with antioxidant properties and has been used to treat cardiovascular diseases for a long time. The aim of this study was to explore the protective role of SMF and the mechanism by which it prevents myocardial injury in UFPM-exposed rats with MI.

Methods: An MI rat model was established. Animals were randomly divided into five groups: sham, UFPM + MI, SMF (1.08 mg/kg·d) + UFPM + MI, SMF (2.16 mg/kg·d) + UFPM + MI, and SMF (4.32 mg/kg·d) + UFPM + MI. SMF or saline was administrated 7 days before UFPM instillation (100 μg/kg), followed by 24 h of ischemia. Physiological and biochemical parameters were measured, and histopathological examinations were conducted to evaluate myocardial damage. We also explored the potential mechanism of the protective role of SMF using a system pharmacology approach and an *in vitro* myoblast cell model with small molecule inhibitors.

Results: UFPM produced myocardial injuries on myocardial infarct size; serum levels of LDH, CK-MB, and cardiac troponin; and OS responses in the rats with MI. Pretreatment with SMF significantly attenuated these damages *via* reversing the biomarkers. SMF also improved histopathology induced by UFPM and significantly altered the PI3K/AKT/MAPK and OS signaling pathways. The expression patterns of *Cat*, *Gstk1*, and *Cyba* in the UFPM model group were reversed in the SMF-treated group. In *in vitro* studies, SMF attenuated UFPM-induced reactive oxygen species production, mitochondrial damage, and OS responses. The PI3K/AKT/p38 MAPK/Nrf2 pathway was significantly changed in the SMF group compared with that in the UFPM group, whereas opposite results were obtained for pathway inhibition.

OPEN ACCESS

Edited by:
Yan Xu,
Cleveland State University, United States

Reviewed by:
Ye Huang,
China Academy of Chinese Medical Sciences, China
Sarawut Kumphune,
Chiang Mai University, Thailand

***Correspondence:**
Yujie Li
yjli@icmm.ac.cn
Xiaoxin Zhu
xxzhu@icmm.ac.cn

[†]These authors have contributed equally to this work

Specialty section:
This article was submitted to Ethnopharmacology, a section of the journal Frontiers in Pharmacology

Received: *20 October 2020*
Accepted: *28 January 2021*
Published: *08 March 2021*

Citation:
Chen L, Guo Y, Qu S, Li K, Yang T, Yang Y, Zheng Z, Liu H, Wang X, Deng S, Zhang Y, Zhu X and Li Y (2021) The Protective Effects of Shengmai Formula Against Myocardial Injury Induced by Ultrafine Particulate Matter Exposure and Myocardial Ischemia are Mediated by the PI3K/AKT/p38 MAPK/Nrf2 Pathway. Front. Pharmacol. 12:619311. doi: 10.3389/fphar.2021.619311

Conclusion: These findings indicate that SMF prevents OS responses and exerts beneficial effects against myocardial injury induced by UFPM + MI in rats. Furthermore, the PI3K/AKT/p38 MAPK/Nrf2 signaling pathway might be involved in the protective effects of SMF.

Keywords: Shengmai formula, myocardial injury, ultrafine particulate matter, oxidative stress, PI3K/AKT/p38 MAPK/Nrf2 pathway

INTRODUCTION

Particulate matter (PM) is a complex mixture composed of coarse particles (diameter, 2.5–10 μm; $PM_{2.5–10}$), fine particles (diameter, ≤2.5 μm; $PM_{2.5}$), and ultrafine particles (diameter, ≤0.1 μm; $PM_{0.1}$ or UFPM). PM is considered an environmental risk factor and a life-threatening public health challenge for humans; PM pollution accounts for approximately 12% of the global burden of disease (Zhou et al., 2019). A growing number of epidemiological studies have demonstrated that UFPM is closely associated with morbidity and mortality due to both acute and chronic cardiovascular diseases (Ruckerl et al., 2007). Chen et al. reported that UFPM could trigger the onset of nonfatal myocardial infarction at a sub-daily timescale (Chen et al., 2020). Short-term acute exposure or long-term exposure to fine PM can cause acute cardiovascular events such as myocardial ischemia (MI), ischemic stroke, and congestive heart failure (Wei et al., 2019), which are favored by the smaller particles (Araujo and Nel, 2009). Consequently, UFPM can exert significant adverse effects on patients with cardiovascular disease, resulting in a large number of deaths.

Several mechanistic pathways are responsible for the cardiovascular effects of acute and chronic exposures to UFPM (Chin, 2015; Hadei and Naddafi, 2020). The translocation of pollutants may increase blood pressure, cause endothelial injury/dysfunction, and induce systemic oxidative stress (OS) (Lee et al., 2014) and inflammation (Tsai et al., 2012), which can cause thrombosis, coagulation (Chiarella et al., 2014), and arterial vasoconstriction (Rao et al., 2014) and decrease the heart rate variability, leading to MI events. Divergence in the toxicological mechanisms of PM could be attributed to the different origins of air particles with distinct chemical components that can trigger various pathways (Ronkko et al., 2018). Although different signaling pathways may be involved, systemic OS plays a major role in the cardiovascular effects of PM pollutants (Li R. et al., 2015; Miller, 2020).

Numerous treatment measures to alleviate the risk of PM exposure have been adapted and evaluated, including the use of masks or air purifiers and antioxidants (Zhong et al., 2017; Bolcas et al., 2019). In addition, extracts of traditional medicinal plants and natural products have been used to attenuate or prevent PM-induced injury in laboratory animals (Lee et al., 2019; Sanjeewa et al., 2020). Zhang reported that walnut protein isolates exerted protective effects in a PM-induced acute lung injury mouse model. The walnut protein isolates inhibited myeloperoxidase (MPO), nitric oxide (NO), interleukin-1β (IL-1β), and interleukin-6 (IL-6) in bronchoalveolar lavage fluid. In addition, pro-inflammatory cytokine production and acyl carrier protein levels were decreased by the walnut extract (Zhang et al., 2019). Tanshinone IIA effectively reduced $PM_{2.5}$ damage to EA.hy926 cells by inhibiting the p38/MAPK pathway (Jia et al., 2012). However, the therapeutic or preventive effects of these agents on MI events following exposure to UFPM have not been reported.

Shengmai formula (SMF) is composed of Ginseng radix et Rhizoma Rubra (*Panax ginseng* C. A. Mey.), Ophiopogonis Radix [*Ophiopogon japonicus* (Thunb.) Ker Gawl.], and Schisandrae Chinensis Fructus [*Schisandra chinensis* (Turcz.) Barll.]. SMF has long been used clinically for the treatment of heart failure and has outstanding curative effects on cardiovascular diseases owing to its free radical scavenging activity (Li F. et al., 2015). In addition, SMF increases superoxide dismutase (SOD) activity and reduces inflammatory and OS activities to protect the myocardium and strengthen the heart (Zhu et al., 2019). SMF is a strong natural antioxidant used in traditional Chinese medicine and has a 2000-year history of use. SMF has cardioprotective properties and strong antioxidant, anti-atherogenic, and immune-modulating effects (Ichikawa et al., 2003).

In the present study, the protective effects of SMF on myocardial injury after exposure to UFPM were tested in rat and H9C2 cell models. The aims of this study were to determine whether SMF could inhibit UFPM-induced OS responses in rats with MI and improve the recovery of myocardial tissue damaged following exposure to UFPM + MI. In addition, the potential mechanism involved in the process was examined. Network pharmacology, RT-qPCR, western blot analysis, and inhibitors were used to investigate the pharmacological effects of SMF on myocardial injury and identify potential therapeutic targets and pathways.

MATERIALS AND METHODS

Animals and Reagents

Healthy adult male Sprague Dawley rats weighing 200 ± 20 g were purchased from the China Institute of Food and Drug Testing. All rats were raised in light-controlled and air-conditioned (23 ± 2°C) rooms and had free access to food and water. This study was approved by the Animal Ethics Committee of the Institute of Chinese Materia Medica, China Academy of Chinese Medical Sciences. All reagents were purchased from Sigma-Aldrich (Missouri, United States) unless otherwise stated. UFPM (NIST® SRM® 1650b) was obtained from MilliporeSigma Corporate Offices (CAS Number 1333-86-4), and chemical characterization of UFPM can be found at https://www-s.nist.gov/srmors/certificates/1650b.pdf.

Quality Control and Preparation of Shengmai Formula

SMF was purchased from Beijing Tongrentang Co., Ltd. (batch number, 16262159). Beijing Tongrentang Co. is a Chinese pharmaceutical company founded in 1669 and is the largest producer of traditional Chinese medicine. The drug is a multi-herbal preparation prepared according to the Pharmacopoeia of the People's Republic of China (Chinese Pharmacopoeia Commission, 2010). High-performance liquid chromatography-mass spectrometry (HPLC-MS) was used to identify the main chemical components of SMF. The active ingredients are shown in **Supplementary Figure S1**; **Supplementary Table S1**. The concentration of two major compounds in SMF, schisandrin ($C_{24}H_{32}O_7$) and ruscogenin ($C_{27}H_{42}O_4$), were 0.022 mg/mg and 0.132 mg/mg, respectively, as determined using HPLC and ultraviolet-visible (UV-Vis) spectrometry. The chromatogram for schisandrin is shown in **Supplementary Figure S1**.

For the preparation of SMF, Ginseng radix et Rhizoma Rubra, Ophiopogonis Radix, and Schisandrae Chinensis Fructus were mixed at a ratio of 1:2:1 (w/w). These three ingredients were pulverized to a coarse powder and macerated in 65% ethanol for 24 h. Approximately 4,500 ml of percolate was collected and concentrated to approximately 250 ml under vacuum. After cooling, the solution was diluted with 400 ml of water and filtered. Next, 300 ml of 60% syrup and a quantity of preservative was added, the pH was adjusted to the specified range, and the volume was adjusted to 1000 ml. After stirring thoroughly, the solution was allowed to stand, filtered, packed, and sterilized. For detailed information on the three herbal ingredients in SMF, see **Supplementary Table S2**. The structures of active compounds in SMF are shown in **Supplementary Figure S2**.

SMF Administration, UFPM Exposure, and Myocardial Infarction Model

The rats were anesthetized with chloral hydrate (60 mg/kg, i.p.), and the specified dose of SMF or saline was given by oral administration daily for 7 days. Twenty-four hours after the final SMF administration, the animals were intubated with a tracheal tube through which 2.0 mg of UFPM suspended in 0.3 ml of saline was instilled (purchased from National Institute of Standards and Technology, Maryland, United States). MI was induced by ligating the left anterior descending coronary artery, as previously described (Wu et al., 2011; Li et al., 2012). The coronary artery was not ligated in the sham group. Specifically, the MI model with UFPM exposure was constructed by ligating the left anterior descending coronary artery, followed by 24 h UFPM exposure. Subsequently, the rats were killed after 24 h of ischemia.

Animal Experimental Design

The rats were randomly divided into five groups (n = 10 each) as follows: sham group; UFPM + MI group, treated with saline for 7 days before administration of UFPM followed by 24 h of ischemia; SMF (1.08 mg/kg·d, orally, 7 days) + UFPM + MI group, treated with SMF for 7 days before UFPM instillation, followed by 24 h of ischemia; SMF (2.16 mg/kg·d, orally, 7 days) + UFPM + MI group, treated with SMF for 7 days before UFPM instillation, followed by 24 h of ischemia; and SMF (4.32 mg/kg·d, orally, 7 days) + UFPM + MI group, treated with SMF for 7 days before UFPM instillation, followed by 24 h of ischemia (**Figure 1A**). To measure the effect of SMF on cardiac function from the pathological and blood indexes of heart tissue, lactate dehydrogenase (LDH), creatine kinase myocardial band (CK-MB), cTnT levels, triphenyl tetrazolium chloride (TTC) staining and hematoxylin and eosin (H&E) assays were performed. To further clarify which biological processes are affected by SMF, we tested the oxidative stress response based on previous reports. Generally, mitochondrial damage can lead to oxidative stress reaction. Therefore, we evaluated mitochondrial function-related indicators [mitochondrial membrane potential (MMP), Seahorse and mitochondrial ultrastructure], levels of myocardial malondialdehyde (MDA), NADPH oxidase (NOX), heme oxygenase-1 (HO-1), catalase (CAT), total SOD (T-SOD), and phospholipid hydroperoxide glutathione peroxidase (GSH-Px) and mRNA levels of *SOD1*, *CAT*, *GSH-Px*, and *NOX* in myocardial tissues. Furthermore, we sought to determine which pathway or molecule mediates the changes in oxidative stress.

Quantification of Infarct Size (Rats)

The infarct size was determined as described previously (Gao et al., 2011). Briefly, the heart was promptly removed after euthanasia and stored for 8 min at −80°C. Then, 2-mm-thick sections were cut, stained with 1% 2,3,5-triphenyl tetrazolium chloride (TTC) in phosphate buffer (pH 7.4) for 20 min at 37°C, and fixed overnight in 10% formalin. Normal myocardium was stained red by TTC, whereas infarcted myocardium was pale in color due to cell membrane damage. Images of the slices were acquired, and the myocardial infarct area was calculated as a percentage of the total area using Image-Pro Plus 6.0.

Measurement of Serum Lactate Dehydrogenase, Creatine Kinase MB, and Cardiac Troponin T Activities

LDH and CK-MB activities in serum were assessed using commercial kits (Nanjing Jiancheng Bioengineering Institute, Nanjing, China) according to the manufacturer's protocols, as described previously (Kim et al., 2017). LDH and CK-MB activities were expressed in U/L. Blood samples were obtained 24 h after MI, and serum cTnT levels were measured (pg/ml) using a commercial assay kit (ab246529, Cambridge MA, United States) according to the manufacturer's instructions, as described previously (Hortmann et al., 2017).

Assessment of Lipid Peroxidation and Antioxidant Enzymes

MD, NOX, HO-1, CAT, T-SOD, and GSH-Px levels in the heart and serum were measured using commercial kits (Nanjing Jiancheng Bioengineering Institute, Nanjing, China).

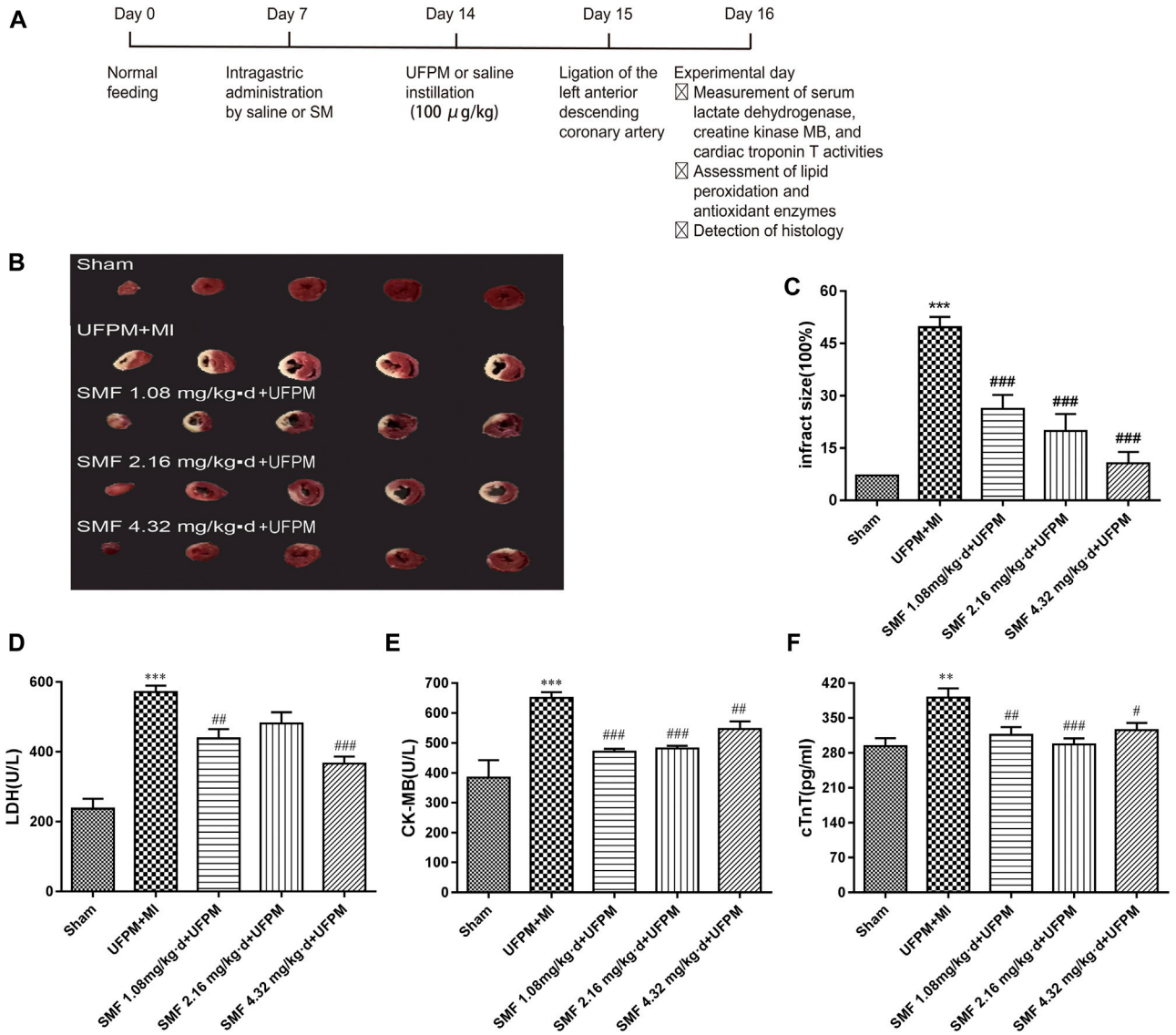

FIGURE 1 | SMF pretreatment protected against MI in UFPM-exposed rats with MI. **(A)** Treatments and endpoints following intratracheal instillation of saline or ultrafine particulate matter (UFPM) with or without repeated Shengmai formula (SMF) pretreatment (administered by oral gavage) in rats with myocardial ischemia (MI). **(B)** Isolated rat hearts taken after LAD ligation followed by 24 h of ischemia were sectioned and stained with TTC. **(C)** Infarct size quantification by TTC staining. Infarct sizes were quantified and expressed as a percentage of the total left ventricle area. Ratios were obtained in six rats per group (means ± SEM). Levels of **(D)** LDH, **(E)** CK-MB, and **(F)** cTnT in rat sera. All values are expressed as mean ± SD, $n = 6$ per group. LAD, left anterior descending; TTC, triphenyltetrazolium chloride. $^{*}p < 0.05$, $^{**}p < 0.01$ vs. sham. $^{\#}p < 0.05$, $^{\#\#}p < 0.01$ vs. UFPM + MI.

Histology

Twenty-four hours after MI induction, the hearts were removed, fixed in 4% paraformaldehyde, and embedded in paraffin. The paraffin-embedded tissues were sliced into 5-mm sections and stained with hematoxylin and eosin (H&E). An optical microscope (Olympus, Japan) was used to observe pathological changes in the tissues. To determine the myocardial ultrastructure, the myocardium was fixed in 3% glutaraldehyde, followed by fixation in 1% osmium tetroxide and dehydration in ethanol. Epoxy resin was used to embed the tissues, followed by the use of a hardener, accelerator, and growth agent. Subsequently, 70-nm-thick sections were cut using an ultra-microtome and stained with a solution containing uranyl acetate and lead citrate. Changes in the myocardial ultrastructure were observed using a JEM-1200EX transmission electron microscope (TEM, JEM 1200EX II, Jeol, Japan).

Network Pharmacology-Based Analysis

An integrated pharmacology network-computing platform for traditional Chinese medicine (TCMIP V2.0, http://www.Tcmip.cn,updated on September, 2019) (Xu et al., 2019) and the SymMap databases (https://www.symmap.org/) (Wu et al.,

2019) were used to collect the SMF compounds. TCMIP V2.0, SymMap, and Swiss Target Prediction (http://www.swisstargetprediction.ch/index.php) databases were used to predict the targets of active ingredients. Disease-associated target prediction was performed using DisGeNET (http://www.disgenet.org/web/DisGeNET/), Therapeutic Target Database (TTD), and Human Phenotype Ontology (HPO) databases and published literature. The potential targets of SMF were predicted using the DrugBank database (http://www.drugbank.ca/, version: 3.0). The relevant protein–protein interaction network was extracted from the Human Protein Reference Database and String databases. This information along with information about the herbs, ingredient-related proteins, and disease-related proteins were entered into a bioinformatics software, Cytoscape (version 3.7.1), to construct a complete network for SMF. The Kyoto Encyclopedia of Genes and Genomes (KEGG) pathway database was used to analyze the disease-related targets of SMF and toxicity-related pathways of UFPM.

Experimental Validation

Oxidative Stress-Related Gene Expression Analysis

Mitochondria of the heart tissue were homogenized and lyzed with Trizol reagent (Life Technologies) to extract total RNA after 24 h of MI. The extracted RNA samples were purified using the spin column-based RNeasy Mini Kit (Qiagen, Hilden, Germany). The quality and concentration of RNA were measured using a NanoDrop® ND-1000 spectrophotometer (Thermo Fisher Scientific, Massachusetts, United States). The A260/280 values of all the RNA samples were 1.8–2.1. cDNA was transcribed using the RT^2 First Strand Kit (Qiagen, Hilden, Germany). The RT^2 Profiler PCR array (Qiagen, 48-well format, catalog no. PARN-065ZA) was used to analyze gene expression using a Stratagene Mx3005P real-time (RT) quantitative polymerase chain reaction (qPCR) system (Agilent Technologies).

RT-qPCR Analysis

RT-qPCR assays for *Nrf2*, *HO-1*, *CAT*, *T-SOD*, *Gpx1*, *NQO1*, *NoX4*, and *GAPDH* (housekeeping gene) were performed for further validation (see **Supplementary Table S3** for primers). RNA was isolated and cDNA was synthesized using the High Capacity cDNA Reverse Transcription Kit (Invitrogen Life Technologies). Gene expression levels were determined by RT-qPCR using the SYBR Green PCR Master Mix (Qiagen, Hilden, Germany) and normalized to the level of the housing gene *GAPDH*. Gene expression levels in the SMF-treated group were expressed as fold-changes when compared with gene expression levels in the UFPM-exposed MI rats using the $2^{-\Delta\Delta CT}$ method. Similarly, the gene expression levels in the UFPM-exposed MI rats were determined by calculating the fold-change when compared with the sham control rats.

Cell Culture and Treatment

Rat myoblast cells (H9C2) were purchased from American Type Culture Collection and cultured in Dulbecco's modified Eagle's medium supplemented with 10% fetal bovine serum, 100 U/mL penicillin, and 100 μg/ml streptomycin (Gibco, Madison, United States) under sterile conditions. The cells were incubated with 5% CO_2 at 37°C. For the cell viability assay, H9C2 cells were exposed to UFPM (25, 50, 100, and 200 mg/ml) for 24 h or SMF (0.28, 0.56, 1.12, and 2.24 mg/ml) for 24 h. Cell Counting Kit 8 (WST-8/CCK8) (ab228554, Abcam) was used for analysis. To analyze the mechanism of SMF, H9C2 cells pre-incubated with either medium or LY294002 (50 μM)/SB 203580 (10 mM) for 4 h were then cultured with medium or SMF for 24 h followed by culture with or without UFPM (50 mg/ml) for 6 h. The lysates from H9C2 were resolved on 10% SDS-PAGE, transferred onto membranes, and blotted with specific antibodies. The supernatants were collected for analysis of OS biomarkers (T-SOD, CAT, GSH-PX, and NOX) using ELISA assays.

Seahorse Assay

The XFe96 Extracellular Flux Analyzer (Seahorse Bioscience) was used to measure oxygen consumption rates (OCRs) and extracellular acidification rates. The cells were diluted to 2× the final optical density, and 90 μl of cell culture was added to XF Cell Culture Microplates pre-coated with poly-D-lysine. The cells were centrifuged for 10 min at 1,400 × *g* in a Heraeus Multifuge ×1R (M-20 rotor) to attach them to the pre-coated plates. After centrifugation, 90 μl of fresh media was added to each well. To achieve uniform cell seeding, the initial OCR was measured for two cycles (7 min) before UFPM exposure. The maximal OCR that can be read on the analyzer is approximately 700–800 pmol/min; above this rate, the consumption rate exceeds the replenishment of the system and the curves show a false declination in OCR, which was excluded from the graphical presentation.

Western Blotting

Proteins were extracted from frozen heart tissues. The bicinchoninic acid protein assay was used to determine the protein concentration using bovine serum albumin as a standard (Pierce Rockford, IL). Equal amounts of proteins were loaded on SDS-PAGE gels; after separation, the proteins were transferred to a polyvinylidene difluoride membrane. The membranes were incubated with anti-MAPK p38 (CST, #8690S), p-MAPK p38 (CST, #4511S), rat anti-AKT (ab8805, Abcam), p-AKT (ab81283, Abcam), rabbit anti-Nrf2 (1:1000, 16396-1-AP, Proteintech), rabbit anti-PCNA (1:1000, 10205-2-AP, Proteintech), rabbit anti-HO-1 (1:1000, #82206S, CST), and rabbit antibody to β-Actin (1:2500, #8457, CST) antibodies. The bands were visualized by enhanced chemiluminescence and scanned using FLUORCHEM™ E (ProteinSimple, United States). The densitometric results were quantified using ImageJ software. The results from western blotting were normalized to the control group.

MAPK inhibitor (SB203580) was purchased from Merck-Millipore (Billerica, MA, United States), and PI3K inhibitor (LY294002, ab120243) was purchased from Abcam.

Statistical Analysis

Data were expressed as mean ± standard error of the mean. One-way analysis of variance was used to analyze the differences

TABLE 1 | Survival rates (%) after SMF pretreatment in UFPM-exposed rats with MI.

Groups[a]	SMF dose (mg/kg·d)	Survival rate (%)
Sham	—	66.7
UFPM + MI	—	45.0
UFPM + MI + SMF	1.08	66.7
	2.16	86.7
	4.32	73.3

[a]n = *15 animals per group. SMF, Shengmai formula; UFPM, ultrafine particulate matter; MI, myocardial ischemia.*

among the experimental groups. Dunnett's multiple comparison test was used for inter-group comparisons. A p-value of less than 0.05 was considered statistically significant.

RESULTS

Effects of UFPM Exposure, MI, and SMF on Survival Rates

Survival rates after UFPM exposure and 24 h of MI are shown in **Table 1**. The survival rate was 45% after UFPM exposure + MI and decreased compared with that in the sham group. Pretreatment with SMF (UFMI + MI + SMF groups) improved survival compared with that in the UFPM + MI group. Survival rates after 1.86, 2.16, and 4.32 mg/kg·d SMF pretreatment were 66.7, 86.7, and 73.3%, respectively.

MI Size Quantification

As shown in **Figures 1B,C**, a significant difference in myocardial infarct size was observed between the experimental and control groups. The myocardial infarct size in the UFPM-exposed MI group (49.69 ± 7.167) was significantly larger than that in the sham group (10.22 ± 2.739). Moreover, the infarct sizes were smaller in the SMF-treated groups than in the UFPM-exposed MI group (26.29 ± 9.684, 19.91 ± 11.92, and 10.56 ± 8.197 in the 1.86, 2.16, and 4.32 mg/kg·d SMF pretreatment groups, respectively). A typical example of a myocardial infarct is shown in **Figure 1B**.

Serum Markers of Myocardial Damage

Serum markers of myocardial damage are shown in. LDH levels significantly increased in the UFPM-exposed MI group compared with that in the sham group. However, SMF pretreatment significantly restored the LDH values to close to sham levels (**Figure 1D**). Furthermore, the CK-MB (212.3 U/L) and cTnT (97.7 pg/ml) levels in the UFPM-exposed MI group were significantly higher than those in the sham group (**Figures 1E,F**). These values were significantly improved by pretreatment with SMF in the UFPM-exposed MI group. These results indicate that SMF attenuated cardiac injury induced by UFPM exposure and MI.

Histopathological Assessment of Heart Tissues

To evaluate the effects of SMF on cardiac morphology, myocardial sections were stained with H&E (**Figure 2A**). The myocardial muscle fibers in the sham group were regularly arranged, and no edema was observed between the cells. In contrast, the tissues in the UFPM-exposed MI group exhibited moderate vascular edema, myocardial fiber edema, connective tissue hyperplasia, and enlarged myocardial fibers with inflammatory cell infiltration. These morphological signs of myocardial injury were attenuated in the SMF pretreated groups. Specifically, heart tissues in the low-dose SMF pretreatment group showed local hemorrhage, myocardial fiber edema, red blood cells between the myocardial fibers, and enlarged myocardial fibers with inflammatory cell infiltration. Myocardial tissues in the middle- and high-dose SMF pretreatment groups showed decreased numbers of red blood cells, reduced intracellular gaps between myocardial fibers, and reduced infiltration of inflammatory cells compared with myocardial tissues in the UFPM-exposed MI group.

The myocardial ultrastructure in rats in the sham group was generally normal (**Figure 2B**). The myocardial cells and nuclear membranes were intact, no edema was detected, the myofibril structure was neatly arranged, the mitochondrial structure was intact, the ridges were dense, and no swelling or vacuole-like changes were observed. The myocardial ultrastructure in rats in the UFPM + MI group demonstrated abnormal changes, including edema in some myocardial cells, blurred light and dark bands of muscle segments, broken myofilaments, swollen mitochondria, dissolved ridges, and vacuole-like changes. In the low-dose SMF pretreatment group, the size and number of lesions were reduced. Specifically, myofibrils were neatly arranged, the sarcomere structure was clear, the mitochondria were slightly swollen, and vacuole-like changes were observed in the low-dose SMF group. In the middle-dose SMF group, the size and number of myocardial lesions were also reduced compared with that in the UFPM + MI group, with fewer mitochondrial lesions, neatly arranged myofibrils, and clearly-structured sarcomeres. Moreover, the mitochondrial structure was found to be swollen occasionally and the palate was regular and dense.

Biomarkers of OS in Heart Tissue

Significant reductions in the levels of T-SOD, CAT, and GSH-Px (lowest levels reaching 13.5, 0.649, and 130 U/mL, respectively) were observed in the UFPM + MI rats compared with that in the sham group (**Figures 3A–C**). However, SMF pretreatment significantly restored the levels of antioxidant enzymes to those in the sham group. The HO-1, NOX, and MDA levels were increased significantly in the UFPM + MI rats compared with those in the sham group ($p < 0.05$), and these changes were attenuated in the SMF pretreatment groups ($p < 0.05$; 26.08 ± 5.0 vs. 33.4 ± 10.8 for NOX, 3.01 ± 0.6 vs. 4.36 ± 0.62 for MDA), as shown in **Figures 3D–F**. These results indicate that pretreatment with SMF improves the OS response to UFPM + MI.

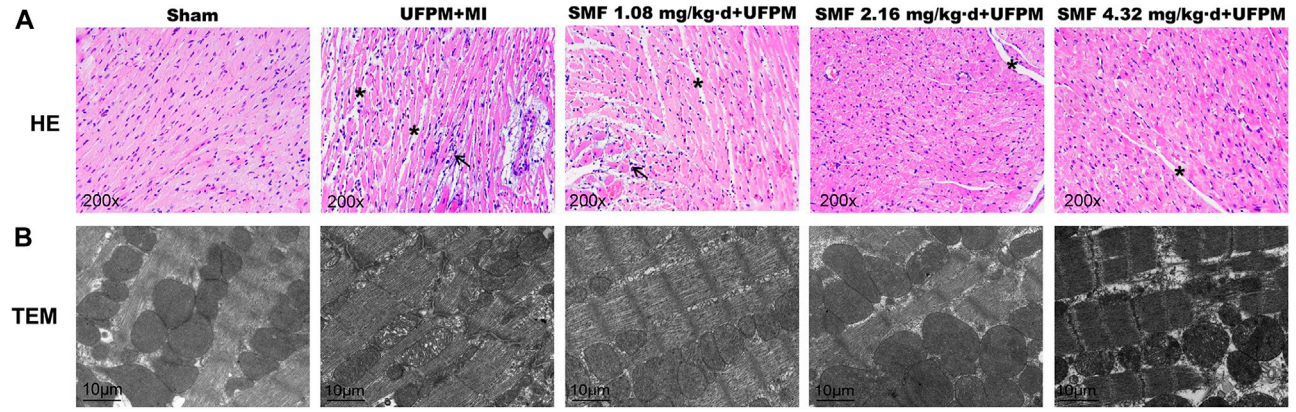

FIGURE 2 | Protective effects of SMF on toxic changes in myocardial tissues in acute UFPM-exposed rats with MI, as shown by hematoxylin and eosin (H&E) staining and transmission electron microscopy (TEM). Representative images of H&E staining (**A**, ×200) and TEM (**B**, bar = 10 μm) in myocardial tissues from the sham or MI groups pretreated with different SMF concentrations before UFPM exposure. MI, myocardial ischemia; SMF, Shengmai formula; UFPM, ultrafine particulate matter.

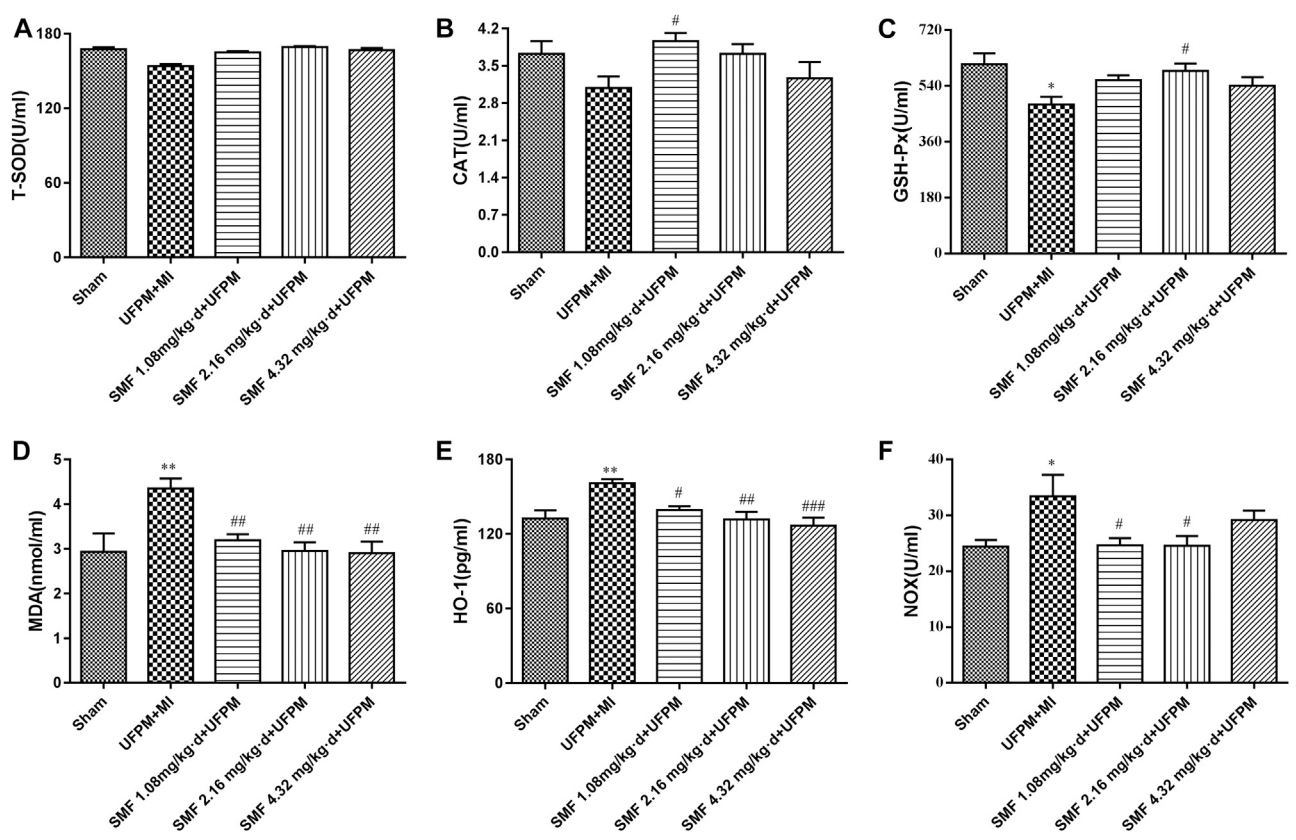

FIGURE 3 | Effects of SMF on UFPM-induced oxidative stress in rats with MI. **(A)** T-SOD (total superoxide dismutase), **(B)** CAT (catalase), and **(C)** glutathione peroxidase (GSH-Px) activity were measured in serum from the five experimental groups.**(D)** Malondialdehyde (MDA), **(E)** Heme oxygenase-1 (HO-1), and **(F)** NADPH oxidase (NOX) were analyzed. Data are represented as mean ± SEM. * and **, significant difference from sham group at $p < 0.05$ and $p < 0.01$; $^{\#, \#\#}$ and $^{\#\#\#}$, significant differences from the UFPM group at $p < 0.05$, $p < 0.01$, and $p < 0.001$, respectively. MI, myocardial ischemia; SMF, Shengmai formula; UFPM, ultrafine particulate matter.

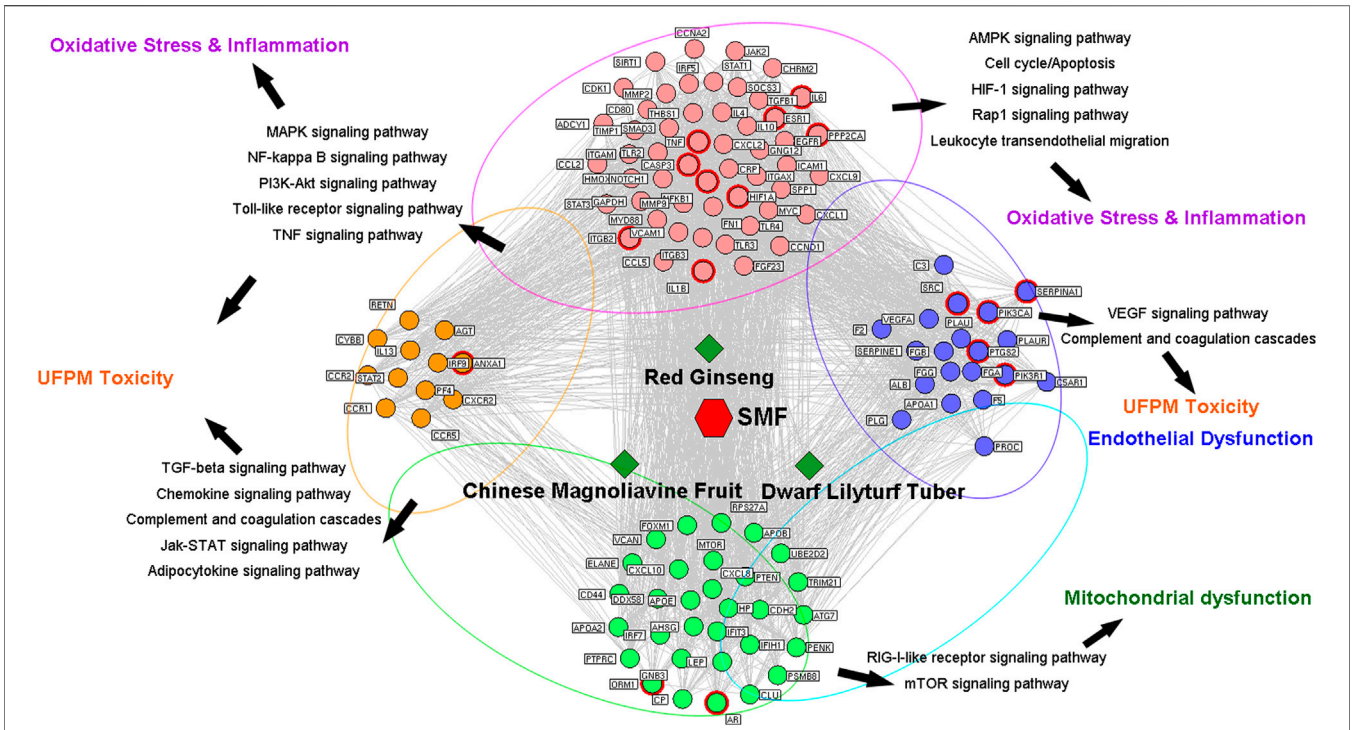

FIGURE 4 | UFPM, Cardiovascular disease-drug target-pathway network. The red node at the center of the figure corresponds to the Shengmai formula and the surrounding green diamond-shaped nodes are the three Chinese herbal medicines (Ginseng radix et Rhizoma Rubra, Ophiopogonis Radix, and Schisandrae Chinensis Fructus). The round nodes represent the key network targets in the "disease gene-drug target interaction network," where the red circles (the marked target genes) are candidates for the Shengmai formula, and the others are disease-related genes. The edges represent interactions among cardiovascular disease genes, herbs, and putative targets for the treatment of cardiovascular disease. The different color ovals represent the main pathways from the enrichment analysis of major targets in the "disease gene-drug target interaction network" and the previously described toxicity pathways of UFPM.

Network Pharmacology Analysis

To identify the molecular mechanism by which SMF attenuates myocardial damage in response to UFPM and MI, a UFPM-cardiovascular-drug target-pathway network analysis was performed based on the related proteins and their signaling pathways. Putative targets of SMF, composed of Ginseng radix et Rhizoma Rubra, Ophiopogonis Radix, and Schisandrae Chinensis Fructus, were predicted using the DrugBank database. A total of 475 putative targets for SMF were identified; 376 genes were predicted as putative targets after removing the duplicates (**Supplementary Table S4**). The cardiovascular-related genes were carefully collected from DisGeNET (3,240 genes), HPO (1,018 genes), and TTD (2,398 genes), and previously published research articles (1,347 genes) are listed in **Supplementary Table S5**. Subsequently, 1,343 genes were collected after removing the duplicates. A network was constructed, including the 376 predicted genes and 1,343 cardiovascular-related genes. The cutoff value was set at 0.626, and a total of 1,214 nodes and 6,370 pairs of interactions were included in the network.

The hubs in a network have excessively high levels of node degree and are likely to be major genes. Based on previous studies, we defined a node as a hub if the node degree was more than twice the median degree of all the nodes in the network (Li S. et al., 2007). Consequently, 354 nodes were identified as hubs, and an interaction network comprising these nodes was constructed (**Supplementary Table S6**). By calculating the topological characteristic values of these nodes based on the hub interaction network ("Degree," "Node betweenness," and "Closeness"), the major nodes and key network targets of SMF action were successfully screened, and 116 key network targets were obtained (**Supplementary Table S7**). A pathway enrichment analysis of the above network targets was performed based on the KEGG pathway by combining the UFPM toxicological pathways in cardiovascular diseases (CVDs) and the literature (**Figure 4**; **Supplementary Table S8**). Among the enriched pathways, the two largest functional modules were OS (PI3K/AKT, MAPK, and AMPK signaling pathways) and inflammation pathways (p53, chemokine, and NOD-like receptor signaling pathways and cytokine–cytokine receptor interactions). The other modules were involved in mitochondrial dysfunction and endothelial dysfunction. For SMF, IL-6, ESR1, PPP2CA, TNF, CASP3, NFKB1, ITGB2, IL-1β, HIF1A, SERPINE1, PIK3CA, PLAU, PTGS2, PIK3R1, and GNB3 were identified as major targets (red circle in **Figure 4**) that play essential roles in OS and inflammation and were regarded as the key markers of SMF treatment in CVD. Notably, the putative targets of TNF, CASP3, NFKB1, and IL-1β were involved in the p38 MAPK signaling pathway and were strongly associated with the pathological, toxicological, and pharmacological mechanisms

of CVD, UFPM, and SMF, respectively. The p38 MAPK signaling pathway can be stimulated by numerous stress signals, including OS, leading to the production of antioxidants. Based on the integrated UFPM-cardiovascular-drug target-pathway network, we propose that the antioxidant effects of SMF in rats subjected to UFPM exposure and MI are associated with key targets (TNF, CASP3, NFKB1, and IL-1β) regulating the OS response.

Furthermore, to gain the main chemical composition, we screened candidate compounds and predicted the gene targets of SMF (**Supplementary Table S9**), and an ingredient-target network of SMF was established. After eliminating all duplicate compounds and overlapping targets, SMF yielded 56 candidate compounds and a total of 290 targets were identified (**Supplementary Figure S3**). Specifically, the network included 155 nodes and 268 ingredient-target interactions. In the network, we found that IL-1β, TNF, CASP3, IL-4, FN1 and CCND1, which were involved in p38 MAPK/PI3K/AKT pathway, were targets of Kaempferol, Ginsenoside Rd, Ginsenoside Rf, Ginsenoside Rg1, Ginsenoside Rh2, 20-Glucosylginsenoside Rf, D-Limonene, Geraniol and Citral-B, as highlighted in **Supplementary Figure S3**. Additionally, by HPLC-MS assay, we identify the main chemical components of SMF, including Ginsenoside Rf, Ginsenoside Rg1, Ginsenoside Rh2, which were described above. Thus, we speculate that Ginsenoside Rf, Ginsenoside Rg1, Ginsenoside Rh2 could be the main chemical composition by which SMF play its protection roles *via* PI3K/AKT/p38 MAPK/Nrf2 pathway.

Experimental Validation

Evaluation of H9C2 Cell Viability After UFPM Exposure and SMF Treatment

H9C2 cells were exposed to various concentrations of UFPM, and alterations in cell viability were observed using the CCK8 assay. A dose-dependent decrease in cell survival was observed following UFPM exposure (**Supplementary Figure S4A**). Cells exposed to high doses of UFPM (50, 100, and 200 mg/ml) demonstrated significant reductions in cell viability ($p < 0.05$). The cell survival rate after 100 μg/ml UFPM exposure was approximately 57%. This group was selected for subsequent *in vitro* studies.

To examine the functional role of SMF, H9C2 cells were pretreated with 0.28, 0.56, 1.12, and 2.24 mg/ml SMF before UFPM exposure and cell viability was measured (**Supplementary Figure S4B**). Pretreatment with SFM resulted in significantly improved viability in UFPM-treated cells (concentrations 0.28, 0.56, and 1.12 mg/ml) compared with the vehicle ($p < 0.05$).

SMF Suppresses UFPM-Induced ROS Production in H9C2 Cells

UFPM induces ROS generation to promote OS. Therefore, we examined whether SMF could decrease ROS generation and the expression levels of ROS-dependent genes. First, we detected ROS by H2DCF-DA staining. **Supplementary Figure S4C** shows that the ROS levels in the H9C2 cells after UFPM exposure were significantly higher than those in the control cells. This effect was attenuated by SMF.

SMF Attenuated UFPM-Induced Mitochondrial Damage in H9C2 Cells

Previous studies showed that UFPM-induced OS promoted changes in the MMP. As shown in **Figures 5A,B**, JC-1 exhibited a monomeric form in UFPM-exposed cells and Δψm significantly decreased ($p < 0.05$). Compared with that in the UFPM group, the red fluorescence intensity in the SMF group increased and the green fluorescence intensity decreased. The red/green fluorescent signal ratios in the control and UFPM cells were 1.109 ± 0.39 and 0.50 ± 0.09, respectively, whereas the signal in the SMF (1.12 mg/ml) + UFPM group was 0.6935 ± 0.22 (**Figure 5B**).

To determine whether the SMF-induced attenuation of mitochondrial dysfunction in UFPM-treated cells was followed by functional changes in energetics, the Seahorse assay was used. We found that SMF increased OCR levels markedly under basal conditions (UFPM control, 33.63 ± 2.11 pmol/min; 0.56 mg/ml SMF, 40.11 ± 3.09; **Figure 5C**) and increased proton leak (UFPM control, 6.073 ± 0.79; 0.28 mg/ml SMF, 9.87 ± 0.58; **Figure 5D**), ATP production (UFPM control, 25.18 ± 1.07; 0.28 mg/ml SMF, 30.68 ± 2.16; **Figure 5E**), and non-mitochondrial respiration (UFPM control, 31.34 ± 2.01; 0.56 mg/ml SMF, 39.61 ± 4.69: **Figure 5F**) compared with that in UFPM-exposed cells.

PCR Array

Changes in the expression levels of several OS-associated genes were evaluated (**Figures 6A,B**). Of the 84 genes assayed in the array, the expression levels of two changed at least 2-fold (*Cyba* and *Ucp3*) and those of five changed 0.5-fold (*Cat*, *Gstk1*, *Cygb*, *Idh1*, and *Sqstm1*) in the UFPM-exposed MI rats compared with those in the sham control rats (**Table 2**). The expression levels of *Cat*, *Mb*, *Ucp3*, and *Txnrd2* were upregulated and the expression levels of *Txn1* and *Cyba* were downregulated in the SMF treatment group compared with those in the UFPM-exposed MI rats ($p < 0.05$; **Table 3**). The genes that exhibited opposite expression patterns in the drug and UFPM model groups were termed contrary genes (*Cat*, *Gstk1*, and *Cyba*). RT-qPCR was performed using these contrary genes to validate the results obtained by the PCR array analysis (**Figures 6C,D**). Trends in the expression levels of these genes confirmed that SMF treatment can maintain oxidative homeostasis.

Involvement of the p38 MAPK, PI3K/AKT, and Nrf2/HO-1 Pathways

We examined the effect of UFPM and SMF on p38 MAPK and PI3K/AKT signaling by measuring the expression levels of phosphorylated (p)-p38 MAPK and AKT in H9c2 cells (**Figures 7A,C**). The expression levels of p-p38 MAPK and p-AKT were significantly higher in the UFPM-treated group than in the untreated cells (**Figures 7B,D**; $p < 0.001$ and $p < 0.01$, respectively). Conversely, treatment with SMF significantly reduced p-p38 MAPK and p-AKT levels compared with those in the UFPM group ($p < 0.05$).

Nrf2/HO-1 is a positive downstream pathway of MAPK and PI3K. We investigated the potential effects of SMF on Nrf2/HO-1 in H9c2 cells by western blot analysis. UFPM exposure resulted in

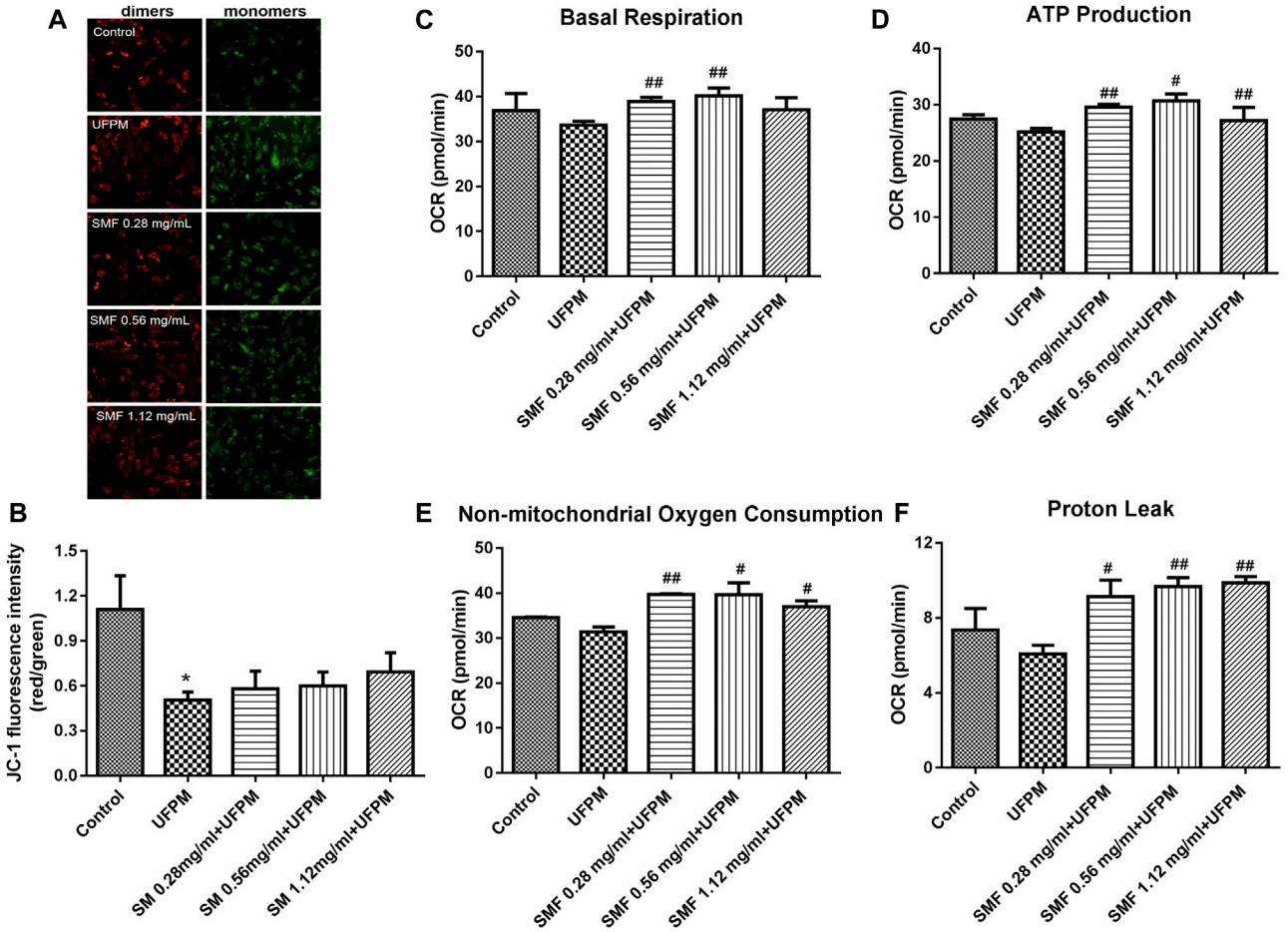

FIGURE 5 | SMF attenuated UFPM-induced mitochondrial damage in H9C2 cells. **(A)** Effects of the indicated concentrations of SMF on mitochondrial membrane potential in H9C2 cells. Representative images are shown. **(B)** The optical density ratio of the red and green fluorescence is shown. $^{*}p < 0.05$, compared to the control group. **(C–F)** SMF improves *in vitro* UFPM-induced mitochondrial activity. Basal respiration, ATP production, non-mitochondrial respiration, and proton leak of cells exposed to UFPM with or without SMF pretreatment. Oxygen consumption rate (OCR) was measured with a Seahorse metabolic analyzer. The data are presented as mean ± standard deviation ($^{*}p < 0.05$, $^{**}p < 0.01$ compared to the control group; $^{\#}p < 0.05$, $^{\#\#}p < 0.01$, $^{\#\#\#}p < 0.001$ compared to the UFPM group). MI, myocardial ischemia; SMF, Shengmai formula; UFPM, ultrafine particulate matter.

a considerable increase in the protein expression of HO-1 and nuclear Nrf2 ($p < 0.01$; **Figures 8A,B**). SMF treatment further increased HO-1 and Nrf2. The effects of p38 MAPK (SB 203580) and PI3K (LY294002) inhibitors on Nrf2/HO-1 expression were evaluated in H9c2 cells. As shown in **Figures 8A,B**, UFPM + SB203580/LY294002 treatment significantly decreased HO-1 and nuclear Nrf2 expression levels compared with those in the UFPM-exposed group ($p < 0.001$). However, SMF treatment significantly reversed this decrease ($p < 0.01$ and $p < 0.05$, respectively). These results suggest that UFPM can act as a stimulating factor for the translocation of free Nrf2 into the nucleus to increase the expression of antioxidant-stress proteins, while SMF can promote this activation. However, inhibitors of p38 MAPK and PI3K prevented these effects.

The combination of UFPM and SB203580/LY294002 significantly increased the levels of T-SOD, CAT, GSH-Px and reduced the level of NOX in the medium compared to UFPM exposure without inhibitors (**Figures 8C–I**). In contrast, when SMF was added to UFPM and SB203580/LY294002 treatment, the level of GSH-Px in the medium decreased (**Figures 8E,H**), compared with that in the SMF and UFPM treatment (without the inhibitors) ($p < 0.01$). Furthermore, SMF + SB203580/LY294002 administration increased the levels of the NOX factors in UFPM-exposed H9c2 cells compared with SMF treatment alone (**Figures 8F,I**), suggesting a slight reversal in the effect of SMF on the expression of NOX factors. These findings indicate that SMF exerts antioxidative effects on UFPM-induced H9c2 cells *via* the PI3K/AKT and p38 MAPK pathways.

DISCUSSION

In this study, we showed that SMF treatment can protect cells against UFPM-induced myocardial injury and OS events both *in vitro* and *in vivo*. In addition, UFPM exposure induced ROS

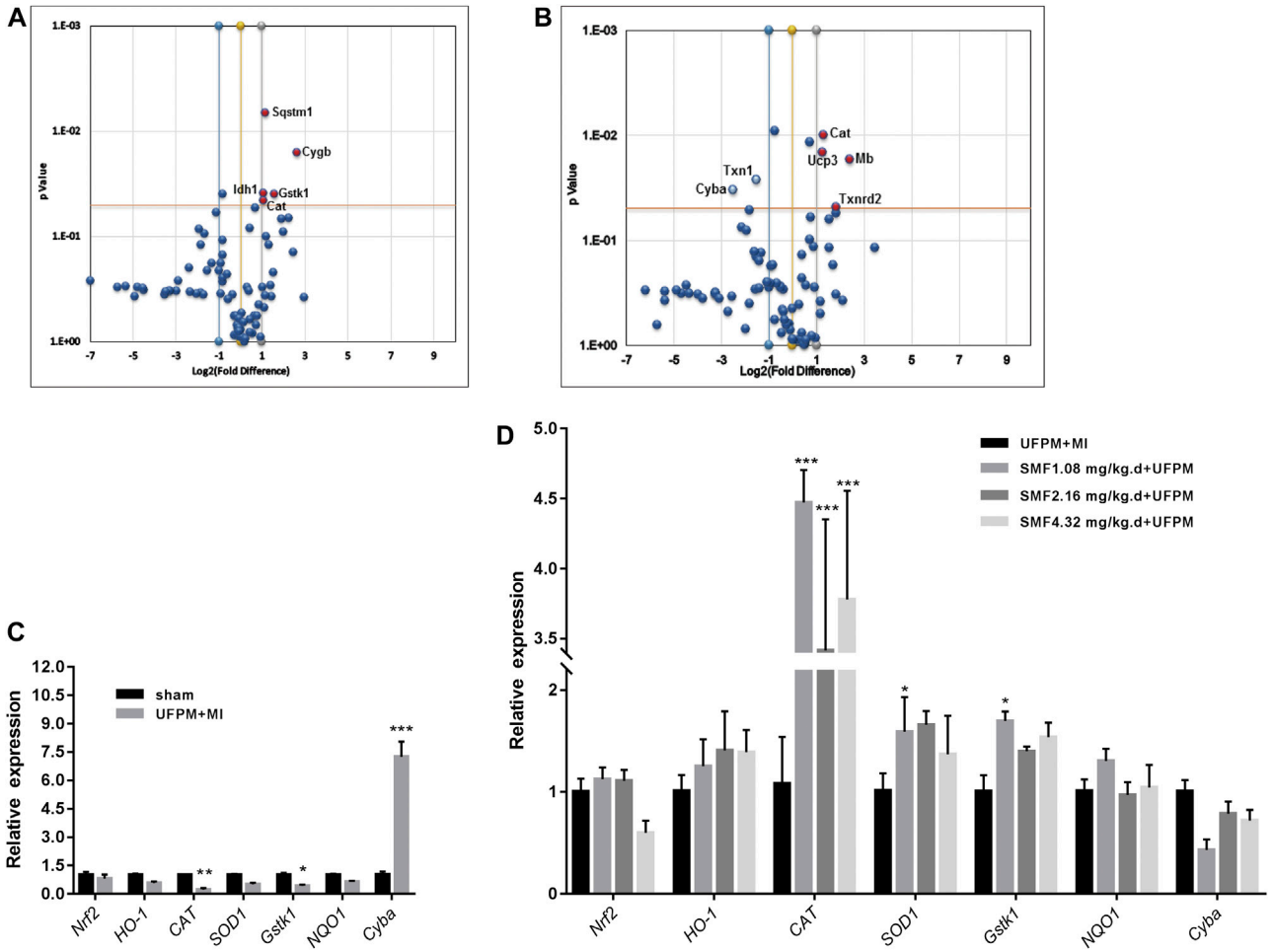

FIGURE 6 | RT^2 Profiler PCR array analysis of oxidative stress-related gene expression in the myocardial tissues of rats. **(A)** A scatter plot comparing the expression of 84 oxidative stress genes from rats exposed to UFPM gene expression in the sham controls. **(B)** A comparison of gene expression in rats pretreated with SMF before UFPM exposure to UFPM-exposed rats. Red solid circles identify genes with at least a 2-fold decrease **(A)** or a 2-fold increase **(B)** in expression. The central line represents unchanged gene expression and the boundaries represent the 2-fold cut-off value for changes in expression. **(C,D)** qRT-PCR validation of some oxidative stress genes. The histogram represents fold-changes in genes up- or downregulated in the UFPM group compared to the sham and SMF groups compared to the UFPM group.

TABLE 2 | Expression of oxidative stress-associated genes in UFPM-exposed rats with MI.

Symbol	Description	Fold-change ($2^{-\Delta\Delta Ct}$)	*p*-value
Cat	Catalase	0.47	0.0454*
Gstk1	Glutathione S-transferase kappa 1	0.34	0.0393*
Cyba	Cytochrome b-245, alpha polypeptide	2.15	0.0598
Ucp3	Uncoupling protein 3 (mitochondrial, proton carrier)	2.29	0.1005
Cygb	Cytoglobin	0.16	0.0159*
Idh1	Isocitrate dehydrogenase 1 (NADP+), soluble	0.48	0.0391*
Sqstm1	Sequestosome 1	0.45	0.007**

** and ** indicate significant differences from the sham group at* $p < 0.05$ *and* $p < 0.01$*, respectively. UFPM, ultrafine particulate matter; MI, myocardial ischemia.*

production, which activated the p38 MAPK/PI3K pathway, increased the expression levels of Nrf2/HO-1, and decreased the expression of antioxidative proteins. In contrast, SMF attenuated the UFPM-induced activation of MAPK/PI3K and increased the expression level of Nrf2, resulting in increased expression of HO-1 and antioxidative proteins.

In the present study, we analyzed the effect of acute exposure to UFPM on cardiovascular endpoints.The toxicity of PM can

TABLE 3 | Expression of oxidative stress-associated genes after SMF treatment in UFPM-exposed rats with MI.

Symbol	Description	Fold-change ($2^{-\Delta\Delta Ct}$)	*p*-value
Cat	Catalase	2.43	0.0100**
Gstk1	Glutathione S-transferase kappa 1	2.91	0.0627
Cyba	Cytochrome b-245, alpha polypeptide	0.18	0.0335*
Ucp3	Uncoupling protein 3 (mitochondrial, proton carrier)	2.40	0.0147*
Mb	Myoglobin	5.31	0.0171*
Txn1	Thioredoxin 1	0.34	0.0266*
Txnrd2	Thioredoxin reductase 2	3.57	0.0482*

** and ** indicate significant differences from the sham group at* $p < 0.05$ *and* $p < 0.01$ *vs. UFPM-exposed MI rats. UFPM, ultrafine particulate matter; MI, myocardial ischemia.*

influence remote organs, includingthe heart (Du et al., 2016). The intratracheal instillation method used in the present study is regarded as an efficient method for the delivery of foreign substances (Driscoll et al., 2000). The dosage of UFPM used in the current study was similar to the dosage in previous studies involving rat models exposed to PM (Adams et al., 2019).

Our data show that acute exposure to UFPM causes significant myocardial damage characterized by increased myocardial infarct size, increased serum CK-MB and cTnT, and histopathological injury to the heart. In the present study, exposure to UFPM resulted in cardiomyocytedamage and mitochondrial dysfunction. In addition, the appearance of hyperplastic connective tissue and increased inflammatory cells suggested that UFPM exacerbates myocardial tissue injury leading to myocardial fiber edema. This may explain the low survival rate after MI in rats and the increased cardiovascular events accompanying urban air pollution. In addition, we examined cTnI, LDH, and CK-MB levels in serum, as specific markers of myocardial damage. The levels of these myocardial damage markers were higher in rats after UFPM exposure and MI compared with sham rats, supporting the involvement of UFPM in myocardial dysfunction. Published studies also demonstrate that PM2.5 exposure aggravates myocardial damage in hyperlipidemia rats (Wang et al., 2019).

The mechanisms by which UFPM induces cardiac damage remain unclear. UFPM may affect extra-pulmonary sites *via* inflammatory factors produced in the lung and secreted into the circulation (Thomson, 2019). Alternatively, UFPM may avoid the normal defenses of the lungs and gain access to the heart or brain (Du et al., 2016). However, one study showed that OS plays a critical role in the toxic mechanism of UFPM; UFPM may induce the formation or aggregation of free radicals (Yang et al., 2014).

In our study, UFPM exposure and MI significantly modified the OS status in rats, as indicated by increased MDA and NOX. Meanwhile, in our *in vitro* study, elevated levels of ROS were

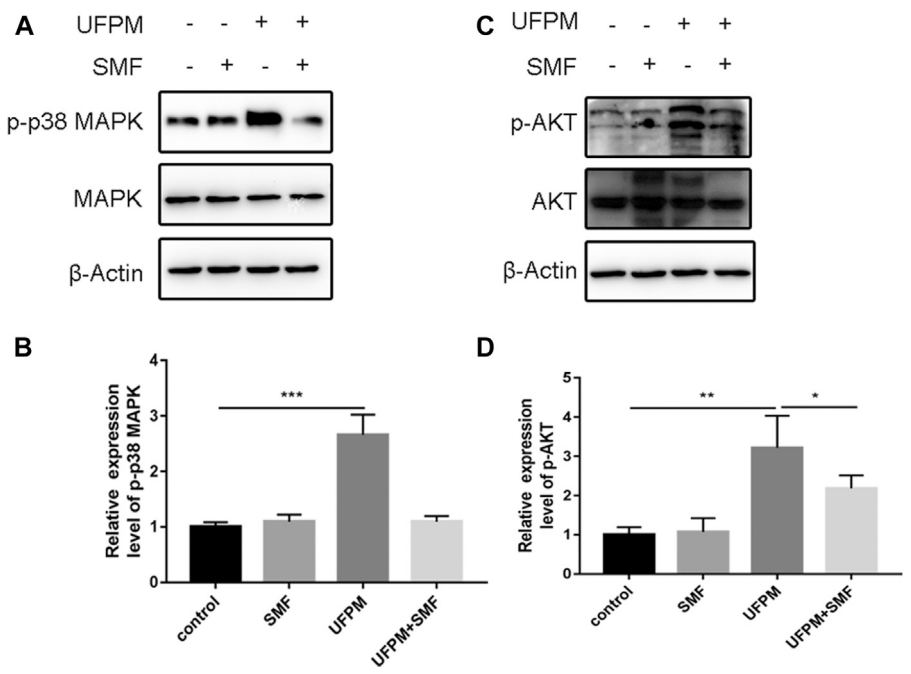

FIGURE 7 | SMF inhibits UFPM-induced p38 MAP kinase and PI3K/AKT activation. H9C2 cells pre-incubated with either medium or SMF (1.12 mg/ml) for 24 h were stimulated with UFPM (50 mg/ml) for 6 h. The lysates from H9C2 were analyzed by western blotting using specific antibodies to **(A)** phospho-p38 MAP kinase (p-p38 MAPK) and **(B)** p-AKT. The cells were cultured with medium (*lane 1*), SMF (*lane 2*), UFPM (*lane 3*), and UFPM and SMF (*lane 4*). Fold increases in amounts of phosphorylated p38 MAP kinase proteins are indicated. The amounts of p-p38 MAPK and p-AKT were quantified using NIH Image Analyzer and are shown as the amounts relative to control cells. Three identical experiments were independently performed providing similar results.

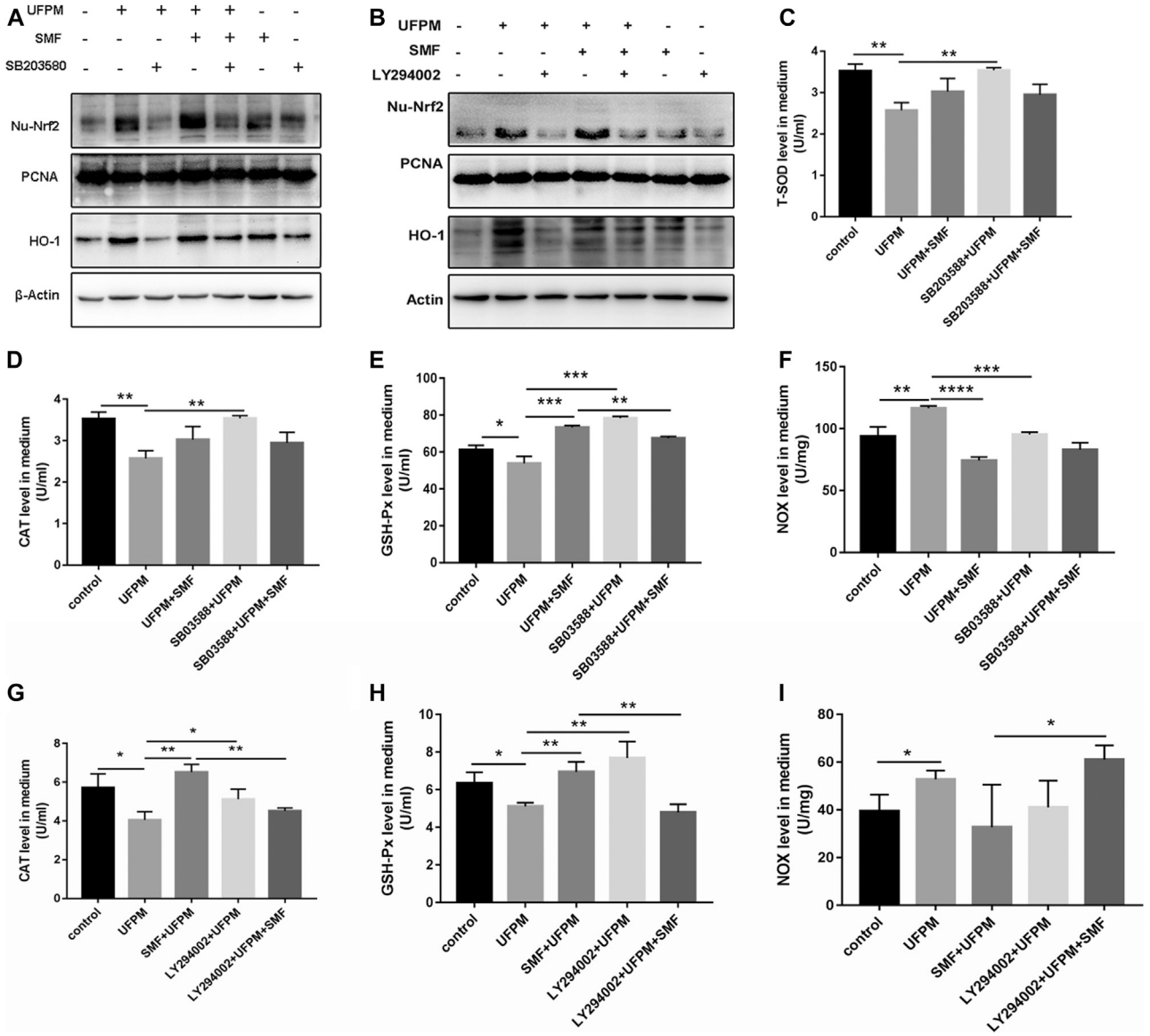

FIGURE 8 | SB 203580, LY294002 and SMF inhibit UFPM-induced HO-1 and Nrf2 expression and T-SOD, CAT, NOX, and GSH-Px production. H9C2 pre-incubated with medium or SB 203580 (10 mM) for 60 min and LY294002 (50 μM) for 4 h were cultured with medium or SMF for 24 h, and then treated with or without UFPM (50 mg/ml) for 6 h **(A,B)** Western blot analysis of HO-1 and Nrf2 expression in cells. T-SOD **(C)**, CAT **(D,G)**, GSH-Px **(E,H)**, and NOX **(F,I)** concentrations in the culture supernatants were determined 6 h after UFPM exposure. The results are expressed as the mean ± SD of three different experiments. Asterisks indicate significant differences by *t*-test, $^{*}p < 0.05$, $^{**}p < 0.01$, $^{***}p < 0.001$.

observed in the H9C2 cells exposed to UFPM, consistent with an imbalance in the oxidation/reduction observed in our *in vivo* study. A previous study demonstrated a significant difference in the expression levels of MDA, CAT, and GSH-Px in lung tissues of PM2.5-treated mice compared with saline-treated control mice (Huang et al., 2019). Similar increases in the levels of HO-1 and NOX in the lung and heart have been reported after particle exposure in rats; the differences were dependent on particulate size (Aztatzi-Aguilar et al., 2015). However, contrary to our findings, a recent study by OG Aztatzi-Aguilar reported a significant increase in SOD2 mRNA expression in the aorta of rats exposed to PM when compared to those in the filtered air group (Aztatzi-Aguilar et al., 2018). One explanation for this discrepancy is that the mRNA expression of SOD2 might have been elevated at the beginning of PM exposure in the previous study to increase the anti-oxidation ability of the myocardial cells and resist free radical damage.

The poor outcomes in response to MI in the current study may be due to the development of pulmonary artery hypertension (PAH) after UFPM exposure. PAH disturbs cardiac function. This is consistent with the findings of a previous study, which showed the general cytotoxicity of PM arising from different

areas, possibly due to the similarities in the species used in the studies (Bein and Wexler, 2015). Several mechanisms may explain PAH-induced toxicity, including antioxidant defense impairment and OS (Holme et al., 2019). The antioxidant system attenuates oxidative injuries. Natural antioxidants have received increased attention over the past ten years. The effective biological activities of natural antioxidants are crucial during conditions that cause OS, such as air pollution (Zhang and Gao, 2014).

SMF is a known potent antioxidant agent; however, the protective effects of SMF on UFPM-induced cardiac damage/OS have not been reported. In the current study, SMF increased the survival rate in rats subjected to UFPM exposure and MI, suggesting that UFPM exposure-induced cardiotoxicity can be reversed by SMF. Cardiac dysfunction after UFPM exposure and MI impacted the survival rate and administration of SMF, which is beneficial in improving the heart function, improved the survival rate (Zhao et al., 2016).

Myocardial infarct size is a key prognostic factor in a wide range of adverse cardiovascular outcomes. Although there is little direct evidence for the induction of cardiac ischemia following exposure to UFPM in humans, experimental animal models have demonstrated an association between PM exposure and infarct size and/or MI. The results of the present study showed that SMF, administered 24 h after an acute single intranasal instillation of UFPM, significantly decreased the myocardium infarct size, indicating a significant recovery of myocardial function in rats with MI. This effect was further demonstrated by measuring LDH, CK-MB, and cTnT levels in the serum and the histopathological evaluation of the myocardial tissue. A previous study reported that three representative components in SMF showed significant protective effects on cardiac function after MI injury (Mo et al., 2015; Li et al., 2018).Thus, our results can be ascribed to specific components of SMF that interact in a complex way to regulate LDH, CK-MB, and cTnT activities. Further assessment is needed to connect the specific chemical components and biological activities.

As described above, UFPM disrupted OS status both in the MI rat model and in H9C2 cells. The disrupted OS status was signified by an imbalance of oxidative markers, mitochondrial membrane potential, and energy metabolism, while SMF prevented these outcomes. These results corroborate the findings of Zhu et al. (2019) (Zhu et al., 2019) demonstrating that the decreased levels of SOD, GSR, and CAT induced by H_2O_2 were upregulated following SMF treatment. The current study provides evidence that co-treatment with SMF in UFPM-exposed MI rats protected the heart from OS injury. Notably, the protective effects of SMF against UFPM-induced cardiotoxicity were not dose-dependent in the present study. This may be because differences in the selected doses in the current study were not large enough; hence, differences in the protective effects of SMF could not be detected.

Because SMF significantly attenuated UFPM effects in the serum and myocardial tissue, we hypothesized that multiple signaling pathways play a key role in the protective effects of SMF in rats exposed to UFPM and MI. To confirm this hypothesis, a herb-major hub-CVD disease-UFPM toxicity-pathway network was constructed to visualize the relationships among SMF herbs, major targets, CVD disease, and PM toxicity. Based on the integrated network-pathway analysis, SMF exerts antioxidant effects by regulating OS, which was identified as an important mechanism involved in UFPM toxicity and MI progression (Li et al., 2005; Kurian et al., 2016). OS was regulated *via* the PI3K/AKT signaling pathway, which was an important functional module with a high enrichment score in our study. In addition, the p38 MAPK pathway had a higher number of genes that were significantly affected but had low enrichment scores. We choose the p38 MAPK pathway based on the findings of previous studies. Austin Nguyen (2019) showed that inter-gene correlation could affect the enrichment score resulting in a pathway with lower expression values but more significantly affected genes (Austin Nguyen, 2019). Furthermore, PM causes a time- and dose-dependent increase in the phosphorylation of p38 MAPK in human pulmonary artery endothelial cells (Li et al., 2005). Marchini et al. (2016) showed that acute exposure to PM increased the levels of TNF-α, IL-6, and IL-1β, increased the ratio of active Caspase 3/pro-Caspase 3, and activated the NFκB pathway (Marchini et al., 2016; Li X. et al., 2017). TNF, CASP3, and NFKB1, which are among the key targets of SMF, are involved in p38 MAPK signaling. In addition, TNF, CASP3, and NFKB1 are targets of Ginseng radix et Rhizoma Rubra, Ophiopogonis Radix, and Schisandrae Chinensis Fructus, suggesting that these three targets play important roles in SMF action.

Because the OS response was also observed in the network analysis, the RT^2 Profiler PCR array of myocardial tissue was designed to analyze a panel of genes related to the OS pathway. Our findings were in agreement with the detection of CAT in the serum of MI rats. A similar study also reported that SMF injection restored the mRNA expression of CAT after suppression by H_2O_2 (Zhu et al., 2019). Furthermore, the present study showed that SMF downregulated the gene expression of Cyba, which was consistent with a dramatic decrease in NOX levels in the serum of PM-treated MI rats. Cyba encodes a subunit of NOX. Thus, downregulation of Cyba reflected the decrease in myocardial OS after SMF treatment. NOX4 is highly expressed in cardiomyocytes and NOX4 activation causes cardiac dysfunction (Lassegue et al., 2012). Therefore, decreased myocardial NOX in the serum and myocardial tissue might help maintain myocardial function, supporting the protective effects of SMF in UFPM-induced oxidative injury. Additionally, the mRNA level of the antioxidant enzyme T-SOD was upregulated after SMF treatment in myocardial tissues of rats subjected to UFPM exposure and MI, in agreement with elevated serum T-SOD.

To further investigate the effects of SMF on the regulation of the OS pathways, we evaluated the p38 MAPK and PI3K/AKT pathways based on the net pharmacological data. UFPM induced the phosphorylation of p38 MAPK and AKT, decreased the levels of antioxidative factors such as GSH-Px, T-SOD, and CAT, and increased NOX production in H9C2 cells. These effects were prevented by SMF treatment. Nrf2 is activated under OS conditions and promotes the expression of numerous antioxidative enzymes such as T-SOD, CAT, and GSH-Px.

Subsequently, protein expression levels of Nrf2/HO-1 were increased in response to SMF in H9C2 cells exposed to UFPM. However, Nrf2/HO-1 levels were also increased in the UFPM-exposed cells, which may be due to the specific components of UFPM and the stress response to acute UFPM exposure. Both SB 203580 and LY294002, specific inhibitors of p38 MAPK and PI3K, respectively, restored the inhibition of UFPM-induced NOX formation and the promotion of GSH-Px and CAT levels in SMF + UFPM-treated H9C2 cells. Meanwhile, SB 203580 and LY294002 decreased the expression levels of Nrf2/HO-1 in SMF + UFPM-treated H9C2 cells. Therefore, we speculated that p38 MAPK and PI3K/AKT might be involved in UFPM-induced OS. Our findings are in line with a previous report, which showed that the PI3K/AKT and p38 MAPK signaling pathways regulate HO-1 expression in RAW264.7 macrophages during anti-inflammatory responses (Li T. et al., 2017). Additionally, our data are consistent with previous studies, which showed the beneficial antioxidant effects of SMF on H_2O_2-induced oxidative injury (Zhu et al., 2019) and cerebral oxidative damage in rats (Ichikawa et al., 2003). Based on the findings that UFPM activated both p38 MAPK and PI3K/AKT, while their inhibitors and SMF inhibited these effects, we assume that the regulation of HO-1 expression and antioxidant proteins is controlled by the PI3K/AKT/p38 MAPK/Nrf2 pathways.

This study presents limitations. We have used the TTC staining method to measure the infarct size of MI rats. However, the normalized of area under ligation should be quality controlled by expressing infarct vs area at risk (AAR) by evan blue dye staning. We make sure that infarct size measurement will be normalized to AAR by evan blue dye staning in our following study. For cardiac injury analysis, flipped LDH combined with cTNT, CK-MB will be used in subsequent tudy rather than total LDH used in this study. In addition, an *in vitro* cell culture model related to MI and UFPM could be advantageous and the best way to present the signaling activation in animal model is to perform western blot analysis using heart tissue homogenate from animal treated with LY294002 or SB203580. Actually, we have tried to establish cell model about MI by hypoxia stimulation, however, most cells with hypoxia were dead after UFPM exposure due to the extremly harsh conditions. Considering that UFPM and MI can both produce the same toxicological effects, i.e., oxidative stress, therefore, we established the *in vitro* model which can reflect the oxidative stress injury by UFPM exposure to be maximally approximation to the true state of *in vivo* study. Meantime, we will perform western blot analysis using heart tissue homogenate from animal treated with LY294002 or SB203580 in our following study. Again, we will analysis mitochondrial respiration in isolated mitochondria from heart tissue of rat exposed to UFPM prior to LAD ligation for demonstrating mitochondrial respiration dysfunction directly.

In conclusion, the present study demonstrated that exposure to UFPM induced myocardial damage and mitochondria dysfunction, increased MDA, and decreased the levels of antioxidant factors in rats with MI. Pretreatment with SMF significantly relieved the cardiac-linked pathologies, inhibited the release of MDA and NOX, elevated the levels of antioxidant factors, and prevented the cardiovascular effects mediated, in part, by the PI3K/AKT/p38 MAPK/Nrf2 signaling pathway. Our results indicate that SMF is a potent antioxidant that protects against the deleterious effects of UFPM in the heart. SMF may be used to prevent and treat the cardiovascular events caused by UFPM exposure.

DATA AVAILABILITY STATEMENT

The original contributions presented in the study are included in the article/**Supplementary Material**, further inquiries can be directed to the corresponding authors.

ETHICS STATEMENT

The animal study was reviewed and approved by Animal Ethics Committee of the Institute of Chinese Materia Medica, China Academy of Chinese Medical Sciences.

AUTHOR CONTRIBUTIONS

CL, YL, and XZ designed the experiment, analyzed the data, and wrote and modified the manuscript. YG, SQ, KL, TY, YY, ZZ, HL, XW, SD, and YZ assisted with the animal experiments. CL carried out the western blot analyses. YG performed the qRT-PCR, H&E staining, and Seahorse analysis. All authors contributed to the manuscript and approved the submitted version.

FUNDING

The authors thank the National Natural Science Foundation of China (Nos. 81673640, 81841001, and 81803814) and the Major National Science and Technology Program of China for Innovative Drug (2017ZX09301012002 and 2017ZX09101002-001-001-3) for their financial support.

SUPPLEMENTARY MATERIAL

The Supplementary Material for this article can be found online at: https://www.frontiersin.org/articles/10.3389/fphar.2021.619311/full#supplementary-material.

REFERENCES

Adams, R. A., Potter, S., Berube, K., Higgins, T. P., Jones, T. P., and Evans, S. A. (2019). Prolonged systemic inflammation and damage to the vascular endothelium following intratracheal instillation of air pollution nanoparticles in rats. *Clin. Hemorheol. Microcirc.* 72 (1), 1–10. doi:10.3233/CH-180377

Araujo, J. A., and Nel, A. E. (2009). Particulate matter and atherosclerosis: role of particle size, composition and oxidative stress. *Part. Fibre. Toxicol.* 6, 24. doi:10.1186/1743-8977-6-24

Austin Nguyen, M. B. (2019). *Analysis of model organism viability through an interspecies pathway comparison pipeline using the dynamic impact approach*. Available at: https://www.biorxiv.org/content/10.1101/2019.12.18.448985v1.

Aztatzi-Aguilar, O. G., Uribe-Ramirez, M., Arias-Montano, J. A., Barbier, O., and De Vizcaya-Ruiz, A. (2015). Acute and subchronic exposure to air particulate matter induces expression of angiotensin and bradykinin-related genes in the lungs and heart: angiotensin-II type-I receptor as a molecular target of particulate matter exposure. *Part. Fibre Toxicol.* 12, 17. doi:10.1186/s12989-015-0094-4

Aztatzi-Aguilar, O. G., Valdés-Arzate, A., Debray-García, Y., Calderón-Aranda, E. S., Uribe-Ramirez, M., Acosta-Saavedra, L., et al. (2018). Exposure to ambient particulate matter induces oxidative stress in lung and aorta in a size- and time-dependent manner in rats. *Toxicol. Res. Appl.* 2, 1–15. doi:10.1177/2397847318794859

Bein, K., and Wexler, A. (2015). Compositional variance in extracted particulate matter using different filter extraction techniques. *Atmos. Environ.* 107, 24–34. doi:10.1016/j.atmosenv.2015.02.026

Bolcas, P. E., Brandt, E. B., Zhang, Z., Biagini Myers, J. M., Ruff, B. P., and Khurana Hershey, G. K. (2019). Vitamin D supplementation attenuates asthma development following traffic-related particulate matter exposure. *J. Allergy Clin. Immunol.* 143 (1), 386–394. doi:10.1016/j.jaci.2018.04.042

Chen, K., Alexandra, S., Josef, C., Kathrin, W., Christa, M., Margit, H., et al. (2020). Hourly exposure to ultrafine particle metrics and the onset of myocardial infarction in Augsburg, Germany. *Environ. Health Perspect.* 128 (1), 17003. doi:10.1289/EHP5478

Chiarella, S. E., Soberanes, S., Urich, D., Morales-Nebreda, L., Nigdelioglu, R., Green, D., et al. (2014). beta(2)-Adrenergic agonists augment air pollution-induced IL-6 release and thrombosis. *J. Clin. Invest.* 124 (7), 2935–2946. doi:10.1172/JCI75157

Chin, M. T. (2015). Basic mechanisms for adverse cardiovascular events associated with air pollution. *Heart* 101 (4), 253–256. doi:10.1136/heartjnl-2014-306379

Chinese Pharmacopoeia Commission (2010). *Pharmacopoeia of the People's Republic of China*. (Beijing: China Medical Science Press), Vol. 1, 2332.

Driscoll, K. E., Costa, D. L., Hatch, G., Henderson, R., Oberdorster, G., Salem, H., et al. (2000). Intratracheal instillation as an exposure technique for the evaluation of respiratory tract toxicity: uses and limitations. *Toxicol. Sci.* 55 (1), 24–35. doi:10.1093/toxsci/55.1.24

Du, Y., Xu, X., Chu, M., Guo, Y., and Wang, J. (2016). Air particulate matter and cardiovascular disease: the epidemiological, biomedical and clinical evidence. *J. Thorac. Dis.* 8 (1), E8–E19. doi:10.3978/j.issn.2072-1439.2015.11.37

Gao, Y., Yao, X., Zhang, Y., Li, W., Kang, K., Sun, L., et al. (2011). The protective role of hydrogen sulfide in myocardial ischemia-reperfusion-induced injury in diabetic rats. *Int. J. Cardiol.* 152 (2), 177–183. doi:10.1016/j.ijcard.2010.07.012

Hadei, M., and Naddafi, K. (2020). Cardiovascular effects of airborne particulate matter: a review of rodent model studies. *Chemosphere* 242, 125204. doi:10.1016/j.chemosphere.2019.125204

Holme, J. A., Brinchmann, B. C., Refsnes, M., Lag, M., and Ovrevik, J. (2019). Potential role of polycyclic aromatic hydrocarbons as mediators of cardiovascular effects from combustion particles. *Environ. Health* 18 (1), 74. doi:10.1186/s12940-019-0514-2

Hortmann, M., Robinson, S., Mohr, M., Haenel, D., Mauler, M., Stallmann, D., et al. (2017). Circulating HtrA2 as a novel biomarker for mitochondrial induced cardiomyocyte apoptosis and ischemia-reperfusion injury in ST-segment elevation myocardial infarction. *Int. J. Cardiol.* 243, 485–491. doi:10.1016/j.ijcard.2017.05.088

Huang, K., Shi, C., Min, J., Li, L., Zhu, T., Yu, H., et al. (2019). Study on the mechanism of curcumin regulating lung injury induced by outdoor fine particulate matter (PM2.5). *Mediators Inflamm.* 2019, 8613523. doi:10.1155/2019/8613523

Ichikawa, H., Wang, X., and Konishi, T. (2003). Role of component herbs in antioxidant activity of shengmai san—a traditional Chinese medicine formula preventing cerebral oxidative damage in rat. *Am. J. Chin. Med.* 31 (4), 509–521. doi:10.1142/S0192415X03001193

Jia, L. Q., Yang, G. L., Ren, L., Chen, W. N., Feng, J. Y., Cao, Y., et al. (2012). Tanshinone IIA reduces apoptosis induced by hydrogen peroxide in the human endothelium-derived EA.hy926 cells. *J. Ethnopharmacol.* 143 (1), 100–108. doi:10.1016/j.jep.2012.06.007

Kim, S. H., Kim, K. J., Kim, J. H., Kwak, J. H., Song, H., Cho, J. Y., et al. (2017). Comparision of doxorubicin-induced cardiotoxicity in the ICR mice of different sources. *Lab. Anim. Res.* 33 (2), 165–170. doi:10.5625/lar.2017.33.2.165

Kurian, G. A., Rajagopal, R., Vedantham, S., and Rajesh, M. (2016). The role of oxidative stress in myocardial ischemia and reperfusion injury and remodeling: revisited. *Oxid. Med. Cell. Longev.* 2016, 1656450. doi:10.1155/2016/1656450

Lassegue, B., San Martin, A., and Griendling, K. K. (2012). Biochemistry, physiology, and pathophysiology of NADPH oxidases in the cardiovascular system. *Circ. Res.* 110 (10), 1364–1390. doi:10.1161/CIRCRESAHA.111.243972

Lee, M. S., Eum, K. D., Fang, S. C., Rodrigues, E. G., Modest, G. A., and Christiani, D. C. (2014). Oxidative stress and systemic inflammation as modifiers of cardiac autonomic responses to particulate air pollution. *Int. J. Cardiol.* 176 (1), 166–170. doi:10.1016/j.ijcard.2014.07.012

Lee, W., Jeong, S. Y., Gu, M. J., Lim, J. S., Park, E. K., Baek, M. C., et al. (2019). Inhibitory effects of compounds isolated from *Dioscorea* batatas Decne peel on particulate matter-induced pulmonary injury in mice. *J. Toxicol. Environ. Health A.* 82 (12), 727–740. doi:10.1080/15287394.2019.1646174

Li, F., Fan, X. X., Chu, C., Zhang, Y., Kou, J. P., and Yu, B. Y. (2018). A strategy for optimizing the combination of active components based on Chinese medicinal formula Sheng-Mai-San for myocardial ischemia. *Cell Physiol. Biochem.* 45 (4), 1455–1471. doi:10.1159/000487572

Li, F., Lv, Y. N., Tan, Y. S., Shen, K., Zhai, K. F., Chen, H. L., et al. (2015). An integrated pathway interaction network for the combination of four effective compounds from ShengMai preparations in the treatment of cardio-cerebral ischemic diseases. *Acta Pharmacol. Sin.* 36 (11), 1337–1348. doi:10.1038/aps.2015.70

Li, R., Kou, X., Geng, H., Xie, J., Tian, J., Cai, Z., et al. (2015). Mitochondrial damage: an important mechanism of ambient PM2.5 exposure-induced acute heart injury in rats. *J. Hazard.Mater.* 287, 392–401. doi:10.1016/j.jhazmat.2015.02.006

Li, S., Zhang, Z. Q., Wu, L. J., Zhang, X. G., Li, Y. D., and Wang, Y. Y. (2007). Understanding ZHENG in traditional Chinese medicine in the context of neuro-endocrine-immune network. *IET Syst. Biol.* 1 (1), 51–60. doi:10.1049/iet-syb:20060032

Li, T., Cheng, X., Du, M., Chen, B., and Mao, X. (2017). Upregulation of heme oxygenase-1 mediates the anti-inflammatory activity of casein glycomacropeptide (GMP) hydrolysates in LPS-stimulated macrophages. *Food Funct.* 8 (7), 2475–2484. doi:10.1039/c7fo00481h

Li, X., Geng, J., Chen, Y., Chen, F., Liu, C., Xu, Q., et al. (2017). Exposure to particulate matter induces cardiomyocytes apoptosis after myocardial infarction through NFkappaB activation. *Biochem. Biophys. Res. Commun.* 488 (1), 224–231. doi:10.1016/j.bbrc.2017.05.047

Li, Y. F., Cao, F. F., Liu, F., Bai, X. Y., and Lu, Y. (2012). Effects of Shexiangbaoxin pills on the expression of cardiac alpha(1)- and beta-adrenergic receptor subtypes in rat hearts with heart failure induced by myocardial infarction. *Chin. Med. J. (Engl.)* 125 (9), 1556–1562. doi:10.3760/cma.j.issn.0366-6999.2012.09.007

Li, Z., Carter, J. D., Dailey, L. A., and Huang, Y. C. (2005). Pollutant particles produce vasoconstriction and enhance MAPK signaling via angiotensin type I receptor. *Environ. Health Perspect.* 113 (8), 1009–1014. doi:10.1289/ehp.7736

Marchini, T., Wolf, D., Michel, N. A., Mauler, M., Dufner, B., Hoppe, N., et al. (2016). Acute exposure to air pollution particulate matter aggravates experimental myocardial infarction in mice by potentiating cytokine secretion from lung macrophages. *Basic Res. Cardiol.* 111 (4), 44. doi:10.1007/s00395-016-0562-5

Miller, M. R. (2020). Oxidative stress and the cardiovascular effects of air pollution. *Free Radic. Biol. Med.* 151, 69–87. doi:10.1016/j.freeradbiomed.2020.01.004

Mo, W. L., Chai, C. Z., Kou, J. P., Yan, Y. Q., and Yu, B. Y. (2015). Sheng-Mai-San attenuates contractile dysfunction and structural damage induced by chronic intermittent hypoxia in mice. *Chin. J. Nat. Med.* 13 (10), 743–750. doi:10.1016/S1875-5364(15)30074-1

Rao, X., Zhong, J., Maiseyeu, A., Gopalakrishnan, B., Villamena, F. A., Chen, L. C., et al. (2014). CD36-dependent 7-ketocholesterol accumulation in macrophages mediates progression of atherosclerosis in response to chronic air pollution exposure. *Circ. Res.* 115 (9), 770–780. doi:10.1161/CIRCRESAHA.115.304666

Ronkko, T. J., Jalava, P. I., Happo, M. S., Kasurinen, S., Sippula, O., Leskinen, A., et al. (2018). Emissions and atmospheric processes influence the chemical composition and toxicological properties of urban air particulate matter in Nanjing, China. *Sci. Total Environ.* 639, 1290–1310. doi:10.1016/j.scitotenv.2018.05.260

Ruckerl, R., Phipps, R. P., Schneider, A., Frampton, M., Cyrys, J., Oberdorster, G., et al. (2007). Ultrafine particles and platelet activation in patients with coronary heart disease—results from a prospective panel study. *Part. Fibre. Toxicol.* 4, 1. doi:10.1186/1743-8977-4-1

Sanjeewa, K. K. A., Jayawardena, T. U., Kim, S. Y., Lee, H. G., Je, J. G., Jee, Y., et al. (2020). *Sargassum horneri* (Turner) inhibit urban particulate matter-induced inflammation in MH-S lung macrophages via blocking TLRs mediated NF-kappaB and MAPK activation. *J. Ethnopharmacol.* 249, 112363. doi:10.1016/j.jep.2019.112363

Thomson, E. M. (2019). Air pollution, stress, and allostatic load: linking systemic and central nervous system impacts. *J. Alzheimers Dis.* 69 (3), 597–614. doi:10.3233/JAD-190015

Tsai, D. H., Amyai, N., Marques-Vidal, P., Wang, J. L., Riediker, M., Mooser, V., et al. (2012). Effects of particulate matter on inflammatory markers in the general adult population. *Part. Fibre. Toxicol.* 9, 24. doi:10.1186/1743-8977-9-24

Wang, Q., Gan, X., Li, F., Chen, Y., Fu, W., Zhu, X., et al. (2019). PM2.5 exposure induces more serious apoptosis of cardiomyocytes mediated by Caspase3 through JNK/P53 pathway in hyperlipidemic rats. *Int. J. Biol. Sci.* 15 (1), 24–33. doi:10.7150/ijbs.28633

Wei, Y., Wang, Y., Di, Q., Choirat, C., Wang, Y., Koutrakis, P., et al. (2019). Short term exposure to fine particulate matter and hospital admission risks and costs in the Medicare population: time stratified, case crossover study. *BMJ* 367, l6258. doi:10.1136/bmj.l6258

Wu, Y., Yin, X., Wijaya, C., Huang, M. H., and McConnell, B. K. (2011). Acute myocardial infarction in rats. *J. Vis. Exp.* 16, e2464. doi:10.3791/2464

Wu, Y., Zhang, F., Yang, K., Fang, S., Bu, D., Li, H., et al. (2019). SymMap: an integrative database oftraditional Chinese medicine enhanced by symptom mapping. *Nucl. Acids Res.* 47, 1110–1117. doi:10.1093/nar/gky1021

Xu, H., Zhang, Y., Liu, Z., Chen, T., Lv, C., Tang, S., et al. (2019). ETCM: an encyclopaedia of traditional Chinese medicine. *Nucl. Acids Res.* 47, 976–982. doi:10.1093/nar/gky987

Yang, A., Jedynska, A., Hellack, B., Kooter, I., Hoek, G., Brunekreef, B., et al. (2014). Measurement of the oxidative potential of PM 2.5 and its constituents: the effect of extraction solvent and filter type. *Atmos. Environ.* 83, 35–42. doi:10.1016/j.atmosenv.2013.10.049

Zhang, X., and Gao, F. (2014). Natural antioxidants for health promotion and disease prevention. *Front. Pharmacol.* 5, 266. doi:10.3389/fphar.2014.00266

Zhang, Y., Liu, M., Fan, R., Zhou, Q., Yang, J., Yang, S., et al. (2019). Walnut protein isolates attenuate particulate matter-induced lung and cardiac injury in mice and zebra fish. *RSC Adv.* 9, 40736–40744. doi:10.1039/C9RA06002B

Zhao, J., Cao, T. T., Tian, J., Chen, H. H., Zhang, C., Wei, H. C., et al. (2016). Shengmai san ameliorates myocardial dysfunction and fibrosis in diabetic db/db mice. *Evid. Based Complement. Alternat Med.* 2016, 4621235. doi:10.1155/2016/4621235

Zhong, J., Karlsson, O., Wang, G., Li, J., Guo, Y., Lin, X., et al. (2017). B vitamins attenuate the epigenetic effects of ambient fine particles in a pilot human intervention trial. *Proc. Natl. Acad. Sci. USA* 114 (13), 3503–3508. doi:10.1073/pnas.1618545114

Zhou, M., Wang, H., Zeng, X., Yin, P., Zhu, J., Chen, W., et al. (2019). Mortality, morbidity, and risk factors in China and its provinces, 1990-2017: a systematic analysis for the Global Burden of Disease Study 2017. *Lancet* 394 (10204), 1145–1158. doi:10.1016/S0140-6736(19)30427-1

Zhu, J., Ye, Q., Xu, S., Chang, Y. X., Liu, X., Ma, Y., et al. (2019). Shengmai injection alleviates H_2O_2 induced oxidative stress through activation of AKT and inhibition of ERK pathways in neonatal rat cardiomyocytes. *J. Ethnopharmacol.* 239, 111677. doi:10.1016/j.jep.2019.01.001

Conflict of Interest: The authors declare that the research was conducted in the absence of any commercial or financial relationships that could be construed as a potential conflict of interest.

Copyright © 2021 Chen, Guo, Qu, Li, Yang, Yang, Zheng, Liu, Wang, Deng, Zhang, Zhu and Li. This is an open-access article distributed under the terms of the Creative Commons Attribution License (CC BY). The use, distribution or reproduction in other forums is permitted, provided the original author(s) and the copyright owner(s) are credited and that the original publication in this journal is cited, in accordance with accepted academic practice. No use, distribution or reproduction is permitted which does not comply with these terms.

frontiers in Pharmacology

ORIGINAL RESEARCH
published: 08 March 2021
doi: 10.3389/fphar.2021.627123

Inhibition of TLR4/MAPKs Pathway Contributes to the Protection of Salvianolic Acid A Against Lipotoxicity-Induced Myocardial Damage in Cardiomyocytes and Obese Mice

Zhen Yang[1,2,3†], Yanli Chen[1,2†], Zhaoyuan Yan[2], Tian Tian Xu[2], Xiangyao Wu[2], Aiwen Pi[2], Qingsheng Liu[4], Hui Chai[2,3], Songtao Li[1,3] and Xiaobing Dou[2,3]**

[1]College of Basic Medicine and Public Health, Zhejiang Chinese Medical University, Hangzhou, China, [2]College of Life Science, Zhejiang Chinese Medical University, Hangzhou, China, [3]Molecular Medicine Institute, Zhejiang Chinese Medical University, Hangzhou, China, [4]Hangzhou Hospital of Traditional Chinese Medicine, Guangxing Hospital Affiliated to Zhejiang University of Traditional Chinese Medicine, Hangzhou, China

The occurrence of lipotoxicity during obesity-associated cardiomyopathy is detrimental to health. Salvianolic acid A (SAA), a natural polyphenol extract of *Salvia miltiorrhiza Bunge* (Danshen in China), is known to be cardioprotective. However, its clinical benefits against obesity-associated cardiomyocyte injuries are unclear. This study aimed at evaluating the protective effects of SAA against lipotoxicity-induced myocardial injury and its underlying mechanisms in high fat diet (HFD)-fed mice and in palmitate-treated cardiomyocyte cells (H9c2). Our analysis of aspartate aminotransferase and creatine kinase isoenzyme-MB (CM-KB) levels revealed that SAA significantly reversed HFD-induced myocardium morphological changes and improved myocardial damage. Salvianolic acid A pretreatment ameliorated palmitic acid-induced myocardial cell death and was accompanied by mitochondrial membrane potential and intracellular reactive oxygen species improvement. Analysis of the underlying mechanisms showed that SAA reversed myocardial TLR4 induction in HFD-fed mice and H9c2 cells. Palmitic acid-induced cell death was significantly reversed by CLI-95, a specific TLR4 inhibitor. TLR4 activation by LPS significantly suppressed SAA-mediated lipotoxicity protection. Additionally, SAA inhibited lipotoxicity-mediated expression of TLR4 target genes, including MyD88 and *p*-JNK/MAPK in HFD-fed mice and H9c2 cells. However, SAA did not exert any effect on palmitic acid-induced SIRT1 suppression and *p*-AMPK induction. In conclusion, our data shows that SAA protects against lipotoxicity-induced myocardial damage through a TLR4/MAPKs mediated mechanism.

Keywords: salvianolic acid A, lipotoxicity, myocardial injury, TLR4, MAPKs

OPEN ACCESS

Edited by:
Yanqiong Zhang,
China Academy of Chinese Medical Sciences, China

Reviewed by:
He-Hui Xie,
Shanghai Jiao Tong University, China
Ye Huang,
China Academy of Chinese Medical Sciences, China

***Correspondence:**
Xiaobing Dou
xbdou77@gmail.com
Songtao Li
lisongtao@zcmu.edu.cn

†These authors have contributed equally to this work

Specialty section:
This article was submitted to Ethnopharmacology, a section of the journal Frontiers in Pharmacology

Received: *08 November 2020*
Accepted: *11 January 2021*
Published: *08 March 2021*

Citation:
Yang Z, Chen Y, Yan Z, Xu TT, Wu X, Pi A, Liu Q, Chai H, Li S and Dou X (2021) Inhibition of TLR4/MAPKs Pathway Contributes to the Protection of Salvianolic Acid A Against Lipotoxicity-Induced Myocardial Damage in Cardiomyocytes and Obese Mice. Front. Pharmacol. 12:627123. doi: 10.3389/fphar.2021.627123

INTRODUCTION

Obesity is a global epidemic that is characterized by excessive amounts of circulating free fatty acids (FFAs), resulting in a variety of metabolic disorders, including lipotoxic cardiomyopathy (Schrammel et al., 2013). Lipotoxicity occurs when FFAs form heterotopic deposits in non-adipose tissues, including the kidney, skeletal muscles, and liver (Sletten et al., 2018). Lipotoxicity-induced myocardial damage accelerates advanced heart disease development. Palmitic acid (PA), the most abundant saturated fatty acid in human diet, has been found to be significantly elevated in blood samples of both obese individuals and high-fat diet (HFD) -fed animals (van Rooijen and Mensink, 2020). Therefore, PA is widely used to induce lipotoxicity *in vitro*.

Although the mechanisms underlying obesity-associated cardiac dysfunction are not fully understood, several factors, including toll-like-receptor 4 (TLR4) have been implicated. TLR4 is a well-known activator of innate immune responses against pathogens and has recently been shown to mediate obesity-induced cardiac inflammation, glucose metabolic derangement and injury (Jackson et al., 2015; Chen et al., 2020; Liu et al., 2020). Palmitate is an endogenous TLR4 ligand that significantly upregulates TLR4 levels in hepatocytes (Dou et al., 2020). Palmitate also enhances TLR4 expression in cardiomyocytes (Wang et al., 2017). Studies on HFD-induced obesity have shown that myocardial damage is significantly alleviated by TLR4 depletion (Wang et al., 2017). MyD88 is an adapter protein that mediates TLR4 signal transduction and activation of mitogen-activated protein kinase (MAPK) signaling pathway. MyD88 or MAPKs (including JNK and ERK1/2) inhibition has been shown to improve lipotoxicity-induced cardiac injury in both obese mice and cultured cardiomyocytes (Liu et al., 2014; Wang et al., 2016). Additionally, adenosine monophosphate activated protein kinase (AMPK), a key cellular energy sensor, has been implicated in HFD-induced cardiac hypertrophy, palmitate-induced apoptosis, and cardiomyocytes lipid deposit (Gélinas et al., 2018; Yang et al., 2018; Zhang et al., 2019). AMPK activation inhibits myocardial hypertrophy by regulating energy metabolism through sirtuin 1 (SIRT1) (Ma et al., 2018).

Salvia miltiorrhiza Bunge (Danshen in China) is a Chinese medicinal herb that has traditionally been used for the treatment of cardiovascular diseases. Salvianolic acid A (SAA) is the main water-soluble component of Danshen. It has been established that SAA has a range of pharmacological effects, including anti-oxidant, anti-inflammatory, anti-fibrotic, and anti-carcinogenic activities (Yang et al., 2012; Zheng et al., 2015; Wang et al., 2019a). Animal models have shown that SAA is cardioprotective, including during ischemic-reperfusion, cardiomyocyte infarction, and arsenic trioxide-induced injury (Ho and Hong, 2011; Feng et al., 2017; Wang et al., 2019b). However, its clinical benefits against lipotoxicity-induced myocardial damage have not been established.

In this study, we investigated the clinical benefits of SAA against lipotoxicity-induced cardiac injuries in both HFD-induced obese mice and palmitate-exposed cardiomyocytes. Our findings highlight the potential therapeutic values of SAA in the prevention and treatment of obesity-associated myocardial damage.

MATERIALS AND METHODS

Animals Studies

Animal care and experiments complied with National Institute of Animal Health guidelines on animal research. Ethical approval was granted by the Animal Ethics Committee at Zhejiang Chinese Medical University. Eight-week old male C57BL/6J mice were housed at 22 ± 2°C and 12-h light/dark cycle. Animals were divided into the following groups (6 mice each); normal diet group (Control), HFD group (HFD), normal diet with 40 mg/kg BW SAA group (SAA), and HFD with 40 mg/kg BW SAA (SAA + HFD) group. The Control group was fed AIN-93G diet. HFD mice were fed 60% fat diet to induce obesity (60% fat, D12492, Research Diets, New Brunswick, NJ), and water enriched with high fructose and sucrose. 42 g/L of carbohydrates was added to drinking water at a ratio of 45% sucrose and 55% fructose (St. Louis, MO) by weight. SAA was dissolved in sterilized physiologic saline to a stock concentration of 20 mg/ml. 100 μL aliquots of the SAA solution or sterilized physiologic saline were intraperitoneally administered to mice every other day for 12 weeks. Body weight was recorded weekly. At the end of the experiment, mice were fasted overnight, anesthetized using sodium pentobarbital (50 mg/kg BW), and sacrificed to obtain plasma and hearts for analysis. The obese mice model was successfully established by the evaluating of body weight and plasma lipids (**Supplementary Figure S1**).

Measurement of Plasma Lipids, AST, CK-MB Level

Mice were sacrificed under anesthesia, blood was obtained and plasma was harvested by centrifugation for 5 min at 3,000 rpm. Plasma AST, CK-MB, triglyceride (TG), free fatty acids (FFA), total cholesterol, high-density lipoprotein-cholesterol (HDL-C), low-density lipoprotein-cholesterol (LDL-C) levels were then measured using commercial kits (Nanjing Jiancheng BioTech. Co. Ltd., Nanjing, China) according to the manufacturers' instructions.

Immunohistochemistry

Hearts were fixed in 4% PFA and embedded in paraffin. Sectioned tissues were then stained using H&E and their myofibers analyzed histologically. H&E sections were examined and imaged under brightfield illumination on a Leica microscope (Carl Zeiss, Gottingen, Germany).

Reagents

Lipopolysaccharides (LPS) was purchased from Selleck Chemicals (Huston, TX). PA, stearic acid (SA), oleic acid (OA), and SAA were purchased from Sigma-Aldrich

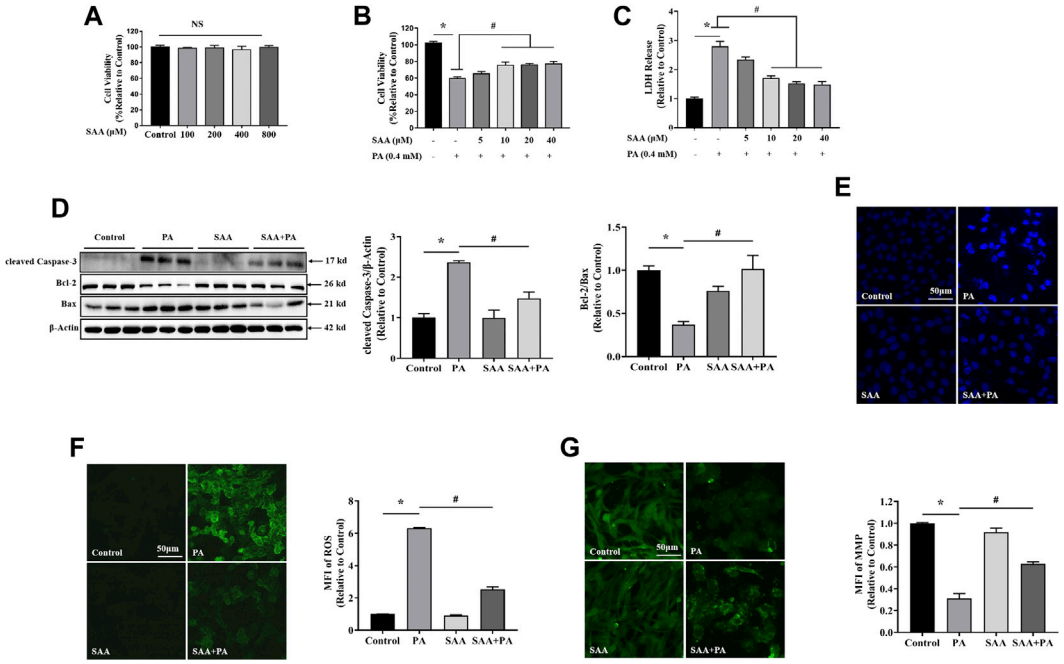

FIGURE 1 | SAA reverses PA-induced lipotoxicity in H9c2 cardiomyocytes **(A)** Cardiomyocytes were seeded onto 24-well plates and grown to 80–90% confluence before treatment with the indicated SAA concentrations for 24 h. Cell viability was determined using MTT. **(B)**, **(C)** Cardiomyocytes were pretreated with indicated SAA concentrations for 1 h and incubated with 0.4 mM palmitic acid (PA) for 12 h and cell viability and LDH release measured. **(D)** Western blot analysis of cleaved Caspase-3, Bcl-2, and Bax. Values are presented as mean ± SD for three or more independent tests. **(E)** Hoechst staining for nuclei. Cell death was detected by morphologic examination after Hoechst staining by fluorescence microscopy (mag = 200X). **(F)** ROS levels were measured using DCFH-DA. **(G)** MFI analysis of mitochondrial membrane potential using Rh123. Values with different superscripts are significantly different at $p < 0.05$. * shows comparison with normal control group while # shows comparison with PA-only treatment group.

(St. Louis, MO). CLI-95 was purchased from Invitrogen (Carlsbad, CA). SA-BSA and PA-BSA were processed as previously described (Dou et al., 2020). Briefly, SA or PA were solubilized in 100% ethanol and saponified with sodium hydroxide. The sodium salt was desiccated and resuspended in PBS. It was then heated at 80°C to achieve complete dissolution. We then added an isovolumetric 20% (w/v) BSA and stirred the mixture at 50°C for 4 h to allow SA or PA to bind BSA. The SA-BSA or PA-BSA complex (3 mmol/L fatty acid:1.5 mmol/L BSA, molar ratio, 2:1) was sterilized by filtration, and aliquoted for use. Oleate was complexed with 10% BSA to produce a stock solution, which was diluted in culture medium prior to use. The control and vehicle groups were treated with equal amounts of solvents (BSA or DMSO).

Cell Culture

H9c2 cells were obtained from Shanghai Institute Cell Bank (Shanghai, China). Cells were cultured in DMEM medium (Gibco, Eggenstein, Germany) containing 5.5 mmol/L D-glucose and supplemented with 10% FBS (Biological Industries, ISR) as well as 100 U/mL/100 mg/ml pen/strep, at 37°C, in a humidified incubator, O_2/CO_2 (19:1) atmosphere.

Cell Death Assay

2×10^5 cells/well were seeded onto a 24-well plate and cultured in normal media or media containing indicated concentrations of palmitate in the presence or absence of SAA (5, 10, 20, 40 μM). After 12 h, 450 μM MTT solution was added into each well and incubated for 4 h. The supernatant was removed and 600 μL DMSO added to dissolve the resulting formazan. Absorbance was then read at 470 nm using FLUOstar Omega (BMG Labtech). For the LDH test, the culture medium was collected and LDH assayed using an LDH assay kit (Thermo Scientific Inc., VA) according to the manufacturers' instructions. Nuclear morphological changes were examined by staining with 5 mg/L Hoechst 33342 for 10 min at 37°C before being imaged under a fluorescent microscope (Leica).

Reactive Oxygen Species (ROS)

ROS levels were evaluated as described before (Li et al., 2014). After treatments, cells were washed and placed in serum free medium. 2, 7-dichlorodi-hydrofluorescein diacetate (DCFH-DA) was added to each well at a final concentration of 10 μM and cells cultured at 37°C for 20 min. They were then washed thrice using ice-cold PBS. Fluorescence intensity was determined using an inverted fluorescent microscope (Leica, Wetzlar, Germany). The

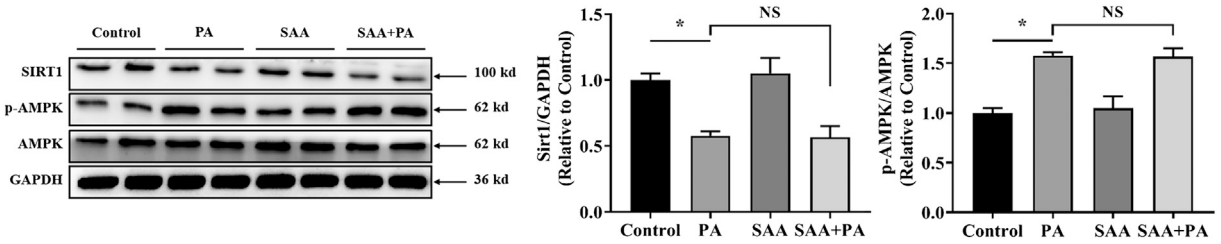

FIGURE 2 | SIRT1/AMPK pathway is not involved in SAA protection from lipotoxicity. Cardiomyocytes were incubated with 0.4 mM palmitic acid (PA) for 12 h. 10 μM SAA was added 1 h before PA treatment. SIRT1, AMPK, and *p*-AMPK, protein levels were determined by western blot. Data were quantified by densitometric analysis as fold changes. Values are presented as mean ± SD for ≥3 independent tests. Bars with different characters are significantly different, $p < 0.05$.

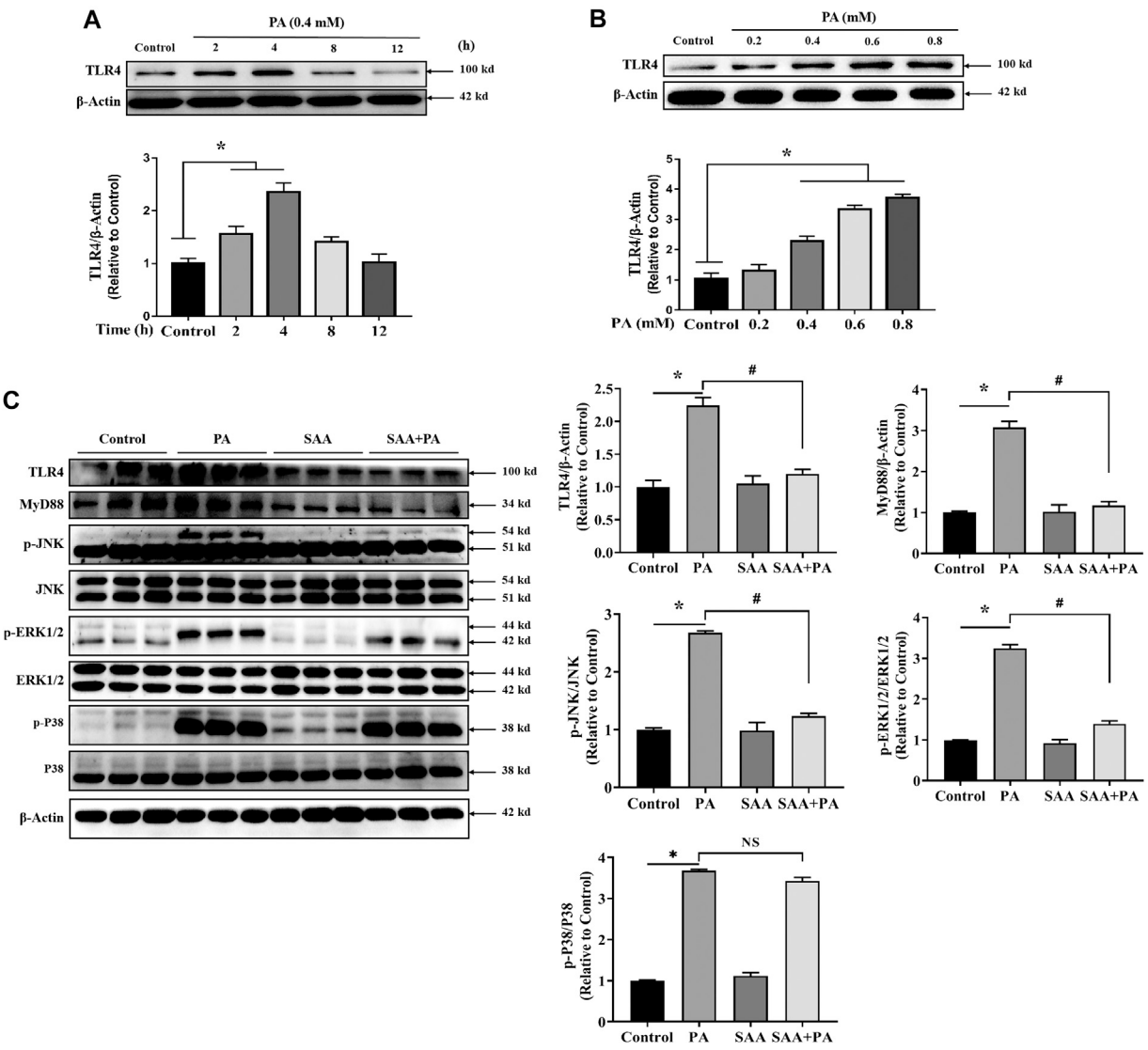

FIGURE 3 | SAA attenuates palmitate-induced TLR4 activation. Cardiomyocytes were seeded onto 24-well plates and grown to 80% confluence before treatment with 0.4 mM PA for 2, 4, 8 and 12 h **(A)** or 0.2, 0.4, 0.6, or 0.8 mM PA for 4 h **(B)** For the detection of anti-lipotoxicity role of SAA, H9c2 cells were incubated with 0.4 mM palmitic acid (PA) for 4 h. 10 μM SAA was added 1 h before free fatty acids treatment. Representative western blot data on TLR4 levels. Data are shown as mean ± SD. Total protein was extracted from myocardial cells. TLR4, MyD88, *p*-JNK, and *p*-ERK1/2 levels were determined by western blot. Values with different superscripts are significantly different at $p < 0.05$. * indicates comparison with normal control group while # indicates comparison with PA-only treatment group.

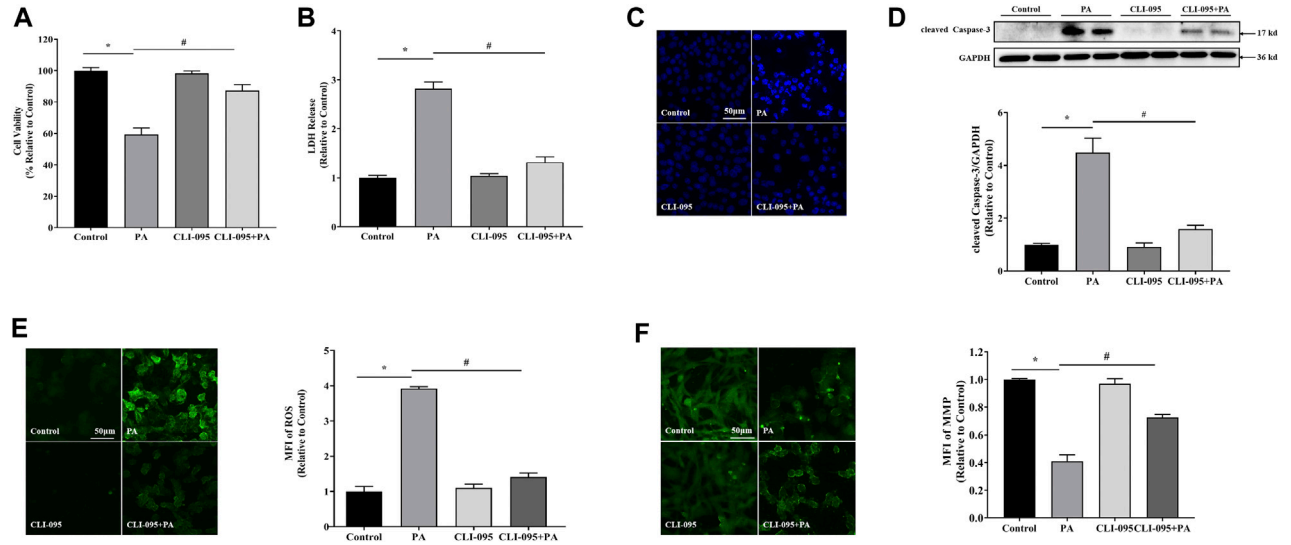

FIGURE 4 | TLR4 was involved in lipotoxicity-induced injury in cardiomyocytes. Cardiomyocyte cells were treated with PA at 0.4 mM for 4 h with or without 1 h CLI-095 preincubation (1 μM). PA-induced cytotoxicity in CLI-095-treated cardiomyocytes was determined using the MTT assay **(A)** and analysis of LDH release into culture medium **(B)**. **(C)** Nuclear staining with Hoechst. **(D)** Representative western blot with densitometric analysis of cleaved Caspase-3 levels in cells. **(E)** ROS levels were measured using DCFH-DA. **(F)** MFI analysis of mitochondrial membrane potential using Rh123. Values are presented as mean ± SD for ≥3 independent tests. * indicates comparison with normal controls while # shows comparison with PA-only treatment. Bars with different characters are significantly different, $p < 0.05$.

mean fluorescence intensity (MFI) of five random fields was determined using ImageJ.

Mitochondrial Membrane Potential (MMP) Assay

MMP was evaluated using Rhodamine123 (Rh123) at a final concentration of 100 μg/ml for 45 min. Fluorescence was measured using a fluorescent microscope (Leica, Wetzlar, Germany). The mean fluorescence intensity (MFI) of five random fields was determined using ImageJ.

Western Blotting

Western blotting was done as previously described (Li et al., 2014) using the following antibodies: anti-β-actin, anti-cleaved-caspase3, anti-Bcl-2, anti-Bax, anti-MyD88, anti-JNK, anti-phospho-JNK, anti-ERK1/2, anti-phospho-ERK1/2, and anti-GAPDH from Cell Signaling Technology; Anti-TLR4, anti-SIRT1, anti-AMPK, anti-phospho-AMPK, from Santa Cruz Biotechnology. β-actin and GAPDH were used as loading controls. Protein levels were detected using HRP-conjugated secondary antibodies, and signal developed using ECL.

Statistical Analysis

Data are presented as mean ± SD for ≥3 independent biological experiments with three replicates per experiment. Statistical analysis was done using SPSS. Student's t-test or one-way ANOVA followed by Tukey test were used for pairwise comparisons between groups. $p < 0.05$ was set as the threshold for statistical significance.

RESULTS

SAA Protects Against Lipotoxicity-Induced Myocardial Cell Injury

First, we tested the cytotoxic effects of various FFAs on myocardial cells with or without SAA. Analysis of LDH levels in the culture media revealed that long-chain saturated fatty acids (LSFAs), including PA and SA, exhibited significant dose-dependent lipotoxicity (**Supplementary Figures S2A–D**). OA, an important representative of long-chain monounsaturated fatty acids, did not exert lipotoxic effects in myocardial cells (**Supplementary Figures S2E,F**). Based on these results, we chose 0.4 mM PA to stimulate myocardial cells. To establish appropriate SAA concentrations for the experiments, we evaluated SAA cytotoxicity in cells without fatty acid treatment, and found that tolerance was up to 800 μM SAA (**Figure 1A**). Cell viability and LDH assays indicated that SAA significantly suppressed PA-induced cell death (**Figures 1B,C**). *In vitro* assays were done using SAA at a maximum concentration of 40 μM. Pretreating cells with SAA significantly reversed PA-induced cytotoxicity in a dose-dependent manner (**Figures 1B,C**). Then, 10 μM of SAA were chosen for the subsequent experiments. It was found that 10 μM SAA inhibited PA-mediated upregulation of cleaved Caspase-3, Bcl-2, Bax, and Bcl2/Bax ratio, indicating suppressed apoptosis (**Figure 1D**). Additionally, PA-stimulated chromatin damage was reversed by SAA pre-treatment (**Figure 1E**). Reduced circulating FFA levels enhanced oxidative stress during cardiomyopathy. This prompted us to assess SAA's capacity to scavenge PA-induced ROS in cardiac cells. The DCFH-DA assay showed that 0.4 mM PA significantly

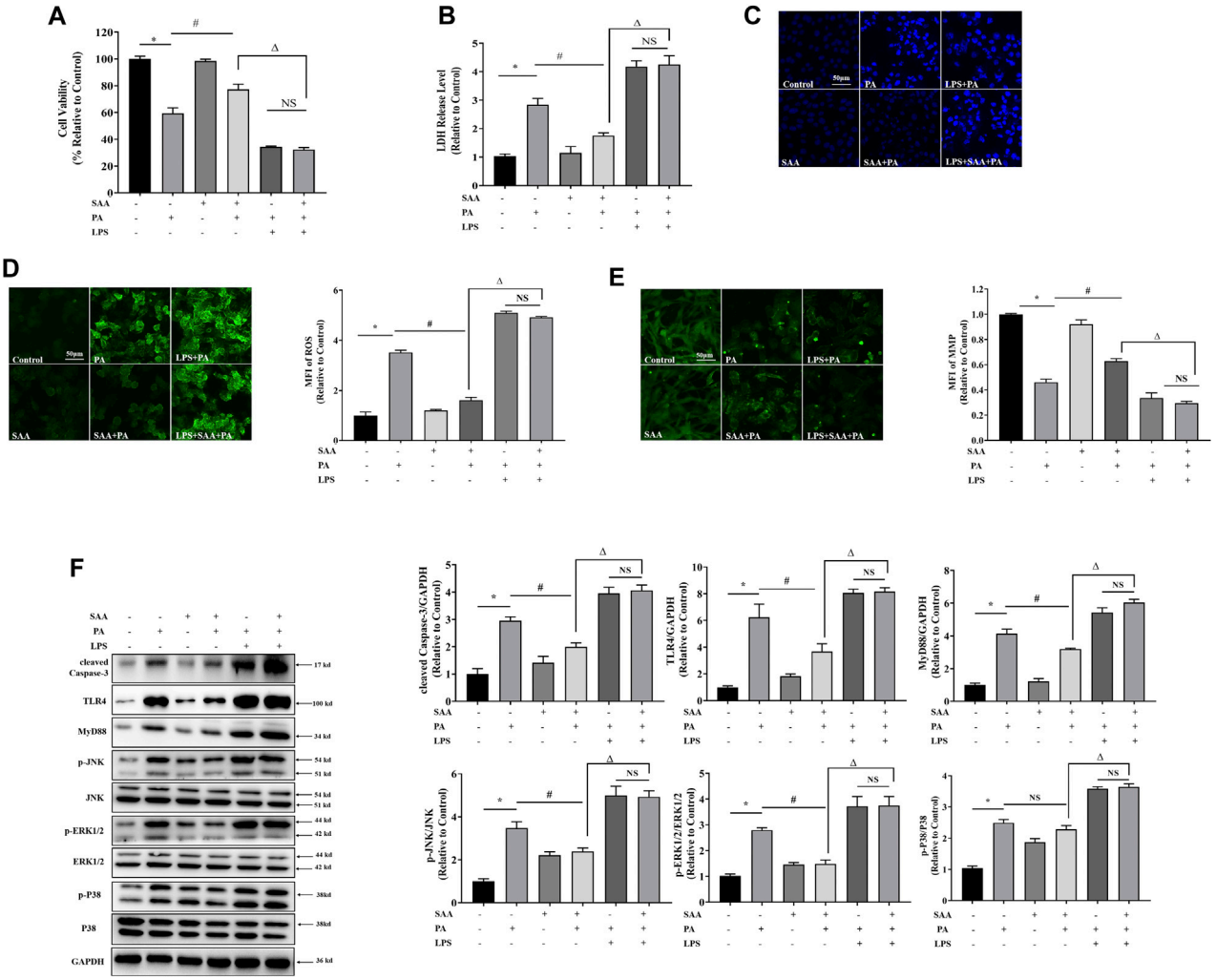

FIGURE 5 | TLR4 activation contributes to SAA protection from lipotoxicity-induced injury in cardiomyocytes. Cardiomyocyte cells were treated with PA at 0.4 mM for 4 h. TLR4 was activated with 100 ng/ml LPS for 2 h before PA treatment. 10 μM SAA was added 1 h before PA treatment. **(A)** Cell viability was tested using MTT. **(B)** LDH release measurement. **(C)** Nuclear staining with Hoechst. Cell death was detected by assessing nuclear morphology by fluorescence microscopy at a ×200 magnification **(D)** ROS levels were measured by DCFH-DA. **(E)** Mitochondrial membrane potential (MMP) was examined by fluorescence microscopy. **(F)** Cleaved Caspase-3, TLR4, MyD88, *p*-JNK, and *p*-ERK1/2 levels were determined by western blot. Values are presented as mean ± SD for ≥3 independent tests. Bars with different characters are significantly different, $p < 0.05$.

increased ROS levels relative to control cells (**Figure 1F**). However, SAA was shown to significantly suppress ROS production. MFI values showed that SAA significantly reduced PA-induced ROS production. Pretreatment with SAA was also shown to significantly reverse PA-induced reduction of mitochondrial membrane potential (MMP) (**Figure 1G**). Together, these data demonstrate the protective effects of SAA against mitochondrial damage, apoptosis, and oxidative stress-mediated injury.

The Protective Role of SAA Is Independent of SIRT1 and AMPK Pathways

Next, we determined whether SIRT1 mediates the beneficial effects of SAA against PA-induced cardiac lipotoxicity and found that SIRT1 levels were significantly reduced in PA-treated cells, while SAA treatment did not reverse SIRT1 suppression by PA (**Figure 2**). Analysis of potential AMPK involvement showed that pretreatment with SAA did not effectively improve PA-induced alteration of AMPK (**Figure 2**), implying that SIRT1 and AMPK did not mediate SAA effects in myocardial cells.

Activation of TLR4/AMPK Signaling Pathway Contributes to SAA Lipo-Protective Effects in Cardiac Cells

TLR4 inhibition is thought to be an SAA target during liver injury. Therefore, we determined if TLR4 signaling modulated

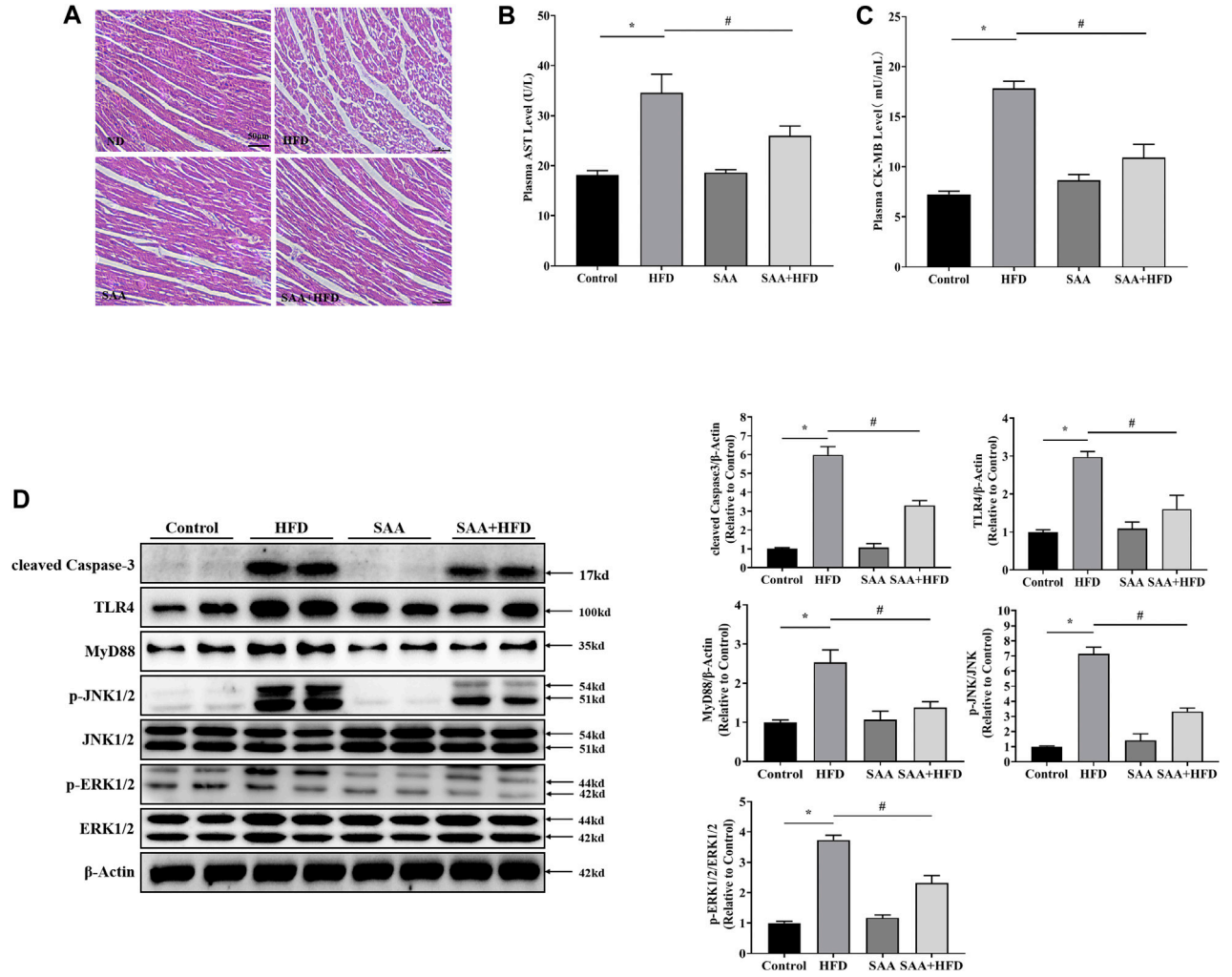

FIGURE 6 | TLR4/MAPKs pathway is involved in SAA protection of cardiomyocytes from lipotoxicity-induced injury in high-fat diet (HFD)-fed mice. Animals were divided into the following groups (6 mice each); normal diet group (Control), HFD group (HFD), normal diet with 40 mg/kg BW SAA group (SAA), and HFD with 40 mg/kg BW SAA (SAA + HFD) group. The Control group was fed AIN-93G diet. HFD mice were fed 60% fat diet to induce obesity (60% fat, D12492, Research Diets, New Brunswick, NJ) and water enriched with high fructose and sucrose. SAA was dissolved in sterilized physiologic saline with a stock concentration of 20 mg/mL. A total volume of 100 μL SAA diluted solution or sterilized physiologic saline was intraperitoneally administered every other day for 12 weeks. **(A)** H/E staining of cardiomyocytes - scale bars = 50 μm. **(B)** Plasma aspartate aminotransferase (AST) level **(C)** plasma creatine kinase, MB (CK-MB) level. **(D)** Cleaved Caspase-3, TLR4, MyD88, JNK, *p*-JNK, ERK1/2 and *p*-ERK1/2 levels in mouse heart tissues were determined by western blot. Values with different superscripts are significantly different at $p < 0.05$. * indicates comparison with normal controls while # shows comparison with HFD-fed group.

the protective effects of SAA against lipotoxicity. Analysis of TLR4 expression levels in PA-treated cardiac cells showed that treatment with PA at 0.4 mM for 2–4 h significantly increased TLR4 levels. At 8–12 h, the expression levels of TLR4 were not found to be significantly different from the untreated cardiac cells (**Figure 3A**). Then, we determined the expression level of TLR4 after the treatment with indicated concentrations (0.2, 0.4, 0.6, 0.8 mM) of *p*A. It was found that TLR4 were significantly up-regulated by PA treatment in a dose-dependent manner (**Figure 3B**). We then tested 0.4 mM concentration of PA on H9c2 cells for 4 h with or without SAA. MAPKs mediate SAA protection of liver injury. Analysis of whether MAPKs signaling mediate SAA protection against PA-induced lipotoxicity showed that SAA pretreatment significantly reversed PA-induced upregulation of MyD88, *p*-JNK and *p*-ERK1/2 levels. This implies that SAA lipo-protective effects are, partly, mediated by TLR4/MyD88/MAPKs signaling (**Figure 3C**).

TLR4 Upregulation Mediates PA-Induced Lipotoxicity in Cardiac Cells

To confirm whether TLR4 regulates lipotoxicity in cardiomyocytes, we inhibited TLR4 using CLI-095 in H9c2 cells. TLR4 inhibition significantly suppressed cytotoxicity and LDH release relative to palmitate-treated cells (**Figures 4A,B**), supporting the observation that TLR4 facilitates PA-induced

lipotoxicity in cardiomyocytes. Moreover, inhibiting TLR4 also suppressed PA-induced elevation of cleaved Caspase-3 and ROS, mitochondrial membrane potential repression, and apoptosis in cardiac cells (**Figures 4C–F**), implying that TLR4 is involved in PA-induced lipotoxicity in cardiac cells.

TLR4/MAPKs Is Involved in SAA Lipo-Protective Effects in Cardiomyocytes

To determine the role of TLR4/MAPKs in SAA's lipo-protective effects in cardiomyocytes, we activated TLR4 using LPS and found that it significantly suppressed the protective properties of SAA against lipotoxicity, including cell viability, LDH release, MMP, ROS formation, apoptosis, and cleaved Caspase-3 levels (**Figures 5A–F**). Moreover, TLR4 upregulation mitigated the lipo-protective effects of SAA through PA-induced targets of MyD88 and MAPKs, including *p*-JNK and *p*-ERK1/2 (**Figure 5F**). These findings confirmed that TLR4 signaling is involved in the exertion of the lipo-protective effects of SAA in cardiomyocytes.

TLR4/MAPKs Mediate SAA Lipo-Protective Effects in Cardiomyocytes of HFD-Fed Mice

To determine the protective effects of SAA in cardiomyocytes of HFD-fed mice, we examined the pathological alterations of cardiomyocytes in various groups using H&E staining. There were structural abnormalities in the cardiomyocytes of HFD-fed mice, including altered cellular structures and broken fibers, which were significantly alleviated by SAA treatment (**Figure 6A**). The plasma levels of AST and CK-MB are indicators of cardiomyocyte injury. We found that SAA significantly reduced HFD-driven increase in plasma AST and plasma CK-MB levels (**Figures 6B,C**). Furthermore, SAA significantly suppressed HFD-induced increase in cleaved Caspase-3 in mouse myocardial tissues (**Figure 6D**), implying that SAA prevented against cardiomyocyte lipotoxicity in HFD fed mice.

We then examined the role of TLR4/MAPKs in SAA anti-lipotoxic effects *in vivo* and found that SAA significantly suppressed HFD-induced elevation of TLR4, MyD88, *p*-JNK and *p*-ERK1/2, consistent with our *in vitro* data (**Figure 6D**). These findings suggest that TLR4/MAPKs inhibition contributes to SAA's protection of cardiomyocytes from lipotoxicity.

DISCUSSION

We have shown that SAA, a phytochemical found in Danshen, protects against lipotoxicity in HFD-fed mice and cultured cardiomyocytes. Its benefits are associated with its effects on TLR4/MAPKs signaling. SAA is a bioactive component of *Salvia miltiorrhiza Bunge*. In traditional Chinese medicine, Danshen is used to enhance blood flow, resolve blood stasis and for the prevention and treatment of cardiovascular diseases. However, the cardioprotective benefits of SAA are not well understood.

Lipotoxicity refers to cellular damage and death caused by free fatty acids elevation and aberrant lipid metabolism. Lipotoxicity by saturated fatty acids (SFAs) promotes myocardial lipotoxic injury. Sustained SFA elevation leads to myocardial lipotoxic injury, resulting in cardiac dysfunction (Wende and Abel, 2010). As documented in literature, PA and SA, but not OA, cause significant myocardial cell injury by suppressing cell viability and enhancing LDH activity in a dose-dependent manner. Moreover, PA elevated Bcl2: Bax ratio, as well as Caspase-3 levels, implying that it mediates cardiomyocyte apoptosis. These data established that SFAs induce myocardial lipotoxic injury *in vitro*. LSFA induction of myocardial injury, mitochondrial dysfunction, and subsequent mitochondrial apoptosis mediate cardiomyopathic pathogenesis (Murphy et al., 2016). We found that cardiomyocytes are susceptible to PA stimulation, causing mitochondrial damage, increased ROS, decreased MMP, and reduced Bcl2/Bax ratio. To our knowledge, a limited number of studies have evaluated the protective effects of SAA against SFA-induced myocardial lipotoxicity. Analysis of the effect of SAA on PA-induced myocardial lipotoxicity revealed that SAA exposure inhibited the PA-induced LDH release and cell viability in a dose-dependent manner by reversing the effect of lipotoxicity on MMP, ROS, and Bcl2/Bax ratio. These findings are in tandem with the role of SAA on PA-induced hepatic lipotoxic injury in NAFLD (Li et al., 2020).

Activation of SIRT1/AMPK signaling may prevent oxidative stress and inflammation during lipotoxicity-related hepatocyte injury (Xu et al., 2020). SAA alleviates insulin resistance and HFD-induced NAFLD through AMPK activation (Li et al., 2020). Moreover, SIRT1/AMPK attenuates palmitate-induced oxidative stress in cardiomyocytes. Multiple bioactive compounds, including curcumin (Zhang et al., 2019) and resveratrol (Feng et al., 2019) protect cardiomyocytes from apoptosis through the AMPK pathway. However, in this study, SAA did not reverse PA-induced activation of SIRT1 and AMPK phosphorylation in cardiomyocytes.

Another potential mechanism for SAA is through the TLR4 axis (Yang et al., 2019). In myocardial cells, TLR4 acts as a cellular injury sentinel and mediates inflammatory responses (Zhou et al., 2020). PA has been reported to be a TLR4 ligand during the induction of myocardial inflammatory responses where it activates TLR4 after HFD-induced injury (Wang et al., 2017). In line with the reports, we found TLR4 expression levels were upregulated in PA-stimulated cardiomyocytes injury, *in vitro*. In addition, TLR4 inhibition using CLI-095 significantly suppressed PA-induced cardiomyocytes mitochondrial dysfunction and apoptosis. This implies that TLR4 inhibition is a potential therapeutic target for lipotoxic heart disease. Interestingly, the cytoprotective effects of SAA in various cellular contexts are attributed to TLR4 inhibition (Zeng et al., 2020). Through modulating TLR4 signaling, SAA reduces oxidative stress, inflammation, and apoptosis in liver tissue during insulin resistance (Yang et al., 2019). Thus, we determined whether TLR4 signaling involved in the protection of SAA against lipotoxicity-induced myocardial damage. Accordingly, SAA significantly alleviated PA-activated TLR4 protein levels,

concurrent with reduction of its downstream factor MyD88 to activate the MAPK family members.

In cardiomyopathy, MAPK signaling activation induces cardiomyocytes apoptosis and promotes inflammation injury (Liang et al., 2019). *In vitro*, MAPKs overactivation has been reported to be involved in LSFAs-induced apoptosis in various cell types, including cardiomyocytes, pharmacologically inhibiting MAPKs or silencing them significantly elevates H_2O_2 levels and LSFAs-induced cell death (Oh et al., 2014). Previously, we have shown that TLR4/MAPK activation contributes to PA-induced cell death in hepatocytes. Analysis of if TLR4/MAPK signaling is mechanistically involved in PA-induced cell death in cardiomyocytes and SAA′s cardioprotective effects found that PA upregulated TLR4/MAPKs expression in H9c2 cells *in vitro*, SAA reversed the expression of TLR4, MAPK and its downstream signals *p*-JNK, ERK1/2.

To further delinate the role of TLR4 in SAA and PA-induced lipotoxicity in cardiomyocytes lipotoxicity, we further dissected potential underlying mechanisms. In our previous study (Dou et al., 2020), activating TLR4 using LPS markedly blocked the lipid-reducing effects of Salidrosid. Consistent with the results, the TLR4 activation by LPS prominently abolished the beneficial role of SAA on TLR4-regulated MAPKs inhibition and myocardial apoptosis, which indicated that TLR4-regulated MAPKs pathway was mechanistically involved in SAA protection against cardiomyocytes lipotoxicity. However, we still do not know how SAA regulates TRL4/MAPKs expression in cardiomyocytes. In addition, LPS is a very strong activator of TLR4 pathway, which induction markedly aggravated PA-induced adverse effects, which might mask the potential protective effect of SAA through other pathways. Therefore, the participation of other potential signaling pathways in SAA-prevented lipotoxicity could also not be excluded, although it seems like that LPS completely abolished the beneficial effects of SAA.

In summary, we show that SAA has anti-inflammatory and anti-mitochondrial dysfunction effects *in vitro* and *in vivo*. Thus, the clinical benefits of SAA are closely associated with its ability to reduce TLR4 and inhibit MAPKs. We provide important insights into the mechanisms by which SAA-mediates myocardial protection against lipotoxic injury, thereby highlighting SAA as a potential dietary supplement or therapeutic agent for preventing and treating lipotoxicity-induced heart diseases.

DATA AVAILABILITY STATEMENT

The original contributions presented in the study are included in the article/**Supplementary Material**, further inquiries can be directed to the corresponding authors.

ETHICS STATEMENT

The animal study was reviewed and approved by the Animal Ethics Committee at Zhejiang Chinese Medical University.

AUTHOR CONTRIBUTIONS

ZY (3rd author) and YC contributed experimental data. ZY (1st author) wrote the first draft of the manuscript; SL, XD wrote sections of the manuscript and revised the whole manuscript. All authors contributed to manuscript revision, read and approved the submitted version.

FUNDING

This work was supported by the National Natural Science Foundations of China (No. 81973041, 81773981, and 81773422), Zhejiang Natural Science Foundations for Distinguished Young Scholars ((No. LR20H260001), and Special Support Program for High Level Talents in Zhejiang Province (No. ZJWR0308092).

SUPPLEMENTARY MATERIAL

The Supplementary Material for this article can be found online at: https://www.frontiersin.org/articles/10.3389/fphar.2021.627123/full#supplementary-material.

REFERENCES

Chen, Y., Feng, B., Yuan, Y., Hu, J., Zhao, W., Jiang, H., et al. (2020). Aloe emodin reduces cardiac inflammation induced by a high-fat diet through the TLR4 signaling pathway. *Mediat. Inflamm.* 2020, 6318520. doi:10.1155/2020/6318520

Dou, X., Ding, Q., Lai, S., Jiang, F., Song, Q., Zhao, X., et al. (2020). Salidroside alleviates lipotoxicity-induced cell death through inhibition of TLR4/MAPKs pathway, and independently of AMPK and autophagy in AML-12 mouse hepatocytes. *J. Funct. Foods* 65. doi:10.1016/j.jff.2019.103691

Feng, L., Ren, J., Li, Y., Yang, G., Kang, L., Zhang, S., et al. (2019). Resveratrol protects against isoproterenol induced myocardial infarction in rats through VEGF-B/AMPK/eNOS/NO signaling pathway. *Free Radic. Res.* 53 (1), 82–93. doi:10.1080/10715762.2018.1554901

Feng, S., Nan, A., Geng, J., Huang, J., Sun, R., Chun, G., et al. (2017). Pharmacokinetic and metabolomic analyses of the neuroprotective effects of salvianolic acid A in a rat ischemic stroke model. *Acta Pharmacol. Sin.* 38 (11), 1435–1444. doi:10.1038/aps.2017.114

Gélinas, R., Mailleux, F., Dontaine, J., Bultot, L., Demeulder, B., Ginion, A., et al. (2018). Bertrand bouchard, christine des rosiers, benoit viollet, kei sakamoto, jean-luc balligand, jean-louis vanoverschelde, christophe beauloye, sandrine horman, luc BertrandAMPK activation counteracts cardiac hypertrophy by reducing O-GlcNAcylation. *Nat. Commun.* 9, 374. doi:10.1038/s41467-017-02795-4

Ho, J. H. C., and Hong, C. Y. (2011). Salvianolic acids: small compounds with multiple mechanisms for cardiovascular protection. *J. Biomed. Sci.* 18 (1), 30. doi:10.1186/1423-0127-18-30

Jackson, E. E., RendinaRuedy, E., Smith, B. J., and Lacombe, V. A. (2015). Loss of toll-like receptor 4 function partially protects against peripheral and cardiac glucose metabolic derangements during a long-term high-fat diet. *PloS One* 10 (11), e0142077. doi:10.1371/journal.pone.0142077

Li, S., Li, J., Shen, C., Zhang, X., Sun, S., Cho, M., et al. (2014). tert-Butylhydroquinone (tBHQ) protects hepatocytes against lipotoxicity via

inducing autophagy independently of Nrf2 activation. *Biochim. Biophys. Acta* 1841 (1), 22–33. doi:10.1016/j.bbalip.2013.09.004

Li, S., Qian, Q., Ying, N., Lai, J., Feng, L., Zheng, S., et al. (2020). Activation of the AMPK-SIRT1 pathway contributes to protective effects of Salvianolic acid A against lipotoxicity in hepatocytes and NAFLD in mice. *Front. Pharmacol.* 30 (11), 560905. doi:10.3389/fphar.2020.560905

Liang, Y., Lp, M. S. M., and Mak, J. C. W. (2019). (-)-Epigallocatechin-3-gallate suppresses cigarette smoke-induced inflammation in human cardiomyocytes via ROS-mediated MAPK and NF-κB pathways. *Phytomedicine* 58 (5), 152768. doi:10.1016/j.phymed.2018.11.028

Liu, H., Jia, W., Tang, Y., Zhang, W., Qi, J., Yan, J., et al. (2020). Inhibition of MyD88 by LM8 attenuates obesity-induced cardiac injury. *J. Cardiovasc. Pharmacol.* 76 (1), 63–70. doi:10.1097/FJC.0000000000000846

Liu, Z., Wang, J., Qiu, C., Guan, G., Liu, X., Li, S., et al. (2014). Matrine pretreatment improves cardiac function in rats with diabetic cardiomyopathy via suppressing ROS/TLR-4 signaling pathway. *Acta Pharmacol. Sin.* 36 (3), 323–333. doi:10.1038/aps.2014.127

Ma, Z., Kong, C., Song, P., Zhang, X., Yuan, Y., and Tang, Q. (2018). Geniposide protects against obesity-related cardiac injury through AMPKα- and sirt1-dependent mechanisms. *Oxid. Med. Cell Longev.* 2018, 6053727. doi:10.1155/2018/6053727

Murphy, E., Ardehali, H., Balaban, R. S., DiLisa, F., Dorn, G. W., Kitsis, R. N., et al. (2016). Mitochondrial function, biology, and role in disease: a scientific statement from the American heart association. *Circ. Res.* 118 (12), 1960–1991. doi:10.1161/RES.0000000000000104

Oh, C. C., Nguy, M. Q., Schwenke, D. C., Migrino, R. Q., Thornburg, K., and Reaven, P. (2014). P38αmitogen-activated kinase mediates cardiomyocyte apoptosis induced by palmitate. *Biochem. Biophys. Res. Commun.* 450 (1), 628–633. doi:10.1016/j.bbrc.2014.06.023

Schrammel, A., Mussbacher, M., Winkler, S., Haemmerle, G., Stessel, H., Wölkart, G., et al. (2013). Cardiac oxidative stress in a mouse model of neutral lipid storage disease. *Biochim. Biophys. Acta* 1831 (11), 1600–1608. doi:10.1016/j.bbalip.2013.07.004

Sletten, A. C., Peterson, L. R., and Schaffer, J. E. (2018). Manifestations and mechanisms of myocardial lipotoxicity in obesity. *J. Intern. Med.* 284 (5), 478–491. doi:10.1111/joim.12728

van Rooijen, M. A., and Mensink, R. P. (2020). Palmitic acid versus stearic acid: effects of interesterification and intakes on cardiometabolic risk markers-A systematic review. *Nutrients* 12 (3), 615. doi:10.3390/nu12030615

Wang, R., Song, F., Li, S., Wu, B., Gu, Y., and Yuan, Y. (2019a). Salvianolic acid A attenuates CCl4-induced liver fibrosis by regulating the PI3K/AKT/mTOR, Bcl-2/Bax and caspase-3/cleaved caspase-3 signaling pathways. *Drug Des. Dev. Ther.* 13, 1889–1900. doi:10.2147/DDDT.S194787

Wang, R., Zhang, J., Wang, S., Wang, M., Ye, T., Du, Y., et al. (2019b). The cardiotoxicity induced by arsenic trioxide is alleviated by salvianolic acid A via maintaining calcium homeostasis and inhibiting endoplasmic reticulum stress. *Molecules* 24 (3), 543. doi:10.3390/molecules24030543

Wang, S., Ding, L., Ji, H., Xu, Z., Liu, Q., and Zheng, Y. (2016). The role of p38 MAPK in the development of diabetic cardiomyopathy. *Int. J. Mol. Sci.* 17 (7), 1037. doi:10.3390/ijms17071037

Wang, Y., Qian, Y., Fang, Q., Zhong, P., Li, W., Wang, L., et al. (2017). Saturated palmitic acid induces myocardial inflammatory injuries through direct binding to TLR4 accessory protein MD2. *Nat. Commun.* 8, 13997. doi:10.1038/ncomms13997

Wende, A. R., and Abel, E. D. (2010). Lipotoxicity in the heart. *Biochim. Biophys. Acta* 1801 (3), 311–319. doi:10.1016/j.bbalip.2009.09.023

Xu, H., Chen, G., Ma, Y., Zhang, H., Zhou, Y., Liu, G., et al. (2020). Hepatic proteomic changes and Sirt1/AMPK signaling activation by oxymatrine treatment in rats with non-alcoholic steatosis. *Front. Pharmacol.* 216 (11), 216. doi:10.3389/fphar.2020.00216

Yang, H., Feng, A., Lin, S., Yu, L., Lin, X., Yan, X., et al. (2018). Fibroblast growth factor-21 prevents diabetic cardiomyopathy via AMPK-mediated antioxidation and lipid-lowering effects in the heart. *Cell Death Dis.* 9 (2), 227. doi:10.1038/s41419-018-0307-5

Yang, L., Jiang, L., Jiang, D., Liu, B., and Jin, S. (2019). The protective effects of salvianolic acid A against hepatic ischemia-reperfusion injury via inhibiting expression of toll-like receptor 4 in rats. *Arch. Med. Sci.* 15 (6), 1599–1607. doi:10.5114/aoms.2019.87412

Yang, L., Li, D., Zhang, Y., Zhu, M., Chen, D., and Xu, T. (2012). Salvianolic acid A inhibits angiotensin II-induced proliferation of human umbilical vein endothelial cells by attenuating the production of ROS. *Acta Pharmacol. Sin.* 33 (1), 41–48. doi:10.1038/aps.2011.133

Zeng, X., Chen, X., Qin, H., Han, Y., Chen, X., Han, Z., et al. (2020). Preventive effects of a natural anti-inflammatory agent Salvianolic acid A on acute kidney injury in mice. *Food Chem. Toxicol.* 135 (1), 110901. doi:10.1016/j.fct.2019.110901

Zhang, J., Wang, Y., Bao, C., Liu, T., Li, S., Huang, J., et al. (2019). Curcumin-loaded PEG-PDLLA nanoparticles for attenuating palmitate-induced oxidative stress and cardiomyocyte apoptosis through AMPK pathway. *Int. J. Mol. Med.* 44 (2), 672–682. doi:10.3892/ijmm.2019.4228

Zheng, X., Chen, S., Yang, Q., Cai, J., Zhang, W., You, H., et al. (2015). Salvianolic acid A reverses the paclitaxel resistance and inhibits the migration and invasion abilities of human breast cancer cells by inactivating transgelin. *Canc. Biol. Ther.* 16 (9), 1407–1414. doi:10.1080/15384047.2015.1070990

Zhou, R., Gao, J., Xiang, C., Liu, Z., Zhang, Y., Zhang, J., et al. (2020). Salvianolic acid A attenuated myocardial infarction-induced apoptosis and inflammation by activating Trx. *Naunyn-Schmiedeberg's Arch. Pharmacol.* 393 (6), 991–1002. doi:10.1007/s00210-019-01766-4

Conflict of Interest: The authors declare that the research was conducted in the absence of any commercial or financial relationships that could be construed as a potential conflict of interest.

Copyright © 2021 Yang, Chen, Yan, Xu, Wu, Pi, Liu, Chai, Li and Dou. This is an open-access article distributed under the terms of the Creative Commons Attribution License (CC BY). The use, distribution or reproduction in other forums is permitted, provided the original author(s) and the copyright owner(s) are credited and that the original publication in this journal is cited, in accordance with accepted academic practice. No use, distribution or reproduction is permitted which does not comply with these terms.

frontiers in Pharmacology

ORIGINAL RESEARCH
published: 26 March 2021
doi: 10.3389/fphar.2021.643482

Palmul-Tang, a Korean Medicine, Promotes Bone Formation via BMP-2 Pathway in Osteoporosis

La Yoon Choi[1], *Mi Hye Kim*[1], *Yeon Kyung Nam*[1], *Ju Hee Kim*[2], *Hea-Young Cho*[2] *and Woong Mo Yang*[1]*

[1]Department of Convergence Korean Medical Science, College of Korean Medicine, Kyung Hee University, Seoul, South Korea, [2]College of Pharmacy, CHA University, Seongnam, South Korea

Osteoporosis is a common skeletal disease in post-menopausal women. *Palmul*-tang, an herbal medicine, has been treated for gynecological disease such as anemia, anorexia, anti-fatigue, unspecified menstruation and female infertility in East Asia. In this study, ameliorative effects of *Palmul*-tang soft extracts (PMT), a Korean Medicine, on osteoporosis were investigated. Ovariectomized (OVX) osteoporotic ICR mice were intragastrically administrated PMT for 4 weeks. The level of bone mineral density (BMD) was analyzed in bone tissues by dual X-ray absorptiometry. The bone medullary cavity and deposition of collagen were investigated by histological analysis. In addition, the BMP-2 signaling-related molecules, osteoblastic differentiation and formation markers, were determined in femoral tissues. The levels of BMD and bone mineral content were significantly increased in tibia, femurs and LV by treatment of PMT. PMT replenished bone marrow cavity and increased collagen deposition in bone marrow cells of femur. In addition, administration of PMT recovered serum ALP, bALP, osteocalcin and calcium levels in osteoporotic mice. Moreover, PMT treatment up-regulated the expressions of BMP-2, RUNX2 and OSX with its downstream factors, ALP, OPN and BSP-1, in the femoral tissues. Taken together, PMT restored the bone minerals and improvement of bone integrity by bone-forming BMP-2 signaling pathway. These results demonstrate that PMT could be an ameliorative agent for osteoporosis.

Keywords: osteoporosis, traditional herbal medicine, palmul-tang, bone integrity, BMP-2

OPEN ACCESS

Edited by:
Hai Yu Xu,
China Academy of Chinese Medical Sciences, China

Reviewed by:
Subhash Chandra Mandal,
Government of West Bengal, India
Jwu-Lai Yeh,
Kaohsiung Medical University, Taiwan
Seon-Yong Jeong,
Ajou University, South Korea

***Correspondence:**
Woong Mo Yang
wmyang@khu.ac.kr

Specialty section:
This article was submitted to Ethnopharmacology, a section of the journal Frontiers in Pharmacology

Received: *18 December 2020*
Accepted: *19 February 2021*
Published: *26 March 2021*

Citation:
Choi LY, Kim MH, Nam YK, Kim JH, Cho H-Y and Yang WM (2021) Palmul-Tang, a Korean Medicine, Promotes Bone Formation via BMP-2 Pathway in Osteoporosis. *Front. Pharmacol. 12:643482. doi: 10.3389/fphar.2021.643482*

INTRODUCTION

Osteoporosis is a skeletal disease by occurring the impairment of osteoblast and osteoclast balances (Chen et al., 2018). During the procession of osteoporosis, the reduction of bone mass and deterioration of bone tissue leads to augmentation of bone fragility, thereby lowering bone mineral density (BMD) and increasing the risk of bone fractures such as wrist, hip and vertebrae (Kanis, 2002; Cheng et al., 2011). More than 30% of women over the age of 50 estrogen deficient which also causes environmental changes such as increased treatment costs and poor quality of life (Dickenson et al., 1981). Accordingly, management and prevention of osteoporosis is the most representative public health issue for the assignment of global strategies (Lewis et al., 2019).

A common prescription for treatment of osteoporosis is hormone therapy, bisphosphonates and supplements such as calcium and vitamin D (Bowring and Francis, 2011). The mode of action by

anti-osteoporosis drugs is associated with improvement of balances for abnormal function of osteoblast and osteoclast that increase the bone mass and offset the bone loss (Tanaka et al., 2005; Nanjundaiah et al., 2013). However, the possibility of experiencing side effects including hot flush, breast cancer, blood clots, heart failure and osteonecrosis of jaw still remains an obstacle to be overcome and drives us to find new prospective drugs for improving osteoporosis (Nam et al., 2012; Tella and Gallagher, 2014).

Traditional herbal medicine in Korea is used to treat various diseases because of its low side effects and high efficacy in prevention and treatment (Yuan et al., 2016). *Palmul*-tang, also known as *Paljin*-tang in Korean, *Hachimotsu-to* in Japanese and *Bawu*-tang in Chinese, is a herbal formula which is consists of eight herbs, *Panax ginseng* C. A. Meyer, *Atractylodes macrocephala* Koidz, *Poria cocos* F. A. Wolf, *Glycyrrhiza uralensis* Fischer, *Rehmannia glutinosa* (Gaertner) Liboschitz, *Paeonia lactiflora* Pallas, *Ligusticum officinale* (Makino) Kitag and *Angelica gigas* Nakai (Eom et al., 2017; Jin et al., 2017). *Palmul*-tang has traditionally been prescribed for anemia, anorexia, anti-fatigue, and nerualgia (Heo et al., 2003; Park et al., 2004a; Park et al., 2004b; Ma et al., 2007b; Shin and Shin, 2012; Kim and Bak, 2015). Especially, *Palmul*-tang has been used for women diseases such as unspecified menstruation, reproductive activities and female infertility (Ma et al., 2007a). Also, *Palmul*-tang was used for women diseases such as unspecified menstruation, reproductive activities and female infertility (Ma et al., 2007a). Recent study showed inhibitory effects of *Palmul*-tang on inflammatory mediator production related to NF-κB, MAPK and HO-1 pathway in macrophages (Oh et al., 2014). According to the traditional theory including Korean medicine, traditional Chinese medicine and Kampo medicine, *Palmul*-tang has been known for improving the basis of metabolism and enhancing the organ activity by nourishing "qi" and enriching "blood." Tonifying "qi" induces bone marrow to nourish the bone, resulting in growth of skeleton (Wang et al., 2016b). Interruption of "blood" circulation is highly involved in increasing osteoclastic activities leading to induction of cumulative bone loss as a crucial factor for bone growth (Fricke and Krokowski, 1975; Alagiakrishnan et al., 2003). In addition, *Palmul*-tang is a combination of *Sagunja*-tang and *Samul*-tang, which is reported to be effective for osteoporosis (Lee et al., 1995; Shim et al., 2011; Yim et al., 2018). Based on the recent studies, we anticipated that *Palmul*-tang soft extracts (PMT) has ameliorative effects on post-menopausal osteoporosis. In the present study, the effects of PMT on bone loss was investigated by assessing BMC and BMD levels and bone-forming BMP-2 signaling pathway-related molecules were determined in bone tissues.

MATERIALS AND METHODS

Samples

PMT (Lot. #8001), which is a standardized Korean medicine for health insurance, was obtained from Kyoungbang pharmacy Inc. (Incheon, Korea). The total volume of PMT is 10 g per pack and composed of *Panax ginseng* C. A. Meyer, *Atractylodes macrocephala* Koidz, *Poria cocos* F. A. Wolf, *Glycyrrhiza uralensis* Fischer, *Rehmannia glutinosa* (Gaertner) Liboschitz, *Paeonia lactiflora* Pallas, *Ligusticum officinale* (Makino) Kitag and *Angelica gigas* Nakai (**Table 1**). Voucher specimen PMT (Lot. #8001) is deposited in our laboratory.

TABLE 1 | Components of *Palmul*-tang soft extract one pack.

Y	Family	Source	Weight (mg)
Panax ginseng C. A. Meyer	Araliaceae	Korea	420
Atractylodes macrocephala Koidz	Asteraceae	Korea	495
Poria cocos F. A. Wolf	Polyporaceae	Korea	225
Glycyrrhiza uralensis Fischer	Fabaceae	Korea	660
Rehmannia glutinosa (Gaertner) Liboschitz	Orobanchaceae	Korea	720
Paeonia lactiflora Pallas	Paeoniaceae	Korea	495
Ligusticum officinale (Makino) Kitag	Apiaceae	Korea	645
Angelica gigas Nakai	Apiaceae	Korea	495

High-Performance Liquid Chromatography

Three packets (45 g) of PMT was thoroughly mixed, extracted and filtered to make a test liquid for injecting into the Alliance HPLC e2695 system with 2489 UV/Vis detector. A full scan spectrum in positive ESI mode was obtained for the main ingredient identification of PMT. Then the reference standards of atractylenolide I and atractylenolide III were accurately weighed and dissolved in methanol. The chromatographic separations of the analytes were conducted on Kromasil C18 column (4.6 × 159 mm, 3.5 μm). The mobile phase consisted of (A) water and (B) acetonitrile (30:70, v/v) flowed at a rate of 1.0 ml/min. Then 10 μL of the sample was injected for the analysis. Contents of atractylenolide I and atractylenolide III were 0.033 ± 0.0010 mg and 0.039 ± 0.0002 mg, respectively (n = 3). (**Supplementary Figure S1**).

Animals

All experiments were conducted with the approval of the Committee on Care and Use of Laboratory Animals of Kyung Hee University, Seoul, Korea (KHSASP-19-097). Female ICR mice aging of 5 weeks old were obtained from RaonBio Inc. (Yongin, Korea). All mice were acclimated at least 1 week under standard housing conditions (22–24°C, 12 h/12 h light/dark cycle) and had freely access food and water. The experimental groups divided into 6 groups (n = 7); 1) sham (blank control), 2) OVX (negative control), E2 (OVX + 17β-estradiol, 10 μg/kg, positive control), PMT 61.7 (OVX + PMT 61.7 mg/kg), PMT 617 (OVX + PMT 617 mg/kg), PMT 6170 (OVX + PMT 6170 mg/kg).

Experimental Protocol

All mice were intraperitoneally injected with avertin (Sigma-Aldrich, St. Louis, United States) and shaved dorsal midline skin. The shaved skins were longitudinally incised and operated sham or removed bilateral ovaries. Exposed skin and muscle were closed with silk 4-0 suture (AILEE co., Busan, Korea) and applied povidone iodine on surgical area to disinfect the skin.

Following induce osteoporosis for 10 weeks, Day 70, OVX-operated groups were assigned to 5 groups in accordance with body weights. The PMT samples were administrated 5 days per week for 4 weeks; sham and OVX groups were orally treated with vehicle, E2 group was intraperitoneally injected with 10 μg/kg of 17β-estradiol, PMT groups were orally treated with dose of 61.7, 617, 6,170 mg/kg of PMT diluted in distilled water. The doses of PMT were selected from formula for dose translation by human equivalent dose (Nair and Jacob, 2016). The dosage of samples in use for human is 30 g/60 kg/day (3 packs). Dosage for human (30 g/60 kg/day) is converted into mice (6,170 mg/kg/day) by using human equivalent dose equation as high dosage of this study. During animal experiments, body weight was monitored by weekly. The body weights of osteoporotic mice showed almost same values in whole experimental periods without any adverse events. At the end of experiments, Day 96, the mice were sacrificed by cervical dislocation. The sacrifice mice dissected blood, tibiae, femora and L4~L6 vertebrae (LV) to analyzed efficacy of PMT on osteoporosis.

Dual Energy X-Ray Absorptiometry Test

To measure bone mineral content (BMC; g) and bone mineral density (BMD; g/cm^2), excised tibiae, femora and LV were detected by using dual energy X-ray absorptiometry (DXA, Medikors, Seongnam, Korea).

Histopathological Examination

Excised left femurs were fixed in 10% neutralized formalin for 24 h and demineralized using 0.1 M ethylene diamine tetra acetic acid (EDTA) for 2 weeks. After decalcification, femurs were dehydrated with a graded series of alcohol, xylene and paraffin. The femurs were embedded for sagittal sections in paraffin and harden in the freezer for 24 h. Paraffin blocks were sliced using microtome into 10 μm-thick and placed on gelatin-coated glass slides. To evaluate the recovery of bone marrow cavity and interstitial collagen, hematoxylin and eosin (H&E) staining and picrosirius red staining were performed. Stained sections were photographed with magnification ×400 under microscope.

ELISA Analysis of Osteoblastic Factors

Collected blood sample were isolated by centrifuge at 17,000 rpm for 20 min and supernatants were kept at −20°C until use. The serum samples were moved at 4°C 1 day before usage. Serum alkaline phosphatase (ALP), bone-specific ALP (bALP) (AnaSpec, United States), osteocalcin (TaKaRa Bio Inc., Japan) and Ca (Nikken SEIL Co., Japan) levels were analyzed using enzyme-linked immunosorbent assay (ELISA) kit. The procedures were conducted according to manufacturer's instructions.

RT-PCR Analysis

To analyze osteoblastic markers, right femurs were pulverized using liquid nitrogen with mortar and pestle into fine powder. Powdered femurs were incubated with trizol (Invitrogen, United States) at 4°C for overnight and homogenized. Total RNA was extracted according to the manufacturer's protocols. Total RNA was measured and synthesized cDNA using 1 μg RNA and Maxime RT premix (Invitrogen). Reverse transcription polymerase chain reaction (RT-PCR) was performed using Maxim PCR premix (Invitrogen). Osteoblastic markers specific primers were as follows: 5′-GCGGTGGACTGCACAGGGAC-3′ and 5′-CTACCCTTCCCCGTGGGGGA-3′ for *bone morphogenetic protein 2* (BMP-2), 5′-CCGCACGACAACCGC ACCAT-3′ and 5′-CGCTCCGGCCCACAAATCTC-3′ for *runt-related transcription factor 2* (RUNX2), 5′-TAATGGGCTCCT TTCACCTG-3′ and 5′-CACTGGGCAGACAGTCAGAA-3′ for *osterix* (OSX), 5′-TGGAGCTTCAGAAGCTCAACACCA-3′ and 5′-ATCTCGTTGTCTGAGTACCAGTCC-3′ for *alkaline phosphatase* (ALP), 5′-CATTGCCTCCTCCCTCCCGGTG-3′ and 5′-GTCATCACCTCGGCCGTTGGGG-3′ for *osteopontin* (OPN), 5′-GAGCCAGGACTGCCGAAAGGAA-3′ and 5′-CCGTTGTCTCCTCCGCTGCTGC-3′ for *bone sialoprotein* (BSP-1), 5′-GGCATGGACTGTGGTCATGA-3′ and 5′-TTC ACCACCATGGAGAAGGC-3′ for *glyceraldehyde 3-phosphate dehydrogenase* (GAPDH). The gene expressions were detected by 1% agarose gel and normalized to housekeeping gene, GAPDH. All bands were analyzed by image J software.

Statistical Analysis

All data are analyzed by using GraphPad Prism 5 software (GraphPad Software Inc., La Jolla, CA, United States). Significance was determined by one-way analysis of variance (ANOVA) and Tukey multiple comparison tests. Data were presented as the mean ± standard error. In all analyses, $p < 0.05$ was taken to indicate statistical significance. All data underlying the study was deposited in our laboratory.

RESULTS

Effects of PMT on BMC and BMD

Femoral, tibial and LV were used to evaluate the levels of BMC and BMD. As shown in **Figure 1A**, levels of femoral, tibial and LV BMC was declined 4.33, 6.01 and 17.31% in OVX group compared to sham group and recovered 5.20, 6.33 and 13.65% in E2 group compared to OVX group. Treatment of PMT up-regulated BMC in femur, tibia and LV compared to OVX group, especially increased 4.69, 5.86 and 11.32% in 6,170 mg/kg of PMT. As similar as result from **Figure 1B**, levels of BMD on femora, tibial and LV were decreased 9.29, 7.12 and 20.87% in OVX group by PMT. Also, treatment of E2 increased levels of BMD by 10.24% in femora, 8.06% in tibiae and 13.10% in LV. In addition, 6,170 mg/kg of PMT improved levels of BMD, 3.97, 3.10 and 11.34%, respectively.

Effects of PMT on Histological Changes

The bone marrow cavity in femoral shaft was used to determine by H&E staining. In **Figure 2A**, OVX group appeared high adiposity of bone marrow compared to sham group, whereas treatment of E2 and PMT ameliorated bone marrow adiposity, particularly treated with 6,170 mg/kg of PMT. Picrosirius red staining showed quantitatively improvement of collagen fibers in femur. As demonstrated

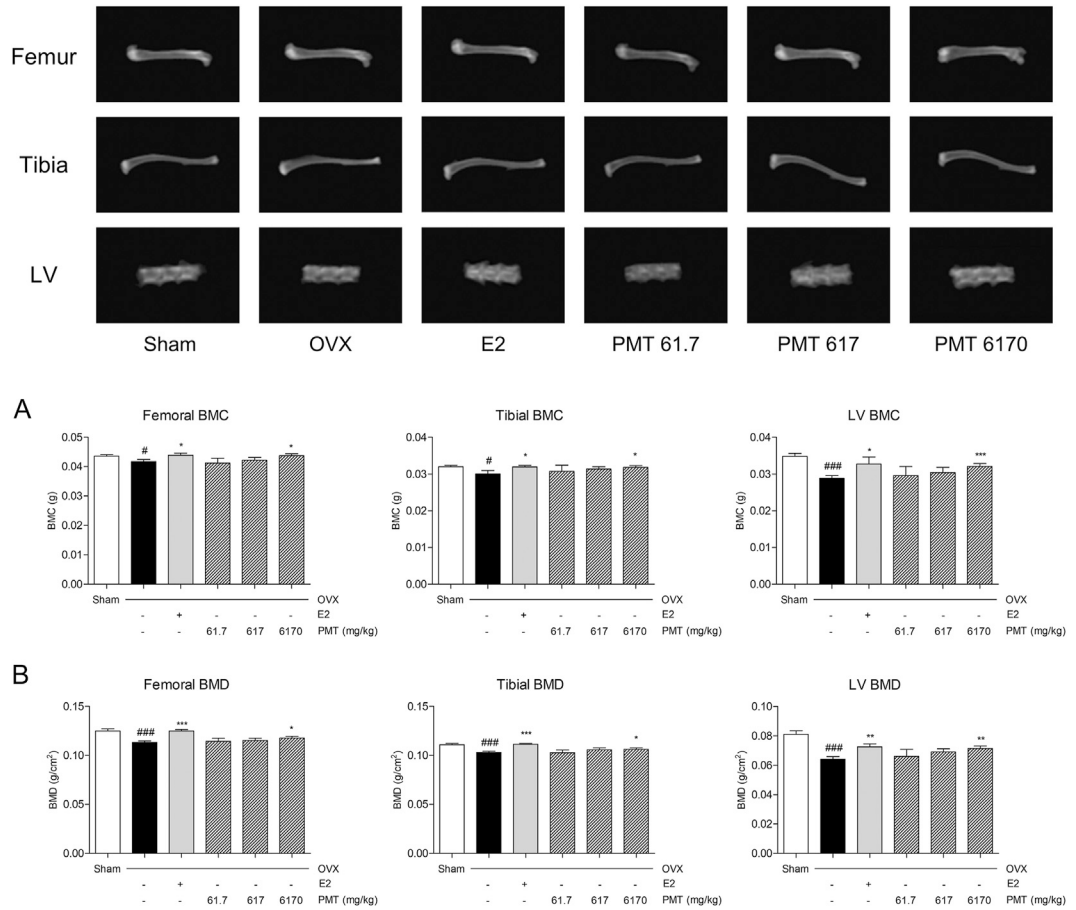

FIGURE 1 | Effects of PMT on BMC and BMD in osteoporotic mice. Bone mineral content and bone mineral density of tibiae, femora and lumbar vertebrae were analyzed by DXA. **(A)** Levels of bone mineral content in tibia, femur and LV. **(B)** Levels of bone mineral density in tibia, femur and LV. Results are presented as mean ± standard error of the mean. $^{\#}p < 0.05$, $^{\#\#}p < 0.01$ and $^{\#\#\#}p < 0.001$ vs. Sham group; $^{*}p < 0.05$, $^{**}p < 0.01$ and $^{***}p < 0.001$ vs. OVX group. OVX, ovariectomized group; E2, 17β-estradiol group; PMT, *Palmul*-tang soft extracts; LV, lumbar vertebrae; BMC, bone mineral content; BMD, bone mineral density.

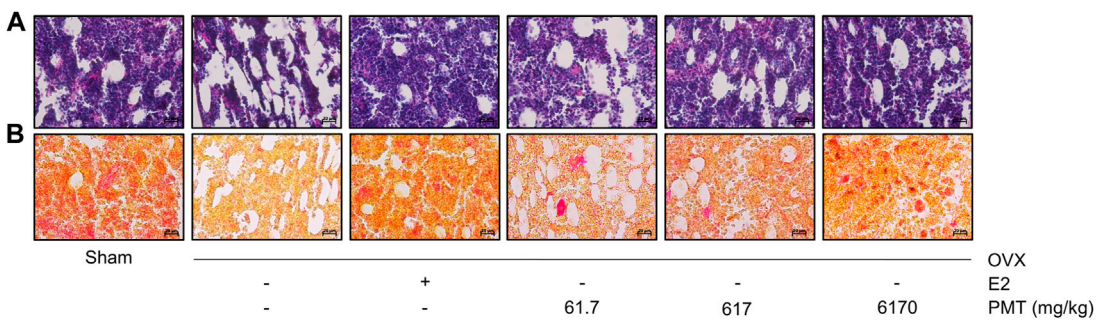

FIGURE 2 | Effects of PMT on histological changes in femur. Evaluation of histological changes using hematoxylin and eosin staining for bone marrow cavity and picrosirius red staining for detecting deposition of collagen. Magnification of images were ×400. OVX, ovariectomized group; E2, 17β-estradiol group; PMT, *Palmul*-tang soft extracts.

in **Figure 2B**, the collagen fibers were markedly aggravated in OVX group compared to sham group. However, treatment of E2 and PMT recovered expression of collagen fibers, especially 6,170 mg/kg of PMT treatment.

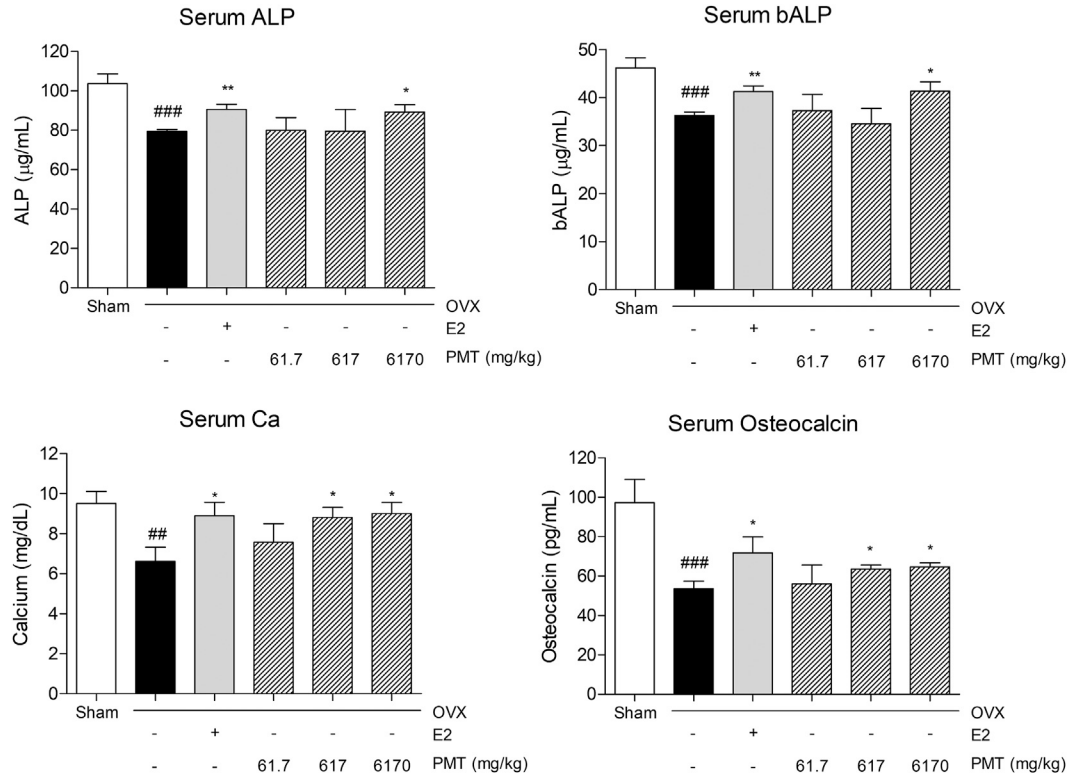

FIGURE 3 | Effects of PMT on bone specific markers in serum. Secretion of bone specific markers in serum was analyzed by ELISA. Results are presented as the mean ± standard error. $^{\#\#}p < 0.01$ and $^{\#\#\#}p < 0.001$ vs. Sham group; $^{*}p < 0.05$ and $^{**}p < 0.01$ vs. OVX group. OVX, ovariectomized group; E2, 17β-estradiol group; PMT, *Palmul*-tang soft extracts; ALP, alkaline phosphatase; bALP, bone-specific alkaline phosphatase.

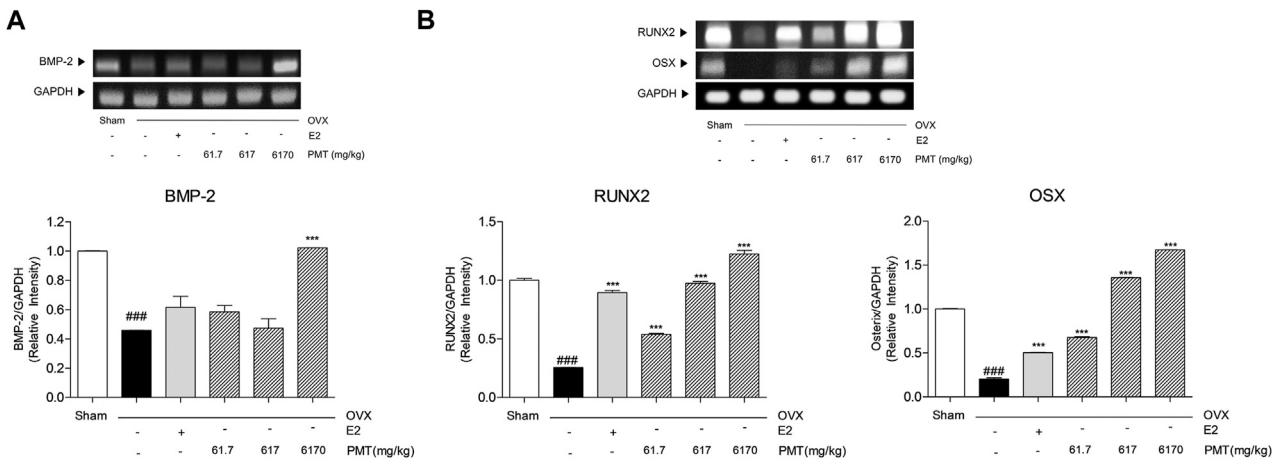

FIGURE 4 | Effects of PMT on osteoblastic differentiation initiation markers in femur. Osteoblastic differentiation initiation markers were analyzed by RT-PCR. Results are presented as the mean ± standard error. $^{\#\#\#}p < 0.001$ vs. Sham group; $^{***}p < 0.001$ vs. OVX group. OVX, ovariectomized group; E2, 17β-estradiol group; PMT, *Palmul*-tang soft extracts; BMP-2, bone morphogenetic protein 2; RUNX2, Runt-related transcription factor 2; OSX, osterix.

Effects of PMT on Bone Specific Markers in Serum

The ALP and bALP levels were decreased in OVX group, 23.29 and 21.43%, respectively, whereas E2 treatment increased levels of ALP and bALP compared to OVX group, 13.89 and 13.59%, respectively. In addition, the levels of ALP and bALP were recovered by administrating PMT compared to OVX group. Particularly 6,170 mg/kg of PMT treatment significantly

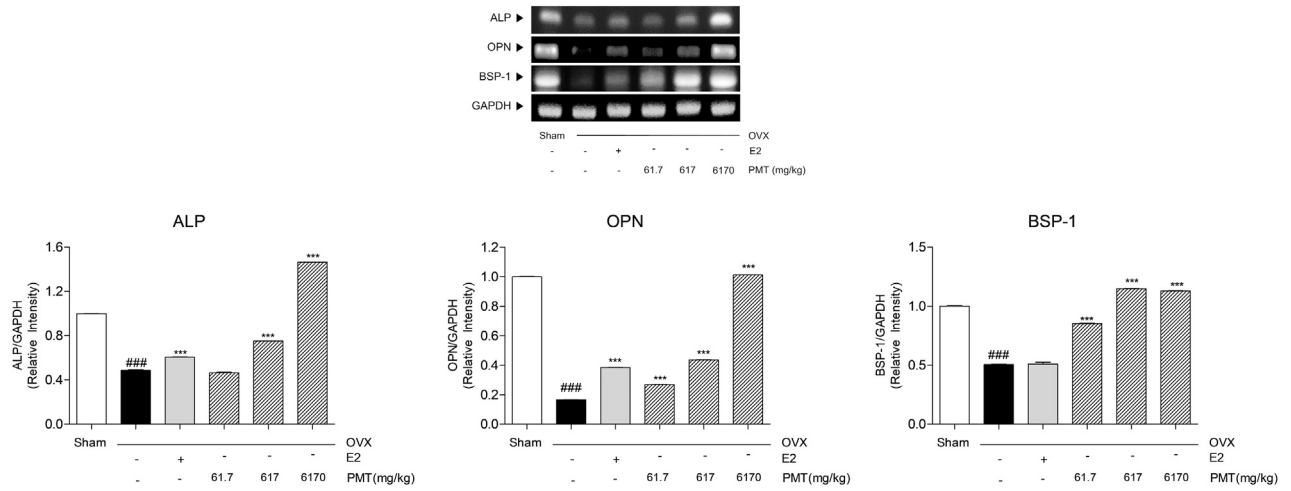

FIGURE 5 | Effects of PMT on osteoblastic production markers in femur. Osteoblastic production markers were analyzed by RT-PCR. Results are presented as the mean ± standard error. $^{###}p < 0.001$ vs. Sham group; $^{***}p < 0.001$ vs. OVX group. OVX, ovariectomized group; E2, 17β-estradiol group; PMT, *Palmul*-tang soft extracts; ALP, alkaline phosphatase; OPN, osteopontin; BSP-1, bone sialoprotein 1.

increased expression levels by 12.31% in ALP and 13.86% in bALP. In addition, serum Ca levels were diminished 30.39% in OVX group, and rise 34.31% in E2 group. Treating PMT remarkably improved levels of Ca 32.96% in PMT 617 group and 36.04% in PMT 6170 group. Serum levels of osteocalcin, similar to Ca, was decreased 44.93% in OVX group and increased 34.07% in E2 group. Treatment with 617 and 6,170 mg/kg of PMT significantly advanced 18.7 and 20.85% Ca levels, respectively, in OVX-induced osteoporotic mice (**Figure 3**).

Effects of PMT on Osteoblastic Markers in Femur

As shown in **Figure 4A**, BMP-2 was expressed in OVX group 54.14% lower than sham group, however, there was no significance in E2 group. While 6,170 mg/kg of PMT treatment recovered 122.63% higher than OVX group. Expression levels of BMP-2 in PMT 6170 group seems to be approximated with sham group. In addition, transcription factors in osteoblast, RUNX2 and OSX, were decreased 74.45 and 79.73%, respectively, in OVX group. Expression of RUNX2 and OSX were significantly increased 250.37 and 148.25%, respectively, treated with E2. The treatment three doses of PMT remarkably up-regulated expressions of RUNX2 and OSX dose-dependent manner, 1.1, 2.81 and 3.79 folds of RUNX2 and 2.34, 5.7 and 7.25 folds of OSX, respectively (**Figure 4B**). By regulating osteoblast differentiation, ALP, OPN and BSP-1 were lowly expressed in OVX group, 51.21, 83.33 and 49.41%, respectively. On the contrary, treatment of E2 highly expressed mRNA levels of ALP and OPN, 24.27 and 130.7%, respectively. However, there was no significance expression of BSP-1 in E2 group. Administration of PMT increased levels of ALP, OPN and BSP-1 dose-dependent manner. These markers were significantly expressed 60.95, 161.13 and 507.68% of OPN and 68.49, 127.12 and 123.36% of BSP-1, respectively. Additionally, expression levels of ALP were increased 54.27 and 200.06% by treating 617 and 6,170 mg/kg of PMT (**Figure 5**).

DISCUSSION

Postmenopausal osteoporosis is a metabolic and skeletal disease that has a high prevalence of age-related bone loss with porous and low levels of bone density (Garnero, 2014). BMD is commonly used in the clinics for the standards of osteoporosis, which is diagnosed with -2.5 or lower levels BMD T-score in the region of the femoral neck and lumbar spine (Kanis, 2002). In addition, the collapse of bone microstructure results in increases of the risk of fractures by reducing bone strength (Chesnut et al., 2001). Moreover, to form of mature osteoblast, collagen is essential extracellular matrix protein for increasing bone strength and remodeling (Elango et al., 2018). In this study, OVX-induced osteoporotic mice group, levels of BMC and BMD in femur, tibia and LV were lowered compared to sham-operated mice group. On the contrary, the levels of BMC and BMD were significantly improved in PMT-treated mice. In addition, PMT reduced bone marrow adiposity, which was promoted the deposition of collagen tissue in the bone marrow. Accordingly, PMT enhanced the levels of BMC, BMD and refilled a cavity with bone mineral which leads to improvement of bone integration.

Impaired osteoporotic bone is the imbalance of osteoblast and osteoclast (Aggarwal et al., 2012). Especially, postmenopausal osteoporosis reveals the inactivation of osteoblasts due to the insufficiency of estrogen, which disrupted the equilibrium of osteoblast and osteoclast (Paschalis et al., 2003). Promotion of osteoblastic activities, which lead to bone proliferation, maturation and formation, is recommended to prioritize for treating post-menopausal osteoporosis (Wang et al., 2016a).

Bone turnover markers including ALP, bALP, Ca and osteocalcin, as specific and sensitive markers of bone formation, have been investigated in clinical and experimental studies in the early and late stages of osteoporosis (Risteli and Risteli, 1993). Several reports related to bone metabolism that the expression of ALP is maximized during bone matrix maturation (Alcantara et al., 2011). In addition, osteocalcin is a calcium-dependent biomarker that has a high affinity for the bone matrix to complete bone formation (Singh et al., 2015). In our study, levels of serum ALP and bone-specific ALP were lowly expressed in osteoporotic mice, while significantly recovered by administering PMT 6170 mg/kg. Additionally, OVX-induced mice treated with PMT augmented that diminished levels of serum Ca and osteocalcin. Thus, osteoblast differentiation is attributed to PMT by increasing levels of serum ALP, bALP, Ca and osteocalcin.

To clarify the underlying mechanism of PMT on the recovery of bone loss, osteoblastogenetic factors were investigated in femoral specimens. BMP-2 activates the expression of RUNX2 and OSX, which are mediated for osteoblast differentiation and new bone formation (Lee et al., 2003; Fan et al., 2013). In addition, bone-specific matrix proteins such as ALP, OPN and BSP-1 are also associated with osteoblast maturation for bone formation (Cowles et al., 1998). Hence, those genes are considered as the key markers of osteoporosis that newly construct a bone matrix. The present study determined that expression of osteoblastic markers BMP-2, RUNX2, OSX, ALP, OPN and BSP-1 were significantly decreased in OVX-induced osteoporosis while treating PMT increased those of osteoblastic markers in a dose-dependent manner. Therefore, PMT influences on osteoblasts to repair the balances of bone homeostasis and the formation of new bone matrix.

CONCLUSION

Taken together, PMT has ameliorative effects on postmenopausal osteoporosis. In the previous study, *P. ginseng*, *P. lactiflora* and *L. officinale*, consists of *Palmul*-tang, is recently reported to enhance the osteoblast activities, leading to generation of new bone matrix (Yen et al., 2007; Kim et al., 2013; Dong et al., 2020). In addition, *A. macrocephala* and *P. cocos*, and decursin derived from *A. gigas* are known to ameliorate the development progress of osteoporosis by inhibiting osteoclast differentiation (Ha et al., 2013; Wang et al., 2016c; Hwang et al., 2020). Moreover, *G. uralensis* and *R. glutinosa* showed protective effects on osteoporosis by maintaining bone mineral density (Lim and Kim, 2013; Galanis et al., 2019). *Palmul*-tang, which is a combination of those eight herbs as a traditional herbal formula, was assumed to exhibit a synergic effect on bone formation in osteoporosis. In this study, PMT ameliorated bone loss in osteoporosis by activating osteoblastic markers such as BMP-2 signaling pathway, leading to improving bone integrity. The bone marrow adiposity cavity filled with collagen fibers to restore the bone marrow tightly. Moreover, the expressions of the BMP-2 signaling pathway were upregulated by PMT treatment, resulting in an increase of bone differentiation and formation. These results might provide evidence of expanding the medical category and the basis of medical insurance in Korea for postmenopausal osteoporosis.

DATA AVAILABILITY STATEMENT

The original contributions presented in the study are included in the article/**Supplementary Material**, further inquiries can be directed to the corresponding author.

ETHICS STATEMENT

The animal study was reviewed and approved by the Committee on Care and Use of Laboratory Animals of Kyung Hee University.

AUTHOR CONTRIBUTIONS

All authors participated in the design, interpretation of the studies and analysis of the data and review of the manuscript; LC, MK, YN and WY contributed to analysis design, LC, YN, JK analyzed data, LC, MK, JK, H-YC and WY drafted the manuscript, and WY provided supervision of study. All authors contributed to manuscript revision, read and approved the revised version.

FUNDING

This work was supported by the National Research Foundation of Korea (NRF) grant funded by the Korea government (MSIT, Ministry of Science and ICT) (No. 2020R1A5A201941311) and a grant of the National Development Institute of Korean Medicine (NIKOM) funded by the Korean Ministry of Health and Welfare (MOHW), Republic of Korea. The funders did not participate in the design of the study, data collection, analysis and interpretation of data or in preparation of the manuscript.

SUPPLEMENTARY MATERIAL

The Supplementary Material for this article can be found online at: https://www.frontiersin.org/articles/10.3389/fphar.2021.643482/full#supplementary-material.

REFERENCES

Aggarwal, R., Lu, J., Kanji, S., Joseph, M., Das, M., Noble, G. J., et al. (2012). Human umbilical cord blood-derived CD34+ cells reverse osteoporosis in NOD/SCID mice by altering osteoblastic and osteoclastic activities. *PLoS One* 7 (6), e39365. doi:10.1371/journal.pone.0039365

Alagiakrishnan, K., Juby, A., Hanley, D., Tymchak, W., and Sclater, A. (2003). Role of vascular factors in osteoporosis. *Journals Gerontol. Ser. A: Biol. Sci. Med. Sci.* 58 (4), M362–M366. doi:10.1093/gerona/58.4.m362

Alcantara, E. H., Shin, M.-Y., Sohn, H.-Y., Park, Y.-M., Kim, T., Lim, J.-H., et al. (2011). Diosgenin stimulates osteogenic activity by increasing bone matrix protein synthesis and bone-specific transcription factor Runx2 in osteoblastic MC3T3-E1 cells. *J. Nutr. Biochem.* 22 (11), 1055–1063. doi:10.1016/j.jnutbio.2010.09.003

Bowring, C. E., and Francis, R. M. (2011). National Osteoporosis Society's Position statement on hormone replacement therapy in the prevention and treatment of osteoporosis. *Menopause Int.* 17 (2), 63–65. doi:10.1258/mi.2011.011012

Chen, X., Wang, Z., Duan, N., Zhu, G., Schwarz, E. M., and Xie, C. (2018). Osteoblast-osteoclast interactions. *Connect. Tissue Res.* 59 (2), 99–107. doi:10.1080/03008207.2017.1290085

Cheng, M., Wang, Q., Fan, Y., Liu, X., Wang, L., Xie, R., et al. (2011). A traditional Chinese herbal preparation, Er-Zhi-Wan, prevent ovariectomy-induced osteoporosis in rats. *J. Ethnopharmacology* 138 (2), 279–285. doi:10.1016/j.jep.2011.09.030

Chesnut, C. H., 3rd, Rosen, C. J., and Bone Quality Discussion, G. (2001). Perspective: reconsidering the effects of antiresorptive therapies in reducing osteoporotic fracture. *J. Bone Miner Res.* 16 (12), 2163–2172. doi:10.1359/jbmr.2001.16.12.2163

Cowles, E. A., DeRome, M. E., Pastizzo, G., Brailey, L. L., and Gronowicz, G. A. (1998). Mineralization and the expression of matrix proteins during *in vivo* bone development. *Calcif Tissue Int.* 62 (1), 74–82. doi:10.1007/s002239900397

Dickenson, R., Hutton, W., and Stott, J. R. (1981). The mechanical properties of bone in osteoporosis. *The J. Bone Jt. Surg. Br. volume* 63-B (2), 233–238. doi:10.1302/0301-620x.63b2.7217148

Dong, X.-L., Yu, W.-X., Li, C.-M., Zhou, L.-P., and Wong, M.-S. (2020). Chuanxiong (rhizome of Ligusticum chuanxiong) protects ovariectomized hyperlipidemic rats from bone loss. *Am. J. Chin. Med.* 48 (2), 463–485. doi:10.1142/S0192415X2050024X

Elango, J., Sanchez, C., de Val, J. E. M. S., Henrotin, Y., Wang, S., Motaung, K. S. C. M., et al. (2018). Cross-talk between primary osteocytes and bone marrow macrophages for osteoclastogenesis upon collagen treatment. *Sci. Rep.* 8 (1), 5318. doi:10.1038/s41598-018-23532-x

Eom, J.-H., Cheon, S.-Y., Chung, K.-S., Kim, M.-D., and An, H.-J. (2017). Bawu decoction (八物汤) ameliorates benign prostatic hyperplasia in rats. *Chin. J. Integr. Med.* 23 (8), 611–616. doi:10.1007/s11655-016-2528-8

Fan, J., Park, H., Tan, S., and Lee, M. (2013). Enhanced osteogenesis of adipose derived stem cells with Noggin suppression and delivery of BMP-2. *PLoS One* 8 (8), e72474. doi:10.1371/journal.pone.0072474

Fricke, M., and Krokowski, E. (1975). [Osteoporosis -- due to reduced blood circulation of bone (author's transl)]. *Z. Orthop. Ihre Grenzgeb* 113 (6), 1043–1050.

Galanis, D., Soultanis, K., Lelovas, P., Zervas, A., Papadopoulos, P., Galanos, A., et al. (2019). Protective effect ofGlycyrrhiza glabraroots extract on bone mineral density of ovariectomized rats. *BioMedicine* 9 (2), 8. doi:10.1051/bmdcn/2019090208

Garnero, P. (2014). New developments in biological markers of bone metabolism in osteoporosis. *Bone* 66, 46–55. doi:10.1016/j.bone.2014.05.016

Ha, H., An, H., Shim, K.-S., Kim, T., Lee, K., Hwang, Y.-H., et al. (2013). Ethanol extract of Atractylodes macrocephala protects bone loss by inhibiting osteoclast differentiation. *Molecules* 18 (7), 7376–7388. doi:10.3390/molecules18077376

Heo, M. K., Hong, H. W., Kam, C. W., and Park, D. I. (2003). Experimental study on the anti-allergic effects of palmul-tang. *Korean J. Oriental Physiol. Pathol.* 17 (4), 1075–1081.

Hwang, Y.-H., Jang, S.-A., Lee, A., Kim, T., and Ha, H. (2020). Poria cocos ameliorates bone loss in ovariectomized mice and inhibits osteoclastogenesis in vitro. *Nutrients* 12 (5), 1383. doi:10.3390/nu12051383

Jin, S. E., Ha, H., and Shin, H.-K. (2017). Effects of traditional herbal formulae on human CYP450 isozymes. *Chin. J. Integr. Med.* 23 (1), 62–69. doi:10.1007/s11655-016-2476-3

Kanis, J. A. (2002). Diagnosis of osteoporosis and assessment of fracture risk. *The Lancet* 359 (9321), 1929–1936. doi:10.1016/S0140-6736(02)08761-5

Kim, T. Y., and Bak, J. P. (2015). Antioxidant and protective effects of palmul-tang on ultraviolet B (UVB)-induced damage in human keratinocytes. *J. Soc. Prev. Korean Med.* 19 (3), 141–154.

Kim, Y., Sohn, S., Yang, S., Kim, H., Shin, Y., and Lee, S. (2013). Effects of Panax ginseng extract on osteoporosis in aged rats. *Planta Med.* 79 (13), 1146. doi:10.1055/s-0033-1351968

Lee, M.-H., Kwon, T.-G., Park, H.-S., Wozney, J. M., and Ryoo, H.-M. (2003). BMP-2-induced Osterix expression is mediated by Dlx5 but is independent of Runx2. *Biochem. Biophysical Res. Commun.* 309 (3), 689–694. doi:10.1016/j.bbrc.2003.08.058

Lee, S. G., Kwon, Y. K., Kim, K. J., and Kim, W. H. (1995). Effect of samultang and yukmizihwangtang on osteoporosis induced by ovariectomy of the rats. *J. Jeahan Oriental Med. Acad.* 1 (1), 31–48. doi:10.18632/oncotarget.20611

Lewis, R., Gómez Álvarez, C. B., Rayman, M., Lanham-New, S., Woolf, A., and Mobasheri, A. (2019). Strategies for optimising musculoskeletal health in the 21st century. *BMC Musculoskelet. Disord.* 20 (1), 164. doi:10.1186/s12891-019-2510-7

Lim, D., and Kim, Y. (2013). Dried root of Rehmannia glutinosa prevents bone loss in ovariectomized rats. *Molecules* 18 (5), 5804–5813. doi:10.3390/molecules18055804

Ma, J. Y., Huang, D. S., Yu, Y. B., Ha, H. K., and Shin, H. K. (2007a). Acute toxicity study on palmul-tang(bawu-tang) in mice. *Kor. J. Herbology* 22 (2), 13–16.

Ma, J. Y., Huang, D. S., Yu, Y. B., Ha, H. K., and Shin, H. K. (2007b). Subacute toxicity study on palmultang(bawu-tang) in SD rats. *Kor. J. Herbology* 22 (4), 59–64.

Nair, A., and Jacob, S. (2016). A simple practice guide for dose conversion between animals and human. *J. Basic Clin. Pharma* 7 (2), 27–31. doi:10.4103/0976-0105.177703

Nam, S. H., Jeong, J.-H., Che, X., Lim, K.-E., Nam, H., Park, J.-S., et al. (2012). Topically administered Risedronate shows powerful anti-osteoporosis effect in ovariectomized mouse model. *Bone* 50 (1), 149–155. doi:10.1016/j.bone.2011.10.017

Nanjundaiah, S. M., Astry, B., and Moudgil, K. D. (2013). Mediators of inflammation-induced bone damage in arthritis and their control by herbal products. *Evidence-Based Complement. Altern. Med.* 2013, 1. doi:10.1155/2013/518094

Oh, Y.-C., Jeong, Y., Cho, W.-K., Gu, M.-J., and Ma, J. (2014). Inhibitory effects of palmultang on inflammatory mediator production related to suppression of NF-κB and MAPK pathways and induction of HO-1 expression in macrophages. *Ijms* 15 (5), 8443–8457. doi:10.3390/ijms15058443

Park, C. H., Bae, I. T., and Jeong, H. W. (2004a). Effects of palmul-tang on the change of cerebral hemodynamics in rats. *Korean J. Oriental Physiol. Pathol.* 18 (4), 1014–1020.

Park, C. H., Kim, G. Y., and Jeong, H. W. (2004b). Mechanism of palmul-tang on the change of cerebral hemodynamics in rats. *Korean J. Oriental Physiol. Pathol.* 18 (6), 1714–1722.

Paschalis, E., Boskey, A., Kassem, M., and Eriksen, E. (2003). Effect of hormone replacement therapy on bone quality in early postmenopausal women. *J. Bone Miner Res.* 18 (6), 955–959. doi:10.1359/jbmr.2003.18.6.955

Risteli, L., and Risteli, J. (1993). Biochemical markers of bone metabolism. *Ann. Med.* 25 (4), 385–393. doi:10.3109/07853899309147301

Shim, K.-S., Ma, C. J., Cho, C.-W., and Ma, J. Y. (2011). Samul-tang suppresses RANKL-induced osteoclast differentiation in RAW264.7 cells. *Biotechnol. Bioproc. E* 16, 603–610. doi:10.1007/s12257-010-0431-2

Shin, Y. J., and Shin, S. H. (2012). Protective effect of palmul-tang on glutamate induced cytotoxicity in C6 glial cells. *Korean J. Oriental Physiol. Pathol.* 26 (4), 475–482.

Singh, S., Kumar, D., and Lal, A. K. (2015). Serum osteocalcin as a diagnostic biomarker for primary osteoporosis in women. *Jcdr* 9 (8), RC04–RC07. doi:10.7860/JCDR/2015/14857.6318

Tanaka, Y., Nakayamada, S., and Okada, Y. (2005). Osteoblasts and osteoclasts in bone remodeling and inflammation. *Cdtia* 4 (3), 325–328. doi:10.2174/1568010054022015

Tella, S. H., and Gallagher, J. C. (2014). Prevention and treatment of postmenopausal osteoporosis. *J. Steroid Biochem. Mol. Biol.* 142, 155–170. doi:10.1016/j.jsbmb.2013.09.008

Wang, C., Meng, H., Wang, X., Zhao, C., Peng, J., and Wang, Y. (2016a). Differentiation of bone marrow mesenchymal stem cells in osteoblasts and adipocytes and its role in treatment of osteoporosis. *Med. Sci. Monit.* 22, 226–233. doi:10.12659/msm.897044

Wang, S. J., Yue, W., Rahman, K., Xin, H. L., Zhang, Q. Y., Qin, L. P., et al. (2016b). Mechanism of treatment of kidney deficiency and osteoporosis is similar by

traditional Chinese medicine. *Curr. Pharm. Des.* 22 (3), 312–320. doi:10.2174/1381612822666151112150346

Wang, X., Zheng, T., Kang, J.-H., Li, H., Cho, H., Jeon, R., et al. (2016c). Decursin from Angelica gigas suppresses RANKL-induced osteoclast formation and bone loss. *Eur. J. Pharmacol.* 774, 34–42. doi:10.1016/j.ejphar.2016.01.008

Yen, P. H., Van Kiem, P., Nhiem, N. X., Tung, N. H., Quang, T. H., Van Minh, C., et al. (2007). A new monoterpene glycoside from the roots ofPaeonia lacti- flora increases the differentiation of osteoblastic MC3T3-E1 cells. *Arch. Pharm. Res.* 30 (10), 1179–1185. doi:10.1007/BF02980258

Yim, N.-H., Gu, M. J., Park, H. R., Hwang, Y.-H., and Ma, J. Y. (2018). Enhancement of neuroprotective activity of Sagunja-tang by fermentation with lactobacillus strains. *BMC Complement. Altern. Med.* 18 (1), 312. doi:10.1186/s12906-018-2361-z

Yuan, H., Ma, Q., Ye, L., and Piao, G. (2016). The traditional medicine and modern medicine from natural products. *Molecules* 21 (5), 559. doi:10.3390/molecules21050559

Conflict of Interest: The authors declare that the research was conducted in the absence of any commercial or financial relationships that could be construed as a potential conflict of interest.

Copyright © 2021 Choi, Kim, Nam, Kim, Cho and Yang. This is an open-access article distributed under the terms of the Creative Commons Attribution License (CC BY). The use, distribution or reproduction in other forums is permitted, provided the original author(s) and the copyright owner(s) are credited and that the original publication in this journal is cited, in accordance with accepted academic practice. No use, distribution or reproduction is permitted which does not comply with these terms.

frontiers in Pharmacology

ORIGINAL RESEARCH
published: 01 April 2021
doi: 10.3389/fphar.2021.590602

An Integrative Pharmacology-Based Strategy to Uncover the Mechanism of Xiong-Pi-Fang in Treating Coronary Heart Disease with Depression

Lihong Zhang[1†], Yu Zhang[1†], Mingdan Zhu[2], Limin Pei[1], Fangjun Deng[1], JinHong Chen[1], Shaoqiang Zhang[2], Zidong Cong[2], Wuxun Du[2] and Xuefeng Xiao[1]**

[1]Tianjin University of Traditional Chinese Medicine, Tianjin, China, [2]Second Affiliated Hospital, Tianjin University of Traditional Chinese Medicine, Tianjin, China

OPEN ACCESS

Edited by:
Yanqiong Zhang,
China Academy of Chinese Medical Sciences, China

Reviewed by:
Nasra Ayuob,
Mansoura University, Egypt
Xinmin Liu,
Chinese Academy of Medical Sciences and Peking Union Medical College, China

***Correspondence:**
Wuxun Du
cnduwux@163.com
Xuefeng Xiao
kai1219@163.com

[†]These authors have contributed equally to this work

Specialty section:
This article was submitted to Ethnopharmacology, a section of the journal Frontiers in Pharmacology

Received: 02 August 2020
Accepted: 11 February 2021
Published: 01 April 2021

Citation:
Zhang L, Zhang Y, Zhu M, Pei L, Deng F, Chen J, Zhang S, Cong Z, Du W and Xiao X (2021) An Integrative Pharmacology-Based Strategy to Uncover the Mechanism of Xiong-Pi-Fang in Treating Coronary Heart Disease with Depression. Front. Pharmacol. 12:590602. doi: 10.3389/fphar.2021.590602

Objectives: This study aimed to explore the mechanism of Xiong-Pi-Fang (XPF) in the treatment of coronary heart disease (CHD) with depression by an integrative strategy combining serum pharmacochemistry, network pharmacology analysis, and experimental validation.

Methods: An ultrahigh performance liquid chromatography-quadrupole-time-of-flight tandem mass spectrometry (UPLC-Q-TOF/MS) method was constructed to identify compounds in rat serum after oral administration of XPF, and a component-target network was established using Cytoscape, between the targets of XPF ingredients and CHD with depression. Furthermore, Gene Ontology and Kyoto Encyclopedia of Genes and Genomes pathway enrichment analyses were performed to deduce the mechanism of XPF in treating CHD with depression. Finally, in a chronic unpredictable mild stress (CUMS)-and isoproterenol (ISO)-induced rat model, TUNEL was used to detect the apoptosis index of the myocardium and hippocampus, ELISA and western blot were used to detect the predicted hub targets, namely AngII, 5-HT, cAMP, PKA, CREB, BDNF, Bcl-2, Bax, Cyt-c, and caspase-3.

Results: We identified 51 compounds in rat serum after oral administration of XPF, which mainly included phenolic acids, saponins, and flavonoids. Network pharmacology analysis revealed that XPF may regulate targets, such as *ACE2*, *HTR1A*, *HTR2A*, *AKT1*, *PKIA*, *CREB1*, *BDNF*, *BCL2*, *BAX*, *CASP3*, cAMP signaling pathway, and cell apoptosis process in the treatment of CHD with depression. ELISA analysis showed that XPF decreased Ang-II content in the circulation and central nervous system, inhibited 5-HT levels in peripheral circulation, and increased 5-HT content in the central nervous system and cAMP content in the myocardia and hippocampus. Meanwhile, western blot analysis indicated that XPF could upregulate the expression levels of PKA, CREB, and BDNF both in the myocardia and hippocampus. TUNEL staining indicated that the apoptosis index of myocardial and hippocampal cells increased in CUMS-and ISO-induced CHD in rats under depression, and XPF could increase the expression of Bcl-2, inhibit the expression of Bax, Cyt-c, and caspase-3, and rectify the injury of the hippocampus and myocardium, which exerted antidepressant and antimyocardial ischemia effects.

Conclusion: Our study proposed an integrated strategy, combining serum pharmacochemistry and network pharmacology to investigate the mechanisms of XPF in treating CHD with depression. The mechanism of XPF in treating CHD with depression may be related to the activation of the cAMP signaling pathway and the inhibition of the apoptosis.

Keywords: integrative pharmacology, serum pharmacochemistry, network pharmacology analysis, Xiong-Pi-Fang, coronary heart disease with depression

INTRODUCTION

Coronary heart disease (CHD) is a chronic and complex disease that poses a serious threat to human health (Mozaffarian et al., 2016; Blais et al., 2020). Traditional risk factors are mainly related to hypertension, hyperlipidemia, diabetes, etc (Li C et al., 2020). Moreover, depression is another independent risk factor for CHD, as it has been shown to diminish the quality of life of patients with CHD and also increase the incidence and mortality of major adverse cardiac events (Su et al., 2018; de Heer et al., 2020). Increasing evidence suggests that the incidence of CHD with depression is increasing, ranging from approximately 15–18%, moreover, approximately 31% of these patients develop major depressive disorder (MDD) (Carney and Freedland, 2017). However, there are no effective chemicals to improve the quality of life and survival rate of patients with comorbid CHD and depression (Lee et al., 2018; Magaard et al., 2018).

The ideal medication for CHD with depression would be integrated, improving myocardial blood supply and regulating nervous system function at the same time (Yeung et al., 2014; Chen M et al., 2018; Xue et al., 2019). Xiong-Pi-Fang (XPF), a classical traditional Chinese medicine (TCM) formula, consists of Radix Bupleuri (Bupleurum chinense DC. and Bupleurum scorzonerifolium Willd.) 15 g; Ligusticum wallichii (Conioselinum anthriscoides 'Chuanxiong' and Ligusticum striatum DC.) 12 g; Rhizoma Cyperi (Cyperus rotundus L.) 12 g; Sanders (Santalum album L..) 9 g; Fructus aurantii (Citrus × aurantium L. and Citrus trifoliata L.) 9 g; Dried tangerine peel (Citrus × aurantium L.) 15 g; Pinellia ternata (Pinellia ternata (Thunb.) Makino) 15 g; Herba Menthae (Mentha haplocalyx Briq.) 10 g; Perilla Stem (Perilla frutescens (L.) Britton) 15 g; Poria Cocos (Wolfiporia extensa (Peck) Ginns) 15 g; Rhizoma Atractylodis Macrocephalae (Atractylodes Macrocephala Koidz) 15 g; Radix Glycyrrhizae (Glycyrrhiza uralensis Fisch.) 9 g. It is widely used in clinical practices, showing satisfactory therapeutic effects in relieving angina pectoris, chest pain, and depression symptoms (Hou et al., 2017). However, it is difficult to fully understand the therapeutic mechanism of XPF for treating CHD with depression solely using traditional pharmacological methods. Hence, an integrated pharmacology-based strategy including computer high-throughput analytical techniques and biological experimental tools was established in this study, which provides a helpful method to reveal the potential bioactive ingredients and modern pharmacological mechanism of TCM (Park et al., 2018; Fang et al., 2019).

Integrative pharmacology, combined with conventional pharmacology, network pharmacology, bioinformatics, and other disciplines, is the systematic study of the overall interactions between drugs and humans at the molecular, cell, organ, and network levels (Hart and Xie, 2016; Zhang R. et al., 2018; Zhang R. et al., 2019). Network pharmacology, characterized by integration, systematization, and emphasis on drug interaction (Yuan et al., 2017), predicts the biological molecular mechanism of drug treatment of diseases from a holistic perspective by constructing an interaction network between active ingredients and disease targets. However, most TCM-related databases provide information on chemical ingredients extracted *in vitro* (Zhang W et al., 2019). Previous studies have shown that the drug ingredients absorbed into the blood circulation may be the main active constituents (Chen et al., 2014; Li et al., 2016). Therefore, it is critical to combine serum pharmacochemistry with a network pharmacology strategy to accurately establish the network.

In this study, an integrated pharmacology strategy employing serum pharmacochemistry, network pharmacological analysis, and experimental validation was conducted to illustrate the therapeutic mechanism of XPF in treating CHD with depression (**Figure 1**). Briefly, An ultrahigh performance liquid chromatography-quadrupole-time-of-flight tandem mass spectrometry (UPLC-Q-TOF/MS) method was established to determine the main active components of XPF in rat serum. Furthermore, a serum pharmacochemistry-based network was constructed and the component–target network between CHD comorbid depression-relevant genes and the targets of active components in XPF was established. Finally, we validated the predicted molecular mechanisms obtained from the network analysis of XPF in treating CHD with depression in a chronic unpredictable mild stress (CUMS)-and isoproterenol (ISO)-induced CHD in a rat model of depression.

MATERIALS AND METHODS

Reagents and Materials

Sertraline hydrochloride (Pfizer Inc., United States), metoprolol (Asilkan, United Kingdom), Isoproterenol (Sigma Aldrich Co., United States) were purchased from the Shanghai Yuanye Biotechnology Co. Ltd (Shanghai, China). UPLC-Q-TOF/MS grade acetonitrile and HPLC grade acetonitrile, methanol, formic acid, were provided by Fisher Scientific International Inc (Fair Lawn, NJ). The ELISA assay kits for Ang-Ⅱ (142191202), 5-HT (106191202), cAMP (202004) were purchased from Tianjin Zihan Biotechnology Co., Ltd. (Tianjin, China). TUNEL assay kit (7E310H9) was purchased from Vazyme Biotech Co., Ltd. (Nanjing, China), Rabbit

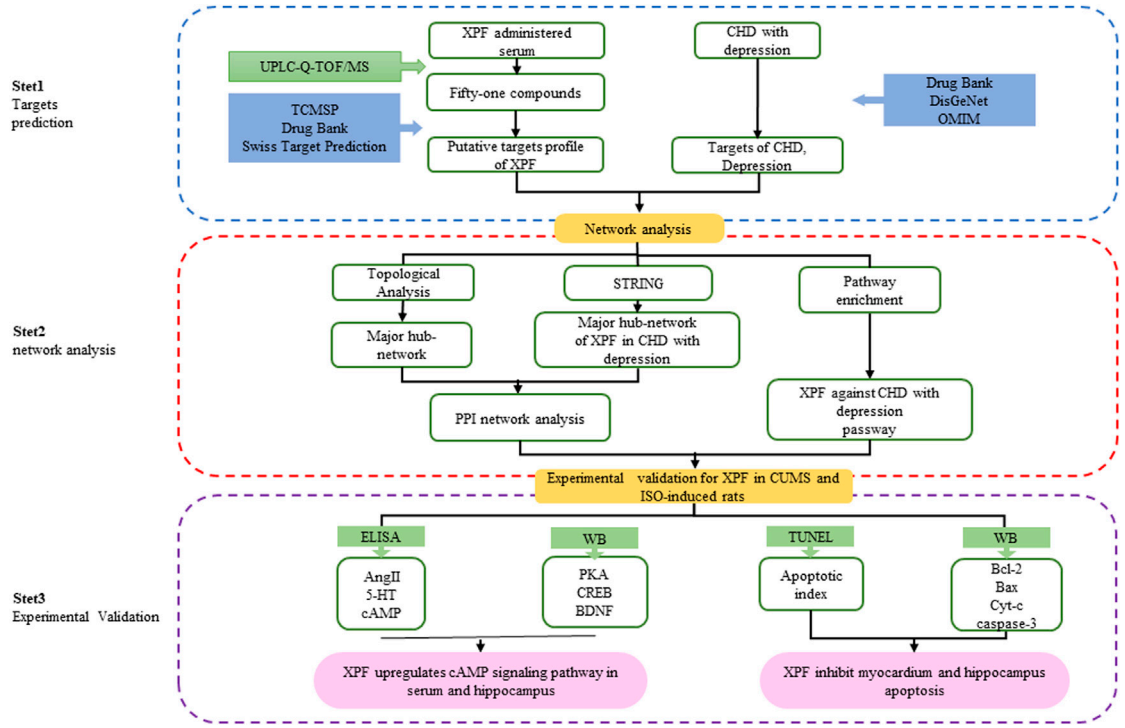

FIGURE 1 | Flowchart of the study.

antihuman monoclonal antibodies PKA (5842), CREB (6188), BDNF (3189), Bcl2 (26,593-1-12p), Bax (50,599–2-1 g), Cytochrome c (10993-1-Ap), and mouse antihuman monoclonal antibodies caspase-3 (66,470-E1g) and β-actin were provided by Proteintech Group, Inc. (Wuhan, China).

Animals

Male Sprague-Dawley rats (weighing 200 ± 20 g) were purchased from the Experimental Animal Center of the Academy of Military Medical Sciences (Beijing, China), and kept in an environmentally controlled room (temperature 22 ± 2°C, humidity 50 ± 10%) with food and water available. This study was carried out in accordance with the principles of the Basel Declaration and the guidelines of the National Institutes of Health. All animal experiments were approved by the Ethics Committee of Tianjin University of Traditional Chinese Medicine (Tianjin, China).

UPLC-Q-TOF/MS Method for Serum Pharmacochemistry Analysis

XPF was prepared by the pharmacy of the Second Affiliated Hospital of Tianjin University of Traditional Chinese Medicine (Tianjin, China). Twelve rats were randomly divided into a control group (n = 6, 0.9% saline IG), and According to the calculation method of equivalent dose coefficient of experimental animals in *Methodology of Pharmacological Experiment* (Xu et al., 2018), the XPF group (n = 6, 32.7 g/kg XPF IG), equivalent to twice the clinical effective dose, for three days (Xu et al., 1997). All rats fasted for 12 h before the experiment and then the serum samples were collected at 120 min after oral administration, via the postorbital venous plexus. The serum samples were centrifuged at 12,000 rpm for 10 min at 4°C. Then, 300 μL of serum was added to three times the amount of acetonitrile, vortexed for 2 min, followed by ultrasonic extraction for 10 min, and centrifugation (12,000 rpm, 10 min). and The supernatant was collected and placed in a N_2 blower to blow dry at 40°C, 50% acetonitrile (50 μL) was added to the residue, vortexed for 3 min, ultrasound for 10 min, centrifugation (12,000 rpm, 10 min), and the supernatant was collected for UPLC-Q-TOF/MS analysis.

UPLC-Q-TOF/MS analysis was analyzed on a Waters ACQUITYTM UPLC BEH C18 (100 mm × 2.1 mm, 1.7 μm) system, maintained at 30 °C. The flow rate was set at 0.45 ml/min, and the injection volume was 5 μL. The mobile phase was consisted of water (A) and methanol (B) both containing 0.1% (v/v) formic acid for astragaloside (0–5 min, 2% B; 5–8 min, 2%–20% B, 8–11 min, 20% B, 11–14 min, 20%–48% B, 14–20 min, 48%–70% B, 20–23 min, 70%–90% B, 23–26 min, 90%–100% B, 26–30 min, 100% B). The mass spectrometer analysis was performed with reaction monitoring both in positive and negative ion modes.

Construction of the Compound-Target and Disease-Target Networks

All targets of active components of XPF determined by serum pharmacochemistry analysis were collected from TCM-related databases, including TCMSP (http://tcmspw.com/tcmsp.php)

TABLE 1 | Identification of absorbed components from XPF in serum of rats.

No	tR (min)	Name	Formula	Heoretical molecular weightigh/Da	[M + H]+		[M-H}-	
					Quasi-molecular ecular	Ppm	Quasi-moecular lecular	Ppm
1	1.42	Succinic acid	C4H6O4	117.0187			117.0185	2.8372
2	3.75	7-Methoxycoumarin	C10H8O3	177.0552	177.0557	2.8239		
3	5.44	Ferulic acid	C10H10O4	193.0501			193.0502	0.5698
4	5.86	Phenylalanine	C9H11NO2	166.0869	166.0865	2.4083		
5	12.48	Benzyl alcohol	C7H8O	131.0473	131.0475	1.5261		
6	15.95	Lonicerin	C27H30O15	593.1507	595.1671	1.1761	593.1488	3.237
7	18.42	Vanillic acid	C8H8O4	167.0344			167.0345	0.2334
8	18.90	Chrysophanol	C15H10O4	255.0658	255.066	0.7841		
9	19.64	Quercetin	C15H10O7	303.0505	303.0508	0.9899		
10	21.5	Liquiritoside	C21H22O9	417.1186	419.1338	1.1929	417.1193	1.6302
11	22.47	Rhoifolin	C27H30O14	577.1558	579.1721	3.6258	577.1557	0.1906
12	23.39	Protocatechuic acid	C7H6O4	153.0187			153.0182	3.8492
13	23.87	Acacetin	C16H12O5	285.0763	285.0753	3.6481		
14	23.87	Physcion	C16H12O5	285.0763	285.0764	0.2104		
15	23.98	Neoisoliquiritin	C21H22O9	417.1186			417.1176	2.4453
16	21.40	Naringin	C27H32O14	579.1714			579.1696	3.2288
17	21.70	Naringenin	C15H12O5	273.0763	273.077	2.5633		
18	24.54	Nobiletin	C21H22O8	403.1394	403.1399	1.2402		
19	25.57	Hesperetin	C16H14O6	303.0869	303.0875	1.9466		
20	25.64	Liquiritigenin	C15H12O4	257.0814	257.0811	1.1669		
21	26.06	Hesperidin	C28H34015	609.1820			609.1802	3.0204
22	26.24	Naringenine-7-rhamnosidoglucoside	C21H22O8	403.1394			403.1389	1.2403
23	26.49	Neoliquiritin	C21H22O9	417.1186			417.1177	2.2775
24	26.61	Formononetin	C16H12O4	269.0814	269.0816	0.6317		
25	27.02	Sinensetin	C20H20O7	373.1288	373.1274	3.7520		
26	27.05	Licochalcone B	C16H14O5	285.0763			285.0769	2.1047
27	27.15	Aloe-emodin	C15H10O5	271.0607	271.0615	2.9513		
28	237.34	Eugenol	C10H12O2	163.076			163.0755	3.3113
29	27.45	Emodin	C15H10O5	271.0607	271.0615	2.9513		
30	27.45	Spathulenol	C15H24O4	267.1597			267.1601	1.4972
31	27.54	Kaempferol	C15H10O6	287.0555	287.0571	5.2603		
32	27.78	Isorhamnetin	C16H12O7	317.0661	317.0652	3.0277		
33	27.81	Isoliquiritigenin	C15H12O4	255.0658			255.0663	1.9602
34	27.89	Angelicin	C11H6O3	187.0395	187.0389	3.2078		
35	28.01	Cerevisterol	C28H46O3	430.0325	430.0311	3.2555		
36	28.13	β-Amyrin acetate	C32H52O2	468.3969	468.3954	3.3732		
37	28.23	(–)-Hesperetin`	C16H14O6	303.0869	303.0867	0.6928		
38	28.45	Rosmarinic acid	C18H16O8	359.0767			359.0771	1.0304
39	28.52	Aesculetin	C9H6O4	179.0345	179.0339	3.5747		
40	28.81	Diosmin	C28H32O15	607.1663			607.1683	3.1622
41	29.13	Atractylenolide-1	C15H18O2	231.1385	231.1387	0.4759		
42	29.18	Saikosaponin A	C42H68O13	779.4584			779.4559	3.2587
43	29.21	4-Hydroxy-3-butylphthalideylphthalide	C12H14O3	207.1021	207.1026	2.0279		
44	29.29	Tangeretin (6Cl)	C42H68O13	779.4584			779.4559	3.2587
45	29.53	α-Cyperone	C15H22O	219.175	219.1759	4.1063		
46	29.57	5,6,4′-trihydroxy-7,8,3′-trimethoxyflavonexy-7,8,3′-trimethoxyflavone	C18H16O8	359.0767			359.0771	1.0304
47	29.78	Menthyl benzoatee	C8H8O2	135.0446			135.0446	0.5183
48	29.83	β-Cyperol	C15H22O	219.175	219.1755	2.2812		
49	29.88	Tangeretin	C20H20O7	373.1288			373.1276	3.216
50	33.2	Natsudaidain	C20H20O7	417.1186	417.1188	0.4794	417.1193	1.6781
51	33.22	5,6,7,8-Tetramethoxy-2-(4-methoxyphenyl)-4-benzopyronethoxy-2-(4-methoxyphenyl)-4-benzopyrone	C20H20O7	373.1288	373.1279	2.4120		

(Ru et al., 2014), DrugBank (https://www.drugbank.ca/) (Wishart et al., 2018), Swiss Target Prediction (http://www.swisstargetprediction.ch/) (Gfeller et al., 2014), and Similarity Ensemble Approach (http://sea.bkslab.org/) (Wang et al., 2016). Known therapeutic targets related to CHD and depression were obtained from the DrugBank database (Wishart et al., 2018), Online Mendelian Inheritance in Man (OMIM) (http://www.omim.org) (Amberger and Hamosh, 2017), DisGeNet database

(http://www.disgenet.org/web/DisGeNET/menu/home) (Li Y et al., 2020), and Therapeutic Target database (TTD) (https://db.idrblab.org/ttd/) (Li et al., 2018). The common potential target of XPF in the treatment of CHD with depression was obtained by comparing the component target with the disease target analysis. Then, the component–target network between the targets of active components in XPF and CHD with depression was established using Cytoscape (Version 3.8.0) (Otasek et al., 2019).

Topological Analysis and Pathway Enrichment Analysis

A network analyzer was used to calculate the topological analysis of the nodes of the component–target network. Nodes with degrees higher than the average number 4) were identified as the core targets, and were brought into the STRING database (https://string-db.org/) (Szklarczyk et al., 2017) to obtain the interacting proteins. Then, the PPI network was constructed using Cytoscape for visual analysis and, according to topological features (degree centrality), the major hub target was extracted. Further, the core targets were brought into the DAVID database (https://david.ncifcrf.gov) (Dennis et al., 2003), and Kyoto Encyclopedia of Genes and Genomes (KEGG) signaling pathway enrichment analysis and Gene ontology (GO) were performed to obtain the representative biological processes and pathways (cutoff at $p < 0.05$) of XPF in treating CHD with depression.

Animal Model Preparation and Drug Treatments

Sixty-four male Sprague-Dawley rats (weighing 200 ± 20 g) were randomly divided into a normal control group (n = 8) and a depressive-like behavioral group (n = 56). Experimental rats (n = 56) were exposed to chronic unpredictable mild stress (CUMS) to induce depression. The regimen consisted of immobilization for 4 h; cage tilting at 45° for 12 h; continuous illumination for 24 h; clip the distal 1 cm rat tails with tongs for 3 min; deprivation of water for 24 h; noise stimulation for 30 min; damp animal bedding for 24 h; foot shock for 3 min; removal of animal bedding for 24 h; high-speed agitation for 10 min; deprivation of food 24 h; and forced cold swim stress for 6 min at 4°C. Each animal received two stressors randomly per day for a total of 28 days. The normal control group (n = 8) remained undisturbed. Subsequently, the CUMS-induced rats were injected with ISO (8 mg/kg) for five days to form the CHD model (Aa et al., 2019; Hu et al., 2020). The rat model for CHD with depression induced by CUMS and ISO was evaluated by measuring rat body weight change, open field test, sucrose preference test, and ST-segment of the electrocardiogram. Then, all CHD with depression rats were randomly divided into a model group (n = 15, 0.9% saline, IG), Ser + Met group (n = 8, sertraline 10 mg/kg + metoprolol 5 mg/kg, IG), Ser group (n = 8, sertraline 10 mg/kg, IG), Met group (n = 8, metoprolol 10 mg/kg, IG), high-dose XPF (XPF-H) group (n = 8, 32.7 g/kg, IG), equivalent to CH 3.13 g/kg, CX 2.5 g/kg, XF 2.5 g/kg, TX 1.88 g/kg, ZQ 3.13 g/kg, CP 3.13 g/kg, BX 3.13 g/kg, BH 2.08 g/kg, FL 3.13 g/kg, BZ 3.13 g/kg, ZS 3.13 g/kg, GC 3.13 g/kg, medium-dose XPF (XPF-M) group (n = 8, 16.35 g/kg, IG), equivalent to CH 1.65 g/kg, CX 1.25 g/kg, XF 1.25 g/kg, TX 0.94 g/kg, ZQ 1.65 g/kg, CP 1.65 g/kg, BX 1.65 g/kg, BH 1.04 g/kg, FL 1.65 g/kg, BZ 1.65 g/kg, ZS 1.65 g/kg, GC 0.94 g/kg, and low-dose XPF (XPF-L) group (n = 8, 8.175 g/kg, IG), equivalent to CH 0.78 g/kg, CX 0.62 g/kg, XF 0.63 g/kg, TX 0.47 g/kg, ZQ 0.78 g/kg, CP 0.78 g/kg, BX 0.78 g/kg, BH 0.52 g/kg, FL 0.78 g/kg, BZ 0.78 g/kg, ZS 0.78 g/kg, GC 0.47 g/kg. The control group received 0.9% saline via oral administration. The drugs were administered daily for three weeks, while the animals were exposed to CUMS, except for the control group. At 24 h after the last treatment, all rats were sacrificed, and the brain, hippocampus, and heart tissues were rapidly extracted from each rat, stored at −80°C until analysis. One part of the brain and heart tissues were placed into a flask containing 4% paraformaldehyde.

TUNEL Staining

TUNEL staining was performed according to the manufacturer's instructions, to determine hippocampus and myocardial apoptosis. The apoptotic cells showed red fluorescence and the nucleus showed blue fluorescence, six high-power fields were selected from each sample. All cells and positive stained cells were counted, the percentage of positively stained cells was apoptotic index (AI) (AI = number of apoptotic cells/total number of nucleated cells).

ELISA Analysis

The level of 5-HT, Ang-II, cAMP in hippocampus and myocardial were quantified by ELISA assay kit, according to the manufacturer's instruction. After color development, the absorbance was measured at 450 nm with fluorescence reader (THERMO USA).

Western Blot Analysis

Hippocampus, hearts tissue proteins were mechanically homogenized in lysis buffer, centrifuged at 12,000 rpm for 10 min at 4 °C, collected the supernatant. BCA protein assay was used to determine protein concentrations. Equal concentrations of protein were resolved on 10% SDS-PAGE gels, and were transferred onto PVDF membranes. These membranes PVDF were soaked in TBST buffer with 5% non-fat skim milk for 2 h, and then These membranes PVDF were incubated in the primary antibodies (PKA, CREB, BDNF, Bcl-2, Bax, Cyt-c, caspase-3, and β-actin) overnight at 4°C. Subsequently, the membrane was washed for 5 times with TBST, followed by secondary antibodies incubated with horseradish peroxidase for 2 h at room temperature. After rewashing with TBST, the membranes were scanned on X-ray film by chemiluminescence reaction, used ImageJ software to analysis the band intensity.

Statistical Analysis

Data were expressed as mean ± SD, Differences between groups were analyzed using a one-way analysis of variance (ANOVA), followed by Dunnett's t test. All data were analyzed statistically

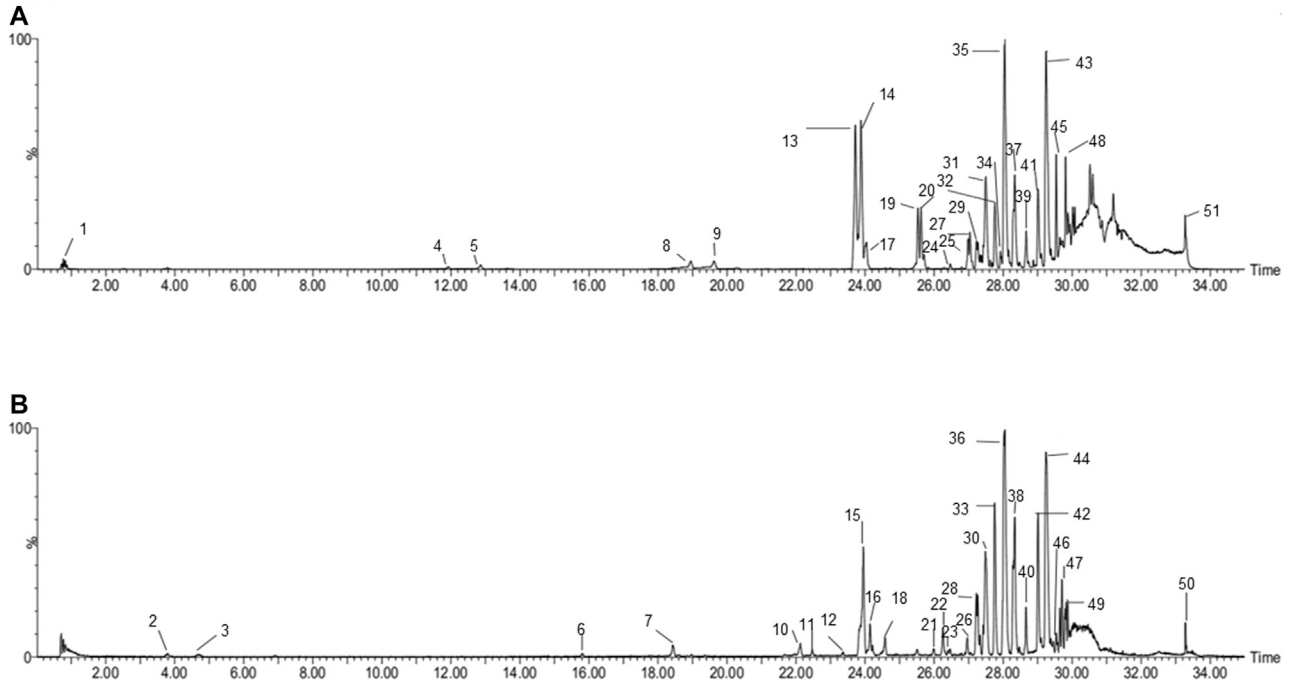

FIGURE 2 | BPI chromatograms of XPF in serum sample in positive **(A)** and negative. **(B)** Ion modes determined by UPLC-Q-TOF/MS.

using GraphPad Prism 8.0 (GraphPad Software, Inc., La Jolla, CA, USA), p-value < 0.05 was considered significant.

RESULTS

Serum Pharmacochemistry Analysis of XPF by UPLC-Q-TOF/MS

Based on the established UPLC-Q-TOF/MS method, 51 serum prototypes of the drugs were analyzed and identified (**Table 1**). These compounds can be roughly divided into three categories: phenolic acids, saponins, and flavonoids. **Figure 2** shows the base peak chromatogram (BPC) of each typical sample in the mode of positive and negative ions, and peaks 1–51 are the original components entering the blood. These 51 compounds of XPF detected in the serum were determined to be the main active components and further selected to predict the targets and pathways using network analysis.

Component-Target Network Construction

In this work, 820 targets for the 51 (Nine of them had no therapeutic targets) components were explored by using TCMSP, Swiss Target Prediction, Drugbank, and Swiss Target Prediction as shown in **Supplementary Table S1**, and 1817 candidate targets of CHD and depression were obtained from Drugbank, OMIM, and DisGeNet databases as shown in **Supplementary Table S2**. Taking the intersection of component targets and candidate targets associated with CHD and depression, 168 consensus targets were generated as potential targets for XPF in treating CHD and depression, which were used to construct a component–target network using Cytoscape. As shown in **Figure 3A**, the network comprised 42 components, 168 targets, and two diseases, and included 212 nodes and 845 edges.

Topological Analysis and Pathway Enrichment Analysis

Among the 168 consensus targets, 75 major targets with degrees higher than the average number 4) were considered as the major targets (**Table 2**). Ten components with degrees higher than 20 were identified as the main active components (Kaempferol and quercetin were not included because they are widely distributed and have many targets, but their pharmacological effects are weak) (**Table 3**). The 75 major targets were brought into the STRING database to obtain protein-protein interaction (PPI) predictions. The PPI network was constructed using Cytoscape, and hide disconnected nodes in the network (5 nodes). A network analyzer was used to calculate topological features (degree) of the 70 major targets (**Figure 3B**). Among these, 10 target genes (*ACE2*, *HTR1A*, *HTR2A*, *AKT1*, *PKIA*, *CREB1*, *BDNF*, *BCL2*, *BAX*, and *CASP3*), with higher degree were recognized as the major hub targets of XPF in treating CHD with depression. KEGG pathway enrichment and GO analyses of the 75 major targets were performed using the DAVID database. GO analysis showed 184 enriched processes (**Supplementary Table S3**), including 126 biological processes, 39 molecular functions, and 19 cellular components. The top 30 according to p-values are shown in **Figure 4A**. KEGG pathway enrichment showed 117 signaling pathways, as shown in **Supplementary Table S4**, and the top 20 pathways according to p-values are shown in **Figure 4B**.

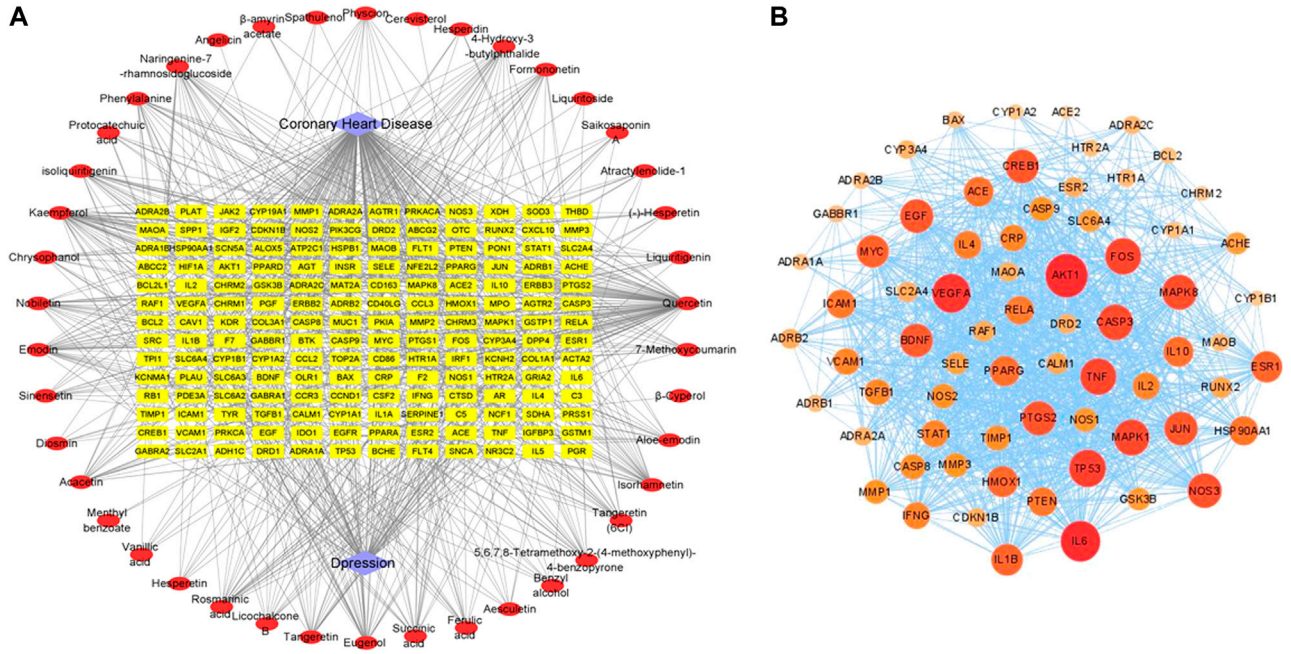

FIGURE 3 | The networks associating with XPF in the treatment of CHD with depression. **(A)** The component-target network consisted of 42 components, 168 targets and 2 diseases including 212 nodes and 845 edges. **(B)** The PPI network of hub targets obtained from STRING database and constructed by Cytoscape.

Experimental Validation

Evaluation of Depressive-like Behaviors of Chronic Stress-Depressed Rats

The open field test can reflect the spatial exploration behavior of rats (Chen et al., 2019), and sucrose preference test could be the objective indicator of hedonic behavior (Gross and Pinhasov, 2016b). All rats were evaluated by open field test, sucrose preference test before and after the CUMS and ISO-induced process, then all CHD with depression rats were randomly divided into 7 groups. After three weeks of administration, open field test and sucrose preference test were performed again of all rats. As shown in **Table 4**, after CUMS and ISO-induced, compared with the control group the open-field test and sucrose preference scores were significantly reduced in the model group and each administration groups ($p < 0.005$). It was shown that the depression model was successfully established. After treatment for 21 days, compared with the model group, XPF administration significantly improve the open-field test and sucrose preference scores ($p< 0.005$).

Effects of XPF on Myocardial and Hippocampal Apoptosis

Apoptosis can cause myocardial and hippocampal injury and dysfunction, which are the major mechanisms of CHD and depression. As shown in **Figure 5**, the myocardial and hippocampus of the CUMS and ISO-induced rats were injured. The effects of XPF on myocardial apoptosis are shown in **Figure 5A**. And the effects of XPF on hippocampal apoptosis are shown in **Figure 5B**. Compared with the control group, the myocardial and TUNEL-positive cells were significantly increased in the model group, as shown in **Figure 5C** ($p < 0.005$). The myocardial apoptotic index of the XPF-H and XPF-M groups was significantly lower than that of the model group ($p < 0.01$). Sertraline 10 mg/kg + metoprolol 5 mg/kg and metoprolol 10 mg/kg also significantly inhibited the apoptosis in the myocardia (**Figure 5C**) ($p < 0.005$). Sertraline (10 mg/kg) and low-dose XPF treatment did not alter myocardial apoptosis.

There were significant differences in the total apoptotic index in the hippocampus after XPF treatment for 21 days. In the model group, the apoptotic index significantly increased compared with the control group, as shown in **Figure 5D**. Furthermore, XPF administration significantly decreased the apoptotic index in the hippocampus. Additionally, sertraline and metoprolol also significantly inhibited apoptosis in the hippocampus ($p < 0.005$).

The results indicated that the brain and myocardial tissues of the rats were injured after CUMS and ISO-induced damage. It was shown that the CHD with depression model was successfully established, while the treatment of XPF can inhibit apoptosis of myocardial and brain tissue simultaneously.

According to key proteins with a higher degree in the PPI network and KEGG pathway enrichment analysis, it is suggested that the mechanism of XPF in the treatment of CHD with depression may be through the regulation of *ACE2*, *HTR1A*, *HTR2A*, *AKT1*, *PKIA*, *CREB1*, *BDNF*, *BCL2*, *BAX*, *CASP3*, cAMP signaling pathway, and the cell apoptosis process. As the second intracellular messenger, cAMP regulates the expression of downstream proteins and plays an important role in cell growth and apoptosis (Zhou et al., 2012). Bcl-2 and Bax, as

TABLE 2 | The topological parameters of 32 major targets.

Swiss prot	Genes/proteins	Description	Degree
P31749	AKT1	RAC-alpha serine/threonine-protein kinase	74
P05231	IL6	Interleukin-6	68
P15692	VEGFA	Vascular endothelial growth factor A	64
P04637	TP53	Cellular tumor antigen p53	61
P01100	FOS	Proto-oncogene c-Fos	59
P01375	TNF	Tumor necrosis factor	59
P28482	MAPK1	Mitogen-activated protein kinase 1	58
P42574	CASP3	Caspase-3	57
P45983	MAPK8	Mitogen-activated protein kinase 8	56
P29474	NOS3	Nitric oxide synthase	55
P35354	PTGS2	Prostaglandin G/H synthase 2	54
P16220	CREB1	Cyclic AMP-responsive element-binding protein 1	53
P01133	EGF	Pro-epidermal growth factor	53
P05412	JUN	Transcription factor AP-1	53
P23560	BDNF	Brain-derived neurotrophic factor	52
P01106	MYC	Myc proto-oncogene protein	50
P01584	IL1B	Interleukin-1 beta	49
P03372	ESR1	Estrogen receptor	48
P09601	HMOX1	Heme oxygenase 1	47
P37231	PPARG	Peroxisome proliferator-activated receptor gamma	45
P22301	IL10	Interleukin-10	45
P12821	ACE	Angiotensin-converting enzyme	44
P07900	HSP90AA1	Heat shock protein HSP 90-alpha	43
P05362	ICAM1	Intercellular adhesion molecule 1	42
P60484	PTEN	Phosphatidylinositol 3,4,5-trisphosphate 3-phosphatase and dual-specificity protein phosphatase PTEN	42
Q04206	RELA	Transcription factor p65	41
P05112	IL4	Interleukin-4	40
P42224	STAT1	Signal transducer and activator of transcription 1-alpha/beta	38
P01579	IFNG	Interferon gamma	38
P60568	IL2	Interleukin-2	38
P19320	VCAM1	Vascular cell adhesion protein 1	37
P02741	CRP	C-reactive protein	37

TABLE 3 | The topological parameters of 20 main active components.

Compounds	Degree
Eugenol	28
Emodin	27
Isorhamnetin	25
Nobiletin	23
Isoliquiritigenin	22
Rosmarinic acid	22
4-Hydroxy-3 -butylphthalide	21
Acacetin	20

targets downstream of CREB and BDNF, regulate apoptosis through the mitochondrial pathway (Mi et al., 2015; Tang et al., 2016). Recent studies have shown that the cAMP-PKA-CREB-BDNF signaling pathway is closely related to depression (Wang et al., 2017; Ye et al., 2017). Meanwhile, the related proteins in the cAMP-PKA-CREB-BDNF signaling pathway can also improve myocardial microcirculation, improve the ability of myocardial cells to resist ischemia and hypoxia, and effectively prevent the development and deterioration of CHD (Huang et al., 2016). To verify whether XPF works in treating CHD with depression by intervening in the cAMP-PKA-CREB-BDNF signaling pathway and cell apoptosis process, the expression of 5-HT, Ang-II, cAMP, PKA, CREB, BDNF, Bcl-2, Bax, Cyt-c, and caspase-3 in the myocardial and hippocampal tissues were detected.

3.4.3 Effects of XPF on the Expression of Ang-II, 5-HT, and cAMP in Myocardial Tissues

As shown in **Figures 6A–C**, it was noted that compared with the control group, the levels of Ang-II and 5-HT were significantly increased in the myocardial tissues in the model group. Compared with the control group, the expression of cAMP in the myocardial tissues was markedly lower in the model group ($p < 0.005$). After treatment for 21 days, high-dose XPF decreased the levels of Ang-II and 5-HT in the myocardium ($p < 0.01$). The treatments with middle-dose XPF solely decreased the levels of Ang-II ($p < 0.05$), whereas low-dose XPF had no effect on the levels of Ang-II and 5-HT in the myocardium. The levels of cAMP were significantly increased, in a dose-dependent manner, in the myocardium of the rats in the XPF-H, XPF-M, and XPF-L groups ($p < 0.005$).

3.4.4 Effects of XPF on the Expression of Ang-II and 5-HT cAMP in the Hippocampus

As shown in **Figures 6D–F**, it was noted that, compared with the control group, the levels of Ang-II were significantly increased in the hippocampus of the model group. Conversely, the expression of 5-HT and cAMP in the hippocampus was markedly lower in the model group. After treatment for 21 days, the treatment with

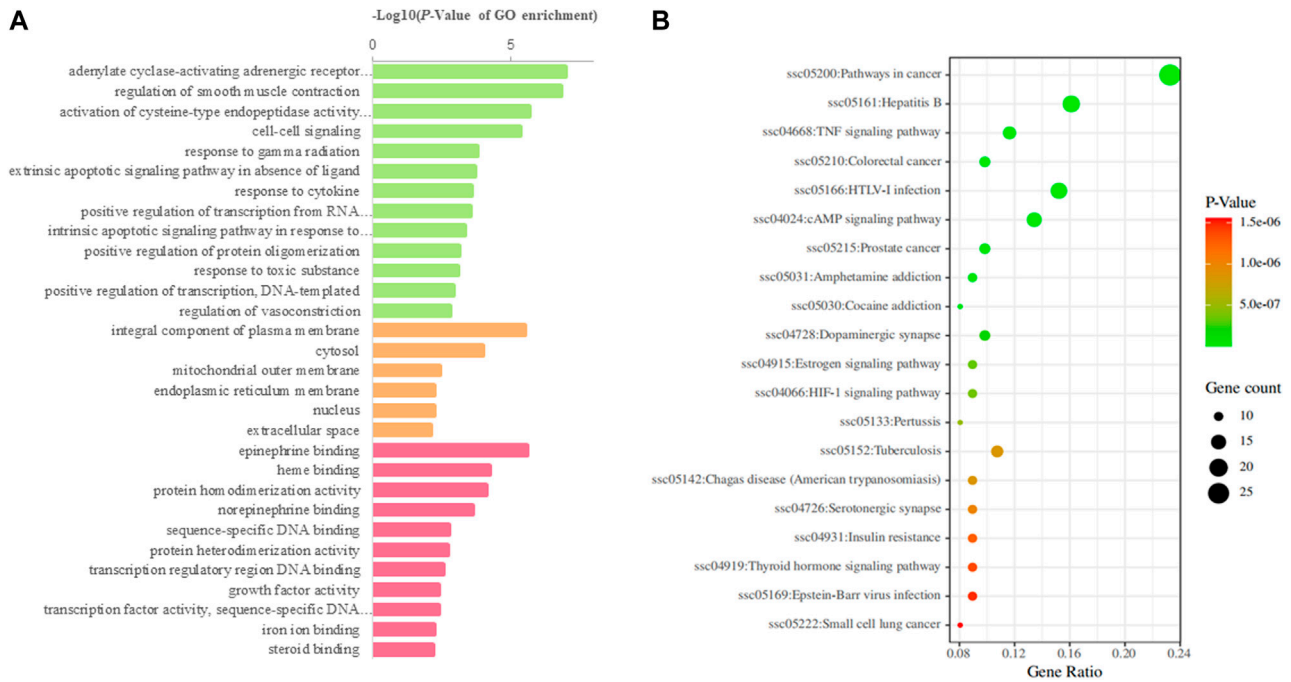

FIGURE 4 | GO and KEGG analysis of the candidate targets. **(A)** Biological process enrichment of candidate targets. **(B)** KEGG pathwayenrichment of candidate targets.

TABLE 4 | The comparison of the open field test scores and sucrose preference of rats in different groups.

Group	Open field test (scores)		Sucrose preference (%)	
	After CUMS and ISO-induced	After treatment	After CUMS and ISO-induced	After treatment
Control	160.17 ± 10.48	158.33 ± 12.4	91.69 ± 3.60	88.49 ± 2.91
Model	79.67 ± 6.80***	58.83 ± 3.06	58.89 ± 2.33***	55.03 ± 1.22
Ser + Met	82.83 ± 4.66$^{***\triangle}$	128.17 ± 8.4$^{\#\#\#}$	57.68 ± 2.79$^{***\triangle}$	81.17 ± 1.93$^{\#\#\#}$
Ser	77.5 ± 9.39$^{***\triangle}$	105.17 ± 7.9$^{\#\#\#}$	59.30 ± 2.69$^{***\triangle}$	76.01 ± 3.68$^{\#\#\#}$
Met	78.17 ± 6.94$^{***\triangle}$	96.67 ± 8.21$^{\#\#\#}$	56.51 ± 1.54$^{***\triangle}$	62.04 ± 1.40$^{\#\#\#}$
XPF-H	83.17 ± 2.63$^{***\triangle}$	148.50 ± 7.66$^{\#\#\#}$	58.25 ± 4.25$^{***\triangle}$	87.07 ± 2.16$^{\#\#\#}$
XPF-M	83.33 ± 0.13$^{***\triangle}$	122 ± 9.63$^{\#\#\#}$	57.39 ± 3.36$^{***\triangle}$	82.13 ± 1.52$^{\#\#\#}$
XPF-L	80.83 ± 7.98$^{***\triangle}$	109 ± 1$^{\#\#\#}$	57.76 ± 2.28$^{***\triangle}$	76.78 ± 1.72$^{\#\#\#}$

Values are expressed as the mean ± SD; n = 6–8 in each group. Compared with controll group after CUMS and ISO-induced.
$^{***}P < 0.005$. *Compared with model group after CUMS and ISO-induced,* $^{\triangle}P > 0.05$. *Compared with model group after treatment,* $^{\#\#\#}P < 0.005$.

high-dose XPF and middle-dose XPF significantly decreased the levels of Ang-II ($p < 0.005$) and increased the levels of 5-HT and cAMP in the hippocampus ($p < 0.05$). Similarly, treatment with metoprolol markedly decreased the levels of Ang-II, and treatment with sertraline increased the levels of 5-HT and cAMP in the hippocampus ($p < 0.05$). However, low-dose XPF had no effect on the levels of Ang-II, 5-HT, and cAMP in the hippocampus.

Effects of XPF on the Expression of PKA, CREB, and BDNF on Myocardial Tissue

As presented in **Figures 7A–C**, the results of the WB analysis indicated that the expression of PKA, CREB, and BDNF in the myocardium in the model group was significantly lower than that of the control group ($p < 0.005$). XPF could upregulate the expression of PKA, CREB, and BDNF compared with the model group ($p < 0.05$).

Effects of XPF on the Expression of PKA, CREB, and BDNF in the Hippocampus

As shown in **Figures 7D–F**, the PKA, CREB, and BDNF protein levels of the model group were significantly lower than those of the control group. High-dose XPF and middle-dose XPF was able to upregulate the expression of PKA, CREB, and BDNF compared with the model group ($p < 0.005$). However, low-dose XPF had no effect on the levels of CREB and BDNF in the hippocampus.

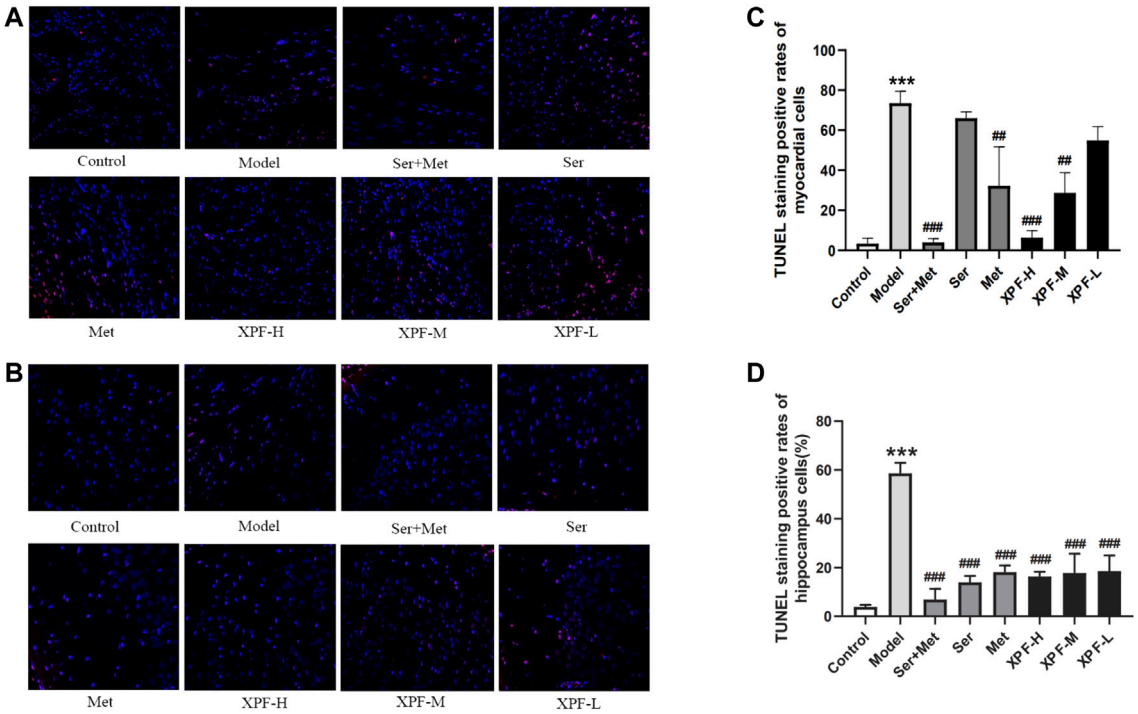

FIGURE 5 | Anti-apoptosis effect of XPF on CUMS and ISO-induced rats (×400). **(A)** Representative images of myocardial apoptosis stained by TUNEL. **(B)** Representative images of hippocampal apoptosis stained by TUNEL. **(C)** Rate of myocardial apoptosis in each group. **(D)** Rate of hippocampal apoptosis in each group. Data wer presented as means ± SD (n = 3). $^{***}p < 0.05$ compared with the control group, $^{\#\#}p < 0.01$, $^{\#\#}p < 0.005$ compared with the model group.

Effects of XPF on the Expression of Bcl-2, Bax, Cyt-C, and Caspase-3 in the Myocardium

As shown in **Figure 8** and **Table 5**, compared with the control group, the levels of Bax, Cyt-c, and caspase-3 were significantly increased in the model group, although Bcl-2 levels significantly decreased. Treatment with XPF significantly increased the levels of Bcl-2 and decreased the levels of Bax, Cyt-c, and caspase-3 ($p < 0.005$), in a dose dependent manner.

Effects of XPF on the Expression of Bcl-2, Bax, Cyt-C, and Caspase-3 in the Hippocampus

As shown in **Figure 9** and **Table 6**, the results of the WB analysis indicated that the expression of Bax, Cyt-c, and caspase-3 was significantly increased in the model group, while Bcl-2 levels were significantly decreased. After treatment for 21 days, high-dose XPF and middle-dose XPF significantly decreased the levels of Bax, Cyt-c, and caspase-3 ($p < 0.005$). High-dose, and middle-dose XPF also increased the levels of Bcl-2 ($p < 0.05$), in a dose-dependent manner. In contrast, low-dose XPF only inhibited the expression of Bax and Cyt-c ($p < 0.005$), but had no effect on the expression of Bcl-2 and caspase-3.

DISCUSSION

XPF, characterized by multiple components and targets, has been shown to have a relatively satisfactory therapeutic effect in treating CHD with depression. XPF can improve myocardial blood supply and mental state of patients at the same time, which reflects the overall concept of traditional Chinese medicine (Hou et al., 2017). Through this study, we found that XPF could protect the myocardium and hippocampus in CUMS and ISO-induced CHD in depression rats, it shows that XPF has the advantages and characteristics of treating the heart and brain at the same time. However, it is difficult to accurately identify and understand the active compounds and mechanisms of XPF in treating CHD with depression solely by using conventional pharmacological methods. Therefore, new research approaches to reveal the interaction between components of TCM and biological system networks are urgently required. Here, an integrated strategy was established by combining serum pharmacochemistry and network pharmacology to comprehensively and systematically investigate the components and mechanisms of XPF in treating CHD with depression, and validated in experiments.

In this study, 51 compounds were detected in rat serum after oral administration of XPF using UPLC-Q-TOF/MS technology. The identified constituents, mainly phenolic acids, saponins, and flavonoids, were determined to be the main active components of XPF. Among them, phenolic acids, such as rosmarinic acid and eugenol, can inhibit vascular smooth muscle cell proliferation and have a cardioprotective effect (Liu Y et al., 2018). Rosmarinic acid can treat neurodegenerative diseases via anti-neuroinflammatory activity (Wei et al., 2018). Furthermore, saponins, such as saikosaponin A, are the major bioactive component extracted from Radix Bupleuri (Chen et al., 2018; Liu R et al., 2018) and

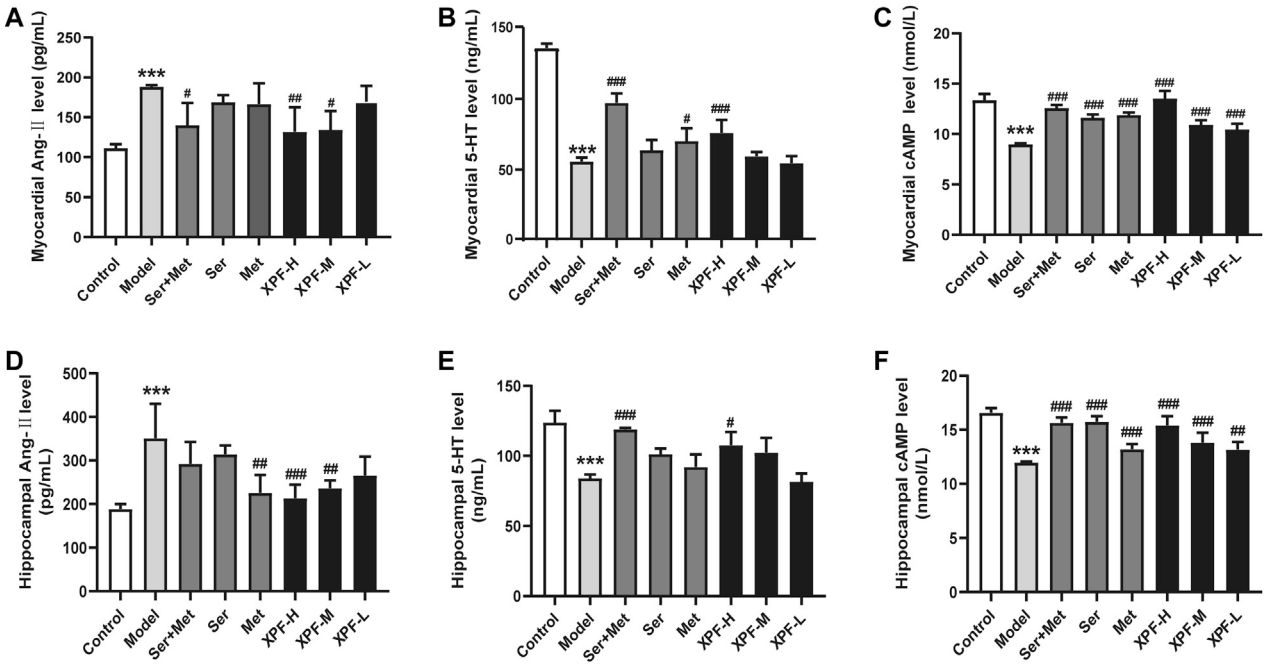

FIGURE 6 | Experimental validation of key targets Ang-II, 5-HT, cAMP in rat myocardium and hippocampus induced by CUMS and ISO. **(A)** The levels of Ang-II in the myocardial were determined by ELISA. **(B)** The levels of 5-HT in the myocardial were determined by ELISA. **(C)** The levels of cAMP in the myocardial were determined by ELISA. **(D)** The levels of Ang-II in the hippocampus were determined by ELISA. **(E)** The levels of 5-HT in the hippocampus were determined by ELISA. **(F)** The levels of cAMP in the hippocampus were determined by ELISA. Data were presented as means ± SD (n = 3). $^{***}p < 0.005$ compared with the control group, $^{\#\#}p < 0.05$, $^{\#\#}p < 0.01$, $^{\#\#\#}p < 0.005$.

have anti-inflammatory and antioxidant pharmacological activities, as well as a good therapeutic effect on many diseases of the central nervous system and cardiovascular system (Guo et al., 2020). Flavonoids, such as hesperidin and hesperetin, can inhibit inflammatory reactions and oxidative stress, and protect nerve cells and vascular endothelium (Hwang et al., 2012; Van Rymenant et al., 2017).

Moreover, the component–target network between the targets of absorbed components in the serum of XPF and CHD with depression was built using Cytoscape, followed by topological parameters and PPI analysis. As a result, 8 components (eugenol, emodin, isorhamnetin, nobiletin, isoliquiritigenin, rosmarinic acid, 4-Hydroxy-3-butylphthalide, and acacetin), with higher degree centrality were determined to be the active ingredients of XPF, and 10 hub targets, including (ACE2, HTR1A, HTR2A, AKT1, PKIA, CREB1, BDNF, BCL2, BAX, CASP3, cAMP) were determined as hub targets of XPF in treating CHD with depression. GO analysis and KEGG pathway enrichment analysis showed that XPF may regulate the cAMP signaling and apoptosis pathways by interfering with the expression of Ang-II, 5-HT, cAMP, PKA, CREB, BDNF, Bcl-2, Bax, Cyt-c, and caspase-3.

In this study, CUMS and ISO-induced CHD in a rat model of depression was used to explore the mechanism of XPF in treating CHD with depression. These rats showed a large number of apoptotic cells in myocardial and hippocampal tissues compared with the control group, which indicated that the CHD with depression model was successfully established. Sertraline and metoprolol were used as positive control drugs to treat CHD in rats with depression. Sertraline can increase the content of 5-hydroxytryptamine (5-HT) in the brain and exert antidepressant-like effects (Sun et al., 2020). Metoprolol is a beta-blocker commonly used in the clinic (Podlesnikar et al., 2019; Qin et al., 2020). Studies have shown that metoprolol could reduce the oxygen consumption of the myocardium and reduce the risk of cardiovascular events (Assimon et al., 2018). However, co-administration of sertraline and metoprolol increases the blood concentration of metoprolol. Therefore, we adjusted the dose of metoprolol in the sertraline and metoprolol groups in this study (Bahar et al., 2018).

Under these experimental conditions, XPF could decrease Ang-II content in the circulation and central system, inhibit 5-HT level in peripheral circulation, and increase 5-HT content in the central nervous system. Meanwhile, XPF could upregulate the expression levels of cAMP, PKA, CREB, and BDNF both in the myocardium and hippocampus, which matched the predicted results of the network pharmacological analysis. Interestingly, sertraline regulated the cAMP, PKA, CREB, and BDNF levels in the hippocampus, but had a limited effect on the myocardium. Metoprolol can regulate the cAMP, PKA, CREB, and BDNF expression in myocardial, but it has a limited effect on the central nervous system. XPF treatment not only activated the cAMP signal pathway, but also further inhibited apoptosis and protected

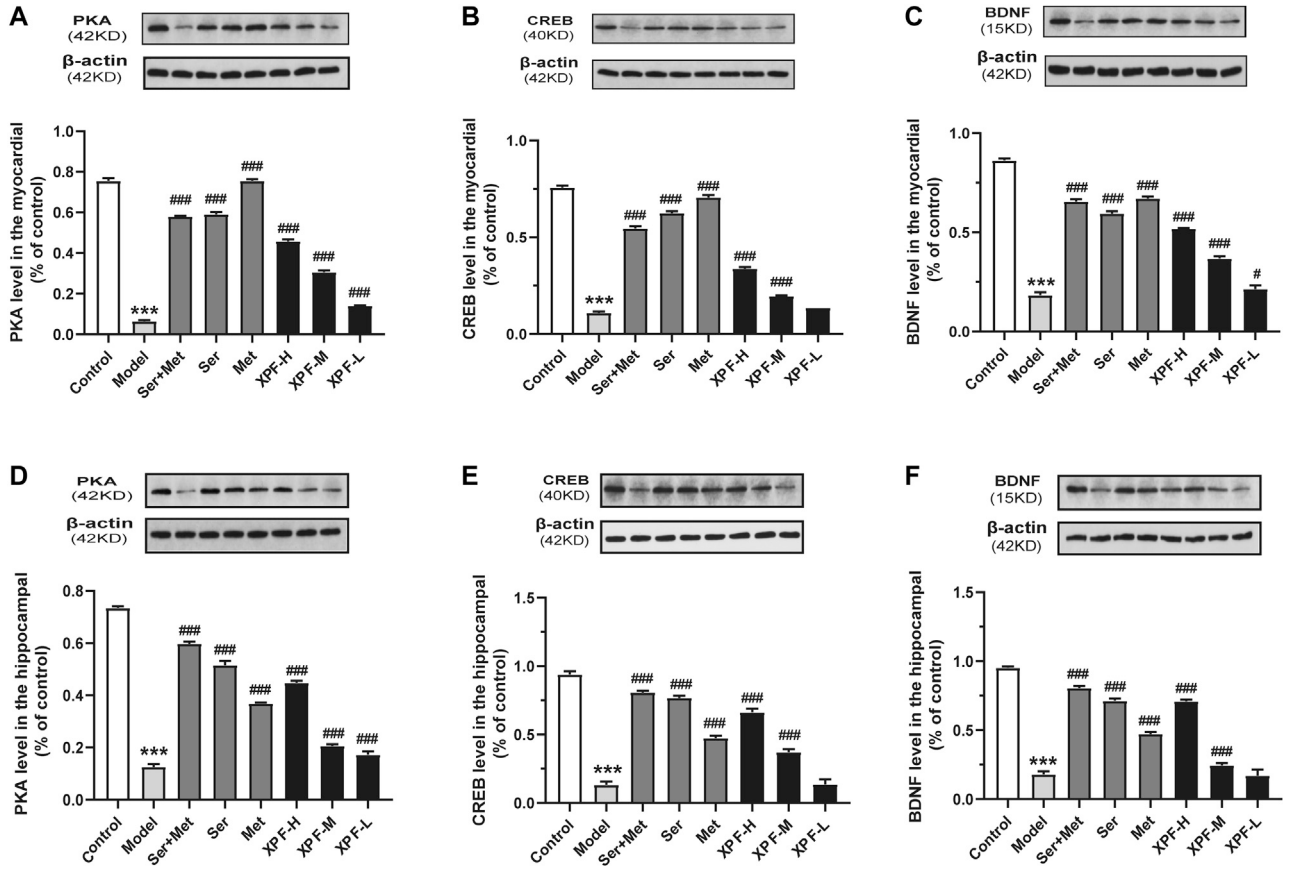

FIGURE 7 | Experimental validation of key targets PKA, CREB, BDNF in rat myocardium and hippocampus induced by CUMS and ISO. **(A)** Quantitative analysis of PKA expression in the myocardial. **(B)** Quantitative analysis of CREB expression in the myocardial. **(C)** Quantitative analysis of BDNF expression in the hippocampal. **(D)** Quantitative analysis of PKA expression in the hippocampal. **(E)** Quantitative analysis of CREB expression in the hippocampal. **(F)** Quantitative analysis of CREB expression in the hippocampal. Data were presented as means ± SD (n = 3). $^{***}p < 0.005$ compared with the control group, $^{\#\#}p < 0.01$, $^{\#\#}p < 0.005$.

the myocardium and hippocampus. The cAMP signaling pathway can increase the expression of Bcl-2 and inhibit the activation of caspase-3 by regulating the expression of CREB and BDNF proteins (Mo et al., 2020; Yang et al., 2020). In this study, XPF rectified the injury of the hippocampus and myocardium caused by CHD in depressed rats, significantly decreasing the hippocampal and myocardial levels of Bax, Cyt-c, caspase-3, and increased Bcl-2 expression, which suggests that XPF may inhibit hippocampal and myocardial apoptosis, improve heart function and nerve function, and exert antidepressant and anti-myocardial ischemia effects.

Chronic stressful life events can stimulate the renin-angiotensin-aldosterone system (RAAS). Evidence has shown that Ang-II levels are significantly higher in patients with CHD and depression. Ang-II is metabolized into Ang-(1–7), which directly interferes with the intestinal uptake of tryptophan and affects the metabolism of 5-HT (Klempin et al., 2018; W et al., 2020). The decrease of 5-HT levels in the central nervous system leads to depression or other mental disorders (Jiao et al., 2019; Wenxiu et al., 2020). 5-HT metabolic disorder inhibits the cAMP signaling pathway (Louiset et al., 2017). The cAMP signaling pathway was observed in both CHD and depression patients (Amare et al., 2017; Wang and Mao, 2019; Sandrini et al., 2020).

Activated cAMP and PKA can phosphorylate the Ca^{2+}channel on the cell membrane, promote calcium flow in cardiomyocytes, promote excitation contraction coupling, enhance myocardial contractility, improve the anti-ischemic effects of cardiomyocytes, and produce protective effects on cardiomyocytes (Inserte et al., 2004; Zhang et al., 2010). At the same time, cAMP and PKA are also widely distributed in the nervous system, which can guide the regeneration of neurons, improve the plasticity of synapses, and play a role in protecting the nervous system (Zhang M et al., 2018). CREB is involved in a wide range of neural plasticity processes, including neuronal survival, neuroprotection, neurogenesis, synaptic plasticity, and regulation of emotional expression (Liu et al., 2016; Tang et al., 2020). BDNF is a classical downstream target gene of CREB, which can nourish nerves and promote the differentiation, increment, and regeneration of neurons (Wang et al., 2019). BDNF also has a modulatory role in cardiovascular function, is involved in angiogenesis maintenance of endothelial integrity (Kaess et al., 2015; Jin et al., 2018), repairing myocardial

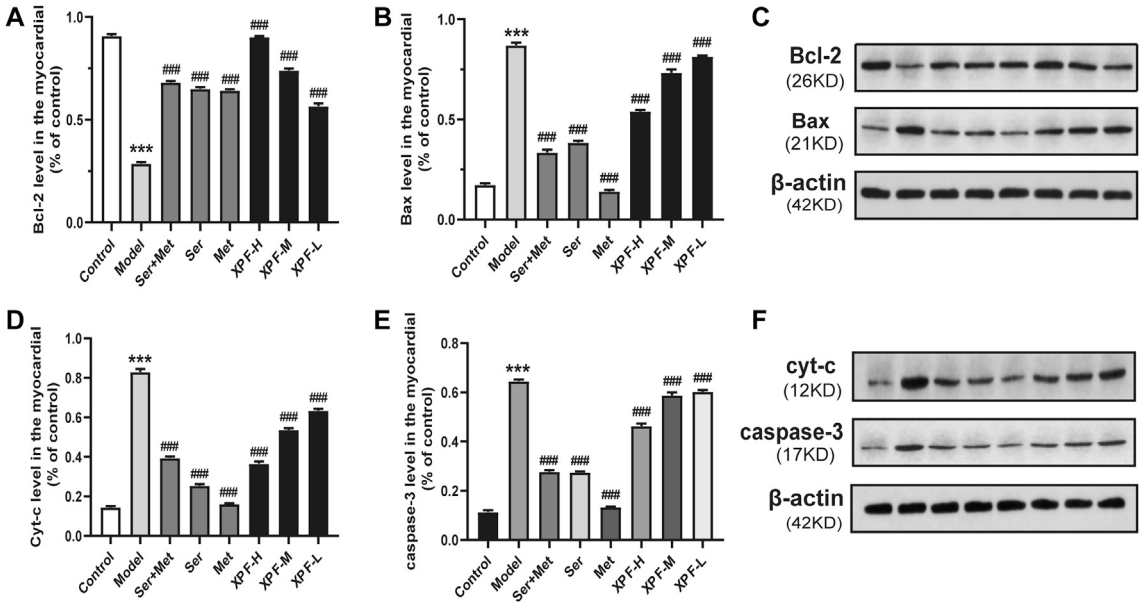

FIGURE 8 | Experimental validation of key targets Bcl-2, BAX, Cyt-c, caspase-3 in rat myocardium induced by CUMS and ISO. **(A)** Quantitative analysis of Bcl-2 expression in the myocardial. **(B)** Quantitative analysis of BAX expression in the myocardial. **(C)** Western blot analysis of Bcl-2 and BAX protein. **(D)** Quantitative analysis of Cyt-c expression in the myocardial. **(E)** Quantitative analysis of caspase-3 expression in the myocardial. **(F)** Western blot analysis of Cyt-c and caspase-3 protein. Data were presented as means ± SD (n = 3). $^{***}p < 0.005$ compared with the control group, $^{\#\#\#}p < 0.005$ compared with the model group.

TABLE 5 | Comparison of gray values of Bcl-2, Bax, Cyt-C and Caspase-3 in myocardium of rats in different groups.

Group	Bal-2/β-actin	Bax/β-actin	Cyt-c/β-actin	Caspase/β-actin
Control	0.9080 ± 0.0083	0.1728 ± 0.0084	0.1437 ± 0.0077	0.1139 ± 0.0071
Model	0.2864 ± 0.0076***	0.8701 ± 0.0143***	0.8300 ± 0.0159***	0.6454 ± 0.0072***
Ser + Met	0.6814 ± 0.0072###	0.3348 ± 0.0142###	0.3945 ± 0.0075###	0.2768 ± 0.0067###
Ser	0.6505 ± 0.0086###	0.3850 ± 0.0085###	0.2534 ± 0.0085###	0.2743 ± 0.0044###
Met	0.6419 ± 0.0067###	0.1408 ± 0.0070###	0.1615 ± 0.0029###	0.1328 ± 0.0029###
XPF-H	0.9032 ± 0.0035###	0.5394 ± 0.0084###	0.3657 ± 0.0113###	0.4630 ± 0.0104###
XPF-M	0.7402 ± 0.0083###	0.7331 ± 0.0173###	0.5366 ± 0.0082###	0.5879 ± 0.0126###
XPF-L	0.5665 ± 0.0130###	0.8143 ± 0.0053###	0.6337 ± 0.0096###	0.6024 ± 0.0069###

Values are expressed as the mean ± SD; n = *3 in each group. Compared with control.*
***P < *0.005, Compared with model.*
###P < *0.005.*

microcirculation, and maintaining myocardial cell function after myocardial injury (Lee et al., 2017). Low expression of CREB and BDNF causes Bax overexpression, Bcl-2 expression is inhibited, and the promotion of the release of apoptosis factors such as cytochrome c (Cyt-c) into the cytoplasm and increased caspase-3. Caspase-3, the final executive factor of apoptosis, leads to apoptosis (Xu et al., 2018). Bcl-2 can form a heterodimer with Bax to inhibit its function, Bcl-2 can also inhibit the activation of caspase-3, and inhibit apoptosis (Abu et al., 2018). Meng (Meng and Wang, 2013) have found that Baishile (BSL) capsule could significantly improve the CUMS rats with depression-like behavior; K252a could block the cAMP signaling pathway to antagonize the antidepressant effect of BSL capsule. Jiang (Jiang et al., 2017) have found that acupuncture could improve depressive-like behaviors via PKA/CREB signaling pathway, H89 could block the PKA/CREB signaling pathway to antagonize the antidepressant effect of acupuncture. Mao (Mao and Zhang, 2014) have found H89 could block the PKA/CREB signaling pathway to antagonize the myocardial protective effect of Danlou tablets. Therefore, enhanced expression of related proteins in the cAMP signaling pathway and inhibition of the cell apoptosis process contributes to the alleviation of angina pectoris, chest pain, and depression symptoms. Essentially, it promotes protection of the cardiovascular and nervous system against coronary heart disease with depression.

The 8 active components (eugenol, emodin, isorhamnetin, nobiletin, isoliquiritigenin, rosmarinic acid, 4-Hydroxy-3-butylphthalide,

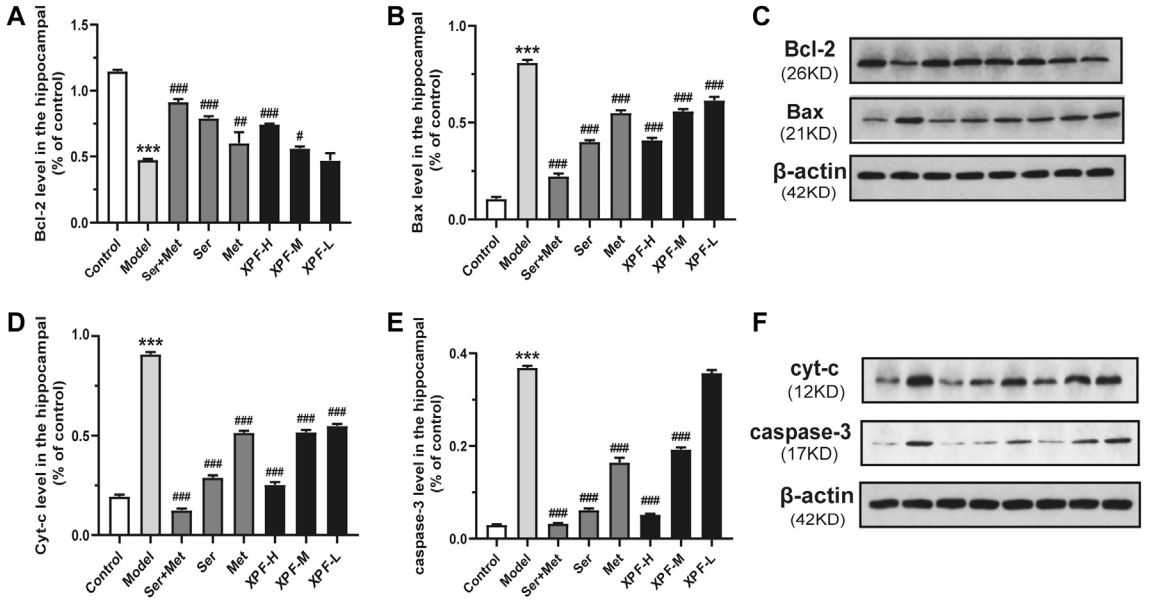

FIGURE 9 | Experimental validation of key targets Bcl-2, BAX, Cyt-c, caspase-3 in rat hippocampus induced by CUMS and ISO. **(A)** Quantitative analysis of Bcl-2 expression in the hippocampal. **(B)** Quantitative analysis of BAX expression in the hippocampal. **(C)** Western blot analysis of Bcl-2 and BAX protein. **(D)** Quantitative analysis of Cyt-c expression in the hippocampal. **(E)** Quantitative analysis of caspase-3 expression in the hippocampal. **(F)** Western blot analysis of Cyt-c and caspase-3 protein. Data were presented as means ± SD (n = 3). ***p < 0.005 compared with the control group, ###p < 0.005 compared with the model group.

TABLE 6 | Comparison of gray values of Bcl-2, Bax, Cyt-C and Caspase-3 in hippocampus of rats in different groups.

Group	Bal-2/β-actin	Bax/β-actin	Cyt-c/β-actin	Caspase/β-actin
Control	1.1464 ± 0.0112	0.1064 ± 0.0098	0.1937 ± 0.0103	0.0301 ± 0.0009
Model	0.4744 ± 0.0081***	0.8098 ± 0.0144***	0.9091 ± 0.0106***	0.3689 ± 0.0040***
Ser + Met	0.9136 ± 0.0217###	0.2226 ± 0.0147###	0.1248 ± 0.0090###	0.0323 ± 0.0015###
Ser	0.7909 ± 0.0143###	0.4004 ± 0.0085###	0.2885 ± 0.0122###	0.0620 ± 0.0038###
Met	0.6014 ± 0.0832##	0.5492 ± 0.0142###	0.5143 ± 0.0094###	0.1646 ± 0.0103###
XPF-H	0.7445 ± 0.0061###	0.4084 ± 0.0119###	0.2529 ± 0.0131###	0.0521 ± 0.0017###
XPF-M	0.5623 ± 0.0151#	0.5590 ± 0.0104###	0.5180 ± 0.0106###	0.1928 ± 0.0043###
XPF-L	0.4703 ± 0.0535	0.6148 ± 0.0181###	0.5496 ± 0.0097###	0.3575 ± 0.0063

Values are expressed as the mean ± SD; n = *3 in each group. Compared with control.*
***P < *0.005, Compared with model,* #P < *0.05,* ##P < *0.01,* ###P < *0.005.*

and acacetin) in XPF have been reported to activate the cAMP signaling pathway of CHD and depression. Eugenol can reverse oxidative stress, inhibit of caspase-3 activity, and it has an anti-myocardial ischemia effect. Emodin opposes CUMS-induced depressive-like behavior in rats by upregulating the levels of hippocampal BDNF (Choudhary et al., 2006; Liu et al., 2017). Isorhamnetin has a positive effect on H/R-induced injury by reducing caspase-3 and attenuating oxidative stress in H9c2 cardiomyocytes (Zhao et al., 2018). Nobiletin and acacetin exerted antidepressant-like effects by increasing the level of 5-HT in the hippocampus (Yi et al., 2011). Isoliquiritigenin has been shown to have neuroprotective effects by increasing the level of cAMP in peripheral nerves (Shindo et al., 1992). Rosmarinic acid can regulate the expression of BDNF in the hippocampus (Makhathini et al., 2018), and inhibit angiotensin-converting enzyme activity (Ferreira et al., 2018).

Increasing evidence has shown a reciprocal causation relationship between CHD and depression. Regulating psychopathy can significantly improve the quality of life of patients with CHD and reduce the incidence of acute cardiovascular events (Kuhlmann et al., 2019). Recently, TCM has attracted increasing attention in treating cardiovascular and psychological diseases because of its holistic approach and satisfactory clinical efficacy. Through this study, we found that XPF could protect the myocardium and hippocampus in CUMS and ISO-induced CHD in depression rats by regulating the cAMP signal cascade. Furthermore, XPF can inhibit cell apoptosis, improve heart function, reduce neuropathy, improve nerve function, and exert an antidepressant and antimyocardial ischemia effect. These results preliminarily show the material basis and mechanism of XPF in the treatment of CHD with depression.

CONCLUSION

In this study, we proposed an integrative systems pharmacology strategy to illustrate the mechanism of XPF in treating CHD with depression by combining serum pharmacochemistry, network analysis, and experimental validation. First, we identified 51 ingredients in rat serum after oral administration of XPF, which was used for the construction and analysis of the component–target network between the targets of absorbed components in serum and CHD with depression. As a result, 10 components with higher degree centrality were determined to be the active ingredients of XPF, and 10 hub genes, including *ACE2*, *HTR1A*, *HTR2A*, *AKT1*, *PKIA*, *CREB1*, *BDNF*, *BCL2*, *BAX*, *CASP3*, and *cAMP* were determined as targets of XPF in treating CHD with depression. Furthermore, the hub targets (AngII, 5-HT, cAMP, PKA, CREB, BDNF, Bcl-2, Bax, Cyt-c, and caspase-3) predicted by network pharmacology analysis were validated. We confirmed the myocardial protective and neuroprotective effects of XPF in treating CHD with depression, which was associated with its activation of the cAMP signaling pathway and inhibition of myocardium and hippocampus apoptosis. In conclusion, these results indicate that the integrated pharmacology strategy provides an efficient approach for exploring the pharmacological mechanisms of TCM.

DATA AVAILABILITY STATEMENT

The raw data supporting the conclusions of this article will be made available by the authors, without undue reservation.

ETHICS STATEMENT

The animal study was reviewed and approved by and the guidelines of the National Institutes of Health. All animal experiments were approved by the Ethics Committee of Tianjin University of Traditional Chinese Medicine. Written informed consent was obtained from the owners for the participation of their animals in this study.

AUTHOR CONTRIBUTIONS

LZ is the first author and performed all the experiments and drafted the manuscript. YZ contributed toward study design and revised the manuscript. LP, FD, and JC helped the first author, prepared the materials of this paper. ZC, SZ, and MZ provided fund support. WD and XX contributed toward study design, experimental setup, results supervision, and manuscript correction.

FUNDING

This work was supported by National Natural Science Foundation of China (81774227); Natural Science Fund of Tianjin City (17JCZDJC34600); Technology program in key areas of Tianjin (20190101); Scientific research project of Tianjin Education Commission (2018KJ014).

ACKNOWLEDGMENTS

The authors would like to acknowledge Editage Language Services for providing language assistance and for proofreading the manuscript.

SUPPLEMENTARY MATERIAL

The Supplementary Material for this article can be found online at: https://www.frontiersin.org/articles/10.3389/fphar.2021.590602/full#supplementary-material.

REFERENCES

Aa, N., Guo, J. H., Cao, B., Sun, R. B., Ma, X. H., Chu, Y., et al. (2019). Compound danshen dripping pills normalize a reprogrammed metabolism of myocardial ischemia rats to interpret its time-dependent efficacy in clinic trials: a metabolomic study. *Metabolomics* 15, 128. doi:10.1007/s11306-019-1577-3

Abu, Z. E., Hussein, M., and Ali, H. (2018). Ascorbic acid protects male rat brain from oral potassium dichromate-induced oxdative DNA damage and apoptotic changes: the expression patterns of caspase-3, P 53, Bax, and Bcl-2 genes. *Environ. Sci. Pollut. Res. Int.* 25, 13056–13066. doi:10.1007/s11356-018-1546-9

Amare, A. T., Schubert, K. O., Klingler-Hoffmann, M., Cohen-Woods, S., and Baune, B. T. (2017). The genetic overlap between mood disorders and cardiometabolic diseases: a systematic review of genome wide and candidate gene studies. *Transl Psychiatry* 7, e1007. doi:10.1038/tp.2016.261

Amberger, J. S., and Hamosh, A. (2017). Searching online mendelian inheritance in man (OMIM): a knowledgebase of human genes and genetic phenotypes. *Curr. Protoc. Bioinformatics* 58, 1–121. doi:10.1002/cpbi.2712.12

Assimon, M. M., Brookhart, M. A., Fine, J. P., Heiss, G., Layton, J. B., and Flythe, J. E. (2018). A comparative study of carvedilol versus metoprolol Initiation and 1-year mortality among individuals receiving maintenance hemodialysis. *Am. J. Kidney Dis.* 72, 337–348. doi:10.1053/j.ajkd.2018.02.350

Bahar, M. A., Kamp, J., Borgsteede, S. D., Hak, E., and Wilffert, B. (2018). The impact of CYP2D6 mediated drug-drug interaction: a systematic review on a combination of metoprolol and paroxetine/fluoxetine. *Br. J. Clin. Pharmacol.* 84, 2704–2715. doi:10.1111/bcp.13741

Blais, C., Rochette, L., Ouellet, S., and Huynh, T. (2020). Complex evolution of epidemiology of vascular diseases, including increased disease burden: from 2000 to 2015. *Can. J. Cardiol.* 36, 740–746. doi:10.1016/j.cjca.2019.10.021

Carney, R. M., and Freedland, K. E. (2017). Depression and coronary heart disease. *Nat. Rev. Cardiol.* 14, 145–155. doi:10.1038/nrcardio.2016.181

Chen, B., Li, J., Xie, Y., Ming, X., Li, G., Wang, J., et al. (2019). Cang-ai volatile oil improves depressive-like behaviors and regulates DA and 5-HT metabolism in the brains of CUMS-induced rats. *J. Ethnopharmacol.* 244, 112088. doi:10.1016/j.jep.2019.112088

Chen, M., Men, L., Ou, L., Li, T., Li, M., Zhong, X., et al. (2018). Effectiveness and safety of modified 'Huoxue Shugan' formulas on coronary heart disease combined with depression: protocol for a systematic review. *BMJ Open* 8, e022868. doi:10.1136/bmjopen-2018-022868

Chen, X. Q., Chen, S. J., Liang, W. M., Wang, M., Li, C. F., Wang, S. S., et al. (2018). Saikosaponin A attenuates perimenopausal depression-like symptoms by chronic unpredictable mild stress. *Neurosci. Lett.* 662, 283–289. doi:10.1016/j.neulet.2017.09.046

Chen, X. Z., Cao, Z. Y., Liao, L. M., Liu, Z. Z., and Du, J. (2014). Application of serum pharmacology in evaluating the antitumor effect of Fuzheng Yiliu

Decoction from Chinese medicine. *Chin. J. Integr. Med.* 20, 450–455. doi:10.1007/s11655-013-1544-1

Choudhary, R., Mishra, K. P., and Subramanyam, C. (2006). Interrelations between oxidative stress and calcineurin in the attenuation of cardiac apoptosis by eugenol. *Mol. Cel. Biochem.* 283, 115–122. doi:10.1007/s11010-006-2386-3

de Heer, E. W., Palacios, J. E., Adèr, H. J., van Marwijk, H. W. J., Tylee, A., and van der Feltz-Cornelis, C. M. (2020). Chest pain, depression and anxiety in coronary heart disease: consequence or cause? A prospective clinical study in primary care. *J. Psychosom. Res.* 129, 109891. doi:10.1016/j.jpsychores.2019.109891

Dennis, G., Sherman, B. T., Hosack, D. A., Yang, J., Gao, W., Lane, H. C., et al. (2003). DAVID: database for annotation, visualization, and integrated discovery. *Genome Biol.* 4, P3. doi:10.1186/gb-2003-4-5-p3

Fang, J., Cai, C., Chai, Y., Zhou, J., Huang, Y., Gao, L., et al. (2019). Quantitative and systems pharmacology 4. Network-based analysis of drug pleiotropy on coronary artery disease. *Eur. J. Med. Chem.* 161, 192–204. doi:10.1016/j.ejmech.2018.10.020

Ferreira, L. G., Evora, P. R. B., Capellini, V. K., Albuquerque, A. A., Carvalho, M. T. M., Gomes, R. A. D. S., et al. (2018). Effect of rosmarinic acid on the arterial blood pressure in normotensive and hypertensive rats: role of ACE. *Phytomedicine* 38, 158–165. doi:10.1016/j.phymed.2017.02.006

Gfeller, D., Grosdidier, A., Wirth, M., Daina, A., Michielin, O., and Zoete, V. (2014). SwissTargetPrediction: a web server for target prediction of bioactive small molecules. *Nucleic Acids Res.* 42, W32–W38. doi:10.1093/nar/gku293

Gross, M., and Pinhasov, A. (2016b). Chronic mild stress in submissive mice: marked polydipsia and social avoidance without hedonic deficit in the sucrose preference test. *Behav. Brain Res.* 298, 25–34. doi:10.1016/j.bbr.2015.10.049

Guo, J., Zhang, F., Gao, J., Guan, X., Liu, B., Wang, X., et al. (2020). Proteomics-based screening of the target proteins associated with antidepressant-like effect and mechanism of Saikosaponin A. *J. Cel. Mol. Med.* 24, 174–188. doi:10.1111/jcmm.14695

Hart, T., and Xie, L. (2016). Providing data science support for systems pharmacology and its implications to drug discovery. *Expert Opin. Drug Discov.* 11, 241–256. doi:10.1517/17460441.2016.1135126

Hou, S. S., Du, W. X., Li, X. X., Zhang, Y., et al. (2017). Professor Du Wuxun's experience in treating climacteric arrhythmia. *J. Sichuan Traditional Chin. Med.* 35, 133–134.

Hu, Y., Dong, X., Zhang, T., Ma, H., Yang, W., Wang, Y., et al. (2020). Kai-Xin-San suppresses matrix metalloproteinases and myocardial apoptosis in rats with myocardial infarction and depression. *Mol. Med. Rep.* 21, 508–516. doi:10.3892/mmr.2019.10807

Huang, H., Hong, Q., Tan, H. L., Xiao, C. R., and Gao, Y. (2016). Ferulic acid prevents LPS-induced up-regulation of PDE4B and stimulates the cAMP/CREB signaling pathway in PC12 cells. *Acta Pharmacol. Sin.* 37, 1543–1554. doi:10.1038/aps.2016.88

Hwang, S. L., Lin, J. A., Shih, P. H., Yeh, C. T., and Yen, G. C. (2012). Pro-cellular survival and neuroprotection of citrus flavonoid: the actions of hesperetin in PC12 cells. *Food Funct.* 3, 1082–1090. doi:10.1039/c2fo30100h

Inserte, J., Garcia-Dorado, D., Ruiz-Meana, M., Agulló, L., Pina, P., and Soler-Soler, J. (2004). Ischemic preconditioning attenuates calpain-mediated degradation of structural proteins through a protein kinase A-dependent mechanism. *Cardiovasc. Res.* 64, 105–114. doi:10.1016/j.cardiores.2004.06.001

Jiang, H., Zhang, X., Wang, Y., Zhang, H., Li, J., Yang, X., et al. (2017). Mechanisms underlying the antidepressant response of acupuncture via PKA/CREB signaling pathway. *Neural Plast.* 2017, 4135164. doi:10.1155/2017/4135164

Jiao, H., Yan, Z., Ma, Q., Li, X., Jiang, Y., Liu, Y., et al. (2019). Influence of Xiaoyaosan on depressive-like behaviors in chronic stress-depressed rats through regulating tryptophan metabolism in hippocampus. *Neuropsychiatr. Dis. Treat.* 15, 21–31. doi:10.2147/NDT.S185295

Jin, H., Chen, Y., Wang, B., Zhu, Y., Chen, L., Han, X., et al. (2018). Association between brain-derived neurotrophic factor and von Willebrand factor levels in patients with stable coronary artery disease. *BMC Cardiovasc. Disord.* 18, 23. doi:10.1186/s12872-018-0762-z

Kaess, B. M., Preis, S. R., Lieb, W., Beiser, A. S., Yang, Q., Chen, T. C., et al. (2015). Circulating brain-derived neurotrophic factor concentrations and the risk of cardiovascular disease in the community. *J. Am. Heart Assoc.* 4, e001544. doi:10.1161/JAHA.114.001544

Klempin, F., Mosienko, V., Matthes, S., Villela, D. C., Todiras, M., Penninger, J. M., et al. (2018). Depletion of angiotensin-converting enzyme 2 reduces brain serotonin and impairs the running-induced neurogenic response. *Cell Mol Life Sci* 75, 3625–3634. doi:10.1007/s00018-018-2815-y

Kuhlmann, S. L., Arolt, V., Haverkamp, W., Martus, P., Ströhle, A., Waltenberger, J., et al. (2019). Prevalence, 12-month prognosis, and clinical management need of depression in coronary heart disease patients: a prospective cohort study. *Psychother. Psychosom.* 88, 300–311. doi:10.1159/000501502

Lee, H. W., Ahmad, M., Wang, H. W., and Leenen, F. H. (2017). Effects of exercise training on brain-derived neurotrophic factor in skeletal muscle and heart of rats post myocardial infarction. *Exp. Physiol.* 102, 314–328. doi:10.1113/EP086049

Lee, S. J., Koh, S., Kim, B. O., Kim, B., and Kim, C. (2018). Effect of type D personality on short-term cardiac rehabilitation in patients with coronary artery disease. *Ann. Rehabil. Med.* 42, 748–757. doi:10.5535/arm.2018.42.5.748

Li, F., Zhang, Y. B., Wei, X., Song, C. H., Qiao, M. Q., and Zhang, H. Y. (2016). Metabolic profiling of Shu-Yu capsule in rat serum based on metabolic fingerprinting analysis using HPLC-ESI-MSn. *Mol. Med. Rep.* 13, 4191–4204. doi:10.3892/mmr.2016.5082

Li, Y., Ge, F., and Wang, S. (2020). Four genes predict the survival of osteosarcoma patients based on TARGET database. *J. Bioenerg. Biomembr.* 52, 291–299. doi:10.1007/s10863-020-09836-6

Li, Y. H., Yu, C. Y., Li, X. X., Zhang, P., Tang, J., Yang, Q., et al. (2018). Therapeutic target database update 2018: enriched resource for facilitating bench-to-clinic research of targeted therapeutics. *Nucleic Acids Res.* 46, D1121–D1127. doi:10.1093/nar/gkx1076

Li, C., Ma, R., Zhang, X., Ma, J., Wang, X., He, J., et al. (2020). Risk of coronary heart disease in the rural population in Xinjiang: a nested case-control study in China. *PLoS One* 15, e0229598. doi:10.1371/journal.pone.0229598

Liu, R., Heiss, E. H., Waltenberger, B., Blažević, T., Schachner, D., Jiang, B., et al. (2018). Constituents of mediterranean spices counteracting vascular smooth muscle cell proliferation: Identification and characterization of rosmarinic acid methyl ester as a novel inhibitor. *Mol. Nutr. Food Res.* 62, e1700860. doi:10.1002/mnfr.201700860

Liu, Y., Gao, L., Zhao, X., Guo, S., Liu, Y., Li, R., et al. (2018). Saikosaponin a protects from pressure overload-induced cardiac fibrosis via inhibiting fibroblast activation or endothelial cell endMT. *Int. J. Biol. Sci.* 14, 1923–1934. doi:10.7150/ijbs.27022

Liu, Y. M., Hu, C. Y., Shen, J. D., Wu, S. H., Li, Y. C., and Yi, L. T. (2017). Elevation of synaptic protein is associated with the antidepressant-like effects of ferulic acid in a chronic model of depression. *Physiol. Behav.* 169, 184–188. doi:10.1016/j.physbeh.2016.12.003

Liu, Z., Qi, Y., Cheng, Z., Zhu, X., Fan, C., and Yu, S. Y. (2016). The effects of ginsenoside Rg1 on chronic stress induced depression-like behaviors, BDNF expression and the phosphorylation of PKA and CREB in rats. *Neuroscience* 322, 358–369. doi:10.1016/j.neuroscience.2016.02.050

Louiset, E., Duparc, C., Lenglet, S., Gomez-Sanchez, C. E., and Lefebvre, H. (2017). Role of cAMP/PKA pathway and T-type calcium channels in the mechanism of action of serotonin in human adrenocortical cells. *Mol. Cel. Endocrinol.* 441, 99–107. doi:10.1016/j.mce.2016.10.008

Magaard, J. L., Löwe, B., Brütt, A. L., and Kohlmann, S. (2018). Illness beliefs about depression among patients seeking depression care and patients seeking cardiac care: an exploratory analysis using a mixed method design. *BMC Psychiatry* 18, 366. doi:10.1186/s11888-018-1936-z

Makhathini, K. B., Mabandla, M. V., and Daniels, W. M. U. (2018). Rosmarinic acid reverses the deleterious effects of repetitive stress and tat protein. *Behav. Brain Res.* 353, 203–209. doi:10.1016/j.bbr.2018.07.010

Mao, Shuai., and Zhang, Minzhou. (2014). *The effect of Danlou tablets and its components on ventricular remodeling after acute coronary syndrome*. Guangzhou; Guangzhou University of Traditional Chinese Medicine.

Meng, P., and Wang, Y.. (2013). The Effect of Baishile capsule on hippocampus nerveregeneration of Chronic Unpredicted Mild Stressdepression model rats by signal pathway of cAMP-CREB-BDNF. *Hunan Univ. traditional Chin. Med.* 8, 35558–35572. doi:10.18632/oncotarget.16009

Mi, L., Chen, Y., Zheng, X., Li, Y., Zhang, Q., Mo, D., et al. (2015). MicroRNA-139-5p suppresses 3T3-L1 preadipocyte differentiation through notch and IRS1/PI3K/akt insulin signaling pathways. *J. Cel. Biochem.* 116, 1195–1204. doi:10.1002/jcb.25065

Mo, F., Tang, Y., Du, P., Shen, Z., Yang, J., Cai, M., et al. (2020). GPR39 protects against corticosterone-induced neuronal injury in hippocampal cells through the CREB-BDNF signaling pathway. *J. Affect Disord.* 272, 474–484. doi:10.1016/j.jad.2020.03.137

Mozaffarian, D., Mozaffarian, D., Benjamin, E. J., Go, A. S., Arnett, D. K., Blaha, M. J., et al. (2016). Executive summary: heart disease and stroke statistics--2016 update: a Report from the American Heart Association. *Circulation* 133, 447–454. doi:10.1161/CIR.0000000000000366

Otasek, D., Morris, J. H., Bouças, J., Pico, A. R., and Demchak, B. (2019). Cytoscape automation: empowering workflow-based network analysis. *Genome Biol.* 20, 185. doi:10.1186/s13059-019-1758-4

Park, S. Y., Park, J. H., Kim, H. S., Lee, C. Y., Lee, H. J., Kang, K. S., et al. (2018). Systems-level mechanisms of action of Panax ginseng: a network pharmacological approach. *J. Ginseng Res.* 42, 98–106. doi:10.1016/j.jgr.2017.09.001

Podlesnikar, T., Pizarro, G., Fernández-Jiménez, R., Montero-Cabezas, J. M., Sánchez-González, J., Bucciarelli-Ducci, C., et al. (2019). Effect of early metoprolol during ST-Segment elevation myocardial infarction on left ventricular strain: feature-tracking cardiovascular magnetic resonance substudy from the METOCARD-CNIC trial. *JACC Cardiovasc. Imaging* 12, 1188–1198. doi:10.1016/j.jcmg.2018.07.019

Qin, W., Zhang, L., Li, Z., Xiao, D., Zhang, Y., Yang, H., et al. (2020). Metoprolol protects against myocardial infarction by inhibiting miR-1 expression in rats. *J. Pharm. Pharmacol.* 72, 76–83. doi:10.1111/jphp.13192

Ru, J., Li, P., Wang, J., Zhou, W., Li, B., Huang, C., et al. (2014). TCMSP: a database of systems pharmacology for drug discovery from herbal medicines. *J. Cheminform* 6, 13. doi:10.1186/1758-2946-6-13

Sandrini, L., Castiglioni, L., Amadio, P., Werba, J. P., Eligini, S., Fiorelli, S., et al. (2020). Impact of BDNF Val66Met polymorphism on myocardial infarction: exploring the macrophage phenotype. *Cells* 9, 1084. doi:10.3390/cells9051084

Shindo, H., Tawata, M., Aida, K., and Onaya, T. (1992). The role of cyclic adenosine 3',5'-monophosphate and polyol metabolism in diabetic neuropathy. *J. Clin. Endocrinol. Metab.* 74, 393–398. doi:10.1210/jcem.74.2.1370506

Su, S. F., Chang, M. Y., and He, C. P. (2018). Social support, unstable angina, and stroke as predictors of depression in patients with coronary heart disease. *J. Cardiovasc. Nurs.* 33, 179–186. doi:10.1097/JCN.0000000000000419

Sun, W., Jin, Y., Wang, C., Zhao, S., Wang, X., Luo, M., et al. (2020). Stereoselective separation of isomeric sertraline with analytical countercurrent chromatography. *J. Chromatogr. A.* 1617, 460834. doi:10.1016/j.chroma.2019.460834

Szklarczyk, D., Morris, J. H., Cook, H., Kuhn, M., Wyder, S., Simonovic, M., et al. (2017). The STRING database in 2017: quality-controlled protein-protein association networks, made broadly accessible. *Nucleic Acids Res.* 45, D362–D368. doi:10.1093/nar/gkw937

Tang, X. H., Zhang, G. F., Xu, N., Duan, G. F., Jia, M., Liu, R., et al. (2020). Extrasynaptic CaMKIIα is involved in the antidepressant effects of ketamine by downregulating GluN2B receptors in an LPS-induced depression model. *J. Neuroinflammation* 17, 181. doi:10.1186/s11974-020-01843-z

Tang, Z., Wei, J., Yu, Y., Zhang, J., Liu, L., Tang, W., et al. (2016). γ-Secretase inhibitor reverts the Notch signaling attenuation of osteogenic differentiation in aged bone marrow mesenchymal stem cells. *Cell Biol. Int.* 40, 439–447. doi:10.1002/cbin.10583

Van Rymenant, E., Grootaert, C., Beerens, K., Needs, P. W., Kroon, P. A., Kerimi, A., et al. (2017). Vasorelaxant activity of twenty-one physiologically relevant (poly)phenolic metabolites on isolated mouse arteries. *Food Funct.* 8, 4331–4335. doi:10.1039/c7fo01273j

Wenxiu, H., Zhijie, W., Ruili, D., Yujin, G., Hailiang, Z., Chunmei, G., et al. (2020). Angiotensin-II and angiotensin-(1-7) imbalance affects comorbidity of depression and coronary heart disease. *Peptides* 131, 170353. doi:10.1016/j.peptides.2020.170353

Wang, C., Guo, J., and Guo, R. (2017). Effect of XingPiJieYu decoction on spatial learning and memory and cAMP-PKA-CREB-BDNF pathway in rat model of depression through chronic unpredictable stress. *BMC Complement. Altern. Med.* 17, 73. doi:10.1186/s11906-016-1543-9

Wang, J. Q., and Mao, L. (2019). The ERK pathway: molecular mechanisms and treatment of depression. *Mol. Neurobiol.* 56, 6197–6205. doi:10.1007/s11035-019-1524-3

Wang, N., Ma, J., Liu, J., Wang, J., Liu, C., Wang, H., et al. (2019). Histamine H3 receptor antagonist enhances neurogenesis and improves chronic cerebral hypoperfusion-induced cognitive impairments. *Front. Pharmacol.* 10, 1583. doi:10.3389/fphar.2019.01583

Wang, Z., Liang, L., Yin, Z., and Lin, J. (2016). Improving chemical similarity ensemble approach in target prediction. *J. Cheminform* 8, 20. doi:10.1186/s13321-016-0130-x

Wei, Y., Chen, J., Hu, Y., Lu, W., Zhang, X., Wang, R., et al. (2018). Rosmarinic acid mitigates lipopolysaccharide-induced neuroinflammatory responses through the inhibition of TLR4 and CD14 expression and NF-κB and NLRP3 inflammasome activation. *Inflammation* 41, 732–740. doi:10.1007/s10753-017-0728-9

Wishart, D. S., Feunang, Y. D., Guo, A. C., Lo, E. J., Marcu, A., Grant, J. R., et al. (2018). DrugBank 5.0: a major update to the DrugBank database for 2018. *Nucleic Acids Res.* 46, D1074–D1082. doi:10.1093/nar/gkx1037

Xu, F., Ren, L., Song, M., Shao, B., Han, Y., Cao, Z., et al. (2018). Fas- and mitochondria-mediated signaling pathway involved in osteoblast apoptosis induced by AlCl3. *Biol. Trace Elem. Res.* 184, 173–185. doi:10.1007/s11011-017-1176-y

Xu, S. Y., Dian, R. L., and Chen, X. (1997). *Methodology of pharmacological experiment*. Bejing: People's Medical Publishing House..

Xue, Y.-j., Xie, Y., Zhao, G.-l., Zhou, B.-d., Li, K., Li, S.-y., et al. (2019). Oral Chinese herbal medicine for depressive disorder in patients after percutaneous coronary intervention: a systematic review and meta-analysis. *Chin. J. Integr. Med.* 26, 617. doi:10.1007/s11655-019-2702-x

Yang, D., Wu, W., Gan, G., Wang, D., Gong, J., Fang, K., et al. (2020). (-)-Syringaresinol-4-O-β-D-glucopyranoside from Cortex Albizziae inhibits corticosterone-induced PC12 cell apoptosis and relieves the associated dysfunction. *Food Chem. Toxicol.* 141, 111394. doi:10.1016/j.fct.2020.111394

Ye, Y. L., Zhong, K., Liu, D. D., Xu, J., Pan, B. B., Li, X., et al. (2017). Huanglian-Jie-Du-Tang extract ameliorates depression-like behaviors through BDNF-TrkB-CREB pathway in rats with chronic unpredictable stress. *Evid. Based Complement. Alternat Med.* 2017, 7903918. doi:10.1155/2017/7903918

Yeung, W. F., Chung, K. F., Ng, K. Y., Yu, Y. M., Ziea, E. T., and Ng, B. F. (2014). A systematic review on the efficacy, safety and types of Chinese herbal medicine for depression. *J. Psychiatr. Res.* 57, 165–175. doi:10.1016/j.jpsychires.2014.05.016

Yi, L. T., Xu, H. L., Feng, J., Zhan, X., Zhou, L. P., and Cui, C. C. (2011). Involvement of monoaminergic systems in the antidepressant-like effect of nobiletin. *Physiol. Behav.* 102, 1–6. doi:10.1016/j.physbeh.2010.10.008

Yuan, H., Ma, Q., Cui, H., Liu, G., Zhao, X., Li, W., et al. (2017). How can synergism of traditional medicines benefit from network pharmacology?. *Molecules* 22. doi:10.3390/molecules22071135

Zhang, L., Xu, C. Q., Hong, Y., Zhang, J. L., Liu, Y., Zhao, M., et al. (2010). Propranolol regulates cardiac transient outward potassium channel in rat myocardium via cAMP/PKA after short-term but not after long-term ischemia. *Naunyn Schmiedebergs Arch. Pharmacol.* 382, 63–71. doi:10.1007/s00210-010-0520-y

Zhang, M., Liu, W., Zhou, Y., Li, Y., Qin, Y., and Xu, Y. (2018). Neurodevelopmental toxicity induced by maternal PM2.5 exposure and protective effects of quercetin and Vitamin C. *Chemosphere* 213, 182–196. doi:10.1016/j.chemosphere.2018.09.009

Zhang, R., Guo, L., Ji, Z., Li, X., Zhang, C., Ma, Z., et al. (2018). Radix scutellariae attenuates CUMS-Induced depressive-like behavior by promoting neurogenesis via cAMP/PKA pathway. *Neurochem. Res.* 43, 2111–2120. doi:10.1007/s11064-018-2635-3

Zhang, R., Zhu, X., Bai, H., and Ning, K. (2019). Network pharmacology databases for traditional Chinese medicine: review and assessment. *Front. Pharmacol.* 10, 123. doi:10.3389/fphar.2019.00123

Zhang, W., Huai, Y., Miao, Z., Qian, A., and Wang, Y. (2019). Systems pharmacology for investigation of the mechanisms of action of traditional Chinese medicine in drug discovery. *Front. Pharmacol.* 10, 743. doi:10.3389/fphar.2019.00743

Zhao, T. T., Yang, T. L., Gong, L., and Wu, P. (2018). Isorhamnetin protects against hypoxia/reoxygenation-induced injure by attenuating apoptosis and oxidative stress in H9c2 cardiomyocytes. *Gene* 666, 92–99. doi:10.1016/j.gene.2018.05.009

Zhou, M. H., Yang, G., Jiao, S., Hu, C. L., and Mei, Y. A. (2012). Cholesterol enhances neuron susceptibility to apoptotic stimuli via cAMP/PKA/CREB-dependent up-regulation of Kv2.1. *J. Neurochem.* 120, 502–514. doi:10.1111/j.1471-4159.2011.07593.x

Conflict of Interest: The authors declare that the research was conducted in the absence of any commercial or financial relationships that could be construed as a potential conflict of

Copyright © 2021 Zhang, Zhang, Zhu, Pei, Deng, Chen, Zhang, Cong, Du and Xiao. This is an open-access article distributed under the terms of the Creative Commons Attribution License (CC BY). The use, distribution or reproduction in other forums is permitted, provided the original author(s) and the copyright owner(s) are credited and that the original publication in this journal is cited, in accordance with accepted academic practice. No use, distribution or reproduction is permitted which does not comply with these terms.

frontiers in Pharmacology

ORIGINAL RESEARCH
published: 15 April 2021
doi: 10.3389/fphar.2021.646489

The Treatment of Rhodiola Mimics Exercise to Resist High-Fat Diet-Induced Muscle Dysfunction via Sirtuin1-Dependent Mechanisms

Baiyang You[1,2], Yaoshan Dun[1,2,3], Siqian Fu[1], Dake Qi[4], Wenliang Zhang[1], Yuan Liu[1], Ling Qiu[1], Murong Xie[1] and Suixin Liu[1,2]**

[1]Division of Cardiac Rehabilitation, Department of Physical Medicine and Rehabilitation, Xiangya Hospital of Central South University, Changsha, China, [2]National Clinical Research Center for Geriatric Disorders, Xiangya Hospital of Central South University, Changsha, China, [3]Division of Preventive Cardiology, Department of Cardiovascular Medicine, Mayo Clinic, Rochester, MN, United States, [4]College of Pharmacy, University of Manitoba, Winnipeg, MB, Canada

Muscle dysfunction is a complication of high-fat diet (HFD)-induced obesity that could be prevented by exercise, but patients did not get enough therapeutic efficacy from exercise due to multiple reasons. To explore alternative or supplementary approaches to prevent or treat muscle dysfunction in individuals with obesity, we investigated the effects of Rhodiola on muscle dysfunction as exercise pills. SIRT1 might suppress atrogenes expression and improve mitochondrial quality control, which could be a therapeutic target stimulated by exercise and Rhodiola, but further mechanisms remain unclear. We verified the lipid metabolism disorders and skeletal muscle dysfunction in HFD feeding mice. Moreover, exercise and Rhodiola were used to intervene mice with a HFD. Our results showed that exercise and Rhodiola prevented muscle atrophy and dysfunction in obese mice and activating the SIRT1 pathway, while atrogenes were suppressed and mitochondrial quality control was improved. EX-527, SIRT1 inhibitor, was used to validate the essential role of SIRT1 in salidroside benefit. Results of cell culture experiment showed that salidroside alleviated high palmitate-induced atrophy and mitochondrial quality control impairments, but these improvements of salidroside were inhibited by EX-527 in C2C12 myotubes. Overall, Rhodiola mimics exercise that activates SIRT1 signaling leading to improvement of HFD-induced muscle dysfunction.

Keywords: salidroside, SIRT1, atrogenes, mitochondrion, rhodiola

OPEN ACCESS

Edited by:
Takashi Sato,
Tokyo University of Pharmacy and Life Sciences, Japan

Reviewed by:
Suresh Kumar Mohankumar,
Swansea University Medical School, United Kingdom
Giuseppe Annunziata,
University of Naples Federico II, Italy

***Correspondence:**
Suixin Liu
liusuixin@csu.edu.cn
Yaoshan Dun
dunyaoshan@csu.edu.cn

Specialty section:
This article was submitted to Ethnopharmacology, a section of the journal Frontiers in Pharmacology

Received: *27 December 2020*
Accepted: *22 March 2021*
Published: *15 April 2021*

Citation:
You B, Dun Y, Fu S, Qi D, Zhang W, Liu Y, Qiu L, Xie M and Liu S (2021) The Treatment of Rhodiola Mimics Exercise to Resist High-Fat Diet-Induced Muscle Dysfunction via Sirtuin1-Dependent Mechanisms. Front. Pharmacol. 12:646489. doi: 10.3389/fphar.2021.646489

INTRODUCTION

Skeletal muscle dysfunction (or muscle wasting) characterized with a reduction of myofibrillar, and mitochondrial dysfunction has been reported as an important complication of high-fat diet (HFD)-induced obesity (Perry et al., 2016). However, compared to its adverse impacts on type 2 diabetes, cardiovascular, or osteoarticular diseases, muscle dysfunction has received less attention. Thus, investigating the mechanisms and potential therapy against HFD-induced muscle dysfunction will have important clinical significance. Though the underlying mechanisms are not thoroughly understood, several factors are well known, for example, the oversupplied energy and impaired lipid metabolism damage the mitochondrial which is essential in maintain muscle quality (Jorgensen et al., 2015).

A major therapeutic strategy against muscle dysfunction is exercise that effectively increases muscle mass, strength, and physical performance (Pillard et al., 2011; Dun et al., 2019a; Dun et al., 2019b). Although the molecular mechanisms of exercise in regulating HFD-induced muscle dysfunction are largely unknown, previous evidence indicated that exercise could decrease transcription of atrogenes, such as muscle-specific RING finger protein 1 (MuRF1) and atrogin1, both of which inhibit protein degradation and facilitate myofibrillar synthesis. Exercise also promotes mitochondrial mass and functions (Sandri et al., 2006). Mitochondrial quality control (MQC), including mitochondrial biogenesis, mitophagy, and fusion/fission, has been used as an important evaluation for mitochondrial function. Our previous studies indicated that exercise activates MQC in skeletal and myocardial muscle (Xie et al., 2019; Jiang et al., 2021). However, exercise lacks a long-term therapeutic efficacy for muscle dysfunction due to poor compliance or disabilities resulted from skeleton-muscle system (Conraads et al., 2012). Therefore, alternative or supplementary approaches to prevent muscle dysfunction in individuals with overweight need to be explored.

Sirtuin 1 (SIRT1), a sirtuin family protein, displays a nicotinamide adenine dinucleotide (NAD) protein deacetylase activity (Milne and Denu, 2008). Thus, it can be activated by changes of NAD+ levels during exercise. SIRT1 is associated with beneficial effects of exercise through resisting protein degradation and improving the quality of mitochondria (Tonkin et al., 2012). Overexpression of SIRT1 reduces muscle dysfunction by inhibiting key atrogenes and activating peroxisome proliferator-activated receptor gamma coactivator 1-α (PGC-1α) in skeletal muscle (Lee and Goldberg, 2013). SIRT1 also modulates transcription factors, such as FOXO3/PINK1/Parkin and MFN1/DRP1 that participate in the regulation of mitophagy and mitochondrial dynamics (Valero, 2014; Lei et al., 2020). Thus, SIRT1 might be a key therapeutic target for muscle atrophy or dysfunction stimulated by exercise.

Rhodiola is a natural plant which has been widely used to treat altitude sickness for hundreds of years (Kelly, 2001). Salidroside, an active ingredient from *Rhodiola* roots, activates the SIRT1 pathway to ameliorate diabetic nephropathy and hypoxia-induced neurodegeneration in mice via promoting mitochondrial biogenesis (Barhwal et al., 2015; Xue et al., 2019). More recently, salidroside was also found to improve denervation-induced muscle proteolysis and muscle atrophy (Wu et al., 2019). Our previous study also indicated that *Rhodiola chrysanthemifolia subsp. sacra (Raym.-Hamet) H.Ohba* (*R. sacra*) supplementary and exercise activated MQC of skeletal muscle, which contributes to the enhancement of exercise capacity and facilitates the muscle ability to resist fatigue in healthy mice (Dun et al., 2017). However, the effects of *R. sacra* on HFD-induced mitochondrial dysfunction and muscle atrophy remain unknown. Thus, in the present study, we explored the role of SIRT1 signaling pathway in mediating muscle dysfunction and compared the potential therapeutic effects of *R. sacra* and exercise.

MATERIALS AND METHODS

Animals

Male C57BL/6J mice (8 weeks old) were purchased from the Laboratory Animal Centre, Xiangya Medical School (Changsha, Hunan, China). The mice were housed in temperature-controlled (22°C ± 2°C) quarters with a 12:12 hour light-dark cycle and free access to water and food. All animal procedures were in accordance with the guidelines for the use of live animals of National Institute of Health and were approved by the Medicine Animal Welfare Committee of Xiangya Medical School, Central South University (Changsha, China) (approval ID: SYXK 2015-0017).

Groups

After one-week feeding adaptation, mice were randomly divided into four groups (n = 16 for each): normal chow (NC), high fat diet (HFD), HFD + *R. sacra* (HFD + RS) and HFD + exercise (HFD+EX). The HFD contains 45% of fat. The mice in the HFD + EX group were trained for exercise as described previously (Dun et al., 2017). In the HFD+RS group, mice were given 50 mg/ml of *R. sacra* per 500 mg/kg weight (Tibet Rhodiola Pharmaceutical Holding Company, Tibet, China) by gavage (0.1 ml/10 g weight) daily between 9 to 10 a.m. as previously described (Dun et al., 2017). The rest groups obtained normal saline by gavage at a dose of 0.1 ml per 10 g weight. Exercise, *R. sacra* and normal saline were administered together with HFD for 8 consecutive weeks. Body weights were weekly monitored during the whole experiment. An additional *R. sacra* treatment to the HFD mice didn't cause any observable change in food intake pattern or gastrointestinal reaction.

After 8 weeks, each group was further divided into two subgroups with or without exhaustive exercise (n = 8). The mice in the EE subgroups further underwent an inverted screen test and load swimming (5% body weight) session as previously described (Dun et al., 2017). After the experiments, all mice were anesthetized via an intraperitoneal injection of 1% pentobarbital sodium (150 mg/kg) and then sacrificed via exsanguination. Blood samples were collected from the inferior vena cava. Gastrocnemius muscle and visceral fat including mesenteric, epididymal, and perirenal fat tissue were dissected and weighted eventually. The protocol has been described in **Figure 1**.

R. Sacra

The highly pure extract from the root of *Rhodiola chrysanthemifolia subsp. sacra (Raym.-Hamet) H.Ohba* (*R. sacra*) was provided by the Tibet Rhodiola Pharmaceutical Holding Company. Root of *R. sacra* was decocted with double distilled water twice, first time for 1.5 hours and second time for 1 hour, then collect the decoction after filtration. The filtrated liquor was concentrated to the relative density 1.25–1.30 (detected in 40°C) and prepared to powder by spray-drying. HPLC-MS analysis revealed that the main effective components are salidroside (C14H20O7, 2.62%) and flavone (C27H30O16, 3.27%) (**Supplementary Figure S1** and

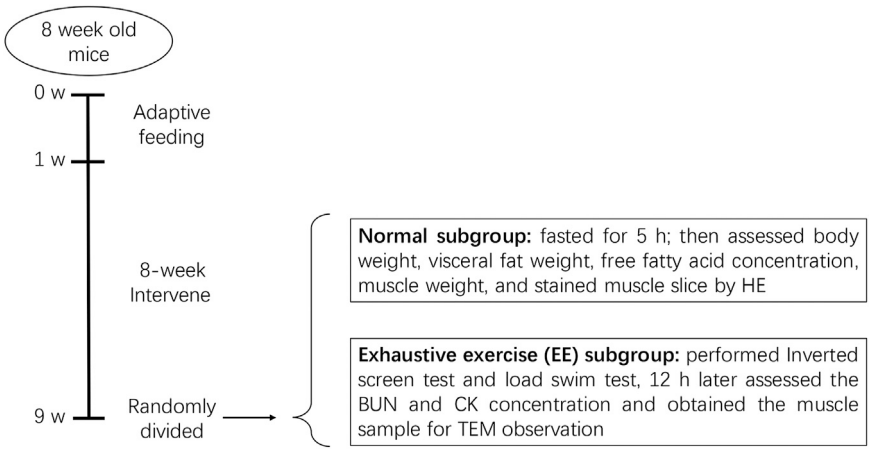

FIGURE 1 | Diagram of animal experiments. After a 1 week adaptive feeding, mice were randomly divided into four groups: normal chow (NC), high-fat diet (HFD), HFD + *R. sacra* (HFD + RS) and HFD + exercise (HFD+EX). 8 weeks later, mice in each group were randomly divided into two subgroups: normal subgroup and exhaustive exercise (EE) subgroup, the subsequent experiments were performed as the diagram showed.

Supplementary Table S1) and the exact preparation complied with The Chinese Pharmacopeia 2015 (inspection report number C1051612067). The extract powder was dissolved in distilled water (50 mg/ml) and it was administered to mice by gavage at a liquid/ body weight ratio of 0.1 ml/10 g for ten consecutive weeks (Every morning between 9 a.m. and 10 a. m.).

Exercise Training

The mice in the HFD + EX group were subjected to a moderate intensity swim training as previously described (Dun et al., 2017). Briefly, the mice were placed in a Morris water maze pool (60 cm high and 120 cm in diameter) (XR-XM101-R, ZSdichuang, Beijing, China) for a swimming training from 10 to 60 min. Swimming exercise was performed between 9 a.m. to 2 p.m. and the mice exhibited minimal variations in aerobic capacity.

Serum Free Fatty Acid

Mouse blood samples were collected and then assayed for serum free fatty acid according to the manufacturer's instructions (A042, Nanjing Jiancheng Bioengineering Institute, China). Free fatty acid and coenzyme A (CoA) reaction and produce acetyl-CoA. Then, acetyl-CoA produce H2O2 with the acetyl CoA oxidase. We used peroxidase to make H_2O_2 colorized and quantify free fatty acid indirectly.

Cross-Sectional Area of Muscle Fibers

Sliced muscle was stained by hematoxylin and eosin. Then, use the image analysis software Image J to measure area of each muscle fiber. Eventually, we statistically analyze the difference among groups.

Inverted Screen Test

Mice were placed on the center of an invertible 40 × 40 cm wire screen with a padded surface. After gently inverting the screen, the time for hanging on and the limb strength was recorded.

Exhaustive Exercise (EE) Program

The mice in EE subgroup (n = 8) performed a forced weight-loaded swimming session. The load composed of a lead sheath (0.8 mm thick, 0.5 cm wide) which is equal to 5% of each mouse body weight. The mice were enforced to swim till exhaustion, defined as the failure to rise the surface of water to breathe for 7 s. The swimming time was recorded and regarded as exercise capacity or muscular endurance.

Transmission Electron Microscope (TEM)

The muscle tissues were resized to 1 × 1 × 3 mm^3 and then fixed by 2.5% Glutaraldehyde and 1% osmic acid. After washed by 0.1 mol/L phosphate buffer, the tissue was dehydrated with acetone at a gradient concentration. Then embedding and solidify the tissue in 37°C for 12 hours and 60°C for 24 hours. After sliced to 50–100 nm and eventually they were examined by a transmission electron microscope (Tecnai G2 Spirit, FEI, United States) (Dun et al., 2017).

Creatine Kinase (CK), and Blood Urea Nitrogen (BUN)

Blood samples were also collected from the EE subgroup 12 h after EE program. The CK concentration was determined via a colorimetric kit according to the manufacturer's instructions (A032-1, Nanjing Jiancheng Bioengineering Institute, Nanjing, China). And the BUN was determined by a urease methods kit (C013-2, Nanjing Jiancheng Bioengineering Institute, Nanjing, China). The urea produced ammonia when exposed to urease, and ammonia could be colorized in the alkaline environment.

Western Blot

Muscle tissues or cells were lysed in radioimmunoprecipitation assay (RIPA) buffer (Beyotime) containing 1 mmol/L phenylmethanesulfonyl fluoride (PMSF; Beyotime) on ice to extract proteins. After SDS-PAGE, the proteins were detected

(Dun et al., 2017) and treated with primary antibodies against SIRT1, myosin heavy chain II (MyHC II), MuRF1, atrogin1, PGC1α, Microtubule-associated proteins 1A/1B light chain 3B (LC3), PTEN-induced kinase 1(PINK1), mitofusin-1 (MFN1), dynamin-related protein 1 (DRP1), citrate synthase (CS), and Glyceraldehyde 3-phosphate dehydrogenase (GAPDH) (Proteintech, Rosemont, IL, USA), respectively. Following HRP-labeled goat anti-rabbit IgG or goat anti-mice IgG (Proteintech), the bands were analyzed using a gel documentation system (Bio-Rad, Hercules, CA, United States).

Adenosine Triphosphate (ATP) Content

The ATP content in muscle tissues and lysed cells were determined via phosphomolybdic acid colorimetric method according to the manufacturer's instructions (A095-1-1, Nanjing Jiancheng Bioengineering Institute, Nanjing, China).

Gene Expression Analysis

Total DNA was isolated from gastrocnemius using a DNeasy Kit (Qiagen). MtCO3 oligos and succinate dehydrogenase complex subunit A (SDHA) were analyzed to evaluate the quantification of mitochondrial and nuclear genomes. The primer sequences for the specific target genes are listed in the following **Table 1**.

Cell Culture

C2C12 mouse myoblasts (Cobioer Biotechnology Ltd, Nanjing, China) were cultured in Dulbecco Modified Eagle Medium (DMEM) containing 10% fetal bovine serum and penicillin/streptomycin (5000U/5000 μg/ml; Gibco, Grand Island, NY, USA). Cells with a 75% confluence were incubated with differentiation media (DMEM containing 2% horse serum, Gibco) for 5 days. Our preliminary data suggested that the concentrations of salidroside (UPLC ≥98%, Sinopharm Chemical Reagent, Shanghai, China) above 50 μg/ml will induce cell death. Thus, our current study only used a concentration of salidroside less than 50 μg/ml to treat differentiated myotubes together with 0.75 mmol/L of palmitate for 24 hours, with or without pretreatment of 10 μmol/L EX-527 (SIRT1 inhibitor, 6-Chloro-2,3,4,9-tetrahydro-1H-Carbazole-1-carboxamide).

TABLE 1 | Primer sequences for qPCR analyses on tissues

Gene	Primer	Product length
M-DNA-mt-Co3	F GCAGGATTCTTCTGAGCGTTCT R GTCAGCAGCCTCCTAGATCATGT	67 bp
M-DNA-Sdha	F TACTACAGCCCCAAGTCT R TGGACCCATCTTCTATGC	194 bp

SIRT1 Activity

Cells' SIRT1 activity was measured by Colorimetric quantitative detection kit (Genmed Scientifics Inc. United States), each procedure follows the instruction.

Immunofluorescence Staining

Cells were seeded on glass coverslips and incubated with anti-MyHC II (Proteintech). Following incubation with a fluorescent secondary antibody (Abcam, Cambridge, United Kingdom), images were acquired using a fluorescence microscope (Eclipse, Nikon, Japan).

Oxygen Consumption Rate (OCR)

C2C12 myoblasts were seeded in XF 24-well microplates (Seahorse Bioscience, Billerica, MA, United States) and

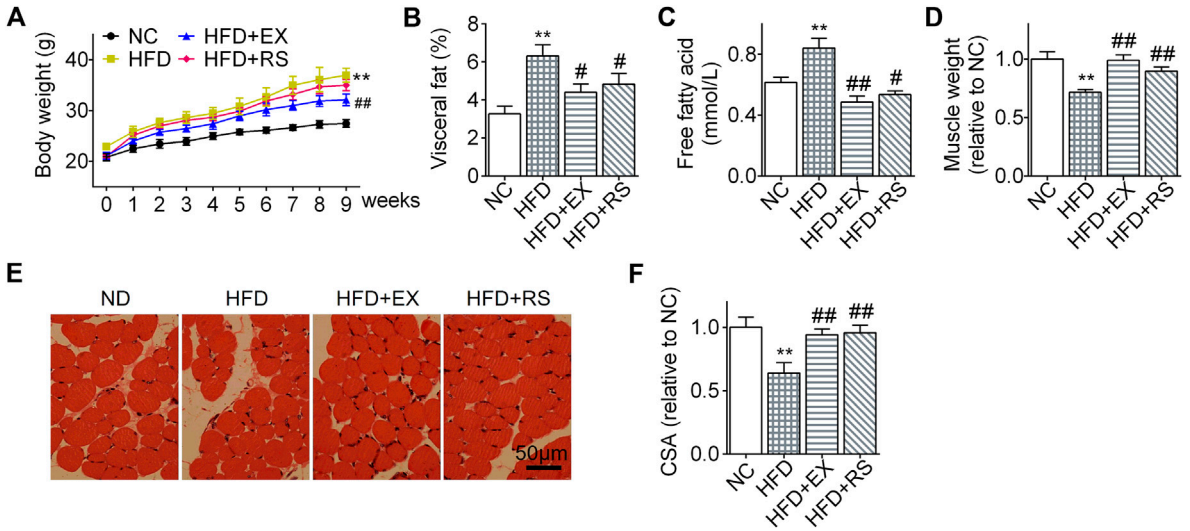

FIGURE 2 | *R. sacra* alleviates HFD-induced muscle atrophy in mice as exercise **(A)** 8 week-old mice were fed normal chow (NC) or high-fat diet (HFD) with either *R. sacra* treatment (RS) or exercise training (EX) for 8 weeks, body weight was monitored in the whole process; **(B)** after 8 weeks, visceral fat/body weight, **(C)** serum free fatty acid, and **(D)** muscle weight/body weight were calculated and assessed; **(E)** Representative gastrocnemius muscle sections were stained with hematoxylin-eosin, **(F)** the cross-sectional area (CSA) of muscle fiber were measured. Scale bar = 50 μm. Data are expressed as Mean ± SEM, n = 8, ** represents $p < 0.01$ in comparison with NC; #, ## represent $p < 0.05$, $p < 0.01$ in comparison with HFD.

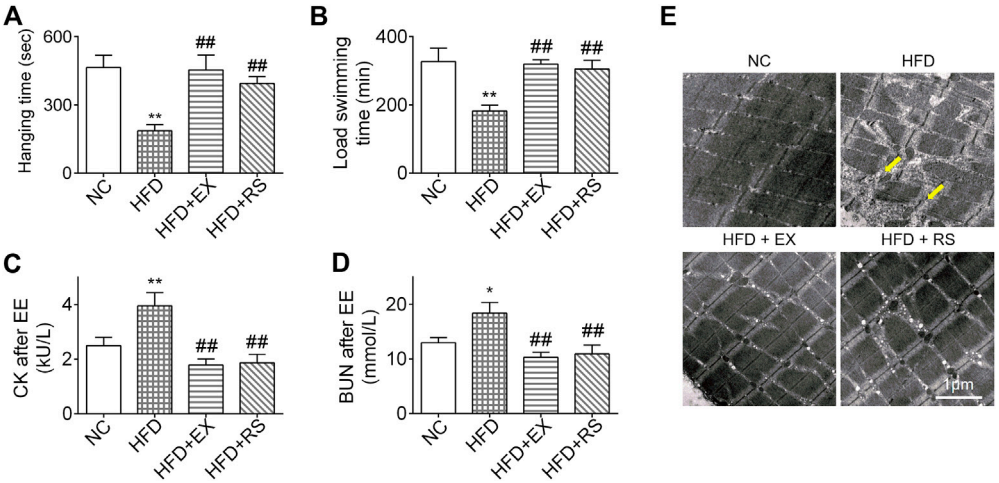

FIGURE 3 | *R. sacra* or exercise improves muscle dysfunction in HFD mice **(A)** 8 week-old mice were fed normal chow (NC) or high-fat diet (HFD) with either *R. sacra* treatment (RS) or exercise training (EX) for 8 weeks, then the inverted screen test was performed and hanging time was analyzed; **(B)** and the forced weight-loaded swimming session were performed, and swimming time was analyzed; **(C)** 12 h after exhaustive exercise (EE), serum creatine kinase (CK), and **(D)** blood urea nitrogen (BUN) of mice were measured; **(E)** meanwhile, the morphology of muscle sample was observed by transmission electron microscope (TEM), and the damaged myofibrils (yellow arrows) were indicated in TEM images, scale bar = 1 μm. Data are expressed as Mean ± SEM, $n = 3$, *, ** represent $p < 0.05$, $p < 0.01$ in comparison with NC; #, ## represent $p < 0.05$, $p < 0.01$ in comparison with HFD.

differentiated. Following treatments of mitochondrial inhibitors, including 1 μmol/L oligomycin, 1 μmol/L Carbonyl cyanide 4-(trifluoromethoxy) phenylhydrazone (FCCP) and 1 μmol/L rotenone/antimycin A, OCRs were measured with extracellular flux analysis (Seahorse Biosciences) every 8 minutes.

Statistical Analysis

The results are expressed as Mean ± SEM. One-way ANOVA plus the Student-Newman-Keuls test was used for statistical analysis. $p < 0.05$ represents statistical significance.

RESULTS

R. sacra Alleviates HFD-Induced Muscle Atrophy in Mice as Exercise

Lipid infiltration induced muscle atrophy in HFD mice (Tong et al., 2019). Exercise has been considered as an effective therapy to limit muscle atrophy or sarcopenia associated with disuse or denervation. However, it remains unclear how exercise affects HFD-induced muscle atrophy. In our present study, following HFD feeding for 8 weeks, mouse body weights increased more profound than normal chow group (**Figure 2A**). However, the body weight gain was significantly inhibited in the HFD group accompanied with exercise. Interestingly, HFD+RS mice showed a decreased tendency of body weight gain when compared to HFD group, but there is no statistical difference. The visceral fat weight (% body weigh) and serum free fatty acid in HFD mice were also increased following HFD. However, *R. sacra* or exercise decreased these two parameters (**Figure 2B**,**1C**). Gastrocnemius muscle weight was decreased following HFD feeding (**Figure 2D**) accompanied with a lower cross-sectional area of muscle fiber (**Figure 2D**). However, exercise training or *R. sacra* treatment significantly ameliorate these pathological conditions as showed in **Figures 2D,E**. These data collectively suggested that *R. sacra* treatment mimics exercise training to improve HFD-induced muscle atrophy.

R. sacra or Exercise Improves Muscle Dysfunction in HFD Mice

We next performed inverted screen test and load swim test to assess muscle strength and endurance. The hanging time was decreased 50% in HFD group compared NC. However, accompanied with exercise or *R. sacra* treatment, the mice following HFD demonstrated a normal hanging time as NC group (**Figure 3A**). A similar result was also observed in the load swimming experiment (**Figure 3B**). Following load swimming, muscle damage was subsequently evaluated by electron microscopy. We found that in HFD group, muscle fiber consistency was disrupted, and mitochondrial membrane was ruptured (**Figure 3E**). In parallel, serum creatine kinase (CK) and BUN were also increased (**Figures 3C,D**). However, neither the morphologic changes in muscle cells nor CK and BUN release occur in HFD+EX or HFD+RS groups (**Figures 3C–E**), suggesting that exercise or *R. sacra* could improve muscle function deficiency induced by HFD.

R. sacra Improves Atrophy Through Activating SIRT1 Signaling Pathway

Atrophy is associated with protein degeneration, inflammation, and mitochondrial dysfunction. SIRT1, a key regulator in nutrients/energy metabolism and cell fate signaling, also

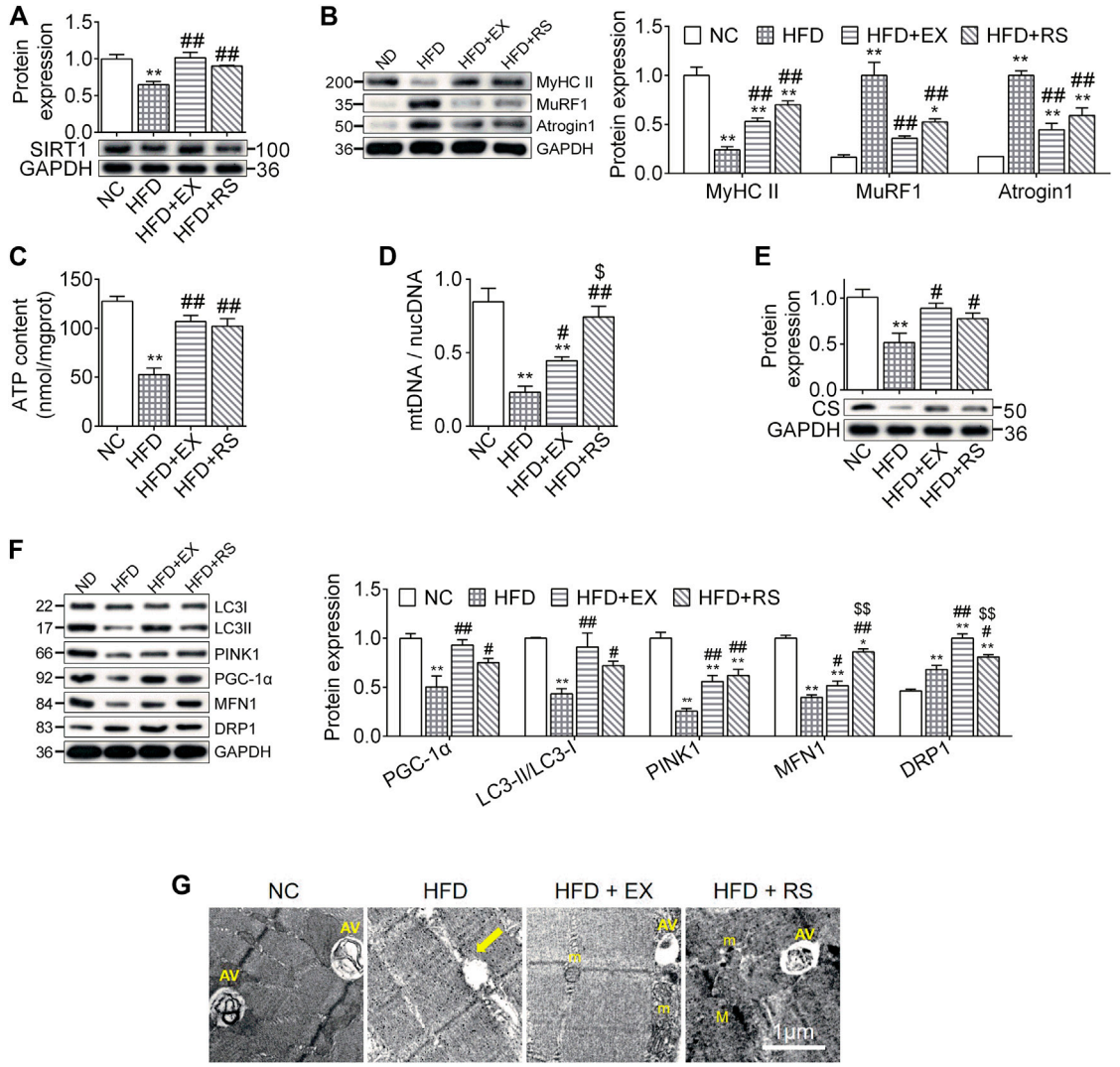

FIGURE 4 | *R. sacra* improves atrophy through activating sirt1 signaling pathway **(A,B)** 8 week-old mice were fed normal chow (NC) or high-fat diet (HFD) with either *R. sacra* treatment (RS) or exercise training (EX) for 8 weeks, then muscle samples were obtained and the relative protein expression of SIRT1, MyHC II, MuRF1, and Atrogin1 were assessed; **(C)** the ATP content is measured; **(D)** the ratio between mitochondrial DNA (mtDNA) and nuclear DNA (nucDNA) determined; **(E,F)** the relative protein expression of CS, PGC-1α, LC3, PINK1, MFN1, and DRP1 were assessed; **(G)** the morphology of muscle sample was observed by transmission electron microscope (TEM), and the damaged mitochondrion (yellow arrows), normal mitochondria (m), autophagic vacuoles (AV), as well as myofilament (M) were indicated in TEM images, scale bar = 1 μm. Data are expressed as Mean ± SEM, $n = 3$, *, ** represent $p < 0.05$, $p < 0.01$ in comparison with NC; #, ## represent $p < 0.05$, $p < 0.01$ in comparison with HFD; $, $$ represent $p < 0.05$, $p < 0.01$ in comparison with HFD+EX.

modulates atrophic genes and mitochondrial homeostasis (Tonkin et al., 2012). We found that SIRT1 protein levels were significantly decreased in skeletal muscle following HFD feeding, and this reduction was inhibited by exercise training or *R. sacra* treatment (**Figure 4A**). MyHC II content was lost almost 76% in muscles isolated from HFD group compared to NC ($p < 0.01$). The protein expression of atrogenes including MuRF1 and atrogin1 were increased in HFD group (**Figure 4B**). All these changes were partially corrected in HFD+EX and HFD+RS groups. Interestingly, exercise training seems to have greater effects than *R. sacra* treatment although there is no statistical significance.

ATP content is an important parameter to evaluate mitochondrial functions. In our study, we found that ATP content was significantly reduced in skeletal muscle isolated from HFD group. This reduction was accompanied with a decrease in the expression of mtDNA/nucDNA and CS (**Figures 4C–E**), suggesting that HFD might induce muscle mitochondrial dysfunction. Exercise or *R. sacra* facilitated mitochondrial function recovery by increasing ATP content, mtDNA/nucDNA and CS. HFD skeletal muscle also demonstrated a reduction in protein expression of mitochondrial biogenesis marker, PGC-1α, mitophagy markers, LC3-II and PINK1, and fusion marker MFN1. The

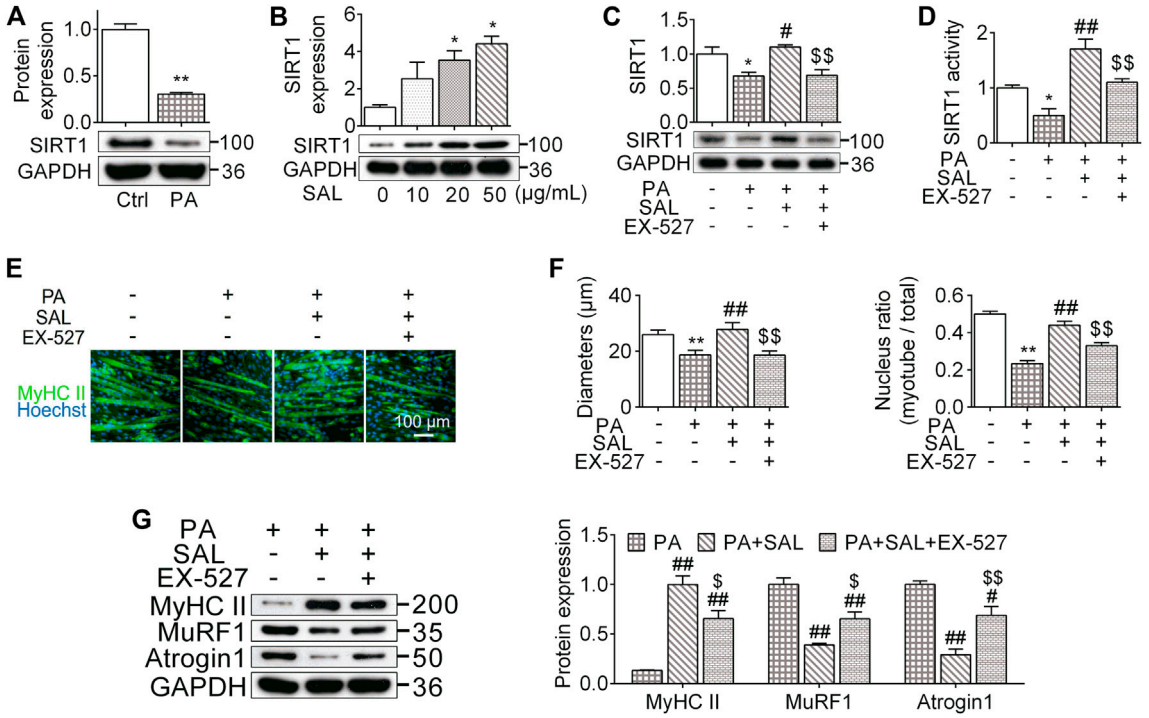

FIGURE 5 | Salidroside prevents myotube atrophy through activating SIRT1 signaling. **(A)** The differentiated myotubes were vehicle (Ctrl) or 0.75 mmol/L palmitate (PA) for 24 hours, SIRT1 expression were subsequently measured; **(B)** the cells were incubated in different concentration of salidroside (SAL), then the protein expression of SIRT1 was measured; **(C,D)** the cells were treated with 50 μg/ml salidroside with or without 10 μmol/L EX-527 in the presence of 0.75mmol/L palmitate for 24 hours, then the protein expression and activity of SIRT1 were measured; **(E,F)** the morphology of differentiated myotubes was observe by MyHC II immunofluorescence, meanwhile the diameters and nucleus ratio of myotubes were calculated; **(G)** the relative protein expression of MyHC II, MuRF1, and Atrogin1 were assessed. Scale bar = 100 μm. Data are expressed as Mean ± SEM, $n = 3$, *, ** represent $p < 0.05$, $p < 0.01$ in comparison with Ctrl; #, ## represent $P < 0.05$, $P < 0.01$ in comparison with PA; $, $$ represent $p < 0.05$, $p < 0.01$ in comparison with PA+SAL.

fission marker DRP1 was increased. Exercise training or *R. sacra* treatment prevent these changes (**Figure 4F**). Eventually, by using TEM, we observed damaged mitochondria characterized with edema and reduction of cristae (yellow arrows) in HFD muscles but autophagic vacuoles (marked by AV) were hardly observed. Autophagic vacuoles were more abundant in NC, HFD+EX and HFD+RS.

Salidroside Prevents Myotube Atrophy Through Activating SIRT1 Signaling

To further investigate the molecular mechanisms by which *R. sacra* prevents HFD-induced muscle dysfunction, C2C12 myotubes were incubated with a high palmitate treatment. We found that high palmitate significantly inhibited the protein expression of SIRT1 in C2C12 myotubes as we observed *in vivo*, suggesting that palmitate might be a direct factor in accelerating muscle cell atrophy (**Figure 5A**). Salidroside, as the major active ingredient of *R. sacra,* activated SIRT1 in myotubes in a dose-dependent manner (**Figure 5B**). We therefore used salidroside to treat C2C12 myotubes with palmitate. We found that salidroside significantly relieve the inhibition of SIRT1 in palmitate-treated cells (**Figures 5B–D**).

We also analyzed the morphology of myotubes following 0.75 mM palmitate treatment. High palmitate significantly decreased the diameter of myotubes around 29% ($P < 0.01$) and reduced the number of nuclei located within the myosin heavy chain positive myotube by 44% ($p < 0.01$) (**Figures 5E**,**4F**). Salidroside abated these morphological alterations. Salidroside also upregulated MyHC II and decreased atrogenes expression (**Figure 5G**). To further clarify the role of SIRT1 signaling pathway in the influences of salidroside, a SIRT1 signaling inhibitor, EX-527, was used with salidroside in the presence of high palmitate in C2C12 myotubes. EX-527 prevented the effects of salidroside on upregulating SIRT1 expression and activity (**Figures 5C,D**). Meanwhile, the effects of salidroside on the myotube morphology, nucleus ratio, MyHC II content, as well as atrogenes were also abolished by EX-527 (**Figures 5E–G**). These data together suggest that salidroside limits myotube atrophy probably through activating the SIRT1 signaling pathway.

Salidroside Activates Mitochondrial Quality Control Through the SIRT1 Signaling

Mitochondria maintain muscle contractile function and remodeling (Gan et al., 2018). In order to evaluate whether

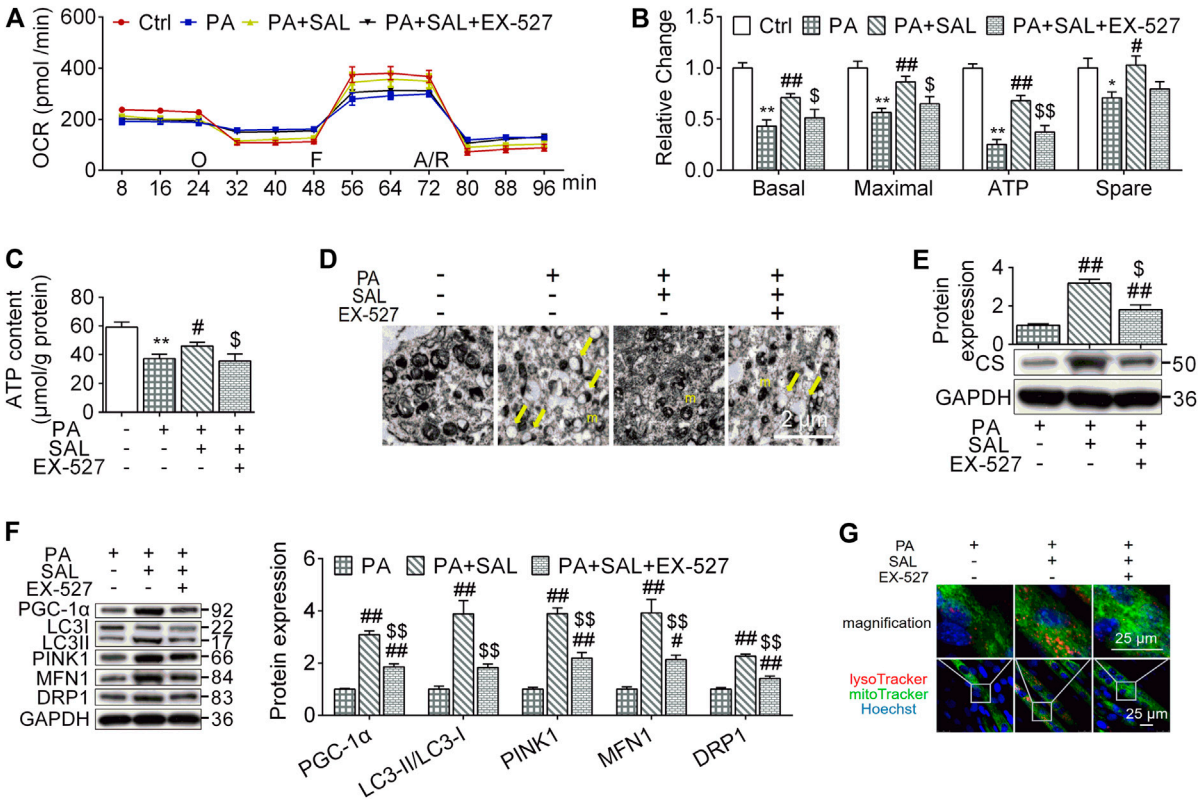

FIGURE 6 | Salidroside activates mitochondrial quality control through the SIRT1 signaling. **(A,B)** the cells were treated with 50 μg/ml salidroside (SAL) with or without 10 μmol/L EX-527 in the presence of 0.75mmol/L palmitate (PA) for 24 hours, oxygen consumption rate (OCR) was measured by seahorse XF analyzer whereas 1 μmol/L oligomycin (O), 1 μmol/L FCCP (F) and 1 μmol/L rotenone/antimycin A (A/R) were added in order, then the basal respiration, maximal respiration, ATP respiration, and spare respiration were calculated from the OCR data; **(C)** ATP content were measured; **(D)** mitochondria in treated cells were directly observed by transmission electron microscope (TEM), and the normal mitochondria (m) as well as damaged mitochondria (yellow arrows) were indicated in TEM images, scale bar = 2 μm; **(D,F)** the protein expression of CS, PGC-1α, LC3, PINK1, MFN1, and DRP1 were measured; **(G)** the treated cells were stained by lysoTracker and mitoTracker, scale bar = 25 μm. Data are expressed as Mean ± SEM, $n = 3$, *, ** represent $p < 0.05$, $p < 0.01$ in comparison with Ctrl; #, ## represent $p < 0.05$, $p < 0.01$ in comparison with PA; $, $$ represent $p < 0.05$, $p < 0.01$ in comparison with PA+SAL.

the beneficial effects of salidroside on skeletal muscle are associated with mitochondrial functions, we quantify mitochondrial functions and MQC-associated parameters. In this study, OCR levels, including basal respiration, maximal respiration, ATP production respiration, and spare respiration as well as ATP content were decreased in myotubes following palmitate-treatment. However, salidroside treatment prevented these reductions (**Figures 6A–C**). Similar results were observed in the expression of CS, the mitochondrial respiratory critical enzyme (**Figure 6E**). In morphology, we found that high palmitate induced a damage in mitochondrial structures characterized with edema and reduction of crista (yellow arrows). Salidroside treatment successfully mitigate the morphological changes in mitochondria (**Figure 6D**). However, EX-527 inhibited the improvement effects of salidroside on mitochondrial structure and functions evaluated by OCR levels, ATP content, CS expression, and TEM.

To explore how the activated SIRT1 signaling by salidroside regulates mitochondrial functions, we evaluated MQC. As shown in **Figure 6F**, salidroside treatment increased MQC quantified by PGC-1α, LC3-II, PINK1, MFN1, and DRP1 compared to PA group while EX-527 abolished this enhancement. Mitolysosome, a mitophagy marker, has been defined as the colocalization of LysoTraker and MitoTracker-stained organelles in cells. In the presence of SAL, Mitolysosomes were more abundant compared to palmitate-treated cells. However, addition of EX-527 reduced mitolysosomes content (**Figure 6G**). These results suggest that SIRT1 is a key regulator in modulating palmitate-induced MQC impairment and salidroside as an activator of SIRT1 might be a potential therapeutic treatment for HFD-induced muscle dysfunction.

DISCUSSION

HFD-induced muscle dysfunction is an important clinical issue due to its prevalence and poor prognosis. Exercise training improves muscle functions against atrophy (Perry et al., 2016). Our present study indicated that a long-term exercise mitigated HFD-induced muscle dysfunction via inhibiting atrogenes and enhancing MQC. Interestingly, *R. sacra* mimics long-term exercise training to mitigate muscle dysfunction and it also

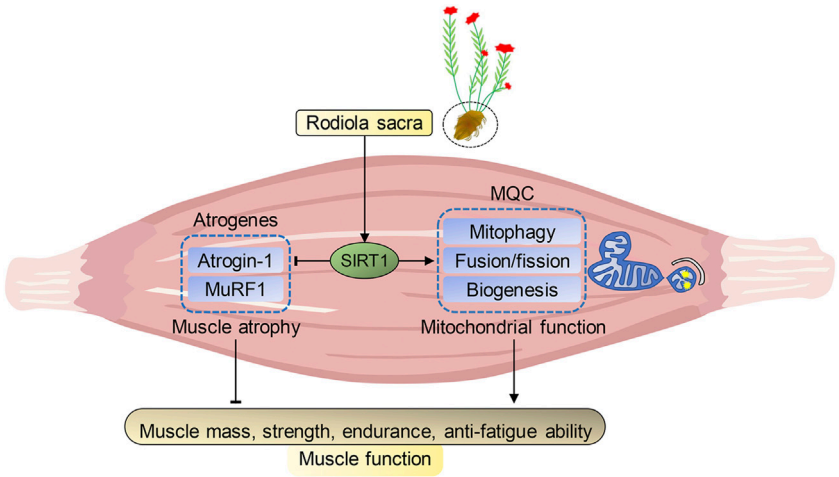

FIGURE 7 | Proposed pathway of Rhodiola effects on HFD-induced muscle dysfunction. Sirtuin1 (SIRT1) is the key regulator of atrophy via mediating atrogenes and mitochondrial hemostasis. During high-fat diet (HFD)-induced obesity, SIRT1 in muscle was inhibited and adversely alteration in atrogenes and mitochondrial quality control (MQC) were observed. However, our data shows exercise training or *R. Sacra* treatment suppress atrogenes and enhances MQC to alleviate HFD-induced muscle dysfunction through activating SIRT1 signaling. Thus, we conclude that *R. sacra* treatment might be a potential exercise mimic or supplement therapy against HFD-induced muscle dysfunction.

modulates SIRT1 signaling pathway, suggesting that *R. sacra* might be a new strategy to replace the long-term exercise training.

Diet containing 45% of fat (mainly lard) was used in this study to induce muscle dysfunction. It is long-chain saturated fatty acids (SFA) instead of unsaturated fatty acid described to be involved in lipotoxic pathways (Listenberger et al., 2003). Palmitate, as the most important SFA in lard (about 24%), was proposed to be an inducement of muscle mitochondrial dysfunction (Nisr et al., 2020). Thus, we used palmitate to establish dysfunctional C2C12 myotubes.

The NAD-dependent protein deacetylase, SIRT1, belongs to the sirtuin family and it performs a wide variety of functions in resisting metabolic disorders, cancer and cardiac stress etc.(Canto and Auwerx, 2012). Activation of SIRT1 by resveratrol also prevents muscle atrophy induced by mechanical unloading and dexamethasone (Lagouge et al., 2006; Momken et al., 2011). SIRT1 blocks FoxO1 and 3 and prevents the induction of key atrogenes atrogin1 and MuRF1 which are muscle-specific ubiquitin ligases contributing to proteolysis (Lee and Goldberg, 2013). Our present study found that SIRT1 activation also alleviates muscle dysfunction induced by HFD by reversing the upregulation of atrogenes in mice, suggesting that SIRT1 is an important signaling pathway in preventing or rescuing muscle dysfunction through the regulation of atrogenes.

Muscle dysfunction is associated with mitochondrial dysfunction (Gan et al., 2018), which is usually characterized with alteration of mitochondrial hemostasis, reduction of mitochondrial contents, and changed expression of mitochondrial genes which are responsible for oxidative metabolism in skeletal muscle (Joseph et al., 2012). Any cellular mechanism which improves mitochondrial functions would have important therapeutic potentials to resist the development of muscle dysfunction. SIRT1 activation protects mitochondrial oxidative functions. Supplementation of nicotinamide riboside, an NAD+ precursor, activates SIRT1 and upregulates mitochondrial energy metabolic genes in mice (Canto et al., 2012). Furthermore, an increase in mitochondrial respiration has been observed in permeabilized skeletal muscle fibers from human subjects following 2 weeks of supplementation with acipimox, another NAD+ precursor (van de Weijer et al., 2015). SIRT1 also improves obesity-associated metabolic diseases through deacetylating and activating mitochondrial biogenetic marker, PGC-1α (Lagouge et al., 2006). Thus, SIRT1-regulated mitochondrial biogenesis and oxidative metabolism may be another important mechanism to prevent or rescue muscle dysfunction.

Exercise counteracts deleterious muscle influence of aging and obesity via resisting lipid-induced protein degeneration or metabolic disorders in skeletal muscle (Heo et al., 2018). Thus, a 12-month exercise training increased thigh cross-sectional area and muscle mass in older-aged patient with diabetes mellitus (Mavros et al., 2014). Exercise also enhances mitochondrial oxidative functions via activating SIRT1 (Gurd, 2011). Indeed, our present study indicated that HFD decreased mitochondrial ATP content, DNA ratio, and CS expression in mouse muscle which are accompanied with attenuated mitochondrial functions. These effects were overcome by additional exercise training. MQC including mitochondrial biogenesis, autophagy, fusion, and fission is key to maintain mitochondrial homeostasis and oxidative function. MQC disorders result in mitochondrial dysfunction and pathological changes. Exercise enhances MQC and improves exercise capacity in healthy mice (Dun et al., 2017). Our present data suggest that MQC-related parameters, PGC-1α, LC3-II, PINK1, DRP1, and MFN1 were inhibited, whereas exercise relieve the MQC impairment, suggesting that exercise training mitigate HFD-induced muscle dysfunction probably through mediating atrogenes and MQC.

Extracts from the root of *Rhodiola* have been traditionally used to improve hypoxic tolerance for the people who ascend to high altitudes (Kelly, 2001). *Rhodiola* also improves exercise performance and anti-stress ability of skeletal muscle in human subjects and animal models which are probably associated with enhanced mitochondrial functions in skeletal muscle (Abidov et al., 2003; Noreen et al., 2013). We previously indicated that *R. sacra* triggered MQC and ultimately improves the exercise capacity and anti-fatigue ability in healthy mice (Dun et al., 2017). However, it remains uncertain whether *R. sacra* is beneficial to HFD-induced muscle dysfunction. In the present study, muscle atrophy and SIRT1 inhibition occurred in HFD-induced obese mice which were significantly mitigate by *R. sacra* treatment or exercise training. In parallel, HFD-impacted mitochondrial function and MQC in obese mice were also improved by *R. sacra* treatment or exercise training, suggesting that *R. sacra* has similar therapeutic effect as exercise training on activating SIRT1 and enhancing mitochondrial functions.

Salidroside is an active ingredient from the roots of *R. sacra*. It ameliorates muscle atrophy in cachexia or denervation via activating mTOR signaling pathway or reducing expression of atrogenes, such as MuRF1 and Atrogin-1 (Chen et al., 2016; Wu et al., 2019). Our previous study also indicated that salidroside resists metabolic disorders in skeletal muscle via upregulating SIRT1-mediated mitochondrial quality control in mice (You et al., 2020). Our present study further showed that in skeletal muscle cells, salidroside abated palmitate-induced SIRT1 inhibition, atrogenes activation, and myotubes atrophy and these therapeutic effects were significantly attenuated by additional EX-527 pre-treatment. These results indicate that salidroside may counteract lipid accumulation-caused atrophic factors and mitochondrial alteration by activating SIRT1 signal pathway. As the LC-MS analysis shown, polyphenols are main bioactive compounds of *R. sacra* too. Moreover, Capó and his colleagues found that polyphenolic extract ameliorate muscle decline in by reducing oxidative stress and oxidative damage (Annunziata et al., 2020). Thus, polyphenols might be responsible for the biological effects of *R. sacra* in the study and could be another potential treatment for HFD-induced muscle atrophy, but more data is needed.

In summary, our present study indicated that *R. sacra* mimics exercise to alleviate HFD-induced muscle dysfunction via inhibiting atrogenes and enhancing MQC via SIRT1 pathway, which was summarized in **Figure 7**. We believe that *R. sacra* treatment may be a potential substitute for long-term exercise training in clinical practice against muscle dysfunction in the future.

DATA AVAILABILITY STATEMENT

The original contributions presented in the study are included in the article/**Supplementary Material**, further inquiries can be directed to the corresponding author.

ETHICS STATEMENT

The animal study was reviewed and approved by the Medicine Animal Welfare Committee of Xiangya Medical School, Central South University.

AUTHOR CONTRIBUTIONS

BY designed and performed most of the study and the wrote the paper; YD analyzed and interpreted the data; YD, SF, WZ, LQ and MX performed part of the study; DQ provided valuable suggestions and comments on the study design and critically revised and edited the manuscript; YD, YL and SL supervised and funded the study.

FUNDING

This work was supported by grants from the National Natural Science Foundation of China (Grant number 81672262 to SL, 82002403 to YD, and 81702241 to YL), the Natural Science Foundation of Hunan Province (Grant number 2018JJ3847 to YL), and the National Development and Reform Commission (No. (201201521 to SL).

SUPPLEMENTARY MATERIAL

The Supplementary Material for this article can be found online at: https://www.frontiersin.org/articles/10.3389/fphar.2021.646489/full#supplementary-material.

REFERENCES

Abidov, M., Crendal, F., Grachev, S., Seifulla, R., and Ziegenfuss, T. (2003). Effect of extracts from Rhodiola rosea and Rhodiola crenulata (Crassulaceae) roots on ATP content in mitochondria of skeletal muscles. *Bulletin of Experimental Biology and Medicine* 136 (6), 585–587. doi:10.1023/b:bebm.0000020211.24779.15

Annunziata, G., Jimenez-García, M., Tejada, S., Moranta, D., Arnone, A., Ciampaglia, R., et al. (2020). Grape Polyphenols Ameliorate Muscle Decline Reducing Oxidative Stress and Oxidative Damage in Aged Rats. *Nutrients* 12 (5), 1280. doi:10.3390/nu12051280

Barhwal, K., Das, S. K., Kumar, A., Hota, S. K., and Srivastava, R. B. (2015). Insulin receptor A and Sirtuin 1 synergistically improve learning and spatial memory following chronic salidroside treatment during hypoxia. *J. Neurochem.* 135 (2), 332–346. doi:10.1111/jnc.13225

Cantó, C., and Auwerx, J. (2012). Targeting Sirtuin 1 to Improve Metabolism: All You Need Is NAD+?. *Pharmacol Rev.* 64 (1), 166–187. doi:10.1124/pr.110.003905

Cantó, C., Houtkooper, R. H., Pirinen, E., Youn, D. Y., Oosterveer, M. H., Cen, Y., et al. (2012). The NAD+ Precursor Nicotinamide Riboside Enhances Oxidative Metabolism and Protects against High-Fat Diet-Induced Obesity. *Cell Metabolism* 15 (6), 838–847. doi:10.1016/j.cmet.2012.04.022

Chen, X., Wu, Y., Yang, T., Wei, M., Wang, Y., Deng, X., et al. (2016). Salidroside alleviates cachexia symptoms in mouse models of cancer cachexia via activating mTOR signalling. *Journal of Cachexia, Sarcopenia and Muscle* 7 (2), 225–232. doi:10.1002/jcsm.12054

Conraads, V. M., Deaton, C., Piotrowicz, E., Santaularia, N., Tierney, S., Piepoli, M. F., et al. (2012). Adherence of heart failure patients to exercise: barriers and possible solutions. *European Journal of Heart Failure* 14 (5), 451–458. doi:10.1093/eurjhf/hfs048

Dun, Y., Liu, S., Zhang, W., Xie, M., and Qiu, L. (2017). Exercise Combined withRhodiola sacraSupplementation Improves Exercise Capacity and Ameliorates Exhaustive Exercise-Induced Muscle Damage through Enhancement of Mitochondrial Quality Control. *Oxidative Medicine and Cellular Longevity* 2017, 1. doi:10.1155/2017/8024857

Dun, Y., Thomas, R. J., Medina-Inojosa, J. R., Squires, R. W., Huang, H., Smith, J. R., et al. (2019a). High-Intensity Interval Training in Cardiac Rehabilitation: Impact on Fat Mass in Patients With Myocardial Infarction. *Mayo Clinic Proceedings* 94 (9), 1718–1730. doi:10.1016/j.mayocp.2019.04.033

Dun, Y., Thomas, R. J., Smith, J. R., Medina-Inojosa, J. R., Squires, R. W., Bonikowske, A. R., et al. (2019b). High-intensity interval training improves metabolic syndrome and body composition in outpatient cardiac rehabilitation patients with myocardial infarction. *Cardiovasc Diabetol* 18 (1), 104. doi:10.1186/s12933-019-0907-0

Gan, Z., Fu, T., Kelly, D. P., and Vega, R. B. (2018). Skeletal muscle mitochondrial remodeling in exercise and diseases. *Cell Res.* 28 (10), 969–980. doi:10.1038/s41422-018-0078-7

Gurd, B. J. (2011). Deacetylation of PGC-1α by SIRT1: importance for skeletal muscle function and exercise-induced mitochondrial biogenesis. *Appl. Physiol. Nutr. Metab.* 36 (5), 589–597. doi:10.1139/h11-070

Heo, J.-W., Yoo, S.-Z., No, M.-H., Park, D.-H., Kang, J.-H., Kim, T.-W., et al. (2018). Exercise Training Attenuates Obesity-Induced Skeletal Muscle Remodeling and Mitochondria-Mediated Apoptosis in the Skeletal Muscle. *Ijerph* 15 (10), 2301. doi:10.3390/ijerph15102301

Jiang, L., Shen, X., Dun, Y., Xie, M., Fu, S., Zhang, W., et al. (2021). Exercise combined with trimetazidine improves anti-fatal stress capacity through enhancing autophagy and heat shock protein 70 of myocardium in mice. *Int. J. Med. Sci.* 18, 1680–1686. doi:10.7150/ijms.53899

Jørgensen, T., Grunnet, N., and Quistorff, B. (2015). One-year high fat diet affects muscle-but not brain mitochondria. *J Cereb Blood Flow Metab.* 35 (6), 943–950. doi:10.1038/jcbfm.2015.27

Joseph, A.-M., Adhihetty, P. J., Buford, T. W., Wohlgemuth, S. E., Lees, H. A., Nguyen, L. M.-D., et al. (2012). The impact of aging on mitochondrial function and biogenesis pathways in skeletal muscle of sedentary high- and low-functioning elderly individuals. *Aging Cell* 11 (5), 801–809. doi:10.1111/j.1474-9726.2012.00844.x

Kelly, G S (2001). Rhodiola rosea: a possible plant adaptogen. *Altern Med Rev.* 6 (3), 293–302.

Lagouge, M., Argmann, C., Gerhart-Hines, Z., Meziane, H., Lerin, C., Daussin, F., et al. (2006). Resveratrol Improves Mitochondrial Function and Protects against Metabolic Disease by Activating SIRT1 and PGC-1α. *Cell* 127 (6), 1109–1122. doi:10.1016/j.cell.2006.11.013

Lee, D., and Goldberg, A. L. (2013). SIRT1 protein, by blocking the activities of transcription factors FoxO1 and FoxO3, inhibits muscle atrophy and promotes muscle growth. *Journal of Biological Chemistry* 288 (42), 30515–30526. doi:10.1074/jbc.M113.489716

Lei, Y., Wang, J., Wang, D., Li, C., Liu, B., Fang, X., et al. (2020). SIRT1 in forebrain excitatory neurons produces sexually dimorphic effects on depression-related behaviors and modulates neuronal excitability and synaptic transmission in the medial prefrontal cortex. *Mol Psychiatry* 25 (5), 1094–1111. doi:10.1038/s41380-019-0352-1

Listenberger, L. L., Han, X., Lewis, S. E., Cases, S., Farese, R. V., Jr., Ory, D. S., et al. (2003). Triglyceride accumulation protects against fatty acid-induced lipotoxicity. *Proceedings of the National Academy of Sciences* 100 (6), 3077–3082. doi:10.1073/pnas.0630588100

Mavros, Y., Kay, S., Simpson, K. A., Baker, M. K., Wang, Y., Zhao, R. R., et al. (2014). Reductions in C-reactive protein in older adults with type 2 diabetes are related to improvements in body composition following a randomized controlled trial of resistance training. *J Cachexia Sarcopenia Muscle* 5 (2), 111–120. doi:10.1007/s13539-014-0134-1

Milne, J. C., and Denu, J. M. (2008). The Sirtuin family: therapeutic targets to treat diseases of aging. *Current Opinion in Chemical Biology* 12 (1), 11–17. doi:10.1016/j.cbpa.2008.01.019

Momken, I., Stevens, L., Bergouignan, A., Desplanches, D., Rudwill, F., Chery, I., et al. (2011). Resveratrol prevents the wasting disorders of mechanical unloading by acting as a physical exercise mimetic in the rat. *FASEB j.* 25 (10), 3646–3660. doi:10.1096/fj.10-177295

Nisr, RB, Shah, DS, and Hundal, HS (2020). Mono- and Polyunsaturated Fatty Acids Counter Palmitate-Induced Mitochondrial Dysfunction in Rat Skeletal Muscle Cells. *Cell Physiol Biochem.* 54 (5), 975–993. doi:10.33594/000000282

Noreen, E. E., Buckley, J. G., Lewis, S. L., Brandauer, J., and Stuempfle, K. J. (2013). The effects of an acute dose of Rhodiola rosea on endurance exercise performance. *J Strength Cond Res.* 27 (3), 839–847. doi:10.1519/JSC.0b013e31825d9799

Perry, B. D, Caldow, M. K, Brennan-Speranza, T. C, Sbaraglia, M, Jerums, G, Garnham, A, et al. (2016). Muscle atrophy in patients with Type 2 Diabetes Mellitus: roles of inflammatory pathways, physical activity and exercise. *Exerc Immunol Rev.* 22, 94–109.

Pillard, F., Laoudj-Chenivesse, D., Carnac, G., Mercier, J., Rami, J., Rivière, D., et al. (2011). Physical activity and sarcopenia. *Clinics in Geriatric Medicine* 27 (3), 449–470. doi:10.1016/j.cger.2011.03.009

Sandri, M., Lin, J., Handschin, C., Yang, W., Arany, Z. P., Lecker, S. H., et al. (2006). PGC-1 protects skeletal muscle from atrophy by suppressing FoxO3 action and atrophy-specific gene transcription. *Proceedings of the National Academy of Sciences* 103 (44), 16260–16265. doi:10.1073/pnas.0607795103

Tong, T., Kim, M., and Park, T. (2019). α-Ionone attenuates high-fat diet-induced skeletal muscle wasting in mice via activation of cAMP signaling. *Food Funct.* 10 (2), 1167–1178. doi:10.1039/c8fo01992d

Tonkin, J., Villarroya, F., Puri, P. L., and Vinciguerra, M. (2012). SIRT1 signaling as potential modulator of skeletal muscle diseases. *Current Opinion in Pharmacology* 12 (3), 372–376. doi:10.1016/j.coph.2012.02.010

Valero, T. (2014). Editorial (Thematic Issue: Mitochondrial Biogenesis: Pharmacological Approaches). *Cpd* 20 (35), 5507–5509. doi:10.2174/1381612820351409111421 18

Van De Weijer, T., Phielix, E., Bilet, L., Williams, E. G., Ropelle, E. R., Bierwagen, A., et al. (2015). Evidence for a Direct Effect of the NAD+Precursor Acipimox on Muscle Mitochondrial Function in Humans. *Diabetes* 64 (4), 1193–1201. doi:10.2337/db14-0667

Wu, C., Tang, L., Ni, X., Xu, T., Fang, Q., Xu, L., et al. (2019). Salidroside Attenuates Denervation-Induced Skeletal Muscle Atrophy Through Negative Regulation of Pro-inflammatory Cytokine. *Front. Physiol.* 10, 665. doi:10.3389/fphys.2019.00665

Xie, M., Jiang, L., Dun, Y., Zhang, W., and Liu, S. (2019). Trimetazidine combined with exercise improves exercise capacity and anti-fatal stress ability through enhancing mitochondrial quality control. *Life Sciences* 224, 157. doi:10.1016/j.lfs.2019.03.027

Xue, H., Li, P., Luo, Y., Wu, C., Liu, Y., Qin, X., et al. (2019). Salidroside stimulates the Sirt1/PGC-1α axis and ameliorates diabetic nephropathy in mice. *Phytomedicine* 54, 240–247. doi:10.1016/j.phymed.2018.10.031

You, B., Dun, Y., Zhang, W., Jiang, L., Li, H., Xie, M., et al. (2020). Anti-insulin resistance effects of salidroside through mitochondrial quality control. *J Endocrinol* 244 (2), 383–393. doi:10.1530/JOE-19-0393

Conflict of Interest: The authors declare that the research was conducted in the absence of any commercial or financial relationships that could be construed as a potential conflict of interest.

Copyright © 2021 You, Dun, Fu, Qi, Zhang, Liu, Qiu, Xie and Liu. This is an open-access article distributed under the terms of the Creative Commons Attribution License (CC BY). The use, distribution or reproduction in other forums is permitted, provided the original author(s) and the copyright owner(s) are credited and that the original publication in this journal is cited, in accordance with accepted academic practice. No use, distribution or reproduction is permitted which does not comply with these terms.

frontiers in Pharmacology

ORIGINAL RESEARCH
published: 19 April 2021
doi: 10.3389/fphar.2021.588587

Galectin-3 Mediated Inflammatory Response Contributes to Neurological Recovery by QiShenYiQi in Subacute Stroke Model

Yule Wang[1,2,3], *Shuang He*[1,2], *Xinyan Liu*[1,2], *Zhixiong Li*[1,2], *Lin Zhu*[1,2], *Guangxu Xiao*[1,2], *Xiaoli Du*[1,2,4], *Hongxia Du*[1,2], *Wen Zhang*[1,5], *Yiqian Zhang*[6], *John Orgah*[1,2], *Yuxin Feng*[1,2], *Boli Zhang*[1] *and Yan Zhu*[1,2]*

[1]*State Key Laboratory of Component-based Chinese Medicine, Tianjin University of Traditional Chinese Medicine, Tianjin, China,* [2]*Research and Development Center of TCM, Tianjin International Joint Academy of Biotechnology and Medicine, Tianjin, China,* [3]*Pharmaceutical Informatics Institute, College of Pharmaceutical Sciences, Zhejiang University, Hangzhou, China,* [4]*Inner Mongolia Medical University, Jinshan Economic and Technological Development District, Inner Mongolia, China,* [5]*State Key Laboratory of Core Technology in Innovative Chinese Medicine, Beijing, China,* [6]*State Key Laboratory of Core Technology in Innovative Chinese Medicine, Tianjin Tasly Holding Group Co., Ltd., Tianjin, China*

OPEN ACCESS

Edited by:
Yanqiong Zhang,
China Academy of Chinese Medical Sciences, China

Reviewed by:
Hamdollah Panahpour,
Ardabil University of Medical Sciences, Iran
Weirong Fang,
China Pharmaceutical University, China
Jiangwen Yin,
Sichuan University, China

***Correspondence:**
Yan Zhu
yanzhu.harvard@icloud.com

Specialty section:
This article was submitted to Ethnopharmacology, a section of the journal Frontiers in Pharmacology

Received: *29 July 2020*
Accepted: *29 January 2021*
Published: *19 April 2021*

Citation:
Wang Y, He S, Liu X, Li Z, Zhu L, Xiao G, Du X, Du H, Zhang W, Zhang Y, Orgah J, Feng Y, Zhang B and Zhu Y (2021) Galectin-3 Mediated Inflammatory Response Contributes to Neurological Recovery by QiShenYiQi in Subacute Stroke Model. Front. Pharmacol. 12:588587. doi: 10.3389/fphar.2021.588587

Effective therapies for stroke are still limited due to its complex pathological manifestations. QiShenYiQi (QSYQ), a component-based Chinese medicine capable of reducing organ injury caused by ischemia/reperfusion, may offer an alternative option for stroke treatment and post-stroke recovery. Recently, we reported a beneficial effect of QSYQ for acute stroke *via* modulation of the neuroinflammatory response. However, if QSYQ plays a role in subacute stroke remains unknown. The pharmacological action of QSYQ was investigated in experimental stroke rats which underwent 90 min ischemia and 8 days reperfusion in this study. Neurological and locomotive deficits, cerebral infarction, brain edema, and BBB integrity were assessed. TMT-based quantitative proteomics were performed to identify differentially expressed proteins following QSYQ treatment. Immunohistochemistry, western blot analysis, RT-qPCR, and ELISA were used to validate the proteomics data and to reveal the action mechanisms. Therapeutically, treatment with QSYQ (600 mg/kg) for 7 days significantly improved neurological recovery, attenuated infarct volume and brain edema, and alleviated BBB breakdown in the stroke rats. Bioinformatics analysis indicated that protein galectin-3 and its mediated inflammatory response was closely related to the beneficial effect of QSYQ. Specially, QSYQ (600 mg/kg) markedly downregulated the mRNA and protein expression levels of galectin-3, TNF-α, and IL-6 in CI/RI brain as well as serum levels of TNF-α and IL-6. Overall, our findings showed that the effective action of QSYQ against the subacute phase of CI/RI occurs partly *via* regulating galectin-3 mediated inflammatory reaction.

Keywords: qishenyiqi, cerebral ischemia/reperfusion injury, TMT-based quantitative proteomics analysis, inflammatory response, galectin-3

INTRODUCTION

Stroke is recognized as one of the main leading causes of death and serious long-term disability, as well as cognitive functional impairment, worldwide (Benjamin et al., 2019). Of all strokes, ischemic stroke incidents account for approximately 87% (Benjamin et al., 2019). Although intensive basic and clinical research has uncovered multiple modifiable risk factors (such as high systolic blood pressure, high fasting plasma glucose, and high total cholesterol) (Feigin et al., 2016), and has revealed many potential molecular mechanisms (such as inflammatory response (Jin et al., 2013), oxidative stress (Li et al., 2018), blood-brain barrier dysfunction (Jiang et al., 2018), activation of apoptotic and autophagic pathways (Kalogeris et al., 2012), mitochondrial dysfunction (Yang et al., 2018), and complement activation of stroke (Ma et al., 2019), effective therapies are still limited. Currently, the standard clinical therapy for appropriate patients with acute ischemic stroke are tissue plasminogen activator (tPA)-mediated intravenous thrombolysis and executing intra-arterial thrombectomy to realize recanalization (Dong et al., 2017; Goda et al., 2020). However, the major problems of the relatively narrow therapeutic time window and a high risk of hemorrhagic transformation in tPA treatment should not be ignored (Dong et al., 2017; Puig et al., 2017). Reperfusion injury following the restoration of blood supply may also result in more adverse stroke outcomes *via* complicated pathological processes (Lin et al., 2016). It is believed that cerebral ischemia/reperfusion injury (CI/RI) has become an increasingly critical challenge for post-stroke recovery (Pan et al., 2007). Thus, it is crucial to discover novel and alternative therapies for ischemic stroke.

In China, herbal remedies have been historically applied in the treatment of stroke and stroke-associated symptoms based on the theory of traditional Chinese medicine (TCM) (Sun et al., 2015; Han et al., 2017a). Qishen Yiqi (QSYQ) formula, which is composed of *Astragalus membranaceus* (Fisch.) Bge. (Huangqi), *Salvia miltiorrhiza* Bge. (Danshen), *Panax notoginseng* (Burk.) F. H. Chen (Sanqi), and *Dalbergia odorifera* T. Chen (Jiangxiang), is a typical component-based Chinese medicine that was approved by the State Food and Drug Administration of China in 2003 for treatment of angina pectoris of coronary heart disease origin with Qi deficiency and blood stasis syndrome (Cao et al., 2017), and secondary prevention of myocardial infarction (Shang et al., 2013). Recently, the major active ingredients in QSYQ, such as astragaloside IV, calycosin, calycosin-7-O-β-D-glycoside, formononetin, salvianolic acid A, salvianolic acid B, tanshinone IIA, notoginsenoside R1, ginsenoside Rg1, and ginsenoside Rb1(Yu et al., 2017; Zhang et al., 2018), have been reported to have therapeutic potential in acute and subacute phases of ischemic stroke *via* various functional mechanisms, especially immune-inflammatory response related mechanism (Han et al., 2017b; Zhang et al., 2020). Furthermore, we have found the protective action of QSYQ against acute ischemic stroke *via* regulating neuroinflammatory network mobilization in a mouse model of cerebral ischemia and reperfusion (Wang et al., 2020).

At present, it is believed that immune-inflammatory response is an important endogenous mechanism involved in the pathophysiological process of CI/RI (Famakin, 2014). An anti-inflammatory strategy appears to be a favorite therapeutic target, given its pleiotropic roles in the acute damage to long term recovery phase of ischemic stroke (Peng et al., 2019). Galectin-3 is a unique chimera-type member of the galectin family and exerts various functions depending on cell type and cellular location (Yip et al., 2017). Recent studies suggested that galectin-3 may serve as a promising prognostic biomarker as well as a potential therapeutic target for cardiovascular and cerebrovascular diseases (Shen et al., 2016; Dong et al., 2018). Accumulated evidence has indicated that galectin-3 appeared to function as a significant regulator participating in the neuroinflammatory reaction caused by cerebral ischemia and reperfusion (Shin, 2013; Rahimian et al., 2018). Interestingly, Burguillos et al. reported that microglia-secreted galectin-3 acted as an endogenous ligand for Toll-like receptor 4 (TLR-4) activation and deteriorated typical TLR4-dependent inflammatory response after cerebral ischemia (Burguillos et al., 2015).

In the present study, we aimed to explore the pharmacodynamic effect of QSYQ against the cerebral injury induced by ischemic stroke in the subacute phase. Subsequently, tandem mass tag (TMT)-based quantitative proteomics analysis followed by experimental verification was executed to explain the galectin-3 mediated neuroinflammatory mechanism of QSYQ treatment in response to CI/RI of the subacute phase.

MATERIALS AND METHODS

Drugs and Reagents

QSYQ (drug approval number: Z20030139; batch number: 20160604), which was supplied by Tasly Pharmaceutical Group Co., Ltd. (Tianjin, China), was prepared according to the ratio of Huangqi: Danshen: Sanqi: Jiangxiang oil = 148.01: 70.35:70.35:11.97 and dissolved in ultrapure water to make a solution at concentrations of 15 mg/ml, 30 mg/ml, and 60 mg/ml for experiments. Nimodipine (Nim) (drug approval number: H14022821) was purchased from Yabao Pharmaceutical Group Co., Ltd. (Taiyuan, China). Chromatographic-grade methanol and acetonitrile were purchased from Merck (Darmstadt, Germany). Water was purified using the Millipore-Q water purification system (Millipore, Milford, MA, United States). Standards of tanshinol, calycosin-7-O-β-D-glycoside, protocatechualdehyde, formononetin, and rosmarinic acid were purchased from the National Institutes for Food and Drug Control of China (Beijing, China). Standards of lithospermic acid, ononin, and calycosin were purchased from Tianjin Shilan Technology Co., Ltd. (Tianjin, China). Standards of salvianolic acid A, salvianolic acid B, salvianolic acid D, salvianolic acid T, and salvianolic acid U were obtained from Tianjin Tasly Pharmaceutical Group Co., Ltd. (Tianjin, China). The purities of the above standards were more than 98%. 2, 3, 5-Triphenyl-2H-Tetrazolium Chloride (TTC) solution (2%, G3005), paraformaldehyde (4%, P1110), RIPA lysis buffer (R0020), PMSF (100mM, P0100), BCA Protein Assay Kit

(PC0020–50T), and SDS-PAGE Gel Kit (P1200–50T) were purchased from Solarbio (Beijing, China). Evans Blue was purchased from Meilunbio (MB4680-5°g, Dalian, China). Isoflurane (Lot No. B506) was purchased from Ruiwode Lifescience Co., Ltd. (Shenzhen, China). Omnipaque (300 mg I/ml, drug approval number: H20000,595) was purchased from GE Pharmaceutical Co., Ltd. (Shanghai, China). Tandem mass tag (TMT) (6-plex) isobaric label reagents were purchased from Thermo Fisher Scientific (Waltham, MA, United States). Sodium dodecyl sulfate (SDS), DL-dithiothreitol (DTT), Iodoaceamide (IAA), Triethylamine borane (TEAB), and urea were obtained from Bio-Rad (Hercules, CA, United,States). Trypsin was obtained from Promega (Madison, WI). Tris was obtained from Sigma (St. Louis, MO, United States). Anti-Galectin-3 antibody was purchased from the Abcam Company (ab53082, Cambridge, United Kingdom). Anti-β-actin antibody was purchased from Cell Signaling Technology (8457S, Beverly, MA, United States). Goat anti-rabbit IgG H&L was purchased from Zhongshan Jingqiao Biotechnology, Inc. (ZB-5301, Beijing, China). Cytokine IL-6 and TNF-α ELLISA kits were obtained from Shanghai Zhuocai Biotechnology Co., Ltd. (Shanghai, China).

High Performance Liquid Chromatography Analysis

Mixed standards were prepared as follows: all standards were weighed accurately and dissolved in 10 ml of methanol. Mixed standards were then filtered using a 0.45 μm filtration membrane before analysis. Samples were extracted as follows: One hundred fifty milligrams of QSYQ was accurately weighed and ultrasonically extracted with 10 ml of 50% (v/v) methanol by ultrasonication for 30 min. After replenishing the lost weight during extraction, samples were filtered using a 0.45 μm filtration membrane for HPLC analysis.

The HPLC analysis of QSYQ was performed using an Agilent 1,290 Infinity LC, which was equipped with a photodiode array ultraviolet-visible detector. A Waters ACQUITY UPLC BEH Shield RP18 column (2.1 × 100 mm, 1.7 μm) was used to perform the chromatography separation using water (A) and acetonitrile (B) as mobile phases. The gradient elution was set as follows: 0–3 min, 15% B; 3–10 min, 15–20% B; 10–12 min, 20% B; 12–18 min, 20–40% B; 18–24 min, 40–70% B; 24–27 min, 70–95% B; and 27–28 min, 95–8% B. The column temperature was maintained at 25°C with an injection volume of 2 μL and a flow rate of 0.4 ml/min for analysis. Dual-wavelength detection was applied in this analysis: channel A was set as 254 nm; channel B was set as 280 nm from 0 to 3 min and 325 nm from to 28 min.

Experimental Animals

Male Sprague-Dawley (SD) rats weighing 200–220 g were obtained from Beijing Vital River Lab Animal Technology Co., Ltd. (Beijing, China, Certificate No: SCXK [Jing] 2014-0013). Rats were housed under a 12 h light/dark cycle in polypropylene cages, which were well ventilated, and there was a controlled in-house temperature of 22 ± 2°C as well as humidity of 40 ± 5%. Commercial rodent chow (Beijing Vital River Lab Animal Technology Co., Ltd.) and clean water were provided ad libitum. Before the surgery, animals were fasted for 12 h, but with free access to water. The behavioral assessment was executed during the rats' active periods.

Middle Cerebral Artery Occlusion Model and Drug Treatment

Before the surgery, rats were anesthetized with 4% isoflurane in 70% nitrous oxide (N_2O)/30% oxygen (O_2). Then, isoflurane was lowered to 2.5% to maintain anesthesia using a small animal anesthesia machine (Matrix VIP 3,000; Midmark, United States). Throughout all surgical procedures, the animal was placed on a heating pad to keep body temperature at 37°C. Surgery was performed using transient MCAO technique as described elsewhere with proper modification (Uluc et al., 2011; Gubskiy et al., 2018; Lopez and Vemuganti, 2018). A ventral midline incision (~1 cm) was made at the sterile neck and the left common carotid artery (CCA), external cerebral artery (ECA), and internal cerebral artery (ICA) were orderly exposed. After temporarily blocking the left CCA and ICA using two microsurgical clips, two sterile 4–0 silk sutures were placed around the left ECA: one tight ligature was tied as distally as possible from the bifurcation and the other loose ligature was put near the bifurcation. Then, a small hole was created between two silk sutures on the left ECA with a microsurgical scissor and a 3.0–5.0 cm length of silicone-coated 4-0 nylon monofilament (diameter with coating 0.32 ± 0.02 mm, Guangzhou Jialing Biotechnology Co., Ltd., Guangzhou, China) was inserted into the left ECA and gently guided toward the ICA. The microsurgical clip from the ICA was removed and advanced toward the monofilament until the tip occluded the origin of the left middle cerebral artery (MCA), resulting in a decline of local cerebral blood flow to 20% of baseline. After 90 min MCAO, the perfusion of blood flow was regained by withdrawing the monofilament. Before its closing, the wound area was moisturized with sterile saline and lidocaine was applied as a topical analgesic. Isotonic saline was intraperitoneally injected to prevent dehydration. After wound closure, bupivacaine was applied along the sutures and the animal was placed in a temperature-controlled recovery chamber to monitor its behavior for 1–2 h. Finally, the rat was put back to the housing cage and moistened rodent chow was placed on the bottom of the cage to facilitate eating. Sham-operated rats were handled in the same way like the model group, although the monofilament was not used to achieve the occlusion of MCA.

Animal Grouping and Drug Treatment

After 22.5 h reperfusion, two independent observers, who were blinded to the experiment, tested the neurological deficits of the animals that had undergone MCAO surgery according to a five-point scale described previously by Longa et al. with a minor modification (Longa et al., 1989). The criteria were set as follows: score 0, no neurological deficit; score 1, mild focal neurological deficit (failure to fully extend contralateral forelimb); score 2, moderate focal neurological deficit (repetitive circling to the contralateral side); score 3, severe focal neurological deficit

(falling to the contralateral side); and score 4, unable to walk spontaneously with a depressed level of consciousness or death. A total of 130 rats with a score between 1 and 2 were selected for the present study. As shown in **Supplementary Figure S1**, apart from the Sham group, the selected experimental rats were randomly divided into five different groups, including I/R (model), Nim (positive control)+I/R, QSYQ low dose (150 mg/kg) + I/R, middle dose (300 mg/kg) + I/R, and high dose (600 mg/kg) + I/R groups. Rats in QSYQ (150 mg/kg, 300 mg/kg, 600 mg/kg) and Nim (12 mg/kg) groups were orally administered their respective dose once daily for 7 days. Meanwhile, the Sham-operated and I/R model groups were given 0.9% normal saline via gavage at a dose of 10 ml/kg.

Neurological Deficits and Mortality Rate

For the evaluation of neurological function, a modified Neurological Severity Score (mNSS) was used on days 1, 3, 5, and 7, respectively after MCAO. The mNSS was a synthetic scale, including motor function, sensory disturbance, balance, and reflection tests, graded on a score of 0–18 (Chen et al., 2001). The details were shown in **Supplementary Table S1**. One point was defined as inability to complete the tasks or no response to tests, while higher scores represented more serious neurological deficit. All tests were assessed by two independent investigators who were blinded to the experimental groups. The mortality rate of each group was calculated for the whole period of the drug treatment.

Behavioral Assay

Open field test was executed to evaluate the locomotor activity of experimental animals (Jin et al., 2015). On the 8th day after stroke, the rats were respectively placed in four open field locomotion chambers (50 cm in length× 50 cm in width× 40 cm wall height) made of plywood. The bottom of the chamber was actually divided by white drawn lines, composing nine equal-area grids. After 5 min adaption to the novel environment, the locomotor data of each rat was automatically recorded for 30 min and calculated using the ANY-maze software (version 4.82, Stoelting, United States). The following parameters were analyzed: total distance traveled by the animals and average speed. The behavioral assessment was performed in a quiet room, from 8:00–12:00 a.m., by two observers who were blinded to the animal experiment.

Gait Analysis

For the gait test, CatWalk XT 9.1 (Noldus Information Technology, Wageningen, Netherlands), an automated quantitative gait analysis system, was performed in this study (Orgah et al., 2019). Prior to surgery, rats were trained for at least three consecutive days to adapt to the walkway in a quiet room. On the 8th day after the MCAO or sham-operation, post-surgery testing was executed in the same conditions as the training period. Each experimental animal was placed individually on the runway and allowed to freely run back and forth until three accepted runs were recorded. The subsequent data analysis was handled using the Catwalk XT 9.1 Software. The main gait parameters, including walking speed (the speed of rats across the runway), base of support (distance between girdle paw pairs), stride length (distance the paw traveled from one step to the next), and stand (time duration of the paw in contact with the floor during a step cycle), were employed for assessing the effects of QSYQ on functional recovery. At least two observers who were blinded to the animal grouping carried out the CatWalk test and data analysis.

Micro-CT Imaging and Analysis

After 8 days post-reperfusion, anesthetized rats were intra-arterially injected with a clinically available iodinated x-ray contrast agent (Omnipaque) at 2.0 ml over a period of 20 s. Subsequently, the micro-Computed Tomography (CT) imaging technique was used to visualize the blood-brain barrier (BBB) disruption and cerebral edema (Park et al., 2014; Orgah et al., 2018). In brief, brain micro-CT imaging was performed using a small animal micro-CT imager (Quantum FX; PerkinElmer, United States) with the following main imaging parameters: voltage for 90 kV, current for 180 μA, field of view (FOV) for 40 mm, and scan for 4.5 min. BBB disruption was detected for Omnipaque leakage and cerebral edema was presented with position offset of midline. Next, the "VOL EDIT" module in Analyze 12.0 image analysis software (Analyze Direct, Overland Park, KS, United States) was applied to make 3D reconstructions of whole-cerebral slide images. The "ROI" measure module was used to calculate the mean micro-CT number (HU) of Omnipaque leakage and cerebral hemisphere volumes.

TTC Staining and Quantification of Infarct Volume

After performing micro-CT imaging, brains were quickly removed. Six pieces of 2 mm-thick coronal cerebral slices were obtained using a rat brain matrix (Shenzhen RWD life technology Co., Ltd., Guangzhou, China) and stained with 2% TTC solution in the dark for 10 min at 37°C. After stained cerebral slices were photographed, ImageJ image processing software (ImageJ 1.51, Wayne Rasband, National Institutes of Health, United States) was applied to measure cerebral infarct area. Ratios of infarct volume were displayed as a percentage (%) of (total cerebral infarct volume/total brain volume) ×100 (Lin et al., 1993).

Assessment of BBB Permeability

BBB permeability was examined by the extravasation of Evans Blue (EB) stain into the brain following the tail-vein injection. After 7 days post-reperfusion, rats were injected with 4% EB solution in 0.9% normal saline (2 ml/kg) via the tail vein. 24 h later, the brains suffering perfusion were cut into 2 mm-thick coronal slices. After recording the EB-stained cerebral sections, the Caliper IVIS Lumina K Series III system was used for fluorescent imaging detection [58]. Then, the Living Image® Software (version 4.3.1) was used to quantify the EB leakage via calculating a total radiant efficiency [(p/s)/(μW/cm2)].

TMT-Based Quantitative Proteomics Analysis

Sample Preparation

According to the above experimental results, rats from the model group (n = 3) and QSYQ high dose group (n = 3) were screened to

further perform proteomic analysis. A total of eight days after MCAO, anesthetized rats were transcardially perfused with prechilled saline and then the brains were immediately removed. The infarcted cerebral hemisphere tissues were separated, snap frozen in liquid nitrogen, and stored at -80°C until use. Protein extraction from the cerebral tissues were carried out referring to a method previously described (Zhu et al., 2014) with some modifications. In brief, all samples were homogenized in ice-cold lysis buffer. Subsequently, the homogenate was sonicated and boiled for 15 min. After centrifugation at 14,000 g for 40 min at 4°C, the supernatant was filtered with 0.22 μm filters. Protein content was determined using the BCA protein assay kit.

Protein Digestion Based on Filter-Aided Sample Preparation

Protein digestion was performed according to the method of filter-aided sample preparation (FASP) (Wisniewski et al., 2009). 200 μg of proteins for each sample were incorporated into 30 μL SDT buffer (4% SDS, 100 mM DTT, 150 mM Tris-HCl pH 8.0). The detergent, DTT, and other low-molecular-weight components were removed using UA buffer (8 M Urea, 150 mM Tris-HCl pH 8.0) by repeated ultrafiltration (Microcon units, 10 kD). Then 100 μL iodoacetamide (100 mM IAA in UA buffer) was added to block reduced cysteine residues and the samples were incubated for 30 min in the dark. The filters were washed with 100 μL UA buffer three times and then 100 μL100 mM TEAB buffer twice. Finally, the protein suspensions were digested with 4 μg trypsin (Promega) in 40 μL TEAB buffer overnight at 37°C, and the resulting peptides were collected as a filtrate. The peptide content was estimated by UV light spectral density at 280 nm using an extinctions coefficient of 1.1 of 0.1% (g/L) solution that was calculated on the basis of the frequency of tryptophan and tyrosine in vertebrate proteins.

TMT Labeling and Peptide Fractionation

According to the manufacturer's instructions, 100 μg peptide mixture of each sample was labeled using tandem mass tags (TMT) isobaric label reagents (Thermo Fisher Scientific). Subsequently, pierce high pH reversed-phase peptide fractionation kit (Thermo Fisher Scientific, Waltham, MA, United States) was used to fractionate TMT-labeled digest samples into 15 fractions by an increasing acetonitrile step-gradient elution according to instructions (Wei et al., 2018). The fractions were dried, lyophilized, and stored at -80 C until LC-MS/MS analysis.

Reversed-Phase Liquid Chromatography-Tandem Mass Spectrometry

The NanoLC-MS/MS analysis of each fraction was performed using a Q Exactive mass spectrometer (Thermo Fisher Scientific) that was coupled to an Easy nLC1000 HPLC system (Thermo Fisher Scientific). The labeled peptides were loaded onto a reverse phase trap column (Thermo Scientific Acclaim PepMap100, 100 μm inner diameter× 2 cm, nanoViper C18) connected to the C18-reversed phase analytical column (Thermo Scientific Easy Column, 10 cm long, 75 μm inner diameter, 3 μm resin) in buffer A (0.1% formic acid) and eluted with a 60 min linear gradient - 0–50% buffer B (84% acetonitrile and 0.1% formic acid), 50 min; 50–100% buffer B, 5 min; 100%–100% buffer B, 5 min - at a flow rate of 300 nL/min controlled by IntelliFlow technology. The mass spectrometer was operated in positive ion mode. MS data was acquired using a data-dependent top 10 method dynamically choosing the most abundant precursor ions from the survey scan (300–1800 m/z) for high-energy collision dissociation (HCD) fragmentation. Automatic gain control (AGC) target value was set to 3×10^6 with a maximum ion injection time of 10 ms. Dynamic exclusion duration was 40.0 s. The survey scans were acquired at a high resolution of 70,000 at m/z 200, resolution for HCD spectra was set to 17,500 at m/z 200, and isolation width was 2 m/z. Normalized collision energy was 30 eV and the underfill ratio, which specified the minimum percentage of the target value likely to be reached at maximum fill time, was defined as 0.1%. The instrument was run with peptide recognition mode enabled.

Protein Identification and Quantification

The MS/MS spectra were searched using MASCOT engine (Matrix Science, London, United Kingdom; version 2.2) embedded into Proteome Discoverer 1.4 (Thermo Fisher Scientific). Trypsin was chosen as the enzyme, allowing up to two missed cleavage sites. Carbamidomethylation (C), TMT 6-plex (N-term), and TMT 6-plex (lysine, K) were chosen as fixed modification. Oxidation (methionine, M) was regarded as a variable modification. The peptide mass tolerances were set at 20 ppm for MS1 spectra acquired, and the fragment mass tolerance for MS2 spectra was set to 0.1 Da. In this study, only rank 1 peptide and a false discovery rate (FDR) of ≤1% were accepted. The protein ratios were calculated as the median of only unique peptides of the protein. All peptide ratios were normalized by the median protein ratio, and the median protein ratio should be 1 after the normalization. Comparisons of the protein identification and quantitation results were done between each QSYQ high dose (H) and the corresponding model (M) groups. Significantly regulated proteins between experimental groups were determined based on their p-value (p-value<0.05). Only proteins with more than 1.20-fold or less than 0.833-fold change compared to control groups were considered differentially regulated.

Bioinformatics Analysis

In this study, Cluster 3.0 (http://bonsai.hgc.jp/~mdehoon/software/cluster/software.htm) and Java Treeview software (http://jtreeview.sourceforge.net) were used to perform hierarchical clustering analysis. Euclidean distance algorithm for similarity measure and average linkage clustering algorithm (clustering uses the centroids of the observations) for clustering were selected when carrying out hierarchical clustering. The acquired protein relative expression data was visualized as a

tree heat map. Then, the data, including significantly differential protein name, *p*-value, and log(fold change), were imported into Ingenuity® Pathway Analysis (IPA) system (http://www.ingenuity.com) to execute further analysis. "Core analysis-Diseases and Functions" module was performed to obtain the top diseases and functions related to the significantly differential proteins. "Build-Connection" module was used to analyze protein-protein interaction (PPI) network.

According to the direct functional degree of each protein, the importance of the protein in the PPI network was displayed. "Path designer" module was used to polish the network images and graphs.

The algorithm of the IPA analysis was based on Fisher's exact test with the enrichment score of *p*-value.

Immunohistochemistry Analysis

After 8 days post-reperfusion, brain tissues were quickly obtained from euthanized rats and then fixed in 4% paraformaldehyde for at least 48 h. The fixed tissues were dehydrated and embedded in paraffin blocks to be cut into 5 μm cerebral coronal paraffin slices. Subsequently, the sections were dewaxed in xylene and rehydrated followed by incubation with 3% hydrogen peroxide at room temperature for 10 min to block intrinsic peroxidase activity. After performing antigen repair, the brain slices were treated with blocking buffer (10% bovine serum) at 37 C for 1 h to block any nonspecific antibody responses. Next step, the sections were incubated overnight at 4 C using anti-galectin-3 antibody diluted with blocking buffer (1:50), then sequentially incubated with secondary antibody (the biotin-conjugated goat anti-rabbit IgG) diluted with blocking buffer (1:200) for 40 min at 37 C. The immunoreactivity of galectin-3 protein was visualized using a DAB substrate kit, followed by counterstaining hematoxylin, differentiation with 1% hydrochloric acid alcohol, dehydration, and sealing. Finally, the optical microscope (Vectra 3, PerkinElmer, United States) was carried out to observe and photograph the brain slices. ImagePro Plus software (National Institutes of Health, Bethesda, MD, United States) was executed to quantify the expression of galectin-3 by calculating the average optical density (AOD) value.

Western Blotting Analysis

The frozen post-ischemic hemisphere tissues (n = 3 per group) were collected in ice-cold RIPA lysis buffer containing serine proteases and acetylcholinesterase inhibitors. The lysates were centrifuged at 12,000 g for 10 min at 4 C. The BCA protein assay kit was used to measure the protein concentration. Equal amounts of 30 μg protein extracts were loaded and separated by 12% sodium dodecyl sulfate-polyacrylamide gels (SDS-PAGE) and transferred to polyvinylidene fluoride (PVDF) blotting membrane (GE Healthcare, Millipore, United States) using an electrophoresis apparatus (Tanon Science and Technology Co., Ltd., Shanghai, China). The membrane was blocked with a 5% non-fat milk-Tris-HCl-buffered saline and Tween 20 (TBST) solution for 3 h at room temperature, and then incubated overnight at C with the antibodies of anti-Galectin-3 (1:1,000) and anti-β-actin (1:2,000). After washing three times with TBST, the membrane was incubated with goat anti-rabbit IgG H&L (1:10,000) as the secondary antibody for 2 h at room temperature. After incubation finished, the membrane was washed three times (10 min each) and visualized using enhanced chemiluminescence detection reagents (TransGen Biotech Co., Ltd., Beijing, China). Western blotting bands were captured using the C-DiGit scanner with Image Studio (Version 5.2) imaging system. The quantification of band intensity was performed according to integrated density by ImageJ image processing software (ImageJ 1.42, Wayne Rasband, National Institutes of Health, United States).

Quantitative Real-Time Polymerase Chain Reaction Analysis

Total RNA samples from the post-ischemic hemisphere tissues were isolated using TRIzol® reagent (Invitrogen, Thermo Fisher Scientific, Inc., Waltham, MA, United States) according to the manufacturer's protocol. Subsequently, the complementary DNA (cDNA) was synthesized from 1 μg total RNA in a 20 μL reaction using Transcriptor First Strand cDNA Synthesis Kit (Roche, Mannheim, Germany).

The Bestar®Sybr Green qPCR Master Mix (DBI®Bioscience, Ludwigshafen, Germany) was used in reverse transcription-quantitative real-time polymerase chain reaction (RT-qPCR) to quantify the mRNA expression levels of LGALS3 (galectin-3), TNF-α, and IL-6 with glyceraldehyde 3-phosphate dehydrogenase (GAPDH) as an internal control. The designed gene-specific primers were obtained by Sangon Biotech (Shanghai, China) and the following oligonucleotide primer sequences were used: for LGALS3 forward 5′-GAG AAC AAC AGA AGA GTC ATC GTG-3′, reverse 5′-GAC CTG TAT TTT GAA TGG TTT GCC-3′; for TNF-α forward 5′-GCG TGT TCA TCC GTT CTC TA-3′, reverse 5′-CGT CTC GTG TGT TTC TGA GC-3′; for IL-6 forward 5′-ACC TGG AGT TTG TGA AGA ACA AC-3′, reverse 5′-GGA AGT TGG GGT AGG AAG GA-3′; for GAPDH forward 5′-GGC CTT CCG TGT TCC TAC C-3′, reverse 5′-CGC CTG CTT CAC CAC CTT C-3′.The amplification and analysis were performed using LightCycler®480 Software Version1.5.0.39 (Roche, Mannheim, Germany) for 45 cycles. The relative mRNA expression levels were calculated using 2−ΔΔCT method, following normalization to the housekeeping gene GAPDH.

Enzyme-Linked Immunosorbent Assay

After 8 days post-reperfusion, the blood samples were collected from anesthetized rats. Then, blood samples were centrifuged at 10,000 rpm for 15 min at 4 C to separate and obtain the serum. In order to measure the expression levels of TNF-α and IL-6 in serum, the rat TNF-α ELISA kit (ZC-37624, ZCi Biotechnology Co., Ltd.) and rat IL-6 ELISA kit (ZC-36404, ZCi Biotechnology Co., Ltd.) were applied according to the manufacturer's instructions. Finally, the protein concentrations of TNF-α and IL-6 in serum were calculated with the reference to the standard curve acquired from a gradient concentration standard substances provided by the assay kit.

Statistical analysis Statistical analysis was performed using Student's two-tailed t-test for comparison between two groups

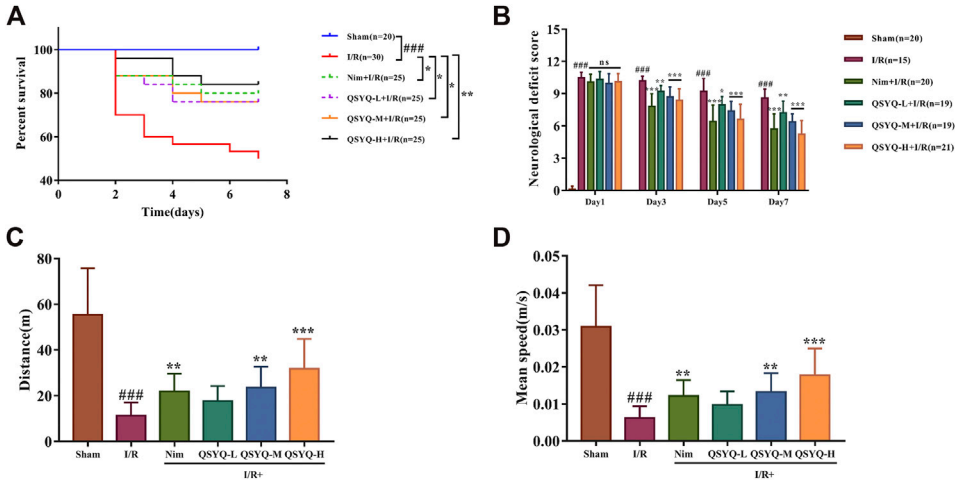

FIGURE 1 | Effect of treatment with QSYQ on survival rate and neurological as well as motor deficits caused by stroke. **(A)** The Kaplan-Meier survival curve of each group. Treatment with QSYQ at all doses or Nim improved the survival rate compared to the model group. **(B)** The mNSS scores on days 1, 3, 5, and 7 after I/R surgery. The model group exhibited serious neurological deficit among six groups on days 3, 5, and 7 after drug treatment, whereas QSYQ and positive control groups showed a distinct reduction in mNSS scores. **(C)** Bar graph representing results of traveled total distance (n = 15). QSYQ at middle and high doses/Nim + I/R groups obviously improved the total traveled distance compared to the stroke rats. **(D)** Bar graph representing results of mean speed (n = 15). QSYQ at middle and high doses/Nim + I/R groups significantly boosted the mean speed compared to the stroke rats. Data are expressed as the mean ± SD. #$p < 0.05$, ##p < 0.01, and ###$p < 0.001$ vs. the sham group; *$p < 0.05$, **$p < 0.01$, and ***$p < 0.001$ vs. the model group. I/R, ischemia/reperfusion; Nim, Nimodipine; QSYQ-L, QSYQ 150°mg/kg-low dose; QSYQ-M, QSYQ 300°mg/kg-middle dose; QSYQ-H, QSYQ 600°mg/kg-high dose.

and using one-way analysis of variance (ANOVA) followed by Dunnett's t-test for comparisons between multiple groups. The mortality was analyzed using the Kaplan-Meier survival curve. A value of $p < 0.05$ was defined as a statistically significant difference. Data from different experiments were expressed either as mean ± SD or mean ± SEM as indicated. GraphPad Prism 7 software (GraphPad Software, Inc., La Jolla, CA, United States) was used to generate all data graphs.

RESULTS

Chemical Profile of Major Ingredients in QSYQ by HPLC

To elucidate the main chemical components in QSYQ, HPLC analysis was performed in this study. A representative HPLC chromatogram was displayed in **Supplementary Figure S2**. Thirteen constituents in QSYQ were successfully identified according to the comparison of the retention times with standard substances, which was similar with the previous report (Zhang et al., 2018).

QSYQ Improved the Survival Rate and Neurological Scores of Subacute Stroke Rats

The Kaplan-Meier survival curve showed the survival proportion of the stroke-induced rats (**Figure 1A**). Rats after MCAO significantly increased mortality, especially during the acute period of reperfusion (first 72 h), compared to the sham group within the 7 day period of data collection. As expected, MCAO rats treated with low and middle doses of QSYQ or Nim obviously improved their survival rate ($p < 0.05$). Furthermore, treatment with QSYQ at high doses (600 mg/kg) increased the survival rate from 50 to 84% ($p < 0.01$; **Figure 1A**). As shown in **Figure 1B**, rats subjected to sham operation behaved normally without neurological deficit symptoms, however, the left side cerebral I/R surgery caused serious neurological deficit of rats in the model group. Compared with the model group, treatment with Nim or different doses of QSYQ markedly decreased scores with better neurological function. Moreover, QSYQ at middle and high doses had similar effects on neurological function to the Nim group (**Figure 1B**). In addition, we also carried out an open field test to measure the locomotor activity of experimental animals on post-stroke day 8. The data of total distance traveled by the animals and average speed within the 30 min indicated severe motor deficits in the model group (**Figures 1C,D**). Fortunately, the Nim, QSYQ middle dose (300 mg/kg), and QSYQ high dose (600 mg/kg) groups significantly enhanced the locomotor activity of stroke rats ($p < 0.01$).

QSYQ Ameliorated Motion Deficits of Subacute Stroke Rats

In this study, we applied CatWalk XT 9.1 system to conduct the gait test of rats in each group 8 days after the MCAO or sham-operation. The collected footprints of rats from each group were automatically labeled by the system as right front paw (RF), right hind paw (RH), left front paw (LF), and left hind paw (LH). Once auto-classification of labeled footprints was finished, we could obtain the corresponding gait parameters of each labeled paw. Then, a one-way between subjects ANOVA was used to compare

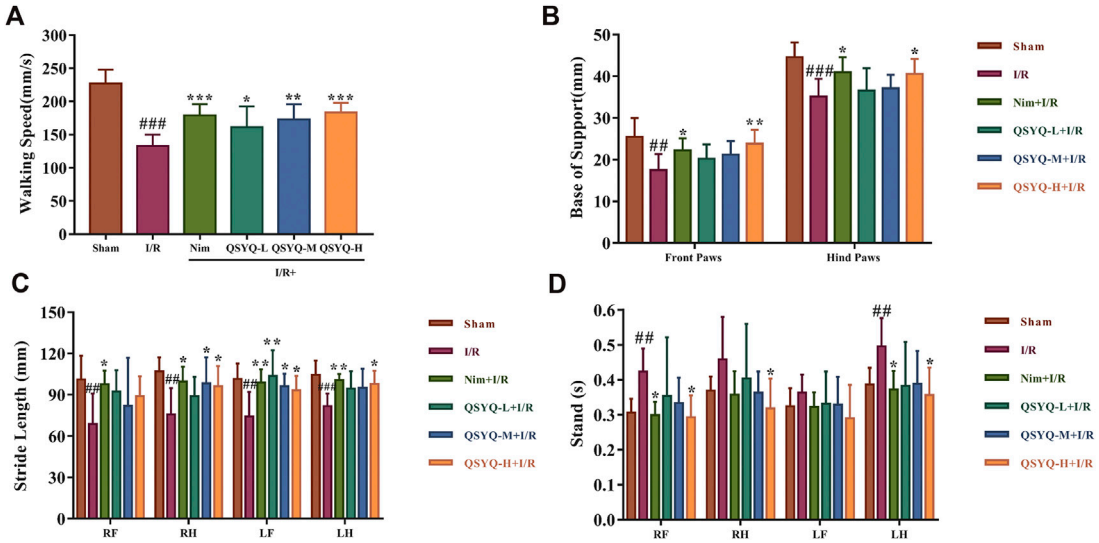

FIGURE 2 | Locomotive gait analysis and functional recovery of QSYQ treated subacute stroke rats. **(A–D)** Bar graph representation of main parameter statistics, including walking speed, BOS, stride length, and stand time, for estimating functional recovery of QSYQ-treated stroke rats (n = 8). Left brain lesion induced by I/R resulted in a significant motion deficits of rats. Fortunately, QSYQ treatment could attenuate the abnormal motion function during the 8th-days post-reperfusion. Data are presented as the mean ± SD. #$p < 0.05$, ##$p < 0.01$, and ###$p < 0.001$ vs. the sham group; *$p < 0.05$, **$p < 0.01$, and ***$p < 0.001$ vs. the model group. I/R, ischemia/reperfusion; Nim, Nimodipine; QSYQ-L, QSYQ 150°mg/kg-low dose; QSYQ-M, QSYQ 300°mg/kg-middle dose; QSYQ-H, QSYQ 600°mg/kg-high dose.

the effect of drugs on the function recovery of post-stroke motion impairment for walking speed, base of support (BOS), stride length, and stand time. In subacute phase of stroke, the rats subjected to MCAO significantly reduced walking speed, BOS, and stride length as well as increased stand time (**Figure 2**). Surprisingly, treatment with QSYQ could dose-dependently enhance walking speed (**Figure 2A**). Secondly, MCAO rats treated with QSYQ at high dose (600 mg/kg) obviously increased BOS of their front paws and hind paws (**Figure 2B**).

For the parameter of stride length, treatment with QSYQ at high dose (600 mg/kg) remarkably improved the impairment of RH, LF, and LH caused by stroke, while treatment with QSYQ at middle dose (300 mg/kg) only increased stride length in RH and LF (**Figure 2C**). Treatment with high doses of QSYQ positively reduced stand time of RF, RH, and LH (**Figure 2D**). As expected, treatment with Nim also obviously improved the deficit of locomotor function induced by cerebral ischemia and reperfusion (**Figure 2**).

QSYQ Reduced Cerebral Infarction Volume and Cerebral Edema in Subacute Stroke Rat Brain

By calculating the cerebral infarction volume in TTC-stained slices and indirectly assessing the severity of brain edema in micro-CT imaging, the brain injury in different groups on the 8th day after MCAO surgery was evaluated. Compared with the sham-operated group, the infarct volume was significantly increased in the experimental ischemic stroke model group (25.87 ± 2.88% of the cerebral volume), whereas treatment with Nim, QSYQ middle dose (300 mg/kg), and high dose (600 mg/kg) could exhibit a positive effect on reducing infarct volume induced by I/R injury (**Figures 3A,B**). According to the cerebral coronal image, we found that the model group presented the most obvious midline offset caused by cerebral edema, however, treatment with QSYQ at all three doses as well as Nim lessened the degree of midline offset (**Figure 3C**). Subsequently, Analyze 12.0 image analysis software was used to calculate the cerebral edema. Compared with the sham group, the ratio of the bilateral cerebral hemisphere volume markedly elevated on account of undergoing left MCAO surgical operation (**Figure 3D**). Similar to the result of Nim, treatment with QSYQ at three doses inhibited the ratio of the bilateral cerebral hemisphere volume, which confirmed that QSYQ treatment reduced cerebral edema in the subacute phase of the experimental animal model of ischemic stroke (**Figure 3D**).

QSYQ Attenuated BBB Disruption in Subacute Stroke Rats

IVIS fluorescent imaging and brain micro-CT imaging techniques were integrated to detect and quantify the BBB integrity. As a control, no EB extravasation, Omnipaque leakage, and detectable spectrum were observed in the sham group, whereas a significant leakage (EB and Omnipaque) of the BBB was detected in the model samples (**Figure 4**). Notably, treatment with both Nim and QSYQ high dose (600 mg/kg) significantly lowered EB extravasation and Omnipaque leakage (**Figure 4**). Treatment with QSYQ at middle dose (300 mg/kg) also reduced Omnipaque leakage, whereas treatment with QSYQ at middle dose (300 mg/kg) attenuated EB leakage to some extent, but did not reach significance (**Figures 4D,E**). The results of EB and Omnipaque extravasation indicated that treatment

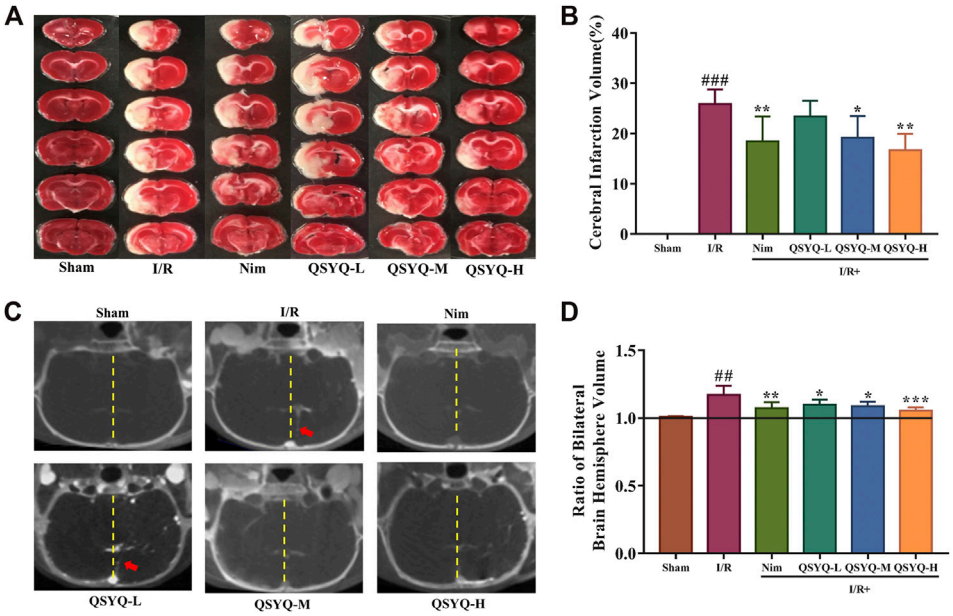

FIGURE 3 | Effect of treatment with QSYQ on cerebral infarction and cerebral edema in subacute stroke rat brain. **(A)** Representative images of TTC-stained brain slices of each group. The infarct areas were in white, whereas normal areas were in red. **(B)** Quantitative analysis of cerebral infarction volumes of each group (n = 6). QSYQ/Nim + I/R group significantly decreased the infarct volumes caused by MCAO. **(C)** Representative coronal cerebral slice image of each group. Yellow dotted line marks the cerebral midline and red arrows indicate offset distance of midline. **(D)** Quantitative analysis of the ratio of bilateral brain hemisphere volume of each group (n = 6). Treatment with QSYQ at three doses as well as Nim decreased the raised values of the ratio of bilateral brain hemisphere volume due to left cerebral I/R injury. TTC staining and cerebral edema data are presented as the mean ± SD. $^{\#}p< 0.05$, $^{\#\#}p< 0.01$, and $^{\#\#\#}p< 0.001$ vs. the sham group; $^{*}p< 0.05$, $^{**}p< 0.01$, and $^{***}p<0.001$ vs. the model group. I/R, ischemia/reperfusion; Nim, Nimodipine; QSYQ-L, QSYQ 150°mg/kg-low dose; QSYQ-M, QSYQ 300°mg/kg-middle dose; QSYQ-H, QSYQ 600°mg/kg-high dose.

with QSYQ at high dose (600 mg/kg) or Nim observably reduced BBB disruption of model rats in the subacute phase of experimental stroke.

Identification of Differentially Expressed Proteins Induced by QSYQ Treatment in the Brain of Subacute Stroke Rats.

To reveal the underlying molecular mechanisms of subacute phase (1.5 h ischemia and 8 days reperfusion) stroke protection against cerebral injury by QSYQ, TMT-based quantitative proteomics analysis was employed on the proteins extracted from ischemic brain tissues of MCAO/reperfusion rats with or without QSYQ treatment. A total of 34,187 unique peptides were detected (only rank 1 peptides and FDR ≤1% were accepted) and 5,813 proteins were identified by one or more unique peptides. Using a strict criteria (fold change >1.20 or <0.833, *p*-value <0.05), a total of 92 differentially expressed proteins in ischemic brain tissues were detected between QSYQ (high dose)-treated and the model groups. Among them, the expression levels of 40 proteins were significantly elevated with a fold change more than 1.20 in H (QSYQ high dose group) vs. M (model group), whereas the expression levels of 52 proteins were dramatically reduced with a fold change less than 0.833 in H (QSYQ high dose group) vs. M (model group), as displayed in a volcano plot in **Figure 5A**. Hierarchical clustering analysis of the acquired protein relative expression data were visualized in a tree heat map (**Figure 5B**), which supported the rationality of selecting differentially expressed proteins. The detailed information of significantly differentially expressed proteins was shown in **Supplementary Table S2**.

Network Pharmacology Analysis Revealed Galectin-3 Mediated Neuroinflammation as a Sey Mechanism of Subacute Stroke Protection by QSYQ.

To discover the molecular mechanisms accounting for the action of QSYQ treatment against ischemia and reperfusion injury, network pharmacology analysis was carried out using IPA system. The "Core analysis-Diseases and Functions" module was executed to gain the top diseases and functions strongly linked to the significantly differentially expressed proteins. Based on the Fisher's exact test algorithm of IPA, the diseases as well as functions were ranked according to corresponding *p*-value scores so as to distinguish the relatedness or importance among these proteins and diverse diseases as well as functions. The top 10 diseases and functions influenced by QSYQ in the order of descending -log (*p*-value) score were inflammatory response, cardiovascular disease, organismal injury and abnormalities, neurological disease, renal and urological disease, cancer, connective tissue disorders, inflammatory disease, skeletal and muscular disorders, and developmental disorder. As the inflammatory response ranked the highest with a -log

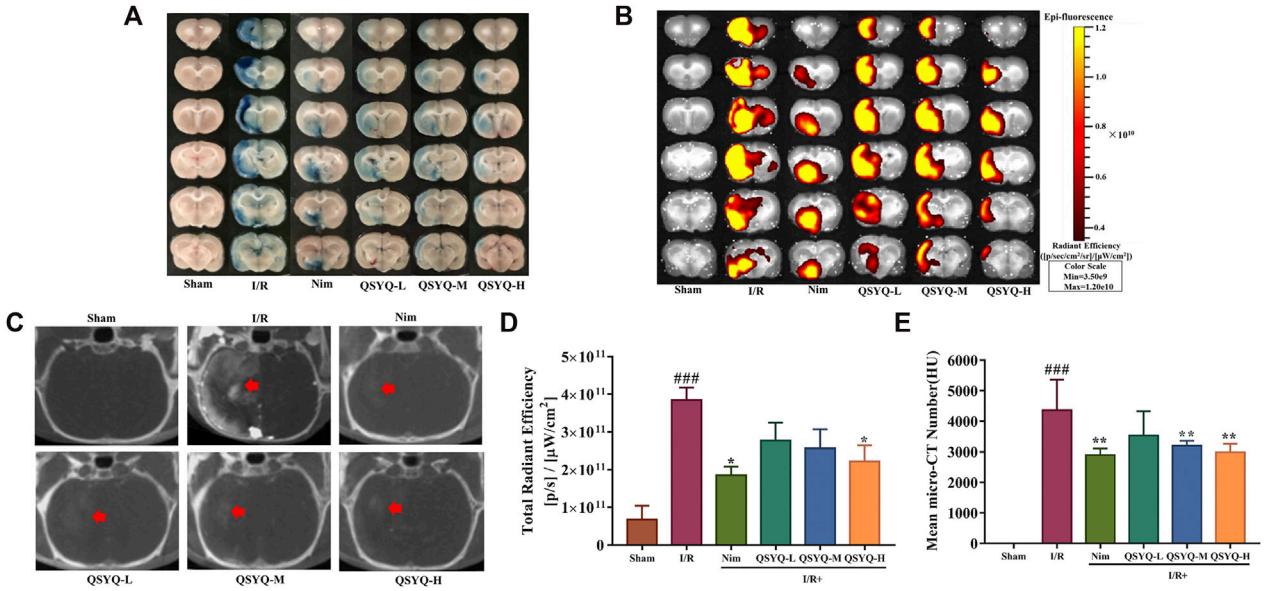

FIGURE 4 | Treatment with QSYQ reduced the BBB breakdown in subacute stroke rats. **(A)** Representative images of cerebral coronal slices of the experimental rats stained with EB dye after undergoing ischemic stroke (n = 5–6). **(B)** The corresponding fluorescent pictures of EB leakage of brain coronal sections (n = 5–6). **(C)** Representative cerebral micro-CT images of Omnipaque extravasation of each group (n = 6). Red arrows indicate the position of Omnipaque extravasation. **(D)** Quantitative analysis of EB leakage of cerebral coronal sections of rats in each group. Treatment with QSYQ at high dose/Nim markedly reduce EB leakage caused by BBB disruption compared with the model group. **(E)** Quantitative analysis of brain Omnipaque leakage of rats from each group. Treatment with QSYQ at middle and high doses as well as Nim significantly lowered Omnipaque extravasation caused by BBB disruption. The data of total radiant efficiency are expressed as mean ± SEM. The data of Omnipaque leakage are presented as mean SD. #$p < 0.05$, ##$p < 0.01$, and ###$p < 0.001$ vs. the sham group; *$p < 0.05$, **$p < 0.01$, and ***$p < 0.001$ vs. the model group. I/R, ischemia/reperfusion; Nim, Nimodipine; QSYQ-L, QSYQ 150°mg/kg-low dose; QSYQ-M, QSYQ 300°mg/kg-middle dose; QSYQ-H, QSYQ 600°mg/kg-high dose.

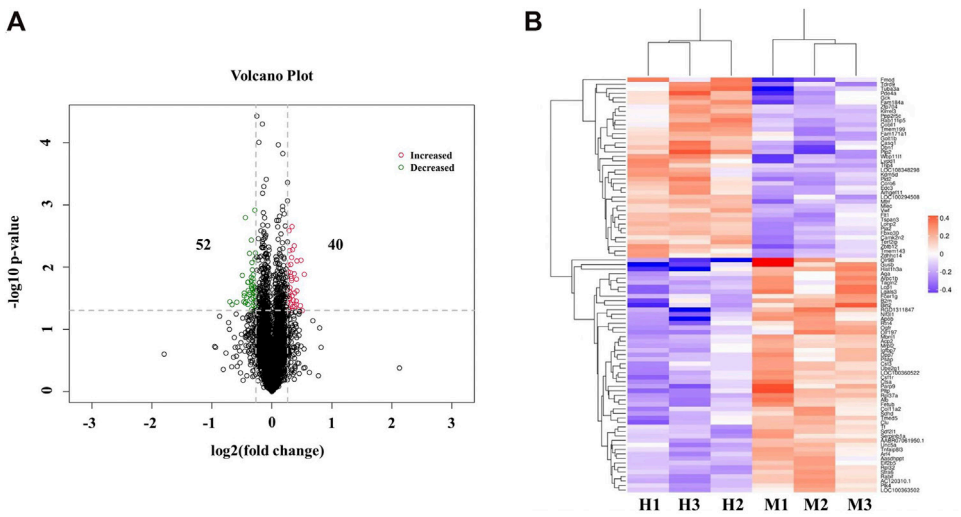

FIGURE 5 | Identification of differentially expressed proteins between QSYQ-treated group and the model group in ischemic brain of subacute stroke rats. **(A)** Volcano plot of differentially expressed proteins regulated by QSYQ treatment. The differentially expressed proteins in tested samples were presented in different colors. Red stands for the proteins of increased expression, green stands for the proteins of decreased expression, and black stands for proteins that are not differently expressed. **(B)** A tree heat map of hierarchical clustering analysis of the individual brain samples (n = 3). X-coordinates represented samples and Y-coordinates represented the gene name of differentially expressed proteins. The log2 (fold change) value of differentially expressed proteins in tested samples was expressed in different colors in the heat map, with red indicating up-regulation and blue indicating down-regulation. H means QSYQ at high dose (600 mg/kg) group; M means model group.

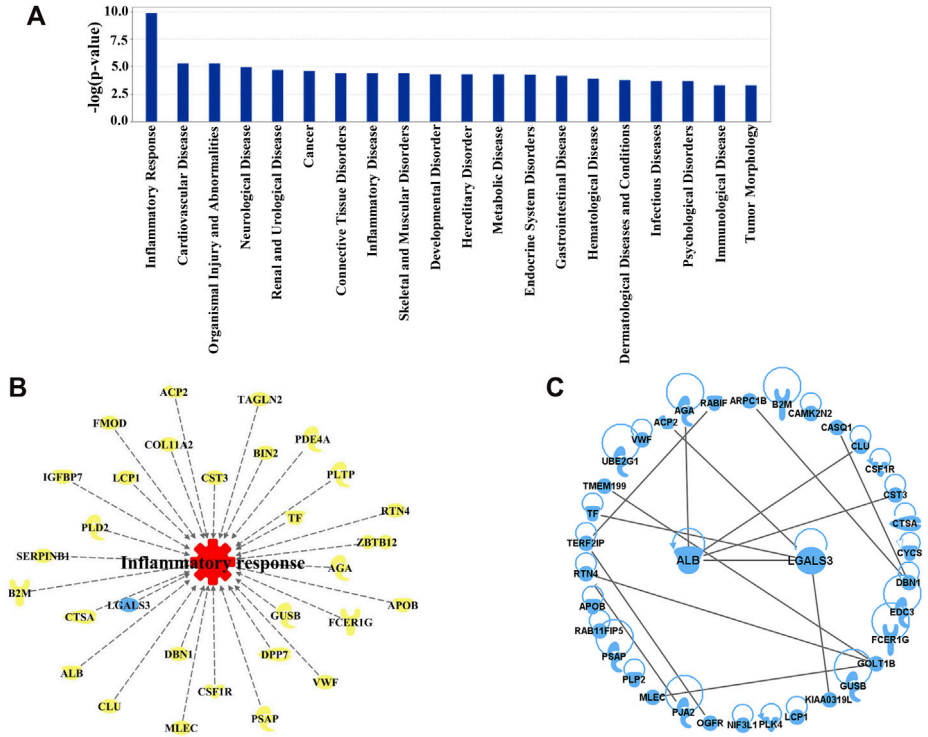

FIGURE 6 | (A) Diseases and Functions affected by QSYQ were ranked according to the Fisher's exact test algorithm. Top 20 diseases and functions were displayed in descending order based on -log (*p*-value) score. Among them, inflammatory response ranked the highest with a -log (*p*-value) score. **(B)** 30 important proteins correlated with inflammatory response picked out from 92 differentially expressed proteins modulated by QSYQ. **(C)** PPI network of the differentially expressed proteins. From the network, galectin-3 (LGALS3) and albumin (ALB) directly interact with the greatest number of proteins.

(*p*-value) score (**Figure 6A**), the result indicated that the anti-inflammatory mechanism could be one of the most vital mechanisms to explain QSYQ effective action against experimental stroke. The corresponding differentially expressed proteins involved in inflammatory response determined by "Build-Grow-Diseases and Functions" module of IPA (**Figure 6B**) showed that 30 proteins, including galectin-3 (LGALS3), albumin (ALB), cathepsin A (CTSA), clusterin (CLU), and transferrin (TF), participated in the inflammatory response. PPI network analysis positioned galectin-3 (LGALS3) and albumin (ALB) as the core proteins regulated by QSYQ since they displayed the most interactions with other significantly differentially expressed proteins revealed by our differential proteomic analysis (**Figure 6C**). The detailed information of PPI network analysis was shown in **Supplementary Table S3**.

QSYQ Reversed Galectin-3 Mediated Neuroinflammation in Subacute Stroke Brain Tissues

Based on the results of network pharmacology analysis, the differentially expressed protein of galectin-3 was found to act as a critical target involved in QSYQ-regulated inflammatory response during subacute stroke recovery. Both immunohistochemistry and western blotting were performed to confirm the results from the TMT-based quantitative proteomics analysis. As shown in **Figures 7A–D**, the protein expression level of galectin-3 was significantly increased in brain tissues of stroke rats in the subacute phase compared with the sham group. Treatment with high dose (600 mg/kg) of QSYQ markedly decreased galectin-3 expression compared to rats that underwent MCAO and reperfusion (**Figures 7A–D**). This was consistent with the above quantitative proteomic datasets. Since published literature reported that galectin-3 activated TLR-4 and downstream inflammatory targets like nuclear factor κB (NF-κB), resulting in an increase in the release of pro-inflammatory cytokines following brain injury (Burguillos et al., 2015), we compared the mRNA expression of the following genes - LGALS3 (galectin-3), TNF-α, and IL-6 - in rat brain samples from the sham group, cerebral I/R injury model group, and model treated with QSYQ (600 mg/kg) group by RT-qPCR. Compared with the sham group, MCAO and reperfusion caused obvious inflammation, as indicated by significant upregulation of these mRNA levels (**Figures 7E–G**). Importantly, treatment with high dose (600 mg/kg) of QSYQ distinctly downregulated mRNA expression of these neuroinflammation-related genes compared to the model group (**Figures 7E–G**).

QSYQ Reduced Proinflammatory Factors TNF-α and IL-6 in Serum

To gain an insight into the regulatory role of QSYQ on galectin-3 mediated inflammation in subacute ischemic stroke, serum levels

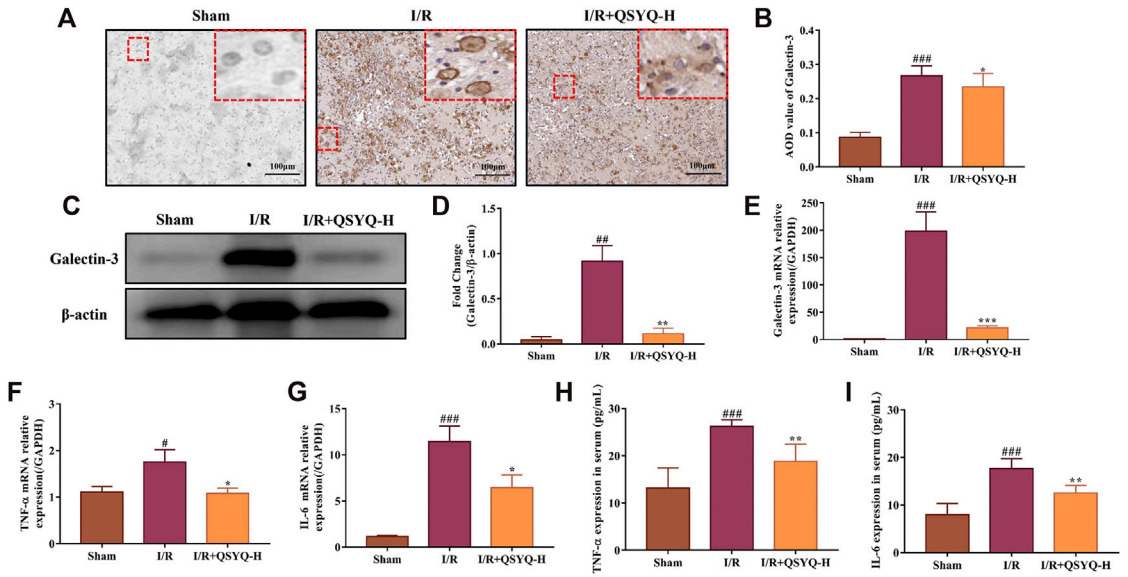

FIGURE 7 | The regulatory role of QSYQ on galectin-3 mediated neuroinflammation in response to cerebral ischemia and reperfusion injury. **(A)** Representative images of immunohistochemical staining of galectin-3 protein expression in brain tissue slices (×200 magnification). **(B)** Quantification of immunohistochemical staining (n = 3). **(C)** Representative images of western blotting of galectin-3. **(D)** The quantitative analysis of western blotting (n = 3). Treatment with high doses of QSYQ significantly reduced the protein expression level of galectin-3 compared with the model group. Relative expression levels of cerebral LGALS3 **(E)**, TNF-α **(F)**, and IL-6 **(G)** mRNA were evaluated by RT-qPCR (n = 3). Results were normalized to GAPDH expression. Treatment with high dose of QSYQ significantly decreased the mRNA expression of galectin-3-mediated inflammation related genes. Quantitative assessment the effect of QSYQ treatment on the release of TNF-α **(H)** and IL-6 **(I)** in rats serum following MCAO and reperfusion using ELISA kits (n = 6). The data of western blotting and ELISA are expressed as mean ± SD. Meanwhile, the data of RT-qPCR are presented as mean $^{\#}p < 0.05$, $^{\#\#}p < 0.01$, and $^{\#\#\#}p < 0.001$ vs. the sham group; $^{*}p < 0.05$, $^{**}p < 0.01$, and $^{***}p < 0.001$ vs. the model group. I/R, ischemia/reperfusion; QSYQ-H, QSYQ 600°mg/kg-high dose.

of TNF-α and IL-6 in different groups were determined by ELISA. As shown in **Figures 7H,I**, concentrations of TNF-α and IL-6 in serum were significantly higher in rats that underwent MCAO/reperfusion compared with that from sham-operated rats. As expected, treatment with QSYQ at high dose (600 mg/kg) markedly lowered the serum concentrations of TNF-α and IL-6 compared with the model group (**Figures 7H,I**).

DISCUSSION

Recovery after stroke is a complex, dynamic, multifactorial, and multicellular process (Alawieh et al., 2018; Sadler et al., 2020). No drugs or therapies have been approved for stroke recovery to date, in part due to inappropriate experimental models and because screen strategies focusing on single targets and drug molecules were used (Cramer, 2015). Our current study tested a hypothesis that a multi-component medicine, such as QSYQ, targeting different biological pathways would be more effective for post-stroke recovery. At present, QSYQ with the function of Qi-tonifying and blood-activating has been widely used to treat cardiovascular disease in clinic (Han et al., 2019). In addition to the cardioprotection against ischemia/reperfusion injury, we recently also reported the protective effect of pretreatment with QSYQ against CI/RI, which may be partly related to the modulation of neuroinflammatory response in an acute stroke model (Chen et al., 2015; Wang et al., 2020). However, questions remain on whether QSYQ contributes to the therapeutic post-stroke recovery and, if so, what the underlying mechanisms are.

To evaluate the efficacy of QSYQ for post-stroke recovery, we chose Nim as a positive control drug in the present study. Nim is a dihydropyridine calcium channel blocker and has been observed for its therapeutic application in stroke. Babu et al. showed that administration of Nim alleviated excitotoxicity and neurological deficits in experimental ischemic stroke rats (Babu and Ramanathan, 2011). Liu et al. found that Nim treatment reduced infarct volume and pathological damage and improved neurological function of subacute stroke animals (Liu et al., 2016). The beneficial effect of Nim on protecting BBB integrity has also been reported (Li et al., 2019). Since neurological and motor deficits are common in stroke patients, improvement of neural and behavioral outcomes are considered as necessary to estimate the action of anti-stroke drugs (Benjamin et al., 2019). Therefore, in addition to the parameters used in our previous acute CI/RI study, mNSS, open field test, and gait test were integrated to systematically evaluate the neuroprotective function of QSYQ on promoting post-stroke recovery in this work. Similar to Nim, the results indicated that treatment with QSYQ at middle (300 mg/kg) and high dose (600 mg/kg) markedly inhibited cerebral infarct volume as well as ameliorated neurological and behavioral impairment in subacute stroke rats (**Figures 1–3**), which revealed the beneficial effect of QSYQ on functional recovery.

BBB dysfunction, characterized by the structural disruption of tight junction protein complexes causing increased permeability, ion transporter dysfunction leading to cerebral edema, and further inflammatory damage induced by the infiltration and accumulation of peripheral immune cells and the activation of resident microglial cells, is a prominent pathological feature of ischemic stroke (Jiang et al., 2018). Damage to BBB permeability after cerebral ischemia and reperfusion is apparent in both the acute and subacute phases of ischemic stroke (~1–7°days) (Jiang et al., 2012). In response to CI/RI, multiple mechanisms may be involved in the restoration of BBB integrity, such as inflammatory response, oxidative stress, and angiogenesis (Jiang et al., 2018). The therapeutic strategies to promote BBB repair may enhance the functional recovery of the subject after ischemic stroke (Boese et al., 2018). In this study, the IVIS fluorescent imaging and brain micro-CT imaging techniques were respectively applied to measure BBB permeability. Significantly, treatment with QSYQ at high dose (600 mg/kg) and Nim obviously reduced the extravasation of EB and Omnipaque on account of BBB breakdown after ischemic stroke, which suggested the positive action of QSYQ against BBB disruption caused by ischemia and reperfusion (**Figure 4**). The data of micro-CT imaging also indicated decreased cerebral edema after three doses of QSYQ treatment, which could be observed in the subacute stage of CI/RI (**Figures 3C,D**).

Proteomics analysis takes a holistic approach to deciphering the complexity of biological systems and to characterizing protein interactions and biological networks that mediate physiological and pathological processes of diseases (Ji et al., 2015). In recent years, it has been increasingly applied to reveal the underlying mechanisms of TCM for multiple therapeutic effects on stroke treatment (Ning et al., 2012; Ji et al., 2015). TMT-based proteomics technique, employing chemical peptide labeling with amine-reactive isobaric tags, is a reliable method for large-scale multiplexed proteins relative quantification between multiple samples within a single experiment (Rauniyar et al., 2013). In this study, we applied TMT-based proteomics (TMT-LC-MS/MS) to label ischemic rat brain tissue samples to identify differentially expressed proteins following QSYQ treatment. As a result, a total of 5,813 proteins were identified, of which 92 were significantly differentially expressed (fold change >1.20 or <0.833, p-value <0.05) (**Figure 5A**). IPA analysis revealed that among the differentially expressed proteins, those with the highest -log (p-value) score were closely associated with inflammatory response, suggesting that post-stroke inflammation may be one of the main mechanisms underlying the beneficial action of QSYQ in enhancing functional recovery after CI/RI (**Figures 6A,B**). Importantly, subsequent PPI network analysis revealed that an inflammation-related protein named galectin-3 (LGALS3) could be tightly networked with other proteins (**Figure 6C**) and serve as a key player of QSYQ action at the subacute phase of stroke.

Inflammation has been recognized as a double-edged sword which could be either detrimental or beneficial depending on the particular stages after a stroke. In response to acute ischemic stroke, resident glial cells activation, infiltration of peripheral immune cells, release of pro-inflammatory cytokines and BBB disruption together orchestrate the post-stroke augmented inflammatory response, which contribute to a series of long-term secondary brain damages and neurological behavioral deficits (Rajkovic et al., 2018; Wang et al., 2018). In the late repair phase of CI/RI, neuroinflammation fundamentally participates in multiple brain recovery processes, including post-stroke neurogenesis, neurovascular unit remodeling, post-stroke synaptogenesis, and axonal sprouting, which synergistically promote neurological behavioral outcomes (Wang et al., 2018). Currently, the regulation of inflammation is considered as a primary target for the development of stroke therapies.

Recently, growing evidence has suggested that galectin-3 could act as an endogenous regulator of brain injury-related inflammation (Shin, 2013; Rahimian et al., 2018). In response to cerebral damage induced by stroke, high level expression of galectin-3 was observed in activated microglial cells localized in the ischemic lesion (Lalancette-Hebert et al., 2012). Burguillos *et al.* showed that microglia-secreted galectin-3 acted as an endogenous ligand for TLR-4 activation to amplify the pro-inflammatory response and led to hippocampal degeneration in the injured brain caused by ischemia (Burguillos et al., 2015). However, galectin-3 deficiency reduced the expression of pro-inflammatory cytokines and exerted a neuroprotective effect (Yip et al., 2017). Prins *et al.* reported that the absence of galectin-3 attenuated neuroinflammation and ameliorated neurological functional recovery after spinal cord injury (Prins et al., 2016). These findings suggested that galectin-3 could be regarded as a major immunomodulatory molecule that played a significant role in the modulation of brain inflammation and neurodegeneration. In this study, we found that treatment with QSYQ (600 mg/kg) distinctly downregulated the high expression level of galectin-3 protein in brain tissues from MCAO/reperfusion rats according to the quantitative proteomics analysis results, which was verified with the methods of RT-qPCR, immunohistochemistry, and western blot analysis (**Figures 7A–E**). The results indicated that the neuroprotective function of QSYQ against the subacute phase of CI/RI might act partly through the regulation of galectin-3-mediated inflammatory response.

The inflammatory cytokines, tumor necrosis factor-alpha (TNF-α) and interleukin-6 (IL-6), are generally considered to be representative contributors to neuroinflammation in ischemic stroke and are therefore promising potential targets in future stroke therapy (Lambertsen et al., 2019). In experimental stroke model of rodents, the increased expression levels of TNF-α mRNA and protein were observed in ischemic brain tissues (Berti et al., 2002; Haddad et al., 2006). In the subacute phase of CI/RI, the upregulated level of TNF-α and IL-6 contents could be detected in damaged brain tissues (Yang et al., 2019). The enhanced serum levels of TNF and IL-6 in stroke patients were tested on days 1, 3, and 7 after stroke when compared to the control group (Jiang et al., 2017). Furthermore, TNF-α was also reported to regulate neuronal networks involved in cognition and behavior (Baune et al., 2008). In the present work, we further showed that treatment with QSYQ (600 mg/kg) significantly reduced the mRNA levels of TNF-α and IL-6 in brain tissues of stroke rats after ischemia and reperfusion (**Figures 7F,G**). Moreover, the serum levels of TNF-α and IL-6

were markedly increased in the subacute phase of stroke, which were reversed by QSYQ (600 mg/kg) (**Figures 7H,I**). The data suggested that the beneficial effects of QSYQ on brain damage and neurological behavioral dysfunction induced by experimental stroke were partly *via* the modulation of galectin-3-mediated inflammatory reaction.

LIMITATION AND FUTURE DIRECTIONS

Although we demonstrated the efficacy and mechanism of QSYQ for post-stroke recovery, there are still limitations to this study. First, the clinical relevance of the rat subacute stroke model we used needs to be tested in human studies. Secondly, models of longer-term recovery are to be established and optimized to evaluate drugs and treatments that will benefit real-time patients. Thirdly, differential contributions of Yiqi (Qi-benefitting, i.e., Huangqi) and Huoxue (Blood-activiting, i.e., Danshen + Sanqi) components of QSYQ need to be distinguished and the active components involved needs defining.

CONCLUSION

In summary, the current work provides the first evidence for the beneficial action of treatment with QSYQ against the subacute phase of CI/RI, which may be closely associated with its potential to inhibit MCAO/reperfusion-induced upregulation of brain-injury-related inflammatory regulator galectin-3, as well as the pro-inflammatory cytokines TNF-α and IL-6. The results suggest that QSYQ exerts a neuroprotective role in the damaged brain caused by experimental stroke probably through modulating the galectin-3-mediated inflammatory response. The fact that QSYQ can improve post-stroke outcome needs further clarification, and more thorough and reliable experimental data are required to support its clinical application. Our study may provide a novel therapeutic agent of ischemic stroke.

DATA AVAILABILITY STATEMENT

All datasets generated for this study are included in the article and the **Supplementary Material**. Besides, the mass spectrometry proteomics data were deposited to the ProteomeXchange via the PRIDE partner repository with the dataset identifier PXD020936.

ETHICS STATEMENT

All animal experiments were performed in accordance with the international regulations, following the guidelines of the Laboratory Animal Ethics Committee of Tianjin University of TCM (Permit number: TCM-LAEC2016036) as well as Tianjin International Joint Academy of Biotechnology and Medicine (Permit number: TJAB-TJU20160024).

AUTHOR CONTRIBUTIONS

YZ designed and funded the study. YW and GX carried out MCAO surgery and brain tissue TTC staining. YQZ prepared the extracts of QSYQ and YW performed drug administration. YW executed micro-CT and IVIS imaging studies. LZ and XL performed the evaluation of the neurological deficits and mortality rate. JO and ZL participated in the open field test and gait analysis. YW performed IPA analysis. XL carried out immunohistochemistry. YW and XD carried out western blotting analysis. YW and SH performed RT-qPCR experiment. YW and HD executed ELISA experiment. WZ and YQZ provided key materials and executed HPLC analysis. JO, YF, and BZ contributed to the review and interpretation of the data. YW wrote the draft manuscript. YZ and YW. edited the final manuscript. All authors have read and agreed with the submission of the manuscript.

FUNDING

This work was supported by grants from the National Science Foundation of China (NSFC 81873037), the National Key Research and Development Plan (2018YFC1704502), the National Science and Technology Major Projects of China (2018ZX01031301), and the China Postdoctoral Science Foundation Grant (2020M681904).

ACKNOWLEDGMENTS

We appreciated Shanghai Applied Protein Technology Co., Ltd. (Shanghai, China) for the technical support of TMT-based quantitative proteomics analysis. We would also like to thank Jian Yang, Pengzhi Dong, and Rui Shao for discussion and suggestions, and the members of our laboratory, particularly Shan Li and Kai Huang, for technical assistance in some experiments.

SUPPLEMENTARY MATERIAL

The Supplementary Material for this article can be found online at: https://www.frontiersin.org/articles/10.3389/fphar.2021.588587/full#supplementary-material.

REFERENCES

Alawieh, A., Zhao, J., and Feng, W. W. (2018). Factors affecting post-stroke motor recovery: implications on neurotherapy after brain injury. *Behav. Brain Res.* 340, 94–101. doi:10.1016/j.bbr.2016.08.029

Babu, C. S., and Ramanathan, M. (2011). Post-ischemic administration of nimodipine following focal cerebral ischemic-reperfusion injury in rats alleviated excitotoxicity, neurobehavioural alterations and partially the bioenergetics. *Int. J. Dev. Neurosci.* 29 (1), 93–105. doi:10.1016/j.ijdevneu.2010.08.001

Baune, B. T., Wiede, F., Braun, A., Golledge, J., Arolt, V., and Koerner, H. (2008). Cognitive dysfunction in mice deficient for tnf- and its receptors. *Am. J. Med. Genet. B. Neuropsychiatr. Genet.* 147B (7), 1056–1064. doi:10.1002/ajmg.b.30712

Benjamin, E. J., Muntner, P., Alonso, A., Bittencourt, M. S., Callaway, C. W., Carson, A. P., et al. (2019). Heart disease and stroke statistics-2019 update: a report from the american heart association. *Circulation* 139 (10), e56–e528. doi:10.1161/CIR.0000000000000659

Berti, R., Williams, A. J., Moffett, J. R., Hale, S. L., Velarde, L. C., Elliott, P. J., et al. (2002). Quantitative real-time rt-pcr analysis of inflammatory gene expression associated with ischemia-reperfusion brain injury. *J. Cereb. Blood Flow. Metab.* 22 (9), 1068–1079. doi:10.1097/00004647-200209000-00004

Boese, A. C., Le, Q. E., Pham, D., Hamblin, M. H., and Lee, J. P. (2018). Neural stem cell therapy for subacute and chronic ischemic stroke. *Stem Cel. Res. Ther.* 9 (1), 154. doi:10.1186/s13287-018-0913-2

Burguillos, M. A., Svensson, M., Schulte, T., Boza-Serrano, A., Garcia-Quintanilla, A., Kavanagh, E., et al. (2015). Microglia-secreted galectin-3 acts as a toll-like receptor 4 ligand and contributes to microglial activation. *Cell. Rep.* 10 (9), 1626–1638. doi:10.1016/j.celrep.2015.02.012

Cao, H., Wang, P., Li, N., Liu, D., Ma, J., Fan, R., et al. (2017). Practice of comparative effectiveness research to identify treatment characteristics of similar chinese patent medicine for angina pectoris. *Evid. Based Complement. Alternat. Med.* 2017, 7062714. doi:10.1155/2017/7062714

Chen, J., Sanberg, P. R., Li, Y., Wang, L., Lu, M., Willing, A. E., et al. (2001). Intravenous administration of human umbilical cord blood reduces behavioral deficits after stroke in rats. *Stroke* 32 (11), 2682–2688. doi:10.1161/hs1101.098367

Chen, J. R., Wei, J., Wang, L. Y., Zhu, Y., Li, L., Olunga, M. A., et al. (2015). Cardioprotection against ischemia/reperfusion injury by qishenyiqi pill® via ameliorate of multiple mitochondrial dysfunctions. *Drug Des. Devel. Ther.* 9, 3051–3066. doi:10.2147/DDDT.S82146

Cramer, S. C. (2015). Drugs to enhance motor recovery after stroke. *Stroke* 46 (10), 2998–3005. doi:10.1161/STROKEAHA.115.007433

Dong, Q., Dong, Y., Liu, L., Xu, A., Zhang, Y., Zheng, H., et al. (2017). The chinese stroke association scientific statement: intravenous thrombolysis in acute ischaemic stroke. *Stroke. Vasc. Neurol.* 2 (3), 147–159. doi:10.1136/svn-2017-000074

Dong, R., Zhang, M., Hu, Q., Zheng, S., Soh, A., Zheng, Y., et al. (2018). Galectin-3 as a novel biomarker for disease diagnosis and a target for therapy (review). *Int. J. Mol. Med.* 41 (2), 599–614. doi:10.3892/ijmm.2017.3311

Famakin, B. M. (2014). The immune response to acute focal cerebral ischemia and associated post-stroke immunodepression: a focused review. *Aging Dis.* 5 (5), 307–326. doi:10.14336/AD.2014.0500307

Feigin, V. L., Roth, G. A., Naghavi, M., Parmar, P., Krishnamurthi, R., Chugh, S., et al. (2016). Global burden of stroke and risk factors in 188 countries, during 1990-2013: a systematic analysis for the global burden of disease study 2013. *Lancet Neurol.* 15 (9), 913–924. doi:10.1016/S1474-4422(16)30073-4

Goda, T., Oyama, N., Kitano, T., Iwamoto, T., Yamashita, S., Takai, H., et al. (2020). Prestroke conditions of acute ischemic stroke patients are associated with functional outcome after mechanical thrombectomy. *J. Stroke. Cerebrovasc. Dis.* 29 (2), 104540. doi:10.1016/j.jstrokecerebrovasdis.2019.104540

Gubskiy, I. L., Namestnikova, D. D., Cherkashova, E. A., Chekhonin, V. P., Baklaushev, V. P., Gubsky, L. V., et al. (2018). MRI guiding of the middle cerebral artery occlusion in rats aimed to improve stroke modeling. *Transl. Stroke. Res.* 9 (4), 417–425. doi:10.1007/s12975-017-0590-y

Haddad, M., Rhinn, H., Bloquel, C., Coqueran, B., Szabo, C., Plotkine, M., et al. (2006). Anti-inflammatory effects of pj34, a poly (adp-ribose) polymerase inhibitor, in transient focal cerebral ischemia in mice. *Br. J. Pharmacol.* 149 (1), 23–30. doi:10.1038/sj.bjp.0706837

Han, S. Y., Hong, Z. Y., Xie, Y. H., Zhao, Y., and Xu, X. (2017a). Therapeutic effect of chinese herbal medicines for post stroke recovery: a traditional and network meta-analysis. *Med. (Baltimore)* 96 (49), e8830. doi:10.1097/MD.0000000000008830

Han, J. Y., Li, Q., Ma, Z. Z., and Fan, J. Y. (2017b). Effects and mechanisms of compound chinese medicine and major ingredients on microcirculatory dysfunction and organ injury induced by ischemia/reperfusion. *Pharmacol. Ther.* 177, 146–173. doi:10.1016/j.pharmthera.2017.03.005

Han, J. Y., Li, Q., Pan, C. S., Sun, K., and Fan, J. Y. (2019). Effects and mechanisms of qishenyiqi pills and major ingredients on myocardial microcirculatory disturbance, cardiac injury and fibrosis induced by ischemia-reperfusion. *Pharmacol. Res.* 147, 104386. doi:10.1016/j.phrs.2019.104386

Ji, Q., Zhu, F., Liu, X., Li, Q., and Su, S. B. (2015). Recent advance in applications of proteomics technologies on traditional chinese medicine research. *Evid. Based. Complement. Alternat. Med.* 2015, 983139. doi:10.1155/2015/983139

Jiang, Q., Ewing, J. R., and Chopp, M. (2012). MRI of blood-brain barrier permeability in cerebral ischemia. *Transl. Stroke. Res.* 3 (1), 56–64. doi:10.1007/s12975-011-0133-10.1007/s12975-011-0133-x

Jiang, C., Kong, W., Wang, Y., Ziai, W., Yang, Q., Zuo, F., et al. (2017). Changes in the cellular immune system and circulating inflammatory markers of stroke patients. *Oncotarget* 8 (2), 3553–3567. doi:10.18632/oncotarget.12201

Jiang, X., Andjelkovic, A. V., Zhu, L., Yang, T., Bennett, M. V. L., Chen, J., et al. (2018). Blood-brain barrier dysfunction and recovery after ischemic stroke. *Prog. Neurobiol.* 163–164, 144–171. doi:10.1016/j.pneurobio.2017.10.001

Jin, R., Liu, L., Zhang, S., Nanda, A., and Li, G. (2013). Role of inflammation and its mediators in acute ischemic stroke. *J. Cardiovasc. Transl. Res.* 6 (5), 834–851. doi:10.1007/s12265-013-9508-6

Jin, Y., Raviv, N., Barnett, A., Bambakidis, N. C., Filichia, E., and Luo, Y. (2015). The shh signaling pathway is upregulated in multiple cell types in cortical ischemia and influences the outcome of stroke in an animal model. *PLoS One* 10 (4), e0124657. doi:10.1371/journal.pone.0124657

Kalogeris, T., Baines, C. P., Krenz, M., and Korthuis, R. J. (2012). Cell biology of ischemia/reperfusion injury. *Int. Rev. Cel. Mol. Biol.* 298, 229–317. doi:10.1016/B978-0-12-394309-5.00006-7

Lalancette-Hebert, M., Swarup, V., Beaulieu, J. M., Bohacek, I., Abdelhamid, E., Weng, Y. C., et al. (2012). Galectin-3 is required for resident microglia activation and proliferation in response to ischemic injury. *J. Neurosci.* 32 (30), 10383–10395. doi:10.1523/JNEUROSCI.1498-12.2012

Lambertsen, K. L., Finsen, B., and Clausen, B. H. (2019). Post-stroke inflammation-target or tool for therapy. *Acta Neuropathol.* 137 (5), 693–714. doi:10.1007/s00401-018-1930-z

Li, P., Stetler, R. A., Leak, R. K., Shi, Y., Li, Y., Yu, W., et al. (2018). Oxidative stress and dna damage after cerebral ischemia: potential therapeutic targets to preserve the genome and improve stroke recovery. *Neuropharmacology* 134, 208–217. doi:10.1016/j.neuropharm.2017.11.011

Li, S., Bian, L., Fu, X., Ai, Q., Sui, Y., Zhang, A., et al. (2019). Gastrodin pretreatment alleviates rat brain injury caused by cerebral ischemic-reperfusion. *Brain Res.* 1712, 207–216. doi:10.1016/j.brainres.2019.02.006

Lin, L., Wang, X., and Yu, Z. (2016). Ischemia-reperfusion injury in the brain: mechanisms and potential therapeutic strategies. *Biochem. Pharmacol. (Los Angel).* 5 (4), 213. doi:10.4172/2167-0501.1000213

Lin, T. N., He, Y. Y., Wu, G., Khan, M., and Hsu, C. Y. (1993). Effect of brain edema on infarct volume in a focal cerebral ischemia model in rats. *Stroke* 24 (1), 117–121. doi:10.1161/01.str.24.1.117

Liu, B., Li, F., Shi, J., Yang, D., Deng, Y., and Gong, Q. (2016). Gastrodin ameliorates subacute phase cerebral ischemia-reperfusion injury by inhibiting inflammation and apoptosis in rats. *Mol. Med. Rep.* 14 (5), 4144–4152. doi:10.3892/mmr.2016.5785

Longa, E. Z., Weinstein, P. R., Carlson, S., and Cummins, R. (1989). Reversible middle cerebral artery occlusion without craniectomy in rats. *Stroke* 20 (1), 84–91. doi:10.1161/01.str.20.1.84

Lopez, M. S., and Vemuganti, R. (2018). Modeling transient focal ischemic stroke in rodents by intraluminal filament method of middle cerebral artery occlusion. *Methods Mol. Biol.* 1717, 101–113. doi:10.1007/978-1-4939-7526-6_9

Ma, Y., Liu, Y., Zhang, Z., and Yang, G. Y. (2019). Significance of complement system in ischemic stroke: a comprehensive review. *Aging Dis.* 10 (2), 429–462. doi:10.14336/AD.2019.0119

Ning, M., Lopez, M., Cao, J., Buonanno, F. S., and Lo, E. H. (2012). Application of proteomics to cerebrovascular disease. *Electrophoresis* 33 (24), 3582–3597. doi:10.1002/elps.201200481

Orgah, J. O., Yu, J., Zhao, T., Wang, L., Yang, M., Zhang, Y., et al. (2018). Danhong injection reversed cardiac abnormality in brain-heart syndrome via local and remote β-adrenergic receptor signaling. *Front. Pharmacol.* 9, 692. doi:10.3389/fphar.2018.00692

Orgah, J. O., Ren, J., Liu, X., Orgah, E. A., Gao, X. M., and Zhu, Y. (2019). Danhong injection facilitates recovery of post-stroke motion deficit via parkin-enhanced mitochondrial function. *Restor. Neurol. Neurosci.* 37 (4), 375–395. doi:10.3233/RNN-180828

Pan, J., Konstas, A. A., Bateman, B., Ortolano, G. A., and Pile-Spellman, J. (2007). Reperfusion injury following cerebral ischemia: pathophysiology, mr imaging, and potential therapies. *Neuroradiology* 49 (2), 93–102. doi:10.1007/s00234-006-0183-z

Park, J. Y., Lee, S. K., Kim, J. Y., Je, K. H., Schellingerhout, D., and Kim, D. E. (2014). A new micro-computed tomography-based high-resolution blood-brain barrier imaging technique to study ischemic stroke. *Stroke* 45 (8), 2480–2484. doi:10.1161/STROKEAHA.114.006297

Peng, T., Jiang, Y., Farhan, M., Lazarovici, P., Chen, L., and Zheng, W. (2019). Anti-inflammatory effects of traditional chinese medicines on preclinical in vivo models of brain ischemia-reperfusion-injury: prospects for neuroprotective drug discovery and therapy. *Front. Pharmacol.* 10, 204. doi:10.3389/fphar.2019.00204

Prins, C. A., Almeida, F. M., and Martinez, A. M. B. (2016). Absence of galectin-3 attenuates neuroinflammation improving functional recovery after spinal cord injury. *Neural Regen. Res.* 11 (1), 92–93. doi:10.4103/1673-5374.175051

Puig, J., Blasco, G., Daunis-I-Estadella, P., van Eendenburg, C., Carrillo-García, M., Aboud, C., et al. (2017). High-permeability region size on perfusion ct predicts hemorrhagic transformation after intravenous thrombolysis in stroke. *PLoS One* 12 (11), e0188238. doi:10.1371/journal.pone.0188238

Rahimian, R., Beland, L. C., and Kriz, J. (2018). Galectin-3: mediator of microglia responses in injured brain. *Drug Discov. Today* 23 (2), 375–381. doi:10.1016/j.drudis.2017.11.004

Rajkovic, O., Potjewyd, G., and Pinteaux, E. (2018). Regenerative medicine therapies for targeting neuroinflammation after stroke. *Front. Neurol.* 9, 734. doi:10.3389/fneur.2018.00734

Rauniyar, N., Gao, B., McClatchy, D. B., and Yates, J. R. (2013). Comparison of protein expression ratios observed by sixplex and duplex tmt labeling method. *J. Proteome. Res.* 12 (2), 1031–1039. doi:10.1021/pr3008896

Sadler, R., Cramer, J. V., Heindl, S., Kostidis, S., Betz, D., Zuurbier, K. R., et al. (2020). Short-chain fatty acids improve poststroke recovery via immunological mechanisms. *J. Neurosci.* 40 (5), 1162–1173. doi:10.1523/JNEUROSCI.1359-19.2019

Shang, H., Zhang, J., Yao, C., Liu, B., Gao, X., Ren, M., et al. (2013). Qi-shen-yi-qi dripping pills for the secondary prevention of myocardial infarction: a randomised clinical trial. *Evid. Based. Complement. Alternat. Med.* 2013, 738391. doi:10.1155/2013/738391

Shen, Y. F., Yu, W. H., Dong, X. Q., Du, Q., Yang, D. B., Wu, G. Q., et al. (2016). The change of plasma galectin-3 concentrations after traumatic brain injury. *Clin. Chim. Acta* 456, 75–80. doi:10.1016/j.cca.2016.02.029

Shin, T. (2013). The pleiotropic effects of galectin-3 in neuroinflammation: a review. *Acta Histochem.* 115 (5), 407–411. doi:10.1016/j.acthis.2012.11.010

Sun, K., Fan, J., and Han, J. (2015). Ameliorating effects of traditional chinese medicine preparation, chinese materia medica and active compounds on ischemia/reperfusion-induced cerebral microcirculatory disturbances and neuron damage. *Acta Pharm. Sin. B* 5 (1), 8–24. doi:10.1016/j.apsb.2014.11.002

Uluc, K., Miranpuri, A., Kujoth, G. C., Akture, E., and Başkaya, M. K. (2011). Focal cerebral ischemia model by endovascular suture occlusion of the middle cerebral artery in the rat. *J. Vis. Exp.* 48, 1978. doi:10.3791/1978

Wang, X., Xuan, W., Zhu, Z. Y., Li, Y., Zhu, H., Zhu, L., et al. (2018). The evolving role of neuro-immune interaction in brain repair after cerebral ischemic stroke. *CNS. Neurosci. Ther.* 24 (12), 1100–1114. doi:10.1111/cns.13077

Wang, Y., Xiao, G., He, S., Liu, X., Zhu, L., Yang, X., et al. (2020). Protection against acute cerebral ischemia/reperfusion injury by qishenyiqi via neuroinflammatory network mobilization. *Biomed. Pharmacother.* 125, 109945. doi:10.1016/j.biopha.2020.109945

Wei, Y., Fang, C. L., Liu, S. J., Yang, W. Q., Wei, L. S., Lei, X. J., et al. (2018). Long-term moderate exercise enhances specific proteins that constitute neurotrophin signaling pathway: a tmt-based quantitative proteomic analysis of rat plasma. *J. Proteomics* 185, 39–50. doi:10.1016/j.jprot.2018.06.017

Wisniewski, J. R., Zougman, A., Nagaraj, N., and Mann, M. (2009). Universal sample preparation method for proteome analysis. *Nat. Methods* 6 (5), 359–362. doi:10.1038/nmeth.1322

Yang, J. L., Mukda, S., and Chen, S. D. (2018). diverse roles of mitochondria in ischemic stroke. *Redox Biol.* 16, 263–275. doi:10.1016/j.redox.2018.03.002

Yang, S., Wang, H., Yang, Y., Wang, R., Wang, Y., Wu, C., et al. (2019). Baicalein administered in the subacute phase ameliorates ischemia-reperfusion-induced brain injury by reducing neuroinflammation and neuronal damage. *Biomed. Pharmacother.* 117, 109102. doi:10.1016/j.biopha.2019.109102

Yip, P. K., Carrillo-Jimenez, A., King, P., Vilalta, A., Nomura, K., Chau, C. C., et al. (2017). Galectin-3 released in response to traumatic brain injury acts as an alarmin orchestrating brain immune response and promoting neurodegeneration. *Sci. Rep.* 7, 41689. doi:10.1038/srep41689

Yu, J., Zhang, W., Zhang, Y., Wang, Y., Zhang, B., Fan, G., et al. (2017). A critical courier role of volatile oils from dalbergia odorifera for cardiac protection in vivo by qishenyiqi. *Sci. Rep.* 7 (1), 7353. doi:10.1038/s41598-017-07659-x

Zhang, Y., Yu, J., Zhang, W., Wang, Y., He, Y., Zhou, S., et al. (2018). An Integrated evidence-based targeting strategy for determining combinatorial bioactive ingredients of a compound herbal medicine qishen yiqi dripping pills. *J. Ethnopharmacol.* 219, 288–298. doi:10.1016/j.jep.2018.02.041

Zhang, B., Saatman, K. E., and Chen, L. (2020). Therapeutic potential of natural compounds from chinese medicine in acute and subacute phases of ischemic stroke. *Neural Regen. Res.* 15 (3), 416–424. doi:10.4103/1673-5374.265545

Zhu, Y., Xu, H., Chen, H., Xie, J., Shi, M., Shen, B., et al. (2014). Proteomic analysis of solid pseudopapillary tumor of the pancreas reveals dysfunction of the endoplasmic reticulum protein processing pathway. *Mol. Cel. Proteomics* 13 (10), 2593–2603. doi:10.1074/mcp.M114.038786

Conflict of Interest: YQZ was employed by Tasly Holding Group Co., Ltd.

The remaining authors declare that the research was conducted in the absence of any commercial or financial relationships that could be construed as a potential conflict of interest.

Copyright © 2021 Wang, He, Liu, Li, Zhu, Xiao, Du, Du, Zhang, Zhang, Orgah, Feng, Zhang and Zhu. This is an open-access article distributed under the terms of the Creative Commons Attribution License (CC BY). The use, distribution or reproduction in other forums is permitted, provided the original author(s) and the copyright owner(s) are credited and that the original publication in this journal is cited, in accordance with accepted academic practice. No use, distribution or reproduction is permitted which does not comply with these terms.

frontiers in Pharmacology

METHODS
published: 22 April 2021
doi: 10.3389/fphar.2021.575726

An Effective Workflow for Differentiating the Same Genus Herbs of Chrysanthemum morifolium Flower and Chrysanthemum Indicum Flower

Jiao He[1], *Qian Zhang*[1], *Cuiying Ma*[2], *Gabriel I. Giancaspro*[2], *Kaishun Bi*[1] *and Qing Li*[1]*

[1]School of Pharmacy, Shenyang Pharmaceutical University, Shenyang, China, [2]Department of Dietary Supplements and Herbal Medicines, Science Division, United States Pharmacopeial Convention, Rockville, MD, United States

C. morifolium flower and *C. indicum* flower are two closely related herbal species with similar morphological and microscopic characteristics but are discriminated in edible and medicinal purpose. However, there is no effective approach to distinguish the two herbs. A novel workflow for quickly differentiating *C. morifolium* flower and *C. indicum* flower was developed. Firstly, the difference in anti-inflammatory effects for *C. morifolium* flower and *C. indicum* flower was characterized using lipopolysaccharide-treated rats. Then HPLC fingerprint analysis for 53 batches of *C. morifolium* flowers and 33 batches of *C. indicum* flower was carried out to deep profile the chemical components. The preliminary markers were screened out by OPLS-DA, identified by HPLC-ESI-QTOF-MS, and quantified by the improved SSDMC (single reference standard to determine multiple compounds) approach. Finally, multiple statistical data mining was performed to confirm the markers and a binary logistic regression equation was built to differentiate *C. morifolium* flower and *C. indicum* flower successfully. In general, the established workflow was rapid, effective and highly feasible, which would provide a powerful tool for herb identification.

Keywords: *Chrysanthemum* morifolium flower, *Chrysanthemum* indicum flower, comparative evaluation, anti-inflammatory, phytochemical analysis

OPEN ACCESS

Edited by:
Javier Echeverria,
University of Santiago, Chile

Reviewed by:
Jen-Tsung Chen,
National University of Kaohsiung, Taiwan
Jingyi Gu,
University College London, United Kingdom

***Correspondence:**
Qing Li
lqyxm@hotmail.com

Specialty section:
This article was submitted to Ethnopharmacology, a section of the journal Frontiers in Pharmacology

Received: *24 June 2020*
Accepted: *29 March 2021*
Published: *22 April 2021*

Citation:
He J, Zhang Q, Ma C, Giancaspro GI, Bi K and Li Q (2021) An Effective Workflow for Differentiating the Same Genus Herbs of Chrysanthemum morifolium Flower and Chrysanthemum Indicum Flower. Front. Pharmacol. 12:575726. doi: 10.3389/fphar.2021.575726

INTRODUCTION

Chrysanthemum morifolium flower [*Chrysanthemum x morifolium* (Ramat.) Hemsl.] and its wild relative, *Chrysanthemum indicum* flower (*Chrysanthemum indicum* L.), are commonly used as medicinal and edible cognate plants in Asia. *C. morifolium* flower and *C. indicum* flower have been widely used as food supplements, as well as herbal teas and health foods in China for 3,000 years (Lin and Harnly, 2010). Modern pharmacological studies indicate that both the two herbs possess various

Abbreviations: 5-HT, 5-hydroxytryptamine; CFDA, china food and drug administration; CIE, *Chrysanthemum indicum* flower exact; CME, *Chrysanthemum. morifolium* flower extract; COX-2, cyclooxygenase-2; DEX, dexamethasone sodium phosphate injection; ESM, external standard method; HIS, histamine; HPLC-DAD, high performance liquid chromatography diode-array detector; HPLC-ESI-QTOF-MS, high performance liquid chromatography-electrospray ionization-quadrupole tandem time-of-flight mass spectrometry; IL-1β (IL-4, IL-6, IL-8, IL-10), interleukin 1β (interleukin 4, 6, 8, 10); LOD, limits of detection; LOQ, limits of quantification; LPS, lipopolysaccharides; NO, nitric oxide; NOS, nitric oxide synthase; OPLS-DA, orthogonal partial least squares discrimination analysis; PGE2, prostaglandin E2; RRF, relative response factor; RRT, relative response time; SSDMC, single reference standard to determine multiple compounds; RSD, relative standard deviation; TNF-α, tumor necrosis factor-α; UV, ultraviolet.

FIGURE 1 | Representative photos of *C. morifolium* flower and *C. indicum* flower.

bioactivities, including anti-inflammation (Su et al., 2012; Han et al., 2015), antioxidation (Cui et al., 2012), cardiovascular protection (He et al., 2012), anticancer (Liu et al., 2018), etc.

In the Chinese Pharmacopoeia, *C. morifolium* flower is used for "scattering cold," "cleaning heat and toxin," and "brightening eyes," and *C. indicum* flower is used to remove toxic heat (Chinese Pharmacopoeia Commission, 2020). Inflammation is the basic pathological changes of all these diseases. Inflammatory cytokines play an important role in the process, which is the interaction between pro-inflammatory cytokines like tumor necrosis factor-α (TNF-α), prostaglandin E2 (PGE2), interleukin (IL)-2, IL-6, IL-17, IL-23, and anti-inflammatory cytokines such as IL-4, IL-10, and IL-13 (Cheng et al., 2005). The dynamic change between pro-cytokines and anti-cytokines determines the ending and outcome of inflammation. Research on cytokines in inflammation especially in infective inflammation is meaningful as it may be the next breakthrough of a thorough cure in inflammatory disease (Gabay and Kushner, 1999; Kim et al., 2015). However, a comparative study of the anti-inflammatory activity of the two herbs remains to be investigated.

Though there are some differences between fresh *C. morifolium* flower and *C. indicum* flower, multiple batches of *C. morifolium* flower and *C. indicum* flower materials were easy to

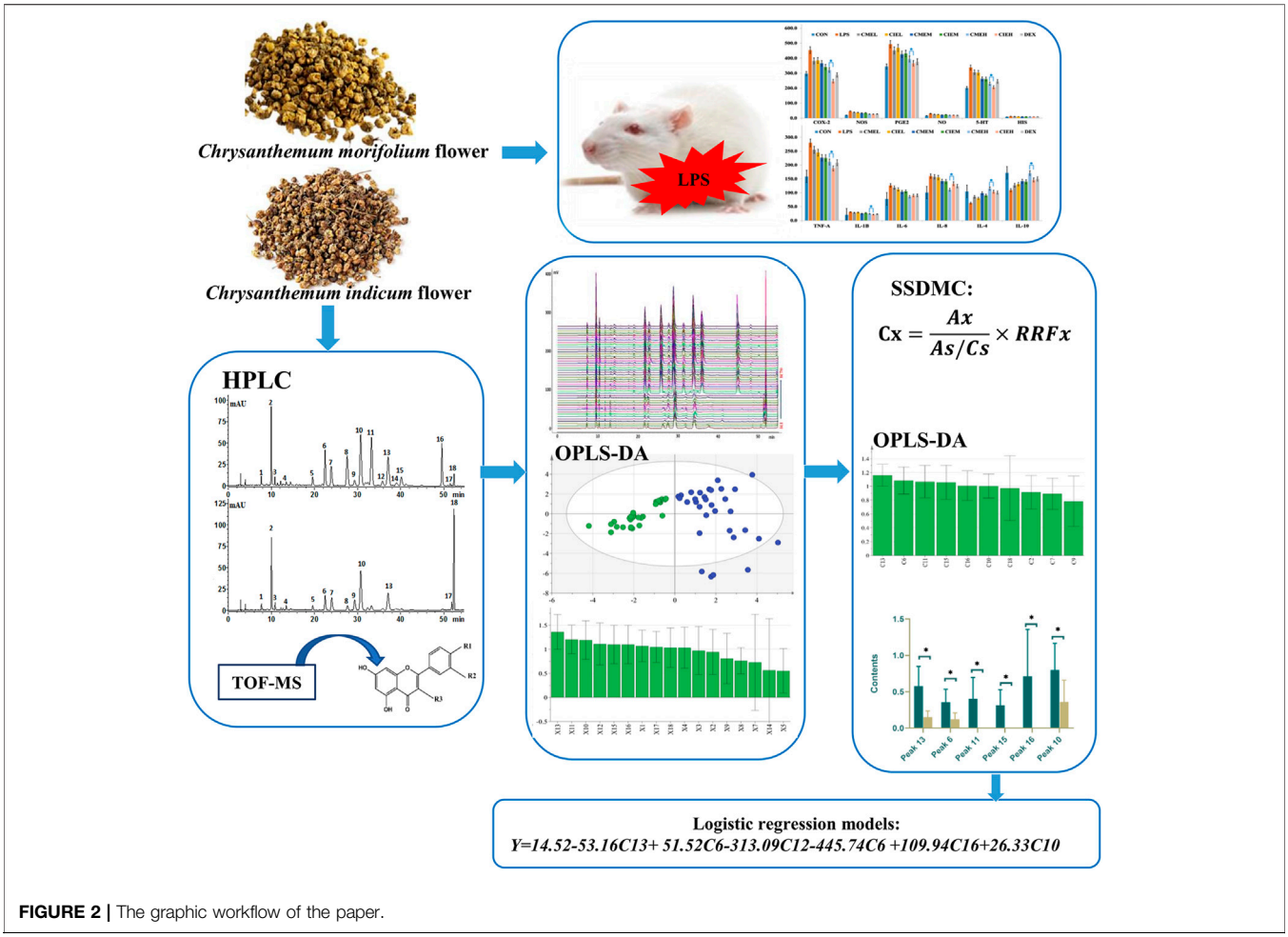

FIGURE 2 | The graphic workflow of the paper.

confuse due to different harvest periods, different origins, different processing or other reasons, especially for non-professionals (Fang et al., 2012; Japanese Pharmacopoeia Commission, 2016; Chinese Pharmacopoeia Commission, 2020). In addition, the commercialized products of *C. morifolium* flower and *C. indicum* flower are often sold in processed form as powder or extract (shown in **Figure 1**), which is more likely to lead to species misidentification and subsequent substitution. Furthermore, the two closely related herbal species have similar chemical compositions but are discriminated in medicinal and tea use due to differences in the contents of active compounds (Committee, C. P. 2015). However, the two herbs are usually assessed independently for quality using one or several marker compounds (Wu et al., 2010; Liu et al., 2013; Committee, C. P. 2015). The markers detected might be not sufficient to distinguish between herbal drugs that have similar appearances and/or chemical compositions (Osathanunkul et al., 2016). Therefore, the development of comparative quality evaluation and characterization methods for *C. morifolium* flower and *C. indicum* flower is essential.

Therefore, the present study aimed to define the chemical composition and pharmacological characteristics for comparative evaluation of *C. morifolium* flower and *C. indicum* flower (shown in **Figure 2**). First, the anti-inflammation activities of *C. morifolium* flower and *C. indicum* flower were systematically compared using lipopolysaccharide-treated rats. Then HPLC fingerprint analysis for 53 batches of *C. morifolium* flowers and 33 batches of *C. indicum* flower was carried out to deep profile the chemical components and differentiate the two herbs. The preliminary markers were screened out by OPLS-DA, identified by HPLC-ESI-QTOF-MS, and quantified by the improved SSDMC (single reference standard to determine multiple compounds) approach. Finally, multiple statistical data mining was performed to confirm the markers and a binary logistic regression equation was built to differentiate *C. morifolium* flower and *C. indicum* flower successfully.

MATERIALS AND METHODS

Chemicals, Reagents and Materials

Isochlorogenic acid A, isochlorogenic acid B, isochlorogenic acid C, chlorogenic acid, luteolin-7-*O*-glucoside, apigenin-7-*O*-glucoside, linarin, luteolin-7-*O*-glucuronide, diosmetin-7-*O*-glucoside, caffeic acid, neochlorogenic acid and cryptochlorogenic acid (purity > 98%) were purchased from

TABLE 1 | Sample information of *C. morifolium* flower and *C. indicum* flower samples.

Group	Sample no	Chinese name	Origins	Morphological characteristics	Similarity (Mean ± SD)
I	G1~19	*Gongju*	Huangshan, Anhui	Flower	0.865 ± 0.031
	H1~9	*Hangbaiju*	Tongxiang, Zhejiang	Flower	0.884 ± 0.035
	H10~18	*Hangbaiju*	Tongxiang, Zhejiang	Flower buds	0.914 ± 0.032
II	K1~16	*Hangbaiju*	Lanxi, Zhejiang, etc.	Flower	0.838 ± 0.142
III	Y1-33	*Yejuhua*	Anhuietc.	Flower or flower buds	0.654 ± 0.121*

I: C. morifolium *flower samples which were Genuine medicinal materials and purchased online or from markets; II:* C. morifolium *flower samples collected from the five introduction districts and provided by Zhejiang Conba Pharmaceutical Co., Ltd; III:* C. indicum *flower samples collected from 13 provinces which were summarized in a previous study (1). The significant difference in similarities between the two herbs was statistically evaluated by the Student's t-test (*p < 0.05).*

Chengdu Must Biological Technology Co. Ltd., (Chengdu, China). Water for HPLC was redistilled. Other chemical reagents were of HPLC grade. Dexamethasone sodium phosphate injection (DEX) (Specification: 1 ml: 2 mg) was purchased from Tianjin pharmaceutical Group Xinzheng Co. Ltd. Lipopolysaccharides (LPS) (*Escherichia coli* 055: B5) was purchased from Beijing Solaibao Biotechnology Co. Ltd., (Beijing, China). ELISA kits of rat 5-Hydroxytryptamine (5-HT), cyclooxygenase-2 (COX-2), Prostaglandin E2 (PGE2), nitric oxide (NO), nitric oxide synthase (NOS), tumor necrosis factor α (TNF-α), Histamine (HIS), interleukin 1β (IL-1β), IL-4, IL-6, IL-8, and IL-10 were purchased from Beijing Qisong Biotechnology Co. Ltd., (Beijing, China).

As listed in **Table 1**, 37 samples of *C. morifolium* flowers were purchased from herb markets, including the two cultivars of "*Gongju*" (from Huangshan City, Anhui Provence) and "*Hangbaiju*" (from Tongxiang County, Zhejiang Provence), which were considered as the genuine medicinal materials. From different farms owned by Zhejiang Conba Pharmaceutical Co. Ltd., 16 samples of *C. morifolium* flower were also collected. In addition, 33 batches of *C. indicum* flower samples were collected from different provinces in China as summarized in a previous study (He et al., 2016). All of these samples were authenticated based on analyses of microscopic and macroscopic characteristics by Professor Jia Ying and deposited at the Centre of Chinese Material Medica at Shenyang Pharmaceutical University.

Apparatus and Chromatographic Conditions

HPLC analysis was performed using a Shimadzu 20A HPLC System (Shimadzu Corporation, Japan) composed of a binary solvent delivery system, an on-line degasser, an auto-sampler, a column temperature controller and a photodiode array detector coupled with Lab solution software. Additional different HPLC instruments were also used, including an Agilent 1260 HPLC system composed of a quaternary solvent delivery system, an on-line degasser, an auto-sampler, a column temperature controller and a photodiode array detector coupled with an analytical workstation. HPLC analysis was performed on a Luna C_{18} column (4.6 × 250 mm, 5 μm, Phenomenex Inc., CA, United States) with a sample injection volume of 10 μl. The detection wavelength was set at 327 nm, the flow rate was 1.0 ml min^{-1}, and the column temperature was maintained at 25°C. The mobile phase consisted of a mixture of solution A (0.1% glacial acetic acid in water) and solution B (acetonitrile) along a linear gradient as follows: 0–10 min (10–18% B), 10–14 min (18–19% B), 14–20 min (19–19% B), 20–35 min (19–20% B), 35–40 min (20–22% B), 40–45 min (22–25% B), 45–55 min (25–35% B), 55–60 min (95–95% B), 60–65 min (10–10% B).

LC–MS^n analysis was performed on an Agilent 1260 HPLC system coupled with a Triple TOF™ 5600 (AB SCIEX, Foster City, CA) with an ESI interface. The mass range was set at *m/z* 50–1,500. The optimum parameters of the MS/MS detector were set as follows: the ion spray voltage was 5000 V for positive ion mode and −4500 V for negative ion mode, the ion source temperature was set at 500°C, ion source gas 1 was set at 50 psi, ion source gas 2 was set at 50 psi, the curtain gas was set at 30 psi, and the declustering potential was set as 90 V. Peak View® Software V. 2.2 was used for data collection and processing.

Sample Preparation for Bioassay

Fifty grams of *C. indicum* flower/*C. morifolium* flower powder was refluxed with1250 ml of 75% EtOH for 2 h, and the extract solution was evaporated in vacuo to an adequate concentration. Then the extract powders were obtained with a freeze-drying method. The yields of *C. indicum* flower and *C. morifolium* flower extracts were 25 and 26%, respectively. For the vivo experiment on inflammatory response, both the *C. indicum* flower exact (CIE) and *C. morifolium* flower extract (CME) were suspended in 0.5% sodium carboxymethylcellulose at the concentration of 80, 40 and 20 mg/ml prior to use.

Sample Preparation for Qualitative and Quantitative Analysis

The reference mixture solutions of chlorogenic acid (0.1782 mg/ml), luteolin-7-*O*-glucoside (0.1110 mg/ml), isochlorogenic acid B (0.1234 mg/ml), isochlorogenic acid A (0.1882 mg/ml), apigenin-7-*O*-glucoside (0.1338 mg/ml), isochlorogenic acid C (0.1122 mg/ml), and linarin (0.2458 mg/ml) were prepared in methanol. The mixed stock solutions were serially diluted to produce calibration standard solutions. All standard solutions were kept at 4°C.

Five hundred milligrams of *C. indicum* flower (No. Y29)/250 g *C morifolium* flower (No. H5) powder was accurately weighed

and transferred into a flask, followed by the addition of 25 ml of 60% methanol and sonication for 30 min. The supernatant was collected and filtered through a 0.22 μm membrane for qualitative and quantitative analysis.

Evaluation of the Anti-Inflammatory Activity *In Vivo*

Sprague Dawley (SD) rats (male, 16 weeks of age, 180–220 g) were provided by the Medical Experiment Animal Center of Shenyang Pharmaceutical University. They were housed under controlled temperature (23–25°C) and 12 h light/12 h dark cycle for a week before the experiment. Food and water were freely available. Experiments were conducted in accordance with the guidelines of the Guiding Principles for the Care and Use of Laboratory Animals approved by the Committee for Animal Experiments in Shenyang Pharmaceutical University.

For the experiment, rats were randomly assigned to nine groups (eight for each). CME (100, 200, and 400 mg/kg) and CIE (100, 200, and 400 mg/kg) were tube-fed for 7 days. The dose of linarin was selected based on previous report [20] and our preliminary study. The normal control, positive control group (DEX) and control group (LPS) were given equal amount of vehicle during this period. 0.5 h after final administration, all of the animals except for rats in normal control groups were injected intraperitoneally with 100 μg/kg LPS to induce acute inflammation. Rats in positive control group were injected with DEX (50 μg/kg) 0.5 h before LPS challenge. All of the animals were anesthetized with pentobarbital sodium and then the blood samples were collected from the abdominal aorta at 6 h after LPS injection. Blood samples were immediately centrifuged at 3,000 rpm for 10 min. Sera were collected, frozen, and kept at −80°C until analysis.

Calculation of Relative Conversion Factors in SSDMC Approach

According to the HPLC test results for the reference compound mixture solutions obtained using the method described in *Apparatus and Chromatographic Conditions*, the relative response factor (RRF_X) could be calculated using the ratio of the peak areas and the ratio of the concentration of the analyte and internal reference substance (**Eq. 1**) (Hou et al., 2014):

$$RRFx = \frac{\sum \left(\frac{Asi}{Csi}\right) \Big/ \left(\frac{Axi}{Cxi}\right)}{N} \quad i = 1 \sim n, \tag{1}$$

where *Asi* and *Axi* are the peak areas of the internal reference substance and analyte, respectively, at the concentration level *i*. The variables *Csi* and *Cxi* are the concentrations (at level *i*) of the internal reference substance and analyte, respectively. N represents the number of concentration levels, which was seven in this work.

With the results of RRFx, the concentration of analyte (C_x) in the samples was calculated based on the following equation:

$$Cx = \frac{Ax}{As/Cs} \times RRFx, \tag{2}$$

where *Ax* and *As* are the peak areas of the analyte and reference component, respectively. *Cx* and *Cs* are the concentrations of the analyte and reference compound in the *sample solution* and *standard solution*, respectively. RRFx is the relative response factor of the analyte vs. the reference compound.

Validation of the Quantitative Analysis Method

Analytical method validation ensures the suitability and ruggedness of the method as a quality measure for use across multiple laboratories. The method developed for quantitative analysis of the major caffeoylquinic acids and flavone glycosides in *C. morifolium* flower and *C. morifolium* flower was validated by tests of linearity, limits of detection (LODs), limits of quantification (LOQs), accuracy, precision (intra- and inter-day variability), robustness and stability.

RESULTS AND DISCUSSION

Anti-inflammatory Activity of C. morifolium Flower and C. indicum Flower Extract in Lipopolysaccharide-treated Rats

Gram-negative bacterial endotoxins or LPS, are associated with tissue injury and fatal outcome in septic shock (Girish, 2013). It has been demonstrated both experimentally and clinically that sepsis causes the production of a series of proinflammatory cytokines (IL-1β, TNF-α, IL-8, and IL-6), anti-inflammatory cytokines (IL-4 and IL-10), inflammatory mediums (NO, HIS, 5-HT, PGE_2), and related enzymes (iNOS, COX-2), which determine the ending and outcome of inflammation (Gouwy et al., 2005; Chen et al., 2018; Dickson and Lehmann, 2019).

In the present study, levels of serum inflammatory cytokines, inflammatory mediums and related enzymes were measured by ELISA at 6 h after LPS injection based on pilot experiments results and the previous reports who demonstrated peaks in serum cytokines concentrations at 4–6 h after LPS injection (Kim et al., 2014). As shown in **Figure 3**, ELISA results displayed that all extracts of *C. morifolium* flower and *C. indicum* flower can cause a dose-dependent decrease in pro-inflammation cytokines, inflammatory mediators and related enzymes, and a dose-dependent increase in anti-inflammatory cytokines for anti-inflammatory effects. Moreover, high dose groups (400 mg/kg) of *C. morifolium* flower and *C. indicum* flower exhibited significant difference in inhibition or promotion of inflammatory mediums (NO, HIS, 5-HT, PGE_2), and related enzymes (iNOS, COX-2) serum cytokines ($p < 0.05$), while low (100 mg/kg) and moderate (200 mg/kg) dose groups of *C. morifolium* flower and *C. indicum* flower showed no significant variation was observed between each other. Comparatively, high dose group of *C. indicum* flower reflected stronger inhibitory effects for COX-2, PEG2, 5-HT, TNF-α, IL-β in serum. While,

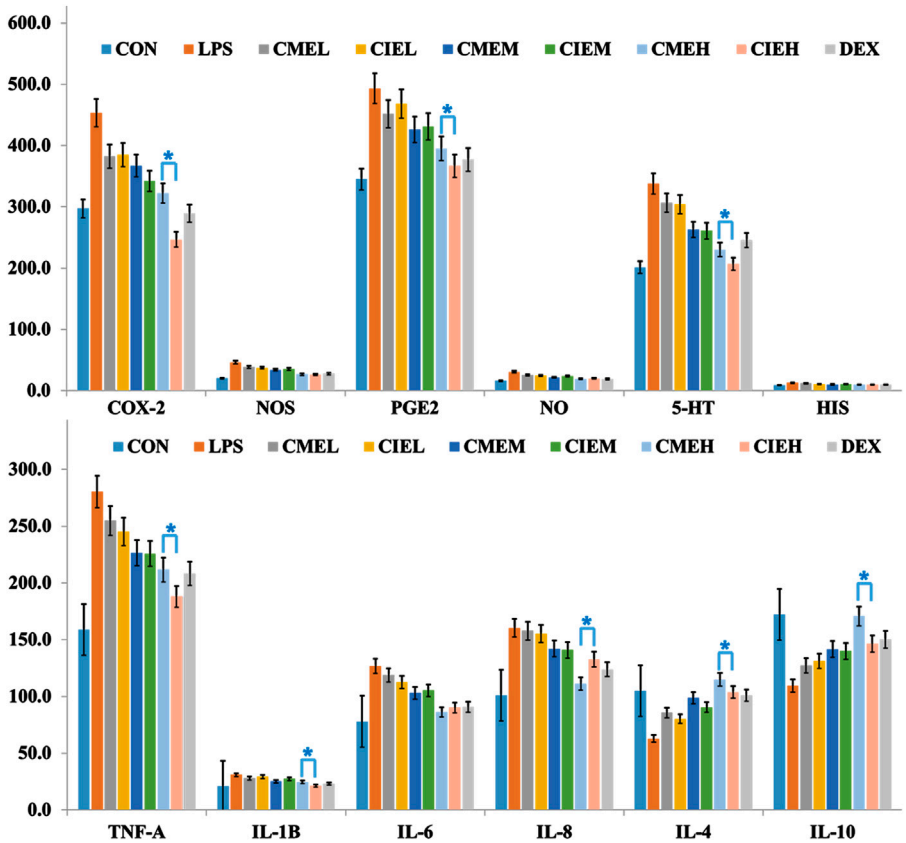

FIGURE 3 | Anti-inflammation effect of *C. morifolium* flower extract (CME) and *C. indicum* flower extract (CIE) in lipopolysaccharide-induced rats. The data are expressed as the mean ± S.D. The significant difference between groups of CME and CIE with different dose was statistically evaluated, respectively, by the Student's *t*-test (*$p < 0.05$).

high dose group of *C. morifolium* flower appeared to show stronger promoting effects for IL-4 and IL-10. In addition, all the groups with the same dose of *C. morifolium* flower and *C. indicum* flower showed no significant difference in expression of NOS, NO, HIS, and IL-6.

HPLC Fingerprint Analysis

In the present work, the HPLC fingerprint analysis was validated and considered to be effective and reliable. Then, 53 batches of *C. morifolium* flower ("*Hangbaiju*" and "*Gongju*") and 33 batches of *C. indicum* flower samples from different regions (**Table 1**) were analyzed under the optimized HPLC conditions. **Figure 4** shows typical fingerprinting chromatograms of *C. morifolium* and *C. indicum* flowers. Eighteen common peaks, which moderately existed in all chromatograms from the samples and indicated similarity among the various samples, were collected from *C. morifolium* flower samples by comparison of the UV spectra and retention times. Chromatograms of *C. indicum* flower confirmed the abundance of peak 18 but showed a deficiency of peaks 11, 12, 14, 15, and 16 compared with the spectra of *C. morifolium* flower samples.

CFDA suggests that all herbal chromatograms should be evaluated in terms of similarity based on a calculation of the correlation coefficient and/or angle cosine value of the original data (Zhao et al., 2011). The similarities (**Table 1**) between the mean chromatogram (both *C. morifolium* flower and *C. indicum* flower) and each herb sample were within a range of 0.341–0.805 (*C. indicum* flower) and 0.816–0.947 (*C. morifolium* flower). These preliminary examinations showed that it was possible to discriminate *C. morifolium* and *C. indicum* flower samples by calculating the correlation coefficients of the main secondary metabolite profiles. It also demonstrated that *C. indicum* flower samples from numerous wild regions had a large fluctuation in quality, while the chromatograms of *C. morifolium* flower samples considered to be genuine were comparatively stable and consistent. In addition, *C. morifolium* flower ("*Hangbaiju*") samples from Zhejiang Province (samples considered to be genuine) had higher correlation coefficients of similarity (0.833–0.947), while samples (K10-15) from Jiangsu and Hubei Provinces (introduction areas) had lower correlation coefficients of similarity (0.624–0.886). The results indicated that there were differences in the internal quality of "*Hangbaiju*" between samples grown in Zhejiang and those grown in the other two provinces of Jiangsu and Hubei.

OPLS-DA was used to preliminarily screen out the markers for differentiating *C. morifolium* and *C. indicum* flower samples

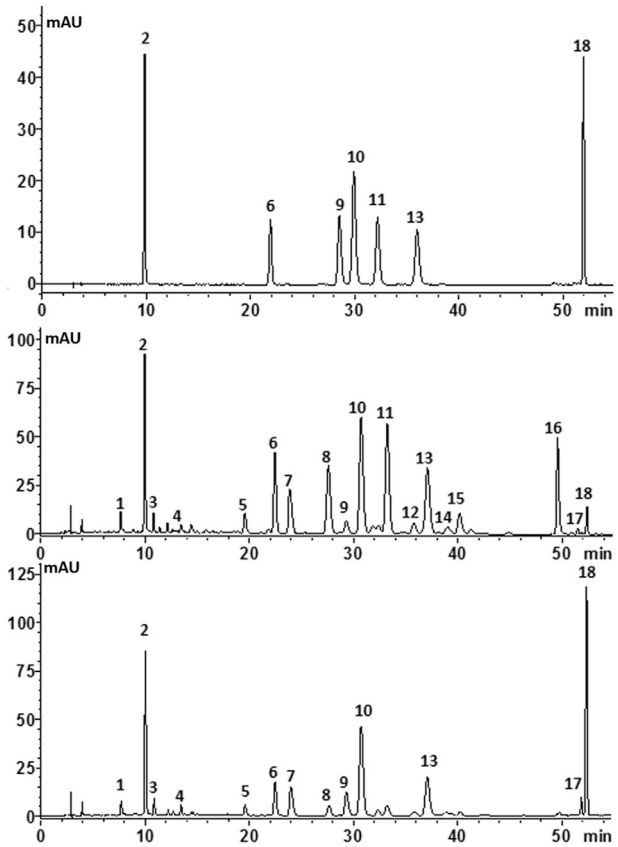

FIGURE 4 | Typical chromatograms of **(A)** mixed standard solution, **(B)** *C. morifolium* flower and **(C)** *C. indicum* flower with the compounds numbered as follows: (1) neochlorogenic acid; (2) chlorogenic acid; (3) cryptochlorogenic acid; (4) caffeic acid; (5) luteolin-7-O-rutinoside; (6) luteolin-7-*O*-glucoside; (7) luteolin-7-*O*- glucuronide; (9) isochlorogenic acid B (10) isochlorogenic acid A (11) apigenin-7-*O*-glucoside; (13) isochlorogenic acid C; (15) diosmetin-7-*O*-glucoside; (16) apigenin-7-*O*-6″-malonylglucoside (18) linarin.

based on the relative peak areas (RPAs) of common peaks. The score plot (**Figure 5A**) showed that *C. morifolium* flower and *C. indicum* flower were separated clearly (R^2X 0.736, R^2Y 0.756, Q^2 0.725). Combined *VIP* value (**Figure 5B**) of OPLS-DA (*VIP* > 1.0) and *p* value of Student's *t*-test ($p < 0.05$), potential marker pool was generated, which contained peaks 13, 11, 10, 12, 15, 16, 1, 17, 18, 4.

Identification of Potential Markers Between *C. morifolium* and *C. indicum* Flowers

Based on HPLC-DAD and HPLC-ESI-QTOF-MS analysis, 14 detected peaks in *C. morifolium* and *C. indicum* flowers were identified or tentatively characterized using the chemical reference standards by comparing UV spectra, retention times, precursors and fragment ion (*m/z*) values. The UV spectrums and extracted ion chromatograms of CM and CI were shown in **Supplementary Figures S1, S2** in Supporting Information. The structures and detailed MS data of the identified components were summarized in **Table 2**. Compounds 1, 2 and 3 yielded $[M\text{-}H]^-$ peaks at *m/z* 353.0876 (calculated for $C_{16}H_{18}O_9$, 353.0873) and fragment ions at *m/z* 191.0559 due to the cleavage of the caffeoyl band, suggesting that monocaffeoylquinic acids were present. Compounds 9, 10, and 13 showed $[M\text{-}H]^-$ peaks at *m/z* 515.1645 (calculated for $C_{25}H_{24}O_{12}$, 353.0873), which produced two successive neutral losses from caffeic acid that yielded two stable fragment ions at 353.0845 $[M\text{-}H\text{-}C_9H_6O_3]^-$ and 191.0536 $[M\text{-}H\text{-}2C_9H_6O_3]^-$, suggesting that dicaffeoylquinic acids were also present. Compound 4 produced $[M\text{-}H]^-$ peaks at *m/z* 179.0351 (calculated for $C_9H_8O_4$), which produced a stable ion fragment at 135.0451 $[M\text{-}H\text{-}CO_2]^-$, suggesting that this compound was caffeic acid. Then, the seven compounds numbered 1, 2, 3, 4, 9, 10, and 13 were unambiguously identified as neochlorogenic acid, chlorogenic acid, cryptochlorogenic acid, caffeic acid, isochlorogenic acid B, isochlorogenic acid A, and isochlorogenic acid C, respectively, based on comparison of the experimental retention times, UV spectra and MS^n data with those of the standards.

Seven major flavonoids were identified in the two herbal medicines, five of which (peaks 6, 7, 13, 15, and 18) were unambiguously identified by comparing the obtained data with those from the reference standards. The produced ions $[M\text{-}H\text{-}308]^-$ at *m/z* 287.0393 ($[M\text{-}H\text{-}glucose]^-$) from compound 5 $[M\text{-}H\text{-}162]^-$ at *m/z* 287.0393 ($[M\text{-}H\text{-}glucoside]^-$) from compound 6, and $[M\text{-}H\text{-}176]^-$ at *m/z* 285.0380 ($[M\text{-}H\text{-}glucuronide]^-$) from compound 7 were indicative of the glucuronide, glucoside and glucuronide of luteolin, respectively. Compound 11 produced an $[M\text{-}H]^-$ ion at *m/z* 431.0954 $[M\text{-}H]^-$ (calculated for $C_{21}H_{20}O_{10}$,

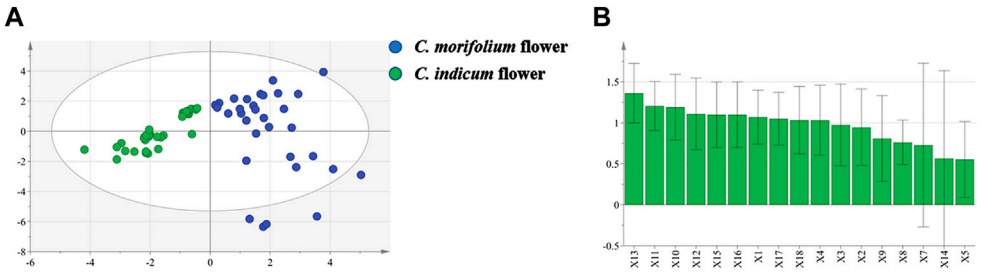

FIGURE 5 | OPLS-DA projection plots in HPLC fingerprint analysis: **(A)** Score plot of 33 samples of *C. indicum* flowers (CI) and 53 samples of *C. morifolium* flowers (CM) from different origins; **(B)***VIP* values of the components in differentiating CM and CI.

TABLE 2 | Characterization of constituents by LC-MSn analysis in negative-ion modes.

No	t_R (min)	Formula	Mass error (ppm)	Fragment ion MS (*m/z*) in negative ion mode	Identification	Structural formula		
Caffeoylquinic acid and caffeic acid						**R_3**	**R_4**	**R_5**
1	7.03	$C_{16}H_{18}O_9$	−1.8	353.0871[M-H]$^-$, 91.0559, 135.0452	Neochlorogenic acid	H	H	*C*
2	9.89	$C_{16}H_{18}O_9$	−3.3	353.0866[M-H]$^-$, 191.0562	Chlorogenic acid	*C*	H	H
3	10.24	$C_{16}H_{18}O_9$	−1.7	353.0875[M-H]$^-$, 191.0562	Cryptochlorogenic acid	H	*C*	H
4	12.14	$C_9H_8O_4$	0.8	179.0351[M-H]$^-$, 135.0451	Caffeic acid			
9	23.96	$C_{25}H_{24}O_{12}$	−3.6	515.1175[M-H]$^-$, 353.0871, 191.0558, 135.0455	3,4-Dicaffeoylquinic acid	*C*	*C*	H
10	26.28	$C_{25}H_{24}O_{12}$	−3.3	515.1177[M-H]–, 353.0853, 191.0544, 135.0446	3,5-Dicaffeoylquinic acid	*C*	H	*C*
13	32.22	$C_{25}H_{24}O_{12}$	−3.0	515.1179[M-H]$^-$, 353.0845, 191.0536	4,5-Dicaffeoylquinic acid	H	*C*	*C*
Flavonoid glycoside						**R_7**	**$R_{3'}$**	**$R_{4'}$**
5	18.86	$C_{27}H_{30}O_{15}$	−1.0	593.1496[M-H]$^-$ 447.0950[M-H-rhamnose]$^-$, 285.0393 [M-H-rutinoside]$^-$	Luteolin-7-*O*-rutinoside	–Rutinose	OH	OH
6	20.45	$C_{21}H_{20}O_{11}$	1.0	447.0911[M-H]$^-$ 285.0393[M-H-glucose]$^-$	Luteolin-7-*O*-glucoside	–Glucoside	OH	OH
7	21.13	$C_{21}H_{18}O_{12}$	−3.4	461.0712[M-H]$^-$ 357.0614[M-H-rutinoside]$^-$ 285.0380[M-H-glucuronide]$^-$	Luteolin-7-*O*-glucuronide	–Glucuronide	OH	OH
11	29.01	$C_{21}H_{20}O_{10}$	−2.2	431.0954[M-H]$^-$ 269.0437[M-H-glucose]$^-$	Apigenin-7-*O*-glucoside	–Glucose	H	OH
15	38.12	$C_{22}H_{22}O_{11}$	−3.8	461.1067[M-H]$^-$ 299.0540[M-H-glucose]$^-$ 284.0300[M-H-glucose-CH3]–	Diosmetin-7-*O*-glucoside	–Glucose	OH	OCH_3
16	45.96	$C_{24}H_{22}O_{13}$	0.2	517.0945[M-H]$^-$ 473.1068[M-H-CO2I]– 431.0970[M-H-malonyl]$^-$ 269.0437[M-H-malonyl-glucose]$^-$	Apigenin-7-*O*-(6″-malonyl) glucoside	–(6″-malonyl) glucose	H	OH
18	52.45	$C_{27}H_{30}O_{15}$	0.1	591.1681[M-H]$^-$ 283.0586[M-H-rutinose]$^-$ 268.0350[M-H-rutinose-CH3]	Linarin (acacetin-7*O*-rutinoside)	–Rutinose	H	OCH_3

465.1033), and moderately abundant [M-H-162]$^-$ product ions at *m/z* 269.0437 were formed through the neutral losses of glucose, indicating that this compound was apigenin-7-*O*-glucoside. Compound 16 produced [M-H-248]$^-$ and [M-H-86]$^-$ fragments due to the loss of malonyl-glucose and malonyl (-$COCH_2COO$-) from their molecular ions, suggesting that this compound was the malonyl glucoside of apigenin. The fragment ions [M-H-162]$^-$ at *m/z* 299.0540 produced from compound 15 were indicative of the glucosides of diosmetin, and the fragment ions at *m/z* 284.0300 were formed by the neutral losses of CH_3. The fragment ions ([M-H-rutinoside]$^-$) at *m/z* 283.0586 from compound 18 were indicative of the rutinoside of acacetin. The fragment ion at *m/z* 151.0021 yielded through the loss of CH_3 showed the existence of a 3′-OCH_3 group. In general, these compounds were identified as glycosylated derivatives of apigenin, luteolin, diosmetin and acacetin.

Quantitative Analysis of Potential Markers Between *C. morifolium* and *C. indicum* Flowers

Considering that all potential markers between *C. morifolium* and *C. indicum* flowers belong to caffeoylquinic acids (Peak 13, 10, 1, and4) or flavone glycosides (Peak 11, 15, 16, and 18), quantitative analysis was conducted for the two types of compounds in the tested samples by improved SSDMC and standard calibration methods.

Calculation of Relative Response Factors and Relative Retention Times

The SDDMC method was mainly developed to simultaneously identify a group of compounds with similar polarity characteristics, UV spectra and chromatographic behaviors (Wang et al., 2015). In this work, chlorogenic acid and luteolin-7-*O*-glucoside, which were stable, accessible, and abundant in the samples, were selected as internal reference substances to determine the other three caffeoylquinic acids (isochlorogenic acid A, isochlorogenic acid B, and isochlorogenic acid C) and two flavone glycosides (apigenin-7-*O*-glucoside and linarin). Based on the series of standard solutions, the final RRF of each analyte was calculated using the average of several RRFs detected from the series of concentrations and calculated according to **Eq. 1**. The calculation of RRT was necessary to identify the peaks using only the internal standard for the SSDMC method. To develop an SSDMC method with general applicability, it was essential to evaluate the ruggedness of the RRT and RRF on different columns (different batches of Luna C_{18}) and equipment. As summarized in **Table 3**, the RRFs for each analyte were quite similar at the detection wavelength of 327 nm across different HPLC instruments, indicating a good consistency of the RRFs. The RRT for each analyte was stable with the RSDs, with deviations of less than 2.0%, and was found to be suitable for use in the identification.

In addition, previous studies showed that the RRFs of flavones presenting the same or similar skeletons and different substituent groups were correlated with molecular weights (Cui et al., 2016). Due to a lack of reference standards, the RRFs of the three flavone glycosides luteolin-7-*O*-glucuronide, diosmetin-7-*O*-glucoside and apigenin-7-*O*-6″- malonylglucoside were calculated based on analytes with highly similar molar absorptivities and molecular weights. For example, the structures of luteolin-7-*O*-glucuronide (Mr = 462.3) and diosmetin-7-*O*-glucoside (Mr =

TABLE 3 | Ruggedness of the RRT and RRF of marker components in C. morifolium/C. indicum flower, $n = 7$.

Analyte	Shimadzu20 A		Agilent1260		RSD (%)	
	RRT	RRF	RRT	RRF	RRT	RRF
Chlorogenic acid[a]	1.00	-	1.00	-	-	-
Isochlorogenic acid B[a]	2.89	0.93	2.90	0.93	0.2	1.4
Isochlorogenic acid A[a]	3.26	0.83	3.27	0.82	0.2	1.6
Isochlorogenic acid C[a]	3.84	0.89	3.85	0.88	0.2	0.8
Luteolin-7-*O*-glucoside[b]	1.00	-	1.00	-	-	-
Apigenin-7-*O*-glucoside[b]	2.89	0.76	2.90	0.77	0.2	1.0
Linarin[b]	3.26	1.04	3.25	1.04	0.2	3.1
Luteolin-7-*O*-glucuronide[b]	1.04	1.03	1.05	1.03	0.7	-
Diosmetin-7-*O*-glucoside[b]	1.65	1.03	1.64	1.03	0.4	-
Apigenin-7-*O*-6″-malonylglucoside[b]	2.65	0.91	2.64	0.91	0.3	-

Components were identified and quantified using chlorogenic acid.
[a]*or luteolin-7-O-glucoside.*
[b]*as internal reference substances.*

462.3) were similar to that of luteolin-7-*O*-glucoside (Mr = 448.3). Thus, the RRFs of the two analytes were both obtained as 1.03 (RRF = 462.3/448.3 × 1.00). The RRF of apigenin-7-*O*-6″-malonylglucoside (Mr = 518.1), which possessed a structure similar to that of apigenin-7-*O*-glucoside (Mr = 432.8), was determined to be 0.91 (RRF = 518.1/432.8 × 0.76). Though the results of the three RRFs may deviate from the true value and are only an approximation, the method was validated as an effective alternative for the quality control of *C. morifolium* flower and *C. indicum* flower when lacking of the sufficient chemical standard substances.

Validation of the Quantitative Analysis Method

For the ESM method, all of the reference standards solutions related to the analytes to be examined should be prepared first. In contrast, only the internal reference solutions were needed for the SSDMC method. The results calculated via the SSDMC method in this experiment were compared to the results obtained with ESM (shown in **Supplementary Tables S1–S8**).

The linearity equation was constructed using a series of standard solutions. The calibration curves calculated by plotting the peak area Y against the concentration x (μg/ml) of each compound were $Y_1 = 2.564\times10^4x + 5.208 \times 10^3$, $Y_2 = 2.006 \times 10^4x + 0.745 \times 10^3$, $Y_3 = 2.756 \times 10^4x + 1.954 \times 10^3$, $Y_4 = 3.129 \times 10^4x + 0.973 \times 10^3$, $Y_5 = 2.628 \times 10^4x + 7.102 \times 10^3$, $Y_6 = 2.918 \times 10^4x + 3.478 \times 10^3$, and $Y_7 = 1.918 \times 10^4x + 7.238 \times 10^3$ for Peak 2, 9,10, 13, 6, 11, and 18, respectively. The calibration curves exhibited good linearity ($r^2 > 0.9993$) within the test range. The LOD (S/N = 3) was 0.49–0.79 ng/ml and the LOQ (S/N = 10) was 1.64–2.65 ng/ml for the seven compounds.

Repeatability was assessed by examining three replicate solutions prepared at three different concentrations (high, medium and low). The *RSD* values for the seven components in samples (H5, Y29) were less than 5.4%. The precision of the method was analyzed by using different operators and performing the analysis on different days, equipment and columns. The *RSD* values were found to be in the range of 1.2–4.2% (in S3–S7 in Supporting Information). The results showed no remarkable differences between the precision of the two methods, SSDMC and ESM, according to the F-test ($p = 0.113 > 0.05$).

The method accuracy was determined using a recovery test by assaying the known added amount of analyte in the sample at three concentration levels (75, 100, and 125%). Three replicates of each concentration in samples (H5, Y29) were examined. Recoveries were in the range 95.0–102.0% with *RSDs* less than 3.2% for the seven analytes in the samples (H5, Y29) (shown in S8-S9 in Supporting Information). The recoveries between the ESM and SSDMC methods showed no remarkable differences using the paired t-test ($p = 0.174 > 0.05$).

The stability of the sample solutions (H5, Y29) was examined by comparing the peak areas of the same sample solutions after storage for different times. The results demonstrated that the sample solutions were stable for almost 24 h with the *RSD*s of peak areas less than 2.6%.

Workflow for Differentiating *C. morifolium* Flower and *C. indicum* Flower

Four caffeoylquinic acids (Peak 2, 9, 10, and 13) and three flavone glycosides (Peak 6, 11, and 18), in the tested samples were simultaneously determined by SSDMC and standard calibration methods. The quantitative results from the two methods were accordant using the t-test ($p = 0.376$, $p > 0.05$). Meanwhile, the other three flavone glycosides (Peak 7, 15, and 16) were determined by the RRFs calculated as described in *Calculation of Relative Response Factors and Relative Retention Times*. All of the results are summarized in **Supplementary Tables S9–S11** in the Supporting Information. Contents of the ten components in the different samples varied greatly, with the total contents of four caffeoylquinic acids ranging from 0.684 to 3.445% in *C. morifolium* flower and 0.166–2.112% in *C. indicum* flower, while the total contents of six flavone glycosides ranged from 0.315 to 4.161% in *C. morifolium* flower and 0.144–2.078% in *C. indicum* flower. The average amount of Peak18 (linarin, 0.636%) in *C. indicum* flower was much higher (approximately six-fold) than that in *C. morifolium* flower but varied significantly among the different samples due to the numerous regions of origin and the variation of wild resources. In contrast, the other five flavone glycosides were detected at significantly lower levels in *C. indicum* flower. Furthermore, the absolute contents of the four caffeoylquinic acids in *C. morifolium* flower samples were

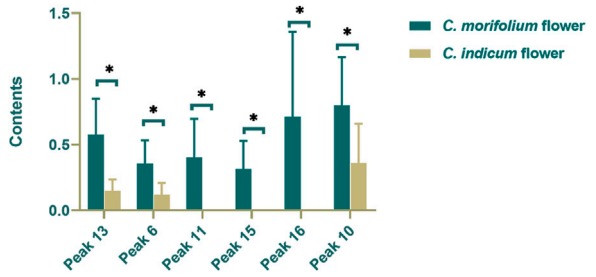

FIGURE 6 | Contents of markers in *C. indicum* flower (CI) and *C. morifolium* flower. (*$p < 0.05$).

significantly higher than those in *C. indicum* flower samples, but the content ratios of the four caffeoylquinic acids were similar in both *C. morifolium* flower and *C. indicum* flower.

Based on the quantitative results, Student's *t*-test and OPLS-DA (R^2X 0.822, R^2Y 0.764, Q^2 0.715) were used to further screen out markers for differentiating *C. morifolium* flower and *C. indicum* flower. Combined *VIP* value and *p* value, peaks 13, 16, 11, 15, 16 and 10 were identified as the markers, whose contents were shown as **Figure 6**. Then to effectively distinguish the two hers from the same genus, a binary logistic regression equation was established as $Y = 14.52 - 53.16C13 + 51.52\ C^6 - 313.09C11 - 445.74\ C6 + 109.94C16 + 26.33C10$ (Cx represents the content of peak x). When the contents of the six markers were substituted into the equation, the sample was determined as *C. morifolium* flower if the result was negative and on the contrary for *C. indicum* flower. The established method was tested with multiple batches of samples collected from different regions, and the accuracy ratewas 100%, which proved the robust of the model.

CONCLUSION

In summary, we demonstrated a systematic study for comparing *C. morifolium* flower and *C. indicum* flower from chemical composition to pharmacological characteristics. The difference in anti-inflammatory activity between the two herbs was firstly characterized. Potential markers for distinguishing *C. morifolium* flower from *C. indicum* flower were preliminarily screened out by HPLC fingerprint analysis combined with statistical methods and identified by HPLC-ESI-QTOF-MS. And improved SSDMC approach was used for quantifying the potential markers of four caffeoylquinic acids and six flavone glycosides. Finally, a binary logistic regression equation based on the contents of markers was built to differentiate *C. morifolium* flower and *C. indicum* flower successfully. The workflow for differentiating *C. morifolium* flower and *C. indicum* flower was effective and would provide a powerful tool for herb identification.

DATA AVAILABILITY STATEMENT

The raw data supporting the conclusion of this article will be made available by the authors, without undue reservation, to any qualified researcher.

AUTHOR CONTRIBUTIONS

JH: Methodology, Validation, Formal analysis, Writing–original draft. QZ: Writing–original draft, Writing–review and editing. CM, GG: Data curation, Supervision. Tao Han: Data curation. KB: Conceptualization. QL: Writing–review and editing, Funding acquisition.

FUNDING

This study was financially supported by Key Technologies of Common Quality Evaluation of New Drugs (Grant No. 2015010201), National and Local Joint Engineering Laboratory for Key Technology of Chinese Material Medica Quality Control, Common Technology Innovation Platform of Biomedical Industry in Liaoning-New Drugs Development Center in Northeast China, and National Natural Science Foundation of China (Grant No. U1508220).

SUPPLEMENTARY MATERIAL

The Supplementary Material for this article can be found online at: https://www.frontiersin.org/articles/10.3389/fphar.2021.575726/full#supplementary-material.

REFERENCES

Chen, L., Deng, H., Cui, H., Fang, J., Zuo, Z., Deng, J., et al. (2018). Inflammatory responses and inflammation-associated diseases in organs. *Oncotarget* 9, 7204–7218. doi:10.18632/oncotarget.23208

Cheng, W., Li, J., You, T., and Hu, C. (2005). Anti-inflammatory and immunomodulatory activities of the extracts from the inflorescence of *Chrysanthemum* indicum Linné. *J. Ethnopharmacol.* 101, 334–337. doi:10.1016/j.jep.2005.04.035

Chinese Pharmacopoeia Commission (2020). *Pharmacopoeia of the people's Republic of China*. Beijing, China: China Medical Science Press.

Cui, G., Niu, Y., Wang, H., Dong, J., Yuki, H., and Chen, S. (2012). Rapid isolation and identification of active antioxidant ingredients from gongju using HPLC-DAD-ESI-MSnand postcolumn derivatization. *J. Agric. Food Chem.* 60, 5407–5413. doi:10.1021/jf300938e

Cui, L., Zhang, Y., Shao, W., and Gao, D. (2016). Analysis of the HPLC fingerprint and QAMS from Pyrrosia species. *Ind. Crops Prod.* 85, 29–37. doi:10.1016/j.indcrop.2016.02.043

Dickson, K., and Lehmann, C. (2019). Inflammatory response to different toxins in experimental sepsis models. *IJMS.* 20, 4341. doi:10.3390/ijms20184341

Fang, H-L., Guo, Q-S., Shen, H-J., and Li, Y-C. (2012). Genetic diversity evaluation of chrysanthemum indicum L. by medicinal compounds and molecular biology tools. *Biochem. Syst. Ecol.* 41, 26–34. doi:10.1016/j.bse.2011.12.013

Gabay, C., and Kushner, I. (1999). Acute-phase proteins and other systemic responses to inflammation. *N. Engl. J. Med.* 340, 448–454. doi:10.1056/NEJM199902113400607

Girish, R. (2013). Gram-positive and gram-negative bacterial toxins in sepsis: a brief review. *Virulence* 5, 213–218. doi:10.4161/viru.27024

Gouwy, M., Struyf, S., Proost, P., and Van Damme, J. (2005). Synergy in cytokine and chemokine networks amplifies the inflammatory response. *Cytokine Growth Factor. Rev.* 16, 561–580. doi:10.1016/j.cytogfr.2005.03.005

Han, Y., Zhou, M., Wang, L., Ying, X., Peng, J., Jiang, M., et al. (2015). Comparative evaluation of different cultivars of Flos Chrysanthemi by an anti-inflammatory-based NF-κB reporter gene assay coupled to UPLC-Q/TOF MS with PCA and ANN. *J. Ethnopharmacol.* 174, 387–395. doi:10.1016/j.jep.2015.08.044

He, D., Ru, X., Wen, L., Wen, Y., Jiang, H., Bruce, I. C., et al. (2012). Total flavonoids of Flos Chrysanthemi protect arterial endothelial cells against oxidative stress. *J. Ethnopharmacol.* 139, 68–73. doi:10.1016/j.jep.2011.10.043

He, J., Wu, X., Kuang, Y., Wang, T., Bi, K., and Li, Q. (2016). Quality assessment of *Chrysanthemum indicum* Flower by simultaneous quantification of six major ingredients using a single reference standard combined with HPLC fingerprint analysis. *Asian J. Pharm. Sci.* 11, 265–272. doi:10.1016/j.ajps.2015.08.010

Hou, J.-J., Wu, W.-Y., Liang, J., Yang, Z., Long, H.-L., Cai, L.-Y., et al. (2014). A single, multi-faceted, enhanced strategy to quantify the chromatographically diverse constituents in the roots of Euphorbia kansui. *J. Pharm. Biomed. Anal.* 88, 321–330. doi:10.1016/j.jpba.2013.08.049

Japanese Pharmacopoeia Commission (2016). *The Japanese Pharmacopoeia*. Tokyo, Japan: Hirogawa Book-shop.

Kim, S-J., Cho, H-I., Kim, S-J., Park, J-H., Kim, J-S., Kim, Y. H., et al. (2014). Protective effect of linarin against D-galactosamine and lipopolysaccharide-induced fulminant hepatic failure. *Eur. J. Pharmacol.* 738, 66–73. doi:10.1016/j.ejphar.2014.05.024

Kim, S. J., Lee, K-T., Choi, H-E., Ha, T. J., Nam, J. H., Hong, S. Y., et al. (2015). Anti-inflammatory effects of flavonoids in Korean *Chrysanthemum* species via suppression of inducible nitric oxide synthase and cyclooxygenase-2 in LPS-induced RAW 264.7 macrophages. *Food Sci. Biotechnol.* 24, 975–985. doi:10.1007/s10068-015-0125-9

Lin, L.-Z., and Harnly, J. M. (2010). Identification of the phenolic components of *Chrysanthemum* flower (*Chrysanthemum morifolium* Ramat). *Food Chem.* 120, 319–326. doi:10.1016/j.foodchem.2009.09.083

Liu, F., Ong, E. S., and Li, S. F. Y. (2013). A green and effective approach for characterisation and quality control of *Chrysanthemum* by pressurized hot water extraction in combination with HPLC with UV absorbance detection. *Food Chem.* 141, 1807–1813. doi:10.1016/j.foodchem.2013.04.083

Liu, Y. H., Mou, X., Zhou, D. Y., Zhou, D. Y., and Shou, C. M. (2018). Extraction of flavonoids from *Chrysanthemum* morifolium and antitumor activity *in vitro*. *Exp. Ther. Med.* 15, 1203–1210. doi:10.3892/etm.2017.5574

Osathanunkul, M., Suwannapoom, C., Osathanunkul, K., Madesis, P., and de Boer, H. (2016). Evaluation of DNA barcoding coupled high resolution melting for discrimination of closely related species in phytopharmaceuticals. *Phytomedicine* 23, 156–165. doi:10.1016/j.phymed.2015.11.018

Su, J-Y., Tan, L-R., Lai, P., Liang, H-C., Qin, Z., Ye, M-R., et al. (2012). Experimental study on anti-inflammatory activity of a TCM recipe consisting of the supercritical fluid CO_2 extract of *Chrysanthemum* indicum, Patchouli Oil and Zedoary Turmeric Oil *in vivo*. *J. Ethnopharmacol.* 141, 608–614. doi:10.1016/j.jep.2011.08.055

Wang, C-Q., Jia, X-H., Zhu, S., Komatsu, K., Wang, X., and Cai, S-Q. (2015). A systematic study on the influencing parameters and improvement of quantitative analysis of multi-component with single marker method using notoginseng as research subject. *Talanta* 134, 587–595. doi:10.1016/j.talanta.2014.11.028

Wu, L. Y., Gao, H. Z., Wang, X. L., Ye, J. H., and Liang, Y. R. (2010). Analysis of chemical composition of *Chrysanthemum indicum* flowers by GC/MS and HPLC. *J. Med. Plant Res.* 4, 421–426. doi:10.1007/s12272-010-0320-4

Zhao, Y-L., Fan, R-H., Yuan, H-X., Yu, M., Bi, K-S., and Yu, Z-G. (2011). Development of the fingerprints for the quality evaluation of Viscum coloratum by high Performance liquid chromatography. *J. Pharm. Anal.* 1, 113–118. doi:10.1016/S2095-1779(11)70020-x

Conflict of Interest: The authors declare that the research was conducted in the absence of any commercial or financial relationships that could be construed as a potential conflict of interest.

Copyright © 2021 He, Zhang, Ma, Giancaspro, Bi and Li. This is an open-access article distributed under the terms of the Creative Commons Attribution License (CC BY). The use, distribution or reproduction in other forums is permitted, provided the original author(s) and the copyright owner(s) are credited and that the original publication in this journal is cited, in accordance with accepted academic practice. No use, distribution or reproduction is permitted which does not comply with these terms.

frontiers in Pharmacology

ORIGINAL RESEARCH
published: 23 April 2021
doi: 10.3389/fphar.2021.658811

Yi-Qi-Jian-Pi Formula Suppresses RIPK1/RIPK3-Complex-Dependent Necroptosis of Hepatocytes Through ROS Signaling and Attenuates Liver Injury *in Vivo* and *in Vitro*

Feixia Wang[1,2†], Li Tang[1,2†], Baoyu Liang[2], Chun Jin[2], Liyuan Gao[2], Yujia Li[2], Zhanghao Li[2], Jiangjuan Shao[2], Zili Zhang[2], Shanzhong Tan[1,2], Feng Zhang[2*] and Shizhong Zheng[2*]*

[1]Department of Integrated TCM and Western Medicine, Nanjing Hospital Affiliated to Nanjing University of Chinese Medicine, Nanjing, China, [2]Jiangsu Key Laboratory for Pharmacology and Safety Evaluation of Chinese Materia Medica, School of Pharmacy, Nanjing University of Chinese Medicine, Nanjing, China

OPEN ACCESS

Edited by:
Hai Yu Xu,
China Academy of Chinese Medical Sciences, China

Reviewed by:
Lei Chen,
Fujian Agriculture and Forestry University, China
Hor Yue Tan,
Hong Kong Baptist University, Hong Kong

***Correspondence:**
Shanzhong Tan
doctortsz@aliyun.com
Feng Zhang
nucmzf@163.com
Shizhong Zheng
nytws@163.com

[†]These authors have contributed equally to this work

Specialty section:
This article was submitted to Ethnopharmacology, a section of the journal Frontiers in Pharmacology

Received: 26 January 2021
Accepted: 07 April 2021
Published: 23 April 2021

Citation:
Wang F, Tang L, Liang B, Jin C, Gao L, Li Y, Li Z, Shao J, Zhang Z, Tan S, Zhang F and Zheng S (2021) Yi-Qi-Jian-Pi Formula Suppresses RIPK1/RIPK3-Complex-Dependent Necroptosis of Hepatocytes Through ROS Signaling and Attenuates Liver Injury in Vivo and in Vitro. Front. Pharmacol. 12:658811. doi: 10.3389/fphar.2021.658811

Acute-on-chronic liver failure (ACLF) is described as a characteristic of acute jaundice and coagulation dysfunction. Effective treatments for ACLF are unavailable and hence are urgently required. We aimed to define the effect of Yi-Qi-Jian-Pi Formula (YQJPF) on liver injury and further examine the molecular mechanisms. In this study, we established CCl_4-, LPS-, and D-galactosamine (D-Gal)-induced ACLF rat models *in vivo* and LPS- and D-Gal-induced hepatocyte injury models *in vitro*. We found that YQJPF significantly ameliorates liver injury *in vivo* and *in vitro* that is associated with the regulation of hepatocyte necroptosis. Specifically, YQJPF decreased expression of receptor-interacting protein kinase 1 (RIPK1), receptor-interacting protein kinase 3 (RIPK3) and pseudokinase mixed lineage kinase domain-like (MLKL) to inhibit the migration of RIPK1 and RIPK3 into necrosome. YQJPF also reduces the expression of inflammatory cytokines IL-6, IL-8, IL-1β, and TNF-α, which were regulated by RIPK3 mediates cell death. RIPK1 depletion was found to enhance the protective effect of YQJPF. Furthermore, we showed that YQJPF significantly downregulates the mitochondrial reactive oxygen species (ROS) production and mitochondrial depolarization, with ROS scavenger, 4-hydroxy-TEMPO treatment recovering impaired RIPK1-mediated necroptosis and reducing the expression of IL-6, IL-8, IL-1β, and TNF-α. In summary, our study revealed the molecular mechanism of protective effect of YQJPF on hepatocyte necroptosis,

Abbreviations: ACLF, Acute-on-chronic liver failure; ALP, Alkaline phosphatase; ALT, Alanine aminotransferase; AST, Aspartate aminotransferase; D-Gal, D-galactosamine; ELISA, Enzyme-linked immunosorbent assay, Glb, Globulin, H&E, Hematoxylin and Eosin, HSCs, Hepatic stellate cells, IL-18, Interleukin-18, IL-1β, Interleukin-1β, IL-6, Interleukin-6, LPS, Lipopolysaccharide, MDA, Malondialdehyde, MLKL, Mixed lineage kinase domain-like protein, PBS, Phosphate-buffered saline, RIPK1, Receptor-interacting protein kinases 1, RIPK3, Receptor-interacting protein kinases 3, RT-qPCR, Real-time quantitative polymerase chain reaction, SOD, Superoxide dismutase, TBIL, Total bilirubin, TNF-α, Tumor Necrosis Factor-α, YQJPF, Yiqijianpi Formula, ROS, Reactive oxygen species, Tempol, 4-hydroxy-TEMPO, HBV, Hepatitis B virus, HCV, Hepatitis C virus, Nec-1, Necrotatin, DMEM, Dulbecco's modified essential medium, FBS, Fetal bovine serum, GAPDH, Glyceraldehyde phosphate dehydrogenase, Co-IP, Co-immunoprecipitation, DCFH-DA, 2′,7′-dichlorodihydrofluorescin diacetate, JC-1, 5.5′,6.6′-tetrachloro-1.1′,3.3′-tetraethylbenzimidazolylcarbocyanine iodide, TEM, Transmission electron microscopy, MMP, Mitochondrial membrane potential, Sou-Medrol, Methylprednisolone

targeting RIPK1/RIPK3-complex-dependent necroptosis *via* ROS signaling. Overall, our results provided a novel perspective to indicate the positive role of YQJPF in ACLF.

Keywords: acute-on-chronic liver failure, reactive oxygen species, inflammation, hepatocytes necroptosis, Yi-Qi-Jian-Pi formula

INTRODUCTION

Acute-on-chronic liver failure (ACLF) is a syndrome characterized by acute decompensation of chronic liver disease, which has a high short-term mortality rate, and it seriously threatens the lives of patients with chronic liver disease (Xiang et al., 2020). However, the pathogenesis of ACLF remains poorly understood. Among Asian countries, the prevalence of hepatitis in China is still high. There are approximately 97 million hepatitis B virus (HBV) carriers and one million hepatitis C virus (HCV)-infected patients in China. Chronic viral hepatitis is still the basis in ACLF (Xie et al., 2019). Virus replication and bacterial infection are the main causes of liver failure. However, no effective therapy for liver failure beyond supportive treatment is currently available; hence, a new treatment or medicine against liver failure is needed. Previous studies have suggested that ACLF develops in patients with cirrhosis as a consequence of precipitating events leading to acute decompensation and multi-organ failure (Sarin and Choudhury, 2016). Despite variations in the definition of ACLF in different regions, progressive, unrelenting hepatocyte injury and death are common hallmarks of ACLF, which have been well-documented as pathobiology of ACLF. Effective treatments to target hepatocyte injury and death due to ACLF are lacking and thus are urgently required. Unlike apoptosis and pyroptosis, necroptosis is a caspase-independent death program (Asrani et al., 2019). The dying cells exhibit none of the morphological characteristics of apoptosis, instead these cells display the swelling associated with necrosis; the dying cell can trigger an innate immune response, cause the release of inflammatory cytokines, and exacerbate tissue damage (Wang et al., 2014). The inhibitors of necroptosis could have therapeutic potential.

Traditional Chinese medicines have received attention worldwide in last few decades because of their satisfactory therapeutic effects, facile availability, and cost-effectiveness (Bajaj et al., 2018; Engelmann et al., 2020). Our previous study confirmed that the treatment with Yi-Qi-Jian-Pi Formula (YQJPF) composed of Huangqi, Taizishen, Baizhu, Chenpi, Danggui, Fulin, Huangqin, and Gancao can ameliorate HBV-ACLF. *Corethrodendron multijugum* (Maxim.) B. H. Choi and H. Ohashi (Huangqi in Chinese) and Pseudostellariae Radix, *Pseudostellaria heterophylla* (Miq.) Pax (Taizishen in Chinese) are Monarch drugs; Angelicae Sinensis Radix, *Angelica sinensis* (Oliv.) Diels (Danggui in Chinese), *Wolfiporia extensa* (Peck) Ginns (Fulin in Chinese), *Atractylodes lancea* (Thunb.) DC (Cangzhu in Chinese) and *Atractylodes macrocephala* Koidz (Baizhu in Chinese) are Ministerial drugs; and Citrus Reticulata, Citrus × aurantium L. (Chenpi in Chinese), Scutellariae Radix *Scutellaria baicalensis* Georgi (Huangqin in Chinese), and licorice, *Glycyrrhiza uralensis* Fisch. ex DC., G. glabra L., and G. inflata Batalin (Gancao in Chinese) are adjuvants. A retrospective cohort study on 60 patients with HBV-ACLF reported that YQJPF could prevent the development of liver failure and improve the Model for End-Stage Liver disease score (Zhang Z. et al., 2014; Lian et al., 2015). However, the regulation mechanism of its effect has not been elucidated. Atractylone is the main sesquiterpenic constituent of *Atractylode japonica*, which is a necessary component of YQJPF. Atractylode japonica was used to treatment of several diseases such as rheumatic diseases, digestive disorders, hepatic protection and influenza for a long history in China. Additionally, atractylone was reported to have anti-inflammatory and anti-hepatotoxic effects (Cheng et al., 2019).

In the present study, we developed *in vivo* and *in vitro* models with D-galactosamine (D-gal)/LPS injection that recapitulate some features of clinical ACLF. In these models, we assessed the features of ACLF in laboratory settings. Further, ACLF models were treated with YQJPF to assess its effect on liver injury. Additionally, we explored the role of inflammation infiltration and hepatocyte necroptosis and the potential mechanisms for the treatment of liver injury in ACLF.

MATERIALS AND METHODS

Reagents and Antibodies

Methylprednisolone was obtained from the Nanjing Hospital affiliated to Nanjing University of Chinese Medicine (Nanjing, Jiangsu China) and was dissolved in PBS to a concentration of 30 mg/ml and was stored at 4°C. Necrotatin-1 (Nec-1) and 4-hydroxy-TEMPO (Tempol) were bought from Sigma-Aldrich (St Louis, MO, United States). Dulbecco's modified essential medium (DMEM), fetal bovine serum (FBS), Opti-MEM medium, phosphate-buffered saline (PBS), and trypsin-EDTA were purchased from GIBCO (Grand Island, NY, United States). The antibodies against β-actin (20536-1-AP), RIPK1 (17519-1-AP), and RIPK3 (17563-1-AP) were purchased from Proteintech Group, Inc (Rosemont, IL, United States). Caspase-3 (#9662), cleaved-caspase-3 (#9664), caspase-8 (#9746), cleaved-caspase-8 (#9748), TNF-α (#11948), IL-18 (#54943), IL-1β (#12242), and IL-6 (#12153) were procured from Cell Signaling Technology (Danvers, MA, United States). Mixed lineage kinase domain-like protein (MLKL; ab243142) were purchased from Abcam Technology (Abcam, Cambridge, United Kingdom).

Preparation and High-Performance Liquid Chromatography of YQJPF for Quality Control

YQJPF was provided by Nanjing University of Chinese Medicine, Nanjing Hospital Affiliated to Nanjing University of Chinese Medicine. YQJPF was prepared from nine commonly used Chinese herbal medicines (**Table 1**). All the herbal

TABLE 1 | The composition of traditional Chinese medicine in Yi-Qi-Jian-Pi Formula (YQJPF).

Components	Latin name	Medical parts	Amount used (g)	Percentage (%)
Huangqi	*Corethrodendron multijugum* (Maxim.) B. H. Choi and H. Ohashi	Root	30	19.6
Taizishen	*Pseudostellaria heterophylla* (Miq.) Pax	Root	30	19.6
Danggui	*Angelica sinensis* (Oliv.) Diels	Rhizome	30	19.6
Baizhu	*Atractylodes macrocephala* Koidz	Root	15	9.8
Fulin	*Wolfiporia extensa* (Peck) Ginns	Sclerotium	15	9.8
Cangzhu	*Atractylodes lancea* (Thunb.)DC	Fruit	10	6.5
Chenpi	*Citrus* × aurantium L.	Pericarp	10	6.5
Huangqin	*Scutellaria baicalensis* Georgi	Root	10	6.5
Gancao	*Glycyrrhiza uralensis* Fisch. ex DC., G. glabra L., and G. inflata Batalin	Root, hizome	3	2.1

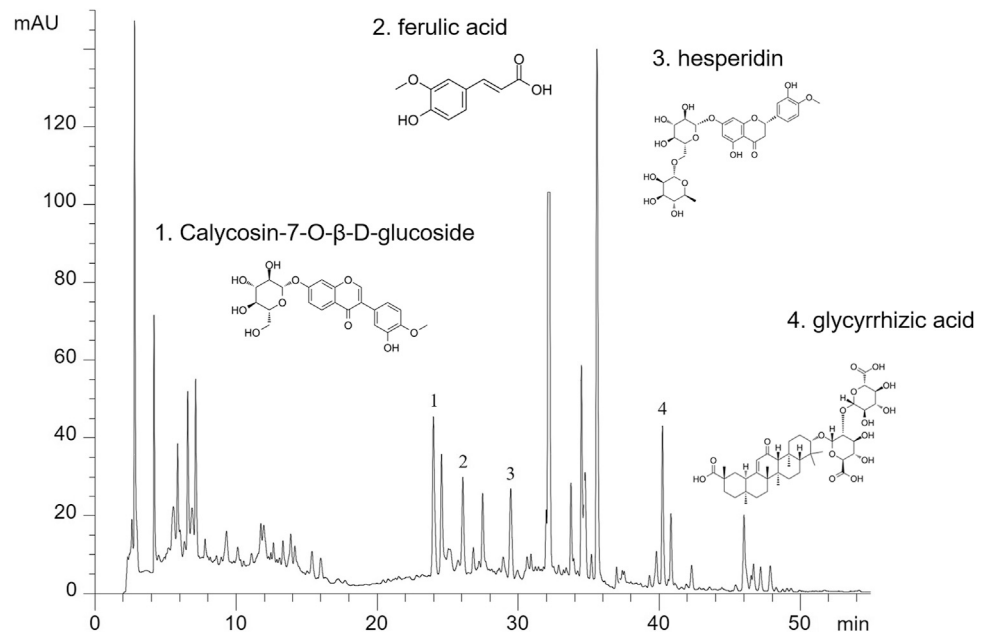

FIGURE 1 | Establishment of a new model of ACLF in rats and the experimental procedures. Rats were randomly divided into the following seven groups (eight rats in each group).

constituents were obtained from the Beijing Tong Ren Tang Co. Ltd. (Beijing, China). Huangqi, Taizishen, Baizhu, Chenpi, Danggui, Fulin, Huangqin, and Gancao were mixed in the ratio 30:30:30:10:15:15:3:10:10.

Then, all herbs were decocted twice and the decoction liquids were concentrated to a density of 2.86 g/ml and was stored at 4°C. For quality control, HPLC analysis was used as previously described (Yao et al., 2018). YQJPF were assessed using an Agilent 1,260 liquid chromatography system (United Kingdom). Briefly, 10 μl YQJPF solution was injected into an apparatus with an auto sampler. Chromatographic separation was implemented at a flow rate of 1 ml/min with an Agilent C18 column (4.6 mm × 250 mm, 5 μm). The separation phase was composed of 0.2% phosphoric acid (A) and acetonitrile (B). The linear concentration solution gradually increases from 2 to 72% of solvent B over the course of 45 min. The separation temperature was 40°C, with a detection wavelength of 254 nm. The results are shown in **Figure 1**.

Animals and Experimental Design

A total of 56 male Sprague-Dawley rats, with the body weight of 180–220 g, were purchased from Beijing Vital River Laboratory Animal Technology Co. Ltd (Beijing, China). All animals were housed with laboratory chow and tap water at 22 ± 2°C under 55 ± 5% humidity-controlled environment and a 12-h light–dark cycle. The experimental design was approved by the Institutional and Local Committee on the Care and Use of Animals of Nanjing University of Chinese Medicine (Nanjing, China). All animals were provided care in compliance with the National Institutes of Health (United States) guidelines. A mixture of CCl_4 and olive oil [1:1 (w/v)] was used to induce liver cirrhosis in rats (1.5 ml/kg body weight). LPS (100 μg/kg) and D-Gal (400 mg/kg) were

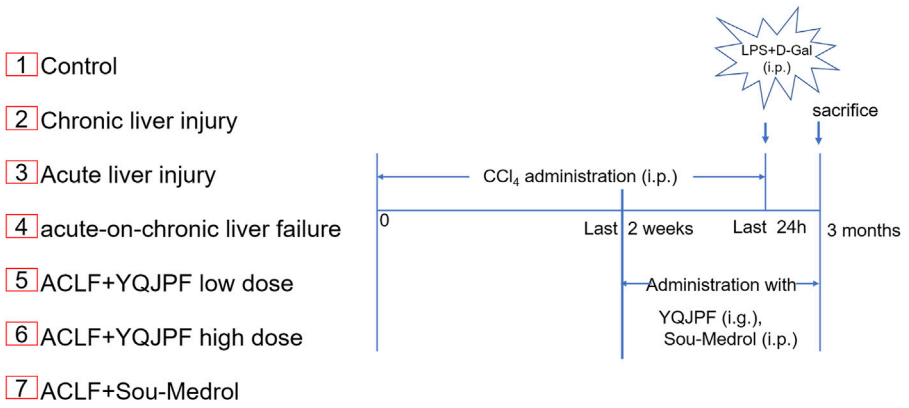

FIGURE 2 | The major components in YQJPF were assessed using HPLC. Calycosin-7-O-β-D-glucoside, ferulic acid, hesperidin, and glycyrrhizic acid were found to be in the amounts of 0.3676, 0.6639, 2.442, and 0.4028 mg/ml, respectively.

used to induce acute liver injury. The mice were randomly divided into seven groups (n = 8 for each group). The experimental groups were as follows (**Figure 2**):

Group 1: control group; i. p. with olive oil.
Group 2: chronic liver injury model group; i. p. with CCl_4 for 12 weeks.
Group 3: acute liver injury model group; i. p. with LPS and D-Gal once.
Group 4: ACLF model group; i. p. with CCl_4 for 12 weeks followed by i. p. with LPS and D-Gal once.
Group 5: YQJPF low-dose treatment group; i. p. with CCl_4 for 12 weeks and i. g. with YQJPF (14.3 g/kg) for 2 weeks followed by i. p. with LPS and D-Gal once.
Group 6: YQJPF high-dose treatment group; i. p. with CCl_4 for 12 weeks and i. g. with YQJPF (28.6 g/kg) for 2 weeks followed by i. p. with LPS and D-Gal once.
Group 7: methylprednisolone treatment group; i. p. with CCl_4 for 12 weeks and i. p. with methylprednisolone (15 mg/kg) for 2 weeks followed by i. p. with LPS and D-Gal once.

Cell Culture

Human LO2 cell line was obtained from the Cell Bank of Chinese Academy of Sciences (Shanghai, China). Cells were cultured in DMEM with 10% FBS and 1% antibiotics and were incubated in 5% CO_2 and 95% air humidified atmosphere at 37°C.

Liver Histopathology

Liver hematoxylin and eosin (H&E) and Masson and Sirius Red staining were performed as per the previously described methods (Jin et al., 2016). Representative pictures of liver sections were displayed.

Serum Biochemistry

Blood samples were collected and incubated at room temperature for 1 h, and extracted serum was collected after centrifugation. Levels of alkaline phosphatase (ALP), aspartate aminotransferase (AST), and alanine aminotransferase (ALT) in serum were measured using enzyme-linked immunosorbent assay kits (Nanjing Jinting Bioengineering Institute, Nanjing, China) according to the manufacturer's protocols.

Determination of Hepatic mtDNA, ATP, Malondialdehyde, and Superoxide Dismutase Levels

Liver tissues were treated according to the treatment regimen mentioned earlier After treatment, hepatic mtDNA, ATP, malondialdehyde (MDA), and superoxide dismutase (SOD) were quantified using corresponding kits (Nanjing Jinting Bioengineering Institute, Nanjing, China) according to the manufacturer's instructions.

Immunohistochemistry

Immunohistochemical staining of liver tissue was performed using antibodies against caspase 8, MLKL, RIPK1, and RIPK3, as previously described (Zhang F. et al., 2014). Representative pictures of liver sections were displayed.

Cell Viability Assay

To assess the effects of different treatments on cell proliferation, Cell viability analysis was performed using MTT. In brief, The LO2 cells were seeded into 96-well plates at a density of 3×10^3 cells per well. After incubating for 24 h, the cells were treated with LPS (10 μg/ml) and D-Gal (10 mg/ml) for 4 h for the hepatocyte injury model. Further, the cells were treated with serial concentration gradients of YQJPF and atractylone for another 24 h, with triplicates for each concentration. Then 5 mg/ml MTT was added in cells, and cells were incubated at 37°C for 4 h, and the absorbance was measured at a wavelength of 490 nm. Independent experiments were performed in triplicates.

Trypan Blue Staining

Cell death was determined using the trypan blue staining assay (Beyotime Biotechnology, Shanghai, China). In brief, after YQJPF treatment, the cells were digested using trypsin without EDTA

TABLE 2 | Primers used for human LO2 cells.

Gene	Forward sequence	Reverse sequence
IL-6	GCTTCCCTCAGGATGCTTGT	ATTAACTGGGGTGCCTGCTC
TNF-α	GAGACAGATGTGGGGGGTGTGAG	TCCTAGCCCTCCAAGTTCCA
IL-1β	AGCCATGGCAGAAGTACCTG	TGAAGCCCTTGCTGTAGTGG
IL-18	CGAGGGAGTGAAGACCCTG	TGGGCGTAAGCTTGGAATGT
GAPDH	TGTCATGGCAGAAGTACCTG	GTTAACTGGGGAGCCTGCTC

followed by centrifugation. The cells were further washed twice with PBS and were resuspended in PBS. Cell suspension and trypan blue solution were mixed gently in 1:1 ratio and allowed to stand for 3 min. A few of the stained cells were counted with a hemocytometer, and photographs were taken in a blinded fashion at random fields. Stained blue cells represented dead cells.

RNA Isolation and Real-Time PCR

Total RNA was extracted from liver tissues and LO2 cells by using Trizol reagent according to the manufacturer's protocol (Sigma-Aldrich, St. Louis, MO, United States) and further reverse-transcribed into cDNA by using PrimeScript RT reagent kit (TaKaRa Biotechnology, Beijing, China). Real-time PCR was performed using the SYBR Green I fluorescent dye (TaKaRa Biotechnology, Beijing, China), according to the manufacturer's protocol. Glyceraldehyde phosphate dehydrogenase (GAPDH) served as an invariant control, and mRNA levels were expressed as fold changes after normalizing to GAPDH. The experiment was performed in triplicates. Primers (Genscript, Nanjing, China) are listed in **Table 2** below.

Western Blot

Cells and liver samples were lyzed using a mammalian lysis buffer (Sigma St. Louis, MO, United States) and were denatured in SDS loading buffer. Then, western blot analysis was performed according to the manufacturer's instructions (Bio-Rad, Hercules, CA, United States). Thereafter, Cells and liver samples were incubated overnight with antibodies against caspase 3, cleaved-caspase-3, caspase 8, cleaved-caspase-8, MLKL, RIPK1, RIPK3, IL-6, IL-18, IL-1β, and TNFα at 4°C. Protein detection, band visualization, and quantification were performed as per the manufacturer's instructions. Anti-β-actin antibody (Danvers, MA, United States) was used as a loading control.

Immunoprecipitation Assay

The immunoprecipitation assay was performed using co-immunoprecipitation (Co-IP) kit (Thermo) as per manufacturer's instructions. Briefly, the cell lysates were incubated with anti-RIPK1 and anti-RIPK3 antibodies. Protein G-agarose beads were added and incubated overnight to precipitate the protein complexes. Western blot analysis was performed to detect the protein complexes expression.

Immunofluorescence Analysis

LO2 cells were seeded on 24-well plates and cultured in DMEM with 10% FBS. Afterward, they were treated with corresponding reagents for 24 h. Then, the cells were fixed with 4% PFA for 30 min at 37°C, permeabilized with PBS-T (0.1% Triton x-100 dissolved in PBS), and blocked with PBS-B (4% BSA dissolved in PBS). The cells were stained with the corresponding antibody (1: 200 dilution) overnight at 4°C, followed by incubation with FITC-labelled goat anti-rabbit IgG (1:100 dilution) for 2 h. Finally, 4′,6-diamidino-2-phenylindole (DAPI) staining was performed by incubation in dark for 5 min, and the fluorescence was observed using a fluorescence microscope (Nikon, Tokyo, Japan) to visualize the nuclei.

Enzyme-Linked Immunosorbent Assay (ELISA)

Levels of IL-6, IL-8, IL-1β, and TNF-α in serum were measured using ELISA kits (Nanjing Jiancheng Bioengineering Institute, Nanjing, China) according to the manufacturer's instructions.

Intracellular ROS Assay

The level of intracellular ROS was determined using an oxidation-sensitive fluorescent probe, 2′,7′-dichlorodihydrofluorescin diacetate (DCFH-DA) (Beyotime Biotechnology, Shanghai, China). Briefly, LO2 cells were seeded in a 24-well plate and pre-treated with ROS scavenger Tempol (10 μM) for 1 h before exposing to YQJPF or selective RIPK1 inhibitor Nec-1. DCFH-DA probe was subsequently incubated with LO2 for 30 min. Subsequently, ROS levels were detected according to the manufacturer's instructions.

Determination of Mitochondrial ROS

We determined mitochondrial ROS production by using a fluorescent probe, MitoSOX, which is a red mitochondrial superoxide indicator for live cell imaging (Molecular Probes; Life technologies). Briefly, LO2 cells were treated with YQJPF or selective RIPK1 inhibitor Nec-1. Further, LO2 cells were incubated with MitoSox reagent (5 μM) for 10 min at 37°C and washed with PBS. The red fluorescence density was detected using a fluorescence microscope (Nikon, Tokyo, Japan) with the rhodamine channel.

Mitochondrial Membrane Potential Assay

The mitochondrial membrane potential (MMP) was determined using 5.5′,6.6′-tetrachloro-1.1′,3.3′-tetraethylbenzimidazolylcarbocyanine iodide (JC-1) (Beyotime Biotechnology, Shanghai, China) staining as per the manufacturer's protocol. LO2 cells were washed with PBS and incubated with JC-1 working solution at 37°C in dark for 20 min. After removing JC-1 solution, the cells were washed with PBS, and images were taken using a fluorescence microscope (Nikon, TiE, Japan) with both red and green channels. The MMP is represented by the average red/green fluorescence intensity ratio.

Transmission Electron Microscopy

LO2 cells were seeded in six-well plates (14,000 cells/well). After the corresponding treatment, transmission electron microscopy (TEM) images were obtained using a JEM 1010 transmission electron microscope (JEOL, Tokyo, Japan). Briefly, LO2 cells were fixed in Karnovsky fixative solution (2% paraformaldehyde and 2.5% glutaraldehyde in 0.15 mol/L sodium cacodylate buffer, pH 7.1–7.3) during 1 h and then washed three times in a

cacodylate buffer for 15 min. Then pellets were embedded into 2% agar and postfixed in 1% osmium tetraoxide in a cacodylate buffer during 1 h. Samples were then dehydrated in 50, 70, 95, and 100% of acetone for 2, 10, 30, and 60 min, respectively, and embedded into Durcupan ACM (Fluka, Analytical Sigma-Aldrich; Switzerland). And the ultrathin sections (70 nm) were placed on nickel grids and examined at 100 keV. For each group, electromicrographs were recorded at a microscope magnification of ×10,000.

Flow Cytometer Analysis

FITC Annexin V apoptosis detection kit (BD Pharmingen™, BD Biosciences) was used for detection of cell apoptosis. Briefly, LO2 cells were seeded in six-well plates in complete medium and allowed to attach for 24 h. Then, cells were treated as indicated. Cells were further incubated for 24 h, in 5% CO_2 at 37°C. After that, cells were trypsinized, washed in PBS and stained according to kit according to the manufacturer's instructions. Stained cells were analyzed using BD Accuri C6 flow cytometer (BD Pharmingen™, BD Biosciences) and data was processed with FlowJo_v10.6.2 software. Each sample was assessed using a collection of 10,000 events. The mean values and standard deviations were calculated from three independent experiments.

Statistical Analysis

Two-tailed Student's tests and one-way ANOVA analysis were performed using GraphPad Prism software v. 7.0 (Graph Pad Software Inc., San Diego, CA). The values and data are presented as the mean ± SEM from three independent experiments. A p value of <0.05 was considered statistically significant.

RESULTS

YPJPF Alleviated Liver Injury *In Vivo*

The ACLF rat model was pre-established through intraperitoneal injection of CCl_4 for 12 weeks. Further, acute liver injury was induced by using a combination of LPS and D-Gal. And YQJPF was given for 2 weeks to investigate the protective effect on ACLF rats. In addition, methylprednisolone (Sou-Medrol) was used as a positive control drug, which has been confirmed as a therapeutic agent for ACLF (Zhao et al., 2012; Jia et al., 2020). And the establishment of a new model of ACLF in rats and the experimental procedures as shown in **Figure 2**. The livers in ACLF model became small and hard accompanied by necrosis, with small nodules on their surface; however, YQJPF and methylprednisolone were found to effectively ameliorate the liver morphology. Pathological examinations were used to manifest the effects of YQJPF on hepatic injury. As shown in H&E staining, YQJPF and methylprednisolone ameliorated the disordered hepatic structure (**Figure 3A**). The effect of YQJPF on liver injury was evaluated. Detection of serum biochemical indicators indicated improvement in liver injury indices such as TBil, ALT, and AST contents after 2 weeks of YQJPF and methylprednisolone treatment in rats with ACLF (**Figures 3B–E**). In summary, YQJPF and methylprednisolone significantly ameliorated liver injury in ACLF model rats.

Protective Effect of YQJPF on LPS- and D-Gal-Induced Hepatocyte *In Vitro*

Generally, massive hepatocyte death is implicated in ACLF. Here, we used LPS (10 μg/ml) and D-Gal (10 mg/ml) to induce liver injury in LO2 cells. MTT assay showed that LPS and D-Gal inhibit cell viability, whereas YQJPF and atractylone could promote cell viability in a dose-dependent manner. YQJPF above 10 μg/ml and atractylone at 5 μM showed a significant effect (**Figures 4A,B**). Light microscopy indicated that the adherent LO2 cells are swollen, and the cell morphology changed after LPS and D-Gal treatment for 4 h. YQJPF and atractylone could improve microscopic performance (**Figure 4C**). Levels of AST and ALT were detected to assess the hepatocytic damage. The levels of ALT, AST, and LDH in the supernatant of cultured LO2 cells were detected by ELISA. Results showed significantly increased levels of ALT, AST, and LDH in the model group and decreased levels of those in YQJPF and atractylone treatment groups (**Figures 4D–F**). Thus, YQJPF and atractylone exerted a protective effect on LPS- and D-Gal-induced hepatocytic injury.

YQJPF Inhibited Necroptosis but Not Apoptosis on LPS- and D-Gal-Induced Hepatocytic Injury *In Vitro*

Necrosis and apoptosis are the most common pathways of death during liver injury (Schwabe and Luedde, 2018). Hence, we first examined which pathway plays a significant role in LPS- and D-Gal-induced hepatocytic injury. The result of the TUNEL assay indicated that YQJPF (10, 20, and 40 μg/ml) and atractylone (5 μM) have no effect on apoptosis (**Figure 5B**). The protein expression of key indicators such as caspase 3, caspase 8, and the cleaved caspase-3 and caspase-8 did not change after LPS and D-Gal treatment (**Figure 5C**). Then, the cell apoptosis was determined by flow cytometry, and results indicated that YQJPF and atractylone have no effect on apoptosis (**Figure 5D**). Therefore, LPS- and D-Gal-induced cell death was not dependent on apoptosis because no obvious apoptotic features could be observed. YQJPF and atractylone prevented cell death without influencing apoptosis. Next, we assessed whether necroptosis plays a role in this process. Positive result in trypan blue staining indicated that membrane permeability is altered by LPS and D-Gal. YQJPF or atractylone treatment significantly decreased the number of dead cells (**Figure 5A**). To confirm our findings, we used TEM analysis to observe cell morphology and structure. The cells exhibited a typical necrotic cell death morphology, including swelling of organelles (especially mitochondria), condensation of chromatin into small, irregular patches, and chromatin margination, after LPS and D-Gal treatment (**Figure 5E**). YQJPF could restore cell morphology

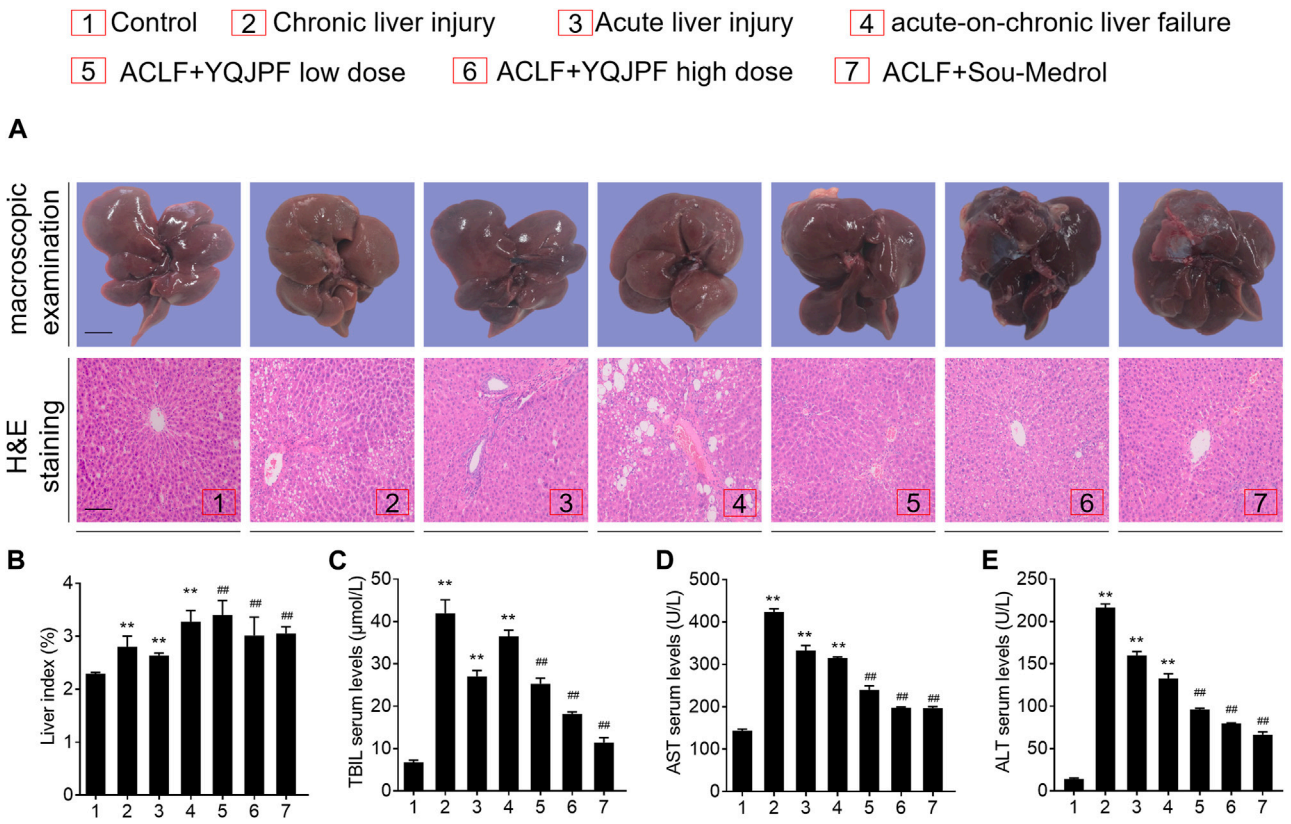

FIGURE 3 | YPJPF alleviated liver injury *in vivo*. **(A)** Ratio of liver weight and body weight. **(B–D)** TBIL, AST, and ALT levels in serum. **(E)** Representative pictures of liver tissues and photograph of H&E-stained sections (Scale bars, 100 μm). Data are expressed as mean ± SD (n = 8) *vs. control group, *vs. ACLF group; $^{*}p < 0.05$, $^{**}p < 0.01$; $^{\#}p < 0.05$, $^{\#\#}p < 0.01$.

and structure in a dose-dependent manner. Atractylone exhibited the same effect. Necroptotic cells underwent organelle breakdown, leading to the leakage of intracellular contents consequently triggering inflammation (Weinlich et al., 2017). Further, we examined some inflammation-associated biomarkers. mRNA and protein levels of pro-inflammatory cytokines IL-1β, IL-6, TNF-α, and IL-18 were detected using RT-qPCR, ELISA, and western blot analysis (**Figures 6A–I**). The results showed that pro-inflammatory cytokines are decreased in YQJPF and atractylone treatment groups compared with the LPS- and D-Gal-induced model group. Above all, we demonstrated that LPS and D-Gal induce hepatocyte necroptosis but not apoptosis and that YQJPF and its active ingredient atractylone could protect hepatocytes from necroptosis by reducing the expression of inflammatory cytokines in hepatocytes.

The RIPK1/RIPK3 Complex Is Required for YQJPF to Inhibit Necroptosis *In Vitro*

The RIPK1/RIPK3 signaling pathway has been reported to be involved in the induction of necroptosis (Lin et al., 2016; Newton et al., 2016). Thus, we investigated using western blot and ELISA whether YQJPF and atractylone alter the expression of RIPK1, RIPK3 and MLKL. As shown in (**Figures 7A–E**), YQJPF or atractylone treatment downregulated the expression of RIPK1, RIPK3 and MLKL. Immunofluorescence staining of RIPK1 and RIPK3 further validated these results. The association between RIPK1 and RIPK3 was analyzed using immunoprecipitation, which indicated that YQJPF and atractylone could inhibit the interaction between RIPK1 and RIPK3 (**Figure 7F**). To identify whether YQJPF and atractylone are dependent on RIPK1/RIPK3-mediated necroptosis, we used the RIPK1 kinase inhibitor necrostatin-1 (Nec-1) to verify the effect of YQJPF and atractylone. The results indicated that Nec-1 and YQJPF work together, and they had the most significant inhibitory effect on LO2 necroptosis induced by LPS and D-Gal (**Figures 8A–E**). We further investigated the interaction between RIPK1 and RIPK3 in YQJPF-treated LO2 cells through immunoprecipitation. RIPK1 and RIPK3 were significantly immunoprecipitated in LPS- and D-Gal-induced cells, which could be impaired by YQJPF and RIPK1 inhibitor Nec-1 (**Figure 8F**). Overall, YQJPF could downregulate the expression of RIPK1 and RIPK3, inhibit their aggregation to form necrosome, and eventually reduce

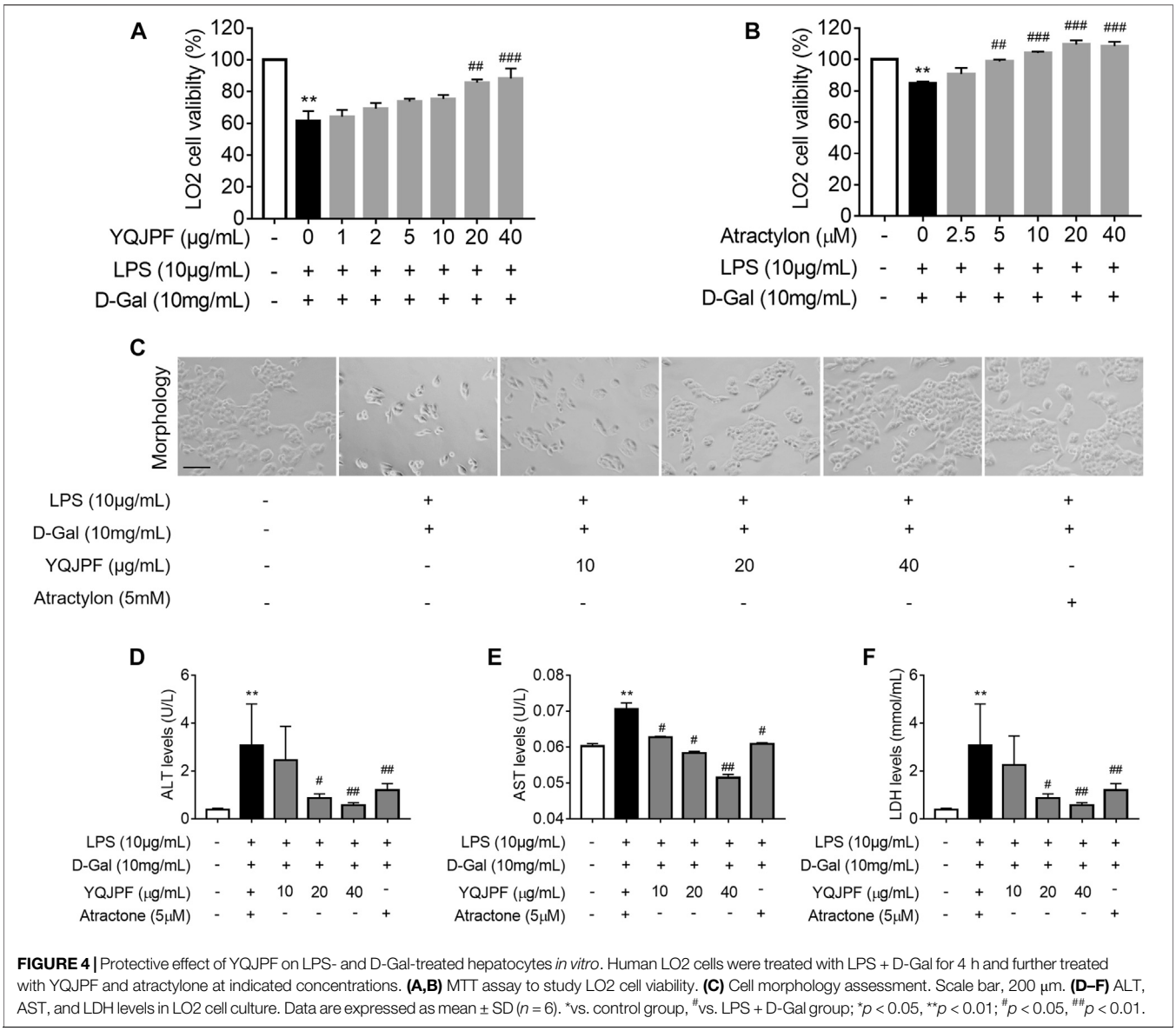

FIGURE 4 | Protective effect of YQJPF on LPS- and D-Gal-treated hepatocytes *in vitro*. Human LO2 cells were treated with LPS + D-Gal for 4 h and further treated with YQJPF and atractylone at indicated concentrations. **(A,B)** MTT assay to study LO2 cell viability. **(C)** Cell morphology assessment. Scale bar, 200 μm. **(D–F)** ALT, AST, and LDH levels in LO2 cell culture. Data are expressed as mean ± SD ($n = 6$). *vs. control group, #vs. LPS + D-Gal group; $^{*}p < 0.05$, $^{**}p < 0.01$; $^{\#}p < 0.05$, $^{\#\#}p < 0.01$.

the expression of pro-inflammatory cytokines by inhibiting RIPK1/RIPK3-mediated necroptosis.

YQJPF Inhibited Hepatocyte Necroptosis Through Inhibition of Mitochondrial ROS Generation and Depolarization *In Vitro*

Numerous studies have shown that ROS production is necessary for necroptosis in several cell lines such as macrophages (Koike et al., 2019), fibrosarcoma L929, HeLa, and human embryonic kidney (HEK) 293 T (Luedde et al., 2014; Zhang et al., 2017). To investigate whether YQJPF reduces ROS production in hepatocytes, we first analyzed the effect of YQJPF on intracellular ROS levels. Observation using fluorescence microscope revealed that YQJPF treatment decreases the ROS level in LO2 cells (**Figures 9B,C**). MitoSox Red staining was used to evaluate the mitochondrial ROS production. As shown in **Figure 9A**, YQJPF caused a significant decrease in mitochondrial superoxide, which had the same effect as selective RIPK1 inhibitor Nec-1. In addition, we found that pre-treatment of cells with YQJPF or Nec-1 significantly reversed LPS- and D-Gal-induced reduction in intracellular GSH and SOD levels. Additionally, YQJPF or Nec-1 inhibited MDA formation (**Figures 9D–F**). The effect of YQJPF on MMP was assessed using JC-1 staining, where a high ratio of red/green indicates an increase in MMP. The result indicated that YQJPF or Nec-1 upregulates MMP, recovers LPS- and D-Gal-induced MMP dissipation, and ameliorates mitochondrial depolarization (**Figure 9G**). The overproduction of ROS triggers serious damages in various cells. We observed that when the cells are pre-treated with ROS scavenger Tempol (10 μM), it could restore necroptosis-associated cell morphology and structure and inhibit

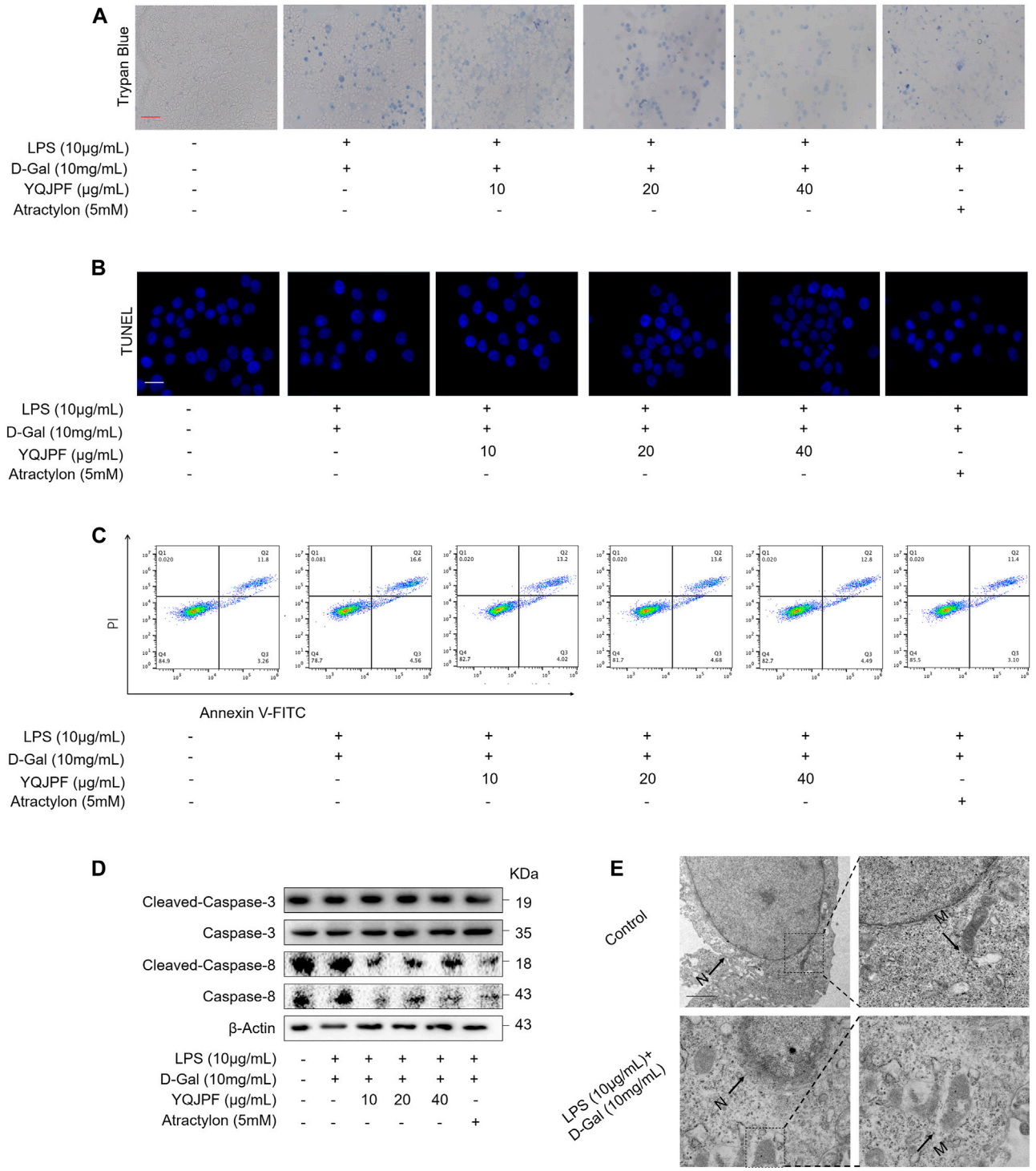

FIGURE 5 | YQJPF inhibited hepatocytic cell death, which was not by apoptosis, in LPS- and D-Gal-treated LO2 cells *in vitro*. Human LO2 cells were treated with LPS + D-Gal for 4 h and further with YQJPF and atractylone. **(A)** Trypan blue staining to detect cell death. Scale bar, 100 μm. **(B)** TUUNEL staining to detect cell apoptosis. **(C)** Western blot analysis of the protein expression of caspases three and eight and cleaved caspases three and eight in the treated human LO2 cells. **(D)** cell apoptosis assay by flow cytometer in the treated human LO2 cells. **(E)** Transmission electron microscopy (TEM) of cells. Black arrows represent swollen mitochondria (M), whereas white arrows represent condensed and marginated chromatins in nuclei (N). Data are expressed as mean ± SD ($n = 3$). *vs. control group, $^{\#}$vs. LPS + D-Gal group; $^{*}p < 0.05$, $^{**}p < 0.01$; $^{\#}p < 0.05$, $^{\#\#}p < 0.01$.

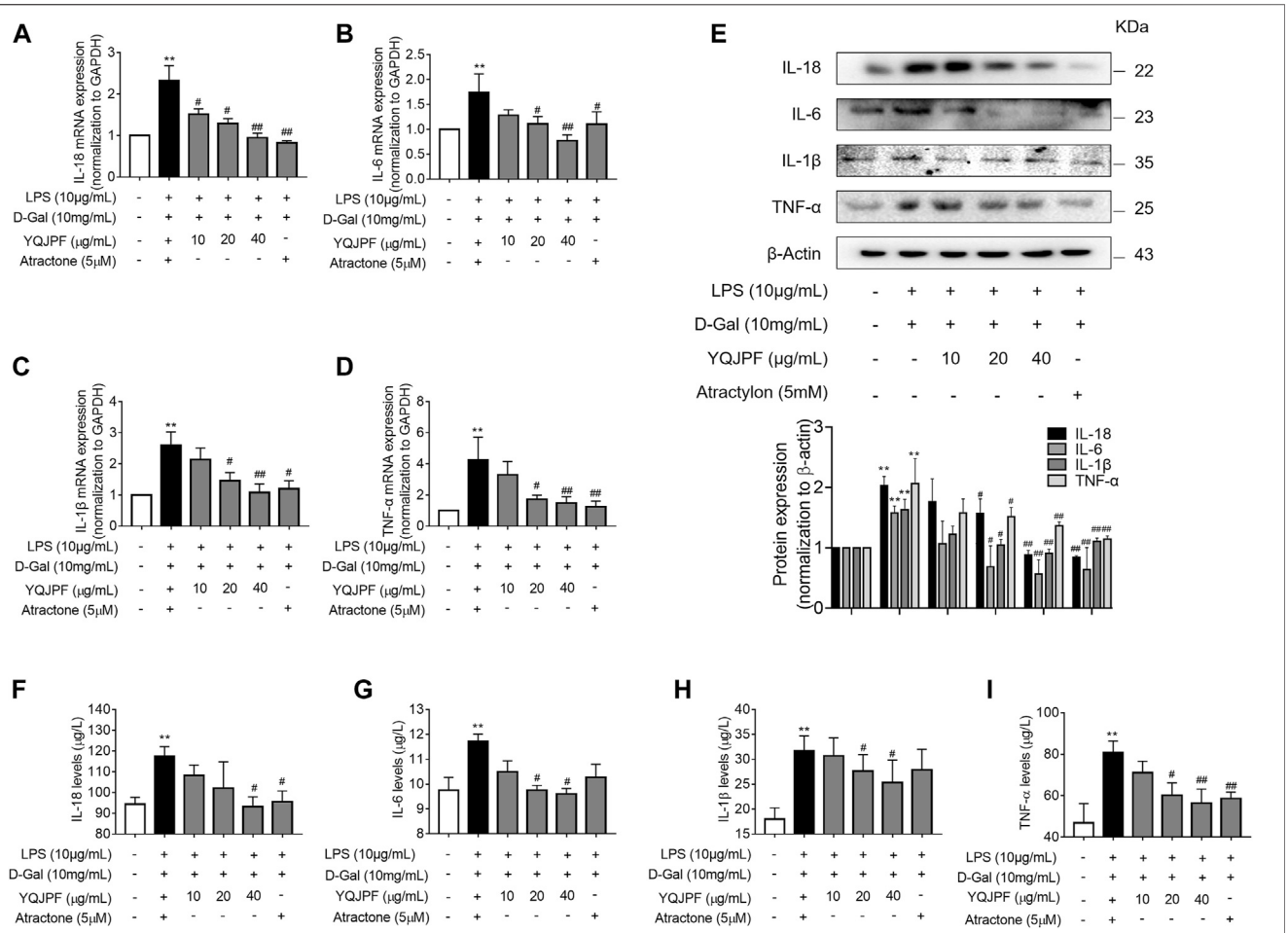

FIGURE 6 | YQJPF inhibited necroptosis of LPS- and D-Gal-treated hepatocytes *in vitro*. Human LO2 cells were treated with LPS + D-Gal for 4 h and further with YQJPF and atractylone. **(A–D)** Real-time PCR analyses of genes of pro-inflammatory cytokines IL-1β, IL-6, TNF-α, and IL-18. **(E)** Western blot analysis and quantitative analysis of the expression of pro-inflammatory cytokines IL-1β, IL-6, TNF-α, and IL-18 (F–I) Expression levels of IL-1β, IL-6, TNF-α, and IL-18 in LO2 were detected by ELISA. Data are expressed as mean ± SD (n = 3). *vs. control group, #vs. LPS + D-Gal group; $^{*}p < 0.05$, $^{**}p < 0.01$; $^{\#}p < 0.05$, $^{\#\#}p < 0.01$.

the expression of pro-inflammatory cytokines IL-1β, IL-6, TNF-α, and IL-18, as revealed by western blot (**Figure 9H**), which had the same effect as that of YQJPF. This suggested that YQJPF reduces the level of ROS in hepatocytes and thus plays a critical role in inhibiting cell death. Collectively, these results suggested that YQJPF inhibits necroptosis by reducing the level of mitochondrial ROS and stabilizing MMP in hepatocytes.

Disruption of Hepatocyte Necroptosis, Instead of Apoptosis, Was Associated with YQJPF Treatment *In Vivo*

The results of *in vivo* studies on the effect of YQJPF on hepatocyte necroptosis were the same as those of *in vitro* results. Protein levels of key caspases did not change under YQJPF treatment. Therefore, reduction in cell death due to YQJPF was independent of apoptosis. Further, we proceeded to investigate whether YQJPF could disrupt hepatocytic death by regulating necroptosis. Western blot analysis of RIPK1, RIPK3, and MLKL, which governed necroptosis, indicated that necroptosis is increased in ACLF *in vivo* (**Figure 10E**). However, it was weakened by YQJPF treatment. Furthermore, immunochemical staining of RIPK1, RIPK3, and MLKL showed that YQJOF reduces hepatocytic RIPK1, RIPK3, and MLKL levels, which were upregulated in chronic liver injury, acute liver injury, and ACLF model (**Figure 10F**). Overall, these results demonstrated that YQJPF decreases the levels of RIPK1, RIPK3, and MLKL and decreases ATP production to ameliorate hepatocyte necroptosis instead of apoptosis in ACLF model. Our previous study revealed that JNK1/2-ROS signaling is involved in HSC necroptosis (Jia et al., 2018). To investigate the role of anti-oxidant response in YQJPF-ameliorated hepatocyte necroptosis, we analyzed the effect of YQJPF on SOD and MDA levels in the liver, which are produced during lipid peroxidation. Observation using SOD and MDA detection kits showed that YQJPF treatment increases the anti-oxidant response in the liver (**Figure 10A**). Interestingly, the levels of ATP and mtDNA decreased significantly in chronic liver injury, acute liver injury, and ACLF model (**Figure 10B**).

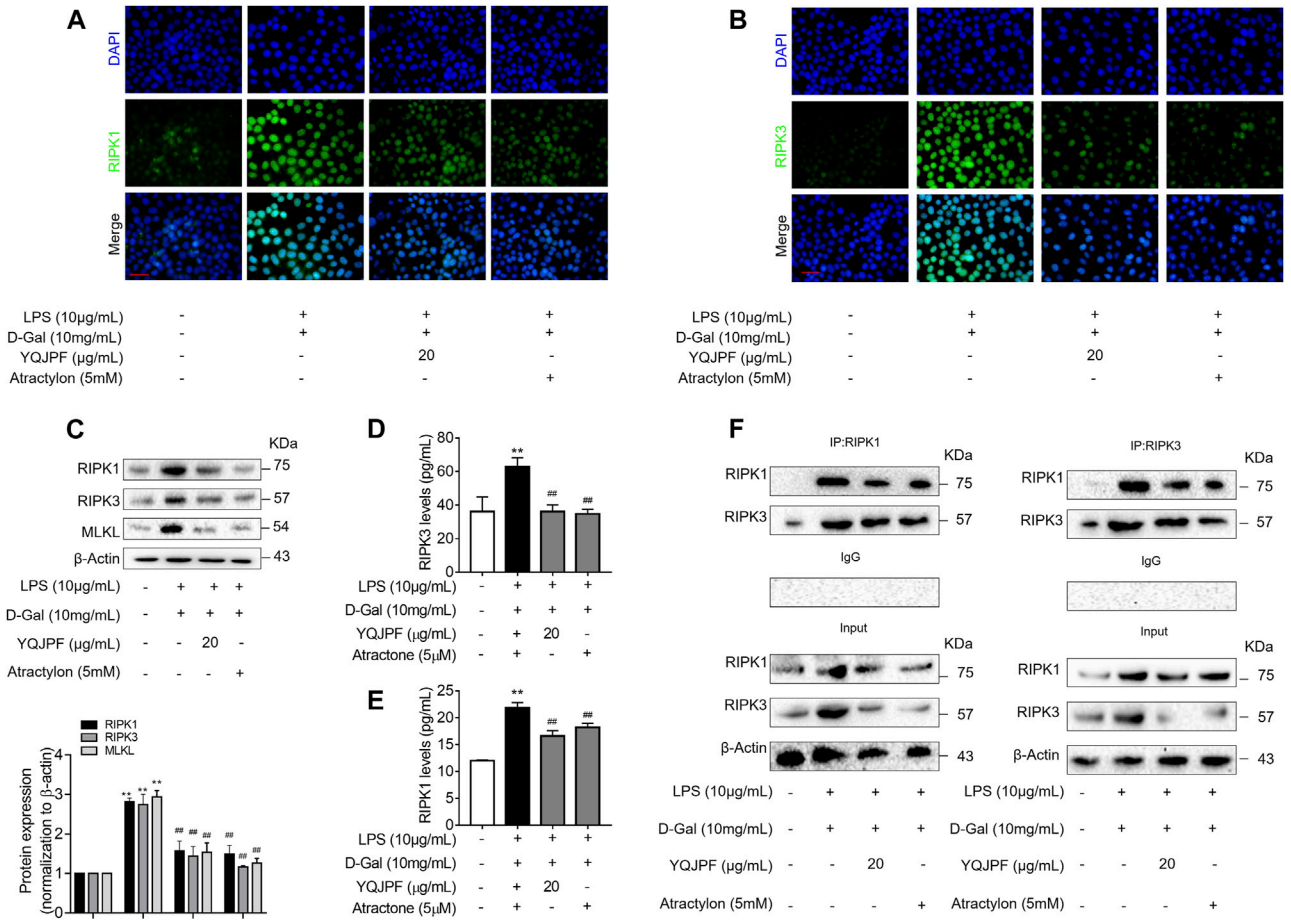

FIGURE 7 | The RIPK1/RIPK3-complex is required for YQJPF to inhibit hepatocyte necroptosis *in vitro*. Human LO2 cells were treated with LPS + D-Gal for 4 h and further with YQJPF and atractylone. **(A,B)** Immunofluorescence staining of RIPK1 and RIPK3 in LO2 cells. Scale bar, 50 μm. **(C)** Western blot analysis and quantitative assessment of RIPK1, MLKL and RIPK3. **(D,E)** Expression levels of RIPK1 and RIPK3 in LO2 were detected by ELISA. **(F)** RIPK1 was immunoprecipitated with its antibody and resulted in co-immunoprecipitation of RIPK3. Immunoprecipitation of RIPK3 with its antibody caused co-immunoprecipitation of RIPK1 in LO2 cells. Data are expressed as mean ± SD (n = 3). *vs. control group, #vs. LPS + D-Gal group; *$p < 0.05$, **$p < 0.01$; #$p < 0.05$, ##$p < 0.01$.

Collectively, these results suggest that anti-oxidant response contributes to the effect of YQJPF on hepatocyte necroptosis. Similar to the *in vitro* results, we observed a significant increase in the serum levels of TNF-α, IL-18, IL-1β, and IL-6 in ACLF rats, but the effect was altered in a concentration dependent-manner by YQJPF treatment (**Figures 10G–J**). These results indicated that YQJPF attenuates hepatic inflammation and liver injury by disrupting hepatocyte necroptosis instead of apoptosis *in vivo*.

DISCUSSION

The pathobiology of ACLF is characterized by hepatic and systemic inflammation; progressive, unrelenting hepatocyte injury; and hepatocyte death. Hepatocyte death typically follows two patterns: necrosis and apoptosis (Vanlangenakker et al., 2008). In our study, we developed ACLF rat models by administering high dose (1.5 ml/kg body weight) of 1:1 (w/v) mixture of CCl_4 and olive oil for 3 months followed by 100 μg/kg LPS and 400 mg/kg D-Gal injection. Hepatocyte injury and cell death index were obvious in the *in vivo* model. Through the successful establishment of the disease model, we first confirmed the protective effect of YQJPF on ACLF liver injury. YQJPF could ameliorate CCl_4-, LPS-, and D-Gal-induced liver injury. Liver tissue morphology improved and serum levels of hepatic ALT, AST, and Tbil decreased after YQJPF treatment. The protective effect of YQJPF was consistent in the *in vitro* experiments. To further clarify the mechanism of action of YQJPF, an *in vitro* hepatocyte injury model was established using LPS (10 μg/ml) and D-Gal (10 mg/ml). YQJPF and atractylone (the main component of YQJPF) could restore the damage to cell viability induced by LPS and D-Gal and decrease ALT, AST, and LDH levels in cell supernatant. These data clearly indicated that YQJPF confers protection against ACLF.

Liver failure is characterized by massive loss of parenchymal cells, and cell death can occur in this pathophysiological context (Schwabe and Luedde, 2018). Necroptosis is defined as the third type of programmed cell death in addition to apoptosis and

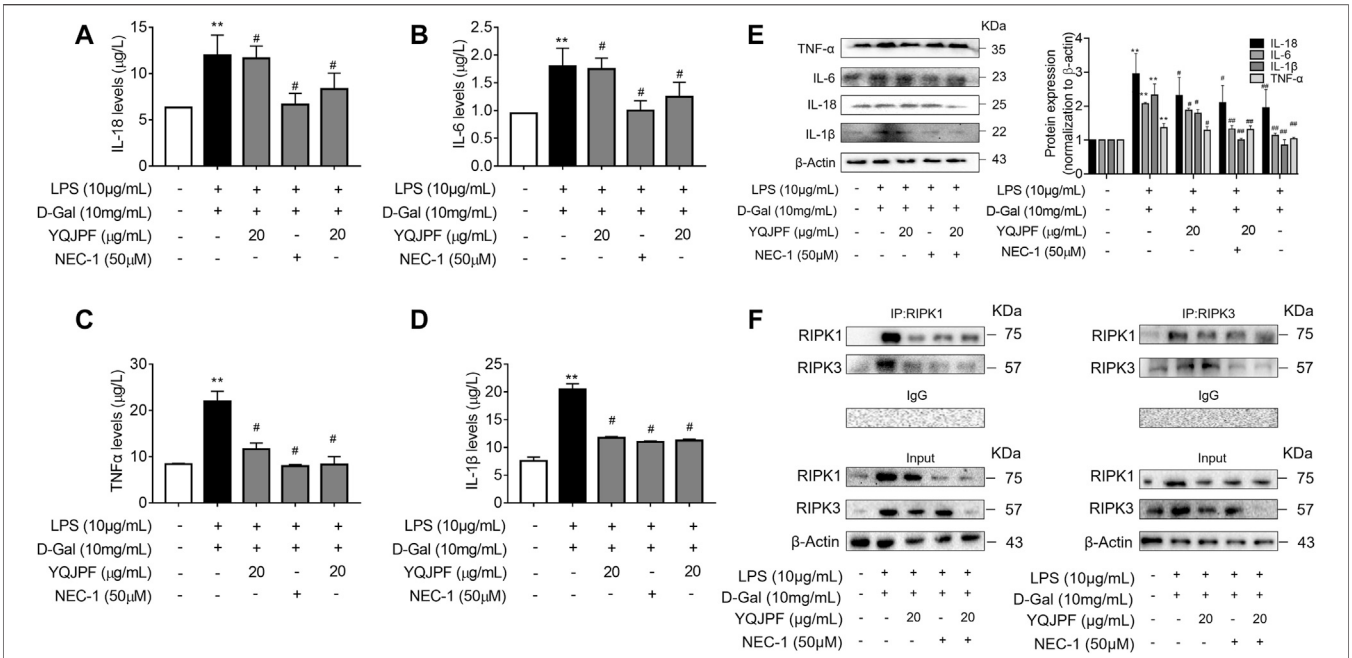

FIGURE 8 | YQJPF inhibited hepatocyte necroptosis in RIPK1-dependent manner *in vitro*. Human LO2 cells were treated with LPS + D-Gal for 4 h and further pre-treated with 50 μM Nec-1 for 1 h, followed by YQJPF or atractylone treatment for 24 h. **(A–D)** Expression levels of IL-1β, IL-6, TNF-α, and IL-18 in LO2 cells were detected by ELISA. **(E)** Western blot and quantitative analysis of IL-1β, IL-6, TNF-α, and IL-18. **(F)** RIPK1 was immunoprecipitated with its antibody and resulted in co-immunoprecipitation of RIPK3. Immunoprecipitation of RIPK3 with its antibody caused co-immunoprecipitation of RIPK1 in LO2 cells. Data are expressed as mean ± SD (n = 3). *vs. control group, #vs. LPS + D-Gal group; $^{*}p < 0.05$, $^{**}p < 0.01$; $^{\#}p < 0.05$, $^{\#\#}p < 0.01$.

necrosis (Galluzzi and Kroemer, 2008). It is also known as programmed necrosis or caspase-independent cell death. Necroptosis is believed to trigger a massive inflammatory response that can cause substantial collateral damage to neighboring cells. Findings of a clinical study indicated that circulating RIPK3 is significantly increased in patients with HBV-ACLF and is associated with a clinical outcome (Chen et al., 2020). However, very few studies on drugs inhibiting necroptosis in the liver are available. This study found that YQJPF could attenuate hepatocyte death but has no effect on the inhibition of the caspases three and eight activity. Therefore, YQJPF-induced hepatocytic cell death inhibition did not result from apoptosis. Moreover, a typical cell necroptosis morphology could be identified, and RIPK3 mediates cell death and regulates inflammatory responses (Zhao et al., 2017). Our study showed that the levels of TNF-α, IL-18, IL-1β, and IL-6 were found to be significantly increased in LPS (10 μg/ml)- and D-Gal (10 mg/ml)-induced models. The effect was altered in a concentration-dependent manner after YQJPF treatment. RIPK1, RIPK3, and MLKL were identified as necroptosis regulators (Wang et al., 2012). Further, we assessed expressions of RIPK1 and RIPK3. Western blot analysis, ELISA, and immunochemical staining of RIPK1 and RIPK3 demonstrated that YQJPF decreases hepatocytes necroptosis in the ACLF model. Moreover, YQJPF inhibited the combination expression of RIPK1 and RIPK3 and blocked the formation of necrosome. As expected, YQJPF-induced inhibition of inflammatory cytokines and necrosome formation were enhanced when RIPK1 activity was inhibited by pharmacological inhibitor Nec-1. Obviously, YQJPF inhibited RIPK1/RIPK3-complex-dependent necroptosis in human LO2 cells.

Oxidative stress, a major contributor of liver injury, can be induced by excessive ROS. Studies have shown that ROS may be considerably involved in the pathogenesis of liver diseases (Chen et al., 2016). ROS have a significant effect on necroptosis, particularly the mitochondrial ROS generated in response to TNF/TNFR1 engagement. Conversely, ROS accumulation is also gradually regarded as the executioner and mediator of necroptosis (Zhu et al., 2018). ROS is mainly produced in mitochondria that in turn leads to the damage of organelles or even cell death. In this study, we found significantly decreased levels of intracellular and mitochondrial ROS after YQJPF treatment. Following pre-treatment with the ROS scavenger-Tempol, the YQJPF-induced inhibition of cell inflammatory cytokines was significantly enhanced. Thus, YQJPF could inhibit ROS accumulation. The association between RIPK1 and RIPK3 upregulation and mPTP opening has been illustrated in several studies (He et al., 2011). ROS has been reported as the primary factor that activates mPTP opening and has been implicated in the process of necroptosis. In addition, RIPK1-RIPK3 interaction could upregulate ROS levels and enhance mitochondrial superoxide production. Hence, we identified that the inhibition of RIPK1 with Nec-1 markedly enhances YQJPF-induced alteration of mitochondrial superoxide. Cellular anti-oxidant machinery mainly includes SOD, MDA, and GPx that can effectively scavenge free radicals (Riordan and Williams, 2003). In this study, SOD,

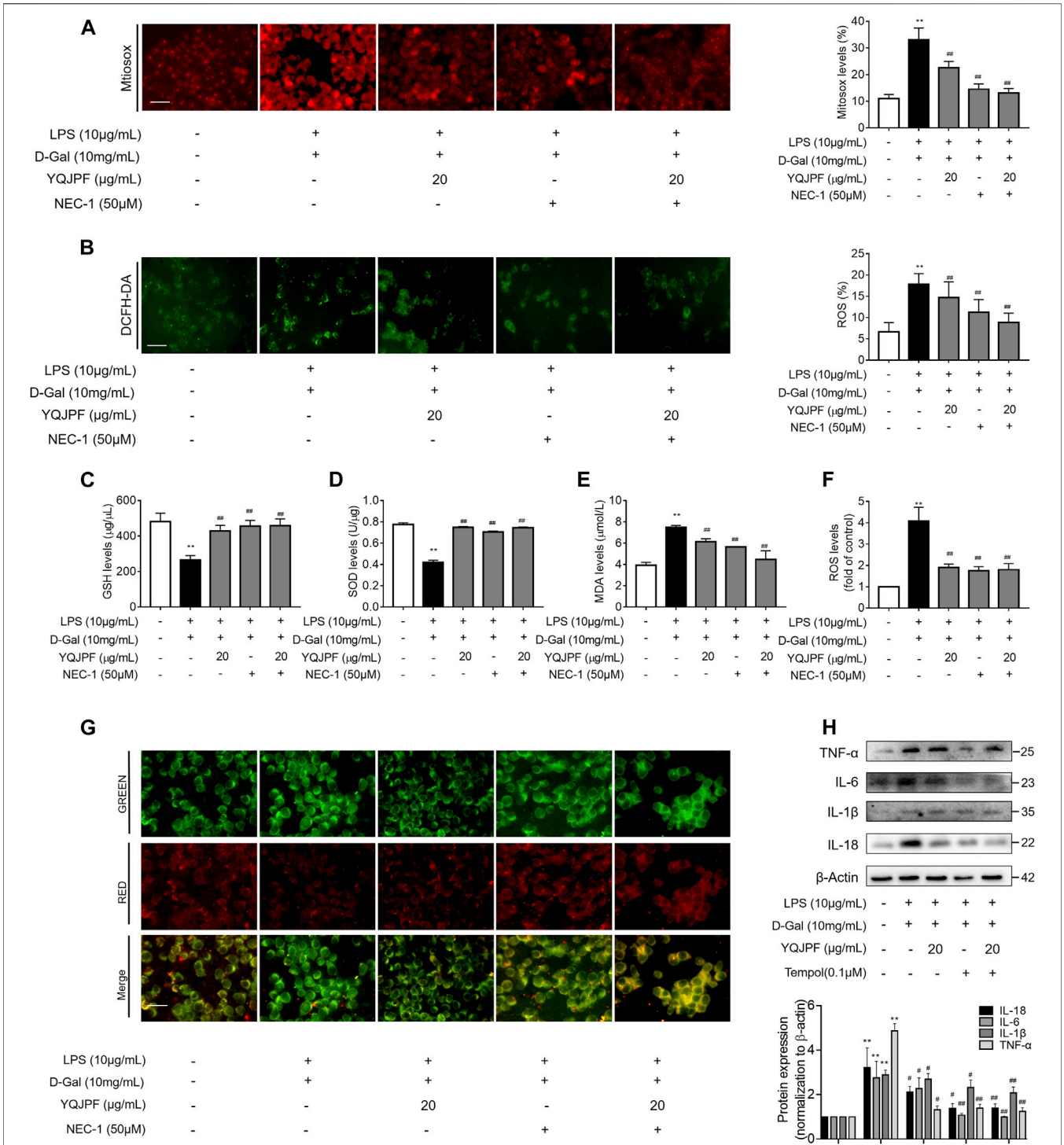

FIGURE 9 | YQJPF inhibited hepatocyte necroptosis through the inhibition of mitochondrial ROS generation and depolarization *in vitro*. Human LO2 cells were treated with LPS + D-Gal for 4 h and further pre-treated with 50 μM Nec-1 for 1 h, followed by YQJPF or atractylone treatment for 24 h. **(A)** Mitochondrial superoxide was detected and quantified through immunofluorescence by using MitoSox Red staining. Scale bar, 50 μm. **(B)** ROS production was assessed and quantified by DCFH-DA staining, Scale bar, 50 μm. **(C–E)** MDA, SOD, and GSH levels were measured by corresponding test kits. **(F)** ROS levels were assessed using ROS test kit. **(G)** Mitochondrial membrane potential was detected by JC-1 staining. Scale bar, 50 μm. **(H)** Western blot and quantitative analysis of the expression of IL-1β, IL-6, TNF-α, and IL-18. Data are expressed as mean ± SD (n = 3). *vs. control group, $^{\#}$vs. LPS + D-Gal group; $^{*}p < 0.05$, $^{**}p < 0.01$; $^{\#}p < 0.05$, $^{\#\#}p < 0.01$.

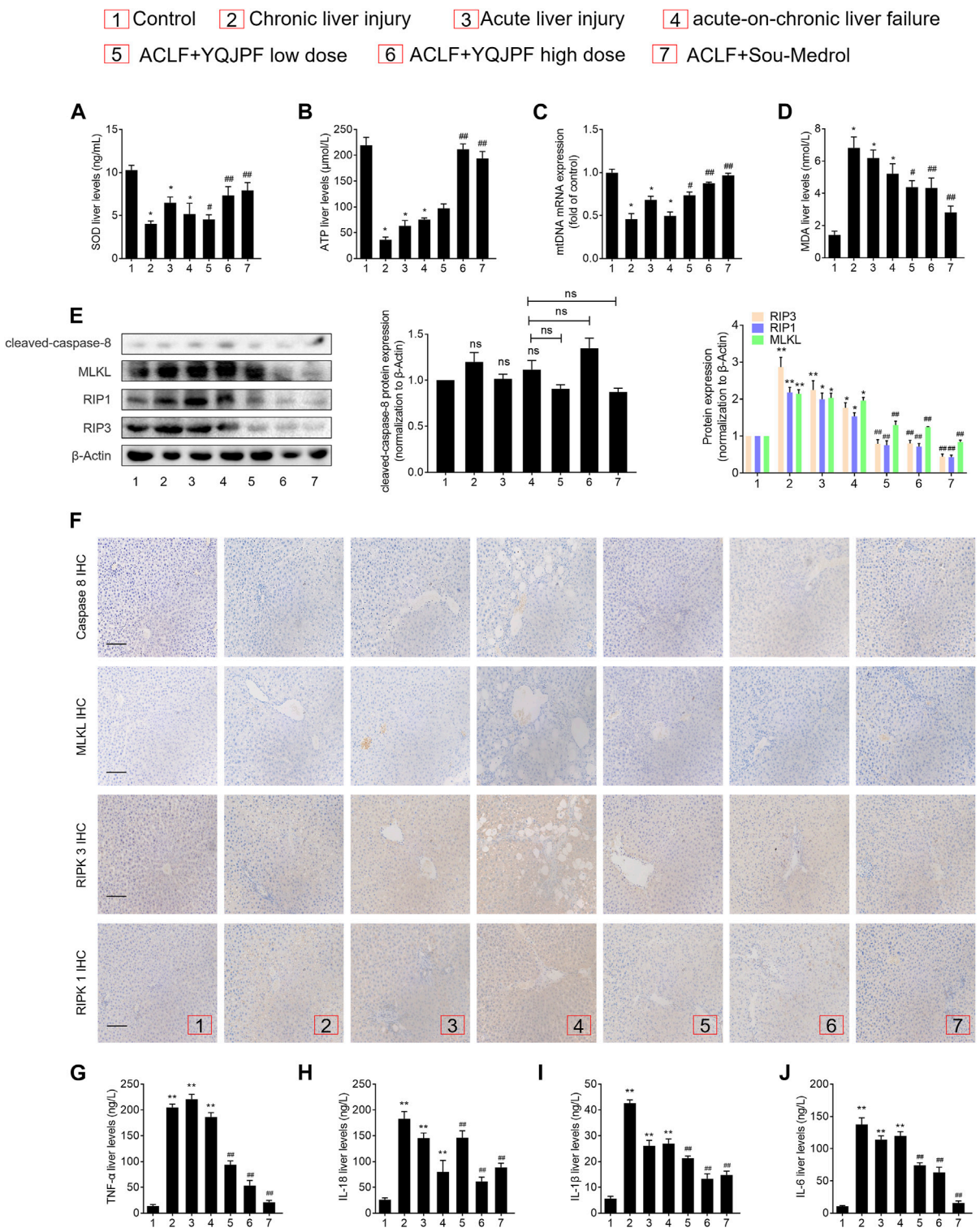

FIGURE 10 | Disruption of hepatocyte necroptosis, and not apoptosis, was required for the action of YQJPF *in vivo*. **(A–D)** MDA, ATP, GSH, and SOD levels in the rat livers were measured. **(E)** Western blot and quantitative analysis of cleaved caspase 8, MLKL, RIPK1, and RIPK3 expression in the rat livers. **(F)** Immunochemical staining and quantitative analysis of caspase 8, MLKL, RIPK1, and RIPK3 in liver tissues. Scale bar, 100 μm. **(G–J)** Expression levels of IL-1β, IL-6, TNF-α, and IL-18 in the rat livers were detected by ELISA. Data are expressed as mean ± SD (n = 8) *vs. control group, $^{\#}$vs. ACLF group; $^{*}p < 0.05$, $^{**}p < 0.01$; $^{\#}p < 0.05$, $^{\#\#}p < 0.01$.

GSH, and MDA levels were assessed, and the results suggested that the anti-oxidant response contributes to the effect of YQJPF on hepatocyte necroptosis. Inhibition of RIPK1 by Nec-1 enhanced the effect. Additionally, these findings were confirmed in the rat models.

Traditional Chinese medicine (TCM) pattern is a physiological regulation network, which contains a regulation center, overall effective target, material basis and functional unit. Its mechanism needs to be indicated by means of TCM pattern prevention and treatment characteristics, multiple organ integration effectiveness, and functional unit network so as to guide clinical practice as well as for inspiring basic research. It is urgently to exploring the efficacy mechanism and regulation with the molecular biology and systems biology. In our research, we conducted a deep study of the pathogenesis, TCM pattern feature and efficacy evaluation of TCM in ACLF. And results showed that YQJPF attenuates liver injury in ACLF. Recently, Chen et al.' reported that flavonoids have been to possess a wide variety of biological activities such as antioxidant activity, anti-inflammatory activity, hepatoprotective effect, antibacterial activity, antiviral activity, anticancer activity, and antidiabetic activity (Chen et al., 2018). Chen et al.' reported that raspberry treatment could ameliorate H2O2-induced oxidative stress in HepG2 cells *via* Keap1/Nrf2 pathway (Chen et al., 2019). In our study, we found that atractylone (one component of YQJPF) has the similar effect with YQJPF, and inhibited necroptosis of hepatocytes *in vitro*. Which revealed the main component of YQJPF could play such effect.

In summary, YQJPF attenuates liver injury by inhibiting hepatic inflammation and necroptosis of hepatocytes *in vivo* and *in vitro*. Mechanistically, YQJPF inhibits hepatocyte necroptosis by blocking the RIPK1/RIPK3 complex formation followed by relieving mitochondrial dysfunction, which ultimately prevents hepatocytic cell death. Most importantly, we confirmed that YQJPF can be used as a medicine for ACLF treatment and provided a scientific basis for the research on the application of YQJPF in ACLF.

DATA AVAILABILITY STATEMENT

The raw data supporting the conclusions of this article will be made available by the authors, without undue reservation.

ETHICS STATEMENT

The animal study was reviewed and approved by the Nanjing University of Chinese Medicine.

AUTHOR CONTRIBUTIONS

All of the authors took part in the experiments. Guarantor of the article: ST, FZ, and SZ. Author contributions: Study concept and design: ST, FZ, and SZ. Acquisition, analysis, and interpretation of data: FW, LT, BL, CJ, LG, YL, ZL, JS, and ZZ. Drafting the manuscript: FW and LT. Obtained funding: ST, FZ, and SZ.

FUNDING

This work was supported by the Leading Talent Project of Jiangsu Province Traditional Chinese Medicine (SLJ0216), the National Natural Science Foundation of China (81870423, 82073914, 82000572), the Major Project of the Natural Science Research of Jiangsu Higher Education Institutions (19KJA310005), the Postgraduate Research & Practice Innovation Program of Jiangsu Province, Grant/Award Number: KYCX20_1493, the Joint Project of Jiangsu Key Laboratory for Pharmacology and Safety Evaluation of Chinese Materia Medica and Yangtze River Pharmaceutical (JKLPSE202005), the Natural Science Foundation of Jiangsu Province (BK20200056).

REFERENCES

Asrani, S. K., Devarbhavi, H., Eaton, J., and Kamath, P. S. (2019). Burden of Liver Diseases in the World. *J. Hepatol.* 70, 151–171. doi:10.1016/j.jhep.2018.09.014

Bajaj, J. S., Moreau, R., Kamath, P. S., Vargas, H. E., Arroyo, V., Reddy, K. R., et al. (2018). Acute-on-Chronic Liver Failure: Getting Ready for Prime Time? *Hepatology* 68, 1621–1632. doi:10.1002/hep.30056

Chen, L., Teng, H., Zhang, K. Y., Skalicka-Woźniak, K., Georgiev, M. I., and Xiao, J. (2016). Agrimonolide and Desmethylagrimonolide Induced HO-1 Expression in HepG2 Cells through Nrf2-Transduction and P38 Inactivation. *Front. Pharmacol.* 7, 513. doi:10.3389/fphar.2016.00513

Chen, L., Cao, Z., Yan, L., Ding, Y., Shen, X., Liu, K., et al. (2020). Circulating Receptor-Interacting Protein Kinase 3 Are Increased in HBV Patients with Acute-On-Chronic Liver Failure and Are Associated with Clinical Outcome. *Front. Physiol.* 11, 526. doi:10.3389/fphys.2020.00526

Chen, L., Li, K., Liu, Q., Quiles, J. L., Filosa, R., Kamal, M. A., et al. (2019). Protective Effects of Raspberry on the Oxidative Damage in HepG2 Cells through Keap1/Nrf2-dependent Signaling Pathway. *Food Chem. Toxicol.* 133, 110781. doi:10.1016/j.fct.2019.110781

Chen, L., Teng, H., Jia, Z., Battino, M., Miron, A., Yu, Z., et al. (2018). Intracellular Signaling Pathways of Inflammation Modulated by Dietary Flavonoids: The Most Recent Evidence. *Crit. Rev. Food Sci. Nutr.* 58, 2908–2924. doi:10.1080/10408398.2017.1345853

Cheng, Y., Chen, T., Yang, X., Xue, J., and Chen, J. (2019). Atractylon Induces Apoptosis and Suppresses Metastasis in Hepatic Cancer Cells and Inhibits Growth In Vivo. *Cmar* Vol. 11, 5883–5894. doi:10.2147/cmar.s194795

Engelmann, C., Mehta, G., and Tacke, F. (2020). Regeneration in Acute-On-Chronic Liver Failure - the Phantom Lost its Camouflage. *J. Hepatol.* 72, 610–612. doi:10.1016/j.jhep.2020.01.003

Galluzzi, L., and Kroemer, G. (2008). Necroptosis: a Specialized Pathway of Programmed Necrosis. *Cell* 135, 1161–1163. doi:10.1016/j.cell.2008.12.004

He, S., Liang, Y., Shao, F., and Wang, X. (2011). Toll-like Receptors Activate Programmed Necrosis in Macrophages through a Receptor-Interacting Kinase-3-Mediated Pathway. *Proc. Natl. Acad. Sci.* 108, 20054–20059. doi:10.1073/pnas.1116302108

Jia, L., Xue, R., Zhu, Y., Zhao, J., Li, J., He, W. P., et al. (2020). The Efficacy and Safety of Methylprednisolone in Hepatitis B Virus-Related Acute-On-Chronic Liver Failure: a Prospective Multi-Center Clinical Trial. *BMC Med.* 18, 383. doi:10.1186/s12916-020-01814-4

Jia, Y., Wang, F., Guo, Q., Li, M., Wang, L., Zhang, Z., et al. (2018). Curcumol Induces RIPK1/RIPK3 Complex-dependent Necroptosis via JNK1/2-ROS Signaling in Hepatic Stellate Cells. *Redox Biol.* 19, 375–387. doi:10.1016/j.redox.2018.09.007

Jin, H., Lian, N., Zhang, F., Chen, L., Chen, Q., Lu, C., et al. (2016). Activation of PPARgamma/P53 Signaling Is Required for Curcumin to Induce Hepatic Stellate Cell Senescence. *Cell Death Dis* 7, e2189. doi:10.1038/cddis.2016.92

Koike, A., Hanatani, M., and Fujimori, K. (2019). Pan-caspase Inhibitors Induce Necroptosis via ROS-Mediated Activation of Mixed Lineage Kinase

Domain-like Protein and P38 in Classically Activated Macrophages. *Exp. Cel Res.* 380, 171–179. doi:10.1016/j.yexcr.2019.04.027

Lian, Y., Xu, L., Tan, S., Xiao, Q., Sun, W., Shen, J., et al. (2015). Effects of Treatment on T Lymphocyte Frequency with Principle of Strengthening Vital Qi and the Spleen Based on the Mechanism of Deficiency in Vital Qi in Patients. JETCM *Chin.* 24, 2106–2108.

Lin, J., Kumari, S., Kim, C., Van, T.-M., Wachsmuth, L., Polykratis, A., et al. (2016). RIPK1 Counteracts ZBP1-Mediated Necroptosis to Inhibit Inflammation. *Nature* 540, 124–128. doi:10.1038/nature20558

Luedde, T., Kaplowitz, N., and Schwabe, R. F. (2014). Cell Death and Cell Death Responses in Liver Disease: Mechanisms and Clinical Relevance. *Gastroenterology* 147, 765–783. doi:10.1053/j.gastro.2014.07.018

Newton, K., Dugger, D. L., Maltzman, A., Greve, J. M., Hedehus, M., Martin-Mcnulty, B., et al. (2016). RIPK3 Deficiency or Catalytically Inactive RIPK1 Provides Greater Benefit Than MLKL Deficiency in Mouse Models of Inflammation and Tissue Injury. *Cell Death Differ* 23, 1565–1576. doi:10.1038/cdd.2016.46

Riordan, S. M., and Williams, R. (2003). Mechanisms of Hepatocyte Injury, Multiorgan Failure, and Prognostic Criteria in Acute Liver Failure. *Semin. Liver Dis.* 23, 203–215. doi:10.1055/s-2003-42639

Sarin, S. K., and Choudhury, A. (2016). Acute-on-chronic Liver Failure: Terminology, Mechanisms and Management. *Nat. Rev. Gastroenterol. Hepatol.* 13, 131–149. doi:10.1038/nrgastro.2015.219

Schwabe, R. F., and Luedde, T. (2018). Apoptosis and Necroptosis in the Liver: a Matter of Life and Death. *Nat. Rev. Gastroenterol. Hepatol.* 15, 738–752. doi:10.1038/s41575-018-0065-y

Vanlangenakker, N., Berghe, T., Krysko, D., Festjens, N., and Vandenabeele, P. (2008). Molecular Mechanisms and Pathophysiology of Necrotic Cell Death. *Cmm* 8, 207–220. doi:10.2174/156652408784221306

Wang, F. S., Fan, J. G., Zhang, Z., Gao, B., and Wang, H. Y. (2014). The Global Burden of Liver Disease: the Major Impact of China. *Hepatology* 60, 2099–2108. doi:10.1002/hep.27406

Wang, Z., Jiang, H., Chen, S., Du, F., and Wang, X. (2012). The Mitochondrial Phosphatase PGAM5 Functions at the Convergence Point of Multiple Necrotic Death Pathways. *Cell* 148, 228–243. doi:10.1016/j.cell.2011.11.030

Weinlich, R., Oberst, A., Beere, H. M., and Green, D. R. (2017). Necroptosis in Development, Inflammation and Disease. *Nat. Rev. Mol. Cel Biol* 18, 127–136. doi:10.1038/nrm.2016.149

Xiang, X., Feng, D., Hwang, S., Ren, T., Wang, X., Trojnar, E., et al. (2020). Interleukin-22 Ameliorates Acute-On-Chronic Liver Failure by Reprogramming Impaired Regeneration Pathways in Mice. *J. Hepatol.* 72, 736–745. doi:10.1016/j.jhep.2019.11.013

Xie, F., Dong, J., Zhu, Y., Wang, K., Liu, X., Chen, D., et al. (2019). HIF1a Inhibitor Rescues Acute-On-Chronic Liver Failure. *Ann. Hepatol.* 18, 757–764. doi:10.1016/j.aohep.2019.03.007

Yao, H., Huang, X., Xie, Y., Huang, X., Ruan, Y., Lin, X., et al. (2018). Identification of Pharmacokinetic Markers for Guanxin Danshen Drop Pills in Rats by Combination of Pharmacokinetics, Systems Pharmacology, and Pharmacodynamic Assays. *Front. Pharmacol.* 9, 1493. doi:10.3389/fphar.2018.01493

Zhang, F., Zhang, Z., Kong, D., Zhang, X., Chen, L., Zhu, X., et al. (2014a). Tetramethylpyrazine Reduces Glucose and Insulin-Induced Activation of Hepatic Stellate Cells by Inhibiting Insulin Receptor-Mediated PI3K/AKT and ERK Pathways. *Mol. Cell Endocrinol.* 382, 197–204. doi:10.1016/j.mce.2013.09.020

Zhang, Y., Su, S. S., Zhao, S., Yang, Z., Zhong, C. Q., Chen, X., et al. (2017). RIP1 Autophosphorylation Is Promoted by Mitochondrial ROS and Is Essential for RIP3 Recruitment into Necrosome. *Nat. Commun.* 8, 14329. doi:10.1038/ncomms14329

Zhang, Z., Zhang, F., Wang, Y., Du, Y., Zhang, H., Kong, D., et al. (2014b). Traditional Chinese Medicine for Stable Angina Pectoris via TCM Pattern Differentiation and TCM Mechanism: Study Protocol of a Randomized Controlled Trial. *Trials* 15, 422. doi:10.1186/1745-6215-15-422

Zhao, J., Zhang, J.-Y., Yu, H.-W., He, Y.-L., Zhao, J.-J., Li, J., et al. (2012). Improved Survival Ratios Correlate with Myeloid Dendritic Cell Restoration in Acute-On-Chronic Liver Failure Patients Receiving Methylprednisolone Therapy. *Cell Mol Immunol* 9, 417–422. doi:10.1038/cmi.2011.51

Zhao, Q., Yu, X., Zhang, H., Liu, Y., Zhang, X., Wu, X., et al. (2017). RIPK3 Mediates Necroptosis during Embryonic Development and Postnatal Inflammation in Fadd -Deficient Mice. *Cel Rep.* 19, 798–808. doi:10.1016/j.celrep.2017.04.011

Zhu, P., Hu, S., Jin, Q., Li, D., Tian, F., Toan, S., et al. (2018). Ripk3 Promotes ER Stress-Induced Necroptosis in Cardiac IR Injury: A Mechanism Involving Calcium overload/XO/ROS/mPTP Pathway. *Redox Biol.* 16, 157–168. doi:10.1016/j.redox.2018.02.019

Conflict of Interest: The authors declare that the research was conducted in the absence of any commercial or financial relationships that could be construed as a potential conflict of interest.

Copyright © 2021 Wang, Tang, Liang, Jin, Gao, Li, Li, Shao, Zhang, Tan, Zhang and Zheng. This is an open-access article distributed under the terms of the Creative Commons Attribution License (CC BY). The use, distribution or reproduction in other forums is permitted, provided the original author(s) and the copyright owner(s) are credited and that the original publication in this journal is cited, in accordance with accepted academic practice. No use, distribution or reproduction is permitted which does not comply with these terms.

frontiers in Pharmacology

ORIGINAL RESEARCH
published: 28 April 2021
doi: 10.3389/fphar.2021.590477

Network Pharmacology-Based Strategy for Elucidating the Molecular Basis Forthe Pharmacologic Effects of Licorice (*Glycyrrhiza* spp.)

Jia Chen[1,2], *Lin-Fu Li*[3], *Xiao-Ru Hu*[2], *Feng Wei*[2]* *and Shuangcheng Ma*[1,2]*

[1]School of Chinese Materia Medica, Beijing University of Chinese Medicine, Beijing, China, [2]Institute for Control of Chinese Traditional Medicine and Ethnic Medicine (ICCTMEM), National Institutes for Food and Drug Control (NIFDC), Beijing, China, [3]College of Pharmacy, Gannan Medical University, Ganzhou, China

OPEN ACCESS

Edited by:
Yanqiong Zhang,
Institute of Chinese Materia Medica, China Academy of Chinese Medical Sciences, China

Reviewed by:
Hai-yu Xu,
Institute of Chinese Materia Medica, China Academy of Chinese Medical Sciences, China
Wei Zhang,
Macau University of Science and Technology, Macau
Shao Li,
School of Information Science and Technology, Tsinghua University, China

***Correspondence:**
Feng Wei
weifeng@nifdc.org.cn
Shuangcheng Ma
masc@nifdc.org.cn

Specialty section:
This article was submitted to Ethnopharmacology, a section of the journal Frontiers in Pharmacology

Received: 01 August 2020
Accepted: 06 April 2021
Published: 28 April 2021

Citation:
Chen J, Li L-F, Hu X-R, Wei F and Ma S (2021) Network Pharmacology-Based Strategy for Elucidating the Molecular Basis Forthe Pharmacologic Effects of Licorice (Glycyrrhiza spp.). Front. Pharmacol. 12:590477. doi: 10.3389/fphar.2021.590477

Licorice (*Glycyrrhiza* spp.) is used widely in traditional Chinese medicine (TCM) due to its numerous pharmacologic effects. However, the mechanisms of action of the chemical constituents of licorice and their structure–function relationships are not fully understood. To address these points, we analyzed the chemical compounds in licorice listed in the TCM Systems Pharmacology database and TCM Integrated database. Target proteins of the compounds were predicted using Integrative Pharmacology-based Research Platform of TCM v2.0. Information on the pharmacologic effects of licorice was obtained from the 2020 *Chinese Pharmacopoeia*, and disease-related genes that have been linked to these effects were identified from the Encyclopedia of TCM database. Pathway analyses using the Kyoto Encyclopedia of Genes and Genomes database were carried out for target proteins, and pharmacologic networks were constructed based on drug target–disease-related gene and protein–protein interactions. A total of 451 compounds were analyzed, of which 211 were from the medicinal parts of the licorice plant. The 241 putative targets of 106 bioactive compounds in licorice comprised 52 flavonoids, 47 triterpenoids, and seven coumarins. Four distinct pharmacologic effects of licorice were defined: 61 major hubs were the putative targets of 23 compounds in heat-clearing and detoxifying effects; 68 were targets of six compounds in spleen-invigorating and qi-replenishing effects; 28 were targets of six compounds in phlegm-expulsion and cough-suppressant effects; 25 compounds were targets of six compounds in spasm-relieving and analgesic effects. The major bioactive compounds of licorice were identified by ultra-high-performance liquid chromatography–quadrupole time-of-flight–tandem mass spectrometry. The anti-inflammatory properties of liquiritin apioside, liquiritigenin, glycyrrhizic acid and isoliquiritin apioside were demonstrated by enzyme-linked immunosorbent assay (ELISA) and Western blot analysis. Liquiritin apioside, liquiritigenin, isoliquiritin, isoliquiritin apioside, kaempferol, and kumatakenin were the main active flavonoids, and 18α- and 18β-glycyrrhetinic acid were the main active triterpenoids of licorice. The former were associated with heat-clearing and detoxifying effects, whereas the latter were implicated in the other three pharmacologic effects. Thus, the compounds in licorice have

distinct pharmacologic effects according to their chemical structure. These results provide a reference for investigating the potential of licorice in treatment of various diseases.

Keywords: licorice, flavonoid, triterpenoid, pharmacologic effects, network pharmacology

INTRODUCTION

Licorice (referred toin Chinese as "GanCao") is a food and dietary supplement that has been used widely in traditional Chinese medicine (TCM) for ~4,000 years. According to the 2020 *Chinese Pharmacopoeia*, licorice refers to the dried root and rhizome of *Glycyrrhiza uralensis* Fisch. ex DC., *G. inflate* Bat., or *G. glabra* L.

As indicated in *Shennong's Materia Medica Classic* (Shennong Bencao Jing), licorice is used predominantly to treat spleen dysfunction, stomach weakness, fatigue, lack of strength, palpitation, dyspnea, cough, profuse sputum, acute pain in the abdominal cavity, limb contracture, carbuncles, and sores, as well as to alleviate drug toxicity (Chinese Pharmacopoeia Commission, 2020). Because of its ability to "harmonize" the effects of different medicines, licorice is an ingredient in nine out of 10 herbal formulations.

The genus *Glycyrrhiza* comprises ~30 species that are native to Eurasia and which have been cultivated in Europe (e.g., Spain, Italy, France), the Middle East (e.g., Syria, Iran, Turkey, Iraq) and Asia (e.g., China) (Chen J. et al., 2019). Eight species in the Leguminosae family are found in China: *G. uralensis* Fisch. ex DC.; *G. inflata* Bat.; *G. glabra* L.; *G. eurycarpa* P.C.Li; *G. aspera* Pall.; *G. yunnanensis* P.C.Li; *G. pallidiflora* Maxim.; *G. squamulosa* Franch. (Zeng et al., 1991; Karami et al., 2015). These species have various chemical constituents, such as flavonoids, triterpenoids, coumarins, and stilbenoids (Zhang and Ye, 2009; Cheng et al., 2012; Qiao et al., 2015).

There have been several reports on the pharmacologic effects and bioactive constituents of licorice, which are mainly flavonoids and triterpenoids (Wang et al., 2020). *In vivo* and *in vitro* experiments have shown that these classes of compound have anti-inflammatory, antimicrobial, antiviral, antioxidant, and antitumor effects. Recent studies have focused on the pathways regulating the pharmacologic effects of the metabolites of flavonoids and triterpenoids in licorice (Hosseinzadeh and Nassiri-Asl, 2015). However, given the diversity and complexity of the bioactive compounds in licorice, high-throughput and network-based approaches are needed to fully elucidate their pharmacologic properties and mechanisms of action.

Network pharmacology is an emerging discipline based on systems biology, analysis of biological networks, and identification of specific network nodes as targets in drug design (Hopkins, 2007; Li and Zhang, 2013). In general, treatment of diseases using TCM is based on integrative and holistic principles as well as the synergistic effects of multiple compounds and herbal formulations (Zhang et al., 2013). Network pharmacology adopts a similar holistic approach in aparadigm shift from "one target, one drug" to "network target, multi-compound" therapeutics (Li et al., 2014). Thus, network pharmacology is used widely to investigate the molecular mechanisms underlying the pharmacologic effects of TCM formulations (Li H. et al., 2014; Xiong et al., 2018; Piao et al., 2019); appropriate TCM prescriptions for the treatment of specific diseases (Li et al., 2007; Li X. et al., 2014; Shi et al., 2014; Ke et al., 2016; Fang et al., 2017a, 2017b; Hu and Sun, 2017; Dai et al., 2018; Shi et al., 2019); bioactive components of medicines (Lv et al., 2014; Zhang Y.-F. et al., 2019; Ma et al., 2019; Song et al., 2019; Guo et al., 2020).

Network pharmacology has been applied to studies on the mechanisms of action of TCM formulations containing licorice such as Sini, Shaoyao-Gancao, Guizhi-Shaoyao-Zhimu, Yinchensini, and Maxing-Ganshi decoctions, among others (Chen S. et al., 2014; Chen G. et al., 2018; Song et al., 2018; Zhang Q. et al., 2019; Zhu et al., 2019) as well as analyses of licorice constituents and their functions (Liu et al., 2013; Chen M. et al., 2019). The molecular mechanisms of licorice components in the context of diseases have also been studied (Li Y. et al., 2019). Those reports focused on compounds present in the overground and underground parts of the plant, which differ considerably (Wang, 2004; Zhou, 2015; Ran, 2019). The medicinal properties of licorice are associated mainly with the underground parts (roots and rhizomes).

Here, we classified the different types of bioactive compounds in the underground parts of the licorice plant. We also analyzed the mechanisms of action underlying the pharmacologic effects of licorice.

MATERIALS AND METHODS

Chemicals, Reagents, and Materials

Ultra-high-performance liquid chromatography–mass spectrometry (UHPLC–MS)-grade acetonitrile and formic acid were supplied by Fisher Scientific (Fairlawn, NJ, United States). Ultrapure water (18.2MΩ) was prepared with a Milli-Q™ water-purification system (Millipore, Milford, MA, United States). All other reagents were of analytical grade and purchased from Sinopharm Chemical Reagents (Shanghai, China).

The reference compounds schaftoside (number 1; lot number, 111,912–201703; purity, 95.60%), calycosin 7-O-β-D-glucopyranoside (4; 111,920–201907; 96.80%), liquiritin (5; 111,610–201908; 95.00%), kaempferol (15; 110,861–202013; 93.20%), formononetin (17; 111,703–201504) and glycyrrhizic acid monoammonium salt (18; 110,731–202021; 96.20%) were supplied by National Institutes for Food and Drug Control (NIFDC; Beijing, China).

The reference compounds neoliquiritin (2; PRF20060,941; 97.88%), liquiritinapioside (3; PRF9050224; 99.95%), isoliquiritin apioside (6; PRF9101021; 97.04%), isoliquiritin (7; PRF20040,923; 98.23%), ononin (8; PRF20060,944; 99.58%), neoisoliquiritin (9; PRF20060,942; 99.25%), licochalcone B (10; PRF8031021; 99.10%), liquiritigenin (11; PRF20042,742;

99.50%), calycosin (12; PRF10072945; 99.70%), naringenin (13; PRF10030641; 99.67%), echinatin (14; PRF10122621; 99.81%), isoliquiritigenin (16; PRF20060,943; 99.87%), licoflavone A (19; PRF8050422; 99.94%), glycycoumarin (20; PRF20060,921; 99.77%), kumatakenin (21; PRF10120925; 99.28%), licochalcone A (25; PRF8041841; 98.65%), 18α-Glycyrrhetinic acid (29; PRF10101201; 99.02%) and 18β-Glycyrrhetinic acid (30; PRF9100841; 99.46%) were purchased from Chengdu BiopurifyPhytochemicals (Chengdu, China).

The reference compounds licoisoflavone A (23; PS010124; 98.46%), glycyrol (26; PS010089; 98.71%) and licoisoflavone B (28; PS200618–01; 98.02%) were obtained from Chengdu Push Biotech (Chengdu, China).

The reference compound licoflavonol (27; MUST-20041,311; 98.86%) was purchased from Chengdu Must Biotechnology (Chengdu, China). The reference compound licoricone (24; 200313G; 99.46%) was obtained from Nanjing Dasf Biotechnology (Nanjing, China). The reference compound licoflavone C (22; P29A9F68905; 99.30%) was purchased from Shanghai Yuanye Biotechnology (Shanghai, China).

Licorice materials were obtained from Elion Resources Group (Inner Mongolia, China) and Gansu JinYoukang Pharmaceutical Technology (Gansu, China). Licorice materials were authenticated as the dried roots of *Glycyrrhiza uralensis* Fisch. ex DC. by Professor Nanping Zhang (NIFDC, Beijing, China). The voucher numbers of licorice from Inner Mongolia wereN2-4-1 to N2-4-10, and from Gansu were G1-5-1 to G1-5-10. Voucher specimens were deposited in the Museum of Chinese Traditional Drugs within the NIFDC (Li X. et al., 2019).

Preparation of Standard and Sample Solutions

Thirty reference compounds were prepared by completely dissolution in 70% methanol and their concentration (in mg/mL)was (compound 1) 0.266; 2) 0.187; 3) 0.178; 4) 0.416; 5) 0.258; 6) 0.186; 7) 0.269; 8) 0.299; 9) 0.166 (10) 0.155 11) 0.277 12) 0.189 13) 0.279 14) 0.222 15) 0.257 16) 0.214 17) 0.431 18) 0.227 19) 0.144 (20) 0.124 21) 0.144 22) 0.233 23) 0.263 24) 0.164 25) 0.221 26) 0.230 27) 0.186 28) 0.164 29) 0.172 (30) 0.337. All solutions were stored at 4°C before analyses.

All samples were pulverized and screened through the 50-mesh sieve. The dried powder (0.5g) was weighed accurately into a 100-ml conical flask with a stopper, and extracted by ultrasonication in 50ml of methanol (70%) for 0.5h. The mixture was centrifuged at 12,000rpm for 10min at room temperature. Finally, the supernatant was filtered through 0.22-μm membrane before injection into aUHPLC–MS/MS system.

Ultra-High-Performance Liquid Chromatography–Quadrupole Time-of-Flight–Tandem Mass spectrometry(UHPLC–QTOF–MS/MS)

Chromatography was undertaken using an Acquity UHPLC HSS T3 C18 column (2.1mm i. d. × 100mm, 1.8μm) within an Acquity UHPLC system (Waters, Milford, MA, United States). The column temperature was maintained at 35°C. The mobile phase (at a flow rate of 0.4ml/min) consisted of solvent A (0.1%formic acid/water) and solvent B (acetonitrile). The conditions of gradient elution were optimized as: 5% B (0–1min), 5–18% B (1–3min), 18–30% B (3–13min), 30–45% B (13–18min), 45–50% B (18–21min), 50–75% B (21–29min), 75–95% B (29–31min), 95–5% B (31–31.5min) and held at 5% B for 3.5min to equilibrate the column. The injection volume was 2μL.

A Synapt™ G2-S QTOF mass spectrometer (Waters MS Technologies, Manchester, UK) was combined with the UHPLC system via the electrospray-ionization source in positive-ion mode. The desolvation-gas rate was set as 600L/h at 500°C. The source temperature was set as 120°C. The capillary voltage was3 kV and the sample cone voltage was set at 30V. Centroided data were acquired from 50 to 1,000Da. Mass data were acquired using LockSpray™ to ensure the mass was recorded accurately. Leucine-enkephalin at a charge/mass ratio (*m/z*) 556.2771 was selected as the lock-mass in positive mode. The accurate mass and composition of precursor ions and fragment ions were calculated using MassLynx V4.1 (Waters), that incorporated with the instrument solution for the acquisition of accurate mass.

Preparation of Bioactive Compounds

Four reference bioactive compounds, liquiritin apioside, liquiritigenin, glycyrrhizic acid and isoliquiritin apioside were prepared by completely dissolution in 0.1% DMSO/water and their concentration were 2mg/ml. The dried licorice extract powder (1.0g) was weighed accurately into a 100-ml conical flask with a stopper, and completely dissolved in 50ml of ultrapure water. All solutions were stored at −20°C before analyses.

Cell Culture and Treatments

Murine macrophage RAW264.7 cells, a widely used *in vitro* model for studies of macrophage and inflammatory cascades, were obtained from the China National Collection of Authenticated Cell Cultures (Shanghai, China). Cells were maintained at 37°C under 5% CO_2 in Dulbecco's modified Eagle's medium (DMEM) supplemented with 10% fetal bovine serum. RAW264.7 cells were treated with 1μg/ml lipopolysaccharide (LPS; Sigma-Aldrich; Merck KGaA, Darmstadt, Germany) for 24h at 37' °C. The cells were rinsed with phosphate buffer saline (PBS) and stimulated with LPS (1ug/ml) to induce pyroptosis. Conditioned cells were collected for measurement of protein expression levels by ELISA and western blot analysis.

ELISA Assay for Cytokines

Interleukin (IL)-1β and tumor necrosis factor (TNF)-α expression levels in the supernatant of treated cells were measured by ELISA assays (IL-1β: Mouse: ml063132-C; TNF-α: Mouse: ml002095-C; Enzyme-linked Biotechnology Co., Ltd., Shanghai, China) according to the manufacturer's instructions.

Western Blot Analysis

The protein expression in RAW264.7 cells were detected by Western blot. Cells (1.6×10^5 cells/well) were plated overnight and then treated with the indicated concentrations of bioactive compounds. After 1h, 1μg/ml LPS were added. Then, the supernatant and precipitation of cells were collected 24h later. Immunoblotting was performed using antibodies against the target proteins, including AKT1 (1:2,500; ab89402; Abcam, Cambridge, MA, United States), p-AKT1 (1:5,000; ab81283; Abcam, Cambridge, MA, United States), PI3K (1:1,000; 4,249; Cell Signaling Technology, Inc., Danvers, MA, United States), p-PI3K (1:1,000; bs-3332R; Bioss Antibodies, Biotechnology, Inc., Beijing, China), NFκB-p65 (1:1,000; sc-8008; Santa Cruz Biotechnology, Inc.,Dallas, TX, United States), p-NFκB-p65 (1:1,000; YP0191; Immuno Way, Biotechnology, Inc., Plano, TX, United States). The blots were developed with an enhanced chemiluminescence kit (ECL, Amersham Biosciences, Buckinghamshire, United Kingdom) and measured by using a luminescent image analyzer (LAS-3000, Fuji Photo Film Co. Ltd., Japan).

Statistical Analyses

All experimental values were presented as the mean ± standard error of the mean. Statistical comparison between two groups was performed by Student's *t*-test, and one-way analysis of variance followed by Bonferroni *post hoc* analyses was performed among multiple groups for parametric data. $P < 0.05$ was considered to indicate a statistically signifcant difference.

Chemical Compounds in Licorice

Candidate chemical compounds in licorice were searched in two phyto chemical databases: Traditional Chinese Medicine Systems Pharmacology (TCMSP; http://tcmspw.com/tcmsp.php) (Ru et al., 2014) and Traditional Chinese Medicines Integrated database (TCMID; www.megabionet.org/tcmid/). Components of the underground parts of the licorice plant were screened from candidate compounds by reviewing the literature. National Center for Biotechnology Information (NCBI) PubMed (https://pubmed.ncbi.nlm.nih.gov/) and China National Knowledge Infrastructure (CNKI; www.cnki.net/) databases were used to find the underground parts of licorice. In the PubMed database, "licorice chemical composition" were used as keywords to search for studies from 2000 to 2020. In the CNKI database, we searched for doctor altheses from 2000 to 2020 under the keyword of "licorice". Two-dimensional (2D) chemical structures were obtained from NCBI PubChem (https://pubchem.ncbi.nlm.nih.gov/) and SciFinder Scholar (https://scifinder.cas.org/scifinder/) databases. If a structure could not be retrieved from these databases, the original research article describing the identification or purification of the compound was searched for. ChemBioDraw Ultra v12.0 (PerkinElmer, Waltham, MA, United States) was used to draw structures, which were saved in sdf or mol2 formats (Xiong et al., 2019).

Putative Targets of Bioactive Compounds in Licorice

The sdf or mol2 files were uploaded to Integrative Pharmacology-based Research Platform of Traditional Chinese Medicine (TCMIP) v2.0 (www.tcmip.cn/). The putative targets of the compounds in licorice were predicted using the drug target-prediction tool of TCMIP. We selected only pairs of compound–putative targets in which the structural similarity score of the compound to known drugs was >0.80 (moderate–high similarity). Detailed information on putative targets are shown in **Supplementary Table S1**.

Disease-Related Genes Associated with Thepharmacologic Effects of Licorice

Disease-related genes associated with the pharmacologic effects of licorice were identified from the Encyclopedia of Traditional Chinese Medicine database (www.nrc.ac.cn:9090/ETCM) (Xu et al., 2019). The genes related to "immune inflammation" imbalance and some psychiatric symptoms were obtained as disease/symptom gene sets corresponding to heat-clearing and detoxifying effects. The genes related to anemia, low resistance, mental disorders, organ dysplasia, reproductive capacity and other symptoms were obtained as disease/symptom gene sets corresponding to spleen-invigorating and qi-replenishing effects. The genes related to the throat, trachea, bronchus, inflammation, lung disease, asthma and other symptoms were obtained as disease/symptom gene sets corresponding to phlegm-expulsion and cough-suppressant effects. The genes related to the chest, abdomen, limb-spasm pain and neurological diseases were obtained as the disease/symptom gene sets corresponding to spasm-relieving and analgesic effects.

Network of Interactions Between Drug Targets and Disease-Related Genes

Networks of interactions between drug targets and disease-related genes were constructed based on the relationships between the putative targets of compounds in licorice and disease-related genes associated with the pharmacologic effects of licorice. Construction and analyses of such networks were carried out with TCMIP v2.0 (www.tcmip.cn). Visualization of such networks was done using Navigator v2.2.1 (Krembil Research Institute, Toronto, ON, Canada). Hubs with a degree greater than two fold the median value of all node degrees were screened, and a network was constructed based on direct interactions between hubs. Three topologic properties of the hub network (degree, betweenness, and closeness) were calculated to identify targets of topologic importance. Major hubs were identified as those with network topology values that were higher than the corresponding median values.

Analyses of Pathway Enrichment

Pathway-enrichment analyses were done using database Visualization and Integrated Discovery v6.7 (http://david.abcc.ncifcrf.gov/home.jsp) based on pathway data obtained from the Kyoto Encyclopedia of Genes and Genomes (KEGG)database (www.genome.jp/kegg; updated on 18 November 2016) (Kanehisa and Goto, 2000; Dennis et al., 2003). Only functional annotations with enrichment *P*-values corrected

with Bonferroni and Benjamini algorithms ($p < 0.05$) were selected for further analyses.

RESULTS AND DISCUSSION

Analyses of Licorice Composition and Compound Screening

A total of 451 compounds were screened from TCMSP and TCMID (**Supplementary Table S2**). Of these, 211 were identified by literature review as compounds present in the medicinal portion of thelicorice plant:134 flavonoids, 49 triterpenoids, 18 coumarins, and 10 stilbenoids (**Supplementary Table S3**). Most network-pharmacology studies on licorice have used a single database to identify itschemical constituents. We compared compounds in TCMSP and TCMID, which are used widely in TCM research and provide the names and 2D structures of compounds. We found that some were commonto both databases whereas others were unique. Some compounds were duplicated in the same database. We obtained 604 compounds from the initial search (280 from TCMSP and 324 from TCMID). We found that 26 compounds were duplicated in TCMID and, therefore, there were actually 298 chemical compounds; 127 were common to both TCMSP and TCMID. Compared with earlier network-pharmacology studies of licorice, our screen of the chemical constituents of licorice was more comprehensive and allowed more accurate prediction of molecular mechanisms. The compounds were grouped according to their2D structure for further analyses of the relationship between the type of compound and pharmacologic effects of licorice.

Putative Targets of Compounds in Licorice

Based on their structural similarity to known chemical compounds, 241 putative targets were identified for 106 chemical compounds in licorice: 52 targeted by flavonoids, 47 by triterpenoids, and seven by coumarins. Detailed information on the bioavailability of these chemical compounds is provided in **Supplementary Table S4** (Ru et al., 2014; Daina et al., 2017; Xu et al., 2019). Enrichment analyses based on the biological pathways in the KEGG database revealed that the putative targets were mainly involved in neuromodulation [neuroactive ligand–receptor interactions ($P = 3.90 \times 10^{-10}$), long-term potentiation ($P = 0.001$), and gap junctions ($P = 0.03$)], energy production and metabolic pathways (nitrogen metabolism ($P = 7.84 \times 10^{-10}$), linoleic-acid metabolism ($P = 1.30 \times 10^{-7}$) and oxidative phosphorylation ($P = 9.47 \times 10^{-4}$) and inflammation/immune-system regulation (Fc epsilon RI ($P = 0.01$), toll-like receptor (TLR; $P = 0.01$) and nucleotide-binding and oligomerization domain-like receptor (NLR; $P = 0.02$) signaling pathways.

Pharmacologic Mechanisms of Compoundsin Licorice

Pharmacologic Mechanisms of Heat-Clearing and Detoxifying Effects

Of the 241 putative targets, 37 were disease-related genes involved in the heat-clearing and detoxifying effects of licorice. The network of interactions of drug target–disease-related genes contained 985 nodes and 3,974 interactions. A total of 299 major hubs were identified based on the values of three topologic features of the network (node degree, betweenness, and closeness). Of these, 61 hubs were the putative targets of 23 chemical compounds in licorice: echinatin, glabrolide, glycycoumarin, glycyrol, glycyrrhizic acid, isoliquiritin, kumatakenin, licoarylcoumarin, licochalcone B, licoricesaponin A3, licoricesaponin B2, licoricesaponin C2, licoricesaponin D3, licoricesaponin E2, licoricesaponin F3, licoricesaponin G2, licoricesaponin J2, licoricesaponin K2, liquiritigenin, liquiritin, methyl glycyrrhetate, neoisoliquiritin, and ononin.

To investigate the mechanisms underlying the heat-clearing and detoxifying effects of licorice, a network was constructed based on direct interactions between major hubs that was divided into four functional modules.

The first nodule was regulation of the balance between inflammation and the immune system. This comprised the genes involved in nuclear factor-kappa B(NF-κB) (Zhang et al., 2015), tumor necrosis factor (TNF) (Graßmann et al., 2017), TLR (Belforte et al., 2013), and NLR signaling pathways (Luan et al., 2018), as well as inflammatory regulation of transient receptor potential (TRP) channels (Sahoo et al., 2019).

The second nodule was modulation of the nervous system. This comprised the genes involved in retrograde endocannabinoid signaling (Musella et al., 2017), neuroactive ligand–receptor interactions (Schüle et al., 2014), γ-aminobutyric acid [GABA]ergic (Streeter et al., 2010) as well as serotonergic synapses and neurotrophin signaling pathways (Kashyap et al., 2018).

The third nodule was regulation of energy production and metabolism. This comprised the genes involved in adipocytokine (Kita et al., 2019) and thyroid-hormone signaling pathways (Mullur et al., 2014).

The fourth nodule was cellular functions. This comprised genes involved in phosphoinositide 3-kinase/protein kinase B ([PI3K/AKT) (Hong et al., 2016) and mitogen-activated protein kinase (MAPK) signaling pathways (Park, 2018) and apoptosis (Kawamoto et al., 2016) (**Figure 1**).

Pharmacologic Mechanisms of Spleen-Invigorating and Qi-Replenishing Effects

Of the 241 putative targets, 78 were disease-related genes associated with the spleen-invigorating and qi-replenishing effects of licorice. The network of interactions of drug target–disease-related genes contained 1,729 nodes and 9,181 interactions. Based on the node degree, betweenness, and closeness values, 534 major hubs were identified, of which 68 were the putative targets of six compounds (18α-and 18β-glycyrrhetinic acid, isoliquiritin apioside, kumatakenin, licoarylcoumarin, and liquiritin apioside).

We wished to investigate the mechanisms underlying the spleen-invigorating and qi-replenishing effects of licorice. Hence, a major hub network was constructed based on the direct interactions between major hubs that were divided into four functional modules.

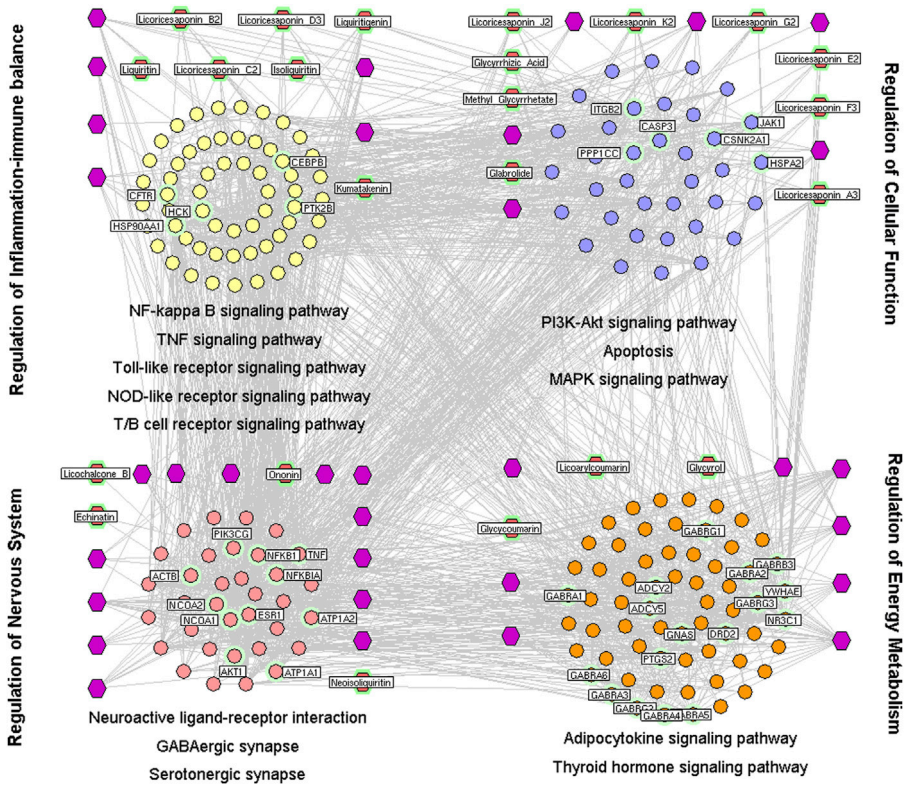

FIGURE 1 | Interaction network of chemical compounds containing licorice and the corresponding major targets associated with its heat-clearing and detoxifying effects. To investigate the mechanisms underlying the heat-clearing and detoxifying effects of licorice, a network was constructed based on direct interactions between major hubs that was divided into four functional modules. Purple hexagons represent chemical components, red hexagons denote representative the chemical components of licorice, yellow circles denote the core targets related to regulation of balance of inflammation and the immune system, and blue circles represent the core targets related to cellular functions. The pink circle represents the core target related to modulation of the nervous system, the orange circle represents the core target related to regulation of energy production and metabolism.

The first functional node was regulation of balance of inflammation and the immune system. This comprised genes involved in PI3K/AKT, MAPK, TNF, Fc epsilon RI (Ben Mkaddem et al., 2019), and NF-κB signaling pathways, and inflammatory regulation of TRP channels.

The second functional node was regulation of energy production and metabolism. This was composed of genes involved in thyroid hormone, cyclic (c)AMP (Alqurashi et al., 2016), insulin (Guo and Guo, 2017), adipocytokine, and 5′ AMP-activated protein kinase (Ke et al., 2018) signaling pathways.

The third functional module was modulation of the nervous system. This comprised genes involved in the neurotrophin signaling pathway, gap junctions (Dong et al., 2018), long-term potentiation/depression (Bliss and Cooke, 2011), and neuroactive ligand–receptor interactions.

The fourth functional module was regulation of angiogenesis and circulation. This comprised genes involved in Ras-associated protein (Rap)1 (Rho et al., 2017), hypoxia-inducible factor (HIF)-1 (Semenza, 2014), and vascular endothelial growth factor (VEGF) signaling pathways (Gianni-Barrera et al., 2014) as well as contraction of vascular smooth muscle and platelet activation (Starlinger et al., 2011) (**Figure 2**).

Pharmacologic Mechanisms of Phlegm Expulsion and Cough-Suppressant Effects

Of the 241 putative targets, nine were disease-related genes involved in the phlegm-expulsion and cough-suppressant effects of licorice. The network of interactions between drug targets and disease-related genes contained 301 nodes and 851 interactions. Ninety-seven major hubs were identified based on the values of the node degree, betweenness, and closeness in the network. Of these, 28 were the putative targets of six compounds in licorice (18α- and 18β-glycyrrhetinic acid, isoliquiritin apioside, kumatakenin, licoarylcoumarin, and liquiritin apioside).

We wished to investigate the mechanistic basis of the phlegm-expulsion and cough-suppressant effects of licorice. A major hub network was constructed based on the direct interactions between major hubs that was divided into three functional modules.

The first functional nodule was regulation of the balance between inflammation and the immune system. This comprised the genes involved in: TNF, NF-κB, T-/B-cell receptors (Lee and Korner, 2019), NLR, and TLR signaling pathways; leukocyte transendothelial migration (Nourshargh and Alon, 2014); *tuberculosis* (Khader et al., 2019); pertussis (Murphy et al., 2020).

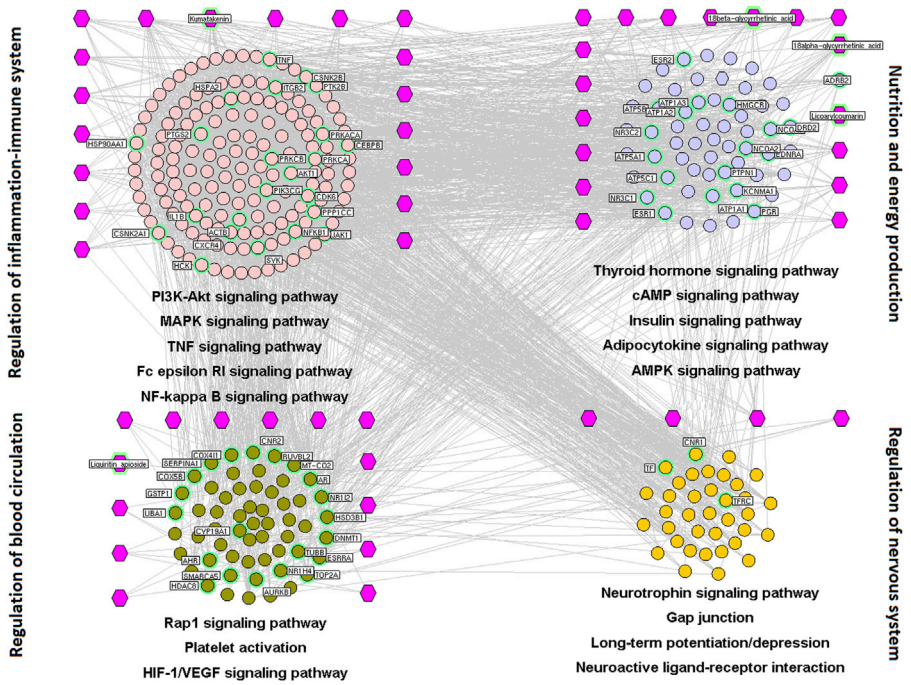

FIGURE 2 | Interaction network of chemical compounds containing licorice and the corresponding major targets associated with spleen-invigorating and qi-replenishing effects. We wished to investigate the mechanisms underlying the spleen-invigorating and qi-replenishing effects of licorice. Hence, a major hub network was constructed based on the direct interactions between major hubs that were divided into four functional modules. Purple hexagons represent chemical components, pink circles denote core targets related to regulation of balance of inflammation and the immune system, blue circles represent core targets related to nutrition and energy production, green circles denote core targets related to regulation of blood circulation, and the orange circle represents the core target related to modulation of the nervous system.

The second functional nodule was regulation of energy production and metabolism. This was composed of the genes involved in thyroid hormone, cAMP, adipocytokine, and glucagon signaling pathways (Kleinert et al., 2019); regulation of lipolysis in adipocytes (Shin et al., 2017) as well asthyroid-hormone synthesis.

The third functional nodulewas modulation of the nervous system. This comprised genes involved in GABAergic synapses (Babaev et al., 2018); retrograde endocannabinoid (Lu and Mackie, 2017) and chemokine (Zigmond and Echevarria, 2019) signaling pathways, as well as neuroactive ligand–receptor interactions (MacKenzie EM et al., 2007) (**Figure 3**).

Pharmacologic Mechanisms of Spasm-Relieving and Analgesic Effects

Of the 241 putative targets, 29 were disease-related genes linked to the spasm-relieving and analgesic effects of licorice. The network of interactions of the drug target and disease-related genes contained 689 nodes and 2,682 interactions. Based on the network topology values of node degree, betweenness, and closeness, 200 major hubs were selected, of which 25 were the putative targets of six compounds in licorice (18α- and 18β-glycyrrhetinic acid, isoliquiritin apioside, kumatakenin, licoarylcoumarin, and liquiritin apioside).

We wished to investigate the mechanisms associated with the spasm-relieving and analgesic effects of licorice. Hence, a network was constructed based on the direct interactions between major hubs that were divided into three functional modules.

The first functional module was modulation of neuroinflammation and neuropathologic pain. This comprised thegenes involved in MAPK, calcium (Navakkode et al., 2018), TNF, and TLR signaling pathways, as well as neuroactive ligand–receptor interactions (Salvalaio et al., 2017).

The second functional module was regulation of energy production and metabolism. This was composed of the genes involved in cAMP and adipocytokine signaling pathways, regulation of lipolysis in adipocytes, and oxidative phosphorylation (Bald et al., 2017).

The third functional module was regulation of angiogenesis and circulation. This comprised the genes involved in Rap1, HIF-1 and VEGF signaling pathways as well as contraction of vascular smooth muscle and platelet activation (**Figure 4**).

Analyses of the Main Bioactive Ingredients of Licorice

The main bioactive components of licorice could be detected by UHPLC–TOF–MS/MS (**Figure 5**). Thirty bioactive compounds were identified by comparing the retention time and quasi-molecular ions with reference standards, respectively. The structures of these compounds are shown in **Figure 6**. Information such as retention time (min), CAS number, molecular formula, *m/z*, and MS^2 fragments is offered in **Supplementary Table S5**.

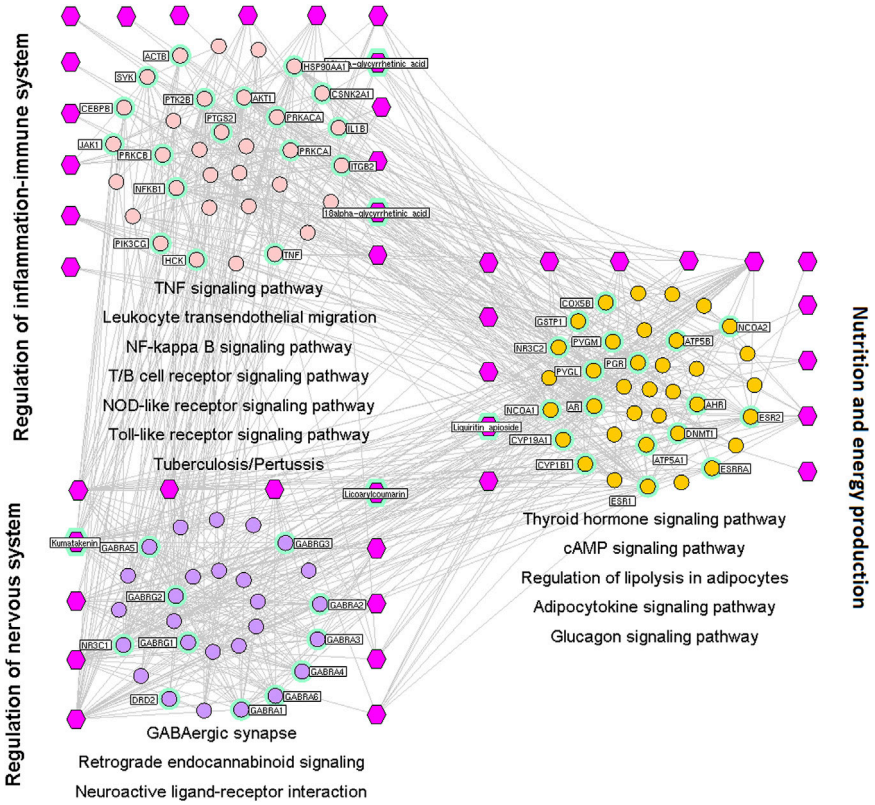

FIGURE 3 | Interaction network of chemical compounds containing licorice and the corresponding major targets associated with phlegm-expulsion and cough-suppressant effects. We wished to investigate the mechanistic basis of the phlegm-expulsion and cough-suppressant effects of licorice. A major hub network was constructed based on the direct interactions between major hubs that was divided into three functional modules. Purple hexagons represent chemical components, pink circles denote core targets related to regulation of balance of inflammation and the immune system, light purple circles represent core targets related to modulation of the nervous system, and orange circles denote core targets related to nutrition and energy production.

Liquiritin apioside and liquiritigenin were the main flavonoids, and 18α- and 18β-glycyrrhetinic acid were the main triterpenoids, in licorice. These compounds were found to be implicated in the various pharmacologic effects of licorice. Liquiritin apioside, which was also present at a high level in licorice, can be used as a marker for the quality assessment of *Glycyrrhiza* species (Jiang et al., 2016). The phlegm-expulsion and cough-suppressant effects of liquiritin apioside have been reported (Kuang et al., 2018; Wei et al., 2020). Also, liquiritin apioside has been linked to TNF, NF-κB, NLR, TLR, and adipocytokine signaling pathways, which have important roles in anti-inflammatory immune activity, energy production, and metabolism (Guan et al., 2012).

Liquiritigenin has potent pharmacologic activity, including inhibitory effects on fibrogenesis and inflammation in the liver (Huang et al., 2019; Lee et al., 2019). We predicted the following proteins to be the putative targets of liquiritigenin in the heat-clearing and detoxifying effects of licorice: AKT1, cyclin-dependent kinase 6, heat-shock protein (HSP)90AA1, HSPA2, Janus kinase, phosphatidylinositol-4,5-bisphosphate 3-kinase catalytic subunit *γ*, casein kinase 2α1, CCAAT enhancer-binding protein β, β-actin, estrogen receptor 1, nuclear receptor coactivator (NCOA)1, and NCOA2. Our analyses suggested that liquiritigenin exerts heat-clearing and detoxifying effects *via* regulation of PI3K/AKT (Shi et al., 2015; Tao et al., 2016; Meng and Lin, 2019), MAPK (Tu et al., 2019), NF-κB (Zhu et al., 2018), TNF (Yu et al., 2015), and neurotrophin (Liu et al., 2009)signaling pathways and apoptosis (Bae et al., 2018).

18α-and 18β-glycyrrhetinic acid are representative triterpenoid saponins present in high concentrations in licorice (Wang and Yang, 2007). They have anti-inflammatory, antiviral, hepatoprotective, and anti-tumor effects. We predicted the following proteins to be the putative targets of 18α-and 18β-glycyrrhetinic acid in the spleen-invigorating and qi-replenishing effects of licorice: NF-κB subunit 1, estrogen receptor1, NCOA1, NCOA2, 3-mydroxy-3-methylglutaryl-coA reductase, integrin subunit β2, and nuclear receptor subfamily 3 group C member 1. These proteins constituted two functional modules. The first functional module was regulation of balance of inflammation and the immune system, with genes involved in PI3K/AKT (Kao et al., 2010; Wang et al., 2011), MAPK (Chen X. et al., 2018; Zhang Y. et al., 2019), TNF (Zhou and Wink, 2019) and NF-κB (Cao et al., 2017) signaling pathways. The second functional module was regulation of energy production and metabolism (Chang et al., 2010, Chen et al., 2014a), with genes involved in thyroid hormone, cAMP, and adipocytokine signaling pathways (Shamsa et al., 1991; Rastegari et al., 2019).

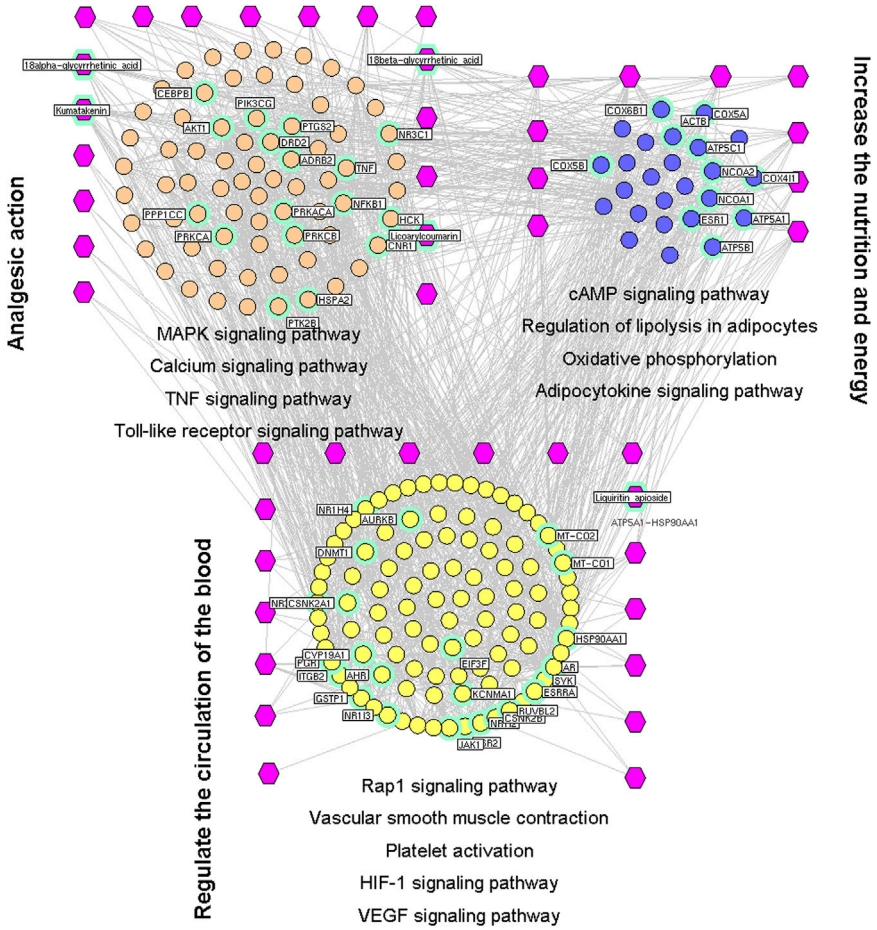

FIGURE 4 | Interaction network of chemical compounds containing licorice and the corresponding major targets associated with spasm-relieving and analgesic effects. We wished to investigate the mechanisms associated with the spasm-relieving and analgesic effects of licorice. Hence, a network was constructed based on the direct interactions between major hubs that were divided into three functional modules. The purple hexagon represents the chemical composition, the pink circle denoted the core target related to analgesic action, the blue circle represents the core target related to nutrition and energy production, and the yellow circle denoted the core target related to regulation of blood circulation.

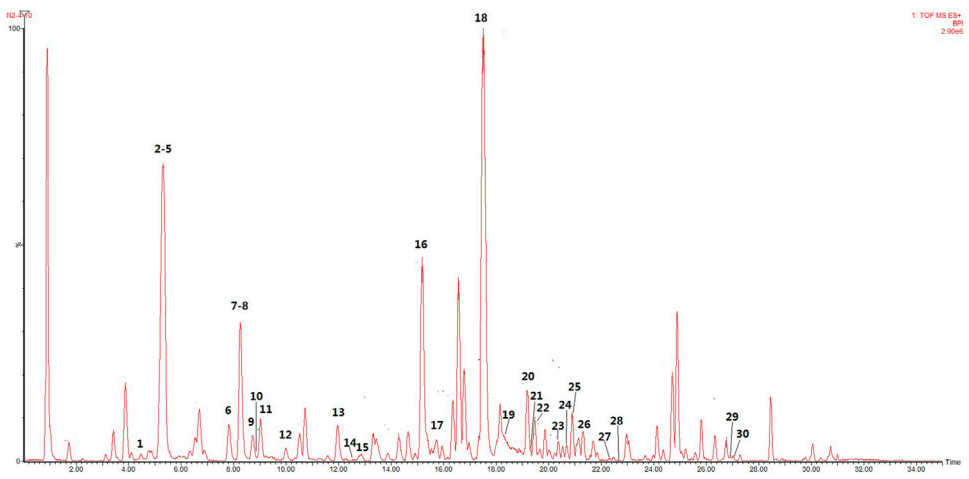

FIGURE 5 | Representative base peak intensity (BPI) chromatograms of licorice derived from UHPLC–QTOF–MS/MS.

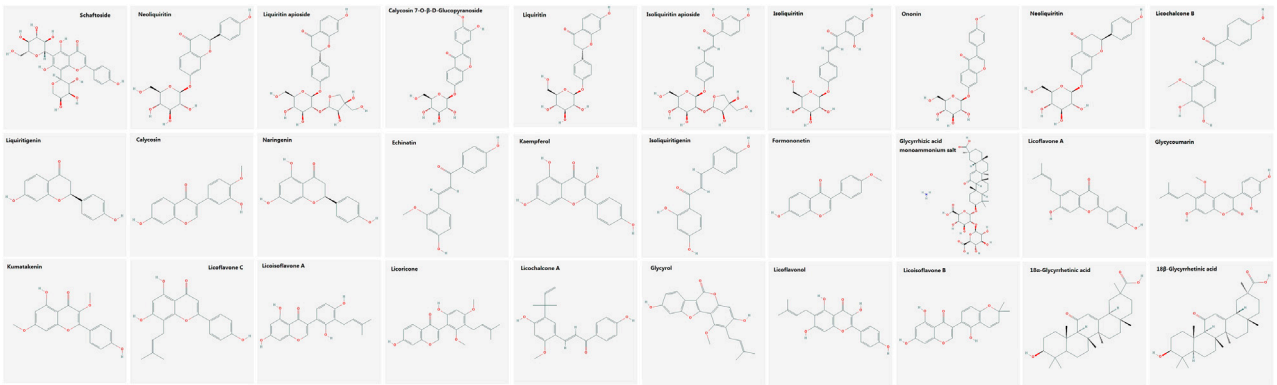

FIGURE 6 | Two-dimensional chemical structures of the bioactive compounds in licorice.

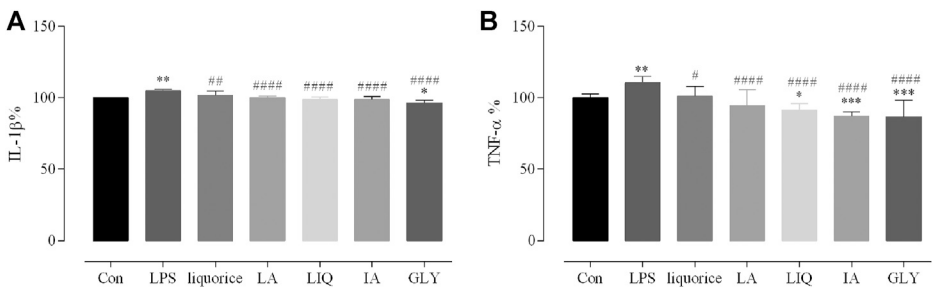

FIGURE 7 | Reduce effects of the main bioactive compounds of licorice on the LPS-induced production of cytokines and chemokines. The supernatants were collected for measuring the levels of IL-1β (A), TNF-α (B) by ELISA. Data are presented as the mean ± standard error of the mean (n = 3). *p < 0.05, **p < 0.01, ***p < 0.001, ****p < 0.001 vs. Con group; #p < 0.05, ##p < 0.01, ###p < 0.001, ####p < 0.0001 vs. LPS group. Liquiritin apioside, LA; Liquiritigenin, LIQ; Isoliquiritin apioside, IA; Glycyrrhizin, GLY; IL, interleukin; LPS, lipopolysaccharide; TNF, tumor necrosis factor.

Liquiritin and glycyrrhizic acid are the main representative chemical components of licorice (Chinese Pharmacopoeia Commission, 2020). We found that liquiritin and glycyrrhizic acid had putative targets, but the number of their putative targets were not as high as those of liquiritin apioside, 18β-glycyrrhetinic acid or other chemical components. The pharmacologic effects of the chemical components of licorice were related not only to the strength of biological activity but also to their concentration. Chemical components with strong biological activity but very low concentration contributed little to the pharmacologic effect. However, the chemical components with moderate activity but very high concentration contributed considerably to the pharmacologic effect. Biological activity and concentration are the most important factors for selecting quality control (QC) markers. We believe that liquiritin and glycyrrhizic acid should be used as QC markers for licorice.

Main Bioactive Ingredients of Licorice Reduce the Inflammatory Responses

Based on the result of network pharmacology, liquiritin apioside, liquiritigenin and isoliquiritin apioside were found as the main bioactive components of licorice. Liquiritin apioside and isoliquiritin apioside comprised the genes involved in NF-κB, TNF and IL-1β, while liquiritigenin comprised the genes involved in PI3K/AKT. Glycyrrhizic acid is the main representative chemical components of licorice which comprised the genes involved in NF-κB and TNF. All of these genes have important roles in anti-inflammatory immune activity.

To determine whether the main bioactive components of licorice can reduce the inflammatory response, the levels of TNF-α and IL-1β were measured in RAW 264.7 by ELISA analysis. Liquiritin apioside, liquiritigenin, glycyrrhizic acid and isoliquiritin apioside were chosen as representative bioactive components. In the vitro experiment, the levels of TNF-α and IL-1β in RAW 264.7 were significantly increased after stimulation with LPS compared with those in the blank control (P < 0.01). The LPS group showed higher levels of TNF-α and IL-1β than those of the four bioactive components-treated and licorice-treated LPS group (P < 0.05), indicating that the excessive secretion of TNF-α and IL-1β induced by LPS could be reduced by liquiritin apioside, liquiritigenin, glycyrrhizic acid, isoliquiritin apioside and licorice (**Figure 7**). According to these results, we found that the inflammatory responses could be reduced by the main bioactive components of licorice treatment.

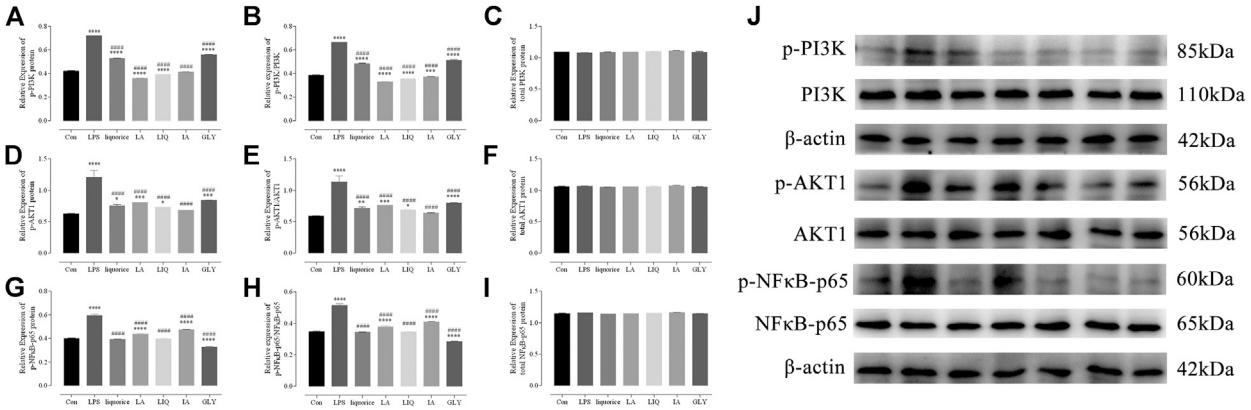

FIGURE 8 | Reduce effects of the main bioactive compounds of licorice on the PI3K/AKT/NFκB signaling pathway. The levels of PI3K, AKT and NF-κB proteins were detected by Western blotting(J). The relative expression of p-PI3K(A), p-AKT1(D), p-NFκB-p65(G) protein and ratio of p-PI3K/PI3K(B), p-AKT1/AKT1(E), p-NFκB-p65/NFκB-p65(H) and total PI3K(C), AKT1(F) and NFκB-p65/NFκB-p65(I) protein were quantified. Data are presented as the mean ± standard error of the mean ($n = 3$). *$p < 0.05$, **$p < 0.01$, ***$p < 0.001$, ****$p < 0.001$ vs. Con group; #$p < 0.05$, ##$p < 0.01$, ###$p < 0.001$, ####$p < 0.0001$ vs. LPS group. Liquiritin apioside, LA; Liquiritigenin, LIQ; Isoliquiritin apioside, IA; Glycyrrhizin, GLY; LPS, lipopolysaccharide.

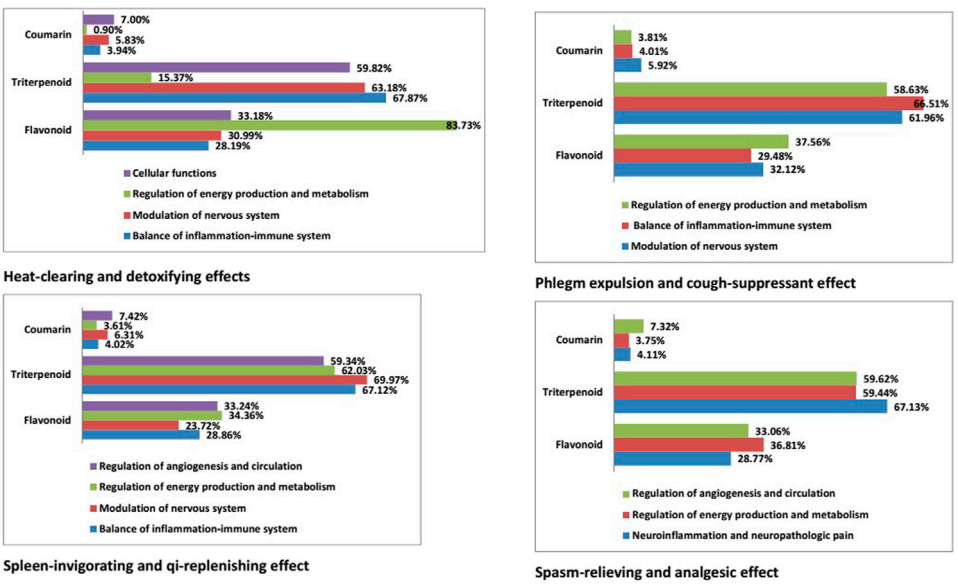

FIGURE 9 | Proportion of different chemical structure types of licorice in various pharmacologic effects.

In order to investigate the mechanisms underlying the anti-inflammatory activities of bioactive components of licorice, Western blotting analysis was used to verify the regulatory effects of the main bioactive components. The results of Western blotting revealed that bioactive components are able to markedly suppressed the PI3K/AKT/NFκB signaling pathway, mediated by p-PI3K (**Figure 8A**), p-AKT1 (**Figure 8D**), p-NFκB-p65 (**Figure 8G**), p-PI3K/PI3K (**Figure 8B**), p-PI3K/PI3K (**Figure 8B**), p-AKT1/AKT1 (**Figure 8E**) and p-NFκB-p65/NFκB-p65 (**Figure 8H**) in LPS-activated macrophages.

The PI3K/AKT/NFκB signaling pathway plays an important role in the regulation of signal transduction and biological processes such as cell proliferation, apoptosis, metabolism and angiogenesis. The regulatory echanisms and biological functions of the PI3K/AKT/NFκB signaling pathway are important in many human diseases, including ischemic brain injury, neurodegenerative diseases, and tumors and play an important role in erythropoiesis and glycolysis (Xie et al., 2019; Xu et al., 2020). Nuclear factor-kappaB (NF-κB) proteins constitute a family of transcription factors that are

stimulated by pro-inflammatory cytokines, chemokines, stress-related factors and extracellular matrix (ECM) degradation products, which has long been considered a prototypical proinflammatory signaling pathway (Toby, 2009; Stella and Athanasios, 2013). These results indicat that the main bioactive components of licorice inhibit the expression of TNF-α and IL-1β in the downstream through the PI3K/AKT/NFκB signaling pathway. Our results further demonstrate that the main bioactive components of licorice have anti-inflammatory properties.

Functions of Different Types of Compound in the Pharmacologic Effects of Licorice

We analyzed the major targets of the chemical compounds associated with the pharmacologic effects of licorice. We showed that the activities of the compounds varied according to their chemical structure, with flavonoids and triterpenoids having the most important role, data that are consistent with results from the work of Wang and colleagues (Wang et al., 2020).

We constructed a network for the heat-clearing and detoxifying effects of licorice comprising four functional modules: cellular functions; modulation of the nervous system; balance between inflammation and the immune system; regulation of energy production and metabolism. Triterpenoids were the predominant type of compound in the first three modules, whereas flavonoids had a leading role in regulation of energy production and metabolism (accounting for 83.73% of compounds within this module). Triterpenoids participated to varying degrees in the different functional modules. In the spleen-invigorating and qi-replenishing effects of licorice, they were important formodulation of the nervous system (69.97%). In the phlegm-expulsion and coughing-suppressant effects, they were responsible for regulating the balance between inflammation and the immune system (66.51%). In the spasm-relieving and analgesic effects, they played a major part in neuroinflammation and neuropathologic pain (67.13%) (**Figure 9**).

CONCLUSION

The pharmacologic effects of licorice arise from the combined action of various types of compounds. Triterpenoids and flavonoids make the greatest contribution, but coumarins are also important. Each pharmacologic effect of licorice comprised multiple functional modules. This finding is consistent with the general premise of TCM that therapeutic mechanisms involve many compounds and targets. We suggest that, for invigorating the spleen and replenishing qi, expelling phlegm and suppressing cough, or relieving spasm and pain, licorice with a higher triterpenoid content may be used. Licorice with higher levels of flavonoids may be more appropriate for heat-clearing and detoxification. Our results provide a reference for the QC of licorice and for investigating its therapeutic potential in the treatment of specific symptoms or diseases.

DATA AVAILABILITY STATEMENT

The original contributions presented in the study are included in the article/**Supplementary Material**, further inquiries can be directed to the corresponding authors.

AUTHOR CONTRIBUTIONS

JC was responsible for the conception and design of the study, data acquisition and analyses, and manuscript drafting. XH and LL assisted with data collection and manuscript revision. FW aided the conception and design of the study. SM aided the conception and design of the study, as well as data analyses and interpretation. All authors approved the final version of the manuscript for submission.

FUNDING

This study was supported financially by the 12th Five-Year China National Significant New Drugs Creation Feature Subjects–Traditional Chinese Medicine Quality Safety Evaluation and Risk Control Technology Platform (2014ZX09304307-002) and National Key Research and Development Plan (2019YFC1711500; "Research and Application of Key Technologies and Intelligent Equipment for Clean Cutting of Traditional Chinese Medicine Materials").

ACKNOWLEDGMENTS

We acknowledge Dr. Xian-Long Cheng from the Institute for Control of Chinese Traditional Medicine and Ethnic Medicine, National Institutes for Food and Drug Control, for his technical assistance in UHPLC-QTOF-MS/MS and processing of MS data.

SUPPLEMENTARY MATERIAL

The Supplementary Material for this article can be found online at: https://www.frontiersin.org/articles/10.3389/fphar.2021.590477/full#supplementary-material

REFERENCES

Alqurashi, M., Gehring, C., and Marondedze, C. (2016). Changes in the *Arabidopsis thaliana* Proteome Implicate cAMP in Biotic and Abiotic Stress Responses and Changes in Energy Metabolism. *Ijms* 17 (6), 852. doi:10.3390/ijms17060852

Babaev, O., Piletti Chatain, C., and Krueger-Burg, D. (2018). Inhibition in the Amygdala Anxiety Circuitry. *Exp. Mol. Med.* 50 (4), 1–16. doi:10.1038/s12276-018-0063-8

Bae, G. D., Park, E.-Y., Baek, D. J., Jun, H.-S., and Oh, Y. S. (2018). Liquiritigenin Prevents Palmitate-Induced Beta-Cell Apoptosis via Estrogen Receptor-Mediated AKT Activation. *Biomed. Pharmacother.* 101, 348–354. doi:10.1016/j.biopha.2018.02.097

Bald, D., Villellas, C., Lu, P., and Koul, A. (2017). Targeting Energy Metabolism in *Mycobacterium tuberculosis*, a New Paradigm in Antimycobacterial Drug Discovery. *MBio* 8 (2), 8. doi:10.1128/mBio.00272-17

Belforte, F. S., ColuccioLeskow, F., Poskus, E., and Penas Steinhardt, A. (2013). Toll-like Receptor 4 D299G Polymorphism in Metabolic Disorders: a Meta-Analysis. *Mol. Biol. Rep.* 40 (4), 3015–3020. doi:10.1007/s11033-012-2374-5

Ben Mkaddem, S., Benhamou, M., and Monteiro, R. C. (2019). Understanding Fc Receptor Involvement in Inflammatory Diseases: From Mechanisms to New Therapeutic Tools. *Front. Immunol.* 10, 811. doi:10.3389/fimmu.2019.00811

Bliss, T. V. P., and Cooke, S. F. (2011). Long-term Potentiation and Long-Term Depression: a Clinical Perspective. *Clinics* 66 (Suppl. 1), 3–17. doi:10.1590/s1807-59322011001300002

Cao, L., Ding, W., Jia, R., Du, J., Wang, T., Zhang, C., et al. (2017). Anti-inflammatory and Hepatoprotective Effects of Glycyrrhetinic Acid on CCl 4 -induced Damage in Precision-Cut Liver Slices from Jian Carp (*Cyprinus carpio* Var . Jian) through Inhibition of the Nf-kB Pathway. *Fish Shellfish Immunol.* 64, 234–242. doi:10.1016/j.fsi.2017.03.007

Chang, Y.-l., Chen, C.-l., Kuo, C.-L., Chen, B.-c., and You, J.-s. (2010). Glycyrrhetinic Acid Inhibits ICAM-1 Expression via Blocking JNK and NF-κB Pathways in TNF-α-Activated Endothelial Cells. *Acta Pharmacol. Sin.* 31, 546–553. doi:10.1038/aps.2010.34

Chen, G., Huang, C., Liu, Y., Chen, T., Huang, R., Liang, M., et al. (2018a). A Network Pharmacology Approach to Uncover the Potential Mechanism of Yinchensini Decoction. *Evidence-Based Complement. Altern. Med.* 2018, 1–14. doi:10.1155/2018/2178610

Chen, H.-J., Kang, S.-P., Lee, I.-J., and Lin, Y.-L. (2014a). Glycyrrhetinic Acid Suppressed NF-κB Activation in TNF-α-Induced Hepatocytes. *J. Agric. Food Chem.* 62, 618–625. doi:10.1021/jf405352g

Chen, J., Wei, F., and Ma, S. (2019a). Application of Analytical Chemistry in the Quality Evaluation of *Glycyrrhiza* Spp. *J. Liquid Chromatogr. Relat. Tech.* 42, 122–127. doi:10.1080/10826076.2018.1531293

Chen, M., Zhu, J., Kang, J., Lai, X., Gao, Y., Gan, H., et al. (2019b). Exploration in the Mechanism of Action of Licorice by Network Pharmacology. *Molecules* 24, 2959. doi:10.3390/molecules24162959

Chen, S., Wu, S., Li, W., Chen, X., Dong, X., Tan, G., et al. (2014b). Investigation of the Therapeutic Effectiveness of Active Components in Sini Decoction by a Comprehensive GC/LC-MS Based Metabolomics and Network Pharmacology Approaches. *Mol. Biosyst.* 10, 3310–3321. doi:10.1039/c4mb00048j

Chen, X., Zhi, X., Yin, Z., Li, X., Qin, L., Qiu, Z., et al. (2018b). 18β-Glycyrrhetinic Acid Inhibits Osteoclastogenesis *In Vivo* and *In Vitro* by Blocking RANKL-Mediated RANK-TRAF6 Interactions and NF-κB and MAPK Signaling Pathways. *Front. Pharmacol.* 9, 647. doi:10.3389/fphar.2018.00647

Cheng, X., Qiao, X., Ye, M., and Guo, D.-A. (2012). [Classification and Distribution Analysis of Components in glycyrrhiza Using Licorice Compounds Database]. *Yao Xue Xue Bao.* 47, 1023–1030. [in Chinese]. doi:10.16438/j.0513-4870.2012.08.007

Chinese Pharmacopoeia Commission (2020). *Pharmacopoeia of the People's Republic of China.* 1st Edition. Beijing, China: Chemical Industry Press, 88–89.

Dai, W., Chen, H.-Y., and Chen, C. Y.-C. (2018). A Network Pharmacology-Based Approach to Investigate the Novel TCM Formula against Huntington's Disease and Validated by Support Vector Machine Model. *Evidence-Based Complement. Altern. Med.* 2018, 1–(29). doi:10.1155/2018/6020197

Daina, A., Michielin, O., and Zoete, V. (2017). SwissADME: a Free Web Tool to Evaluate Pharmacokinetics, Drug-Likeness and Medicinal Chemistry Friendliness of Small Molecules. *Sci. Rep.* 7, 42717. doi:10.1038/srep42717

Dennis, G., Jr, Sherman, B. T., Hosack, D. A., Yang, J., Gao, W., Lane, H. C., et al. (2003). DAVID: Database for Annotation, Visualization, and Integrated Discovery. *Genome Biol.* 4, P3. doi:10.1186/gb-2003-4-9-r60

Dong, A., Liu, S., and Li, Y. (2018). Gap Junctions in the Nervous System: Probing Functional Connections Using New Imaging Approaches. *Front. Cel. Neurosci.* 12, 320. doi:10.3389/fncel.2018.00320

Fang, J., Gao, L., Ma, H., Wu, Q., Wu, T., Wu, J., et al. (2017a). Quantitative and Systems Pharmacology 3. Network-Based Identification of New Targets for Natural Products Enables Potential Uses in Aging-Associated Disorders. *Front. Pharmacol.* 8, 747. doi:10.3389/fphar.2017.00747

Fang, J., Wang, L., Wu, T., Yang, C., Gao, L., Cai, H., et al. (2017b). Network Pharmacology-Based Study on the Mechanism of Action for Herbal Medicines in Alzheimer Treatment. *J. Ethnopharmacology* 196, 281–292. doi:10.1016/j.jep.2016.11.034

Gianni-Barrera, R., Bartolomeo, M., Vollmar, B., Djonov, V., and Banfi, A. (2014). Split for the Cure: VEGF, PDGF-BB and Intussusception in Therapeutic Angiogenesis. *Biochem. Soc. Trans.* 42 (6), 1637–1642. doi:10.1042/BST20140234

Graßmann, S., Wirsching, J., Eichelmann, F., and Aleksandrova, K. (2017). Association between Peripheral Adipokines and Inflammation Markers: A Systematic Review and Meta-Analysis. *Obesity* 25 (10), 1776–1785. doi:10.1002/oby.21945

Guan, Y., Li, F.-F., Hong, L., Yan, X.-F., Tan, G.-L., He, J.-S., et al. (2012). Protective Effects of Liquiritin Apioside on Cigarette Smoke-Induced Lung Epithelial Cell Injury. *Fundam. Clin. Pharmacol.* 26, 473–483. doi:10.1111/j.1472-8206.2011.00956.x

Guo, C. A., and Guo, S. (2017). Insulin Receptor Substrate Signaling Controls Cardiac Energy Metabolism and Heart Failure. *J. Endocrinol.* 233 (3), R131–R143. doi:10.1530/JOE-16-0679

Guo, X., Ji, J., Feng, Z., Hou, X., Luo, Y., and Mei, Z. (2020). A Network Pharmacology Approach to Explore the Potential Targets Underlying the Effect of Sinomenine on Rheumatoid Arthritis. *Int. Immunopharmacology* 80, 106201. doi:10.1016/j.intimp.2020.106201

Hong, S. Y., Yu, F.-X., Luo, Y., and Hagen, T. (2016). Oncogenic Activation of the PI3K/Akt Pathway Promotes Cellular Glucose Uptake by Downregulating the Expression of Thioredoxin-Interacting Protein. *Cell Signal.* 28 (5), 377–383. doi:10.1016/j.cellsig.2016.01.011

Hopkins, A. L. (2007). Network Pharmacology. *Nat. Biotechnol.* 25, 1110–1111. doi:10.1038/nbt1007-1110

Hosseinzadeh, H., and Nassiri-Asl, M. (2015). Pharmacological Effects ofGlycyrrhizaspp. And its Bioactive Constituents: Update and Review. *Phytother. Res.* 29, 1868–1886. doi:10.1002/ptr.5487

Hu, R.-F., and Sun, X.-B. (2017). Design of New Traditional Chinese Medicine Herbal Formulae for Treatment of Type 2 Diabetes Mellitus Based on Network Pharmacology. *Chin. J. Nat. Medicines* 15, 436–441. doi:10.1016/S1875-5364(17)30065-1

Huang, Z., Zhao, Q., Chen, M., Zhang, J., and Ji, L. (2019). Liquiritigenin and Liquiritin Alleviated Monocrotaline-Induced Hepatic Sinusoidal Obstruction Syndrome via Inhibiting HSP60-Induced Inflammatory Injury. *Toxicology* 428, 152307. doi:10.1016/j.tox.2019.152307

Jiang, Z., Wang, Y., Zheng, Y., Yang, J., and Zhang, L. (2016). Ultra High Performance Liquid Chromatography Coupled with Triple Quadrupole Mass Spectrometry and Chemometric Analysis of Licorice Based on the Simultaneous Determination of Saponins and Flavonoids. *J. Sep. Sci.* 39, 2928–2940. doi:10.1002/jssc.201600246

Kanehisa, M., and Goto, S. (2000). KEGG: Kyoto Encyclopedia of Genes and Genomes. *Nucleic Acids Res.* 28, 27–30. doi:10.1093/nar/28.1.27

Kao, T.-C., Shyu, M.-H., and Yen, G.-C. (2010). Glycyrrhizic Acid and 18β-Glycyrrhetinic Acid Inhibit Inflammation via PI3K/Akt/GSK3β Signaling and Glucocorticoid Receptor Activation. *J. Agric. Food Chem.* 58, 8623–8629. doi:10.1021/jf101841r

Karami, Z., Emam-Djomeh, Z., Mirzaee, H. A., Khomeiri, M., Mahoonak, A. S., and Aydani, E. (2015). Optimization of Microwave Assisted Extraction (MAE) and Soxhlet Extraction of Phenolic Compound from Licorice Root. *J. Food Sci. Technol.* 52, 3242–3253. doi:10.1007/s13197-014-1384-9

Kashyap, M. P., Roberts, C., Waseem, M., and Tyagi, P. (2018). Drug Targets in Neurotrophin Signaling in the Central and Peripheral Nervous System. *Mol. Neurobiol.* 55 (8), 6939–6955. doi:10.1007/s12035-018-0885-3

Kawamoto, Y., Nakajima, Y.-i., and Kuranaga, E. (2016). Apoptosis in Cellular Society: Communication between Apoptotic Cells and Their Neighbors. *Ijms* 17 (12), 2144. doi:10.3390/ijms17122144

Ke, R., Xu, Q., Li, C., Luo, L., and Huang, D. (2018). Mechanisms of AMPK in the Maintenance of ATP Balance during Energy Metabolism. *Cell Biol Int.* 42 (4), 384–392. doi:10.1002/cbin.10915

Ke, Z., Zhang, X., Cao, Z., Ding, Y., Li, N., Cao, L., et al. (2016). Drug Discovery of Neurodegenerative Disease through Network Pharmacology Approach in Herbs. *Biomed. Pharmacother.* 78, 272–279. doi:10.1016/j.biopha.2016.01.021

Khader, S. A., Divangahi, M., Hanekom, W., Hill, P. C., Maeurer, M., Makar, K. W., et al. (2019). Targeting Innate Immunity for Tuberculosis Vaccination. *J. Clin. Invest.* 129 (9), 3482–3491. doi:10.1172/JCI128877

Kita, S., Maeda, N., and Shimomura, I. (2019). Interorgan Communication by Exosomes, Adipose Tissue, and Adiponectin in Metabolic Syndrome. *J. Clin. Invest.* 129 (10), 4041–4049. doi:10.1172/JCI129193

Kleinert, M., Sachs, S., Habegger, K. M., Hofmann, S. M., and Müller, T. D. (2019). Glucagon Regulation of Energy Expenditure. *Ijms* 20 (21), 5407. doi:10.3390/ijms20215407

Kuang, Y., Li, B., Fan, J., Qiao, X., and Ye, M. (2018). Antitussive and Expectorant Activities of Licorice and its Major Compounds. *Bioorg. Med. Chem.* 26, 278–284. doi:10.1016/j.bmc.2017.11.046

Lee, A. Y. S., and Körner, H. (2019). The CCR6-CCL20 axis in Humoral Immunity and T-B Cell Immunobiology. *Immunobiology* 224 (3), 449–454. doi:10.1016/j.imbio.2019.01.005

Lee, E. H., Park, K.-I., Kim, K.-Y., Lee, J.-H., Jang, E. J., Ku, S. K., et al. (2019). Liquiritigenin Inhibits Hepatic Fibrogenesis and TGF-β1/Smad with Hippo/YAP Signal. *Phytomedicine* 62, 152780. doi:10.1016/j.phymed.2018.12.003

Li, H., Zhao, L., Zhang, B., Jiang, Y., Wang, X., Guo, Y., et al. (2014a). A Network Pharmacology Approach to Determine Active Compounds and Action Mechanisms of Ge-Gen-Qin-Lian Decoction for Treatment of Type 2 Diabetes. *Evidence-Based Complement. Altern. Med.* 2014, 1-12. doi:10.1155/2014/495840

Li, S., Fan, T.-P., Jia, W., Lu, A., and Zhang, W. (2014). Network Pharmacology in Traditional Chinese Medicine. *Evidence-Based Complement. Altern. Med.* 2014, 1–2. doi:10.1155/2014/138460

Li, S., and Zhang, B. (2013). Traditional Chinese Medicine Network Pharmacology: Theory, Methodology and Application. *Chin. J. Nat. Medicines* 11, 110–120. doi:10.1016/S1875-5364(13)60037-0

Li, S., Zhang, Z. Q., Wu, L. J., Zhang, X. G., Wang, Y. Y., and Li, Y. D. (2007). Understanding ZHENG in Traditional Chinese Medicine in the Context of Neuro-Endocrine-Immune Network. *IET Syst. Biol.* 1, 51–60. doi:10.1049/iet-syb:20060032

Li, X., Liu, H., Shao, Y., Ma, G., Song, D., Xu, G., et al. (2019a). Wide Identification of the Compounds in Licorice and Exploration of the Mechanism for Prostatitis Treatment by Combining UHPLC-LTQ-Orbitrap MS with Network Pharmacology. *ChemistrySelect* 4, 3011–3017. doi:10.1002/slct.201802661

Li, X., Wu, L., Liu, W., Jin, Y., Chen, Q., Wang, L., et al. (2014b). A Network Pharmacology Study of Chinese Medicine QiShenYiQi to Reveal its Underlying Multi-Compound, Multi-Target, Multi-Pathway Mode of Action. *PLoS ONE* 9, e95004. doi:10.1371/journal.pone.0095004

Li, Y., Liu, Y., Han, X., Jin, H., and Ma, S. (2019b). Arsenic Species in Cordyceps Sinensis and its Potential Health Risks. *Front. Pharmacol.* 10, 1471. doi:10.3389/fphar.2019.01471

Liu, H., Wang, J., Zhou, W., Wang, Y., and Yang, L. (2013). Systems Approaches and Polypharmacology for Drug Discovery from Herbal Medicines: An Example Using Licorice. *J. Ethnopharmacology* 146, 773–793. doi:10.1016/j.jep.2013.02.004

Liu, R.-t., Zou, L.-b., and Lü, Q.-j. (2009). Liquiritigenin Inhibits Aβ25-35-Induced Neurotoxicity and Secretion of Aβ1-40 in Rat Hippocampal Neurons. *Acta Pharmacol. Sin.* 30, 899–906. doi:10.1038/aps.2009.74

Lu, H.-C., and Mackie, K. (2016). An Introduction to the Endogenous Cannabinoid System. *Biol. Psychiatry* 79 (7), 516–525. doi:10.1016/j.biopsych.2015.07.028

Luan, J., Zhang, X., Wang, S., Li, Y., Fan, J., Chen, W., et al. (2018). NOD-like Receptor Protein 3 Inflammasome-dependent IL-1β Accelerated ConA-Induced Hepatitis. *Front. Immunol.* 9, 758. doi:10.3389/fimmu.2018.00758

Lv, Y.-N., Li, S.-X., Zhai, K.-F., Kou, J.-P., and Yu, B.-Y. (2014). Network Pharmacology-Based Prediction and Verification of the Molecular Targets and Pathways for Schisandrin against Cerebrovascular Disease. *Chin. J. Nat. Medicines* 12, 251–258. doi:10.1016/S1875-5364(14)60051-0

Ma, C., Xu, T., Sun, X., Zhang, S., Liu, S., Fan, S., et al. (2019). Network Pharmacology and Bioinformatics Approach Reveals the Therapeutic Mechanism of Action of Baicalein in Hepatocellular Carcinoma. *Evidence-Based Complement. Altern. Med.* 2019, 1–15. doi:10.1155/2019/7518374

MacKenzie, E. M., Odontiadis, J., Le Mellédo, J.-M., Prior, T. I., and Baker, G. B. (2007). The Relevance of Neuroactive Steroids in Schizophrenia, Depression, and Anxiety Disorders. *Cell Mol Neurobiol.* 27 (5), 541–574. doi:10.1007/s10571-006-9086-0

Meng, F.-C., and Lin, J.-K. (2019). Liquiritigenin Inhibits Colorectal Cancer Proliferation, Invasion, and Epithelial-To-Mesenchymal Transition by Decreasing Expression of Runt-Related Transcription Factor 2. *Oncol. Res.* 27, 139–146. doi:10.3727/096504018X15185747911701

Mullur, R., Liu, Y.-Y., and Brent, G. A. (2014). Thyroid Hormone Regulation of Metabolism. *Physiol. Rev.* 94 (2), 355–382. doi:10.1152/physrev.00030.2013

Murphy, K. L., Fischer, R., Swanson, K. A., Bhatt, I. J., Oakley, L., Smeyne, R., et al. (2020). Synaptic Alterations and Immune Response Are Sexually Dimorphic in a Non-pertussis Toxin Model of Experimental Autoimmune Encephalomyelitis. *Exp. Neurol.* 323, 113061. doi:10.1016/j.expneurol.2019.113061

Musella, A., Fresegna, D., Rizzo, F. R., Gentile, A., Bullitta, S., De Vito, F., et al. (2017). A Novel Crosstalk within the Endocannabinoid System Controls GABA Transmission in the Striatum. *Sci. Rep.* 7 (1), 7363. doi:10.1038/s41598-017-07519-8

Navakkode, S., Liu, C., and Soong, T. W. (2018). Altered Function of Neuronal L-type Calcium Channels in Ageing and Neuroinflammation: Implications in Age-Related Synaptic Dysfunction and Cognitive Decline. *Ageing Res. Rev.* 42, 86–99. doi:10.1016/j.arr.2018.01.001

Nourshargh, S., and Alon, R. (2014). Leukocyte Migration into Inflamed Tissues. *Immunity* 41 (5), 694–707. doi:10.1016/j.immuni.2014.10.008

Park, W. (2018). MAPK Inhibitors, Particularly the JNK Inhibitor, Increase Cell Death Effects in H2O2-Treated Lung Cancer Cells via Increased Superoxide Anion and Glutathione Depletion. *Oncol. Rep.* 39 (2), 860–870. doi:10.3892/or.2017.6107

Piao, C.-L., Luo, J.-L., Jin, D., Tang, C., Wang, L., Lian, F.-M., et al. (2019). Utilizing Network Pharmacology to Explore the Underlying Mechanism of Radix Salviae in Diabetic Retinopathy. *Chin. Med.* 14, 58. doi:10.1186/s13020-019-0280-7

Qiao, X., Song, W., Ji, S., Wang, Q., Guo, D.-a., and Ye, M. (2015). Separation and Characterization of Phenolic Compounds and Triterpenoid Saponins in Licorice (*Glycyrrhiza* Uralensis) Using Mobile Phase-dependent Reversed-phase×reversed-phase Comprehensive Two-Dimensional Liquid Chromatography Coupled with Mass Spectrometry. *J. Chromatogr. A.* 1402, 36–45. doi:10.1016/j.chroma.2015.05.006

Ran, F. J. (2019). Studies on the Chemical Constituents and Biological Activities of the Aerial Parts of *Glycyrrhiza* Uralensis Fisch. M.Sc. Thesis. Beijing, China: Beijing University of Chinese Medicine.

Rastegari, A., Mottaghitalab, F., Dinarvand, R., Amini, M., Arefian, E., Gholami, M., et al. (2019). Inhibiting Hepatic Gluconeogenesis by Chitosan Lactate Nanoparticles Containing CRTC2 siRNA Targeted by Poly(ethylene Glycol)-Glycyrrhetinic Acid. *Drug Deliv. Transl. Res.* 9, 694–706. doi:10.1007/s13346-019-00618-1

Rho, S.-S., Ando, K., and Fukuhara, S. (2017). Dynamic Regulation of Vascular Permeability by Vascular Endothelial Cadherin-Mediated Endothelial Cell-Cell Junctions. *J. Nippon Med. Sch.* 84 (4), 148–159. doi:10.1272/jnms.84.148

Ru, J., Li, P., Wang, J., Zhou, W., Li, B., Huang, C., et al. (2014). TCMSP: a Database of Systems Pharmacology for Drug Discovery from Herbal Medicines. *J. Cheminform* 6. doi:10.1186/1758-2946-6-13

Sahoo, S. S., Majhi, R. K., Tiwari, A., Acharya, T., Kumar, P. S., Saha, S., et al. (2019). Transient Receptor Potential Ankyrin1 Channel Is Endogenously Expressed in T Cells and Is Involved in Immune Functions. *[J] Biosci. Rep.* 39 (9), 39. doi:10.1042/BSR20191437

Salvalaio, M., D'Avanzo, F., Rigon, L., Zanetti, A., D'Angelo, M., Valle, G., et al. (2017). Brain RNA-Seq Profiling of the Mucopolysaccharidosis Type II Mouse Model. *Ijms* 18 (5), 1072. doi:10.3390/ijms18051072

Schüle, C., Nothdurfter, C., and Rupprecht, R. (2014). The Role of Allopregnanolone in Depression and Anxiety. *Prog. Neurobiol.* 113, 79–87. doi:10.1016/j.pneurobio.2013.09.003

Semenza, G. L. (2014). Hypoxia-Inducible Factor 1 and Cardiovascular Disease. *Annu. Rev. Physiol.* 76, 39–56. doi:10.1146/annurev-physiol-021113-170322

Shamsa, F., Nagata, N., Oh-Ishi, M., and Ohtsuki, K. (1991). The *In Vitro* Effects of Glycyrrhizin and the Derivatives of Glycyrrhetinic Acid on the Activity of cAMP-dependent Protein Kinase and Phosphorylation of Cellular Polypeptide by the Kinase from Ehrlich Ascites Tumor Cells. *Tohoku J. Exp. Med.* 165, 305–318. doi:10.1620/tjem.165.305

Shi, H., Wu, Y., Wang, Y., Zhou, M., Yan, S., Chen, Z., et al. (2015). Liquiritigenin Potentiates the Inhibitory Effects of Cisplatin on Invasion and Metastasis via Downregulation MMP-2/9 and PI3 K/AKT Signaling Pathway in B16F10 Melanoma Cells and Mice Model. *Nutr. Cancer* 67, 761–770. doi:10.1080/01635581.2015.1037962

Shi, S.-h., Cai, Y.-p., Cai, X.-j., Zheng, X.-y., Cao, D.-s., Ye, F.-q., et al. (2014). A Network Pharmacology Approach to Understanding the Mechanisms of Action of Traditional Medicine: Bushenhuoxue Formula for Treatment of Chronic Kidney Disease. *PLoS ONE* 9, e89123. doi:10.1371/journal.pone.0089123

Shi, X.-Q., Yue, S.-J., Tang, Y.-P., Chen, Y.-Y., Zhou, G.-S., Zhang, J., et al. (2019). A Network Pharmacology Approach to Investigate the Blood Enriching Mechanism of Danggui Buxue Decoction. *J. Ethnopharmacology* 235, 227–242. doi:10.1016/j.jep.2019.01.027

Shin, H., Ma, Y., Chanturiya, T., Cao, Q., Wang, Y., Kadegowda, A. K. G., et al. (2017). Lipolysis in Brown Adipocytes Is Not Essential for Cold-Induced Thermogenesis in Mice. *Cel Metab.* 26 (5), 764–777. doi:10.1016/j.cmet.2017.09.002

Song, W., Ni, S., Fu, Y., and Wang, Y. (2018). Uncovering the Mechanism of Maxing Ganshi Decoction on Asthma from a Systematic Perspective: A Network Pharmacology Study. *Sci. Rep.* 8, 17362. doi:10.1038/s41598-018-35791-9

Song, X., Zhang, Y., Dai, E., Du, H., and Wang, L. (2019). Mechanism of Action of Celastrol against Rheumatoid Arthritis: A Network Pharmacology Analysis. *Int. Immunopharmacology* 74, 105725. doi:10.1016/j.intimp.2019.105725

Starlinger, P., Alidzanovic, L., Schauer, D., Brugger, P., Sommerfeldt, S., Kuehrer, I., et al. (2011). Platelet-Stored Angiogenesis Factors: Clinical Monitoring Is Prone to Artifacts. *Dis. Markers* 31 (2), 55–65. doi:10.3233/DMA-2011-079810.1155/2011/535109

Stella, R., and Athanasios, G. P. (2013). The NF-κB Signalling Pathway in Osteoarthritis [J]. *Int. J. Biochem. Cel Biol.* 45, 2580–2584. doi:10.1016/j.biocel.2013.08.018

Streeter, C. C., Whitfield, T. H., Owen, L., Rein, T., Karri, S. K., Yakhkind, A., et al. (2010). Effects of Yoga versus Walking on Mood, Anxiety, and Brain GABA Levels: A Randomized Controlled MRS Study. *J. Altern. Complement. Med.* 16 (11), 1145–1152. doi:10.1089/acm.2010.0007

Tao, W., Dong, Y., Su, Q., Wang, H., Chen, Y., Xue, W., et al. (2016). Liquiritigenin Reverses Depression-like Behavior in Unpredictable Chronic Mild Stress-Induced Mice by Regulating PI3K/Akt/mTOR Mediated BDNF/TrkB Pathway. *Behav. Brain Res.* 308, 177–186. doi:10.1016/j.bbr.2016.04.039

Toby, L. (2009). The Nuclear Factor NF-kB Pathway in Inflammation [J]. *Cold Spring Harb Perspect. Biol.* 1 (6), a001651. doi:10.1101/cshperspect.a001651

Tu, C., Ma, Y., Song, M., Yan, J., Xiao, Y., and Wu, H. (2019). Liquiritigenin Inhibits IL-1β-induced Inflammation and Cartilage Matrix Degradation in Rat Chondrocytes. *Eur. J. Pharmacol.* 858, 172445. doi:10.1016/j.ejphar.2019.172445

Wang, C.-Y., Kao, T.-C., Lo, W.-H., and Yen, G.-C. (2011). Glycyrrhizic Acid and 18β-Glycyrrhetinic Acid Modulate Lipopolysaccharide-Induced Inflammatory Response by Suppression of NF-κB through PI3K P110δ and P110γ Inhibitions. *J. Agric. Food Chem.* 59, 7726–7733. doi:10.1021/jf2013265

Wang, C., Chen, L., Xu, C., Shi, J., Chen, S., Tan, M., et al. (2020). A Comprehensive Review for Phytochemical, Pharmacological, and Biosynthesis Studies onGlycyrrhizaspp. *Am. J. Chin. Med.* 48, 17–45. doi:10.1142/S0192415X20500020

Wang, W. (2004). Study on the Effective Components of *Glycyrrhiza* Uralensis Fisch. M.Sc. Thesis. Harbin, China: Northeast Forestry University.

Wang, Y.-C., and Yang, Y.-S. (2007). Simultaneous Quantification of Flavonoids and Triterpenoids in Licorice Using HPLC. *J. Chromatogr. B.* 850, 392–399. doi:10.1016/j.jchromb.2006.12.032

Wei, W., Gao, X., Zhao, L., Zhuang, J., Jiao, Y., and Xu, F. (2020). Liquiritin Apioside Attenuates Laryngeal Chemoreflex but Not Mechanoreflex in Rat Pups. *Am. J. Physiology-Lung Cell Mol. Physiol.* 318, L89–L97. doi:10.1152/ajplung.00306.2019

Xie, Y., Shi, X., Sheng, K., Han, G., Li, W., Zhao, Q., et al. (2019). PI3K/Akt Signaling Transduction Pathway, Erythropoiesis and Glycolysis in Hypoxia (Review). *Mol. Med. Rep.* 19 (2), 783–791. doi:10.3892/mmr.2018.9713

Xiong, Y., Hu, Y., Chen, L., Zhang, Z., Zhang, Y., Niu, M., et al. (2018). Unveiling Active Constituents and Potential Targets Related to the Hematinic Effect of Steamed Panax Notoginseng Using Network Pharmacology Coupled with Multivariate Data Analyses. *Front. Pharmacol.* 9, 1514. doi:10.3389/fphar.2018.01514

Xiong, Y., Yang, Y., Xiong, W., Yao, Y., Wu, H., and Zhang, M. (2019). Network Pharmacology-based Research on the Active Component and Mechanism of the Antihepatoma Effect ofRubia cordifoliaL. *J. Cel Biochem.* 120, 12461–12472. doi:10.1002/jcb.28513

Xu, F., Na, L., Li, Y., and Chen, L. (2020). Roles of the PI3K/AKT/mTOR Signalling Pathways in Neurodegenerative Diseases and Tumours. *Cell Biosci.* 10, 54. doi:10.1186/s13578-020-00416-0

Xu, H.-Y., Zhang, Y.-Q., Liu, Z.-M., Chen, T., Lv, C.-Y., Tang, S.-H., et al. (2019). ETCM: an Encyclopaedia of Traditional Chinese Medicine. *Nucleic Acids Res.* 47, D976–D982. doi:10.1093/nar/gky987

Yu, J.-Y., Ha, J., Kim, K.-M., Jung, Y.-S., Jung, J.-C., and Oh, S. (2015). Anti-Inflammatory Activities of Licorice Extract and its Active Compounds, Glycyrrhizic Acid, Liquiritin and Liquiritigenin, in BV2 Cells and Mice Liver. *Molecules* 20, 13041–13054. doi:10.3390/molecules200713041

Zeng, L., Lou, Z.-C., and Zhang, R.-Y. (1991). [Quality Evaluation of Chinese Licorice]. *Yao Xue Xue Bao.* 26, 788–793. doi:10.16438/j.0513-4870.1991.10.013

Zhang, G.-b., Li, Q.-y., Chen, Q.-l., and Su, S.-b. (2013). Network Pharmacology: A New Approach for Chinese Herbal Medicine Research. *Evidence-Based Complement. Altern. Med.* 2013, 1–9. doi:10.1155/2013/621423

Zhang, M., Huang, J., Tan, X., Bai, J., et al. (2015). Common Polymorphisms in the NFKBIA Gene and *Cancer* Susceptibility: A Meta-Analysis. *Med. Sci. Monit.* 21, 3186–3196. doi:10.12659/msm.89525710.12659/msm.895257

Zhang, Q., Li, R., Peng, W., Zhang, M., Liu, J., Wei, S., et al. (2019a). Identification of the Active Constituents and Significant Pathways of Guizhi-Shaoyao-Zhimu Decoction for the Treatment of Diabetes Mellitus Based on Molecular Docking and Network Pharmacology. *Cchts* 22, 584–598. doi:10.2174/1386207322666191022101613

Zhang, Q., and Ye, M. (2009). Chemical Analysis of the Chinese Herbal Medicine Gan-Cao (Licorice). *J. Chromatogr. A* 1216, 1954–1969. doi:10.1016/j.chroma.2008.07.072

Zhang, Y.-F., Huang, Y., Ni, Y.-H., and Xu, Z.-M. (2019c). Systematic Elucidation of the Mechanism of Geraniol via Network Pharmacology. *Ddt* 13, 1069–1075. doi:10.2147/DDDT.S189088

Zhang, Y., Yang, S., Zhang, M., Wang, Z., He, X., Hou, Y., et al. (2019b). Glycyrrhetinic Acid Improves Insulin-Response Pathway by Regulating the Balance between the Ras/MAPK and PI3K/Akt Pathways. *Nutrients* 11, 604. doi:10.3390/nu11030604

Zhou, B. (2015). Study on the above Ground Chemical Constituents of *Glycyrrhiza* Uralensis Fisch.and *Glycyrrhiza* Inflata Bat. M.Sc. Thesis. Tarim, China: Tarim University.

Zhou, J.-X., and Wink, M. (2019). Evidence for Anti-inflammatory Activity of Isoliquiritigenin, 18β Glycyrrhetinic Acid, Ursolic Acid, and the Traditional Chinese Medicine Plants *Glycyrrhiza* Glabra and Eriobotrya Japonica, at the Molecular Level. *Medicines* 6, 55. doi:10.3390/medicines6020055

Zhu, N., Hou, J., Ma, G., and Liu, J. (2019). Network Pharmacology Identifies the Mechanisms of Action of Shaoyao Gancao Decoction in the Treatment of Osteoarthritis. *Med. Sci. Monit.* 25, 6051–6073. doi:10.12659/MSM.915821

Zhu, X., Shi, J., and Li, H. (2018). Liquiritigenin Attenuates High Glucose-Induced Mesangial Matrix Accumulation, Oxidative Stress, and Inflammation by Suppression of the NF-κB and NLRP3 Inflammasome Pathways. *Biomed. Pharmacother.* 106, 976–982. doi:10.1016/j.biopha.2018.07.045

Zigmond, R. E., and Echevarria, F. D. (2019). Macrophage Biology in the Peripheral Nervous System after Injury. *Prog. Neurobiol.* 173, 102–121. doi:10.1016/j.pneurobio.2018.12.001

Conflict of Interest: The authors declare that the research was conducted in the absence of any commercial or financial relationships that could be construed as a potential conflict of interest.

Copyright © 2021 Chen, Li, Hu, Wei and Ma. This is an open-access article distributed under the terms of the Creative Commons Attribution License (CC BY). The use, distribution or reproduction in other forums is permitted, provided the original author(s) and the copyright owner(s) are credited and that the original publication in this journal is cited, in accordance with accepted academic practice. No use, distribution or reproduction is permitted which does not comply with these terms.

frontiers in Pharmacology

ORIGINAL RESEARCH
published: 29 April 2021
doi: 10.3389/fphar.2021.590994

Qing-Yi Decoction in the Treatment of Acute Pancreatitis: An Integrated Approach Based on Chemical Profile, Network Pharmacology, Molecular Docking and Experimental Evaluation

Tian-Fu Wei[1,2†], Liang Zhao[3†], Peng Huang[1,2], Feng-Lin Hu[1,2], Ju-Ying Jiao[1,2], Kai-Lai Xiang[3], Zhi-Zhou Wang[1,2], Jia-Lin Qu[1] and Dong Shang[1,2,3]**

[1]Laboratory of Integrative Medicine, The First Affiliated Hospital of Dalian Medical University, Dalian, China, [2]Institute (College) of Integrative Medicine, Dalian Medical University, Dalian, China, [3]Department of General Surgery, Pancreatic-Biliary Center, The First Affiliated Hospital of Dalian Medical University, Dalian, China

Background: Qing-Yi Decoction (QYD) is a classic precompounded prescription with satisfactory clinical efficacy on acute pancreatitis (AP). However, the chemical profile and overall molecular mechanism of QYD in treating AP have not been clarified.

Methods: In the present study, a rapid, simple, sensitive and reliable ultra-performance liquid chromatography coupled with quadrupole time-of-flight mass spectrometry (UHPLC-QTOF-MS)-based chemical profile was first established. An integration strategy of network pharmacology analysis and molecular docking based identified ingredients was further performed to screen out the potential targets and pathways involved in the treatment of QYD on AP. Finally, SD rats with acute pancreatitis were constructed to verify the predicted results through a western blot experiment.

Results: A total of 110 compounds, including flavonoids, phenolic acids, alkaloids, monoterpenes, iridoids, triterpenes, phenylethanoid glycosides, anthraquinones and other miscellaneous compounds were identified, respectively. Eleven important components, 47 key targets and 15 related pathways based on network pharmacology analysis were obtained. Molecular docking simulation indicated that ERK1/2, c-Fos and p65 might play an essential role in QYD against AP. Finally, the western blot experiments showed that QYD could up-regulate the expression level of ERK1/2 and c-Fos, while down-regulate the expression level of p65.

Conclusion: This study predicted and validated that QYD may treat AP by inhibiting inflammation and promoting apoptosis, which provides directions for further experimental studies.

Keywords: Qing-Yi decoction, acute pancreatitis, chemical profile, network pharmacology, molecular docking, p65, ERK1/2, c-fos

OPEN ACCESS

Edited by:
Michael Heinrich, UCL School of Pharmacy, United Kingdom

Reviewed by:
Hua Yang, China Pharmaceutical University, China
Jianming Guo, Nanjing University of Chinese Medicine, China
Zhihong Yao, Jinan University, China

****Correspondence:***
Dong Shang
shangdong@dmu.edu.cn
Jia-Lin Qu
jialin_qu@126.com

†These authors have contributed equally to this work

Specialty section:
This article was submitted to Ethnopharmacology, a section of the journal Frontiers in Pharmacology

Received: *03 August 2020*
Accepted: *29 March 2021*
Published: *29 April 2021*

Citation:
Wei T-F, Zhao L, Huang P, Hu F-L, Jiao J-Y, Xiang K-L, Wang Z-Z, Qu J-L and Shang D (2021) Qing-Yi Decoction in the Treatment of Acute Pancreatitis: An Integrated Approach Based on Chemical Profile, Network Pharmacology, Molecular Docking and Experimental Evaluation. Front. Pharmacol. 12:590994. doi: 10.3389/fphar.2021.590994

INTRODUCTION

Acute pancreatitis (AP) is a common clinical disease caused by a variety of factors, including cholelithiasis, excessive drinking, obesity, smoking, etc (Sadr-Azodi et al., 2012; Yadav and Lowenfels, 2013; Lankisch et al., 2015; Forsmark et al., 2016), which is manifested by acute epigastric pain, nausea, vomiting and fever (Lankisch et al., 2015). The overall incidence rate of AP is 13–45 per 100,000 persons and is increasing year by year (Yadav and Lowenfels, 2013; Lankisch et al., 2015).

At present, the western medicine treatment of AP is mainly focused on spasmolysis, pain relief, inhibition of pancreatin secretion and fluid resuscitation. In severe cases, surgical treatment will be used (Lankisch et al., 2015; Brunschot et al., 2018). However, the therapeutic effect of these schemes is limited because they can only control the symptoms without an ultimate cure. Furthermore, there is no specific drug available yet. Therefore, it is imperative to develop safer and more effective drugs to treat AP. Traditional Chinese medicine (TCM), which has a history of clinical application for thousands of years in China, has been gradually accepted in the treatment of AP in view of its characteristics of holism concept and pattern differentiation (Wang and Zhang, 2017) as well as advantages of less side effects and systemic regulation.

Qing-Yi Decoction (QYD) is a classic precompounded prescription that consists of eight herbs, namely, *Rheum officinale* Baill. (da-huang in Chinese), *Bupleurum chinense* DC. (chai-hu in Chinese), *Scutellaria baicalensis* Georgi (huang-qin in Chinese), *Paeonia lactiflora* Pall. (bai-shao in Chinese), *Aucklandia costus* Falc. (mu-xiang in Chinese), *Corydalis yanhusuo* (Y. H. Chou and Chun C. Hsu) W. T. Wang ex Z. Y. Su and C. Y. Wu (yan-hu-suo in Chinese), *Gardenia jasminoides* J. Ellis (zhi-zi in Chinese) and *Natrii* Sulfas (mang-xiao in Chinese). Previous studies reported that it could treat AP by reducing the production of various inflammatory mediators, blocking inflammatory signaling pathways, and improving intestinal mucosal barrier and motility effectively (Zhang et al., 2015). In clinical practice, QYD is more widely used than similar prescriptions such as Da-Cheng-Qi Decoction because of its advantages of targeting symptomatic infection by heat-clearing, detoxifying and removing stasis by purgation. (Qu et al., 2007; Chen et al., 2015). However, there are some shortages in the current research on QYD. For one thing, the pharmacodynamic material basis and quality evaluation system related to drug efficacy of QYD have not been established. For another, the current reports are mostly limited to a single target, which is difficult to reflect the "holism" characteristics of QYD as a compound preparation with multiple constituents, multiple targets and multiple pathways, and lacks convincing power. The above problems hindered the development and application of QYD. Therefore, it is necessary to characterize and reveal its chemical constituents and overall mechanism systematically.

Network pharmacology was proposed by Andrew Hopkins in 2007. Its core idea is to optimize treatment strategies depends on a biological network formed by disease features, bioactive agents and drug targets that connect to each other (Hopkins, 2007). It has been introduced to evaluate the constituents and action mechanisms of TCM in view of its systematic and holistic coincides (Li et al., 2011; Li and Zhang, 2013; Cai et al., 2018a). Molecular docking is a technology of drug design and screening based on computer data simulation through the interaction and affinity between receptor macromolecules and drug micromolecules (Chen et al., 2014; Lionta et al., 2014; Saikia and Bordoloi, 2019; Reddyrajula and Dalimba, 2020). At present, their combined use has been successfully applied in the research of Traditional Chinese medicine and their compound preparation (Liang et al., 2019; Wang et al., 2019).

In this study, we systematically expounded the possible targets and related pathways of QYD in treating AP by integrating the ultra-performance liquid chromatography coupled with quadrupole time-of-flight mass spectrometry (UHPLC-QTOF-MS), network pharmacology, molecular docking analysis and experimental evaluation using molecular biology. The schematic diagram of this study was shown in **Figure 1**.

MATERIALS AND METHODS

Chemicals, Reagents and Materials

Methanol and acetonitrile of HPLC grade were purchased from Merck Company Inc. (Darmstadt, Germany). The chemical of formic acid was MS grade and purchased from Fisher Scientific Company Inc. (Fairlawn, NJ). All other reagents were of analytical grade and supplied by Tianjin Concord Technology Co., Ltd. (Tianjin, China). Ultra-pure water (18.2 MΩ) was prepared daily with a Milli-Q water purification system (Millipore, Milford, MA, United States).

Gallic acid (**3**), catechin (**18**), chlorogenic acid (**19**) (+)-epicatechin (**28**), scutellarin (**36**), tetrahydropalmatine (**47**), jatrorrhizine (**48**), baicalin (**62**), palmatine (**72**), baicalein (**88**), aloe-emodin (**93**), rhein (**94**), saikosaponin a (**96**), wogonin (**97**), emodin (**104**), chrysophanol (**107**), and physcion (**108**) were obtained from the National Institutes for Food and Drug Control (Beijing, China). Syringin (**22**), albiflorin (**29**), paeoniflorin (**31**), rutin (**35**) and benzoylpaeoniflorin (**85**) were purchased from Chengdu Pufei De Biotech (Chengdu, Sichuan, China). The purity of each reference standard was above 98%.

All the eight herbs of QYD, including *Rheum officinale* Baill. (batch No. 160702), *Bupleurum chinense* DC. (batch No. 170509), *Scutellaria baicalensis* Georgi (batch No. 170505), *Paeonia lactiflora* Pall. (batch No. 170308), *Aucklandia costus* Falc. (batch No. 170503), *Corydalis yanhusuo* (Y. H. Chou and Chun C. Hsu) W. T. Wang ex Z. Y. Su and C. Y. Wu (batch No. 170307), *Gardenia jasminoides* J. Ellis (batch No. 170305) and *Natrii* Sulfas (batch No. 170609) were purchased from the First Affiliated Hospital of Dalian Medical University (Dalian, Liaoning Province, China), and authenticated by Professor Aijing Leng (Department of Chinese medicine, The First Affiliated Hospital of Dalian Medical University). Their voucher specimens were deposited at the author's laboratory.

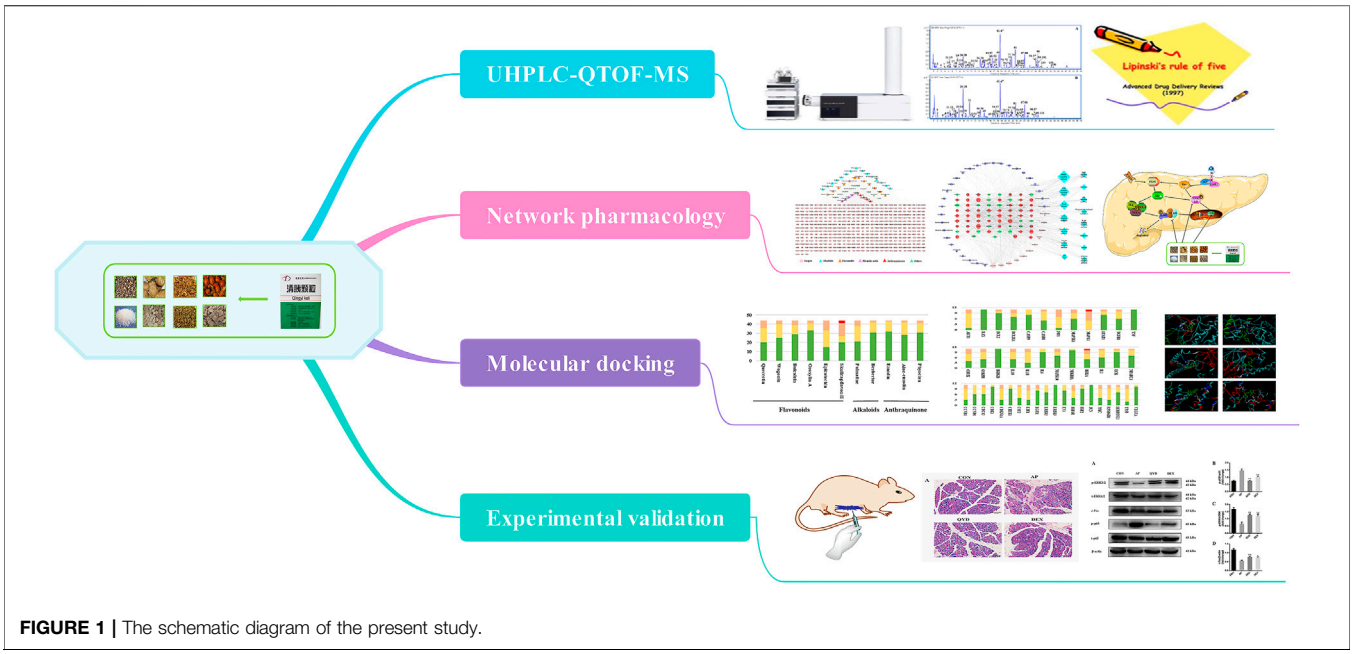

FIGURE 1 | The schematic diagram of the present study.

Preparation of Qing-Yi Decoction Extract and Standard Solution

Raw herbs for the formula (containing *Bupleurum chinense* DC., 15 g; *Scutellaria baicalensis* Georgi, 12 g; *Paeonia lactiflora* Pall., 15 g; *Aucklandia costus* Falc, 15 g; *Corydalis yanhusuo* (Y. H. Chou and Chun C. Hsu) W. T. Wang ex Z. Y. Su and C. Y. Wu, 15 g; and *Gardenia jasminoides* J. Ellis, 15 g) was soaked and extracted by boiling with 10-fold mass of water (870 ml) for 1 h. After filtered with six-layer absorbent gauze, the residue was re-extracted with 8-fold mass of water in the same way for 0.5 h. Then *Rheum officinale* Baill. (20 g) was added into the extract and boiled for additional 0.5 h. After being filtered with six-layer absorbent gauze and added by *Natrii* Sulfas (10 g) when solution was hot, the two filtrates were combined and concentrated under vacuum to 120 ml (equal to 1 g crude herb/ml), and finally the concentrate was subjected to freeze-dry. The extract was obtained with a yield of 29.5% and kept in the desiccator before use.

A 1.0 g of the freeze-dried powder was accurately weighted and extracted with 50 ml of methanol/water (1:1, v/v) for 30 min under ultrasound. The extract solution was centrifuged at 13,000 rpm for 10 min at 4°C and the supernatant was filtered through a 0.22 μm membrane filters. Finally, 1.0 μl of filtrate was injected into UHPLC-QTOF-MS for analysis.

Ultra-Performance Liquid Chromatography Coupled With Quadrupole Time-of-Flight Mass Spectrometry Condition

Chromatographic separation was carried out on an Agilent 1,290 Infinity LC system (Agilent, United States) using an Agilent Zorbax Eclipse Plus C18 column (100 × 2.1 mm i.d., 3.5 μm) at 40°C with a flow rate of 0.3 ml/min. The mobile phase consisted of water containing 0.1% formic acid (solvent system A) and acetonitrile (solvent system B) were performed with gradient elution program as follows: 0–5 min, 3–10% B; 5–13 min, 10–18% B; 13–20 min, 18–25% B; 20–35 min, 25–70% B; 35–40 min, 70–99% B; 40–42 min, 99–3% B; 42–45 min, 3% B. 2 μl of sample solution was injected for analysis.

Mass detection was performed using an Agilent 6530b Accurate-Mass Quadrupole Time-of-Flight (Q-TOF) mass spectrometer (Agilent Corp., United States) equipped with a Dual AJS ESI source operating in both positive and negative mode with the following operating parameters: drying gas (N_2) flow rate, 10.0 L/min; drying gas (N_2) temperature, 350°C; nebulizer, 35 psig; sheath gas (N_2) temperature, 400°C; fragmentor voltage, 120 V; skimmer voltage, 65 V; Octopole RF, 750 V. The capillary voltage was set at 4 kV or −3.5 kV under positive or negative mode, respectively. The nozzle voltage was set at +500 V or −1000 V, respectively; The quasi-molecular ions $[M - H]^-$ and $[M + H]^+$ were selected as precursor ions and subjected to target-MS/MS analyses with different collision energies ranging from 10 to 60 V to acquire sufficient product ions. MS spectra were recorded over the m/z range of 50–1,100. All data was processed by MassHunter workstation software version B.06.00 (Agilent Technologies, Germany).

Network Pharmacology Analysis

Establishment of Component Target Database for Qing-Yi Decoction

Briefly, the constituents contained in QYD identified by UHPLC-QTOF-MS were input into the Molispiration Smiles database (https://www.molinspiration.com/cgi-bin/properties), and the active constituents were screened out through the Lipinski's rule of five (Lipinski et al., 2001). Then, the Canonical SMILES structure formats of these constituents were obtained from Pubchem database (https://www.ncbi.nlm.nih.gov/pubmed/), and the component targets were found out by inputting them into Swiss

Target Prediction Database (http://www.swisstargetprediction.ch/). To obtain more target information, the names of the ingredients were also input into Traditional Chinese Medicine Systems Pharmacy Database and Analysis Platform (TCMSP) (http://LSP.nwu.edu.cn/tcmsp.php). Finally, the UniProt Knowledgebase (http://www.uniprot.org/) was used to convert the protein names into official gene symbols (*Homo sapiens*).

Establishment of Therapeutic Target Database for Acute Pancreatitis

The information of therapeutic target was searched by using "acute pancreatitis" as the keyword. After integration of search-derived target data and elimination of the repeated genes, the therapeutic targets database can be obtained. The databases that used in this study were shown below.

1) OMIM database (http://omim.org/)
2) GeneCards database (https://www.genecards.org/)
3) DisGeNET database (http://www.disgenet.org/web/DisGeNET/menu)
4) GAD database (https://geneticassociationdb.nih.gov/)

The Protein-Protein Interactions Network Analysis

To clarify the relationship between intersection targets, an intersection targets protein-protein interactions (PPI) network of acute pancreatitis and QYD component was constructed and analyzed using STRING database (https://string-db.org/). Species were defined as Homo sapiens. PPIs with a confidence score greater than 0.95 were selected and topology analyses were carried out to ensure the accuracy of the results. Finally, targets with a degree value greater than twice the median were chosen for subsequent network construction and analysis (Lu et al., 2017; Li et al., 2018a).

Enrichment Analysis

In order to clarify the signaling pathways related to key targets, Kyoto Gene and Genome Encyclopedia (KEGG) enrichments analysis was performed based on Database for Annotation, Visualization and Integrated Discovery (DAVID, https://david.ncifcrf.gov/home.jsp, ver. 6.8) (Huang et al., 2009).

Network Construction and Analysis

To visualize the research data, we process the data by employing the network visualization software Cytoscape 3.2.1 (Demchak et al., 2014), which supplies a method for data integration, analysis, and visualization for complex network analysis. The two networks were constructed as follows: 1) constituents-putative targets network of QYD; 2) active constituents-intersection target PPIs-pathways network. In these network diagrams, constituents, targets, and pathways were all represented by nodes, while the edges indicate the interactions between different nodes. The "degree" of a node was determined by the number of connected edges.

Molecular Docking

The Surflex-docking module in SYBYL-X 2.0 (Boström, 2001) was performed to evaluate the binding ability between the screened core constituents and targets. First of all, the 2D structure of the compound was obtained from the PubChem database (https://www.ncbi.nlm.nih.gov/pubmed/) in SDF format and then converted into the 3D structure in mol2 format by SYBYL-X 2.0 software for the preparation of micromolecule ligand compounds. Next, the protein crystal structure of core targets was obtained from the RCSB Protein Data Bank database (http://www.rcsb.org) after searching PDB ID in the uniport database (http://www.uniprot.org/). Finally, a series of treatments include removing water molecules and original ligands, adding hydrogen, repairing amino acids and forming binding pockets were performed to complete the preparation of macromolecular receptor target proteins. "Total Score" given by software was used as the indicator for docking results. The higher the score, the stronger the binding effect.

Experiments Evaluation

Animals and Drug Treatments

Twenty four male Sprague-Dawley (SD) rats (240 ± 10 g body weight about 6–8 weeks-old) purchased from the Laboratory Animal Center of Dalian Medical University (License number: SCXK (Liao) 2018-0003) were maintained in a breeding room under controlled temperature (22 ± 2°C), humidity (55 ± 5%) and lighting (12 h light-dark cycles) conditions. To be acclimatized, rats were allowed food and water *ad libitum* for one week before the experiments. All experimental protocol was approved by the Ethics Review Committee for Animal Experimentation of Dalian Medical University.

SD rats were randomly divided into four groups including the control (CON) group, acute pancreatitis (AP) group, Qing-Yi Decoction-treated (QYD) group and dexamethasone-treated (DEX) group (n = 6 in each group). AP model was induced by retrograded injection of 3.5% sodium taurocholate (STC) into the pancreatic duct according to the previous report (Huang et al., 2017). For the CON group, only the traction of the duodenum was conducted, and injection of the drug wasn't given. QYD extract was orally administrated to rats at a dosage of 10 g crude drug/kg/day when awakening after modeling. DEX that dissolved with normal saline by ultrasound was used as a positive drug at a dose of 10 mg/kg by intravenous tail injection. QYD and DEX were given repeated 12 h later. Rats in the control and model group were given physiological saline, which had the same volume as QYD and DEX.

After modeling for 24 h, rat serum was collected by centrifugation at 3,000 rpm for 10 min at 4°C. Meanwhile, part of pancreatic tissues was collected and fixed in 4% paraformaldehyde solution for histopathological staining. The remaining ones were immediately frozen and stored at −80°C for western blot analysis.

Histopathological Examination and Biochemical Analysis

Pancreatic was observed under an optical microscope (Olympus, Japan) with a magnification of 200 times after embedded in paraffin and stained with hematoxylin and eosin. Finally, the previous scoring system was used to evaluate the damage degree of pancreatic tissue with edema, inflammation and vacuolation as indexes (Rongione et al., 1997). Also, the serum of rats was diluted 100 times, and then the amylase level was determined according to the instructions of the kit (Jiancheng, Nanjing, China).

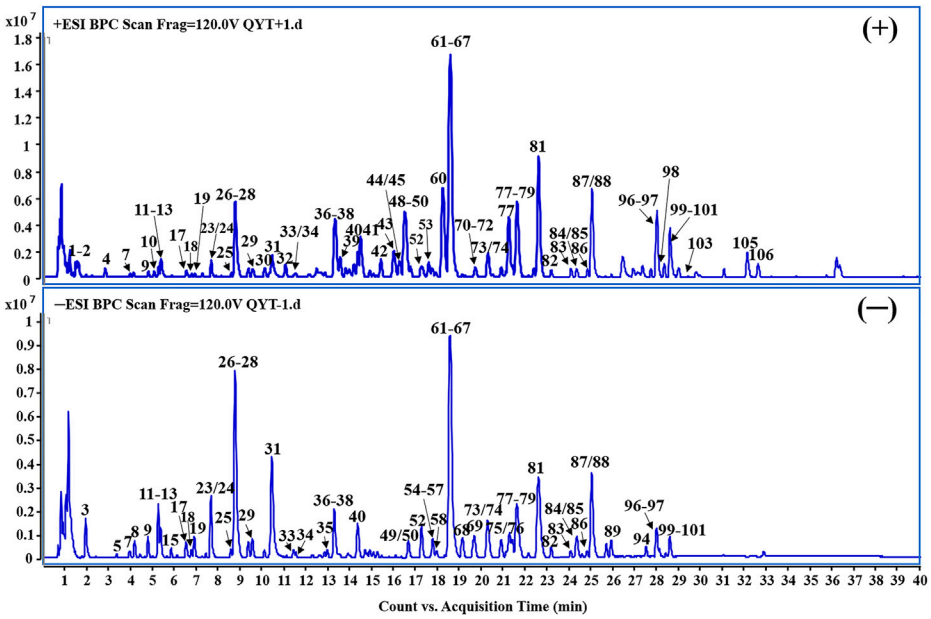

FIGURE 2 | Representative base peak chromatogram (BPC) of QYD in the positive and negative ions mode, respectively.

Western Blot Analysis

Total protein was extracted from pancreas tissues with cold lysis buffer and PMSF protease inhibitor. Next, the protein concentration was determined using the BCA protein assay kit. The protein samples were fractionated by SDS-PAGE (8–10%) and then transferred to PVDF membranes. The membranes were blocked with 5% non-fat milk for 1.5 h and incubated overnight at 4°C with the following primary antibodies: p65, p-p65, ERK1/2, p-ERK1/2, c-Fos, β-actin (1:1,000 dilution). The membranes were incubated 1 h at room temperature with secondary antibodies and protein expression was probed with an ECL method and placed in a Tanon-5200 Imaging System (Tanon, Shanghai, China).

Statistical Analysis

Statistical analysis was carried out with SPSS 20.0 software. All the data in the experiment are expressed as mean ± standard deviation. F-test was used to analyze the variance homogeneity of the data. Then one-way ANOVA's "LSD test" or "Games-Howell test" was used to compare the differences between the two groups according to the results. Values of $p < 0.05$ were considered statistically significant.

RESULTS

Chemical Profile of Qing-Yi Decoction by Ultra-Performance Liquid Chromatography Coupled With Quadrupole Time-of-Flight Mass Spectrometry

Under the optimized conditions, a total of 110 constituents including 28 flavonoids, 16 phenolic acids, 15 alkaloids, 15 monoterpenes, 11 iridoids, eight triterpenes, five phenylethanoid glycosides, five anthraquinones and seven miscellaneous compounds that originate from seven herbs were identified or tentatively characterized according to the in-house constituents database established for QYD (**Figure 2**, **Supplementary Table S1**). While the typical constituents of *Natrii* Sulfas ($Na_2SO_4{\cdot}10H_2O$) were not detected.

Among them, 22 compounds (compounds **3**, **18**, **19**, **22**, **28**, **29**, **31**, **35**, **36**, **47**, **48**, **62**, **72**, **85**, **88**, **93**, **94**, **96**, **97**, **104**, **107** and **108**) were identified as gallic acid, catechin, chlorogenic acid, syringing (+)-epicatechin, albiflorin, paeoniflorin, rutin, scutellarin, tetrahydropalmatine, jatrorrhizine, baicalin, palmatine, benzoylpaeoniflorin, baicalein, aloe-emodin, rhein, saikosaponin a, wogonin, emodin, chrysophanol and physcion by comparing the retention time, quasi-molecular ions with authentic standards, respectively. While the others were tentatively deduced based on their high-accurate quasi-molecular ion such as $[M - H]^-$ $[M + HCOO]^-$ $[M + Cl]^-$ $[M]^+$ $[M + H]^+$ and $[M + Na]^+$ with those of the known published compounds recorded in the in-house library. Information regarding the 110 constituents, such as t_R (min), identification, formula, negative ion (m/z), positive ion (m/z) and botanical source, is offered in **Supplementary Table S1**.

Network Pharmacology Analysis

Qing-Yi Decoction Component Targets Network and Acute Pancreatitis Related Therapeutic Targets

Based on the chemical profile of QYD characterized by UHPLC/QTOF-MS, 541 targets associated with the 110 constituents were predicted as potential targets of QYD (**Supplementary Table S2**, **Supplementary Figure S1**). In order to focus on more important information, a total of 47 active constituents were screened out

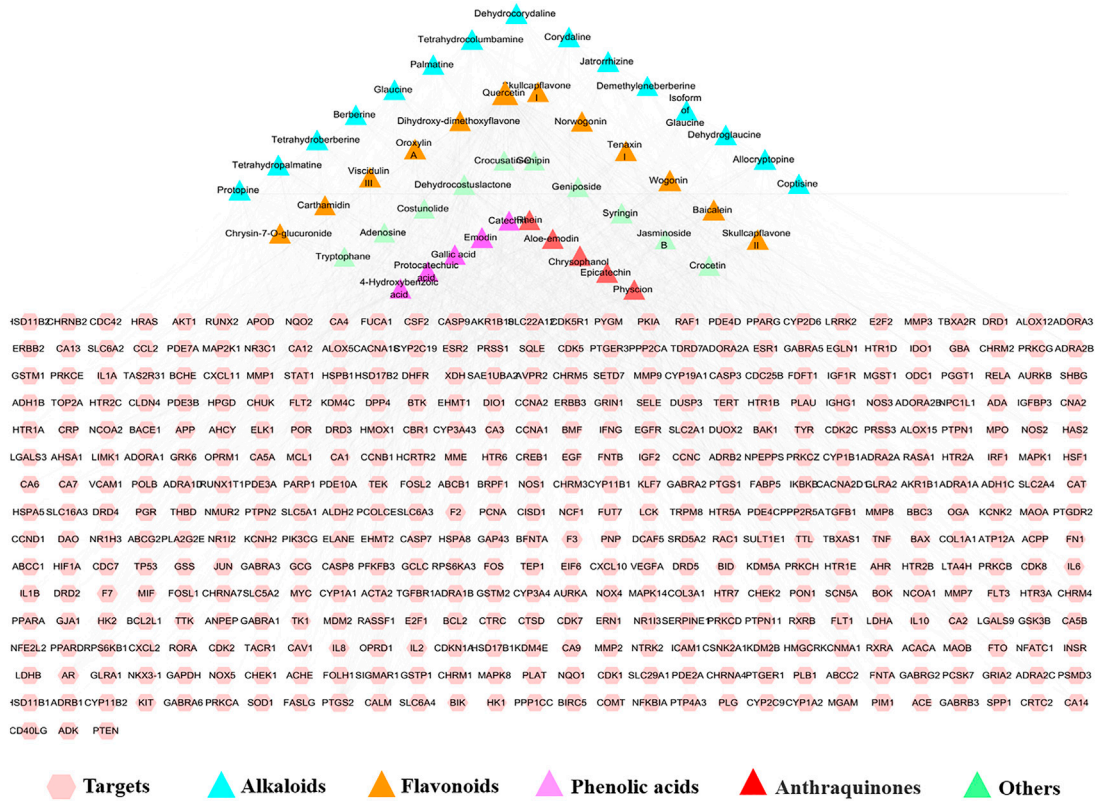

FIGURE 3 | Compound-target network of QYD (Pink circle represents target; Triangle represents compound in QYD. It's a positive proportional relationship that between the node size and the degree).

according to the Lipinski's rule of five. Correspondingly, the potential targets of the constituents were reduced to 423. The active constituents-potential targets network of QYD for AP was constructed and shown in **Figure 3**. Similarly, 6593AP-related targets obtained from OMIM, GeneCards, DisGeNET and GAD databases were collected after searching, integrating and de-duplicating steps. (**Supplementary Table S3**).

Acquisition of Candidate Targets and Core Constituents for Qing-Yi Decoction Against Acute Pancreatitis

For the acquisition of the core targets for QYD against AP, the constituents-targets and disease-targets databases were intersected by Cytoscape 3.2.1 software, and 350 intersection targets were obtained. The PPI network of intersection targets was analyzed by the STRING database (https://string-db.org/) and the targets with confidence score >0.95 were screened for network construction. As a result, 236 nodes and 666 edges were involved in this network. More crucial targets were obtained based on the degree value of network topology analysis. Among them, 69 targets with degree values greater than twice the median were considered as candidate targets (**Supplementary Figure S2**). Forty constituents that had direct effects on 69 candidate targets were screened out for further identified as the key active constituents of QYD in treating AP. Among them, 11 constituents including quercetin (**33**), wogonin (**97**), baicalein (**88**), emodin (**104**), epicatechin (**28**), aloe-Emodin (**93**), berberine (**71**), palmatine (**72**), oroxylin A (**101**), physcion (**108**) and skullcapflavon II (**100**) were considered to be the key active constituents because their degree value was more than twice the median value.

Analysis of Related Pathways of Potential Targets

DAVID website was used to carry out KEGG pathway enrichment analysis on potential targets and 63 pathways were obtained. Of which 59 were statistically significant ($p < 0.05$). Associations among active constituents, potential targets and the top 15 pathways (excepted cancer pathways) were shown in **Figure 4**. It could be seen that 11 key active ingredients could regulate relevant pathways by acting on 47 targets, and the MAPK signaling pathway, T cell receptor signaling pathway, Focal adhesion, Toll-like receptor signaling pathway and Apoptosis were involved. The details of their interactions were listed in **Supplementary Table S4**.

Molecular Docking Analysis

RCSB Protein Data Bank database was used to investigate the relationship between active constituents and potential targets by collecting the crystal structure of the target (**Supplementary Table S5**), and SYBYL-X 2.0 platform was applied to analyze

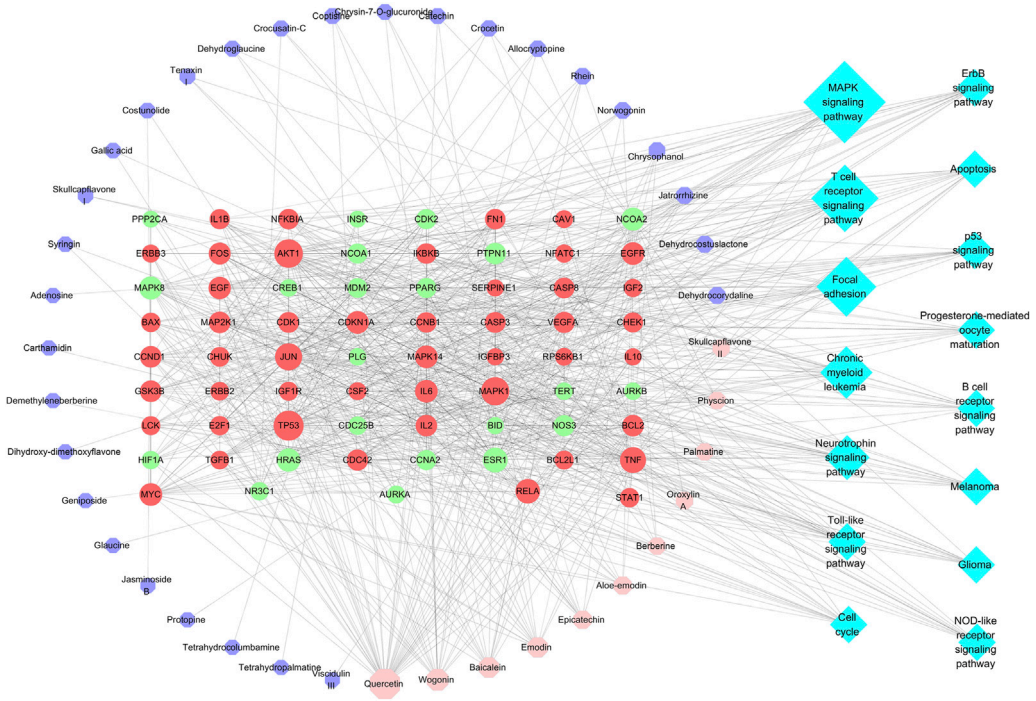

FIGURE 4 | Compound-target-pathway network (Pink octagon represents the key compound; purple octagon represents common compound; red circles represents key target; green circles represents common target; blue diamond represents pathway. It's a positive proportional relationship that between the node size and the degree).

the docking relationship. As shown in **Figure 5A**, the binding ability of components with targets were divided into three levels, which contain strong interaction (>6.0), medium interaction (5.0–6.0), weak interaction (4.0–5.0) and no interaction (<4.0). In this study, 5.0 was set as the screening value to obtain more critical targets. As a result, skullcapflavon II (a characteristic ingredient derived from *Scutellaria baicalensis* Georgi), palmatine (from *Corydalis yanhusuo* (Y. H. Chou and Chun C. Hsu) W. T. Wang ex Z. Y. Su and C. Y. Wu), and physcion (from *Rheum officinale* Baill.), showed better binding ability in flavonoids, alkaloids and anthraquinone compounds, respectively. As for the targets, MAPK1 (ERK, PDB ID: 6slg), FOS (c-Fos, PDB ID: 1a02), and RELA (p65, PDB ID: 4kv1) possess higher binding activity (**Figure 5B**). The representative three-dimensional patterns of docking combinations (MAPK1-physcion, FOS-skullcapflavon II, and RELA-palmatine) were shown in **Figure 5C**.

It was seen that there are four hydrogen bonds between MAPK1 and physcion (**108**), and three of which are the interaction between hydroxyl and MET108, ASP106 and GLN105, the other one is the interaction between MET108 and carbonyl. Three interactions consist in the combination of MAPK1 and the positive drug LM22B-10, namely MET108, ASP106 and LY654. In addition, in the binding pocket of FOS and skullcapflavon II (**100**), five hydrogen bonds formed by two amino acid residues (ARG286 and ILE535) and phenolic hydroxyl groups were found. Similarly, five hydrogen bonds were also found between FOS and the positive drug LM22B-10, which were formed by phenolic hydroxyl groups bond with ASP174, ASP464 and ILE535. For RELA, three hydrogen bonds were found connection with palmatine (**72**) with GLN127, LYS72 and THR134. In the docking combination of RELA and positive Licochalcone D, four hydrogen bonds formed by RELA and ASN116, ASN117, GLN127 and GLN64 were shown.

Experimental Evaluation

Histopathological Examination and Biochemical Analysis

In pancreatic tissue of AP rats, the acinar cell injury, vacuolation, hemorrhage and inflammatory cell infiltration occurred was observed. When compared with the AP group, different degrees of improvement in QYD and DEX treatment groups were seen, and the QYD group possess a better effect. As shown in **Figure 6A**, edema and hemorrhage were not observed between the cells; the structure of the pancreatic lobules was clear and without infiltrated by inflammatory cells in the CON group. For the AP group, obvious edema among histiocytes was observed, a large number of red blood cells was overflowed, and the pancreatic tissue was infiltrated by numerous neutrophils and lymphocytes. The structure of pancreatic lobules was fuzzy and uniform, and a large quantity of necrotic pancreatic cells was found. In the QYD group, there was mild edema among tissue cells, the pancreas was infiltrated by a small number of inflammatory cells, and some areas were calcified. As for the DEX group, there was edema between cells, the pancreas was infiltrated by a few inflammatory cells, and the infiltration was

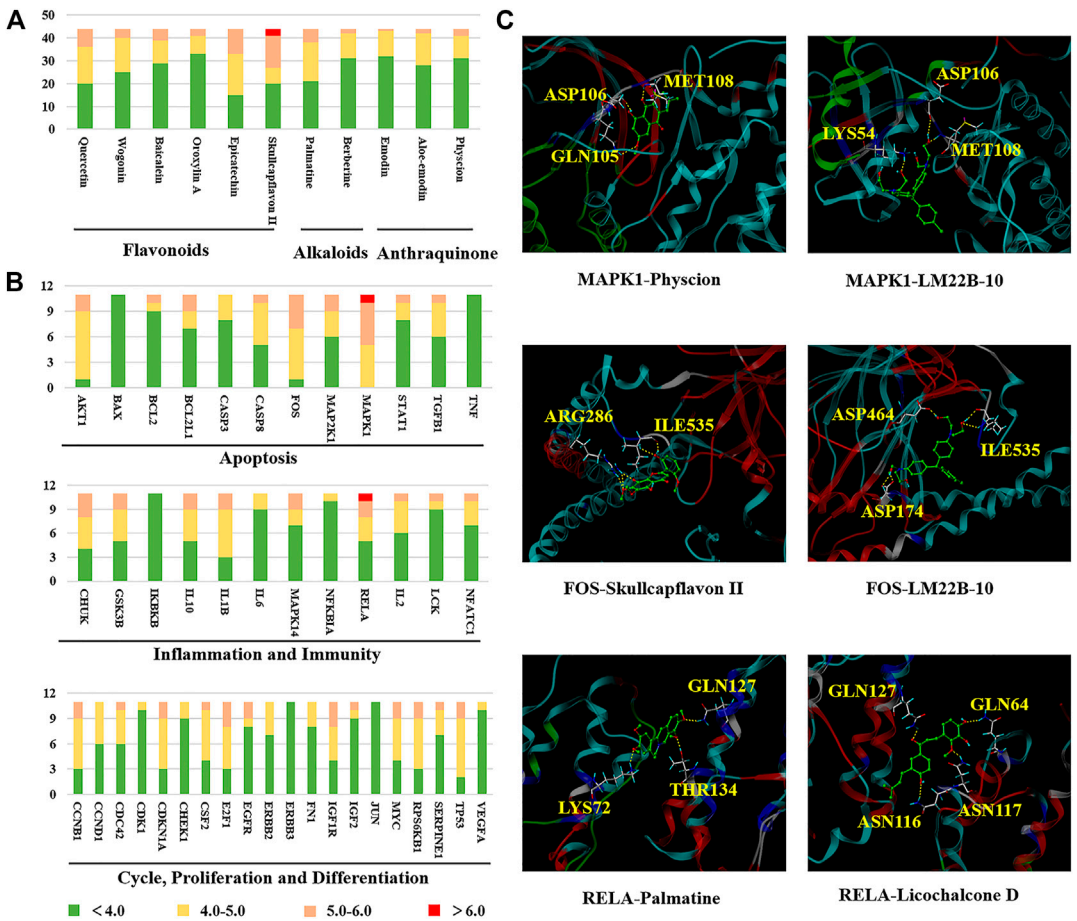

FIGURE 5 | The binding modes of key compounds with related proteins were analyzed by SYBYL-X 2.0 software. **(A)** Component docking score; **(B)** Target docking score; **(C)** Representative docking combinations.

distributed in the lesion. Calcification was seen in some areas, and a small number of red blood cells are spilled around the blood vessels. Also, its histopathological score is shown in **Figure 6B**.

Besides, an abnormal increase of serum amylase level is an essential basis for the diagnosis of AP. In this experiment, the serum amylase level of rats was detected by the starch-iodine colorimetric method. The results showed (**Figure 6C**) that amylase levels in the AP group were significantly higher than those in the CON group ($p < 0.01$). In addition, compared with the AP group, QYD treatment could significantly inhibit the activity of amylase ($p < 0.01$).

Western Blot Analysis

The western blotting analysis was used to evaluate related protein levels in the pancreas. As shown in **Figure 7**, p-p65 expression was markedly up-regulated, and p-ERK1/2 and c-Fos expression were notably down-regulated in AP rats following STC infusion ($p < 0.01$). As expected, QYD and DEX treatment significantly increased p-ERK1/2 and c-Fos levels and decreased p-p65 levels compared to the AP group ($p < 0.01$), and QYD treatment group possesses a better effect. The results suggest that the therapeutic effect of QYD on AP may be related to inhibiting the expression of p-p65 and promoting the expression of p-ERK1/2 and c-Fos.

DISCUSSION

As a common critical disease of the digestive system, AP should attract our attention. Although the pathogenesis and clinical treatment of AP has been widely developed in recent basic and clinical research, satisfactory results are still not obtained. Therefore, it has become a significant challenge in clinical and scientific research to explore the mechanism of AP occurrence and development and provide new treatment suggestions for AP patients.

According to TCM theory, the pathogenesis of AP belongs to the category of Yang ming fu-viscera excess syndrome, which should be treated following the principles of soothing liver, regulating qi, clearing heat, detoxifying and removing stasis by purgation. QYD is developed based on the classic prescription Da-Cheng-Qi decoction of "Shang Han Lun", which is composed of eight herbs and obtained a significant effect in the clinical treatment of AP. However, its material basis and the overall mechanism of action

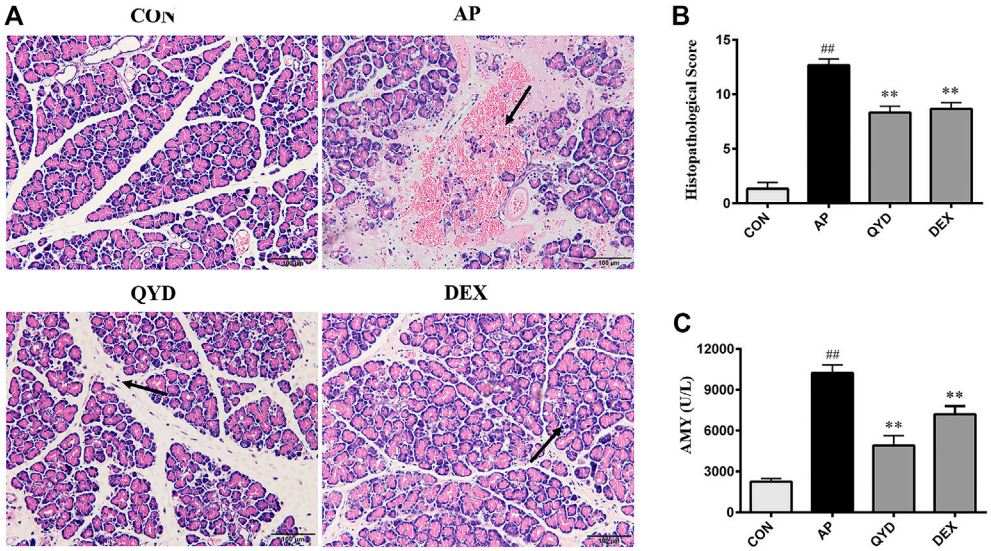

FIGURE 6 | Histopathological examination and biochemical analysis. **(A)** Histopathological observation of pancreatic tissue in four groups (HE, ×200); **(B)** Histological score of pancreatic tissue in four groups (HE, ×200). **(C)** Serum amylase level in rats. Data are presented as the mean ± SD ($n = 3$), $^{**}p < 0.01$ *vs.* AP group. $^{\#\#}p < 0.01$ *vs.* CON group.

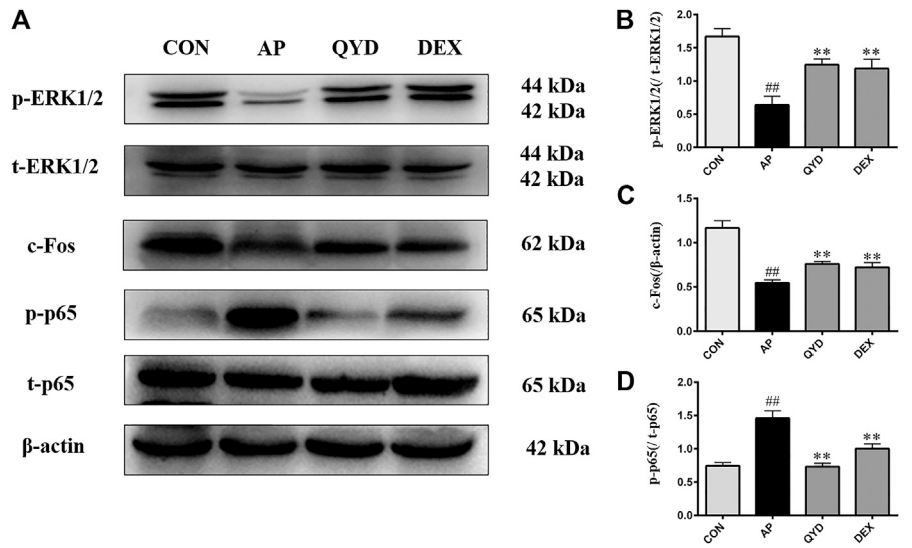

FIGURE 7 | QYD extracts protect pancreas tissue of SD rats by regulated inflammation and cell apoptosis. **(A)** Effects of QYD extracts on p-p65, t-p65, p-ERK1/2, t-ERK1/2, c-Fos protein levels in STC-induced acute pancreatitis model based on the western blotting assay; **(B–D)** Statistical analysis of the effects of QYD extracts on protein expressions levels. Data are presented as the mean ± SD ($n = 3$), $^{**}p < 0.01$ *vs.* AP group. $^{\#\#}p < 0.01$ *vs.* CON group.

remain a mystery. In this study, a combined strategy of phytochemistry, network pharmacology, molecular docking and basic experiment was used to assess the active constituents and potential molecular mechanisms of QYD on AP step by step. Firstly, the chemical composition of QYD was characterized by UHPLC-QTOF-MS for the first time. A total of 110 constituents were identified, of which 47 conform to the Lipinski's rule of five and mainly belong to alkaloids, flavonoids, and anthraquinones. Next, 11 key components were further filtered through network pharmacology, which contained six flavonoids that mainly from *Scutellaria baicalensis* Georgi [quercetin (**33**), wogonin (**97**), baicalein (**88**), epicatechin (**28**), oroxylin A (**101**), skullcapflavon II (**100**)], three anthraquinones that mainly from *Rheum officinale* Baill. [emodin (**104**), aloe-emodin (**93**), physcion (**108**)], and two alkaloids that mainly from *Corydalis yanhusuo* (Y. H. Chou and Chun C. Hsu) W. T. Wang ex Z. Y. Su and C. Y. Wu [berberine (**71**),

palmatine (**72**)]. Interestingly, the effects of *Scutellaria baicalensis* Georgi, *Rheum officinale* Baill. and *Corydalis yanhusuo* (Y. H. Chou and Chun C. Hsu) W. T. Wang ex Z. Y. Su and C. Y. Wu in TCM are similar to the primary efficacy of QYD, which suggests that these three drugs play a significant role in QYD treatment of AP. This makes the prediction results of network pharmacology more convincing. Also, the main components of these three herbs have been preliminarily explored in the treatment of AP. Two previous studies found that baicalein (**88**) and quercetin (**33**) from *Scutellaria baicalensis* Georgi could alleviate the symptoms of AP by promoting cell apoptosis and inhibiting inflammation (Zheng et al., 2018; Pu et al., 2019). In addition, emodin (**104**) from *Rheum officinale* Baill. played an antioxidant and anti-inflammatory role in AP (Xia et al., 2019). Moreover, berberine (**71**) from *Corydalis yanhusuo* (Y. H. Chou and Chun C. Hsu) W. T. Wang ex Z. Y.Su and C. Y. Wu had analgesic effects, which involved relieving the pancreatic pain of QYD on AP (Choi et al., 2016). The above discussion fully affirmed the therapeutic potential of QYD in AP.

Apoptosis, inflammatory response, immune regulation, cell proliferation and differentiation are essential characteristics of AP development (Xiang et al., 2017). In this study, KEGG pathway enrichment analysis showed that 11 key components in the QYD regulate the information transmission of 15 signaling pathways by targeting 47 targets. Combined the results of KEGG and molecular docking, we found that the top targets in docking scores were near related to apoptosis and inflammation.

As is known to all, the AP's development process is related to apoptosis and necrosis of pancreatic acinar cells, the MAPK signaling pathway and Apoptosis signaling pathway were enriched by apoptosis-related proteins such as AKT1, CASP3, FOS, etc. Our molecular docking results showed that a high overall score existed in MAPK1 (ERK1/2) and FOS (c-Fos) when docking with 11 key components, which suggested that they may play an essential role in QYD against AP. Previous studies have confirmed that ERK1/2 is a crucial target for MAPK signaling pathways. It is an important carrier that transfers transmitting signals from cell surface receptors to the nucleus, which could be activated by upstream signaling molecules and regulate corresponding biological functions like cell proliferation and apoptosis (Ma et al., 2013; Tanaka and Iino, 2015; Li et al., 2018b). Some other researchers have found that the process of apoptosis could be regulated by promoting phosphorylation of ERK1/2 (Damiano et al., 2018; Kim et al., 2019). Similarly, apoptosis could be promoted after c-Fos being activated, which is a downstream target of ERK1/2 (Pandey and Wang, 1995; Wagner, 2010; Ren et al., 2013). It has also been reported that accelerating apoptosis is beneficial to the disease remission in the early stage of AP because it delays the process of cell necrosis to some extent (Cai et al., 2018b) Consistent with this, our molecular biology experiments showed that there was a significantly decreased in the expression of ERK1/2 and c-Fos when AP occurred, while QYD restored their expression to some extent. Other critical proteins related to apoptosis, such as BCL-2 and caspase family, were also predicted (Morishima et al., 2002). It suggested that QYD treatment of AP may be partially achieved by promoting the process of apoptosis.

The NF-KB signaling pathway is one of the typical inflammatory response pathways and the inflammatory response is a typical feature of AP. Although this pathway did not show in the results of KEGG pathway enrichment analysis, it exists in the multiple signal pathways that have been enriched and play a vital role in them, such as MAPK signal pathway, T cell receptor signal pathway, Toll-like receptor signal pathway, and NOD-like receptor signaling pathway. RELA (p65) is an essential molecule in NF-KB signaling pathways who is responsible for the expression of proinflammatory mediators (Jakkampudi et al., 2016). When docking with critical components, it exhibited high binding activity. In some studies, inflammatory cascade reaction shows the importance to aggravate AP. The binding of p65 and IKB is inhibited under normal conditions. However, when something stimulates the cell, IKB will be degraded by IKK, p65 will be released and enter the nucleus quickly to binding with the DNA so that the transcription is initiated and a large number of inflammatory cells factors such as TNF-α, IL-6 and IL-1B are released. Then, the p65 is further activated, and the inflammatory response is gradually amplified (Hayden and Ghosh, 2008; Rotstein, 2014). Hence, we can see that inhibition of p65 expression could attenuate the severity of the inflammatory response and alleviate the symptoms of AP, which was also supported by the results of our experiment. In addition, other targets such as CHUK and GSK3B were also involved in inflammation and the AP process.

In recent years, more and more researches have focused on the human immune system. A study found that the disturbance of the immune regulation mechanism is one reason that aggravates the severity of AP and even leads to death (Kylänpää et al., 2010). AP could be improved by timely adjustment of the immunosuppressive state because it will urge a dynamic balance between the proinflammatory and anti-inflammatory responses (Munir et al., 2020). Other studies had shown that IL2, NFATC1 and LCK played a vital role in the T cell receptor signaling pathway. Among them, IL2 is necessary for T cell proliferation and other immune regulation, and it could stimulate B cells, monocytes and natural killer cells. And NFATC1 is very important for the induction of IL2 gene transcription. The differentiation and apoptosis of T cells was regulated by it (Chuvpilo et al., 1999). Besides, Lck is an src-related protein tyrosine kinase, which regulates T cells' survival status by binding to CD4 molecules and the inflammatory response of AP (Bai et al., 2014; Bozso et al., 2020).

It is worth noting that among the targets predicted in this study, some proteins were related to the cell cycle, cell proliferation and cell differentiation. Among the multiple proteins, the CCNB1, CDC42, CDKN1A, E2F1, EGFR, MYC, and TP53 had a higher docking score. Previous studies believed that inflammation was closely related to immunity and the unfavorable supervision of the immune system is an advantage for tumorigenesis (Padoan et al., 2019). Meanwhile, repeated episodes of AP can lead to chronic pancreatitis, and scholars such as Kleeff J believed that chronic pancreatitis is an important risk factor for pancreatic ductal adenocarcinoma. Moreover, obvious binding effects between key components and tumor-related proteins suggested that QYD may have unexpected effects in preventing the transformation of pancreatitis from inflammation to cancer (Kleeff et al., 1965; Tarasiuk and Fichna 2019).

There are still two shortcomings in this study. On one hand, in terms of the research dimension, there is a lack of the validation from clinical and cellular molecular aspects. On the other hand, in

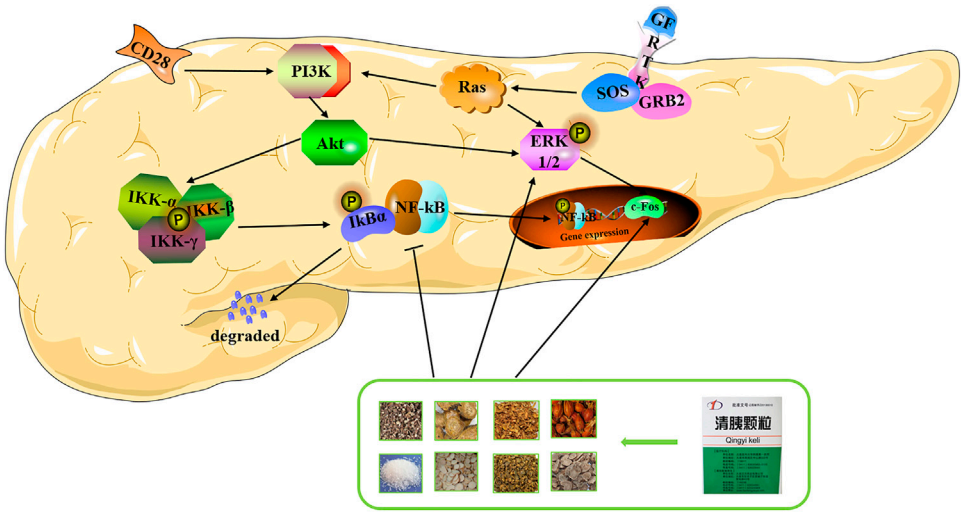

FIGURE 8 | Overview of potential mechanisms underlying the protective effects of QYD on STC-induced acute pancreatitis.

terms of the research technology, network pharmacology ignores the dose-effect relationship of multi-components in formula when they exert the therapeutic effects. These deficiencies will be improved in subsequent studies.

In conclusion, our molecular biology experiments showed that QYD could reduce the expression of p-p65 and promote the expression of p-ERK1/2 and c-Fos significantly, which is consistent with the results of the prediction of network pharmacology and molecular docking. Based on this, we propose a plausible molecular mechanism for the multi-target effects of QYD on AP, namely, QYD may protect the pancreas from injury by promoting apoptosis and inhibiting inflammation (**Figure 8**).

CONCLUSION

Chinese medicine plays a crucial role in preventing and treating AP. In this study, 110 chemical components of QYD were identified by UHPLC-QTOF-MS for the first time, and then 11 important components and 47 key targets were screened based on network pharmacological analysis. Molecular docking showed that QYD may influence the process of apoptosis and inflammation by regulating the expression of ERK1/2, c-Fos and p65, thus protecting pancreatic injury caused by AP. This result has been confirmed in molecular biology experiments. To sum up, our research not only provides a comprehensive understanding of the active components and molecular mechanism of QYD, but also provides experimental basis and new idea for further development and clinical application of QYD.

DATA AVAILABILITY STATEMENT

The raw data supporting the conclusions of this article will be made available by the authors, without undue reservation, to any qualified researcher.

ETHICS STATEMENT

The animal study was reviewed and approved by the Animal Care and Welfare Committee of Dalian Medical University. Written informed consent was obtained from the owners for the participation of their animals in this study.

AUTHOR CONTRIBUTIONS

T-FW and LZ are the co-first author and performed all the experiments like identification of traditional Chinese medicine components, network pharmacological analysis, molecular docking analysis and animal experiments, etc. PH, F-LH, J-YJ, K-LX and Z-ZW helped the first author in different steps of experiments. J-LQ and DS designed the experiments, analyzed and supervised the results and corrected the manuscript. All the authors read and approved the final version of the manuscript.

FUNDING

This work was financially supported by grants from National Natural Science Foundation of China (Nos. 81703675, 81873156), National Key Research and Development Program of China (No. 2018YFE0195200) and Dalian Municipal Medical Research Foundation (No. 17Z2001).

SUPPLEMENTARY MATERIAL

The Supplementary Material for this article can be found online at: https://www.frontiersin.org/articles/10.3389/fphar.2021.590994/full#supplementary-material.

REFERENCES

Bai, X. W., Song, Z. F., Zhou, Y. M., Pan, S. H., Wang, F., Guo, Z. M., et al. (2014). The apoptosis of peripheral blood lymphocytes promoted by hyperbaric oxygen treatment contributes to attenuate the severity of early stage acute pancreatitis in rats. *Apoptosis* 19 (1), 58–75. doi:10.1007/s10495-013-0911-x

Boström, J. (2001). Reproducing the conformations of protein-bound ligands: a critical evaluation of several popular conformational searching tools. *J. Comput. Aided Mol. Des.* 15 (12), 1137–1152. doi:10.1023/a:1015930826903

Bozso, S. J., Kang, J. J. H., and Nagendran, J. (2020). The role of competing mechanisms on lck regulation. *Immunol. Res.* 68 (5), 289–295. doi:10.1007/s12026-020-09148-2

Brunschot, V. S., Grinsven, V. J., Santvoort, H. C. V., Bakker, O. J., Besselink, M. G., and Boermeester, M. A. (2018). Endoscopic or surgical step-up approach for infected necrotising pancreatitis: a multicentre randomised trial. *Lancet* 391 (10115), 51–58. doi:10.1016/s0140-6736(17)32404-2

Cai, F. F., Zhou, W. J., Wu, R., and Su, S. B. (2018a). Systems biology approaches in the study of Chinese herbal formulae. *Chin. Med.* 13 (1), 65. doi:10.1186/s13020-018-0221-x

Cai, S. W., Han, Y., and Wang, G. P. (2018b). Mir-148a-3p exhaustion inhibits necrosis by regulating pten in acute pancreatitis. *Int. J. Clin. Exp. Pathol.* 11 (12), 5647–5657.

Chen, L. W., Du, J., Dai, Q. W., Zhang, H. C., Pang, W. S., and Hu, J. (2014). Prediction of anti-tumor chemical probes of a traditional Chinese medicine formula by HPLC fingerprinting combined with molecular docking. *Eur. J. Med. Chem.* 83, 294–306. doi:10.1016/j.ejmech.2014.06.037

Chen, W. W., Yang, X. N., Huang, L., Xue, P., Wan, M. H., Guo, J., et al. (2015). Qing-Yi decoction in participants with severe acute pancreatitis: a randomized controlled trial. *Chin. Med.* 10 (1), 11. doi:10.1186/s13020-015-0039-8

Choi, S. B., Bae, G. S., Jo, I. J., Wang, S. F., Song, H. J., and Park, S. J. (2016). Berberine inhibits inflammatory mediators and attenuates acute pancreatitis through deactivation of JNK signaling pathways. *Mol. Immunol.* 74, 27–38. doi:10.1016/j.molimm.2016.04.011

Chuvpilo, S., Avots, A., Berberich-Siebelt, F., Glöckner, J., Fischer, C., Kerstan, A., et al. (1999). Multiple NF-ATc isoforms with individual transcriptional properties are synthesized in T lymphocytes. *J. Immunol.* 162 (12), 7294–7301. doi:10.1016/S0010-7824(02)00314-

Damiano, S., Sasso, A., Felice, B. D., Gregorio, L. D., Rose, G. L., Lupoli, G. A., et al. (2018). Quercetin increases MUC2 and MUC5AC gene expression and secretion in intestinal goblet cell-like LS174T via PLC/PKCα/ERK1-2 pathway. *J. Immunol.* 9, 357. doi:10.3389/fphys.2018.00357

Demchak, B., Hull, T., Reich, M., Liefeld, T., Smoot, M., Ideker, T., et al. (2014). Cytoscape: the network visualization tool for GenomeSpace workflows. *F1000Res* 3, 151. doi:10.12688/f1000research.4492.2

Forsmark, C. E., Vege, S. S., and Wilcox, C. M. (2016). Acute pancreatitis. *N. Engl. J. Med.* 375, 1972–1981. doi:10.1056/NEJMra1505202

Hayden, M. S., and Ghosh, S. (2008). Shared principles in NF-κB signaling. *Cell* 132, 344–362. doi:10.1016/j.cell.2008.01.020

Hopkins, A. L. (2007). Network pharmacology. *Nat. Biotechnol.* 25 (10), 1110–1111. doi:10.1038/nbt1007-1110

Huang, C. L., Chen, J., Wang, J. J., Zhou, H., Lu, Y. Y., Lou, L. H., et al. (2017). Dysbiosis of intestinal microbiota and decreased antimicrobial peptide level in paneth cells during hypertriglyceridemia-related acute necrotizing pancreatitis in rats. *Front. Microbiol.* 8, 776. doi:10.3389/fmicb.2017.00776

Huang, D. W., Sherman, B. T., and Lempicki, R. A. (2009). Systematic and integrative analysis of large gene lists using DAVID bioinformatics resources. *Nat. Protoc.* 4 (1), 44–57. doi:10.1038/nprot.2008.211

Jakkampudi, A., Jangala, R., Reddy, B. R., Mitnala, S., Reddy, D. N., and Talukdar, R. (2016). NF-κB in acute pancreatitis: mechanisms and therapeutic potential. *Pancreatology* 16, 477–488. doi:10.1016/j.pan.2016.05.001

Kim, S. H., Yoo, E. S., Woo, J. S., Han, S. H., Lee, J. H., Jung, S. H., et al. (2019). Antitumor and apoptotic effects of quercetin on human melanoma cells involving JNK/P38 MAPK signaling activation. *Eur. J. Pharmacol.* 860, 172568. doi:10.1016/j.ejphar.2019.172568

Kleeff, J., Whitcomb, D. C., and Shimosegawa, T. (1965). Chronic pancreatitis. *Lancet* 19 (11), 318. doi:10.1159/000078369

Kylänpää, M. L., Repo, H., and Puolakkainen, P. A. (2010). Inflammation and immunosuppression in severe acute pancreatitis. *World J. Gastroenterol.* 16 (23), 2867. doi:10.3748/wjg.v16.i23.2867

Lankisch, P. G., Apte, M., and Banks, P. A. (2015). Acute pancreatitis. *The Lancet* 386, 85–96. doi:10.1016/s0140-6736(14)60649-8

Li, S., and Zhang, B. (2013). Traditional Chinese medicine network pharmacology: theory, methodology and application. *Chin. J. Nat. Medicines* 11 (2), 110–120. doi:10.1016/s1875-5364(13)60037-0

Li, S., Zhang, B., and Zhang, N. B. (2011). Network target for screening synergistic drug combinations with application to traditional Chinese medicine. *BMC Syst. Biol.* 5 (Suppl. 1), S10. doi:10.1186/1752-0509-5-s1-s10

Li, X. X., Yin, J., Tang, J., Li, Y., Yang, Q., Xiao, Z., et al. (2018a). Determining the balance between drug efficacy and safety by the network and biological system profile of its therapeutic target. *Front. Pharmacol.* 9, 1245. doi:10.3389/fphar.2018.01245

Li, Y. B., Li, Y. M., Lu, W. L., Li, H. B., Wang, Y. M., Luo, H. M., et al. (2018b). Integrated network pharmacology and metabolomics analysis of the therapeutic effects of zi dian fang on immune thrombocytopenic purpura. *Front. Pharmacol.* 9, 597. doi:10.3389/fphar.2018.00597

Liang, J. W., Wang, M. Y., Olounfeh, K. M., Zhao, N., Wang, S., and Meng, F. H. (2019). Network pharmacology-based identifcation of potential targets of the flower of Trollius chinensis Bunge acting on anti-inflammatory effectss. *Sci. Rep.* 9 (1), 8109. doi:10.1038/s41598-019-44538-z

Lionta, E., Spyrou, G., Vassilatis, D. K., and Cournia, Z. (2014). Structure-based virtual screening for drug discovery: principles, applications and recent advances. *Ctmc* 14 (16), 1923–1938. doi:10.2174/1568026614666140929124445

Lipinski, C. A., Lombardo, F., Dominy, B. W., and Feeney, P. J. (2001). Experimental and computational approaches to estimate solubility and permeability in drug discovery and development settings. *Adv. Drug Deliv. Rev.* 46, 3–26. doi:10.1016/s0169-409x(00)00129-0

Lu, C. L., Zheng, Q., Shen, Q., Song, C., and Zhang, Z. M. (2017). Uncovering the relationship and mechanisms of Tartary buckwheat (Fagopyrum tataricum) and Type II diabetes, hypertension, and hyperlipidemia using a network pharmacology approach. *PeerJ* 5 (1), e4042. doi:10.7717/peerj.4042

Ma, B., Wu, L., Lu, M., Gao, B., Qiao, X., Sun, B., et al. (2013). Differentially expressed kinase genes associated with trypsinogen activation in rat pancreatic acinar cells treated with taurolithocholic acid 3-sulfate. *Mol. Med. Rep.* 7 (5), 1591–1596. doi:10.3892/mmr.2013.1355

Morishima, N., Nakanishi, K., Takenouchi, H., Shibata, T., and Yasuhiko, Y. (2002). An endoplasmic reticulum stress-specific caspase cascade in apoptosis. Cytochrome c-independent activation of caspase-9 by caspase-12. *J. Biol. Chem.* 277, 34287–34294. doi:10.1074/jbc.M204973200

Munir, F., Jamshed, M. B., Shahid, N., Hussain, H. M., Muhammad, S. A., Mamun, A. A., et al. (2020). Advances in immunomodulatory therapy for severe acute pancreatitis. *Immunol. Lett.* 217, 72–76. doi:10.1016/j.imlet.2019.11.002

Padoan, A., Plebani, M., and Basso, D. (2019). Inflammation and pancreatic cancer: focus on metabolism, cytokines, and immunity. *Ijmsint J. Mol. Sci.* 20 (3), 676. doi:10.3390/ijms20030676

Pandey, S., and Wang, E. (1995). Cells en route to apoptosis are characterized by the upregulation ofc-fos, c-myc, c-jun, cdc2, and RB phosphorylation, resembling events of early cell-cycle traverse. *J. Cel. Biochem.* 58 (2), 135–150. doi:10.1002/jcb.240580203

Pu, W. L., Bai, R. Y., Zhou, K., Peng, M. Y., Li, W. H., Gao, X. M., et al. (2019). Baicalein attenuates pancreatic inflammatory injury through regulating MAPK, STAT 3 and NF-κB activation. *Int. Immunopharmacology* 72, 204–210. doi:10.1016/j.intimp.2019.04.018

Qu, Z. L., Fu, Q., and Xia, Q. (2007). Practical guidelines for management of severe acute pancreatitis by integrated traditional Chinese and western medicine (protocol specifications). *Chin. J. Surg. Integrated Traditional West. Med.* 8. doi:10.3969/j.issn.1007-6948.2007.03.009

Reddyrajula, R., and Dalimba, U. (2020). The bioisosteric modification of pyrazinamide derivatives led to potent antitubercular agents: synthesis via click approach and molecular docking of pyrazine-1,2,3-triazoles. *Bioorg. Med. Chem. Lett.* 30 (2), 126846. doi:10.1016/j.bmcl.2019.126846

Ren, X. X., Song, W., Liu, W. J., Guan, X., Miao, F., Miao, S. Y., et al. (2013). Rhomboid domain containing 1 inhibits cell apoptosis by upregulating AP-1 activity and its downstream target Bcl-3. *FEBS Lett.* 587 (12), 1793–1798. doi:10.1016/j.febslet.2013.04.033

Rongione, A. J., Kusske, A. M., Kwan, K., Ashley, S. W., Reber, H. A., and McFadden, D. W. (1997). Interleukin 10 reduces the severity of acute pancreatitis in rats. *Gastroenterology* 112 (3), 960–967. doi:10.1053/gast.1997.v112.pm9041259

Rotstein, O. D. (2014). Circulating cytokines in predicting development of severe acute pancreatitis. *Crit. Care* 18 (5), 575. doi:10.1186/s13054-014-0575-0

Sadr-Azodi, O., Andrén-Sandberg, Å., Orsini, N., and Wolk, A. (2012). Cigarette smoking, smoking cessation and acute pancreatitis: a prospective population-based study. *Gut* 61 (2), 262–267. doi:10.1136/gutjnl-2011-300566

Saikia, S., and Bordoloi, M. (2019). Molecular docking: challenges, advances and its use in drug discovery perspective. *Cdt* 20 (5), 501–521. doi:10.2174/1389450119666181022153016

Tanaka, T., and Iino, M. (2015). Sec8 regulates cytokeratin8 phosphorylation and cell migration by controlling the ERK and p38 MAPK signalling pathways. *Cell Signal.* 27 (6), 1110–1119. doi:10.1016/j.cellsig.2015.02.015

Tarasiuk, A., and Fichna, J. (2019). Effectiveness and therapeutic value of phytochemicals in acute pancreatitis: a review. *Pancreatology* 19 (4), 481–487. doi:10.1016/j.pan.2019.04.010

Wagner, E. F. (2010). Bone development and inflammatory disease is regulated by AP-1 (Fos/Jun). *Ann. Rheum. Dis.* 69 (Suppl. 1), i86–i88. doi:10.1136/ard.2009.119396

Wang, W.J., and Zhang, T. (2017). Integration of traditional Chinese medicine and western medicine in the era of precision medicine. *J. Integr. Med.* 15 (1), 1–7. doi:10.1016/S2095-4964(17)60314-5

Wang, Y., Sun, Y. W., Wang, Y. M., Ju, Y., and Meng, D. L. (2019). Virtual screening of active compounds from *Artemisia* argyi and potential targets against gastric ulcer based on Network pharmacology. *Bioorg. Chem.* 88, 102924. doi:10.1016/j.bioorg.2019.102924

Xia, S. L., Ni, Y. J., Zhou, Q., Liu, H., Xiang, H., Sui, H., et al. (2019). Emodin attenuates severe acute pancreatitis via antioxidant and anti-inflammatory activity. *Inflammation* 42 (6), 2129–2138. doi:10.1007/s10753-019-01077-z

Xiang, H., Zhang, Q. K., Qi, B., Tao, X. F., Xia, S. L., Song, H. Y., et al. (2017). Chinese herbal medicines attenuate acute pancreatitis: pharmacological activities and mechanisms. *Front. Pharmacol.* 8, 216. doi:10.3389/fphar.2017.00216

Yadav, D., and Lowenfels, A. B. (2013). The epidemiology of pancreatitis and pancreatic cancer. *Gastroenterology* 144 (6), 1252–1261. doi:10.1053/j.gastro.2013.01.068

Zhang, J. W., Zhang, G. X., Chen, H. L., Liu, G. L., Owusu, L., Wang, Y. X., et al. (2015). Therapeutic effect of Qingyi decoction in severe acute pancreatitis-induced intestinal barrier injury. *Wjg* 21 (12), 3537–3546. doi:10.3748/wjg.v21.i12.3537

Zheng, J. J., Xu, H., Huang, C. L., Fan, J. J., Mei, Q. X., Lu, Y. Y., et al. (2018). Quercetin protects against intestinal barrier disruption and inflammation in acute necrotizing pancreatitis through TLR4/MyD88/p38 MAPK and ERS inhibition. *Pancreatology* 18 (7), 742–752. doi:10.1016/j.pan.2018.08.001

Conflict of Interest: The authors declare that the research was conducted in the absence of any commercial or financial relationships that could be construed as a potential conflict of interest.

Copyright © 2021 Wei, Zhao, Huang, Hu, Jiao, Xiang, Wang, Qu and Shang. This is an open-access article distributed under the terms of the Creative Commons Attribution License (CC BY). The use, distribution or reproduction in other forums is permitted, provided the original author(s) and the copyright owner(s) are credited and that the original publication in this journal is cited, in accordance with accepted academic practice. No use, distribution or reproduction is permitted which does not comply with these terms.

frontiers in Pharmacology

SYSTEMATIC REVIEW
published: 29 April 2021
doi: 10.3389/fphar.2021.630896

Evaluation of the Efficacy and Safety of Chinese Herbal Injection Combined With Trimetazidine for Viral Myocarditis: A Network Meta-Analysis

Kerui Wu[1], *Dingwei Deng*[2], *Binghui Yu*[1], *Ziyun Han*[1], *Lanlin Huang*[1], *Yaxing He*[1], *Xia Yan*[2]* *and Dawei Wang*[3]*

[1]The Second Clinical College of Guangzhou University of Chinese Medicine, Guangzhou, China, [2]The Second Affiliated Hospital of Guangzhou University of Chinese Medicine, Guangdong Provincial Hospital of Chinese Medicine, Guangzhou, China, [3]Shunde Affiliated Hospital of Guangzhou University of Chinese Medicine, Shunde, China

Background: Viral myocarditis (VMC) is a common emergency of cardiovascular disease. Current treatment for VMC includes the prohibition of exercise plus supportive and symptomatic treatment, given the lack of specific antiviral therapeutic options and insufficient evidence for the use of novel immunosuppressive therapies. Trimetazidine, a drug used to improve myocardial energy metabolism, is frequently used for the treatment of viral myocarditis. In China, Chinese herbal injections (CHIs) are often used in combination with trimetazidine. Therefore, we evaluate the efficacy and safety of CHI combined with trimetazidine in the treatment of VMC through the method of network meta-analysis.

Methods: We searched PubMed, the Cochrane Library, Embase, China National Knowledge Infrastructure (CNKI), Wanfang Database, Chinese Scientific Journals Full-text Database (VIP), and China Biology Medicine Database (CBM) databases from inception to September 1, 2020, to identify eligible randomized controlled trials. The Cochrane risk of bias tool was used to assess the risk of bias among selected studies and the Stata 16.0 software was used to perform the network meta-analysis.

Results: A total of 29 studies were included, representing data from 2,687 patients. The effectiveness rate, level of myocardial injury marker, and the adverse reaction rate were evaluated. Compared with conventional treatment or conventional treatment combined with trimetazidine, CHIs combined with trimetazidine appeared to have a better therapeutic effect, with higher effectiveness rate and better reduction of the levels of creatine kinase, creatine kinase-MB, and lactate dehydrogenase. Based on surface under the cumulative ranking, Shenmai injection combined with trimetazidine appeared to be superior in terms of effective rate, while *Astragalus* injection or *Salviae miltiorrhizae* and *ligustrazine hydrochloride* injection combined with trimetazidine appeared most effective in

OPEN ACCESS

Edited by:
George Qian Li,
Western Sydney University, Australia

Reviewed by:
Xu-Dong Zhou,
Hunan University of Chinese Medicine, China
Yan Lin,
Guizhou Medical University, China

***Correspondence:**
Xia Yan
387808457@qq.com
Dawei Wang
davidwang33@139.com

Specialty section:
This article was submitted to Ethnopharmacology, a section of the journal Frontiers in Pharmacology

Received: 18 November 2020
Accepted: 24 February 2021
Published: 29 April 2021

Citation:
Wu K, Deng D, Yu B, Han Z, Huang L, He Y, Yan X and Wang D (2021) Evaluation of the Efficacy and Safety of Chinese Herbal Injection Combined With Trimetazidine for Viral Myocarditis: A Network Meta-Analysis. Front. Pharmacol. 12:630896. doi: 10.3389/fphar.2021.630896

Abbreviations: VMC, viral myocarditis; CHI, Chinese herbal injection; TCM, traditional Chinese medicine; RCTs, randomized controlled trials; CNKI, China National Knowledge Infrastructure; VIP, Chinese Scientific Journals Full-Text Database; CBM, China Biology Medicine; CK, creatine kinase; CK-MB, creatine kinase-MB; LDH, lactate dehydrogenase; cTnI, cardiac troponin I; OR, odds ratios; SMD, standard mean difference; CI, confidence intervals; IF, inconsistency factors; SUCRA, surface under the cumulative ranking.

reducing myocardial injury markers. There was no significant difference in safety between the interventions. However, a lack of safety monitoring in some selected studies meant that the safety of some interventions could not be fully evaluated.

Conclusion: CHIs combined with trimetazidine may have therapeutic value in the treatment of viral myocarditis, and Shenmai injection, *Astragalus* injection, and *Salviae miltiorrhizae* and *ligustrazine hydrochloride* injection may represent the most effective CHIs. Further clinical investigation is required to confirm these results.

Keywords: randomized controlled trials, network meta-analysis, viral myocarditis, trimetazidine, Chinese herbal injection

INTRODUCTION

Viral myocarditis (VMC) is a localized or diffuse myocardial inflammatory lesion caused by viral infection. Its clinical manifestations vary widely, from asymptomatic in mild cases to heart failure and even sudden cardiac death in severe cases. The most common manifestations are chest pain, heart failure, and fatigue dyspnea (Grün et al., 2012; Society of Cardiovascular Diseases, China Association of Chinese Medicine, 2020). Viral infection is believed to be the main cause of VMC, and the common viruses are coxsackievirus B, parvovirus B19, herpesvirus, and so on (Leone et al., 2019). Relevant epidemiological data show that the incidence of VMC is about 10–22 per 100,000 people, and the population is mainly young and middle-aged (Global Burden of Disease Study 2013 Collaborators, 2015; Olejniczak et al., 2020). As severe cases of VMC can lead to heart failure and sudden cardiac death, which seriously affect the life of patients, the timely treatment of it is very important. Current treatment for viral myocarditis remains founded on the prohibition of exercise plus supportive and symptomatic treatment, given the lack of specific antiviral therapeutic options and insufficient evidence for the use of novel immunosuppressive therapies (Tschöpe et al., 2019).

Trimetazidine, an oxidation inhibitor of free fatty acids, is often used in the treatment of heart disease with the effect of improving myocardial energy metabolism and protecting myocardium (Marzilli et al., 2019). Some studies have shown that trimetazidine has a curative effect in the treatment of VMC, which can increase the clinical effectiveness rate, improve clinical symptoms, and promote the recovery of myocardial zymogram (Yu et al., 2014). In China, traditional Chinese medicine (TCM) also has significant advantages in the treatment of VMC, showing good therapeutic effects in anti-inflammation, protecting myocardium, enhancing immune function and so on (Cao et al., 2015). Chinese herbal injection (CHI), the product of the combination of traditional Chinese medicine and modern technology, is a kind of innovative preparation with high bioavailability and good curative effect (Li et al., 2017). It is an innovative application of Chinese medicine and has been widely used in the treatment of VMC. In recent years, a large number of clinical practices have combined trimetazidine with CHI in the treatment of VMC, showing a better therapeutic effect. Liu et al (2015) conducted a meta-analysis of the efficacy and safety of *Astragalus* injection combined with trimetazidine for VMC, and the results showed that compared with conventional treatment or conventional treatment combined with trimetazidine, *Astragalus* injection combined with trimetazidine improved the clinical efficacy and reduced the cardiac zymogram level significantly. Cheng (2015) researched the efficacy of trimetazidine combined with Shenmai injection in the treatment of VMC, and the results showed that the combination could significantly shorten the improvement time of clinical symptoms and signs, and reduced B-type natriuretic peptide (BNP) and C-reactive protein (CRP) levels. Wang (2019) showed that trimetazidine combined with *Breviscapine* injection in the treatment of acute VMC is superior to trimetazidine alone in controlling the level of inflammatory cytokines, improving myocardial zymogram and relieving symptoms and so on.

Although a variety of CHIs have shown considerable efficacy in the treatment of VMC, previous studies have only explored the efficacy and safety of a single CHI combined with trimetazidine. To date, no direct or indirect comparison of different CHIs combined with trimetazidine has been reported for the treatment of VMC, meaning that it remains unclear which CHIs are most effective in the treatment of this condition. In view of this, the study aims to indirectly compare the efficacy and safety of different CHIs combined with trimetazidine in the treatment of VMC though network meta-analysis and hopes to provide some reference for clinical treatment.

MATERIALS AND METHODS

Inclusion Criteria

All published clinical randomized controlled trials (RCTs) of CHI combined with trimetazidine in the treatment of VMC were selected. No restrictions were imposed on nationality, age, gender, and race. The control group was treated with conventional treatment or conventional treatment combined with trimetazidine. Conventional treatment included one or more of the following therapies: rest, sedation, antiarrhythmic therapy, myocardial protection, antioxidant therapy, antiviral therapy, and so on. The experimental group was treated with trimetazidine and CHI on the basis of the conventional treatment used in the control group. All the included literature should report any one of the primary or secondary outcome indicators. The primary outcome indicator was the effectiveness rate. The main reference criteria were as follows: markedly effective:

clinical symptoms improved or disappeared, myocardial injury markers (myocardial zymogram or cardial troponin) returned to normal; effective: clinical symptoms relieved, myocardial injury markers improved partially, but did not fully return to normal; invalid: clinical symptoms did not improve or even further worsened, myocardial injury markers did not improve. Effectiveness rate = N (the number of markedly effective and effective cases)/N (total number of cases) × 100%. The secondary outcomes were as follows: 1) myocardial injury markers: creatine kinase (CK), creatine kinase-MB (CK-MB), lactate dehydrogenase (LDH), and cardiac troponin I (cTnI); 2) adverse reactions.

Exclusion Criteria

1) Studies on treatment combined with other TCM-related treatment measures, such as TCM decoction, Chinese patent medicines, and acupuncture were excluded; 2) participants complicated with other diseases, such as coronary heart disease and diabetes; 3) literature works published with duplicate data; 4) the reported data were incomplete and impossible to be acquired; 5) the reported data were inconsistent with the conclusion.

Search Strategies

To obtain RCTs of CHI combined with trimetazidine in the treatment of VMC, we searched PubMed, the Cochrane Library, Embase, China National Knowledge Infrastructure (CNKI), Wanfang database, Chinese Scientific Journals Full-Text Database (VIP), and China Biology Medicine Database (CBM) from inception to September 1, 2020. The search terms in English database were as follows: "Viral myocarditis," "Myocarditides," "Carditis," "Myocarditis," "Trimetazidine," "Centrophène," "Trimetazidine Dihydrochloride," "Dihydrochloride, Trimetazidine," "Vastarel," "Trimétazidine Irex," "Vasartel," and "Idaptan." The search terms in Chinese database included "bing du xing xin ji yan," "qu mei ta qin," "yan suan qu mei ta qin," "wan shuang li," and "san jia yang bian qin." The search strategy of each database is shown in **Supplementary Table S1**.

Literature Screening and Data Extraction

After literature retrieval, two evaluators independently conducted literature screening according to the inclusion and exclusion criteria. A preliminary screening was carried out according to the title and abstract, and then rescreening was carried out by reading the full text. Any differences in the screening results of the two evaluators were resolved by discussion with a third evaluator. After determining the included studies, the data of literature was extracted as follows: title, authors, year of publication, baseline status, methodological information, sample size, intervention measures, the course of treatment, and outcomes.

Bias Risk Assessment

Two evaluators independently assessed the risk of bias in the included studies by using the Cochrane risk of bias tool (Higgins et al., 2011), which consisted of the following items: 1) random sequence generation; 2) allocation hiding; 3) blinding of outcome evaluators; 4) blinding of patients and trial personnel; 5) incomplete result data; 6) selective reporting; and 7) other biases. The risk assessment criteria are divided into low, high, and uncertain bias risk. Any differences in the assessment results of the two evaluators were resolved by discussion with a third evaluator. The bias risk assessment results of the included studies were visualized by RevMan5.3 software.

Statistical Analysis

All statistical analysis was performed using Stata 16.0 software (Stata Company). For dichotomous variables (effectiveness rate and adverse reaction rate), odds ratios (OR), and 95% confidence intervals (CI) were used to assess effect size, whereas the effect size of continuous variables (myocardial injury markers) was assessed using the standard mean difference (SMD) and 95% CI. Considering the expected heterogeneity in the included studies, a random-effects model was used for statistical analysis. If the data could not be meta-analyzed, we would conduct a descriptive analysis. Based on the classical frequency, the random-effects model was selected under the "Network" command in the analysis software to perform the network meta-analysis. A network diagram of interventions was constructed to show the relationships between interventions. Where no closed loop was formed, the consistency model was used for analysis. When a closed loop was observed, an overall inconsistency check was performed. If p value > 0.05, it indicated that the overall inconsistency was not significant, otherwise, it indicated that the overall inconsistency was significant. At the same time, the inconsistency test of the loop was carried out to determine inconsistency between direct and indirect evidence by calculating the absolute difference between these types of evidence, expressed as an inconsistency factor (IF). Whereas 95% CI of the IF values contained 0, and the inconsistency of direct and indirect evidence was considered not significant. Otherwise, the inconsistency was deemed significant. When no inconsistency was apparent, the consistency model was used for analysis. Otherwise, the inconsistency model was selected for analysis. The value of surface under the cumulative ranking (SUCRA) was subsequently calculated and the number of iterations set at 5,000. Intervention measures were sorted based on SUCRA value. The larger the SUCRA value, the higher the ranking, indicating that the intervention was more likely to be the best intervention. Funnel plots were used to evaluate publication bias in the included studies.

RESULTS

Literature Search and Screening

A total of 904 literature works were obtained. Among them, there were 3 from PubMed, 7 from the Cochrane Library, 4 from Embase, 453 from CNKI, 172 from Wanfang database, 135 from VIP, and 130 from CBM. After screening, a total of 29 studies were included. The literature screening process is shown in **Figure 1**.

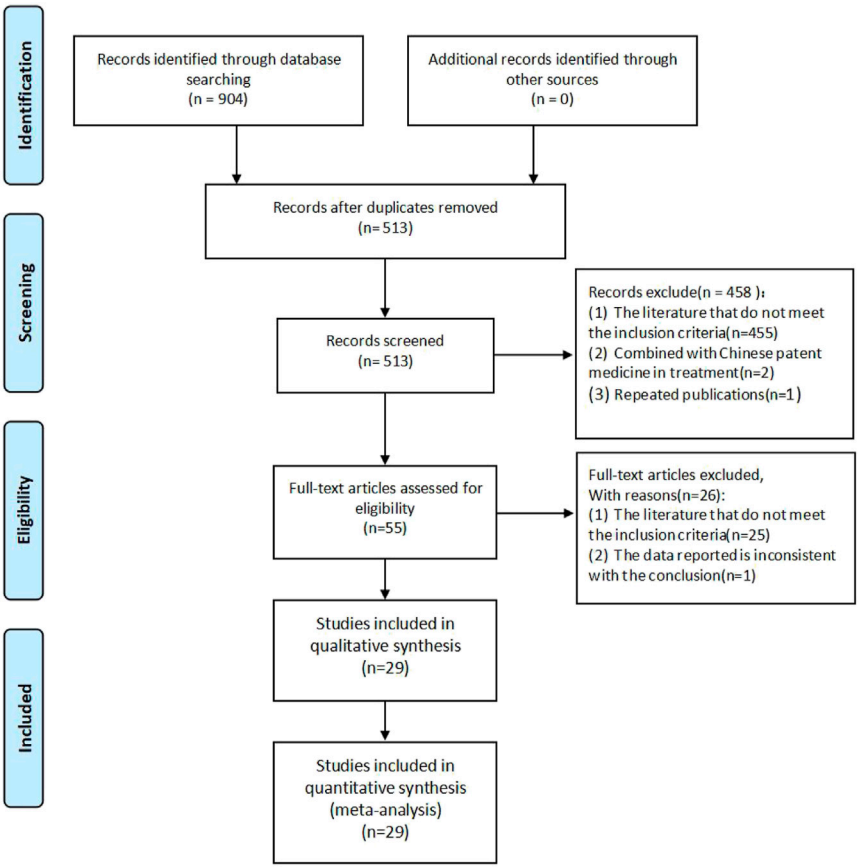

FIGURE 1 | Flow diagram of literature screening process.

Basic Characteristics of Included Studies

29 studies enrolled a total of 2,687 patients. All the included studies were conducted in China, and the literature was published from 2009 to 2020. The baselines of all studies were comparable between the experimental and control groups. In terms of intervention measures, the control groups of 18 studies were treated with conventional treatment alone, whereas the experimental groups were treated with CHI and trimetazidine on the basis of the control groups. Among them, 14 studies were combined with *Astragalus* injection, 3 studies combined with Shenfu injection, and 1 study combined with Shenmai injection. In the other 11 studies, the control groups were treated with conventional treatment combined with trimetazidine, whereas the experimental groups were treated with CHI on the basis of the control group. Among them, 4 studies combined with *Astragalus* injection, 4 studies combined with *Salviae miltiorrhizae* and *ligustrazine hydrochloride* injection, 2 studies combined with *Breviscapine* injection, and 1 study combined with Shenmai injection. The detailed information of CHIs used in included studies and the chemical analysis of them are shown in **Supplementary Tables S2, S3**. In the course of treatment, the shortest was 2 weeks and the longest was 8 weeks. In the outcome indicators, 25 studies reported the effectiveness rate, 10 studies reported the level of CK, 12 studies reported the level of CK-MB, 13 studies reported the level of LDH, 8 studies reported the level of cTnI, and 20 studies reported the adverse reactions during treatment. The basic characteristics of included studies are detailed in **Table 1**. For the convenience of description, A refers to conventional treatment, B refers to conventional treatment combined with trimetazidine and *Astragalus* injection, C refers to conventional treatment combined with trimetazidine and Shenfu injection, D refers to conventional treatment combined with trimetazidine, E refers to conventional treatment combined with trimetazidine and *Salviae miltiorrhizae* and *ligustrazine hydrochloride* injection, F refers to conventional treatment combined with trimetazidine and *Breviscapine* injection, and G refers to conventional treatment combined with trimetazidine and Shenmai injection. The network diagrams of the seven interventions in different outcome indicators are shown in **Figure 2**.

Bias Risk Assessment of Included Studies

The methodological quality of the included studies was generally low. In the generation of random sequences, 9 studies used random number tables, and 1 study used lottery randomization, so they were at low bias risk. Other studies only mentioned randomness and did not describe random methods, so they were at uncertain bias risk. None studies

TABLE 1 | Basic characteristics of the included studies.

Study	Age (mean or range)	Sample size	Intervention		Courses	Outcome
	C/E	C/E	C	E		
Chen (2011)	17–46/17–46	32/32	Conventional treatment	Conventional treatment + trimetazidine 20 mg/d + *Astragalus* injection 40 ml/d	*Astragalus* injection 2 w Others 8 w	(1) (4) (6)
Chen (2014)	57.8/57.8	80/80	Conventional treatment	Conventional treatment + trimetazidine 20 mg/d + *Astragalus* injection 50 ml/d	1 m	(1) (6)
Dai (2018)	25.4 ± 8.6/ 25.6 ± 7.9	20/20	Conventional treatment	Conventional treatment + trimetazidine 60 mg/d + *Astragalus* injection 50 ml/d	1 m	(1) (2) (3) (4) (6)
Ge,et al. (2010)	27.2 ± 11.2/ 26.8 ± 10.7	30/30	Conventional treatment	Conventional treatment + trimetazidine 20 mg/d + *Astragalus* injection 40 ml/d	*Astragalus* injection 2w Others 8w	(1) (6)
Ma (2012)	22.48 ± 7.2/ 23.56 ± 8.5	46/62	Conventional treatment	Conventional treatment + trimetazidine 60 mg/d + *Astragalus* injection 20 g/d	2w	(1) (3) (5) (6)
Pu (2013)	—	67/79	Conventional treatment	Conventional treatment + trimetazidine 60 mg/d + *Astragalus* injection 50 ml/d	4w	(1) (6)
Shao,et al. (2012)	27 ± 11/28 ± 7	48/50	Conventional treatment	Conventional treatment + trimetazidine 60 mg/d + *Astragalus* injection 10–20 ml/d	*Astragalus* injection 2w Others 8w	(1) (6)
Sun (2013)	30 ± 5/28 ± 5	40/40	Conventional treatment	Conventional treatment + trimetazidine 60 mg/d + *Astragalus* injection 20 g/d	4w	(1) (6)
Wang (2016)	55.6 ± 2.4/ 56.3 ± 2.8	37/37	Conventional treatment	Conventional treatment + trimetazidine 60 mg/d + *Astragalus* injection 20 ml/d	2w	(1) (3) (5) (6)
Wang (2010)	31 ± 10/30 ± 10	50/50	Conventional treatment	Conventional treatment + trimetazidine 60 mg/d + *Astragalus* injection 30 ml/d	3w	(1) (6)
Xu and Zhang (2011)	14–40/13–41	30/60	Conventional treatment	Conventional treatment + trimetazidine 60 mg/d + *Astragalus* injection 40 ml/d	2w	(1) (4)
Yang (2009)	31 ± 10/32 ± 10	43/45	Conventional treatment	Conventional treatment + Trimetazidine 60 mg/d + *Astragalus* injection 50 ml/d	4w	(1) (6)
Zhang,et al. (2015)	25.2 ± 8.5/ 26.2 ± 8.5	30/30	Conventional treatment	Conventional treatment + trimetazidine 60 mg/d + *Astragalus* injection 30 ml/d	—	(1)
Yu (2014)	32.4 ± 5.6/ 32.9 ± 6.1	51/51	Conventional treatment	Conventional treatment + trimetazidine 60 mg/d + *Astragalus* injection 50 ml/d	4w	(1) (3) (5) (6)
Zhang,et al. (2016)	44.1 ± 7.2/ 44.5 ± 7.8	40/40	Conventional treatment	Conventional treatment + trimetazidine 60 mg/d + Shenfu injection 50 ml/d	4w	(1) (2) (3) (4)
Sun and Sun (2018)	53.1 ± 5.8/ 52.4 ± 5.3	51/51	Conventional treatment	Conventional treatment + trimetazidine 60 mg/d + Shenfu injection 50 ml/d	Shenfu injection 2w Others 4w	(1)
Gao (2019)	46.21 ± 2.57/ 46.73 ± 2.10	39/39	Conventional treatment	Conventional treatment + trimetazidine 60 mg/d + Shenfu injection 40–200 ml/d	—	(1) (2) (3) (4)
Pang and Huang (2013)	10 m–12/ 10 m–12	33/33	Conventional treatment	Conventional treatment + trimetazidine 0.3–0.5 mg/kg/d + Shenmai injection 0.5–1 ml/kg/d	2w	(1)
Wang (2012)	60 ± 9/55 ± 11	35/35	Conventional treatment + trimetazidine 60 mg/d	Conventional treatment + trimetazidine 60 mg/d + *Astragalus* injection 50 ml/d	4w	(1) (6)
Zheng (2019)	49.15 ± 16.18/ 48.47 ± 15.25	44/45	Conventional treatment + trimetazidine 60 mg/d	Conventional treatment + trimetazidine 60 mg/d + *Astragalus* injection 10–20 ml/d	6w	(3) (4) (6)
Cui (2018)	55.2 ± 6.5/ 54.8 ± 6.3	35/35	Conventional treatment + trimetazidine 60 mg/d	Conventional treatment + trimetazidine 60 mg/d + *Astragalus* injection 40 ml/d	4w	(2) (3) (4) (5)
Wei,et al. (2020)	70.3 ± 7.8/ 70.9 ± 7.5	90/90	Conventional treatment + trimetazidine 60 mg/d	Conventional treatment + trimetazidine 60 mg/d + *Astragalus* injection 20 ml/d	2w	(1) (3) (4) (5) (6)
Zhu,et al. (2020)	5.81 ± 1.22/ 5.7 ± 1.15	46/46	Conventional treatment + trimetazidine 20 mg/d	Conventional treatment + trimetazidine 20 mg/d + *Salviae miltiorrhizae* and *ligustrazine hydrochloride* injection 5 ml/d	30 d	(1) (2) (3) (4) (5) (6)
Wang (2020)	9.91 ± 1.27/ 9.89 ± 1.31	50/50	Conventional treatment + trimetazidine 60 mg/d	Conventional treatment + trimetazidine 60 mg/d + *Salviae miltiorrhizae* and *ligustrazine hydrochloride* injection 5 ml/d	30 d	(2) (3) (4) (5)
Chen and Zeng (2018)	41.2 ± 6.8/ 41.8 ± 6.9	49/49	Conventional treatment + trimetazidine 60 mg/d	Conventional treatment + trimetazidine 60 mg/d + *Salviae miltiorrhizae* and *ligustrazine hydrochloride* injection 5 ml/d	1 m	(1) (2) (4)
Li and Gao (2016)	43.9 ± 7.9/ 43.3 ± 7.5	55/55	Conventional treatment + trimetazidine 20 mg/d	Conventional treatment + trimetazidine 20 mg/d + *Salviae miltiorrhizae* and *ligustrazine hydrochloride* injection 5 ml/d	30 d	(1) (2) (4) (6)
Miao (2019)	51.17 ± 2.67/ 50.64 ± 3.2	49/49	Conventional treatment + trimetazidine 60 mg/d	Conventional treatment + trimetazidine 60 mg/d + *Breviscapine* injection 5 ml/d	1 m	(2) (6)

(Continued on following page)

TABLE 1 | (*Continued*) Basic characteristics of the included studies.

Study	Age (mean or range)	Sample size	Intervention		Courses	Outcome
	C/E	C/E	C	E		
Wang (2017)	42.1 ± 15.9/ 43.2 ± 15.6	62/62	Conventional treatment + trimetazidine 60 mg/d	Conventional treatment + trimetazidine 60 mg/d + *Breviscapine* injection 5 ml/d	4 w	(1) (2) (3) (4) (5) (6)
He (2014)	33.52 ± 1.14/ 33.52 ± 1.14	30/30	Conventional treatment + trimetazidine 60 mg/d	Conventional treatment + trimetazidine 60 mg/d + Shenmai injection 2–4 ml/d	4 w	(1) (6)

C: control group; E: experimental group; d: day; w: week; m: month; (1): effectiveness rate; (2): CK; (3): CK-MB; (4): LDH; (5): cTnl; (6): adverse reactions.

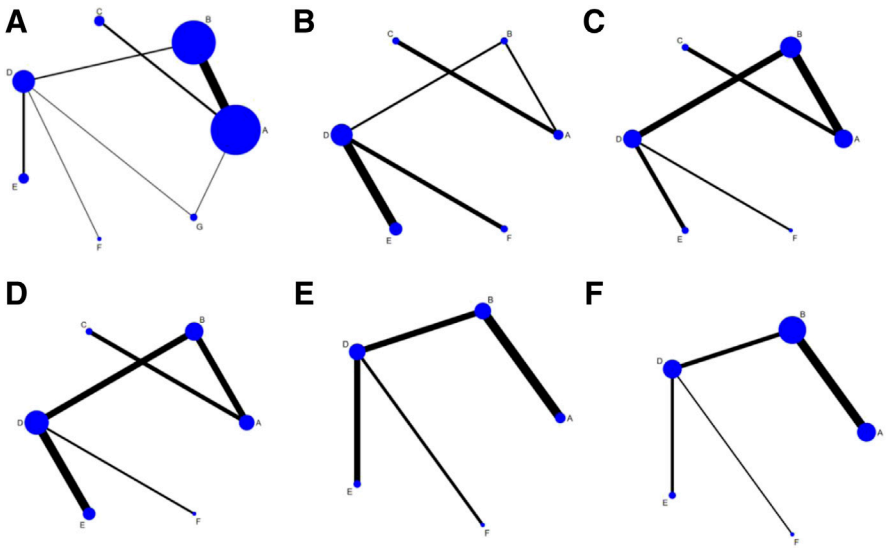

FIGURE 2 | Network diagrams of outcome indicators.**(A)** effectiveness rate; **(B)** CK; **(C)** CK-MB; **(D)** LDH; **(E)** cTnl; **(F)** adverse reaction rate. A: conventional treatment; B: conventional treatment + trimetazidine + *Astragalus* injection; C: conventional treatment + trimetazidine + Shenfu injection; D: conventional treatment + trimetazidine; E: conventional treatment + trimetazidine + *Salviae miltiorrhizae* and *ligustrazine hydrochloride* injection; F: conventional treatment + trimetazidine + *Breviscapine* injection; G: conventional treatment + trimetazidine + Shenmai injection.

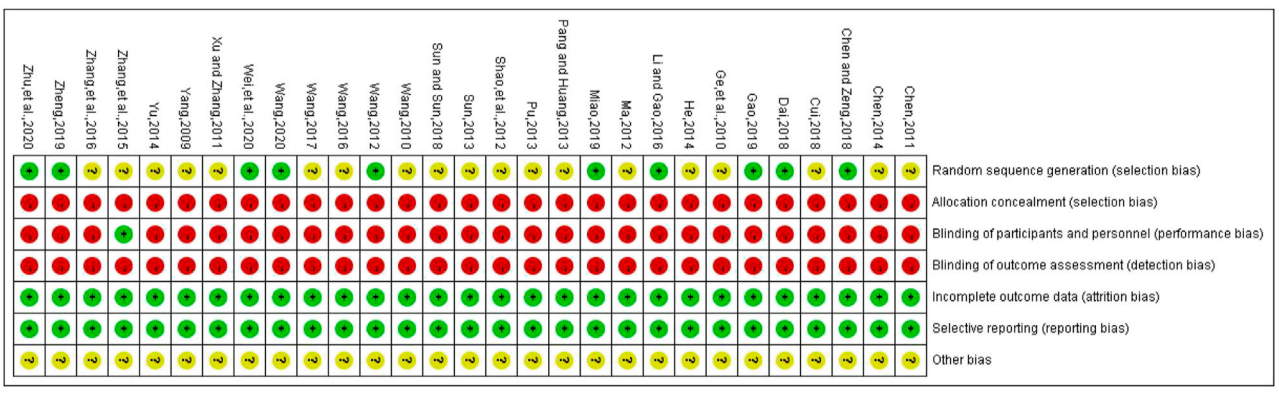

FIGURE 3 | Risk of bias for each included study. Red represents high risk of bias; green represents low risk of bias; yellow represents uncertain risk of bias.

adopted random allocation hiding and blinding to outcome evaluators, which belonged to high risk bias. One study applied blinding to patients and trial personnel, which belonged to low bias risk, while other studies did not adopt blinding, and they all belonged to high bias risk. All the data were reported completely, and there were no evidences to support the

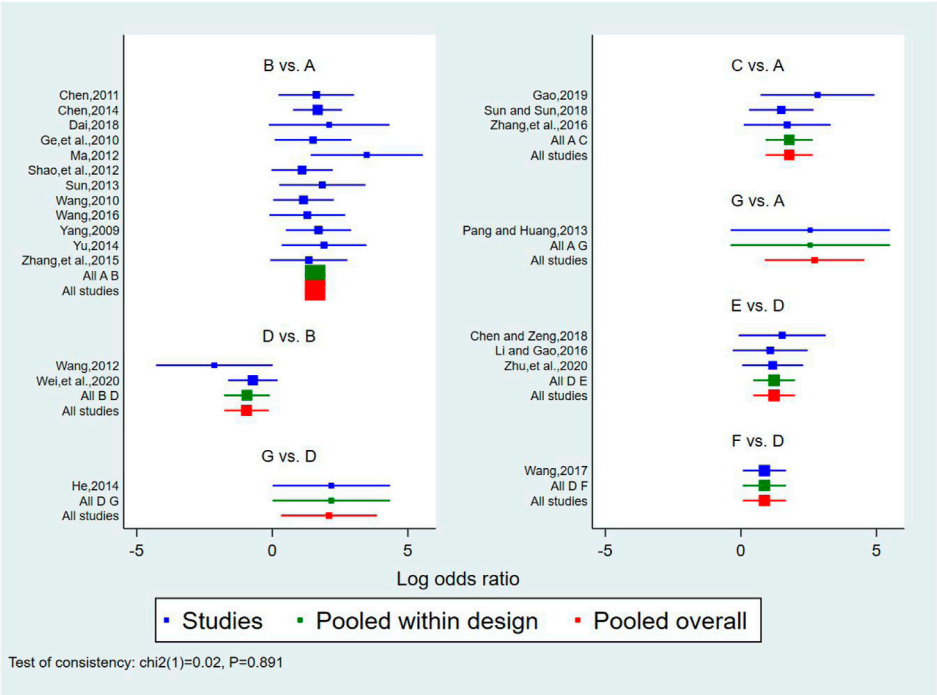

FIGURE 4 | Forest diagram of direct comparison of effectiveness rate. A: conventional treatment; B: conventional treatment + trimetazidine + *Astragalus* injection; C: conventional treatment + trimetazidine + Shenfu injection; D: conventional treatment + trimetazidine; E: conventional treatment + trimetazidine + *Salviae miltiorrhizae* and *ligustrazine hydrochloride* injection; F: conventional treatment + trimetazidine + *Breviscapine* injection; G: conventional treatment + trimetazidine + Shenmai injection.

FIGURE 5 | The result of loop inconsistency test. A: conventional treatment; B: conventional treatment + trimetazidine + *Astragalus* injection; D: conventional treatment + trimetazidine; G: conventional treatment + trimetazidine + Shenmai injection.

selective reporting of outcomes, so it belonged to low bias risk. Whether there were other biases in all included studies could not be judged clearly, so they were at uncertain bias risk. The bias risk assessment results of included studies are detailed in **Figure 3**.

Outcome Indicators

Effectiveness Rate

A total of 25 studies reported effectiveness rate, of which 2 studies (Xu and Zhang, 2011; Pu, 2013) had data distortion and were not

TABLE 2 | The network meta-analysis results of the outcome indicators.

Intervention	Outcome indicators (OR/SMD, 95% CI)					
	Effectiveness rate	**CK**	**CK-MB**	**LDH**	**cTnI**	**Adverse reaction rate**
G vs. F	3.40, (0.49, 23.72)	—	—	—	—	—
G vs. E	2.38, (0.34, 16.40)	—	—	—	—	—
G vs. D	**8.09, (1.38, 47.59)**	—	—	—	—	—
G vs. C	2.54, (0.33, 19.44)	—	—	—	—	—
G vs. B	3.14, (0.50, 19.52)	—	—	—	—	—
G vs. A	**15.17, (2.41, 95.25)**	—	—	—	—	—
F vs. D	**2.38, (1.07, 5.28)**	**−1.90, (−3.07, −0.72)**	−1.68, (−4.24, 0.87)	−0.97, (−3.86, 1.92)	−3.33, (−57.22, 50.56)	0.23, (0.03, 2.18)
F vs. C	0.75, (0.17, 3.29)	−1.15, (−4.17, 1.88)	−1.54, (−5.26.2.19)	−0.93, (−5.21, 3.35)	—	—
F vs. B	0.92, (0.29, 2.89)	0.21, (−1.87, 2.28)	1.04, (−1.93.4.01)	0.36, (−2.98, 3.70)	−0.48, (−66.28, 65.33)	0.19, (0.02, 2.14)
F vs. A	**4.46, (1.34, 14.80)**	−2.73, (−5.51, 0.05)	−2.45, (−5.69.0.80)	−1.89, (−5.64, 1.87)	−31.67, (−104.23, 40.89)	0.19, (0.02, 2.34)
E vs. F	1.43, (0.47, 4.32)	−0.17, (−1.61, 1.28)	−0.62, (−3.77.2.52)	**−3.52, (−6.77, −0.27)**	1.08, (−64.92, 67.08)	6.57, (0.55, 78.19)
E vs. D	**3.40, (1.58, 7.34)**	**−2.06, (−2.90, −1.22)**	**−2.31, (−4.13, −0.48)**	**−4.49, (−5.97, −3.00)**	−2.25, (−40.36, 35.86)	1.54 (0.52.4.53)
E vs. C	1.07, (0.25, 4.64)	−1.31, (−4.22, 1.60)	−2.16, (−5.42.1.10)	**−4.45, (−7.94, −0.96)**	—	—
E vs. B	1.32, (0.43, 4.06)	0.04, (−1.87, 1.95)	0.42, (−1.95.2.78)	**−3.16, (−5.40, −0.92)**	0.61, (−53.04, 54.25)	1.28, (0.32.5.15)
E vs. A	**6.38, (1.96, 20.77)**	**−2.90, (−5.55, −0.24)**	**−3.07, (−5.78, −0.36)**	**−5.40, (−8.23, −2.58)**	−30.59, (−92.34, 31.16)	1.27, (0.27.6.02)
C vs. D	3.18, (0.91, 11.10)	−0.75, (−3.54, 2.04)	−0.15, (−2.85.2.56)	−0.04, (−3.20, 3.12)	—	—
C vs. A	**5.96, (2.50, 14.23)**	**−1.59, (−2.78, −0.40)**	−0.91, (−2.73.0.91)	−0.95, (−3.01, 1.10)	—	—
B vs. C	0.81, (0.31, 2.10)	−1.35, (−3.55, 0.85)	**−2.58, (−0.33, −4.82)**	−1.29, (−3.98, 1.39)	—	—
B vs. D	**2.58, (1.14, 5.86)**	**−2.10, (−3.81, −0.39)**	**−2.73, (−4.23, −1.22)**	−1.33, (−3.01, 0.34)	−2.86, (−40.76, 35.05)	1.21, (0.50.2.91)
B vs. A	**4.83, (3.30, 7.09)**	**−2.94, (−4.79, −1.09)**	**−3.49, (−4.80, −2.17)**	**−2.25, (−3.97, −0.53)**	−31.19, (−62.36, −0.03)	0.99, (0.50.1.98)
A vs. D	0.53, (0.22, 1.31)	0.84, (−1.68, 3.36)	0.76, (−1.24.2.76)	0.92, (−1.49, 3.32)	28.34, (−20.43, 77.11)	1.21, (0.40.3.72)

OR, odds ratio; SMD, standardized mean difference; CI, confidence interval; A, conventional treatment; B, conventional treatment + trimetazidine + Astragalus injection; C, conventional treatment + trimetazidine + Shenfu injection; D, conventional treatment + trimetazidine; E, conventional treatment + trimetazidine + Salviae miltiorrhizae and ligustrazine hydrochloride injection; F, conventional treatment + trimetazidine + Breviscapine injection; G, conventional treatment + trimetazidine + Shenmai injection.

combined in the analysis. The remaining 23 studies constituted 7 pairs of direct comparisons, which involved 5 types of CHIs. Four types of intervention measures (A and G) formed a quadrilateral closed loop, as shown in **Figure 2A**. The overall inconsistency test result had a p value = 0.891, indicating that the inconsistency was not significant, as shown in **Figure 4**. The inconsistency test of the loop resulted in an IF = 0.26 and 95% CI (0.00, 4.03), indicating that the inconsistency between the direct and indirect evidence was not significant, as shown in **Figure 5**. The consistent model was therefore adopted for network meta-analysis.

A total of 21 pairs were compared among the 7 intervention measures, 9 of which showed statistically significant differences ($p < 0.05$). On the basis of conventional treatment, combining with *Astragalus* injection and trimetazidine [OR = 4.83, 95% CI (3.30, 7.09)], or Shenfu injection and trimetazidine [OR = 5.96, 95% CI (2.50, 14.23)], or *Salviae miltiorrhizae* and *ligustrazine hydrochloride* injection and trimetazidine [OR = 6.38, 95% CI (1.96, 20.77)], or *Breviscapine* injection and trimetazidine [OR = 4.46, 95% CI (1.34, 14.80)], or Shenmai injection and trimetazidine [OR = 15.17, 95% CI (2.41, 95.25)] was superior to conventional treatment alone with respect to effectiveness rate. In addition to the Shenfu injection, on the basis of conventional treatment plus trimetazidine, combining with *Astragalus* injection [OR = 2.58, 95% CI(1.14, 5.86)], or *Salviae miltiorrhizae* and *ligustrazine hydrochloride* injection [OR = 3.40, 95% CI(1.58, 7.34)] or *Breviscapine* injection [OR = 2.38, 95% CI (1.07, 5.28)], or Shenmai injection [(OR = 8.09, 95% CI (1.38, 47.59)] was superior to conventional treatment plus trimetazidine in terms of effectiveness rate. The comparisons among the 5 types of injections and between conventional treatment and conventional treatment plus trimetazidine showed no statistically significant difference ($p > 0.05$). The above results are detailed in **Table 2**.

Ranking the 5 types of injections according to the SUCRA resulted in the following hierarchy: Shenmai injection (89.2%), *Salviae miltiorrhizae* and *ligustrazine hydrochloride* injection (69.1%), Shenfu injection (65.5%), *Astragalus* injection (55.2%), and *Breviscapine* injection (52.3%), as shown in **Figure 6A**.

Creatine Kinase

A total of 10 studies reported the level of CK, which constituted 5 pairs of direct comparisons, involved 4 types of CHIs and 6 types of intervention measures. The network diagram formed is shown in **Figure 2B**. Since it did not form a closed loop, no inconsistency test was carried out.

A total of 15 pairs were compared among the 6 intervention measures, 6 of which showed statistically significant differences ($p > 0.05$). On the basis of conventional treatment, combining with *Astragalus* injection and trimetazidine [SMD = −2.94, 95% CI (−4.79,−1.09)], or Shenfu injection and trimetazidine [SMD = −1.59, 95% CI (−2.78, −0.40)], or *Salviae miltiorrhizae* and *ligustrazine hydrochloride* injection and *trimetazidine* [SMD = −2.90, 95% CI (−5.55,−0.24)] was superior to conventional treatment alone on reducing the level of CK. On the basis of conventional treatment plus trimetazidine, combining with *Astragalus* injection [SMD = −2.10, 95% CI (−3.81, −0.39)], or *Salviae miltiorrhizae* and *ligustrazine hydrochloride* injection

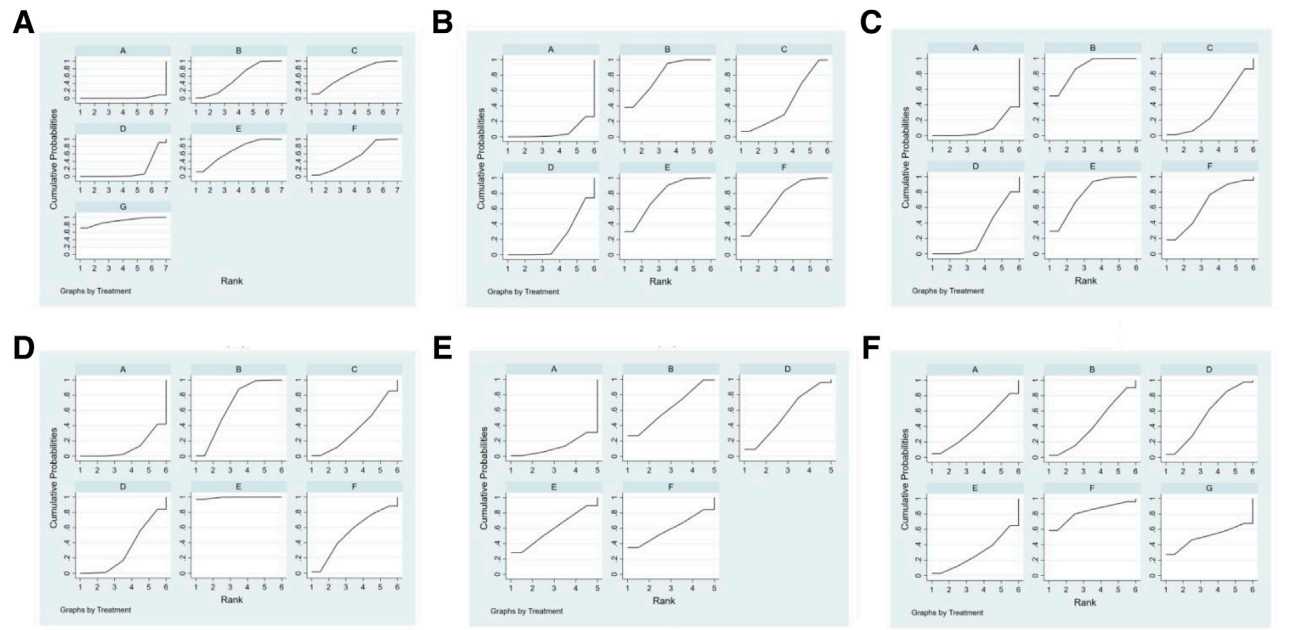

FIGURE 6 | SUCRA of outcome indicators.**(A)**:effectiveness rate; **(B)**:CK; **(C)**: CK-MB; **(D)**: LDH; **(E)**: cTnI; **(F)**: adverse reaction rate. A: conventional treatment; B: conventional treatment + trimetazidine + *Astragalus* injection; C: conventional treatment + trimetazidine + Shenfu injection; D: conventional treatment + trimetazidine; E: conventional treatment + trimetazidine + *Salviae miltiorrhizae* and *ligustrazine hydrochloride* injection; F: conventional treatment + trimetazidine + *Breviscapine* injection; G: conventional + treatment + trimetazidine + Shenmai injection.

[SMD = −2.06, 95% CI (−2.90, −1.22)] or *Breviscapine* injection [SMD = −1.90, 95% CI (−3.07, −0.72)] was superior to conventional treatment plus trimetazidine on reducing the level of CK. The comparisons among the 4 types of injections and between conventional treatment and conventional treatment plus trimetazidine showed no statistically significant difference ($p > 0.05$). The above results are detailed in **Table 2**.

Ranking the 4 injections based on the SUCRA value, the results were as follows: *Astragalus* injection (79.5%), *Salviae miltiorrhizae* and *ligustrazine hydrochloride* injection (77.1%), *Breviscapine* injection (71.7%), and Shenfu injection (44.5%), as shown in **Figure 6B**.

Creatine Kinase-MB

A total of 12 studies reported the level of CK-MB, which constituted 5 pairs of direct comparisons, involved 4 types of CHIs and 6 types of intervention measures. The network diagram formed is shown in **Figure 2C**. It did not form a closed loop, so there was no inconsistency test.

A total of 15 pairs of comparisons were formed among the 6 intervention measures, 5 of which were statistically significant ($p < 0.05$). On the basis of conventional treatment, combining with *Astragalus* injection and trimetazidine [SMD = −3.49, 95% CI (−4.80,−2.17)], or *Salviae miltiorrhizae* and *ligustrazine hydrochloride* injection and trimetazidine [SMD = −3.07, 95% CI (−5.78,−0.36)] was superior to conventional treatment alone on reducing the level of CK-MB. On the basis of conventional treatment plus trimetazidine, combining with *Astragalus* injection [SMD = −2.73, 95% CI (−4.23,−1.22)], or *Salviae miltiorrhizae* and *ligustrazine hydrochloride* injection [SMD = −2.31, 95% CI (−4.13, −0.48)] was superior to conventional treatment plus trimetazidine on reducing the level of CK-MB. The comparisons among the 4 types of injections showed that on the basis of conventional treatment plus trimetazidine, combining with *Astragalus* injection was superior to Shenfu injection [SMD = −2.58, 95% CI (−0.33, −4.82)] on reducing the level of CK-MB. The other 10 pair comparisons showed no statistically significant difference ($p > 0.05$). The above results are detailed in **Table 2**.

Based on the SUCRA value, the 4 types of injections were ranked as follows: *Astragalus* injection (87.5%), *Salviae miltiorrhizae* and *ligustrazine hydrochloride* injection (77.9%), *Breviscapine* injection (64.3%), and Shenfu injection (33.9%), as shown in **Figure 6C**.

Lactate Dehydrogenase

A total of 13 studies reported the level of LDH, which constituted 5 pairs of direct comparisons, involved 4 types of CHIs and 6 types of intervention measures. The network diagram formed is shown in **Figure 2D**. No closed loop was constituted and no inconsistency test was performed.

A total of 15 pairs of comparisons were formed among the 6 intervention measures, 6 of which were statistically significant ($p < 0.05$). On the basis of conventional treatment, combining with *Astragalus* injection and trimetazidine [SMD = −2.25, 95% CI (−3.97, −0.53)], or *Salviae miltiorrhizae* and *ligustrazine hydrochloride* injection and trimetazidine [SMD = −5.40, 95%

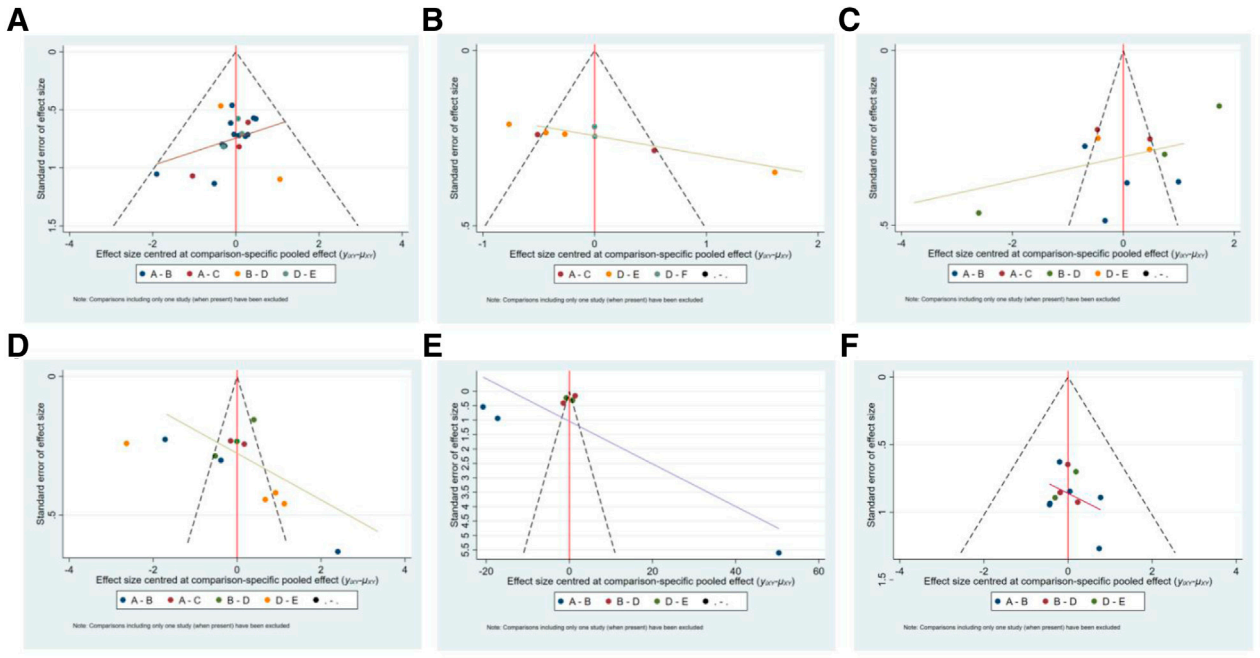

FIGURE 7 | The funnel plot of outcome indicators. **A**:effectiveness rate; **B**:CK; **C**:CK-MB; **D**:LDH; **E**:cTnI; **F**:adverse reaction rate. A: conventional treatment; B: conventional treatment + trimetazidine + *Astragalus* injection; C: conventional treatment + trimetazidine + Shenfu injection; D: conventional treatment + trimetazidine; E: conventional treatment + trimetazidine + *Salviae miltiorrhizae* and *ligustrazine hydrochloride* injection; F: conventional treatment + trimetazidine + *Beviscapine* injection.

CI (−8.23, −2.58)] was superior to conventional treatment alone on reducing the level of LDH. On the basis of conventional treatment plus trimetazidine, combining with *Salviae miltiorrhizae* and *ligustrazine hydrochloride* injection [SMD = −4.49, 95% CI (−5.97,−3.00)]was superior to conventional treatment plus trimetazidine on reducing the level of LDH. The comparisons among the 4 types of injections showed that on the basis of conventional treatment plus trimetazidine, combining with *Salviae miltiorrhizae* and *ligustrazine hydrochloride* injection was superior to *Astragalus* injection [SMD = −3.16, 95% CI (−5.40, −0.92)] or Shenfu injection [SMD = −4.45, 95% CI (−7.94, −0.96)] or *Breviscapine* injection [SMD = −3.52, 95% CI (−6.77, −0.27)] on reducing LDH. The other 9 pairs comparisons were not statistically significant ($p > 0.05$). The above results are detailed in **Table 2**.

Ranking the 4 injections based on the SUCRA value, the results were as follows: *Salviae miltiorrhizae* and *ligustrazine hydrochloride* injection (99.4%), *Astragalus* injection (66.7%), *Breviscapine* injection (54.3%), and Shenfu injection (36.4%), as shown in **Figure 6D**.

Cardiac Troponin I

A total of 8 studies reported the level of cTnI, which constituted 4 pairs of direct comparisons, involved 3 types of CHIs and 5 types of intervention measures. The network diagram formed is shown in **Figure 2E**. Since it did not constitute a closed loop, the inconsistency test was not performed.

The results showed that there were no statistically significant differences among 10 pairs of comparisons of the 5 intervention measures ($p > 0.05$). The above results are detailed in **Table 2**.

Based on the SUCRA value, the 3 injections were ranked as follows: *Astragalus* injection (63.2%), *Salviae miltiorrhizae* and *ligustrazine hydrochloride* injection (59.4%), and *Breviscapine* injection (59.4%), as shown in **Figure 6E**.

Adverse Reaction Rate

Eight studies reported no adverse reactions during treatment, and 12 studies reported the number of cases of adverse reactions. The adverse reactions mainly include dizziness, headache, abdominal discomfort, nausea and vomiting, poor appetite, diarrhea, and rash. In terms of the adverse reaction rate, 12 studies consisted 4 pairs of comparisons, involved 3 types of CHIs and 5 types of intervention measures. The network diagram formed is shown in **Figure 2F**. Since it did not constitute a closed loop, the inconsistency test was not performed. The results showed that there were no statistically significant differences among 10 pairs comparisons of the 5 intervention measures (p > 0.05). The above results are detailed in **Table 2**.

Ranking the three injections based on the SUCRA value, the results were as follows: *Breviscapine* injection (90.4%), *Astragalus* injection (39.3%), and *Salviae miltiorrhizae* and *ligustrazine hydrochloride* injection (26.1%), as shown in **Figure 6F**.

Assessment of Publication Bias

The funnel plots have poor symmetry, indicating that there was some publication bias in the included studies, which may be caused by small sample effects, as shown in **Figure 7**.

DISCUSSION

In the present study, we conducted a search of the RCTs of CHIs combined with trimetazidine in the treatment of VMC, and adopted a network meta-analysis approach to evaluate the clinical efficacy and safety of different CHIs combined with trimetazidine. A total of 29 RCTs were included in this analysis, representing 7 types of intervention measures and 5 types of CHIs. Our findings indicate that, in terms of effectiveness rate and reduction of the CK and CK-MB levels, *Astragalus* injection or *Salviae miltiorrhizae* and *ligustrazine hydrochloride* injection combined with trimetazidine was superior to conventional treatment alone or conventional treatment combined with trimetazidine. Moreover, *Salviae miltiorrhizae* and *ligustrazine hydrochloride* injection combined with trimetazidine was also superior to conventional treatment or conventional treatment combined with trimetazidine in reducing the level of LDH, and *Astragalus* injection combined with trimetazidine was also superior to conventional treatment in reducing the level of LDH. Shenmai injection or *Breviscapine* injection combined with trimetazidine was better than conventional treatment or conventional treatment combined with trimetazidine in terms of effectiveness rate. *Breviscapine* injection combined with trimetazidine was superior to conventional treatment combined with trimetazidine in reducing the level of CK. Shenfu injection combined with trimetazidine was superior to conventional treatment alone in terms of effectiveness rate and reduction of CK level. The comparison of different CHIs showed that *Astragalus* injection was superior to Shenfu injection in reducing the level of CK-MB. In reducing the level of LDH, *Salviae miltiorrhizae* and *ligustrazine hydrochloride* injection was superior to *Astragalus* injection, Shenfu injection, and *Breviscapine* injection. In terms of safety, there was no significant difference among different interventions. Based on the ranking of the SUCRA value, Shenmai injection may be superior to other injections in terms of effectiveness rate, *Astragalus* injection and *Salviae miltiorrhizae* and *ligustrazine hydrochloride* injection may be superior to other injections in reducing myocardial injury markers. However, different CHIs have different properties. Some tend to replenish qi, some tend to activate blood circulation, some tend to tonify yang, and some tend to nourish yin. Therefore, for the selection of CHI, it is better to choose based on the performance of patients and syndrome differentiation of traditional Chinese medicine in clinical practice, which may be able to harvest a better clinical efficacy.

As a myocardial metabolic agent, trimetazidine can optimize the oxidation of fatty acids and glucose, improve myocardial metabolism, inhibit cardiomyocyte apoptosis, reduce cardiac remodeling, improve cardiac function and so on, which is often used in the treatment of cardiovascular diseases (Li et al., 2020). *Astragalus* injection is extracted from the root of *Astragalus mongholicus Bunge*. Previous studies have shown that the application of *Astragali Radix* can improve the survival rate and relieve the pathological changes of mice with VMC induced by coxsackievirus B3 (Chen et al., 2006). Astragaloside IV plays a cardioprotective role in experimental animals with VMC through a variety of signal pathways, such as antimyocardial remodeling, antivirus, anti-oxidation, anti-inflammation, anti-apoptosis, and reducing myocardial fibrosis (Zhuang et al., 2019). *Salviae miltiorrhizae* and *ligustrazine hydrochloride* injection is a compound preparation composed of *ligustrazine hydrochloride* and the extract of *Salvia miltiorrhiza Bunge*. *Salviae miltiorrhizae Radix et Rhizoma* is a standard Chinese herbal medicine for promoting blood circulation and removing blood stasis, and is thus widely used in the treatment of cardiovascular diseases. Previous studies have shown that several active components of *Salviae miltiorrhizae Radix et Rhizoma* have significant anti-inflammatory and antioxidant activities (MEIm et al., 2019). Tanshinone IIA can reduce myocardial apoptosis and myocardial remodeling caused by overload (Feng et al., 2016) and has been shown to alleviate cardiac dysfunction in septic mice by inhibiting inflammatory response (Huang et al., 2015). Tanshinol enhances antioxidant activity by activating serine/threonine kinase/extracellular signaling-regulated kinase1/2/nuclear factor erythroid-2-related factor 2 (Akt/ERK1/2/Nrf2) signal pathway, thus exerting a cardioprotective function (Yu et al., 2015). *Ligustrazine hydrochloride* can reduce cardiomyocyte apoptosis and injury in coxsackievirus B3–induced VMC by downregulating the expression of membrane surface molecules in mouse cardiomyocytes (Jiang et al., 2014). *Breviscapine* injection, which is extracted from *Erigeron breviscapus* (*Vaniot.*) *Hand–Mazz.*, has been shown in previous studies to have pharmacological effects, such as anti-inflammation, endothelial protection, myocardial protection, and reduction of cardiac remodeling, leading to its widespread use in the treatment of cardiovascular disease (Gao et al., 2017). Shenmai injection is derived from *Panax ginseng C. A. Mey*. and *Ophiopogon japonicus* (*Thunb.*) *Ker Gawl*., and has been shown in systematic reviews to be of use in the treatment of VMC (Lu et al., 2014). Ginsenoside Rb3, an active components of *Ginseng Radix et Rhizoma*, can inhibit endothelial to mesenchymal transformation of cardiac microvascular cells following coxsackievirus B3 infection through protein-rich tyrosine kinase 2-phosphoinositide-3-kinase/serine/threonine kinase (Pyk2-PI3K-AKT) signal pathway (Yang et al., 2019). Finallly, Shenfu injection is derived from *Panax ginseng C. A. Mey* and *Aconitum carmichaeli Debeaux*, and is widely used in China for the treatment of acute and critical cardiovascular diseases. Studies have shown that Shenfu injection may play a role in antiviral myocarditis by regulating multiple metabolic pathways, such as sphingolipid metabolism, glycerophospholipid metabolism, arachidonic acid metabolism, tryptophan metabolism, amino acyl RNA biosynthesis, and the citrate cycle (Tan et al., 2018).

Although the present study compared the efficacy and safety of different types of CHIs combined with trimetazidine in the treatment of VMC by network meta-analysis and provided some reference for the selection of CHI in clinic, there are still some limitations in this study. First, the methodological quality of the included studies was generally low. The method of generating random sequences in most studies is not clear, and all studies have no random allocation hiding, which may lead to selective bias in the determination of subjects. Almost all the included studies have not blinded the patients, trial personnel, and outcome evaluator, which may lead to expectation bias due

to the influence of subjective factors in the evaluation of outcome indicators. Second, there may be some clinical heterogeneity because of some differences in the age of participators, drug dosage, and course of treatment in the included studies. Some studies do not monitor safety, leading to the failure to assess the safety of some CHIs. In addition, there may be a small sample effect, resulting in some publication bias in the included study. In view of the above limitations, we suggest that more high-quality, large-sample, standardized clinical randomized controlled trials should be carried out in the future, to provide strong evidence for the efficacy and safety of CHIs combined with trimetazidine for the treatment of VMC.

CONCLUSION

The results of our network meta-analysis showed that CHI combined with trimetazidine may have therapeutic effect in the treatment of VMC. Compared with conventional treatment alone or conventional treatment combined with trimetazidine, the clinical effectiveness rate of CHI combined with trimetazidine is higher, with a greater effect on reducing myocardial zymogram level and no significant difference in safety. Among these CHIs evaluated in our analysis, Shenmai injection, *Astragalus* injection, and *Salviae miltiorrhizae* and *ligustrazine hydrochloride* injection may be the most effective. Given the limitations in the design of the included studies, our conclusions require further verification in larger, multicenter, and randomized controlled trials.

AUTHOR CONTRIBUTIONS

Conception and design: DW and XY. Literature retrieval, data extraction, and analysis: KW, BY, ZH, LH, and YH. Interpretation of results: DD and KW. Manuscript writing: KW, DD, and BY.

FUNDING

This work is supported by The High-Level Key Disciplines Project of Guangzhou University of Chinese Medicine (No. A1-AFD018171Z11089 to DW) and Scientific Research Project of Traditional Chinese Medicine Bureau of Guangdong Province (NO:20184015).

ACKNOWLEDGMENTS

We thank Clare Cox, from Liwen Bianji, Edanz Editing China (www.liwenbianji.cn/ac), for editing the English text of the draft of this manuscript.

SUPPLEMENTARY MATERIAL

The Supplementary Material for this article can be found online at: https://www.frontiersin.org/articles/10.3389/fphar.2021.630896/full#supplementary-material.

REFERENCES

Cao, Y., Xu, X., and Zhang, P. (2015). Advances in the traditional Chinese medicine-based management of viral myocarditis. *Cell Biochem. Biophys.* 73 (1), 237–243. doi:10.1007/s12013-015-0620-x

Chen, C. L. (2011). 32 cases of acute viral myocarditis with the treatment of traditional Chinese medicine combined with western medicine. *China's Naturopathy* 19 (07), 57. doi:10.19621/j.cnki.11-3555/r.2011.07.059

Chen, P. G. (2014). Efficacy of trimetazidine combined with *Astragalus* injection in the treatment of viral acute myocarditis. *Chin. Foreign Med. Res.* 12 (01), 105–106. doi:10.14033/j.cnki.cfmr.2014.01.048

Chen, X.-J., Bian, Z.-P., Lu, S., Xu, J.-D., Gu, C.-R., Yang, D., et al. (2006). Cardiac protective effect of *Astragalus* on viral myocarditis mice: comparison with perindopril. *Am. J. Chin. Med.* 34 (3), 493–502. doi:10.1142/s0192415x06004028

Chen, X. H., and Zeng, Y. S. (2018). Efficacy of *Salviae Miltiorrhizae* and *Ligustrazine hydrochloride* injection combined with trimetazidine in the treatment of VMC in acute stage. *Shenzhen J. Integrated Traditional Chin. West. Med.* 28 (21), 36–37. doi:10.16458/j.cnki.1007-0893.2018.21.016

Cheng, L. X. (2015). Efficacy of trimetazidine combined with Shenmai injection in the treatment of acute viral myocarditis. *Cardiovasc. Dis. J. integrated traditional Chin. West. Med.* 3 (27), 36–37. doi:10.16282/j.cnki.cn11-9336/r.2015.27.021

Cui, S. Q. (2018). Effect of trimetazidine combined with *Astragalus* injection on resisting inflammation and oxygen radicals in patients with acute viral myocarditis. *J. Hainan Med. Univ.* 24 (07), 337–739. doi:10.13210/j.cnki.jhmu.20180322.001

Dai, M. M. (2018). Analysis of the Efficacy of trimetazidine combined with *Astragalus* injection in the treatment of myocarditis. *China Foreign Med. Treat.* 37 (28), 110–112. doi:10.16662/j.cnki.1674-0742.2018.28.110

Feng, J., Li, S., and Chen, H. (2016). Tanshinone IIA inhibits myocardial remodeling induced by pressure overload via suppressing oxidative stress and inflammation: possible role of silent information regulator 1. *Eur. J. Pharmacol.* 791, 632–639. doi:10.1016/j.ejphar.2016.09.041

Gao, J., Chen, G., He, H., Liu, C., Xiong, X., Li, J., et al. (2017). Therapeutic effects of *Breviscapine* in cardiovascular diseases: a review. *Front. Pharmacol.* 8, 289. doi:10.3389/fphar.2017.00289

Gao, Y. (2019). Efficacy evaluation of trimetazidine combined with Shenfu injection in the treatment of viral myocarditis. *Modern Digestion and Intervention* (A02) 24, 2120–2121.

Ge, H. Z., Xu, Y., and Qin, H. Y. (2010). Clinical observation of *Astragalus* injection combined with trimetazidine in treating 60 cases of acute viral myocarditis. *HeiLong Jiang Med. J.* 34 (2), 134–136. doi:10.3969/j.issn.1004-5775.2010.02.023

Global Burden of Disease Study 2013 Collaborators (2015). Global, regional, and national incidence, prevalence, and years lived with disability for 301 acute and chronic diseases and injuries in 188 countries, 1990-2013: a systematic analysis for the Global Burden of Disease Study 2013. *Lancet* 386 (9995), 743–800. doi:10.1016/S0140-6736(15)60692-4

Grün, S., Schumm, J., Greulich, S., Wagner, A., Schneider, S., Bruder, O., et al. (2012). Long-term follow-up of biopsy-proven viral myocarditis. *J. Am. Coll. Cardiol.* 59 (18), 1604–1615. doi:10.1016/j.jacc.2012.01.007

He, L. (2014). Clinical observation of trimetazidine combined with Shenmai injection in the treatment of viral myocarditis. *China Health Care and Nutrition* 24 (4), 2249. doi:10.3969/j.issn.1004-7484(x).2014.04.559

Higgins, J. P. T., Altman, D. G., Gotzsche, P. C., Jüni, P., Moher, D., Oxman, A. D., et al. (2011). Cochrane bias methods group, and Cochrane statistical methods GroupThe Cochrane collaboration's tool for assessing risk of bias in randomised trials. *Bmj* 343, d5928. doi:10.1136/bmj.d5928

Huang, L., Zheng, M., Zhou, Y., Zhu, J., Zhu, M., Zhao, F., et al. (2015). Tanshinone IIA attenuates cardiac dysfunction in endotoxin-induced septic mice via inhibition of NADPH oxidase 2-related signaling pathway. *Int. Immunopharmacol.* 28 (1), 444–449. doi:10.1016/j.intimp.2015.07.004

Jiang, H., Chen, X. X., and Wang, J. Y. (2014). Effects of *Ligustrazine hydrochloride* on cardiomyocyte apoptosis in mice infected with Coxsackie virus B3. *Chin. J. Nosocomiol.* 24 (13), 3121–3123. doi:10.11816/cn.ni.2014-134233

Leone, O., Pieroni, M., Rapezzi, C., and Olivotto, I. (2019). The spectrum of myocarditis: from pathology to the clinics. *Virchows Arch.* 475 (3), 279–301. doi:10.1007/s00428-019-02615-8

Li, H., Ma, Z., Zhai, Y., Lv, C., Yuan, P., Zhu, F., et al. (2020). Trimetazidine ameliorates myocardial metabolic remodeling in isoproterenol-induced rats through regulating ketone body metabolism via activating AMPK and PPAR α. *Front. Pharmacol.* 11, 1255. doi:10.3389/fphar.2020.01255

Li, J. P., Liu, Y., Guo, J. M., Shang, E. X., Zhu, Z. H., Zhu, K. Y., et al. (2017). A comprehensive strategy to evaluate compatible stability of Chinese medicine injection and infusion solutions based on chemical analysis and bioactivity assay. *Front. Pharmacol.* 8, 833. doi:10.3389/fphar.2017.00833

Li, Q., and Gao, X. F. (2016). Clinical observation of *Salviae Miltiorrhizae* and *Ligustrazine hydrochloride* injection combined with trimetazidine in the treatment of acute viral myocarditis. *China Pharm.* 27 (32), 4568–4570. doi:10.6039/j.issn.1001-0408.2016.32.34

Liu, S., Niu, H., and Zhang, J. G. (2015). Meta-analysis of the efficacy and safety of *Astragalus* injection combined with trimetazidine in the treatment of viral myocarditis. *China Pharmary* 26 (36), 5113–5116. doi:10.6039/j.issn.1001-0408.2015.27.26

Lu, L. Y., Zheng, G. Q., and Wang, Y. (2014). An overview of systematic reviews of Shenmai injection for healthcare. *Evid. Based Complement. Alternat. Med.* 2014, 1–9. doi:10.1155/2014/840650

Ma, Z. X. (2012). Clinical observation on 62 cases of viral myocarditis treated by trimetazidine combined with *Astragalus* injection. *Chin. J. Coal Industry Med.* 15 (03), 380–381.

Marzilli, M., Vinereanu, D., Lopaschuk, G., Chen, Y., Dalal, J. J., Danchin, N., et al. (2019). Trimetazidine in cardiovascular medicine. *Int. J. Cardiol.* 293, 39–44. doi:10.1016/j.ijcard.2019.05.063

MEIm, X.-D., Cao, Y.-F., Che, Y.-Y., Li, J., Shang, Z.-P., Zhao, W.-J., et al. (2019). Danshen: a phytochemical and pharmacological overview. *Chin. J. Nat. Med.* 17 (1), 59–80. doi:10.1016/s1875-5364(19)30010-x

Miao, Y. J. (2019). Effects of *Breviscapine* injection combined with trimetazidine on the improvement of symptoms and changes of myocardial enzyme levels in patients with acute viral myocarditis. *Capital Med.* 26 (07), 49. doi:10.3969/j.issn.1005-8257.2019.07.041

Olejniczak, M., Schwartz, M., Webber, E., Shaffer, A., and Perry, T. E. (2020). Viral myocarditis-incidence, diagnosis and management. *J. Cardiothorac. Vasc. Anesth.* 34 (6), 1591–1601. doi:10.1053/j.jvca.2019.12.052

Pang, M. X., and Huang, Z. (2013). Clinical observation of trimetazidine combined with Shenmai injection in the treatment of viral myocarditis in children. *J. Youjiang Med. Coll. Nationalities* 68 (2), 207–208. doi:10.3969/j.issn.1001-5817.2013.02.052

Pu, X. H. (2013). Analysis of the clinical effect of trimetazidine combined with *Astragalus* injection in the treatment of 134 cases of myocarditis. *China Health Industry* 10 (06), 69. doi:10.16659/j.cnki.1672-5654.2013.06.094

Shao, L. L., Han, L. Y., Xin, S. L., Chang, C., Li, Z. M., and Liu, L. J. (2012). Analysis of trimetazidine combined with *Astragalus* injection in the treatment of myocarditis. *Zhejiang Clin. Med. J.* 14 (09), 1106–1107. doi:10.3969/j.issn.1008-7664.2012.09.040

Society of Cardiovascular Diseases, China Association of Chinese Medicine (2020). International clinical practice guideline of traditional Chinese medicine·viral myocarditis. *Chin. J. Exp. Traditional Med. Formulae* 26 (18), 91–97. doi:10.13422/j.cnki.syfjx.20201062

Sun, X. P. (2013). Clinical observation of trimetazidine and *Astragalus* in the treatment of acute viral myocarditis. *Contemp. Med.* 19 (07), 148–149. doi:10.3969/j.issn.1009-4393.2013.7.113

Sun, X., and Sun, J. L. (2018). Efficacy of trimetazidine combined with Shenfu injection in the treatment of viral myocarditis. *Chin. Community Doctors* 34 (3), 80–81. doi:10.3969/j.issn.1007-614x.2018.3.50

Tan, G., Zhou, Q., Liu, K., Dong, X., Li, L., Liao, W., et al. (2018). Cross-platform metabolic profiling deciphering the potential targets of Shenfu injection against acute viral myocarditis in mice. *J. Pharm. Biomed. Anal.* 160, 1–11. doi:10.1016/j.jpba.2018.07.042

Tschöpe, C., Cooper, L. T., Torre-Amione, G., and Van Linthout, S. (2019). Management of myocarditis-related cardiomyopathy in adults. *Circ. Res.* 124 (11), 1568–1583. doi:10.1161/circresaha.118.313578

Wang, J. (2017). Efficacy of trimetazidine combined with *Breviscapine* injection in the treatment of acute viral myocarditis. *Mod. J. Integrated Traditional Chin. West. Med.* 26 (8), 879–881. doi:10.3969/j.issn.1008-8849.2017.08.029

Wang, J. F. (2020). Effects of *Salviae Miltiorrhizae* and *Ligustrazine hydrochloride* combined with trimetazidine on serum lipid peroxides, IFN-γ and myocardial enzymes in patients with viral myocarditis. *Chin J. Clin. Rational Drug Use* 13 (2B), 51–53. doi:10.15887/j.cnki.13-1389/r.2020.08.028

Wang, Q. (2012). Efficacy and safety of trimetazidine combined with *Astragalus* injection in treating acute viral myocarditis. *Chin. J. Gerontol.* 32 (9), 1820–1821. doi:10.3969/j.issn.1005-9202.2012.09.018

Wang, Q. J. (2016). Clinical effects and safety of trimetazidine combined with *Astragalus* radix injection in treating acute viral myocarditis. *Chin. J. Clin. Rational Drug Use* 9 (3C), 8–9. doi:10.15887/j.cnki.13-1389/r.2016.09.004

Wang, Y. C. (2019). Clinical effect of trimetazidine combined with *Breviscapine* injection in treating acute viral myocarditis. *Mod. Diagn. Treat.* 30 (24), 4320–4322.

Wang, Z. X. (2010). Clinical observation of trimetazidine combined with *Astragalus* injection in the treatment of myocarditis. *J. China Traditional Chin. Med. Inf.* 2 (28), 134.

Wei, A., Li, Q., Ding, L. X., Tan, X. H., Guo, D. M., Gu, Q., et al. (2020). Effect of *Astragalus* injection combined with trimetazidine on NLRP3 inflammasome and related downstream pathways in peripheral blood of elderly patients with viral myocarditis. *Mod. J. Integrated Traditional Chin. West. Med.* 29 (8), 815–818. doi:10.3969/j.issn.1008-8849.2020.08.005

Xu, W. M., and Zhang, S. F. (2011). *Astragalus* injection combined with Wanshuangli in the treatment of 60 cases of viral myocarditis. *Contemp. Med.* 17 (19), 39–40. doi:10.3969/j.issn.1009-4393.2011.19.021

Yang, L., Liu, Q., Yu, Y., Xu, H., Chen, S., and Shi, S. (2019). Ginsenoside-Rb3 inhibits endothelial-mesenchymal transition of cardiac microvascular endothelial cells. *Herz* 44 (1), 60–68. doi:10.1007/s00059-017-4628-4

Yang, S. Y. (2009). Observation on the curative effect of *Astragalus* injection combined with trimetazidine in the treatment of acute viral myocarditis-Analysis of 45 cases. *New Med.* 40 (2), 101–103.

Yu, J., Wang, L., Akinyi, M., Li, Y., Duan, Z., Zhu, Y., et al. (2015). Danshensu protects isolated heart against ischemia reperfusion injury through activation of Akt/ERK1/2/Nrf2 signaling. *Int. J. Clin. Exp. Med.* 8 (9), 14793–14804.

Yu, K., Wang, Y. N., Ren, Y., Zhang, X. W., Zhang, X. F., and Zhang, H. (2014). Trimetazidine:a meta-analysis of randomized controlled trial to the patients with viral myocarditis. *Chin. J. Nosocomiol* 24 (24), 6139–6141. doi:10.11816/cn.ni.2014-143898

Yu, X. L. (2014). Clinical observation of *Astragalus* injection combined with trimetazidine for the treatment of acute viral myocarditis. *Int. J. Virol.* 21 (5), 226–230. doi:10.3706/cma.j.issn.1673-4092.2014.05.010

Zhang, H. X., Guan, S. C., and Zhao, L. X. (2015). Therapeutic effect of trimetazidine combined with *Astragalus* injection on acute viral myocarditis. *Contemp. Med.* 21 (13), 122–123. doi:10.3969/j.issn.1009-4393.2015.13.081

Zhang, Y. J., Fu, Y. Z., and Chen, J. D. (2016). Efficacy analysis of trimetazidine combined with Shenfu injection in treating viral myocarditis. *China Med. Eng.* 24 (4), 101–102. doi:10.19338/j.issn.1672–2019.2016.04.045

Zheng, X. M. (2019). Efficacy of trimetazidine combined with *Astragalus* injection on viral myocarditis. *Med. J. Chin. People's Health* 31 (9), 11–12. doi:10.3969/j.issn.1672-0369.2019.09.005

Zhu, Q. B., Huang, H. F., Xu, Y., Pan, Z. H., and Xiang, J. H. (2020). Effects of *Salviae Miltiorrhizae* and *Ligustrazine hydrochloride* on expression of myocardial enzymes, oxidative stress and inflammatory factors in children with viral myocarditis. *Matern. Child Health Care China* 35 (2), 259–262. doi:10.19829/j.zgfybj.issn.1001-4411.2020.02.021

Zhuang, Z., Wang, Z. H., Deng, L. H., Zheng, Q., Zheng, G. Q., and Wang, Y. (2019). Astragaloside IV exerts cardioprotection in animal models of viral myocarditis: a preclinical systematic review and meta-analysis. *Front. Pharmacol.* 10, 1388. doi:10.3389/fphar.2019.01388

Conflict of Interest: The authors declare that the research was conducted in the absence of any commercial or financial relationships that could be construed as a potential conflict of interest.

Copyright © 2021 Wu, Deng, Yu, Han, Huang, He, Yan and Wang. This is an open-access article distributed under the terms of the Creative Commons Attribution License (CC BY). The use, distribution or reproduction in other forums is permitted, provided the original author(s) and the copyright owner(s) are credited and that the original publication in this journal is cited, in accordance with accepted academic practice. No use, distribution or reproduction is permitted which does not comply with these terms.

frontiers in Pharmacology

ORIGINAL RESEARCH
published: 04 May 2021
doi: 10.3389/fphar.2021.665398

Gegen Qinlian Decoction Ameliorates Hyperuricemia-Induced Renal Tubular Injury via Blocking the Inflammatory Signaling Pathway

Xiao-Jun Wang[1,2†], Yi-Ding Qi[3†], Hao-Chen Guan[4†], Hua-Gang Lin[5], Pei-Qing He[1], Kang-Wei Guan[1], Lei Fu[2], Mao-Qing Ye[2,3*], Jing Xiao[2,5*] and Tao Wu[1,2*]*

[1]Department of Traditional Chinese Medicine, Huadong Hospital Affiliated to Fudan University, Shanghai, China, [2]Shanghai Key Laboratory of Clinical Geriatric Medicine, Huadong Hospital Affiliated to Fudan University, Shanghai, China, [3]Department of Cardiology, Huadong Hospital Affiliated to Fudan University, Shanghai, China, [4]Department of Nephrology, Shanghai General Hospital, Shanghai Jiao Tong University School of Medicine, Shanghai, China, [5]Department of Nephrology, Huadong Hospital Affiliated to Fudan University, Shanghai, China

OPEN ACCESS

Edited by:
Yan Xu,
Cleveland State University,
United States

Reviewed by:
Kai Xiao,
Second Military Medical University,
China
Xu-Dong Zhou,
Hunan University of Chinese Medicine,
China

***Correspondence:**
Lei Fu
sabrinafl@msn.com
Mao-Qing Ye
yemaoqing@fudan.edu.cn
Jing Xiao
jingxiao13@fudan.edu.cn
Tao Wu
taowuh@hotmail.com

[†]These authors have contributed equally to this work

Specialty section:
This article was submitted to Ethnopharmacology, a section of the journal Frontiers in Pharmacology

Received: 08 February 2021
Accepted: 25 March 2021
Published: 04 May 2021

Citation:
Wang X-J, Qi Y-D, Guan H-C, Lin H-G, He P-Q, Guan K-W, Fu L, Ye M-Q, Xiao J and Wu T (2021) Gegen Qinlian Decoction Ameliorates Hyperuricemia-Induced Renal Tubular Injury via Blocking the Inflammatory Signaling Pathway. Front. Pharmacol. 12:665398. doi: 10.3389/fphar.2021.665398

Background: Gegen Qinlian decoction (GGQLD) is a typical traditional Chinese medicine (TCM) prescription documented in *Shang Han Lun*. Clinically, GGQLD has been utilized to manage the inflammatory symptoms of metabolic diseases and to protect against renal damage in China. In the present study, a hypothesis was proposed that the multi-target solution of GGQLD produced anti-inflammatory effects on ameliorating hyperuricemia (HUA).

Methods: A total of 30 primary HUA patients receiving GGQLD treatment (two doses daily) for 4 weeks were selected. Then, differences in uric acid (UA) levels and expression of peripheral blood mononuclear cells (PBMCs) and urinary exosomes before and after treatment were analyzed. The therapeutic indexes for the active ingredients in GGQLD against HUA were confirmed through pharmacological subnetwork analysis. Besides, the HUA rat model was established through oral gavage of potassium oxonate and treated with oral GGQLD. In addition, proximal tubular epithelial cells (PTECs) were stimulated by UA and intervened with GGQLD for 48 h. Subsequently, RNA-seq, flow cytometry, and confocal immunofluorescence microscopy were further conducted to characterize the differences in UA-mediated inflammation and apoptosis of human renal tubular epithelial cells pre- and post-administration of GGQLD. In the meanwhile, quantitative real-time PCR (qPCR) was carried out to determine gene expression, whereas a western blotting (WB) assay was conducted to measure protein expression.

Results: Our network analysis revealed that GGQLD treated HUA via the anti-inflammatory and antiapoptotic pathways. Additionally, NLPR3 expression significantly decreased in PBMCs and urinary exosomes of HUA patients after GGQLD treatment. *In vivo*, GGQLD treatment alleviated HUA-induced renal inflammation, which was associated with decreased expression of NLRP3 inflammasomes and apoptosis-related mRNAs. Moreover, GGQLD promoted renal UA excretion by inhibiting the activation of GSDMD-

dependent pyroptosis induced by NLRP3 inflammasomes and by reducing apoptosis via the mitochondrial apoptosis signaling pathway *in vitro*.

Conclusion: This study indicates that GGQLD efficiently reduces inflammatory responses while promoting UA excretion in HUA. Our findings also provide compelling evidence supporting the idea that GGQLD protects against the UA-mediated renal tubular epithelial cell inflammation through the mitochondrial apoptosis signaling pathways. Taken together, these findings have demonstrated a novel therapeutic method for the treatment of HUA.

Keywords: Gegen Qinlian decoction, hyperuricemia, NLRP3, apoptosis, pharmacological network analysis

INTRODUCTION

Hyperuricemia (HUA) is a factor that independently predicts the risk of kidney diseases (Prasad and Qing, 2015; Srivastava et al., 2018; Tsai et al., 2018). Generally, HUA is manifested as macrophage infiltration, tubular damage, and upregulated inflammatory mediator levels (Zhou et al., 2012; Xiao et al., 2018; Braga et al., 2020). The renal proximal tubule plays a pivotal role in transporting renal urate, which is a major site of urate reabsorption (Lipkowitz, 2012) and exerts a remarkable role in HUA occurrence and development. In our previous study, soluble uric acid (UA) triggers NLRP3 inflammasome production, IL-1β expression, and caspase-1 activation in human PTECs, which could thus induce the secretion of pro-inflammatory cytokines and activate the innate immunity (Xiao et al., 2015; Xiao et al., 2016). Therefore, it is of importance to develop a treatment against HUA to prevent renal tubular injury in the future. Till the present, numerous patients have experienced a relapse after the withdrawal of anti-hyperuricemic drugs such as benzbromarone.

For thousands of years, combination therapy has been promoted in traditional Chinese medicine (TCM) to treat different disorders. Among them, Gegen Qinlian decoction (GGQLD), one of the typical TCM prescriptions, was originally documented in the *Treatise on Exogenous Febrile Disease* in the Han Dynasty (202 BC–220 CE). GGQLD comprises *Pueraria montana* var. *lobata* (Gegen), *Scutellaria baicalensis Georgi* (Huangqin), *Glycyrrhiza uralensis Fisch. ex DC* (Gancao), and *Coptis chinensis Franch* (Huanglian). It has been extensively utilized for the clinical treatment of gastrointestinal diseases for approximately 2,000 years, in particular for damp-heat syndrome–related diarrhea (Bi et al., 2013; Tian et al., 2016). Moreover, the clinical efficacy of GGQLD in treating ulcerative colitis (UC) has been verified (Zhao et al., 2020). Experiments *in vitro* and *in vivo* suggest that some active ingredients in GGQLD, like berberine, baicalin, and puerarin, obviously mitigate oxidative stress (OS) and inflammation (Dinesh and Rasool, 2017; Guarino et al., 2017; Yu et al., 2021). We previously discovered that GGQLD exerted diabetes-mitigating (Xu et al., 2011; Li et al., 2013; Zhang et al., 2013) and anti-inflammation effects through its active ingredients (Tian et al., 2013; Ryuk et al., 2017; Wu et al., 2019). Besides, inflammatory response, lipid, and glucose metabolic disorders are also important for HUA. Therefore, guided by the TCM theory of "treating different diseases with the same therapy," GGQLD can be sometimes used to treat HUA. However, the underlying mechanism of action has not been clarified.

By network pharmacology, we discovered that GGQLD might treat HUA via the anti-inflammatory and antiapoptotic pathways. Further experiments showed that GGQLD alleviated the inflammatory state of HUA patients and improved renal inflammation in HUA rats. Moreover, *in vitro* experiment confirmed that GGQLD played a role in the inflammation and apoptosis of PTECs induced by UA.

MATERIALS AND METHODS

Materials and Reagents

Cell culture medium and human primary renal PTECs were provided by ScienCell (San Diego, CA, United States). Anti-SLC2A9 (URAT1) antibodies, TSG101, CD63, caspase-1, GSDMD, IL-1β, caspase-3, caspase-8, caspase-9, cytochrome c, Bcl-2, and Bax were purchased from ABclonal (Wuhan, China). Oxonic acid (OA) and UA were provided by Sigma (St. Louis, MO, United States). CIAS1/NALP3, GAPDH, and anti-GLUT9 were provided by Abcam (Cambridge, United Kingdom). In addition, the CCK-8 assay kit was provided by Jiwei Biological Technology (Shanghai, China).

Preparation of GGQLD

GGQLD, a famous decoction documented in the *Treatise on Exogenous Febrile Disease* around 1,900 years ago, was used and approved by the Huadong Hospital Affiliated to Fudan University. The dried herbs, including *Pueraria montana* var. *lobata* (Gegen), *Scutellaria baicalensis Georgi* (Huangqin), *Glycyrrhiza uralensis Fisch. ex DC* (Gancao), and *Coptis chinensis Franch* (Huanglian), in the ratio of 8:3:3:2 (w/w/w/w), were first soaked in distilled water with 15-fold volumes of herbs (v/w) for 30 min and then extracted by decoction twice, 2 h for the first time and 2 h for the second time, with 8-fold volumes of water to herbs (v/w). After filtration, the solution was evaporated under reduced pressure to a suspension with a final density of 1 g/ml and stored at 4°C for further use (Xie et al., 2006).

High-Performance Liquid Chromatography (HPLC)

Puerarin, baicalin, liquiritin, and berberine (all purities >98%) were provided by Shanghai Yuanzhi Biotechnology Co., Ltd.

(Shanghai, China). **Supplementary Figure S1** presents the chemical structures of the ingredients. Acetonitrile, formic acid, and methanol of HPLC grade were provided by Merck Company (Darmstadt, Germany). The Milli-Q system (Millipore, Milford, MA, United States) was utilized to obtain deionized water. Other reagents of analytical grade were acquired from commercial sources. To identify the components of GGQLD, we performed HPLC analysis using an Agilent 1260 Infinity brand chromatographic chain with a C18 chromatographic column (250 × 4:6 mm, 5 μm, Thermo Fisher Scientific, NY, United States), along with a column oven, a binary pump, a diode array detector, and an autosampler (Agilent 1100 series). Thereafter, 20 ml ethanol extract was added to the column. Throughout the whole chromatographic analysis process, the column injector was maintained at 25°C. The mobile phase comprised the ammonium formate solution (10 mmol/l, pH 3.0, A) and acetonitrile. For the components, their detection wavelength was set at 270 nm. Subsequently, we identified each compound according to the pure standard absorbance spectra and retention time (Guo et al., 2019).

Systemic Pharmacological Analysis of GGQLD

We searched the active ingredients of Gegen, Huangqin, Huanglian, and Gancao in GGQLD against the TCMSP database (http://tcmspw.com/index.php) by the thresholds of druglikeness (DL, also known as the similarity between the known medicines and the components) ≥0.18 and oral bioavailability (OB, medicine component oral availability) ≥30%. Based on the TCMSP database (Yao et al., 2013; Liu et al., 2020), we aligned the GGQLD active ingredients with the candidate targets separately, then retrieved targets of diverse origins against the UniProt database (http://www.uniport.org), and acquired the official target gene symbols to perform subsequent assays. A total of 196 HUA-associated targets were identified from the DisGeNET (http://www.disgenet.org) and NCBI databases. Cytoscape 3.8.0 software is the openly accessible bioinformatics platform used to visualize the molecular interaction networks (Deng et al., 2020). In the current study, we adopted Cytoscape to construct the active ingredient–target–disease–medicine interaction network. GO functional annotations and KEGG pathway analyses on the critical therapeutic targets in GGQLD against HUA were analyzed by adopting the DAVID 6.8 database (Komada et al., 2018).

Participants and Setting

From January 1st, 2020 to October 31st, 2020, a total of 30 male patients with asymptomatic hyperuricemia were enrolled from the Inpatient and Outpatient Departments of the Huadong Hospital Affiliated to Fudan University (Shanghai, China). The patient inclusion criteria are shown below, those aged 18–75 years with a diagnosis of HUA (serum uric acid, SUA > 420 μmol/l). For patients receiving anti-HUA treatment, they should receive washout for 2 weeks, and we only enrolled patients with SUA > 420 μmol/l post-washout. The patient exclusion criteria were as follows: 1) those with an allergic physique or previous allergic history to benzbromarone or TCM, 2) serum creatinine >1.5 mg/dl, 3) two-fold elevation of ALT compared with the normal upper limit, 4) serious stiffness or deformity due to gouty arthropathy, 5) clinically significant arrhythmia, and 6) alcohol abuse history. In addition, patients confirming to any one of the following conditions were also excluded: 1) those having serious concurrent diseases in the hematopoietic system, liver, cerebrovascular system, or kidney, mental diseases, or malignant cancers; 2) those taking salicylate or aspirin (>325 mg/d)-containing medications; 3) those taking hypouricemic medications, 6-mercaptopurine, or azathioprine; and 4) those who had been involved in additional clinical trials in the last 3 months.

In this study, 30 patients were given GGQLD treatment (two doses daily for 4 weeks). SUA and urine uric acid (UUA) were adopted for evaluating the therapeutic efficacy (**Table 1**). The Local Ethical Committee of Huadong Hospital Affiliated to Fudan University approved our study protocols (No. 20190037).

Peripheral Blood Mononuclear Cell Isolation by Ficoll-Paque Density Gradient Centrifugation

The Local Ethical Committee of Huadong Hospital Affiliated to Fudan University approved our experimental protocols on human blood (No. 20190037). To be specific, whole blood was centrifuged at 500 × g for 5 min at room temperature to separate the plasma. Thereafter, the equivalent amount of 1× PBS (under ambient temperature) was used to dilute the rest blood samples, followed by Ficoll-Paque underlaying (under ambient temperature) and 30 min of centrifugation (2,000 rpm, 21°C) using a Heraeus Multifuge X3R (Thermo Fisher Scientific), with the deceleration and acceleration being set at 0 and 5, respectively. Afterward, we obtained PBMCs from the interface between plasma and Ficoll-Paque in the 15 ml tube and used 1× PBS to wash the cells twice for 10 min (1,500 rpm, 4°C).

Purification and Characterization of Urine Exosomes and Pellets

We collected urinary exosomes from 8 controls and 8 GGQLD-intervened HUA patients. Later, 40 ml freshly prepared urine samples were collected to obtain urinary cell pellets. Thereafter, the supernatants were subjected to 30 min of centrifugation at 12,000 × g, followed by standing to isolate the urinary exosomes. ExoQuick-TC for tissue culture media and urine (Exiqon, Woburn, MA, United States) was used to isolate urinary exosomes in accordance with specific protocols. To validate the protocols for exosome purification, we performed cryo-transmission electron microscopy to analyze the size, shape, and morphology of urinary exosomes. The isolation of exosomes was characterized by WB using NanoSight.

Animal Model and Measurement

A total of 15 male SPF SD rats (age, 8 weeks; weight, 200–250 g) were raised at the Animal Center of Shanghai

Rat and Mouse Biotech Co., Ltd. Then, all animals were randomized into three groups, including the 1) Cont, 2) OA (8-week administration of OA at 750 mg/kg/day), and 3) OA + GGQLD (8-week administration of OA at 750 mg/kg/day + 4-week administration of GGQLD at 10 ml/kg/day initiating in week 5) groups, with five in every group. At the end of week 8, each animal was terminated. The 24-h urine was sampled from animals in metabolic cages. Subsequently, the levels of sUA, uUA, serum creatinine (Scr), blood urea nitrogen (BUN), and urinary creatinine (Ucr) were measured through the enzymatic colorimetric assay using a fully automatic chemistry analyzer (MODULAR D/P, Roche). Afterward, the freshly prepared renal cortical samples were obtained immediately after the animals were terminated to measure UA in accordance with specific protocols. Part of the tissues was stained with hematoxylin–eosin (HE) or Masson's trichrome stain for light microscopy. Next, the dissected tissue samples were preserved at −80°C to carry out immunoblotting and RT-PCR assays. Each animal experiment was approved by the Animal Care and Use Committee of Shanghai Rat and Mouse Biotech Co., Ltd. following guidelines of the National Institutes of Health (NIH Pub. No. 85-23, revised 1996).

Cell Culture

The epithelial cell medium, which was supplemented with basal medium (500 ml), fetal bovine serum (10 ml, FBS), penicillin/streptomycin (5 ml), and epithelial cell growth supplement (5 ml), was used to culture human primary PTECs. Then, we incubated cells under 37°C and 5% CO_2 conditions. A 24-h "growth arrest" period was observed within the serum-free medium before stimulation in each experiment.

Soluble UA Preparation

Previously, we dissolved UA into 1M NaOH to the final concentration of 50 mg/ml (Xiao et al., 2015). Then, we examined the solution so as to ensure that there was no mycoplasma and also filtered the solution (pore size, 22 μm) prior to use. No detectable crystal was observed under polarizing microscopy or in the process of cell incubation.

Cell Viability Assay on Cells Treated With Different Doses of GGQLD

A Cell Counting Kit-8 (CCK-8, Beijing Solarbio Science and Technology Co., Ltd.) assay was conducted to assess cell viability after GGQLD treatments at diverse doses. Cells (1 × 104 cells/well) were cultivated within the 96-well plate for 24–48 h. The microplate reader was used to measure absorbance (OD) at 450 nm. All experiments were conducted thrice.

RNA Sequencing

After GGQLD treatment, we harvested PTECs and washed them twice with ice-cold PBS. We collected six samples altogether, among which three were from the GGQLD group while three were from the control group. Trizol reagent (Takara, Dalian, China) was employed to extract total RNA in accordance with specific protocols. Libraries were constructed and mRNA was sequenced by Nuohe Zhiyuan Technology Company (Beijing, China). In addition, DESeq (version 1.30.0) was utilized to identify differentially expressed genes (DEGs). The false discovery rate (FDR) was applied to adjust p value, and the significance thresholds of fold change (FC) ≥ 2 and $p < 0.05$ were applied.

TABLE 1 | Clinical data of HUA patients before and after GGQLD treatment.

	Before treatment with GGQLD Mean ± SD	After treatment with GGQLD Mean ± SD	*p* value[#]
SUA	497.70 ± 39.47	418.93 ± 69.64	<0.001
UUA	424.81 ± 157.10	641.62 ± 272.83	0.0128
Scr	85.84 ± 14.28	83.88 ± 12.34	0.3699
BUN	5.37 ± 1.28	5.84 ± 2.42	0.3518
eGFR	85.38 ± 17.35	87.33 ± 13.34	0.4198
TG	2.22 ± 1.08	1.81 ± 0.69	0.0263
TC	4.59 ± 1.04	4.34 ± 0.95	0.1458
IL1β	9.13 ± 1.06	4.67 ± 1.15	0.0005
IL6	7.43 ± 5.80	2.35 ± 0.70	0.0389
IL8	20.58 ± 13.35	6.40 ± 0.77	0.0206
ALT	35.22 ± 33.16	24.96 ± 17.38	0.0380
AST	26.46 ± 15.28	20.87 ± 9.02	0.1043

Annexin V-FITC/PI Double-Labeled Flow Cytometry

Flow cytometric analysis was conducted with an Annexin V-FITC apoptosis detection kit (DOJINDO; Kyushu, Japan) to analyze cell apoptosis under specific instructions. After UA and GGQLD treatments, PTECs were harvested and rinsed with ice-cold PBS, followed by staining using the binding buffer that contained Annexin V-FITC/PI at 4°C for 15 min in the dark. Finally, flow cytometric analysis (Beckman Coulter, Fullerton, CA, United States) was performed to record cells.

Confocal Immunofluorescence Microscopy

Cells were cultured onto a laser confocal cell culture dish (Thermo Fisher Scientific, NY, United States) in accordance with specific protocols. 24 h later, the cells were washed with PBS and fixed by 4% paraformaldehyde in PBS. Thereafter, 10% BSA contained within PBS was utilized to block the cells for 30 min, whereas the GSDMD and NLRP3 antibodies in 10% BSA were used to incubate the cells at 4°C overnight. Then, the cells were rinsed with PBS thrice and incubated with goat anti-rabbit antibodies (Invitrogen, Grand Island, NY, United States) for 1 h in the dark. The cells were washed consecutively thrice, and a confocal imaging system (LSM 780;Carl Zeiss, Jena, Germany) was employed to examine the dishes.

RNA Extraction and Quantitative Real-Time PCR

Trizol (Life Technologies, United States) was employed to isolate total cellular and tissue RNA in accordance with specific

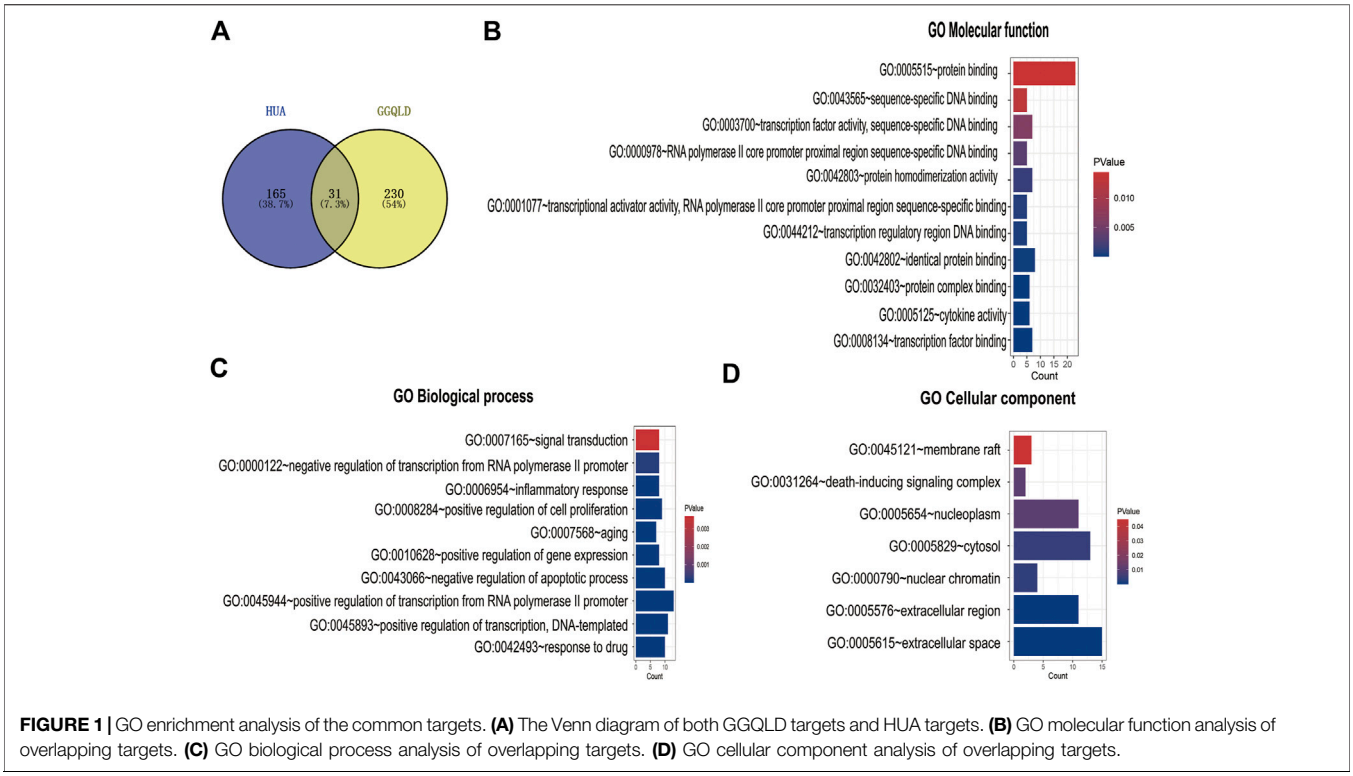

FIGURE 1 | GO enrichment analysis of the common targets. **(A)** The Venn diagram of both GGQLD targets and HUA targets. **(B)** GO molecular function analysis of overlapping targets. **(C)** GO biological process analysis of overlapping targets. **(D)** GO cellular component analysis of overlapping targets.

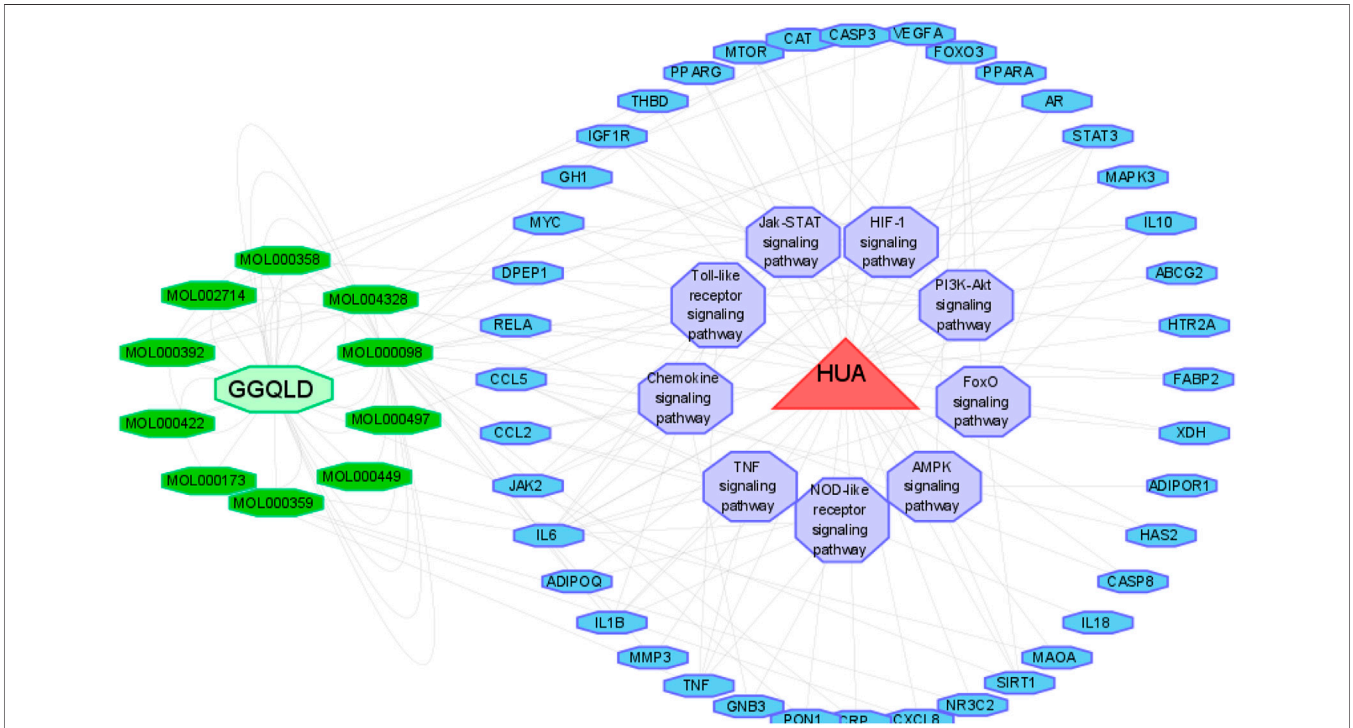

FIGURE 2 | Potential therapeutic mechanisms of GGQLD in hyperuricemia. **(A)** Bubble chart of the top 35 signaling pathways screened by using the KEGG enrichment analysis. **(B)** Venn diagram showing the overlap genes between five types of pathways. **(C)** Protein–protein interaction and gene coexpression network.

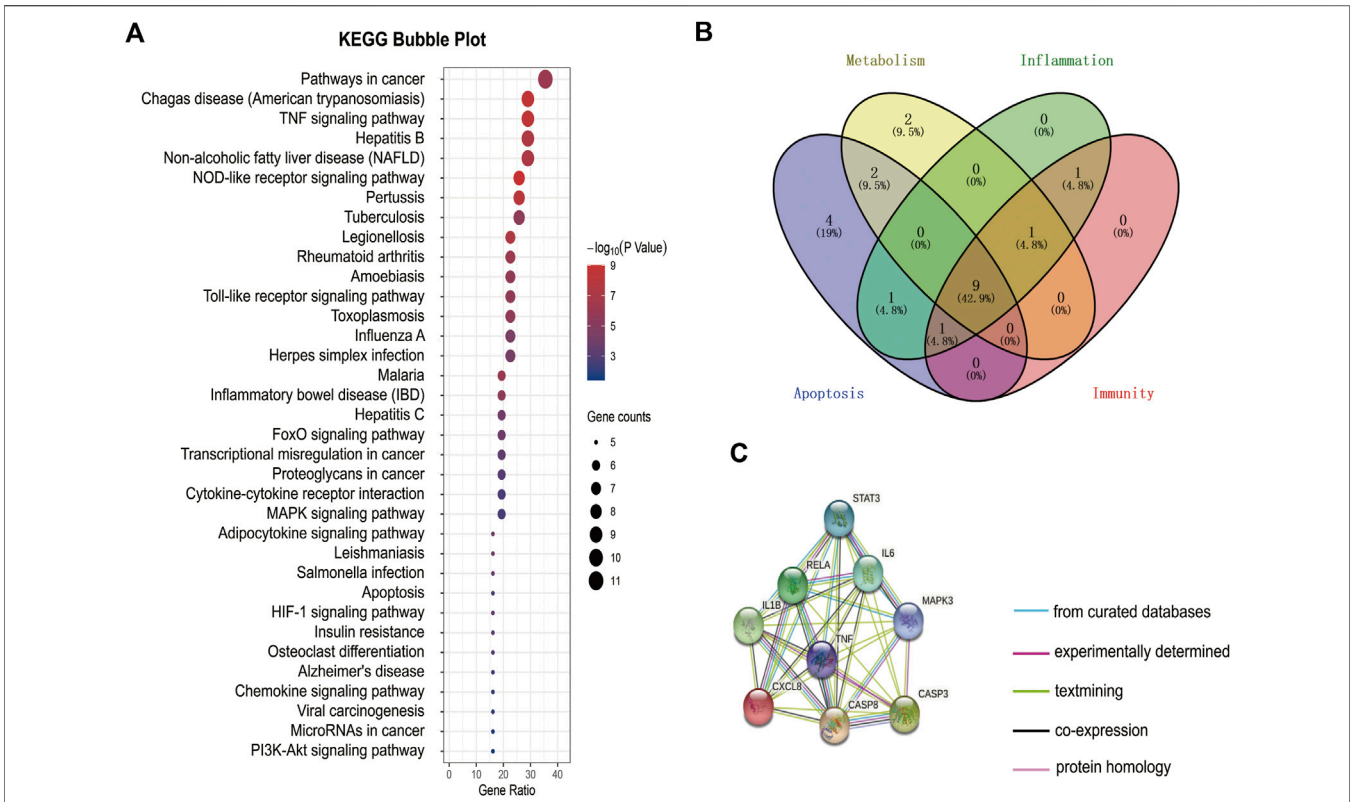

FIGURE 3 | Drug–compound–target–disease network map.

protocols. The content and purity of RNA were detected through a NanoDrop 2000 (Thermo Fisher Scientific, United States). To carry out mRNA quantification, we applied a reverse transcription kit (Vazyme, China) for the reverse transcription of total RNA according to specific instructions. Afterward, SYBR Green Master Mix (Vazyme, China) was utilized to perform qPCR, whereas a Roche Light Cycler system (Roche, Switzerland) was adopted for analysis, with GAPDH being an endogenous control. **Table 2** lists the primer sequences. Gene expression was normalized to the GAPDH level, which was presented in the manner of FC ($2-\Delta\Delta CT$). All results were repeated thrice.

WB Analysis of the Cultured Human PTECs

Supernatants of cell culture were collected according to the previous description and then the lysis buffer supplemented with protease inhibitor cocktails (Sigma, St Louis, MO, United States) was used to lyse the rest cells. After collecting total proteins, we carried out WB analysis according to the previous description (Xiao et al., 2015). In the present work, the following primary antibodies (all were diluted at 1:1,000) were adopted, including rabbit pAb Glut9, rabbit pAb URAT1, rabbit pAb caspase-1, rabbit pAb caspase-3, rabbit pAb NLRP3, rabbit pAb IL-1β, rabbit pAb GSDMD, rabbit pAb Bax, rabbit pAb caspase-8, rabbit pAb cytochrome c, rabbit pAb Bcl-2, and rabbit pAb caspase-9.

Statistical Analysis

Data were presented in the manner of means ± SD, except as otherwise noted. SPSS19.0 (SPSS, Inc., Chicago, IL, United States) was applied for all statistical analyses. For continuous variables, multivariate ANOVA was utilized to assess the differences between the groups. $p < 0.05$ indicated that a difference was statistically significant. GraphPad Prism 5.0 was employed for drawing plots.

RESULTS

Acquisition of Potential Active Ingredients in GGQLD and Common Targets of HUA

A total of 907 ingredients were discovered in GGQLD through the TCMSP database, including 62, 123, 178, and 278 in Gegen, Huangqin, Huanglian, and Gancao, respectively. The thresholds of DL ≥ 0.18 and OB ≥ 30% were used to screen the active ingredients. Finally, 372 candidate active ingredients conformed to our preset screening thresholds. A total of 196 genes in HUA were screened from the database (DisGeNET). In TCM, a medication displays diverse pharmacological effects via various targets. Therefore, it is greatly significant to determine the TCM medication mechanisms in treating complicated diseases based on network analysis. Previously, we acquired a total of 196 targets

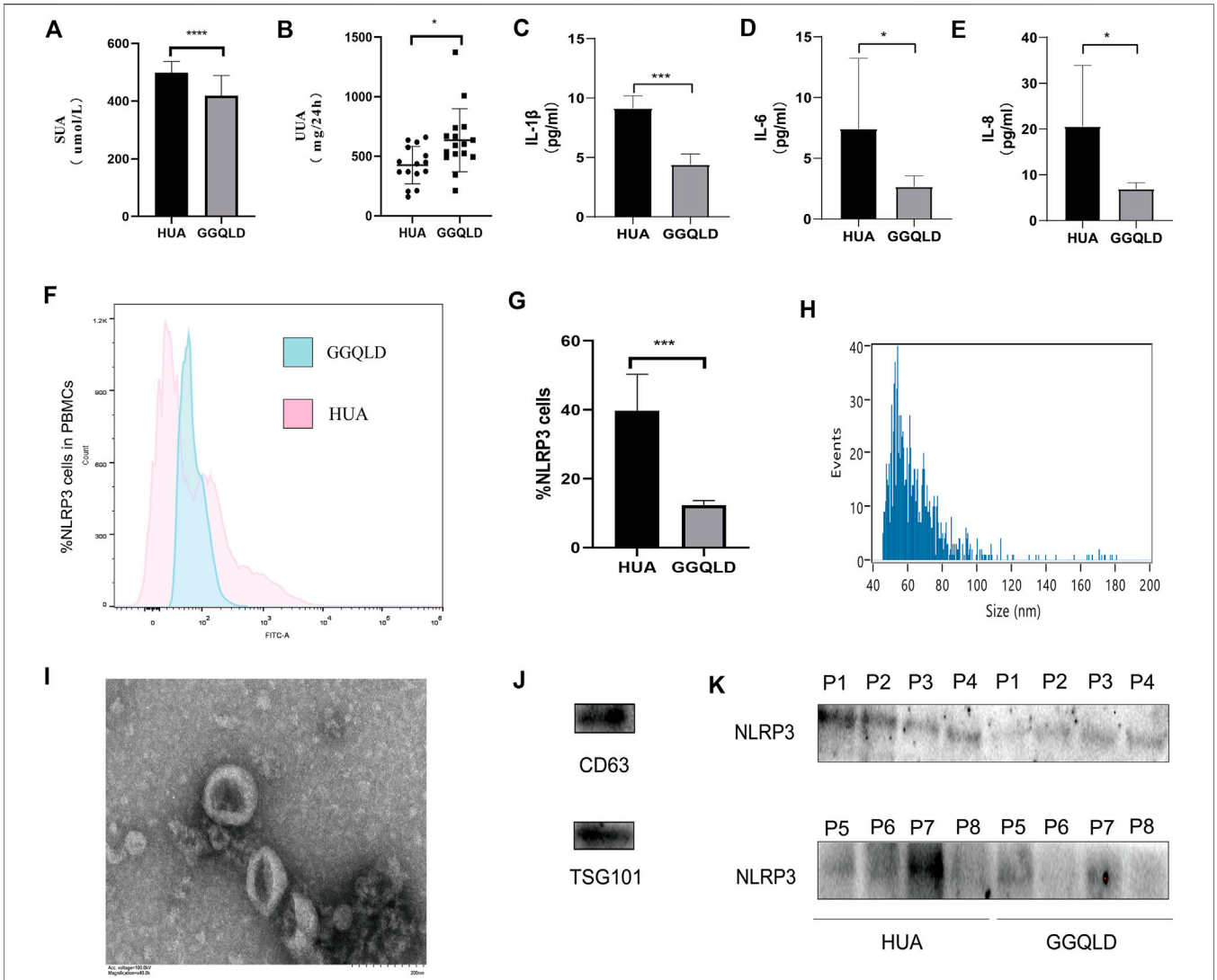

FIGURE 4 | NLRP3 expression is suppressed in HUA patients after GGQLD treatment. **(A–E)** Serum uric acid, 24 h urine uric acid, IL-1β, IL-6, and IL-8 were studied before and after medication. **(F)** PBMCs, freshly isolated by Ficoll–Paque density gradient centrifugation, were stained with mAbs conjugated with FITC and data acquired by flow cytometry. Cells were gated as shown in Figure. **(G)** The expression of NLRP3 inflammatory protein in PBMCs of HUA patients was significantly reduced after GGQLD treatment. **(H–J)** Exosome nanoparticle tracking analysis; Exosomes under electron microscope; the characterization exosomes with related markers. **(K)** The expression of NLRP3 inflammatory protein in urinary exosomes of HUA patients was significantly reduced after GGQLD treatment. For **(K)**, $n = 3$ independent experiments per group. In all statistical plots, data are expressed as the mean ± SD, $^{*}p < 0.05$, $^{**}p < 0.01$, $^{***}p < 0.001$, $^{****}p < 0.0001$.

for HUA from the DisGeNET database. Then, targets were predicted by incorporating 372 active ingredients in the UniProt database. Consequently, 31 overlapped targets between GGQLD and HUA were obtained by VENN map (**Figure 1A**).

Potential Therapeutic Mechanisms of GGQLD in HUA

We performed GO functional annotations of the 31 identified genes, suggesting their involvements in cell components (CCs), biological processes (BPs), and molecular functions (MFs). To be specific, these genes were mainly involved in various BPs, including inflammatory response and negative regulation of the apoptotic process (**Figures 1B–D**). In addition, according to KEGG pathway analysis, the intersected genes were mainly associated with 40 pathways. Among them, 35 pathways with the most significant *p*-values are shown in **Figure 2A** including cancers, apoptosis, and inflammatory signaling pathways. In addition, we also constructed the active ingredient–target–disease network by adopting Cytoscape 3.8.0 software, obtaining the interactions among drugs, compounds, diseases, and targets. The results are shown in **Figure 3**. Obviously, 17 targets were related to the apoptosis pathways, 14 to the metabolism pathways, 13 to the inflammation pathways, 13 to the immunity pathways, and 14 to the signal transduction pathways. As illustrated by the VENN map, we acquired 8 intersected targets in the

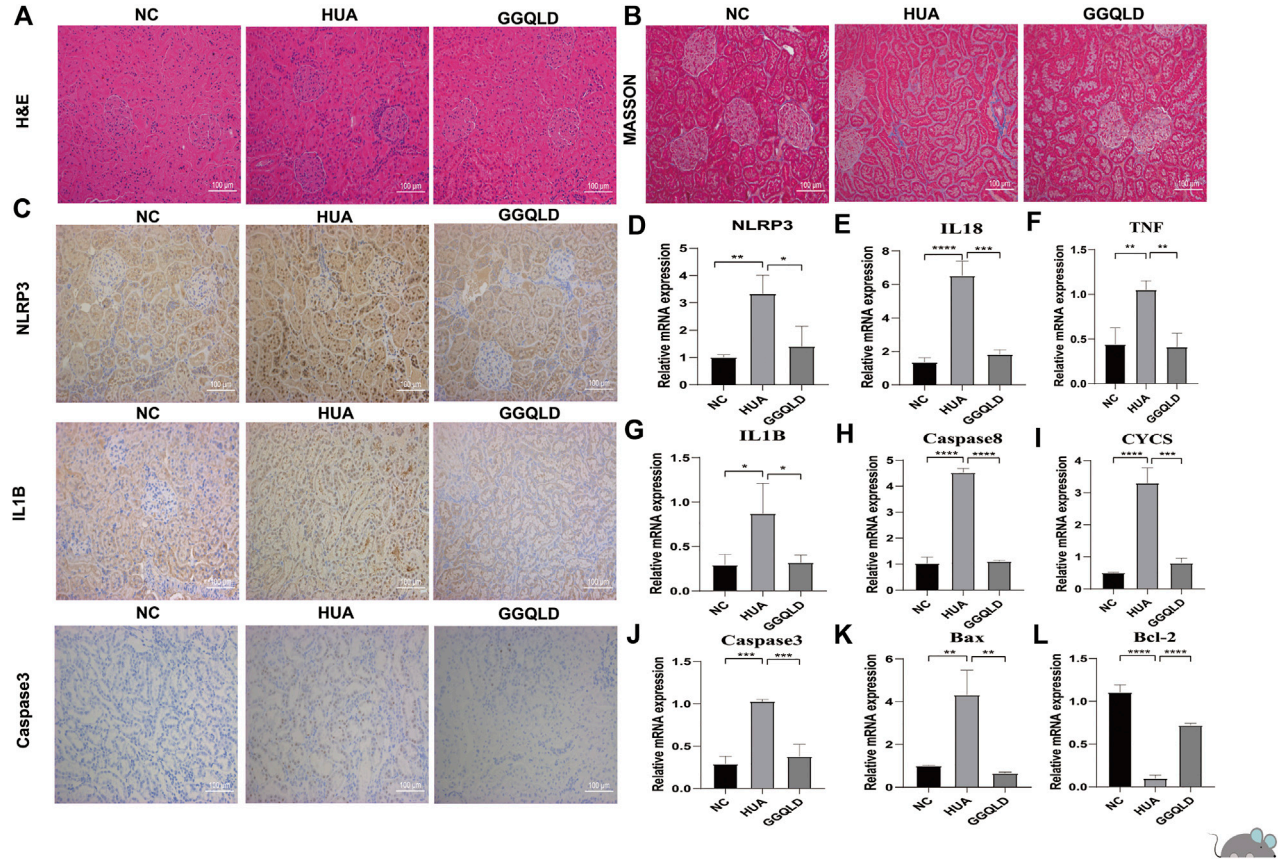

FIGURE 5 | GGQLD therapy inhibits NLRP3 expression and expression of the apoptosis gene *in vivo*. **(A)** The renal histological injury of three groups was measured by HE staining. **(B)** The renal fibrosis of four groups was determined by Masson trichrome staining. **(C)** Representative immunohistochemical staining images of NLRP3, IL1β, and caspase-3 expression in renal tissue. *N* = 3 rats/group. Scale bars, 100 mm. **(D,E,G)** GGQLD protected the kidney through suppressing the relative mRNA levels of NLRP3 inflammasomes, IL-1β, and IL-18 in HUA rats. **(F,H–L)** GGQLD alleviated the relative mRNA levels of apoptosis-related genes caspase-3, caspase-8, and TNF and simultaneously alleviated the mRNA levels of mitochondrial apoptosis-related genes Bax, Bcl-2, and CYCS in HUA rats. For **(D–L)**, *n* = 3 independent experiments per group. In all statistical plots, data are expressed as the mean ± SD, $^{*}p < 0.05$, $^{**}p < 0.01$, $^{***}p < 0.001$, $^{****}p < 0.0001$.

5 pathways (**Figure 2B**). Moreover, the STRING platform was adopted to establish the protein–protein interaction (PPI) (**Figure 2C**).

GGQLD Downregulated the Expression of NLPR3 in PBMCs and Urinary Exosomes in HUA Patients

We found that the SUA and UUA levels (**Figures 4A,B**) in HUA patients were reduced after GGQLD treatment. Besides, the levels of, IL-6, and IL-8 (**Figures 4C–E**) also significantly decreased in the GGQLD group. According to our previous study, soluble UA induced NLRP3 inflammasome production. To define the possible therapeutic approaches of HUA-induced renal tubular injury, the present study analyzed the expression of NLRP3 in PBMCs and that of urinary exosome protein in HUA patients before and after GGQLD treatment. By isolating PBMCs and extracting urinary exosomes from HUA patients before and after treatment, this study conducted flow cytometry and WB assays to analyze two groups of PBMCs and urinary exosomes. As a result, GGQLD downregulated the expression of NLRP3 in HUA patients (**Figure 4F,G,K**).

HPLC Profiles of GGQLD and Its Fractions

We obtained GGQLD extract through the purification of chromatographic grade methanol, since saponin and flavone were the major bioactive ingredients in GGQLD. Besides, HPLC analysis was performed to investigate the chemical features of GGQLD extract, with methanol being the eluent. To obtain the superb efficiency and favorable separation selectivity of HPLC analysis, we optimized the composition of the mobile phase (10 mmol/l acetonitrile–water contained within the ammonium formate solution). According to **Supplementary Figure S1**, the major bioactive ingredient puerarin was identified in Gegen, baicalin in Huangqin, berberine in Huanglian, and liquiritin in Gancao, which were later adopted to construct a combined standard approach. Accordingly, we detected four peaks of GQT extract from the HPLC chromatogram and adopted related chemical standards to quantify levels of puerarin, liquiritin, berberine, and baicalin (Peaks A–D), respectively. To be

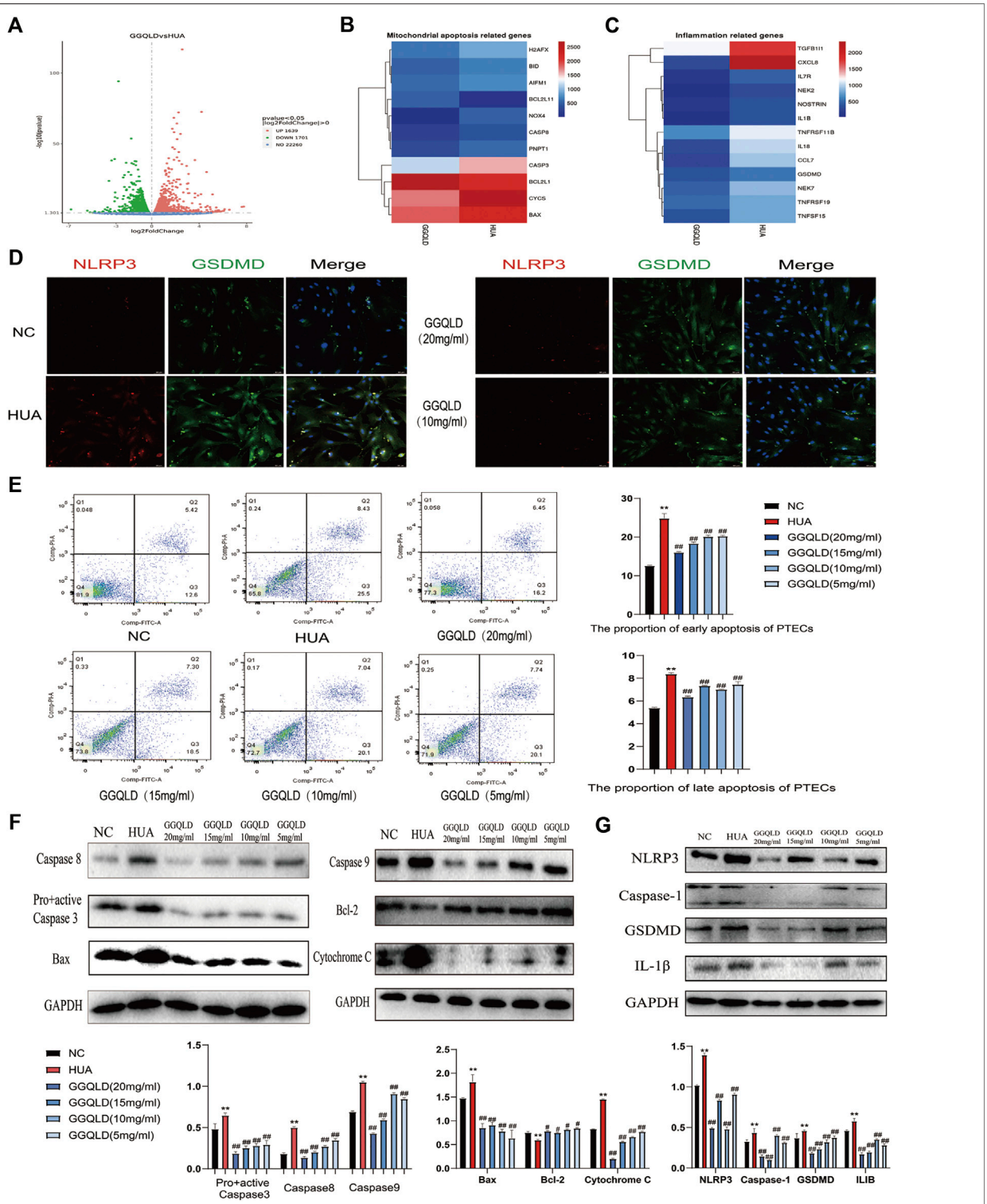

FIGURE 6 | GGQLD inhibits mitochondrial apoptosis and inflammation in PTECs. **(A)** Gene expression profile was compared between cells in response to GGQLD treatment, and heat maps were generated based on expression of the significantly changed genes related to inflammatory response and the mitochondrial apoptosis process **(B,C)**. **(D)** GGQLD alleviating inflammasome-induced pyroptosis through inhibiting the NLRP3/GSDMD signal in UA-stimulated PTECs. **(E)** GGQLD alleviated early and late apoptosis. **(F,G)** GGQLD also reduced Bcl-2, Bax, cytochrome c, pro + active caspase-3, cleaved caspase-3, caspase-9, and caspase-8 expression in UA-stimulated PTECs. The levels of key proteins of the NLRP3 signaling cascade in PTECs by GGQLD treatment. For **(D–G)**, $n = 3$ independent experiments per group. $^{*}p < 0.05$ vs. NC, $^{**}p < 0.01$ vs. NC, $\#p < 0.05$ vs. HUA, $\#\#p < 0.01$ vs. HUA.

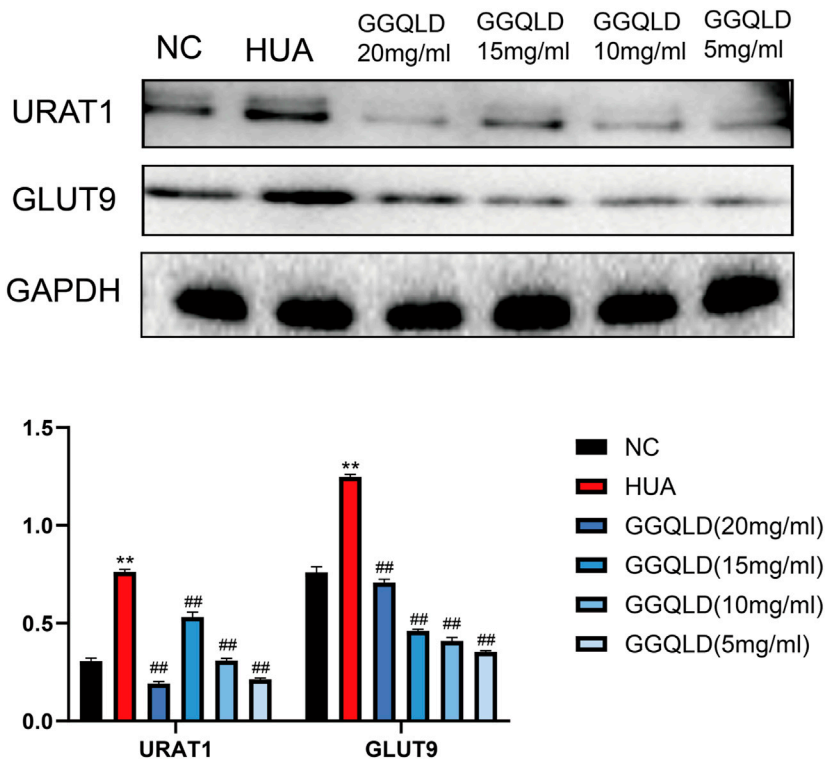

FIGURE 7 | GGQLD alleviated urate transporter expression in UA-stimulated PTECs. GGQLD significantly reduced URAT1 and GLUT9 expressions. $n = 3$ independent experiments per group. $^{*}p < 0.05$ vs. NC, $^{**}p < 0.01$ vs. NC, $\#p < 0.05$ vs. HUA, $\#\#p < 0.01$ vs. HUA.

specific, the contents of the above four active ingredients were 3.9, 0.3, 2.9, and 1.0 mg/ml in GGQLD extract, respectively (**Table 3**).

GGQLD Alleviated HUA-Induced Renal Tubular Inflammation and Apoptosis *In Vivo*

Furthermore, the current work verified the protection of GGQLD against HUA in rat models. In brief, gastric OA at 750 mg/kg/day was given to male SD rats for eight consecutive weeks. Meanwhile, GGQLD at 10 ml/kg/day initiating on week 5 was given for four consecutive weeks. As a result, NLRP3 staining and mRNA expression increased in renal cortical tissues of OA rats (**Figures 5C,D**). GGQLD reduced the NLRP3 expression in OA-treated rats (**Figures 5C,D**). GGQLD significantly attenuated the mRNA expression and staining of IL-1β and caspase-3 in renal tissues of UA rats (**Figures 5C,G,J**). Additionally, it was found that GGQLD significantly alleviated the mRNA expression of TNF, caspase-3, caspase-8, Bax, Bcl-2, and CYCS in renal tissues of HUA rats (**Figures 5F,H–L**).

GGQLD Inhibited Mitochondrial Apoptosis and Inflammation of PTECs

According to the CCK-8 results, different doses of GGQLD (20, 15, 10, and 5) were used to treat the UA-induced PTECs (**Supplementary Figure S2**). Based on our RNA-seq data, GGQLD was found to suppress BPs related to mitochondrial apoptosis and inflammatory response (**Figures 6A–C**). Moreover, GGQLD significantly reduced the expression of NLRP3 and GSDMD compared with UA (**Figure 6D**). UA remarkably promoted apoptosis at the early and late stages (**Figure 6E**), while GGQLD had the opposite effect (**Figure 6E**). Besides, we also investigated the effect of GGQLD on the UA-induced expression of Bcl-2 and caspase gene family proteins in PTECs. Consequently, as further confirmed by WB assays, GGQLD significantly reduced the UA-induced NLRP3 expression (**Figures 6F,G**).

GGQLD Down-Regulated the Expression of Urate Transporter in UA-Stimulated PTECs

UA is mainly regulated by urate transporters. To explore the effect of GGQLD on HUA, this study investigated its effects on URAT1 and GLUT9. As a result, GGQLD significantly downregulated the expression of URAT1 and GLUT9 (**Figure 7**) in comparison with the HUA group.

DISCUSSION

In the present study, clinical data proved that GGQLD reduced the SUA levels and NLRP3 expression in PBMCs and urinary exosomes in asymptomatic HUA patients. In addition, it could also be demonstrated that GGQLD significantly suppressed NLRP3 inflammasome production within the renal cortical

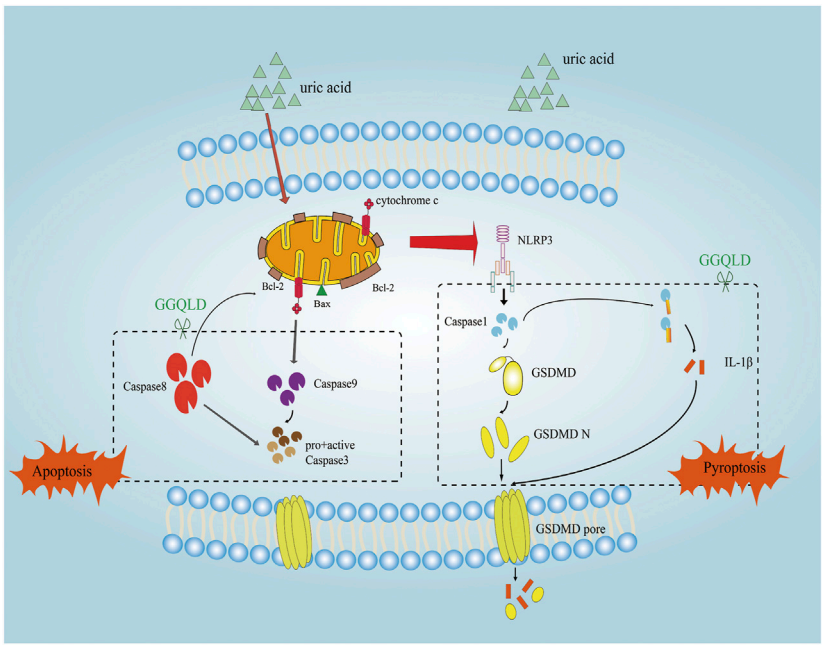

FIGURE 8 | The mechanism of the protective effect of GGQLD in HUA-induced renal injury. The increased UA led to PTEC mitochondrial apoptosis and assembled NLRP3 inflammasomes and facilitated IL-1β maturation and thus inflamed the cells, which damaged the mitochondria and caused pyroptosis to lead to renal tubule damage. GGQLD protected cells from inhibiting the mitochondrial apoptotic pathways through capsase-9, caspase-8, and Bcl-2/Bax/caspase-3, thus alleviating inflammation via inhibition of NLRP3/caspase-1/IL-1β/GSDMD.

TABLE 2 | Primers for real-time PCR.

Gene	Forward primer	Reverse primer
NLRP3	GCAGCGATCAACAGGCGAGAC	TCCCAGCAAACCTATCCACTCCTC
IL1β	CTCCACCTCCAGGGACAGGATATG	TCATCTTTCAACACGCAGGACAGG
IL18	GCTGCTGAACCAGTAGAAGACA	TGCCAAAGTAATCTGATTCCAGGT
TNF	TGGCGTGGAGCTGAGAGATAACC	CGATGCGGCTGATGGTGTGG
Bax	GACGCATCCACCAAGAAGCTGAG	GCTGCCACACGGAAGAAGACC
Bcl2	GGGCTACGAGTGGGATACTGGAG	TCGGTTGCTCTCAGGCTGGAAG
CYCS	AAAGGGAGGCAAGCACAAGACTG	ATTGGCGGCTGTGTAAGAGTATCC
CASP8	TCTACGGAACGGATGGGAAGGAAG	CAGGCACAGGCACCGCTTTC
CASP3	GTGGAGGCCGACTTCTTGTATGC	TGGCACAAAGCGACTGGATGAAC

tissues in HUA rats and UA-stimulated PTECs. GGQLD significantly prevented the UA-induced renal inflammation, which caused apoptosis via the NLRP3 signaling pathway and the mitochondrial-dependent pathway. The HUA-induced renal injury was significantly alleviated by GGQLD *in vitro* and *in vivo*.

It is beneficial to inhibit receptors and inflammasomes to reduce renal fibrosis and inflammation. Knocking down Aim2 and NLRP3 can alleviate renal fibrosis, inflammation, and injury (Kopalli et al., 2016; Cao et al., 2021). In clinical settings, GGQLD has frequently been adopted for the treatment of diabetes and UC (Xu et al., 2011; Zhao et al., 2020). GGQLD has been suggested to suppress the inflammatory signal transduction pathway and promote the antioxidant effect, thus improving UC. Additionally, GGQLD promotes glucose metabolic disorders, protects pancreatic β cells, and elevates the insulin sensitivity index, thereby exerting an important role in treating diabetes (Ahmed et al., 2017). On this basis, we performed bioinformatics analysis to identify potential therapeutic targets of GGQLD. Our results of the systemic pharmacological analysis proved that the treatment of GGQLD mainly involved the anti-inflammatory and antiapoptotic pathways. In our previous study, NLRP3 was found to be related to the pathogenesis of HUA. Therefore, we hypothesized that GGQLD targeted NLRP3 to exert its anti-inflammatory activity.

NLRP3 is one of the key elements during the activation of inflammation, which can interact with an apoptotic speck-like protein that contains a caspase recruitment domain (CARD) (ASC) through the pyrin domain (PYD). Later, ASC will recruit and activate pro-caspase-1 via CARD. The aforementioned interaction constitutes the NLRP3 inflammasome, which is a kind of great cytosolic protein complex (Csak et al., 2011; Wree et al., 2014; Shi et al., 2015; Abraham et al., 2016). Afterward, the

TABLE 3 | Contents of the four major compounds in GGQLD.

Sample name	Puerarin (mg/ml)	Liquiritin (mg/ml)	Baicalin (mg/ml)	Berberine (mg/ml)
Sample 1	3.971	0.310	2.970	1.047
Sample 2	3.967	0.312	2.983	1.051
Sample 3	3.969	0.306	2.967	1.048

activation of NLRP3 inflammasomes can activate caspase-1. First, caspase-1 cleaves gasdermin D (GSDMD), which can be activated for releasing the active N-terminal protein, and the latter can mediate pyroptosis (Derangère et al., 2014; Ding et al., 2016; Sborgi et al., 2016; Liu et al., 2017). Second, the activation of caspase-1 will recruit and activate the inflammatory molecules like IL-1β, while inducing inflammatory responses. Pyroptosis, also called cellular inflammatory necrosis, can promote the release of cellular contents to activate the inflammatory response (Shi et al., 2017; Wang et al., 2018). Evidence from previous studies shows that the NLRP3 inflammasome-induced GSDMD-dependent pyroptosis, accompanied by IL-1β processing, is responsible for renal tubular epithelial cell injury (Miao et al., 2019; Wang et al., 2019; Yasukawa and Koshiba, 2021). In our study, we first compared the difference of NLRP3 expression in PBMCs and urinary exosomes of HUA patients before and after treatment, finding that the expression of NLRP3 significantly decreased after treatment, providing that GGQLD exhibited significant anti-inflammation activity. We further validated and demonstrated that GGQLD significantly reduced the expression of NLRP3, caspase-1, GSDMD, and IL-1β in the UA-stimulated PTEC model *in vitro*, suggesting that GGQLD alleviated IL-1β processing and the subsequent amplification of inflammatory cascades. Some scholars have proved that GGQLD exerts an anti-inflammatory effect, and we confirmed that GGQLD showed anti-inflammatory effect by targeting NLRP3-induced GSDMD-dependent pyroptosis in the treatment of HUA.

The mitochondrion is an organelle with multiple functions, which is involved in a lot of biological processes, such as energy metabolism and cell suicide (Dagvadorj et al., 2021). It is currently proposed that mitochondrial damage accounts for an important determining factor for the activation of NLRP3 inflammasomes (Mohan et al., 2012). The NLRP3 stimuli–induced mitochondrial destruction contributes to exposing mitochondrial DNA (mtDNA) into cytoplasm and generating reactive oxygen species (ROS). The mtDNA in cytoplasm can colocalize with NLRP3, which can thus promote IL-1β release, whereas the oxidized mtDNA can serve as the stronger factor to induce IL-1β secretion. Till the present, mtDNA is only associated with the activation signal related to the responses of NLRP3 inflammasomes. According to the network pharmacology analysis, it is considered that GGQLD exhibited protective effects on uric acid–induced renal injury through the apoptotic pathway. Therefore, we speculated that GGQLD may protect HUA-induced renal injury through the antimitochondrial apoptosis pathway.

Proteins in the Bcl-2 family, which include the proapoptotic proteins (like Bad, Bal, and Bax) and the antiapoptotic proteins (like Bcl-2, Mcl-1, and Bcl-xl), are responsible for regulating mitochondrial disruption (Degenhardt et al., 2002; Vucicevic et al., 2016; Peña-Blanco and García-Sáez, 2018). Among them, the proapoptotic proteins play the roles of the mitochondrial pathway promoters. After being stimulated, Bak and Bax will be transported in the mitochondrial membrane, which increases the permeability of the mitochondrial outer membrane, causing caspase cascade activation and cytochrome c release (Dairaku et al., 2004; Fang et al., 2012). In addition, the antiapoptotic proteins play the roles of suppressors through suppressing cytochrome c release (Mo et al., 2019). Bcl-2 is reported to directly reduce mitochondrial membrane permeability through binding to the mitochondrial outer membrane protein voltage-dependent anion channel 1 (VDAC1). Therefore, inducing Bax transport in mitochondria and inhibiting Bcl-2 transport in mitochondria can serve as two approaches for inducing the mitochondria-regulated apoptosis. In our study, we found that GGQLD significantly attenuated the miRNA expression of caspase-3, caspase-8, Bax, Bcl-2, and CYCS in renal tissue from HUA rats. We also examined the effect of GGQLD on the UA-induced expression of Bcl-2 and caspase gene family proteins in PTECs. It can be demonstrated that GGQLD can protect HUA-induced renal epithelial cells by inhibiting mitochondrial apoptosis.

In summary, GGQLD positively affects HUA by suppressing apoptosis and enhancing renal inflammation, which provides laboratory data supporting its clinical application. All the medicinal herbs in GGQLD have been utilized in TCM for thousands of years. Therefore, GGQLD is regarded to be safe and tolerable. GGQLD treatment reduces IL-1β production, NLRP3, caspase-1, and GSDMD expression depending on its concentration. In addition, GGQLD inhibits the apoptosis of PTECs, upregulates the expression of Bcl-2, and downregulates that of Bax, cytochrome c, and caspase-3/8/9. The present work suggests that GGQLD is the best treatment for HUA, which exerts its effects through suppressing apoptosis and renal inflammation. More studies are warranted to examine the systemic molecular mechanisms of GGQLD via the selection of diverse blockers and development of experimental technologies.

DATA AVAILABILITY STATEMENT

The data presented in the study are deposited in the ENA repository, accession number is PRJEB43968.

ETHICS STATEMENT

The studies involving human participants were reviewed and approved by The Local Ethical Committee of Huadong Hospital Affiliated to Fudan University (No. 20190037). The patients/participants provided their written informed consent to participate in this study. The animal study was reviewed and approved by The Institutional Animal Care and Use Committee (License: SYXK(H)2016-0004).

AUTHOR CONTRIBUTIONS

LF, M-QY, and JX conceived and designed the study. X-JW, Y-DQ, H-CG, and H-GL performed the experiments. P-QH and K-WG provided the samples. X-JW wrote the paper. IW, M-QY, and JX reviewed and edited the manuscript. All authors read and approved the manuscript.

FUNDING

This study was supported by a grant of the Shanghai Municipal Commission of Health and Family Planning Project Grant (No. 2018LQ003).

SUPPLEMENTARY MATERIAL

The Supplementary Material for this article can be found online at: https://www.frontiersin.org/articles/10.3389/fphar.2021.665398/full#supplementary-material

REFERENCES

Abraham, N. G., Junge, J. M., and Drummond, G. S. (2016). Translational significance of heme oxygenase in obesity and metabolic syndrome. *Trends Pharmacol. Sci.* 37, 17–36. doi:10.1016/j.tips.2015.09.003

Ahmed, S. M. U., Luo, L., Namani, A., Wang, X. J., and Tang, X. (2017). Nrf2 signaling pathway: pivotal roles in inflammation. *Biochim. Biophys. Acta (Bba) - Mol. Basis Dis.* 1863, 585–597. doi:10.1016/j.bbadis.2016.11.005

Bi, Y., Li, M., Wang, T., Wang, T., Xu, Y., Wang, L., et al. (2013). Prevalence and control of diabetes in Chinese adults. *JAMA* 310, 948–959. doi:10.1001/jama.2013.168118

Braga, T. T., Foresto-Neto, O., and Camara, N. O. S. (2020). The role of uric acid in inflammasome-mediated kidney injury. *Curr. Opin. Nephrol. Hypertens.* 29, 423–431. doi:10.1097/mnh.0000000000000619

Cao, Z., Zeng, Z., Wang, B., Liu, C., Liu, C., Wang, Z., et al. (2021). Identification of potential bioactive compounds and mechanisms of GegenQinlian decoction on improving insulin resistance in adipose, liver, and muscle tissue by integrating system pharmacology and bioinformatics analysis. *J. Ethnopharmacol* 264, 113289. doi:10.1016/j.jep.2020.113289

Csak, T., Ganz, M., Pespisa, J., Kodys, K., Dolganiuc, A., and Szabo, G. (2011). Fatty acid and endotoxin activate inflammasomes in mouse hepatocytes that release danger signals to stimulate immune cells. *Hepatology* 54, 133–144. doi:10.1002/hep.24341

Dagvadorj, J., Mikulska-Ruminska, K., Tumurkhuu, G., et al. (2021). Recruitment of pro-IL-1α to mitochondrial cardiolipin, via shared LC3 binding domain, inhibits mitophagy and drives maximal NLRP3 activation. *Proc. Natl. Acad. Sci. U S A.* 1181 (1), e2015632118. doi:10.1073/pnas.2015632118

Dairaku, N., Kato, K., Honda, K., Koike, T., Iijima, K., Imatani, A., et al. (2004). Oligomycin and antimycin A prevent nitric oxide-induced apoptosis by blocking cytochrome C leakage. *J. Lab. Clin. Med.* 143 (3), 143–151. doi:10.1016/j.lab.2003.11.003

Degenhardt, K., Sundararajan, R., Lindsten, T., Thompson, C., and White, E. (2002). Bax and Bak independently promote cytochrome cRelease from mitochondria. *J. Biol. Chem.* 277 (16), 14127–14134. doi:10.1074/jbc.m109939200

Deng, Y., Li, Q., Li, M., Han, T., Li, G., and Liu, Q. (2020). Network pharmacology identifies the mechanisms of sang-xing-zhi-ke-fang against pharyngitis. *Evid. Based Complement. Alternat Med.* 2020, 2421916. doi:10.1155/2020/2421916

Derangère, V., Chevriaux, A., Courtaut, F., Bruchard, M., Berger, H., Chalmin, F., et al. (2014). Liver X receptor β activation induces pyroptosis of human and murine colon cancer cells. *Cell Death Differ* 21 (12), 1914–1924. doi:10.1038/cdd.2014.117

Dinesh, P., and Rasool, M. (2017). Berberine, an isoquinoline alkaloid suppresses TXNIP mediated NLRP3 inflammasome activation in MSU crystal stimulated RAW 264.7 macrophages through the upregulation of Nrf2 transcription factor and alleviates MSU crystal induced inflammation in rats. *Int. Immunopharmacology* 44, 26–37. doi:10.1016/j.intimp.2016.12.031

Ding, J., Wang, K., Liu, W., She, Y., Sun, Q., Shi, J., et al. (2016). Pore-forming activity and structural autoinhibition of the gasdermin family. *Nature* 535, 111–116. doi:10.1038/nature18590

Fang, H., Wu, Y., Guo, J., Rong, J., Ma, L., Zhao, Z., et al. (2012). T-2 toxin induces apoptosis in differentiated murine embryonic stem cells through reactive oxygen species-mediated mitochondrial pathway. *Apoptosis* 17 (8), 895–907. doi:10.1007/s10495-012-0724-3

Guarino, G., Strollo, F., Carbone, L., Della Corte, T., Letizia, M., Marino, G., et al. (2017). Bioimpedance analysis, metabolic effects and safety of the association Berberis aristata/Bilybum marianum: a 52-week double-blind, placebo-controlled study in obese patients with type 2 diabetes. *J. Biol. Regul. Homeost Agents* 31 (2), 495–502.

Guo, W., Huang, J., Wang, N., Tan, H. Y., Cheung, F., Chen, F., et al. (2019). Integrating network pharmacology and pharmacological evaluation for deciphering the action mechanism of herbal formula zuojin pill in suppressing hepatocellular carcinoma. *Front. Pharmacol.* 10, 1185. doi:10.3389/fphar.2019.01185

Komada, T., Chung, H., Lau, A., Platnich, J. M., Beck, P. L., Benediktsson, H., et al. (2018). Macrophage uptake of necrotic cell DNA activates the AIM2 inflammasome to regulate a proinflammatory phenotype in CKD. *Jasn* 29, 1165–1181. doi:10.1681/asn.2017080863

Kopalli, S. R., Kang, T.-B., and Koppula, S. (2016). Necroptosis inhibitors as therapeutic targets in inflammation mediated disorders - a review of the current literature and patents. *Expert Opin. Ther. Patents* 26, 1239–1256. doi:10.1080/13543776.2016.1230201

Li, Y. M., Fan, X. M., Wang, Y. M., Liang, Q. L., and Luo, G. A. (2013). [Therapeutic effects of gegen qinlian decoction and its mechanism of action on type 2 diabetic rats]. *Yao Xue Xue Bao.* 48 (9), 1415–1421.

Lipkowitz, M. S. (2012). Regulation of uric acid excretion by the kidney. *Curr. Rheumatol. Rep.* 14 (2), 179–188. doi:10.1007/s11926-012-0240-z

Liu, W., Fan, Y., Tian, C., Jin, Y., Du, S., Zeng, P., et al. (2020). Deciphering the molecular targets and mechanisms of HGWD in the treatment of rheumatoid arthritis via network pharmacology and molecular docking. *Evid. Based Complement. Alternat Med.* 2020, 7151634. doi:10.1155/2020/7151634

Liu, Z., Gan, L., Xu, Y., Luo, D., Ren, Q., Wu, S., et al. (2017). Melatonin alleviates inflammasome-induced pyroptosis through inhibiting NF-κB/GSDMD signal in mice adipose tissue. *J. Pineal Res.* 63 (1), e12414. doi:10.1111/jpi.12414

Miao, N., Yin, F., Xie, H., Wang, Y., Xu, Y., Shen, Y., et al. (2019). The cleavage of gasdermin D by caspase-11 promotes tubular epithelial cell pyroptosis and urinary IL-18 excretion in acute kidney injury. *Kidney Int.* 96 (5), 1105–1120. doi:10.1016/j.kint.2019.04.035

Mo, X.-Y., Li, X.-M., She, C.-S., Lu, X.-Q., Xiao, C.-G., Wang, S.-H., et al. (2019). Hydrogen-rich saline protects rat from oxygen glucose deprivation and reperusion-induced apoptosis through VDAC1 via Bcl-2. *Brain Res.* 1706 (1706), 110–115. doi:10.1016/j.brainres.2018.09.037

Mohan, S., Abdelwahab, S. I., Kamalidehghan, B., Syam, S., May, K. S., Harmal, N. S. M., et al. (2012). Involvement of NF-κB and Bcl2/Bax signaling pathways in

the apoptosis of MCF7 cells induced by a xanthone compound Pyranocycloartobiloxanthone A. *Phytomedicine* 19 (11), 1007–1015. doi:10.1016/j.phymed.2012.05.012

Peña-Blanco, A., and García-Sáez, A. J. (2018). Bax, Bak and beyond: mitochondrial performance in apoptosis. *FEBS J.* 285 (3), 416–431. doi:10.1111/febs.14186

Prasad, S., and Qing, Y. (2015). Associations between hyperuricemia and chronic kidney disease: a review. *Nephrourol Mon* 7 (3), 27233. doi:10.5812/numonthly.7(3)2015.27233

Ryuk, J. A., Lixia, M., Cao, S., Ko, B.-S., and Park, S. (2017). Efficacy and safety of Gegen Qinlian decoction for normalizing hyperglycemia in diabetic patients: a systematic review and meta-analysis of randomized clinical trials. *Complement. Therapies Med.* 33, 6–13. doi:10.1016/j.ctim.2017.05.004

Sborgi, L., Rühl, S., Mulvihill, E., Pipercevic, J., Heilig, R., Stahlberg, H., et al. (2016). GSDMD membrane pore formation constitutes the mechanism of pyroptotic cell death. *EMBO J.* 35, 1766–1778. doi:10.15252/embj.201694696

Shi, J., Gao, W., and Shao, F. (2017). Pyroptosis: gasdermin-mediated programmed necrotic cell death. *Trends Biochem. Sci.* 42 (4), 245–254. doi:10.1016/j.tibs.2016.10.004

Shi, J., Zhao, Y., Wang, K., Shi, X., Wang, Y., Huang, H., et al. (2015). Cleavage of GSDMD by inflammatory caspases determines pyroptotic cell death. *Nature* 526, 660–665. doi:10.1038/nature15514

Srivastava, A., Kaze, A. D., McMullan, C. J., Isakova, T., and Waikar, S. S. (2018). Uric acid and the risks of kidney failure and death in individuals with CKD. *Am. J. Kidney Dis.* 71 (3), 362–370. doi:10.1053/j.ajkd.2017.08.017

Tian, J., Lian, F., Yu, X., Cui, Y., Zhao, T., Cao, Y., et al. (2016). The efficacy and safety of Chinese herbal decoction in type 2 diabetes: a 5-year retrospective study. *Evid. Based Complement. Alternat Med.* 2016, 5473015. doi:10.1155/2016/5473015

Tian, N., Wang, J., Wang, P., Song, X., Yang, M., and Kong, L. (2013). NMR-based metabonomic study of Chinese medicine Gegen Qinlian Decoction as an effective treatment for type 2 diabetes in rats. *Metabolomics* 9 (6), 1228–1242. doi:10.1007/s11306-013-0535-8

Tsai, C.-W., Chiu, H.-T., Huang, H.-C., Ting, I.-W., Yeh, H.-C., and Kuo, C.-C. (2018). Uric acid predicts adverse outcomes in chronic kidney disease: a novel insight from trajectory analyses. *Nephrol. Dial. Transpl.* 33 (2), 231–241. doi:10.1093/ndt/gfx297

Vucicevic, K., Jakovljevic, V., Colovic, N., Tosic, N., Kostic, T., Glumac, I., et al. (2016). Association of Bax expression and bcl2/bax ratio with clinical and molecular prognostic markers in chronic lymphocytic leukemia. *J. Med. Biochem.* 35 (2), 150–157. doi:10.1515/jomb-2015-0017

Wang, Y., Zhu, X., Yuan, S., Wen, S., Liu, X., Wang, C., et al. (2019). TLR4/NF-κB signaling induces GSDMD-related pyroptosis in tubular cells in diabetic kidney disease. *Front. Endocrinol.* 10, 603–611. doi:10.3389/fendo.2019.00603

Wang, Y., Yin, B., Li, D., Wang, G., Han, X., and Sun, X. (2018). GSDME mediates caspase-3-dependent pyroptosis in gastric cancer. *Biochem. Biophysical Res. Commun.* 495 (1), 1418–1425. doi:10.1016/j.bbrc.2017.11.156

Wree, A., McGeough, M. D., Peña, C. A., Schlattjan, M., Li, H., Inzaugarat, M. E., et al. (2014). NLRP3 inflammasome activation is required for fibrosis development in NAFLD. *J. Mol. Med.* 92, 1069–1082. doi:10.1007/s00109-014-1170-1

Wu, Y., Wang, D., Yang, X., Fu, C., Zou, L., and Zhang, J. (2019). Traditional Chinese medicine Gegen Qinlian decoction ameliorates irinotecan chemotherapy-induced gut toxicity in mice. *Biomed. Pharmacother.* 109, 2252–2261. doi:10.1016/j.biopha.2018.11.095

Xiao, J., Han, R., Fu, C. S., Zhang, X., Chen, W., Ye, Z., et al. (2016). Uric acid induces TLR4- dependent innate immune response but not HLA-DR and CD40 activation in renal proximal tubular epithelial cells. *Int. J. Clin. Exp. Pathol.* 20169, 940–949.

Xiao, J., Zhang, X.-L., Fu, C., Han, R., Chen, W., Lu, Y., et al. (2015). Soluble uric acid increases NALP3 inflammasome and interleukin-1β expression in human primary renal proximal tubule epithelial cells through the Toll-like receptor 4-mediated pathway. *Int. J. Mol. Med.* 35, 1347–1354. doi:10.3892/ijmm.2015.2148

Xiao, J., Zhang, X., Fu, C., Yang, Q., Xie, Y., Zhang, Z., et al. (2018). Impaired Na+−K+-ATPase signaling in renal proximal tubule contributes to hyperuricemia-induced renal tubular injury. *Exp. Mol. Med.* 50 (3), e452. doi:10.1038/emm.2017.287

Xie, P., Chen, S., Liang, Y.-z., Wang, X., Tian, R., and Upton, R. (2006). Chromatographic fingerprint analysis-a rational approach for quality assessment of traditional Chinese herbal medicine. *J. Chromatogr. A* 1112, 171–180. doi:10.1016/j.chroma.2005.12.091

Xu, X., Gao, Z., Yang, F., Yang, Y., Chen, L., Han, L., et al. (2011). Antidiabetic effects of gegen qinlian decoction via the gut microbiota are attributable to its key ingredient berberine. *Genomics Proteomics Bioinformatics* 17 (4), 249–251. doi:10.1016/j.gpb.2019.09.007

Yao, Y., Zhang, X., Wang, Z., Zheng, C., Li, P., Huang, C., et al. (2013). Deciphering the combination principles of Traditional Chinese Medicine from a systems pharmacology perspective based on Ma-huang Decoction. *J. Ethnopharmacology* 150 (2), 619–638. doi:10.1016/j.jep.2013.09.018

Yasukawa, K., and Koshiba, T. (2021). Mitochondrial reactive zones in antiviral innate immunity. *Biochim. Biophys. Acta (Bba) - Gen. Subjects* 1865, 129839. doi:10.1016/j.bbagen.2020.129839

Yu, Z.-M., Wan, X.-M., Xiao, M., Zheng, C., and Zhou, X.-L. (2021). Puerarin induces Nrf2 as a cytoprotective mechanism to prevent cadmium-induced autophagy inhibition and NLRP3 inflammasome activation in AML12 hepatic cells. *J. Inorg. Biochem.* 217 (217), 111389. doi:10.1016/j.jinorgbio.2021.111389

Zhang, C.-H., Xu, G.-L., Liu, Y.-H., Rao, Y., Yu, R.-Y., Zhang, Z.-W., et al. (2013). Anti-diabetic activities of Gegen Qinlian Decoction in high-fat diet combined with streptozotocin-induced diabetic rats and in 3T3-L1 adipocytes. *Phytomedicine* 20, 221–229. doi:10.1016/j.phymed.2012.11.002

Zhao, Y., Luan, H., Gao, H., Wu, X., Zhang, Y., and Li, R. (2020). Gegen Qinlian decoction maintains colonic mucosal homeostasis in acute/chronic ulcerative colitis via bidirectionally modulating dysregulated Notch signaling. *Phytomedicine* 68, 153182. doi:10.1016/j.phymed.2020.153182

Zhou, Y., Fang, L., Jiang, L., Wen, P., Cao, H., He, W., et al. (2012). Uric acid induces renal inflammation via activating tubular NF-kappaB signaling pathway. *PloS one* 7 (6), e39738. doi:10.1371/journal.pone.0039738

Conflict of Interest: The authors declare that the research was conducted in the absence of any commercial or financial relationships that could be construed as a potential conflict of interest.

Copyright © 2021 Wang, Qi, Guan, Lin, He, Guan, Fu, Ye, Xiao and Wu. This is an open-access article distributed under the terms of the Creative Commons Attribution License (CC BY). The use, distribution or reproduction in other forums is permitted, provided the original author(s) and the copyright owner(s) are credited and that the original publication in this journal is cited, in accordance with accepted academic practice. No use, distribution or reproduction is permitted which does not comply with these terms.

frontiers in Pharmacology

ORIGINAL RESEARCH
published: 07 May 2021
doi: 10.3389/fphar.2021.649732

Integrated Pharmacological Analysis on the Mechanism of Fuyou Formula in Treating Precocious Puberty

Chunyan Guo[1], Ning Sun[1], Kaili Hu[2], Guoliang Bai[1], Meng Zhang[1], Qian Wang[1], Qian Ding[1], Jing Liu[3], Xiaoling Wang[1] and Libo Zhao[1]**

[1]Department of Pharmacy, National Center for Children Health, Beijing Children's Hospital, Capital Medical University, Beijing, China, [2]School of Traditional Chinese Medicine Department, Beijing University of Chinese Medicine, Beijing, China, [3]Department of Traditional Chinese medicine, National Center for Children Health, Beijing Children's Hospital, Capital Medical University, Beijing, China

Fu-you formula (FY), a Traditional Chinese Medicine (TCM) formula composed of 12 herbs, as an in-hospital preparation, has been used treat to precocious puberty (PP) for decades. However, the lack of phytochemical characterization and mechanism of FY remains the main limitation for its spreading. In this study, we analyze the components and mechanisms of FY in PP, based on the integrated pharmacology. Investigated main constituents, targets, pathways of FY by using an integrative pharmacology, and recognized main constituents by HPLC-MS/MS. Then, observed the levels of Follicle-stimulating hormone (FSH), luteinizing hormone (LH), and estrogen (E_2) in danazol-induced PP in Sprague–Dawley (SD) rats. Lastly, retrospective study analyzed the clinical data of 575 patients who were diagnosed PP, treated by the FY, and followed-up in our hospital from 2014–2020. The result that total of 116 important candidate targets were selected based on pharmacological analysis. Selected the top 10 values key targets such as the estrogen receptor alpha (ESR1) and insulin-like growth factor 1 (IGF1), were localized and the related gene functions were determined. Gene functions were associated with biological regulation, a cellular process, or signaling pathway, such as the Estrogen signaling pathway, MAPK signaling pathway and PI3K-Akt signaling pathway. By recognizing the five compounds related to the ESR1 and IGF1, which are Quercetin, kaempferol, Luteolin, Apigenin, and Emodin. The results of the molecular docking study further showed that the flavonoids had a strong binding affinity for ESR1 and IGF1 after docking into the crystal structure. The results showed that the FY could effectively reduce E_2, LH, and FSH levels in SD rats. Furthermore, the results of the retrospective analysis of medical records showed that the FY could remarkably reduce E_2 levels in girls with PP.

Keywords: integrated pharmacology, precocious puberty, Chinese medicine, protein-protein interaction network, Fuyou formula

OPEN ACCESS

Edited by:
Yanqiong Zhang,
Institute of Chinese Materia Medica, China

Reviewed by:
Chengliang Zhang,
Huazhong University of Science and Technology, China
Li Zhiling,
Shanghai Children's Hospital, China

****Correspondence:***
Xiaoling Wang
wangxiaoling@bch.com.cn
Libo Zhao
lb.zhao@163.com

Specialty section:
This article was submitted to Ethnopharmacology, a section of the journal Frontiers in Pharmacology

Received: *05 January 2021*
Accepted: *21 April 2021*
Published: *07 May 2021*

Citation:
Guo C, Sun N, Hu K, Bai G, Zhang M, Wang Q, Ding Q, Liu J, Wang X and Zhao L (2021) Integrated Pharmacological Analysis on the Mechanism of Fuyou Formula in Treating Precocious Puberty. Front. Pharmacol. 12:649732. doi: 10.3389/fphar.2021.649732

INTRODUCTION

Precocious puberty (PP) is a common endocrine disorder among children. It occurs before the age of eight years in girls and before the age of 9 years in boys. In recent years, the annual incidence of this condition has been on the rise, and the incidence among girls is 5–10 times that among boys (Chinese Society of Pediatric Endocrinology and Metabolism (CSPEM), 2015). At present, early initiation of

the gonadal axis is believed to be the cause of PP. Therefore, modern medicine holds the view that the administration of a gonadotropin releasing hormone antagonist (GnRHa) in the treatment of PP is the most effective method. However, clinical results show that the long-term use of a GnRHa has inhibitory effects on growth and the thyroid in children. In addition, some children require simultaneous treatment with growth hormone or even thyroxine. Clinical studies on the FY as a treatment for girls with PP at our hospital have shown that it can control the early symptoms, and effectively reduce estrogen levels and bone age (Liu et al., 2009; Pan et al., 2019). At present, the literature comprises mostly clinical reports and observations of curative effects. However, in-depth research on the effective components, key targets, and mechanisms of action of the FY are still lacking. Integrative pharmacology could enhance our comprehension and facilitate the prediction of potential targets, pathways, and effects, which might provide clues for the design of subsequent research studies. In the present study, we used an integrative pharmacological approach to understand the systemic, organ-related, and molecular effects of the FY. The components and mechanisms of the FY in the treatment of PP were preliminarily analyzed and explored. The TCM integrated pharmacology platform was used and a TCM-component-network target-disease multi-level network was considered as the underlying framework.

MATERIALS AND METHODS

Materials and Reagents

Danazol was obtained from the A&D Technology Corporation (Beijing, China). Leuprorelin acetate microspheres for injection were purchased from Livzon (Zhuhai, China). FSH, LH, and E_2 ELISA kits were obtained from Cloud-Clone Corp (Wuhan, China). The TCM standards Quercetin (serial number: 100081–201610, purity: 99.90%), Luteolin (serial number: 111520–202006, purity: 94.40%), kaempferol (serial number: 110861–202013, purity: 93.20%) and Emodin (serial number: 110756–201913, purity: 96.0%) were purchased from the National Institutes for Food and Drug Control (Beijing, China). Apigenin (serial number: B20981–20 mg, purity: 98.00%) was purchased from the Shanghai Yuanye Bio-Technology Co., Ltd. (Shanghai, China).

Plant Materials and Fu-you Formula Preparation

The FY was an in-hospital preparation (Approval number: Z20053679). It comprised a mixture of *Prunella vulgaris* L. (Xiakucao); *Carapax Trionycis* (Cubiejia); *Gentiana scabra* Bunge (Longdan); *Chrysanthemum morifolium* (Ramat.) Hemsl (Juhua); *Lycium chinense* Mill (Digupi); *Alisma plantago-aquatica* L (Zexie); *Scrophularia ningpoensis* Hemsl (Xuanshen); *Paeonia suffruticosa Andrews* (Mudanpi); *Rehmannia glutinosa* (Gaertn.) DC (Shengdihuang); *Hordeum vulgare* L (Maiya); *Concha oetreae* (Muli); *Thalluslaminariae* (Kunbu) (1.5:1:0.6:0.6:1:1:1.5:0.6:1.2:2:3:1). All herbs were purchased from the Beijing Bencao Fangyuan Pharmaceutical Group Co. Ltd. and the FY was prepared by the Preparation Center of the Beijing Children's Hospital (Lot number: 20201202).

Construction of the Compound-Target and Disease-Target Database

To identify the corresponding targets of the 12 active ingredients of the FY, several approaches combining chemometric methods, information integration, and data mining were implemented. First, all active compounds were submitted to the TCM-IP platform (http://www.tcmip.cn/TCMIP/index.php/Home/Index/index.html) Xu et al. (2019), as well as the TCMSP (http://tcmspw.com/tcmsp.php) Ru et al. (2014), and TCMID (http://119.3.41.228:8000/tcmid/search/) Huang et al. (2018) to mine compound-target interactions. The biological targets of the active ingredients were obtained from the STITCH (http://stitch.embl.de/) Szklarczyk et al. (2016); SwissTarget (http://www.swisstargetprediction.ch/) Gfeller et al. (2014); CTD (http://tcmspw.com/index.php) Yan et al. (2019); and SymMap (https://www.symmap.org/) Wu et al. (2019) databases. Known therapeutic targets for PP were obtained from the DrugBank (http://www.drugbank.ca/) Wishart et al. (2018); Online Mendelian Inheritance in Man (OMIM) (http://www.omim.org) Hamosh et al. (2005); and DisGeNET (https://www.disgenet.org/home/) Janet et al. (2020) databases.

Protein-Protein Interaction Network Construction

The protein-protein interaction (PPI) data were imported from the STRING (https://string-db.org/cgi/input.pl?sessionId=rEkaDRgfV0vC&input_page_show_search=on) PPI databases. An interactive network for the candidate drug targets and known PP-related targets of the FY was constructed based on their interaction data and was visualized using the Cytoscape software (Shannon et al., 2003). Interactions between the targets of the traditional Chinese medicine components of the FY and the targets related to PP were determined. Furthermore, the gene interaction network of the Chinese medicine components of the FY and PP was established. The degree centrality (DC) equal to two times the median value, was applied as the core for selection of the network nodes (hubs node). Thus, the median of node connectivity, closeness centrality, and betweenness centrality were the key values that determined the selection of nodes. Nodes that met three values simultaneously were selected as the candidate key targets of the FY in the treatment of PP.

Gene Oncology Enrichment and Pathway Analysis

We performed gene ontology (GO) analysis of the non-repetitive putative targets of the FY using the database for Annotation, Visualization, and Integrated Discovery (DAVID) to gain insights into their involvement in two different categories namely, biological process and molecular function (Sherman and Lempicki, 2009). Tissue enrichment analysis was performed

using the FunRich software (http://www.funrich.org) (Pathan et al., 2015). We then performed Kyoto Encyclopedia of Genes and Genomes (KEGG) signaling pathway enrichment analysis of the candidate targets of the FY after topological analysis. A *P*-value < 0.05 was considered significant, and the enriched GO terms were identified using the hypergeometric test. A bubble chart was plotted using the OmicShare tools, a free online platform for data analysis (www.omicshare.com/tools).

Chemical Components Analysis

Characterization of main chemical components in FY was assayed by HPLC-MS/MS (AB SCIEX QTRAP 5500). Chromatographic separation was performed on a Hypersil Gold C18 column (150 × 2.1 mm, 5 μm) (Thermo Scientific), with column temperature set at 40°C. The mobile phase was solution A, 2 mM ammonium acetate in water containing 0.4‰ formic acid, and solution B, methanol. Gradient elution program was: 0–1.5 min, 60–10% A; 1.5–3.5 min, 10% A; 3.5–3.51 min, 10–60% A; 3.51–6.0 min, 60% A. The flow rate of mobile phase was 0.4 ml/min. The mass spectrometer was operated in negative ion mode with a needle potential of -4,500 V; the source temperature was set at 500°C. Nitrogen was used as the sheath gas and auxiliary gas at pressures of 50 and 40 psi. Multiple reactions monitoring (MRM) mode was used to identify the five compounds by monitoring their transitions from the molecular ions to product ions. The proper amounts of standard substance were weighed and dissolved in methanol-water (1:1, v/v) to prepare standard solutions at 1 μg/ml. Meanwhile, 10 μL of FY was mixed with 1 ml of methanol-water (1:1, v/v) by vortexing for 10 min, then centrifuge for 15 min at 15,000 rpm. The supernatant fluid was used as sample solution. The chromatograms of standard solution and sample solution were used to compounds matching.

In Silico Molecular Docking

In silico molecular docking studies of bio-active peptides or chemical drug molecules that exert their action by binding with specific receptors provides evidence on binding conformation, pattern and affinity. To identify the binding ability of active constituents with PP related targets, the crystal structures of ESR1 (PDB code: 6VIG) and IGF-1 (PDB code: 1IMX) were obtained from RCSB Protein Data Bank (http://www.rcsb.org/), and three main compounds structure of Quercetin, Apigenin and Luteolin were obtained from PubChem (https://pubchem.ncbi.nlm.nih.gov/) to establish molecular docking model with Discovery Studio 4.5. The CDOCKER module of Dock Ligands in Discovery Studio 4.5 was used to do the docking. The kinetic method was used to randomly search the small molecule conformation, and then the simulated annealing method was used to optimize each conformation in the receptor active site region, so as to make the docking results more accurate.

Animals

At postnatal day (PND) 3, female Sprague-Dawley rats and their mothers were obtained from SPF Biotechnology Co., Ltd. (Beijing, license no: SYXK (Beijing) 2016–0038). The rats were housed in the laboratory animal room and maintained at 24 ± 2°C, with 42 ± 5% humidity on a 12-h light/dark cycle (lights on from 07:30 to 19:30) in a specific-pathogen-free animal room. The animals were supplied food and water *ad libitum* and acclimated for three days before the start of the experiments. All animal experiments were performed in strict compliance with Chinese guidelines, including the standards for Laboratory Animals (GB14925–2001), and the Guideline on the Humane Treatment of Laboratory Animals (MOST 2006a). All animal procedures were approved by the Beijing Administration Office for Laboratory Animals.

Animal Grouping and Drug Administration

The animals were randomly divided into four groups: the control group, model group, positive control (leuprorelin) group, and FY group. At PND 5, the rats in the three experimental groups were given a single subcutaneous injection of 300 μg/25 μL danazol (ethylene glycol:ethanol = 1:1, v/v). The rats in the control group were given a subcutaneous injection of 25 μL of glycol/ethanol (Morishita et al., 1993; Ju et al., 2019). The rats in the positive control (leuprorelin) group were subcutaneously injected with 100 μg/kg leuprorelin. The rats in the FY group were given a solution formulated with dry ointment powder, by intragastric administration every day. The rats in the control and model groups were given the same amount of normal saline. The rats that exhibited vaginal opening were sacrificed at diestrus after a complete estrous cycle. The remaining rats were sacrificed at the same time point. All rats were anesthetized with an intraperitoneal injection of 2% pentobarbital sodium. Blood samples were collected from the abdominal aorta before sacrifice. Blood serum was separated by centrifugation (3,500 rpm, 20 min, 4°C) and preserved at −80°C for further analysis of serum hormone levels.

Drug dosage: The Fy dose was calculated according to the clinical dosage administered to 6-year-old girls. According to the following formula:

$$d_B = d_A \mathrm{dA} \times R_B / R_A \times (W_A / W_B)^{1/3}$$

with d_B representing the animal/human body weight dose, d_A representing the known human/animal body weight dose, W_A and W_B representing known human and animal weights, respectively, and R_A and R_B representing known human/animal body shape coefficients, respectively. Every two days, the animals were weight, and the dose was recalculated.

Serum Hormone Level Detection

After anesthesia, blood was collected from the abdominal aorta, and the serum was centrifuged at 4°C and stored at −20°C until further analysis. The serum concentrations of FSH, LH, and E_2 were measured using ELISA kits, according to the manufacturers' instructions. The ELISA kits, which employ a competitive inhibition enzyme immunoassay technique, were purchased from Cloud-Clone Corp (Wuhan, China).

Retrospective Analysis of Cases

Children with PP, treated with the FY at the outpatient department of our hospital from 2014 to 2020 were also evaluated. The inclusion criteria were as follows: 1) continuous

TABLE 1 | Composition of the FY.

Chinese name	Scientific name	Family	Lot No	Place of origin	Parts of plant used
Xia Ku Cao	*Prunella vulgaris* L.	Lamiaceae	20201010	Jiangsu, China	Dried erial parts
Cu Bie Jia	*Carapax Trionycis*	Trionyxsinensis Wiegmann	20201018	Hubei, China	Carapace
Long Dan	*Gentiana scabra* Bunge	Gentianaceae	20200927	Yunan, China	Dried roots and rhizomes
Ju Hua	*Chrysanthemum morifolium* (Ramat.) Hemsl	Compositae	20201027	Anhui, China	Capitulum
Di Gu Pi	*Lycium chinense* Mill	Solanaceae	20201105	Hebei, China	Dried root bark
Ze Xie	*Alisma plantago-aquatica* L	Alismataceae	20201126	Fujian, China	Dried tuber
Xuan Shen	*Scrophularia ningpoensis* Hemsl	Scrophulariaceae	20201019	Zhejiang, China	Dried root tuber
Mu Dan Pi	*Paeonia suffruticosa* Andrews	Paeoniaceae	20201123	Anhui, China	Dried root bark
Sheng Di Huang	*Rehmannia glutinosa* (Gaertn.) DC	Plantaginaceae	20201104	Henan, China	Dried root tuber
Mai Ya	*Hordeum vulgare* L	Triticum	20201030	Hebei, China	Dried ripe fruit
Mu Li	*Concha oetreae*	Ostrea	20200917	Guangdong, China	Shell
Kun Bu	*Thalluslaminariae*	Laminaria	20200922	Fujian, China	Dried lobes

TABLE 2 | Basic data on the components and targets of traditional Chinese medicines.

TCM	Number of components	Number of targets
Prunella vulgaris L.	39	10,189
Carapax Trionycis	16	374
Gentiana scabra Bunge	45	1289
Chrysanthemum morifolium (Ramat.) Hemsl	101	11,384
Lycium chinense Mill	22	1358
Alisma plantago-aquatica L	26	795
Scrophularia ningpoensis Hemsl	25	564
Paeonia suffruticosa Andrews	36	9072
Rehmannia glutinosa (Gaertn.) DC	49	1777
Hordeum vulgare L	32	496
Concha oetreae	10	56
Thalluslaminariae	12	114

use of the FY for 1 year; and 2) evaluation of sex hormone levels every 6 months. The exclusion criteria were as follows: 1) the presence of other endocrine diseases; 2) the presence of ovarian cysts. This retrospective study was approved by the Medical Ethics Committee of Beijing Children's Hospital, Capital Medical University.

Statistical Analysis

All results were presented as the mean ± SD. Differences were analyzed using one-way ANOVA. The data were further analyzed and plotted using the SPSS 19.0 software (IBM SPSS Software, New York, United States). Differences were considered statistically significant at $p < 0.05$.

RESULTS

Formula Analysis of Fu-you Formula

Prunella vulgaris L.and *Carapax Trionycis* act on the liver and relieves congestion, nourishes yin and clears heat; *Gentiana scabra* Bunge, *Chrysanthemum morifolium* (Ramat.) Hemsl, *Lycium chinense* Mill, *Alisma plantago-aquatica* L, *Scrophularia ningpoensis* Hemsl., *Paeonia suffruticosa* Andrews, *Rehmannia glutinosa* (Gaertn.) DC, which clear heat and removes dampness, nourishes yin, and cools the blood; *Hordeum vulgare L*, *Concha oetreae* and *Thalluslaminariae* act on the liver and relieves congestion, used as an adjuvant. All herbs combined act on the liver, clear congestion, nourish yin, and clear heat, can reduce the size of nodules in the breast, eliminate vaginal secretions, and dissipate scrofula, and reduce sputum production. The TCM composition are listed in **Table 1**.

Chemical Composition and Prediction Target Analysis

Four hundred and thirteen chemical components were detected from 12 TCM in the FY. Furthermore, 37,468 predicted drug targets were obtained. The predicted target information and the characterization of each herb were derived from data on the TCM-component-targets, as shown in **Table 2**. Analysis of the common targets among the predicted targets, yielded a total of 4,741 predicted targets, among the 12 TCM. No common intersection targets were detected among the 12 TCM. 97 targets were detected between the two key herbs, which each had common targets with other herbs, as shown in **Table 3**.

TABLE 3 | Number of common targets.

TCM	*Prunella vulgaris* L.	*Carapax Trionycis*	*Gentiana scabra* Bunge	*Chrysanthemum morifolium* (Ramat.) Hemsl	*Lycium chinense* Mill	*Alisma plantago-aquatica* L	*Scrophularia ningpoensis* Hemsl	*Paeonia suffruticosa* Andrews	*Rehmannia glutinosa* (Gaertn.) DC	*Hordeum vulgare* L	*Concha oetreae*	*Thalluslaminariae*
Prunella vulgaris L.	—	97	358	3975	417	262	168	3991	293	181	25	61
Carapax Trionycis	97	—	48	95	58	37	30	88	43	41	7	16

Construction and Analysis of Compound-Target Network of Fu-you Formula

After removing redundant targets, 4,741 targets obtained from 12 herbs intersected with 166 disease targets to obtain 79 mapped-genes. We then explored the predicted therapeutic targets of the FY, using multiple online databases as previously described. A network of potential targets of the compounds in the FY was then constructed using the Cytoscape software, as shown in **Figure 1A**. Based on the 1,224 core nodes obtained, 116 key candidate targets for the treatment of PP girls were screened out, 75 were direct targets and 41 were predicted targets. The degree values were determined for the top 10 hub genes, two of the most important targets are ESR1 and IGF1. After further analysis, there were 96 chemical components acting on 10 hub genes in the formula, and 42 chemical components acting on ESR1 and IGF1, which the five components most widely distributed in medicinal materials were Luteolin, Quercetin, Apigenin, Kaempferol and Emodin. The interaction relationships between targets were determined and a network map of the hub targets for the treatment of PP in girls was constructed (**Figure 1B**).

Gene Oncology and Kyoto Encyclopedia of Genes and Genomes Enrichment Analysis of Hub Targets for the Fu-you Formula in Precocious Puberty

Based on the results of GO and KEGG pathway analyses, the enriched pathways were determined. A total of 2,462 hub genes were identified based on the GO analysis, which were associated with the target genes or proteins of cells (cellular component), molecular functions (function), or biological processes (in process). Gene function information is presented in **Figure 1C**. A total of 133 KEGG pathways were enriched, which were associated with key candidate targets. The top 20 pathways were sorted by *P*-value, as shown in **Figure 1D**.

Construction and Analysis of the Multi-Layer Network Correlation Diagram of Traditional Chinese Medicine-Core Component-Hub Target-Main Pathways in the Treatment of PP With the Fu-you Formula

The KEGG pathways of the top 30 key candidate targets, based on their *P*-values were selected to construct the multi-level network association diagram of the "traditional Chinese medicine-core component-key target-main pathways" for the FY in the treatment of PP in girls (**Figure 1E**). The *P*-values were used to sort 30 KEGG pathways, which included 10 hub genes.

Phytochemical Characterization of Fu-you Formula

To identify the main constituents of FY, we analyzed the FY using HPLC-MS/MS. Five compounds were recognized from FY as

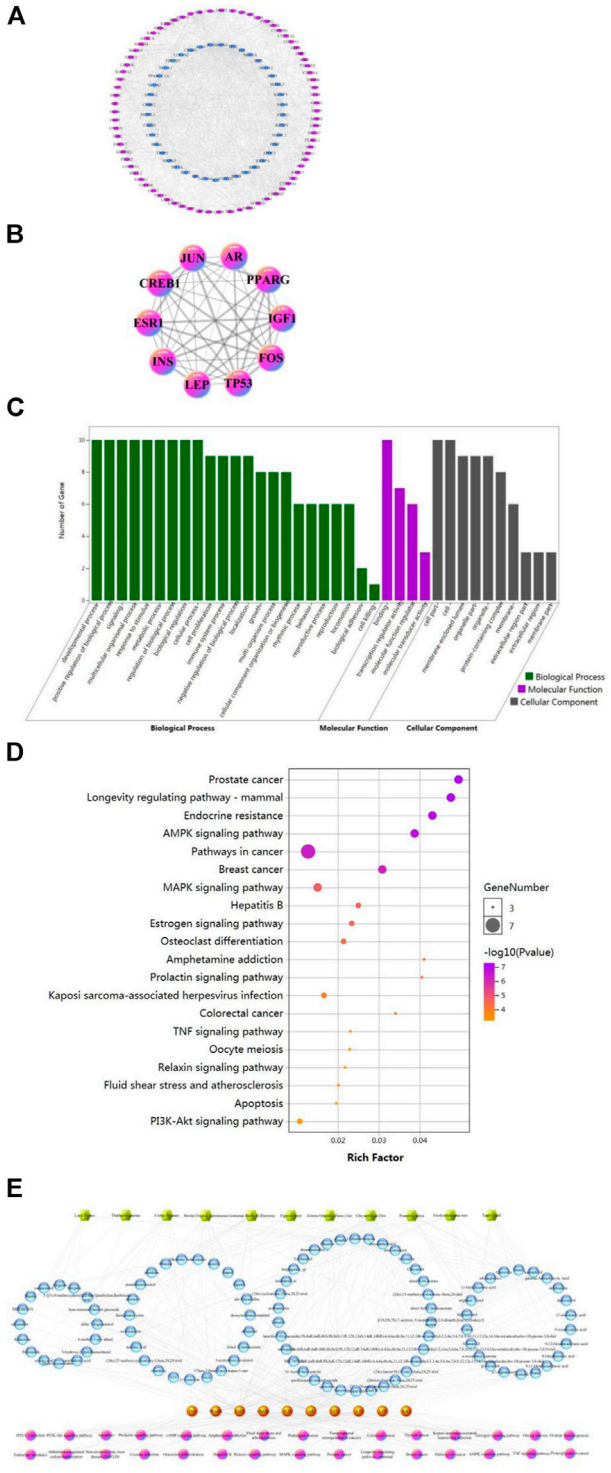

FIGURE 1 | Compound-target interaction network and preliminary gene ontology (GO) analysis of drug targets. **(A)** Compound-key target network of the FY. **(B)** Compound-hub target network of the FY. **(C)** GO analysis of drug targets classified into three categories: biological process, molecular function, and cellular component. **(D)** Kyoto Encyclopedia of Genes and Genomes (KEGG) pathway analysis of core targets of the FY in the treatment of PP. **(E)** Chinese medicinal materials-core component-key target-main pathways.

TABLE 4 | MRM transitions for identify of the target compounds.

Analyte	Precursorion (m/z)	Production (m/z)	DP	EP	CE	CXP
Luteolin	284.8	132.8	−150	−2	−40	−40
Quercetin	300.9	150.8	−120	−2	−27	−40
Apigenin	269.0	116.8	−150	−2	−40	−40
Kaempferol	284.9	93.0	−180	−2	−40	−40
Emodin	268.9	224.8	−150	−2	−36	−40

shown in **Table 4**. The standard solution and the sample solution were analyzed by the HPLC-MS/MS method upper to identify the five constituents of FY. Accroding to the chromatograms (**Figure 2**), the consistent chromatographic peaks of the five compounds could be recognized in standard solution and sample solution, including of Luteolin, Quercetin, Apigenin, Kaempferol and Emodin. Therefore, it is convincing that FY contains these five constituents.

Molecular Docking

To further validate the potential targets possessing good affinity to the ingredients, molecular docking was performed for 3 high content ingredients with the 2 high relevance degree proteins. The docking results of the 3 flavonoids with the target proteins ESR1 and IGF1 are shown in **Table 5** and **Figure 3**. As shown in the results, all the active compounds have favorable binding energy (<0 Kcal/moL) with their relative potential target proteins, and 3 flavonoids interact with ESR1 more stronger, which adds chips to the reliability of the virtual screening results.

Serum Test Results

Compared with the normal control group, E_2, LH, and FSH levels in the model group were significantly increased ($p < 0.01$), indicating that the model of PP was successfully established. After treatment with the FY, the E_2 and LH levels in rats with PP were significantly reduced compared with the model group ($p < 0.01$); and FSH levels were significantly reduced ($p < 0.05$), compared with the model group. However, in the leuprorelin group, only the LH levels showed a reduction ($p < 0.05$) (**Figure 4A** and **Figure 4B**).

Retrospective Analysis of Cases

Retrospective analysis showed that 575 children who met the inclusion criteria were included. It showed that E_2, LH, and FSH levels were significantly reduced after 12 months treatments ($p < 0.01$). Significant differences were noted in E_2 levels between groups ($p < 0.01$). The FSH levels were significantly lower at 12 months after treatment compared with 6 months after treatment ($p < 0.05$) (**Figures 4C,D**).

DISCUSSION

The results of the analysis of the common targets of the FY revealed a total of 97 targets for Prunella vulgaris L. and *Carapax Trionycis*, which had common targets with other drugs. These

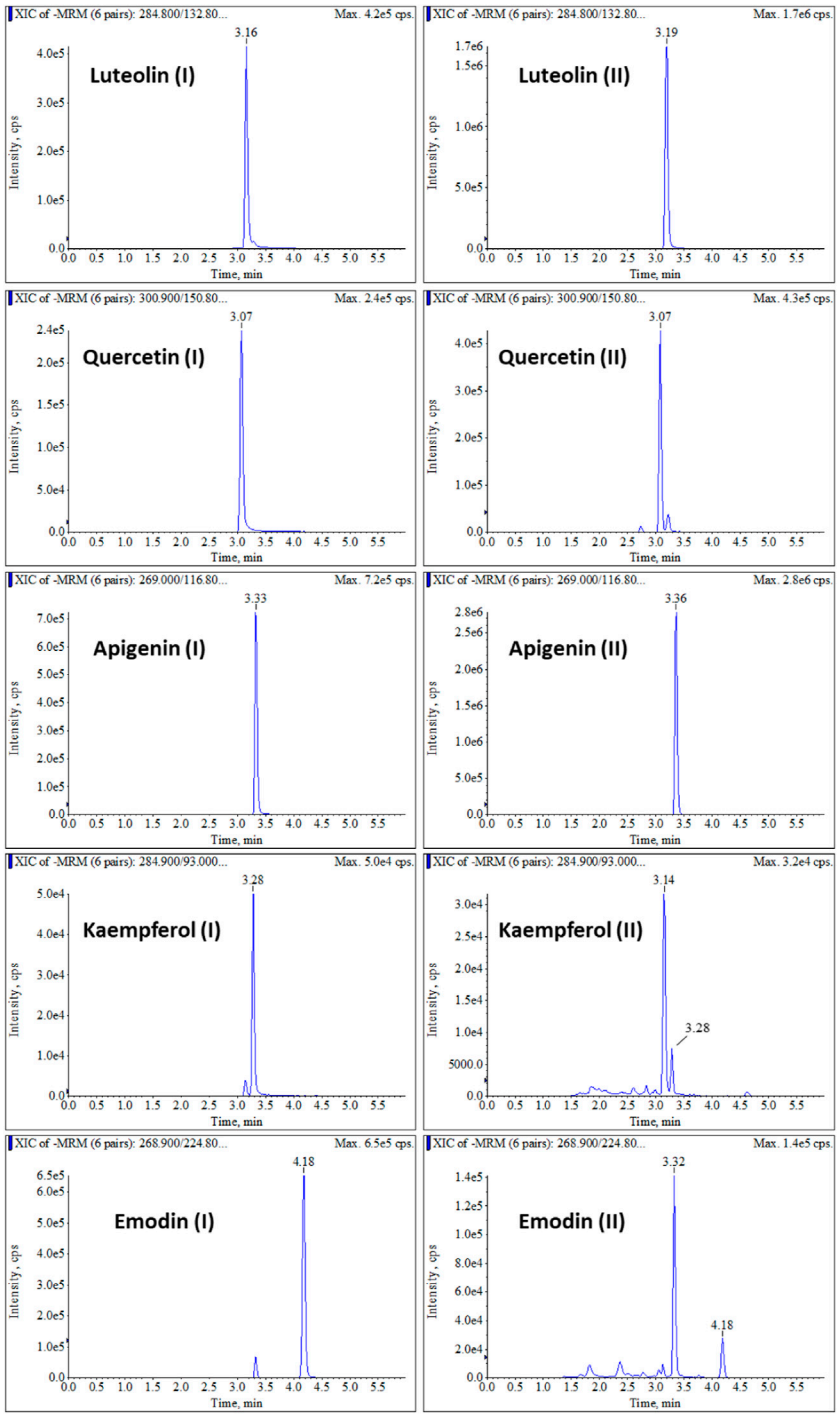

FIGURE 2 | Chromatograms of HPLC-MS/MS of FY. [(I) Standard solution; (II) Sample solution of FY; Retention time of Kaempferol and Emodin were 3.28 and 4.18 min, respectively].

findings suggest that these herbs had close synergistic effects with the other herbs. The following herbs: *Gentiana scabra Bunge, Chrysanthemum morifolium (Ramat.) Hemsl., Lycium chinense Mill, Alisma plantago-aquatica L, Scrophularia ningpoensis Hemsl, Paeonia suffruticosa Andrews* and *Rehmannia glutinosa (Gaertn.) DC* had a total of 51 targets. These findings indicate that these 7 herbs in the prescription also had synergistic effects. Furthermore, no common targets were detected for *Hordeum vulgare L, Concha Etreae, and Thalluslaminariae,* indicating that these 3 herbs are not key active ingredients in the formulation.

TABLE 5 | Molecular docking results of target and active compounds.

Active compounds	Binding energy (Kcal/moL)	
	IGF1	ESR1
Quercetin	−9.81275	−41.9021
Apigenin	−16.8225	−43.4102
Luteolin	−13.2934	−40.1986

Our previous study about data mining showed that the most frequently used herbs were *Anemarrhena asphodeloides Bunge*, *Rehmannia glutinosa (Gaertn.) DC*, *Phellodendron chinense C.K. Schneid*, *Paeonia suffruticosa Andrews*, and *Prunella Vulgaris L.* Common medicinal were cold and bitter, mostly attributed to the liver and kidney. The core of the herbs based on Zhibai Dihuangwan, and there were 4 kinds of herbs with FY.

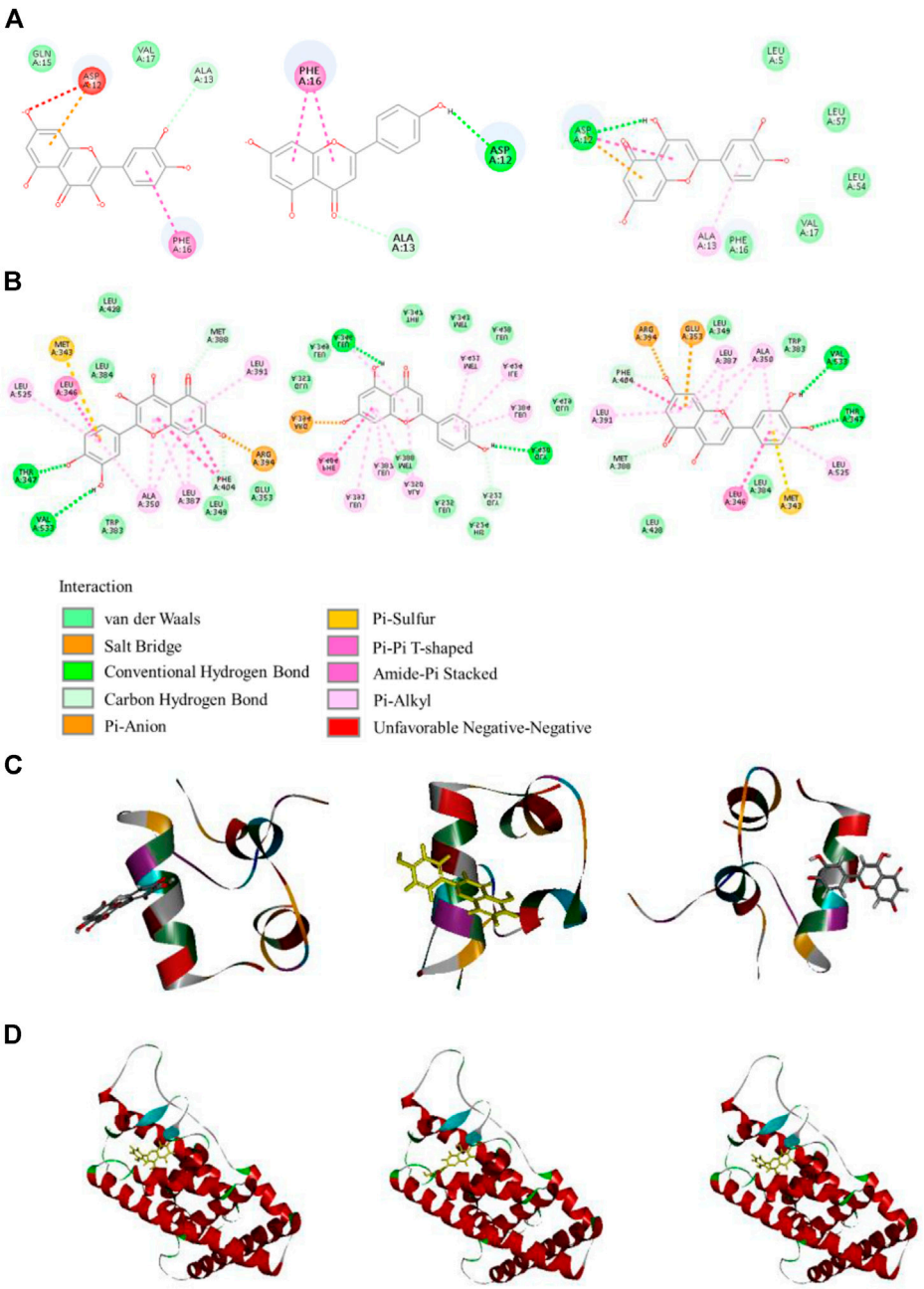

FIGURE 3 | (A) Active binding sites of compounds with IGF1. **(B)** Active binding sites of compounds with ESR1. **(C)** Molecular docking patterns of compounds and IGF1. **(D)** Molecular docking patterns of compounds and ESR1.

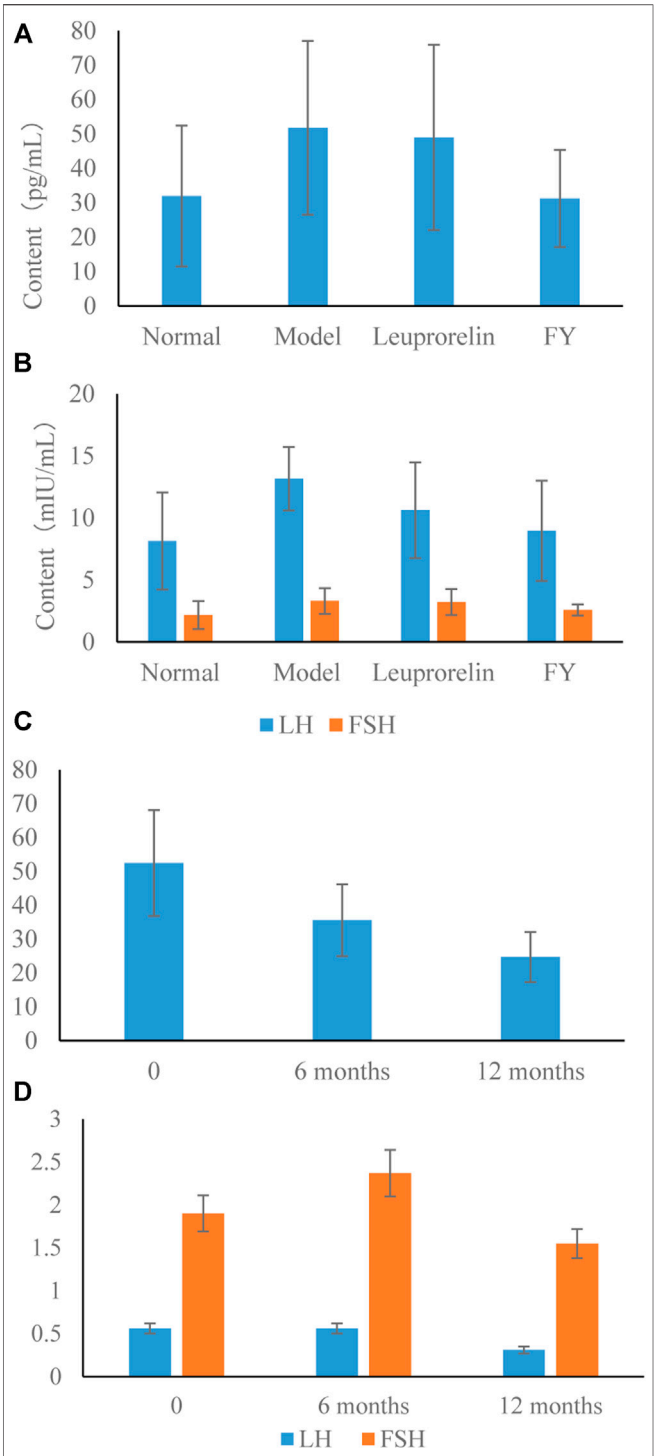

FIGURE 4 | Effects of the FY on sex hormone levels in PP. **(A)** Serum estrogen (E_2) levels among all groups of rats. **(B)** Serum luteinizing hormone (LH) and follicle-stimulating hormone (FSH) levels among all groups of rats. **(C)** Serum E_2 levels among all groups of children. **(D)** Serum LH and FSH were detected among all groups of children.

At present, GnRHa is recommended to treat CPP, but not incompleteness precocious puberty in the relevant guidelines. The premature thelarche is the most common type of incomplete precocious puberty, 14–23% of which will develop to CPP (Zhu et al., 2008). So intervene as early as possible is the present clinical needs to solve the problem. Literature shows that Zhibai Dihuang Pill and Dabuyin Pill can treat precocious puberty (Liu and Wang, 2018; Wang and Zhao, 2019; Wang et al., 2020), but there is no indication for this in their instructions, so it belongs to off-label drug use.

The above-mentioned number of common targets of each herb is consistent with compatibility principles of the formulation. We identified main chemical constituents of FY using HPLC-MS/MS and confirmed that the main constituents related to the key targets in FY are Quercetin, kaempferol, Luteolin, Apigenin and Emodin. Analysis of the formulation reveals that the core components are mainly flavonoids, as well as kaempferol and quercetin, which are all phytoestrogens. Modern pharmacological studies have shown that phytoestrogens can make two-way adjustments, as they are similar to endogenous estrogen in structure and function. When the level of estrogen in the body is lower than the normal level, it can play an estrogen-like role, which can prevent and cure women's menopausal syndrome, prostate cancer, osteoporosis and cardiovascular diseases. On the other hand, when the level of estrogen in the body is higher than the normal level. such as breast hyperplasia, uterine fibroids and other diseases, it can produce estrogen antagonism and effectively weaken the response of target cells to estrogen (Chen et al., 2017; Cai and Zhanf, 2020).

Among the top 10 core targets selected, ESR1, IGF1 and other direct therapeutic targets are reportedly related to the onset and development of PP (Ye et al., 2011; Yang and Zhao, 2013; Wang et al., 2016), and are important targets in the treatment of PP. We further analyzed and clarified the core targets of biological function, gene function, and signal pathways. The results showed that the key components of the FY alone or combined were associated with transcription factor binding, transcription factor regulation, biological and cellular processes, such as GO or biological process-related gene/protein molecular function, and the estrogen signaling pathway, MAPK signaling pathway, and PI3K-Akt signaling pathways. These pathways mediate hormones that act on target tissues to achieve endocrine regulation. The E_2 hormone binds with ESR1 to form a hormone-receptor complex that activates the estrogen signaling pathway. The MAPK signaling pathway and PI3K-Akt signaling pathway regulate the secretion of GnRH, LH, and FSH, as well as metabolic processes associated with bones. In addition, the growth hormone-insulin-like growth factor-1 (GH-IGF1) is the most important neuroendocrine factor associated with growth and development. Excessive IGF1 levels can inhibit GH secretion, and thereby inhibiting the growth of articular cartilage and epiphyseal cartilage, and retard growth in children (Su et al., 2017).

Treatment with GnRH analogues, such as Leuproline, which act by downregulating pituitary GnRH receptors (Carel et al., 2009), represent the standard of care for the treatment of CPP. The integrated pharmacological results suggest that the mechanism of the FY in the treatment of PP may include:

competitive binding of E_2 with ESR1and reduction in serum IGF1 concentrations. At the same time, animal experiments showed that the FY could reduce E_2, LH, and FSH levels in rats with PP. Retrospective analysis of the medical records also showed that the FY could control the early symptoms of PP, and effectively inhibit E_2 levels. The results of the animal experiments and retrospective analysis of medical records have confirmed the feasibility of studies of the mechanism of action of Chinese herbal compounds by integrative pharmacological methods.

In addition, the complex key targets of the FY and predictions based on the KEGG pathway analysis results show that the treatment may have effects on ovarian steroidogenesis, prostate and breast cancer, and other signaling pathways. These results are consistent with our previous clinical studies, which have shown that the effects of complex mixtures in girls with PP and ovarian cysts may be a more favorable intervention. Mixtures such as the FY may diminish ovarian cysts, regulate character development, improve liver function and qi stagnation, alleviate yin deficiencies and heat symptoms, reduce levels of E_2, and retard bone aging and maturation. The present findings also provide a novel basis for the clinical application, and further research and development of the FY.

However, this study has some limitations that are worth mentioning. First, the reliability of the effects of FY against PP depends on database, so biological verification is necessary to evaluate the reliability of bioinformatics analysis *in vitro, in vivo* and *in silico*. Secondly, quantitative analysis of the synergistic effect of the main compounds should be investigated in the future.

CONCLUSION

In conclusion, we combined methods of big data discovery with biological validation to study the mechanism of actions of the FY in PP at the systemic level. We used the TCM-IP database for the treatment of PP and considered various components and molecular mechanisms in the preliminary analysis. We determined that the FY acts through multiple component interactions with targets. The mixture also exerts its effects through multiple pathways involved in the regulation of PP, and may thus play a role in treatment of the condition. Whether other pathways or mechanisms predicted in this network pharmacological approach also contribute to the beneficial effects of the FY requires further investigation.

DATA AVAILABILITY STATEMENT

The original contributions presented in the study are included in the article/Supplementary Material, further inquiries can be directed to the corresponding author.

ETHICS STATEMENT

The animal study was reviewed and approved by the animal experimental design and protocols of this study was reviewed and approved by the Ethics Review Committee for Animal Experimentation of Beijing University of Chinese Medicine (BUCM-4–2017090116–3016).

AUTHOR CONTRIBUTIONS

LZ and XW designed the experiments. CG and NS analyzed the data and wrote the manuscript. YH helped to conduct the animal experiments. MZ and GB provided technical support. QW, QD, and JL helped to construct the illustrations and revised the manuscript.

FUNDING

This work was supported by the National Major Science and Technology Projects of China (grant no. 2018ZX09721003) and Beijing TCM Science and Technology Development Fund Project (grant no. QN-2020–26).

ACKNOWLEDGMENTS

The authors thank Beijing University of Traditional Chinese Medicine and the Chinese Academy of Traditional Chinese Medicine for their support.

REFERENCES

Cai, X.-Y., and Zhanf, Z.-J. (2020). Pharmacological Effects of Phytoestrogens and Research Progress of Related Traditional Chinese Medicine. *Chin. Med. J. Res. Prac.* 34 (2), 75–78. doi:10.13728/j.1673-6427.2020.02.015

Carel, J.-C., Eugster, E. A., Rogol, A., Ghizzoni, L., and Palmert, M. R. (2009). Consensus Statement on the Use of Gonadotropin-Releasing Hormone Analogs in Children. *Pediatrics* 123 (4), e752–e762. doi:10.1542/peds.2008-1783

Chen, M., Zhao, P.-W., Zhao, D., and Wu, H.-B. (2017). Research Progress on Pharmacological Action of Phytoestrogens in Traditional Chinese Medicine. *Jiangsu J. Traditional Chin. Med.* 49 (4), 82–85. doi:10.3969/j.issn.1672-397X.2017.04.032

Chinese Society of Pediatric Endocrinology and Metabolism (CSPEM) (2015). Consensus on Diagnosis and Treatment of Central Precocious Puberty. *Chin. J. Pediatr.* 53 (6), 412–418. doi:10.3760/cma.j.issn.0578-1310.2015.06.004

Gfeller, D., Grosdidier, A., Wirth, M., Daina, A., Michielin, O., and Zoete, V. (2014). SwissTargetPrediction: a Web Server for Target Prediction of Bioactive Small Molecules. *Nucleic Acids Res.* 42 (W1), W32–W38. doi:10.1093/nar/gku293

Hamosh, A., Scott, A. F., Amberger, J. S., Bocchini, C. A., and McKusick, V. A. (2004). Online Mendelian Inheritance in Man (OMIM), a Knowledgebase of Human Genes and Genetic Disorders. *Nucleic Acids Res.* 33 (Suppl. l_1), D514–D517. doi:10.1093/nar/gki033

Huang, L., Xie, D., Yu, Y., Liu, H., Shi, Y., Shi, T., et al. (2018). TCMID 2.0: a Comprehensive Resource for TCM. *Nucleic Acids Res.* 46 (D1), D1117–D1120. doi:10.1093/nar/gkx1028

Janet, P., Juan, M. R., Josep, S., Francesco, R., Emilio, G., Ferran, S., et al. (2020). The DisGeNET Knowledge Platform for Disease Genomics: 2019 Update. *Nucleic Acids Res.* 48 (D1), D845–D855. doi:10.1093/nar/gkz1021

Liu, H.-L., Liu, J., and Liu, G.-Q. (2009). Clinical Research on 60 Cases of Girls with Central Precocious Puberty Treated with Fuyou Mixture. *Beijing J. Traditional Chin. Med.* 28 (8), 588–589. doi:10.16025/j.1674-1307.2009.08.035

Liu, J.-P., and Wang, H. (2018). Clinical Effect and Safety of Zhibai Dihuang Pill Combined with Dabuyin Pill in the Sexual Precocity of Girls. *Chin. J. Hum. Sex.* 27 (1), 64–67. doi:10.3969/j.issn.1672-1993.2018.01.019

Morishita, H., Takemoto, M., Kondo, H., Higuchi, K., and Aono, T. (1993). Induction of True Precocious Puberty by Neonatal Treatment with Danazol in Female Rats. *Neurosci. Lett.* 157 (1), 33–36. doi:10.1016/0304-3940(93)90636-y

Pan, Y.-C., Liu, J., and Liu, H.-L. (2019). Clinical Observation on the Treatment of Girl Ovarian Cysts Complicated with Precocious Puberty with Traditional Chinese Medicine Fuyou Mixture. *Beijing J. Traditional Chin. Med.* 38 (7), 700–703. doi:10.16025/j.1674-1307.2019.07.021

Pathan, M., Keerthikumar, S., Ang, C.-S., Gangoda, L., Quek, C. Y. J., Williamson, N. A., et al. (2015). FunRich: An Open Access Standalone Functional Enrichment and Interaction Network Analysis Tool. *Proteomics* 15 (15), 2597–2601. doi:10.1002/pmic.201400515

Ru, J., Li, P., Wang, J., Zhou, W., Li, B., Huang, C., et al. (2014). TCMSP: a Database of Systems Pharmacology for Drug Discovery from Herbal Medicines. *J. Cheminform* 6 (1), 13. doi:10.1186/1758-2946-6-13

Shannon, P., Markiel, A., Ozier, O., Baliga, N.-S., Wang, J.-T., Ramage, D., et al. (2003). Cytoscape: a Software Environment for Integrated Models of Biomolecular Interaction Networks. *Genome Res.* 13 (11), 2498–2504. doi:10.1101/gr.1239303

Sherman, B. T., and Lempicki, R. A. (2009). Systematic and Integrative Analysis of Large Gene Lists Using DAVID Bioinformatics Resources. *Nat. Protoc.* 4 (1), 44. doi:10.1038/nprot.2008.211

Su, H.-R., Tang, L.-L., Yuan, R.-F., Chen, X.-X., Wei, Q.-S., and Deng, W.-M. (2017). A Kidney-tonifying Herbal Fufang Effects the Bone Mineral Density in Senile Osteoporosis Mice by GH/IGF-1 axis. *J. Pract. Med.* 33 (15), 2459–2464. doi:10.3969/j.issn.1006-5725.2017.15.009

Szklarczyk, D., Santos, A., von Mering, C., Jensen, L. J., Bork, P., and Kuhn, M. (2016). STITCH 5: Augmenting Protein-Chemical Interaction Networks with Tissue and Affinity Data. *Nucleic Acids Res.* 44 (D1), D380–D384. doi:10.1093/nar/gkv1277

Wang, W.-H., Xiang, N., Deng, Y.-P., Tang, J.-Q., Zhou, Y.-N., Zhou, G.-W., et al. (2016). Effect of Nourishing Yin and Shugan Prescription on Hypothalamus-Pituitary-Gonadal axis and Body Mass in Female Central Precocious Rats. *Chin. J. Integrated Traditional West. Med. Intensive Crit. Care* 23 (1), 71–75. doi:10.3969/j.issn.1008-9691.2016.01.017

Wang, X.-J., Li, P.-O., and Feng, C.-Z. (2020). Ultrasound Evaluation of the Clinical Efficacy of Zhibai Dihuang Pill Combined with Dabuyin Pill in the Treatment of Central Precocious Puberty in Girls. *J. PEDIATRICS TCM.* 16 (3), 72–76. doi:10.16840/j.issn1673-4297.2020.03.21

Wang, Y.-H., and Zhao, X. (2019). Effect of Zhibai Dihuang Pills Combined with Diphereline in the Treatment of Childhood Precocious Puberty and Their Effect on Serum Hormone Levels. *Med. J. Wuhan Univ.* 40 (3), 444–448. doi:10.14188/j.1671-8852.2018.0973

Wishart, D. S., Feunang, Y. D., Guo, A. C., Lo, E. J., Marcu, A., Grant, J. R., et al. (2018). DrugBank 5.0: a Major Update to the DrugBank Database for 2018. *Nucleic Acids Res.* 46 (D1), D1074–D1082. doi:10.1093/nar/gkx1037

Wu, Y., Zhang, F., Yang, K., Fang, S., Bu, D., Li, H., et al. (2019). SymMap: an Integrative Database of Traditional Chinese Medicine Enhanced by Symptom Mapping. *Nucleic Acids Res.* 47 (D1), D1110–D1117. doi:10.1093/nar/gky1021

Xu, H.-Y., Zhang, Y.-Q., Liu, Z.-M., Chen, T., Lv, C.-Y., Tang, S.-H., et al. (2019). ETCM: an Encyclopaedia of Traditional Chinese Medicine. *Nucleic Acids Res.* 47 (D1), D976–D982. doi:10.1093/nar/gky987

Yan, X.-N., Tian, G.-X., He, H.-R., Liu, X.-M., Zhang, J., and Lv, J. (2019). CTD Database Architecture and Data Acquisition Query and Extraction Method. *Chin. J. Evid. Based Cardiovasc. Med.* 11 (8), 905–909. doi:10.3969/j.issn.1674-4055.2019.08.03

Yang, L.-Z., and Zhao, M.-F. (2013). Effect of Zhizao Granules on Serum Levels of Growth Hormone and Insulin-like Growth Factor 1 in Rats with Early Sexual Maturation. *J. Changchun Univ. Traditional Chin. Med.* 29 (1), 15–17. doi:10.3969/j.issn.1007-4813.2013.01.007

Ye, J., Han, X.-M., Li, Y.-Q., Yang, L.-L., and Wu, Y.-M. (2011). Effect of Kangzao Granule on Sex Hormone Level in Female Precocious Rats. *Lishizhen Med. Materia Med. Res.* 22 (3), 618–619. doi:10.3969/j.issn.1008-0805.2011.03.045

Zhu, S.-Y., Du, M.-L., and Lin, A.-H. (2008). An Analysis of Risk Factors for Premature Thelarche Converting into Complete Central Precocious Puberty. *Chin. J. Pract. Pediatr.* 23 (3), 174–176. doi:10.3969/j.issn.1005-2224.2008.03.007

Conflict of Interest: The authors declare that the research was conducted in the absence of any commercial or financial relationships that could be construed as a potential conflict of interest.

Copyright © 2021 Guo, Sun, Hu, Bai, Zhang, Wang, Ding, Liu, Wang and Zhao. This is an open-access article distributed under the terms of the Creative Commons Attribution License (CC BY). The use, distribution or reproduction in other forums is permitted, provided the original author(s) and the copyright owner(s) are credited and that the original publication in this journal is cited, in accordance with accepted academic practice. No use, distribution or reproduction is permitted which does not comply with these terms.

frontiers in Pharmacology

CLINICAL TRIAL
published: 07 May 2021
doi: 10.3389/fphar.2021.646310

Clinical Efficacy of *Cortex Daphnes (Zushima)* Patch in Patients With Symptomatic Knee Osteoarthritis: A Multicenter Non-Inferiority Randomized Controlled Clinical Trial

Yan-Ting Li[1†], Juan Jiao[2†], Yi Zhang[1], Ci-Bo Huang[3], Hai-Dong Wang[4], Bei Wang[5], Xiao Su[6], Hui Song[7], Mian-Song Zhao[8], De-Xun Jiang[9], Jia-Qiang Wang[10] and Quan Jiang[2]**

[1]College of Basic Medical Science, Zhejiang Chinese Medical University, Hangzhou, China, [2]Department of Rheumatology, Guang'anmen Hospital, China Academy of Chinese Medical Sciences, Beijing, China, [3]Department of Rheumatology, Beijing Hospital, Beijing, China, [4]Department of Rheumatology and Osteopathy, Gansu Provincial Hospital of TCM, Lanzhou, China, [5]Department of Rheumatology and Immunology, Beijing Hospital of Traditional Chinese Medicine, Capital Medical University, Beijing, China, [6]Department of Rheumatology, Shanghai Municipal Hospital of Traditional Chinese Medicine, Shanghai University of Traditional Chinese Medicine, Shanghai, China, [7]Department of Rheumatology and Immunology, Beijing Jishuitan Hospital, Beijing, China, [8]Department of Rheumatology and Clinical Immunology, Beijing Shijitan Hospital, Capital Medical University, Beijing, China, [9]Department of Rheumatism and Immunology, Seventh Medical Center of PLA General Hospital, Beijing, China, [10]Gansu Taikang Pharmaceutical Co., Ltd., Lan Zhou, China

Background: Osteoarthritis (OA) is imposing substantial burdens on individuals and society with the aging population. Cortex Daphnes patch is widely used for symptomatic knee OA in China with a satisfying clinical efficacy; however, there is scant clinical evidence supporting its use. To evaluate its efficacy, we conducted a multicenter, non-inferiority, randomized, parallel-group study comparing Cortex Daphnes patch with topical nonsteroidal anti-inflammatory drugs in patients with knee OA (NCT02770950).

Methods: A total of 264 symptomatic knee OA patients were treated with Cortex Daphnes or indomethacin cataplasms applied to affected sites once daily for 2 weeks. The primary outcome was improvement in knee pain on walking as assessed using a visual analog scale (VAS). The non-inferiority margin based on the full analysis population was set as –5 mm on the pain VAS. The secondary outcomes were changes of the Western Ontario and McMaster Universities Osteoarthritis Index (WOMAC) total score, WOMAC scores for pain, function and stiffness, the 36-item Short Form Health Survey (SF-36), and global assessment of knees by the patients. Responder rates for pain VAS, WOMAC total score, and WOMAC pain were also included in the secondary outcomes.

Results: The Cortex Daphnes patch was non-inferior to indomethacin cataplasms for the primary outcome with a group difference (Cortex Daphnes patch–indomethacin cataplasm) of 2.1 mm (95% confidence interval: 2.1–6.4); similar results were found in the per-protocol population. For all other outcomes, no significant differences were found in the full analysis set or in the per-protocol analysis set, except the responder rates for WOMAC pain was higher in the Cortex Daphnes patch group than in the indomethacin cataplasm group (78.4 vs. 64.7%, p = 0.022) in the per-protocol analysis set. Overall,

OPEN ACCESS

Edited by:
Yanqiong Zhang,
China Academy of Chinese Medical Sciences, China

Reviewed by:
Yin Su,
Peking University People's Hospital, China
Xinping Tian,
Peking Union Medical College Hospital (CAMS), China
Yuan Jia,
Peking University People's Hospital, China

***Correspondence:**
Jia-Qiang Wang
wangjiaqiang@jzyyjt.com
Quan Jiang
doctorjq@126.com

†These authors have contributed equally to this work and share first authorship

Specialty section:
This article was submitted to Ethnopharmacology, a section of the journal Frontiers in Pharmacology

Received: 26 December 2020
Accepted: 08 March 2021
Published: 07 May 2021

Citation:
Li Y-T, Jiao J, Zhang Y, Huang C-B, Wang H-D, Wang B, Su X, Song H, Zhao M-S, Jiang D-X, Wang J-Q and Jiang Q (2021) Clinical Efficacy of Cortex Daphnes (Zushima) Patch in Patients With Symptomatic Knee Osteoarthritis: A Multicenter Non-Inferiority Randomized Controlled Clinical Trial. Front. Pharmacol. 12:646310. doi: 10.3389/fphar.2021.646310

28.8% patients in the Cortex Daphnes patch group and 9.8% in the indomethacin cataplasm group reported treatment-related adverse events, the vast majority of which were mild-to-moderate skin irritation, resulting in only 3.8 and 0.8% of patients dropping out, respectively.

Conclusion: The Cortex Daphnes patch, which provides satisfactory analgesic efficacy and enhances the physical function of the knee, as well as improving quality of life, may be a promising alternative to knee OA.

Keywords: knee osteoarthritis, nonsteroidal anti-inflammatory drugs, Cortex Daphnes patch, pain, non-inferiority trial design

INTRODUCTION

Osteoarthritis (OA) is a progressive disease of joints, common in middle and old age, that leads to joint capsule and ligament contracture, resulting in joint pain and functional impairment, as well as social and economic burdens (Dieppe and Lohmander, 2005; Hunter et al., 2014; Sharif et al., 2017). The joint pain, deformity, and motor dysfunction caused by OA can further increase the incidence of cardiovascular events and all-cause mortality (Xing et al., 2016; Liu et al., 2017). Knee OA is the most common type of OA; symptomatic knee OA is associated with considerable morbidity both in China and elsewhere (Cooper and Arden., 2011; Tang et al., 2016), with the result of an almost 90% increase in all-cause mortality (Liu et al., 2015). There is no specific treatment for osteoarthritis so far. Nonsteroidal anti-inflammatory drugs (NSAIDs) have been recognized as a good choice to manage symptomatic knee OA; however, oral NSAIDs are associated with higher risk of gastrointestinal, cardiovascular, and renal injury than placebo (Cepeda et al., 2006). Topical NSAIDs can avoid many of the adverse effects associated with systemic medications, can be considered as alternative therapy by patients with knee OA (Ringdahl and Pandit, 2011), but in fact, topical NSAIDs were less effective than oral NSAIDs (Lin et al., 2004). Therefore, it is of great significance to develop novel and more efficient therapeutic strategies for treatment of knee OA.

Traditional Chinese medicine has been accepted as a complementary therapy for knee OA, owing to its effects on relieving pain and improving functions of knee joint (Wang et al., 2020). Topical Chinese herbal preparation, as a representative form of traditional Chinese medicine, is commonly used in patients with symptomatic knee OA. Also known as Zushima (pronounced/zu-shi-ma:/), Cortex Daphnes is the processed stem and root barks of Daphne giraldii Nitsche., Daphne tangutica Maxim., and Daphne retusa Hemsl., all of which belong to the genus Daphne (Thymelaeaceae) (Pharmacopoeia of the People's Republic of China, 1977).

According to Chinese medicine theory, the function of Cortex Daphnes herb is to remove blood stasis and relieve pain, removing cold-wind and dredge collaterals. It is used to treat headache, stomach ache, bruises, limb numbness, joint pain, and others. Although Cortex Daphnes patch has been widely used to treat arthritis in China, there have been few clinical studies reporting its effect and safety. The first published clinical study of Cortex Daphnes patch was in the 1980s, reporting the effects of pain relief in Chinese patients with soft tissue injury (Wang, 1986). Only one low-quality randomized controlled trial in patients with knee OA reported satisfactory clinical efficacy of Cortex Daphnes patch when combined with acupuncture (Wang and Zhan, 2014).

The aim of the present study is to evaluate whether Cortex Daphnes patch has the potential to be a valuable topical intervention for patients with knee OA. For this reason, we conducted a multicenter, non-inferiority, randomized controlled trial to compare the safety and efficacy of the Cortex Daphnes patch to indomethacin cataplasms for the treatment of knee OA.

MATERIALS AND METHODS

Plant Material, Handling, and Phytochemical Analysis

Cortex Daphnes is majorly derived from the field-grown root bark and stem bark of Daphne giraldii Nitsche., which were collected in the plateau region of Gansu Province, China, and processed as described in the standard of Chinese medicinal materials in Gansu Province (Gansu Medical Products Administration, 2009). The main processing methods include rinsing, drying, and cutting pharmaceutical materials. Cortex Daphnes patch is the inheritance and innovation of traditional techniques of the black plaster. The black plaster, as a representative form of topical Chinese herbal preparation, has been used in China for at least thousands of years. The processing and extraction of Cortex Daphnes patch mainly include the following steps: Cortex Daphnes decoction pieces are cut off and boiled twice with water. Then, the decoction is filtered, concentrated, and dried. Finally, the Cortex Daphnes dry powder is added to the traditional black plaster matrix that is refined and smeared in the center of the plaster cloth. Cortex Daphnes patch is made by adding water-extracted Cortex Daphnes dry powder instead of the traditional frying extraction method, so as to avoid extreme damage to the active ingredients. Cortex Daphnes patch in the current study was produced by Gansu Taikang Pharmaceutical Co., Ltd. (China, batch number: 20150679). Preparation and assay methods of Cortex Daphnes patch are based on the pharmaceutical standards of the Ministry of Health of the

People's Republic of China (Standard No. WS3-B-3456-98; Pharmacopoeia Committee of National Health, 1998). Its phytochemical content (daphnetin) in each patch, according to extraction and assay methods, was 600 μg dry weight. The chemical profiling of Cortex Daphnes patch was detected using LC/MS/MS method, and the details were provided in supplementary material.

Study Design

This was a multicenter, randomized, active controlled trial with duration of 2 weeks to evaluate the efficacy and safety/tolerability of Cortex Daphnes patch in patients with symptomatic knee OA. The study was conducted at eight sites in China from May 2016 to December 2017.

Among those NSAIDs used for local treatment of OA, topical administration of indomethacin has been widely prescribed for pain in China. According to package instructions, the dose of indomethacin cataplasm was one patch for one site once daily for 24 h.

Selection Criteria

Participants were all outpatient patients who visited doctors complaining of knee pain. Patients were aged 40–75 years who met the 1995 American College of Rheumatology combined clinical and radiographic criteria for knee OA (Hochberg et al., 1995) and had symptoms in both knees. The inclusion criteria were knee pain of no less than 20 mm on a 100-mm visual analog scale (VAS) when walking flat. Patients taking oral NSAIDs prior to the breakthrough period (one week before starting) were included. The exclusion criteria included swollen and hot knees at the time of recruitment and patients with other joint diseases, such as rheumatoid arthritis, ankylosing spondylitis, congestive heart failure and edema, and advanced renal disease. We also excluded patients who were allergic to any ingredient in Cortex Daphnes patch (Cortex Daphnes and substrates including lithargite, linseed oil, and red lead) and in indomethacin cataplasm, as well as those who had punctured knee skin or other skin diseases.

Randomization and Masking

This was a multicenter and active-controlled design. Using the block randomization method, a random number table was generated by an independent third party, the Clinical Evaluation Center of China Academy of Chinese Medical Sciences, using SAS 9.4 software (SAS Institute, Cary, NC, United States). The randomized assignment sequence was placed in a sealed opaque envelope and was kept by the scientific research management department of the research unit and can be reproduced upon request. Eligible patients were randomized 1:1 to either Cortex Daphnes or indomethacin cataplasm topical treatment. Prior to recruitment, study investigators, site staff, and patients were blinded to the details of the allocation sequence. In order to avoid patient's preference for treatment method, we discussed all the interventions (the Cortex Daphnes patch and the indomethacin cataplasm) involved in this study with each participant, and informed them that all the treatments may benefit them. Furthermore, we asked a staff member not to discuss the intervention with participants when dispensing the medicine. The therapeutic and side effects were evaluated by a trained staff member of each site who was blinded to group allocation.

Outcome Measures

The study included a screening visit to determine eligibility, a baseline visit, and a 2-week visit. Patient-reported outcome measures were collected at baseline and at the 2-week visit. Unscheduled visits were also possible at any time during the study treatment if required.

The primary outcome was change in the patient's global assessment of pain intensity score from baseline to posttreatment. The Patient's Global Assessment of Pain Intensity score employed a 100-mm VAS pain scale evaluating knee pain when walking flat (0 for no pain and 100 for pain as bad as it could possibly be) (Cao et al., 2009). The secondary outcomes included changes in the Western Ontario and McMaster Universities Osteoarthritis Index (WOMAC) total score, WOMAC scores for three subscales (pain, function, and stiffness), the 36-item Short Form Health Survey (SF-36), and the patient's global assessment of knees from baseline to posttreatment. Responder rates for pain VAS (at least a 30% improvement from baseline), WOMAC total score (at least a 30% improvement from baseline), and WOMAC pain (at least a 30% improvement from baseline) were also included in the secondary outcomes. The WOMAC is a 24-item disease-specific patient-reported outcome measure with five questions assessing pain (range 0–20), two assessing stiffness (range 0–8), and 17 assessing function (range 0–68) (Bellamy et al., 1988). The WOMAC total score ranges from 0 to 96, with higher scores indicating greater burden of knee OA (Bellamy et al., 1988). The SF-36 is a generic quality of life instrument with eight health domains. It consists of 36 questions and assesses eight dimensions: physical functioning, role physical, pain index, general health, vitality, social functioning, role emotional, and mental health index (Li et al., 2002). It also provides two summary measures of physical and mental components, physical component score and mental component score, ranging from 0 to 100, with higher scores indicating better health status (Li et al., 2002). The participants were all self-assessed using VAS score to document the overall symptom severity of their knees at the beginning of the study and after treatment.

Safety evaluations included monitoring of adverse events (AEs), treatment discontinuations, measurement of skin irritation, and the assessment of clinical laboratory investigations. Skin irritation intensity evaluation criteria were used to record adverse skin events, which were the most commonly expected side effects. According to these criteria, the degree of the irritation symptoms including erythema, edema, and pruritus, were divided into mild, moderate, and strong irritation and were assessed by a trained physician (Bureau of Drug Policy and Administration of the People's Republic of China, 1994). The specific laboratory assessments included complete blood counts and urinalyses, as well as

measurements of glutamic-pyruvic transaminase, glutamic-oxalacetic transaminase, creatinine, and blood urea nitrogen.

Treatment

Patients whose eligibility was confirmed at the baseline visit were randomly assigned to treatment with one or the other intervention. During the treatment period, participants were instructed to apply the Cortex Daphnes patch or the indomethacin cataplasm (Nipro Patch CO. LTD. Japan, batch number: EM002) onto clean skin overlying the affected sites on both knees every night and keep it in place for 24 h. The standard operation procedure for the application of Cortex Daphnes patch has been established. As shown in **Figure 1**, instructions were offered to every participant in the Cortex Daphnes patch group to standardize the external use site, the administration time, and the method of placing and removing the patch to ensure the consistency of application.

No other treatments for knee OA were permitted during the treatment period: systemic and topical NSAIDs; opioid analgesics; acetaminophen; oral and intra-articular injection of corticosteroids; intra-articular knee injections (hyaluronic acid injection and local anesthetics); surgical or physiotherapeutic therapies; acupuncture; and aspirin. All AEs were recorded in detail and were monitored regularly until properly resolved or the condition was stable.

Sample Size Calculation

The sample size was determined using the primary endpoint of the change of VAS pain score. The literature showed that the effect for Cortex Daphnes patch with the same primary endpoint was 44.6 mm (SD: 33.4 mm) and it was 35.3 mm (SD: 30.4 mm) for indomethacin cataplasms at week 2 (Wang et al., 2016). Assuming a non-inferiority margin of -5 mm and that the ratio of the Cortex Daphnes patch group and the indomethacin cataplasm group was 1:1, using a two-sided test with a significance level (α) of 0.05 and a power (1–β) of 0.90, the required sample size was estimated at 105 cases in each group. Allowing for a dropout of 20%, the Cortex Daphnes patch group and the indomethacin cataplasm group each required 132 patients, a total of 264 patients.

Statistical Analysis of Data

Statistical analyses were performed using SAS version 9.4 (SAS Institute, Cary, NC, USA). The full analysis set (FAS) and per-protocol (PP) analysis set were analyzed. The FAS population included all participants who were randomized and underwent the assigned treatment. Non-inferiority of the primary endpoint (change of VAS pain score of Cortex Daphnes patch vs. indomethacin cataplasm) was determined if the lower limit of the 95% CI for the difference was not less than the cutoff value of -5 mm. The changes of primary and secondary endpoints at week 2 from baseline were analyzed using an analysis of covariance (ANCOVA) model with the treatment group and the study center as factors and the baseline score as a covariate. The point estimate, the least squares (LS) means, and the two-sided 95% CI based on the ANCOVA model were provided for the difference between treatment groups. The 30% responders were defined as patients who experienced a 30% reduction of WOMAC pain score,

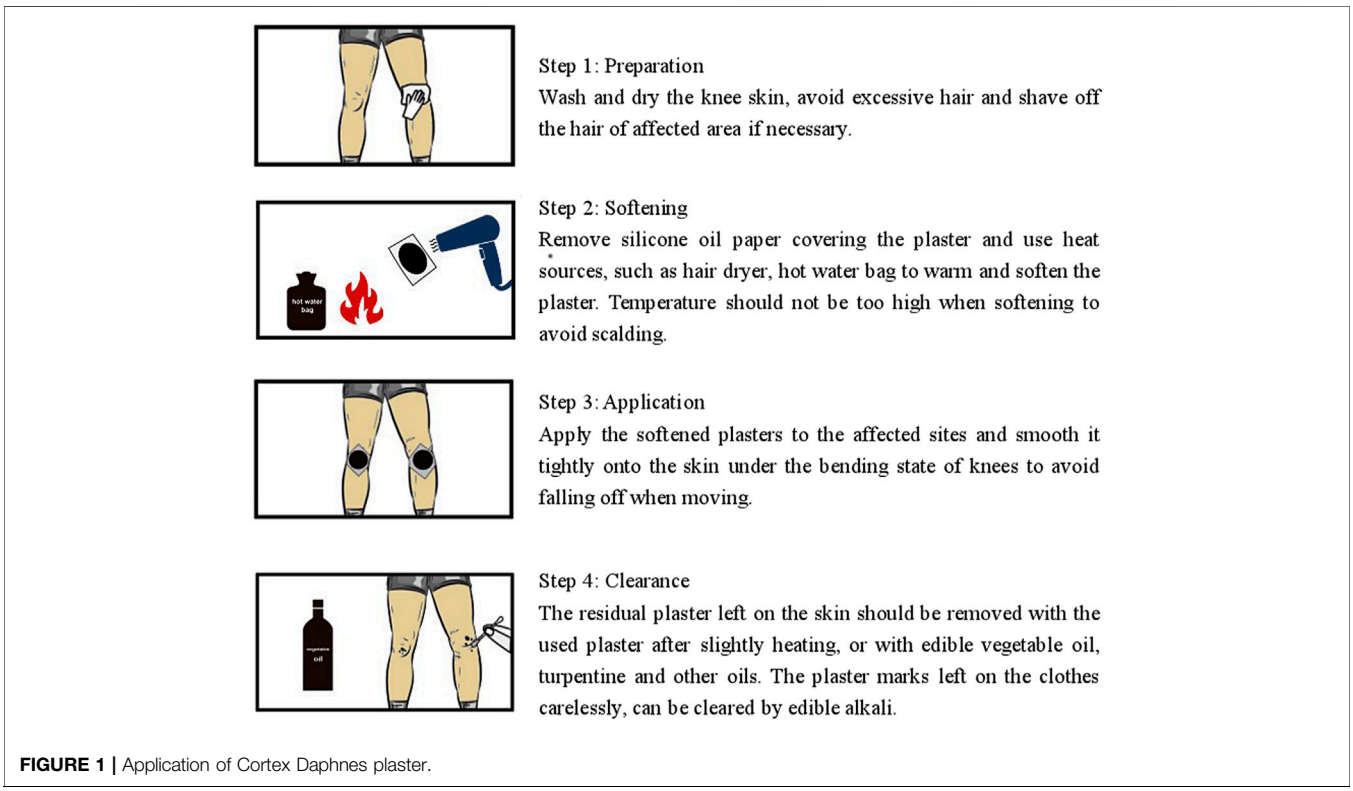

FIGURE 1 | Application of Cortex Daphnes plaster.

TABLE 1 | Demographic and baseline clinical characteristics of patients in FAS population.

Variable	Cortex Daphnes patch group (*n* = 132)	Indomethacin cataplasm group (*n* = 132)	*p*-value
Age (years, mean (SD))	59.8 (7.8)	59.5 (8.6)	0.81
Gender (n (%))			0.15
Male	19 (14.4)	28 (21.2)	
Female	113 (85.6)	104 (78.8)	
Race (n (%))			0.31
Han	129 (97.7)	131 (99.2)	
Non-Han	3 (2.3)	1 (0.8)	
Duration of knee pain (month, median (Qd))	36 (48.0)	36 (52.5)	0.93
Weight (kg, mean (SD))	64.1 (8.8)	66.1 (11.7)	0.13
Height (cm, mean (SD))	162.1 (6.5)	161.9 (5.8)	0.83
BMI (kg/m^2, mean (SD))	24.4 (3.0)	25.2 (4.1)	0.08
Kellgren/Lawrence scale (n (%))			0.79
Grade 1	37 (28.0)	42 (31.8)	
Grade 2	60 (45.5)	45 (34.1)	
Grade 3	22 (16.7)	33 (25.0)	
Grade 4	1 (0.8)	0 (0)	
Unknown	12 (9.1)	12 (9.1)	
Pain VAS[a] (mean (SD))	63.1 (14.0)	64.0 (16.1)	0.48
NRS[b] (n (%))			0.30
NRS-mild pain	1 (0.8)	5 (3.8)	
NRS-moderate pain	78 (59.1)	63 (67.7)	
NRS-severe pain	53 (40.2)	64 (48.5)	
Patient's global assessment of knee OA (mean (SD))	62.0 (14.3)	63.5 (16.5)	0.34
WOMAC[c] (mean (SD))			
Total score	31.5 (15.2)	33.3 (15.5)	0.25
Pain	6.7 (3.2)	7.4 (3.6)	0.09
Stiffness	2.6 (1.8)	2.7 (1.8)	0.53
Function	22.3 (11.4)	23.2 (11.5)	0.42
SF-36[d] (mean (SD))			
PCS	53.11 (8.8)	49.9 (19.7)	0.16
MCS	59.3 (18.3)	55.1 (22.6)	0.33

Abbreviations: FAS = full analysis set; BMI = body mass index; pain VAS = pain visual analog scale; NRS = numerical rating scale for pain; OA = osteoarthritis. WOMAC = Western Ontario and McMaster Universities Osteoarthritis Index; SF-36 = Short Form-36 Health Status Questionnaire; PCS = physical component score; MCS = mental component score.

[a]*Pain VAS is a measurement for body pain. Scores range from 0 to 100 mm, with higher score indicating greater pain.*

[b]*The NRS allows a person to describe the intensity of his/her pain, as a number ranging from 0 to 10. "0" indicates "no pain," "1 to 3" "mild pain," "4 to 6" "moderate pain," "7 to 9" "severe pain," and "10" "bad as it could be."*

[c]*The WOMAC is a 24-item disease-specific outcome measure and the higher score indicates greater burden of knee OA. Scores range from 0 to 96 with five questions assessing pain (range 0–20), two assessing stiffness (range 0–8), and 17 assessing function (range 0–68).*

[d]*SF-36 is a self-administered, 36-item questionnaire that assesses the physical and mental quality of life. Both of physical and mental component summaries can be combined ranging from 0 to 100, with higher scores indicating better health status.*

WOMAC total score, and VAS score from baseline for each respective outcome. A p-value of <0.05 was considered statistically significant. All patients who received at least one dose of the study drug were included in the safety set (SS). Incidence of AEs, treatment-related AEs, and discontinuation rate due to AEs were compared between the two groups using the Pearson chi-square test and Fisher's exact model.

RESULTS

Baseline of Clinical Cohorts

All patients were Chinese. Among 292 patients with symptomatic knee OA who were initially screened, 264 eligible patients were enrolled and constituted the FAS population. There were no statistically significant differences between the groups with respect to demographic and baseline clinical characteristics (**Table 1**). There were 21 (15.9%) patients in the Cortex Daphnes patch group and 13 (9.8%) patients in the indomethacin cataplasm group who did not complete the 2-week treatment, resulting in an overall dropout rate of 12.9% (**Figure 2**). Finally, 230 patients were included in the PP population for the efficacy analyses.

Treatment Effects

The Primary Outcome: Patient's Global Assessment of Pain Intensity

In the FAS population, the LS mean changes from baseline in the pain VAS score at week 2 was −25.4 mm in patients receiving the Cortex Daphnes patch and −23.3 mm in patients receiving indomethacin cataplasms. The treatment difference (Cortex Daphnes patch−indomethacin cataplasm) in the FAS population was 2.1 mm and the two-sided 95% CI for the treatment difference was −2.1–6.4 mm. In the PP population, the result was similar (treatment difference and two-sided 95% CI: 3.8 [−0.6 to 8.2] mm). The lower limit of the 95% CI was

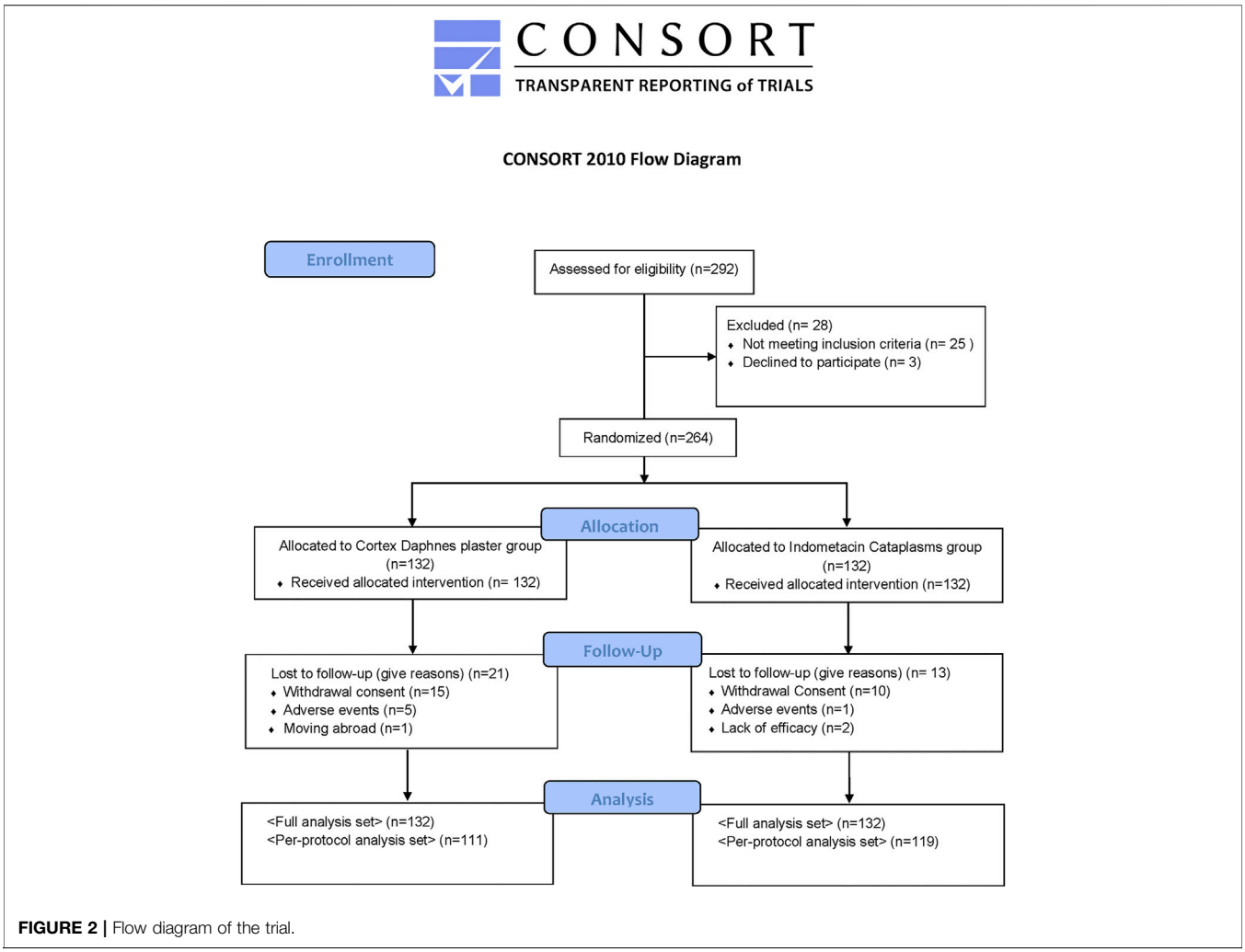

FIGURE 2 | Flow diagram of the trial.

TABLE 2 | Outcomes changes from baseline and difference in LS mean change of Cortex Daphnes patch from indomethacin cataplasms in FAS population posttreatment.

Outcomes	LS mean (95% CI) change from baseline		Between-group difference	*p*-value
	Cortex Daphnes patch group (n = 132)	Indomethacin cataplasm group (n = 132)	LS mean difference from control (95% CI)	
Pain VAS[a]	–25.4 (–28.4, –22.4)	–23.3 (–26.3, –20.3)	2.1 (–2.1, 6.4)	0.33
Patient's global assessment	–24.6 (–27.6, –21.6)	–23.2 (–26.2, –20.3)	1.4 (–2.8, 5.6)	0.52
WOMAC[b]				
Total score	–13.9 (–15.7, –12.2)	–12.6 (–14.4, –10.8)	1.3 (–1.2, 3.8)	0.29
Pain	–3.1 (–3.5, –2.7)	–2.7 (–3.1, –2.3)	0.4 (–0.1, 1.0)	0.12
Stiffness	–1.2 (–1.4, –1.0)	–1.1 (–1.3, –0.9)	0.1 (–0.2, 0.4)	0.41
Function	–9.7 (–11.0, –8.3)	–8.9 (–10.2, –7.5)	0.8 (–1.1, 2.7)	0.41
SF-36[c]				
PCS	9.3 (7.2, 11.4)	8.7 (6.6, 10.8)	–0.6 (–3.6, 2.4)	0.70
MCS	5.8 (4.0, 7.8)	5.2 (3.3, 7.2)	–0.6 (–3.4, 2.1)	0.66

All values are means (95% confidence intervals). Abbreviations: FAS = full analysis set; WOMAC = Western Ontario and McMaster Universities Osteoarthritis Index; SF-36 = Short Form-36 Health Status Questionnaire; PCS = physical component score; MCS = mental component score.

[a]Pain VAS is a measurement for body pain. Scores range from 0 to 100 mm, with higher scores indicating greater pain.

[b]The WOMAC is a 24-item disease-specific outcome measure and the higher score indicates greater burden of knee OA. Scores range from 0 to 96 with five questions assessing pain (range 0–20), two assessing stiffness (range 0–8), and 17 assessing function (range 0–68).

[c]SF-36 is a self-administered, 36-item questionnaire that assesses the physical and mental quality of life. Both of physical and mental component summaries can be combined ranging from 0 to 100, with higher scores indicating better health status.

TABLE 3 | Outcomes changes from baseline and difference in LS mean change of Cortex Daphnes patch from indomethacin cataplasms in PP population posttreatment.

Outcomes	LS mean (95% CI) change from baseline		Between-group difference	p-value
	Cortex Daphnes patch group (n = 111)	Indomethacin cataplasm group (n = 119)	LS mean difference from control (95% CI)	
Pain VAS[a]	−29.4 (−32.6, −26.3)	−25.6 (−28.6, −22.6)	3.8 (−0.6, 8.2)	0.09
Patient's global assessment	−28.6 (−31.7, −25.5)	−25.5 (−28.5, −22.5)	3.1 (−1.2, 7.4)	0.16
WOMAC[b]				
Total score	−16.0 (−17.9, −14.2)	−13.8 (−15.6, −12.1)	2.2 (−0.4, 4.7)	0.10
Pain	−3.5 (−3.9, −3.1)	−2.9 (−3.4, −2.5)	0.6 (−0.0, 1.2)	0.06
Stiffness	−1.3 (−1.5, −1.1)	−1.2 (−1.4, −1.0)	0.1 (−0.2, 0.4)	0.39
Function	−11.2 (−12.6, −9.8)	−9.7 (−11.1, −8.4)	1.5 (−0.5, 3.4)	0.14
09SF-36[c]				
PCS	11.1 (8.7, 13.5)	10.0 (7.7, 12.4)	−1.1 (−4.4, 2.3)	0.53
MCS	7.1 (4.9, 9.4)	5.9 (3.7, 8.1)	−1.2 (−4.3, 1.9)	0.45

All values are means (95% confidence intervals).

Abbreviations: FAS = full analysis set; WOMAC = Western Ontario and McMaster Universities Osteoarthritis Index; SF-36 = Short Form-36 Health Status Questionnaire; PCS = physical component score; MCS = mental component score.

[a]Pain VAS is a measurement for body pain. Scores range from 0 to 100 mm, with higher scores indicating greater pain.

[b]The WOMAC is a 24-item disease-specific outcome measure and the higher score indicates greater burden of knee OA. Scores range from 0 to 96 with 5 questions assessing pain (range 0–20), 2 assessing stiffness (range 0–8), and 17 assessing function (range 0–68).

[c]SF-36 is a self-administered, 36-item questionnaire that assesses the physical and mental quality of life. Both of physical and mental component summaries can be combined ranging from 0 to 100, with higher scores indicating better health status.

−5 mm, which indicates that Cortex Daphnes patch was non-inferior to indomethacin cataplasm for the treatment of Chinese patients with knee OA.

Secondary Outcomes

In the FAS population, there were no significant differences between groups with respect to any secondary endpoint after 2-week treatment (**Table 2**). The LS mean change from baseline in WOMAC total score was −13.9 in the Cortex Daphnes patch group and it was −12.6 in the indomethacin cataplasm group. WOMAC pain, stiffness, and function subscales were −3.1, −1.2, and −9.7 in the Cortex Daphnes patch group and −2.7, −1.1, and −8.9 in the indomethacin cataplasm group, respectively. The LS mean changes from baseline in SF-36 physical component scores and mental component scores were 9.3 and 5.8 in the Cortex Daphnes patch group and 8.7 and 5.2 in the indomethacin cataplasm group, respectively. The LS mean change from baseline in patient's global assessment of disease activity was −24.6 in the Cortex Daphnes patch group and −23.2 in the indomethacin cataplasm group. In the PP population, the treatment differences between the groups for all secondary endpoints were similar (**Table 3**).

In the FAS population, no differences between groups were significant in terms of responder rates for pain VAS, WOMAC total score, and pain subscale ($p > 0.05$) (**Figure 3**). In the PP population, no significant differences were found, except that the percentage of 30% responder WOMAC pain subsacle was higher

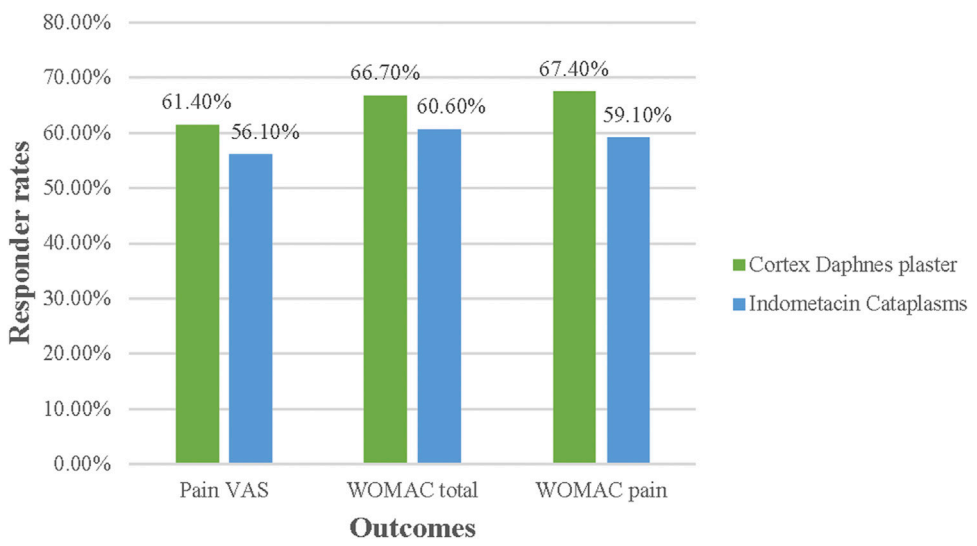

FIGURE 3 | Responder rates for Pain VAS, WOMAC total, and pain score in FAS population posttreatment.

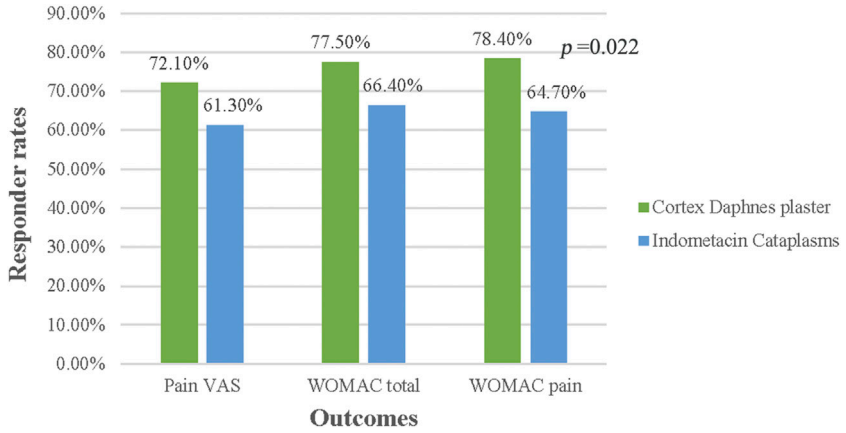

FIGURE 4 | Responder rates for Pain VAS, WOMAC total, and pain score in PP population.

in the Cortex Daphnes patch group than in the indomethacin cataplasm group (78.4 vs. 64.7%, p = 0.022; **Figure 4**).

Safety Profile

AEs are displayed in **Table 4**. AEs were documented 60 times during the study with a higher rate in the Cortex Daphnes patch group than in the indomethacin cataplasm group (29.5 vs. 19.5%, p = 0.008). The majority of these 60 events (51, 85%) were skin irritation and all were treatment-related AEs reported by 38 patients in the Cortex Daphnes patch group and 13 patients in the indomethacin cataplasm group. Routine laboratory examinations indicated that no patients in either group developed abnormalities. Most of the skin irritation AEs were mild-to-moderate in intensity with only five patients in the Cortex Daphnes patch group and one patient in the indomethacin cataplasm group discontinuing treatment.

The severity for skin AEs of erythema, itching, and edema are summarized in **Table 5**. Most expected side effects were slight in severity and resolved within 7 days without any additional intervention. The occurrence and severity of skin irritation, including erythema, itching, and edema tended to be higher in the Cortex Daphnes patch group than in the indomethacin cataplasm group. However, there were 38 patients in the Cortex Daphnes patch group reporting skin irritation symptoms. Among them, the knee skins of only 4 patients were allergic to the black plaster, while the other 34 patients reported that the knee skin around the plaster was allergic due to the mount material used in the Cortex Daphnes patch. Erythema and itching skin AEs resulting from black plaster were less likely to occur when using indomethacin cataplasms. There was one severe erythema and one itching skin AE in the Cortex Daphnes patch group due to black plaster, while no severe skin AEs occurred due to indomethacin cataplasms.

DISCUSSION

Current international and Chinese guidelines support the use of topical NSAIDs as an early treatment option for symptomatic relief of the management of knee OA (Hochberg et al., 2012; McAlindon et al., 2014; Joint Surgery Group of Chinese Orthopedic Association, 2018). Despite extensive clinical applications, definitive evidence of the efficacy of the Cortex

TABLE 4 | Number of patients experiencing adverse events during treatment.

Adverse effect	Cortex Daphnes patch group (*n* = 132)	Indomethacin cataplasm group (*n* = 132)	p-value
With AEs (n (%))	39 (29.5)	21 (15.9)	0.008
Skin irritation	38 (28.8)	13 (9.8)	<0.001
Sinus bradycardia	0 (0.0)	3 (2.3)	0.12
Upper respiratory infection	0 (0.0)	3 (2.3)	0.12
Gastrointestinal reaction	1 (0.8)	0 (0.0)	1.00
Thrombocytopenia	0 (0.0)	1 (0.8)	1.00
Pharyngitis	0 (0.0)	1 (0.8)	1.00
Treatment-related AEs (n (%))			
Skin irritation	38 (28.8)	13 (9.8)	<0.001
Discontinued due to AEs (n (%))			
Skin irritation	5 (3.8)	1 (0.8)	0.21

Abbreviations: AEs = adverse events.

TABLE 5 | The severity for the reported skin irritation.

Skin irritation	Cortex Daphnes patch group (n = 38)		Indomethacin cataplasm group (n = 13)
	Due to mount material (n = 34)	Due to black plaster (n = 4)	
Erythema			
Mild	9 (23.7)	0 (0.0)	6 (4.5)
Moderate	17 (44.7)	2 (5.2)	2 (1.5)
Severe	3 (7.9)	1 (2.6)	0 (0.0)
In total	29 (76.3)	3 (7.9)	8 (61.5)
Itching			
Mild	21 (55.3)	1 (2.6)	7 (5.3)
Moderate	8 (21.1)	1 (2.6)	1 (0.8)
Severe	1 (2.6)	1 (2.6)	0 (0.0)
In total	30 (78.9)	3 (7.9)	8 (61.5)
Edema			
Mild	5 (13.2)	1 (2.6)	1 (0.8)
Moderate	3 (7.9)	1 (2.6)	1 (0.8)
Severe	3 (7.9)	0 (0.0)	0 (0.0)
In total	11 (28.9)	2 (5.2)	2 (1.6)

Daphnes patch as an alternate option has yet to be provided. Against this background, the current multicenter, randomized clinical trial showed that the Cortex Daphnes patch was not inferior to indomethacin cataplasms with respect to efficacy, and its safety profile was also favorable, with no serious AEs being observed. These observations strongly support the existing evidence to the effect that Cortex Daphnes patch may be a potential alternative topical application for treatment of knee OA.

Our results suggest that the Cortex Daphnes patch can effectively relieve the symptoms of knee OA, in line with the findings of previous clinical studies. Cui et al. demonstrated that a 2-week regimen of Cortex Daphnes patch could relieve pain, swelling, and restricted movement in patients with knee synovitis when compared with infrared radiation therapy (Cui and Liu, 2017). A randomized controlled clinical trial with a short duration of about 2 weeks reported that, when combined with acupuncture, Cortex Daphnes patch was superior to glucosamine sulfate in terms of pain relief and joint function improvement in patients with knee OA (Wang and Zhan, 2014). Due to its warm property, Cortex Daphnes patch even reduced wrist joint pain, swelling, and stiffness in cold-type patients with rheumatoid arthritis (Wang et al., 2016), as well as alleviating lumbar pain and promoting functional status when combined with herb decoction in cold-type patients with chronic lumbar muscle strains (Wu et al., 2020). The key differences between the current and previous studies involve differences in use of the Cortex Daphnes patch as well as different target patient populations. In our study, we used a single Cortex Daphnes patch in patients suffering from knee OA; the previous studies used single Cortex Daphnes patches in patients with other chronic pain or arthritis diseases, and in the only study of knee OA study, the intervention was Cortex Daphnes patch combined with acupuncture. Using a higher quality of design and well-recognized outcome measures, the current study is the first clinical evidence to suggest the effectiveness of Cortex Daphnes patch for treatment of symptomatic knee OA.

Our findings show that Cortex Daphnes patch has a favorable anti-inflammatory analgesic effect. In recent years, daphnetin, coumarins, lignins, flavonoids, diterpenes, and other chemical components have been isolated and identified from Cortex Daphnes. Daphnetin, the main phytochemical component of Cortex Daphnes, has provided dramatic improvement in percutaneous absorption results *in vivo* and *in vitro* experiments. Pharmacological activity experiments showed that prostaglandin E2 generation was inhibited by extract of Cortex Daphnes by inhibiting the expression of cyclooxygenase-2 (Yuan et al., 2009). An animal experiment showed that daphnetin significantly reduced the swelling of feet and the severity of arthritis in adjuvant-induced arthritis rat model (Gao et al., 2008). Daphnetin, a natural product, inhibits not only lipoxygenase and cyclooxygenase but also neutrophil-dependent superoxide anion generation (Fylaktakidou et al., 2004).

In recent years, more than 250 chemical constituents have been identified from the genus Daphne. The most important classes of compounds obtained from this genus include coumarins, flavonoids, lignans, terpenoids, and several other less common groups (Xu et al., 2011; Moshiashvili et al., 2020) Coumarins are among the most common compounds in the Daphne genus and major toxic components. Daphne genus–related potential risks include hepatotoxicity, nephrotoxicity, burning in the pharynx, gastrointestinal discomfort (nausea, vomiting, burning of stomach, gastroenteritis, and diarrhea), internal bleeding, muscle spasms and paralysis, and skin irritation (redness, swelling, and blusters). In severe cases, circulatory arrest and coma may be observed "(Goel et al., 2007; Xu et al., 2011; Moshiashvili et al., 2020; Wink, 2009; Stefanachi et al., 2018)." Therefore, we should pay more attention to the safety of the Cortex Daphnes patch. In the study, the safety profiles suggested a trend toward higher frequency and more severity of treatment-related adverse effects in the Cortex Daphnes patch group. Although skin irritation was the most frequently reported treatment-related adverse effect in both treatment groups, the material used in the Cortex Daphnes patch predisposes patients to increased risk of developing erythema and edema, as well as itching of the contact skin, especially after fixing the plasters for 24 h daily, for 2 weeks, on knee skin.

Fortunately, those skin side effects were mostly mild in severity, were transient, and did not require intervention. Moreover, the skin reactions may be alleviated after discontinuation of the Cortex Daphnes patches. These findings suggest a rest time for skin is needed when using the Cortex Daphnes patch, and the components containing the Cortex Daphnes patch should be changed to be milder and less irritating.

There are some limitations with respect to the design of this non-inferiority study. First, the completely different physical characteristics and smell between the Cortex Daphnes patch and the indomethacin cataplasm prevented double-dummy design from being applied. Nevertheless, considering that those two medicines and their topical simulators could not be used on the knee simultaneously, or even used separately on each knee, an enormous difference in efficacy might result in a substantial decline in compliance with the treatment plan. Therefore, to ensure the reliability of evaluation measurements, instead of using the double-dummy design, a staff member who dispensed the investigational medicine was trained not to discuss the intervention with participants, and the therapeutic effects and side effects were evaluated by another blinded trained staff member. Second, its long-term efficacy remains unclear due to a paucity of follow-up. Third, we did not pay attention on the average time for skin irritation after medication and relevant data need to be supplemented in the following Cortex Daphnes patch-related research.

CONCLUSION

The Cortex Daphnes patch exerts favorable effects in decreasing knee pain and improving joint function for patients with knee OA, especially with mild-to-moderate knee OA, which were non-inferior to the therapeutic effects of a recognized treatment for knee OA. The clinical evidence presented here highlights the promising therapeutic efficacy of the Cortex Daphnes patch for the treatment of pain and symptoms associated with knee OA, particularly as part of a changing healthcare landscape that seeks to identify effective and safe plant medicines to treat chronic pain.

DATA AVAILABILITY STATEMENT

The raw data supporting the conclusion of this article will be made available by the authors, without undue reservation.

ETHICS STATEMENT

The studies involving human participants were reviewed and approved by the Ethics Review Committee of the Guang'anmen Hospital. The patients/participants provided their written informed consent to participate in this study.

AUTHOR CONTRIBUTIONS

QJ, JJ, C-BH, and H-DW designed the multicenter, randomized placebo-controlled trial. QJ, JJ, C-BH, H-DW, BW, XS, HS, M-SZ, and D-XJ conducted the research, Y-TL and JJ collected the documents and wrote the paper. Y-TL drew the figures. YZ was responsible for the statistical analyses. J-QW provided free research drugs. Y-TL and JJ are co-first author and contribute equally. All authors commented on the manuscript. All authors participated in the manuscript revision and approved the final version of manuscript.

FUNDING

This work was supported by the grant from the science and technology project of Gansu (18ZD2FH020).

SUPPLEMENTARY MATERIAL

The Supplementary Material for this article can be found online at: https://www.frontiersin.org/articles/10.3389/fphar.2021.646310/full#supplementary-material

REFERENCES

Bellamy, N., Buchanan, W. W., Goldsmith, C. H., Campbell, J., and Stitt, L. W. (1988). Validation study of WOMAC: a health status instrument for measuring clinically important patient relevant outcomes to antirheumatic drug therapy in patients with osteoarthritis of the hip or knee. *J. Rheumatol.* 15 (12), 1833–1840.

Bureau of Drug Policy and Administration of the People's Republic of China (1994). *Research guidelines for the new Chinese medicines (pharmacy, pharmacology, toxicology)*. Beijing China: Bureau of drug policy & administration of the People's Republic of China, 210–212.

Cao, H., Xing, J., and Liu, J. (2009). Application of visual analogue scales in assessment of symptomatic outcome data. *J. Traditional Chin. Med.* 50 (07), 600–602. doi:10.13288/j.11-2166/r.2009.07.001

Cepeda, M. S., Camargo, F., Zea, C., and Valencia, L. (2006). Tramadol for osteoarthritis. *Cochrane Database Syst. Rev.* 5 (3), CD005522. doi:10.1002/14651858.CD005522

Cooper, C., and Arden, N. K. (2011). Excess mortality in osteoarthritis. *Bmj* 342, d1407. doi:10.1136/bmj.d1407

Cui, X. D., and Liu, X. F. (2017). Clinical study on treatment of synovitis of knee joint with Chinese herbal medicine Ta Zi therapy. *ACTA Chin. Med.* 32 (9), 1770–1773. doi:10.16368/j.issn.1674-8999.2017.09.466

Dieppe, P. A., and Lohmander, L. S. (2005). Pathogenesis and management of pain in osteoarthritis. *The Lancet* 365 (9463), 965–973. doi:10.1016/S0140-6736(05)71086-2

Fylaktakidou, K., Hadjipavlou-Litina, D., Litinas, K., and Nicolaides, D. (2004). Natural and synthetic coumarin derivatives with anti-inflammatory/antioxidant activities. *Cpd* 10 (30), 3813–3833. doi:10.2174/1381612043382710

Gansu Medical Products Administration (2009). *Gansu provincial standard for Chinese medicinal materials (2009 edition)*. Lan Zhou: Gansu Culture Press, 290.

Gao, Q., Shan, J., Di, L., Jiang, L., and Xu, H. (2008). Therapeutic effects of daphnetin on adjuvant-induced arthritic rats. *J. Ethnopharmacology* 120 (2), 259–263. doi:10.1016/j.jep.2008.08.031

Goel, G., Makkar, H. P. S., Francis, G., and Becker, K. (2007). Phorbol esters: structure, biological activity, and toxicity in animals. *Int. J. Toxicol.* 26 (4), 279–288. doi:10.1080/10915810701464641

Hochberg, M. C., Altman, R. D., April, K. T., Benkhalti, M., Guyatt, G., McGowan, J., et al. (2012). American College of Rheumatology 2012 recommendations for the use of nonpharmacologic and pharmacologic therapies in osteoarthritis of the hand, hip, and knee. *Arthritis Care Res.* 64 (4), 465–474. doi:10.1002/acr.21596

Hochberg, M. C., Altman, R. D., Brandt, K. D., Clark, B. M., Dieppe, P. A., Griffin, M. R., et al. (1995). Guidelines for the medical management of osteoarthritis. *Arthritis Rheum.* 38 (11), 1541–1546. doi:10.1002/art.1780381104

Hunter, D. J., Schofield, D., and Callander, E. (2014). The individual and socioeconomic impact of osteoarthritis. *Nat. Rev. Rheumatol.* 10 (7), 437–441. doi:10.1038/nrrheum.2014.44

Joint Surgery Group of Chinese Orthopaedic Association (2018). Guidebook for the diagnosis and treatment of osteoarthritis (2018 edition). *Orthopaedic Surg.* 38 (12), 705–715.

Li, L., Wang, H., and Shen, Y. (2002). Development and psychometric tests of a Chinese version of the SF-36 health Survey scales. *Zhonghua Yu Fang Yi Xue Za Zhi* 36 (2), 109–113.

Lin, J., Zhang, W., Jones, A., and Doherty, M. (2004). Efficacy of topical non-steroidal anti-inflammatory drugs in the treatment of osteoarthritis: meta-analysis of randomised controlled trials. *BMJ* 329 (7461), 324. doi:10.1136/bmj.38159.639028.7C

Liu, Q., Niu, J., Huang, J., Ke, Y., Tang, X., Wu, X., et al. (2015). Knee osteoarthritis and all-cause mortality: the wuchuan osteoarthritis study. *Osteoarthritis and Cartilage* 23 (7), 1154–1157. doi: doi:10.1016/j.joca.2015.03.021

Liu, Q., Niu, J., Li, H., Ke, Y., Li, R., Zhang, Y., et al. (2017). Knee symptomatic osteoarthritis, walking disability, NSAIDs use and all-cause mortality: population-based wuchuan osteoarthritis study. *Sci. Rep.* 7 (1), 3309. doi:10.1038/s41598-017-03110-3

McAlindon, T. E., Bannuru, R. R., Sullivan, M. C., Arden, N. K., Berenbaum, F., Bierma-Zeinstra, S. M., et al. (2014). OARSI guidelines for the non-surgical management of knee osteoarthritis. *Osteoarthritis and cartilage* 22 (3), 363–388. doi:10.1016/j.joca.2014.01.003

Moshiashvili, G., Tabatadze, N., and Mshvildadze, V. (2020). The genus Daphne: a review of its traditional uses, phytochemistry and pharmacology. *Fitoterapia* 143, 104540. doi:10.1016/j.fitote.2020.104540

Pharmacopoeia Committee of National Health (1998). Commission of the People's Republic of China. *Natl. Drug Stand. Chin. Med. prescription preparations* 18, 233.

Pharmacopoeia of the People's Republic of China (1977). *China Pharmacopoeia committee*.

Ringdahl, E., and Pandit, S. (2011). Treatment of knee osteoarthritis. *Am. Fam. Physician* 83 (11), 1287–1292.

Sharif, B., Garner, R., Hennessy, D., Sanmartin, C., Flanagan, W. M., and Marshall, D. A. (2017). Productivity costs of work loss associated with osteoarthritis in Canada from 2010 to 2031. *Osteoarthritis and Cartilage* 25 (2), 249–258. doi:10.1016/j.joca.2016.09.011

Stefanachi, A., Leonetti, F., Pisani, L., Catto, M., and Carotti, A. (2018). Coumarin: a natural, privileged and versatile scaffold for bioactive compounds. *Molecules* 23 (2), 250. doi:10.3390/molecules23020250

Tang, X., Wang, S., Zhan, S., Niu, J., Tao, K., Zhang, Y., et al. (2016). The prevalence of symptomatic knee osteoarthritis in China: results from the China health and retirement longitudinal study. *Arthritis Rheumatol.* 68 (3), 648–653. doi:10.1002/art.39465

Wang, F. (1986). Cortex Daphnes for the treatment of closed soft tissue injury. *Shanxi J. Traditional Chin. Med.* 7, 367.

Wang, H. D., Nian, F. H., and Jin, F. M. (2016). Zushima plaster in treating wrist symptoms of 40 patients with rheumatoid arthritis of cold-ampness stagnation pattern. *West. J. Traditional Chin. Med.* 29 (10), 107–109.

Wang, M., Liu, L., Zhang, C. S., Liao, Z., Jing, X., Fishers, M., et al. (2020). Mechanism of traditional Chinese medicine in treating knee osteoarthritis. *Jpr* 13, 1421–1429. doi:10.2147/JPR.S247827

Wang, Y. J., and Zhan, F. J. (2014). Clinical observation of 120 cases of knee osteoarthritis treated by acupuncture combined with Cortex Daphnes patch. *Pract. Clin. J. Integrated Traditional Chin. West. Med.* 14 (5), 28–29. doi:10.13638/j.issn.1671-4040.2014.05.017

Wink, M. (2009). Mode of action and toxicology of plant toxins and poisonous plants. *Mitt. Julius Kühn Inst.* 421, 93–112.

Wu, D. Y., Zhang, T. B., and Li, L. (2020). Clinical evaluation of Yaoning decoction combined with Zushima plaster in treatment of chronic lumbar muscle strain of cold-dampness and blood stasis type. *Chin. Arch. Traditional Chin. Med.* 38 (4), 181–183. doi:10.13193/j.issn.1673-7717.2020.04.042

Xing, D., Xu, Y., Liu, Q., Ke, Y., Wang, B., Li, Z., et al. (2016). Osteoarthritis and all-cause mortality in worldwide populations: grading the evidence from a meta-analysis. *Sci. Rep.* 6, 24393. doi:10.1038/srep24393

Xu, W. C., Shen, J. G., and Jiang, J. Q. (2011). Phytochemical and biological studies of the plants from the genus Daphne. *Chem. Biodiversity* 8, 1215–1233. doi:10.1002/cbdv.201000117

Yuan, F., Chen, J., Xu, G. M., Zheng, J. J., and Long, Q. C. (2009). Anti-inflammatory mechanism of total glycosides of Acanthopanax Giraldii. *Chin. J. Integr. Med.* 15 (3), 210–215. doi:10.1007/s11655-009-0210-0

Conflict of Interest: Author J-QW was employed by the company Gansu Taikang Pharmaceutical Co., Ltd.

The remaining authors declare that the research was conducted in the absence of any commercial or financial relationships that could be construed as a potential conflict of interest.

The handling editor declared a shared affiliation with several of the authors (JJ and QJ) at time of review.

Copyright © 2021 Li, Jiao, Zhang, Huang, Wang, Wang, Su, Song, Zhao, Jiang, Wang and Jiang. This is an open-access article distributed under the terms of the Creative Commons Attribution License (CC BY). The use, distribution or reproduction in other forums is permitted, provided the original author(s) and the copyright owner(s) are credited and that the original publication in this journal is cited, in accordance with accepted academic practice. No use, distribution or reproduction is permitted which does not comply with these terms.

frontiers in Pharmacology

SYSTEMATIC REVIEW
published: 10 May 2021
doi: 10.3389/fphar.2021.649470

Comparative Efficacy of Oral Chinese Patent Medicine for Chronic Prostatitis/Chronic Pelvic Pain Syndrome With Sexual Dysfunction: A Bayesian Network Meta-Analysis of Randomized Controlled Trials

*Yang Zhang[1], Hongzhao Ma[2], Tao Nan[2], Yongqiang Li[2], Wei Zheng[2], Zhihui Zhou[2] and Xiaoyong Gong[2]**

[1]Shaanxi University of Chinese Medicine, Xianyang, China, [2]The Second Affiliated Hospital of Shaanxi University of Chinese Medicine, Xianyang, China

OPEN ACCESS

Edited by:
Takashi Sato,
Tokyo University of Pharmacy and Life Sciences, Japan

Reviewed by:
Junaid Wazir,
Nanjing University, China
Hongjun Li,
Peking Union Medical College Hospital (CAMS), China
Xiansheng Zhang,
First Affiliated Hospital of Anhui Medical University, China

***Correspondence:**
Xiaoyong Gong
miwai99@163.com

Specialty section:
This article was submitted to Ethnopharmacology, a section of the journal Frontiers in Pharmacology

Received: 04 January 2021
Accepted: 22 April 2021
Published: 10 May 2021

Citation:
Zhang Y, Ma H, Nan T, Li Y, Zheng W, Zhou Z and Gong X (2021) Comparative Efficacy of Oral Chinese Patent Medicine for Chronic Prostatitis/Chronic Pelvic Pain Syndrome With Sexual Dysfunction: A Bayesian Network Meta-Analysis of Randomized Controlled Trials. Front. Pharmacol. 12:649470. doi: 10.3389/fphar.2021.649470

Background: Oral Chinese patent medicine (OCPM) combined with western medicine (WM) are believed to be effective for the therapy of chronic prostatitis/chronic pelvic pain syndrome (CP/CPPS) with sexual dysfunction (SD). These western medicines mainly involve antibiotics, phosphodiesterase type-5 inhibitor (PDE-5i), α-blockers. But there is no randomized controlled trial (RCT) that directly compares the efficacy of different OCPM. Hence, we operated a network meta-analysis (NMA) to contrast the efficacy of different OCPM for CP/CPPS with SD.

Methods: Relevant studies were searched in PubMed, Cochrane Library, Web of Science, Embase, China National Knowledge Infrastructure (CNKI), Chinese Scientific Journal Database (VIP), and Wanfang database. All of the RCTs concentrated on the use of OCPM to cure CP/CPPS with SD from the inception of the databases to November 2020. We appraised the risk of bias under the Cochrane Handbook and CONSORT statement. The data were statistically analyzed *via* STATA 13.0 and WinBUGS 1.4.3 instrument.

Results: Altogether, 30 pieces of literature with 2,996 participants containing 11 oral Chinese patent medicine and 11 interventions were included in the NMA. In terms of The National Institutes of Health chronic prostatitis symptom index (NIH-CPSI), Qianlie Shutong Capsules (QLSTC) + WM had the most possible of being the optimal treatment. In the light of the International Index of Erectile Function (IIEF-5), Congrong Yishen Granules (CRYSG) + WM had the most possible of being the optimal treatment. Shugan Yiyang Capsules (SGYYC) + WM performed the highest likelihood efficacy under cluster rank graph combined NIH-CPSI and IIEF-5. Liuwei Dihuang Pills/Yougui capsules (LWDHP/YGC) + WM had highly possible to be the optimal treatment not only for the clinical effective rate of CP/CPPS but also for the clinical effective rate of SD. Considering four outcomes, QLSTC, CRYSG, SGYYC, LWDHP/YGC, Qianlie Beixi Capsules (QLBXC) plus WM were the best

therapy approach for CP/CPPS with SD, especially LWDHP/YGC + WM and QLBXC + WM.

Conclusion: Based on the NMA, QLSTC, CRYSG, SGYYC, LWDHP/YGC, QLBXC plus WM demonstrated the maximum probability of being the optimal therapies. Owing to the limitations of this research, these results should be confirmed by elaborate RCTs.

Systematic Review Registration: [https://www.crd.york.ac.uk/prospero/], identifier [CRD42021224060].

Keywords: network meta-analysis, chronic prostatitis/chronic pelvic pain syndrome, sexual dysfunction, oral medicine, Chinese patent medicine

INTRODUCTION

"Prostatitis is classified as acute bacterial prostatitis (category I), chronic bacterial prostatitis (category II), chronic prostatitis (CP)/chronic pelvic pain syndrome (CPPS, category III, inflammatory IIIA, noninflammatory IIIB) and asymptomatic inflammatory prostatitis (category IV), according to the National Institutes of Health (NIH) classification system for prostatitis" (Krieger et al., 1999). CP/CPPS, a very common urinary system disease, with small and complex symptoms, which seriously affect patient's quality of life. Furthermore, "men with CP/CPPS had a high probability to suffer sexual dysfunction (SD) than those without, such as erectile dysfunction (ED), premature ejaculation (PE), decreased sexual desire, ejaculatory pain and so on" (Li and Kang, 2016). "A meta-analysis involving 11,189 men showed that the prevalence of sexual dysfunction in men with CP/CPPS was high (SD was 62%, ED was 29% and PE was 40%), even though overall SD demonstrated a slightly decreasing trend, ED prevalence rate had an increasing trend in recent years" (Li and Chen, 2016). "A questionnaire survey was conducted among 1786 men indicated that the prevalence rate of SD in Chinese men with CP/CPPS is high (SD was 49%, ED was 15% and PE was 26%) and related to age" (Liang et al., 2004). Sexual dysfunction (SD) in our studies mainly refer to self-reported erectile dysfunction (ED) or premature ejaculation (PE), or both.

The studies on CP/CPPS with SD mainly concentrated on "epidemiology" (Liang et al., 2010; Hao et al., 2011), "risk factors" (Zhang et al., 2015a; Ma et al., 2020), and "relationship" (Chung et al., 2012), researches focus on therapeutics are scarce. "The National Institutes of Health (NIH) reached the consensus about prioritization of treatments for chronic prostatitis, rank 1 is antimicrobials (e.g., antibiotics), rank 2 is α-blockers (e.g., terazosin)" (Nickel et al., 1999). Lately, "α-blockers, antibiotics, and combinations of these therapies appear to achieve the greatest improvement in clinical symptom scores compared with placebo" (Anothaisintawee et al., 2011; Qin et al., 2016). However, the effectiveness of α-blockers and antibiotics has been controversial. Additionally, due to the long treatment time, we need to choose some drugs with fewer side effects and a longer course of treatment, so "Chinese patent medicine has become the best choice for us to treat chronic prostatitis with sexual dysfunction" (Zhong et al., 2013). "Oral Chinese patent medicine (OCPM) combined with western medicine (WM) has the beneficial effects for CP/CPPS with SD" (Wang et al., 2012; Feng et al., 2013).

"Under traditional Chinese medicine (TCM) theories, CP means damp-heat and blood stasis syndromes" (Wang et al., 2016). Therefore, the top priority of treatment is to activate blood circulation and remove dampness. TCM combines syndrome differentiation with disease differentiation was more favorable to us to understand and treat CP. Syndrome differentiation is used to identify different types of a single disease to create a specific treatment plan. Hence, our research evaluated the clinical curative effect of OCPM combined with WM in patients who meet the standard therapy of CP/CPPS with SD: syntheses, individualization, and sequencing. Yet, there is no direct evidence showing the optimal OCPM for CP/CPPS with SD treatment. It is difficult to decide the superiority of treatment under a meta-analysis of pairwise comparisons. A network meta-analysis (NMA) combines existing evidence makes it possible to compare different treatment options at the same time. So, our research compared the curative effect of 11 OCPM combined with WM through NMA to reveal the optimal OCPM for CP/CPPS with SD and provide more perspectives for the choice of CP/CPPS with SD. The graphic workflow in our research is illustrated in **Figure 1**.

METHODS

Eligibility Criteria

The RCTs that were published in English or Chinese were included if they met the following standard: 1) "Participants met criteria for CP/CPPS categories IIIA or IIIB according to the National Institutes of Health classification" (Krieger et al., 1999); 2) Participants met criteria for SD categories "erectile dysfunction (ED)" (Rosen et al., 1999) or "premature ejaculation (PE)" (Screponi et al., 2001), or both; 3) The interventions of experiment group involve OCPM add WM, the interventions of control group consist of WM alone or another OCPM plus WM. Besides, "these OCPMs must be included in the Pharmacopoeia of the People's Republic of China"(Lin et al., 2020) or the data query system of the National Medical Products Administration website https://www.nmpa.gov.cn/; 4) The full text could be found and had sufficient data for collection,

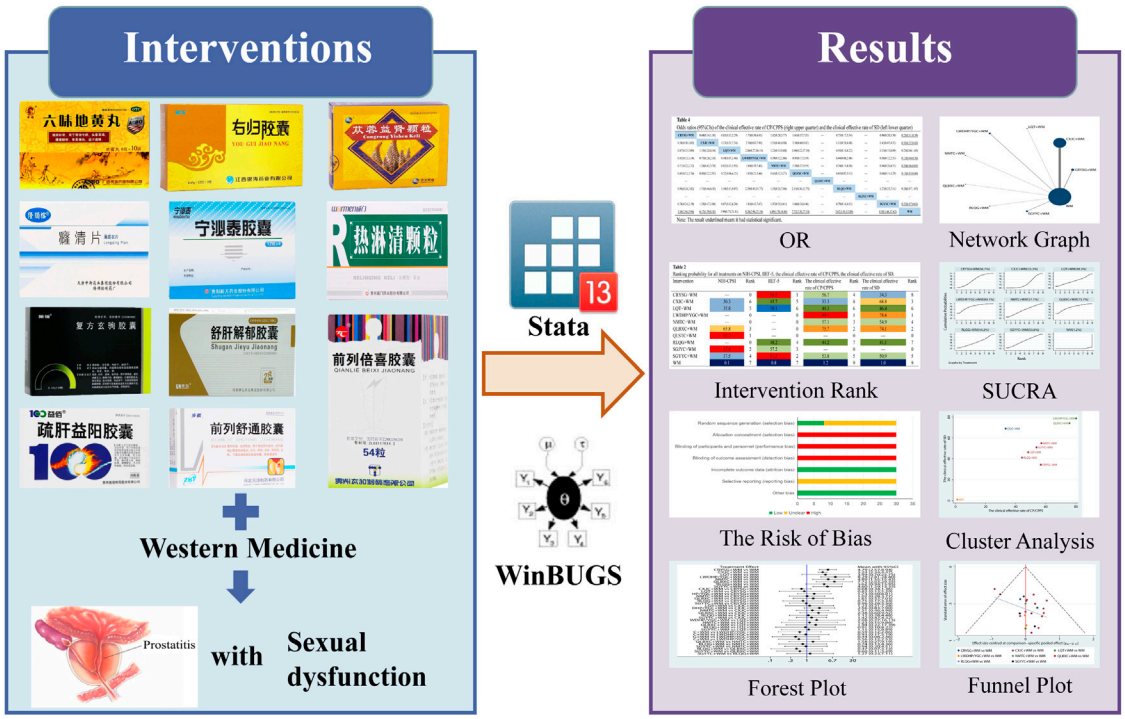

FIGURE 1 | Graphic workflow for the NMA.

including the number of patients, age of patients, duration of therapy; 5) The study contained any of the following outcomes: NIH-CPSI scores, IIEF-5 scores, the clinical effectiveness of CP/CPPS, the clinical effectiveness of SD. The following formula was utilized: the clinical effectiveness (%) = (quantity of recovered patients + quantity of improved patients)/total quantity × 100%, The clinical effective rate of SD = the clinical effective rate of ED + the clinical effective rate of PE. The clinical effective rate of CP/CPPS was primary according to the reduction of the NIH-CPSI score, the clinical effective rate of ED was based on the increase of the IIEF-5 score and the clinical effective rate of PE was on the basis of the increase of Chinese Index of Premature Ejaculation (CIPE-5) score. These scores could be divided into three grades: recovery, improvement, and inefficiency. For response to treatment, various definitions were used in the original studies; recovery was determined when the decrements of the NIH-CPSI score >50%, recovery definition to reach the IIEF-5 score >21, recovery definition to reach the CIPE-5 score >17; improvement was defined when the decreases of the NIH-CPSI score >25%, improvement definition to reach the IIEF-5 score >15, improvement definition to meet 4-unit score increases in the CIPE-5 from baseline; the rest was inefficiency.

The following studies were excluded: studies involving patients who had 1) major psychological or somatic diseases; 2) the use of drugs that influence sexual function; 3) the use of antibiotics during the preceding 2 weeks; 4) missing or incorrect data; 5) experimental research, retrospective studies, conference abstracts, case reports, and reviews or meta-analyses.

Data Sources and Retrieval Strategy

This research retrieves literature by employing the following databases from inception to November 2020: PubMed, Web of Science, Embase, Cochrane Library, CNKI, VIP, and Wanfang database. The free text words and medical subject headings (MeSH) were adopted. The restriction of language includes English and Chinese. Besides, we manually retrieved the reference of involved researches.

After overlaps were removed by EndNote X9, two researchers browsed the titles and abstracts of involved researches respectively. Besides, we also confirmed the potential articles. Any divergence could be solved through discussions or negotiations with a superior researcher.

Data Extraction and Quality Evaluation

This information was extracted on the basis of the designed table: identity document (author's name and year), participant's characteristics (number of patients, age of patients, chronic prostatitis category, and sexual dysfunction category), methods of intervention, duration, outcomes, the random method.

Two authors evaluated the risk of bias. The intervention was systematically evaluated in randomized controlled trials and Cochrane Handbook. "The quality evaluation of the included RCTs focused on several key domains: selection bias (sequence generation and allocation concealment), performance bias (blinding of patients and personnel), detection bias (blinding of outcome assessors), attrition bias (incomplete outcome data), reporting bias (selective reporting), and other biases" (Higgins et al., 2011). Each of these options was evaluated as high, low or

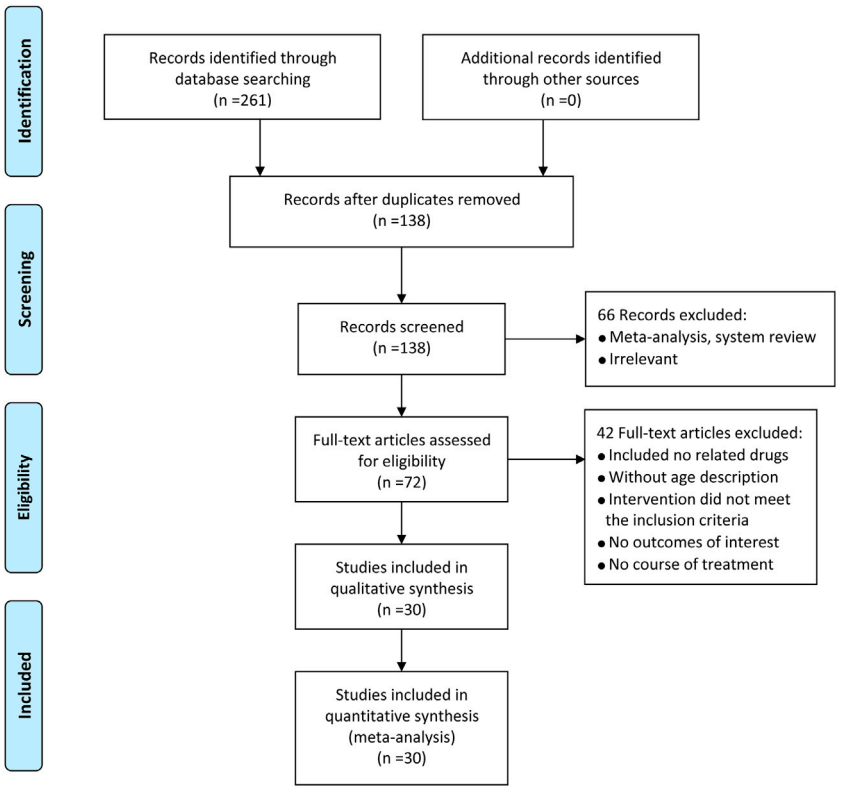

FIGURE 2 | PRISMA flow diagram for eligible RCTs.

unclear. When described a valid generation of random number, blinding, and results, they will be categorized as low-risk, otherwise, they will be high-risk. Once described an ambiguous information, they will be categorized as an unclear risk. Any divergence could be solved through discussions or negotiations with a superior researcher.

Statistical Analysis

The article adopted a Bayesian frame structure employing WinBUGS 1.4.3 and Stata 13.0 instrument to compute the outcomes. As for statistical processes, Random and fixed effects model was adopted for continuous and dichotomous variables, respectively. Simulation iterations were commanded to 200,000, adaptation iterations were required to10,000. Dichotomous variables or count data made use of odds ratios (ORs), continuous variables or measuring data chose mean difference (MD), as well as used their 95% confidence intervals (95% CIs). In addition, "the ranking probability of each treatment in different results was evaluated through the surface under the cumulative ranking area (SUCRA) value, a larger SUCRA value indicating a better treatment option" (Rücker and Schwarzer, 2015). Cluster analysis about variable results could be used to determine an optimal OCPM about therapy of CP/CPPS with SD under conducting a SUCRA. We didn't implement the hypothesis of consistency because of non-close loops. Meanwhile, funnel graphs were plotted to identify the presence of publication bias. The forest graph, the risk of bias graph, and network plot were also illustrated.

RESULTS

Study Characteristics of the Involved Researches

All of 261 pieces of literature from seven databases, 72 reserved by removing overlaps, reviews, unrelated researches, and research on animal. What's more, 42 articles were removed on account of the following causes: no related drugs, without age description, the intervention did not meet the inclusion conditions, no results of interest, no course of treatment. Ultimately, 30 (Liu et al., 2009; Sa et al., 2009; Li et al., 2011; Guo, 2012; Li et al., 2012; Luo, 2012; Wang et al., 2012; Yang, 2012; Feng et al., 2013; Zheng and Li, 2013; Zhong et al., 2013; Chen et al., 2014; Zhang et al., 2014a; Zhang et al., 2014b; Chen et al., 2015; Lang and Xia, 2015; Zhang et al., 2015b; Liu and Chen, 2016; Liu et al., 2016a; Liu et al., 2016b; Su et al., 2016; Wu et al., 2017; Liu et al., 2018; Zhou, 2018; Li et al., 2019; Liu et al., 2019; Hong and Liu, 2020; Wang, 2020; Xia et al., 2020; Zhao, 2020) two-arm randomized controlled trials presented in China from 2009 to 2020 were covered in our study. The PRISMA flow diagram was depicted in **Figure 2**.

Thirty studies with 2,996 patients (1,507 cases in the experimental group, 1,489 cases in the control group)

TABLE 1 | Characteristics of included studies.

Study ID	Sample size/ experiment/ control	Age (Mean ± SD)		Prostatitis type	Sexualdysfunction type	Intervention		Duration(weeks)	Outcomes
		Experiment	Control			Experiment	Control		
Zhao (2020)	47/48	40.36 ± 1.41 (27~66)	39.89 ± 1.47 (26~66)	CP/CPPS	ED	QLSTC+WM	WM	12	①
Xia et al. (2020)	43/43	20 ~ 45	20 ~ 45	IIIB	ED	LQT+WM	WM	8	①②③④
Wang (2020)	51/51	45.77 ± 5.45 (30~60)	45.90 ± 5.23 (31~60)	CP/CPPS	SD	RLQG+WM	WM	4	②③④⑦
Hong and Liu (2020)	28/28	33.1 ± 2.4 (17~55)	32.1 ± 2.3 (18~50)	IIIB	SD	SGJYC+WM	WM	8	①②⑥
Liu et al. (2019)	40/40	33.18 ± 4.56	32.84 ± 4.71	CP/CPPS	ED	CXJC+WM	WM	6	①②③④⑦
Li et al. (2019)	44/43	29.28 ± 4.07 (26~38)	28.43 ± 4.43 (25~38)	CP/CPPS	PE	QLSTC+WM	WM	3	①⑤
Liu et al. (2018)	50/50	22 ~ 51	21 ~ 49	CP/CPPS	ED	SGYYC+WM	WM	8	①②③④⑦
Zhou (2018)	49/49	34.57 ± 3.48 (24~51)	34.82 ± 3.37 (23~52)	CP/CPPS	SD	LWDHP/ YGC+WM	WM	12	③④
Wu et al. (2017)	68/68	44.36 ± 5.22 (21~64)	45.12 ± 5.04 (22~66)	CP/CPPS	ED	CXJC+WM	WM	4	②
Su et al. (2016)	38/38	36.48 ± 5.21 (28~54)	36.29 ± 5.34 (29~52)	CP/CPPS	SD	CXJC+WM	WM	4	①②③④
Liu et al. (2016b)	43/43	23 ± 5 (18~48)	23 ± 5 (18~48)	IIIB	PE	QLBXC+WM	WM	4	①③④⑥
Liu and Chen, (2016)	52/48	28.6 ± 4.3 (22~43)	28.6 ± 4.3 (22~43)	CP/CPPS	SD	CRYSG+WM	WM	6	②③④
Liu et al., (2016a)	75/65	29 (19 ~ 41)	29 (19 ~ 41)	CP/CPPS	SD	CRYSG+WM	WM	8	④
Zhang et al. (2015b)	50/46	34.30 ± 8.15 (21 ~ 53)	34.30 ± 8.15 (21 ~ 53)	CP/CPPS	PE	CXJC+WM	WM	8	①③④⑥
Lang and Xia (2015)	49/49	32.4 ± 8.2 (21 ~ 52)	31.1 ± 8.9 (19 ~ 54)	IIIB	SD	SGJYC+WM	WM	8	①②⑥
Chen et al. (2015)	60/60	33.2 ± 8.7 (18 ~ 51)	32.2 ± 7.9 (19 ~ 54)	CP/CPPS	SD	CXJC+WM	WM	4	①②③④⑤⑦
Zhang et al. (2014b)	30/30	34.5 (20 ~ 56)	34.5 (20 ~ 56)	CP/CPPS	ED	CXJC+WM	WM	6	①②③④⑦
Zhang et al. (2014a)	93/105	30.2 (18 ~ 50)	30.2 (18 ~ 50)	CP/CPPS	ED	CXJC+WM	WM	8	①②③④⑦
Chen et al., 2014	45/45	35.32 ± 3.43 (26 ~ 45)	35.34 ± 3.41 27 ~ 45)	CP/CPPS	SD	CXJC+WM	WM	4	③④⑤
Feng et al. (2013)	40/40	25.5 ± 6.3 (16 ~ 41)	24.2 ± 5.9 (15 ~ 39)	CP/CPPS	ED	SGYYC+WM	WM	8	①②③④
Zeng ZF, 2013	40/40	23 ~ 47	23 ~ 47	CP/CPPS	SD	CXJC+WM	WM	4	③④
Zhong et al. (2013)	60/60	17.10 ± 5.16 (21 ~ 51)	(16.81 ± 5.26) (21 ~ 51)	CP/CPPS	SD	LWDHP/ YGC+WM	WM	12	③④
Yang (2012)	49/49	32.4 (23 ~ 54)	31.8 (22 ~ 52)	CP/CPPS	PE	NMTC+WM	WM	8	③④⑦
Wang et al. (2012)	62/70	33.9 (19 ~ 58)	33.9 (19 ~ 58)	CP/CPPS	ED	CXJC+WM	WM	8	①②③④⑦
Luo (2012)	64/56	28 (20 ~ 43)	28 (20 ~ 43)	CP/CPPS	SD	CRYSG+WM	WM	8	③④
Li (2012)	50/40	35.2 (18 ~ 49)	35.2 (18 ~ 49)	CP/CPPS	SD	CXJC+WM	WM	6	③④⑤

(Continued on following page)

TABLE 1 | (*Continued*) Characteristics of included studies.

Study ID	Sample size/ experiment/ control	Age (Mean ± SD)		Prostatitis type	Sexualdysfunction type	Intervention		Duration(weeks)	Outcomes
		Experiment	Control			Experiment	Control		
Guo (2012)	20/20	36 (25 ~ 48)	34 (25 ~ 46)	CP/CPPS	SD	CXJC+WM	WM	4	③④
Li (2012)	31/31	31.5 (22 ~ 41)	31.5 (22 ~ 41)	CP/CPPS	PE	CXJC+WM	WM	4	③④
Sa (2009)	66/64	34.5 (19~49)	34.5 (19 ~ 49)	CP/CPPS	ED	CXJC+WM	WM	6	③④
Liu (2009)	70/70	34.3 (20~49)	34.3 (20 ~ 49)	CP/CPPS	SD	CXJC+WM	WM	6	③④⑤

①*NIH-CPSI*, ②*IIEF-5*, ③*the clinical effective rate of CP/CPPS*, ④*the clinical effective rate of SD*, ⑤*SAS*, ⑥*CIPE-5*, ⑦*adverse reaction*.

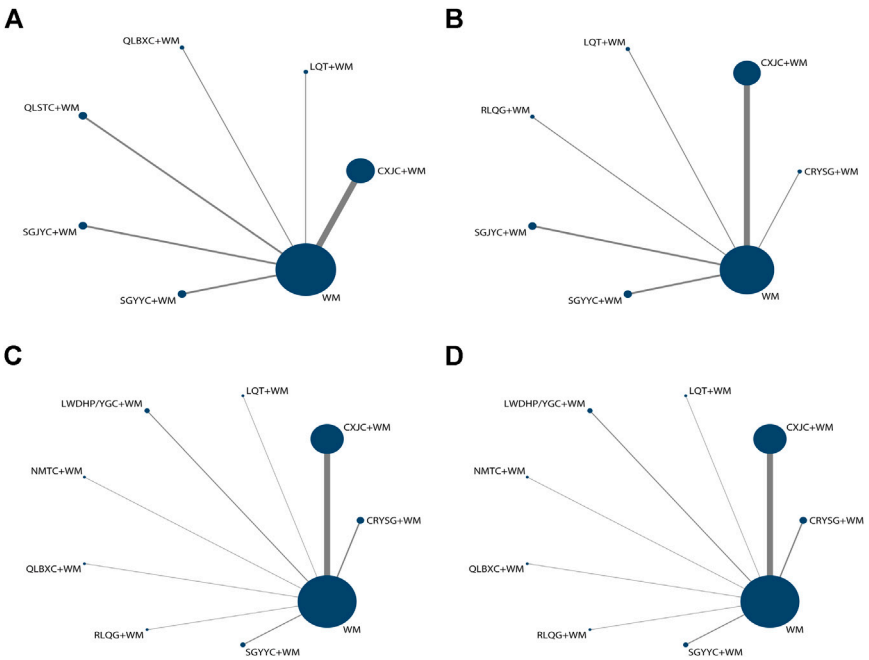

FIGURE 3 | Network graphs for various outcomes **(A)** NIH-CPSI; **(B)** IIEF-5; **(C)** the clinical effective rate of CP/CPPS; **(D)** the clinical effective rate of SD.

involving 11 oral Chinese patent medicine and 11 interventions (LWDHP/YGC was one intervention based on syndrome differentiation, LWDHP for kidney-yin deficiency, YGC for kidney-yang deficiency) with CP/CPPS with SD (include PE = 5, ED = 10, SD = 15) were included in this NMA. The age range of the participants was approximately 15 to 66, and the young and middle-aged crowd made up the majority. Ten comparisons were appraised: Compound Xuanju Capsules+WM vs. WM (n = 15), Congrong Yishen Granules+WM vs. WM (n = 3), Liuwei Dihuang Pills/Yougui capsules+WM vs. WM (n = 2), Longqing Tablets+WM vs. WM (n = 1), Ningmitai Capsules+WM vs. WM (n = 1), Qianlie Beixi Capsules+WM vs. WM (n = 1), Qianlie Shutong Capsules+WM vs. WM (n = 2), Relinqing Granules+WM vs. WM (n = 1), Shugan Jieyu Capsules+WM vs. WM (n = 2) and Shugan Yiyang Capsules+WM vs. WM (n = 2). Western medicine regimen contained antibiotics, α-blockers, phosphodiesterase type-5 inhibitor (PDE-5i), an anti-inflammatory drug, pollen extract, etc. All the eligible Chinese patent medicine were taken orally, and the course of treatment ranged from 3 to 12 weeks, and most of the studies were 8 weeks. The detailed characteristics of included researches are demonstrated in **Table 1**, the patented formulations of involved literature are listed in **Supplementary Table S1** and the network plots about diverse results could be found in **Figure 3**.

Quality Assessment

Two authors appraised the risk of bias in contained researches respectively by utilizing the Cochrane Risk of Bias Tool proposed by the Cochrane Handbook 5.1. Items assessed were as follows: Low-risk items: 1) seven studies about selective bias (explained utilized table of random numbers) and one study in selection bias (stated adopted lottery method). 2) All studies in attrition bias (reported outcome data completely). 3) All studies in other biases

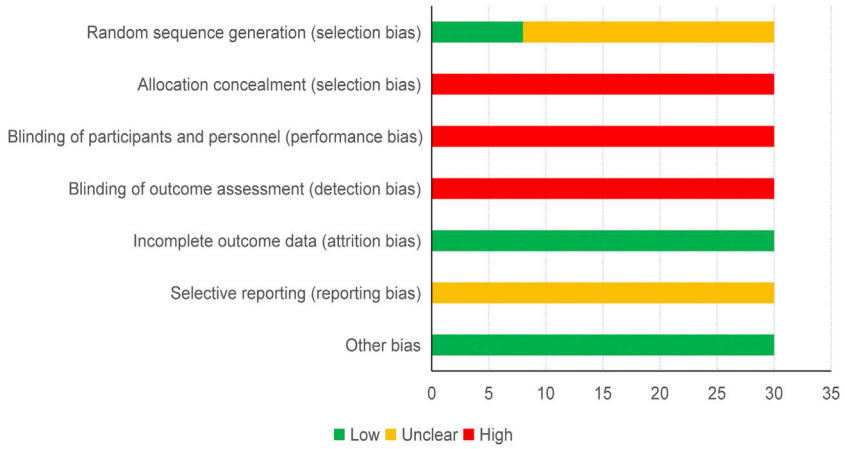

FIGURE 4 | Risk of bias graph.

TABLE 2 | Mean difference (95% CIs) of NIH-CPSI (right upper quarter) and IIEF-5 (left lower quarter).

CRYSG+WM	—	—	—	—	—	—	—	—	—	—
2.42 (−0.99, 5.84)	**CXJC+WM**	—	−0.25 (−2.86, 2.35)	—	−2.42 (−4.94, 0.10)	−5.05 (−7.14, −2.95)	—	−4.59 (−7.57, −1.61)	−0.35 (−2.51, 1.81)	2.88 (1.78, 3.98)
—	—	**LWDHP/ YGC+WM**	—	—	—	—	—	—	—	—
3.62 (−0.79, 8.03)	1.20 (−2.13, 4.52)	—	**LQT+WM**	—	−2.17 (−5.44, 1.10)	−4.80 (−7.76, −1.84)	—	−4.34 (−7.98, −0.70)	−0.10 (−3.10, 2.90)	3.13 (0.77, 5.49)
—	—	—	—	**NMTC+WM**	—	—	—	—	—	—
—	—	—	—	—	**QLBXC+WM**	−2.63 (−5.51, 0.26)	—	−2.17 (−5.75, 1.41)	2.07 (−0.85, 5.00)	5.30 (3.03, 7.57)
—	—	—	—	—	—	**QLSTC+WM**	—	0.46 (−2.84, 3.75)	4.70 (2.15, 7.24)	7.93 (6.14, 9.71)
2.39 (−1.78, 6.56)	−0.04 (−3.04, 2.97)	—	−1.23 (−5.33, 2.87)	—	—	—	**RLQG+WM**	—	—	—
1.92 (−1.96, 5.81)	−0.50 (−3.08, 2.09)	—	−1.69 (−5.50, 2.11)	—	—	—	−0.46 (−3.99, 3.06)	**SGJYC+WM**	4.24 (0.91, 7.57)	7.47 (4.70, 10.24)
0.61 (−3.15, 4.36)	−1.82 (−4.21, 0.58)	—	−3.01 (−6.69, 0.66)	—	—	—	−1.78 (−5.17, 1.60)	−1.32 (−4.34, 1.71)	**SGYYC+WM**	3.23 (1.38, 5.08)
6.33 (3.16, 9.50)	3.91 (2.63, 5.18)	—	2.71 (−0.36, 5.78)	—	—	—	3.94 (1.22, 6.66)	4.40 (2.16, 6.65)	5.72 (3.70, 7.75)	**WM**

The result underlined meant it had statistical significant.

(stated a baseline of randomized controlled trials). High-risk events: 1) All studies about selection bias (did not adopt allocation concealment). 2) All studies in performance bias (did not utilize blinding of participants and personnel). 3) All researches in detection bias (did not report blinding of outcome assessment). Unclear risk items: 1) 22 studies in selection bias (did not state specific random method). 2) All studies in reporting bias (unclear selective reporting). A detailed description of the risk of bias evaluation is shown in **Figure 4**.

Outcomes

NIH-CPSI Score

All 15 pieces of research including six OCPM and seven interventions recorded the NIH-CPSI score. As the dominating results, the NIH-CPSI score was depicted in the right upper quarter of **Table 2** and **Figure 5A**, CXJC+WM, LQT+WM, QLBXC+WM, QLSTC+WM, SGJYC+WM, and SGYYC+WM were better than the WM regimen alone in terms of the NIH-CPSI score. These results were statistically

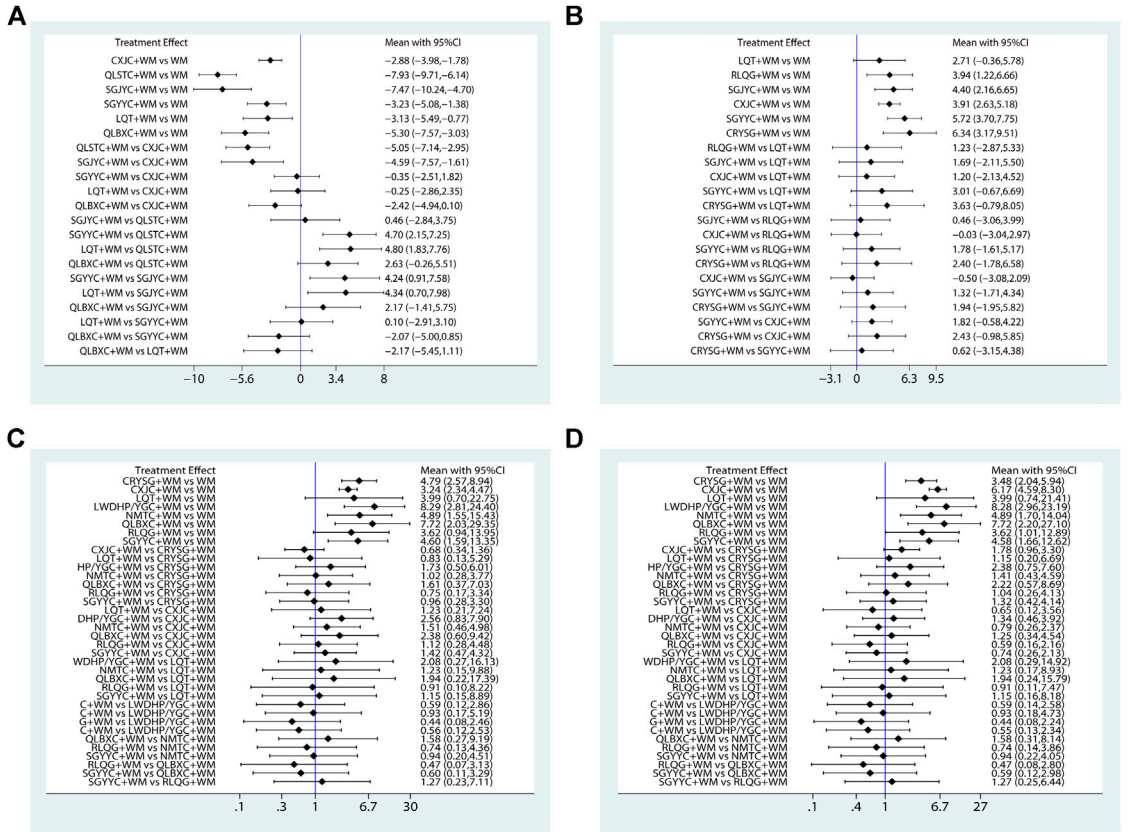

FIGURE 5 | Forest graphs of Meta-analysis **(A)** NIH-CPSI; **(B)** IIEF-5; **(C)** the clinical effective rate of CP/CPPS; **(D)** the clinical effective rate of SD.

significant, MD and 95% CIs were 2.88 (1.78, 3.98), 3.13 (0.77, 5.49), 5.30 (3.03, 7.57), 7.93 (6.14, 9.71), 7.47 (4.70, 10.24) and 3.23 (1.38, 5.08), respectively. Additionally, QLSTC+WM was more effective than LQT+WM (MD = −4.80, 95% CI = −7.76 to −1.84) and CXJC+WM (MD = −5.05, 95% CI = −7.14 to −2.95; SGJYC+WM was more effective than LQT+WM (MD = −4.34, 95% CI = −7.98 to −0.70) and CXJC+WM (MD = −4.59, 95% CI = −7.57 to −1.61). According to the calculated probabilities of **Figure 6A** and **Table 3**, QLSTC+WM (92.7%) was the optimal combination in decreasing NIH-CPSI score, SGJYC+WM (87.8%) was number two, and QLBXC+WM (65.8%) was the third.

IIEF-5 Score

All 14 pieces of literature including six OCPM and seven interventions recorded the IIEF-5 score. As the other dominating outcomes, the IIEF-5 score was demonstrated in the left lower quarter of **Table 2** and **Figure 5B**, CRYSG+WM, CXJC+WM, RLQG+WM, SGJYC+WM, and SGYYC+WM were better than the WM regimen by itself according to the IIEF-5 score. These results were statistically significant, MD and 95% CIs were 6.33 (3.16, 9.50), 3.91 (2.63, 5.18), 3.94 (1.22, 6.66), 4.40 (2.16, 6.65), and 5.72 (3.70, 7.75), respectively. No statistical significance was proved in the rest of the treatments. Relying on the ranking probabilities of **Figure 6B** and **Table 3**, CRYSG+WM (86.5%) was the best combination in increasing the IIEF-5 score, followed by SGYYC+WM (81.5%) and SGJYC+WM (57.2%).

The Clinical Effective Rate of CP/CPPS

All 24 pieces of research including nine OCPM and nine interventions recorded the clinical effective rate of CP/CPPS. It was considered to the main outcomes, was displayed in the right upper quarter of **Table 4** and **Figure 5C**, CRYSG+WM, CXJC+WM, LWDHP/YGC+WM, NMTC+WM, QLBXC+WM, and SGYYC+WM were better than the WM regimen alone according to the clinical effective rate of CP/CPPS. These results were statistically significant, ORs and 95% CIs were 0.21 (0.11, 0.39), 0.31 (0.22, 0.43), 0.12 (0.04, 0.36), 0.20 (0.06, 0.65), 0.13 (0.03, 0.49), and 0.22 (0.07, 0.63), respectively. Nevertheless, other interventions had no statistical difference. On the basis of the ranking probabilities of **Figure 6C** and **Table 3**, LWDHP/YGC+WM (80.1%) was the optimum combination in improving the clinical effective rate of CP/CPPS, QLBXC+WM (75.7%) was number two, and NMTC+WM (57.1%) was the third.

The Clinical Effective Rate of SD

All 24 pieces of literature including nine OCPM and nine interventions recorded the clinical effective rate of SD. As the

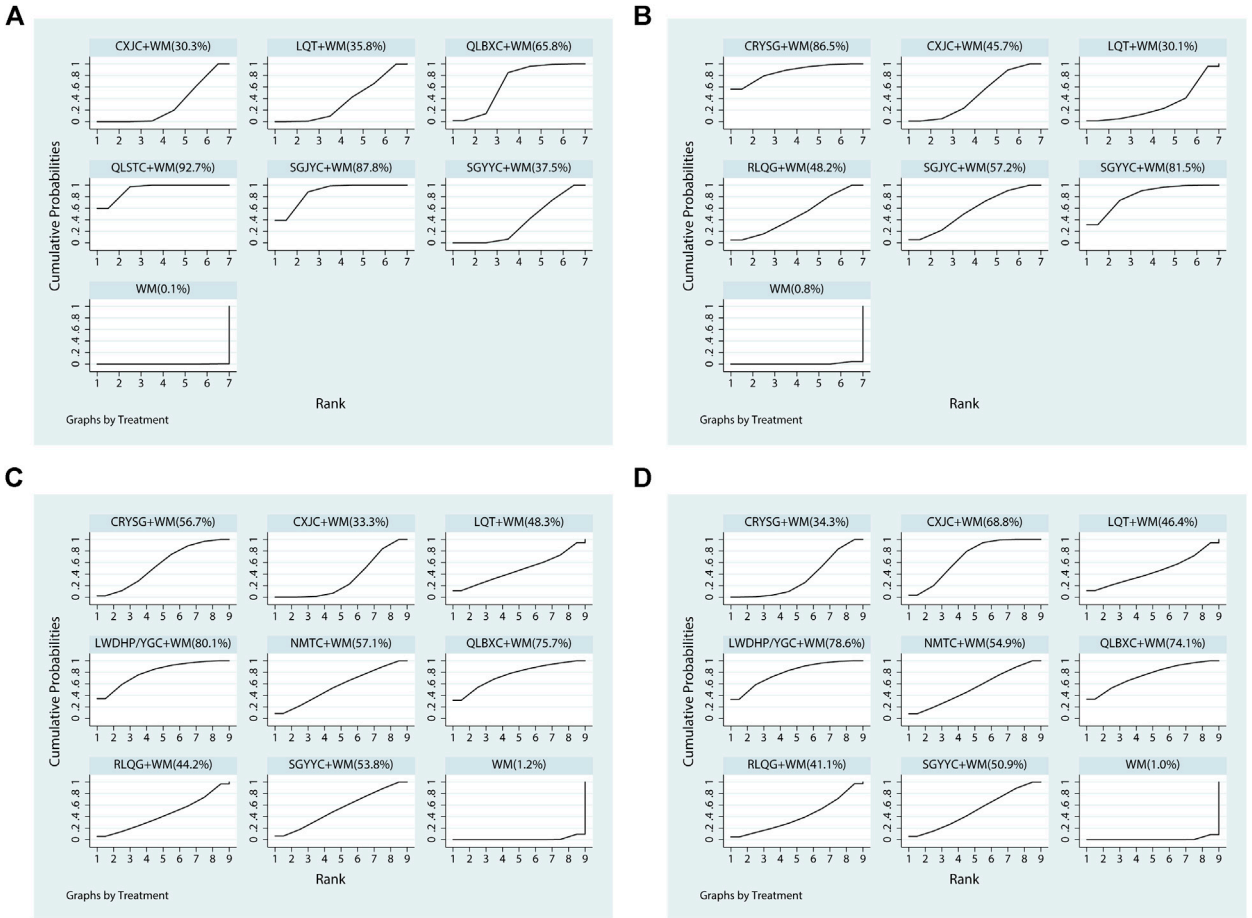

FIGURE 6 | Plots of the surface under the cumulative ranking curves for all treatments **(A)** NIH-CPSI; **(B)** IIEF-5; **(C)** the clinical effective rate of CP/CPPS; **(D)** the clinical effective rate of SD.

TABLE 3 | Ranking probability for all treatments on NIH-CPSI, IIEF-5, the clinical effective rate of CP/CPPS, the clinical effective rate of SD.

Intervention	NIH-CPSI	Rank	IIEF-5	Rank	The clinical effective rate of CP/CPPS	Rank	The clinical effective rate of SD	Rank
CRYSG+WM	—	0	86.5	1	56.7	4	34.3	8
CXJC+WM	30.3	6	45.7	5	33.3	8	68.8	3
LQT+WM	35.8	5	30.1	6	48.3	6	46.4	6
LWDHP/YGC+WM	—	0	—	0	80.1	1	78.6	1
NMTC+WM	—	0	—	0	57.1	3	54.9	4
QLBXC+WM	65.8	3	—	0	75.7	2	74.1	2
QLSTC+WM	92.7	1	—	0	—	0	—	0
RLQG+WM	—	0	48.2	4	44.2	7	41.1	7
SGJYC+WM	87.8	2	57.2	3	—	0	—	0
SGYYC+WM	37.5	4	81.5	2	53.8	5	50.9	5
WM	0.1	7	0.8	7	1.2	9	1.0	9

other staple outcomes, the clinical effective rate of SD was depicted to the left lower part of **Table 4** and **Figure 5D**, CRYSG+WM, CXJC+WM, LWDHP/YGC+WM, NMTC+WM, QLBXC+WM, RLQG+WM, and SGYYC+WM were better than the WM regimen alone accordance with the clinical effective rate of SD. These results were statistically significant, ORs and 95% CIs were 3.48 (2.04, 5.94), 6.17 (4.59, 8.30), 8.28 (2.96, 23.19), 4.89 (1.70, 14.04), 7.72 (2.20, 27.10), 3.62 (1.01, 12.89), and 4.58 (1.66,

TABLE 4 | Odds ratios (95% CIs) of the clinical effective rate of CP/CPPS (right upper quarter) and SD (left lower quarter).

CRYSG+WM	0.68 (0.34, 1.36)	0.83 (0.13, 5.29)	1.73 (0.50, 6.01)	1.02 (0.28, 3.77)	1.61 (0.37, 7.03)	—	0.75 (0.17, 3.34)	—	0.96 (0.28, 3.30)	0.21 (0.11, 0.39)
0.56 (0.30, 1.05)	**CXJC+WM**	1.23 (0.21, 7.24)	2.56 (0.83, 7.90)	1.51 (0.46, 4.98)	2.38 (0.60, 9.42)	—	1.12 (0.28, 4.48)	—	1.42 (0.47, 4.32)	0.31 (0.22, 0.43)
0.87 (0.15, 5.09)	1.55 (0.28, 8.54)	**LQT+WM**	2.08 (0.27, 16.13)	1.23 (0.15, 9.88)	1.94 (0.22, 17.39)	—	0.91 (0.10, 8.22)	—	1.15 (0.15, 8.89)	0.25 (0.04, 1.43)
0.42 (0.13, 1.34)	0.75 (0.26, 2.18)	0.48 (0.07, 3.46)	**LWDHP/ YGC+WM**	0.59 (0.12, 2.86)	0.93 (0.17, 5.19)	—	0.44 (0.08, 2.46)	—	0.56 (0.12, 2.53)	0.12 (0.04, 0.36)
0.71 (0.22, 2.32)	1.26 (0.42, 3.78)	0.82 (0.11, 5.93)	1.69 (0.39, 7.40)	**NMTC+WM**	1.58 (0.27, 9.19)	—	0.74 (0.13, 4.36)	—	0.94 (0.20, 4.51)	0.20 (0.06, 0.65)
0.45 (0.12, 1.76)	0.80 (0.22, 2.91)	0.52 (0.06, 4.21)	1.07 (0.21, 5.44)	0.63 (0.12, 3.27)	**QLBXC+WM**	—	0.47 (0.07, 3.13)	—	0.60 (0.11, 3.29)	0.13 (0.03, 0.49)
—	—	—	—	—	—	**QLSTC+WM**	—	—	—	—
0.96 (0.24, 3.82)	1.71 (0.46, 6.30)	1.10 (0.13, 9.07)	2.29 (0.45, 11.77)	1.35 (0.26, 7.06)	2.13 (0.36, 12.75)	—	**RLQG+WM**	—	1.27 (0.23, 7.11)	0.28 (0.07, 1.07)
—	—	—	—	—	—	—	—	**SGJYC+WM**	—	—
0.76 (0.24, 2.39)	1.35 (0.47, 3.88)	0.87 (0.12, 6.20)	1.81 (0.43, 7.67)	1.07 (0.25, 4.61)	1.68 (0.34, 8.46)	—	0.79 (0.16, 4.01)	—	**SGYYC+WM**	0.22 (0.07, 0.63)
3.48 (2.04, 5.94)	6.17 (4.59, 8.30)	3.99 (0.74, 21.41)	8.28 (2.96, 23.19)	4.89 (1.70, 14.04)	7.72 (2.20, 27.10)	—	3.62 (1.01, 12.89)	—	4.58 (1.66, 12.62)	**WM**

The result underlined meant it had statistical significant.

12.62), respectively. No statistical significance was testified in the rest of the treatments. According to the ranking probabilities of **Figure 6D** and **Table 3**, LWDHP/YGC+WM (78.6%) was the first-rank combination in improving the clinical effective rate of SD, followed by QLBXC+WM (74.1%) and CXJC+WM (68.8%).

SAS, CIPE-5, and Adverse Reaction

All five pieces of research including 2 OCPM and 3 interventions recorded the Self-rating anxiety scale (SAS), four studies involving three OCPM, and four interventions reported the Chinese Index of Premature Ejaculation (CIPE-5) and eight studies involving four OCPM and five interventions reported the adverse reaction. No statistical analysis was performed on these secondary outcomes on account of the scarcity of studies and inconsistent evaluation criteria.

Cluster Analysis

The influences of interventions in two diverse results were synthetically contrasted by cluster analysis. Two sets of cluster analyses were conducted in our study, containing NIH-CPSI and IIEF-5, the clinical effective rate of CP/CPPS and the clinical effective rate of SD, respectively. The results are shown in **Figure 7**. Through synthetical analysis by means of cluster analysis, SGJYC+WM had the better efficacy in decreasing the NIH-CPSI score, SGYYC+WM had the better curative effect in increasing the IIEF-5 score. Nevertheless, there was no optimum combination associated with a preferable response in both aspects. On the other group of cluster analysis, LWDHP/YGC+WM might possess the best efficacy in improving the clinical effective rate of CP/CPPS and SD, QLBXC+WM was in hot pursuit, their efficacy in the therapy of CP/CPPS with SD is worthy of attention.

Publication Bias

A funnel graph for four major outcomes was presented in **Figure 8** to evaluate publication bias. All of the funnel graphs were not completely symmetrical visually, and each of the adjusted auxiliary lines was not perpendicular to the centerline. Thus, there may be significant publication bias.

DISCUSSION

Summary of Main Findings

According to the information from 30 involved pieces of research with four primary outcomes, this article systematically appraised the efficacy of 11 commonly used OCPM (CRYSG, CXJC, LQT, LWDHP, NMTC, QLBXC, QLSTC, RLQG, SGJYC, SGYYC, and YGC) combined with WM in treating CP/CPPS with SD by taking advantage of network meta-analysis method. It's worth noting that LWDHP/YGC belonged to one intervention through adopting dialectical treatment, LWDHP for kidney-yin deficiency, YGC for kidney-yang deficiency. On the account of the result of NMA, most OCPM combined with WM presented better results than utilizing WM by itself in various outcomes, and these results between groups were statistical differences. On the

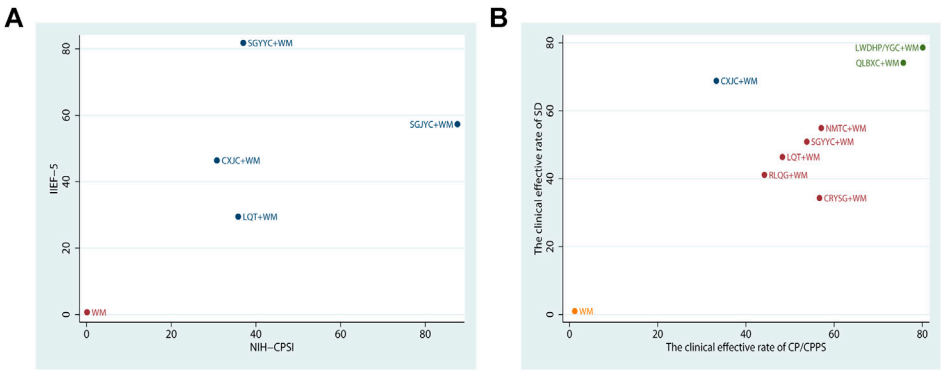

FIGURE 7 | Cluster analysis plots. Interventions located in the upper right corner indicate optimal combination therapy for two different outcomes.

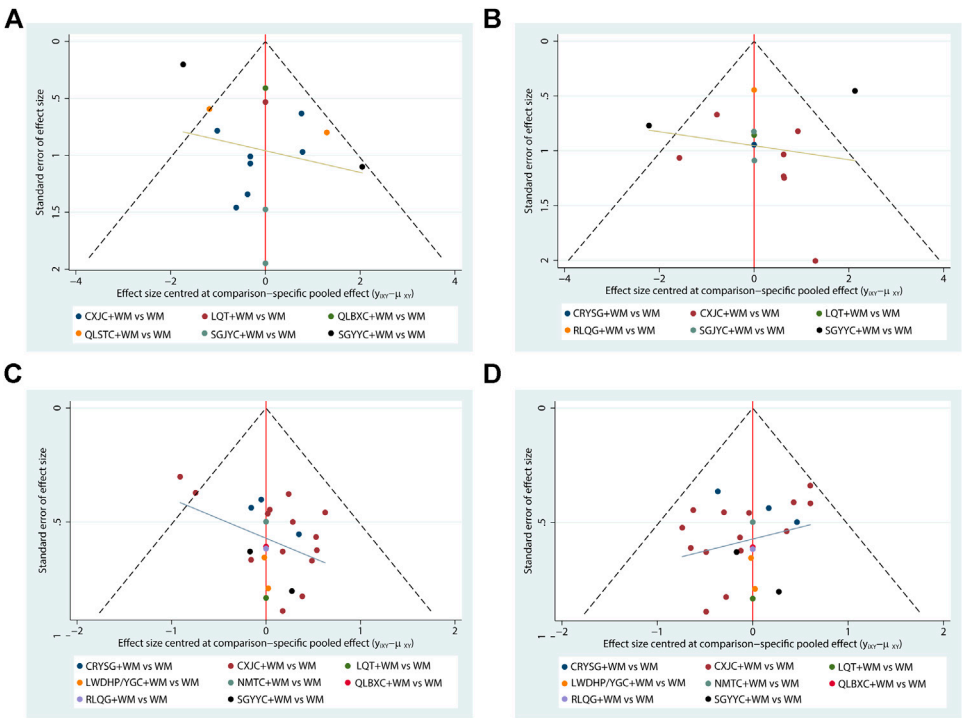

FIGURE 8 | Funnel plots **(A)** NIH-CPSI; **(B)** IIEF-5; **(C)** the clinical effective rate of CP/CPPS; **(D)** the clinical effective rate of SD.

account of SUCRA results, QLSTC + WM had the maximum probability to be the best treatment in the NIH-CPSI. While in IIEF-5, CRYSG + WM intervention might be the best intervention. LWDHP/YGC had highly possible to be the optimal therapy in both the clinical effective rate of CP/CPPS and the clinical effective rate of SD. The clustered ranking according to NIH-CPSI compared with IIEF-5 showed there was no optimum combination better than any other combination. Fortunately, the clustered ranking based on the clinical effective rate of CP/CPPS compared with the clinical effective rate of SD showed LWDHP/YGC + WM had highly possible to be the best treatment on both sides. Considering four outcomes, QLSTC, CRYSG, SGYYC, LWDHP/YGC, Qianlie Beixi Capsules (QLBXC) plus WM were the optimum treatment regimens for CP/CPPS with SD, especially LWDHP/YGC + WM and QLBXC + WM. Therefore, the efficacy of LWDHP/YGC + WM and QLBXC + WM in the therapy of CP/CPPS with SD was worthy of attention, but clinicians should also select appropriate methods on the basis of specific situations of clinical patients.

Research Significance and Importance

This article utilizes a network meta-analysis approach to appraise the curative effect of OCPM for treating CP/CPPS with SD for the

first time. Meanwhile, our studies involved utilized treatment based on syndrome differentiation in Traditional Chinese Medicine (TCM) theories (e.g., LWDHP for kidney-yin deficiency, YGC for kidney-yang deficiency) and "obtained satisfactory curative effect" (Zhong et al., 2013; Zhou, 2018). In fact, "From the diagnosis of TCM, it included primarily type of syndrome, pathogen, position or name of a disease, such as wind-chill virus cold, wind-heat mycoplasma pneumonia" (Hou and Liu, 2013). Meanwhile, "Western medicine also developed a six-point clinical phenotyping of CP/CPPS to create a specific symptomatic treatment plan (UPOINT system), these clinical domains contained urinary symptoms, psychosocial dysfunction, organ-specific findings, infection, neurologic/systemic, and tenderness of muscles" (Shoskes and Nickel, 2013). "People have different opinions on whether to add SD into the UPOINT system" (Magri et al., 2010; Ersan et al., 2016). Basing on the above theory and method of integrated Chinese and Western medicine, we ranked the outcomes for the sake of offer evidence and recommendations for clinical medication. Furthermore, from the view of mechanisms, on the one hand, antibiotics could control infection and α-blockers could relaxes smooth muscles in areas such as the prostate and bladder and improves lower urinary tract symptoms and pain except anxious emotion, on the other hand, traditional Chinese medicine theory believes that anxiety is related to liver stagnation, OCPM could regulate liver stagnation and improves deficiency of kidney and spleen to relieves anxious emotion, improves erectile function and inhibit premature ejaculation ultimately. So as to say, OCPM and WM complement each other, physiotherapy and psychotherapy are as important as pharmacotherapy in the therapy of CP/CPPS with SD, "multi-disciplinary treatment (MDT) schema is expected to be preferred treatment in future" (Cheng and Zhang, 2018; Yan et al., 2019).

Limitations

Nevertheless, this research also possessed limitations. In the first place, among 30 literature, only eight literature that utilized the correct method of a random number, none of them adopted allocation concealment, applied the blind method (blind to participants and personnel), and reported blinding of outcome evaluation. The quality of the involved researches might not be high, which reduced the persuasiveness of research results. In the second place, limited by application area of OCPM, all researches were reported in China and published in a Chinese journal, lacking the resource in other languages, which is not beneficial to the international promotion of study outcomes. In the third place, most RCTs studied on OCPM + WM vs. WM, lacking direct study on comparisons between diverse OCPM combined with WM. Finally, this research didn't limit the phenotyping of CP/CPPS (include III = 26, IIIB = 4) and SD (include PE = 5, ED = 10, SD = 15). Therefore, we need to further analyze the efficacy of various OCPM on CP/CPPS with SD in the future.

Prospects

Eventually, we propound the following recommendations: firstly, multicenter randomized double-blind tests should be implemented in rigorous in the light of regulations when conducting RCTs. The method of a random number, allocation concealment, and blind method performance are committed steps that need to be attentive in the future study program. Secondly, it is important to perform more clinical researches compared to the effect of different OCPM to make up for the absence of study in this domain. Finally, because of recurrent frequently of CP/CPPS with SD, a subsequent program should be carried out to supervise the prognosis of participants.

CONCLUSION

By means of this NMA, OCPM combined with WM offered significant benefits compared to WM by itself in the therapy of chronic prostatitis/chronic pelvic pain syndrome (CP/CPPS) with sexual dysfunction (SD). What's more, among the OCPM, LWDHP/YGC + WM and QLBXC + WM should be worthy of attention. But, on account of the limitations of this article, these conclusions were supposed to be certified *via* multicenter, high-quality, and larger-sample randomized controlled trials.

DATA AVAILABILITY STATEMENT

The original contributions presented in the study are included in the article/**Supplementary Material**, further inquiries can be directed to the corresponding author.

AUTHOR CONTRIBUTIONS

YZ, HM, and TN were involved in the design and conception of the network meta-analysis. YZ was responsible for the conduct of the network meta-analysis. YL and WZ took charge of the quality evaluation of the NMA. YZ and TN saw to the analysis of study information. YZ and HM took charge of the writing of the article. ZZ and XG saw to the revision of the article. All authors read and approved the final version of the manuscript.

FUNDING

Subject Innovation Team of the Second Affiliated Hospital of Shaanxi University of Chinese Medicine (Grant No. 2020XKTD-B01) and Natural Science Foundation of Shaanxi Province (Grant No. 2019JM-224).

SUPPLEMENTARY MATERIAL

The Supplementary Material for this article can be found online at: https://www.frontiersin.org/articles/10.3389/fphar.2021.649470/full#supplementary-material

REFERENCES

Anothaisintawee, T., Attia, J., Nickel, J. C., Thammakraisorn, S., Numthavaj, P., McEvoy, M., et al. (2011). Management of Chronic Prostatitis/chronic Pelvic Pain Syndrome: a Systematic Review and Network Meta-Analysis. *JAMA*. 305 (1), 78–86. doi:10.1001/jama.2010.1913

Chen, W. J., Yang, B., Tong, J. F., and Lin, Y. F. (2014). Effect of Compound Xuanju Capsule in the Treatment of Type III Prostatitis-Related Sexual Dysfunction. *Chin. J. Hum. Sex.* 23 (05), 6–8. doi:10.5246/jcps.2014.09.077

Chen, Y. Q., Chen, C. R., Yan, Q. X., and Xian, Y. J. (2015). The Study of the Efficacy of 60 Cases Patients of Prostatitis and Sexual Dysfunction with Compound Xuanju Capsules. *Chin. J. Ethnomedicine Ethnopharmacy*. 24 (15), 97–98+100.

Cheng, J. H., and Zhang, W. L. (2018). Research Progress on Chronic Prostatitis/chronic Pelvic Pain Syndrome Accompanied by Sexual Dysfunction. *J. Med. Postgra* 31 (11), 1222–1227.

Chung, S.-D., Keller, J. J., and Lin, H.-C. (2012). A Case-Control Study on the Association between Chronic Prostatitis/chronic Pelvic Pain Syndrome and Erectile Dysfunction. *BJU Int.* 110 (5), 726–730. doi:10.1111/j.1464-410x.2011.10807.x

Ersan, A., Basri, C., Tuncay, T., Sinan, E., and Sami, U. B. (2016). Use of the UPOINT Classification in Turkish Chronic Prostatitis or Chronic Pelvic Pain Syndrome Patients. *Urology*. 97, 227–231. doi:10.1016/j.urology.2016.07.023

Feng, Y. G., Chen, L., and Zhou, Z. H. (2013). Clinical Efficacy of Shuganyiyang Capsule Combined with Western Medicine for the Treatment of Type III Prostatitis Complicated by Erectile Dysfunction. *Zhonghua Nan Ke Xue*. 19 (11), 1034–1038.

Guo, S. Z., and F, S. (2012). Effect of Compound Xuanju Capsule in the Treatment of Prostatitis-Related Sexual Dysfunction. *Drugs Clin.* (03), 233–234.

Hao, Z.-Y., Li, H.-J., Wang, Z.-P., Xing, J.-P., Hu, W.-L., Zhang, T.-F., et al. (2011). The Prevalence of Erectile Dysfunction and its Relation to Chronic Prostatitis in Chinese Men. *J. Androl.* 32 (5), 496–501. doi:10.2164/jandrol.110.012138

Higgins, J. P. T., Altman, D. G., Gotzsche, P. C., Jüni, P., Moher, D., Oxman, A. D., et al. (2011). The Cochrane Collaboration's Tool for Assessing Risk of Bias in Randomised Trials. *Bmj.* 343, d5928. doi:10.1136/bmj.d5928

Hong, T. L., and Liu, L. L. (2020). Clinical Efficacy of Alpha-Blockers Combined with Shugan Jieyu Capsules for Patients with Type IIIB Chronic Prostatitis and Sexual Dysfunction. *Chin. J. Clin. Rational Drug Use*. 13 (30), 128–129.

Hou, A. C., and Liu, X. H. (2013). Standardized Diagnosis and Treatment of Children's Respiratory Tract Infection with Wind-Cold and Wind-Heat Combined with Traditional Chinese Medicineand Western Medicine. *J. Clin. Exp. Med.* 12 (09), 723–724+726.

Krieger, J. N., Nyberg, L., Jr., and Nickel, J. C. (1999). NIH Consensus Definition and Classification of Prostatitis. *JAMA*. 282 (3), 236–237. doi:10.1001/jama.282.3.236

Lang, W. H., and Xia, H. B. (2015). Shugan Jieyu Capsules Combined with Conventional Therapy for Type III B Prostatitis Complicated by Sexual Dysfunction. *Zhonghua Nan Ke Xue*. 21 (06), 545–548.

Li, F. D., Kong, F. Y., Zhang, B., Cao, Z. G., and Wang, Y. M. (2019). Clinical Observation of Qianlie Shutong Capsule Combined with Tamsulosin on Chronic Prostatitis with Premature Ejaculation. *Med. J. NDFNC* 40 (01), 20–24.

Li, H.-J., and Kang, D.-Y. (2016). Prevalence of Sexual Dysfunction in Men with Chronic Prostatitis/chronic Pelvic Pain Syndrome: a Meta-Analysis. *World J. Urol.* 34 (7), 1009–1017. doi:10.1007/s00345-015-1720-3

Li, H. F., Wu, Z. Q., Yan, W., and Chen, Y. (2011). Efficacy of Compound Xuanju Capsules in the Treatment of Type IIIA Prostatitis with Premature Ejaculation. *All Health*. 5 (15), 10–12.

Li, X. D., Shao, H. L., Song, G. J., and Wang, L. N. (2012). Efficacy of Compound Xuanju Capsule on Type-III Prostatitis-Related Sexual Dysfunction. *Natl. J. Androl.* 18 (07), 665–668. doi:10.1016/s1353-8020(11)70586-7

Liang, C.-Z., Hao, Z.-Y., Li, H.-J., Wang, Z.-P., Xing, J.-P., Hu, W.-L., et al. (2010). Prevalence of Premature Ejaculation and its Correlation with Chronic Prostatitis in Chinese Men. *Urology*. 76 (4), 962–966. doi:10.1016/j.urology.2010.01.061

Liang, C.-Z., Zhang, X.-J., Hao, Z.-Y., Shi, H.-Q., and Wang, K.-X. (2004). Prevalence of Sexual Dysfunction in Chinese Men with Chronic Prostatitis. *BJU Int.* 93 (4), 568–570. doi:10.1111/j.1464-410x.2003.04662.x

Lin, S. S., Liu, C. X., Zhang, J. H., Wang, X. L., and Mao, J. Y. (2020). Efficacy and Safety of Oral Chinese Patent Medicine Combined with Conventional Therapy for Heart Failure: An Overview of Systematic Reviews. *Evid. Based Complement. Alternat Med.* 2020, 8620186. doi:10.1155/2020/8620186

Liu, A. Q., Li, J., Chen, T., Zhu, Q. F., Ma, D. Y., and Wu, X. F. (2019). Curative Effect of Sildenafil Combined with Compound Xuanju Capsules for Patients with Type III Chronic Prostatitis and Erectile Dysfunction. *Chin. J. Hum. Sex.* 28 (05), 12–14.

Liu, C. M., Xiong, Y., Liu, Y. H., and Wang, T. (2016a). Clinical Observation of Congrong Yishen Granules Combined with Erythrocin and Naftopidil for Patients with Chronic Prostatitis and Sexual Dysfunction. *World Latest Med. Inf.* 16 (65), 173

Liu, Z., An, K., Wang, X. S., and Liu, P. (2016b). Clinical Efficacy of Qianlie Beixi Capsules for Patients with Type IIIB Chronic Prostatitis and Premature Ejaculation. *China J. Pharm. Econ.* 11 (09), 38–40.

Liu, G. L., Xie, H. J., Sun, R. W., and Zhang, B. Q. (2018). Clinical Observation on Traditional Chinese Medicine Scheme in the Treatment of Prostatitis Complicated with Erectile Dysfunction. *CJGMCM*. 33 (15), 2150–2152.

Liu, K., and Chen, J. (2016). Clinical Observation of Congrong Yishen Granules Combined with Levofloxacin for Patients with Chronic Prostatitis and Sexual Dysfunction. *World Latest Med. Inf.* 16 (64), 114–115.

Liu, X. K., Yang, S. B., Li, Z. L., and Bi, J. B. (2009). Study on Treatment of Prostatitis-Related Sexual Dysfunction by Fufang Xuanju Capsule. *Natl. J. Androl.* 23 (12), 53–55.

Luo, J. F. (2012). 64 Cases of Administrating Congrong Yishen Granula with Levofloxacin and Tamsulosin Hydrochloride for Treating Chronic Prostatitis Accompaned with Sexual Dysfunction. *Herald Med.* 31 (03), 328–329.

Ma, C. Q., Cai, Z. L., Xiong, J., and Li, H. J. (2020). History of Prostatitis Is an Independent Risk Factor for Erectile Dysfunction: A Cross-Sectional Study. *Biomed. Res. Int.* 2020, 8964673. doi:10.1155/2020/8964673

Magri, V., Wagenlehner, F., Perletti, G., Schneider, S., Marras, E., Naber, K. G., et al. (2010). Use of the UPOINT Chronic Prostatitis/chronic Pelvic Pain Syndrome Classification in European Patient Cohorts: Sexual Function Domain Improves Correlations. *J. Urol.* 184 (6), 2339–2345. doi:10.1016/j.juro.2010.08.025

Nickel, J. C., Nyberg, L. M., and Hennenfent, M. (1999). Research Guidelines for Chronic Prostatitis: Consensus Report from the First National Institutes of Health International Prostatitis Collaborative Network. *Urology*. 54 (2), 229–233. doi:10.1016/s0090-4295(99)00205-8

Qin, Z. S., Wu, J. N., Tian, J. H., Zhou, J., Liu, Y. L., and Liu, Z. S. (2016). Network Meta-Analysis of the Efficacy of Acupuncture, Alpha-Blockers and Antibiotics on Chronic Prostatitis/Chronic Pelvic Pain Syndrome. *Sci. Rep.* 6, 35737. doi:10.1038/srep35737

Rosen, R., Cappelleri, J., Smith, M., Lipsky, J., and Peña, B. (1999). Development and Evaluation of an Abridged, 5-item Version of the International Index of Erectile Function (IIEF-5) as a Diagnostic Tool for Erectile Dysfunction. *Int. J. Impot Res.* 11 (6), 319–326. doi:10.1038/sj.ijir.3900472

Rücker, G., and Schwarzer, G. (2015). Ranking Treatments in Frequentist Network Meta-Analysis Works without Resampling Methods. *BMC Med. Res. Methodol.* 15, 58. doi:10.1186/s12874-015-0060-8

Sa, Y. L., Ye, X. X., Xue, Y. G., and Hu, X. Y. (2009). Efficacy of Compound Xuanju Capsules in the Treatment of Chronic Prostatitis with Erectile Dysfunction. *Natl. J. Androl.* 23 (12), 64–65.

Screponi, E., Carosa, E., Di Stasi, S. M., Pepe, M., Carruba, G., and Jannini, E. A. (2001). Prevalence of Chronic Prostatitis in Men with Premature Ejaculation. *Urology*. 58 (2), 198–202. doi:10.1016/s0090-4295(01)01151-7

Shoskes, D. A., and Nickel, J. C. (2013). Classification and Treatment of Men with Chronic Prostatitis/chronic Pelvic Pain Syndrome Using the UPOINT System. *World J. Urol.* 31 (4), 755–760. doi:10.1007/s00345-013-1075-6

Su, J. X., Wang, X., Chen, S. Q., and Xie, Z. X. (2016). Clinical Observation of Compound Xuanju Capsules on Chronic Prostatitis with Sexual Dysfunction. *Shenzhen J. Integrated Traditional Chin. West. Med.* 26 (23), 35–36.

Wang, J. X. (2020). Effect of Relinqing Granule on Inflammatory Factors and Sexual Dysfunction in Patients with Chronic Prostatitis. *Chin. J. Hum. Sex.* 29 (10), 129–132.

Wang, L., Liang, P., Yang, W., Zhou, P., Huang, X. K., Liu, J. W., et al. (2012). Efficacy of Compound Xuanju Capsule in the Treatment of Chronic Prostatitis with Erectile Dysfunction. *Zhonghua Nan Ke Xue* 18 (10), 950–952.

Wang, Z., Yuan, L., Wang, Y., Yang, B., Dong, X., and Gao, Z. (2016). Efficacy and Safety of Chinese Herbal Medicine for Chronic Prostatitis Associated with Damp-Heat and Blood-Stasis Syndromes: a Meta-Analysis and Literature Review. *Patient Prefer Adherence.* 10, 1889–1902. doi:10.2147/ppa.s108699

Wu, X. F., Weng, Z. L., Chen, T., and Lou, J. (2017). Effect of Compound Xuanju Capsules on Erectile Dysfunction, Sperm Quality and Urodynamics of Patients with Chronic Prostatitis. *J. New Chin. Medi.* 49 (09), 60–62. doi:10.3758/s13428-016-0849-3

Xia, K., Pang, R., Mo, J. F., Wu, C. K., and Wu, L. Q. (2020). Clinical Sthdy of Longqing Tablet Conbined with Vardenafil in the Treatment of Type IIIB Chronic Prostatitis Complicated with Erectile Dysfunction. *Chongqing Med.* 49 (14), 2298–2301.

Yan, B., Zhang, J. W., Gao, Q. H., and Wang, F. (2019). Research Progress on the Mechanism on Chronic Prostatitis/chronic Pelvic Pain Syndrome Accompanied by Sexual Dysfunction. *Chin. J. Androl.* 33 (02), 69–72.

Yang, J. L. (2012). Comparison of Efficacy of Two Drug Regimens for Premature Ejaculation Secondary to Chronic Non-bacterial Prostatitis. *Contemp. Med.* 18 (01), 131–132.

Zhang, Q., Qiang, Z. Y., Ma, L. H., and Han, L. Z. (2014a). Therapeutic Efficacy of Compound Xuanju Capsule on Type III Prostatitis Related Erectile Dysfunction. *Ningxia Med. J.* 36 (05), 401–403.

Zhang, X. J., Chen, H. J., Wang, J., and Yang, N. G. (2014b). Efficacy of Compound Xuanju Capsules in the Treatment of Chronic Prostatitis with Erectile Dysfunction. *Chin. Prim. Health Care* 28 (09), 110–111.

Zhang, Z., Li, Z., Yu, Q., Wu, C., Lu, Z., Zhu, F., et al. (2015a). The Prevalence of and Risk Factors for Prostatitis-like Symptoms and its Relation to Erectile Dysfunction in Chinese Men. *Andrology.* 3 (6), 1119–1124. doi:10.1111/andr.12104

Zhang, W. H., Liu, N., and Su, Y. S. (2015b). Efficacy of Compound Xuanju Capsules Conbined Tamsulosin in the Treatment of Chronic Prostatitis with Premature Ejaculation. *Med. J. NDFNC* 36 (05), 291–293.

Zhao, X. J. (2020). Clinical Observation of Sildenafil Combined with Qianlie Shutong Capsules for Patients with Type III Chronic Prostatitis and Erectile Dysfunction. *Pract. Clin. J. Integrated Traditional Chin. West. Med.* 20 (11), 21–22.

Zheng, Z. F., and Li, Z. J. (2013). Effect of Compound Xuanju Capsule in the Treatment of Prostatitis-Related Sexual Dysfunction. *Mod. Diagn. Treat.* 24 (04), 792

Zhong, W., Mai, T. J., Liu, J. B., Zhu, Z. R., Li, Z., Zhang, C. G., et al. (2013). Efficacy of Chinese Herbal Medicine on Chronic Prostatitis Complicated with. *Chin. J. Hum. Sex.* 22 (07), 46–47+67.

Zhou, J. H. (2018). Clinical Observation on Chinese Medicine in the Treatment of Chronic Prostatitis with Sexual Dysfunction. *CJGMCM.* 33 (09), 1275–1276.

Conflict of Interest: The authors declare that the research was conducted in the absence of any commercial or financial relationships that could be construed as a potential conflict of interest.

Copyright © 2021 Zhang, Ma, Nan, Li, Zheng, Zhou and Gong. This is an open-access article distributed under the terms of the Creative Commons Attribution License (CC BY). The use, distribution or reproduction in other forums is permitted, provided the original author(s) and the copyright owner(s) are credited and that the original publication in this journal is cited, in accordance with accepted academic practice. No use, distribution or reproduction is permitted which does not comply with these terms.

GLOSSARY

CI Credible interval

CIPE-5 Chinese Index of Premature Ejaculation

CNKI China National Knowledge Infrastructure

CP/CPPS Chronic prostatitis/chronic pelvic pain syndrome

CRYSG Congrong Yishen Granules

CXJC Compound Xuanju Capsules

ED Erectile dysfunction

IIEF-5 The International Index of Erectile Function

LQT Longqing Tablets

LWDHP/YGC Liuwei Dihuang Pills/Yougui capsules

MD Mean difference

NIH-CPSI The National Institutes of Health chronic prostatitis symptom index

NMA Network meta-analysis

NMTC Ningmitai Capsules

OCPM Oral Chinese patent medicine

ORs Odds ratios

PDE-5i phosphodiesterase type-5 inhibitor

PE Premature ejaculation

QLBXC Qianlie Beixi Capsules

QLSTC Qianlie Shutong Capsules

RCT Randomized controlled trial

RLQG Relinqing Granules

SAS Self-rating anxiety scale

SD Sexual dysfunction

SGJYC Shugan Jieyu Capsules

SGYYC Shugan Yiyang Capsules

SUCRA Surface under the cumulative ranking area

TCM Traditional Chinese medicine

WM Western medicine

frontiers in Pharmacology

ORIGINAL RESEARCH
published: 10 May 2021
doi: 10.3389/fphar.2021.602543

Exploring the Mechanism of Zhibai Dihuang Decoction in the Treatment of Ureaplasma Urealyticum-Induced Orchitis Based on Integrated Pharmacology

Dong-hua Bin[1,2†], Shi-ying Zhang[2,3,4†], Min Zhan[1†], Ling Li[2], Ying-qiu Li[5], Xing Zhou[1], Fang-guo Lu[5], Qing Zhou[1] and Qing-hu He[6]**

[1]Surgery of traditional Chinese Medicine, The First Affiliated Hospital of Hunan University of Chinese Medicine, Changsha, China, [2]College of traditional Chinese Medicine, Hunan University of Chinese Medicine, Changsha, China, [3]Department of Traditional Chinese Medicine, Shenzhen Luohu People's Hospital, Shenzhen, China, [4]Department of Traditional Chinese Medicine, The Third Affiliated Hospital of Shenzhen University, Shenzhen, China, [5]Medical School, Hunan University of Chinese Medicine, Changsha, China, [6]College of Integrated Traditional Chinese and Western Medicine, Hunan University of Chinese Medicine, Changsha, China

OPEN ACCESS

Edited by:
Takashi Sato,
Tokyo University of Pharmacy and Life Sciences, Japan

Reviewed by:
Jen-Tsung Chen,
National University of Kaohsiung, Taiwan
Ashutosh Pandey,
Rutgers Biomedical and Health Sciences, United States

***Correspondence:**
Qing Zhou
supergoon@163.com
Qing-hu He
hqh19651111@163.com

[†]These authors share first authorship

Specialty section:
This article was submitted to Ethnopharmacology, a section of the journal Frontiers in Pharmacology

Received: 03 September 2020
Accepted: 24 March 2021
Published: 10 May 2021

Citation:
Bin D, Zhang S, Zhan M, Li L, Li Y, Zhou X, Lu F, Zhou Q and He Q (2021) Exploring the Mechanism of Zhibai Dihuang Decoction in the Treatment of Ureaplasma Urealyticum-Induced Orchitis Based on Integrated Pharmacology. Front. Pharmacol. 12:602543. doi: 10.3389/fphar.2021.602543

Background: Ureaplasma urealyticum (UU) infection is the most common cause of male infertility. Zhibai Dihuang Decoction (ZBDHD) can improve the rate of forwarding motility sperm, sperm deformity rate, seminal plasma zinc and refined berry sugar levels.

Methods: The potential targets of ZBDHD are obtained from The Encyclopedia of Traditional Chinese Medicine (ETCM). Orchitis-related targets were collected from the Genecards and OMIM databases. The Cytoscape and the Database for Annotation, Visualization and Integrated Discovery (DAVID) were utilized to construct and analyzed the networks. Finally, a rat model of orchitis caused by UU infection was used to detect related indicators of mitochondrial energy metabolism using TUNEL apoptosis detection technology, loss cytometry, Real-Time Quantitative Reverse Transcription PCR (qRT-PCR) and Western Blot.

Results: A total of 795 ZBDHD targets and 242 orchitis-related targets were obtained. The "ZBDHD- orchitis PPI network" was constructed and analyzed. ZBDHD can regulate signaling pathways and biological processes related to mitochondrial energy metabolism. The results of experimental studies have shown that ZBDHD maintains the integrity of sperm mitochondrial respiratory chain function by enhancing mitochondrial Na^+-K^+-ATPase and $Ca2^+$-Mg^{2+}-ATPase activities, promotes the synthesis of mitochondrial ATP, and improves sperm energy supply, thereby improving the motility, vitality and survival rate of sperm, and effectively improving the quality of semen in UU-infected rats ($p < 0.05$).

Conclusion: This study discovered the multi-pathway mechanism of ZBDHD intervention in UU-induced orchitis through integrated pharmacological strategies, which provides a reference for further research on the mechanism of ZBDHD intervention in orchitis in the direction of mitochondrial energy metabolism.

Keywords: Zhibai Dihuang decoction, ureaplasma urealyticum, orchitis, integrated pharmacological, bioinformatics, Chinese medicine, herb medicine

INTRODUCTION

With the development and progress of society, the influence of many factors such as psychology, environment, diet, bad living habits, etc., human reproductive function shows a downward trend year by year, and about one-sixth of couples suffer from infertility (Moridi et al., 2020). This has an adverse effect on family harmony and social stability. Therefore, infertility has become a serious public health problem. Among the many factors that cause infertility, males account for about 30–50% (Huang et al., 2016), among which low sperm motility and reduced sperm count are important reasons for male infertility (Huang et al., 2015). Reproductive system infection is one of the important causes of male infertility, and Ureaplasma urealyticum (UU) infection is the most common (Gdoura, et al., 2007; Lee et al., 2013). The pathogenesis and treatment of low sperm motility caused by UU infection are still problems facing the medical community. Due to the continuous increase of antibiotic resistance and the existence of the blood-testis barrier, the efficacy of antibiotics in the treatment of UU infectious infertility has been affected. Although it has a certain effect in killing UU, it is not effective in improving sperm motility (Zhu et al., 2012; Kokkayil and Dhawan, 2015; He et al., 2016). Therefore, an important topic in the field of male diseases is to reveal its pathogenesis in depth and to find efficient, stable and durable treatments (Wang, 2017). Traditional Chinese medicine (TCM) treatment is unique in that it emphasizes a holistic view, uses multiple channels for adjustment, and two-way balance adjustment. It is of great significance to use TCM to prevent and treat UU infectious infertility to enhance sperm "vitality" (Bin et al., 2016; Wang, 2017).

Zhibai Dihuang Decoction (ZBDHD) comes from "The Golden Mirror of Medicine". Current research shows that: ZBDHD is a classic prescription for nourishing yin and nourishing kidneys, clearing heat and reducing fire, and it has significant clinical treatment effects on various diseases (such as urinary system, endocrine system, gynecology, andrology, pediatrics, skin diseases, and venereal diseases, etc.) (Gao et al., 2020; Wu et al., 2020). The pharmacological mechanisms involved in ZBDHD include lowering blood sugar, enhancing immunity, anti-oxidation, anti-fatigue, regulating neuroendocrine, anti-tumor, etc. (Liu et al., 2018a; Liu et al., 2018b; Gao et al., 2020; Wu et al., 2020). Our previous research also found that ZBDHD can improve the rate of forwarding motility sperm, sperm deformity rate, seminal plasma zinc and refined berry sugar levels (Sheng and He, 2019; Li et al., 2019). However, its specific mechanism is still unknown.

At present, integrated pharmacology, as a new discipline, is a discipline that studies the interaction of multi-component drugs with the body and its integration laws and principles of action (Zeng and Yang, 2017). It emphasizes multi-level and multi-link integrated research such as "whole and part," "*in vivo* and *in vitro*," "*in vivo* process and activity evaluation," which is in line with the overall and systematic treatment of TCM (Yang et al., 2020; Zeng et al., 2020). Previously, we have explored the mechanism of multi-component Chinese herbal medicines in infectious diseases, endocrine diseases and immune diseases by using integrated pharmacology (Zhang et al., 2020a; Zhang et al., 2020b). In this study, we would use the strategy of integrating pharmacology and multi-directional pharmacology to study the mechanism of ZBDHD intervention in UU-induced orchitis. The process of this research is shown in **Figure 1**.

MATERIALS AND METHODS

Potential Targets and Orchitis-Related Targets Collection

The potential targets of ZBDHD were collected from the Encyclopedia of Traditional Chinese Medicine (ETCM, http://www.tcmip.cn/ETCM/index.php) (Xu et al., 2018). ETCM is a database that include comprehensive and standardized information for the commonly used herbs and formulas of TCM, as well as their ingredients. The Orchitis-related targets were collected from Genecards (http://www.genecards.org) (Stelzer et al., 2018), andOnline Mendelian Inheritance in Man (OMIM) (http://omim.org/) databases (Hamosh et al., 2015). The proteins were introduced into UniProt (https://www.uniprot.org/) to correct their official gene symbols. Finally, a total of 795 ZBDHD targets and 242 orchitis-related targets were obtained (**Supplementary Tables S1, S2**).

Network Construct and Analysis Methods

The protein-protein interaction (PPI) information of ZBDHD targets and orchitis-related targets were collected from String 11.0 (https://string-db.org) Szklarczyk et al., 2015). The drug target-disease target PPI network (such as ZBDHD-orchitis PPI network) were constructed by Cytoscape 3.7.2 (www.cytoscape.org/) (Bader and Hogue, 2003). The ZBDHD-orchitis PPI network was analyzed by the "Network Analyzer" and "MCODE" plug in of Cytoscape to obtain the degree of each node and clusters of this network. Finally, the Database for Annotation, Visualization and Integrated Discovery (DAVID) ver 6.8 (https://david.ncifcrf.gov/) and the "ClueGO", plug-in of Cytoscape, were utilized to perform Kyoto Encyclopedia of Genes and Genomes (KEGG) pathway enrichment analysis and Gene Ontology (GO) enrichment analysis (Huang et al., 2009).

Experimental Materials

Instruments and Reagents

The UU standard strain and UU culture medium were provided by the Department of Microbiology, Nanhua University, and the reagents required for electron microscopy were provided by the Electron Microscopy Room of Xiangya Medical College, Central South University. Mitochondrial membrane potential (mitochondrial membrane potential, MMP) detection reagent JC-1, PCR kit, and reverse transcription kit were all purchased from Kilton Biotechnology (Shanghai) Co., Ltd. BCA protein quantification kit, mouse anti-rat MRPS22 monoclonal antibody, and HRP-labeled goat anti-mouse IgG were purchased from Biyuntian Biotechnology Co., Ltd. C 18 column Diamonsil, sum, 250 × 4.6 mm; ADP reference substance (SIGMA company A2754, content 95%), ATP reference substance

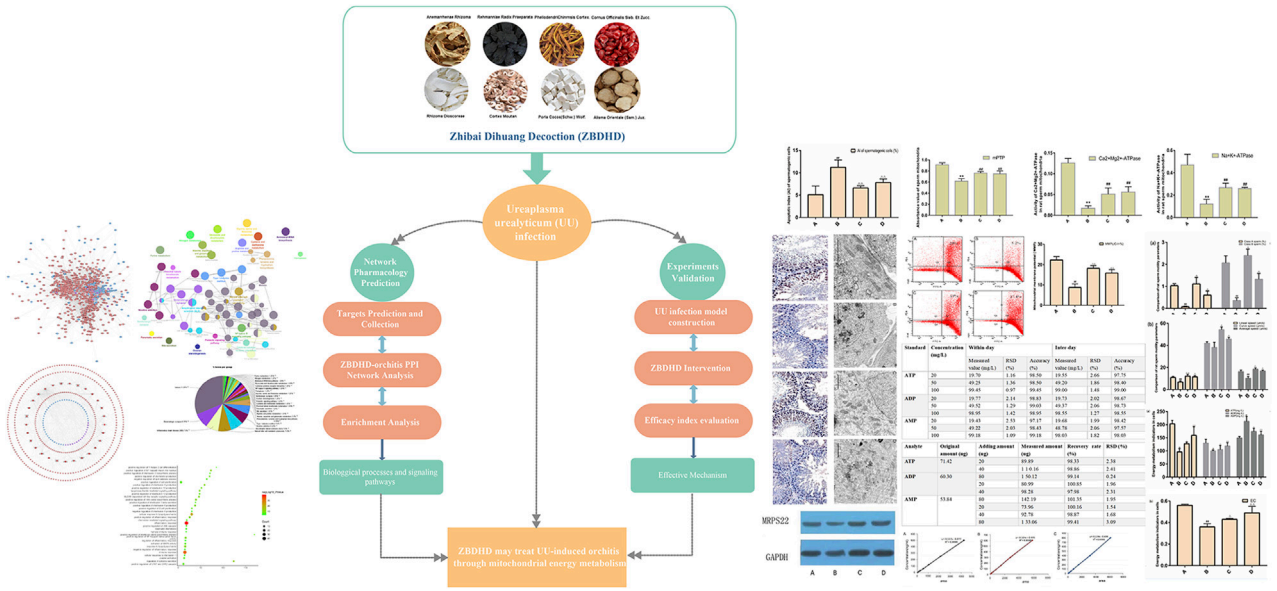

FIGURE 1 | Flow chart of this research.

(SIGMA company A26209, the content is 99%), AMP reference substance (SIGMA company 01930, content is 99%). CytC ELISA kit (BOSTER Biological Technology co. ltd.). Loganin reference substance (China Institute for the Control of Pharmaceutical and Biological Products, batch number 111640-201602). Tissue Mitochondrial Isolation Kit (Cat. No.: 050217171026, Biyuntian Biotechnology Company). Purified mPTP Colorimetric Detection Kit (Cat. No.: 6-4267-11, GENMED Technology Company).

Azithromycin tablets were purchased from CSPC Ouyi Pharmaceutical Company (Lot No.: 001120941), and were formulated with normal saline to make 25 mg/ml. ZBDHD is composed of *Rehmanniae Radix Praeparata, Cornus Officinalis Sieb. Et Zucc., Rhizoma Dioscoreae, Alisma Orientale (Sam.) Juz., Cortex Moutan, Poria Cocos(Schw.) Wolf., Anemarrhenae Rhizoma, Phellodendri Chinrnsis Cortex* with ratio 24:12:12:9:9:9:6:6. The medicinal materials are provided by the First Affiliated Hospital of Hunan University of Chinese Medicine. They are appraised by Chinese pharmacists and processed in strict accordance with traditional methods. The medicinal materials are decocted in distilled water. Finally, ZBDHD was concentrated to 1 g crude drug/ml, and stored in a refrigerator at 4°C for later use.

HT7700 transmission electron microscope (Hitachi Inc.), FACSAria flow cytometer (BD Inc.), electrophoresis (Bio-Rad), ABI-7300 Real-time detector (ABI Inc.). Other instruments are provided by the Central Laboratory of Hunan University of Chinese Medicine. High performance liquid chromatograph (HPLC) (Waters company, model Waters 1525); UV detector (U.S. Waters company, model Waters 2489).

Experimental Animals

60 specific pathogen free (SPF) SD male rats were purchased from Hunan Slack Jingda Experimental Animal Company, 4–5 months old, weight (208 ± 15) g, laboratory animal production license number: SCXK (Xiang) 2011-0003. The animals were kept in the Special Animal Room for Pathogenic Microorganisms of Hunan University of Chinese Medicine [Permit No.: SYXK (Xiang) 2009-0001]. All animal care and use procedures comply with the National Institutes of Health (NIH) guidelines for the care and use of experimental animals and have been approved by the Institutional Animal Ethics Committee of Hunan University of Chinese Medicine.

ZBDHD Quality Control by HPLC

Preparation of Sample Solution

Loganin solution: The loganin reference substance was added to 50% methanol to make a reference solution containing 50 μg per 1 ml.

ZBDHD solution: ZBDHD solution was prepared according to the aforementioned method.

HPLC Condition

Shim-Pack CLCODS column (150 mm × 4.6 mm, 5 μm); acetonitrile: water (15:85) as mobile phase, flow rate 1.0 ml·min-1, detection wavelength 232 nm, column temperature at room temperature. Under these conditions, the loganin peak in the sample chromatogram reached baseline separation without interference (**Figure 2**).

Experimental Methods

Animal Modeling

First, UU titer titration was performed. The UU standard strain (freeze-dried product) was resuscitated, inoculated into liquid culture medium under aseptic conditions, cultured at 37°C for 16–24 h, and the logarithmic phase bacteria were taken. When the culture medium appears orange-red and clear bacterial liquid,

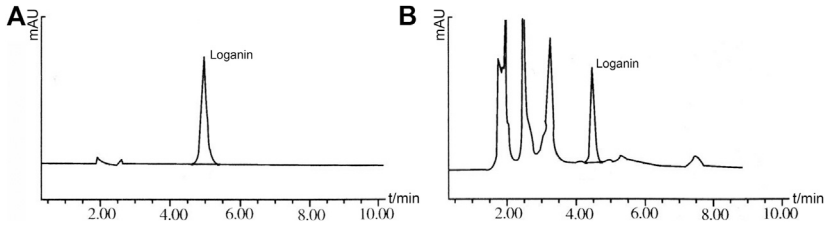

FIGURE 2 | The results of HPLC. **(A)**: Loganin solution; **(B)**: ZBDHD solution.

the multiple dilution was implemented. The color change unit of the bacterial liquid with a titer of $10^{*}10^{6}$ ccu/ml is used in the *in vitro* experiment. Then, the UU standard strain suspension was injected into the bladder to establish a UU infection animal model. The rats were fasted for 12 h before modeling. After the rats were anesthetized with 2% pentobarbital sodium (0.2 ml/100 g) and disinfected, the abdominal cavity was opened and the bladder was freed. The residual urine in the bladder was drained with a syringe, and 2 ml of normal saline or UU standard strain was injected into the bladder, and finally the abdominal cavity was sutured.

After the inoculation, the testicular puncture fluid was taken after routine feeding for 7 days and inoculated in UU culture medium at 37°C and 5% CO2. If the culture medium turns from yellow to red and is transparent and clear, 0.2 ml UU is transferred to solid medium after filtering through a microporous membrane. After culturing at 37°C and 5% CO2 for 72 h, the colonies were observed under a low-power microscope to confirm whether there was UU growth in the testicular tissue.

Animal Grouping and Intervention

Successfully modeled UU-infected rats were randomly divided into model group, ZBDHD group, and positive control group. At the same time, normal rats were used as normal group, with 15 rats in each group. Gavage was started on the 10th day after the successful model building, once daily. According to Sellami et al., 2014, (Guo et al., 2017) the dose of ZBDHD group is 1 g/(kg d) [i.e. ZBDHD 1 ml/(kgd)], the dose of positive control group is 0.105 g/(kg d) [i.e. azithromycin suspension 1 ml/(kgd)]. The normal group and the model group were given corresponding volume of normal saline by gavage. The testes of the rats were removed, the testis capsule and blood vessels were thoroughly stripped, and the testes were placed in a cell culture dish, and 3 ml PBS was added to completely soak the testes for later use.

Detection of Spermatogenic Cell Apoptosis

The prepared rat testis tissue sections were tested for spermatogenic cell apoptosis according to the instructions of the TUNEL detection kit. The cells with brown particles in the nucleus were apoptotic cells. Twenty seminiferous tubules were randomly selected from each section, and the number of positive spermatogenic cells apoptosis in the total spermatogenic cells was counted, and the positive cell rate was calculated, which was the apoptotic index (AI).

Preparation of Spermatogenic Cell Suspension and Sperm Motility Test

The testicular tissue was collected under aseptic conditions to prepare a spermatogenic cell suspension, which was placed in a 32°C, 5% CO2 incubator for 5 min to diffuse for use. Sperm suspension was diluted with PBS solution in a ratio of 1:9, fully shaken. Color sperm dynamic detection system was used to measure sperm motility parameters.

Detection of MMP and Mitochondrial Structure of Spermatogenic Cells

Alexa Fluor 488 and R-phycoerythrin are excited by the 488 nm light of the flow cytometer to detect the fluorescence signal at 520 nm and analyze the MMP of spermatogenic cells. A long strip specimen of the middle part of the left testis of the rat was taken out, and ultra-thin sections were made according to the requirements of electron microscopy. The ultra-thin sections were stained with uranyl acetate and lead nitrate, and then electron microscopy observations and photographs were performed to observe the mitochondrial structure of spermatogenic cells.

Detection of MRPS22 mRNA in Spermatogenic Cells by Real-Time Quantitative Reverse Transcription PCR

The total RNA of the spermatogenic cell suspension was extracted and subjected to RTPCR detection. The data obtained in the experiment was analyzed by ABI's own RQ software, and the relative quantification of target gene expression was analyzed by the 2-ΔΔCt method. Each sample was repeated 3 times in parallel, and the average was taken for analysis.

Detection of MRPS22 Protein in Spermatogenic Cells by Western Blot

The spermatogenic cell suspension was lysed and homogenized, and the MRPS22 protein of spermatogenic cells was detected by Western blotting. Using β-actin as the internal reference, the Image-pro Plus processing software was used to analyze the image information and calculate the relative expression level.

Quantitative Detection of ATP, ADP, AMP in Sperm Mitochondria

A random number table was used to select 5 rats in each group, and the contents of ATP, ADP, and AMP in sperm mitochondria were detected by HPLC, and proceeded in accordance with the

procedures of each kit. Energy charge (EC) value: EC = (ATP +0.5 ADP)/(ATP + ADP + AMP).

Determination of Sperm CytC Content by ELISA

The content of CytC in rat testis tissue was tested according to the operation steps of the ELISA test kit.

Mitochondrial Permeablity Transition Pore Opening Detection

After the purified mitochondrial sample to be tested was prepared, 100 μl of the mitochondrial sample (a total of 0.2 mg) was transferred to a 1.5 ml centrifuge tube, 10 μl of staining solution (Reagent A) was added, and the mixture was evenly mixed. Then, it was incubated in a cell incubator at 37°C in the dark for 15 min, and then centrifuged in a miniature benchtop centrifuge at 4°C for 5 min at a speed of 16,000 g, and the supernatant was removed. Then the pre-heated preservation solution (Reagent C) at 37°C was added to mix the particles. Finally, 100 μl of the above suspension was transferred to a black 96-well plate, and put into a fluorescence microplate reader for detection (Excitation wavelength 488 nm, emission wavelength 505 nm). If the relative fluorescence units (RFU) decreases, it indicates that mPTP is enhanced.

Sperm Mitochondrial Na^+-K^+-ATPase, Ca^{2+}-Mg^{2+}-ATPase Detection

After the sperm suspension is prepared, the sperm mitochondria are separated by a differential fractionation method and placed in an ice tank for later use. The determination of Na^+-K^+-ATPase and Ca^{2+}-Mg^{2+}-ATPase activity is strictly in accordance with the instructions of the mitochondrial Na^+-K^+-ATPase and Ca^{2+}-Mg^{2+}-ATPase kit instructions.

Statistical Analysis

SPSS 17. 0 is used for statistical analysis, and the measurement data is expressed as x ± s. The independent sample t test was used to compare the difference in means between two groups. One-way ANOVA is used to compare the mean difference between multiple groups, and the LSD test is used for pairwise comparison between multiple groups. Pearson analysis was used to analyze the correlation between MRPS22 and MMP. All tests are two-sided tests, and $p \leq 0.05$ is considered statistically significant.

RESULTS

ZBDHD-Orchitis PPI Network Analysis

ZBDHD-Orchitis PPI Network Construction

ZBDHD-orchitis PPI network consists of 946 nodes (726 ZBDHD target nodes, 194 orchitis target nodes and 26 ZBDHD-orchitis target nodes) and 18,098 edges (**Figure 3**). The targets are arranged in descending order according to their degree, the top 20 can be divided into 3 category: 1) ZBDHD target: GAPDH (294 edges), INS (290 edges), AKT1 (253 edges), MAPK3 (199 edges), SRC (166 edges), EGF (157 edges), CASP3 (153 edges); 2) Orchitis related targets: ALB (276 edges), CXCL8 (188 edges), IL10 (180 edges), STAT3 (167 edges), CAT (160 edges), IL2 (158 edges), IL4 (151 edges), HSP90AA1 (147 edges); 3) ZBDHD-orchitis target: IL6 (249 edges), TNF (227 edges), VEGFA (192 edges), IL1B (173 edges), TLR4 (168 edges).

Biological Processes of ZBDHD-Orchitis PPI Network

The ZBDHD-orchitis PPI network was analyzed by MCODE and 27 clusters were obtained (**Figure 4** and **Table 1**). The targets and genes of top 10 clusters were input into DAVID and ClueGO to perform GO enrichment analysis so as to obtain the biological processes of each cluster.

Cluster 1, 6 and 9 is related to inflammation and immune response. Cluster 2, 4 and 5 are associated with mitochondria and energy metabolism. Cluster 8 are associated with mitochondria and nutrient metabolism. Cluster 3 and 10 did not return any orchitis-related biological processes (**Supplementary Table S3**). The *p*-value, fold enrichment and count of biological processes in cluster 1 were shown in **Figure 5** as an example.

Pathway of ZBDHD-Orchitis PPI Network

The targets in ZBDHD- orchitis PPI network were input into DAVID and ClueGo to perform pathway enrichment analysis and a lot of human signaling pathways returned (**Figure 6**).

The pathway enrichment analysis showed that ZBDHD can regulate a lot of orchitis -related signaling pathways, such as Metabolic pathways, Neuroactive ligand-receptor interaction, Arginine biosynthesis, Alanine, aspartate and glutamate metabolism, Glutamatergic synapse, Biosynthesis of amino acids, Arginine and proline metabolism, cAMP signaling pathway, 2-Oxocarboxylic acid metabolism, Glycine, serine and threonine metabolism (**Figure 7** and **Supplementary Table S4**). The *p*-value, fold enrichment and count of each signaling pathways were shown in **Figure 8**.

Evaluation of Establishment of UU Infection Rat Model

Seven days after the rat bladder was inoculated with UU, the testicular puncture fluid changed from yellow to red and the culture medium was transparent and clear after cultured in the UU liquid culture medium. After the solid medium was filtered through a microporous filter membrane, fried egg-like colonies were observed under a low power microscope, confirming that the rat testis tissue had UU growth, and the model was successful.

UU Infection Rate in Rats

After treatment, rats in each group were sacrificed, and the epididymal tissue fluid was cut and cultured for UU. The results showed that UU was not cultured in the normal group, the positive rate of UU in the model group was 93.3% (14/15), the positive rate of UU in the ZBDHD group was 33.3% (5/15), and the positive rate of UU in the positive control group was 26.7% (4/15). Compared with the normal group, the positive rate of UU in the model group was higher, and the difference between the two groups was statistically significant ($p < 0.01$). Compared with the model group, the positive rates of UU in the ZBDHD group and the positive control group were reduced, and the difference was statistically significant ($p < 0.05$).

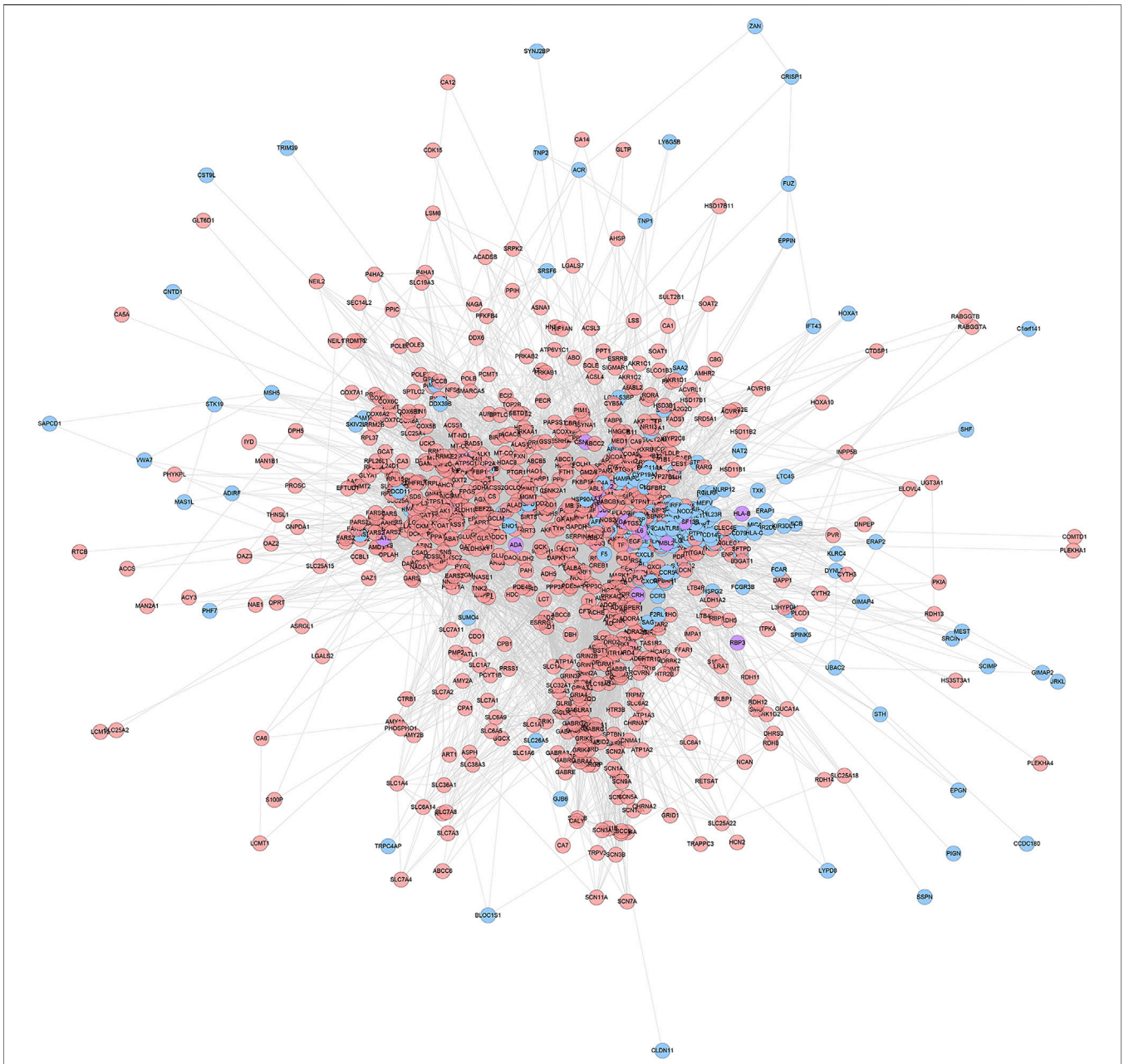

FIGURE 3 | ZBDHD-orchitis PPI Network (Pink circles stand for ZBDHD target, Blue circles stand for orchitis targets, purple circles stand for ZBDHD-orchitis target).

Comparison of Rat Sperm Quality and Sperm Motility Parameters

Compared with the normal group, the rats in the model group had fast-moving sperm (A-grade sperm), slow-moving sperm (B-grade sperm), linear speed, and average speed decreased ($p < 0.05$, $p < 0.01$). After treatment, compared with the model group, the sperm motility parameters of each treatment group increased, and the difference was statistically significant ($p < 0.05$, $p < 0.01$) (**Figure 9**).

Apoptosis of Rat Spermatogenic Cells

The results of TUNEL method showed that there was spermatogenic cell apoptosis in the testicular tissues of each group, and the model group was the most serious. The AI of spermatogenic cells in the testis of the model group was significantly higher than that of the ZBDHD group and the positive control group ($p < 0.01$), while the AI of the positive control group was significantly higher than that of the ZBDHD group ($p < 0.05$) (**Figures 10**, **11**).

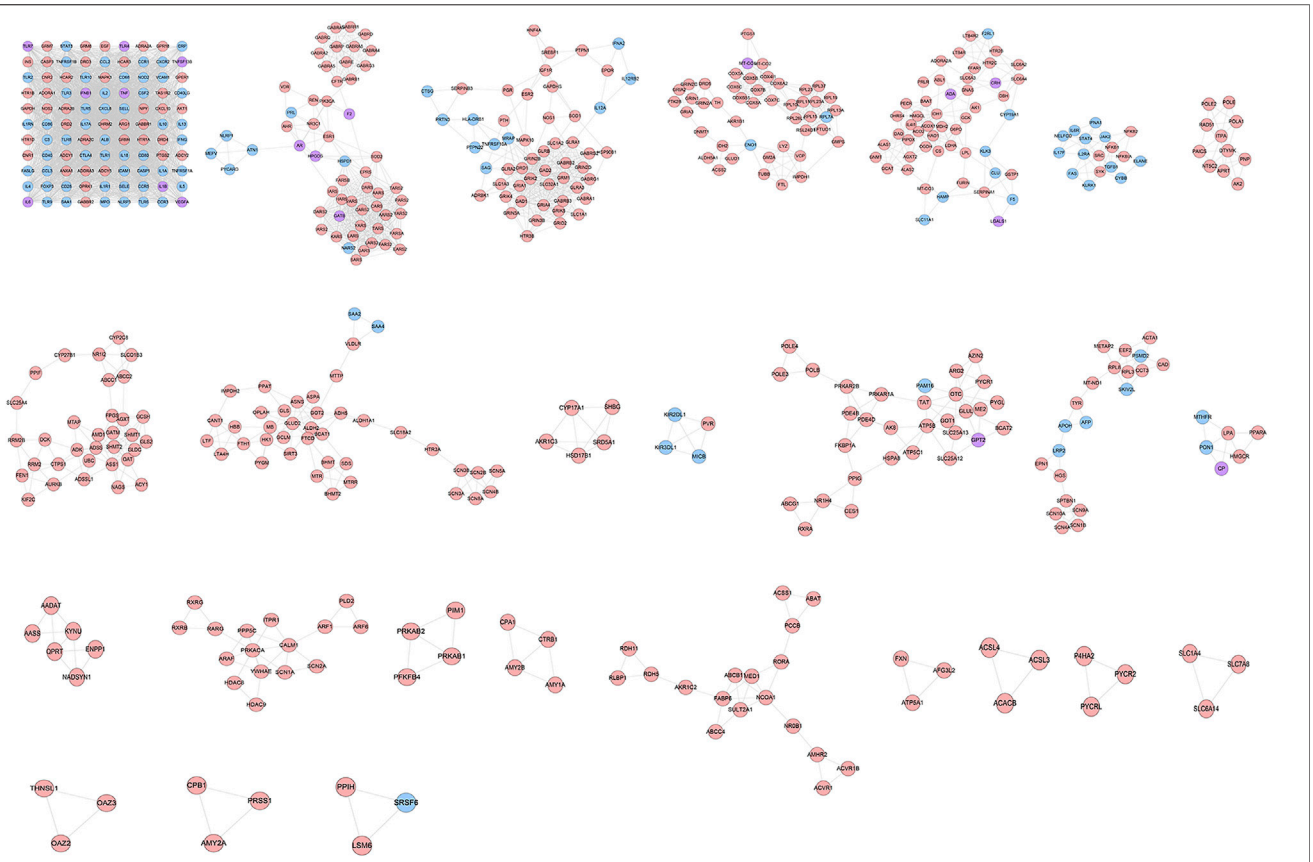

FIGURE 4 | Clusters of ZBDHD-orchitis PPI Network (Pink circles stand for ZBDHD target, Blue circles stand for orchitis targets, purple circles stand for ZBDHD-orchitis target).

The Ultrastructure of Rat Spermatogenic Cell Mitochondria

In the normal group, the morphology and structure of spermatogenic cells at all levels were normal, and mitochondria could be observed in the cytoplasm with normal structure and abundant numbers and orderly arrangement. In the model group, spermatogenic cells at all levels showed obvious swelling and mitochondria with vacuolated ridges, and the membrane structure was unclear. In the positive control group, the arrangement, cell morphology and structure of spermatogenic cells were basically normal, and the size and number of mitochondria were basically normal; the mitochondria were slightly swollen but the mitochondrial cristae structure was still clear (**Figure 12**).

Rat Spermatogenic Cell MMP

The results of flow cytometry showed that the MMP level of spermatogenic cells in the model group was significantly lower than that of the control group ($p < 0.01$), and the MMP level of the ZBDHD group was significantly higher than that of the model group and the positive control group ($p < 0.01$) (**Figure 13**).

Expression of MRPS22 mRNA and Protein in Rat Spermatogenic Cells

Expression of MRPS22 mRNA

The expression of MRPS22 mRNA was the lowest in the model group ($p < 0.01$), and the expression of MRPS22 mRNA in ZBDHD was significantly higher than that of the positive control group ($p < 0.01$) (**Figure 14A**).

Expression of MRPS22 Protein

The MRPS22 protein of the model group was significantly lower than that of the control group, ZBDHD group and the positive control group ($p < 0.01$). There was no significant difference between the MRPS22 protein of the ZBDHD group and the control group, but they were significantly higher than that of the positive control group ($p < 0.01$) (**Figure 14B** and **Figure 15**).

Effect of ZBDHD on the Energy Metabolism Index of Rat Sperm

Methodological Quality Control

Under the aforementioned HPLC conditions, the precision, accuracy, stability, repeatability and recovery experiments were

TABLE 1 | Clusters of DGBXD known Target-AS PPI Network.

Cluster	Score	Nodes	Edges	Targets and genes
1	56.878	99	2,787	IL18, ADORA1, IL1RN, GAPDH, ADORA3, CD40LG, IL4, CXCL8, NOS2, TLR2, CASP1, MPO, NLRP3, FOXP3, IL2, IL17A, CD68, IL1A, IL1R1, IL13, SAA1, IFNG, ALB, ICAM1, FASLG, TNFRSF1B, INS, VCAM1, IL5, ARG1, MAPK3, SELL, TLR4, TLR7, IL1B, TLR3, CCL2, CD40, CXCL10, CXCR2, C3, CCR3, CD28, CNR1, CNR2, TLR1, TNF, TLR8, TLR5, CCR5, CTLA4, TLR9, NPY, GPR18, CSF2, HTR1A, HTR1B, SELE, HTR1D, ADRA2A, ADRA2B, TLR6, ADRA2C, CD86, GPER1, CD80, TLR10, GRM4, CCL3, GRM7, GRM8, CHRM2, IL6, IFNB1, PTGS2, GABBR1, GABBR2, ANXA1, CASP3, TNFSF13B, AKT1, VEGFA, TAS1R2, STAT3, EGF, ADCY1, ADCY2, ADCY5, DRD2, DRD3, DRD4, OPRK1, IL10, TNFRSF1A, NOD2, HCAR2, HCAR3, CRP, CCR1
2	17.309	56	476	GABRP, GABRQ, AR, PIK3CA, LARS, GABRR1, TARS, GABRB1, REN, CARS2, AHR, F2, GARS, CARS, GATB, NLRP1, YARS, ATN1, PYCARD, FARS2, EARS2, ESR1, HARS, DARS, VARS, PARS2, YARS2, PRL, FARSA, FARSB, TARS2, IARS2, IARS, AARS, LARS2, GABRG3, AARS2, VDR, HSPD1, DARS2, SOD2, GABRA2, GABRA3, GABRA4, GABRA5, GABRA6, NR3C1, KARS, SARS, NARS2, MEFV, HPGDS, EPRS, CFTR, GABRD, GABRE
3	12.231	53	318	HNF4A, NOS1, SLC32A1, IGF1R, PTPN1, GABRB2, GABRB3, IFNA2, GAD1, GAD2, GRID2, PGR, PRTN3, ESR2, EPOR, MRAP, GRIN3A, GRIN3B, HSP90B1, GABRG1, GABRG2, PTH, SLC1A1, SLC1A2, SLC1A3, GRIK2, HLA-DRB1, GRIK4, SOD1, GRIK5, PTPN22, GLRB, GRIA1, ADRBK1, GLRA1, GLRA2, GLRA3, TNFRSF10A, GRIA4, GAPDHS, HTR3B, DRD1, GABRA1, SERPINB3, CTSG, MAPK10, SAG, IL12RB2, GRIN2B, GRIN2D, SREBF1, GRM1, IL12A
4	8.311	46	187	COX5A, ENO1, VCP, COX5B, FTL, GM2A, MT-CO1, GRIN1, MT-CO2, GRIA2, GRIA3, COX8A, PTGS1, COX6C, PTK2B, COX6B1, LYZ, COX4I1, RPL11, RPL23A, GMPS, RPL15, TUBB, COX6A2, DNMT1, EFTUD1, DRD5, GRIN2A, ACSS2, RPL19, RPL37, TH, COX7B, IDH2, GRIN2C, COX7C, RPL13A, RPL26L1, RPL7A, AKR1B1, GLUD1, RPL23, IMPDH1, ALDH5A1, RSL24D1, RPL10L
5	6.72	51	168	GSTP1, ACO2, LTB4R2, SLC6A2, SLC6A3, SLC6A4, MT-CO3, FURIN, HTR2B, DHRS4, HTR2C, GNMT, ADA, GNAS, IL4I1, SERPINA1, AGXT2, DAO, CRH, F2RL1, PIPOX, LGALS1, ADORA2A, CYP19A1, CLU, KLK3, LDHA, PRLR, PECR, LTB4R, AK1, SLC11A1, ALAS1, ALAS2, F5, GCK, FFAR1, DBH, BAAT, ACOX1, GCAT, HAO1, G6PD, OGDH, HAMP, LPL, ABL1, CS, IDH1, MDH2, HMGCL
6	6	17	48	SYK, NFKBIA, SRC, IFNA1, NFKB1, IL6R, CYBB, NFKB2, ELANE, TGFB1, NELFCD, JAK2, IL17F, FAS, IL2RA, KLRK1, STAT4
7	6	11	30	POLE2, POLA1, DTYMK, PAICS, PNP, NT5C2, APRT, AK2, RAD51, POLE, ITPA
8	5.438	33	87	GLDC, FPGS, KIF2C, UBC, SHMT1, FEN1, SHMT2, GLS2, ADSSL1, ABCC1, ASS1, ABCC2, ADK, CTPS1, SLCO1B3, ACY1, CYP2C8, NAGS, RRM2B, AURKB, DCK, NR1I2, CYP27B1, GATM, MTAP, OAT, SLC25A4, GCSH, AMD1, PPIF, RRM2, AGXT, ADSS
9	4.833	25	58	IL23R, TNFAIP3, ITGB2, HSP90AA1, PLG, NOS3, CD4, IRF8, LCK, B2M, ITGAL, CAMP, CREB1, PPARG, S100B, IL12RB1, LCN2, THBD, GPT, LGALS3, CD1E, KITLG, CAT, ACE, CTSB
10	4.718	40	92	ALDH1A1, SCN5A, SIRT3, ASNS, OPLAH, BHMT, GOT2, PPAT, FTCD, ALDH2, HBB, MTR, SCN3A, SCN3B, LTF, SLC18A2, HTR3A, SDS, CANT1, GCLM, ASPA, GLS, SAA4, BCAT1, MTRR, PYGM, SAA2, ADH5, LTA4H, VLDLR, GLUD2, BHMT2, FTH1, IMPDH2, MTTP, SCN8A, SCN2B, MB, HK1, SCN4B
11	4.5	5	9	SHBG, SRD5A1, AKR1C3, HSD17B1, CYP17A1
12	4	4	6	PVR, KIR2DL1, MICB, KIR3DL1
13	3.933	31	59	PRKAR2B, GOT1, ATP5C1, RXRA, HSPA8, OTC, CES1, TAT, AK8, SLC25A12, PAM16, SLC25A13, ATP5B, ABCG1, GLUL, PDE4B, PDE4D, PYCR1, NR1H4, FKBP1A, POLB, ARG2, PYGL, BCAT2, POLE3, POLE4, PPIG, GPT2, ME2, AZIN2, PRKAR1A
14	3.9	21	39	ACTA1, SCN1B, MT-ND1, TYR, SKIV2L, HGS, PSMD2, CCT3, LRP2, CAD, SCN10A, EEF2, AFP, RPL3, METAP2, SPTBN1, RPL8, APOH, SCN4A, SCN9A, EPN1
15	3.6	6	9	PPARA, LPA, CP, HMGCR, PON1, MTHFR
16	3.6	6	9	AADAT, KYNU, AASS, NADSYN1, ENPP1, QPRT
17	3.333	16	25	YWHAE, ITPR1, SCN1A, CALM1, PLD2, RARG, HDAC8, HDAC9, RXRB, RXRG, ARAF, PRKACA, PPP5C, ARF1, SCN2A, ARF6
18	3.333	4	5	PRKAB1, PRKAB2, PFKFB4, PIM1
19	3.333	4	5	CPA1, AMY1A, AMY2B, CTRB1
20	3.059	18	26	AKR1C2, ACVR1B, ACVR1, NCOA1, RDH5, ABAT, MED1, PCCB, ACSS1, FABP6, RDH11, NR0B1, RLBP1, ABCB11, AMHR2, ABCC4, RORA, SULT2A1
21	3	3	3	ATP5A1, FXN, AFG3L2
22	3	3	3	ACSL4, ACACB, ACSL3
23	3	3	3	PYCR2, PYCRL, P4HA2
24	3	3	3	SLC6A14, SLC7A8, SLC1A4
25	3	3	3	OAZ3, THNSL1, OAZ2
26	3	3	3	CPB1, PRSS1, AMY2A
27	3	3	3	PPIH, SRSF6, LSM6

performed. The accuracy is controlled above 95%, the recovery rate is controlled above 95%, and the RSD is controlled within 4%, indicating that the instrument has good precision and reliable experimental methodology (**Tables 2–4**).

Quantitative Analysis

Equal volumes of ATP, ADP, and AMP standard solutions are mixed and diluted into a series of working solutions for injection analysis. The standard curve is drawn (**Supplementary Figure**

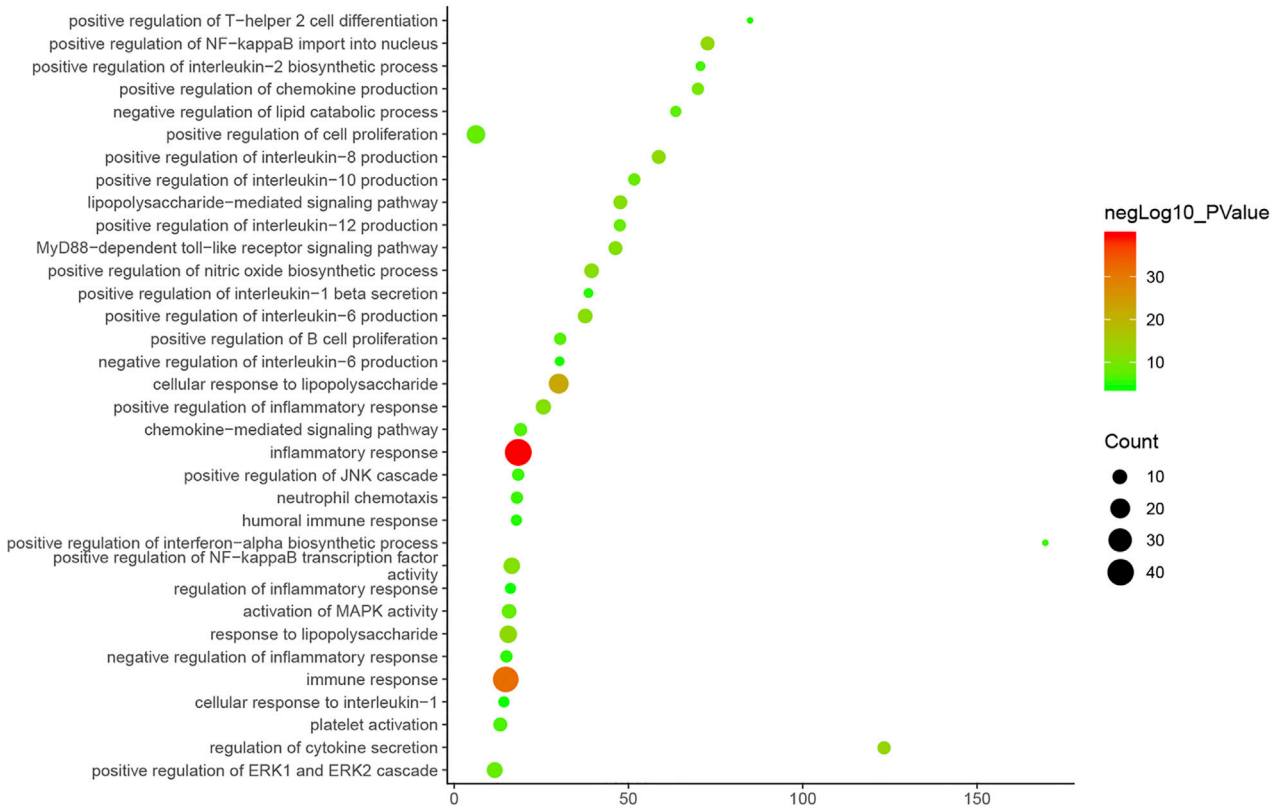

FIGURE 5 | Bubble chart of biological processes in cluster 1 (X-axis stand for fold enrichment).

S1) with the concentration as the x-axis and the area under the peak area as the Y-axis:

1) ATP regression equation: y = 0.117x−0.077, correlation coefficient R2 = 0.9999 (**Supplementary Figure S1A**);
2) ADP regression equation: y = 0.104x+0.695, correlation coefficient R2 = 0.998 (**Supplementary Figure S1B**);
3) AMP regression equation: y = 0.128x−0.606, correlation coefficient R2 = 0.9998 (**Supplementary Figure S1C**).

Compared with the normal group, the sperm ATP and EC values of the model group decreased, and the AMP value increased ($p < 0.01$). Compared with the model group, the sperm ATP and EC values of the positive control group increased, while the AMP value decreased ($p < 0.05$, $p < 0.01$), while the AMP value of the ZBDHD group decreased ($p < 0.05$) (**Supplementary Figure S2**).

Effect of ZBDHD on CytC in UU Infection Model Rat Sperm

Compared with the normal group, the CytC content of the model group and the positive control group was significantly increased ($p < 0.01$). Compared with the model group, the CytC content in the ZBDHD group decreased ($p < 0.05$). It shows that ZBDHD can inhibit sperm apoptosis and reduce the release of CytC from mitochondria in UU infection model rats (**Supplementary Figure S3**).

Effect of ZBDHD on the Opening of Mitochondria mPTP in UU Infection Model Rat Sperm

Compared with the sham operation group, the absorbance of sperm mitochondria in the model group decreased ($p < 0.01$). Compared with the model group, the absorbance of sperm mitochondria of rats in each treatment group increased ($p < 0.01$) (**Supplementary Figure S4**).

Effect of ZBDHD on the Activities of Na^+-K^+-ATPase and Ca^{2+}-Mg^{2+}-ATPase in UU Infection Model Rat Sperm

Compared with the sham operation group, the sperm Na^+-K^+-ATPase and Ca^{2+}-Mg^{2+}-ATPase activities of the model group were reduced ($p < 0.01$). Compared with the model group, the sperm Na^+-K^+-ATPase and Ca^{2+}-Mg^{2+}-ATPase activities of rats in each treatment group increased ($p < 0.01$) (**Supplementary Figure S5**).

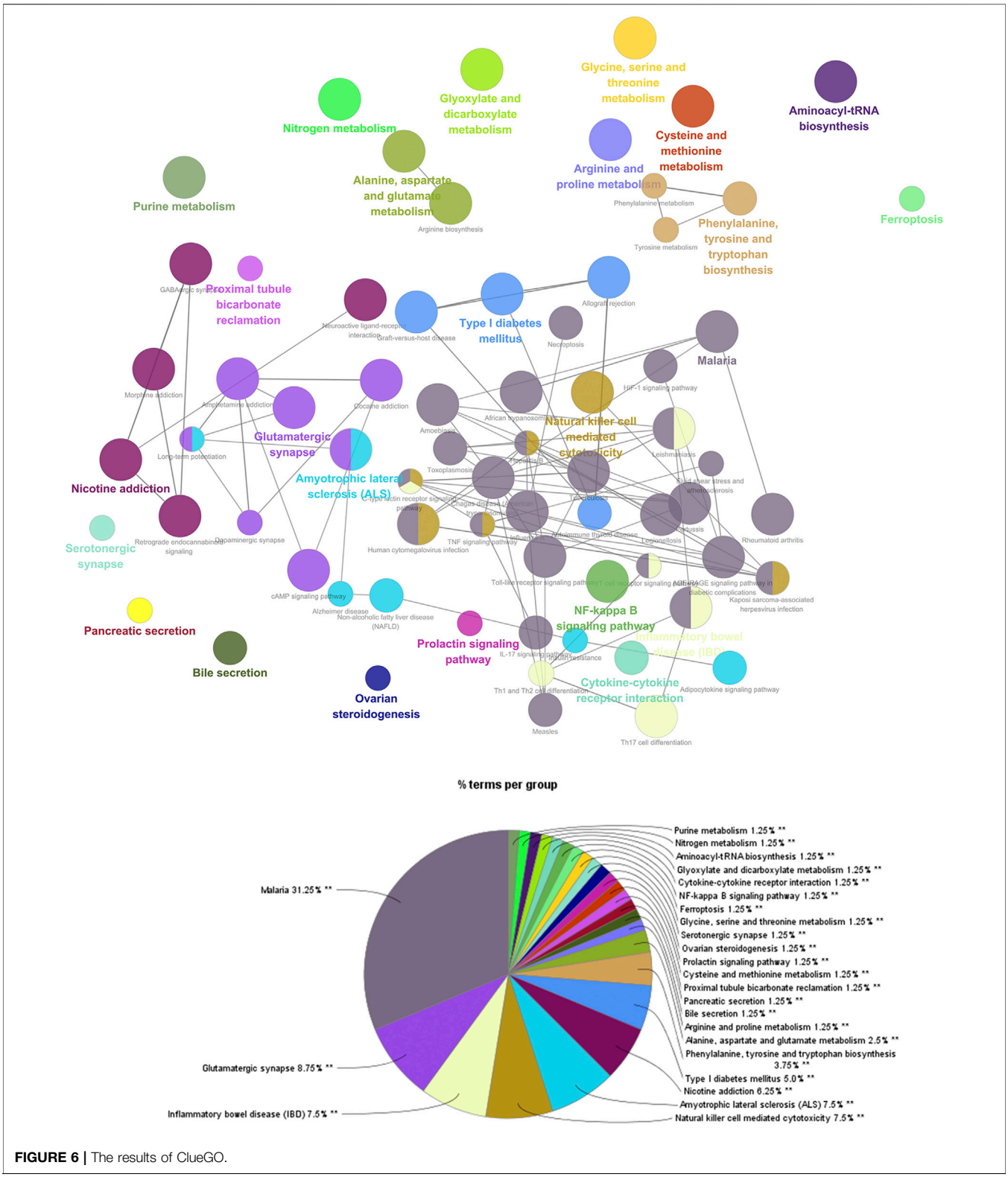

FIGURE 6 | The results of ClueGO.

DISCUSSION

The morphology, structure and function of sperm are important indicators to measure the ability of sperm to fertilize. Normal sperm structure and function are important conditions for fertilization (Manochantr et al., 2012). UU is adsorbed on the sperm surface, the lecithin lipid on the sperm membrane will be decomposed by the phospholipase A and C on the cell membrane,

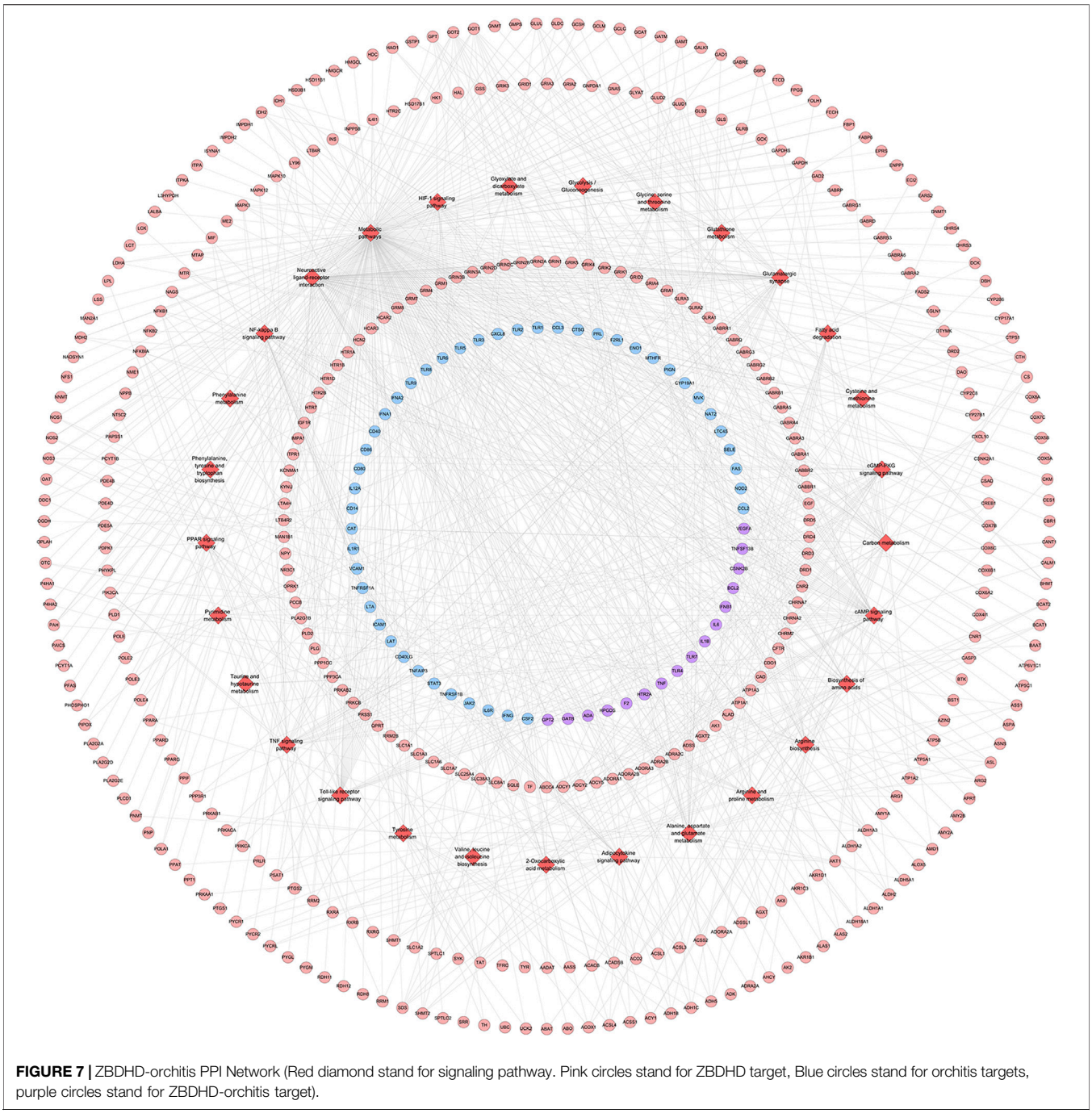

FIGURE 7 | ZBDHD-orchitis PPI Network (Red diamond stand for signaling pathway. Pink circles stand for ZBDHD target, Blue circles stand for orchitis targets, purple circles stand for ZBDHD-orchitis target).

and the integrity of the sperm structure will be affected and it will fuse with the protoplasm. Toxic substances in the UU cytoplasm will enter the sperm cytoplasm, which will affect the development, maturation and normal physiological functions of the sperm, resulting in a decline in sperm motility and penetration ability (Xu et al., 1997; Wu et al., 2004). UU can survive and migrate in mammals, and can survive for a long period of time in testicular tissues, and can cause extensive lesions of seminiferous tubules. UU adheres to the spermatogenic cells, which can cause the latter to fall off the seminiferous tubules (Zhang et al., 2011; Qian et al., 2016). At the same time, UU can lead to the formation of multinucleated giant cells and sperm cell nucleus, seminal convoluted tubule atrophy, interstitial edema and exudation and other pathological changes, leading to oligospermia, azoospermia, and affecting sperm maturation. Meanwhile, UU infection can severely damage the morphology and function of sperm, and also make the acrosome membrane

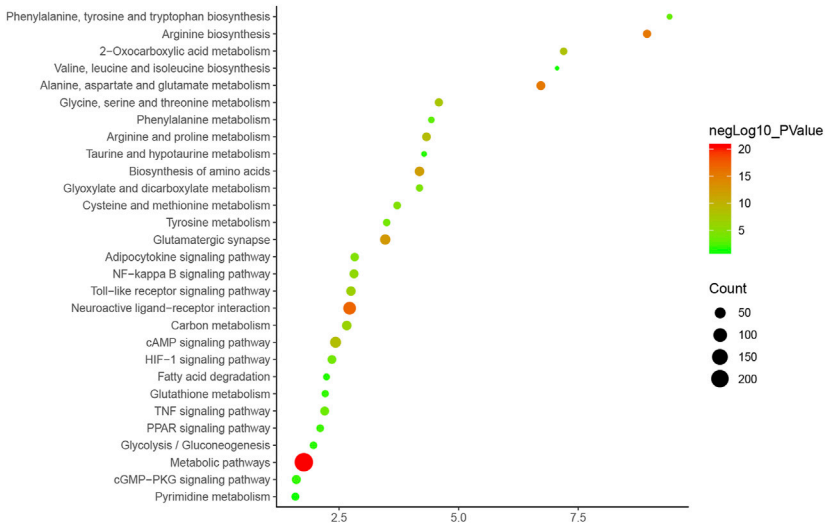

FIGURE 8 | Bubble chart of signaling pathway (X-axis stand for fold enrichment).

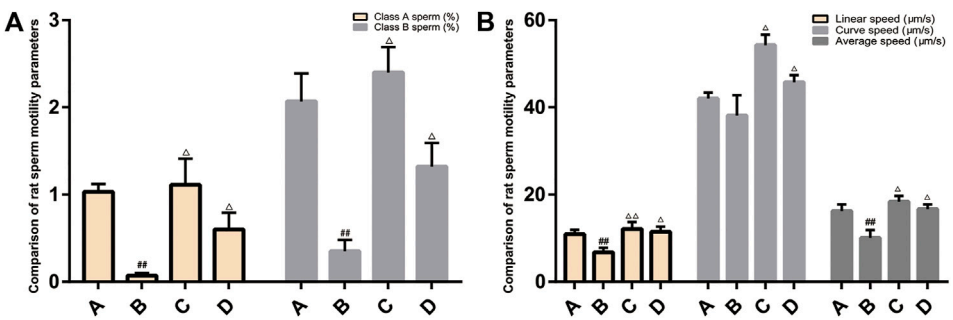

FIGURE 9 | Comparison of rat sperm quality and sperm motility parameters. **(A)**: normal group; **(B)**: model group; **(C)**:ZBDHD group; D:positive control group. Compared with normal group ##$p < 0.01$; compared with model group △$p < 0.05$, △△$p < 0.01$).

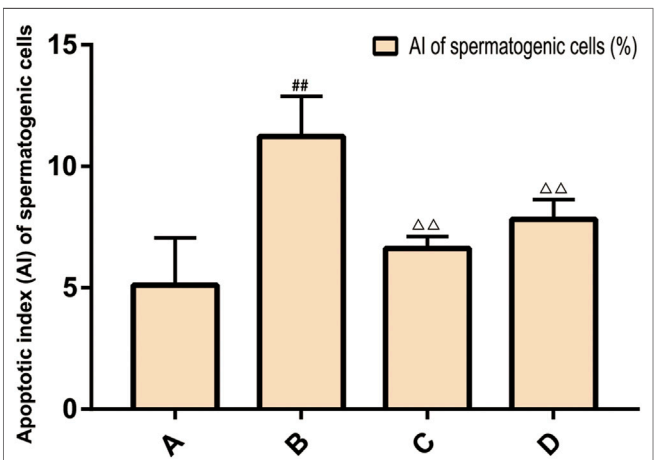

FIGURE 10 | The AI of spermatogenic cells. **(A)**: normal group; **(B)**: model group; **(C)**: ZBDHD group; **(D)**:positive control group. Compared with normal group ##$p < 0.01$; compared with model group, △△$p < 0.01$).

and the plasma membrane unable to fuse normally, the acrosome and the nuclear membrane are separated, the double-layer structure is partially interrupted, and the structure of part of the sperm head is damaged, which increases the rate of sperm deformity (Yang et al., 2018). UU infection has an impact on sperm density, sperm motility and forward motility, which can lead to a decrease in semen quality (Zhou et al., 2018).

Mitochondria regulate the energy production and apoptosis of eukaryotic cells, and provide energy for sperm movement. Normal mitochondrial structure is the basis for spermatogenic cells to exert their respiratory function to produce energy, which is directly related to the motility of sperm (du Plessis et al., 2015). UU infection can affect the structure and function of sperm mitochondria in many ways. UU enzymes and toxins can damage the sperm mitochondrial membrane, thereby affecting the production of sperm motility energy (Burrello et al., 2009). UU infection reduces the mitochondrial membrane potential (MMP) of sperm cells and hinders mitochondrial function (La

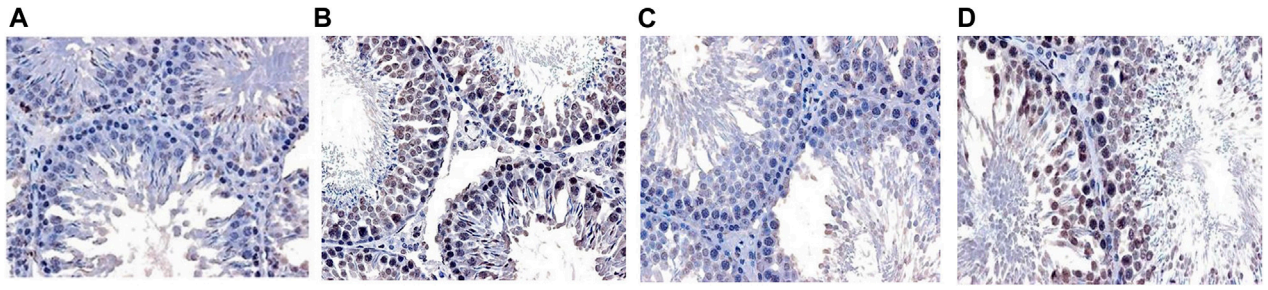

FIGURE 11 | The Apoptosis of rat spermatogenic cells [TUNEL × 400. **(A)**: normal group; **(B)**: model group; **(C)**: ZBDHD group; **(D)**: positive control group].

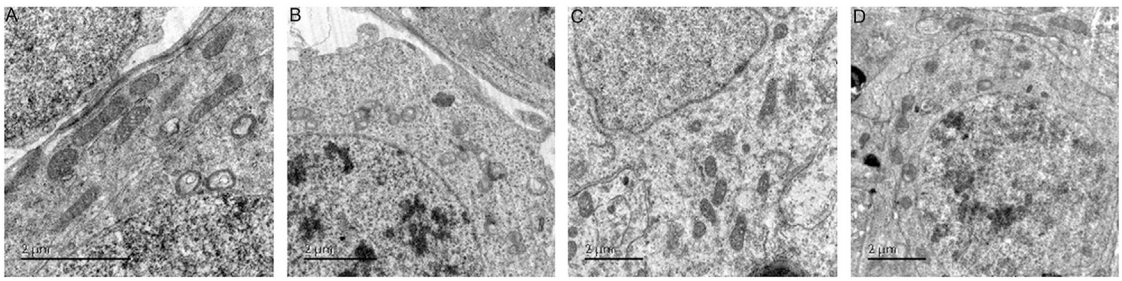

FIGURE 12 | The ultrastructure of rat spermatogenic cell mitochondria [× 12,000 **(A)**: normal group; **(B)**: model group; **(C)**: ZBDHD group; **(D)**: positive control group].

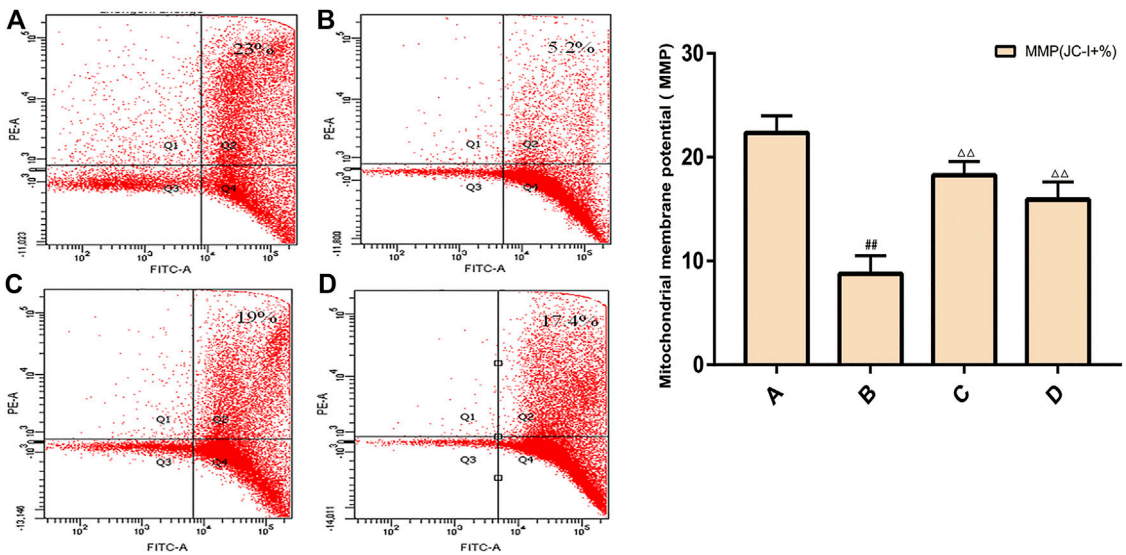

FIGURE 13 | Rat spermatogenic cell MMP. **(A)**: normal group; **(B)**: model group; **(C)**: ZBDHD group; **(D)**: positive control group. Compared with normal group ##p < 0.01; compared with model group, △△p < 0.01.

Vignera et al., 2012). When the MMP of sperm cells decreases, the arrangement of mitochondria in the sperm tail will be disordered, the mitochondrial sheath will be missing, and the mitochondrial morphology and position will also be abnormal (La Vignera et al., 2012). UU infection will increase the content of reduced coenzyme oxidase that transfers single electrons in the

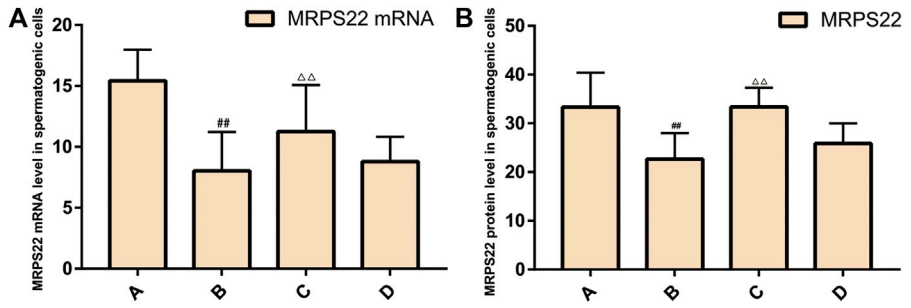

FIGURE 14 | Expression of MRPS22 mRNA and proteins. **(A)**: MRPS22 mRNA; **(B)**: MRPS22 protein. A: normal group; B: model group; C: ZBDHD group; D: positive control group. Compared with normal group ##$p < 0.01$; compared with model group, △△$p < 0.01$.

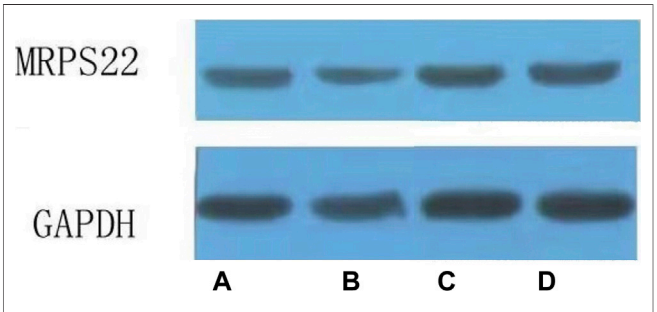

FIGURE 15 | Expression of MRPS22 proteins. **(A)**: normal group; **(B)**: model group; **(C)**: ZBDHD group; **(D)**: positive control group.

reproductive system, and produce a series of reactive oxygen specie (ROS). ROS can promote the lipid peroxidation of unsaturated fatty acids on the inner and outer membranes of sperm mitochondria, resulting in sparse lipid arrangement of the membrane, reduced inner membrane ridges, and reduced ATP synthesis. MMP is negatively correlated with ROS content, so excessive production of reactive oxygen species in sperm is one of the important reasons for the decline of mitochondrial membrane potential (MMP). Sperm mitochondrial membrane may be damaged by reactive oxygen and insufficient energy supply and decreased vitality (La Vignera et al., 2012; Sellami et al., 2014). Mitochondrial energy synthesis will be affected by abnormal mitochondrial structure, so sperm motility and fertilization ability decrease (Agarwal and Said, 2005). MMP reflects the tricarboxylic acid cycle that generates energy in the mitochondria. Its decrease means that the mitochondrial energy supply is impaired, and it is a sensitive indicator for evaluating mitochondrial function. Studies have shown that there is a positive correlation between MMP and sperm viability, motility and sperm fertilization rate (Brahem et al., 2012). According to classical theory, the mitochondrial sheath in the middle of the sperm, synthesized by oxidative phosphorylation, is the source of energy required by the flagella of the sperm tail during sperm movement (Gong et al., 2017).

The permeability and fluidity of mitochondrial membrane are the guarantee for maintaining the structure and function of mitochondria. Abnormal mitochondrial permeability transition (MPT) can cause mitochondrial dysfunction. MPT is achieved through two mechanisms: the opening of the mPTP and the activation of Bax and Bak proteins to increase the permeability of the mitochondrial outer membrane (Baines et al., 2007). The abnormal opening of mPTP would cause the decrease of mitochondrial membrane potential, cell energy metabolism level and cell activity (Shen et al., 2014). mPTP is a transmembrane multi-protein complex pore, mainly composed of adenine nucleotide translocase (ANT) in the inner membrane, voltage-dependent anion channel (VDAC)

TABLE 2 | Precision and accuracy (n = 6).

Standard	Concentration (mg/l)	Within-day			Inter-day		
		Measured value (mg/l)	RSD (%)	Accuracy (%)	Measured value (mg/l)	RSD (%)	Accuracy (%)
ATP	20	19.70	1.16	98.50	19.55	2.66	97.75
	50	49.25	1.36	98.50	49.20	1.86	98.40
	100	99.45	0.97	99.45	99.00	1.48	99.00
ADP	20	19.77	2.14	98.83	19.73	2.02	98.67
	50	49.52	1.29	99.03	49.37	2.06	98.73
	100	98.95	1.42	98.95	98.55	1.27	98.55
AMP	20	19.43	2.53	97.17	19.68	1.99	98.42
	50	49.22	2.03	98.43	48.78	2.06	97.57
	100	99.18	1.09	99.18	98.03	1.82	98.03

TABLE 3 | Stability experiment and repeatability experiment RSD (%) (n = 5).

Standard	Stability	Repeatability
ATP	3 .60	2 .80
ADP	3 .49	1 .38
AMP	3 .36	2 .24

in the outer membrane, cyclosporin A receptor D (cyclophilin-D, CyP-D) in the mitochondrial matrix (Lam et al., 2015). mPTP is normally closed to maintain the integrity of the mitochondrial structure, which is a necessary condition for mitochondria to undergo oxidative stress, ATP synthesis, and achieve their physiological functions (Lam et al., 2015). The synthesis of ATP and the electron transfer in the respiratory chain are carried out in the mitochondria. ATP and ADP are effectively exchanged and transported between the mitochondria and the cytoplasm, so that the cell respiration and the coupling of the respiratory chain are maintained normal (Halestrap and Brenner, 2003). The transport of ATP and ADP depends on the ANT/VDAC transporter complex formed by the adenine nucleotide carrier ANT and VDAC. The former is located in the inner mitochondrial membrane and the latter is located in the outer mitochondrial membrane (Halestrap and Brenner, 2003; Veenman et al., 2007). As a transmembrane protein with abundant content in the outer mitochondrial membrane, VDAC is involved in many physiological and pathological mechanisms, including energy metabolism and cell apoptosis (Vyssokikh and Brdiczka, 2003). In a certain pathological state, the continuous opening of the mitochondrial outer membrane VDAC reduces the mitochondrial inner membrane potential, that is, energy production decreases, respiratory function decreases, cytochrome C leaks, cell energy metabolism level decreases, and cell activity decreases. The excessive opening of mPTP leads to a decrease in the ratio of ATP/ADP, mitochondrial respiratory function is inhibited, the H^+ gradient inside and outside the mitochondria disappears, the respiratory chain is uncoupled, and energy production is interrupted (Neginskaya et al., 2019). When the stimulation was mild, the number of irreversible openings of mPTP was small or it is temporarily opened and then closed again, and the intracellular ATP concentration did not decrease significantly, and apoptosis can only be induced by releasing CytC.

Our research shows that ZBDHD can improve sperm motility. After successful UU infection modeling, the proportion of sperm cells in the model group with decreased MMP was higher. After ZBDHD treatment, the proportion of sperm cells with decreased MMP in each group decreased. After successful UU infection modeling, the sperm ROS level of the model group was higher, which was significantly different from the normal group. After treatment with ZBDHD, the sperm ROS level of rats in each group decreased, which proved that ZBDHD can reduce the sperm ROS level of UU infection model rats and reduce the sperm ROS production of UU infection model rats. After successful modeling of UU infection, the content of CytC in sperm of the model group was higher, indicating that UU infection can increase sperm apoptosis and cause the release of CytC. After ZBDHD treatment, the content of CytC in sperm of rats decreased, suggesting that ZBDHD can inhibit sperm apoptosis and reduce the release of CytC from mitochondria in UU infection model rats.

In summary, the results of this study indicate that UU infection can lead to increased sperm MMP reduction ratio, ROS level and CytC content increase, and ZBDHD can reduce the production of sperm ROS, reduce the pathological damage of ROS to sperm membrane and function, and improve sperm MMP. This increases the energy synthesis of sperm mitochondria, reduces sperm apoptosis, and inhibits the release of CytC, so as to achieve the goal of anti-oxidation to increase sperm density, viability and vitality. This may be one of the mechanisms of ZBDHD in the treatment of male infertility caused by UU infection.

CONCLUSION

This study discovered the multi-pathway mechanism of ZBDHD intervention in UU-induced orchitis through integrated pharmacological strategies, which provides a reference for further research on the mechanism of ZBDHD intervention in orchitis in the direction of mitochondrial energy metabolism. At the same time, it provides new research ideas for the research of classic famous TCM prescriptions.

TABLE 4 | Recovery rate experiment results (n = 2).

Analyte	Original amount (ug)	Adding amount (ug)	Measured amount (ug)	Recovery rate (%)	RSD (%)
ATP	71.42	20	89.89	98.33	2.38
		40	1 1 0.16	98.86	2.41
ADP	60.30	80	1 50.12	99.14	0.24
		20	80.99	100.85	1.96
		40	98.28	97.98	2.31
AMP	53.84	80	142.19	101.35	1.95
		20	73.96	100.16	1.54
		40	92.78	98.87	1.68
		80	1 33.06	99.41	3.09

DATA AVAILABILITY STATEMENT

The original contributions presented in the study are included in the article/**Supplementary Material**, further inquiries can be directed to the corresponding authors.

ETHICS STATEMENT

The animal study was reviewed and approved by the Institutional Animal Ethics Committee of Hunan University of Chinese Medicine.

AUTHOR CONTRIBUTIONS

D-hB, S-yZ, MZ, QZ, and Q-hH are responsible for concept and design. D-hB, S-yZ, MZ, LL, Y-qL, XZ, F-gL, QZ, and Q-hH are responsible for data analysis and interpretation. D-hB, S-yZ, and MZ drafted the paper; QZ and Q-hH supervised the study; all authors participated in the analysis and interpretation of data and approved the final paper.

FUNDING

The National Natural Science Foundation of China (No. 81973863, No. 81603634 and No. 81774324), Science Research Program of Hunan Education Department (19B418), Scientific research project of Hunan Health Committee (20200745).

SUPPLEMENTARY MATERIAL

The Supplementary Material for this article can be found online at: https://www.frontiersin.org/articles/10.3389/fphar.2021.602543/full#supplementary-material

REFERENCES

Agarwal, A., and Said, T. M. (2005). Oxidative stress, DNA damage and apoptosis in male infertility: a clinical approach. *BJU Int.* 95 (4), 503–507. doi:10.1111/j.1464-410X.2005.05328.x

Bader, G. D., and Hogue, C. W. (2003). An automated method for finding molecular complexes in large protein interaction networks. *BMC Bioinformatics* 4, 2. doi:10.1186/1471-2105-4-2

Baines, C. P., Kaiser, R. A., Sheiko, T., Craigen, W. J., and Molkentin, J. D. (2007). Voltage-dependent anion channels are dispensable for mitochondrial-dependent cell death. *Nat. Cell Biol* 9 (5), 550–555. doi:10.1038/ncb1575

Bin, D. H., Han, Z., and He Qing, H. (2016). The application of Zhibai Dihuang Wan in male infertility. *Chin. Sex. Sci.* 25 (12), 84–87. doi:10.3969/j.issn.1672-1993.2016.12.028

Brahem, S., Jellad, S., Ibala, S., Saad, A., and Mehdi, M. (2012). DNA fragmentation status in patients with necrozoospermia. *Syst. Biol. Reprod. Med.* 58 (6), 319. doi:10.3109/19396368.2012.710869

Burrello, N., Salmeri, M., Perdichizzi, A., Bellanca, S., Pettinato, G., D'Agata, R., et al. (2009). *Candida* albicans experimental infection: effects on human sperm motility, mitochondrial membrane potential and apoptosis. *Reprod. BioMedicine Online* 18 (4), 496–501. doi:10.1016/s1472-6483(10)60125-3

du Plessis, S., Agarwal, A., Mohanty, G., and van der Linde, M. (2015). Oxidative phosphorylation versus glycolysis: what fuel do spermatozoa use? *Asian J. Androl.* 17 (2), 230–235. doi:10.4103/1008-682X.135123

Gao, G. Y., Bai, Y. Y., and Kang, Y. X. J. (2020). Research progress in clinical application of Zhibai Dihuang decoction. *New Chin. Med.* 52 (09), 30–32. doi:10.13457/j.cnki.jncm.2020.09.008

Gdoura, R., Kchaou, W., Chaari, C., Znazen, A., Keskes, L., Rebai, T., et al. (2007). Ureaplasma urealyticum, Ureaplasma parvum, Mycoplasma hominis and Mycoplasma genitalium infections and semen quality of infertile men. *BMC Infect. Dis.* 7, 129. doi:10.1186/1471-2334-7-129

Gong, Y., Guo, H., Zhang, Z., Zhou, H., Zhao, R., and He, B. (2017). Heat stress reduces sperm motility via activation of glycogen synthase kinase-3α and inhibition of mitochondrial protein import. *Front. Physiol.* 8, 718. doi:10.3389/fphys.2017.00718

Guo, J., Li, Y., and Guo, X. (2017). The effect of Zhibai Dihuang Decoction on mitochondrial cytochrome oxidase in spermatogenic cells of rats infected with Ureaplasma urealyticum. *Chin. J. Androl.* 23 (8), 722–727.

Halestrap, A., and Brenner, C. (2003). The adenine nucleotide translocase: a central component of the mitochondrial permeability transition pore and key player in cell death. *Curr. Med. Chem.* 10 (16), 1507–1525. doi:10.2174/0929867033457278

Hamosh, A., Scott, A. F., Amberger, J. S., Bocchini, C. A., McKusick, V. A., and McKusick, V. A. (2005). Online Mendelian Inheritance in Man (OMIM), a knowledgebase of human genes and genetic disorders. *Nucleic Acids Res.* 33, D514–D517. doi:10.1093/nar/gki033

He, M., Xie, Y., Zhang, R., Gao, S., Xu, G., Zhang, L., et al. (2016). Prevalence and antimicrobial resistance of Mycoplasmas and Chlamydiae in patients with genital tract infections in Shanghai, China. *J. Infect. Chemother.* 22 (8), 548–552. doi:10.1016/j.jiac.2016.05.007

Huang, C., Long, X., Jing, S., Fan, L., Xu, K., Wang, S., et al. (2016). Ureaplasma urealyticum and Mycoplasma hominis infections and semen quality in 19,098 infertile men in China. *World J. Urol.* 34 (7), 1039–1044. doi:10.1007/s00345-015-1724-z

Huang, C., Zhu, H. L., Xu, K. R., Wang, S. Y., Fan, L. Q., and Zhu, W. B. (2015). Mycoplasma and ureaplasma infection and male infertility: a systematic review and meta-analysis. *Andrology* 3 (5), 809–816. doi:10.1111/andr.12078

Huang, D. W., Sherman, B. T., and Lempicki, R. A. (2009). Systematic and integrative analysis of large gene lists using DAVID bioinformatics resources. *Nat. Protoc.* 4, 44–57. doi:10.1038/nprot.2008.211

Kokkayil, P., and Dhawan, B. (2015). Ureaplasma: current perspectives. *Indian J. Med. Microbiol.* 33 (2), 205–214. doi:10.4103/0255-0857.154850

La Vignera, S., Condorelli, R., D'Agata, R., Vicari, E., and Calogero, A. E. (2012). Semen alterations and flow-citometry evaluation in patients with male accessory gland infections. *J. Endocrinol. Invest.* 35 (2), 219–223. doi:10.3275/7924

Lam, C. K., Zhao, W., Liu, G.-S., Cai, W.-F., Gardner, G., Adly, G., et al. (2015). HAX-1 regulates cyclophilin-D levels and mitochondria permeability transition pore in the heart. *Proc. Natl. Acad. Sci. U.S.A.* 112 (47), E6466–E6475. doi:10.1073/pnas.1508760112

Lee, J. S., Kim, K. T., Lee, H. S., Yang, K. M., Seo, J. T., and Choe, J. H. (2013). Concordance of ureaplasma urealyticum and mycoplasma hominis in infertile couples: impact on semen parameters. *Urology* 81 (6), 1219–1224. doi:10.1016/j.urology.2013.02.044

Li, Z., He, Q., Donghua, B., Zhou, Q., Zhou, Xing., Ling, Li., et al. (2019). Clinical observation of Zhibai Dihuang pills in treating kidney yin deficiency type semen non-liquefaction. *J. Hunan Univ. Tradit. Chin. Med.* 39 (01), 73–76.

Liu, C.-M., Chen, J., Yang, S., Jiang, T.-T., Chen, Z.-L., Tu, H.-H., et al. (2018a). iTRAQ-based proteomic analysis to identify the molecular mechanism of Zhibai Dihuang Granule in the Yin-deficiency-heat syndrome rats. *Chin. Med.* 13, 2. doi:10.1186/s13020-017-0160-y

Liu, C.-M., Chen, J., Yang, S., Mao, L.-G., Jiang, T.-T., Tu, H.-H., et al. (2018b). The Chinese herbal formula Zhibai Dihuang Granule treat Yin-deficiency-heat syndrome rats by regulating the immune responses. *J. Ethnopharmacology* 225, 271–278. doi:10.1016/j.jep.2018.05.001

Manochantr, S., Chiamchanya, C., and Sobhon, P. (2012). Relationship between chromatin condensation, DNA integrity and quality of ejaculated spermatozoa from infertile men. *Andrologia* 44 (3), 187–199. doi:10.1111/j.1439-0272.2010.01128.x

Moridi, K., Hemmaty, M., Azimian, A., Fallah, M. H., Khaneghahi Abyaneh, H., and Ghazvini, K. (2020). Epidemiology of genital infections caused by Mycoplasma hominis, M. genitalium and Ureaplasma urealyticum in Iran; a systematic review and meta-analysis study (2000-2019). *BMC Public Health* 20 (1), 1020. doi:10.1186/s12889-020-08962-5

Neginskaya, M. A., Solesio, M. E., Berezhnaya, E. V., Amodeo, G. F., Mnatsakanyan, N., Jonas, E. A., et al. (2019). ATP synthase C-Subunit-Deficient mitochondria have a small cyclosporine A-sensitive channel, but lack the permeability transition pore. *Cell Rep.* 26 (1), 11–17. doi:10.1016/j.celrep.2018.12.033

Qian, L., Bian, G.-R., Li, H.-B., Zhou, Y., Dong, S.-D., Wang, W.-J., et al. (2016). Effects ofUreaplasma urealyticumInfection on sperm quality and concentrations of nitric oxide and cytokine in the semen of infertile males. *Am. J. Reprod. Immunol.* 75 (6), 605–608. doi:10.1111/aji.12500

Sellami, H., Znazen, A., Sellami, A., Mnif, H., Louati, N., Zarrouk, S. B., et al. (2014). Molecular detection of *Chlamydia trachomatis* and other sexually transmitted bacteria in semen of male partners of infertile couples in Tunisia: the effect on semen parameters and spermatozoa apoptosis markers. *PLoS One* 9 (7), e98903. doi:10.1371/journal.pone.0098903

Shen, J., Du, T., Wang, X., Duan, C., Gao, G., Zhang, J., et al. (2014). α-Synuclein amino terminus regulates mitochondrial membrane permeability. *Brain Res.* 1591, 14–26. doi:10.1016/j.brainres.2014.09.046

Sheng, W., and He, Q. (2019). Discussion on the treatment of Ureaplasma urealyticum infectious infertility based on "yin-ping-yang secret". *Chin. J. Inf. Tradit. Chin. Med.* 26 (3), 128–129. doi:10.3969/j.issn.1005-5304.2019.03.029

Stelzer, G., Rosen, R., Plaschkes, I., Zimmerman, S., Twik, M., Fishilevich, S., et al. (2016). The GeneCards suite: from gene data mining to disease genome sequence analysis. *Curr. Protoc. Bioinformatics* 54, 1301–1303. doi:10.1002/cpbi.5

Szklarczyk, D., Franceschini, A., Wyder, S., Forslund, K., Heller, D., Huerta-Cepas, J., et al. (2015). STRING v10: protein-protein interaction networks, integrated over the tree of life. *Nucleic Acids Res.* 43, D447–D452. doi:10.1093/nar/gku1003

Veenman, L., Papadopoulos, V., and Gavish, M. (2007). Channel-like functions of the 18-kDa translocator protein (TSPO): regulation of apoptosis and steroidogenesis as part of the host-defense response. *Curr. Pharm. Des.* 13 (23), 2385–2405. doi:10.2174/138161207781368710

Vyssokikh, M. Y., and Brdiczka, D. (2003). The function of complexes between the outer mitochondrial membrane pore (VDAC) and the adenine nucleotide translocase in regulation of energy metabolism and apoptosis. *Acta Biochim. Pol.* 50 (2), 389–404. doi:10.18388/abp.2003_3693

Wang, L. W. (2017). *Co-word cluster analysis of research on acupuncture and moxibustion intervention in male infertility[D]*. Guangzhou: Guangzhou University of Chinese Medicine.

Wu, P. P., Ye, L., Shao, Y. J., Lai, Y. H., Ji, J. J., Ding, B., et al. (2020). Study on the mechanism of Zhibai Dihuang Decoction in the treatment of Yin deficiency and fire prosperous syndrome by regulating the ARE signaling pathway to activate cellular antioxidant response. *J. Zhejiang Univ. Traditional Chin. Med.* 44 (04), 316–323. doi:10.16466/j.issn1005-5509.2020.04.002

Wu, T., Lu, M., Hu, Y., Guo, Q., and Xu, C. (2004). [Influence of Ureaplasma urealyticum infection on the sperm-egg binding associated molecule, sulfogalactosylglycerolipid]. *Zhonghua Nan Ke Xue* 10 (9), 651–654. doi:10.13263/j.cnki.nja.2004.09.002

Xu, C., Sun, G. F., Zhu, Y. F., and Wang, Y. F. (1997). The correlation of ureaplasma urealyticum infection with infertility. *Andrologia* 29 (4), 219–226. doi:10.1111/j.1439-0272.1997.tb00319.x

Xu, H.-Y., Zhang, Y.-Q., Liu, Z.-M., Chen, T., Lv, C.-Y., Tang, S.-H., et al. (2018). ETCM: an encyclopaedia of traditional Chinese medicine. *Nucleic Acids Res.* 47, D976. doi:10.1093/nar/gky987

Yang, K., Zeng, L., Ge, A., Bao, T., Xu, T., Xie, X., et al. (2020). Exploring the regulation mechanism of xihuang pill, olibanum and β-boswellic acid on the biomolecular network of triple-negative breast cancer based on transcriptomics and chemical informatics methodology. *Front. Pharmacol.* 11, 825. doi:10.3389/fphar.2020.00825

Yang, T., Zou, Y., Zhou, W., Ruan, Z., Kong, Y., Zhou, Y., et al. (2018). Clonal diversity of Ureaplasma species and its relationship with oligozoospermia and semen quality in Chinese infertile males. *Eur. J. Clin. Microbiol. Infect. Dis.* 37 (10), 1957–1963. doi:10.1007/s10096-018-3331-6

Zeng, L., and Yang, K. (2017). Exploring the pharmacological mechanism of yanghe decoction on HER2-positive breast cancer by a network pharmacology approach. *J. Ethnopharmacology* 199, 68. doi:10.1016/j.jep.2017.01.045

Zeng, L., Yang, K., Liu, L., Zhang, T., Liu, H., Tan, Z., et al. (2020). Systematic biological and proteomics strategies to explore the regulation mechanism of Shoutai Wan on recurrent spontaneous Abortion's biological network. *J. Ethnopharmacol.* 263, 113156. doi:10.1016/j.jep.2020.113156

Zhang, S. Y., Li, L., Zhang, N., Xia, H. T., Lu, F. G., and Li, W. Q. (2020a). Systematic pharmacological strategies to explore the regulatory mechanism of ma xing Shi Gan decoction on COVID-19. *Digital Chin. Med.* 3 (02), 96–115. doi:10.1016/j.dcmed.2020.06.004

Zhang, S.-y., Yang, K.-l., Long, Z.-y., Li, W.-q., and Huang, H.-y. (2020b). Use of a systematic pharmacological methodology to explore the mechanism of shengmai powder in treating diabetic cardiomyopathy. *Med. Sci. Monit.* 26, e919029. doi:10.12659/MSM.919029

Zhang, Z.-H., Zhang, H.-G., Dong, Y., Han, R.-R., Dai, R.-L., and Liu, R.-Z. (2011). Ureaplasma urealyticum in male infertility in jilin province, north-east China, and its relationship with sperm morphology. *J. Int. Med. Res.* 39 (1), 33–40. doi:10.1177/147323001103900104

Zhou, Y. H., Ma, H. X., Shi, X. X., and Liu, Y. (2018). Ureaplasma spp. in male infertility and its relationship with semen quality and seminal plasma components. *J. Microbiol. Immunol. Infect.* 51 (6), 778–783. doi:10.1016/j.jmii.2016.09.004

Zhu, C., Liu, J., Ling, Y., Dong, C., Wu, T., Yu, X., et al. (2012). Prevalence and antimicrobial susceptibility of Ureaplasma urealyticum and Mycoplasma hominis in Chinese women with genital infectious diseases. *Indian J. Dermatol. Venereol. Leprol.* 78 (3), 406–407. doi:10.4103/0378-6323.95480

Conflict of Interest: The authors declare that the research was conducted in the absence of any commercial or financial relationships that could be construed as a potential conflict of interest.

Copyright © 2021 Bin, Zhang, Zhan, Li, Li, Zhou, Lu, Zhou and He. This is an open-access article distributed under the terms of the Creative Commons Attribution License (CC BY). The use, distribution or reproduction in other forums is permitted, provided the original author(s) and the copyright owner(s) are credited and that the original publication in this journal is cited, in accordance with accepted academic practice. No use, distribution or reproduction is permitted which does not comply with these terms.

frontiers in Pharmacology

SYSTEMATIC REVIEW
published: 21 May 2021
doi: 10.3389/fphar.2021.610745

Efficacy of Chinese Herbal Injections for Elderly Patients With pneumonia—A Bayesian Network Meta-analysis of Randomized Control Trials

Yang Yuan[1], Quan Zheng[2], Zhilin Si[2], Juhua Liu[2], Zhi Li[2], Lian Xiong[3], Pan Liu[1], Xu Li[2], Chengshi He[1] and Jinghong Liang[4]**

[1]Hospital of Chengdu University of Traditional Chinese Medicine, Chengdu, China, [2]The First People's Hospital of Suining City, Suining, China, [3]Chengdu Second People's Hospital, Chengdu, China, [4]Department of Maternal and Child Health, School of Public Health, Sun Yat-sen University, Guangzhou, China

OPEN ACCESS

Edited by:
Myeong Soo Lee, Korea Institute of Oriental Medicine (KIOM), South Korea

Reviewed by:
Bo Yang, Zhejiang University, China
Boram Lee, Korea Institute of Oriental Medicine (KIOM), South Korea

***Correspondence:**
Chengshi He
hcs6512@126.com
Jinghong Liang
liangjh78@mail2.sysu.edu.cn

Specialty section:
This article was submitted to Ethnopharmacology, a section of the journal Frontiers in Pharmacology

Received: *27 September 2020*
Accepted: *31 March 2021*
Published: *21 May 2021*

Citation:
Yuan Y, Zheng Q, Si Z, Liu J, Li Z, Xiong L, Liu P, Li X, He C and Liang J (2021) Efficacy of Chinese Herbal Injections for Elderly Patients With pneumonia—A Bayesian Network Meta-analysis of Randomized Control Trials. Front. Pharmacol. 12:610745. doi: 10.3389/fphar.2021.610745

Background: Pneumonia is a prevalent and complicated disease among adults, elderly people in particular, and the debate on the optimal Chinese herbal injections (CHIs) is ongoing. Our objective is to investigate the comparative effectiveness of various CHIs strategies for elderly patients with pneumonia.

Methods: A comprehensive search strategy was executed to identify relevant randomized controlled trials (RCTs) by browsing through several databases from their inception to first, Feb 2020; All of the direct and indirect evidence included was rated by Network meta-analysis under a Bayesian framework.

Results: We ultimately identified 34 eligible randomized controlled trials that involved 3,111 elderly participants and investigated 4 CHIs combined with Western medicine (WM) (Xiyanping injection [XYP]+WM, Yanhuning injection [YHN]+WM, Tanreqing injection [TRQ]+WM, Reduning injection [RDN]+WM), contributing 34 direct comparisons between CHIs. Seen from the outcome of Clinical effective rate and time for defervescence, patients taking medicine added with CHIs [Clinical effective rate, XYP + WM(Odd ratio (OR): 0.74, 95%Credible intervals (CrIs):0.55–0.98), YHN + WM(OR: 0.66, 95%CrI: 0.45–0.95), TRQ + WM(OR: 0.65, 95%CrI: 0.50–0.83), RDN + WM(OR: 0.60, 95%CrI: 0.40–0.89); Time for defervescence, YHN + WM(Mean difference (MD): −2.11, 95%CrI: −3.26 to −0.98), XYP + WM(MD: −2.06, 95%CrI: −3.08 to −1.09), RDN + WM(MD: −1.97, 95%CrI: −3.61 to −0.35), TRQ + WM(MD: −1.69, 95%CrI: −2.27 to −1.04)] showed statistically better effect compared with participants in the Control group (CG) who only took WM. Meanwhile, based on the time for disappearance of cough, 3 out of 4 CHIs [TRQ + WM(MD: −2.56, 95%CrI: −3.38 to −1.54), YHN + WM(MD: −2.36, 95% CrI: −3.86 to −1.00) and XYP + WM(MD: −2.21, 95%CrI: −3.72 to −1.10)] strategies indicated improvement of clinical symptoms. Only XYP + WM(MD −1.78, 95%CrI: −3.29 to −0.27) and TRQ + WM (MD: −1.71, 95%CrI: −2.71 to −0.73) could significantly shorten the time for disappearance of pulmonary rales.

Conclusion: According to the statistical effect size (The surface under the cumulative ranking), we found that XYP + WM was presumably to be the preferable treatment for treating elderly patients with pneumonia compared with WM alone in terms of clinical effective rate. Our findings were based on very limited evidence and thus should be interpreted with caution. The application of the findings requires further research.

Keywords: elderly people, pneumonia, tradional medicine, chinese herbal injections, bayesian network meta-analysis

Background

Pneumonia, a common disease with detrimental effect among adults worldwide, particularly elderly people, is posing substantial healthcare costs, and social burdens globally (GBD Diarrheal Diseases Collaborators, 2017). Study indicated that the number of old people aged over 80 hit the highest hospital admission rate record (16.4 cases/1,000 persons per year) for Community Acquired Pneumonia (CAP), a figure higher than that for common adults whose rate was 2.5 cases/1,000 people per year (Jain et al., 2015). To make matters worse, the global outbreak of coronavirus disease 2019, a relevant pneumonia, namely Severe Acute Respiratory Syndrome Coronavirus 2, is rapidly evolving and expanding on a global scale (Ronco et al., 2020). The ever-increasing cases of pneumonia imposes much stress on intensive care management and urges a systematical method to help policy-makers and clinicians in making the optimal decisions among numerous available therapies (Mandell et al., 2007). To further complicate the situation, despite the extensive use of drugs to treat the pneumonia patients, such as antiseptics, statins, as well as antibiotics, a first-tier preferred treatment was of huge benefit to patients' health but it also brought about a great risk of drug resistance and various adverse drug reactions (ADRs) (Labeau et al., 2011; Zampieri et al., 2015). The number of people who were diagnosed with pneumonia was going upwards rather than downwards, which directly exacerbated both the financial and resources burden on healthcare system (GBD 2016 Causes of Death Collaborators, 2017).

In the past decade, owing to the unsatisfactory response to current treatments, a considerable amount of research have focused on Chinese herbal medicine (CHM) to address a series of clinical symptoms of pneumonia patients (Zhou et al., 2000). As a potent, selective and promising formulation, Chinese herbal injection (CHI) was obtained via extracting and purifying the effective and active herbs compounds. The CHIs have gained more popularity in China due to their instant effects, few side effects and remarkable tonic function, and their efficacy was supported by previous studies not only on respiratory system, but also on many other systems (Zhao et al., 2013; Li et al., 2016). However, up to now, evidence that proves the efficacy of CHIs treating pneumonia has remained scarce among older adults. There is no study comparing the efficacy of CHIs in elderly adults with pneumonia. The necessity to bridge this gap via Network meta-analysis (NMA) is as follows: CHI combined with Western medicine (WM) was considered as a comprehensive therapy that is relatively effective and safe for treating pneumonia. However, the conventional meta-analysis can merely group various CHIs into a comprehensive CHI and analyze them separately while NMA can evaluate each CHI individually and compare them simultaneously. Consequently, our study used Bayesian NMA method to ascertain exactly whether such CHIs are truly helpful in preventing pneumonia among elderly people and to rank the efficacy of them.

METHOD

Search Strategies

Based on the Pubmed, embase, Cochrane Central register of controlled trials, Wan Fang database, China National Knowledge Infrastructure database, Chinese Biomedical Literature database, Chinese Scientific Journal database, we adopted a comprehensive search strategy from their inception to first, Feb 2020 to identify the eligible randomized controlled trials (RCTs) which scrupulously evaluate the efficacy of CHIs among elderly people with pneumonias according to various proper diagnostic criteria.

Without any language restriction, the following Medical Subject Heading (MeSH) terms incorporating with keywords by using the framework of Boolean logical operators were adopted: "Pneumonias", "Pneumonitis", "Lung Inflammations", "Chinese herbal", "Chinese drugs", "Chinese plant extracts", "Traditional medicine", "Randomized controlled trials", additional text-terms as well. We additionally implemented a recursive manual-search to retrieve full-text studies from the bibliographies of obtained trails or the similar systematic reviews in order to check the potentially eligible studies we missed at first. Details of the search strategy was introduced in **Supplementary File S1**. At the same time, all the records were collected and processed in **Endnote X9** (Thompson ISI Research Soft, Philadelphia, PA) software.

Inclusion and Exclusion Criteria

We defined the satisfactory randomized controlled trials based on the predetermined selection rules that met the following PICOS criterion:

Population: Pneumonitis was diagnosed by any proper clinical criteria, such as "Guidelines for diagnosis and treatment of community acquired pneumonia (Chinese revision)" (Academy RBoCM, 2006). Aged over 60 years old, without sex, race or region restriction.

Intervention: Based on the basis of literature and a pre-search we conducted before, patients with pneumonitis treated by numerous CHIs were conceptualized in four main CHIs, namely, Tanreqing injection (TRQ), Xiyanping injection (XYP), Yanhuning injection (YHN) and Reduning injection

(RDN) (Ye, 2016; Xia, 2017; Yao, 2017; Zhou, 2017), while the other CHIs failed to report the sufficient available data for our analysis. We excluded the studies in which either different CHIs are combined or the definition of CHI is vague.

Comparison: CHIs or the control group alone. Placebo and most of them were WM.

Outcomes: Primary outcome: The clinical effective rate [CER, CER = (Total sample size of patients–total sample size of patients ineffective)/total sample size of patients * 100%]; Secondary outcomes: Clinical symptom disappearance time (cough disappearance, lung rale disappearance time).

Study design: We confined our study design to RCTs published without year and language restriction. Non-randomized controlled studies such as case-control studies, cohort studies, full-text but unpublished studies were all excluded.

Initially, two investigators respectively screened the collected studies by title and abstract. Duplications were removed primarily according to their titles and the first author's name. Through a full-text review, all the potentially relevant articles were further perused and assessed at length. Our study adheres to the Network Meta-analysis of the Preferred Reporting Items for Systematic Reviews and Meta Analyses (PRISMA-NMA) (See in **Supplementary File S2**) and the Cochrane Handbook for Systematic Reviews of Interventions (Higgins and Green, 2011; Hutton et al., 2015). All analyses were based on previous published studies and therefore no ethical approval and patients' consent were required.

Data Extraction and Quality Assessment

Following the Cochrane consumers and Communication Review Group's data extraction template, two investigators independently implemented a data extraction form to collect the relevant data of the included studies such as Essential publication information (name of first author, year of publication), characteristic of participants (Total sample size, baseline age), and quality of the RCT. Any conflict or discrepancy regarding screening reached consensus after discussion, or was judged by an expert as a third author.

The Cochrane Risk of Bias tool (ROB) was utilized to assess the quality of each trial, which divided ROB into seven items, and all trials were rated as low, unclear or high bias level (HGGS, 2011). For the selection bias, studies would be accepted as low risk of bias if they had described the details of sequence generation and approach of allocation concealment. Otherwise, the studies would be regarded as high risk of bias. We judged the items Performance and Detection Bias based on whether the study was blind or not to the participants, personnel and outcome assessors. For the attrition bias, we rated studies as high-risk whose data was insufficient for contributing to the analysis especially the primary outcome. For judging other biases, if the study had an imprecize study design, or reported an obvious inconsistency compared with the previous studies, they would be rated as high risk of bias. We assessed selective biases by detecting whether the included studies reported the raw data for analysis. All the 7 items were rated as "unclear risk" when the study did not mention the relevant items. We focused on the selection bias and attrition bias due to their specificity in the assessment of ROB. Any disagreement generated during the procession of assessment was resolved by team-discussion.

Statistical Analyses

Our study first carried out a conventional pairwise meta-analysis to analyze the direct evidence by synthesizing the available data from the included studies. I^2 statistics were set to judge the magnitude of heterogeneity with higher values indicating more heterogeneity (Higgins and Thompson, 2002). The sensitivity analysis was conducted to test if there was any heterogeneity existing and to explore its sources. A network geometry was constructed firstly to provide comparative evidence among treatments, with distinguishing treatments expressed by different nodes whose size corresponded to the sample of participants, and studies were connected by appropriate lines. Moreover, in order to assess whether other publication biases or small-study biases were generated in our study, we created comparison-adjusted funnel plots to detect whether the scatter distributed to the vertical axis is asymmetric in the funnel plot (*X*-axis is sample size, *Y*-axis is effect) (Seagroatt and Stratton, 1998). The above analyses were conducted by using STATA/SE version 15.0 (Stata, corp, College Station, TX).

The Transitivity Assumption was applied to the appraisal of the robustness and reliability of the NMA by comparing the clinical similarity (e.g., patients, sample size and origin) and the methodological characteristics (e.g., random method, outcome and bias) among the studies involved (Caldwell et al., 2005). For outcomes presented as the numerical variable and the categorical variable, we generated a pooled Mean difference (MD) (Hedge's *g*) and Odd ratio (OR) following 95% Credible intervals (CrIs) as a conservative estimate to summarize the treatment and effects respectively. Based on the maximum likelihood and Bayesian estimation, the approach of Markov-chain Monte Carlo with prior non-informative distributions were performed in our NMA (Salanti et al., 2008; Mavridis and Salanti, 2013). We set up three parallel chains running in our model simultaneously by means of Gibbs sampling and different initial values during the beginning period, through stimulation to obtain their target distributions (Valkenhoef and Kuiper, 2016). Each chain was put into 100,000 interactions and the first 20,000 were discarded to minimize the bias which may be produced at the initial stage. The Brooks-Gelman-Rubin diagnostic statistics were used to spot the convergence of model by checking the density plot and tract plot (Brooks and Gelman, 1998). The surface under the cumulative ranking (SUCRA), a concisely hierarchical curve, was produced to rank the possible efficacy of each treatment and it was found that higher SUCRA values denoted greater efficacy (Dias et al., 2012). Finally, the inconsistency of our NMA was examined by the split-node method and the *p*-value was obtained to indicate whether a

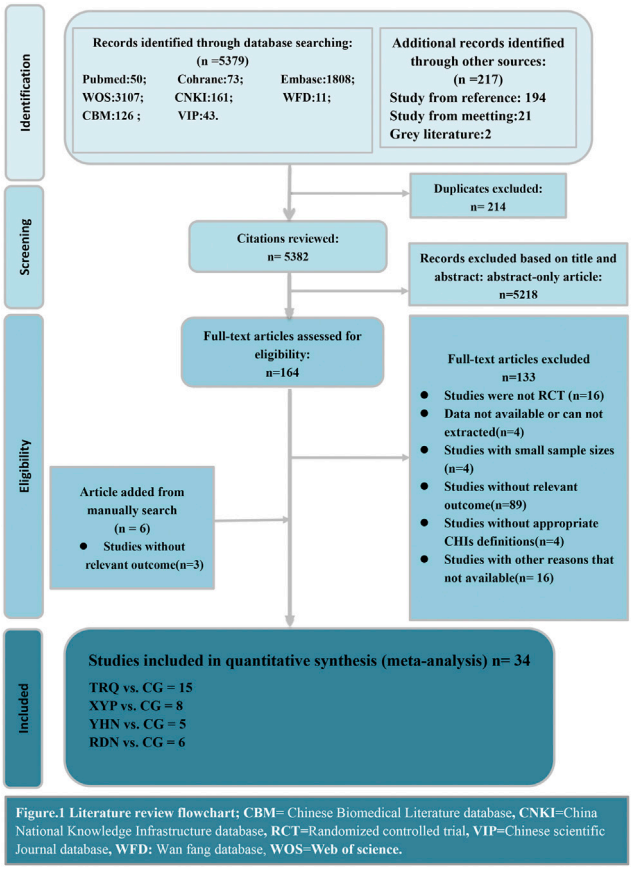

FIGURE 1 | Literature review flowchart. CBM, Chinese Biomedical Literature database; CNKI, China National Knowledge Infrastructure database; RCT, Randomized controlled trial; VIP, Chinese scientific Journal database; WFD, Wan fang database; WOS, Web of science.

significant inconsistency existed (Valkenhoef et al., 2016). All Bayesian analyses were done in R Version 3.32 (X64) with package "Gemtc"and WinBUGS Version1.4.3 (MRC Biostatistics Unit, Cambridge, United Kingdom) (Coreteam, 2014), and details of code were shown in **Supplementary File S3**.

RESULTS

Study Selection

We obtained 5,596 records initially and reviewed 164 potentially relevant studies in full-text after screening the titles and abstracts. Overall, 214 nonduplicate citations were identified, and we retrieved 6 relevant articles by hand-search in case of omitting the eligible research we probably left out in the electronic database. 34 RCTs eventually met our pre-established criteria after a rigorous full-text review, which consisted of 4 CHIs treatments. The details of literature screen were depicted in **Figure 1**. All the investigators involved reached a unanimous approval for the selection and the assessment of the studies.

Study Characteristics and Risk of Bias Quality Assessment

Supplementary Table S1 revealed the detailed demographic characteristics of 34 included studies. All the 34 parallel randomized controlled trials took place in China from 2008 to 2019. In total, 682 participants were randomly assigned to TRQ + WM group, 425 to XYP + WM, 213 to YHN + WM and 247 to RDN + WM whereas 1,544 were categorized into the CG (All the CG were conducted with WM only). Our NMA comprised 1,030 males participants and 2081 female participants, all of whom were qualified in terms of age according to the definition offered by World Health Organization (WHO) (WHO, 2017) that elderly people are those aged at least 60, The mean of all participants ranged from 60 to 85. Most trials (22/34, 64.71%) recruited participants with CAP, but few of them (4/34, 11.76%) considering the patients with Hospital Acquired Pneumonia (HAP). The citations of the included studies are introduced in detail in **Supplementary File S4**.

The overwhelming majority of the trials rendered a low risk of bias in "Random sequence generation" and all trials reflected a low risk of bias in Incomplete Outcome Data with sufficient original data. Notably, two studies were judged to be high-risk bias of "selective reporting" because their data for our analysis were calculated by transforming the original data manually (Li, 2010; Zhou, 2019). Due to their less rigorous study design, three studies (Huang, 2014; Zhang, 2014; Tian, 2016) were rated as high-risk bias in "other bias" items, among which the first two (Zhang, 2014; Tian, 2016) had less precise definition on pneumonia with one (Tian, 2016) not further reporting the calculation procedures for its relevant outcomes, and the third (Huang, 2014) had a bad representativeness of cases compared with other included studies since it recruited all the participants with pneumonia for a long-term period from 2000 to 2013. The remaining two items ("Allocation Concealment", "Blinding of Participants and Personnel") were generally ranked as unclear-to-moderate risk of bias. Full details regarding risk of bias for each RCT were shown in **Supplementary Figure S1** and summarized in **Supplementary Figure S2**, respectively. Funnel plots throughout the included studies based on the four endpoints showed a relatively symmetric distribution (**Supplementary Figure S3**).

Network Meta-analysis

Figure 2 presented all the primary evidence between each CHI, and all the CHIs had at least one comparison with CG while all of CHIs lacked a closed loop between them. According to the network geometries of clinical effective rate, CG (1,544) obtained the largest sample size (SS) compared with other three CHIs whereas YHN + WM(213) got a relative lower SS throughout the entire network.

Primary Outcome

Clinical Effective Rate

In terms of the outcome of CER, all four CHIs had significant benefits to patients with pneumonia compared with CG. XYP + WM(OR:0.74, 95%CrI:0.55–0.98), YHN + WM(OR: 0.66, 95%

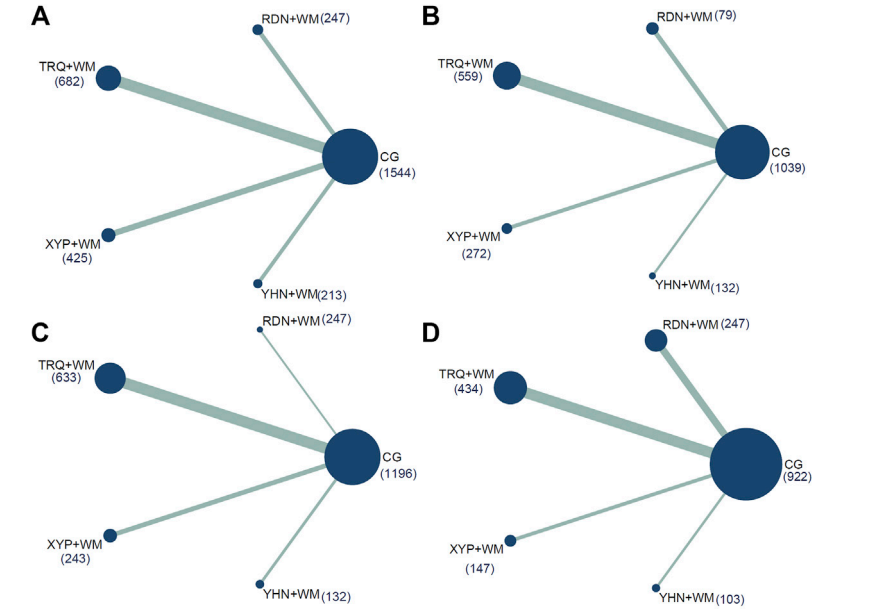

FIGURE 2 | Network plot of all the trials based on the outcomes. **(A)** Clinical effective rate; **(B)** time for defervescence; **(C)** disappearance time of cough; **(D)** disappearance time of pulmonary rales. CG, Control group; RDN, Reduning injection; TRQ, Tanreqing injection; XYP, Xiyanping injection; YHN, Yanhuning injection; WM, Western medicine. Each node represented a CHI and its size depended on the number of patients that is directly examined. The nodes were joined by different thickness lines which generated to show whether there existed a direct relationship between treatments and the thickness was weighted according to the available direct evidence between them.

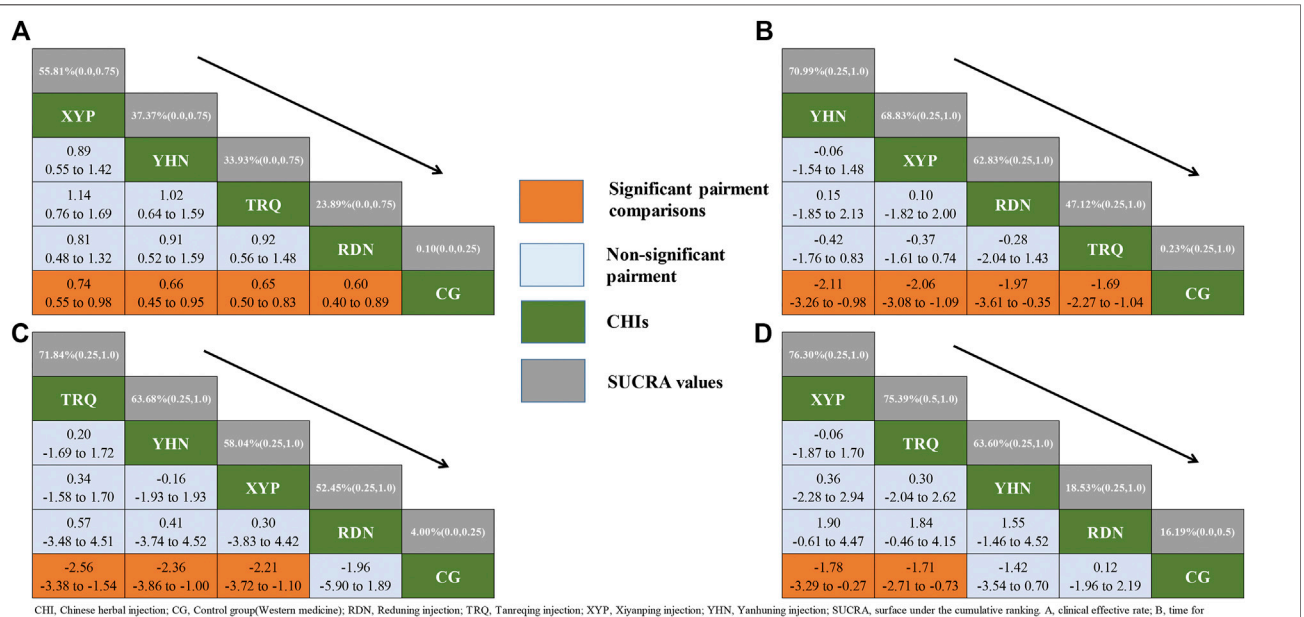

FIGURE 3 | Relative effect sizes of efficacy at post-treatment according to network meta-analysis. CHI, Chinese herbal injection; CG, Control group (Western medicine); RDN, Reduning injection; TRQ, Tanreqing injection; XYP, Xiyanping injection; YHN, Yanhuning injection; SUCRA, surface under the cumulative ranking. **(A)** Clinical effective rate; **(B)** time for defervescence; **(C)** disappearance time of cough; **(D)** disappearance time of pulmonary rales; Highest probability of being the most efficient CHI(With high SUCRA values) and Lowest probability of being the most efficient CHI(With low SUCRA values).

CrI: 0.45–0.95), TRQ + WM(OR: 0.65, 95%CrI: 0.50–0.83), RDN + WM(OR: 0.60, 95%CrI: 0.40–0.89) (See in **Supplementary Table S2**). However, no significant difference was observed in any comparison among CHIs(See in **Figure 3**). Based on the SUCRA values, XYP + WM(SUCRA = 55.81%) took the lead in the effect on pneumonia patients in terms of CER compared with other three CHIs, closely followed by two equally remarkable CHIs, namely, YHN + WM(SUCRA = 37.37%) and TRQ + WM(SUCRA = 33.93%) while RDN + WM(SUCRA = 23.89%) lagged behind (See in **Figure 3** and **Supplementary Figure S4**).

Secondary Outcomes

The Time for Clinical Symptoms to Disappear

With regarding to the time for defervescence, all CHIs, similar to the above outcome, produced a significant efficacy compared with CG. YHN + WM(MD: −2.11, 95%CrI: −3.26 to −0.98), XYP + WM(MD: −2.06, 95%CrI: −3.08 to −1.09), RDN + WM(MD: −1.97, 95%CrI: −3.61 to −0.35), TRQ + WM(MD: −1.69, 95%CrI: −2.27 to −1.04) (See in **Supplementary Table S2**).

For cough disappearance, only TRQ + WM(MD: −2.56, 95% CrI: −3.38 to −1.54), YHN + WM(MD: −2.36, 95%CrI: −3.86 to −1.00) and XYP + WM(MD: −2.21, 95%CrI: −3.72 to −1.10) were associated with a significant improvement among patients. However, the results didn't show statistical difference between RDN + WM (MD: −1.96, 95%CrI: −5.89 to 1.89) injection and other groups (See in **Supplementary Table S2**).

As for the time for disappearance of pulmonary rales, only XYP + WM(MD: −1.78, 95%CrI: −3.29 to −0.27) and TRQ + WM(MD: −1.71, 95%CrI: −2.71 to −0.73) had desirable performance in accelerating the disappearance of pulmonary rales (See in **Supplementary Table S2**).

Based on the SUCRA values, it seemed that among these CHIs injections, YHN + WM(SUCRA = 70.99%), TRQ + WM(SUCRA = 71.84%) and XYP + WM (SUCRA = 76.30%) became the optimal CHI compared to CG for the outcome of time for defervescence, cough disappearance and pulmonary rales disappearance, respectively. Conversely, TRQ + WM(SUCRA = 47.12%), RDN + WM(SUCRA = 52.45%) and RDN + WM(SUCRA = 18.53%) were most likely to be the least efficacious for defervescence, cough disappearance and pulmonary rales disappearance, respectively (See in **Figure 3** and **Supplementary Figure S4**). According to the four endpoints, forest plot was conducted in order to display the efficacy of each CHI for improving the clinical symptoms among patients (**Supplementary Table S2**). Relative effect sizes of treatments efficacy according to all outcomes were shown in **Figure 3**.

DISCUSSION

This NMA has adopted a consecutive Bayesian model which involves 34 parallel randomized controlled trials to appraise 4 CHIs with four outcomes by comparing their effect among elderly patients with pneumonia. Considering the primary outcome, XYP + WM seemed to be most promising CHI in helping the elderly with pneumonia to improve their clinical symptoms whereas YHN + WM and TRQ + WM are suboptimal and can be regarded as complementary therapies.

Pneumonia represents a progressive and prevalent clinical condition due to its relatively high morbidity and mortality, and high incidence was found among elderly adults due to their higher susceptibility (Thomas et al., 2012). As the first-line preferred therapy which is widely used for respiratory disease, antibiotic is a double-edged sword, because though improving the clinical symptom of patients, it, as the same time, causes some adverse effects (AEs) (Mandell et al., 2007). Due to the fault of current treatment and much attention being concentrated on the efficacy of CHIs, our study was attempted to achieve relatively objective evidence in the hope of seeking the optimal CHI among elderly people in order to offer an evidence-base mirror.

From the perspective of Traditional Chinese Medicine (TCM), pneumonia belongs to the category of asthma and cough, and its clinical symptoms such as cough, expectoration, fever and asthma should be treated; Other symptoms caused by exogenous pathogens invading the lung should be focused on the way of allaying fever and soothing the lung (Feng, 2014). Modern pharmacology shows that CHIs have multiple effects on antipyretic and analgesic, antiviral and antibacterial symptoms (Li et al., 2017), such as XYP injection. As a derivative of andrographolid with the characteristics of antipyretic and anti-inflammatory, it holds the most likelihood to be the optimal CHI injection among 4 CHIs, which enhances the immunity of the body. Moreover, XYP can improve the smooth muscle spasm, relax the smooth muscle, control the symptoms of cough and resolve phlegm by reducing the recreation of serous fluid (Zhang, 2011; L, 2017). TRQ classifies Chinese herbal into five categories: Scutellaria, Bear(bile) powder, Cornu gorais, honeysuckle and forsythia, with the efficacy of heat-clearing and detoxicating. It also has a positive effect on fever, cough and sore throat triggered by pulmonary disease (Huang, 2018). Patients with pneumonia would ameliorate their symptom by the usage of YHN injection or RDN injection, which was corroborated by numerous studies. But the two aforementioned CHIs got a relatively poor ranking in our study, possibly due to that they two mainly played a role in inhibiting respiratory viruses and blocking bacterial growth among patients with viral pneumonia rather than with the ability of anti-inflammatory, antipyretic and immunoregulatory effects among CAP patients (Gao et al., 2011; Nie, 2018). Although conclusions drawn by numerous studies showed consistency with our study that most such CHIs were preferable in the clinical treatment for patients with pneumonia when compared with CG (Sun, 2019; Wang, 2018). But there is no significant difference detected in any comparison between CHIs due to the absence of the indirect evidence among them. XYP + WM seem to be the most effective CHI for the outcome of clinical effective rate and the disappearance time of pulmonary rales while based on the results of time for defervescence and the disappearance time of cough that YHN + WM and TRQ + WM got the highest possibility become the most effective for improving these clinical symptoms, respectively. In spite of the evidence regarding the effectiveness of YHN + WM on reducing the fever is limited,

some relatively convincing evidence can account for it that YHN + WM is an effective extract of Andrographis paniculate which was recommended by Chinese medicine as one of the most effective herbal with the function of clearing away heat and toxic material (Tian, 2011). Compared with other CHIs, the main function of TRQ is diluting the sputum which makes the sputum thinner and easier to cough up and further improves the patients' breath, so that the clinical symptoms of cough can disappear in a short time (Ye, 2016). One previous study has compared the effect of various CHIs on CAP for all age groups and our study only shared similar analysis methods with it. Focusing on elderly people and all the types of pneumonia, our study arrived at a conclusion that XYP + WM might be the best CHI for improving elderly people with pneumonia, which was inconsistent with the results of the previous study that YHN + WM was the best CHI for treating pneumonia (Huang et al., 2019). The difference of research subjects may account for the different conclusions between our study and the former one since our study was more specifically targeted at elderly patients rather than patients of all ages. As we mentioned before, although YHN had rapid onset of action, as well as good bioavailability widely used in clinical, but it had a greater incidence of toxicities or AEs (Nie, 2018). One study indicated that YHN injection had the highest incidence of AEs among numerous CHIs (Xiong et al., 2016), and the Food and Drug Administration of China also indicated the usage of YHN was accompanied with substantial AEs especially the systemic damage (China Tfadao, n d). The above findings would diminish metabolizing capacity and excretory functions in the elderly patients since metabolism and excretion are significant parameters to evaluate the transformation and delivery of drugs in the body (Gao, 2017; Gao et al., 2017). As a result, it was more likely to lead to accumulation of drugs in elderly bodies and increased their risk of AEs compared with ordinary adults, and thus decreased the effectiveness of TCM for elderly people in terms of population (Gao, 2017). We may hypothesize that elderly population was probably sensitive and fragile to be affected by the acceptability of TCM especially the drug toxicology of TCMs. Therefore, the XYP + WM is the most effective based on the result of our study while the previous study focus on ordinary adults is in favor of YHN + WM.

Strength and Limitations

Instead of performing a traditional meta-analysis, our study lies in the fact that we structured a Bayesian framework to evaluate the effectiveness of current CHIs simultaneously for pneumonia patients among elderly population based on several endpoints. Moreover, we enriched the way of search strategy in order that more potentially eligible trials would be found for the establishment of the literature basis of our NMA.

The limitations across our study also should not be ignored. First, we have not registered our study either in Cochrane central or PROSPERO, which may indirectly influence the generalization of our results. Due to the fact that the topic of our study is CHI, all trials were simply conducted in China and our NMA therefore might not apply to cases in other countries. We have not collected and analyzed the data regarding AEs, because only two studies mentioned the AEs(One study conducted with XYP + WM found a patient getting a rash during the therapy duration while the other study reported several patients with bloating, nausea, vomiting and facial flushing after taking YHN + WM) and we could not estimate it without sufficient data (Yuan, 2010; Wang, 2014). Quality of several studies would possibly weaken the reliability and robustness of our results. Only two studies mentioned the blind method (Zhang, 2010; Guo, 2019a), and two studies were rated as low risk of bias in selection bias (Li, 2018; Guo, 2019b). Moreover, there were three trials with a high risk of bias with regard to other biases (Huang, 2014; Zhang, 2014; Tian, 2016).

CONCLUSION

In summary, based on the clinical effective rate, our NMA suggested that XYP + WM probably was the better CHI choice among numerous CHIs for elderly patients with pneumonia when compared to WM. Meanwhile, it worth mentioning that this finding should be interpreted with caution due to the limited evidence. Besides, the present study put emphasis on the need of future guidelines to optimize their management and further similar high-quality trials should be carried out to confirm our results.

DATA AVAILABILITY STATEMENT

The original contributions presented in the study are included in the article/**Supplementary Material**, further inquiries can be directed to the corresponding authors.

AUTHOR CONTRIBUTIONS

YY conducted the database search, screened and extracted data for the meta-analysis, prepared extracted data for the procedures, and had primary responsibility in writing this article. QZ and ZS performed statistical analysis and interpretation of data. JL, ZL. LX, PL and XL contributed to the discussion and editing. CH and JL critically revised the draft manuscript. All authors read and approved the final manuscript.

SUPPLEMENTARY MATERIAL

The Supplementary Material for this article can be found online at: https://www.frontiersin.org/articles/10.3389/fphar.2021.610745/full#supplementary-material

REFERENCES

Academy RBoCM (2006). [Guidelines for the Diagnosis and Treatment of Community-Acquired Pneumonia: Learning and Practicing]. *Zhonghua Jie He He Hu Xi Za Zhi* 29 (10), 649–650. CNKI:SUN:ZHJH.0.2006-10-001.

Brooks, S. P., and Gelman, A. (1998). General Methods for Monitoring Convergence of Iterative Simulations. *J. Comput. Graphical Stat.* 7, 434–455. doi:10.1080/10618600.1998.10474787

Caldwell, D. M., Ades, A. E., and Higgins, J. P. T. (2005). Simultaneous Comparison of Multiple Treatments: Combining Direct and Indirect Evidence. *BMJ* 331 (7521), 897–900. doi:10.1136/bmj.331.7521.897

China Tfadao (n d). *The Safety of Chuanhuning and Yanhuning Injection*. Adverse drug reaction information circular. http://wwwcdr-adrorgcn/xxtb_255/ypblfyxxtb/2 00909/t20090902_2841html 2016/5/17.

Coreteam, D. (2014). *A Language and Environment for Statistical Computing*

Dias, S., Sutton, A. J., Ades, A. E., and Welton, N. J. (2012). Evidence Synthesis for Decision Making 2. *Med. Decis. Making* 33, 607–617. doi:10.1177/0272989X12458724

Feng, J. (2014). Research Progress in the Diagnosis and Treatment of Pneumonia with Traditional Chinese Medicine. *J. Emerg. Traditional Chin. Med.* 23 (4), 670–672. CNKI:SUN:ZYJZ.0.2014-04-047.

Gao, W., Wang, S., Cui, Z., Cao, J., and Tian, H. (2011). [Reduning Injection for Community-Acquired Pneumonia: Meta-Analysis]. *Zhongguo Zhong Yao Za Zhi* 36 (24), 3539–3543. CNKI:SUN:ZGZY.0.2011-24-034.

Gao, Z. (2017). *Adverse Reactions of Yanhuning Injection-A Meta-Analysis*. Zhengzhou University.

Gao, Zhongli., Hou, Guiqin., and Cao, Z. (2017). Adverse Reactions of Yanhuning Injection-Ameta-Analysis. *Journala Chin. patent Med.* 39 (003), 486–491. CNKI:SUN:ZCYA.0.2017-03-009.

GBD 2016 Causes of Death Collaborators (2017). Global, Regional, and National Age-Sex Specific Mortality for 264 Causes of Death, 1980-2016: a Systematic Analysis for the Global Burden of Disease Study 2016. *Lancet* 390 (10100), 1151–1210. doi:10.1016/S0140-6736(17)32152-9

GBD Diarrhoeal Diseases Collaborators (2017). Estimates of the Global, Regional, and National Morbidity, Mortality, and Aetiologies of Lower Respiratory Tract Infections in 195 Countries: a Systematic Analysis for the Global Burden of Disease Study 2015. *Lancet Infect. Dis.* 17 (11), 1133–1161. doi:10.1016/S1473-3099(17)30396-1

Guo, J. (2019a). Effects of Moxifloxacin and Xiyanping on Community Acquired Pneumonia Among Elderly People. *Chin. Med. Sci. J.* 18, 63–04. CNKI:SUN:GYKX.0.2019-18-017.

Guo, Y. (2019b). Clinical Effect of Tanreqing Injection Combined with Shenfu Injection in the Treatment of Senile Severe Pneumonia. *Chin. Contemp. Med.* 3 (B), 0151–0104. CNKI:SUN:ZGUD-08-047.0.2019.

HGGS. *Cochrane Handbook for Systematic Reviews of Interventions* Version 5.1.0 London: The Cochrane Collaboration; 2011. doi: doi:10.1002/9780470712184

Higgins, J., and Green, S. E. (2011). Cochrane Handbook for Systematic Reviews of Interventions Version 5.1.0. *The Cochrane Collaboration* **(Eds)**. Naunyn Schmiedebergs Arch Exp Pathol Pharmakol, S38. doi:10.1002/9780470712184

Higgins, J. P. T., and Thompson, S. G. (2002). Quantifying Heterogeneity in a Meta-Analysis. *Statist. Med.* 21, 1539–1558. doi:10.1002/sim.1186

Huang, W. (2014). Clinical Effect of Moxifloxacin Injection Combined with Yanhuning Injection on the Treatment of Elderly Acquired Pneumonia Patients. *J. Yunnan Chin. traditional Med.* 35 (12), 0016–0002. doi:10.16254/j.cnki.53-1120/r.2014.12.050

Huang, X. (2018). Clinical Evaluation of Tanreqing Injection Combined with Antibiotics in the Treatment of Community Acquired Pneumonia Elderly People-A Meta-Analysis. *J. Pharmacoepidemiol.* 27 (12), 777–784. CNKI:SUN:YWLX.0.2018-12-001.

Huang, X., Duan, X., Zhu, Y., Wang, K., Wu, J., Tian, X., et al. (2019). Comparative Efficacy of Chinese Herbal Injections for the Treatment of Community-Acquired Pneumonia: A Bayesian Network Meta-Analysis of Randomized Controlled Trials. *Phytomedicine* 63, 153009. doi:10.1016/j.phymed.2019.153009

Hutton, B., Salanti, G., Caldwell, D. M., Chaimani, A., Schmid, C. H., Cameron, C., et al. (2015). The PRISMA Extension Statement for Reporting of Systematic Reviews Incorporating Network Meta-Analyses of Health Care Interventions: Checklist and Explanations. *Ann. Intern. Med.* 162 (11), 777–784. doi:10.7326/M14-2385

Jain, S., Self, W. H., Wunderink, R. G., Fakhran, S., Balk, R., Bramley, A. M., et al. (2015). Community-Acquired Pneumonia Requiring Hospitalization Among U.S. Adults. *N. Engl. J. Med.* 373 (5), 415–427. doi:10.1056/NEJMoa1500245

L, X. (2017). Efficacy of Xiyanping Combined with Azithromycin in the Treatment of Community Acquired Pneumonia Among Elderly People-A Meta-Analysis. *Traditional Chin. Med.* 30 (12), 69–04. CNKI:SUN:ZYYJ.0.2017-12-031.

Labeau, S. O., Van de Vyver, K., Brusselaers, N., Vogelaers, D., and Blot, S. I. (2011). Prevention of Ventilator-Associated Pneumonia with Oral Antiseptics: a Systematic Review and Meta-Analysis. *Lancet Infect. Dis.* 11 (11), 845–854. doi:10.1016/S1473-3099(11)70127-X

Li, D. M., Tang, S. H., Liao, Q., Chen, W., and Zhang, H. C. (2017). [Literature Study on Prevention and Treatment of Community Acquired Pneumonia by Traditional Chinese Medicine]. *Zhongguo Zhong Yao Za Zhi* 42 (8), 1418–1422. doi:10.19540/j.cnki.cjcmm.2017.0037

Li, J. (2010). Clinical Observation of Xiyanping in the Treatment of 32 Cases of Senile Pneumonia. *Aerosp Med.* 21 (12), 063, 2010 . SUN:HKHT.0.2010-12-064

Li, P. (2018). Levofloxacin Combined with Reduning Injection in the Treatment of Community Acquired Pneumonia Among Elderly People. *J. Hubei Univ. nationalities* 35 (3), 0025–0003. doi:10.13501/j.cnki.42-1590/r.2018.03.007

Li, W., Li, C., Zheng, H., Chen, G., and Hua, B. (2016). Therapeutic Targets of Traditional Chinese Medicine for Colorectal Cancer. *J. Tradit Chin. Med.* 36 (2), 243–249. doi:10.1016/S0254-6272(16)30034-6

Mandell, L. A., Wunderink, R. G., Anzueto, A., Bartlett, J. G., Campbell, G. D., Dean, N. C., et al. (2007). "Infectious Diseases Society of America/American Thoracic Society Consensus Guidelines on the Management of Community-Acquired Pneumonia in Adults," in *Clinical Infectious Diseases* (An official publication of the Infectious Diseases Society of America), 44, S27–S72. doi:10.1086/511159

Mavridis, D., and Salanti, G. (2013). A Practical Introduction to Multivariate Meta-Analysis. *Stat. Methods Med. Res.* 22 (2), 133–158. doi:10.1177/0962280211432219

Nie, Z. (2018). Yanhuning in the Treatment of Community Acquired Pneumonia Among Elderly People. *Pharm. reasearch* 06 (C), 0001–0074. doi:10.16659/j.cnki.1672-5654.2012.18.078

Ronco, C., Reis, T., and Husain-Syed, F. (2020). Management of Acute Kidney Injury in Patients with COVID-19. *Lancet Respir. Med.* doi:10.1016/S2213-2600(20)30229-0

Salanti, G., Higgins, J. P., Ades, A., and Ioannidis, J. P. (2008). Evaluation of Networks of Randomized Trials. *Stat. Methods Med. Res.* 17 (3), 279–301. doi:10.1177/0962280207080643

Seagroatt, V., and Stratton, I. (1998). Bias in Meta-Analysis Detected by a Simple, Graphical Test. Test Had 10% False Positive Rate. *BMJ (Clinical research ed)* 316 (7129), 470–471. doi:10.1002/sim.1186

Sun, Y. (2019). Comparative Efficacy of Four Chinese Herbal Injections for Treating Virus Pneumonia: a Network Meta-Analysis of Randomized Controlled Trials *Chinese. Arch. traditional Chineses Med.* 09 (44), 24. doi:10.13193/j.issn.1673-7717.2020.07.029

Thomas, C. P., Ryan, M., Chapman, J. D., Stason, W. B., Tompkins, C. P., Suaya, J. A., et al. (2012). Incidence and Cost of Pneumonia in Medicare Beneficiaries. *Chest* 142 (4), 973–981. doi:10.1378/chest.11-1160

Tian, J. (2011). Clinical Analysis of the Therapeutic Effect of Yanhuning Injection on the Elderly Patients with Community Acquired Pneumonia and its Influence on H S-CRP and IL-6. *Chin. traditional Med. Community* 36, 190, 2011 . CNKI:SUN:ZGSQ.0.2011-36-191

Tian, Y. (2016). Effect of Moxifloxacin Combined with Xiyanping on Serum Inflammatory Factors and T Lymphocyte Subsets in Elderly Patients with Community Acquired Pneumonia. *Chin. J. Hosp. Infect.* 26 (15), 3389–3303. doi:10.11816/cn.ni.2016-160103

Valkenhoef, G., Dias, S., Ades, A. E., and Welton, N. J. (2016). Automated Generation of Node-splitting Models for Assessment of Inconsistency in Network Meta-analysis. *Res. Syn. Meth.* 7 (1), 80–93. doi:10.1002/jrsm.1167

Valkenhoef, G. V., and Kuiper, J. (2016). *Gemtc: Network Meta-Analysis Using Bayesian Methods*. John Wiley & Sons. http://mirrors.nic.cz/R/web/packages/gemtc/index.html.

Wang, B. (2018). Network Meta-Analysis of Heat-Clearing and Detoxifying Chinese Herbal Injections in the Treatment for Pediatric Viral Pneumonia.

Chin. traditional patent Med. 40 (122), 2644–2649. CNKI:SUN:ZCYA.0.2018-12-007

Wang, R. (2014). Clinical Observation of Yanhuning Injection in the Treatment of Severe Pneumonia Among Elderly People. *Chin. Community doctors* 34, 61. doi:10.3969/j.issn.1007-614x.2016.34.61

WHO (2017). *WHO Guidelines on Integrated Care for Older People (ICOPE) [EB/OL]*. Available at: http://wwwwhoint/ageing/publications/guidelines-icope/en/2017.

Xia, L. (2017). Early Application of Shenfu Injection Combined with Yanhuning for Injection in the Treatment of Severe Community-Acquired Pneumonia Among Old People. *J. Hebei Chineses traditional Med.* 39 (12), 1801–1806. doi:10.3969/j.issn.1002-2619.2017.12.009

Xiong, Z., Tu, F., and Yu, D. (2016). Adverse Reactions for 65 Types of Traditional Chinese Medicine and its Preparations. *Contemp. Med.* 22 (35), 184–186. CNKI:SUN:DDYI.0.2016-35-120

Yao, Z. (2017). Impact of Xiyanping Injection Combined with Cefoperazone and Sulbactam Sodium on Elderly Patients with Community ? Acquired Pneumonia. *Pract. J. Card. Cereb. Pneumal Vasc. Dis. Prev.* 25 (10), 155–157. CNKI:SUN:SYXL.0.2017-10-050

Ye, M. (2016). Clinical Effect of Tanreqing Injection on Community Acquired Pneumonia. *Med. recapitulate* 22 (12), 2463–2404. CNKI:SUN:YXZS.0.2016-12-055

Yuan, J. (2010). Meropenem Combined with Xiyanping in the Treatment of 62 Elderly Stroke Patients with Hospital Acquired Pneumonia. *Chin. J. Difficult Complicated Cases* 09 (06), 441–442. CNKI:SUN:YNBZ.0.2010-06-026.

Zampieri, F. G., Nassar Jr, A. P., Jr, Gusmao-Flores, D., Taniguchi, L. U., Torres, A., and Ranzani, O. T. (2015). Nebulized Antibiotics for Ventilator-Associated Pneumonia: a Systematic Review and Meta-Analysis. *Crit. Care* 19, 150. doi:10.1186/s13054-015-0868-y

Zhang, B. (2010). Clinical Observation of Tanreqing Injection in the Treatment of Community Acquired Pneumonia Among Elderly People. *Clin. Med. Res.* 19 (09B), 1155–1102. CNKI:SUN:SXLC.0.2010-18-003.

Zhang, F. (2014). Analysis of the Clinical Effect of Reduning Injection on the Elderly Community Acquired Pneumonia with Fever. *J. Mod. Drug Appl.* 8 (22), 89–90. doi:10.14164/j.cnki.cn11-5581/r.2014.22.264

Zhang, L. (2011). Clinical Observation on Xiyanping Injection in the Treatment of Severe Pneumonia Among Elderly People. *J. Emerg. Traditional Chin. Med.* 24 (12), 2289–2290. CNKI:SUN:ZYJZ.0.2015-12-082.

Zhao, Z. Q., Mao, J. Y., Wang, X. L., and Hou, Y. Z. (2013). [Application and Evaluation of Chinese Medicine in Treatment of Chronic Heart Failure]. *Zhongguo Zhong Xi Yi Jie He Za Zhi* 33 (12), 1701–1704. CNKI:SUN:ZZXJ.0.2013-12-032.

Zhou, J. (2017). Clinical Observation of Reduning Injection in the Treatment of Senile Severe Pneumonia. *Mod. Diagn. Treat.* 06, 1013–1002. CNKI:SUN:XDZD.0.2017-06-017.

Zhou, Y. (2019). Clinical Study of Yanhuning Injection Combined with Etimicin in the Treatment of Community Acquired Pneumonia in the Elderly Adults. *Drugs&Clinic* 34 (11), 3271–3204. CNKI:SUN:GWZW.0.2019-11-016.

Zhou, Z., Gao, N., Wang, Y., Chang, P., Tong, Y., and Fu, S. (2000). Clinical Research for Elderly People with Pneumonia Based on the Treatment of Traditional Chinese Medicine. *Henan traditional Chin. Med.* 20 (5), 70–72. CNKI:SUN:HNZY.0.2000-05-078.

Conflict of Interest: The authors declare that the research was conducted in the absence of any commercial or financial relationships that could be construed as a potential conflict of interest.

Copyright © 2021 Yuan, Zheng, Si, Liu, Li, Xiong, Liu, Li, He and Liang. This is an open-access article distributed under the terms of the Creative Commons Attribution License (CC BY). The use, distribution or reproduction in other forums is permitted, provided the original author(s) and the copyright owner(s) are credited and that the original publication in this journal is cited, in accordance with accepted academic practice. No use, distribution or reproduction is permitted which does not comply with these terms.

frontiers in Pharmacology

CLINICAL TRIAL
published: 25 May 2021
doi: 10.3389/fphar.2021.679588

Traditional Chinese Medicine Qingre Huoxue Treatment vs. the Combination of Methotrexate and Hydroxychloroquine for Active Rheumatoid Arthritis: A Multicenter, Double-Blind, Randomized Controlled Trial

Xun Gong[1†], Wei-Xiang Liu[1†], Xiao-Po Tang[1], Jian Wang[1], Jian Liu[2], Qing-Chun Huang[3], Wei Liu[4], Yong-Fei Fang[5], Dong-Yi He[6], Ying Liu[7], Ming-Li Gao[8], Qing-Jun Wu[9], Shi Chen[10], Zhen-Bin Li[11], Yue Wang[12], Yan-Ming Xie[13], Jun-Li Zhang[14], Cai-Yun Zhou[15], Li Ma[16], Xin-Chang Wang[17], Chi Zhang[18] and Quan Jiang[1]**

[1]Guang'anmen Hospital China Academy of Chinese Medical Sciences, Beijing, China, [2]The First Affiliated Hospital of Anhui University of Chinese Medicine, Hefei, China, [3]Guangdong Provincial Hospital of Traditional Chinese Medicine, Guangzhou, China, [4]The First Affiliated Hospital of Tianjin University of Traditional Chinese Medicine, Tianjin, China, [5]Affiliated Hospital of the Third Military Medical University of the Chinese People's Liberation Army, Chongqing, China, [6]Shanghai Guanghua Hospital of Integrated Traditional Chinese and Western Medicine, Shanghai, China, [7]The Affiliated Hospital of Shandong University of Traditional Chinese Medicine, Jinan, China, [8]The Affiliated Hospital of Liaoning University of Traditional Chinese Medicine, Shandong, China, [9]Peking Union Medical College Hospital, Beijing, China, [10]Peking University People's Hospital, Beijing, China, [11]Bethune International Peace Hospital, Shijiazhuang, China, [12]Jiangsu Provincial Hospital of Traditional Chinese Medicine, Beijing, China, [13]Institute of Basic Research in Clinical Medicine, China Academy of Chinese Medical Sciences, Beijing, China, [14]The Fifth Hospital of Xi'an, Xi'an, China, [15]Xiyuan Hospital China Academy of Chinese Medical Sciences, Beijing, China, [16]China-Japan Friendship Hospital, Beijing, China, [17]The Second Affiliated Hospital of Zhejiang University of Chinese Medicine, Hangzhou, China, [18]Dongzhimen Hospital Beijing University of Chinese Medicine, Beijing, China*

Traditional Chinese medicine (TCM) has been used successfully to treat rheumatoid arthritis (RA). Qingre Huoxue treatment (Qingre Huoxue decoction (QRHXD)/Qingre Huoxue external preparation (QRHXEP)) is a therapeutic scheme of TCM for RA. To date, there have been few studies comparing the efficacy and safety of QRHXD and conventional synthetic disease-modifying antirheumatic drugs (csDMARDs) for the treatment of active RA. This was investigated in a multicenter, double-blind, randomized controlled trial involving 468 Chinese patients with active RA [disease activity score (DAS)-28 > 3.2] treated with QRHXD/QRHXEP (TCM group), methotrexate plus hydroxychloroquine [Western medicine (WM) group], or both [integrative medicine (IM) group]. Patients were followed up for 24 weeks. The primary outcome measure was the change in DAS-28 from baseline to 24 weeks. The secondary outcome measures were treatment response rate according to American College of Rheumatology 20, 50, and 70% improvement criteria (ACR-20/50/70) and the rate of treatment-related adverse events (TRAEs). The trial was registered at ClinicalTrials.gov (NCT02551575). DAS-28 decreased in all three groups after treatment ($p < 0.0001$); the score was lowest in the TCM group ($p < 0.05$), while no difference was observed between

OPEN ACCESS

Edited by:
Yanqiong Zhang,
China Academy of Chinese Medical Sciences, China

Reviewed by:
Liwei Lu,
The University of Hong Kong, China
Hua Zhou,
The University of Hong Kong, Hong Kong

***Correspondence:**
Quan Jiang
jiang.quan@hotmail.com
Chi Zhang
sage618@126.com

[†]These authors have contributed equally to this work

Specialty section:
This article was submitted to Ethnopharmacology, a section of the journal Frontiers in Pharmacology

Received: 12 March 2021
Accepted: 10 May 2021
Published: 25 May 2021

Citation:
Gong X, Liu W-X, Tang X-P, Wang J, Liu J, Huang Q-C, Liu W, Fang Y-F, He D-Y, Liu Y, Gao M-L, Wu Q-J, Chen S, Li Z-B, Wang Y, Xie Y-M, Zhang J-L, Zhou C-Y, Ma L, Wang X-C, Zhang C and Jiang Q (2021) Traditional Chinese Medicine Qingre Huoxue Treatment vs. the Combination of Methotrexate and Hydroxychloroquine for Active Rheumatoid Arthritis: A Multicenter, Double-Blind, Randomized Controlled Trial. Front. Pharmacol. 12:679588. doi: 10.3389/fphar.2021.679588

the WM and IM groups ($p > 0.05$). At week 24, ACR-20 response was 73.04% with TCM, 80.17% with WM, and 73.95% with IM (based on the full analysis set [FAS], $p > 0.05$); ACR-50 responses were 40.87, 47.93, and 51.26%, respectively, (FAS, $p > 0.05$); and ACR-70 responses were 20.87, 22.31, and 25.21%, respectively, (FAS, $p > 0.05$). Thus, treatment efficacy was similar across groups based on ACR criteria. On the other hand, the rate of TRAEs was significantly lower in the TCM group compared to the other groups ($p < 0.05$). Thus, QRHXD/QRHXEP was effective in alleviating the symptoms of active RA—albeit to a lesser degree than csDMARDs—with fewer side effects. Importantly, combination with QRHXD enhanced the efficacy of csDMARDs. These results provide evidence that QRHXD can be used as an adjunct to csDMARDs for the management of RA, especially in patients who experience TRAEs with standard drugs.

Clinical Trial Registration: ClinicalTrials.gov, identifier NCTNCT025515.

Keywords: qingre huoxue decoction, damp-heat-stasis syndrome, active rheumatoid arthritis, comprehensive treatment., randomized controlled trial

INTRODUCTION

Rheumatoid arthritis (RA) is the most common autoimmune inflammatory arthritis in adults. RA has significant negative impacts on the ability of patients to perform daily activities—including work and home tasks—and health-related quality of life, and increases the risk of mortality (Singh et al., 2016). The incidence of RA is about 1% globally (van der Woude and van der Helm-van Mil, 2018) and 0.28–0.40% in China (Chinese Rheumatology Association, 2018), with no fewer than five million people in China living with the disease. In traditional Chinese medicine (TCM), clinical manifestations of active RA such as joint swelling and tenderness, morning stiffness, and local skin redness constitute a "damp-heat-stasis syndrome" that is similar to the active period of RA [i.e., disease activity score (DAS)-28 > 3.2]. TCM has been used successfully to treat RA. Specifically, Qingre Huoxue decoction (QRHXD) may prevent bone destruction by modulating inflammation, and short-term application of a cream prepared from *Tripterygium wilfordii*—the source of a QRHXEP component—was shown to be an effective and safe adjunctive treatment (Jiang et al., 2012; China Association of Chinese Medicine, 2017; Jiao et al., 2019). Oral Chinese medicines were found to relieve joint symptoms with minimal adverse reactions in combination with topical formulations for improved disease control (Xing et al., 2020).

The goals of RA treatment are to achieve disease remission or low disease activity and ultimately control the disease, reduce the disability rate, and improve patients' quality of life (Smolen et al., 2020). Conventional synthetic disease-modifying antirheumatic drugs (csDMARDs) are the first-line treatment for RA in China and elsewhere (Singh et al., 2016; Chinese Rheumatology Association, 2018; Lau et al., 2019; Smolen et al., 2020). Methotrexate (MTX) is the anchor drug (Pincus et al., 2003) while hydroxychloroquine (HCQ) is mainly used in combination treatment regimens (95%) (Zhang et al., 2013); the utilization rates of these drugs are 55.9 and 30.4%, respectively, (Jin et al., 2017). However, MTX and HCQ have adverse effects such as gastrointestinal discomfort (e.g., nausea and diarrhea) (Giraud et al., 2020), hepatitis, interstitial pneumonitis, cytopenias, and retinopathy (Abbasi et al., 2019); as such, the vast majority of RA patients in China are willing to receive TCM treatment (Lu et al., 2019).

Qingre Huoxue treatment (QRHXD plus QRHXEP) is a therapeutic scheme of TCM for RA that have been routinely used in clinical practice for at least 40 years at Guang'anmen Hospital, China Academy of Chinese Medical Sciences. However, there have been few blinded trials systematically comparing the efficacy and safety of Qingre Huoxue treatment and csDMARDs in RA treatment. Thus, the aim of this investigation was to evaluate the effects of Qingre Huoxue treatment vs. MTX plus HCQ in patients with active RA.

MATERIALS AND METHODS

Trial Design

This multicenter, double-blind, randomized controlled clinical trial has been registered at ClinicalTrials.gov (NCTNCT02551575). The study was conducted in accordance with the principles outlined in the Declaration of Helsinki, Good Clinical Practice Guidelines of the International Conference on Harmonization, and local regulatory requirements. This study followed CONSORT. The protocol was approved by the ethics committee at Guang'anmen Hospital, China Academy of Chinese Medical Sciences (no. 2013EC122). A study period of 24 weeks was selected based on pilot clinical trials.

Participants

Men and women aged 18–65 years were considered for enrollment if they met the American College of Rheumatology (ACR) criteria for RA (Arnett et al., 1988; Lu and Jiao, 1996; Aletaha et al., 2010) as well as TCM criteria for the diagnosis of RA "damp-heat-stasis syndrome" (Zheng, 2002) (**Supplementary Material**). The trial was conducted at 16 hospitals. An independent committee monitored the trial for safety and scientific integrity. The inclusion criteria were as follows: 1) DAS-28 score > 3.2; 2) patients were taking csDMARDs for at least 3 months at a

stable dose, and continued the same treatment for the duration of the present study; and 3) patients voluntarily participated in the study and signed an informed consent form. Exclusion criteria were as follows: 1) patients with skin burst or allergies; 2) patients with cancer or other malignant diseases such as cardiovascular, hematopoietic, liver, or kidney disease or psychopathy; 3) patients with active or chronic infection, including HIV, hepatitis C virus, hepatitis B virus, or tuberculosis; 4) treatment with *Tripterygii*, glucocorticoid, or biologic DMARDs in the prior 3 months; 5) previous treatment with MTX or HCQ; and 6) patients with retinopathy. Patients who met the following criteria were not allowed to continue receiving the therapy as part of the study, but were followed up until the end of the trial: 1) patients who experienced intolerable adverse events (AEs), complications, or physiologic changes, and had discontinued the study drug for more than 14 days; 2) patients who demonstrated poor compliance (the number and course of medication were not between 80 and 120%); 3) patients who were unwilling to continue participating in the study or were lost to follow-up; and 4) patients who used a nonprescribed range of combined medications that could affect the efficacy and safety assessments.

Treatment

Eligible patients obtained sequence numbers from the trial coordinator and were allocated to 1 of the 3 following groups by computer-generated sequence randomization: 1) TCM group (TCM plus MTX and HCQ placebos); 2) Western medicine (WM) group (12.5 mg MTX once weekly plus 200 mg HCQ twice daily combined with TCM placebo); and 3) integrative medicine (IM) group (TCM combined with 12.5 mg MTX once weekly plus 200 mg HCQ twice daily). MTX and HCQ tablets were obtained from Shanghai Xinyi Pharmaceutical Co. (Shanghai, China) and Shanghai Zhongxi Pharmaceutical Co. (Shanghai, China), respectively, and were taken orally. TCM Qingre Huoxue treatment for RA "damp-heat-stasis syndrome" with QRHXD and QRHXEP optimized by the Guang'anmen Hospital China Academy of Chinese Medical Sciences were used in this study. QRHXD was processed into granules that were packaged in a tin foil bag by Sichuan New Green Pharmaceutical Technology Development Co. (Chengdu, China). QRHXEP was processed into a gel formulation and packaged in a plastic tube at Guang'anmen Hospital China Academy of Chinese Medical Sciences (batch no. 15011303). QRHXD was taken twice daily—at breakfast and 0.5 h after dinner—for 24 weeks (1 bag boiled in water for each dose). QRHXEP was applied topically once daily 1 h after dinner for 12 weeks [20 g (1 stick) daily in weeks 1–4 and 10 g (half a stick) daily in weeks 5–12] to the skin surface of affected joints, while avoiding the face and temporomandibular joint.

QRHXD has 12 components including animal drug wugong (*Centipede* [4 g]) and the botanical drugs species or TCM plant preparations tufuling (*Smilax glabra Roxb* [30 g]), yinhua (Lonicera japonica Thunb [30 g]), huangqi (*Astragalus mongholicus* [30 g]), chaocangzhu (bran-fried *Atractylodes chinensis* [15 g]), huangbo (*Phellodendron amurense* [9 g]), chishao (*Paeonia lactiflora* [15 g]), bixie (*Dioscoreae hypoglaucae rhizoma* [15 g]), danshen (*Salvia miltiorrhiza* [15 g]), ezhu (*Curcuma zedoaria* [9 g]), qingfengteng (*Sinomenium acutum* (Thunb.) [15 g]), and fengfang (*Nidus vespae* [5 g]). The granules were packaged as 10-g bags, with each bag containing 96 g of crude product. QRHXEP is composed of six botanical drugs including leigongteng (*T. wilfordii* [120 g]), chuanxiong (*Ligusticum wallichii* [60 g]), baizhi (*Angelica dahurica* [60 g]), dahuang (*Rheum officinale* [30 g]), ruxiang (*Boswellia carterii* [30 g]), and bohe (*Fructus forsythiae* [30 g]), as well as the resin moyao (*Myrrh* [30 g]) and mineral mangxiao (*Mirabilite* [120 g]). *T. wilfordii*, *R. officinale*, and *A. dahurica* were refluxed in a volume of 75% ethanol eight times the combined weight of the three components for 1 h. The extracts were combined and filtered, and the ethanol was separated from the filtrate and set aside with the residue stored in another container. *L. wallichii*, *B. carterii*, and myrrh were added to a volume of water 6 times the combined weight of the three components and the volatile oils were extracted for 8 h, and the liquid was filtered and set aside. The residues of *L. wallichii*, *B. carterii*, and *Myrrh* were combined with those of *T. wilfordii*, *R. officinale*, and *A. dahurica*; *Mirabilite* was added along with a 6 × volume of water. The mixture was decocted for 1 h and filtered; the filtrate was combined with the extract liquids that had been set aside, concentrated to a relative density of 1.055–1.075 (75°C), and filtered through a 100-mesh sieve and set aside. *F. forsythiae* was steam-distilled and frozen, and partially decapitated to obtain 0.3 ml peppermint oil. The volatile oils extracted from *L. wallichii*, *B. carterii*, and *Myrrh* were combined with the peppermint oil and ethyl benzoate and dissolved in ethanol. Carboxymethyl cellulose sodium and glycerol were added with stirring. Water was then added to the concentrated extract liquid up to a weight of 1,000 g with continuous stirring until a gel was obtained. The names of the TCM ingredients in Chinese and English are listed in **Supplementary Material**.

QRHXD placebo granules were composed of lactose, starch, edible colorant, and bitter taste agents packaged in a tin foil bag identical to the one containing QRHXD granules and had the same color, texture, taste, and smell as the actual medicine. The QRHXEP placebo gel was prepared from viscous agent with cane sugar color added so that it had the same color, texture, and smell as the actual QRHXEP gel. The MTX and HCQ placebo tablets were composed of lactose, starch, carboxymethyl starch sodium, and magnesium stearate and had the same color, texture, taste, and smell as the actual drugs.

The quality of the TCM granules and gel was evaluated according to the 2005 Chinese pharmacopoeia (Chinese Pharmacopoeia Commission, 2005). Before the start of the trial, the TCM granules and gel were tested for heavy metals, microbial contamination, and residual pesticides, and were determined to meet the safety standards in China. Laboratory personnel were blinded to the identity of the TCM granules and gel. QRHXD and QRHXEP and their placebos were prepared by the same manufacturer. The medicines were distributed to the 16 study sites from the same source.

Measurements

The patients were observed for 24 weeks. The primary outcome measure was the change in DAS-28 from baseline to week 24, and the secondary outcome measures were ACR-20, ACR-50, and ACR-70 (ACR criteria for 20, 50, and 70% improvement, respectively), which were evaluated at week 24. DAS-28 was based on erythrocyte sedimentation rate (ESR), 28 tender and swollen joint counts (TJC and SJC, respectively), general health (GH; patient assessment of disease activity according to a 100-mm visual analogue scale with 0 = best and 100 = worst), and levels of acute phase reactant (ESR [mm/h]), and was calculated as $0.56 \times \sqrt{(TJC28)} + 0.28 \times \sqrt{(SJC28)} + 0.014 \times GH + 0.70 \times \ln(ESR)$ (Wells et al., 2009). The ACR-20/50/70 response was defined as ≥ 20%/50%/70% improvement in both the TJC and SJC and ≥ 20%/50%/70% improvement in three of the five other core measures (resting pain, patient's global assessment, physician's global assessment, Health Assessment Questionnaire [HAQ] score, and ESR/C-reactive protein ratio) (Felson et al., 1995). Physical function was assessed at baseline and at week 24 with the HAQ (Bruce and Fries, 2005). Safety was assessed based on routine blood and urine tests, liver (alanine aminotransferase and aspartate aminotransferase) and renal (blood urea nitrogen and creatinine) function, electrocardiogram, and treatment-related (TR)AEs at week 24.

Sample Size

The sample size was determined by the primary outcome. Assume that the ratio of the three groups is 1:1:1, using a two-sided test with a significance level (α) of 0.05 and a power (1-β) of 0.90, and the required sample size is estimated by SAS 9.4 software for 129 cases in each group. Allowing for a dropout of about 20%, and the TCM group, WM group and the IM group each required 156 cases, a total of 468 cases.

Statistical Analysis

Intention-to-treat (ITT) approach was performed using in all of analyses. Continuous data was presented as mean (SD), and categorical data was presented as numbers and/or percentages. A one-way ANOVA or Kruskal–Wallis rank test combined with the t or Wilcoxon rank test for post hoc testing was used in analyzing the continuous data. The chi-square or Fisher exact test was used in analyzing the categorical data. The Kruskal–Wallis test combined with the Wilcoxon rank test for post hoc testing was used in analyzing the ordinal data. A one-way ANOVA or Kruskal–Wallis rank test combined with the t or Wilcoxon rank test for post hoc testing was used in analyzing difference value (change before and after the treatment) among three groups. For this three-arm clinical study (groups TCM, WM, and IM), we care about whether there are differences in the efficacy of the three groups. Therefore, after completing the difference test for the three groups, it is necessary to further conduct multiple comparisons between the three groups. In order to avoid false positive results, it is necessary to adjust the test level in the multiple comparison. The Bonferroni method is one of the classic methods for the test level adjustment. The processing method is as follows: the accepted test level is divided by the times of multiple comparisons, and then used as the adjusted test level for multiple comparisons. In this paper, it is necessary to complete the pairwise comparison between the three groups, TCM-WM, TCM-IM, and WM-IM, the test level is adjusted to 0.0167 (0.05/3). That is, the analysis method for two independent samples is used to test the differences between the TCM-WM, TCM-IM, and WM-IM groups. At this time, only when $p < 0.0167$, the difference is considered to be statistically significant. This method can effectively control the generation of false positive results. Statistical analyses were performed using SAS v9.4 software (SAS Institute, Cary, NC, United States).

RESULTS

Phytochemical Analysis

Preparation and assay methods of QRHXD and QRHXEP are based on the Pharmaceutical standards of the Ministry of Health of the People's Republic of China (Pharmacopoeia of the people's Republic of China [2010]). The chemical profiling of QRHXD and QRHXEP was detected using LC/MS/MS method, and the details were provided in **Supplementary Material**.

Study Participants

Subjects were recruited at 16 medical research centers nationwide (**Supplementary Material**) from November 2013 to November 2015; the 24-week clinical observation period for all patients was completed in May 2016. A total of 522 patients were screened and 468 were enrolled (156 per group); treatment was discontinued for 109 patients (TCM group, $n = 40$; WM group, $n = 33$; IM group, $n = 36$) and 8 cases were excluded (TCM group, $n = 3$; WM group, $n = 2$; IM group $n = 3$) (**Figure 1**). There were no significant differences in baseline characteristics between the three groups (**Table 1**).

Primary Outcome Measure (Disease Activity Score-28)

There was no significant difference in DAS-28—the primary outcome measure—among the three groups at baseline (**Tables 2**, **3**). At week 24, DAS-28 was decreased in all three groups compared to the baseline score ($p < 0.0001$). The rank order of DAS-28 at week 24 was IM < WM < TCM ($p < 0.05$) (**Tables 4**, **5**); the score was decreased to 4.20 ± 1.56 in the TCM group, 3.58 ± 1.28 in the WM group, and 3.39 ± 1.27 in the IM group (all $p < 0.0001$ vs. baseline). The difference value of DAS-28 (i.e., change in score from baseline to week 24) was greater in the IM (2.10 ± 1.12) and WM (2.24 ± 1.40) groups than in the TCM group (1.60 ± 1.17) ($p < 0.05$), while no difference was observed between the former two groups ($p > 0.05$) (**Figure 2**).

Secondary Outcome Measures

American College of Rheumatology-20/50/70

There was no significant difference in ACR-20, ACR-50, and ACR-70 between the three groups at 24 weeks ($p > 0.05$) based on the full analysis set (FAS) (**Tables 6**, **7**). ACR-20 and ACR-70 responses at 12 weeks were lower in the TCM group than in the WM and IM groups ($p < 0.05$). There was no significant

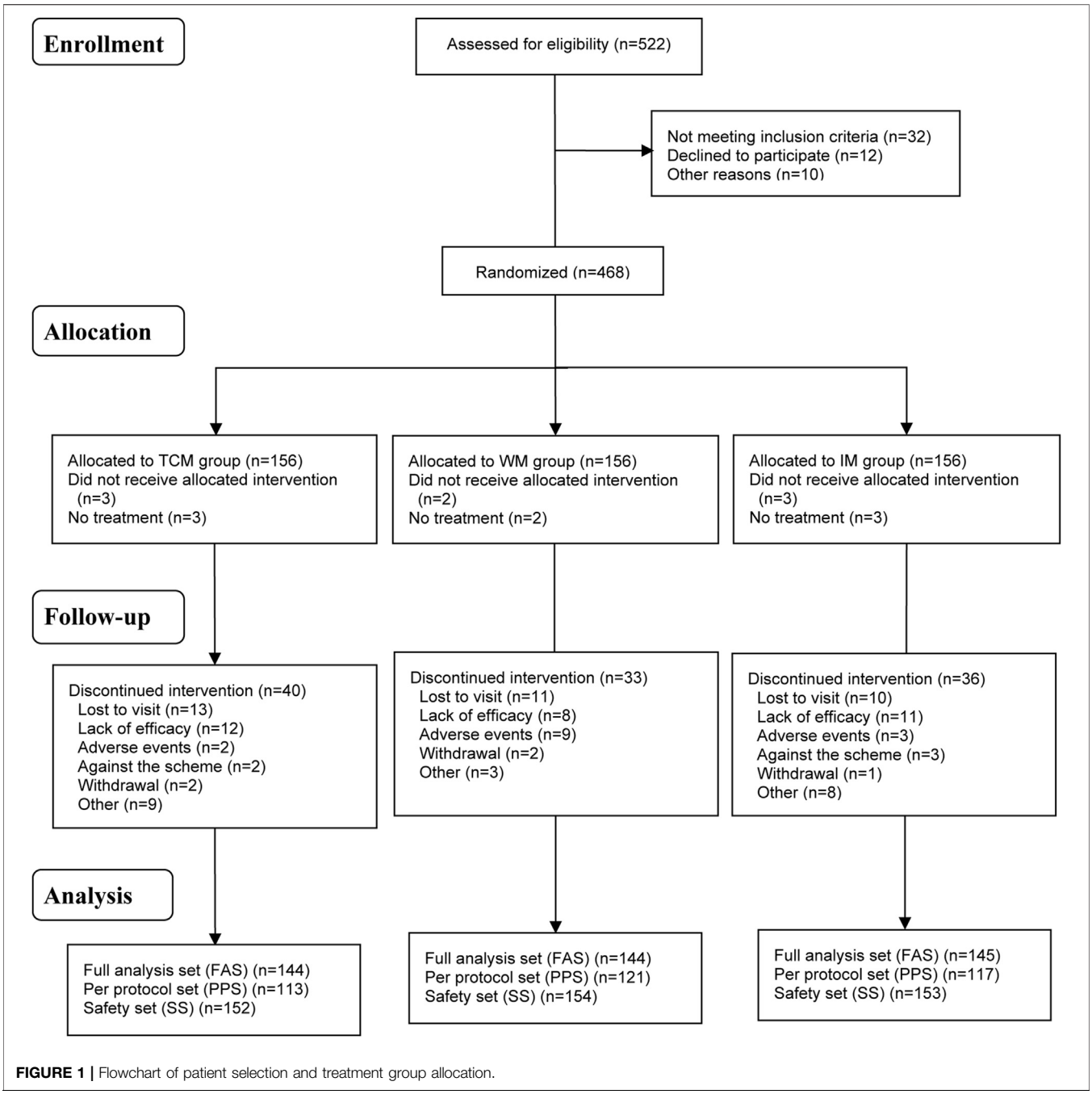

FIGURE 1 | Flowchart of patient selection and treatment group allocation.

difference in ACR-50 between the WM and IM groups at 12 weeks ($p > 0.05$). At 24 weeks, there were no differences in ACR responses among the TCM, WM, and IM groups (ACR-20: 73.04, 80.17, and 73.95%, respectively, $p = 0.3764$; ACR-50: 40.87, 47.93, and 51.26%, respectively, $p = 0.2674$; ACR-70: 20.87, 22.31, and 25.21%, respectively, $p = 0.7218$).

Based on the per protocol set (PPS), ACR-20 response at 12 weeks was significantly lower in the TCM group than in the WM and IM groups ($p < 0.05$) (**Tables 8**, **9**). There was no significant difference in ACR-50 and ACR-70 between the latter two groups at 12 weeks ($p > 0.05$). Similarly, at 24 weeks there were no differences in ACR responses among the TCM, WM, and IM groups (ACR-20: 73.45, 80.00, and 74.36%, respectively, $p = 0.4431$; ACR-50: 40.71, 48.33, and 51.28%, respectively, $p = 0.2540$; ACR-70: 20.35, 22.50, and 24.79%, respectively, $p = 0.7237$).

Safety

No patients died during the study period. More patients in the WM group ($n = 12$) discontinued treatment because of TRAEs than in the IM ($n = 3$) and TCM ($n = 2$) groups ($p < 0.05$) (**Tables 10**, **11**). Fewer patients in the TCM group reported gastrointestinal discomfort ($n = 4$) compared to the WM group (n = 18) and

TABLE 1 | Baseline characteristics of the study population (analysis based on full analysis set or safety set).

Characteristic	TCM group		WM group		IM group		P Value
	N (missing)	Mean (SD)/n (%)	N (missing)	Mean (SD)/n (%)	N (missing)	Mean (SD)/n (%)	
Age, years	139 (5)	47.86 (10.70)	139 (5)	48.74 (10.76)	141 (4)	48.11 (10.64)	0.7506
Male sex, n (%)	144 (0)	13 (9.03)	144 (0)	22 (15.28)	145 (0)	25 (17.24)	0.1082
Height, cm	144 (0)	160.43 (5.62)	143 (1)	161.05 (6.04)	145 (0)	161.96 (7.07)	0.2170
Weight, kg	144 (0)	59.39 (10.75)	143 (1)	60.21 (10.35)	145 (0)	60.16 (11.60)	0.7339
SBP, mmHg	149 (3)	121.38 (14.08)	153 (1)	120.99 (14.33)	150 (3)	121.39 (12.74)	0.9124
DBP, mmHg	149 (3)	77.06 (8.79)	153 (1)	77.37 (8.68)	150 (3)	77.19 (9.16)	0.8919
HR, bpm	148 (4)	78.91 (11.68)	150 (4)	76.92 (10.81)	145 (8)	78.10 (9.19)	0.1974
Respiration, times/min	146 (6)	18.42 (1.37)	150 (4)	18.65 (1.37)	147 (6)	18.58 (1.47)	0.3916
Duration, months	141 (3)	21.60 (17.40)	141 (3)	22.17 (19.21)	140 (5)	21.59 (17.78)	0.9832
Patients receiving other drugs, n (%)	140 (4)	66 (51.97)	133 (11)	62 (49.21)	139 (6)	56 (44.44)	0.4804
RF	127 (17)	280.81 (465.01)	127 (17)	321.01 (566.27)	129 (16)	222.66 (436.05)	0.7110
Anti-CCP	76 (68)	523.94 (797.23)	60 (84)	458.42 (756.70)	68 (77)	465.16 (651.49)	0.6533
ESR	140 (4)	42.54 (26.80)	144 (0)	41.68 (27.35)	143 (2)	42.25 (26.37)	0.9437
CRP	143 (1)	20.16 (27.38)	137 (7)	19.17 (26.40)	139 (6)	16.94 (19.76)	0.7649
Resting pain (VAS score, mm)	143 (1)	58.32 (17.11)	144 (0)	54.84 (19.01)	144 (1)	54.70 (18.76)	0.1660
Patient's global assessment (VAS score, mm)	143 (1)	59.60 (17.62)	144 (0)	56.91 (19.01)	144 (1)	60.22 (19.54)	0.2638
Physician's global assessment (VAS score, mm)	143 (1)	58.95 (15.18)	144 (0)	54.92 (17.41)	144 (1)	56.41 (18.61)	0.0899
Tender joint count	143 (1)	10.59 (6.62)	144 (0)	9.86 (5.88)	144 (1)	10.56 (6.95)	0.8209
Swollen joint count	143 (1)	7.41 (5.25)	144 (0)	6.80 (5.09)	144 (1)	7.40 (5.31)	0.4422
HAQ score	143 (1)	1.12 (0.65)	144 (0)	0.98 (0.64)	144 (1)	1.03 (0.65)	0.1328

Data are presented as mean (SD) unless otherwise indicated.
CCP, cyclic citrullinated peptide; CRP, C-reactive protein; DBP, diastolic blood pressure; ESR, erythrocyte sedimentation rate; HAQ, Health Assessment Questionnaire; HR, heart rate; IM, integrative medicine; RF, rheumatoid factor; SBP, systolic blood pressure; SD, standard deviation; TCM, traditional Chinese medicine; VAS, visual analog scale; WM, Western medicine.

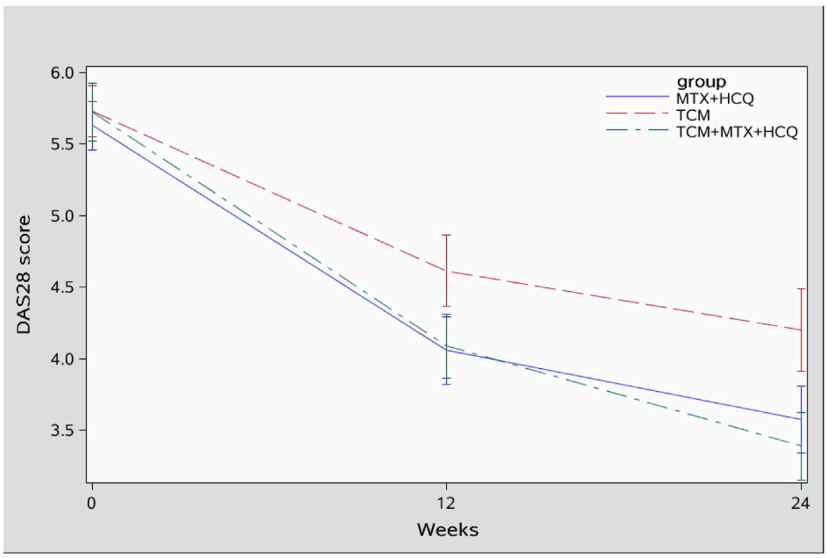

FIGURE 2 | Change in DAS-28 score (full analysis set). TCM, TCM group; MTX+HCQ, WM group; TCM+MTX+HCQ, IM group.

IM group ($n = 16$) ($p < 0.05$). Nausea occurred in one patient treated with TCM compared to eight patients in the WM group and 10 in IM the group ($p < 0.05$). Bacteriuria was also reported at a lower rate in patients treated with TCM ($n = 8$ vs. 20 with WM and 19 with IM) ($p < 0.05$). There was no significant difference in the frequency of other TRAEs among the groups. The overall rate of TRAEs was lower in the TCM group than in the other two groups ($p < 0.05$).

DISCUSSION

The pathogenesis of RA is unknown. The aims of currently recommended treatments are mainly to reduce inflammation, suppress disease activity and delay progression, and prevent bone deformity. RA is classified as "Bi syndrome" in TCM, which refers to a group of diseases involving joint and muscle pain such as RA,

TABLE 2 | Distribution of DAS-28 scores and their decline in patients (analysis based on full analysis set).

DAS 28	TCM group			WM group			IM group			*P* Value
	N (missing)	Mean (SD)	*P* Value	N (missing)	Mean (SD)	*P* Value	N (missing)	Mean (SD)	*P* Value	
DAS-28 score										
0 weeks	143 (1)	5.73 (1.08)	–	144 (0)	5.63 (1.02)	–	143 (2)	5.72 (1.23)	–	0.7013
12 weeks	127 (17)	4.61 (1.42)	<0.0001	124 (20)	4.06 (1.32)	<0.0001	129 (16)	4.09 (1.27)	<0.0001	0.0011*
24 weeks	115 (29)	4.20 (1.56)	<0.0001	120 (24)	3.58 (1.28)	<0.0001	113 (32)	3.39 (1.27)	<0.0001	0.0003*
DAS-28 difference value										
12 weeks	127 (17)	1.07 (1.11)	–	124 (20)	1.61 (1.12)	–	128 (17)	1.63 (1.29)	–	0.0005*
24 weeks	115 (29)	1.60 (1.17)	–	120 (24)	2.10 (1.12)	–	112 (33)	2.24 (1.40)	–	0.0006*

*p < *0.05*.

DAS, disease activity score; IM, integrative medicine; SD, standard deviation; TCM, traditional Chinese medicine; WM, Western medicine.

TABLE 3 | Distribution of DAS-28 scores and their decline in patients (analysis based on per protocol set).

DAS 28	TCM group			WM group			IM group			*P* Value
	N (missing)	Mean (SD)	*P* Value	N (missing)	Mean (SD)	*P* Value	N (missing)	Mean (SD)	*P* Value	
DAS-28 score										
0 weeks	113 (0)	5.82 (1.05)	–	121 (0)	5.68 (0.99)	–	116 (1)	5.65 (1.11)	–	0.4055
12 weeks	108 (5)	4.64 (1.45)	<0.0001	118 (3)	4.05 (1.32)	<0.0001	115 (2)	4.10 (1.26)	<0.0001	0.0016*
24 weeks	113 (0)	4.21 (1.57)	<0.0001	119 (2)	3.57 (1.28)	<0.0001	111 (6)	3.41 (1.27)	<0.0001	0.0005*
DAS-28 difference value										
12 weeks	108 (5)	1.17 (1.03)	–	118 (3)	1.64 (1.11)	–	114 (3)	1.57 (1.14)	–	0.0031*
24 weeks	113 (0)	1.62 (1.18)	–	119 (2)	2.10 (1.13)	–	110 (7)	2.23 (1.37)	–	0.0011*

*p < *0.05*.

DAS, disease activity score; IM, integrative medicine; SD, standard deviation; TCM, traditional Chinese medicine; WM, Western medicine.

TABLE 4 | Comparisons of the decline in DAS-28 score between treatment groups (analysis based on full analysis set).

DAS 28	TCM vs. MTX + HCQ		MTX + HCQ vs. TCM + MTX + HCQ		TCM vs. TCM + MTX + HCQ	
	Statistic (Z/t)	*P* Value	Statistic (Z/t)	*P* Value	Statistic (Z/t)	*P* Value
DAS-28 score						
0 weeks	0.79 (t)	0.4283	0.83 (Z)	0.4037	0.04 (t)	0.9656
12 weeks	3.21 (t)	0.0015*	–0.18 (t)	0.8576	3.12 (t)	0.0020*
24 weeks	2.93 (Z)	0.0034*	1.12 (t)	0.2640	–3.85 (Z)	0.0001*
DAS-28 difference value						
12 weeks	3.50 (Z)	0.0005*	0.27 (Z)	0.7881	–3.20 (Z)	0.0014*
24 weeks	–3.28 (Z)	0.0010*	0.53 (Z)	0.5978	–3.74 (t)	0.0002*

*p < *0.05*.

DAS, disease activity score; HCQ, hydroxychloroquine; MTX, methotrexate; TCM, traditional Chinese medicine.

TABLE 5 | Comparisons of the decline in DAS-28 score between treatment groups (analysis based on per protocol set).

DAS 28	TCM vs. MTX + HCQ		MTX + HCQ vs. TCM + MTX + HCQ		TCM vs. TCM + MTX + HCQ	
	Statistic (Z/t)	*P* Value	Statistic (Z/t)	*P* Value	Statistic (Z/t)	*P* Value
DAS-28 score						
0 weeks	1.11 (t)	0.2668	0.18 (t)	0.8608	1.21 (t)	0.2294
12 weeks	3.20 (t)	0.0016*	–0.30 (t)	0.7623	2.98 (t)	0.0032*
24 weeks	2.99 (Z)	0.0028*	0.91 (t)	0.3622	–3.68 (Z)	0.0002*
DAS-28 difference value						
12 weeks	–3.17 (Z)	0.0015*	–0.49 (Z)	0.6240	–2.67 (Z)	0.0075*
24 weeks	–3.13 (Z)	0.0017*	0.50 (Z)	0.6198	–3.57 (t)	0.0004*

*p < *0.05*.

DAS, disease activity score; HCQ, hydroxychloroquine; MTX, methotrexate; TCM, traditional Chinese medicine.

TABLE 6 | ACR-20, ACR-50, and ACR-70 measurements (analysis based on full analysis set).

ACR	TCM group		WM group		IM group		*P* Value
	N (missing)	Effective no. (%)	N (missing)	Effective no. (%)	N (missing)	Effective no. (%)	
ACR-20							
12 weeks	135 (9)	59 (43.70)	129 (15)	77 (59.69)	135 (10)	81 (60.00)	0.0092*
24 weeks	115 (29)	84 (73.04)	121 (23)	97 (80.17)	119 (26)	88 (73.95)	0.3764
ACR-50							
12 weeks	135 (9)	25 (18.52)	129 (15)	33 (25.58)	135 (10)	33 (24.44)	0.3362
24 weeks	115 (29)	47 (40.87)	121 (23)	58 (47.93)	119 (26)	61 (51.26)	0.2674
ACR-70							
12 weeks	135 (9)	5 (3.70)	129 (15)	13 (10.08)	135 (10)	15 (11.11)	0.0578
24 weeks	115 (29)	24 (20.87)	121 (23)	27 (22.31)	119 (26)	30 (25.21)	0.7218

*p < *0.05*.

ACR-20/-50/-70, American College of Rheumatology 20%/50%/70% improvement criteria; IM, integrative medicine; TCM, traditional Chinese medicine; WM, Western medicine.

TABLE 7 | ACR-20, ACR-50, and ACR-70 measurements (analysis based on per protocol set).

ACR	TCM group		WM group		IM group		*P* Value
	N (missing)	Effective no. (%)	N (missing)	Effective no. (%)	N (missing)	Effective no. (%)	
ACR-20							
12 weeks	113 (0)	52 (46.02)	121 (0)	74 (61.16)	117 (0)	73 (62.39)	0.0205*
24 weeks	113 (0)	83 (73.45)	120 (1)	96 (80.00)	117 (0)	87 (74.36)	0.4431
ACR-50							
12 weeks	113 (0)	21 (18.58)	121 (0)	31 (25.62)	117 (0)	29 (24.79)	0.3832
24 weeks	113 (0)	46 (40.71)	120 (1)	58 (48.33)	117 (0)	60 (51.28)	0.2540
ACR-70							
12 weeks	113 (0)	5 (4.42)	121 (0)	13 (10.74)	117 (0)	12 (10.26)	0.1619
24 weeks	113 (0)	23 (20.35)	120 (1)	27 (22.50)	117 (0)	29 (24.79)	0.7237

*p < *0.05*.

ACR-20/-50/-70, American College of Rheumatology 20%/50%/70% improvement criteria; IM, integrative medicine; TCM, traditional Chinese medicine; WM, Western medicine.

TABLE 8 | Comparisons of ACR-20, ACR-50, and ACR-70 standard remission between treatment groups (analysis based on full analysis set).

ACR	TCM vs. MTX + HCQ		MTX + HCQ vs. TCM + MTX + HCQ		TCM vs. TCM + MTX + HCQ	
	Statistic (χ^2)	*P* Value	Statistic (χ^2)	*P* Value	Statistic (χ^2)	*P* Value
ACR-20						
12 weeks	6.75(χ2)	0.0094*	0.00(χ2)	0.9590	7.18(χ2)	0.0074*
24 weeks	1.67(χ2)	0.1958	1.31(χ2)	0.2520	0.02(χ2)	0.8752
ACR-50						
12 weeks	1.92(χ2)	0.1659	0.05(χ2)	0.8311	1.41(χ2)	0.2358
24 weeks	1.19(χ2)	0.2750	0.27(χ2)	0.6063	2.54(χ2)	0.1109
ACR-70						
12 weeks	4.22(χ2)	0.0400*	0.07(χ2)	0.7851	5.40(χ2)	0.0201*
24 weeks	0.07(χ2)	0.7876	0.28(χ2)	0.5981	0.62(χ2)	0.4308

*p < *0.05*.

ACR-20/-50/-70, American College of Rheumatology 20%/50%/70% improvement criteria; HCQ, hydroxychloroquine; MTX, methotrexate; TCM, traditional Chinese medicine.

osteoarthritis, soft tissue damage, etc. The philosophy of TCM is to maintain overall health and intervene at early stages of disease to prevent progression. However, there is no professional term of "active RA" in TCM. Joint swelling and pain caused by inflammation in RA is considered to be related to dampness, heat, and stasis, which are similar to the active (inflammatory) period of RA (Liu and Jiang, 2020). Therefore, we take the internationally recognized disease activity evaluation standard DAS-28 > 3.2 as the objective identification of RA "damp-heat-stasis syndrome".

The results of this study demonstrate that TCM treatment is both effective and safe for the treatment of active RA compared to

TABLE 9 | Comparisons of ACR-20, ACR-50, and ACR-70 standard remission between treatment groups (analysis based on per protocol set).

ACR	TCM vs. MTX + HCQ		MTX + HCQ vs. TCM + MTX + HCQ		TCM vs. TCM + MTX + HCQ	
	Statistic (χ^2)	P Value	Statistic (χ^2)	P Value	Statistic (χ^2)	P Value
ACR-20						
12 weeks	5.39(χ2)	0.0203*	0.04(χ2)	0.8445	6.21(χ2)	0.0127*
24 weeks	1.40(χ2)	0.2364	1.07(χ2)	0.3006	0.02(χ2)	0.8755
ACR-50						
12 weeks	1.67(χ2)	0.1958	0.02(χ2)	0.8823	1.30(χ2)	0.2543
24 weeks	1.37(χ2)	0.2419	0.21(χ2)	0.6499	2.59(χ2)	0.1078
ACR-70						
12 weeks	3.29(χ2)	0.0699	0.02(χ2)	0.9024	2.86(χ2)	0.0910
24 weeks	0.16(χ2)	0.6901	0.17(χ2)	0.6787	0.65(χ2)	0.4218

*p < *0.05*.

ACR-20/-50/-70, American College of Rheumatology 20%/50%/70% improvement criteria; HCQ, hydroxychloroquine; MTX, methotrexate; TCM, traditional Chinese medicine.

TABLE 10 | Adverse events (analysis based on safety set).

Adverse event	TCM group (*n* = 152)	WM group (*n* = 154)	IM group (*n* = 153)	*P* Value
Deaths	0	0	0	
SAEs	0	0	0	
Discontinuation due to AE	2 (1.32)	12 (7.79)	3 (1.96)	0.0042*
Discontinuation due to SAEs	0	0	0	
Gastrointestinal	4 (2.63)	18 (11.69)	16 (10.46)	0.0078*
Nausea	1 (0.66)	8 (5.19)	10 (6.54)	0.0261*
Vomit	0 (0.00)	5 (3.25)	3 (1.96)	0.1063
Hiccup	0 (0.00)	1 (0.65)	0 (0.00)	1.0000
Abdominal pain	0 (0.00)	1 (0.65)	0 (0.00)	1.0000
Stomachache	1 (0.66)	2 (1.30)	0 (0.00)	0.6638
Diarrhea	0 (0.00)	1 (0.65)	2 (1.31)	0.6638
Constipation	0 (0.00)	0 (0.00)	1 (0.65)	0.6645
Acid reflux	0 (0.00)	2 (1.30)	3 (1.96)	0.3372
Anorexia	0 (0.00)	5 (3.25)	4 (2.61)	0.0852
Epigastric distension	1 (0.66)	0 (0.00)	0 (0.00)	0.3312
Epigastric discomfort	2 (1.32)	2 (1.30)	1 (0.65)	0.8746
Infection	3 (1.97)	7 (4.55)	6 (3.92)	0.4419
Cold	2 (1.32)	6 (3.90)	2 (1.31)	0.3408
Pulmonary infection	0 (0.00)	0 (0.00)	1 (0.65)	0.6645
Urinary infection	1 (0.66)	3 (1.95)	3 (1.96)	0.7081
Other	7 (4.61)	20 (12.99)	16 (10.46)	0.0360*
Headache	0 (0.00)	3 (1.95)	2 (1.31)	0.3790
Fatigue	0 (0.00)	1 (0.65)	1 (0.65)	1.0000
Arrhythmia	1 (0.66)	0 (0.00)	3 (1.96)	0.1813
Insomnia	0 (0.00)	0 (0.00)	2 (1.31)	0.2198
Hair loss	1 (0.66)	2 (1.30)	3 (1.96)	0.7910
Mouth ulcer	0 (0.00)	1 (0.65)	1 (0.65)	1.0000
Cough	0 (0.00)	1 (0.65)	1 (0.65)	1.0000
Dry mouth	0 (0.00)	0 (0.00)	1 (0.65)	0.6645
Dry eye	0 (0.00)	1 (0.65)	0 (0.00)	1.0000
Rash	1 (0.66)	4 (2.60)	2 (1.31)	0.5149
Pigmentation	0	0	0	
Leukopenia	2 (1.32)	3 (1.95)	1 (0.65)	0.7910
Abnormal liver function	2 (1.32)	2 (1.30)	0 (0.00)	0.4776
Menstrual disorder	0 (0.00)	1 (0.65)	2 (1.31)	0.6638
Operation	0 (0.00)	0 (0.00)	1 (0.65)	0.6645
Frequent urination	0 (0.00)	2 (1.30)	0 (0.00)	0.3319
Joint swelling and pain	1 (0.66)	0 (0.00)	0 (0.00)	0.3312
Hyperthyroidism	0 (0.00)	1 (0.65)	0 (0.00)	1.0000
Pleural effusion	0 (0.00)	1 (0.65)	0 (0.00)	1.0000
Anemia	0 (0.00)	0 (0.00)	1 (0.65)	0.6645

Data are presented as n (%).

*p < *0.05*.

AE, adverse event; IM, integrative medicine; SAE, serious adverse event; TCM, traditional Chinese medicine; WM, Western medicine.

TABLE 11 | Laboratory parameters (analysis based on safety set).

Adverse event	TCM group (*n* = 152)	WM group (*n* = 154)	IM group (*n* = 153)	*P* Value
Hematologic abnormalities	24 (15.79)	19 (12.34)	13 (8.50)	0.2178
Abnormal WBC count	9 (5.92)	9 (5.84)	7 (4.58)	0.9205
Abnormal HGB level	8 (5.26)	4 (2.60)	4 (2.61)	0.4183
Abnormal platelet count	12 (7.89)	7 (4.55)	4 (2.61)	0.1375
Routine urinalysis	22 (14.47)	34 (22.08)	37 (24.18)	0.2914
Hematuria	13 (8.55)	11 (7.14)	12 (7.84)	0.9922
Proteinuria	6 (3.95)	13 (8.44)	17 (11.11)	0.1982
Bacteriuria	8 (5.26)	20 (12.99)	19 (12.42)	0.0297*
Liver function	11 (7.24)	14 (9.09)	9 (5.88)	0.2996
Abnormal ALT (>40 U/l)	7 (4.61)	10 (6.49)	4 (2.61)	0.2531
Abnormal AST (>35 U/l)	8 (5.26)	8 (5.19)	8 (5.23)	0.4544
Renal function	21 (13.82)	13 (8.44)	9 (5.88)	0.0624
Abnormal creatinine (>84 μmol/l)	14 (9.21)	6 (3.90)	8 (5.23)	0.2291
Abnormal urea nitrogen (>8.2 mmol/l)	7 (4.61)	8 (5.19)	2 (1.31)	0.3191
Abnormal ECG	10 (6.58)	9 (5.84)	10 (6.54)	0.9516

Data are presented as n (%).

**p<0.05.*

AE, adverse event; ALT, alanine aminotransferase; AST, aspartate aminotransferase; ECG, electrocardiogram; HGB, hemoglobin; IM, integrative medicine; SAE, serious adverse event; TCM, traditional Chinese medicine; WBC, white blood cell; WM, Western medicine.

csDMARDs. DAS-28 at 24 weeks was lower in patients treated with QRHXD alone than in those treated with MTX plus HCQ; thus, Qingre Huoxue treatment did not have the expected therapeutic advantage over standard RA treatments. However, it is worth noting that the score was lower in the IM group than in the WM group at the end of the treatment period, suggesting that QRHXD can enhance the efficacy of csDMARDs. It was previously reported that QRHXD is suitable for the treatment of "damp-heat-stasis" as it delayed disease activity by reducing inflammation and potentially conferred bone protection (Jiang et al., 2012). In line with the comprehensive treatment approaches used in TCM, patients received QRHXD and QRHXEP during the active period of RA. QRHXEP should not be ignored in efficacy assessments; however, as a topical formulation, its effects begin to decline after about 4 weeks and last only 12 weeks; thus, by the end of the 24-week study period, QRHXD was likely responsible for the observed therapeutic effects of TCM.

In order to standardize the evaluation of "damp-heat-stasis syndrome", we used DAS-28 > 3.2 to define the active period of RA. DAS-28 (Prevoo et al., 1995), which is based on a count of 28 swollen and tender joints and ranges from 0 to 9.4, can be used to objectively evaluate a patient's response to treatment (Fransen and van Riel, 2009). The European League Against Rheumatism response criteria combine the DAS-28 score at the time of evaluation with the change in DAS-28 score between two time points, which is a more useful measure of treatment response (van Gestel et al., 1998). Combining DAS-28 score and ACR-20/50/70 can provide more information on the therapeutic benefit of TCM for the treatment of RA beyond its effect on joints (He et al., 2007; He et al., 2008; He et al., 2014).

This is the first registered randomized controlled trial investigating the efficacy and safety of TCM Qingre Huoxue treatment compared to csDMARDs in active RA. Given the large sample size and the involvement of numerous medical centers, the results are representative of the Chinese population. We found that the TCM Qingre Huoxue treatment improved DAS-28 from baseline to week 24, whether it was administered alone or in combination with MTX and HCQ. In the FAS, ACR-20 was 73.04%, ACR-50 was 40.87%, and ACR-70 was 20.87% with TCM Qingre Huoxue treatment at 24 weeks; the TCM efficacy at the end of the study was only slightly lower than that observed in the WM and IM groups. In this study, we found that Qingre Huoxue treatment can improve DAS-28 score and ACR-20/50/70 by improving joint tenderness, joint swelling, ESR and CRP. According to other studies (He et al., 2007; He et al., 2014), ACR-20 and ACR-50 responses with WM treatment were higher at 24 weeks than in the TCM group. Whether a therapeutic advantage of TCM over MTX and HCQ will be revealed with a longer follow-up period remains to be determined. At 24 weeks, ACR-20/50/70 was similar in patients treated with QRHXD alone to in those treated with MTX plus HCQ. In clinical practice, we often use QRHXD as a prescription for RA patients from active stage to remission stage, whether a longer follow-up might show further benefit for QRHXD treatment can only be answered with such a longer study.

In our study, subjects in the WM group received a combination the csDMARDs MTX and HCQ (Singh et al., 2016). In China, most rheumatologists choose to use two kinds of csDMARDs combined with drugs in the treatment of active RA patients, and MTX alone is only used for RA patients with mild condition. The combination of MTX and HCQ is the most commonly used prescription. Therefore, MTX + HCQ is more representative in China. With this treatment, DAS-28 score in the FAS decreased and ACR-20/50/70 responses were 80.17, 47.93, and 22.31%, respectively, at 24 weeks, which is in line with results obtained in other studies (O'Dell et al., 2002; Hua et al., 2020; Zhang et al., 2020). In one study, an ACR-20 of 71.4% was reported after 24 weeks with MTX treatment alone, which was lower than the response achieved with the combination of MTX and HCQ (Westhovens et al., 2021). In our study, there were no differences in ACR-20/50/70 among the three groups at 24 weeks.

The TCM group had the lowest rate of TRAEs. Patients in the WM group were more likely to discontinue treatment due to TRAEs,

and reported significantly higher rates of gastrointestinal discomfort (e.g., nausea) and bacteriuria along with the IM group compared to patients treated with TCM. These data suggest that TCM is more suitable for RA patients with poor gastrointestinal function or urinary tract bacterial infection, especially as the use of TCM did not increase the risk of infections (**Table 10**).

CONCLUSION

The results of this study provide evidence that Qingre Huoxue treatment (QRHXD plus QRHXEP) is effective for the treatment of patients with active RA, with a better safety profile than MTX and HCQ. While the efficacy of QRHXD alone was lower than that of the two csDMARDs, combining QRHXD with MTX and HCQ yielded the greatest improvement in disease activity. The efficacy of QRHXD alone was similar to that of MTX + HCQ in achieving ACR-20/50/70. Thus, QRHXD is a useful adjunct that should be considered as a viable option in the management of RA.

DATA AVAILABILITY STATEMENT

The original contributions presented in the study are included in the article/**Supplementary Material**, further inquiries can be directed to the corresponding authors.

ETHICS STATEMENT

The studies involving human participants were reviewed and approved by the ethics committee at Guang'anmen Hospital, China Academy of Chinese Medical Sciences. The patients/participants provided their written informed consent to participate in this study.

AUTHOR CONTRIBUTIONS

QJ and CZ designed the study. X-PT, JW, JL, Q-CH, WL, Y-FF, D-YH, YL, M-LG, Q-JW, SC, Z-BL, YW, Y-MX, J-LZ, C-YZ, LM, and X-CW performed the experiments. Feng Tian and W-XL analyzed the data. XG and W-XL wrote the manuscript. All authors read and approved the final version of the manuscript for publication.

FUNDING

This study was supported by the National Key Research and Development Program (No. 2018YFC1705202; "Clinical Cohort and Efficacy Evaluation Study of Traditional Chinese Medicine in the Treatment of Rheumatoid Arthritis") and the Chinese National Science and Technology Support Program (No. 2013BAI02B06; "Study on the Regularity of TCM Disease and Syndromes and Comprehensive Treatment of Rheumatoid Arthritis").

ACKNOWLEDGMENTS

We thank Feng Tian at Beijing CreateMed Medicine Technology Co. (Beijing, China) for assistance with statistical analyses and manuscript preparation.

SUPPLEMENTARY MATERIAL

The Supplementary Material for this article can be found online at: https://www.frontiersin.org/articles/10.3389/fphar.2021.679588/full#supplementary-material

REFERENCES

Abbasi, M., Mousavi, M. J., Jamalzehi, S., Alimohammadi, R., Bezvan, M. H., Mohammadi, H., et al. (2019). Strategies toward Rheumatoid Arthritis Therapy; the Old and the New. *J. Cel. Physiol.* 234, 10018–10031. doi:10.1002/jcp.27860

Aletaha, D., Neogi, T., Silman, A. J., Funovits, J., Felson, D. T., Bingham, C. O., 3rd, et al. (2010). 2010 Rheumatoid Arthritis Classification Criteria: An American College of Rheumatology/European League against Rheumatism Collaborative Initiative. *Arthritis Rheum.* 62, 2569–2581. doi:10.1002/art.27584

Arnett, F. C., Edworthy, S. M., Bloch, D. A., McShane, D. J., Fries, J. F., Cooper, N. S., et al. (1988). The American Rheumatism Association 1987 Revised Criteria for the Classification of Rheumatoid Arthritis. *Arthritis Rheum.* 31, 315–324. doi:10.1002/art.1780310302

Bruce, B., and Fries, J. F. (2005). The Health Assessment Questionnaire (HAQ). *Clin. Exp. Rheumatol.* 23, S14–S18.

Chinese Pharmacopoeia Commission (2005). [*Pharmacopoeia of the People's Republic of China*]. Beijing: People's Medical Publishing House.

Chinese Rheumatology Association (2018). 2018 Chinese Guideline for the Diagnosis and Treatment of Rheumatoid Arthritis. *Zhonghua Nei Ke Za Zhi* 57, 242–251. article in Chinese. doi:10.3760/cma.j.issn.0578-1426.2018.04.004

China Association of Chinese Medicine. (2017). [Guidelines for Diagnosis and Treatment of Rheumatoid Arthritis Based on Combination of Disease and Syndrome]. *Chin. Med. (Cptcm)* 10, 1–9. article in Chinese.

Felson, D. T., Anderson, J. J., Boers, M., Bombardier, C., Furst, D., Goldsmith, C., et al. (1995). American College of Rheumatology Preliminary Definition of Improvement in Rheumatoid Arthritis. *Arthritis Rheum.* 38, 727–735. doi:10.1002/art.1780380602

Fransen, J., and van Riel, P. L. C. M. (2009). The Disease Activity Score and the EULAR Response Criteria. *Rheum. Dis. Clin. North America* 35, 745–757. doi:10.1016/j.rdc.2009.10.001

Giraud, E. L., Jessurun, N. T., van Hunsel, F. P. A. M., van Puijenbroek, E. P., van Tubergen, A., Ten Klooster, P. M., et al. (2020). Frequency of Real-World Reported Adverse Drug Reactions in Rheumatoid Arthritis Patients. *Expert Opin. Drug Saf.* 19, 1617–1624. doi:10.1080/14740338.2020.1830058

He, Y.-t., Ou, A.-h., Yang, X.-b., Chen, W., Fu, L.-y., Lu, A.-p., et al. (2014). Traditional Chinese Medicine versus Western Medicine as Used in China in the Management of Rheumatoid Arthritis: A Randomized, Single-Blind, 24-week Study. *Rheumatol. Int.* 34, 1647–1655. doi:10.1007/s00296-014-3010-6

He, Y., Lu, A., Zha, Y., and Tsang, I. (2008). Differential Effect on Symptoms Treated with Traditional Chinese Medicine and Western Combination Therapy in RA Patients. *Complement. Therapies Med.* 16, 206–211. doi:10.1016/j.ctim.2007.08.005

He, Y., Lu, A., Zha, Y., Yan, X., Song, Y., Zeng, S., et al. (2007). Correlations between Symptoms as Assessed in Traditional Chinese Medicine (TCM) and ACR20 Efficacy Response. *J. Clin. Rheumatol.* 13, 317–321. doi:10.1097/RHU.0b013e31815d019b

Hua, L., Du, H., Ying, M., Wu, H., Fan, J., and Shi, X. (2020). Efficacy and Safety of Low-Dose Glucocorticoids Combined with Methotrexate and Hydroxychloroquine in the Treatment of Early Rheumatoid Arthritis. *Medicine (Baltimore)* 99, e20824. doi:10.1097/MD.0000000000020824

Jiang, Q., Zhou, X.-y., Wang, L., Yu, W., Wang, P., Cao, W., et al. (2012). A One-Year Evaluation of Radiographic Progression in Patients with Rheumatoid Arthritis Treated by Qingre Huoxue Decoction. *Chin. J. Integr. Med.* 18, 256–261. doi:10.1007/s11655-011-0793-0

Jiao, J., Tang, X., Gong, X., Yin, H., Jiang, Q., and Wei, C. (2019). Effect of Cream, Prepared with *Tripterygium Wilfordii* Hook F and Other Four Medicinals, on Joint Pain and Swelling in Patients with Rheumatoid Arthritis: A Double-Blinded, Randomized, Placebo Controlled Clinical Trial. *J. Tradit. Chin. Med.* 39, 89–96.

Jin, S., Li, M., Li, M., Fang, Y., Li, Q., Liu, J., et al. (2017). Chinese Registry of Rheumatoid Arthritis (CREDIT): II. Prevalence and Risk Factors of Major Comorbidities in Chinese Patients with Rheumatoid Arthritis. *Arthritis Res. Ther.* 19, 251. doi:10.1186/s13075-017-1457-z

Lau, C. S., Chia, F., Dans, L., Harrison, A., Hsieh, T. Y., Jain, R., et al. (2019). 2018 Update of the APLAR Recommendations for Treatment of Rheumatoid Arthritis. *Int. J. Rheum. Dis.* 22, 357–375. doi:10.1111/1756-185X.13513

Liu, W. X., and Jiang, Q. (2020). Exploration of the Pathogenesis Theory of "Dampness-heat-stasis" in Rheumatoid Arthritis. *J. Tradit. Chin. Med.* 61, 2148–2153. article in Chinese.

Lu, M.-C., Livneh, H., Chiu, L.-M., Lai, N.-S., Yeh, C.-C., and Tsai, T.-Y. (2019). A Survey of Traditional Chinese Medicine Use Among Rheumatoid Arthritis Patients: A Claims Data-Based Cohort Study. *Clin. Rheumatol.* 38, 1393–1400. doi:10.1007/s10067-018-04425-w

Lu, Z. Z., and Jiao, S. D. (1996). *Diagnostic Criteria of National Integrated Traditional and Western Academic Conference on Rheumatism (1988).* Beijing, China: People Public Health Publishing Company, Vol. 456, 16..

O'Dell, J. R., Leff, R., Paulsen, G., Haire, C., Mallek, J., Eckhoff, P. J., et al. (2002). Treatment of Rheumatoid Arthritis with Methotrexate and Hydroxychloroquine, Methotrexate and Sulfasalazine, or a Combination of the Three Medications: Results of a Two-Year, Randomized, Double-Blind, Placebo-Controlled Trial. *Arthritis Rheum.* 46, 1164–1170. doi:10.1002/art.10228

Pincus, T., Yazici, Y., Sokka, T., Aletaha, D., and Smolen, J. S. (2003). Methotrexate as the "Anchor Drug" for the Treatment of Early Rheumatoid Arthritis. *Clin. Exp. Rheumatol.* 21, S179–S185.

Prevoo, M. L. L., Van'T Hof, M. A., Kuper, H. H., van Leeuwen, M. A., van de Putte, L. B. A., and van Riel, P. L. C. M. (1995). Modified Disease Activity Scores that Include Twenty-Eight-Joint Counts Development and Validation in a Prospective Longitudinal Study of Patients with Rheumatoid Arthritis. *Arthritis Rheum.* 38, 44–48. doi:10.1002/art.1780380107

Singh, J. A., Saag, K. G., Bridges, S. L., Jr, Akl, E. A., Bannuru, R. R., Sullivan, M. C., et al. (2016). 2015 American College of Rheumatology Guideline for the Treatment of Rheumatoid Arthritis. *Arthritis Rheumatol.* 68, 1–26. doi:10.1002/art.39480

Smolen, J. S., Landewé, R. B. M., Bijlsma, J. W. J., Burmester, G. R., Dougados, M., Kerschbaumer, A., et al. (2020). EULAR Recommendations for the Management of Rheumatoid Arthritis with Synthetic and Biological Disease-Modifying Antirheumatic Drugs: 2019 Update. *Ann. Rheum. Dis.* 79, 685–699. doi:10.1136/annrheumdis-2019-216655

van der Woude, D., and van der Helm-van Mil, A. H. M. (2018). Update on the Epidemiology, Risk Factors, and Disease Outcomes of Rheumatoid Arthritis. *Best Pract. Res. Clin. Rheumatol.* 32, 174–187. doi:10.1016/j.berh.2018.10.005

van Gestel, A. M., Haagsma, C. J., and van Riel, P. L. C. M. (1998). Validation of Rheumatoid Arthritis Improvement Criteria that Include Simplified Joint Counts. *Arthritis Rheum.* 41, 1845–1850. doi:10.1002/1529-0131(199810)41:10<1845::aid-art17>3.0.co;2-k

Wells, G., Becker, J.-C., Teng, J., Dougados, M., Schiff, M., Smolen, J., et al. (2009). Validation of the 28-joint Disease Activity Score (DAS28) and European League against Rheumatism Response Criteria Based on C-Reactive Protein against Disease Progression in Patients with Rheumatoid Arthritis, and Comparison with the DAS28 Based on Erythrocyte Sedimentation Rate. *Ann. Rheum. Dis.* 68, 954–960. doi:10.1136/ard.2007.084459

Westhovens, R., Rigby, W. F. C., van der Heijde, D., Ching, D. W. T., Stohl, W., Kay, J., et al. (2021). Filgotinib in Combination with Methotrexate or as Monotherapy versus Methotrexate Monotherapy in Patients with Active Rheumatoid Arthritis and Limited or No Prior Exposure to Methotrexate: The Phase 3, Randomised Controlled FINCH 3 Trial. *Ann. Rheum. Dis.*, doi:10.1136/annrheumdis-2020-219213

Xing, Q., Fu, L., Yu, Z., and Zhou, X. (2020). Efficacy and Safety of Integrated Traditional Chinese Medicine and Western Medicine on the Treatment of Rheumatoid Arthritis: A Meta-Analysis. *Evidence-Based Complement. Altern. Med.* 2020, 1–15. doi:10.1155/2020/4348709

Zhang, L., Chen, F., Geng, S., Wang, X., Gu, L., Lang, Y., et al. (2020). Methotrexate (MTX) Plus Hydroxychloroquine versus MTX Plus Leflunomide in Patients with MTX-Resistant Active Rheumatoid Arthritis: A 2-year Cohort Study in Real World. *J. Inflamm. Res.* Vol. 13, 1141–1150. doi:10.2147/JIR.S282249

Zhang, S., Wang, X., Li, C., An, Y., Zhou, Y. S., Liu, J., et al. (2013). Investigation of Hydroxychloroquine Use in Rheumatoid Arthritis Patients in China. *Chin. J. Rheumatol.* 17, 585–590. article in Chinese.

Zheng, X. Y. (2002). Clinical Research Criteria on Treating RA by Chinese Herbs. *Med. Sci. Technol. Press. China* 5, 115–119.

Conflict of Interest: The authors declare that the research was conducted in the absence of any commercial or financial relationships that could be construed as a potential conflict of interest.

The handling editor declared a shared affiliation with several of the authors XG WL XT JW YX CZ, and QJ at time of review.

Copyright © 2021 Gong, Liu, Tang, Wang, Liu, Huang, Liu, Fang, He, Liu, Gao, Wu, Chen, Li, Wang, Xie, Zhang, Zhou, Ma, Wang, Zhang and Jiang. This is an open-access article distributed under the terms of the Creative Commons Attribution License (CC BY). The use, distribution or reproduction in other forums is permitted, provided the original author(s) and the copyright owner(s) are credited and that the original publication in this journal is cited, in accordance with accepted academic practice. No use, distribution or reproduction is permitted which does not comply with these terms.

frontiers in Pharmacology

ORIGINAL RESEARCH
published: 04 June 2021
doi: 10.3389/fphar.2021.669551

Identification of the Main Active Components and Mechanism of Wang Bi Tablet in Treating Rheumatoid Arthritis Based on Integrative Pharmacology

*Yuanyuan Jiao[1,2†], Jia Xu[3†], Hong Chen[1,4†], Qiuyan Guo[1], Xiaofang Deng[1], Tong Zhang[1], Jingbo Zhang[1], Chenjing Shi[1] and Ping Wang[1]**

[1]Institute of Chinese Materia Medica, China Academy of Chinese Medical Sciences, Beijing, China, [2]College of Traditional Chinese Medicine, Tianjin University of Traditional Chinese Medicine, Tianjin, China, [3]Affiliated Hospital of Guizhou Medical University, Guiyang, China, [4]College of Traditional Chinese Medicine, Shenyang Pharmaceutical University, Shenyang, China

OPEN ACCESS

Edited by:
Yan Xu,
Cleveland State University,
United States

Reviewed by:
Jihan Huang,
Shanghai University of Traditional Chinese Medicine, China
Augusto Zuluaga-Vélez,
Technological University of Pereira, Colombia
Retno Widyowati,
Airlangga University, Indonesia

***Correspondence:**
Ping Wang
hudielanwp@sina.com

[†]These authors have contributed equally to this work.

Specialty section:
This article was submitted to Ethnopharmacology, a section of the journal Frontiers in Pharmacology

Received: *19 February 2021*
Accepted: *28 April 2021*
Published: *04 June 2021*

Citation:
Jiao Y, Xu J, Chen H, Guo Q, Deng X, Zhang T, Zhang J, Shi C and Wang P (2021) Identification of the Main Active Components and Mechanism of Wang Bi Tablet in Treating Rheumatoid Arthritis Based on Integrative Pharmacology. Front. Pharmacol. 12:669551. doi: 10.3389/fphar.2021.669551

Wang Bi tablet (WBT) is used to treat rheumatoid arthritis (RA) in China. We employed integrative pharmacology, including rapid analysis of chemical composition, pharmacological experiment, and network pharmacology analysis, to elucidate the active components and mechanism underlying the effect of WBT against RA. The chemical fingerprint of WBT was revealed by UPLC-QTOF-MS/MS, and the chemical composition was identified. The anti-inflammatory effect of WBT was evaluated in TNF-α-stimulated RAW264.7 cells by ELISA and transcriptome sequencing. Network pharmacology analysis, functional enrichment analysis, and network visualization were performed. A total of 293 chemical constituents were preliminarily identified or tentatively characterized in WBT extract, and they effectively inhibited inflammatory response in TNF-α-stimulated RAW264.7 cells. Forty-eight key active constituents were identified based on high-frequency binding to hub targets and their corresponding targets number. Next, 135 corresponding hub genes, which may be the putative targets of WBT in treating RA, were selected. Functionally, the putative targets were significantly associated with the inflammatory immune response regulation module, energy metabolism regulation module, and cell function regulation module, corresponding to the traditional efficacy of WBT. In summary, this study revealed, for the first time using integrative pharmacology, that WBT may attenuate RA through the inflammation-immune regulation system.

Keywords: TCMIP, integrative pharmacology strategy, UPLC-QTOF-MS/MS, rheumatoid arthritis, Wang Bi Tablet

INTRODUCTION

Rheumatoid arthritis (RA) is a chronic autoimmune disease characterized by synovial hyperplasia, inflammatory cell infiltration, pannus formation, and destruction of articular cartilage and bone matrix, and this disease develops symmetrically and destructively, eventually leading to articular deformity and loss of function (Smolen et al., 2016; Burmester and Pope, 2017; McInnes and Schett, 2017; Aletaha and Smolen, 2018). RA has a worldwide prevalence of approximately 0.5–1%, affects women 2–3 times more often than men, and occurs in adolescents, adults, and the elderly, with a high

incidence in people aged 40–60 years (Saraux et al., 2006; Myasoedova et al., 2010). Globally, the overall age-standardized prevalence and incidence rates of RA have been increasing since 1990 (Safiri et al., 2019). Between 2005–2014, the overall incidence of RA was stable compared with that in the previous decade, possibly owing to the changing prevalence of lifestyle factors, such as smoking and obesity (Myasoedova et al., 2020). As RA is a chronic, progressive disease, patients with RA have serious comorbid conditions, such as infection (Au et al., 2011), osteoporosis (Jin et al., 2018), cardiovascular disease (England et al., 2018), respiratory disease (Chatzidionisyou and Catrina, 2016), and cancer (Askling, 2007). Early diagnosis and treatment could slow down the progression of arthritic damage in 90% of RA patients, thereby preventing irreversible disability (Goekoop-Ruiterman et al., 2005). However, only a few patients can achieve long-term remission without long-term medical treatment (Matcham et al., 2014). At present, the western drugs for RA can be divided into five generations according to the development time and principles: nonsteroidal anti-inflammatory drugs, glucocorticoids, disease-modifying antirheumatic drugs, early biological agents mainly composed of TNF-α inhibitors, and new biological agents directly targeting T cells. In recent years, the development of effective biologics and small-molecule kinase inhibitors has markedly improved both the management and long-term prognosis of RA. However, these treatments are mainly used to relieve symptoms, and they cause adverse side effects including vomiting, rash, leukopenia, and liver and kidney damage. Therefore, it is urgent to find a safe and effective treatment strategy to improve both the management and long-term prognosis of RA.

Traditional Chinese medicine (TCM) is a medical and pharmaceutical system with unique theories and techniques that reflect the Chinese nations understanding of life, health, and disease. Wang Bi was first proposed by Mr. Shude Jiao in 1981 in China, mainly refers to RA and other diseases with joint deformation and bone damage, such as ankylosing spondylitis, tuberculous arthritis, and Kashin-Beck disease (Jiao and Wang, 2009). Owing to its minor side effects and reasonable treatment expenditure, TCM has become a significant strategy for treating chronic, complex, and geriatric diseases, such as RA, diabetes, emphysema, and chronic nephritis. Herbal TCMs, such as Danggui Sini decoction (Cheng et al., 2017), Guizhi Fuzi decoction (Peng et al., 2013), Huangqi Guizhi Wuwu decoction (Wang et al., 2010), and Wang Bi tablet (WBT) (Yang et al., 2009; Kang et al., 2011; Wu and Shen, 2011; Liu et al., 2012), have a long history of use in the treatment of RA. WBT is a Chinese patent medicine produced exclusively by Liaoning Haohushi Pharmaceutical (Group) Co., Ltd., and it has been recorded in the Pharmacopeia of the People's Republic of China from the 2010 edition. WBT is composed of 17 herbal medicines, including *Rehmannia glutinosa* (Gaertn.) DC (Sheng Dihuang, SDH) 15.4g, processed *R. glutinosa* (Shu Dihuang, SD) 15.4g, *Dipsacus asper* Wall. ex DC (Xu Duan, XD) 11.5g, *Aconitum carmichaelii* Debeaux (Fu Zi, FZ) 11.5g, *Angelica pubescens* Maxim (Du Huo, DH) 7.7g, *Drynaria fortunei* (Kunze ex Mett.) J. Sm (Gu Suibu, GSB) 11.5 g, *Cinnamomum cassia* (L.). J. Presl (Gui Zhi, GZ) 7.7g, *Epimedium brevicornu* Maxim (Yin Yanghuo, YYH) 11.5g, *Saposhnikovia divaricata* (Turcz.) Schischk (Fang Feng, FF) 7.7g, *Clematis chinensis* Osbeck (Wei Lingxian, WLX) 11.5 g, *Gleditsia sinensis* Lam (Zao Jiaoci, ZJC) 7.7g, *Paeonia lactiflora* Pall (Bai Shao, BS) 9.2 g, *Cibotium barometz* (L.). J. Sm (Gou Ji, GJ) 11.5g, *Anemarrhena asphodeloides* Bunge (Zhi Mu, ZM) 11.5 g, *Lycopodium japonicum* Thunb (Shen Jincao, SJC) 7.7g, *Carthamus tinctorius* L. (Hong Hua, HH) 7.7g, and goat or sheep bones 15.4g.

Accumulating evidence from clinical practices has proved the efficacy of WBT against RA (Yang et al., 2009; Wu and Shen, 2011) and its ability to enhance the therapeutic efficacy of western medicines, such as methotrexate (Li, 2013; Zhang, 2016; Fan, 2019), in the treatment of RA. Until now, WBT research has been focused on the clinical practice. Thus, at present, basic research on WBT is still lacking in China. There is only one report on analysis of the chemical composition of WBT, in which 138 compounds were characterized by UPLC-Q-TOF-MS (Wang et al., 2019). Research on the pharmacological mechanism of WBT is limited to the NF-κB and JAK-STAT3 signaling pathways (Guan et al., 2018; Shen et al., 2019) as well as the balance between Th1 and Th2 cells (Wang et al., 2020). As a consequence, the pharmacological mechanism of WBT is largely unclear.

Integrative pharmacology, first proposed in 2014 (Xu and Yang 2014), is an interdisciplinary science that comprehensively explores the interactions between multiple constituents of TCM and the body at multiple levels, such as molecules, cells, tissues, organs, and animals (Wang et al., 2018). Integrative Pharmacology-based Network Computational Research Platform of Traditional Chinese Medicine (TCMIP v2.0, http://www.tcmip.cn/), which is composed of five databases (Xu et al., 2019) and seven functional modules (Xu et al., 2017), could assist the identification of chemical constituents and the elucidation of the molecular mechanisms of TCM (Mao et al., 2019; Feng et al., 2020; Ma et al., 2020). In the Database of TCM ingredients, we have introduced a characteristic parameter, namely "quantitative estimate of drug-likeness" (QED) to evaluate the druggability of our herbal components. QED includes ADME, water solubility, plasma protein binding rate, blood brain barrier permeability, inhibition of hepatic drug enzymes, hepatotoxicity, and intestinal absorption rate (Bickerton et al., 2012; Doak et al., 2014; Doak et al., 2016).

Therefore, we aimed to systematically analyze the chemical compositions of WBT and explore its molecular mechanisms against RA through the following scheme, as shown in **Figure 1**: 1) analyzing the chemical components of WBT via UPLC-QTOF-MS/MS and identifying the main chemical components by using the UNIFI 1.8 software; 2) evaluating the anti-inflammatory activity of WBT in TNF-α-stimulated RAW264.7 cells via transcriptome sequencing; 3) predicting the putative targets of the identified chemical components of WBT and collecting the putative targets of RA using TCMIP; 4) constructing a network of "Anti-inflammatory Core Genes-Putative Targets-RA genes" to identify the hub genes; 5) selecting key active constituents according to the binding frequency between hub targets and WBT components, and 6) conducting a functional enrichment analysis to investigate whether the molecular mechanisms of

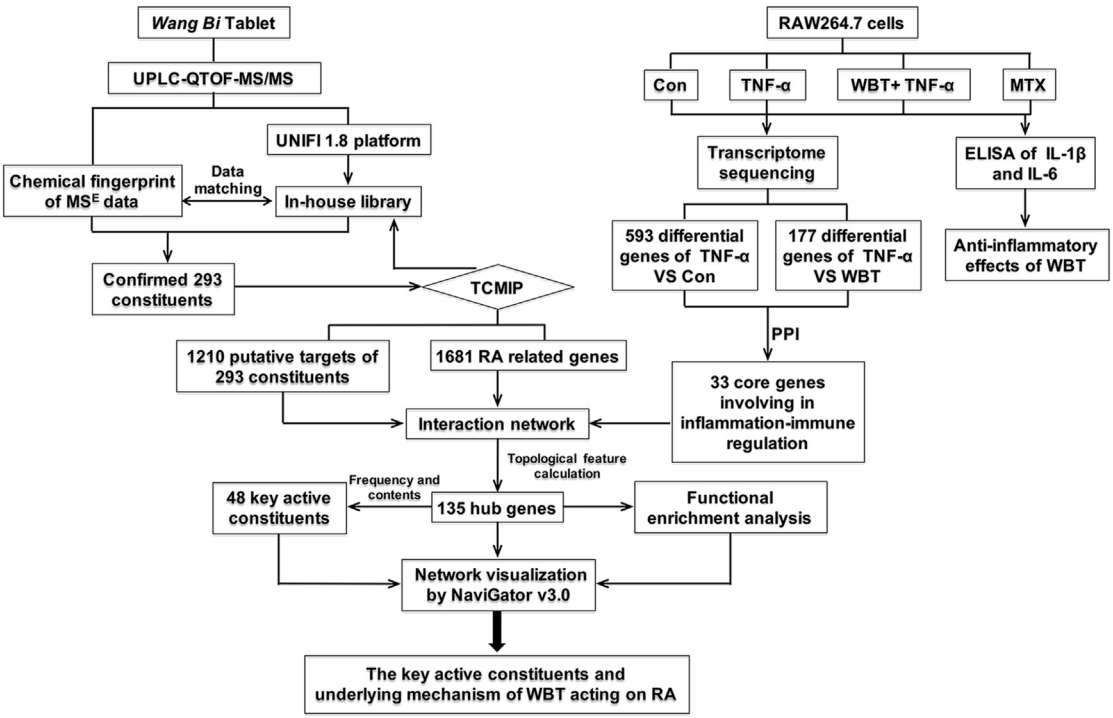

FIGURE 1 | The scheme of the present study based on the "integrative pharmacology strategy" to elucidate the main active components and mechanism of WBT in treating RA.

WBT against RA is mediated via regulation of its candidate targets. The findings of this study would advance our understanding of the pharmacological mechanism of WBT against RA.

MATERIALS AND METHODS

Chemicals and Reagents

HPLC-grade methanol and acetonitrile were purchased from Fisher Scientific Co. (Loughborough, United Kingdom). HPLC-grade formic acid was purchased from Sigma-Aldrich (St. Louis, MO, United States of America). Distilled water was purchased from Watsons Water Co., Ltd. (Shenzhen, China). SDH, SD, XD, FZ, DH, GSB, GZ, YYH, FF, WLX, ZJC, BS, GJ, ZM, SJC, HH, and goat or sheep bones were purchased from Shanghai Traditional Chinese Medicine Co., Ltd. (Shanghai, China). The herbal medicines were identified by Mrs. Xirong He, a research assistant at the China Academy of Chinese Medical Sciences (Beijing), and the voucher specimens were deposited at the Institute of Chinese Materia Medica, China Academy of Chinese Medical Sciences.

Recombinant human TNF-α (catalog #300-01A) was purchased from PeproTech, Inc (Rocky Hill, NJ, United States of America). An MTT assay kit (ab211091) as well as IL-1β (ab46052) and IL-6 (ab178013) ELISA kits were purchased from Abcam (Burlingame, CA, United States). Dulbecco's modified eagle medium (DMEM) (LOT26019006), 0.25% trypsin (LOT10519010), penicillin streptomycin solution (LOT30002341), and phosphate buffer saline (PBS) (LOT18919010) were purchased from Corning, Inc (NY, United States). Fetal bovine serum (LOT10099-141) was purchased from Gibco BRL Co. (Boise, Idaho, United States). Methotrexate was purchased from Sigma-Aldrich (St. Louis, MO, United States of America).

Preparation of Herbal Extracts

WBT preparation was conducted in complete compliance with that recorded in the Chinese Pharmacopeia (P985-986, 2015 edition). The procedure was as follows. Briefly, SDH 15.4 g, SD 15.4 g, GSB 11.5 g, GJ 11.5 g, and goat or sheep bones 15.4 g were decocted twice in eight and six volumes of water for 1.5 h. The decoctions were filtered and then combined to obtain extract S1. The remaining 12 herbal medicines were decocted as before to obtain extract S2. Next, S2 was evaporated under reduced pressure to the weight of the original herbal medicines in a rotary evaporator and then mixed with three volumes of EtOH. The mixture was allowed to stand for 16.0 h, and then the EtOH in the supernatant was recovered under reduced pressure to obtain extract S3. S1 and S3 were combined and concentrated under reduced pressure to obtain a thick paste (S4) with a relative density of 1.27–1.30 (50°C). BS 46 g and ZM 57.5 g were ground into powder and then filtered through a 100-mesh sieve. The fine powder was mixed thoroughly with S4 before freeze drying, and the

lyophilized powder was screened through a 40-mesh sieve. Six batches of herbal medicines were extracted in parallel.

The fine lyophilized powder of WBT was ultrasonically extracted using 20 volumes of 70% MeOH for 0.5 h before centrifugation at 12,000 ×*g* for 10 min in an Eppendorf 5415D centrifuge (Eppendorf Co., Hamburger, Germany). After the supernatant was filtered through a 0.22 μm filter (Pall Corporation, Beijing, China), 2 μl aliquots were transferred to the UPLC-QTOF-MS/MS system for analysis. The quality control (QC) samples of WBT were prepared by mixing the six batches of herbal medicines.

Instrumentation and UPLC-QTOF-MS/MS Conditions

The UPLC separation was performed using a Waters Acquity UPLC HSS T3 column (100 mm × 2.1 mm, i. d. 1.8 μm) on a Waters Acquity UPLC I-Class system (Waters Corp., Milford, United States of America). The column was maintained at 40°C. The mobile phases consisted of eluent A (0.1% formic acid in deionized water, v/v) and eluent B (0.1% formic acid in acetonitrile, v/v), and the linear gradient program was as follows: 0–1 min, 1% B; 1–10 min, 1–20% B; 10–20 min, 20–40% B; 20–25 min, 40–50% B; 25–28 min, 50–100% B; 28–33 min, 100% B; 33–33.1 min, 1% B; 33.1–35 min, 1% B. The flow rate was 0.5 ml/min, and the injection volume was 2 μl.

The MS experiment was performed on a Waters Xevo G2-S Q-TOF Mass System (Manchester, United Kingdom) equipped with electrospray ionization (ESI). The data acquisition modes were MS^E centroid for all samples and the extra continuum mode for QC samples in both the ESI^+ and ESI^- ionization modes. The operating parameters were set as follows: mass range, 50–1,500 Da; source temperature, 100°C; desolvation temperature, 400°C; desolvation gas flow, 800 L/h; sampling cone, 40 V; capillary voltage, 2.5 KV for ESI^-, 0.5 KV for ESI^+. At low CE scan, the auto MS collision energy was 6 eV. At high CE scan, the collision energy was 15–45 eV ramp for ESI^+ and ESI^-.

Leucine enkephalin was selected as the lock-mass at a concentration of 200pg/ml in acetonitrile (0.1% formic acid): H_2O (0.1% formic acid) (50:50, v/v) for the positive ion mode ($[M + H]^+$ = 556.2771) and negative ion mode ($[M-H]^-$ = 554.2615) via a lock spray interface.

Cell Culture

RAW264.7 murine macrophage-like cells were obtained from Cell Resource Center, IBMS, CAMS/PUMC (Beijing, China) and cultured in DMEM supplemented with 10% heat-inactivated fetal bovine serum and antibiotics (100 U/ml penicillin and 100 U/ml streptomycin) at 37°C in a biochemical incubator (LRH-150, Shanghai, China) with humidified atmosphere containing 95% O_2 and 5% CO_2.

MTT Assay

The cytotoxicity of WBT was analyzed via MTT assay. RAW264.7 cells (1×10^5 cells/well) were plated in 96-well plates ($p = 6$) and incubated for 24 h. After washing with PBS, WBT (12.8, 25.6, 128, 640, 3200, 1.6×10^4, 8.0×10^4, 4.0×10^5, 2.0×10^6, 1.0×10^7 ng/ml) or PBS was added to the cells, which were then incubated for another 24 h. Cell viability was evaluated using an MTT assay kit (#ab211091; Abcam) according to the manufacturer's protocol, and the absorbance was detected by a PerkinElmer EnVision multimode plate reader (2104, Wellesley, MA).

Drug Treatment

RAW264.7 cells were seeded on 96-well plates ($p = 6$) at a density of 1×10^5 cells per well and incubated for 24 h. Next, the medium was discarded, and the cells were washed with PBS. The cells were subsequently incubated with PBS, TNF-α (20 ng/ml), TNF-α (20 ng/ml) + WBT (0.001, 0.01, 0.1, 1.0, or 10 μg/ml), or TNF-α (20 ng/ml) + methotrexate (MTX, 0.2 μg/ml) for another 24 h. Finally, the supernatant was collected for measurement of IL-1β and IL-6 using ELISA kits according to the manufacturer's instructions.

RNA Extraction and Quality Control

Total RNA was isolated using a RNeasy mini kit (Qiagen, Germany) according to the manufacturer's protocol. RNA integrity was evaluated using an Agilent 2100 Bioanalyzer (Agilent Technologies, Santa Clara, CA, United States of America). The quantity of total RNA in the samples was measured using a Qubit®3.0 Fluorometer (Thermo Fisher Scientific, United States of America) and NanoDrop One (Wilmington, DE, United States of America).

mRNA-Seq

Paired-end libraries were synthesized using a TruSeq™ RNA Sample Preparation Kit (Illumina, United States of America) following the TruSeq™ RNA Sample Preparation Guide. Briefly, poly A-containing mRNA molecules were purified using poly T oligo-attached magnetic beads. Following purification, the mRNA was fragmented into small pieces using divalent cations at 94°C for 8min. The cleaved RNA fragments were copied into first-strand cDNA using reverse transcriptase and random primers. This was followed by second-strand cDNA synthesis using DNA Polymerase I and RNase H. These cDNA fragments then went through an end-repair process, the addition of a single 'A' base, and then ligation of the adapters. The products were then purified and amplified via PCR to create the final cDNA library. Purified libraries were quantified using a Qubit® 2.0 Fluorometer (Life Technologies, United States of America) and validated using an Agilent 2100 Bioanalyzer (Agilent Technologies) to confirm the insert size and calculate the mole concentration. Clusters were generated by cBot with the library diluted to 10 pM and then sequenced on an Illumina NovaSeq 6000 (Illumina, United States of America). The sequencing work was performed by Beijing Zhimei Yinuo Biotechnology Co., Ltd. (Beijing, China). The sequencing data has been uploaded to GEO website with Series record GSE165272.

Bioinformatic Analysis

Bioinformatic analysis was also undertaken by Zhimei Yinuo Biotechnology Co., Ltd. The whole procedure is shown in **Figure 2**.

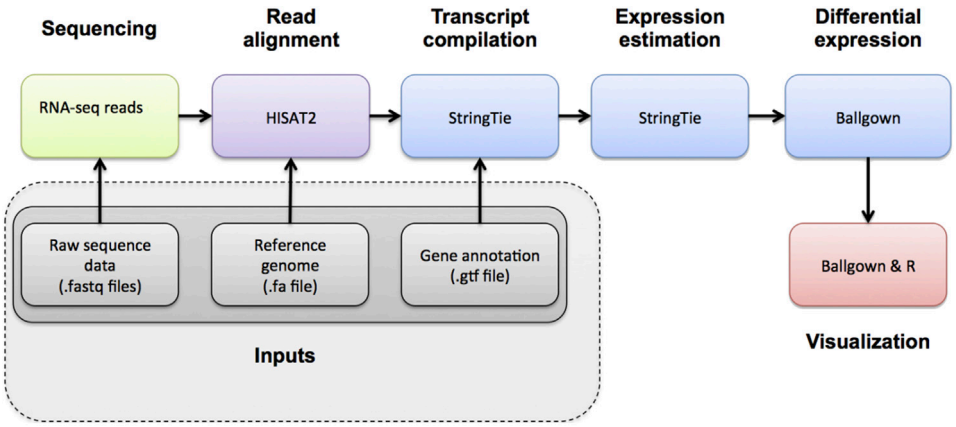

FIGURE 2 | The whole procedure of bioinformatic analysis of transcriptomics.

Prediction the Putative Targets of the Chemical Constituents of WBT

The TCM target prediction and function analysis module (TTFM) of TCMIP was employed to predict the putative targets of the compounds preliminarily identified in WBT. The prediction accuracy was set at 0.80 (moderate to high similarity) to select constitute-putative target pairs, and these genes were saved in the customer center. Simultaneously, the QED value was set at 0.49, and constituents with QED <0.49 will be filtered out.

Collection of RA-Related Genes From TCMIP

The disease name "rheumatoid arthritis" and symptom nouns, such as "joint swelling", "morning stiffness", and "arthralgia" were selected to search in TCMIP in order to obtain RA-related genes among those saved in the personal user center.

Network Visualization and Functional Enrichment Analysis

NaviGator v3.0 was employed to establish a network, and the Database for Annotation, Visualization and Integrated Discovery (DAVID) v6.8 (https://david.ncifcrf.gov) was used to elucidate the biological functions of the core efficacy gene set.

Data Analysis

The UPLC-QTOF-MS/MS system was controlled by the Masslynx 4.1 software (Waters Corp.). The MS^E continuum data were processed by UNIFI 1.8 (Waters Corp.). The processes included data acquisition, data mining, library searching, and report generation. The chemical information of the 16 herbal medicines (except for goat or sheep bones) was collected in a list consisting of molecular name/formulae/weights and chemical structures (mol. format) from the literature and the Encyclopedia of Traditional Chinese Medicine (http://www.nrc.ac.cn:9090/ETCM/) (Xu et al., 2019). The list, as a customized library that could facilitate chemical identification, is shown in **Supplementary Excel S1** $[M+H]^+$, $[M+K]^+$, $[M+Na]^+$, $[2M+H]^+$, and $[M-e]^+$ were selected as additive ions in the positive ion mode. $[M+COOH]^-$, $[M-H]^-$, and $[2M-H]^-$ were selected in the negative ion mode. The allowable maximum error range was 5 mDa/10 ppm, and the matched constituents were given the predicted fragments from the structure. The functional module of the mass fragment could facilitate the chemical identification of unmatched constituents based on the isotopic abundance, elemental composition, and i-FIT score.

RESULTS

Characterization and Identification of Chemical Constituents in WBT

A total of 293 compounds were identified or tentatively characterized in both the positive (165) and negative 229) ion modes, including flavonoids, alkaloids, glycosides, coumarins, saponins, phenolic acid, and iridoids. The base peak intensity (BPI) chromatograms of WBT in two ion modes are depicted in **Figures 3A,B**. Among the 293 constituents characterized, 45 were identified in SDH or SD, 28 in XD, 23 in FZ, 23 in DH, 15 in GSB, 14 in GZ, 36 in YYH, 22 in FF, 7 in WLX, 8 in ZJC, 28 in BS, 8 in GJ, 26 in ZM, 16 in SJC, and 31 in HH. Detailed information of the 293 compounds is listed in **Supplementary Excels S2, S3**, including RT, M/Z, error, response, adducts, formula, name, fragments, category, and origin.

The BPI chromatograms of the water extract of WBT corresponding to the positive and negative ion modes are shown in **Figures 3A,B**. The mass spectra of two compounds are shown below. The ion at RT = 15.37 and $[M + H]^+$ = 823.3022 was primarily identified as baohuoside VI ($C_{39}H_{50}O_{19}$) in ESI^+ after matching with data from the customized database (**Supplementary Excel S4**) of UNIFI. The main fragments were m/z 677.2438 $[M + H\text{-rha}]^+$, 531.1860 $[M + H\text{-2rha}]^+$, 369.1328 $[M + H\text{-Glc-2rha}]^+$, and 313.0703 $[M + H\text{-Glc-2rha-}C_4H_7]^+$, which were consistent with those in literature (Yu et al., 2016). In the same way, the ion at RT = 17.27 and $[M-H]^-$ = 927.4931 was primarily identified as akebiasaponin D ($C_{47}H_{76}O_{18}$) in ESI^-. The main fragments were

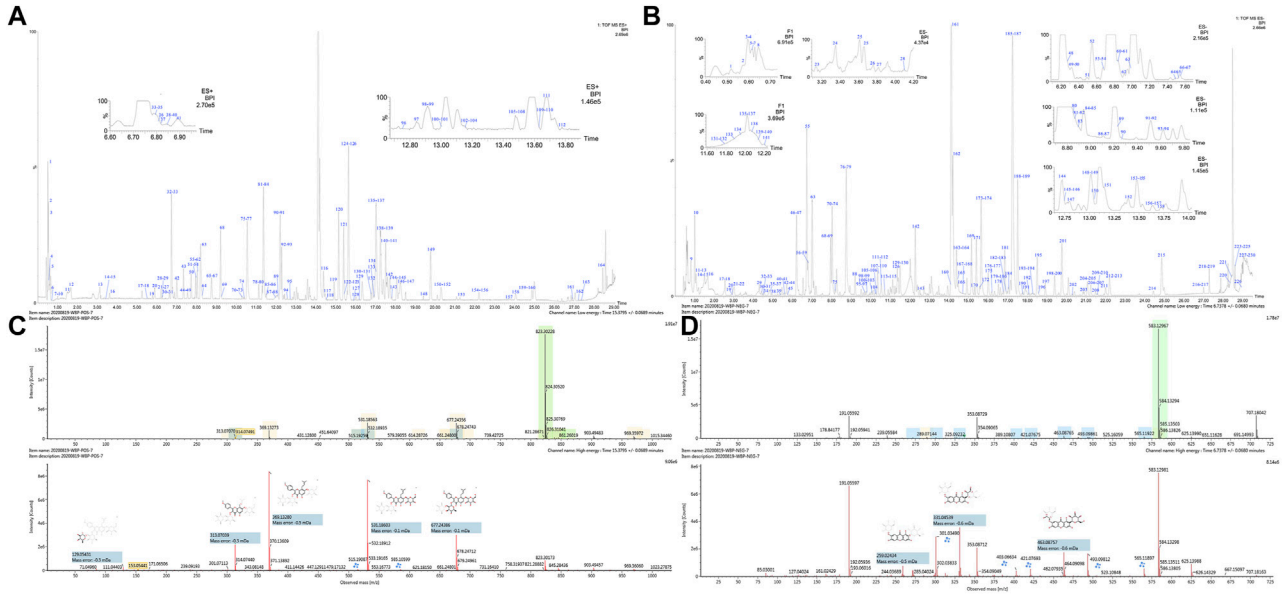

FIGURE 3 | BPI chromatograms of WBT extracts **(A)** ESI^+; **(B)** ESI^-), and spectrum information of baohuoside VI **(C)** and akebiasaponin D **(D)** automatically provided by UNIFI™.

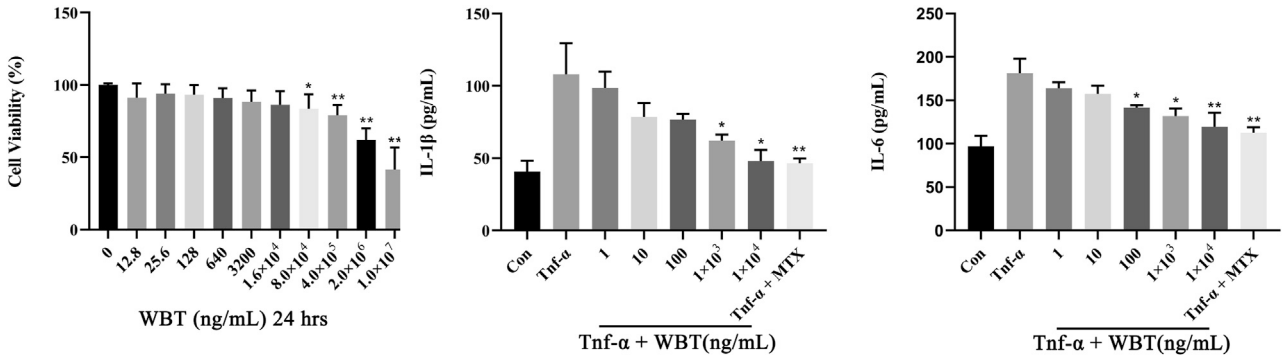

FIGURE 4 | WBT prevents inflammatory response induced by TNF-α in RAW264.7 cells in a dose-dependent manner. Cell viability was determined by MTT assay **(A)**. The levels of IL-1β **(B)** and IL-6 **(C)** in cell culture supernatant were detected by ELISA kits (Mean ± SD, $p < 0.05$*, $p < 0.01$**).

m/z 603.3904 $[M\text{-}H\text{-}2Glc]^-$, 323.0984 $[M\text{-}H\text{-}Glc\text{-}C_4H_8O_4]^-$, and 179.0563 $[M\text{-}H\text{-}Glc\text{-}C_3H_6O_3]^-$, which were consistent with those in literature (Yang et al., 2016). The mass spectra and structures of the two compounds are displayed in **Figures 3C,D**.

WBT Reduces the Release of IL-1β and IL-6 in TNF-α Stimulated RAW264.7 Cells

The MTT assay showed that WBT exerted no significant cytotoxicity to RAW264.7 cells even at a concentration as high as 1.6×10^4 ng/ml (**Figure 4A**). Therefore, WBT concentrations ranging from 0.001 to 10 μg/ml were selected for the examination of the anti-inflammatory activity of WBT in TNF-α-stimulated RAW264.7 cells. In RAW264.7 cells stimulated with TNF-α (20 ng/ml) for 24 h, IL-1β and IL-6 levels in the culture medium were significantly increased ($p < 0.01$) compared with that in the control group. MTX, as a positive drug, exhibited an excellent effect against inflammatory responses, suggesting a good pharmacodynamic evaluation system. In RAW264.7 cells co-cultured with TNF-α and WBT at 0.1, 1, and 10 μg/ml, IL-1β and IL-6 levels were significantly reduced ($p < 0.01$) in a dose-dependent manner. WBT at a low dose (0.001, 0.01 μg/ml) did not exhibit any anti-inflammatory effects (**Figures 4B,C**).

RNA-Seq Transcriptional Comparison Between Different Groups and Functional Enrichment Analysis of Core Genes

To elucidate the mechanism by which WBT altered the transcriptomic profile of RAW264.7 cells simulated by TNF-α,

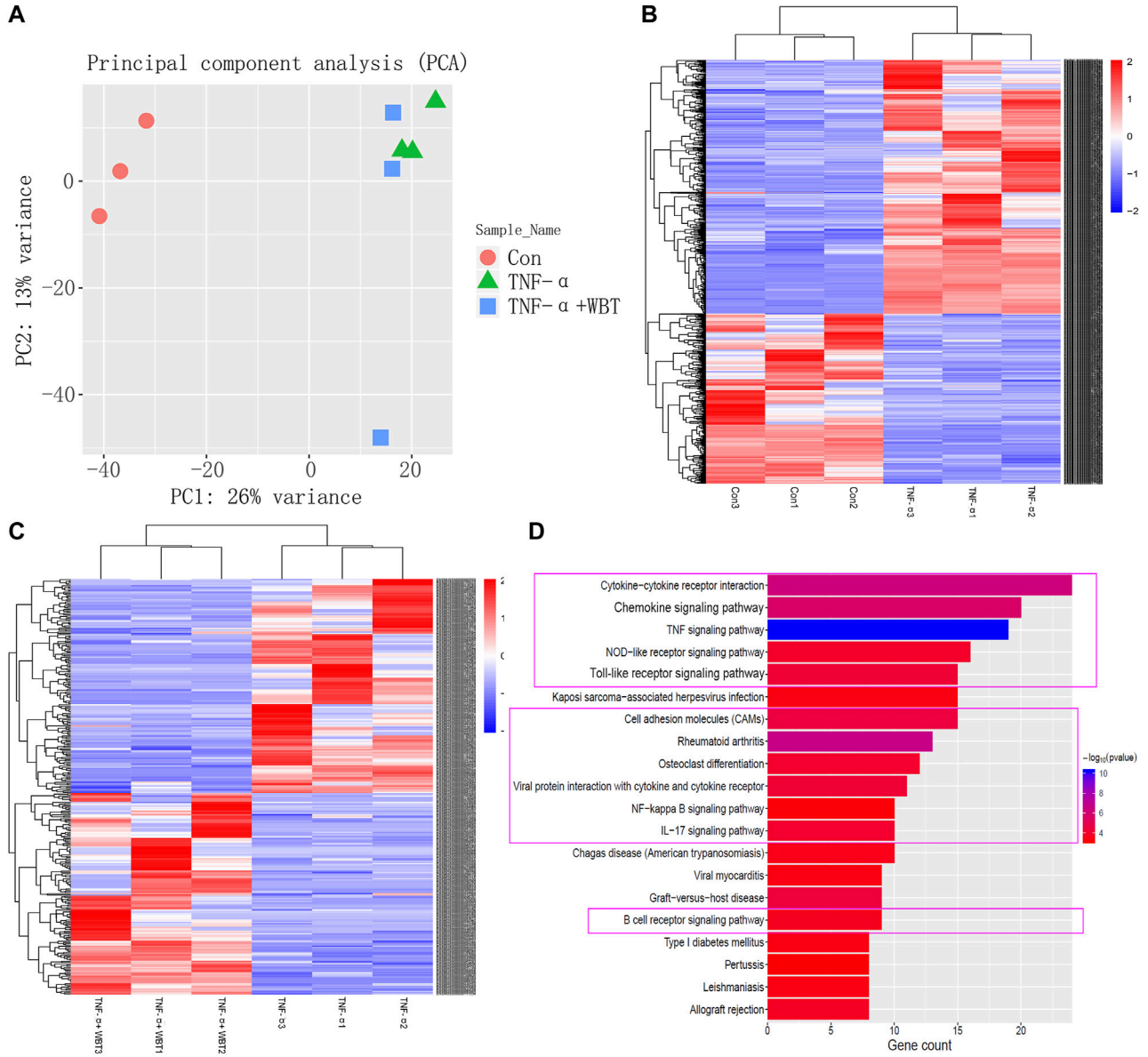

FIGURE 5 | RNA-seq transcriptional comparison between different groups, and functional enrichment analysis based on network pharmacology. Principal component analysis of transcriptome sequencing results **(A)**. Differential gene expression profiles of TNF-α vs. Con **(B)** and TNF-α+WBT vs. TNF-α **(C)** were visualized in heat maps (fold change ≥2, $p < 0.05$). Pathway enrichment analysis of the hub genes responsible for the anti-inflammatory effect of WBT. The purple box indicated the pathways closely related to the occurrence and development of RA **(D)**.

RNA-seq experiments were performed. The control, TNF-α, and TNF-α + WBT (1.0 μg/ml) groups were selected as the biological samples according to the level of inflammatory factors. To ensure the accuracy of the analysis, we set three biological replicates for RNA-seq, a fold change of more than 2, and a *p* value of less than 0.05. Principal component analysis showed good separation between different groups and good consistency in the same group (**Figure 5A**). After treatment, 593 and 177 genes were differentially regulated between TNF-α vs. Con and between TNF-α+WBT vs. TNF-α, respectively (**Supplementary Excel S5, S6**). Between TNF-α vs. Con, 376 genes were upregulated, and 217 genes were downregulated; these genes were regarded as "Inflammatory Immune Dysregulation Genes." Between TNF-α+WBT vs. TNF-α, 92 genes were upregulated, and 85 genes were downregulated; these genes were regarded as "Anti-inflammatory Effect Genes." Heat maps were generated to visualize the gene expression patterns in the three groups (**Figures 5B,C**). Interestingly, 45 genes that were differentially expressed between TNF-α vs. Con were significantly counter-regulated by WBT; thus, these genes may be the potential gene set responsible for the efficacy of WBT in reducing inflammatory responses. The 593 and 177 different genes were imported into

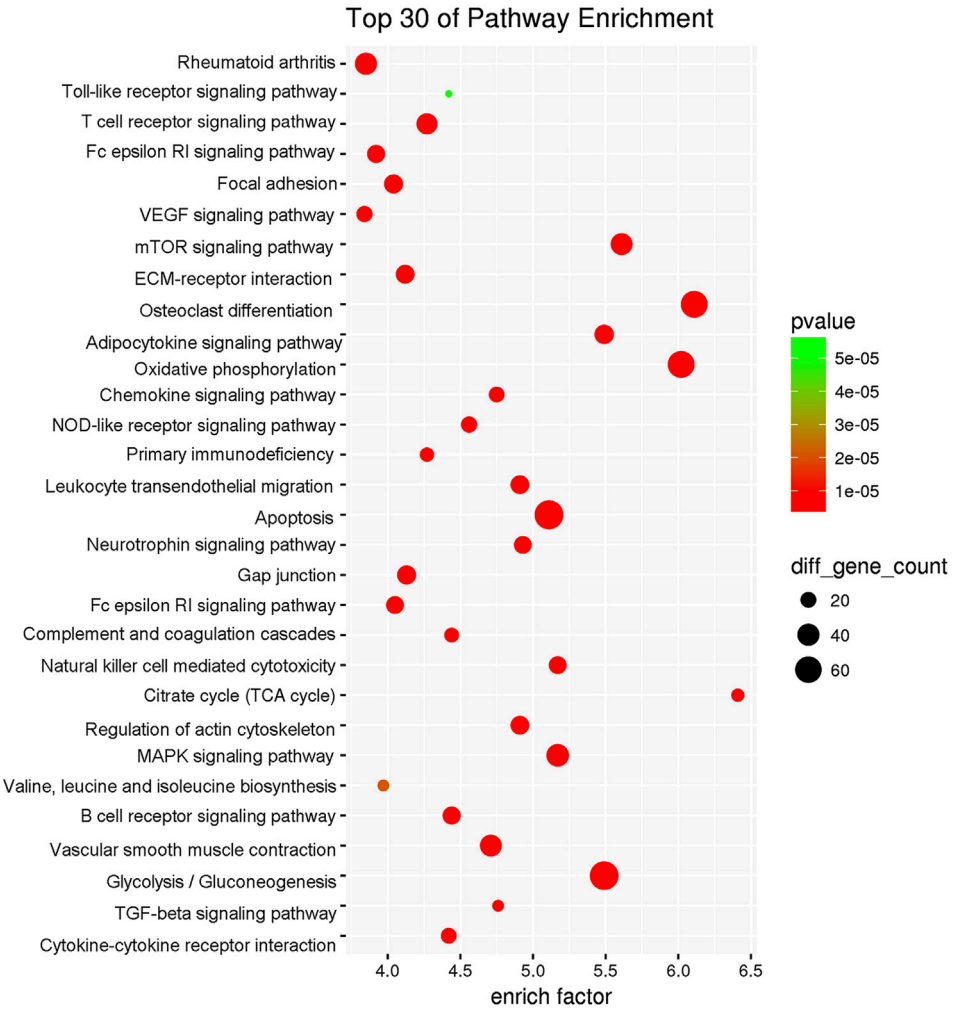

FIGURE 6 | Top 30 enriched pathways for the 135 hub genes in the effect of WBT against RA.

the STRING database for construction of a PPI network including 264 nodes and 599 edges (**Supplementary Excel S7**). Thirty-three core nodes of the network were obtained by calculating the topological feature values, including degree, betweenness, and closeness. Generally, the node with a degree value of two-fold the median as well as betweenness and closeness values of one-fold the median is selected as the hub node. The 33 hub nodes included ABL1, ACTG2, ALDH1A7, B2M, C3, CCL2, CCL20, CCL5, CCL9, CES2C, CSF1, CXCL1, CXCL10, CXCR3, EPHA3, EPHA5, H2-K1, HVCN1, IRF7, JUN, MFI2, MMP3, MMP9, NMUR1, OLFM4, PLXNB3, RAB27A, RHBDF2, SEMA3G, THY1, TLR2, TRF, and VCAM1. Based on functional enrichment analysis, these 33 genes were mainly involved in the inflammation-immune regulation module, and the purple box indicates that the pathway information was closely related to the occurrence and development of RA (**Figure 5D**), such as cytokine-cytokine receptor interaction, chemokine signaling pathway, TNF signaling pathway, NOD-like receptor signaling pathway, and Toll-like receptor signaling pathway.

Underlying Mechanism and Key Active Components of WBT in Treating RA

By using the TTFM of TCMIP, we predicted a total of 1,210 putative targets based on the chemical structures of the 293 identified compounds (**Supplementary Excel S8**). Moreover, a total of 1681 RA-related genes were collected from the Disease-related Gene Database of TCMIP, as shown in **Supplementary Excel S9.** To illustrate the underlying mechanisms of WBT against RA, an interaction network of "Anti-inflammatory Hub Genes-Putative Targets- Disease Genes" was constructed using the TCM Association Network Mining Module of TCMIP. The interaction network included 2,251 nodes and 53,254 edges, with a network density of 0.011. A total of 566 core nodes of the network were obtained by calculating the topological feature values. In addition, a PPI network of the 566 core nodes was

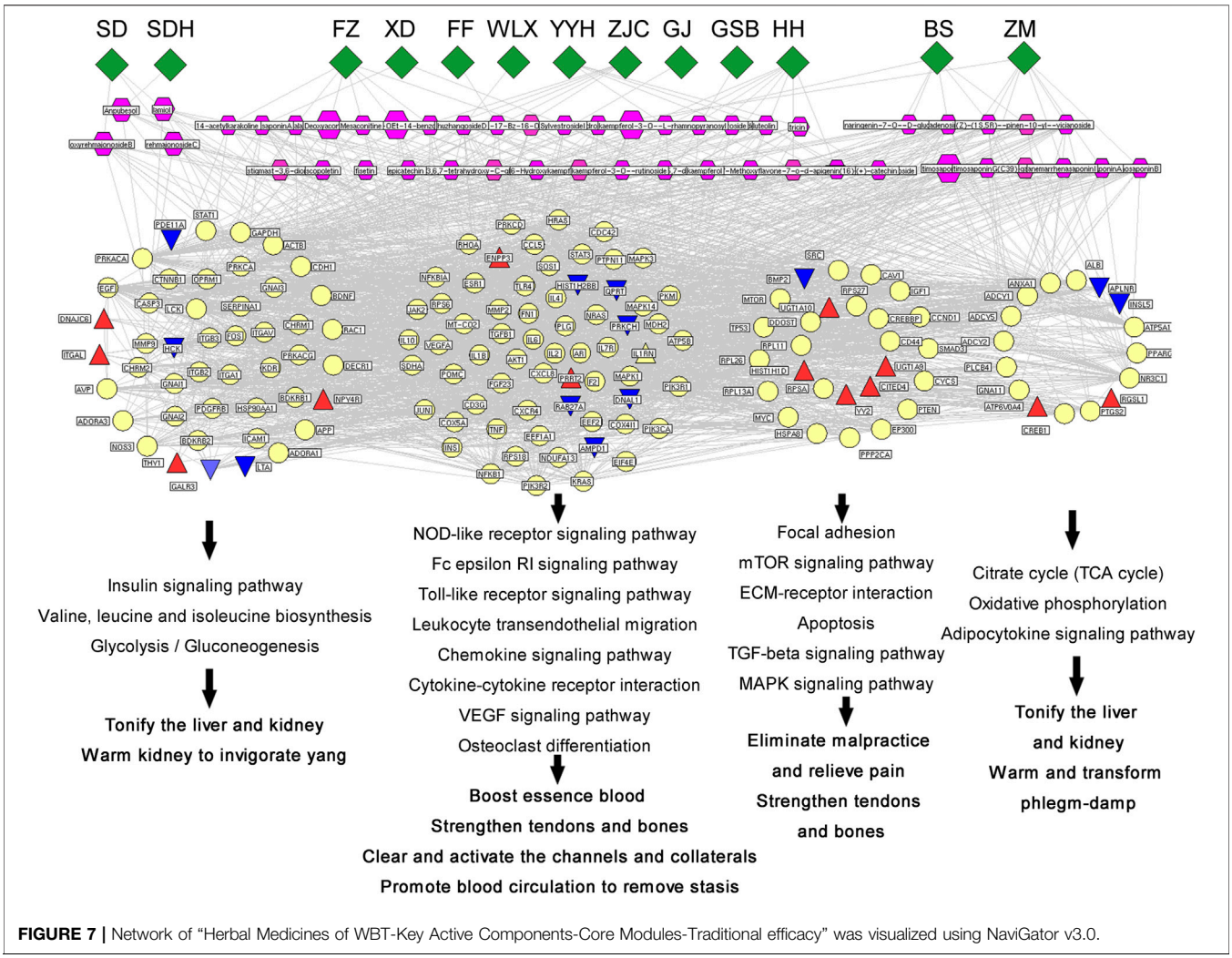

FIGURE 7 | Network of "Herbal Medicines of WBT-Key Active Components-Core Modules-Traditional efficacy" was visualized using NaviGator v3.0.

constructed, which included 566 nodes and 23,558 edges and had a network density of 0.074, which was significantly higher than that of the initial network (density 0.011) and in accordance with network centrality of hub nodes. Finally, 135 hub nodes were obtained by calculating the topological feature values, of which 81 were putative targets of WBT corresponding to 225 chemical constituents.

To explore the biological function of these 135 hub genes, DAVID v6.8 was employed for KEGG analysis. As shown in **Figure 6**, the pathway information could be divided into five function modules: 1) the synovial inflammation-immune imbalance regulation module. It was the most significant functional module that included NOD-like receptor signaling pathway, B cell receptor signaling pathway, T cell receptor signaling pathway, Fc epsilon RI signaling pathway, Toll-like receptor signaling pathway, primary immunodeficiency, leukocyte transendothelial migration, chemokine signaling pathway, complement and coagulation cascades, natural killer cell-mediated cytotoxicity, regulation of actin cytoskeleton, Fc gamma R-mediated phagocytosis, and cytokine-cytokine receptor interaction; 2) energy metabolism regulation module, including citrate cycle (TCA cycle), oxidative phosphorylation, adipocytokine signaling pathway, neurotrophin signaling pathway, insulin signaling pathway, valine, leucine and isoleucine biosynthesis, glycolysis/gluconeogenesis, and pyrimidine metabolism; 3) cell function regulation module, including focal adhesion, mTOR signaling pathway, ECM-receptor interaction, apoptosis, TGF-beta signaling pathway, and MAPK signaling pathway; 4) synovial pannus formation module, including VEGF signaling pathway and vascular smooth muscle contraction; 5) bone destruction regulation module, including osteoclast differentiation.

The constituents that showed high-frequency binding to hub targets and had high content were selected as the key constituents (the target frequency and content were higher than the corresponding medians). A total of 48 key active constituents were selected, which corresponded to 13 herbal medicines. The detailed information is shown in **Supplementary Excel S10.** A multidimensional association network of "Herbal Medicines of WBT-Key Active Components-Core Targets-Functional Modules-Traditional efficacy" was visualized using NaviGator v3.0, as shown in **Figure 7**. Among the hub targets, 13 red

triangles and 13 blue triangles represented the genes upregulated or downregulated, respectively, by WBP in the transcriptome data. These hub targets involved in different pathways were divided into four functional models corresponding to different traditional efficacies. The insulin signaling pathway; valine, leucine, and isoleucine biosynthesis; and glycolysis/gluconeogenesis were related to the tonifying of the liver and kidney as well as warming of the kidney to invigorate *yang*. The focal adhesion mTOR signaling pathway, ECM-receptor interaction apoptosis, TGF-beta signaling pathway, and MAPK signaling pathway were consistent with the elimination of malpractice, relief of pain, and strengthening of tendons and bones. The TCA cycle, oxidative phosphorylation, and adipocytokine signaling pathway were related to tonifying of the liver and kidney as well as warming and transforming of phlegm-damp. The other pathways were consistent with the boosting of blood essence, strengthening of tendons and bones, clearing and activation of the channels and collaterals, and promotion of blood circulation to remove stasis.

DISCUSSION

In the present study, we analyzed the chemical compositions of WBT and explore its molecular mechanisms against RA using integrative pharmacology. This is the first study to explore the active constituents and underlying mechanism of WBT in treating RA using integrative pharmacology, including rapid analysis of chemical composition, transcriptome sequencing, and network pharmacology analysis. In this study, the BPI chromatogram of WBT extracts was obtained by UPLC-QTOF-MS/MS, and 293 chemical compounds were preliminarily identified or tentatively characterized by matching the MS^E raw data to in-house library data using the UNIFI 1.8 software. WBT at 0.1, 1.0, and 10 μg/ml significantly reduced IL-1β and IL-6 levels in RAW264.7 cells stimulated by TNF-α. Moreover, 593 and 177 differential genes were screened between TNF-α vs. Con and between TNF-α+WBT vs. TNF-α based on transcriptome sequencing analysis. An interaction network of "Inflammatory Immune Dysregulation Genes" and "Anti-inflammatory Effect Genes" was constructed, and the hub nodes, as calculated by the topological feature values, were mainly involved in the inflammation-immune regulation module, which is closely related to the occurrence and development of RA. To explore the underlying mechanism of WBT against RA and identify its key pharmaceutically active substances, a multidimensional association network of Real-World Medicines of WBT-Key Active Components-Core Targets-Functional Modules-RA Pathology" was visualized using NaviGator v3.0. A total of 48 key active constituents were obtained based on their high-frequency binding to hub targets and contents in WBT, and 135 hub corresponding genes were selected, which may be the putative targets of WBT in treating RA. Functionally, the 135 putative targets were significantly associated with the inflammatory immune response regulation module, energy metabolism regulation module, and cell function regulation module, corresponding to their traditional efficacy.

WBT is composed of 17 herbal medicines that fit the compatibility principle of Monarch, Minister, Assistant, and Guide. We herein discuss the mechanism of WBT in treating RA according to this principle, as the 48 key active constituents were mainly involved in 13 herbal medicines: SDH and SD are Monarch drugs; YYH, XD, GJ, FZ, DH, FF, WLX, ZC, HH, and BS are Minister drugs; and ZM and BS are Assistant and Guide drugs. The other three herbal medicines and one animal drug may exert therapeutic effects through other pathways or systems than the inflammation-immune regulation system. 21 of the 48 key active constituents belong to flavonoids, 7 alkaloid, 7 steroidal saponin, 3 monoterpenoid, 3 iridoid, 2 coumarins, 1 ribonucleoside, 1 sterol, and 1 tannin. According to our experience, flavonoids may have greater potential against RA. RAW 264.7 cell which we all know is one of the media for RA testing. Inflammation is an important pathological process of RA, so we selected TNF-α as inflammatory inducer.

Interestingly, the enrichment pathways are consistent with the traditional efficacy of the corresponding herbal medicines (**Figure 7**.). For example, 20 hub genes corresponding to 5 chemical constituents of SDH and DH, are correlated with the regulation of glucose and lipid metabolism and blood circulation, which are consistent with the traditional effect of SDH and SD in "tonifying the liver and kidney, benefiting essence and blood". 32 hub genes corresponding to 9 chemical constituents of FZ, FF and WLX, are mainly involved in signal transduction and inflammatory response of the nervous system, which are consistent with the traditional effect of the three herbs in "clearing and activating the channels and collaterals". 24 hub genes corresponding to 8 chemical constituents of YYH, XD, GSB and GJ, are correlated with various regulation pathways and energy metabolism in the body, such as the citrate cycle; oxidative phosphorylation; adipocytokine signaling pathway; neurotrophin signaling pathway; insulin signaling pathway, which consistent with the "warming the kidney and strengthening *yang*" efficacy of Minister drugs. 44 hub genes corresponding to 19 chemical constituents of ZC and BS, are mainly involved in inflammatory immune regulation pathways, signal transduction, and neuroinflammatory response, which are related to the effects of warm channels and freeing of vessels, invigorating blood circulation and dispersing stasis. 48 hub genes corresponding to 14 chemical constituents of ZM and BS, were mainly involved in the regulatory pathways of nutrients and energy metabolism, blood circulation regulation pathway, which were related to the overall regulation of physical fitness and the enhancement of the effects of other drugs.

In the transcriptome sequencing experiment, we found that IL-13Rα2, Tnfaip3, Tnfrsf14, and Tnfrsf9 were upregulated in TNF-α-stimulated RAW264.7 cells, which was related with the development of inflammation (Wilson et al., 2011). The expression of Il1rn was upregulated in WBT + TNF-α-stimulated RAW264.7 cells, suggesting WBT could ameliorate inflammatory conditions stimulated by TNF-α

(Matsuki et al., 2005; Hada et al., 2020). These findings were consistent with ELISA results about IL-1β and IL-6. Moreover, IL-1β and IL-6 were involved in 4 prediction pathways, including cytokine-cytokine receptor interaction, TNF signaling pathway, NOD-like receptor signaling pathway, and Toll-like receptor signaling pathway.

There were two putative genes among the hub targets of WBT, which were also the drug effect genes identified by sequencing, namely hematopoietic cell kinase (HCK) and bone morphogenetic protein 2 (BMP2). The expression level of HCK was significantly downregulated, whereas that of BMP2 was remarkably upregulated after the treatment of RAW264.8 cells with WBT. HCK, a member of the Src family of non-receptor tyrosine kinases, is primarily expressed in myeloid cells and B lymphocytes. Moreover, HCK participates in the regulation of immune function by binding to the FC terminal of immunoglobulin (Ernst et al., 2002). HCK is highly expressed in macrophages, and its expression is further augmented during macrophage activation. HCK has been reported to be involved in various inflammatory reactions (English et al., 1993). The results of transcriptome sequencing showed that after inflammation was induced by TNF-α, cellular immunity was enhanced, and the expression level of was significantly increased. After WBT intervention, however, HCK expression level was effectively inhibited. BMP2, a member of the transforming growth factor-β (TGF-β) superfamily (Koseki et al., 2002), plays an important role in the recruitment and differentiation of undifferentiated mesenchymal cells and osteoblasts (Lyons et al., 1995; Deng et al., 2008). In the early stage of bone formation, BMP2 not only induced undifferentiated stromal cells to accumulate into bone-forming centers and differentiate into osteogenic cells but also reversed the differentiation of fibroblasts, myoblasts, and bone marrow basal cells into osteoblasts. For osteoblasts, BMP2 maintains its unique cell phenotype, induces an increase in osteoblast markers, and promotes extracellular matrix calcification. In the late stage of bone formation, BMP2, as an osteoclast differentiation factor, directly or indirectly stimulates osteoclast differentiation together with other osteoclast differentiation supporting factors, and participates in bone reconstruction. It has been reported that the expression of BMP-2 decreases upon bone and cartilage destruction in the pathogenesis of RA (Sun et al., 2019). After intervention with anchoring agents or other cytokine inhibitors, the expression of BMP-2 increased significantly as the of the disease progressed, which was consistent with the transcriptome sequencing results of WBT in this study.

Although the current study reveals these important findings, there are still several potential limitations. Firstly, it is difficult to determine whether the correlation between herbs and their corresponding targets is direct or indirect. Secondly, it is difficult to confirm whether the interaction between herbs and their corresponding targets is positive or negative. Therefore, further experiments are needed to verify the results of this preliminary study.

CONCLUSION

In summary, the 48 key active constituents contained in WBT may attenuate the major pathological changes in RA through their 135 candidate targets, which were involved the inflammation-immune regulation system, energy metabolism regulation module, and cell function regulation module. TCMIP v2.0 undoubtedly accelerates the process of chemical composition identification and network analysis, and transcriptome sequencing increases the accuracy of network prediction. This research strategy provides an efficient way to analyze chemical constituents and explore the pharmacological mechanism of TCM.

DATA AVAILABILITY STATEMENT

The datasets presented in this study can be found in online repositories. The names of the repository/repositories and accession number(s) can be found below: https://www.ncbi.nlm.nih.gov/geo/query/acc.cgi?acc=GSE165272

AUTHOR CONTRIBUTIONS

PW performed the experimental design and drafted the manuscript. YJ and HC performed the analysis of chemical constituents. JX and HC performed the analysis of network pharmacology. QG performed the cell experiment. XD, TZ, JZ. and CS helped to identify the chemical constituents. All authors read and approved the final manuscript.

FUNDING

This work was supported by grants from the National Key Research and Development Program of China (2017YFC1702104), National Natural Science Foundation of China (81774201), National Key Research and Development Program of China (2017YFC1702303), and the National Natural Science Foundation of China (81830111). The funding agencies had no role in the study design, the collection, analysis, or interpretation of data, the writing of the report, or the decision to submit the article for publication.

ACKNOWLEDGMENTS

Thank Liaoning Haohushi Pharmaceutical (Group) Co., Ltd. for providing WBT samples.

SUPPLEMENTARY MATERIAL

The Supplementary Material for this article can be found online at: https://www.frontiersin.org/articles/10.3389/fphar.2021.669551/full#supplementary-material

REFERENCES

Aletaha, D., and Smolen, J. S. (2018). Diagnosis and Management of Rheumatoid Arthritis. *JAMA* 320 (13), 1360–1372. doi:10.1001/jama.2018.13103

Askling, J. (2007). Malignancy and Rheumatoid Arthritis. *Curr. Rheumatol. Rep.* 9 (5), 421–426. doi:10.1007/s11926-007-0067-1

Au, K., Reed, G., Curtis, J. R., Kremer, J. M., Greenberg, J. D., Strand, V., et al. (2011). High Disease Activity Is Associated with an Increased Risk of Infection in Patients with Rheumatoid Arthritis. *Ann. Rheum. Dis.* 70 (5), 785–791. doi:10.1136/ard.2010.128637

Bickerton, G. R., Paolini, G. V., Besnard, J., Muresan, S., and Hopkins, A. L. (2012). Quantifying the Chemical Beauty of Drugs. *Nat. Chem* 4 (2), 90–98. doi:10.1038/nchem.1243

Burmester, G. R., and Pope, J. E. (2017). Novel Treatment Strategies in Rheumatoid Arthritis. *The Lancet* 389 (10086), 2338–2348. doi:10.1016/S0140-6736(17)31491-5

Chatzidionisyou, A., and Catrina, A. I. (2016). The Lung in Rheumatoid Arthritis, Cause or Consequence? *Curr. Opin. Rheumatol.* 28 (1), 76–82. doi:10.1097/BOR.0000000000000238

Cheng, B., Zheng, H., Wu, F., Wu, J., Liu, X., Tang, C., et al. (2017). Metabolomics Analysis of Danggui Sini Decoction on Treatment of Collagen-Induced Arthritis in Rats. *J. Chromatogr. B* 1061-1062, 282–291. doi:10.1016/j.jchromb.2017.07.043

Deng, Z.-L., Sharff, K. A., Tang, N., Song, W. X., Luo, J., Luo, X., et al. (2008). Regulation of Osteogenic Differentiation during Skeletal Development. *Front. Biosci.* 13, 2001–2021. doi:10.2741/2819

Doak, B. C., Over, B., Giordanetto, F., and Kihlberg, J. (2014). Oral Druggable Space beyond the Rule of 5: Insights from Drugs and Clinical Candidates. *Chem. Biol.* 21 (9), 1115–1142. doi:10.1016/j.chembiol.2014.08.013

Doak, B. C., Zheng, J., Dobritzsch, D., and Kihlberg, J. (2016). How beyond Rule of 5 Drugs and Clinical Candidates Bind to Their Targets. *J. Med. Chem.* 59 (6), 2312–2327. doi:10.1021/acs.jmedchem.5b01286

England, B. R., Thiele, G. M., Anderson, D. R., and Mikuls, T. R. (2018). Increased Cardiovascular Risk in Rheumatoid Arthritis: Mechanisms and Implications. *BMJ* 361, k1036. doi:10.1136/bmj.k1036

English, B. K., Ihle, J. N., Myracle, A., and Yi, T. (1993). Hck Tyrosine Kinase Activity Modulates Tumor Necrosis Factor Production by Murine Macrophages. *J. Exp. Med.* 178 (3), 1017–1022. doi:10.1084/jem.178.3.1017

Ernst, M., Inglese, M., Scholz, G. M., Harder, K. W., Clay, F. J., Bozinovski, S., et al. (2002). Constitutive Activation of the SRC Family Kinase Hck Results in Spontaneous Pulmonary Inflammation and an Enhanced Innate Immune Response. *J. Exp. Med.* 196 (5), 589–604. doi:10.1084/jem.20020873

Fan, F. (2019). Clinical Observation of Wangbi Pian Combined with Methotrexate in Treating Rheumatoid Arthritis. *China's Naturopathy* 027 (001), 64–65. doi:10.19621/j.cnki.11-3555/r.2019.0138

Feng, X., Ma, G., Shi, H., Wang, Y., and Chao, X. (2020). An Integrative Serum Pharmacology-Based Approach to Study the Anti-tumor Activity of B. Paniculatum Aqueous Bulb Extract on the Human Hepatocellular Carcinoma Cell Line BEL-7404. *Front. Pharmacol.* 11, 01261. doi:10.3389/fphar.2020.01261

Goekoop-Ruiterman, Y. P. M., de Vries-Bouwstra, J. K., Allaart, C. F., van Zeben, D., Kerstens, P. J. S. M., Hazes, J. M. W., et al. (2005). Clinical and Radiographic Outcomes of Four Different Treatment Strategies in Patients with Early Rheumatoid Arthritis (The BeSt Study): a Randomized, Controlled Trial. *Arthritis Rheum.* 52 (11), 3381–3390. doi:10.1002/art.21405

Guan, Y. Y., Zhang, Y., Liu, L. X., Li, H. D., Xue, D., Bao, W. L., et al. (2018). Suppressive Effects of Wang-Bi Tablet on Adjuvant-induced Arthritis in Rats via NF-κB and STAT3 Signaling Pathways. *Int. J. Mol. Med.* 42 (3), 1666–1674. doi:10.3892/ijmm.2018.3723

Hada, Y., Uchida, H. A., Mukai, T., Kojima, F., Yoshida, M., Takeuchi, H., et al. (2020). Inhibition of Interleukin-6 Signaling Attenuates Aortitis, Left Ventricular Hypertrophy and Arthritis in Interleukin-1 Receptor Antagonist Deficient Mice. *Clin. Sci. (Lond).* 134 (20), 2771–2787. doi:10.1042/CS20201036

Jiao, S. D., and Wang, W. G. (2009). Study on Disease Name Wangbi and its Treatment Discipline. *J. Zhejiang Chin. Med. Univ.* 33 (05), 681–685. doi:10.16466/j.issn1005-5509.2009.05.015

Jin, S., Hsieh, E., Peng, L., Yu, C., Wang, Y., Wu, C., et al. (2018). Incidence of Fractures Among Patients with Rheumatoid Arthritis: a Systematic Review and Meta-Analysis. *Osteoporos. Int.* 29 (6), 1263–1275. doi:10.1007/s00198-018-4473-1

Kang, X. Z., Wu, Q. F., and Jie, H. Y. (2011). Clinical Study on the Treatment of Knee Osteoarthritis by Wangbi Tablet. *Chin. J. Integr. Med.* 31 (9), 1205–1208.

Koseki, T., Gao, Y., Okahashi, N., Murase, Y., Tsujisawa, T., Sato, T., et al. (2002). Role of TGF-β Family in Osteoclastogenesis Induced by RANKL. *Cell Signal.* 14 (1), 31–36. doi:10.1016/s0898-6568(01)00221-2

Li, S. H. (2013). Observation on the Curative Effect of Wangbi Tablet Combined with Methotrexate in the Treatment of Rheumatoid Arthritis. *Liaoning J. TCM* 040 (2), 297–298. doi:10.13192/j.ljtcm.2013.02.111.lishh.079

Liu, D. M., Yang, L. L., and Xue, H. X. (2012). Efficacy of Wangbipian on Knee Osteoarthritis. *Pract. Pharm. Clin. Remedies* 15 (6), 380–381. doi:10.14053/j.cnki.ppcr.2012.06.014

Lyons, K. M., Hogan, B. L. M., and Robertson, E. J. (1995). Colocalization of BMP 7 and BMP 2 RNAs Suggests that These Factors Cooperatively Mediate Tissue Interactions during Murine Development. *Mech. Development* 50 (1), 71–83. doi:10.1016/0925-4773(94)00326-i

Ma, C., Wang, X., Xu, T., Zhang, S., Liu, S., Zhai, C., et al. (2020). An Integrative Pharmacology-Based Analysis of Refined Qingkailing Injection against Cerebral Ischemic Stroke: A Novel Combination of Baicalin, Geniposide, Cholic Acid, and Hyodeoxycholic Acid. *Front. Pharmacol.* 11, 519. doi:10.3389/fphar.2020.00519

Mao, X., Xu, H., Li, S., Su, J., Li, W., Guo, Q., et al. (2019). Exploring Pharmacological Mechanisms of Xueshuan-Xinmai-Ning Tablets Acting on Coronary Heart Disease Based on Drug Target-Disease Gene Interaction Network. *Phytomedicine* 54, 159–168. doi:10.1016/j.phymed.2018.09.018

Matcham, F., Scott, I. C., Rayner, L., Hotopf, M., Kingsley, G. H., Norton, S., et al. (2014). The Impact of Rheumatoid Arthritis on Quality-Of-Life Assessed Using the SF-36: a Systematic Review and Meta-Analysis. *Semin. Arthritis Rheum.* 44 (2), 123–130. doi:10.1016/j.semarthrit.2014.05.001

Matsuki, T., Isoda, K., Horai, R., Nakajima, A., Aizawa, Y., Suzuki, K., et al. (2005). Involvement of Tumor Necrosis Factor-α in the Development of T Cell-dependent Aortitis in Interleukin-1 Receptor Antagonist-Deficient Mice. *Circulation* 112 (9), 1323–1331. doi:10.1161/CIRCULATIONAHA.105.564658

McInnes, I. B., and Schett, G. (2017). Pathogenetic Insights from the Treatment of Rheumatoid Arthritis. *The Lancet* 389 (10086), 2328–2337. doi:10.1016/S0140-6736(17)31472-1

Myasoedova, E., Crowson, C. S., Kremers, H. M., Therneau, T. M., and Gabriel, S. E. (2010). Is the Incidence of Rheumatoid Arthritis Rising?: Results from Olmsted County, Minnesota, 1955-2007. *Arthritis Rheum.* 62 (6), 1576–1582. doi:10.1002/art.27425

Myasoedova, E., Davis, J., Matteson, E. L., and Crowson, C. S. (2020). Is the Epidemiology of Rheumatoid Arthritis Changing? Results from a Population-Based Incidence Study, 1985-2014. *Ann. Rheum. Dis.* 79 (4), 440–444. doi:10.1136/annrheumdis-2019-216694

Peng, D. P., Tang, X. H., and Yan, Y. M. (2013). Effects of Guizhi Fuzi Decoction on Tumor Necrosis Factor in Rheumatoid Arthritis. *Chin. J. Basic Med. Tradit Chin. Med.* 19 (10), 1136–1138.

Safiri, S., Kolahi, A. A., Hoy, D., Smith, E., Bettampadi, D., Mansournia, M. A., et al. (2019). Global, Regional and National Burden of Rheumatoid Arthritis 1990-2017: a Systematic Analysis of the Global Burden of Disease Study 2017. *Ann. Rheum. Dis.* 78 (11), 1463–1471. doi:10.1136/annrheumdis-2019-215920

Saraux, A., Devauchelle-Pensec, V., Engerran, L., and Flipo, R. M. (2006). Most Rheumatologists Are Conservative in Active Rheumatoid Arthritis Despite Methotrexate Therapy: Results of the PRISME Survey. *J. Rheumatol.* 33 (7), 1258–1265.

Shen, W., Guan, Y.-Y., Wu, R.-M., Liu, L.-X., Li, H.-D., Bao, W.-L., et al. (2019). Protective Effects of Wang-Bi Tablet on Bone Destruction in Collagen-Induced Arthritis by Regulating Osteoclast-Osteoblast Functions. *J. Ethnopharmacology* 238, 111861. doi:10.1016/j.jep.2019.111861

Smolen, J. S., Aletaha, D., and McInnes, I. B. (2016). Rheumatoid Arthritis. *The Lancet* 388 (10055), 2023–2038. doi:10.1016/S0140-6736(16)30173-8

Sun, Z., Wang, W., Yu, D., and Mao, Y. (2019). Differentially Expressed Genes between Systemic Sclerosis and Rheumatoid Arthritis. *Hereditas* 156, 17. doi:10.1186/s41065-019-0091-y

Wang, H., Guan, Y., Wu, R., Lv, X., Shen, X., and Ye, G. (2019). UPLC-Q-TOF/MS Characterization of Efficacy Substances on Osteoblasts Differentiation and Function in Rat Serum after Administration of Wang-Bi Tablet. *Biomed. Chromatogr.* 33 (10), e4628. doi:10.1002/bmc.4628

Wang, J., Luo, J., Xu, Y., Yan, Z., Qu, X., Chen, M., et al. (2020). Wang-Bi Tablet, a Patented Chinese Medicine, Maintains the Balance of Th1/Th2 in Mice with Collagen-Induced Arthritis. *J. Tradit Chin. Med.* 40 (3), 401–406. doi:10.19852/j.cnki.jtcm.2020.03.006

Wang, P., Tang, S. H., Su, J., Zhang, J. Q., Cui, R. Y., Xu, H. Y., et al. (2018). [Modern Research Progress of Traditional Chinese Medicine Based on Integrative Pharmacology]. *Zhongguo Zhong Yao Za Zhi* 43 (7), 1297–1302. doi:10.19540/j.cnki.cjcmm.2018.0052

Wang, W. P., Shi, S. M., Liu, J., and Zhang, Q. Q. (2010). Treatment of 31 Cases of Rheumatoid Arthritis of Qi-Blood Deficiency by Internal and External Administration of Modified "Huangqi Guizhi Wuwu Decoction". *Shanghai J. Tradit Chin. Med.* 44 (5), 43–45. doi:10.16305/j.1007-1334.2010.05.014

Wilson, M. S., Ramalingam, T. R., Rivollier, A., Shenderov, K., Mentink–Kane, M. M., Madala, S. K., et al. (2011). Colitis and Intestinal Inflammation in IL10−/− Mice Results from IL-13Rα2-Mediated Attenuation of IL-13 Activity. *Gastroenterology* 140 (1), 254–264. doi:10.1053/j.gastro.2010.09.047

Wu, J. W., and Shen, T. (2011). Clinical Study on the Treatment of Rheumatoid Arthritis with Wangbi Tablet. *Liaoning J. TCM* 38 (12), 2392–2393. doi:10.13192/j.ljtcm.2011.12.90.wujw.032

Xu, H.-Y., Zhang, Y.-Q., Liu, Z.-M., Chen, T., Lv, C.-Y., Tang, S.-H., et al. (2019). ETCM: an Encyclopaedia of Traditional Chinese Medicine. *Nucleic Acids Res.* 47 (D1), D976–D982. doi:10.1093/nar/gky987

Xu, H. Y., Liu, Z. M., Fu, Y., Zhang, Y. Q., Yu, J. J., Guo, F. F., et al. (2017). [Exploiture and Application of an Internet-Based Computation Platform for Integrative Pharmacology of Traditional Chinese Medicine]. *Zhongguo Zhong Yao Za Zhi* 42 (18), 3633–3638. doi:10.19540/j.cnki.cjcmm.2017.0141

Xu, H. Y., and Yang, H. J. (2014). [Integrative Pharmacology: New Paradigm of Modernization of Chinese Medicine]. *Zhongguo Zhong Yao Za Zhi* 39 (3), 357–362. doi:10.4268/cjcmm20140302

Yang, B., Liu, Z., Shang, S., Qin, X., and Xia, P. (2016). Quantification of Neomangiferin in Rat Plasma by Liquid Chromatography-Tandem Mass Spectrometry and its Application to Bioavailability Study. *J. Pharm. Anal.* 6 (5), 335–340. doi:10.1016/j.jpha.2016.03.005

Yang, M., Ji, H. W., Cao, X. J., Luo, Q., Yi, L., Lei, P., et al. (2009). Clinical Study of Wangbi Pills in the Treatment of Rheumatoid Arthritis (Yin Deficiency in Liver and Kidney, Blood Stasis Stagnation Syndrome), *Mod. Tradit Chin. Med.* 29, 21–23.

Yu, X. E., Qin, J. P., Li, J. C., Huang, W. Z., Wang, Z. Z., and Xiao, W. (2016). [Rapid Analysis on Chemical Constituents in Yinyanghuo Zonghuangtong Capsule by UPLC/Q-TOF-MS/MS]. *Zhongguo Zhong Yao Za Zhi* 41 (24), 4587–4597. doi:10.4268/cjcmm20162417

Zhang, X. M. (2016). Wangbi Tablets Combined with Methotrexate and Leflunomide in the Treatment of Rheumatoid Arthritis for 17 Cases. *Chin. Med. Mod. Distance Education China* 14 (1), 90–91. doi:10.3969/j.issn.1672-2779.2016.01.047

Conflict of Interest: The authors declare that the research was conducted in the absence of any commercial or financial relationships that could be construed as a potential conflict of interest.

Copyright © 2021 Jiao, Xu, Chen, Guo, Deng, Zhang, Zhang, Shi and Wang. This is an open-access article distributed under the terms of the Creative Commons Attribution License (CC BY). The use, distribution or reproduction in other forums is permitted, provided the original author(s) and the copyright owner(s) are credited and that the original publication in this journal is cited, in accordance with accepted academic practice. No use, distribution or reproduction is permitted which does not comply with these terms.

frontiers in Pharmacology

ORIGINAL RESEARCH
published: 07 June 2021
doi: 10.3389/fphar.2021.667433

Qian Yang Yu Yin Granule Improves Renal Injury of Hypertension by Regulating Metabolic Reprogramming Mediated by HIF-1α/PKM2 Positive Feedback Loop

Lichao Qian†, Shuai Ren†, Zhongchi Xu, Yawei Zheng, Lihua Wu, Ying Yang, Yixuan Wang, Jie Li, Shihai Yan and Zhuyuan Fang**

Jiangsu Province Hospital of Chinese Medicine, Affiliated Hospital of Nanjing University of Chinese Medicine, Nanjing, China

OPEN ACCESS

Edited by:
Takashi Sato, Tokyo University of Pharmacy and Life Sciences, Japan

Reviewed by:
Omar Estrada, Instituto Venezolano de Investigaciones Científicas, Venezuela
Guang-Bo Ge, Shanghai University of Traditional Chinese Medicine, China

***Correspondence:**
Shihai Yan
sea-y@qq.com
Zhuyuan Fang
fangzhuyuan@njucm.edu.cn

†These authors have contributed equally for this work

Specialty section:
This article was submitted to Ethnopharmacology, a section of the journal Frontiers in Pharmacology

Received: *13 February 2021*
Accepted: *21 May 2021*
Published: *07 June 2021*

Citation:
Qian L, Ren S, Xu Z, Zheng Y, Wu L, Yang Y, Wang Y, Li J, Yan S and Fang Z (2021) Qian Yang Yu Yin Granule Improves Renal Injury of Hypertension by Regulating Metabolic Reprogramming Mediated by HIF-1α/PKM2 Positive Feedback Loop. Front. Pharmacol. 12:667433. doi: 10.3389/fphar.2021.667433

Protection against hypoxia injury is an important therapeutic strategy for treating hypertensive nephropathy. In this study, the effects of Qian Yang Yu Yin granule (QYYY) on spontaneously hypertensive rats fed with high salt diet and HEK293T cells exposed to hypoxia were investigated. After eight weeks' treatment of QYYY, blood pressure, serum creatinine, serum cystatin C, blood urea nitrogen, urinary β2-microglobulin, urinary N-acetyl-β-glucosaminidase, and urinary microalbumin were assessed. The changes of hypoxia-inducible factor-1α (HIF-1α), pyruvate kinase M2 (PKM2), glucose transport 1 (GLUT1), lactate dehydrogenase A (LDH-A), connective tissue growth factor (CTGF), transforming growth factor-β1 (TGF-β1), ATP, lactate, pyruvate, and pathology were also assessed *in vivo*. HEK293T cells pre-treated with QYYY and/or HIF-1α over expressing cells were cultured in a three gas hypoxic incubator chamber (5% CO_2, 1% O_2, 94% N_2) for 12 h and then the expressions of HIF-1α, PKM2, GLUT1, LDH-A, CTGF, TGF-β1, ATP, lactate, and pyruvate were detected. Our results showed that QYYY promoted the indicators of renal inflammation and fibrosis mediated by HIF-1α/PKM2 positive feedback loop *in vivo* and *vitro*. Our findings indicated that QYYY treated hypertensive nephropathy by regulating metabolic reprogramming mediated by HIF-1α/PKM2 positive feedback loop.

Keywords: hypertensive nephropathy, metabolic reprogramming, HIF-1α, PKM2, Qian Yang Yu Yin granule

INTRODUCTION

Hypertension is a commonly observed cardiovascular disease and kidney damage is one of the major complications found in patients with hypertension. Hypertension is one of the important causes of chronic kidney disease. Statistics from the American Nephrology Association in 2009 showed that about 28% of patients with end-stage kidney disease were induced by hypertension (Mahmoodi et al., 2012). Traditional Chinese medicine (TCM) has its unique curative effects in the treatment of hypertensive renal damage, but the mechanism of TCM in the treatment of hypertensive renal damage is insufficient (Guo et al., 2019). Under the guidance of the theory of "blood stasis and heat" in TCM, Qian Yang Yu Yin granule (QYYY) was created and applied as hospital preparation and has been widely used in clinical practice for more than 20 years in Jiangsu Province Hospital of Chinese

Medicine. It is safe and effective in treating hypertensive kidney injury. Previous studies of our project group showed that QYYY had antioxidant, anti-inflammatory and anti fibrosis effects (Chen et al., 2013; Wang et al., 2014; Yan D et al., 2014; Ding et al., 2015; Yan et al., 2018; Liu et al., 2019; Zhang et al., 2020).

Metabolic reprogramming refers to the change of cell metabolic mode. In normal cells, when oxygen is sufficient, cells primarily obtain energy through the process of oxidative phosphorylation. However, under hypoxia, cells obtain energy through glycolysis, pentose phosphate and other pathways. This switch of cell energy acquisition mode has been termed as metabolic reprogramming (Vander et al., 2009; Krisher and Prather, 2012). Kidney is an organ that requires high-energy consumption. Therefore, the normal and optimal energy metabolism system serves as an important biochemical basis to maintain the specific structure and physiological functions of the kidney. A number of previous studies have reported that alteration in renal cell metabolism from oxidative phosphorylation to glycolysis is the main feature of cell activation during renal fibrosis and inhibition of renal cell glycolysis can significantly reduce renal fibrosis (Ding et al., 2017). Moreover, gene and protein analyses have showed that the expression of glycolytic enzyme was significantly up-regulated in renal interstitial fibroblasts treated with unilateral ureteral obstruction (UUO) or transforming growth factor-β1 (TGF-β1). In nephropathy caused by UUO or renal interstitial fibroblasts treated with TGF-β1, the aerobic glycolysis flux was increased with glucose uptake and lactate production and it was reported to be positively correlated with the fibrosis process. Glycolysis inhibitors can be used as a potential anti fibrosis strategy.

Protection against hypoxia injury is an important therapeutic strategy for treating hypertensive nephropathy (Watson et al., 2019). Hypoxia inducible factor-1α (HIF-1α) is a special protein distributed in mammalian cells. Knockout or inhibition of HIF-1α effectively improved hypertensive renal injury (Huang et al., 2019). In renal injury model, HIF-1α mediated gene expression in renal medulla such as glucose transporter 1 (GLUT1), pyruvate kinase M2 (PKM2), connective tissue growth factor (CTGF), TGF-β1, and other related genes were increased. A related study showed that long-term over-expression of HIF-1α was a pathogenic factor leading to chronic kidney injury and stimulating the expression of HIF-1α in cells induced renal injury, hypertension and disease progression (Armutcu et al., 2019). Moreover, a related study found that the level of serum HIF-1α may reflect the degree of damage of chronic glomerulonephritis and actively participate in the occurrence and development of chronic glomerulonephritis (Dallatu et al., 2014). It has been reported that an increase of HIF-1α level could participate in the formation of proteinuria, promote metabolic reprogramming and renal fibrosis, and thereby aggravate the progressive deterioration of renal function. Our previous study found that HIF-1α was highly expressed in hypertensive renal injury model (Wu, 2020). Therefore, we speculated that HIF-1α is a key target of metabolic reprogramming of renal cell in hypertensive renal injury model.

A large number of studies have confirmed that HIF-1α is closely related to PKM2 (Luo et al., 2011). For instance, Hasan D found that the antisense chain of the first intron of PKM gene contained hypoxia response element (HRE), and proved that HIF-1α significantly promoted the expression of PKM2, which also formed a positive feedback mechanism at the gene level and played a key role in cell metabolic reprogramming (Hasan et al., 2018). In another study, Chai Xin Xin used shikonin, a specific inhibitor of PKM2, to down-regulate the expression of PKM2. They found that the down-regulation of PKM2 in breast cancer cells caused the down-regulation of HIF-1α (Chai et al., 2019). Therefore, we speculated that HIF-1α/PKM2 positive feedback is the key pathway of metabolic reprogramming of renal cell in hypertension.

MATERIALS AND METHODS

Preparation of Qian Yang Yu Yin

QYYY (Batch No. Z20100007) was obtained from Jiangsu Province of Chinese Medicine. It is made up of *Cyathula officinalis* K. C. Kuan [Amaranthaceae; cyathulae radix], *Scrophularia ningpoensis* Hemsl [Scrophulariaceae; scrophulariae radix], *Bidens pilosa* L. [Asteraceae; *Bidens bipinnata* L.], *Cornus officinalis* Siebold and Zucc [Cornaceae; corni fructus], *Alisma plantago-aquatica* subsp. orientale (Sam.) Sam. [Alismataceae; alismatis rhizoma] and *Reynoutria multiflora* (Thunb.) Moldenke [Polygonaceae; polygoni multiflori radix] (Rivera et al., 2014). Detailed information on the components of QYYY is listed in **Table 1**. The preparing process of QYYY was as below: six ingredients were mixed together. Then the mixture was decocted with 12 times of the amount of water twice, for 1 h each time. The supernatant obtained by high-speed centrifugation was concentrated to a relative density of 1.2 g/ml at 60°C. After stevioside was added to a concentration of 1% (weight/volume), the concentrated supernatant was mixed with dextrin and granulated in a fluidized bed granulator. The obtained particles were dried at 60°C for 1 h and then stored at 4°C (Ding et al., 2015). High performance liquid chromatogram (HPLC) was established to determine the active components in QYYY and 2,3,5,4′-tetra-hydroxystilbene-2-O-β-Dglucopyranoside (2,3,5,4-TDG), morroniside, harpgide, ecdysterone, and hyperin were detected. The quality evaluation of QYYY is shown in **Table 2** (Zhang et al., 2020).

Animals and Treatment

50 spontaneously hypertensive rats (SHR), 10 Wistar-Kyoto rats (WKY), 8 weeks old, male, weighing 200 ± 30 g, were purchased from Beijing Weitong Lihua Experimental Animal Technology Co., Ltd. After four weeks of adaptive feeding, the rats were weighed and administrated. SHR were randomly divided into five groups: model group, QYYY (low, medium and high dose) group and valsartan group. Wistar-Kyoto rats (WKY) of the same age were used as the control group. WKY were fed with normal salt diet (0.4% NaCl) while SHR were fed with high salt diet (4% NaCl) for 8 weeks to establish hypertensive nephropathy model

TABLE 1 | The components of Qian Yang Yu Yin.

Components	Chinese name	Family	Amount used (g)
Cyathula officinalis K. C. Kuan	Chuan Niu Xi	Amaranthaceae	170
Scrophularia ningpoensis Hemsl	Xuan Shen	Scrophulariaceae	180
Bidens pilosa L.	Gui Zhen Cao	Asteraceae	110
Cornus officinalis Siebold and Zucc	Shan Zhu Yu	Cornaceae	108
Alisma plantago-aquatica subsp. orientale (Sam.) Sam	Ze Xie	Alismataceae	180
Reynoutria multiflora (Thunb.) moldenke	He Shou Wu	Polygonaceae	180

TABLE 2 | Quality evaluation of Qian Yang Yu Yin.

Major constituents	Method of determination	Quality specifications
2,3,5,4-TDG	HPLC	>6 mg per 10 g QYYY
Morroniside	HPLC	Contained
Harpgide	HPLC	Contained
Ecdysterone	HPLC	Contained
Hyperin	HPLC	Contained

HPLC: high performance liquid chromatogram.

and then be treated with QYYY or valsartan for another 8 weeks. QYYY group: QYYY granule (low dose 3.2 g/kg/d, medium dose 6.4 g/kg/d, high dose 12.8 g/kg/d) was given by gavage; valsartan group: valsartan (17 mg/kg/d) was given by gavage. This dose was 10 folds of clinic dosage according to the pharmacology experimental methodology of TCM which had obvious curative effect based on the results of the previous studies (Wang, 2020). After 8 weeks' treatment of QYYY or valsartan, serum creatinine (S-Cr), serum cystatin C (CysC), blood urea nitrogen (BUN), urinary β2-microglobulin (β2-MG), urinary N-acetyl-β-glucosaminidase (NAG), and urinary microalbumin (mALB) were assessed. The changes of HIF-1α, GLUT1, CTGF, IL-6, TGF-β1, ATP, lactate, pyruvate, and pathology were also assessed *in vivo*. The Experimental Animal Ethics Committee of Affiliated Hospital of Nanjing University of Chinese Medicine approved all animal experiments.

Cell Culture

HEK293T cell was purchased from Cell Bank of the Chinese Academy of Sciences (Shanghai, China) and cultured with Dulbecco's modified Eagle's medium (DMEM; Gibco, United States of America) containing 10% fetal bovine serum (FBS; Gibco, United States of America) in a humidified 5% CO_2 atmosphere at 37°C.

Preparation of Qian Yang Yu Yin-Containing Serum

Thirty 8 week-old Sprague Dawley rats (SD), male, weighing 200 ± 30 g, were purchased from Beijing Weitong Lihua Experimental Animal Technology Co., Ltd. After four weeks of adaptive feeding, the rats were weighed and administrated. SD were randomly divided into five groups: blank group (n = 10), positive control group (n = 5) and QYYY group (n = 15). Blank group: pure water was given with 1 ml/100 g by gavage; positive control group: valsartan was given according to 17 mg/kg/d; QYYY group: QYYY granule was given by gavage according to 12.8 g/kg/d. Each group was given drug intervention for seven consecutive days. Thereafter, the rats were anesthetized and their blood was drawn from abdominal aorta. 5–8 ml blood was collected from each rat and kept in the blood collection tube at room temperature for 2 h. After centrifugation at 3,000 rpm for 10 min, the upper serum was aspirated, and the serum of the same group was mixed, filtered with 0.22 μM filter, placed into 1.5 ml sterile centrifuge tube and stored at -20°C.

Hypoxia Treatment

We determined the optimal anoxia time according to the expression of HIF-1α. HEK 293T cells were placed in a hypoxia cultivator containing a gaseous mixture of 5% CO_2, 1% O_2, and 94% N_2 at 37°C for durations of 0, 6, 12, 24, and 36 h respectively. Subsequently, the proteins from HEK 293T cells were extracted with RIPA lysis buffer (Beyotime, China) and subjected to western blot analysis to analyze HIF-1a expression. We considered the time with the highest HIF-1α expression as our optimal anoxic exposure time. In our study, we found that HIF-1α expression peaked at 12 h of hypoxia, so we performed our experiments at 12 h of hypoxia in this study. Hypoxia was induced using a three-gas hypoxia incubator chamber (5% CO_2, 1% O_2, and 94% N_2). For drug intervention, cultured HEK 293T cells were pre-treated with QYYY for 1 h before hypoxia. Cells were randomly divided into following groups: Model group (Hypoxia + 10% blank serum); QYYY group (Hypoxia + 5% QYYY-containing serum + 5% blank serum) and valsartan group (Hypoxia + 10% Valsartan-containing serum). The control group was maintained in a humidified atmosphere of 5% CO_2 at 37°C till end of study.

MTT Assay

The proliferation abilities of HEK 293T cells for 0, 6, 12, 24, and 36 h in the anoxic incubator were assessed by MTT assay. HEK293T cells were cultured in 96-well plates with 10% FBS in a three-gas hypoxia incubator chamber (5% CO_2, 1% O_2, and 94% N_2) for 0, 6, 12, 24, and 36 h, respectively. Then 20 μl MTT was added and then cultured for another 4 h. Finally, 150 μl DMSO was added. Plates were shaken for 10 min at room temperature. We used microplate reader to measure absorbance at 570 nm.

Western Blot

The protein was extracted by RIPA lysis buffer (Beyotime Biotechnology, Shanghai, China) mixed with

phenylmethanesulfonyl fluoride (PMSF). The quantity of proteins was measured using the BCA assay (Beyotime Biotechnology, Shanghai, China). 10% sodium dodecyl sulfate polyacrylamide gel electrophoresis were used to separate different molecular weight proteins. Gels were then transferred onto PVDF membranes. Nonfat milk was used of for 1 h then and the membranes were incubated with the primary antibody against HIF-1α, PKM2, GLUT1, LDH-A, IL-6, and GAPDH at 4°C overnight. Peroxidase-conjugated second antibody were uesd for 1 h on the shaking table at room temperature. Protein bands were detected by ChemiDoc XRS imaging system (Bio-Rad, United States of America) after using ECL reagents.

Real-Time Quantitative PCR Analysis

The total RNA was extracted by using Trizol (Ambion, United States). The High Capacity cDNA Reverse Transcription Kit (Vazyme, Nanjing, China) was used to conduct the reverse transcription. SYBR Green chemistry (Vazyme, Nanjing, China) on a 7,500 fast RT-PCR system was used to perform amplified reaction. The primers (Invitrogen Co, Shanghai, China) were listed in **Supplementary Table S1**. The ratio of the mRNA expression of the target gene vs that of β-actin was defined as $2^{-\triangle\triangle Ct}$.

Lentiviral Transduction to Establish Stable Cell Lines

HIF-1α-overexpression, PKM2-overexpression, HIF-1α-knockdown, and PKM2-knockdown lentiviruses were generated by Genechem Co.,Ltd (Shanghai, China). Thereafter, over-expression and silencing lentiviral vectors of HIF-1α were transfected into 293T cells when multiplicity of infection was 10. Green fluorescent protein was then expressed in all the lentiviral vectors. We also collected other lentiviral vectors without carrying HIF-1α or PKM2 for excluding the influence of lentivirus itself on transfection. The stable cell lines were selected by using 2 μg/ml puromycin (VWR, America) in medium. The levels of HIF-1α and PKM2 were detected by using qPCR and western blotting.

Kits for ATP, Lactate and Pyruvate

Levels of ATP, lactate and pyruvate were measured using an the assay kits (Nanjing Jiancheng Bioengineering Institute, Nanjing, China) according to the instruction of manufacturer.

HE Staining

The kidney tissues were fixed with 4% paraformaldehyde for 24 h, dehydrated gradiently in turn, and embedded in the paraffin wax blocks. The blocks were labelled based on the different treatment groups. The wax block was thereafter sliced, dewaxed and washed. Hematoxylin staining and eosin staining were used in a sequence.

Masson Staining

The kidney tissues were fixed and sectioned as described above under HE staining. Weigert's iron hematoxylin staining was used to stain the nucleus, and ponceau S was used thereafter for 5–10 min. After rinsing with distilled water, they were treated with molybdophosphoric acid for 3–5 min. The samples were then stained using Aniline blue again for 5 min and treated with 1% glacial acetic acid for 1 min. The slides were then dried, mounted. The samples were finally observed by microscope and the images were analyzed.

Immunofluorescence Staining

For immunocytochemistry, cells were seeded on poly-D-lysine precoated cell climbing films (Shanghai wohong Biotechnology Co., Ltd) in 12-well culture plate. The medium was removed and the cells were washed with PBS three times for 5 min each and then fixed with 4% paraformaldehyde for 15 min at room temperature. After washing with PBS three times for 5 min each, the fixed cells were blocked by using 0.3% Triton X-100/PBS for 1 h. Cells were incubated with the primary antibody, HIF-1α (Proteintech: 20960-1-AP), PKM2 (Proteintech: 60268-1-Ig), GLUT-1 (Proteintech: 66290-1-Ig), LDH-A (Proteintech: 19987-1-AP) diluted in 1% BSA in PBS overnight at 4°C. After washing three times with PBS, cells were incubated for 1.5 h with CoraLite488-conjugated Affinipure Goat Anti-Rabbit IgG (H + L) (Proteintech: SA00013-2) or CoraLite594-conjugated Goat Anti-Mouse IgG (H + L) (Proteintech: SA00013-3) secondary antibodies. The unbound secondary antibody was removed with three washes of PBS for 5 min each. Next, the samples were counterstained with DAPI (Beyotime Biotechnology). Samples were visualized on fluorescence microscopes (Nikon, Japan). The intensity was quantified using ImageJ software.

Immunohistochemistry

The rat kidney tissues were fixed and processed as described above for HE staining. The tissue sections were then placed in EDTA antigen repair buffer (pH = 9.0) for 15 min. After cooling, the slides were placed in PBS (pH = 7.4). The slides were shaken and washed for three times on the shaking table for 5 min each time. The slides were then placed in 3% hydrogen peroxide solution and incubated for 25 min at room temperature in the dark. The slides were shaken and washed for three times as before. The tissues were incubated with the primary antibody overnight at 4°C in a wet box. After washing three times with PBS, the tissues were incubated with secondary antibodies for 50 min at room temperature. The secondary antibody was removed by washing three times with PBS for 5 min each. After the slides have dried, DAB solution was added to observe the color, and then stained with hematoxylin for 3 min. Thereafter, dehydration was carried out, and the slides were observed under microscope, and the images were collected and analyzed. The optical density of immunohistochemical images was analyzed by ImageJ software.

Bioinformatics Analysis and Network Pharmacology of Qian Yang Yu Yin

All of the compound data of the six botanical drugs contained in QYYY were retrieved from TCMSP and Chemistry database, and their corresponding ADME indices, including oral bioavailability (OB) and drug likeness (DL), were collected. The screening

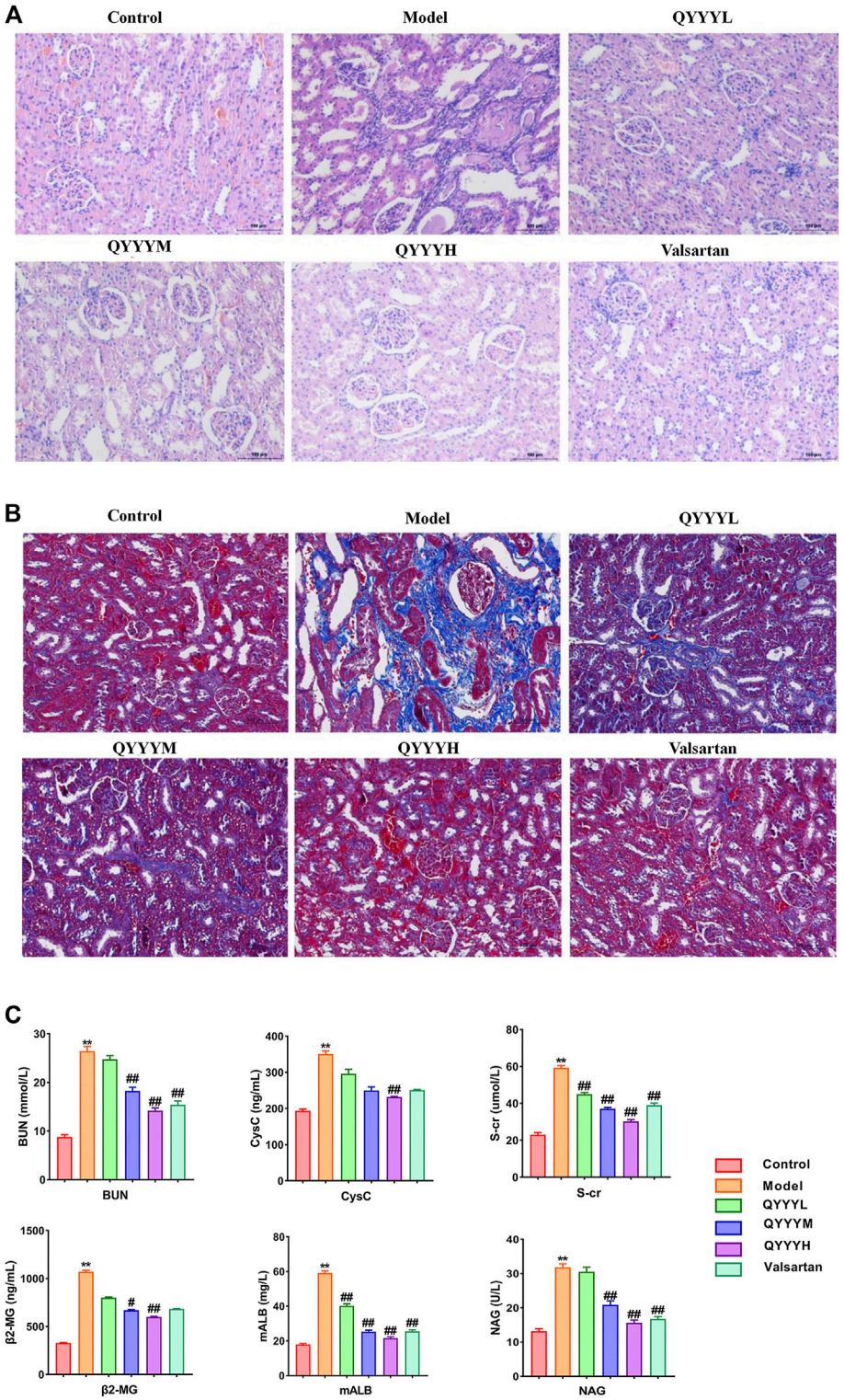

FIGURE 1 | QYYY promoted pathology, fibrosis and renal function *in vivo*. SHR were randomly divided into five groups: Model group, QYYYL (low dose 3.2 g/kg/d), QYYYM (middle dose 6.4 g/kg/d), QYYYH (high dose 12.8 g/kg/d) group and valsartan group (17 mg/kg/d). WKY of the same age were used as the control group. WKY were fed with normal salt diet (0.4% NaCl) while SHR were fed with high salt diet (4% NaCl) for 8 weeks to establish hypertensive nephropathy model and then be treated with QYYY or valsartan for another 8 weeks. **(A)** Effects of QYYY on renal histomorphology in rats. **(B)** Effects of QYYY on masson staining method for staining renal fibrosis. **(C)** Effects of QYYY on renal function in SHR. $^{*}p < 0.05$ and $^{**}p < 0.01$ as compared with the control group. $^{\#}p < 0.05$ and $^{\#\#}p < 0.01$ as compared with the model group.

conditions were OB ≥ 30% and DL ≥ 0.18. The putative target proteins of these active compounds were searched through TCMSP. The putative target proteins names were converted into gene names through UniProt database. With the help of Cytoscape 3.7.0 software, a network was constructed to connect the candidate compounds of QYYY with the putative targets. All of the hypertensive nephropathy-associated genes were obtained from the OMIM and GeneCards databases. The acquired genes were overlapped with the putative target proteins from QYYY. Upload the intersection target genes to the STRING platform to perform KEGG enrichment analysis and structure protein-protein interaction network.

Statistical Analysis

SPSS 20 software was used to statistical analysis. The differences were considered statistically significant when $p < 0.05$.

RESULTS

Qian Yang Yu Yin Promoted Blood Pressure, Pathology, Fibrosis, Renal Functions *In Vivo*

Firstly, we successfully established the model by 12-week-old SHR which were fed with high salt diet (4% NaCl) for 8 weeks. We observed the effects of QYYY on BP, pathology, fibrosis and renal function *in vivo* to identify the effects of QYYY on hypertensive nephropathy. Effects of QYYY on renal histomorphology in rats were shown in **Figure 1A**. In model group, the arrangement of renal tubules was observed to be loose and the volume of epithelial cells was relatively smaller. In QYYYH and valsartan group, the atrophy of glomeruli was not obvious and the vacuoles in renal small cysts were improved (**Figure 1A**). After observing the effects of QYYY on masson staining method for staining renal fibrosis, it was found QYYY and valsartan effectively improved the renal fibrosis (**Figure 1B**). The effects of QYYY on indicators of BP and renal function including S-Cr, CysC, BUN, β2-MG, NAG, and mALB in rats were shown in **Supplementary Tables S2 and S3**; **Figure 1C**. The resluts showed that QYYY significantly decreased the levels of S-cr, CysC, BUN, mALB, NAG, and β2-MG in SHR. These data suggest that QYYY can treat hypertensive nephropathy effectively.

Network Pharmacology Prediction of the Potential Active Compounds in Qian Yang Yu Yin and Corresponding Pathways Related to Hypertensive Nephropathy

After identifying that QYYY can effectively treat hypertensive nephropathy, we performed a network pharmacology investigation of QYYY to determine its candidate active compounds and the corresponding pathways underlying the progression of hypertensive nephropathy. Firstly, a library for active compounds of the six botanical drugs in QYYY was constructed based on online databases and literature mining. Only compounds with favorable pharmacokinetic parameters of oral bioavailability (OB ≥ 30%) and drug-likeness (DL ≥ 0.18) were included (**Figure 2A**) and their chemical information are listed (**Supplementary Table S4**). Secondly, we screened 181 putative target proteins from the 46 active compounds in QYYY and 30 candidate compounds were identified. To elucidate the multiple interactions of these target proteins, we constructed a Drug–Compound–Target (D–C–T) network (**Figure 2B**). To further identify the effects of QYYY on hypertensive nephropathy, 2,456 hypertensive nephropathy-associated genes were extracted from databases and 120 of these genes were overlapped with putative target proteins of QYYY (**Figure 2C**). KEGG analysis of the 120 gene targets (**Figure 2D**) showed that pathways involved in HIF-1 signaling pathway. PPI network (**Figure 2E**) was established to understand the possible regulatory mechanism and its relationship.

Qian Yang Yu Yin Promoted HIF-1α, PMK2, Metabolic Markers, Renal Inflammation and Fibrosis *In Vivo*

According to the results of the above network pharmacology prediction and some related studies. We speculated that QYYY can improve HIF-1α, PKM2 and related metabolism, inflammation, and fibrosis indexes. Therefore, we observed the effects of QYYY on HIF-1α, PMK2, metabolic markers, renal inflammation, and fibrosis *in vivo*. Western blot results indicated that QYYY significantly decreased the expression of HIF-1α, PKM2, GLUT1, LDH-A, and IL-6 in SHR (**Figure 3A**). The nucleoprotein expression of HIF-1α, PKM2 were significantly increased and cytoplasmic protein of HIF-1α, PKM2 were significantly decreased in model group. It triggered the nuclear translocation and increased the transcriptional activity of HIF-1α and PKM2 in model group. QYYY significantly increased the cytoplasmic level of HIF-1α compared to model group and blocked HIF-1α nuclear accumulation significantly (**Figure 3F**). The resluts by using kits for ATP, lactate and pyruvate indicated that QYYY significantly increased the production of ATP and decreased the production of pyruvate and lactate in SHR (**Figure 3B**). QPCR results showed that QYYY significantly decreased the expression of HIF-1α, PKM2, CTGF, TGF-β1, and TNF-α in SHR (**Figure 3C**). Immunohistochemistry showed that QYYY significantly decreased the expression of HIF-1α and PKM2 in SHR (**Figures 3D,E**). These data suggest that QYYY can improve metabolic markers, renal inflammation and fibrosis *in vivo* to treat hypertensive nephropathy.

Qian Yang Yu Yin Promoted HIF-1α, PMK2, Metabolic Markers, Renal Inflammation and Fibrosis *In Vitro*

To further determine the effects of QYYY on HIF-1α, PMK2, metabolic markers, renal inflammation, and fibrosis in hypertensive nephropathy. We also observed the curative effect *in vitro*. Hypoxia can stimulate the proliferation of mesangial and epithelial cells, thereby modulating the

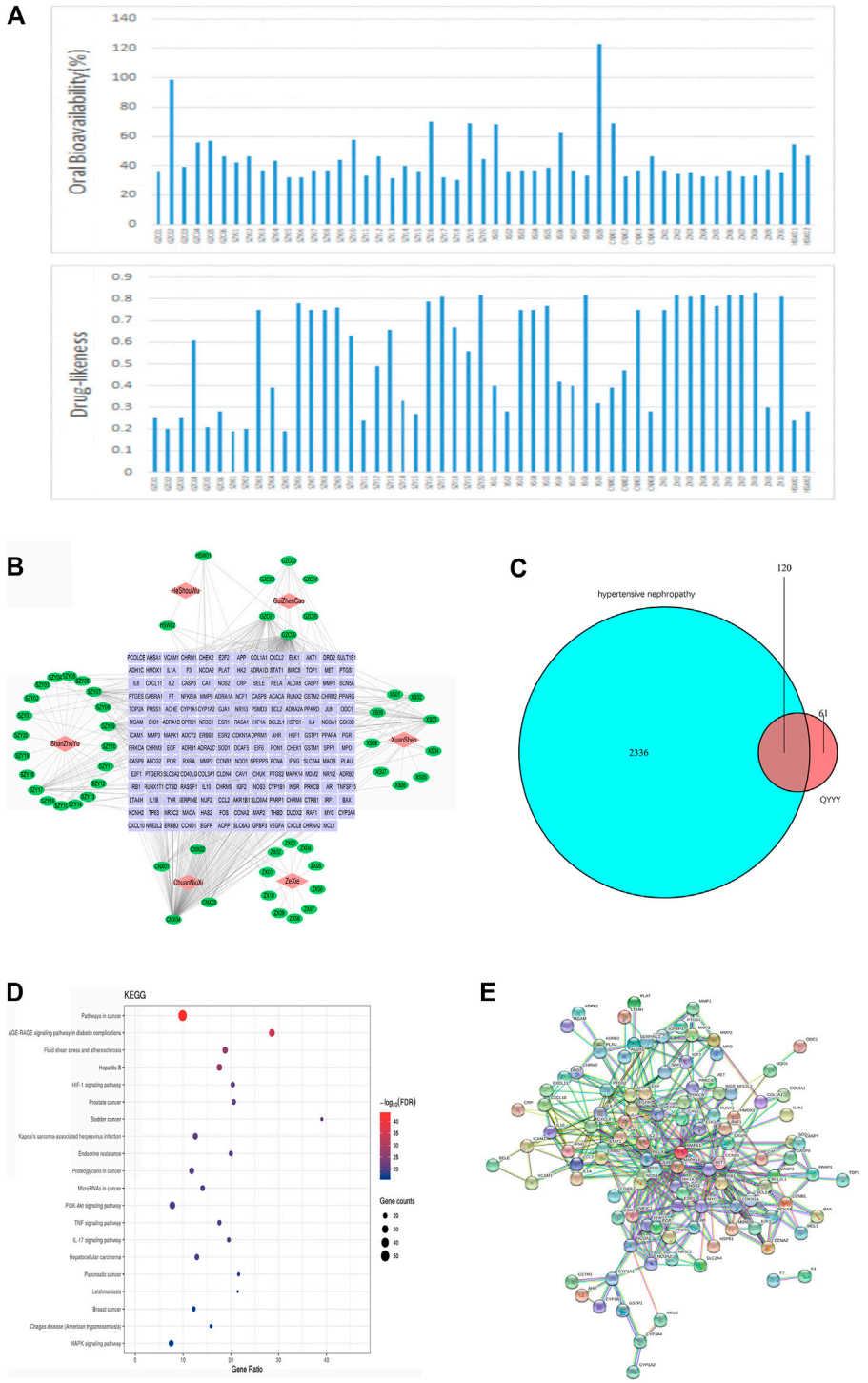

FIGURE 2 | Network pharmacology prediction of the potential active compounds in QYYY and corresponding pathways related to hypertensive nephropathy. **(A)** Active compounds in QYYY with oral bioavailability (OB) ≥ 30% and drug-likeness (DL) ≥ 0.18. **(B)** Drug–Compound–Target Network: the nodes represent drug (red diamond), candidate compounds (green ellipse), and the targets proteins (purple rectangle). **(C)** Venn diagram of 2,456 hypertension nephropathy-associated genes and 181 putative target proteins screened from candidate compounds of QYYY. **(D)** KEGG analysis of the 120 gene targets. **(E)** PPI network of the 120 gene targets.

glomerular hemodynamics and leading to glomerular sclerosis and stimulation of tubular epithelial cells and renal interstitial fibroblasts to synthesize a large number of extracellular matrix components and reduce their degradation. HEK293T cells, human renal epithelial cells, was chosen to be the model of renal damage of the hypertension in the current study. The

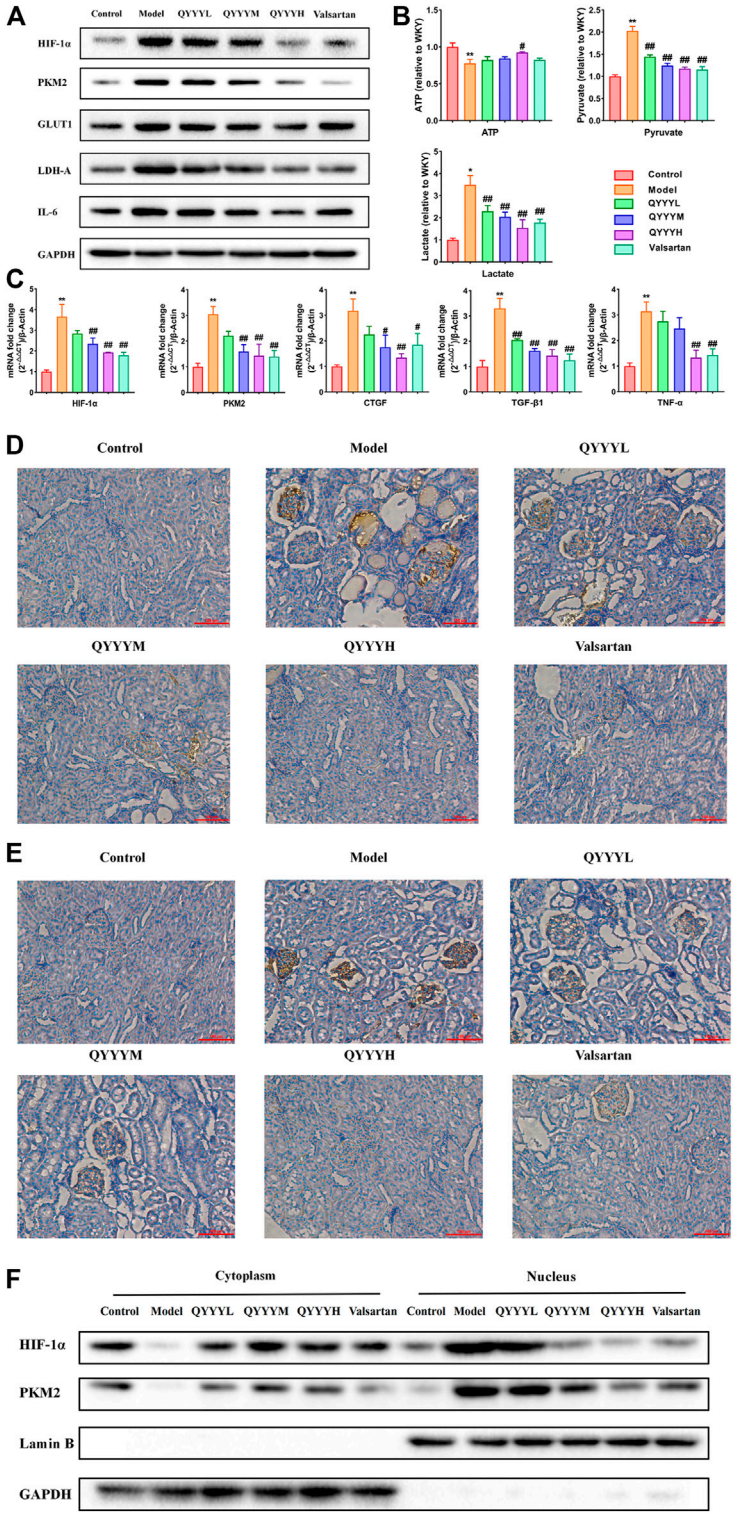

FIGURE 3 | QYYY promoted HIF-1α, PKM2, metabolic markers, renal inflammation and fibrosis *in vivo*. **(A)** Effects of QYYY on protein expression of HIF-1α, PKM2, GLUT1, LDH-A, and IL-6 in SHR were examined using western blotting. **(B)** Effects of QYYY on changes of ATP, pyruvate and lactate using kits. **(C)** Effects of QYYY on mRNA levels of HIF-1α, PKM2, CTGF, TGF-β1 and TNF-α in SHR were examined using qPCR. **(D)** Effects of QYYY on protein level of HIF-1α in SHR were examined by immunohistochemistry. **(E)** Effects of QYYY on protein level of PKM2 in SHR were examined by immunohistochemistry. **(F)** Effects of QYYY on nuclear and cytoplasmic protein expression of HIF-1α, PKM2 in SHR were examined using western blotting. $^{*}p < 0.05$ and $^{**}p < 0.01$ as compared with the control group. $^{\#}p < 0.05$ and $^{\#\#}p < 0.01$ as compared with the model group.

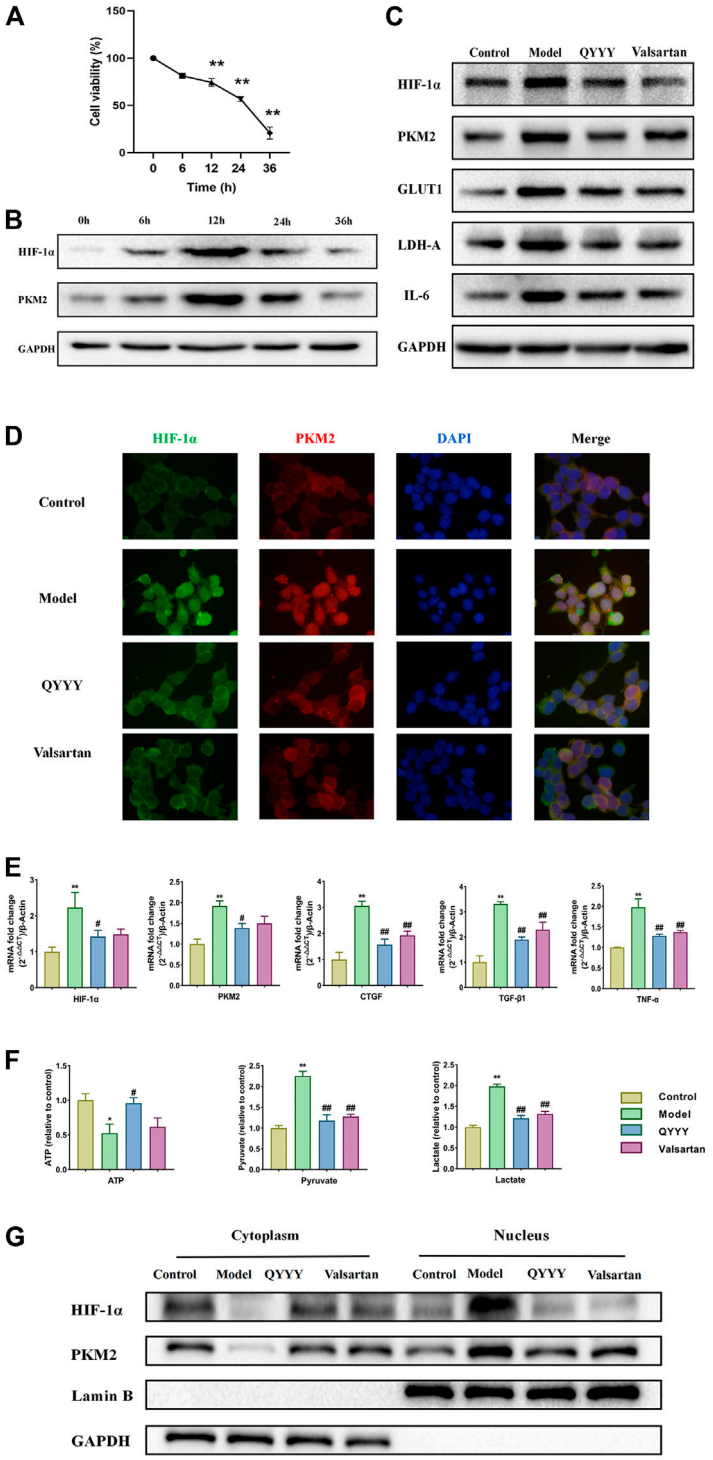

FIGURE 4 | QYYY promoted HIF-1α, PMK2, metabolic markers, renal inflammation and fibrosis *in vitro*. Cells were divided into following groups: Model group (Hypoxia + 10% blank serum); QYYY group (Hypoxia + 5% QYYY-containing serum + 5% blank serum) and valsartan group (Hypoxia + 10% Valsartan-containing serum). The control group was maintained in a humidified atmosphere of 5% CO_2 at 37°C till end of study. **(A)** Effects of anoxia time on the cell viability of HEK293T were examined by using MTT. **(B)** Effects of anoxia time on the protein expression of HIF-1α and PKM2 of hypoxic HEK293T cells were examined by using western blotting. **(C)** Effects of QYYY on protein expression of HIF-1α, PKM2, GLUT1, LDH-A, and IL-6 in hypoxic HEK293T cells were examined by using western blotting. **(D)** Effects of QYYY on immunofluorescence staining of HIF-1α and PKM2 in hypoxic HEK293T cells. **(E)** Effects of QYYY on mRNA levels of HIF-1α, PKM2, CTGF, TGF-β1, and TNF-α in hypoxic HEK293T cells were examined by using qPCR. **(F)** Effects of QYYY on changes of ATP, pyruvate and lactate using kits. **(G)** Effects of QYYY on nuclear and cytoplasmic protein expression of HIF-1α and PKM2 in hypoxic HEK293T cells were examined by using western blotting. $^{*}p < 0.05$ and $^{**}p < 0.01$ as compared with the control group. $^{\#}p < 0.05$ and $^{\#\#}p < 0.01$ as compared with the model group.

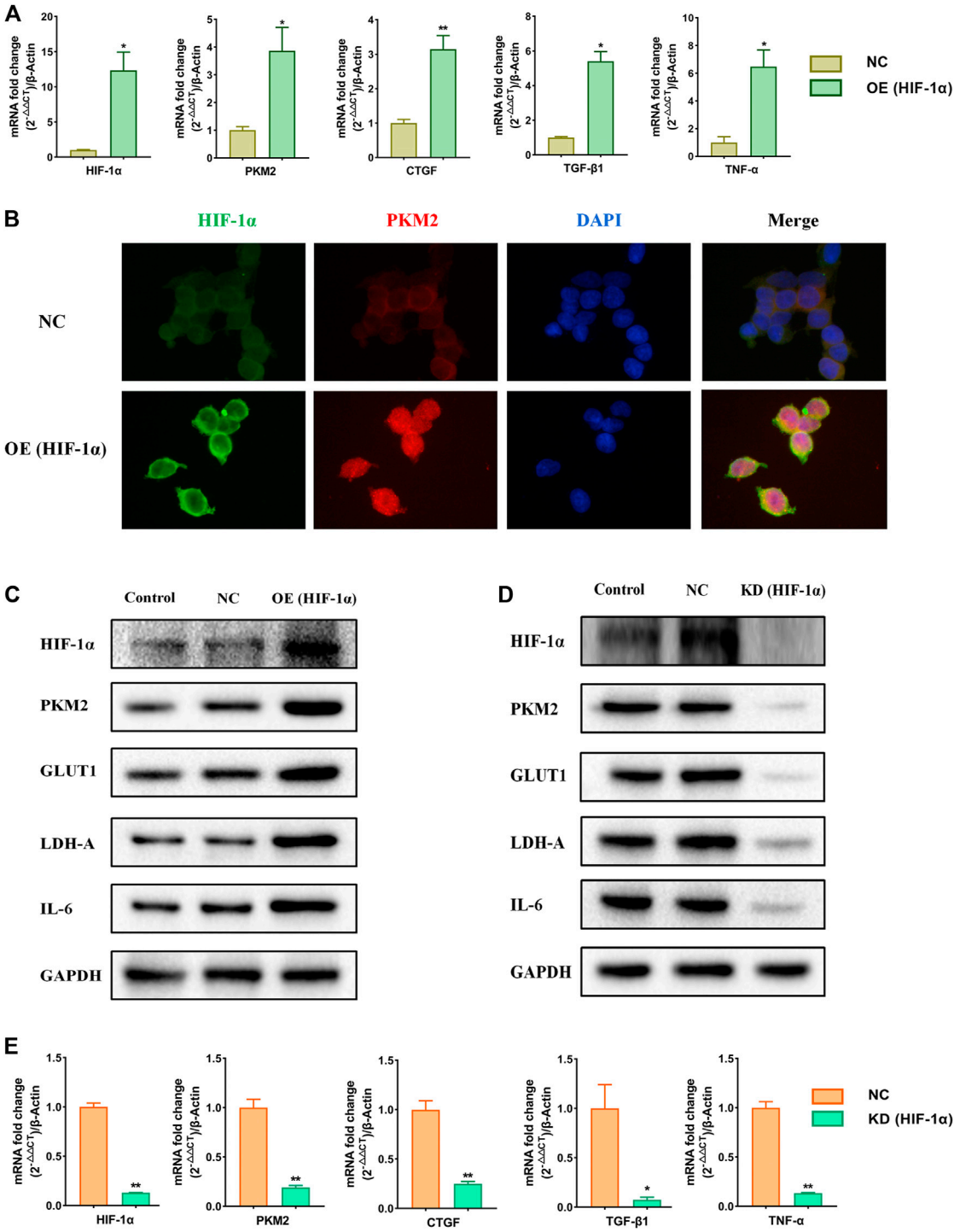

FIGURE 5 | Effects of over-expression and knockdown of HIF-1α on relative markers in HEK293T cells. Cells were divided into following groups: conrtol, negative control (NC), HIF-1α-overexpression group (OE) and HIF-1α-knockdown group (KD). **(A)** Effects of over-expression of HIF-1α on mRNA levels of HIF-1α, PKM2, CTGF, TGF-β1, and TNF-α were examined by using qPCR. **(B)** Effects of over-expression of HIF-1α on immunofluorescence staining of HIF-1α and PKM2. **(C)** Effects of over-expression of HIF-1α on proteins of HIF-1α, PKM2, GLUT1, LDH-A, and IL6 in HEK293T cells were examined by using western blotting. **(D)** Effects of knockdown of HIF-1α on proteins of HIF-1α, PKM2, GLUT1, LDH-A, and IL6 in HEK293T cells were examined by using western blotting. **(E)** Effects of knockdown of HIF-1α on mRNA levels of HIF-1α, PKM2, CTGF, TGF-β1, and TNF-α in HEK293T cells were examined by using qPCR. *$p < 0.05$ and **$p < 0.01$.

effects of different anoxia time on the viability of HEK293T cells were detected via MTT assay. We found there was no significant change in HEK293T cell viability at 6 h, but the cell viability was significantly decreased when treated for 12, 24, and 36 h (**Figure 4A**). We investigated the effect of anoxia time on HEK293T cells, which were exposed to the incremental durations of anoxia time of 0, 6, 12, 24, 36 h. The results showed that HIF-1α and PKM2 reached its peak level at 12 h of anoxia which suggested a steady anoxic condition (**Figure 4B**). Hence, we selected 12 h as an optimal anoxia time-point in the following study. QPCR and western blot results indicated that QYYY significantly decreased the expression of HIF-1α, PKM2, GLUT1, LDH-A, CTGF, TGF-β1, TNF-α, and IL-6 in hypoxic HEK293T cells (**Figures 4C,E**).The nucleoprotein expression of HIF-1α, PKM2 were significantly increased and cytoplasmic protein of HIF-1α, PKM2 were significantly decreased in model group. Hypoxia also triggered the nuclear translocation and increased the transcriptional activity of HIF-1α and PKM2 *in vitro*. The cytoplasmic level of HIF-1α were significantly increased compared to model group and HIF-1α nuclear accumulation was significantly blocked by using QYYY (**Figures 4D,G**). The resluts by using kits for ATP, lactate and pyruvate indicated that QYYY significantly increased the production of ATP and decreased the production of pyruvate and lactate *in vitro* (**Figure 4F**). These data suggest that QYYY can also improve HIF-1α, PKM2, metabolic markers, renal inflammation and fibrosis *in vitro*.

Effects of Over-Expression and Knockdown of HIF-1α on Relative Markers in HEK293T Cells

To further study the role of HIF-1α in the metabolic reprogramming, HIF-1α-overexpression and HIF-1α-knockdown lentiviruses were constructed (**Supplementary Figure S1**). We analyzed the changes of the expression of HIF-1α, PKM2, GLUT1, LDH-A, CTGF, TGF-β1, TNF-α, and IL-6 when HIF-1α was over expressed or knockdowned respectively. The results showed that the expressions of HIF-1α, PKM2, GLUT1, LDH-A, CTGF, TGF-β1, TNF-α, and IL-6 were increased significantly following the HIF-1α over-expression (**Figures 5A–C**). Over-expression of HIF-1α triggered the nuclear translocation and increased the transcriptional activity of PKM2 (**Figure 5B**). After knockdowning HIF-1α, the expression of HIF-1α, PKM2, GLUT1, LDH-A, CTGF, TGF-β1, TNF-α, and IL-6 was significantly decreased (**Figures 5D,E**). The results suggest that HIF-1α is the up-stream in the metabolic reprogramming and plays a very important role in hypertensive nephropathy.

Effects of Over-Expression and Knockdown of PKM2 on Relative Markers in HEK293T Cells

A large number of studies have confirmed that HIF-1α is closely related to PKM2 and there is a strong mutual influence between them. Therefore, we speculated that HIF-1α/PKM2 positive feedback is the key pathway of metabolic reprogramming of renal cell in hypertension (Luo et al., 2011). As is shown above, the results showed that the expressions of PKM2 was increased significantly following the HIF-1α over-expression. After knockdowning HIF-1α, the expression of PKM2 was significantly decreased. To further study the influence of PKM2 on HIF-1α and the role of PKM2 in the metabolic reprogramming, PKM2-overexpression and PKM2-knockdown lentiviruses were constructed (**Supplementary Figure S2**). We analyzed the changes of the expression of HIF-1α, PKM2, ATP, pyruvate and lactate when PKM2 was over expressed or knockdowned respectively. The results showed that the expressions of HIF-1α, PKM2, pyruvate and lactate were increased and ATP was decreased significantly following the PKM2 over-expression (**Figures 6A–D**). Over-expression of PKM2 triggered the nuclear translocation and increased the transcriptional activity of HIF-1α (**Figure 6C**). After knockdowning PKM2, the expressions of HIF-1α, PKM2, pyruvate, and lactate were significantly decreased and ATP was significantly increased (**Figures 6E–G**). The results suggest that the relationship of HIF-1α and PKM2 was positive feedback.

Rescue Assays Certify HIF-1α as a Target of Qian Yang Yu Yin in Hypertensive Nephropathy

As is shown above, the relationship of HIF-1α and PKM2 was positive feedback. To further verify that HIF-1α was a target of QYYY in hypertensive nephropathy and study the role of HIF-1α and PKM2 in the metabolic reprogramming, we observed the effect of QYYY on HIF-1α and its downstream PKM2, GLUT1, LDH-A, and IL-6 in hypoxic HEK 293T cells in which HIF-1α was over expressed and found that over-expression of HIF-1α partially abolished the effects of QYYY on hypertensive nephropathy. The results showed that the protein expressions of HIF-1α, PKM2, GLUT1, LDH-A, IL-6, and levels of pyruvate and lactate in Hypoxia + QYYY were significantly lower than those in HIF-1α-OE + Hypoxia + QYYY. The level of ATP in Hypoxia + QYYY were significantly higher than those in HIF-1α-OE + Hypoxia + QYYY (**Figure 7**). These data suggest that HIF-1α is a target of QYYY and HIF-1α/PKM2 positive feedback palys an important role in improving renal injury of hypertension by regulating metabolic reprogramming.

DISSCUSSION

Our experimental data demonstrated that QYYY improved renal injury of hypertension by regulating metabolic reprogramming mediated by HIF-1α/PKM2 positive feedback *in vivo* and *in vitro*.

In TCM, hypertension mostly belongs to “vertigo” and “headache” category. Based on clinical and epidemiological studies of TCM, QYYY has been reported to exert the effect of tonifying the liver and kidney, promoting blood circulation and dredging collaterals. It has been awarded the national invention patent (Patent No: ZL 201010205024.2) and the Preparation Certificate of Jiangsu food and drug administration. Clinical

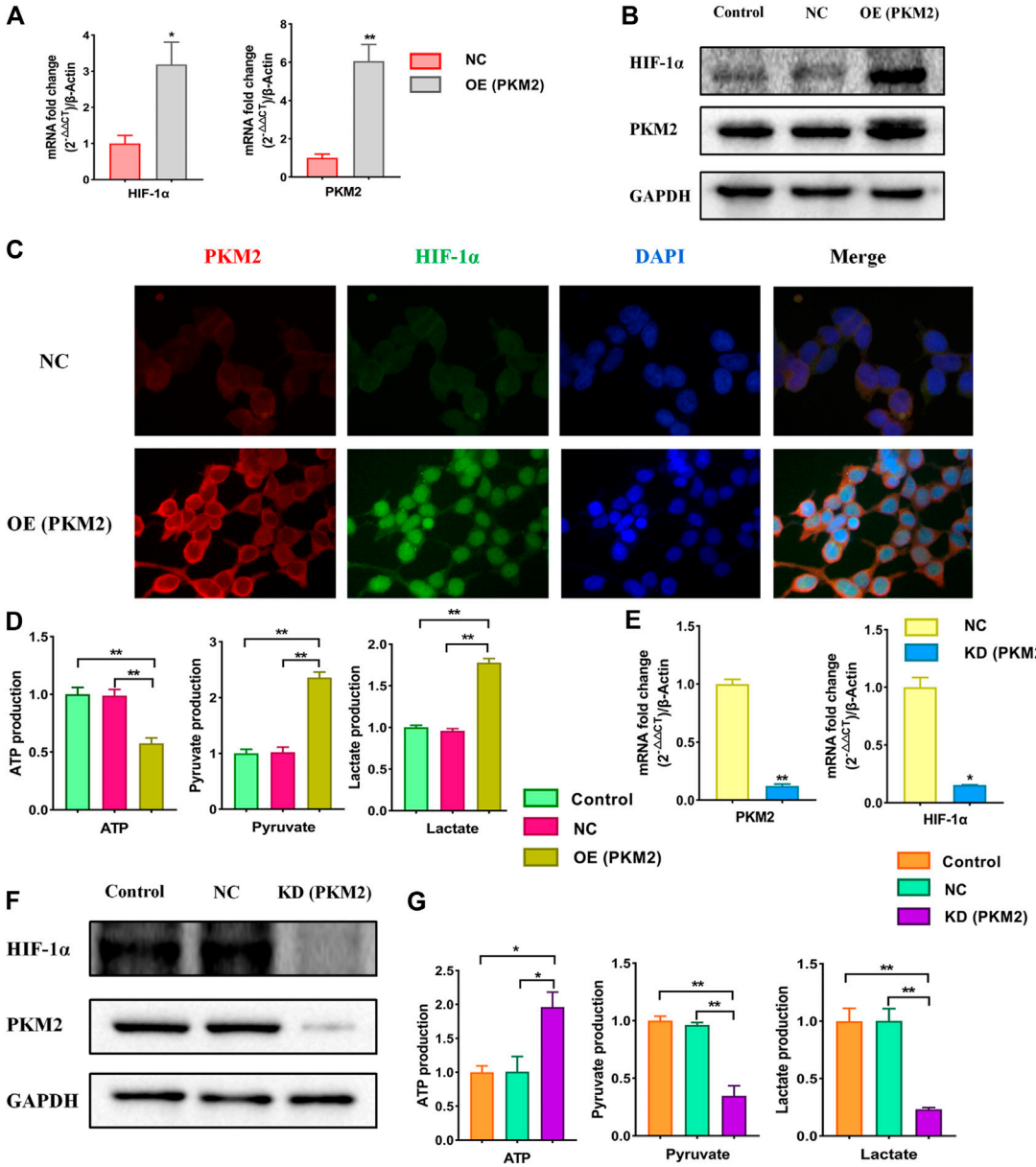

FIGURE 6 | Effects of over-expression and knockdown of PKM2 on relative markers in HEK293T cells. Cells were divided into following groups: conrtol, negative control (NC), PKM2-overexpression group (OE) and PKM2-knockdown group (KD). **(A)** Effects of over-expression of PKM2 on mRNA levels of HIF-1α and PKM2 were examined by using qPCR. **(B)** Effects of over-expression of PKM2 on proteins of HIF-1α and PKM2 in HEK293T cells were examined by using western blotting. **(C)** Effects of over-expression of PKM2 on immunofluorescence staining of HIF-1α and PKM2. **(D)** Effects of over-expression of PKM2 on changes of ATP, pyruvate and lactate using kits. **(E)** Effects of knockdown of PKM2 on mRNA levels of HIF-1α and PKM2 in HEK293T cells were examined by using qPCR. **(F)** Effects of knockdown of PKM2 on proteins of HIF-1α and PKM2 in HEK293T cells were examined by using western blotting. **(G)** Effects of knockdown of PKM2 on changes of ATP, pyruvate and lactate using kits. *$p < 0.05$ and **$p < 0.01$.

research showed that QYYY significantly improved the early renal damage of hypertension. QYYY contains six Chinese medical botanical drugs. HPLC was established to determine the active components in QYYY and 2,3,5,4-TDG, morroniside, harpgide, ecdysterone, and hyperin were detected (Zhang et al., 2020). In recent years, a number of previous studies have reported that 2,3,5,4-TDG can protect the kidney by reducing the expression of TGF-β1 mRNA (Li et al., 2010; Stanton, 2011). 2,3,5,4-TDG is also closely related to HIF-1 and a related study (Yang and Liu, 2016) has found that it can significantly reduce the production of HIF-1, thus delaying the progression of the disease. Morroniside also has been reported to be useful in protecting the kidney (Liu et al., 2018; Jin et al., 2019). Moreover, disorder of glucose metabolism is still a difficult problem in medical field. Ecdysterone can significantly enhance glucose metabolism, improve the excretion of urinary albumin, inhibit the

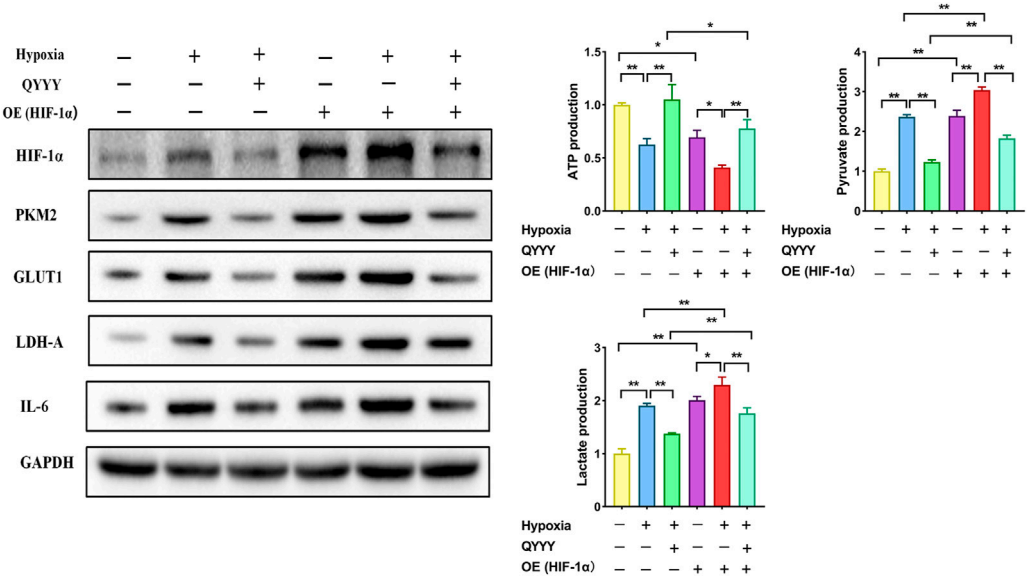

FIGURE 7 | Rescue assays certify HIF-1α as a target of QYYY in hypertensive nephropathy. Over-expression of HIF-1α partially abolished the effects of QYYY on hypertensive nephropathy. *$p < 0.05$ and **$p < 0.01$.

expression of CTGF and collagen Ⅳ, and has the potential effect of improving renal fibrosis. It acts as a potential fibrosis antagonist for the renal proximal tubule cells. It might also act through suppressing post-receptor signaling of TGF-β1 and restoring the tubule epithelial character (Zou et al., 2010; Hung et al., 2012; Chen et al., 2017). Hyperin can inhibit renal fibrosis in the rats effectively. It can reduce *a*-smooth muscle actin and fibronectin and improve the renal fibrosis (Yan et al., 2014). Therefore, we assume that improvement of metabolic disorder and anti-fibrosis of these compounds may be involved in the inhibitory effect of QYYY on treating renal injury of hypertension. Firstly, we successfully established the model by 12-week-old SHR which were fed with high salt diet (4% NaCl) for 8 weeks and we found QYYY improved BP, pathology, fibrosis, and renal function *in vivo*. In the present study, QYYYL (low dose 3.2 g/kg/d), QYYYM (middle dose 6.4 g/kg/d) and QYYYH (high dose 12.8 g/kg/d) were used and we found that the curative effects were statistically significant when administered in low dosage *in vivo*. In recent years, more and more authoritative studies have emphasized that the metabolic rate of rodents is higher and the results may be meaningless when the starting dose of rodents is too high. The evaluation of doses that are much higher than what can be achieved in humans may have no translational value from a therapeutic point of view. The importance of reasonable initial dosage for experiment was highlighted by relevant authoritative experts (Zou et al., 2012; White and Kearney, 2014; Nair and Jacob, 2016; Heinrich et al., 2020), therefore it is very necessary for us to use a lower starting dose in future experiments. From the existing experimental results, it was identified QYYY had good effects on hypertensive nephropathy. As a TCM, the components present in QYYY are complex and there are many related targets in QYYY, so it is difficult to decipher the mechanism of actions of QYYY as a whole. In recent years, the advent of network pharmacology has provided a novel method to identify the various active components of TCM, predict its related targets, and decipher its molecular mechanisms, which could be helpful to understand the different complex interactions between the biological systems, drugs and complex diseases from the perspective of network (Li and Zhang, 2013; Boezio et al., 2017; Guo et al., 2019; Zhang et al., 2019; Zhang et al., 2019; Luo et al., 2020). So we then performed a network pharmacology investigation of QYYY to determine its candidate active compounds and the corresponding pathways underlying the progression of hypertensive nephropathy. And the results showed that HIF-1 signaling pathway is a key pathway of QYYY. Moreover, our previous study also found that QYYY improved the early renal damage of hypertension by inhibiting inflammatory reaction and reducing the expression of HIF-1α, some inflammatory factors and fibrosis indexes (Ding et al., 2015; Yan et al., 2018; Wu, 2020). Many literatures also have shown the strong mutual influence between HIF-1α and PKM2 and positive feedback of HIF-1α and PKM2. HIF-1α/PKM2 positive feedback may be involved in the regulation of hypertensive renal damage by enhancing cell glycolysis (Zhu et al., 2012; Prigione et al., 2014; Wang et al., 2014; Zhu et al., 2014; Luo et al., 2015). Therefore, we speculated that QYYY may affect hypertensive nephropathy via metabolic reprogramming mediated by HIF-1α/PKM2 positive feedback. As expected, our resluts showed QYYY significantly improved the metabolic indexes, inflammatory fibrosis factors related to HIF-1α/PKM2 positive feedback *in votro* and *vivo*.

Metabolic reprogramming refers to the change of cell metabolism, which has been extensively studied and an in-depth understanding of this process has been achieved in tumor biology and other fields (Biswas, 2015; Georgoudaki et al., 2016; Li and Zhang, 2016; Schito

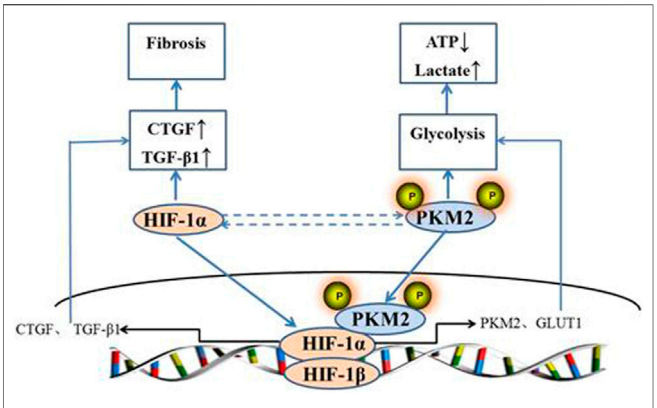

FIGURE 8 | Schematic diagram of metabolic reprogramming of hypertensive kidney injury promoted by HIF-1α/PKM2 positive feedback.

and Semenza, 2016; Vaupel et al., 2019; Jin et al., 2020). However, it is still in its infancy in the field of research related to the kidney diseases, some evidences have shown that metabolic reprogramming plays an important role in the development of kidney diseases. As a result, novel studies elucidating the possible role of metabolic reprogramming in hypertensive nephropathy is of great significance for the treatment of renal damage of hypertension. Kidney is a high-energy consuming organ and optimal energy metabolism system is the biochemical basis for maintaining the specific structure and physiological function of kidney. During the early stage of chronic kidney disease, the glomerulus is generally characterized by high filtration and high perfusion. The glomerulus needs more energy. Fibroblasts are often activated and can proliferate rapidly in the renal interstitium. The local area of glomerular hypertrophy represents an anoxic state. In addition, when the glomerulus is in a state of hyperfiltration, the proton pump, which plays the role of renal tubular reabsorption, can also effectively reabsorb a large number of different ions in the urine and thereby increase the consumption of ATP in kidney. Under pathological conditions, the normal oxidative phosphorylation of glucose cannot provide sufficient energy or carbon groups to enable cell proliferation, so the ratio of glycolysis pathway increases. Although the increased ratio of glycolysis pathway can provide sufficient energy and necessary materials for maintaining cell proliferation and division, a few studies have reported that glycolysis pathway can increase renal fibrosis. Additionally, Some studies have also verified the potential relationship between glycolysis and renal fibrosis both *in vivo* and *in vitro*. These reports used mice with UUO as the model of renal fibrosis and found that with an increase of the degree of renal fibrosis, the levels of glucose metabolism related enzymes in the renal tissue increased synchronously. Additionally, the findings *in vitro* experiments have suggested that TGF-β1 could potentially induce renal fibroblast fibrosis and metabolic reprogramming thus increasing glycolysis pathway (Yin et al., 2018). It has been suggested that metabolic reprogramming occurs in the process of renal fibrosis and the enhancement of glycolysis can increase renal fibrosis. Therefore, inhibition of renal glycolysis may function as a new target for the treatment of chronic kidney disease. For instance, Hui Peng found that the renal injury and fibrosis could be significantly improved by improving renal energy metabolism (Peng et al., 2017). PKM2 is a key rate-limiting enzyme involved in the process of glycolysis, which could directly regulate the occurrence of glycolysis and has been reported to be closely related to embryonic development, tissue fibrosis, tumor, and glucose metabolism (Luo et al., 2011). Our data suggested that the total protein expression of PKM2 *in vivo* and *vitro* was upregulated and nuclear translocation of PKM2 was enhanced, thereby affecting glycolysis, decreasing ATP, increasing pyruvic acid and lactic acid and aggravated inflammation and fibrosis. QYYY effectively improved hypertensive renal damage through metabolic reprogramming. Glycolysis inhibitors can be used as a potential anti fibrosis strategy. Thus, the process of metabolic reprogramming has a significant potential in the study of hypertensive renal damage.

HIF is a special protein discovered by Semenza in 1992 (Semenza, 1999). HIF-1α is ubiquitously found in the mammalian cells and plays a role in multiple signaling pathways (Liu et al., 2020). In recent years, the role of HIF-1α in hypertensive renal damage has attracted more and more attention. Many factors present in the disease microenvironment, such as hypoxia, reactive oxygen species, nitric oxide, and some metabolites can increase the protein level of HIF-1α and thus enhance cellular erobic glycolysis, which is a significant feature of renal injury (Gerald et al., 2004; Hsu and Sabatini, 2008; Semenza, 2013; Briggs et al., 2016; Oh et al., 2016; Magistroni and Boletta, 2017). The activation of HIF-1α signaling pathway may be involved in the regulation of hypertensive renal damage by enhancing cell glycolysis. A large number of studies have confirmed that HIF-1α is closely related to PKM2. A few studies have suggested that HIF-1α can potentially regulate reprogramming through early translocation of glycolysis and up regulation of PKM2. For instance, Luo W upregulated the expression of PKM2 through viral transfection and found that the fluorescence level of HIF-1α was significantly enhanced but the transcriptional activity of HIF-1α was significantly reduced by knockout of PKM2. Proline hydroxylase 3 can hydroxylate the proline at position 403 and 408 of PKM2, which can facilitate the binding of PKM2 with HIF-1α, and thereby promote the binding of HIF-1α with HRE, thus regulating the transcription of downstream genes such as lactate dehydrogenase and glucose transporter. The relationship between HIF and PKM is positive feedback (Prigione et al., 2014). Our data identified the role of HIF-1α and PKM2 in the metabolic reprogramming in hypertensive renal damage. QYYY played an important role in the treatment of hypertensive renal damage by regulating metabolic reprogramming mediated by HIF-1α/PKM2 positive feedback loop and HIF-1α is a key target in the treatment of renal damage of hypertension by QYYY. We found that QYYY inhibited total protein expression of HIF-1α as well as PKM2 and caused a significant increase in the accumulation of nuclear protein of HIF-1α and PKM2, thereby improving their downstream target genes by regulating metabolic reprogramming such as erobic glycolysis induced by HIF-1α and PKM2 and inhibited inflammation and fibrosis of kidney tissue. And the schematic diagram of metabolic reprogramming of hypertensive kidney injury promoted by HIF-1α/PKM2 positive feedback is shown in **Figure 8**.

CONCLUSIONS

The present study demonstrated the effects of QYYY on the progress of hypertensive nephropathy and we investigated the underlying mechanisms involved in HIF-1α/PKM2 positive feedback. Our present findings clearly indicated that QYYY inhibited the positive feedback of HIF-1α and PKM2, reduced the nuclear accumulation of HIF-1α and PKM2, regulated metabolic reprogramming, and then suppressed renal inflammatory fibrosis and improved hypertensive renal injury. In total, our study provides the basis for the treatment of hypertensive renal injury with TCM by regulating metabolic reprogramming mediated by HIF-1α/PKM2 positive feedback.

DATA AVAILABILITY STATEMENT

The original contributions presented in the study are included in the article/**Supplementary Material**, further inquiries can be directed to the corresponding authors.

ETHICS STATEMENT

The animal study was reviewed and approved by The Experimental Animal Ethics Committee of Nanjing University of Chinese Medicine approved all animal experiments.

AUTHOR CONTRIBUTIONS

Conceptualization: LQ, SY, ZF. Data curation: SY, SR. Formal analysis: LW, YZ, ZX, YY. Project administration: LQ, ZF. Supervision: ZF, SY. Writing-original draft: LQ, SR. Writing-review and editing: ZX, SY, YW, JL.

FUNDING

National Natural Science Foundation of China (81873258, 82074320, 81603310, 81904113), Postgraduate Research and Practice Innovation Program of Jiangsu Province (KYCX20_1455 and KYCX20_1477), A Project Funded by the Priority Academic Program Development of Jiangsu Higher Education Institutions (PAPD), The Open Projects of the Discipline of Chinese Medicine of Nanjing University of Chinese Medicine Supported by the Subject of Academic priority discipline of Jiangsu Higher Education Institutions (NO.ZYX03KF073), Natural Science Foundation of Jiangsu Province (BK20201498 and BK20181095).

SUPPLEMENTARY MATERIAL

The Supplementary Material for this article can be found online at: https://www.frontiersin.org/articles/10.3389/fphar.2021.667433/full#supplementary-material

REFERENCES

Armutcu, F., Demircan, K., Yildirim, U., Namuslu, M., Yagmurca, M., and Celik, H. T. (2019). Hypoxia Causes Important Changes of Extracellular Matrix Biomarkers and ADAMTS Proteinases in the Adriamycin-induced Renal Fibrosis Model. *Nephrology* 24, 863–875. doi:10.1111/nep.13572

Biswas, S. K. (2015). Metabolic Reprogramming of Immune Cells in Cancer Progression. *Immunity* 43, 435–449. doi:10.1016/j.immuni.2015.09.001

Boezio, B., Audouze, K., Ducrot, P., and Taboureau, O. (2017). Network-based Approaches in Pharmacology. *Mol. Inf.* 36, 1700048. doi:10.1002/minf.201700048

Briggs, K. J., Koivunen, P., Cao, S., Backus, K. M., Olenchock, B. A., Patel, H., et al. (2016). Paracrine Induction of HIF by Glutamate in Breast Cancer: EglN1 Senses Cysteine. *Cell* 166, 126–139. doi:10.1016/j.cell.2016.05.042

Chai, X. X., Le, Y. F., Wang, J. C., Mei, C. X., Feng, J. F., Zhao, H., et al. (2019). Carpesium Abrotanoides (L.) Root as a Potential Source of Natural Anticancer Compounds: Targeting Glucose Metabolism and PKM2/HIF-1α Axis of Breast Cancer Cells. *J. Food Sci.* 84, 3825–3832. doi:10.1111/1750-3841.14953

Chen, L., Zheng, S., Huang, M., Ma, X., Yang, J., Deng, S., et al. (2017). β-Ecdysterone from Cyanotis Arachnoidea Exerts Hypoglycemic Effects through Activating IRS-1/Akt/GLUT4 and IRS-1/Akt/GLUT2 Signal Pathways in KK-Ay Mice. *J. Funct. Foods* 39, 123–132. doi:10.1016/j.jff.2017.09.061

Chen, Y., Fang, Z., Yan, S., Jiang, W., Yan, D., and Liu, Z. (2013). Effect of Qianyang Yuyin Granules Medicated Serum on Angiotensin Ⅱ-induced Apoptosis and Expression of fas/fasL in Human Umbilical Vein Endothelial Cells. *Chin. Traditional Patent Med.* 35, 1381–1385. doi:10.3969/j.issn.1001-1528.2013.07.006

Dallatu, M. K., Nwokocha, E., Agu, N., Myung, C., Newaz, M. A., Garcia, G., et al. (2014). The Role of Hypoxia-Inducible Factor/Prolyl Hydroxylation Pathway in Deoxycorticosterone Acetate/Salt Hypertension in the Rat. *J. Hypertens.* 03, 184. doi:10.4172/2167-1095.1000184

Ding, H., Jiang, L., Xu, J., Bai, F., Zhou, Y., Yuan, Q., et al. (2017). Inhibiting Aerobic Glycolysis Suppresses Renal Interstitial Fibroblast Activation and Renal Fibrosis. *Am. J. Physiology-Renal Physiol.* 313, F561–F575. doi:10.1152/ajprenal.00036.2017

Ding, K., Wang, Y., Jiang, W., Zhang, Y., Yin, H., and Fang, Z. (2015). Qian Yang Yu Yin Granule-Containing Serum Inhibits Angiotensin II-Induced Proliferation, Reactive Oxygen Species Production, and Inflammation in Human Mesangial Cells via an NADPH Oxidase 4-dependent Pathway. *BMC Complement. Altern. Med.* 15, 81. doi:10.1186/s12906-015-0619-2

Georgoudaki, A-M., Prokopec, K. E., Boura, V. F., Hellqvist, E., Sohn, S., Östling, J., et al. (2016). Reprogramming Tumor-Associated Macrophages by Antibody Targeting Inhibits Cancer Progression and Metastasis. *Cel. Rep.* 15, 2000–2011. doi:10.1016/j.celrep.2016.04.084

Gerald, D., Berra, E., Frapart, Y. M., Chan, D. A., Giaccia, A. J., Mansuy, D., et al. (2004). JunD Reduces Tumor Angiogenesis by Protecting Cells From Oxidative Stress. *Cell* 118, 781–794. doi:10.1016/j.cell.2004.08.025

Guo, F., Zhang, W., Su, J., Xu, H., and Yang, H. (2019). Prediction of Drug Positioning for Quan-Du-Zhong Capsules against Hypertensive Nephropathy Based on the Robustness of Disease Network. *Front. Pharmacol.* 10, 49. doi:10.3389/fphar.2019.00049

Hasan, D., Gamen, E., Abu Tarboush, N., Ismail, Y., Pak, O., and Azab, B. (2018). PKM2 and HIF-1α Regulation in Prostate Cancer Cell Lines. *PLoS One* 13, e0203745. doi:10.1371/journal.pone.0203745

Heinrich, M., Appendino, G., Efferth, T., Fürst, R., Izzo, A. A., Kayser, O., et al. (2020). Best Practice in Research - Overcoming Common Challenges in Phytopharmacological Research. *J. Ethnopharmacology* 246, 112230. doi:10.1016/j.jep.2019.112230

Hsu, P. P., and Sabatini, D. M. (2008). Cancer Cell Metabolism: Warburg and beyond. *Cell* 134, 703–707. doi:10.1016/j.cell.2008.08.021

Huang, H., Fan, Y., Gao, Z., Wang, W., Shao, N., Zhang, L., et al. (2019). HIF-1α Contributes to Ang II-Induced Inflammatory Cytokine Production in Podocytes. *BMC Pharmacol. Toxicol.* 20, 59. doi:10.1186/s40360-019-0340-8

Hung, T-J., Chen, W-M., Liu, S-F., Liao, T-N., Lee, T-C., Chuang, L-Y., et al. (2012). 20-Hydroxyecdysone Attenuates TGF-B1-Induced Renal Cellular Fibrosis in Proximal Tubule Cells. *J. Diabetes its Complications* 26, 463–469. doi:10.1016/j.jdiacomp.2012.06.014

Jin, D., Huang, W.-J., Meng, X., Yang, F., Bao, Q., Zhang, M-z., et al. (2019). Chinese Herbal Medicine Tangshen Formula Treatment for Type 2 Diabetic Kidney Disease in the Early Stage: Study Protocol for a Randomized Controlled Trial. *Trials* 20, 756. doi:10.1186/s13063-019-3821-6

Jin, T., Wang, C., Tian, Y., Dai, C., Zhu, Y., and Xu, F. (2020). Mitochondrial Metabolic Reprogramming: An Important Player in Liver Cancer Progression. *Cancer Lett.* 470, 197–203. doi:10.1016/j.canlet.2019.11.029

Krisher, R. L., and Prather, R. S. (2012). A Role for the Warburg Effect in Preimplantation Embryo Development: Metabolic Modification to Support Rapid Cell Proliferation. *Mol. Reprod. Dev.* 79, 311–320. doi:10.1002/mrd.22037

Li, C., Cai, F., Yang, Y., Zhao, X., Wang, C., Li, J., et al. (2010). Tetrahydroxystilbene Glucoside Ameliorates Diabetic Nephropathy in Rats: Involvement of SIRT1 and TGF-B1 Pathway. *Eur. J. Pharmacol.* 649, 382–389. doi:10.1016/j.ejphar.2010.09.004

Li, S., and Zhang, B. (2013). Traditional Chinese Medicine Network Pharmacology: Theory, Methodology and Application. *Chin. J. Nat. Medicines* 11, 110–120. doi:10.1016/S1875-5364(13)60037-0

Li, Z., and Zhang, H. (2016). Reprogramming of Glucose, Fatty Acid and Amino Acid Metabolism for Cancer Progression. *Cell. Mol. Life Sci.* 73, 377–392. doi:10.1007/s00018-015-2070-4

Liu, J., Li, B., Du, J., and Jiang, W. (2019). Clinical Study of Qianyang Yuyin Granules Treating Early Renal Damage Patients with Yin Deficiency and Yang Hyperactivity Type Hypertension. *J. Nanjing Univ. Traditional Chin. Med.* 35, 262–265. doi:10.14148/j.issn.1672-0482.2019.0262

Liu, M., Galli, G., Wang, Y., Fan, Q., Wang, Z., Wang, X., et al. (2020). Novel Therapeutic Targets for Hypoxia-Related Cardiovascular Diseases: The Role of HIF-1. *Front. Physiol.* 11, 774. doi:10.3389/fphys.2020.00774

Liu, P., Peng, L., Zhang, H., Tang, P. M.-K., Zhao, T., Yan, M., et al. (2018). Tangshen Formula Attenuates Diabetic Nephropathy by Promoting ABCA1-Mediated Renal Cholesterol Efflux in Db/db Mice. *Front. Physiol.* 9, 343. doi:10.3389/fphys.2018.00343

Luo, R., Zhang, W., Zhao, C., Zhang, Y., Wu, H., Jin, J., et al. (2015). Elevated Endothelial Hypoxia-Inducible Factor-1α Contributes to Glomerular Injury and Promotes Hypertensive Chronic Kidney Disease. *Hypertension* 66, 75–84. doi:10.1161/HYPERTENSIONAHA.115.05578

Luo, T-t., Lu, Y., Yan, S.-k., Xiao, X., Rong, X.-l., and Guo, J. (2020). Network Pharmacology in Research of Chinese Medicine Formula: Methodology, Application and Prospective. *Chin. J. Integr. Med.* 26, 72–80. doi:10.1007/s11655-019-3064-0

Luo, W., Hu, H., Chang, R., Zhong, J., Knabel, M., O'Meally, R., et al. (2011). Pyruvate Kinase M2 Is a PHD3-Stimulated Coactivator for Hypoxia-Inducible Factor 1. *Cell* 145, 732–744. doi:10.1016/j.cell.2011.03.054

Magistroni, R., and Boletta, A. (2017). Defective Glycolysis and the Use of 2-Deoxy-D-Glucose in Polycystic Kidney Disease: from Animal Models to Humans. *J. Nephrol.* 30, 511–519. doi:10.1007/s40620-017-0395-9

Mahmoodi, B. K., Matsushita, K., Woodward, M., Blankestijn, P. J., Cirillo, M., Ohkubo, T., et al. (2012). Associations of Kidney Disease Measures with Mortality and End-Stage Renal Disease in Individuals with and without Hypertension: a Meta-Analysis. *The Lancet* 380, 1649–1661. doi:10.1016/S0140-6736(12)61272-0

Nair, A., and Jacob, S. (2016). A Simple Practice Guide for Dose Conversion between Animals and Human. *J. Basic Clin. Pharma* 7, 27–31. doi:10.4103/0976-0105.177703

Oh, E.-T., Kim, J-w., Kim, J. M., Kim, S. J., Lee, J-S., Hong, S.-S., et al. (2016). NQO1 Inhibits Proteasome-Mediated Degradation of HIF-1α. *Nat. Commun.* 7, 13593. doi:10.1038/ncomms13593

Peng, H., Wang, Q., Lou, T., Qin, J., Jung, S., Shetty, V., et al. (2017). Myokine Mediated Muscle-Kidney Crosstalk Suppresses Metabolic Reprogramming and Fibrosis in Damaged Kidneys. *Nat. Commun.* 8, 1493. doi:10.1038/s41467-017-01646-6

Prigione, A., Rohwer, N., Hoffmann, S., Mlody, B., Drews, K., Bukowiecki, R., et al. (2014). HIF1α Modulates Cell Fate Reprogramming Through Early Glycolytic Shift and Upregulation of PDK1-3 and PKM2. *Stem Cells* 32, 364–376. doi:10.1002/stem.1552

Rivera, D., Allkin, R., Obón, C., Alcaraz, F., Verpoorte, R., and Heinrich, M. (2014). What Is in a Name? the Need for Accurate Scientific Nomenclature for Plants. *J. Ethnopharmacology* 152, 393–402. doi:10.1016/j.jep.2013.12.022

Schito, L., and Semenza, G. L. (2016). Hypoxia-Inducible Factors: Master Regulators of Cancer Progression. *Trends Cancer* 2, 758–770. doi:10.1016/j.trecan.2016.10.016

Semenza, G. L. (2013). HIF-1 Mediates Metabolic Responses to Intratumoral Hypoxia and Oncogenic Mutations. *J. Clin. Invest.* 123, 3664–3671. doi:10.1172/JCI67230

Semenza, G. L. (1999). Regulation of Mammalian O2Homeostasis by Hypoxia-Inducible Factor 1. *Annu. Rev. Cel Dev. Biol.* 15, 551–578. doi:10.1146/annurev.cellbio.15.1.551

Stanton, R. C. (2011). Oxidative Stress and Diabetic Kidney Disease. *Curr. Diab. Rep.* 11, 330–336. doi:10.1007/s11892-011-0196-9

Vander, H. M., Cantley, L. C., and Thompson, C. B. (2009). Understanding the Warburg Effect: the Metabolic Requirements of Cell Proliferation. *Science* 324, 1029–1033. doi:10.1126/science.1160809

Vaupel, P., Schmidberger, H., and Mayer, A. (2019). The Warburg Effect: Essential Part of Metabolic Reprogramming and central Contributor to Cancer Progression. *Int. J. Radiat. Biol.* 95, 912–919. doi:10.1080/09553002.2019.1589653

Wang, X., Fang, Z., Yan, S., Chen, Y., and Zhang, S. (2014). Impact of Qianyang Yuyin Granules Containing Serum on Ang Ⅱ Inducing HUVEC Injuring NO. *Chin. Traditional Patent Med.* 36, 2467–2470. doi:10.3969/j.issn.1001-1528.2014.12.005

Wang, Y. (2020). *Effect of Qianyang Yuyin Granule on Hypertensive Renal Injury by Affecting Podocyte Autophagy*. Nanjing: Nanjing University of traditional Chinese Medicine. doi:10.27253/d.cnki.gnjzu.2020.000124

Wang, Z., Zhu, Q., Li, P.-L., Dhaduk, R., Zhang, F., Gehr, T. W., et al. (2014). Silencing of Hypoxia-Inducible Factor-1α Gene Attenuates Chronic Ischemic Renal Injury in Two-Kidney, One-Clip Rats. *Am. J. Physiology-Renal Physiol.* 306, F1236–F1242. doi:10.1152/ajprenal.00673.2013

Watson, A. M. D., Gould, E. A. M., Penfold, S. A., Lambert, G. W., Pratama, P. R., Dai, A., et al. (2019). Diabetes and Hypertension Differentially Affect Renal Catecholamines and Renal Reactive Oxygen Species. *Front. Physiol.* 10, 309. doi:10.3389/fphys.2019.00309

White, C. R., and Kearney, M. R. (2014). Metabolic Scaling in Animals: Methods, Empirical Results, and Theoretical Explanations. *Compr. Physiol.* 4, 231–256. doi:10.1002/cphy.c110049

Wu, L. (2020). *Effect of Qianyang Yuyin Granule on Hypertensive Renal Damage Based on the Regulation of Oxidative Stress by Sestrin2 Signaling Pathway*. Nanjing: Nanjing University of traditional Chinese Medicine. doi:10.27253/d.cnki.gnjzu.2020.000251

Yan, D., Fang, Z., Yan, S., and Chen, Y. (2014). Effect of Qianyang Yuyin Granules Medicated Serum on Angiotensin Ⅱ-induced NADPH, AKT, TNF-α and IL-6 in Human Umbilical Vein Endothelial Cells. *Chin. Traditional Patent Med.* 36, 1809–1813. doi:10.3969/j.issn.1001-1528.2014.09.004

Yan, D., Yue, B., Qian, M., Zhao, L., Zhang, Z., Qian, H., et al. (2018). JYYS Granule Mitigates Renal Injury in Clinic and in Spontaneously Hypertensive Rats by Inhibiting NF-Kb Signaling-Mediated Microinflammation. *Evidence-Based Complement. Altern. Med.* 2018, 1–13. doi:10.1155/2018/8472963

Yan, Y., Feng, Y., Li, W., Che, J-P., Wang, G-C., Liu, M., et al. (2014). Protective Effects of Quercetin and Hyperoside on Renal Fibrosis in Rats with Unilateral Ureteral Obstruction. *Exp. Ther. Med.* 8, 727–730. doi:10.3892/etm.2014.1841

Yang, X. Y., and Liu, N. (2016). Effect of TSG on Protein Expression of APP in APP/PS1 Double Transgenic AD Mice Brain Tissues. *Chin. J. Geriatr.* 36, 536–539. doi:10.3969/j.issn.1005-9202.2016.03.009

Yin, X. N., Wang, J., Cui, L. F., and Fan, W. X. (2018). Enhanced Glycolysis in the Process of Renal Fibrosis Aggravated the Development of Chronic Kidney Disease. *Eur. Rev. Med. Pharmacol. Sci.* 22, 4243–4251. doi:10.26355/eurrev_201807_15419

Zhang, R., Zhu, X., Bai, H., and Ning, K. (2019). Network Pharmacology Databases for Traditional Chinese Medicine: Review and Assessment. *Front. Pharmacol.* 10, 123. doi:10.3389/fphar.2019.00123

Zhang, S-F., Mao, X-J., Jiang, W-M., and Fang, Z-Y. (2020). Qian Yang Yu Yin Granule Protects against Hypertension-Induced Renal Injury by Epigenetic Mechanism Linked to Nicotinamide N-Methyltransferase (NNMT) Expression. *J. Ethnopharmacology* 255, 112738. doi:10.1016/j.jep.2020.112738

Zhang, W., Huai, Y., Miao, Z., Qian, A., and Wang, Y. (2019). Systems Pharmacology for Investigation of the Mechanisms of Action of Traditional Chinese Medicine in Drug Discovery. *Front. Pharmacol.* 10, 743. doi:10.3389/fphar.2019.00743

Zhu, Q., Hu, J., Han, W-Q., Zhang, F., Li, P-L., Wang, Z., et al. (2014). Silencing of HIF Prolyl-Hydroxylase 2 Gene in the Renal Medulla Attenuates Salt-Sensitive Hypertension in Dahl S Rats. *Am. J. Hypertens.* 27, 107–113. doi:10.1093/ajh/hpt207

Zhu, Q., Liu, M., Han, W-Q., Li, P-L., Wang, Z., and Li, N. (2012). Overexpression of HIF Prolyl-Hydoxylase-2 Transgene in the Renal Medulla Induced a Salt Sensitive Hypertension. *J. Cel. Mol. Med.* 16, 2701–2707. doi:10.1111/j.1582-4934.2012.01590.x

Zou, D. P., Xu, Z. Z., Cao, L., and Chen, Q. (2010). Effect of Ecdysterone on Early Diabetic Nephropathy in Rats. *Chin. J. New Drugs Clin. Remedies* 29, 842–846. doi:10.21275/v5i3.nov161951

Zou, P., Yu, Y., Zheng, N., Yang, Y., Paholak, H. J., Yu, L. X., et al. (2012). Applications of Human Pharmacokinetic Prediction in First-In-Human Dose Estimation. *AAPS. J.* 14, 262–281. doi:10.1208/s12248-012-9332-y

Conflict of Interest: The authors declare that the research was conducted in the absence of any commercial or financial relationships that could be construed as a potential conflict of interest.

Copyright © 2021 Qian, Ren, Xu, Zheng, Wu, Yang, Wang, Li, Yan and Fang. This is an open-access article distributed under the terms of the Creative Commons Attribution License (CC BY). The use, distribution or reproduction in other forums is permitted, provided the original author(s) and the copyright owner(s) are credited and that the original publication in this journal is cited, in accordance with accepted academic practice. No use, distribution or reproduction is permitted which does not comply with these terms.

frontiers in Pharmacology

ORIGINAL RESEARCH
published: 09 June 2021
doi: 10.3389/fphar.2021.611722

Synthesis of Icariin-Zinc and its Protective Effect on Exercise Fatigue and Reproductive System Related Glands in Male Rats

Juntao Zhang[1,2†], Chao Zhang[2†], Aifeng Liu[2], Qiang Ji[3], Lixia Ren[4], Chuanrui Ma[2], Hengyu Zhang[1], Chaochao Wu[3], Donglin Zhang[3], Man Shang[5] and Feng He[1]**

[1]Academy of Medical Engineering and Translational Medicine, Tianjin University, Tianjin, China, [2]Orthopedics Department, The First Teaching Hospital of Tianjin University of Traditional Chinese Medicine, Tianjin, China, [3]Graduate College, Tianjin University of Traditional Chinese Medicine, Tianjin, China, [4]School of Materials Science and Engineering, Tianjin University, Tianjin, China, [5]Department of Pharmacology, School of Basic Medical Sciences, Tianjin Medical University, Tianjin, China

OPEN ACCESS

Edited by:
Yanqiong Zhang,
China Academy of Chinese Medical Sciences, China

Reviewed by:
Abdulkerim Kasim Baltaci,
Selcuk University Medical Faculty Departmensi, Turkey
Rasim Mogulkoc,
Selçuk University, Turkey

***Correspondence:**
Man Shang
shangman@tmu.edu.cn
Feng He
heaven@tju.edu.cn

[†]These authors have contributed equally to this work

Specialty section:
This article was submitted to Experimental Pharmacology and Drug Discovery, a section of the journal Frontiers in Pharmacology

Received: 29 September 2020
Accepted: 17 May 2021
Published: 09 June 2021

Citation:
Zhang J, Zhang C, Liu A, Ji Q, Ren L, Ma C, Zhang H, Wu C, Zhang D, Shang M and He F (2021) Synthesis of Icariin-Zinc and its Protective Effect on Exercise Fatigue and Reproductive System Related Glands in Male Rats. Front. Pharmacol. 12:611722. doi: 10.3389/fphar.2021.611722

Background: Icariin, a traditional Chinese medicine, plays a protective role in the treatment of exercise fatigue. Zinc, a trace element, plays an important role in the reproductive system. Therefore, we aimed to synthesize an Icariin-Zinc complex (by chemical means) and verify its protective effect on exercise fatigue and the reproductive system using animal experiments.

Methods: The icariin-zinc complex was prepared by the reaction of icariin carbonyl and zinc ions (molar ratio 1:3). The molecular formula and structural formula of the complex were identified and tested. Fifty-six rats selected by swimming training were randomly divided into six groups: static control, exercise control, icariin, gluconate zinc (G-Zn group), icariin glucose zinc and icariin-zinc exercise (low, high dose/L-E group, H-E group) groups. These groups respectively received the following doses: 1 ml/100 g, daily gavage with NS (for the first two groups), 45 mg/kg icariin, 110 mg/kg Gluconate Zinc, Icariin glucose zinc (45 mg/kg Icariin and 110 mg/kg Gluconate Zinc), 60 mg/kg icariin zinc and 180 mg/kg icariin zinc. After 3 weeks of gavage, we conducted 6 weeks of exhaustive swimming training. Test indices such as exhaustive swimming time of rats and body weight were evaluated after the last training exercise. The seminal vesicles, testes, and prostate gland were weighed, and their indices were calculated. The levels of testosterone (in the plasma) and glycogen (in the liver and muscle homogenates) were also evaluated using ELISA.

Results: Compared with the static control group, the exhaustive swimming time of the rats in each group was prolonged. Compared with the other groups, the exhaustive swimming time of the L-E and H-E groups was significantly longer ($p < 0.01$); the Icariin-Zinc complex significantly increased the exhaustive swimming time of the rats. Compared with the static control group, the plasma testosterone content of the L-E and H-E groups increased significantly ($p < 0.05$). Compared with the exercise control group and G-Zn group, the

Abbreviations: ICA: icariin;; ICP-OES: inductively coupled plasma-optic emission spectrometer; NS: normal saline;; ELISA: enzyme linked immunosorbent assay; H&E: hematoxylin & eosin;; SD: standard deviation;; SPF: specific pathogen free;; ROS: reactive oxygen species.

plasma testosterone content of the H-E group also increased significantly ($p < 0.01$). The Icariin-Zinc complex significantly increased the serum levels of testosterone in rats. Compared with the control group, the muscle glycogen reserves of each group decreased, indicating that the muscle glycogen reserves of the rats decreased after swimming. Compared with other groups, the Icariin-Zinc complex can reduce the level of glycogen in the muscles, indicating that it can increase the utilization efficiency of glycogen in muscles. Compared with the static control and exercise control groups, the testicular weight of rats in the administration groups increased slightly. The Icariin-Zinc complex increased the testicular weight, indicating that the function of the reproductive system was improved to some extent.

Conclusion: Icariin-Zinc can significantly prolong the exhaustive swimming time, improve exercise ability, and increase the plasma testosterone level (which is beneficial for improving the reproductive ability of male rats). Moreover, the beneficial effect of Icariin-Zinc on the glycogen content, testis index, and other reproductive system glands is dose-dependent.

Keywords: icariin-zinc, synthesis, protective effect, exercise fatigue, reproductive system

BACKGROUND

Fatigue is a complex physiological and pathological that seriously affects human health. Epimedium is a perennial herb belonging to the family Berberidaceae. It has been used for thousands of years to promote male potency. Traditional Chinese medicines are believed to help in tonifying the kidneys and invigorating the Yang, and they have been used to treat impotence, premature ejaculation, lumbago and leg pain, neurasthenia, forgetfulness, and other diseases. Icariin (ICA) is the main active component extracted from Herba Epimedii (herbal medicine made from dried aerial parts of Epimedium). ICA has many functions such as neuroprotection, antitumoral activity, antioxidative activities, immunomodulation, and promotion of reproductive functions (especially in male mice). It has become a research hotspot at home and abroad (Liu et al., 2004; Tan et al., 2016).

Many in vivo studies have shown the beneficial effect of ICA on reproductive functions (Kang et al., 2012; Chen et al., 2014). ICA increases the epididymal sperm count and testosterone level in male rats (Chen et al., 2014). Mechanistically, the improved sexual function of male mice mediated by ICA might be associated with the hypothalamic-pituitary-gonadal axis and the PI3K/AKT/eNOS/NO signaling pathway (Ding et al., 2017). In addition, ICA could protect human sperm from being damaged by $FeSO_4/H_2O_2$ (Zhan et al., 2014). It can maintain the "Raman fingerprint" of human sperm, suggesting that ICA may serve as a tonifying and replenishing agent of herbal origin that enhances reproductive functions. These show that ICA can promote the function of human and animal reproductive systems and provide a basis for animal experiments.

Zinc is a component of more than 300 types of metal enzymes in the human body (Hennigar and Kelleher, 2012). Zinc is reported to be an essential element for the normal function of the male reproductive system and sperm. It plays an important role in the production, storage, secretion, and function of male sex hormones (Chu et al., 2016). Studies have shown that there is a relationship between sexual dysfunction and physical fatigue (Young et al., 2017; Fairbanks et al., 2017).

Based on the protective effect of Icariin and Zinc on the reproductive system, we hypothesized that an Icariin-Zinc combination might have a synergistic protective effect on the reproductive system and exercise fatigue.

METHODS

Experimental Animals and Drugs

All procedures were performed in accordance with the NIH guidelines for the Care and Use of Laboratory Animals (NIH Publications No. 80–23, revised 1996), and the research protocol was approved by the Ethics Committee of Tianjin University of Traditional Chinese Medicine (TCM-LAEC2019069). Sixty-six Wistar male rats weighing 200–220 g were obtained from the Academy of Military Medical Science in Beijing and housed in special cages in a specific-pathogen-free (SPF) environment, allowing free movement and ad libitum access to food and drink. Icariin (purity ≥ 98%, Lot No. 181209, Shanghai Mochi Biotechnology Co., Ltd.), zinc chloride (GR, lot No. G1820107, Shanghai Alading Biochemical Technology Co., Ltd.), zinc reagent (AR, H08F9S54539, Shanghai Yuanye Biotechnology Co., Ltd.), distilled water, anhydrous ethanol (Shandong lierkang Medical Technology Co., Ltd.), 75% ethanol (Shandong lierkang Medical Technology Co., Ltd.), and 0.9% sodium chloride (NS, batch number 19012523, China Otsuka Pharmaceutical Co., Ltd.) were the main chemicals used in the experiment.

Experimental Instruments

The main instruments used in the experiment were a constant temperature magnetic stirrer (78HW-1, Hangzhou instrument and

TABLE 1 | ICP-OES Instrument Operating Conditions.

Working Parameters	Setting Conditions	Working Parameters	Setting Conditions
Power	1200 W	Reading stability delay	10 s
Cooling gas (AR) flow	15.0 L/min	Injection stability delay	20 s
Auxiliary gas (AR) flow	1.5 L/min	Pump speed	15 rpm
Atomizing gas (AR) pressure	200 kPa	Cleaning time	310 s
Observation height	10 mm	Number of readings	3times
Reading time	10 s		

motor company), a rotary vaporizer (re-2000e, Gongyi Yuhua Instrument Co., Ltd.), a circulating water multi-purpose vacuum pump (SHB-3, Gongyi Yuhua Instrument Co., Ltd.), an electronic analysis balance (BS210s, Beijing Saiduolis Balance Co., Ltd.), mobile phone timer (COR-Al10, honor), swimming sink (L×W×H=100 × 50 × 60 cm), and a water pump (Jiabao "AP1500" type).

Preparation and Detection of the Icariin-Zinc Complex

Preparation and Extraction of Icariin-Zinc

Three thousand milligrams of icariin and 1200 mg of zinc chloride were mixed (presumably the molar ratio of icariin to zinc chloride is 2:1 or 1:1 in theory). To make icariin fully react, 1: 2.5 mixture ratio was selected and dissolved in 500 ml (volume fraction is 45%) of ethanol solution, and a constant temperature magnetic stirrer was used (the parameters were set at 400 rpm, 70°C [range 60–80°C] oil bath) to stir the mixture for at least 24 h. The reacting solution was then placed in a water bath at 45°C. The final icariin-zinc product was obtained by centrifugation and was repeatedly washed with pure water to remove unreacted icariin.

Preparation of the Zinc Reagent Solution

Zinc reagent (0.1 mg) was weighed and dissolved in 125 ml anhydrous ethanol. After it had completely dissolved, it was stored in a brown bottle.

Identification of Compounds (Colorimetry)

The reaction between the zinc reagent solution and zinc ion was used for identification. The reactant (that is, final icariin-zinc product) was completely dissolved in anhydrous ethanol after the last washing. Adding the zinc reagent solution to it turned the color of the mixture blue; meanwhile, adding the zinc reagent solution to the last washing solution did not change its color to blue. As such, it could be concluded that the reactant was the icariin-zinc complex and that there was no zinc chloride residue in the reactant.

Molecular Formula and Structural Formula of the Icariin-Zinc Complex

Sample Pretreatment

A 0.05-g sample of the compound was placed in a microwave digestion tank made up of polytetrafluorethylene. The sample was soaked for 2 h in mixture of 6 ml of nitric acid and 1 ml of hydrogen peroxide. Subsequently, it was digested for 20 min at 190°C. Acid removal, constant volume to 100 ml. This needs to be determined. ICP-OES on-line measurement: A VISTA-MPX inductively coupled plasma spectrometer (Varian Company, United States), referred to as ICP-OES was used to determine the formula (see **Table 1**).

The measured wavelength was 213 nm. The average of three results were taken.

The Zn^{2+} content was 4.6%. Combining the structural formula and molecular weight of icariin, we found that icariin and Zn are 2-coordinated (that is, two carbonyls (C=O) and one Zn^{2+} coordinate). The molecular formula is $(C_{33}H_{40}0_{15})_2Zn^{2+}$, with a relative molecular weight of 1417 (**Figure 1**).

Experimental Groups

After 3 days of adaptive feeding and 3 days of swimming training (the rats were trained 20 min/d), the rats were randomly divided into 7 groups with 8 rats in each group. Each group received a basic feeding and distilled water, and was fed freely every day. Each group was treated with different doses of 1 ml/100 g by gavage for 3 weeks (see **Table 2**, Experimental grouping and intervention).

Anti-Fatigue Experimental Method (Surhio et al., 2017)

The control group did not undergo any training. In the other groups, a swimming trough of 100 × 50 × 60 cm was used as the swimming training device for the rats, and the water depth was set at 50 cm. The water temperature was 31 ± 2°C, and a water pump was installed at the bottom of the water tank to cause the water to flow (the aim was to prevent rats from floating on the water surface). Swimming training to exhaustion was performed every week for a total of 6 weeks. The parameters were changed every week. The first week, the rats exercised without weight, the second week with 2% weight, the third week with 4% weight, and the fourth to the sixth week with 5% weight. Each time, the swimming training was performed to exhaustion. The last time, all groups performed exhaustion swimming training without weight, and the time of swimming before exhaustion was measured. The time from the beginning of swimming to exhaustion which is a measure of the exhaustion exercise ability, was used as an index of anti-exercise fatigue ability. The standard used to determine exhaustion was the inability of the rats to show up on the water surface 10 seconds after sinking.

Test Indices and Methods of Measurement (Xi et al., 2018)

Each group was weighed 24 h after the last training. Blood samples were taken from the inner canthi of the rats and

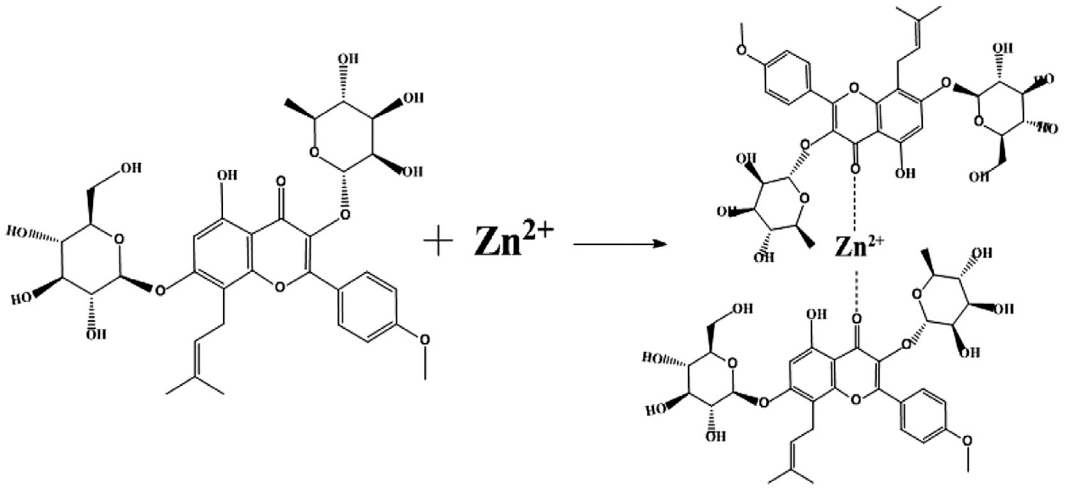

FIGURE 1 | Chemical Synthesis Route of the Icariin-Zinc complex.

TABLE 2 | Experimental grouping and intervention.

Grouping	Intervention measures
Control group	Normal saline
Exercise group	Normal saline
Icariin group	45 mg/kg Icariin
G-Zn group	110 mg/kg Gluconate Zinc
Icariin glucose zinc	45 mg/kg Icariin, 110 mg/kg Gluconate Zinc
Low dose Icariin zinc exercise group (L-E group)	60 mg/kg Icariin zinc
High dose Icariin zinc exercise group (H-E group)	180 mg/kg Icariin zinc

sodium citrate solution added to prevent coagulation. The samples were incubated in a 37°C water bath for 30 min, centrifuged at 3000 R/min for 10 min, and plasma was separated. The plasma testosterone levels were measured.

All rats were administered with an overdose of 2,2,2-tribromoethanol (640 mg/kg, intraperitoneal injection) for anesthesia. The seminal vesicles, testes, prostate, liver, and the deep quadriceps femoris muscles (without the fascia) were removed. These organs were washed in precooled normal saline to remove the blood stains, dried with filter paper, and stored in a refrigerator at −20°C. The seminal vesicle, testis, and prostate glands were weighed, and their indices (the ratio of seminal vesicle gland, testis, and prostate gland weights to body weight) were calculated.

To prepare the liver and muscle tissue homogenate, appropriate amounts of tissues (0.2–1 g) and precooled normal saline (NS) were added into a beaker in a tissue mass (g) to liquid volume (ml) homogenate medium proportion of 1/9. The tissue was then quickly cut into pieces (the above operations were carried out in an iced water bath). The supernatant was separated and extracted by centrifugation at 4°C, 3000 rpm for 15 min and then refrigerated at 4°C or frozen at −20°C for standard. The supernatant was used to measure the glycogen content of the liver or muscle homogenate.The remaining mice were killed (anesthetized and euthanized in a CO_2 chamber).

RESULTS

Observation of the Feeding and Swimming Behavior

The rats in each group were fed for 6 weeks. At the third week, the rats in each group were more excited, the amount of activity in the cages increased, the fighting phenomenon appeared, the number of squeaks increased, their voices became louder, and they struggled more strongly when grasped and during weighing. The amount of food and drinking water given to the icariin-zinc group and the exercise control group was slightly more than that in the static control group. The swimming abilities of the rats in each group were observed, and the rats in the icariin-zinc group were found to be more active, to jump out of the water and squeak more frequently, and their relative swimming distances were longer.

Effect of Icariin-Zinc on Body Weight of Rats

Before the beginning of the experiment, the average body weight of the rats in each group was approximately 250 g. After continuous feeding for 3 weeks, the average body weight of rats increased steadily to approximately 320 g, and there was no significant difference in body weight between the three groups. After 6 weeks of weight-bearing swimming training, the body weight was taken before the last exhaustive swimming. The average body weight of the static control group had increased by about 4% meanwhile that of the exercise control group had reduced. After the administration of the different concentrations of icariin-zinc, the average body weight of rats in the L-E and H-E groups decreased compared with the exercise control group (**Figure 2**).

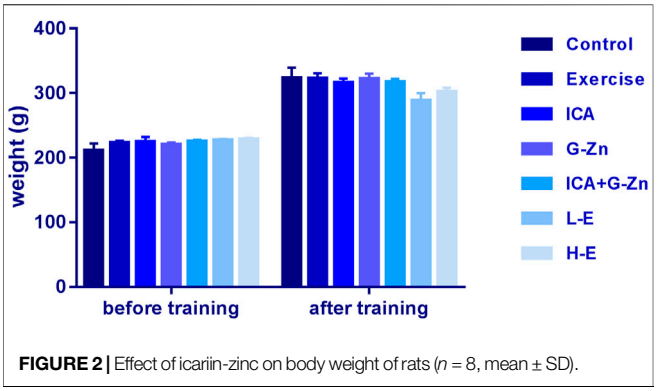

FIGURE 2 | Effect of icariin-zinc on body weight of rats (n = 8, mean ± SD).

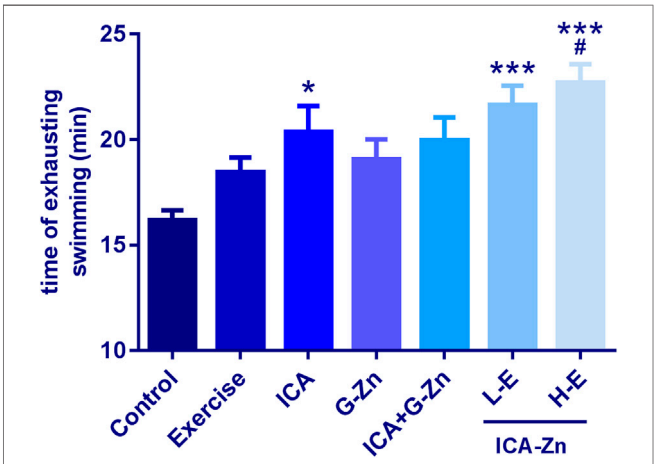

FIGURE 3 | Effect of icariin-zinc on anti-fatigue of rats (n = 8, mean ± SD). $^{*}p < 0.01$, $^{***}p < 0.001$ vs. Control ; $^{\#}p < 0.05$ vs. Exercise.

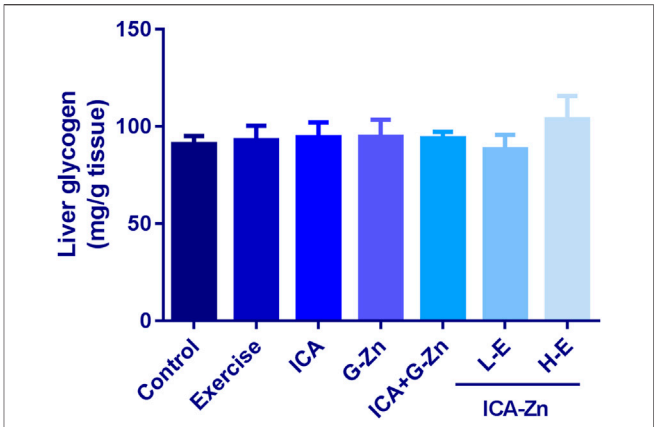

FIGURE 4 | Effect of icariin-zinc on liver glycogen level in rats (n = 8, mean ± SD).

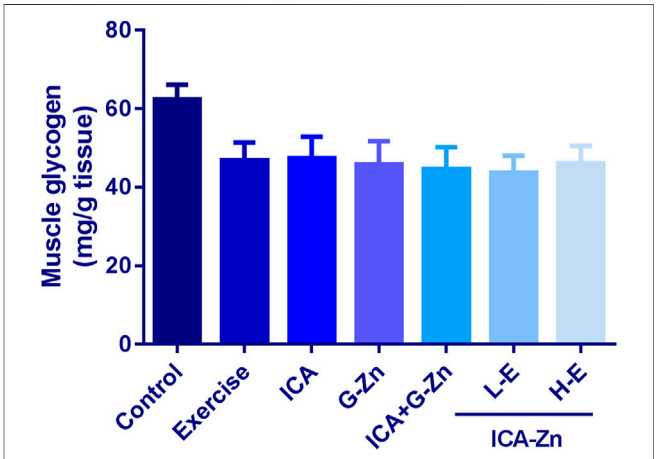

FIGURE 5 | Effect of icariin-zinc on muscle glycogen level in rats (n = 8, mean ± SD).

The Effect of Icariin-Zinc on Anti-Fatigue in Rats

Compared with the static control, the exhaustive swimming time of rats in each group was prolonged. After administration of the icariin-zinc, the exhaustive swimming times of the L-E and H-E groups were significantly prolonged (p <0.01), just as that of the ICA group (**Figure 3**). It is suggested that icariin-zinc has the same function as ICA in improving the exercise ability of rats. The swimming abilities of rats in each group were observed, and the rats in the icariin-zinc group were more active, jumped out of the water more frequently during swimming, had a longer relative swimming distance, and had a more prolonged exhaustive swimming time. These showed that the physical functional reserves of the rats were better and their exercise ability was enhanced.

The Effect of Exercise and Icariin-Zinc on Glycogen Storage in the Liver and Muscle of Rats

The content of liver glycogen was the same in all the groups but for the H-E group there was an increasing trend (**Figure 4**). Compared with the control group, the muscle glycogen reserves of each group decreased after swimming (**Figure 5**). A comparative evaluation showed that icariin-zinc had no significant effect on liver glycogen and muscle glycogen storage in rats.

There was no significant difference between the testicular weights of the different groups when compared with the control (**Figure 6**). Hematoxylin and eosin (HE) staining showed normal morphologies of Leydig and Sertoli cells, continuous and complete membrane of the seminiferous tubules, and a regular arrangement of germ cells. These findings suggest that icariin-zinc does not affect testes histopathology (**Figure 7**).

The Effect of Icariin-Zinc on the Testicular Weight and Index of Rats

Compared with the static control group and exercise control group, the testicular index of rats in the treatment group increased slightly (**Figure 8**). Testicular index = testis/weight x

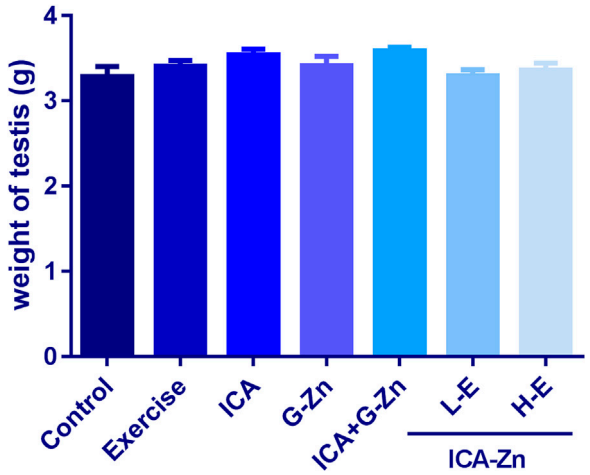

FIGURE 6 | Effect of icariin-zinc on testis weight in rats (n = 8, mean ± SD).

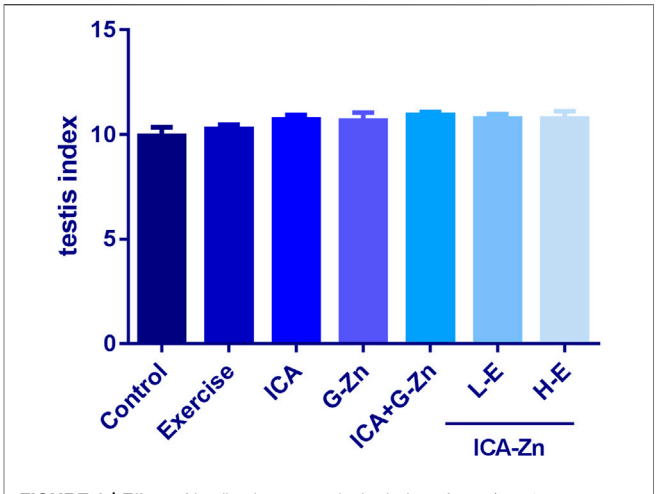

FIGURE 8 | Effect of icariin-zinc on testicular index of rats (n = 8, mean ± SD).

1000. Testicular index measurement helps to eliminate the influence of animal weight, and can be used to evaluate the function of the rat's reproductive system. The results showed that after intragastric administration of ICA, G-Zn, icariin glucose, zinc, and icariin-zinc, the testicular index increased, indicating that icariin-zinc could improve reproductive function in male rats.

The Effect of Exercise and Icariin-Zinc on the Weights of the Seminal Vesicle and Prostate Gland in Rats

Compared with the exercise control group, the average weight of the seminal vesicles of rats in the L-E group increased significantly, indicating that the sperm reserve of the rats in the L-E group was larger. This phenomenon was not observed in the HE group (**Figure 9**). However, icariin-zinc had no significant effect on prostate weight in rats (**Figure 10**).

The Effect of Exercise and Icariin-Zinc on the Plasma Testosterone Level in Rats

The concentration of testosterone in the plasma of rats was measured by ELISA, and the standard curve was obtained with good correlation (r = 0.9985) (**Figure 11**). Compared with the static control group, the plasma testosterone content of the L-E and H-E groups increased significantly ($p< 0.05$). Compared with the exercise control group and G-Zn group, the plasma testosterone content of the H-E group also increased significantly ($p< 0.01$). The above experimental results show that icariin-zinc can significantly

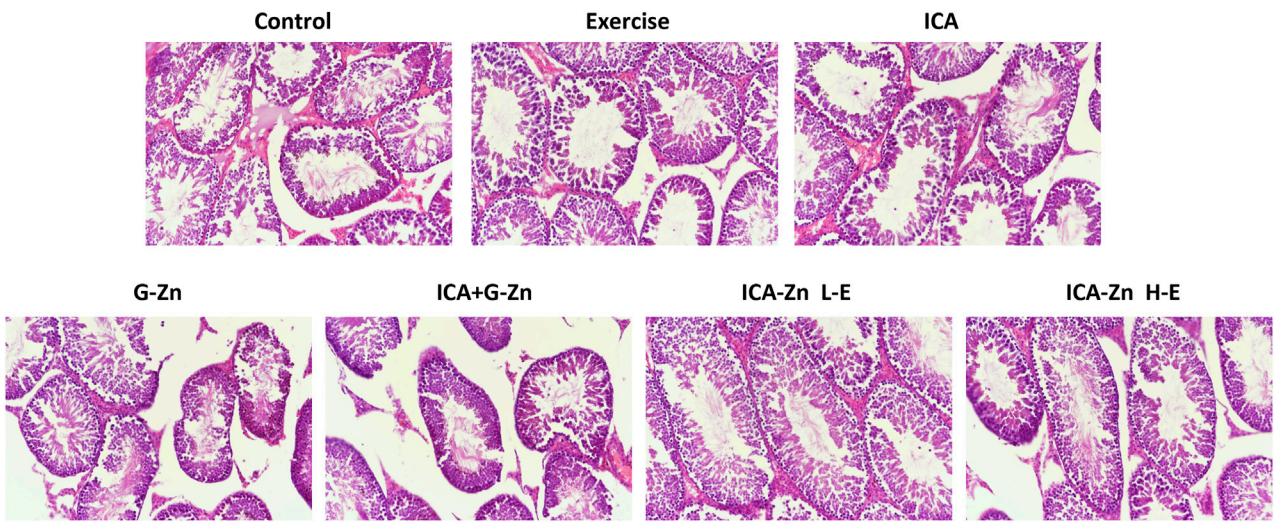

FIGURE 7 | HE staining of testes in rats (200x).

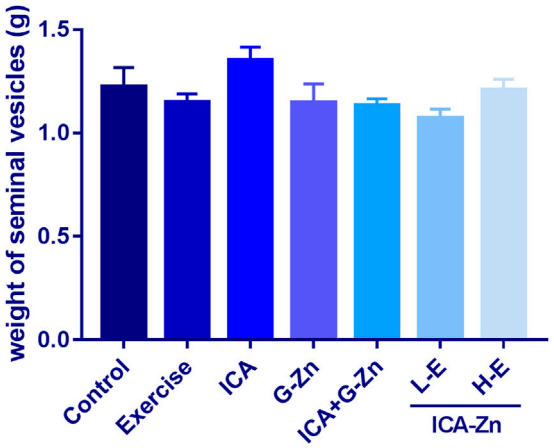

FIGURE 9 | Effect of icariin-zinc on the weight of the seminal vesicle weight in rats (n = 8, mean ± SD).

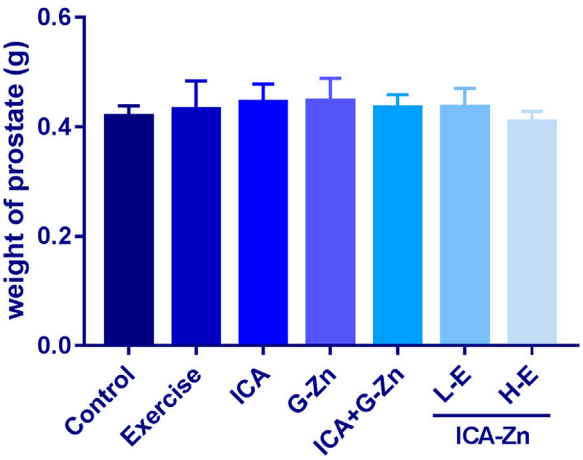

FIGURE 10 | Effect of icariin zinc on the weight of the prostate gland in rats (n = 8, mean ± SD).

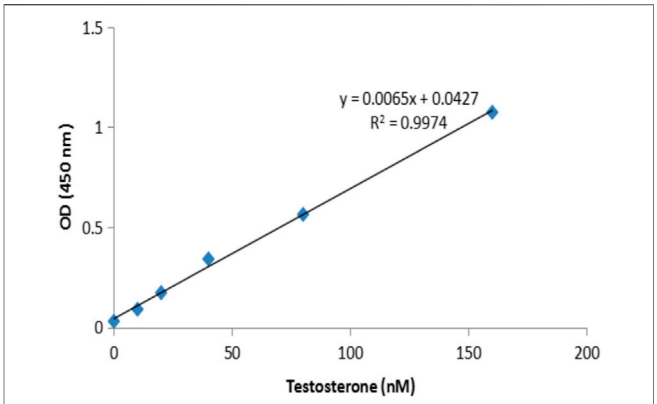

FIGURE 11 | Testosterone standard curve.

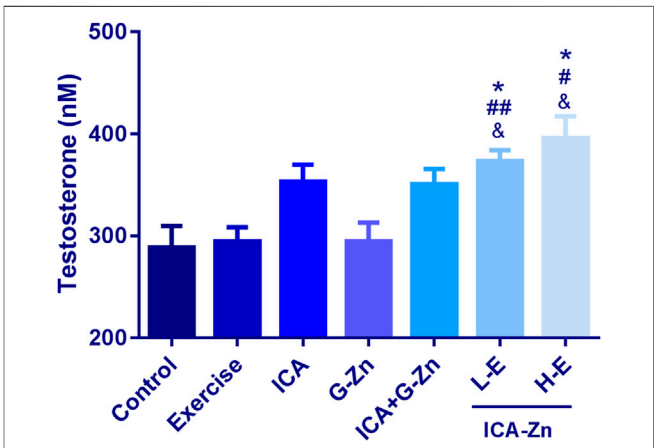

FIGURE 12 | Effect of exercise and icariin-zinc on the plasma testosterone content of rats (n = 8, mean ± SD). $^{*}p < 0.05$ vs. Control; $^{\#}p < 0.05$, $^{\#\#}p < 0.01$ vs. exercise; $^{\&}p < 0.05$, $^{\&\&}p < 0.01$ vs. G-Zn.

improve the plasma testosterone level in rats, largely than icariin alone and zinc agents such as zinc gluconate (**Figure 12**).

DISCUSSION

Icariin is the main extract and active component of the herbaceous plant epimedium which among others, plays a role in tonifying the kidney, strengthening the yang, and slowing down aging. Longh et al. (2018) found that icariin improved erectile function of SHR (Long et al., 2018). Zinc is a part of the structural composition of many proteins. It helps in the recovery of the nervous system. Zinc also plays an important biological role in male reproductive physiology and endocrine system (Santos and Teixeira, 2019). In this study, icariin and zinc were combined to produce a synergistic effect. Icariin-zinc was prepared by chemical synthesis. It was formed by the combination of two molecules of icariin with one molecule of divalent zinc ion through ionic and coordination bonds (**Figure 13**). The hydroxyl group provides an electron pair and forms a coordination bond with zinc, giving the compound a good chemical stability. After chemical synthesis, the structure of each particle is the same, uniform, and easy to absorb. Physical mixing has different rules, and makes it difficult to achieve a uniform mixing proportion thus impacting the experimental data. Through the study of its effects on body weight, exercise exhaustive time, testicular and seminal vesicle weight, and glycogen storage, we were able to put into evidence preliminary improvements in anti-fatigue and sexual function in rats.

Body weight is an important indicator of the skeletal, muscular, and functional states, and overall development of the body. A change in body weight can reflect the adaptation of the body to sports training and the degree of its influence on the body. It is one of the most important indicators of animal growth and nutritional

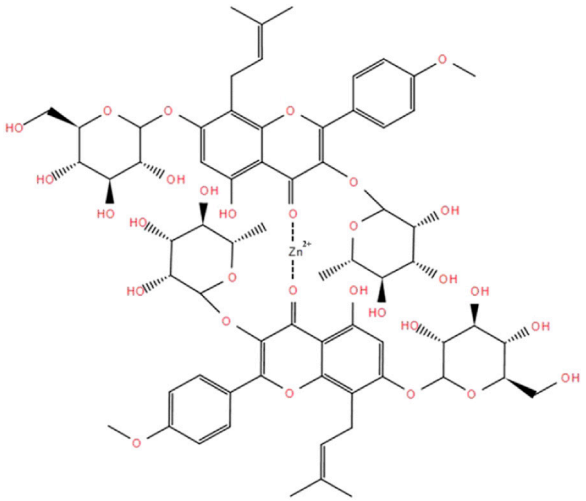

FIGURE 13 | Molecular structure of Icariin-Zinc.

state. Our results showed that there was no significant difference between the body weights of the rats in the different groups during the first three weeks. It was considered that the normal development of the body weight had occurred. At the end of the 6th week, the body weight of rats in the L-E and H-E groups decreased, which was due to the increase in excitability and activity. In the process of feeding, the rats in the icariin-zinc group began to show hyperactivities (increased activity, fighting, and frequent squeaking) compared with the exercise control group and the static control group during the third week. This indicates that icariin-zinc can improve the excitability and exercise ability of male rats. The rats' body weight change, and daily amounts of food and water consumed were similar in both the icariin-zinc and exercise control groups. The change in body weight was slightly higher in the control group. This was because the compound promotes the development of the body, increases the basal metabolic rate, appetite, and amount of exercise.

Exercise fatigue is the physiological decline in working ability, activity ability, and range of activity after a strenuous exercise (Narkhede et al., 2016; Górski et al., 2017). The recovery time of exercise fatigue is relatively long and this has an impact on human life and work. Exercise exhaustive time is an important sign reflecting the body's exercise ability. It can be used as an index to measure the anti-exercise fatigue ability of animals.

The exhaustion training resulted in the maintenance of the rats in both the icariin-zinc and exercise control groups in a state of exercise fatigue, and so, the exercise function could not be effectively recovered. Theoretically, in a short period of time, the exhaustion time would be shorter than that of the control group. The results of the anti-fatigue experiment showed that the exhaustive swimming time of rats in the exercise control group was shortened as expected. However, after the administration of icariin-zinc, the exhaustive swimming time of the L-E group was prolonged. Considering the hyperexcited state of the H-E group, the rats in the exercise control group struggled more violently during the exhaustion swimming training, jumped out of the water more frequently incurring great energy losses, and failed to rest for a long period of time. Because they could not store enough energy for exhaustive training, the both H-E and L-E groups exhaustive times were not prolonged. Our results showed that the concentration of the icariin-zinc was very important, and high concentrations would cause high excitability, which was not conducive for physical recovery. Low concentration can enhance the anti-exercise fatigue abilities, a consequence of the improvement of the exercise level in skeletal muscles.

Glycogen is a form of energy storage in organisms. Glycogen in the skeletal muscle is an important form of energy storage. In long-term aerobic exercise, muscle glycogen consumption often occurs and is related to the inability to maintain muscle contractility (Britto et al., 2018). In long-term and high-intensity sports, the storage of muscle glycogen before exercise determines the time of exhaustion, which directly affects endurance training and competition. The importance of glycogen in exercise ability is reflected in endurance exercise. During exercise, glycogen decomposition is accelerated, and glucose is released into blood by the liver to maintain blood glucose balance. Our results showed that after swimming, the glycogen reserves in the liver and muscle of rats in the exercise control group decreased to the lowest level. However, the glycogen reserves increased in each group after the administration of different concentrations of icariin-zinc, especially in the H-E group.

These results indicate that icariin-zinc can promote glycogen synthesis in rats undergoing training. The possible mechanism is that icariin-zinc can enhance the oxidation and absorption of glucose, thus promoting the synthesis of muscle glycogen and liver glycogen.

The testis is a male internal reproductive organ and plays a role in the development of male secondary sexual characteristics and physiological function. The seminal vesicle is an important accessory gland of men, and is involved in the process of semen accumulation and release. Seminal vesicle secretion accounts for about 50–80% of the volume of semen, and thus closely influences the quality and quantity of sperm (Zhao et al., 2019). Our results showed that the testicular weights and indices of the L-E and H-E groups were increased. This could be because icariin-zinc promotes testicular development and spermatogenesis. We found that, compared with other administration groups, the weight of the seminal vesicle of rats in the L-E group increased significantly. This was probably due to the increase in seminal vesicle secretion caused by Icariin-Zinc.

Testosterone is one of the main components of androgen. It promotes spermatogenesis, stimulates the growth and development of reproductive organs, maintains normal sexual desire, and promote protein synthesis. From this experiment, we found that icariin-zinc can significantly improve the plasma testosterone level of rats, and this effect is significantly better than when icariin and zinc agents, such as zinc gluconate, are administered separately. It is suggested that ICA can promote the secretion of testosterone. ICA is a flavonoid that can protect the synthesis of testosterone in mouse Leydig cells (by the effects of 2-ethylhexyl phthalate). It protects mouse testes from the damage induced by DEHP by blocking ROS and promoting the secretion of testosterone (Sun et al., 2019). It can be concluded that icariin-

zinc may promote testosterone secretion by protecting rat testicular cells from damage.

To sum up, sports fatigue and men's health problems are of great concern, and they often affect each other. Male sexual dysfunction can cause other functional abnormalities in the body and thus, influence mental and physical health. Hence, it is a problem that requires an urgent solution. Therefore, it will be of great significance if a fast and effective drug that improves anti-fatigue and sexual abilities was found. Based on the behavior of animals in this study, and the analyses of specific experimental data, we believe that the combination of icariin and zinc ion can improve the motor and anti-fatigue abilities of male rats (through the improvement of the functions of skeletal muscles and joint). In addition, it can promote the index and function of the glands of the reproductive system (especially increase in testicular and seminal vesicle weights, increase the glycogen reserve in rats, and improve exercise ability). The mechanisms of action may be related to zinc induced oxidative stress mechanism, or improvement of sexual function by the regulation of the hypothalamic pituitary gonadal axis and the PI3K/Akt/eNOS/NO signal pathway by ICA (Ding et al., 2018). In the future, these mechanisms will be further studied in terms of enhancing testicular function, including steroid production, sperm count, sperm motility, and spermatogenesis in male rats. Therefore, the preparation and application of icariin-zinc provides a new idea to explore for increasing anti-fatigue ability, enhancing exercise ability, and solving male reproductive health problems.

CONCLUSION

In this experiment, icariin-zinc was successfully prepared, and the reaction rate was positively related to the reaction temperature, reactant concentration, and reaction time. An appropriate amount of icariin-zinc compounds can promote development in male rats, improve their excitability, promote their recovery from the fatigue state, and enhance their anti-fatigue ability.

Icariin-zinc can significantly prolong the exhaustive swimming time, improve the exercise ability, and increase the content of testosterone in the plasma of male rats. However, there was no significant effect on glycogen content, testicular index, and other reproductive glands (such as the prostate gland and seminal vesicle). Moreover, icariin-zinc was better than zinc gluconate in prolonging exhaustive swimming time, and increasing plasma testosterone content. Compared with icariin, the effect of high-dose zinc is more significant. It is suggested that in the application of the icariin-zinc complex, the dosage should be strictly controlled to obtain the best drug effect without affecting the reproductive system organs.

DATA AVAILABILITY STATEMENT

The original contributions presented in the study are included in the article/Supplementary Material, further inquiries can be directed to the corresponding authors.

ETHICS STATEMENT

The animal study was reviewed and approved by the Ethics Committee of Tianjin University of Traditional Chinese Medicine (TCM-LAEC2019069).

AUTHOR CONTRIBUTIONS

JZ, DM designed the research associated with the project, QJ,LX performed the acquisition and analysis in the experiment. MS and CZ, AF performed acquisition, analysis and interpretation of data. HY interpreted the data. CC,DL drafted the work and revised it. All authors have read and approved the submitted version of manuscript. And all authors have agreed their contributions in the manuscript.

FUNDING

This work was supported by National Natural Science Foundation of China (51573137, 82074470, 81873316).

ACKNOWLEDGMENTS

We thank Professor Guanwei Fan for technical assistance in the research and manuscript preparation.

REFERENCES

Britto, F. A., Cortade, F., Belloum, Y., Blaquière, M., Gallot, Y. S., Docquier, A., et al. (2018). Glucocorticoid-dependent REDD1 Expression Reduces Muscle Metabolism to Enable Adaptation under Energetic stress. *BMC Biol.* 16 (1), 65. doi:10.1186/s12915-018-0525-4

Chen, M., Hao, J., Yang, Q., and Li, G. (2014). Effects of Icariin on Reproductive Functions in Male Rats. *Molecules* 19, 9502–9514. doi:10.3390/molecules19079502

Chu, Q., Chi, Z.-H., Zhang, X., Liang, D., Wang, X., Zhao, Y., et al. (2016). A Potential Role for Zinc Transporter 7 in Testosterone Synthesis in Mouse Leydig Tumor cells. *Int. J. Mol. Med.* 37 (6), 1619–1626. doi:10.3892/ijmm.2016.2576

Ding, J., Tang, Y., Tang, Z., Zu, X., Qi, L., Zhang, X., et al. (2018). Icariin Improves the Sexual Function of Male Mice through the PI3K/AKT/eNOS/NO Signalling Pathway. *Andrologia*. 50 (1), e12802. doi:10.1111/and.12802

Fairbanks, F., Andres, M. P., Caldeira, P., Abdo, C., and Podgaec, S. (2017). Sexual Function, Anxiety and Depression in Women with Benign Breast Disease. A Case-Control Study. *Rev. Assoc. Med. Bras.* 63, 876–882. doi:10.1590/1806-9282.63.10.876

Górski, W., Mokros, Ł., Kumor-Kisielewska, A., Pietras, T., and Piotrowski, W. J. (2017). The Utility of Selected Questionnaires in the Assessment of Fatigue, Depression and Health Quality in post-sarcoidosis Fatigue Syndrome. *Adv. Respir. Med.* 85 (6), 313–321. doi:10.5603/arm.2017.0054

Hennigar, S. R., and Kelleher, S. L. (2012). Zinc Networks: the Cell-specific Compartmentalization of Zinc for Specialized Functions. *Biol. Chem.* 393, 565–578. doi:10.1515/hsz-2012-0128

Kang, H. K., Choi, Y.-H., Kwon, H., Lee, S.-B., Kim, D.-H., Sung, C. K., et al. (2012). Estrogenic/antiestrogenic Activities of a Epimedium Koreanum Extract and its Major Components: In Vitro and In Vivo Studies. *Food Chem. Toxicol.* 50, 2751–2759. doi:10.1016/j.fct.2012.05.017

Liu, Z. Q., Luo, X. Y., Sun, Y. X., Wu, W., Liu, C. M., Liu, Z. Q., et al. (2004). The Antioxidative Effect of Icariin in Human Erythrocytes against Free-Radical-Induced Haemolysis. *J. Pharm. Pharmacol.* 56 (12), 1557–1562. doi:10.1211/0022357044869

Long, H., Jiang, J., Xia, J., and Jiang, R. (2018). Icariin Improves SHR Erectile Function via Inhibiting eNOS Uncoupling. *Andrologia* 50 (9), e13084. doi:10.1111/and.13084

Narkhede, A. N., Jagtap, S. D., Nirmal, P. S., Giramkar, S. A., Nagarkar, B. E., Kulkarni, O. P., et al. (2016). Anti-fatigue Effect of Amarkand on Endurance Exercise Capacity in Rats. *BMC Complement. Altern. Med.* 16, 23. doi:10.1186/s12906-016-0995-2

Santos, H. O., and Teixeira, F. J. (2019). Use of Medicinal Doses of Zinc as a Safe and Efficient Coadjutant in the Treatment of Male Hypogonadism. *Aging Male* Feb 15, 1–10. doi:10.1080/13685538.2019.1573220

Sun, J., Wang, D., Lin, J., Liu, Y., Xu, L., Lv, R., et al. (2019). Icariin protects mouse Leydig cell testosterone synthesis from the adverse effects of di(2-ethylhexyl) phthalate. *Toxicol. Appl. Pharmacol.* 378, 114612. doi:10.1016/j.taap.2019.114612

Surhio, M. M., Wang, Y., Fang, S., Li, J., and Ye, M. (2017). Anti-fatigue Activity of a Lachnum Polysaccharide and its Carboxymethylated Derivative in Mice. *Bioorg. Med. Chem. Lett.* 27, 4777–4780. doi:10.1016/j.bmcl.2017.07.034

Tan, H. L., Chan, K. G., Pusparajah, P., Saokaew, S., Duangjai, A., Lee, L-H., et al. (2016). Anti-Cancer Properties of the Naturally Occurring Aphrodisiacs: Icariin and its Derivatives. *Front. Pharmacol.* 7, 191. doi:10.3389/fphar.2016.00191

Xi, X., Guo, S., Guo, H., Cui, X., Cao, H., Xu, F., et al. (2018). Anti-exercise-fatigue and Promotion of Sexual Interest Activity of Total Flavonoids from Wasps Drone-Pupae in Male Mice. *Biomed. Pharmacother.* 107, 254–261. doi:10.1016/j.biopha.2018.07.172

Young, C. A., Tennant, A., Mills, R., Rog, D., Ford, H., and Orchard, K. (2017). Sexual Functioning in Multiple Sclerosis: Relationships with Depression, Fatigue and Physical Function. *Mult. Scler.* 23, 1268–1275. doi:10.1177/1352458516675749

Zhan, S. H., Heng, J. X., Tao, Q., Hu, Z. M., Li, H., Chen, Y. L., et al. (2014). Antioxidative Protective Effect of Icariin on the $FeSO_4/H_2O_2$ Damaged Human Sperm Based on Confocal Raman Micro-spectroscopy. *J. Huazhong Univ. Sci. Technol.* 34, 755–780. doi:10.1007/s11596-014-1348-3

Zhao, S. Y., Liao, L. X., Tu, P. F., Li, W. W., and Zeng, K. W. (2019). Icariin Inhibits AGE-Induced Injury in PC12 Cells by Directly Targeting Apoptosis Regulator Bax. *Oxid Med. Cel. Longev.* 2019, 7940808. doi:10.1155/2019/7940808

Conflict of Interest: The authors declare that the research was conducted in the absence of any commercial or financial relationships that could be construed as a potential conflict of interest.

Copyright © 2021 Zhang, Zhang, Liu, Ji, Ren, Ma, Zhang, Wu, Zhang, Shang and He. This is an open-access article distributed under the terms of the Creative Commons Attribution License (CC BY). The use, distribution or reproduction in other forums is permitted, provided the original author(s) and the copyright owner(s) are credited and that the original publication in this journal is cited, in accordance with accepted academic practice. No use, distribution or reproduction is permitted which does not comply with these terms.

frontiers in Pharmacology

METHODS
published: 17 June 2021
doi: 10.3389/fphar.2021.673729

Developing Placebos for Clinical Research in Traditional Chinese Medicine: Assessing Organoleptic Properties of Three Dosage Forms (Oral Liquid, Capsule and Granule)

Mengli Xiao[1,2], *Jiake Ying*[1,2], *Yang Zhao*[1,2], *Qingna Li*[1,2], *Yingpan Zhao*[3], *Rui Gao*[1,2]* and *Fang Lu*[1,2]*

[1]NMPA Key Laboratory for Clinical Research and Evaluation of Traditional Chinese Medicine, Xiyuan Hospital of China Academy of Chinese Medical Sciences, Beijing, China, [2]National Clinical Research Center for Chinese Medicine Cardiology, Xiyuan Hospital of China Academy of Chinese Medical Sciences, Beijing, China, [3]Department of Gastroenterology, Xiyuan Hospital of China Academy of Chinese Medical Sciences, Beijing, China

OPEN ACCESS

Edited by:
Yan Xu,
Cleveland State University,
United States

Reviewed by:
Godwin Upoki Anywar,
Makerere University, Uganda
Rolf Teschke,
Hospital Hanau, Germany

***Correspondence:**
Rui Gao
ruigao@126.com
Fang Lu
deerfang@126.com

Specialty section:
This article was submitted to Ethnopharmacology, a section of the journal Frontiers in Pharmacology

Received: 28 February 2021
Accepted: 07 June 2021
Published: 17 June 2021

Citation:
Xiao M, Ying J, Zhao Y, Li Q, Zhao Y, Gao R and Lu F (2021) Developing Placebos for Clinical Research in Traditional Chinese Medicine: Assessing Organoleptic Properties of Three Dosage Forms (Oral Liquid, Capsule and Granule). Front. Pharmacol. 12:673729. doi: 10.3389/fphar.2021.673729

Background: The successful application of randomized, double-blind placebo-controlled studies requires maximum blinding. Organoleptic properties of the placebo should be similar to the drug, making it difficult to distinguish between the two. The uniqueness of traditional Chinese medicine (TCM) preparations makes it challenging to prepare placebo. Evaluation of the TCM placebo simulation effect can determine whether the preparation of placebo can be genuinely blind in clinical trials. There is still a lack of well-established methods to evaluate TCM placebos. Hence, this study aimed to explore the evaluation methodology of TCM placebo simulation.

Methods: An independent evaluation method and three comparative evaluation methods were proposed, and three dosage forms (oral liquid, capsule, and granule) were tested. The independent evaluation, in which each person was given an experimental drug or a placebo, gave an overall assessment of organoleptic properties in a blind state. We comparatively evaluated the similarity in organoleptic properties between the experimental drug and placebo. According to different distribution methods, we divided comparative evaluation methods into three. In method 1, the evaluator was given the experimental drug and placebo and was told that there must be a placebo among them. In method 2, each evaluator was randomly assigned to the combination group or two investigational drugs group. In method 3, the evaluator was assigned to a set of three coded samples, numbered by random three-digit numbers, each different, two of which were identical, and the two samples were equally frequent.

Results: In the independent evaluation, there was no difference between TCM placebo and experimental drugs in a blind state at the level of $p = 0.05$. Even though the comparative evaluation methods enabled identification of potential differences between the two samples, methods 2 and 3 were better than method 1 in eliminating psychological factors. Also, in method 3, the completely random method combined with the blind

method eliminated the subjectivity and objectivity bias and improved the experiment's credibility compared with the previous two methods.

Conclusion: Regardless of the methods that could evaluate the placebo's simulated effect in actual clinical trials, we suggest that independent evaluation and comparative evaluation (method 3) should be combined to reflect better whether the placebo is truly blind.

Keywords: traditional Chinese medicine, placebo, simulation effect, evaluation, organoleptic properties

INTRODUCTION

Masking of participants and researchers has long been used in randomized clinical trials (RCTs) to eliminate the potential impacts of nondrug effects, including the natural course of the disease; the evaluator and researchers; and subjective factors in treatment, diagnosis, and clinical assessment (Jamshidian et al., 2014; Dube et al., 2007). In the past 40 years, at least 17,000 RCTs have been conducted in China to assess the efficacy and safety of traditional Chinese medicine (TCM), including Chinese herbal medicine, acupuncture, massage, moxibustion, Qigong, and other therapies, most of which are related to Chinese herbal medicine (Wang et al., 2007). Regardless of the increasing number of TCM studies, their reliability has been challenged because of the lack of rigorous evidence (Wang et al., 2007; Teschke et al., 2015; Liu et al., 2015). Inadequate randomization, insufficient sample sizes, and the lack of proper blinding make the research results vulnerable to the selection, reporting, and assessor bias.

A more recent review of TCM uncovered that many studies often lacked true blindness (Teschke et al., 2015). To meet the requirements for blinding, it is necessary to prepare a convincing TCM placebo, and these must be similar to the investigational drug in terms of visual attributes, dosage form features, and smell/taste attributes. Compared with western medicine placebo drugs, the unique odor, taste, and color of TCM preparations make it challenging to prepare placebo. At present, there are two forms of placebo preparation: no pharmacodynamic components and low-dose pharmacodynamic components. The placebo prepared by the simple excipient method placebo does not contain pharmacodynamic components. Generally, it uses flavorants (edible additives), colorants (edible pigments), and volatiles (agents to simulate a placebo) (Lu et al., 2018). The other is to use the drug with excipients in a low proportion. It is feasible to dilute the drug substance by 10 or 20 times, use it as a placebo, or use materials with certain pharmacological activities unrelated to the investigational drug's effect to prepare the placebo (Nakaya et al., 2003). To explore whether the organoleptic properties of the placebo are exactly the same as those of experimental drugs, it is imperative to evaluate the TCM placebo's simulation effect. Nevertheless, there is a lack of recognized evaluation methods and standards for TCM placebos (Wang et al., 2014).

At present, there are mainly two clinical evaluation methods: artificial and objective evaluation. For artificial evaluation, some researchers have proposed a placebo quality checklist (Brinkhaus et al., 2008), but this has never been appropriately validated. Some Chinese researchers have proposed to allow healthcare professionals, pharmaceutical companies, and patients to score placebos, and the results should be used to determine whether the placebo simulation is successful (Tang et al., 2009; Wang et al., 2011; Jin et al., 2014a; Song et al., 2014; Yang, 2014; Sun et al., 2019; Yan and Zhang, 2020). For objective evaluation, some researchers have begun to use intelligent sensory analysis to evaluate placebo quality, including visual sensors, electronic tongue sensors, and other technologies. These are used to assess placebo consistency with the investigational drug in organoleptic properties, and they can transform subjective evaluation reports into objective data to standardize evaluations (Luo, 2012; Jin et al., 2014b; Liu et al., 2014; Fan, 2018).

Manual placebo evaluation can maximize the simulation of the patient judgment of drugs in the real clinical environment. Here, we proposed four methods for evaluating the simulated effect of placebo in TCM, including an independent evaluation method and three comparative evaluation methods. In the independent evaluation, only one of the two drugs, including experimental drug and placebo, was given to the evaluator. In contrast, in the comparative evaluation, the evaluator was given multiple boxes of drugs, including various possibilities. To fully explore whether the four evaluation methods identified and evaluated the simulation effect of TCM preparations stably, we took three commonly used TCM preparations (oral liquid, granule, and capsule) as an example to conduct the simulation effect evaluation test. We provided our insights and considerations for evaluating the manufacture and simulated effects of TCM placebos.

MATERIALS AND METHODS

Evaluation of Different Dosage Forms of Traditional Chinese Medicine Placebo

This study was intended to evaluate three different dosage forms of TCM placebo used in clinical studies and the following were in each: 1) Fufang Ejiao Syrup (FFEJJ) oral solution (batch number: Z37021371); this product is a brown to dark brown liquid, sweet in taste, and comes in 20 ml vials. The ingredients and contents in placebo FFEJJ oral solution (20 ml) are listed in **Table 1**. Shandong Dong-e E-Jiao Co., Ltd., produced both the investigational drug and placebo. 2) Zhizhu Kuanzhong (ZZKZ) capsules (batch number: Z20020003); this product is light grayish brown, slightly bitter, salty and comes in 0.43 g/grains. The ingredients and contents in placebo ZZKZ capsules (0.43 g) are listed in **Table 2**. The investigational drug and

TABLE 1 | Ingredients and their contents of FFEJ placebo in each placebo bottle (20 ml).

Ingredients	Content	Role(s)
Gelatina nigra syrup	0.9 ml	Equivalent to 5% of the original formula
Caramel pigment	0.8 g	Pharmaceutical excipient/food additive
Stevioside	0.025 g	Pharmaceutic adjuvant

placebo were produced by Langzhi Group Shuangren Pharmaceutical Co., Ltd., 3) Billing Weitong (BLWT) granules (batch number: Z19990069); this product is brown to tan granules with a bitter taste and comes in 5 g/bags. Ingredients and content contained in each placebo sachet (5 g) of BLWT granules are listed in **Table 3**. Both the investigational drug and placebo were prepared by Yangtze River Pharmaceutical Group Jiangsu Pharmaceutical Co., Ltd.

Evaluation Methods of Placebo Simulation Effect of Traditional Chinese Medicine

The placebo should be completely consistent with the tested TCM in terms of appearance, color, odor, taste, packaging, usage, and dosage, so it was necessary to evaluate whether the placebo successfully mimicked the investigational drug by independent assessment and comparative effectiveness evaluation. Independent evaluation was required to determine if the actual medication was simulated. The evaluator determind whether a sample in the investigational drug or placebo was an investigational drug under a blinded state; for comparative effect evaluation, they evaluated the similarity of the investigational drug and placebo at different levels such as appearance texture, color, odor, and taste.

Independent Evaluation

Three dosage forms of FFEJJ oral solution, ZZKZ capsules, BLWT granules, and their placebos were evaluated. The investigational drug or placebo was randomly distributed to 20 evaluators ($n = 10$ each). The evaluators were randomly selected from the target evaluator for which the drug was acting. The evaluator made an overall assessment of the possibility that the sample was the investigational drug under a blinded state. There were two evaluation options: probably an investigational drug or probably a placebo. After unblinding, judgment accuracy was compared between the placebo and the investigational drug groups to determine whether there was a difference between them.

For the qualification criteria of the placebo simulation effect, the methods listed in **Table 4** were adopted. Twenty evaluators (10 each for placebo and investigational drug) were used to calculate the difference in the proportion of the investigational drug and placebo judged as the investigational drug in the blinded state ($p < 0.05$). Assuming that the numbers of the evaluators who judged investigational drug as the investigational drug were 5, 6, 7, 8, 9, and 10, the cut-off value of the number of the evaluators who judged the placebo as the investigational drug varied from 0 to 5, indicating a significant difference at the 0.05 level. That is, when the number of evaluators was 20, and 5 evaluators judged the investigational drug as the investigational drug, the number of the evaluators who judged placebo as the investigational drug was at least 1, indicating there was no difference in the proportion of the evaluators who judged the placebo and investigational drug as the investigational drug in the blinded state at the 0.05 level. When all evaluators judged the investigational drug as the investigational drug, the number of the evaluators who judged the placebo as the investigational drug was at least 6, which means there was no difference in the proportion of evaluators who judged the placebo and the investigational drug as the investigational drug in the blinded state at the 0.05 level.

Comparably, if the number of evaluators was increased to 20 each for placebo and the investigational drug, with an assumption that the numbers of patients judged the investigational drug as the investigational drug were 10, 12, 14, 16, 18, and 20, and there was a difference in the proportion of the evaluators who judged both

TABLE 2 | Ingredients and their contents of ZZKZ placebo in each placebo grain (0.43 g).

Ingredients	Proportion	Role(s)
Microcrystalline cellulose	1	Filler (no pharmacological activity)
Starch	2	Filler (no pharmacological activity)
Magnesium stearate	0.5%	Lubricant (no pharmacological activity)
Food-grade pigment solution	--	Food additive

TABLE 3 | Ingredients and their contents of BLWT placebo in each placebo pack (5 g).

Ingredients	Content (g)	Proportion (%)	Role(s)
Dextrin	3.19	63.8	Pharmaceutic adjuvant
Sucrose	1.0	20.0	Pharmaceutic adjuvant
BLWT fine powder	0.375	7.5	Equivalent to 7.5% of the original formula
Povidone K30	0.25	5.0	Pharmaceutic adjuvant
Caramel	0.125	2.5	Pharmaceutical excipient/food additive
Low-substituted hydroxypropylcellulose	0.06	1.2	Pharmaceutic adjuvant

TABLE 4 | Cut-off values of the difference in the number of evaluators who judged the investigational drug and placebo as the investigational drug at the 0.05 level.

	No. of evaluators = 20 (50/50 received investigational drug and placebo)		No. of evaluators = 40 (50/50 received investigational drug and placebo)	
	Investigational drug	Placebo	Investigational drug	Placebo
Investigational drug	10	0	20	0
Placebo	5	5	15	5
Investigational drug	9	1	18	2
Placebo	3	7	11	9
Investigational drug	8	2	16	4
Placebo	2	8	9	11
Investigational drug	7	3	14	6
Placebo	1	9	6	14
Investigational drug	6	4	12	8
Placebo	0	10	4	16
Investigational drug	5	5	10	10
Placebo	0	10	3	17

the investigational drug and placebo as the investigational drug in the blinded state ($p< 0.05$), the cut-off value of the number of evaluators who judged the placebo as the investigational drug varied from 3 to 15, suggesting a significant difference at the level of 0.05. That is, when 10 evaluators judged the investigational drug as the investigational drug, the number of evaluators who identified the placebo as the investigational drug was at least 4, which suggested there was no significant difference at the 0.05 level. When all evaluators judged the investigational drug as the investigational drug and the number of evaluatiors who thought the placebo was the investigational drug was at least 16, it was considered that there was no difference in the proportion of the evaluators who judged the investigational drug in the blinded state at the 0.05 level.

Comparative Evaluation

Method 1

All 20 evaluators were distributed an investigational drug and a placebo and the evaluators were told that one of them was a placebo, but they did not know which one was a placebo. Also, they were allowed to open the drug package. The evaluators scored the sensory similarities in terms of drug appearance, odor, taste, and characteristics. The judgment criteria were as follows: complete consistency corresponded to a score of 10.0 points, comparative consistency was 7.5 points, uncertainty scored 5.0 points, a large difference corresponded to 2.5 points, and complete inconsistency was 0 points. If the single evaluation content was < 5 points, it was considered that there were certain differences between the two samples.

Method 2

The evaluators were randomly distributed into two groups, and there were two scenarios in each: 1) both samples were the investigational drug; and 2) one sample was the investigational drug and the other was the placebo. The patients had an equal chance of obtaining either sample in both scenarios. There were a total of 20 evaluators. Each assessed the placebo/investigational drug or the investigational drug/investigational drug simultaneously, and they were allowed to open the packaging. The evaluators considered the similarities between the placebo and investigational drug in terms of packaging, label, strength, drug form, color, odor and taste; they were instructed to determine if the placebo was similar to the investigational drug and whether the placebo could be identified. The judgment criteria were as follows: complete consistency corresponded to a score of 10.0 points, comparative consistency was 7.5 points, uncertainty scored 5.0 points, a large difference corresponded to 2.5 points, and complete inconsistency was 0 points. The 0.05 level was used to determine whether there was a difference in scores between the two groups.

Method 3

A three-point test method was used to evaluate the slight differences between the two samples. Evaluation steps: the evaluator was provided with a group of three samples that were coded with a random three-digit number that was different each time. Two of the samples had the same numbers. The evaluators were required to pick out the sample different from the other two, with an equal occurrence rate of the three samples: BAA, ABB, ABA, BAB, AAB, and BBA. The statistical null hypothesis was that it is impossible to distinguish between these two samples based on their characteristic strength. In this case, the probability of correctly identifying an individual sample was $p = 0.33$. The alternative hypothesis was that these two samples could be distinguished based on their characteristic strength. The probability of correctly identifying a control sample, in this case, was $p > 0.33$. Finally, the number of correct responses and the total number of evaluators was statistically analyzed. When the number of correct responses was greater than or equal to the corresponding value at a certain level of the table tested by the three-point test method, the null hypothesis was rejected, and the alternative hypothesis was accepted at the significant level. A total of 36 samples were included, and the cut-off value for a difference between the two samples was 18 at the 0.05 level.

RESULTS

Independent Evaluation

In the independent evaluation of three dosage forms of TCM placebos, there were no significant differences across the groups

TABLE 5 | Basic information of patients independently evaluating FFEJJ placebo.

		Placebo (n = 10)	Investigational drug (n = 10)
Sex	Male	2	2
	Female	8	8
Age (yr)	—	30.67 ± 4.485	38.87 ± 13.967
Evaluation time (seconds)	Mean ± SD	38.87 ± 13.967	23.20 ± 9.414
	Min, max	14, 29	10, 35
Prior FFEJJ use	Yes	3	0
	No	7	10

TABLE 6 | Basic information of patients independently evaluating ZZKZ placebo.

		Placebo (n = 10)	Investigational drug (n = 10)
Sex	Male	3	5
	Female	7	5
Age (yr)	—	37.8 ± 17.0	40.7 ± 16.6
Evaluation time (seconds)	Mean ± SD	51.10 ± 27.225	40.90 ± 12.749
	Min, max	30, 61	20, 55
Prior ZZKZ use	Yes	2	2
	No	8	8
Open capsule	Yes	6	8
	No	4	2

TABLE 7 | Basic information of patients independently evaluating BLWT placebo.

		Placebo (n = 10)	Investigational drug (n = 10)
Sex	Male	4	5
	Female	6	5
Age (yr)	—	34.4 ± 7.88	39.7 ± 13.57
Evaluation time (seconds)	Mean ± SD	46 ± 56.6	33 ± 34
	Min, max	10, 200	10, 120
Prior BLWT granule use	Yes	0	0
	No	10	10

about the evaluator gender or age, or the time to make a judgment on whether the dispensed drug was the investigational drug or placebo. Three evaluators had taken FFEJJ before the study (all in the placebo group), and four evaluators had taken ZZKZ before evaluation (two in the placebo group). See **Tables 5–7** for specific information.

With regard to the evaluation of the FFEJJ oral placebo simulation effect, when the compound was actually the placebo, three of 10 evaluators judged it as the investigational drug, and when it was actually the investigational drug, seven of 10 evaluators judged both of them as investigational drugs.

Next, we evaluated the placebo simulation effect of ZZKZ capsules. When the compound was actually the placebo, eight of 10 evaluators judged it as the investigational drug; when it was actually the investigational drug, five of 10 evaluators judged it as the investigational drug.

Finally, we evaluated the placebo simulation effect of BLWT granules. When granules were the placebo and investigation drug, respectively, four and seven of 10 evaluators chose it as the investigational drug.

If the cut-off value of the evaluators who judged the investigational drug and placebo as the investigational drug was different at the 0.05 level, it was considered that there was no significant difference between the three different TCM preparations placebos, and the study was appropriately blinded (**Tables 4**, **8**).

Comparative Evaluation

Method 1

A total of 20 evaluators participated in the placebo evaluation of ZZKZ capsule (10 male and 10 female, age range 27–69 years, mean 44.8 ± 12.2 years). Four evaluators had taken capsules before participating in the evaluation. Eighteen of the 20 evaluators opened the capsules and evaluated the similarity of the compounds. For the ZZKZ capsule similarity evaluation, 13 evaluators correctly identified the placebo (**Table 9**). If the score in a single evaluation was<5 points, it was identified as a difference. The ZZKZ capsule placebo was generally consistent or indefinitely different in appearance and content characteristics with the investigational drug, with some taste and odor differences.

Method 2

A total of 20 evaluators participated in the comparative evaluation of the placebo simulation effect of ZZKZ capsules; three evaluators in the experimental group had previously taken the capsules. The patients in both groups who participated in the evaluation opened the capsule for discrimination, and the results of appearance, contents, odor, and taste are shown in **Table 10**. Eight evaluators in the combination group identified the placebo, and nine evaluators in the two investigational drugs group mistook the investigational drug as a placebo. Since psychological effects were ruled out, the investigational drug was not considered to be different from the placebo in appearance, but there were some differences between the two in taste, content traits, and odor.

Method 3

A total of 36 evaluators (16 male, 20 female; age range 18–76 years, mean age 41.72 ± 13.403) participated in the comparative evaluation. None of them had taken the investigational drug before completing the evaluation. The evaluators selected one different sample or two identical samples from each test package regarding appearance, texture, color, odor, and taste. The number of evaluators with correct judgment was less than half of the total, so the comprehensive evaluation result was pass for BLWT granules vs. placebo (**Table 11**).

DISCUSSION

An ideal placebo has no active ingredients but is identical to the investigational drug in organoleptic properties. In clinical investigations of western medicine, the active ingredients are clear, so the placebo only needs to use the corresponding excipients (e.g., starch, glucose, etc.,) and the difficulty coefficient is not high (Qi et al., 2008). However, for TCM studies, the Chinese materia medica composition is often several or even dozens of components, and many traditional forms (e.g., decoctions, pills and powders) have special odors and tastes, and ensuring that the placebo is similar can be

TABLE 8 | Independent evaluation results of evaluators who judged the investigational drug and placebo as the investigational drug.

		No. of evaluators = 20 (50/50 received investigational drug and placebo)	
		Investigational drug	Placebo
FFEJJ	Investigational drug	7	3
	Placebo	3	7
ZZKZ	Investigational drug	5	5
	Placebo	8	2
BLWT	Investigational drug	7	3
	Placebo	4	6

TABLE 9 | Comparative evaluation results of ZZKZ for method 1

	Number of evaluators = 20 (50/50 received investigational drug and placebo)			
	Mean	SD	Min	Max
Appearance	8.38	1.81	2.5	10.0
Characteristics	5.25	2.64	2.5	9.0
Odor	4.40	2.83	0.0	10.0
Taste	4.95	2.32	2.5	9.0

TABLE 10 | Comparative evaluation results of ZZKZ for method 2

	No. of evaluators = 10 (investigational drug and placebo)	No. of evaluators = 10 (only assessed the investigational drug)	*p* Values
Appearance (Mean ± SD)	8.650 ± 2.015	8.700 ± 1.207	0.947
Characteristics (Mean ± SD)	3.500 ± 2.134	8.850 ± 1.226	<0.0001
Odor (Mean ± SD)	0.500 ± 1.054	7.550 ± 2.047	<0.0001
Taste (Mean ± SD)	3.600 ± 2.558	6.800 ± 2.394	0.010

TABLE 11 | Comparative evaluation results of BLWT for method 3

Comparative evaluation content	No. of evaluators who made the correct judgment	Eligibility criteria	Pass or fail
A. Appearance	A = 4	A < 18	Pass
B. Texture	B = 3	B < 18	Pass
C. Color	C = 12	C < 18	Pass
D. Odor	D = 12	D < 18	Pass
E. Taste	E = 16	E < 18	Pass
S. Comprehensive assessment	S = 9.4	S < 18	Pass

difficult. There is large variability, which makes placebo preparation even more difficult. Special consideration should be given to the design of a placebo to ensure a good simulation effect.

In actual clinical trials, uniform criteria are often used for the specification, packaging, usage, and dosage of the placebo and investigational drug. The evaluation mainly focuses on whether the placebo has drug activity and whether it is consistent with the investigational drug in terms of appearance, color odor, and taste. Nevertheless, there is no recognized evaluation method for placebo quality evaluation. In addition to avoiding placebo effects, attention should also be paid to nocebo effects during double-blind RCTs. The nocebo effect is defined as a harmful result of patients' doubts or negative expectations about the treatment (Blasini et al., 2018). Evidence has been found that both the placebo and nocebo effects can substantially affect the efficacy of the drug as well as nondrug treatments (Amanzio et al., 2001; Aslaksen et al., 2015). Therefore, nocebo effects can affect the accurate determination and evaluation of therapeutic drugs. Determining how to scientifically and consistently design placebos and evaluate their simulation effects is particularly important.

Although the objective evaluation method can make the data more objective and reduce the degree of deviation, there are some differences between the objective evaluation method and clinical practice. The patients' potential psychological factors cannot be

100% simulated, affecting the test results. Also, the standardization and objective quantification of simulation effects still need to be improved (Wang et al., 2003). So, the present study used the artificial evaluation method. By pre-investigating a small number of target evaluators in advance, researchers can predict whether they will distinguish the difference between the placebo and the experimental drug in the actual clinical study. Considering whether the placebo's simulation effect would be affected if there were simultaneous exposure to two drugs, we provided three different contrast evaluation methods. All of them enabled identifying potential differences between the two samples, and they all have some differences. For the first method, the evaluators knew that there must be a placebo included, so they would pay more attention to finding the differences between the two, and the probability of unblinding was increased. The second method used to deal with this limitation was semi-randomized and evaluated if the two (the investigational drug and placebo, or two investigational drugs) were the same. To make this judgment, both the difference and the consistency, or both of them, had to be considered, making up for the limitation of the first method that only looked for different points. The difference reflects the inconsistencies between the two and the investigational drug, and the consistency expresses the degree of the similarities between the two and the investigational drug. With smaller differences comes higher consistency. The purpose of the evaluation was achieved by using one of the analyses in actual operation. Nevertheless, semi-randomization may also produce some biases, because of the infeasibility of true randomization in a strict sense. The third method adopted complete randomization, eliminateing nonuniformity error, order error caused by the sampling method, and allocation error due to improper allocation. It also reduced subjective and objective biases by combining the blinding approach, thus significantly improving data reliability. We believe that the completely random simulated evaluated better whether the placebo was more consistent with the experimental drug by discussing several comparative evaluation methods. In the actual clinical application, we suggest that the combination of independent and comparative evaluation can be closer to the real double-blind placebo-controlled studies, so as to avoid the placebo and nocebo effects to the greatest extent. Nevertheless, evaluators may have different psychological tendencies and have varying sensitivities to the organoleptic properties of Chinese materia medica so that the manual evaluation method can be affected by subjective factors. Also, in this study, the sample size was small, and more samples are needed for verification.

Concerning the evaluation criteria, there are currently two primary forms. One compares the investigational drug and placebo in terms of shape, color, odor, taste and other aspects to determine whether the differences were significant. The second is to define the value of either artificially, but there is no uniform definition of evaluation criteria cut-off values. This study was mainly based on the relevant literature and statistical indicators in early-stage investigations. There are some doubts about the scientific validity and reliability of this approach, which must be continuously explored in the future.

The literature suggests that evaluators should be asked to indicate whether they think they took the investigational drug or placebo after the trial. The statistical analyses should then estimate and adjust for postrandomization confounding factors that could influence treatment effect according to the causal inference framework to obtain the unbiased efficacy estimate and more easily explain the estimate (Hubbard et al., 2012). At present, there is little evidence that RCTs are actually double-blinded (Hrobjartsson et al., 2007). Our next focus will be to investigate whether it is necessary to specify the evaluation results of the placebo simulation effect along with articles, which should provide better references to readers.

CONCLUSION

A blind method is an essential link to a high-quality TCM clinical trial. The simulation effect of the placebo will directly affect whether the blind method can be realized. Evaluation of the TCM placebo's simulation effect can judge whether the placebo preparation achieves complete consistency in visual attributes, dosage form features and smell/taste attributes. We proposed an independent evaluation method and three comparative evaluation methods, and three dosage forms (oral liquid, capsule and granule) were tested. Regardless of the methods can evaluate well the simulated effect of placebos, in actual clinical trials, we suggest that independent evaluation and comparative evaluation (method 3) should be combined to reflect better whether the placebo is truly blind. This study can provide a new choice for the simulation evaluation of TCM placebo in the future and further improve the quality of TCM clinical trials.

DATA AVAILABILITY STATEMENT

The original contributions presented in the study are included in the article/Supplementary Material, further inquiries can be directed to the corresponding authors.

ETHICS STATEMENT

Ethical review and approval was not required for the study on human participants in accordance with the local legislation and institutional requirements. Written informed consent for participation was not required for this study in accordance with the national legislation and the institutional requirements.

AUTHOR CONTRIBUTIONS

FL and RG conceived and designed the study. JY, QL, and YiZ collected and evaluated data. YaZ analyzed the data. MX wrote the paper. All authors revised the paper.

FUNDING

The work is supported by Special Research on Modernization of Traditional Chinese Medicine in the National Key Research and Development Program in China's 13th Five-Year Plan Demonstrative Research on TCM-related International Cooperation with Countries along the Belt and Road (No.2017YFC1703703).

REFERENCES

Amanzio, M., Pollo, A., Maggi, G., and Benedetti, F. (2001). Response Variability to Analgesics: a Role for Non-specific Activation of Endogenous Opioids. *Pain*. 90 (3), 205–215. doi:10.1016/S0304-3959(00)00486-3

Aslaksen, P. M., Zwarg, M. L., Eilertsen, H.-I. H., Gorecka, M. M., and Bjørkedal, E. (2015). Opposite Effects of the Same Drug: Reversal of Topical Analgesia by Nocebo Information. *Pain*. 156 (1), 39–46. doi:10.1016/j.pain.0000000000000004

Blasini, M., Peiris, N., Wright, T., and Colloca, L. (2018). The Role of Patient-Practitioner Relationships in Placebo and Nocebo Phenomena. *Int. Rev. Neurobiol.* 139, 211–231. doi:10.1016/bs.irn.2018.07.033

Brinkhaus, B., Pach, D., Lüdtke, R., and Willich, S. N. (2008). Who Controls the Placebo? Introducing a Placebo Quality Checklist for Pharmacological Trials. *Contemp. Clin. Trials*. 29 (2), 149–156. doi:10.1016/j.cct.2007.06.005

Fan, L. J. (2018). Application of Computer Color Matching Technology in Color Simulation of Chinese Materia Medica Placebo. Dissertation/Master's Thesis. China (Beijing): China Academy of Chinese Medical Sciences.

Hrobjartsson, A., Forfang, E., Haahr, M., Als-Nielsen, B., and Brorson, S. (2007). Blinded Trials Taken to the Test: an Analysis of Randomized Clinical Trials that Report Tests for the success of Blinding. *Int. J. Epidemiol.* 36 (3), 654–663. doi:10.1093/ije/dym020

Hubbard, A., Jamshidian, F., and Jewell, N. (2012). Adjusting for Perception and Unmasking Effects in Longitudinal Clinical Trials. *Int. J. Biostat.* 8 (2), 1–20. doi:10.2202/1557-4679.1376

Jamshidian, F., Hubbard, A. E., and Jewell, N. P. (2014). Accounting for Perception, Placebo and Unmasking Effects in Estimating Treatment Effects in Randomised Clinical Trials. *Stat. Methods Med. Res.* 23 (3), 293–307. doi:10.1177/0962280211413449

Jin, G. Q., Sun, L., and Xia, L. H. (2014a). Preparation and Evaluation of Placebos for Shenbawei Capsules. *Chin. Pharmacist.* 17 (05), 734–736.

Jin, G. Q., Xia, L. H., and Sun, L. (2014b). Preparation Method and Effect Evaluation of Placebo for Sicaotongmai Capsule. *Chin. Pharmacist.* 17 (12), 2013–2015.

Liu, J., Zhang, G.-L., Huang, G.-Q., Li, L., Li, C.-P., Wang, M., et al. (2014). Therapeutic Effect of Jinzhen Oral Liquid for Hand Foot and Mouth Disease: a Randomized, multi-center, Double-Blind, Placebo-Controlled Trial. *PLoS One*. 9 (4), e94466. doi:10.1371/journal.pone.0094466

Liu, X.-T., Zhang, X., Wen, S., Peng, L., Hong, Q., and Kang, D. (2015). Impact of the Consolidated Standards of Reporting Trials (CONSORT) Checklist on Reporting of Randomized Clinical Trials in Traditional Chinese Medicine. *J. Evidence-Based Med.* 8 (4), 192–208. doi:10.1111/jebm.12173

Lu, F., Tang, J. Y., Zhao, Y., Li, Q. N., and Gao, R. (2018). Evaluation and Thinking of Placebo Simulation Effect in Clinical Trials of New Drugs of TCM. *Chin. J. Evid-based Med.* 18 (11), 1163–1168. doi:10.7507/1672-2531.201804065

Luo, D. (2012). Placebo Evaluation and Preparation Process Study of TCM Granules. Dissertation/Master's thesis. China: Chengdu University of TCM. doi:10.1002/9781118313367

Nakaya, K., Liu, J. J., and Guo, Y. M. (2003). Questions about Clinical Trials of TCM. *Introduction Jpn. Med.* 24 (02), 91–93.

Qi, G., We, D., Chung, L., and Fai, C. (2008). Placebos Used in Clinical Trials for Chinese Herbal Medicine. *Recent Pat Inflamm Allergy Drug Discov.* 2 (2), 123–127. doi:10.2174/187221308784543700

Song, J. J., Chen, T., Wu, J., and Yan, X. M. (2014). Preparation and Evaluation of Placebo for Chinese Herbal Decoction. *Liaoning J. Chin. Med.* 10, 2188–2189. doi:10.13192/j.issn.1000-1719.2014.10.067

Sun, M. Y., Lu, F., Zhao, Y., Chai, L. L., Li, Q. N., Zhang, J. B., et al. (2019). Placebo Preparation and Simulation Effect Evaluation of Ginkgo Biloba Dripping Pills. *Chin. Tradit. Herbal Drugs*. 50 (20), 4884–4888. doi:10.7501/j.issn.0253-2670.2019.20.007

Tang, X. D., Bian, L. Q., Gao, R., and Guan, S. J. (2009). Discussion on Placebo Preparation in Clinical Trials of TCM. *Chin. J. Integr. Tradit. Chin. West. Med.* 29 (07), 656–658.

Teschke, R., Wolff, A., Frenzel, C., Eickhoff, A., and Schulze, J. (2015). Herbal Traditional Chinese Medicine and its Evidence Base in Gastrointestinal Disorders. *World J. Gastroenterol.* 21 (15), 4466–4490. doi:10.3748/wjg.v21.i15.4466

Wang, G., Mao, B., Xiong, Z.-Y., Fan, T., Chen, X.-D., Wang, L., et al. (2007). The Quality of Reporting of Randomized Controlled Trials of Traditional Chinese Medicine: a Survey of 13 Randomly Selected Journals from mainland China. *Clin. Ther.* 29 (7), 1456–1467. doi:10.1016/j.clinthera.2007.07.023

Wang, R. R., Liu, Y. J., Yang, T. J., He, Z. X., and Wu, C. J. (2014). Thinking on Objective Quantification of Placebo Evaluation of Chinese Materia Medica. *World Sci. Technology/Modernization Traditional Chin. Med. Materia Med.* 16 (03), 485–489. doi:10.11842/wst.2014.03.005

Wang, X. F., Dong, D., Liu, F., Li, J., and Lu, Y. (2003). Preliminary Study on Placebo Preparation in Clinical Trial of Chinese Materia Medica. *Liaoning J. Chin. Med.* 30 (12), 966–967. doi:10.13192/j.ljtcm.2003.12.15.wangxf.008

Wang, Y. F., Ruan, X. M., Wu, H. L., Ou, A. H., Cao, B. J., Mu, Q. Y., et al. (2011). Study on the Preparation Method and Effect Evaluation of Chinese Materia Medica Placebo in Large-Scale Double-Blind Clinical Trial. *Tradit. Chin. Drug Res. Clin. Pharmacol.* 22 (03), 255–258. doi:10.19378/j.issn.1003-9783.2011.03.007

Yan, X. N., and Zhang, H. R. (2020). Preparation and Evaluation of Placebo for TCM Granules in Double-Blind Clinical Trials. *Food Drug* 22 (02), 108–111. doi:10.3969/j.issn.1672-979X.2020.02.005

Yang, T. T. (2014). Study on the Preparation Method and Effect Evaluation of Chinese Materia Medica Placebo in Large-Scale Double-Blind Clinical Trial. *Asia-pac. Tradit. Med.* 10 (23), 22–23.

Conflict of Interest: The authors declare that the research was conducted in the absence of any commercial or financial relationships that could be construed as a potential conflict of interest.

Copyright © 2021 Xiao, Ying, Zhao, Li, Zhao, Gao and Lu. This is an open-access article distributed under the terms of the Creative Commons Attribution License (CC BY). The use, distribution or reproduction in other forums is permitted, provided the original author(s) and the copyright owner(s) are credited and that the original publication in this journal is cited, in accordance with accepted academic practice. No use, distribution or reproduction is permitted which does not comply with these terms.

frontiers in Pharmacology

ORIGINAL RESEARCH
published: 25 June 2021
doi: 10.3389/fphar.2021.652989

Metabolic and Network Pharmacological Analyses of the Therapeutic Effect of *Grona styracifolia* on Calcium Oxalate-Induced Renal Injury

Wei Chen[1†], *Yachen Si*[1†], *Jin Cheng*[1†], *Jiarong Ding*[1], *Hongxia Zhao*[2], *Wenrui Liu*[1], *Qishan Lin*[3], *Jiebin Hou*[4*] and *Zhiyong Guo*[1*]

[1]*Department of Nephrology, Shanghai Changhai Hospital, Navy Medical University, Shanghai, China,* [2]*School of Pharmacy, Navy Medical University, Shanghai, China,* [3]*RNA Epitranscriptomics and Proteomics Resource, Department of Chemistry, University at Albany, Albany, NY, United States,* [4]*Department of Nephrology, The Second Medical Centre (National Clinical Research Center for Geriatric Diseases), Chinese PLA General Hospital, Beijing, China*

OPEN ACCESS

Edited by:
Yan Xu,
Cleveland State University,
United States

Reviewed by:
Yanming Wei,
Gansu Agricultural University, China
Chanderdeep Tandon,
Amity University, India

***Correspondence:**
Jiebin Hou
drhoujiebin@163.com
Zhiyong Guo
drguozhiyong@163.com

[†]*These authors have contributed equally to this work*

Specialty section:
This article was submitted to Ethnopharmacology, a section of the journal Frontiers in Pharmacology

Received: *13 January 2021*
Accepted: *07 June 2021*
Published: *25 June 2021*

Citation:
Chen W, Si Y, Cheng J, Ding J, Zhao H, Liu W, Lin Q, Hou J and Guo Z (2021) Metabolic and Network Pharmacological Analyses of the Therapeutic Effect of Grona styracifolia *on Calcium Oxalate-Induced Renal Injury. Front. Pharmacol. 12:652989. doi: 10.3389/fphar.2021.652989*

Grona styracifolia (Osbeck) Merr. (GS), a popular folk medicine, is clinically applied to treat nephrolithiasis. In this study, a urinary metabolic analysis was performed in a mouse model of renal calcium oxalate (CaOx) crystal deposition to identify the differentially altered metabolites in mice with oxalate-induced renal injury and explore the therapeutic mechanisms of GS against nephrolithiasis. Twenty-four mice were randomly divided into the control, oxalate and GS-treated groups. A metabolomics approach based on ultra-high-performance liquid chromatography coupled with quadrupole-time-of-flight mass spectrometry (UHPLC-Q-TOF/MS) was used to analyze the metabolic profiles of the urine samples. In addition, network pharmacology analysis was performed with different databases. As a result, the protective effects of GS were verified by measuring biochemical parameters and detecting crystal deposition. Fifteen metabolites were identified as the differentially altered metabolites in mice with crystal-induced renal injury. Most were involved in amino acid and fatty acid metabolism. Thirteen of these metabolites showed a reversal trend following GS treatment. A component-target-metabolite network was further constructed and nine overlapping target proteins of GS and the differentially altered metabolites were discovered. Among these proteins, the expression of estrogen receptor 2 (ESR2) in renal tissues was significantly down-regulated while androgen receptor (AR) expression was obviously increased in the oxalate group compared with the control group. These changes were reversed by the GS treatment. In conclusion, GS exerts its therapeutic effect by regulating multiple metabolic pathways and the expression of ESR and AR in mice with oxalate-induced renal injury.

Keywords: traditional medicine, biological network, metabolomics, integrative pharmacology, renal injury

Abbreviations: CaOx, calcium oxalate; GS, *Grona styracifolia* (Osbeck) Merr; H. Ohashi and K. Ohashi; UHPLC-Q-TOF/MS, ultra-high-performance liquid chromatography coupled with quadrupole-time-of-fight mass spectrometry; MS/MS, tandem mass spectrometry; RSD, relative standard derivation; ESI, electrospray ionization source; PCA, principle component analysis; PLS-DA, partial least squares discriminate analysis; VIP, variable importance in the projection; EIC, extracted ion chromatogram; TIC, total ion chromatogram; ESR2, estrogen receptor 2; AR, androgen receptor.

INTRODUCTION

Kidney stone disease, also known as nephrolithiasis, is a common disease jeopardizing the health of 7–13% of the population worldwide (Sorokin et al., 2017). Nephrolithiasis is considered a systemic disease because of its significant association with chronic kidney disease, cardiovascular events and metabolic syndrome (including type 2 diabetes, obesity, hypertension and dyslipidemia), as reported by numerous epidemiological studies (Sakhaee, 2008). Calcium oxalate (CaOx) is the most common inorganic matrix found in kidney stones and crystals. CaOx crystals, an early form of kidney stones, have also been shown to cause apoptosis in renal tubular cells (Mulay et al., 2013). The supersaturation of the urine is the first step in the formation of kidney crystals, followed by the progression of nucleation, growth and aggregation (Kolbach-Mandel et al., 2015). Renal injury induced by kidney stones has been observed throughout the process of stone formation. Metabolic disturbances are also promoted by crystal-induced renal injury. Thus, metabolic disturbances resulting from renal injury during crystal formation should be addressed.

Grona styracifolia (Osbeck) H. Ohashi and; K. Ohashi (GS), a popular traditional medicine (also known as "Guang Jin Qian Cao" in Chinese), is widely distributed in southern China and is clinically applied to treat nephrolithiasis. GS has been shown in a previous study to alleviate CaOx deposition in a murine model and has been reported to effectively relieve the apoptosis of tubular cells and prevent the oxidative stress changes induced by crystals (Zhou et al., 2018). However, no studies have been performed to evaluate the effects of GS on nephrolithiasis from the perspective of metabolism.

Metabolomics is a scientific study of the systemic metabolic changes in complex living systems in response to pathophysiological stimuli and has been effectively applied to reveal metabolic changes in diverse types of renal injury (Fan et al., 2018). In addition, the concept of network pharmacology has been developed due to the rapid development of bioinformatics. Network pharmacology is more effective for establishing a "compound-protein/gene-disease" network and revealing the regulatory effects of small molecules in a high-throughput manner. This approach is very powerful for the analysis of drug combinations, especially traditional medicinal herbs (Zhang et al., 2019). A combination of network pharmacology and metabolomics can establish the relationships of herb targets and endogenous metabolic responses to further reveal the molecular mechanisms of the herb based on a component-target-metabolite network. In the present study, a urinary metabolomics-based approach integrated with network pharmacology was conducted to investigate the potential effects of GS on a mouse model of crystalline nephropathy characterized by renal CaOx deposition.

MATERIALS AND METHODS

Preparation and Quality Control of GS

Grona styracifolia (Osbeck) H. Ohashi and K. Ohashi (GS) was purchased from Anguo (Hebei, China) and was authenticated by Prof. Lianna Sun (School of Pharmacy, Navy Medical University, Shanghai, China). The purchased herbs were extracted using standard methods according to the Chinese Pharmacopoeia (Yu et al., 2015). First, the entire GS plant was ground into a powder and was filtered through a 250 μm mesh. Next, 200 g of the powder was extracted with 1,000 ml of 80% methanol for 2 h using a ultrasonicator. The extract solution was filtered and then concentrated using a rotary evaporator, followed by drying to a powder under a vacuum at 60°C. The GS was parallel-extracted six times and the average yield of the methanol extract was 13.1% (w/w).

The ultra-high-performance liquid chromatography coupled with quadrupole-time-of-flight mass spectrometry (UHPLC-Q-TOF/MS) approach was used to test the reproducibility of GS extraction. Based on previous research and the literature (Zhou et al., 2012; Yu et al., 2015), four major constituents of GS, including schaftoside, isovitexin, luteolin, and apigenin, were selected for further analysis. The relative standard derivation (RSD) values of the peak areas of each component of the product were calculated in six parallel extracts of GS. The standard substances (NatureStandard, Shanghai, China) of these four constituents were also analyzed for comparison. A detailed description of the methodology is provided in the Supplemental Materials section (**Supplementary Methods S1**).

Cell Model and Treatment

The human proximal tubular cell line, HK-2 cells were obtained from the ATCC (Manassas, United States). Cells were incubated with sodium oxalate (NaOx) at 1 mM for 12 h to establish a cell model. Potassium citrate (K3Cit) is known for preventing the formation of kidney stone and was used as a positive control. HK-2 cells were divided into five groups (six wells per group): control groups (no treatment), model group (NaOx), K3Cit group (NaOx +1.0 mg/ml K3Cit), 25 μg/ml GS group (NaOx +25 μg/ml GS), 50 μg/ml GS group (NaOx +50 μg/ml GS) and 100 μg/ml GS group (NaOx +100 μg/ml GS). The levels of IL-6 and TNF-α in the cell supernatant were detected using ELISA kits (MultiSciences, Hangzhou, China). Simultaneously, lactate dehydrogenase (LDH) release was determined according to the instructions provided with the kits (Jiancheng Bioengineering, Nanjing, China).

Animal Experiment and Sample Collection

This experiment was approved by the Animal Ethics Committee of Navy Medical University (license: SCXK (Hu) 2017-0004) and was performed in accordance with the Guiding Principles for the Care and Use of Laboratory Animals. Twenty-four wild-type male C57B/L6 mice aged seven to eight weeks were purchased from the Shanghai SLAC Laboratory Animal Co., Ltd. (production license: SCXK (Hu) 2017-0005), provided with standard food and water, and housed at a temperature of 20–25°C and relative humidity of 55–65%. After one week, the 24 mice were randomly divided into four groups: the control group, oxalate group, oxalate + low dose GS group and oxalate + high dose GS group (n = 6).

The mice were intraperitoneally injected with 100 mg/kg glyoxylate once daily for seven days to establish the oxalate-induced renal injury model (n = 18), while the mice in the control

group received an equal volume of saline. Two days after the first injection of glyoxylate, the mice received a daily gastric perfusion of the GS extract at a low dose of 10 ml/kg (equivalent to 500 mg/kg body weight of the whole plant powder, $n = 6$) and a high dose of 2 0 ml/kg (equivalent to 1,000 mg/kg body weight of the whole plant powder, $n = 6$) for five consecutive days, while the mice in the control and oxalate groups received an equal volume of saline. After the last gavages, all the mice were placed in metabolic cages for 24 h to collect urine samples, which were stored at −80°C until the biochemical and metabolic analysis. Then, the mice were all anesthetized with sodium thiopental. Blood samples were collected and separated by centrifugation at 3,000 rpm for 10 min and stored at −80°C until the biochemical analysis. After *in situ* cardiac perfusion, the right kidneys were immediately removed and stored at −80°C until further biochemical analysis and western blot. Next, the left kidneys were removed and fixed with 10% buffered formalin for pathological analysis.

Biochemical Analysis and Detection of Crystal Deposition

Serum creatinine (SCr) and blood urea nitrogen (BUN) levels were detected using creatinine assay and urea assay kits, respectively (Jiancheng Bioengineering, Nanjing, Jiangsu, China). The urine calcium and creatinine levels were measured using kits (Jiancheng Bioengineering, Nanjing, Jiangsu, China) and the ratio of urine calcium to creatinine (UCa/Cr) was calculated. The renal tissues were placed in prechilled normal saline and phosphate-buffered saline (PBS, pH = 7.4) to produce 10% kidney homogenates. Then, calcium contents in renal tissues were determined with kits (Jiancheng Bioengineering, Nanjing, Jiangsu, China).

The kidney samples were embedded in paraffin and sectioned at a thickness of 3 μm. The deposition of CaOx crystals in representative sections was identified using a polarizing microscope.

Reverse Transcription-Quantitative Polymerase Chain Reaction

Total RNA was extracted from the renal tissues using TRIzol reagent (Invitrogen, Carlsbad, CA, United States) according to the manufacturer's instructions. The RNA concentration and purity were determined by measuring the absorbance at 260/280 nm. Reverse transcription kits (Vazyme, Nanjing, Jiangsu, China) were used to reverse transcribe RNA into cDNAs. The expression of kidney injury molecule 1 (KIM-1; forward: 5′-ATG AATCA-GATTCAAGTCTTC-3′ and reverse: 5′-TCTGGTTTG TGAGTCCATGTG-3′) was determined using the SYBR Green PCR kit (Yeasen, Shanghai, China).

UHPLC-Q-TOF/MS Analysis of Urine Samples

The UHPLC-Q-TOF/MS analysis was performed on an Agilent 1,290 Infinity LC system equipped with an Agilent 6,538 Accurate Mass Quadrupole Time-of-Flight mass spectrometer (Agilent Technologies, Santa Clara, CA, United States). Chromatographic separations were performed at 40°C on an ACQUITY UPLC HSS T3 column (2.1 mm × 100 mm, 1.8 μm, Waters, Milford, MA, United States). The mobile phase consisted of 0.1% formic acid (A) and ACN modified with 0.1% formic acid (B). The optimized UPLC elution conditions were as follows: 0–1 min, 2% B; 1–6 min, 2–20% B; 6–9 min, 20–50% B, 9–13 min, 50–95% B; and 13–15 min, 95% B. The post time was set to 5 min for system equilibration. The flow rate was set to 0.35 ml/min, and the injection volume was 4 μL. The auto-sampler was maintained at 4°C.

An electrospray ionization source (ESI) was used both in positive and negative mode. The optimized conditions were as follows: capillary voltage, 4 kV in the positive mode and 3.5 kV in the negative mode; drying gas flow, 11 L/min; gas temperature, 350°C; nebulizer pressure, 45 psig; fragmentor voltage, 120 V; and skimmer voltage, 60 V. Data were collected in the profile mode from 50 to 1,100 m/z. Potential metabolites were further analyzed using MS/MS, and the collision energy ranged from 10 to 40 eV.

Data Processing and Statistical Analysis

The raw UPLC data were converted into a common data format (mzData files) using Agilent Mass Hunter Qualitative software, in which the isotope interferences were excluded with a threshold set to 0.1%. The XCMS program (http://metlin.scripps.edu/download/) was used for peak detection, retention time (RT) alignment and peak integration to generate a visual data matrix. After filtering the ions based on an 80% rule, the data from each sample were normalized to the total intensity to correct for the MS response shift. Then, the three-dimensional data, including RT-m/z pair, sample name, and normalized ion intensity, were imported into SIMCA-P software (version 11.0, Umetrics, Umea, Sweden) for principle component analysis (PCA) and partial least squares discriminate analysis (PLS-DA). The variable importance in the projection (VIP) values were generated and represented the contribution to the intergroup discrimination of each metabolite ion. Metabolite ions with VIP values greater than 1.0 were selected for further analysis.

All data are presented as the means ± standard errors of the means (SEM). Statistical significance of the mean values was assessed using a one-way analysis of variance (ANOVA) or the Kruskal-Wallis H test as appropriate to assess differences among groups in SPSS 17.0 statistical software (SPSS Inc., Chicago, IL, United States) under the conditions of $p < 0.05$.

Identification of Metabolites

The identification of potential urinary metabolites is important and challenging. Therefore, we identified the mass metabolites in a stepwise manner. First, we confirmed the ions based on the extracted ion chromatogram (EIC). Second, we input the accurate molecular mass of the ions into online databases, such as Metlin (http://metlin.scripps.edu/), Human Metabolome Database (http://www.hmdb.ca/), and the Mass Bank (http://www.massbank.jp/), to search for possible metabolites. Third, we compared the MS/MS spectra with the MS/MS information from databases to verify the structure of some putative metabolites.

Network Analysis

The 15 main compounds of GS and their potential targets were acquired as described in our previous research (Hou et al., 2018). In the present study, the interacting proteins of differentially altered metabolites were further searched using the Search Tool for Interactions of Chemicals (STITCH, http://stitch.embl.de) database (Szklarczyk et al., 2016). Subsequently, the interacting proteins of differentially altered metabolites were pooled with the targets of components of GS to construct the component-target-metabolite network using Cytoscape software (http://cytoscape.org).

Western Blot

Acquired renal tissues were homogenized in lysis buffer (KeyGEN, Nanjing, China) containing protease inhibitors and phosphatase inhibitors. The lysates were centrifuged at 12,000 rpm for 5 min at 4°C and the supernatant was collected. The protein concentrations of mixed lysates were determined using a BCA protein assay kit (Thermo Fisher Scientific). Equal amounts of total protein were separated on SDS-PAGE gels and transferred onto nitrocellulose membranes (GE Healthcare Life Sciences). After blocking, the membrane was incubated with rabbit polyclonal anti-ESR2 (1:1,000, Boster Biological Technology), anti-ESR1 (1:1,000, Santa Cruz Biotechnology), anti-AR (1:500, Cloud-Clone), anti-MAOB (1:1,000, Wuhan USCN), anti-PGR (1:1,000, Abcam), anti-GBA (1:1,000, Wuhan USCN), anti-THRB (1:1,000, Abcam), anti-ALB (1:1,000, Cell Signaling Technology), anti-CMA1 (1:1,000, Wuhan USCN) and anti-GAPDH (1:1,000, Wuhan USCN) antibodies at 4°C overnight. After washes with TBST, the membrane was incubated with a fluorescent dye-conjugated secondary anti-rabbit antibody (1:10,000, Licor) for 60 min at room temperature. The signals were visualized using the Odyssey Infrared Imaging System (Licor, NE, United States) and quantitatively analyzed by normalizing them to GAPDH levels using ImageJ software.

Immunohistochemical Staining

For IHC staining, renal sections were incubated at 4°C overnight with primary antibodies against ESR2 (1:50; Cloud-clone, Wuhan, Hubei, China) and AR (1:50; Cloud-clone, Wuhan, Hubei, China), and then washed with PBS. The specimens were subsequently incubated with an HRP-conjugated goat anti-rabbit antibody (1:500, Proteintech, Chicago, IL, United States) at 37°C for 1 h. Next, the sections were stained with 3,3′-diaminobenzidine (DAB; Boster, Wuhan, Hubei, China) for 6 min.

RESULTS

Quality Control of the GS Extract

The GS was parallel-extracted six times, and an UHPLC-Q-TOF/MS approach was used to test the reproducibility of the extraction of GS. As shown in **Figures 1A,B**, the EIC of the four standard substances and the GS extraction visually showed a very similar profile of retention time, which demonstrated that all of these standard substances could be found in the GS extraction. Each RSD value of the peak area was below 3.2%, as shown in **Table 1**, which indicated that the UHPLC-Q-TOF system was stable and repeatable and that the extraction of GS was reproducible and reliable. Tandem mass spectrometry (MS/MS) was further performed and was shown to be matched between the standard substances and GS extraction (**Figures 1C,D**). More information about the MS/MS is provided in the Supplemental Materials section (**Supplementary Figure S1**).

Cell Model and Treatment

LDH is a cytoplasmic enzyme that can be released outside when cells are damaged or dead. The number of injured and dead cells is proportional to the level of LDH released to the culture medium. As shown in **Supplementary Figure S2A**, the release of LDH in NaOx-treated cells was significantly higher than that in the control group. The treatment of GS and K3Cit (as a positive control) significantly inhibited the LDH release stimulated by oxalate. The secretion of TNF-α and IL-6 of the oxalate-stimulated HK-2 cells was significantly increased, compared with nontreated cells. However, the secretion of these cytokines was significantly inhibited by the treatment of GS and K3Cit (**Supplementary Figures S2B,C**).

Biochemical Analysis

The levels of SCr, BUN, UCa/Cr, renal KIM-1 mRNA and the calcium contents in renal tissues in the oxalate group were markedly increased compared to the control group, but were significantly reduced by the GS treatment, especially at a high dose (**Figures 2A–E**).

Detection of Crystal Deposition

Using a polarizing microscope, CaOx crystal deposition was clearly present in the renal corticomedullary junction in the oxalate group, while the crystal deposition was obviously alleviated by the GS treatment, especially at a high dose (**Figure 2F**).

Metabolic Profile of Urine

A UHPLC-Q-TOF/MS analysis was performed in both positive and negative modes to explore the metabolic changes in the pathological process of oxalate-induced kidney injury and the mechanism of the protective effects of high-dose GS. As shown in the total ion chromatogram (TIC) and the corresponding spectra collected in positive mode of the control group, oxalate group and oxalate + high-dose GS group were similar (**Figure 3** and **Supplementary Figure S3**). After preprocessing the data, PCA was performed to extract systematic variations and to visualize the general relationships between the control group, oxalate group and oxalate + high-dose GS group (**Figure 4A** and **Supplementary Figure S4A**). Furthermore, PLS-DA was applied to screen the potential metabolites, and the three-dimensional score plot showed that the oxalate group was obviously separated from the control group (**Figure 4B** and **Supplementary Figure S4B**). However, the oxalate + high-dose GS group was close to the control group, revealing that GS rectified the metabolic deviations and protected against crystal-induced kidney injury.

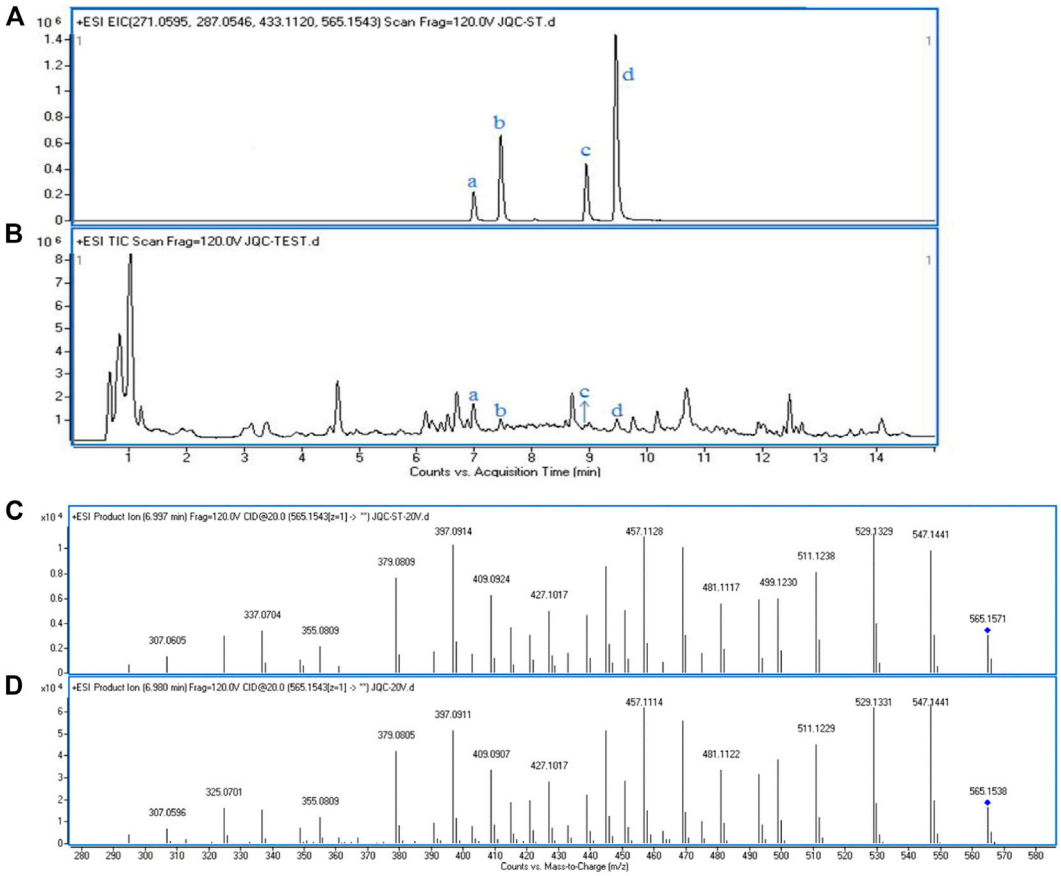

FIGURE 1 | The EICs and the MS/MS spectrum of standard substances and GS extraction. **(A)** EICs of four standard substances in positive mode. **(B)** Total ion chromatogram of GS extraction in positive mode: a. Schaftoside, b. Isovitexin, c. Luteolin, d. Apigenin. Tandem spectrum of standard, Schaftoside **(C)** and GS extraction **(D)** in positive mode.

TABLE 1 | The peak area and RSD values of components.

Compound	Schaftoside	Isovitexin	Luteolin	Apigenin
Area[a]	4984479.83 ± 84153.52	2769191 ± 69812.83	381927 ± 12104.72	696599.5 ± 17078.66
RSD (%)	1.69	2.52	3.17	2.45

[a]*The peak area of each standard substance.*

The MS-based identification of the potential metabolites was conducted using online databases. Fifteen metabolites that were differentially present between the control group and oxalate group were finally identified as differentially altered metabolites associated with crystal-induced renal injury (**Table 2**). Among these metabolites, creatine and pantothenic acid were verified based on the MS/MS spectra (**Figure 5**). These fifteen endogenous metabolites were mainly involved in amino acid metabolism and fatty acid metabolism. A metabolic network covering all of the differentially altered metabolites was constructed to comprehensively understand the metabolic disturbances that accompanied the occurrence of crystalline nephropathy (**Figure 6**). In addition, these differentially altered metabolites were further analyzed using network pharmacology.

Among the 15 metabolites associated with renal injury, the trends of 13 metabolites were reversed by the GS intervention. The level of L-tyrosine methyl ester decreased after oxalate stimulation and displayed a significant tendency to be reversed by GS treatment. In addition, levels of L-fucose increased considerably in response to oxalate stimulation and exhibited a significant tendency to be corrected to a normal level after GS treatment.

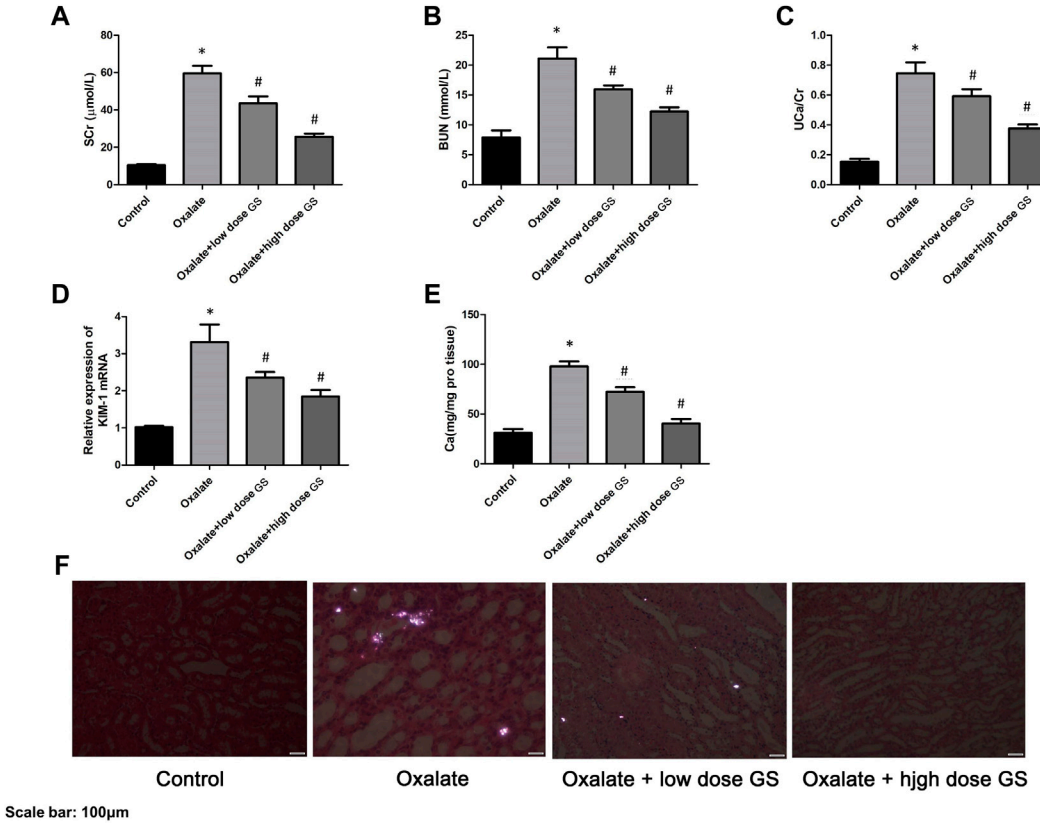

FIGURE 2 | GS protected renal function and alleviated crystal deposition. The levels of SCr **(A)** and BUN **(B)** in the serum, UCa/Cr **(C)** in the urine, renal KIM-1 mRNA **(D)** and calcium contents **(E)** in the renal tissues in the control group, oxalate group, oxalate + low-dose GS group, and oxalate + high-dose GS group. **(F)** Detection of renal CaOx crystal deposition in the four groups with a polarizing microscope. The results are presented as means ± SEM. Statistical comparisons were performed using a Newman-Keuls test (*$p < 0.05$ compared with the control group and $^{\#}p < 0.05$ compared with the oxalate group).

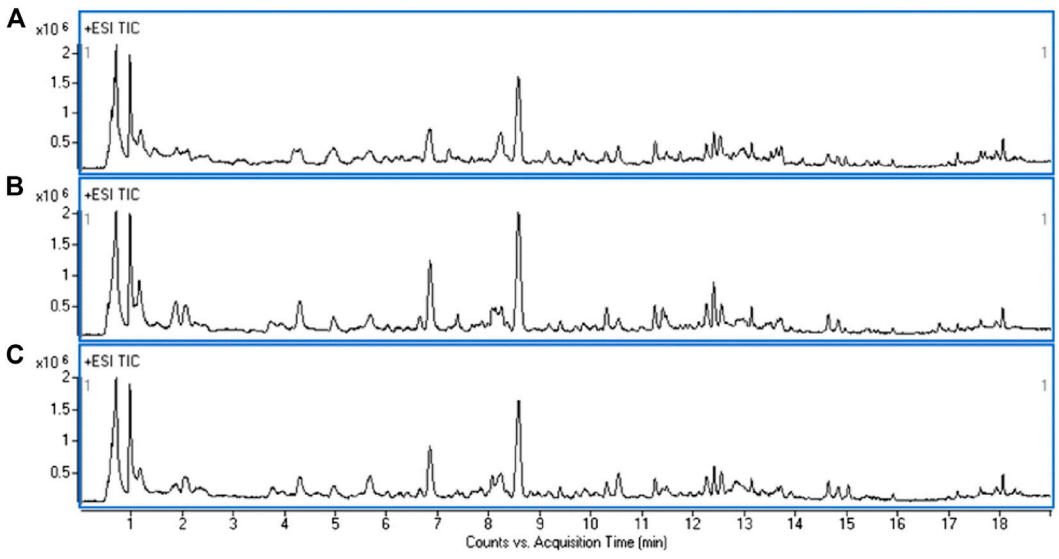

FIGURE 3 | Representative TIC obtained for the ESI-positive ion in the control group **(A)**, oxalate group **(B)** and oxalate + high-dose GS group **(C)**.

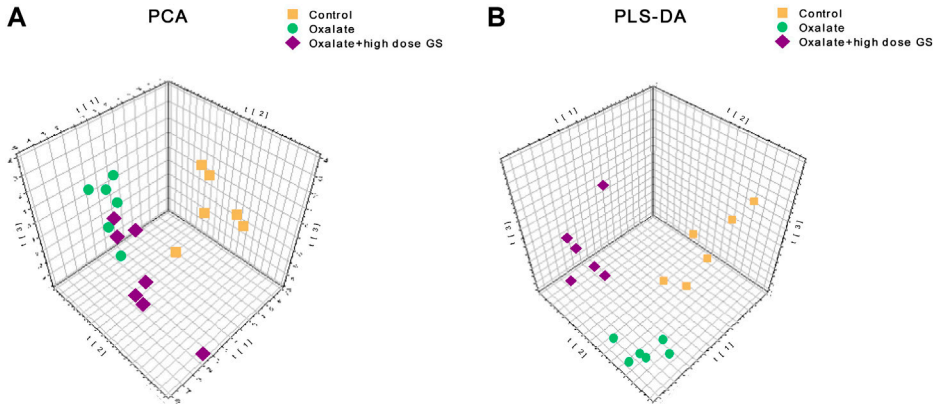

FIGURE 4 | PCA and PLS-DA score plots in ESI positive ion mode. **(A)** PCA score plots based on the urine metabolic profiles of the control group, oxalate group and oxalate + high-dose GS group. **(B)** PLS-DA score plots of urine samples obtained from the control group, oxalate group and oxalate + high-dose GS group.

Network Pharmacology Analysis

Potential targets of the components of GS were previously acquired using PharmMapper Server (Hou et al., 2018). Proteins that interacted with differentially altered metabolites were obtained from the STITCH database (**Supplementary Table S1**). Nine overlapping related proteins interacting with GS and metabolites were identified by constructing a Venn diagram (**Figure 7A**). A component-target-metabolite network was constructed with Cytoscape software to visually reveal the interactions among the components of GS, target proteins and differentially altered metabolites (**Figure 7B** and **Supplementary Table S2**). In the network, nine overlapping target proteins, including ESR2, ESR1, AR, MAOB, PGR, GBA, THRB, ALB and CMA1, were identified for further analysis. This network indicated that the components of GS might regulate multiple metabolic pathways through multiple targets to exert various therapeutic effects.

Validation of Potential Targets

The nine overlapping proteins were further verified by western blotting. As illustrated in **Supplementary Figure S5**, a significantly decreased level of ESR2 and increased level of AR were observed in the oxalate group. These changes were reversed by the GS treatment. However, the expression of the other seven overlapping proteins was not significantly different.

The expression of ESR2 and AR was further investigated using IHC staining, and the expression of ESR2 in the tubular cells was significantly decreased in the oxalate group compared with the control group, but was increased by the GS treatment, especially at a high dose (**Figure 8A**). In addition, AR expression in the nuclei of tubular cells was obviously increased in the oxalate group compared to the control group, and this change was reversed by GS, especially at a high dose (**Figure 8B**).

DISCUSSION

Amino Acid Metabolism

Amino acid metabolism participates in the processes of protein synthesis and degeneration, energy supply, gluconeogenesis, ketogenesis and biosynthesis of some signaling molecules. In the model group, the levels of several amino acids and their endogenous relative metabolites were noticeably changed. In our study, the involved pathways, including tyrosine metabolism, lysine metabolism, tryptophan metabolism, arginine metabolism and glutamate metabolism, were substantially altered.

As an essential amino acid in mammals, tryptophan was shown to play a notable role in the pathological processes of many kidney diseases, such as chronic kidney disease and nephrotoxicity, because it can be further transformed into many biological molecules and has an important function in homeostasis (Bossola and Tazza, 2015). In the model group, levels of L-tyrosine methyl ester, serotonin and 5-hydroxyindoleacetic acid, the endogenous biological derivative of tryptophan, were reduced (Fernandez-Canon et al., 2002). Based on our present work, we propose that the metabolism of these amino acids is inseparably connected with oxalate-induced renal injury. Levels of all of these amino acids were restored to the normal level after the intervention with GS, indicating that GS has therapeutic efficacy in maintaining normal tryptophan metabolism.

Tyrosine is a semi-essential amino acid in our body, along with tryptophan, and it is also an aromatic amino acid that has been documented to be associated with renal diseases (Zhan et al., 2002). In the model group, the levels of 3-methoxytyrosine and L-tyrosine methyl ester were significantly decreased. In contrast, GS treatment significantly increased the levels of those metabolites, suggesting that the disturbed metabolic state in the urine from mice with oxalate-induced crystal-related kidney injury was in the process of returning to normal after the GS intervention.

Both 1, 3-dimethyluracil and N2, N2-dimethylguanosine are metabolites of glutamic acid and were reduced in the model group. Meanwhile, they were shifted toward the baseline level in the control group after the GS treatment. Glutamic acid was recognized many years ago as a basic amino acid participating in protein biosynthesis that is converted into α-ketoglutarate through multiple pathways, and it is an essential metabolic intermediate in the tricarboxylic acid cycle (TCA) (Curthoys, 2001). Therefore, the changes in the levels of 1, 3-dimethyluracil

TABLE 2 | The differentially altered metabolites related to oxalate-induced nephrotoxicity and their metabolic pathways.

Class	No	Rt/min	Quasi-molecular ion (m/z)[a]		Ions	Error (ppm)	Formula	Metabolite	Assignment based on	VIP	Fold change[b]	
			Observed	Theoretical							Oxalate/ Control	High dose GS/Oxalate
Amino acids	1	0.68	132.0775	132.0768	[M + H]+	5	$C_4H_9N_3O_2$	Creatine	AM[c], TM[d]	1.76	[e]0.72	[e]1.94
	2	0.85	130.086	130.0863	[M + H]+	1	$C_6H_{11}NO_2$	L-Pipecolic acid	AM	1.31	[e]0.85	1.37
	3	8.03	194.0809	194.0823	[M-H]-	7	$C_{10}H_{13}NO_3$	L-Tyrosine methyl ester	AM	2.16	[e]0.36	[e]976.00
	4	4.81	212.092	212.0917	[M + H]+	1	$C_{10}H_{13}NO_4$	3-Methoxytyrosine	AM	1.45	[e]0.42	1.03
Organic acids and derivatives	5	3.83	188.0918	188.0917	[M + H]+	0	$C_8H_{13}NO_4$	2-Keto-6-acetamidocaproate	AM	1.05	[e]1.68	1.05
Aromatic heteromonocyclic compounds	6	0.9	141.0658	141.0659	[M + H]+	0	$C_6H_8N_2O_2$	1,3-Dimethyluracil	AM	1.66	[e]0.40	1.78
Aromatic heteropolycyclic compounds	7	7.49	214.0477	214.0475	[M + Na]+	1	$C_{10}H_9NO_3$	5-Hydroxyindoleacetic acid	AM	1.77	[e]0.69	5.08
	8	10.53	228.0634	228.0631	[M + Na]+	1	$C_{11}H_{11}NO_3$	5-Methoxyindoleacetate	AM	1.11	[e]2.44	2.27
	9	1.42	177.1018	177.1022	[M + H]+	2	$C_{10}H_{12}N_2O$	Serotonin	AM	1.58	[e]0.36	1.3
Lipids	10	1.01	182.0787	182.0788	[M + Na]+	0	$C_7H_{13}NO_3$	5-Acetamidopentanoate	AM	1.79	[e]3.91	0.29
	11	1.21	153.0654	153.0659	[M + H]+	0	$C_7H_8N_2O_2$	Prostaglandins	AM	1.13	[e]0.81	[e]1.06
	12	6.37	218.1389	218.1387	[M + H]+	0	$C_{10}H_{19}NO_4$	Propanoyl-carnitine	AM, +/−[f]	1.41	[e]1.82	0.81
Nucleosides	13	2.85	312.1308	312.1302	[M + H]+	0	$C_{12}H_{17}N_5O_5$	N_2,N_2-dimethylguanosine	AM	1.26	[e]0.56	1.41
Carbohydrates and carbohydrate conjugates	14	0.69	163.0601	163.0612	[M-H]-	6	$C_6H_{12}O_5$	L-fucose	AM	1.93	[e]2.84	[e]0.552
Aliphatic acyclic compounds	15	2.45	220.1182	220.1179	[M + H]+	0	$C_9H_{17}NO_5$	Pantothenic acid	AM, TM	1.58	[e]0.67	1.37

[a]*Quasi-molecular ions (m/z) in this table include three species, namely, [M + H]+ or [M + Na]+ (ES + mode) and [M–H] – (ES– mode).*

[b]*Statistical comparisons were performed using a Tukey post hoc test.*

[c]*Accurate mass.*

[d]*Tandem mass spectrometry.*

[e]$p < 0.05$.

[f]*ESI^+ and ESI^- mode cross-assist analysis.*

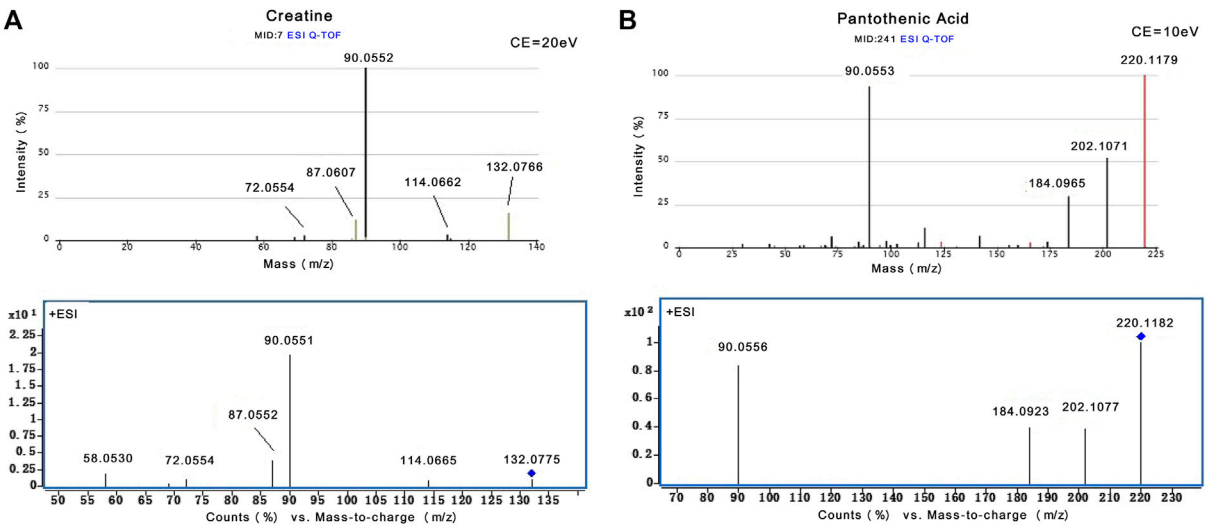

FIGURE 5 | The identification of creatine and pantothenic acid. **(A)** MS/MS spectra of creatine from Metlin database and actual collection (m/z 132.08). **(B)** MS/MS spectra of pantothenic acid from Metlin database and actual collection (m/z 220.12).

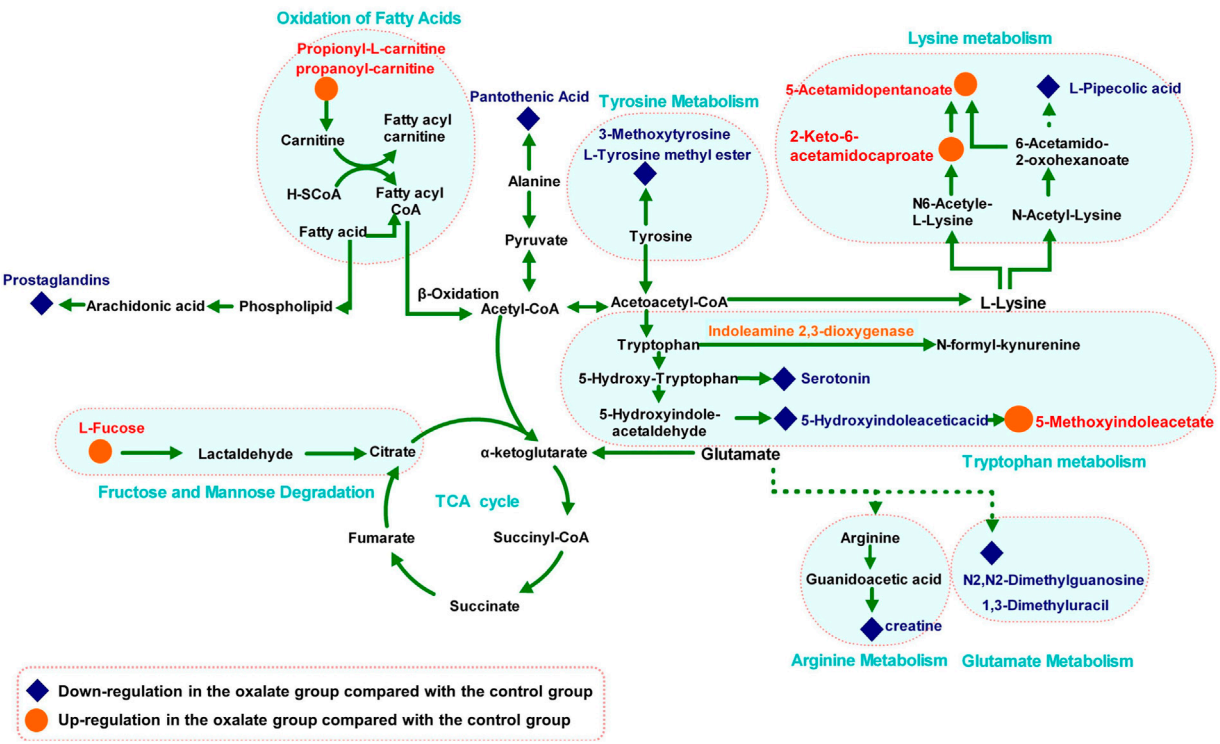

FIGURE 6 | Metabolic pathway network related to oxalate crystal-induced kidney injury. The levels of metabolites in the oxalate group compared with those in the control group are labeled in red (up-regulated) and blue (down-regulated).

and N2, N2-dimethylguanosine may indicate that energy metabolism was affected during the pathological process.

L-arginine plays important roles in the body, as it participates in the disposal of ammonia and is converted to glucose and glycogen under conditions of an inadequate energy supply. Furthermore, arginine is also the precursor of creatine in the urea cycle (Karamat et al., 2015). Levels of serotonin, creatinine and pantothenic acid, the metabolic derivatives of arginine, were decreased in the crystal kidney injury group. Arginine is transformed into acetyl-coenzyme A through pyruvate, which

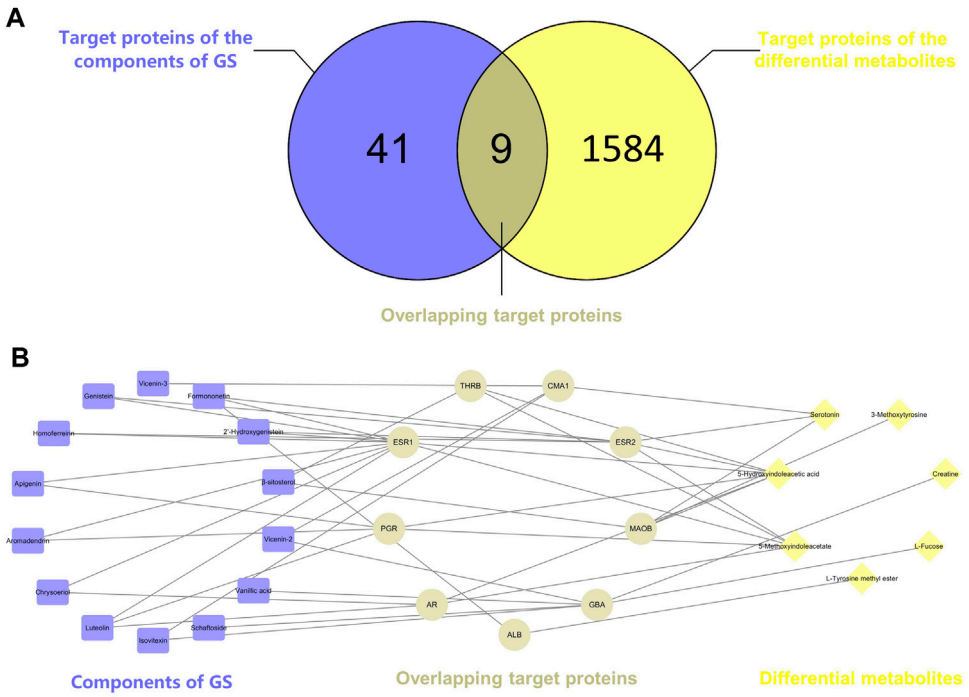

FIGURE 7 | (A) Venn diagram. The intersection of two circles represents the overlapping target proteins of the components of GS and the differentially altered metabolites. **(B)** The component-target-metabolite network in the treatment of oxalate-induced kidney injury by GS. The purple nodes (14) represent the components of GS, the yellow nodes **(C)** represent the differentially altered metabolites, and the gray nodes **(D)** represent the overlapping proteins.

acts as the starting point for a series of physiological reactions known as the TCA (Schneider et al., 2011). The abnormal levels of these metabolites were rectified by GS, which further normalized amino acid metabolism. Therefore, we have many reasons to speculate that the therapeutic efficacy of the targeted GS intervention against crystal-induced kidney injury is mainly mediated by normalizing the disordered TCA through changes in the arginine and glutamate metabolic pathways.

Fatty Acid Metabolism

Fatty acid metabolism has a direct relationship with the energy supply in organisms through fat mobilization and β-oxidation. In this process, L-carnitine is a key factor because it helps transport long-chain fatty acids into the mitochondrial matrix for the utilization of fatty acids through β-oxidation (Knottnerus et al., 2018). Therefore, an increased intracellular level of carnitine provides an additional energy supply. In the model group, levels of propionyl-L-carnitine, a product of the enzymatic esterification of carnitine, increased significantly, which indicated the presence of a pathological process induced by the glyoxylate intervention. The subsequent CaOx deposition pushed the organism into a high metabolic state to satisfy the energy requirement by increasing the β-oxidation process in the mitochondria. However, large quantities of reactive oxidants were produced during the process of β-oxidation, leading to severe oxidative injury to the renal epithelial cells. Following treatment with GS, the increased propionyl-L-carnitine level was significantly reduced, suggesting that the disordered fatty acid metabolism induced by glyoxylate was in the process of returning to a normal state.

Component-Target-Metabolite Network Analysis

According to the network construction, we identified nine overlapping proteins might play important roles in the therapeutic effects of GS on CaOx crystal-induced renal injury. Interestingly, ESR1, ESR2 and AR are the predicted targets of the components of GS among these overlapping targets. Since nephrolithiasis is more common in men than in women, sex hormones and their receptors may play important roles in kidney stone formation and CaOx crystal-induced renal injury. Estrogen has been indicated to protect against kidney stone formation by lowering urinary CaOx saturation through a decrease in the urinary excretion of calcium and oxalate (Heller et al., 2002). In addition, ESR2 was reported to suppress renal CaOx crystal deposition by reducing hepatic oxalate biosynthesis and to alleviate crystal-induced injury by inhibiting reactive oxygen species production (Zhu et al., 2019b). However, androgen and AR signaling may promote kidney stone formation and aggravate renal injury since the plasma testosterone level and AR expression in the kidneys are up-regulated in men with nephrolithiasis (Li et al., 2010). Similarly, a previous study suggested that AR increased

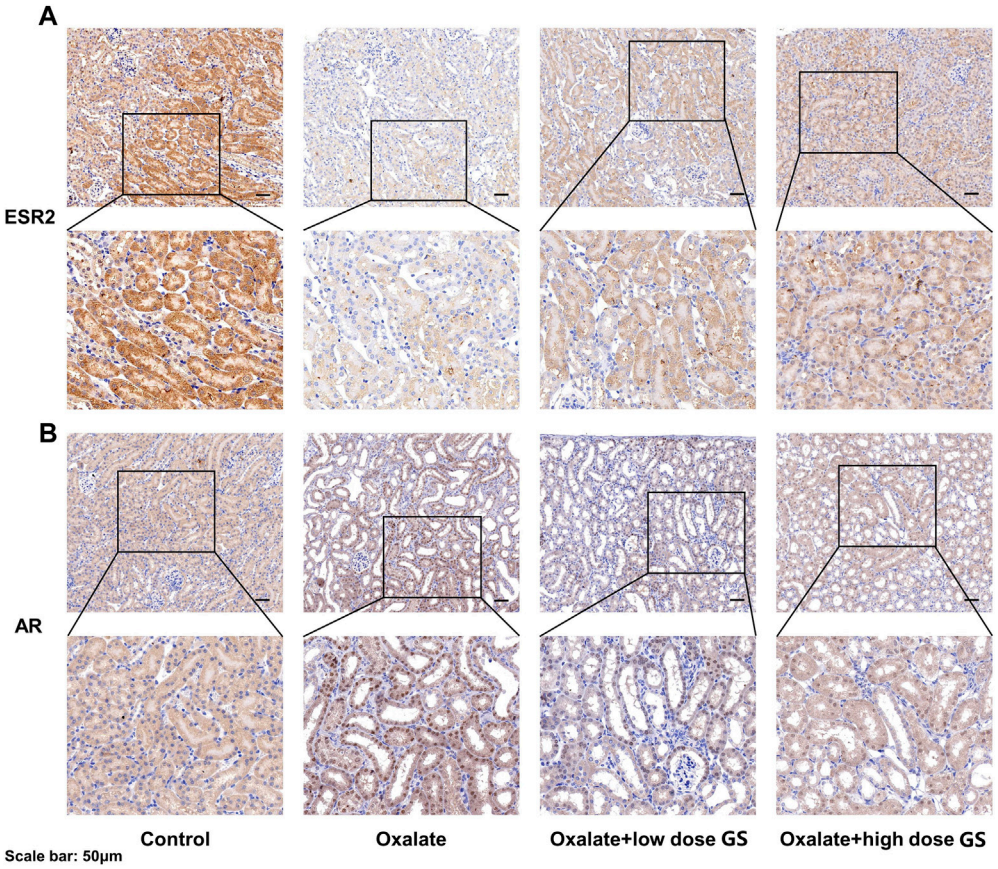

FIGURE 8 | The expression of ESR2 **(A)** and AR **(B)** in the renal tissues from the control group, oxalate group, oxalate + low-dose GS group, and oxalate + high-dose GS group detected using IHC staining.

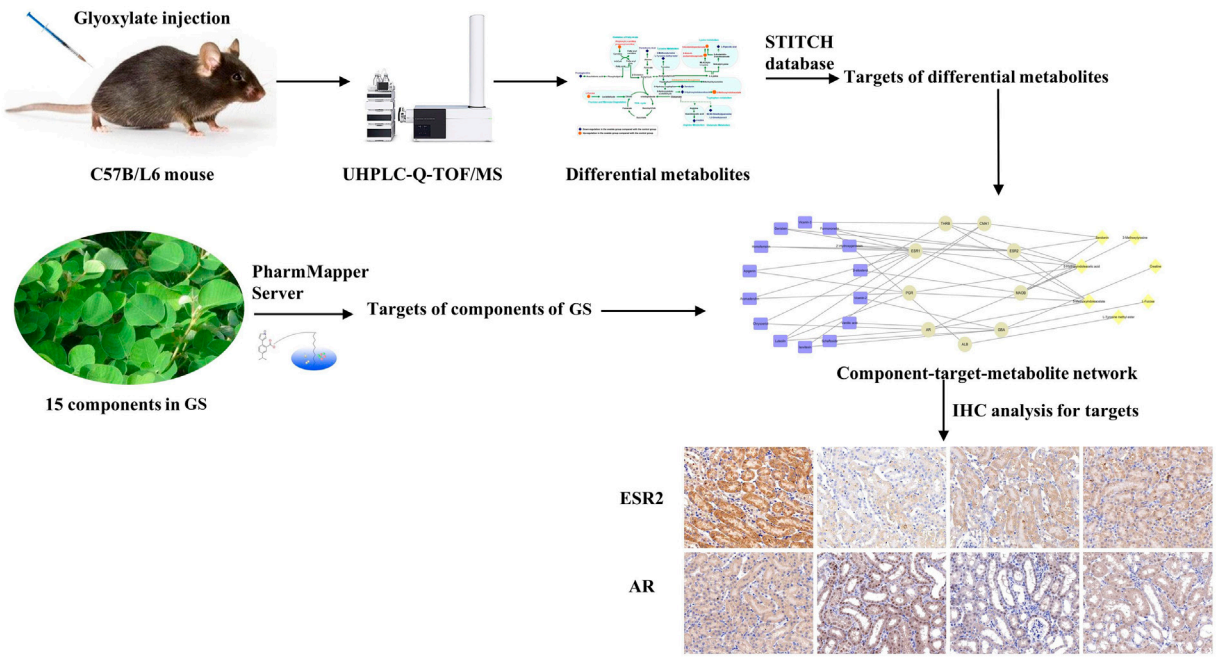

FIGURE 9 | Roadmap of this study.

CaOx crystal deposition by increasing oxalate biosynthesis and oxidative stress (Liang et al., 2014). Moreover, the loss of AR suppressed renal CaOx crystal deposition by promoting M2 macrophage recruitment/polarization (Zhu et al., 2019a). In our study, ESR2 expression in renal tissues was down-regulated while the AR expression in the nuclei of tubular cells was increased in the oxalate group compared with the control group, changes that were reversed by GS. Therefore, we speculated that GS might exert its protective effect on CaOx crystal-induced renal injury by activating ESR2 and decreasing the nuclear translocation of AR.

CONCLUSION

In the present study, GS was verified to alleviate renal injury induced by CaOx. The roadmap of this study is shown in **Figure 9**. We employed an integrative pharmacology-based strategy combining network pharmacology and metabolomics to decipher the underlying mechanism. Fifteen metabolites involved in amino acid and fatty acid metabolism were identified as potential biomarkers of crystal-induced renal damage and the changes in the levels of 13 metabolites were reversed by the GS intervention. By integrating network pharmacology, a component-target-metabolite network was constructed. Among the nine overlapping target proteins, two crucial targets (ESR2 and AR) were differentially expressed in the kidney of oxalate group, but these trends were reversed by the GS treatment. In conclusion, GS exerts its therapeutic effect by regulating multiple metabolic pathways and the expression of ESR and AR in mice with oxalate-induced renal injury. Our findings might help us consider novel potential targets when treating nephrolithiasis and obtain a better understanding of the mechanism underlying the curative effect of GS.

DATA AVAILABILITY STATEMENT

The raw data supporting the conclusion of this article will be made available by the authors, without undue reservation.

ETHICS STATEMENT

The animal study was reviewed and approved by the Animal Ethics Committee of Navy Medical University.

AUTHOR CONTRIBUTIONS

Conceptualization, WC; methodology, JC and HZ; software, YS and JH; validation, WL; formal analysis, QL; investigation, JC; data curation, YS and JD; writing and editing, JH; project administration, ZG and WC; funding acquisition, ZG, WC, and JH.

FUNDING

This study was supported by grants from the National Natural Science Foundation of China (Nos. 81903962 and 82070692), and Panfeng project of Changhai hospital (No. 2019YXK043).

SUPPLEMENTARY MATERIAL

The Supplementary Material for this article can be found online at: https://www.frontiersin.org/articles/10.3389/fphar.2021.652989/full#supplementary-material

REFERENCES

Bossola, M., and Tazza, L. (2015). Fatigue and Plasma Tryptophan Levels in Patients on Chronic Hemodialysis. *Kidney Int.* 88, 637. doi:10.1038/ki.2015.186

Curthoys, N. P. (2001). Role of Mitochondrial Glutaminase in Rat Renal Glutamine Metabolism. *J. Nutr.* 131, 2491S–2495S. Discussion 2496S-2497S. doi:10.1093/jn/131.9.2491s

Fan, W., Hou, J., Zhu, W., Zhang, S., Shao, K., Quan, F., et al. (2018). The Mechanism of the Preventive Effect of Shen'an Capsule on the Calcium Oxalate crystal-induced Early Renal Injury Based on Metabolomics. *Biomed. Chromatogr.* 32, e4374. doi:10.1002/bmc.4374

Fernández-Cañón, J. M., Baetscher, M. W., Finegold, M., Burlingame, T., Gibson, K. M., and Grompe, M. (2002). Maleylacetoacetate Isomerase (MAAI/GSTZ)-deficient Mice Reveal a Glutathione-dependent Nonenzymatic Bypass in Tyrosine Catabolism. *Mol. Cel Biol* 22, 4943–4951. doi:10.1128/mcb.22.13.4943-4951.2002

Heller, H. J., Sakhaee, K., Moe, O. W., and Pak, C. Y. C. (2002). Etiological Role of Estrogen Status in Renal Stone Formation. *J. Urol.* 168, 1923–1927. doi:10.1016/s0022-5347(05)64264-4

Hou, J., Chen, W., Lu, H., Zhao, H., Gao, S., Liu, W., et al. (2018). Exploring the Therapeutic Mechanism of Desmodium Styracifolium on Oxalate Crystal-Induced Kidney Injuries Using Comprehensive Approaches Based on Proteomics and Network Pharmacology. *Front. Pharmacol.* 9, 620. doi:10.3389/fphar.2018.00620

Karamat, F. A., Van Montfrans, G. A., and Brewster, L. M. (2015). Creatine Synthesis Demands the Majority of the Bioavailable L-Arginine. *J. Hypertens.* 33, 2368. doi:10.1097/HJH.0000000000000726

Knottnerus, S. J. G., Bleeker, J. C., Wust, R. C. I., Ferdinandusse, S., IJlst, L., Wijburg, F. A., et al. (2018). Disorders of Mitochondrial Long-Chain Fatty Acid Oxidation and the Carnitine Shuttle. *Rev. Endocr. Metab. Disord.* 19, 93–106. doi:10.1007/s11154-018-9448-1

Kolbach-Mandel, A. M., Kleinman, J. G., and Wesson, J. A. (2015). Exploring Calcium Oxalate Crystallization: a Constant Composition Approach. *Urolithiasis* 43, 397–409. doi:10.1007/s00240-015-0781-5

Li, J.-Y., Zhou, T., Gao, X., Xu, C., Sun, Y., Peng, Y., et al. (2010). Testosterone and Androgen Receptor in Human Nephrolithiasis. *J. Urol.* 184, 2360–2363. doi:10.1016/j.juro.2010.08.009

Liang, L., Li, L., Tian, J., Lee, S. O., Dang, Q., Huang, C.-K., et al. (2014). Androgen Receptor Enhances Kidney Stone-CaOx Crystal Formation via Modulation of Oxalate Biosynthesis & Oxidative Stress. *Mol. Endocrinol.* 28, 1291–1303. doi:10.1210/me.2014-1047

Mulay, S. R., Kulkarni, O. P., Rupanagudi, K. V., Migliorini, A., Darisipudi, M. N., Vilaysane, A., et al. (2013). Calcium Oxalate Crystals Induce Renal Inflammation by NLRP3-Mediated IL-1β Secretion. *J. Clin. Invest.* 123, 236–246. doi:10.1172/jci63679

Sakhaee, K. (2008). Nephrolithiasis as a Systemic Disorder. *Curr. Opin. Nephrol. Hypertens.* 17, 304–309. doi:10.1097/mnh.0b013e3282f8b34d

Schneider, R., Meusel, M., Betz, B., Kersten, M., Möller-Ehrlich, K., Wanner, C., et al. (2011). Nitric Oxide-Induced Regulation of Renal Organic Cation

Transport after Renal Ischemia-Reperfusion Injury. *Am. J. Physiology-Renal Physiol.* 301, F997–F1004. doi:10.1152/ajprenal.00264.2011

Sorokin, I., Mamoulakis, C., Miyazawa, K., Rodgers, A., Talati, J., and Lotan, Y. (2017). Epidemiology of Stone Disease across the World. *World J. Urol.* 35, 1301–1320. doi:10.1007/s00345-017-2008-6

Szklarczyk, D., Santos, A., von Mering, C., Jensen, L. J., Bork, P., and Kuhn, M. (2016). STITCH 5: Augmenting Protein-Chemical Interaction Networks with Tissue and Affinity Data. *Nucleic Acids Res.* 44, D380–D384. doi:10.1093/nar/gkv1277

Yu, J., Ma, Y., Wang, P., Wang, L., Wang, X., Wang, Z., et al. (2015). *Chinese Pharmacopoeia*. Beijing: China Medical Science Press, 44–45.

Zhan, Y., Kim, S., Kawano, H., and Iwao, H. (2002). Enhancement of Glomerular Platelet-Derived Growth Factor β-Receptor Tyrosine Phosphorylation in Hypertensive Rats and its Inhibition by Calcium Channel Blocker. *Hypertens. Res.* 25, 295–301. doi:10.1291/hypres.25.295

Zhang, R., Zhu, X., Bai, H., and Ning, K. (2019). Network Pharmacology Databases for Traditional Chinese Medicine: Review and Assessment. *Front. Pharmacol.* 10, 123. doi:10.3389/fphar.2019.00123

Zhou, C., Luo, J.-G., and Kong, L.-Y. (2012). Quality Evaluation of Desmodium Styracifolium Using High-Performance Liquid Chromatography with Photodiode Array Detection and Electrospray Ionisation Tandem Mass Spectrometry. *Phytochem. Anal.* 23, 240–247. doi:10.1002/pca.1349

Zhou, J., Jin, J., Li, X., Zhao, Z., Zhang, L., Wang, Q., et al. (2018). Total Flavonoids of Desmodium Styracifolium Attenuates the Formation of Hydroxy-L-Proline-Induced Calcium Oxalate Urolithiasis in Rats. *Urolithiasis* 46, 231–241. doi:10.1007/s00240-017-0985-y

Zhu, W., Zhao, Z., Chou, F. J., Zuo, L., Liu, T., Bushinsky, D., et al. (2019b). The Protective Roles of Estrogen Receptor β in Renal Calcium Oxalate Crystal Formation via Reducing the Liver Oxalate Biosynthesis and Renal Oxidative Stress-Mediated Cell Injury. *Oxid Med. Cel Longev* 2019, 5305014. doi:10.1155/2019/5305014

Zhu, W., Zhao, Z., Chou, F., Zuo, L., Liu, T., Yeh, S., et al. (2019a). Loss of the Androgen Receptor Suppresses Intrarenal Calcium Oxalate Crystals Deposition via Altering Macrophage recruitment/M2 Polarization with Change of the miR-185-5p/CSF-1 Signals. *Cell Death Dis* 10, 275. doi:10.1038/s41419-019-1358-y

Conflict of Interest: The authors declare that the research was conducted in the absence of any commercial or financial relationships that could be construed as a potential conflict of interest.

Copyright © 2021 Chen, Si, Cheng, Ding, Zhao, Liu, Lin, Hou and Guo. This is an open-access article distributed under the terms of the Creative Commons Attribution License (CC BY). The use, distribution or reproduction in other forums is permitted, provided the original author(s) and the copyright owner(s) are credited and that the original publication in this journal is cited, in accordance with accepted academic practice. No use, distribution or reproduction is permitted which does not comply with these terms.

frontiers in Pharmacology

ORIGINAL RESEARCH
published: 25 June 2021
doi: 10.3389/fphar.2021.601846

Exploring the Regulatory Mechanism of *Hedysarum Multijugum Maxim.-Chuanxiong Rhizoma* Compound on HIF-VEGF Pathway and Cerebral Ischemia-Reperfusion Injury's Biological Network Based on Systematic Pharmacology

Kailin Yang[1†], *Liuting Zeng*[1†], *Anqi Ge*[2†], *Yi Chen*[1†], *Shanshan Wang*[1†], *Xiaofei Zhu*[1,3†] *and Jinwen Ge*[1,4*]

[1]*Key Laboratory of Hunan Province for Integrated Traditional Chinese and Western Medicine on Prevention and Treatment of Cardio-Cerebral Diseases, Hunan University of Chinese Medicine, Changsha, China,* [2]*Galactophore Department, The First Hospital of Hunan University of Chinese Medicine, Changsha, China,* [3]*School of Graduate, Central South University, Changsha, China,* [4]*Shaoyang University, Shaoyang, China*

OPEN ACCESS

Edited by:
Takashi Sato,
Tokyo University of Pharmacy and Life Sciences, Japan

Reviewed by:
Hui Zhao,
Capital Medical University, China
Maria Luisa Del Moral,
University of Jaén, Spain

***Correspondence:**
Jinwen Ge
001267@hnucm.edu.cn

[†]*These authors share first authorship*

Specialty section:
This article was submitted to Ethnopharmacology, a section of the journal Frontiers in Pharmacology

Received: *01 September 2020*
Accepted: *17 May 2021*
Published: *25 June 2021*

Citation:
Yang K, Zeng L, Ge A, Chen Y, Wang S, Zhu X and Ge J (2021) Exploring the Regulatory Mechanism of Hedysarum Multijugum Maxim.-Chuanxiong Rhizoma *Compound on HIF-VEGF Pathway and Cerebral Ischemia-Reperfusion Injury's Biological Network Based on Systematic Pharmacology. Front. Pharmacol. 12:601846. doi: 10.3389/fphar.2021.601846*

Background: Clinical research found that *Hedysarum Multijugum Maxim.-Chuanxiong Rhizoma* Compound (HCC) has definite curative effect on cerebral ischemic diseases, such as ischemic stroke and cerebral ischemia-reperfusion injury (CIR). However, its mechanism for treating cerebral ischemia is still not fully explained.

Methods: The traditional Chinese medicine related database were utilized to obtain the components of HCC. The Pharmmapper were used to predict HCC's potential targets. The CIR genes were obtained from Genecards and OMIM and the protein-protein interaction (PPI) data of HCC's targets and IS genes were obtained from String database. After that, the DAVID platform was applied for Gene Ontology (GO) enrichment analysis and pathway enrichment analysis. Finally, a series of animal experiments were carried out to further explore the mechanism of HCC intervention in CIR.

Results: The prediction results of systematic pharmacology showed that HCC can regulate CIR-related targets (such as AKT1, MAPK1, CASP3, EGFR), biological processes (such as angiogenesis, neuronal axonal injury, blood coagulation, calcium homeostasis) and signaling pathways (such as HIF-1, VEGF, Ras, FoxO signaling). The experiments showed that HCC can improve the neurological deficit score, decrease the

Abbreviations: CIR, cerebral ischemia-reperfusion injury; DL, drug-likeness; GO, Gene Ontology; HCC, Hedysarum Multijugum Maxim.-Chuanxiong Rhizoma Compound; HPLC, high performance liquid chromatography; IRI, Ischemia-reperfusion injury; MVD, microvessel density; NMDA, N-methyl-D-aspartic acid; OB, oral bioavailability; PPI, protein-protein interaction; RT-PCR, Reverse Transcription-Polymerase Chain Reaction; TCM, traditional Chinese medicine; TNF, tumor necrosis factor; TXB2, thromboxane B2.

volume of cerebral infarction and up-regulate the expression of HIF-1α/VEGF and VEGFR protein and mRNA ($p < 0.05$).

Conclusion: HCC may play a therapeutic role by regulating CIR-related targets, biological processes and signaling pathways found on this study.

Keywords: hedysarum multijugum maxim-chuanxiong rhizoma compound, cerebral ischemia-reperfusion injury, Ischemic stroke, cerebral ischemia, HIF-VEGF pathway, systematic pharmacology, chinese medicine

INTRODUCTION

Cerebrovascular disease is a common disease in the clinic, which seriously endangers human health and life. As the population of aging increases, the morbidity, mortality and disability rate of cerebrovascular disease were increasing year by year (Thomas, 1996; Sacco and Rundek, 2012; Liu et al., 2015). Among them, ischemic cerebrovascular disease accounts for a large proportion. The key to cerebral ischemia treatment is to quickly restore cerebral blood perfusion and maintain smooth blood flow (Frizzell, 2005; Behravan et al., 2014). However, the brain injury may be further aggravated after the restoration of blood flow perfusion, that is cerebral ischemia-reperfusion injury (CIR). Ischemia-reperfusion injury (IRI) refers to the pathological phenomenon that the degree of tissue damage is increased after the blood supply to the ischemic tissue is restored for a certain period of time (Wu et al., 2018). The harm of CIR is huge. It involves many complicated links and factors, which has been the focus of scientists' research for many years. With the deepening of the research, while looking for neuroprotective drugs, a variety of comprehensive intervention strategies for CIR such as mild hypothermia, atmospheric hyperbaric therapy and ischemic preconditioning and ischemic postconditioning were also proposed (Lapi and Colantuoni, 2015; Patel and McMullen, 2017; Leech et al., 2019); the drugs include: N-methyl-D-aspartic acid (NMDA) receptor antagonist, Ca_2 + channel blocker, ICAM-1 antibody, CDP-choline, and so on (Lapi and Colantuoni, 2015; Patel and McMullen, 2017). At present, natural plant ingredients have been found to improve microcirculation barriers after CIR, and Chinese medicine formulations have gradually become a new direction for new drug development (Wang et al., 2019).

Hedysarum Multijugum Maxim.-Chuanxiong Rhizoma Compound (HCC) was first used by the First Affiliated Hospital of Hunan University of Chinese Medicine. Clinical research showed that HCC has definite curative effect on cerebral ischemic diseases (such as ischemic stroke and CIR), and its clinical effective rate is over 90% (Ge, 2014). This Chinese medicine formula is composed of *Hedysarum Multijugum Maxim.* [*Leguminosae; Astragali Radix* (Huang Qi)], *Ligusticum striatum DC.* [*Apiaceae; Chuanxiong Rhizoma* (Chuan Xiong)], *Pheretima Aspergillum (E.Perrier)* [*Megascolecidae*; *Pheretima* (Di Long)], *Bombyx Batryticatus* [A desiccated body formed by the 4–5 instar larvae of *Bombyx mori Linnaeus* (family: *Bombycidae*) infected with white *Beauveria bassiana (Bals.) Vuillant*; (Jiang Can)], and can reduce serum tumor necrosis factor (TNF) -α and plasma thromboxane B2 (TXB2) levels and increase plasma 6-Keto-PGF1α (He et al., 2002). Our previous research also found that HCC can protect neurons in the hippocampal CA_2 region by regulating Fpn expression to balance iron levels after cerebral ischemia. This suggests that imbalance of intracellular iron balance may be a new mechanism of cerebral ischemia (Liao et al., 2015). However, the mechanism of HCC in treating cerebral ischemia is still not fully explained. Systematic pharmacology is an emerging discipline based on the intersection and integration of multidisciplinary technologies such as classic pharmacology, computer technology, bioinformatics, and network pharmacology, which systematically studies the interactions between drugs and the human body at multiple levels, including molecules, cells, organs, and networks (Zeng et al., 2017; Zeng and Yang, 2017; Bao et al., 2019; Yang et al., 2019a; Yang et al., 2019b). Our previous research used systematic pharmacological strategies to reveal the mechanism of Chinese medicine formula in the treatment of complex diseases in the fields of oncology and cardiovascular (Zeng et al., 2017; Zeng and Yang, 2017; Bao et al., 2019; Yang et al., 2019a; Yang et al., 2019b). Therefore, this study hopes to reveal the complex mechanism of HCC through a systematic pharmacology strategy (integrating network pharmacology experimental pharmacology).

MATERIALS AND METHODS

HCC's Compounds Collection

The components of HCC were collected from the traditional Chinese Medicine (TCM) Database at Taiwan (http://tcm.cmu.edu.tw/zh-tw/) (Chen et al., 2014) and the Traditional Chinese Medicine Systems Pharmacology Database (TcmSPTM, http://tcmspw.com/tcmsp.php) (Ru et al., 2014). The components with oral bioavailability (OB) ≥ 30%, Caco-2 permeability > −0.4 and drug-likeness (DL) ≥ 0.18 were considered as the potential bioactive compounds of HCC (Walters and Murcko, 2002; Ano et al., 2004; Hu et al., 2009; Xu et al., 2012; Ru et al., 2014). Meanwhile, since the application of biological models to predict HCC compounds has limitations (Metodiewa et al., 1997), a large number of references were searched to supplement oral absorbable compounds with pharmacological activity (Shi et al., 2014; Tong et al., 2019). The components of HCC were shown in **Table 1**.

HCC's Potential Targets Prediction and CIR Genes Collection

The molecular structure was drawn by ChemBioDraw according to their structure in SciFinder (http://scifinder.cas.org) and saved

TABLE 1 | Components of HCC.

Drug name	Species	Family	Components
Astragali Radix (Huang Qi)	*Hedysarum Multijugum Maxim*	*Leguminosae*	1,7-Dihydroxy-3,9-dimethoxy pterocarpene, 3,9-di-O-methylnissolin, 64474–51-7, 64997–52-0, 73340–41-7, 7-O-methylisomucronulatol, astragaloside IV, Bifendate, Calycosin, Calycosin 7-O-glucoside, Formononetin, Hederagenin, Isodalbergin, Isorhamnetin, Jaranol, Kaempferol, Mairin, Ononin, Quercetin
Chuanxiong Rhizoma (Chuan Xiong)	*Ligusticum striatum DC.*	*Apiaceae*	Butylidenephthalide, Butylphthalide, Chlorogenic acid, Coniferyl Ferulate, Ferulic acid, Ligustilide, Ligustrazine, Mandenol, Myricanone, Perlolyrine, Senkyunolide A, Senkyunolide H, Senkyunolide I, Senkyunone, Sitosterol, Wallichilide
Pheretima (Di Long)	*Pheretima Aspergillum (E.Perrier)*	*Megascolecidae*	4-Guanidino-1-butanol, Cholesteryl ferulate, Guanosine, Hyrcanoside, Xanthinin
Bombyx Batryticatus (Jiang Can)[a]	-	-	Bassianin, Beauvericin, Ecdysterone, Ergotamine, Lupeol acetate

[a]Bombyx Batryticatu *is the desiccated body formed by the 4–5 instar larvae of* Bombyx mori Linnaeus *(family:* Bombycidae*) infected with white* Beauveria bassiana (Bals.) Vuillant.

as "mol2" file format. The "mol2" files of HCC's components were input into PharmMapper (http://lilab-ecust.cn/pharmmapper) for potential targets prediction (Wang X. et al., 2017). OMIM database (http://omim.org/) and Genecards (http://www.genecards.org) were utilized to collect the CIR-related disease genes and targets (Hamosh et al., 2005; Stelzer et al., 2016). The PDB ID number of HCC's protein target and the name of CIR-related targets were input into UniProt KB (https://www.uniprot.org/uniprot/) to obtain the official gene symbol of each target. (see **Supplementary Table S1** and **Supplementary Table S2** in Supplementary Material).

Network Construction and Analysis Methods

The protein-protein interaction (PPI) data of targets were obtained from String 11.0 (http://string-db.org/) (Szklarczyk et al., 2015). The CIR gene, HCC compounds and potential targets, and PPI data were imported into Cytoscape 3.7.1 software (https://cytoscape.org/) for network construction (Bader and Hogue, 2003). The networks were analyzed by the plugin MCODE to obtain cluster. The definition and the methodology of acquisition of clusters were described in our previous work (Zeng et al., 2017; Zeng and Yang, 2017; Bao et al., 2019; Yang et al., 2019a; Yang et al., 2019b), such as "Exploring the Pharmacological Mechanism of Quercetin-Resveratrol Combination for Polycystic Ovary Syndrome: A Systematic Pharmacological Strategy-Based Research" (Yang et al., 2019a) and "Uncovering the Pharmacological Mechanism of *Astragalus* Salvia Compound on Pregnancy-Induced Hypertension Syndrome by a Network Pharmacology Approach" (Zeng et al., 2017).

The HCC targets and CIR genes in the network were input into the Database for Annotation, Visualization and Integrated Discovery (DAVID, https://david-d.ncifcrf.gov, ver. 6.8) for Gene Ontology (GO) enrichment analysis and pathway enrichment analysis (Huang et al., 2009).

Experimental Materials

Instruments and Reagents

Instruments: BX51 optical microscope, Motic Image Advanced 3.0 image analysis system (Olympus, Japan); Tgradient PCR instrument (Biomatra); KD2258 paraffin slicer (Zhejiang Jinhua); LEICA DM LB2 binocular microscope (Leica, Germany); JY3002 electronic balance (Shanghai Precision Scientific Instrument Co., Ltd.); HHS-2 electronic constant temperature stainless steel Water bath (Shanghai Nanyang Instrument Co., Ltd.); S2-93 automatic double pure water distiller (Shanghai Yarong Biochemical Instrument Factory). Eppendorf benchtop cryogenic microcentrifuge (Eppendorf Inc.); high speed benchtop centrifuge (Beckman Inc.); micropipette (Eppendorf Inc.) ultrapure water meter (Millipore Inc.); ultra clean bench (Suzhou Purification Equipment Co., Ltd.); −80°C ultra-low temperature refrigerator (Zhongke Meiling Cryogenic Technology Co., Ltd.). Column: Welch Vltimate XB-C18 (HS), 4.6 x 250 nm. 5 μm; High Performance Liquid Chromatograph: Agilent, Germany angilent1260 (Diode Array Detector).

Reagents: TRIzol was purchased from Invitrogen Inc., United States; RT-PCR kit was purchased from MBI Inc, United States; HIF-1α (batch number: bs-0737R), VEGF (batch number: bs-1957R) and VEGFR (batch number: bs-0565R) antibody were purchased from Beijing Boaosen Biotechnology Co., Ltd.; vWF monoclonal antibody (batch number: F3520), rhodamine red (lot number: 83697), isothiocyanate fluorescent yellow (FITC, batch number: P5282) were purchased from Sigma Inc., United States; BrdU monoclonal antibody (NA61) was purchased from Chemicon, United States; immunohistochemistry kit was purchased from Beijing Boaosen Biotechnology Co., Ltd.; Standards: Ligustrazine Hydrochloride 110817–201608, ferulic acid 110773–201614, astragaloside 110781–201717, all from China Food and Drug Testing Institute.

Animal

One hundred and twenty (120) Sprague-Dawley (SD) rat with 7 ~ 8 week old and body weight 280~300 g (without limited to male and female) were purchased from Shanghai Xipuer-Bikai Laboratory Animal Co., Ltd. [Animals permit number: SCXK (Shanghai) 2018–0016]. All animals were housed in clean cages and housed under a 12 h light/dark cycle at a temperature of 21–25°C and a humidity of 45–65%. Free drinking, feeding, and adaptive feeding for 1 week. The experiment was approved by the Ethics Committee of Hunan University of Chinese Medicine

(Changsha, China) (Approval No: 201404163). Animal experiments are strictly in accordance with the ethics committee guidelines and laboratory animal care and use guidelines.

Preparation of HCC Extract

Hedysarum Multijugum Maxim. (Specimen number: 2014062101), *Chuanxiong Rhizoma* (Specimen number: 2014062410), *Pheretima* (Specimen number: 2014062205), *Bombyx Batryticatus* (Specimen number: 20140622307), with ratio 4:1:1.5:1.5, was purchased from the Chinese Pharmacy of the First Affiliated Hospital of Hunan University of Chinese Medicine. The herbs were verified by Professor Bing Dai. The HCC extract was prepared by the Department of Pharmacy, the First Affiliated Hospital of Hunan University of Chinese Medicine. The specific experimental procedure refers to our previous study (Chen, 2005). When in use, the HCC dry extract and physiological saline are formulated into an HCC solution.

High Performance Liquid Chromatography

Three representative compounds in HCC were identified by high performance liquid chromatography (HPLC) for quality control: astragaloside IV, ferulic acid, and ligustrazine. Conditions: Ultimate XB-C18 column (5 μm, 4.6 × 250 mm), A: acetonitrile; B: 0.2% phosphoric acid-water; gradient elution flow rate: 1 ml/min; Detection wavelength: 198, 201, 280, 290, 315, 320 nm; injection volume: 10 μl.

The HPLC of HCC is shown in **Supplementary Figure S1**. The main compounds of HCC were quantified: astragaloside IV 13.72 mg/200g, ferulic acid 2.52 mg/200g, ligustrazine 0.36 mg/200g.

Experimental Methods

Animal Grouping, Model Preparation and Intervention Methods

One hundred and twenty (120) rats were randomly divided into normal group (n = 12), sham operation group (n = 12), CIR model group (n = 48) and HCC group (n = 48). The model group and the HCC group were divided into four subgroups (1, 3, 5, and 7 days after reperfusion) with 12 rats in each group. All animals were trained for 3 days with reference (Bederson et al., 1986; Huang et al., 2009) before modeling. The specific method is: suspending the tail of the rat about 1 m from the ground, and observing the flexion of the forelimb. The cages where the animals are kept are marked with letters, and the drugs are also marked with letters, and they are kept by a third person before the end of the experiment. The animal experiment operator, data collector, and indicator tester do not know the group and intervention drugs.

Scoring criteria: 0 points: Rat forelimbs extended to the ground, no other symptoms; 1) point: The forelimb of the injured hemisphere of the rat suffered from flexion, and its posture changed from slight lumbar flexion and a certain degree of adduction to the shoulder of the elbow, to complete flexion of the waist and elbow and internal rotation of the shoulder; 2) points: Put the rat on a piece of soft plastic paper, lift the tail, apply a soft force on the shoulder, and the resistance of the rat to the external force which causes it to slide toward the diseased side is weakened; 3) points: The rat has a clear consciousness, making a rear-end movement to the right or falling to the right; 4) points: accompanied by disturbance of consciousness, no spontaneous activity; 5) points: death. The entire test process takes 3–5 min, and the rats with scores of 1–3 were enrolled. When the rat died and the sample size was insufficient, random replacement was performed. The left middle cerebral artery occlusion (MCAO) model was prepared by referring to Longa et al. (1989). Rats were fasted before operation and anesthetized. The body temperature was maintained by a constant temperature circulating water system. The rat had a median neck incision, exposed the left external carotid artery and its branches (occipital artery and superior thyroid artery) and the common carotid artery bifurcation. The occipital artery and the superior thyroid artery were ligated, and the carotid artery bifurcation was cut at the bifurcation of the common carotid artery and a smooth nylon thread (1.85 ± 1.5) cm with a diameter of 0.26 mm was inserted into the internal carotid artery. Stop sending the line when the resistance is felt, and record the time. Two hours after the middle cerebral artery was blocked, the suture was withdrawn to restore perfusion. The sham operation group only inserted the fishing line about 1 cm, and the others were the same as the model group. The success rate of modeling is about 80%, and the failure model is randomly replaced. After the model is prepared, the animals are kept in cages.

Administration method: HCC group: the dose given to rats was calculated according to the animal body surface area dose conversion algorithm, the formula is D2 = D1 × R2 ÷ R1 (D2 is the desired dose, D1 is the known dose, R1 is the corresponding known value, and R2 is the ratio of the surface area of the corresponding animal body). The daily dose for rats (0.72 g/ml, 1 ml/100 g) is equivalent to twice the dose for adults. It was calculated from the ratio of 80 g of the daily dose of a 70 kg adult to the body surface area of 300 g rat. The first dose was given 2 h after waking anesthesia. The HCC group was intragastrically administered with HCC extract, and the rest were given the same amount of physiological saline, and were given once a day for 7 days.

Specimen Collection and Section Preparation

One (1) hour after the last administration, the rats were anesthetized with 1% sodium pentobarbital (2.75 ml/kg, intraperitoneal injection), and then sacrificed by cervical dislocation. The brain tissue was then quickly collected. The specimen was divided into two parts, one was rinsed with 1‰ DEPC water and immediately placed in liquid nitrogen; the other was fixed in 4% paraformaldehyde to make a 5 μm thick paraffin section for HE staining, immunohistochemical staining and BrdU/vWF fluorescence double labeling.

Detection Indicators and Methods

Neurological Deficit Score

Neurological deficits were assessed by a five-point, four-point scoring method by Longa et al. (1989). 0 points: no symptoms of

neurological deficits; 1) point: When the rat is suspended from the tail, the contralateral forelimb of the lesion is flexed and raised, the shoulder is adducted, and the elbow is straight; 2) points: rotate to the opposite side of the lesion; 3) points: fall to the opposite side of the lesion; 4) points: no spontaneous activity and decreased level of consciousness. The score was performed at 1, 3, 5, and 7 days after surgery. Rats with a score of 1–3 were selected for inclusion in the results.

Volume of Cerebral Infarction

The volume of cerebral infarction was assessed by TTC staining. The brain tissues were and placed in a refrigerator at −20°C for 10 min. Then the brain tissue was deceived and placed in a 1% TTC solution, strictly protected from light, incubated at 37°C for 30 min, and then placed in 10% formaldehyde for 3 h. The stain-free area is infarct tissue. The area of infarct size was calculated by multimedia color image analysis system. The infarct volume was calculated according to formula V = S × D (S is the infarct area of each slice and D is the slice thickness). The infarct size of each brain slice was measured on a computer by area measurement software, and the sum of the infarct volumes of all brain slices was the total volume of the infarct.

Microvessel Density Detection

Microvessels were observed by immunohistochemical methods, and microvessel density (MVD) counts were performed according to Weidner et al. (1991). The test was carried out according to the instructions of the immunohistochemistry kit. vWF is labeled as a brownish-yellow particle in the cytoplasm of vascular endothelial cells, and any endothelial cell or endothelial cell cluster that is stained brown by the vWF antibody is considered to be a blood vessel count. Using the MIAS medical image analysis system, five sections were taken at each time point, and each section was selected for 4 high-magnification (× 400) fields around the same cortical ischemic area for microvessel counting. Referring to the Weidener counting method, the number of microvessels per 1 mm^2 was calculated and then averaged. The results of 15 slices per group at each time point were obtained.

Immunofluorescence Staining for Expression of BrdU and vWF

After Brdu is dissolved in normal saline, the dose is determined at 100 mg/kg/day, and intraperitoneal injection is performed. The sections of brain tissue were immersed in 3% H2O2 deionized water for 10 min; washed with PBS for 5 min × 3 times; immersed in 2 mol/L HCl at 37°C for 15 min. Then, the sections were wash with PBS for 5 min × 3 times; 5% goat serum was blocked at room temperature for 30 min, and the liquid was aspirated. After that, BrdU monoclonal antibody (1: 100) 10 μl were added and incubated in 37°C water bath. Then, FITC (luminescence wavelength 520~530 nm, yellow-green light) staining was performed, 37°C water bath for 30 min, after washing, the sections were blocked with 5% goat serum at room temperature for 30 min vWF antibody (1: 100) 10 μl were added and incubated in37 °C water bath for 3 h. Rhodamine (light emission wavelength 570~590 nm, red light) staining was performed, 37°C water bath for 30 min. Finally, the slices were packaged with glycerin and observed with an OLYMPUS BX51 fluorescence microscope by the corresponding color filters at 520 and 580 nm, respectively. FITC is green and rhodamine is red. The image is taken in Key Lab of Hunan Province for Prevention and Treatment of Cardio-cerebral Diseases with Integrated Traditional Chinese and Western Medicine, Hunan University of Chinese Medicine, and the images obtained under the two excitation lights are superimposed to obtain a yellow signal as a common signal.

Detection of HIF-1α, VEGFA and VEGFR mRNA Levels

The total RNA was extracted from the infarcted side of the brain by the guanidinium isothiocyanate method. The mRNA expression was determined by Reverse Transcription-Polymerase Chain Reaction (RT-PCR).

PCR product analysis: 5 μl PCR amplification products were analyzed on 2.5% agarose gel electrophoresis (voltage 50 V, 30–45 m, ethidium bromide staining). The electrophoresis strips were taken under UV light and the negatives were scanned with a laser density scanner. The expression levels of HIF-1α, VEGF and VEGFR mRNA were calculated using the following formula: Relative product content = HIF-1α (VEGF, VEGFR) amplification product optical density value/GAPDH amplification product optical density value × 100%. The Primers were designed with reference to the computer gene library nucleotide sequence data, and were synthesized by Shanghai Shenggong Bioengineering Co., Ltd. (**Table 2**).

Detection of HIF-1α, VEGFA and VEGFR Protein by Immunohistochemistry

The brain tissue was embedded by paraffin, sliced (5 μm), conventional dewaxed. Then it was soaked in 3% hydrogen peroxide for 10 min at room temperature and washed twice with distilled water. After heat repairing the antigen, the primary antibody (rabbit anti-VEGF 1:300; rabbit anti-VEGFR2 1:200; rabbit anti-HIF-1α1:200) and the biotinylated secondary antibody were added sequentially. Then the horseradish enzyme-labeled streptavidin solution was added and incubated in 20~37°C for 20 min. The color was developed by DAB at room temperature, and the reaction time was controlled under the microscope (5–30 min). Finally, the slices were lightly counterstained with hematoxylin, dehydrated, and transparent, and sealed with a neutral gum. The expression of HIF-1α, VEGFA and VEGFR was observed under a microscope.

Statistical Analysis

The data were processed by SPSS 19.0 statistical software, and the measurement data were expressed as mean ± standard deviation. Variance homogeneity tests were performed for comparison between groups. If the variances are homogeneous, multiple comparisons using a completely random design analysis of variance or a grouped t test are used for data processing. If the variances are not homogeneous, the rank sum test is used.

TABLE 2 | Primer design.

Gene primer sequence	Product size	/bp
VEGF-A	F: 5'-CGCCAAGCCCGGAAGATTAG-3'R: 5'-CCAGGGATGGGTTTGTCGTG-3'	392
VEGFR2	F: 5'-CTGTGCTGTTTCCTACCCTAATC-3'R: 5'-CTTTACCGTCGCCACTTGAC-3'	275
HIF-1α	F: 5'-TACTGATTGCATCTCCACCTTCTAC-3'R: 5'-CTGCTCCATTCCATCCTGTTC-3'	210
GAPDH	F: 5'-AACTCCCTCAAGATTGTCAG-3R: 5'-GGGAGTTGCTTGAAGTCACA-3'	448

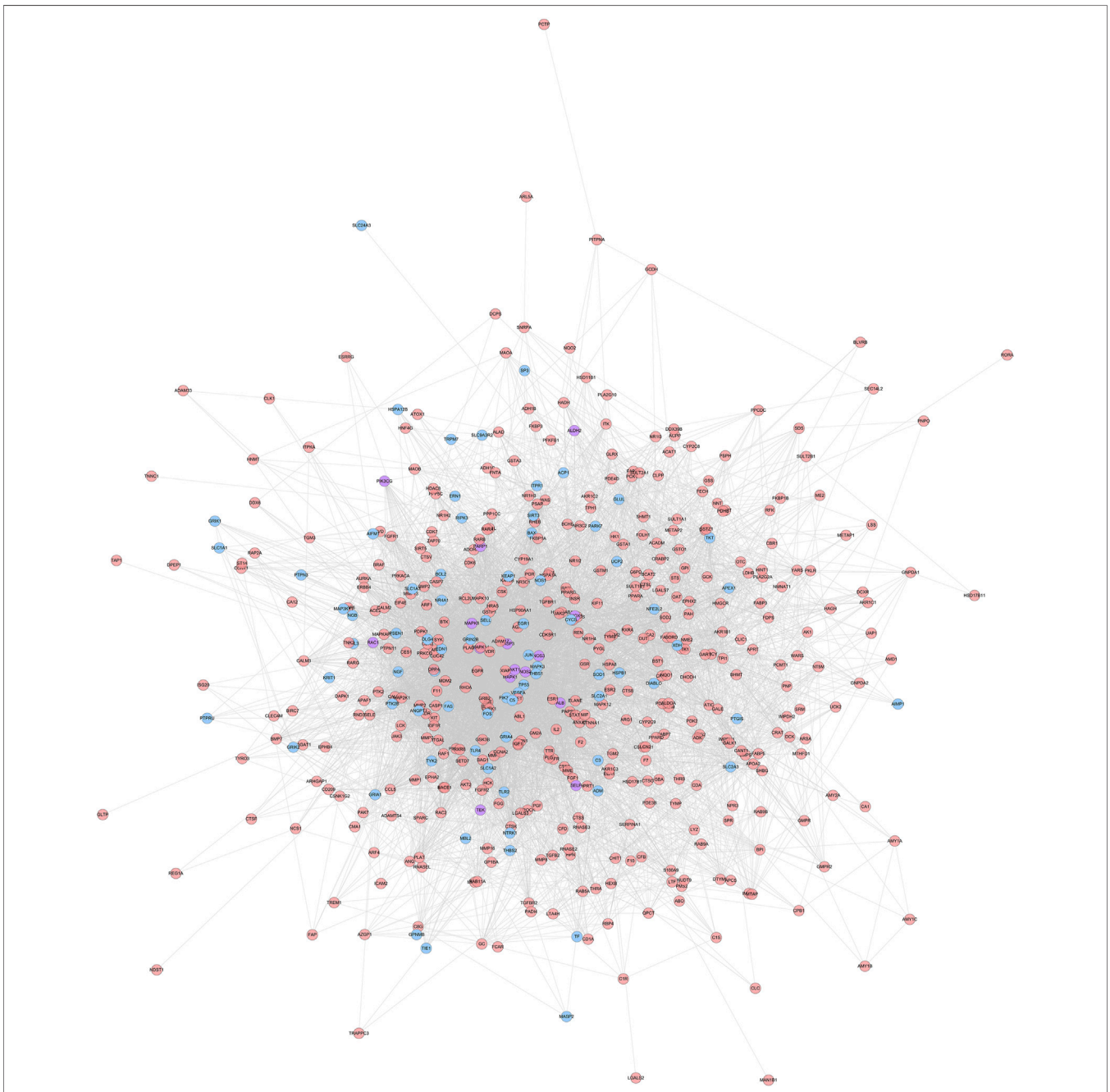

FIGURE 1 | HCC-CIR PPI Network (Blue, pink, purple circles stand for CIR genes, HCC targets and HCC-CIR targets, respectively).

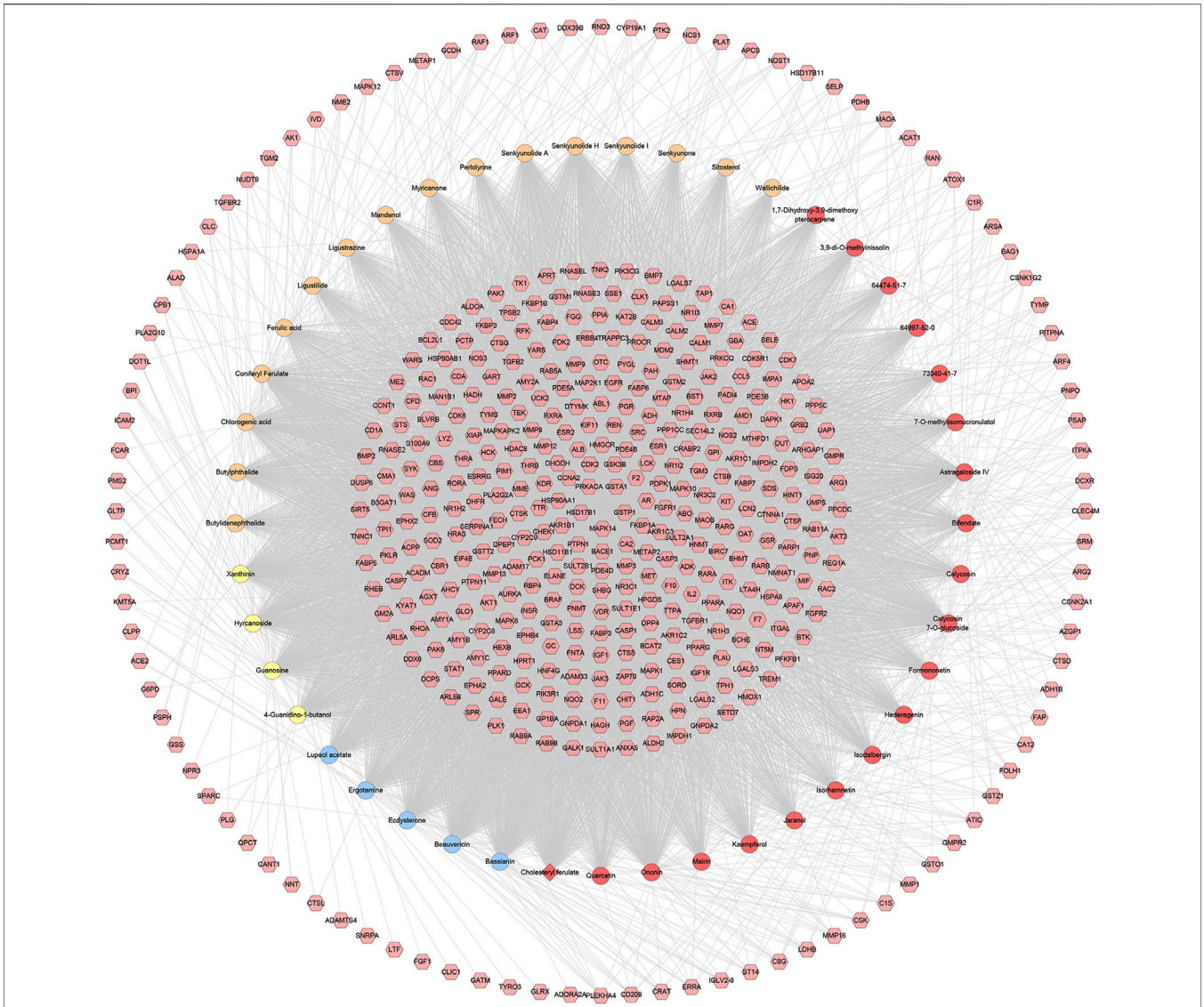

FIGURE 2 | Potential compounds-potential targets network of HCC (The red circle stands for compound of *Hedysarum Multijugum Maxim.*; the blue circle stands for compound of *Bombyx Batryticatus*; the yellow circle stands for compound of *Pheretima*; the orange circle stands for compound of *Chuanxiong Rhizoma*. The red diamond stands for the common compound of *Pheretima* and *Bombyx Batryticatus*. The pink hexagon stands for potential targets.).

RESULTS AND DISCUSSION

Potential Targets of HCC and CIR Genes

Ninety CIR-related genes were obtained from GeneCards and OMIM database (see **Supplementary Table S2**). After the potential target prediction, totally 440 potential targets were obtained. The relationship among potential compounds and potential targets was shown in **Figure 1**. This network consists of 440 compound targets, 45 potential compounds and 8,759 edges. The targets near the center are regulated by more compounds than ones in the peripheral. For example, the targets in the center are: AR (45 edges), BACE1 (45 edges), CA2 (45 edges), CDK2 (45 edges), F2 (45 edges), FKBP1A (45 edges), GSK3B (45 edges), GSTA1 (45 edges), GSTP1 (45 edges), HSD17B1 (45 edges), MAPK14 (45 edges), PRKACA (45 edges), AKR1B1 (44 edges), CCNA2 (44 edges), HSP90AA1 (44 edges), MMP3 (44 edges), PDE4D (44 edges), PTPN1 (44 edges), AKR1C3 (43 edges), FGFR1 (43 edges), LCK (43 edges), METAP2 (43 edges), PDPK1 (43 edges); the targets in the peripheral (ADAMTS4, ADORA2A, CLIC1, FGF1, GATM, GLRX, LTF) are regulated only by one compound. The compounds in herbs can regulate multiple targets. The top five compounds in each herb are: *Hedysarum Multijugum Maxim.*: Astragaloside IV (298 edges), Calycosin 7-O-glucoside (295 edges), Ononin (294 edges), Bifendate (162 edges), Isorhamnetin (151 edges); *Chuanxiong Rhizoma*: Senkyunolide

TABLE 3 | Cluster of HCC-CIR PPI Network.

Cluster	Score	Nodes	Edges	Genes and targets
1	35.244	46	793	MAPK14, SOD2, MAPK8, MDM2, SRC, MET, PLG, EGFR, TP53, CASP3, CAT, HMOX1, MMP2, ESR1, MMP3, HSPB1, CCNA2, HPGDS, FOS, TLR4, MAPK3, HRAS, JUN, AKT1, AKT2, CDC42, PTK2, ALB, HSP90AA1, PTPN11, CYCS, NOS3, IGF1, IGF1R, IL2, RAF1, EDN1, JAK2, RHOA, NGF, TLR2, VEGFA, GRB2, PGR, MAP2K1, MAPK1
2	11	47	253	MAPK10, ABL1, ACE, PLAU, THBS1, STAT1, EIF4E, MMP1, CASP1, MMP13, CASP7, PPARG, ERBB4, ESR2, CCL5, MMP7, MMP9, CDK2, PTK2B, PTPN1, NOS2, HSPA8, NQO1, CHEK1, RAC1, FGFR2, ANXA5, APAF1, NR3C1, AR, XIAP, CRYZ, CSK, JAK3, REN, EGR1, KDR, SOD1, KIT, PARP1, LCK, PIK3CA, BCL2L1, SELE, BMP2, GSK3B, GSR
3	7.932	60	234	BRAF, SLC2A1, GSTA1, BTK, NOS1, GSTP1, ANGPT1, CALM1, HCK, HEXB, PRKCQ, FAS, CDK6, HSP90AB1, HSPA1A, C3, RAC2, IMPDH1, INSR, RARA, DIABLO, PARK7, RHEB, CTSB, RNASE2, RNASE3, CTSG, LGALS3, LYZ, SELP, ADAM17, ELANE, EPHA2, SYK, TEK, AKR1B1, TGFBR1, F2, FABP5, TTR, FGF1, FGFR1, VDR, G6PD, ARG1, ZAP70, ARSA, BAX, ATIC, NTRK1, AURKA, NFE2L2, GLRX, GM2A, PDPK1, KEAP1, PGF, PIK3CG, BPI, PIK3R1
4	7.714	15	54	TKT, TYMP, IMPDH2, UCK2, DTYMK, UMPS, APRT, PNP, APEX1, GART, ADK, GLO1, GMPR, TK1, DCK
5	5.579	20	53	SIRT5, CHIT1, SPARC, DUT, CANT1, BCL2, HK1, PPIA, CTSD, AIFM1, HPRT1, TGM2, CTSS, CDA, LTA4H, LTF, SIRT3, ALDOA, UCP2, QPCT
6	4.4	6	11	CYP2C8, GSTA3, CYP2C9, ADH1B, GSTO1, ADH1C
7	3.846	14	25	TYMS, PKLR, SORD, NT5M, CALM2, YARS, PPP1CC, LDHB, MTHFD1, PDE5A, GMPR2, GPI, PYGL, SHMT1
8	3.333	4	5	PSEN1, GRIA1, BACE1, DLG4
9	3.176	18	27	FECH, DHFR, GRIK2, DHODH, C1R, C1S, C5, FGG, PAH, AHCY, GLUL, SLC1A3, ALAD, BHMT, GRIK1, SERPINA1, TPI1, GRIA4
10	3	3	3	GSTM2, GSS, GSTM1
11	3	3	3	EEA1, RAB11A, RAB5A
12	3	3	3	UAP1, GNPDA1, GNPDA2
13	2.909	12	16	GC, GRIN2B, TGFB2, TGFBR2, FKBP1A, APOA2, RBP4, CALM3, DAPK1, TF, BMP7, CFD
14	2.875	17	23	MBL2, APCS, RARB, RARG, STS, OTC, ARG2, SULT2A1, GATM, F11, RXRA, AKR1C3, F7, THRB, PSPH, CDK7, CFB

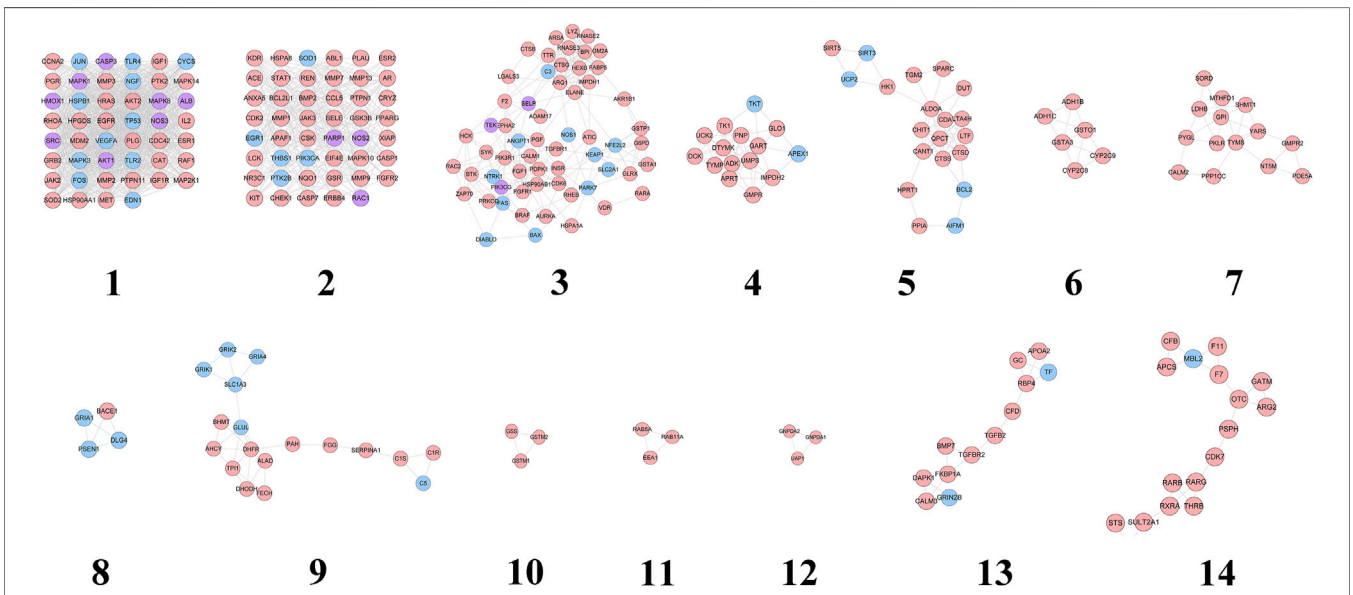

FIGURE 3 | Cluster of HCC-CIR PPI Network (Blue, pink, purple circles stand for CIR genes, HCC targets and HCC-CIR targets, respectively).

H (297 edges), Coniferyl Ferulate (295 edges), Chlorogenic acid (295 edges), Senkyunolide A (219 edges), Butylphthalide (218 edges); *Pheretima*: Hyrcanoside (298 edges), Cholesteryl ferulate (295 edges), Xanthinin (288 edges), Guanosine (283 edges), 4-Guanidino-1-butanol (255 edges); *Bombyx Batryticatus*: Ergotamine (297 edges), Ecdysterone (297 edges), Beauvericin (296 edges), Bassianin (295 edges), Lupeol acetate (228 edges) (**Figure 2**).

HCC-CIR PPI Network Analysis

HCC-CIR PPI Network

HCC potential targets, CIR genes and their PPI data were input into Cytoscape to construct HCC-CIR PPI network. This network contains 502 nodes 75 CIR gene nodes, 412 HCC target nodes and 15 HCC-CIR targets nodes) and 7,762 edges (**Figure 1**) The top 20 targets of degree are selected and divided into three categories: 1) CIR targets: TP53 (189 edges), VEGFA (166 edges), MAPK3 (164

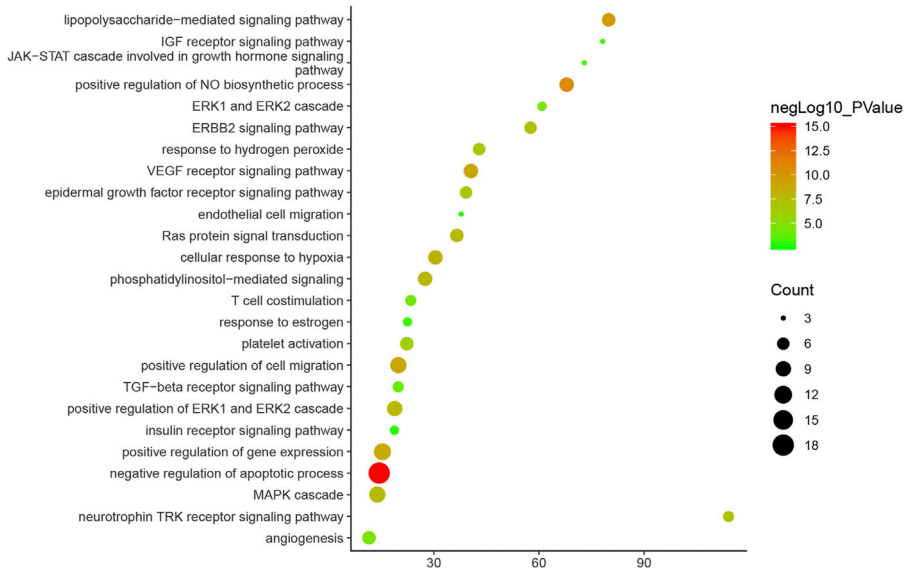

FIGURE 4 | Bubble chart of biological processes (*X*-axis stands for fold enrichment).

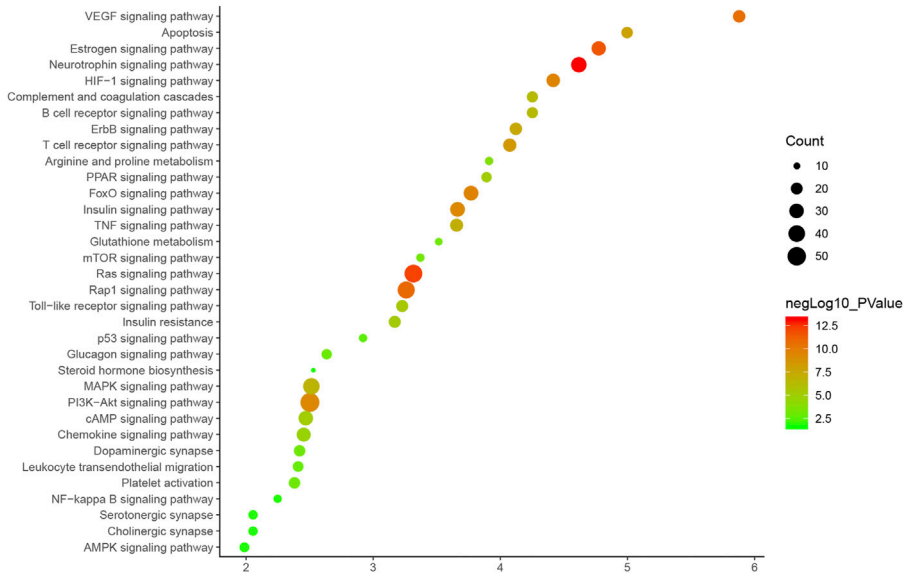

FIGURE 5 | Bubble Chart of Signaling Pathway (*X*-axis stands for fold enrichment).

edges), JUN (133 edges), CYCS (109 edges); 2) HCC genes: EGFR (155 edges), HSP90AA1 (135 edges), HRAS (127 edges), IGF1 (126 edges), CAT (123 edges), MMP9 (122 edges), ESR1 (116 edges), RHOA (104 edges), MAPK14 (102 edges); 3) HCC-CIR targets: ALB (215 edges), AKT1 (205 edges), MAPK1 (156 edges), SRC (143 edges), CASP3 (141 edges), MAPK8 (137 edges).

Clusters of HCC-CIR PPI Network

The HCC-CIR PPI network was analyzed by MCODE, and returns 14 clusters (**Table 3** and **Figure 3**).

These genes in each cluster were input into DAVID database to undergo GO enrichment analysis. After that, several biological processes were obtained. Cluster 1 is associated with negative regulation of neuronal apoptosis, nitric oxide production and metabolism, angiogenesis, hypoxia induction, neurotrophicity, platelet activation, and CIR-related signaling pathways (such as NF-kB signaling pathway). Cluster 2 is related to cell proliferation, hypoxia-induced, cell migration, and CIR-related signaling pathways (ERK1/2 signaling and PI3K signaling, EGF receptor signaling, and VEGF receptor signaling pathways). Cluster 3

TABLE 4 | Effect of HCC on the score of neurological deficits in rats after CIR at different time points (n = 5, x ± s).

Group	1 day	3 days	5 days	7 days
Normal	0	0	0	0
Sham operation	0	0	0	0
CIR model	1.6 ± 0.54[a]	1.6 ± 1.67[a]	0.75 ± 0.5[a]	0.6 ± 0.55[a]
HCC	1.5 ± 1.00[a]	0.5 ± 0.35[b]	0.4 ± 0.54	0.4 ± 0.54

[a]*compared with the Sham operation group,* p < *0.05.*
[b]*compared with the CIR model group,* p < *0.05.*

mainly involves inflammation, platelet activation, nerve cell survival, angiogenesis, oxidative stress, neuronal axonal injury, hypoxia-induced stress, blood coagulation, calcium homeostasis. Cluster 4 is associated with nucleic acid metabolism. Cluster 5 is related to oxidative stress, neuronal apoptosis, ischemia induction, cytokines and NF-κB signaling pathway. Cluster 8 mainly includes the biological processes of synaptic transmission. Cluster 9 is associated with chemical synapses and neurotransmitters. Cluster 13 mainly involves angiogenesis. Cluster 6, 7, 10, 11, 12, 14 do not return CIR-related biological processes (see **Supplementary Table S3**).

Since cluster 1 is the most important one, it is used as an example to show its main biological processes on bubble chart (**Figure 4**).

Pathway of HCC-CIR PPI Network

Thirty-four CIR signaling pathways are obtained. The signaling pathway is arranged according to the degree of enrichment (based on p-value) and count, and the Neurotrophin signaling pathway is found to have the highest enrichment and contained 34 targets (p-value = 7.15*10^-14; Count = 34). According to the sorting, the other signaling pathways (top 10) are: Ras signaling pathway (p-value = 6.74*10^-13; Count = 46), Estrogen signaling pathway (p-value = 2.82*10^-12; Count = 29), Rap1 signaling pathway (p-value = 1.49*10^-11; Count = 42), VEGF signaling pathway (p-value = 2.54*10^-11; Count = 22), FoxO signaling pathway (p-value = 2.86*10^-10; Count = 31), HIF-1 signaling pathway (p-value = 3.04*10^-10; Count = 26), Insulin signaling pathway (p-value = 6.15*10^-10; Count = 31), PI3K-Akt signaling pathway (p-value = 6.46*10^-10; Count = 53), T cell receptor signaling pathway (p-value = 4.18*10^-09; Count = 25) (See **Figure 5**). (**Supplementary Table S4**).

Through chemical informatics technology, combined with the prediction and analysis of active ingredients and potential targets, protein interaction analysis and gene annotation enrichment analysis, we systematically explored the pharmacological substance basis and potential biological mechanism of HCC for CIR. Estrogen signaling pathways are involved in CIR's blood-brain barrier, neuroprotection, and oxidative stress

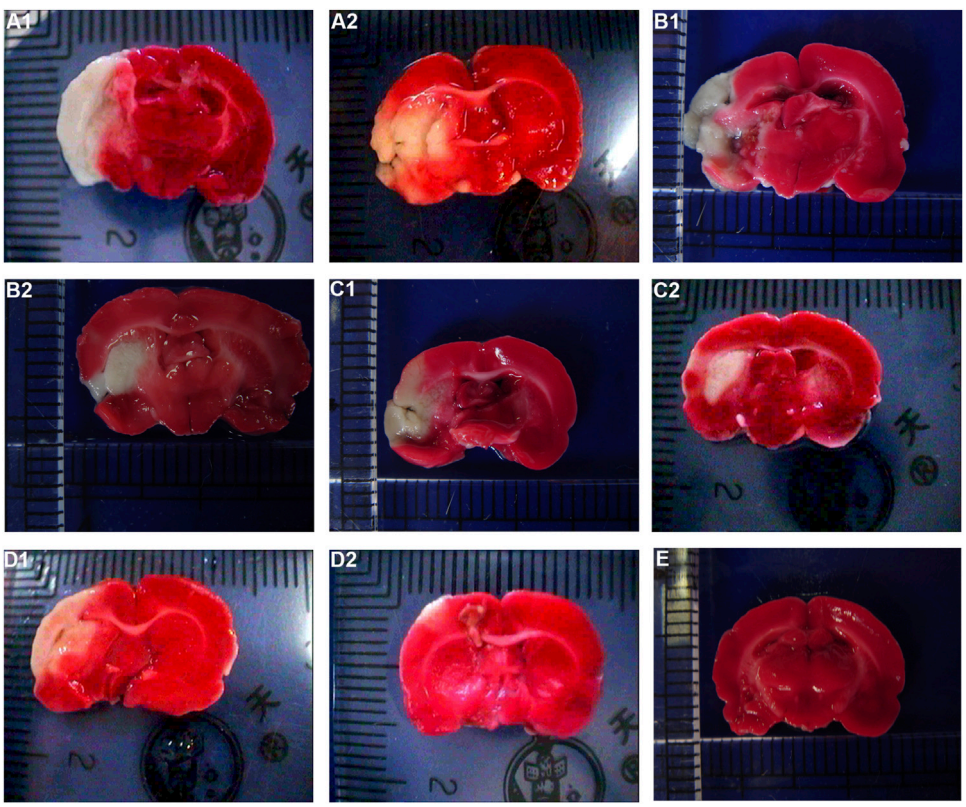

FIGURE 6 | Effect of HCC on cerebral infarction volume in rats at different time after CIR (TCC staining. **(A1)**: Model group 1 day; **(A2)**: HCC group 1 day; **(B1)**: Model group 3 days; **(B2)**: HCC group 3 days; **(C1)**: Model group 5 days; **(C2)**: HCC group 5 days; **(D1)**: Model group 7 days; **(D2)**: HCC group 7 days. **(E)**: Sham operation group).

TABLE 5 | Effect of HCC on cerebral infarction volume at different time points after CIR (n = 5, mm 3, x ± s).

Group	1 day	3 days	5 days	7 days
Normal	0	0	0	0
Sham operation	0	0	0	0
CIR model	23.59 ± 10.42[a]	26.52 ± 18.03[a,b]	25.91 ± 13.61[a,b]	22.47 ± 8.70[a,b]
HCC	22.14 ± 12.75[a]	12.54 ± 9.04	12.40 ± 4.56	10.19 ± 7.2

[a]*compared with the Sham operation group,* p < *0.05.*
[b]*compared with the HCC group,* p < *0.05.*

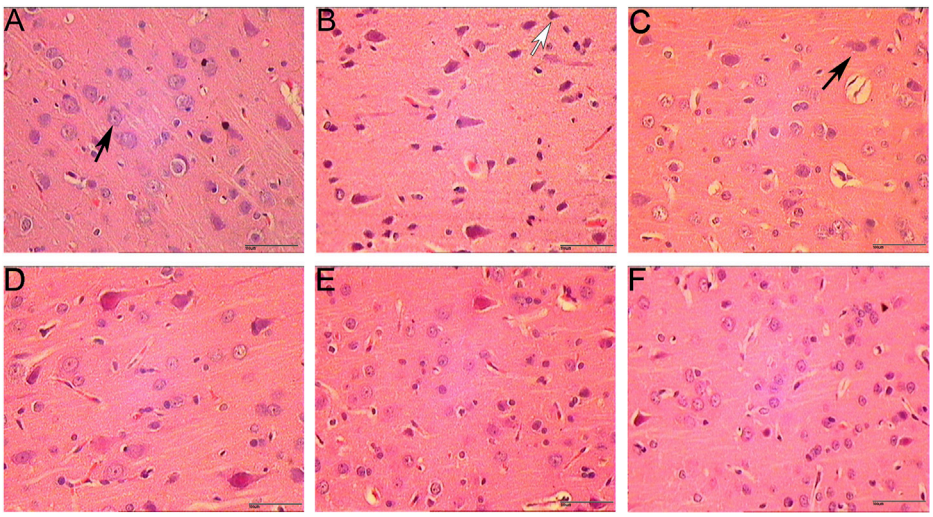

FIGURE 7 | Pathological changes in cerebral cortex (HE staining. 400 x **(A)**: Sham operation group 1 day; **(B)**: Model group; **(C)**: HCC group 1 day; **(D)**: HCC group 3 days; **(E)**: HCC group 5 days; **(F)**: HCC group 7 days; Black arrows indicate normal cells; white arrows indicate cells with pyknotic nucleus.).

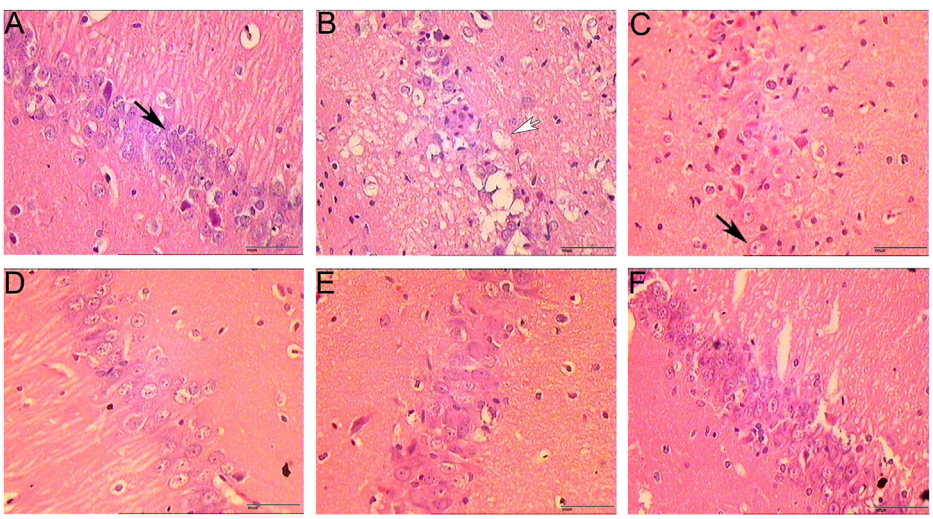

FIGURE 8 | Pathological changes in hippocampus (HE staining. 400 x **(A)**: Sham operation group 1 day; **(B)**: Model group; **(C)**: HCC group 1 day; **(D)**: HCC group 3 days; **(E)**: HCC group 5 days; **(F)**: HCC group 7 days; Black arrows indicate normal cells; white arrows indicate neuronal cells with vacuolar changes.).

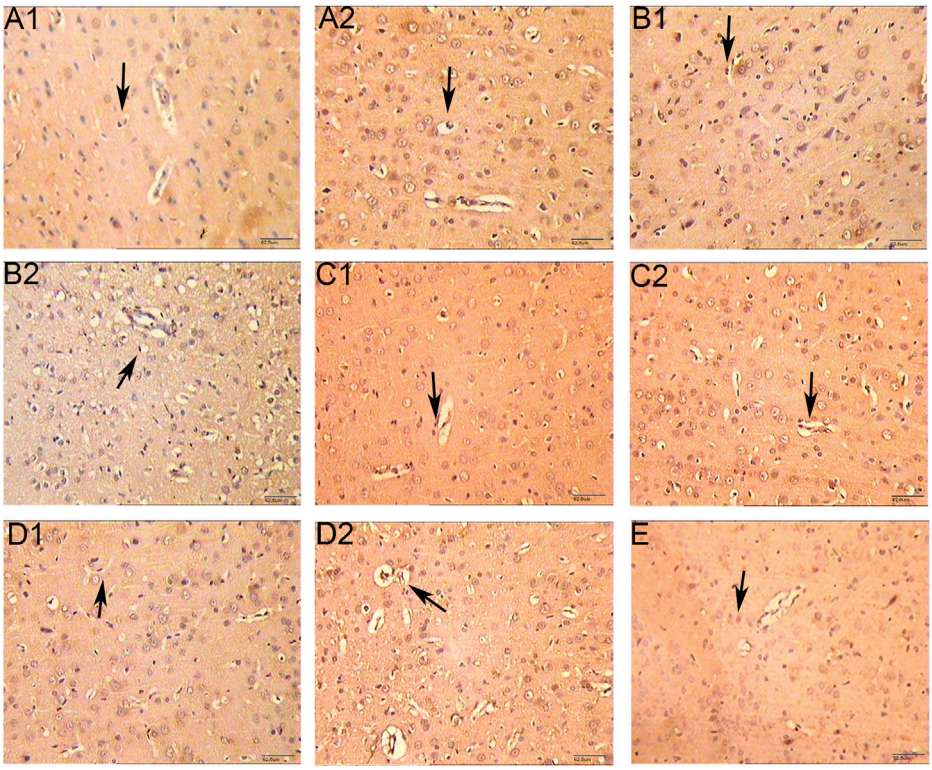

FIGURE 9 | Effect of HCC on MVD at different time points in rat ischemic peripheral area (immunohistochemistry staining. 250 x A1: Model group 1 day; **(A2)**: HCC group 1 day; B1: Model group 3 days; B2: HCC group 3 days; C1: Model group 5 days; C2: HCC group 5 days; D1: Model group 7 days; D2: HCC group 7 days. E: Sham operation group. The arrow points to endothelial cells.).

TABLE 6 | Effect of HCC on MVD at different time points in rat ischemic peripheral area (n = 5, number of blood vessels/mm2, x ± s).

Group	1 day	3 days	5 days	7 days
Sham operation	-	-	-	39.0 ± 13.32
CIR model	45.0 ± 11.02	47.2 ± 11.67	57.8 ± 7.32	60.2 ± 10.37[a]
HCC	46.6 ± 12.70	60.8 ± 16.31[a]	67.8 ± 10.18[b]	67.9 ± 10.03[b]

[a]*compared with the Sham operation group,* $p < 0.05$.
[b]*compared with the Sham operation group,* $p < 0.01$.

(Yang et al., 2005; Wiklund et al., 2012). VEGF signaling pathway is involved in angiogenesis after CIR (Sun et al., 2015; Ho et al., 2017). FoxO signaling pathway is involved in oxidative stress in CIR (Yoo et al., 2012; Zhou et al., 2019). HIF-1 signaling pathway is involved in the induction of hypoxia after CIR (Singh et al., 2012). Insulin signaling pathways are involved in vascular endothelial apoptosis (White et al., 2000). The PI3K-Akt signaling pathway and T cell receptor signaling pathway are involved in cell damage of CIR (Huang et al., 2007; Zhou et al., 2015). HCC may play a therapeutic role by regulating these CIR-related signaling pathways.

Recent studies have also shown that *Astragalus* injection can promote cerebral vascular regeneration in CIR rats, the mechanism of which may be that *Astragalus* injection activates the HIF-1α/VEGF signaling pathway (Wu et al., 2016). Astragaloside IV can promote the proliferation and differentiation of neural stem cells in the hippocampus, inhibit the activation of astrocytes and microglia after CIR in rats and the release of inflammatory factors, and protect the integrity of the blood-brain barrier (Qu et al., 2009; Li et al., 2017; Huang et al., 2018; Li et al., 2018). It can also increase the expression of brain-derived neurotrophic factor (BDNF), vascular endothelial growth factor (VEGF) and VEGF receptor 2 (VEGFR2) after CIR, promote the formation of new blood vessels, improve the survival environment of nerve cells, and inhibit apoptosis or necrosis of ischemic hypoxic neurons (Yang L. et al., 2019). Astragaloside IV may protect CIR by reducing catalase (CAT), superoxide dismutase (SOD), glutathione peroxidase (GSH-Px) activity, malondialdehyde (MDA) content in brain tissue, lactate dehydrogenase (LDH) and creatine kinase (CK) content in

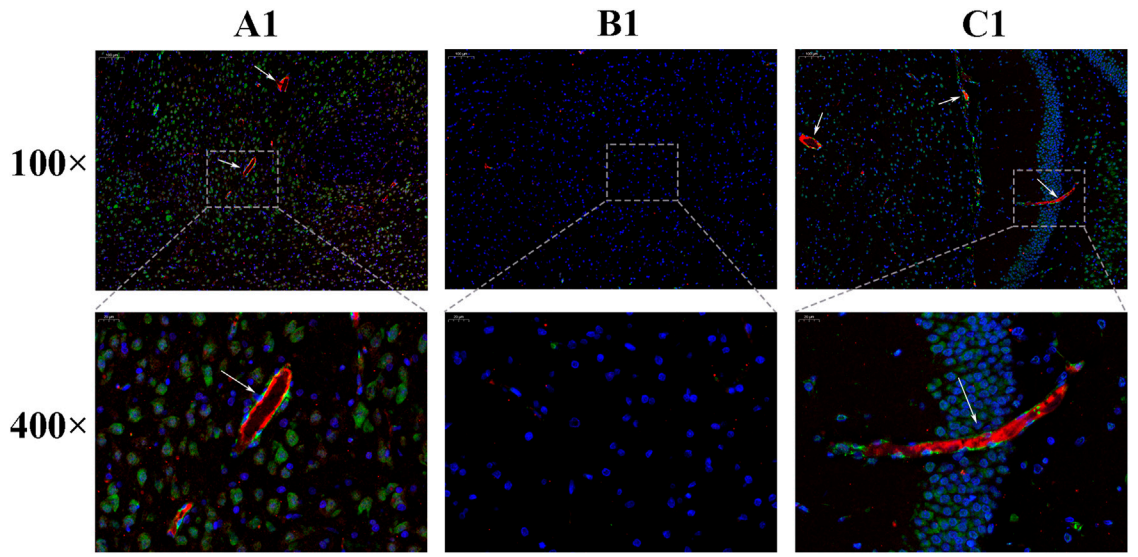

FIGURE 10 | Expression of Brdu and vWF [**(A)**: sham operation group; **(B)**: Model group; **(C)**: HCC group. The areas indicated by the arrows are Brdu (green) and vWF (red)].

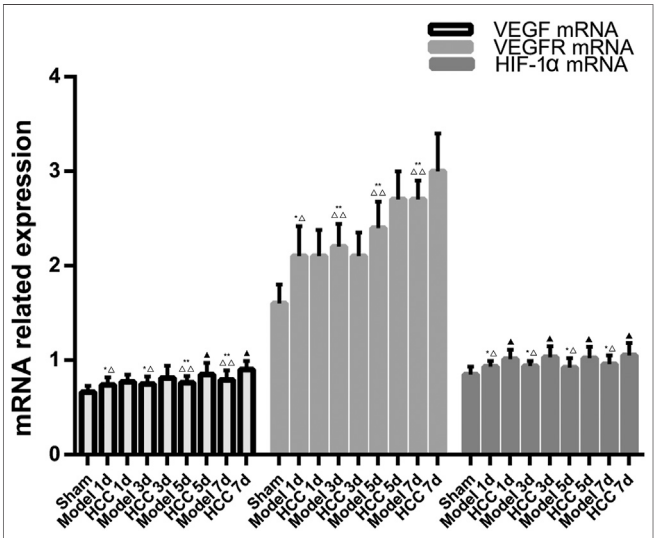

FIGURE 11 | The Expression of VEGF, VEGFR and HIF-1α mRNA (compared with the normal group, $^{*}p < 0.05$, $^{**}p < 0.01$; compared with the Sham operation group, $\triangle p < 0.05$, $\triangle\triangle p < 0.01$; compared with CIR group $\blacktriangle p < 0.05$).

serum, and reduce the expression of NF-κB protein in the brain due to CIR (Shao et al., 2014). This also indirectly confirms the reliability of our reverse pharmacophore docking technology in chemical informatics. Ligustrazine, as the main compound of Chuanxiong Rhizoma, can alleviate the energy metabolism disorder of CIR (Wang Z. et al., 2017), reduce excitatory amino acid toxicity, inhibit apoptosis and the synthesis of inflammatory cells and pro-inflammatory cytokines IL-1 and TNF-α, and fight against inflammatory damage caused by IL-1 and TNF-α (Wang A. et al., 2017; Zhao et al., 2018). Ligustrazine can also induce adrenocortical hormone production, control multiple links of the inflammatory response, increase SOD activity in the brain, reduce NOS expression, and affect nitric oxide (NO) content (Peng et al., 1996; Zhou et al., 2000; Wang A. et al., 2017).

In addition, this study also found that there may be a potential synergy between HCC active compounds. For example, astragaloside IV and ferulic acid can jointly regulate: AURKA, CBS, HPGDS, RAC2, DCK, PDE4B, AMY1A, OTC, CCL5, ANG, AGXT, AMD1, ELANE, PDE4D, PTPN1, MMP3, RARG, UCK2, AMY2A, REN, PDE5A, HMGCR, SHMT1, F7, ADK, GLO1, LYZ, RHOA, EPHA2, TPI1, et al. Ferulic acid and ligustrazine can jointly regulate: HSP90AA1, PDE4D, GPI, MME, FKBP1A, AR, DCK, ABO, CCNA2, AMY1B, GSTP1, EGFR, F2, PPP1CC, PDE4B, SDS, PDPK1, GLO1, LCK, CA2, PRKACA, AMY1C, PIM1, REN, HDAC8, GCK, MMP3, MAPK10, CYP2C9, GSTT2, et al. Recent research has confirmed some of our results. Wang (2012) found that electrospun fibers carrying astragaloside IV and ferulic acid can promote angiogenesis. Gong et al. Found that astragaloside IV and ferulic acid can improve blood lipids, protect the cardiovascular system, and have anti-atherosclerotic effects in New Zealand rabbits (Gong and Huang, 2017). In terms of angiogenesis, ligustrazine combined with astragaloside IV can promote angiogenesis of chick embryo chorionic urea capsule (Zhang et al., 2010). Yang et al. Found that the combination of Hedysarum Multijugum Maxim. And Chuanxiong Rhizoma can significantly improve the morphology of hypoxic rat brain microvascular endothelial cells (RBMVECs), effectively enhance the activity of SOD, inhibit the G1/S phase arrest of RBMVECs induced by hypoxia, significantly reduce cell apoptosis, and reduce the expression of caspase-3 and caspase-8 genes (Yang et al., 2015). The results of their orthogonal experiments showed that the preferred combination was ligustilide 5 μg/ml, ligustrazine 10 μg/ml, ferulic acid 20 μg/ml, calycosin 10 μg/ml, astragaloside IV 10 μg/ml (Yang et al., 2015). These have brought

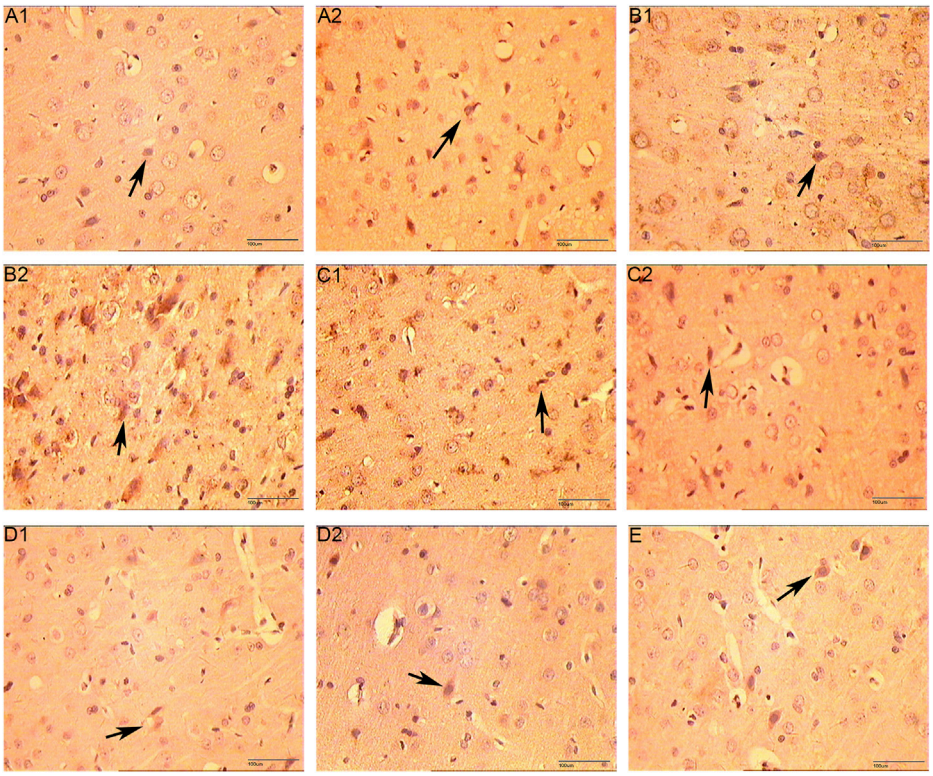

FIGURE 12 | The Expression of VEGF (immunohistochemistry staining. 400 x **(A1)**: Model group 1 day; **(A2)**: HCC group 1 day; **(B1)**: Model group 3 days; **(B2)**: HCC group 3 days; **(C1)**: Model group 5 days; **(C2)**: HCC group 5 days; **(D1)**: Model group 7 days; **(D2)**: HCC group 7 days. **(E)**: Sham operation group; The arrow points to positive expression).

huge opportunities for the research and development of new drugs in the future.

The Effect of HCC on The Score of Neurological Deficit in Rats

The scores of neurological deficits of rats in the sham operation group were 0 points 1 day to 7 days after reperfusion. At 1 d, the scores of neurological deficits in HCC group and CIR model group were higher than those in sham operation group ($p < 0.05$), but the difference between the two groups had no statistical significance. At 3 d, the scores of the neurological deficits in the HCC group were lower than those in the CIR model group ($p < 0.05$). At 5 d and 7 d, the scores of the HCC group and CIR model group decreased, but the scores of CIR model group was still higher than that of sham operation group ($p < 0.05$). The results are shown in **Table 4**.

Pathological Changes

For the volume of cerebral infarction in rats: after staining with TTC, the uninfarcted area was red and the infarcted area was white. No significant cerebral infarction was seen in the sham operation group. There was no significant difference in cerebral infarction volume between HCC group and model group at 1 d ($p > 0.05$). Compared with model group in the same phase, cerebral infarction volume of the HCC group decreased from 3 days to 7 days ($p < 0.05$). See **Figure 6** and **Table 5**.

The results of HE staining showed that the morphology and structure of the cerebral cortex and hippocampus of the sham operation group were basically normal. In the model group, most of the cells in the cerebral cortex and hippocampus showed pyknosis and vacuole-like changes in nuclei. In the HCC group, there were significantly more normal cells in the cerebral cortex and hippocampus than in the model group, and only a few cells showed nuclear constriction changes (**Figures 7**, **8**).

The Effect of HCC on Brain MVD in Rats

The microvessels were irregular in shape and the lumen was surrounded by endothelial cells stained with brownish yellow. In the hemispheric cortex of cerebral infraction, the expression of vWF-stained vascular endothelial cells increased significantly. At 1 day after CIR, the number of microvessels in CIR group and HCC group was increased compared with the sham operation group, but the difference was not statistically significant ($p > 0.05$). Compared with the sham operation group, the number of microvessels in the HCC group increased at 3 days ($p < 0.05$); At 5 and 7 days, the number of microvessels in the HCC group increased significantly ($p < 0.01$). The CIR group also showed an upward trend. At 7 days, the MVD of the CIR group was higher than that of the sham operation group ($p < 0.05$) (**Figure 9** and **Table 6**).

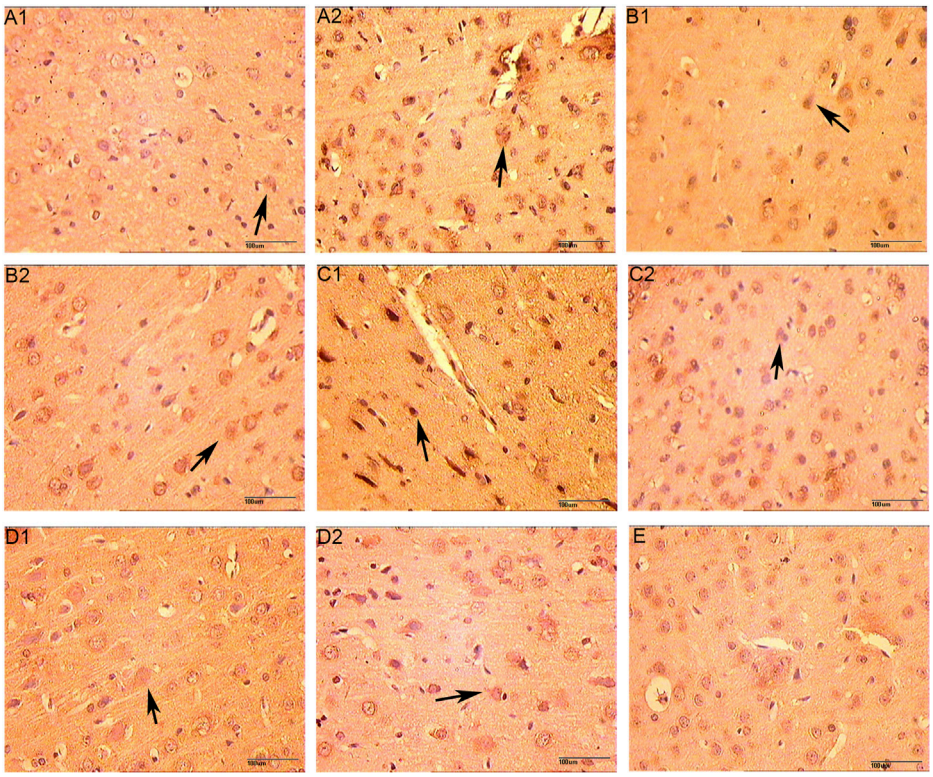

FIGURE 13 | The Expression of VEGFR (immunohistochemistry staining. 400 x **(A1)**: Model group 1 day; **(A2)**: HCC group 1 day; **(B1)**: Model group 3 days; **(B2)**: HCC group 3 days; **(C1)**: Model group 5 days; **(C2)**: HCC group 5 days; **(D1)**: Model group 7 days; **(D2)**: HCC group 7 days. **(E)**: Sham operation group; The arrow points to positive expression).

The Expression of Brdu and vWF

Under immunofluorescence, the Brdu and vWF double-stained signals appeared in the CIR group, and it was considered that there were neovascular endothelial cells. The number of positive signals in the HCC group was higher than that in the CIR group, indicating that the number of new blood vessels increased after drug treatment (**Figure 10**).

The Expression of VEGF, VEGFR and HIF-1α mRNA

Compared with the normal group and the sham operation group, the expression of VEGF, VEGFR and HIF-1α mRNA in the CIR group was enhanced ($p < 0.01$, $p < 0.05$). Compared with the model group, the expression of VEGF mRNA increased on the 5th and 7th day in HCC group ($p < 0.05$), and the expression of HIF-1α mRNA increased at each time point ($p < 0.05$). (**Figure 11**).

The Expression of VEGF, VEGFR and HIF-1α Protein

The positive expression of VEGF and VEGFR-2 is light yellow cytoplasm with brownish brown particles. HIF-1α is positive for brown-yellow particles mainly in the nucleus and a small amount in the cytoplasm. Compared with the normal group and the sham operation group, the expression of VEGF protein was increased on 5 days of the CIR group ($p < 0.05$), the expression of VEGFR protein was increased on 7 days ($p < 0.05$), and the expression of HIF-1α protein was increased on 3 and 5 days ($p < 0.05$). Compared with the CIR group, the expression of VEGF protein was increased on 1 and 3 days of the HCC group ($p < 0.01$), the expression of HIF-1α protein was increased on 1 day ($p < 0.01$), and the expression of VEGFR protein was increased on 5 days ($p < 0.01$). (**Table 5** and **Figures 12–15**).

The effect of HCC on CIR angiogenesis was discovered through a systematic pharmacological method in previous section. Then, animal experiments were carried out to clarify the mechanism of HCC, and further explored the upstream pathways that HCC promotes VEGF expression. Current research found that vascular endothelial cells play an important role in vascular regeneration and maintenance of vascular morphology and function. The upstream of VEGF expression is regulated by a variety of factors. Under hypoxia, HIF-1α can promote the regeneration of blood vessels, and HIF-1α can also be used as a regulator to promote the expression of downstream VEGF (Lee et al., 2017; Chen et al., 2018; Fan et al., 2019). This experimental pharmacology section explores whether HCC can promote VEGF expression by up-regulating HIF-1α. The results showed that after CIR, the express of HIF-1α mRNA and protein increased, and HCC could further promote this effect. After

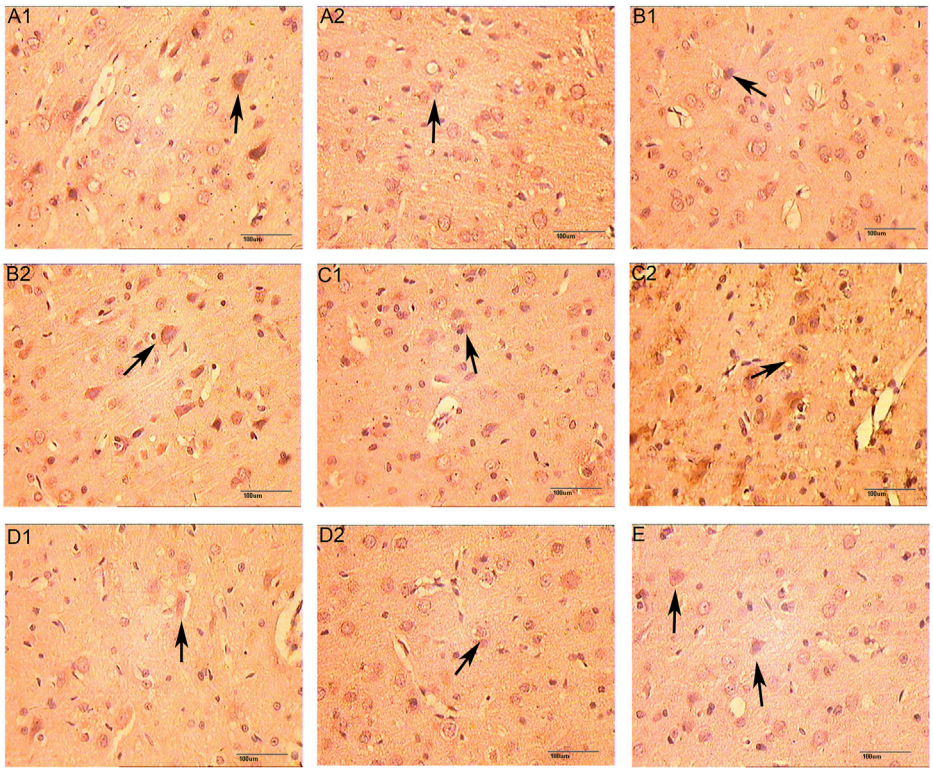

FIGURE 14 | The Expression of HIF-1α (immunohistochemistry staining. 400 x **(A1)**: Model group 1 day; **(A2)**: HCC group 1 days; **(B1)**: Model group 3 days; **(B2)**: HCC group 3 days; **(C1)**: Model group 5 days; **(C2)**: HCC group 5 days; **(D1)**: Model group 7 days; **(D2)**: HCC group 7 days. **(E)**: Sham operation group; The arrow points to positive expression).

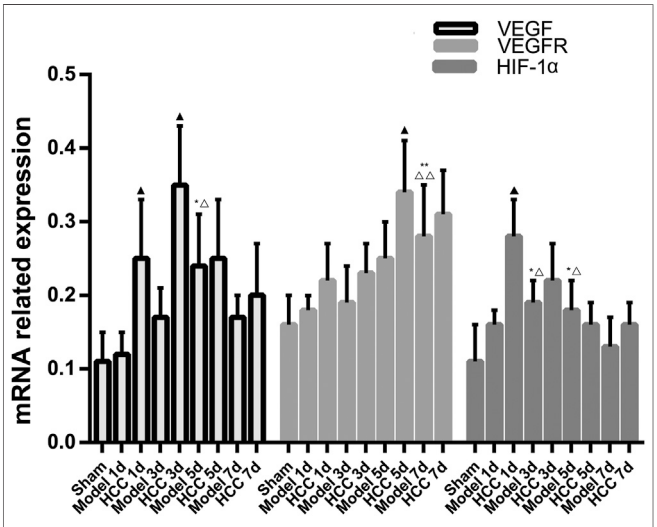

FIGURE 15 | The Expression of VEGF, VEGFR and HIF-1α proteins (compared with the normal group, $*p < 0.05$, $**p < 0.01$; compared with the Sham operation group, $\triangle p < 0.05$, $\triangle\triangle p < 0.01$; compared with CIR group $\blacktriangle p < 0.05$).

CIR, the changes in VEGF and VEGFR were the same as above. Compared with the model group, the difference in HIF-1α mRNA expression in the HCC group increased on the first day after CIR, while the difference in VEGF mRNA expression appeared on the fifth day.

CONCLUSION

The systematic pharmacology prediction results showed that HCC may regulate CIR-related targets (such as AKT1, MAPK1, CASP3, EGFR), biological processes (such as inflammation, platelet activation, nerve cell survival, angiogenesis, oxidative stress, neuronal axonal injury, hypoxia-induced stress, blood coagulation, calcium homeostasis) and signaling pathways (such as HIF-1, VEGF, Ras, FoxO signaling). The experiments also showed that HCC may promote angiogenesis by up-regulating the expression of HIF-1α/VEGF and VEGFR, and finally achieves the role of prevention and treatment of CIR. Hence, this research may provide new reference information for the treatment of CIR by Chinese medicine.

Declare

The work described has not been submitted elsewhere for publication, in whole or in part, and all the authors listed have approved the manuscript that is enclosed.

DATA AVAILABILITY STATEMENT

The original contributions presented in the study are included in the article/**Supplementary Material**, further inquiries can be directed to the corresponding authors.

ETHICS STATEMENT

The animal study was reviewed and approved by the Ethics Committee of Hunan University of Chinese Medicine (Changsha, China).

AUTHOR CONTRIBUTIONS

KY, LZ, YC, XZ, AG and JG are responsible for the study concept and design. KY, LZ, XZ, SW, AG are responsible for data analysis and interpretation in the network pharmacology section; SW, YC and JG are responsible for data analysis and interpretation in experiments. KY, LZ, YC, XZ, AG drafted the paper; JG supervised the study; all authors participated in the analysis and interpretation of data and approved the final paper. XZ, KY, LZ, YC, SW, AG should be considered joint first author.

FUNDING

This work is supported by the National Natural Science Foundation of China (No. 81774174) and the National Key Research and Development Project of China (No. 2018YFC1704904).

SUPPLEMENTARY MATERIAL

The Supplementary Material for this article can be found online at: https://www.frontiersin.org/articles/10.3389/fphar.2021.601846/full#supplementary-material

REFERENCES

Ano, R., Kimura, Y., Shima, M., Matsuno, R., Ueno, T., and Akamatsu, M. (2004). Relationships between Structure and High-Throughput Screening Permeability of Peptide Derivatives and Related Compounds with Artificial Membranes: Application to Prediction of Caco-2 Cell Permeability. *Bioorg. Med. Chem.* 12, 257–264. doi:10.1016/j.bmc.2003.10.002

Bader, G. D., and Hogue, C. W. (2003). An Automated Method for Finding Molecular Complexes in Large Protein Interaction Networks. *BMC Bioinf.* 4, 2. doi:10.1186/1471-2105-4-2

Bao, T., Yang, K., Long, Z., Zeng, L., and Li, Y. (2019). Systematic Pharmacological Methodology to Explore the Pharmacological Mechanism of Siwu Decoction for Osteoporosis. *Med. Sci. Monit.* 25, 8152–8171. doi:10.12659/MSM.917393

Bederson, J. B., Pitts, L. H., Tsuji, M., Nishimura, M. C., Davis, R. L., and Bartkowski, H. (1986). Rat Middle Cerebral Artery Occlusion: Evaluation of the Model and Development of a Neurologic Examination. *Stroke* 17 (3), 472–476. doi:10.1161/01.str.17.3.472

Behravan, E., Razavi, B. M., and Hosseinzadeh, H. (2014). Review of Plants and Their Constituents in the Therapy of Cerebral Ischemia. *Phytother. Res.* 28 (9), 1265–1274. doi:10.1002/ptr.5187

Chen, F. P., Chang, C. M., and Hwang, S. J. (2014). Chinese Herbal Prescriptions for Osteoarthritis inTaiwan: Analysis of NationalHealth Insurance Dataset. *BMC Complement. Altern. Med.* 14, 91. doi:10.1186/1472-6882-14-91

Chen, M., Zou, W., Chen, M., Cao, L., Ding, J., Xiao, W., et al. (2018). Ginkgolide K Promotes Angiogenesis in a Middle Cerebral Artery Occlusion Mouse Model via Activating JAK2/STAT3 Pathway. *Eur. J. Pharmacol.* 833, 221–229. doi:10.1016/j.ejphar.2018.06.012

Chen, Z. (2005). *Quantitative Study of Chemical Constituents in Naotaifang Decoction and Capsules [D]*. Changsha City: Hunan University of Traditional Chinese Medicine. [in chinese]

Fan, J., Lv, H., Li, J., Che, Y., Xu, B., Tao, Z., et al. (2019). Roles of Nrf2/HO-1 and HIF-1α/VEGF in Lung Tissue Injury and Repair Following Cerebralischemia/reperfusion Injury. *J. Cel. Physiol.* 234 (6), 7695–7707. doi:10.1002/jcp.27767

Frizzell, J. P. (2005). Acute Stroke: Pathophysiology, Diagnosis, and Treatment. *AACN Clin. Issues* 16 (4), 421–440. doi:10.1097/00044067-200510000-00002

Ge, J. (2014). *Chinese Medicinal Composition for Treating Ischemic Apoplexy and its Preparation Method.* CN102846699B. Available at: https://patents.google.com/patent/CN102846699B/en (Accessed 2014-08-27). doi:10.1109/chicc.2014.6895705

Gong, T. D., and Huang, S. Q. (2017). Basic Research on Anti-atherosclerotic Compatibility of Effective Components of Danggui Buxue Decoction. *New J. Traditional Chin. Med. Clin. Pharmacol.* 4, 64–68. [in chinese]. doi:10.19378/j.issn.1003-9783.2017.04.012

Hamosh, A., Scott, A. F., Amberger, J. S., and BocchiniMcKusick, C. A. V. A. (2005). Online Mendelian Inheritance in Man (OMIM), a Knowledgebase of Human Genes and Genetic Disorders. *Nucleic Acids Res.* 33, D514–D517. doi:10.1093/nar/gki033

He, Y. H., Ge, J. W., Cheng, Z. Y., and Hao, X. Y. (2002). Effect of Naotaifang on Plasma TXB_2, 6-Keto-PGF_ (1α) and Serum TNF-α Contents in Patients with Qi Deficiency and Blood Stasis Cerebral Infarction [J]. *China J. Traditional Chin. Med. Mag.* 2002 (04), 16–17. doi:10.3969/j.issn.1005-5304.2002.04.006

Ho, W. M., Reis, C., Akyol, O., Akyol, G. Y., Applegate, R., Stier, G., et al. (2017). Pharmacological Management Options to Prevent and Reduce Ischemic Hemorrhagic Transformation. *Curr. Drug Targets* 18 (12), 1441–1459. doi:10.2174/1389450117666160818115850

Hu, G. X., Zhang, C. H., and Zhao, W. N. (2009). QSPR Study on the Permeability of Drugs across Caco-2 Monolayer. *J. Zhejiang Univ.* 3, 304–308. doi:10.1360/972009-470

Huang, Y., Rabb, H., and Womer, K. L. (2007). Ischemia-reperfusion and Immediate T Cell Responses. *Cell Immunol.* 248 (1), 4–11. doi:10.1016/j.cellimm.2007.03.009

Huang, D. W., Sherman, B. T., and Lempicki, R. A. (2009). Systematic and Integrative Analysis of Large Gene Lists Using DAVID Bioinformatics Resources. *Nat. Protoc.* 4, 44–57. doi:10.1038/nprot.2008.211

Huang, F., Lan, Y., Qin, L., Dong, H., Shi, H., Wu, H., et al. (2018). Astragaloside IV Promotes Adult Neurogenesis in Hippocampal Dentate Gyrus of Mouse through CXCL1/CXCR2 Signaling. *Molecules* 23 (9), E2178. doi:10.3390/molecules23092178

Lapi, D., and Colantuoni, A. (2015). Remodeling of Cerebral Microcirculation after Ischemia-Reperfusion. *J. Vasc. Res.* 52 (1), 22–31. doi:10.1159/000381096

Lee, J. C., Tae, H. J., Kim, I. H., Cho, J. H., Lee, T. K., Park, J. H., et al. (2017). Roles of HIF-1α, VEGF, and NF-κB in Ischemic Preconditioning-Mediated Neuroprotection of Hippocampal CA1 Pyramidal Neurons Against a Subsequent Transient Cerebral Ischemia. *Mol. Neurobiol.* 54 (9), 6984–6998. doi:10.1007/s12035-016-0219-2

Leech, T., Chattipakorn, N., and Chattipakorn, S. C. (2019). The Beneficial Roles of Metformin on the Brain with Cerebral Ischaemia/reperfusion Injury. *Pharmacol. Res.* 146, 104261. doi:10.1016/j.phrs.2019.104261

Li, M., Li, H., Fang, F., Deng, X., and Ma, S. (2017). Astragaloside IV Attenuates Cognitive Impairments Induced by Transient Cerebral Ischemia and Reperfusion in Mice via Anti-inflammatory Mechanisms. *Neurosci. Lett.* 639, 114–119. doi:10.1016/j.neulet.2016.12.046

Li, C., Yang, F., Liu, F., Li, D., and Yang, T. (2018). NRF2/HO-1 Activation via ERK Pathway Involved in the Anti-neuroinflammatory Effect of Astragaloside IV in LPS Induced Microglial Cells. *Neurosci. Lett.* 666, 104–110. doi:10.1016/j.neulet.2017.12.039

Liao, J., Xia, X., Wang, G. Z., Shi, Y. M., and Ge, J. W. (2015). Naotaifang Extract Treatment Results in Increased Ferroportin Expression in the hippocampus of Rats Subjected to Cerebral Ischemia. *Mol. Med. Rep.* 11 (6), 4047–4052. doi:10.3892/mmr.2015.3309

Liu, W., Wong, A., Law, A. C., and Mok, V. C. (2015). Cerebrovascular Disease, Amyloid Plaques, and Dementia. *Stroke* 46 (5), 1402–1407. doi:10.1161/STROKEAHA.114.006571

Longa, E. Z., Weinstein, P. R., Carlson, S., and Cummins, R. (1989). Reversible Middle Cerebral Artery Occlusion without Craniectomy in Rats. *Stroke* 20 (1), 84–91. doi:10.1161/01.str.20.1.84

Metodiewa, D., Kochman, A., and Karolczak, S. (1997). Evidence for Antiradical and Antioxidant Properties of Four Biologically Active N,N-Diethylaminoethyl Ethers of Flavaone Oximes: A Comparison with Natural Polyphenolic Flavonoid Rutin Action. *IUBMB Life* 41, 1067–1075. doi:10.1080/15216549700202141

Patel, R. A. G., and McMullen, P. W. (2017). Neuroprotection in the Treatment of Acute Ischemic Stroke. *Prog. Cardiovasc. Dis.* 59 (6), 542–548. doi:10.1016/j.pcad.2017.04.005

Peng, W., Hucks, D., Priest, R. M., Kan, Y. M., and Ward, J. P. (1996). Ligustrazine-induced Endothelium-dependent Relaxation in Pulmonary Arteries via an NO-Mediated and Exogenous L-arginine-dependent Mechanism. *Br. J. Pharmacol.* 119 (5), 1063–1071. doi:10.1111/j.1476-5381.1996.tb15778.x

Qu, Y. Z., Li, M., Zhao, Y. L., Zhao, Z. W., Wei, X. Y., Liu, J. P., et al. (2009). Astragaloside IV Attenuates Cerebral Ischemia-Reperfusion-Induced Increase in Permeability of the Blood-Brain Barrier in Rats. *Eur. J. Pharmacol.* 606 (1-3), 137–141. doi:10.1016/j.ejphar.2009.01.022

Ru, J., Li, P., and Wang, J. (2014). TCMSP: a Database of Systems Pharmacology for Drug Discovery from Herbal Medicines. *J. Cheminform.* 6, 13. doi:10.1186/1758-2946-6-13

Sacco, R. L., and Rundek, T. (2012). Cerebrovascular Disease. *Curr. Opin. Neurol.* 25 (1), 1–4. doi:10.1097/WCO.0b013e32834f89b1

Shao, A., Guo, S., Tu, S., Ammar, A. B., Tang, J., Hong, Y., et al. (2014). Astragaloside IV Alleviates Early Brain Injury Following Experimental Subarachnoid Hemorrhage in Rats. *Int. J. Med. Sci.* 11 (10), 1073–1081. doi:10.7150/ijms.9282

Shi, X., Tang, Y., Zhu, H., Li, W., Li, W., Li, Z., et al. (2014). Pharmacokinetic Comparison of Seven Major Bio-Active Components in normal and Blood Deficiency Rats after Oral Administration of Danggui Buxue Decoction by UPLC-TQ/MS. *J. Ethnopharmacol.* 153 (1), 169–177. doi:10.1016/j.jep.2014.02.004

Singh, N., Sharma, G., and Mishra, V. (2012). Hypoxia Inducible Factor-1: its Potential Role in Cerebral Ischemia. *Cell Mol. Neurobiol.* 32 (4), 491–507. doi:10.1007/s10571-012-9803-9

Stelzer, G., Rosen, R., Plaschkes, I., Zimmerman, S., Twik, M., Fishilevich, S., et al. (2016). The GeneCards Suite: From Gene Data Mining to Disease Genome Sequence Analysis. *Curr. Protoc. Bioinformatics* 54, 1–30. doi:10.1002/cpbi.5

Sun, K., Fan, J., and Han, J. (2015). Ameliorating Effects of Traditional Chinese Medicine Preparation, Chinese Materia Medica and Active Compounds on Ischemia/reperfusion-Induced Cerebral Microcirculatory Disturbances and Neuron Damage. *Acta Pharm. Sin. B* 5 (1), 8–24. doi:10.1016/j.apsb.2014.11.002

Szklarczyk, D., Franceschini, A., Wyder, S., Forslund, K., Heller, D., Huerta-Cepas, J., et al. (2015). STRING V10:protein-Protein Interaction Networks, Integrated over the Tree of Life. *Nucleic Acids Res.* 43, D447–D452. doi:10.1093/nar/gku1003

Thomas, W. B. (1996). Cerebrovascular Disease. *Vet. Clin. North. Am. Small Anim. Pract.* 26 (4), 925–943. doi:10.1016/s0195-5616(96)50057-4

Tong, Y. F., Xu, S. M., Liang, Y. C., Chen, H. P., Chen, L., and Liu, Y. (2019). Determination of 10 Chemical Constituents in Ligusticum Chuanxiong Hort by Different HPLC Methods. *China Pharm.* 30 (6), 92–97. doi:10.6039/j.issn.1001-0408.2019.06.17

Walters, W. P., and Murcko, M. A. (2002). Prediction of 'drug-Likeness. *Adv. Drug Deliv. Rev.* 54, 255–271. doi:10.1016/s0169-409x(02)00003-0

Wang, A., Zhu, G., Qian, P., and Zhu, T. (2017). Tetramethylpyrazine Reduces Blood-Brain Barrier Permeability Associated with Enhancement of Peripheral Cholinergic Anti-inflammatory Effects for Treating Traumatic Brain Injury. *Exp. Ther. Med.* 14 (3), 2392–2400. doi:10.3892/etm.2017.4754

Wang, J., Xu, J., Gong, X., Yang, M., Zhang, C., and Li, M. (2019). Biosynthesis, Chemistry, and Pharmacology of Polyphenols from Chinese Salvia Species: A Review. *Molecules* 24 (1), E155. doi:10.3390/molecules24010155

Wang, X., Shen, Y., and Wang, S. (2017). PharmMapper 2017 Update: a Web Server for Potential Drug Target Identification with a Comprehensive Target Pharmacophore Database. *Nucleic Acids Res.* 45 (W1), W356–W360. doi:10.1093/nar/gkx374

Wang, Z., Zhou, Z., Wei, X., Wang, M., Wang, B. O., Zhang, Y., et al. (2017). Therapeutic Potential of Novel Twin Compounds Containing Tetramethylpyrazine and Carnitine Substructures in Experimental Ischemic Stroke. *Oxid. Med. Cel. Longev.* 2017, 1–15. doi:10.1155/2017/7191856

Wang, H. (2012). *Study on the Promotion of Angiogenesis by Electrospun Fibers Carrying Astragaloside IV and Ferulic Acid [D]*. Chengdu City: Southwest Jiaotong University. [in chinese]

Weidner, N., Semple, J. P., Welch, W. R., and Folkman, J. (1991). Tumor Angiogenesis and Metastasis-Correlation in Invasive Breast Carcinoma. *N. Engl. J. Med.* 324 (1), 1–8. doi:10.1056/nejm199101033240101

White, B. C., Sullivan, J. M., DeGracia, D. J., O'Neil, B. J., Neumar, R. W., Grossman, L. I., et al. (2000). Brain Ischemia and Reperfusion: Molecular Mechanisms of Neuronal Injury. *J. Neurol. Sci.* 179 (S 1-2), 1–33. doi:10.1016/s0022-510x(00)00386-5

Wiklund, L., Martijn, C., Miclescu, A., Semenas, E., Rubertsson, S., and Sharma, H. S. (2012). Central Nervous Tissue Damage after Hypoxia and Reperfusion in Conjunction with Cardiac Arrest and Cardiopulmonary Resuscitation: Mechanisms of Action and Possibilities for Mitigation. *Int. Rev. Neurobiol.* 102, 173–187. doi:10.1016/B978-0-12-386986-9.00007-7

Wu, J., Ke, X., Ma, N., Wang, W., Fu, W., Zhang, H., et al. (2016). Formononetin, an Active Compound of Astragalus Membranaceus (Fisch) Bunge, Inhibits Hypoxia-Induced Retinal Neovascularization via the HIF-1α/VEGF Signaling Pathway. *Drug Des. Devel. Ther.* 10, 3071–3081. doi:10.2147/dddt.s114022

Wu, M. Y., Yiang, G. T., Liao, W. T., Tsai, A. P., Cheng, Y. L., Cheng, P. W., et al. (2018). Current Mechanistic Concepts in Ischemia and Reperfusion Injury. *Cell Physiol. Biochem.* 46 (4), 1650–1667. doi:10.1159/000489241

Xu, X., Zhang, W., Huang, C., Li, Y., Yu, H., Wang, Y., et al. (2012). A Novel Chemometric Method for the Prediction of Human Oral Bioavailability. *Int. J. Mol. Sci.* 13, 6964–6982. doi:10.3390/ijms13066964

Yang, S. H., Liu, R., Perez, E. J., Wang, X., and Simpkins, J. W. (2005). Estrogens as Protectants of the Neurovascular Unit against Ischemic Stroke. *Curr. Drug Targets CNS Neurol. Disord.* 4 (2), 169–177. doi:10.2174/1568007053544174

Yang, Z., Zhou, H., Zhou, P., Yang, J. H., Wan, H. T., Guan, M. G., et al. (2015). Effects of Effective Components of Chuanxiong and Astragalus Membranaceus on Hypoxic Cerebral Microvascular Endothelial Cells. *Chin. Tradit. Herb. Drugs* 46 (09), 1326–1332. [in chinese]. doi:CNKI:SUN:ZCYO.0.2015-09-018

Yang, K., Zeng, L., Bao, T., Long, Z., and Jin, B. (2019a). Exploring the Pharmacological Mechanism of Quercetin-Resveratrol Combination for Polycystic Ovary Syndrome: A Systematic Pharmacological Strategy-Based Research. *Sci. Rep.* 9 (1), 18420. doi:10.1038/s41598-019-54408-3

Yang, K., Zeng, L., Ge, A., Chen, Z., Bao, T., Long, Z., et al. (2019b). Investigating the Regulation Mechanism of Baicalin on Triple Negative Breast Cancer's Biological Network by a Systematic Biological Strategy. *Biomed. Pharmacother.* 118, 109253. doi:10.1016/j.biopha.2019.109253

Yang, L., Liu, N., Zhao, W., Li, X., Han, L., Zhang, Z., et al. (2019). Angiogenic Function of Astragaloside IV in Rats with Myocardial Infarction Occurs via the PKD1-HDAC5-VEGF Pathway. *Exp. Ther. Med.* 17 (4), 2511–2518. doi:10.3892/etm.2019.7273

Yoo, K. Y., Kwon, S. H., Lee, C. H., Yan, B., Park, J. H., Ahn, J. H., et al. (2012). FoxO3a Changes in Pyramidal Neurons and Expresses in Non-pyramidal Neurons and Astrocytes in the Gerbil Hippocampal CA1 Region after Transient Cerebral Ischemia. *Neurochem. Res.* 37 (3), 588–595. doi:10.1007/s11064-011-0648-2

Zeng, L., and Yang, K. (2017). Exploring the Pharmacological Mechanism of Yanghe Decoction on HER2-Positive Breast Cancer by a Network Pharmacology Approach. *J. Ethnopharmacol.* 199, 68–85. doi:10.1016/j.jep.2017.01.045

Zeng, L., Yang, K., and Ge, J. (2017). Uncovering the Pharmacological Mechanism of Astragalus Salvia Compound on Pregnancy-Induced Hypertension Syndrome by a Network Pharmacology Approach. *Sci. Rep.* 7 (1), 16849. doi:10.1038/s41598-017-17139-x

Zhang, Y., Yang, J., Yu, D., and Wan, H. T. (2010). Experimental Study on the Anticoagulant and Fibrinolytic Effects of Ligustrazine and Astragaloside IV on Hypoxic Human Umbilical Vein Endothelial Cells [C]/Basic and Clinical Research of Collateral Disease. [in chinese]. Available at: https://kns.cnki.net/kcms/detail/detail.aspx?dbcode=IPFD&dbname=IPFD9914&filename=ZHLB201009001085&v=MQ742d%25mmd2FFK1B94%25mmd2FsarAtjbblvsZ0PEUeVLSaYTegTePKnPc8mPBk3oCf3fbD8AYCWDVk3d1pT4Gk%3d

Zhao, T., Fu, Y., Sun, H., and Liu, X. (2018). Ligustrazine Suppresses Neuron Apoptosis via the Bax/Bcl-2 and Caspase-3 Pathway in PC12 Cells and in Rats with Vascular Dementia. *IUBMB Life* 70 (1), 60–70. doi:10.1002/iub.1704

Zhou, S., Shao, W., and Zhang, W. (2000). Clinical Study of Astragalus Injection Plus Ligustrazine in Protecting Myocardial Ischemia Reperfusion Injury. *Zhongguo Zhong Xi Yi Jie He Za Zhi* 20 (7), 504–507. [in Chinese]

Zhou, J., Du, T., Li, B., Rong, Y., Verkhratsky, A., and Peng, L. (2015). Crosstalk between MAPK/ERK and PI3K/AKT Signal Pathways during Brain Ischemia/Reperfusion. *ASN Neuro.* 7 (5). 1759091415602463. doi:10.1177/1759091415602463

Zhou, H., Wang, X., Ma, L., Deng, A., Wang, S., and Chen, X. (2019). FoxO3 Transcription Factor Promotes Autophagy after Transient Cerebral Ischemia/reperfusion. *Int. J. Neurosci.* 129 (8), 738–745. doi:10.1080/00207454.2018.1564290

Conflict of Interest: The authors declare that the research was conducted in the absence of any commercial or financial relationships that could be construed as a potential conflict of interest.

The reviewer HZ declared a shared affiliation with one of the authors KY to the handling editor at time of review.

Copyright © 2021 Yang, Zeng, Ge, Chen, Wang, Zhu and Ge. This is an open-access article distributed under the terms of the Creative Commons Attribution License (CC BY). The use, distribution or reproduction in other forums is permitted, provided the original author(s) and the copyright owner(s) are credited and that the original publication in this journal is cited, in accordance with accepted academic practice. No use, distribution or reproduction is permitted which does not comply with these terms.

frontiers in Pharmacology

ORIGINAL RESEARCH
published: 28 June 2021
doi: 10.3389/fphar.2021.680640

Components and Pharmacodynamical Mechanism of Yinfupian Based on Liquid Chromatography-Mass Spectrometry and Proteomics Analyses

Heng-li Tong[1†], *Hao Chen*[1†], *Fei-peng Gong*[2], *Ling-yun Zhong*[1*], *Jing Zhu*[1*] and *Song-hong Yang*[1]

[1]Laboratory of Traditional Chinese Medicine Preparation, School of Pharmacy, Jiangxi University of Traditional Chinese Medicine, Nanchang, China, [2]Department of Orthopedic, Jiangxi Provincial People's Hospital, Nanchang, China

OPEN ACCESS

Edited by:
Yan Xu,
Cleveland State University,
United States

Reviewed by:
Ina Yosifova Aneva,
Bulgarian Academy of Sciences,
Bulgaria
Donglin Chen,
Sichuan University, China

***Correspondence:**
Ling-yun Zhong
ly1638163@163.com
Jing Zhu
277836041@qq.com

[†]These authors have contributed equally to this work

Specialty section:
This article was submitted to Ethnopharmacology, a section of the journal Frontiers in Pharmacology

Received: 15 March 2021
Accepted: 02 June 2021
Published: 28 June 2021

Citation:
Tong H, Chen H, Gong F, Zhong L, Zhu J and Yang S (2021) Components and Pharmacodynamical Mechanism of Yinfupian Based on Liquid Chromatography-Mass Spectrometry and Proteomics Analyses. Front. Pharmacol. 12:680640. doi: 10.3389/fphar.2021.680640

Objective: According to the treatment records of Yang deficiency syndrome (YDS) with characteristic decoction pieces of lateral root of *Aconitum carmichaelii*—Yinfupian (YF) in traditional Chinese medicine prepare school, known as "Jianchangbang". The aim of this study was to investigate differences in the composition and therapeutic mechanism of the unprocessed lateral root of *Aconitum carmichaelii* (ULRA) and its processed product (YF).

Methods: Ultra-performance liquid chromatography-quadrupole time-of-flight mass spectrometry and orthogonal partial least squares discriminant analysis method were used to determine and screen the main components of ULRA and YF. Changes in the histological structure and morphology of gonads in rats were observed using hematoxylin-eosin. Enzyme-linked immunosorbent assay was used to determine the contents of serum cyclic adenosine monophosphate and cyclic guanosine monophosphate in YDS rats treated with ULRA and YF. Tandem mass tag proteomics analysis was used to identify the differentially expressed proteins in YDS rats treated with ULRA and YF.

Results: Both ULRA and YF exerted certain therapeutic effects on rats with YDS. They improved the gonadal morphology and increased the contents of serum cyclic adenosine monophosphate and cyclic guanosine monophosphate. After processing of ULRA into YF, the content of C19-diester-diterpenoid alkaloids decreased (converted into C19-monoester-diterpenoid alkaloids and C19-alkylol amine-diterpenoid alkaloids), whereas that of C20-diterpene alkaloids increased. Proteomics analysis showed that cytochrome P450 and aldehyde oxidase 3 (AOX3) were downregulated, whereas cathepsin G (CTSG) was upregulated in rats with YDS. Treatment with ULRA mainly downregulated the expression of α-actinin, fast skeletal troponin, creatine kinase, and myosin. Treatment with YF mainly upregulated the expression of mitochondrial ribosomal protein and mitochondrial inner membrane protein.

Conclusion: ULRA and YF exerted good therapeutic effects on YDS; the main difference in components between these preparations was in C19-diterpenoid alkaloids. ULRA

mainly acts on the muscle contraction-related proteins and is closely related to inflammation and myocardial injury. YF mainly acts on the mitochondrial proteins and is closely related to adenosine triphosphate energy metabolism.

Keywords: Aconitum, preparation, chemical components, pharmacology, proteomics, yang deficiency

INTRODUCTION

Yang deficiency syndrome (YDS) is a physical state characterized by chilly sensation (i.e., cold limbs) and dysfunction of the viscera. The main clinical manifestations are "dread cold, coolness of extremities, fatigued body and lack of strength, depression, hypomnesis, clear and large amount of urine" (Shi et al., 2018). This condition is associated with heart failure, hypothyroidism, chronic gastritis, primary nephrotic syndrome, infertility, and other diseases (Xia et al., 2010; Yang et al., 2010; Zou et al., 2011; Fan, 2014; Weng, 2014). Physiological, biochemical, and genomic studies on YDS (Zhang et al., 2019) have shown that YDS is associated with hypofunction of the hypothalamic-pituitary-adrenal, hypothalamic-pituitary-thyroid, and hypothalamic-pituitary-gonad axes, as well as disturbance of the cyclic nucleotide system and immune function. Polymorphisms of susceptibility genes in patients with YDS have been linked to the levels of cyclic adenosine monophosphate (c-AMP) and cyclic guanosine monophosphate (c-GMP), memory, metabolic energy status, and immune function (Yao et al., 2015).

Aconitum had been used medicinally and as a poison in both Western and Eastern countries for centuries. It is currently used medicinally in different parts of the world, such as China and Solčavsko (Slovenia) (Zhou et al., 2014; Povšnar et al., 2017). The lateral root of *Aconitum carmichaelii* (LRA) is termed "Fuzi" in traditional Chinese medicine; it is also called "Bushi" and "Kyeong-PoBuja" in Japan and Korea, respectively. It has shown efficacy in reviving the Yang for resuscitation, tonifying fire, and helping Yang, as well as dispersing cold and relieving pain (Chinese Pharmacopoeia Commission, 2020). The application of LRA has a long history, with remarkable therapeutic effects. The primary active component of *Aconitum* is alkaloid, mainly used to treat rheumatoid arthritis and cardiovascular diseases (Zhou et al., 2014). The diterpenoid alkaloids of LRA can be divided into diester, monoester, and alkylol amine alkaloids, according to the presence or absence of an ester bond at the C4 and C8 positions (Hu et al., 2010). Alkylol amine alkaloids and other water-soluble nitrogen-containing organic compounds are collectively referred to as water-soluble alkaloids. It has been reported that higenamine (Kosuge and Yokota, 1976), coryneine chloride (Konno et al., 1979), salsolinol (Cheng and Liang, 1982), uracil (Nizhenkovska, 2015), and fuzinoside (Li et al., 2015) are the cardiotonic active components of LRA. In recent years, further studies have shown that the water-soluble diterpenoid alkaloids found in LRA, including beiwutinine, mesaconine, karakoline, aconine, isotalatizidine, hypaconine, and 3-deoxyaconine, are cardiotonic active components (He et al., 2014a; He et al., 2014b; Wang et al., 2014). Fuziline, neoline (Xiong et al., 2012), talatisamine (Chen et al., 2014), and neoline also have significant analgesic effect (Suzuki et al., 2016). Songorine exerts anti-inflammatory, analgesic, and anti-anxiety effects (Yu et al., 2014; Khan et al., 2018). Fuziline has demonstrated efficacy against shock and improves myocardial ischemia (Gong et al., 2016). In addition, the water-soluble alkaloids found in LRA have anti-arrhythmic and anti-hypertensive effects (Fujita et al., 2009; Li et al., 2014). Therefore, this plant has broad prospects for the development of new drugs and applications. For centuries, Fuzi has been effectively used in treating various diseases associated with YDS. Jianchangbang is an ancient school of medicine in the south of China. Its method of preparing LRA through steaming with ginger juice is unique and famous. It is well established that Yinfupian (YF) has high efficacy and low toxicity, and is suitable for the treatment of YDS in clinical practice. At present, the impact of the components of *Aconitum* on proteins related to YDS remains unclear. The aim of this study was to investigate changes in the components of LRA before and after preparation, content of serum cyclic nucleotides, gonadal tissue morphology, and the relationship between components and proteins in rats with YDS. The proteomic changes in liver tissue were detected using tandem mass tag (TMT) mass spectrometry (MS). Proteomics may provide new information for high-throughput analysis, and it has been used in investigating the pathogenesis of YDS with great coverage of the proteome (Huang and Liang, 2005; Lu et al., 2012; Li et al., 2017). These research studies provide new data for the therapeutic value of LRA and its processed products in diseases related to YDS, and promote the development of new potential biomarkers for abnormalities related to Yang deficiency.

MATERIALS AND METHODS

Preparation of Medicinal Materials

Salted LRA (LRA soaked in bittern water; Batch No. 20180918) and ginger (fresh rhizomes of *Zingiber officinale Roscoe*) was purchased from the Chinese medicinal materials market of Zhangshu (China). All materials were authenticated by Professor Qianfeng Gong of Jiangxi University of Traditional Chinese Medicine (Nanchang, China). Unprocessed LRA (ULRA) was obtained by rinsing the salted LRA. ULRA was moistened with 15% fresh ginger juice (quality %) for 12 h and steamed for 8 h to obtain YF.

Administered solution: ULRA and YF were respectively soaked in water (×10 their volume) for 1 h, boiled for 30 min, and filtered. The obtained residues were soaked again in water (×6 their volume), boiled for 30 min, and filtered. The filtrates were combined and concentrated to 1.2 g/ml. The concentrated solution was stored at 4°C.

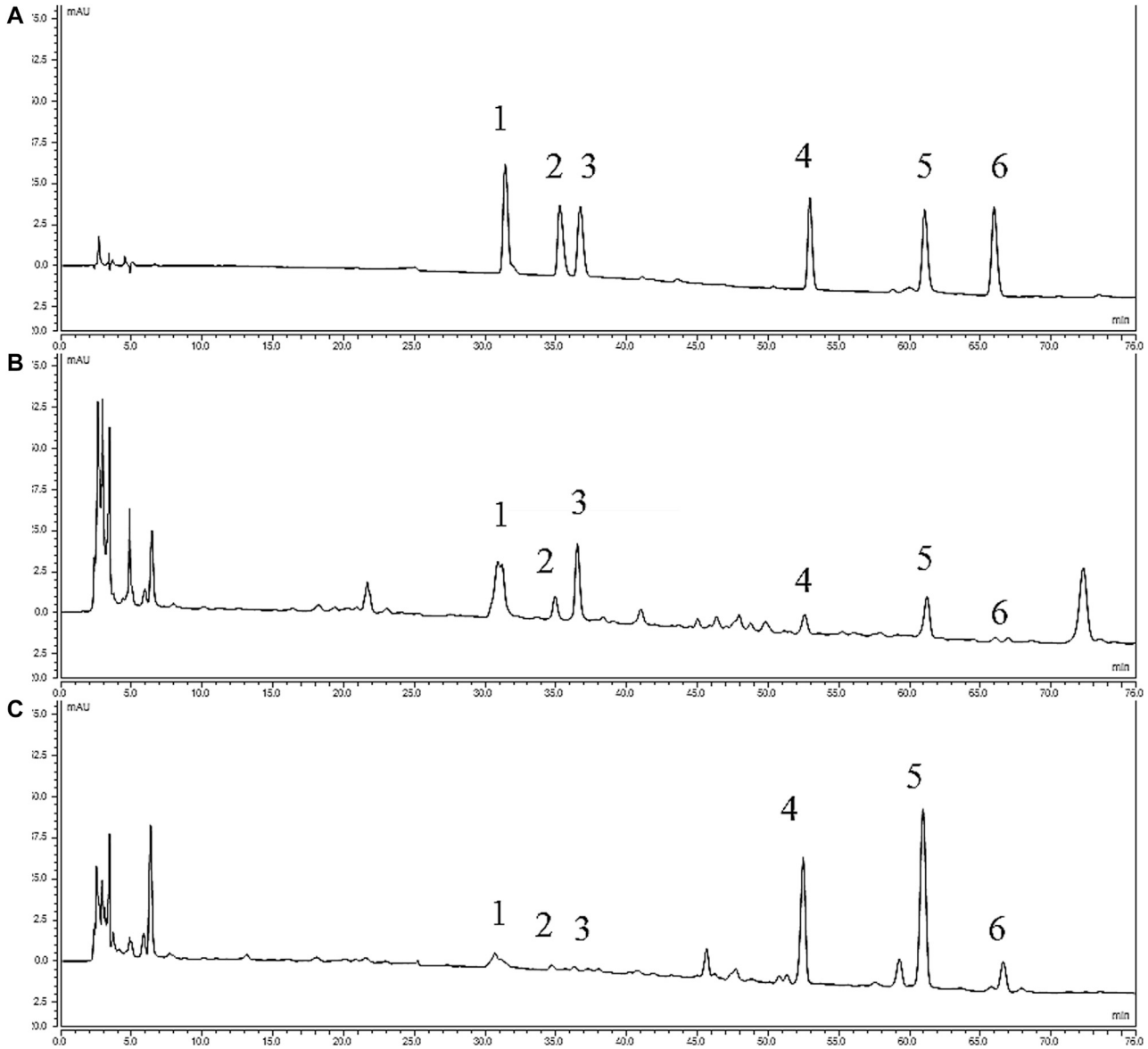

FIGURE 1 | HPLC chromatograms of various alkaloids. **(A)** Standards; **(B)** YF; **(C)** ULRA; (1), Benzoylmesaconine; (2), Benzoylhypaconine; (3), Benzoylaconine; (4), Mesaconitine; (5), Aconitine; (6), Hypaconitine; HPLC, high performance liquid chromatography; ULRA, unprocessed lateral root of *Aconitum carmichaelii*; YF, Yinfupian.

Standard solution: All standards (Weikeqi biotech Co., Ltd., Chengdu, China) were weighed and added isopropanol-dichloromethane (1:1) mixed solution to prepare solution contained 10.32 μg/ml aconitine (Batch NO. 130723), 37.38 μg/ml mesaconitine (Batch NO.130402), 5.75 μg/ml hypaconitine (Batch NO. 130509), 33.34 μg/ml benzoylaconine (Batch NO. 130516), 7.92 μg/ml benzoylmesaconine (Batch NO. 130505), and 5.38 μg/ml benzoylhypaconine (Batch NO. 130401).

Sample solution for HPLC: ULRA and YF were respectively soaked in water (×10 the volume) for 1 h, boiled for 30 min, and filtered. The obtained residues were soaked again in water (×6 the volume), boiled for 30 min, and filtered. The filtrates were combined, concentrated and dried into powers. The powders (2 g) of ULRA and YF decoction mixed with ammonia (3 ml), and immersed in isopropanol-ethyl acetate (1:1) mixed solution (50 ml) extracted under ultrasonic condition for 30 min, and then filtered. The filtrate (25 ml) evaporated to dryness under 40°C and low pressure condition. The obtained residue dissolved by isopropanol-dichloromethane (1:1) mixed solution (5 ml), and then filtrated through a filter membrane (0.22 μm).

Sample solution for UPLC-quadrupole-TOF-MS: The medicine (100 g of ULRA or YF) and 15 times the volume of water (×15 their volume) were placed into round bottom flasks, soaked for 30 min, subjected to heat reflux, decocted for 30 min, filtered and concentrated to 1 g/ml. Subsequently, 5.0 ml of the above concentrated solutions were transferred into 50 l volumetric flasks. Water was added to

TABLE 1 | Calibration curves of various alkaloids.

Alkaloids	Regression equations	R^2
Aconitine	Y = 0.2050X+0.3294	0.9994
Mesaconitine	Y = 0.3915X+0.4621	0.9992
Hypaconitine	Y = 0.4043X+0.8154	0.9996
Benzoylaconine	Y = 0.6271X+0.3214	0.9992
Benzoylmesaconine	Y = 0.7897X+0.7180	0.9996
Benzoylhypaconine	Y = 0.3405X+0.1127	0.9993

dissolve the concentrated solution. The supernatants were filtered using a 0.22-microporous membrane. The primary filtrates were discarded and the remaining filtrates were stored as sample solution.

Conditions of Chromatography and Mass Spectrometry

An Ultimate 3000 high performance liquid chromatography (HPLC) (Dionex, Sunnyvale, CA, United States), equipped with a PDA-3000 diode array ultraviolet detector (Dionex, Sunnyvale, CA, United States) and a chromeleom workstation was used. Symmetry C18 column (5 μm, 4.6 mm × 250 mm, Waters Corporation, Milford, MA, United States) was used to determine the six alkaloids standards and the components of ULRA and YF.

The following gradient system was used with 100% acetonitrile (solvent A) and 0.04 mol/L Ammonium acetate aqueous solution (PH = 10, Adjusted by ammonia water) (solvent B): 0–8 min: 18% of A; 8–35 min: linear 18–35% of A; 35–45 min: linear 35–45% of A; 45–55 min: linear 45–50% of A; 55–65 min: linear 50–55% of A; 65–75 min: 55% of A. The flowing rate was 1.0 ml/min, the detection wavelength was at 235 nm, the column temperature was at 35°C, and the injection volumn was 20 μl. The chromatograms are shown in **Figure 1**.

An ultra-high performance liquid chromatography (UPLC) tandem four-stage rod time-of-flight (TOF) mass spectrometer (Triple TOF 5600+; AB Sciex), equipped with an Analyst1.6 Chromatographic workstation and MS analysis software (PeakView v1.2; AB Sciex), was used. Nexera UPLC LC-30 (Shimadzu Corporation, Kyoto, Japan) and ACQUITY UPLC® BEH C18 column (1.7 μm, 2.1 mm × 100 mm; Waters Corporation, Milford, MA, United States) were used to determine the components of ULRA and YF.

The gradient system was 0.1% formic acid aqueous solutions (solvent A)-100% acetonitrile (solvent B): 0–25 min, 95–60% A; 25–32 min, 60–5% A; 32–35 min, 5–95% A; Experiment: Positive Ion Mode, Electron Spray Ionization, ionization temperature: 500 °C, curtain gas: 40 psi, ion source gas1: 50 psi, ion source gas2: 50 psi, ion spray voltage: 5,500 eV, collision energy: 40 eV, declustering potential: 100 eV, mass scan range: *m/z* 100–1,000. The flow rate was 0.5 L/min, the column temperature was 40°C, and the injection volume was 2 μl.

Calibration of Six Alkaloids and Method Evaluation

Standard samples of alkaloids were prepared into appropriate concentration, and the calibration curve for each alkaloid was performed with six quantities by plotting the peak area vs. the concentrations of the alkaloids. The results of all calibration curves are shown in **Table 1**.

Precision and stability was calculated within 24 h (n = 6) with the standard solution of the six alkaloids. Repeatability and average recovery was tested by sample solutions of ULRA and standard solutions of the six alkaloids, and they were injected six times. All indexes of method evaluation evaluated by calculating the relative standard deviation (RSD) (**Table 2**).

Data Collection and Analysis of Ultra-High Performance Liquid Chromatography-Quadrupole-Time-of-Flight-Mass Spectrometry

The original data were imported into MarkView v1.2.1 and PeakView v1.2 software (both from AB Sciex) to determine the retention time, mass-to-charge ratio, intensity data, and information of two-stage MS (MS2). The total ion chromatogram of ULRA and YF is shown in **Figure 2**. Subsequently, the data were imported into Simca-p 14.1 software. To observe the contour differences between groups and more effectively identify differences in markers, orthogonal partial least squares discriminant analysis (OPLS-DA) was performed. This analysis yielded the OPLS-DA score chart and similarity-plot (S-plot) diagram, which could directly reflect the contribution rate of differences between groups. The markers with variable important in projection (VIP) > 1 and p-values <0.05 were considered potentially highly related to differences in the decoction pieces. The qualitative analysis of these markers was performed by comparing evidence form the literature and data retrieved from databases.

Experimental Animal Treatments and Sample Collection

The animal study was approved by the Ethics Committee on Laboratory Animals of Jiangxi University of Traditional Chinese Medicine. Sprague–Dawley rats (24 males and 24 females, each weighing 200 ± 20 g; laboratory animal license no. 3700920018,748) were purchased from Jinan Pengyue Experimental Animal Breeding Co., Ltd. (Jinan, China) (license key number: SCXK (Lu) 2014 0007). All rats after acclimatizing in normal atmospheric temperature for 5 days and divided randomly into four groups containing equal numbers of male and female animals, namely the blank (B) group (n = 12), model (M) group (n = 12), ULRA group (n = 12), and YF group (n = 12).

Rats in the model and treatment groups received *Rheum officinale* (dried roots and rhizomes of *Rheum officinale* Baill) powder 1.0 g and goldthread (dried rhizomes of *Coptis chinensis* Franch) powder 1.0 g (namely, 2 g of herb powder/8 ml water suspension, 1 ml/100 g body weight, once daily for 7 days, at the same time) through oral gavage. After the administration, the rats were subjected to exhaustive swimming once daily to establish the model of YDS. Rats in the blank group received the same amount of distilled water daily through oral gavage. On day 8, rats in the

TABLE 2 | RSD of method evaluation for various alkaloids (n = 6).

Alkaloids	Precision (%)	Stability (%)	Repeatability (%)	Average recovery (%)
Aconitine	1.08	0.38	0.35	0.16
Mesaconitine	0.75	0.52	0.43	0.63
Hypaconitine	0.25	0.73	0.86	1.40
Benzoylaconine	0.65	0.46	0.74	0.59
Benzoylmesaconine	0.54	0.23	0.65	0.30
Benzoylhypaconine	1.02	0.35	0.47	1.30

treatment groups received ULRA and YF concentrated solution at 12 g (crude medicine)/kg (bodyweight) per day. Rats in the blank and model groups received the same amount of distilled water by oral gavage for 7 days.

Blood samples were collected from the abdominal aorta after anesthesia using 5% pentobarbital sodium (5 mg/100 g bodyweight, intraperitoneally). Next, the liver tissues were rapidly excised, frozen in liquid nitrogen, and stored at −80°C for protein extraction. Subsequently, testicular and ovarian tissues were excised, sectioned, embedded in paraffin, and stained with hematoxylin-eosin. Serum was separated by centrifugation at 3,000 rpm for 5 min at 4°C after standing for 15 min to detect c-Amp and c-GMP using enzyme-linked immunosorbent assay kits (LOT: 20191108; Nanjing Jiancheng Bioengineering Institute, Nanjing, China). Throughout the experimental period, there was no occurrence of death in the animals. At the end of the experiment, euthanasia was performed under anesthesia with sodium pentobarbital. The data are expressed as the mean ± standard deviation, and comparison between groups was performed using one-way analysis of variance.

Tandem Mass Tag-Based Proteomics

Liver tissues were added to SDT lysis buffer (4% sodium dodecyl sulfate [SDS; 161-0302; Bio-Rad, Hercules, CA, United States]; 100 mM Tris-HCl [A6141; Sigma, Saint Louis, MO, United States]; 1 mM dithiothreitol [DTT; 161-0404; Bio-Rad, Hercules, CA, United States]; pH 7.6), transferred into a 2-ml centrifuge tube with an appropriate amount of quartz sand (MP 6910-050; MP Biomedicals, Santa Ana, CA, United States) and 1/4-inch ceramic bead (MP 6540-034; MP Biomedicals, Santa Ana, CA, United States), and crushed into homogenate (24 × 2, 6.0 M/S, 60 s, twice) using a MP fastprep-24 homogenizer (MP Biomedicals). Samples were subjected to ultrasound with an ultrasonic crusher (JY92-II; Scientz, Ningbo, China) (power: 80 W, duration: 10 s, intervals: 15 s, repetitions: 10) and placed in boiling water for 15 min. The homogenate was centrifuged at 14,000×g for 40 min, the supernatant was filtered with a 0.22-μm membrane, and the filtrate was collected. The bicinchoninic acid (BCA) method (BCA quantitative Kit; P0012; Beyotime, Nanjing, China) was used for protein quantification. The samples were stored at −80°C.

Protein from each group (20 μg) was added to 5× buffer solution (10% SDS, 0.5% bromophenol blue, 50% glycerin, 500 mM DTT, 250 mM Tris-HCL, pH 6.8) and placed in boiling water for 5 min. Next, 12.5% SDS-polyacrylamide gel electrophoresis (constant current, 14 Ma, 90 min; eps601; GE Healthcare, Marlborough, MA, United States) and Coomassie brilliant blue staining were performed.

Protein solutions (30 μl) were obtained from each group. DTT was added to reach a final concentration of 100 mM. Subsequently, the solutions were placed in boiling water for 5 min and cooled to room temperature. Uric acid (UA) buffer (200 μl; 8 M urea [161-0731 Bio-Rad]; 150 mM Tris-HCl; pH 8.0) was added, mixed well, transferred into a 10 kDa ultrafiltration centrifuge tube (Sartorius, Gottingen, Germany), and centrifuged at 14,000×g for 15 min; the filtrate was discarded (this step was repeated once). Iodoacetamide buffer (100 μl; 100 mM iodoacetamide [163-2109; Bio-Rad] in UA) was added, oscillated at 600 rpm for 1 min, reacted in the dark at room temperature for 30 min, and centrifuged at 14,000 × g for 15 min. UA buffer (100 μl) was added and centrifuged at 14,000 × g for 15 min; this step was repeated twice. Subsequently, 100 mM triethylamonium bicarbonate (TEAB) buffer (100 μl) was added, and the mixture was centrifuged at 14,000 × g for 15 min; this step was repeated twice. Trypsin buffer (40 μl; 4 μg trypsin [317107; Promega coporation, Madison, WI, United States) in 40 μl 100 mM TEAB buffer) was added, oscillated at 600 rpm for 1 min, and placed at 37°C for 16–18 h. The collection tubes were replaced, the samples were centrifuged at 14,000 × g for 15 min; ×10 diluted 100 mM TEAB buffer (40 μl) was added, and the samples were centrifuged again at 14,000 × g for 15 min; the filtrates were collected for peptide quantification (OD280).

Peptides (100 μg) were obtained from each sample and labeled according to the instructions provided by the manufacturer (TMT Mass Tagging Kits and Reagents; Thermo Fisher Scientific, Waltham, MA, United States). The labeled peptides in each group were mixed in equal amount and graded using a high pH reversed-phase spin column. Following lyophilization, peptides (100 μg) were diluted in 0.1% trifluoroacetic acid (T6508; Sigma) (300 μl), transferred to the high pH reversed-phase spin column, and centrifuged to collect the flow-through compositions. After adding 300 μl of pure water, the washed compositions were collected by centrifugation, and gradient elution was performed. Following lyophilization, the samples were re-dissolved in 0.1% formic acid (06450; Fluka, Seelze, Germany) (12 μl), and the concentration of the peptide was determined at OD280.

Each sample was separated by HPLC Easy nLC (Thermo Fisher Scientific) at a nl flow rate. Buffer solution A was 0.1% formic acid aqueous solution, while buffer solution B was 0.1%

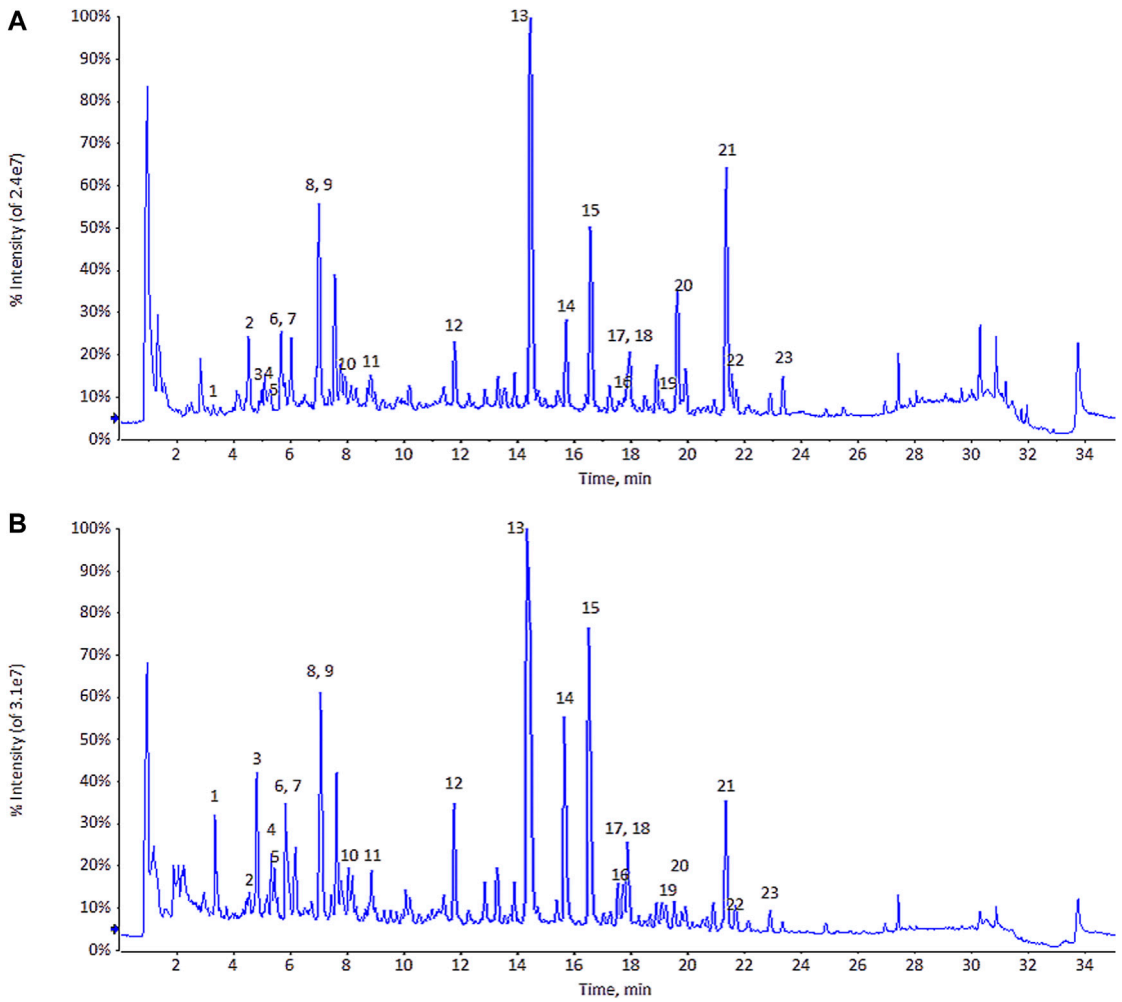

FIGURE 2 | The total ion chromatogram (TIC) of ULRA **(A)** and YF **(B)**. ULRA, unprocessed lateral root of *Aconitum carmichaelii*; YF, Yinfupian.

formic acid acetonitrile aqueous solution (acetonitrile was 84%). The chromatographic column was equilibrated with 95% A solution. The sample was loaded from the automatic injector to the loading column (Acclaim PepMap100, 100 μm × 2 cm, nanoViper C18; Thermo Fisher Scientific) and separated by the analytical column (EASY column, 10 cm, ID75 μm, 3 μm, C18-A2; Thermo Fisher Scientific) at a flow rate of 300 nl/min. For gradient elution, the linear gradient of solution B ranged 0–55% for 0–80 min, 55–100% for 80–85 min, and 100% for 85–90 min.

The samples were separated by chromatography and analyzed using a Q-Exactive mass spectrometer (Thermo Fisher Scientific). The analysis time was 60 min. The detection method was positive ion mode; scanning range of the parent ion was 300–1,800 m/z; resolution of primary MS was 70,000 at 200 m/z; AGC target was 3e6; primary maximum IT was 10 ms; number of scan ranges was 1; and dynamic exclusion was 40.0 s. The mass-to-charge ratios of polypeptide and polypeptide fragments were collected using the following method: 10 MS2 scans were collected after each full scan; the MS2 activation type was higher-energy collisional dissociation; isolation window was 2 m/z; resolution of secondary MS was 35,000 at 200 m/z (TMT6plex, Thermo Fisher Scientific); microscan was 1; secondary maximum IT was 60 ms; normalized collision energy was 30 eV; and underfill was 0.1%.

The raw data of MS were obtained in RAW files, and identified and quantitatively analyzed by Mascot2.2 and Proteome Discoverer 1.4 (Thermo Fisher Scientific). Blast2GO (Götz et al., 2008) was used to perform the Gene Ontology (GO) annotation of the target protein set. The Kyoto Encyclopedia of Genes and Genomes (KEGG) Automatic Annotation Server (Moriya et al., 2007) was used to perform the KEGG pathway annotation of the target protein set. The target protein sequence was classified through KEGG Orthology (KO) by comparison with data obtained from the KEGG GENES database. Information on the pathway involved in the target protein sequence was automatically obtained according to the KO classification. Fisher's exact test was used to compare the distribution of each GO classification or KEGG pathway in the target protein set, as well as the overall protein set for

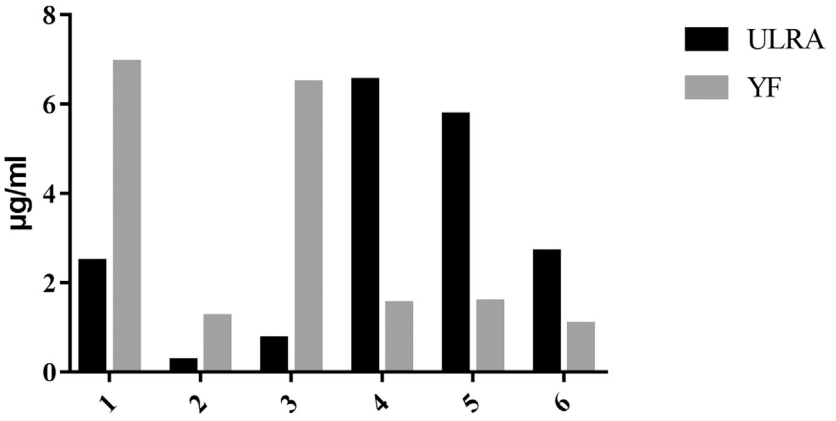

FIGURE 3 | Results of content determination of six alkaloids (n = 3). (1), Benzoylmesaconine; (2), Benzoylhypaconine; (3), Benzoylaconine; (4), Mesaconitine; (5), Aconitine; (6), Hypaconitine.

evaluating the significance level of protein enrichment of a GO term or KEGG pathway. Firstly, the quantitative information of the target protein set was normalized (normalized to the [−1, 1] region). Secondly, the Cluster 3.0 software was used to classify the two dimensions of sample and protein expression (distance algorithm: Euclidean; connection mode: average linkage). Finally, the hierarchical clustering heat map was generated using the Java Treeview software, and the gene symbol of the target protein was obtained from the database of the source of the target protein sequence. These gene symbols were used in the IntAct (http://www.ebi.ac.uk/intact/main.xhtml) or Search Tool for the Retrieval of Interacting Genes (STRING; http://string-db.org/) database to search for direct and indirect interactions between target proteins; the interaction network was generated and analyzed using the Cytoscape 3.2.1 software.

RESULTS

High Performance Liquid Chromatography Analysis of Alkaloids Contents in Unprocessed Lateral Root of *Aconitum carmichaelii* and Yinfupian

The contents of six alkaloids in ULRA and YF are calculated by the calibration curves (**Table 1**), and the results are shown in **Figure 3**. When comparing of ULRA with YF, the contents of aconitine, mesaconitine, and hypaconitine in YF were lower than those of them in ULRA. The contents of benzoylaconine, benzoylmesaconine, and benzoylhypaconine in YF were obvious higher than those of them in ULRA. The diester alkaloids (aconitine, mesaconitine, and hypaconitine) in "Fuzi" were decreased after "Fuzi" processed into YF, and the diester alkaloids may turned into monoester alkaloids, therefore the contents of benzoylaconine, benzoylmesaconine, and benzoylhypaconine in YF are high.

Analysis of Markers of Differential Components

In the OPLS-DA analysis, there were no abnormal samples that were excluded (all samples were within the confidence interval). The score and S-plot chart, which can directly reflect the differences between two groups and the contribution rate of differences in components, were obtained. All the samples of the score chart were clearly distinguished, suggesting that the two groups of samples were significantly different (**Figure 4**), Two principal components were obtained: R2X = 0.701, R2Y = 0.999, Q2 = 0.991. In the S-plot chart (**Figure 5**), closer proximity to the two corners of the S-plot indicated a larger VIP value of the variable (i.e., the component with great difference).

According to the data obtained by HPLC-quadrupole-TOF-MS, a comparative analysis was performed between the ULRA and YF groups. The VIP value of the OPLS-DA model principal component (threshold value > 1) and the p-value of the t-test (threshold: <0.05) were used to screen different components, combined with literature, MassBank database, and other searches. The structure of the differential substances was finally identified as representative of the difference in components (**Table 3**).

Identification of components: The inference process was illustrated using chuanfumine as an example. Compound 1 produced 394.3 $[M+H]^+$ with high sensitivity at 40 eV collision energy. In the MS2 spectrum, the peak produced 376.2479 $[M+H-H_2O]^+$, 358.2385 $[M+H-2H_2O]^+$, and 340.2278 $[M+H-3H_2O]^+$, according to the literature (Liu et al., 2011; Zhang et al., 2012). There was no $[M+H-CH_3OH-H_2O]^+$, which is a characteristic ion of karakolidine ($C_{22}H_{35}NO_5$). Therefore, it was inferred that compound 1 was chuanfumine.

Histomorphological Changes in the Gonads of Rats Induced by Yang Deficiency Syndrome

Ovarian and testicular tissues were obtained from female and male rats, respectively. In the blank group, the histological

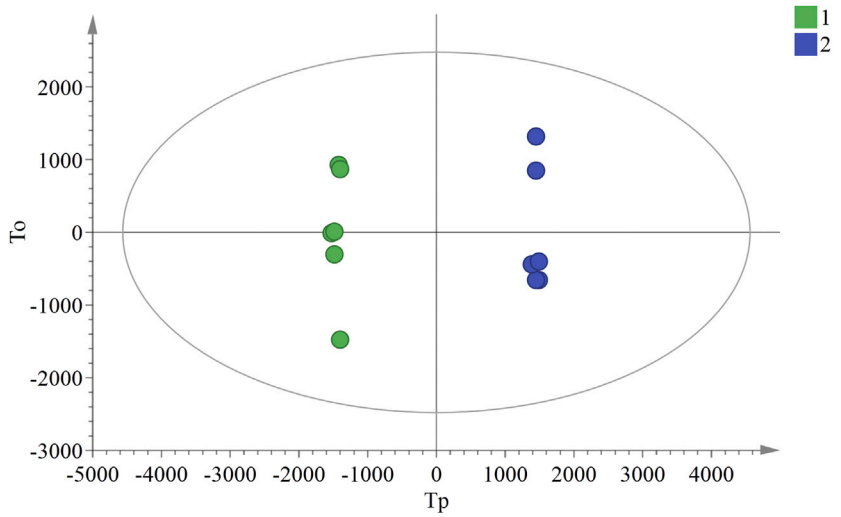

FIGURE 4 | OPLS-DA score chart of ULRA and YF groups. Green dots are ULRA group, and blue dots are YF group. OPLS-DA, partial least squares discrimination analysis; ULRA, unprocessed lateral root of *Aconitum carmichaelii*; YF, Yinfupian.

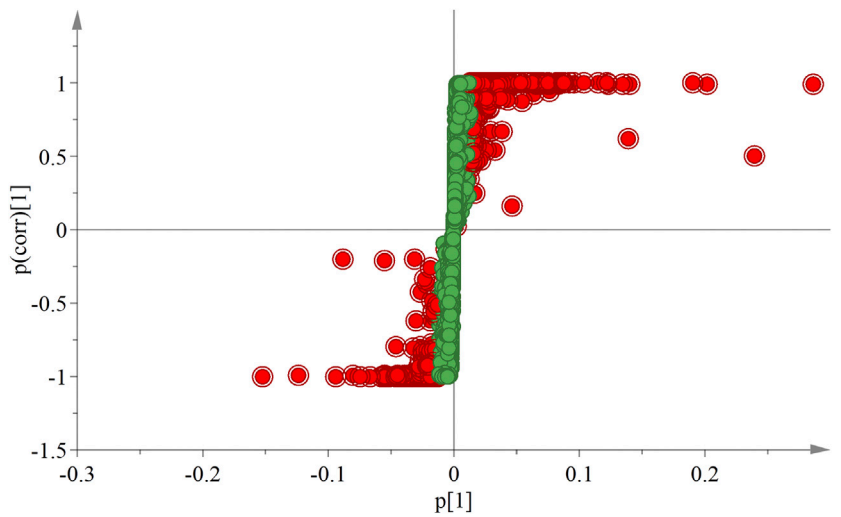

FIGURE 5 | S-plot chart of ULRA and YF groups. The VIP value of red dots is greater than 1. ULRA, unprocessed lateral root of *Aconitum carmichaelii*; YF, Yinfupian; VIP, variable important in projection.

structure of the testes was normal, and the division of spermatogenic cells in the seminiferous tubules was active with rich and obvious layers (**Figure 6A**). In the model group, the number of spermatogenic cells and sperm cells was significantly lower, and the arrangement was loose with vacuoles (**Figure 6B**).

Compared with the model group, the number of spermatogenic cells and sperm cells in the ULRA and YF groups was significantly increased and orderly arranged, similar to the blank group, and recovered significantly (**Figures 6C,D**).

In the blank group, the number and morphology of ovarian follicles at all levels were normal; the ovarian follicles grew actively, and there were abundant layers of granulosa cells (**Figure 7A**). In the model group, the volume of the ovary decreased, and the number of ovarian follicles and granulosa cells in different layers decreased significantly (**Figure 7B**).

Compared with the model group, the ovarian volume and the number of granulosa cells in the ULRA group increased (**Figure 7C**). The volume of ovary and the number of

TABLE 3 | Screening and analysis of the components of ULRA and YF.

No	t_R/ min	Type	Name	Formula	$[M + H]^+$ (m/z)	Main fragment ions (m/z)	ULRA/ YF	References
1	3.3	C_{20}DA	Chuanfumine	$C_{22}H_{35}NO_5$	394.3	376.2479 $[M+H-H_2O]^+$, 358.2385 $[M+H-2H_2O]^+$, 340.2278 $[M+H-3H_2O]+$	↓	Liu et al. (2011); Tan et al. (2011); Zhang et al. (2012); Huang et al. (2015)
2	4.5	C_{19}ADA	Senbusine A	$C_{23}H_{37}NO_6$	424.3	406.2580 $[M+H-H_2O]^+$, 388.2484 $[M+H-2H_2O]^+$, 374.2337 $[M+H-H_2O-CH_3OH]^+$, 360.2179 $[M+H-2CH_3OH]^+$, 356.2223 $[M+H-2H_2O-CH_3OH]^+$	↓	Tan et al. (2011); Huang et al. (2015)
3	4.8	C_{19}ADA	Mesaconine	$C_{24}H_{39}NO_9$	486.3	468.2589 $[M+H-H_2O]^+$, 454.2425 $[M+H-CH_3OH]^+$, 436.2312 $[M+H-CH_3OH-H_2O]^+$, 422.2170 $[M+H-2CH_3OH]^+$, 404.2057 $[M+H-2CH_3OH-H_2O]^+$, 378.1907 $[M+H-C_2O_2-3H_2O]^+$	↓	Tan et al. (2011); Huang et al. (2015)
4	5.3	C_{19}ADA	Karakoline	$C_{22}H_{35}NO_4$	378.3	360.2519 $[M+H-H_2O]^+$, 332.2219 $[M+H-CH_3-CH_3O]^+$, 328.2267 $[M+H-CH_3OH-H_2O]^+$, 310.2173 $[M+H-CH_3OH-2H_2O]^+$	↓	Huang et al. (2015)
5	5.4	C_{19}ADA	Isotalatizidine	$C_{23}H_{37}NO_5$	408.3	390.2641 $[M+H-H_2O]^+$, 372.2550 $[M+H-2H_2O]^+$, 358.2389 $[M+H-H_2O-CH_3OH]^+$	↓	Tan et al. (2011); Huang et al. (2015)
6	5.8	C_{20}DA	Songorine	$C_{22}H_{31}NO_3$	358.2	340.2266 $[M+H-H_2O]^+$, 322.2178 $[M+H-2H_2O]^+$	↓	Tan et al. (2011); Zhang et al. (2012); Huang et al. (2015)
7	5.9	C_{19}ADA	Aconine	$C_{25}H_{41}NO_9$	500.3	482.2748 $[M+H-H_2O]^+$, 468.2592 $[M+H-CH_3OH]^+$, 450.2479 $[M+H-CH_3OH-H_2O]^+$, 436.2335 $[M+H-2CH_3OH]^+$, 418.2229 $[M+H-2CH_3OH-H_2O]^+$	↓	Huang et al. (2015)
8	7.0	C_{19}ADA	Fuziline	$C_{24}H_{39}NO_7$	454.3	436.2669 $[M+H-H_2O]^+$, 418.2591 $[M+H-2H_2O]^+$, 404.2420 $[M+H-CH_3OH-H_2O]^+$, 386.2327 $[M+H-CH_3OH-2H_2O]^+$, 354.2066 $[M+H-2CH_3OH-2H_2O]^+$	↓	Tan et al. (2011); Sun et al. (2012); Huang et al. (2015)
9	7.0	C_{19}ADA	Hypaconine	$C_{24}H_{39}NO_8$	470.3	438.2470 $[M+H-CH_3OH]^+$, 406.2217 $[M+H-2CH_3OH]^+$, 388.2114 $[M+H-2CH_3OH-H_2O]^+$, 378.1903 $[M+H-2CH_2O-CH_3OH]^+$, 374.1961 $[M+H-3CH_3OH]^+$, 356.1853 $[M+H-3CH_3OH-H_2O]^+$	↓	Huang et al. (2015)
10	8.0	C_{19}ADA	Neoline	$C_{24}H_{39}NO_6$	438.3	420.2737 $[M+H-H_2O]^+$, 402.2648 $[M+H-2H_2O]^+$, 388.2474 $[M+H-H_2O-CH_3OH]^+$, 374.2341 $[M+H-2CH_3OH]^+$, 370.2382 $[M+H-2H_2O-CH_3OH]^+$, 356.2220 $[M+H-2CH_3OH-H_2O]^+$	↓	Liu et al. (2011); Tan et al. (2011); Huang et al. (2015)
11	8.8	C_{19}ADA	Talatizamine	$C_{24}H_{39}NO_5$	422.3	390.2644 $[M+H-CH_3OH]^+$, 372.2546 $[M+H-CH_3OH-H_2O]^+$, 358.2395 $[M+H-2CH_3OH]^+$, 340.2289 $[M+H-2CH_3OH-H_2O]^+$	↓	Tan et al. (2011); Sun et al. (2012); Huang et al. (2015)
12	11.7	C_{19}MDA	14-Benzoyl-10-OH–mesaconine	$C_{31}H_{43}NO_{11}$	606.3	588.2788 $[M+H-H_2O]^+$, 574.2636 $[M+H-CH_3OH]^+$, 556.2515 $[M+H-CH_3OH-H_2O]^+$, 542.2376 $[M+H-2CH_3OH]^+$, 524.2262 $[M+H-2CH_3OH-H_2O]^+$	↓	Tan et al. (2011)
13	14.3	C_{19}MDA	Benzoylmesaconine	$C_{31}H_{43}NO_{10}$	590.3	558.2683 $[M+H-CH_3OH]^+$, 540.2571 $[M+H-CH_3OH-H_2O]^+$, 526.2430 $[M+H-2CH_3OH]^+$, 508.2316 $[M+H-2CH_3OH-H_2O]^+$	↓	Tan et al. (2011); Huang et al. (2015)
14	15.6	C_{19}MDA	Benzoylaconine	$C_{32}H_{45}NO_{10}$	604.3	586.3005 $[M+H-H_2O]^+$, 572.2836 $[M+H-CH_3OH]^+$, 540.2591 $[M+H-2CH_3OH]^+$, 554.2726 $[M+H-CH_3OH-H_2O]^+$, 522.2477 $[M+H-2CH_3OH -H_2O]^+$	↓	Tan et al. (2011); Huang et al. (2015)
15	16.5	C_{19}MDA	Benzoylhypaconine	$C_{31}H_{43}NO_9$	574.3	542.2733 $[M+H-CH_3OH]^+$, 524.2661 $[M+H-CH_3OH-H_2O]^+$, 510.2482 $[M+H-2CH_3OH]^+$, 492.2391 $[M+H-2CH_3OH-H_2O]^+$	↓	Tan et al. (2011); Huang et al. (2015)
16	17.7	C_{19}MDA	14-Benzoyl-13-deoxyhyaconine	$C_{31}H_{43}NO_8$	558.3	526.2807 $[M+H-CH_3OH]^+$, 508.2718 $[M+H-CH_3OH-H_2O]^+$, 494.2548 $[M+H-2CH_3OH]^+$, 476.2449 $[M+H-2CH_3OH-H_2O]^+$	↓	Tan et al. (2011)
17	17.9	C_{19}MDA	Benzoyldeoxyaconine	$C_{32}H_{45}NO_9$	588.3	556.2900 $[M+H-CH_3OH]^+$, 538.2832 $[M+H-CH_3OH-H_2O]^+$, 524.2650 $[M+H-2CH_3OH]^+$, 496.2347 $[M+H-2CH_3OH-H_2O]^+$	↓	Tan et al. (2011); Huang et al. (2015)
18	17.9	C_{19}DDA	Beiwutine	$C_{33}H_{45}NO_{12}$	648.3	616.2781 $[M+H-CH_3OH]^+$, 598.2683 $[M+H-CH_3OH-H_2O]^+$, 588.2822 $[M+H-2CH_2O]^+$,	↑	Huang et al. (2015)

(Continued on following page)

TABLE 3 | (*Continued*) Screening and analysis of the components of ULRA and YF.

No	t_R/ min	Type	Name	Formula	$[M + H]^+$ (m/z)	Main fragment ions (m/z)	ULRA/ YF	References
						556.2563 $[M+H-2CH_2O-CH_3OH]^+$, 538.2457 $[M+H-2CH_2O-CH_3OH-H_2O]^+$		
19	19.4	C_{19}MDA	Dehydrated-benzoylhypaconine	$C_{31}H_{41}NO_8$	556.3	524.2641 $[M+H-CH_3OH]^+$, 492.2391 $[M+H-2CH_3OH]^+$	↓	Huang et al. (2015)
20	19.7	C_{19}DDA	Mesaconitine	$C_{33}H_{45}NO_{11}$	632.3	600.2823 $[M+H-CH_3OH]^+$, 582.2740 $[M+H-CH_3OH-H_2O]^+$, 572.2874 $[M+H-2CH_2O]^+$, 540.2626 $[M+H-2CH_2O-CH_3OH]^+$	↑	Sun et al. (2012); Huang et al. (2015)
21	21.3	C_{19}DDA	Hypaconitine	$C_{33}H_{45}NO_{10}$	616.3	584.2844 $[M+H-CH_3OH]^+$, 556.2879 $[M+H-2CH_2O]^+$, 524.2621 $[M+H-2CH_2O-CH_3OH]^+$, 492.2373 $[M+H-C_2O_2-CH_3OH-2H_2O]^+$	↑	Tan et al. (2011); Huang et al. (2015)
22	21.5	C_{19}DDA	Aconitine	$C_{34}H_{47}NO_{11}$	646.3	628.3069 $[M+H-H_2O]^+$, 596.2855 $[M+H-CH_3OH-H_2O]^+$, 586.3053 $[M+H-AcOH]^+$, 568.2895 $[M+H-AcOH-H_2O]^+$, 554.2785 $[M+H-AcOH-CH_3OH]^+$, 536.2693 $[M+H-2CH_2O-CH_3OH-H_2O]^+$	↑	Tan et al. (2011); Sun et al. (2012); Huang et al. (2015)
23	23.3	C_{19}DDA	Deoxyaconitine	$C_{34}H_{47}NO_{10}$	630.3	598.3029 $[M+H-CH_3OH]^+$, 570.3061 $[M+H-AcOH]^+$, 538.2804 $[M+H-AcOH-CH_3OH]^+$, 506.2549 $[M+H-AcOH-2CH_3OH]^+$	↑	Tan et al. (2011); Huang et al. (2015)

Note: ULRA compared with YF, ↑, the content increased; ↓, the content decreased; C_{19}ADA, C19-alkylol amine-diterpenoid alkaloid; C_{19}DDA, C19-monoester-diterpenoid alkaloid; C_{19}MDA, C19-monoester-diterpenoid alkaloid; C_{20}DA, C20-diterpene alkaloid; ULRA, unprocessed lateral root of Aconitum carmichaelii*; YF, Yinfupian.*

granulosa cells, corpus luteum, and ovarian follicles increased in the YF group (**Figure 7D**).

Serum cyclic Adenosine Monophosphate and cyclic Guanosine Monophosphate Levels in Rats with Yang Deficiency Syndrome

Compared with the blank group, the levels of c-AMP and c-GMP in the model group were significantly decreased. There was no significant difference between the ULRA and model groups. Compared with the model group, the levels of c-AMP in the YF group increased significantly, whereas those of c-GMP exhibited an upward trend.

Differentially Expressed Proteins

According to the standard of expression <1.2-fold (upregulated by >1.2-fold or downregulated by <0.83-fold) and p-value <0.05, a total of 4,673 differentially expressed proteins were identified. The number of differentially expressed proteins in each group is shown in **Table 4**.

Gene Ontology Analysis

The results of GO analysis for the blank group vs. the model group revealed that the functions of these potential targets are related to numerous biological processes that may be important for the occurrence and development of YDS. The top 20 generally changed GO terms were compared. The most significantly enriched biological process terms were associated with detoxification, stress response to metal ion, cellular response to zinc ion, lauric acid metabolic process, and arginine catabolic process. With respect to molecular function, the most significantly enriched terms included iron ion binding, heme binding, tetrapyrrole binding, arachidonic acid binding, icosanoid binding, and icosatetraenoic acid binding. For the cellular component, the most enriched terms were delta DNA polymerase complex, C-fiber, histone locus body, cytoskeleton, nuclear inner membrane, and DNA polymerase complex (**Figure 8A**).

Comparison of the ULRA and model groups showed that the most enriched biological process terms were associated with muscle contraction, muscle system process, myosin filament assembly and organization, myofibril assembly, sarcomere organization, and cellular component assembly involved in morphogenesis. The representative terms related to molecular function were actin binding and structural constituent of muscle. For the cellular component, the most enriched terms were myofibril, contractile fiber, sarcomere, and muscle myosin complex (**Figure 8B**).

In the YF group vs. model group analysis, the most significantly enriched biological process terms were associated with muscle contraction, cell fate specification, myosin filament assembly and organization, sarcomere organization, and cellular component assembly involved in morphogenesis. The most significantly enriched molecular function terms were associated with actin binding and transmembrane transporter activity. The representative terms related to cellular component were supramolecular structure,

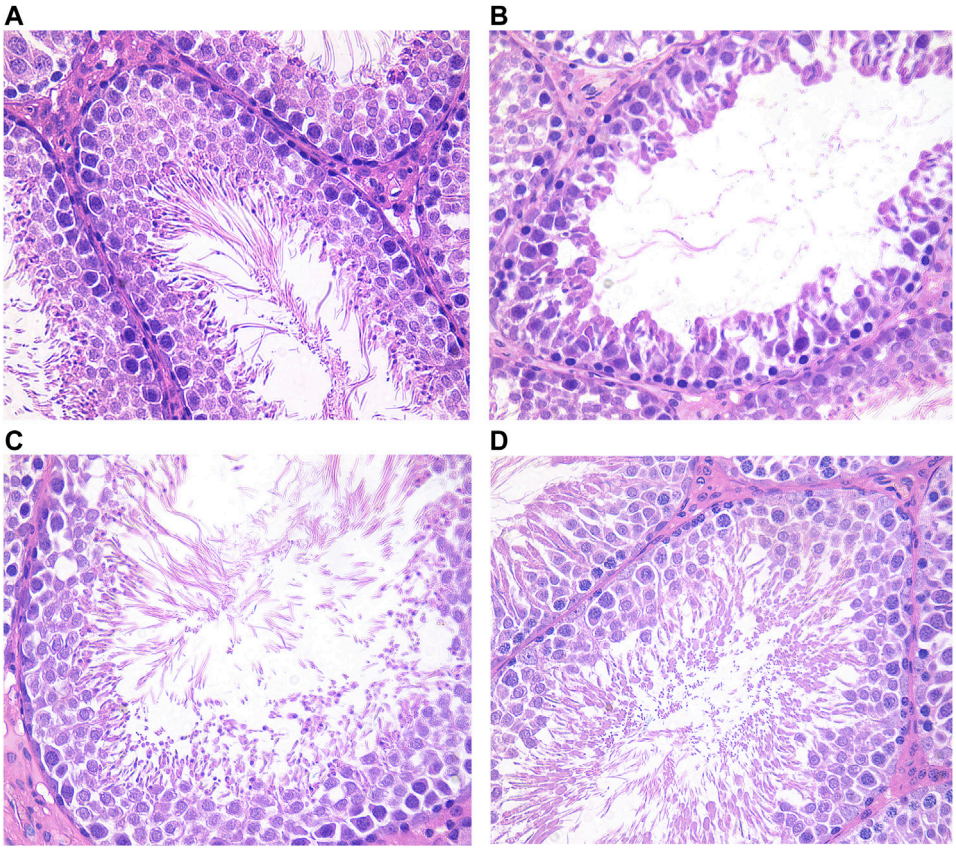

FIGURE 6 | Testis histological changes of male rats in each group (HE×400). **(A)** Blank group; **(B)** Model group; **(C)** ULRA group; **(D)** YF group. HE, hematoxylin-eosin staining; ULRA, unprocessed lateral root of *Aconitum carmichaelii*; YF, Yinfupian.

contractile fiber part, keratin filament, and myofibril (**Figure 8C**).

Kyoto Encyclopedia of Genes and Genomes Analysis

The KEGG analysis demonstrated that a number of pathways were significantly enriched in the model group compared with the blank group. These included some classical pathways, such as the nicotinate and nicotinamide metabolism, peroxisome proliferator activated receptor (PPAR) signaling pathway, drug metabolism cytochrome P450 (CYP), steroid hormone biosynthesis, arachidonic acid metabolism, and retinol metabolism (**Figure 9A**).

Comparison of the ULRA and model groups revealed that the inflammatory mediator regulation of transient receptor potential (TRP) channels, hypoxia inducible factor 1 (HIF1) signaling pathway, tight junction, glycolysis/gluconeogenesis, and cardiac muscle contraction were significantly enriched according to the differentially expressed proteins. Moreover, we found some disease-related pathways, such as type I diabetes mellitus, hypertrophic cardiomyopathy, dilated cardiomyopathy, allograft rejection, graft-versus-host disease, autoimmune thyroid disease, and African trypanosomiasis, which indicate that raw aconite has a potential application in other diseases (**Figure 9B**).

Comparison of the YF and model groups showed neuroactive ligand-receptor interaction and nucleotide excision repair (**Figure 9C**).

Protein–Protein Interaction

To investigate the interactions between differentially expressed proteins in each group, several protein–protein interaction networks were established based on differentially expressed proteins using the Cytoscape v3.2.1 software. Comparison of the model and blank groups revealed complex interactions with CYP 4A2 and 4A8 (downregulation), aldehyde oxidase 3 (AOX3) (downregulation), cathepsin G (CTSG) (upregulation), fatty acid binding protein 5 (FABP5) (upregulation), lysozyme 2 (LYZ2) (upregulation), etc. In the comparison of the ULRA and model groups, the protein network based on differentially expressed proteins revealed complex interactions with actinin alpha 3 (ACTN3) (downregulation), actinin alpha 2 (ACTN2) (downregulation), troponin C2 fast skeletal type (TNNC2) (downregulation), troponin I2 fast skeletal type (TNNI2) (downregulation), troponin T3 fast skeletal type (TNNT3) (downregulation), creatine kinase M-type (CKM) (downregulation), myosin light chain 1 (MYL1) (downregulation), myosin heavy chain 1 (MYH1) (downregulation), etc. Comparison of

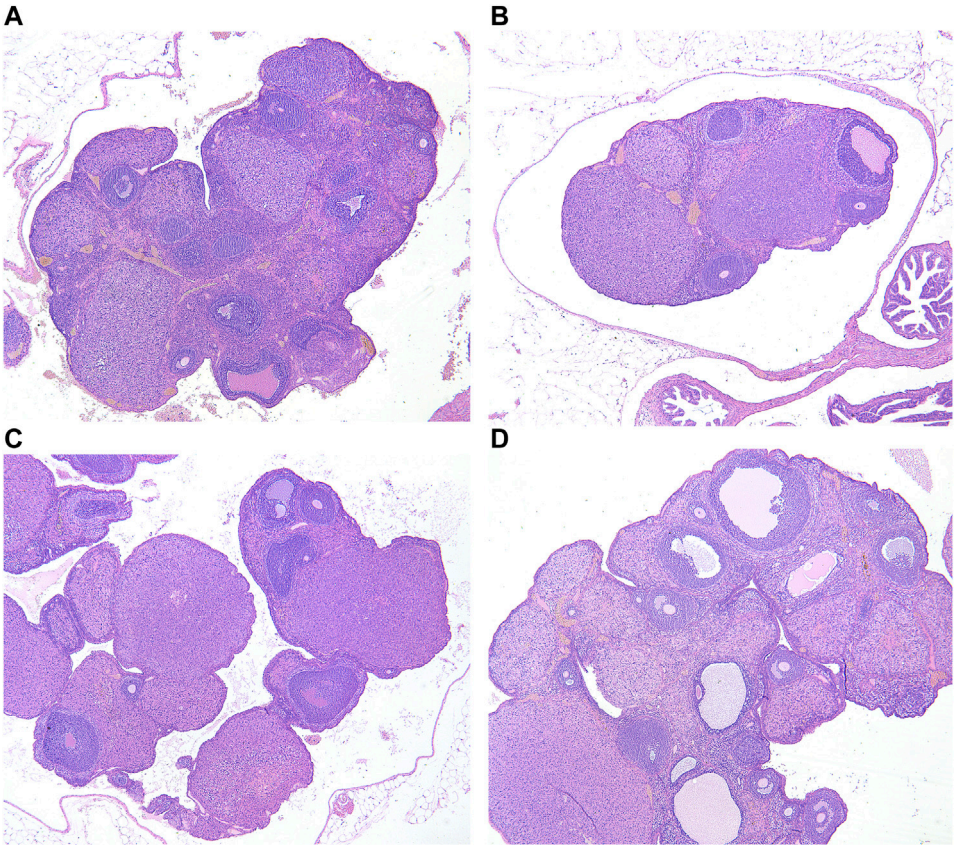

FIGURE 7 | Ovarian histological changes of female rats in each group (HE×40). **(A)** Blank group; **(B)** Model group; **(C)** ULRA group; **(D)** YF group; HE, hematoxylin-eosin staining; ULRA, unprocessed lateral root of *Aconitum carmichaelii*; YF, Yinfupian.

TABLE 4 | Protein expression results.

Comparison (group)	Upregulation	Downregulation	All
B vs. M	30	35	65
ULRA vs. M	27	135	162
YF vs. M	52	46	98

Note: Upregulation, upregulated differentially expressed proteins; Downregulation, downregulated differentially expressed proteins; All, all differentially expressed proteins; B, blank group; M, model group; ULRA, unprocessed lateral root of Aconitum carmichaelii*; YF, Yinfupian.*

the YF and model groups showed complex interactions with keratin 5 (KRT5) (upregulation), KRT16 (upregulation), KRT17 (upregulation), KRT72 (upregulation), mitochondrial ribosomal protein L28 (MRPL28) (upregulation), MRPL4 (upregulation), MRPL38 (upregulation), OXA1L mitochondrial inner membrane protein (OXA1L) (upregulation), etc.

DISCUSSION

Aconitum alkaloids can be rapidly absorbed and widely distributed in the body. There is a large quantity of C19-diester-diterpenoid alkaloid (C_{19}DDA) in ULRA; C_{19}DDA has been associated with acute toxicity. Hydrolysis of C_{19}DDA into C19-monoester-diterpenoid alkaloid (C_{19}MDA) decreases the toxicity. Through further hydrolysis, the alkaloids are converted into C19-alkylol amine-diterpenoid alkaloid (C_{19}ADA) with almost no toxicity (Huang et al., 2015; Wu et al., 2018). According to the results of composition analysis (**Table 1**), the levels of mesaconitine, hypaconitine, aconitine, and other C_{19}DDAs were significantly decreased in YF compared with the ULRA. In contrast, the levels of C_{19}MDAs (e.g., benzoylaconine, benzoylhypaconine, benzoylmesaconine), C_{19}ADAs (e.g., fuziline, mesaconine, and neoline), and C20-diterpene alkaloids (e.g., chuanfumine and songorine) were significantly increased. The components of *Aconitum* alkaloids underwent obvious changes in the process of preparation. Hydrolysis of C_{19}DDA reduced the toxicity of ULRA, while the increase in the levels of C_{19}MDA, C_{19}ADA, and C20-diterpene alkaloid also ensured the pharmacological activity. This confirmed the importance of preparation in reducing the toxicity and increasing efficiency of ULRA in terms of chemical composition.

Previous studies have shown that YDS can affect gonad and related functions, as well as damage male testicular function and female ovarian function (Nakada and Adachi. 1999; Liu et al., 2018; Song et al., 2019). The vitality of spermatogenic cells and

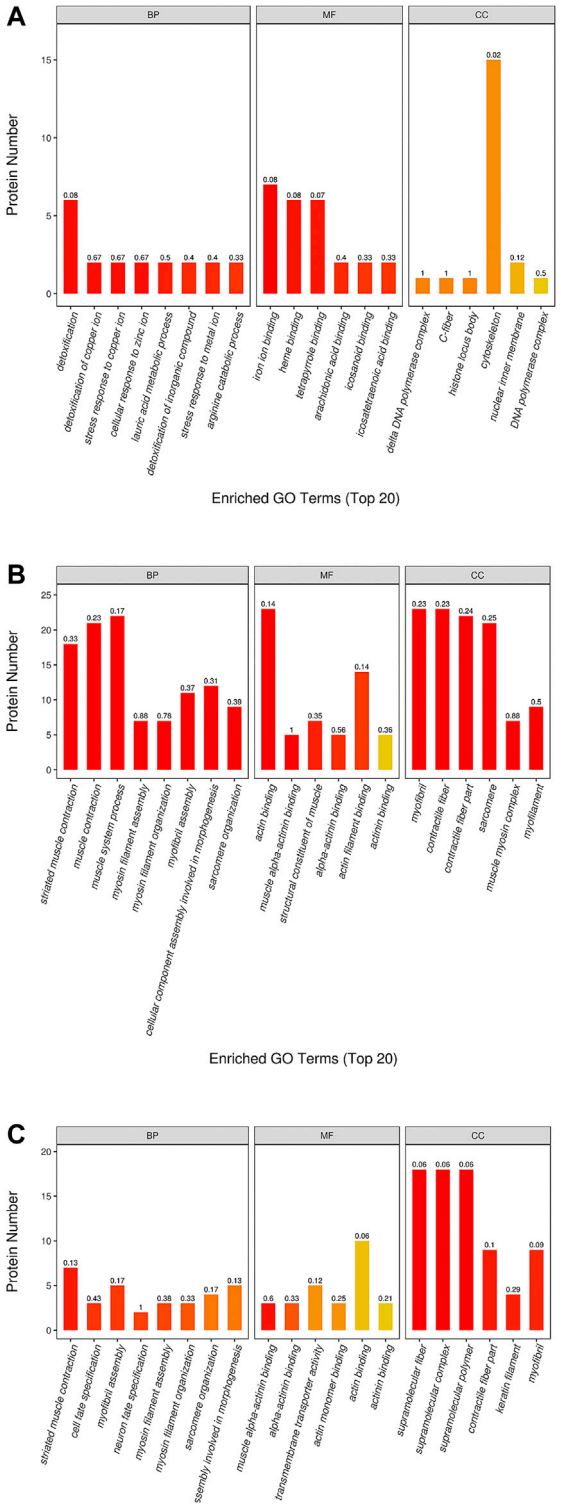

FIGURE 8 | The GO (gene ontology) function classification of the differential protein identified by the TMT-based proteomics. The GO enrichment analysis of proteins from the liver samples was performed according to the BP (biological process), MF (molecular function) and CC (cellular component). The comparison between the **(A)** blank group and model group, between the **(B)** ULRA group and model group, between the **(C)** YF group and model group was performed. ULRA, unprocessed lateral root of *Aconitum carmichaelii*; YF, Yinfupian.

ovarian cells in the testes and ovaries of rats with YDS was inhibited, and the numbers of cells were significantly reduced (**Figures 3**, **4**). Moreover, following treatment with ULRA and YF, the morphology of the testes and ovaries recovered well in rats with YDS, suggesting good efficacy.

c-AMP is a signal transduction substance formed by the dephosphorylation of adenosine triphosphate (ATP) under the catalysis of adenylate cyclase It activates protein kinase (PKA) and phosphorylates target cell proteins, thus regulating the cell response. c-GMP is another signal transduction substance formed by guanosine triphosphate under the catalysis of guanylate cyclase. It activates protein kinase PKG and phosphorylates proteins in target cells, thus regulating cell reaction. Both transduction substances, termed cyclic nucleotides, are involved in regulating the physiological function and metabolism of cells. They have a wide range of biological effects and participate in a variety of physiological and pathological processes. During this period, numerous neurotransmitters, hormones and some active substances need to exert their corresponding physiological effects on target cells through cyclic nucleotides (Burhenne et al., 2011; Rondina and Weyrich, 2012). The content of c-AMP and c-GMP in rats with YDS decreased significantly, thereby leading to the inhibition of physiological function and metabolism to a certain extent. The body reaction caused by this change was consistent with the symptoms of YDS, and YF could significantly increase the content of c-AMP and c-GMP (**Figures 10**, **11**). The above results indicate that YF has an obvious therapeutic effect on YDS.

The GO and KEGG pathway enrichment analyses revealed that YDS mainly affects detoxification, heme-related compositions (i.e., iron ion, heme, tetrapyrrole) binding, response to metal ion, CYP, steroid hormone biosynthesis, nicotinate and nicotinamide metabolism, PPAR signaling pathway, as well as the combination and metabolism of some unsaturated fatty acids. The present findings are consistent with those of previous research studies on YDS (Zhang et al., 2019; Liang et al., 2020). GO analysis showed that both ULRA and YF influenced the movement of muscle tissues. KEGG pathway analysis found that ULRA mainly affects the inflammatory mediator regulation of TRP channels, HIF1 signaling pathway, tight junction, glycolysis/gluconeogenesis, and cardiac muscle contraction, and was related to some disease-related pathways, such as type I diabetes mellitus, hypertrophic cardiomyopathy, dilated cardiomyopathy, allograft rejection, graft-versus-host disease, autoimmune thyroid disease, and African trypanosomiasis. YF was mainly associated with neuroactive ligand-receptor interaction and nucleotide excision repair. The above results may be closely related to the content of alkaloids in RAC. The high content of C_{19}DDA in ULRA has been linked to strong anti-inflammatory activity (Hikino et al., 1982; Komoda et al., 2003), anti-tumor activity (Du et al., 2013; Ji et al., 2016), and damage to myocardial cells (Ma et al., 2018). The high content of C_{19}MDA in YF exerts a protective effect on nerve cells (Jiang et al., 2012). C_{19}ADA can increase the viability of myocardial cells, and improve myodynamia and ventricular diastolic function (Liu et al., 2012; Xiong et al., 2012).

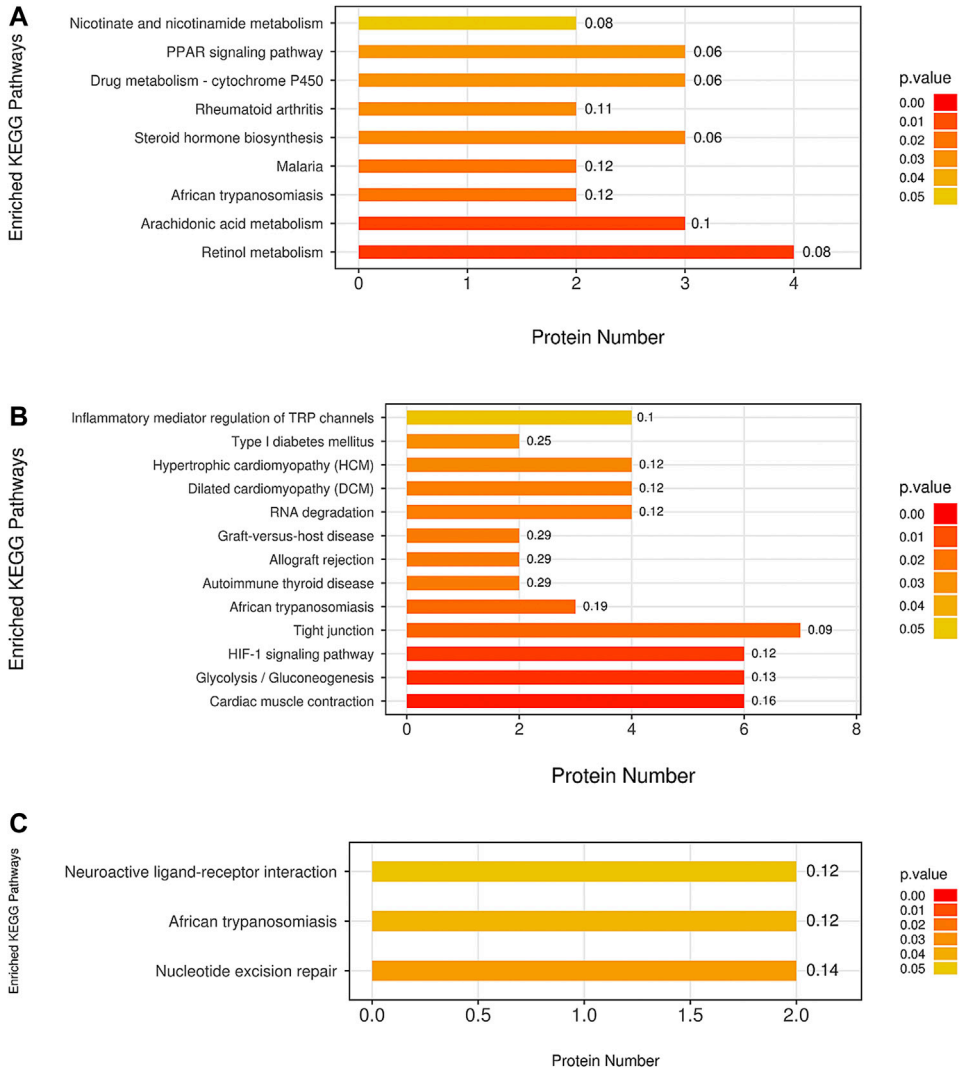

FIGURE 9 | The pathway analysis of all differentially expressed proteins was based on the KEGG (Kyoto Encyclopedia of Genes and Genomes) database. The comparison between the **(A)** M group and B group, between the **(B)** ULRA group and model group, and between the **(C)** YF and model groups was performed. ULRA, unprocessed lateral root of *Aconitum carmichaelii*; YF, Yinfupian.

CYP has two main biological functions. The first is the metabolism of heterologous substances. Lipid soluble drugs can only be excreted after biotransformation in the kidneys (Modi and Dawson, 2015). CYP can reduce the hydrophobicity of compounds and form intermediate metabolites for easy excretion. The second function is the biosynthesis of bioactive molecules, including the metabolism of steroids, vitamins, and fatty acids (Albertolle and Guengerich, 2018). The CYP4A family metabolizes arachidonic acid into ω-hydroxyeicosatetraenoic acid in kidneys (Ying et al., 2008). 20-hydroxyeicosatetraenoic acid plays an important role in skeletal muscle and vascular myogenic response, and regulates blood circulation (Imig et al., 1996). In addition, studies have shown that specific inhibition of CYP4A can treat myocardial injury induced by advanced glycation end product (Wang et al., 2019). Aldehyde oxidase is an important enzyme system involved in drug metabolism (Garattini et al., 2003). *In vivo* studies showed that CTSG inhibitors decreased cardiac inflammation and improved cardiac function after myocardial ischemia-reperfusion injury (Hooshdaran et al., 2017), indicating that CTSG may promote inflammation. FABP is a sensitive marker for the early diagnosis of myocardial infarction (Mad et al., 2007; Figiel et al., 2008). Following the occurrence of myocardial ischemia, fatty acids are mobilized to supply energy, thereby increasing the levels of heart-type FABP. LYZ is widely distributed in the human body because of its antibacterial, antiviral, anti-inflammatory, and immunity-enhancing properties (Eichenberger et al., 2010).

The downregulation of CYP and AOX in the model group may indicate that YDS can inhibit the metabolic activities in the body.

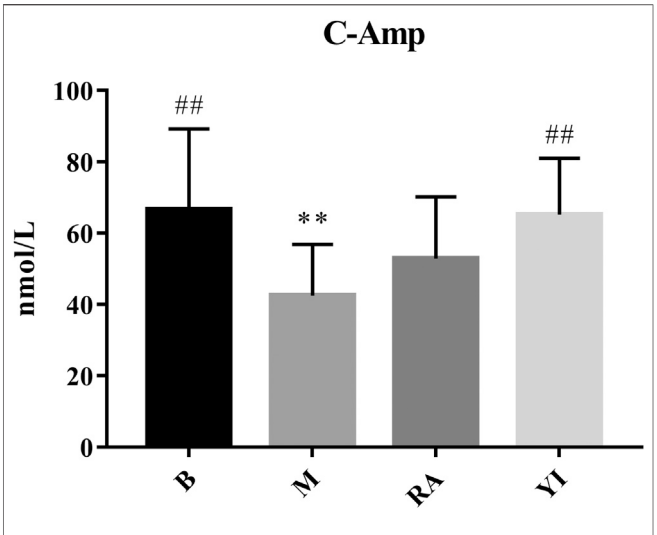

FIGURE 10 | Changes of serum c-AMP levels. B, blank group; M, model group; RA, ULRA group; YI, YF group. Compared with B group, **: $p < 0.01$; Compared with M group, ##: $p < 0.01$. c-AMP, cyclic adenosine monophosphate; ULRA, unprocessed lateral root of *Aconitum carmichaelii*; YF, Yinfupian.

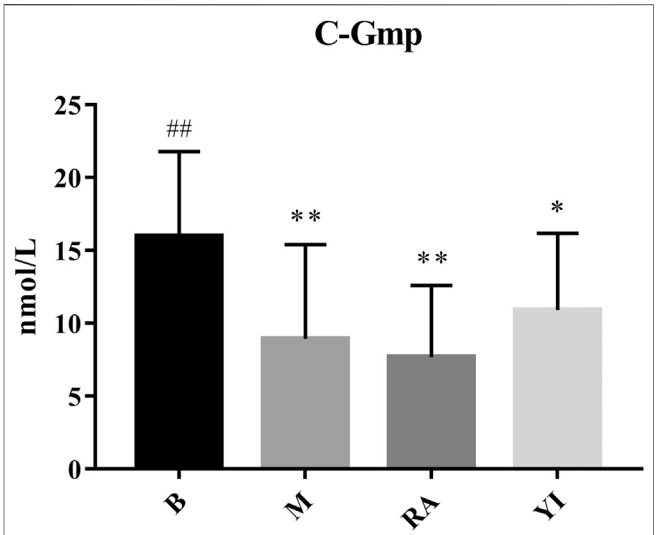

FIGURE 11 | Changes of serum c-GMP levels. B, blank group; M, model group; RA, ULRA group; YI, YF group. Compared with B group, *: $p < 0.05$, **: $p < 0.01$; Compared with M group, ##: $p < 0.01$. c-GMP, cyclic guanine monophosphate; ULRA, unprocessed lateral root of *Aconitum carmichaelii*; YF, Yinfupian.

Upregulation of CTSG expression can aggravate the inflammatory reaction. The upregulation of FABP and LYZ may be related to the self-regulation and response of the body in the state of YDS. CYP was downregulated in the ULRA group compared with the model group. This finding was consistent with those of previous studies stating that C_{19}DDA can inhibit the activity of CYP and affect its mRNA levels. Its toxic targets are ion channels, substructures, enzymes, and receptors (Yen and Ewald, 2012; Chang et al., 2019). The expression of AOX3 was significantly increased in the ULRA group compared with the model group. The levels of CTSG were significantly decreased in the YF group compared with the model group, suggesting that YF may exert an anti-inflammatory effect by downregulating the expression of CTSG.

Together, α-actinin and actin form the main cytoskeleton protein of cells, maintain the special morphology of cells, and endow the cells with toughness and strength (Dixson et al., 2003). For myocardial cells, actinin is located on the myocardial cell membrane and Z-band through a variety of actin connexins to perform myocardial contractile and diastolic functions. α-actinin is one of the connexins; following change, α-actinin directly affects the systolic and diastolic functions of myocardial cells and leads to myocardial remodeling. Spatial regularity disorder of α-actinin-2 has been found in cardiac myocytes of patients with heart failure (Dobrev and Nattel, 2010), indicating that the plasticity of α-actinin-2 may occur in cardiac structural remodeling. TNNT contains the binding site of protomyosin; TNNI is an inhibitor of actin ATPase, which inhibits the interaction between actin and myosin. TNNC binds to Ca^{2+} and regulates the interaction between TNNT, TNNI, and other components of the systolic system (Perry, 1998; Perry, 1999). Creatine kinase (CK) is closely related to energy metabolism in mammals. It is involved in glycolysis control, mitochondrial respiration, and energy supply for muscle contraction. CK is one of the key enzymes in the metabolism of the ATP-creatine phosphate system. Its role is to catalyze the reversible transfer of a high-energy bond between ATP and creatine phosphate (Cheng et al., 2020). Myosin is the structural protein and the main contractile protein of the myocardium. It is composed of two heavy chains and four light chains. Typically, the body can produce immune tolerance to myosin. However, under pathological conditions, myosin can be an autoantigen causing an autoimmune reaction, stimulating the production of anti-myosin antibody, and mediating myocardial immune injury. Studies (Wang et al., 2003) suggested that myosin can be an autoantigen mediating myocardial injury, which can transform myocarditis into dilated cardiomyopathy.

Studies have shown that aconitine can inhibit the expression of α-actinin (Zhang et al., 2020). This may be due to the effects of aconitine on protein expression in the myofilaments of cardiomyocytes, resulting in dysfunction of myofilaments; this may be the mechanism of aconitine-induced cardiotoxicity. The expression levels of troponin and CK were downregulated in the ULRA group, indicating that ULRA could inhibit the contraction and relaxation of muscle. Moreover, the downregulation of myosin may be involved in the anti-inflammatory effect of ULRA.

Mammalian mitochondrial ribosomal proteins are synthesized in cytoplasmic ribosomes and transported to mitochondria by special protein complexes. They are combined with rRNA and assembled into ribosomes. Moreover, they are responsible for the translation of 13 membrane proteins encoded by mitochondrial DNA and participate in the oxidative phosphorylation reaction (Christian and Spremulli, 2011; De et al., 2015). Mitochondrial

inner membrane protein is essential for the activity and assembly of cytochrome oxidase; it is also necessary for the correct biogenesis of ATP synthase and complex I in mitochondria (Bonnefoy et al., 1994; Stiburek et al., 2007).

In the YF group, the expression of Mammalian mitochondrial ribosomal proteins was significantly upregulated. Studies have shown that benzoylaconine can increase the mitochondrial quality and induce mitochondrial biogenesis in mice by activating the adenosine monophosphate-activated protein kinase (AMPK) signaling cascade (Deng et al., 2019). It is suggested that YF can promote the production of ATP, and the increase in benzoylaconine is an important step for mitochondrial energy metabolism.

As a medicinal plant with documented efficacy and toxicity, the chemical composition and effects of LRA have been investigated in recent years, shedding light on its material basis and the pharmacological and toxicological mechanisms. However, further studies are warranted to overcome some current limitations. Regarding chemical constituents, despite the availability of detailed studies on various alkaloids, the extraction of many compounds remains difficult, and there are challenges in the hydrolysis and transformation of C_{19}DDA, C_{19}MDA, and C_{19}ADA. Therefore, it is necessary to further investigate the dynamic transformation law of different types of alkaloids to increase efficiency and reduce toxicity in the process of component transformation. Concerning medicinal activity, although the overall pharmacological and toxicological effects of LRA have been extensively studied, there is a lack research on the target mechanism of most monomer compounds. Hence, it is necessary to further clarify the mechanisms of interaction between multiple components and multiple targets.

DATA AVAILABILITY STATEMENT

The datasets presented in this study can be found in online repositories. The names of the repository/repositories and accession number(s) can be found at [iProX (www.iprox.org), ID: PXD026321].

ETHICS STATEMENT

The animal study was reviewed and approved by Ethics Committee on Laboratory Animals of Jiangxi University of Traditional Chinese Medicine.

AUTHOR CONTRIBUTIONS

H-lT and HC performed the experiments, analyzed the data, and wrote the manuscript. F-pG and S-hY revised the manuscript. L-yZ and JZ designed the research and performed the analyses.

FUNDING

This study was supported by the National Natural Science Foundation of China (Nos. 81660663; 81860703).

REFERENCES

Albertolle, M. E., and Peter Guengerich, F. (2018). The Relationships between Cytochromes P450 and H 2 O 2 : Production, Reaction, and Inhibition. *J. Inorg. Biochem.* 186, 228–234. doi:10.1016/j.jinorgbio.2018.05.014

Bonnefoy, N., Kermorgant, M., Groudinsky, O., Minet, M., Slonimski, P. P., and Dujardin, G. (1994). Cloning of a Human Gene Involved in Cytochrome Oxidase Assembly by Functional Complementation of an Oxa1- Mutation in *Saccharomyces cerevisiae*. *Proc. Natl. Acad. Sci.* 91, 11978–11982. doi:10.1073/pnas.91.25.11978

Burhenne, H., Tappe, K., Beste, K., Voigt, U., Spangler, C., Tsikas, D., et al. (2011). Quantitation of Cyclic Nucleotides in Mammalian Cells and in Human Urine by High-Performance Liquid Chromatography/Mass Spectrometry. *BMC Pharmacol.* 11 (S1), 12–13. doi:10.1186/1471-2210-11-S1-P12

Chang, W.-C., Chu, M.-T., Hsu, C.-Y., Wu, Y.-J. J., Lee, J.-Y., Chen, T.-J., et al. (2019). Rhein, an Anthraquinone Drug, Suppresses the NLRP3 Inflammasome and Macrophage Activation in Urate Crystal-Induced Gouty Inflammation. *Am. J. Chin. Med.* 47 (1), 135–151. doi:10.1142/S0192415X19500071

Chen, X., Cao, Y., Zhang, H., Zhu, Z., Liu, M., Liu, H., et al. (2014). Comparative Normal/Failing Rat Myocardium Cell Membrane Chromatographic Analysis System for Screening Specific Components that Counteract Doxorubicin-Induced Heart Failure from Acontium Carmichaeli. *Anal. Chem.* 86 (10), 4748–4757. doi:10.1021/ac500287e

Cheng, D. H., and Liang, X. T. (1982). Studies on the Constituents of Lateral Root of Aconitum Carmichaelii Debx. (FUZI). I. Isolation and Structural Determination of Salsolinol. *Acta Pharm. Sin.* 17 (10), 792–794. doi:10.1017/S0031182000048393

Cheng, Y., Li, R., Lin, Z., Chen, F., Dai, J., Zhu, Z., et al. (2020). Structure-activity Relationship Analysis of Dammarane-type Natural Products as Muscle-type Creatine Kinase Activators. *Bioorg. Med. Chem. Lett.* 30 (17), 127364. doi:10.1016/j.bmcl.2020.127364

Chinese Pharmacopoeia Commission (2020). *Pharmacopoeia of P.R. China:* I. Beijing: The Medicine Science and Technology Press of China.

Christian, B. E., and Spremulli, L. L. (2012). Mechanism of Protein Biosynthesis in Mammalian Mitochondria. *Biochim. Biophys. Acta (Bba) - Gene Regul. Mech.* 1819 (9-10), 1035–1054. doi:10.1016/j.bbagrm.2011.11.009

De Silva, D., Tu, Y. T., Amunts, A., Fontanesi, F., and Barrientos, A. (2015). Mitochondrial Ribosome Assembly in Health and Disease. *Cell Cycle* 14, 2226–2250. doi:10.1080/15384101.2015.1053672

Deng, X.-h., Liu, J.-j., Sun, X.-j., Dong, J.-c., and Huang, J.-h. (2019). Benzoylaconine Induces Mitochondrial Biogenesis in Mice via Activating AMPK Signaling Cascade. *Acta Pharmacol. Sin.* 40 (5), 658–665. doi:10.1038/s41401-018-0174-8

Dixson, J. D., Forstner, M. R. J., and Garcia, D. M. (2003). The α-Actinin Gene Family: A Revised Classification. *J. Mol. Evol.* 56 (1), 1–10. doi:10.1007/s00239-002-2374-5

Dobrev, D., and Nattel, S. (2010). New Antiarrhythmic Drugs for Treatment of Atrial Fibrillation. *The Lancet* 375, 1212–1223. doi:10.1016/S0140-6736(10)60096-7

Du, J., Lu, X., Long, Z., Zhang, Z., Zhu, X., Yang, Y., et al. (2013). *In Vitro* and *In Vivo* Anticancer Activity of Aconitine on Melanoma Cell Line B16. *Molecules* 18 (1), 757–767. doi:10.3390/molecules18010757

Eichenberger, A. P., Gattin, Z., Yalak, G., and van Gunsteren, W. F. (2010). Molecular Dynamics Simulation of Ester-Linked Hen Egg White Lysozyme Reveals the Effect of Missing Backbone Hydrogen Bond Donors on the Protein Structure. *Hca* 93 (10), 1857–1869. doi:10.1002/hlca.201000077

Fan, W. Q. (2014). Research on Correlation of Primary Nephrotic Syndrome and Traditional Chinese Medical Constitution. Master's thesis. Fuzhou: Fujian University of Traditional Chinese Medicine.

Figiel, Ł., Kasprzak, J. D., Peruga, J., Lipiec, P., Drozdz, J., Krzemińska-Pakuła, M., et al. (2008). Heart-type Fatty Acid Binding Protein-A Reliable Marker of Myocardial Necrosis in a Heterogeneous Group of Patients with Acute Coronary Syndrome without Persistent ST Elevation. *Kardiol. Pol.* 66 (3), 253–261. doi:10.1002/ccd.1810270318

Fujita, Y., Terui, K., Kakizaki, A., Takahashi, K., Aoki, H., and Endo, S. (2007). Correlation between Time of Ingestion or the Ingested Aconite Plant Parts and Aconite Poisoning-Induced Arrhythmia. *Jpn. J. Pharm. Health Care Sci.* 33 (12), 1027–1031. doi:10.5649/jjphcs.33.1027

Garattini, E., Mendel, R., Romão, M. J., Wright, R., and Terao, M. (2003). Mammalian Molybdo-Flavoenzymes, an Expanding Family of Proteins: Structure, Genetics, Regulation, Function and Pathophysiology. *Biochem. J.* 372 (Pt1), 15–32. doi:10.1042/BJ20030121

Gong, X.-h., Li, Y., Li, Y.-x., Yuan, A., Zhao, M.-j., Zhang, R.-q., et al. (2016). Development and Validation of an UPLC-Q-TOF-MS Method for Quantification of Fuziline in Beagle Dog after Intragastric and Intravenous Administration. *J. Chromatogr. Sci.* 54 (3), bmv156–412. doi:10.1093/chromsci/bmv156

Götz, S., García-Gómez, J. M., Terol, J., Williams, T. D., Nagaraj, S. H., Nueda, M. J., et al. (2008). High-throughput Functional Annotation and Data Mining with the Blast2GO Suite. *Nucleic Acids Res.* 36 (10), 3420–3435. doi:10.1093/nar/gkn176

He, S., Dai, O., Liu, J. L., Zhou, Y. X., Gong, X. H., Du, Q. H., et al. (2014a). Effects of Acontum Fischeri Mankshood Water-Solubility Alkaloid on Acute Heart Failure. *Pharmacol. Clin. Chin. Mater. Clin. Med.* 30 (2), 89–92. doi:10.13412/j.cnki.zyyl.2014.02.028

He, S., Xie, X. F., Zhang, X., and Peng, C. (2014b). Therapeutic Effects of Water-Solubility Alkaloid of Aconitum Carmichaelii on Heart-Failure Cell Model. *Chin. J. Exp. Tradit. Med. Form.* 16 (20), 127–131. doi:10.13422/j.cnki.syfjx.2014160127

Hikino, H., Takata, H., Fujiwara, M., Konno, C., and Ohuchi, K. (1982). Mechanism of Inhibitory Action of Mesaconitine in Acute Inflammations. *Eur. J. Pharmacol.* 82 (1-2), 65–71. doi:10.1016/0014-2999(82)90553-2

Hooshdaran, B., Kolpakov, M. A., Guo, X., Miller, S. A., Wang, T., Tilley, D. G., et al. (2017). Dual Inhibition of Cathepsin G and Chymase Reduces Myocyte Death and Improves Cardiac Remodeling after Myocardial Ischemia Reperfusion Injury. *Basic Res. Cardiol.* 112 (6), 62–74. doi:10.1007/s00395-017-0652-z

Hu, R., Zhao, J., Qi, L.-W., Li, P., Jing, S.-L., and Li, H.-J. (2009). Structural Characterization and Identification of C19 - and C20 -diterpenoid Alkaloids in Roots of Aconitum Carmichaeli by Rapid-Resolution Liquid Chromatography Coupled with Time-Of-Flight Mass Spectrometry. *Rapid Commun. Mass. Spectrom.* 23 (11), 1619–1635. doi:10.1002/rcm.4038

Huang, L. M., and Liang, H. (2005). Proteomic Considerations and Methods of Different Diseases with Same Syndrome of Kidney-Yang Deficiency. *Shanghai J. Tradit. Chin. Med.* 5, 44–46. doi:10.16305/j.1007-1334.2005.05.019

Huang, Z. F., Tang, X. L., Luo, H., Zhang, Y. H., Liu, Y. H., Chen, Y., et al. (2015). Chemical Constituents of Aconite Lateralis Radix and Changing Regularities during Decoction Process by HPLC-Q-TOF-MS. *Chin. J. Exp. Tradit. Med. Form.* 21 (1), 57–63. doi:10.13422/j.cnki.syfjx.2015010057

Imig, J. D., Zou, A. P., Stec, D. E., Harder, D. R., Falck, J. R., and Roman, R. J. (1996). Formation and Actions of 20-hydroxyeicosatetraenoic Acid in Rat Renal Arterioles. *Am. J. Physiology-Regulatory, Integr. Comp. Physiol.* 270 (1Pt2), R217–R227. doi:10.1152/ajpregu.1996.270.1.R217

Ji, B. L., Xia, L. P., Zhou, F. X., Mao, G. Z., and Xu, L. X. (2016). Aconitine Induces Cell Apoptosis in Human Pancreatic Cancer via NF-Kb Signaling Pathway. *Eur. Rev. Med. Pharmacol. Sci.* 20 (23), 4955–4964.

Jiang, B., Lin, S., Zhu, C., Wang, S., Wang, Y., Chen, M., et al. (2012). Diterpenoid Alkaloids from the Lateral Root of Aconitum Carmichaelii. *J. Nat. Prod.* 75 (6), 1145–1159. doi:10.1021/np300225t

Khan, H., Nabavi, S. M., Sureda, A., Mehterov, N., Gulei, D., Berindan-Neagoe, I., et al. (2018). Therapeutic Potential of Songorine, A Diterpenoid Alkaloid of the Genus Aconitum. *Eur. J. Med. Chem.* 153 (10), 29–33. doi:10.1016/j.ejmech.2017.10.065

Komoda, Y., Nosaka, S., and Takenoshita, M. (2003). Enhancement of Lidocaine-Induced Epidural Anesthesia by Deoxyaconitine in the Rabbit. *J. Anesth.* 17 (4), 241–245. doi:10.1007/s00540-003-0184-6

Konno, C., Shirasaka, M., and Hikino, H. (1979). Cardioactive Principle of Aconitum Carmichaeli Roots1. *Planta Med.* 35 (2), 150–155. doi:10.1055/s-0028-1097196

Kosuge, T., and Yokota, M. (1976). Studies on Cardiac Principle of Aconite Root. *Chem. Pharm. Bull.* 24 (1), 176–178. doi:10.1248/cpb.24.176

Li, X.-H., He, P., Liu, X.-Y., Chao, R.-B., and Wang, F.-P. (2015). Synthesis and Cardiac Activity Evaluation of the Proposed Structures of Fuzinoside. *Tetrahedron* 71 (45), 8661–8668. doi:10.1016/j.tet.2015.09.009

Li, X. Y., Zhao, Q. H., Lv, L. L., Wang, Y., Feng, Q., Yan, M., et al. (2014). Experimental Study on "Dose- Time- Efficacy" Relationship of Blood Pressure Induced by Aconite Water Extract. *Chin. J. Pharmacovigil.* 11 (10), 584–586+591. doi:10.19803/j.1672-8629.2014.10.003

Li, Y., Su, X., Wu, P., Wang, J., Guo, Y., Zhu, J., et al. (2017). Proteomics Analysis of IBS-D with Spleen and Kidney Yang Deficiency. *J. Traditional Chin. Med. Sci.* 4 (1), 39–49. doi:10.1016/j.jtcms.2017.05.006

Liang, H., Wang, Y., Zhu, M. X., Xi, W., and Li, Z. G. (2020). Proteomics on the Material Basis of Kidney-Yang Deficiency Syndrome Based on the Relevance of Formula and Syndrome. *Chin. Arch. Tradit. Chin. Med.* 38 (12), 10–13+275. doi:10.13193/j.issn.1673-7717.2020.12.002

Liu, A. Q., Ma, J., Dong, H. J., Cao, L., Jia, C. G., Chen, C. B., et al. (2018). Expression of G-Protein Coupled Estrogen Receptor in the Testis of the Male Mouse with Kidney Yin or Kidney Yang Deficiency and its Impact on the Reproductive Function of the Mouse. *Natl. J. Androl.* 24 (2), 156–162. doi:10.13263/j.cnki.nja.2018.02.012

Liu, H., Su, J., Yang, X., He, Y.-J., Li, H.-Y., Ye, J., et al. (2011). A Novel Approach to Characterize Chemical Consistency of Traditional Chinese Medicine Fuzi Lizhong Pills by GC-MS and RRLC-Q-TOFMS. *Chin. J. Nat. Medicines* 9 (4), 267–273. doi:10.1016/S1875-5364(11)60063-0

Liu, X.-X., Jian, X.-X., Cai, X.-F., Chao, R.-B., Chen, Q.-H., Chen, D.-L., et al. (2012). Cardioactive C19-Diterpenoid Alkaloids from the Lateral Roots of Aconitum Carmichaeli "Fu Zi". *Chem. Pharm. Bull.* 60 (1), 144–149. doi:10.1248/cpb.60.144

Lu, D. H., Song, J. L., Wang, P. E., Yang, Z., Tang, L. H., Li, Y., et al. (2012). Analysing the Serum Proteomics between Hyperthyroidism of Yin Deficiency in Liver and Kidney and Hypothyroidism of Yang Deficiency in Spleen and Kidney. *J. Zhejiang. Chin. Med. Univ.* 36 (01), 23–26. doi:10.16466/j.issn1005-5509.2012.01.016

Ma, L.-Q., Yu, Y., Chen, H., Li, M., Ihsan, A., Tong, H.-Y., et al. (2018). Sweroside Alleviated Aconitine-Induced Cardiac Toxicity in H9c2 Cardiomyoblast Cell Line. *Front. Pharmacol.* 9, 1138–1148. doi:10.3389/fphar.2018.01138

Mad, P., Domanovits, H., Fazelnia, C., Stiassny, K., Russmüller, G., Cseh, A., et al. (2007). Human Heart-type Fatty-Acid-Binding Protein as a point-of-care Test in the Early Diagnosis of Acute Myocardial Infarction. *Q. J. Med.* 100 (4), 203–210. doi:10.1093/qjmed/hcm007

Modi, A. R., and Dawson, J. H. (2015). Oxidizing Intermediates in P450 Catalysis: A Case for Multiple Oxidants. *Adv. Exp. Med. Biol.* 851, 63–81. doi:10.1007/978-3-319-16009-2_2

Moriya, Y., Itoh, M., Okuda, S., Yoshizawa, A. C., and Kanehisa, M. (2007). KAAS: An Automatic Genome Annotation and Pathway Reconstruction Server. *Nucleic Acids Res.* 35, W182–W185. doi:10.1093/nar/gkm321

Nakada, Y., and Adachi, T. (1999). Effect of Experimentally Induced Renal Failure on Testicular Testosterone Synthesis in Rats. *Arch. Androl.* 43, 37–45. doi:10.1080/014850199262715

Nesterova, Y. V., Povet'yeva, T. N., Suslov, N. I., Zyuz'kov, G. N., Pushkarskii, S. V., Aksinenko, S. G., et al. (2014). Analgesic Activity of Diterpene Alkaloids from Aconitum Baikalensis. *Bull. Exp. Biol. Med.* 157 (4), 488–491. doi:10.1007/s10517-014-2598-6

Nizhenkovska, I. (2015). The Influence of a New Uracil Derivative Carbicyl on Myocardium Bioenergetic Processes. *Ajcem* 3 (4), 162–166. doi:10.11648/j.ajcem.20150304.16

Perry, S. V. (1999). Troponin I: Inhibitor or Facilitator. *Mol. Cel. Biochem.* 190 (1-2), 9–32. doi:10.1023/A:1006939307715

Perry, S. V. (1998). Troponin T: Genetics, Properties and Function. *J. Muscle Res. Cel Motil.* 19 (6), 575–602. doi:10.1023/A:1005397501968

Povšnar, M., Koželj, G., Kreft, S., and Lumpert, M. (2017). Rare Tradition of the Folk Medicinal Use of Aconitum Spp. Is Kept Alive in Solčavsko, Slovenia. *J. Ethnobiol. Ethnomed.* 13 (1), 45–59. doi:10.1186/s13002-017-0171-x

Rondina, M. T., and Weyrich, A. S. (2012). Targeting Phosphodiesterases in Anti-platelet Therapy. *Exp. Pharm.* 210 (210), 225–238. doi:10.1007/978-3-642-29423-5_9

Shi, S. L., Cao, J. X., Dai, P. J., Ruan, Y. Y., and He, Y. X. (2018). Research Progress of Acupoint Sticking Therapy on Yang Deficiency Constitution. *Guangming. J. Chin. Med.* 33 (05), 746–750. doi:10.3969/j.issn.1003-8914.2018.05.065

Song, J., Xiang, S., Yang, Y., and Sun, Z. (2019). Assessment of Follicular Fluid Metabolomics of Polycystic Ovary Syndrome in Kidney Yang Deficiency Syndrome. *Eur. J. Integr. Med.* 30, 100944. doi:10.1016/j.eujim.2019.100944

Stiburek, L., Fornuskova, D., Wenchich, L., Pejznochova, M., Hansikova, H., and Zeman, J. (2007). Knockdown of Human Oxa1l Impairs the Biogenesis of F1Fo-ATP Synthase and NADH: Ubiquinone Oxidoreductase. *J. Mol. Biol.* 374, 506–516. doi:10.1016/j.jmb.2007.09.044

Sun, H., Wang, M., Zhang, A., Ni, B., Dong, H., and Wang, X. (2012). UPLC-Q-TOF-HDMS Analysis of Constituents in the Root of Two Kinds ofAconitumUsing a Metabolomics Approach. *Phytochem. Anal.* 24, 263–276. doi:10.1002/pca.2407

Suzuki, T., Toshiaki, K., Yokoyama, N., Sugi, M., Kagioka, A., Kitao, Y., et al. (2016). Processed Aconite Root and its Active Ingredient Neoline May Alleviate Oxaliplatin-Induced Peripheral Neuropathic Pain. *J. Ethnopharmacology* 186, 44–52. doi:10.1016/j.jep.2016.03.056

Tan, G., Lou, Z., Jing, J., Li, W., Zhu, Z., Zhao, L., et al. (2011). Screening and Analysis of Aconitum Alkaloids and Their Metabolites in Rat Urine after Oral Administration of Aconite Roots Extract Using LC-TOFMS-Based Metabolomics. *Biomed. Chromatogr.* 25 (12), 1343–1351. doi:10.1002/bmc.1607

Wang, L., Ding, J. Y., Liu, X. X., Tang, M. H., Chao, R. B., and Wang, F. P. (2014). [Identification of Aminoalcohol-Diterpenoid Alkaloids in Aconiti Lateralis Radix Praeparata and Study of Their Cardiac Effects]. *Yao Xue Xue Bao* 49 (12), 1699–1704. doi:10.1007/s00063-010-1142-3

Wang, R., Wang, L., He, J., Li, S., Yang, X., Sun, P., et al. (2019). Specific Inhibition of CYP4A Alleviates Myocardial Oxidative Stress and Apoptosis Induced by Advanced Glycation End-Products. *Front. Pharmacol.* 10, 876–887. doi:10.3389/fphar.2019.00876

Wang, Z. H., Liao, Y. H., Dong, J. H., Li, S. L., Wang, J. P., and Michael, L. X. (2003). Clinical Significance and Pathogenicrole of Anticardiac Myosin Autoantibady in Dilated Cardiomyopathy. *Chin. Med. J.* 116 (4), 499–502. doi:10.1097/00000441-200304000-00011

Weng, S. Z. (2014). Preliminary Study of TCM Constitution and Syndrome Element Differences of Different Types of Chronic Gastritis. Master's thesis. Fuzhou: Fujian University of traditional Chinese Medicine.

Wu, J.-j., Guo, Z.-z., Zhu, Y.-f., Huang, Z.-j., Gong, X., Li, Y.-h., et al. (2018). A Systematic Review of Pharmacokinetic Studies on Herbal Drug Fuzi : Implications for Fuzi as Personalized Medicine. *Phytomedicine* 44, 187–203. doi:10.1016/j.phymed.2018.03.001

Xia, Z. Y., Wang, Q., Guo, Q., and Pang, J. (2010). TCM Constitutional Types of Hyperthyroidism and Hypothyroidism. *J. Beijing Univ. Tradit. Chin. Med.* 33 (4), 280–282. doi:10.3788/HPLPB20102202.0415

Xiong, L., Peng, C., Xie, X.-F., Guo, L., He, C.-J., Geng, Z., et al. (2012). Alkaloids Isolated from the Lateral Root of Aconitum Carmichaelii. *Molecules* 17 (8), 9939–9946. doi:10.3390/molecules17089939

Yang, M., He, Y. P., Huang, L. S., and You, J. X. (2010). Epidemiological Investigation of Constitution of Sterility Patients. *J. N. Chin. Med.* 42 (5), 55–56. doi:10.13457/j.cnki.jncm.2010.05.067

Yao, S.-l., Wang, Q., Zhang, Z.-z., Wu, J.-x., Cheng, N., Xu, X., et al. (2015). Genome-wide Association Study on Susceptibility Genes Associated with Yang-Deficiency Constitution: A Small Sample Case-Control Study. *Chin. J. Integr. Med.* 21 (8), 601–609. doi:10.1007/s11655-014-1957-5

Yen, M., and Ewald, M. B. (2012). Toxicity of Weight Loss Agents. *J. Med. Toxicol.* 8, 145–152. doi:10.1007/s13181-012-0213-7

Ying, C.-J., Noguchi, T., Aso, H., Ikeda, K., Yamori, Y., and Nara, Y. (2008). The Role of Cytochrome P-450 in Salt-Sensitive Stroke in Stroke-Prone Spontaneously Hypertensive Rats. *Hypertens. Res.* 31 (9), 1821–1827. doi:10.1291/hypres.31.1821

Zhang, B. Q., Chen, L., Ran, F. Y., Du, K. H., Yu, F., Chen, W., et al. (2020). Effects of Aconitine on H9c2 Cell Differentiation. *Anhui Med. Pharm. J.* 24 (07), 1287–1290+1485. doi:10.3969/j.issn.1009-6469.2020.07.004

Zhang, J. M., Li, L., Gao, F., Li, Y., He, Y., and Fu, C. M. (2012). [Chemical Ingredient Analysis of Sediments from Both Single Radix Aconiti Lateralis Decoction and Radix Aconiti Lateralis - Radix Glycyrrhizae Decoction by HPLC-MS]. *Yao Xue Xue Bao* 47 (11), 1527–1533. doi:10.16438/j.0513-4870.2012.11.007

Zhang, J. Y., Hong, C. L., Chen, H. S., Zhou, X. J., Zhang, Y. J., Efferth, T., et al. (2019). Target Identification of Active Constituents of Shen Qi Wan to Treat Kidney Yang Deficiency Using Computational Target Fishing and Network Pharmacology. *Front. Pharmacol.* 10, 650–668. doi:10.3389/fphar.2019.00650

Zhou, G., Tang, L., Zhou, X., Wang, T., Kou, Z., and Wang, Z. (2015). A Review on Phytochemistry and Pharmacological Activities of the Processed Lateral Root of Aconitum Carmichaelii Debeaux. *J. Ethnopharmacology* 160, 173–193. doi:10.1016/j.jep.2014.11.043

Zou, X., Pan, G. M., Sheng, X. G., Lai, R. K., and Wu, Y. (2011). Clinical Epidemiologic Investigation on Chinese Medicine Syndrome Laws in Patients with Chronic Heart Failure. *Chin. J. Integr. Tradit. West. Med.* 31 (7), 903–908. doi:10.1007/s10570-010-9464-0

Conflict of Interest: The authors declare that the research was conducted in the absence of any commercial or financial relationships that could be construed as a potential conflict of interest.

Copyright © 2021 Tong, Chen, Gong, Zhong, Zhu and Yang. This is an open-access article distributed under the terms of the Creative Commons Attribution License (CC BY). The use, distribution or reproduction in other forums is permitted, provided the original author(s) and the copyright owner(s) are credited and that the original publication in this journal is cited, in accordance with accepted academic practice. No use, distribution or reproduction is permitted which does not comply with these terms.

frontiers in Pharmacology

ORIGINAL RESEARCH
published: 15 July 2021
doi: 10.3389/fphar.2021.598200

TCMIP v2.0 Powers the Identification of Chemical Constituents Available in Xinglou Chengqi Decoction and the Exploration of Pharmacological Mechanisms Acting on Stroke Complicated With Tanre Fushi Syndrome

Ping Wang[1†], *Shuang Wang*[1,2†], *Hong Chen*[1,3†], *Xiaofang Deng*[1], *Luoqi Zhang*[1], *Haiyu Xu*[1,4*] *and Hongjun Yang*[5]

[1]Institute of Chinese Materia Medica, China Academy of Chinese Medical Sciences, Beijing, China, [2]College of Pharmacy, Heilongjiang University of Chinese Medicine, Harbin, China, [3]College of Traditional Chinese Medicine, Shenyang Pharmaceutical University, Shenyang, China, [4]Shaanxi Institute of International Trade and Commerce, Xianyang, China, [5]Experimental Research Center, China Academy of Chinese Medical Sciences, Beijing, China

OPEN ACCESS

Edited by:
Yan Xu,
Cleveland State University,
United States

Reviewed by:
Aihua Zhang,
Heilongjiang University of Chinese Medicine, China
Xuezhong Zhou,
Beijing Jiaotong University, China

***Correspondence:**
Haiyu Xu
hyxu@icmm.ac.cn

[†]These authors have contributed equally to this work

Specialty section:
This article was submitted to Ethnopharmacology, a section of the journal Frontiers in Pharmacology

Received: 24 August 2020
Accepted: 21 June 2021
Published: 15 July 2021

Citation:
Wang P, Wang S, Chen H, Deng X, Zhang L, Xu H and Yang H (2021) TCMIP v2.0 Powers the Identification of Chemical Constituents Available in Xinglou Chengqi Decoction and the Exploration of Pharmacological Mechanisms Acting on Stroke Complicated With Tanre Fushi Syndrome. Front. Pharmacol. 12:598200. doi: 10.3389/fphar.2021.598200

Xinglou Chengqi (XLCQ) decoction, composed of three botanical drugs and one inorganic drug, is used in clinics during the treatment of acute stroke complicated with Tanre Fushi (TRFS) syndrome in China. However, its active ingredients and the molecular mechanism have not been clarified. So, we aimed to preliminarily characterize its chemical constituents and investigate its pharmacological mechanisms using an integrative pharmacology strategy, including component analysis, network prediction, and experimental verification. We employed UPLC-QTOF-MS/MS to describe the chemical profile of XLCQ, Integrative Pharmacology-based Network Computational Research Platform of Traditional Chinese Medicine (TCMIP v2.0, http://www.tcmip.cn/), to assist in identifying the chemical components and predict the putative molecular mechanism against acute stroke complicated with TRFS, and LPS-stimulated BV-2 cells to verify the anti-neuroinflammatory effects of luteolin, apigenin, and chrysoeriol. Altogether, 197 chemical compounds were identified or tentatively characterized in the water extraction of XLCQ, 22 of them were selected as the key active constituents that may improve the pathological state by regulating 27 corresponding targets that are mainly involved in inflammation/immune-related pathways, and furthermore, luteolin, apigenin, and chrysoeriol exhibited good anti-neuroinflammatory effects from both protein and mRNA levels. In summary, it is the first time to employ an integrative pharmacology strategy to delineate 22 constituents that may improve the pathological state of stroke with TRFS by regulating 27 corresponding targets, which may offer a highly efficient way to mine the scientific connotation of traditional Chinese medicine prescriptions. This study might be a supplement for the deficiency of the basic research of XLCQ.

Keywords: TCMIP, integrative pharmacology strategy, UPLC-QTOF-MS/MS, Xinglou Chengqi decoction, Tanre Fushi syndrome

INTRODUCTION

Stroke, characterized by a high incidence rate, high mortality, and a high disability rate, is a devastating cerebrovascular event that occurs as a result of cerebral vascular occlusion (ischemic stroke) or burst/bleeding (hemorrhagic stroke), leading to cerebral blood flow disruption, physical disability, and multiple functional impairment, which seriously threatens human health and quality of life (Feigin et al., 2016). At present, the main treatment to ischemic stroke is early thrombolysis to restore blood flow and achieve vascular recanalization, but most patients cannot get thrombolytic therapy due to the limitation of treatment time window or other contraindications. Therefore, it is particularly urgent to find safe and effective drugs for stroke prevention and treatment with a clear mechanism.

Traditional Chinese medicine (TCM), characterized by lower side effects, is often thought to be an alternative pharmacotherapy for prevention and rehabilitation intervention of ischemic stroke in China (Liu et al., 2018). As early as in 1981, Academician Yongyan Wang observed that about 74.2% of stroke patients were accompanied by "Tanre Fushi" (TRFS) syndrome (Wang, 1981) that manifests as abdominal distension, constipation, bad breath, and dry throat, and then he developed the "Huatan Tongfu" treatment strategy in the following year (Wang et al., 1982). In 1986, he created "Huatan Tongfu" decoction, which was later renamed as "Xinglou Chengqi" (XLCQ) decoction, to treat acute stroke in clinics. At the same time, the indication and opportunity for the correct application of XLCQ decoction were given (Wang et al., 1986). XLCQ decoction is composed of three botanical drugs and one inorganic drug, namely, *Trichosanthes kirilowii* Maxim. (Gualou, GL) 30–40 g, *Arisaema erubescens* (Wall.) *Schott* (Dannanxing, DNX) 6–10 g, *Rheum palmatum L.* (DaHuang, DH) 10–15 g, and *Natrii sulfas* (Mangxiao, MX) 10–15 g. The main component of *Natrii sulfas* is $Na_2SO_4 \bullet 10H_2O$, which belongs to a mineral medicine.

Accumulating clinical practices have proven that the effective power of the Western medicine treatment for acute stroke could be enhanced obviously when combined with XLCQ, especially when the patient is suffering with TRFS (Chen et al., 2017; Zhen, 2017; Liu and Lei, 2019; Wang et al., 2020a; Han, 2020; Jiang et al., 2020; Lu and Wang, 2020; Yao et al., 2020). Although XLCQ has almost been used for 40 years in clinics, its chemical composition has not been systematically characterized, and its pharmacological mechanism is limited to anti-inflammatory (Du et al., 2009; Wand, 2016; Zhen, 2017; Zhao et al., 2018), anti–free radical injury (Wu and Jiang, 2005; Zhou et al., 2016), inhibition of neuronal damage (Liu et al., 2012a; Yu et al., 2018), and anti-neuronal apoptosis (Liu et al., 2012b).

Therefore, in the present study, we aimed to describe the chemical profiles and explore the underlying pharmacological mechanisms of XLCQ acting on stroke with TRFS through the following scheme, as shown in **Figure 1**: 1) analyzing XLCQ chemical components by UPLC-QTOF-MS/MS, 2) collecting the information of chemical components from Integrative Pharmacology-based Network Computational Research Platform of Traditional Chinese Medicine (TCMIP v2.0, http://www.tcmip.cn/), 3) predicting the putative targets of the identified components and collecting the genes of stroke and TRFS from TCMIP, 4) constructing a "component targets-stroke/TRFS genes" network to select the candidate targets and the main active components of XLCQ, 5) functional enrichment analysis for investigating the underlying molecular mechanisms of XLCQ acting on stroke complicated with TRFS, and 6) verifying the anti-neuroinflammatory effects of luteolin, apigenin, and chrysoeriol based on LPS-simulated BV-2 cells.

MATERIALS AND METHODS

Chemicals and Reagents

HPLC-grade acetonitrile and methanol were purchased from Merck KGaA (Darmstadt, Germany); HPLC-grade formic acid from Sigma-Aldrich (St. Louis, MO, United States); chloroform (100068), isopropanol (80109218), and anhydrous alcohol (10009218) from Sinopharm (Beijing, China); and DEPC-treated water (sc-204391) from Santa Cruz Biotechnology (CA, United States). Deionized water (18.2 MΩ cm) was purified by a Milli-Q system (Millipore Co., Billerica, United States). *Trichosanthes kirilowii* Maxim. (place of production: Hebei Province; batch number: 190112010), *Arisaema erubescens* (Wall.) Schott (place of production: Sichuan Province; batch number: D180903001), *Rheum palmatum L.* (place of production: Sichuan Province; batch number: 18111201), and *Natrii Sulfas* (place of production: Sichuan Province; batch number: DD0181) were purchased from Shengshi Baicao Pharmaceutical Co., Ltd. and authenticated by Mrs. Xirong He, a research assistant of China Academy of Chinese Medical Sciences (Beijing). The voucher specimens were deposited in the Institute of Chinese Materia Medica, China Academy of Chinese Medical Sciences.

Fetal bovine serum (FBS,10270–106), penicillin–streptomycin (10,000 U/mL, 15140122), and 0.05% trypsin-EDTA (1X, 25300–054) from Gibco BRL Co. (Boise, Idaho, United States); Dulbecco's Modified Eagle's Medium-high glucose (DMEM/High Glucose, SH30022.01) from HyClone Laboratories (Logan, UT, United States); dry powder of phosphate-buffered saline (PBS, P1010), dimethyl sulfoxide (DMSO, D8371), and sterile deionized water (F0025) from Solarbio Life Sciences (Beijing, China); lipopolysaccharide (LPS, 0111:B4, L2630) from Sigma-Aldrich Crop. (St. Louis, MO, United States).

Luteolin (BT1191), apigenin (BT443), and chrysoeriol (BT2582) were borrowed from Beijing Beite Renkang Biomedical Technology Co., Ltd. (Beijing, China); IL-1β (CSB-E08054m) and TNF-α (CSB-E04741) ELISA kits from Cusabio (Beijing, China); CCK-8 kit from Dojindo (Kumamoto ken, Japan); and TB Green® Premix Ex Taq™ (RR420A) from TAKARA BIO INC. (Chiryu Shi, Japan).

Preparation of Herbal Extracts

The prescription is composed of GL, DNX, DH, and MX with a dose proportion of 15:3:5:5. GL and DNX were soaked in 10 volumes of water for 60 min before boiling for 30 min. Then DH was added and boiling was maintained for another 30 min. MX

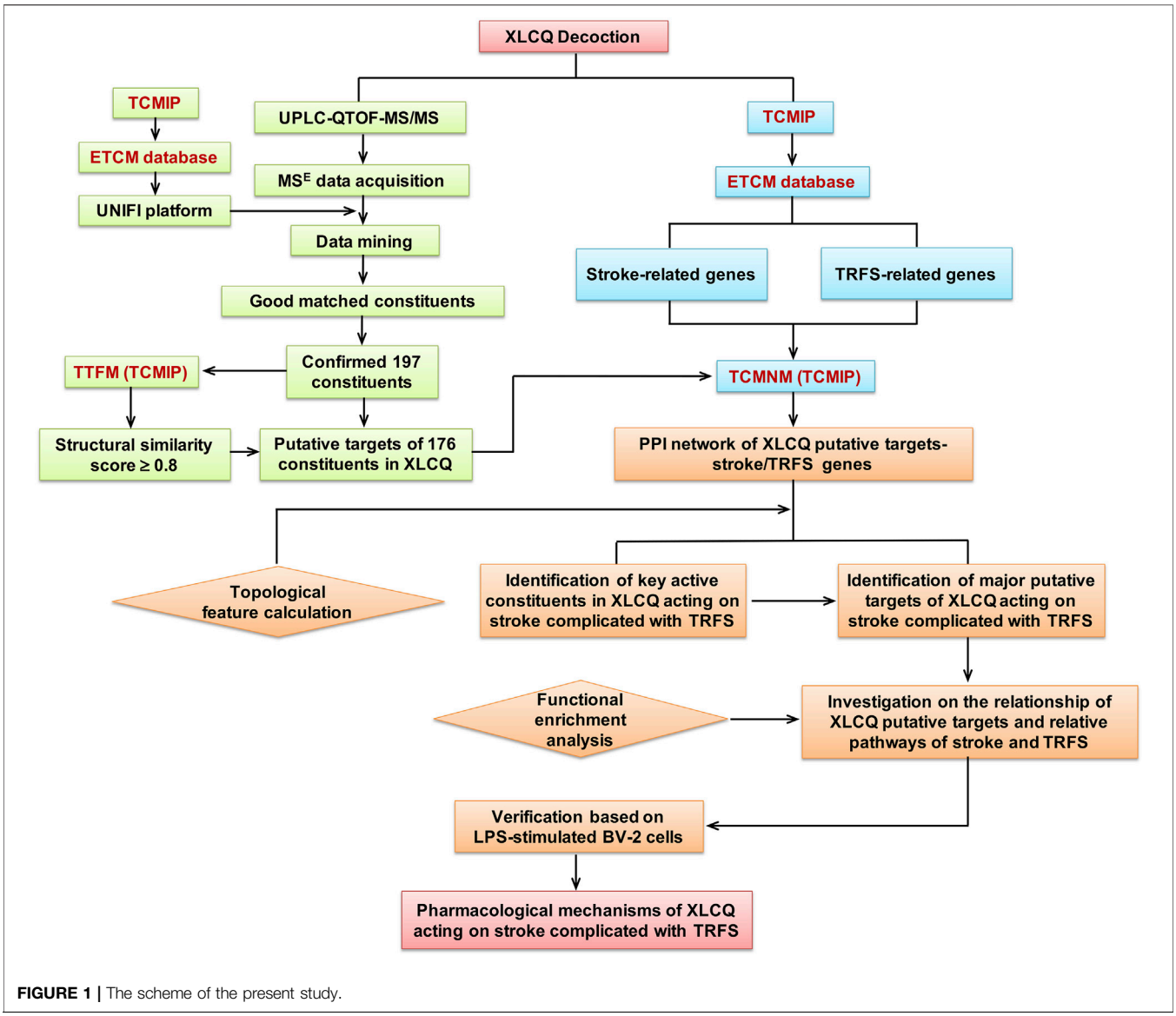

FIGURE 1 | The scheme of the present study.

was dissolved in the decoction that was filtered by eight layers of gauze. The residue was boiled with 8 volumes of water for another 30 min, and the decoction was filtered as before. The two combined filtrates were freeze-dried (Lab-1D-80E; Beijing boyaikang Experimental Instrument Co., Ltd., Beijing, China) at −80°C with a paste rate at 26.96%, and the powder was pressed through a 60-mesh sieve. The fine powder was dissolved into 10 volumes of 70% MeOH and extracted with an ultrasonic wave for 15 min before 1-μl aliquots were transferred to autosampler vials for analysis.

Instrumentation and UPLC-QTOF-MS/MS Conditions

The analysis was performed on a Waters Acquity UPLC I-Class system (Waters Corp., Milford, United States) equipped with a binary pump, an online vacuum degasser, an autosampler, and an automatic thermostatic column oven, coupled with a Waters Xevo G2-S Q-TOF Mass System (Manchester, United Kingdom) equipped with electrospray ionization (ESI). The data were recorded by Masslynx V4.1 (Waters Corporation, Milford, United States). Unifi software (Waters Corporation, Milford, United States) was used for peak detection and compound preliminary identification.

Chromatographic separation was performed on a Waters Acquity UPLC HSS T3 column (100 mm × 2.1 mm, i.d., 1.8 μm) maintained at 35°C, and a linear gradient of (A) 0.1% (v/v) formic acid in deionized water and (B) acetonitrile containing 0.1% (v/v) formic acid was used for the elution procedure, as follows: 0–3 min, 0.2–2% B; 3–5 min, 2–5% B; 5–6 min, 5–8% B; 6–10 min, 8–16% B; 10–10.2 min, 16–19% B; 10.2–14.5 min, 19–25% B; 14.5–15 min, 25–30% B; 15–15.5 min, 30–40% B; 15.5–18 min, 40–50% B; 18–20 min, 50–70% B; 20–21 min, 70–98% B; 21–24 min, 98% B; 24–24.1 min, 98–0.2%

TABLE 1 | Primers used in this study.

Primer name	Nucleotide sequence (5′-3′)	Product size
IL-1β forward	GCAACTGTTCCTGAACTCAACT	89bp
IL-1β reverse	ATCTTTTGGGGTCCGTCAACT	
TNF-α forward	CCCTCACACTCACAAACCAC	133bp
TNF-α reverse	ACAAGGTACAACCCATCGGC	
PIK3CA forward	TATGTCTACCCTCCAAATGTCG	128bp
PIK3CA reverse	TACTTCTGCTTGTCGTTGTTTG	
AKT1 forward	ATGAACGACGTAGCCATTGTG	116bp
AKT1 reverse	TTGTAGCCAATAAAGGTGCCAT	
NF-κB1 forward	CAAAGACAAAGAGGAAGTGCAA	203bp
NF-κB1 reverse	GATGGAATGTAATCCCACCGTA	
NF-κB2 forward	CAAGGACATGACTGCTCAATTT	92bp
NF-κB2 reverse	GCCTCTGAAGTTTCTGGATCAT	
CREB1 forward	AGCAGCTCATGCAACATCATC	152bp
CREB1 reverse	AGTCCTTACAGGAAGACTGAACT	
HSP90AA1 forward	TGTTGCGGTACTACACATCTGC	116bp
HSP90AA1 reverse	GTCCTTGGTCTCACCTGTGATA	
β-actin forward	GGCTGTATTCCCCTCCATCG	154bp
β-actin reverse	CCAGTTGGTAACAATGCCATGT	

B; and 24.1–26 min, 0.2% B. The flow rate was set at 0.5 ml/min, and a 1-μl aliquot was set as the injection volume.

The QTOF-MS data were collected in a full scan auto mode from 0 to 26 min in both positive and negative ion modes. Based on the best response for most of the compounds, the optimal parameters were set as follows: mass range, 50–1,500 Da; source temperature, 100 °C; desolvation temperature, 450°C; desolvation gas flow, 900 l/h; sampling cone, 40 V; ESI^- capillary voltage, 2.5 KV; and ESI^+ capillary voltage, 0.5 KV. At low CE scan, the auto MS collision energy was 6 eV. At high CE scan, the collision energy was 30–50 eV ramp for ESI^+ and 80–100 eV ramp for ESI^-.

Leucine enkephalin was employed as lock mass at a concentration of 200 pg/ml in acetonitrile (0.1% formic acid): H_2O (0.1% formic acid) (50:50, v/v) for the positive ion mode ($[M + H]^+ = 556.2771$) and negative ion mode ($[M-H]^- = 554.2615$) *via* a lock spray interface.

Data Processing

UPLC-QTOF-MS/MS system was controlled by the Masslynx 4.1 platform. The MS^E data collected in a continuum mode were processed using the apex peak detection and alignment algorithms in UNIFI 1.8, which enabled quasi-molecular ion peaks, salt adduct ions, and dehydration fragment ions to be analyzed as a single entity. The analysis process includes data acquisition, data mining, library searching, and report generation.

The information of chemical components GL, DNX, and DH including molecular name, molecular formulas, molecular weights, and chemical structures (mol. format) was collected from ETCM (Xu et al., 2019) (http://www.nrc.ac.cn:9090/ETCM/), as a customized library listed in **Supplementary Excel S1**, to assist the chemical identification, which were transferred to the UNIFI form later (**Supplementary Excel S2**). The additive ions of $[M + H]^+$, $[M + K]^+$, $[M + Na]^+$, $[2M + H]^+$, and $[M-e]^+$ were selected in a positive ion mode and $[M + COOH]^-$, $[M-H]^-$, and $[2M-H]^-$ in a negative ion mode. A margin of error up to 5 mDa/10 ppm for identified components was allowed, and the matched components would be generated as predicted fragments from the structure. For unmatched components, the functional module of elemental composition and mass fragment could further assist the chemical identification. Based on the isotopic abundance, the elemental composition calculator could provide a number of possible formulas for an accurate mass peak. Mass fragment could provide fragment structures which assist the chemical identification. The final list of possible formulas could provide relative confidence denoted by an i-FIT score and 0.8 as the threshold value.

Prediction of the Putative Targets of Chemical Constituents Available in XLCQ

The mol. formats of identified compounds were uploaded to the customer center of TCMIP to predict the putative targets using TCM target prediction and function analysis module (TTFM) according to the chemical structure similarity comparison with known drugs on the market. In order to improve the prediction accuracy, we set the structural similarity score at 0.80 (moderate~high similarity) to select the constitute–putative target pairs (Mao et al., 2019).

Network Construction of XLCQ Putative Target-Stroke/TRFS Gene

To investigate the relationship of XLCQ putative targets and stroke/TRFS genes, we collected a list of stroke-related genes and TRFS-related genes from disease-related gene database of TCMIP. The key words of stroke were "stroke, ischemic stroke, brain injury, cerebral ischemia, and cerebral hemorrhage." TRFS syndrome was a combination of Yang Ming Fushi syndrome, phlegm heat obstructing lung syndrome, and wind-phlegm syndrome. So, the symptomatic phenotypes of three syndromes were used as the key words to collect the related genes, including "fever, delirium, abdominal pain, dysphoric mood, hyperhidrosis, constipation, wheezing, cough, vertigo, vomiting, abnormality of salivation, syncope, facial paralysis, and hemiplegia."

An interaction network of XLCQ putative target–stroke/TRFS-related gene was constructed based on the links among the three gene sets using the TCM Association Network Mining Module (TCMNM) of TCMIP, which directly exhibits the major hub network according to three topological features of each node gene, including "degree," "betweenness," and "closeness." Generally, the node that has the degree value 2-fold the median, and betweenness and closeness value 1-fold the median is selected as the major hub.

Network Visualization and Functional Enrichment Analysis

To better exhibit the common targets among XLCQ, stroke, and TRFS, the Venn diagram was performed using the "Calculate and draw custom Venn diagrams" website (http://bioinformatics.psb.ugent.be/webtools/Venn/). To better exhibit the interactions of the major hubs, the network visualization was performed using CytoScape V3.8.0. To elucidate the biological functions of XLCQ putative

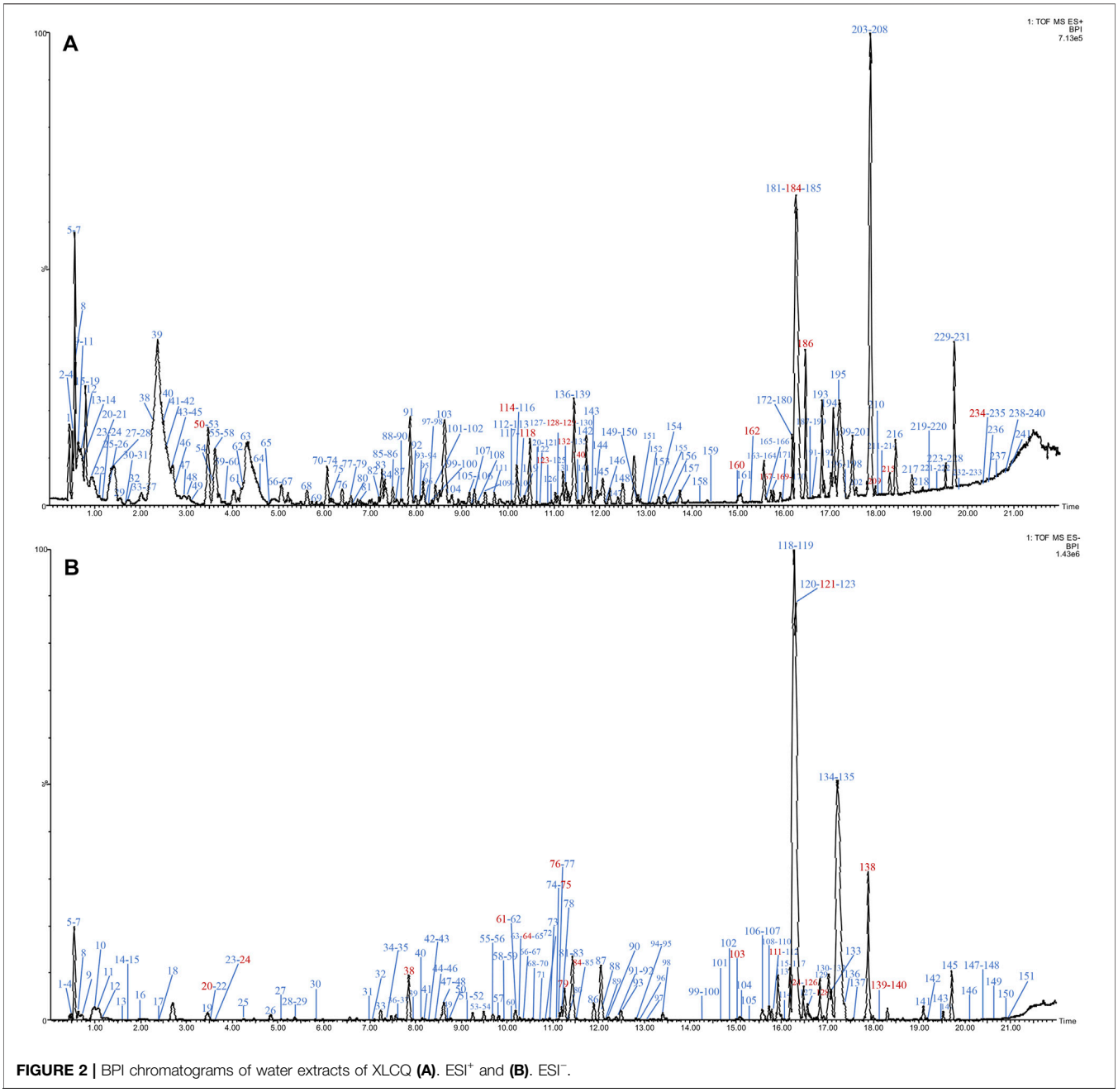

FIGURE 2 | BPI chromatograms of water extracts of XLCQ **(A)**. ESI^+ and **(B)**. ESI^-.

targets, the functional enrichment analysis was performed using the database for annotation, visualization, and integrated discovery (DAVID) v6.8 (https://david.ncifcrf.gov).

Cell Viability Evaluation

Murine BV-2 microglia cells were obtained from the Institute of Materia Medica-Chinese Academy of Medical Science (Beijing, China) and cultured in DMEM supplemented with 10% heat-inactivated FBS and antibiotics (100 U/ml streptomycin and 100 U/ml penicillin) at 37°C in an incubator [Sanyo MCO-18AIC (UV), Osaka, Japan] with a humidified atmosphere containing 5% CO_2 and 95% O_2. BV-2 cells were plated in 96-well plates with density at 1×10^4 cells/well and incubated in the abovementioned conditions for 24 h. Luteolin, apigenin, and chrysoeriol solutions were added to different wells with final concentrations at 80, 40, 20, 10, and 5 μM and incubated for another 24 h. Cell viability was evaluated by a CCK-8 kit, and the absorbance was determined at 450 nm 2 h later by a ThermoFisher Scientific Multiskan FC Microplate Reader (MA, United States).

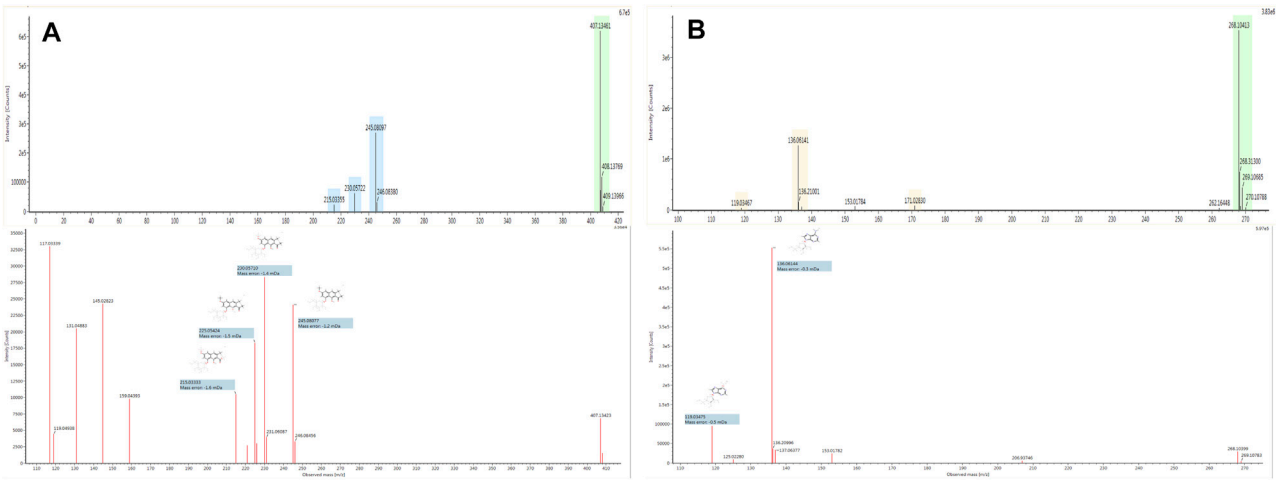

FIGURE 3 | Spectrum information of torachrysone-8-O-β-D-glucoside **(A)** and arginine **(B)** automatically provided by UNIFI™.

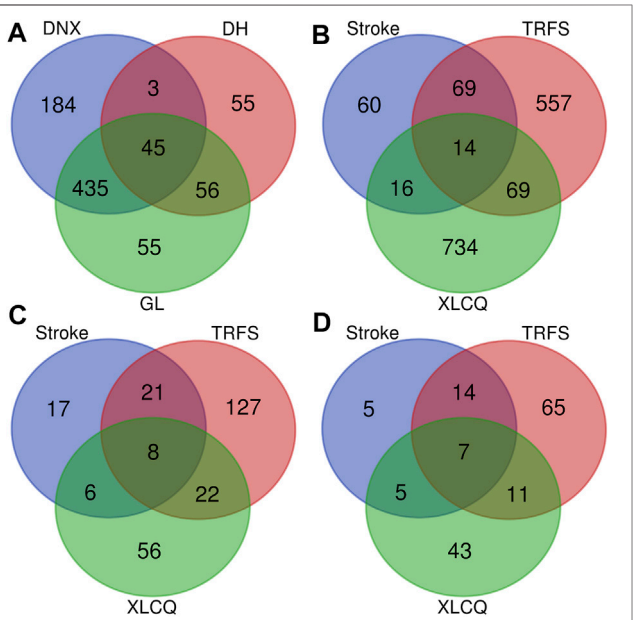

FIGURE 4 | The Venn diagram of putative targets of the three herbs available XLCQ **(A)**; the Venn diagram of XLCQ putative targets, known stroke/TRFS-related genes **(B)**; the Venn diagram of 257 major hubs **(C)**; and the Venn diagram of 150 key hubs **(D)**. [GL: *Trichosanthes kirilowii Maxim.*; DNX: *Arisaema erubescens (Wall.) Schott*; DH: *Rheum palmatum L.*].

Drug Treatment

BV-2 cells were plated in 24-well plates with the density at 1.5×10^5 cells/well and incubated for 24 h. Luteolin, apigenin, and chrysoeriol solutions were added with final concentrations at 10 μM and incubated for 1 h. Then LPS was added to induce neuroinflammation with a final concentration of 1 μg/ml, and incubated for another 24 h. Finally, the supernatant was collected by centrifugation at 12,000 r and 4 °C for 10 min, which was used for IL-1β and TNF-α analyses according to the instructions of ELISA kits.

Real-Time Reverse Transcription–Polymerase Chain Reaction (RT-qPCR)

The total RNA was isolated using TRNzol Universal Reagent (TIANGEN, DP424, China), and 1 μg RNA was reverse-transcribed to cDNA using FastKing gDNA Dispelling RT SuperMix (TIANGEN, KR118-02, China) by Veriti 96-Well Thermal Cycler PCR (Thermo Fisher, 4375786, United States) according to the manufacturer's instructions. A single-stranded cDNA was amplified by PCR with primers for IL-1β, TNF-α, PIK3CA, AKT1, NFKB1, NFKB2, CREB1, HSP0AA1, and β-actin, whose primer sequences are shown in **Table 1**. PCR was performed using a real-time fluorescence quantitative PCR instrument (Roche, LightCycler480 II, Germany) by the following two-step PCR amplification procedure: 1 cycle of pre-degradation at 95°C for 30 s, 40 cycles of denaturation at 95°C for 5 s (ramp rate: 4.4°C/s), and then, annealing and extension at 60°C for 30 s (ramp rate: 2.2°C/s, acquisition mode: single). β-actin was selected as an internal control to evaluate the expression of the eight genes. Primers were purchased from Beijing Qingke Biotechnology Co., Ltd. (Beijing, China).

RESULTS

Characterization and Identification of Chemical Constituents Available in XLCQ

The base peak intensity (BPI) chromatograms of water extraction of XLCQ corresponding to the positive and

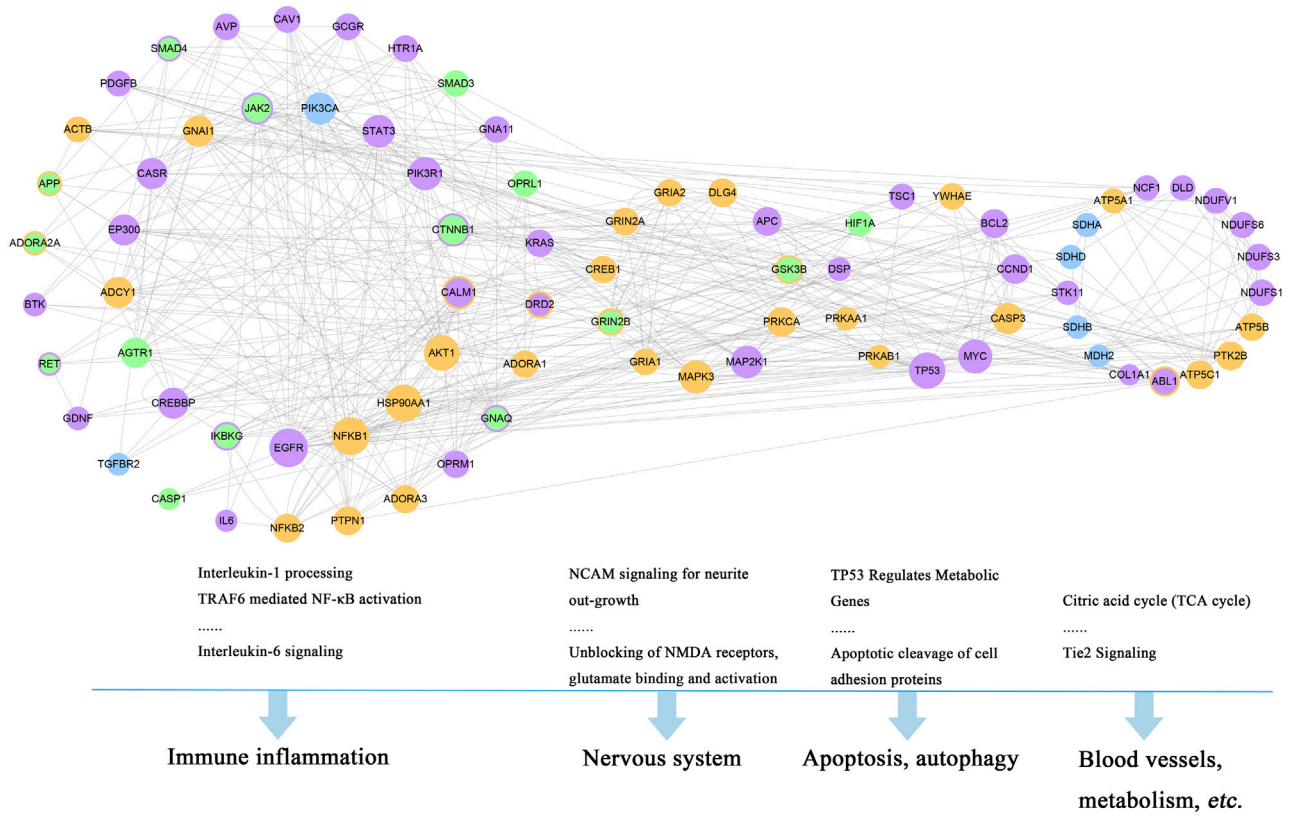

FIGURE 5 | Four functional modules involved in 82 major hubs and the corresponding pathological events during the progression of stroke complicated with TRFS. (Orange nodes refer to putative targets of XLCQ; green nodes refer to known therapeutic targets of stroke; purple nodes refer to known therapeutic targets of TRFS; blue nodes refer to the common genes of three sets; and the color-overlay nodes refer to common genes of two sets.)

negative ion modes are shown in **Figure 2**. The MS^E raw data obtained by UPLC-QTOF-MS/MS were processed using the UNIFI 1.8 software automatically to quickly identify the constituents by matching the detailed information with the customized library (**Supplementary Excel S2**). Altogether, a total of 197 compounds (152 in ESI^+ and 116 in ESI^-) were identified or tentatively characterized, of which 56 originated from GL, 63 from DNX, and 78 from DH. The detailed information of chemical compounds is listed in **Supplementary Tables S1, S2**, containing RT, M/Z, error, response, adducts, formula, name, fragments, category, and origination. The identified constituents, especially the isomers, were verified by the characteristic fragments reported in the literatures. Taking two compounds as examples, the secondary fragment information was exhibited in detail. The ion at RT = 15.56 and $[M-H]^-$ = 407.1334 was primarily identified as torachrysone-8-O-β-D-glucoside ($C_{20}H_{24}O_9$) in ESI^- after searching in the scientific database of UNIFI collected from ETCM, and the main fragments were m/z 245.0600 $[M-H-Glc]^-$, 230.0560 $[M-H-Glc-CH3]^-$, 215.0324 $[M-H-Glc-2CH_3]^-$, 159.0431 $[M-H-Glc-2CH_3-2CO]^-$, and 141.0483 $[M-H-Glc-2CH_3-3CO]^-$ (**Figure 3A**), which were consistent with the literature report (Gao, 2012). In the same way, ion at RT = 3.46 and $[M + H]^+$ = 268.1046 was primarily identified as arginine ($C_{10}H_{13}N_5O_4$) in ESI^+, and the main fragments were m/z 136.0624 and 119.0349 (**Figure 3B**), corresponding to loss $-C_5H_7O_4$ and $-NH_3$ in turn, which were consistent with the literature report (Wang and Han, 2018).

Putative Targets of Chemical Constituents Available in XLCQ

Altogether, a total of 833 putative targets were predicated based on the chemical structures of 197 primarily identified compounds using the TCM Target Prediction and Function Analysis Module of TCMIP (**Supplementary Excel S3**). Only 176 compounds (52 from GL, 51 from DNX, and 73 from DH) had putative targets when the Tanimoto score was set at 0.8 (moderate~high similarity). The putative targets of GL, DNX, and DH were 591, 667, and 159, respectively. Interestingly, the three herbs had a number of common putative targets according to the prediction, indicating the potential drug–drug interactions through their common targets (**Figure 4A**).

The Gene Set of Stroke and TRFS Syndrome

A total of 159 stroke-related genes and 709 TRFS-related genes were collected from the disease-related gene database of TCMIP

TABLE 2 | Active constituents of XLCQ and their putative targets.

NO.	Active constituents	Putative targets	Number of targets	Targets frequency	Category
1	**Guanosine** (–/24)[a]	MAPK3; DLG4; CREB1; AKT1; PIK3CA; ADORA3; ADORA2A; ADORA1; PRKAB1; PRKAA1; ADCY1; GNAI1; ABL1	13	42	*Trichosanthes kirilowii Maxim.Arisaema erubescens (Wall.) Schott*
2	**Adenosine** (50,20)	MAPK3; CREB1; AKT1; PIK3CA; ADORA3; ADORA2A; ADORA1; PRKAB1; PRKAA1; GSK3B; ADCY1; ABL1	12	39	*Trichosanthes kirilowii Maxim. Arisaema erubescens (Wall.) Schott*
3	5α-Stigmast-7-En-3-β-Ol (123/-)	GRIN2B; GRIN2A; NFKB1; NFKB2	4	24	*Trichosanthes kirilowii Maxim*
4	**Kaempferol** (160/103)	AKT1; HSP90AA1; ACTB; PTK2B; PRKCA; ATP5B; ATP5C1; ATP5A1	8	23	*Trichosanthes kirilowii Maxim*
5	Arvenin **III** (169/111)	NFKB1; NFKB2; CASP3; YWHAE	4	19	*Trichosanthes kirilowii Maxim*
6	Arvenin I (186/126)	NFKB1; NFKB2; CASP3; YWHAE	4	19	*Trichosanthes kirilowii Maxim*
7	Dihydroisocucurbitacin B (–/140)	NFKB1; NFKB2; CASP3; YWHAE	4	19	*Trichosanthes kirilowii Maxim*
8	3-epi-isocucurbitacin B (209/138)	NFKB1; NFKB2; CASP3	3	17	*Trichosanthes kirilowii Maxim*
9	23,24-dihydrocucurbitacinD (–/124)	NFKB1; NFKB2; CASP3	3	17	*Trichosanthes kirilowii Maxim*
10	**Resveratrol** (114/61)	AKT1; APP	2	15	*Trichosanthes kirilowii Maxim*
11	**Procyanidin B-1-3-O-gallate** (118/64)	HSP90AA1; ACTB; PRKCA; ATP5B; ATP5C1; ATP5A1	6	13	*Trichosanthes kirilowii Maxim*
12	**Procyanidin B-2 3, 3′-di-O-gallate** (129/76)	HSP90AA1; ACTB; PRKCA; ATP5B; ATP5C1; ATP5A1	6	13	*Trichosanthes kirilowii Maxim*
13	**Procyanidin B-4 3′-O-gallate** (140/84)	HSP90AA1; ACTB; PRKCA; ATP5B; ATP5C1; ATP5A1	6	13	*Trichosanthes kirilowii Maxim*
14	**Bryonolic acid** (234/–)	GRIN2B; GRIN2A; NFKB1; NFKB2	4	24	*Rheum palmatum L*
15	**Luteolin** (162/–)	AKT1; HSP90AA1; ACTB; PTK2B; PRKCA; ATP5B; ATP5C1; ATP5A1	8	23	*Rheum palmatum L*
16	**Apigenin** (167/–)	AKT1; HSP90AA1; ACTB; PTK2B; ATP5B; ATP5C1; ATP5A1	7	20	*Rheum palmatum L*
17	Chrysoeriol (184/121)	AKT1; HSP90AA1; ACTB; PTK2B; ATP5B; ATP5C1; ATP5A1	7	20	*Rheum palmatum L*
18	**(–)-epicatechin 3-O-gallate** (132/79)	AKT1; HSP90AA1; ACTB; PTK2B; ATP5B; ATP5C1; ATP5A1	7	20	*Rheum palmatum L*
19	**(+)-catechin** (–/38)	AKT1; HSP90AA1; ACTB; PTK2B; ATP5B; ATP5C1; ATP5A1	7	20	*Rheum palmatum L*
20	23,24-dihydrocucurbitacin B (215/139)	NFKB1; NFKB2; CASP3; YWHAE	4	19	*Rheum palmatum L*
21	23,24-dihydrocucurbitacin E (-/128)	NFKB1; NFKB2; CASP3; YWHAE	4	19	*Rheum palmatum L*
22	**Procyanidin C-1 3′, 3″-di-O-gallate** (128/75)	HSP90AA1; ACTB; PRKCA; ATP5B; ATP5C1; ATP5A1	6	13	*Rheum palmatum L*

[a]*The number is corresponding to* ***Supplementary Tables S1, S2****.*

(**Supplementary Excel S3**). The distribution of the 1519 genes was exhibited in the Venn diagram (**Figure 4B**), with XLCQ 734, stroke 159, and TRFS 709. Whereas "stroke" was a disease, "TRFS" was a syndrome, and there were still 83 common targets, indicating they may have the possible effects targets. XLCQ had 30 common targets with that of stroke and 83 with that of TRFS, indicating the possible direct targets of XLCQ acting on stroke complicated with TRFS. The common targets of XLCQ with TRFS were more than those of XLCQ with stroke, indicating that the therapeutic effect of XLCQ on TRFS may be stronger than that of stroke.

Underlying Mechanisms of XLCQ Acting on Stroke Complicated With TRFS Syndrome

To illustrate the underlying mechanisms of XLCQ acting on stroke complicated with TRFS, an interaction network of drug target genes and disease/syndrome-related genes was constructed based on the interactions among three gene sets using the TCM Association Network Mining Module of TCMIP, and the network topological features were calculated automatically by TCMIP. Altogether, 257 hubs were selected, and detailed information is provided in **Supplementary Excel S3**. The target distribution of the 257 genes was exhibited in the Venn diagram (**Figure 4C**). The target number of XLCQ, stroke, and TRFS was 92, 52, and 178, respectively, with 30 common targets between XLCQ and TRFS, 14 between XLCQ and stroke, and 29 between stroke and TRFS.

To improve the prediction accuracy, 150 major hubs whose degree value ≥12 were selected from the 257 hubs (**Supplementary Excel S3**, marked in red). Among them, 31 nodes were stroke-related genes, 97 were TRFS-related genes, and 66 were XLCQ putative targets (**Figure 4D**).

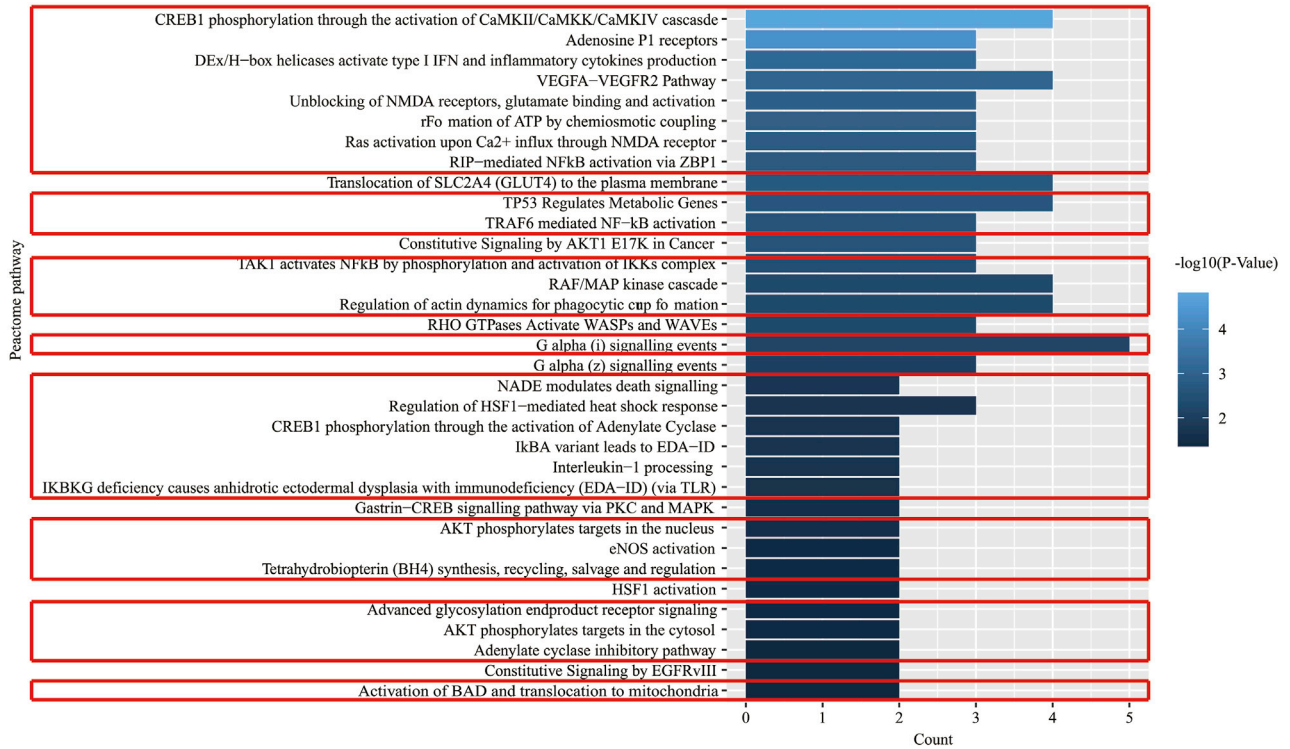

FIGURE 6 | Pathway enrichment analysis of key effect genes of XLCQ in the treatment of stroke complicated with TRFS.

The functional enrichment analysis of the 150 genes was investigated by DAVID v6.8. Altogether, 85 pathways were obtained based on the Reactome Pathway Database. Among them, 52 pathways (**Supplementary Excel S3**, marked in bold) containing 82 genes were involved in the corresponding pathological events during the progression of stroke and TRFS, which were divided into four functional modules, including immune inflammation module, nervous system module, apoptosis, and autophagy module (**Figure 5**).

Selection of Key Active Constituents of XLCQ Acting on Stroke Complicated With TRFS Syndrome

There were 60 chemical components corresponding to 150 major hubs. According to the number of major hubs and its frequency appearing in different pathways, the threshold was set at 2 and 13. That was, if a chemical constituent had more than two hubs and simultaneously the frequency of these hubs was more than 13, this chemical constituent was regarded as a key active constituent of XLCQ acting on stroke complicated with TRFS. Altogether, a total of 22 key active constituents and 28 corresponding targets were selected (**Table 2**). Twenty-seven of the 28 putative targets were enriched in 27 pathways (**Figure 6**, **Supplementary Excel S3**). The multi-dimensional network of 22 key active constituents, the corresponding 27 key targets, and 27 pathways was constructed as shown in (**Figure 7**). The GO functional analysis showed that these targets were mainly involved in immune inflammation (regulation of cellular response to heat, Fc-γ receptor signaling pathway involved in phagocytosis), the growth and development of the nervous system (ionotropic glutamate receptor signaling pathway, adenosine receptor signaling pathway, and cellular response to nerve growth factor stimulus), apoptosis (negative regulation of apoptotic process, MAPK cascade), and signal transduction (**Figure 8**).

Luteolin, Apigenin, and Chrysoeriol Reduce the Release of IL-1β and TNF-α in LPS-Stimulated BV-2 Cells

The CCK-8 assay kit was employed to evaluate the cytotoxicity to select the appropriate concentration of luteolin, apigenin, and chrysoeriol. As shown in **Figure 9A**, apigenin showed cytotoxicity to BV-2 cells at 40 μM, and luteolin and chrysoeriol showed cytotoxicity at 20 μM, so 10 μM was selected for a later anti-inflammatory study. Pro-inflammatory cytokine levels of IL-1β ($p < 0.0001$) and TNF-α ($p < 0.05$) were significantly increased after BV-2 cells were stimulated by LPS (1 μg/ml) for 24 h, and reversed by pretreatment with luteolin, apigenin, and chrysoeriol at 10 μM for 1 h, suggesting these three compounds had anti-neuroinflammatory activities (**Figure 9B**).

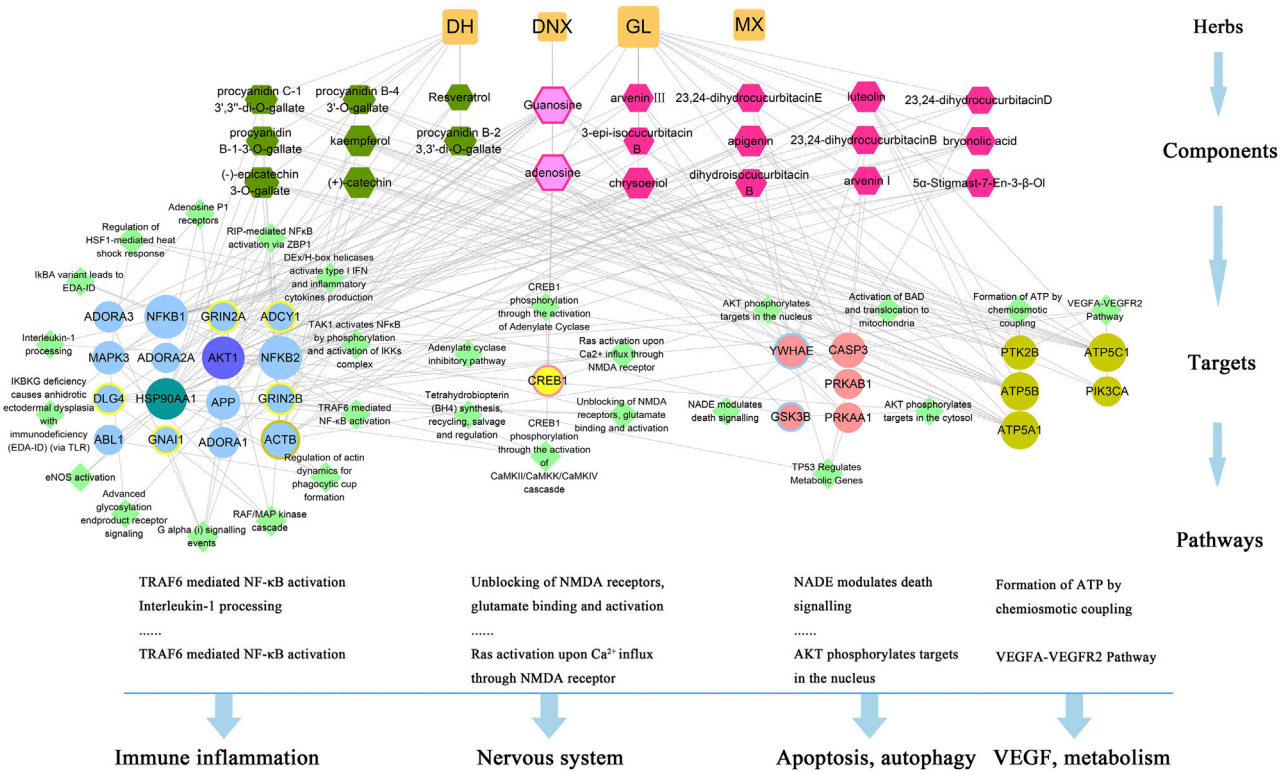

FIGURE 7 | The network of interactions among 22 key active constituents of XLCQ, the corresponding 27 key targets and 27 pathways. [Square nodes refer to herbal medicine; hexagon nodes refer to key active constituents contained in three herbal medicines; circular nodes refer to putative targets (blue refers to inflammation-related, pink refers to apoptosis-related, yellows refer to nerve-related, brown refers to others, the color-overlay nodes refer to common genes of two sets, and purple or blue-green refers to three gene sets); and diamond nodes refer to pathways of putative gene enrichment].

Luteolin, Apigenin, and Chrysoeriol Downregulate the mRNA Expression of IL-1β, TNF-α, PIK3CA, AKT1, NFKB1, NFKB2, CREB1, and HSP0AA1

As shown in **Figure 10A**, the mRNA expression of IL-1β, TNF-α, PIK3CA, AKT1, NFKB1, and NFKB2 was 7.4-fold, 7.1-fold, 4.3-fold, 1.5-fold, 3.2-fold, 10.7-fold, 1.6-fold, and 2.3-fold increases, respectively, after the LPS stimulation, while pretreatment with these three compounds significantly reversed the above states. The pathway diagram is shown in **Figure 10B**.

DISCUSSION

In the present study, 197 chemical compounds were identified or tentatively characterized in the water extraction of XLCQ analyzed by UPLC-QTOF-MS/MS, and 176 of them had putative targets (Tanimoto score ≥0.8). *Natrii sulfas* had no putative targets as sodium sulfate was hydrolyzed to produce sulfate ion, which was not easily absorbed by the intestinal wall. *Natrii sulfas* remains in the intestine as a hypertonic solution to prevent the absorption of water in the intestine and increases the intestinal volume, thus causing mechanical stimulation and promoting the secretion of the intestinal wall. Subsequently, the heat pathogens and toxins in the body are discharged from the body. 833 putative targets corresponding to 176 components were predicted (Tanimoto Score ≥0.8) using TCMIP, and 159 stroke-related genes and 709 TRFS-related genes were collected from TCMIP. Twenty-two key active constituents were selected based on the interactions among the three abovementioned gene sets, which may improve the pathological state of stroke patients with TRFS syndrome by regulating the 27 corresponding targets that mainly involved in inflammation–immune-related pathways. Luteolin, apigenin, and chrysoeriol, as the predicted components, exhibited good anti-neuroinflammatory effects based on LPS-stimulated BV-2 cells.

"Integrative pharmacology" is an interdisciplinary science that comprehensively explores the interactions between the multiple constituents of TCM and the body at multiple levels (Xu et al., 2021). TCMIP, as an important part of integrative pharmacology, is an intelligent data mining platform that integrates big data management and pharmacology computing services, which consists of five databases and seven functional modules. The five database resources

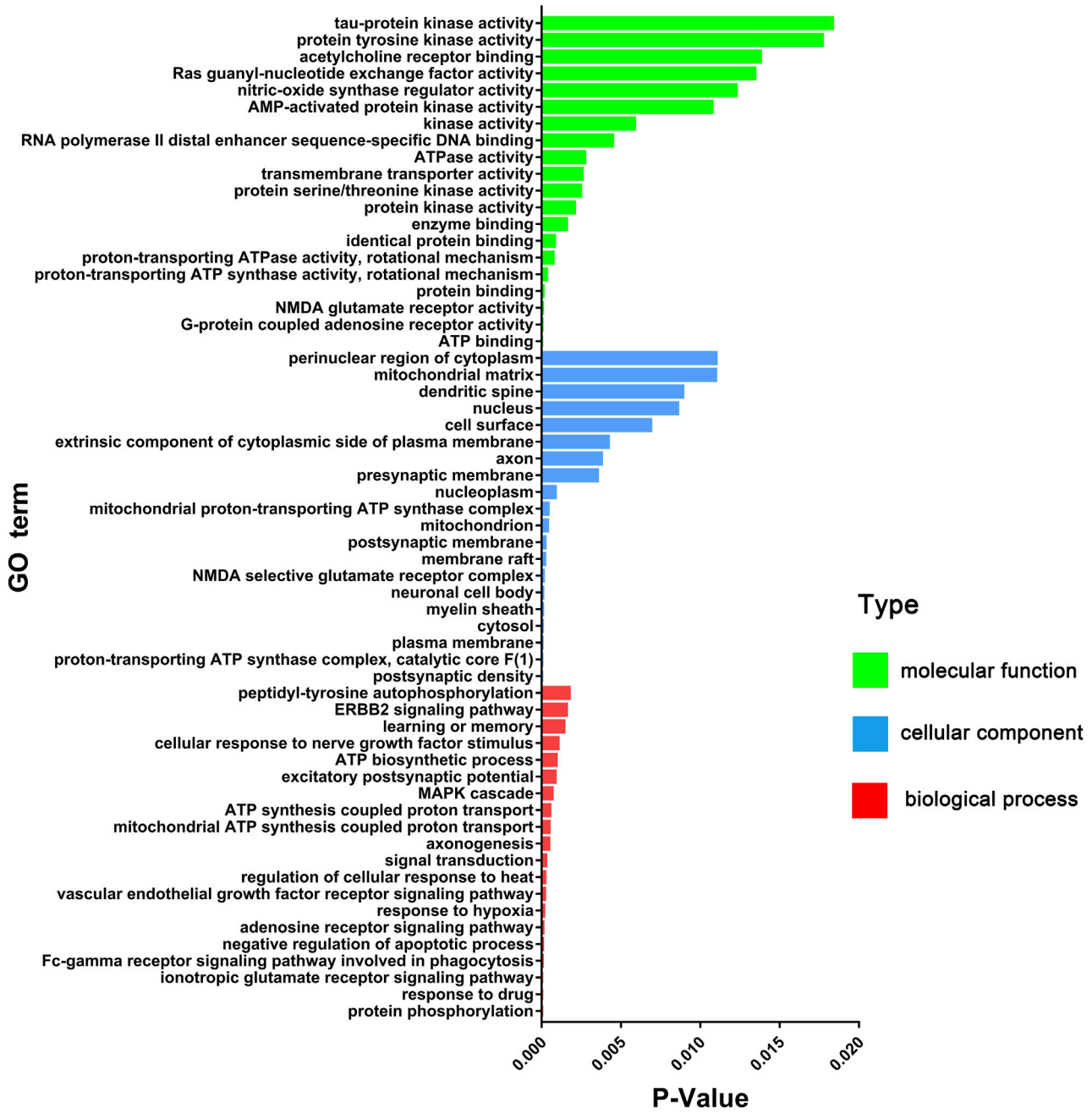

FIGURE 8 | GO enrichment analysis (molecular function, cellular component, and biological process) of key effect genes of XLCQ in the treatment of stroke complicated with TRFS.

come from the encyclopedia of TCM (ETCM) (Xu et al., 2019), an international authoritative database, which provides the basic information of TCM, including chemical compounds, putative targets, corresponding disease, and syndrome. The seven functional modules can be used to query and mine the biological basis and mechanisms of disease, syndrome, and TCM.

Among the 22 constituents, ten of them have been reported to exert some protective effect on experimental cerebral ischemia (**Table 2**, marked in red), and their mechanisms were involved in several stroke-related targets and pathways, which was consistent with our corresponding targets and pathways. Guanosine, adenosine, luteolin, and kaempferol were reported to play a protective role in ischemic stroke by reducing neuroinflammation, oxidative stress, and excitotoxicity (Zhao et al., 2011; Bettio et al., 2016; Luo et al., 2019; Wang et al., 2020b). Apigenin protects from cerebral ischemia by reducing apoptosis and

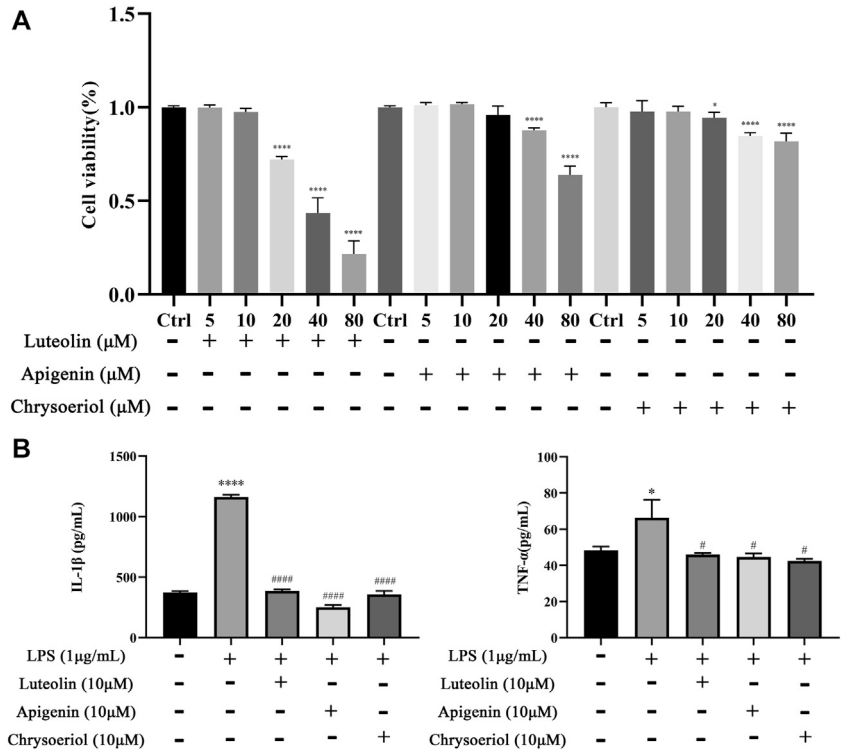

FIGURE 9 | Luteolin, apigenin, and chrysoeriol prevents the neuroinflammatory response by LPS in BV-2 cells. Cytotoxicity was detected by the CCK-8 assay **(A)**. IL-1β and TNF-α levels were detected by ELISA kits **(B)**. (Mean ± SD, $p < 0.05^{*/\#}$, $p < 0.0001^{****/\#\#\#\#}$).

autophagy to promote cell regeneration through the Caveolin-1/VEGF pathway (Zachary, 2005; Pang et al., 2018; Cárdenas-Rivera et al., 2019). (−)-Epicatechin 3-O-gallate alleviated ischemia-reperfusion injury by promoting cell proliferation, angiogenesis, and migration, and inhibiting cell apoptosis and autophagy (Fu et al., 2019). (+)-Catechin could inhibit inflammatory biomarkers or cytokines, such as C-reactive protein, Lp-PLA2, IL-6, and TNF-α, to reduce ischemic injury (Tu et al., 2018). Resveratrol, a multifunctional biological polyphenol, was regarded as a potential drug for stroke-related diseases, which could alleviate hemorrhagic brain injury by inhibiting neuronal apoptosis (Zhao et al., 2019). It was reported that bryonolic acid could inhibit Ca^{2+} influx and regulate the gene expression in the Ca^{2+}-CaMKII-CREB signaling pathway against cerebral ischemia (Que et al., 2016). Finally, procyanidins exert antioxidant activity against traumatic brain injury (Mao et al., 2015). The mechanisms of these ten chemical components covered most aspects of the pathological process of stroke, and the target and pathway information involved were consistent with our prediction results (**Table 2**; **Figure 6**), suggesting an integrative pharmacology strategy has certain prediction accuracy.

AKT1 and *PIK3CA* had high frequency in our study, and were involved in several signaling pathways, including TP53-regulated metabolic genes, AKT phosphorylates targets in the nucleus, AKT phosphorylates targets in the cytosol, activation of BAD and translocation to the mitochondria, eNOS activation, tetrahydrobiopterin (BH4) synthesis, recycling, salvage and regulation, and VEGFA-VEGFR2 pathway, which associated with apoptosis, inflammation, and nerves, and basically covers all mechanisms of stroke/TRFS, suggesting PI3K/Akt signaling pathways may play an important role in stroke formation (Yu et al., 2016; Lv et al., 2017; Pompura and Dominguez-Villar, 2018; Wen et al., 2018). PIK3CA was the only common target of key constituents and candidate stroke/TRFS targets, which may play an extremely important role in the treatment of XLCQ acting on stroke complicated with TRFS and needed to be focused on in the further experiment. MAPK3 was involved in encoding the proteins of the MAP kinase family. NFKB1 and NFKB2 were involved in encoding the NF-κB protein complex, which is an important nuclear transcription factor in cells, participating inflammatory response, immune response, apoptosis, stress response, *etc.* (Oeckinghaus and Ghosh, 2009; Mitchell et al., 2016). GSK3B was involved in the inflammation-related pathway regulation of HSF1-mediated heat shock response and apoptosis-related pathway AKT 101ylates targets in the cytosol. ATP5C1, ATP5A1, and ATP5B were involved in encoding a subunit of mitochondrial ATP synthase (Neupane et al., 2019). ADORA3, ADORA2A, and ADORA1, as adenosine receptors, were involved in inflammatory response, neuroprotection, apoptosis, and other intracellular signaling pathways (Chen et al., 2006; Blackburn et al., 2009; Sebastião and Ribeiro, 2009; González-Fernández et al., 2014; Feliu et al., 2019). CASP3 and HSP90AA1 were involved in the process of apoptosis and inflammation

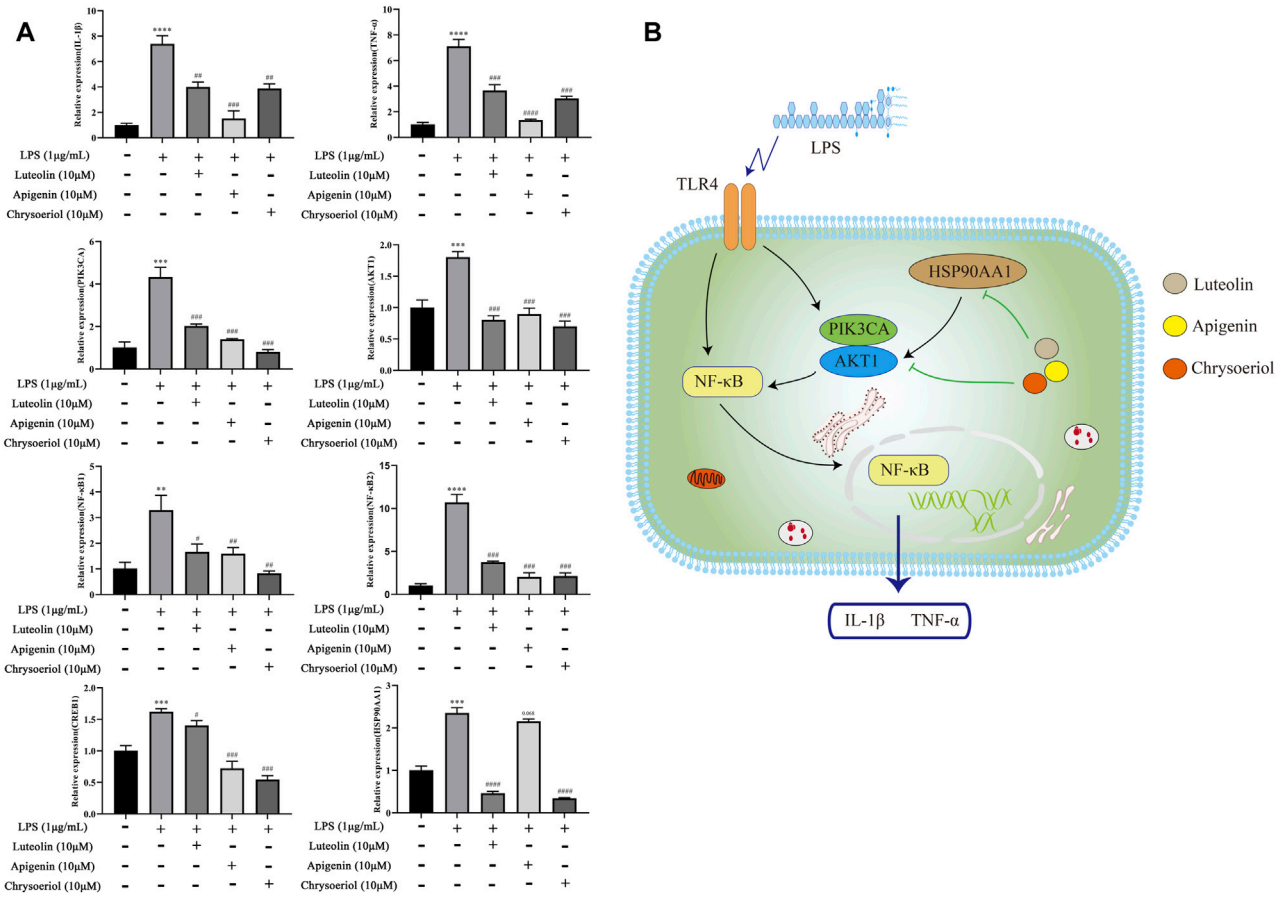

FIGURE 10 | Luteolin, apigenin, and chrysoeriol downregulate the mRNA expression of IL-1β, TNF-α, PIK3CA, AKT1, NFKB1, NFKB2, CREB1, and HSP0AA1 **(A)**, and the pathway diagram is shown in **(B)**.

(Triantafilou et al., 2001; Creagh et al., 2003; Khurana and Bhattacharyya, 2015; Man and Kanneganti, 2016).

According to the prediction results, the rest 9 of the 22 constituents may be involved in anti-inflammatory, regulating energy metabolism, and antiapoptotic by regulating NFKB1, NFKB2, ATP5C1, ATP5A1, AKT1, HSP90AA1, *etc.* (**Table. 2**). We select three compounds (luteolin, apigenin, and chrysoeriol) with high response values (**Supplementary Tables S1, S2**) to perform some verification experiments. Luteolin and apigenin have been reported to restore ischemic brain injury of rodents (Ha et al., 2008; Luo et al., 2019). Chrysoeriol has been reported to reverse skin inflammation (Wu et al., 2020), arthritis (Ananth et al., 2016), and macrophage inflammation (Yoon and Park, 2021), except for neuroinflammatory effects. Inflammatory cascade is one of the major characteristics of stroke. Therefore, we evaluated their anti-neuroinflammatory effects based on LPS-stimulated BV-2 cells. TLR4 and PI3K/Akt signaling pathways were involved in regulating the activation of microglia and related cytokines in the process of neuroinflammation (Troutman et al., 2012; García et al., 2016; Rahimifard et al., 2017; Zhong et al., 2020). Excessive secretion of proinflammatory cytokines from BV-2 leads to a detrimental effect on neuronal cells (Wang et al., 2019). In our study, luteolin, apigenin, and chrysoeriol at 10 μM inhibited the release of IL-1β and TNF-α, as well as downregulated the mRNA expression of IL-1β, TNF-α, PIK3CA, AKT1, NFKB1, NFKB2, CREB1, and HSP0AA1. The TCM prescription emphasizes the synergistic effect of multi component, especially when treating complex diseases. An important research content of integrative pharmacology strategy is network prediction and verification. We delineate 22 key active constituents based on the integrative pharmacology strategy. Each component may only work for a certain link, and functional superposition of multiple components plays an overall effect. We selected three components with a high content for verification, which, of course, do not represent the efficacy of the whole prescription or directly reduce the infarct volume. Similarly, these three compounds are common in other botanical drugs and may have other effects.

In the present study, we just did some basic research about XLCQ, but the particular interactions between the active constituents and the corresponding targets, and if the 22 compounds could represent the whole prescription, still need to be verified in the near future.

CONCLUSION

It is the first time to systematically analyze the chemical composition of XLCQ and to explore the pharmacological mechanisms of XLCQ acting on stroke complicated with TRFS using an integrative pharmacology strategy. The twenty-two key active constituents may improve the pathological state by regulating 27 corresponding targets that are mainly involved in inflammation–immune-related pathways. The integrative pharmacology strategy may offer a highly efficient way to mine the scientific connotation of traditional Chinese medicine prescriptions. This study might be a supplement for the deficiency of the basic research of XLCQ.

DATA AVAILABILITY STATEMENT

The original contributions presented in the study are included in the article/**Supplementary Material**; further inquiries can be directed to the corresponding author.

AUTHOR CONTRIBUTIONS

PW and HX performed the experimental design, and PW drafted the manuscript. PW and SW performed the analysis of chemical constituents. PW and HC performed the analysis of network pharmacology. HC and XD performed the cell experiment. LZ helped to identify the chemical constituents. HY participated in the design and coordination. All authors read and approved the final manuscript.

FUNDING

This work was supported by grants from the National Natural Science Foundation of China (Grant Nos. 81774201 and 81830111), the National Key Research and Development Program of China (2017YFC1702104 and 2017YFC1702303), and the Youth Innovation Team of Shaanxi Universities and Shaanxi Provincial Science and Technology Department Project (No. 2016SF-378). The funding agencies had no role in the study design, the collection, analysis, or interpretation of data; the writing of the report; or the decision to submit the article for publication.

SUPPLEMENTARY MATERIAL

The Supplementary Material for this article can be found online at: https://www.frontiersin.org/articles/10.3389/fphar.2021.598200/full#supplementary-material

REFERENCES

Ananth, D. A., Rameshkumar, A., Jeyadevi, R., Aseervatham, G. S. B., Sripriya, J., Bose, P. C., et al. (2016). Amelioratory Effect of Flavonoids Rich Pergularia Daemia Extract against CFA Induced Arthritic Rats. *Biomed. Pharmacother.* 80, 244–252. doi:10.1016/j.biopha.2016.03.019

Bettio, L. E., Gil-Mohapel, J., and Rodrigues, A. L. (2016). Guanosine and its Role in Neuropathologies. *Purinergic Signal.* 12 (3), 411–426. doi:10.1007/s11302-016-9509-4

Blackburn, M. R., Vance, C. O., Morschl, E., and Wilson, C. N. (2009). Adenosine Receptors and Inflammation. *Handb Exp. Pharmacol.* (193), 215–269. doi:10.1007/978-3-540-89615-9_8

Cárdenas-Rivera, A., Campero-Romero, A. N., Heras-Romero, Y., Penagos-Puig, A., Rincón-Heredia, R., and Tovar-Y-Romo, L. B. (2019). Early Post-stroke Activation of Vascular Endothelial Growth Factor Receptor 2 Hinders the Receptor 1-Dependent Neuroprotection Afforded by the Endogenous Ligand. *Front Cel Neurosci* 13, 270. doi:10.3389/fncel.2019.00270

Chen, G. J., Harvey, B. K., Shen, H., Chou, J., Victor, A., and Wang, Y. (2006). Activation of Adenosine A3 Receptors Reduces Ischemic Brain Injury in Rodents. *J. Neurosci. Res.* 84 (8), 1848–1855. doi:10.1002/jnr.21071

Chen, P., Ling, L., Ren, Y., Jiang, L., Wu, S., Wang, W., et al. (2017). Efficacy and Safety of Xinglouchengqi Decoction for Acute Ischemic Stroke with Constipation: Study Protocol for a Randomized Controlled Trial. *J. Tradit Chin. Med.* 37 (6), 810–818. doi:10.1016/S0254-6272(18)30045-1

Creagh, E. M., Conroy, H., and Martin, S. J. (2003). Caspase-activation Pathways in Apoptosis and Immunity. *Immunol. Rev.* 193, 10–21. doi:10.1034/j.1600-065x.2003.00048.x

Du, Z., Zhao, B., and Yin, H. (2009). Effect of Xinglouchengqi Decoction on Expression of ICAM-1 and NF-Kb in Rat with Cerebral Ischemia-Reperfusion. *Heb J. Traditional Chin. Med.* 31 (04), 613–615. doi:10.3969/j.issn.1002-2619.2009.04.093

Feigin, V. L., Roth, G. A., Naghavi, M., Parmar, P., Krishnamurthi, R., Chugh, S., et al.Global Burden of Diseases, Injuries and Risk Factors Study 2013 and Stroke Experts Writing Group (2016). Global burden of Stroke and Risk Factors in 188 Countries, during 1990-2013: a Systematic Analysis for the Global Burden of Disease Study 2013. *Lancet Neurol.* 15 (9), 913–924. doi:10.1016/S1474-4422(16)30073-4

Feliu, C., Peyret, H., Poitevin, G., Cazaubon, Y., Oszust, F., Nguyen, P., et al. (2019). Complementary Role of P2 and Adenosine Receptors in ATP Induced-Anti-Apoptotic Effects against Hypoxic Injury of HUVECs. *Int. J. Mol. Sci.* 20 (6), 1446. doi:10.3390/ijms20061446

Fu, B., Zeng, Q., Zhang, Z., Qian, M., Chen, J., Dong, W., et al. (2019). Epicatechin Gallate Protects HBMVECs from Ischemia/Reperfusion Injury through Ameliorating Apoptosis and Autophagy and Promoting Neovascularization. *Oxid Med. Cel Longev* 2019, 7824684. doi:10.1155/2019/7824684

Gao, L. (2012). *Chemical Constituents and Bioactivities of Rheum Tanguticum, Rheum Officinale and Rheum Palmatum.* Beijing: Peking Union Medical College.

García Bueno, B., Caso, J. R., Madrigal, J. L., and Leza, J. C. (2016). Innate Immune Receptor Toll-like Receptor 4 Signalling in Neuropsychiatric Diseases. *Neurosci. Biobehav Rev.* 64, 134–147. doi:10.1016/j.neubiorev.2016.02.013

González-Fernández, E., Sánchez-Gómez, M. V., Pérez-Samartín, A., Arellano, R. O., and Matute, C. (2014). A3Adenosine Receptors Mediate Oligodendrocyte Death and Ischemic Damage to Optic Nerve. *Glia* 62 (2), 199–216. doi:10.1002/glia.22599

Ha, S. K., Lee, P., Park, J. A., Oh, H. R., Lee, S. Y., Park, J. H., et al. (2008). Apigenin Inhibits the Production of NO and PGE2 in Microglia and Inhibits Neuronal Cell Death in a Middle Cerebral Artery Occlusion-Induced Focal Ischemia Mice Model. *Neurochem. Int.* 52 (4-5), 878–886. doi:10.1016/j.neuint.2007.10.005

Han, M. (2020). Effect of Xinglou Chengqi Decoction on TCM Syndrome Score and Nerve Function in Patients with Acute Cerebral Infarction. *J. Pract. Traditional Chin. Intern. Med.* 34 (2), 50–52. doi:10.13729/j.issn.1671-7813.Z20190566

Jiang, C., Chen, X., Bai, C., Zhang, J., Liu, R., Zhao, S., et al. (2020). Effect of Modified Xinglou Chengqi Decoction on Neurological Function in Patients with Acute Cerebral Infarction. *J. Emerg. Tradit Chin. Med.* 29 (3), 460–462.

Khurana, N., and Bhattacharyya, S. (2015). Hsp90, the Concertmaster: Tuning Transcription. *Front. Oncol.* 5, 100. doi:10.3389/fonc.2015.00100

Liu, J., Li, J., Yu, W., Hei, C., Liu, H., Ren, F., et al. (2012a). Effects of Xinglou Chengqi Decoction and Buyang Huanwu Decoction on the Injury of Hippocampal Neurons in Rats with Cerebral Ischemia. *Chin. J. Exp.*

Traditional Med. Formulae 18 (12), 233–237. doi:10.13422/j.cnki.syfjx.2012.12.072

Liu, J., Li, J., Yu, W., Hei, C., Liu, H., Ren, F., et al. (2012b). Effects of Xinglou Chengqi Decoction and Buyang Huanwu Decoction on Fas/Fasl and Caspase-3 Pathway of Apoptosis in Rats with Cerebral Ischemia. *Chin. J. Exp. Traditional Med. Formulae* (23), 187–191. doi:10.13422/j.cnki.syfjx.2012.23.079

Liu, T., Ding, Y., and Wen, A. (2018). Traditional Chinese Medicine for Ischaemic Stroke. *Lancet Neurol.* 17 (9), 745. doi:10.1016/S1474-4422(18)30290-4

Liu, X., and Feng, L. (2019). Clinical Observation of Xinglou Chengqi Decoction in Treatment of Stroke at Acute Stage of Phlegm Heat Excess Pattern. *World J. Integrated Traditional West. Med.* 14 (4), 537–539. doi:10.13935/j.cnki.sjzx.190422

Lu, H., and Wang, L. (2020). Clinical Effect Analysis of Xinglou Chengqi Decoction in Treating Acute Stage of Ischemic Stroke. *Clin. J. Traditional Chin. Med.* 32 (5), 931–933. doi:10.16448/j.cjtcm.2020.0531

Luo, S., Li, H., Mo, Z., Lei, J., Zhu, L., Huang, Y., et al. (2019). Connectivity Map Identifies Luteolin as a Treatment Option of Ischemic Stroke by Inhibiting MMP9 and Activation of the PI3K/Akt Signaling Pathway. *Exp. Mol. Med.* 51 (3), 1–11. doi:10.1038/s12276-019-0229-z

Lv, M.-R., Li, B., Wang, M.-G., Meng, F.-G., Yu, J.-J., Guo, F., et al. (2017). Activation of the PI3K-Akt Pathway Promotes Neuroprotection of the δ-opioid Receptor Agonist against Cerebral Ischemia-Reperfusion Injury in Rat Models. *Biomed. Pharmacother.* 93, 230–237. doi:10.1016/j.biopha.2017.05.121

Man, S. M., and Kanneganti, T. D. (2016). Converging Roles of Caspases in Inflammasome Activation, Cell Death and Innate Immunity. *Nat. Rev. Immunol.* 16 (1), 7–21. doi:10.1038/nri.2015.7

Mao, X., Hao, S., Zhu, Z., Zhang, H., Wu, W., Xu, F., et al. (2015). Procyanidins Protects against Oxidative Damage and Cognitive Deficits after Traumatic Brain Injury. *Brain Inj.* 29 (1), 86–92. doi:10.3109/02699052.2014.968621

Mao, X., Xu, H., Li, S., Su, J., Li, W., Guo, Q., et al. (2019). Exploring Pharmacological Mechanisms of Xueshuan-Xinmai-Ning Tablets Acting on Coronary Heart Disease Based on Drug Target-Disease Gene Interaction Network. *Phytomedicine* 54, 159–168. doi:10.1016/j.phymed.2018.09.018

Mitchell, S., Vargas, J., and Hoffmann, A. (2016). Signaling via the NFκB System. *Wiley Interdiscip. Rev. Syst. Biol. Med.* 8 (3), 227–241. doi:10.1002/wsbm.1331

Neupane, P., Bhuju, S., Thapa, N., and Bhattarai, H. K. (2019). ATP Synthase: Structure, Function and Inhibition. *Biomol. Concepts* 10 (1), 1–10. doi:10.1515/bmc-2019-0001

Oeckinghaus, A., and Ghosh, S. (2009). The NF-kappaB Family of Transcription Factors and its Regulation. *Cold Spring Harb Perspect. Biol.* 1 (4), a000034. doi:10.1101/cshperspect.a000034

Pang, Q., Zhao, Y., Chen, X., Zhao, K., Zhai, Q., and Tu, F. (2018). Apigenin Protects the Brain against Ischemia/Reperfusion Injury via Caveolin-1/VEGF *In Vitro* and *In Vivo*. *Oxidative Med. Cell. longevity* 2018, 7017204. doi:10.1155/2018/7017204

Pompura, S. L., and Dominguez-Villar, M. (2018). The PI3K/AKT Signaling Pathway in Regulatory T-Cell Development, Stability, and Function. *J. Leukoc. Biol.* 103, 1065–1076. doi:10.1002/JLB.2MIR0817-349R

Que, J., Ye, M., Zhang, Y., Xu, W., Li, H., Xu, W., et al. (2016). Bryonolic Acid, a Triterpenoid, Protect against N-Methyl-D-Aspartate-Induced Neurotoxicity in PC12 Cells. *Molecules* 21 (4), 418. doi:10.3390/molecules21040418

Rahimifard, M., Maqbool, F., Moeini-Nodeh, S., Niaz, K., Abdollahi, M., Braidy, N., et al. (2017). Targeting the TLR4 Signaling Pathway by Polyphenols: A Novel Therapeutic Strategy for Neuroinflammation. *Ageing Res. Rev.* 36, 11–19. doi:10.1016/j.arr.2017.02.004

Sebastião, A. M., and Ribeiro, J. A. (2009). Adenosine Receptors and the central Nervous System. *Handbook Exp. Pharmacol.* (193), 471–534. doi:10.1007/978-3-540-89615-9_16

Triantafilou, K., Triantafilou, M., and Dedrick, R. L. (2001). A CD14-independent LPS Receptor Cluster. *Nat. Immunol.* 2 (4), 338–345. doi:10.1038/86342

Troutman, T. D., Bazan, J. F., and Pasare, C. (2012). Toll-like Receptors, Signaling Adapters and Regulation of the Pro-inflammatory Response by PI3K. *Cell Cycle* 11 (19), 3559–3567. doi:10.4161/cc.21572

Tu, S., Xiao, F., Min, X., Chen, H., Fan, X., and Cao, K. (2018). Catechin Attenuates Coronary Heart Disease in a Rat Model by Inhibiting Inflammation. *Cardiovasc. Toxicol.* 18 (5), 393–399. doi:10.1007/s12012-018-9449-z

Wand, W. (2016). Effect of XingLou ChengQi Decoction on Serum D-Lactate Level of the Patients with Acute Cerebral Ischemia at SIRS Stage. *West. J. Traditional Chin. Med.* 36 (11), 2729–2931. doi:10.3969/j.issn.1004-6852.2016.10.033

Wang, J., Mao, J., Wang, R., Li, S., Wu, B., and Yuan, Y. (2020b). Kaempferol Protects against Cerebral Ischemia Reperfusion Injury through Intervening Oxidative and Inflammatory Stress Induced Apoptosis. *Front. Pharmacol.* 11, 424. doi:10.3389/fphar.2020.00424

Wang, J., Sun, Y., Zhang, H., Gong, F., Li, T., et al. (2020a). Effect of Jiawei Xinglou Chengqi Decoction on Nerve Function, Blood Lipid and Hemorheology in Patients with Acute Ischemic Stroke. *Prog. Mod. Biomed.* 20 (5), 992–995. doi:10.13241/j.cnki.pmb.2020.05.043

Wang, P., Zhang, J., Guo, F., Wang, S., Zhang, Y., Li, D., et al. (2019). Lipopolysaccharide Worsens the Prognosis of Experimental Cerebral Ischemia via Interferon Gamma-Induced Protein 10 Recruit in the Acute Stage. *BMC Neurosci.* 20 (1), 64. doi:10.1186/s12868-019-0547-z

Wang, Y. (1981). Clinical Observation on 120 Cases of Acute Ischemic Cerebrovascular Disease Treated with TCM. *J. Traditional Chin. Med.* 26 (4), 31–33. doi:10.13288/j.11-2166/r.1981.04.015

Wang, Y., Deng, Z., Dong, J., Jiao, S., et al. (1982). Discussion on Syndrome Differentiation and Treatment of Ischemic Stroke. *Shanghai J. Traditional Chin. Med.* 27 (4), 4–5. doi:10.16305/j.1007-1334.1982.04.003

Wang, Y., and Huang, H. (2018). Analysis of Main Chemical Components in Gualou Xiebai Banxia Decoction Based on UPLC-Q-TOF/MS. *Chin. J. Hosp. Pharm.* 38 (019), 2017–2021. doi:10.13286/j.cnki.chinhosppharmacyj.2018.19.07

Wang, Y., Li, X., Deng, Z., Sun, S., Long, C., Ren, Z., et al. (1986). Clinical Observation on 158 Cases of Stroke Treated by Huatan Tongfu Method. *China J. Traditional Chin. Med. Pharm.* 1 (2), 22–24.

Wen, Z., Hou, W., Wu, W., Zhao, Y., Dong, X., Bai, X., et al. (2018). 6'-O-Galloylpaeoniflorin Attenuates Cerebral Ischemia Reperfusion-Induced Neuroinflammation and Oxidative Stress via PI3K/Akt/Nrf2 Activation. *Oxidative Med. Cell. longevity* 2018, 8678267. doi:10.1155/2018/8678267

Wu, H., and Jiang, W. (2005). Influence of Xinglou Chengqi Decoction on Cerebral Edema and Metabolism of Free Radicals of Experimental Rat with Cerebral Hemorrhage. *Heb J. Traditional Chin. Med.* 27, (05), 388–390. doi:10.3969/j.issn.1002-2619.2005.05.051

Wu, J. Y., Chen, Y. J., Bai, L., Liu, Y. X., Fu, X. Q., Zhu, P. L., et al. (2020). Chrysoeriol Ameliorates TPA-Induced Acute Skin Inflammation in Mice and Inhibits NF-Kb and STAT3 Pathways. *Phytomedicine* 68, 153173. doi:10.1016/j.phymed.2020.153173

Xu, H. Y., Zhang, Y. Q., Liu, Z. M., Chen, T., Lv, C. Y., Tang, S. H., et al. (2019). ETCM: an Encyclopaedia of Traditional Chinese Medicine. *Nucleic Acids Res.* 47 (D1), D976–D982. doi:10.1093/nar/gky987

Xu, H. Y., Zhang, Y. Q., Wang, P., Zhang, J. H., Chen, H., Zhang, L. Q., et al. (2021). A Comprehensive Review of Integrative Pharmacology-Based Investigation: A Paradigm Shift in Traditional Chinese Medicine. *Acta Pharmaceutica Sinica B* 11, 1379–1399. doi:10.1016/j.apsb.2021.03.024

Yao, Y., Zhou, B., Fu, G., Guo, K., et al. (2020). Systematic Evaluation of Xinglou Chengqi Decoction in the Treatment of Acute Ischemic Stroke with Tanre Fushi Syndrome. *Beijing J. TCM* 39 (1), 50–55. doi:10.16025/j.1674-1307.2020.01.016

Yoon, H. S., and Park, C. M. (2021). Chrysoeriol Ameliorates COX-2 Expression through NF-Kb, AP-1 and MAPK Regulation via the TLR4/MyD88 Signaling Pathway in LPS-Stimulated Murine Macrophages. *Exp. Ther. Med.* 22 (1), 718. doi:10.3892/etm.2021.10150

Yu, M., Zhou, X., and Cui, H. (2018). Effect of Xinglou Chengqi Decoction on the Blood Brain Barrier Permeability, Nerve Damage and Neurotrophy in Rats with Cerebral Hemorrhage. *J. Hainan Med. Univ.* 24 (15), 1387–1390. doi:10.13210/j.cnki.jhmu.20180525.004

Yu, Z. H., Cai, M., Xiang, J., Zhang, Z. N., Zhang, J. S., Song, X. L., et al. (2016). PI3K/Akt Pathway Contributes to Neuroprotective Effect of Tongxinluo against Focal Cerebral Ischemia and Reperfusion Injury in Rats. *J. Ethnopharmacol* 181, 8–19. doi:10.1016/j.jep.2016.01.028

Zachary, I. (2005). Neuroprotective Role of Vascular Endothelial Growth Factor: Signalling Mechanisms, Biological Function, and Therapeutic Potential. *Neurosignals* 14 (5), 207–221. doi:10.1159/000088637

Zhao, G., Zang, S. Y., Jiang, Z. H., Chen, Y. Y., Ji, X. H., Lu, B. F., et al. (2011). Postischemic Administration of Liposome-Encapsulated Luteolin Prevents against Ischemia-Reperfusion Injury in a Rat Middle Cerebral Artery Occlusion Model. *J. Nutr. Biochem.* 22 (10), 929–936. doi:10.1016/j.jnutbio.2010.07.014

Zhao, R., Zhao, K., Su, H., Zhang, P., and Zhao, N. (2019). Resveratrol Ameliorates Brain Injury via the TGF-β-Mediated ERK Signaling Pathway in a Rat Model of Cerebral Hemorrhage. *Exp. Ther. Med.* 18 (5), 3397–3404. doi:10.3892/etm.2019.7939

Zhao, X., Liu, B., Sun, H., Wu, X., and Wang, J. (2018). Effects of Xinglou Chengqi Decoction on Serum Tissue Inhibitor of Metalloproteinase-3, Matrix Metalloprotei-Nase-9, and Aquaporin-4 in Intracerebral Hemorrhage Rats. *Heb J. TCM.* 40 (3), 411–415. doi:10.3969/j.issn.1002-2619.2018.03.021

Zhen, Y. (2017). Clinical Observation of Xinglou Chengqi Decoction in the Treatment of Acute Ischemic Stroke with Tanre Fushi Syndrome. *Clin. J. Chin. Med.* 9 (22), 101–102. doi:10.3969/j.issn.1674-7860.2017.22.050

Zhong, J., Qiu, X., Yu, Q., Chen, H., and Yan, C. (2020). A Novel Polysaccharide from Acorus Tatarinowii Protects against LPS-Induced Neuroinflammation and Neurotoxicity by Inhibiting TLR4-Mediated MyD88/NF-Kb and PI3K/Akt Signaling Pathways. *Int. J. Biol. Macromol* 163, 464–475. doi:10.1016/j.ijbiomac.2020.06.266

Zhou, X., Li, B., Lv, Y., and Li, N. (2016). Effect of Xinglou Chengqi Decoction on Free Radical Metabolism and Brain Edema in Rats with Ischemic Stroke. *J. Emerg. Tradit Chin. Med.* 25 (05), 846–848. doi:10.3969/j.issn.1004-745X.2016.05.028

Conflict of Interest: The authors declare that the research was conducted in the absence of any commercial or financial relationships that could be construed as a potential conflict of interest.

The reviewer AZ declared a shared affiliation, with no collaboration, with one of the authors, SW, to the handling editor at the time of review.

Copyright © 2021 Wang, Wang, Chen, Deng, Zhang, Xu and Yang. This is an open-access article distributed under the terms of the Creative Commons Attribution License (CC BY). The use, distribution or reproduction in other forums is permitted, provided the original author(s) and the copyright owner(s) are credited and that the original publication in this journal is cited, in accordance with accepted academic practice. No use, distribution or reproduction is permitted which does not comply with these terms.

frontiers in Pharmacology

ORIGINAL RESEARCH
published: 28 July 2021
doi: 10.3389/fphar.2021.670146

Feasibility and Mechanism Analysis of Shenfu Injection in the Treatment of Idiopathic Pulmonary Fibrosis

Peipei Liu[1,2,3,4,5†], *Shengnan Yang*[1,2,3,4,6†], *Zai Wang*[7*], *Huaping Dai*[1,2,3,4*] and *Chen Wang*[1,2,3,4,5,6*]

[1]Department of Pulmonary and Critical Care Medicine, Center of Respiratory Medicine, China-Japan Friendship Hospital, Beijing, China, [2]National Center for Respiratory Medicine, Beijing, China, [3]Institute of Respiratory Medicine, Chinese Academy of Medical Sciences, Beijing, China, [4]National Clinical Research Center for Respiratory Diseases, Beijing, China, [5]Chinese Academy of Medical Sciences, Peking Union Medical College, Beijing, China, [6]Harbin Medical University, Harbin, China, [7]Institute of Clinical Medical Sciences, China-Japan Friendship Hospital, Beijing, China

OPEN ACCESS

Edited by:
Hai Yu Xu,
China Academy of Chinese Medical Sciences, China

Reviewed by:
Yang Xu,
Renmin Hospital of Wuhan University, China
Mengcheng Cai,
Second Military Medical University, China

***Correspondence:**
Huaping Dai
daihuaping@ccmu.edu.cn
Zai Wang
wzai_163pass@163.com
Chen Wang
cyh-birm@263.net

†These authors have contributed equally to this work

Specialty section:
This article was submitted to Ethnopharmacology, a section of the journal Frontiers in Pharmacology

Received: 11 March 2021
Accepted: 14 July 2021
Published: 28 July 2021

Citation:
Liu P, Yang S, Wang Z, Dai H and Wang C (2021) Feasibility and Mechanism Analysis of Shenfu Injection in the Treatment of Idiopathic Pulmonary Fibrosis. Front. Pharmacol. 12:670146. doi: 10.3389/fphar.2021.670146

Background: Idiopathic pulmonary fibrosis (IPF) is disease with high mortality, and its effective treatment is limited. Shenfu injection is a traditional Chinese medicine which can improve circulation and protect cells. In this study, we aimed to investigate the feasibility and mechanism of Shenfu injection in the treatment of IPF.

Methods: The components and targets of Shenfu injection were mainly retrieved from the Traditional Chinese Medicine Systems Pharmacology Database and Analysis Platform (TCMSP) database. The targets of Shenfu injection were standardized by UniProt database. The Genecards and OMIM databases was used to search for IPF-related genes. The Venn diagram of gene intersection was drawn using the OmicStudio tools, and the protein-protein interaction network was visualized using the Cytoscape 3.7.2 software. Moreover, the metascape online software was applied to explore the enriched Gene Ontology (GO) terms and Kyoto Encyclopedia of Genes and Genomes (KEGG) pathways, and the Cytoscape 3.7.2 software was used to construct the target-pathway network. Molecular docking was used to visualize the interactions between the main active compounds and targeted proteins. Animal experiments were performed to validate the effects and mechanisms of Shenfu injection.

Results: We obtained 46 co-targets of Shenfu injection and IPF. Among the hub target genes, several genes with important functions were enriched, including TNF, IL-6, IL-1B, TP53, JUN, CASP3 and CASP8. The pathway enrichment analysis for the hub target genes identified pathways in infection/inflammation, apoptosis and cancer. Molecular docking results showed that the main active compound Ginsenoside Re had high affinity to the core target proteins. These results suggested that Shenfu injection may have a positive effect in the treatment of IPF. Consistent with this finding, animal experiments showed that Shenfu injection significantly reduced pulmonary fibrosis in a mouse model with inhibition of

Abbreviations: GO, gene ontology; IPF, idiopathic pulmonary fibrosis; KEGG, kyoto encyclopedia of genes and genomes; PPI, protein-protein interaction; TCMSP, traditional chinese medicine systems pharmacology database and analysis platform.

apoptosis and inflammation by downregulating IL-1β, caspase-3 and phosphorylated NF-κB.

Conclusion: Our results demonstrated that Shenfu injection efficiently alleviate bleomycin-induced pulmonary fibrosis through multi-targets in inflammation-, apoptosis- and cancer-related pathways, which provided first evidence and reference to the feasibility of Shenfu injection in the treatment of IPF.

Keywords: idiopathic pulmonary fibrosis, Shenfu injection, network pharmacology, inflammation, apoptosis

INTRODUCTION

Idiopathic pulmonary fibrosis (IPF) is a progressive fibrosis lung disease with the clinical symptoms of cough and progressive dyspnea. It is common in old men with median age of 65 years. For patients with IPF, the median survival time after diagnosis is between 2 and 4 years (Richeldi et al., 2017). At present, lung transplantation is the only effective treatment for IPF. Pirfenidone and nintedanib are recommended to treat IPF (Behr et al., 2018). However, many patients can hardly afford the burden of lung transplantation and drugs.

Shenfu injection is a traditional Chinese medicine injection that has been approved in 1987 (approval code: SFDA approval number Z20043117, package: 50 ml per bottle) and applied in clinical for 30 years. It is taken from Shenfu decoction and used in clinical acute conditions such as shock, cardiopulmonary resuscitation and heart failure. A prospective randomized controlled study aimed at efficacy and safety found that Shenfu injection can improve 28- and 90-days survival, shorten hospital stays, improve clinical outcomes in patients and has no serious drug-related adverse reactions (Zhang et al., 2017b). Shenfu injection also enhances cellular immunity. Another study in sepsis or septic patients found that Shenfu injection reduced the duration of vasopressor use and ICU stay, increased $CD4^+$ and $CD8^+$T cell counts in peripheral blood (Zhang et al., 2017a). In a clinical research, Shenfu injection was used to treat elderly severe pneumonia. It could decrease the blood level of IL-6, TNF-α and IL-8, improve the vital signs of the patients, shorten the ICU hospital stays and reduce the mortality of the patients (Lv et al., 2017). Cumulative studies have shown that Shenfu injection possesses anti-inflammatory effect through multiple targets and pathways, especially inhibiting the NF-kappa B (Li et al., 2016). Ginsennoside is considered as the effective compound in Shenfu injection. Researchers found that Ginsennoside Rd could down-regulate caspase-3 expression and decrease the expression level of IL-6, TNF-α and IL-1β in a rat model of Alzheimer disease. It also has the function of anti-inflammation, anti-oxidation and anti-apoptosis (Liu et al., 2012).

Network pharmacology analyze drug effect through multiple disciplines, which provides a method to discover drugs for complex diseases (Hopkins, 2007). Shenfu injection can be used in the treatment of acute respiratory distress syndrome and acute exacerbation of chronic obstructive pulmonary disease as recommended by expert consensus. Therefore, we explored the feasibility and mechanism of Shenfu injection for the treatment of IPF using network pharmacology analysis and experiments in IPF mouse model. In this study, we performed network pharmacology analysis on the Shenfu injection in the treatment of IPF, and used protein-protein network analysis and enrichment analysis to identify hub genes and potential pathways, which may help to better understand the mechanism of Shenfu injection in the treatment of IPF. We further validated that Shenfu injection could significantly reduce pulmonary fibrosis in a mouse model.

MATERIALS AND METHODS

Collection of Compounds and Target Genes for Shenfu Injection

Since Shenfu injection is used by intravenous injection, all of its components were analyzed. Traditional Chinese Medicine Systems Pharmacology Database and Analysis Platform (Ru et al., 2014) (TCMSP) were used to collect all compounds of Panax ginseng C.A. Mey (hongshen) and Aconitum carmichaelii Debeaux (fuzi). Because the Chinese names of hongshen and Fuzi have special latin names in database of TCMSP, we used Ginsen Radix Et Rhizoma Rubra (hongshen) and Aconiti Lateralis Radix Praeparata (Fuzi) to obtain their related target proteins (**Table 1**). Then the target proteins were standardized to human-related genes through the Uniprot database (UniProt Consortium, 2018).

Screening of Idiopathic Pulmonary Fibrosis-Related Genes

We utilized "idiopathic pulmonary fibrosis" as a keyword to collect genes from the Genecards (https://www.genecards.org/) and OMIM (Hamosh et al., 2005) databases on April 2020, and chose "*Homo sapiens*" as the species option.

Screening of Idiopathic Pulmonary Fibrosis-Related Genes Targeted by Shenfu Injection

The Venn diagram visualizing the intersection of genes between Shenfu injection and IPF was drawn by the OmicStudio tools at https://www.omicstudio.cn/tool.

Analysis of Protein-Protein Interaction Network

The String database (Szklarczyk et al., 2019) was used to analyze the PPI network of the intersected target genes, organism was selected as "*Homo sapiens*" and the minimum required interaction

TABLE 1 | Information of Shenfu injection.

Latin name	English name	TCMSP name	Chinese name	Origin of place
Panax ginseng C.A. Mey	*Radix ginseng rubra*	*Ginsen Radix Et Rhizoma Rubra*	Hongshen	Jilin, China
Aconitum carmichaelii Debeaux	*Aconitine*	*Aconiti Lateralis Radix Praeparata*	Fuzi	Sichuan, China

TABLE 2 | Quality analysis of Shenfu injection (Batch Number: 18120501007).

Item	Content	Quality control
Finger print consistency	0.9	≥0.9
Total saponins	1.0 mg/ml	0.7–1.7 mg/ml
Ginsenoside Rg1	0.1 mg/ml	≥0.08 mg/ml
Ginsenoside Re	0.1 mg/ml	≥0.06 mg/ml

**Data were derived from product inspection report of Ya'an 999 Pharmaceutical Group Co. Ltd. Sichuan Province, China.*

score was selected as "medium confidence 0.4." Moreover, the Cytoscape 3.7.2 software was used to visualize the PPI network.

Enrichment Analysis of Target Genes

The Metascape platform (Zhou et al., 2019) online analytical tool was used for gene functional enrichment and Kyoto Encyclopedia of Genes and Genomes (KEGG) pathway enrichment. The hub genes were uploaded to the online tool and the significant pathways or functions were obtained based on the minimum overlap value of three and *p* value cutoff less than 0.01. Then the Cytoscape 3.7.2 software was applied to visualize the network of KEGG pathways and related target genes.

Molecular Docking

The docking studies of the representative compounds and targets were performed with AutoDock 4.2. The BIOVIA Discovery Studio (San Diego: Dassault Systèmes) was used for pre-processing the chemical structures and biomolecules. The metal ions and/or substrate molecules (if any) were kept in the binding pocket of the targets. The Lamarckian genetic algorithm search was employed for the docking. The key residues of the binding pocket were kept flexible. The center of the binding pockets of the individual targets was selected for the grid placement. A total of 60 runs along with 2.5 million energy evaluation steps were employed. The representative pose selection was carried out based on the cluster analysis of the docked poses. The PyMOL Molecular Graphics System (Version 1.8.4.0, Schrödinger, LLC) and PLIP webserver (Salentin et al., 2015) were used for the visualizations and graphics generations.

Shenfu Injection

Shenfu injection (batch number:18120501007) is a solution extracted from Panax ginseng C.A.Mey and Aconitum carmichaeli Debeaux. Its quality meets the standard of China Food and Drug Administation (approval No: WS3-B-3427-98-2013 and P.ZL.205-001) (**Table 2**). Panax ginseng C.A.Mey and Aconitum carmichaeli Debeaux were soaked and extracted to the solution respectively, then mixed together to form Shenfu injection. The specimens were stored in the herbarium of Ya'an 999 Pharmaceutical Group Co. Ltd. (Sichuan Province, China).

Pulmonary Fibrosis Mouse Model

C57BL/6 mice (male, 25 ± 2 g, 8–9 weeks old, Vital River Laboratory Animal Technology Co., Ltd. Beijing, China) were fed with the standard diet under SPF conditions (60–70% humidity, 24 ± 1°C, 12/12 h dark-light cycle). The mice were divided into three groups (8 mice per group): control group, model group and Shenfu injection therapy group. Intratracheal instillation of bleomycin (Zhejiang HISUN Pharmaceuticals Co., Ltd.) was used at 15 USP/kg to induce pulmonary fibrosis in mice. Intraperitoneal injection of Shenfu injection (Ya'an 999 Pharmaceutical Group Co. Ltd. Sichuan Province, China) was given at 10 ml/kg once daily after bleomycin injection from day 1 to day 7. The dosage of Shenfu injection was based on a previous study (Xu et al., 2020). The animals were sacrificed on day 4 (n = 3 mice per group) or 14 (n = 5 mice per group). The left lung was used for hematoxylin-eosin staining, Masson's trichrome stain, Sirius red staining, immunohistochemical staining and TdT-mediated dUTP nick end labeling (TUNEL) staining; and the right lung was used for Western blot. The Animal Studies Committee of China-Japan Friendship Hospital (Approval certificate number: zryhyy12-20-07-2) approved all the animal experiments in our study. All experimental procedures were performed according to the Principles of Laboratory Animal Care.

Histological Staining and Immunostaining

The left lung of mice was dehydrated, paraffin-embedded and cut into 4-μm sections. Then the lung sections were subjected with H&E staining, Masson's trichrome stain, Sirius red staining and immunohistochemical staining. Primary antibodies used were anti-α-SMA (ab124964, Abcam) and anti-collagen I (ab88147, Abcam).

TUNEL Staining

The apoptotic cells in the lung tissues were detected by TUNEL staining (CF488 TUNEL Cell Apoptosis Detection Kit, Servicebio) according to the manufacturer's instructions. Frozen lung sections (4-μm) were defrosted for 20 min at room temperature, permeabilized with 0.2% Triton X-100 for 5 min on ice, and washed twice for 5 min in PBS. Then the samples were stained with TUNEL reaction mixture for 60 min at 37°C in dark, washed twice for 5 min in PBS and mounted with Mounting Medium with DAPI (ab104139, Abcam). The slides were visualized and fluorescent images were captured with fluorescence microscope (ZEISS).

Western Blot

The right lungs of mice were lysed and the protein concentrations were measured by BCA Protein Assay Kit (P0010, beyotime). An

TABLE 3 | Composite compounds of Shenfu injection.

—	—	Compounds	—
Acetoacetate	Deoxyaconitine	Lactose	Tetracosane
Acetylcholine or isomer	Deoxyandrographolide	Leucine	Threonine
Aconitate	Deoxycytidine diphosphate	L-NG-monomethylarginine	Thymidine
Aconitine	Dimethyl glycine	Lysine	Thymidine isomer
Adenine	DNOP	Malate	Thymine
Adenosine	EIC	Maleamate	TMPEA
ADP	Farnesene	Maleate	trimethylamine-N-oxide
Agidol 7	Ferulate	Malonate	Tryptophan
Alanine	Ferulate isomer	Maltose	Tyrosine
Alloaromadedrene	Ferulate isomer	Mesaconitine	Tyrosine isomer
Alpha-guaiene	Folate	Methylsuccinate	UDP
Anthranilate	Fructose	Mevalonate	UNAL
Arabinose	Fructose 1,6-bisphosphate	Myristic acid	Uracil
Arachic acid	Fumarate	Neojiangyouaconitine	Uracil
Arginine	Fuzitine	Neokadsuranic acid B	Uridine
Argininosuccinate or isomer	GABA	Neoline	Valine
Ascorbate	Galactitol	Neopterin or isomer	Vetol
Asparagine	Gallate	Niacinamide	Xanthine or isomer
Aspartate	Gentisate	Nicotinate	Xylose
Asymmetric dimethylarginine, symmetric dimethylarginine or isomer	Ginsenoside R0	Nonacosane	Zoba 3 GA
Beiwutine	Ginsenoside R0_qt	Notoginsenoside R2	Zoba EG
Benzoate	Ginsenoside Rb1	Notoginsenoside R2_qt	Zoomaric acid
Benzoylaconine	Ginsenoside Re	NSC692928	α-santalene
Benzoylhypaconine	Ginsenoside Rf	0ctacosane	β-cedrene
Benzoylmesaconine	Ginsenoside Rg2	o-isoprenyl benzophenone	β-guaiene
Benzoylnapelline	Ginsenoside Rg2_qt	Ornithine	()-aromadendrene
Beta-caryophyllene	Ginsenoside Rg3	Orotate or isomer	(1S,2S)-2-isopropenyl-4-isopropylidene-1-methyl-1-vinylcyclohexane
Beta-elemene	Ginsenoside Rg3_qt	Oxaloacetate	(2R,3R,4S,5S,6R)-2-[[(3S,5R,6S,8R,9R,10R,12R,13R,14R,17S)-3,12-dihydroxy-17-[(2S)-2-hydroxy-6-methylhept-5-en-2-yl]-4,4,8,10,14-pentamethyl-2,3,5,6,7,9,11,12,13,15,16,17-dodecahydro-1h-cyclopenta [a]phenanthren-6-yl]oxy]-6-(hydroxymethyl)oxane-3,4,5-triol
Betaine	Ginsenoside Rh2	Palmitic acid	(2S,3R,4S,5S,6R)-2-[(2S)-2-[(3S,5R,8R,9R,10R,12R,13R,14R,17S)-3-[(2R,3R,4S,5S,6R)-4,5-dihydroxy-6-(hydroxymethyl)-3-[(2S,3R,4S,5S,6R)-3,4,5-trihydroxy-6-(hydroxymethyl)oxan-2-yl]oxyoxan-2-yl]oxy-12-hydroxy-4,4,8,10,14-pentamethyl-2,3,5,6,7,9,11,12,13,15,1
Beta-sitosterol	Ginsenoside Rh4	Panaxydol	(3R,5R,8R,9R,10R,12R,13R,14R,17S)-17-[(2S)-2-hydroxy-6-methylhept-5-en-2-yl]-4,4,8,10,14-pentamethyl-2,3,5,6,7,9,11,12,13,15,16,17-dodecahydro-1H-cyclopenta [a]phenanthrene-3,12-diol
Biotin	Ginsenoside Rh4_qt	Panaxynol	(3R,8S,9R,10R,13R,14S,17R)-3-hydroxy-4,4,9,13,14-pentamethyl-17-[(E,2R)-6-methyl-7-[(2R,3R,4S,5S,6R)-3,4,5-trihydroxy-6-[[(2R,3R,4S,5S,6R)-3,4,5-trihydroxy-6-(hydroxymethyl)oxan-2-yl]oxymethyl]oxan-2-yl]oxyhept-5-en-2-yl]-1,2,3,7,8,10,12,15,16,17-decahydr
Butyrate or isobutyrate	Ginsenoside Rs1	Pantothenate	(3R,9R,10R)-heptadec-1-en-4,6-diyne-3,9,10-triol
cAMP	Ginsenoside Rs1_qt	Pentadecylic acid	(3S,5R,6S,8R,9R,10R,12R,13R,14R,17S)-17-[(2R)-2-hydroxy-6-methylhept-5-en-2-yl]-4,4,8,10,14-pentamethyl-2,3,5,6,7,9,11,12,13,15,16,17-dodecahydro-1H-cyclopenta [a]phenanthrene-3,6,12-triol
Carnitine or isomer	Ginsenoside-Rb2	Phenylalanine	(3S,5R,6S,8R,9R,10R,12R,13R,14R,17S)-17-[(2S)-2-hydroxy-6-methylhept-5-en-2-yl]-4,4,8,10,14-pentamethyl-2,3,5,6,7,9,11,12,13,15,16,17-dodecahydro-1H-cyclopenta [a]phenanthrene-3,6,12-triol
Carnosifloside I_qt	Ginsenoside-Rc	Phosphoenolpyruvate	(3S,5R,8R,9R,10R,12R,13R,14R,17S)-17-[(2S)-2-hydroxy-6-methylhept-5-en-2-yl]-4,4,8,10,14-pentamethyl-2,3,5,6,7,9,11,12,13,15,16,17-dodecahydro-1H-cyclopenta [a]phenanthrene-3,12-diol
Carnosine	Ginsenoside-Rh1	Phosphotyrosine	(4aR,9aS)-2,9,9-trimethyl-5-methylene-4,4a,6,7,8,9a-hexahydro-3h-benzo [7]annulene

(Continued on following page)

TABLE 3 | (*Continued*) Composite compounds of Shenfu injection.

—	Compounds		—
Cedrol	Ginsenoside-Rh1_qt	p-hydroxyphenyllactate or isomer	(6Z,10E,14E,18E)-2,6,10,15,19,23-hexamethyltetracosa-2,6,10,14,18,22-hexaene
cGMP	Globulol	p-hydroxyphenyllactic acid or isomer	(butylsulfonyl)ethynylbenzene
Chasmaconitine	Glucose	Piperonal	(R)-Norcoclaurine
Chasmanine	Glutamate	Proline	11,14-Eicosadienoic acid
Cinnamate	Glutamine	p-tert-Butylanisole	13-Deoxo-13 alpha-acetyloxy-1-deoxynortaxine I
Citrate	Glutarate	Pyridoxal-5-P	14-acetyltalatisamine
Citrulline or isomer	Glyceraldehyde	Pyridoxine or isomer	14-Deoxy-11,12-didehydroandrographolide
Clovene	Glycine	Pyrrolezanthine	1-Ethenyl-1-methyl-2-(1-methylethenyl)-4-(isopropyl)-cyclohexane
Coryneine	Guanine	Quinolinate or isomer	1-Methylhistamine
Coumaran	Guanosine	Reduced glutathione or isomer	1-Methylhistamine or isomer
Creatine	Heptacosane	Rhamnose or isomer	2,7-Dideacetyl-2,7-dibenzoyl-taxayunnanine F
Creatinine	Hetisine	Salicylate	20(R)-ginsenoside Rg2
Cysteine	Hexacosane	Salicylurate	20(S)-ginsenoside Rg3
Cytidine	Histamine or isomer	Salsolinol	20(S)-ginsenoside Rg3_qt
Cytosine	Histidine	Sanchinoside C1	20(S)-Ginsenoside-Rh1_qt
Daturic acid	Histidine isomer	Senbusine A	2-aminoadipate
Delavaconitine	Hokbusine A	Senbusine B	2-Deoxyadenosine
Delbruline	Homogentisate	Senbusine C	2-Deoxycytidine
Delbrusine	Homoserine	Serine	2-Isopropylmalate
Delcorine	Hydroxyproline	Shikimate	3,4-Dihydrobenzoate
Delphamine	Hypaconitine	Sitosterol	3,4-Dihydroxyphenylacetate
Delphin	Ignavine	Songorine	3-Oh-anthranilate or isomer
delphin_qt	Inosine	Sorbitol	3-Phosphoglycerate
Delsemine B	Inositol	Sorbitol or isomer	4-Hydroxybenzoate or isomer
Delsoline	Isoleucine	Spathulenol	4-Pyridoxic acid
Delta-amorphene	Isotalatizidine	Stockin-53073	58,924_fluka
Deltamine	Jesaconitine	Succinate	5-Hydroxytryptophan
Deltoin	Karakoline	Sucrose	5-Phenyl-4E-pentenol
Demethyldelavaine A	Karanjin	Talatizamine	6-Demethyldesoline
Demethyldelavaine B	Kynurenate	Tamarixinol	—
Denudatine	Lactate	Taurine or isomer	—

**Data were from the TCMSP database and a reference using column-switching HILIC–RPLC-MS/MS system as in the identification method (Song et al., 2015).*

equivalent amount of protein samples were separated by 4–15% BeyoGel™ Plus Precast PAGE (Polyacrylamide gel electrophoresis) Gel (P0465S, beyotime), electrotransferred to PVDF membranes and incubated for 2 h at room temperature with primary antibodies: caspase-3 antibody (9662, Cell Signaling Technology), IL-1β antibody (31,202, Cell Signaling Technology), Phospho-NF-κB p65 antibody (3033, Cell Signaling Technology), NF-κB p65 antibody (BS1253, Bioworld) and GAPDH antibody (60004-1-Ig, Proteintech). Then, the membranes were incubated with secondary antibodies for 1 h at room temperature and exposured with the ChemiDoc XRS + System (Bio-Rad). The results were quantified using ImageJ system (1.52a).

Quantitative Real-time PCR (qPCR)

Total RNA was extracted using the Trizol reagent according to the manufacturer's instructions (15596026, Invitrogen), and transcribed into cDNA (11120ES60, Yeasen). qPCR was performed using SYBR Green Master Mix (11202ES08, Yeasen), and analyzed on the ABI-7500 Real-Time PCR System. PCR primer sequences were listed in **Supplementary Table 1**.

Statistical Analysis

Data were presented as mean ± standard deviation (SD). Group comparisons were analyzed with one-way ANOVA after Shapiro-Wilk normality test for normality and Bartlett's test for the homogeneity of variance. The analysis was performed by GraphPad Prism 8. p value <0.05 was considered statistically significant.

RESULTS

Compounds and Target Genes for Shenfu Injection

We obtained 137 compounds and 119 target proteins of Shenfu injection from TCMSP after duplicates exclusion. In addition to the hydrophobic compounds, we also list the hydrophilic compounds including mainly amino acids and nucleosides identified by column-switching HILIC–RPLC-MS/MS system (Song et al., 2015) (**Table 3**). Since the hydrophobic compounds were considered to be the main active ingredients, we identified 88 target genes based on the 137 compounds obtained from TCMSP after standardization on the Uniprot database.

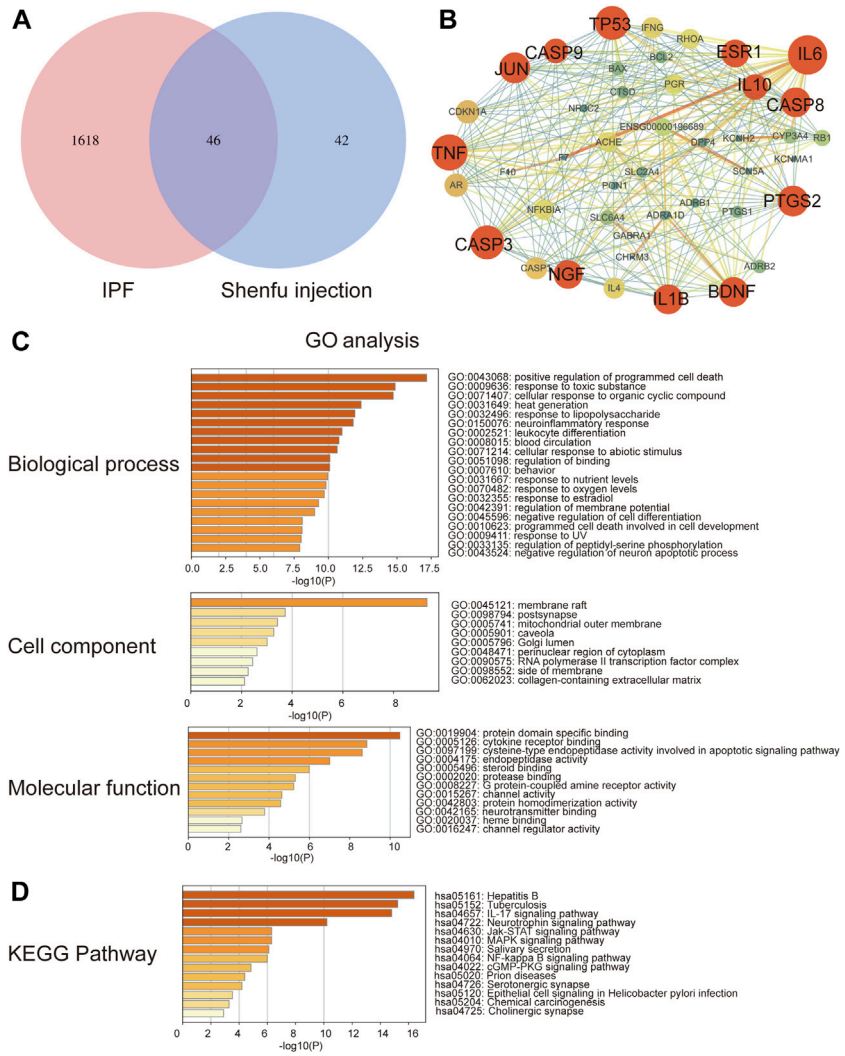

FIGURE 1 | Network pharmacology analysis of Shenfu injection and IPF. **(A)** The intersection of targeted genes between Shenfu injection and IPF shown as Venn diagram. **(B)** The PPI network analysis: the node represents the protein and the edge represents the connection between proteins; the size of the node represents the importance of the gene in the network. **(C)** GO enrichment analysis of potential targets genes including biological process, cellular components and molecular function. **(D)** KEGG pathway enrichment analysis of the top 14 pathways.

Idiopathic Pulmonary Fibrosis-Related Genes

We first identified 2793 genes from the Genecards database, and then we retained 1396 genes with median target score greater than or equal to 4.86 (Target Score: maximum:124.57; minimum: 0.24; median:4.86). In addition, we obtained 322 genes from the OMIM database. Finally, a total of 1664 genes were obtained after eliminating the duplicates.

Gene Intersection of Shenfu Injection and Idiopathic Pulmonary Fibrosis

In order to obtain the intersected genes between Shenfu injection and IPF, we performed a venn analysis on the target genes of Shenfu injection and IPF. As shown in **Figure 1A**, a total of 46 genes were identified as intersected genes of Shenfu injection and IPF.

Protein-Protein Interaction Network Analysis of Gene Intersection

To explore the relationship of the target genes, we constructed a PPI network using the string database. The PPI network contained 46 nodes and 272 edges and the average node degree was 11.8. We further visualized the PPI network by Cytoscape 3.7.2 software (**Figure 1B**). The red circles represent the hub genes. The bigger the circle, the more important the gene is in the PPI network. In the PPI network, the clustering coefficient was 0.613, and the network density and centralization were 0.288 and 0.454, respectively. Considering that the higher the node degree, the more important it is in the

TABLE 4 | Characterization parameters of hub genes.

Target gene	Degree	Betweenness centrality	Closeness centrality
IL6	31	0.2075	0.7544
TNF	28	0.0782	0.6825
TP53	26	0.0498	0.6615
CASP3	26	0.0475	0.6615
JUN	23	0.0185	0.6143
PTGS2	23	0.0210	0.6324
CASP8	22	0.0178	0.5811
IL1B	22	0.0344	0.6324
BDNF	22	0.0751	0.6418
NGF	21	0.0286	0.6232
ESR1	20	0.0219	0.5972
IL10	18	0.0096	0.5658
CASP9	17	0.0094	0.5584

**Data were analyzed by Cytoscape 3.7.2 software.*

network, we then selected the degree of node as the evaluation parameter. As a result, we screened out 13 hub genes including IL-6, TNF, TP53, CASP3, JUN, PTGS2, CASP8, IL-1B, BDNF, NGF, ESR1, IL10 and CASP9 with degrees higher than average (median degree = 16) (**Table 4**).

Gene Ontology and Kyoto Encyclopedia of Genes and Genomes Pathway Enrichment Analysis

The GO analysis enriched 1048 biological processes, 34 cellular components and 67 molecular function items ($p < 0.01$) by using the Metascape platform (**Figure 1C**). Among the top five enrichments, in biological processes, genes were involved in cell death and response to stimuli, including positive regulation of programmed cell death, response to toxic substance, cellular response to organic cyclic compound, heat generation and response to lipopolysaccharide. In the cellular components, genes were enriched in the membrane-associated subcellular structures, including membrane raft, postsynapse, mitochondrial outer membrane, caveola and Golgi lumen. In the molecular functions, genes were enriched in protein domain specific binding; exogenous signal transduction pathways, including cytokine receptor binding and steroid binding; apoptosis-related functions including cysteine-type endopeptidase activity involved in apoptotic signaling pathway and endopeptidase activity.

Moreover, we performed KEGG enrichment analysis and found that the hub genes were mainly involved in infection and inflammation pathways. The top five enrichments include hpatitis B, tuberculosis, IL-17 signaling pathway, JAK-STAT signaling pathway and neurotrophin signaling pathway (**Figure 1D**).

Network of Target Genes and Pathways

After obtaining the pathways from the Metascape platform, we further used Cytoscape 3.7.2 software to visualize the relationships between the pathways and genes. As shown in **Figure 2A**, the red circles represent the target genes and the purple diamonds represent the pathways. There were 89 nodes in the network (55 pathways, 34 target genes), and the median of genes degree was 16.5. Among them, target genes with degrees higher than average were TNF, JUN, IL-6, IL-1B, NFKBIA, TP53, CASP3, IFNG, BCL2, CASP8 and BAX (**Table 5**), which may be important targets for Shenfu injection in the treatment of IPF. The median of pathways degree was nine. Pathways with degrees higher than average included pathways in cancer, infection/inflammation including tuberculosis, hepatitis B and IL-17 signaling pathway; and apoptosis (**Table 6**).

Molecular Docking of Active Compounds and Targeted Proteins

We used Cytoscape 3.7.2 software to analyze active compounds (**Table 7**). We selected compounds including beta-sitosterol, beta-elemene, myristic acid, TMPEA and the main content Ginsenoside Re as active compounds targeting TNF, IL-6, IL-1B, CASP3 and NFKBIA proteins. Generally, the negative value of the docking score means that they can bind to each other, and the positive value means that they cannot bind. The smaller the score value, the stronger the binding force is. Molecular docking results showed that these five compounds could bind to the target proteins. The docking score of Ginsenoside Re- NFKBIA was −9.046 kcal/mol, Ginsenoside Re- CASP3 was −9.273 kcal/mol, and Ginsenoside Re- IL-1B was −7.806 kcal/mol, showing that Ginsenoside Re had a relatively strong affinity with NFKBIA, CASP3 and IL-1B (**Figure 2B**). These results indicated that Shenfu injection may be functional in the treatment of IPF by targeting NFKBIA, CASP3 and IL-1B by its main content Ginsenoside Re. The docking details were recorded in **Table 8** and **Supplementary Table 2**.

Shenfu Injection Reduces BLM-Induced Pulmonary Fibrosis in Mice

We established bleomycin-induced pulmonary fibrosis on a mouse model. H&E staining of lung sections showed that bleomycin induced destruction of alveolar structures in mice, and the alveolar space was filled with fibrous tissue (**Figure 3A**). Shenfu injection-treated group showed lower score than bleomycin-treated group as assessed by Ashcroft scoring ($p < 0.05$, **Figure 3F**). Masson's trichrome staining showed the deposition of extensive collagen fibers in the lung interstitium (**Figure 3B**). Sirius red staining showed birefringent red collagen I and green collagen III under polarized light microscopy (**Figure 3C**). Shenfu injection treatment remarkably ameliorated these pathological injuries and alleviated collagen deposition (**Figure 3G,H**). The expression of α-SMA and collagen I was analyzed by immunohistochemical staining on the lung sections. Our data showed that the expression of α-SMA and collagen I increased in bleomycin-treated group, and Shenfu injection treatment significantly inhibited the expression of α-SMA and collagen I in the lung sections compared with bleomycin-treated group (**Figure 3D,E,I,J**).

Shenfu Injection Reduces Pulmonary Fibrosis by Inhibiting Inflammation and Apoptosis

To verify the mechanisms of Shenfu injection in the treatment of pulmonary fibrosis proposed by network pharmacology analysis,

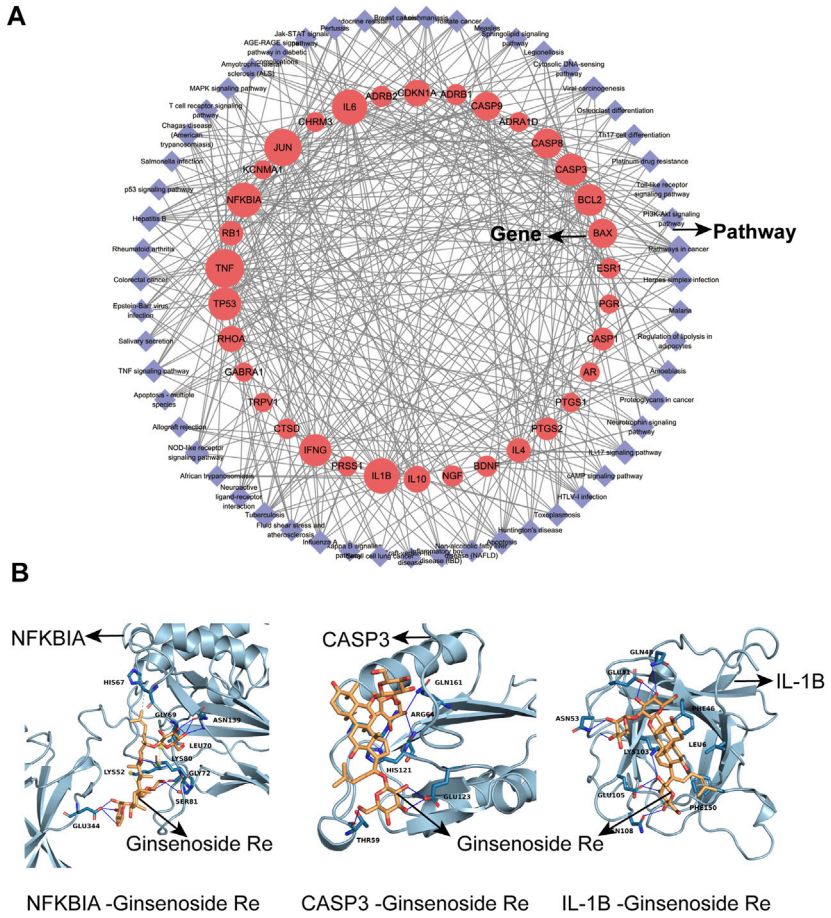

FIGURE 2 | The network of target gene-pathway interactions and molecular docking analysis. **(A)** The network of target gene-pathway interactions. Red circle stands for target genes and purple diamond stands for pathways. The size of the red circle represents the importance of the target gene in this network. **(B)** Molecular docking analysis. 3D visualization of NFKBIA-Ginsenoside Re, CASP3-Ginsenoside Re and IL-1B-Ginsenoside Re interactions are presented.

TABLE 5 | Target gene network and node characterization parameters.

Target gene	Degree	Betweenness centrality	Closeness centrality
TNF	32	0.1041	0.4607
JUN	30	0.1537	0.4809
IL6	27	0.0689	0.4334
IL-1B	27	0.0571	0.4251
NFKBIA	26	0.1079	0.4512
TP53	23	0.0572	0.4055
CASP3	22	0.0426	0.3982
IFNG	22	0.0415	0.4055
BCL2	21	0.0440	0.3946
CASP8	18	0.0260	0.3810
BAX	17	0.0221	0.3777

**Data were analyzed by Cytoscape 3.7.2 software.*

we performed TUNEL staining to observe the apoptotic cells in the lung sections, qPCR to examine the mRNA level of NFKBIA, CASP3, and IL-1B, and Western blot to examine the expression levels of inflammation-related proteins, including caspase-3, IL-1β, phosphorylated NF-κB and total NF-κB in the lung tissues from the three groups. The results showed that the number of TUNEL-positive cells increased in BLM-treated group compared with the control, and Shenfu injection significantly reduced the number of TUNEL-positive cells induced by BLM treatment. (**Figure 4**). The mRNA and protein level of caspase-3 was also upregulated in BLM-treated group, and could be reversed in Shenfu injection-treated group ($p < 0.05$, **Figure 5A,D,G**). These results indicated that BLM treatment could induce apoptosis in pulmonary cells, and Shenfu injection inhibited the apoptosis process, which may be one of its mechanisms to alleviate subsequent pulmonary fibrosis.

For the regulation of inflammatory process, we found that BLM treatment upregulated the protein and mRNA level of IL-1β, and Shenfu injection treatment significantly reduced the increased expression of IL-1β ($p < 0.05$, **Figure 5A,E,H**). In addition, BLM treatment upregulated mRNA level of NF-κB, and Shenfu injection treatment significantly reduced the mRNA level. Interestingly, the total protein level of NF-κB did not changed significantly. Since the phosphorylated NF-κB is the active form of this protein, we detected the protein level of phosphorylated NF-κB. It increased in BLM-treated group, and this increasement was significantly inhibited by Shenfu injection

TABLE 6 | KEGG Pathway network and node characterization parameters.

Pathway	Degree	Betweenness centrality	Closeness centrality
Pathways in cancer	14	0.0498	0.4444
Tuberculosis	12	0.0247	0.4231
Hepatitis B	12	0.0182	0.4314
Apoptosis	11	0.0243	0.4272
IL-17 signaling pathway	10	0.0208	0.4314

**Data were analyzed by Cytoscape 3.7.2 software.*

TABLE 7 | Main active compounds characterization parameters.

Pathway	Degree	MOL ID	Betweenness centrality	Closeness centrality
Beta-sitosterol	38	MOL000358	0.1951	0.4669
Beta-elemene	26	MOL000908	0.1311	0.4273
Myristic acid	24	MOL001393	0.0691	0.4075
TMPEA	19	MOL002399	0.0529	0.4099

**Data were analyzed by Cytoscape 3.7.2 software.*

TABLE 8 | Molecular docking score (kcal/mol).

Gene	PDB	Molecules				
		MOL000358	MOL000908	MOL001393	MOL002399	MOL005338
NFKBIA	1SVC	−1.962	−0.309	−1.315	−1.826	−9.046
TNF	6X81	No binding	−0.946	1.245	−3.494	No binding
IL-6	1ALU	No binding	−0.853	−1.382	−1.967	No binding
IL1B	1ITB	−1.440	−0.682	−0.449	−2.405	−7.806
CASP3	2XYP	−2.493	−1.406	−0.923	−3.653	−9.273

(**Figure 5A–C,F**), indicating that instead of affecting the total protein amount of NF-κB, Shenfu injection may function through inhibiting its phosphorylation. The above results together demonstrated that inhibition of inflammatory response is another mechanism of Shenfu in the treatment of pulmonary fibrosis.

DISCUSSION

Shenfu injection is a pure Chinese patent medicine modified from the classical Chinese medicine "Shenfu decoction" and extracted from ginseng and Fuzi by using the modern pharmaceutical technology. As "Extension of Famous Medical Prescriptions" records: "There is nothing as good as ginseng to nourish acquired Qi, and there is nothing as good as Fuzi to replenish innate Qi," Shenfu injection is mainly used in infectious diseases, haemorrhage, hemorrhagic shock and other Yang Qi burst off Syndromes in clinics. It is also applied in the Qi deficiency Syndrome, such as cough, shock, panic, stomachache, diarrhea and so on. In traditional Chinese medicine, IPF is considered to be in the category of pulmonary arthralgia and cough, and its root is Qi deficiency of the lung and spleen. Therefore, Shenfu injection might have some effects on IPF based on the theory of traditional Chinese medicine. Based on the studies with modern medical research methods, the therapeutic mechanism of Shenfu injection could be attributed to the promotion of cell repair and inhibition of cell apoptosis, as well as inhibition of inflammation, oxidation, ischemia and hypoxia (Liu et al., 2012; Lv et al., 2017; Chen et al., 2020). For instance, a recent study found that Shenfu injection inhibited TLR4/NF-κB signaling pathway, reduced systemic inflammatory response and played a protective role in the post-resuscitation myocardial dysfunction (Gu et al., 2021). Apoptosis of alveolar epithelial cells and the abnormal repair of alveolar injury is considered to be the pathological basis of IPF, while inflammation plays an important role in the induction and acute exacerbation of IPF. These characteristics are also consistent with the therapeutic mechanism of the Shenfu injection.

In this study, network pharmacological analysis revealed 46 genes correlated with Shenfu injection and IPF. The results indicated that Shenfu injection has a potential therapeutic effect on IPF, and its curative effect may be exerted through anti-inflammation and anti-cell apoptosis, involving pathways in tuberculosis, hepatitis B, apoptosis and IL-17 signaling.

As IL-6 and TNF co-stimulate MIP1-α expression of alveolar macrophages in bleomycin-induced mice, researchers proposed that IL-6 and TNF are part of the cytokine network in bleomycin-induced pulmonary pathophysiology (Smith et al., 1998). IL-6 and TNF-α polymorphism analysis in IPF patients showed that

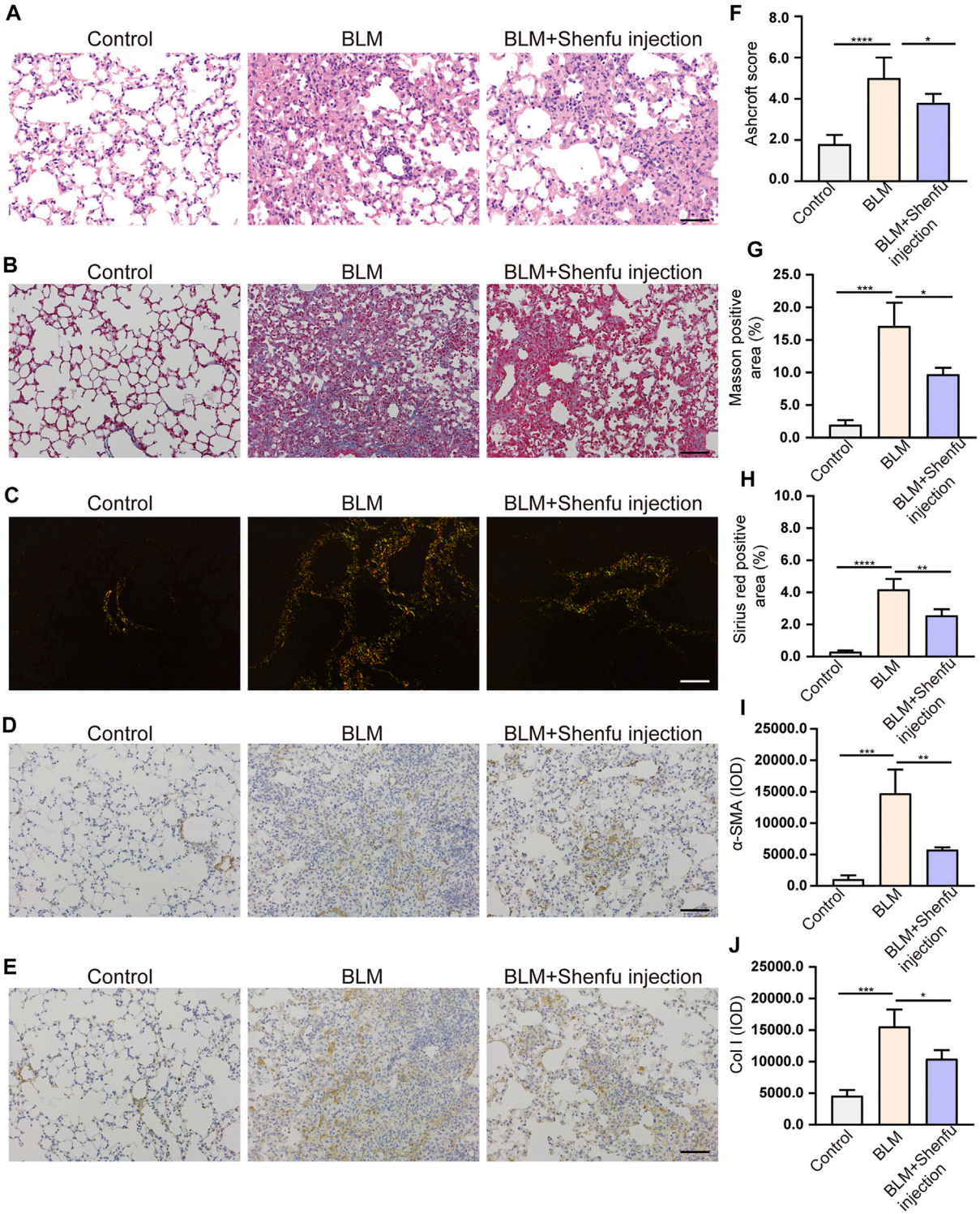

FIGURE 3 | Shenfu injection alleviates pulmonary fibrosis. Representative photomicrographs of H&E staining **(A)** ($n = 5$), Masson's trichrome staining **(B)** ($n = 3$) and Sirius red staining **(C)** ($n = 3$). Representative immunohistochemistry photomicrographs of α-SMA **(D)** ($n = 3$) and collagen I **(E)** ($n = 3$). Quantification of pulmonary fibrosis by Ashcroft score **(F)**, Masson positive area **(G)**, Sirius red positive area **(H)**, α-SMA positive signals **(I)** and collagen I positive signals **(J)**. Scale bar: 100 μm. The results are expressed as mean ± SD. $^{****}p < 0.0001$; $^{***}p < 0.001$; $^{**}p < 0.01$; $^{*}p < 0.05$. IOD, integrated optical density.

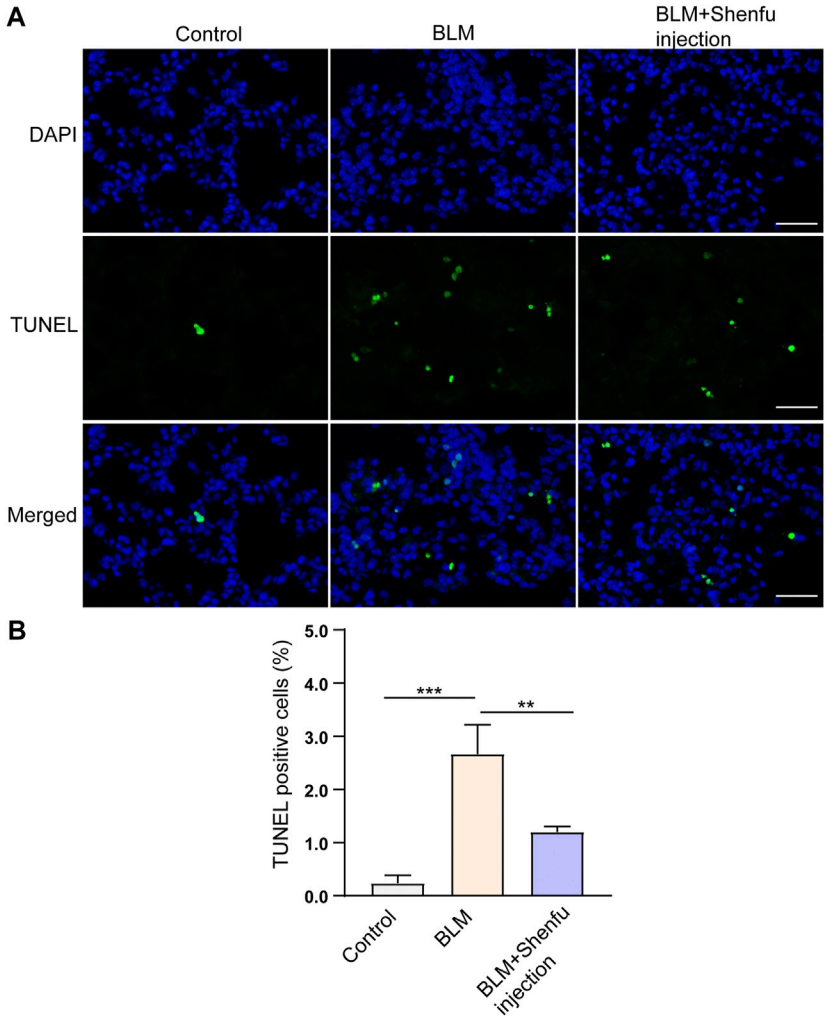

FIGURE 4 | Shenfu injection suppresses BLM-induced apoptosis. **(A)** Representative TUNEL staining using lung tissues 4 days after BLM treatment. **(B)** Quantification of TUNEL positive cells. Scale bar: 50 μm. The results are expressed as mean ± SD (n = 3 mice per group). ***p < 0.001, **p < 0.01.

IL-6 and TNF-α genes differed between the IPF and normal population and both related to the progression of IPF (Pantelidis et al., 2001). In lung tissue specimens, TNF-α and IL-1β were overexpressed in acute pulmonary fibrosis while presented a low expression level in old IPF patients, suggesting that TNF-α and IL-1β may be involved in the initiation of pulmonary fibrosis. Besides, the serum and BALF level of IL-1β is higher in IPF patients than healthy controls (Pan et al., 1996; Barlo et al., 2011). Shenfu injection alleviated lung injury in a rat systemic inflammatory response syndrome model by inhibiting NF-B activation and decreasing the plasma level of IL-6 and TNF-α (Wang et al., 2008). In a vascular endothelial cell damaging model, Shenfu injection cloud increase the level of Bcl2 protein and reduce caspase-3 and Bax levels, demonstrating that Shenfu injection has the function of anti-apoptosis and anti-oxidance (Hong et al., 2015). The molecular docking results showed that compounds of Shenfu injection could bind to these targets, especially its main content Ginsenoside Re had strong affinity with NFKBIA, CASP3 and IL-1B. Our results showed that Shenfu injection may interfere with inflammatory response and cell apoptosis by targeting NFKBIA, CASP3 and IL-1B.

IPF has the common photomechanics of epithelial damage, abnormal repairment and epithelial-mesenchymal transition with lung cancer, and it is considered to be associated with lung cancer. Researchers observed TP53 status in surgical resection of lung cancer in IPF patients, and found that the peripheral parts of fibrotic zone had high mutation rate of TP53 gene. Another research found that lung cancer with interstitial lung diseases had high risk for pleural invasion (Kawasaki et al., 2001; Hata et al., 2017). Moreover, a meta-analysis evaluated the function of Shenfu injection by objective tumor response, disease control rate, karnofsky performance score, adverse effects and indicators of cellular immune function, and the result indicated that Shenfu injection could improve immune function of lung cancer patients and reduce adverse effect of chemotherapy (Cao

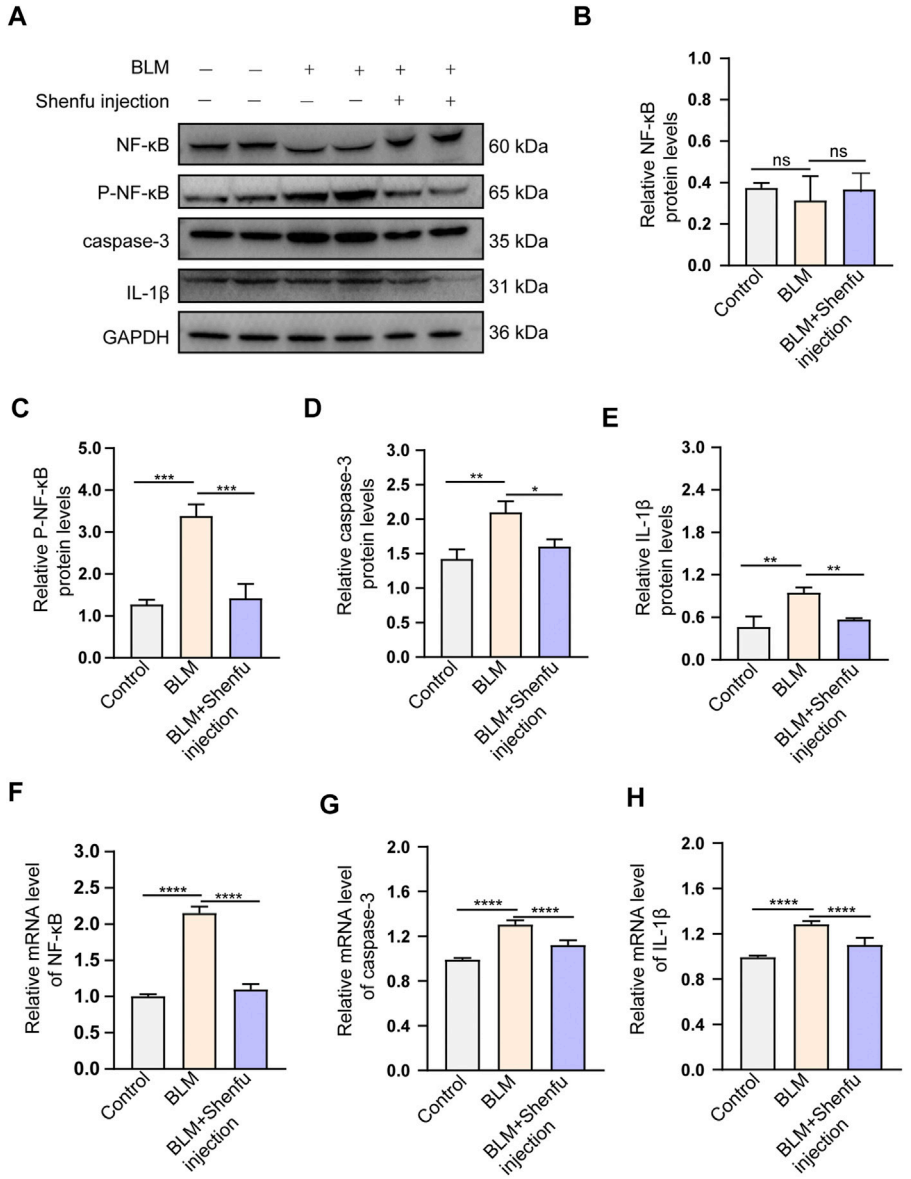

FIGURE 5 | Shenfu injection inhibits BLM-induced pulmonary fibrosis by targeting NFKBIA, CASP3 and IL-1B. **(A)** Western bot analysis of total NF-κB, Phospho-NF-κB, caspase-3 and IL-1β in each group. **(B–E)** Quantitative analysis of total NF-κB **(B)**, Phospho-NF-κB **(C)**, caspase-3 **(D)** and IL-1β **(E)** protein levels in each group ($n = 3$ mice per group). **(F–H)** Quantification of relative mRNA levels of NF-κB **(F)**, caspase-3 **(G)** and IL-1β **(H)** in each group ($n = 3$ mice per group). Data are presented as mean ± SD. ****$p < 0.0001$; ***$p < 0.001$; **$p < 0.01$; *$p < 0.05$.

et al., 2017). The interaction mechanism between Shenfu injection and lung cancer are still unclear. A cohort study found that IPF has a high risk of lung cancer. After adjusting the risk of smoking, the rate ratio (RR) for the incidence of IPF with lung cancer was 8.25 (890 IPF patients, 5884 control participants, 95% CI 4.70–11.48) (Hubbard et al., 2000). Our results showed that Shenfu injection may exert anti-tumor function by regulating P53 and JUN, which may add beneficial effects to the treatment of IPF.

Notably, infection, inflammation and apoptosis participate in the process of IPF. Viral and bacterial infections play a role in the process of IPF by causing alveolar injury and apoptosis. A meta-analysis from 20 studies (634 IPF patients, 653 controls) analyzed 19 virus species, demonstrating that the incidence of IPF increased by the infection of Epstein-Barr virus (EBV), cytomegalovirus (CMV), human herpesvirus 7 (HHV7) and human herpesvirus 8 (HHV8) (Sheng et al., 2020). Tuberculosis and hepatitis B are a global health problem, especially in China. Tuberculosis induces pulmonary fibrosis *via* macrophage apoptosis, recruiting TNF-α, TGF-β, Th1 and Th2 cytokines. Chronic hepatitis B causes defective T cell to affect the immune system and accelerates the progress of live fibrosis

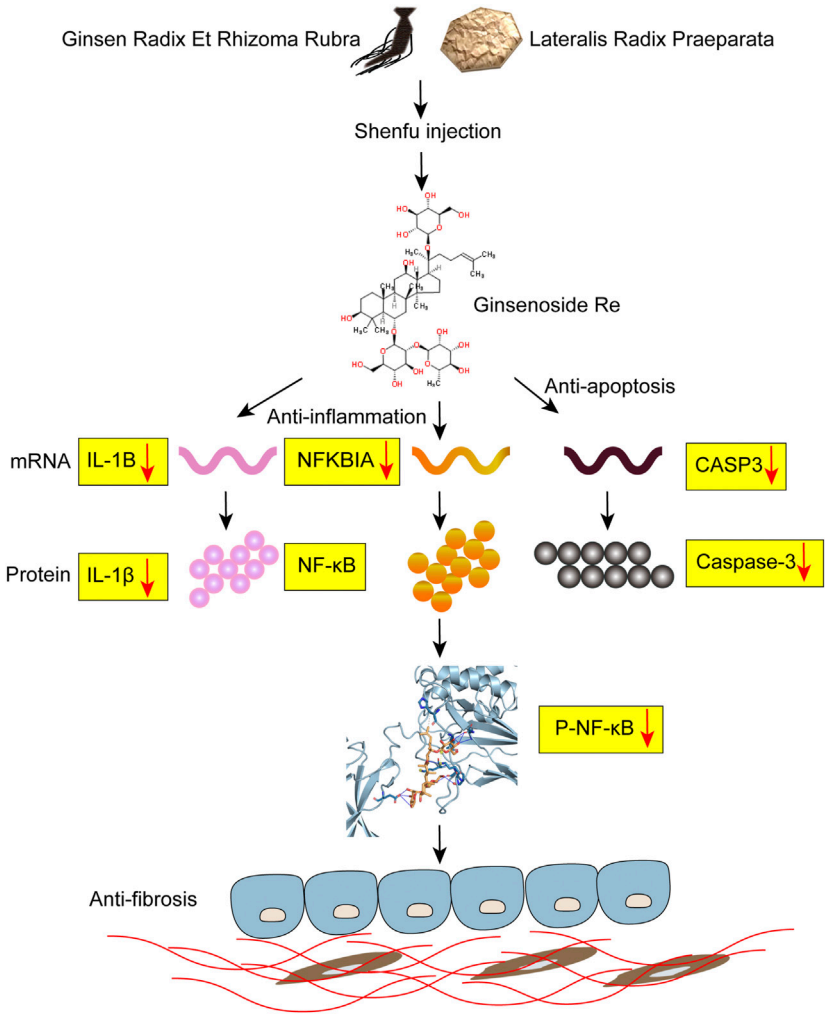

FIGURE 6 | Potential mechanism of Shenfu injection alleviating BLM-induced pulmonary fibrosis. Shenfu injection may have the function of anti-inflammation and anti-apoptosis by targeting NFKBIA, CASP3 and IL-1B, and alleviate BLM-induced pulmonary fibrosis.

(Dheda et al., 2005; Nebbia et al., 2012). Besides, researchers found that B cell activating factor (BAFF, one member of the TNF family) played a key role in bleomycin-induced lung fibrosis model by regulating the IL-1β and IL-17 pathway, and the expression of BAFF increased in BALF of IPF patients (François et al., 2015). Our results showed that Shenhua injection may interfere with tuberculosis, hepatitis B, apoptosis and IL-17 signaling to treat IPF.

Finally, to examine the effect of Shenfu injection *in vivo*, we used bleomycin-induced pulmonary fibrosis mouse model and applied Shenfu injection as daily treatment. Our data showed that Shenfu injection ameliorated the expression of α-SMA and collagen I, and remarkably reduced pulmonary fibrosis. We further validated that Shenfu injection inhibited the mRNA level of NFKBIA, CASP3, and IL-1B, it also inhibited NF-κB activation and reduced the protein expression levels of caspase-3 and IL-1β. Interestingly, our WB result of total protein NF-κB did not change significantly in the BLM-treated group and the Shenfu injection-treated group. Since the mRNA level may not always be consistent with the protein level, we considered that the total protein level of NFKBIA may be affected by other post-transcriptional modifications. At the same time, we found that Ginsenoside Re—the main component of Shenfu injection—could bind to NFKBIA and inhibit its phosphorylation. Therefore, we proposed a new mechanism from network pharmacology and our experiment that Shenfu injection may influence the activity of NFKBIA by inhibiting its phosphorylation by binding it with Ginsenoside Re, instead of affecting the total amount of NFKBIA protein. Inflammation plays an important role in IPF pathogenesis, and NF-κB coordinate with the expression of inflammation genes, that contribute to pulmonary fibrosis (Li and Verma, 2002). Besides, in human IPF and BLM-induced animal lung samples, excess alveolar epithelial cell apoptosis promotes pulmonary fibrosis (Hosseinzadeh et al., 2018). Our results validated the effectiveness of Shenfu injection in the treatment

of IPF, and verified its mechanism as inhibiting inflammation and apoptosis as proposed by targeting NFKBIA, CASP3, and IL-1B (**Figure 6**). Currently, the interaction of cancer-related pathways and IPF is not clear. How Shenfu injection ameliorates pulmonary fibrosis by regulating cancer-related genes such as JUN and TP53 is worth study in the future.

CONCLUSION

According to network pharmacology-based analysis and animal experiment, we discovered that Shenfu injection has the therapeutic potential for IPF and provided possible mechanisms underlined. This is the first evidence for the feasibility of Shenfu injection in the treatment of IPF.

DATA AVAILABILITY STATEMENT

The original contributions presented in the study are included in the article/**Supplementary Material**, further inquiries can be directed to the corresponding authors.

ETHICS STATEMENT

The animal study was reviewed and approved by the Committee of China-Japan Friendship Hospital.

AUTHOR CONTRIBUTIONS

PL and SY contributed equally to this study, they designed the project, conducted the experiment and wrote the manuscript. ZW, HD, and CW contributed to the conception of the study, the interpretation of experiment results, the revision and the approval of the final submitted version of manuscript.

FUNDING

This work was supported by Chinese Academy of Medical Sciences, Science and Technology Innovation in Medicine and Health Project (Major Collaborative Innovation Project 2018-I2M-1-0001) and the National Natural Science Foundation of China (No. 81870056).

ACKNOWLEDGMENTS

We thank the Ya'an 999 for providing the Shenfu injection.

SUPPLEMENTARY MATERIAL

The Supplementary Material for this article can be found online at: https://www.frontiersin.org/articles/10.3389/fphar.2021.670146/full#supplementary-material

REFERENCES

Barlo, N. P., van Moorsel, C. H. M., Korthagen, N. M., Heron, M., Rijkers, G. T., Ruven, H. J. T., et al. (2011). Genetic Variability in the IL1RN Gene and the Balance between Interleukin (IL)-1 Receptor Agonist and IL-1β in Idiopathic Pulmonary Fibrosis. *Clin. Exp. Immunol.* 166, 346–351. doi:10.1111/j.1365-2249.2011.04468.x

Behr, J., Günther, A., Bonella, F., Geißler, K., Koschel, D., Kreuter, M., et al. (2018). German Guideline for Idiopathic Pulmonary Fibrosis - Update on Pharmacological Therapies 2017. *Pneumologie* 72, 155–168. doi:10.1055/s-0043-123035

Cao, A., He, H., Jing, M., Yu, B., and Zhou, X. (2017). Shenfu Injection Adjunct with Platinum-Based Chemotherapy for the Treatment of Advanced Non-small-cell Lung Cancer: A Meta-Analysis and Systematic Review. *Evidence-Based Complement. Altern. Med.* 2017, 1–12. doi:10.1155/2017/1068751

Chen, R.-J., Rui, Q.-L., Wang, Q., Tian, F., Wu, J., and Kong, X.-Q. (2020). Shenfu Injection Attenuates Lipopolysaccharide-Induced Myocardial Inflammation and Apoptosis in Rats. *Chin. J. Nat. Medicines* 18, 226–233. doi:10.1016/S1875-5364(20)30025-X

Dheda, K., Booth, H., Huggett, J. F., Johnson, M. A., Zumla, A., and Rook, G. A. W. (2005). Lung Remodeling in Pulmonary Tuberculosis. *J. Infect. Dis.* 192, 1201–1209. doi:10.1086/444545

François, A., Gombault, A., Villeret, B., Alsaleh, G., Fanny, M., Gasse, P., et al. (2015). B Cell Activating Factor Is central to Bleomycin- and IL-17-mediated Experimental Pulmonary Fibrosis. *J. Autoimmun.* 56, 1–11. doi:10.1016/j.jaut.2014.08.003

Gu, W., Hou, X.-m., and Li, C.-s. (2021). Effects of Shenfu Injection (参附注射液) on Inflammatory Response during Post-Resuscitation Myocardial Dysfunction after Cardiac Arrest in Swine. *Chin. J. Integr. Med.* 27, 417–423. doi:10.1007/s11655-021-2855-2

Hamosh, A., Scott, A. F., Amberger, J. S., Bocchini, C. A., and McKusick, V. A. (2004). Online Mendelian Inheritance in Man (OMIM), a Knowledgebase of Human Genes and Genetic Disorders. *Nucleic Acids Res.* 33, D514–D517. doi:10.1093/nar/gki033

Hata, A., Suzuki, H., Nakajima, T., Tanaka, K., Fujiwara, T., Wada, H., et al. (2017). Concomitant Interstitial Lung Disease Is a Risk Factor for Pleural Invasion in Lung Cancer. *Ann. Thorac. Surg.* 103, 967–974. doi:10.1016/j.athoracsur.2016.08.074

Hong, F. F., Guo, F. X., Zhou, Y., Min, Q. H., Zhang, D. L., Yang, B., et al. (2015). Shenfu Injection Protects Human ECV304 Cells from Hydrogen Peroxide via its Anti-apoptosis Way. *J. Ethnopharmacol.* 163, 203–209. doi:10.1016/j.jep.2015.01.032

Hopkins, A. L. (2007). Network Pharmacology. *Nat. Biotechnol.* 25, 1110–1111. doi:10.1038/nbt1007-1110

Hosseinzadeh, A., Javad-Moosavi, S. A., Reiter, R. J., Yarahmadi, R., Ghaznavi, H., and Mehrzadi, S. (2018). Oxidative/nitrosative Stress, Autophagy and Apoptosis as Therapeutic Targets of Melatonin in Idiopathic Pulmonary Fibrosis. *Expert Opin. Ther. Targets* 22, 1049–1061. doi:10.1080/14728222.2018.1541318

Hubbard, R., Venn, A., Lewis, S., and Britton, J. (2000). Lung Cancer and Cryptogenic Fibrosing Alveolitis. *Am. J. Respir. Crit. Care Med.* 161, 5–8. doi:10.1164/ajrccm.161.1.9906062

Kawasaki, H., Ogura, T., Yokose, T., Nagai, K., Nishiwaki, Y., and Esumi, H. (2001). p53 Gene Alteration in Atypical Epithelial Lesions and Carcinoma in Patients with Idiopathic Pulmonary Fibrosis. *Hum. Pathol.* 32, 1043–1049. doi:10.1053/hupa.2001.28246

Li, P., Lv, B., Jiang, X., Wang, T., Ma, X., Chang, N., et al. (2016). Identification of NF-Kb Inhibitors Following Shenfu Injection and Bioactivity-Integrated UPLC/Q-TOF-MS and Screening for Related Anti-inflammatory Targets *In Vitro* and In Silico. *J. Ethnopharmacology* 194, 658–667. doi:10.1016/j.jep.2016.10.052

Li, Q., and Verma, I. M. (2002). NF-κB Regulation in the Immune System. *Nat. Rev. Immunol.* 2, 725–734. doi:10.1038/nri910

Liu, J., Yan, X., Li, L., Zhu, Y., Qin, K., Zhou, L., et al. (2012). Ginsennoside Rd Attenuates Cognitive Dysfunction in a Rat Model of Alzheimer's Disease. *Neurochem. Res.* 37, 2738–2747. doi:10.1007/s11064-012-0866-2

Lv, S. J., Lai, D. P., Wei, X., Yan, Q., and Xia, J. M. (2017). The Protective Effect of Shenfu Injection against Elderly Severe Pneumonia. *Eur. J. Trauma Emerg. Surg.* 43, 711–715. doi:10.1007/s00068-016-0713-2

Nebbia, G., Peppa, D., and Maini, M. K. (2012). Hepatitis B Infection: Current Concepts and Future Challenges. *Qjm* 105, 109–113. doi:10.1093/qjmed/hcr270

Pan, L.-H., Ohtani, H., Ohtani, H., Yamauchi, K., and Nagura, H. (1996). Co-expression of TNFα and IL-1β in Human Acute Pulmonary Fibrotic Diseases: An Immunohistochemical Analysis. *Pathol. Int.* 46, 91–99. doi:10.1111/j.1440-1827.1996.tb03584.x

Pantelidis, P., Fanning, G. C., Wells, A. U., Welsh, K. I., and Du Bois, R. M. (2001). Analysis of Tumor Necrosis Factor- α , Lymphotoxin- α , Tumor Necrosis Factor Receptor II, and Interleukin-6 Polymorphisms in Patients with Idiopathic Pulmonary Fibrosis. *Am. J. Respir. Crit. Care Med.* 163, 1432–1436. doi:10.1164/ajrccm.163.6.2006064

Richeldi, L., Collard, H. R., and Jones, M. G. (2017). Idiopathic Pulmonary Fibrosis. *The Lancet* 389, 1941–1952. doi:10.1016/s0140-6736(17)30866-8

Ru, J., Li, P., Wang, J., Zhou, W., Li, B., Huang, C., et al. (2014). TCMSP: a Database of Systems Pharmacology for Drug Discovery from Herbal Medicines. *J. Cheminform.* 6, 13. doi:10.1186/1758-2946-6-13

Salentin, S., Schreiber, S., Haupt, V. J., Adasme, M. F., and Schroeder, M. (2015). PLIP: Fully Automated Protein-Ligand Interaction Profiler. *Nucleic Acids Res.* 43, W443–W447. doi:10.1093/nar/gkv315

Sheng, G., Chen, P., Wei, Y., Yue, H., Chu, J., Zhao, J., et al. (2020). Viral Infection Increases the Risk of Idiopathic Pulmonary Fibrosis. *Chest* 157, 1175–1187. doi:10.1016/j.chest.2019.10.032

Smith, R. E., Strieter, R. M., Phan, S. H., Lukacs, N., and Kunkel, S. L. (1998). TNF and IL-6 Mediate MIP-1α Expression in Bleomycin-Induced Lung Injury. *J. Leukoc. Biol.* 64, 528–536. doi:10.1002/jlb.64.4.528

Song, Y., Zhang, N., Shi, S., Li, J., Zhang, Q., Zhao, Y., et al. (2015). Large-scale Qualitative and Quantitative Characterization of Components in Shenfu Injection by Integrating Hydrophilic Interaction Chromatography, Reversed Phase Liquid Chromatography, and Tandem Mass Spectrometry. *J. Chromatogr. A* 1407, 106–118. doi:10.1016/j.chroma.2015.06.041

Szklarczyk, D., Gable, A. L., Lyon, D., Junge, A., Wyder, S., Huerta-Cepas, J., et al. (2019). STRING V11: Protein-Protein Association Networks with Increased Coverage, Supporting Functional Discovery in Genome-wide Experimental Datasets. *Nucleic Acids Res.* 47, D607–D613. doi:10.1093/nar/gky1131

UniProt Consortium, T. (2018). UniProt: the Universal Protein Knowledgebase. *Nucleic Acids Res.* 46, 2699. doi:10.1093/nar/gky092

Wang, J., Qiao, L.-f., and Yang, G.-t. (2008). Role of Shenfu Injection (参附注射液) in Rats with Systemic Inflammatory Response Syndrome. *Chin. J. Integr. Med.* 14, 51–55. doi:10.1007/s11655-008-0051-2

Xu, P., Zhang, W.-Q., Xie, J., Wen, Y.-S., Zhang, G.-X., and Lu, S.-Q. (2020). Shenfu Injection Prevents Sepsis-Induced Myocardial Injury by Inhibiting Mitochondrial Apoptosis. *J. Ethnopharmacology* 261, 113068. doi:10.1016/j.jep.2020.113068

Zhang, N., Liu, J., Qiu, Z., Ye, Y., Zhang, J., and Lou, T. (2017). Shenfu Injection for Improving Cellular Immunity and Clinical Outcome in Patients with Sepsis or Septic Shock. *Am. J. Emerg. Med.* 35, 1–6. doi:10.1016/j.ajem.2016.09.008

Zhang, Q., Li, C., Shao, F., Zhao, L., Wang, M., and Fang, Y. (2017). Efficacy and Safety of Combination Therapy of Shenfu Injection and Postresuscitation Bundle in Patients with Return of Spontaneous Circulation after In-Hospital Cardiac Arrest. *Crit. Care Med.* 45, 1587–1595. doi:10.1097/CCM.0000000000002570

Zhou, Y., Zhou, B., Pache, L., Chang, M., Khodabakhshi, A. H., Tanaseichuk, O., et al. (2019). Metascape Provides a Biologist-Oriented Resource for the Analysis of Systems-Level Datasets. *Nat. Commun.* 10, 1523. doi:10.1038/s41467-019-09234-6

Conflict of Interest: The authors declare that the research was conducted in the absence of any commercial or financial relationships that could be construed as a potential conflict of interest.

Publisher's Note: All claims expressed in this article are solely those of the authors and do not necessarily represent those of their affiliated organizations, or those of the publisher, the editors and the reviewers. Any product that may be evaluated in this article, or claim that may be made by its manufacturer, is not guaranteed or endorsed by the publisher.

Copyright © 2021 Liu, Yang, Wang, Dai and Wang. This is an open-access article distributed under the terms of the Creative Commons Attribution License (CC BY). The use, distribution or reproduction in other forums is permitted, provided the original author(s) and the copyright owner(s) are credited and that the original publication in this journal is cited, in accordance with accepted academic practice. No use, distribution or reproduction is permitted which does not comply with these terms.

frontiers in Pharmacology

ORIGINAL RESEARCH
published: 30 July 2021
doi: 10.3389/fphar.2021.688746

Poria cum Radix Pini Rescues Barium Chloride-Induced Arrhythmia by Regulating the cGMP-PKG Signalling Pathway Involving ADORA1 in Zebrafish

Ning-Juan Yang[1†], *Yan-Ru Liu*[1†*], *Zhi-Shu Tang*[1*], *Jin-Ao Duan*[2], *Ya-Feng Yan*[1], *Zhong-Xing Song*[1], *Ming-Geng Wang*[3], *Yu-Ru Zhang*[1], *Bai-Jin Chang*[1,4], *Meng-Li Zhao*[1] *and Yan-Ting Zhao*[1]

[1]*Shaanxi Province Key Laboratory of New Drugs and Chinese Medicine Foundation Research, Shaanxi Collaborative Innovation Center Medicinal Resources Industrialization, Shaanxi University of Chinese Medicine, Xianyang, China,* [2]*Key Laboratory for High Technology Research of TCM Formulae and Jiangsu Collaborative Innovation Center of Chinese Medicinal Resources Industrialization, Nanjing University of Chinese Medicine, Nanjing, China,* [3]*Shandong Buchang Pharmaceutical Co. Ltd, Xi'an, China,* [4]*Changchun University of Chinese Medicine, Changchun, China*

The traditional Chinese medicine *Poria cum Radix Pini* (PRP) is a fungal medicinal material that has been proven to play an important role in the treatment of arrhythmia. However, the mechanism of its effect on arrhythmia is still unclear. In this study, network pharmacology and metabolomics correlation analysis methods were used to determine the key targets, metabolites and potential pathways involved in the effects of PRP on arrhythmia. The results showed that PRP can significantly improve cardiac congestion, shorten the SV-BA interval and reduce the apoptosis of myocardial cells induced by barium chloride in zebrafish. By upregulating the expression of the ADORA1 protein and the levels of adenosine and cGMP metabolites in the cGMP-PKG signalling pathway, PRP can participate in ameliorating arrhythmia. Therefore, we believe that PRP shows great potential for the treatment of arrhythmia.

Keywords: arrhythmia, *Poria cum Radix Pini*, ADORA1, cGMP-PKG signalling pathway, zebrafish

OPEN ACCESS

Edited by:
Hai Yu Xu,
Institute of Chinese Materia Medica, China

Reviewed by:
Aiping Li,
Shanxi University, China
Gaosong Wu,
Shanghai University of Traditional Chinese Medicine, China
Xiaoxia Gao,
Shanxi University, China

***Correspondence:**
Yan-Ru Liu
yanzi_2203@aliyun.com
Zhi-Shu Tang
tzs6565@163.com

[†]These authors have contributed equally to this work

Specialty section:
This article was submitted to Ethnopharmacology, a section of the journal Frontiers in Pharmacology

Received: *31 March 2021*
Accepted: *19 July 2021*
Published: *30 July 2021*

Citation:
Yang N-J, Liu Y-R, Tang Z-S, Duan J-A, Yan Y-F, Song Z-X, Wang M-G, Zhang Y-R, Chang B-J, Zhao M-L and Zhao Y-T (2021) Poria cum Radix Pini *Rescues Barium Chloride-Induced Arrhythmia by Regulating the cGMP-PKG Signalling Pathway Involving ADORA1 in Zebrafish. Front. Pharmacol. 12:688746. doi: 10.3389/fphar.2021.688746*

INTRODUCTION

Arrhythmia is one of the most serious diseases of the cardiovascular system. Its negative effects include not only aggravating original heart disease and affecting the quality of life of patients but also inducing sudden cardiac death, which seriously threatens the life of patients (Krittayaphong et al., 2016). Approximately 600,000 people die from sudden cardiac death in China every year and

Abbreviations: ADORA1, Adenosine A1 Receptor; AO, acridine orange; BA, bulbus arteriosus; BP, biological processes; CC, cellular components; CT, cycle threshold; FA, formic acid; GO, gene Ontology; IP3R, inositol triphosphate receptor; MF, molecular functions NOS, nitric oxide synthase; PBS, phosphate-buffered saline; PI3K/Akt, phosphoinositide 3-kinase/protein kinase B; PLS, partial least squares; PPI, protein-protein interaction; PRP, *Poria cum Radix Pini*; PRP-H, PRP high-dose group; PRP-L, PRP low-dose group; PRP-M, PRP medium-dose group; RT-PCR, reverse transcription polymerase chain reaction; SPSS, statistical program for the social sciences; SV, sinus venosus; UPLC/Q-TOF-MS, ultraperformance liquid chromatography/quadrupole time-of flight mass spectrometry; VIP, variable importance in projection.

approximately 390,000 people die from malignant arrhythmia every year in the United States (Wang et al., 2018; Kusumoto et al., 2018). The pathogenesis of arrhythmia is complicated. Molecular biology studies have revealed cardiac autonomic nerve dysfunction, such as excitement of the vagus nerve and inhibition of sympathetic nerves (de Araújo et al., 2018; Janssens and Michels, 2019). Abnormal structure and function of ion channels can cause arrhythmia (Torrente et al., 2020). The clinical treatment of arrhythmia is based mainly on Western medicine, such as propafenone, calcium channel blockers, and β-receptor blockers, but medical research has shown that antiarrhythmic drugs also have arrhythmic effects and that their improper use can cause more serious adverse reactions. Although the long-term use of these drugs can relieve symptoms, it results in an unsatisfactory prognosis and may even increase mortality, so there is an urgent need to explore new anti-arrhythmia treatment strategies (Brugada et al., 2020).

Poria cum Radix Pini (PRP) is a traditional Chinese medicine with a long history that was first referenced in the "Famous Doctors". PRP consists of the white part of *Poria cocos (Schw.) Wolf* with pine roots in the middle (Ping, Guixin, Spleen Channel). Research shows that PRP has significant antitumour, spleen and stomach invigoration, swelling relief, mind-calming and tranquilization, immunity-enhancing and bacterium-inhibiting effects (Changhe, 2009).Pharmacological and clinical medicine research has shown that PRP can prolong sleep time and shows a synergistic effect with pentobarbital sodium. It has a good effect on most people who exhibit insomnia and difficulty falling asleep or who wake up easily (Shah et al., 2014). In addition, it can also inhibit tumour growth and exert antitumour effects by enhancing the body's immune function. Triterpenes and polysaccharide compounds are the main active components of PRP (Xu et al., 2020; Yi et al., 2020). Studies have shown that triterpenes (poria cocoic acid) can inhibit the secretion of IL-2 and IFN-γ and affect the killing of target cells by cytotoxic T cells and the apoptosis of cardiomyocytes (Wu et al., 2014). *Poria cocos* polysaccharides can inhibit the occurrence of cardiac hypertrophy, improve haemodynamics, enhance myocardial systolic function, improve myocardial diastolic function and increase cardiac output in rats (Zhao et al., 2020b). Ergosterol compounds also exhibit good curative antitumour effects and prevent cardiovascular diseases (Kim et al., 2019), which shows that PRP presents great potential for the treatment of arrhythmia. However, the mechanism and core pathways involved in the PRP-based treatment of arrhythmia have not yet been reported, and further investigation is needed.

Databases such as the Encyclopedia of Traditional Chinese Medicine (ETCM) and the Bioinformatics Analysis Tool for Molecular Mechanisms of Traditional Chinese Medicine (BATMAN-TCM) are commonly used for network pharmacological analysis (Gong et al., 2019; Xu et al., 2019). This study is based on the use of these databases to predict the potential targets and biological pathways of PRP-based treatment of arrhythmia. Ultra-performance liquid chromatography/quadrupole time-of-flight mass spectrometry (UPLC/Q-TOF-MS) positive and negative detection modes were used to analyse alcohol extracts of PRP, and the main active ingredients were determined (Zhang et al., 2020). In addition, since zebrafish heart have a very similar electrophysiological behaviour to the human heart, thus, it has become a very interesting model for human heart system pathologies researches, like cardiomyopathy, arrhythmia, heart failure, structural and congenital heart disease etc (Gut et al., 2017; Cassar et al., 2020; Echeazarra et al., 2020). Specially, the advantage of zebrafish embryos is transparency which offer a possibility to observe heart physiology and pathology characteristics directly (Matrone et al., 2015; Crowcombe et al., 2016). Therefore, in our experiments, we prefer to use the BaCl2-induced arrhythmia zebrafish model to explore PRP treatment functions (Khisatmutdinova et al., 2006; Huang et al., 2013). A biological arrhythmia model in zebrafish was established with barium chloride (Liu et al., 2014). Then, through the correlation analysis of network pharmacology and metabolomics, the main pathway involved in the PRP-based treatment of arrhythmia was identified, and the mechanism of action of the PRP-based treatment of arrhythmia was further clarified through the quantitative analysis of key targets and metabolites in the pathway by reverse transcription polymerase chain reaction (RT-PCR) and metabolomics (Shi et al., 2020).

MATERIALS AND METHODS

Chemicals and Reagents

Verapamil hydrochloride was purchased from Shanghai Hefeng Pharmaceutical Co., Ltd. (Shanghai, China). Barium chloride was obtained from Chongqing Maoye Chemical Reagent Co., Ltd. Optimal LC grade acetonitrile was obtained from Merck (Merck, Darmstadt, Germany). Isopropanol, formic acid and nucleotides for metabolite analyses were purchased from Sigma-Aldrich (Spruce St., St Louis, MO, United States).

Preparation of *Poria cum Radix Pini* Extracts

PRP was obtained from Shaanxi Xingshengde Co., Ltd. (Shannxi, China) and identified by Prof. Ji-Qing Bai. The specimens were deposited at Shaanxi University of Chinese Medicine (Shaanxi, China). PRP was prepared via the following steps: precise weighing of 0.8 g PRP in a 50 ml conical bottle, dilution with 25 ml methanol, weighing, soaking for 30 min, ultrasonic processing for 60 min, cooling, and weighing again. Next, the solution was brought up to the desired weight with methanol and filtered. A 15 ml aliquot was then absorbed by continuous filtration, evaporated to approximately 1 ml in an evaporation dish in a water bath, diluted with methanol in a 5 ml capacity bottle, shaken, evaporated in an evaporating pan in a water bath, and then dissolved in deionized water for animal experiments.

Zebrafish Embryos and Treatment

Zebrafish embryos 72 h post fertilization (hpf) were purchased from Shanghai Fish Biotechnology Co., Ltd. and maintained in

Holt buffer solution (15 mM NaCl, 0.5 mM KCl, 1 mM $MgSO_4$, 1 mM $CaCl_2$, 0.15 mM KH_2PO_4, 0.05 mM Na_2HPO_4, 0.7 mM $NaHCO_3$, 5% methylene blue; pH 7.5) on a 14 h light/10 h dark cycle at 28 ± 1°C and pH 7.5 ± 0.5.

Zebrafish embryos were randomized into six groups and placed on 48-well cell culture plates (ten embryos per group, five embryos per well): control, model (barium chloride sterile saline solution 2.1 μg/ml, 2 ml), positive control (model + 0.45 μg/ml verapamil hydrochloride), and three treatment groups (PRP-H: model + PRP extract 162.60 μg/ml, PRP-M: model + PRP extract 121.95 μg/ml, PRP-H: model + PRP extract 97.56 μg/ml). Technical details of the establishment protocol for the barium chloride-induced arrhythmia model establishment protocol and the PRP treatment dosage design are shown in **Supplementary File S1**. After 24 h of incubation with sterile saline solution of barium chloride, verapamil hydrochloride, or PRP extract, the morphology of the zebrafish embryo hearts was observed. All animal handling and experimental conditions were approved by the Laboratory Animal Care and Use Committee of Shaanxi University of Chinese Medicine.

Identification of the Chemical Components of *Poria cum Radix Pini*

The concentration of PRP extract was 9.6 mg/ml. The PRP extract solution was analysed on a Waters Acquity H-Class UltraPerformance LC (Waters, MA, USA)/tandem 5600^+ triple-quadruple time-of-flight mass spectrometer (QTOF-MS) system (AB SCIEX, MA, United States) using a Waters BEH C_{18} column (50 mm × 2.1 mm, 1.7 μm) with a gradient mobile phase of 0.1% formic acid aqueous solution (A) and 0.1% formic acid-acetonitrile solution (B) at a flow rate of 0.3 ml/min and a 30°C column temperature. The gradient program was as follows: 0–1 min, 2% B; 1–42 min, 2–100% B; 42–44 min, 100% B; 44–48 min, 100–2% B; 48–50 min, 2% B. The full scan and MS/MS experiments were performed under positive and negative modes by using an electrospray ionization (ESI) ion source. Information-dependent data (IDA) acquisition mode was used to switch automatically between MS and MS/MS acquisition with the following parameters: ion spray voltage floating: +5500 or −4500 V, declustering potential (DP): 40 V, ion source gas 1 and ion source gas 2 both set as nitrogen: 50 psi, curtain gas: 35 psi, source temperature: 500°C. The scanning range of parent ions (TOF-MS) was 100–2000 m/z. The eight strongest peaks exceeding 100 cps were collected by MS^2, and the scanning range was 100–2000 m/z. Data were acquired using Analyst TF software (version 1.7.1, AB SCIEX). Component identification was performed by using PeakView™ software (version 2.2, AB SCIEX) and MasterView™ software (version 1.1, AB SCIEX) coupled with the TCM library database (version 1.0, AB SCIEX).

Network Pharmacology Prediction for *Poria cum Radix Pini* Therapy

According to the UPLC-TOF-MS/MS identification results, the screening for active components of PRP and the PRP target prediction for arrhythmia treatment were performed by network pharmacology analysis on ETCM (http://www.tcmip.cn/ETCM/index.php/Home/Index/), BATMAN-TCM (http://bionet.ncpsb.org.cn/batman-tcm/index.php) , Traditional Chinese Medicine Systems Pharmacology Database and Analysis Platform (TCMSP, http://tcmspw.com/tcmsp.php), Therapeutic Targets Database (TTD, http://db.idrblab.net/ttd/) and Genecards (https://www.genecards.org/) (Liu et al., 2016).

Common targets were identified between the screened active component-related targets and disease targets ('arrhythmia') by VENNY 2.1.0 (https://bioinfogp.cnb.csic.es/tools/venny/), and a relationship among these targets was generated by the STRING 11.0 database (https://string-db.org/). Then, the component-disease-target association network was constructed by Cytoscape software (version 3.7.2). Finally, the enrichment of Gene Ontology (GO) functions and pathways of selected key targets were examined by using the clusterProfiler package of R software (version 3.6.1) for RPR treatment function prediction (Yu et al., 2012).

Cardiovascular Morphological Observation and Sinus Venosus-Bulbus Arteriosus Distance Measurement

After incubation with Holt buffer solution from 60 to 72 hpf, zebrafish embryos were randomly selected ($n = 10$ each group) for the observation of cardiac morphology. The zebrafish embryos were fixed with 3% methylcellulose (AlfaAesar, Shanghai, China), and cardiac morphology observations (pericardial oedema, abnormal circulation, thrombosis, haemorrhage, etc.) and sinus venosus-bulbus arteriosus (SV-BA) distance measurement for heart tube looping quantification were performed on an ABX51 electron microscope (Olympus, Tokyo, Japan), and images were acquired under a DD71 digital camera (Olympus, Tokyo, Japan). The pericardial congestion area and the SV-BA straight line distance were calculated with ImageJ software (version 1.8.0, NIH, USA). Each experimental treatment was repeated three times (Lin et al., 2007; Gut et al., 2017; Echeazarra et al., 2020).

Acridine Orange Staining for Apoptosis Evaluation

Acridine orange (AO) is a nucleic acid-selective metachromatic dye: AO-stained apoptotic cells show yellow-green fragments, while normal cells show uniform green or yellow-green fluorescence (Antonio et al., 2017). To evaluate the cardiomyocyte apoptosis of zebrafish embryos after barium sodium exposure and rescue treatment, five live zebrafish embryos at 96 hpf from each group were randomly selected and washed with phosphate-buffered saline (PBS, pH 7.4) to remove exposure residues and then incubated in 2.5 mg/L AO solution at 28°C in the dark for 30 min. Next, the embryos were rinsed thoroughly in PBS twice and fixed in 3% methyl cellulose solution. Images of the dorsal side of fixed zebrafish were acquired under a BX51 push-around-type electronic fluorescence microscope (Tokyo, Japan) coupled with a DD71

digital camera under a green light source. The average fluorescence density of the particle number was calculated by Image J software (Jin et al., 2019).

Untargeted Metabolomic Analysis

Sample Preparation

For significant endometabolite selection, 30 live 72 hpf zebrafish embryos from each group were randomly selected and washed with PBS (pH 7.4) to remove exposure residues, placed in 1.5 ml centrifuge tubes, mixed with 1 ml of PBS solution, and centrifuged at 12,000 r/min for 10 min. Next, the PBS solution was aspirated, 1 ml of 80% methanol solution was added, and the mixture was ground and centrifuged at 12,000 r/min at 4°C for 10 min. Finally, the supernatant was extracted, concentrated and freeze-dried until use.

Untargeted Metabolomics UPLC-Q/TOF-MS Analysis

The freeze-dried zebrafish embryo sample was mixed with 250 μl of acetonitrile:water (1:1) solution prior to untargeted metabolomics analysis. The prepared samples were separated on a UPLC-QTOF-MS/MS system using a Waters UPLC® HSS T3 C_{18} column (2.1 × 100 mm, 1.7 μm), with a gradient mobile phase of aqueous solution +2 mM ammonium acetate+0.05% aqueous formic acid (A)-acetonitrile: isopropanol = 1:1 + 2 mM ammonium acetate-0.05% aqueous formic acid (B), at a flow rate of 0.3 ml/min and a column temperature of 40°C. The gradient program was as follows: 0–1.5 min, 2% B; 1.5–23 min, 1–60% B; 23–24 min, 60–98% B; 24–27 min, 98% B; 27–27.1 min, 27.1–33 min, 1% B. Full scans and MS/MS experiments with information-dependent data (IDA) acquisition mode were performed by using an ESI ion source with the following parameters: ion spray voltage floating: +5500or −4500 V, declustering potential (DP): 40 V, ion source gas 1 and ion source gas 2 both set as nitrogen: 50 psi, curtain gas: 35 psi, source temperature: 500°C. The scanning range of parent ions was 70–1200 m/z. The twelve strongest peaks exceeding 100 cps were collected by MS^2, and the scanning range was 70–1200 m/z. Data were acquired using Analyst TF software (version 1.7.1, AB SCIEX). Metabolites were identified by using PeakView™ software (version 2.2, AB SCIEX) and MasterView™ software (version 1.1, AB SCIEX) coupled with "the Accurate Mass Metabolite Spectral Library" (version 1.0, AB SCIEX). The combined score of confidence setting parameters were as follows: mass error 40%, retention time 0%, isotope 20%, library hit 40%, and formula finder 0%.

Untargeted Differential Metabolome Screening

To identify targeted endo-metabolites, metabolite database matching data were extracted and converted to Excel files (*.xls) for matrix formation. Then, the pretreatment matrix was subjected to SIMCA-P 14.0 (Umetrics, Sweden) software for partial least squares (PLS) analysis between the control and model groups to identify the differential metabolome that corresponded to a statistical p value of < 0.05 and a variable importance in projection (VIP) value of > 1.0 (Liu et al., 2019). To select the therapeutic-related endo-metabolites among the control, model, positive control, PRP-H, PRP-M and PRP-L groups, the differential metabolome was next distinguished by PCA on the MetaboAnalyst 4.0 online platform (http://www.metaboanalyst.ca) (Xia et al., 2009).

Metabolic Pathway Enrichment

Further analyses were conducted to identify and visualize the effect of the PRP extract on the metabolic pathways related to arrhythmia. The differential metabolites screened by metabolomics and the key targets predicted on the basis of network pharmacology were input into the MetaboAnalyst database, with p <0.05 as the card value, and the pathway library (Kyoto Encyclopedia of Genes and Genomes (KEGG)) was selected for pathway enrichment analysis.

Targeted Metabolites Determination

To analyse the targeted metabolomic selection results, potential metabolite markers were quantitated by comparison to the areas of the peaks for the external standards (method validation is shown in **Supplementary File S2**, **Supplementary Table S1**).

Quantitative Reverse Transcriptase Polymerase Chain Reaction Analysis

After treatment at 96 hpf, zebrafish embryos were randomly selected (n = 30 each group) for qRT-PCR analysis. Thirty milligrams of zebrafish embryos was homogenized in TRIzol reagent (Servicebio Technology Co., Ltd., Wuhan, China) to extract total RNA. The extracted RNA was used as a template, and cDNA was synthesized by reverse transcription with appropriate primers according to the instructions of the Servicebio® RT First Strand cDNA Synthesis Kit (G3330, Servicebio, Wuhan, China). qRT-PCR was performed in an ABI 7900HT Fast Real-Time PCR system (Bio-Rad Bole Gradient, California, America). The primer sequences were as follows (ref. NM_001128584.1, 242 bp, 60°C, Servicebio): TTC TGACCCAAAGTTCCATCCT (forward) and CTCAAACTG GCAGGTGACGAT (reverse). Levels of the Adenosine A1 Receptor (ADORA1) mRNAs were normalized to the GAPDH mRNA level and determined using the $2^{-\Delta\Delta Ct}$ method, and all reactions were performed in triplicate.

Statistical Analysis

Statistical Program for the Social Sciences (SPSS) 26.0 was used for statistical analysis. All the data are expressed as the mean ± SD. One-way analysis of variance (ANOVA) was used to compare the data among the groups. GraphPad Prism 8 software was used to generate all graphics, and $p < 0.05$ was considered statistically significant.

RESULTS

UPLC/Q-TOF-MS Components Identification of *Poria cum Radix Pini*

Under the optimized chromatographic and mass spectrometry conditions, UPLC/Q-TOF-MS in positive and negative detection

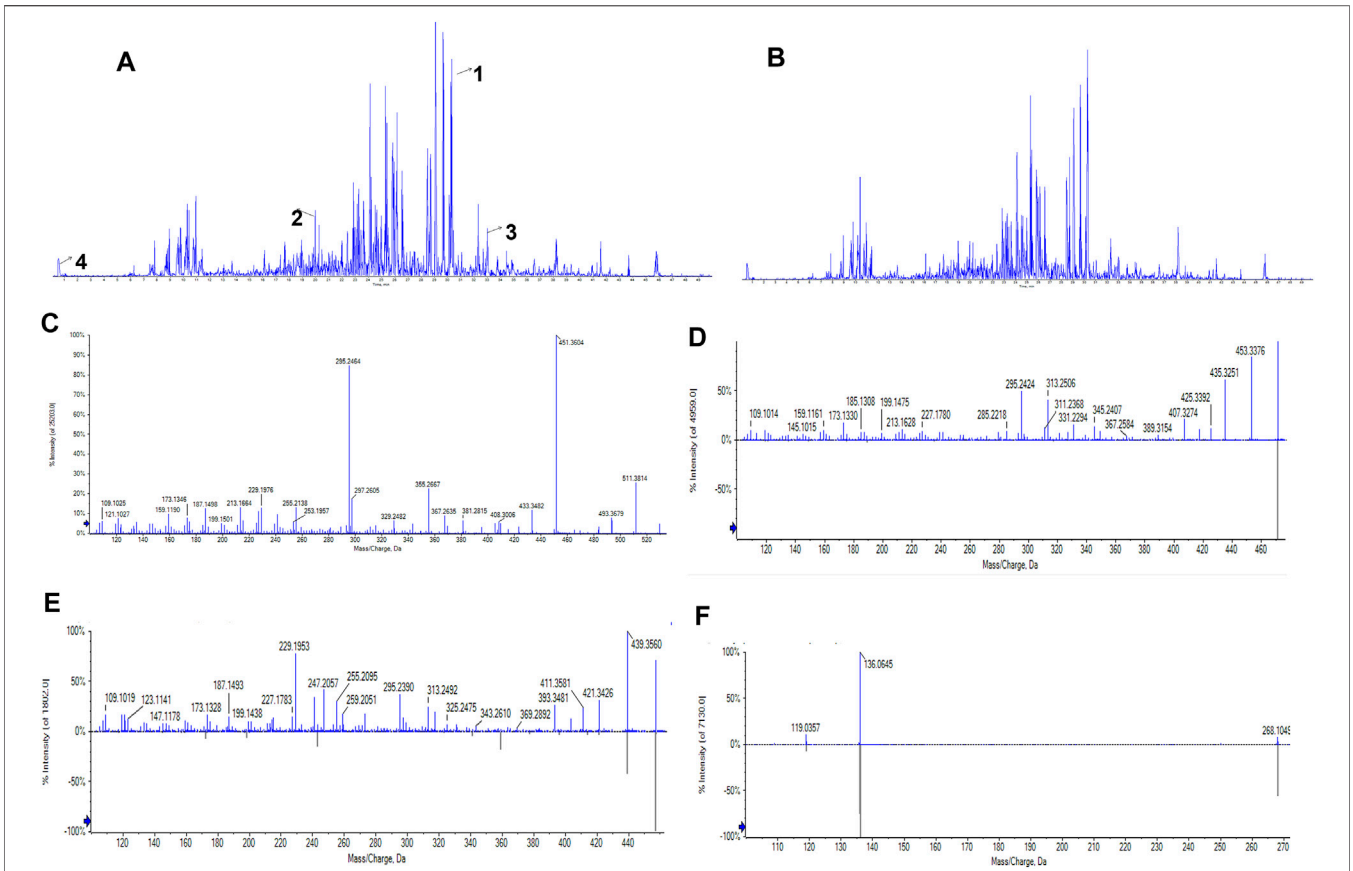

FIGURE 1 | UPLC/Q-TOF-MS total ion current chromatogram of the PRP alcohol extract. **(A)** Total ion current chromatogram in positive ion mode. Numbers represent the following compounds:1. Pachymic acid, 2. Glycyrrhetinic acid, 3. Oleanolic acid, 4. Adenosine. **(B)** Total ion current chromatogram in negative mode. The retention times of the four compounds were 30.317, 19.867, 33.012, and 0.55 min, respectively. **(C)** MS/MS spectrum of pachymic acid; **(D)** MS/MS spectrum of glycyrrhetinic acid; **(E)** MS/MS spectrum of oleanolic acid; **(F)** MS/MS spectrum of adenosine.

TABLE 1 | Chemical identification combining component characterization and database search.

Number	Name	Molecular Formula	Mass (Da)	Source
1	Pachymic Acid	$C_{33}H_{52}O_5$	529.38875	MS、MS2、TCMSP、ETCM
2	Oleanolic acid	$C_{30}H_{48}O_3$	457.3676	MS、MS2
3	Glycyrrhetinic acid	$C_{30}H_{46}O_4$	471.34688	MS、MS2
4	Adenine	$C_5H_5N_5$	136.06177	MS、BATMAN-TCM、ETCM
5	Ergotamine	$C_{33}H_{35}N_5O_5$	581.26382	ETCM
6	Lauric Aldehyde	$C_{12}H_{24}O$	184.18272	TCMSP、ETCM
7	Adenosine	$C_{10}H_{13}N_5O_4$	268.10402	MS、MS2
8	Palmitic acid	$C_{16}H_{32}O_2$	256.24023	TCMSP、ETCM
9	Lauric acid	$C_{12}H_{24}O_2$	200.17763	TCMSP、ETCM
10	Caprylic acid	$C_8H_{16}O_2$	144.11503	TCMSP、ETCM
11	Tumulosic acid	$C_{31}H_{50}O_4$	486.37091	TCMSP、ETCM

modes was used to analyse the PRP extracts (**Figures 1A,B**). The results showed that 31 compounds were identified in positive ion mode and 5 in negative ion mode (**Supplementary File S3**, **Supplementary Table S2**). According to the molecular weight, retention time, and MS/MS data, four compounds were identified: pachymic acid, glycyrrhetinic acid, oleanolic acid and adenosine (**Figures 1C–F**) (**Supplementary File S3**, **Supplementary Table S3**) (Qian et al., 2018).

Network Pharmacological Analysis for *Poria cum Radix Pini* Therapy

By combining UPLC/Q-TOF-MS identification and database search results, 11 compounds were identified and selected (**Table 1**). For these compounds, 606 putative targets were predicted from the ETCM, TCMSP and Batman-TCM databases (**Supplementary File S4**, **Supplementary Table S4**). A total of 316 targets related to arrhythmia were obtained against

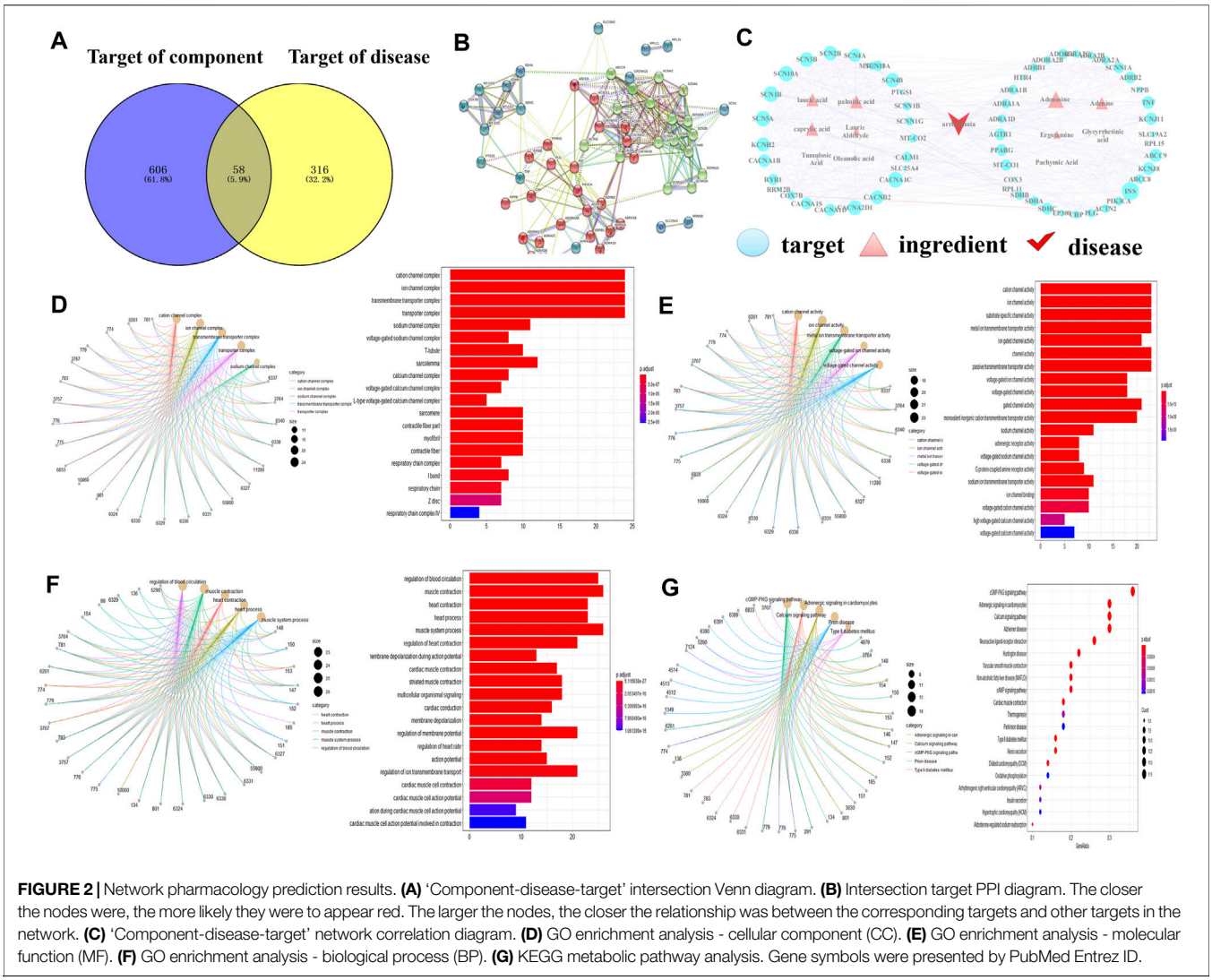

FIGURE 2 | Network pharmacology prediction results. **(A)** 'Component-disease-target' intersection Venn diagram. **(B)** Intersection target PPI diagram. The closer the nodes were, the more likely they were to appear red. The larger the nodes, the closer the relationship was between the corresponding targets and other targets in the network. **(C)** 'Component-disease-target' network correlation diagram. **(D)** GO enrichment analysis - cellular component (CC). **(E)** GO enrichment analysis - molecular function (MF). **(F)** GO enrichment analysis - biological process (BP). **(G)** KEGG metabolic pathway analysis. Gene symbols were presented by PubMed Entrez ID.

the ETCM, TTD, and GeneCards databases (**Supplementary File S4**, **Supplementary Table S5**). In **Figure 2A**, we first extracted 58 intersection targets from the overlaps between the disease gene set and PRP target sets (**Supplementary File S4**, **Supplementary Table S6**). In the following study, the relationships of these 58 targets were connected as a PPI network for importance evaluation (**Supplementary File S4**, **Supplementary Table S7**). As shown in **Figure 2B**, the PPI k-means classification results suggested that 25 genes, iADORA1, ADORA2B, ADRA1A, ADRA1B, and ADRA1D, play a more important role in arrhythmia pathology and PRP treatment.

To further explore PRP multicomponent and multitarget therapy functions, all 58 targets of the PPI network were mapped to "component-disease" connections, and then the "component-disease-target" network of PRP therapy was constructed by Cytoscape software (**Figure 2C**). This network included 70 nodes, which illustrated potential interplay among 1 disease type, 11 chemical components, and 58 targets. Since the node size is proportional to the importance of nodes involved in the pathway, 7 components involved in the therapy pathway, including adenosine, palmitic acid, caprylic acid, lauric acid, and adenine. In addition, 58 targets, such as ADORA1, ADORA2B, and CACNA1B, were considered potential therapeutic targets (**Supplementary File S4**, **Supplementary Table S8**).

GO analysis revealed that the targets were significantly enriched in 581 pathways for PRP therapy, specifically "complex ion channels and transmembrane transporters", "ion channel activity and metal ion transmembrane transport protein activity", and "myocardial contraction, the regulation of myocardial contractility and the regulation of blood circulation" (**Figures 2D–F**, **Supplementary File S4**, **Supplementary Table S9**). Similarly, KEGG pathway enrichment analysis showed that the targets were significantly enriched in 193 pathways for PRP therapy, specifically the "cGMP-PKG signalling pathway" and "calcium ion signalling pathway" (**Figure 2G**, **Supplementary File S4**, **Supplementary Table S10**). As the GO and KEGG analyses suggested that most adenosine receptors (ADORAs) under PRP treatment were involved in arrhythmia-related pathways, these 58 targets were used to perform metabolomic joint pathway analysis.

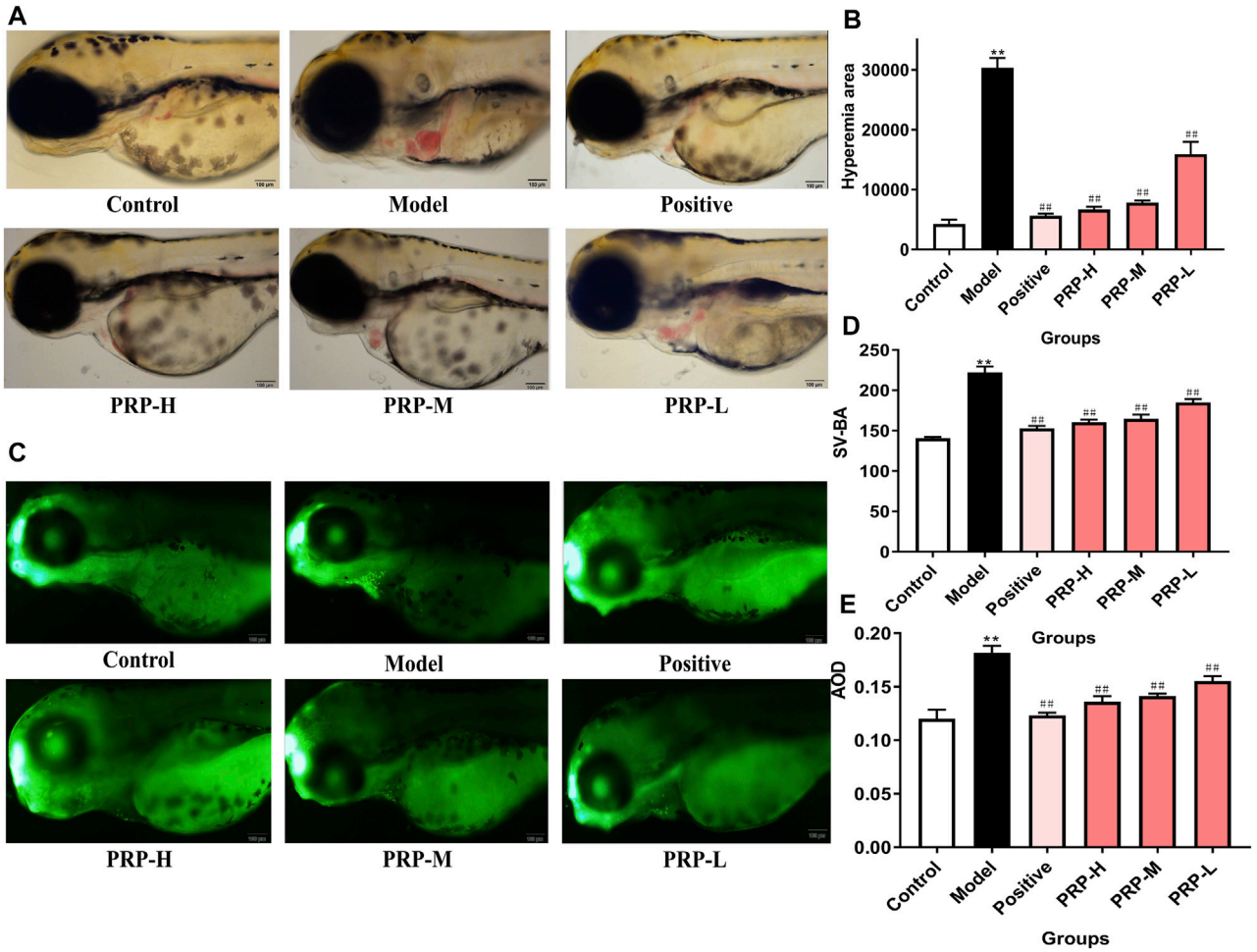

FIGURE 3 | The effect of PRP on the heart development of zebrafish embryos following barium chloride treatment. **(A)** Morphological observations of the heart development of zebrafish embryos under a microscope, with the heart shown in the yellow box (X10). **(B)** The cardiac congestion area of zebrafish embryos was calculated. **(C)** The results of acridine orange staining. The apoptosis of zebrafish embryos cardiomyocytes observed under fluorescence microscopy is shown in the yellow box (X10). **(D)** The SV-BA distance was measured. **(E)** The average fluorescence density was calculated.All data are presented as means ± SD, $n = 6$. $^{*}p < 0.05$, $^{**}p < 0.01$, control versus model; $^{\#}p < 0.05$, $^{\#\#}p < 0.01$, model versus positive, PRP-H, PRP-M, and PRP-L.

Poria cum Radix Pini can Rescue Barium Chloride-induced Cardiac Defects in Zebrafish Embryos

In the morphological phenotype observation, PRP extracts showed a significant and dose-dependent rescue function against barium chloride-induced morphological phenotypes (**Figure 3A**). Calculating the cardiac congestion area in zebrafish showed that the cardiac congestion area was 605.42% larger in the zebrafish model group than in the control group. However, the cardiac congestion areas in the positive control group, PRP-H group, PRP-M group and PRP-L group showed decreases of 81.44, 78.05, 74.22 and 47.54%, respectively, compared to that in the model group. These findings further proved that PRP can lessen the degree of cardiac congestion induced by barium chloride in zebrafish (**Figure 3B**, **Supplementary File S5**, **Supplementary Tables S11, S11-1, S11-2**). Compared with the control group, the model group zebrafish showed a 58.10% increase in the SV-BA distance. Compared to the model group, the SV-BA distance in the verapamil exposure group led to a significant 31.30% decrease, while the PRP-H, PRP-M, and PRP-L treatment groups showed 27.83, 25.96, and 16.82% decreases, respectively (**Figure 3D**, **Supplementary File S5**, **Supplementary Tables S12, S12-1, S12-2**).

Poria cum Radix Pini can Inhibit Cardiomyocyte Apoptosis in Zebrafish Embryos

After AO staining, compared with the control group, a large number of apoptotic cells (green debris particles) were found in zebrafish embryo hearts, and the average fluorescence density was 51.18% higher than that in the control group. At 96 hpf, the

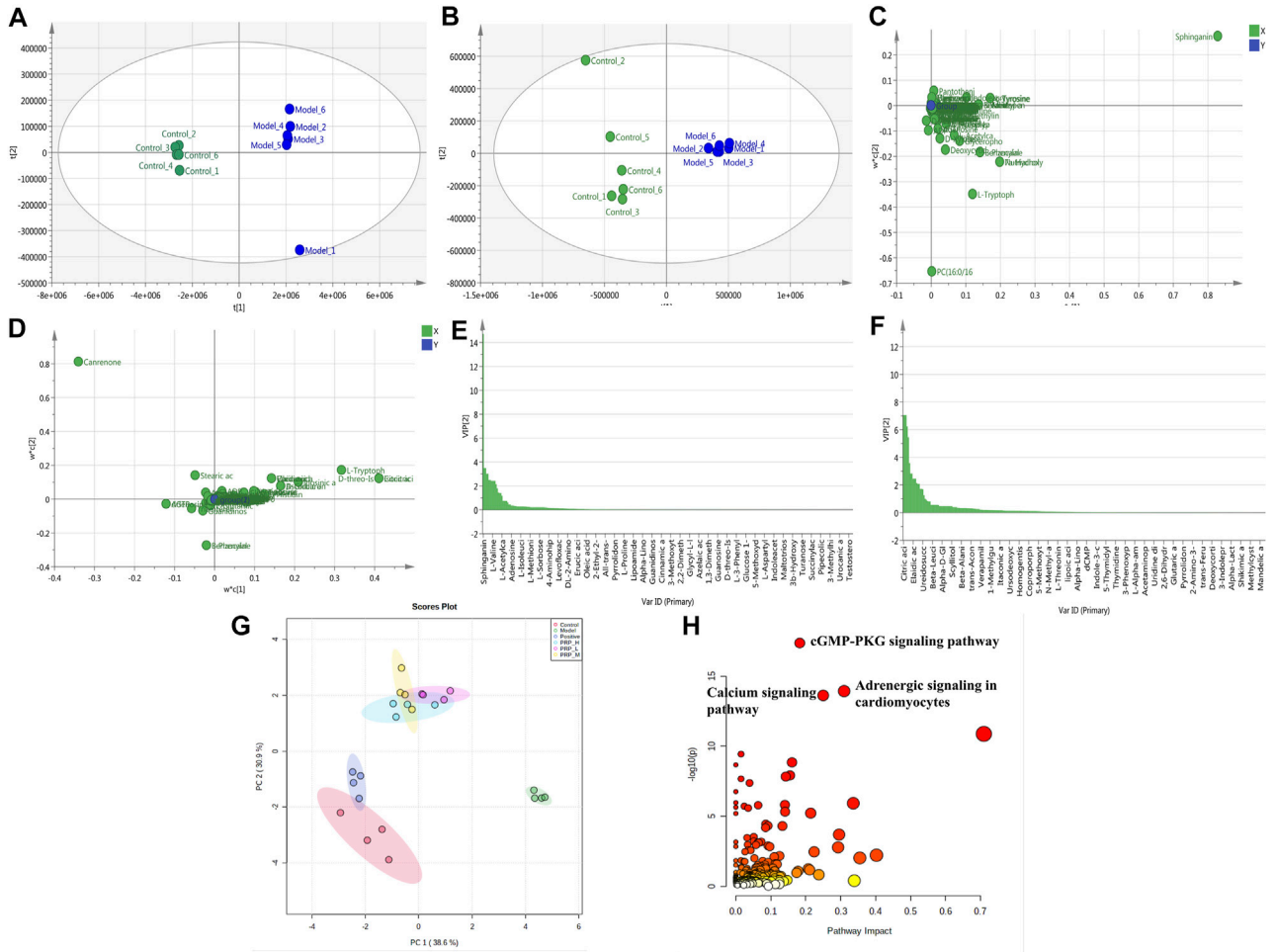

FIGURE 4 | Effects of PRP on metabolite alterations induced by barium chloride in zebrafish embryos. $R^2Y = 0.999$, $Q^2 = 0.995$ in positive ion mode; $R^2Y = 0.986$, $Q^2 = 0.984$ in negative ion mode; **(A)** 2D scores plot in positive ion mode; **(B)** 2D scores plot in negative ion mode; **(C)** Loading plot in positive ion mode; **(D)** Loading plot in negative ion mode; **(E)** VIP diagram in positive ion mode; **(F)** VIP diagram in negative ion mode; **(G)** PCA scores plot of different metabolites in each group; **(H)** Metabolic pathway enrichment analysis diagram.

numbers of apoptotic cells in zebrafish embryo hearts were significantly and dose-dependently decreased in the PRP treatment group. Compared to the model group, the average fluorescence density of the PRP-H, PRP-M and PRP-L groups showed declines of 25.13, 22.20 and 14.50%, respectively. These results indicated that PRP could rescue barium chloride-induced apoptosis in the hearts of zebrafish embryos in a concentration-dependent manner (**Figures 3C,E**, **Supplementary File S5**, **Supplementary Tables S13, S13-1, S13-2**).

Poria cum Radix Pini can Regulate Metabolite Disorders Induced by Barium Chloride in Zebrafish Embryos

PLS analysis of the untargeted metabolome showed a distinct change in metabolite profiles between the model embryos and control embryos, represented by the substantial metabolomic perturbation of the cardiac system observed in these embryos (three experiments, **Figures 4A,B**). Then, significant features were selected based on a selected criterion with an adjusted *p*-value cut-off of <0.05. Statistical analysis of the metabolomics data from the barium chloride-treated group and the control group indicated significant differences in ions between these two groups, as shown in the loading plot (**Figures 4C,D**). The VIP values were also used to calculate the feature importance by the cut-off value of weight VIP > 1 (**Figures 4E,F**). Following the selection flow, a total of 17 potential differential metabolites were identified in positive and negative ion modes (**Table 2**), including amino acid components such as L-tyrosine, L-valine, L-tryptophan, indoleacrylic acid, and L-histidine and choline components such as glycerophosphocholine, L-acetylcarnitine and adenosine triphosphate.

Furthermore, to clarify whether PRP administration can regulate barium chloride-induced metabolite alterations, comparisons among the control group, model group, positive control group and PRP-H, PRP-M and PRP-L groups were

TABLE 2 | Potential differential metabolites induced by barium chloride in zebrafish embryos.

Number	Name	Formula	m/z	Adduct	VIP	*p* Value
1	L-Tyrosine	$C_9H_{11}NO_3$	181.0739	+H	3.02665	3.2307×10^{-14}
2	Nutriacholic acid	$C_{24}H_{38}O_4$	390.2770	+H	3.50493	3.154×10^{-05}
3	Indoleacrylic acid	$C_{11}H_9NO_2$	187.0633	+H	1.79193	1.8004×10^{-06}
4	L-Valine	$C_5H_{11}NO_2$	117.0790	+H	2.42267	6.938×10^{-06}
5	Benzocaine	$C_9H_{11}NO_2$	165.0790	+H	2.49461	2.0293×10^{-06}
6	Glycerophosphocholine	$C_8H_{20}NO_6P$	257.1028	+H	1.45259	2.2183×10^{-4}
7	L-Acetylcarnitine	$C_9H_{17}NO_4$	203.1158	+H	1.16715	1.6222×10^{-04}
8	Ascorbic acid	$C_6H_8O_6$	176.0321	-H	2.83443	7.0845×10^{-12}
9	Adenosine triphosphate	$C_{10}H_{14}N_5O_7P$	347.0631	-H	2.07961	6.416×10^{-04}
10	Ureidosuccinic acid	$C_5H_8N_2O_5$	176.0433	-H	1.69662	3.963×10^{-10}
11	Glutathione	$C_{10}H_{17}N_3O_6S$	307.0838	-H	1.26381	6.9709×10^{-10}
12	Triamterene	$C_{12}H_{11}N_7$	253.1076	-H	1.01154	3.853×10^{-10}
13	Citric acid	$C_{10}H_8O_7$	240.0270	-H	7.06906	2.5526×10^{-03}
14	Inosinic acid	$C_{10}H_{13}N_4O_8P$	348.0471	-H	3.59027	1.9504×10^{-12}
15	L-Histidine	$C_6H_9N_3O_2$	155.0695	-H	2.152	1.2383×10^{-04}
16	L-Tryptophan	$C_{11}H_{12}N_2O_2$	204.0899	-H	5.46315	1.26×10^{-14}
17	Canrenone	$C_{22}H_{28}O_3$	340.2038	-H	6.2536	2.257×10^{-02}

analysed by using the MetaboAnalyst database. As shown in **Figure 4G**, the PCA score plot showed obvious sample clusters among the control, model, positive control and PRP-treated groups, where the PRP-H group and PRP-M group were close to the control group but separated from the model group. The results indicated that PRP treatment could improve barium chloride-induced metabolomic profile imbalance in zebrafish embryos.

Poria cum Radix Pini Rescues Metabolite Profiles From the ADORA1-Mediated cGMP-PKG Signalling Pathway

To further investigate the roles of the enriched metabolite pathways and dissect which of the screened targets contributed to these pathways, the candidate targets from the network pharmacology selection were mapped to 17 differential endometabolites by joint-pathway analysis on the MetaboAnalyst database (**Figure 4H**). Gene-metabolic pathway correlation analyses showed that the "cGMP-PKG signalling pathway" ($p < 0.001$) was highly enriched among the 72 enriched metabolic pathways. In this pathway, ADORA1 is a highly ranked protein that acts as an adenosine receptor to reduce cardiomyocyte calcium overload in the occurrence of arrhythmia diseases, and adenosine and cGMP are highly ranked metabolites (Szentmiklosi et al., 2015; Deb et al., 2019).

Next, by quantifying the levels of adenosine and cGMP in embryo samples using LC-MS in multiple reaction monitoring (MRM) mode, barium chloride induced a significant decreasing trend in adenosine by 63.30% and cGMP by 78.86% compared with the control ones. PRP therapy significantly reversed these changes: the adenosine and cGMP levels in the PRP-H group were increased by 75.84 and 231.35%, in the PRP-M group were increased by 66.71 and 159.57%, and in the PRP-L group were increased by 41.71 and 78.86%, respectively (**Figures 5A,B**, **Supplementary File S6**, **Supplementary Tables S14–S15-2**). ADORA1 expression was determined using qRT-PCR assays to examine how PRP treatment influenced barium chloride-induced arrhythmia in zebrafish embryos (**Figure 5C**, **Supplementary File S6**, **Supplementary Tables S16, S16-1, S16-2**). Interestingly, ADORA1 expression was significantly decreased by 81.65% ($p < 0.01$) in the model group. PRP therapy restored ADORA1 expression at three dosages, with increases of 320.53, 261.96, 184.56 and 154.58%, respectively. The results showed that PRP could increase the expression level of ADORA1 in the cGMP-PKG signalling pathway. These findings indicated that barium chloride disturbed the cGMP-PKG signalling pathway, which resulted in arrhythmia. This was attributed to ADORA1 downregulation associated with adenosine and cGMP decline and PRP treatment rescued these trends towards an imbalance.

DISCUSSION

PRP is a traditional fungal medicinal material that is often used as the key medicine for the treatment of arrhythmia. Modern pharmacological studies have shown that PRP water decoction shows a similar central inhibitory effect to synergistic pentobarbital sodium, which further demonstrates its anti-arrhythmic effects, and it can be used together with *Poria cocos* to treat heart palpitations caused by deficiencies of the heart and spleen (Shah et al., 2014). In addition, its main active components, such as triterpenoids and polysaccharides, have been proven to play an important role in the treatment of arrhythmia (Wu et al., 2014; Li et al., 2015). Studies have indicated that cardiomyocyte apoptosis plays an important role in arrhythmia, and the severity of apoptosis is positively correlated with the arrhythmia score (Niu et al., 2020). In addition, zebrafish heart congestion, an extended SV-BA distance, pericardial oedema and other cardiac morphological changes can cause heart damage and arrhythmia. In this study, by observing the heart morphology of zebrafish with arrhythmia induced by barium chloride, it was found that PRP

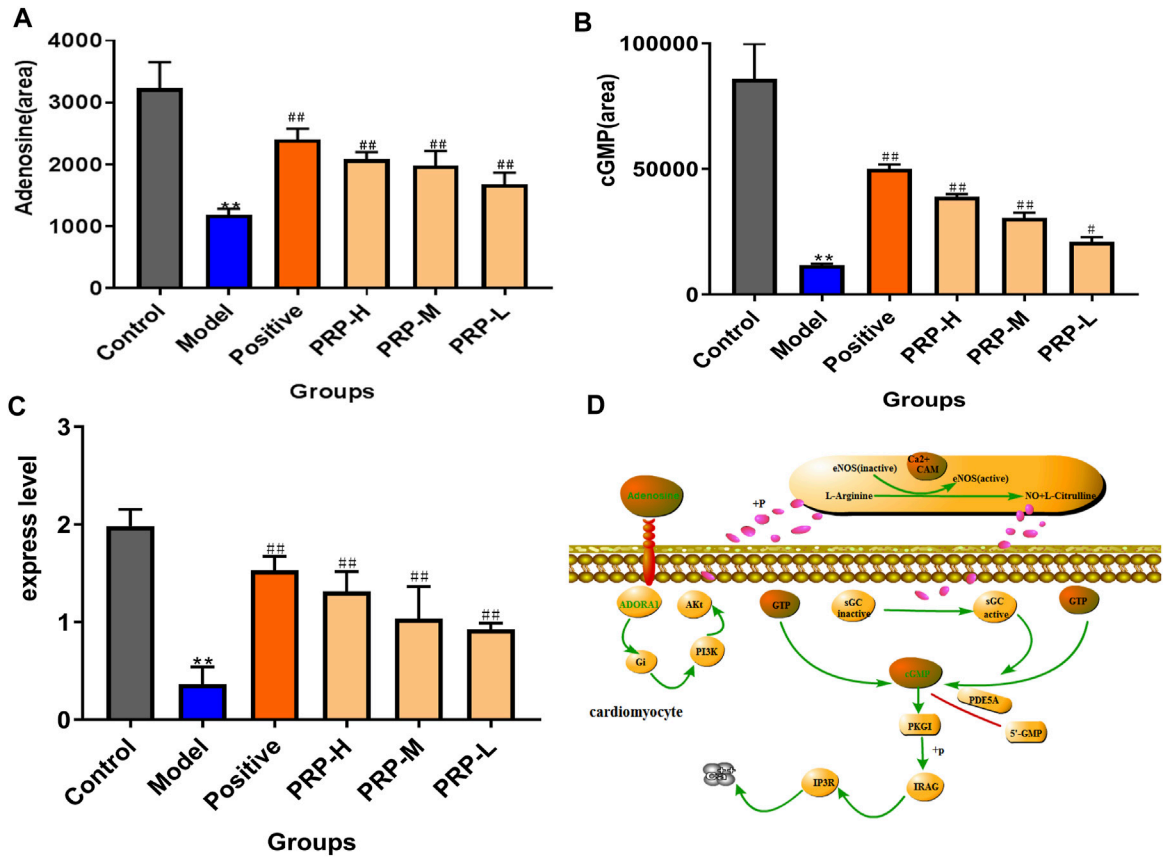

FIGURE 5 | PRP-mediated regulation of the levels of adenosine and cGMP metabolites and the expression level of ADORA1 in the cGMP-PKG signalling pathway. **(A)** Quantitative evaluation of adenosine metabolism; **(B)** quantitative evaluation of cGMP metabolic levels; **(C)** expression levels of ADORA1 in zebrafish determined by reverse transcription polymerase chain reaction; **(D)** ADORA1-mediated cGMP-PKG pathway map.

administration could significantly improve the cardiac congestion area, the SV-BA interval and the degree of myocardial cell apoptosis and promote the normal development of the heart in zebrafish, which further indicated the great potential of PRP for the treatment of arrhythmia. However, due to the complex pathogenesis of arrhythmia and the efficacy characteristics of multicomponent, multitarget and multipathway drugs, it is still a great challenge to explain the mechanism underlying the effects of PRP in the treatment of arrhythmia.

In the analysis of PPI and component-disease-target network pharmacology results, we found that the ADORA1 protein may be the main target in the PRP-based treatment of arrhythmia and that it participates in multiple signalling pathways, such as the cGMP-PKG, cAMP, and cardiac muscle contraction pathways. These pathways all play important roles in heart disease (Zhu et al., 2020). In addition, we verified through PCR that the expression levels of the ADORA1 protein in the PRP-treated groups were significantly higher than those in the model group. Studies have indicated that calcium overload in cardiomyocytes is one of the important causes of arrhythmias and that not only does adenosine affect the intracellular calcium ion current, but adenosine receptors can also cause arrhythmias by affecting calcium ion homeostasis (Greene et al., 2016). Among the adenosine receptors, ADORA1 shows the highest affinity for adenosine, which is mainly distributed in the sinoatrial and atrioventricular nodes and the atrial muscle of the heart and can play a role in myocardial protection by regulating oxygen free radicals, heat shock proteins, interleukins and L-type calcium channels (Goldman et al., 2010). Therefore, we highlight the finding that PRP can significantly restore the high gene expression of ADORA1 and thereby play a role in the treatment of arrhythmia.

In this study, the enrichment analysis of KEGG metabolic pathways showed that PRP can regulate a variety of signalling pathways, including the cGMP-PKG signalling pathway, the adrenergic signalling pathway in cardiomyocytes, and the calcium ion signalling pathway. Among these pathways, the cGMP-PKG signalling pathway showed the highest significance and can be regarded as one of the most critical signalling pathways in the PRP-based treatment of arrhythmia. The results of network pharmacology and metabolomics correlation analysis showed that the cGMP-PKG signalling pathway was the most significant, which was consistent with the network pharmacology prediction results, indicating that PRP may participate in the treatment of arrhythmia by

regulating proteins and metabolites in the cGMP-PKG signalling pathway (**Figure 5D**). The adenosine receptor protein ADORA1 is activated and conjugates with the Gi protein to promote the phosphoinositide 3-kinase/protein kinase B (PI3K/Akt) signalling pathway. Studies have shown that the PI3K/Akt/eNOS signalling pathway has myocardial protective effects, such as antioxidative and antiapoptotic effects (Yao et al., 2014; Zhang and Zhang, 2021). NO is a factor that regulates heart relaxation. Its formation process involves L-arginine and nitric oxide synthase (NOS). Following the catalytic synthesis of NO and L-citrulline, calcium ions enter the cell and bind with calmodulin to form a complex to activate eNOS. The resulting NO diffuses into the intercellular space and crosses the membrane of adjacent target cells to activate SGC and convert GTP into cGMP (Silberman et al., 2010). cGMP activates the most important downstream target, PKG I. Activated PKG I acts on its downstream targets to regulate the inositol triphosphate receptor (IP3R) in cardiomyocytes and increase calcium ion regeneration in the sarcoplasmic reticulum, thereby inhibiting platelet activation, reducing cell apoptosis and exerting a negative inotropic effect on cardiomyocytes to protect the cardiovascular system (Zhang et al., 2007). Studies have also shown that the cGMP-PKG signalling pathway plays an important role in the cardioprotective mechanism of pretreatment and posttreatment. It can prevent cell necrosis-induced stress, reduce cell apoptosis and negative inotropic effects on cardiomyocytes, protect the cardiovascular system and reduce the occurrence of arrhythmias (Yu et al., 2018).

In the cGMP-PKG signalling pathway, the metabolites adenosine and cGMP play extremely important roles. In this study, the levels of adenosine and cGMP in zebrafish with arrhythmia were quantitatively determined after various treatments and were shown to be significantly higher in the PRP-treated groups than in the model group. These findings indicated that PRP could increase adenosine and cGMP metabolism, improve heart shape, and reduce the occurrence of arrhythmia in zebrafish. As an anti-arrhythmic drug, adenosine can induce independent potassium currents in the atrioventricular node, reduce the influx of calcium ions, slow atrioventricular conduction and reduce the occurrence of arrhythmia. Studies have indicated that inflammation and oxidative stress can be reduced by increasing adenosine levels and that drugs with such effects exert a protective effect against myocardial ischaemia-reperfusion injury in mice (Zhao et al., 2020a). The metabolite cGMP can activate protein kinase G to activate phosphodiesterase (PDE), cleave cAMP, inhibit the phosphorylation of muscle fibre membrane proteins, and reduce the intake of calcium ions through the cell membrane, thereby protecting the heart. Studies have shown that after administration, the release of cGMP in the isolated hearts of rats with myocardial ischaemia is increased, which inhibits ischaemia-induced cardiac sympathetic hyperactivity and cardiac electrophysiological instability and attenuates arrhythmia (He et al., 2020). Therefore, we believe that PRP can play a role in the treatment of arrhythmia by increasing the metabolic levels of adenosine and cGMP in the cGMP-PKG pathway.

The main advantage of this study was that we used the methods of network pharmacology and metabolomics correlation analysis to determine the pathways underlying the effects of PRP on arrhythmia and experimentally verified the key target ADORA1 and the main metabolites adenosine and cGMP in the pathway. PRP can interfere with arrhythmia by regulating the protein level of ADORA1 and the metabolic levels of adenosine and cGMP in the cGMP-PKG pathway. The above findings indicated that PRP is a Chinese herbal medicine with great potential for preventing and reducing the occurrence of arrhythmias.

CONCLUSION

This study used network pharmacology and metabolomics correlation analysis to explain the mechanism of PRP in arrhythmia. The results showed that PRP can significantly improve barium chloride-induced zebrafish cardiac congestion, shorten SV-BA spacing, and reduce myocardial apoptosis. By upregulating the expression level of the ADORA1 target and the metabolic levels of adenosine and cGMP in the cGMP-PKG signalling pathway, PRP plays a role in reducing arrhythmia. Therefore, we believe that PRP shows great potential as an adjuvant for the treatment of arrhythmia.

DATA AVAILABILITY STATEMENT

The raw data supporting the conclusions of this article will be made available by the authors, without undue reservation, to any qualified researcher.

ETHICS STATEMENT

The animal study was reviewed and approved by the Laboratory Animal Care and Use Committee of the Shaanxi University of Chinese Medicine.

AUTHOR CONTRIBUTIONS

Y-RL, Z-ST, and J-AD designed the research; N-JY, Y-RL, Y-FY, and Y-TZ performed the main experiments; B-JC, M-LZ, Z-XS, and Y-TZ analysed the data; N-JY and Y-RL wrote the paper.

FUNDING

This study was supported by the Special Support Program for High-Level Personnel Recruitment and the National Youth Talent Support Program supported by Shaanxi Province (No. The Organization Department of CPC Shaanxi Committee Notice (2018) 33), the Key Research and Development

Program of Shaanxi Province (No. 2020ZDLSF05-08), and the Major Project of National Science and Technology on New Drug Creation (2019ZX09301-133).

ACKNOWLEDGMENTS

We acknowledge the support from the Shaanxi Province Key Laboratory of New Drugs and Chinese Medicine Foundation Research and the Shaanxi Collaborative Innovation Center of Chinese Medicinal Resource Industrialization.

SUPPLEMENTARY MATERIAL

The Supplementary Material for this article can be found online at: https://www.frontiersin.org/articles/10.3389/fphar.2021.688746/full#supplementary-material

REFERENCES

Antonio, M., Teresa, C., C, G. M., Valentina, S., and Ida, F. (2017). Neurodegeneration in Zebrafish Embryos and Adults after Cadmium Exposure. *Eur. J. Histochem. : EJH* 61.

Brugada, J., Katritsis, D. G., Arbelo, E., Arribas, F., Bax, J. J., Blomström-Lundqvist, C., et al. (2020). 2019 ESC Guidelines for the Management of Patients with Supraventricular tachycardiaThe Task Force for the Management of Patients with Supraventricular Tachycardia of the European Society of Cardiology (ESC). *Eur. Heart J.* 41, 655–720. doi:10.1093/eurheartj/ehz467

Cassar, S., Adatto, I., Freeman, J. L., Gamse, J. T., Iturria, I., Lawrence, C., et al. (2020). Use of Zebrafish in Drug Discovery Toxicology. *Chem. Res. Toxicol.* 33, 95–118. doi:10.1021/acs.chemrestox.9b00335

Changhe, Z. X. R. L. (2009). Research Progress on Chemical Components and Pharmacological Action of *Poria Cum Radix Pini*. *Progress In the Study of Chemical Constituents and Pharmacological Effects of Fuzia. J. Zhengzhou Coll. Anim. Husbandry Eng.*, 25–27.

Crowcombe, J., Dhillon, S. S., Hurst, R. M., Egginton, S., M Ller, F., Sik, A., et al. (2016). 3D Finite Element Electrical Model of Larval Zebrafish ECG Signals. *PLoS One* 11, e0165655. doi:10.1371/journal.pone.0165655

de Araújo, L. J. T., Nagaoka, M. R., Borges, D. R., and Kouyoumdjian, M. (2018). Participation of Hepatic α/β-adrenoceptors and AT1 Receptors in Glucose Release and portal Hypertensive Response Induced by Adrenaline or Angiotensin II. *Braz. J. Med. Biol. Res.* 51, e7526. doi:10.1590/1414-431X20187526

Deb, P. K., Deka, S., Borah, P., Abed, S. N., and Klotz, K.-N. (2019). Medicinal Chemistry and Therapeutic Potential of Agonists, Antagonists and Allosteric Modulators of A1 Adenosine Receptor: Current Status and Perspectives. *Cpd* 25, 2697–2715. doi:10.2174/1381612825666190716100509

Echeazarra, L., Hortigón-Vinagre, M. P., Casis, O., and Gallego, M. (2020). Adult and Developing Zebrafish as Suitable Models for Cardiac Electrophysiology and Pathology in Research and Industry. *Front. Physiol.* 11, 607860. doi:10.3389/fphys.2020.607860

Goldman, N., Chen, M., Fujita, T., Xu, Q., Peng, W., Liu, W., et al. (2010). Adenosine A1 Receptors Mediate Local Anti-nociceptive Effects of Acupuncture. *Nat. Neurosci.* 13, 883–888. doi:10.1038/nn.2562

Gong, X., Xiong, H., Liu, S., Liu, Y., Yin, L., Tu, C., et al. (2019). Qingpeng Ointment Ameliorates Inflammatory Responses and Dysregulation of Itch-Related Molecules for its Antipruritic Effects in Experimental Allergic Contact Dermatitis. *Front. Pharmacol.* 10, 354. doi:10.3389/fphar.2019.00354

Greene, S. J., Sabbah, H. N., Butler, J., Voors, A. A., Albrecht-Küpper, B. E., Düngen, H.-D., et al. (2016). Partial Adenosine A1 Receptor Agonism: a Potential New Therapeutic Strategy for Heart Failure. *Heart Fail. Rev.* 21, 95–102. doi:10.1007/s10741-015-9522-7

Gut, P., Reischauer, S., Stainier, D. Y. R., and Arnaout, R. (2017). LITTLE FISH, BIG DATA: ZEBRAFISH AS A MODEL FOR CARDIOVASCULAR AND METABOLIC DISEASE. *Physiol. Rev.* 97, 889–938. doi:10.1152/physrev.00038.2016

He, Y., Liu, Y., Zhou, M., Xie, K., Tang, Y., Huang, H., et al. (2020). C-type Natriuretic Peptide Suppresses Ventricular Arrhythmias in Rats with Acute Myocardial Ischemia. *Peptides* 126, 170238. doi:10.1016/j.peptides.2019.170238

Huang, W., Wang, Y., Cao, Y.-G., Qi, H.-P., Li, L., Bai, B., et al. (2013). Antiarrhythmic Effects and Ionic Mechanisms of Allicin on Myocardial Injury of Diabetic Rats Induced by Streptozotocin. *Naunyn-schmiedeberg's Arch. Pharmacol.* 386, 697–704. doi:10.1007/s00210-013-0872-1

Janssens, U., and Michels, G. (2019). Adrenalin bei Patienten mit prähospitalem Herz-Kreislauf-Stillstand. *Med. Klin Intensivmed Notfmed* 114, 63–67. doi:10.1007/s00063-018-0478-y

Jin, M., Ji, X., Zhang, B., Sheng, W., Wang, R., and Liu, K. (2019). Synergistic Effects of Pb and Repeated Heat Pulse on Developmental Neurotoxicity in Zebrafish. *Ecotoxicology Environ. Saf.* 172, 460–470. doi:10.1016/j.ecoenv.2019.01.104

Khisatmutdinova, R. Iu., Baschenko, N. Zh., Zarudiĭ, F. S., Gabdrakhmanova, S. F., Makara, N. S., and Sapozhnikova, T. A. (2006). [Some Aspects of the Antiarrhythmic Effect of Glialin]. *Eksp Klin Farmakol* 69, 26–28.

Kim, J. H., Sim, H. A., Jung, D. Y., Lim, E. Y., Kim, Y. T., Kim, B. J., et al. (2019). Poria Cocus Wolf Extract Ameliorates Hepatic Steatosis through Regulation of Lipid Metabolism, Inhibition of ER Stress, and Activation of Autophagy via AMPK Activation. *Int. J. Mol. Sci.* 20. doi:10.3390/ijms20194801

Krittayaphong, R., Rangsin, R., Thinkhamrop, B., Hurst, C., Rattanamongkolgul, S., Sripaiboonkij, N., et al. (2016). Prevalence and Associating Factors of Atrial Fibrillation in Patients with Hypertension: a Nation-wide Study. *BMC Cardiovasc. Disord.* 16, 57. doi:10.1186/s12872-016-0232-4

Kusumoto, F. M., Bailey, K. R., Chaouki, A. S., Deshmukh, A. J., Gautam, S., Kim, R. J., et al. (2018). Systematic Review for the 2017 AHA/ACC/HRS Guideline for Management of Patients with Ventricular Arrhythmias and the Prevention of Sudden Cardiac Death. *Circulation* 138, e392–e414. doi:10.1161/cir.0000000000000550

Li, F.-F., Yuan, Y., Liu, Y., Wu, Q.-Q., Jiao, R., Yang, Z., et al. (2015). Pachymic Acid Protects H9c2 Cardiomyocytes from Lipopolysaccharide-Induced Inflammation and Apoptosis by Inhibiting the Extracellular Signal-Regulated Kinase 1/2 and P38 Pathways. *Mol. Med. Rep.* 12, 2807–2813. doi:10.3892/mmr.2015.3712

Lin, C., Hui, M., and Cheng, S. (2007). Toxicity and Cardiac Effects of Carbaryl in Early Developing Zebrafish (*Danio rerio*) Embryos. *Toxicol. Appl. Pharmacol.* 222, 159–168. doi:10.1016/j.taap.2007.04.013

Liu, B., Li, S., Su, Y., Xiong, M., and Xu, Y. (2014). Comparative Study of the Protective Effects of Terfenadine and Amiodarone on Barium Chloride/aconitine-Induced Ventricular Arrhythmias in Rats: a Potential Role of Terfenadine. *Mol. Med. Rep.* 10, 3217–3226. doi:10.3892/mmr.2014.2640

Liu, H., Zeng, L., Yang, K., and Zhang, G. (2016). A Network Pharmacology Approach to Explore the Pharmacological Mechanism of Xiaoyao Powder on Anovulatory Infertility. *Evid. Based Complement. Alternat Med.* 2016, 2960372. doi:10.1155/2016/2960372

Liu, Y.-R., Tang, Z.-S., Duan, J.-A., Chen, L., Sun, J., Zhou, R., et al. (2019). ER-depletion Lowering the 'hypothalamus-Uterus-Kidney' axis Functions by Perturbing the Renal ERβ/Ptgds Signalling Pathway. *Aging* 11, 9500–9529. doi:10.18632/aging.102401

Matrone, G., Wilson, K. S., Mullins, J. J., Tucker, C. S., and Denvir, M. A. (2015). Temporal Cohesion of the Structural, Functional and Molecular Characteristics of the Developing Zebrafish Heart. *Differentiation* 89, 117–127. doi:10.1016/j.diff.2015.05.001

Niu, S., Xu, L., Yuan, Y., Yang, S., Ning, H., Qin, X., et al. (2020). Effect of Down-Regulated miR-15b-5p Expression on Arrhythmia and Myocardial Apoptosis after Myocardial Ischemia Reperfusion Injury in Mice. *Biochem. Biophysical Res. Commun.* 530, 54–59. doi:10.1016/j.bbrc.2020.06.111

Qian, Q., Zhou, N., Qi, P., Zhang, Y., Mu, X., Shi, X., et al. (2018). A UHPLC-QTOF-MS/MS Method for the Simultaneous Determination of Eight Triterpene Compounds from Poria Cocos (Schw.) Wolf Extract in Rat

Plasma: Application to a Comparative Pharmacokinetic Study. *J. Chromatogr. B* 1102-1103, 34–44. doi:10.1016/j.jchromb.2018.10.011

Shah, V. K., Choi, J. J., Han, J.-Y., Lee, M. K., Hong, J. T., and Oh, K.-W. (2014). Pachymic Acid Enhances Pentobarbital-Induced Sleeping Behaviors via GABAA-Ergic Systems in Mice. *Biomolecules Ther.* 22, 314–320. doi:10.4062/biomolther.2014.045

Shi, Y.-p., Zhang, Y.-g., Li, H.-n., Kong, H.-t., Zhang, S.-s., Zhang, X.-m., et al. (2020). Discovery and Identification of Antithrombotic Chemical Markers in Gardenia Fructus by Herbal Metabolomics and Zebrafish Model. *J. Ethnopharmacology* 253, 112679. doi:10.1016/j.jep.2020.112679

Silberman, G. A., Fan, T.-H. M., Liu, H., Jiao, Z., Xiao, H. D., Lovelock, J. D., et al. (2010). Uncoupled Cardiac Nitric Oxide Synthase Mediates Diastolic Dysfunction. *Circulation* 121, 519–528. doi:10.1161/circulationaha.109.883777

Szentmiklosi, A. J., Galajda, Z., Cseppento, Á., Gesztelyi, R., Susán, Z., Hegyi, B., et al. (2015). The Janus Face of Adenosine: Antiarrhythmic and Proarrhythmic Actions. *Curr. Pharm. Des.* 21, 965–976. doi:10.2174/1381612820666141029100346

Torrente, A. G., Mesirca, P., Bidaud, I., and Mangoni, M. E. (2020). Channelopathies of Voltage-Gated L-type Cav1.3/α1D and T-type Cav3.1/α1G Ca2+ Channels in Dysfunction of Heart Automaticity. *Pflugers Arch. - Eur. J. Physiol.* 472, 817–830. doi:10.1007/s00424-020-02421-1

Wang, Z., Chen, Z., Wang, X., Zhang, L., Li, S., Tian, Y., et al. (2018). The Disease Burden of Atrial Fibrillation in China from a National Cross-Sectional Survey. *Am. J. Cardiol.* 122, 793–798. doi:10.1016/j.amjcard.2018.05.015

Wu, Z.-L., Ren, H., Lai, W.-Y., Lin, S., Jiang, R.-Y., Ye, T.-C., et al. (2014). Sclederma of Poria Cocos Exerts its Diuretic Effect via Suppression of Renal Aquaporin-2 Expression in Rats with Chronic Heart Failure. *J. Ethnopharmacology* 155, 563–571. doi:10.1016/j.jep.2014.05.054

Xia, J., Psychogios, N., Young, N., and Wishart, D. S. (2009). MetaboAnalyst: a Web Server for Metabolomic Data Analysis and Interpretation. *Nucleic Acids Res.* 37, W652–W660. doi:10.1093/nar/gkp356

Xu, H.-Y., Zhang, Y.-Q., Liu, Z.-M., Chen, T., Lv, C.-Y., Tang, S.-H., et al. (2019). ETCM: an Encyclopaedia of Traditional Chinese Medicine. *Nucleic Acids Res.* 47, D976–d982. doi:10.1093/nar/gky987

Xu, H., Wang, Y., Zhao, J., Jurutka, P. W., Huang, D., Liu, L., et al. (2020). Triterpenes from Poria Cocos Are Revealed as Potential Retinoid X Receptor Selective Agonists Based on Cell and In Silico Evidence. *Chem. Biol. Drug Des.* 95, 493–502. doi:10.1111/cbdd.13610

Yao, H., Han, X., and Han, X. (2014). The Cardioprotection of the Insulin-Mediated PI3K/Akt/mTOR Signaling Pathway. *Am. J. Cardiovasc. Drugs* 14, 433–442. doi:10.1007/s40256-014-0089-9

Yi, Y., Hua, H., Sun, X., Guan, Y., and Chen, C. (2020). Rapid Determination of Polysaccharides and Antioxidant Activity of Poria Cocos Using Near-Infrared Spectroscopy Combined with Chemometrics. *Spectrochimica Acta A: Mol. Biomol. Spectrosc.* 240, 118623. doi:10.1016/j.saa.2020.118623

Yu, G., Wang, L.-G., Han, Y., and He, Q.-Y. (2012). clusterProfiler: an R Package for Comparing Biological Themes Among Gene Clusters. *OMICS: A J. Integr. Biol.* 16, 284–287. doi:10.1089/omi.2011.0118

Yu, L.-m., DI, W.-c., Dong, X., Li, Z., Zhang, Y., Xue, X.-d., et al. (2018). Melatonin Protects Diabetic Heart against Ischemia-Reperfusion Injury, Role of Membrane Receptor-dependent cGMP-PKG Activation. *Biochim. Biophys. Acta (Bba) - Mol. Basis Dis.* 1864, 563–578. doi:10.1016/j.bbadis.2017.11.023

Zhang, J., and Zhang, X. (2021). Ischaemic Preconditioning-induced Serum Exosomes Protect against Myocardial Ischaemia/reperfusion Injury in Rats by Activating the PI3K/AKT Signalling Pathway. *Cell Biochem Funct.* 39, 287–295. doi:10.1002/cbf.3578

Zhang, L., Miao, X., Li, Y., Dai, H., Shang, X., Hu, F., et al. (2020). Toxic and Active Material Basis of Aconitum Sinomontanum Nakai Based on Biological Activity Guidance and UPLC-Q/TOF-MS Technology. *J. Pharm. Biomed. Anal.* 188, 113374. doi:10.1016/j.jpba.2020.113374

Zhang, Q., Scholz, P. M., Pilzak, A., Su, J., and Weiss, H. R. (2007). Role of Phospholamban in Cyclic GMP Mediated Signaling in Cardiac Myocytes. *Cell Physiol Biochem.* 20, 157–166. doi:10.1159/000104163

Zhao, C., Yang, Y., An, Y., Yang, B., and Li, P. (2020a). Cardioprotective Role of Phyllanthin against Myocardial Ischemia-Reperfusion Injury by Alleviating Oxidative Stress and Inflammation with Increased Adenosine Triphosphate Levels in the Mice Model. *Environ. Toxicol.* 36, doi:10.1002/tox.23008

Zhao, J., Niu, X., Yu, J., Xiao, X., Li, W., Zang, L., et al. (2020b). Poria Cocos Polysaccharides Attenuated Ox-LDL-Induced Inflammation and Oxidative Stress via ERK Activated Nrf2/HO-1 Signaling Pathway and Inhibited Foam Cell Formation in VSMCs. *Int. Immunopharmacology* 80, 106173. doi:10.1016/j.intimp.2019.106173

Zhu, D., Zhu, R., Zhou, X., Shi, E., Zhang, X., Zhou, Z., et al. (2020). Exchange Protein Directly Activated by cAMP (Epac) Mediates Cardiac Repolarization and Arrhythmogenesis during Chronic Heart Failure. *Can. J. Physiol. Pharmacol.* 99(7), 729–736. doi:10.1139/cjpp-2020-0122

Conflict of Interest: M-GW was employed by the company Shandong Buchang Pharmaceutical Co. Ltd.

The remaining authors declare that the research was conducted in the absence of any commercial or financial relationships that could be construed as a potential conflict of interest.

Publisher's Note: All claims expressed in this article are solely those of the authors and do not necessarily represent those of their affiliated organizations, or those of the publisher, the editors and the reviewers. Any product that may be evaluated in this article, or claim that may be made by its manufacturer, is not guaranteed or endorsed by the publisher.

Copyright © 2021 Yang, Liu, Tang, Duan, Yan, Song, Wang, Zhang, Chang, Zhao and Zhao. This is an open-access article distributed under the terms of the Creative Commons Attribution License (CC BY). The use, distribution or reproduction in other forums is permitted, provided the original author(s) and the copyright owner(s) are credited and that the original publication in this journal is cited, in accordance with accepted academic practice. No use, distribution or reproduction is permitted which does not comply with these terms.

frontiers in Pharmacology

SYSTEMATIC REVIEW
published: 06 August 2021
doi: 10.3389/fphar.2021.682732

Efficacy and Safety of Chinese Patent Medicine Combined With Oseltamivir in Treatment of Children With Influenza: A meta-Analysis

Nai-fan Duan[1,2†], Bin Liu[1†], Xiao-na Li[1,2], Yi-bai Xiong[1,2], Yan Zhang[1,2], Chi Zhang[3], Li LI[1,2], Cheng Lu[1,2] and Jueni Lyu[4]*

[1]Institute of Basic Research in Clinical Medicine, China Academy of Chinese Medical Science, Beijing, China, [2]China Center for Evidence Based Traditional Chinese Medicine, Beijing, China, [3]Dongzhimen Hospital, Beijing University of Chinese Medicine, Beijing, China, [4]HKU Business School, The University of Hong Kong, Pok Fu Lam, Hong Kong

OPEN ACCESS

Edited by:
Yan Xu,
Cleveland State University,
United States

Reviewed by:
Ambrose Okem,
University of the Witwatersrand, South Africa
Bunleu Sungthong,
Mahasarakham University, Thailand

***Correspondence:**
Cheng Lu
lv_cheng0816@163.com

[†]*These authors have contributed equally to this work.*

Specialty section:
This article was submitted to Ethnopharmacology, a section of the journal Frontiers in Pharmacology

Received: *19 March 2021*
Accepted: *14 June 2021*
Published: *06 August 2021*

Citation:
Duan N, Liu B, Li X, Xiong Y, Zhang Y, Zhang C, LI L, Lu C and Lyu J (2021) Efficacy and Safety of Chinese Patent Medicine Combined With Oseltamivir in Treatment of Children With Influenza: A meta-Analysis. Front. Pharmacol. 12:682732. doi: 10.3389/fphar.2021.682732

Background: Recently, Chinese patent medicines (CPMs) have been widely used to treat children with influenza in China, with curative effects. Therefore, the efficacy and safety of such treatment require further evaluation. The present meta-analysis integrated data from several independent studies to determine overall treatment trends in children with influenza.

Methods: The following databases were searched for randomized controlled trials (RCTs) published from their inception to December 12, 2020: CNKI, Wanfang, SinoMed, PubMed, Cochrane library, and Embase. Two researchers independently extracted the data, assessed the methodological quality of the studies, and conducted a meta-analysis of the results using Review Manager 5.2. The results were assessed using forest plots, and publication bias was evaluated using a funnel plot.

Results: A total of 21 RCTs involving 2960 cases were included. Compared to oseltamivir alone, CPMs combined with oseltamivir reduced the duration of symptoms, including that of fever (mean difference [MD] = −0.64, 95% confidence interval [CI]: −0.86 to −0.41, $P < 0.00001$), cough (MD = −0.82, 95% CI: −1.02 to −0.62, $P < 0.00001$), nasal obstruction (MD = −0.88, 95% CI: −1.15 to −0.61, $P < 0.00001$), and sore throat (MD = −0.92, 95% CI: −1.26 to −0.57, $P < 0.00001$). Combined therapy also reduced the time of viral shedding (MD = −0.53, 95% CI: −0.70 to −0.36, $P < 0.00001$) and the occurrence of adverse drug reactions (ADRs) (RR=0.53, 95% CI: 0.34 to 0.83, $P = 0.005$).

Conclusions: CPMs combined with oseltamivir reduced the duration of symptoms, shortened the time of viral shedding, and reduced the number of ADRs. However, these results should be considered with caution because there was marked heterogeneity and publication bias in the research data. More rigorous RCTs should be designed to verify the effect of CPMs in children with influenza.

Keywords: influenza, children, Chinese patent medicine, oseltamivir, meta-analysis

INTRODUCTION

Influenza is an acute respiratory infectious disease caused by influenza virus. The disease is common worldwide and its main symptoms include fever, cough, nasal congestion, and sore throat (National Health Commission of the People's Republic of China, 2018). During the influenza season, children are particularly vulnerable. According to data from the World Health Organization, the annual incidence of influenza in children ranges from 20 to 30% worldwide. In severe influenza seasons, the annual influenza infection rate in children can be as high as 50% (COMMITTEE ON INFECTIOUS DISEASES, 2018). Generally, children with influenza are treated using oseltamivir, peramivir, or zanamivir, with oseltamivir being the most commonly used (COMMITTEE ON INFECTIOUS DISEASES, 2019). Oseltamivir carboxylate, the active metabolite of oseltamivir, inhibits the neuraminidase activity of influenza virus and reduces transmission by preventing the release of the virus from infected cells. The best effect is achieved when drug treatment is initiated within 24 h of symptom onset. However, influenza virus has gradually developed resistance to oseltamivir (Govorkova et al., 2001; Kiso et al., 2004; Moscona, 2004; Moscona, 2009; Panning, 2013; Lina et al., 2018), and some patients have shown adverse drug reactions (ADRs) (Zhou et al., 2019). Therefore, oseltamivir may not remain a viable treatment for influenza in the long run, and new therapies should be developed to improve influenza treatment in children and reduce the use of antiviral drugs.

In Chinese patent medicines (CPMs), traditional Chinese medicine (TCM) based raw materials are processed into defined dosages and forms according to prescriptions. They are chemically stable; have a definite curative effect with relatively less toxicity and side effects; and can be carried and stored easily (Zhang, 2018). In general, children infected with influenza mostly manifest mild symptoms, such as fever, respiratory symptoms such as cough, sore throat, runny nose, and nasal congestion. A small proportion of children manifest gastrointestinal symptoms, such as nausea, vomiting, and diarrhea. The clinical symptoms of influenza in infants are often atypical. Neonatal influenza is relatively rare, but it can lead to pneumonia and symptoms of sepsis, such as lethargy, refusal to eat, and apnea. Children of different ages present different clinical manifestations at different stages of influenza. Many types of CPMs are used to treat influenza in children at different ages and disease stages (Cao et al., 2015). Such treatments have marked advantages and significant effects, reducing symptoms, shortening the disease course, and reducing complications (Yao et al., 2015; Rong et al., 2017; Wu 2018). Moreover, several RCTs have indicated that CPMs combined with oseltamivir have some curative effects in children with influenza (Xiong et al., 2020). For example, *Xiaoer Chiqiao Qingre* granules are generally used to treat children with symptoms such as fever, cough, nasal congestion, sore throat, and constipation. Evidence shows that *Xiaoer Chiqiao Qingre* granules can improve symptoms in children with acute upper respiratory tract infections and reduce the levels of inflammatory factors in the serum of these children; hence, their use can be promoted in clinical practice (Wang, 2019). Another study has shown that *Xiaoer Chiqiao Qingre* granules have a significant antipyretic effect in children with viral upper respiratory tract infections, quickening symptom improvement and showing high drug safety (Han et al., 2018). In another investigation, *Lianhua Qingwen* granules combined with oseltamivir have been shown to shorten the time to fever resolution, reduce the duration of symptoms. The children tolerated the combined treatment, hence, they can be used in clinical practice (Wang et al., 2020). *Yinqiao San* consists of Chinese medicines, such as *Lonicera japonica* (Thunb) and *Forsythia suspensa* (Thunb, Vahl). Studies have shown that it has inhibitory effects on various viruses. In animal experiments, it slightly protected mice from influenza A virus infection. Among the 17 chemical components separated from *Yinqiao San*, the main antiviral active components were identified as lignans and flavonoids. Specifically, the active components liquiritin and arctiin have relatively weak antiviral effects, reflecting the synergistic effect of TCM prescriptions (Shi et al., 2003). To a certain extent, the above research conclusions provide evidence for the use of CPMs in the treatment of children with influenza.

As the current clinical evidence is relatively scattered, no systematic evidence is available to support the role of CPMs in influenza treatment. The present study gathered and comprehensively evaluated data from clinical trials to increase the level of evidence and, thus, better evaluate the efficacy and safety of CPMs combined with oseltamivir in the treatment of children with influenza. In brief, we conducted a meta-analysis of the available published clinical evidence.

METHODS

Study Registration

This systematic review was registered in the PROSPERO (registration number: CRD42020188184).

Search Strategy

The following databases were searched from their inception to December 12, 2020: CNKI, Wanfang, SinoMed, PubMed, Cochrane library, and Embase. The following terms were searched in the abstract or title of the study (Influenza, Human OR Human Influenzas OR Influenzas, Human OR Influenza OR Influenzas OR Human Flu OR Flu, Human OR Human Influenza OR Influenza in Humans OR Influenza in Human OR Grippe) AND (Medicine, Chinese Traditional OR Traditional Chinese Medicine OR Traditional Medicine, Chinese OR Zhong Yi Xue OR Chinese Traditional Medicine OR Chinese Medicine, Traditional OR Chinese patent medicine OR Chinese Proprietary Medicine) AND (Oseltamivir OR GS 4104 OR GS4104 OR GS-4104 OR Tamiflu OR GS 4071 OR GS4071 OR GS-4071). We also manually searched for studies that met our inclusion criteria from other sources that were not included in the aforementioned databases. Two researchers (Duan N. F. and Liu B.) independently selected the eligible studies. The studies were retrieved in any language.

Inclusion and Exclusion Criteria

This systematic review was conducted according to the Preferred Reporting Items for Systematic Review and Meta-Analysis Statement (Moher et al., 2009). The inclusion criteria were as follows: 1) RCT study design; 2) patient age >1 year and <14 years (Cao et al., 2015; Geneva, 2017); 3) treatment group treated using oral CPMs combined with oseltamivir and control group treated with oseltamivir alone; 4) main outcome of time to fever resolution; secondary outcomes of duration of cough, nasal congestion, and sore throat and time of viral shedding; and safety outcome of any ADR; 5) meeting the influenza diagnostic criteria as follows: fever accompanied by acute respiratory symptoms, such as cough, nasal congestion, or sore throat, and positive nucleic acid test results; 6) time of <48 h from symptom onset to randomization (Ma et al., 2015); 7) twice daily oral oseltamivir dosage of 30 mg in patients weighing <15 kg, 45 mg in those weighing 15–23 kg, 60 mg in those weighing 24–40 kg, and 75 mg in those weighing >41 kg; 8) treatment course of 3–7 days (Cao et al., 2015). The exclusion criteria were as follows: 1) other antiviral drugs; 2) CPM injections; 3) outcome data format that failed to meet the requirements of the statistical analysis; 4) missing data on the key outcome of time to fever resolution.

Data Extraction and Risk of Bias Assessment

According to standard information extraction tables, two researchers (Duan N. F. and Liu B.) independently extracted the data. Throughout the process, disagreements were resolved by discussion or by involving another researcher (Lu C.). The basic information extracted from the articles included data on authors' names, publication year, published region, type of study design, virus detection results, number of cases, age, time from symptom onset to randomization, course of treatment, randomization method, patient blinding method, researcher blinding method, inclusion and exclusion criteria, diagnostic criteria, efficacy evaluation criteria, therapeutic schedule, outcome indicators, and ADRs.

Two reviewers (Duan N. F. and Liu B.) independently assessed the risk of bias in each study using the criteria outlined in the Cochrane Handbook, (2019). Any disagreements were resolved by discussion or by involving another author (Lu C.). The risk of bias was assessed according to the following domains: 1) random sequence generation; 2) attrition bias; 3) allocation concealments; 4) blinding of participants and personnel; 5) blinding of outcome assessment; 6) incomplete outcome data; 7) selective outcome reporting; 8) other biases. Each potential source of bias was graded as high, low, or unclear, providing a quote from the study report and a justification of our judgment in the "risk of bias" table. In the table, red represents high risk, yellow represents unclear risk, and green represents low risk. We also added notes in the table when information on the risk of bias was related to unpublished data or correspondence with a trial author. When evaluating treatment effects, we considered the risk of bias in studies that contributed to the outcome.

Data Synthesis and Analysis

Review Manager 5.2 software was used to produce the risk of bias summary and calculate a summary statistic for each outcome in the meta-analysis. Risk ratios (RRs), Mantel–Haenszel tests, and 95% confidence intervals (CI) were used to analyze dichotomous data. Mean difference (MD), inverse variance, and 95% CI were used to determine continuous variables. The I^2 values ranged from 0 to 100% and were categorized as follows: I^2 <40%, might

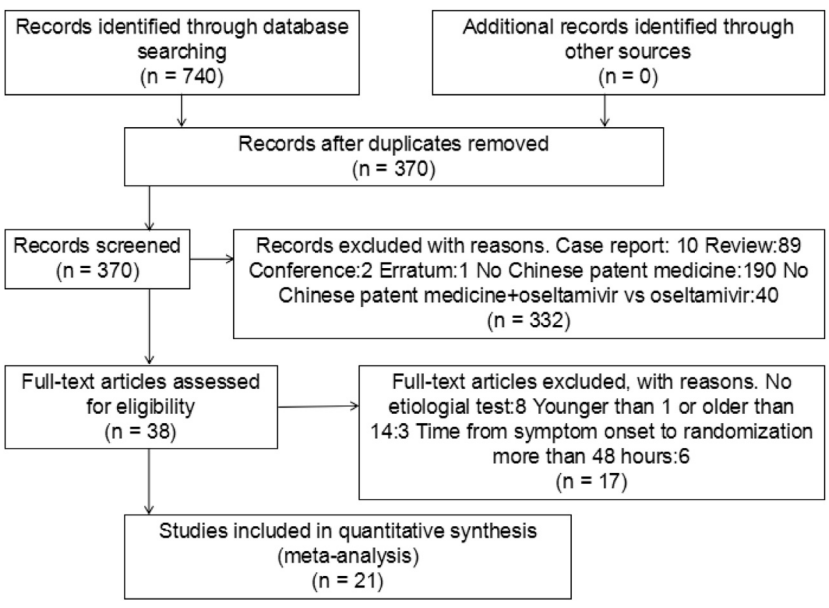

FIGURE 1 | Flow chart of including and excluding studies.

TABLE 1 | Characteristics of included studies.

Study year region	Type	Types of Chinese patent medicine	Influenza virus	Cases (Treatment group/ Control group)	Age (Treatment group/ Control group)	Time from symptom onset to randomization (h)	Dosage		Course of treatment	Outcomes	Adverse reactions	
							CPMs	Oseltamivir			Treatment group	Control group
Song (2018) China	RCT	Xiaoer Chiqiao Qingre Granules	+	68/60	1~14(6.93 ± 4.26)/ 1~14(5.13 ± 4.82)	2~48(15.31 ± 9.54)/2~ 48(13.22 ± 7.21)	1~3 years old, 2~3 g/time; 4~6 years old, 3~4 g/time; 7~9 years old, 4~5 g/time; >10 years old, 6 g/time; 3 times/d	<15 kg 30 mg/time, 15~23 kg 45 mg/time, 24~40 kg 60 mg/time, >41 kg 75 mg/time, 2 times/d	5	A13	NA	NA
Zhang (2018) China	RCT	Xiaoer Chiqiao Qingre Granules	+	46/46	1~12(7 ± 2.6)/1~12(6.4 ± 2.5)	(18.4 ± 7)/(19 ± 7.2)	1~3 years old, 2~3 g/time; 4~6 years old, 3~4g/time; 7~9 years old, 4~5 g/time; >10 years old, 6 g/time; 3 times/d	<15 kg 30 mg/time, 15~23 kg 45 mg/time, 24~40 kg 60 mg/time, >41 kg 75 mg/time, 2 times/d	5	A1235	3 cases of nausea,vomiting and diarrhea	3 cases of nausea,vomiting and diarrhea 2 cases of diarrhea
Zhangy (2018) China	RCT	Xiaoer Chiqiao Qingre Granules	+	57/57	1~12(3.5 ± 0.53)/ 1~12(3.5 ± 0.53)	(36.96 ± 10.08)/ (36.96 ± 10.08)	1~3 years old, 2 g/time; 4~6 years old, 4 g/time; 7~9 years old, 5 g/time; >10 years old, 6 g/time; 3 times/d	<15 kg 30 mg/time, 15~23 kg 45 mg/time, 24~40 kg 60 mg/time, >41 kg 75 mg/time, 2 times/d	5	A	NA	NA
Su (2011) China	RCT	Xiaoer Chiqiao Qingre Granules	+	53/53	1~12(6.7 ± 3.2)/1~13(6.9 ± 3.1)	5~35(19.5 ± 3.8)/ 7~36(19.8 ± 3.6)	<3 years old 2 g/ time, 3~6 years old 3 g/time, 7~10 years old 4 g/time, >11 years old 6 g/ time, 3 times/d	<15 kg 30 mg/time, 15~2 3kg 45 mg/time, 24~40 kg 60 mg/time, >41 kg 75 mg/time, 2 times/d	5	A12	NA	NA
Yin (2011) China	RCT	Xiaoer Chiqiao Qingre Granules	+	30/30	1~10(5.2 ± 1.3)/1~9(4.9 ± 1.6)	6~35/6~32	1~3 years old, 2~3 g/time, 4~6 years old, 3~4 g/time, 7~9 years old, 4~5 g/ time, >10 years old, 6 g/time, 3 times/d	<15 kg 30 mg/time, 15~23 kg 45 mg/time, 24~40 kg 60 mg/time, >41 kg 75 mg/time, 2 times/d	5	A135	1 case of nausea and vomiting. 1 case of abdominal pain	2 cases of nausea and vomiting. 1 case of diarrhea

(Continued on following page)

TABLE 1 | (*Continued*) Characteristics of included studies.

Study year region	Type	Types of Chinese patent medicine	Influenza virus	Cases (Treatment group/ Control group)	Age (Treatment group/ Control group)	Time from symptom onset to randomization (h)	Dosage		Course of treatment	Outcomes	Adverse reactions	
							CPMs	Oseltamivir			Treatment group	Control group
Zhou (2019) China	RCT	Xiaoer Chiqiao Qingre Granules	+	118/118	1~12(6.5 ± 0.7)/1~12 (6.8 ± 0.5)	3~47(22.8 ± 3.5)/ 4~48(22.5 ± 3.7)	<3 years old, 2~3 g/time; 3~6 years old, 3~4 g/time; 6~10 years old, 4~5 g/time; >10 years old, 6 g/time, 3 times/d	<15 kg 30 mg/time, 15~23 kg 45 mg/time, 24~40 kg 60 mg/time, >41 kg 75 mg/time, 2 times/d	5	A45	2 cases of nausea and vomiting. 2 cases of abdominal pain	4 cases of nausea and vomiting. 4 cases of abdominal pain. 2 cases of diarrhea
Zhau (2019) China	RCT	Xiaoer Chiqiao Qingre Granules	+	75/75	1~14(7.2 ± 3.5)/1~13(7.8 ± 4.1)	7~37(19.67 ± 9.56)/9~36(19.28 ± 8.97)	1~3 years old, 2~3 g/time, 4~6 years old, 3~4 g/time, 7~9 years old, 4~5 g/time, >10 years old, 6 g/time, 3 times/d	<15 kg 30 mg/time, 15~23 kg 45 mg/time, 24~40 kg 60 mg/time, >41 kg 75 mg/time, 2 times/d	5	A125	3 cases of nausea and vomiting. 1 case of abdominal pain. 2 cases of diarrhea	4 cases of nausea and vomiting. 3 cases of abdominal pain. 1 case of diarrhea
Long (2020) China	RCT	Xiaoer Chiqiao Qingre Granules	+	92/92	(6.5 ± 0.7)/ (6.4 ± 0.9)	(19.06 ± 0.61)/ (19.16 ± 0.51)	1~3 years old, 2~3 g/time, 4~6 years old, 3~4 g/time, 7~9 years old, 4~5 g/time, >10 years old, 6 g/time, 3 times/d	<15 kg 30 mg/time, 15~23 kg 45 mg/time, 24~40 kg 60 mg/time, >41 kg 75 mg/time, 2 times/d	5	A1235	1 case of nausea. 1case of vomiting. 1 case of diarrhea	2 cases of nausea. 1 case of vomiting. 1 case of diarrhea. 1 case of abdominal pain
Liu (2020) China	RCT	Xiaoer Chiqiao Qingre Granules	+	69/69	1~13(7.4 ± 1.9)/1~11(7.3 ± 1.8)	7~42(18.6 ± 4.4)/ 6~39(18.3 ± 4.2)	1~3 years old, 2~3 g/time, 4~6 years old, 3~4 g/time, 7~9 years old, 4~5 g/time, >10 years old, 6 g/time, 3 times/d	<15 kg 30 mg/time, 15~23 kg 45 mg/time, 24~40 kg 60 mg/time, >41 kg 75 mg/time, 2 times/d	5	A1235	2 cases of nausea. 1 case of diarrhea	2 cases of nausea. 2 cases of diarrhea
Qian (2020) China	RCT	Xiaoer Chiqiao Qingre Granules	+	50/50	2~12(7.2 ± 1.2)/1~12(7.4 ± 1.2)	<48/<48	1~3 years old, 2~3 g/time, 4~6 years old, 3~4 g/time, 7~9 years old, 4~5 g/time, >10 years old, 6 g/time, 3 times/d	<15 kg 30 mg/time, 15~23 kg 45 mg/time, 24~40 kg 60 mg/time, >41 kg 75 mg/time, 2 times/d	5	A125	1 case of nausea and vomiting. 1 case of abdominal pain	4 cases of nausea and vomiting. 3 cases of abdominal pain. 1 case of diarrhea

(Continued on following page)

TABLE 1 | (*Continued*) Characteristics of included studies.

Study year region	Type	Types of Chinese patent medicine	Influenza virus	Cases (Treatment group/ Control group)	Age (Treatment group/ Control group)	Time from symptom onset to randomization (h)	Dosage		Course of treatment	Outcomes	Adverse reactions	
							CPMs	Oseltamivir			Treatment group	Control group
Wu (2020) China	RCT	Xiaoer Chiqiao Qingre Granules	+	33/32	1~13(6.7 ± 2.1)/1~12(6.6 ± 2.1)	7~35(21.2 ± 4.1)/ 7~35(21.2 ± 4.1)	1~3 years old, 2~3 g/time, 4~6 years old, 3~4 g/time, 7~9 years old, 4~5 g/time, >10 years old, 6 g/time, 3 times/d	<15 kg 30 mg/time, 15~23 kg 45 mg/time, 24~40 kg 60 mg/time, >41 kg 75 mg/time, 2 times/d	5	A235	1 case of nausea. 1 case of diarrhea	3 cases of nausea. 5 cases of diarrhea
Chen (2019) China	RCT	Kanggan Granules	+	31/31	1~14/1~14	3~45(22.1 ± 6.0)/ 5~48(22.8 ± 6.3)	1~5 years old, 2.5 g/time, 6~9 years old, 5 g/time, 10~14 years old, 7.5 g/time,3 times/d	<15 kg 30 mg/time, 15~23 kg 45 mg/time, 24~40 kg 60 mg/time, >41 kg 75 mg/time, 2 times/d	5	A	NA	NA
Li (2019) China	RCT	Kanggan Granules	+	193/193	2~6/2~6	<48/<48	1~5 years old, 2.5 g/time, 6~9 years old, 5 g/time, 3 times/d	<15 kg 30 mg/time, 15~23 kg 45 mg/time, 24~40 kg 60 mg/time, >41 kg 75 mg/time, 2 times/d	5	A	NA	NA
Yan (2020) China	RCT	Kanggan Granules	+	45/45	1~10(5.15 ± 2.19)/1~11 (5.19 ± 2.1)	3~43(23.52 ± 4.81)/3~45(23.82 ± 4.83)	1~3 years old, 2.5 g/time, 4~7 years old, 5 g/time, 8~11 years old, 7.5 g/time,3 times/d	<15 kg 30 mg/time, 15~23 kg 45 mg/time, 24~40 kg 60 mg/time, >41 kg 75 mg/time, 2 times/d	7	23	NA	NA
Zhu (2019) China	RCT	Lianhua Qingwen Granules	+	110/110	3~13(9.10 ± 2.06)/ 3~14(9.03 ± 2.12)	4~48(22.08 ± 9.52)/3~46(21.35 ± 9.64)	≤23 kg 3 g/time, >23 kg 6 g/time, 3 times/d	<15 kg 30 mg/time, 15~23 kg 45 mg/time, 24~40 kg 60 mg/time, >41 kg 75 mg/time, 2 times/d	3	A134	NA	NA

(Continued on following page)

TABLE 1 | (*Continued*) Characteristics of included studies.

Study year region	Type	Types of Chinese patent medicine	Influenza virus	Cases (Treatment group/ Control group)	Age (Treatment group/ Control group)	Time from symptom onset to randomization (h)	Dosage		Course of treatment	Outcomes	Adverse reactions	
							CPMs	Oseltamivir			Treatment group	Control group
Liu 2020 China	RCT	Lianhua Qingwen Granules	+	34/34	(4.78 ± 1.39)/ (4.76 ± 1.33)	(19.64 ± 4.72)/ (18.65 ± 4.32)	1~6 years old, 3 g/ time,6~8 years old, 6 g/time, 3 times/d	<15 kg 30 mg/time, 15~23 kg 45 mg/time, 24~40 kg 60 mg/time, 2 times/d	7	A13	NA	NA
Fang (2018) China	RCT	Xiaoer Resuqing Granules	+	66/65	2~12 (5.81 ± 2.73)/2~12 (5.63 ± 2.95)	1~46(20.45 ± 12.77)/1~46 (18.78 ± 10.52)	1~3 years old, 1~2 g/time, 4~6 years old, 2~3 g/time, 7~12 years old, 3~4 g/time, 3~4 times/d	<15 kg 30 mg/time, 15~23 kg 45 mg/time, 24~40 kg 60 mg/time, >41 kg 75 mg/time, 2 times/d	3	A	NA	NA
Liu (2018) China	RCT	Xiaoer Resuqing oral liquid	+	85/85	2~11(6.54 ± 2.22)/ 1~12(6.57 ± 2.19)	4~37(19.26 ± 3.49)/6~35(19.31 ± 3.54)	1~3 years old, 1~2 g/time, 4~7 years old, 2~3 g/time, 8~12 years old, 3~4 g/time, 3 times/d	<15 kg 30 mg/time, 15~23 kg 45 mg/time, 24~40 kg 60 mg/time, >41 kg 75 mg/time, 2 times/d	7	1234	NA	NA
Gao (2020) China	RCT	Xiaoer Shuanghuanglian Mixture	+	45/45	3~10(5.1 ± 2.4)/2~11(5.3 ± 2.0)	12~48(28.8 ± 2.4) 7.2~48(31.2 ± 4.8)	1~3 years old, 10 ml/time, >3 years old, 20 ml/time, 3 times/d	<15 kg 30 mg/time, 15~23 kg 45 mg/time, 24~40 kg 60 mg/time, >41 kg 75 mg/time, 2 times/d	7	A15	1 case of abdominal distension 1 case of skin pruritus	1 case of diarrhea
Kuang (2020) China	RCT	Siji Kangbingdu Mixture	+	110/110	1~12(6.50 ± 3.41)/ 1~12(6.49 ± 3.39)	2~48(25.44 ± 8.20)/3~48(25.47 ± 8. 21)	<2 years old, 3~5 ml/time, 2~5 years old, 5 ml/time, 5~7 years old, 5~10 ml/time, >7 years old, 10~20 ml/time, 3 times/d	<15 kg 30 mg/time, 15~23 kg 45 mg/time, 24~40 kg 60 mg/time, >41 kg 75 mg/time, 2 times/d	5	A12	NA	NA

(Continued on following page)

TABLE 1 | (*Continued*) Characteristics of included studies.

Study year region	Type	Types of Chinese patent medicine	Influenza virus	Cases (Treatment group/ Control group)	Age (Treatment group/ Control group)	Time from symptom onset to randomization (h)	Dosage		Course of treatment	Outcomes	Adverse reactions	
							CPMs	Oseltamivir			Treatment group	Control group
Du (2020) China	RCT	Xiaoer Niuhuang Qingxin Powder	+	75/75	2~6(3.8 ± 2.46)/ 2~6(3.69 ± 2.17)	8~45(18.05 ± 6.17)/6~48 (18.33 ± 6.29)	<1 years old, 0.15 g/time, 1~3 years old, 0.3 g/time, 3~8 years old, 0.45 g/time, 2 times/d	<15 kg 30 mg/time, 15~23 kg 45 mg/time, 24~40 kg 60 mg/time, >41 kg 75 mg/time, 2 times/d	5	A123	NA	NA

Notes:
The "+" means positive for the influenza virus.
The outcomes are time of defervescence, the easing time of cough, the easing time of nasal obstruction, the easing time of sore throat, the time of viral shedding and adverse reactions, that are denoted by "A" "1" "2" "3" "4" and "5" respectively.

not be important; 30% < I^2 <60%, moderate heterogeneity; 50% <I^2 <90%, substantial heterogeneity; and 75% < I^2 <100%, considerable heterogeneity (Higgins and Green, 2011). A fixed-effect model was used to pool the estimates. Potential sources of heterogeneity were identified using subgroup and sensitivity analyses. A random effects model was used to aggregate the results and, thus, minimize potential clinical heterogeneity. Differences were considered statistically significant at *p*-values of <0.05. We conducted a subgroup analysis of each CPM (Chinese patent medicine). The results are presented as forest plots. A funnel chart was used to analyze publication bias.

RESULTS

Search Results and Study Characteristics

A total of 740 studies were identified using the search strategy, including 160 from CNKI, 284 from Wanfang, 194 from SinoMed, 14 from PubMed, 4 from the Cochrane library, and 84 from embase. Of these 370 duplicate studies were excluded, and 332 more studies were excluded after abstract review. Of the remaining 38 studies, 17 were excluded after full text review. Ultimately, 21 RCTs involving 2,960 cases were included (Song and Zhang, 2018; Zhang, B. Y. et al., 2018; Zhang, Y. H. et al., 2018; Su, 2019; Yin, 2019; Zhou, 2019; Zhao et al., 2019; Long, 2020; Liu, 2020; Qian, 2020; Wu, 2020; Chen et al., 2019; Li, 2019; Yan, 2020; Zhu et al., 2019; Liu et al., 2020; Fang, 2018; Liu, 2018; Gao and Wang, 2020; Kuang and Wang, 2020; Du et al., 2020). The flowchart of the screening process is presented in **Figure 1**. Two researchers independently extracted the data from the literature. There were 1,485 and 1,475 cases in the treatment and control groups, respectively. All 21 RCTs were published in China and included seven kinds of CPMs: *Xiaoer Chiqiao Qingre* granules, *Kanggan* granules, *Lianhua Qingwen* granules, *Xiaoer Resuqing* granules (oral liquid), *Xiaoer Shuanghuanglian* mixture, *Siji Kangbingdu* mixture, and *Xiaoer Niuhuang Qingxin* powder. The data were published between 2018 and 2020. All cases tested positive for influenza virus. The treatment course was 3–7 days. Nine studies reported ADRs (Zhang, B. Y. et al., 2018; Yin, 2019; Zhou, 2019; Zhao et al., 2019; Long, 2020; Liu, 2020; Qian, 2020; Wu, 2020; Gao and Wang, 2020). The baseline characteristics were consistent across the studies. The detailed characteristics of the studies are presented in **Table 1**.

Methodological Quality Assessment

Assessment of the risk of bias in the 21 trials (**Figure 2**) showed that all studies implemented randomized grouping, 12 trials used random number tables, while the remaining nine trials did not report a specific random allocation method. One study (Zhou, 2019) used a blinding method, but it was unclear whether single or double blinding was implemented. The remaining studies did not provide blinding information. Regarding allocation concealment, 12 studies used a random number table method (Zhang, B. Y. et al., 2018; Su, 2019; Zhao et al., 2019; Long, 2020; Chen et al., 2019; Zhu et al., 2019; Liu et al., 2020; Fang, 2018; Liu, 2018; Gao and Wang, 2020; Kuang and Wang, 2020; Du et al.,

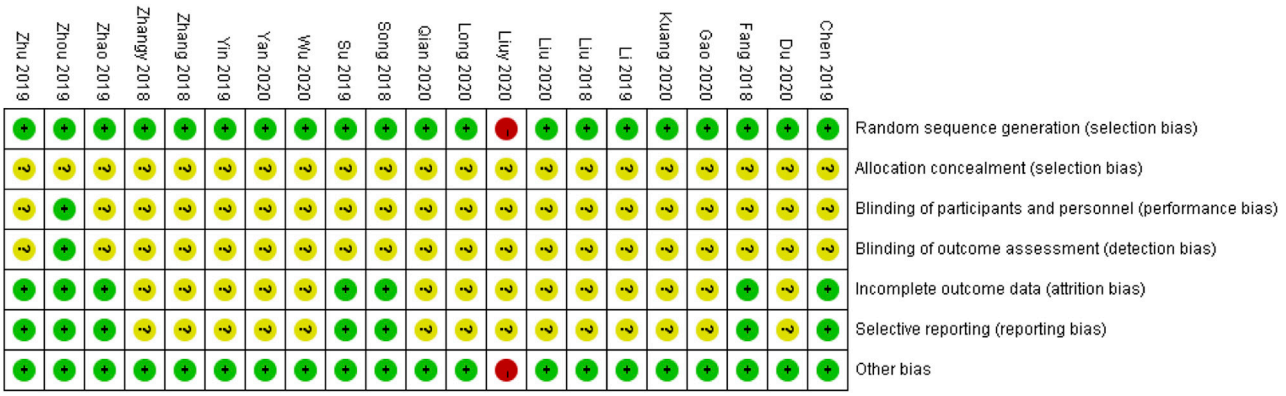

FIGURE 2 | Assessment of risk of bias in the 21 trials.

2020), but it was unclear whether the randomly assigned researchers and allocation concealment researchers were third-party personnel. Therefore, the studies were rated as having an unclear risk. The remaining studies were also rated as having an unclear risk. With regard to incomplete outcome data and selective reporting, seven studies reported the results according to preset outcome indicators and were, thus, rated as having a low risk (Fang, 2018; Song and Zhang, 2018; Chen et al., 2019; Su, 2019; Zhao et al., 2019; Zhou, 2019; Zhu et al., 2019). The remaining studies failed to clarify whether the outcome indicators were established in advance and were, therefore, rated as having an unclear risk. With regard to other biases, one study was suspected of reporting plagiarized data and, therefore, was rated as having a high risk. The remaining studies showed no obvious other biases and, thus, were rated as having a low risk.

Primary Outcome

Time to Fever Resolution

Nineteen studies involving 2,700 cases reported the time to fever resolution (Song and Zhang, 2018; Zhang, B. Y. et al., 2018; Zhang, Y. H. et al., 2018; Su, 2019; Yin, 2019; Zhou, 2019; Zhao et al., 2019; Long, 2020; Liu, 2020; Qian, 2020; Wu, 2020; Chen et al., 2019; Li, 2019; Zhu et al., 2019; Liu et al., 2020; Fang, 2018; Gao and Wang, 2020; Kuang and Wang, 2020; Du et al., 2020). The forest plot showed significant differences between the treatment and control groups (MD = −0.64, 95% CI: 0.86 to −0.41, $p < 0.00001$; **Figure 3**). The heterogeneity was high (I^2 = 99%, $p < 0.00001$). A random effects model was used to analyze the data.

Secondary Outcomes

Duration of Cough

Fourteen studies involving 1876 cases reported the duration of cough (Song and Zhang, 2018; Zhang, B. Y. et al., 2018; Su, 2019; Yin, 2019; Zhao et al., 2019; Long, 2020; Liu, 2020; Qian, 2020; Zhu et al., 2019; Liu et al., 2020; Liu, 2018; Gao and Wang, 2020; Kuang and Wang, 2020; Du et al., 2020). The forest plot (**Figure 4**) showed significant differences between the treatment and control groups (MD = −0.82, 95% CI: 1.02 to −0.62, $p < 0.00001$), and the heterogeneity was high ($p < 0.00001$, I^2 = 94%). The random effects model was used to analyze the data.

Duration of Nasal Congestion

Eleven studies involving 1,245 cases reported the duration of nasal congestion (Zhang, B. Y. et al., 2018; Su, 2019; Zhao et al., 2019; Long, 2020; Liu, 2020; Qian, 2020; Wu, 2020; Yan, 2020; Liu, 2018; Kuang and Wang, 2020; Du et al., 2020). The forest plot (**Figure 5**) showed significant differences between the treatment and control groups (MD = −0.88, 95% CI: 1.15 to −0.61, $p < 0.00001$), and the heterogeneity was high (I^2 = 96%, $p < 0.00001$). The random effects model was used to analyze the data.

Duration of Sore Throat

Eleven studies involving 1,365 cases reported the duration of sore throat (Song and Zhang, 2018; Zhang, B. Y. et al., 2018; Yin, 2019; Long, 2020; Liu, 2020; Wu, 2020; Yan, 2020; Zhu et al., 2019; Liu, 2020; Liu, 2018; Du et al., 2020). The forest plot (**Figure 6**) showed significant differences between the treatment and control groups (MD = −0.92, 95% CI: 1.26 to −0.57, $p < 0.00001$), and the heterogeneity was high (I^2 = 98%, $p < 0.00001$). The random effects model was used to analyze the data.

Time of Viral Shedding

Three studies involving 626 cases reported the time of viral shedding (Liu, 2018; Zhou, 2019; Zhu et al., 2019). The forest plot (**Figure 7**) showed significant differences between the treatment and control groups (MD = −0.53, 95% CI: 0.70 to −0.36, $p < 0.00001$). The heterogeneity was low (I^2 = 15%, p = 0.31); therefore, we used the fixed effects model to analyze the data.

Safety Analysis: ADRs

Nine studies involving 1,115 cases reported ADRs (Zhang, B. Y. et al., 2018; Yin, 2019; Zhou, 2019; Zhao et al., 2019; Long, 2020; Liu, 2020; Qian, 2020; Wu, 2020; Gao and Wang, 2020). The forest plot (**Figure 8**) showed significant differences between the treatment and control groups (RR = 0.53, 95% CI: 0.34 to 0.83, p = 0.005). There was no heterogeneity (I^2 = 0%, p = 0.81); therefore, we used the fixed effects model to analyze the data.

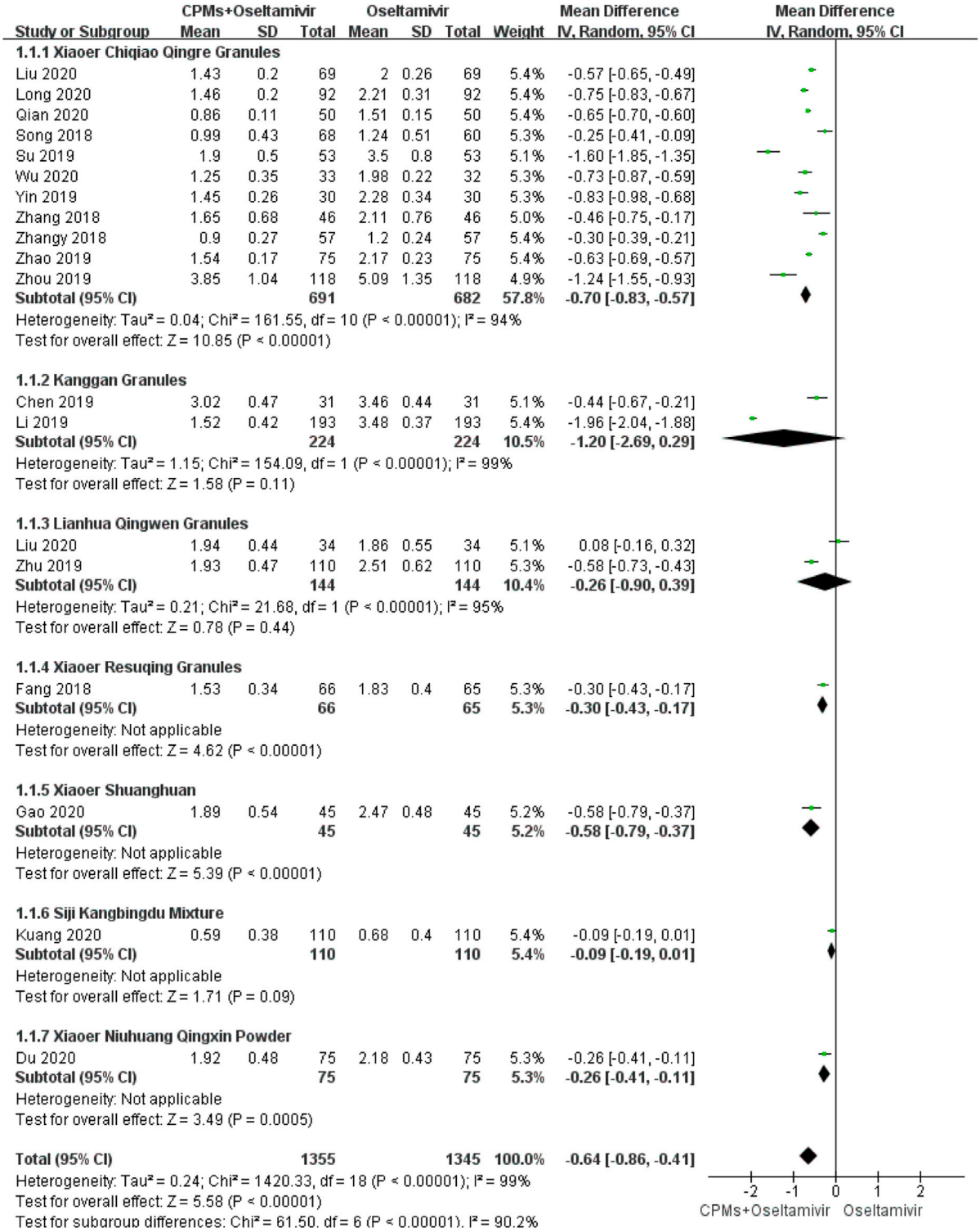

FIGURE 3 | Forest plot of time to fever resolution.

Subgroup Analysis

We conducted a subgroup analysis of each CPM. There were subgroup differences in terms of time to fever resolution (90.2%), duration of cough (92.4%), nasal congestion (93%), and sore throat (81.5%). Regarding time to fever resolution, 11 studies were included in the *Xiaoer Chiqiao Qingre* granules subgroup, with 94% heterogeneity within the subgroup, two studies were included in the *Kanggan* granules subgroup, with 99%

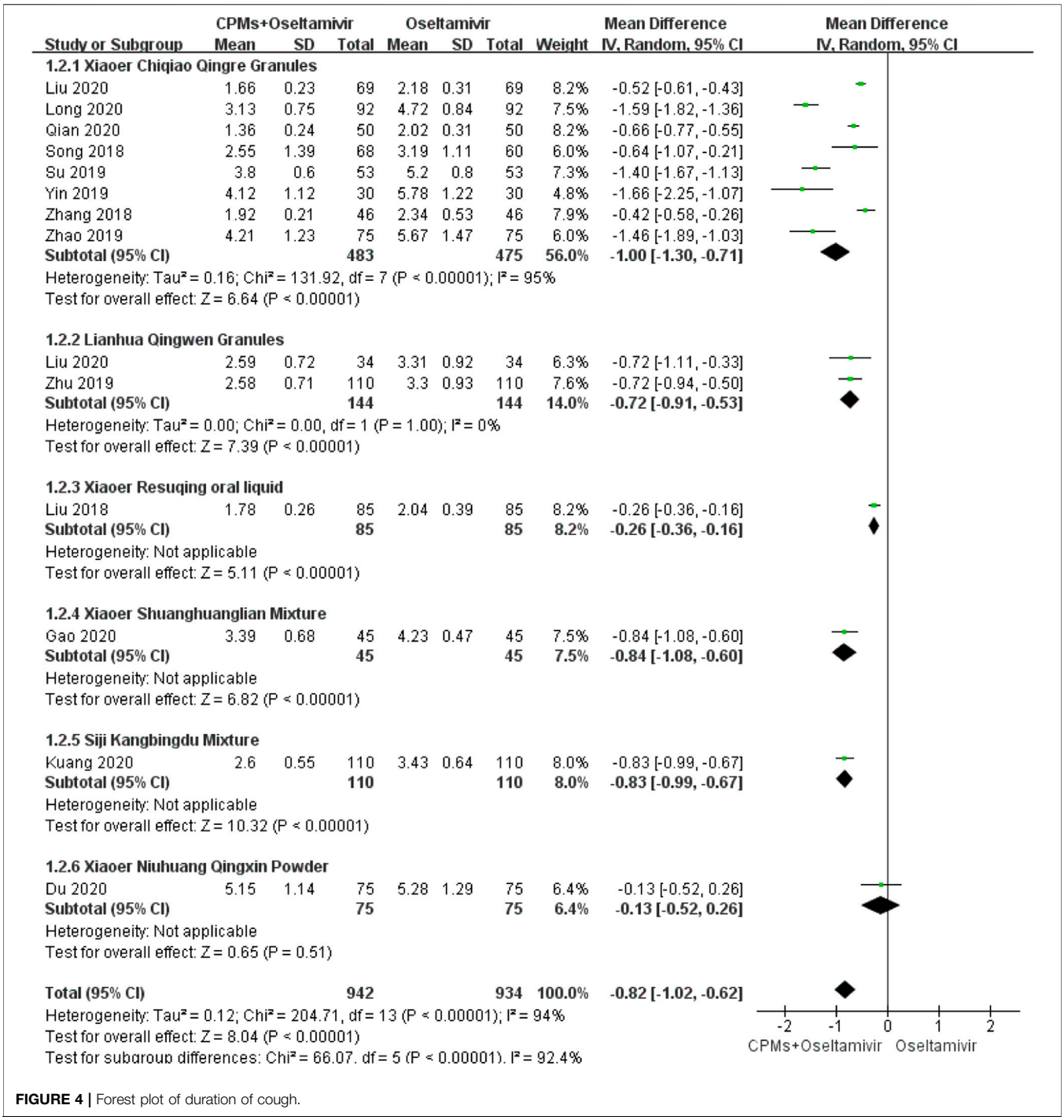

FIGURE 4 | Forest plot of duration of cough.

heterogeneity within the subgroup, and two were included in the *Lianhua Qingwen* granules subgroup, with 99% heterogeneity within the subgroup. Regarding duration of cough, eight studies were included in the *Xiaoer Chiqiao Qingre* granules subgroup, with 95% heterogeneity within the subgroup, and two studies were included in the *Lianhua Qingwen* granules subgroup, with 0% heterogeneity within the subgroup. Regarding duration of nasal congestion, seven studies were included in the *Xiaoer Chiqiao Qingre* granules subgroup, with 96% heterogeneity within the subgroup. Regarding duration of sore throat, six studies were included in the *Xiaoer Chiqiao Qingre* granules subgroup, with 99% heterogeneity within the subgroup. The remaining subgroups had only one study each, hence, within-group heterogeneity could not be analyzed.

Sensitivity Analysis

Sensitivity analysis was performed to investigate potential sources of heterogeneity by observing changes in data after deletion of

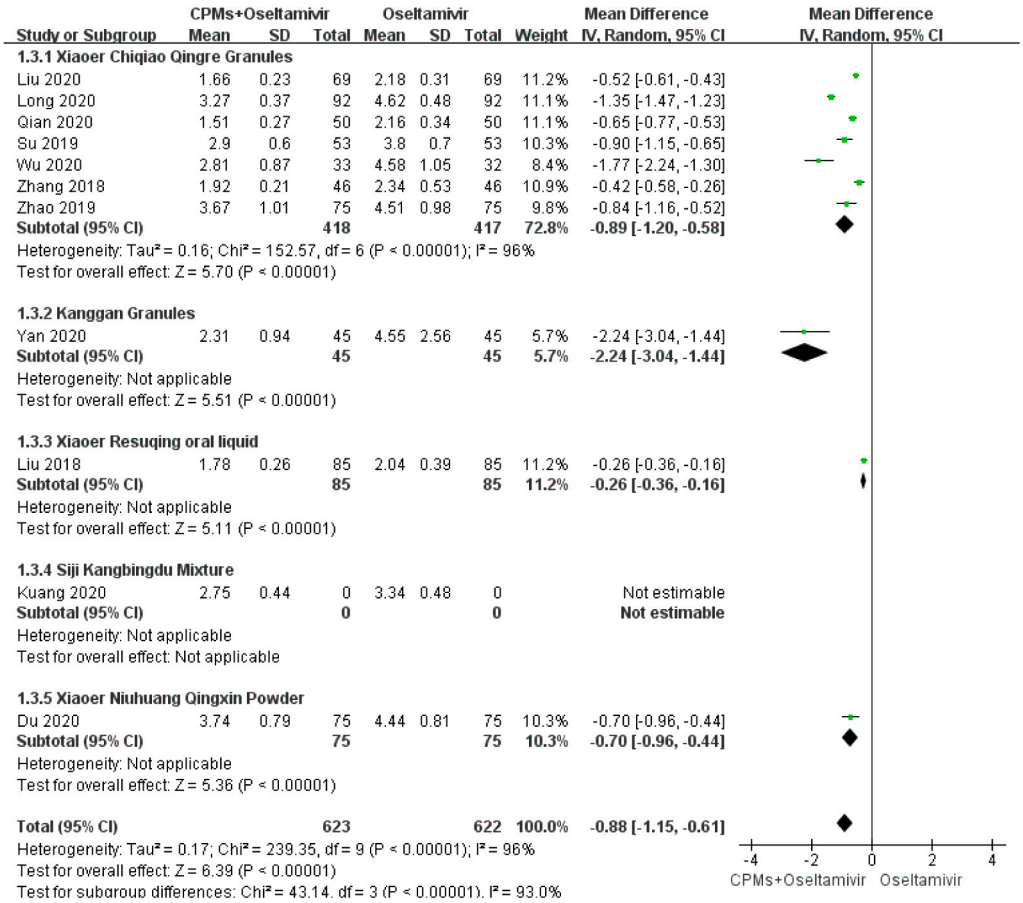

FIGURE 5 | Forest plot of duration of nasal congestion.

individual studies one by one. With regard to fever, cough, nasal congestion, and sore throat, the heterogeneity remained >90% after removal of individual studies one by one (details are shown in **Supplementary Table 2**). The heterogeneity results did not change significantly.

Evaluation of Publication Bias

Time to fever resolution was used as the outcome; 19 studies were included (Song and Zhang, 2018; Zhang, B. Y. et al., 2018; Zhang, Y. H. et al., 2018; Su, 2019; Yin, 2019; Zhou, 2019; Zhao et al., 2019; Long, 2020; Liu, 2020; Qian, 2020; Wu, 2020; Chen et al., 2019; Li, 2019; Zhou, 2019; Liu, 2020; Fang, 2018; Gao and Wang, 2020; Kuang and Wang, 2020; Du et al., 2020), and the effect size MD was used as the horizontal axis to create a funnel chart (**Figure 9**). The graph was not completely symmetrical, indicating the possibility of publication bias.

DISCUSSION

In the present meta-analysis, the MD values for fever, cough, nasal congestion, sore throat, and viral shedding were >0.5, as shown in the forest plots, indicating that the combination of drugs shortened the course of influenza by 0.5 days. The above data reflects the trend of time reduction. In terms of ADRs, the RR was 0.53, indicating that the combination of drugs can reduce ADRs by half (Dobson et al., 2015). These results showed that, compared with oseltamivir alone, CPMs combined with oseltamivir shortened the time to fever resolution, shortened the time of symptom relief, shortened the time of viral shedding, and reduced the occurrence of ADRs, indicating that CPMs play an active role in the treatment of influenza in children. But due to the uneven quality of the current research, it will affect the reliability of the results. In order to get more accurate recommendations, we need more clinical data in the future.

However, the four outcomes of fever, cough, nasal congestion, and sore throat showed high heterogeneity. Different CPMs have different drug compositions and treatment directions, which may lead to high clinical heterogeneity (Hu et al., 2010). Therefore, we take each CPM as a subgroup and performed subgroup analysis to observe the level of heterogeneity. Differences were high among the subgroups, and subgroup analysis did not reduce the heterogeneity, possibly because there was uneven distribution among the subgroups in terms of the number of studies and cases. Except for the *Xiaoer Chiqiao*

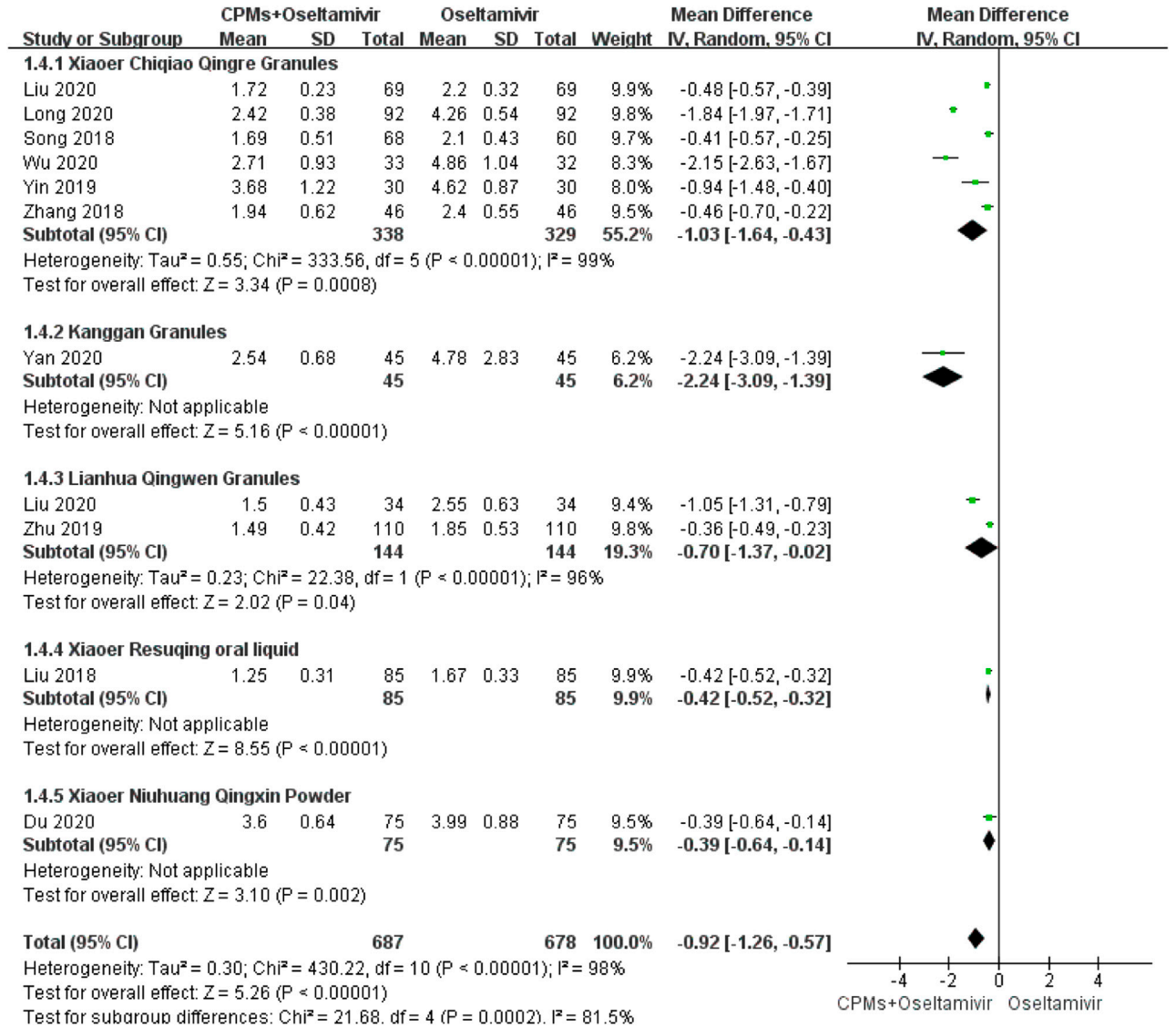

FIGURE 6 | Forest plot of duration of sore throat.

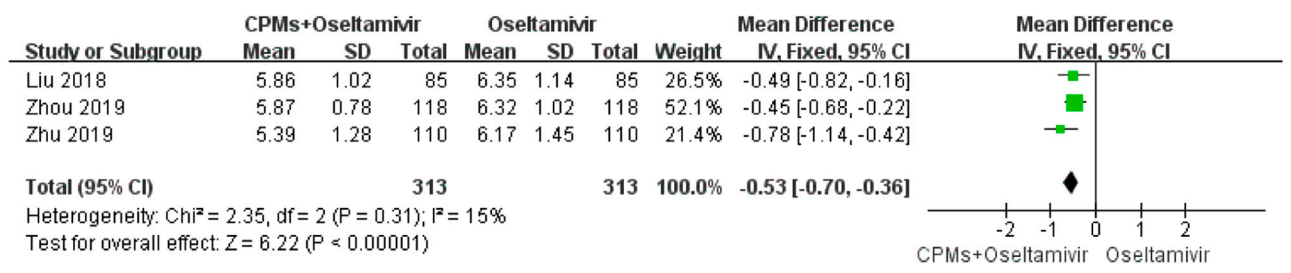

FIGURE 7 | Forest plot of time of viral shedding.

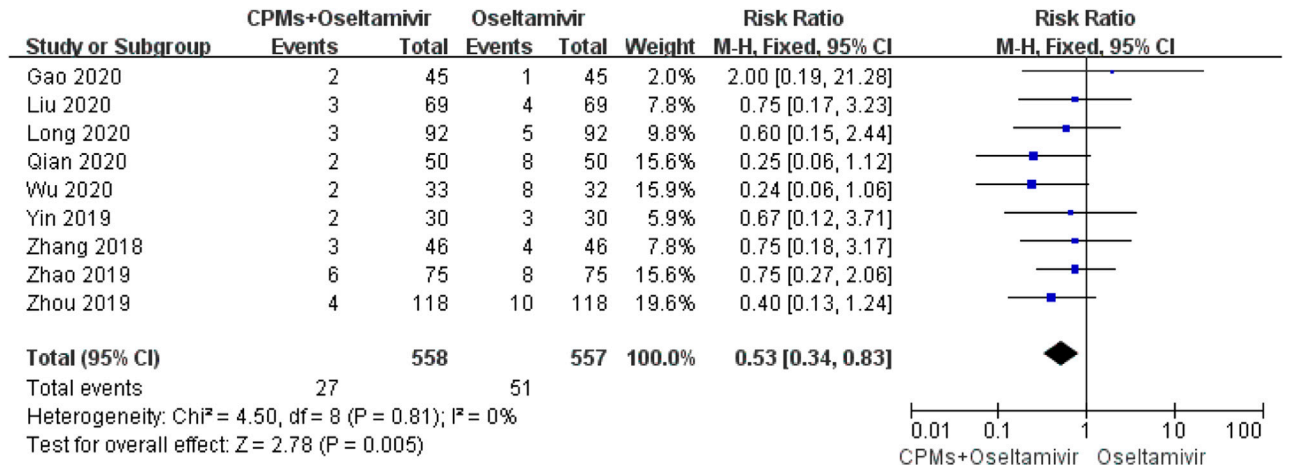

FIGURE 8 | Forest plot of ADRs.

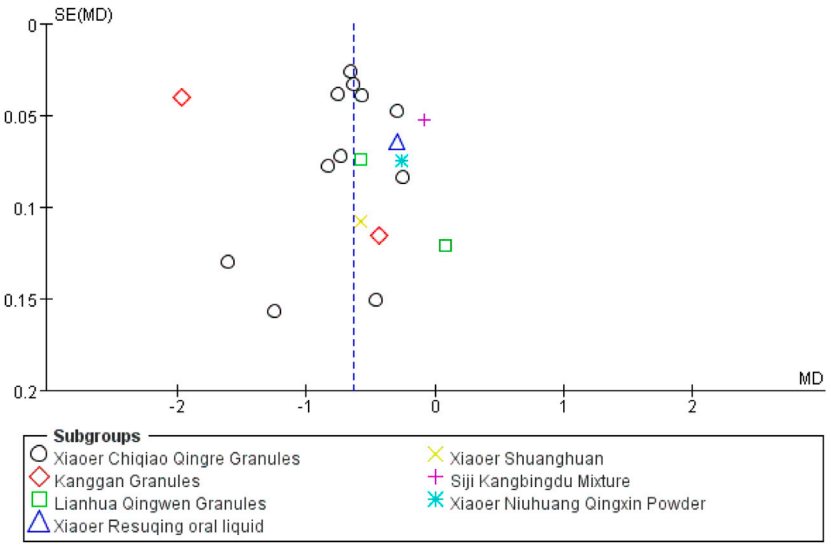

FIGURE 9 | Funnel plot of time to fever resolution.

Qingre granules, *Kanggan* granules, and *Lianhua Qingwen* granules subgroups, all subgroups only included one study each; therefore, further comparative studies are needed to further evaluate the sources of heterogeneity. In the *Xiaoer Chiqiao Qingre* granules subgroup, which included the largest number of studies and cases, the heterogeneity was high. Taking time to fever resolution as an example, there were 11 studies in the *Xiaoer Chiqiao Qingre* granules subgroup, and the heterogeneity within the group was high ($p < 0.00001$, $I^2 = 94\%$), possibly because the statistical unit of the outcome was time; hence, it was possible that the statistician could not accurately measure time data or that the children could not accurately express their own feelings, misleading the statistician's judgment. Some studies did not clearly indicate whether the child was hospitalized. Moreover, when children's data are reported by the family, the error is greater, resulting in inaccurate data (Kang et al., 2000).

We attempted to identify another source of heterogeneity. By contrast detailed characteristics of included studies, it was found that the reason for the large heterogeneity maybe due to the difference in age range and the fluctuation range of the time from onset of symptoms to randomization (Wang et al., 2009; Wang et al., 2008). The age range in the present study was 1–14 years, and the time from symptom onset to randomization was <48 h. Children of different ages have different immunity, and the time of appearance and disappearance of symptoms after infection also differs. Such a large age and time span may lead to greater data differences and increased heterogeneity. Therefore, we analyzed subgroups stratified according to age. However, in the included

studies, the average age of the patients was concentrated in the 5–10 years age range, and the standard deviation values of age were uneven; hence, accurate grouping was not possible (details are shown in **Supplementary Figure 10**). We also planned to use time from symptom onset to randomization in subgroup analysis, but the average time was concentrated around 24 h, and the standard deviation values were uneven in some cases; hence, accurate grouping could not be performed (details are shown in **Supplementary Figure 11**). For both sets of data, age and time from symptom onset to randomization, the values recorded in the studies were averages; hence, we could not eldetermine the number of cases in each age subgroup and the specific time from symptom onset to randomization. More detailed information could not be obtained from the original text of each study, and no reply was received after sending the email. Both the above factors may have led to greater heterogeneity, the source of which could not be clarified. Later, we conducted sensitivity analysis and found that the heterogeneity results lacked significant changes, indicating that the included studies were relatively stable, but also that no source of heterogeneity was found. Finally, the four outcomes were combined using the random effects model. Finally, the four outcomes are combined using a random effects model. The main reason is that the RCTs of each study are not rigorous in the details of certain links. Future RCTs of children should be divided into age groups as much as possible. Every RCT should be registered. The test process and details have been carefully described to make the research more accurate and rigorous (Li et al., 2007; Liu and Xia, 2007).

To assess methodological quality, we tried to contact the corresponding authors of each study by phone or email to inquire about the details of the trials, but we did not received responses. Therefore, it was unclear whether strict operating procedures, such as allocation concealment and blinding methods, were used during the tests. The methodological quality of the included studies was poor; therefore, the reliability of the results is questionable and it is unclear whether the studies were actual RCTs (Tang et al., 1999; Moher et al., 2009).

A comprehensive analysis of the funnel chart results revealed publication bias. There were gaps in the upper left and lower right corners of the graph, indicating that some negative results were not published. In a further search for unpublished studies, we found no unpublished negative results in previous studies, possibly because there is a lack of awareness of registration in clinical research or because there are limited studies on this subject, making it impossible to obtain comprehensive evidence and, thus, leading to publication bias.

The composition of CPMs is diverse (details are shown in **Supplementary Table 3**), and different ingredients act through different mechanisms in the human body. The combination of modern biomedical technology and TCM has shown a synergistic effect. Using omics and network pharmacology theory, researchers have gradually discovered the mechanisms of some Chinese medicines. Both *Lonicera japonica* (Thunb) and *Forsythia suspensa* (Thunb, Vahl) have significant synergistic benefits, conferring antipyretic and anti-free radical damage effects and improving immunity (Duan and Ma, 2009; Zhou et al., 2015). The mechanisms underlying the antipyretic effects of *Bupleurum chinense* (DC) and *Scutellaria baicalensis Georgi* are regulation of PGE2 and cAMP and inhibition of the synthesis or release of the endogenous pyrogens TNF-α and β-EP (Yang, 2012; Zhu et al., 2015; Yao et al., 2018). *Forsythia suspensa* (Thunb, Vahl) has been shown to have antipyretic effects (Wang and Zhao, 2010). One experiment confirmed that phillyrin, the active ingredient of *Forsythia suspensa* (Thunb, Vahl), can inhibit influenza A virus infection, most likely by downregulating a certain gene (Duan et al., 2012). Baicalin combined with phillyrin can downregulate the expression of the influenza A virus nucleoprotein gene transfected into HeLa cells, and it showed a synergistic effect within a certain concentration range (Huang et al., 2018). Studies have found that (R, S)-goitrin in *Isatis tinctoria L* inhibits influenza virus replication by increasing the production of IFN-β and interferon-induced transmembrane 3 (Luo et al., 2019). Modern pharmacological studies have found that *Isatis tinctoria L* has anti-inflammatory, anti-viral, antipyretic, and immunity enhancement effects, and is often used clinically to treat various infections, such as pharyngitis and tonsillitis (Yang, 2016). Studies have shown that the effect of *Platycodon grandiflorus* (Jacq.) A.DC in reducing phlegm and relieving cough is positively correlated with the content of platycodin (Xie et al., 2019). Platycodin capsules can reduce the frequency of cough and asthma, and increase the excretion of phenol red in the respiratory tract. The excretion of phenol red can indirectly reflect the amount of secretion in the respiratory tract. At this time, the amount of secretion in the respiratory tract increases, which is conducive to thinning the thick sputum attached to the respiratory tract mucosa, making it easier to fall off from the airway wall, which has the effect of reducing phlegm and relieving cough (Jin and Chen, 2015). Studies have shown that pulegone, the active ingredient of *Nepeta tenuifolia Benth*, has a good anti-inflammatory protective effect on Lipopolysaccharide poisoning model mice, which can inhibit the release of inflammatory factors and reduce inflammatory cell infiltration. The mechanism of its anti-inflammatory effect is related to the intervention and regulation of the activation of NLRP3 inflammasome (Wen, 2017). When influenza virus is combined with bacterial infection, combined prescription drugs can show the therapeutic advantage. The six CPMs included in the present study contain *Forsythia suspensa* (Thunb, Vahl). Among them, *Lianhua Qingwen* granules, *Xiaoer Resuqing* granules, and *Xiaoer Shuanghuanglian* mixture use *Lonicera japonica* (Thunb) and *Forsythia suspensa* (Thunb, Vahl) in combination. *Xiaoer Chiqiao Qingre* granules and *Xiaoer Resuqing* granules use *Bupleurum chinense* (DC) and *Scutellaria baicalensis Georgi* in combination. The drug composition of *Lianhua Qingwen* granules and *Xiaoer Resuqing* granules contains *Isatis tinctoria L*. *Nepeta tenuifolia Benth* is contained in the medicine composition of both *Xiaoer Chiqiao Qingre* granules and *Siji Kangbingdu* Mixture. By combining ancient theory and modern technology, researchers can possibly clarify the drug mechanisms of TCM, thereby guiding treatment with clinical prescription drugs.

In future clinical practice, combination medications may provide new ideas to treat children with influenza, promoting the use of CPMs and TCM for this purpose (Ru et al., 2017; Gao and Wang, 2018; Liu et al., 2019). They are especially effective at shortening the time to fever resolution and relieving the symptoms of influenza (Wang et al., 2010; Duan et al., 2011; Wang et al., 2011; He et al., 2019; Yoshino et al., 2019). This is consistent with the conclusions of the present study.

CONCLUSION

In conclusion, the present meta-analysis demonstrated the efficacy and safety of CPMs combined with oseltamivir in the treatment of children with influenza. It provides evidence that combination therapy can be used to treat children with influenza. However, because most of the studies included in this analysis were of low quality and the analysis results showed high heterogeneity, there is no strong evidence to support this conclusion, which needs to be verified in future high-quality, well-designed, multi-center RCTs. At the same time, future studies should focus on improving objectivity in outcome measurements and methodological quality by adopting a rigorous experimental design. In future clinical research, the publication of RCTs should follow strict registration procedures, and standards should be unified as much as possible.

DATA AVAILABILITY STATEMENT

The datasets presented in this study can be found in online repositories. The names of the repository/repositories and accession number(s) can be found in the article/**Supplementary Material**.

AUTHOR CONTRIBUTIONS

CL, ND, and BL: conceived and designed this study. ND, XL, and BL: performed the data extraction, analysis, interpretation and wrote the initial draft. YX and YZ: were responsible for literature checking and data entry. CL, CZ, and LL: assisted with data interpretation. JL: helped with data analysis and result discussion. All authors contributed to the final article. ND and BL. contributed equally to this work.

FUNDING

Supported by the Fundamental Research Funds for the Central public welfare research institutes (No. ZZ13-024-1, Z0653), National Key Research & Development Plan (2019YFC1712000) and the National Science and Technology Major Project (No. ZZ13-024-1,Z0653, 2019YFC1712000, 2018ZX10101001-005-003 and 2018ZX10101001-005-004). National Key R & D Program of China (2020YFE0205100).

ACKNOWLEDGMENTS

We sincerely thank the school China Academy of Chinese Medical Sciences for its convenience. Thanks to everyone in the research group for their help. National Key R & D Program of China (2020YFE0205100)

SUPPLEMENTARY MATERIAL

The Supplementary Material for this article can be found online at: https://www.frontiersin.org/articles/10.3389/fphar.2021.682732/full#supplementary-material

REFERENCES

Cao, L., Xu, B. P., Liu, G., Zhu, C. M., Yu, H., Zhong, W., et al. (2015). Expert Consensus on Diagnosis and Treatment of Influenza in Children (2015 Edition). *Chin. J. Appl. Clin. Pediatr. (Chin)*. 30, 1296–1303. doi:10.3760/cma.j.issn.2095-428X.2015.17.005

Chen, D. Z., Cheng, Y. Y., Wei, G. Y., Wei, M., and Ma, M. Y. (2019). Clinical Study on Kanggan Granules Combined with Oseltamivir in Treatment of Infantile Influenza. *Drugs Clinic*. 04 (34), 1029–1033. doi:10.7501/j.issn.1674-5515.2019.04.031

Cochrane Handbook (2019). Assessing Risk of Bias in a Randomized Trial. *Cochrane Handbook Syst. Rev. Interventions* 2, 205–228. doi:10.1002/9781119536604.ch8

COMMITTEE ON INFECTIOUS DISEASES (2018). Influenza in Children and Vaccination—Interpretation of AAP Committee on Infectious Diseases Recommendations for Prevention and Control of Influenza in Children (2018—2019). *Chin. Gen. Pract.* 22 (06), 621–626. doi:10.1542/peds.2018-2367

COMMITTEE ON INFECTIOUS DISEASES (2019). Recommendations for Prevention and Control of Influenza in Children (2019–2020). *Pediatrics* 144 (4), e20192478. doi:10.1542/peds.2019-2478

Dobson, J., Whitley, R. J., Pocock, S., and Monto, A. S. (2015). Oseltamivir Treatment for Influenza in Adults: a Meta-Analysis of Randomised Controlled Trials. *The Lancet*. 385, 1729–1737. doi:10.1016/S0140-6736(14)62449-1

Du, Y., Wu, Y. L., Song, W. C., Zhang, Y. X., and Zhang, Y. (2020). Clinical Study on Xiaoer Niuhuang Qingxin Powder Combined with Oseltamivir Phosphate Granules for Influenza in Children. *JOURNAL NEW CHINESE MEDICINE*. 22 (52), 101–103. doi:10.13457/j.cnki.jncm.2020.22.028

Duan, H., and Ma, C. (2009). Experimental Study on the Antipyretic Mechanism of the Compatibility of Honeysuckle and Forsythia. *Mod. J. Integrated Traditional Chin. West. Med.* 18 (11), 1214–1216. doi:10.3969/j.issn.1008-8849.2009.11.005

Duan, L. J., Zhang, Q., Wang, N. R., Yang, B., He, S. J., and Sun, J. (2012). Effect of Phillyrin on Gene Expression of Influenza A Virus Nucleoprotein. *Chin. Gen. Prac* 15 (18), 2082–2084. doi:10.3969/j.issn.1007-9572.2012.06.101

Duan, Z. P., Jia, Z. H., Zhang, J., Liu, S., Chen, Y., Liang, L. C., et al. (2011). Natural Herbal Medicine Lianhuaqingwen Capsule Anti-influenza A (H1N1) Trial: a Randomized, Double Blind, Positive Controlled Clinical Trial. *Chin. Med. J. (Engl)* 124 (18), 2925–2933.

Fang, L. (2018). Clinical Observation of Xiaoer Resuqing Granules for Influenza A with Syndrome of Wind-Heat Invading the Wei-Exterior in Children. *J. New Chin. Med.* 50 (4), 140–142. doi:10.13457/j.cnki.jncm.2018.04.038

Gao, Y. L., and Wang, L. (2020). Effect of Children Shuanghuanglian Mixture Combined with Oseltamivir Phosphate in the Treatment of Influenza. *J. Clin. Pathological Res.* 40 (02), 332–336. doi:10.3978/j.issn.2095-6959.2020.02.012

Gao, Y., and Wang, R. (2018). Research Progress of Traditional Chinese Medicine in the Treatment of Influenza. *Clin. Medication J.* 16 (01), 17–20. doi:10.3969/j.issn.1672-3384.2018.01.004

Geneva, W. H. O. (2017). *Global Accelerated Action for the Health of Adolescents (AA-HA!): Guidance to Support Country Implementation*. Available at: https://www.who.int/

Govorkova, E. A., Leneva, I. A., Goloubeva, O. G., Bush, K., and Webster, R. G. (2001). Comparison of Efficacies of RWJ-270201, Zanamivir, and Oseltamivir against H5N1, H9N2, and Other Avian Influenza Viruses. *Antimicrob. Agents Chemother.* 45 (10), 2723–2732. doi:10.1128/AAC.45.10.2723-2732.2001

Han, D. G., Guo, Q., Ju, H., and Shen, Y. (2018). Observation on the Effect of Xiaoer Chiqiao Qingre Granules in Treating Fever (Wind-heat Stagnation Pattern) in Children with Viral Upper Respiratory Tract Infection. *J. Chin. Med. Mater.* 41 (08), 2011–2013. doi:10.13863/j.issn1001-4454.2018.08.051

He, J., Li, Z., Huang, W., Guan, W., Ma, H., Yang, Z. F., et al. (2019). Efficacy and Safety of Chou-Ling-Dan Granules in the Treatment of Seasonal Influenza via Combining Western and Traditional Chinese Medicine: Protocol for a Multicentre, Randomised Controlled Clinical Trial. *BMJ Open*. 9 (4), e24800. doi:10.1136/bmjopen-2018-024800

Higgins, J. P. T., and Green, S. (2011). *Cochrane Handbook for Systematic Reviews of Interventions 5.1.0*. Chichester, United Kingdom: The Cochrane Collaboration. Available at: http://www.cochrane-handbook.org

Hu, D., Kang, D. Y., and Hong, Q. (2010). Heterogeneity Analysis of Systematic Reviews on Traditional Chinese Medicine. *Chin. J. Evid-based Med.* 04, 488–491. doi:10.3969/j.issn.1672-2531.2010.04.022

Huang, Z. S., Yang, B., Zhang, Q., and Sun, J. (2018). Effect of Baicalin Combined with Phillyrin on the Gene Expression of Influenza A Virus Nucleoprotein. *J. Med. Postgraduates* 10, 1033–1037. doi:10.16571/j.cnki.1008-8199.2018.10.005

Jin, X., and Chen, Q. (2015). New Progress of Research on Pharmacological Effects of Platycodon Grandiflorus (Jacq.) A.DC. *Res. Pract. Chin. Medicines* 29 (02), 79–82. doi:10.13728/j.1673-6427.2015.02.025

Kang, D. Y., Wang, J. L., Hong, Q., and Liu, G. J. (2000). Study on Heterogeneity Evaluation in Meta-Analysis of Clinical Trials. *West China Med. J.* 02, 143–145. doi:10.3969/j.issn.1002-0179.2000.02.012

Kiso, M., Mitamura, K., Sakai-Tagawa, Y., Shiraishi, K., Kawakami, C., Kimura, K., et al. (2004). Resistant Influenza A Viruses in Children Treated with Oseltamivir: Descriptive Study. *The Lancet*. 364 (9436), 759–765. doi:10.1016/s0140-6736(04)16934-1

Kuang, M. L., and Wang, S. (2020). Efficacy of Siji Kangbingdu Mixture Combined with Oseltamivir on Children with Influenza. *Henan Med. Res.* 29 (09), 1659–1660. doi:10.3969/j.issn.1004-437X.2020.09.058

Li, G. F. (2019). Observation on the Effect of Kanggan Granule Combined with Oseltamivir in the Treatment of Children with Influenza. *Diabetes World* 16 (6), 70.

Li, Y. Q., Liu, X. M., Zhang, M. M., Ma, J. X., Du, L., and Zhou, Y. D. (2007). Assessment of Systematic Reviews and Meta-Analyses on Traditional Chinese Medicine Published in Chinese Journals. *Chin. J. Evid-based Med.* 03, 180–188. doi:10.3969/j.issn.1672-2531.2007.03.006

Lina, B., Boucher, C., Osterhaus, A., Monto, A. S., Schutten, M., Whitley, R. J., et al. (2018). Five Years of Monitoring for the Emergence of Oseltamivir Resistance in Patients with Influenza A Infections in the Influenza Resistance Information Study. *Influenza Other Respi Viruses*. 12 (2), 267–278. doi:10.1111/irv.12534

Liu, J. P., and Xia, Y. (2007). Quality Appraisal of Systematic Reviews or Meta-Analysis on Traditional Chinese Medicine Published in Chinese Journals. *Chin. J. Integr. Trad West. Med.* 04, 306–311. doi:10.3321/j.issn:1003-5370.2007.04.007

Liu, J., Wang, H., Dong, S., and Jiang, Y. (2019). Research Progress of Chinese Medicine in Treating Children with Influenza. *J. Liaoning Univ. Traditional Chin. Med.* 21 (07), 217–221. doi:10.13194/j.issn.1673-842x.2019.07.057

Liu, X. H. (2018). Clinical Efficacy of Xiaoer Resuqing Oral Liquid Combined with Oseltamivir in the Treatment of Influenza. *Xiandaiyangsheng.* 18, 96–97. doi:10.3969/j.issn.1671-0223(x).2018.09.065

Liu, Y. (2020). Analysis of the Effect of Oseltamivir Combined with Xiaoer Chiqiao Qingre Granules in Treating Children with Influenza. *Guide China Med.* 04 (18), 81–82. doi:10.15912/j.cnki.gocm.2020.04.063

Liu, Y., Yang, J., Zhao, X. K., and Zhou, M. Y. (2020). Clinical Analysis of Lianhua Qingwen Granule Combined with Oseltamivir Phosphate in the Treatment of Pediatric Influenza A. *JOURNAL CHINA PRESCRIPTION DRUG* 11 (18), 128–130. doi:10.3969/j.issn.1671-945X.2020.11.070

Long, M. (2020). Effect of Xiaoer Chiqiao Qingre Granules Combined with Oseltamivir on the Recovery Time of Clinical Symptoms in Children with Influenza. *JOURNAL NORTH PHARMACY*. 02 (17), 97–98. doi:10.3969/j.issn.1672-8351.2020.02.070

Luo, Z., Liu, L.-F., Wang, X.-H., Li, W., Jie, C., Chen, H., et al. (2019). Epigoitrin, an Alkaloid from Isatis Indigotica, Reduces H1N1 Infection in Stress-Induced Susceptible Model *In Vivo* and *In Vitro*. *Front. Pharmacol.* 10, 78. doi:10.3389/fphar.2019.00078

Ma, R., Hu, S., Ding, Y., Xiang, X., Yang, J., Xue, Z., et al. (2015). Guideline on Evaluation of Chinese Materia Medica Research for Treatment of Acute Upper Respiratory Tract Infection in Children. *Drug Eval. Res.* 38 (01), 8–16.

Moher, D., Liberati, A., Tetzlaff, J., and Altman, D. G. (2009). The PRISMA Group (2009). Preferred Reporting Items for Systematic Reviews and Meta-Analyses: The PRISMA Statement. *Plos Med.* 6 (6), e1000097. doi:10.1371/journal.pmed1000097

Moscona, A. (2009). Global Transmission of Oseltamivir-Resistant Influenza. *N. Engl. J. Med.* 360 (10), 953–956. doi:10.1056/NEJMp0900648

Moscona, A. (2004). Oseltamivir-resistant Influenza?. *The Lancet*. 364 (9436), 733–734. doi:10.1016-S0140-6736(04)16947-X10.1016/s0140-6736(04)16947-x

National Health Commission of the People's Republic of China (2018). Guideline for Diagnosis and Treatment of Infuenza (Revision 2018). *Infect. Dis. Inf.* 31 (06), 500–504. doi:10.3969/j.issn.1671-9638.2018.02.020

Panning, M. (2013). Influenza heute und in Zukunft. *Pneumologe*. 10 (5), 314–325. doi:10.1007/s10405-013-0674-7

Qian, M. H. (2020). Observation on the Curative Effect of Xiaoer Chiqiao Qingre Granules Combined with Oseltamivir in the Treatment of Children with Influenza. *RENOWNED DOCTOR*. 11, 296–297.

Rong, P., Ma, R., Liu, Q., Yan, H., Hu, S., Li, X., et al. (2017). A Review of Studies on Chinese Patent Medicines in the Treatment of Acute Upper Respiratory Tract Infections in Children. *China J. Chin. Materia Med.* 42 (08), 1455–1466. doi:10.19540/j.cnki.cjcmm.2017.0042

Ru, L., Chen, X., Qiu, Z., Shan, Y., and Li, J. (2017). Research Progress in Traditional Chinese Medicine for Influenza. *Hebei J. Traditional Chin. Med.* 39 (02), 313–317. doi:10.3969/j.issn.1002-2619.2017.02.039

Shi, Y., Shi, R. B., Liu, B., Lu, Y. R., and Du, L. J. (2003). Isolation and Elucidation of Chemical Constituents with Antiviral Action from Yinqiao San on Influenza Virus. *China J. Chin. Materia Med.* 01, 47–51. doi:10.3321/j.issn:1001-5302.2003.01.017

Song, W. S., and Zhang, H. Y. (2018). Analysis of the Clinical Efficacy of Xiaoer Chiqiao Qingre Granules Combined with Oseltamivir in the Treatment of Children with Influenza. *J. Clin. Med. Lit.* 5 (60), 161–162. doi:10.16281/j.cnki.jocml.2018.60.134

Su, D. B. (2019). Xiaoer Chiqiao Qingre Granules Combined with Oseltamivir in the Treatment of Children with Influenza. *Mod. Diagn. Treat.* 30 (4), 525–527.

Tang, J.-L., Zhan, S.-Y., and Ernst, E. (1999). Review of Randomised Controlled Trials of Traditional Chinese Medicine. *Bmj*. 319 (7203), 160–161. doi:10.1136/bmj.319.7203.160

Wang, C., Cao, B., Liu, Q.-Q., Zou, Z.-Q., Liang, Z.-A., Gu, L., et al. (2011). Oseltamivir Compared with the Chinese Traditional Therapy Maxingshigan-Yinqiaosan in the Treatment of H1N1 Influenza. *Ann. Intern. Med.* 155 (4), 217–225. doi:10.7326/0003-4819-155-4-201108160-00005

Wang, H. X. (2019). Observation of Xiaoer Chiqiao Qingre Granules in Improving the Clinical Symptoms and Inflammatory Factors in Children with Acute Upper Respiratory Tract Infection (Exogenous Wind-Heat Stagnation Pattern). *Strait Pharm. J.* 31 (01), 199–201. doi:10.3969/j.issn.1006-3765.2019.01.109

Wang, J. W., Wang, T. F., and Liu, J. P. (2008). Systematic Review of Studies of Microcosmic Syndrome Differentiation in Traditional Chinese Medicine: Some New Ideas. *J. Evidence-Based Med.* 02, 101–103. doi:10.3969/j.issn.1671-5144.2008.02.011

Wang, J. Y., Qu, J. X., Mou, Z. Y., Zong, H. X., Zhao, X. D., Wang, X. Y., et al. (2009). Stock Identity. *Chin. J. Evid-based Med.* 10, 1115–1118. doi:10.1016/b978-0-12-373553-9.00255-8

Wang, J., and Zhao, C. (2010). Study on the Correlation between the Content of Forsythin in Shuanghuanglian Preparations and the Antipyretic Effect. *China Pharmacist* 10 (13), 1405–1408. doi:10.3969/j.issn.1008-049X.2010.10.008

Wang, L., Zhang, R.-M., Liu, G.-Y., Wei, B.-L., Wang, Y., Cai, H.-Y., et al. (2010). Chinese Herbs in Treatment of Influenza: A Randomized, Double-Blind, Placebo-Controlled Trial. *Respir. Med.* 104 (9), 1362–1369. doi:10.1016/j.rmed.2010.05.015

Wang, Y., Wang, Y. F., Ma, J., Zhang, X., Kang, K. G., and Chen, X. G. (2020). Efficacy of Lianhua Qingwen Granules Combined with Oseltamivir in the Treatment of Children with Influenza Virus Infection and its Influence on the Expression Levels of NO, IFN-γ and IL-17. *Chin. Arch. Traditional Chin. Med.* 38 (01), 214–216. doi:10.13193/j.issn.1673-7717.2020.01.052

Wen, T. (2017). *Study on Mechanism of Essential Oils of Schizonepeta Tenuifolia Briq. And Pulegone in Anti-inflammatory Effect of LPS-Induced Endotoxin Poisoning Mice Based on NLRP3 Signaling Pathway*. Chengdu University of TCM.

Wu, L. (2018). Chinese Patent Medicine Treatment of Children with Influenza. *Clin. Medication J.* 16 (01), 21–24. doi:10.3969/jissn16723384201801005

Wu, M. (2020). Efficacy of Oseltamivir Combined with Xiaoer Chiqiao Qingre Granules in Treating Children with Influenza. *ELECTRONIC JOURNAL CLINICAL MEDICAL LITERATURE*. 202016 (7), 165. doi:10.16281/j.cnki.jocml.2020.16.144

Xie, X. X., Zhang, C., Zeng, J. X., Zhang, C. H., Mao, Z., He, J. W., et al. (2019). Antitussive and Expectorant Activities and Saponinson Components of Various Extract Fractions from Platycodon Grandiflorus (Jacq.) A.DC. *Chin. J. New Drug* 28 (13), 1647–1653. doi:10.3969/j.issn.1003-3734.2019.13.018

Xiong, Y., Li, N. X., Duan, N., Liu, B., Zhu, H., Zhang, C., et al. (2020). Traditional Chinese Medicine in Treating Influenza: From Basic Science to Clinical Applications. *Front. Pharmacol.* 11 (2020), 575803. doi:10.3389/FPHAR.2020.575803

Yan, J. (2020). The Effect of Kanggan Granule Combined with Oseltamivir on the Improvement of Clinical Symptoms in Children with Influenza. *JOURNAL NORTH PHARMACY*. 04 (17), 67–68. doi:10.3969/j.issn.1672-8351.2020.04.045

Yang, C. W. (2016). Research Progress in Pharmacology of *Isatis Tinctoria L. Chin. J. Mod. Drug Appl.* 10 (09), 282–283. doi:10.14164/j.cnki.cn11-5581/r.2016.09.214

Yang, J. (2012). Study on the Effective Parts of Bupleurum-Scutellaria Baicalensis on Antipyretic and its Compatibility Mechanism. *Beijing Univ. Chin. Med. BUCM*. 10, 67–69.

Yao, J., Zhang, H., Ma, L., Mu, X., Wang, Y., Lu, Y., et al. (2018). Effect of Traditional Chinese Medicine Bupleurum in the Treatment of Influenza A (H1N1). *Pak J. Pharm. Sci.* 31 (4), 1713–1717.

Yao, J., Xiu, X., Duan, X., Wang, R., Zhang, Y., Sun, L., et al. (2015). Current Status of Clinical Application of Chinese Patent Medicine in Children with Upper Respiratory Tract Infection. *Matern. Child Health Care China* 30 (15), 2468–2470. doi:10.7620/zgfybj.j.issn.1001-4411.2015.15.64

Yin, Z. X. (2019). Evaluation of Clinical Effect and Adverse Reaction of Xiaoer Chiqiao Qingre Granules in Treating Influenza. *Med. Diet Health*. 17, 116–117.

Yoshino, T., Arita, R., Horiba, Y., and Watanabe, K. (2019). The Use of Maoto (Ma-Huang-Tang), a Traditional Japanese Kampo Medicine, to Alleviate Flu Symptoms: a Systematic Review and Meta-Analysis. *BMC Complement. Altern. Med.* 19 (1), 68. doi:10.1186/s12906-019-2474-z

Zhang, B. Y., He, J. E., Wang, W., and Gao, C. Y. (2018). Observation on the Clinical Efficacy of Oseltamivir Combined with Xiaoer Chiqiao Qingre Granules in the Treatment of Children with Influenza. *J. Ningxia Med. Coll.* 12 (40), 1441–1443. doi:10.16050/j.cnki.issn1674-6309.2018.12.021

Zhang, J. L. (2018). *Chinese Patent Medicines*. Beijing, China: China Traditional Chinese Medicine Publishing House, 5–10. IBSN: 9787513244046

Zhang, Y. H., Ji, J. W., and Chen, J. L ((2018). Observation on the Curative Effect of Xiaoer Chiqiao Qingre Granules Combined with Oseltamivir in the Treatment of Children with Influenza. *Med. Aesthetics Beauty*. 27 (6), 2–3. URL: https://www-wanfangdata-com-cn–bjtu.naihes.cn/details/detail.do?_type=perio&id=yxmxmr18201806002

Zhao, Y. C., Wu, J., Zhang, S., Xie, J., and Huang, Z. (2019). Observation on Curative Effect of Oseltamivir Combined with Xiaoer Chiqiao Qingre Keli in Treatment of Children with Influenza. *China Med. Pharm.* 9 (2), 38–40. doi:10.3969/j.issn.2095-0616.2019.02.010

Zhou, H., Xu, N., Zhang, X., Chen, G., Liu, Y., Yu, X., et al. (2019). Data Analysis of Oseltamivir Adverse Reactions in 55 Cases. *Chin. J. Pharmacovigilance*. 16 (07), 420–424. doi:10.19803/j.1672-8629.2019.07.007

Zhou, J. Y. (2019). Clinical Effect Analysis of Oseltamivir Phosphate Combined with Xiaoer Chiqiao Qingre Granules in Treating Influenza A. *Clin. Res.* 27 (9), 128–129.

Zhou, Z., Li, X., Liu, J., Dong, L., Chen, Q., Liu, J., et al. (2015). Honeysuckle-encoded Atypical microRNA2911 Directly Targets Influenza A Viruses. *Cell Res.* 25 (1), 39–49. doi:10.1038/cr.2014.130

Zhu, H.-y., Han, L., Shi, X.-l., Wang, B.-l., Huang, H., Wang, X., et al. (2015). Baicalin Inhibits Autophagy Induced by Influenza A Virus H3N2. *Antiviral Res.* 113, 62–70. doi:10.1016/j.antiviral.2014.11.003

Zhu, S. J., Li, S., and Li, W. (2019). Lianhua Qingwen Granule Combined with Oseltamivir Phosphate in the Treatment of Influenza A in Children. *Chin. J. Clin. Res.* 32 (08), 1099–1101. doi:10.13429/j.cnki.cjcr.2019.08.024

Conflict of Interest: The authors declare that the research was conducted in the absence of any commercial or financial relationships that could be construed as a potential conflict of interest.

Publisher's Note: All claims expressed in this article are solely those of the authors and do not necessarily represent those of their affiliated organizations, or those of the publisher, the editors and the reviewers. Any product that may be evaluated in this article, or claim that may be made by its manufacturer, is not guaranteed or endorsed by the publisher.

Copyright © 2021 Duan, Liu, Li, Xiong, Zhang, Zhang, LI, Lu and Lyu. This is an open-access article distributed under the terms of the Creative Commons Attribution License (CC BY). The use, distribution or reproduction in other forums is permitted, provided the original author(s) and the copyright owner(s) are credited and that the original publication in this journal is cited, in accordance with accepted academic practice. No use, distribution or reproduction is permitted which does not comply with these terms.

frontiers in Pharmacology

ORIGINAL RESEARCH
published: 16 August 2021
doi: 10.3389/fphar.2021.683645

A Systematic Study of the Mechanism of Acacetin Against Sepsis Based on Network Pharmacology and Experimental Validation

Yuanshuo Ouyang[1,2,3†], *Yi Rong*[1,2,3†], *Yanming Wang*[1,2,3], *Yanli Guo*[1,2,3], *Liya Shan*[1,2,3], *Xiushi Yu*[1,2,3], *Li Li*[1], *Junqiang Si*[1,2,3], *Xinzhi Li*[1,2,4*] *and Ketao Ma*[1,2,3*]

[1]*Key Laboratory of Xinjiang Endemic and Ethnic Diseases, Ministry of Education, Shihezi University School of Medicine, Shihezi, China,* [2]*NHC Key Laboratory of Prevention and Treatment of Central Asia High Incidence Diseases, First Affiliated Hospital, Shihezi University School of Medicine, Shihezi, China,* [3]*Department of Physiology, Shihezi University School of Medicine, Shihezi, China,* [4]*Department of Pathophysiology, Shihezi University School of Medicine, Shihezi, China*

Sepsis is a dysregulated systemic response to infection, and no effective treatment options are available. Acacetin is a natural flavonoid found in various plants, including *Sparganii rhizoma*, *Sargentodoxa cuneata* and *Patrinia scabiosifolia*. Studies have revealed that acacetin potentially exerts anti-inflammatory and antioxidative effects on sepsis. In this study, we investigated the potential protective effect of acacetin on sepsis and revealed the underlying mechanisms using a network pharmacology approach coupled with experimental validation and molecular docking. First, we found that acacetin significantly suppressed pathological damage and pro-inflammatory cytokine expression in mice with LPS-induced fulminant hepatic failure and acute lung injury, and *in vitro* experiments further confirmed that acacetin attenuated LPS-induced M1 polarization. Then, network pharmacology screening revealed EGFR, PTGS2, SRC and ESR1 as the top four overlapping targets in a PPI network, and GO and KEGG analyses revealed the top 20 enriched biological processes and signalling pathways associated with the therapeutic effects of acacetin on sepsis. Further network pharmacological analysis indicated that gap junctions may be highly involved in the protective effects of acacetin on sepsis. Finally, molecular docking verified that acacetin bound to the active sites of the four targets predicted by network pharmacology, and *in vitro* experiments further confirmed that acacetin significantly inhibited the upregulation of p-src induced by LPS and attenuated LPS-induced M1 polarization through gap junctions. Taken together, our results indicate that acacetin may protect against sepsis *via* a mechanism involving multiple targets and pathways and that gap junctions may be highly involved in this process.

Keywords: sepsis, acacetin, network pharmacology, molecular docking, macrophage

OPEN ACCESS

Edited by:
Hai Yu Xu,
Institute of Chinese Materia Medica, China Academy of Chinese Medical Sciences, China

Reviewed by:
Cheorl-Ho Kim,
Sungkyunkwan University, South Korea
Qingjun Pan,
Affiliated Hospital of Guangdong Medical University, China

***Correspondence:**
Ketao Ma
maketao@hotmail.com
Xinzhi Li
lixinzhi@shzu.edu.cn

[†]*These authors have contributed equally to this work*

Specialty section:
This article was submitted to Ethnopharmacology, a section of the journal Frontiers in Pharmacology

Received: *21 March 2021*
Accepted: *02 August 2021*
Published: *16 August 2021*

Citation:
Ouyang Y, Rong Y, Wang Y, Guo Y, Shan L, Yu X, Li L, Si J, Li X and Ma K (2021) A Systematic Study of the Mechanism of Acacetin Against Sepsis Based on Network Pharmacology and Experimental Validation. Front. Pharmacol. 12:683645. doi: 10.3389/fphar.2021.683645

INTRODUCTION

Sepsis is a severe systemic inflammatory response to microbial infection, and lipopolysaccharide (LPS) is well known to induce this phenomenon (Chen et al., 2020). D-Galactosamine (GalN)-sensitized mice administered LPS and mice administered only LPS by intratracheal instillation are recognized as promising experimental models of fulminant hepatic failure (FHF) and acute lung injury (ALI) (Zhang et al., 2019; Liu et al., 2020a). Macrophage polarization is involved in the pathogenesis of sepsis, an uncontrolled inflammatory response caused by infection or acute insult (Fan et al., 2020). Excessive M1 polarization may lead to exacerbated inflammatory reactions and initiate injury in the host.

Acacetin (5,7-dihydroxy-40-methoxyflavone), an O-methylated flavone monomer, is a bioactive constituent found in various plants, including *Sparganii rhizoma, Sargentodoxa cuneata* and *Patrinia scabiosifolia* (Hu et al., 2020; Lu et al., 2021). Acacetin has diverse biological functions, including anti-inflammatory, antioxidant, and anti-microbial activity, and exerts protective effects on cardiac tissue and neurons (Singh et al., 2020). Various studies have reported the anti-inflammatory activity of acacetin *in vitro* and *in vivo*. For example, acacetin was shown to attenuate ALI in LPS-induced mice *via* augmenting haem oxygenase-1 (HO-1) activity (Sun et al., 2018) and to protect against GalN/LPS-induced liver injury by suppressing the TLR4 signalling pathway (Cho et al., 2014). Moreover, acacetin strongly inhibited the expression of the pro-inflammatory cytokines inducible nitric oxide synthase (iNOS) and COX-2 in LPS-activated RAW264.7 cells and in a mouse model of tetradecanoyl phorbal acetate (TPA)-induced tumours (Pan et al., 2006). These results suggest that acacetin ameliorates sepsis by inhibiting inflammation and promoting redox homeostasis, but the underlying molecular mechanism remains unclear.

Network pharmacology is an effective method for screening drug-disease targets and for predicting the possible underlying mechanisms *via* bioinformatics analyses (Li et al., 2020; Xia et al., 2020; Zhang et al., 2021). For example, acacetin was shown to be a bioactive compound in *Sparganii rhizoma*, which has anti-gastric cancer activity as determined by network pharmacology analysis (Lu et al., 2021). Acacetin is also the active ingredient in *Sargentodoxa cuneata* and *Patrinia scabiosifolia,* which improve pelvic inflammatory diseases related to dampness-heat stasis syndrome as determined by network pharmacology analysis (Hu et al., 2020). In this study, we investigated the potential targets of acacetin in subjects with sepsis and predicted the underlying mechanisms by network pharmacology coupled with molecular docking and experimental validation.

MATERIALS AND METHODS

Reagents

Acacetin (MedChemExpress, molecular weight: 284.26 g/mol), LPS (Sigma, 055:B5, L2880), and Gap27 (MedChemExpress) were used in the experiments.

Animals and Model Treatment

Healthy male C57BL/6 mice (8–12 weeks old, 24–26 g) were purchased from the Animal Experimental Centre of the Fourth Military Medical University, China. All mice were bred in a specific pathogen-free animal facility at the Department of Biochemistry and Molecular Biology, School of Basic Medical Science, Xi'an Jiaotong University Health Science Center. All animal experiments were approved by the Institutional Animal Ethics Committee of Xi'an Jiaotong University (no. 2017–666). All animal experiments were performed in accordance with standard animal research guidelines. C57BL/6 mice were randomly assigned to one of six groups (n = 5): the control group, acacetin treatment group, LPS-induced ALI model group, LPS + acacetin treatment group, LPS/GalN-induced FHF model group and LPS/GalN + acacetin treatment group. ALI was induced by the intratracheal injection of LPS (5 mg/kg) (Zhang et al., 2019), and FHF was induced by the intraperitoneal injection of GalN (800 mg/kg) and LPS (40 μg/kg) (Liu et al., 2020a). An equivalent amount of PBS was administered to mice in the control group. Two hours before the intraperitoneal injection of acacetin (50 mg/kg) to the solvent comparison and treatment groups, acacetin was dissolved in 5% core oil. The mice were sacrificed at 10 h after ALI modelling and at 6 h after FHF modelling.

Histology

The lung and liver tissues were collected and fixed in a 4% paraformaldehyde solution for 48 h. The tissues were dehydrated, embedded in paraffin, and sliced into 5 μm-thick sections. The sections were stained with haematoxylin and eosin (H & E) reagent and visualized under a light microscope.

ELISA

To assess the effects of acacetin on pro-inflammatory mediators, appropriate ELISA kits (Jioin, Shanghai, China) were used. The levels of the pro-inflammatory mediators TNF-α, IL-6, and IL-1β in lung and liver homogenates from LPS-induced mice were measured.

Cell Culture

RAW264.7 macrophages were obtained from academician Rikard Holmdahl (Sweden Medical Inflammation Research of the Karolinska Institute). The cells were cultured in a thermostatic incubator at 37°C and 5% CO_2. This cell line, used to screen for molecular mechanisms, was cultured in DMEM (Gibco, Thermo Fisher Scientific, Inc.) supplemented with 10% FBS (Gibco, Carlsbad, CA, United States) and 1% streptomycin/penicillin. The cells were passaged when they reached 70–80% confluence.

MTT Assay

RAW264.7 cells were cultured in a 96-well plate at 5×10^3 cells/well. Cells in the treatment groups were administered different amounts of acacetin (1, 5, and 10 μMol) dissolved in DMSO, while those in the model group were administered LPS (100 ng/ml), and those in the control and blank (no cells) groups were administered an equivalent amount of medium before growth for an additional 24 h. Then, MTT solution was added and

continuously incubated at 37°C for 4 h. The medium in each well was discarded, after which 150 μl of DMSO was added, and the cells were shocked on a microvibrator for 5 min. The optical density at 490 nm was determined with a plate reader (VICTOR X5, PerkinElmer, MA, United States).

Flow Cytometry

The experimental groups were divided into a control group, an LPS model group, and treatment groups that were administered different amounts of acacetin (1, 5, 10 μMol). Groups other than the control and LPS model groups were pre-treated with acacetin for 4 h and then stimulated with LPS (100 ng/ml) for 24 h. Flow cytometry was performed on single-cell suspensions of RAW264.7 macrophages. For intracellular staining, cells were fixed and permeabilized using BD Cytofix/Cytoperm solution (BD Biosciences, NJ, United States). The following monoclonal antibodies were used: the M1-type surface markers CD86-PE (1: 150; BD Biosciences, NJ, United States) and iNOS-PEcy7 (1:150; BD Biosciences, NJ, United States). Samples were measured by flow cytometry (Guava, Millipore), and the data were analysed using Flow Jo software (TreeStar Inc., OR, United States).

Western Blotting

The cell grouping, stimulation, and culture were carried out as described for the flow cytometry experiment. The cells were harvested and lysed with radioimmunoprecipitation assay (RIPA) buffer and phenyl methyl sulfonyl fluoride (PMSF), and the protein content was confirmed by the BCA method. Equivalent amounts of protein from each sample were loaded onto 10% SDS-PAGE gels and then transferred onto PVDF membranes (EMD Millipore, CA, United States). After being blocked with 10% skimmed milk for 2 h, the blots were probed with the following primary antibodies: CD86 (1:1,000; cat. no. ab53004; Abcam), iNOS (1:800; cat. no. ab15323; Abcam), p65 (1: 1,000; cat. no. ab16502; Abcam), p-p65 (1:1,000; cat. no. ab86299; Abcam), Src (1:1,000; cat. no. 2109T; CST), p-Src (1:1,000; cat. no. 6943T; CST), Cx43 (1:1,000; cat. no. AP1541b; Abcepta) and GAPDH (1:2,000; cat. no. bs-2188R; BIOSS). The cells were gently incubated overnight at 4 °C and subsequently incubated with the corresponding secondary antibodies diluted 1:5,000 with 5% skimmed milk. The membranes were washed with TBST, incubated with ECL reagent (GE Healthcare Life Sciences, United Kingdom) and developed. Quantity One software (Bio-Rad, Hercules, CA, United States) was used to analyse the collected images.

Quantitative RT-PCR

The cell culture and stimulation were performed as described for Western blot analysis. Only one acacetin (10 μmol) treatment group was used. After stimulation, the cells were harvested with TRIzol reagent (Life Technologies, CA, United States), and total RNA was extracted and reverse transcribed into cDNA using a ReverTraAce RT kit (Thermo Fisher, MA, United States). Real-time quantitative PCR was carried out using SYBR Green Master Mix (Roche, Germany) according to the manufacturer's protocols. The following gene primer sequences were obtained from Shanghai Gene Pharma: CD86, 5′-ACGGAGTCAATG AAGATTTCCT-3′ (forward), 5′-GATTCGGCTTCTTGTGAC-ATAC-3′ (reverse); iNOS, 5′-GTTTACCATGAGGCTGAAATC C-3′ (forward), 5′-CCTCTTGTCTTT-GACCCAGTAG-3′ (reverse); and β-actin, 5′-CACGATGGAGGGGCCGGACTC ATC-3′ (forward), 5′-TAAAGACCTCTATGCCAACACAGT-3′ (reverse). mRNA abundance was quantified using the Ct values obtained by $2^{-\Delta\Delta}$Ct comparative method.

Network Pharmacology Approach

The acacetin chemical formula was imported into the Swiss Target Prediction database (http://swisstargetprediction.ch/) for drug-target prediction analysis, and the keyword "sepsis" was then searched in the Gene Cards database (https://www.genecards.org/) to identify disease targets. The overlapping targets among compound and sepsis targets were used to draw a Venn diagram.

The protein-protein interaction (PPI) network was obtained by introducing these potential overlapping targets of acacetin and sepsis into the STRING database (https://string-db.org) with the species limited to "*Homo sapiens*" and a confidence score >0.9. The results were further visualized by Cytoscape 3.7.0. The degree of freedom was reflected by the node size and colour. Subsequently, the top four key targets were identified as hub targets based on their degree, centrality and proximity to hub proteins.

The hub targets were converted into their Ensembl gene names (www.ensembl.org/biomart/), and the OmicShare server (http://www.omicshare.com/) was then used for the analysis. The converted Ensembl gene names were used as input, and Gene Ontology (GO) enrichment and Kyoto Encyclopaedia of Genes and Genomes (KEGG) enrichment analyses were performed. The molecular function (MF), biological process (BP) and cellular component (CC) terms enriched in the targets were determined, and pathway enrichment of the top 20 pathways was visualized with the R package.

These results were summarized and loaded into Cytoscape 3.7.0 to construct the acacetin-target-GO-KEGG-sepsis network. In the network, edges represent interactions between nodes, and nodes represent drugs, diseases, BPs, pathways and targets.

Molecular Docking

The 3D crystal structures of ESR1 (PDB code: 5ACC), COX-2 (gene: PTGS2, PDB code: 4RRX), SRC (PDB code: 4U5J) and EGFR (PDB code: 6JZ0) were obtained from the Protein Data Bank (PDB). The 2D structure of acacetin was downloaded from the ZINC15 database (https://zinc15docking.org/). The original ligand active site residues were identified from the PDB coordinates and recorded. The protein structures were prepared by removing all nonreceptor atoms, including water, ions, and miscellaneous compounds, using Discover Studio Visualizer. Docking experiments were performed using CDOCKER with receptor-ligand interactions. The -CDOCKER_INTERACTION_ENERGY value was determined to evaluate bonding. The binding results were visualized as 3D and 2D diagrams using Discovery Studio Visualization version 4.5 (Accelrys, Inc., San Diego, CA 92121, CA, United States).

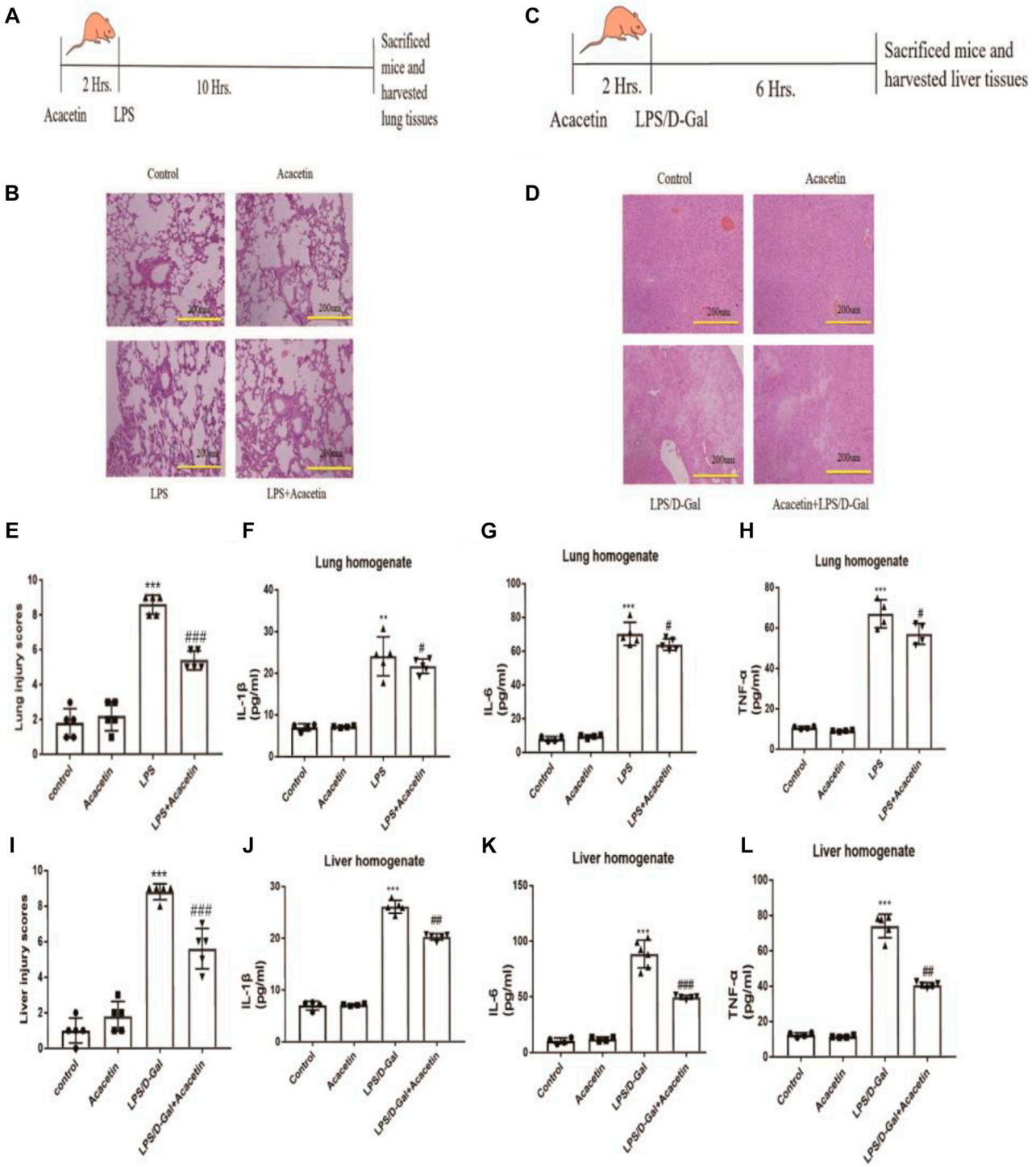

FIGURE 1 | The protective effect of acacetin against sepsis *in vivo*. **(A)** and **(C)** Methods to generate two inflammatory models and diagram showing the drawing time. **(B)** and **(D)** Histopathological damage to the lung (× 200) and liver (× 200). **(E)** and **(I)** Lung and liver injury scores. The lung **(F)** and liver **(J)** homogenate levels of IL-1β **(G)**, **(K)** IL-6 **(H)**, and **(L)** TNF-α were determined by ELISA. The data are expressed as the mean ± SEM (n = 5). $^{*}p < 0.05$, $^{**}p < 0.01$, $^{***}p < 0.001$, compared with the control group; $^{\#}p < 0.05$, $^{\#\#}p < 0.01$, $^{\#\#\#}p < 0.001$, compared with the LPS-stimulated group.

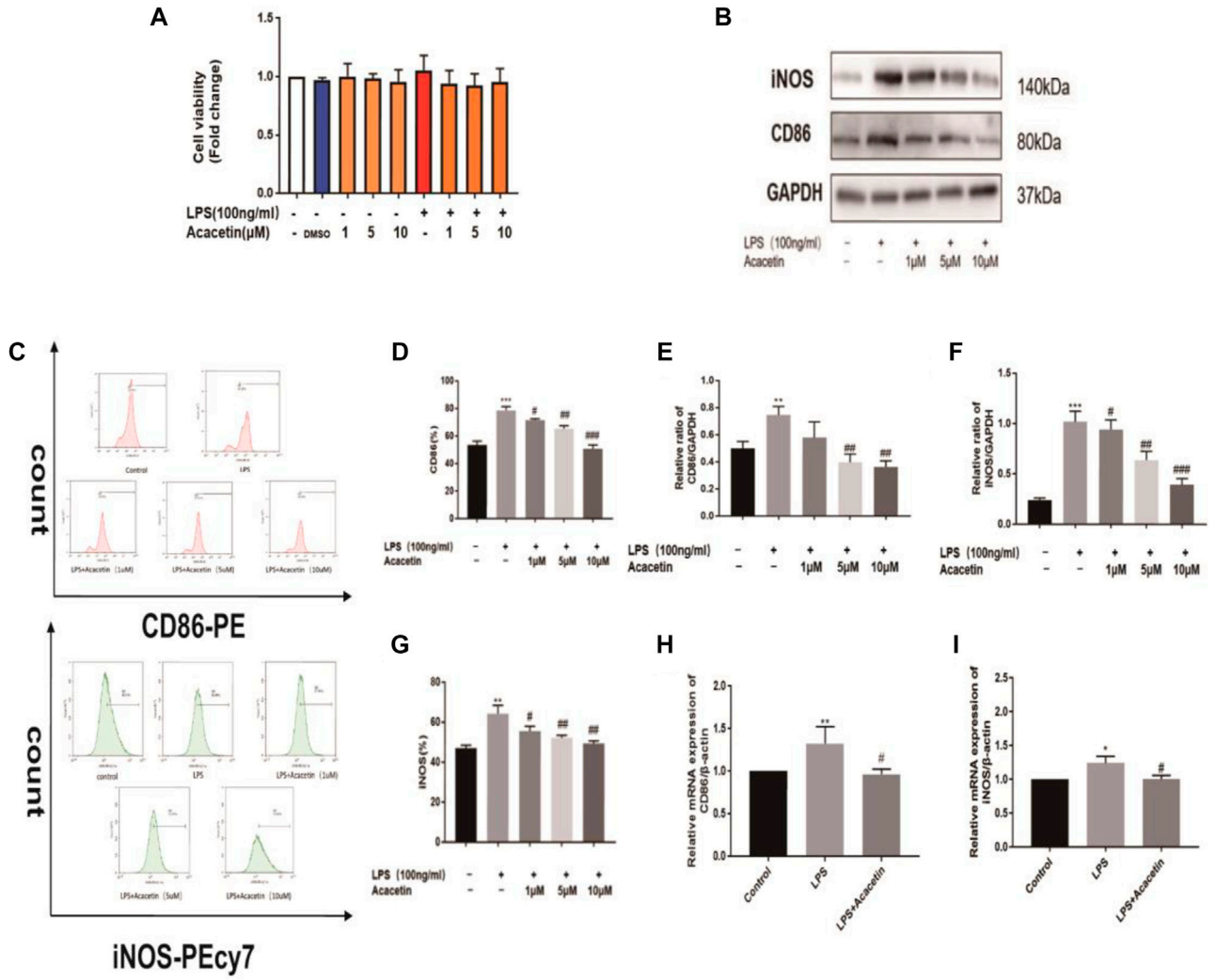

FIGURE 2 | The protective effect of acacetin against sepsis *in vitro*. **(A)** The effect of acacetin on cell viability as determined by the MTT assay. The protein levels **(B, E, F)**, positive cells identified by FACS **(C, D, G)**, and mRNA levels **(H, I)** of the M1 polarization markers CD86 and inducible nitric oxide synthase (iNOS) in RAW264.7 cells. The data are expressed as the mean ± SEM ($n = 3$). $^{*}p < 0.05$, $^{**}p < 0.01$, and $^{***}p < 0.001$ compared with the control group; $^{\#}p < 0.05$, $^{\#\#}p < 0.01$, $^{\#\#\#}p < 0.001$ compared with the LPS-stimulated group.

Statistical Analyses

Statistical evaluations were performed using the GraphPad Prism 5 package (GraphPad Software Inc., San Diego, CA, United States). Multiple comparisons were performed by one-way ANOVA followed by Tukey's post hoc significant difference test. p values less than 0.05 indicate statistical significance.

RESULTS

Protective Effect of Acacetin Against Sepsis *in vivo*

To assess the protective effect of acacetin against sepsis, we utilized LPS-induced FHF and ALI models. Compared with the control group, the FHF model group showed congestion, oedema, inflammatory cell infiltration, and a broadened pulmonary interval ($p < 0.05$), and the ALI model group showed more inflammatory areas in the portal vein and more necrotic hepatocytes ($p < 0.05$). Compared with the FHF and ALI model groups, the acacetin group showed less severe lung and liver injury symptoms as determined by HE staining (**Figures 1B,D**), and the injury scores of the acacetin group were significantly lower than those of the model group (**Figures 1E,I**; $p < 0.05$). The levels of IL-1β, IL-6 and TNF-α in the liver and lung tissues of the model group were significantly higher than those in the control group tissues, while those in the acacetin group were decreased compared to those in the control group (**Figures 1F–H,J–L** $p < 0.05$). These results indicated that acacetin improves liver and lung injury by decreasing the levels of IL-1β, IL-6 and TNF-α.

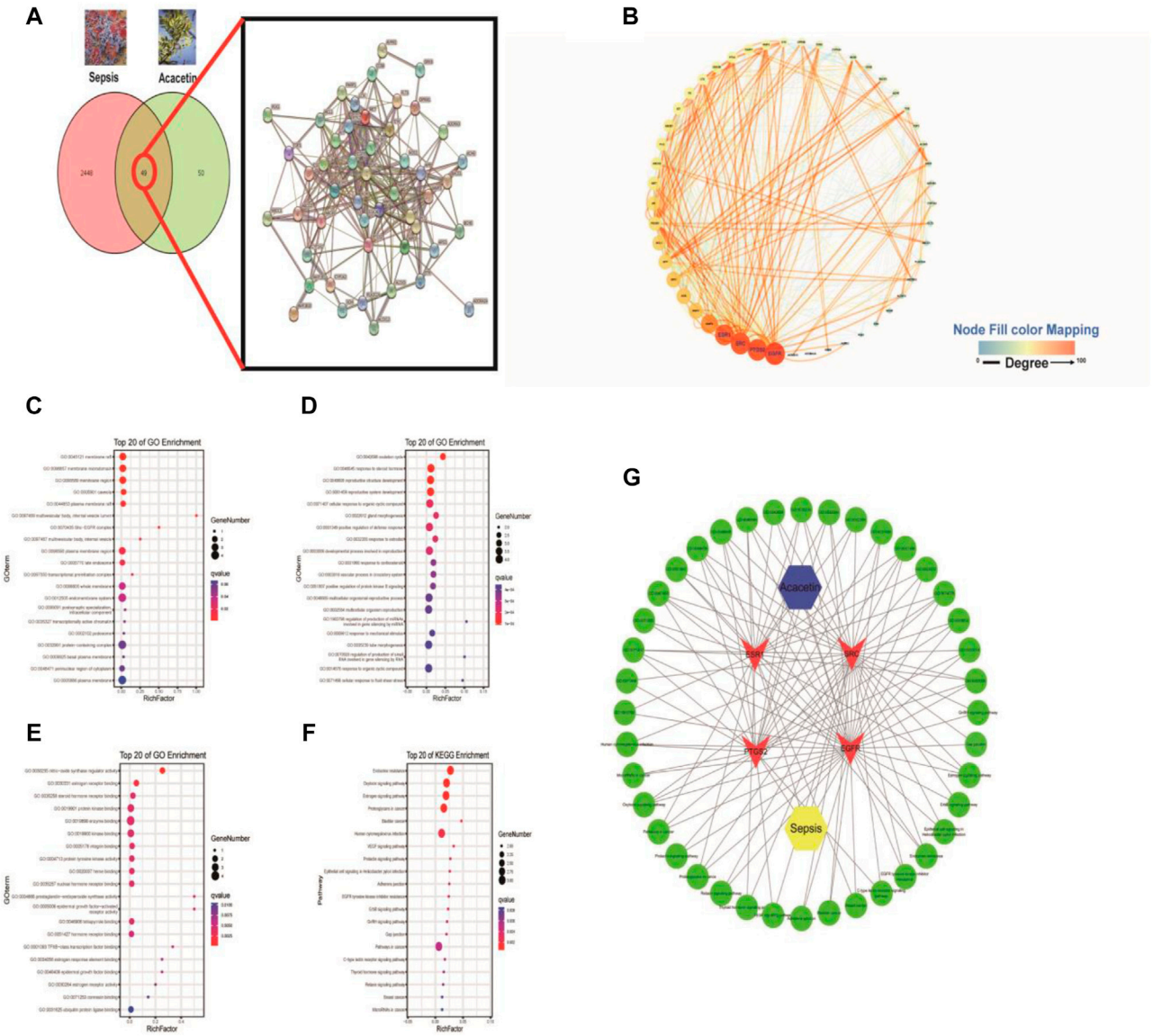

FIGURE 3 | The underlying mechanisms by which acacetin affects sepsis as determined by a network pharmacology approach. **(A)** All of the targets of acacetin and sepsis and the 49 intersecting targets of acacetin and sepsis were identified *via* a Venn diagram and PPI network. **(B)** The top four hub genes/targets of both acacetin and sepsis were identified and arranged according to their degree value with an algorithm using Cytoscape software. **(C–F)** With the OmicShare service R-language packages, the four core targets were subjected to GO analyses of cellular component (CC), biological process (BP), and molecular function (MF) terms and KEGG pathway analysis. The bubble diagram shows the top 20 terms related to the activity of acacetin against sepsis. **(G)** Network constructed from the bioinformatics analysis results highlighting the detailed interactions between acacetin-targets-GO-KEGG-sepsis. Hub targets are represented by a red V, and the top 20 BP terms and pathways involved in the activity of acacetin against sepsis are shown in green.

Protective Effect of Acacetin Against Sepsis *in vitro*

Macrophage polarization is involved in the pathogenesis of sepsis. To assess the protective effect of acacetin on sepsis and the underlying mechanism *in vitro*, we observed its effect on M1 macrophage polarization induced by LPS in RAW264.7 cells. As shown in **Figure 2A**, treatment with 1, 5, and 10 μMol acacetin had no toxic effects, and the agent was thus used at these nontoxic concentrations in further experiments. Compared with those in the control group, the CD86 and iNOS protein levels, number of positive cells determined by flow cytometry, and mRNA levels were increased in the LPS-stimulated group. Compared with LPS, acacetin attenuated the CD86 and iNOS protein levels (**Figures 2B,E,F**), the number of positive cells determined by fluorescence-activated cell sorting (FACS) (**Figures 2C,D,G**) and the mRNA levels (**Figures 2H,I**). Additionally, exposure to various doses of acacetin (1, 5, and 10 μMol) attenuated the expression of CD86 and iNOS in M1-type cells in a concentration-dependent manner

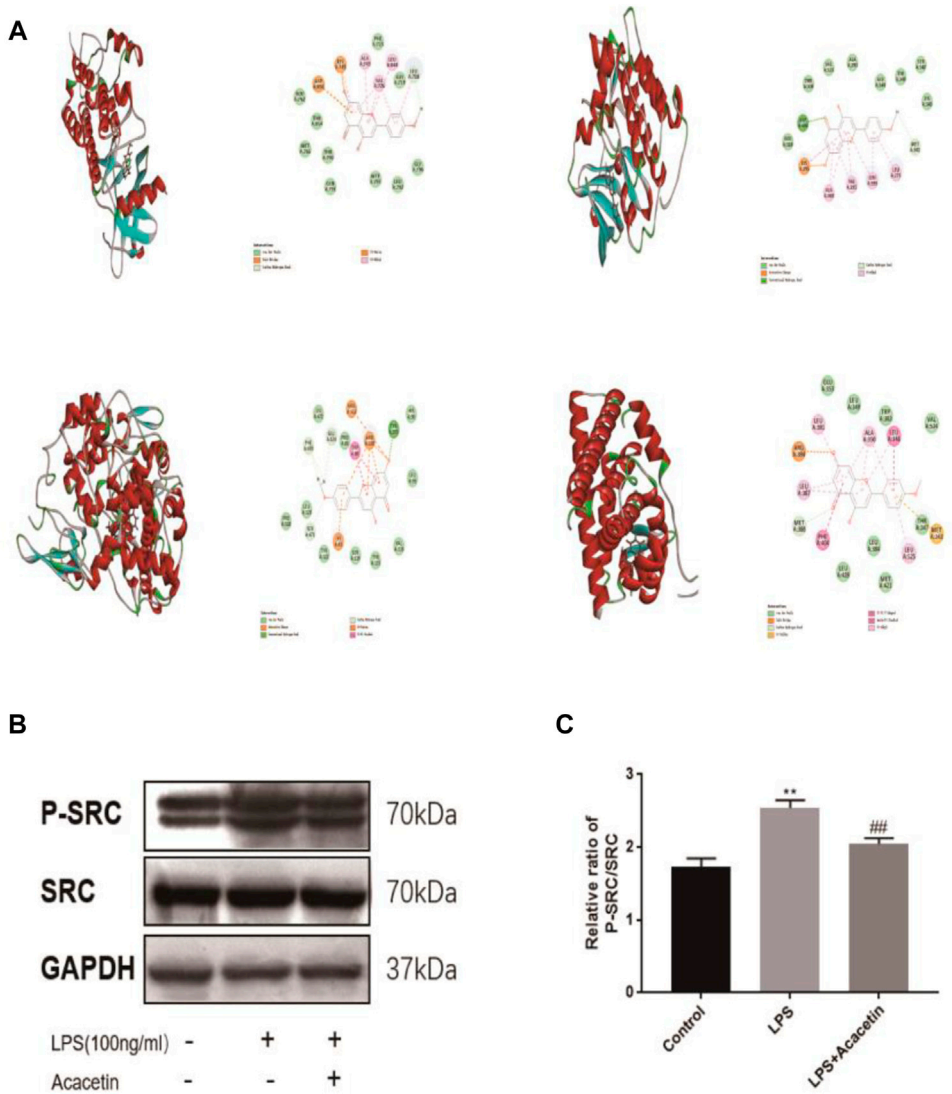

FIGURE 4 | Molecular docking and experimental validation of acacetin binding core targets predicted by network pharmacology. **(A)** EGFR, SRC, PTGS2 and ESR1. All pictures show the 3D docking of ligands in the active binding pocket, with the hydrophobic effect area and the 2D interaction patterns between the ligands and proteins and the important interactions between the ligand atoms and amino acid residues of the proteins being displayed. **(B–C)** The expression levels of Src and phosphorylated Src were assessed via Western blotting. The data are expressed as the mean ± SEM ($n = 3$). $^{*}p < 0.05$, $^{**}p < 0.01$, and $^{***}p < 0.001$ compared with the control group; $^{\#}p < 0.05$, $^{\#\#}p < 0.01$, $^{\#\#\#}p < 0.001$ compared with the LPS-stimulated group.

($p < 0.05$). These phenomena revealed that acacetin helped to quickly reduce the CD86 and iNOS levels in M1-type macrophages.

Elucidating the Mechanisms Underlying the Effects of Acacetin on Sepsis *via* a Network Pharmacology Approach

The canonical SMILES string for acacetin was input into the Swiss Target Prediction database to identify the targets of acacetin, and a total of 99 potential drug targets were found. There were 2,497 potential targets of sepsis in the GeneCards database. As shown in **Figures 3A**,**4** common targets were included in the acacetin-sepsis target Venn diagram. The 49 intersectional targets were imported into the STRING database to explore the relationships among these targets (**Figure 3A**). A PPI network of the 49 common targets between acacetin and sepsis was constructed based on degree value screening, and EGFR, PTGS2, SRC and ESR1 were identified as the core targets (**Figure 3B**). GO and KEGG analyses were performed, and the core targets of EGFR, PTGS2, SRC and ESR1 were input into the Omicshare database to identify the possible mechanism by which acacetin affects sepsis. GO analysis of the CC terms showed that the four core targets were mainly associated with membrane rafts, the membrane microdomain and the membrane region (**Figure 3C**). GO analysis of BP terms showed that the four core targets were mainly related to the ovulation cycle, steroid

TABLE 1 | Interaction of acacetin and hub targets by discovery studio

Targets	Acacetin CDCOKER interaction energy	Positive compare CDOCKER interaction energy
EGFR	37.6692	29.7857
SRC	40.6193	58.7556
PTGS2	49.4521	34.7360
ESR1	37.7927	36.4148

hormones and reproductive structure development (**Figure 3D**). GO analysis of MF terms showed that the four core targets were mainly associated with connexin (Cx) binding, NOS activity regulation, oestrogen receptor binding and protein kinase binding (**Figure 3E**). KEGG analysis revealed that the four core targets were closely associated with the gap junction, endocrine resistance, oxytocin signalling, proteoglycans in cancer, bladder cancer and human cytomegalovirus infection pathways (**Figure 3F**). **Figure 3G** shows the acacetin-sepsis-target-GO-KEGG network.

Molecular Docking and Experimental Validation of the Binding of Core Acacetin Targets Predicted by Network Pharmacology

Molecular docking was carried out to investigate potential binding modes and interactions between acacetin and its key targets (**Figure 4A**). For the docking interaction energy score, the targets were ranked as PTGS2 > SRC > ESR1 > EGFR (**Table 1**). The carbonyl, methoxy and hydroxy groups are thought to be the key groups that bind residues containing H donor moieties at the terminus (Zhao et al., 2019); (Lin et al., 2019); (Duan et al., 2014); (De Savi et al., 2015); (Blobaum et al., 2015) For the specific proteins in the EGFR complex, the residues involved in the formation of H-bonds included ALA 743, THR 790, VAL726, and THR 854. With regard to the SRC docking results, the key residues involved in H-bonds were MET 341, VAL 281 and LEU 393. In the ESR1 complex, THR 347 and MET343 emerged as key residues between the methoxyl group at the 4' position of acacetin and the target. In the COX-2 (PTGS2) complex, TYR 355 was identified as the only key residue involved in H-bonds. Moreover, known standard or positive molecules of the four targets were subjected to the same simulation (**Supplementary Figure S1**). The molecular docking results indicated that acacetin can interact with PTGS2, SRC, ESR1 and EGFR to form compact complexes. Src is a prototype of the highly conserved Src family kinase (SFK) proteins, and our results indicated that the expression of p-src in RAW264.7 cells was significantly increased after LPS stimulation and reduced after treatment with acacetin (**Figures 4B,C**; $p < 0.05$).

Experimental Validation of the Acacetin Binding Signalling Pathway Predicted by Network Pharmacology

Further network pharmacological analysis and GO and KEGG analyses indicated that gap junctions may be highly involved in the protective effects of acacetin against sepsis. We confirmed the role of gap junctions in the effects of acacetin on LPS-induced M1 polarization in RAW264.7 cells. As shown in **Figures 5A,D**, the expression levels of Cx43 were significantly increased after LPS stimulation but reduced after treatment with acacetin. As shown in **Figures 5B,C,E,F** the protein expression levels of CD86, iNOS, p65, and p-p65 were revealed by Western blotting. Notably, p-p65, CD86 and iNOS protein expression was significantly decreased in the Gap27 group compared with the LPS group ($p < 0.05$). Together, these results suggest a prospective role for gap junctions in attenuating the effect of acacetin on M1-type macrophages.

DISCUSSION

Sepsis is a global healthcare issue and continues to be the leading cause of death from infection. In clinical practice, the use of antimicrobial agents to fight infection is key to the treatment of sepsis. Over the past few decades, natural products, such as anti-bacterial and anti-inflammatory drugs, have been used for the herbal treatment and prevention of human diseases (McBride Margaret et al., 2020). Acacetin is a natural flavonoid found in various plants, including *Sparganii rhizoma*, *Sargentodoxa cuneata* and *Patrinia scabiosifolia*. Our results indicated that acacetin improved liver and lung injury by decreasing the levels of IL-1β, IL-6 and TNF-α, and acacetin expedited the reduction in CD86 and iNOS expression in M1-type macrophages. Previous reports have indicated that acacetin has anti-inflammatory effects. For example, acacetin was shown to suppress the LPS-induced upregulation of iNOS and COX-2 in murine macrophages and TPA-induced tumour promotion in mice (Pan et al., 2006). Acacetin was also shown to attenuate mouse ALI induced by endotoxin by augmenting HO-1 activity (Wu et al., 2018) and to block kv1.3 channels and inhibit human T cell activation (Zhao et al., 2014). These results demonstrate that acacetin has anti-inflammatory and antioxidative effects on sepsis, but the underlying molecular mechanism remains unclear.

We herein further investigated the mechanisms underlying the effects of acacetin on sepsis by performing network pharmacology analysis coupled with experimental validation and molecular docking. All potential targets of acacetin and sepsis were methodically obtained, and the top four overlapping targets in the PPI network were EGFR, PTGS2, SRC and ESR1. EGFR prevents the translocation of gut-residing pathogenic and cancer-associated protein kinases and is a key target for late-onset neonatal sepsis and cancer (Knoop et al., 2020; Singh et al., 2021). Our results identified ALA 743, THR790, VAL726, THR854 and ASP855 as the key EGFR residues in the binding pocket. PTGS2, also known as COX-2, has been reported to have an anti-inflammatory effect, and acacetin can reportedly relieve sepsis by inhibiting COX-2 activity (Pan et al., 2006; Wu et al., 2018; Fatemi et al., 2020). Due to the structural specificity of the COX-2 protein, only TYR 355 was identified as the key residue involved in H-bonds.

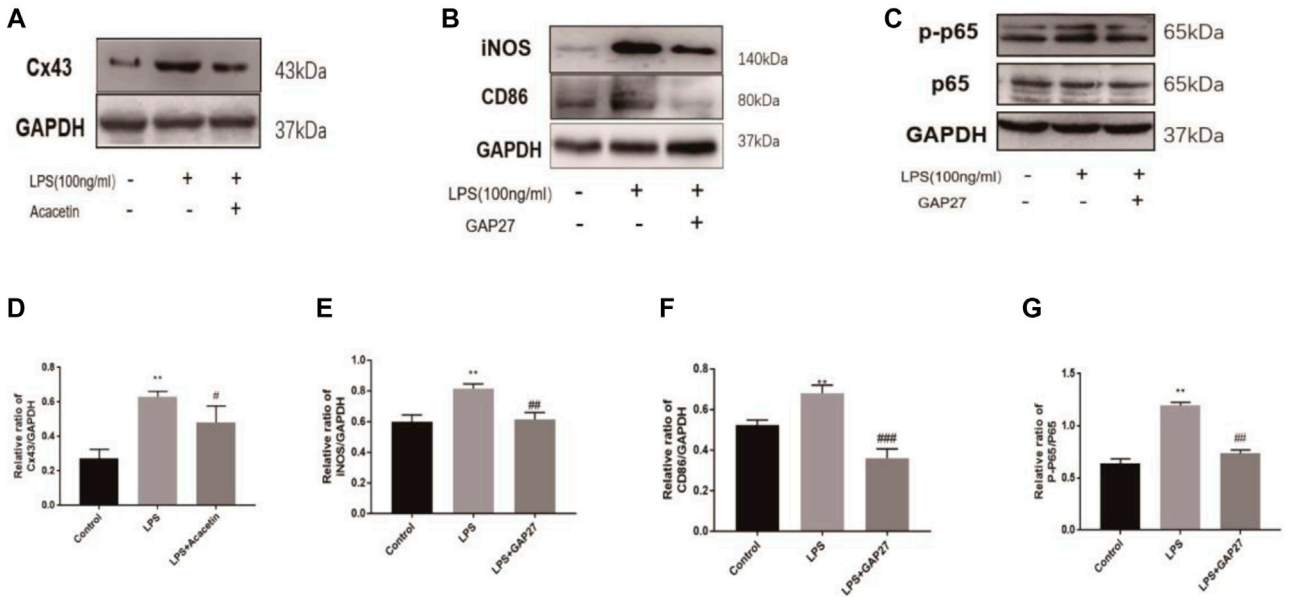

FIGURE 5 | Experimental validation of the acacetin binding signalling pathway predicted by network pharmacology. The expression levels of Cx43, CD86, iNOS, P65 and phosphorylated P65 **(A–G)** were assessed via Western blotting. The data are expressed as the mean ± SEM ($n = 3$). $^{*}p < 0.05$, $^{**}p < 0.01$, and $^{***}p < 0.001$ compared with the control group; $^{\#}p < 0.05$, $^{\#\#}p < 0.01$, $^{\#\#\#}p < 0.001$ compared with the LPS-stimulated group.

Moreover, ESR1, as the target of the *ShenFuHuang* formulation in a zebrafish model, was associated with septic syndrome in patients with COVID-19 (Liu et al., 2020b). Our results highlighted THR 347 and MET343 as the key residues residing between the methoxyl group at the 4' position of acacetin and ESR1, which is also consistent with the binding site for the original ligand. Additionally, cellular Src is the prototype of highly conserved SFK proteins. Evidence suggests that siglec-G deficiency ameliorates hyperinflammation and immune collapse in patients with sepsis by regulating Src activation (Li et al., 2019). With regard to the Src docking results, MET 341, VAL 281 and LEU 393 were identified as the key residues of the binding pocket with the original ligand ruxolitinib. Thus, based on its prediction as a core target and its association with macrophages and sepsis, Src deserves to be further studied *in vitro*. Our western blot results suggested that phosphorylated Src plays an important role in the anti-septic activity of acacetin. Together, our results showed that acacetin had a preferential affinity for all four targets, confirming the prediction results obtained by network pharmacology analysis.

GO and KEGG analyses were performed to analyse the interactions among multiple targets and pathways, and the top 20 enriched BPs and signalling pathways were shown to be associated with the therapeutic effects of acacetin on sepsis. Membrane raft, oestrogen receptor activity, and human cytomegalovirus infection are related to the effects of acacetin on sepsis. In a previous study, lipid raft microdomains were shown to be essential components of phagolysosomal macrophage membranes and to play an essential role in antifungal immunity (Schmidt et al., 2020). Moreover, human cytomegalovirus infection was shown to potentially impact immunity (Cox et al., 2021). Thus, our subsequent research will be performed using macrophages. Further network pharmacological analysis indicated that gap junctions may be highly involved in the protective effects of acacetin against sepsis. Cxs are basic components of gap junctions, and Cx43 is a common Cx family member that is widely expressed in immune cells and involved in a variety of immune regulatory processes (Glass et al., 2015). In a previous study, ATP release through Cx43 was reported to be important for inhibiting inflammation and bacterial burden (Balázs et al., 2015). Our results showed that the gap junction selective blocker gap27 could significantly decrease the protein expression of p-p65, CD86 and iNOS. p-p65 is the key target of the classic inflammation-related NF-κB signalling pathway, CD86 is a surface marker of M1-polarized macrophages, and iNOS is a pro-inflammatory molecule associated with the inflammatory process. Our previous research on Cx43 showed that carbenoxolone decreased monocrotaline-induced pulmonary inflammation in rats by decreasing the expression of Cxs in T lymphocytes (Zhang et al., 2020). Angiotensin II induced RAW264.7 macrophage polarization toward the M1 phenotype through the Cx43/NF-κB pathway (Wu et al., 2020). Our findings highlighted gap junctions in macrophages as a new potential target for sepsis, and most importantly, showed that acacetin inhibited the LPS-induced increase in Cx43 expression. Interestingly, the anti-inflammatory effect of acacetin via gap junctions has not been reported. Together, these results suggest that gap junctions attenuate the effects of acacetin on sepsis.

CONCLUSION

Our results suggest that acacetin protects against sepsis *via* a mechanism involving multiple targets and pathways and that gap junctions are highly involved in this process.

DATA AVAILABILITY STATEMENT

The original contributions presented in the study are included in the article/**supplementary files**, further inquiries can be directed to the corresponding authors.

ETHICS STATEMENT

The studies involving human participants were reviewed and approved by Institutional Animal Ethics Committee of Xi'an Jiaotong University No. 2017–666. The patients/participants provided their written informed consent to participate in this study. The animal study was reviewed and approved by Institutional Animal Ethics Committee of Xi'an Jiaotong University No. 2017–666. Written informed consent was obtained from the owners for the participation of their animals in this study. Written informed consent was obtained from the individual(s), and minor(s)' legal guardian/next of kin, for the publication of any potentially identifiable images or data included in this article.

AUTHOR CONTRIBUTIONS

KM and XL conceived and designed the experiments. YO, YW and YG were involved in the study design. YO and YR performed the experiments. YO, YW, YG, LS and XY analysed the data. YO, YW, YG, LL, JS and KM wrote and revised the manuscript. KM and XL received the funding. All authors have read and approved the final manuscript.

FUNDING

This work was supported by the National Natural Science Foundation of China (nos. 81860085 and 81860286), the Corps Science and Technology Cooperation Project of China (no. 2020BC004), and the Central Research Institute Fund of Chinese Academy of Medical Sciences (no. 2020-PT330-003).

ACKNOWLEDGMENTS

We thank the Key Laboratory of Xinjiang Endemic and Ethnic Diseases, NHC Key Laboratory of Prevention and Treatment of Central Asia High Incidence Diseases, the Department of Physiology and Pathophysiology of Shihezi University School of Medicine, and the Department of Biochemistry and Molecular Biology, School of Basic Medical Science, Xi'an Jiaotong University Health Science Center for their support.

SUPPLEMENTARY MATERIAL

The Supplementary Material for this article can be found online at: https://www.frontiersin.org/articles/10.3389/fphar.2021.683645/full#supplementary-material

REFERENCES

Balázs, Csóka., Németh Zoltán, H., Gábor, Törő., Idzko, M., Zech, A., Koscsó, B., et al. (2015). Extracellular ATP Protects against Sepsis through Macrophage P2X7 Purinergic Receptors by Enhancing Intracellular Bacterial Killing. *[J]. FASEB J.* 29, 3626–3637.

Blobaum, A. L., Xu, S., Rowlinson, S. W., Duggan, K. C., Banerjee, S., Kudalkar, S. N., et al. (2015). Action at a Distance. *J. Biol. Chem.* 290, 12793–12803. doi:10.1074/jbc.m114.635987

Chen, W., Wang, Y., Zhou, T., Xu, Y., Zhan, J., and Wu, J. (2020). CXCL13 Is Involved in the Lipopolysaccharide-Induced Hyperpermeability of Umbilical Vein Endothelial Cells. *Inflammation* 43 (5), 1789–1796. doi:10.1007/s10753-020-01253-6

Cho, H.-I., Park, J.-H., Choi, H.-S., Kwak, J. H., Lee, D.-U., Lee, S. K., et al. (2014). Protective Mechanisms of Acacetin Againstd-Galactosamine and Lipopolysaccharide-Induced Fulminant Hepatic Failure in Mice. *J. Nat. Prod.* 77, 2497–2503. doi:10.1021/np500537x

Cox, M., Kartikasari Apriliana, E. R., Gorry Paul, R., Flanagan, K. L., Plebanski, M., et al. (2021). Potential Impact of Human Cytomegalovirus Infection on Immunity to Ovarian Tumours and Cancer Progression. *[J]. Biomedicines* 9. doi:10.3390/biomedicines9040351

De Savi, C., Bradbury, R. H., Rabow, A. A., Norman, R. A., de Almeida, C., Andrews, D. M., et al. (2015). Optimization of a Novel Binding Motif to (E)-3-(3,5-Difluoro-4-((1R,3R)-2-(2-fluoro-2-methylpropyl)-3-methyl-2,3,4,9-tetrahydro-1H-pyrido [3,4-b]indol-1-yl)phenyl)acrylic Acid (AZD9496), a Potent and Orally Bioavailable Selective Estrogen Receptor Downregulator and Antagonist. *J. Med. Chem.* 58, 8128–8140. doi:10.1021/acs.jmedchem.5b00984

Duan, Y., Lin, C., Chen, Y., and Fan, X. G., (2014). c-Src Binds to the Cancer Drug Ruxolitinib with an Active Conformation. *[J]. PLoS One* 9, e106225. doi:10.1371/journal.pone.0106225

Fan, H., Wu, Q., Peng, L., Li, D., Dong, Y., Cao, M., et al. (2020). Phyllolobium Chinense Fisch Flavonoids (PCFF) Suppresses the M1 Polarization of LPS-Stimulated RAW264.7 Macrophages by Inhibiting NF-κB/iNOS Signaling Pathway. *[J]. Front Pharmacol.* 11, 864. doi:10.3389/fphar.2020.00864

Fatemi, F., Golbodagh, A., Dadkhah, R. A., Akbarzadeh, K., Dini, S., and Malayeri, M. R. M. (2020). Anti-inflammatory Effects of Deuterium-Depleted Water Plus Rosa Damascena Mill. Essential Oil via Cyclooxygenase-2 Pathway in Rats. *Turk J. Pharm. Sci.* 17, 99–107. doi:10.4274/tjps.galenos.2018.24381

Glass, A. M., Snyder, E. G., and Taffet, S. M. (2015). Connexins and Pannexins in the Immune System and Lymphatic Organs. *Cell. Mol. Life Sci.* 72, 2899–2910. doi:10.1007/s00018-015-1966-3

Hu, L., Chen, Y., Chen, T., Huang, D., Li, S., Cui, S., et al. (2020). Sargentodoxa Cuneata A Systematic Study of Mechanism of and against Pelvic Inflammatory Disease with Dampness-Heat Stasis Syndrome via Network Pharmacology Approach. *[J]. Front Pharmacol.* 11, 582520. doi:10.3389/fphar.2020.582520

Knoop, K. A., Coughlin, P. E., Floyd, A. N., Ndao, I. M., Hall-Moore, C., Shaikh, N., et al. (2020). Maternal Activation of the EGFR Prevents Translocation of Gut-Residing pathogenicEscherichia Coliin a Model of Late-Onset Neonatal Sepsis. *Proc. Natl. Acad. Sci. USA* 117, 7941–7949. doi:10.1073/pnas.1912022117

Li, R., Guo, C., Li, Y., Qin, Z., and Huang, W. (2020). Therapeutic Targets and Signaling Mechanisms of Vitamin C Activity against Sepsis: a Bioinformatics Study. *[J] Brief Bioinform* 22. doi:10.1093/bib/bbaa079

Li, W., Li, Y., Qin, K., Du, B., Li, T., Yuan, H., et al. (2019). Siglec-G Deficiency Ameliorates Hyper-Inflammation and Immune Collapse in Sepsis via Regulating Src Activation. [J]. *Front. Immunol.* 10, 2575. doi:10.3389/fimmu.2019.02575

Lin, S.-Y., Chang Hsu, Y., Peng, Y.-H., Ke, Y.-Y., Lin, W.-H., Sun, H.-Y., et al. (2019). Discovery of a Furanopyrimidine-Based Epidermal Growth Factor Receptor Inhibitor (DBPR112) as a Clinical Candidate for the Treatment of Non-small Cell Lung Cancer. *J. Med. Chem.* 62, 10108–10123. doi:10.1021/acs.jmedchem.9b00722

Liu, B., Lu, Y., Chen, X., Muthuraj, P. G., Li, X., Pattabiraman, M., et al. (2020). Protective Role of Shiitake Mushroom-Derived Exosome-like Nanoparticles in D-Galactosamine and Lipopolysaccharide-Induced Acute Liver Injury in Mice. *Nutrients* 12 (2), 477. doi:10.3390/nu12020477

Liu, T., Guo, Y., Zhao, J., He, S, Bai, Y., Wang, N., et al. (2020). Systems Pharmacology and Verification of ShenFuHuang Formula in Zebrafish Model Reveal Multi-Scale Treatment Strategy for Septic Syndrome in COVID-19. [J]. *Front. Pharmacol.* 11, 584057. doi:10.3389/fphar.2020.584057

Lu, X., Zheng, Y., Wen, F., Huang, W., Chen, X., Ruan, S., et al. (2021). Study of the Active Ingredients and Mechanism of Sparganii Rhizoma in Gastric Cancer Based on HPLC-Q-TOF-MS/MS and Network Pharmacology. *[J]. Sci Rep.* 11, 1905. doi:10.1038/s41598-021-81485-0

McBride Margaret, A., Patil Tazeen, K., Bohannon Julia, K., Hernandez, A., Sherwood, E. R., Patil, N. K., et al. (2020). Immune Checkpoints: Novel Therapeutic Targets to Attenuate Sepsis-Induced Immunosuppression. [J]. *Front. Immunol.* 11, 624272. doi:10.3389/fimmu.2020.01043

Pan, M.-H., Lai, C.-S., Wang, Y.-J., and Ho, C.-T. (2006). Acacetin Suppressed LPS-Induced Up-Expression of iNOS and COX-2 in Murine Macrophages and TPA-Induced Tumor Promotion in Mice. *Biochem. Pharmacol.* 72, 1293–1303. doi:10.1016/j.bcp.2006.07.039

Schmidt, F., Thywißen, A., Cunha, M. C., Cseresnyés, Z., Schmidt, H., Rafiq, M., et al. (2020). Flotillin-Dependent Membrane Microdomains Are Required for Functional Phagolysosomes against Fungal Infections. *Cel Rep.* 32, 108017. doi:10.1016/j.celrep.2020.108017

Singh, S., Gupta, P., and Luqman, A. S. (2020). Acacetin, a Flavone with Diverse Therapeutic Potential in Cancer, Inflammation, Infections and Other Metabolic Disorders. *Food Chem. Toxicol.* 145, 111708. doi:10.1016/j.fct.2020.111708

Singh, S., Meena, A., and Meena, S. A. (2021). Acacetin and Pinostrobin as a Promising Inhibitor of Cancer-Associated Protein Kinases. *Food Chem. Toxicol.* 151, 112091. doi:10.1016/j.fct.2021.112091

Sun, L. C., Zhang, H. B., Gu, C. D., Guo, S. D., Li, G., Lian, R., et al. (2018). Protective Effect of Acacetin on Sepsis-Induced Acute Lung Injury via its Anti-inflammatory and Antioxidative Activity. *Arch. Pharm. Res.* 41, 1199–1210. doi:10.1007/s12272-017-0991-1

Wu, D., Wang, Y., Zhang, H., Du, M., and Li, T. (2018). Acacetin Attenuates Mice Endotoxin-Induced Acute Lung Injury via Augmentation of Heme Oxygenase-1 Activity. *Inflammopharmacol* 26, 635–643. doi:10.1007/s10787-017-0398-0

Wu, L., Chen, K., Xiao, J., Xin, J., Zhang, L., Li, X., et al. (2020). Angiotensin II Induces RAW264.7 Macrophage Polarization to the M1-type through the C-onnexin 43/NF-κB P-athway. *Mol. Med. Rep.* 21, 2103–2112. doi:10.3892/mmr.2020.11023

Xia, Q. D., Xun, Y., Lu, J. L., Lu, Y. C., Yang, Y. Y., Zhou, P., et al. (2020). Network Pharmacology and Molecular Docking Analyses on Lianhua Qingwen Capsule Indicate Akt1 Is a Potential Target to Treat and Prevent COVID-19. *Cell Prolif* 53, e12949. doi:10.1111/cpr.12949

Zhang, D., Lee, H., Wang, X., Groot, M., Sharma, L., Dela Cruz, C. S., et al. (2019). A Potential Role of Microvesicle-Containing miR-223/142 in Lung Inflammation. *Thorax* 74 (9), 865–874. doi:10.1136/thoraxjnl-2018-212994

Zhang, F.-x., Li, Z.-t., Xie, X. Z.-n., Chen, M.-h., Yao, Z.-h., Chen, J.-x., et al. (2021). Discovery of Anti-flu Substances and Mechanism of Shuang-Huang-Lian Water Extract Based on Serum Pharmaco-Chemistry and Network Pharmacology. *J. Ethnopharmacology* 268, 113660. doi:10.1016/j.jep.2020.113660

Zhang, L. Z., Fan, Z. R., Wang, L., Liu, L. Q., Li, X. Z., Li, L., et al. (2020). Carbenoxolone Decreases Monocrotaline-induced P-ulmonary I-nflammation and P-ulmonary A-rteriolar R-emodeling in R-ats by D-ecreasing the E-xpression of C-onnexins in T L-ymphocytes. *Int. J. Mol. Med.* 45, 81–92. doi:10.3892/ijmm.2019.4406-**Ru**

Zhao, N., Dong, Q., Fu, X.-X., Du, L.-L., Cheng, X., Du, Y.-M., et al. (2014). Acacetin Blocks kv1.3 Channels and Inhibits Human T Cell Activation. *Cell Physiol Biochem* 34, 1359–1372. doi:10.1159/000366343

Zhao, Z., Liu, G., Meng, Y., Tian, J., Chen, X., Shen, M., et al. (2019). Synthesis and Anti-tyrosinase Mechanism of the Substituted Vanillyl Cinnamate Analogues. *Bioorg. Chem.* 93, 103316. doi:10.1016/j.bioorg.2019.103316

Conflict of Interest: The authors declare that the research was conducted in the absence of any commercial or financial relationships that could be construed as a potential conflict of interest.

Publisher's Note: All claims expressed in this article are solely those of the authors and do not necessarily represent those of their affiliated organizations, or those of the publisher, the editors and the reviewers. Any product that may be evaluated in this article, or claim that may be made by its manufacturer, is not guaranteed or endorsed by the publisher.

Copyright © 2021 Ouyang, Rong, Wang, Guo, Shan, Yu, Li, Si, Li and Ma. This is an open-access article distributed under the terms of the Creative Commons Attribution License (CC BY). The use, distribution or reproduction in other forums is permitted, provided the original author(s) and the copyright owner(s) are credited and that the original publication in this journal is cited, in accordance with accepted academic practice. No use, distribution or reproduction is permitted which does not comply with these terms.

frontiers in Pharmacology

ORIGINAL RESEARCH
published: 26 August 2021
doi: 10.3389/fphar.2021.665635

Study on the Effect of Macrophages on Vascular Endothelium in Mice With Different TCM Syndromes of Dyslipidemia and its Biological Basis Based on RNA-Seq Technology

*Jing Chen[1], Chao Ye[2], Zheng Yang[3], Tieshan Wang[4], Bing Xu[5], Pengyang Li[2], Shan Zhang[3] and Xiaolin Xue[3]**

[1]Preventive Treatment of Disease Department, The Third Affiliated Hospital, Beijing University of Chinese Medicine, Beijing, China, [2]Orthopedics Department, Dongzhimen Hospital, Beijing University of Chinese Medicine, Beijing, China, [3]School of Traditional Chinese Medicine, Beijing University of Chinese Medicine, Beijing, China, [4]Beijing Research Institute of Chinese Medicine, Beijing University of Chinese Medicine, Beijing, China, [5]Traditional Chinese Medicine Department, Tibetology Research Center of Beijing Tibetan Medicine Hospital, Beijing, China*

OPEN ACCESS

Edited by:
Hai Yu Xu,
China Academy of Chinese Medical Sciences, China

Reviewed by:
Huimin Yang,
Beijing University of Chinese Medicine, China
Lingru Li,
Beijing University of Chinese Medicine, China

***Correspondence:**
Xiaolin Xue
bjxuexiaol@163.com

Specialty section:
This article was submitted to Ethnopharmacology, a section of the journal Frontiers in Pharmacology

Received: *08 February 2021*
Accepted: *12 August 2021*
Published: *26 August 2021*

Citation:
Chen J, Ye C, Yang Z, Wang T, Xu B, Li P, Zhang S and Xue X (2021) Study on the Effect of Macrophages on Vascular Endothelium in Mice With Different TCM Syndromes of Dyslipidemia and its Biological Basis Based on RNA-Seq Technology. Front. Pharmacol. 12:665635. doi: 10.3389/fphar.2021.665635

Background: "Treating the same disease with different methods" is a Traditional Chinese medicine (TCM) therapeutic concept suggesting that, while patients may be diagnosed with the same disease, they may also have different syndromes that require distinct drug administrations.

Objective: This study aimed to identify the differentially expressed genes and related biological processes in dyslipidemia in relation to phlegm–dampness retention (PDR) syndrome and spleen and kidney Yang deficiency (SKYD) syndrome using transcriptomic analysis.

Methods: Ten ApoE$^{-/-}$ mice were used for the establishment of dyslipidemic disease–syndrome models via multifactor-hybrid modeling, with five in the PDR group and five in the SKYD group. Additionally, five C57BL/6J mice were employed as a normal control group. Test model-quality aortic endothelial macrophages in mice were screened using flow cytometry. Transcriptomic analysis was performed for macrophages using RNA-Seq.

Results: A quality assessment of the disease–syndrome model showed that levels of lipids significantly increased in the PDR and SKYD groups, compared to the normal control group, $p < 0.05$. Applying, in addition, hematoxylin and eosin staining of aorta, the disease model was also successfully established. A quality assessment of the syndrome models showed that mice in the PDR group presented with typical manifestations of PDR syndrome, and mice in the SKYD group had related manifestations of SKYD syndrome, indicating that the syndrome models were successfully constructed as well. After comparing the differentially expressed gene expressions in macrophages of the dyslipidemic mice with different syndromes, 4,142 genes were identified with statistical significance, $p < 0.05$. Gene ontology analysis for the differentially expressed genes showed that the biological process of difference between the PDR group and the SKYD group included both adverse and protective processes.

Conclusion: The differentially expressed genes between PDR syndrome and SKYD syndrome indicate different biological mechanisms between the onsets of the two syndromes. They have

distinctive biological processes, including adverse and protective processes that correspond to the invasion of pathogenic factors into the body and the fight of healthy Qi against pathogenic factors, respectively, according to TCM theory. Our results provide biological evidence for the TCM principle of "treating the same disease with different treatments."

Keywords: macrophages, traditonal Chinese medicine, dyslipidemia, phlegm-dampness retention syndrome, spleen and kidney Yang deficiency syndrome, RNA-Seq

INTRODUCTION

As life quality increases and dietary patterns change, multiple factors are beginning to give rise to a growing morbidity of dyslipidemia in humans. A recent epidemiological study has shown that dyslipidemia is closely linked to cardiovascular and cerebrovascular diseases, including coronary atherosclerotic heart disease and cerebral infarction (Li et al., 2019). It is estimated that the overall morbidity of dyslipidemia in Chinese adults has reached 40.40% and is continuing to rise (Chu et al., 2016).

Dyslipidemia is characterized by abnormalities in the quantity and quality of lipids in the plasma, including lower high-density lipoprotein cholesterol (HDL-C) levels and higher triglyceride (TG), total cholesterol (TC), and low-density lipoprotein cholesterol (LDL-C) levels (Sarzynski et al., 2015). Lipid and cholesterol accumulation (Pantos et al., 2007) in the vascular wall may lead to endothelial dysfunction. Dyslipidemia is an independent and changeable risk factor shortening the onset time of atherosclerosis (Ciccone et al., 2011). The 2013 American College Foundation of Cardiology and American Heart Association guidelines on the management of blood lipids in atherosclerotic cardiovascular disease recommended that management of dyslipidemia is the key to controlling risk factors for ischemic cardiovascular events (Stone et al., 2014).

Numerous clinical studies and laboratory experiments have ascertained the satisfactory efficacy of TCM with respect to dyslipidemia, enriching the therapies available for the disease (He et al., 2018). Taking berberine orally has been shown to lower TG and cholesterol levels (Hu et al., 2012), and the oral administration of *Monascus* rice has also been found to significantly reduce the levels of blood lipids and to be well tolerated (Lin et al., 2005). An important effect of TCM lies in the accurate discrimination of TCM syndromes of dyslipidemia, which is the basis of TCM diagnosis and treatment. The differentiation of syndromes is brought about through the collection of clinical information (i.e., "TCM symptoms") of patients via integrated TCM diagnostic methods, including looking, listening, and questioning the individual, and feeling their pulse, as well as analyzing and summarizing the etiological factors and pathogenesis according to the TCM theoretical approach.

As individuals present with different TCM symptoms, dyslipidemic patients may exhibit various syndromes that can be considered different TCM subtypes of dyslipidemia. For example, spleen and kidney Yang deficiency (SKYD) syndrome and phlegm–dampness retention (PDR) syndrome are both common in patients with dyslipidemia. In addition, the vascular endothelium is responsible for delivering nutrients in a dynamic way (Eelen et al., 2020), while dyslipidemia acts as a risk factor of cardiovascular disease, potentially by promoting endothelium dysfunction—a prerequisite for the occurrence of atherosclerotic manifestations (Scicchitano et al., 2019). A critical mechanism of endothelium dysfunction is oxidative stress. Excessive nitric oxide (NO) binding with hyperoxides can form a peroxynitrite anion (ONOO−), and ONOO− triggers oxidative stress of the vascular endothelium and endothelial injury through its oxidative effect (nitrification) on proteins, exacerbating the endothelial injury. Accordingly, the severity of endothelial injury can be indicated by ONOO− levels.

Our team has been studying the integration of TCM differentiation and Western medicine diagnosis alongside investigating endothelial injury differences as the characteristics between SKYD syndrome and PDR syndrome in dyslipidemia. Findings from our previous research have suggested that dyslipidemic patients with SKYD syndrome and PDR syndrome exhibit different serum ONOO− concentrations,

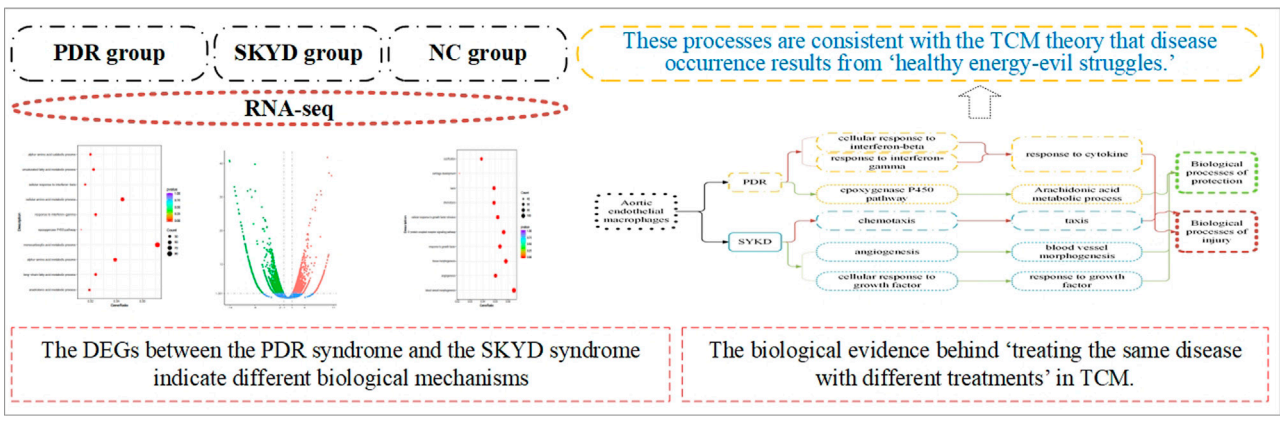

GRAPHICAL ABSTRACT |

reflecting the difference in TCM syndromes in a certain sense (Chen et al., 2016). Consequently, we theorize that different syndromes of dyslipidemia may correspond to different degrees of endothelial injury. In dyslipidemia, macrophages play a pivotal role in the process of endothelial injury. Recognizing this critical effect of macrophages, and following on from our previous study series, the present study focuses on aortic endothelial macrophages and explores the characteristics of the endothelial injury between individuals with SKYD syndrome and those with PDR syndrome as well as dyslipidemia.

In dyslipidemia, monocytes that migrate to the endothelium differentiate into macrophages via macrophage colony stimulating factors, and then damage the vascular endothelium. Macrophages consist of two subtypes, M1 and M2 macrophages (Davies and Taylor, 2015). Lactate dehydrogenase stimulates the expression of adhesion molecules and chemokines, thereby differentiating monocytes into macrophages through various pathways. M1 macrophages can release inflammatory factors that facilitate the progression of inflammation and further impair vascular endothelial cells (Pesce et al., 2009). M2 macrophages release anti-inflammatory factors that are involved in angiogenesis and tissue growth and delay the progression of inflammation (Moore and West, 2019). A prior study established that macrophages are indispensable in the formation of atherosclerosis (Yamada et al., 1998). Moreover, according to TCM theory, the two subtypes exhibit antagonistic characteristics, corresponding to "healthy Qi" (the ability to combat evils, preventing disease) versus "evil Qi" (pathogenetic factors, factors damaging healthy Qi). The interactions between healthy Qi and evil Qi are characterized by "healthy energy–evil struggles, mutually opposing and constraining, and the rule of waxing and waning" in the occurrence and development of diseases and syndromes.

Disease–syndrome combination is a significant mode for TCM diagnosis and treatment in the clinic. Furthermore, in this context, the in-depth investigation of diseases and syndromes requires biological studies using disease–syndrome animal models in agreement with the traits of TCM theories to apprehend the underlying mechanisms. The characteristics of such models, such as rigorous controls, high repeatability, and success rates, make it easier to regulate the research cycle, repetitively perform experiments, collect more data, and comprehensively analyze the data. Hence, the establishment of an appropriate disease–syndrome animal model is increasingly attracting research attention.

An important element of TCM syndrome research is the investigation of biological mechanisms and the characteristics of syndromes using animal models. Accordingly, we developed a disease–syndrome animal model in the present study for analysis. The quality of a disease–syndrome animal model can affect the accuracy and credibility of any study based on it. We employed multifactor-hybrid modeling and established dyslipidemic mouse models featuring SKYD syndrome and PDR syndrome, based on the model used in our previous study, so that the quality of the animal models could be ensured as much as possible. The disease model replicated the core physiopathologic process present during the occurrence and development of a disease, and the syndrome models each simulated the core etiology and pathology during the onset of a syndrome.

Transcriptomics is a technique used to study gene transcription and regulation related to TCM syndromes and is conducive to in-depth biological research toward a better understanding of the pathogenesis of TCM syndromes, and so warrants more prevalent application in TCM syndrome research (Jiang and Li, 2020). Gan et al. (2020) studied Yin deficiency–heat syndrome using transcriptomics technology and obtained its potential biomarkers. Currently, though, studies concerning the characteristics of SKYD syndrome and PDR syndrome in relation to dyslipidemia are rarely reported. Our study focuses on the two-way impacts between the severity of endothelial injury and macrophages, and analyzes the differences in biological processes and signaling pathways between different TCM syndromes (subtypes) of dyslipidemia using transcriptomic techniques. Thus, this study provides a reference for in-depth mechanical research of TCM syndromes and studies of the targets of TCM drugs.

MATERIALS AND METHODS

Figure 1 presents an overview of the study's materials and methods, described in full below.

Experimental Animals

The animals featured in the research comprised 10 apolipoprotein E knockout ($ApoE^{-/-}$) mice—male, 6 weeks old, body mass about 20 ± 5 g—and five C57BL/6J mice of the same strain—male, 6 weeks old, body mass about 20 ± 5 g. All animals were raised in the Beijing Changyang Xishan Farm; the rearing environment incorporated a room temperature of 21–25°C, 50%–70% humidity, and 12 h of alternating shade. The ethics of this study were approved by the animal ethics review committee of the Institute of Basic Theories of Chinese medicine, Chinese Academy of Chinese Medical Sciences, approval no. 201908006 (Beijing, China).

Experimental Reagents and Model-Making Feed

Main Reagents for the Experiment

LDL cholesterol test kit (Nanjing Jiancheng Bioengineering Institute Co., Ltd.); total cholesterol lipoprotein test kit (Nanjing Jiancheng Bioengineering Institute Co., Ltd.); HDL cholesterol test kit (Nanjing Jiancheng Bioengineering Institute Co., Ltd.); triglyceride test kit (Nanjing Jiancheng Bioengineering Institute Co., Ltd.); FITC anti-mouse F4/80 antigen (BM8.1) (Tonbo Biosciences Co., Ltd.); PE anti-human/mouse CD11b (M1/70) (Tonbo Biosciences Co., Ltd.); hematoxylin–eosin (HE) staining solution (Aijia Biotechnology Co., Ltd.).

Experimental Modeling Feed

The dyslipidemic feed formula consisted of 63.6% basal feed +15% lard +20% sucrose +1.2% cholesterol +0.2% sodium cholate, provided by Beijing Keaoxieli Feed Co.

Modeling and Evaluation Methods of Animal Models of Diseases and Syndromes

Modeling Methods

The PDR Group

Five ApoE knockout mice were randomly selected and fed a high-fat diet for 4 weeks, from Weeks 1–4 (the disease model was constructed at 2 weeks, and the syndrome model was constructed at 2 weeks).

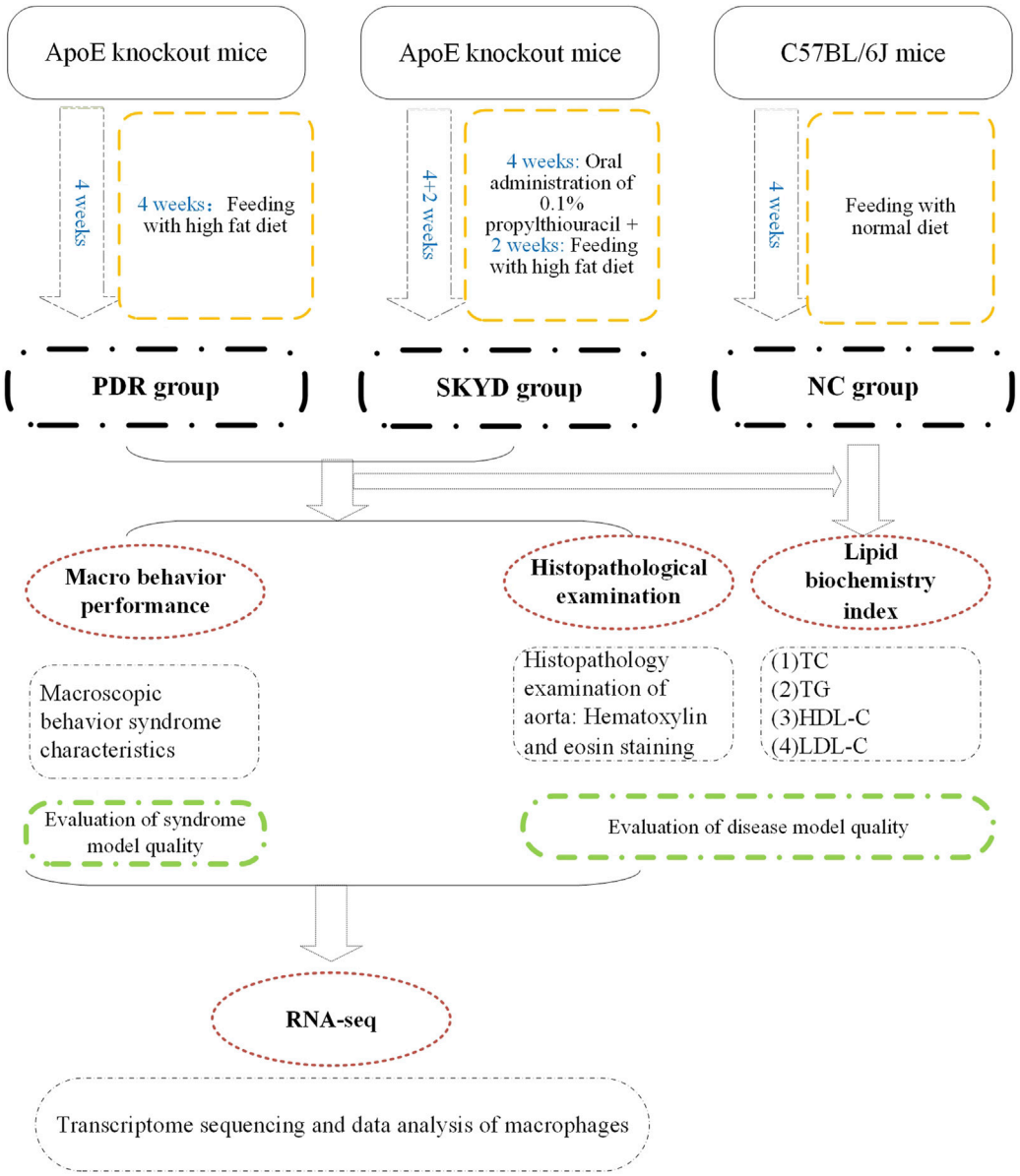

FIGURE 1 | Flowchart of the study.

The SKYD Group

Five ApoE knockout mice were randomly selected and given 0.1% propylthiouracil by gavage at a dose of 10 mg/(kg·d) during Weeks 1–4 (constructing the syndrome model), and high-fat chow for 2 weeks during Weeks 5 and 6 (constructing the disease model).

The Normal Control Group

Five C57BL/6J mice were given normal chow for modeling for a total of 4 weeks from Weeks 1–4.

Model Evaluation Methods

Model evaluation was completed as follows: 1) evaluation of model quality of dyslipidemia by means of serum lipid index testing and aortic pathology staining; 2) evaluation of model quality of the PDR group and the SKYD group by observing the characteristic manifestations of the syndromes.

Sampling and Macrophage Screening Methods

Mice were fasted without water for 18 h before sampling and given anesthesia for execution.

Animal Serum

Animals in the PDR group, the SKYD group, and the NC group, after taking whole blood, placed in conventional serum tubes, 3,000 rpm for 10 min, separated serum, divided and immediately stored in −80°C refrigerator.

Animal Tissues
Aortic tissues were taken from animals in the PDR group and the SKYD group.

Macrophages
Aorta of animals from the PDR group and the SKYD group were isolated and removed intact, digested by adding trypsin, sieved and ground, digestion was terminated, centrifuged, supernatant was decanted, re-suspended by adding PBS, centrifuged again, supernatant was decanted, and labeled with FITC anti-mouse F4/80 antigen (BM8.1) and PE anti-human/mouse CD11b (M1/70), blown and re-suspended, and stored away from light. After labeling the macrophages, the macrophages were screened by fluorescence-activated cell sorting (FACS) using the MoFlo XDP Ultra-Fast Flow Cell Sorting System (Beckman Coulter Co., Ltd.). (See **Supplementary Material S1**).

Measurement of Indicators
General Observation of the Model
Observing and recording mental status, body hair glossiness, movement, feces, etc.

Lipid Index Testing
Serum testing of TG, TC lipoprotein, HDL-C, and LDL-C levels in each group.

Aortic Histopathology
Specimens were fixed in 10% neutral formalin at room temperature for 24 h. The specimens were fixed for 48 h at room temperature using freshly prepared 4% formaldehyde, followed by paraffin embedding and sectioning. Specimens were cut into 4 mm-thick sections and subjected to histological HE staining to observe the morphological features of the vascular endothelium.

After staining, the slices were photographed and examined using an optical microscope (AE41; Motic) equipped with a digital scanner (Panoramic MIDI; 3DHISTECH) to record images of the stained slices.

Macrophage Transcriptomic Sequencing and Data Analysis
Total RNAs of macrophages were extracted in accordance with the TRIzol® manual (Life Technologies, Inc., Gaithersburg, MD, United States). Preparation of library and sequencing of transcriptomes were carried out using Illumina HiSeq X Ten (Novogene Bioinformatics Technology Co., Ltd., Beijing, China). The mapping of 100-bp paired-end reads to genes was undertaken using HTSeq v0.6.0 software, while fragments per kilo base of transcript per million fragments mapped (FPKM) were also analyzed. Raw reads from RNA-Seq libraries were trimmed to remove the adaptor sequence and the reads with adaptor contaminants and low-quality reads (the mass value Q score <5 of the base number accounts for more than 50%) and reads from N (N indicates that the base information that cannot be determined) which was >10%.

After filtering, reference genome and gene model annotation files were downloaded from a genome website browser (NCBI/UCSC/Ensembl). Indexes of the reference genome were built using Bowtie (version 2.0.6) and paired-end clean reads were aligned to the reference genome using TopHat (version 2.0.9). Bowtie was used for a Burrows–Wheeler transform algorithm for mapping reads to the genome, and TopHat can generate a database of splice junctions based on the gene model annotation file and thus achieve a better mapping result than other non-splice mapping tools.

For the quantification of gene expression level, HTSeq (version 0.6.1) was used to count the read numbers mapped for each gene. The reads per kilo base of transcript per million mapped reads (RPKM) of each gene was calculated based on the gene read counts mapped to this gene. A differential expression analysis was performed using the DESeq R package (3.18.1). The p values were adjusted using the Benjamini and Hochberg method. A corrected p value of 0.05 and absolute fold change of 2 were set as the threshold for significantly differential expression.

Gene ontology (GO) enrichment analysis of differentially expressed genes (DEGs) was implemented using the clusterProfiler R package, in which gene length bias was corrected. GO terms with a corrected p value of less than 0.05 were considered significantly enriched by DEGs.

Statistical Methods
Subject-related data were statistically processed by applying SPSS (version 19.0) statistical software. The measurement data were expressed as the mean plus or minus the standard deviation. A one-way analysis of variance with randomized group design was used for comparison between groups; Fisher's least significant difference test was used for two-way comparison, if the data variance was the same; Tamhane's test was used for two-way comparison, if the variance was not the same; and the difference was considered statistically significant at $p < 0.05$. The test level was $\alpha = 0.05$, and the confidence interval for parameter estimation was 95%.

RESULTS
General Information and Macro Behavioral Performance
Ten ApoE knockout mice and five C57BL/6J mice of the same strain without deletion were used in the experiment, with 15 mice entering into the resulting analysis. Before sampling, the mice in the PDR group had exhibited loss of body hair brightness, lethargy, and laziness; the mice in the SKYD group had showed arching of the back and curling up, tranquil, lethargy, lying down, and a propensity to pile up.

Comparison of Blood Lipid Indexes
Evaluating the lipid indexes, compared with the NC group, TG, TC, and LDL-C levels were found to be significantly higher in the PDR group and the SKYD group, $p < 0.05$. Compared with the NC group, no significant statistical differences were perceived between the HDL-C indexes of the PDR and SKYD groups. No significant statistical differences were seen between the PDR and SKYD groups when comparing TG, TC, and HDL-C levels. Also, no statistically significant differences were found in the

TABLE 1 | Total cholesterol index in three groups of mice (mean ± standard deviation).

Group	TG index
PDR group	23.32 ± 2.33[a]
SKYD group	29.32 ± 6.32[b,c]
NC group	2.38 ± 0.38
F	65.82
p	0.000

[a]*was compared with NC group,* p *<0.05;*
[b]*was compared with NC group,* p *<0.05;*
[c]*was compared with PDR group,* p *>0.05.*

TABLE 2 | Triglycerides index in three groups of mice (mean ± standard deviation).

Group	TC index
PDR group	2.96 ± 0.11[a]
SKYD group	4.71 ± 1.15[b,c]
NC group	0.80 ± 0.79
F	43.07
p	0.000

[a]*was compared with NC group,* p *<0.05;*
[b]*was compared with NC group,* p *<0.05;*
[c]*was compared with PDR group,* p *>0.05;*

TABLE 3 | HDL-C index in three groups of mice (mean ± standard deviation).

Group	HDL-C index
PDR group	5.17 ± 2.15
SKYD group	3.03 ± 1.92[a]
NC group	3.55 ± 0.68
F	2.13
p	0.162

Note:
[a]*was compared with PDR group,* p *>0.05;*

TABLE 4 | LDL-C index in three groups of mice (mean ± standard deviation).

Group	LDL-C index
PDR group	2.54 ± 0.22[a]
SKYD group	3.60 ± 1.39[b,c]
NC group	0.89 ± 0.12
F	13.88
p	0.001

Note:
[a]*was compared with NC group,* p *<0.05;*
[b]*was compared with NC group,* p *<0.05*
[c]*was compared with PDR group,* p *>0.05.*

comparisons of the TG, TC, HDL-C, LDL-C, and LDL-C indexes between the PDR and SKYD groups. These results are summarized in **Tables 1–4**.

Comparison of HE Staining Examination

The aortas from the PDR group and the SKYD group were examined using HE staining. The endothelial surface of the vessels was observed to be smooth, the inner, middle, and outer membranes showed clear, and no obvious lipid deposition or lipid streak production was seen. See **Figure 2**.

Transcriptome Sequencing Analysis of Macrophages in Mice With Dyslipidemia Syndrome Model

Analysis of DEGs in Macrophages of Mice With Different Syndromes of Dyslipidemia Generated by RNA Sequencing

After comparing the DEG expressions in macrophages in dyslipidemic mice with different syndromes, 4,142 genes were identified with statistical significance, $p < 0.05$. Among them, 1,781 genes were upregulated and 2,361 genes were downregulated. See **Figure 3**.

Through additional reference to bioinformatics information, a total of 284 DEGs were selected in this study for in-depth analysis of content related to vascular endothelial injury. In a comparison of the 74 DEGs between the PDR group and the SKYD group, the number of reads in the PDR group was statistically higher than that in the SKYD group, $p < 0.05$. See **Supplementary Material S2**.

GO Enrichment Analysis of DEGs Associated With Vascular Endothelial Injury in Macrophages

Through GO enrichment analysis based on DEGs, macrophage sequencing data of mice in the PDR group and the SKYD group were analyzed, focusing on the enrichment results of biological processes related to vascular endothelial injury.

The differential pathways that were upregulated in the PDR group compared to the SKYD group primarily included the arachidonic acid (AA) metabolic process, epoxygenase P450 pathway, response to interferon-gamma, and cellular response to interferon-beta, as illustrated in **Figure 4**.

The differential pathways that were upregulated in the SKYD group compared to the PDR group primarily included blood vessel morphogenesis, angiogenesis, response to growth factor, cellular response to growth factor stimulus, chemotaxis, and taxis. See **Figure 5**.

DISCUSSION

Dyslipidemia may significantly increase the morbidity and mortality associated with cardiovascular diseases (Lee et al., 2017). Prior research has found that effective control of blood lipid levels may reduce the possibility of relapsed coronary heart disease and its mortality (Mozaffarian et al., 2015). Therefore, proactive diagnosis and treatment for dyslipidemia, the most critical risk factor of atherosclerosis, is essential for decreasing the incidence and mortality of coronary heart disease and cerebral infarction (Rhee et al., 2019).

Treatment based on syndrome differentiation is the quintessence of TCM (Xu et al., 2021). Syndromes as a distinctive concept in TCM are the core content of the theory and provide vital evidence for treatment and prescription. TCM treatment has been shown to offer advantages in the management of dyslipidemia (Sham et al., 2014; Xu et al., 2019). The predominant mechanisms encompass inhibiting

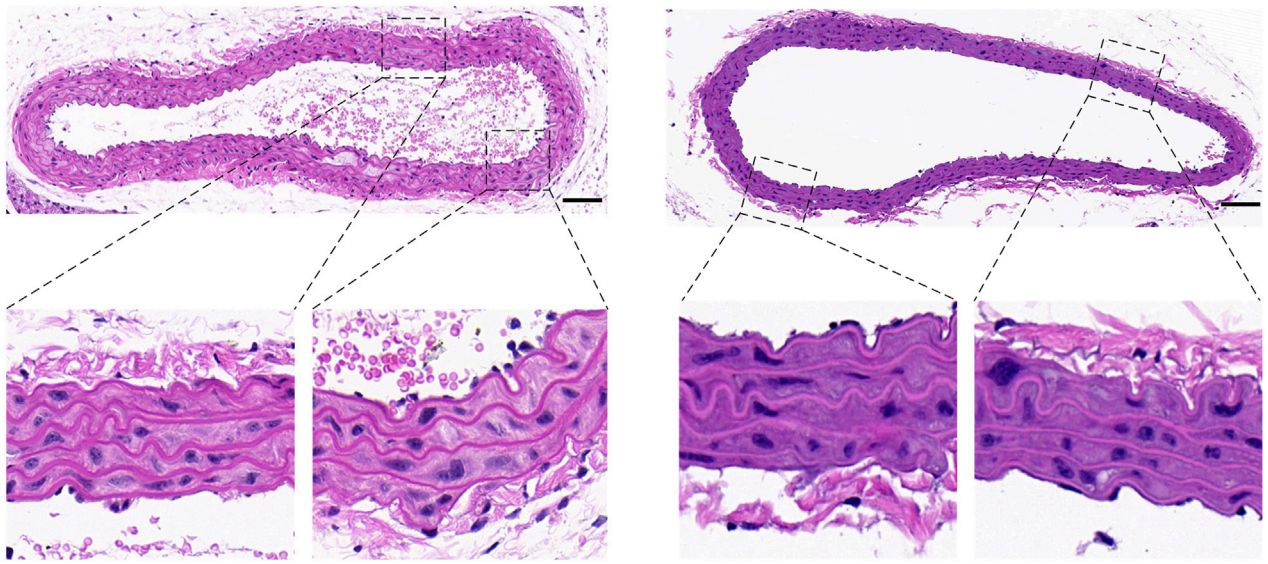

FIGURE 2 | The aorta was stained with hematoxylin and eosin. Scale bars represent 100 μm.

cholesterol absorption in the intestines and biological synthesis of endogenous lipids, regulating lipoprotein lipase activity and cholesterol transport, promoting the conversion of cholesterol into bile acids and cholesterol emission, and the regulatory effects of lipid metabolism-related transcription factors in TCM drugs (Bei et al., 2012). Syndromes represent conclusions made regarding the location and nature of the current stage of a disease, focusing on the pathological changes of the body's response state at a certain stage of a disease. In the context of the current study, the precise discrimination of exact TCM syndromes of dyslipidemia is the prerequisite and basis of TCM treatment. Therefore, TCM syndrome research is a critical link in TCM modernization, wherein biological syndrome research is most significant, providing evidence for the onset and evolution of syndromes and effective mechanisms behind specific interventions for syndromes.

RNA-Seq is a next-generation approach using high throughput sequencing available for low-abundance genomes. It is sensitive for gene structure analysis and gene expression and function assessments to unveil internal molecular mechanisms behind specific biological processes and the pathogenesis of diseases. The features of these genes consist of classic genetic features (nucleotide sequence changes) and epigenetic features (heritable phenotype changes without nucleotide sequence alterations). Transcriptomics can provide gene expression information under certain conditions and reveal the mechanism of action of specific genes, which is consistent with the TCM theory that diseases express different syndromes under the influence of internal and external causes. Our study investigated the syndrome–biological mechanism of dyslipidemia using RNA-Seq.

Our previous serum metabonomics studies of dyslipidemic patients with PDR syndrome and SKYD syndrome found that the accumulation of harmful metabolites is the predominant metabolic trait in patients with PDR syndrome, while a lack of protective metabolites is the main metabolic feature in patients with SKYD syndrome. Further analysis has shown that oxidation and inflammatory responses are essential contributors to the different metabolic characteristics between the two syndromes (Chen et al., 2019). Thus, in-depth study of SKYD syndrome and PDR syndrome in dyslipidemia necessitates research concerning oxidation and inflammatory responses.

Macrophages are pivotal in the formation of atherosclerosis following oxidative stress damage to the vascular endothelium. M1 macrophages can promote inflammation and tissue damage, while M2 macrophages can release anti-inflammatory factors and enhance plaque stability. Endothelial dysfunction and the subsequent oxidative inflammatory reaction represent the core pathological mechanism of dyslipidemia. Macrophages are recruited toward endothelial cells, which is an early stimulus of atheromatous plaque formation (Tiwari et al., 2008) and the chief basis of the incidence of atherosclerosis. Based on our previous research, in the present study, we established the disease–syndrome animal models for and explored the characteristics of the aortic endothelial macrophages between PDR syndrome and SKYD syndrome of dyslipidemia, using RNA-Seq. Our findings from the current research are presented in the following subsections.

Quality Assessment of the Dyslipidemia Disease Model Using Serum Lipids Analysis and HE Staining of the Aorta Revealed Success in Disease Modeling

Compared with the NC group, TG, TC, and LDL-C levels significantly increased in mice of the PDR and SKYD groups and exceeded the upper limit of the normal range, in conformity to the diagnostic criterion of dyslipidemia. The HE staining of the aorta revealed a smooth endothelial surface and clear borders between inner, medial, and outer layers in mice from the PDR and SKYD groups, without

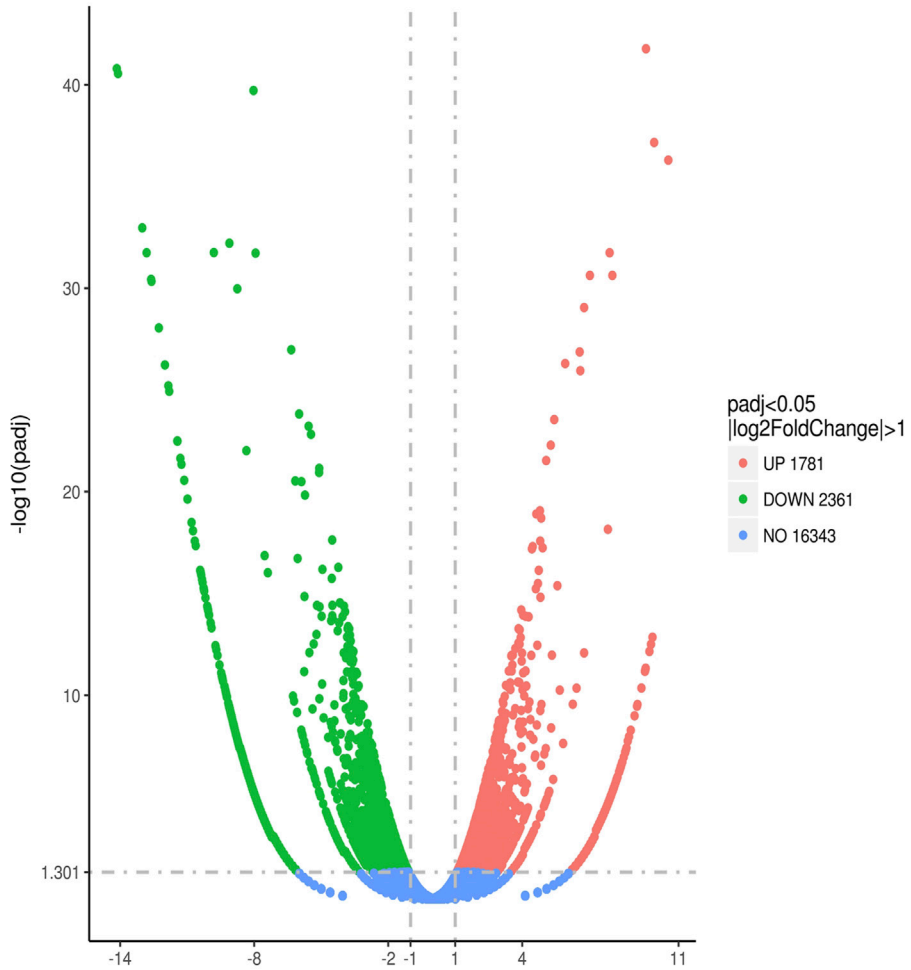

FIGURE 3 | Quantitative comparison of gene expression levels in aortic macrophages of mice with dyslipidemia: PDR group vs. SKYD group.

pronounced lipid accumulation and fatty streaks. These results indicated that there were no pathological manifestations of atherosclerosis in the mice of the two groups. The HE staining results implied the satisfactory quality of the dyslipidemia modeling.

However, there were no significant differences in TG, TC, HDL-C, and LDL-C levels between the PDR and SKYD groups. Therefore, the differences in transcriptomic traits and biological results between the two groups based on RNA-Seq in subsequent studies may not be caused by the disease itself, but by syndromes (subtypes).

Quality Assessment of the Two Syndrome Models (PDR, SKYD) Through Behavioral Tests Indicated the Feasibility of Syndrome Modeling

The characteristics of mice in the PDR group included their being fat in body shape, with a reduced brightness of hair, lethargy, slow responses, lazy to move, as well as soft, formed, and sticky feces, consistent with clinical manifestations of PDR syndrome. The behavioral features of mice in the SKYD group incorporated matted hair, slight paw and nail coloration, shrinking of the body, tranquil, fatigue, sleepiness, sticking together, low-temperature tail, decrease in food and water intake, and loose and watery stools. These were in agreement with clinical manifestations of SKYD syndrome. These results indicate that syndrome modeling can simulate typical symptoms of the corresponding syndrome.

Transcriptomic Data of Macrophages Showed Pro-Inflammatory Activities in the Vascular Endothelium in Dyslipidemic Mice With PDR Syndrome and SKYD Syndrome, but the Mechanisms Were Different

IFN-γ and IFN-β Expressions Were Upregulated in Macrophages in Dyslipidemic Mice With PDR Syndrome, Promoting Endothelial Inflammation

It is known that interferon gamma (IFN-γ) can facilitate the progression of inflammatory diseases—for example, inflammatory bowel disease and atherosclerosis. *In-vitro* and *in vivo* studies have found IFN-γ may damage epithelial cells

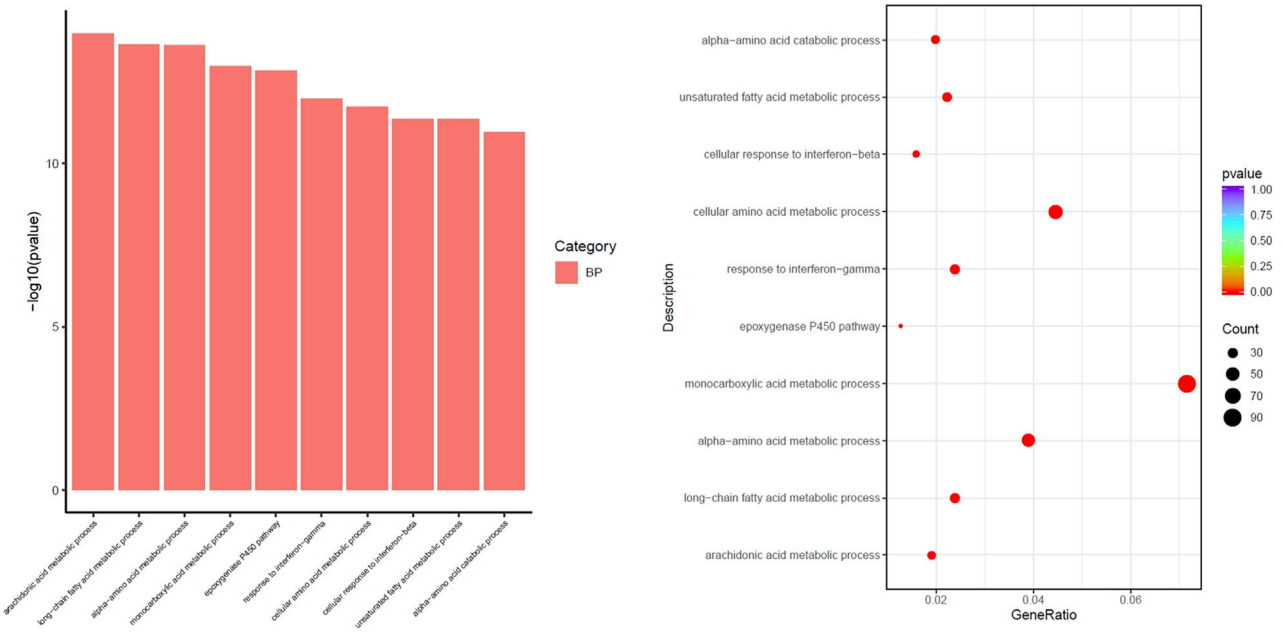

FIGURE 4 | Different biological process of upregulation in the group with PDR syndrome compared with the group with SKYD syndrome.

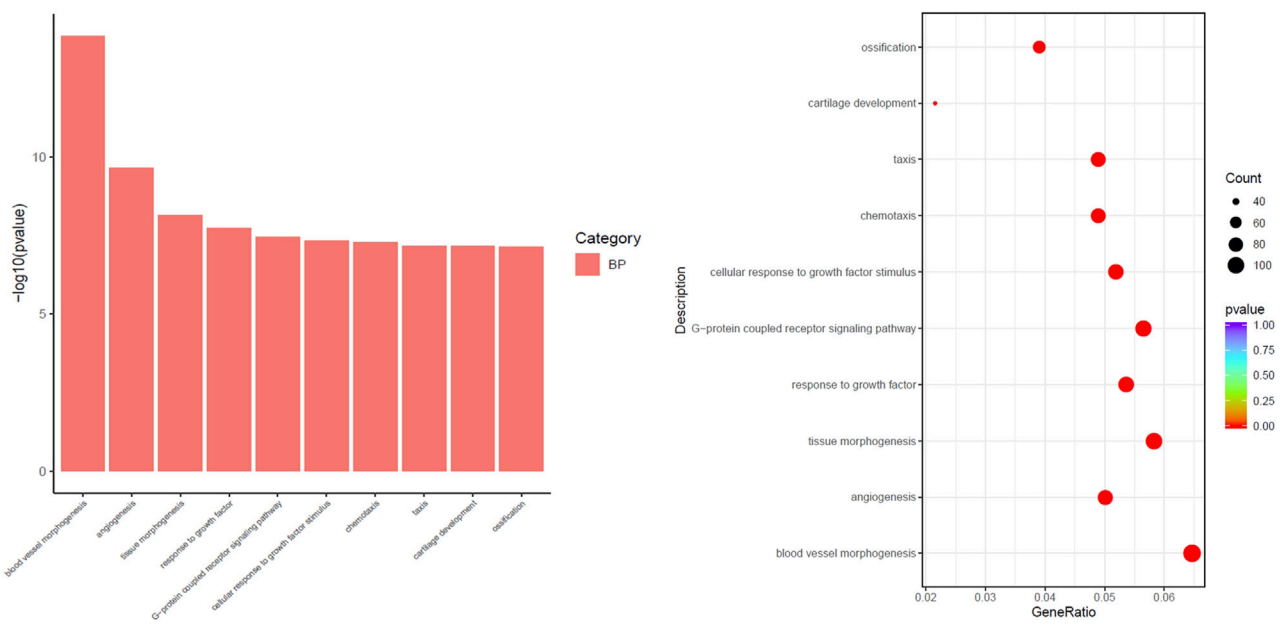

FIGURE 5 | Different biological process of upregulation in the group with SKYD syndrome compared with the group with PDR syndrome.

and endothelial barrier integrity (Ng et al., 2015). Moreover, IFN-γ exerts significant impacts on the biological properties of the vascular endothelial cells. It may initiate vascular remodeling around microvascular endothelial cells (Chrobak et al., 2013). Monocyte-derived macrophages are induced by the pro-inflammatory factor IFN-γ, which are of vital significance during plaque formation. Both IFN-γ and macrophages are major players in oxidative stress. Just like other pro-inflammatory factors, IFN-γ acts as a significant trigger of the synthesis and release of reactive oxygen species (Schroecksnadel et al., 2006).

Interferon beta (IFN-β) mRNA can effectively induce endothelial chemokine expression (Buttmann et al., 2007). It enhances endothelial cell adhesion to eosinophils mainly

through upregulating vascular cell adhesion molecule-1 and intercellular adhesion molecule-1 expressions (Kobayashi et al., 2008). IFN-β fuels the formation of macrophage foam cells via a macrophage scavenger receptor class A (SR-A)-mediated cholesterol influx and an ATP-binding cassette transporter (ABCA1)-mediated efflux of mechanisms, thus expediting the incidence of atherosclerosis (Boshuizen et al., 2016).

Under TCM, PDR syndrome is a type of sthenia syndrome. The phlegm evil is both the pathological product and pathogenic factor, impeding the delivery and movement of Qi, thus resulting in body fluid stagnation and hydrops or damp evil accumulation and phlegm. Turbid phlegm can block the vessels and bring about damage that causes blood vessels to be blocked. This then affects the operation of Qi and blood, resulting in their poor operation, which can lead to the occurrence of diseases over time. Finally, the vascular endothelium is impaired.

Our results showed that IFN-γ and IFN-β expressions in macrophages were upregulated in dyslipidemic mice with PDR syndrome, and at significantly higher levels than in mice with SKYD syndrome. This finding suggests that vascular endothelial injury induced by IFN-γ and IFN-β overexpression in vascular endothelial macrophages is a characteristic of PDR syndrome in dyslipidemia.

Macrophage Chemotaxis and Taxis Were Enhanced in Dyslipidemic Mice With SKYD Syndrome, Promoting Endothelial Inflammation

Macrophages are inflammatory cells, and their accumulation can stimulate cytokine and chemokine release, initiating immune responses and accelerating plaque formation (Liehn et al., 2006). The secreted chemokines infiltrate atherosclerotic plaques at an early stage (Weber et al., 2008). Despite the role in lipid accumulation, macrophage foam cells also release pro-inflammatory factors and chemokines, further stimulating vascular endothelial cells, fueling vascular endothelial inflammation, and exacerbating the disease (Kleemann et al., 2008). A prior study found that resveratrol could exert a protective effect on the heart via inhibiting endothelial cell migration and monocyte chemotaxis (Cicha et al., 2011).

The TCM mechanism of SKYD syndrome in dyslipidemia refers to spleen–kidney Yang deficiency. The spleen and kidneys are weak, which will cause the loss of Qi and Yang. The deficiency of spleen Yang and kidney Yang can lead to the loss of a warm body. The function of Qi is abnormal, which causes the decrease of its protective effect. Furthermore, as the body lacks warmth from Yang–Qi and corresponding protection, the vascular endothelium can be easily injured.

Our results showed that macrophage chemotaxis and taxis were significantly enhanced in dyslipidemic mice with SKYD syndrome, compared with the PDR mice. This finding suggests that vascular endothelial injury induced by enhanced macrophage chemotaxis and taxis was the main characteristic of the SKYD syndrome in dyslipidemia.

The above results demonstrate that different biological processes resulted in vascular endothelial injury in PDR syndrome and SKYD syndrome with dyslipidemia, indicating different injury mechanisms of the two syndromes. These results also imply that there exist biological bases behind the pathogenesis of TCM syndromes.

Transcriptomic Data of Macrophages Showed Protection for the Vascular Endothelium in Dyslipidemic Mice With PDR Syndrome and SKYD Syndrome, but the Mechanisms Were Different

AA Metabolic Process and Epoxygenase P450 Pathway Levels Increased in Macrophages in Dyslipidemic Mice With PDR Syndrome, Exerting Protection Effects on the Vascular Endothelium

Growing evidence has shown that AA metabolism is crucial in maintaining vascular homeostasis, closely associated with the occurrence and development of cardiovascular diseases (Xue et al., 2015). AA is an amphiphilic compound affecting endothelial cell migration; without the involvement of receptor-specific signaling, it affects endothelial cell metabolism and membrane viscosity (Jensen et al., 2007). AA metabolic pathways are pivotal in platelet activation and gastric damage (Rukoyatkina et al., 2018). Suppressing AA metabolism can further block endothelial cell migration, inducing cell apoptosis (Jantke et al., 2004). A recent study has reported that *Panax notoginseng* saponins combined with aspirin inhibited platelet activity via enhancing AA metabolism (Wang et al., 2021).

Cytochromes P450 (CYP450) refer to a third pathway for AA metabolism (Roman, 2002). CYP450 metabolites of AA in endothelial cells may impact endothelial function. AA is metabolized by CYP450 and cyclooxygenase (COX) into bioactive eicosanoids, exerting vascular protection effects (Spiecker and Liao, 2005). AA is also metabolized by CYP450 and COX into four regioisomeric epoxyeicosatrienoic acids (EETs) used for bioprotection and cardioprotection (Xu et al., 2011). EETs have multiple nutritive functions, including the anti-inflammatory effect, in their cardioprotection (Node et al., 1999). Decreases in EETs expressions may lead to the onset of cardiovascular diseases and endothelial dysfunction (Bellien et al., 2012).

Our analysis showed significant upregulations of AA metabolic process and epoxygenase P450 pathway levels in macrophages in dyslipidemic mice with PDR syndrome, compared to the SKYD mice. These results indicate that endothelial protection from macrophages *via* AA and CYP450 overexpressions is another trait of PDR syndrome in dyslipidemia.

Biological Process Items, Including Angiogenesis, Blood Vessel Morphogenesis, Response to Growth Factor, and Cellular Response to Growth Factor Stimulus, Whose Activities Were Significantly Enhanced for Macrophages in Dyslipidemic Mice With SKYD Syndrome, Which Facilitated Angiogenesis and Vascular Repair

Angiogenesis consists of multiple, intricate, highly coordinated processes in which endothelial cells with dynamic changes are of great importance (Potente et al., 2011). Angiogenesis may occur in the pathological environment (Alvarez Arroyo et al., 1998) and be initiated by endothelial cell activation. The genetic program of endothelial cells triggers the modulation of angiogenic phenotype. Macrophages are significant regulators for tissue homeostasis, growth and repair, and morphogenesis. The growing endothelial cells can respond to extracellular signaling molecules, such as extracellular

matrix molecules, chemokines, growth factors, and cell adhesion molecules (Jeong et al., 2017). Growth factors and cytokines secreted from macrophages (Lucas et al., 2010) may promote the formation of new blood vessels via recruiting new blood vessels and modifying the extracellular matrix (Corliss et al., 2016). Vascular endothelial growth factors (VEGFs) are considered the most robust booster for angiogenesis, increasing the survival of endothelial cells and enhancing mitosis (Dvorak, 2005). Numerous studies have demonstrated that VEGFs are expressed in macrophages (Guo et al., 2018). They can stimulate assorted cell functions of endothelial cells via high-affinity binding to two tyrosine kinase receptors, VEGF receptor (VEGFR) 1 and VEGFR2 (Zachary, 2003).

Our study found that the top biological process items enriched in macrophages in dyslipidemic mice with SKYD syndrome were angiogenesis, blood vessel morphogenesis, response to growth factor, and cellular response to growth factor stimulus, whose activities were significantly enhanced, compared to the PDR group. This finding suggested that angiogenesis and vascular repair via enhancing macrophage chemotaxis and taxis are another critical feature of SKYD syndrome in dyslipidemia.

The above results indicate that vascular protection mechanisms are distinct between PDR syndrome and SKYD syndrome in dyslipidemia. This further implies different protection mechanisms in the two syndromes, which in turn further corroborates that there exist biological bases behind the pathogeneses of TCM syndromes.

According to the results presented in Sections *Transcriptomic Data of Macrophages Showed Pro-Inflammatory Activities in the Vascular Endothelium in Dyslipidemic Mice With PDR Syndrome and SKYD Syndrome, but the Mechanisms Were Different* and *Transcriptomic Data of Macrophages Showed Protection for the Vascular Endothelium in Dyslipidemic Mice With PDR Syndrome and SKYD Syndrome, but the Mechanisms Were Different*, vascular endothelial injury was induced by different biological processes in PDR syndrome versus SKYD syndrome in dyslipidemia. But there was also found to be angiogenesis and vascular repair in the pathogenetic process. The two opposite processes—injury and repair—are consistent with the TCM tenet that "healthy Qi and evil Qi are struggling throughout the incidence and dynamic development of diseases and syndromes." As the injury effect outweighs the repairing effect, the state of diseases takes place.

Different Transcriptomic Characteristics of Aortic Endothelial Macrophages Between Dyslipidemic Mice With PDR Syndrome and SKYD Syndrome are Manifested by Distinct Biological Control Processes During Both Harmful and Protective Biological Processes, Indicating Different Biological Bases Behind Different Syndromes of the Same Disease and Providing Biological Evidence for the TCM Principle of "Treating the Same Disease With Different Treatments"

See **Figure 6**.

In the TCM clinic, Western medicine diagnosis is often combined with TCM syndrome diagnosis for the management of a disease. Research about the association between Western diseases and TCM syndromes is believed to be one of the most important steps for modern TCM diagnostics studies. Based on the confirmation of a Western disease, disease–syndrome research can not only elucidate the biological bases for TCM differentiation but also help to advance innovative research on the "disease–syndrome therapy formula" and thereby provide precise and rational treatment.

Previous TCM syndrome research has emphasized harmful factors in a syndrome scenario, without much attention to the body's self-protection in this process. The present study, however, did both, focusing on an analysis of harmful factors and protective factors, and thereby providing an innovative dimension. The unity of opposites—protective and harmful effects—is achieved through dynamic balancing between healthy Qi and evil Qi via mutual conflicts, mutual restriction, and mutual repulsion. Diseases can occur when evil Qi outstrips healthy Qi, per the TCM principle that affirms, "when there is sufficient healthy Qi inside, pathogenic factors have no way to invade the body; where pathogenic factors accumulate, the parts of the body must be deficient in the healthy Qi." TCM treatment should be implemented based on the accurate discrimination of diseases and syndromes and precisely resolve issues by correcting an imbalance between healthy Qi and evil Qi through prescriptions and formulas.

Our transcriptomic analysis of aortic endothelial macrophages in dyslipidemic mice with PDR syndrome and SKYD syndrome provided notable results, as follows. First, DEGs were identified between dyslipidemic mice with PDR syndrome versus SKYD syndrome, proving different biological mechanisms during the pathogenesis of different syndromes, from the perspective of syndrome research. Second, there were found to exist different biological processes between PDR syndrome and SKYD syndrome in dyslipidemic patients, including harmful and protective biological processes. When evil Qi invades the body to produce harmful effects, healthy Qi also responds to it and thereby generates protective responses in a syndrome scenario, which corresponds with the TCM principle that "healthy Qi and evil Qi are struggling throughout the incidence and dynamic development of diseases and syndromes." Therefore, the occurrence of syndromes can be understood to be a result of healthy energy–evil struggles. This, in turn, may help to explain why TCM treatment for one disease with various therapies and formulas can achieve satisfactory efficacy, in that it could be attributed to different drugs targeting different biological processes. Our work offers biological mechanisms for the TCM theories "treating different syndromes with different treatments" and "formula corresponding to the syndrome." Third, though patients may be diagnosed with the same disease (i.e., dyslipidemia), different formulas should be selected according to their particular syndromes (i.e., giving consideration to the distinct biological processes occurring within PDR syndrome vs. SKYD syndrome). Our study provides biological evidence behind the TCM principle of "treating the same disease with different treatments," embodying the scientificity of "treatment based on syndrome differentiation."

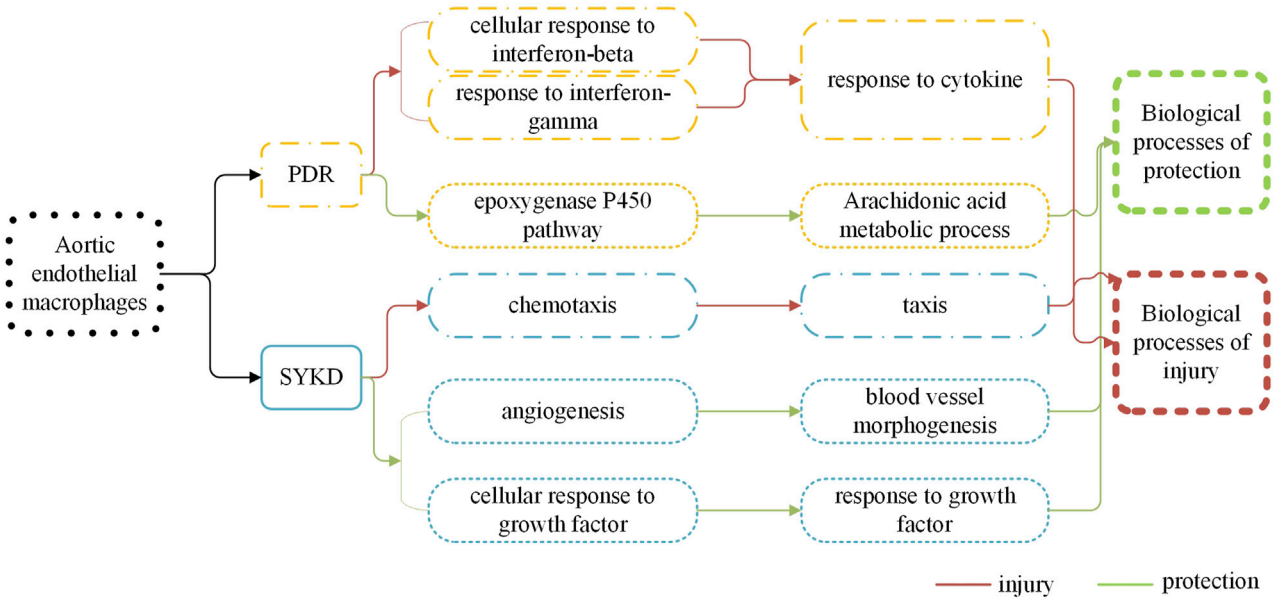

FIGURE 6 | There are different biological processes of macrophages in the dyslipidemia PDR syndrome group and the SKYD group.

DATA AVAILABILITY STATEMENT

The datasets presented in this study can be found in online repositories. The names of the repository/repositories and accession number(s) can be found below: NCBI [accession: https://www.ncbi.nlm.nih.gov/geo/query/acc.cgi?acc=GSE180802].

ETHICS STATEMENT

The animal study was reviewed and approved by the animal ethics review committee of the Institute of Basic Theories of Chinese medicine, Chinese Academy of Chinese Medical Sciences, approval no. 201908006 (Beijing, China).

AUTHOR CONTRIBUTIONS

XX and JC conceived and designed the study. JC, CY, SZ, and PL performed the modeling and evaluation of animal models of diseases and syndromes. JC, TW, ZY, and BX performed the sampling and macrophage screening. JC, CY, ZY, BX, PL, and XX acquired the data. JC, CY, ZY, and BX analyzed and interpreted data. JC and CY drafted the manuscript. PL and ZY critically revised the manuscript for important intellectual content. All authors read and approved the final manuscript.

FUNDING

This study was supported by the National Natural Science Foundation of China (no. 82004237), Fundamental Research Funds for the Central Universities (no. 2018-JYBZZ-JS182), Beijing University of Chinese Medicine Xin-ao Award Fund (no. 2018-XAJLJJ-026).

ACKNOWLEDGMENTS

The authors would like to thank Tong-Jin Zhao (Institute of Metabolism and Integrative Biology (IMIB), Fudan University, Shanghai, China) for technical assistance with this study.

SUPPLEMENTARY MATERIAL

The Supplementary Material for this article can be found online at: https://www.frontiersin.org/articles/10.3389/fphar.2021.665635/full#supplementary-material

REFERENCES

Alvarez Arroyo, M. V., Caramelo, C., Angeles Castilla, M., González Pacheco, F. R., Martín, O., and Arias, J. (1998). Role of Vascular Endothelial Growth Factor in the Response to Vessel Injury. *Kidney Int. Suppl.* 68, S7–S9. doi:10.1046/j.1523-1755.1998.06804.x

Bei, W. J., Guo, J., Wu, H. Y., and Cao, Y. (2012). Lipid-regulating Effect of Traditional Chinese Medicine: Mechanisms of Actions. *Evid. Based Complement. Alternat Med.* 2012, 970635. doi:10.1155/2012/970635

Bellien, J., Iacob, M., Remy-Jouet, I., Lucas, D., Monteil, C., Gutierrez, L., et al. (2012). Epoxyeicosatrienoic Acids Contribute with Altered Nitric Oxide and Endothelin-1 Pathways to Conduit Artery Endothelial Dysfunction in Essential Hypertension. *Circulation* 125 (10), 1266–1275. doi:10.1161/CIRCULATIONAHA.111.070680

Boshuizen, M. C., Hoeksema, M. A., Neele, A. E., van der Velden, S., Hamers, A. A., Van den Bossche, J., et al. (2016). Interferon-β Promotes Macrophage Foam Cell Formation by Altering Both Cholesterol Influx and Efflux Mechanisms. *Cytokine* 77, 220–226. doi:10.1016/j.cyto.2015.09.016

Buttmann, M., Berberich-Siebelt, F., Serfling, E., and Rieckmann, P. (2007). Interferon-beta Is a Potent Inducer of Interferon Regulatory Factor-1/2-dependent IP-10/CXCL10 Expression in Primary Human Endothelial Cells. *J. Vasc. Res.* 44 (1), 51–60. doi:10.1159/000097977

Chen, J., Ye, C., Hu, X., Huang, C., Yang, Z., Li, P., et al. (2019). Serum Metabolomics Model and its Metabolic Characteristics in Patients with Different Syndromes of Dyslipidemia Based on Nuclear Magnetic Resonance. *J. Pharm. Biomed. Anal.* 167, 100–113. doi:10.1016/j.jpba.2018.12.042

Chen, J., Ye, C., Yang, Z., Xue, X., Sun, Q., Li, P., et al. (2016). The Correlation between the Traditional Chinese Medicine (TCM) Syndrome and the Concentration of Adiponectin and Peroxynitrite in Dyslipidemia Patients. *Eur. J. Integr. Med.* 8 (6), 973–979. doi:10.1016/j.eujim.2016.04.009

Chrobak, I., Lenna, S., Stawski, L., and Trojanowska, M. (2013). Interferon-γ Promotes Vascular Remodeling in Human Microvascular Endothelial Cells by Upregulating Endothelin (ET)-1 and Transforming Growth Factor (TGF) β2. *J. Cel Physiol* 228 (8), 1774–1783. doi:10.1002/jcp.24337

Chu, J., G, . R., and Zhao, S. (2016). Guidelines for the Prevention and Treatment of Dyslipidemia in Chinese Adults (Revised Edition in 2016). *Chin. Circ. J.* 31 (10), 937–953.

Ciccone, M. M., Miniello, V., Marchioli, R., Scicchitano, P., Cortese, F., Palumbo, V., et al. (2011). Morphological and Functional Vascular Changes Induced by Childhood Obesity. *Eur. J. Cardiovasc. Prev. Rehabil.* 18 (6), 831–835. doi:10.1177/1741826711398180

Cicha, I., Regler, M., Urschel, K., Goppelt-Struebe, M., Daniel, W. G., and Garlichs, C. D. (2011). Resveratrol Inhibits Monocytic Cell Chemotaxis to MCP-1 and Prevents Spontaneous Endothelial Cell Migration through Rho Kinase-dependent Mechanism. *J. Atheroscler. Thromb.* 18 (12), 1031–1042. doi:10.5551/jat.8136

Corliss, B. A., Azimi, M. S., Munson, J. M., Peirce, S. M., and Murfee, W. L. (2016). Macrophages: An Inflammatory Link between Angiogenesis and Lymphangiogenesis. *Microcirculation* 23 (2), 95–121. doi:10.1111/micc.12259

Davies, L. C., and Taylor, P. R. (2015). Tissue-resident Macrophages: Then and Now. *Immunology* 144 (4), 541–548. doi:10.1111/imm.12451

Dvorak, H. F. (2005). Angiogenesis: Update 2005. *J. Thromb. Haemost.* 3 (8), 1835–1842. doi:10.1111/j.1538-7836.2005.01361.x

Eelen, G., Treps, L., Li, X., and Carmeliet, P. (2020). Basic and Therapeutic Aspects of Angiogenesis Updated. *Circ. Res.* 127 (2), 310–329. doi:10.1161/CIRCRESAHA.120.316851

Gan, L., Jiang, T. T., Yi, W. J., Lu, R., Xu, F. Y., Liu, C. M., et al. (2020). Study on Potential Biomarkers of Energy Metabolism-Related to Early-Stage Yin-Deficiency-Heat Syndrome Based on Metabolomics and Transcriptomics. *Anat. Rec. (Hoboken)* 303 (8), 2109–2120. doi:10.1002/ar.24355

Guo, L., Akahori, H., Harari, E., Smith, S. L., Polavarapu, R., Karmali, V., et al. (2018). CD163+ Macrophages Promote Angiogenesis and Vascular Permeability Accompanied by Inflammation in Atherosclerosis. *J. Clin. Invest.* 128 (3), 1106–1124. doi:10.1172/JCI93025

He, C., Fu, P., Zhang, K., Xia, Q., Yang, Y., and Xie, L. (2018). Chinese Herbal Medicine for Dyslipidemia: Protocol for a Systematic Review and Meta-Analysis. *Medicine (Baltimore)* 97 (44), e13048. doi:10.1097/MD.0000000000013048

Hu, Y., Ehli, E. A., Kittelsrud, J., Ronan, P. J., Munger, K., Downey, T., et al. (2012). Lipid-lowering Effect of Berberine in Human Subjects and Rats. *Phytomedicine* 19 (10), 861–867. doi:10.1016/j.phymed.2012.05.009

Jantke, J., Ladehoff, M., Kürzel, F., Zapf, S., Kim, E., and Giese, A. (2004). Inhibition of the Arachidonic Acid Metabolism Blocks Endothelial Cell Migration and Induces Apoptosis. *Acta Neurochir (Wien)* 146 (5), 483–494. doi:10.1007/s00701-004-0238-z

Jensen, L. D., Hansen, A. J., and Lundbaek, J. A. (2007). Regulation of Endothelial Cell Migration by Amphiphiles - Are Changes in Cell Membrane Physical Properties Involved?. *Angiogenesis* 10 (1), 13–22. doi:10.1007/s10456-006-9060-y

Jeong, H. W., Hernández-Rodríguez, B., Kim, J., Kim, K. P., Enriquez-Gasca, R., Yoon, J., et al. (2017). Transcriptional Regulation of Endothelial Cell Behavior during Sprouting Angiogenesis. *Nat. Commun.* 8 (1), 726. doi:10.1038/s41467-017-00738-7

Jiang, T. T., and Li, J. C. (2020). Review on the Systems Biology Research of Yin-deficiency-heat Syndrome in Traditional Chinese Medicine. *Anat. Rec.*, 1–6. doi:10.1002/ar.24354

Kleemann, R., Zadelaar, S., and Kooistra, T. (2008). Cytokines and Atherosclerosis: a Comprehensive Review of Studies in Mice. *Cardiovasc. Res.* 79 (3), 360–376. doi:10.1093/cvr/cvn120

Kobayashi, T., Takaku, Y., Yokote, A., Miyazawa, H., Soma, T., Hagiwara, K., et al. (2008). Interferon-beta Augments Eosinophil Adhesion-Inducing Activity of Endothelial Cells. *Eur. Respir. J.* 32 (6), 1540–1547. doi:10.1183/09031936.00059507

Lee, J. S., Chang, P. Y., Zhang, Y., Kizer, J. R., Best, L. G., and Howard, B. V. (2017). Triglyceride and HDL-C Dyslipidemia and Risks of Coronary Heart Disease and Ischemic Stroke by Glycemic Dysregulation Status: The Strong Heart Study. *Diabetes Care* 40 (4), 529–537. doi:10.2337/dc16-1958

Li, Z., Zhao, T., Tan, X., Lei, S., Huang, L., and Yang, L. (2019). Polymorphisms in PCSK9, LDLR, BCMO1, SLC12A3, and KCNJ1 Are Associated with Serum Lipid Profile in Chinese Han Population. *Int. J. Environ. Res. Public Health* 16 (17), 3207. doi:10.3390/ijerph16173207

Liehn, E. A., Zernecke, A., Postea, O., and Weber, C. (2006). Chemokines: Inflammatory Mediators of Atherosclerosis. *Arch. Physiol. Biochem.* 112 (4-5), 229–238. doi:10.1080/13813450601093583

Lin, C. C., Li, T. C., and Lai, M. M. (2005). Efficacy and Safety of Monascus purpureus Went rice in Subjects with Hyperlipidemia. *Eur. J. Endocrinol.* 153 (5), 679–686. doi:10.1530/eje.1.02012

Lucas, T., Waisman, A., Ranjan, R., Roes, J., Krieg, T., Müller, W., et al. (2010). Differential Roles of Macrophages in Diverse Phases of Skin Repair. *J. Immunol.* 184 (7), 3964–3977. doi:10.4049/jimmunol.0903356

Moore, E. M., and West, J. L. (2019). Harnessing Macrophages for Vascularization in Tissue Engineering. *Ann. Biomed. Eng.* 47 (2), 354–365. doi:10.1007/s10439-018-02170-4

Mozaffarian, D., Benjamin, E. J., Go, A. S., Arnett, D. K., Blaha, M. J., Cushman, M., et al. (2015). Heart Disease and Stroke Statistics--2015 Update: a Report from the American Heart Association. *Circulation* 131 (4), e29–322. doi:10.1161/CIR.0000000000000152

Ng, C. T., Fong, L. Y., Sulaiman, M. R., Moklas, M. A., Yong, Y. K., Hakim, M. N., et al. (2015). Interferon-Gamma Increases Endothelial Permeability by Causing Activation of P38 MAP Kinase and Actin Cytoskeleton Alteration. *J. Interferon Cytokine Res.* 35 (7), 513–522. doi:10.1089/jir.2014.0188

Node, K., Huo, Y., Ruan, X., Yang, B., Spiecker, M., Ley, K., et al. (1999). Anti-inflammatory Properties of Cytochrome P450 Epoxygenase-Derived Eicosanoids. *Science* 285 (5431), 1276–1279. doi:10.1126/science.285.5431.1276

Pantos, J., Efstathopoulos, E., and Katritsis, D. G. (2007). Vascular wall Shear Stress in Clinical Practice. *Curr. Vasc. Pharmacol.* 5 (2), 113–119. doi:10.2174/157016107780368253

Pesce, J. T., Ramalingam, T. R., Mentink-Kane, M. M., Wilson, M. S., El Kasmi, K. C., Smith, A. M., et al. (2009). Arginase-1-expressing Macrophages Suppress Th2 Cytokine-Driven Inflammation and Fibrosis. *Plos Pathog.* 5 (4), e1000371. doi:10.1371/journal.ppat.1000371

Potente, M., Gerhardt, H., and Carmeliet, P. (2011). Basic and Therapeutic Aspects of Angiogenesis. *Cell* 146 (6), 873–887. doi:10.1016/j.cell.2011.08.039

Rhee, E. J., Kim, H. C., Kim, J. H., Lee, E. Y., Kim, B. J., Kim, E. M., et al. (2019). 2018 Guidelines for the Management of Dyslipidemia in Korea. *Korean J. Intern. Med.* 34 (5), 1171. doi:10.3904/kjim.2019.188.e1

Roman, R. J. (2002). P-450 Metabolites of Arachidonic Acid in the Control of Cardiovascular Function. *Physiol. Rev.* 82 (1), 131–185. doi:10.1152/physrev.00021.2001

Rukoyatkina, N., Shpakova, V., Panteleev, M., Kharazova, A., Gambaryan, S., and Geiger, J. (2018). Multifaceted Effects of Arachidonic Acid and Interaction with Cyclic Nucleotides in Human Platelets. *Thromb. Res.* 171, 22–30. doi:10.1016/j.thromres.2018.09.047

Sarzynski, M. A., Schuna, J. M., Jr., Carnethon, M. R., Jacobs, D. R., Jr., Lewis, C. E., Quesenberry, C. P., Jr., et al. (2015). Association of Fitness with Incident Dyslipidemias over 25 Years in the Coronary Artery Risk Development in Young Adults Study. *Am. J. Prev. Med.* 49 (5), 745–752. doi:10.1016/j.amepre.2015.04.022

Schroecksnadel, K., Frick, B., Winkler, C., and Fuchs, D. (2006). Crucial Role of Interferon-Gamma and Stimulated Macrophages in Cardiovascular Disease. *Curr. Vasc. Pharmacol.* 4 (3), 205–213. doi:10.2174/157016106777698379

Scicchitano, P., Cortese, F., Gesualdo, M., De Palo, M., Massari, F., Giordano, P., et al. (2019). The Role of Endothelial Dysfunction and Oxidative Stress in Cerebrovascular Diseases. *Free Radic. Res.* 53 (6), 579–595. doi:10.1080/10715762.2019.1620939

Sham, T. T., Chan, C. O., Wang, Y. H., Yang, J. M., Mok, D. K., and Chan, S. W. (2014). A Review on the Traditional Chinese Medicinal Herbs and Formulae with Hypolipidemic Effect. *Biomed. Res. Int.* 2014, 925302. doi:10.1155/2014/925302

Spiecker, M., and Liao, J. K. (2005). Vascular Protective Effects of Cytochrome P450 Epoxygenase-Derived Eicosanoids. *Arch. Biochem. Biophys.* 433 (2), 413–420. doi:10.1016/j.abb.2004.10.009

Stone, N. J., Robinson, J. G., Lichtenstein, A. H., Bairey Merz, C. N., Blum, C. B., Eckel, R. H., et al. (2014). 2013 ACC/AHA Guideline on the Treatment of Blood Cholesterol to Reduce Atherosclerotic Cardiovascular Risk in Adults: a Report of the American College of Cardiology/American Heart Association Task Force on Practice Guidelines. *Circulation* 129, S1–S45. doi:10.1161/01.cir.0000437738.63853.7a

Tiwari, R. L., Singh, V., and Barthwal, M. K. (2008). Macrophages: an Elusive yet Emerging Therapeutic Target of Atherosclerosis. *Med. Res. Rev.* 28 (4), 483–544. doi:10.1002/med.20118

Wang, W., Yang, L., Song, L., Guo, M., Li, C., Yang, B., et al. (2021). Combination of Panax Notoginseng Saponins and Aspirin Potentiates Platelet Inhibition with Alleviated Gastric Injury via Modulating Arachidonic Acid Metabolism. *Biomed. Pharmacother.* 134, 111165. doi:10.1016/j.biopha.2020.111165

Weber, C., Zernecke, A., and Libby, P. (2008). The Multifaceted Contributions of Leukocyte Subsets to Atherosclerosis: Lessons from Mouse Models. *Nat. Rev. Immunol.* 8 (10), 802–815. doi:10.1038/nri2415

Xu, X., Zhang, X. A., and Wang, D. W. (2011). The Roles of CYP450 Epoxygenases and Metabolites, Epoxyeicosatrienoic Acids, in Cardiovascular and Malignant Diseases. *Adv. Drug Deliv. Rev.* 63 (8), 597–609. doi:10.1016/j.addr.2011.03.006

Xu, H. Y., Zhang, Y. Q., Liu, Z. M., Chen, T., Lv, C. Y., Tang, S. H., et al. (2019). ETCM: An Encyclopaedia of Traditional Chinese Medicine. *Nucl. Acids Res.* 47 (D1), D976–D982. doi:10.1093/nar/gky987

Xu, H., Zhang, Y., Wang, P., Zhang, J., Chen, H., Zhang, L., et al. (2021). A Comprehensive Review of Integrative Pharmacology-Based Investigation: A Paradigm Shift in Traditional Chinese medicine. *Acta Pharm. Sin B* 11 (6), 1379–1399. doi:10.1016/j.apsb.2021.03.024

Xue, S. S., He, J. L., Zhang, X., Liu, Y. J., Xue, F. X., Wang, C. J., et al. (2015). Metabolomic Analysis Revealed the Role of DNA Methylation in the Balance of Arachidonic Acid Metabolism and Endothelial Activation. *Biochim. Biophys. Acta* 1851 (10), 1317–1326. doi:10.1016/j.bbalip.2015.07.001

Yamada, Y., Doi, T., Hamakubo, T., and Kodama, T. (1998). Scavenger Receptor Family Proteins: Roles for Atherosclerosis, Host Defence and Disorders of the central Nervous System. *Cell Mol Life Sci* 54 (7), 628–640. doi:10.1007/s000180050191

Zachary, I. (2003). VEGF Signalling: Integration and Multi-Tasking in Endothelial Cell Biology. *Biochem. Soc. Trans.* 31 (Pt 6), 1171–1177. doi:10.1042/bst0311171

Conflict of Interest: The authors declare that the research was conducted in the absence of any commercial or financial relationships that could be construed as a potential conflict of interest.

The reviewers LL and HY declared a shared affiliation with several of the authors, JC, CY, ZY, TW, PL, SZ, and XX, to the handling editor at time of review.

Publisher's Note: All claims expressed in this article are solely those of the authors and do not necessarily represent those of their affiliated organizations, or those of the publisher, the editors and the reviewers. Any product that may be evaluated in this article, or claim that may be made by its manufacturer, is not guaranteed or endorsed by the publisher.

Copyright © 2021 Chen, Ye, Yang, Wang, Xu, Li, Zhang and Xue. This is an open-access article distributed under the terms of the Creative Commons Attribution License (CC BY). The use, distribution or reproduction in other forums is permitted, provided the original author(s) and the copyright owner(s) are credited and that the original publication in this journal is cited, in accordance with accepted academic practice. No use, distribution or reproduction is permitted which does not comply with these terms.

frontiers in Pharmacology

REVIEW
published: 19 October 2021
doi: 10.3389/fphar.2021.675350

Kaempferia galanga L.: Progresses in Phytochemistry, Pharmacology, Toxicology and Ethnomedicinal Uses

Si-Yu Wang[1,2†], Hui Zhao[3†], Hong-Tao Xu[4], Xiao-Dong Han[1], Yun-Shan Wu[1,2], Fang-Fang Xu[1,2], Xiao-Bo Yang[1,5,6], Ulf Göransson[7*] and Bo Liu[1,2,5,6*]*

[1]The Second Clinical Medical College, and Guangdong Provincial Key Laboratory of Clinical Research on Traditional Chinese Medicine Syndrome, Guangzhou University of Chinese Medicine, Guangzhou, China, [2]Guangzhou Key Laboratory of Chirality Research on Active Components of Traditional Chinese Medicine, Guangzhou, China, [3]College of Basic Medical Science, Guangzhou University of Chinese Medicine, Guangzhou, China, [4]Shanghai Institute for Advanced Immunochemical Studies, ShanghaiTech University, Shanghai, China, [5]State Key Laboratory of Dampness Syndrome of Chinese Medicine, Guangzhou, China, [6]Guangdong-Hong Kong-Macau Joint Lab on Chinese Medicine and Immune Disease Research, Guangzhou University of Chinese Medicine, Guangzhou, China, [7]Division of Pharmacognosy, Biomedical Center, Uppsala University, Uppsala, Sweden

K. galanga is an aromatic medicinal herb. It is locally to India and distributed in China, Myanmar, Indonesia, Malaysia, and Thailand. *K. galanga* is a Traditional Chinese Herb Medicine (TCHM), which has been applied to treat cold, dry cough, toothaches, rheumatism, hypertension and so on. In addition, it has been used widely as spices since its highly aromas. The aim of this review is to compile and update the current progresses of ethnomedicinal uses, phytochemistry, pharmacology and toxicology of *K. galanga*. All the data on *K. galanga* were based on different classical literary works, multiple electronic databases including SciFinder, Web of Science, PubMed, etc. The results showed that ninety-seven compounds have been identified from rhizome of *K. galanga*, including terpenoids, phenolics, cyclic dipeptides, flavonoids, diarylheptanoids, fatty acids and esters. Modern pharmacology studies revealed that extracts or secondary metabolites of the herb possessed anti-inflammatory, anti-oxidant, anti-tumorous, anti-bacterial, and anti-angiogenesis effects, which were closely related to its abundant ethnomedicinal uses. In conclusion, although previous research works have provided various information of *K. galanga*, more in-depth studies are still necessary to systemically evaluate phytochemistry, pharmacological activities, toxicity and quality control of this herb.

Keywords: *Kaempferia galanga* L., ethnomedicinal uses, phytochemistry, pharmacology, toxicology

OPEN ACCESS

Edited by:
Takashi Sato,
Tokyo University of Pharmacy and Life Sciences, Japan

Reviewed by:
Sandeep Rawat,
Govind Ballabh Pant National Institute of Himalayan Environment and Sustainable Development, India
Germain Sotoing Taiwe,
University of Buea, Cameroon

***Correspondence:**
Xiao-Bo Yang
yangxiaobomd@163.com
Ulf Göransson
ulf.goransson@fkog.uu.se
Bo Liu
doctliu@263.net

†*These authors have contributed equally to this work*

Specialty section:
This article was submitted to Ethnopharmacology, a section of the journal Frontiers in Pharmacology

Received: *03 March 2021*
Accepted: *23 August 2021*
Published: *19 October 2021*

Citation:
Wang S-Y, Zhao H, Xu H-T, Han X-D, Wu Y-S, Xu F-F, Yang X-B, Göransson U and Liu B (2021) Kaempferia galanga *L.: Progresses in Phytochemistry, Pharmacology, Toxicology and Ethnomedicinal Uses. Front. Pharmacol. 12:675350. doi: 10.3389/fphar.2021.675350*

INTRODUCTION

K. galanga is from a dried rhizome of herb *Kaempferia galanga* L., belonging to the important family Zingiberaceae and genus *Kaempferia*. It also called sand ginger, aromatic ginger in different areas. *K. galanga* is native to India, and commonly found in China, Myanmar, Indonesia, Malaysia, and Thailand (Wang and Tang, 1980; Santhoshkumari and Devi, 1991). In Southern China, such as Guangxi, Guangdong, Yunnan are the main producing areas of *K. galanga*. In China, being a source of valuable bioactive compounds, it was used as a folk medicine due to its good curative effect on rheumatism, dry cough, colic, muscle pain, inflammations, as well as tumors (Park et al., 2005; Liu et al., 2010; He et al., 2012). In India, *K. galanga* was used in the treatment of intestinal wounds and urticarial (Nazar et al., 2008; Seth and Maurya, 2014). In Malaysia, *K. galanga* was also applied for

abdominal pain and postpartum care in woman (Hirschhorn, 1983). Moreover, it could also be used as food condiment. According to Sivarajan and Balachandran (1994), *K. galanga* was used to treat phlegm, fever, cough, meanwhile, it also exerts good effect as a diuretic, anabolic, and carminative.

To date, phytochemical studies have discovered many chemical compounds of the plant, mainly terpenoids, phenolics, diarylheptanoids and flavonoids. Also, it has revealed that the components or extracts from *K. galanga* exhibit anti-inflammatory, anti-oxidant, anti-tumorous, anti-angiogenesis, and other effects in **Figure 1** (Umar et al., 2014; Wu et al., 2015; Zhou et al., 2015; Yao et al., 2018; Srivastava et al., 2019). However, pharmacological researches mainly focus on the crude extracts and characteristic compounds especially *trans* ethyl p-methoxycinnamate. Furthermore, many active components in the extracts of *K. galanga* have not been fully investigated yet as well as the mechanisms of action. In addition, biological evaluations should take appropriate effective dose, the frequency of administration and duration of treatment into consideration. Thus, there are many issues worthy of further study.

Although previous reports provided great inspiration and help for us (Umar et al., 2011; Munda et al., 2018; Elshamy et al., 2019; Kumar, 2020), we are more concerned about the application of *K. galanga* in ethnomedicine, its relationship with phytochemistry, modern pharmacology, and its toxicity. Herein, we conducted a comprehensive review on the phytochemistry, pharmacology, toxicology and ethnomedicinal uses of *K. galanga*. We also discuss the limitations of the current studies of the herb and suggest areas of interest for potential future research. We hope to provide valuable information for future in-depth investigations and applications of the herb.

REVIEW METHODOLOGY

The literature for this review was collected from different classical literary works, multiple electronic databases including SciFinder, Web of Science, PubMed, Science Direct, Wiley, Springer, CNKI, and PhD, MSc dissertations in Chinese and Pharmacopoeias prior to December 2020 on phytochemistry, pharmacology, toxicology and ethnomedicinal uses of *K. galanga*. A total of 97 publications were collected after preliminary screening, among them, 24 publications used for traditional uses, 34 publications used for phytochemistry, 39 publications used for pharmacological activities. The search terms "*Kaempferia galanga* L" and "*K. galanga* essential oils" were used with no exact time limit. Identify potential full-texts of eligible papers, and check additional and unpublished citations for all relevant references.

ETHNOMEDICINAL USES

K. galanga has been considered as an important herbal medicine with a long history in China, on the basis of its wide spectrum of biological activities. *K. galanga* was listed in the Chinese medical classic "Compendium of Materia Medica" (Ming dynasty), and it had a good effect on the treatment of pains and cold-damp dysentery. According to the Pharmacopoeia of the People's Republic of China, *K. galanga* is pungent, warm natured in flavor and belonging to the stomach meridian, and has the action of activating Qi, warm interior, remove digestion and relieve pain.

In addition, *K. galanga* showed significant increase in urine volume and also increased level of sodium and potassium in urine which proves as a strong diuretic agent. Therefore, the results provided a quantitative basis to explain the traditional folkloric use of *K. galanga* as a diuretic agent (Mohammad et al., 2016).

The traditional methods of *K. galanga* are to decoct in water or mash for external use, and a dose of 6–9 g for oral medication is recommended by the Chinese Pharmacopoeia (China Pharmacopoeia Commission, 2015). In addition, although *K. galanga* was widely used, there were few studies on its side effects. The ethnomedicinal uses of *K. galanga* are listed in **Table 1**.

PHYTOMEDICINAL FORMULATIONS

K. galanga has been used as a phyto-ingredient in some classical medicinal formulations. It was combined with other herb to treat common pains, cold, digestive disorders as formulations, and these formulations could be made into different dosage forms or decocted with water depending on the maximum efficacy to use them. (Kanjanapothi et al., 2004). The traditional formulations containing *K. galanga* are listed in **Table 2**.

TOXICOLOGY

Although *K. galanga* has long been used as TCHM, its systematic toxicity and safety evaluations are still unclear. The acute and subacute toxicity tests of its rhizomes ethanol extract (maximum single oral dose up to 5,000 mg/kg (b. w.), and daily dose of 1,000 mg/kg (b. w.) for 30 consecutive days) showed that it has no significant toxicity regarding to the morbidity and mortality (Amuamuta et al., 2017).

Similarly, Kanjanapothi et al. have reported that the maximum tolerated dose (MTD) of ethanol extract of rhizomes of *K. galanga* was up to 5,000 mg/kg and no death occurred in rats by oral administration. Hematological analysis showed no difference in any parameter tested between control and test group in male and female. Moreover, no abnormal in pathology and histopathology, and no irritation in the skin. Besides, in 28 days subacute toxicity studies, there was no death occurred when the ethanolic *K. galanga* extract was treated the dosage of 25, 50 or 100 mg/kg (Kanjanapothi et al., 2004). Therefore, *K. galanga* is safe for the vital organs during treatment depending on the above toxicological studies.

PHYTOCHEMISTRY

Chemical characteristics of *K. galanga* showed the existence of various types of secondary metabolites such as terpenoids, phenolics, cyclic dipeptides, diarylhaptanoids, flavonoids,

TABLE 1 | Ethnomedicinal uses of *K. galanga.*

Locality	Traditional uses	Part used	Method of preparation	References
India	Pain (chest pain, cholera, headache, toothache and abdominal pain)	Rhizome	Rhizomes used as much	Vittalrao et al. (2011); Tewtrakul et al. (2005)
India	Diarrhoea	Rhizome	Intact part used for the management of diarrhoea	Dash et al. (2014)
India	Ulcer	Rhizome	Intact parts used as much	Ogiso and Kobayashi (1994)
Manoko in West Java	Inflammation	Rhizome	Consuming herb tea of this plant rhizome	Levita et al. (2015)
Thailand	Ophthalmia	Leaf	Leaves are used for ophthalmia, Fever and sore throat in the form of lotions and poultices	Kanjanapothi et al. (2004); Warrier et al. (1995)
Malaysia	Swelling and muscular rheumatism	Rhizome	Rhizomes of this plant are boiled with other roots to treat Swelling and muscular rheumatism	Mustafa et al. (1996)
Malaysia	Sore throat	Leaf	The air dried powdered leaves (40 g) soaked in distilled water (1: 10; w/v)	Sulaiman et al. (2008)
Thailand	Indigestion, colds	Rhizome	The extract of rhizome	Kanjanapothi et al. (2004)
Japan	Smooth muscle relaxant	Rhizome	Rhizomes used as smooth muscle relaxant	Hashimoto et al. (1986)
Malaysia	Swollen breasts, coughs	Leaf	The ashes of leaves are rubbed on swollen breasts after childbirth while fresh leaves are chewed for relieving coughs	Sulaiman et al. (2008)
Indonesia	Osteoarthritis	Rhizome	Intact part used for treatment for osteoarthritis	Akmal et al. (2017)
Indonesia	Recurrent aphthous stomatitis (RAS)	Rhizome	Rhizome's extract is effective in treating minor RAS	Laurenzia and Wilda (2016)
Thailand	Cardiotonic	Rhizome	Rhizomes used as cardiotonic and central nervous system (CNS) stimulants	Mokkhasmit et al. (1971)
Malaysia	Hypertension	Rhizome	Intact part used for treating Hypertension	Othman et al. (2002)
India	Hepatoprotection	Rhizome	Rhizome's constituents have promising application in hepatoprotection	Manigaunha et al. (2010)
India	Hypolipidemia	Rhizome	Rhizomes extracts shows significant activity for treating hypolipidemic	Achuthan and Padikkala (1997)
Malaysia	Tumor	Rhizome	Rhizomes used as much	Omar et al. (2017)
India	Washing hairs	Leaf	Leaves are used as a perfume in washing hairs	Warrier et al. (1995)
Bangladesh	Pregnancy	Leaf	Leaf infusions can be used as a beneficial drink for women	Rahman et al. (2004)
China	Dyspepsia	Rhizome	Rhizomes have been used as an aromatic stomachic to promote digestion	China Pharmacopeia Commission (2015)
China	Anxiety	Rhizome	Its aroma has also been used for a long history in relieving anxiety	He et al. (2012)

TABLE 2 | Classic prescriptions of *K. galanga.*

Formulations	Uses	Mode of uses	Locality	References
Quercus infectoria, *Glycyrrhiza uralensis*, *Kaempferia galanga* and *Coptis chinensis*	Four plant powders are consisting of traditional Thai herbal remedy for aphthous ulcer	Powders (oral)	Thailand	Aroonrerk and Kamkaen (2009)
Kaempferia galanga L (Kencur) and *Boesenbergia pandurata* (Roxb) Schlecht (Temu kunci)	Combination of kencur and temu lawak ethanol extract with ratio (80%:20%) or (70%:30%) as Sunscreen	Cream (external use)	Southeast Asia, such as Indonesia and Thailand	Shintia et al. (2018)
Plumbago indica, *Garcinia mangostana*, *Dracaena loureiri*, *Dioscorea membranacea*, *Artemisia annua*, *Piper chaba*, *Myristica fragrans* and *Kaempferia galanga*	Eight powdered medicinal plants showed potent antimalarial activity	Powders (oral)	Thailand	Thiengsusuk et al. (2013)

polysaccharides, and essential oils. A total of 97 compounds have been obtained from the rhizome of *K. galanga*. In this article, we will present each types of compounds in **Table 3**, and structures in **Figures 2**-**7**.

Volatile Constituents

The species of the chemical constituents of essential oils has been studied for many years. They were isolated by steam distillation or supercritical fluid extraction, and analyzed by GC-MS. Volatile oils are generally composed of esters, hydrocarbons, terpenes and aromatic compounds. The 19 major compounds of essential oils are esters and terpenoids such as ethyl cinnamate, p-methoxycinnamate, pentadecane, δ-selinene, borneol, eucalyptol (Fan et al., 2005; Zhou et al., 2006; Zhang, 2007; Cui et al., 2008; Wang et al., 2009; Sutthanont et al., 2010; Liu et al., 2014; Luo et al., 2014; Raina and Abraham, 2016; Yang et al., 2018) **(Table 4**; **Figure 2**).

These essential oils show various promising pharmacological and therapeutic potentials, particularly, ethyl cinnamate and p-methoxycinnamate (Peter, 2004; Raina and Abraham, 2016).

TABLE 3 | Chemical constituents isolated from *K. galanga*.

No	Chemical component	Chemical formula	References
Terpenoids			
1	3-caren-5-one	$C_{10}H_{14}O$	Kiuchi et al. (1987)
2	(3*R*,4*R*,6*S*)-3,6-dihydroxy-1-menthene	$C_{10}H_{18}O_2$	Yao (2018)
3	(1*R*,2*S*,4*R*)-p-menth-5-ene-1,2,8-triol	$C_{10}H_{18}O_3$	Yao (2018)
4	oxyphyllenodiol B	$C_{14}H_{22}O_3$	Yao (2018)
5	hedytriol	$C_{15}H_{28}O_3$	Yao (2018)
6	kaemgalangol A	$C_{20}H_{30}O_3$	Ningombam et al. (2018)
7	6β-hydroxypimara-8(14),15-diene-1-one	$C_{20}H_{30}O_2$	Ningombam et al. (2018)
8	sandaracopimaradien-6β,9α-diol-l-one	$C_{20}H_{30}O_3$	Ningombam et al. (2018)
9	(-)-sandaracopimaradiene	$C_{20}H_{32}$	Ningombam et al. (2018)
10	sandaracopimaradiene-9α-ol	$C_{20}H_{32}O$	Ningombam et al. (2018)
11	kaempulchraol I	$C_{20}H_{32}O$	Ningombam et al. (2018)
12	kaempulchraol E	$C_{20}H_{32}O_2$	Ningombam et al. (2018)
13	8(14),15-sandaracopimaradiene-1α,9α-diol	$C_{20}H_{32}O_2$	Ningombam et al. (2018)
14	kaempulchraol L	$C_{21}H_{34}O_2$	Ningombam et al. (2018)
15	2α-acetoxy sandaracopimaradien-1α-ol	$C_{22}H_{34}O_3$	Ningombam et al. (2018)
16	1,11-dihydroxypimara-8(14),15-diene	$C_{20}H_{32}O_2$	Ningombam et al. (2018)
17	6β,14α-dihydroxyisopimara-8(9),15-diene	$C_{20}H_{32}O_2$	Tungcharoen et al. (2020)
18	6β,14β-dihydroxyisopimara-8(9),15-diene	$C_{20}H_{32}O_2$	Tungcharoen et al. (2020)
19	1α-hydroxy-14α-methoxyisopimara-8(9),15-diene	$C_{21}H_{34}O_2$	Tungcharoen et al. (2020)
20	1α,14α-dihydroxyisopimara-8(9),15-diene	$C_{20}H_{32}O_2$	Tungcharoen et al. (2020)
21	boesenberol I	$C_{20}H_{32}O_2$	Ningombam et al. (2018)
22	boesenberol J	$C_{20}H_{32}O_2$	Ningombam et al. (2018)
23	6β-acetoxysandaracopimaradiene-9α-ol	$C_{22}H_{34}O_3$	Tungcharoen et al. (2020)
24	6β-acetoxysandaracopimaradiene-9α-ol-1-one	$C_{22}H_{32}O_4$	Tungcharoen et al. (2020)
25	6β-acetoxysandaracopimaradiene-1α,9α-diol	$C_{22}H_{34}O_4$	Tungcharoen et al. (2020)
26	6β-acetoxy-1α-14α-dihydroxyisopimara-8(9),15-diene	$C_{22}H_{34}O_4$	Yao (2018)
Phenolics			
27	p-metho-xybenzoicacid	$C_8H_8O_3$	Yao et al. (2018)
28	p-hydroxybenzoic acid	$C_7H_6O_3$	Yao et al. (2018)
29	vanillic acid	$C_8H_8O_4$	Yao et al. (2018)
30	methyl 3,4-dihydroxybenzoate	$C_8H_8O_4$	Yao et al. (2018)
31	4-methoxybenzyl-O-β-D-glucopyranoside	$C_{14}H_{20}O_7$	Yao et al. (2018)
32	methyl (2*R*,3*S*)-2,3-dihydroxy-3-(4-methoxyphenyl) propanoate	$C_{11}H_{14}O_5$	Yao et al. (2018)
33	ethyl (2*R*,3*S*)-2,3-dihydroxy-3-(4-methoxyphenyl) propanoate	$C_{12}H_{16}O_5$	Yao et al. (2018)
34	*trans* ethyl p-methoxycinnamate	$C_{12}H_{14}O_3$	Yao et al. (2018)
35	ferulic acid	$C_{10}H_{10}O_4$	Yao et al. (2018)
36	*trans* p-hydroxycinnamic acid	$C_9H_8O_3$	Yao et al. (2018)
37	*trans* p-methoxycinnamic acid	$C_{10}H_{10}O_3$	Yao et al. (2018)
38	*trans* ethyl cinnamate	$C_{11}H_{12}O_2$	Wu (2016)
39	*cis* ethyl p-methoxycinnamate	$C_{12}H_{14}O_3$	Wu (2016)
40	4-methoxy-benzyl (*E*)-3-(4-methoxyp-henyl) acrylate	$C_{18}H_{18}O_4$	Wu (2016)
41	1-O-4-carboxylphenyl-(6-O-4-hydroxybenzoyl)-β-D-glucopyranoside	$C_{20}H_{20}O_{10}$	Yao et al. (2018)
Cyclic Dipeptides			
42	cyclo-(L-Val-L-Phe)	$C_{14}H_{18}N_2O_2$	Yao (2018)
43	cyclo-(L-Leu-L-Ile)	$C_{12}H_{22}N_2O_2$	Yao (2018)
44	cyclo-(L-Val-L-Leu)	$C_{11}H_{20}N_2O_2$	Yao (2018)
45	cyclo-(L-Val-L-Val)	$C_{10}H_{18}N_2O_2$	Yao (2018)
46	cyclo-(L-Ala-L-Ile)	$C_9H_{16}N_2O_2$	Yao (2018)
47	cyclo-(L-Ala-L-Leu)	$C_9H_{16}N_2O_2$	Yao (2018)
48	cyclo-(L-Ala-L-Phe)	$C_{12}H_{14}N_2O_2$	Yao (2018)
49	cyclo-(L-Val-L-Ala)	$C_8H_{14}N_2O_2$	Yao (2018)
50	cyclo-(L-Phe-L-Tyr)	$C_{18}H_{18}N_2O_3$	Yao (2018)
51	cyclo-(L-Leu-L-Tyr)	$C_{15}H_{20}N_2O_3$	Yao (2018)
52	cyclo-(L-Val-L-Tyr)	$C_{14}H_{18}N_2O_3$	Yao (2018)
53	cyclo-(L-Asp-OCH_3-L-Phe)	$C_{14}H_{16}N_2O_4$	Yao (2018)
54	cyclo-(L-Tyr-L-Ile)	$C_{15}H_{20}N_2O_3$	Yao (2018)
55	cyclo-(L-Pro-L-Tyr)	$C_{14}H_{16}N_2O_3$	Yao (2018)
56	cyclo-(L-Leu-L-Phe)	$C_{15}H_{20}N_2O_2$	Yao (2018)
57	cyclo-(L-Glu-OCH_3-L-Phe)	$C_{15}H_{18}N_2O_4$	Yao (2018)
Flavonoids			
58	kaempferol	$C_{15}H_{10}O_6$	Wu (2016)
59	luteolin	$C_{15}H_{10}O_6$	Wu (2016)
60	kaempferide	$C_{16}H_{12}O_6$	Jiao et al. (2017)

(Continued on following page)

TABLE 3 | (*Continued*) Chemical constituents isolated from *K. galanga*.

No	Chemical component	Chemical formula	References
Diarylheptanoids			
61	(1*R*,3*R*,5*R*)-1,5-epoxy-3-hydroxy-1-(3,4-dihydroxyphenyl)-7-(3,4-dihydroxyphenyl) heptane	$C_{19}H_{22}O_6$	Yao et al. (2018)
62	(1*R*,3*R*,5*R*)-1,5-epoxy-3-hydroxy-1-(3,4-dihydroxyphenyl)-7-(4-hydroxyphenyl) heptane 3-O-β-D-glucopyranoside	$C_{25}H_{32}O_{10}$	Yao et al. (2018)
63	phaeoheptanoxide	$C_{19}H_{22}O_5$	Yao (2018)
64	hedycoropyran B	$C_{20}H_{24}O_7$	Yao (2018)
65	1-(4-hydroxy-3-methoxyphenyl)-7-(4-hydroxyphenyl) heptane-1,2,3,5,6-pentaol	$C_{20}H_{26}O_8$	Yao et al. (2018)
66	(3*R*,5*S*)-3,5-dihydroxy-1,7-bis(3,4-dihydroxyphenyl) heptane	$C_{19}H_{24}O_6$	Yao (2018)
67	kaempsulfonic acid A	$C_{20}H_{24}O_8S$	Wang et al. (2013)
68	kaempsulfonic acid B	$C_{20}H_{24}O_8S$	Wang et al. (2013)
Fatty Acids and Esters			
69	stearic acid	$C_{18}H_{36}O_2$	Wu (2016)
70	dec-5-enoic acid	$C_{10}H_{18}O_2$	Wu (2016)
71	2-tetradecenoic acid	$C_{14}H_{26}O_2$	Wu (2016)
72	linolenic acid	$C_{18}H_{30}O_2$	Yao (2018)
73	linoleic acid	$C_{18}H_{32}O_2$	Yao (2018)
74	ethyl icosanoate	$C_{22}H_{44}O_2$	Wu (2016)
75	monopalmitin	$C_{19}H_{38}O_4$	Wu (2016)
76	5,6-dimethyl citrate	$C_8H_{12}O_7$	Yao (2018)
77	3-carboxyethyl-3-hydroxyglutaric acid 1,5-dimethyl ester	$C_{10}H_{16}O_7$	Yao (2018)
78	trimethyl citrate	$C_9H_{14}O_7$	Yao (2018)
79	1,5-dimethyl citrate	$C_8H_{12}O_7$	Yao (2018)
Polysaccharides			
80	fucose	$C_6H_{12}O_5$	Yang et al. (2018)
81	arabinose	$C_5H_{10}O_5$	Yang et al. (2018)
82	xylose	$C_5H_{10}O_5$	Yang et al. (2018)
83	rhamnose	$C_6H_{12}O_5$	Yang et al. (2018)
84	mannose	$C_6H_{12}O_6$	Yang et al. (2018)
85	galactose	$C_6H_{12}O_6$	Yang et al. (2018)
86	glucose	$C_6H_{12}O_6$	Yang et al. (2018)
87	glucuronic acid	$C_6H_{10}O_7$	Yang et al. (2018)
88	galacturonic acid	$C_6H_{10}O_7$	Yang et al. (2018)
Others			
89	L-p Glu-L-Leu-OCH_3	$C_{13}H_{23}N_2O_4$	Yao (2018)
90	pyroglutamyl-phenylalanine methyl ester	$C_{16}H_{21}N_2O_4$	Yao (2018)
91	pyroglutamyl-tyrosine methyl ester	$C_{16}H_{21}N_2O_5$	Yao (2018)
92	benzoic acid	$C_7H_6O_2$	Wu (2016)
93	phenylmethanol	C_7H_8O	Wu (2016)
94	dibutyl phthalate	$C_{16}H_{22}O_4$	Wu (2016)
95	furan-2-carboxylic acid	$C_5H_4O_3$	Yao (2018)
96	β-sitosterol	$C_{29}H_{50}O$	Yao (2018)
97	β-daucosterol	$C_{35}H_{60}O_6$	Yao (2018)

What's more, *K. galanga.* has always been used as food flavoring and aromatic, due to its flavor and fragrances, which might be up to ethyl p-methoxycinnamate (Srivastava et al., 2019).

Terpenoids

Terpenoids were the representative class of compounds isolated from *K. galanga*. To date, 26 terpenoids (**1–26**, **Figure 3**) have been isolated and identified, which included monoterpenoids, sesquiterpenoids and diterpenoids. Most of them were isopimarane type diterpenoids with the typical structural features of two double bonds of $\triangle^{15(16)}$, $\triangle^{8(9)}$ and/or $\triangle^{8(14)}$.

Among them, 3-caren-5-one (**1**) was a monoterpene ketone, which was isolated from methanolic extract of *K. galanga* firstly (Kiuchi et al., 1987). More recently, four new diterpenoids **6**, **19**, **20**, **26** were isolated and elucidated. Kaemgalangol A (**6**) was isolated from the chloroform fraction of methanol extract of *K. galanga*, and it was remarkable that **6** contained a rare 9,10-seco-isopimarane skeleton (Ningombam et al., 2018). From the hexane fraction of 95% ethanol extract of *K. galanga*, diterpenoids **19** and **20** were also identified (Tungcharoen et al., 2020). Compound **26** was isolated from the chloroform fraction of 75% ethanol extract of *K. galanga* (Yao, 2018).

Phenolics

Phenolics (**27–41**, **Figure 4**) are compounds with a phenolic hydroxyl group (Li et al., 2017a; Hua et al., 2018). Depending on the existing literatures, 16 phenolic chemical constituents were found. Among them, **27–29** were hydroxybenzoic acids, and **35–37** were hydroxycinnamic derivatives. In addition, phenolic acids may be found in plants as in the form of glycosides (Masullo et al., 2015), such as **31** and **41** (Yao et al., 2018). Besides, **40** and

41 were first isolated and their structures were elucidated by the NMR, HR-MS and IR (Wu, 2016; Yao et al., 2018).

Cyclic Dipeptides

Cyclic dipeptides (**42–57**, **Figure 5**) are formed by cyclization of two amino acids through peptide bonds. They are the simplest members in the most common cyclic peptide family found in nature. A total of 16 cyclic dipeptides have been reported (Yao, 2018).

Flavonoids

The parent nucleus structure of flavonoids is 2-phenylchromone. The flavonoids isolated from *K. galanga* were all free monomers (**58–60**, **Figure 5**), and the substituents are usually methoxy and phenolic hydroxyl groups (Wu, 2016; Jiao et al., 2017). Kaempferol (**58**) (Chen et al., 2012) and luteolin (**59**) (Liu et al., 2018) had protective effects on lung injury by regulating multiple cellular pathways. Moreover, **58** (Schwarz et al., 2014) have been reported to exert anti-corona virus effects, indicating its potential in the treatment of COVID-19. Similarly, its relative, compound **59** could dose-dependently inhibit the SARS coronavirus cleavage activity with low micromole inhibitory activity (EC_{50} = 10.6 μM) (Yi et al., 2004), particularly, it could also inhibit the 3CLPro of SARS-CoV2 with IC_{50} value of 20.2 μM (Ryu et al., 2010). In silicon docking indicated that **59** could interact with a series of key targets of SARS-CoV-2 (3CLpro, PLpro, Spro and RdRp) to exert potential anti-corona virus activity (Yu et al., 2020).

Diarylheptanoids

Diarylheptanoids (**61–68**, **Figure 6**) have a 1,7-diphenylheptane skeleton. Based on the skeleton, diarylheptanoids could be divided into linear and cyclic structural types. Linear diarylheptanoids occurred frequently in plants of Zingiberaceae family, and all the diarylheptanoids isolated from *K. galanga* were linear.

The first report of two novel sulfonated diarylheptanoid epimers focused on the identification of kaempsulfonic acid A (**67**) and B (**68**) (Wang et al., 2013). More recently, cyclic diarylheptanoids were isolated and elucidated. The two compounds, **62** and **61** were very similar to each other, while the difference was the substituents, **62** had one phenolic hydroxyl replaced by one glucosyl moiety. In addition, a linear diarylheptanoid **65** was isolated and elucidated (Yao, 2018; Yao et al., 2018).

Fatty Acids and Esters

Fatty acid and esters were included in *K. galanga*, currently, 11 fatty acid and esters (**69–79**, **Figure 6**) have been analyzed and identified from *K. galanga* (Wu, 2016; Yao, 2018).

Polysaccharides

Recently, the water-soluble polysaccharides (**80–88**, **Figure 7**) from *K. galanga*. (KGPs) were extracted and purified for the first time, and further investigated by different spectroscopic techniques such as HPGPC, FTIR, IC. Results showed that fucose (80), arabinose (81), xylose (82), rhamnose (83), mannose (84), galactose (85), glucose (86), glucuronic acid (87), and galacturonic acid (88) were the main components of KGPs, and their the molar ratio is 0.37: 3.12: 1.23: 3.09: 1.00: 6.39: 1.36: 0.91: 1.27, which significantly indicated that KGPs were heterogeneous acidic polysaccharides (Yang et al., 2018).

Other Compounds

Apart from those chemical constituents mentioned above (**1–88**), *K. galanga* also contained other eight compounds (**89–97** **Figure 7**). Three pyroglutamic acids (**89–91**), two steroids (**96–97**) and three aromatic compounds (**92–95**) have been isolated and identified (Wu, 2016; Yao, 2018).

Molecular docking assay was used to investigate the effect of **92** as coronavirus polymerase (RdRp) inhibitor, and the results showed its potential anti-coronavirus activity with the binding energies showed −5.54 kcal/mol. Moreover, further studies are required to determine the potential uses of **92** in COVID-19 treatment (El-Aziz et al., 2020). Meanwhile, β-sitosterol (**96**) have been reported to have inhibitory activity against the SARS-CoV 3CLpro with IC_{50} value of 47.8 μg/ml (Lin et al., 2005).

Elemental Composition

K. galanga was abounded with mineral elements K, P, Mg, Ca, Al, Fe, Na and Mn, and the content of K was the highest, amounting to 18,600 μg/g (Huang et al., 2012).

PHARMACOLOGICAL ACTIVITIES

K. galanga have gained much attention with its comprehensive pharmacological potential to treat a variety of human diseases. Modern pharmacological investigations have revealed that the extracts and natural products identified from *K. galanga* exhibited comprehensive bioactivities, including antitumor, antioxidant, anti-inflammatory and anti-tuberculosis, etc. Besides, the aqueous extract from its leaves have been reported to exert antinociceptive activity and anti-inflammatory activities in a dose dependently manner, supporting its traditional uses in the remedy of treat pain and mouth ulcer (Sulaiman et al., 2008). In addition, the kill of booklice by its essential oil, indicating its potential in the development of a natural insecticide and repellent for controlling stored grain pests (Liu et al., 2014). The more detailed pharmacological reviews were as follows.

Antitumor Activity

According to the previous reports, the extracts and active components of *K. galanga* showed potential inhibitory effects on many types of tumors, such as gastric cancer, colon carcinogenesis, oral cancer and multiple myeloma. Although *K. galanga* preparations traditionally are used as an alternative medicine for tumor, there is little scientific evidence available about the use of *K. galanga* as an anticancer agent. Reports indicate that the anticancer signaling mechanisms of *K. galanga* extracts and

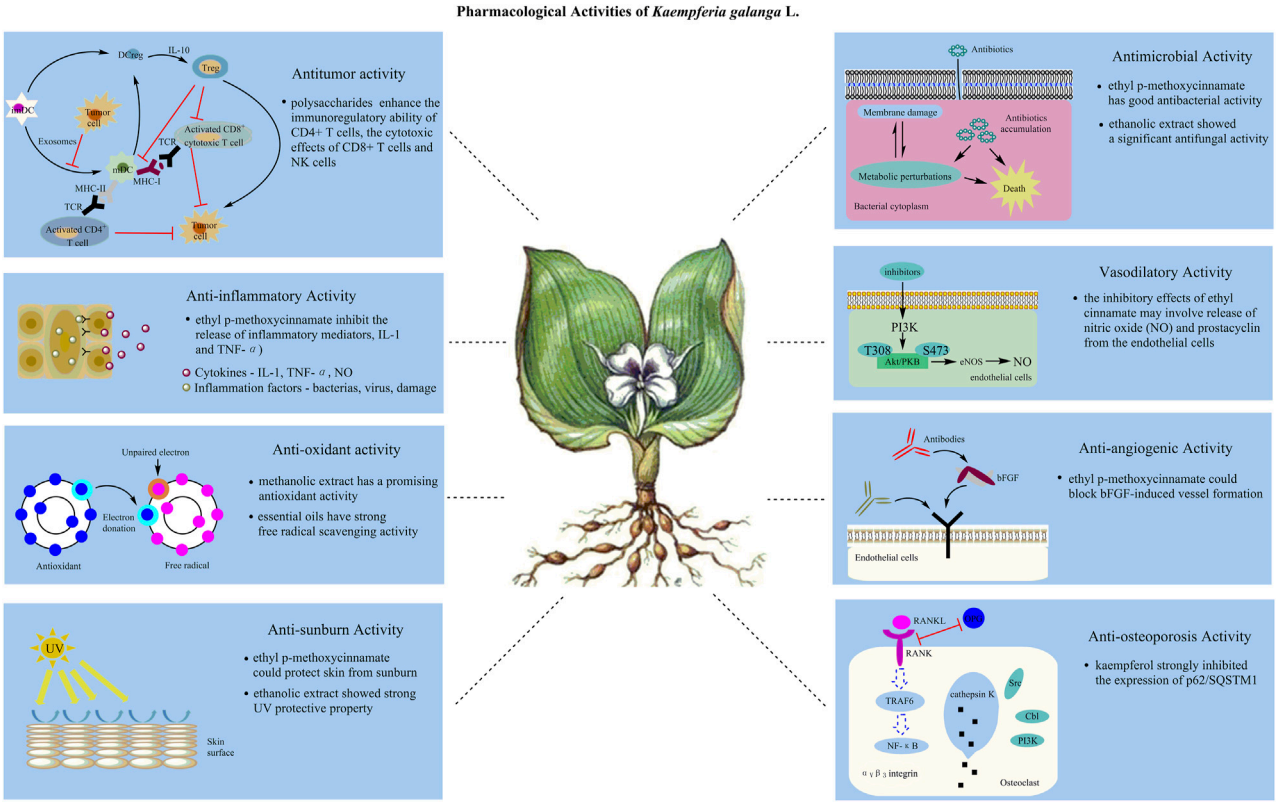

FIGURE 1 | Primary reactions and constituents supporting various biological effects of *K. galanga*. The TCHM shows antitumor, anti-inflammatory, anti-oxidant, anti-sunburn, antimicrobial, vasodilatory, anti-angiogenic and anti-osteoporosis activities, et al. Multiple types of constituents (see **Table 3**) are contributed to such evident pharmacological profiles of this plant.

compounds include inhibition of the growth of tumor cells, apoptosis and cytotoxicity, among others.

Multiple constituents isolated from *K. galanga* showed antitumor activity. It is reported that both *trans*-and *cis*-ethyl p-methoxycinnamate (**34**, **39**) could exert anti-carcinogeneic effect in an *in vitro* EBV assay with IC_{50} values of 5.5 and 9.5 μM (Xue and Chen, 2002). *Trans*-ethyl p-methoxycinnamate (**34**) was examined on HSC-3 and Ca922 lines by MTT assay. The MTT assay showed **34** could exert potent cytotoxicity in HSC-3 (IC_{50} = 0.075 mg/ml) and Ca922 (IC_{50} = 0.085 mg/ml) cell lines (Ichwan et al., 2019). In addition, **34** could also dose dependently induce apoptosis, and affected the cell cycle progress of the cell cycle of HepG2 cells (Liua et al., 2010). *Trans*-p-methoxycinnamic acid (**37**) (40 mg/kg b.w.) exhibited ameliorating anticancer effects in DMH-induced rat colon carcinogenesis by regulating of various processes, such as proliferation, invasion, angiogenesis, apoptosis and inflammation (Gunasekaran et al., 2019). The diarylheptanoid compounds sandaracopimaradiene-9α-ol (**10**), kaempulchraol I (**11**), kaempulchraol L (**14**) revealed anti-cancer effect in human HeLa (IC_{50} = 75.1, 74.2 and 76.5 μM, respectively) and HSC-2 cancer cells (IC_{50} = 69.9, 53.3 and 58.2 μM, respectively) by using MTT assay (Ningombam et al., 2018).

The essential oils from the *K. galanga* have displayed moderate antitumor activity. Flow cytometry (FCM) was used to evaluate the effect of volatile oil on cell cycle and apoptosis of MKN-45 cells. The growth inhibition rates of gastric cancer were 57.2, 28.0 and 5.0% respectively in the high-, medium-, and low-dose volatile oil-treated groups (1.56, 0.78, 0.39 g/d), and the gastric cancer cells (MKN-45 cells) were arrested at G0/G1phase. The results showed the high-dose volatile oil-treated group was effective for inhibiting the growth of gastric cancer by comparing to cyclophospha (CTX)-treated group (78.9%) (Xiao et al., 2006). The ethanolic extract of *K. galanga* and its major bioactive constituent *trans*-ethyl p-methoxycinnamate (**34**) could exert cytotoxic activity against cholangiocarcinoma cells (CL-6). The ethanolic extract inhibited CL-6 cell growth at doses of 125 and 250 μg/ml, with 80 and 94% inhibitory, and IC_{50} values of 64.2 and 49.19 μg/ml, respectively (Amuamuta et al., 2017). Recently, the methanolic and acetonic extracts of *K. galanga* leaves have been reported to exert moderate cytotoxic activities (LC_{50} = 4.78 and 0.11 μg/ml, respectively) in the brine shrimp lethality bioassay (Rahman et al., 2019). The water-soluble polysaccharides isolated from *K. galanga* could inhibit the growth of H22 solid tumors, while exert protective effects on the thymus and spleen of solid tumor bearing mice (Yang et al., 2018).

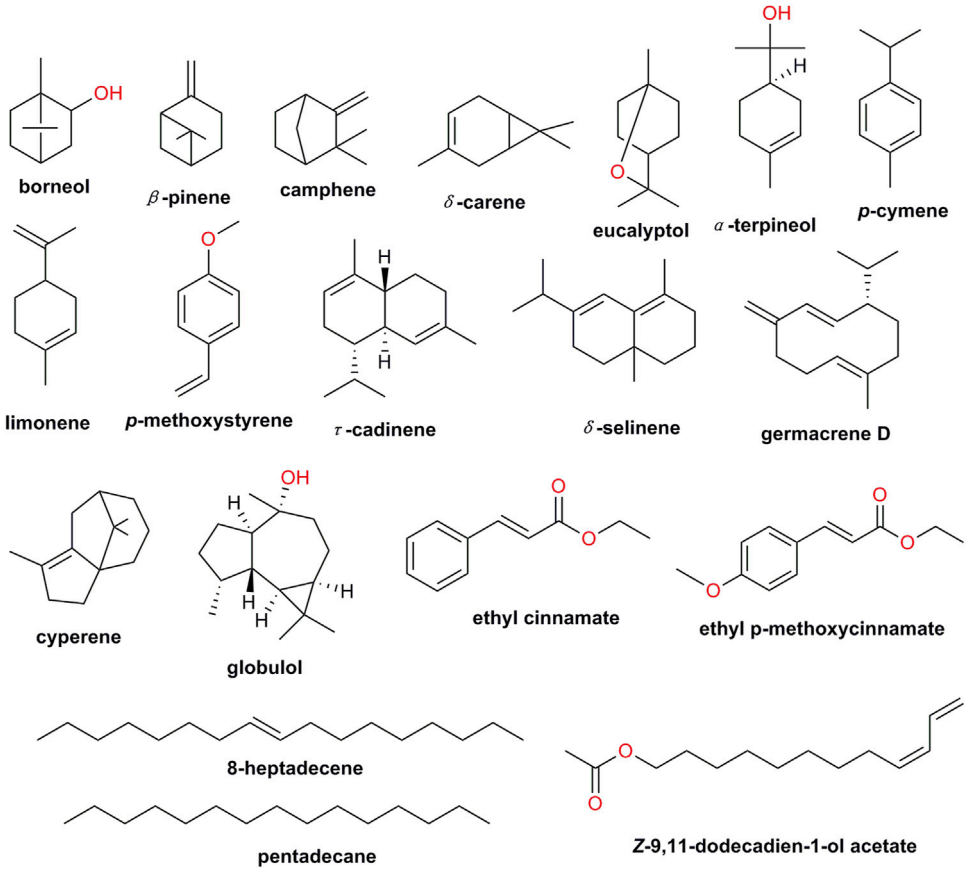

FIGURE 2 | Chemical structures of main volatile components in *K. galanga*.

Anti-Inflammatory Activity

The traditional applications of *K. galanga* in the remedy of abdominal pains and toothache are mostly depend on its anti-inflammatory effects. The mechanism behind the anti-inflammatory action of *K. galanga* is associated with the presence of bioactive metabolites by inhibiting the release of inflammatory factors.

The anti-inflammatory effect of *trans*-ethyl p-methoxycinnamate (**34**) was assessed using the cotton pellet granuloma assay in rats *in vivo*, and *in vitro* using the human macrophage cell line (U937). It strongly inhibited granuloma tissue formation in rats and the release of IL-1 and TNF-α, which were significantly inhibited in both *in vivo* and *in vitro* models (Umar et al., 2014). Kaempferol (**58**) exerted potent inhibitory activity on HMC-1 mast cell-mediated inflammatory response stimulated by lipopolysaccharide (LPS) demonstrated by MTT assay. The release of IL-6, IL-8, IL-1β and TNF-α significantly decreased at the dose of 40 μmol/L (Zhou et al., 2015). Moreover, diarylheptanoids **61**, **63**, **65**, **66**, have been reported to inhibit nitric oxide (NO) production on LPS-induced macrophage RAW264.7 cell lines with IC_{50} values of 27.85, 46.98, 26.98 and 17.26 μM, respectively (Yao et al., 2018).

The leaves of *K. galanga* have been reported to exert potent anti-inflammatory activity in a modified carrageenan-induced paw-edema test, supporting its traditional applications of ulcers and pains (Sulaiman et al., 2008). The various extracts of *K. galanga* exerted anti-inflammatory effects *in vivo*. In carrageenan induced acute inflammation test, the successive petroleum ether fraction (SPEF) showed 39.16% effect (300 mg/kg b.w., p.o.), followed by the successive ethyl acetate fraction (SEAF), alcohol fraction (SAF) and alcoholic extract with respective 10.0, 22.5 and 5.0% effects. In adjuvant-induced chronic inflammation test, the SPEF and diclofenac extract obviously reduced inflammation (5 and 100 mg/kg b.w., p.o., 7 days) (Jagadish et al., 2016).

Anti-Oxidant Activity

The anti-oxidant activity is an important value for the further development of natural products, since oxidation reactions are associated with many diseases (Liu and Ng, 2000). In the past few years, crude extracts with anti-oxidant activity from *K. galanga* has been evaluated using several methods as follows.

It is reported that the essential oil extracted by ultrasound-enhanced subcritical water extraction (USWE) exerted significant DPPH, free radical and superoxide anion radical scavenging effects, suggesting its strong anti-oxidant effects (Ma et al., 2015). The methanolic extract of *K. galanga* showed high antioxidant activity

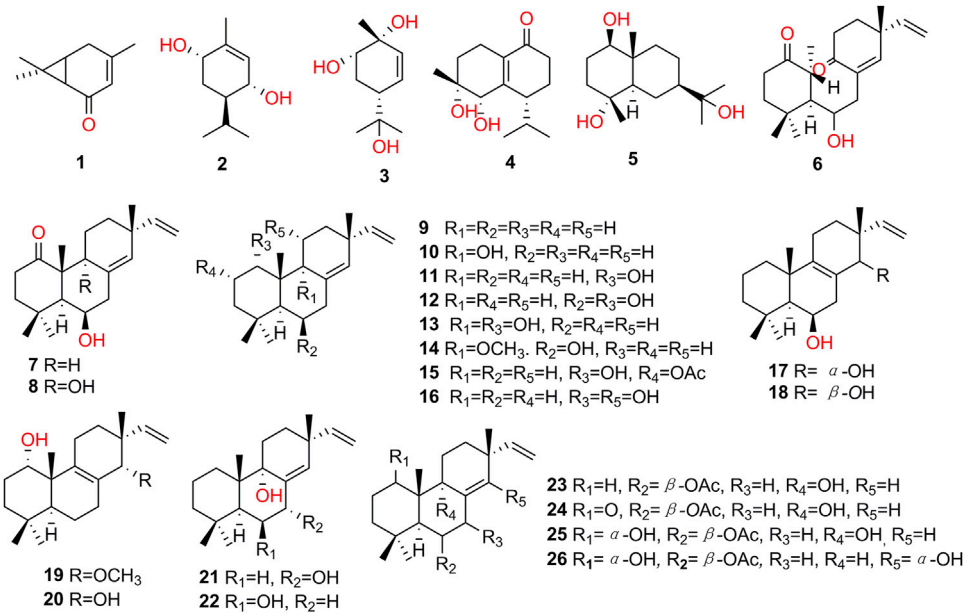

FIGURE 3 | Structures of terpenoids isolated from *K. galanga*.

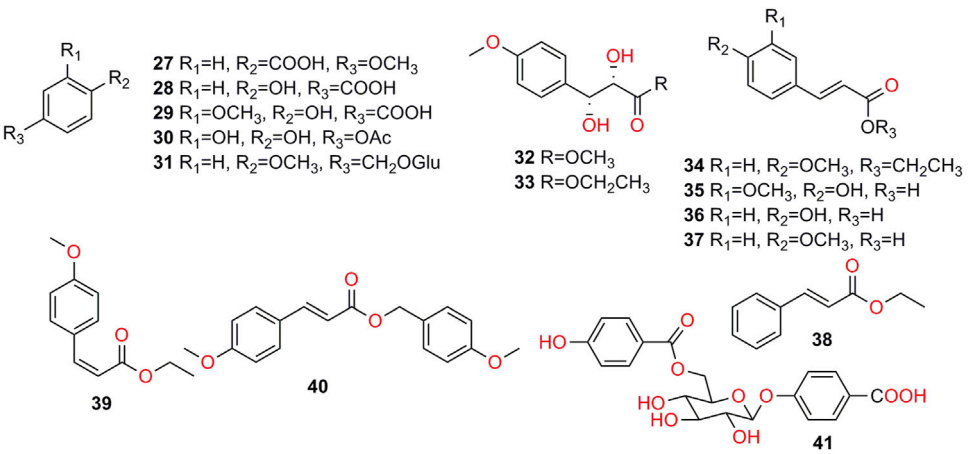

FIGURE 4 | Structures of phenolics isolated from *K. galanga*.

in DPPH, ABTS, and NO scavenging assays (IC_{50} = 16.58, 8.24 and 38.16 μg/ml, respectively) (Ali et al., 2018). Further, the *K. galanga* leaves showed weakly antioxidant activity in DPPH scavenging assay, and IC_{50} values were 611.82 and 702.79 μg/ml, respectively (Rahman et al., 2019). The antioxidant activity of various extracts of *K. galanga* were tested by DPPH and ABTS assays respectively. The results showed that *K. galanga* had good antioxidant activity, among the five extracts, the activity of chloroform fraction was the best, and its SC_{50} on DPPH and ABTS were about 4 and 2 times that of the positive control (V_C) respectively, followed by the ethyl acetate, n-butanol fraction, while petroleum ether fraction was poor and the water fraction was basically inactive (Xiang et al., 2018).

Insecticidal and Repellent Activity

The methanolic extract and essential oil of *K. galanga* rhizome, as well as their isolates *trans*-ethyl p-methoxycinnamate (**34**) and *trans*-ethyl cinnamate (**38**) exhibited strong insecticidal and repellent properties.

Two compounds **34** and **38** with excellent nematicide activity had been obtained from petroleum hexane extracts. After treatment 72 h, the LC_{50} of **34** against *Meloidotyne incongnita*, *Bursaphelenchus xylophilus*, *Ditylenchus destructor*, *M. eloidogyne hainensis*, *M. enterolobii* were 1.49, 2.81, 10.09, 26.67 and 14.47 mg/L. The LC_{50} values of **38** against *M. incongnita*, *B. xylophilus*, *D. destructor*, *M. eloidogyne hainensis*, *M. enterolobii* were 17.79, 29.70, 43.21, 57.64 and 36.94 mg/L, respectively

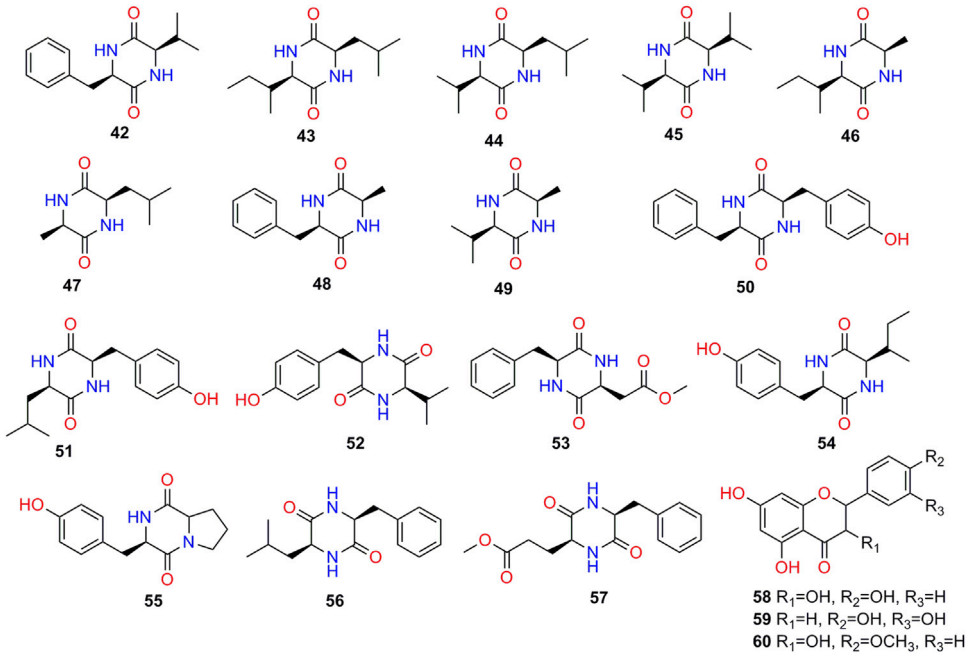

FIGURE 5 | Structures of cyclic dipeptides and flavonoids isolated from *K. galanga*.

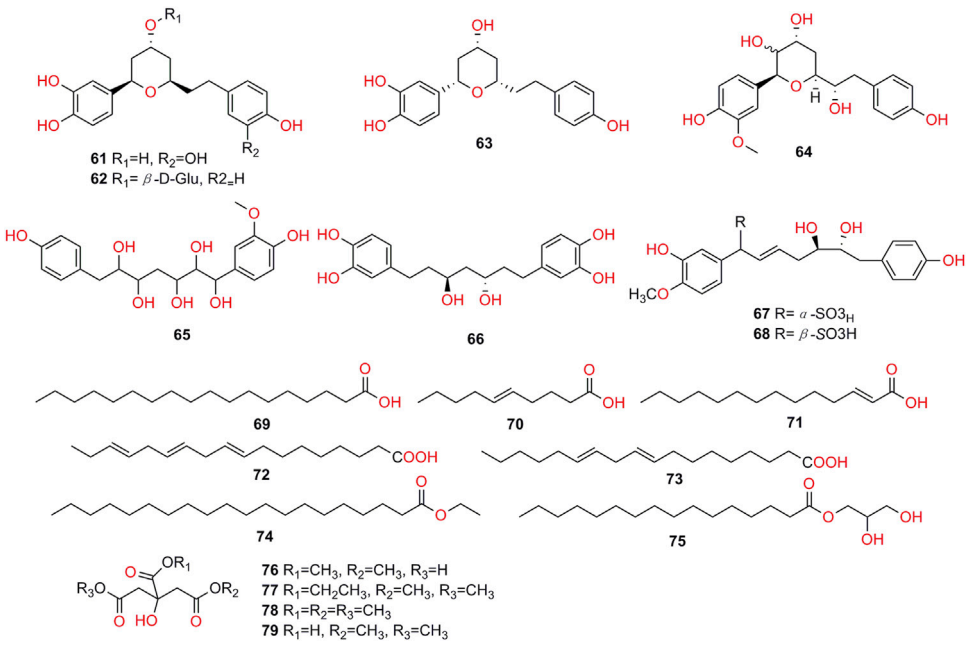

FIGURE 6 | Structures of diarylheptanoids, fatty acids and esters isolated from *K. galanga*.

(Zhang et al., 2010). **34** and **38** also had potent insecticidal activity against the larvae of polyphagous insect *Spodoptera littoralis* (Noctuidae) (LD_{50} = 0.47 and 0.65 μg/mL, respectively) (Pandji et al., 1993).

The essential oil, and its main constituents, **38**, **34** and **39** showed contact toxicity against the booklouse *Liposcelis bostrychophila* Badonnel. Among them, **38** was the most effective with LC_{50} value of 21.4 g/cm^2, **34**, **39** and the essential oil exhibited moderately effects with LC_{50} value of 44.6 and 43.4 68.6 g/cm^2, respectively. In addition, fumigant toxicity (LC_{50} = 1.5 mg/L air) of the essential oil against the booklouse also was observed (Liu et al., 2014). The essential oil as well as **34** and **38**

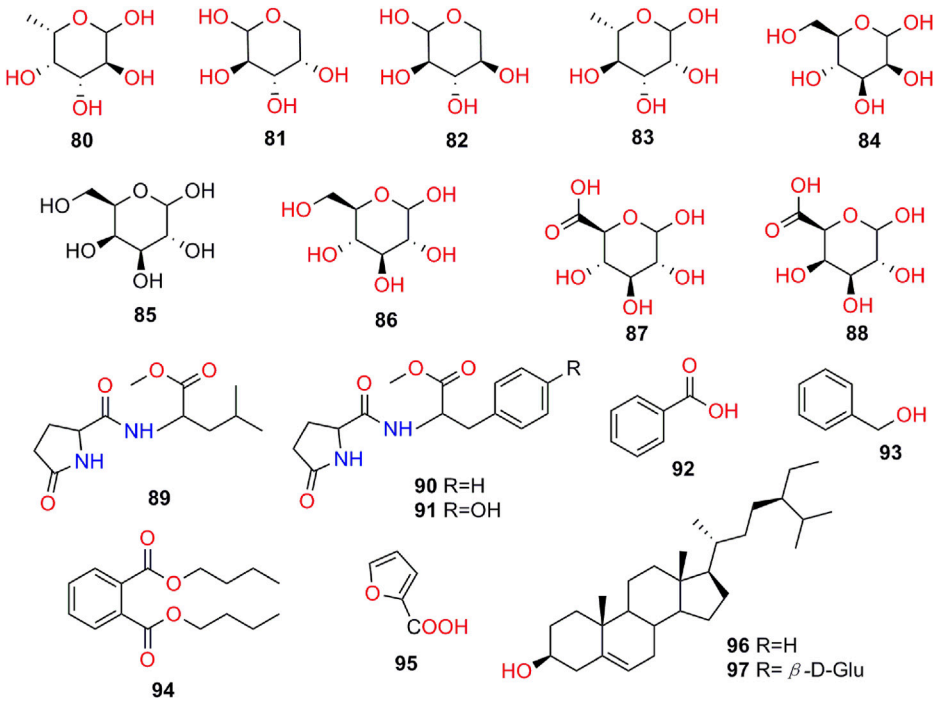

FIGURE 7 | Structures of polysaccharides and other compounds isolated from *K. galanga*.

showed nematicidal activity against the cereal cyst nematode with LC_{50} value of 91.78, 83.04 and 100.60 μg/ml, respectively, while borneol and 1, 8-cineole only showed slight nematicidal toxicity (LC_{50} = 734.89 and 921.21 μg/ml, respectively) (Li et al., 2017b).

The toxicity of the methanol extracts against *Bursaphelenchus xylophilus* and *Meloidotyne incongnita* were tested. The results showed that the mortality of extracts from *K. galanga* against *B. xylophilus* and *M. incongnita* with 100% mortality at 1,000 mg/L after 24 h (Choi et al., 2006).

Antimicrobial Activity

Trans-ethyl p-methoxycinnamate (**34**) exerted potent antibacterial activity against *Pseudomonas aeruginosa*, *Escherichia coli*, *Staphyloccocus aureus*, *Aspergillus niger* and *Monilia albican* in disk diffusion and test tube experiments, and the MIC values were 0.625 1.25, 2.5, 2.5 and 10 mg/ML, respectively (Han et al., 2011). The essential oil of *K. galanga* showed potent antimicrobial activity against *Candida albicans* (fungus); *Staphylococcus aureus* ATCC 25923, *S. faecalis* and *Bacillus subtilis* (three Gram-positive bacteria); *Salmonella typhi*, *Shigella flexneri*, *Escherichia coli* ATCC 25922 (three Gram-negative bacteria) in agar disc diffusion test, with the inhibition zones was 12–16 mm and 8–12 mm against Gram-positive and Gram-negative bacteria respectively, while it potently inhibited *C. albicans* with an inhibition zone of 31 mm, comparing to that (25 mm) of standard antifungal (Clotrimazole) (Tewtrakul et al., 2005). Similarly, agar well diffusion test was employed to assess antifungal potential of ethanolic extract of *K. galanga*, and the results showed a potent antifungal effect of this extract against *Malassezia* spp. (MIC = 5 mg/ml) (Parjo et al., 2018).

Antidiabetic Activity

Diabetes has become the third major non-infective disease threatening human health after cardiovascular disease and tumor (World Health Organization, 2013). The effect of kaempferol (**58**) on the correlation factors of chronic complications of type 2 diabetic rats was observed. Rats in administration group were given respective drug (50, 100, 200 mg/kg) every day, and set the model, normal control, and positive control (metformin hydrochloride 0.2 g/kg) groups. After 10 weeks, compared with diabetic model group, **58** administration could reduce blood lipid levels, along with reducing MDA, AR, TNF-α, and IL-6 levels and increasing SOD levels. Moreover, **58** could prevent and treat the chronic complications of type 2 diabetic rats by reducing blood glucose, insulin resistance, reducing the AR pathway as well as anti-oxidation and anti-inflammation. The antidiabetic activity of **58** was comparable to that of positive control at the dose of 200 mg/kg (Wu et al., 2015).

Anti-Tuberculosis Activity

The anti-tuberculosis effect of **34** was determined by resazurin microtitre assay (REMA) on *Mycobacterium tuberculosis* H37Ra and H37Rv strains. The results demonstrated that **34** had a significant anti-tuberculosis activity, and its MIC values were in the range of 0.242–0.485 mM. This study showed *K. galanga* and

TABLE 4 | Major compounds of essential oils of *K. galanga*.

No	Chemical constituent	Area						References
		Kerala and Karnataka (India)	Chiang Mai (Tailand)	Guangdong (China)	Guangxi (China)	Hainan (China)	Guizhou (China)	
1	borneol	1.0–2.4%	1.03%	0.17% 1.39%	2.79% 1.62%	—	—	Raina and Abraham, 2016; Sutthanont et al. (2010); Fan et al. (2005); Zhou et al. (2006); Zhang (2007)
2	β-pinene	0.1–0.3%	0.11%	0.12%	0.13%	—	0.01%	Raina and Abraham, 2016; Sutthanont et al. (2010); Zhou et al. (2006); Luo et al. (2014)
3	camphene	0.1–0.9	0.37	0.9	1.07	0.82	—	Raina and Abraham, 2016; Sutthanont et al. (2010); Zhou et al. (2006); Cui et al. (2008)
4	δ-carene	0.1–6.5	—	6.61	8.21	5.27	0.10	Raina and Abraham, 2016; Zhou et al. (2006); Cui et al. (2008); Luo et al. (2014)
5	eucalyptol	0.2–5.2	2.12	0.01 0.56	1.59 0.16	—	—	Raina and Abraham, 2016; Sutthanont et al. (2010); Fan et al. (2005); Zhou et al. (2006); Zhang (2007)
6	α-terpineol	0.1–0.3%	—	—	–0.23	—	—	Raina and Abraham, 2016; Zhang (2007)
7	p-cymene	0.1–1.1	—	0.65	0.79 0.93	—	0.01	Raina and Abraham, 2016; Zhou et al. (2006); Zhang (2007); Luo et al. (2014)
8	limonene	0.1–0.7	—	0.52	0.76 0.10	1.36	0.02	Raina and Abraham, 2016; Zhou et al. (2006); Zhang (2007); Cui et al. (2008); Luo et al. (2014)
9	p-methoxystyre-ne	—	—	0.46	0.78	—	—	Zhou et al. (2006)
10	τ-cadinene	0.3–0.5	—	0.15	1.25	—	0.15	Raina and Abraham, 2016; Fan et al. (2005); Zhang (2014)
11	δ-selinene	—	—	0.29	0.35	—	0.14	Zhou et al. (2006); Luo et al. (2014)
12	germacrene D	0.5–0.9	—	1.48	—	—	0.06	Raina and Abraham, 2016; Fan et al. (2005); Luo et al. (2014)
13	cyperene	—	—	0.63	1.464	—	0.95	Fan et al. (2005); Zhang (2007); Luo et al. (2014)
14	globulol	—	—	—	2.35	—	—	Zhang (2007)
15	ethyl cinnamate	11.5–26.6	—	5.27 23.68	27.74 28.30	19.32	—	Raina and Abraham, 2016; Fan et al. (2005); Zhou et al. (2006); Zhang (2007); Cui et al. (2008)
16	ethyl p-methoxycinn-amate	28.4–70.0	25.96	59.24 59.96	48.30 33.84	49.12	—	Raina and Abraham, 2016; Sutthanont et al. (2010); Fan et al. (2005); Zhou et al. (2006); Zhang (2007); Luo et al. (2014)
17	8-heptadecene	0.2–0.6	0.71	0.78	1.08	—	—	Raina and Abraham, 2016; Sutthanont et al. (2010); Fan et al. (2005); Zhang (2007)
18	pentadecane	6.0–16.5	26.1	21.67	14.85	15.02	—	Raina and Abraham, 2016; Sutthanont et al. (2010); Fan et al. (2005); Zhang (2007); Cui et al. (2008)
19	*Z*-9,11-dodecadien-1-ol acetate	—	—	0.99	—	—	—	Fan et al. (2005)

its isolate **34** had anti-tuberculosis effects, however, the molecular mechanisms of action of **34** should be further explored by in-depth studies and clinical trials (Lakshmanan et al., 2011).

Vasodilatory Activity

Previous reports have shown that *trans*-ethyl cinnamate (**38**) could exert vasorelaxant activity, which was in line with traditional role of *K. galanga* in the treatment of high blood pressure. It could dose dependently inhibit the tonic contractions induced by high concentrations of K^+ and phenylephrine (PE) (IC_{50} = 0.3 ± 0.05 and 0.38 ± 0.04 mM, respectively). Mechanistic studies revealed that its vasorelaxant activity could be attributed to the inhibition of influx of Ca^{2+} into vascular cells and the release of prostacyclin and NO from the endothelial cells. Hence, the traditional use of the herb in treating hypertention may be explained well by the vasorelaxant activity of **38** (Othman et al., 2002). In the anaesthetized rats, the dichloromethane extract of *K. galanga* could exert vasorelaxant activity by lowering the basal mean arterial pressure (MAP). Moreover, the active compound, **38** was identified by bioassay-guided fractionation and isolation (Othman et al., 2006).

Sedative Activity

The hexane extract of *K. galanga* demonstrated potent sedative effects (1.5 and 10 mg) by reducing the activity of locomotor. Moreover, *trans*-ethyl p-methoxycinnamate (**34**) and *trans*-ethyl cinnamate (**38**) as well as showed significant sedative activity (14 and 12 μg) (Huang et al., 2008). The acetone extract of *K. galanga* exerted sedative activity at the dose of 200 mg/kg in mice (b.w., p.o.) (Ali et al., 2015).

Anti-Angiogenic Activity

The anti-angiogenic effects of ethanol extract, *trans*-ethyl p-methoxycinnamate (**34**) and kaempferol (**58**) of *K. galanga* exhibited potent anti-angiogenic effect assessed by zebrafish angiogenic assay. Further investigations for action mechanism of **34** indicated that it inhibited the migration and tube formation of human umbilical vein endothelial cells *in vitro*, and blocked vessel formation induced by bFGF on Matrigel plug assay *in vivo* (He et al., 2012).

Anti-Osteoporosis Activity

Kaempferol (**58**) showed inhibitory effects of osteoclastogenesis in the autophagy inhibition process of RAW 264.7 cells in the presence of 50 μM, and obviously inhibited the expression of p62/SQSTM1. Moreover, the potential role of **58** for the treatment of bone metabolism disorders could be explored through in-depth study of the role of p62/SQSTM1 in autophagy (Chang-Ju et al., 2018). Kaempferide (**60**) could prevent osteolysis induced by titanium particle and inhibit osteoclast genesis in mice at 12.5 μM, indicating a potential agent with anti-osteoporosis activity (Jiao et al., 2017).

Antithrombotic Effect

The ethanolic extract of *K. galanga* was orally administered (7, 14 and 28 mg/20 g b.w.) in a mouse thrombotic model induced by collagen-epinephrine. Bleeding time prolongation and the survival rate of mice was observed after 7 days extract pre-treatment. The results showed the greatest antithrombotic potency of *K. galanga* extract had similarities with the positive control (aspirin) at its highest dose (28 mg/20 g b.w.). Thus, the herb had great chance to be an antithrombotic agent in further studies (Saputri and Avatara, 2018).

Hypopigmentary Effect

Kaempferol (**58**) was investigated for the effect on tyrosinase activity, melanin content, and cell proliferation in human normal melanocytes. The effects of various concentration (1–100 μM) of kaempferol upon proliferation, melanin synthesis and tyrosinase activity in human normal melanocytes were observed. The results showed **58** could strongly inhibit tyrosinase activity and melanin content of melanocyte without more toxicity or adverse side effect on proliferation of melanocytes, and suggested **58** was a promising tyrosinase inhibitor (Shang et al., 2011).

Anti-Sunburn Activity

It was reported that *trans*-ethyl p-methoxycinnamate (**34**) could protect skin from sunburn. In order to investigated anti-sunburn activity of **34**, *in vitro* percutaneous solution was established, and the percutaneous absorption of **34** was studied. Modified Franz diffusion cells were used for *in vitro* permeation studies, and the nude mouse skin was used as transdermal barrier. The concentration of **34** in the receptor solution was determined by HPLC, and it also displayed a certain extent of sunscreen efficacy. The results showed that, accumulative permeation amount of **34** within 10 h was 0.2949 mg/cm^2 and indicated it was suitable for the development of natural sunscreen cosmetic products (Li et al., 2013).

The ethanolic rhizome extract of *K. galanga* and its main constituent **34** were evaluated for their UV protective properties. The results demonstrated *K. galanga* presented high UVB protection with SPF range of 8.57–22.34 μg/ml, and its main constituent **34** also demonstrated UV protective effect (Panyakaew et al., 2020).

CONCLUSION AND PERSPECTIVE

This review summarizes the latest researches of different extracts and active compounds of *K. galanga* in the fields of ethnomedicine uses, phytochemistry, toxicology and pharmacology. As stated above, the ninety-seven bioactive phytochemicals including terpenoids, phenolics, cyclic dipeptides, flavonoids, diarylheptanoids, fatty acids and esters, and others, have been isolated and identified from *K. galanga*, suggesting the presence of potential structural diversity of *K. galanga*, among them, isopimarane-type diterpenoids as the mainly characteristic constituents. Furthermore, numerous pharmacological studies have revealed that various crude extracts and some chemical components exerted multiple biological activities, in particular, antitumor, anti-inflammatory and anti-oxidant activities.

Although phytochemistry studies have isolated some compounds from the rhizomes of this plant, no study has documented the constituents separated from the leaves. Thus, the chemical studies on the leaves of this plant are necessary to strengthen. Besides, new compounds are need to be explored for enriching material basis of *K. galanga*.

Most pharmacological studies of *K. galanga* concentrated on the activities of its crude extracts, particularly volatile oil and ethanol extract. However, the underlying mechanisms of activities and exact chemical constituents are still little knowledge. Therefore, further elucidating the relationships of pharmacological mechanisms of bioactive constituents are still required. Gratefully, an emerging technology, DNA-encoded library (DEL) and especially the natural product DNA-encoded library (*n*DEL) has already showed their potential in identification of protein targets of natural products, thus could be used to handle this issue (Ma et al., 2019; Xie et al., 2020). Compounds that isolated from *K. galanga* could be efficiently annotated with unique DNA tags by using the *n*DEL technology to form a *K. galanga* focused *n*DEL. Screening of the *K. galanga* focused *n*DEL against various protein targets will definitely help to illuminate the target network of *K. galanga* in the future.

With regard to the safety profile of *K. galanga*, existing studies have provided only limited information. More systematic toxicology studies are still needed to be carried out in the future on the extracts and purified compounds of *K. galanga*.

For further improving the species, the following aspects also need to be paid attention to. Innovative breeding designs supported by information on the genomic resources and appropriate technologies could play a potential role to realize stable growth

in *K. galanga* productivity and quality (Bohra et al., 2020). In addition, to develop an agrotechnology to commercialize the production of *K. galanga* and bioprospect in *K. galanga* is required to identify secondary metabolite and develop novel technologies to overcome some diseases (Jnanesha and Kumar, 2018). On the other hands, clarifying biosynthetic pathways of bioactive natural products will make a significant contribution to pave the way for their manufacture. (Thomford et al., 2018; Gao and Lei, 2020). Moreover, plant proteomics of *K. galanga* could open new perspectives for ethnobotanical and phytomedicine research purposes, indicating the use of medicinal plants for the treatment of certain diseases (Pedrete, et al., 2019).

In terms of quality control, the information about the cultivation environment, cultivars, processing, transportation, storage time, and quantitative studies of the index components are scarcely in the existing studies. It is worth noting that the dual quality control, chemical benchmark and effect benchmark has been generally accepted (Li et al., 2019; Zhu et al., 2019). Therefore, the quality standard of it could be supported by the effect benchmark. Moreover, the effect benchmark offer basis to Q-biomarker research strategy, which could provide reference of methodology for the quality control study of *K. galanga* (Geng et al., 2019; Lu et al., 2020).

In summary, this review provides a comprehensive analysis on ethnomedicinal uses, phytochemistry, pharmacology and toxicology of *K. galanga*, and proposed future research directions. Based on this, we hope to highlight the potential value of *K. galanga* and provide some new research directions in further studies.

AUTHOR CONTRIBUTIONS

S-YW, H-TX, UG, and BL conceived the presented research. S-YW, H-TX, and BL designed the structure of the paper. S-YW, HZ, and H-TX drafted the manuscript. Y-SW, X-DH, and F-FX provided critical revision of this article. X-BY, UG, and BL supervised the findings of the work, and approved the manuscript for submission. All authors agreed with the final version of this manuscript.

FUNDING

This work was supported by the Key-Area Research and Development Program of Guangdong Province (No. 2020B1111110007); the National Natural Science Foundation of China (Nos. 81202398, 81974565, and 81974571); The special foundation of Guangzhou Key Laboratory (No. 202002010004); Science and Technology Planning Project of Guangdong Province(No. 2017B030314166); the Specific Research Project of State Administration of TCM of China (No. JDZX2015207); Special Funds for State Key Laboratory of Dampness Syndrome of Chinese Medicine (Nos. SZ2021ZZ33, SZ2021ZZ36, SZ2021ZZ40, and SZ2021ZZ46); the Specific Research Fund for TCM Science and Technology of Guangdong Provincial Hospital of Chinese Medicine (No. YN2019MJ05) and the collaborative innovation project of "Double first class" and High-level University Construction of Guangzhou University of Chinese Medicine (Nos. 2021XK69 and 2021XK08).

SUPPLEMENTARY MATERIAL

The Supplementary Material for this article can be found online at: https://www.frontiersin.org/articles/10.3389/fphar.2021.675350/full#supplementary-material

REFERENCES

Achuthan, C. R., and Padikkala, J. (1997). Hypolipidemic Effect of Alpinia Galanga (Rasna) andKaempferia Galanga (Kachoori). *Indian J. Clin. Biochem.* 12 (1), 55–58. doi:10.1007/BF02867956

Akmal, N. S., Citra, K. D., and Nurpudji, A. T. (2017). The Effects of *Kaempferia Galanga* L. Extract on Pain, Stiffness and Functional Physic in Patient with Knee Osteoarthritis: Double Blind Randomized Clinical Trial. *Int. J. Sci. Healthc. Res.* 2, 37–43.

Ali, H., Yesmin, R., Satter, M. A., Habib, R., and Yeasmin, T. (2018). Antioxidant and Antineoplastic Activities of Methanolic Extract of *Kaempferia Galanga* Linn. Rhizome against Ehrlich Ascites Carcinoma Cells. *J. King Saud Univ. - Sci.* 30 (3), 386–392. doi:10.1016/j.jksus.2017.05.009

Ali, M. S., Dash, P. R., and Nasrin, M. (2015). Study of Sedative Activity of Different Extracts of *Kaempferia Galanga* in Swiss Albino Mice. *BMC Complement. Altern. Med.* 15 (1), 158. doi:10.1186/s12906-015-0670-z2015

Amuamuta, A., Plengsuriyakarn, T., and Na-Bangchang, K. (2017). Anticholangiocarcinoma Activity and Toxicity of the *Kaempferia Galanga* Linn. Rhizome Ethanolic Extract. *BMC Complement. Altern. Med.* 17 (1), 213–224. doi:10.1186/s12906-017-1713-4

Aroonrerk, N., and Kamkaen, N. (2009). Anti-inflammatory Activity of *Quercus Infectoria, Glycyrrhiza Uralensis, Kaempferia Galanga* and *Coptis Chinensis*, the Main Components of Thai Herbal Remedies for Aphthous Ulcer. *J. Health Res.* 23 (1), 17–22.

Bohra, A., Saxena, K. B., Varshney, R. K., and Saxena, R. K. (2020). Genomics-assisted Breeding for Pigeonpea Improvement. *Theor. Appl. Genet.* 133, 1721–1737. doi:10.1007/s00122-020-03563-7

Chen, X., Yang, X., Liu, T., Guan, M., Feng, X., Dong, W., et al. (2012). Kaempferol Regulates MAPKs and NF-Kb Signaling Pathways to Attenuate LPS-Induced Acute Lung Injury in Mice. *Int. Immunopharmacol* 14 (2), 209–216. doi:10.1016/j.intimp.2012.07.007

China Pharmacopoeia Commission (2015). *Pharmacopoeia of the People's Republic of China*. Beijing: China Medical Science Press.

Choi, I.-H., Park, J.-Y., Shin, S.-C., and Park, I.-K. (2006). Nematicidal Activity of Medicinal Plant Extracts and Two Cinnamates Isolated from Kaempferia Galanga L. (Proh Hom) against the pine wood Nematode, Bursaphelenchus Xylophilus. *Nematol* 8 (3), 359–365. doi:10.1163/156854106778493402

Cui, B. Q., Lin, Y. Z., and Guo, X. L. (2008). Determination of Chemical Constituents of Galanga Resurrectionlily Rhizome from Hainan Province by GC- MS. *China Pharm.* 19 (3), 215–216.

Dash, P. R., Nasrin, M., Raihan, S. Z., and Ali, M. S. (2014). Study of Antidiarrhoeal Activity of Two Medicinal Plants of Bangladesh in Castor-Oil Induced Diarrhoea. *Int. J. Pharm. Sci. Res.* 5 (9), 3864–3868. doi:10.13040/IJPSR.0975-8232.5(9).3864-68

El-Aziz Abd, N. M., Mohamed, G. S., Awad, O. M. E., and El-Sohaimy, S. A. (2021). Inhibition of COVID-19 RNA-dependent RNA Polymerase by Natural Bioactive Compounds: Molecular Docking Analysis. *Egypt. J. Chem.* 64 (4), 1989–2001. doi:10.21608/ejchem.2021.45739.2947

Elshamy, A. I., Mohamed, T. A., Essa, A. F., Abd-ElGawad, A. M., Alqahtani, A. S., Shahat, A. A., et al. (2019). Recent Advances in *Kaempferia* Phytochemistry and Biological Activity: A Comprehensive Review. *Nutrients* 11 (10), 2396. doi:10.3390/nu11102396

Fan, Y. M., Ren, S. X., Chen, Y. H., Li, L. M., He, C. Y., Li, H. P., et al. (2005). Analysis of Chemical Components of Volatile Oil from *Kaempferia Galanga* L. In South China by GC/MS. *Food Sci.* 26 (6), 196–198.

Gao, L., and Lei, X. (2020). Biosynthetic Intermediate Probes for Visualizing and Identifying the Biosynthetic Enzymes of Plant Metabolites. *ChemBioChem* 21, 1–4. doi:10.1002/cbic.202000530

Geng, Z. K., Li, Y. Q., Sun, Q. H., Rong, R., and Tian, J. Z. (2019). Analysis for Chemical Constituents of Ge-Gen Decoction by HPLC-Q-TOF-MS and Study on the Spectrum-Efficacy Relationship of its Different Extracts against RSV. *Chin. J. Tradit. Chin. Med.* 34 (5), 1944–1950.

Gunasekaran, S., Venkatachalam, K., and Namasivayam, N. (2019). Anti-inflammatory and Anticancer Effects of P-Methoxycinnamic Acid, an Active Phenylpropanoid, against 1,2-Dimethylhydrazine-Induced Rat colon Carcinogenesis. *Mol. Cel. Biochem.* 451 (1-2), 117–129. doi:10.1007/s11010-018-3398-5

Han, H. M., Nan, Y. P., Zhao, Z. M., Zhu, L. P., Cen, S., He, G. R., et al. (2011). Preparation and Measurement of Antimicrobial Activity of Ethyl-P-Methoxycinnamate. *China Surfactant Deterg Cosme* 41 (4), 272–274. doi:10.1080/17415993.2010.547197

Hashimoto, T., Hirata, M., Itoh, T., Kanmura, Y., and Kuriyama, H. (1986). Inositol 1,4,5-trisphosphate Activates Pharmacomechanical Coupling in Smooth Muscle of the Rabbit Mesenteric Artery. *J. Physiol.* 370 (1), 605–618. doi:10.1113/jphysiol.1986.sp015953

He, Z. H., Yue, G. G., Lau, C. B., Ge, W., and But, P. P. (2012). Antiangiogenic Effects and Mechanisms of *Trans*-ethyl P-Methoxycinnamate from *Kaempferia Galanga* L. *J. Agric. Food Chem.* 60 (45), 11309–11317. doi:10.1021/jf304169j

Hirschhorn, H. H. (1983). Botanical Remedies of the Former Dutch East Indies (Indonesia). Part II: Dicotyledones up to and Including Leguminosae. *J. Ethnopharmacol* 8, 65–96. doi:10.1016/0378-8741(83)90090-9

Hua, S., Zhang, Y., Liu, J., Dong, L., Huang, J., Lin, D., et al. (2018). Ethnomedicine, Phytochemistry and Pharmacology of *Smilax Glabra*: An Important Traditional Chinese Medicine. *Am. J. Chin. Med.* 46 (2), 261–297. doi:10.1142/S0192415X18500143

Huang, Q. Y., Chen, S. D., and Liu, H. T. (2012). Determination of Inorganic Elements in *Kaempferia Galanga* Linn. By ICP-MS/ICP-AES with Microwave Digestion. *Chin. J. Spectrosc. Lab.* 29 (3), 1413–1415.

Huang, L. F., Yagura, T., and Chen, S. L. (2008). Sedative Activity of Hexane Extract of *Keampferia galanga* L. and its Active Compound. *J. Ethnopharmacol* 120 (1), 123–125.

Ichwan, S. J. A., Husin, A., Suriyah, W. H., LestariOmar, W. M. N., Omar, M. N., and Kasmuri, A. R. (2019). Anti-neoplastic Potential of Ethyl-P-Methoxycinnamate of Kaempferia Galanga on Oral Cancer Cell Lines. *Mater. Today Proc.* 16 (4), 2115–2121. doi:10.1016/j.matpr.2019.06.100

Jagadish, P. C., Latha, K. P., Mudgal, J., and Nampurath, G. K. (2016). Extraction, Characterization and Evaluation of *Kaempferia Galanga* L. (Zingiberaceae) Rhizome Extracts against Acute and Chronic Inflammation in Rats. *J. Ethnopharmacol.* 194, 434–439. doi:10.1016/j.jep.2016.10.010

Jiao, Z., Xu, W., Zheng, J., Shen, P., Qin, A., Zhang, S., et al. (2017). Kaempferide Prevents Titanium Particle Induced Osteolysis by Suppressing JNK Activation during Osteoclast Formation. *Sci. Rep.* 7 (1), 16665. doi:10.1038/s41598-017-16853-w

Jnanesha, A. C., and Kumar, A. (2018). "Agrotechnology and Bioprospecting in Important Medicinal Plants," in (ICAAASTSD) International Conference on Advances in Agriculture and Allied Science Technologies for Sustainable Development (Hyderabad, India: Genesis Urban and Rural Development Society Hyderabad).

Kanjanapothi, D., Panthong, A., Lertprasertsuke, N., Taesotikul, T., Rujjanawate, C., Kaewpinit, D., et al. (2004). Toxicity of Crude Rhizome Extract of *Kaempferia Galanga* L. (Proh Hom). *J. Ethnopharmacol.* 90 (2-3), 359–365. doi:10.1016/j.jep.2003.10.020

Kim, C. J., Shin, S. H., Kim, B. J., Kim, C. H., Kim, J. H., Kang, H. M., et al. (2018). The Effects of Kaempferol-Inhibited Autophagy on Osteoclast Formation. *Int. J. Mol. Sci.* 19 (1), 125–138. doi:10.3390/ijms19010125

Kiuchi, F., Nakamura, N., and Tsuda, Y. (1987). 3-Caren-5-one from *Kaempferia Galanga*. *Phytochemistry* 26 (12), 3350–3351. doi:10.1016/S0031-9422(00)82505-4

Kumar, A. (2020). Phytochemistry, Pharmacological Activities and Uses of Traditional Medicinal Plant Kaempferia Galanga L. - an Overview. *J. Ethnopharmacol.* 253, 112667. doi:10.1016/j.jep.2020.112667

Lakshmanan, D., Werngren, J., Jose, L., Suja, K. P., Nair, M. S., Varma, R. L., et al. (2011). Ethyl P-Methoxycinnamate Isolated from a Traditional Anti-tuberculosis Medicinal Herb Inhibits Drug Resistant Strains of *Mycobacterium tuberculosis In Vitro*. *Fitoterapia* 82 (5), 757–761. doi:10.1016/j.fitote.2011.03.006

Levita, J., K. Wijaya, L., Celcilia, S., and Mutakin, M. (2015). Inhibitory Activity of *Kaempferia Galanga* and *Hibiscus sabdariffa* on the Rate of PGH2 Formation. *J. Appl. Sci.* 15 (7), 1032–1036. doi:10.3923/jas.2015.1032.1036

Li, C. Y., Suzuki, K., Hung, Y. L., Yang, M. S., Yu, C. P., Lin, S. P., et al. (2017a). Aloe Metabolites Prevent LPS-Induced Sepsis and Inflammatory Response by Inhibiting Mitogen-Activated Protein Kinase Activation. *Am. J. Chin. Med.* 45 (4), 847–861. doi:10.1142/S0192415X17500458

Li, Q., Han, H. M., Sun, Y. J., Guo, W. Y., and Yang, D. P. (2013). Study on *In Vitro* Percutaneous Absorption of Ethyl-P-Methoxycinnamate from *Kaempferia Galangal* L. *Flavour Fragrance Cosmet.* 5, 43–65.

Li, X. J., Huang, Y. Y., Yang, Z., Wu, X., Zhuang, P. W., and Zhang, Y. J. (2019). Research Strategy for Quality-Biomarkers of Traditional Chinese Medicine Based on Effect Benchmarks. *Acta Pharm. Sin.* 54 (2), 204–210. doi:10.1016/j.phymed.2018.01.018

Li, Y. C., Ji, H., Li, X. H., Zhang, H. X., and Li, H. T. (2017b). Isolation of Nematicidal Constituents from Essential Oil of *Kaempferia Galanga* L Rhizome and Their Activity against *Heterodera Avenae* Wollenweber. *Trop. J. Pharm. Res.* 16, 59–65. doi:10.4314/tjpr.v16i1.8

Lin, C. W., Tsai, F. J., Tsai, C. H., Lai, C. C., Wan, L., Ho, T. Y., et al. (2005). Anti-SARS Coronavirus 3C-like Protease Effects of *Isatis Indigotica* Root and Plant-Derived Phenolic Compounds. *Antivir. Res* 68 (1), 36–42. doi:10.1016/j.antiviral.2005.07.002

Liu, B., Liu, F., Chen, C., and Gao, H. (2010). Supercritical Carbon Dioxide Extraction of Ethyl P-Methoxycinnamate from *Kaempferia Galanga* L. Rhizome and its Apoptotic Induction in Human HepG2 Cells. *Nat. Prod. Res.* 24 (20), 1927–1932. doi:10.1080/14786419.2010.490913

Liu, B., Liu, F., Chen, C., and Gao, H. (2010). Supercritical Carbon Dioxide Extraction of Ethyl P-Methoxycinnamate from *Kaempferia Galanga* L. Rhizome and its Apoptotic Induction in Human HepG2 Cells. *Nat. Prod. Res.* 24 (20), 1927–1932. doi:10.1080/14786419.2010.490913

Liu, B., Yu, H., Baiyun, R., Lu, J., Li, S., Bing, Q., et al. (2018). Protective Effects of Dietary Luteolin against Mercuric Chloride-Induced Lung Injury in Mice: Involvement of AKT/Nrf2 and NF-Kb Pathways. *Food Chem. Toxicol.* 113, 296–302. doi:10.1016/j.fct.2018.02.003

Liu, F., and Ng, T. B. (2000). Antioxidative and Free Radical Scavenging Activities of Selected Medicinal Herbs. *Life Sci.* 66 (8), 725–735. doi:10.1016/S0024-3205(99)00643-8

Liu, X. C., Liang, Y., Shi, W. P., Liu, Q. Z., Zhou, L., and Liu, Z. L. (2014). Repellent and Insecticidal Effects of the Essential Oil of *Kaempferia Galanga* Rhizomes to *Liposcelis Bostrychophila* (Psocoptera: Liposcelidae). *J. Econ. Entomol.* 107 (4), 1706–1712. doi:10.1603/EC13491

Lu, D. B., Kong, J., Li, S. T., Fan, Y. Y., Huang, Y. J., Sun, R. D., et al. (2020). Quality Evaluation of *Perillae Folium* Based on Representation Model of Effective Characteristic Spectrum of Reference. *J. Beijing Univ. Traditi. Chin. Med.* 43 (2), 148–162.

Luo, J., Wu, D., and Zhong, Y. K. (2014). Analysis of Volatile Components of *Kaempferia Galanga* L. From Guizhou by Solid Phase Microextraction and Gas Chromatography-Mass Spectrometry. *Mod. Food Sci. Technol.* 30 (12), 271–276.

Ma, P., Xu, H., Li, J., Lu, F., Ma, F., Wang, S., et al. (2019). Functionality-Independent DNA Encoding of Complex Natural Products. *Angew. Chem. Int. Ed. Engl.* 58 (27), 9254–9261. doi:10.1002/anie.201901485

Ma, Q., Fan, X.-D., Liu, X.-C., Qiu, T.-Q., and Jiang, J.-G. (2015). Ultrasound-enhanced Subcritical Water Extraction of Essential Oils from *Kaempferia Galangal* L. And Their Comparative Antioxidant Activities. *Separat. Purif. Technol.* 150, 73–79. doi:10.1016/j.seppur.2015.06.013

Manigaunha, A., Ganesh, N., and Kharya, M. D. (2010). Hepatoprotection by *Kaempferia Galanga* against Carbon Tetrachloride Induced Liver Damage in Rats. *Indian Drugs* 47 (4), 55–60.

Masullo, M., Montoro, P., Mari, A., Pizza, C., and Piacente, S. (2015). Medicinal Plants in the Treatment of Women's Disorders: Analytical Strategies to Assure Quality, Safety and Efficacy. *J. Pharm. Biomed. Anal.* 113, 189–211. doi:10.1016/j.jpba.2015.03.020

Mohammad, S. P., Harindran, J., Kannaki, K. S., and Revathy, R. (2016). Clinical Data Analysis of Vitamin D and Ferritin in Different Age Group People in

South Indian Population. *World J. Pharm. Pharm. Sci.* 5 (4), 1161–1169. doi:10.20959/wjpps20164-6327

Mokkhasmit, M., Swatdimongkol, K., and Satrawah, P. (1971). Study on Toxicity of Thai Medicinal Plants. *Bull. Dept Med. Sci.* 12, 36–65.

Munda, S., Saikia, P., and Lal, M. (2018). Chemical Composition and Biological Activity of Essential Oil of *Kaempferia Galanga*: a Review. *J. Essent. Oil Res.* 30 (5), 303–308. doi:10.1080/10412905.2018.1486240

Mustafa, M. R., Mustafa, A. M., and Hashim, S. (1996). Vasorelaxant Effects of the Chloroform Extract of *Kaempferia Galangal* on Smooth Muscles of the Rat Aora. *Asia Pac. J. Pharmacol.* 11 (3-4), 97–101.

Nazar, S., Ravikumar, S., and Prakash Williams, G. (2008). Ethnopharmacological Survey of Medicinal Plants along the Southwest Coast of India. *J. Herbs, Spices Med. Plants* 14 (3–4), 219–239. doi:10.1080/10496470802598917

Nor Omar, M., Abdul Rahman, S. M. M., Ichwan, S. J. A., Hasali, N. H. M., Abdul Rasid, F., and Abdul Halim1, F. (2017). Cytotoxicity Effects of Extracts and Essential Oil of Kaempferia Galanga on Cervical Cancer C33A Cell Line. *Orient. J. Chem.* 33 (4), 1659–1664. doi:10.13005/ojc/330409

Ogiso, A., and Kobayashi, S. (1994). Anti-ulcer Agents from Alpina Seeds. *Chem. Abstr.* 81, 339.

Othman, R., Ibrahim, H., Mohd, M. A., Awang, K., Gilani, A. U., and Mustafa, M. R. (2002). Vasorelaxant Effects of Ethyl Cinnamate Isolated from Kaempferia Galanga on Smooth Muscles of the Rat Aorta. *Planta Med.* 68 (7), 655–657. doi:10.1055/s-2002-32900

Othman, R., Ibrahim, H., Mohd, M. A., Mustafa, M. R., and Awang, K. (2006). Bioassay-guided Isolation of a Vasorelaxant Active Compound from *Kaempferia Galanga* L. *Phytomedicine* 13 (1-2), 61–66. doi:10.1016/j.phymed.2004.07.004

Pandji, C., Grimm, C., Wray, V., Witte, L., and Proksch, P. (1993). Insecticidal Constituents from Four Species of the Zingiberaceae. *Phytochemistry* 34 (2), 415–419. doi:10.1016/0031-9422(93)80020-S

Panyakaew, J., Chalom, S., Sookkhee, S., Saiai, A., Chandet, N., Meepowpan, P., et al. (2020). Kaempferia Sp. Extracts as UV Protecting and Antioxidant Agents in Sunscreen. *J. Herbs, Spices Med. Plants* 27 (3), 37–56. doi:10.1080/10496475.2020.1777614

Parjo, N. B., Mohamed Zulkifli, R., Md Salleh, M., and Tencomnao, T. (2018). Antidandruff Potential of Kaempheria Galanga Ethanolic Extracts for Hair Cream Formulation. *Jurnal Teknologi* 80 (3), 41–46. doi:10.11113/jt.v80.9998

Park, K. M., Choo, J. H., Sohn, J. H., Lee, S. H., and Hwang, J. K. (2005). Antibacterial Activity of Panduratin A Isolated from *Kaempferia Pandurata* against *Porphyromonas Gingivalis*. *Food Sci. Biotechnol.* 14, 286–289. doi:10.1081/FRI-200051897

Pedrete, T. A., Hauser-Davis, R. A., and Moreira, J. C. (2019). Proteomic Characterization of Medicinal Plants Used in the Treatment of Diabetes. *Int. J. Biol. Macromol.* 140, 294–302. doi:10.1016/j.ijbiomac.2019.08.035

Peter, K. V. (2004). *Handbook of Herbs and Spices. GBR*. Cambridge: Wood head Publishing, Limited.

Rahman, I., Kabir, T., Islam, N., Muqaddim, M., Sharmin, S., Ullah, M. S., et al. (2019). Investigation of Antioxidant and Cytotoxic Activities of *Kaempferia Galanga* L. *Rese. Jour. Pharm. Technol.* 12 (5), 2189–2194. doi:10.5958/0974-360X.2019.00365.2

Rahman, M. M., Amin, M. N., Ahamed, T., Ali, M. R., and Habib, A. (2004). Efficient Plant Regeneration through Somatic Embryogenesis from Leaf Base-Derived Callus of Kaempferia Galanga L. *Asian J. Plant Sci.* 3 (6), 675–678. doi:10.3923/ajps.2004.675.678

Raina, A. P., and Abraham, Z. (2016). Chemical Profiling of Essential Oil of *Kaempferia galanga* L. Germplasm from India. *J. Essent. Oil Res.* 28 (1), 29–34. doi:10.1080/10412905.2015.1077165

Ryu, Y. B., Jeong, H. J., Kim, J. H., Kim, Y. M., Park, J. Y., Kim, D., et al. (2010). Biflavonoids from Torreya Nucifera Displaying SARS-CoV 3CL(pro) Inhibition. *Bioorg. Med. Chem.* 18 (22), 7940–7947. doi:10.1016/j.bmc.2010.09.035

Santhoshkumari, K. S., and Devi, K. S. (1991). Pharmacological and Biochemical Effects of Few Indigenous Drugs. *Indian J. Pharm.* 23, 160–163.

Saputri, F. C., and Avatara, C. (2018). Antithrombotic Effect of *Kaempferia Galanga* L. And *Curcuma Xanthorrhiza* Roxb. on Collagen-Epinephrine Induced Thromboembolism in Mice. *Pharmacognosy J.* 10 (6), 1149–1153. doi:10.5530/pj.2018.6.196

Schwarz, S., Sauter, D., Wang, K., Zhang, R., Sun, B., Karioti, A., et al. (2014). Kaempferol Derivatives as Antiviral Drugs against the 3a Channel Protein of Coronavirus. *Planta Med.* 80 (2/3), 177–182. doi:10.1055/s-0033-1360277

Seth, A., and Maurya, S. K. (2014). Potential Medicinal Plants and Trditional Ayaurvedic Ap-Proach towards Urticaria, an Allergic Skin Disorder. *Int. J. Pharm. Pharmaceut. Sci.* 6 (5), 172–177.

Shang, J., Xin, Y., Feng, H. X., and Wang, Z. Y. (2011). Comparative Study of Kaempferol and Arbutin in Action of Melanocytes. *Chin. J. Derm. Venereol.* 25 (3), 185–191.

Shintia, L. C., Wiranti, S. R., and Retno, W. (2018). Determination of Sun protection Factor and Antioxidant Properties of Cream Formulation of Kencur (*Kaempferia Galanga* L) and Temu Kunci (*Boesenbergia Pandurata* (Roxb.) Schlecht) Rhizomes Extract. *Pharmaciana* 8 (2), 320–331. doi:10.12928/pharmaciana.v%vi%i.11891

Sivarajan, V. V., and Balachandran, I. (1994). Ayurvedic Drugs and Their Plant Sources. New Delhi: Oxford and IBH Publishing Co, 97–99.

Srivastava, N., Ranjana, S. S., Singh, S., Gupta, A. C., Shanker, K., Bawankule, D. U., et al. (2019). Aromatic Ginger (*Kaempferia Galanga* L.) Extracts with Ameliorative and Protective Potential as a Functional Food, beyond its Flavor and Nutritional Benefits. *Toxicol. Rep.* 6, 521–528. doi:10.1016/j.toxrep.2019.05.014

Sulaiman, M. R., Zakaria, Z. A., Daud, I. A., Ng, F. N., Ng, Y. C., and Hidayat, M. T. (2008). Antinociceptive and Anti-inflammatory Activities of the Aqueous Extract of *Kaempferia Galanga* Leaves in Animal Models. *J. Nat. Med.* 62 (2), 221–227. doi:10.1007/s11418-007-0210-3

Sutthanont, N., Choochote, W., Tuetun, B., Junkum, A., Jitpakdi, A., Chaithong, U., et al. (2010). Chemical Composition and Larvicidal Activity of Edible Plant-Derived Essential Oils Against the Pyrethroid-Susceptible and -Resistant Strains of Aedes aegypti (Diptera: Culicidae). *J. Vector Ecol.* 35 (1), 106–115. doi:10.1111/j.1948-7134.2010.00066.x

Swapana, N., Tominaga, T., Elshamy, A. I., Ibrahim, M. A. A., Hegazy, M.-E. F., Brajakishor Singh, C., et al. (2018). Kaemgalangol A: Unusual Seco-Isopimarane Diterpenoid from Aromatic Ginger *Kaempferia Galanga*. *Fitoterapia* 129, 47–53. doi:10.1016/j.fitote.2018.06.010

Tambunan, L. V., and Lubis, W. H. (2016). Effectiveness of *Kaempferia Galanga* Linn Rhizome's Extract towards the Healing of Minor Recurrent Aphthous Stomatitis in RSGMP USU's Patients. *Uip Heath Med.* 1 (1), 100–103. doi:10.7454/uiphm.v1i0.35

Tewtrakul, S., Uuenyongsawad, S., Kummee, S., and Atsawajaruwan, L. (2005). Chemical Components and Biological Activities of Volatile Oil of *Kaempferia Galangal* Linn. *Songklanakarin J. Sci. Technol.* 27 (Suppl. 2), 503–507. doi:10.1007/s10870-005-6145-1

Thiengsusuk, A., Chaijaroenkul, W., and Na-Bangchang, K. (2013). Antimalarial Activities of Medicinal Plants and Herbal Formulations Used in Thai Traditional Medicine. *Parasitol. Res.* 112 (4), 1475–1481. doi:10.1007/s00436-013-3294-6

Thomford, N. E., Senthebane, D. A., Rowe, A., Munro, D., Seele, P., Maroyi, A., et al. (2018). Natural Products for Drug Discovery in the 21st Century: Innovations for Novel Drug Discovery. *Int. J. Mol. Sci.* 19, 1578–1606. doi:10.3390/ijms19061578

Tungcharoen, P., Wattanapiromsakul, C., Tansakul, P., Nakamura, S., Matsuda, H., and Tewtrakul, S. (2020). Anti-inflammatory Effect of Isopimarane Diterpenoids from Kaempferia Galanga. *Phytother. Res.* 34 (3), 612–623. doi:10.1002/ptr.6549

Umar, I., Asmawi, M. Z. B., Sadikun, A., Altaf, R., and Iqbal, M. A. (2011). Phytochemistry and Medicinal Properties of Kaempferia Galanga L. (Zingiberaceae) Extracts. *Afr. J. Pharm. Pharmacol.* 5 (14), 1638–1647. doi:10.5897/AJPP11.388

Umar, M. I., Asmawi, M. Z., Sadikun, A., Majid, A. M., Al-Suede, F. S., Hassan, L. E., et al. (2014). Ethyl-p-methoxycinnamate Isolated from Kaempferia Galanga Inhibits Inflammation by Suppressing Interleukin-1, Tumor Necrosis Factor-α, and Angiogenesis by Blocking Endothelial Functions. *Clinics (Sao Paulo)* 69 (2), 134–144. doi:10.6061/clinics/2014(02)10

Vittalrao, A. M., Shanbhag, T., Kumari, M., Bairy, K. L., and Shenoy, S. (2011). Evaluation of Antiinflammatory and Analgesic Activities of Alcoholic Extract of *Kaempferia Galanga* in Rats. *Indian J. Physiol. Pharmacol.* 55 (1), 13–24.

Wang, F. L., Luo, J. G., Wang, X. B., and Kong, L. Y. (2013). A Pair of Sulfonated Diarylheptanoid Epimers from *Kaempferia Galanga*. *Chin. J. Nat. Med.* 11 (2), 171–176. doi:10.1016/s1875-5364(13)60045-x

Wang, F. Z., and Tang, J. (1980). *Flora of China*. Beijing: Science Publishing House.

Wang, Y., Jiang, Z.-T., Li, R., and Guan, W.-Q. (2009). Composition Comparison of Essential Oils Extracted by Microwave Assisted Hydrodistillation and Hydrodistillation fromKaempferia galangaL. Grown in China. *J. Essent. Oil Bearing Plants* 12 (4), 415–421. doi:10.1080/0972060X.2009.10643739

Warrier, P. K., Nambiar, V. P. K., and Ramankutty, C. (1995). *Indian Medicinal Plants - A Compendium of 500 Species*. India: Orient Longman 3, 274.

World Health Organization (2013). *ES Fact Sheet 312: Diabetes*. Geneva, Switzerland.: World Health Organization.

Wu, H. D. (2016). "Study on the Chemical Constituents of Rhizoma *Kaempferiae*," (Wuhan: Huazhong University of Science and Technology). Master's thesis.

Wu, Q. M., Jin, Y. M., and Ni, H. X. (2015). Effect of Kaempferol on Correlation Factors of Chronic Complications of Type 2 Diabetic Rats. *Chin. Tradit. Herb. Drugs* 46 (12), 1086–1089.

Xiang, Z. B., Wu, X. L., Zhang, L., and Wang, C. Y. (2018). Study on Antioxidant Active Fraction of *Kaempferia Galanga* L. *Sci. Technol. Food Ind.* 39 (24), 62–66.

Xiao, Y., Wei, P. K., Li, J., Shi, J., Yu, Z. H., and Lin, H. M. (2006). Effects of Rhizoma Kaempferiae Volatile Oil on Tumor Growth and Cell Cycle of MKN-45 Human Gastric Cancer Cells Orthotopically Transplanted in Nude Mice. *Zhong Xi Yi Jie He Xue Bao* 4 (4), 384–387. doi:10.3736/jcim20060413

Xie, J., Wang, S., Ma, P., Ma, F., Li, J., Wang, W., et al. (2020). Selection of Small Molecules that Bind to and Activate the Insulin Receptor from a DNA-Encoded Library of Natural Products. *IScience* 23 (6), 101197. doi:10.1016/j.isci.2020.101197

Xue, Y., and Chen, H. (2002). Study on the Anti-carcinogenic Effects of Three Compounds in Kaempferia Galanga L. *Wei Sheng Yan Jiu* 31 (4), 247–251. doi:10.1016/s0045-7930(00)00013-x

Yang, X., Ji, H., Feng, Y., Yu, J., and Liu, A. (2018). Structural Characterization and Antitumor Activity of Polysaccharides from *Kaempferia Galanga* L. *Oxid Med. Cel Longev* 2018, 9579262. doi:10.1155/2018/9579262

Yang, Y., Tian, S., Wang, F., Li, Z., and Li, Y. (2018). Chemical Composition and Antibacterial Activity of *Kaempferia Galanga* Essential Oil. *Int. J. Agric. Biol.* 20 (2), 457–462. doi:10.17957/IJAB/15.0560

Yao, F., Huang, Y., Wang, Y., and He, X. (2018). Anti-inflammatory Diarylheptanoids and Phenolics from the Rhizomes of Kencur (*Kaempferia Galanga* L.). *Ind. Crops Prod.* 125, 454–461. doi:10.1016/j.indcrop.2018.09.026

Yao, F. Z. (2018). "Study on the Chemical Constituents of the Rhizome of *Kaempferia Galanga* L," (Guangzhou: Guangdong Pharmaceutical University). Master's thesis.

Yi, L., Li, Z., Yuan, K., Qu, X., Chen, J., Wang, G., et al. (2004). Small Molecules Blocking the Entry of Severe Acute Respiratory Syndrome Coronavirus into Host Cells. *J. Virol.* 78 (20), 11334–11339. doi:10.1128/JVI.78.20.11334-11339.2004

Yu, R., Chen, L., Lan, R., Shen, R., and Li, P. (2020). Computational Screening of Antagonists against the SARS-CoV-2 (COVID-19) Coronavirus by Molecular Docking. *Int. J. Antimicrob. Agents* 56, 106012. doi:10.1016/j.ijantimicag.2020.106012

Zhang, G. Z. (2007). Analysis of Constituents of Essential Oils in Rhizoma Kaempferiae by GC-MS. *Asia-Pacific Traditional Med.* 3 (7), 56–59.

Zhang, G. Z., Meng, Q. H., and Zou, J. (2014). Analysis of Volatile Oil of Processed Zingiberis Rhizoma by GC-MS. *China Health Care & nutrition* 24 (3), 1781–1782.

Zhang, T. Z., Zeng, Y., Zhu, F. W., Hu, M. Y., and Weng, Q. F. (2010). Isolation and Identification of Nematicide Component from *Kaempferia Galanga* L. *Acta Bot. Boreali-occident. Sin.* 30 (12), 2524–2529. doi:10.3724/SP.J.1206.2010.00266

Zhou, X., Song, F. Y., and Zhong, Z. J. (2006). Analysis of Constituents of Essential Oil in *Kacmpferia Galanga* L. From Various Habitats. *J. Mod. Food Pharm.* 16 (2), 2–4.

Zhou, Y. J., Wang, H., Li, L., Sui, H. H., and Huang, J. J. (2015). Inhibitory Effect of Kaempferol on Inflammatory Response of Lipopolysaccharide-Stimulated Human Mast Cells. *Yao Xue Xue Bao* 50 (6), 702–707.

Zhu, J. Y., Wang, Z. G., Zhang, H., Zhang, J. Q., Wu, F., and Shen, L. (2019). Quality Evaluation of Coix Seed Based on Correlation Analysis of the Contents of Active Ingredients with Anti-tumor and Antioxidant Activity. *Lishizhen Med. Mater. Med. Res.* 30 (1), 1–5.

Conflict of Interest: The authors declare that the research was conducted in the absence of any commercial or financial relationships that could be construed as a potential conflict of interest.

Publisher's Note: All claims expressed in this article are solely those of the authors and do not necessarily represent those of their affiliated organizations, or those of the publisher, the editors and the reviewers. Any product that may be evaluated in this article, or claim that may be made by its manufacturer, is not guaranteed or endorsed by the publisher.

Copyright © 2021 Wang, Zhao, Xu, Han, Wu, Xu, Yang, Göransson and Liu. This is an open-access article distributed under the terms of the Creative Commons Attribution License (CC BY). The use, distribution or reproduction in other forums is permitted, provided the original author(s) and the copyright owner(s) are credited and that the original publication in this journal is cited, in accordance with accepted academic practice. No use, distribution or reproduction is permitted which does not comply with these terms.

frontiers in Pharmacology

ORIGINAL RESEARCH
published: 09 February 2022
doi: 10.3389/fphar.2021.639580

Circadian Pharmacological Effects of Paeoniflorin on Mice With Urticaria-like Lesions

Li Peng[1,2†], Lijuan Wen[3†], Jie Zhang[1,2†], Xiaotong Zhang[1,2], Qin Wei[1,2], Jing Guo[2,4] and Jinhao Zeng[2,5]**

[1]Hospital of Chengdu University of Traditional Chinese Medicine, Chengdu, China, [2]Chengdu University of Traditional Chinese Medicine, Chengdu, China, [3]Clinical Skills Center, Hospital of Chengdu University of Traditional Chinese Medicine, Chengdu, China, [4]Dermatological Department, Hospital of Chengdu University of Traditional Chinese Medicine, Chengdu, China, [5]Geriatric Department, Hospital of Chengdu University of Traditional Chinese Medicine, Chengdu, China*

Paeoniflorin (PF) is a monoterpene glucoside with various biological properties, and it suppresses allergic and inflammatory responses in a rat model of urticaria-like lesions (UL). In the present study, we treated OVA-induced mice presenting UL with PF at four circadian time points (ZT22, ZT04, ZT10, and ZT16) to determine the optimal administration time of PF. The pharmacological effects of PF were assessed by analyzing the scratching behavior; histopathological features; allergic responses such as immunoglobulin E (IgE), leukotriene B4 (LTB4), and histamine (HIS) release; inflammatory cell infiltration [mast cell tryptase (MCT) and eosinophil protein X (EPX)]; and mRNA levels of inflammatory cytokines such as interleukin (IL)-12, IL-6, interferon-γ (IFN-γ), and IL-4. It was demonstrated that PF significantly alleviated scratching behavior and histopathological features, and ZT10 dosing was the most effective time point in remission of the condition among the four circadian time points. Moreover, PF decreased the serum levels of IgE, LTB4, and HIS, and PF administration at ZT10 produced relatively superior effectiveness. PF treatment, especially dosing at ZT10, significantly reduced the number of mast cells and granules and diminished the infiltration of MCT and EPX in the skin tissues of mice with UL. Furthermore, the oral administration of PF effectively decreased the inflammatory cytokine levels of IL-12 mRNA. In conclusion, different administration times of PF affected its efficacy in mice with UL. ZT10 administration demonstrated relatively superior effectiveness, and it might be the optimal administration time for the treatment of urticaria.

Keywords: urticaria-like lesion, paeoniflorin, allergic response, inflammatory cell infiltration, inflammatory cytokine, chronotherapeutic

OPEN ACCESS

Edited by:
Yanqiong Zhang,
Institute of Chinese Materia Medica, China

Reviewed by:
Haolong Liu,
Peking University Health Science Centre, China
Osamu Kaminuma,
Hiroshima University, Japan

****Correspondence:***
Jing Guo
guojing66@cdutcm.edu.cn
Jinhao Zeng
zengjinhao@cdutcm.edu.cn

†These authors have contributed equally to this work and share first authorship

Specialty section:
This article was submitted to Ethnopharmacology, a section of the journal Frontiers in Pharmacology

Received: *09 December 2020*
Accepted: *22 December 2021*
Published: *09 February 2022*

Citation:
Peng L, Wen L, Zhang J, Zhang X, Wei Q, Guo J and Zeng J (2022) Circadian Pharmacological Effects of Paeoniflorin on Mice With Urticaria-like Lesions. Front. Pharmacol. 12:639580. doi: 10.3389/fphar.2021.639580

INTRODUCTION

Urticaria is characterized by the rapid appearance of pale to bright wheals, erythema, and pruritus on the skin (Schaefer, 2017). Sometimes, the condition is life-threatening and has detrimental effects on the quality of life of patients (Maurer et al., 2011) with angioedema and intense pruritus. Immunoglobulin E (IgE) mediates the accumulation and degranulation of mast cells play a

Abbreviations: EPX, eosinophil protein X; HIS, histamine; IgE, Immunoglobulin E; IL, interleukin; IOD, integrated optical density; IFN, interferon; i.p, intraperitoneally; LTB4, leukotriene B4; MCT, mast cell tryptase; NC, normal control; OVA, ovalbumin; PF, paeoniflorin; UL, urticaria-like lesions; ZT, zeitgeber time.

central role in the pathogenesis of urticaria, which results in the release of histamine (HIS) and other inflammatory mediators (Church et al., 2018). Furthermore, urticarial lesions are characterized by lymphocytic infiltration. Antihistamines or monoclonal antibodies are usually prescribed to treat urticaria. However, occasionally, little response, recurrence of symptoms, and side effects such as headache, drowsiness have been observed in some patients (Maurer et al., 2013; Bernstein et al., 2014; Cordeiro Moreira et al., 2016). Moreover, urticaria exacerbates nocturnally, displaying changing patterns in symptom attacks during the day and night (Maurer et al., 2009). Therefore, a safe, effective, selective, and optimal timing of therapy for urticaria has gained attention.

The physiological events and disorders of all creatures on the earth are interlinked to circadian rhythms, such as the sleep-wake cycle, body temperature, immune responsiveness, and anaphylactic reactions (Nakao et al., 2015). Although specific cellular and molecular mechanisms remain largely undefined, the circadian clock was regarded as a potent regulator of IgE/mast cell-mediated allergic reaction (Nakao et al., 2015). Nocturnal symptoms are common in atopic dermatitis and asthma, being related to the diurnal rhythm of inflammatory cell populations (Mackay et al., 1994; Lissoni et al., 1998; Raherison et al., 2006; Fishbein et al., 2015). Moreover, urticaria-like symptoms such as itching, wheals (hives), angioedema, or both, undergo circadian variations, and they exacerbate more frequently at night (Maurer et al., 2009). It has been long recognized that pharmacological effects could be enhanced by time-varying administering drugs of the disease displaying diurnal rhythmicity in severity (Koyanagi et al., 2003). We posit that time-varying drugs may function the treatment efficacy in urticaria.

Paeoniflorin (PF), extracted from the roots of *Paeonia lactiflora* Pall. (Shi et al., 2014; Wang et al., 2015), is a monoterpene glucoside with many biological properties. PF is one of the principal bioactive components of total glucosides, and it has been prescribed for redness, fever, and pain in rheumatoid arthritis patients in China for many years (Wang et al., 2015). Crucially, PF has been found to exhibit the therapeutic effects of various allergic diseases, such as asthma and contact dermatitis in mice. It was demonstrated that PF ameliorated asthma *via* the signaling pathway of phosphoinositide 3 kinase and serine/threonine kinase 1, to regulate the abnormal proliferation and migration of airway smooth muscle cells (Zhou et al., 2018). And PF acts as an immune-modulator to regulate the imbalanced secretion of inflammatory cytokines, such as interleukin (IL)-2, IL-4, IL-10, and IL-17, to treat allergic contact dermatitis in mice (Wang et al., 2015). Additionally, PF inhibits the maturation of dendritic cells and promotes their tolerogenic effects by inhibiting IL-12 production and enhancing the expression of anti-inflammatory cytokines such as IL-10 and transforming growth factor-β (Shi et al., 2014).

In this study, we assessed the ability of PF as a chronotherapeutic to influence the ovalbumin (OVA) induced urticaria-like lesions (UL) in animal models. We explored whether and how the PF exerted effects on histopathological features either in the morning (ZT02) or evening (ZT14) to establish a UL mouse model then dosed at four circadian time points. We also demonstrated whether and how the PF played the medicinal effect on allergic responses among time-varying administering drugs. We identified the role of PF played in the regulation of the Th1 and Th2 expression varied with different dosing time points. Our work may provide experimental evidence for optimal administration time of PF in UL treatment.

MATERIALS AND METHODS

Reagents and Chemicals

Aluminum hydroxide was dissolved in 0.9% NaCl solution to obtain a final concentration of 10 g/L. Furthermore, OVA (5 mg per mouse) (Merck KGaA, Darmstadt, Germany) was added to the mixture to obtain the resulting solution, which will be injected into animals. PF, with a purity quotient of ≥98%, was obtained from the Beijing Solarbio Science and Technology Co., Ltd. (Beijing, China). To obtain the stock solution, PF was dissolved in 50 ml of sterilized 0.9% NaCl at a concentration of 2000 mg/ml (Shi et al., 2015). The working solutions were diluted with saline.

Animals

One hundred and forty-four BALB/c mice (male) were purchased from Chengdu Dashuo Experimental Animal Co., Ltd. (Chengdu, China), and were housed in the Animal Experimental Center, Chengdu University of Traditional Chinese Medicine (Chengdu, China). All mice were maintained at a temperature of 22 ± 2°C and relative humidity of 55 ± 10% with a 12-h light/dark cycle [lights on at 7:00 am (zeitgeber time (ZT) 0) and lights off at 7:00 pm (ZT12)], and *ad libitum* access to water and food was provided. All mice were 8–9 weeks old, and their body weights were 16–20 g. All procedures were approved by the Institutional Animal Care and Use Committee of Chengdu University of Traditional Chinese Medicine (approval no. 2019-11).

Induction and Treatment of Animal Models for Urticaria

After 7 days of adaptation, one hundred and forty-four male BALB/c mice were randomly divided into the following groups (n = 6 in each group): normal control (NC) groups treated with saline, including 1) NC ZT22, 2) NC ZT04, 3) NC ZT10, and 4) NC ZT16; model groups injected intraperitoneally (i.p.) with OVA/aluminium hydroxide, including 5) OVA + saline ZT22, 6) OVA + saline ZT04, 7) OVA + saline ZT10, and 8) OVA + saline ZT16; and PF groups induced with OVA/aluminium hydroxide and treated with 100 mg/kg of PF per day (Shi et al., 2015), including 9) OVA + PF ZT22, (10) OVA + PF ZT04, 11) OVA + PF ZT10, and 12) OVA + PF ZT16. To induce UL, all mice except the controls were sensitized at ZT02 or ZT14 on days 8, 10, and 12 using an i.p. injection of 1 ml aluminium hydroxide solution containing 1 mg of OVA, and were challenged at ZT02 or ZT14 on day 22 with an i.p. injection containing 2 mg of OVA in aluminium hydroxide solution. All animals were orally administered saline or PF solution from day 13 to day 22 for

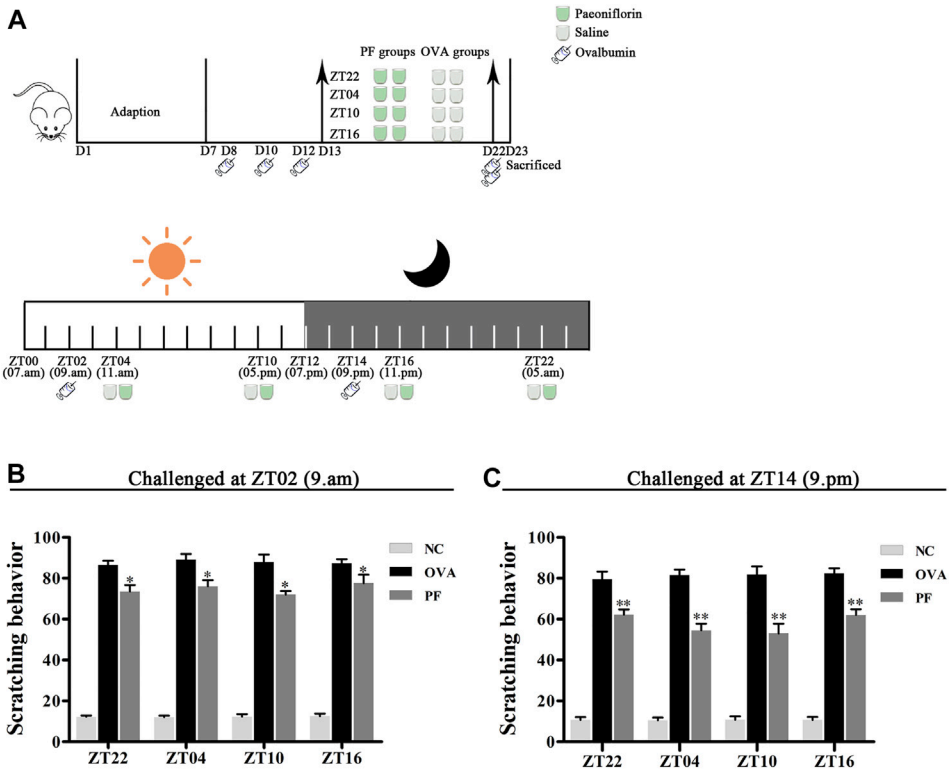

FIGURE 1 | Experimental design **(A)** and Effect of PF treatment on scratching frequency **(B,C)**. 144 male BALB/c mice (urticaria-like animals) were randomly divided into 12 groups as follows modeled at ZT02 or ZT14 ($n = 6$ in each group): normal control (NC) groups treated with saline, including 1) NC ZT22, 2) NC ZT04, 3) NC ZT10, and 4) NC ZT16; model groups injected intraperitoneally (i.p.) with ovalbumin (OVA)/aluminium hydroxide, including 5) OVA + saline ZT22, 6) OVA + saline ZT04, 7) OVA + saline ZT10, and 8) OVA + saline ZT16; and PF groups induced with OVA/aluminium hydroxide and treated with 100 mg/kg per day of paeoniflorin (PF), including 9) OVA + PF ZT22, 10) OVA + PF ZT04, 11) OVA + PF ZT10, and 12) OVA + PF ZT16. To induce urticaria-like lesions (UL), all mice except those in NC groups were sensitized i.p. with 1 ml of aluminium hydroxide solution containing 1 mg of OVA at ZT02 or ZT14 on days 8, 10, and 12, and they were challenged i. p. with 2 mg OVA in aluminium hydroxide at ZT02 or ZT14 on day 22. All animals were orally administered saline or PF solution from day 13 to day 22 for 10 days once a day at ZT22, ZT04, ZT10, and ZT16. As shown in **(A)**, on day 23, the dorsal region of all animals were shaved. After ZT14, 500 μL of the blood sample was collected through the cardiac puncture, and skin tissues were obtained under anesthesia with sodium pentobarbital (60 mg/kg i.p.). Furthermore, animals were humanely euthanized *via* cervical dislocation after sampling. The PF treatment significantly inhibited OVA/aluminium hydroxide-induced scratching reaction. Data are displayed as mean ± SEM ($n = 6$). $^{*}p < 0.05$, $^{**}p < 0.01$ versus OVA mice at the same time points.

10 days once a day at ZT22, ZT04, ZT10, and ZT16. On day 23, the dorsal region of all animals was shaven (**Figure 1A**). After ZT14, 500 μL of blood samples were collected through the cardiac puncture, and skin tissues were obtained by inducing anesthesia using pentobarbital sodium (60 mg/kg i.p., Merck KGaA, Darmstadt, Germany). Furthermore, animals were humanely authorized *via* cervical dislocation after sampling.

Assessment of Scratching Behavior

After challenging for 10 min on day 22, the frequencies of scratching and foot licking were measured for 20 min. The lifting of paws; rubbing of dorsal skin, hind paws, nose, or ears; and then returning the paws to the floor is defined as scratching (Choi et al., 2018; Purushothaman et al., 2018).

Histopathological Analysis

For histopathological observation, the dorsal skin lesions were dissected, dipped in 10% paraformaldehyde (Chengdu Cologne Chemical Co., Ltd., Chengdu, China) overnight, hydrated with ethanol, embedded in paraffin wax (Shanghai Hualing Rehabilitation Equipment Factory, Shanghai, China), and cut into thin sections (3 μm). Skin sections were stained with hematoxylin (Wuhan Seville Biotechnology Co., Ltd., Wuhan, China) and eosin (Zhuhai Bezo Biotechnology Co., Ltd., Zhuhai, China) for detection of edema and inflammatory cell infiltration, images were captured randomly by the pathologist using a light microscope (OLYMPUS, Tokyo, Japan), and they were viewed at a magnification of ×100 (×10ocular lens and ×10 objective lens). The degree of edema, telangiectasia, and inflammatory cell infiltration was scored on a subjective scale of 0–3 as follows which from three fields per hematoxylin and eosin-stained sections: 0, no edema; no telangiectasia; no inflammatory cell infiltration; 1, slight edema; slight telangiectasia; slight inflammatory cell infiltration; 2, moderate edema; moderate telangiectasia; moderate inflammatory cell infiltration; 3, severe edema; severe telangiectasia; severe inflammatory cell infiltration. The histologic score of each animal was the average of the total scores of 3 pathological features from 3 visual fields.

Determination of Serum IgE, Leukotriene B4 (LTB4), and HIS Levels

Blood samples from mice with UL were centrifuged at 3,000 x g to obtain the serum samples, which were then stored at −80°C until quantitative analysis. The serum levels of IgE, LTB4, and HIS were detected using the respective ELISA kits (ZCI BIO, Shanghai, China), and their optical densities (ODs) were determined using a microplate reader (Shanghai Jizhou chemical industry technology co., ltd., Shanghai, China) at 450 nm according to the manufacturer's instructions. The concentrations of IgE, LTB4, and HIS were determined based on their standard curves.

Mast Cell Detection

To evaluate the number and degranulation of mast cells, the skin tissues were fixed with 10% paraformaldehyde (Chengdu Cologne Chemical Co., Ltd., Chengdu, China), dehydrated with ethanol, embedded in paraffin, sectioned, stained with toluidine blue (Shanghai Ruji Biological Technology Development Co., Ltd., Shanghai, China) solution at 37°C for 10 min, and then sealed with a resin. Stained mast cells were enumerated using a microscope (OLYMPUS, Tokyo, Japan) by randomly observing three fields per section at a magnification of ×100 and 400×.

Detection of Mast Cell Tryptase (MCT) and Eosinophil Protein X (EPX)

After the skin tissues were dewaxed, they were stored in 0.01 mol/L citrate to retrieve the antigen, microwaved for 20 min to expose the antigen, immersed in 0.03% H_2O_2 for 15 min to inactivate endogenous peroxidase, and blocked with goat serum blocking solution for 20 min at room temperature. Subsequently, sections were incubated with primary mouse monoclonal anti-MCT antibody (Abcam, Cambridge, United Kingdom) and rabbit polyclonal anti-EPX antibody (Biorbyt, Cambridge, United Kingdom) at 4°C overnight. After rewarming at 37°C for 1 h, samples were washed with phosphate-buffered saline, incubated with a secondary antibody and biotin-labeled goat anti-rabbit IgG at 37°C for 30 min, incubated with biotin-labeled streptavidin at 37°C for 30 min, developed with a DAB kit (ZSGB Bio, Beijing, China), counterstained with hematoxylin, and sealed with a neutral resin. Microphotographs were obtained using a light microscope. Images of each slide were photographed randomly for three fields using a light microscope at ×200 magnification. Image-Pro Plus 6.0 software (MEDIA CYBERNETICS, Maryland, USA) was used to detect the integrated optical density (IOD) of each field. The mean IOD of the three fields was displayed as the semi-quantitative levels of MCT and EPX.

Measurement of Th2/ Th1 Expression in the Dorsal Skin

The mRNA levels of IL-12, IL-6, interferon (IFN)-γ, and IL-4 in the dorsal tissues were detected using qRT-PCR. Fresh skin tissues were lysed with TRIzol (Hefei Bomei Biotechnology Co., Ltd., Hefei, China) to extract total RNA. PrimeScript RT Reagent Kit (Baori Medicine Biotechnology Co., Ltd., Beijing, China) was used to perform reverse transcription experiments to obtain cDNA for each sample. The cDNA was diluted 10-fold, and it was used as a template for qRT-PCR, which was performed using the Thermo Scientific PikoReal software real-time fluorescent quantitative PCR instrument (Thermo Fisher, Waltham, MA, USA) according to the manufacturer's instructions. The following cycle was performed 45 times: predegeneration at 95°C for 30 s, degeneration at 95°C for 5 s, annealing at 55°C for 30 s, and extension at 72°C for 30 s. β-actin (Sangon Biotech (Shanghai) Co., Ltd., Shanghai, China), and GAPDH (Wuhan servicebio technology Co., Ltd., Wuhan, China) were used as the reference and internal control mRNA, and the $2^{-\Delta\Delta CT}$ method was used to count the relative mRNA expression. The primer sequences were used as follows: β-actin, 5′-GAAGATCAA GATCATTGCTCC-3' (sense) and 5′-TACTCCTGCTTGCTGATC CA-3' (anti- sense); GAPDH, 5′-CCTCGTCCCGTAGACAAA ATG-3' (sense) and 5′- TGAGGTCAATGAAGGGGTCGT-3' (anti- sense); 5′-CCTCGTCCCGTAGACAAAATG-3' (sense) and 5′-TGAGGTCAATGAAGGGGTCGT-3' (anti- sense); IL-12, 5′-TCCAGCATGTGTCAATCACGCTACCT-3' (sense) and 5′-AGC CAGGCAACTCTCGTTCTTGTGTA-3' (anti- sense); 5′-CCATCA ACGCAGCACTTCAGA-3' (sense) and 5′-GCTCAGATAGCC CATCACCCT-3' (anti- sense); IL-6, 5′-TGGAGCCCACCAAGA ACGATAGTCAA-3' (sense) and 5′-TGTCACCAGCATCAGTCC CAAGAAGG-3' (anti- sense); 5′-CCCCAATTTCCAATGCTC TCC-3' (sense) and 5′-CGCACTAGGTTTGCCGAGTA-3' (anti-sense); IL-4, 5′-AGGAGCCATATCCACGGATGCGACAA-3' (sense) and 5′-GCGAAGCACCTTGGAAGCCCTACAG-3' (anti-sense); 5′-GATAAGCTGCACCATGAATGAGT-3' (sense) and 5′-CCATTTGCATGATGCTCTTTAGG-3' (anti- sense); IFN-γ, 5′-GCCATCAGCAACAACATAAGCGTCAT-3' (sense) and 5′-CCC GAATCAGCAGCGACTCCTTT-3' (anti- sense); 5′-CTCAAGTGG CATAGATGTGGAAG-3' (sense) and 5′-TGACCTCAAACTTGG CAATACTC-3' (anti- sense);

Statistical Analysis

All statistical analyses were performed using SPSS 25.0 software (IBM, New York, USA), and data were presented as mean ± SEM. One-way analysis of variance was used to compare the mean statistical differences between experimental groups at the same time point and between PF groups at different time points. A p-value < 0.05 was considered as statistically significant. A factorial design was applied to compare the effects of time and treatment (time × treatment). A p-value < 0.05 was considered as statistically significant. Levene's test was used to assess homoscedasticity, least significant difference test was used to assess the data variance, and Dunnett's t-test was used to assess unequal variances.

RESULTS

Effect of PF on Scratching Behavior

In the scratching test, after being challenged with OVA/ aluminium hydroxide solution, an obvious scratching reaction was observed in the mice in the OVA and PF groups at all dosing time points as compared with those in the NC groups both modeled in the morning (ZT02) and evening (ZT14). Compared

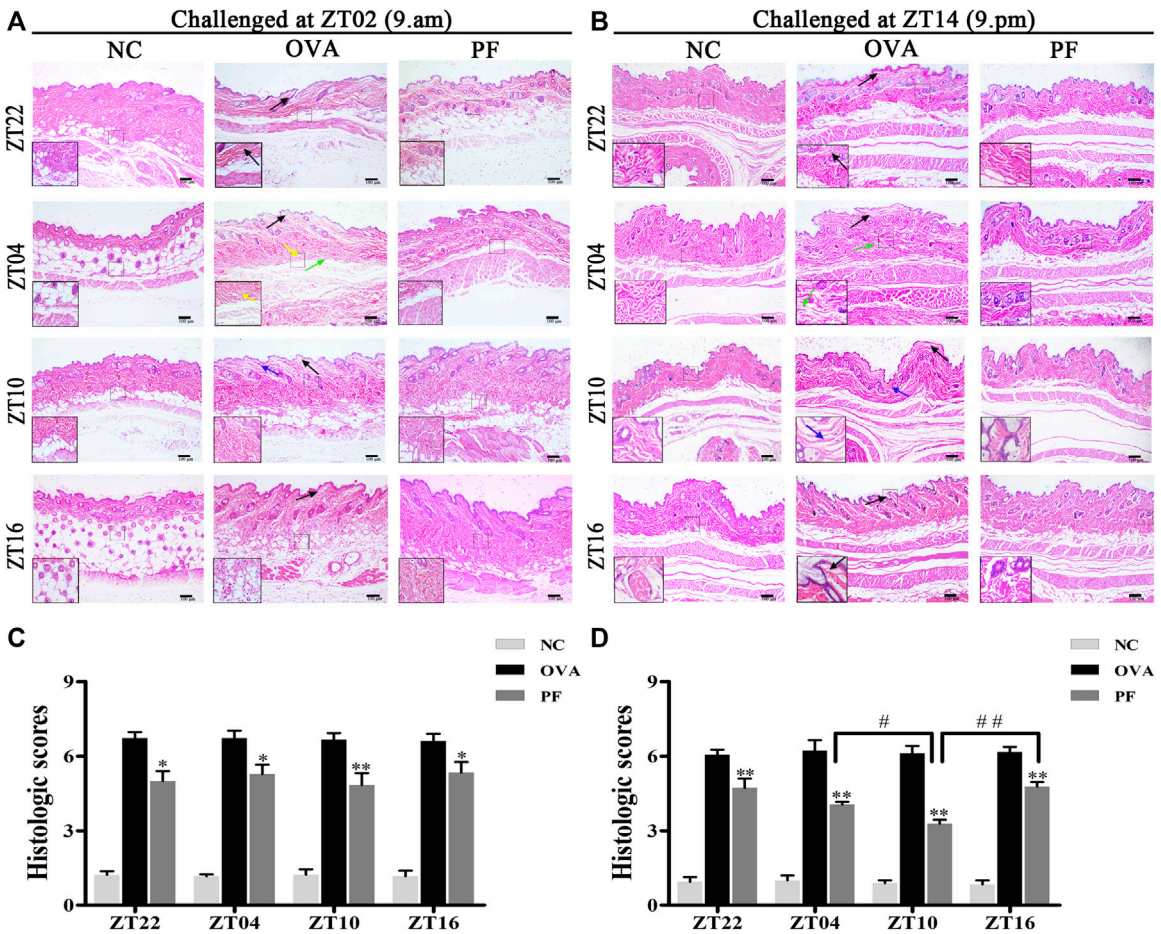

FIGURE 2 | Effect of PF treatment on histopathological features **(A,B)** and histologic scores **(C,D)** in OVA/aluminium hydroxide-induced urticaria-like mice. Representative images of hematoxylin and eosin staining in the dorsal skin. BALB/c mice in the NC group, showing normal architecture. OVA-treated urticaria-like mice showed obvious edema in the upper dermis (black arrows), widening of collagen fiber bundles (blue arrows), with telangiectasia (green arrows), and inflammatory cell infiltration (yellow arrows). PF treatment, especially at ZT10, improved the wheal conditions. The magnification were ×100 and 400×. NC groups have noted less or even no edema, telangiectasia, or inflammatory cell infiltration, OVA groups displayed increased histologic scores, while PF induced significant inhibition of the histologic scores. $^{*}p < 0.05$, $^{**}p < 0.01$ versus OVA mice at the same time points. $^{\#}p < 0.05$, $^{\#\#}p < 0.01$ represents the comparison of PF ZT10 versus the other three PF indicated time points.

to the OVA groups, both PF groups demonstrated a significant decrease in scratching number ($p < 0.05$, modeled at ZT02, and $p < 0.01$, modeled at ZT14). However, the PF dose at four circadian time points showed no significance in comparison with each other among the two challenged time points (**Figures 1B,C**). The scratching behaviors demonstrated that PF relieved the pruritus of the mice with UL, and ZT10 dosing showed the best results (**Figures 1B,C**).

Effect of PF on the Histopathological Features and Histologic Scores of UL

Oral administration of PF significantly inhibited the UL in mice induced by OVA/aluminium hydroxide at ZT02 (resting phase) and ZT14 (active phase). Following hematoxylin and eosin staining, compared to the NC groups, obvious edema, mainly in the upper dermis, and widening of collagen fiber bundles with light pink staining was observed in many OVA groups. At the same time, telangiectasia and inflammatory cell infiltration in skin tissues were observed using light microscopy. As expected, PF showed pharmacological effects on the UL in mice at different dosing time points. The dose at ZT10 improved the histopathological conditions as compared with that at other circadian time points regardless of the modeling time in the morning (ZT02) or evening (ZT14) (**Figures 2A,B**).

The histological findings demonstrated that the NC groups have noted less or even no edema, telangiectasia, or inflammatory cell infiltration while the OVA groups displayed apparent edema, telangiectasia, and inflammatory cell infiltration at all dosing time points, both performed OVA at ZT02 and ZT14. Whereas PF induced significant inhibition of the histologic scores [PF dosing at ZT22 ($p < 0.05$, modeled at ZT02 and $p < 0.01$, modeled at ZT14), PF dosing at ZT04 ($p < 0.05$, modeled at ZT02 and $p < 0.01$, modeled at ZT14), PF dosing at ZT10 ($p < 0.01$, modeled at

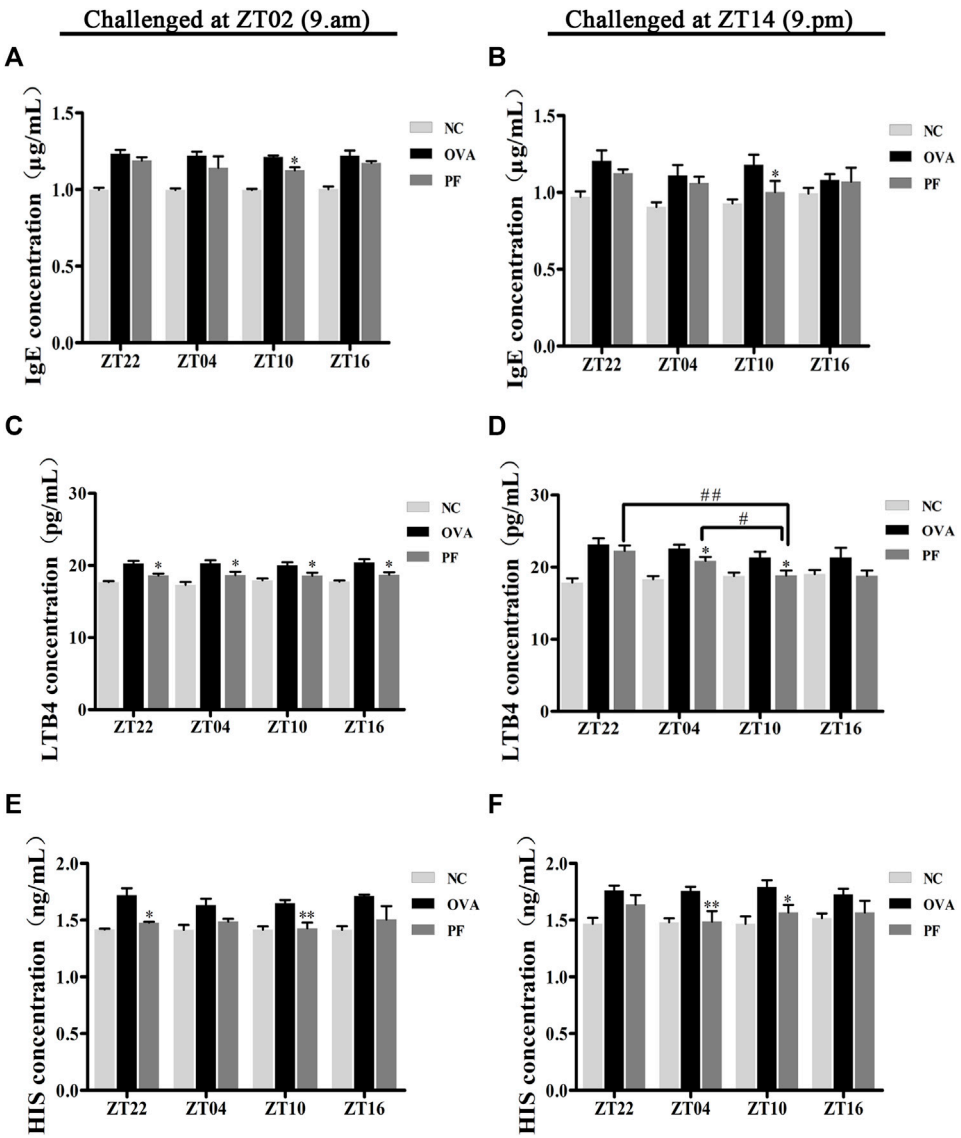

FIGURE 3 | Effect of PF treatment on the secretion of allergic cytokines such as **(A,B)** immunoglobulin E (IgE), **(C,D)** leukotriene B4 (LTB4), and **(E,F)** histamine (HIS) from the serum samples of OVA/aluminium hydroxide-challenged mice. PF downregulated the expression of allergic cytokines. Data are expressed as mean ± SEM (n = 6). $^{*}p < 0.05$, $^{**}p < 0.01$ versus OVA mice at the same time points. $^{\#}p < 0.05$, $^{\#\#}p < 0.01$ represents the comparison of PF ZT10 versus the other three PF groups.

ZT02 and ZT14), PF dosing at ZT16 ($p < 0.05$, modeled at ZT02 and $p < 0.01$, modeled at ZT14)], compared with the OVA groups among all the dosing time points. Furthermore, when sensitized at ZT14, histologic scores were significantly inhibited by PF dosing at ZT10 ($p < 0.05$ *vs.* ZT04 and $p < 0.01$ *vs.* ZT16, $p = 0.052$ *vs.* ZT22). PF dosing at four indicated time points did not differ significantly among sensitized at ZT02, but ZT10 showed slightly better efficacy than others (**Figures 2C,D**).

Effect of PF on the Serum Levels of IgE, LTB4, and HIS

Since IgE, HIS, and LTB4 play major roles in the etiology of urticaria, their expression varies greatly with the time of the day. Thus, the study of the effect of PF administration at different time points on anti-allergic response markers is of great interest. The levels of IgE, LTB4, and HIS in the serum of urticaria-like animal models were determined using ELISA. Dosing at ZT22 ($p < 0.01$), modeled at ZT02 and ZT14), ZT04 ($p < 0.01$, modeled at ZT02 and $p < 0.05$, at ZT14), and ZT10 ($p < 0.01$, modeled at ZT02 and ZT14), and ZT16 ($p < 0.01$, modeled at ZT02) increased the IgE levels in OVA groups as compared to those in the NC groups, respectively (**Figures 3A,B**). A decrease in IgE excretion was observed in PF-treated mice as compared to that of the OVA group at ZT10 ($p < 0.05$, modeled at ZT02 and ZT14) (**Figures 3A,B**). However, the levels of IgE at the other three circadian time points did not decrease in PF groups statistically significant, compared with the OVA groups (**Figures 3A,B**). The levels of

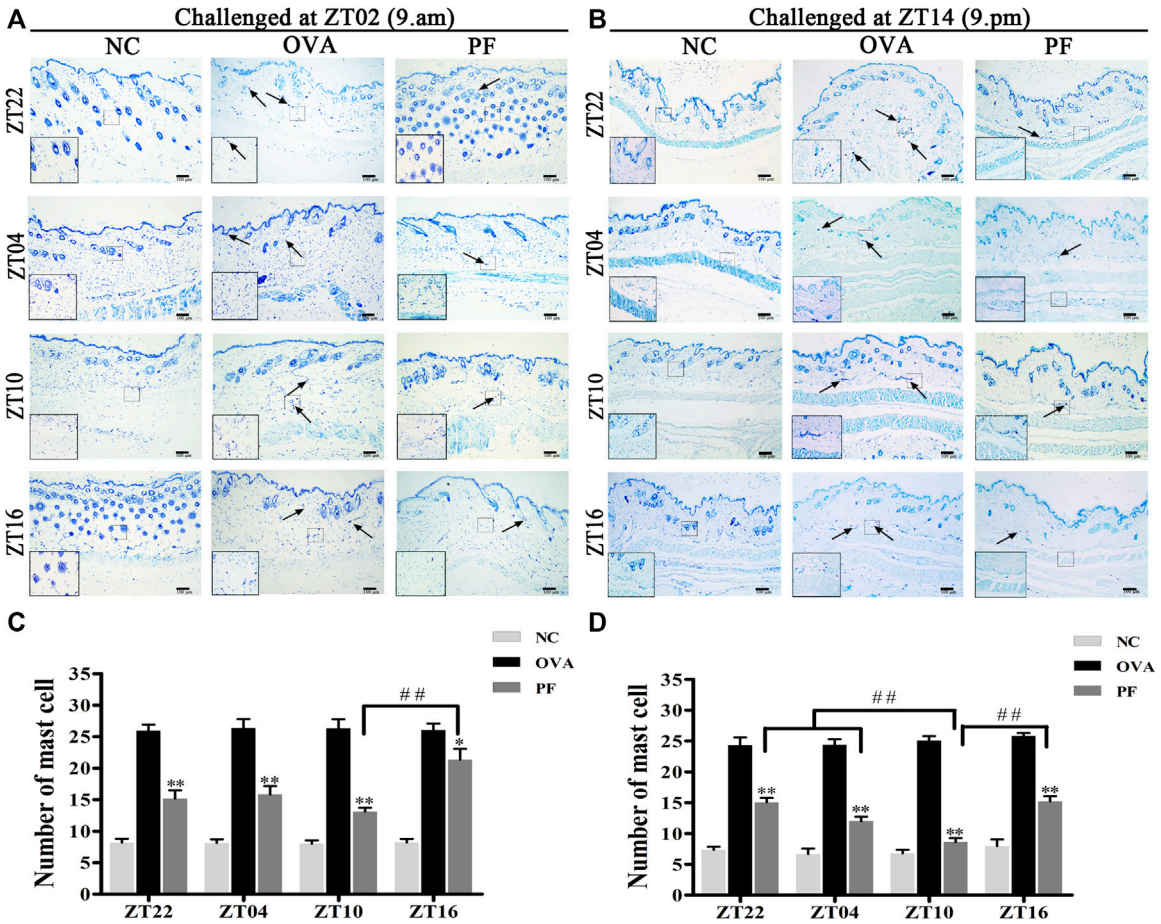

FIGURE 4 | Representative low-magnification light photomicrographs **(A,B)**, and numbers **(C,D)** displaying toluidine blue staining of mast cell degranulation (black arrows). The mast cell degranulation increased with OVA/aluminium hydroxide administration. Oral administration of PF resulted in a significant reduction in mast cell degranulation. Data are expressed as mean ± SEM ($n = 6$). $^{*}p < 0.05$, $^{**}p < 0.01$ versus OVA mice at the same time points. $^{\#\#}p < 0.01$ represents the comparison of PF ZT10 versus the other three PF groups. The magnification were ×100 and 400×.

LTB4 at the four circadian time points were much higher in the OVA groups [ZT22 ($p < 0.01$, modeled at ZT02 and ZT14), ZT04 ($p < 0.01$, modeled at ZT02 and ZT14), ZT10 ($p < 0.01$, modeled at ZT02 and $p < 0.05$, modeled at ZT14), and ZT16 ($p = 0.004$, modeled at ZT02 and $p = 0.103$, modeled at ZT14)] than those in the NC groups. The levels of the serum LTB4 are reduced in both ZT22 ($p < 0.05$, modeled at ZT02), PF ZT04 ($p < 0.05$, modeled at ZT02 and ZT14), and ZT10 ($p < 0.05$, modeled at ZT02 and ZT14), and ZT16 ($p < 0.05$, at ZT02) as compared to the OVA treated mice. However, treatment with PF at ZT22 and ZT16 showed no significant difference in the levels of LTB4 between the OVA groups modeled at ZT14. Furthermore, the PF dosing at ZT10 led to a lower serum level of LTB4 compared to the doses at ZT22 ($p < 0.01$) and ZT04 ($p < 0.05$) modeled in the evening (**Figures 3C,D**). Compared with the NC groups, the OVA groups showed an increase in the expression of HIS [ZT22 ($p < 0.05$), ZT04 ($p < 0.05$), ZT10 ($p<0.01$), ZT16 ($p<0.01$) modeled at ZT02, ZT22 ($p < 0.01$), ZT04 ($p < 0.01$), ZT10 ($p < 0.01$) modeled at ZT14]. PF ZT22 ($p < 0.05$, modeled at ZT02), ZT04 ($p < 0.01$, modeled at ZT14) and PF ZT10 ($p < 0.01$, modeled at ZT02, and $p < 0.05$, modeled at ZT14) dosing significantly repressed the expression of HIS in the PF groups compared to that in the OVA groups. However, PF-treated at different circadian time points showed no significance in comparison with each other (**Figures 3E,F**). These results indicate that PF treatment alleviates the allergic conditions of UL mice (**Figure 3**).

Effect of PF on Mast Cell Infiltration and Degranulation

Urticaria is a mast cell-driven disease. MCT is the most abundant serine protease in mast cells, with mature and immature forms. In urticaria, activated mast cells secrete mature tryptase. One of the biological functions of MCT is correlated with pro-inflammatory effects, involving tissue edema and remodeling, chemokine secretion, and neutrophil recruitment. To determine the infiltration and degranulation of mast cells, we performed toluidine blue staining (**Figures 4A,B**) to analyze the numbers

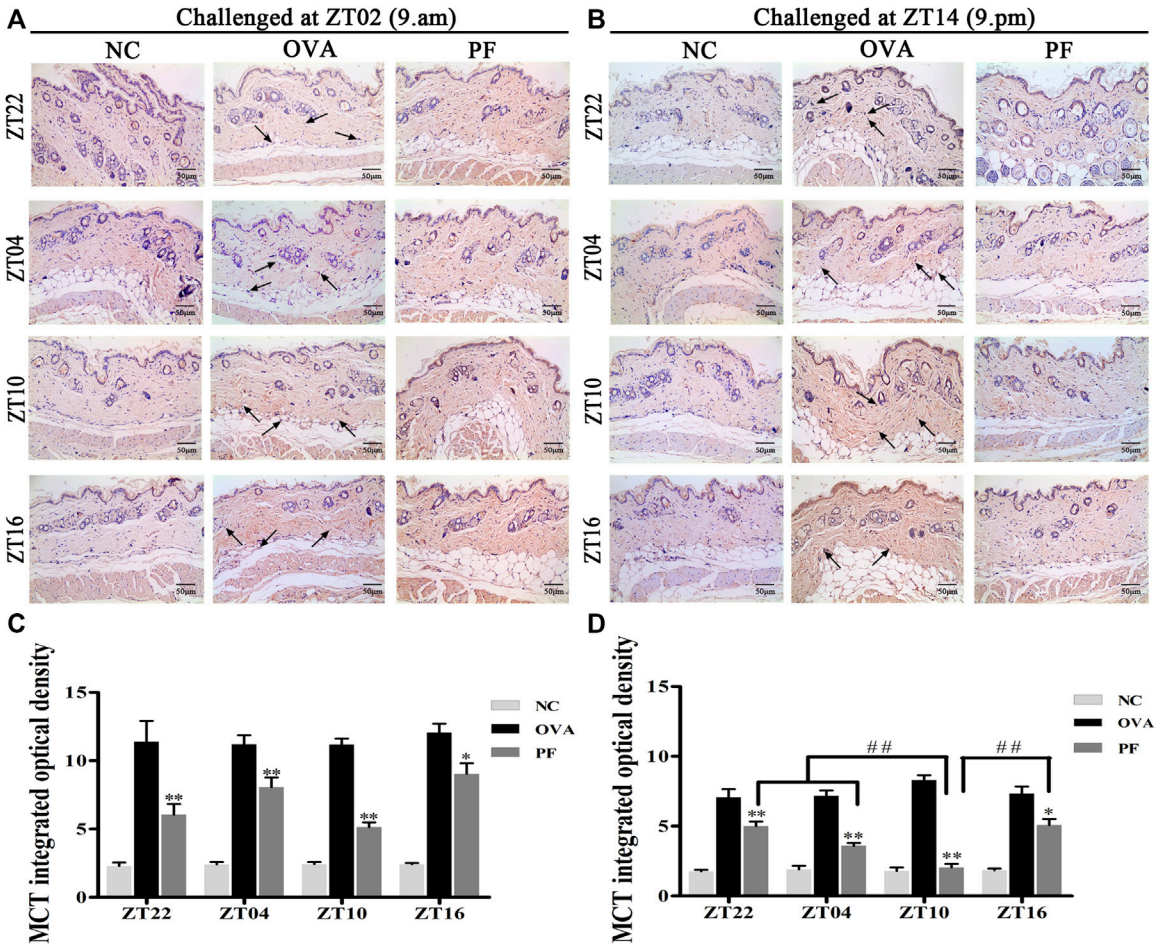

FIGURE 5 | Representative low-magnification light photomicrographs **(A,B)** and integrated optical density **(C,D)** displaying immunohistochemistry of mast cell tryptase (MCT) (black arrows). The PF treatment at ZT10 did possess the best effect on the release of MCT than the other three PF circadian time points. Data are expressed as mean ± SEM (n = 6). *p < 0.05, **p < 0.01 versus OVA mice at the same time points. $^{\#\#}p$ < 0.01 represents the comparison of PF ZT10 versus the other three PF groups. The magnification was ×200.

and degranulation of mast cells and immunohistochemistry to determine the IOD of MCT (**Figures 5A,B**). The OVA challenged in the morning and evening [ZT22 (p < 0.01), ZT04 (p < 0.01), ZT10 (p < 0.01), and ZT16 (p < 0.01)] resulted in a marked and significant increase of mast cell granules compared with the observations in the NC groups. Treatment of mice with PF resulted in a significant reduction in the number of mast cells and granules at ZT22 (p < 0.01 *vs.* OVA), ZT04 (p < 0.01 *vs.* OVA), ZT10 (p < 0.01 *vs.* OVA), with modeling at ZT02 and ZT14, and ZT16 (p < 0.05 *vs.* OVA, modeled at ZT02, and p < 0.01 *vs.* OVA, modeled at ZT14). At ZT10, PF induced a significant reduction [(p < 0.01 *vs.* ZT16) modeled at ZT02, (p < 0.01 *vs.* ZT22), (p < 0.01 *vs.* ZT04), and (p < 0.01 *vs.* ZT16) modeled at ZT14] in mast cell granules in comparison with other three circadian time points (**Figures 4C,D**). The results of MCT were consistent with these results in the OVA groups [ZT22 (p < 0.01 *vs.* NC), ZT04 (p < 0.01 *vs.* NC), ZT10 (p < 0.01 *vs.* NC), and ZT16 (p < 0.01 *vs.* NC)] with modeling in the morning and evening. Compared to the OVA groups, PF [ZT22 (p < 0.01), ZT04 (p < 0.01), ZT10 (p < 0.01), and ZT16 (p < 0.05) modeled at ZT02 and ZT14] significantly decreased the IOD of MCT. The PF dosing at ZT10 [ZT22 (p < 0.01), ZT04 (p < 0.01), and ZT16 (p < 0.01), modeled at ZT14] displayed the best treatment efficacy to decrease the IOD of MCT (**Figures 5C,D**).

Effect of PF on EPX in Skin Tissues

To assess the effect of dosing time on EPX, mice with UL were administered PF using an oral gavage at four circadian time points (ZT16, ZT22, ZT04, and ZT10). EPX as an eosinophilic marker, and released by activated eosinophils, which function in immune responses (Weller and Spencer, 2017; Kim et al., 2020). The IOD of EPX in the OVA groups both for the two challenged time points [ZT22 (p < 0.01), ZT04 (p < 0.01), ZT10 (p < 0.01), and ZT16 (p < 0.01)] was significantly elevated at the four circadian time points compared to that in NC groups. However, the expression levels of EPX reduced in all circadian time groups after treatment with PF [ZT22 (p < 0.01), ZT04 (p < 0.01), ZT10 (p < 0.01), and ZT16 (p < 0.05) modeled at ZT02 and ZT22 (p < 0.05), ZT04 (p < 0.01), ZT10

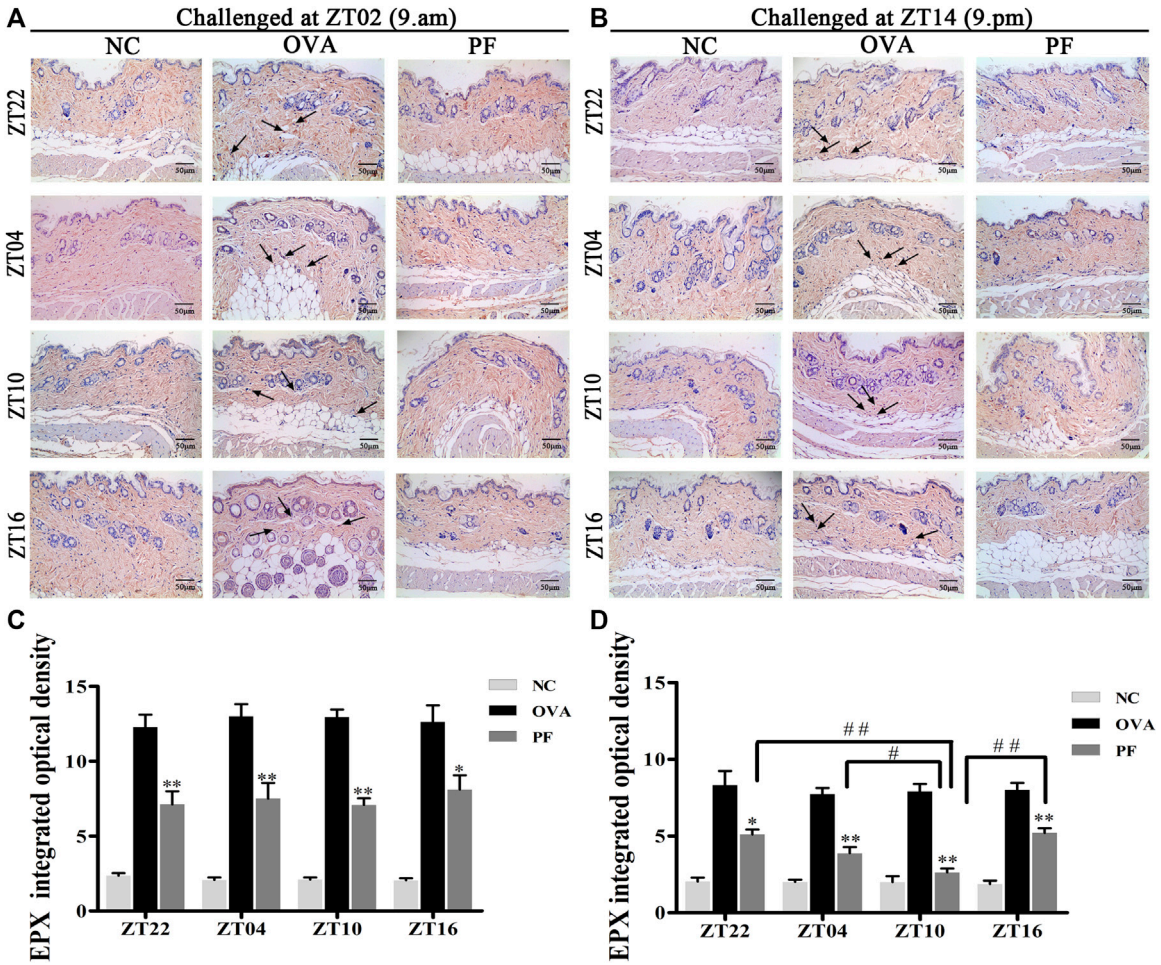

FIGURE 6 | Representative low-magnification light photomicrographs **(A,B)** and integrated optical density **(C,D)** displaying immunohistochemistry of eosinophil protein X (EPX) (black arrows). The PF treatment at ZT10 had a greater effect on EPX production. Data are expressed as mean ± SEM ($n = 6$). $^{*}p < 0.05$, $^{**}p < 0.01$ versus OVA mice at the same time points. $^{\#}p < 0.05$, $^{\#\#}p < 0.01$ represents the comparison of PF ZT10 versus the other three PF groups. The magnification was ×200.

($p < 0.01$), and ZT16 ($p < 0.01$), modeled at ZT14]. Furthermore, PF ZT10 [($p < 0.01$ *vs.* ZT22), ($p < 0.05$ *vs.* ZT04), and ($p < 0.01$ *vs.* ZT16), modeled at ZT14] dosing was more effective in decreasing the IOD levels of EPX (**Figures 6A–D**).

Effect of PF on the mRNA Levels of IL-12, IL-6, IFN-γ, and IL-4

To elucidate the effects of PF on the inflammatory cytokine release in urticaria, we measured the mRNA levels of IL-12, IL-6, IFN-γ, and IL-4 in skin lesions using qRT-PCR. Dosing at ZT22 ($p < 0.05$), ZT04 ($p < 0.05$), ZT10 ($p < 0.01$) modeled at ZT02, and dosing at ZT22 ($p < 0.01$), ZT04 ($p < 0.01$), and ZT10 ($p < 0.05$), ZT16 ($p < 0.05$) modeled at ZT14 expressed a higher IL-12 mRNA level in the OVA groups with UL as compared to that in the NC groups (**Figures 7A,B**). However, the expression of IL-12 mRNA at PF ZT04 ($p < 0.05$, modeled at ZT02), ZT10 ($p < 0.01$, modeled at ZT02), and PF ZT04 ($p < 0.05$, modeled at ZT14) decreased as compared to that in the OVA-treated animals (**Figures 7A,B**). As compared with OVA-treated, no significant differences of PF-treated were observed in the other dosing circadian time points. Additionally, no significant difference was observed in the PF groups between the dosing at ZT16, ZT22, ZT04, and ZT10. For the two indicated model time points, the IL-6 mRNA levels were higher in the OVA-induced mice than that in the NC mice. Moreover, PF treatment at the four dosing circadian time points reduced the levels of IL-6 mRNA. However, the results were not statistically significant (**Figures 7C,D**). The levels of IFN-γ mRNA elevated in OVA-induced UL mice, and they were reduced after PF administration. However, the data presented no statistical significance (**Figures 7E,F**). The levels of IL-4 mRNA showed no statistical difference in OVA-induced UL mice when compared to the levels in the NC groups at the four circadian time points. When compared with the OVA groups, PF groups showed no administration time-dependent effects on regulating the expression of IL-4 mRNA (**Figures 7G,H**).

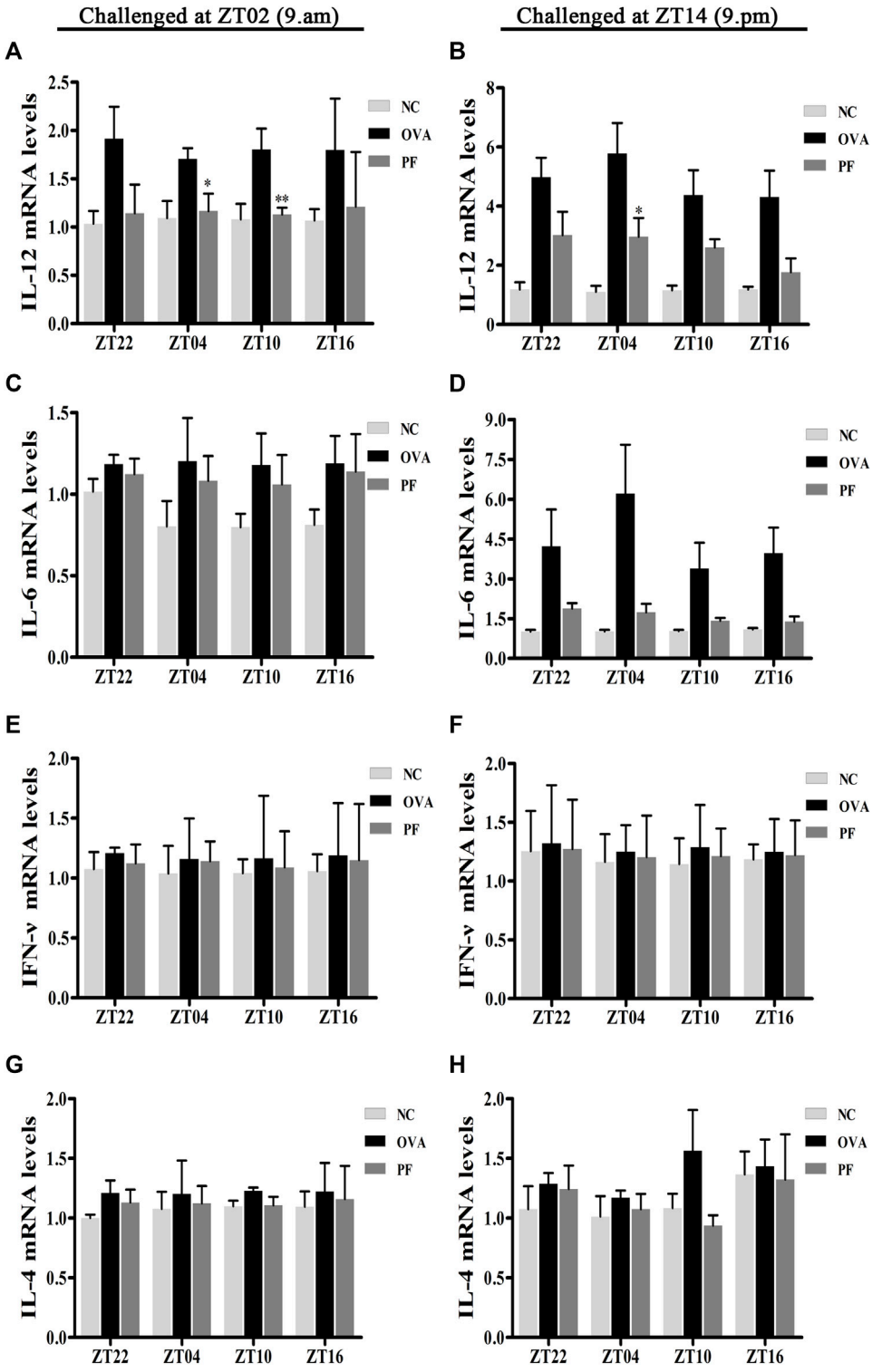

FIGURE 7 | Effect of PF treatment on the release of inflammatory cytokines such as **(A,B)** interleukin (IL)-12, **(C,D)** IL-6, **(E,F)** interferon (IFN)-γ, and **(G,H)** IL-4 from the skin tissues of OVA/aluminium hydroxide-challenged mice. PF reduced the expression of IL-12 mRNA at ZT04 and ZT10. Data are expressed as mean ± SEM ($n = 6$). $^{*}p < 0.05$, $^{**}p < 0.01$ versus OVA mice at the same time points.

DISCUSSION

The prevalence of chronic urticaria ranges from 0.5 to 5% among the general population, leading to a heavy economic burden on the patients. At 19 hospitals in different provinces of China, 60% of urticaria patients experienced their nocturnal attack as reported (Zhong et al., 2014). Nocturnal symptoms attack predominantly around 9 p.m. (ZT14), from another statistical data of 352 patients in China (Huang et al., 2016). The mice were sensitized and challenged at ZT14 to be synchronized with nocturnal symptoms of humans. In our study, the pharmacological effects of PF on urticaria-like symptoms varied with different dosing time points, and PF dosing at ZT10 demonstrated better effects than that at other circadian time points.

Urticaria, a common immune-mediated inflammatory skin disease, causing edema and itching, is associated with IgE-mediated mast cell degranulation and histamine release. IgE is regarded as a potential trigger for the development of urticaria due to its ability to transfer allergen reactivity (Galli and Tsai, 2012; Platts-Mills et al., 2016) and stimulate the degranulation of mast cells. Activated mast cells can secrete pro-inflammatory triggers such as HIS, prostaglandin E- 2, and LTB4 to initiate and amplify hypersensitivity (Galli et al., 2005). MCT, released by mast cells during degranulation, is regarded as a pro-inflammatory mediator in allergic diseases. EPX is a cytotoxic preformed protein, released by the potent pro-inflammatory cells, eosinophil granulocytes. High concentrations of EPX can maintain the secretory activity of mast cells by dissolving mast cells and binding the dissolved matter (Henderson et al., 1980). Injection of OVA and aluminum hydroxide solution stimulated UL in mice at ZT02 or ZT14, leading to an increase in scratching behavior, histopathological changes such as edema, inflammatory cell infiltration, increase in the levels of IgE, HIS, and LTB4, enhance the number of mast cell granules, and concentration of MCT and EPX. These results concur with published data in the literature (Goto et al., 1997; Gu et al., 2004; Hayashi and Fujii, 2008). In addition, abnormalities of the above-mentioned indicators in UL mice were reduced after PF treatment, especially at ZT10.

The circadian rhythm is exhibited by almost all tissues and organs in our body, and disorders in the rhythm induce diseases including urticaria (Smolensky et al., 2015). Metabolic, endocrine, and behavioral functions are governed by circadian rhythms. The number of lymphocytes, T cells, and EPX in human peripheral blood and activation of mast cells exhibit nocturnal peak levels (Pelegrí et al., 2003; Wolthers and Heuck, 2003; Baumann et al., 2013). Pro-inflammatory cytokine levels of IL-12 and IFN-γ are high in the late evening or early morning in human blood (Petrovsky et al., 1998). In addition, blood histamine peaks at the end of the light phase and maintains throughout the dark phase in rats (Friedman and Walker, 1969). These modifications may be responsible for nighttime symptoms, such as itching, wheals.

In our study, oral administration of PF once a day exerted therapeutic effects on mice with UL, although pharmacokinetic study revealed that PF with characteristics of fast absorption rate, short retention time, and low bioavailability (below 5%) (Wang et al., 2008; Wu et al., 2009). *In vivo*, PF is distributed rapidly and widely in various tissues such as the stomach, intestine, spleen, pancreas, and ovary in rats after oral administration of total glycosides of paeony. Besides, the amount of drug in immune organs, such as the spleen and thymus, is greater than in plasma, suggesting that PF may have immune-modulating effects *in vivo* (Fei et al., 2016). Studies also provided the most promising evidence that PF has been widely used as the immune-regulatory agent in immune disorder diseases, including inflammatory bowel disease, psoriasis, asthma, and so on (Gu et al., 2017; Yu et al., 2017; Shou et al., 2018).

Previous studies have reported an imbalance in Th1 and Th2 cells contribute to the progression of UL. IL-4 potentially triggers and sustains mast cells, programs the Th2 cytokine differentiation (Morawetz et al., 1996), and switches B cells to the IgE isotype to induce allergic reactions (Bradding, 1996). IFN-γ, a Th1 effector cytokine, is related to the mitigation of allergic diseases (Teixeira et al., 2005). It is well known that IL-12 promotes Th1 cell polarization, which is associated with the secretion of IFN-γ by T cells (Youssef et al., 2002; Cho et al., 2010). The levels of IL-4, IFN-γ, and IL-6 significantly increase in the dorsal skin of animals with inflammatory diseases such as atopic dermatitis (Choi et al., 2018). In our study, the level of IL-12 mRNA, IL-6 mRNA, IFN-γ mRNA, and IL-4 mRNA were on the rise in UL mice. And PF administration produced a decreasing trend of the cytokines, although our data showed no significance. The persistence of Th1 or Th2 cells predominate is the leading cause of chronic course in some diseases. Th1 cells have been reported to persist in chronic inflammatory diseases, are potent inducers of inflammation due to being repeatedly activated (Niesner et al., 2008; Yamada et al., 2008). And persistent Th2 cells infiltration was associated with the allergic responses of asthma (Wells et al., 2009). Th1 and Th2 are the effector cell subsets of CD4+T cells through the differentiation, which were promoted by cytokines (Mosmann et al., 1986). Furthermore, memory CD4+T cells retain a lifelong ability to mediate protective immunity after vaccination in lymphoid tissues (Amara et al., 2004; Lees and Farber, 2010). To sum up, regulating CD4+T cells is essential for their long-lasting property. Considering the high concentration of PF in the immune organs, and PF-induced regulatory effects on the imbalance in Th1 and Th2 cells, we speculated that PF may exert a continuing medicinal effect through immunoregulatory.

The literature recorded that the intestine could absorb an amount of PF, the unabsorbed fraction is mainly metabolized in intestinal bacteria (Takeda et al., 1997). Bacteroide is one of the intestinal bacteria, playing an important role to convert PF to metabolites (Hattori et al., 1985). It has been reported that gut characteristic metabolite of PF (Benzoic acid) could through the blood-brain barrier to alleviate depressive symptoms in the central nervous system (Yu et al., 2019). Furthermore, gut microbiota and the immune system interact with each other (Kehrmann et al., 2020). *Bacteroides fragilis*-derived Polysaccharide A can differentiate CD4+T-cell into Treg cells, which are a major role in decreasing inflammation (Lahl et al., 2007; Round and Mazmanian, 2010). Another significant aspect is that the majority of the bacterial strains persist for years or even for a lifetime in the host body, which may influence biological functions. In addition, microbiota changed over

time, but, more than 70% of bacterial strains remain stable over 1 year for the individual's microbiota (Faith et al., 2013). The evidence implied that gut microbiota may contribute to the therapeutic role of PF on UL mice persist for some time, which warrants further development.

The activation of mast cells, lymphocytes, T cells, EPX, and cytokines exhibit circadian variations in allergic reactions, showing a high level at night than day. On the other hand, PF is distributed rapidly in the stomach and intestine, the absorption capability of which was high at night compared with day in mice (Hussain and Pan, 2009; Pan and Hussain, 2009). The abundance of bacteroidetes experience diurnal oscillation, peaking at ZT16, troughing around ZT0 in mice, continue to rise during ZT0 to ZT8, slightly fall to ZT12, then rise to ZT16 (Liang et al., 2015). PF dosing at ZT10, therefore, experienced a period of relatively longer detention time to be absorbed then underwent the phase of abundant metabolites producing, which may reinforce the effect. The above information provided some explanation to dosing at ZT10 demonstrated better effects on prophylaxis and treatment than others before symptom onset.

The primary outcome of interest in our experiment was the efficacy of PF on the nocturnal seizures with urticaria, the mice were therefore sensitized and challenged at ZT14 so as to mimic nocturnal symptoms. In order to get more detailed information about antigen challenge and phenotype evaluation at different circadian time points, we performed OVA challenged at ZT02 corresponding to ZT14 so as to imitate morning symptoms of urticaria, and then administrated at ZT22, ZT04, ZT10, and ZT16. The supplementary experiment indicated that the symptoms, histopathological features, mast cell infiltration were severe during the morning, and they were resolved after PF treatment. PF dosing at ZT10 demonstrated better efficacy in comparison to the other three treated indicated time points. Once more, these results provided strong evidence that PF administration at ZT10 produced relatively superior effectiveness to the urticaria symptoms (**Figure 1B**; **Figures 2A,C**; **Figures 3A,C,E**; **Figures 4A,C**; **Figures 5A,C**; **Figures 6A,C**; **Figures 7A,C,E,G**).

The present study preliminarily revealed the circadian pharmacological effects of PF on mice with UL. However, there were some limitations noted. For instance, detailed mechanisms underlying the circadian pharmacological effects of PF remain to be elucidated. Moreover, since the pathogenesis of urticaria involves a complex multistep process which is affected by many target cells, we wound investigate the mechanism of the optimal administration time of PF specific to a single target cell in subsequent studies. The expression of IL-6 mRNA, IFN-γ mRNA, IL-4 mRNA showed no statistical differences, which may be due to the small sample size or the possibility that the cytokines were not the targets for PF-induced therapeutic effects.

In summary, the symptoms, pathologies factors, and metabolism express diurnal rhythmicity may be the reasons for the difference induced among circadian PF administration timing. In our study, oral administration of PF at four circadian time points (ZT22, ZT04, ZT10, and ZT16) alleviated UL mice, including pruritus, histopathological changes, decreased the levels of IgE, LTB4, and HIS, mast cell infiltration, MCT, EPX, and regulated disorders of Th1 and Th2 cells. It is worth noting that PF administration at ZT10 produced relatively superior effectiveness regardless of whether the UL symptoms attack in the morning or the evening. PF may be used as a potential natural alternative for the prevention and treatment of urticaria before their nocturnal symptoms outbreak.

DATA AVAILABILITY STATEMENT

The datasets presented in this study can be found in online repositories. The names of the repository/repositories and accession number(s) can be found in the article/ **Supplementary Material**.

ETHICS STATEMENT

The animal study was reviewed and approved by the Institutional Animal Care and Use Committee of Chengdu University of Traditional Chinese Medicine.

AUTHOR CONTRIBUTIONS

LP, LW, and JZe designed the experiments. LP and QW carried out the experiments. XZ collected the details. LW and JZh carried out the statistical analysis. LP accomplished manuscript. JG and JZe revised the contents. All authors read and approved the submitted manuscript.

FUNDING

This work was supported by the National Natural Science Foundation of China (grant nos. 82074443 and 81873310), the Sichuan Provincial Central Government Leading Local Science and Technology Development Special Project (grant nos. 2021ZYD0089), the "Xing-lin Scholars" Project of Chengdu University of TCM (grant nos. QNXZ2019017 and ZYTS2019009) and the "Hundred Talents Program" of the Hospital of Chengdu University of Traditional Chinese Medicine (grant nos. 21-Y17, 20-B01, 20-Q03 and 20-Q05).

ACKNOWLEDGMENTS

We greatly acknowledge the statistical analyses assistance from Miss Tian Ren. We would like to thank Editage (www.editage.com) for English language editing. We also thank the editors of *frontiers* for their work on this article.

SUPPLEMENTARY MATERIAL

The Supplementary Material for this article can be found online at: https://www.frontiersin.org/articles/10.3389/fphar.2021.639580/full#supplementary-material

REFERENCES

Amara, R. R., Nigam, P., Sharma, S., Liu, J., and Bostik, V. (2004). Long-lived Poxvirus Immunity, Robust CD4 Help, and Better Persistence of CD4 Than CD8 T Cells. *J. Virol.* 78 (8), 3811–3816. doi:10.1128/jvi.78.8.3811-3816.2004

Baumann, A., Gönnenwein, S., Bischoff, S. C., Sherman, H., Chapnik, N., Froy, O., et al. (2013). The Circadian Clock Is Functional in Eosinophils and Mast Cells. *Immunology* 140 (4), 465–474. doi:10.1111/imm.12157

Bernstein, J. A., Lang, D. M., Khan, D. A., Craig, T., Dreyfus, D., Hsieh, F., et al. (2014). The Diagnosis and Management of Acute and Chronic Urticaria: 2014 Update. *J. Allergy Clin. Immunol.* 133 (5), 1270–1277. doi:10.1016/j.jaci.2014.02.036

Bradding, P. (1996). Human Mast Cell Cytokines. *Clin. Exp. Allergy* 26 (1), 13–19. doi:10.1111/j.1365-2222.1996.tb00051.x

Cho, Y. C., You, S. K., Kim, H. J., Cho, C. W., Lee, I. S., and Kang, B. Y. (2010). Xanthohumol Inhibits IL-12 Production and Reduces Chronic Allergic Contact Dermatitis. *Int. Immunopharmacol* 10 (5), 556–561. doi:10.1016/j.intimp.2010.02.002

Choi, Y. Y., Kim, M. H., Lee, H., Jo, S. Y., and Yang, W. M. (2018). (R)-(+)-pulegone Suppresses Allergic and Inflammation Responses on 2,4-Dinitrochlorobenzene-Induced Atopic Dermatitis in Mice Model. *J. Dermatol. Sci.* 91 (3), 292–300. doi:10.1016/j.jdermsci.2018.06.002

Church, M. K., Kolkhir, P., Metz, M., and Maurer, M. (2018). The Role and Relevance of Mast Cells in Urticaria. *Immunol. Rev.* 282 (1), 232–247. doi:10.1111/imr.12632

Cordeiro Moreira, A. S., Rosmaninho Lopes de Soares E Silva, M. I., Pereira Guilherme, M. A., da Silva Ferreira, J. A., and Fonseca Moreira da Silva, J. P. (2016). Use of Omalizumab in the Treatment of Chronic Urticaria. *Eur. Ann. Allergy Clin. Immunol.* 48 (6), 242–246.

Faith, J. J., Guruge, J. L., Charbonneau, M., Subramanian, S., Seedorf, H., Goodman, A. L., et al. (2013). The Long-Term Stability of the Human Gut Microbiota. *Science* 341 (6141), 1237439. doi:10.1126/science.1237439

Fei, F., Yang, H., Peng, Y., Wang, P., Wang, S., Zhao, Y., et al. (2016). Sensitive Analysis and Pharmacokinetic Study of the Isomers Paeoniflorin and Albiflorin after Oral Administration of Total Glucosides of White Paeony Capsule in Rats. *J. Chromatogr. B Analyt Technol. Biomed. Life Sci.* 1022, 30–37. doi:10.1016/j.jchromb.2016.04.005

Fishbein, A. B., Vitaterna, O., Haugh, I. M., Bavishi, A. A., Zee, P. C., Turek, F. W., et al. (2015). Nocturnal Eczema: Review of Sleep and Circadian Rhythms in Children with Atopic Dermatitis and Future Research Directions. *J. Allergy Clin. Immunol.* 136 (5), 1170–1177. doi:10.1016/j.jaci.2015.08.028

Friedman, A. H., and Walker, C. A. (1969). Rat Brain Amines, Blood Histamine and Glucose Levels in Relationship to Circadian Changes in Sleep Induced by Pentobarbitone Sodium. *J. Physiol.* 202 (1), 133–146. doi:10.1113/jphysiol.1969.sp008799

Galli, S. J., Kalesnikoff, J., Grimbaldeston, M. A., Piliponsky, A. M., Williams, C. M., and Tsai, M. (2005). Mast Cells as "tunable" Effector and Immunoregulatory Cells: Recent Advances. *Annu. Rev. Immunol.* 23, 749–786. doi:10.1146/annurev.immunol.21.120601.141025

Galli, S. J., and Tsai, M. (2012). IgE and Mast Cells in Allergic Disease. *Nat. Med.* 18 (5), 693–704. doi:10.1038/nm.2755

Goto, N., Kato, H., Maeyama, J., Shibano, M., Saito, T., Yamaguchi, J., et al. (1997). Local Tissue Irritating Effects and Adjuvant Activities of Calcium Phosphate and Aluminium Hydroxide with Different Physical Properties. *Vaccine* 15 (12-13), 1364–1371. doi:10.1016/s0264-410x(97)00054-6

Gu, P., Zhu, L., Liu, Y., Zhang, L., Liu, J., and Shen, H. (2017). Protective Effects of Paeoniflorin on TNBS-Induced Ulcerative Colitis through Inhibiting NF-kappaB Pathway and Apoptosis in Mice. *Int. Immunopharmacol* 50, 152–160. doi:10.1016/j.intimp.2017.06.022

Gu, Y., Zhang, X., Ma, Y., and Liu, R. (2004). Effects of Different Immunization Times on Serum Total IgE and Specific IgE in Rats. *Lab. Anim. Comp. Med.* 24 (4), 234–235+239. article number: 1004-8448 (2004) 04-0234-02. (in Chinese).

Hattori, M., Shu, Y. Z., Shimizu, M., Hayashi, T., Morita, N., Kobashi, K., et al. (1985). Metabolism of Paeoniflorin and Related Compounds by Human Intestinal Bacteria. *Chem. Pharm. Bull. (Tokyo)* 33 (9), 3838–3846. doi:10.1248/cpb.33.3838

Hayashi, T., and Fujii, T. (2008). Acute Urticaria[corrected]-like Lesions in Allergen-Unexposed Cutaneous Tissues in a Mouse Model of Late Allergic Rhinitis. *Int. J. Exp. Pathol.* 89 (3), 188–200. doi:10.1111/j.1365-2613.2008.00577.x

Henderson, W. R., Chi, E. Y., and Klebanoff, S. J. (1980). Eosinophil Peroxidase-Induced Mast Cell Secretion. *J. Exp. Med.* 152 (2), 265–279. doi:10.1084/jem.152.2.265

Huang, G., Ye, T., Chen, B., and Zhang, J. (2016). Time Characteristic of 352 Cases of Chronic Urticaria. *J. Chin. Pract. Diagn. Ther.* 30 (08), 760–761. doi:10.13507/j.issn.1674-3474.2016.08.011

Hussain, M. M., and Pan, X. (2009). Clock Genes, Intestinal Transport and Plasma Lipid Homeostasis. *Trends Endocrinol. Metab.* 20 (4), 177–185. doi:10.1016/j.tem.2009.01.001

Kehrmann, J., Effenberg, L., Wilk, C., Schoemer, D., Ngo Thi Phuong, N., Adamczyk, A., et al. (2020). Depletion of Foxp3+ Regulatory T Cells Is Accompanied by an Increase in the Relative Abundance of Firmicutes in the Murine Gut Microbiome. *Immunology* 159 (3), 344–353. doi:10.1111/imm.13158

Kim, D. K., Jo, A., Lim, H. S., Kim, J. Y., Eun, K. M., Oh, J., et al. (2020). Enhanced Type 2 Immune Reactions by Increased IL-22/IL-22Ra1 Signaling in Chronic Rhinosinusitis with Nasal Polyps. *Allergy Asthma Immunol. Res.* 12 (6), 980–993. doi:10.4168/aair.2020.12.6.980

Koyanagi, S., Kuramoto, Y., Nakagawa, H., Aramaki, H., Ohdo, S., Soeda, S., et al. (2003). A Molecular Mechanism Regulating Circadian Expression of Vascular Endothelial Growth Factor in Tumor Cells. *Cancer Res.* 63 (21), 7277–7283.

Lahl, K., Loddenkemper, C., Drouin, C., Freyer, J., Arnason, J., Eberl, G., et al. (2007). Selective Depletion of Foxp3+ Regulatory T Cells Induces a Scurfy-like Disease. *J. Exp. Med.* 204 (1), 57–63. doi:10.1084/jem.20061852

Lees, J. R., and Farber, D. L. (2010). Generation, Persistence and Plasticity of CD4 T-Cell Memories. *Immunology* 130 (4), 463–470. doi:10.1111/j.1365-2567.2010.03288.x

Liang, X., Bushman, F. D., and FitzGerald, G. A. (2015). Rhythmicity of the Intestinal Microbiota Is Regulated by Gender and the Host Circadian Clock. *Proc. Natl. Acad. Sci. U S A.* 112 (33), 10479–10484. doi:10.1073/pnas.1501305112

Lissoni, P., Rovelli, F., Brivio, F., Brivio, O., and Fumagalli, L. (1998). Circadian Secretions of IL-2, IL-12, IL-6 and IL-10 in Relation to the Light/dark Rhythm of the Pineal Hormone Melatonin in Healthy Humans. *Nat. Immun.* 16 (1), 1–5. doi:10.1159/000069464

Mackay, T. W., Wallace, W. A., Howie, S. E., Brown, P. H., Greening, A. P., Church, M. K., et al. (1994). Role of Inflammation in Nocturnal Asthma. *Thorax* 49 (3), 257–262. doi:10.1136/thx.49.3.257

Maurer, M., Ortonne, J. P., and Zuberbier, T. (2009). Chronic Urticaria: an Internet Survey of Health Behaviours, Symptom Patterns and Treatment Needs in European Adult Patients. *Br. J. Dermatol.* 160 (3), 633–641. doi:10.1111/j.1365-2133.2008.08920.x

Maurer, M., Rosén, K., Hsieh, H. J., Saini, S., Grattan, C., Gimenéz-Arnau, A., et al. (2013). Omalizumab for the Treatment of Chronic Idiopathic or Spontaneous Urticaria. *N. Engl. J. Med.* 368 (10), 924–935. doi:10.1056/NEJMoa1215372

Maurer, M., Weller, K., Bindslev-Jensen, C., Giménez-Arnau, A., Bousquet, P. J., Bousquet, J., et al. (2011). Unmet Clinical Needs in Chronic Spontaneous Urticaria. A GA^{2}LEN Task Force Report. *Allergy* 66 (3), 317–330. doi:10.1111/j.1398-9995.2010.02496.x

Morawetz, R. A., Gabriele, L., Rizzo, L. V., Noben-Trauth, N., Kühn, R., Rajewsky, K., et al. (1996). Interleukin (IL)-4-independent Immunoglobulin Class Switch to Immunoglobulin (Ig)E in the Mouse. *J. Exp. Med.* 184 (5), 1651–1661. doi:10.1084/jem.184.5.1651

Mosmann, T. R., Cherwinski, H., Bond, M. W., Giedlin, M. A., and Coffman, R. L. (19861950). Two Types of Murine Helper T Cell Clone. I. Definition According to Profiles of Lymphokine Activities and Secreted Proteins. *J. Immunol.* 136 (7), 2348–2357.

Nakao, A., Nakamura, Y., and Shibata, S. (2015). The Circadian Clock Functions as a Potent Regulator of Allergic Reaction. *Allergy* 70 (5), 467–473. doi:10.1111/all.12596

Niesner, U., Albrecht, I., Janke, M., Doebis, C., Loddenkemper, C., Lexberg, M. H., et al. (2008). Autoregulation of Th1-Mediated Inflammation by Twist1. *J. Exp. Med.* 205 (8), 1889–1901. doi:10.1084/jem.20072468

Pan, X., and Hussain, M. M. (2009). Clock Is Important for Food and Circadian Regulation of Macronutrient Absorption in Mice. *J. Lipid Res.* 50 (9), 1800–1813. doi:10.1194/jlr.M900085-JLR200

Pelegrí, C., Vilaplana, J., Castellote, C., Rabanal, M., Franch, A., and Castell, M. (2003). Circadian Rhythms in Surface Molecules of Rat Blood Lymphocytes. *Am. J. Physiol. Cel Physiol* 284 (1), C67–C76. doi:10.1152/ajpcell.00084.2002

Petrovsky, N., McNair, P., and Harrison, L. C. (1998). Diurnal Rhythms of Pro-inflammatory Cytokines: Regulation by Plasma Cortisol and Therapeutic Implications. *Cytokine* 10 (4), 307–312. doi:10.1006/cyto.1997.0289

Platts-Mills, T. A. E., Schuyler, A. J., Erwin, E. A., Commins, S. P., and Woodfolk, J. A. (2016). IgE in the Diagnosis and Treatment of Allergic Disease. *J. Allergy Clin. Immunol.* 137 (6), 1662–1670. doi:10.1016/j.jaci.2016.04.010

Purushothaman, B., Arumugam, P., and Song, J. M. (2018). A Novel Catecholopyrimidine Based Small Molecule PDE4B Inhibitor Suppresses Inflammatory Cytokines in Atopic Mice. *Front. Pharmacol.* 9, 485. doi:10.3389/fphar.2018.00485

Raherison, C., Abouelfath, A., Le Gros, V., Taytard, A., and Molimard, M. (2006). Underdiagnosis of Nocturnal Symptoms in Asthma in General Practice. *J. Asthma* 43 (3), 199–202. doi:10.1080/02770900600566744

Round, J. L., and Mazmanian, S. K. (2010). Inducible Foxp3+ Regulatory T-Cell Development by a Commensal Bacterium of the Intestinal Microbiota. *Proc. Natl. Acad. Sci. U S A.* 107 (27), 12204–12209. doi:10.1073/pnas.0909122107

Schaefer, P. (2017). Acute and Chronic Urticaria: Evaluation and Treatment. *Am. Fam. Physician* 95 (11), 717–724.

Shi, D., Li, X., Li, D., Zhao, Q., Shen, Y., Yan, H., et al. (2015). Oral Administration of Paeoniflorin Attenuates Allergic Contact Dermatitis by Inhibiting Dendritic Cell Migration and Th1 and Th17 Differentiation in a Mouse Model. *Int. Immunopharmacol* 25 (2), 432–439. doi:10.1016/j.intimp.2015.02.031

Shi, D., Ma, A., Zheng, H., Huo, G., Yan, H., Fu, H., et al. (2014). Paeoniflorin Inhibits the Maturation and Immunostimulatory Function of Allergen-Induced Murine Dendritic Cells. *Int. Immunopharmacol* 19 (2), 221–232. doi:10.1016/j.intimp.2014.02.001

Shou, Q., Jin, L., Lang, J., Shan, Q., Ni, Z., Cheng, C., et al. (2018). Integration of Metabolomics and Transcriptomics Reveals the Therapeutic Mechanism Underlying Paeoniflorin for the Treatment of Allergic Asthma. *Front. Pharmacol.* 9, 1531. doi:10.3389/fphar.2018.01531

Smolensky, M. H., Portaluppi, F., Manfredini, R., Hermida, R. C., Tiseo, R., Sackett-Lundeen, L. L., et al. (2015). Diurnal and Twenty-Four Hour Patterning of Human Diseases: Acute and Chronic Common and Uncommon Medical Conditions. *Sleep Med. Rev.* 21, 12–22. doi:10.1016/j.smrv.2014.06.005

Takeda, S., Isono, T., Wakui, Y., Mizuhara, Y., Amagaya, S., Maruno, M., et al. (1997). In-vivo Assessment of Extrahepatic Metabolism of Paeoniflorin in Rats: Relevance to Intestinal floral Metabolism. *J. Pharm. Pharmacol.* 49 (1), 35–39. doi:10.1111/j.2042-7158.1997.tb06748.x

Teixeira, L. K., Fonseca, B. P., Barboza, B. A., and Viola, J. P. (2005). The Role of Interferon-Gamma on Immune and Allergic Responses. *Mem. Inst. Oswaldo Cruz* 100 (Suppl. 1), 137–144. doi:10.1590/s0074-02762005000900024

Wang, C., Yuan, J., Wu, H. X., Chang, Y., Wang, Q. T., Wu, Y. J., et al. (2015). Total Glucosides of Paeony Inhibit the Inflammatory Responses of Mice with Allergic Contact Dermatitis by Restoring the Balanced Secretion of Pro-/anti-inflammatory Cytokines. *Int. Immunopharmacol* 24 (2), 325–334. doi:10.1016/j.intimp.2014.12.026

Wang, C. H., Wang, R., Cheng, X. M., He, Y. Q., Wang, Z. T., Wu, C., et al. (2008). Comparative Pharmacokinetic Study of Paeoniflorin after Oral Administration of Decoction of Radix Paeoniae Rubra and Radix Paeoniae Alba in Rats. *J. Ethnopharmacol* 117 (3), 467–472. doi:10.1016/j.jep.2008.02.035

Weller, P. F., and Spencer, L. A. (2017). Functions of Tissue-Resident Eosinophils. *Nat. Rev. Immunol.* 17 (12), 746–760. doi:10.1038/nri.2017.95

Wells, J. W., Choy, K., Lloyd, C. M., and Noble, A. (2009). Suppression of Allergic Airway Inflammation and IgE Responses by a Class I Restricted Allergen Peptide Vaccine. *Mucosal Immunol.* 2 (1), 54–62. doi:10.1038/mi.2008.69

Wolthers, O. D., and Heuck, C. (2003). Circadian Variations in Serum Eosinophil Cationic Protein, and Serum and Urine Eosinophil Protein X. *Pediatr. Allergy Immunol.* 14 (2), 130–133. doi:10.1034/j.1399-3038.2003.02038.x

Wu, H., Zhu, Z., Zhang, G., Zhao, L., Zhang, H., Zhu, D., et al. (2009). Comparative Pharmacokinetic Study of Paeoniflorin after Oral Administration of Pure Paeoniflorin, Extract of Cortex Moutan and Shuang-Dan Prescription to Rats. *J. Ethnopharmacol* 125 (3), 444–449. doi:10.1016/j.jep.2009.07.019

Yamada, H., Nakashima, Y., Okazaki, K., Mawatari, T., Fukushi, J. I., Kaibara, N., et al. (2008). Th1 but Not Th17 Cells Predominate in the Joints of Patients with Rheumatoid Arthritis. *Ann. Rheum. Dis.* 67 (9), 1299–1304. doi:10.1136/ard.2007.080341

Youssef, S., Stüve, O., Patarroyo, J. C., Ruiz, P. J., Radosevich, J. L., Hur, E. M., et al. (2002). The HMG-CoA Reductase Inhibitor, Atorvastatin, Promotes a Th2 Bias and Reverses Paralysis in central Nervous System Autoimmune Disease. *Nature* 420 (6911), 78–84. doi:10.1038/nature01158

Yu, J., Xiao, Z., Zhao, R., Lu, C., and Zhang, Y. (2017). Paeoniflorin Suppressed IL-22 via P38 MAPK Pathway and Exerts Anti-psoriatic Effect. *Life Sci.* 180, 17–22. doi:10.1016/j.lfs.2017.04.019

Yu, J. B., Zhao, Z. X., Peng, R., Pan, L. B., Fu, J., Ma, S. R., et al. (2019). Gut Microbiota-Based Pharmacokinetics and the Antidepressant Mechanism of Paeoniflorin. *Front. Pharmacol.* 10, 268. doi:10.3389/fphar.2019.00268

Zhong, H., Song, Z., Chen, W., Li, H., He, L., Gao, T., et al. (2014). Chronic Urticaria in Chinese Population: a Hospital-Based Multicenter Epidemiological Study. *Allergy* 69 (3), 359–364. doi:10.1111/all.12338

Zhou, H., Wu, Q., Wei, L., and Peng, S. (2018). Paeoniflorin Inhibits PDGF-BB-induced H-uman A-irway S-mooth M-uscle C-ell G-rowth and M-igration. *Mol. Med. Rep.* 17 (2), 2660–2664. doi:10.3892/mmr.2017.8180

Conflict of Interest: The authors declare that the research was conducted in the absence of any commercial or financial relationships that could be construed as a potential conflict of interest.

Publisher's Note: All claims expressed in this article are solely those of the authors and do not necessarily represent those of their affiliated organizations, or those of the publisher, the editors and the reviewers. Any product that may be evaluated in this article, orclaim that may be made by its manufacturer, is not guaranteed or endorsed by the publisher.

Copyright © 2022 Peng, Wen, Zhang, Zhang, Wei, Guo and Zeng. This is an open-access article distributed under the terms of the Creative Commons Attribution License (CC BY). The use, distribution or reproduction in other forums is permitted, provided the original author(s) and the copyright owner(s) are credited and that the original publication in this journal is cited, in accordance with accepted academic practice. No use, distribution or reproduction is permitted which does not comply with these terms.

Advantages of publishing in Frontiers

OPEN ACCESS
Articles are free to read for greatest visibility and readership

FAST PUBLICATION
Around 90 days from submission to decision

HIGH QUALITY PEER-REVIEW
Rigorous, collaborative, and constructive peer-review

TRANSPARENT PEER-REVIEW
Editors and reviewers acknowledged by name on published articles

Frontiers
Avenue du Tribunal-Fédéral 34
1005 Lausanne | Switzerland

Visit us: www.frontiersin.org
Contact us: frontiersin.org/about/contact

REPRODUCIBILITY OF RESEARCH
Support open data and methods to enhance research reproducibility

DIGITAL PUBLISHING
Articles designed for optimal readership across devices

FOLLOW US
@frontiersin

IMPACT METRICS
Advanced article metrics track visibility across digital media

EXTENSIVE PROMOTION
Marketing and promotion of impactful research

LOOP RESEARCH NETWORK
Our network increases your article's readership